dam world 2025

Fifth International
Dam World Conference

Preserving life through dams

Proceedings of the Fifth International DAM WORLD Conference

Volume 1

edited by:
Carlos Pina
Eliane Portela
Laura Caldeira

LABORATÓRIO NACIONAL
DE ENGENHARIA CIVIL

PORTUGAL • LISBON • LNEC

SPONSORS

SILVER

Turismo de Lisboa

Eletrobras

movhera | ENGIE

Iberdrola

CIMPOR

ÁGUAS DE PORTUGAL

BRONZE

willowstick

carpi

AQUALOGUS Engenharia e Ambiente

apa agência portuguesa do ambiente

Campbell SCIENTIFIC

tpf

Hibbard Inshore
Delivering unmanned solutions for manmade obstacles, worldwide.

WORTHINGTON Waterway Barriers

GROUP coba

KINEMETRICS
Advancement through Innovation

CDA ACB
Canadian Dam Association | Association canadienne des barrages

edp

InfraLab
laboratório de materiais de construção civil e obras públicas

LABORATÓRIO NACIONAL
DE ENGENHARIA CIVIL

dam world 2025

PORTUGAL • LISBON • LNEC

Proceedings of the
Fifth International DAM WORLD Conference
Preserving life through dams

Volume 1

edited by:
Carlos Pina, Eliane Portela, Laura Caldeira

Legal Notice
The scientific quality and content of the papers published herein are of the entire responsibility of their authors. Therefore, the publisher accepts no responsibility or liability whatsoever with regard to the information contained in this publication.
The total or partial reproduction, and any representation of the substantial or partial content of the present publication, by any process or means whatsoever, including copy or transfer, without the express consent of the publisher, is prohibited and constitutes an infringement sanctioned by the Law.

Copyright © LABORATÓRIO NACIONAL DE ENGENHARIA CIVIL, I. P.
Divisão de Divulgação Científica e Técnica
AV DO BRASIL 101 • 1700-066 LISBOA
e-e: livraria@lnec.pt
www.lnec.pt

Publisher: LNEC

Collection: National and international Meetings

Series: RNI 118

1st. edition: 2025 (pdf)

Descriptors: Dams safety / Dams behaviour / Concrete dam / Embankment dam / International congress
Descritores: Segurança de barragens / Comportamento de barragens / Barragem de betão / Barragem de aterro / / Congresso internacional

CDU 627.82(063)(100)
ISBN 978-972-49-2332-1
DOI 10.34638/084d-e697

Preface

The DAM WORLD Conference Series serves as a leading forum for sharing the latest scientific and technical advancements, as well as discussing the key challenges and solutions facing the dam engineering sector.

The inaugural DAM WORLD Conference took place in Brazil in 2012. The subsequent events, held inPortugal in 2015 and Brazil in 2018, were both highly successful. The Fourth International DAM WORLD Conference, originally scheduled as an in-person event in Lisbon in 2020, was instead held as an online event – the DAM WORLD Webinar – due to the global pandemic.

The National Laboratory for Civil Engineering (LNEC) is honoured to host the Fifth International DAM WORLD Conference. Continuing the tradition of its predecessors, this event will provide a platform for delegates from around the world to exchange valuable knowledge and expertise. The theme of DW2025 is "Preserving Life Through Dams," and we are committed to exceeding your expectations. Canada will be the invited country, with distinguished experts and representatives sharing their insights and advancements in dam engineering.

In addition to technical sessions, the conference will feature keynote lectures and pre-conference oneday courses, all designed to enhance professional practice.

The proceedings of the Fifth International DAM WORLD Conference will be published in two volumes. All included papers have undergone a rigorous peer-review process, and only those that were accepted will be presented at the conference and included in the official proceedings.

The Conference Organising Committee would like to extend their appreciation to all the authors for their contributions and dedication in preparing and submitting their papers. We also wish to express our sincere gratitude to the members of the Scientific Committee for their thorough and thoughtful review of the papers featured in these proceedings.

Laura Caldeira
Conference Chair

Organisation

Conference Chair
Laura Caldeira, Portugal

Conference Co-Chairs
António Batista, Portugal
João Bilé Serra, Portugal
José Marques Filho, Brazil
Miguel Augusto Zydan Sória, Brazil
Teresa Viseu, Portugal
Túlio Bittencourt, Brazil

Organising Committee
Andrea Brito, Portugal
Carlos Serra, Portugal
Eliane Portela, Portugal
José Lucas Marques, Brazil
José Rocha Afonso, Portugal
Sílvia Amaral, Portugal

Scientific Committee

President

Carlos Pina, Portugal

Ahmed Chraibi, Morocco
Alberto Marulanda, Colombia
Alberto Sayão, Brazil
Ali Noorzad, Iran
Andy Small, Canada
Anthony Burnett, Canada
António Bettencourt Ribeiro, Portugal
António Pinheiro, Portugal
António Tavares de Castro, Portugal
Bettina Geisseler, Germany
Caius Priscu, Canada
Carlos Fava, Argentina
Carlos Granell, Spain
Claudio Fattor, Argentina
Daniele Cazzuffi, Italy
David Rivera Pantoja, Spain
Devendra Kumar Sharma, India
Diego Antônio Fonseca Balbi, Brazil
Domingos Silva Matos, Portugal
Enrique Cifres, Spain
Etienne Grimal, France
Feng Jin, China
Fernanda Rocha, Portugal
Francesco Federico, Italy
Gensheng Zhao, China
Gerald Zenz, Austria
Giovanni De Cesare, Switzerland
Giovanni Ruggeri, Italy
Gonçalo Tavares, Portugal
Grégory Coubard, France
Humberto Marengo-Mogollon, Mexico
Ignacio Escuder, Spain
Isabelle Levesque, Canada
Jean-Pierre Tournier, Canada
João Cunha, Portugal
João Marcelino, Portugal
João Portugal, Portugal
Jorge Saldanha Matos, Portugal
Jorge Vasquez, Portugal
José Falcão de Melo, Portugal
José Machado do Vale, Portugal
José Mateus de Brito, Portugal
José Vieira de Lemos, Portugal
Louis Hattingh, South Africa
Luca Pagano, Italy
Luis de la Torre Abietar, Spain
Luís Lamas, Portugal
Luiz Paniago Neves, Brazil
Lurdes Pimenta, Portugal
Marc Smith, Canada
Marcelo Giulian Marques, Brazil
Marco André Argenta, Brazil
Margaret Trias, Canada
Paulo Castro, Portugal
Ricardo Pimentel, Portugal
Robin Charlwood, USA
Rogério Menescal, Brazil
Sandra Soares Frazão, Belgium
Stefan Felder, Australia
Teresa Fusaro, Brazil
Tetsuya Ishida, Japan
Tony Bennett, Canada
Travis Bowser, Canada

Conference Themes

Main Themes

T1 Concrete and Masonry Dams
T2 Embankment Dams and Levees
T3 Hydraulics for Dams
T4 Tailings Dams
T5 Environmental and Social Issues
T6 Regulation and Governance
T7 Dams and Climate Change

Topics

ST1 Design and Modelling
ST2 Design Innovation and New Materials
ST3 Geology and Dam Foundation
ST4 Underground Works
ST5 Hydrology and Appurtenant Works
ST6 Seismic Analysis
ST7 Instrumentation and Monitoring
ST8 Dam Safety Evaluation
ST9 Construction and Rehabilitation
ST10 Operation and Maintenance
ST11 Deterioration
ST12 Decommissioning and Dam Removal
ST13 Dam Management Systems and New Technologies
ST14 River and Integrated Reservoir Management
ST15 Risk Assessment
ST16 Dam Failure and Emergency Action Plans (EAP)
ST17 Sedimentation in Reservoirs
ST18 Dams and Climate Change Adaptation
ST19 Hydro, Solar and Wind Energy Associated to Dams

Index

Volume 1

Keynotes

Wadi Derna Disaster (Lybia Sept. 2023) 1
Lino, Michel; Chraibi, Ahmed Fouad

Water Scarcity, Climate Change Adaptation, and the Role of Dams and Reservoirs 3
Oliveira, Rodrigo

Deterioration of Dams Affected by Concrete Swelling. The Role of Observation and Modelling in Safety Control and Rehabilitation 27
Lopes Batista, António

Geomechanical Behaviour of Tailings Storage Facilities 65
Świdziński, Waldemar

Concrete Dams and Earthquake: Numerical Analysis Techniques and Practical Advices for Engineers 67
Robbe, Emmanuel

The Failure Modes of Flood Protection Levees, Consequences on Management and Engineering 99
Tourment, Rémy

Special Session Canada

Simplified Analysis of Selected ASR PFMS 117
Curtis, Dan

Canadian Dam Association and Dams in Canada 119
Smith, Marc; Trias, Margaret

Failure Modes: a Canadian Perspective, Case Study on Internal Erosion 121
Smith, Marc

Tailings Dam Safety - Developments in Canada 123
Al-Mamun, Mohammad; Burnett, Anthony

Dam Safety Management Systems 125
Bennett, Tony

Public Safety Around Dams: Practical Guidance for Meeting Owner Responsibilities in Canada 127
Bennett, Tony

Panel Discussion: Challenges in Developing Dam Safety Guidelines 129
Priscu, Caius

Tailings Dam Safety- Developments in Canada 131
Burnett, Anthony

T1 Concrete and Masonry Dams

The Frost and Leaching Deterioration of Dams in Altitude: Case Studies 133
Paglia, Christian; Antonietti, Samuel

Rock-Filled Concrete (RFC) Arch Dams With or Without Contraction Joints 147
Jin, Feng; Zhang, Quanyi

Rehabilitation Study of Temengor and Chenderoh Dam for Their Safety Enhancement and Life Extension 157
Siskos, Ioannis; Du, Chongjiang

Dam FPO Geomembrane After 14 Years Exposure 169
Favre, Pierre; Eckl, Martin

The Strength at the Base of an Old Concrete Dam, Based on the Spanish Experience With Large-Scale In Situ Shear Tests 181
Asanza Izquierdo, Enrique; Laina Gómez, Carlos; Díez Torres, Juan Antonio; Escudero Merino, Diego; Antón Sempere, José

Structural Solution for the Rehabilitation of Spillway Piers Subjected to Corrosion of the Prestressing Cables in the Trunnion Girder 201
Dalcin, Marcos; Takase, Kauê; Generoso, Bianca

Design and Construction of Hardfill Cofferdam on River Alluvium Deposits 213
Du, Chongjiang; Beck, Sebastian; Jung, Uysung

Pathology Mapping in Concrete Dams through Digital Photogrammetry and Image Processing 223
Roque, Dora; Henriques, Maria João

Safety Verification by 3D Dynamic Analysis of a 100-Year-Old Masonry Arch–Gravity Concrete Dam 233
Iwata, Naoki; Kiyota, Ryoji; Kawasaki, Hideaki; Kurihara, Masaharu

Continuous Ambient Vibration Measurements: Experimental Set Up and First Results on an Arch Dam 249
Steck, Barthelemy; Robbe, Emmanuel; Humbert, Nicolas

Preventive Maintenance with ROV and Sonar Underwater Inspections: a Strategic Approach to Reducing Downtime and Costs in Hydraulic Tunnels Failures 269
Iannotta, Fabio; Malak, David

Automated Defect Change Detection and Quantification for Large Gravity Dams and Spillways – a Pathway to Deterioration Modelling 287
Fowler, Joshua; Aparicio, Javier

A Study on the Influence of the Reservoir Water Level on the Seismic Performance of a Large Double Curvature Arch Dam 303
Oliveira, Sérgio; Ramos, Rafael; Alegre, André; Proença, Jorge; Mendes, Paulo; Silva, João; Serra, Carlos

From Sensor Data to Actionable Information with KMIDam. Seismic Event Reporting and Long-Term Structural Health Monitoring of Dams 323
Alegre, André; Skolnik, Derek; Ciudad-Real, Mauricio; Franke, Mathias; El Idrissi, Mohamed

Dynamic Behaviour of a Concrete Dam: Development of Statistical and Machine Learning Models for Interpretation of Monitoring Data 343
Sejas, Andres Mauricio Guzman; Pereira, Sérgio; Mata, Juan; Cunha, Álvaro

How Effective is Monitoring Concrete Dams with GNSS in 3D Mode? 357
Lima, José Nuno

Analysis of the Dynamic Characteristics of Trapezoidal CSG Dams Using Seismic Records 377
Yasuda, Nario; Cao, Zengyan; Kozaki, Yuya

Creep Tests in Daivões Dam 389
Serra, Carlos; João, Silva

Local and Global Parameter Sensitivity for Concrete Hydraulic Structures Under Seismic Loading Considering Structure and Material Variation 407
de AlmeidaTorres Filho, Rodrigo José; Segura, Rocio; Paultre, Patrick

GIS-Based Database for Improved Dam Management in Cabo Verde 427
Correia e Silva, Carlos Filipe; Tavares, Emanuel; Delgado, Adlisa; Fernandes, João Nuno; Dias, Ivo Figueiredo

Relations Between Seismic Input Motion, Dam Pattern, and Seismically Induced Sliding of Gravity Dams in European Context 437
Labbé, Pierre

Analysis and Interpretation of the Structural Behaviour of Daivões Dam During the First Filling of the Reservoir 455
Serra, Carlos; Mata, Juan

Contributions to the Analysis of the Exothermic-Mechanical Phenomenon in Mass Concrete 475
Mamede Pereira Gomes, Flávio

Evaluation Method for Safety of Concrete Slab Stress Based on Multi-axial Strength Criterion 503
Mi, Zhankuan; Wei, Kuangmin; Wang, Fang

Adaptive Warning Thresholds in Dam Safety Using Kernel Density Estimation 523
Silva Cancino, Nathalia; Irazabal, Joaquín; Salazar, Fernando; Mata, Juan

Rehabilitation of Sordo Dam 535
Costa, André; Cordeiro, José; Vale, José Machado do; Nicolau, Luís; Gonçalves, Sofia

Influence of Fine Materials Addition on the Coefficient of Thermal Expansion of Repair Mortars 571
Goulart Gomes de Oliveira, Rafaela; Reginato, Luan; Funchal de Faria, Étore; Luiz Willrich, Fábio; Parapinski dos Santos, Ana

Development of Improvements in Flow Meter Devices for Dam Monitoring 581
Antônio Sucapuca Aracayo, Luis; João Arenhardt, Bruno; Miranda Rojas, Ricardo; Liska Darli, Diego; Reginato, Luan

Hydrological Risk of Floods and Collapse due to Overtopping of the Ribeira de Principal Dam on Santiago Island in Cape Verde 595
Fernandes, Manuel; Silva, Francisco

Deterioration Due to Simultaneous Expansive Reactions in Dam Concrete: Evaluations on Prototypes 613
Funahashi Júnior, Eduardo Issamu; Pagan Hasparyk, Nicole; Gambale, Patrícia; Possan, Edna; Chapira Kuperman, Selmo

Yes, There Appear to be Options to Stop or Control ASR in Some Dams! 635
Charlwood, Robin; Godart, Bruno; Isgor, Burkan; Grimal, Etienne

A 3D Point Cloud Model of Santa Luzia Dam and Its Contribution for Improving the Finite Element Mesh 657
Henriques, Maria; Dias, Ivo; Roque, Dora; Gomes, Alexandre

Applications of GNSS Technology in Dam Monitoring: a Systematic Literature Review 673
Moreira, Hanna Barreto de Araújo Falcão; Quental Coutinho, Roberto; Silva Alves, Jailson; Aragão Júnior, Wilson Ramos

Dam Safety: How a Good Contractual Design and a Thorough Project Execution Management Can Contribute to it 687
Geisseler, Bettina

Caculo Cabaça Hydropower Project - Evaluation of the Susceptibility of Aggregates for Participation in Expansive Alkali-silica Reaction 695
Custódio, João; Bettencourt Ribeiro, António; Chico, Augusto; Costa, Cristina; Mateus, Gonçalo; Liu, Wen

River Diversion of the Caculo Cabaça Hydropower Project 719
Costa, Maria Cristina; Mateus, Gonçalo; Amador, António; Morgado, António; Chico, Augusto; Zebin, Xiong; Wen, Liu

LNEC Support to the Design Adaptation of Alto Tâmega Dam Due to the Rock Slide on the Right Bank Slope 739
Muralha, José; Lamas, Luís; Batista, António Lopes; Mata, Juan; Serra, Carlos

First Infilling of the Underground Structures of the Gouvães Hydroeletric Scheme - Monitoring and Observed Behaviour 759
Pereira, Renato; Muralha, José; Lamas, Luís

Assessment of Concrete Dam Foundation Discharges for Different Reservoir Levels Following a Hydromechanical Discrete Model 775
Braga Farinha, Maria Luísa; Monteiro Azevedo, Nuno; Oliveira, Sérgio

Stability Analysis of Concrete Dam Foundations Following a Hybrid Discrete Element/Finite Element Approach 791
Monteiro Azevedo, Nuno; Braga Farinha, Maria; Oliveira, Sérgio

Implementation of 3D Thermal Models in the Construction of the Alto Tamega Dam 811
Capinha, Luis; Chacón LLorente, Rafael; Siguenza Ibañez, Alicia; de la Torre Abietar, Luis; Vinagre Alba, Emilio José

T2 Embankment Dams and Levees

Prediction Models for the Hydraulic Behavior of Irapé Dam 833
Marcelino, João; Divino, Paula Luciana; Balbi, Diego

Notes on the Application of New Zealand's 2022 NSHM in Slope Stability 845
Dirikolu, Tarik; Zabolotnii, Elena; Sivathayalan, Siva; Read, John; Venter, Julian

Tropical Lateritic and Saprolitic Soils – The Brazilian Experience 863
Freitas Jr, Manoel; Pastore, Eraldo

Micro Seismic Resonance (MSR) - A Helpful and Complimentary Tool for Mapping Seepage Through, Beneath and Around Dams, Embankments & Levees 883
K. Hughes, Andy; Blanchard, Ryan

The Use of Leakage Detection Systems to Improve Reservoir Safety and Direct Remedial Works 901
Hughes, Andy

Selection of the Critical State Parameter M for Deformation Analysis Under Generalized Stress Paths 915
Murali, Aravind; Bangera, Vinayak; Zabolotnii, Elena; Sivathayalan, Siva

Advanced Geomembrane Systems for Dams and Reservoirs of New Pumped Hydro Storage Schemes 929
Vaschetti, Gabriella; Jackson, A.; Blanco, Alejandro

Experimental Investigation of Sediment Propagation in case of Homogeneous Earth-fill Dam Break by Piping 945
Büyüker, Zehra; Taşkaya, Ebru; Bombar, Gökçen; Tayfur, Gökmen

Embankment Dam Monitoring Using Electrical Resistivity Tomography for Abnormal Seepage Analysis 965
Abdulamit, Altan; Pisculidis, Tudor; Obreja, Razvan

Integration and Challenges in the Slope Health Monitoring System (SHMS) 985
Carneiro, Samuel; Guimarães, Filipe; Penha, Iggor; Faria, Silvia; Thimotio, Flavio; Souza, Camila; Pereira, Vinicius

Codegua, a Compendium of the Chilean Experience in CFRD Dams 999
San Martin, Luis; Materon, Bayardo

Development of an Integrated System for Risk Management and Decision-Making: an FMEA/FMECA and PFMA-Based Approach 1019
Etchegaray Mendes, Daniel

Simplified Analytical Solutions of Free Surface Migration Within Originally Dry, Coarse Grain Sized, Embankment Dam Materials 1039
Federico, Francesco; Cesali, Chiara

Advanced Limit Equilibrium 2D Analyses to Assess Global Sliding Safety of Embankment Dams Under Seismic Actions 1059
Federico, Francesco; Cesali, Chiara; Caushi, Herald

In-situ Estimation of Breach Outflow Hydrographs From Fluvial Dike Failures: a Methodology Integrating Real-time Monitoring and Physical Modelling 1077
Jónatas, Ricardo; Amaral, Sílvia; Aleixo, Rui; Bilé Serra, João; Ferreira, Rui

Lime Treatment for Hydraulic Structures: Benefits, Challenges, and Long-Term Performance 1101
Bertola, Federica; Nicaise, Sylvie; Saussaye, Lucile; Verelst, Kristof; van Hemert, Henk

Brief Insights: In-situ Permeability Test in Weathered and Poorly-Graded Rockfill 1117
Laina-Gómez, Carlos; Escudero-Merino, Diego; Asanza-Izquierdo, Enrique; Díez Torres, Juan Antonio

The Design and Construction of 71 Ndúe Dam – Angola 1129
Costa, Rui; Sousa Cruz, Jorge; A. Henriques, Nuno

Main Failure Modes in Embankment Dams, Mappable with Drone Survey 1145
Leite, Daniel; Marcelino, João; Guerra, Nuno; Manso, João; Sardinha, Ricardo

Construction of an Asphalt Core Dam in a Seismic Zone 1163
Graça, Newton; Moreira, Jose; Carleto, Bruno; Pantoja, Tarcisio

Geological and Geotechnical Studies in Dams Design. Foundation, Reservoir and Construction Materials 1181
Roque, Magda

Application of a Cost-Effective In-Place Inclinometer System on a Zoned Earth Dam 1197
Palma, João; Correia dos Santos, Ricardo; Marcelino, João; Marques, Nuno

Setting an Earthquake Magnitude Threshold and Evaluating its Impact on a Rockfill Dam 1219
Pandey, Binaya Raj; Zenz, Gerald

Occurrence of Canaliculi and Treatments in the Foundations of the Belo Monte Hydroelectric Complex During Construction and Operation 1233
Braga Boaventura, Marcelo; Pimenta de Ávila, Joaquim; Abrahão, Ricardo Antonio; Charone Junior, Wady; Lellis dos Santos, Wagner; Diogo Krajewski, Erlene; Carvalho Lima, Leandro

Developing a Remote Sensing Tool for Reservoir Volume Evaluation 1249
Pimenta, João; Fernandes, João; Azevedo, Alberto

Optimizing Seismic Intensity Measures for Fragility Analysis of Earth Dams: a Comprehensive Evaluation Incorporating Functionality Metrics 1259
Segura, Rocio; Veylon, Guillaume

Geostatistical Spatial Prediction Models of Resurgence and Canaliculus in the Dikes Surrounding the Intermediate Reservoir of the Belo Monte Hydroelectric Plant 1277
Silva Junior, Edivaldo; Fernandes, Débora; Januário, Adriana; Rodrigues, Rodrigo; Reginato, Luan; Concepcion, Candy; Krajewski, Erlene; Boaventura, Marcelo; Lima, Leandro

The Effects of Hypothetical Ochre Clogging of Drainage System on Slope Stability of the Itumbiara Dam, Brazil 1291
Mendonça, Marcos Barreto; Cavalcanti, Maria do Carmo Reis; Machado, Gabriela Wolguemuth

Let's Talk About FMEA 1303
Fusaro, Teresa Cristina; Vaz de Melo, Alexandre; Etchegaray Mendes, Daniel

Quxue Dam 2D FEM Analysis - Asphalt Core Displacements Comparison with Similar Structures 1321
Cavalcanti, Maria do Carmo; Barreto de Mendonça, Marcos; Silva Drumond, Fernanda

Numerical Simulation of Dam Behavior During the Reservoir Filing Until Reaching Steady-State Conditions 1337
da Conceição Rodriguez Moreira, Pablo Henrique; Cavalcanti, Maria do Carmo; Barreto de Mendonça, Marcos

Arching Effect Induced by a Concrete Gallery Inside Tullaroop Dam - Three-dimensional Finite Element Analysis 1357
Nogueira Rodrigues, Gabriel; Cavalcanti, Maria do Carmo

InSAR Monitoring and FEM Modeling of the Vadomojón Earthfill Dam (Córdoba, Spain) 1373
Esteban Mateos, Elías; González Tejada, Ignacio; Lamas-Fernández, Francisco; Ruiz-Armenteros, Antonio; Marchamalo-Sacristán, Miguel; Martínez-Marín, Rubén; Sancho, Candela; Fernández-Landa, Alfredo; Granados, Alfredo; Granados, Isabel; Jorda, Luis

A CFD Account of the Mean Flow and Turbulence over Breached Embankment Dam 1387
L Ferreira, Rui M; Martins, Nuno M; Alvarez, Teresa; Viseu, Teresa

Critical Aspects of Using Vibrating Wire Piezometers in Geotechnical Monitoring of Dams: How to Meet Basic Operating Principles of the Devices and Avoid Common Errors that Compromise Monitoring 1405
Bastos, Wellerson; Pimenta Filho, Marcos; de Almeida, Luiza; Ferreira, Marina; Santos Junior, Mauro

Reinforcement of the Foundation Waterproofing of the Alvorninha Dam 1427
Romeiro, Manuel; Candeias Portugal, João

Drone Survey of an Embankment Dam To Detect Surface Changes 1441
Henriques, Maria; Silva, Hugo

A Detailed Safety and Risk Assessment of Pequenos Libombos Dam 1459
Falcao de Melo, Jose; Sardinha, Ricardo; Pimenta, Lurdes; Duarte, Alexandre; M. Freitas, Rui; Juízo, Dinis; Martins, Amiro; Sengo, D.; Timba, J.; Mabunda, Luís

A Detailed Safety and Risk Assessment of Massingir Dam 1479
Sardinha, Ricardo; Falcao de Melo, Jose; Pimenta, Lurdes; Duarte, Alexandre; M. Freitas, Rui; Juízo, Dinis; Martins, Amiro; Miguel, F.; Cuna, I.; Mabunda, Luís

Design of Raghai Embankment Dam in a Complex Geological and Geotechnical Framework (Tunisia) 1501
Rebelo, Virgílio; Antunes, Joana; Morgado, António; El Ghali, Abdessalem; Yahia, Ali; Pinto, Sónia; Naguindás, Febin; Khlifi, Rabii

Calucuve Dam – Geotechnical Conditions and Design 1525
Sardinha, Ricardo; Badry, Hesham; Pimenta, Lurdes; Abreu, Rui; Leite, Daniel; Custódio, Hugo; Naguindás, Febin

Design, Supervision, and Technical Assistance to Construction of IRCL Southern Expansion 1545
Antunes, Joana; Repsold, Lucas; Almeida, Lúcia; Sardinha, Ricardo; Oliveira, Mafalda

The Use of Sentinel-1 Radar Images Associated With the Insar Technique to Monitor Surface Displacements of a Dam in Brazil 1567
Viana, Deivid Reis; Mendonça, Marcos Barreto; Silva, Wagner Barreto; Rocha, Carlos Henrique Oliveira

Evaluation of a Geophysical Study Involving Electrical Resistivity and Spontaneous Potential Tests for Piping Identification on the Whater Dam on Mato Grosso do Sul - Brazil 1581
Mestnik, Yuri; Ribeiro, Andre Batistela

Slope Stabilization on the Left Bank Upstream of the Caniçada Dam – Considerations on Constraints, Quality and Maintenance of Ground-anchored Structures 1599
Rodrigues de Carvalho, Mariana; Escaleira Esteves, Carlos; Caldeira, Laura

Volume 2

T3 Hydraulics for Dams

Development of Innovative Siphon Spillway for Existing Dams 1623
Kawasaki, Hideaki

Climate Shift Impacts on Hydrological Patterns in Mining Areas Located in Northern Brazil 1641
Costa, Denis; Rodrigues, Francisco; Ferrari, Darym; Oliveira, Keyla; Portes, Andrea; Yokozawa, Stephanie; Sol, Fernanda; Gomide, Paulo

Investigation of the Breach Shape Effects on the Flood Propagation in the Case of the Distorted Physical Model of Ürkmez Dam 1655
Arkış, Tanıl; Bombar, Gökçen; Güney, Mehmet Şükrü; Tayfur, Gökmen

A Methodology to Determine the Flow Curves for a River Barrage in Potentially Submerged Conditions 1673
Zuccalà, David; Gatti, Daria; Scuppa, Isabella; Cirillo, Carlo

Freeboard and Spillway Capacity Progressive Reductions for the Lago Verde Rockfill Dam, Due to the Crest Settlements After Several Decades of Operation 1693
Cesali, Chiara; Federico, Francesco; Maestri, Marina

Extraordinary Maintenance of San Mauro's Dam (Italy): Replacement of the Main Tainter Gates and Restoration of the Safety Conditions of the Structure 1709
Munari, Stefano; Vallese, Gaetano; Bianco, Lorenzo

Analysis of the Influence of Manning's Coefficient in Dam Failure Simulations Using Remote Sensing Data .. 1721
Salgado, Sérgio; Carvalho, Elsa; Viseu, Maria Teresa; de Oliveira, Othon Fialho

Ontime Modeling of the 14 de Julho Partial Dam-Break in South of Brazil 1733
Moecke, Giorgia; De Lara, Pedro; Diniz, Felipe

Development of the Combined Fish Pass of Fratel's Dam using Numerical and Physical Modelling 1745
Falcao de Melo, Jose; Sassetti Mendes, Lourenço; Muralha, António; Pinto, Pedro; Oliveira, João Miguel; Carvalho, Liliana Benites; Almeida, Pedro Raposo; Quintella, Bernardo; Alexandre, Carlos M.; Rato, Ana Sofia

Spillway Modeling: Comparing RNG and LES Turbulence Models 1777
Quaresma, Ana; Pinheiro, António

Overall Hydraulic Model Test of Caculo Cabaça Hydropower Project 1793
Haiyan, Yang; Liqun, Wang; Amador, António; Costa, Maria Cristina; Chico, Augusto; Wen, Liu

Strengthening Key Water Infrastructure in Mozambique: Risk Analysis of Massingir Dam Downstream Valley 1813
Amaral, Sílvia; Rocha, Fernanda; Viseu, Teresa; Juízo, Dinis; Saimone, Francisco; Pimenta, Lurdes; Miguel, Fernando; Cuna, Ivan; Mabunda, Luis

Strengthening Key Water Infrastructure in Mozambique: Risk Analysis of Pequenos Libombos Dam Downstream Valley 1827
Amaral, Sílvia; Rocha, Fernanda; Viseu, Teresa; Juízo, Dinis; Saimone, Francisco; Pimenta, Lurdes; Sengo, Delário; Timba, Jaime; Mabunda, Luis

T4 Tailings Dams

Optimizing Tailings Dam Safety: Integrating Human Factors and Evolving Hazards 1841
Oboni, Franco; Oboni, Cesar

Containment of Concrete Dams Compacted with Roller Using Iron Aggregate 1859
Pereira, Frank; Carmo, João; Andrade, Walton

Mining Dam's Classification & the Brazilian Practice 1889
Rangel Bittencourt, Lucas; Zic, Kresimir

Decommissioning of Tailings Dams: Case Study and Critical Analysis of the Decommissioning Stages of the Samambaia Dam 1911
Pires, Ian Henrique; Romanini, Augusto

Influence of Soil and Climate Variability on Earth Dam Design in Brazil 1929
Campos, Darym Junior Ferrari de; Sol, Fernanda Rocha Reis; Veras, José Dias Diego; Costa, Denis Duda; Ferreira, Stephanie Yumi Yokozawa; Gomide, Paulo Cesar Riquelme

Emergency Action Plan and the Precautionary Principle in Protecting Lives 1947
Sant'Ana, Marcelo; Velloso, Verônica; Motta Velloso, Márcia; Lopes, Daniela

ITRB Experience at Vale Mineração Tailings Storage Facilities 1957
Eleoterio, Marcos; Costa, Filipe; Marques, Eduardo

Comparative Study of 2D and 3D Slope Stability Analyses Applied to a Tailings Dam 1969
de Melo, Rayssa; Carneiro, Ananda; Almeida, Eduarda; Ferraz, Roberto; Marques, Eduardo

Evaluation of Slope Stability in Tailings Dam Construction and Decommissioning Stages Using 3D Limit Equilibrium and Strength Reduction Factor: a Comparative Analysis 1983
Barbosa, Jaime; Dantas, Marcelle; Carvalho, Wesley; Norena, Nilthson

From 2-D to 3-D Limit Equilibrium Analyses on Tailings Dam Stability: Assumptions, Benefits and Uncertainties 2003
Ferreira, Gonçalo

Evaluating 3D Effects on Tailings Dam Stability: a Comparative Analysis Using FS_{3D}/FS_{2D} Ratios 2023
Conceição, Raul; Ferreira, Gonçalo; Camões Lourenço, João; Lopes, Henrique

Technical and Economic Feasibility of Using Iron Mining Waste as Borrow Material for Dam Decharacterization 2045
Pereira, Frank; Tacco, Rafaela; Ribeiro, Adriana; Mazon, Alessandra; Carmo, João Bosco; Guerra, Felipe; Cavalcante, André; Torres, Vidal; Cristiane, Sebastião; Leal, Ana

Geotechnical Risk Assessment of Tailing Storage Facilities - Lessons Learned 2065
Esfehani, Morteza; Figueiredo, Luis Melges de; Carnavale, Thiago de Souza

Sensitivity Analysis of a Tailing Dam Stability Properties Using Sobol Indices and Sensitivity Factors 2099
Rodrigues Leal, Gabriela; Torrico Siacara, Adrian

Dam Raising Using a Reinforced Soil Containment Structure 2113
Ribeiro Paulino, Gustavo; Vilela Wanderley Neto, Ronaldo; Tozetti Franco, Ciro Gabriel; Tozetti Franco, João Emílio; Fernando Fanaya Dluhosch, André; Margarete Magalhães de Oliveira Cadavez, Camyla; Eduardo Pimentel, Victor

Geotechnics 4.0: Use of Big Data and Artificial Intelligence in Geotechcnical Investigations at Dams in Mining 2125
Biondo, Marieli; Piton, Rafael; Costa, Viviane

Evaluation of the Impact of Changing the Tailings Disposal Method in the Reservoir of a Rock Soil Dam 2143
Cruz, Mateus; Franco, Ciro; Flores, Katherine

Historical Cases of Liquefaction in Dams: Lessons Learned 2157
Lima Ferreira, Renata; Muniz de Faria, Thiago; Pereira, Luana

Rescue Systems: the Challenge of Performing Geotechnical Surveys in Tailings Dams at an Emergency Level 2173
Santos, Fernando; Biondo, Marieli; Sousa, Eduardo

A Mathematical Way to Claim Our Experience: Following the Bayesian Approach 2191
Viegas, Jeniffer; Gallardo, António

Technological Challenges in Tailings Dams in the Brazilian Amazon 2213
Pino Véliz, Pedro; Kong Diaz, Patricia

Tailings Dams Engineering: Amazon vs. Non-Amazon Challenges 2241
Pino Véliz, Pedro; Kong Diaz, Patricia

Construction of the Southern Expansion of the Cerro do Lobo Waste Facility 2249
Manso, Joao; Brito, Andrea; Barroso, Madalena; Marcelino, João; Galrão, Rui; Oliveira, Mafalda

Southern Expansion of the Cerro do Lobo Waste Facility. Mechanical Characterization of Soil-Rockfill Mixtures 2261
Brito, Andrea; Manso, João; Marcelino, João; Galrão, Rui; Oliveira, Mafalda

Applications of InSAR Technology in Dam Monitoring: a Systematic Literature Review 2273
Silva Alves, Jailson; Quental Coutinho, Roberto; M. Ruiz-Armenteros, Antonio; Barreto de Araújo Falcão Moreira, Hanna; Ramos Aragão Júnior, Wilson

Automated Geotechnical Monitoring Project of a Brazilian Mining Tailings Dams 2285
Silva, André; Gonçalves, Rachel; Orsseti Dias, Carlos; Meireles, Henrille

Safety Evaluation of an Upstream Raised Red Mud Tailings Dam 2303
Bottaro, Lucas; Lopes, Isabel; Tavares, Goncalo; Garcia, Marta

L-Band SAR Derived Soil Moisture Maps for the Monitoring of Earthen Dams in Scandinavia 2319
Hinton, Mark; Lynch, Jonathan; Rabinovitch, Yonatan

T5 Environmental and Social Issues

A GIS-Grid Nonpoint Pollution and Self-Purification Model for Hydropower Reservoirs 2331
Ribas, José Roberto; Fariña, Maria Elena Arce; Severo, Juliana C Ribas; Garcia, Andrés Suárez

Decharacterization Programs for Dams in Brazil: Solutions and Challenges 2345
Schaefer Santos, Felipe; Sayuri Tanabe Nishijima, Paula; Coelho de Campos, Gisleine; Shoji Iyomasa, Wilson

Sustainable Reservoir Operation: Balancing Power Generation and Downstream Environmental Maintenance - The Case of the Cahora Bassa Dam 2367
Guale, Rosaque; Carvalho, Elsa; Alves, Elsa

Rethinking Economic Risk for Amazonian Tailings Dams 2385
Pino Véliz, Pedro; Kong, P.

Enhancing Tailings Dam Classification for GISTM and ESG Conformance Using Generative AI 2401
Bachu, Lakshmin

T6 Regulation and Governance

The Development of Reservoir Legislation in the UK – Past, Present & Future – A Critical Review and Recommendations 2417
Hughes, Andy

Evaluation of Dam Safety Practices in Mozambique Through Risk Assessment 2439
Mabunda, Luis António; Escuder-Bueno, Ignacio; Morales-Torres, Adrián; Mancini, Davide; Romero-Duque, Sergio Andrés; Silva, Marco

Proposal to Obtain a Correlation of Concrete Properties from Standardized Radiological Testing 2455
Moreira do Carmo, João Bosco; Meira Belo, Luiz Claudio; Soares Lameiras, Fernando; Marques Filho, José

Emergency Action Protocol Implemented by Inea at the Açude da Concórdia Dam 2463
Dias, Fernanda Spitz; Amaral, Daniele Pereira Batista; Alves da Silva, Milena; Bielschowsky, Cauê; Pereira, Thiago Henrique Zampieri

The Challenges of the Brazilian Electric Energy Regulatory Agency on Mitigate Effects from 2024 Rio Grande do Sul Floods 2481
Leite, Sérgio; da Silva, Ludimila; Gomes, Luiz Rogério

The Role of the Brazilian Electric Energy Agency in Dam Safety - A Review of Recent Years and Prospects for the Future 2507
Leite, Sérgio; da Silva, Ludimila; Mendes, Marcelo

Developments of Interest for Dam Industry Regarding Seismic Action in the Eurocode 8 of Next Generation 2533
Labbé, Pierre

Opportunities and Challenges in Applying BIM Methodologies Within the Portuguese Dam Safety Framework 2551
Serra, Carlos; Silva, João; Carvalho, Jorge

Dona Francisca HPP Crisis Management: Extreme Flood Event Response 2569
Moecke, Giorgia; de Lara, Pedro Guilherme; Fonseca, Maria Eduarda

GISTM Requirements Conformance and the Influence of the Key Roles for the Tailings Governance Framework: a Statistic Approach 2583
Borges, Marina; Menezes, Danielle; Delgado, Bruno; Mota, Hernani

General Criteria for Implementation of Dam Safety Management System 2593
Sieber, Luiz

Eletrobras' Experience in Implementing Emergency Action Plans for Dams 2609
Fernandes, Roberta Fonseca Santos; Peplau, Guilherme Rocha; Azevedo, Lizandra Prado de; Deotti, Leonardo de Oliveira Guerra; Vianna, Vinicius Ferreira

Dam Safety KPI at Eletrobras: Development and Application of Tactical Key Performance Indicadors 2625
Fernandes, Roberta Fonseca Santos; Deotti, Leonardo de Oliveira Guerra; Vianna, Vinicius Ferreira; Peplau, Guilherme Rocha; Azevedo, Lizandra Prado de

T7 Dams and Climate Change

Planning the Semi-arid Region: Land Use Capability Allied to Underground Dams as a Measure for Mitigating Deterioration 2643
Costa e Silva, Danilo

21st Century Climate Challenges and Debris Disasters: Assessing Legacy Dams Amid Record Climate Events 2657
McCully, Jared; Meeks, Paul; Rollins, Paul

Impact of Climatic Drift on Arch Dams Behaviour 2675
Suchier, Louis; Robbe, Emmanuel; Simon, Alexandre; Coubard, Grégory

Increasing Reservoir Storage Capacity by Using the Fusegate® System in the Brazilian State of Bahia 2693
De Simone, Cesare; Del Rey, Franck

Climate Resilience in Reservoirs: Recommendations from Chile 2713
Garrido, Carlos; San Martin, Luis

Urban Water Dams Decommissioning Using Nature-based Solutions: the Case of Monjolinho Dam, in Brazil 2733
Povinelli, Silvia Claudia Semensato; Vasconcelos, Anaí Floriano; Mattos, Sergio Henrique Vannucchi Leme de; Rother, Débora Cristina; Gonçalves, Luciana Márcia

State-of-the-Art Review on Advancements Dam Monitoring Technologies 2751
Silva, André; Levesque, Christiane

Diversifying Electricity Sources in Water-Stressed Regions: a Multi-Criteria Approach for the São Francisco River Basin 2769
Barbosa Souza Júnior, Clécio

Fifth International Dam World Conference
PORTUGAL • LISBON • LNEC • APRIL 13-17, 2025
dam world 2025

WADI DERNA DISASTER (LYBIA SEPT. 2023)

Michel Lino[2]
ICOLD

Ahmed Fouad Chraibi[2]
ICOLD

ABSTRACT

On September 10-11, 2023, Storm Daniel caused catastrophic flooding in Libya, particularly in Derna, where over 4,000 lives were lost due to the collapse of the cascade Abu Mansur and Derna dams. UNESCO, with the support of ICOLD, deployed experts to assess the disaster's causes and recommend remedial measures. As direct site inspections were not possible, the analysis relied on documents related to dams' design and monitoring provided by local authorities.

Both dams, built on karstic limestone, had known structural weaknesses, including excessive settlement and leaks reported since the 1980s. Both dams were in such a weak condition that the flood of September 2023 was almost a trigger that led to their failure. Unfortunately, this flood was so massive that the dam failures resulted in a tragedy.

Challenges in estimating rainfall, such as spatial variability and limited reliable data, added uncertainty to determining the event's return period, which ranged from 500 to 5,000 years. Due to poor bedrock conditions, it was recommended that the foundation conditions should be carefully assessed before building new dams upstream of this heavily urbanized area. The design flood should be reassessed in a conservative approach taking into account the effect of climate change. It is noted that efficient flood protection does not necessarily mean rebuilding storage dams. If a new dam is to be considered, it should be designed to withstand overtopping.

Keywords: Wadi Derma disaster.

[1]lino@isl.fr, France
[2]ach@damtech.ma, Morocco

Fifth International Dam World Conference
PORTUGAL • LISBON • LNEC • APRIL 13-17, 2025
dam world 2025

WATER SCARCITY, CLIMATE CHANGE ADAPTATION, AND THE ROLE OF DAMS AND RESERVOIRS

Rodrigo Proença de Oliveira[1]
CERIS – Civil Engineering Research and Innovation for Sustainability
Instituto Superior Técnico, Universidade de Lisboa

ABSTRACT

Water scarcity, exacerbated by climate change, population growth, and economic development, remains a critical global challenge. As water shortages manifest themselves in various forms and over different time scales, it is essential to clearly define and distinguish between the concepts of drought, water scarcity, water stress and aridity to effectively address this complex challenge.

This paper investigates methodologies for accurately assessing water scarcity, emphasizing the importance of accounting the role reservoirs play in mitigating water scarcity, especially in highly regulated river basins characterized by Mediterranean climates.

Reservoirs have traditionally played a pivotal role in addressing water scarcity, particularly in Mediterranean climates where irrigation is vital for agriculture. These regions often endure extended dry seasons, making dependable water storage essential for maintaining crop production. In response to climate change, farmers are increasingly shifting toward irrigated permanent crops, which are generally more valuable but reduce water management flexibility. This shift places additional pressure to construct new dams, as irrigated farming is a cornerstone of local and regional economies, particularly in sparsely populated areas where agriculture dominates economic activity.

Despite their benefits, reservoirs and dams come with notable environmental and economic costs. Their construction can disrupt ecosystems, lead to biodiversity loss, and displace communities, while requiring substantial financial investments and ongoing maintenance. These factors highlight the need for rigorous cost-benefit analyses when considering new reservoir projects, ensuring that their advantages outweigh their negative impacts and that alternative solutions are also evaluated.

Beyond reservoirs, additional strategies can address water scarcity effectively. Demand control measures, such as water pricing and conservation initiatives, promote efficiency in water use. Desalination technology provides a vital alternative for arid and coastal areas, though it remains energy-intensive and should be used judiciously. Water reuse and recycling systems, which treat wastewater for agricultural, industrial, or even potable purposes, further diversify water supply options.

Improving water efficiency is crucial across all sectors. In agriculture, adopting advanced irrigation techniques like drip or sprinkler systems can significantly reduce water consumption while maintaining productivity. Such measures are particularly vital in sparsely populated agricultural regions, where efficient water use directly impacts the livelihoods of local communities and regional economic stability.

By integrating reservoirs with alternative solutions and prioritizing water efficiency, decision-makers can create a more resilient and sustainable approach to water management. This holistic strategy not only addresses current water scarcity challenges but also supports the economic and ecological needs of future generations.

Keywords: Scarcity, indicators, water accounting, dams and reservoirs, economic instruments

[1] rpoliveira@tecnico.ulisboa.pt, Portugal

1. INTRODUCTION

A significant portion of the world's population faces inadequate access to water, negatively affecting their health, well-being, and economic prosperity. Climate change and growing demands for water, driven by improved living standards and changing lifestyles, further intensify these challenges. Additionally, ecosystems suffer greatly from insufficient water availability.

Water shortages manifest themselves in various forms and over different time scales. To effectively address this complex challenge, it is essential to clearly define and distinguish between the concepts of drought, water scarcity, water stress and aridity.

A drought event is defined as a period when a climate variable, namely precipitation, deviates from a reference condition which may lead to a temporary water shortage. The key aspects highlighted in this definition is the temporary duration and the natural cause of the drought.

Water scarcity refers to a prolonged condition resulting from excessive water use relative to its availability. Unlike drought, it is a persistent, human-induced issue that arises due to overconsumption, limited natural water resources, or inadequate infrastructure and institutional frameworks that fail to meet existing consumptive and non-consumptive demands. Within this context, it is useful to differentiate between absolute (or physical) scarcity, where natural water resources are insufficient to satisfy water demands, and economic scarcity, which stems from inadequate infrastructure, insufficient institutional and legal structures, or a shortage of skilled human resources required for effective water resource management.

Water scarcity may reveal itself when rivers, reservoirs and aquifers contain insufficient water of adequate quality to satisfy existing water needs, but also when the water in the soil is unable to support crop growth. This distinction highlights the concepts of blue water—referring to surface water and groundwater resources—and green water, which denotes water stored in the soil that is available for plant uptake. It also emphasizes that water scarcity may arise from contamination and inadequate sanitation infrastructures.

The term water stress typically describes a situation where available water resources may be insufficient to meet the demands of both human activities and ecosystem maintenance. The primary distinction between water stress and water scarcity lies in the explicit consideration of ecosystem requirements in the definition of water stress. However, these two terms are frequently used interchangeably.

Finally, aridity is defined as long term lack of available, life-sustainable moisture in terrestrial ecosystems (UNCCD, 2024).

This paper investigates methodologies for accurately assessing water scarcity, emphasizing the critical importance of mathematical models to account effectively for the role reservoirs play in mitigating water scarcity, especially in highly regulated river basins characterized by Mediterranean climates.

More broadly, the paper explores both the potential and the limitations of reservoirs in addressing water scarcity as a global challenge. While acknowledging the substantial benefits reservoirs can offer, it cautions against the risks inherent in prioritizing dam construction over simpler, more cost-effective, and readily implementable water management alternatives. The paper advocates for adopting a comprehensive strategy aligned with integrated water resources management (IWRM) principles. It stresses that decisions to build new reservoirs must be based on rigorous cost-benefit analyses that thoroughly evaluate economic, environmental, and social impacts, along with the socio-economic value of the activities supported.

Lastly, the paper underscores the necessity of establishing appropriate financing mechanisms and integrating economic instruments. These tools are essential for managing water demand efficiently, allocating water to its most socially and economically beneficial uses, and securing sustained resources for infrastructure maintenance.

2. HOW TO EVALUATE WATER SCARCITY

2.1. Aridity, drought and water scarcity indices

Several indexes have been proposed in the literature to assess the vulnerability of water systems to aridity, droughts, water scarcity or water stress.

Aridity is usually quantified by the *Aridity Index* (AI), defined as the ratio between long term averages of precipitation and potential evapotranspiration. A study by UNCCD concluded that between 1961-1990 and 1991-2020 drylands, defined as those having an AI less than 0.65, have expanded 4.3 million km^2 and reached 40% of global land (excluding Antarctica). People living in drylands doubled in number, reaching 2.3 billion (more than a quarter of global population). Climate models suggest that as many as 5 billion people could inhabit dryland by 2100 (UNCCD, 2024). This trend primarily resulted from rising air temperatures and increased variability in precipitation, leading to elevated evapotranspiration rates and reduced infiltration and soil moisture. Additionally, higher atmospheric CO_2 concentrations contributed by altering stomatal function in plants.

Drought indexes use precipitation and other meteorological variables to evaluate the frequency, severity, and duration of drought events defined as periods when the climate variable, namely precipitation, deviates from a reference condition (Mishra and Singh, 2010).

Among the drought indexes, the most widely used are the Palmer Drought Severity Index (PDSI) (Palmer, 1965), the Standardized Precipitation Index (SPI) (Mckee et al., 1993), and the Standardized Precipitation Evapotranspiration Index (SPEI) (Vicente-Serrano et al., 2010). Drought indexes based on runoff estimates have also been proposed by Shukla and Wood (2008), Wu et al. (2018) and Zou et al. (2018).

Finally, water scarcity indexes aim to assess the level of human-induced quantitative pressures on the river basin water resources, usually by comparing water demands or withdrawals with water availability. These indexes explicitly include estimates of water withdrawals or demands on their definition or include proxy variables, such as the population data. Most of the times, water availability is quantified by a long-term annual average of total runoff in natural conditions, to consider both surface and groundwater resources.

A complete review of several water scarcity indexes can be found in Rijsberman (2006), Pedro-Monzonís et al. (2015), Damkjaer and Taylor (2017), Liu et al. (2017) and Hussain et al. (2022).

2.2. Water Stress Index

The most well know water scarcity index, is the Water Stress Index proposed by Falkenmark et al. (1989), which measures the amount of water available in a watershed per capita. It is determined by the ratio between the long-term mean annual water availability (AWA^i) and the population (Pop^i) of watershed *i* (Equation 1).

$$WSI^i = \frac{AWA^i}{Pop^i} \quad (1)$$

AWA is defined as the long-term average of total annual flow (surface and groundwater flows), under natural conditions. In a hydrological year, the total annual flow is expected to be the streamflow annual volume, as the variation of groundwater storage is assumed to be small. As such AWA, may be determined from monitoring records of streamflow or from the results of a hydrological model.

The index aims at evaluating the capacity to supply basic human needs, such as drinking water, sanitary services, and food preparation. The authors proposed threshold values of 1 700 m³, 1 000 m³ and 500 m³ per capita per year, below which a country experiences water stress, scarcity and absolute scarcity, respectively (Rijsberman, 2006). The use of the expression “water stress” does not follow the above-mentioned distinction between water scarcity and water stress.

2.3. Criticality Ratio or the Water Exploitation Index

The Criticality Ratio (Alcamo et al., 2000) or the Water Exploitation Index *(WEI)* (EEA, 2010) is another index widely used that measures the level of water scarcity by the ratio of annual

water withdrawals to annual water availability. The ratio is also known as the Withdrawal-to-Availability ratio (*WTA)* (Damkjaer and Taylor, 2017) or the Water Resources Vulnerability Index (Raskin et al., 1997; Rijsberman, 2006). It is used to measure the achievement of target 6.4 of the Sustainable Development Goals (SDG), which seeks to ensure sustainable withdrawals and supply of freshwater to address water scarcity. In that context it is known as indicator 6.4.2 or Water Stress Indicator (FAO, 2019), not to be confused with the Water Stress Index, from Falkenmark (1989).

The Water Exploitation Index (WEI) is defined as the ratio of average annual water withdrawals for agriculture, industry and urban uses ($\bar{A}^i$) to annual water availability (Alcamo et al., 2000) (Eq.2).

$$WEI^i = \frac{\bar{A}^i}{AWA^i} \quad (2)$$

Higher values of *CR* indicate more water uses in a river basin and more shortages during low flow periods. The authors define severe levels of water stress when CR > 0.4. A discussion surrounding threshold values persist since some experts believe that water resources can be used with CR up to 0.6. Other experts say that the sustainability of water resources can only be achieved with CR< 0.2 (Alcamo et al., 2000).

By using population as a proxy to water use, WSI is hardly suitable to evaluate water scarcity at a sub-basin level, when significant man-made transfers exist, but WEI can accommodate this situation by including transfers to external basins in the withdrawals of the donor basin, and by including resources originating from external basins in the receiving basin water sources.

Mekonnen and Hoekstra (2016) have computed global water scarcity on a monthly basis at the level of grid cells of 30 × 30 arc min (Figure 1). They have found that two thirds of the global population (4 billion people) experience severe water scarcity at least one month per year and that half a billion people face severe water scarcity all year round.

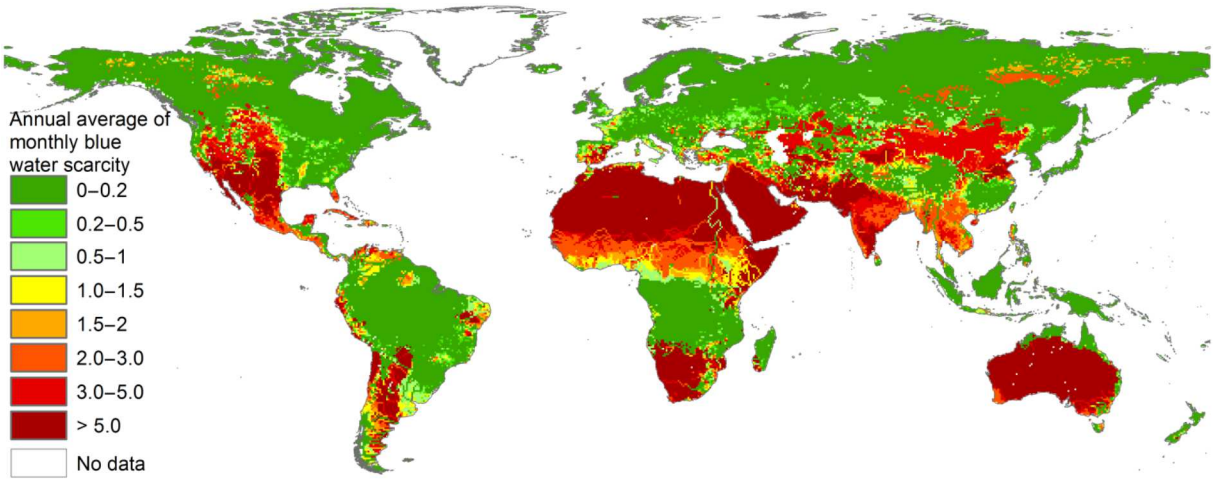

Figure 1 - Annual average monthly blue water scarcity at 30 × 30 arc min resolution. Period: 1996–2005 (Mekonnen and Hoeskstra, 2016)

2.4. Water Exploitation Index +

The Water Stress Index (WSI) and the Water Exploitation Index (WEI) do not consider flow variability, seasonality, nor the regulating capacity of reservoirs. Consequently, they are inadequate for assessing water scarcity in regions with a Mediterranean climate, such as Southern Europe.

WEI+, an improved version of WEI, addresses these issues. It was proposed by the Working Group on Water Scarcity and Droughts of the Common Implementation Strategy for the Water Framework Directive to evaluate water stress conditions in Europe (EEA, 2019a).

The WEI+ quantifies the renewable water resources and the water use for consumptive uses at a monthly time step to better capture water-scarce periods when abstractions surpass water resources availability (Bariamis et al., 2016; Zal et al., 2017). It also assumes regulated conditions, instead of natural conditions.

Instead of water abstractions, *WEI+* considers net consumption for consumptive uses, determined by deduction return flows, R_t^i, from water abstractions, A_t^i. The use of net water consumption, instead of water abstraction (gross values), provides a more accurate and less pessimistic view of water scarcity, as net abstractions correspond to a percentage of total water abstraction, which can be as low as 10-20% for urban uses (Pérez-Blanco et al., 2020). The non-consumed fractions of water abstraction contribute to the satisfaction of downstream uses.

WEI+ also considers ecosystem needs by deducting environmental flow requirements, $Qenv_t^i$, from the renewable water resources, RWR_t^i, as this volume is not available for consumptive uses.

Equation 5 is used to determine the value of WEI+ at sub-basin *i*, in month *t*.

$$WEI^{+}{}_{t}^{i} = \frac{A_t^i - R_t^i}{RWR_t^i - Qenv_t^i} \quad (5)$$

The WEI+ value varies between 0 and 1. A non-stressed period is defined when the WEI+ value is below 20%; a severe water stress period occurs when WEI+ value exceeds 40%; and a highly stressed period occurs when WEI+ value is above 60% (Faergemann, 2012).

Water abstractions for consumptive uses, A_t^i, includes water abstraction for cooling of power plants but not water used for hydropower generation (Faergemann, 2012). However, as water allocation for hydropower generation and other non-consumptive uses affects streamflow and water storage in reservoirs, hydropower generation is indirectly included in WEI+ computations.

Calculating WEI+ values is a complex task, and relatively few studies have provided detailed applications of this indicator. Initially proposed by the European Commission and the European Environment Agency (EEA), the WEI+ index is predominantly applied within Europe but is gradually gaining attention globally. The European Commission and the EEA have been working to use the WISE Water Accounts database and the LISFLOOD hydrological model in assessing WEI+ for various European river basins. Several researchers have applied WEI+ across major European river basins. Bariamis et al. (2016), de Roo et al. (2012), and Zal et al. (2017) have estimated WEI+ values for Europe's larger river basins. Bisselink et al. (2018) and Karabulut et al. (2016) specifically applied WEI+ assessments to the Danube River basin. Beyond Europe, Sun and Zhou (2020) employed WEI+ to evaluate water scarcity in China's Jinghe River basin. Additionally, alternative and simplified methods for estimating WEI+ were proposed by Casadei et al. (2020) for the Upper Tiber River basin and by De Roo et al. (2016) for the Sava River basin.

Applications of WEI+ in river basins characterized by Mediterranean climates remain rare. Noted examples include studies by Contreras and Hunink (2015) on the Segura River basin in Spain and by Sondermann and Oliveira (2022) on the transboundary Tagus River basin.

The substantial data requirements of WEI+ computations require the adoption of mathematical models to supplement and enhance ground-based and satellite monitoring data. Hydrological models estimate natural water flows, including evapotranspiration, groundwater recharge, and streamflow. In parallel, water allocation and management models provide insights into reservoir storage volumes, water withdrawals, consumption, and return flows, offering a comprehensive perspective on water distribution and usage. Decisions on the modelling approach may influence the WEI+ computations, especially in what concerns the simulation of groundwater flow and the river-aquifer interaction.

2.5. Economic and social water scarcity indexes

In addition to the above-mentioned indicators that focus on absolute or physical water scarcity, additional indexes were developed to capture the impacts of water capacity and the societal capacity to deal with them. The Social Water Scarcity Index (Ohlsson, 2000) and the Water Poverty Index (Sullivan, 2002) are examples of these indexes.

Ohlsson (2000) proposed the Social Water Scarcity Index (SWSI) by dividing the Water Stress Index (WSI)—which measures per capita water availability—by the Human Development Index (HDI), an indicator of a country's achievements in the fundamental dimensions of human development: longevity, education, and standard of living. The SWSI thus highlights societal capacity to effectively manage and respond to water scarcity challenges.

The Water Poverty Index (WPI) is a composite indicator calculated as a weighted sum of five components: resources, access, capacity, use, and environment. Collectively, these components evaluate water availability, accessibility, the capacity to effectively manage and use water, and the environmental condition of water bodies. Analysing WPI results enables differentiation between countries that, despite having limited water resources, possess robust institutional frameworks and technological capacities for efficient water management, and those with abundant water resources yet inadequate means or strategies to utilize them sustainably.

The added complexity in collecting data and the difficulty in understanding some variables and results hinders the widespread application of these indexes.

2.6. Water accounting

Water accounting offers a streamlined and user-friendly framework for reporting water availability and allocation within a river basin. It offers a detailed view of how water is used in a country, river basin, water resource system or a specific water body and the amount that remains available for additional uses. The approach is based in a water balance framework that accounts for the water inputs and outputs within a basin, including flows associated with various water uses. Molden (1997), Molden and Sakthivadivel (2010) and Karimi et al. (2012) present the main principles of water accounting.

By consolidating and presenting water resource data in a structured and organized manner, it facilitates a comprehensive understanding of how water is distributed and utilized across various sectors and regions, which is valuable for identifying critical management challenges such as water scarcity, inefficiencies, and imbalances in allocation and to support informed decision-making, especially in basins already experiencing water stress (Momblanch et al., 2014). If the water accounting system also includes economic data, it is possible to assess water productivity and the water footprint of services and products (Craswell et al., 2007).

To effectively represent a river basin water balance, water accounting must ensure completeness, consistency, transparency, and relevance. A thorough evaluation of all components of the natural water cycle—including precipitation, evapotranspiration, surface water, and groundwater—is essential. Additionally, human-influenced flows such as reservoir storage, water withdrawals, and allocations must be included. This comprehensive assessment should achieve precise closure of the water balance and integrate both quantitative and qualitative analyses.

Water accounting methodologies should utilize consistent and standardized approaches with clearly documented data sources, enabling comparability across different regions and time periods. Molden and Sakthivadivel (2010) and Perry (2010) highlight the importance of using accurate and consistent terminology to facilitate cross-sectoral understanding of water flows and water balances, laying the groundwork for consensus-driven solutions in integrated river basin management.

Incorporating verification mechanisms strengthens the credibility and reliability of the data. Lastly, the outputs must be relevant and actionable, directly supporting decision-makers and aligning with governance frameworks. This approach ensures that the needs of diverse water users—such as agriculture, industry, ecosystems, and domestic sectors—are effectively addressed.

Multiple water accounting methodologies have been developed by national and international organizations, each emphasizing different components of water accounting. Delavar et al. (2022), Karimi et al. (2013) and Momblanch et al. (2018) review some of the available water account methodologies. Much of the literature focuses on water use in agriculture, a natural emphasis given that it is the largest water-consuming sector and involves complex flow patterns which challenge some concepts such as efficiency and productivity (Perry, 2010). In contrast, Lyu et al. (2023) discuss the application of these methodologies in analysing industrial water use. Some frameworks also integrate economic data, allowing for assessments of water productivity and the water footprint of goods and services (Craswell et al., 2007). This diversity offers flexibility to accommodate different analytical objectives and data availability contexts but can compromise standardization and the sharing of concepts.

The first widespread water accounting framework is the *System of Environmental-Economic Accounting for Water (SEEA-Water),* proposed by the United Nations as a subset of its environmental accounting systems in the *Handbook of National Accounting: Integrated Environmental and Economic Accounting* (UN, 2012). SEEA-Water provides a robust structure for integrating hydrological and economic data, enabling comprehensive assessments of water supply, demand, and usage by human activities. It facilitates cross-country and temporal

comparability, making it a valuable tool for evaluating water resource allocation and linking water management with economic planning.

The framework addresses the stock and flows of water between the environment and the economy, emphasizing water abstraction, discharge, supply, use, and reuse in economic activities. By organizing hydrological and economic data into a set of core standard tables recommended for all countries, along with supplementary tables addressing social aspects and experimental data, SEEA-Water effectively connects water resource systems with economic activities. Its flexibility allows it to be applied across diverse contexts and at various spatial scales, such as river basins or administrative regions.

However, the SEEA-Water framework also has limitations. Notably, environmental flow requirements—essential for sustaining freshwater ecosystems—are not explicitly included in the standard SEEA-Water tables. This omission reduces the framework's suitability for addressing environmental sustainability priorities without incorporating additional analyses or supplementary tables. Furthermore, because economic accounts are typically compiled at the administrative region level, the framework is less effective when applied to non-administrative boundaries, such as river basins. This constraint may limit its utility in integrated water management planning (Esen and Hein, 2020b; Momblanch et al., 2018; Pedro-Monzonís et al., 2016b; Vicente et al., 2019b, 2016b)

Different from the globally standardized SEEA-Water framework, the Australian Water Accounting Standard (AWAS) framework was primarily developed to support detailed water management in Australia (BoM, 2010). Currently, there are some applications in other countries, for instance in Spain and South Africa (Godfrey and Chalmers, 2012; Momblanch et al., 2014). AWAS is a governance-oriented framework that focuses on water reporting to various stakeholders, particularly users, by applying principles of financial accounting to specific needs of water resource management, emphasizing accountability and transparency. The framework includes elements like water assets, liabilities, changes in storage and water rights, and it explicitly incorporates water rights, entitlements, and liabilities, reflecting the water governance system in Australia, where water trading and allocations are key features.

Finally, the Water Accounting (WA) framework, developed by the International Water Management Institute (IWMI), was designed to track green water use (evapotranspiration) and to minimize errors in evaluating return flows (Molden and Sakthivadivel, 2010). An enhanced version, known as Water Accounting Plus (WA+), offers a simplified and user-friendly framework (Karimi et al., 2013). The WA+ methodology has been widely applied to river basins and agricultural systems in water-scarce regions, at both local and regional scales (Karimi et al., 2013; Molden and Sakthivadivel, 2010).

The WA+ framework organizes its outputs into four sheets to summarise the water balance and management situation, each one with a specific purpose. These are the resource base, the withdrawals, the evapotranspiration and the productivity sheets.

The *Resource Base Sheet* provides hydrological information on water inflows and outflows, depletion processes and available water within a domain. The *Withdrawal Sheet* describes the consumptive use of surface and groundwater sources to urban hubs, irrigation, and industries, without neglecting evaporation losses from reservoirs and return flows to surface and groundwater systems. The *Evapotranspiration Sheet* and the *Productivity Sheet* focus on green water outflows through evaporation and transpiration and biomass production in crop lands, pastures, forests and other natural landscapes. The *Evapotranspiration Sheet* outlines the volumes related to *Interception*, *Evaporation*, and *Transpiration*, assessing whether these processes contribute to *Beneficial* or *Non-Beneficial* water uses, while the *Productivity Sheet* reports agricultural production per unit of water, focusing on *Biomass Services* and *Benefits*, while excluding *Water Productivity* in other sectors.

Figure 2 presents the scheme of the resources base sheet, proposed by Karimi et al. (2013).

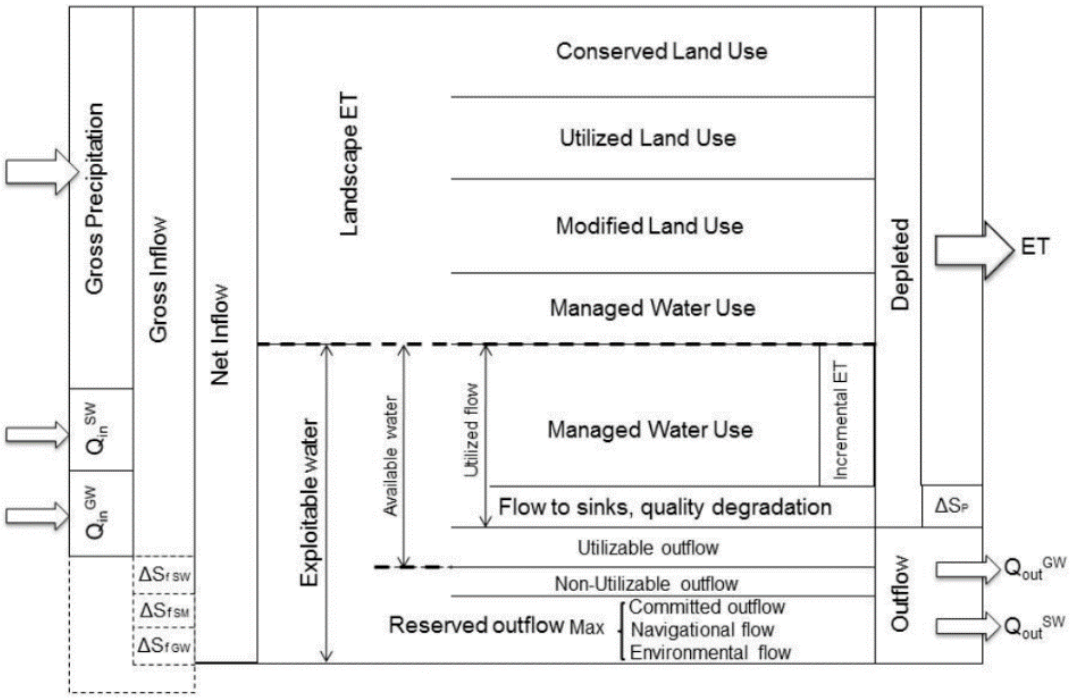

Figure 2 - Scheme of the water accounting methodology (Karimi et al., 2013)

Gross Inflow encompasses all incoming water to the system, primarily from precipitation which feeds surface and groundwater sources. *Net Inflow* accounts for changes in water storage, making it smaller than *Gross Inflow* when water is stored in reservoirs or aquifers, and larger when water is released from storage. *Net Inflow* is divided into two main components: *Green*

Water, representing water lost to the atmosphere through landscape evapotranspiration and unavailable for further use, and *Blue Water*, which refers to the exploitable surface and ground water, whose returns after use remain accessible for downstream uses. *Water Diversions* describe the allocation of water to consumptive and non-consumptive uses, part of it returns to the system and may be further used. The part that does not return due to evaporation or to its inclusion in products, is designated *Water Depletion*. *Water Depletion* also includes contaminated water bodies and contaminated returned volumes to an extent that it is unfit for certain uses, as well as evaporation from water bodies or deep percolation to unreachable underground layers. The difference between *Net Inflow* and *Landscape Evapotranspiration* is the *Exploitable Water,* which corresponds to the volume accessible for current or future consumptive or non-consumptive uses. The water available for consumptive uses (*Available Water*) is determined by deducting from *Exploitable Water* the *Non-Utilisable Flow* (e.g., flow during flood events which is not retained in reservoirs) and the committed or *Reserved Flows* for downstream uses, hydropower, navigation, and environmental purposes. These uses must be viewed collectively as the water flowing in rivers meet different non-consumptive uses simultaneously or in sequence. *Utilisable Water r*efers to uncommitted water which is still available for additional use*.* Finally, *Water Outflow* encompasses both *Reserved Outflow* and *Utilisable Water*.

Under the **WA+ framework**, each sheet generates a set of indicators that offer detailed insights into water resource availability and allocation to different uses (Karimi et al., 2013). The growing demand to increase water productivity and to achieve the best use of water by the various stakeholders requires a deep analysis of economic, environmental, and social benefits of both consumptive and non-consumptive water uses. By summarizing and standardizing data, water accounting serves as an important first step toward achieving this goal. However, the difficulties in obtaining consistent economic data across the different sectors and in estimating the cost and benefits of ecosystems services remain a challenge.

2.7. Discussion

The limitations of these water scarcity indexes have been extensively discussed in the literature.

The WSI and WEI indices were developed to facilitate rapid comparisons between countries or large river basins without extensive data collection efforts. However, their inherent simplicity overlooks many critical details, resulting in significant limitations.

The WSI and WEI indices do not account for the impact of seasonal variability on water availability and demand. Seasonality can significantly reduce abstraction volumes, which is especially critical in river basins with Mediterranean climates. Even in regions with relatively

stable flow regimes, estimating water availability based on the long-term annual mean of total runoff can result in overestimation errors, since it includes extreme high-flow values from unusable flood events. To mitigate this issue, some authors suggest estimating water availability as a percentage of mean annual runoff or by calculating the mean annual runoff during dry years (Saft et al., 2015).

Conversely, these indices overlook flow redistribution provided by hydraulic infrastructures (Damkjaer and Taylor, 2017; Liu et al., 2017; Savenije, 2000) and ignore inter-basin transfers.

They are also insensitive to the importance of green water which is available in the unsaturated zone (soil moisture) to plants and argued for an expansion of these indexes to cover this extra component of water availability and water use (Rockström and Falkenmark, 2015; Savenije, 2000; Vanham et al., 2018). They also usually fail to consider alternative water resources such as desalination and wastewater reuse, which are crucial for water supply in certain regions (Rijsberman, 2006).

Moreover, WSI and WEI typically do not account for water scarcity induced by water quality degradation. While historical and future trends influence water availability and demand, urbanization and agricultural activities have increasingly polluted water resources, thus limiting their safe use. To address this issue, Zeng et al. (2013) introduced a Quantity-Quality Water Scarcity Index, composed of a blue water scarcity index (the ratio of water withdrawals to freshwater resources) and a grey water scarcity index (the ratio of grey water footprint to freshwater resources). Here, grey water represents the volume of freshwater necessary to dilute and assimilate pollutants. Expanding on this concept, Liu et al. (2016) proposed a Quantity-Quality-EFR Water Scarcity Index, incorporating environmental flow requirements into water availability calculations. Wang et al. (2023) further demonstrated the significance of quality-induced scarcity, showing that in 2010, 984 sub-basins experienced scarcity based solely on quantity, whereas 2,517 sub-basins faced scarcity due to combined quantity and quality factors.

Concerning the water use component, the use of water abstraction as a synonym for water use is also a major criticism, as it does not consider water returns from consumptive uses, nor instream water uses (Liu et al., 2017; Rijsberman, 2006; Vanham et al., 2018). However, uncertainties are added when considering net abstractions, because the exact return volume and the exact location of return are usually unknown.

As a result, water scarcity conditions in highly regulated basins may be inaccurately assessed by these indices.

WEI+ offers added value to WSI and WEI, overcoming some of the criticism of these indexes. By considering storage capacity in reservoir and aquifer systems, seasonality and returns from

water use, the index can present a more accurate picture of water scarcity in highly regulated river basins with significant seasonality. WEI+ values highlight hydrological information at smaller spatial and temporal scales and reveal a water-scarce situation that is underestimated when the results are presented on an annual or spatial aggregated basis (Pedro-Monzonís et al., 2016; Rijsberman, 2006).

However, the estimation of WEI+ is not trivial and, in the absence of comprehensive monitoring records on water availability and uses which rarely exist, requires the detailed modelling of water management and allocation in the river basin, including groundwater systems.

The improvements included in WEI+ demand more data and add difficulties to its calculation, especially in complex river basin systems with aquifer-river interactions and major hydrological alteration arising from reservoir storage, water abstractions and returns and inter-basin transfers (Bariamis et al., 2016; RBMP-Cyprus, 2016). The lack of data can be partially overcome with different techniques, such as satellite data, remote sensing and hydrological modelling(Contreras and Hunink, 2015).

In addition to higher data requirements, the WEI+ definition also has certain limitations. While calculating water scarcity at a sub-basin level offers a more precise representation by minimizing estimation errors due to spatial aggregation, the spatial discretization itself can influence WEI+ values. This discretization may obscure dependencies of sub-basins on inflows from external basins, potentially resulting in misinterpretations of actual water scarcity conditions. Such inaccuracies are particularly significant in sub-basins with upstream-downstream dynamics, where increased upstream water consumption exacerbates scarcity downstream. This constitutes a critical issue in transboundary river basins, such as the international Iberian River basins.

The inclusion of environmental flow requirements within WEI+ computation enables its use by policymakers and stakeholders to better manage water allocation while respecting the environmental status of all water bodies. However, WEI+ is significantly dependent on the assumptions or decisions regarding environmental flow requirements, which vary widely. A clear understanding of this dependence is needed when evaluating WEI+ values.

Among the methodologies that have been proposed in the literature, hydrologically based methodologies, which define environmental flow requirements as a percentage of monthly flow, are the most used due to their simplicity and low cost. However, assumptions vary across river regimes (Vicente et al., 2019). For instance, Richter et al. (2012) suggest 80% of monthly runoff, while Pastor et al. (2014) use between 25% and 46% of mean annual flows (Vanham et al., 2018).

In addition, the computation of WEI+ may lead to values greater than one when $Qenv_t^i$ close to RWR_t^i and to negative values when $Qenv_t^i$ is greater than RWR_t^i. These situations are not unusual in southern European river basins with highly variable streamflow regimes, when $Qenv_t^i$ is defined as a fixed percentage of mean monthly flows. ${WEI^+}_t^i$ was set to one in these cases, depicting a situation where all renewable water resources are being used, even though not all demands are being fully satisfied.

Finally, the use of WEI+ to evaluate potential pressures on water bodies may clearly miss poor conditions resulting from significant changes in the hydrological regime induced by hydropower plants. WEI+ only considers water allocated to consumptive demands as water uses. Instream uses such as hydropower are reflected in the reservoir operating policies, but this is insufficient to measure the impacts that hydropower systems, with a large storage capacity, impose on the water dependent ecosystems and other uses.

The water accounting framework also has its limitations. Water accounting primarily relies on average estimates of stocks and flows, neglecting crucial concepts such as water supply reliability, vulnerability, and resilience. These factors are particularly important in basins with a Mediterranean climate, where water availability is highly variable, and acute water scarcity is common. While water managers rely on reservoir and aquifer storage to meet demands, dry periods frequently result in demands being only partially met. Effective water management requires a more comprehensive understanding of variability and risk to ensure sustainable and reliable resource use.

3. WATER USE TRENDS

Global freshwater use has increased significantly since 1950 due irrigation and improved life conditions, but it seems it has plateaued since 2020 (Figure 3). Although irrigated area went on growing, gains from improved efficient seem to have compensate this growth (FAO, 2024). From 2015 to 2021 global water use has marginally decreased by 0.1% and agriculture water use as decrease 0.6%. Water use efficiency, measured by gross value added by cubic meter, rose 19.3% from 2015 to 2021, with agriculture showing the highest percentage change, followed by the industrial sector and the service sector (FAO, 2024). Nevertheless, renewable freshwater resources have decreased, mainly due to population growth (Figure 4)

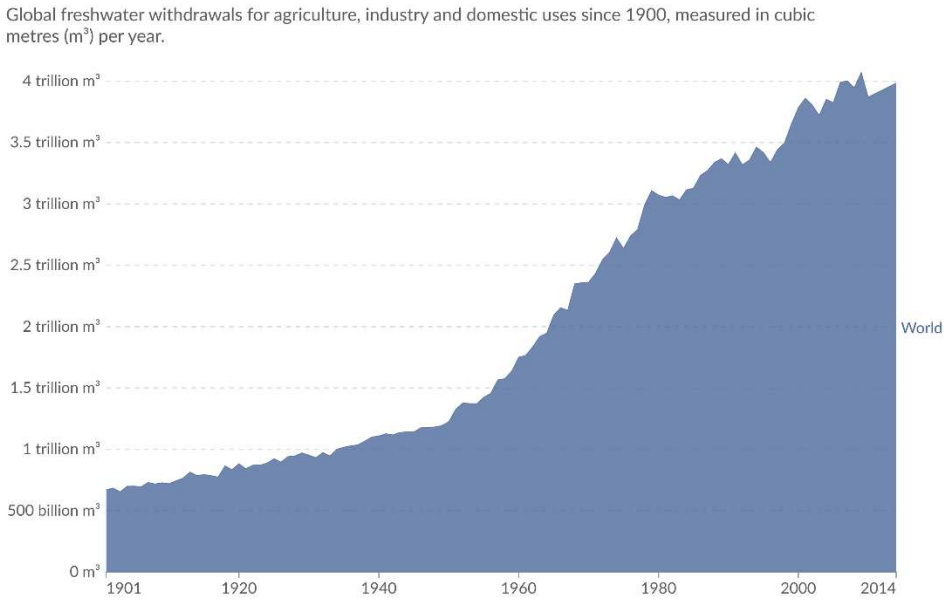

Figure 3 – Global freshwater use over the long run (source: Global International Geosphere-Biosphere Programme (IGB), processed by Our World in Data).

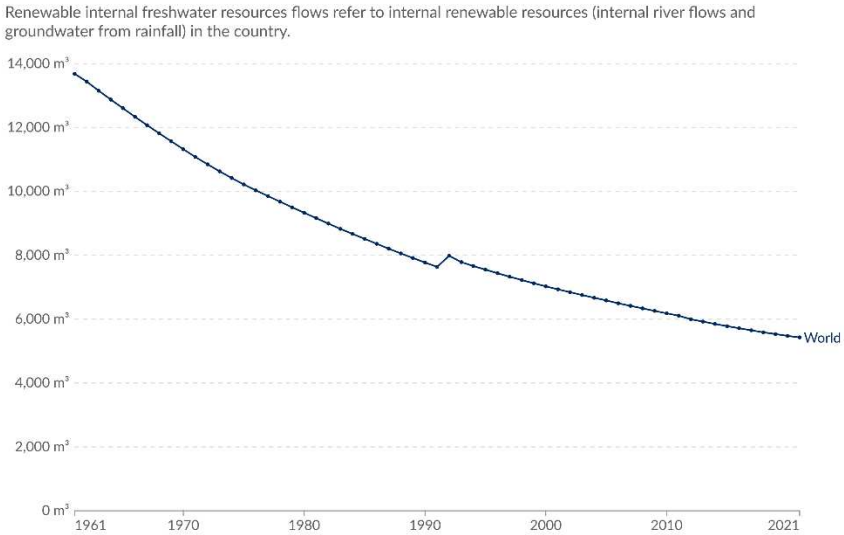

Figure 4 – Renewable freshwater resources per capita (source: Food and Agriculture Organization (via World Bank), processed By Our Word in Data (2025).

In Europe, the picture is clearer. Land equipped for irrigation has plateaued since 1985 (Figure 5). Water use efficiency has increased in agriculture, electricity production, industry, mining, public water supply and tourism, as Figure 6 shows (EEA 2021). Since 2000, water abstractions and consumption have decreased, particularly the former. Water consumption by these sectors was 16 % lower in 2017 (the last year for which EU-wide statistics are available) than in 1995 (baseline), while production in these sectors grew by 20 % in terms of net value added.

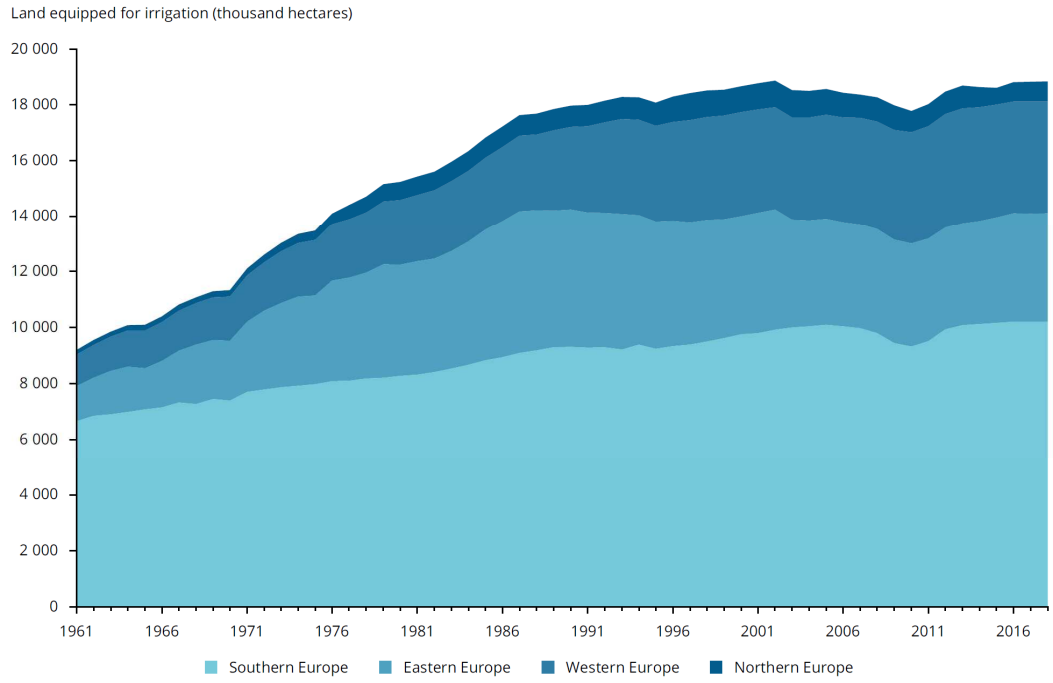

Figure 5 – Irrigable area in the EU-27 and the UK since 1961 (source: FAO)

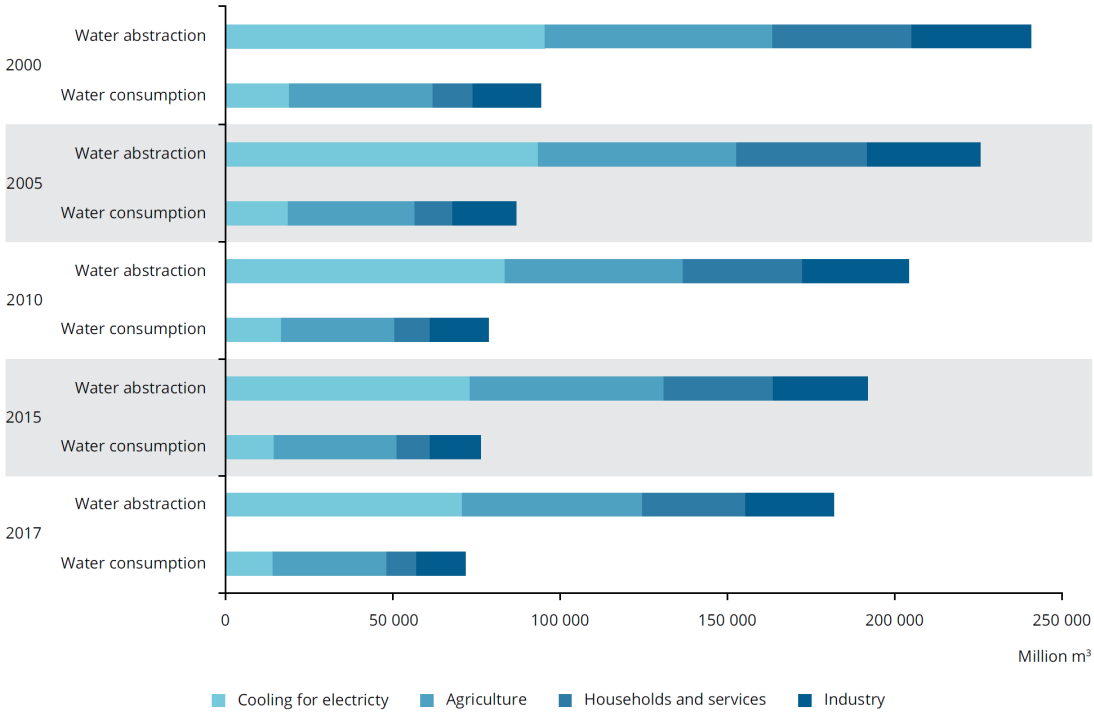

Figure 6 – Trends in water abstraction and water consumption in Europe (EEA-28 and the UK) (source: EEA (2019, 2021), Eurostat, 2020)

These recent trends in water abstraction and improvements in water-use efficiency provide valuable guidance for addressing the growing challenges of water scarcity. The indicators and approaches discussed in this paper can be utilized to evaluate current conditions, set clear objectives, and identify specific regions or basins requiring targeted actions. Additionally, they

can serve as tools for monitoring progress toward achieving these objectives. Among the reviewed approaches, the WEI+ and water accounting offer the most comprehensive analysis by considering the role of reservoirs and inter-basin transfers, which is particularly critical in highly regulated basins. Their study should be complemented with other elements of analysis to overcome their weaknesses.

4. FINAL COMMENTS

Growing population needs and climate change significantly impacts water resources, affecting both water availability and quality.

The growth in water demand and the increasing variability in water availability has led certain sectors to advocate for the construction of new dams to enhance water storage and regulate resources, or to transfer water from wetter regions to drier ones. Despite their benefits, reservoirs and dams come with notable environmental and economic costs, as their construction and operation can displace communities, disrupt ecosystems, lead to biodiversity loss, while requiring substantial financial investments and ongoing maintenance.

Storage-based solutions may be necessary in certain situations, but only after rigorous risk assessments addressing reservoir replenishment and potential future water shortages in donor regions have been conducted. When considering new reservoir projects, it is essential to perform comprehensive cost-benefit analyses to ensure that the advantages clearly outweigh any negative impacts and that alternative solutions have been thoroughly evaluated.

Additional measures contribute significantly to control water scarcity effectively beyond reservoirs, if framed within a diverse, yet coherent, set of initiatives targeting water demand, supply, and quality. This approach requires active involvement from governments, user associations, the private sector, and local communities. It embodies the concept of Integrated Water Resources Management (IWRM), formally introduced during the International Conference on Water and the Environment in Dublin, Ireland, in 1992.

Some measures are widely agreed upon, such as improving water use efficiency and effectively reducing physical water losses from supply and distribution networks in the short term. Taking stock on the improved water use efficiency of the recent decades, additional gains in water productivity and in the preservation of soil moisture are essential. To achieve this, it is crucial to expand traditional farmers' access to micro-irrigation technologies, climate-resilient seed varieties, and sustainable cropping practices (GCEC, 2024).

Another priority area involves enhancing groundwater monitoring to prevent overuse and increasing water availability by integrating the management of surface and groundwater resources.

Within water supply measures, source diversification should be promoted. The reuse of treated wastewater and seawater desalination are emerging strategies in some parts of the world, although expanding these solutions globally presents certain challenges. Typically, desalination plants and wastewater treatment facilities are located near coastal areas and major urban centres. Therefore, using this water in inland regions requires transporting it over potentially significant distances, adding transportation and storage costs to the already substantial treatment and desalination expenses. Furthermore, utilizing this water for agricultural purposes poses additional challenges due to aligning a relatively steady water supply with the seasonal variability of agricultural demand. Thus, treated or desalinated water should ideally complement other water sources or be linked to robust water storage infrastructure.

Finally, managing water demand will require the use of economic instruments that internalize water-related costs in decision-making processes. The Global Commission on the Economics of Water has called for a new economics of water to value water properly to reflect its scarcity and the multiple benefits it provides as the Earth's most precious resource, to tackle externalities caused by the misuse and pollution of water and to spur a wave of innovations, capacity-building and investments (GCEW, 2024). The commission stresses that the widespread underpricing of water today encourages its profligate use across the economy and unwisely skew the locations of the most water-intensive crops to areas most at risk of water stress.

The introduction of intelligent tariff schemes reflecting ideal or recommended water allocations per usage category can encourage responsible water consumption across all sectors. While incremental increases in water pricing may be feasible, provisions must ensure affordability for essential needs and public interest scenarios. A core shift is to correctly price water and allocate subsidies to achieve both its efficient use and access for all.

5. REFERENCES

Alcamo, J., Henrichs, T., Rösch, T., 2000. World Water in 2025 Global modeling and scenario analysis for the World Commission on Water for the 21st Century. Kassel, Germany.

Bariamis, G., Panagos, D., Zachos, A., Baltas, E., 2016. Use of Freshwater Resources in Europe 2002-2012. Supplementary document to the European Environment Agency's core set indicator 018. ETC/ICM Technical Report 1/2016, Magdeburg: European Topic Centre on inland, coastal and marine waters.

Bisselink, B., Bernhard, J., Gelati, E., Jacobs, C., Mentaschi, L., Roo, A. De, 2018. Impact of a changing climate , land use , and water usage on water resources in the Danube river basin. Publications Office of the European Union, Luxembourg. https://doi.org/10.2760/89828

BoM, 2010. Bureau of Meteorology. Australian Water Accounting Standard. Canberra: Commonwealth of Australia.

Casadei, S., Peppoloni, F., Pierleoni, A., 2020. A New Approach to Calculate the Water Exploitation Index (WEI +). Water. https://doi.org/10.3390/w12113227

Contreras, S., Hunink, J., 2015. Water accounting at the basin scale: Water use and supply (2000-2010) in the Segura River Basin using the SEEA framework., Future Water Technical Report. Cartagena (Murcia), Spain.

Craswell, E., Bonell, M., Bossio, D., Demuth, S., van de Giesen, N., 2007. Integrated Assessment of Water Resources and Global Change, Springer. ed, Integrated Assessment of Water Resources and Global Change. Springer Netherlands, Dordrecht, The Netherlands. https://doi.org/10.1007/978-1-4020-5591-1

Damkjaer, S., Taylor, R., 2017. The measurement of water scarcity: Defining a meaningful indicator. Ambio A J. Hum. Environ. 46, 513–531. https://doi.org/10.1007/s13280-017-0912-z

De Roo, A., Bisselink, B., Beck, H., Bernhard, J., Burek, P., Reynaud, A., Pastori, M., Lavalle, C., Jacobs-Crisioni, C., Baranzelli, C., Zajac, Z., Dosio, A., 2016. Modelling water demand and availability scenarios for current and future land use and climate in the Sava River Basin. Joint Research Centre, Ispra, Italy.

Delavar, M., Eini, M.R., Kuchak, V.S., Zaghiyan, M.R., Shahbazi, A., Nourmohammadi, F., Motamedi, A., 2022. Model-based water accounting for integrated assessment of water resources systems at the basin scale. Science of The Total Environment 830, 154810. https://doi.org/10.1016/j.scitotenv.2022.154810

EEA, 2010. Water exploitation index (WEI). — European Environment Agency [WWW Document]. URL https://www.eea.europa.eu/data-and-maps/figures/water-exploitation-index-wei-3 (accessed 9.17.21).

EEA, 2019. Indicators. European Environment Agency. https://www.eea.europa.eu/data-and-maps/indicators/#c0=30&c12-operator=or&b_start=0&c6=wei. Accessed 5 Nov 2020.

EEA, 2021. Water resources across Europe — confronting water stress: an updated assessment, European Environment Agency, Report 12/2021.

Faergemann, H., 2012. Faergemann, H., 2012. — European Environment Agency [WWW Document]. URL https://www.eea.europa.eu/data-and-maps/indicators/use-of-freshwater-resources-3/faergemann-h-2012 (accessed 2.2.21).

Falkenmark, M., Lundqvist, J., Widstrand, C., 1989. Macro-scale water scarcity requires micro-scale approaches. Aspects of vulnerability in semi-arid development. Nat. Resour. Forum 13, 258–267. https://doi.org/10.1111/J.1477-8947.1989.TB00348.X

FAO, 2019. Step-by-step monitoring methodology for indicator 6.4.2. Food and Agricultural Organization of the United Nations, Rome.

GCEW, 2024. The economics of water. Valuing the Hydrological Cycle as a Global Common Good. Global Comission on the Economics of Water.

Godfrey, J.M., Chalmers, K., 2012. Water Accounting: International Approaches to Policy and Decision-making. Water Account. Int. Approaches to Policy Decis. 1–318. https://doi.org/10.4337/9781849807500

Hussain, Z., Wang, Z., Wang, J., Yang, H., Arfan, M., Hassan, D., Wang, W. Azam, M.I., Faisal, M. 2022. A comparative Appraisal of Classical and Holistic Water Scarcity Indicators, Water Resources Management. DOI: 10.1007/s11269-022-03061-z.

Karabulut, A., Egoh, B.N, Lanzanova, D., Grizzetti, B., Bidoglio, G., Pagliero, L., Bouraoui, F., Aloe, A., Reynaud, A., Maes, J., Vandecasteele, I., Mubareka, S., 2016. Mapping water provisioning services to support the ecosystem–water–food–energy nexus in the Danube river basin, Ecosystem Service.

Karimi, P., Bastiaanssen, W.G.M., Molden, D., 2013. Water Accounting Plus (WA+)-a water accounting procedure for complex river basins based on satellite measurements. Hydrol. Earth Syst. Sci 17, 2459–2472. https://doi.org/10.5194/hess-17-2459-2013

Karimi, P., Bastiaanssen, W.G.M., Molden, D.J., Cai, X., 2012. Water accounting to assess use and productivity of water: Evolution of a concept and new frontiers. https://doi.org/10.4337/9781849807494.00012

Lawrence, Meigh and Sullivan 2002, The Water Poverty Index: An International Comparison, Keele Economic Research Papers.

Liu, J., Liu, Q., Yang, H., 2016. Assessing water scarcity by simultaneously considering environmental flow requirements, water quantity, and water quality. Ecol. Indic. 60, 434–441. https://doi.org/10.1016/j.ecolind.2015.07.019

Liu, J., Yang, H., Gosling, S.N., Kummu, M., Flörke, M., Pfister, S., Hanasaki, N., Wada, Y., Zhang, X., Zheng, C., Alcamo, J., Oki, T., 2017. Water scarcity assessments in the past, present, and future. Earth's Futur. 5, 545–559. https://doi.org/10.1002/2016EF000518

Lyu, F., Zhang, H., Dang, C., Gong, X., 2023. A novel framework for water accounting and auditing for efficient management of industrial water use. J Clean Prod 395, 136458. https://doi.org/10.1016/J.JCLEPRO.2023.136458

Mekonnen, M.M., Hoekstra, A.Y., 2016. Sustainability: Four billion people facing severe water scarcity. Sci. Adv. 2. https://doi.org/10.1126/SCIADV.1500323

Mishra, A.K., Singh, V.P., 2010. A review of drought concepts. J. Hydrol. 391, 202–216. https://doi.org/10.1016/J.JHYDROL.2010.07.012

Molden, D., 1997. Accounting for water use and productivity, SWIM Paper 1. Colombo, Sri Lanka: International Irrigation Management Institute.

Molden, D., Sakthivadivel, R., 2010. Water Accounting to Assess Use and Productivity of Water. http://dx.doi.org/10.1080/07900629948934 15, 55–71. https://doi.org/10.1080/07900629948934

Momblanch, A., Andreu, J., Paredes-Arquiola, J., Solera, A., Pedro-Monzonís, M., 2014. Adapting water accounting for integrated water resource management. The Júcar Water Resource System (Spain). J Hydrol (Amst) 519, 3369–3385. https://doi.org/10.1016/J.JHYDROL.2014.10.002

Momblanch, A., Pedro-Monzonís, M., Solera, A., Andreu, J., 2018. Water Accounting for Integrated Water Resources Management: Experiences and Recommendations. Advances in Chemical Pollution, Environmental Management and Protection 3, 63–96. https://doi.org/10.1016/BS.APMP.2018.08.001

Ohlsoon, L. 2000. Water conflicts and social resource scarcity. Phys. Chem. Earth, Vol 25, Nº 3.

Palmer, W.C., 1965. Meteorological Drought, US. Department of Commerce. U.S. Weather Bureau, Washington, D.C.

Pastor, A.V., Ludwig, F., Biemas, H., Kabat, P. 2014, Accounting for environmental flow requirements in global water assessments, Hydrology and Earth System Sciences, 18, 5041–5059.

Pedro-Monzonís, M., Jiménez-Fernández, P., Solera, A., Jiménez-Gavilán, P., 2016a. The use of AQUATOOL DSS applied to the System of Environmental-Economic Accounting for Water (SEEAW). J Hydrol (Amst) 533, 1–14. https://doi.org/10.1016/j.jhydrol.2015.11.034

Pedro-Monzonís, M., Solera, A., Ferrer, J., Estrela, T., Paredes-Arquiola, J., 2015. A review of water scarcity and drought indexes in water resources planning and management. J. Hydrol. 527, 482–493. https://doi.org/10.1016/j.jhydrol.2015.05.003

Pedro-Monzonís M, Solera A, Ferrer J, et al (2016) Water accounting for stressed river basins based on water resources management models. Sci Total Environ 565:181–190. https://doi.org/10.1016/j.scitotenv.2016.04.161

Pedro-Monzonís, M., Solera, A., Ferrer, J., Andreu, J., Estrela, T., 2016b. Water accounting for stressed river basins based on water resources management models. Science of the Total Environment 565, 181–190. https://doi.org/10.1016/j.scitotenv.2016.04.161

Perry, C., 2010. Accounting for water use: Terminology and implications for saving water and increasing production. Agric Water Manag 98, 1840–1846. https://doi.org/10.1016/j.agwat.2010.10.002

Raskin, P., Gleick, P., Kirshen, P., Pontius, G., Strzepek, K., 1997. Comprehensive Assessment of the Freshwater Resources on the World. Water Futures: Assessment of Long-range Patterns and Problems. Stockholm Environment Institute, Sweden.

Richter, B.D., Davis, M.M., Apse, C., Konrad, C., 2012. A presumptive standard for environmental flow protection. River Res. Appl. 28, 1312–1321. https://doi.org/10.1002/RRA.15111046/j.1523-1739.1996.10041163.x.

Rijsberman, F.R., 2006. Water scarcity: Fact or fiction? Agric. Water Manag. 80, 5–22. https://doi.org/10.1016/j.agwat.2005.07.001

Rockström, J., Falkenmark, M., 2015. Agriculture: Increase water harvesting in Africa. Nature 519, 283–285. https://doi.org/10.1038/519283A

Saft, M., Western, A.W., Zhang, L., Peel, M.C., Potter, N.J., 2015. The influence of multiyear drought on the annual rainfall-runoff relationship: An Australian perspective. Water Resour. Res. 51, 2444–2463. https://doi.org/10.1002/2014WR015348

Savenije, H.H.G., 2000. Water scarcity indicators; the deception of the numbers. Phys. Chem. Earth, Part B Hydrol. Ocean. Atmos. 25, 199–204. https://doi.org/10.1016/S1464-1909(00)00004-6

Sondermann, M.N., Oliveira, R.P. de, 2021. A Shared Vision on the Transboundary Water Management Challenges of the Tagus River Basin. Water Resources Management 35, 4647–4664. https://doi.org/10.1007/S11269-021-02973-6

Sondermann, M.N., Oliveira, R.P. de, 2022a. Using the WEI+ index to evaluate water scarcity at highly regulated river basins with conjunctive uses of surface and groundwater resources. Science of The Total Environment 836, 155754. https://doi.org/10.1016/J.SCITOTENV.2022.155754

Sondermann, M.N., Oliveira, R.P. de, 2022b. Climate Adaptation Needs to Reduce Water Scarcity Vulnerability in the Tagus River Basin. Water (Basel) 14. https://doi.org/10.3390/W14162527

Sullivan, C, 2002. Calculating a Water Poverty Index, *World Development*, 30,7:1195-1211.

Sun, C., Zhou, X., 2020. Characterizing Hydrological Drought and Water Scarcity Changes in the Future: A Case Study in the Jinghe River Basin of China. Water 12. https://doi.org/10.3390/w12061605

UN, 2012. SEEA-Water|System of Environmental-Economic Accounting for Water asdf. United Nations.

UNCCD, 2024. The Global Threat of Drying Lands Regional and global aridity trends and future projections, United Nations Convention to Combat Desertification.

UNCCD, 2024. World Drought Atlas, United Nations Convention to Combat Desertification.

Vanham, D., Hoekstra, A.Y., Wada, Y., Bouraoui, F., de Roo, A., Mekonnen, M.M., van de Bund, W.J., Batelaan, O., Pavelic, P., Bastiaanssen, W.G.M., Kummu, M., Rockström, J., Liu, J., Bisselink, B., Ronco, P., Pistocchi, A., Bidoglio, G., 2018. Physical water scarcity metrics for monitoring progress towards SDG target 6.4: An evaluation of indicator 6.4.2 “Level of water stress.” Sci. Total Environ. 613–614, 218–232. https://doi.org/10.1016/J.SCITOTENV.2017.09.056

Vicente-Serrano, S.M., Beguería, S., López-Moreno, J.I., 2010. A multiscalar drought index sensitive to global warming: The standardized precipitation evapotranspiration index. J. Clim. 23, 1696–1718. https://doi.org/10.1175/2009JCLI2909.1

Vicente, D.J., Rodríguez-Sinobas, L., Garrote, L., Sánchez, R., 2019. Applying water accounting methods through statistical data and simulation models: The Douro transboundary watershed. Adv. Chem. Pollution, Environ. Manag. Prot. 3. https://doi.org/https://doi.org/10.1016/bs.apmp.2018.06.001

Wang, M., Bodirsky B.l., Rijneveld, R., Beier, F., Bak, M.O., Batool, M., Droppers, B., Popp, A., van Vliet, M.T.H., Strokal, M., 2023 A triple increase in global river basins with water scarcity due to future pollution, Nature Comunications.

Wu, J., Miao, C., Tang, X., Duan, Q., He, X., 2018. A nonparametric standardized runoff index for characterizing hydrological drought on the Loess Plateau, China. Glob. Planet. Change 161, 53–65. https://doi.org/10.1016/J.GLOPLACHA.2017.12.006

Zal, N., Zachos, A., Bariamis, G., Baltas, E., 2017. Use of Freshwater Resources in Europe - An assessment based on water quantity accounts. European Topic Centre on Inland, Coastal and Marine Waters – ETC/ICM, Magdeburg, Germany.

Zeng, Z., Liu, J., Savenije, H.H.G., 2013. A simple approach to assess water scarcity integrating water quantity and quality. Ecol. Indic. 34, 441–449. https://doi.org/10.1016/j.ecolind.2013.06.012

Zou, L., Xia, J., She, D., 2018. Analysis of Impacts of Climate Change and Human Activities on Hydrological Drought: a Case Study in the Wei River Basin, China. Water Resour. Manag. 32. https://doi.org/10.1007/s11269-017-1877-1

Fifth International Dam World Conference
PORTUGAL • LISBON • LNEC • APRIL 13-17, 2025
dam world 2025

DETERIORATION OF DAMS AFFECTED BY CONCRETE SWELLING. THE ROLE OF OBSERVATION AND MODELLING IN SAFETY CONTROL AND REHABILITATION

António Lopes Batista[1]
National Laboratory for Civil Engineering (LNEC)

ABSTRACT

The most common chemical reactions of internal origin in concrete that cause expansion can be grouped into two main types: alkali-silica reactions (ASR) and internal sulphatic reactions (ISR). Both reactions require water to develop, making concrete dams particularly vulnerable structures.

In dams equipped with well-designed monitoring systems, the proper handling of observation inputs, such as monitoring data, and inspection and specific tests results, helps the quantification of the structural effects of concrete swelling. Adequate modelling of the expansion development and its structural consequences makes it possible to assess the safety of the structures, predict their future behaviour, and guide the study of the best intervention solutions when needed.

On the other hand, the structural effects of concrete swelling are difficult to manage, as there are no fully effective methods to either mitigate the development of the reactions themselves or to repair the damaged structures. Over the past few decades, engineering has developed a set of measures that, when applied judiciously, allow for limiting, in many cases, the adverse effects of these reactions. In the case of severely damaged structures, a range of rehabilitation techniques can be employed to restore structural performance and extend the useful lifespan of dams.

This paper details the role of observation and modelling in supporting studies and decisions to manage the functionality, safety, and durability of dams affected by concrete swelling.

Keywords: Concrete swelling, Dams, Structural effects, Observation, Modelling, Safety control, Deterioration, Rehabilitation.

[1]albatista@lnec.pt, Portugal.

1. INTRODUCTION

1.1. Observation and modelling as the basis for safety control

Large concrete dams may originate catastrophes of important consequences if an eventual rupture in the operation stage occurs; even minor incidents, whose resulting damages may be repaired before degenerating in dangerous situations, may involve a considerable amount of direct and indirect losses. Therefore, it is necessary to avoid the occurrence of this type of situations, through safety control, which usually involves observation and modelling.

The observation should be understood as the set of activities to follow up the dam´s behaviour, involving monitoring, inspection and testing.

The interpretation of the observed behaviour of dams is done through models. These models can be very simple, considering empirical relationships between causes and effects, or very elaborate, usually supported on structural mechanics. These ones are, in the case of large structures, based on the finite element method.

Safety control, to be carried out during dam´s lifetime, by comparing parameters defining the observed behaviour with pre-established requirements, is thus indispensable to guarantee a good structural performance under serviceability and extreme operation conditions and allows a deeper knowledge of dam´s behaviour, which is of great importance, namely in structures with deterioration problems.

Dam deterioration processes can have different causes. In recent decades it has been found that, in an increasing number of cases, it is the internal expansion of concrete that causes major damage to dams. If fact, concrete dams are very stiff structures and were not designed to withstand the effects of concrete expansions, which can be significant and compromise functionality, durability and safety.

1.2. Structural effects of concrete swelling in dams

The most common chemical reactions of internal origin in concrete that cause expansion can be grouped into two main types: alkali-silica reactions (ASR) and internal sulphatic reactions (ISR). Both reactions require water to develop, making concrete dams particularly vulnerable structures.

Macroscopic evidence of the effects of concrete expansive reactions in dams, which are generally similar for the ASR and the ISR, are as follows [1]:

i) surface cracking, diffuse and generalized (map), due to the local heterogeneity of the expansion, sometimes with concrete spalling and formation of small craters, and linear cracking due to the global structural response to prescribed strains;

ii) in structural contraction joints and in decks above the spillways, generalized closing and slippage between blocks (in particular the misalignments at the crest), with crushing of infills and spalling of edges, due to absolute and relative displacements;

iii) in spans and power plants, namely in ducts, orifices and dischargers, ovalization of the ducts section, misalignment of parts and respective fixings, and closing and distortion of holes and shutters, causing problems in supports and in equipment clearances and jamming the gates;

iv) leakage of water through cracks and rupture of reinforcements for expansive reactions of greater magnitude;

iv) discoloration of concrete surfaces affected by the ASR; and

v) efflorescence and exudation of gel (ASR) on the surfaces, generally in cavities, crevices and joints.

The effects of the expansive reactions are reflected in the results of the monitoring of concrete dams, specifically in the evolution of the following quantities [1]:

i) absolute displacements, i.e. vertical displacement upwards and radial displacement towards upstream (except in buttress dams);

ii) relative displacements between blocks, i.e. closing of contraction joints, elevation of higher blocks in relation to the lower ones, and horizontal displacement towards upstream of the central (higher) blocks in relation to the lateral (lower) ones;

iii) concrete deformations, in active and in no-stress strain meters; and

iv) stress field.

Expansions may not be the only source of concrete deterioration. Therefore, it is important to identify, in each case, which causes contribute to unexpected behaviours and the effects of each of them.

1.3. Interventions in dams affected by concrete swelling

The effects of the ASR and the ISR in concrete structures are difficult to deal with, since there are no fully effective methods either to mitigate the development of the expansive reactions, or to repair deteriorated structures. However, engineering has developed a set of measures that, when used judiciously, allow to limit, in many cases, the unfavourable effects of expansive reactions, and adequately manage the functionality, safety and durability of the structures.

The measures to mitigate the concrete swelling reactions mostly consist in limiting the development of these chemical reactions by reducing the involved reagents. Techniques for

repairing and reinforcing deteriorated structures, which often include structural modifications, are often associated with mitigation measures, so they are addressed in an integrated manner.

The physical limitation of the reagents of the reactions can be accomplished by: i) preventing the access of water, in its liquid and vapor forms; and ii) allowing to change, with advantage, the characteristics of the alkaline solution (only to control the ASR). When it is not feasible to prevent access to water, drainage can be done, although this measure is less effective. Regarding other techniques that can mitigate expansive reactions, the following ones should be mentioned: i) controlling the temperature of the setting and hardening of concrete; and ii) increasing the confinement of the concrete, through appropriate construction of elements and/or imposed compression. These types of measures, often used together, usually produce very beneficial effects.

Preventing the access of water to the concrete can be done by using coatings and surface protections, waterproofing membranes and/or protection panels. The drainage of concrete generally consists in creating specific holes. Changing the characteristics of the alkaline solution, to mitigate the ASR, can be done by injecting chemical compounds, even though this is currently only feasible (due to costs) in small structural parts. Controlling the temperature of the concrete, although not common in the operation stage of dams, can be achieved using specific coatings and panels. Increasing the confinement of concrete can be accomplished, as a rule, using concrete, steel, or synthetic fiber elements (steel and synthetic fiber elements can be passive or prestressed).

Regarding the repair of the most deteriorated structures, mass regeneration can be undertaken through injection and replacement of parts or volumes considered irrecoverable. The demolition and total reconstruction, in extreme situations of deterioration, often involves, in the case of concrete dams, new structures with different and optimized structural solutions.

Structural reinforcement, when necessary, generally comprises the addition of linear or laminar elements of steel and carbon fibers, passive or active, as well as concrete lining, which can be simple, reinforced and/or pre-stressed. In all these cases, the confinement is also increased, resulting in the mechanical limitation of the expansion.

The structural changes are intended to endow the structures with the capacity to minimize the mechanical effects of the expansion. The most common interventions are the slot cutting of the concrete, which allows to release the stresses and to reverse the deformations caused by expansion, and the modification of supports and connections of equipment (generator units, gates, etc.).

1.4. Experience worldwide with dams damaged by concrete swelling

The country most affected by concrete expansion in dams is Canada, due to the type of aggregates used in concrete mix. The USA also has many dams that have deteriorated due to this type of causes. This is because there was a large increase in dam construction in the first half of the last century, when there was still no knowledge about this type of phenomenon. It is reported that countries such as France, Switzerland, Italy, Spain and Portugal also have many dams affected. Outside North America and Europe, there are also numerous cases in Brazil and Africa. Table 1 summarizes the most relevant interventions in dams affected by expansive reactions of concrete [1].

Table 1 does not include the known cases of replaced dams, notably the Drum Afterbay, Wild Horse and American Falls in the USA, Maentwrog in Wales, Lady Evelyn in Canada, Stolsvatn in Norway, Serra in Switzerland, Alto Ceira in Portugal, and the arch structure of the emergency spillway of the Fontana dam in the USA [1].

It should be noted, firstly, that most of the dams that were intervened were deteriorated by the ASR. On the other hand, major interventions took place in very old dams (most of them built in the first half of the 20th century) and old ones (the most recent in the previous table dates from 1977). The only dam that underwent all types of interventions listed in Table 1, covering all areas (dam body, spillway, water intake and powerhouse), was the Mactaquac dam, in Canada, due to the great magnitude of the concrete expansions and its particularities, although it is one of the most recent (construction completed in 1968).

In sections 3 and 4 the cases of Alto Ceira and Cahora Bassa dams are respectively presented. They will illustrate the role of observation and modelling in the safety control and in supporting the interventions. The case of Alto Ceira dam, in Portugal, underwent a major deterioration process, leading to its demolition and replacement by a new one. The case of Cahora Bassa dam in Mozambique, which was affected by moderate rate expansions, has already required local interventions in the spillway gates. In the two cases, the behaviour of the dams was properly observed, with monitoring data carefully interpreted through mathematical modelling, within the scope of safety control. These results supported the decisions to carry out local interventions (Cahora Bassa case) and the dam replacement (Alto Ceira case).

Table 1 – Summary of the most relevant interventions in dams affected by expansive reactions of concrete [1]

Dam	Country	Year of cons-truction	Height (m) and structural type	Type of reaction	Affected zones	Follow up / Interventions					
						Strenghting with tendons and rebars	Concrete replacement or regeneration (grouting)	Slot cuts	Coatings or membranes	Interventions in gates	Improvements in monitoring and modelling
Illsee	Switzerland	1927	25 (A+G)	ASR +ISR	B	X	X	X	X		X
Santeetlah	USA	1928	61 (A+G)	ASR	B + S	X	X	X		X	X
Lago Colombo	Italy	1928	31 (AG)	ASR	B		X	X			X
Stewart Mount.	USA	1930	63 (A)	ASR	B	X	X				X
Beauharnois	Canada	1932	21 (G)	ASR	B + W + P	X	X	X			X
Chambon	France	1935	137 (G)	ASR	B + S	X	X	X	X	X	X
Billings-Pedras	Brazil	1936	31 (G)	ASR	B + S + P		X		X	X	X
Simenoe	USA	1939	90 (A)	ASR	B + W		X		X		X
Chickamauga	USA	1940	39 (G)	ASR+ACR	B + S + L	X	X	X		X	X
Hiwassee	USA	1940	94 (G)	ASR	B + S			X		X	X
Friant	USA	1942	97 (G)	ASR	B + S					X	X
Fontana	USA	1944	146 (G)	ASR	B + S	X	X	X			X
Poglia	Italy	1950	50 (B)	ASR	B			X	X		X
Center Hill	USA	1951	76 (G)	ASR+ACR	B + S			X			X
Temple-sur-Lot	France	1951	35 (G)	ASR	B + S	X	X		X	X	X
Pracana	Portugal	1951	60 (B)	ASR+ISR	B + S	X	X		X		X
Bimont	France	1952	86 (A)	ISR	B	X	X		X		X
Salanfe	Switzerland	1952	52 (G)	ASR	B	X	X	X			X
Pian Telessio	Italy	1955	80 (AG)	ASR	B			X			X
San Esteban	Spain	1955	115 (AG)	ISR	B + S		X		X		X
Roanoke Rapids	USA	1955	22 (G)	ASR	B + S	X	X				X
Kariba	Zambia/ Zimbabwe	1959	128 (A)	ASR	B + S					X	X
Matala	Angola	1959	16 (G)	ASR	B + S	X	X			X	
Saunders	Canada	1958	52 (G)	ASR	B + S + W			X			X
Mactaquac	Canada	1968	55 (G)	ASR	B + S + W + P	X	X	X	X	X	X
Pedra	Brazil	1968	60 (G)	ASR	B + S			X		X	X
Cahora Bassa	Mozambique	1975	166 (A)	ASR	B + S + P					X	X
Moxotó	Brazil	1977	30 (G)	ASR	B + S + P	X	X	X		X	X

Structural type: G – gravity; A – arch; AG – arch-gravity; B – Buttress
Reaction type: ASR – alkali-silica reaction; ACR – alkali-carbonate reaction; ISR – internal sulphatic reaction
Affected zones: B – dam's body; S - Spillway; W – Water intake; P – Powerhouse; L - Lock

2. OBSERVATION AND MODELLING IN SAFETY CONTROL

2.1. General remarks

Structural safety of dams is understood as the capacity of the dam-foundation system to sustain the actions that may occur during its lifetime, satisfying the structural requirements with the stated levels of reliability [2].

The structural behaviour of concrete dams in normal operation conditions is usually conditioned by the main actions, namely the ones related to the water level in the reservoir and the seasonal temperature variations. The correspondent loads, forces and prescribed strains, could be estimated by means of action models that could consider coupled effects resulting of mechanical, hydraulic and thermal phenomena. To represent operation scenarios, a set of action combinations are usually considered at the design stage.

Structural models of different types, simple or complex, must be used for the interpretation of the monitored behaviour during operation, considering the effects of a set of simultaneous actions and comparing its results with the observed data. However, for better behaviour interpretation, the identification of each action effect is required, which may be done by statistical or structural mechanics models.

As a consequence of design criteria to satisfy serviceability and safety requirements, the stress levels on dam's body, in serviceability conditions, are limited to low values (about 1 to 1.5 MPa for maximum tension and 6 to 10 MPa for maximum compression). Nevertheless, dam monitoring shows that non-elastic and localized rupture phenomena can develop during the dam's lifetime. These effects may be associated, among other causes, with: i) strain increase due to creep under the applied forces; ii) decrease of structural and material properties under permanent load conditions; iii) internal concrete reactions that originate volume changes, as swelling; and iv) stress concentrations at some specific zones due to geometry and actions. Thus, to be able to interpret the dam’s behaviour, structural models must take into account non-linear material behaviour.

2.2. Statistical approach in the treatment of monitoring data

The preliminary analysis and interpretation of the dam’s monitoring data is usually carried out using a statistical approach of quantitative interpretation of the most important data measured over time, namely displacements (measured by geodetic methods, rod extensometers and plumb lines). Quantitative interpretation consists of the analysis of a behaviour mathematical model by which a functional relationship is established between the quantities or effects observed and the actions that originate them. The principle of superposition is assumed, considering that the actions corresponding to hydrostatic pressures and seasonal variations in

temperature cause reversible effects and that the irreversible effects, due to non-elastic phenomena, depend only on time [3]. In the statistical model, a function of the type can be adopted,

$$E_{calc}\left(h, t^{'}, t\right) = \sum_{i=1}^{N} a_i\, h^i + \mathrm{b}_1 \cos\frac{2\pi\, t'}{365} + b_2 \sin\frac{2\pi\, t'}{365} + \sum_{j=1}^{M} c_j\, t^j + d\left(1 - e^{-\frac{t^n}{\beta}}\right) + k \quad (1)$$

where $E_{calc}(h, t', t)$ represents the calculated response, h is the hydrostatic action usually represented by the upstream water level (when important the downstream level must also be considered), t' is the number of days since the beginning of the year and t is the number of days counted from the initial observation date. The parameters a_i, b_1, b_2, c_j, d and k are calculated by linear regression, performed by the least-squares method. N and M represent the degree of the polynomials used to represent the hydrostatic pressure and time effects, respectively, the terms in sine and cosine are intended to represent the effect of the annual thermal wave, a polynomial expression is considered to reproduce the time effects, and an exponential term is used to represent the effects of the expansive action (n and β define the shape of the correspondent sigmoid curve).

The differences between the values observed in the prototype $E_{obs}(h, t', t)$ and the values calculated by the statistical model are the residuals r, defined by,

$$r = E_{obs}(h, t', t) - E_{cal}(h,\ t', t) \quad (2)$$

The coefficient of determination R^2 of a quantitative interpretation, which assesses the significance of the regression, is expressed by,

$$R^2 = 1 - \frac{\sum_{i=1}^{n}\left(E_{cal}(h, t',\ t) - E_{obs}(h, t', t)\right)^2}{\sum_{i=1}^{n}\left(E_{obs}(h, t',\ t) - \bar{E}_{obs}(h, t', t)\right)^2} \quad (3)$$

where n is the number of observations and $\bar{E}_{obs}(h, t', t)$ is the average of the observed values. The closer the value of R^2 is to 1, the better the model fits to the observed values.

This formulation allows, in general, a reasonable separation of the thermal, the time and the elastic and the viscoelastic water pressure effects, when the water level remains approximately constant in time. Otherwise, the equation (1) must be improved, considering the dependence between the elastic and the creep effects (Fig. 1). This approach requires a reasonable knowledge of the concrete creep function [3,4]. However, the knowledge of the creep function is necessary in analysis based on structural mechanics, as it is explained in the next subsection.

$$u = a_4 h^4 + a_3 h^3 + b_1 \cos\frac{2\pi t'}{365} + b_2 \sin\frac{2\pi t'}{365} + a_4 \sum_{t_f}^{t} \phi(t,t')\,\Delta h^4 + a_3 \sum_{t_f}^{t} \phi(t,t')\,\Delta h^3 + d_2 (1 - e^{-\frac{t^n}{\beta}}) + K$$

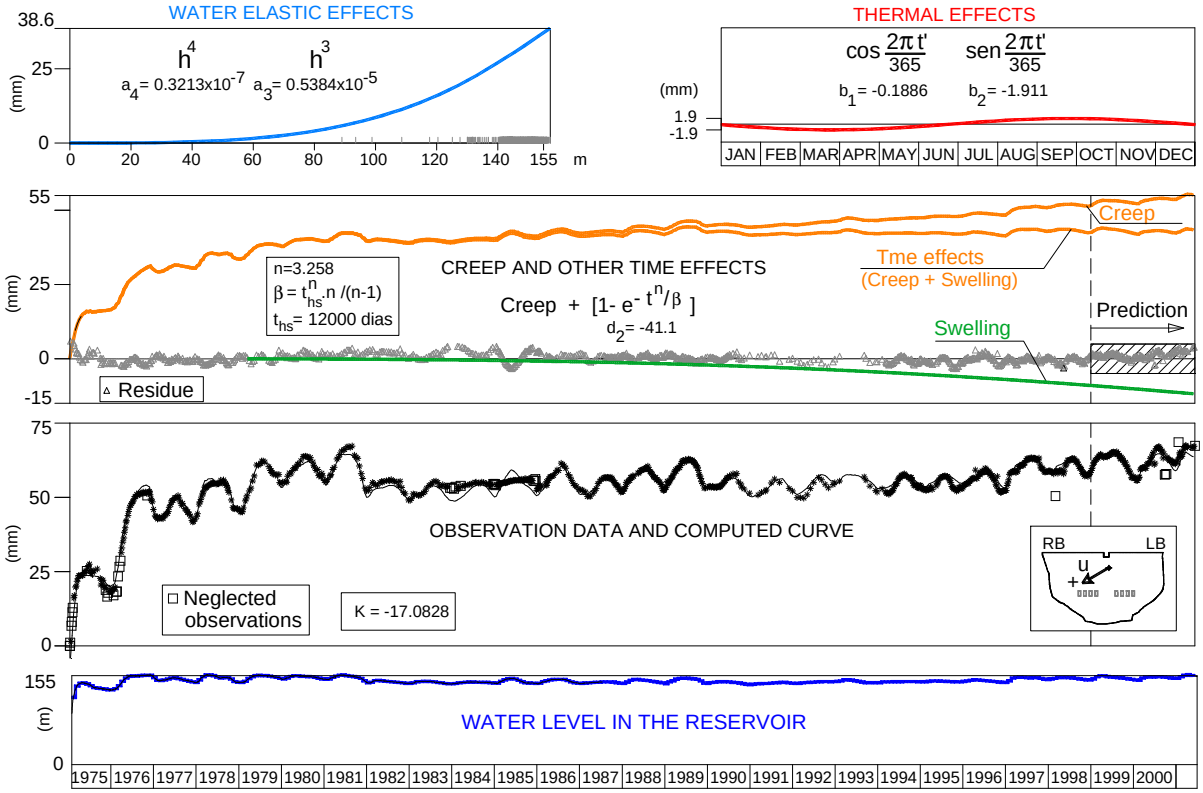

Fig. 1 – Interpretation and prediction of radial displacements in a large arch dam by quantitative analysis of monitoring data [4]

2.3. Structural mechanics models

Structural models used on dam safety control are usually based on the structural mechanics governing equations, whose solution can be obtained numerically by the finite element method or another numerical procedure.

In these models, a set of hypotheses related to actions, material properties and structural behaviour should be considered, namely: i) the dams and their foundations have a 3D behaviour and are composed by an assembly of a set of continuous and homogeneous blocks, possibly linked by joints; ii) the boundary conditions may be idealized as rigid or elastic supports; iii) concrete instantaneous behaviour is non-linear, in tension and compression (with softening, damage, irreversible strain accumulation under cyclic loading, etc.); and iv) concrete delayed behaviour is dependent on changes at rheological properties due to maturing effect and is also influenced by micro-cracking or damage induced by another causes. Some aspects of this type of models, as those developed at the National Laboratory for Civil Engineering (LNEC), are given below [5,6,7,8].

The softening behaviour of concrete on the tensile branch should be considered, to simulate cracking. This non-linear behaviour can be represented by scalar damage models. High efficiency can be obtained using damage formulations with two independent scalar damage variables, one in compression and the other in tension.

Concrete behaviour over time, to represent creep for applied loads and relaxation for prescribed strains, can be well represented by a maturing viscoelastic model.

Interfaces behaviour model must be able to simulate the non-linearity associated to the movements of opening-closure and of sliding on foundation discontinuities and on dam contraction joints. This can be done by an elastoplastic model, with shear stresses defined by the Mohr-Coulomb criterion and the tension strength limited by the Rankine criterion.

Nowadays, in dam applications, 3D solid finite elements and joint elements (to represent contraction joints and, if necessary, construction joints between concrete layers), are often used. Linear finite elements are also useful to simulate tendons and rebars (Fig. 2).

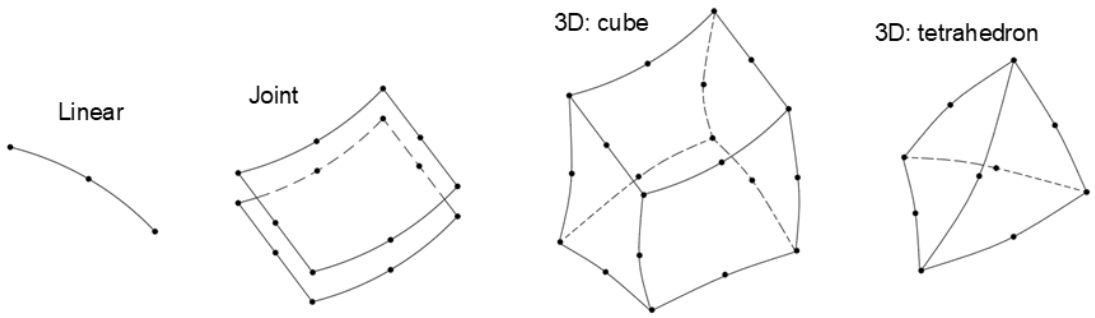

Fig. 2 - Some finite elements available in LNEC´s computational codes

In viscoelastic analysis the concrete creep function is advantagously approached by Dirichlet series to avoid the storage of the whole loading history during the step-by-step time analysis. The non-linear behaviour of structural concrete and joints is considered, in each increment, by an iterative scheme.

To improve reliability of safety control analysis it could be useful to use systematically and in an integrated way the referred statistical and structural approaches. For a satisfactory safety control judgement, the behaviour interpretation can be done with: i) quantitative interpretation results; ii) comparison of results from quantitative analysis and from structural models; and iii) the direct comparison between the observed data and the results obtained from linear or non-linear and viscoelastic analysis.

2.4. Specific models for concrete expansion

Modelling structures affected by concrete swelling also requires the consideration of an expansion model, to include a set of dependencies. At the macro scale the concrete swelling

can be considered a prescribed strain ε_{exp}, whose development over time mainly depends on: the chemistry of the process Q, that is essentially influenced by the concrete composition (type of cement, aggregates, and admixtures, W/C ratio, placing conditions, etc.); the temperature T; the internal humidity, represented by the relative humidity H; the stress field σ; and the time t. This dependency can be expressed by the generic equation,

$$\varepsilon_{exp}(t) = f(Q, T, H, \sigma, t) \quad (4)$$

Assuming some simplifications [1], equation (4) can be rewritten by considering the uncoupled effects of the chemistry $\varepsilon_{exp,\infty}\, \xi_{exp}(t)$, the temperature g_T, the internal humidity g_H and the stress state g_σ,

$$\varepsilon_{exp}(H, T, \sigma, t) = \varepsilon_{exp,\infty}\, \xi_{exp}(t)\, g_H(H)\, g_T(T)\, g_\sigma(\sigma) \quad (5)$$

where $\varepsilon_{exp,\infty}$ is the long-term expansion and ξ_{exp} is a function representing the expansion kinetics.

This concrete swelling model (5) requires the knowledge of some intrinsic characteristics of concrete, to estimate the expansion kinetics and its long-term value, and of the thermal, humidity and stress fields, so its influence in the expansion development can be evaluated through proper functions g.

As mentioned before, the analysis must be performed incrementally (step-by-step) over time, so the loads must be updated as well as the materials behaviour. If needed, the structural topology can also be updated, either to simulate the construction sequence or to include modifications during lifetime. In this context, Equation (5) is then applied in each sampling point of the finite element mesh and for each time step. The thermal, humidity and stress fields can be obtained by resorting to specific finite element models to solve the thermal, hygrometric and structural problems, respectively (Fig. 3).

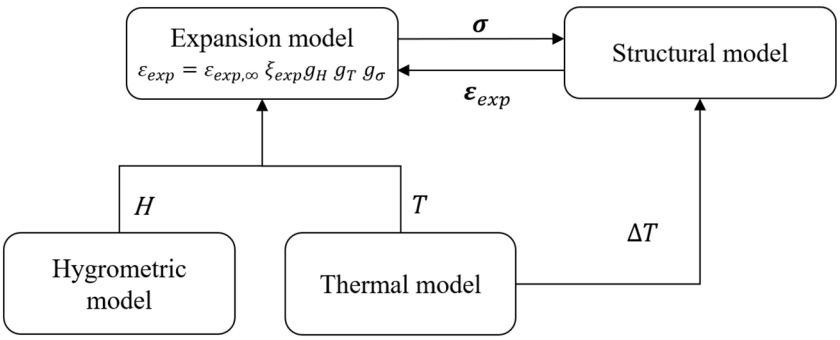

Fig. 3 - Expansion model interaction diagram

The thermal model solves the transient heat conduction equation, also known as heat diffusion equation, considering the evolution of thermal actions in the external faces, the air and water

temperatures and the effects of the solar radiation. If the construction sequence is modelled, the heat generated during concrete hydration should also be considered.

The hygrometric model allows to compute the concrete internal humidity taking in account the reservoir level, the environmental humidity and the effects of rainfall. If the concrete is sound, the hygrometric phenomenon can be modelled using a diffusion equation (Fick's second law of diffusion), which is mathematically equivalent to the heat diffusion equation.

In the case of large, damaged structures, the evaluation of concrete swelling itself and its structural effects should be complemented, beyond the interpretation of monitoring data and structural mathematical modelling, by: i) laboratory, physical and chemical analyses and tests on concrete samples extracted from the dam's body; and ii) "in situ" tests.

3. ALTO CEIRA DAM, PORTUGAL

3.1. The dam and its deterioration process

Alto Ceira dam, built in 1949 and deactivated in 2013 (through demolition of its central section), was a slender arch with a height of 36 m (Fig. 4).

Fig. 4 – Alto Ceira dam. Downstream view and central cantilever cross-section

The dam was founded on a schistose rock mass. In its construction, concrete produced with quartzite aggregates was used. Since the 1960s, the behaviour observed of the dam has been characterized by progressive displacements, vertically upwards and radially towards upstream. The concrete cracking became more accentuated over time, reaching a very advanced stage at the beginning of this century, with leakage through the cracks mainly located in the bearing zones, at mid-height (Fig. 5).

The first laboratory, physical and chemical tests, carried out on concrete samples extracted from the dam's body in 1986 confirmed the seriousness of the deterioration of the concrete and its high remaining potential for expansion [9]. In 1990, a new campaign of sampling and testing of the dam's concrete was carried out. The results of the accelerated expansion tests, carried out by immersing the concrete specimens in a saturated solution of sodium chloride and in distilled water, in an oven at 50ºC, are shown in Fig. 6 [10]. In specimens produced from

samples extracted from the left bank, maximum remaining expansions of about 1400x10^{-6} were then obtained.

Fig. 5 – Alto Ceira dam. Diffuse cracking at the crest (on left) and weirs on the downstream face to collect water passing through cracks (on right)

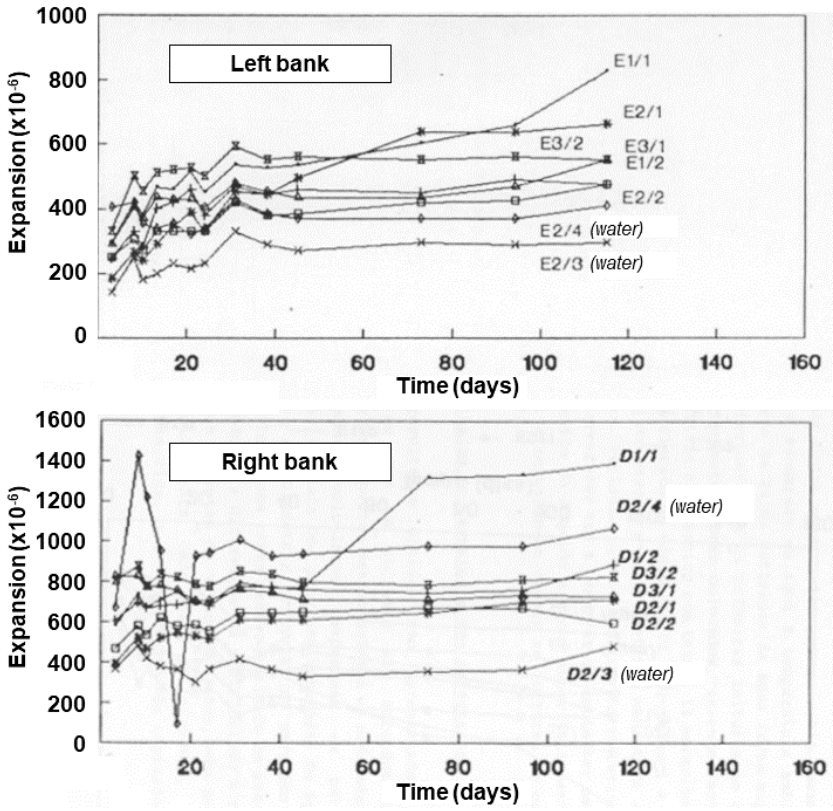

Fig. 6 – Alto Ceira dam. Main results of the accelerated expansion tests of concrete specimens (extracted in 1990) immersed in a saturated solution of sodium chloride and in distilled water, in an oven at 50ºC (adapted from [10])

The absolute displacements of the dam were monitored by geodetic methods since the first filling of the reservoir, in 1950. The radial displacements showed, over time, a great progressivity towards upstream. Fig. 7 shows the evolution of horizontal displacements observed by geodetic methods in the upper targets of the arch (elevation 663.00 m), between 1950 and 1993.

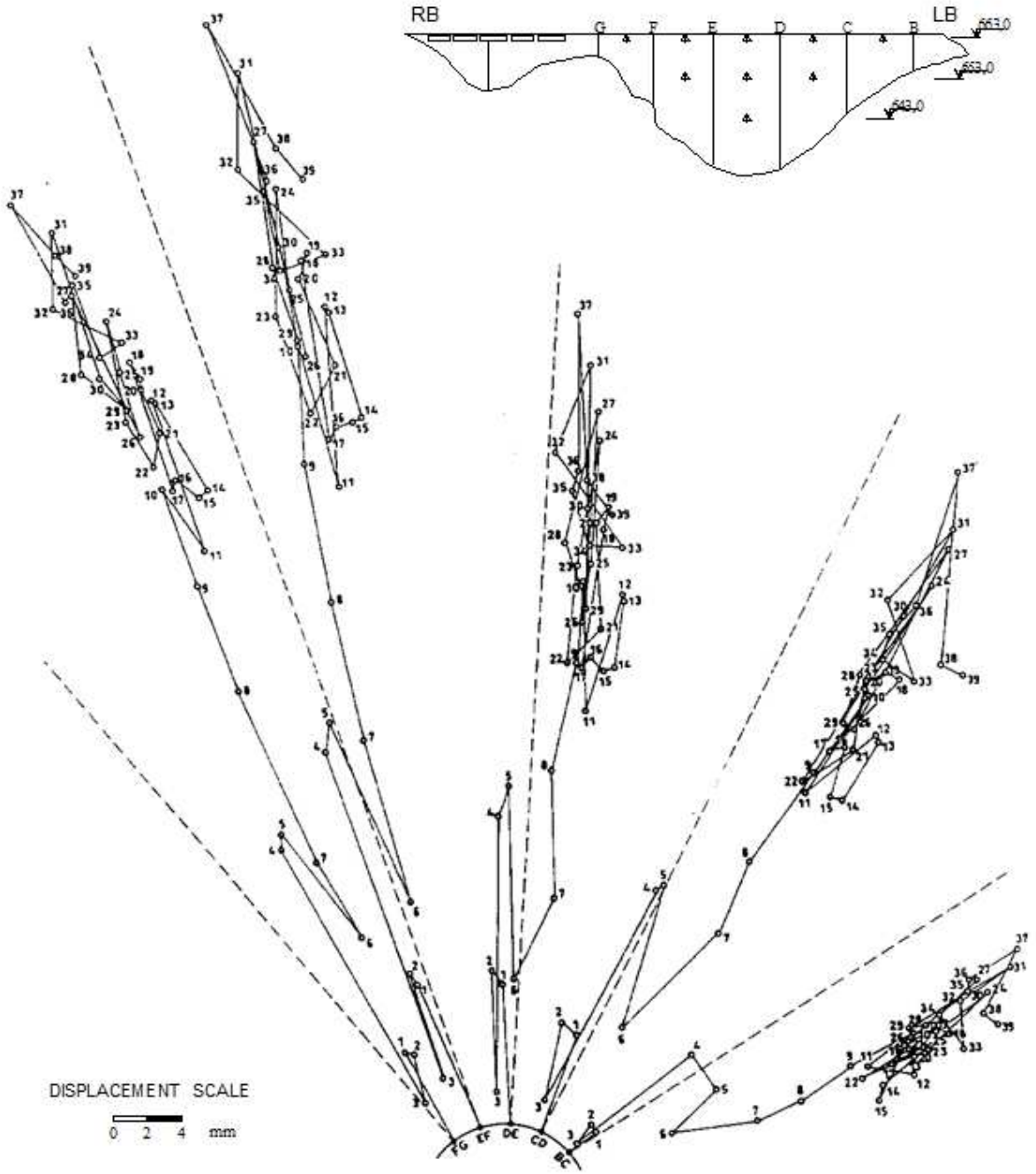

Geodetic survey	Date	Water level in the reservoir (m)
1	15-09-1950	659.0
2	24-09-1950	630.0
3	29-11-1950	658.6
4	22-08-1963	657.5
5	29-08-1963	630.0
6	20-11-1963	659.0
7	18-05-1970	656.1
8	26-09-1974	654.9
9	28-09-1978	654.9
10	10-08-1983	655.2
11	17-05-1984	658.2
12	24-01-1985	658.0
13	25-10-1985	654.8

Geodetic survey	Date	Water level in the reservoir (m)
14	15-01-1986	659.0
15	16-01-1986	659.0
16	24-03-1986	655.6
17	25-03-1986	658.8
18	7-10-1986	658.2
19	22-10-1986	630.0
20	23-10-1986	630.0
21	3-12-1986	658.3
22	7-01-1987	658.6
23	11-06-1987	658.5
24	11-08-1987	655.0
25	8-10-1987	658.6
26	8-03-1988	658.7

Geodetic survey	Date	Water level in the reservoir (m)
27	8-09-1988	658.4
28	12-10-1988	658.4
29	10-01-1989	659.2
30	4-05-1989	658.7
31	22-08-1989	658.0
32	20-09-1989	658.3
33	19-02-1990	658.7
34	15-03-1990	658.7
35	18-10-1990	659.4
36	10-04-1991	658.7
37	25-07-1991	658.5
38	19-10-1992	658.4
39	27-04-1993	658.9

Fig. 7 – Alto Ceira dam. Evolution of the horizontal displacements monitored by geodetic methods in the upper targets of the arch (elevation 663.00 m), between 1950 and 1993 (adapted from [11])

Fig. 8 presents the evolution of the radial displacements at the point where they had the greatest values (next to the crest of EF block), including a function adjusted to the values observed between 1984 and 2011. The irreversible value of the radial displacement at this point reached, in this period, about 50 mm.

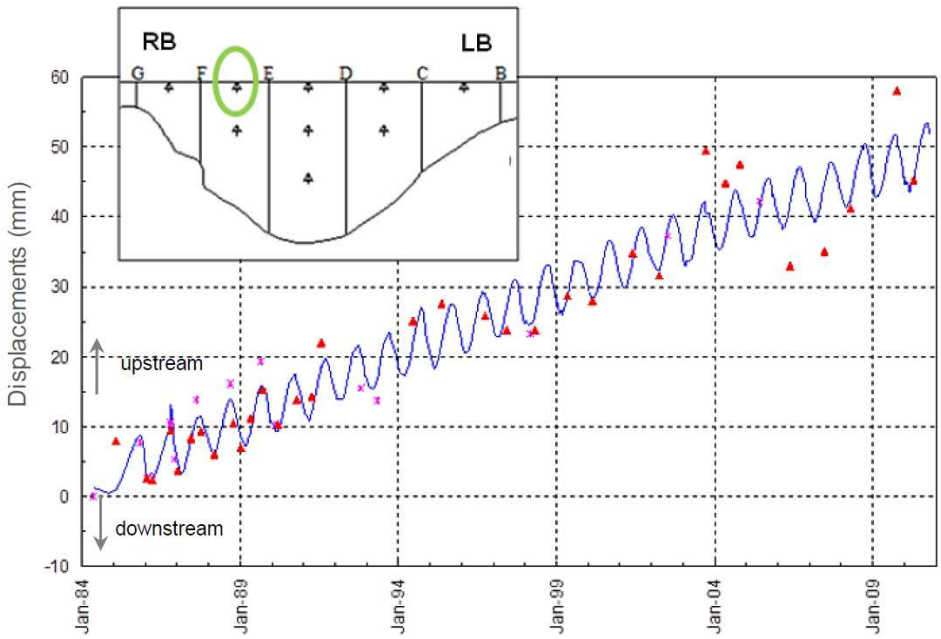

Fig. 8 – Alto Ceira dam. Function adjusted to the radial displacements monitored by geodetic methods in the upper target of the EF block, located near the crest, from 1984 to 2011

Fig. 9 shows the evolution of the vertical displacements at the crest, obtained by precision geometric levelling, between 1950 and 2012. A tendency to blistering has been observed since the early years of operation, but rates have increased substantially since 1983. In the central zone (block DE), the accumulated vertical displacement was about 20 mm (average vertical expansion, including concrete and cracks, of about 500×10^{-6}), but in block FG, on the right bank, the displacement reached about 70 mm, which corresponds to an average vertical expansion (concrete and cracks) of about 4000×10^{-6}.

Regarding the leakage on the downstream face, Fig. 10 shows the evolution of the discharges in the lower section of the BC block (collected at the CE1 weir, see Fig. 5, on the right side), from 1997 to 2013. In the last years of operation, the discharges reached maximum values of about 5 l/min, with seasonal average values between 2 l/min and 4 l/min. The passage of water through cracks enhances the degradation of the concrete.

Fig. 11 shows the main cracks on the downstream face, identified during the surveys carried out in 1994 and 2001. The main cracks had a horizontal direction on the face, being parallel to the insertion surface in the bearing zones at mid-height. Block BC, on the left bank, and blocks FG and GH, on the right bank, were the most cracked ones.

In 2005, a mapping of occurrences was carried out on the downstream face, using georeferenced digital photography (Fig. 12) [12,13]. It can be noted that the main cracks were clearly identified, as well as leakages and carbonate deposits.

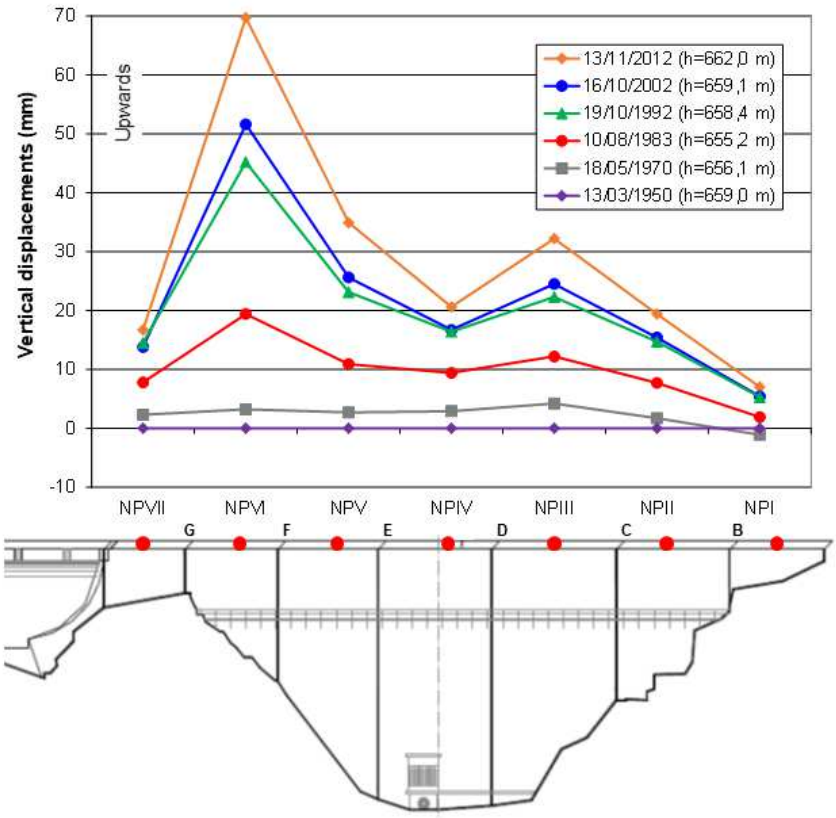

Fig. 9 – Alto Ceira dam. Vertical displacements monitored by precision geometric levelling, between 1950 and 2012

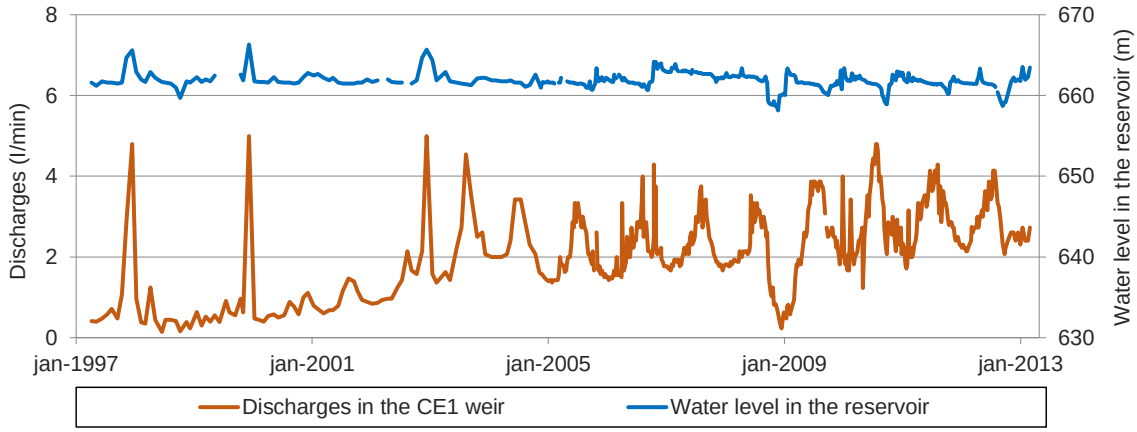

Fig. 10 – Alto Ceira dam. Discharges through cracks at the bottom of BC block, collected in the CE1 weir, between 1997 and 2013

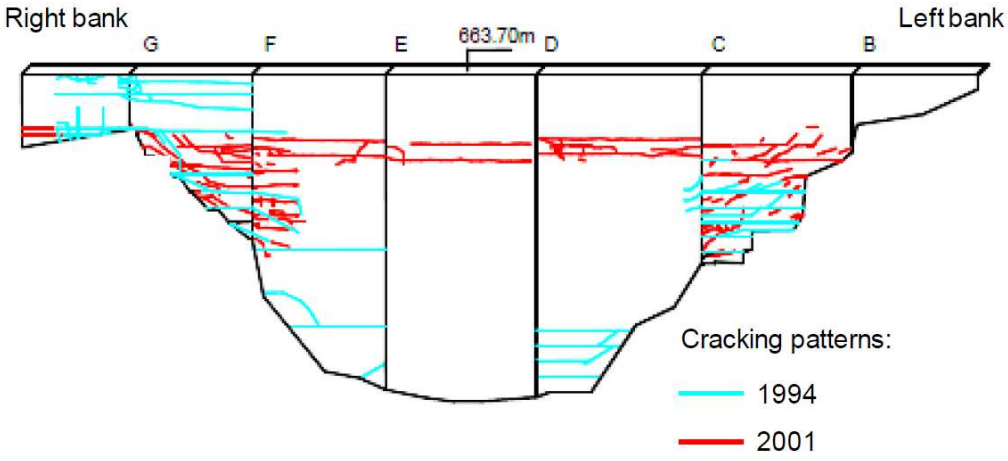

Fig. 11 – Alto Ceira dam. Main cracks on the downstream face, identified during the surveys carried out in 1994 and 2001, using traditional techniques [12]

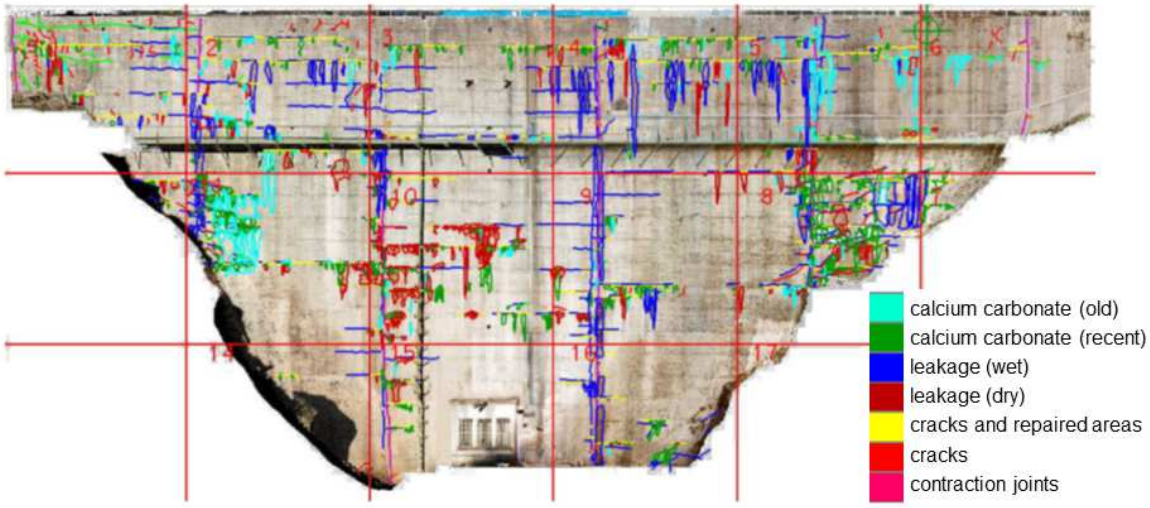

Fig. 12 – Alto Ceira dam. Results of occurrence survey of the downstream face, carried out in 2005, using georeferenced digital photography [12,13]

3.2. Summary of structural analysis studies

The behaviour modelling and structural safety assessment studies of the dam, performed in 1994 [11], was made with the calculation capabilities then available at LNEC. The finite element method was used, considering a continuous three-dimensional mesh of the dam, the spillway and the rock mass foundation (Fig. 13). The non-linear concrete behaviour was supposed to be elastoplastic, defined by a Rankine criterion, in tension, and the Mohr-Coulomb criterion, in compression-shear. The yielding surface was defined for compressive and tensile strengths of 30 MPa and 2 MPa, respectively.

The zoning and the swelling strains accumulated over time, for the dam's body and for the grouted part of the rock mass foundation on right bank, were estimated from the interpretation of the vertical displacements (Fig. 14).

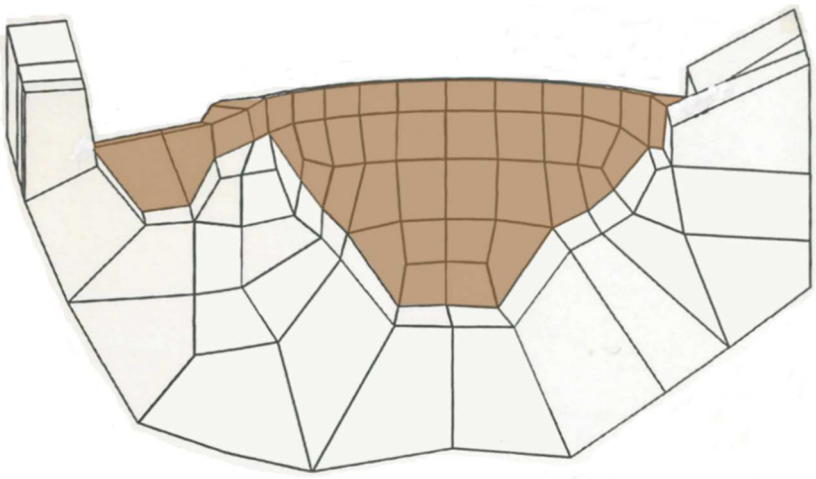

Arch (concrete)
$E_c = 30\ GPa$
$\upsilon_c = 0.2$

Spillway (masonry)
$E_m = 10\ GPa$
$\upsilon_m = 0.2$

Foundation (right bank)
$E_{fr} = 30\ GPa$
$\upsilon_{fr} = 0.2$

Foundation (left bank)
$E_{fl} = 10\ GPa$
$\upsilon_{fl} = 0.2$

Fig. 13 – Alto Ceira dam. Finite element mesh and material properties considered in the studies carried out in 1994 (adapted from [11])

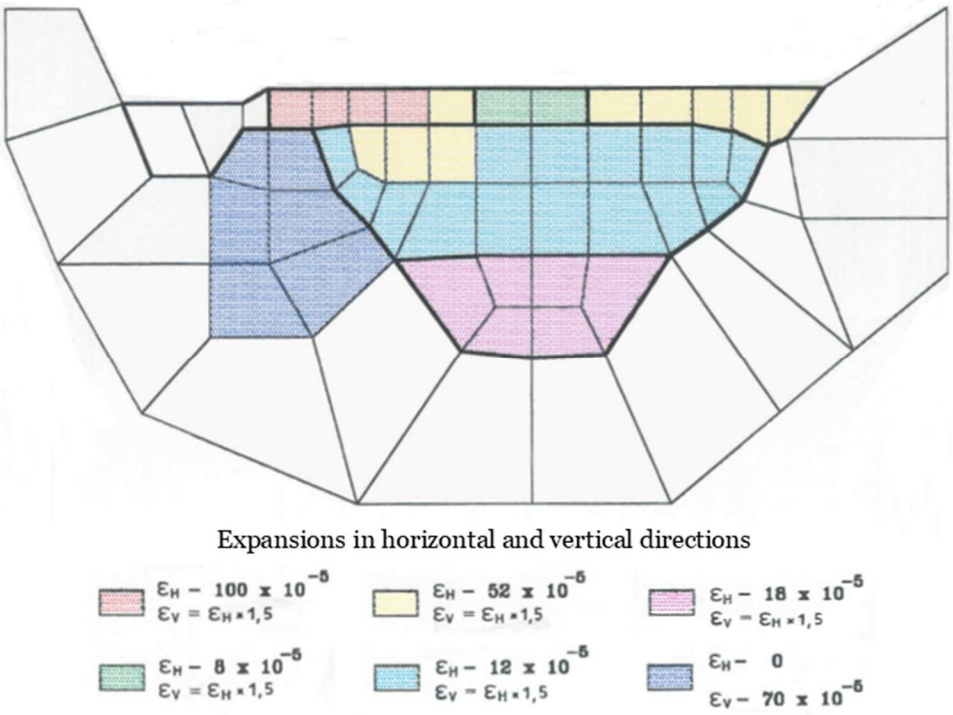

Fig. 14 – Alto Ceira dam. Zoning and accumulated swelling strains estimated for the dam's body and for the grouted part of the rock mass foundation on the right bank [11]

Fig. 15 shows the principal stress on dam's surfaces, and the correspondent tensile rupture zones, obtained considering the actions of the dead weight of concrete, the hydrostatic pressure on the upstream surface, the seasonal temperature variations and the swelling strains. It can be noted that the most cracked areas of the dam coincide with the areas where tensile ruptures were calculated.

In 2004, these studies were updated [14], confirming the evolution of the structural degradation computed about a decade earlier.

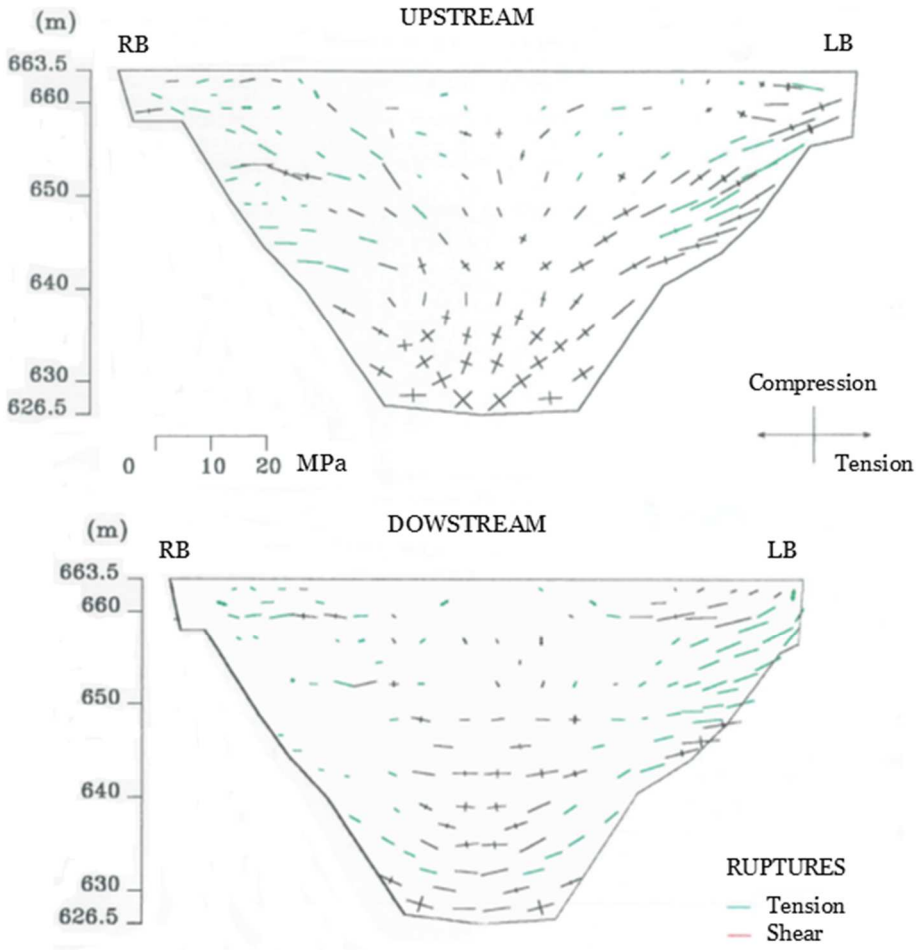

Fig. 15 – Alto Ceira dam. Principal stresses on dam's surfaces (and tensile rupture zones) [11]

3.3. Dam replacement

Given the depth of the main cracks and the progressive evolution of the water leakages in the bearing zones at mid-height, it was recommended to the dam's owner to carry out studies aiming for the dam's rehabilitation or even its replacement.

Subsequent studies by the owner concluded that the location and the characteristics of the dam, associated with the great magnitude of displacements and opening of cracks, made its rehabilitation impracticable [15]. In fact, several rehabilitation alternatives were considered (e.g., crack grouting, slot cuts to release stresses, or waterproofing the upstream face); however, none was considered feasible because the dam was thin and it was more advantageous to build a new dam downstream (and the damaged dam was used as a cofferdam during the construction of the new one), without stopping dam operation.

The owner then proceeded with the design of the new dam, also of the arch type, which was built about 300 m downstream (Fig. 16), between 2011 and 2013 [16]. The old dam was deactivated through the demolition of the central section of the structure. This is the only case

of replacement of a concrete dam, in Portugal, due to structural deterioration. A compilation of all the studies carried out over time on this dam was recently made [17].

Fig. 16 – Alto Ceira dam. View of the new dam (called Alto Ceira II dam) and of the old dam (partially demolished), after the first filling of the reservoir, in July 2014

4. CAHORA BASSA DAM, MOZAMBIQUE

4.1. Characteristics of the dam

The Cahora Bassa dam (Fig. 17) is a part of a hydroelectric scheme located on the Zambezi River, close to Songo village, Tete province, Mozambique.

Fig. 17 – Cahora Bassa dam. Downstream view

The structure is a double curvature arch dam with a 166 m maximum height, from the bottom level of the foundation. The crest is 303 m long, having a chord/height ratio of 1.54 and a thickness ranging, in the main cantilever, from 4 m at the crest to 23 m at the base [18]. The crest and the retention water level (RWL) are located at levels 331.00 m and 326.00 m, respectively. The dam is equipped with a small surface spillway, of the “volet” type, and a mid-bottom spillway with 8 orifices (Fig. 18). The rock mass foundation is of very good quality and mainly consists of gneissic granite. The rocks are sound and the rock mass is poorly fragmented. The reservoir has a large volume of about 66000 hm^3.

The dam was built between September 1972 and March 1975. The first filling of the reservoir began on the 7th of December 1974, before its completion. Since then, the water level has been approximately constant and near the maximum (326.00 m).

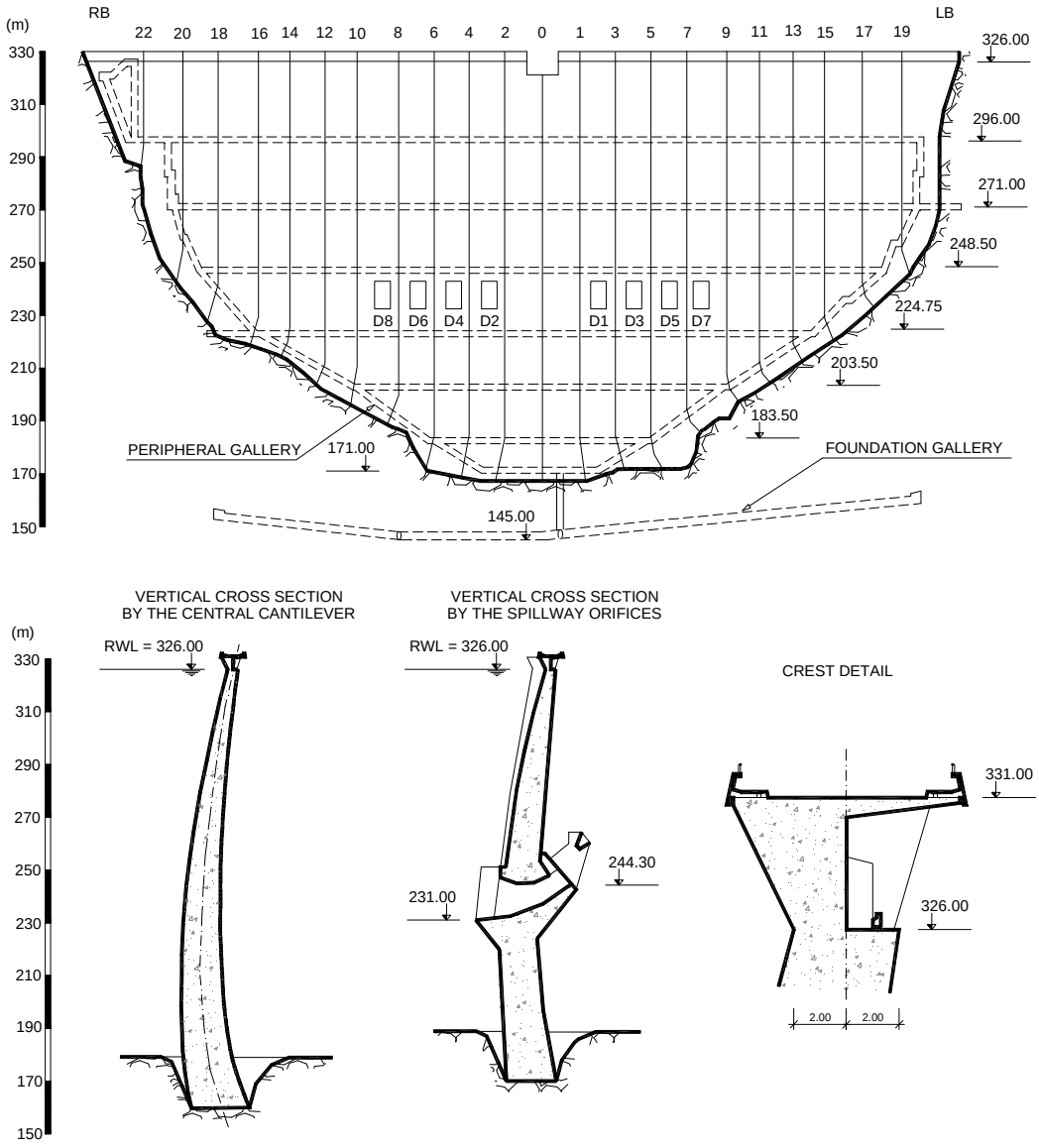

Fig. 18 – Cahora Bassa dam. Downstream elevation, vertical cross-sections and crest detail

The dam monitoring system allows the evaluation of the actions and the determination of the thermal, structural and hydraulic responses, by measuring: i) the upstream and downstream levels, by staff gauges and water level recorders; ii) air temperatures, by both thermometers and thermograph; iii) uplifts, by simple piezometers and by piezometer fans; iv) horizontal displacements, by coordimeter bases installed at the intersection of the five plumb lines with the inspection galleries; v) horizontal displacements by geodetic methods; vi) vertical displacements, by precision geometric levelling in some galleries, and by rod extensometers installed at the central cantilever of the dam and at the foundation, from the peripheral gallery; vii) convergences, by convergence meters installed close to the spillway orifices; viii) joint movements, using devices for measuring the movement of joints and deformeters; ix) temperatures in the concrete, by thermometers, by devices for measuring the movement of joints, by strain meters and stress meters; x) strains, by groups of two, five or nine Carlson strain meters; xi) stress, by stress meters; and xii) discharged and infiltrated flows, by drains and seepage measuring weirs. The dam is also equipped with a rain gauge, for measuring rainfall, as well as with an earthquake monitoring system and a dynamic response monitoring system, formed by a seismometer network. Figs. 19 and 20 show the monitoring system to measure displacements, strains and stresses,

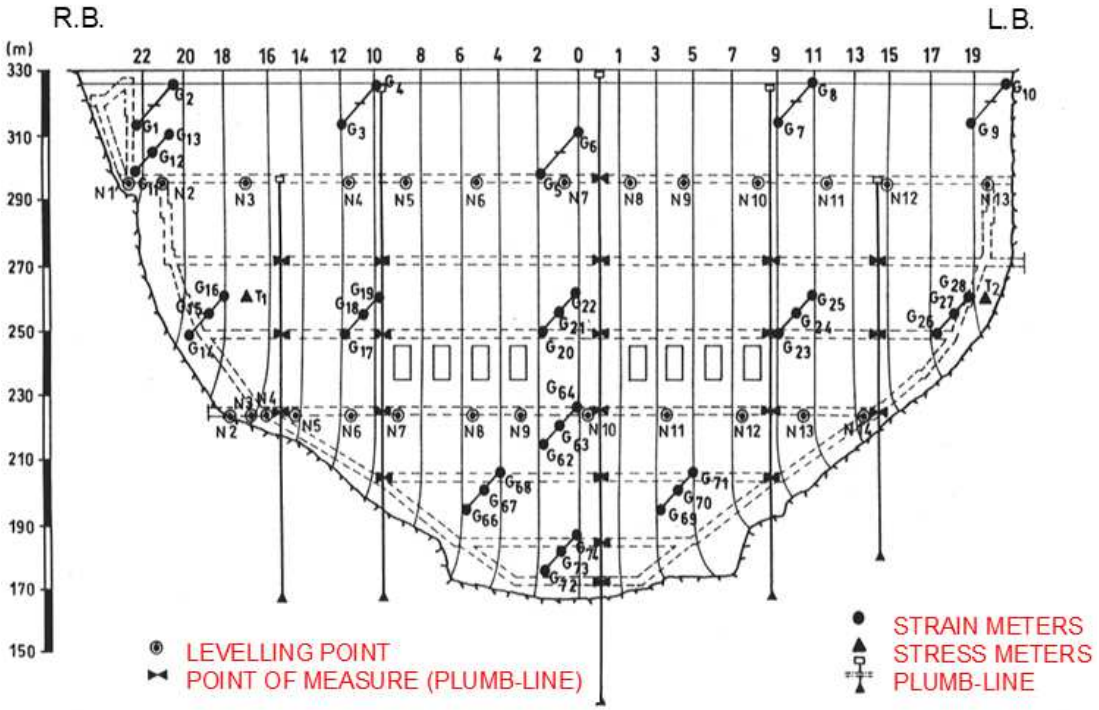

Fig. 19 – Cahora Bassa dam. Monitoring system for displacements, strains and stresses

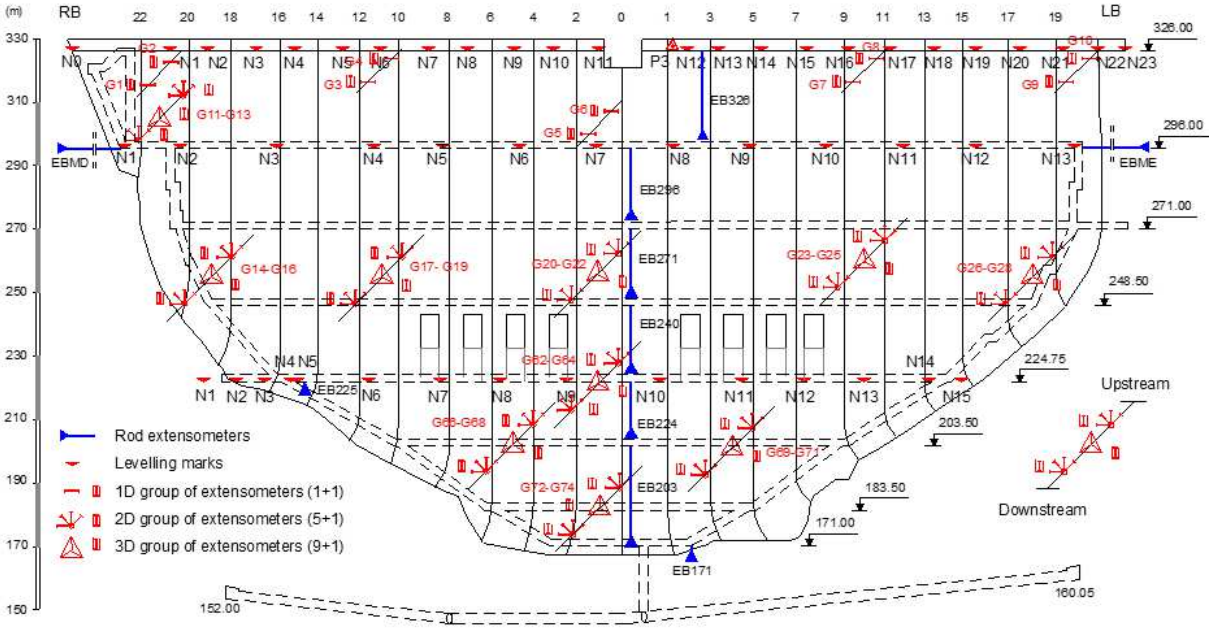

Fig. 20 – Cahora Bassa dam. Monitoring system for vertical displacements and strains

4.2. Sequence of studies about the dam´s concrete swelling and its structural effects

The swelling process of internal origin in the concrete of the dam was identified in the late 1980s, about 15 years after the first filling of the reservoir. Its characterization, from the monitoring results and through physical and chemical tests, was carried out in three stages, the first in the early 1990s, the second at the end of that decade and the third between 2017 and 2021 [19]. In parallel with these studies, the modelling of the structural behaviour of the dam was carried out, to know the evolution of the swelling effects. The structural analysis was performed in 1991, 2002, 2009, 2017 and 2021, considering the knowledge about the swelling phenomenon itself and the development of the numerical capabilities to its simulation [20, 21, 22, 23, 24, 25, 26]. The upgraded model of 2021 was also used to forecast the behaviour of the dam in the next decade [27].

In fact, a few years after the beginning of the dam operation, signs of an unusual structural behaviour were identified, related with the existence of progressive vertical displacements upwards, measured by precision geometric levelling, and increasing strains, monitored by means of stress-free Carlson strain-meters. From the set of studies then performed, it was concluded that a swelling process was on going in the dam's concrete, due to alkali-aggregate reactions (AAR) of the alkali-silica (ASR) type. These studies were mainly developed by LNEC, in Lisbon, which has been providing technical support to the owner over the years.

The technical and scientific knowledge about the concrete swelling processes, when the design and the construction were developed, was still in a rudimentary state. Following the knowledge of that time, testing of the materials (cement, aggregates, water and additives) of

the concrete placed at Cahora Bassa dam and appurtenant works was properly done to determine their chemical composition and the ideal dosage of each material in order to avoid or limit the development of ASR in the concrete.

The sand and coarse aggregates used for the dam's concrete came from crushing the rock blocks of the excavations for the foundations, tunnels and caverns. The maximum size of the aggregates was 150 mm in almost the entire dam´s body, with 215 to 265 kg of cement content per cubic metre of concrete. The aggregates are mainly gneiss of good physical and mechanical proprieties, with uniaxial compressive strength that reached 135 to 150 MPa. The structural concrete of the dam also has a good quality, with a long term uniaxial compressive strength of about 50 MPa.

The large percentage of the free calcium oxide on the cement, identified during the works between 1971 and 1972, required a strict control of the expansibility of the concrete. From 1972 to 1975 the amount of alkalis of the cement used in the dam concrete (Na_2O %+0.658 K_2O %) has annual average values ranging from 0.32% to 0.52%. However, further specific studies of the dam´s concrete confirmed the existence of the swelling phenomenon, which has been developing in a slow process, reaching nowadays values of about $600x10^{-6}$ to $900x10^{-6}$, that can be considered moderate. From the results of recent tests, long term maximum values of about $1400x10^{-6}$ are expected [19, 27].

4.3. Finite element model

A homogeneous continuous structural finite element model was used to support the analysis, interpretation and prediction of the dam behaviour. The continuous model is suitable for the analysis because of the very small movements occurring at the contraction joints since the first filling of the reservoir, which in turn are related to the small variations of the main loads (water level and thermal effects) and also to the concrete swelling, that contributes for closing the dam joints.

The concrete rheological behaviour was simulated by using a viscoelastic model, characterized by the creep function (1) and a Poisson ratio ν_c = 0.2. For the rock mass foundation, also considered homogeneous and continuous, the time effects were not considered, being used a Young's modulus E_f = 50.0 GPa and a Poisson ratio ν_f = 0.2.

From the results of creep tests performed at LNEC, data about the concrete composition, results of continuous monitoring, swelling quantification and structural modelling, the following Bazant e Panula creep function $J(t, t_0)$ was adjusted for the dam concrete,

$$J(t, t_0) = \frac{1}{50.0}(1 + 3.0\ (t_0^{-0.34} + 0.042)(t - t_0)^{0.18}) \qquad (\mathrm{GPa}^{-1}) \qquad (6)$$

which is represented in Fig. 21 for three ages of loading, as well as the corresponding relaxation curves R, obtained through numerical inversion (t_0 is the age of loading). Mention must be made for the fact that the concrete presents considerable creep rates for high load ages, which also corresponds to a good stress relaxation capacity for prescribed strains.

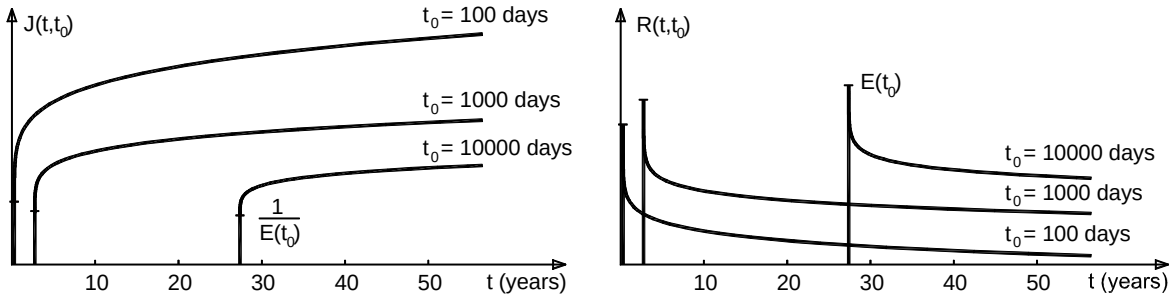

Fig. 21 – Cahora Bassa dam. Creep and relaxation curves of Cahora Bassa dam's concrete

Since the expansive process in the dam concrete is of moderate magnitude, it was assumed that the mechanical properties of the concrete are not affected by internal damages due to swelling. The concrete non-linear behaviour, due to tensile cracking, was also not considered in this study, because structural cracking occurs only in some localized zones of the dam, not affecting its global behaviour.

The upgraded finite element mesh includes the rock mass foundation and the mid-bottom spillway structures. Two elements were considered throughout the dam's thickness, which allows a better representation of the crest geometry (Figs. 22 and 23). The mesh has a total of 20775 nodal points for 4942 volumetric finite elements (1320 of the 20-node hexahedral type, from which 586 corresponding to the dam's body and 734 to the rock mass foundation, and 3622 of the 10-node tetrahedral type, representing the mid-bottom spillway structures).

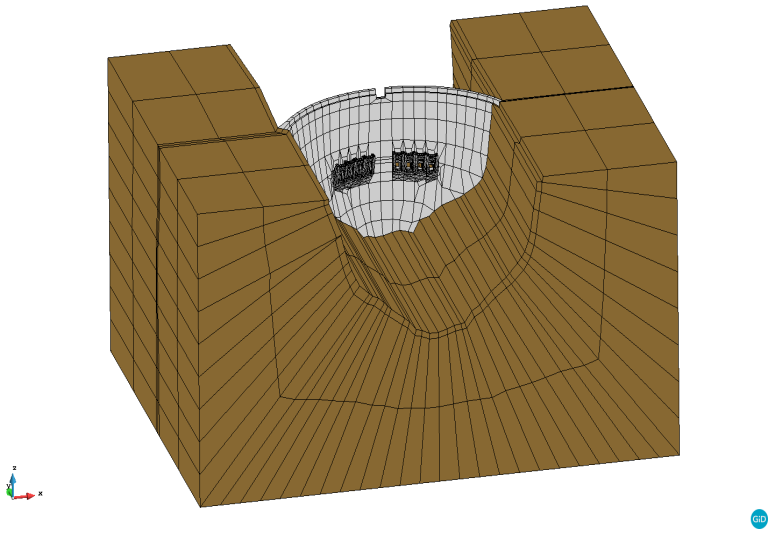

Fig. 22 – Cahora Bassa dam. Downstream view of the finite element mesh of the dam and its rock mass foundation

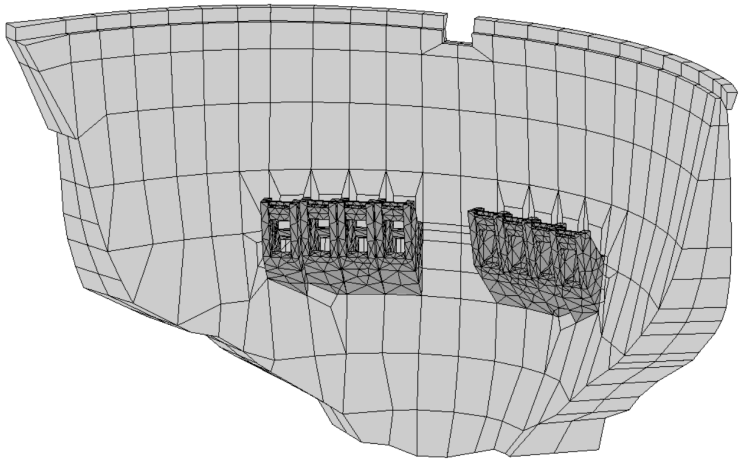

Fig. 23 – Cahora Bassa dam. Downstream view of the finite element mesh of the dam and the mid-bottom spillway structures

4.4. Loads

For analysing the dam behaviour, since the beginning of the first filling of the reservoir to the end of 2030, the following loads were considered: i) the concrete dead weight; ii) the prestressing forces in the spillway structures; iii) the hydrostatic pressure on the upstream surface; iv) the temperature variations due to the annual waves in the air and in the reservoir water; and v) the concrete swelling due to alkali-aggregate reactions.

The dead weight of concrete was represented by means of vertical body forces (γ_c = 24 kN/m^3).

The water pressure was simulated by surface loads, applied on the upstream face of the dam and on the spillway gates (γ_w = 10 kN/m^3). To forecast the behaviour of the dam until 2030, the level of the reservoir was considered equal to the average water level in the period between mid-2003 and October 2015, approximately 323 m (Fig. 24).

The prestressing forces were considered as punctual loads in the mesh nodes corresponding to tendons anchorages and deviations (Fig. 25). For each tendon, a long-term prestressing of about 3500 kN was predicted, that corresponds to a service stress of about 1000 MPa. The used steel has a rupture stress of 1780 MPa.

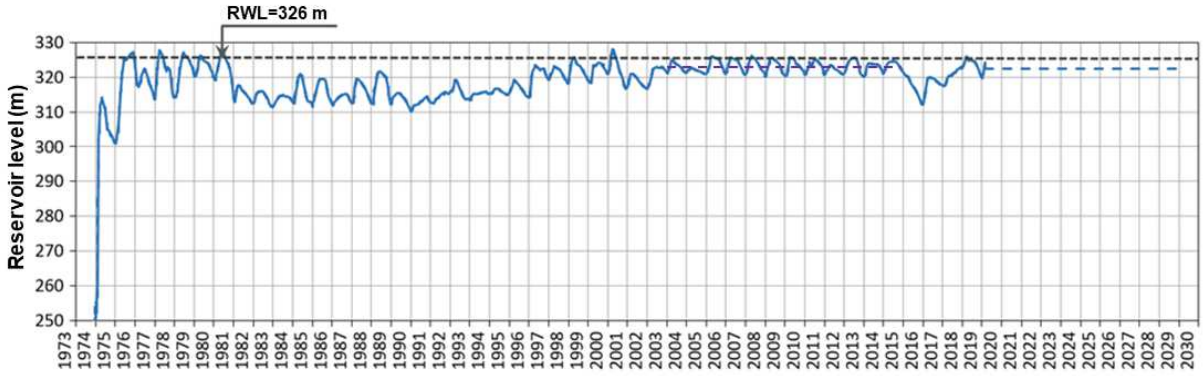

Fig. 24 – Cahora Bassa dam. Monthly discretization of the reservoir level since 1975 until 2030

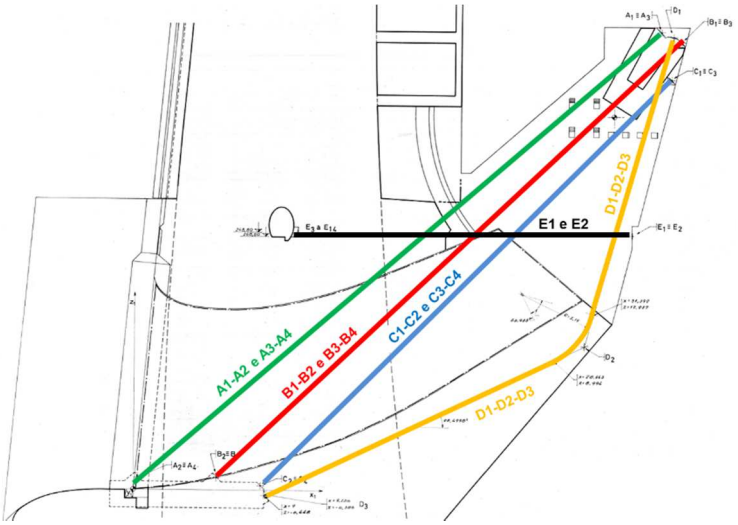

Fig. 25 – Cahora Bassa dam. Elevation of the prestressing tendons connecting the spillway structures to the dam's body

The thermal actions on the dam surfaces were represented by sinusoidal waves of annual period for the air and water. The wave parameters were numerically determined by the least square method based on the temperatures observed on air and water thermometers (Fig. 26). For the concrete thermal dilation coefficient was considered a value of $\alpha = 1.0 \times 10^{-5}$ /ºC.

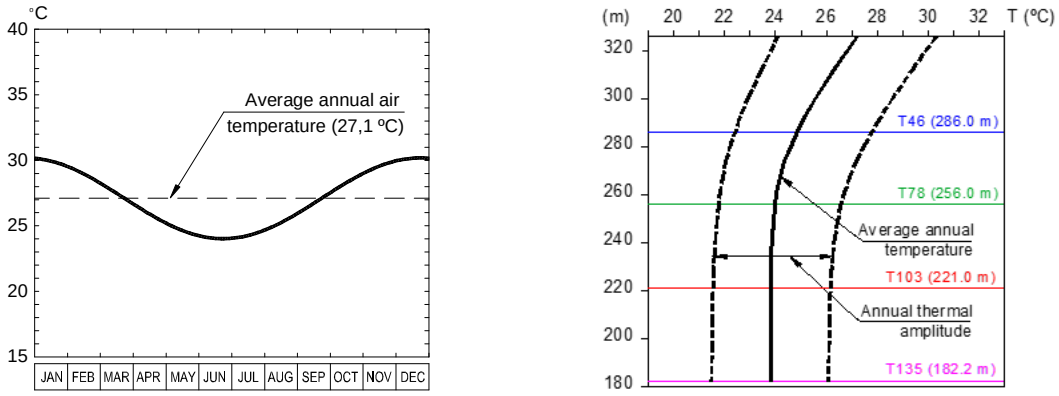

Fig. 26 – Cahora Bassa dam. Average annual thermal wave on air (left) and variation of the average annual thermal wave amplitude with the reservoir water depth (right), evaluated from the monitoring data

The concrete expansion was represented in the model by means of prescribed free-swelling deformations. The evolution of the concrete free-swelling in four different zones (Fig. 27) was estimated on the basis of the information about the concrete composition (in particular the amount of cement and alkali), the results from chemical tests, observations at stress free strain meters and geometric levelling, and also from results obtained with the numerical modelling. The estimated free expansions have long-term maximum values of about 1400×10^{-6}.

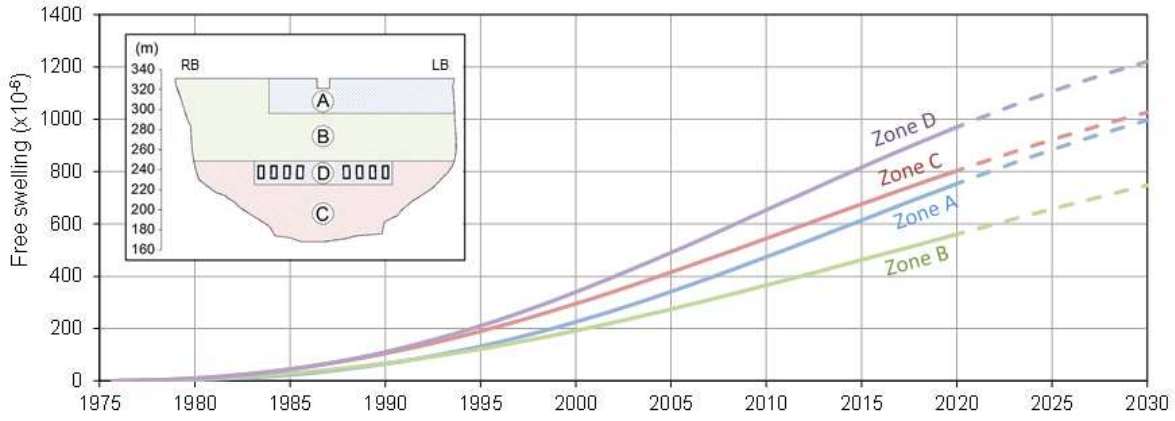

Fig. 27 – Cahora Bassa dam. Zoning and evolution over time of free swelling strains in dam's body

The water level and the free swelling strains time discretization were done monthly.

The influence of stress field on swelling evolution was considered, as in previous studies, according to the relation proposed by Larive [28], based on experimental data (Fig. 28). Changes on the concrete rheological behaviour were not considered since the swelling magnitude is still moderate.

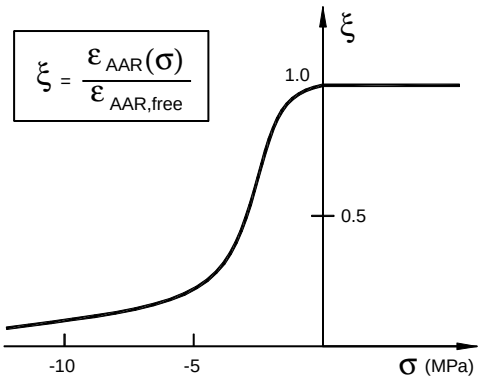

Fig. 28 – Cahora Bassa dam. Relationship considered for taking into account the influence of the stress field on the swelling development

4.5. Results from structural modelling and monitoring

The results computed by the structural model, together with the data provided by the dam monitoring system, support the analysis and interpretation of the dam behaviour until 2020.

The second plot of Fig. 29 shows the evolution of the radial displacements since the first filling of the reservoir until 2020, monitored in the central plumb line I1 at elevation 296.0 m, along with the values computed with the numerical model until 2030, considering the combined loads of the dead weight, water pressure, swelling and their delayed effects. The good agreement between the computed and observed results, until 2020, is remarkable. The computed response is also depicted in the third plot of the same figure, where the effects are separately

represented, so the relative influence of each effect can be appreciated. The delayed response is higher than the elastic response while the swelling effects starts assuming relevant values. The elastic response is consistent with the evolution of the reservoir level, shown in the first plot of the figure.

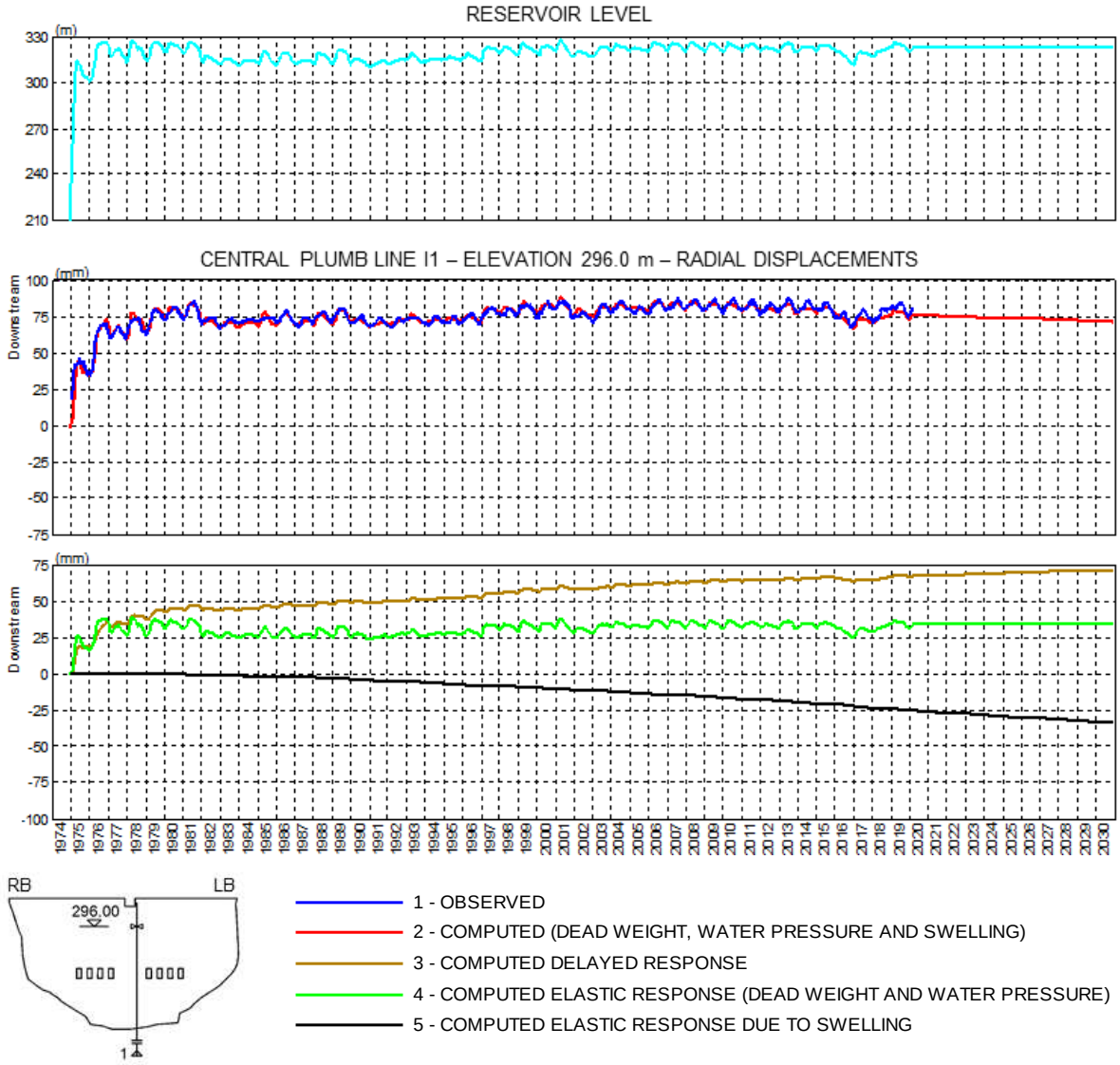

Fig. 29 – Cahora Bassa dam. Central cantilever radial displacements at 296.0 m elevation, measured on the plumb line I1 until 2020 and computed since 1975 until 2030

Fig. 30 presents the evolution of the vertical displacement at the point corresponding to the levelling mark N11 of the gallery at elevation 326.0 m. The plots have an organization similar to Fig. 29, omitting the evolution of the reservoir water level. The first plot shows that the computed vertical displacements compare well with those observed by the geometric levelling, until 2020. The second plot, where the effects are separately represented, shows that the vertical displacements are almost entirely due to swelling effects.

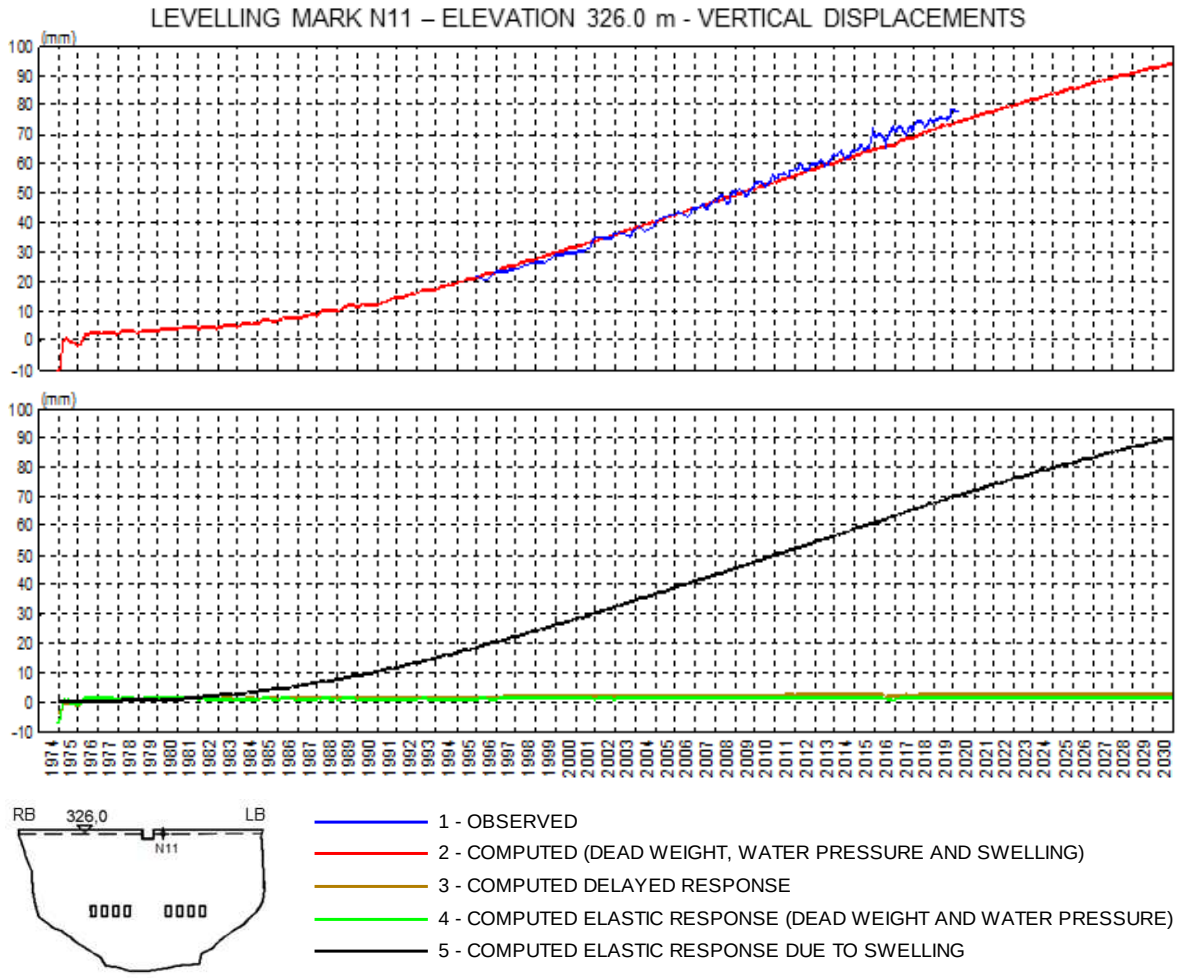

Fig. 30 – Cahora Bassa dam. Vertical displacements at 326.0 m elevation, at the point corresponding to the levelling mark N11, measured until 2020 and computed since 1975 until 2030

The left side of Fig. 31 presents the principal stresses on the upstream and downstream faces, calculated in 2020, due to the combined loads of the dead weight, hydrostatic pressure and swelling, as well as their delayed effects. The stress field is generally compressive except for the upper part of downstream face, where tensile stresses occur. In compression, the maximum values reach 23 MPa and 22 MPa on the upstream and downstream faces, respectively, near the left bank bearing. At the closure of the arches, above the spillway orifices, the maximum compressive stresses are about 11 MPa, upstream. The tensile stresses are vertical and lower than 2 MPa at the closure of the upper arches, and diagonal and superior to 2 MPa near the bearings, with values reaching 5 MPa in some localized zones.

The right side of Fig. 31 presents the principal stresses on the upstream and downstream faces calculated in 2020, due only to swelling and corresponding delayed effects, in particular relaxation. Stresses with significant values appear along the dam insertion. The higher compressive stresses are located at the bearings of the upper arches, reaching values of about

22 MPa at the left bank, upstream, while the higher tensile stresses, of about 4 MPa, were computed downstream with orientation normal to the foundation surface.

In a similar way to the previous figure, Fig. 32 shows the predicted stress fields for 2030. The maximum compressive stresses of 23 MPa will increase to 28 MPa. As the concrete strength is about 50 MPa, no safety problems are expected. The localized areas with relevant tensile stresses will have a very limited progression.

Fig. 33 shows a detail of the stress fields on the downstream face, at the upper arches near the left bearing. In the zone connecting the open gallery, at the elevation 326 m, with the left bank access, diagonal tensile stresses of about 5.0 MPa take place in 2020, justifying the cracks in the dam faces as well as their dominant direction. In the right bank, there are also tensile stresses of about 4.0 MPa in the zone corresponding to the beginning of the bearing enlargement, which also justify the small cracks identified in this zone.

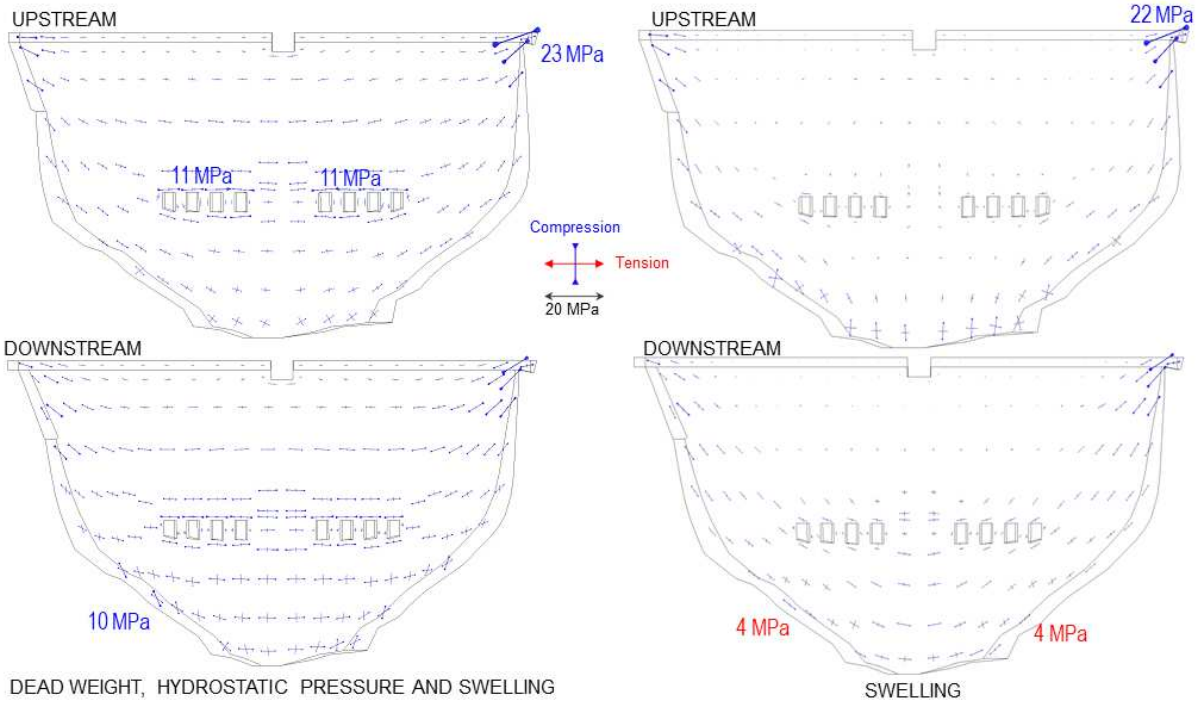

Fig. 31 – Cahora Bassa dam. Principal stresses on dam faces computed in 2020, due to the combined loads of the dead weight, hydrostatic pressure and swelling (left side) and only due to swelling (right side)

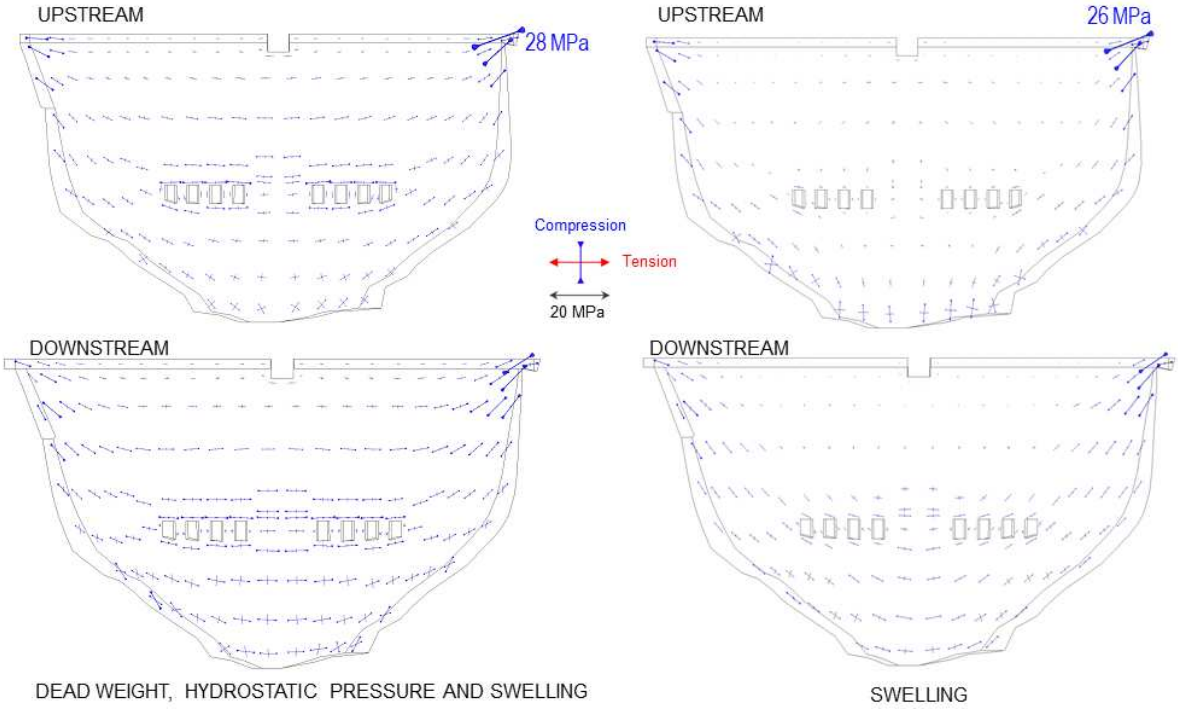

Fig. 32 – Cahora Bassa dam. Principal stresses on dam faces predicted for 2030, due to the combined loads of the dead weight, hydrostatic pressure and swelling (left side) and only due to swelling (right side)

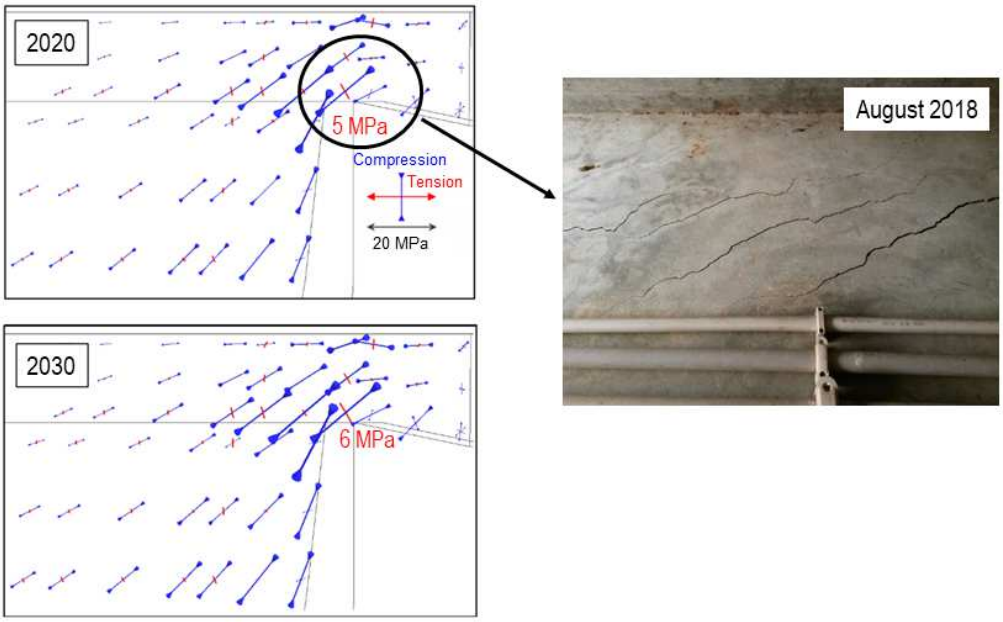

Fig. 33 – Cahora Bassa dam. Detail of the stress fields on the downstream face of the upper arches near the left bearing, computed in 2020 and in 2030, due to the combined loads of the dead weight, hydrostatic pressure and swelling, and view of the main cracks of this zone in August 2018

The convergences of the spillway structures were measured between the vertical interior surfaces of the structures, close to the orifices, from 1994 to 2004. After an interruption period

the monitoring was restarted in 2011 for the orifices 1, 2 and 4. Fig. 34 plots the relative displacements between the spillway structures, corresponding to the first orifice, showing that the swelling effect contributes for the progressive approximation of the lateral surfaces of the mid-bottom spillway orifices.

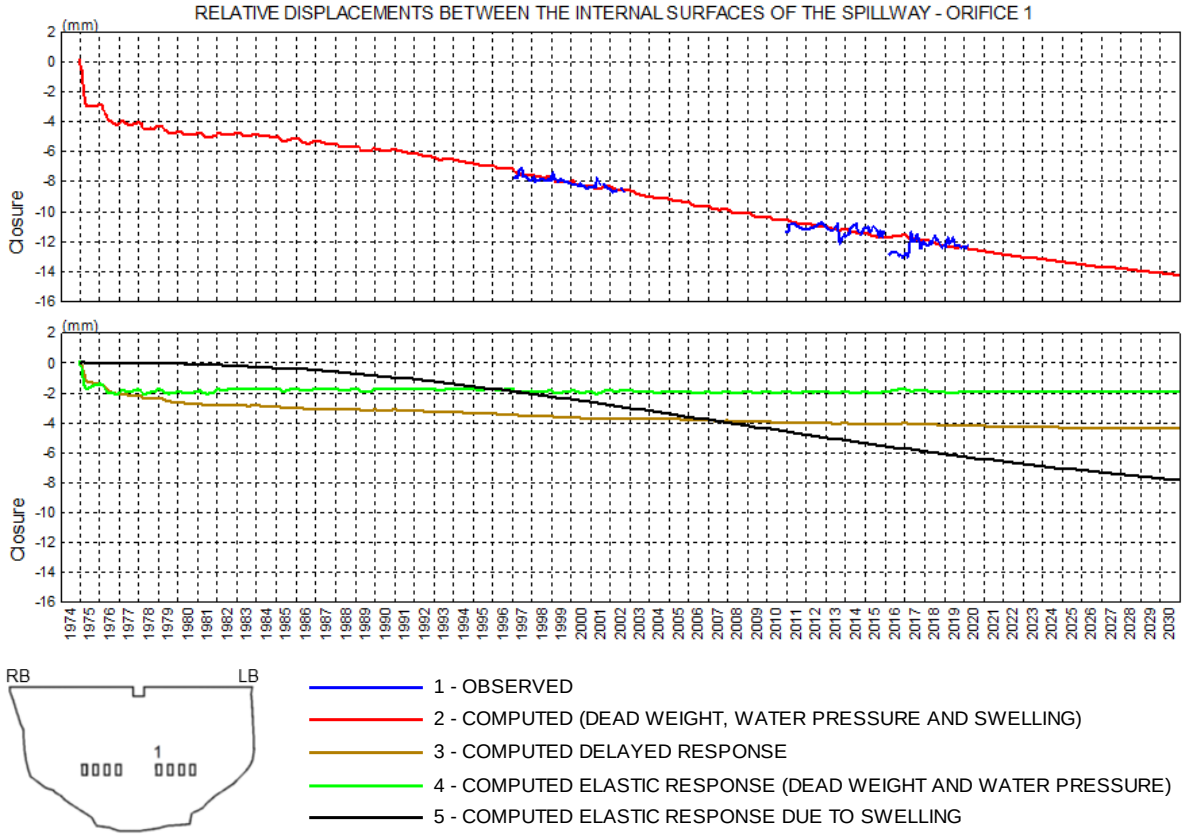

Fig. 34 – Cahora Bassa dam. Relative displacements between the internal surfaces of the spillway structures, corresponding to the first orifice of the mid-bottom spillway, monitored between 1996 and 2002 and between 2010 and 2020, and computed since 1975 until 2030

Due to the swelling effects, an increase of about 260 MPa in the tensile stresses of the prestressing tendons was estimated, in the long term. The maximum stresses will reach about 1260 MPa, which is about 70% of the rupture strength of steel (1780 MPa).

It should also be noted that, in 2017, the measurement of in situ stresses in the dam's concrete was carried out by the overcoring technique, and the values of the high compressive stresses were confirmed [29].

4.6. Intervention in the mid-bottom spillway

In the last decade, a major intervention was carried out on the mid-bottom spillway, involving punctual concrete repairs and waterproofing painting of the apparent surfaces, and corrections to the operation and functioning of the gates.

Regarding the mid-bottom spillway orifices, the progressive approximation of the lateral surfaces, associated with some inaccuracies in the initial installation of the gates, led to lateral wear in some zones of their steel linings. Fig. 35 shows a schematic plan with the gate position, obtained from the displacements computed for its downstream bearings and from topographic surveys, and in Fig. 36 views of the lateral steel linings of the mid-bottom spillway are presented. There were signs of friction between the gates and the lining, before the intervention. Notches in the steel plates, to allow an adequate gate operation, were done.

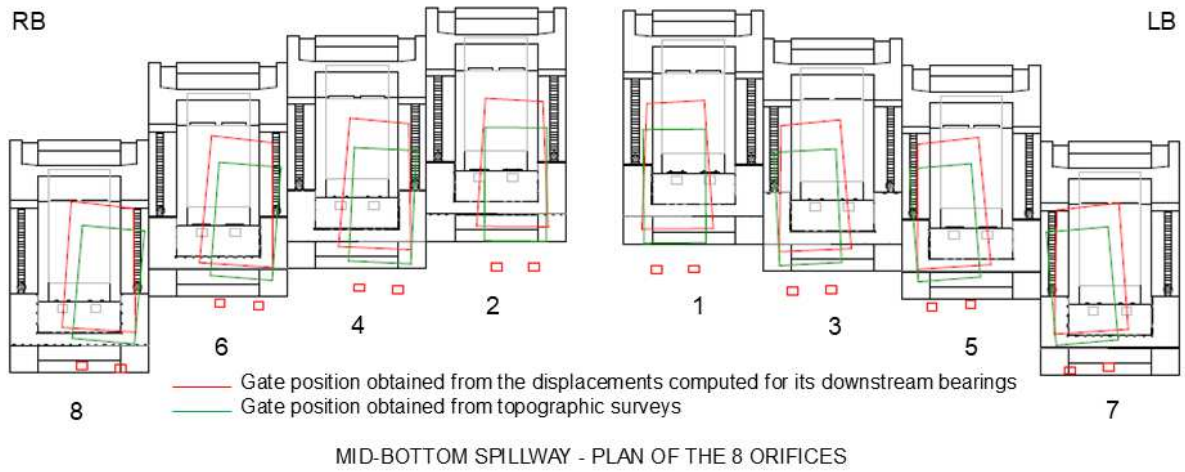

Fig. 35 – Cahora Bassa dam. Schematic plan with the gate position, obtained from the displacements computed for its downstream bearings and from topographic surveys

Fig. 36 – Cahora Bassa dam. Views of the lateral steel linings of the mid-bottom spillway: on the left, before the intervention, with signs of friction between the gates and the lining; on the right, the notches that allow an adequate gate operation

The corrections done in the lateral steel linings of the orifices are expected to guarantee the good operation of the radial gates for the next decades.

5. FINAL REMARKS AND NEW CHALLENGES

The experience accumulated in observing and modelling the behaviour of dams affected by concrete expansions, with a view to controlling their safety and planning and carrying out interventions, allows us to draw the following general conclusions:

- the monitoring systems designed in accordance with ICOLD guidelines [30], allow, in general, the early detection of the structural effects of the swelling phenomena;
- the use of statistical models allows the interpretation of the monitoring results and the preliminary quantification of the expansions themselves and their effects;
- appropriate structural modelling is needed to interpret properly the observed behaviour and to support the safety control and the study of the most appropriate interventions;
- there is a set of techniques for mitigating the development of expansions and for rehabilitating the most deteriorated dams which, if used judiciously, allows for the extension of their useful life.

There are recent developments in the fields of automatic monitoring and assisted inspections, with great interest in knowing the condition of dams. Techniques supported by digital images stand out, which allow the automatic characterization of the surfaces pathologies and help in the definition of the calculation meshes in structures with few design and construction elements [31,32].

In the domain of new challenges, it seems that the following three should be highlighted:

- increasing the natural or the artificial drying of concrete as a measure to limit the swelling development in some dams [33];
- study the influence of spatial variability of expansions on the behaviour and safety of concrete dams [1,34]; and
- study the seismic behaviour of concrete dams deteriorated by expansions, considering, in an integrated manner, the simulation models of the expansions and of the dynamic effects [35].

REFERENCES

[1] Batista, A.L. (2021). Deterioration and rehabilitation of dams affected by internal swelling reactions in concrete (in Portuguese). Research programme, LNEC, Lisbon.

[2] Pedro, J.O.; Azevedo, M.C. (1982). Criteria and models for safety evaluation of concrete dams. 14th International Congress on Large Dams (ICOLD), Q52-R33, Rio de Janeiro, Brazil.

[3] Mora Ramos, J.; Pinho, J.S. (1987). A new method for quantitative analysis of dam displacements. 3rd International Conference on Computational Methods and Experimental Measurements, Porto Carras, Greece.

[4] Batista. A.L.; Mora Ramos, J.; Oliveira, S.; Piteira Gomes, J. (2002). Models for safety control of concrete dams. 3th International Conference on Dam Engineering, Singapore.

[5] Batista, A.L. (1998). Analysis of arch dams' behaviour over time (in Portuguese). PhD thesis, Instituto Superior Técnico, Universidade de Lisboa, Lisbon.

[6] Oliveira, S. (2000). Models to analyse the behaviour of concrete dams considering cracking and time effects. Damage formulation (in Portuguese). PhD thesis, Faculdade de Engenharia da Universidade do Porto, Porto.

[7] Piteira Gomes, J. (2007). Structural behaviour modelling of concrete dams subject to swelling reactions (in Portuguese). PhD thesis, Faculdade de Ciências e Tecnologia, Universidade Nova de Lisboa, Lisbon.

[8] Dias, I.F.; Batista, A.L. (2025). Modelling of concrete swelling effects in dams, considering the influence of temperature, humidity, stress field, viscoelasticity and cracking. Magazine of Concrete Research (accepted for publication).

[9] Tavares de Castro, A.; Mora Ramos, J.; Oliveira, S. (2001). Evaluation of the behaviour of an arch dam affected by a swelling process in the concrete. ICOLD European Symposium, Geiranger, Norway.

[10] LNEC (Reis, M.O.B.) (1991). Study of the concrete of Alto Ceira dam. Collaboration of the Chemistry Unit (in Portuguese). Report 170/1991, Lisbon.

[11] LNEC (Oliveira, S.; Pina, C.; Mora Ramos, J.; Tavares de Castro, A.) (1995). Study of the behaviour of Alto Ceira dam. Structural safety assessment (in Portuguese). Report 41/1995, Lisbon.

[12] Berberan, A.; Portela, E.; Boavida, J. (2006). Assisted visual inspection of dams as a tool for structural safety control. A case study. Hydro2006, Porto Carras, Greece.

[13] LNEC (Henriques, M.J.) (2013). Thermal survey of concrete dam faces to support the control of the evolution of pathologies (in Portuguese). Report 425/2013, Lisbon.

[14] LNEC (Leitão, N.; Tavares de Castro, A.) (2004). Structural safety assessment of Alto Ceira dam (in Portuguese). Report 412/2004, Lisbon.

[15] Cunha, J.; Silva Matos, D. (2008). The new Alto Ceira dam. An example of the substitution of an existing dam. Hydro2008, Ljubljana, Slovenia.

[16] Silva Matos, D.; Cunha, J. (2015). The substitution of an existing dam affected by AAR. The case of Alto Ceira dam. 25th International Congress on Large Dams (ICOLD), Q99-R35, Stavanger, Norway.

[17] Custódio, J.; Mata, J.; Serra, C.; Ribeiro, A.B.; Tavares de Castro, A.; Batista, A.L. (2025). Insights into the diagnosis and prognosis of the alkali–silica reaction (ASR) in concrete dams, highlighting the case of the demolished Alto Ceira dam in Portugal. Buildings 2025, 15, 460, doi.org/10.3390/buildings15030460.

[18] Fernandes, J.S.; Molico, A.A. (1970). Cahora-Bassa arch dam. Study of different criteria for a design solution. 10th International Congress on Large Dams (ICOLD), Q39-R33, Montreal, Canada.

[19] LNEC (Custódio, J.; Costa, D.) (2021). Cahora Bassa dam. Characterization of the properties and the internal swelling reactions in the concrete. Final report (in Portuguese). Report 34/2021, LNEC, Lisbon.

[20] Tavares de Castro, A.; Batista, A.L.; Mora Ramos, J.; Pinho, J.S. (1990). Parameter identification of a rheological model of the dam's concrete from prototype observation (in Portuguese). 2º Encontro Nacional sobre a Análise Experimental de Tensões, Lisbon.

[21] Batista, A.L., Pina, C.; Mora Ramos J. (1992). Creep analysis of arch dams. Technical paper N. 780, LNEC, Lisbon.

[22] Batista A.L.; Mora Ramos J. (2001). Structural analysis of swelling processes in arch dams. Concreep-6@MIT, Boston, USA.

[23] Batista, A.L.; Piteira Gomes, J.; Mora Ramos, J. (2002). Analysis of the structural behaviour of Cahora Bassa dam (in Portuguese). Encontro Nacional Betão Estrutural - BE2002, Lisbon.

[24] Batista, A.L., Piteira Gomes, J.; Carvalho, E.F.; Tembe, I.M. (2012). Analysis and interpretation of the structural behaviour of Cahora Bassa dam (Mozambique). First International Dam World Conferece, Maceió, Brazil.

[25] Batista, A.L.; Fernandes, E.F.; Tembe, I.M. (2016). Comprehensive assessment of the Cahora Bassa dam's concrete swelling process. 15th International Conference on Alkali-Aggregate Reaction in Concrete (ICAAR 2016), São Paulo, Brazil.

[26] Batista, A.L.; Dias, I.F.; Piteira Gomes, J.; Carvalho, E.F.; Tembe, I.M. (2018). Updating of the behaviour analysis and interpretation of Cahora Bassa dam (Mozambique) considering the mid-bottom spillway structures. Third International Dam World Conference, Foz do Iguaçu, Brazil.

[27] Dias, I.F.; Batista, A.L.; Carvalho, E.F. (2022). Analysis, interpretation and prediction of the structural behaviour of Cahora Bassa dam (Mozambique), affected by concrete swelling. 16th International Conference on Alkali-Aggregate Reaction in Concrete (ICAAR 2020-2022), Lisbon, Portugal.

[28] Larive, C. (1997). Combined contribution of experimentation and modelling to the understanding of the alkali-reaction and its mechanical effects (in French). PhD Thesis, Ecole Nationale des Ponts et Chaussées, Paris, France.

[29] Lamas, L.; Gomes, J.P.; Carvalho, E.F.; Batista, A.L.; Matsinhe, B. (2019). Measurement of in situ stresses in the concrete of the Cahora Bassa dam. 87th ICOLD Annual Meeting, Ottawa, Canada.

[30] ICOLD (International Commission on Large Dams) (1989). Monitoring of dams and their foundations. Bulletin 68, Paris, France.

[31] Roque, D.; Henriques, M.J. (2025). Pathology mapping in concrete dams through digital photogrammetry and image processing. Fifth International Dam World Conference, Lisbon.

[32] Henriques, M.J.; Dias, I.F.; Roque, D.; Gomes, A. (2025). A 3d point cloud model of Santa Luzia dam and its contribution for improving the finite element mesh. Fifth International Dam World Conference, Lisbon.

[33] Charlwood, R.; Godart, B.; Grimal, E.; Isgor, B. (2025). Yes, there appear to be options to stop or control ASR in some dams! Fifth International Dam World Conference, Lisbon.

[34] Saouma, V.; Hariri-Ardebili, M.; Graham-Brady, L. (2020). Stochastic analysis of concrete dams with alkali aggregate reaction. Cement and Concrete Research, 132 (2020) doi.org/10.1016/j.cemconres.2020.106032.

[35] Pourbehi, M.S.; Gideon, P.; Strasheim, J. (2019). Analysis of combined action of seismic loads and alkali-silica reaction in concrete dams considering the key chemical-physical-mechanical factors and fluid-structure interaction. Engineering Structures, 195 (2019), doi.org/10.1016/j.engstruct.2019.05.087.

Fifth International
Dam World Conference
PORTUGAL • LISBON • LNEC • APRIL 13-17, 2025
dam world 2025

GEOMECHANICAL BEHAVIOUR OF TAILINGS STORAGE FACILITIES

Waldemar Świdziński[1]
Institute of Hydro-Engineering,
Polish Academy of Sciences

ABSTRACT

Currently, there are over 3,500 active Tailings Storage Facilities (TSFs) worldwide. Since 1915, 257 TSF failures have occurred, releasing approximately 250 million cubic meters of tailings, destroying areas covering up to 5,000 km², causing an estimated 2,650 fatalities, and impacting around 317,000 people [1]. Despite ongoing efforts, the number of TSF failures has increased since 2000. In recent years, several catastrophic TSF failures, including the Brumadinho disaster in Brazil and the Mount Polley disaster in Canada, have raised serious concerns about the safety and environmental risks associated with these sites. One of the main contributing factors to these failures is the inadequate recognition and understanding of the geomechanical behavior of the tailings deposited in these facilities.

In this keynote lecture, we will discuss the specific geomechanical characteristics of tailings, drawing on 40 years of experience advising on the operation and development of the Żelazny Most TSF in Poland. This facility is one of the largest of its kind in the world and is operated by KGHM Polska Miedź S.A.

The focus will be on the reliable assessment of the mechanical behavior of the tailings deposited in the facility, with particular attention to the impact of fine content and its associated challenges, such as susceptibility to liquefaction—one of the main causes of TSF failures. A robust assessment of the mechanical properties of tailings, particularly its potential for liquefaction, is closely linked to all stages of material testing. This includes the collection of undisturbed samples, their transportation, laboratory testing under various stress conditions, and the final interpretation of the results. The role of the gel-push sampler in collecting truly undisturbed samples, which are especially important for low-cohesion soils like tailings, will also be emphasized. The response of fully saturated and partially saturated tailings to monotonic and cyclic loading will be explored as well.

Next, we will explore proper stability assessment techniques, addressing various failure mechanisms along potential slip surfaces to reliably assess the stability of external dams and internal embankments. The cases of diverse soil responses, including triaxial compression, extension, and simple shearing, depending on the position along the failure mechanism running through tailings mass and foundation soils, will be considered. The stability assessment process will incorporate static, pseudo-static, pseudo-dynamic, and full dynamic approaches, all based on 2D and 3D numerical simulations.

[1] waldemarswidzinski@ibwpan.gda.pl, Poland

Special attention will also be given to the role of monitoring systems throughout the life of the facility, ensuring the safe operation and continuous development of TSFs. Finally, the necessity of supporting the analysis of monitored parameters with GIS-driven professional database systems will be discussed.

Keywords: Tailings dams, geomechanical behaviour, monitoring.

[1] Hudson-Edwards, K.A. et al., “Tailings storage facilities, failures and disaster risk”, Nature Reviews Earth & Environment, 5, 612-530, 2024.eld.

Fifth International Dam World Conference
PORTUGAL • LISBON • LNEC • APRIL 13-17, 2025
dam world 2025

CONCRETE DAMS AND EARTHQUAKES: NUMERICAL ANALYSIS TECHNIQUES AND PRACTICAL ADVICES FOR ENGINEERS

Emmanuel Robbe[1]
EDF

ABSTRACT

This paper addresses the seismic assessment of concrete dams, focusing on advanced numerical methods such as finite-element analyses and non-linear approaches. It highlights the importance of soil-structure and fluid-structure interactions in accurately modelling dam behavior under seismic loads. Through case studies and international benchmarks, the paper examines current practices and challenges in seismic evaluation, particularly for dams exposed to moderate seismic hazards. The findings suggest that well-designed and constructed concrete dams generally perform well under seismic stress, although specific studies and reinforcements may be required for older structures or those with particular pathologies. The paper underscores the need for international collaboration and data sharing to enhance seismic safety practices for dams.

Keywords: Seismic, concrete, modelling, damping, numerical analyses.

[1]emmanuel.robbe@edf.fr, France

1. INTRODUCTION

The aim of this paper is to summarize the work done at EDF over the last 20 years related to the seismic analyses of concrete dams while providing practical advice for engineers, useful references, and identification of fields that require additional work and research . This work is based on:

- Seismic assessment of dams in France under moderate seismic hazard levels.
- Development of in-house numerical tools and practical methods for engineers based on state-of-the-art techniques.
- Participation in benchmark workshops dedicated to seismic analyses of concrete dams (ICOLD, USSD conferences, collaboration between the French and Japanese committees on large dams).

Feedback from these activities is summarized in this paper, grouped under the following themes:

- State of the art in the numerical analyses of dams: tips for the elaboration and validation of numerical models and methods.
- The interest of gathering earthquake records on dams and performing back analyses.
- Calibration of numerical models using ambient vibration measurements.
- Damping: the main parameter for seismic analyses.
- Non-linear analyses
- Seismic assessment of concrete dams
- Performance of concrete dams

2. NUMERICAL ANALYSES OF CONCRETE DAMS : STATE OF THE ART

For the seismic assessment of concrete dams, the complexity of numerical analyses has gradually increased over time, evolving from pseudo-static to pseudo-dynamic analyses, and finally to time-history analyses using finite-element models. This level of analysis is now considered state-of-the-art for important dams under significant seismic hazard.

In this framework, to correctly take into account fluid-structure and soil structure interaction, three main approaches are considered accurate, replacing the outdated approach involving massless foundation and Westergaard added masses :

- Substructure approach [1]: This method simulates the foundation as an elastic substructure, considering stiffness and damping components at the dam-rock interface, with uniform seismic inputs distributed at the dam base.

- The approach using the analysis code LS-DYNA, with earthquake excitation applied by the effective seismic input method (ESIM) and perfectly matched layers (PML), described in [2] and extensively used in north America.
- Direct finite-element method: Proposed by Løkke and Chopra [3][4][5], this method involves viscous-spring boundaries.

The first approach is the historical method proposed by Chopra [6] to correctly solve the soil-structure and fluid-structure for dam analyses using the EACD programs with limited computing resources. The last two approaches represent the most up-to-date practices in dam engineering: they are less optimized regarding computing resources but more flexible, particularly for non-linear analyses. For these two methods, the references provided not only describe the methods and equations needed but also include test cases for validation, such as: (Figure 1) :

- Flat foundation boxes [4], comparing the motion at the free-field surface,
- Idealized 2D 120m high gravity dam [3], comparing the frequency response function at the crest of the dam for different seismic load, with or without the impounded reservoir,
- Semicylindrical canyon cut in halfspace [2][4], comparing the free-field motion at the canyon surface.

From the author's point of view, such test cases are mandatory for engineers dealing with seismic analyses using any software to regularly ensure the software (generally with regular updates) still provides the expected results. It is also an excellent practice for young engineers to understand the assumptions behind the methods, such as the propagation of compression and shear waves in the foundation and the absorption of waves at the model boundaries.

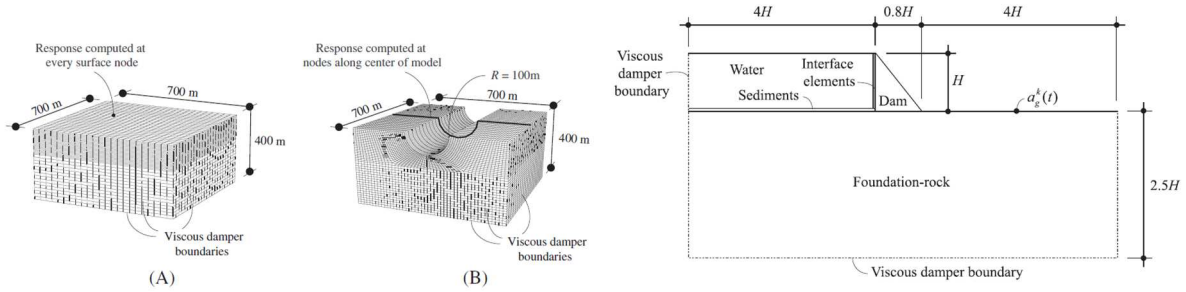

Figure 1 flat box, semicylindrical canyon and gravity dam test cases from Looke and Chopra [3] [4]

In addition to these reference test cases for validating the basic capabilities of the software, benchmark workshops on numerical analyses of dams are organized by ICOLD every two years. These workshops allow engineering groups, researchers, and software developers to compare their results on chosen topics, including seismic analyses of concrete dams. Recent workshops include:

- 2017 in Stockhlom: 3D analyses of Janneh gravity-arch dam
- 2019 in Milan: 2D analyses of Pine Flat gravity dam [7],
- 2025 in Sofia: 3D analyses of Tsankov Kamak arch dam

The 2019 benchmark workshop on Pine Flat dam seismic analyses [7] provided an excellent test case with several sub-cases of increasing complexity, ranging from the analysis of the linear foundation only to the non-linear time-history analysis of the entire dam-foundation-reservoir system.

At EDF, numerical analyses of concrete dams have been performed for 20 years using the in-house and open-source finite-element software Code_Aster. Originally developed for nuclear activities, dedicated features have gradually been developed for concrete dam analyses. While the substructure approach was available early (in the 2000s) in Code_Aster (using MISS3D software), it was not fully operational for industrial use, and engineers continued using massless foundations and Westergaard added masses for seismic analyses. Comparisons between finite-element analyses and earthquake records on Japanese dams (described in §3) confirmed that such methods strongly overestimated the dam's response. Consequently, a method similar to the direct finite-element method was implemented in Code_Aster, using viscous spring boundaries, plane waves for seismic input (compression and shear waves), and fluid elements. Several benchmarks were addressed using Code_Aster [22][26][29][32], gradually improving and correcting the methods, allowing regular use for industrial applications, particularly for arch dam analyses in France (detailed in §7.2).

For engineering use, a balance should always be maintained between the complexity of a new method (such as the direct finite-element method here) and the risk of misuse by engineers if the level of complexity is too high. In this spirit, the following simplifications of the method are generally considered:

- When possible, homogeneous material without damping is considered for the foundation. In this special case, a vertically propagating plane wave does not attenuate, implying that the incident earthquake motion at the bottom boundary is equal to one-half the surface control motion, except for a time shift. This simplification avoids the deconvolution of the surface motion. Considering most of the damping in the foundation comes from absorbing boundaries, the material damping of the rock remains marginal.
- Rigorously, the effective earthquake forces should be computed at each boundary of the foundation (Figure 2) using 1D columns and then 2D faces to correctly represent the canyon's effect. Nevertheless, comparative analyses show that ignoring the canyon's effect is acceptable [5]. Combined with the previous simplification, this allows for a straightforward simulation of the seismic input in the 3D model.

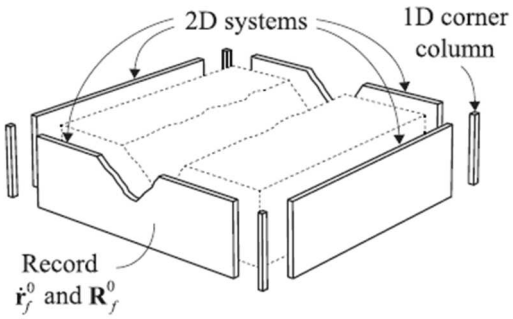

Figure 2 Procedure for computing effective earthquake forces (from Løkke & Chopra [5])

3. RECORDS ON DAMS AND BACK ANALYSES

From 2013 to 2014, the French and Japanese committees on large dams collaborated on the topic of assessing dams under earthquake conditions. JCOLD provided a significant set of earthquake records on dams and foundations [9], which were used in two types of analyses regarding concrete dams:

- Analyses of earthquake records on dams: This involves evaluating the dam's response using transfer functions between records at the crest and at the foundation.
- Back analyses of dams: Using finite-element analyses as previously described (§2) and records in the foundation as earthquake input, with the goal of achieving a good match between recorded and computed accelerations at the crest of the dam.

In Japan, and generally when earthquake sensors are installed on dams, accelerations are recorded at the crest and near the foundation. Several methods of analysis were tested on Tagokura gravity dam and Kurobe arch dam (Figure 3) in [27], concluding that the transfer function is the best way to identify the natural frequencies of the dam from such earthquake records. The transfer function is the ratio of the response at the crest of the dam divided by the input in the frequency domain (conversion from temporal to frequency is done with Discrete Fourier Transformation). The difficulty is that earthquake records are generally short (a few seconds), leading to imprecise transfer functions. While this is generally sufficient for natural frequency evaluation, damping evaluation can be very imprecise.

Since then, it should be highlighted that a more advanced method was proposed [10] using a Transfer Function Matrix, which requires several records in three directions but allows a much more precise evaluation of damping. This will be discussed in §5.

In addition to these analyses, and in a very simplified way, analyses of accelerations records on gravity dams in Japan [31] (Figure 4) allows the author to propose a very simple formula to roughly estimate the maximum crest acceleration (Pca) expected for a conventional gravity

dam (height H) with a known pic ground acceleration (Pga) : $Pca = Pga \times 0{,}07 \times H$. This is a useful tool to get some order of magnitude of the crest accelerations expected.

Figure 3 Kurobe arch dam (left) and Tagokura gravity dam (right) sensor's location

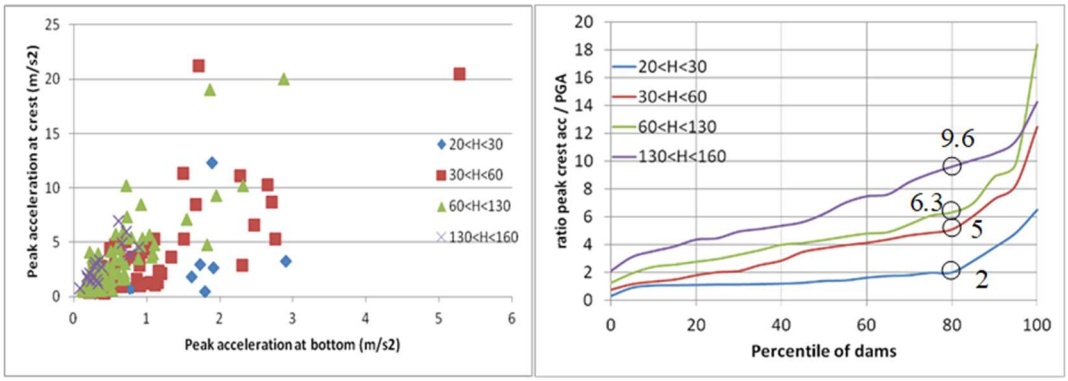

Figure 4 Evolution of the ratio between crest and bottom peak accelerations for Japanese records on concrete gravity dams

Based on Japanese earthquake records, back analyses of Kurobe and Tagokura concrete dams were also performed [28]. Considering the absence of non-linear behavior observed on the dams during the relatively moderate earthquakes recorded, linear elastic analyses are considered sufficient. Using previously described transfer functions, the first frequency of the dam is evaluated, and the Young's modulus of the rock and foundation is adjusted to fit the computed natural frequency.

Analyses confirmed that conventional engineering practices using simplified massless foundations, Westergaard added masses, and 5% modal damping greatly overestimate the dam's response compared to records. In comparison, analyses performed with the compressibility of the water, foundation models with mass, stiffness, certain size, and radiative boundary conditions can better represent the behavior of the dams under earthquake conditions. For the low-intensity earthquakes studied, low concrete damping (1% with Rayleigh damping) was chosen to fit the records, but the overall damping of the model (mainly due to the radiative boundary introduced) is between 10 and 20% depending on the frequency for a

gravity dam, but much lower for the arch dam: around 3%. Figure 5 shows a rather good agreement in the frequency domain between the model and the earthquake records for Kurobe arch dam on March 25, 2007.

Additional earthquakes (5 for Tagokura and 3 for Kurobe) were computed with comparisons of several parameters linked to the dynamic behavior of the dam at the accelerometer locations:

- peak acceleration (PGA),
- peak displacement (PGD),
- acceleration spectrum in three frequency domains: 1-5 Hz, 5-10 Hz and 10-15 Hz
- energy.

For each characteristic, a ratio between the computed and recorded values is evaluated. The ratios, computed for each direction, are then displayed in a circular chart (Figure 6 for Tagokura and Figure 7 for Kurobe). Where the finite element results match the records perfectly, a regular circle should appear.

While the analyses were able to correctly reproduce the dynamic behavior of Tagokura dam under several earthquakes, Kurobe analyses for the arch dam clearly show some differences between finite-element analyses and records depending on the earthquake considered.

Seismic back analyses on Monticello arch dam (organized by United Society of Dams – USSD) in 2016 [19] and on Cabril arch dam [34] also demonstrate that even with up-to-date models (such as described in §2), numerical analyses can sometimes overestimate the response of a dam, requiring an increase in concrete damping beyond realistic values (higher than 10% for Cabril dam for a very distant earthquake (0.002 g)). A possible reason for these results might be that the chosen input, generally recorded in the vicinity of the dam, might contain some frequency content of the dam, which gets even more amplified.

Finally, considering concrete dams are generally built on sound rock, earthquake records in the nearby foundation will provide quality data to improve propagation laws from the fault to the dam site used in seismic hazard assessments. Such laws are generally based on devices not located on sound ground.

Obviously, back analyses of dams remain an excellent way to better understand the behavior of dams under seismic loads. As presented here, there is a lot of room for improvement, even when sticking to elastic analyses for low to moderate earthquakes that did not trigger any non-linearity. Such analyses also require a good knowledge of the static behavior of the dam to be pertinent for dynamic loads. In the meantime, technological improvements in recording devices make it more affordable to install an earthquake recording system on-site, even if continuous monitoring remains challenging in the long term (more than 10 years). In that spirit, the author

proposed to create a database (DamQuake [33]) to gather worldwide records on dams based on the following considerations:

- Seismic behavior can be significantly different depending on dams, foundations, and even earthquake events for the same dam. To be useful and analyzed, a high number of records is required.
- Except in countries with high seismic hazard (such as Japan), significant earthquakes occurring on dams remain a very rare event. A dam owner with few instrumented dams would only have a few records available after several years.
- Analyses of earthquake records involving time-history series require specific knowledge and tools, rarely mastered by dam engineers, even more so in the long term.

Regarding these considerations, it would be useful to gather and share earthquake data to provide a sufficient amount of data to be analyzed, improving knowledge related to the dynamic behavior of dams under earthquakes. At the time of this proposal, the authors did not manage to convince any dam owner to share their records. It should be noted that Japan regularly updates their database on records of dams and foundations [9]; the last update provided 5649 accelerograms recorded on 257 dams. Such practices should be encouraged.

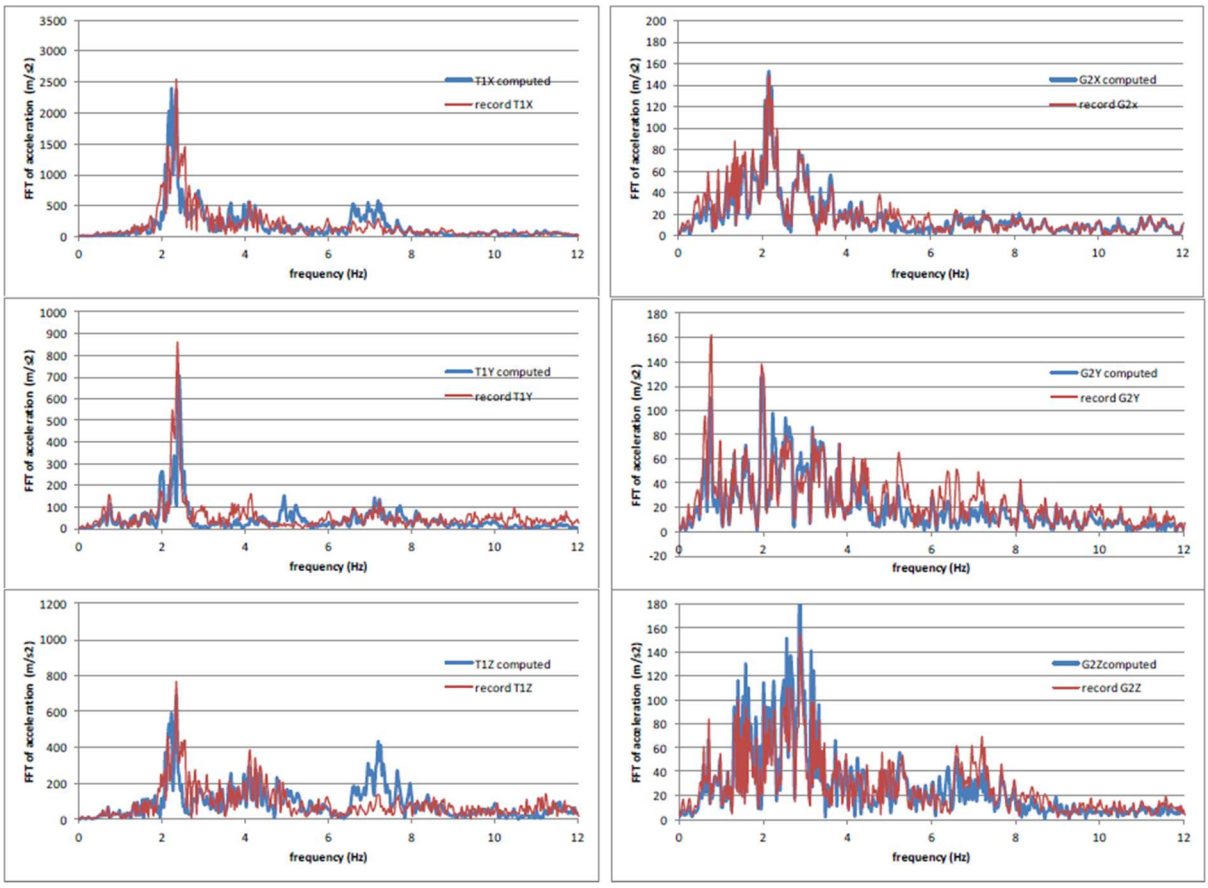

Figure 5 back analyses of Kurobe dam : comparison of the FFT of the horizontal acceleration,

T1 crest sensor (left) and G2 abutment sensor (right), 3 directions u/s (top), dam axis (middle), vertical (bottom)

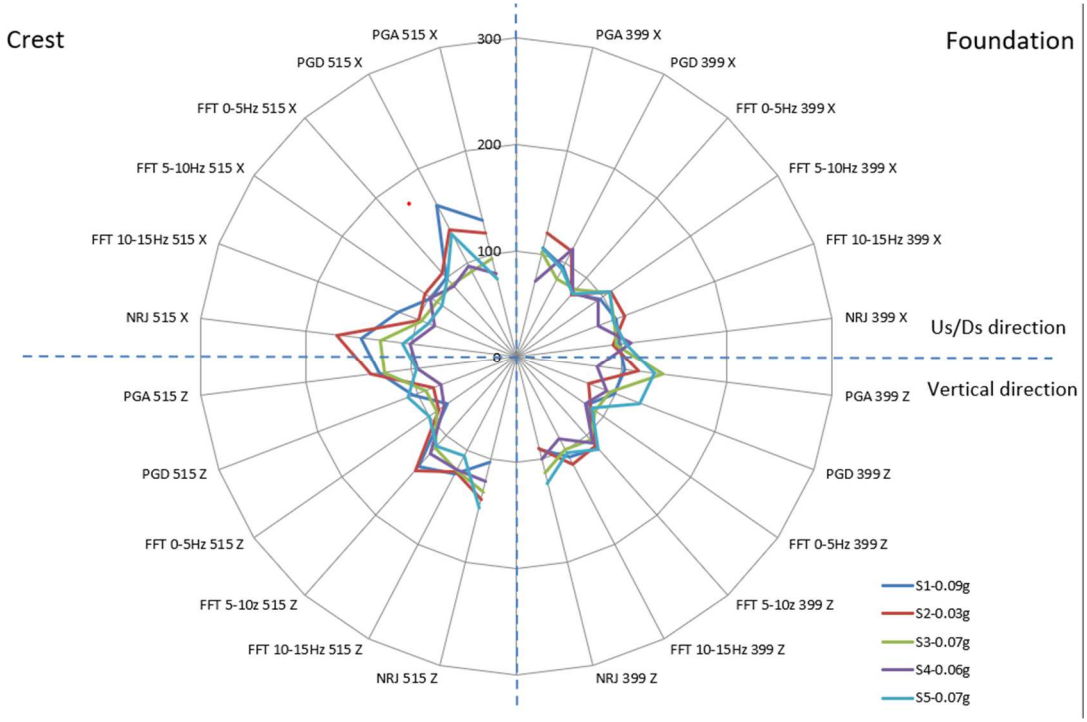

Figure 6 Ratio (%) between computed and recorded response for Tagokura dam for 5 earthquakes (pga 0.03 to 0.09g)

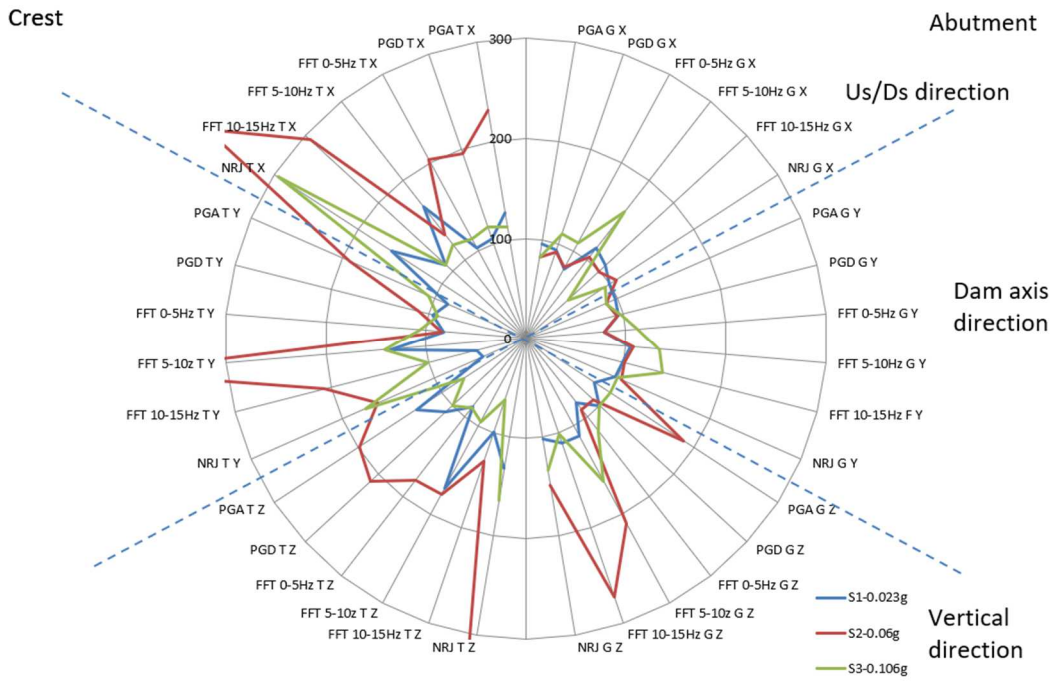

Figure 7 Ratio (%) between computed and recorded response for Kurobe dam for 3 earthquakes (pga 0.02 to 0.1g)

4. CALIBRATION OF NUMERICAL ANALYSES USING AMBIENT VIBRATION MEASURMENT

For the static assessment of existing concrete dams using finite-element analyses, the physical properties of the numerical model are usually adjusted to reproduce the monitored behavior of the dam. This is generally done by adjusting the Young's modulus of concrete and rock to match the monitored displacement of the dam under hydrostatic load (usually obtained through statistical analyses of the monitored displacements). This approach ensures that the numerical model accurately represents the dam's static behavior.

For seismic analyses, until recently, analyses were rarely calibrated against any measurements. An increase in material stiffness was generally assumed, with the dynamic deformation modulus considered to be 1.25 times the static value (this ratio comes from core sample tests [13]). To address this gap, measurements and computations of the first frequencies of the structure provide an interesting way to perform such calibration. As with static analyses, comparisons with measurements at the scale of the whole structure are more relevant than measurements of the dynamic properties of concrete on core samples, due to size effects and the behavior of vertical joints, for instance. Gravity and arch dams are relatively simple structures with relatively simple modal shapes for the first modes, with the highest displacement located at the crest of the dam. This is why ambient vibration measurements at the crest of the dam (usually easily accessible) are a very convenient way to evaluate the first natural frequencies. On the other hand, numerical modal analyses are also easy to perform with any finite-element analysis software, allowing multiple analyses to evaluate the best set of parameters to fit the first frequencies.

Often, people argue that frequencies evaluated from ambient vibration measurements cannot be used for earthquake analyses due to the differences in motion (small motions for ambient vibration, much higher for earthquakes). However, evaluation of the first frequency of a gravity dam in Japan [12] (Figure 8) showed no clear difference between the first-order natural frequencies estimated based on seismic motion records and those based on ambient vibration measurement records. It should be noted that water level and temperature conditions can cause variations in the natural frequency.

Regarding EDF's practice on ambient vibration measurements, feedback from measurements on 20 concrete dams is summarized in [36]. EDF chose to purchase several recording devices so that engineers can directly perform measurements while visiting dams subjected to seismic analyses. Often, records from the crest are sufficient to capture the first frequencies of the structure. Analyses of ambient vibration records require some processing (described in [36]), involving filtering, sampling, windowing, computing Power Spectral Density, and finally peak

picking for modal identification to determine frequency and damping. EDF developed its own in-house software for this purpose.

For arch dams, the first two frequencies are generally very close: symmetrical and anti-symmetrical modes are described in Figure 9 for Vouglans arch dam. Records at the center of the dam only show the symmetrical 2nd mode at 2.8 Hz, while records near the abutment only show the first anti-symmetrical mode at 2.7 Hz. In between, records show both peaks simultaneously.

For six arch dams with heights ranging from 45 to 150 meters, first frequencies range from 2.7 to 4.5 Hz, depending on the height, the shape of the valley, and the fineness of the arch. Water level and thermal conditions also cause variations in the frequencies. When comparing static modulus calibrated on static displacement and dynamic modulus calibrated on measured first frequency of arch dams (Figure 9), the ratio ranges from 1 to 1.8. This is a significant change compared to the previously mentioned misguided 1.25 ratio.

For four gravity dams (50 to 72 meters high), values range from 5.4 to 8.6 Hz. Comparison with simplified formulas (Figure 11) highlights that with uncertainty in the stiffness of the materials, the gap between measured and computed frequencies can be quite significant, between 1 and 2 Hz, and even higher for gravity dams in narrow valleys.

To summarize, from the author's point of view, calibration of dynamic finite-element analyses using ambient vibration measurements is highly recommended for seismic assessment. This approach not only ensures the numerical model is reliable but also that it accurately represents the real structure's behavior.

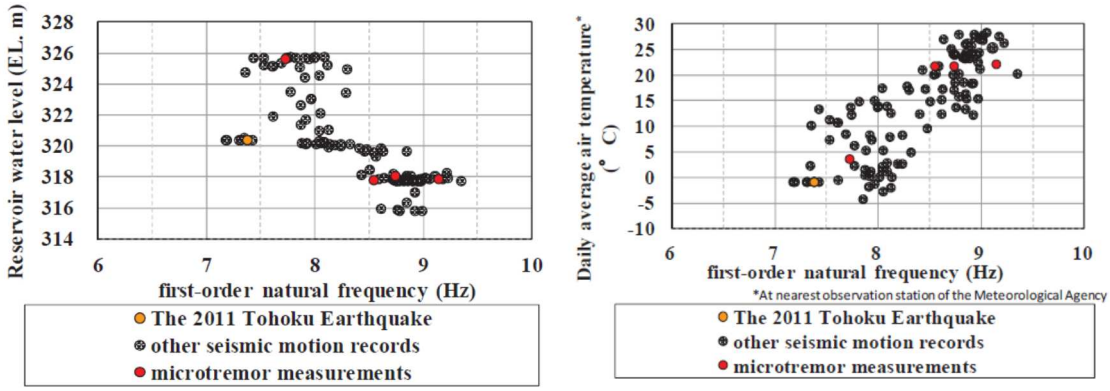

Figure 8 comparison of the natural frequency estimated from seismic event or ambient vibration measurements (depending on the effect of the reservoir water level and the temperature). From [12]

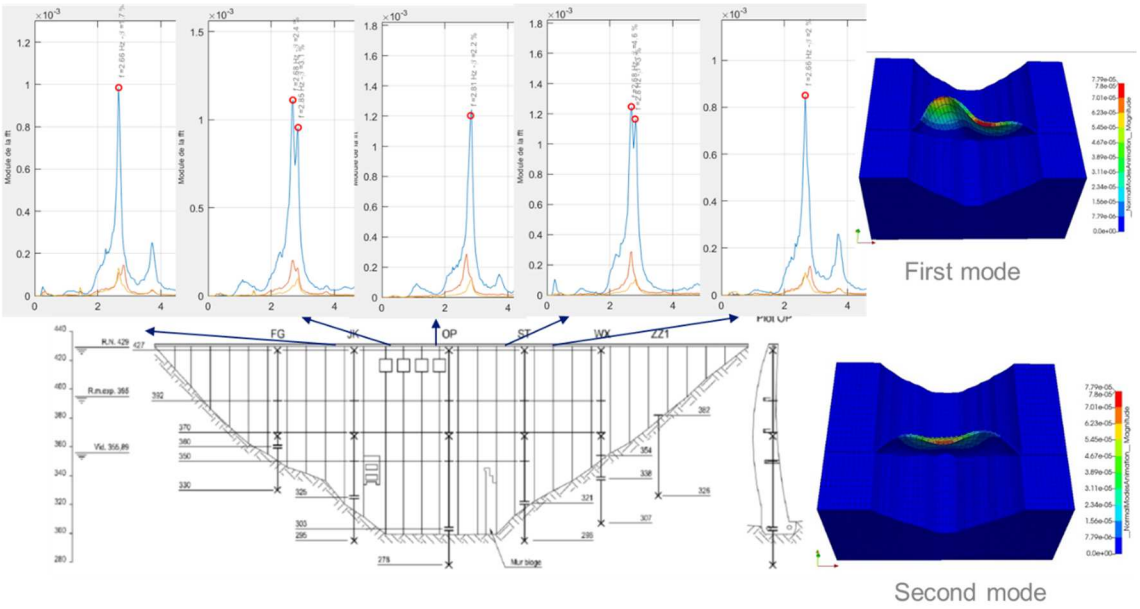

Figure 9 Vouglans frequency content: 2 first modes very close (2.7 & 2.8 Hz) [36]

Dam	first mode frequency (Hz)	modulus from static calibration(GPa)		Dynamic / static ratio from frequency calibration
		concrete	foundation	
Lanoux	4.5 & 4.8	20	(*)	1.75
Roselend	3.0 & 3.5	35	25, 12 & 8	1.8(**)
Saint Guerin	3.8 & 3.9	32.5	15	1
Vouglans	2.7 & 2.8	38.5	32.5	1.5

(*) specific assumptions are considered due to the orthotropy of the foundation
(**) value with Westergaard added masses

Figure 10 dynamic/static ratio from calibration

Dam	Height(m)	Frequency measured (hz)	Density (kg/m3)	Frequency computed from Chopra (Hz)			Frequency computed from Tardieu (Hz)		
				Ec20/Ef15	Ec30/Ef25	Ec35/Ef35	Ec20	Ec30	Ec40
Guerledan	46.8	6.5	2200	4.9	5.8	6.1	7.1	8.7	10.0
Eguzon	62.1	6.8	2300	3.8	4.5	4.8	5.2	6.4	7.4
Gittaz	66	8.6	2400	3.6	4.2	4.5	4.8	5.9	6.8
Gnioure	72	5.4	2400	3.2	3.7	4.0	4.4	5.4	6.2

Figure 11 Comparison between frequencies measured and computed from Chopra and Tardieu formulas with sev-eral assumptions (Ec=concrete modulus, Ef=foundation modulus)

5. DAMPING

Damping is probably the parameter that has the greatest influence on the results of seismic analyses. However, it is also the parameter with the least general agreement among engineers. During the era of massless foundation and Westergaard methods, 5% modal damping was commonly used. However, more advanced types of analyses, such as those described in §2, which introduce radiation damping, require reconsideration of such practices.

Løkke and Chopra [5] discuss this matter, explaining that damping in the numerical model for the dam-water-foundation system should be consistent with measured values at the dam determined from low-amplitude motions—within the linear range of response—recorded during forced vibration tests, ambient vibrations, or small earthquakes. These measured values represent the overall damping in the system, including material damping, radiation damping, and energy loss at the reservoir boundaries, considering experimental data on the contributions of individual sources are generally not available. They compiled damping measurements at 32 concrete dams, reproduced in Figure 12: the range for each dam shows the minimum and maximum damping values measured in the first few (1 to 5) resonant frequencies. This clearly highlights that measured damping is between 1 to 5%, with an average around 3%. For Løkke, this value is representative of the overall damping (material + radiation damping), but this remains (from the author's point of view) a matter of discussion, considering low-amplitude motions from vibration tests or ambient vibration are not likely to mobilize material far away from the dam.

With this in mind, and for the analyses of dams in France with moderate seismic hazard, a value of 3% for concrete damping is considered at EDF. This value appears to be a good compromise given our still limited understanding of damping at present.

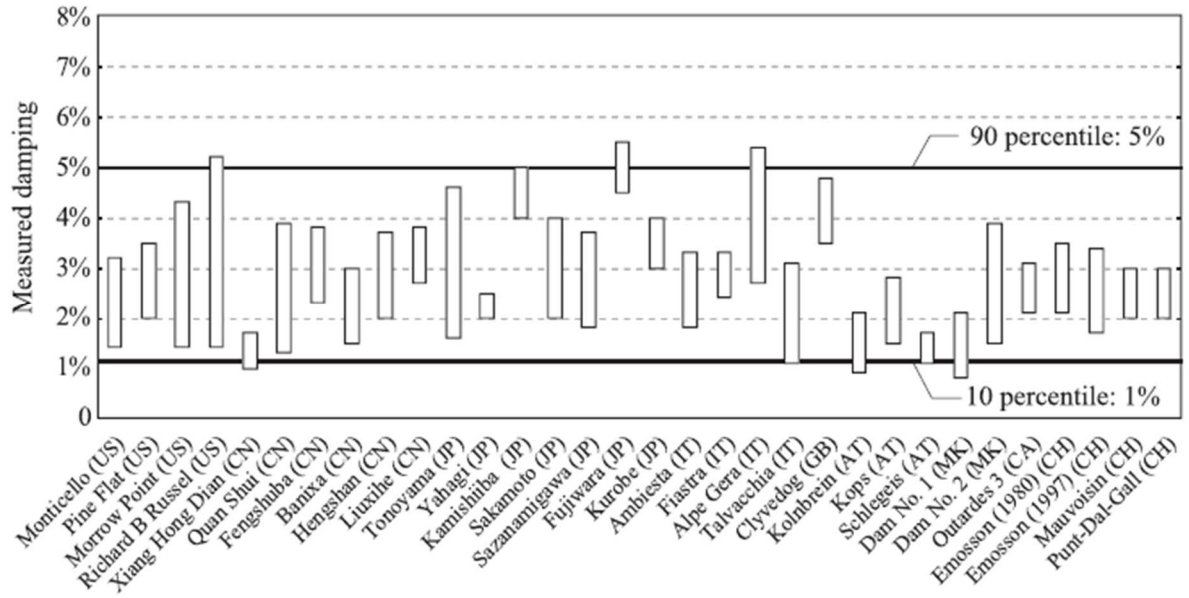

Figure 12 Damping at 32 concrete dams measured during forced vibration field tests and estimated from ambient vibration measurements, compiled by Løkke [5]

Nevertheless, back analyses of dams (§3) highlight that damping values can vary significantly from one dam to another, and even for the same dam under different earthquakes. To progress in this field, analyses of dam records appear promising and, as mentioned before, would be useful for evaluating damping across many dams and seismic events. Evaluating damping

from earthquake records remains a challenging task due to the short duration of such events, requiring the development of different methods than those generally used for ambient vibration measurements. Unfortunately, few authors are working on this challenge. From the author's point of view, promising work has been proposed by Japanese authors [10][11], developing a method called the Transfer Function Matrix (Figure 13), which allows a much more reliable evaluation of damping compared to the half-bandwidth method. This method, which requires at least three sets of records for calibration, is particularly suitable for Japanese dams with a high number of recorded earthquakes. The results look promising, and rigorous analyses of damping compared to acceleration should finally be able to answer the most important question about damping: is there a proven direct correlation between damping and acceleration/earthquake loads, justifying the gradual increase in damping when considering strong earthquake loads?

Figure 14 shows the evaluation of damping values for Kazeya gravity dam and Sakamoto arch dam for several earthquakes, as a function of the maximum peak acceleration. The lack of records at significant accelerations makes it difficult to reach any solid conclusions. For small earthquakes, a high variability in the computed damping is remarkable, potentially explaining the difficulty in matching numerical analyses and records as described in §3, and strongly reminding us that we are still far from understanding the mechanisms behind the concrete dam’s response under seismic load.

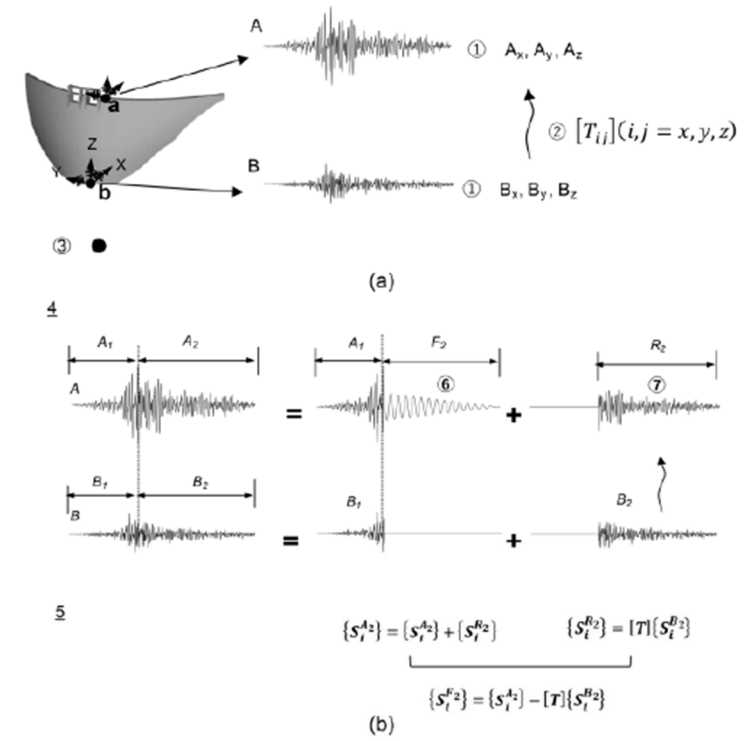

Fig. 1
Schematic view of dam response due to earthquakes.
Vue schématique de la réaction du barrage aux séismes.

1 Monitored behavior during earthquakes, 3-directional components
2 Transfer function matrix
3 Seismograph
4 Time domains
5 Frequency domains, $\{S_i^{A_2}\}$ denotes a spectrum of $A_2(i=X,Y,Z)$ etc.
6 Free vibration
7 Forced vibration

1 Comportement observé durant les séismes, éléments à 3 directions
2 Matrice de la fonction de transfert
3 Séismographe
4 Domaines temps
5 Domaines fréquence, $\{S_i^{A_2}\}$ dénote un spectre de $A2(i=X,Y,Z)$ etc.
6 Vibration libre
7 Vibration forcée

Figure 13 Transfer Function Matric from [10]

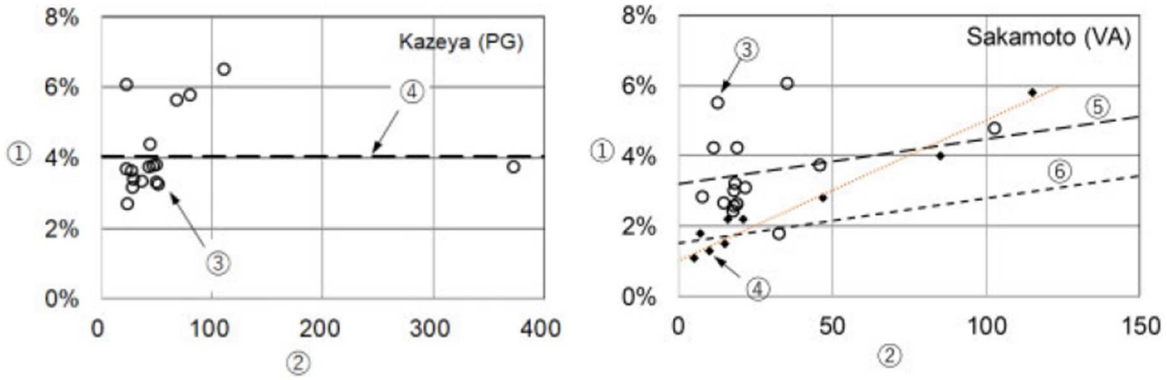

Figure 14 damping function of max acceleration (in cm/s^2) for Kazeya gravity dam and Sakamoto arch dam from[10]

6. NON-LINEAR ANALYSES

While concrete dams have rarely exhibited non-linear behavior under earthquakes in the past (discussed in §8), seismic assessment of dams under strong earthquakes might lead engineers to use non-linear analyses. The aim of this chapter is not to discuss or recommend the most up-to-date methods but to remind that such analyses should be used with caution and to propose some steps to follow.

Based on the experience of several ICOLD benchmark workshops, every theme involving non-linear analyses of concrete dams (static or dynamic) highlights the scatter of the results proposed by the participants. For example, non-linear seismic analyses of Pine Flat dam in 2019 [7] showed significant differences in damage maps (Figure 15), not to mention that some participants did not manage to reach convergence for the entire earthquake. This is because results are strongly dependent on the chosen non-linear behavior, their parameters (including fracture energy), and the mesh of the model. This means that engineers should be very cautious when using non-linear analyses and progress step by step to ensure the model responds as expected, with reference to linear analyses first. In that spirit, linear analyses should always be performed first, and comparisons of time-history key results (such as crest displacements in Figure 16) should be carried out to ensure results are similar during the initial low-intensity phase of the earthquake.

For non-linear analyses of concrete dams, two types of models are generally used:

- Joint elements or contact: These represent the non-linearity at the dam-foundation interface, vertical joints, and possibly some horizontal lift joints. The non-linearity is only located at selected interfaces while the rest of the materials remain elastic. Mohr-Coulomb behavior is generally considered. These are the most reliable kinds of analyses.
- Damage model for concrete material: If previous linear analyses show high tensile stresses outside the previous interface, a damage model can be used for concrete material. For concrete dams, and particularly arch dams, the model should have at least the following characteristics:
    - The damage should not be isotropic to allow the opening of cracks in the direction of principal stresses while the behavior remains more or less elastic in other directions.
    - The model should handle the closure of cracks considering the expected cyclic behavior under earthquakes.

The combination of non-linear models and soil-fluid-structure requirements described in §2 remains a challenging task and requires substantial computational capabilities.

The combination of non-linear models and soil-fluid-structure requirements described in §2 remains a challenging task and requires substantial computational capabilities.

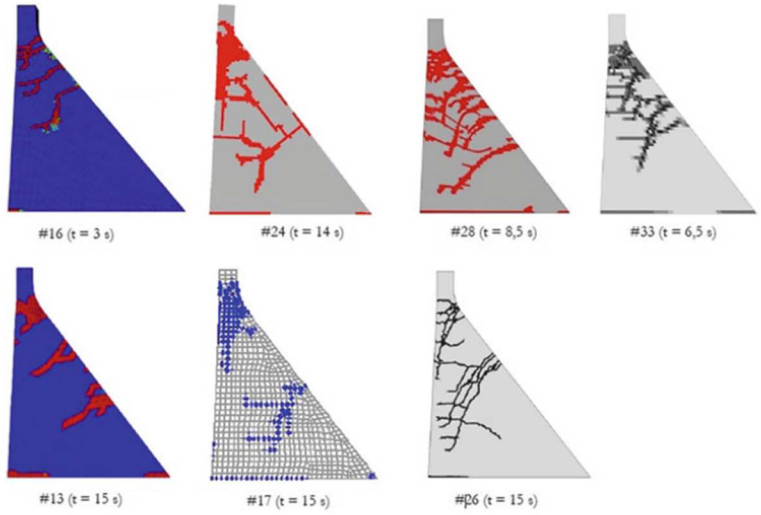

Figure 15 non-linear results of several participants (EDF is #13) on Pineflat dam at the ICOLD benchmark workshop in Milan 2019 [7]

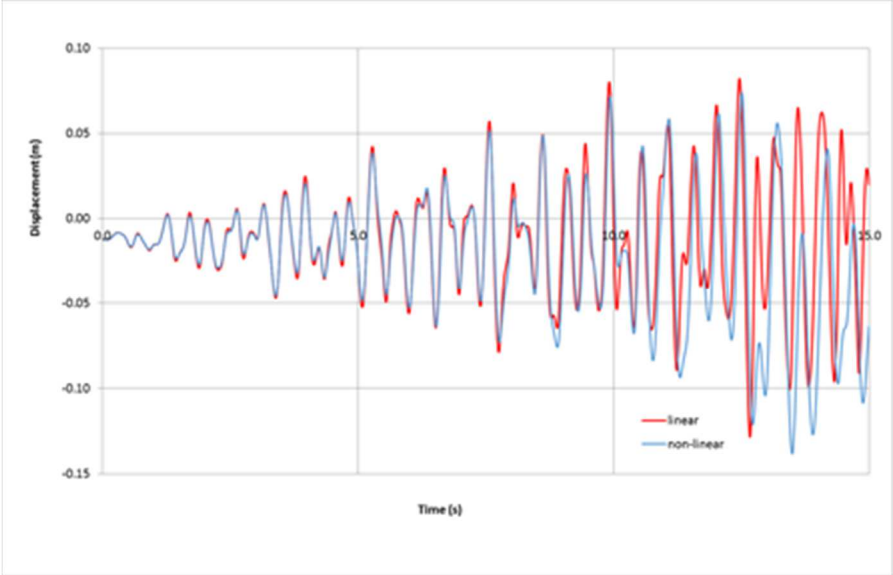

Figure 16 comparison between linear and non-linear analyses for the crest displacement of Pineflat with ETAF load [32]

7. SEISMIC ASSESSMENT OF CONCRETE DAMS

7.1. Gravity dam

For the static assessment of gravity dams, stability assessments are conducted using simple and practical methods considering 2D rigid profiles. Forces are computed on several sections, generally at the dam-foundation interface and lift joints, including uplift. Linearized stresses are then computed using beam theory, and sliding stability is evaluated with the ratio of stabilizing

forces to destabilizing forces. For seismic assessment, extensions of this method have been developed, introducing:

- Pseudo-static analyses: Dynamic loading is represented by the application of static forces considered equivalent to the maximum dynamic forces supported by the structure. Inertial forces are those of a rigid solid subjected to constant acceleration. Fluid-structure forces are computed using Westergaard added masses with the assumption of a rigid body and non-compressible water.
- Pseudo-dynamic analyses (or Response spectrum analyses): Developed by Chopra in 1986 and updated in [14] by Løkke with additional comparisons with finite-element analyses and new sets of parameters. Without going into detail, the aim of the method is to compute maximum and minimum earthquake-induced stresses along the downstream and upstream faces with a correct representation of soil-fluid-structure interaction and the flexibility of the dam in a simplified way using precomputed parameters.

Regarding the pseudo-static method, it is important to remind the origin of an important assumption: the value of the seismic coefficient (α = 2/3) that multiplies the peak ground acceleration for the evaluation of inertial forces in the equation $F = \alpha.PGa.V.\rho$. (with PGa the peak ground acceleration in m/s^2, V the volume of the structure and ρ the density of the concrete). The 2/3 value comes from the work of Tinawi, Léger & Leclerc [15] involving experimentation on concrete specimens with cold lift joints on a shaking table to study the sliding behavior under quasi-static and dynamic loads. Several tests were conducted using North American eastern (high frequency) and western (low frequency) acceleration records, respectively Saguenay and El Centro records. Based on these tests, they introduced the concept of effective or sustained accelerations ($\alpha.PGa$) aiming to define the α value that multiplies the PGA of the seismic record to verify if significant sliding displacements (greater than 1 mm) are expected. Their studies demonstrated that coefficients $\alpha = 0.67$ or $\alpha = 0.5$, for low and high frequency records respectively, should be use. The 0.67 value was then introduced in the Canadian safety guidelines and later in other countries' guidelines (including French guidelines for safety assessment of gravity dams). However, while this method (and the chosen coefficient) was designed for sliding evaluation (with many assumptions and simplifications), engineers started using it to compute stresses on the upstream and downstream faces of dams, which is beyond the scope of this method.

To summarize, from the author's point of view, the following steps should be followed for the seismic assessment of gravity dams when using simplified methods:

- Pseudo-static analyses: For sliding evaluation only, in the vicinity of the dam-foundation interface, considering the rigid body assumption is not valid near the crest of the dam.
- Irreversible displacement evaluation: If the sliding safety factor from the pseudo-static evaluation reaches 1.0, additional analyses should be carried out to evaluate irreversible displacement. A simplified method was proposed by Mevel and compared with finite-element analyses results with Code_Aster [30] (Figure 18).
- Response spectrum analyses (RSA): Should be carried out for the evaluation of maximum stresses at the upstream and downstream faces of the dam.
- Finite-element analyses: If RSA highlights higher than acceptable stresses, then finite-element analyses should be carried out: first with elastic behavior, then with non-linear behavior if stresses remain too high.

When assessing the seismic safety of a gravity dam using finite-element analyses, stress analyses are always challenging because they are strongly dependent on the mesh size, and values are generally not comparable with those computed from simplified static analyses. To solve this problem, it is possible to extract forces from the time-history finite-element analysis, which can be used in the simplified approach to compute linearized upstream and downstream stresses and the sliding safety factor at each time-step (without any coefficient).

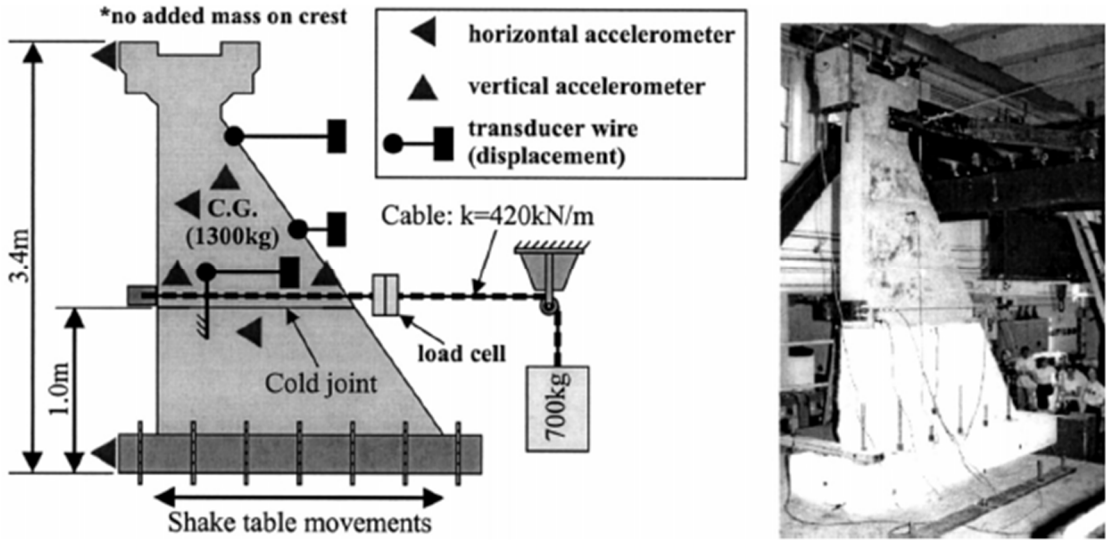

Figure 17 experimental setup for shaking table test from [15]

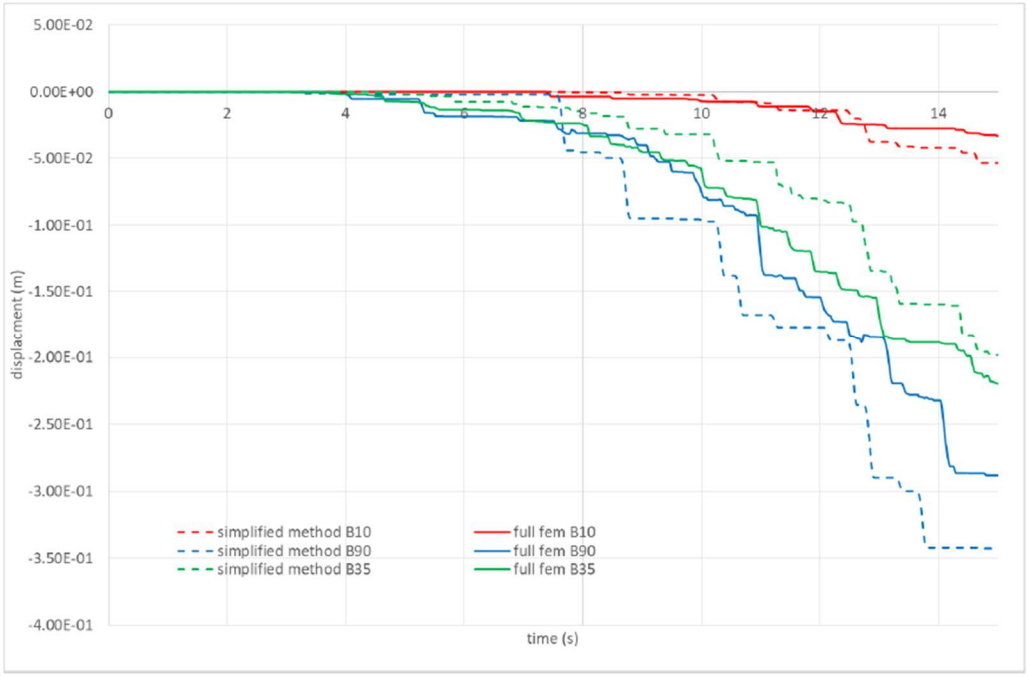

Figure 18 Comparison of the irreversible displacement computed by simplified method and FE analyses for the 3 case-study dams

7.2. Arch dam

The aim of this chapter is to present the main findings regarding the seismic assessment of arch dams in France with a moderate seismic hazard. The focus is on numerical analyses involving finite-element analyses with a time-history approach as described in §2. Results from the seismic analyses on six arch dams with PGA ranging from 0.15 to 0.34g are presented.

For several studies summarized here, the combination of advanced soil-fluid-structure interaction and non-linearities led to unacceptable computing times and required simplification of the problem. Therefore, a few analyses were performed using simplified methods such as Westergaard added masses and/or massless foundation, despite the recommended methodology detailed in §2. The following assumptions were considered:

- For the evaluation of the static behavior of the dam, static modulus are calibrated based on monitored static displacement.
- Regarding the dynamic properties of the concrete and the foundation, if ambient vibration measurements were available, dynamic moduli are adjusted by fitting the computed and measured frequencies. Without any measurements, dynamic moduli are deduced from the static moduli using the equation: Ed=1.25*Es.
- For low to moderate earthquakes, 3% damping of the concrete is considered when radiative damping is taken into account. For simplified approaches such as massless foundation, 5% damping is considered.

- Regarding seismic hazard evaluation, EDF uses a deterministic approach based on historical earthquakes. From the target spectrum, synthetic accelerograms are generated based on the methodology used for the nuclear industry. For linear behavior, analyses are performed using three sets of accelerograms; five sets are required for non-linear behavior.

Table 1 summarizes the arch dams subject to seismic analyses involving time-history analyses with the finite-element software Code_Aster. Figure 19 provides a quick overview of the different meshes of the analyzed arch dams.

Table 1 Summary of arch dams studied

Dam	Height (m)	Pga (g)	Concrete dampin g	Soil-structure interaction	Fluid-structure interaction	Behavior
R	150	0.18	3%	Absorbing boundaries	Added masses	Non-linear at the dam-foundation
L	45	0.23	5%	Massless foundation	Added masses	Non-linear at vertical joints
S	70	0.15	5%	Massless foundation	Added masses	linear
C	101	0.34	3%	Absorbing boundaries	Fluid elements	linear
V	130	0.22	3%	Absorbing boundaries	Fluid elements	Non-linear at the dam-foundation
M	153	0.26	3%	Absorbing boundaries	Fluid elements	linear

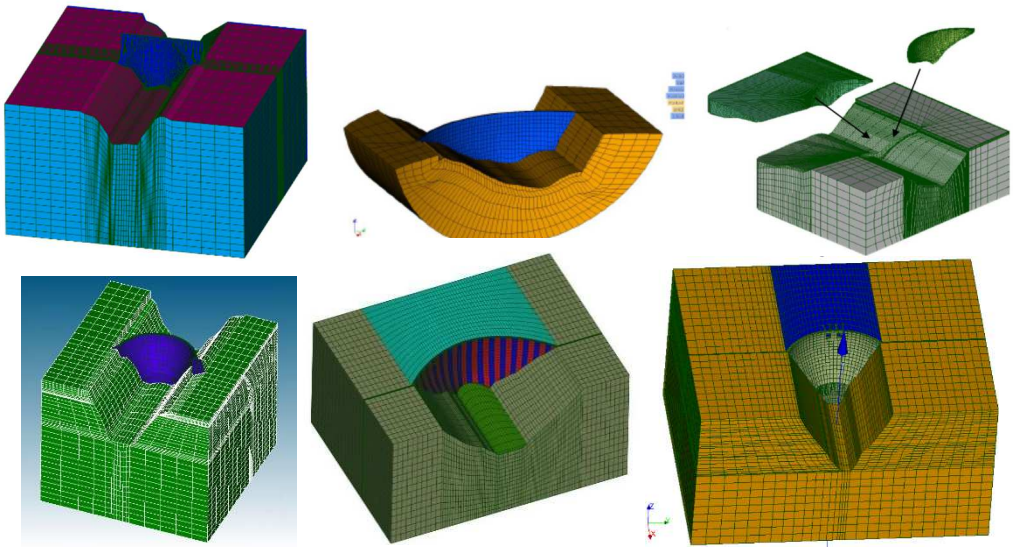

Figure 19 view of the meshes

Table 2 summarizes the main results from the seismic analyses, providing a good overview of values that can be expected regarding the seismic behavior of arch dams under moderate seismic hazard. Peak accelerations at the crest are 6 to 12 times the peak ground accelerations. This leads, even for moderate seismic hazard, to quite high accelerations at the crest of the dam, ranging from 1.5g to almost 3g. Crest displacements toward the downstream under seismic load are generally lower than under hydrostatic load. Nevertheless, two dams (M dam and C dam) out of six show higher crest displacement under earthquakes for the following reasons:

- M dam: This is a thick arch dam involving small displacement of the crest under static load, while crest displacements under earthquake are driven by the second mode, mainly involving the top part of the dam.
- C dam: Maximum displacements are not computed at the crest, while the visualization of the first two modes highlights that maximum displacement under earthquake will occur at the crest.
- Other dams: These are quite slender dams with the first symmetric mode shape similar to the deformed shape of the dam under static load. In such cases, considering that the earthquake load remains generally lower than the hydrostatic load for moderate seismic hazard (Figure 20), displacements under earthquake are lower than under hydrostatic load.

The increase in maximum compression stresses due to earthquake load is moderate, ranging from 1.5 MPa to 5 MPa. Regarding these results, two configurations appear:

- Near the abutments: Maximum compression stresses under earthquake are located near the abutments where maximum values under static load were already identified, as shown

in Figure 21 on the downstream face for V dam. Stresses increase from 9.5 MPa to 13.5 MPa with the addition of earthquake load.

- Upper part of the dam: Maximum compression stresses under earthquake are located at the upper part of the dam, influenced by the deformed shape of higher modes, as shown in Figure 21 on the upstream face of V dam. Under static loads only, maximum compression stresses were around 5.5 MPa at the middle elevation of the central cantilevers. With earthquake loads, compression rises up to 10 MPa near the crest of the central cantilever.

Table 2 Main results on arch dams

Dam	1st frequency (Hz)	Peak acceleration (g)		Max crest displacment toward downstream (mm)		Max compression stress (MPa)	
		Ground	Crest	Hydrostatic load	Seismic load	Hydrostatic load	Static +Seismic load
R	2.4(*)	0.18	1.5 (x8)	55	40	11	16.1
L	3.3(*)	0.23	2.8(x12)	59	34	5.6	10.2
S	3.8 (*)	0.15	1.8(x12)	19	6	8.6	10
C	4.4	0.34	2.0(x6)	7.1	15	4.6	8.6
V	2.3 (*)	0.22	2 (x10)	73.6	29.4	9.4	13.6
M	2.9	0.26	2 (x7.6)	17.9	30.1	7.5	10.6

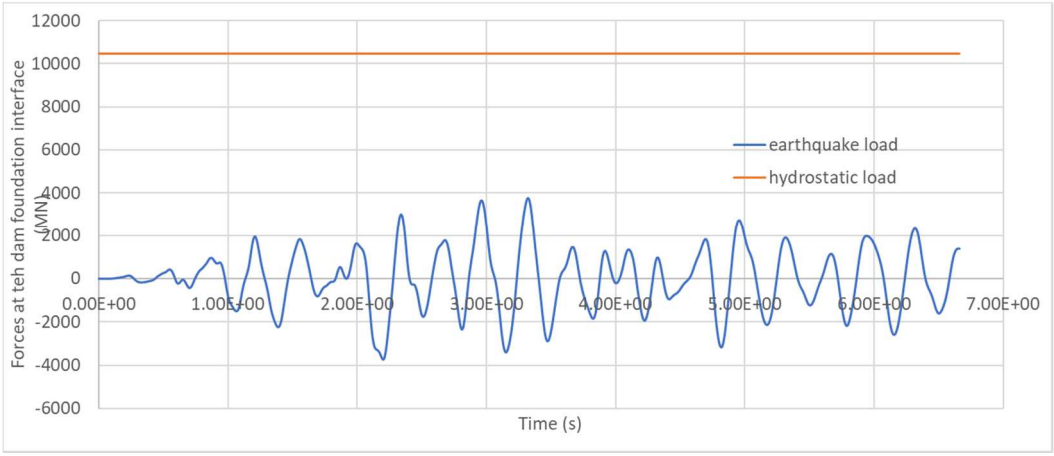

Figure 20 comparison between earthquake load and hydrostatic load for M dam

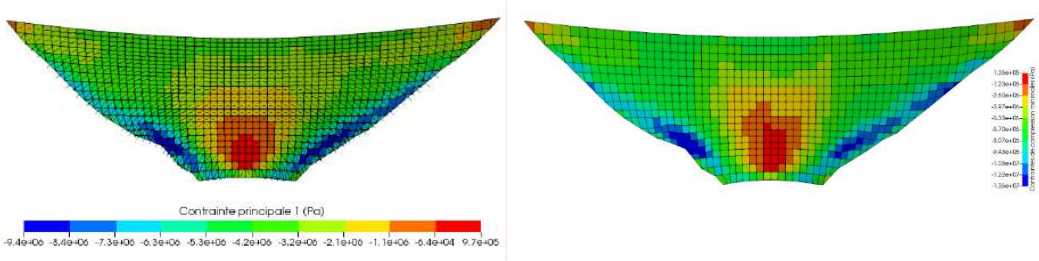

Figure 21 maximum principal compression stresses under static (left) and under static + EQ. loads (right) on the downstream face of V dam

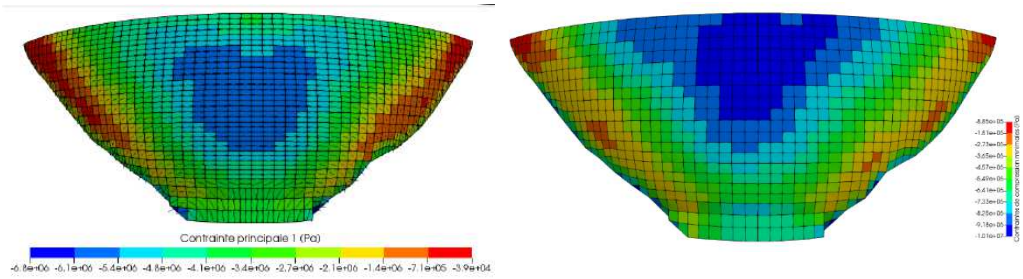

Figure 22 maximum principal compression stresses under static (left) and under static + eq. loads (right) on the upstream face of V dam

Even for moderate earthquake loads, linear analyses compute tensile stresses near the tensile strength of concrete, raising the question of whether such values are acceptable: will they lead to superficial cracks that are acceptable for such events, or to significant damage that could trigger a failure mechanism?

The demand capacity ratio tool provides an interesting way to answer this question. Figure 23 shows an example of demand capacity ratio evaluation for the tensile stress at the middle of the central cantilever, on the downstream face. Considering the exceedance of the criteria and that it was mainly vertical tensile stresses leading to horizontal cracks, kinetic block analyses were performed to evaluate the risk of failure triggered by such cracks. Similar analyses were performed for two of the analyzed dams, considering tensile strength was reached but did not exceed the defined criteria.

Table 3 summarizes the results for the four dams for which this kind of analysis was performed. For moderate earthquakes, results show that block velocities are one order of magnitude lower compared to the velocity required for the block to overturn in the upstream direction.

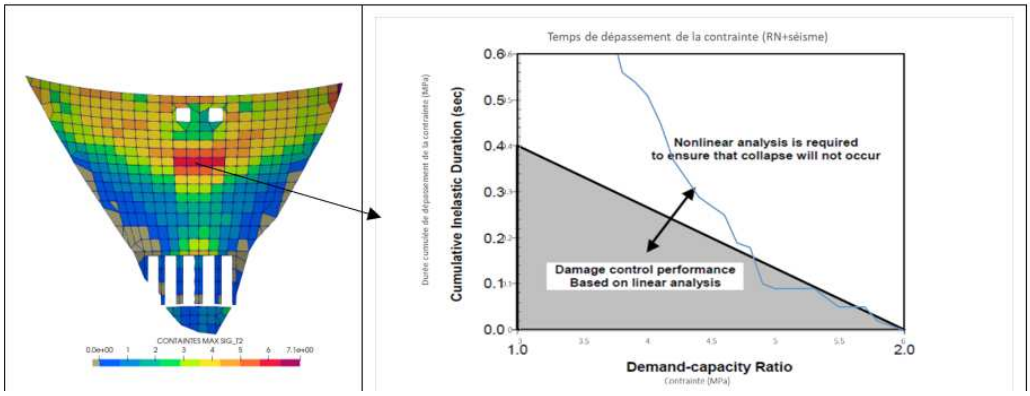

Figure 23 demand capacity ratio for M dam

Table 3 kinetic blocks analyses results

Dam	Block max velocity (m/s)	Critical velocity (m/s)
R	0.5	4.1
L	0.4	3.2
C	0.5	
M	0.5	11.9

7.3. Structure Gate dam

While the seismic behavior of concrete arch dams and conventional gravity dams (with a triangular shape) should be easily assessed for low to moderate seismic hazard (see also §8 about the performance of concrete dams under earthquake), the seismic behavior of old structure gate dams might pose a problem. Tuilières and Cize-Bolozon dams, presented in Figure 24, are representative of such dams, built at the beginning of the 20th century with slender piers on top of which a system of winches allows vertical movement of Stoney gates out of the flow in case of flood. In the case of Tuilières dam, piers are built in masonry, while Cize-Bolozon dam is made of concrete but without any reinforcement for the top part. At the time of their design, seismic considerations were not included, and the aim of this part was only to handle vertical forces. Such design also leads to locating masses on top of the structure, which is particularly unfavorable under seismic load.

Finite-element analyses of these dams were performed [23] :

- Tuilières dam: A new bracing was designed as part of a global rehabilitation project for the dam.
- Cize-Bolozon dam: Analyses showed that there might be a risk of gradually damaging the corners of the superstructure part with several cycles of rocking, gradually reducing the section.

Even for low to moderate seismic hazard, the seismic behavior of such dams should be considered with care.

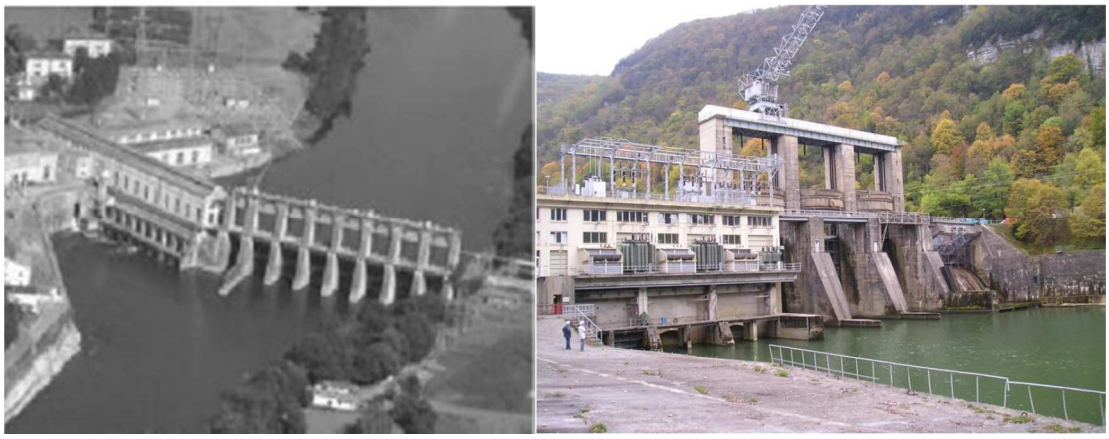

Figure 24 Tuilieres (left) and Cize-Bolozon (right) structure gate dams

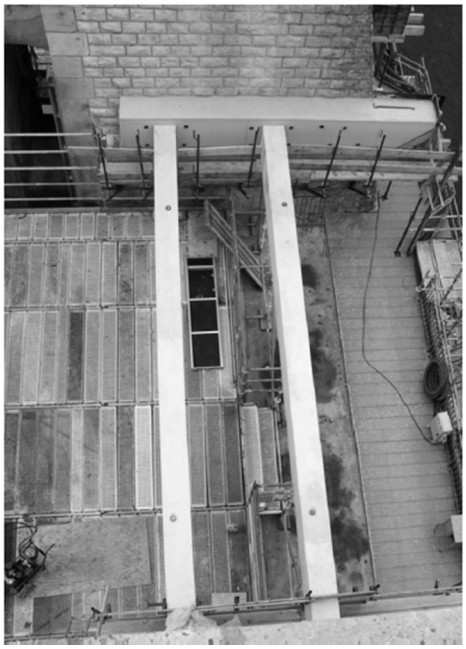

Figure 25 new bracing at Tuilières dam

8. THE PERFORMANCE OF CONCRETE DAMS UNDER EARTHQUAKE

From the previous chapters of this paper, the reader should now realize that performing numerical analyses of a concrete dam to assess its safety under earthquake conditions remains a complex task with a lot of uncertainty, which can be particularly time-consuming for engineers. On the contrary, the performance of concrete dams under earthquake conditions is excellent. This opposition raises the question underlined by Bremen [17]: *It is thus questionable why the dam community has, for various decades, focused on the dynamic safety of dams much more than on other domains causing far more dam failures.*

Regarding the performance of concrete dams under earthquake conditions, USSD in 2014 [18] highlighted that approximately 20 concrete dams experienced earthquakes with PGA higher than 0.3g, with 19 of them analyzed by Nuss [19]: 11 gravity dams, 7 arch dams, and 2 buttress dams. Among them, Kasho gravity dam experienced 0.5–0.6g near the foundation, resulting in 2.0g at the crest.

On an international scale, among all concrete dams that have undergone very high stress, the only failure is that of the Shih Kang dam, which was built on a fault that exhibited a multi-meter displacement. Significant damage was observed on only four other structures, namely Koyna, Pacoima, and two buttress dams. The other 14 structures performed well and showed no structural damage during post-seismic inspections.

In conclusion, Nuss et al. [19] indicate that the damage threshold for well-designed and well-constructed gravity and arch concrete dams is probably well above 0.3g, and that for buttress dams, cracking is possible in the upper part of the structure, at the slope break between the buttresses and the vertical part of the dam. Hansen [20] observes that in no case has a concrete dam been damaged for a PHGA (Peak Horizontal Ground Acceleration) below 0.5g. Based on this observation, he even questions the need for seismic studies on well-designed concrete dams for PHGA values below this threshold.

Among the lessons highlighted in Nuss et al. [19] and Hansen [20], it is particularly noted that for concrete dams:

- Damage, when it occurs, happens in the upper part of the structures where accelerations can be strongly amplified, and often at the level of ancillary structures such as gutters, monitoring rooms, control rooms, and valve operation facilities.
- Conversely, little increase in leakage or significant pressure rise has been observed in the foundation, and these have always been temporary.
- Crest accelerations can exceed 2g (measured on at least three structures: Pacoima, Kasho, and Takou).
- No additional damage has been observed during aftershocks or another major seismic event.

From these lessons and in the frame of the French metropolitan territory with a moderate seismic hazard (bellow 0.3g for French seismic hazard map), Humbert [16] proposed that complexe finite-element analyses should not be mandatory for dams well designed and after a qualitative bases on the following point :

- Robustness of design and quality of construction/implementation
    - Foundation treatment: foundation on "good rock," quality of the concrete/rock interface (treatment, injections, etc.).

    - Absence of geometric or design singularities (e.g., no significant change in inertia in the upper part of the structure, slenderness of the structures).
    - Absence of active faults under the structure (construction on active faults is generally not permitted in France...).
- Analysis of the historical behavior of the structure since impoundment through an auscultation system and appropriate monitoring. Absence of marked pathological behavior (absence of irreversible displacement, high piezometry, significant leakage flows, etc.).
- Analysis of the dam's condition (level of cracking, etc.).
- Stability study under normal conditions demonstrating the existence of usual safety margins with a reasonable set of assumptions.
- Seismic level: a sufficiently low PGA (typically <0.35-0.4g, which is the case in mainland France).

Conversely, many concrete structures may require advanced studies and sometimes physical reinforcements. For example, the Chambon gravity dam is affected by a marked swelling pathology and vertical cracking patterns that could raise concerns about the destabilization of an "upstream" slab. The dam has been the subject of complex studies for many years and several phases of mitigation work, including reinforcement of the upper part in 2015. Some old dams are equipped with flat gates with slender piers such as described in §7.3. These piers are sometimes made of masonry, sometimes hollow, and sometimes of unreinforced concrete. These structures generally deserve complex specific studies that can sometimes demonstrate the stability of these piers, or conversely, require reinforcements (as in the case of the Whakamaru gravity dam in New Zealand or the Chancy-Pougny dam in Switzerland).

9. CONCLUSION

Seismic analyses of concrete dams reveal that, despite significant stresses, most well-designed and well-constructed structures effectively withstand earthquakes. Advanced methods, such as finite-element analyses and non-linear approaches, enhance our understanding of the dynamic behavior of dams and help identify vulnerable areas. However, specific studies and reinforcements may be necessary for older structures or those with particular pathologies. International collaboration and data sharing are crucial for improving practices and ensuring the safety of dams during seismic events. In regions with moderate seismic hazards, such as mainland France, simplified methods may suffice for well-designed dams, while more complex analyses should be reserved for structures with identified vulnerabilities.

10. ACKNOWLEDGEMENTS

I want to mention that all the work I managed to do on that topic would not have been possible without the trust and the time allocated by EDF. A special thanks to Nicolas Humbert and all my colleagues involved in seismic analyses at EDF providing part of the results summarized here, not to forget a lot of interns involved in benchmark workshop analyses. I also benefited a lot from the discussions at several conferences with Arnkjell Løkke, Osmar Penner, Najib Bouaanani, Pierre Leger and Pr. Chopra. Special thoughts to Eric Bourdarot, my mentor for the first 10 years at EDF.

REFERENCES

[1] Fok K.L.; Chopra, A.K. (1986). Earthquake analysis of arch dams including dam-water interaction, reservoir boundary absorption and foundation flexibility. Earthq. Eng. Struct. Dyn., vol. 14, p.155-184

[2] Shahbazi, M. Penner O., Bergman B. Seismic input and topographic effects : a rigorous approach to simulating 3D dal-foundation interaction in LS-DYNA, USSD annual conference 2019

[3] Løkke, A. Chopra A.K. Direct finite element method for nonlinear analysis of semi-unbounded dam–water–foundation rock systems, Earthquake engineering and structural dynamics 2017

[4] Løkke, A. Chopra A.K. Direct finite element method for nonlinear earthquake analysis of 3-dimensional semi-unbounded dam–water–foundation rock systems, Earthquake engineering and structural dynamics 2017

[5] Løkke, A. Chopra A.K. Direct finite element method for nonlinear earthquake analysis of concrete dams: Simplification, modeling, and practical application, Earthquake engineering and structural dynamics 2018

[6] Fenves G, Chopra AK. Effects of reservoir bottom absorption and dam–water–foundation rock interaction on frequency response functions for concrete gravity dams. Earthquake Engineering & Structural Dynamics 1985; 13(1):13–31. DOI:10.1002/eqe.4290130104.

[7] Bolzon, G. Et cie, Numerical analyses of dams, Proceedings of the 15th ICOLD International Benchmark Workshop

[8] www.code-aster.org

[9] JCOLD, Acceleration Records on Dams and Foundations No.3, the Japan Commission on Large dams 2014

[10] Kashiwayanagi, M. Cao, Z. Investiguation of damping characteristics of dams evaluated by DE/TFM method, Q106-R29, 27th ICOLD Congress, Marseille 2022

[11] Kashiwayanagi, M. Yoda, M. Cao, Z.Examination of damping characteristics of concrete dams in dam-reservoir-foundation system, 91st Annual ICOLD Meeting – Gothenburg 13-14 June 2023

[12] Takeshi Kashima T. Effects of reservoir water level and temperature on vibration characteristics of concrete gravity dam, ICOLD Symposium Bali, 2014

[13] ICOLD Bulletin The physical properties of hardened conventional concrete in dams 2009

[14] Løkke, A. Chopra A.K., Response Spectrum Analysis of Concrete Gravity Dams Including Dam-Water-Foundation Interaction, PEER 2013/17 JULY 2013

[15] Tinawi, R. Leger, P., Seismic safety of gravity dams : from shake table experiments to numerical analyses

[16] Humbert, H., Kolmayer, K, Laugier, F., Analyse de risque proportionnée des barrages vis-à-vis du séisme en France métropolitaine, zone faiblement à modérément sismique – Valorisation du retour d'expérience. Colloque CFBR sûreté des barrages et enjeux 2025

[17] Bremen, R. Consequences on the design practices of worldwide dam accidents. Proceedings of the 27th ICOLD Congress, Marseille, France 2022.

[18] USSD. Observed Performance of Dams During Earthquakes – Volume III. 2014

[19] Nuss, L.K., et al. Shaken, but not stirred: Earthquake performances of concrete dams. 2012

[20] Hansen, K.D. Seismic Safety Evaluation of Concrete Dams: An awakening to reality. Concrete International, September, pp. 33-41. 2022

[21] Robbe, E. Rehabilitation of Tuilières Dam : behaviour under seismic load, 2nd international congress on dam maintenance and rehabilitation, Zaragoza 2010

[22] Diallo A. Robbe, E. Fluid Structure Interaction Arch Dam – Reservoir at Seismic Loading, 12th ICOLD Benchmark workshop, Gratz 2013

[23] Robbe, E. Behaviour of two gate-structure dams under seismic load, 2nd European conference on earthquake engineering and seismology, Istanbul 2014

[24] Diallo A. Robbe, E. Influence of dam-réservoir interactions for seismic analysis of arch dams, 2nd European conference on earthquake engineering and seismology, Istanbul 2014

[25] Fouqué, J. Robbe, E. Seismic safety evaluation of a concrete dam based on guidelines, 13th ICOLD Benchmark workshop, Lausanne 2015

[26] Robbe, E. Miot, M. Static and seismic analyses of an arch-gravity dam with Code_Aster, 14th ICOLD Benchmark workshop, Stockholm 2017

[27] Pallu, B Robbe E et al. Analyses of earthquake records on two japanese concrete dams, 16th World Conference on Earthquake, Santiago Chile 2017

[28] Robbe, E. et al. Seismic analyses of concrete dam, comparison between finite-element analyses and seismic records, 16th World Conference on Earthquake, Santiago Chile 2017

[29] Robbe, E. Seismic back analysis of Monticello arch dam – blind prediction workshop and additional analyses, USSD annual conference, 2017

[30] Robbe, E. Behavior of concrete dams under earthquake : lessons learned from japanese records on dams, USSD annual conference, 2018

[31] Robbe, E Mevel S., Behavior of concrete dams under earthquake : lessons learned from the CFBR-JCOLD cooperation and proposition of a simplified method for the safety evaluation; ICOLD conference, Vienne 2018

[32] Robbe, E. Grimal E. Devesa, G. Seismic analyses of Pine Flat Dam : Simplified use of Viscous Spring boundaries and anisotropic damage in the principal directions with the ability of cracks re-closure, 15th ICOLD Benchmark workshop, Milan 2019

[33] Robbe, E. Humbert, H. DamQuake: More than just a database, a powerful tool to analyze and compare earthquake records on dams, ICOLD annual conference, Ottawa 2019

[34] Alegre, A., Robbe, E., Oliveira, S. Seismic analyses of Cabril dam. Measured response and comparison with numerical results from Code_Aster and DamDySSA, Damworld Lisbon 2020

[35] Robbe, E. Mevel, S. Assessement of a simplified method to evaluate the sliding of gravity dams under earthquake, 17th World Conference on Earthquake, Sendai Japan 2021

[36] Robbe, E. Humbert, H. Ambient vibration measurements: feedbacks from measurements on 20 concrete dams and comparisons with finite-element analyses, 16th ICOLD Benchmark workshop, 2020

[37] Humbert, H. Robbe, E. Ambient vibration: feedbacks from measurements on 20 concrete dams and comparisons with finite-element analyses Focus on one year of recording on an arch, EVACES 2023

[38] Robbe, E. Humbert, H. Cherubini S. Effect of non vertical propagating seismic waves on the behavior of gravity and arch dams, 18th World Conference on Earthquake engineering Milan 2024

[39] Humbert, H. Robbe, E. Chalamet L. Push-over analysis on dams: interest, limitations, and proposition of a method, International symposium on dams and earthquakes, Athens 2024

Fifth International
Dam World Conference
PORTUGAL • LISBON • LNEC • APRIL 13-17, 2025
dam world 2025

THE FAILURE MODES OF FLOOD PROTECTION LEVEES, CONSEQUENCES ON MANAGEMENT AND ENGINEERING

Rémy Tourment[1]
INRAE

ABSTRACT

The keynote lecture presents levee failure modes: how elementary mechanisms can interact in complex failure scenarios, and the activities of levee performance assessments and risk analysis, both including failure mode analysis. Potential failure modes are among the most critical information to be taken into account for both design and management of levees. Examples of design and management actions to prevent some of the main failure modes are presented during the lecture. In introduction, this extended abstract gives additional information about the general context of flood protection levees, while the lecture gives more details and examples related to failure modes.

Keywords: Levees, Failure modes, Mechanisms, Scenarios, Design, Management.

[1] remy.tourment@inrae.fr

1. INTRODUCTION: DEFINITION AND IMPORTANCE OF LEVEES

According to the International Levee Handbook (ILH) [1], levees (sometimes called flood defence embankments, dikes or other more local names) are raised, predominantly earth, structures whose primary objective is to protect against fluvial and coastal flood events along coasts, rivers and artificial waterways that are not reshaped under normal conditions by the action of waves and currents. Levees form part of flood defence systems that may also include flood walls, pumping stations, closure structures, natural features, etc. Different flood defence systems are presented in Figure 1, all based on levees but also including other elements.

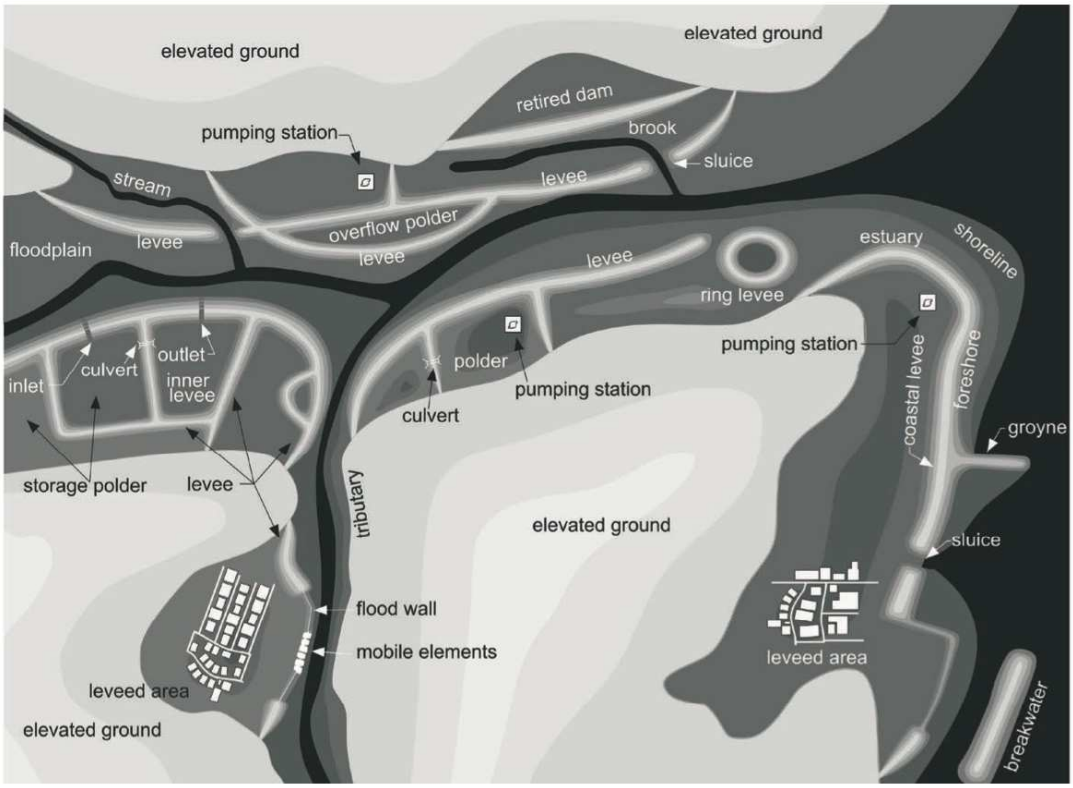

Fig. 1 – Different flood defence systems based on levees (from [1])

Levees avoid a lot of damage to life and goods, while their failure can have catastrophic consequences. According to a report of the EUCOLD working group on levees and flood defences [2] expanded in a bulletin of the ICOLD Technical Committee on Levees [3], the total length of levees across the world is over half a million kilometres. At least 20 countries have a major levee portfolio of over 1000 km of levees, with some of the earliest levees constructed over 4000 years ago. Levees provide flood risk reduction to over 700 million people, about 10% of the world's population. Several countries have experienced major flooding associated with levee failures in recent decades. In France, the 1999 Aude River Flood caused 25 casualties, in 2002/2003, 3 floods along downstream Rhone River caused 14 casualties and 2 billion euro in damages, in 2010 the Xynthia storm and coastal flooding caused 59 casualties

and 1-3 billion Euro damages, all associated to levee failures. More examples from other countries can be found in [2] and [3].

To avoid loss of life and property, effective management, operation and maintenance of levees and, when necessary, renovation and replacement are required. This importance of the safe management and sound design of levees is now recognized in many countries as well as internationally, as in ICOLD for instance, which in 2018 created its Technical Committee on Levees and had the same year a Congress Question on the theme of "Small Dams and Levees" [4].

2. COMPARISON BETWEEN DAMS AND LEVEES

Levees are embankment water retaining structures with many similarities but also many differences with dams, whether reservoir dams or flood storage dams. The Technical Committee of ICOLD on Levees is working on a series of bulletins comparing dams and levees, detailing both their similarities and differences. This comparison deals with all principal aspects: general functional and descriptive, governance, design and construction, management, and assessments. Actually, the family of hydraulic structures is quite large and includes many others like for instance canals and offline reservoirs, and it is a little caricatural to oppose dams and levees as entirely different types of structures as we can find some examples sharing specific features of both dams and levees. Anyway, as a simple discriminating function, it can be said that dams can store water (keep water in) while levees protect from water (keep water out).

Some of the major differences between dams and levees are presented in the list below, these are not always true, as it is always possible a specific dam and a specific levee where it is the opposite. Compared to dams:

- levees are usually much longer and lower,
- water loading on levees is usually only occasional,
- levees are often old structures built by the local population, without proper engineering,
- over time, many levees have suffered multiple breaches during major flood events; they also often have been raised after the flood and repairs, which leads to a general heterogeneity in materials, in all dimensions (an example can be seen in Figure 2),
- in many countries, there is no regulation related to levee safety,
- levee management is often fragmented (not at the scale of the actual system) and sometimes we can even find "orphan" levees, as it is easy after many decades or

centuries without major flood events to remember their usefulness and sometimes even their existence;

- levee systems are rarely equipped with a spillway and so are not resilient to overtopping/overflowing;
- levees are usually built upon alluvial foundations without important treatment, these foundations can sometimes be very deep, much deeper than the levee height.

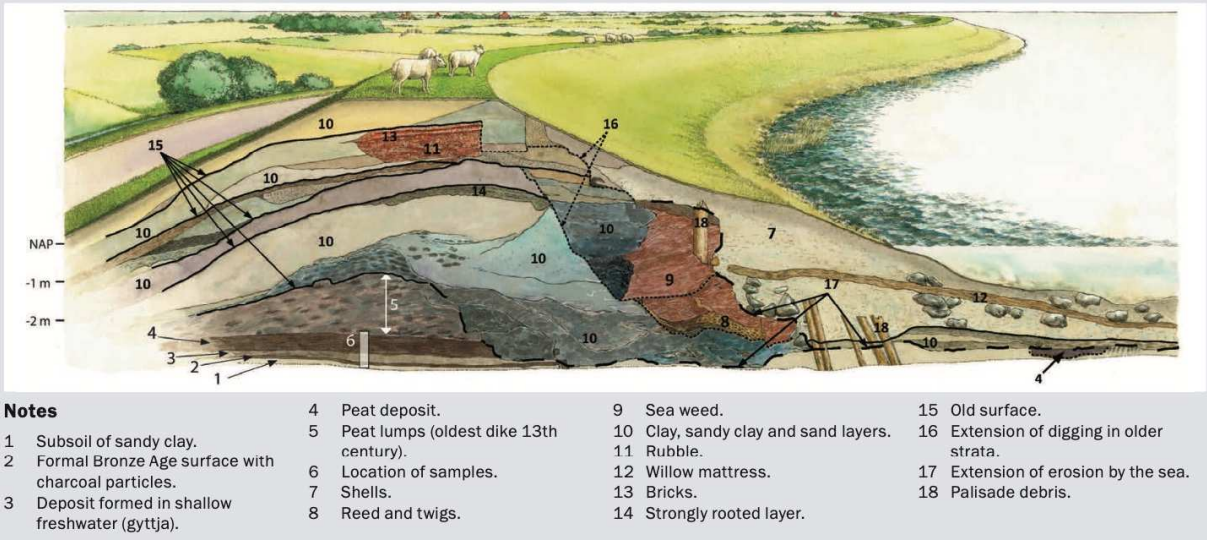

Fig. 2– Example of a cross section of an old and heterogenous levee (from [1])

Most importantly, embankment dams and levees share similar individual deterioration and failure mechanisms related to their similar materials, but, as their environments and loading conditions, are different, as well as other characteristics, their failure modes (scenarios) differ.

3. FAILURE: MECHANISMS AND SCENARIOS

Knowledge about failure modes is essential for dams and more generally for all types of hydraulic structures, as all activities in terms of design, construction, inspection, assessments, and maintenance are oriented toward preventing these failures. The history of dam (and related hydraulic structures) engineering has, unfortunately, made progress after major failures with the understanding of a previously unknown or poorly understood failure mode.

3.1. Hydraulic and structural failure

While working on the content of the International Levee Handbook [1], the teams of authors has identified a need for a more structured approach to the concepts related to "levee failure", detailed in chapter 3 of the ILH and summarized in [5]. A gradation in the possible deterioration of the physical state of a levee was defined as deterioration, damage, or breach. As an approximative simplification, deterioration can be dealt with by regular maintenance, while

damage needs heavier repair works, and a breach is a gap in the levee, allowing water to pass through.

A general definition of failure is "the inability to achieve a defined performance threshold (response to a given loading) or performance indicator for a given function". For levees, it was identified two types of failure:

- Hydraulic failure (failure of the protection function), which happens when the protected area is flooded before the intended level of protection is reached; this is about the whole protection system rather than an individual levee;
- Structural failure, which happens when a levee or a levee component reaches an ultimate state incompatible with its required threshold of structural performance;
- Hydraulic and structural failures are not independent but need to be identified and dealt with separately in a functional approach.

3.2. Mechanisms leading to failure

A structural failure in a levee, the result of one or more often several mechanisms of deterioration or rupture of the materials that compose it, results in a breach in the structure, that is to say, an opening which can allow the passage of water through the levee into the protected area; consequently, in this case, the structure can no longer fulfil its protective function.

NB: from this point onward, we will mostly deal with the physical failure of embankment levees.

The different mechanisms of deterioration or rupture of embankment materials are generally classified into three families: external erosion (by current, waves, shocks, overflow or crossing paths), internal erosion (suffusion, contact erosion, internal regressive erosion, conduit erosion) and instability (shear leading to sliding or collapse, liquefaction, etc.). This list is not exhaustive as many mechanisms are still poorly identified and/or need to be better analysed, like those caused by freeze-thaw or humidity-drought cycles.

3.3. Levee failure modes

Usually, the four classic failure modes of river levees were named after a mechanism [6], or even after the action which was at their origin: overflow (more precisely: erosion by overflow), external erosion, internal erosion, and slope sliding. In reality, in many cases, the failure of a levee is caused by a complex scenario involving different mechanisms acting successively or simultaneously [7]. The Technical Committee 201 on Levees of ISSMGE has worked on a report [8][1] in which a "generic" flowchart presenting the main mechanisms in embankments is

[1] the term "failure path" was chosen in this report to speak about failure scenarios.

proposed and how they can interact within a levee failure scenario; this flowchart is presented in Figure 3. It is generally recommended to show the complex failure scenarios in the form of trees, where all mechanisms are presented, and other items like hydraulic actions, as well as deteriorated states of the levee or its components.

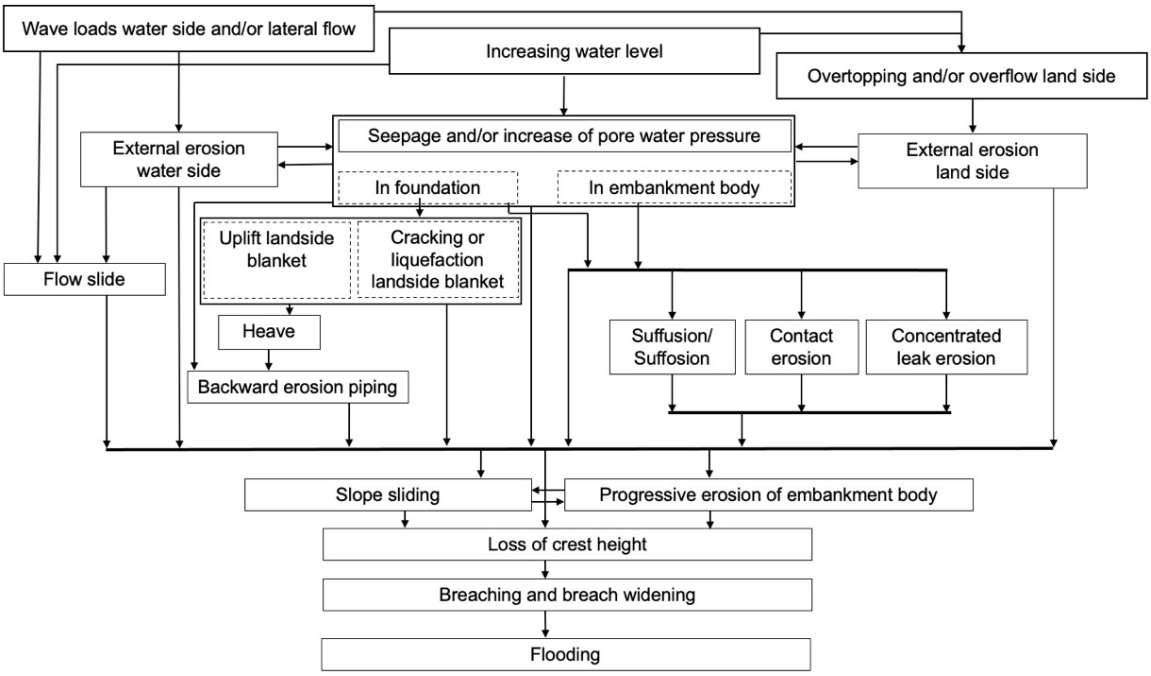

Fig. 3 – The ISSMGE TC201 failure paths flowchart

Examples of scenarios involving different mechanisms are described in [7] and [8] and are presented during the lecture, including some unusual ones.

3.4. Levee environment and scenarios

Levees exist in different environments (rivers, seas, lakes, torrents, …) with specific characteristics in terms of hydraulic behaviour: waves, sediment transport, discharge and the variation speed of discharge and/or level. These have an influence, as well as the nature of the levee material and its foundation on the more probable failure scenarios on a specific levee. In a torrential environment, scour (external erosion of the levee toe or its foundation) is usually a leading mechanism, while internal erosion or external erosion by overflowing are more common on river levees, as external erosion by wave shock or overtopping is more common on coastal levees.

Some environments have characteristics of some of the environments listed above; for instance, estuaries have characteristics of rivers and seas, torrential rivers have characteristics of fluvial rivers and torrents, and lakes can have characteristics of seas and rivers.

4. PERFORMANCE ASSESSMENT AND RISK ANALYSIS

4.1. Definitions

Performance assessment, in both terms of hydraulic and structural performances, and risk analyses are essential activities that inform decisions regarding the management and engineering of levees. The general concepts and frameworks of levee assessments and risk analysis have been developed at the international level in chapter 5 of the ILH [1]; the framework for levee systems risk analysis has been presented in [9], and a comparison of different national approaches in [10]. In France detailed assessments and risk analyses are mandatory for all levee systems, in a report in a specific format defined by the regulation "hazard studies" ("études de dangers" in French).

Performance assessments help determine the following:

- the structural performance of a levee: resistance to all structural failure scenarios,
- the hydraulic performance of a levee system:
  - identification of the protected area and the protection level, or levels, in the case when parts of the protected area have different protection levels,
  - behaviour in terms of controlled flooding once the protection level level has been exceeded and if no breach occurs.

A risk analysis is based on such assessments, but it additionally aims to identify the consequence in terms of flooding in the protected area for different loading events with various probabilities, whether the flooding occurs by a simple exceeding of the protection level without breach or in the case of different breaching scenarios.

In France, it is customary (but not mandatory) to identify, in addition to the protection level of a levee system, the safety level and danger level of its different levee segments. The safety level is defined as the water loading up to which a breach is very unlikely, while the danger level is on the opposite defined as the water loading that will very probably cause a breach.

4.2. Identification of potential failure scenarios

So, it is necessary to identify the possible structural failure scenarios of a levee to conduct an assessment and a risk analysis of the system it belongs to. On a given levee or system, there are different ways to identify the failure modes to be considered in a risk analysis. The simplest one is to rely on "classical" levee failure modes described in the literature (like in [6]), and another which is a little more time consuming relies on an accidentology analysis of the studied system or of some similar systems.

We proposed a more analytical approach and described in detail in [11] a method based on a structural decomposition of the levee followed by a functional analysis of the levee components, then followed by a failure modes analysis based on this functional analysis. This failure mode analysis starts by identifying the failure modes of the different functions of the various components, which are then combined in the complex failure scenarios of the levee itself. Such a structured method allows for identifying many more potential failure modes, including some very specific to the studied levee. Complex scenarios involve different mechanisms.

An example of the application of the result of this method on a levee of the Loire River is presented in figure 4, up to the point of identification of the failure modes of the components.

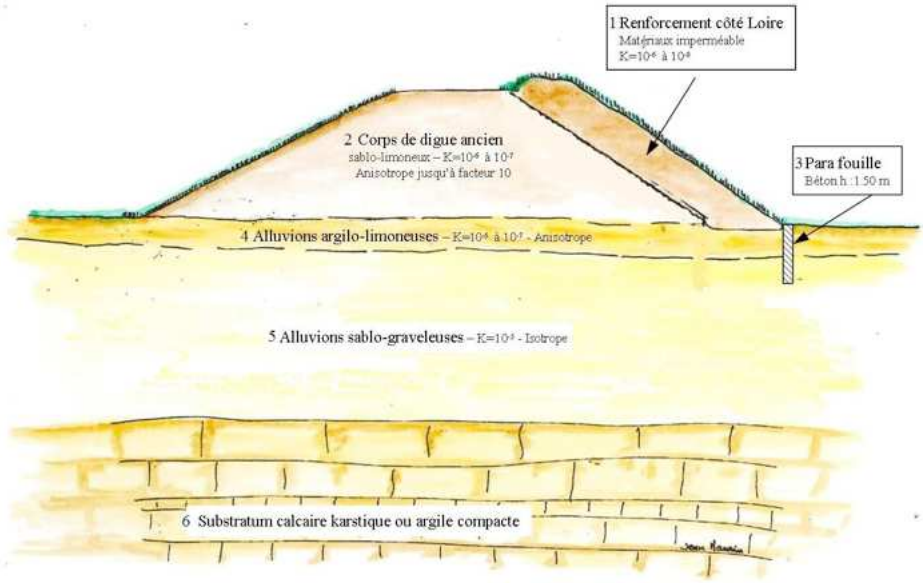

	Levee component	Component functions	Function failure modes
1	Waterside levee slope reinforcement	- Stability - Impermeability - Auto-filtration	- Loss of stability - Permeability increase - Possible migration of particles
2	Levee body (ancient structure)	- Stability - Impermeability - Auto-filtration	- Loss of stability - Permeability increase - Possible migration of particles
3	Waterside levee toe protection	- Impermeability - Scour protection	- Permeability augmentation - Scour
4	Clay-silt foundation	- Stability - Impermeability - Auto-filtration	- Loss of stability - Permeability augmentation - Possible migration of particles
5	Sand-silt foundation	- Stability - Auto-filtration	- Loss of stability - Possible migration of particles
6	Limestone substratum	- Stability	- Loss of stability

Fig. 4 – Structural decomposition, functional analysis and failure mode analysis of a levee components

4.3. Forensic identification of failure scenarios

This analytic method can be applied not only to identify all potential failure modes of a specific levee during an assessment or a risk analysis, but also to help experts during a forensic analysis of deteriorations, damages or breaches on levees to identify complex scenarios at the origin of the problem. An example of such possible complex scenarios is presented in figure 5. This case of the sandboils near the Agly river levees was described in more detail in [8].

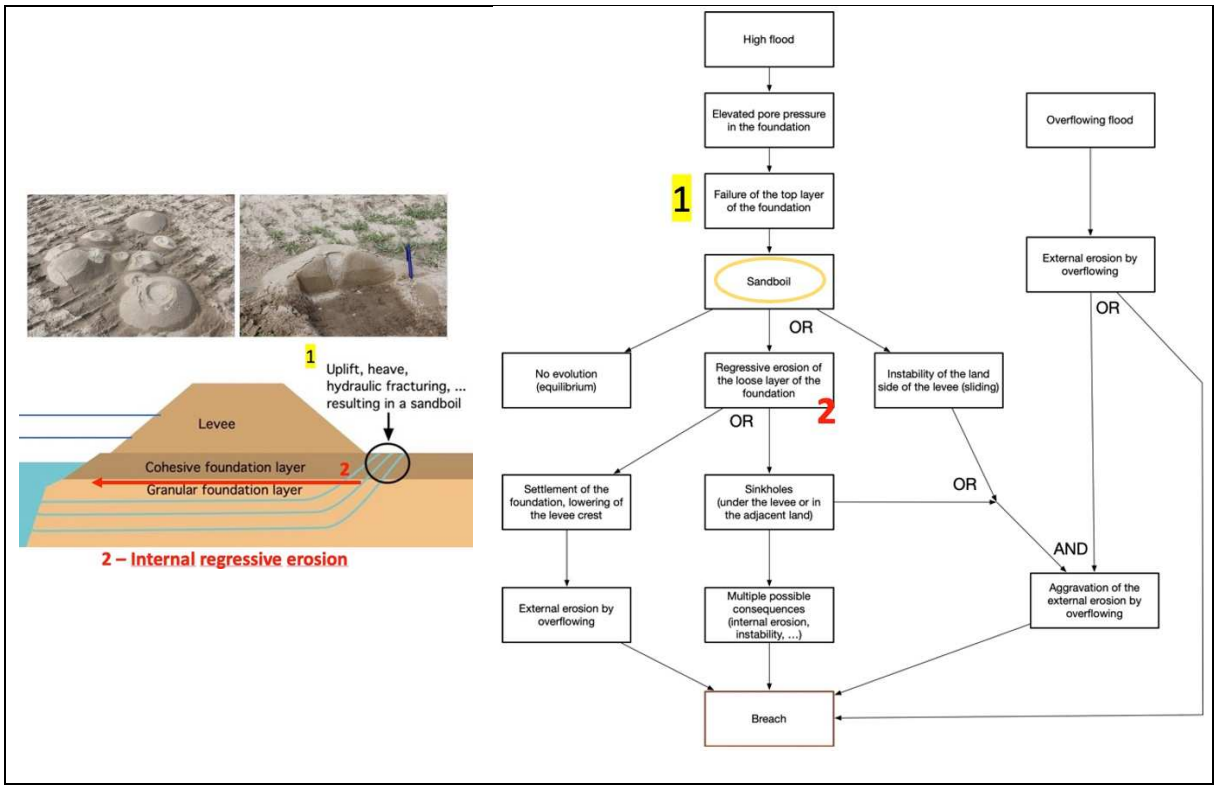

Fig. 5 – Sandboils near the Agly river levees, failure tree involving a sand boil

5. ENGINEERING

The general knowledge of levee failure modes and related mechanisms is the basis of the design and construction of embankment levees. The mechanisms involved in levee failures are the same for embankment dams, it is the way they are combined in scenarios and the relative importance of these different scenarios that differ between dams and levees and also depends of the environment (torrents, fluvial rivers, sea, lakes, …).

CFBR, the French committee on dams and reservoirs, has published guidelines for the justification of embankment dams and levees [12]. These guidelines deal with different mechanisms, scenarios and limit states, including sliding, deformation (settlement and lack of bearing) and hydraulic uplift of the downstream toe. CFBR is now working on a similar document oriented toward erosion (internal and external).

5.1. New levees

When designing a new levee, it is usual to consider all mechanisms and justify the resistance of the structure and its different components to all of these mechanisms. Justification can be simplified in the case of some mechanisms if it can be demonstrated that they can only appear in scenarios that have proven impossible (or sufficiently improbable).

5.2. Retrofitting or repairing existing levees

Considering the presence and importance in terms of protection of many old levees that have not been adequately designed and/or maintained for some time, a lot of the engineering activities related to levees are oriented toward retrofitting or improving existing levees. It also unfortunately happens that, during a flood, levees are damaged or even breached. In these cases, repairs are necessary after the flood and sometimes, when possible, strengthening during the flood.

In all cases, an assessment is necessary to design adequate works. In the case of an actual problem the assessment must identify its causes: the involved scenario and its individual mechanisms; in the case of an old levee without visible problems, the assessment has to identify the possible scenarios with their individual mechanisms. Then, based on the result of this assessment, the principle of the works can be determined in terms of the functions that need to be improved or restored in order to protect against these scenarios. Finally, a technique (or different techniques) can be chosen, corresponding to these functions. Figure 6 presents these various steps. CFBR has published a guide presenting principles and methods for reinforcing and repairing levees [13].

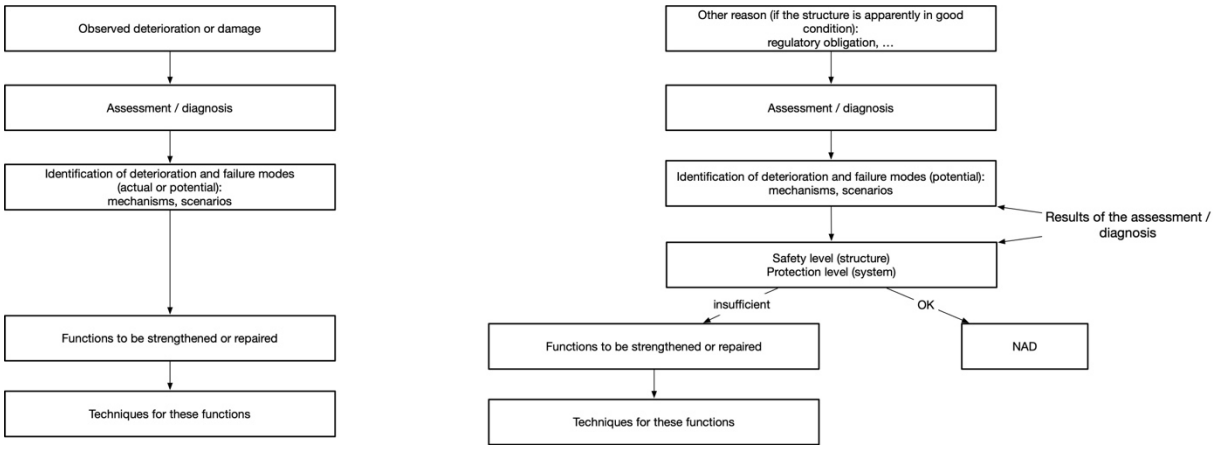

Fig. 6 – Insertion of assessment and its results in the process of choosing techniques for a repair (left) or a reinforcement (right)

The lecture presents different examples of works on existing levees.

Repairs or reinforcements on a levee can be done with a more or less detailed level of investigations, assessment and engineering design, according to the time available. It is possible to make the difference between different levels of urgency:

- Normal situation (in the absence of a recent or ongoing flood event): in order to obtain a functional and durable structure requiring only routine maintenance, investigations, assessment, design and works can take some months or even a few years,
- Urgent situation: after a flood or some damage, to improve the resistance of the levee in preparation for the next event (a few days, weeks or months, according to the local situation),
- Emergency situation: during or just before the loading event, to avoid a breach and a flooding of the protected area (immediate action, need preparedness).

After works conducted in an urgent or emergency situation, there is a need for a specific assessment in order to understand if these works can be considered as reliable for a long term performance of the levee or if some additional works have to be planned.

5.3. Some specific levee failure modes and how to deal with them

- Overflowing/overtopping[2]

Most existing levee systems are not resilient to overflowing/overtopping: as soon as the water passes over the crest, erosion of the crest and/or the land side slope and/or the nearby natural ground begins, which can lead to a breach, if the discharge is important enough and the flood event is long enough.

To avoid failures by overflowing, almost all dams are equipped with a safety spillway to prevent overflowing on the embankment. Overtopping on dams is prevented by adding a sufficient freeboard above the maximum water level. To make levee systems resilient to overflowing and overtopping, it is now more and more common to design levee systems with a spillway or a levee segment resisting overtopping, which has the same function but is a vocabulary more readily accepted by the population in the protected area. We published a guide on spillways on river levees [14], detailing all relevant aspects. At the same time, this issue in other environments needs more attention in the future, particularly on coastal and torrent levees. Figure 7 presents a spillway recently built on the Mosson River upstream of the city of Lattes

[2] At the international level, the vocabulary is not consistent in different countries. The ILH makes a difference between these two words, and we recommend to use these definitions: overflowing is defined as "Passing of water over the top of a structure as a result of a water level higher than the crest of the structure" while overtopping is defined as " Passing of water over the top of a structure as a result of wave action, surge or wind. The water level in front of the structure is lower than the crest level of the structure.". The difference of these two types of phenomena is important in terms of consequences on a levee, as well on their relative probability of occurrence in a specific case.

(France). This spillway feeds into a canal that goes into a coastal pond, contrary to many spillways (or levees resistant to overflowing) that flow directly into the protected area; in this last case, it is important to note that flooding a protected area in a controlled way by a spillway has much less damaging consequences that a breach in terms of hydraulics (discharge volume, duration) and of flood emergency management (because of the unpredictable location of the breaches).

Fig. 7 – The spillway on the left bank of the Lez River, near Lattes (France)

- External erosion by flow on the water side

Contrary to dams where external erosion related to water flows is limited to some specific zones near the spillway, river levees can be subjected to this action all along their length. A difference between scouring (erosion of the toe of the water slope or the bank) is a more critical issue than the erosion of the water side slope itself, as scouring can happen at any hydraulic condition and induce other damaging mechanisms (slope sliding, for instance). In contrast, erosion of the levee slope only happens during floods.

External erosion on the water side is one of the main causes of failure on torrent levees, which, by the way, are often built to control lateral displacements of the torrent in its debris cone more than to avoid flooding.

One of the most efficient ways to fight against erosion on the water side and particularly scouring, which also is beneficent for other issues, is to move the levees away from the river bed when possible. Other solutions exist but are much more costly: sheet piles (an example is presented in figure 8), riprap, gabions, masonry, concrete slabs,…

Fig. 8 – Protection against scouring by sheet piles along a levee on the Loire River

- External erosion of the water side by wave action

On most river levees, wave action rarely causes important problems, contrary to dams, where it is an important issue on the water level fluctuation range, and coastal levees, where waves are usually higher than the water level increase during a storm event.

In this case, solutions are similar to those for protection: placing the levee far from the land/sea interface (bank, beach) or protection revetment in hard material.

- Internal erosion

Internal erosion is, with overflowing/overtopping, one of the main causes of failure on river levees. One or more of the four mechanisms of internal erosion can be involved in a scenario [7] [8], as presented in figure 9. Internal erosion on a levee is more critical than a dam that stores water (so excluding flood storage dams), as seepage in a dam can be detected and interpreted by monitoring, while for a structure like a levee (or flood storage dam) being usually "dry" there is no indication of possible seepage.

To avoid internal erosion, it is possible to act on sealing (upstream or internal) and/or on filtration.

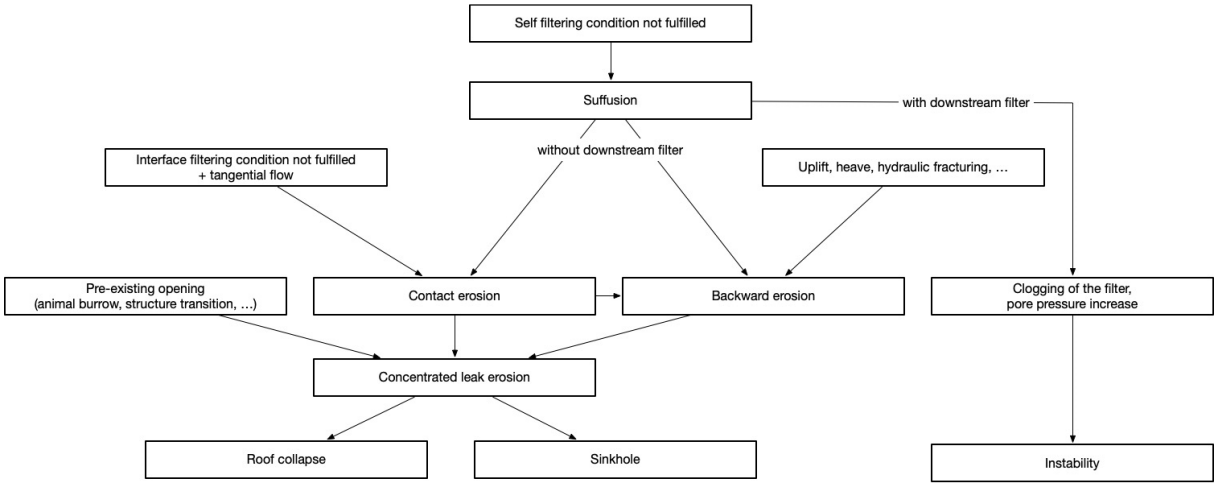

Fig. 9 – The different possible interactions between internal erosion mechanisms (from [8])

- Transitions

Because of the levees' length, the way they are in relation to their environment, including multiple networks, buildings and activities, and their history (raising, repairing), many transitions exist in levees. Transitions have caused many levee failures, with failure modes sometimes specific to them. The typology of transitions and their influence on failure modes has been analysed by the European FP7 research project FloodProBE, a summary has been presented in [15]. The two transitions families are: between a "hard" structure and the embankment and between different types of embankments; figure 10 presents some transition types. The more common types of transitions are crossing structures and transitions between two levee segments with a different cross section. Internal erosion is the more common failure mode associated to transitions.

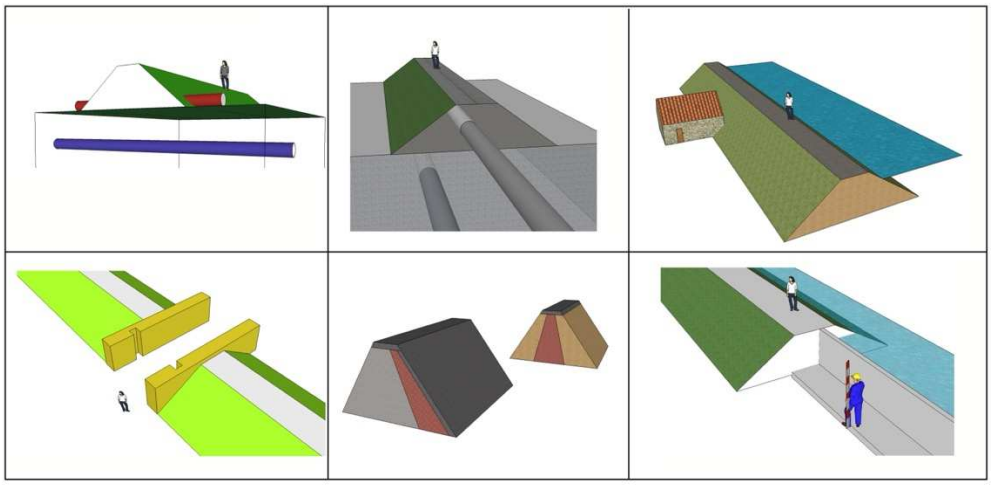

Fig. 10 – Different types of transitions (from the FloodProBE EU research project)

Avoiding transitions is the best solution to avoid problems related to transitions, which is not always possible. If not, it is needed to analyse the failure modes associated with a specific transition type to design it properly.

- Foundation issues

Levee failures often include their foundation. Foundations must be considered simultaneously with levees when analysing the resistance to failure modes, unlike dams, where specific failure modes consider only the dam OR the foundation.

Complete sealing of the foundation of the foundation is not necessary, in particular in terms of depth. It has to be sufficiently impermeable and deep to prevent all mechanisms related to water (internal erosion, slope sliding,…). Still, it does not need to cut off water circulation underground completely, and in the case of river levees, it SHOULD not, as communication between the river and the aquifer in the protected area must be maintained.

6. MANAGEMENT

As for engineering (design and construction), knowledge about levee failure modes, the possible mechanisms, and the specific failure scenarios possible on a given levee (identified via an assessment and/or risk analysis) is the basis for sound management, in terms of safety and resource economy.

6.1. Knowledge, data

Methods related to identifying potential failure modes on levees exist, but they rely on the knowledge related to the individual mechanisms. Some mechanisms are rather well known, like slope sliding, while others have been the effort of research with good results, but it is still ongoing, like the different mechanisms of internal erosion. Others are still poorly known, at least in terms of their characterization and how to consider them in levee design and assessment, like cracking. Desiccation cracks can be as deep as 1 metre; climate change makes this situation more and more likely. Researchers are actively working; decision makers are increasingly aware of the associated risk.

In parallel to methods, assessments and design need specific data related to a given levee, mostly (but not limited to) geotechnical and hydrological/hydraulic data. A levee system manager needs to store and organize all technical data, and when necessary, research historical documents and/or launch specific investigations. The failure or near failure of levees also provides interesting information, so it is necessary to analyze such events.

6.2. Inspections, maintenance

Inspections provide valuable data input for assessments. Levee systems are vulnerable to deterioration and eventual failure. Inspections strive to interrupt this continuum by observing deterioration before failure occurs so that an intervention can prevent failure. Inspections can be conducted in different situations: a normal situation, if time permits (flood warning) before a flood event, if time (flood warning) and safety of the staff permits during the flood event, and in any case after a flood event, this last situation giving particularly important information.

Potential failure modes on a levee are useful to optimize future inspections. It is important that some detailed inspections, conducted every one or a few years, look at all symptoms related to deteriorations, precursors or results. During the more frequent inspections and in particular during flood events, it is more efficient to look for symptoms linked to the more probable failure modes.

Based on the consequences of failure at different locations that can be found in the results of a risk analysis, it is possible to prioritize sectors in terms of frequency.

Some examples of specific observations during inspections:

- in sectors where overflowing or overtopping has been found possible, and before a solution can be implemented, inspectors will pay a particular attention when the water level gets near the crest,
- in sectors where internal erosion has been found possible, during floods, inspectors will look out for seepage, and in the case of seepage if the water is clear or contains soil particles,
- in sectors where external erosion of the water side has been found possible, for instance on the external side of a river curve, inspectors will look for signs of scouring.

More detail on inspection principles and methods can be found in [6] and in the section 5.4 of the ILH [1].

6.3. Monitoring

Unlike dams that permanently retain water, monitoring of levees rarely involve measures in relation to internal hydraulics (water levels, seepage discharge measures), because of the infrequent loading. On the other hand, topographical measurements are possible and may give information. Research is ongoing on specific monitoring techniques, like fiber optics or measurements by drone using different captors. Fiber optics allows the monitoring of temperature and deformation, drones can for instance measure topography (by LIDAR or photogrammetry), temperature (by infra-red) and some geophysical methods. Both

technology, data management and treatment are still in development, but the future is promising.

Understanding what mechanism or failure scenario is happening based on monitoring measurements and analysis requires some expert analysis as it is often needed to integrate the measurements of different sources to understand what's happening inside the levee.

7. CONCLUSIONS

Levee failure modes can be complex and often involve more than one mechanism that interact in a failure scenario.

It is important to conduct initial and regular performance assessments of levees and risk analyses of existing levee systems to be aware of possible and more probable mechanisms and failure scenarios. Based on these, inspection and maintenance of the levees can be optimized. Specific performance assessments of levees and risk analyses of existing levee systems conducted when a problem is detected allow to optimize design of the repairs or reinforcements.

In terms of general knowledge, the community of dams and levees, particularly researchers and engineers but with the feedback from owners and managers, needs to keep on working on improving knowledge on mechanisms and on methods for analysis and for design.

REFERENCES

[1] CIRIA, MEDDE, USACE (2013). The International Levee Handbook. ISBN: 978-0-86017-734-0. CIRIA, London.

[2] EUCOLD Working Group on Levees and Flood Defences (2018). European and US levees and flood defences - Characteristics, Risks and Governance. ISBN 979-10-96371-08-2. Edition CFBR.

[3] ICOLD Technical Committee on Levees (2025). Levees around the world - Characteristics, Risks and Governance. ICOLD Bulletin 196 (approved in 2022, will be published in 2025, available on the ICOLD website in the meantime).

[4] Tourment, R. (2018). Small Dams and Levees - General Report Q103. International Commission on Large Dams – 26th International Congress on Large Dams, July 4th-6th, Vienna (Austria). ISBN: 978-1-138-61228-0

[5] Simm, J., Wallis, M., Smith, P., Tourment, R., Veylon, G., Deniaud, Y., Durand, E., McVicker, J., Herch-Burdick, R. (2013). "The significance of failure modes in the design and management of levees—a perspective from the International Levee Handbook

team", Comprehensive Flood Risk Management, ISBN: 9780415621441, CRC Press: 291-300

[6] Mériaux P., Royet P., Folton C. (2007). Surveillance, maintenance and diagnosis of flood protection dikes - A practical handbook for owners and operators, Éditions Quae, Versailles. 162 p.

[7] Tourment, R. (2024). Levee failure scenarios - Complex levee failure scenarios and examples. CDMX 2024 - The synergy between theory and practice, September 5-7th, 2024, Mexico City. ISBN: 978-607-59398-7-2

[8] Van, M.A., Rosenbrand, E., Tourment, R., Smith, P., Zwanenburg, C. (2022). Failure paths for levees. International Society of Soil Mechanics and Geotechnical Engineering (ISSMGE) – Technical Committee TC201 'Geotechnical aspects of dikes and levees', February 2022. https://doi.org/10.53243/R0006

[9] Tourment, R., Wallis, M., Beullac, B., Kortenhaus, A., Schaaf, D.M., Schelfhout, H. - 2014. The risk analysis of levee systems. 3rd IAHR Europe Congress 14/04/2014-16/04/2014, Porto, PRT. 3rd IAHR Europe Congress, Book of Proceedings 2014. 13 p.

[10] Tourment, R., Beullac, B., de Leeuw, A., Diermanse, F., Gouldby, B., Wallis, M. (2016). The risk analysis of levee systems: a comparison of international best practices. 3rd European Conference on Flood Risk Management FLOODrisk 2016 17/10/2016-21/10/2016, Lyon, FRA. E3S Web Conf. Volume 7, 2016. 3rd European Conference on Flood Risk Management (FLOODrisk 2016). 10 p.

[11] Tourment R., Beullac B. (2019). Inondations - Analyse de risque des systèmes de protection - Application aux études de dangers, ISBN : 978-2-7430-2365-2. Lavoisier, Paris, 356 p.

[12] CFBR (2016). Guidelines for the justification of embankment dams and levees. ISBN 979-10-96371-01-3. Edition CFBR.

[13] CFBR (2021). Methods and techniques for reinforcing and repairing protection levees. ISBN : 979-10-96371-17-4. Edition CFBR.

[14] Degoutte, G., Tourment, R. (2021). Spillways on river levees. ISBN 978-2-7592-1885-1. Éditions Quae.

[15] Tourment, R., Morris, M.W., Royet, P. (2012). Levee failures related to structure transitions: Typology, levee performance evaluation and improvements. 2nd European Conference on Flood Risk Management FLOODrisk2012, 19-23 November 2012, Rotterdam, Netherlands. In "Comprehensive Flood Risk Management. Research for policy and practice" p. 407-414. CRC Press.

Fifth International
Dam World Conference
Portugal•Lisbon•LNEC•13-17 April, 2025
dam world 2025

SIMPLIFIED ANALYSIS OF SELECTED ASR PFMS

Dan D. Curtis[1]
Canadian Dam Association

ABSTRACT

Numerous concrete dams and other water-retaining structures are affected by Alkali Aggregate Reaction (AAR). Currently, very sophisticated 3D nonlinear concrete growth finite element (FE) models are available to analyse these structures. However, detailed FE AAR models require numerous input parameters which are often not well known, and these models require significant time and computational resources for model calibration and predictive analyses. This paper presents the results from simplified 2D non-linear concrete growth analyses of realistic “hypothetical” dam structures. These simplified analyses can be done very quickly, and they allow a very good initial understanding of potential failure modes.

The paper provides a brief discussion of important features to be approximated in AAR modelling, including the effects of AAR kinetics, temperature, humidity, creep, and stress on AAR modelling requirements. Some of these effects can be approximated as fixed pre-defined input parameters in the simplified concrete growth analyses for consideration in a PFMA study. The paper provides a summary and interpretation of results from a recent concrete coring shear strength test program. The knowledge obtained from the evaluation of the core testing results is used to help validate a simplified nonlinear 2D AAR model.

[1] dan@ddcurtisconsulting.com, Canada

The model is used to analyse a known issue where AAR caused severe cracking of a spillway end pier adjacent to a concrete intake structure. The importance of structure geometry is further examined by considering the same spillway pier geometry adjacent to a concrete non-overflow concrete section rather than an intake. The response of these two structures to AAR effects is quite different due to the differences in the flow of AAR-induced stresses and this is an important consideration for AAR-induced PFMs.

The effect of AAR concrete expansion on radial gated spillway piers is also examined. In this case, the effect of AAR on a passive gate trunnion anchor system is analysed. The effects of variations in concrete expansion on the spillway pier is discussed as it may affect gate operation which is another important and potentially new PFM.

Keywords: Concrete Dams, AAR, ASR, Shear Strength

Fifth International
Dam World Conference
Portugal • Lisbon • LNEC • 13-17 April, 2025
dam world 2025

CANADIAN DAM ASSOCIATION AND DAMS IN CANADA

Marc Smith[1]
WSP Canada and
Canadian Dam Association

Margaret Trias[2]
Canadian Dam
Association

ABSTRACT

There are over 15,000 dams in Canada of which over 1,160 are categorised as “large” dams under the ICOLD definition. These dams are owned by the federal and provincial governments, electric utilities, industrial and mining companies, irrigation districts, municipalities and private individuals. Some of the largest dams in the world are associated with Canadian hydroelectric and mine tailings developments. Other dam structures in Canada include small and medium embankments for agricultural and water supply usage. In all cases the dams must be designed, operated and maintained so that they do not pose an unacceptable risk to the downstream populations.

The Canadian Dam Association (CDA) is a not-for-profit association of almost 1500 members including dam owners, operators, regulators, consultants, contractors, academia and suppliers. CDA provides leadership, encourages co-operation, advances technical knowledge and builds competency related to dams.

With over a century of experience with major dam developments, the Canadian dam sector is strong and mature. Our dam professionals have extensive experience in dam design, construction, operation and maintenance. Many existing dams are now undergoing rehabilitation and improvement to counter the effects of aging and to meet current safety

[1] marc.smith.2@wsp.com, Canada
[2] margaret.trias.hault.com, Canada

standards and practices. Dam-building and management require the integrated and interdisciplinary engineering skills that Canadian engineers can provide.

CDA has been highly successful in leveraging member expertise in dams and dam safety, for both water retaining and tailings dams, to promote knowledge transfer around the world. This has kept CDA members in touch with advances in practice.

Keywords: Canada, Canadian Dam Association, Capacity Building

Fifth International
Dam World Conference
Portugal•Lisbon•LNEC•13-17 April, 2025
dam world 2025

FAILURE MODES: A CANADIAN PERSPECTIVE, CASE STUDY ON INTERNAL EROSION

Marc Smith[1]
WSP Canada and
Canadian Dam Association

ABSTRACT

The main geotechnical Dam Safety vulnerabilities and uncertainties for a dam rehabilitation project during its construction were related to potential for increased internal erosion risks at the two 16 m-high central till core zoned embankment dykes, in the wrap-around sections at the spillway extremities. These risks were assessed in terms of potential failure mechanisms as a tool for geotechnical design of interventions to decrease uncertainties and minimize core disturbance as well as to provide lines of defense against initiation, continuation, and progression of internal erosion.

An instrumentation program was implemented during design to decrease geotechnical uncertainties. Instruments were installed to allow pre-construction baseline monitoring as well as dyke behaviour assessment during construction. Soil sampling and testing was also performed as well as 3D stress-deformation analyses. Design features and construction methods that minimize core disturbance and loading were adopted as a first line of defense against potential increase of internal erosion risks. Other lines of defense included ensuring adequate contact between the dyke cores and the spillway structure, ensuring filter compatibility in the dykes as well as placement of additional downstream filter zones.

This paper presents a case study on how geotechnical risks during construction project were assessed to address geotechnical vulnerabilities and uncertainties during design as well as to

[1] marc.smith.2@wsp.com, Canada

identify performance parameters to be monitored during construction. Dyke behaviour during construction in terms of displacements, seepage detection and pore pressures is also presented.

Keywords: Embankment Dams, Failure Modes, Internal Erosion, Rehabilitation

TAILINGS DAM SAFETY- DEVELOPMENTS IN CANADA

Mohammad Al-Mamun[1]
Canadian Dam Association

ABSTRACT

Canada has a strong mining industry which brings economic and material benefits, but there are also risks associated with the by-products – mine tailings, which are usually retained within containment structures such as tailings or mining dams. These structures can pose a significant risk of failure causing loss of life and impacts to environment, as well financial damages.

The Canadian Dam Association (CDA) has been instrumental in promoting improvements in dam safety practices for mining and tailings dams, since the 2007 introduction of tailings dam guidance to Dam Safety Guidelines. This was followed in 2014 by Application of Dam Safety Guidelines to Mining Dams, which was one of first technical bulletins on the design, construction, operations, closure of tailings dam in the world. Since that time, the CDA Mining Dams Committee has developed several technical bulletins and has been very active on the ICOLD Committee on Tailings Dams and Waste Lagoons, developing guidance for international application.

CDA's bulletin on Tailings Dam Breach Analysis has filled a gap in guidance for an activity that is important for understanding the potential consequences of tailings dam failure, classification of the dams, and emergency management. This presentation will touch upon some of the challenges and successes that the working group encountered over the 12 years of consultation and development. It will also highlight the ongoing advances in the science of tailings.

[1] mamun.almamun@tetratech.com, Canada

Currently, CDA's Mining Dams Committee and Dam Safety Committee are collaborating to develop updated Dam Safety Guidelines and associated bulletins that cover the need for guidance related to both tailings dams and water-retaining dams.

In parallel with leadership shown by CDA and other organizations such as the Mining Association of Canada (MAC), the provincial and territorial governments have made significant changes in the dam safety regulations for tailings dams in Canada. Some of these regulatory changes followed the 2014 failure of the Mount Polley Tailings Storage Facility in the province of British Columbia.

This presentation will provide an overview of the advances in good practices and regulation for tailings and mining dams, and the challenges still being faced.

Keywords: Tailings, Mining, Guidelines, Dam

Fifth International
Dam World Conference
Portugal•Lisbon•LNEC•13-17 April, 2025
dam world 2025

DAM SAFETY MANAGEMENT SYSTEMS

Tony Bennett[1]
T&L Consulting and
Canadian Dam Association

ABSTRACT

A comprehensive Dam Safety Management System (DSMS) is essential to ensure the safety, reliability, and longevity of dams, as it integrates policies, processes, data and tools to monitor, assess, and mitigate potential dam safety risks.

The role of policy is paramount in driving the other elements of a DSMS: planning, operation, monitoring and verification, safety assessment, portfolio management, program review and reporting, and continual improvement. Policy is developed in the context of the regulatory framework and standards of good practice; it must include clear reporting structures, and a commitment to safety and continuous improvement. These policies guide the prioritization of maintenance, remedial actions, and emergency response strategies, ensuring that the safety management system remains effective and responsive.

Continuity of knowledge is central to the implementation of the DSMS. As new data becomes available from safety assessments, inspections, monitoring, and incident reports, the safety management system must be dynamic, incorporating the latest information within a knowledge bank. This enables continuous learning that addresses evolving threats, such as those arising from aging infrastructure, climate change, or operational changes. It allows decision-making across a portfolio with the appropriate priority and urgency.

Keywords: Dam Safety Management System

[1] bennett.tony8@gmail.com, Canada

Fifth International
Dam World Conference
Portugal • Lisbon • LNEC • 13-17 April, 2025
dam world 2025

PUBLIC SAFETY AROUND DAMS: PRACTICAL GUIDANCE FOR MEETING OWNER RESPONSIBILITIES IN CANADA

Tony Bennett[1]
T&L Consulting and
Canadian Dam Association

ABSTRACT

Dams benefit society and play a crucial role in water resource management, flood control, and power generation, but dam failure and operation also pose potential risks to public safety. While the focus of dam safety programs is often on the prevention of catastrophic failure, in many jurisdictions including Canada, it is the hazards posed by dam operation, or the public's interaction with the dam, that historically has resulted in more fatalities and accidents. In fact, there have been 112 documented fatalities associated with dams and their operation in Canada since the year 2000, while there are only 37 fatalities known to have been caused by dam failure dating back to the 1800's, with the most recent being in 1966.

In Canada, water management, including dams, generally comes under the jurisdiction of the individual provinces and territories. However, despite the provinces having the legislative accountability for dams, less than 50% have enacted dam safety regulations. Rather, the approach of dam owners is to rely on industry guidance developed by the Canadian Dam Association (CDA) which defines good practice. The CDA Dam Safety Guidelines provide a framework for dam design, operation, maintenance, performance monitoring, emergency management and periodic assessment – including the practice of managing public safety around dams. The guidance includes the CDA Guidelines for Public Safety Around Dams (2011). While compliance is voluntary, following industry good practice does assist owners in demonstrating that due diligence requirements have been met in the prevention of accidents that could result in loss of life or significant property damage.

[1]bennett.tony8@gmail.com, Canada

The CDA Guidelines for Public Safety Around Dams, are structured around a formal risk assessment to document the public activities and identify non-failure hazards associated with the dam and its operation.

The presentation will outline practical guidance and considerations for dam owners to meet their responsibilities with respect to public safety for non-failure scenarios, focusing on the process for risk assessment, identification of control measures, and the implementation of management strategies.

Keywords: Dam Safety Management System, Failure Modes

Fifth International
Dam World Conference
Portugal•Lisbon•LNEC•13-17 April, 2025
dam world 2025

PANEL DISCUSSION: CHALLENGES IN DEVELOPING DAM SAFETY GUIDELINES

Caius Priscu[1]
Moderator, Priscu & Associates

ABSTRACT

Many jurisdictions and organizations have faced the challenges of developing Dam Safety Guidelines that represent good practice and then applying them to the range of dams and circumstances that exist. Authors of such guidance need to navigate the various needs of key stakeholders including regulators, dam owners, operators, consultants and ultimately the public.

These are amongst the issues that the Canadian Dam Association is facing while undertaking a major review and updating of its Dam Safety Guidelines. A Panel format will be used to solicit perspectives of the international audience at Dam World 2025 to address questions such as:

- Do the same principles and guidance apply to water retaining and mine tailings dams? What are the fundamental differences?
- What common principles can we agree on, even if there is no “one size fits all” solution?
- How to reconcile with the requirements of different international organizations – e.g. ICOLD, national guidelines, GISTM, ICMM?
- How does the legal country or state/province framework affect the way guidance is presented?
- Are we clear on differences between standards and guidelines?

[1] cpriscu@priscuengineers.com, Canada

- Is there too much guidance out there? Are they conflicting recommendations?

The audience will be encouraged to engage in the discussion, comment and pose additional questions.

Keywords: Panel Discussion, Guidelines, Water Retaining Dams, Mine Tailings Dams

Fifth International
Dam World Conference
Portugal•Lisbon•LNEC•13-17 April, 2025
dam world 2025

TAILINGS DAM SAFETY- DEVELOPMENTS IN CANADA

Anthony Burnett
Suncor Energy Ltd. and
Canadian Dam Association

ABSTRACT

Syncrude Canada (Operated by Suncor) Geotechnical Review Board first met in November 1972, over 50 years ago and some five years before mine production began. The Board's initial 13 members, each a recognized expert in geotechnical engineering representing a different owner of the Syncrude consortium, worked together to advise Syncrude on pit-slope angles and highwall stability to answer the question: Would 50-metre-tall highwalls be stable enough for dragline mining in the oil sands? Building on advice from the Board, and after excavating and monitoring a large, instrumented oil sands dragline test pit, Syncrude selected dragline mining.

Over the decades, the Board's membership has been streamlined and its mandate broadened to include tailings risk management, waste dumps, mine closure, geoenvironmental issues, and risks associated with hydrogeology. For most of its existence, the Board operated with an implicit mandate, one that was recently formalized. While mining is still a major focus, the Board now spends most of its time reviewing the design, construction, performance, and closure of tailings facilities in support of Syncrude's commitment to developing and using the latest technologies and techniques. Though long a staple of major civil projects, review boards were unusual in the mining sector 50 years ago.

Today, mining geotechnical and tailings review boards are commonplace, and their achievements have both influenced and been influenced by the successes at Syncrude. Syncrude has learned the keys to an effective geotechnical review board. This article explains

[1] anburnett@suncor.com, Canada

these lessons, celebrates the last 50 years, and provides a case history for other companies and their review boards.

Keywords: Independent Review, Geotechnical Design, Risk Assessments, Failure Modes

Fifth International
Dam World Conference
PORTUGAL • LISBON • LNEC • APRIL 13-17, 2025
dam world 2025

THE FROST AND LEACHING DETERIORATION OF DAMS IN ALTITUDE: CASE STUDIES

Christian Paglia [1]
University of Applied Sciences of Southern Switzerland, DACD, V. F. Ruchat 15, 6850 Mendrisio

Samuel Antonietti [2]
University of Applied Sciences of Southern Switzerland, DACD, V. F. Ruchat 15, 6850 Mendrisio

ABSTRACT

Dam concrete is planned to resist the service and atmospheric conditions over time. In the mountain regions, arch dams are built in altitude along narrow valleys and are exposed to severe environmental conditions. The concrete conservation state of a dam tunnel spillway, an upstream face of a second dam both with a service life beyond 60 years and a downstream face dam located up to 2600 meters above the sea level were investigated. The concrete was produced with local materials CEM I, gneiss, quarzite, mica-schist, micas and amphibols. The cement content was 250-300 kg/m3 and the W / C ratio > 0.60. The spillway exhibits a deep delamination of the tunnel concrete and the high variability of the compressive strength indicates a dishomogeneity of the concrete. Indicatively, the concrete did not comply with the actual standard of water permeability requirements for conventional concrete. In spite of the potential AAR reaction triggered by cement alkalis and Na+ released by the albite from gneiss, AAR damage was not detected. The secondary ettringite formation was not present, due to the low water sulphate content. Frost damage and leaching were the main damages emphasized by the low quality of concrete and the turbulent water flow thorough the spillway. The dam upstream face exhibits similar variable and local variations in the concrete quality, due to the casting procedure. Leaching promoted by the CO2-rich waters and the frost damage with local scaling of the surface, promote the local exposure of aggregates in zones with a high water saturation level. The downstream face exhibited a critical saturation level, depending on the rain prior to freezing. A dynamic change in the surface concrete microstructure, due to thermal variations and porosity re-arrangement during time, promoted the formation of sub-vertical cracks for the increased entrance of water, that promoted main expansion cracks, subparallel to the surface.

Keywords: dam, leaching, frost, damage, microstructure

[1] christian.paglia@supsi.ch, Switzerland
[2] samuel.antonietti@supsi.ch, Switzerland

1 INTRODUCTION

The dams are among the massive structures present worldwide, that were mainly built in the second half of the last century. During time, the dams are exposed to several actions, that lead to ageing of the infrastructure. The damage can be related to earthquake events, soil settlement and concrete issues. The concrete is mostly affected by the alkali-silica rection and the cracking pattern that may arise as well as the sulphate attack, due to the sulfur and sulphates present within the soil minerals. The CO_2-rich water may also deteriorate the concrete. In altitude, the frost action may lead to relevant surface scaling and damage of the concrete surface. Air entraining agents may partially improve the frost resistance of the concrete. Closely space parallel cracks may be a clear indication of freeze / thaw damage, while the cyclic thermal expansion, the frost action and the wetting and drying may contribute to the general disintegration of the concrete, especially at a surface level.

On the other hand, alkali-silica reaction is a major damage in dams worldwide [1] and low reactive aggregates, low alkalis cements and supplementary cementitious materials may reduce the damage [2]. The ASR reaction may exhibit a relevant damage also in depth, especially in the upstream face, where water is more present. Stress relief wire sawing was applied to partially release the stress of big dams [3], while water proofing linings on the upstream surface do not seem a reasonable, durable and cost-effective solution to mitigate the expansion. Sulphate attack is also a damage, that occurs in spillways, due to soils and water chemistry [4]. Thaumasite attack in a cold climate and in the presence of carbonates may lead to concrete disintegration. However, cementitious materials disintegration is observed for both Sodium ad Magnesium sulphate, similarly as for shotcrete in tunnels [5]. Concrete abrasion along the dam waterways and cavitation as well as aggregate pop outs along spillways, due to the high water flow velocity, are also major durability issues. This latter form of deterioration can be partially limited by introducing water aeration devices. On the other hand, a service life of a dam cannot be indefinitely extended [6].

The frost damage continues to be a concern, in spite of the technological improvement of the concrete and the chemical admixtures. Concrete scaling is observed at the water line and well below the water level, in the upstream face of dams. Concrete may exhibit scaling of the surface, due to frost action, when in contact with unfrozen water. Frost damage occurs, if the critical water saturation level is reached [7]. The frost damage appears to increase, due to the water leaching effect. Low heat cement and air entraining agents improved the frost resistance of Swedish dams, with minor damage along the water level [8]. Leaching and coarse aggregate

exposure as well as the main damage is largely seen within the waterline changing level. Sunlight largely influences a more frequent freeze / thaw cycles with higher damage present in the South facades as compared to the North facades in dams located in Norway [9]. Furthermore, the damage seems higher in the downstream as compared to the upstream side. The upstream side is often covered by the insulating effect of ice, thus reducing the freeze / thaw cycles, as observed in Finland [10]. An asymmetry in the deterioration of infrastructures is often present [11]. The formation of ice lenses causes internal frost attack, independently of the concrete water to cement ratio. The surface scaling of the concrete can also be observed below the waterline and the presence of air entraining agents does not always exhibit a significant improvement of the frost resistance. On the other hand, the damage speed tends to be relatively low with time [12].

The water saturation level of concrete is an important factor, that controls the freeze / thaw damage susceptibility. The submerged section of the upstream water surface is saturated. A concrete water saturation level below 91.7% seems to limit the detrimental frost damage [13]. Most of the dam concrete is unsaturated. Nonetheless, rain is often followed by freezing in the winter seasons and the water may enter the concrete infrastructure by capillary adsorption and increase the saturation level. The concrete capillary water adsorption up to 10 days before the freezing action exceeded the 91.7% level near the water adsorption surface. The critical depths for the concrete water saturation below the water adsorption surface seem to range from 1.2 cm to 1.8 cm [14].

The aim of the work is to present and discuss some case studies of damaged dams present in the alpine region with respect to the interaction between leaching and frost damage. Both type of deterioration are also coupled with abrasion and the atmospheric changing conditions in altitude. An investigation on a microstructural level was also done to clarify some damaging mechanisms, especially for the frost action on real dam infrastructures.

2 EXPERIMENTAL PROCEDURE

The determination of the damage degree is generally done by means of a visual inspection. Binocular lenses, optical microscopy and a scanning electron microscope (SEM) in back scattered mode were used. The working distance ranged from 7 mm to 9 mm at 15 KV voltage and a pressure of 60 Pa. The compressive strength is determined on cored concrete specimens with a diameter of 50 mm and a length of 50 mm [15]. The porosity and water permeability tests were performed on cylinders after 28 days of hydration. The samples were immersed and

dried to obtain different degrees of saturation. Through weighting carried out in the air and in water, the characteristic quantities of water absorption, porosity and density were determined [16].

3 RESULTS AND DISCUSSION

An arch dam built in 1963 located at 1700 above sea level with a basin volume of 0.3 Mio m^3 a height of 39 m, and a length of 115 m exhibits a relevant damage of the spillway, especially along the lateral tunnel wall curvature (Fig. 1 left). A large zone of calcium carbonate deposition indicates a high humidity presence and water infiltration (Fig. 1 right). The carbonate forms a superficial thick crust along the walls. The deposition is caused by the cyclic wetting and drying, which promotes Calcium dissolution, Ca-hydrogen carbonate formation and re-precipitation in form of carbonates, in contact with the atmosphere.

Fig. 1 – Spillway curvature (left) and calcium carbonate precipitation along the lateral walls (right).

The concrete exhibits a delamination, which is mainly located in the lower parts of the walls, at a height < 1.5 m from the pavement. The detachments and scaling reach relevant dimensions up to 20 cm. A high water velocity also act as an abrasive medium to the concrete causing concrete scaling (Fig. 2 left), well beyond the local cavitation phenomena of the concrete surface. Advanced and deep detachment of the concrete surface with the formation of relevant craters are seen (Fig. 2 right).

Fig. 2 – Spillway wall concrete scaling (left) and detachment (right).

Concrete sampling in the undamaged and deteriorated zones, indicates multiple surface cracking in the deteriorated zones (Fig. 3 left). The spillway tunnel concrete could be detached by hand (Fig. 3 right). Nonetheless, the cement dosage is not low. The estimation ranges from 250 kg/m^3 to 400 kg/m^3, the water to cement ratio is 0.60, no mineral additions are detected, while the relative density exhibits sligthly low values from 2'215 kg/m^3 to 2'213 kg/m^3.

Fig. 3 – Spillway surface cracking pattern on cored specimens in the deteriorated zone (left) and concrete detachment (right).

The compressive strength was mesured in 2011 after the dam was 50 years old. The concrete exhibits relatively low values as compared to today's infrastructures. The estimated compressive strength class during construction appears to be a C20/25. The compressive strength of the less deteriorated zones shows a mean value of 27.7 ± 2.8 MPa (Table 1 left). Conversely, the mean compressive strength of the deteriorated zones shows a lower mean value of 8.8 ± 3.1 Mpa (Table 1 right).

Table 1 – Compressive strength of the low damaged (left) and highly deteriorated zones (right)

Table 1 left

ID	Sampling zone	Density [kg/m^3]	Compressive strength [N/mm^2]
1	Less deteriorated zone	2227	28.7
2	Less deteriorated zone	2246	29.5
3	Less deteriorated zone	2253	24.5
4	Less deteriorated zone	2225	24.2
5	Less deteriorated zone	2229	29.1
6	Less deteriorated zone	2254	30.3
Mean value and Std			**27.7 ± 2.8**

Table 1 right

ID	Sampling zone	Density [kg/m^3]	Compressive strength [N/mm^2]
7	Highly deteriorated zones	2092	11.0
8	Highly deteriorated zones	2092	6.6
Mean value and Std			**8.8 ± 3.1**

The saturable and the total porosity range from 18.3 % to 22.7 %, while the water permeability from 22.2 to 25.6 g/m^{2}h. The values are relatively high as compared to conventional transportation infrastructure concrete. The limit of 10 g/m^{2}h, set by the actual concrete standard [17] for a waterproofing concrete, is not attained. On the other hand, the concrete technology and requirements of the past and the type of infrastructure, were slightly different

from today. A direct correlation between porosity and water peremability does not always exists. A highly deteriorated zone may indicate a lower water permeability and a higher porosity as compared to a less damaged zone. This may be due to the abrasion and transportaiion of the crumbly and damaged material away from the concrete surface.

Table 2 – Porosity and water permeability of the slightly deteriorated and highly damaged zones.

ID	Sampling zone	Saturable pores U_E [vol.%]	Non-saturable pores LP [vol.%]	Total porosity n [vol.%]	Water permability qw [g/m²h]
CI18A 7409 01	Less deteriorated zone	20.7 ± 0.8	2.0 ± 0.4	22.7 ± 0.5	**24.4 ± 1.7**
CI18A 7409 02	Less deteriorated zone	18.3 ± 3.7	1.2 ± 0.2	19.5 ± 3.8	**25.6 ± 5.2**
CI18A 7409 03	Deteriorated zone	19.5 ± 1.0	1.4 ± 0.5	20.9 ± 0.6	**22.2 ± 0.1**

The microstructure exhibits aggregates such as, gneiss, quarzite or micaschist (quartz-feldspar rocks, with micas and amphibols) with an angular and sub-angular shape. A high capillary porosity and no reactions between the cementitious matrix and the aggregates, not even with the siliceous components, were seen. Sometimes, secondary calcite recrystallization with air pores and locally rare cracks < 5 µm were observed. The leaching of the cementitious matrix leads to the formation of a wide capillary porosity and crack formation (Fig. 4). Multilayers of calcite deposition were also seen.

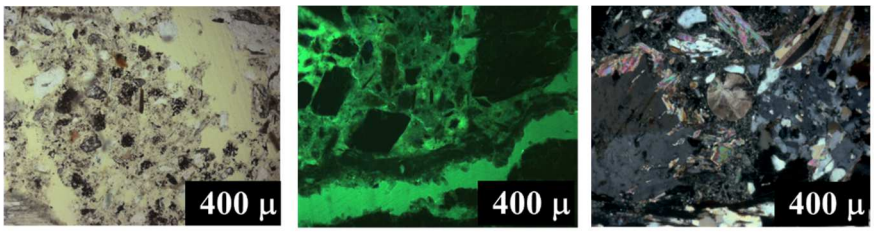

Fig. 4 – Leaching of the cementitious matrix (left). Capillary porosity, due to the cementitious matrix leaching (centre). Secondary crystallization of calcite. Nearby pores and cracks, due to the lack of cementitious matrix (right).

The water analysis shows a slightly acidic pH < 6.3 and CO_2 enrichments, typical for a slightly aggressive water, that may promote the leaching. The content of ions (SO_4^{2-}), (NH_4^+) and (Mg^{2+}) indicates a limited aggressivity, corresponding to an exposition class XA1 [17].

The relevant delamination is locally intense and is caused by the relatively low compressive strength, the dishomogeneity of the concrete and the high porosity, due to a relatively high water to cement ratio. The cyclic water flow and the relatively frequent high water saturation level along the spillway, the increased tunneling wind freezing effects as well as the abrasion and the frost, promote the main damage. The relevant leaching also belongs to one of the main reasons of the degradation.

An arc dam basin with a water capacity of 63 million m^3, built in 1956, with a height of 130 m, a length of 363 m and a dam volume of 775'000 m^3 exhibits a scaling of the concrete surface along the upstream face. Leaching is observed at different levels on the upstream face (Fig. 5 left). The process leads to the exposition of the coarse aggregates (Fig. 5 right). The local scaling of the concrete indicates a frost action taking place across the water level fluctuations.

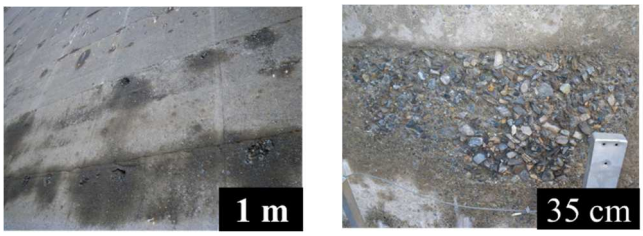

Fig. 5 – Leaching and scaling of the upstream dam concrete and exposition of the coarse aggregates, due to leaching (right).

The concrete compressive strength exhibits a mean value of 28.6 ± 8.5 MPa (Table 3 left), while the saturable porosity indicates a mean value of 14.0 ± 2.9 %. The water permeability shows a mean value of 18.4 ± 4.2 g/m^2h (Table 3 right).

Table 3 left

ID	Density [kg/m^3]	Compressive strength [N/mm^2]
7696-03	2390	33.9
7696 -04B	2360	33.1
7696 -06B	2350	18.8
	Meann value and std	**28.6 ± 8.5**

Table 3 right

Cetificate nr.	Saturable porosity U_E [vol.%]	Non -saturable porosity LP [vol.%]	Total porosity n [vol.%]	Water permeability q_w [g/m^2h]
CI18A 7696 01	14.0 ± 2.9	1.6 ± 0.3	15.6 ± 3.2	**18.4 ± 4.2**

The compresive strength reaches satisfactory values, while the water permeability is above 10 g/m^2h. The sulphates extraction is done through gravimetry, concentrated hydrochloric acid, hot water and Barium chloride precipitation. The sulphate content of the concrete exhibits a mean value of 0.237 ± 0.1 %. Therefore, sulphate attack and expansion as well as disintegra-

tion, can be excluded. A cement Portland content of 300 kg/m^3 is estimated from the microstructural investigation. A medium-high porosity and a rare shrinkage cracking, shows a width from 5 µm to 10 µm. No signs of reaction between the aggregates and the cementitious matrix are seen. The capillary porosity increases along the aggregate-cement matrix interface, while the carbonation depth is measured up to 8 mm. The carbonation is likely due to the cyclic variation of the water level. The pores and cavities exhibit a trend towards agglomeration. The pores exhibit the crystallization of portlandite and some ettringite, with no relevant consequences on the expansion and cracking.

The relative higher compressive strength and lower water permeability of this concrete does not protect the dam from leaching and frost damage. The presence of porosity detected with the microstructural investigation does not allow to determine the addtion of air entraining agents during the concrete casting. These chemical admixtures may mitigate the frost action, but they cannot completely avoid it, due to the changes in the surface concrete micristrcutre with time, especially in the harsh environments. On the other hand, the frequently water saturated parts of the upstream dam façade [7] is highly exposed to the alternate freezing. Conversely, in very cold regions the ice sheet may reduce the cyclinc exposure to the frost action [10].

A dam located at 2600 meters above the sea level (Fig. 6 left) exhibits a significant scaling of the concrete surface in the downstream dam face (Fig. 6 right). The scaling is widespread along the entire dowstream surface.

Fig. 6 – Alpine dam (left) and extensive surface scaling of the downstream face (right).

The scaling is also present along the concrete junctions (Fig. 7 left) and reaches 2 cm in depth. This depth well correlates with the water critical depth up until 1.8 cm of water saturated concrete regions [14], although the downstream face appears generally unsaturated. The saturation may occur during rainy days or through the permeation of water through the decades

across the dam. Nonetheless, carbonate precipitation along junctions is not frequent. Therefore, the saturation seems to derive from rainy atmospheric conditions. The debris fall down along the dam face and accumulate at the bottom of the dam (Fig. 7 right).

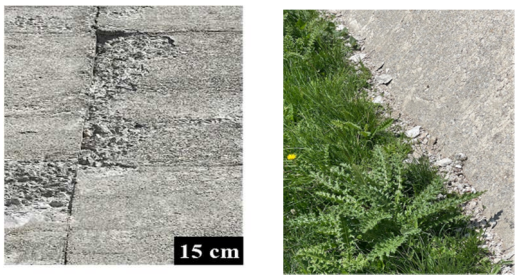

Fig. 7 – Surface scaling along the junctions (left) and debris accumulation at the bottom of the dam (right).

The downstream face is exposed to harsh and extreme atmospheric cyclic conditions and the concrete surface exhibits a dynamic change in the microstructural features, with microcracks formation and closure as well as phases dissolution and phases precipitation (Fig 8 left). The air entraining agents, that are added to the concrete mixture, modify the whole microstructure of the bulk concrete, including the surface, by promoting the formation of a uniformly distributed interconnected porosity. On the other hand, the surface porosity does not remain the same during time. Microcracks formation as well as dissolution-precipitation takes place on the surface and this process may partially mitigate the positive effects of the air entraining agents. This is the reason why the addition of a chemical admixture to increase the frost resistance does not always provide the expected freeze / thaw resistance. However, a relative low speed of the frost damage is generally seen [12]. The leaching of the cementitious component and the exposition of the stone aggregates (Fig. 8 right) may further accelerate the water penetration and contribute to the saturation and frost action during the cooling phase.

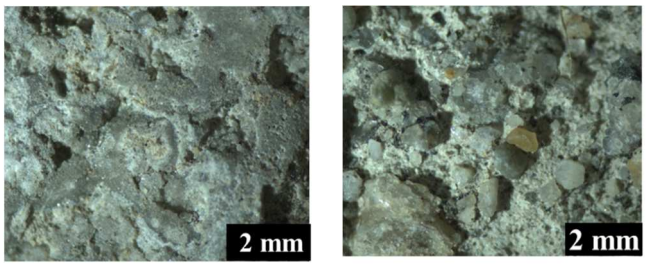

Fig. 8 – Active dynamic crystallization (left) and dissolution of the cementitious component on the surface (right). Binocular lenses images.

The microcracks tend to form with a sub-parallel orientation with respect to the surface. However, they convey the water to main cracks with a wider opening, where the main expansion and scaling takes place (Fig. 9 left). Usually, this main psuedo-horizontal cracking occurs within 0.5 and 2 cm beolw the surface and is mainly controlled by the lack of availability of enough pores to accomodate the expansion and a critical water saturation level. During time, the original porosity distribution of the surface is partially modified by a combination of fine cracking with wide openings towards the surface, formed during the thermal excursions and the slight re-precipitation of phases, that closes a part of the pores and the cavities. Therefore, a re-arrangement of the surface porosity at a micrometer level occurs. This may be one of the reason for the reduced frost resistance of some air entrained concretes. Cracks propagate along the cementitious matrix, along the hydrated cement paste-aggregate interface (Fig. 9 centre), and across the aggregates (Fig. 9 right), depending on the local stresses. Some cracks tend to stop against the aggregates, if the stress field decreases.

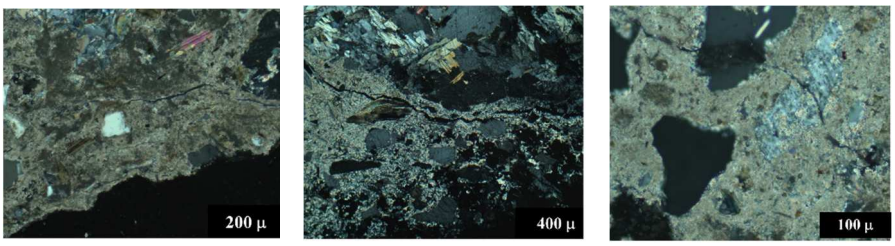

Fig. 9 – A crack pattern close to the concrete surface (left). Crack propagation along the cement paste-aggregate interface (centre) and across the aggregates (right). Optical microscopy images.

A fine cracking formation close to the surface with a sub-vertical orientation (Fig.10 left) tends to improve the water penetration and to increase the water saturation level within the concrete. In the critical water saturated depths and in the presence of frost, a wider crack opening appears to form with a pseudo-horizontal orientation and causes scaling of the concrete surface (Fig.10 right).

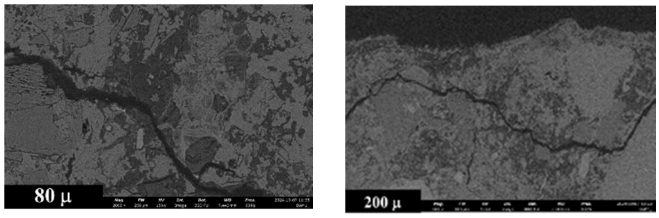

Fig. 10 – Sub vertical fine cracks (left) and horizontal mean expansion crack with resulting scaling of the concrete surface (right) at the critical water saturation level.

On the superior part of the detached flakes, that suffered scaling from the concrete surface, a clear leaching of the cementitious paste and the exposition of the aggregates is seen (Fig,11 left). Cracks with a wide opening towards the surface mainly form within the cementitious paste (Fig. 11 centre), due to the thermal excursion of the concrete. A combination of leaching and fine crack formation, likely also partially caused by the freezing action, is observed along the downstream part of the dam, although these side of the dam is less prone to reach water critical saturation levels. In the downstream face, the critical level is mainly reached through the action of rain [13, 14]. In the inferior parts of the flakes, a widespread presence of fine cracks is seen (Fig. 11 right).

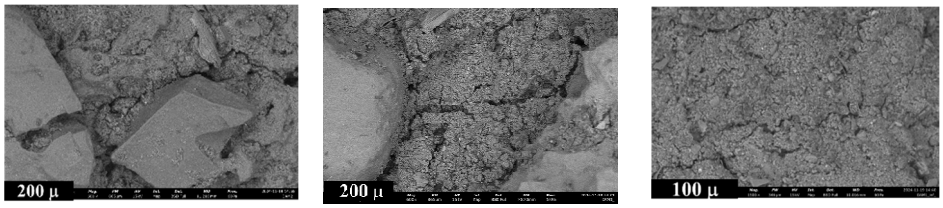

Fig. 11 – Superior part of the detached flakes. Leaching of the cementitious paste and aggregate exposition (left). Cracks surface wide openings within the cementitious paste (centre). In the inferior part of the flakes, a widespread presence of fine cracks is seen.

4 CONCLUSIONS

The dams exhibit a local medium and dishomogeneous concrete quality, likely due to the large dimensions of such infrastructures and the casting as well as the material technology present in the past. A relative high porosity and a high water to cement ratio used in the past, produced some concrete zones with a higher water permeability as compared to today's standards. No chemical reactions, such as delayed ettringite expansion, due to sulphate attack or alkali-aggregate reactions were found, due to the low sulphate concentration of the water and the low susceptibility of the cementitious paste as well as the aggregates with respect to these degradation reactions. A combination of leaching and frost damage was caused by the critical water saturation also in the downstream side of a dam, mainly exposed to rainy conditions, rather than only in the upstream face, almost in permanent contact with water. The concrete surface exhibits a dynamic change and formation of fine cracks, due to the wide thermal excursions at such altitudes. Re-precipitation of phases also occur and the pore presence as well as the pore interconnectivity may change with time, regardless of the presence of air entraining agents. Pseudo-vertical cracks may increase the water penetration and the water saturation

level. In the case of frost, the water conveyed towards the critical depth, ranging from 0.5 cm to 2 cm, freezes and causes main expansion cracks running pseudo-horizontally to the concrete surface. In this case, a relevant scaling is seen.

Acknowledgements

A special thanks to the technicians of the Institute of materials and construction, SUPSI and Guido Corredig for a part of the optical micrographs as well as Chiara D'Erme for the SEM pictures.

REFERENCES

[1] Thomas, M. D. H., Fournier, B. and Folliard, K. (2013). Alkali aggregate Reactivity-ARR Fact Book. U.S. Department of Transportation, Federal Highway Department. Report No. FHW-HIF-13-019, pp.1-5, March.

https://www.fhwa.dot.gov/pavement/cocrete/asr/pubs/hif13019.pdf

[2] Dolen, T. P., Gregg, A., S., von Fay, K.F. and Hamilton, B. (2003). Effects of Concrete Deterioration on Safety of Dams, Alkali-Aggregate Reactions. Dam Safety Office Report No. DSO-03-05 Draft, p.8, Department of the Interior Bureau of Reclamation December.

https://www.usbr.gov/ssle/damsafety/TechDev/DSOTechDev/DSO-03-05.pdf

[3] Stress relief for big dams, Wire Sawing Relieves Concrete Stress Caused by AAR, Concrete openings, vol. 21, n. 4, December 2012.

[4] Dolen, T. P., Gregg, A. S., Von Fay, K.F. and Hamilton, B. (2003). Effects of Concrete Deterioration on Safety of Dams-Sulfate Attack. Dam Safety Office Report No. DSO-03-05 Draft, P 8, Department of the Interior Bureau of Reclamation December.

https://www.usbr.gov/ssle/damsafety/TechDev/DSOTechDev/DSO-03-05.pdf.

[5] C. S. Paglia, F. Wombacher, H. Boehni (2003), The Influence of Alkali-free and Alkaline Shotcrete Accelerators within Cement Systems. Influence of the Temperature on the Sulfate Attack Mechanisms and Damage, Cem. and Concr. Res., 33, pp. 387-395.

[6] Nasrat Adamo, Nadhir Al-Ansari, Varoujan Sissakian, Jan Laue and Sven Knutsson, Dam Safety (2020): Technical Problems of Ageing Concrete Dams, Journal of Earth Sciences and Geotechnical Engineering, Vol. 10, No. 6, 241-279 ISSN: 1792-9040 (print version), 1792-9660 (online) Scientific Press International Limited.

[7] Fagerlund, G. (1977): The International Cooperative Test of the Critical Degree of Saturation Method of Assessing the Freeze/Thaw Resistance of Concrete, Materials and Structures, Vol.4:231-253.

[8] Bergström, S.G. & Nilsson, L.B. (1962) : Cracking and Frost Damage of Concrete in Hydro Power Structures, VAST nr 61:269 (in Swedish).

[9] Heggstad, R. & Myran, R. (1967): Investigations on 132 Norwegian Concrete Dams, 9th International Congress on Large Dams, Istanbul.

[10] Lehtinen, P. (1979): On the Deterioration of Concrete Observed in Dams and Hydraulic Structures in Finland, 13th International Congress on Large Dams, New Delhi.

[11] C. Paglia, The deterioration asymmetry of engineering structures, Case Studies in Construction Materials, Volume 16, June 2022, e00980.

[12] Rosenqvist, M., Nordström, E., Hassanzadeh, M. (2013), Observations and investigations of frost damage mechanisms of concrete dams in Sweden, ICOLD Symposium, 14 August, Seattle, USA.

[13] G. Fagerlund, The significance of critical degrees of saturation at freezing of porous and brittle materials, Acids Struet J., 1975, 13-66.

[14] Yaoying Huang, Zhengyuan Yu, Qian Ding, Shimei Xu, A study of the saturation levels of concrete at different depths on the downstream zone of a dam under low-temperature conditions, Case Studies in Construction Materials 17 (2022) e01689.

[15] Standard EN 12504-1:2019, Testing concrete in structures - Part 1: Cored specimens - Taking, examining and testing in compression.

[16] Swiss Standard Sia 262/1, Concrete construction, complimentary specifications, appendix A. Porosity and water permeability.

[17] Standard EN 206:2021, Concrete - Specification, performance, production and conformity.

Fifth International Dam World Conference
PORTUGAL • LISBON • LNEC • APRIL 13-17, 2025
dam world 2025

ROCK-FILLED CONCRETE (RFC) ARCH DAMS WITH OR WITHOUT CONTRACTION JOINTS

Feng Jin[1]
Tsinghua University

Quanyi Zhang
Zunyi Survey and Design Institute of Water Conservancy and Hydropower

ABSTRACT

As a rapidly developing concrete dam construction technology, Rock-Filled Concrete (RFC) can be used to construct either a gravity dam or an arch dam, achieved by pouring High-performance Self-Compacting Concrete (HSCC) into the voids among preplaced large rock blocks with a grain size larger than 300 mm. To date, 181 dams have either been completed or are under construction, with 13 of them being arch dams. The Baijia dam stands as the tallest completed RFC arch dam at 69 m, while the Yongfeng dam, currently under construction, is set to reach 83 m in height. One notable advantage of RFC is its low hydration thermal rise, which allows for extended distances between contraction joints, typically exceeding 40 m that is significantly larger than that in a CVC arch dam. Under moderate weather conditions, medium or low RFC arch dams can be constructed in whole lifts without contraction joints. Five RFC arch dams without contraction joints impounded in recent years and have all performed very well. For example, Shaqian arch dam with a crest length of 205 m, was constructed during extreme hot season with daily air temperatures exceeding 40°C. Despite the lack of contraction joints and cooling pipes, it remains crack-free with minimal seepage in the bottom gallery. No closure grouting is required as there are no contraction joints in these dams. The unique thermal action considerations for RFC dams without contraction joints distinguish them from conventional arch dams, where contraction joints are typically grouted at a design closure temperature. The consideration in design RFC arch dams and the proposed calculation method for RFC arch dams without contraction joints are presented in this paper. Onsite measurements, including ambient temperature, internal temperatures within the rock blocks and the voids among them, and compactness of RFC, further validate the outstanding performance of RFC arch dams.

Keywords: Rock-Filled Concrete, arch dam, trial load method, contraction joint, thermal action

[1]jinfeng@tsinghua.edu.cn, China

1. INTRODUCTION

Rock-Filled Concrete (RFC) was invented at Tsinghua University, China in 2003 [1], which combined the advantages of masonry and concrete. Several studies have been conducted since then [2–6]. RFC technology utilizes a large number of rock blocks to reduce cement consumption, lower hydration temperature rise, and minimize concrete shrinkage. The employment of Self-Compacting Concrete (SCC) significantly reduces manpower requirements by eliminating the need for vibrating or roller compaction. The SCC employed in RFC is referred to as high-performance SCC (HSCC), as it has higher requirements for fluidity, stability, and anti-segregation, and entails lower cement consumption and reduced heat of hydration. HSCC must flow and be driven by its self-weight to fill the narrow and bent voids, including the fine ends of the voids among the rock blocks.

More than 181 RFC large dams, including 13 arch dams, have been constructed or are under construction, following the completion of a small RFC dam, 14.5 m high, in Beijing in 2005. In the early stages of RFC arch dam construction, the design of RFC arch dams followed that of CVC arch dams. Baijia RFC arch dam stands 69 m high and is divided into 7 monoliths, which was constructed from 2014 to 2016. Based on the engineering experience and monitoring data analysis in Dagutai RFC gravity dam, an innovative concept for constructing arch dams without contraction joints was proposed during the design of the Lyutang RFC arch dam in 2015. Subsequently, several arch dams, including Longdongwan, Shaqian, Taoyuan, and Fengguang, were constructed using the same technology. The design parameters of these RFC arch dams can be found in Table 1.

Table 1 – Design parameters of some RFC arch dams

S/N	Project Name	Dam height（m）	Crest length(m)	Number of contraction joints	Completion year/month
1	Mengshan Reservoir	24.5	129.8	7	2013.03
2	Baijia hydropower station	69	203.0	6	2016.04
3	Lyutang Reservoir	53.5	181.4	0	2018.11
4	Goujiang Reservoir	41	127.4	6	2019.05
5	Xiaoyuanli Reservoir	46.6	116.0	5	2020.05
6	Fengguang Reservoir	48.5	112.0	0	2021.08
7	Longdongwan Reservoir	48	174.7	0	2020.12
8	Niudongkou Reservoir	64	128.25	2	2021.08
9	Taoyuan Reservoir	37	113.0	0	2021.10
10	Longyuan Reservoir	40.5	148.6	8	2022.01
11	Shaqian Reservoir	66	205.0	0	2023.01
12	Qiaodui Reservoir	45	136.5	2	2023.04
13	Yongfeng Reservoir	83	253.4	4	Under construction

2. PRACTICE OF RFC ARCH DAM WITH CONTRACTION JOINTS

2.1. Niudongkou RFC arch dam impounded

Niudongkou RFC arch dam is located on Luoyu river, Hunan province, China [7]. The canyon at dam site is V-shaped, with both slopes steeply inclined at about 75°. The width of the canyon at the bottom and dam crest are 33 m and 110 m, respectively. The lower and upper parts of the canyon consist of limestone and breccia limestone, respectively. The rocks exhibit similar properties with a saturated compressive strength of 45 MPa and a deformability modulus of 5 to 8 GPa in the weakly weathered zone, and a saturated compressive strength of 65 MPa and a modulus of 12 to 15 GPa in the slightly weathered zone.

The dam is a double curvature arch dam with arches of multi-center. The maximum central angle is 102.204° and crest arc length is 169.38 m. The dam height is 64 m. The thickness of the central cantilever at the bottom and crest are 13.40m and 3.86 m, respectively. The shape of dam was determined using the traditional trial load method. The allowance compressive and tensile stresses are 3.8 MPa and 1.2 MPa for the fundamental loading combination, and 4.5 MPa and 1.5 MPa for the check loading combination, respectively. The crown deformation under the loading combination of water pressure at normal pool level and thermal decrease is 39.86 mm downstream, while the monitored crown deformation was 21.40 mm when normal pool level was first reached.

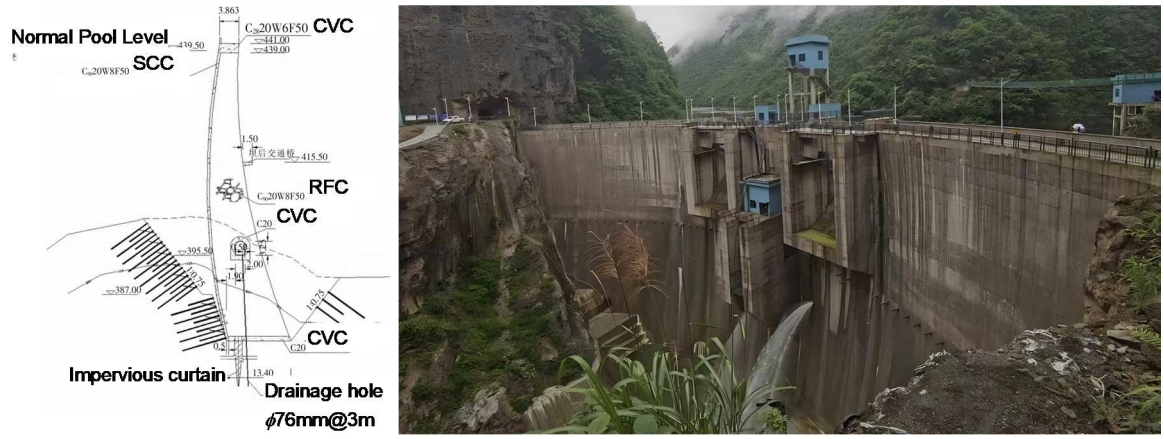

Fig. 1 – Profile and photo of Niudongkou RFC arch dam

An impervious zone, 0.5 m thick, of SCC is set at the upstream face of the dam. At the bottom, a gallery for the grouting curtain, monitoring, and inspection is provided. A CVC bottom cushion with 1 m thick and a crest layer with 2 m thick are set as shown in Fig. 1. The compressive strength class for all types of concrete is designed as 20 MPa for the 150 mm standard cubic specimen. Two contraction joints, spaced 54.80 m apart, are set at the arch dam. Keys, copper waterstops, and a grouting system are provided in the joints. The quality of the RFC dam body was checked using a water-pressure test. The test results ranged from 0.53 to 1.11 Lu, which meet the design requirement of 3 Lu. The density of RFC drilling cores is 2.45 t/m^3.

The height of lift is 1.5 m and the dam is raised at the rate of 1.5 m per 7 days. The unit cost of RFC is about 370 RMB per cum, which is similar to that of masonry and significantly lower than that of CVC. The excavated weakly weathered rocks were used in RFC.

On August 26, 2023, during the largest flood since 1998, the pool level was 0.2 m higher than the check pool level. This RFC arch dam performed exceptionally well, demonstrating the quality of both its design and construction.

2.2. Yongfeng RFC arch dam under construction

Yongfeng RFC arch dam is located on Lyuxi river, Fujian province, China. Given the sound granite rock foundation, a double curvature RFC arch dam with a height of 83 m was designed, making it the highest RFC arch dam under construction. The width of the canyon at the dam crest is about 180 m. The saturated compressive strengths of granite in lower and upper part are 65 to 70 MPa and 60 to 65 MPa, respectively. The arches were designed as parabolic curve with varying thicknesses. The crest thickness ranges from 5.0 to 5.564 m. The bottom thickness of the crown cantilever is 19.898 m, and the ratio of thickness to height of the arch dam is 0.24.

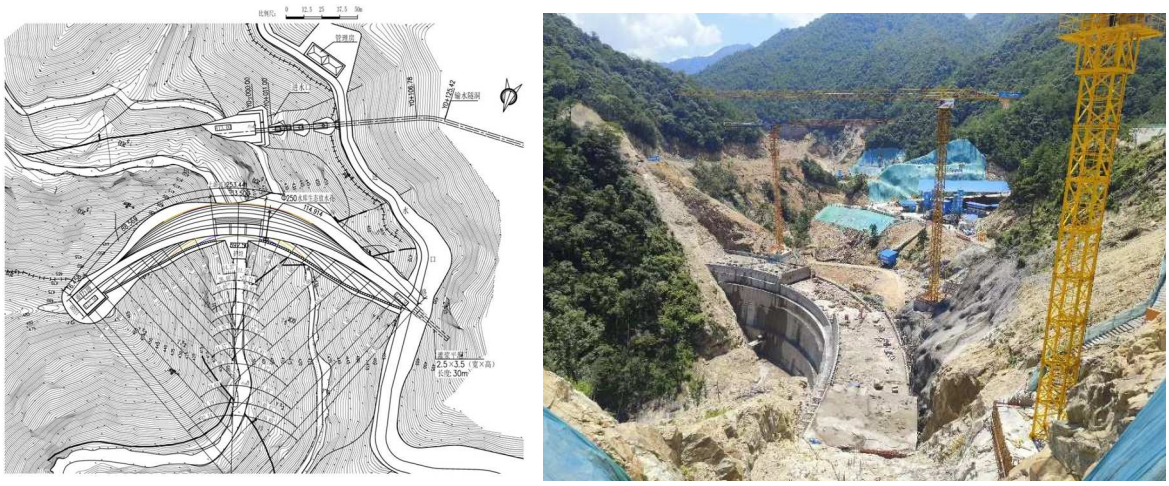

Fig. 2 – Plan and photo of Yongfeng RFC arch dam under construction

Four contraction joints with keys, copper and plastic waterstops, and grouting systems are set in this dam. Closure grouting will be conducted after the temperature of the RFC dam body drops below 15 °C. Walls made of precast concrete blocks, each measuring 300×300×500 mm, are used as formworks. A 1 m thick impervious SCC zone is set near the upstream formwork. A spillway with 3 spans is provided at the central crest. No galleries are provided due to the thin dam body.

The arch dam is constructed with RFC, which has a compressive strength of 15 MPa at 90 days for the 150 mm standard cubic specimen. The design seepage resistance of RFC is W8.

3. STRESS ANALYSIS FOR RFC DAMS WITHOUT CONTRACTION JOINTS

3.1. Mechanism of arch closure for traditional arch dams with contraction joints

Traditional arch dams are constructed as monolith, which are separated by contraction joints. The dam body is cooled to a designed relative cold temperature, known as the arch closure temperature, using embedded cooling pipes before the contraction joints grouting. The arches begin to function once all contraction joints are grouted. The loads acting on the dam before arch closure, such as the dead load, are borne by the cantilevers alone. The mechanism of arch dams was incorporated into the trial load method, which has been the basic stress analysis method for arch dams in China.

3.2. Arch-closure temperature of arch dams without contraction joints

When an arch dam is constructed in a whole lift without contraction joints, the mechanism of arch closure changes. The arches begin to function as soon as the concrete hardens. The traditional trial load method cannot accurately calculate the stress if the arch-closure temperature of arch dams is not determined.

According to the assumptions in the trial load method, the arch-closure temperature shall be the temperature at which arch begin to function and the thermal stress in the arches approaches to zero. In practice, the determination of arch-closure temperature is challenging, as it is influenced by the initial temperature of fresh concrete, the hydration process, and the structure of arches. However, the trial load method is used to determine the shape of an arch dam. Therefore, the requirements for thermal load in the method are not precise. Based on on-site temperature monitoring and analysis [8], a simplified arch-closure temperature calculation process was presented for the trial load method to determine the shape of medium or low arch dams.

The arch-closure temperature can be determined by the formula below [9]

$$T_a = T_p + (1 - \frac{E_1}{E_2})\Delta T \qquad (1)$$

where T_p is initial temperature of RFC, which can be calculated by the average of initial temperature of SCC and the temperature of rock blocks when SCC pouring. The temperature of rock blocks can be taken as the daily average air temperature based on onsite monitoring data. ΔT is the hydration thermal rise of RFC, which can range from 4 to 5 °C in the cold season and 7 to 8 °C in the hot season in the mild weather zone of China, according to the monitoring data. E_1 and E_2 are the average elastic modulus of RFC at pre- and post-peak temperatures, respectively. $1 - \frac{E_1}{E_2}$ can be chosen as 1/3 or 1/4.

It should be noted that the arch-closure temperature calculated by Eq. (1) accounts for the thermal stresses before arch closure during construction. Thus, the criteria of allowance tensile stresses should be changed to 1.5 to 2.0 MPa, instead of the 1.2 MPa as per Chinese code for design of concrete arch dams.

3.3. Stress analysis results of arch dams without contraction joints

The calculated stresses using the trial load method, considering the arch-closure temperature for several RFC arch dams without contraction joints are listed in Table 2. These 4 RFC arch dams have performed well during their operation. All of these dams were impounded in recent years.

Table 2 – Stresses from the trial load method for some RFC arch dams without joints (MPa)

Project	Lyutang			Longdongwan			Shaqian			Fengguang		
Case	TD	TI	CK	TD	TI	CK	TD	TI	CK	TD	TI	CK
σ_1	-1.25	-0.63	-0.77	-1.71	-1.28	-1.30	-1.75	-1.60	-1.66	-1.48	-0.53	-0.54
σ_3	2.62	2.86	3.15	2.78	2.72	2.76	2.57	3.68	3.79	2.27	2.21	2.24

Note: The cases TD, TI and CK refer to the working conditions of water pressure at the design pool level with temperature decease in winter and temperature increase in summer, and water pressure at the check pool level with temperature increase in summer, respectively. The +/- symbol indicates compressive or tensile stresses.

4. PRACTICE OF RFC DAMS WITHOUT CONTRACTION JOINTS

4.1. Lyutang RFC arch dam impounded

Lyutang RFC single curvature arch dam is located on Maoguan river, Guizhou province, China, and is the first RFC arch dam without contraction joints. The foundation consists of a V-shape canyon of limestone with a thin layer of mudstone. The average air temperature at the dam site is 15.7°C. The dam stands 53.5 m in height. The thickness at the bottom of the cantilever is 16.0 m and the thickness-to-height ratio is 0.299. The crest length is 186.31 m. A spillway is set at the crest as shown in Fig. 3. The total volume of RFC is about 68000 m^3.

(a) Completed upstream view (b) Impounded downstream view

Fig. 3 – Photos of Lyutang RFC arch dam

Instead of traditional steel formwork, walls made of precast concrete blocks were used as formworks. An onsite test was conducted to verify that the height of the precast wall, consisting of four layers of blocks, is approximately 1.28 m. The first RFC lift of Lyutang dam was cast in December 10, 2017. On November 28, 2018, Lyutang completed the final RFC lift. All RFC lifts were cast in whole lift without contraction joints.

Due to a shortage of funds for resettlement, the reservoir impoundment had to be delayed by 5 years. The thermal monitor data demonstrate that the thin upper part of the dam cooled to a stable temperature field after one winter, while the thick lower part cooled to a stable temperature after 2 or 3 winters. In 2024, the initial impoundment was completed and the arch dam has performed very well.

4.2. Shaqian RFC arch dam impounded

Shaqian RFC arch dam is also located in Guizhou province. However, the weather at Shaqian is hotter than at Lyutang, as the elevation of Shaqian dam site is lower. The sandstone canyon is V-shaped.

(a) Onsite filling test

(b) RFC casting on the rock foundation

(c) HSCC casting in whole lift

(d) Flood discharge of Shaqian

Fig. 3 –photos of Shaqian RFC arch dam

To study the impact of small rock blocks on SCC filling, an onsite filling test was conducted. The test lift was divided into 2 parts. One part used large rock blocks along with some small rock blocks with grain size less than 300 mm, and the other part used more small rock blocks and placed the small rock blocks in concentrate manner. The inspection results demonstrate that small rock blocks have minimal impact on the compactness of RFC. However, some voids existed after SCC pouring if small rock blocks were placed in a concentrate manner. Therefore, limiting the number of small rock blocks in unit volume during placement is important. Another innovation of Shaqian dam is that RFC was used as the cushion concrete on the sandstone foundation, instead of CVC as other RFC dams done.

Shaqian RFC dam was constructed using the same process as Lyutang dam. The Shaqian dam has a height of 66 m and a crest length of 205 m, both larger than those of the Lyutang dam. The dam construction spanned a very hot summer in 2022, during which there were 20 consecutive days with daily air temperatures exceeding 40 °C. The temperature at the top 200 mm thick of rock blocks was recorded over 60 °C due to sunlight, while the highest temperature of rock blocks below the surface was about 40 °C. No SCC was poured during the hot period from 12:00 to 17:00 to avoid excessively high placement temperatures of RFC. No additional temperature control measures, such as cooling pipes or pre-cooling of aggregates, were employed. Before the first impoundment, a comprehensive inspection was conducted for the dam face and no cracks were found. The bottom gallery remained dry even when the pool level exceeded the normal level and was discharging flood. The displacement of the dam crest, as well as seepage and seepage pressure monitoring data during the impoundment, all remained within the design range. The performance of Shaqian RFC arch dam during operation has been excellent.

5. CONCLUSIONS

RFC technology is an innovative approach that can be used to construct both gravity and arch dams. Some RFC arch dam with or without contraction joints were described in this paper. Due to the low hydration thermal rise, RFC dams, including arch dams, can be cracking-free constructed without temperature control measures. A scheme to estimate the arch-closure temperature was proposed for the trial load method that is the fundamental calculation method used in the design of Chinese arch dams. The practice of 5 RFC arch dams without contraction joints demonstrated that these integral casting arch dams can be constructed for low and medium-height dams under mild weather condition. It is suggested to reduce the number of contraction joints for high RFC arch dams, although a no-joint layout for high dams is not recommended.

REFERENCES

[1] Jin F., An X. H., Shi J.J. and Zhang C.H. (2005). Study on rock-filled concrete dam. Journal of Hydraulic Engineering, 78-83 (in Chinese)

[2] Jin F. and Huang D.R. (2022) Rock-Filled Concrete Dam, Springer Nature, Singapore. doi:10.1007/978-981-16-8298-8.

[3] Xie Y.T., Corr D.J., Chaouche M., Jin F. and Shah S.P. (2014). Experimental study of filling capacity of self-compacting concrete and its influence on the properties of rock- filled concrete. Cement and Concrete Research. 56, 121–128.

doi：10.1016/j.cemconres.2013.11.010.

[4] Jin F., Zhou H. and An X.H. (2019). Research on rock-filled concrete dam. International Journal of Civil Engineering. 17, 495–500. doi: 10.1007/s40999-018-0313-0.

[5] Wang Y.P., Liang T. and Jin F. (2024). Void effect study on the compressive behavior of RFC based on the 3D four-phase mesoscopic finite element model. Construction and Building Materials. 417, 135145. doi: 10.1016/j.conbuildmat.2024.135145

[6] Xu X.R., Xiao A.R., Zhu Y.L., Xu C., Zhang L. and Jin F. (2024). Heterogeneous temperature characteristics considering rainfall effect during construction of an integrally-poured rock-filled concrete arch dam. Construction and Building Materials. 450, 138626. doi: 10.1016/j.conbuildmat.2024.138626

[7] Li, J. L. (2024). Design and construction of Niudongkou RFC double curvature arch dam. Hunan Water Resource and Hydropower, No. 3 (in Chinese)

doi: 10.16052/j.cnki.hnslsd.2024.03.030

[8] Jin F., Zhang G.X. and Zhang Q.Y. (2020). Temperature analysis for Lyutang RFC arch dam in construction period, Journal of Hydraulic Engineering, Vol. 51, 749-756 (in Chinese)

[9] Jin F., Zhang G.X., Lou S.J., He T.H. and Zhang Q.Y. (2020). Trial load analysis for integral casting RFC arch dams, Journal of Hydraulic Engineering, Vol. 51, 1307-1314 (in Chinese)

Fifth International
Dam World Conference
PORTUGAL • LISBON • LNEC • APRIL 13-17, 2025
dam world 2025

REHABILITATION STUDY OF TEMENGOR AND CHENDEROH DAM FOR THEIR SAFETY ENHANCEMENT AND LIFE EXTENSION

Ioannis Siskos[1]
Tractebel Engineering Ltd.

Chongjiang Du[2]
Tractebel Engineering Ltd.

ABSTRACT

For operation of old dams, it is necessary to assess the actual structural safety of dams in accordance with the current state-of-the-art standards and latest recommendations of safety regulation authority. This paper provides case studies for Temengor and Chenderoh dam, and the respective rehabilitation measures are developed to enhance their safety and extend their life. During the time when the dams were designed and constructed, the seismic hazard and probable maximum floods were not considered. In addition, the problems of aging and weathering of materials significantly impact the dam safety. Thus, the topic is significant. The case studies emphasize the safety investigations including the visual inspection of the dams, comprehensive site and laboratory investigations, updating the study of seismic hazard and hydrological conditions. Based on the studies, the required rehabilitation measures are tailored. The study has shown that timely review of the structural conditions and implementation of remedial works can allow for safe extension of the operational life of hydroelectric projects, which may be taken as a reference for other similar projects. The rehabilitation measures are essential and economical. It is confident that the dams can be safely operated for another 30 years with the proposed rehabilitation measures. The discussions in this paper provide information and recommendations on principles and procedures, which is benefitable to owners, designers and constructors of dams.

Keywords: dams, aging, deterioration, rehabilitation, dam safety, dam engineering

[1]ioannis.siskos@tractebel.engie.com; Germany
[2]chongjiang.du@tractebel.engie.com, Germany

1. INTRODUCTION

Sungai Perak Hydroelectric Scheme is situated on Perak River of the Malaysian Peninsula and consists of four existing hydropower plants, namely, Temengor, Bersia, Kenering and Chenderoh dam, forming the Sungai Perak Cascade [1,2]. The projects were constructed from 1920s to 1980s. The old dam structures were designed using simplified design criteria and parameters. Therefore, the actual safety of dam structures shall be assessed in accordance with the current state-of-the-art standards and latest recommendations of safety regulation authority. In this regard, Tractebel Engineering Ltd. in Germany was commissioned to perform the dam safety enhancement study. The main task of the Service was to carry out technical study on integrity and stability of the dam and appurtenant structures, so as to extend the operational life of the hydroelectric plants at least for another 30 years by improving the safety of Dam and Appurtenant Structures to meet currently acceptable standards of safety and functionality. This paper describes the technical studies for the Chenderoh and Temengor dam. Current conditions and problems of the structures are studied, and remedial measures are proposed with preparing the tender documents.

2. BRIEF DESCRIPTIONS OF PROJECTS

Chenderoh HEP (Fig. 1 left) is the first dam on Perak River and the most downstream dam in the cascade, located about 250 km North of Kuala Lumpur. It was the oldest dam and hydropower plant in Malaysia and South-East Asia built from 1927 to 1930 and was considered the largest industrial undertaking in the Malay Peninsula at that time. The power plant has a total installed capacity of 40.5 MW. The water retaining structure is an Ambursen type dam – a type of concrete hollow buttress dams constructed by concrete buttresses and inclined deck slabs. It is founded on granite rock with gated and ungated overflow spillway sections over the crest. The maximum height is 23 m, and the overall crest length is 390 m. Short concrete gravity dam sections close the valley towards the abutments. The powerhouse is constructed at the toe of dam on the right bank.

Temengor HEP (Fig. 1 right) was completed in 1978. It is the upmost dam in the cascade. The main features include a 127m high rockfill dam with a central clay core with a crest length of 537m. The reservoir has a volume of about 6.06×10^9 m³. The appurtenant structures comprise a surface powerhouse at the dam toe with an open-air switchyard, a power intake and four headrace tunnels, a spillway, a saddle dam and a cut-off structure. The free overflow ski-jump spillway with a chute and flip bucket is arranged on the right bank slope in a distance from the dam by means of cutting through the ridge.

Fig. 1 – Chenderoh (left) and Temengor (right) dam

3. TECHNICAL STUDIES

The technical studies included review and evaluation of the existing data, performing visual inspection of the dams, appurtenant structures and the project area, field investigation and laboratory study of the actual conditions of the dams, hydrological study to determine the probable maximum flood (PMF) and a seismic hazard assessment to determine safety evaluation earthquake (SEE), which were not considered in the initial design of the dams. The integrity and stability analysis were then carried out to check whether the dam and appurtenant structures comply with today‘s design and safety criteria. The details are described as follows.

3.1. Hydrological Study

In 1920s and in early 1970s as the two dams were designed, the term PMF was not proposed or popular for dam designers. Accordingly, PMF was not calculated during the design. Nowadays, the PMF has been taken as an important design criterium and is thus studied in the present dam safety assessment. The PMF is derived from the probable maximum precipitation (PMP). Major input for the model were rainfall data up to study date from seven stations inside and adjacent to the catchment area as well as monthly temperature data from the ERA5-L and reanalysis dataset.

Necessary catchment runoffs for model calibration were derived from turbine and spill discharges and from reservoir volume changes. Assessment of the performance parameters of the model calibration and validation lead to satisfactory results. The statistical Hershfield method, which is based on observed maximum precipitation data, has been applied for estimating PMPs for rainfall durations from 1 to 5 days. From reservoir operation simulations combined with hydraulic modelling, the Inflow Design Flood (IDF) of each reservoir of the scheme was defined. The method used to identify the IDF is the Incremental Hazard Potential method recommended by the FEMA guidelines [3].

The Temengor reservoir is classified as a high hazard potential reservoir. The hazard potentials have been estimated for different floods pertaining to the cascade system as 30%

PMF, 50% PMF, 75% PMF and 100% PMF. The flood plain inundations were modelled using HEC-RAS software version 5.0.7.

The other three dams downstream in the cascade system were modelled at once. The simulation was conducted both with and without dam break, assuming that the reservoir water levels are at their Full Supply Levels with normal streamflow conditions. The model covers the flood plains from the Temengor Dam ending at the Sea. As the Temengor dam is not going to be overtopped, the failure mode was set to “piping”. Considering high volume of the most upstream reservoir, complete wash out of the downstream dams were considered in the dam breach scenario. The results of dam break analysis is used for decision-making.

Spillway gate operations at the Chenderoh dam were considered with 0.3m steps. The simulations calculate the inundation areas due to each flood with and without dam breach. Flood inundation was converted to hazard based on the flood hazard rating[4]. The incremental hazard potential is decreasing with the increase of flood magnitude but, at the PMF, the incremental hazard is still about 28% of the total hazard. It is therefore recommended to use the PMF as the IDF for the respective reservoirs of Sungai Perak Cascade system. Simulations with the recommended IDF come out that the maximum water level in the Temengor and Chenderoh reservoirs are not critical. It is therefore concluded that the existing spillway capacities are adequate to discharge the IDF with no overtopping of the dams. The stability analysis of dam is performed in consideration of the PMF, and the stability is proven.

3.2. Seismic Hazard Assessment

A new Seismic Hazard Assessment (SHA) was performed to fill the gap in the initial design. As peninsular Malaysia is not seismically active, the number of recorded earthquakes in a circular area with a radius of 200 km is less than 20 with a maximum magnitude of M5.0. A distance range with a radius of 500 km was used for the probabilistic analysis, where the major seismic source was defined as the area including the earthquakes on Great Sumatran Fault Zone. For the deterministic analysis, a hypothetical critical scenario was adopted considering the local faults of an M5.0 quake at a depth of 15 km. Based on the above, the peak ground acceleration (PGA) of SEE was determined and used in the stability and integrity analysis for the dams.

3.3. Visual Inspection

A visual inspection was carried out for the dams to assess their physical integrity and performance and define necessary site investigations for the integrity and stability studies. The inspection focused on the visible parts at dam crest, including alignment of axis, upstream and downstream face, as well as the dam internal hollow space of Chenderoh dam.

The 90-year-old Chenderoh dam is approaching the usual design lifespan of 100 years. The underwater area of upstream face was not visible at the time of inspection; its condition will be inspected with other means in future. The inspection revealed that the outer faces of concrete showed general aging and weathering. Minor aging with old cracks was identified in the concrete on left and right abutment as well as in the power intake area, while serious aging and weathering of concrete can be observed in the spillway downstream faces. In the left free-spillway, concrete was seriously aging, drying and weathering with abundant of horizontal cracks. The horizontal crack width extended up to 10 mm in a spacing roughly 10 to 20 cm, as shown in Fig. 2. The aging, weathering and cracking lead to the loss of strength and abrasion-resistance, decrease of permeability and reduction of durability of the facing concrete. It is reasonable to suspect that the reinforcing bars (rebar) embedded in the concrete may be corroded and the reinforced concrete condition not be satisfactory.

Fig. 2 – Deterioration of concrete in spillway face concrete of Chenderoh dam

The visual inspection demonstrated that Temengor main dam is in good condition. No misalignments at the dam crest were observed. The upstream and downstream slopes of the embankment were in a good condition and minor settlements were observed at the downstream slope. The condition of the riprap was found acceptable. The dam instrumentation works in an acceptable way -according to the operational personnel- and readings were taken monthly. Also, the concrete of spillway chute and side walls is in a good condition. Although there are some limited areas with minor spalling, the stability of the spillway structure is considered ensured.

3.4. Field and Laboratory Investigation

For Temengor main dam, it is not necessary to perform further investigations. For the spillway, the previous study results with boreholes were used to justify the concrete strength at its chute.

For Chenderoh dam, various tests were performed, including the carbonation tests to check the deterioration depth of concrete; concrete cores to check the compressive strength, modulus of elasticity, splitting tensile strength, Poisson's ratio, visually check the existing reinforcement condition and tensile strength of rebars. Moreover, the core specimens were extracted from the concrete-rock interface for the direct shear testing for the shear strength of the base contact. Besides, concrete cores were extracted from the downstream face of the spillway slabs to investigate the current conditions of concrete. The cores were spread along the length of the dam to provide an indication of the concrete deterioration in different areas of the exposed concrete surface.

Direct shear tests from three borehole cores have been performed. The shear tests indicated that the shear strength of the foundation rock is significantly high. A careful assessment of the shear parameters after testing results led to the use of conservative values of angle of internal friction Ø=52° and cohesion c=600 kN/m². The tests of compressive strength, modulus of elasticity, splitting tensile strength and Poisson's ratio as well as carbonation tests of concrete were carried out with the nine cores. The concrete strength is understood as the ultimate strength. The evaluation of the test results led to a design characteristic strength about C20/25. The carbonation test results showed that carbonation depth of the facing concrete varies from 50 to 335 mm, deeper than the concrete cover of reinforcement, which indicates that the reinforcement corrosion has initiated.

To visually check the existing reinforcement condition, the downstream facing concrete in an area of LxWxD=80x80x20 cm of the left free spillway was exposed. From the exposure area it could be clearly seen that the rebars embedded into the facing concrete are corroded, confirming the results of carbonation tests. This means that the surface cracking has reached the depth of rebar mesh, so that the water and moisture infiltrates to the rebars. Corrosion of the rebars has physical consequences such as decreased ultimate strength and serviceability of the concrete structures.

3.5. Stability and Integrity Analysis for Chenderoh Dam

The Chenderoh concrete hollow buttress dam was constructed according to the design and construction principle of the hollow reinforced concrete structure of Ambursen type [5, 6], based on which the dam was deemed stable. No stability analysis was performed, and the available design and construction data are very limited. In the current study, the bore holes are drilled through the dam and its foundation, The test results of foundation rock mass are used in the analysis. The CADAM software was used for the stability analysis in a way to reduce computational cost that would be required for a full 3D analysis. The structure was simulated by making ingenious use of the functions of CADAM software as follows:

- The buttress walls were simulated as gravity dam sections.
- The concrete slabs between two adjacent buttresses were approximately simplified as concentrated masses provided in the CADAM software acting on the buttress faces to add vertical forces in a static analysis and inertia forces in a seismic analysis. The spacing of the masses is limited to a sloped distance of 1.5 m, with which the accuracy must be ensured.
- The loads on the slabs between the buttresses were calculated and applied onto the buttress faces by means of a load combination factor provided in the software.

In this way, both the slabs and loads were simulated and applied on the buttress walls. The computational models are shown in Fig. 3.

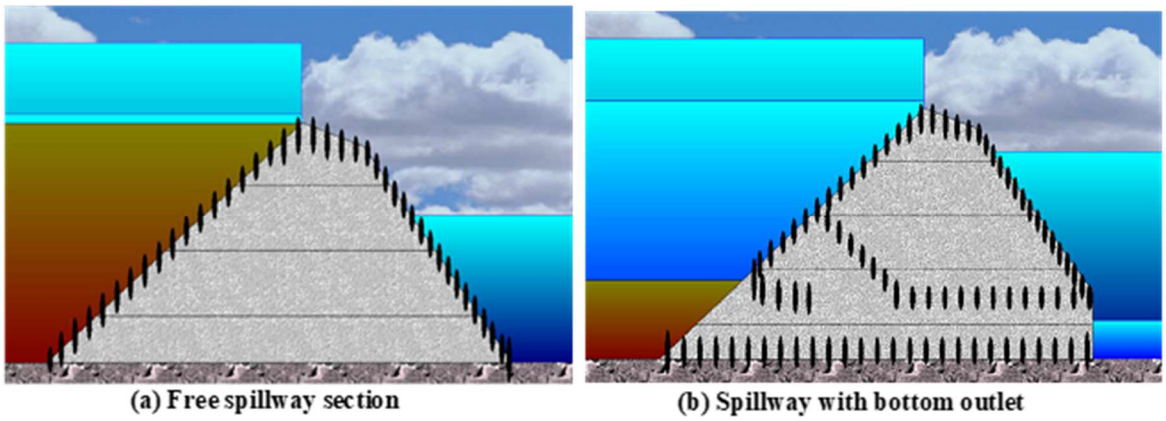

Fig. 3 – Computational models of Ambursen concrete hollow buttress dam at Chenderoh

The results of the stability and stress analysis demonstrated that factors of safety against sliding and overturning meet the requirements for dam design of US Army Corps of Engineers [7]. The maximum compressive stresses at the dam-foundation interface are far below the allowable bearing capacity of the dam concrete and foundation rock. No tensile stress develops apart for SEE seismic loading. The minimum factors of safety against sliding on any plane within the dam body are greater than the required minimum values, and the compressive stresses are far below the permissible stresses. Therefore, the dam stability is ensured.

In the verification of integrity of dam structure, the structural analysis for the concrete slabs between the buttresses was performed in accordance with EN 1992-1-1 [8]. The present test results of concrete and reinforcement extracted from the dam were used. The required reinforcement was calculated firstly with a yield strength of 500 N/mm² (S500 steel). The calculated required reinforcement area was then converted to the existing reinforcement with the yield strength of 221 N/mm² in the dam construction time. The analysis revealed that the tensile strength of existing reinforcement in the slabs [5,6] exceeds that required by the current standard. Therefore, the load-carrying capacity of the concrete slabs is ensured.

3.6. Stability Analysis for Temengor Embankment Dam

The traditional slip circle method was used in the stability analysis and finite element method was applied in the deformation calculations. The material parameters were defined based mainly on the original design parameters, as summarized in Table 1.

Table 1 – Material Parameters for Embankment Dams

Zone	Cohesion (kPa)	Friction Angle (^{0})	Elast. Modulus (MPa)
Impervious Fill (Core)	-	29	50
Filter and Transition Zones	-	29	150
Rockfill	-	40	150
Rockfill (Deep)	-	38	150
Foundation Rock	400	40	2 000

The results obtained for the embankment dam provided acceptable safety factors above 1.5 for the static cases and above 1.0 for the dynamic cases. The results of the dynamic analyses indicated that the deformations of the dam bodies are small after earthquake loading. The calculated permanent settlement at the crest of dam is 18 cm or less, which is much smaller than the freeboard of 4.0 m.

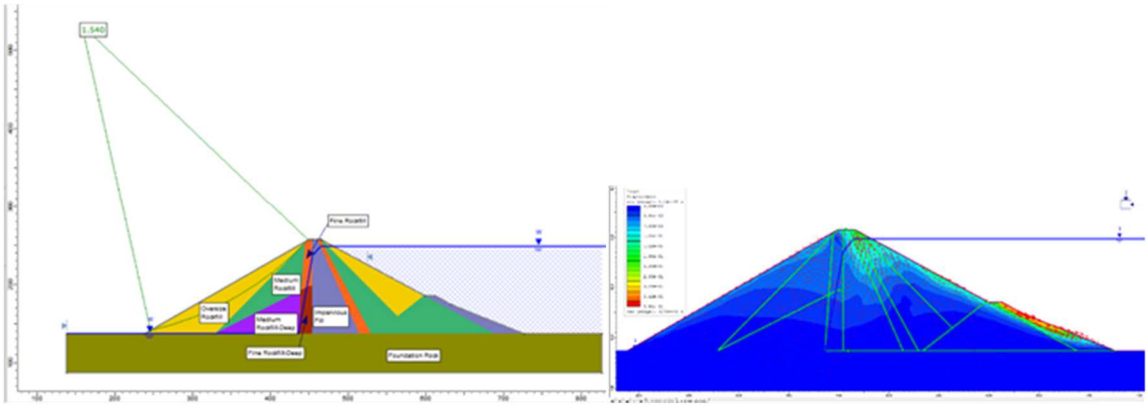

Fig. 4 – (a) Stability and (b) stress – strain dynamic analysis for Temengor Dam

3.7. Assessment of Temengor Spillway

Hydraulic analysis demonstrated that the high-velocity flow of up to 40 m/s may occur in the spillway chute at Temengor which may cause serious problems in the existing bottom concrete slabs. Among others, the existing structures may suffer repeated cavitation damage with a cavitation index of 0.2 or less, deserving special attention. Under such a high velocity flow, cavitation and serious abrasion is expected to occur, causing serious damage to the spillway concrete. In addition, calculations on the effect of possible abrupt stagnation pressures in the

transverse contraction joints of chute concrete slabs indicated that the high stagnation pressures may penetrate into the transverse contraction joints of bottom slabs and slab foundation in case of an unfavourable joint offset, which may create high uplift pressures beneath the bottom slabs. The hydraulic jacking may cause uplifting and throwing out the slabs and the subsequent erosion of foundation. The high stagnation pressures can also occur in cracks formed by differential settlement of erosion of the upstream portion of the joint by cavitation. The concrete slabs were constructed with low grade of concrete which may fail under above actions. Therefore, rehabilitation of the spillway concrete is necessary.

4. REHABILITATION CONCEPT FOR TEMENGOR SPILLWAY

The available information and the test results of drilling cores extracted from the spillway demonstrated that the existing facing concrete of slabs should have a strength class of C25/30 to C30/37. Such a concrete cannot withstand the high-velocity flow with cavitation. The concrete of spillway chute slabs shall be rehabilitated. The basic concept includes: (i) installation of aerators to introduce air into the water flow, so as to increase the cavitation index to decrease cavitation potential; (ii) placement of the abrasion-resistant concrete of C50/60 to the facing of spillway bottom slabs; and (iii) the transverse joints shall be rectified with the installation of water stops at the joints.

The facing concrete of the bottom slabs of 30 to 40 cm in thickness including the reinforcement shall be chipped off and removed. Dowels and anchors shall be installed on the chipped surface into the remaining concrete, and new reinforcement mesh shall be placed along the slope and connected with the dowels/anchors. The surface shall be thoroughly cleaned. Immediately before placing the new concrete, a layer of epoxy agent shall be smeared on the surface to improve the bonding and new concrete with higher strength (C50/60) shall be placed. At the transverse contraction joints, PVC water stops shall be installed.

To produce the abrasion-resistant concrete of C50/60 at 28 days, silica fume may be used to decrease the cement content and increase the abrasion resistance. The concrete placement shall be started from the most downstream block. Within one block, the concrete shall be placed from the downstream (lower) end, progressively to the upstream (upper) end. The finished surface shall be smooth with an offset not higher than 2 mm. The higher offsets shall be smoothened by grinding into a smooth slope of not steeper than 1(V):100(H).

5. REHABILITATION CONCEPT FOR CHENDEROH DAM

The results of site investigation and laboratory tests indicated that the downstream facing concrete of spillway slabs is seriously deteriorated and reinforcing steel is corroded. Consequently, the integrity of the concrete slabs may not be ensured for the succeeding 30

years, although they can work within a short period. To ensure the integrity of the spillway, the following remedial measures are recommended (see Fig. 5).

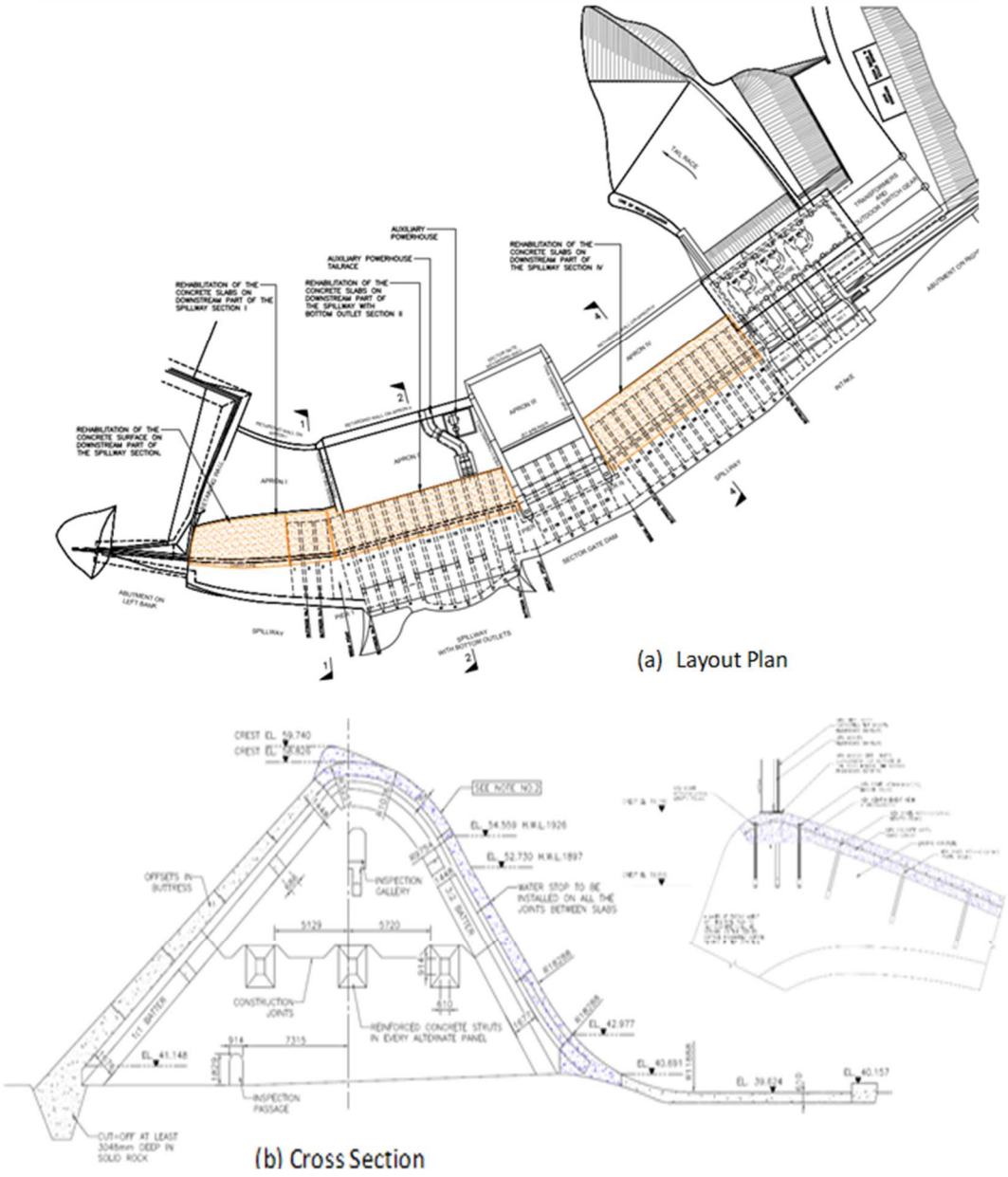

Fig. 5 – Rehabilitation measures for downstream face concrete of Chenderoh dam spillway

The downstream facing concrete of the free spillway in a thickness of 20 to 25 cm up to the crest level including the reinforcement shall be chipped off, and the surface shall be thoroughly cleaned and treated. Dowels shall be installed on the remaining existing concrete surface, and new reinforcement mesh shall be placed along the slope and connected with the dowels. Immediately before placing the new concrete, a layer of epoxy agent shall be smeared on the surface, and new concrete with a strength class of C30/37 shall be placed. At the joints, water stops shall be installed. The remaining existing part of the concrete slabs is working as form works. Through the construction plan with section- to-section rehabilitation work, the upstream water level can remain unchanged, so that the plant operation is not interrupted.

6. CONCLUDING REMARKS

The Chenderoh dam is experiencing serious deterioration of concrete for the reasons, including aging, weathering and cracking, which cause corrosion of steel reinforcement embedded in the concrete as well. Although the stability of the dam itself is not a concern, the existing structure is no longer in condition to maintain its long-term integrity. The concrete slabs of spillway chute of Temengor dam contains high risk of cavitation and stagnation pressure during large floods. Rehabilitation of the spillway structures of both dams are thus necessary besides the routine maintenance. The comprehensive study in this paper discusses the identification of the deterioration of concrete, determination of PMF, seismic hazard assessment, stability and integrity analysis and proposes the best cost-effective rehabilitation measures. While the proposed solution is not challenging from a structural and construction point of view, the simplicity of the proposed rehabilitation measures involves a few relevant advantages, in particular, the rehabilitation can be performed without interruption of the operation of hydropower plants.

REFERENCES

[1] Du, C. & Siskos, I. (2023). Life Extension and Rehabilitation Study for Chenderoh Dam. Proceedings of the 91th ICOLD Annual Meeting (Symposium “Management for Safe Dams”), Gothenburg, Sweden, 13-14 June 2023: 1110-1118

[2] Sisko, I., Du, C., Dibrani, B. & Radzi, MRM. (2023). Dam Safety Enhancement of Sungai Perak Hydro Electric Stations. Proceedings of the Eighth International Conference and Exhibition on Water Resources and Renewable Energy Development in Asia (ASIA 2013), Kuala Lumpur, Malaysia, 14 to 16 March 2023: paper No. 18.03

[3] FEMA (2013). Guidelines for Selecting and Accommodating Inflow Design Floods for Dams. Federal Emergency Management Agency, FEMA P-94, USA.

[4] Kun, C.F. & Saroni, M.J. (2003). Rehabilitation of Chenderoh Dam and Spillway. Dam Maintenance and Rehabilitation (eds. By Lianos et al.). Swets & Zeitlinger: 639-645

[5] Hellstrom, M. (1935). The Perak River Hydro-Electric Power Scheme. Proceedings of the Institution of Civil Engineers. Paper 4974, Vol. 239: 253-312

[6] Rennie, W.J.H. (1935). The construction of the Chenderoh Hydro-Electric Power Scheme. Proceedings of the Institution of Civil Engineers. Paper 4969, Vol. 239: 313-355

[7] US Army Corps of Engineers. (1995). Gravity Dam Design. Design Manual EM 1110-2-2200, Washington D.C.

[8] Eurocode 2 (Part 1). (1994). Design of Concrete Structures - General Rules and Rules for Buildings. EN 1992-1-1

Fifth International
Dam World Conference
PORTUGAL • LISBON • LNEC • APRIL 13-17, 2025
dam world 2025

DAM FPO GEOMEMBRANE AFTER 14 YEARS EXPOSURE

Pierre Favre[1]
Sika Services AG

Martin Eckl
Sika Technology AG

ABSTRACT

A long service life of dams requires durability of all components. The waterproofing of the structure plays a major role in dam construction and upstream sealing of the dam with geosynthetic membranes is an increasingly sought after solution for new and refurbished structures. This paper describes the investigation of the exposed FPO membrane laid 14 years ago on the upstream face of the Porto Dam in Spain. Samples were subjected to detailed examination.

Mechanical properties, watertightness and the quality of the welded seams were determined as well as the welding ability with new membrane. In 2010, ageing tests (autoclave test, test duration 2 years) on a membrane with the same material basis as the Porto Dam membrane have yielded service life forecasts for up to 100 years. The results from mechanical testing on the Porto Dam samples are in line with those forecasts.

14 years of service life has not affected the properties of the FPO membrane, and its waterproofing function can be expected to last for many more decades.

Keywords: dam, waterproofing, FPO membrane, durability.

[1] favre.pierre@ch.sika.com, Switzerland

1. INTRODUCTION

Dams are complex and expensive constructions. Their ability to retain water is their main characteristic but safety of such structures is paramount due to the enormous consequences of a catastrophic collapse. In this regard, waterproofing of the dam is important for the stability of the structure and its integrity.

In 1959, the dramatic collapse of the Vega de Tera Dam in the province of Zamora, Spain, took the life of 144 people. Following this catastrophic failure, investigations were conducted on dams nationwide and measures have been taken to reduce the risks associated with this type of dams. Over the years, one such measure has been the installation of geomembranes on the upstream face of dams.

Less than 100 km from the Vega de Tera Dam, the Porto Dam was selected to receive such a supplementary waterproofing layer. Due to the foresight of the engineers at the time, an extra area of the dam was covered with the waterproofing membrane for future analyses of the durability of the system. This paper deals with the testing of the aged membrane's material properties and discusses further service life perspectives.

A reinforced polyolefin (FPO/TPO) geomembrane was selected for the dam waterproofing due to specific characteristics such as:

- FPO/TPO membranes do not contain any liquid raw materials such as low-molecular plasticizers, which can migrate out of the membrane over the period of use. Such plasticizer migrations are typically associated with a stiffening of the membrane, which can impair cold flexibility or dimensional stability.
- In principle, the water vapor permeability of FPO/TPO is considerably lower than that of PVC-p Composite.
- The product structure of the FPO/TPO membrane used here, with a glass fleece reinforcement between the upper and lower surfaces, offers the best conditions for minimizing the effects of any changes in tensile strength/elongation, burst strength, tear strength and thermal expansion.
- Unlike PVC-p Composite, FPO/TPO membranes are not sensitive to the influence of microorganisms.
- Especially in applications with changing water levels / strongly flowing water together with solar radiation, FPO/TPO is less critical compared to PVC-p Composite.

2. PROJECT DESCRIPTION

The Porto dam is one component of the Moncabril hydroelectric system, which uses the water resources of the Alta Sanabria plain, now owned by ENDESA, the largest Spanish multinational electric utility company. It was built in 1955. Following the collapse of the Vega de Tera Dam in 1959, it was decided to reduce the water capacity to 2'500'000 m^3 by creating a lower spillway and improving its waterproofing by carrying out a series of actions. In 2009, a new external waterproofing geomembrane was mounted on the upstream face of the dam. A specialist applicator of geosynthetic membranes, used the following construction system:

- Preparation of the dam surface to receive the waterproofing membrane post-tensioning elements with a single-component, cement-based, thixotropic low permeability repair micro-concrete with silica fume and polymer, meeting the requirements of Class R4 of EN 1504-3 for structural and non-structural repair of concrete structures [1].
- Installation of a drainage board with nodules ("egg cups") to allow circulation of water both in the hypothetical case of loss of impermeability of the geomembrane and possible condensation due to thermal changes or other reasons. It also allows a control function of the watertightness criteria of the installed membrane system.
- Placement of a cushion layer made of a polypropylene-based, highly resistant to ageing, needle-punched non-woven geotextile.
- Installation of a 2.5 mm thick single ply flexible polyolefin (FPO) geomembrane made of polyethylene with a glass fleece inlay, complying with the harmonised standard EN 13361 for reservoirs and dams [2]. The inlay increases the physical and thermal stability of the geomembrane and provides, together with the separately installed cushioning layer, additional puncture resistance.
- The geomembrane liner is fixed to the upstream face using a vertically installed tensioning profile anchorage system. Once fully installed, the profile pulls the liner to the dam face and tensions the membrane liner between anchorage profile lines, creating a firm system across the upstream face. A geomembrane cover strip is then welded over the external profile, producing a watertight seal over each profile line.

Fig. 1 – Installation of the geomembrane

A few years after the installation of the geomembrane, the applicator repaired with a few patches the areas damaged by the movement of ice at the water surface. A system of buoys was installed in front of the membrane to prevent further damages from ice formation.

Fig. 2 – Repaired area

Following the installation of the waterproofing membrane, the applicator, in collaboration with the membrane manufacturer installed a few square meters of membrane on the dam wall at the location of the spillway for future analysis of the behaviour of the waterproofing layer over time.

The drainage system behind the waterproofing surface is used to control the watertightness of the membrane. To this date, there has been no report of specific increase of drainage water.

In July 2023, an inspection of the waterproofing membrane was organized. The membrane on the water side was intact and visually in good condition. At this occasion, samples were

removed from the spillway. Another disregarded sample was found half buried at the foot of the dam. Moreover, samples were cut out from a roll of virgin material stored in the applicator's warehouse. All these 14-year-old samples were given to the original manufacturer for mechanical and chemical analyses. The samples received were visually in good condition, except for the sample found half-buried, which was obviously very dirty after so many years.

Fig. 3 – Removal of samples at the spillway

Fig. 4 – Spillway sample & buried sample

3. TEST PROCEDURE

The samples were cleaned with running water and left to dry at room temperature. They were tested at the manufacturer's R&D centre with test methods according to actual European standard procedures. The relevant properties determined were:

- Thickness with embossing
- Thickness without embossing

- Mass per unit area
- Tensile strength & elongation
- Resistance to impact
- Foldability at low temperature
- Peel resistance

The welding ability of the old geomembrane was determined by hot air welding of a new geomembrane onto the samples. After cooling down, the strength of the samples was tested by peeling. The criterion of a good seam is that the break occurs outside the seam (EN 12316-2 [3]).

Table 1 – Properties of Sikaplan® WT 5210-25 CE samples from Porto Dam

Property	Test method	Spillway samples	Warehouse samples	Buried samples	Production specification
Thickness with embossing	EN 1849-2 [4]	2.61 mm	2.53 mm	2.69 mm	2.38 – 2.75 mm
Thickness without embossing	EN 1849-2 [4]	2.45 mm	2.41 mm	2.48 mm	Nob height: 0.1 – 0.4 mm
Mass per unit area	EN 1849-2 [4]	2396 g/m^2	2429 g/m^2	2477 g/m^2	2210 – 2560 g/m^2
Tensile strength (MD)	EN 12311-2 [5]	10.1 N/mm^2	10.1 N/mm^2	8.6 N/mm^2	9.5 – 12.5 N/mm^2
Tensile strength (CMD)	EN 12311-2 [5]	9.0 N/mm^2	8.5 N/mm^2	8.5 N/mm^2	8 – 11 N/mm^2
Elongation at break (MD)	EN 12311-2 [5]	541 %	512 % *	442 % *	≥ 450 %
Elongation at break (CMD)	EN 12311-2 [5]	595 %	566 % *	555 % *	≥ 450 %
Resistance to impact (hard surface)	EN 12691 [6]	1000 mm	1500 mm	**	
Foldability at low temperature	EN 495-5 [7]	≤ -50 °C	≤ -50 °C	≤ -50 °C	
Peel resistance	EN 12316-2 [3]	586 N/50mm ***			

* Direction unknown
** Not tested (sample too small)
*** Failure mode C (delamination within the membrane)

Fig. 5 – Peel test of the seam from the spillway samples

3.1. Mechanical properties

The measurements have shown that the exposed samples from the spillway and the buried sample have thicknesses that are all within the specification of the virgin material.

The same applies to the measured basis weights (weights per unit area). Here too, the values are all within the specification of the virgin material.

Thicknesses and basis weights show that the physical integrity of the dam waterproofing is unchanged from the very beginning.

Usually, in the case of FPO geomembranes, one would not expect significant changes in thickness over the service life because, unlike PVC-P, FPO does not contain any low-molecular plasticizers that can migrate and thus lead to a reduction in thickness.

The strength of the spillway sample is exactly at the level of the warehouse sample. This applies to both machine direction (MD) and cross machine direction (CMD). This shows that the mechanical functionality of the membrane is unchanged from the very beginning even after 14 years of outdoor weathering.

The change in the resistance to impact from 1500 mm to 1000 mm seems to be significant but is due to sampling (limited sample size taken from the spillway vs availability of the full width

of the membrane roll from the warehouse as requested by the test standard) and the scattering of the test results associated with this particular test.

The values for the buried sample are slightly lower, but still close to the specification of the virgin material. Here it is not clear what impact the sample was exposed to. It should also be noted that the tensile elongation measurement shows a scattering of around 10%.

The elongation at break is also at the level of virgin material. The spillway sample is even slightly higher than the warehouse sample. No change here either from the very beginning.

The behaviour of the spillway sample in cold bending does not show any change either compared to the initial value. The flexibility is unchanged from the very beginning.

The quality of the welded seams on the Porto Dam was also checked. The sample from the spillway contains such a seam. This was tested for seam strength using a peel test.

The seam failed according to failure type C in accordance with EN 12316-2 [3], i.e. peeling occurred in between top - and bottom layer of the welded membrane, but not in the thermally welded area. The peel strength achieved high values.

3.2. Durability

The long-term resistance of the waterproofing membrane defines its ability to maintain its characteristics under exposure of the predictable environmental influences during its service life. Plastic materials durability depends on various mechanisms that cause some degradation such as reduction of mechanical and/or hydraulic performances. However, specific groups of materials are affected by these various degradation mechanisms in different ways, which means that the ageing process differs from each other. For instance, one of the main degradation mechanisms for PVC-p is the immersing and leaching of plasticizers in various media, while one degradation mechanism for polyolefin materials is the oxidation at high temperatures.

FPO membranes for waterproofing of dams that are exposed to weathering are subject to the following impacts:

1. Heat impact, followed by oxidation of the polymer chains
2. Impact of UV radiation, combined with moisture and heat (= weathering), which also leads to breakage of the polymer chains

In 2010, Sika conducted a study in which FPO tunnel membranes were exposed to drastic conditions in a so-called autoclave test over almost 2 years. The membranes were stored in pH 10 water at temperatures of up to 80°C and simultaneously exposed to elevated oxygen pressure. This was to investigate the behaviour against oxidation.

For this purpose, samples were taken at regular intervals to test the residual tensile strength.

After extrapolating the test results according to Arrhenius, it was found that the FPO membranes have a service life expectancy of 120 years at an ambient temperature of 40°C [8].

The FPO membranes tested have the same material basis as the Porto Dam membranes. The 2010 study can therefore be used as a reference for heat exposure.

We therefore also expect the Porto Dam membrane to have a long service life. This is confirmed by the tests described above. After 14 years of installation, the tear resistance of the spillway sample is exactly at the same level as the initial value, which so far confirms the predictions of the autoclave test.

To withstand the effects of weathering (UV radiation, moisture, ice/snow, and low/high temperatures), the membrane is additionally equipped with weathering stabilizers.

These weathering stabilizers continue to function perfectly even after 14 years. Microscopic examination of the surface of the spillway sample at 20x magnification revealed no surface cracks, which are usually associated with reduction of the tear resistance of geomembranes.

This geomembrane has been used successfully for years to waterproof water reservoirs in the Alps, e.g. reservoirs for snow cannons. In this application, the membrane is also exposed to weathering and daily changes of the waterline, as is the case of the Porto Dam. The membrane has proven itself in these applications to date. There are projects in which the membrane continues to perform its function 25 years after installation.

Fig. 6 – Water reservoir sealed with Sikaplan® WT 5210-25 CE in the Alps

4. CONCLUSION

The Porto Dam in Spain was retrofitted in 2009 with an exposed FPO waterproofing geomembrane on its upstream face. After 14 years, samples taken from the site were analysed to determine the main characteristics of the geomembrane and its behaviour over the years.

The thickness and weight measurements showed that the geomembrane is still within the specifications of the virgin material.

The tensile strength of the exposed geomembrane is at the same level of retained samples stored in the applicator's warehouse since 2009. This indicates that the functionality of the membrane is unchanged after all these years of outdoor exposure. The elongation at break is also at the level of the virgin material. As also shown by the cold bending test, the flexibility of the membrane is still unchanged.

A welded seam was checked. The peel strength achieved high values, and the failure did not occur in the thermally welded area.

14 years of service life has not affected the properties of the membrane.

In 2010, ageing tests in autoclave up to 2 years on a membrane with the same material basis as the Porto Dam geomembrane have yielded service life forecasts for up to 100 years.

The same geomembrane used in Porto Dam is also being used to seal water reservoirs in the Alps. Because of its long-lasting weather stabilizers, this type of membrane continues to perform its waterproofing function after 25 years.

Based on these facts, the FPO geomembrane used at the Porto Dam will continue to fulfil its sealing function for decades to come in this environment.

REFERENCES

[1] EN 1504-3:2006. Products and systems for the protection and repair of concrete structures – Definitions, requirements, quality control and evaluation of conformity – Part 3: Structural and non-structural repair.

[2] EN 13361:2004/A1:2006. Geosynthetic barriers - Characteristics required for use in the construction of reservoirs and dams.

[3] EN 12316-2:2013. Flexible sheets for waterproofing - Determination of peel resistance of joints - Part 2: Plastic and rubber sheets for roof waterproofing.

[4] EN 1849-2:2019. Flexible sheets for waterproofing - Determination of thickness and mass per unit area - Part 2: Plastics and rubber sheets for roof waterproofing.

[5] EN 12311-2:2013. Flexible sheets for waterproofing - Determination of tensile properties - Part 2: Plastic and rubber sheets for roof waterproofing.

[6] EN 12691:2018. Flexible sheets for waterproofing - Bitumen, plastic and rubber sheets for roof waterproofing - Determination of resistance to impact.

[7] EN 495-5:2013. Flexible sheets for waterproofing - Determination of foldability at low temperature - Part 5: Plastic and rubber sheets for roof waterproofing.

[8] Retzlaff, J. (2012). Durability of Sikaplan WT 2200-22HL2, GEOscope GmbH & Co.

Fifth International
Dam World Conference
PORTUGAL • LISBON • LNEC • APRIL 13-17, 2025
dam world 2025

THE STRENGTH AT THE BASE OF AN OLD CONCRETE DAM, BASED ON THE SPANISH EXPERIENCE WITH LARGE-SCALE IN SITU SHEAR TESTS

Asanza-Izquierdo, Enrique[1]	Escudero-Merino, Diego	Laina-Gómez, Carlos	Díez-Torres, Juan Antonio
CEDEX	CEDEX	CEDEX	CEDEX
	Sánchez-Caro, F. Javier	Antón-Sempere, José	
	CHJ	CHJ	

ABSTRACT

This paper discusses the experience gained over decades in Spain on the setting-up and interpretation of large-scale in situ shear tests in dam engineering and addresses the advantages and disadvantages of different arrangements. Besides, it presents a specific test for Amadorio Dam, an old gravity dam in the province of Alicante (Spain). As a result of the rising of the dam crest, geotechnical concern on the choice and reliability of the strength parameters led to the testing of four 1x1m concrete blocks downstream, on a rock outcrop with features like the dam foundation. Novel monitoring system is described as well as the interpretation, that follows the saw-toothed model. Distinction is made between peak and post-peak mobilised strength; the role of dilation angle is highlighted and the gradual degradation of the sliding surface.

Keywords: shear tests, sliding, dilatancy, interface, strength parameters.

[1]enrique.asanza@cedex.es, Spain.

1. INTRODUCTION

1.1. General scope of the Spanish dam

Proper management of water resources provides a wide range of benefits to countries, irrespective of its degree of development, being reservoirs and dams key elements of any national hydraulic network. There are approximately 1300 dams in Spain, with as many as 500 (~38%) of them exceeding 50 years of age, with an average age of 45 years. Regarding the type, approximately 65 % of them are gravity dams. Most of the Spanish dams are State-owned and operated by nine National River Basin Authorities (Confederaciones Hidrográficas, CH) reporting to the Department for Environment. Thus, maintenance in Spain is an issue of major concern of the National Administration that relies on codes of inspection, monitoring and surveillance. The Centro de Estudios y Experimentación de Obras Públicas (CEDEX), a technical agency sponsored by both the Department for Transportation and the Department for Environment, provides institutional support and promotes R&D in civil engineering, and particularly in the scope of dams and water management.

The so-called “Normas Técnicas de Seguridad de Presas, RD 264/21” in Spain, that came into force in 2021, consolidated two previous national guidelines and codes. Such recent regulation enforces comprehensive inspections at specific year intervals of every dam, regardless of its ownership or use.

1.2. Sources of uncertainties linked to sliding of gravity dams

The shear strength parameters at the base of gravity dams, either along a discontinuity plane within the rock mass or at the rock-concrete interface, are the main source of uncertainty; in some cases, it may have not received due attention. Moreover, the critical sliding plane might have even undergone degradation, losing cementitious bonds or developing tensile cracks further inwards from the upstream toe.

It is well known, on the other hand, that decades ago water infrastructure used to be designed for climate conditions whose recurrence at present seems to depart from patterns assumed in the past, not only in semiarid countries like Spain; total rainfall events tend to decrease in volume (droughts) while increase in intensity, with a trend of reduction in the flood return period. Although hydrological failure is, by far, more severe in earth dams, the discharge flow rate of spillways of gravity dams needs re-evaluation and, subsequently, the effect of the increased hydrostatic thrust and uplift forces on the modes of failure, especially sliding.

1.3. Background and purpose

CEDEX was commissioned by the River Basin Authority (CH del Júcar) to carry out desk studies with an updated hydrological database from the Amadorio River Basin whereby the inferred flow rate at several return periods could be checked against the maximum discharge capacity of the spillway of Amadorio dam, a gravity dam close to the river mouth (near Benidorm, Mediterranean Sea). Such studies concluded that the dam crest should be raised 4 m, so that the spillway can discharge the 10000-year inflow design flood without exceeding the minimum free board. During such extreme events, due to the unfavourable increase of the hydrostatic and uplift forces (gravity forces remain unaltered), the safety factor against sliding drops. In this context, the geotechnical concern on the choice and reliability of the strength parameters inevitably arises.

This paper addresses the practice and experience gained in Spain over decades on large-scale in situ shear tests at the rock/concrete interface of dams, and how it was advantageously put into practice for the reassessment of the strength parameters regarding the sliding stability of Amadorio Dam.

2. LARGE-SCALE IN SITU SHEAR TESTS

2.1. Principles of the direct shear tests

Direct shear tests are aimed at measuring the mobilised shear strength (τ_{mob}) at the interface of two bodies in contact, due to both frictional forces (being φ the angle of friction), which is proportional to the normal stress (σ_n) , and adhesion forces or effective cohesion (c'), following the Coulomb failure criteria:

$$\tau_{mob} = c' + \sigma_n \cdot \tan\varphi \quad (1)$$

When dealing with particulate material (soils), which is not the case, samples are placed in a box, horizontally split into two halves. The standard laboratory direct shear apparatus has a 20mm-thick box of internal dimensions 60×60mm. Larger boxes are uncommon and costly and, therefore, they can only be found in certain research centres. The Laboratorio de Geotecnia (LG-CEDEX) has two shear apparatuses with boxes 15x30x30cm in size, suitable for coarse granular soils; LG-CEDEX holds a much larger box as well, 120x100x100cm in size (Fig. 1), which has been intensively used to test the shear strength of rockfills for dams and other earthen structures [1].

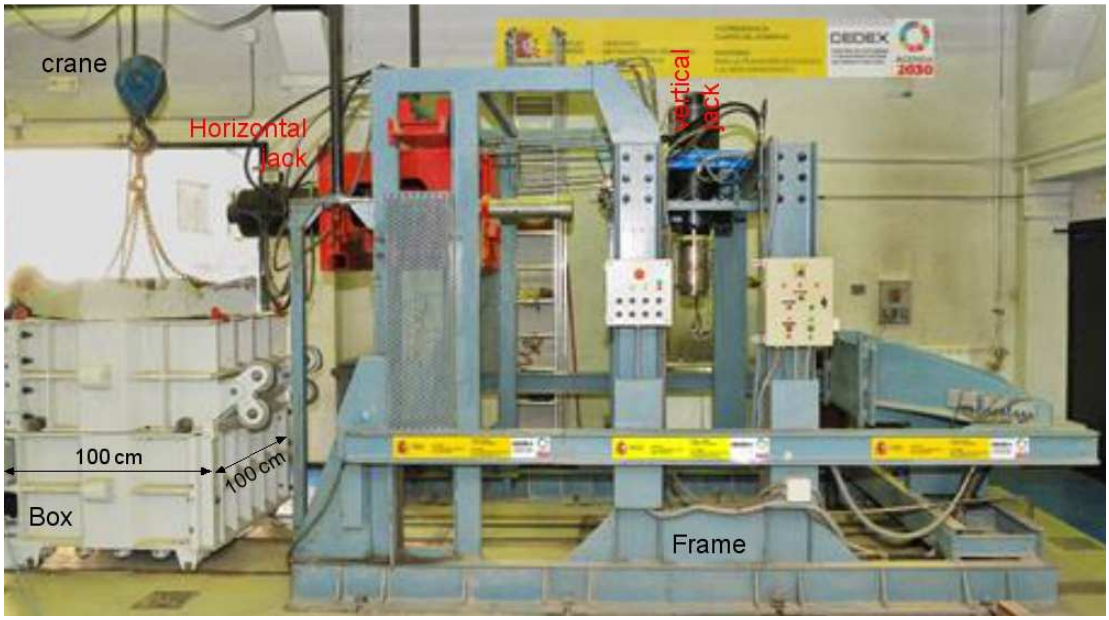

Fig. 1 – Large box (120x100x100 cm) at Laboratorio de Geotecnia (CEDEX)

Once a vertical stress is applied onto a distribution plate resting on the sample, the test is carried out by shearing the two box halves, relative to each other, by means of a motor-driven ram acting upon the bottom half at a programmed constant displacement rate. The opposing shear force that gradually develops within the tested plane is measured throughout the test; vertical displacement is likewise measured, as it accounts for dilation, which yields extra strength due to grain interlocking or large-scale roughness in the case of rock discontinuities (saw-toothed model [2], see Fig. 2).

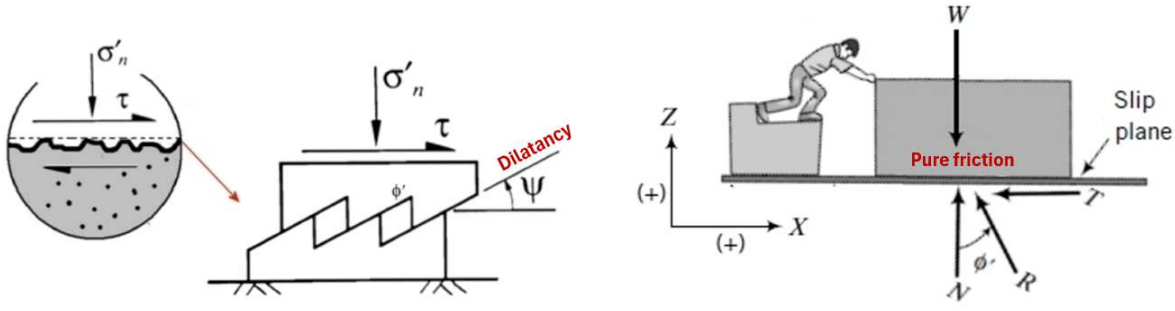

Fig. 2 – Dilatancy envisaged as a saw-toothed model (modified from [3])

2.2. Difficulties facing large-scale in situ shear tests

Distinction should be made when comparing standard laboratory and large-scale in situ shear tests, with samples usually between 0,5 and 1m. Despite their likeness, the high level of forces applied, the space that it takes up and the budget constraints of the latter prevent proper compliance with a laboratory standard shear test. Four basic requirements are exceedingly hard to attain when planning a large-scale in situ shear test, so it must be born in mind at the engineer's desk:

1. Representativeness: the location of the test is of utmost importance, as it has to fulfil accessibility and representativity of the rock mass: Two basic location are the choices: inside one of the dam galleries, free of lining; or outside, on an outcrop of rock of the same nature and conditions, downstream in the vicinity of the dam (Fig. 3).

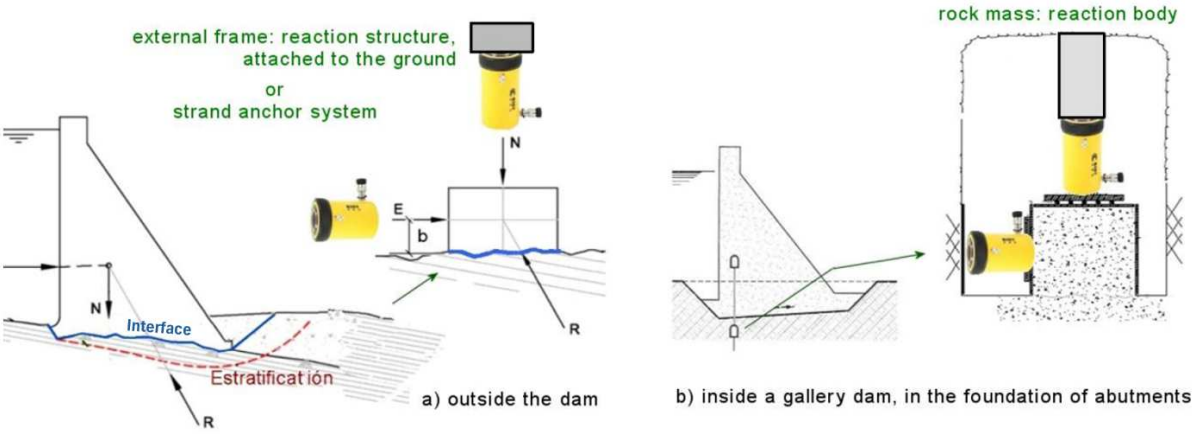

Fig. 3 – The two basic location of a large-scale shear tests

2. Running the shearing force at a constant displacement rate; such testing mode allows a controlled post-peak failure and, therefore, detailed information throughout the test. Explanations of the advantages of failure tests at constant strain rate can be found in [4] and [5], so, whenever possible, it is the preferable mode in the laboratory. However, when handling large loads (from hundreds to thousands of kilonewtons) constant strain rate turns unaffordable in the field (setting up high-performance servo-controlled motor would be needed); a sequence of load increments by a hand-operated hydraulic pump that supplies pressure to a hydraulic ram is used instead, although the control is partially lost. This procedure is accepted in suggested methods and standards [6, 7]. At the peak resistance threshold, however, as the hydraulic pump cannot restore right away the loss pressure caused by sudden displacements, it results in a gap of relevant information. In fact, this is what happened in the tests shown here. However, the loss of information has been minimized by increasing the sampling frequency, yet at the expense of processing sizeable log files.
3. Maintaining the vertical load strictly constant during the shear. Unlike standard shear tests apparatuses, which apply them by means of dead weights on a hanger attached to a lever, large-scale in situ test designs often resort as well to a hydraulic ram, fitted to an external rigid reaction body: rock mass in a gallery or a reaction frame (Fig. 3). However, such rigidity prevents the free and (expected) vertical movements associated to dilation, unless the hydraulic ram releases the excess pressure on the go, so as to counterbalance the subsequent increase of vertical load over the target value. Such operations seem unpractical with hand-operated hydraulic pump; for this reason,

alternatives with strand anchor systems (Fig. 4), due to their high flexibility (compared with bar anchors) have been successfully used in Spain. Some drawbacks, however, have be argued on the grounds of occupational hazards, stress concentration and costs when no anchoring machinery is at hand.

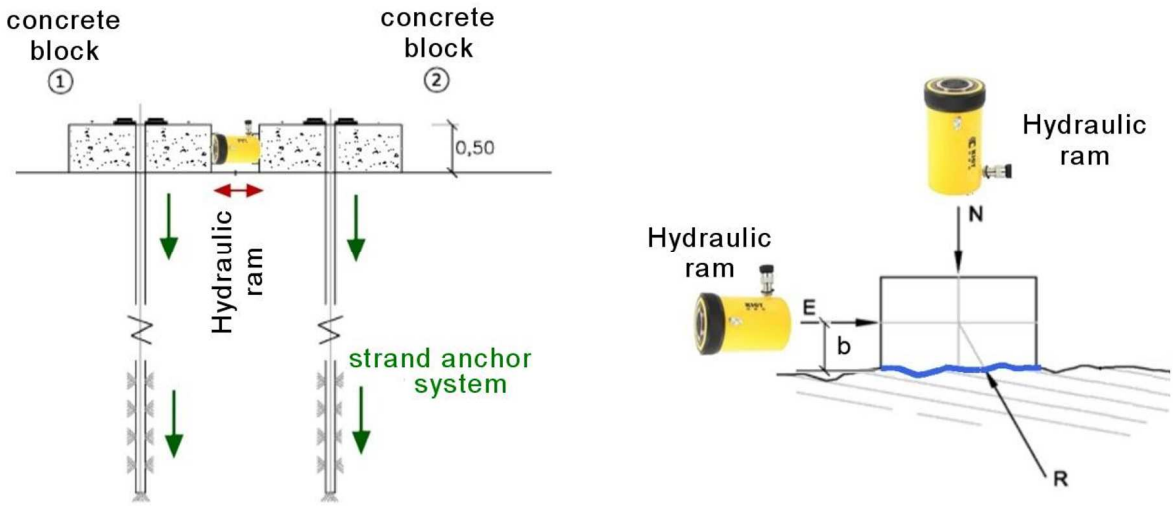

(A) **(B)**

Fig. 4 – Alternatives for applying vertical load

4. Keeping the shear force coplanar to the shearing plane, which is solved with standard laboratory shear tests boxes. If the situ shear test is arranged such that the lateral hydraulic ram is placed horizontally, an overturning moment is unavoidable and might distort the results [8]. Recommended methods and guides suggest [7, 9] tilting the lateral shearing load slightly ($\alpha \sim 15°$) with the resultant line passing through the centre of the sheared plane, so that the load is evenly distributed at the base of the block. Such restriction certainly complicates the setting-up completely, especially when it is carried out outside the dam, as a reaction wall with overhanging face is needed. Leaving aside by now the increase of vertical load when using a rigid reaction body, a tilted lateral load (G_{LAT}) itself entails an increase of the initial vertical load as the test progresses, hence the correction of the true shear load and the total vertical load (Fig. 5):

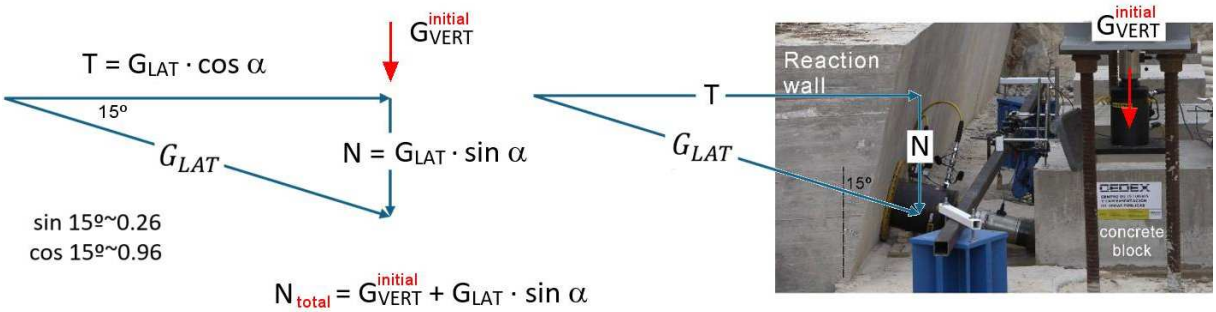

Fig. 5 – Lateral shearing force (tilted 15º): decomposition into horizontal and vertical forces

Fig. 6 shows the setting-up of the large-scale in situ shear test at Amadorio dam, which follows such arrangement.

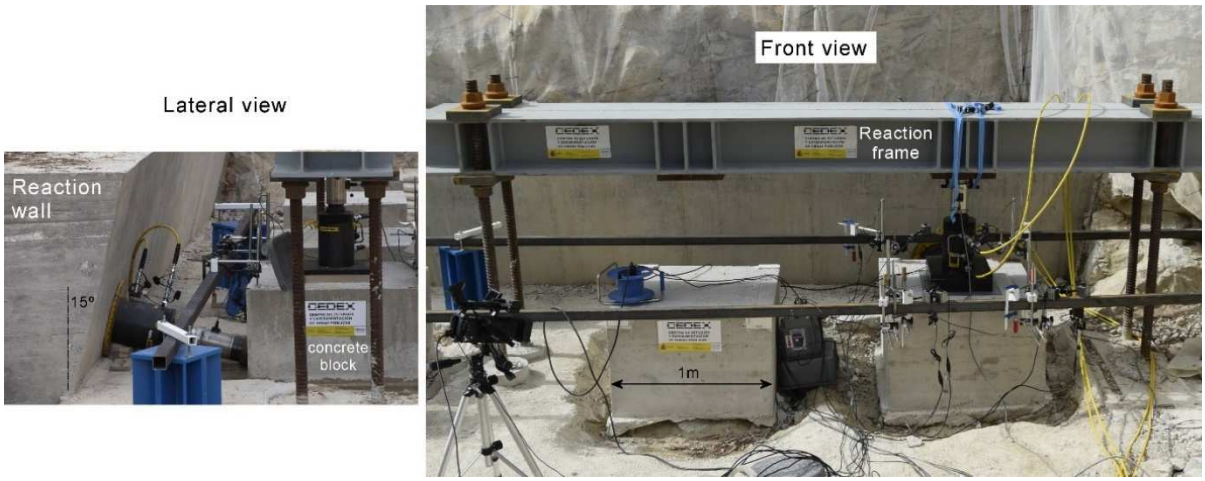

Fig. 6 – Large-scale shear test downstream Amadorio dam. Setting-up: rigid frame and tilted lateral force

3. AN OVERVIEW OF THE SPANISH EXPERIENCE

In Spain, one of the two basic arrangements depicted in Fig. 4 are generally followed in the scope of dam engineering. According to the authors´ experience gained, the advantages and disadvantages of both arrangements are listed in Table 1.

Table 1 – In situ shear test in Spain (outside the dam). Advantages and disadvantages

	Advantages	Disadvantages
With external rigid frame	Stresses evenly distributed Free of overturning moments	Complex Costly Vertical load varies during the test
With strand anchors	Due to the anchor flexibility, vertical load nearly constant Useful if bearing capacity is to be assessed; Relatively inexpensive Simple	Anchor head, require distribution load Overturning moments Vertical load prefixed, not adjustable during the test

Practice in Spain concerning the choice of the strength parameters at the concrete/rock interface has mostly relied on expertise judgement of the excavated fresh rock and inspection pits by comparable experience. Note that laboratory tests on rock cores fall short of the determination of strength parameters. As a result, in situ large-scale shear tests have been successfully carried out as well for a number of concrete dams. Table 2 summarises the large-scale in situ shear tests reported in Spain, to the authors' knowledge; shear test along rock masses discontinuities are included as well, because the procedure hardly differs from those

aimed at testing the interface between concrete surface and rock. Besides, some field tests include both types of interfaces. Fortunately, no gravity dam failures have been reported in our country due to, strictly speaking, sliding along its foundation.

Several sources for compared judgement can be found in the literature ([10]; [11]; [12]; [13]; [14]). In addition, a series of PhD dissertations have gained fair insight in well documented tests in Spain ([15], [16]; [17]).

Table 2 – Large-scale in situ shear test in Spain

	Type/height (m)	Year	River Basin	test	Ref.
El Atance	RCC, 45	1997	Tajo	50x50 cm Quartzite and schist	[18]
Itóiz	Gavity,125	1995	Ebro	50x50 cm Anchors and inclined	[19]
Rules	Arch-gravity, 132	1992	Guadalfeo	Quartzite and schist	[8, 20]
Arraiz	Gravity, 64	1985	Ebro	80x50 cm Argilite Inclined 15º	[21]
Castrovido	Gravity, 95	2009	Duero	80x80 cm Sandstone and siltstone	[22]
Enciso	RCC, 104	2019	Ebro		[23]
Mequinenza	Gravity, 81	1968	Ebro	400x400 cm 100x100 cm Limestone and lignite	[24]
Montearagón	Arc-gravity, 86	2005	Ebro	Sandstone and Marl	
La Rambla Gallinera	Gravity, 58	2013	Júcar		[25]
Albagés	Earthfill dam	2017	Ebro		[26]

4. THE LARGE-SCALE IN SITU TEST AT AMADORIO DAM

4.1. Main features of the dam and purpose

The Amadorio dam, constructed between 1948 and 1960, is located in Villajoyosa (Alicante), on the course of the Amadorio River, a tributary of Júcar River, with a reservoir of around 16 hm^3. It is a gravity dam with a straight profile, approximately 65 meters high from its foundations and a crest length of about 335 meters. Due to the scarcity at that time (Spanish post-war

period) it was built with lean concrete (UCS~10 MPa) poorly mixed. Fig. 7 shows a cross section of the dam.

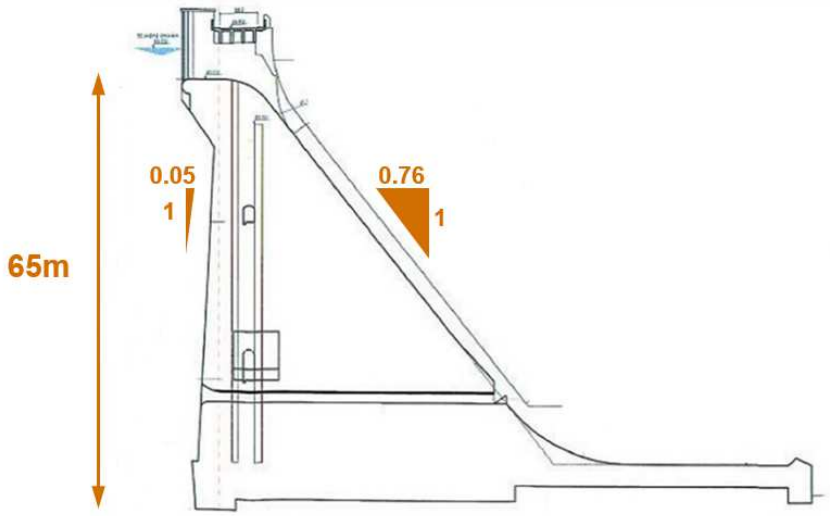

Fig. 7 – Cross section of Amadorio dam

The dam foundation consists of alternated layers of limestone, marly limestones and calcarenites with thickness ranging from centimetres to decimetres. The average dip there is 20° downstream. In general, according to the scarce information available, the rock mass is not weathered, especially on the right bank. Hardly any other information can be found concerning the foundation condition prior to pouring the concrete.

As a result of the recent safety inspections, the issue of the proper choice of the strength parameters at the dam foundation was raised, as some disagreement had been found in the three inspection reports at hand. Table 3 shows the strength parameters (values unaffected by reduction factors) proposed by the three reports:

Table 3 – Strength parameters suggested by the three reports

Report	Angle of friction (º)	Cohesion (kPa)	Remarks
Consultant A (2002)	39	500	
Consultant B (2018)	34	250	
Consultant C (2021)	36,5	350	(1)

(1) Recommended a large-scale shear test; C, previously engaged in such tests for other dams

4.2. Basic arrangement of the test

The test area was located downstream the dam (Fig. 8), on the right bank where representative massive marly limestone outcrops at the base of the slope (Fig. 9). Minor excavation work and ground levelling was needed prior to prepare the test area, where an array of four cast-in-place concrete reinforced blocks 1x1x0,6m in size were programmed to be tested.

Fig. 8 – Location of the test, downstream the dam. The blue rectangle is a canopy for shading

(A) **(B)**

Fig. 9 – (A) Another view of the test site before executing the civil works. (B) Outcrop of the rock at the contact plane of one of the blocks.

The test requires two reaction structures (Fig. 6):

- a passive reinforced single-face (workform overhanging 15º) cast-in-place concrete wall, 4 m long and 1,40 m high, densely reinforced; the opposite side was an open rock excavation, previously examined, as all the passive thrust relies on it;
- and a reaction frame: consisted of 2 twin welded steel HEB-340 beams 5 m long, spanning two concrete blocks; the twin beams are pinned at their ends on four threaded steel bars (Ø63,5 mm St670/800) with flat bearing plates and a nut on each side. The twin beams are detachable and movable to cover the span of the other two concrete blocks with another pair of bars. All six bars, which absorb the uplift force of the vertical hydraulic ram, are grouted 8 m into the rock mass. Fig. 10 shows the design drawings of the reaction frame and the cast-in-place wall.

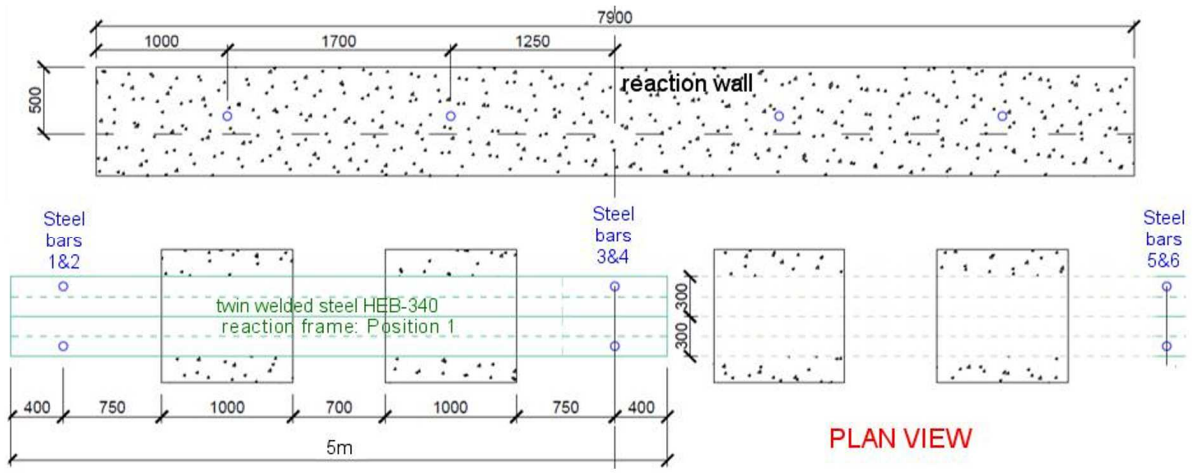

(A)

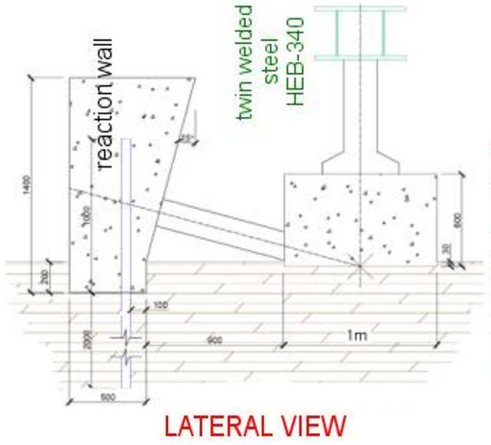

(B)

Fig. 10 – Design drawings of the reaction frame and the concrete wall: (A) Plan view, (B) Lateral View

4.3. Load and monitoring system

The increments of lateral load were applied with a hydraulic ram assisted by a hand-operated hydraulic pump with a capacity of 2,680 kN, whereas the vertical load, with another one of 1,680 kN. Reaction pads and plates to avoid concentrated loads were used. In addition, special efforts were made to create a smooth surface between the top face of the block and the load distribution plate, as the lack of vertical alignment might damage the hydraulic ram; on the top of the block, it proved to work successfully with the placement of a thin aluminium plate, meant to absorb lack of flatness and grain indentation, under a “sandwich” of two thick distribution plates with viscous grease in between. Nonetheless, both hydraulic rams are equipped with a ball-and-socket joint to allow for minor adjustment.

Although during the test the loads can be obtained by the pressures displayed at both pump gauges, electronic load cells were attached between the ram and the distribution plates and connected to the data acquisition system. With regard to the displacement readings, six regular

dial gauges (0,01 mm accuracy; stroke 100 mm) were installed at the tested block: four vertically, at each edge of its top face (dilatancy and tilting); and two horizontally, at the front face near its top corners, to obtain an averaged displacement. All six dial gauges were paired to webcams which, in turn, were connected to a closed-circuit television (CCTV) and recorded (Fig. 11). Load values and dial gauges readings were noted down at intervals throughout the test as back-up. All six webcams, displayed altogether on a screen provide useful information to track the test (Fig. 12) and spare operators from any hazards, as reading are taken off the testing site. In addition, another set of six LVDT were as well installed next to each sister dial gauges and connected to the data acquisition system with a high reading frequency, so as not to miss out uncontrolled brittle failures. The tip of the LVDTs and dial gauges plungers rest on pieces of china tiles glued to the block on avoidance of surface roughness.

4.4. Commented test procedure

The vertical loads applied to the four concrete blocks should cover the range of average effective stress at the base of a 65 m dam at its worst scenarios. Although the desired target vertical loads were aimed at 250, 400, 550 y 700 kN (effective stress: ~250,400, 500 and 700 kPa), the true vertical load at failure can be neither known nor closely narrowed down in advance: on one hand, the inclined lateral load contributes unavoidably with a vertical component (see Fig. 5); and, on the other, the frame itself causes unpredictable extra vertical loads once the adhesive/cohesive forces have been broken after minor shear displacements, since a minimal uplift movement along its saw-toothed surface is partly frustrated in proportion to the frame stiffness.

Fig. 11 – Arrangement of the monitoring system

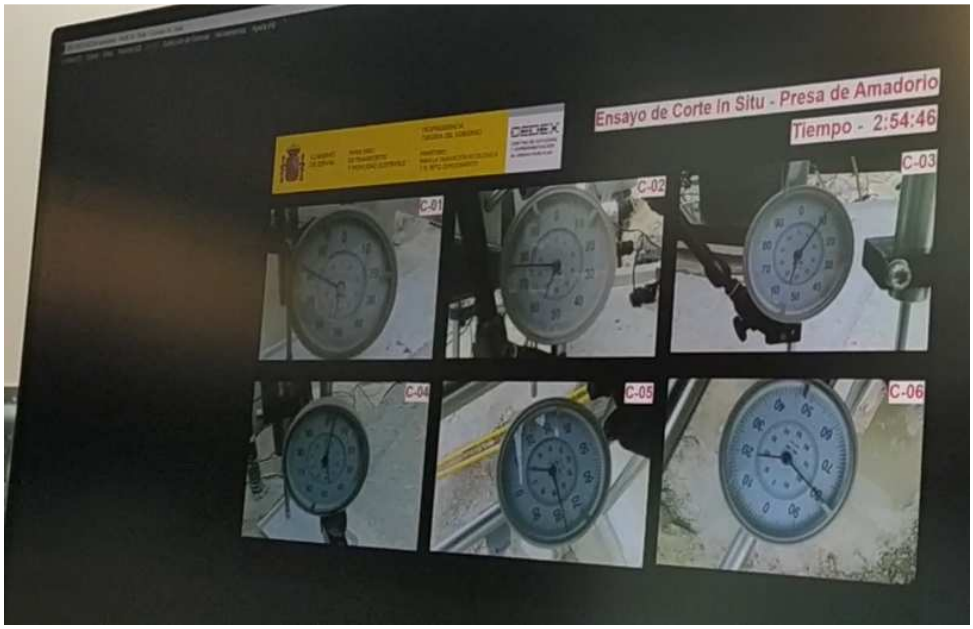

Fig. 12 – All six dial gauges displayed on a PC screen at a safety distance from the test

In fact, it seems hard to set clearly apart cohesive and frictional forces. Even so, basic rationale suggests that, as mass concrete yields at 0,2 % approximately, the cohesive/adhesive forces developed by the concrete at the calcareous rock surface might well reach such range of distortion. Hence, after 1% of relative horizontal distortion (10mm, along a 1m-long stiff concrete block) such forces should have vanished completely, being the remaining forces at the interface purely of frictional nature. In this regard, the tests were intended to reach at least a horizontal displacement of 10 mm and, if possible, 25 mm, which eventually was accomplished. Apparently, the friction angle, due to a (somehow) grinding effect, decays towards a “residual” value. Altarejos-García (2009) made insightful research in this regard, which is in good agreement with the previous reasoning and the results of the present tests, as shown later.

5. RESULTS AND ANALYSIS

5.1. Results. Peak values

Table 4 summarises basic conditions and results of the four tests, while Fig. 13 (left) plots the total force paths (vertical vs horizontal) followed by the 4 tests beyond the peak failure, as well as the peak strength envelope (right). Nonetheless, such “peak” (and brittle as well) envelope, obtained through linear fit, overestimates the true strength parameters (it yields $c' \sim 1$ MPa; $\phi_{peak} \sim 55^{o}$) (see Fig. 13 right), as the cementitious bonds at the dam base may have decayed or been broken by tensile cracks near the upstream toe. Besides, the block is made of concrete of a much higher quality than the old dam itself. So, the true adhesion/cohesion, if any, would have reached values far lower than 1 MPa.

As shown in Table 4, shear strains at peak strength ranges from 0,2 to 0,7 %, as previously predicted; thus, further displacements occur with total lack of adhesion/cohesion forces while dilative strength develops (see Fig. 2). Test with Block 1, as shown in Fig. 14 (vertical vs horizontal displacements), seems to follow such behaviour. In fact, the response of the other 3 blocks do not differ substantially from Fig. 14. The dilation angle is obtained from the ratio vertical/horizontal.

Table 4 –Summary of the main characteristics and observations of the tests

Test	date	Initial vertical Load (1) (kN)	Horizontal force at peak failure (kN)	Displacement at peak failure (mm)	Remarks
Block 1	24/04/2024	25	~2,050	2	Brittle failure
Block 2	28/02/2024	50	~1,760	4	Brittle failure
Block 3	05/03/2024	25	~2,150	7	
Block 4	17/04/2024	25	~1,940	5	Prior, test of rock mass deformability

(1) Self-weight of the concrete block included

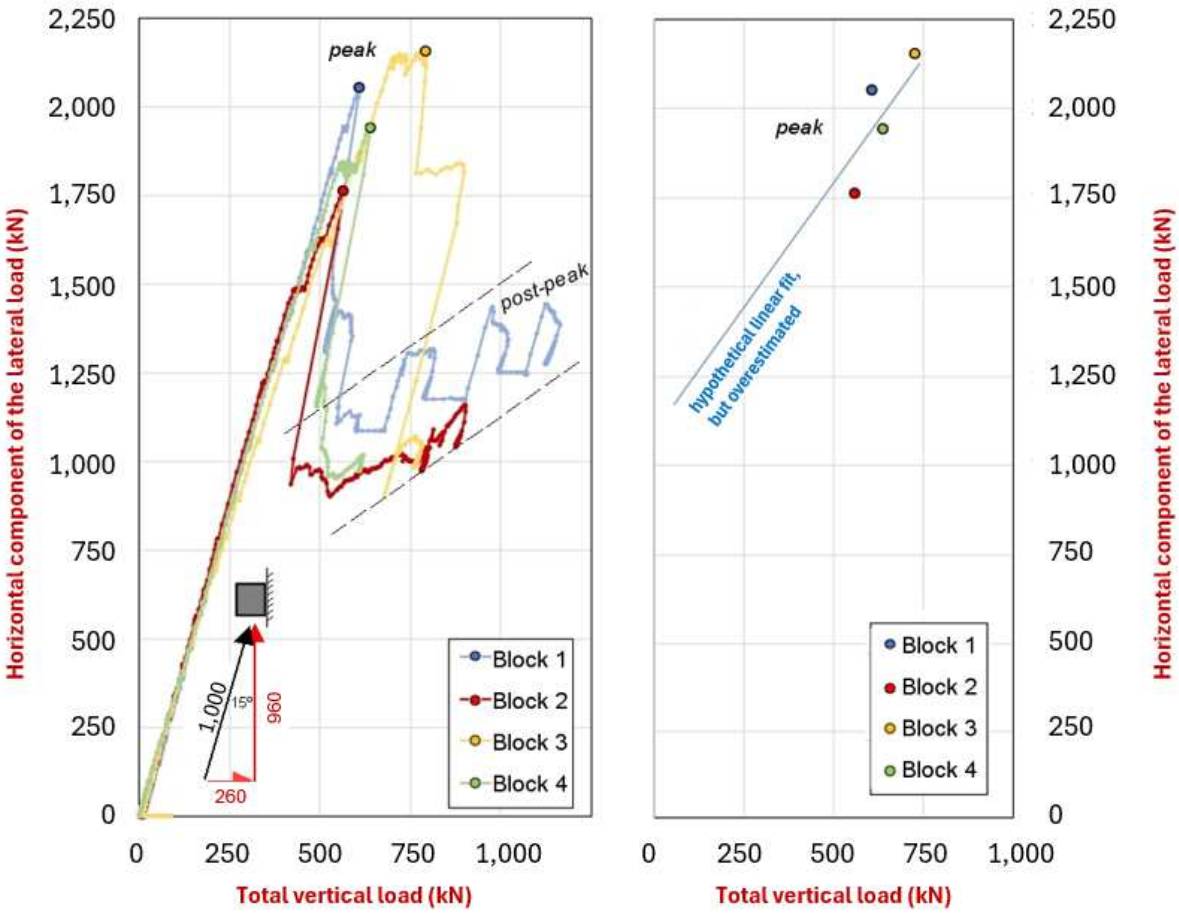

Fig. 13 – Load paths (vertical vs horizontal) followed by the 4 blocks and peak envelope

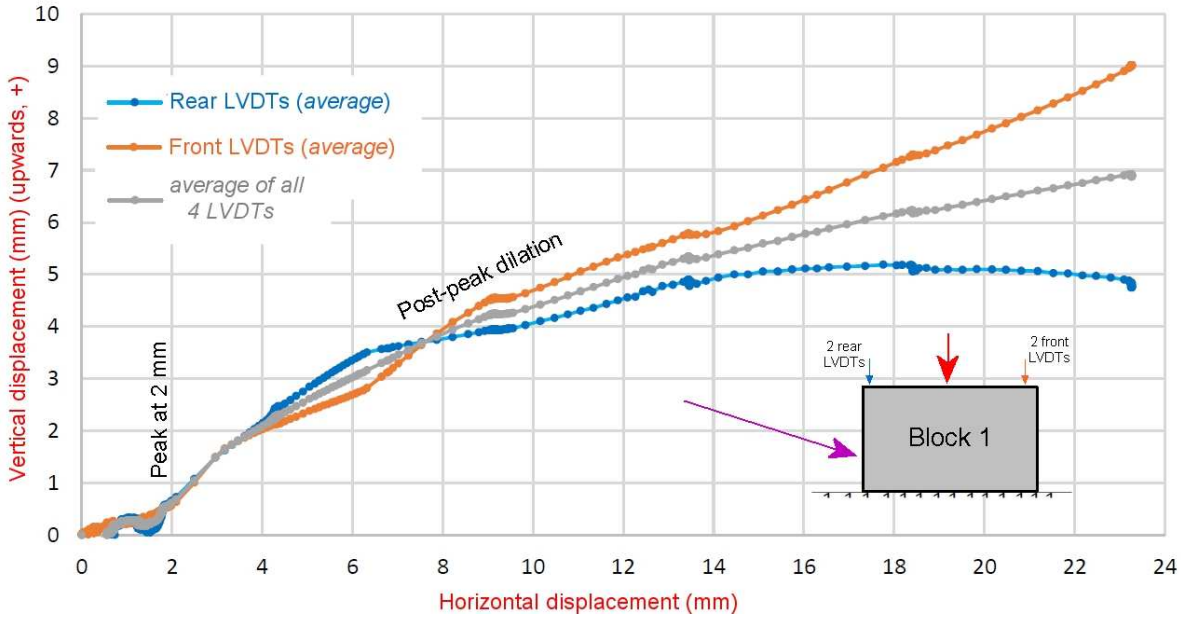

Fig. 14 – Relationship between vertical and horizontal displacements in the test with Block 1.

5.2. Results. Post-peak strength

The post-peak strength was analysed with: Taylor's model [27], based on energy balance; the Barton-Bandis model [28], which is more appropriate for natural discontinuities; and finally, the saw-toothed model (Fig. 2), which seems the most suitable. Taylor's model is highly conceptual, and rather aimed at granular soils, whose dilative response is sensitive to density. Ultimately, the saw-toothed model can be reduced to the contribution of two additive angles:

$$\phi_{mov} = \psi + \phi \quad (2)$$

where ψ is Dilation angle; ϕ, Friction true (or "basic" defined by Barton/Bandis) angle; and ϕ_{mov}, Mobilised angle.

Theoretically, the true angle should not vary as the shear continues, whereas the dilation angle should decay due to the grinding effect, unless the rock matrix is hard enough. Fig. 15 shows the evolution of the three angles throughout the test with block 1. The mobilised angle and the dilation angle are obtained with the ratios shown in Fig. 15 and, therefore, the (true) friction angle is readily inferred as a subtraction. Degraded angles could be roughly derived if large shear displacements have been achieved (>20 mm).

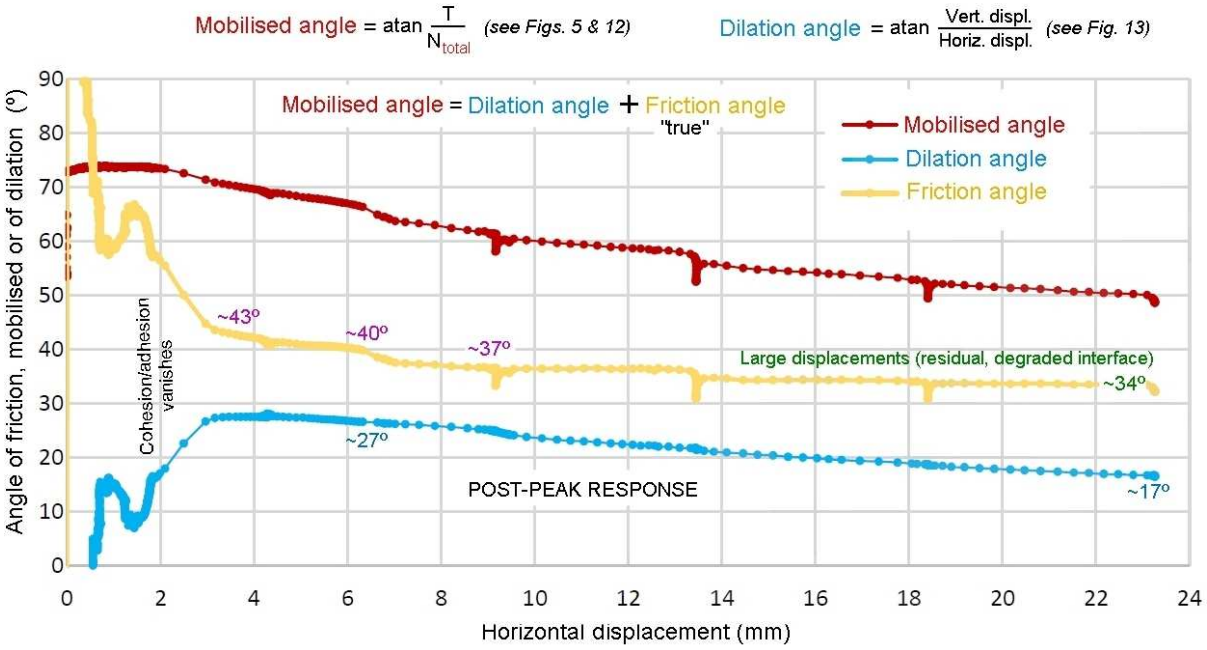

Fig. 15 – Relationship between angle of friction, mobilised, of dilation and horizontal displacements in the test with Block 1.

Table 5 summarises the angles obtained with the four blocks. The true or basic friction angle, as seen as a "plain" angle, free of any geometrical contribution, is a good estimation for design purposes in the safe side. It seems sensible, due to uncertainties, to neglect cohesive/adhesive force. Undoubtedly, irregularities during the foundation clearing and certain cohesive forces are likely to contribute to the sliding stability, yet only a rough guess can be attempted.

Table 5 – Angles (º) obtained from the large-scale shear test

Test	ϕ	$\phi_{degraded}$	ψ	$\psi_{degraded}$
Block 1	40-43	34	27	17
Block 2	38-48 (1)	34	28	19
Block 3	38	32	29	22
Block 4	45	<35 (2)	23	(2)
(1) Vague results; (2) limited displacement;				

6. CONCLUSIONS

Practice in Spain concerning the choice of the strength parameters at the concrete/rock interface has mostly relied on expertise judgement of the excavated fresh rock and inspection pits by comparable experience, yet for decades large-scale in situ test have been successfully carried out to narrow down uncertainties. Details during the setting-up is crucial, as discussed in the paper.

ACKNOWLEDGMENTS

The authors would like to thank all the divisions at CEDEX Geotechnical Laboratory for their collaboration in the development of this work, with special thanks to Pedro Juan García Guzmán, José Luis Amores Martín, Felipe García Matas, Juan María Gutiérrez Fernández, Silvia Ajates Rodríguez, Eva Marull Hernández, Enrique Hernández Suárez de Cepeda, and Marcos Asperilla Moro.

REFERENCES

[1] Muñiz-Menéndez, M., & Estaire, J. (2021). Experimental study on the shear strength of medium-coarse rockfill. In Proceedings of the 20th International Conference on Soil Mechanics and Geotechnical Engineering (Sydney).

[2] Patton, F.D. 1966. Multiple modes of shear failure in rock. Proc. 1st congr. Int. Soc. Rock Mech., Lisbon 1, 509-513.

[3] Budhu, M. (2010). Soil mechanics and foundations (3rd ed.). Wiley.

[4] Serrano, A. (1998). Mecánica de rocas (Tomo I). ETSICCP (UPM).

[5] Hudson, S. L., Crouch, C., & Fairhurst, J. A. (1972). Soft, stiff and servo-controlled testing machines: A review with reference to rock failure. Engineering Geology, 6(3), 155-189.

[6] ASTM International. (2002). ASTM D 4554 – 02: Standard test method for in situ determination of direct shear strength of rock discontinuities. ASTM International.

[7] ISRM. (2007). The complete ISRM suggested methods for rock characterization, testing and monitoring: 1974–2006. In R. Ulusay & J. A. Hudson (Eds.), Suggested methods prepared by the Commission on Testing Methods. ISRM.

[8] Soriano, A. (1997). Panel discussion: Shallow foundations of retaining structures on weak rocks. In Proceedings of the 14th International Conference on Soil Mechanics and Foundation Engineering (Hamburg).

[9] Brady, B. H. G., & Brown, E. T. (2004). Rock mechanics for underground mining (3rd ed.). Springer.

[10] Rocha, M. (1964). Statement of the physical problem of the arch dam. In Proceedings of the Symposium on Theory of Arch Dams (Southampton).

[11] Link, H. (1969). The sliding stability of dams, part III. International Water Power and Dam Construction, 21(5), 172-179.

[12] Lo, K. Y., Lukajic, B., Wang, S., Ogawa, T., & Tsui, K. K. (1990). Evaluation of strength parameters of concrete-rock interface for dam safety assessment. In Proceedings of the Canadian Dam Safety Conference (pp. 71-94). Toronto.

[13] Stone & Webster Engineering Corporation. (1992). Uplift pressures, shear strengths and tensile strengths for stability analysis of concrete gravity dams (Electric Power Research Institute, TR-100345, Vol. 1, Project 2917-05). Palo Alto, California: Electric Power Research Institute.

[14] ICOLD. (2004). Sliding safety of existing gravity dams: Final report. ICOLD European Club.

[15] Zeballos, M. (1992). Comportamiento y caracterización de macizos rocosos de alta deformabilidad empleados como cimientos de presas de fábrica (Tesis doctoral, Escuela Técnica Superior de Ingenieros de Caminos, Canales y Puertos de la Universidad Politécnica de Madrid, UPM). Madrid.

[16] Sánchez Caro, F. J. (2007). Seguridad de presas: Aportación al análisis y control de deformaciones como elemento de prevención de patologías de origen geotécnico (Tesis doctoral, Escuela Técnica Superior de Ingenieros de Caminos, Canales y Puertos de la Universidad Politécnica de Madrid, UPM). Madrid.

[17] Altarejos García, L. (2009). Contribución a la estimación de la probabilidad de fallo de presas de hormigón en el contexto del análisis de riesgos (Tesis doctoral, Universidad Politécnica de Valencia, España).

[18] CEDEX. (1997). Informe técnico. DG Obras Hidráulicas. Seguimiento del comportamiento de la cimentación y de los materiales de diques en presas seleccionadas. Estudio de la cimentación de la presa de El Atance (Guadalajara), Clave: 81-496-1-008.

[19] Castilla, J., Araoz, A., del Campo, F., Portillo, E., & Bernal, A. (1993). Ensayos de corte in situ en la cimentación de la Presa de Itoiz. En IV Jornadas de Presas (pp. 17-32). CNEGP-SPANCOLD. Murcia, España.

[20] Nevot, A. (2004). La presa de Rules. Revista de Obras Públicas, 3441.

[21] Castilla, J., Rodríguez Ibáñez, F., Bernal, A., Bolinaga, F., & Hector, B. (1993). Ensayos in situ de mecánica de rocas en la cimentación de la Presa de Arraiz. En IV Jornadas de Presas (CNEGP SPANCOLD, 4-5 mayo). Murcia, España.

[22] Alonso, E., Puigmartí, N., & Pineda, J. (2013). Foundation of a gravity dam on layered soft rock: Shear strength of bedding planes in laboratory and large “in situ” tests. Geotechnical and Geological Engineering, 32, 10.1007/s10706-013-9670-2.

[23] Soriano Peña, A., & Soriano Martínez, A. (2014). Personal communication.

[24] Uriel, S. (1964). La geotecnia aplicada a las grandes presas. Revista de Obras Públicas, 112.

[25] Sánchez Caro, F. J. (2024). Personal communication.

[26] Pinyol, N., & Alonso, E. E. (2018). Design, construction, monitoring and modelling of Albagés earth dam: A case history. International Journal of Civil Engineering.

[27] Taylor, D. W. (1948). Fundamentals of soil mechanics. John Wiley & Sons.

[28] Barton, N. R., & Bandis, S. C. (1990). Review of predictive capabilities of JRC-JCS model in engineering practice. In N. Barton & O. Stephansson (Eds.), Rock joints: Proceedings of the International Symposium on Rock Joints (pp. 603-610). Rotterdam: Balkema.

Fifth International
Dam World Conference
PORTUGAL • LISBON • LNEC • APRIL 13-17, 2025
dam world 2025

STRUCTURAL SOLUTION FOR THE REHABILITATION OF SPILLWAY PIERS SUBJECTED TO CORROSION OF THE PRESTRESSING CABLES IN THE TRUNNION GIRDER

M. A. Dalcin
Intertechne Consultores S.A.

K. Takase
Intertechne Consultores S.A.

B. Generoso[1]
Intertechne Consultores S.A.

ABSTRACT

As the service life of a prestressed structure progresses, due to potential imperfections in the filling of the prestressing ducts, the prestressing cables may be exposed to water infiltration, salts, chlorides, oxygen, and eventually lead to a corrosion episode of the strands. During a safety inspection, this scenario was identified in the trunnion girders of a Brazilian hydroelectric project following the observation of efflorescence in the region where the prestressing anchorage heads are located. With a careful and diligent procedure following the identification of the pathology, it was concluded that structural intervention was necessary. Considering the specific characteristics of the project, the most suitable solution for this case was the construction of a prestressed buttress downstream of the trunnion beams. This alternative was designed to ensure the operability of the gates in the event of the damaged cables breaking and to ensure full load transfer to the reinforcement. The buttress construction does not interfere with the spillway operation during most of the construction period, providing low hydrological risk during this interval. Thus, the proposed solution not only restores the structural integrity of the beam but also increases its durability and operational safety with minimal impact on the plant's generation activities.

Keywords: Spillway, Trunnion Girder, Corrosion, Prestressing, Buttress.

[1]bge@intertechne.com.br, Brazil

1. INTRODUCTION

Trunnion girders play a critical role in controlled spillway piers, as they are responsible for supporting the entire thrust of the reservoir acting on the radial gates. The high magnitude of these acting forces, combined with deformation constraints, makes prestressing a common solution for structures of this type. In this process, strands are inserted into ducts and tensioned to resist the loads generated by the support of the gates. Subsequently, the ducts are filled with grout [2] to prevent cable corrosion.

Among the most common pathologies observed in trunnion girders are the loss of bond and corrosion of the prestressing cables. In extreme cases of cable failure, the potential consequences can be severe, such as gate jamming, damage to piers, loss of operational capacity of the spillway structure, or, ultimately, a loss of reservoir control due to the abrupt failure of the radial gate.

Different reinforcement alternatives were studied, each one with distinct techniques and schedules, and one was selected for the development of the basic design. The prestressed buttress was chosen as the preferred alternative for combining technical feasibility with execution practicality and adherence to the selected hydrological window. Specific characteristics of the project, such as the level of intervention required in the controlled spillway structure, the strength of the existing concrete, the hydrological risks associated with the works, and the operational rules of the gates, were decisive in selecting the most appropriate solution.

Although the other alternatives are valid and applicable in different situations, in this specific case, they presented disadvantages when compared to the prestressed buttress solution. This solution proved superior due to its ability to ensure structural stability and durability, addressing the specific challenges and requirements of the plant’s operation.

In this context, the structural reinforcement of trunnion girders is an increasingly pressing need, especially in older dams or those with poorly executed prestressing systems. This article aims to present a review of an executive design for reinforcement, with the objective of restoring the capacity of trunnion girders affected by a corrosion process in a Brazilian hydroelectric power plant, exploring its advantages, limitations, and the tests conducted.

2. THE PROBLEM

In Brazil, dam safety legislation establishes criteria and safety measures that must be followed in hydroelectric plants [3]. In compliance with this law, during an inspection conducted at a Brazilian project, only four years after it began operating, ferruginous efflorescence was

observed on the surface of the secondary-stage concrete of the trunnion girders, specifically in the downstream anchorage niches of the longitudinal prestressing, as shown in Figure 1.

Fig. 1 – Efflorescence on the downstream face of the trunnion girder beam

The efflorescence indicated the occurrence, either past or present, of water seepage through the secondary-stage concrete, while its coloration suggested the presence of iron oxide. Based on this observation, an extensive investigation program was initiated, involving progressive stages of testing and evaluations.

Laboratory tests revealed that carbonation was superficial and oxide levels were within normal ranges, indicating that the deposits were associated with interlayer seepage rather than the concrete matrix itself. Subsequently, the secondary-stage concrete (which protects the prestressing anchorages) was removed, and a visual inspection of the metal components revealed oxidation on both the anchorage plates and the exposed ends of the prestressing strands, as well as water seepage through the strands themselves (Figure 2).

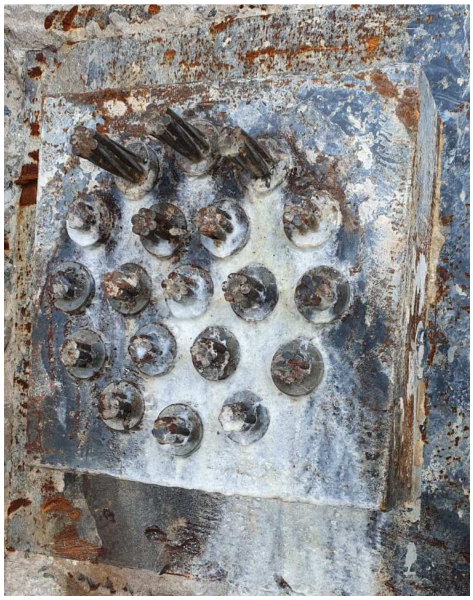

Fig. 2 – Moisture and carbonation marks on strands and exposed anchorage plate

During the months in which the anchorages remained exposed, significant water seepage and continuous carbonate deposition were observed. This finding reinforced the urgency of identifying the water source and mitigating its seepage into the prestressing cables. The primary hypothesis for the anomaly was water infiltration through the upstream prestressing niche's secondary-stage concrete, allowing direct contact between the cables and the reservoir water level.

As a preventive measure, the face of the spillway piers in the region of these niches, between the cofferdam and radial gates, was waterproofed. Figure 3 illustrates the typical arrangement of the structure in question.

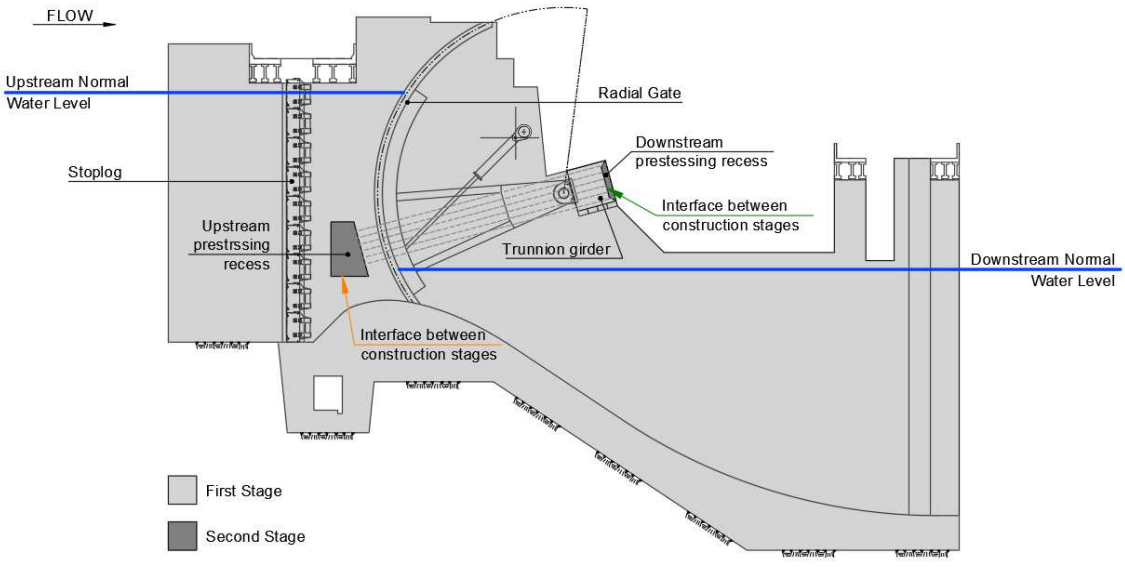

Fig. 3 – Arrangement of the analyzed spillway – Side view

As part of the investigative process, various methods were considered to evaluate the integrity of the prestressing cables, ranging from more invasive approaches, such as opening an inspection window in the spillway pier, to less precise, indirect tests. It was concluded that the Reflectometric Impulse Measurement Technique (RIMT) would be the most suitable method for the project context.

RIMT is a non-destructive test used to identify corrosion levels in strands and detect voids along the cables, indicating areas where the grout inside the ducts is not adequately filled.

The procedure involves transmitting short-duration electromagnetic waves through the prestressing cable by sending an electrical pulse via direct contact of the equipment with the cable at the anchorage region. Although effective, the results obtained through RIMT are qualitative, highlighting areas along the cable affected by oxidation or voids without providing numerical parameters for section loss or strength reduction.

To address this limitation, an empirical methodology was developed to correlate RIMT qualitative data with numerical values, enabling the estimation of the percentage of cable strength loss under different failure scenarios.

Figure 4 illustrates the results obtained for one of the cables in the trunnion girder of the central pier. It can be observed that regions near the upstream prestressing niche exhibited higher concentrations and severity of corrosion, indicating that water infiltration predominantly occurs at the interface between the different stages of concrete present in this area.

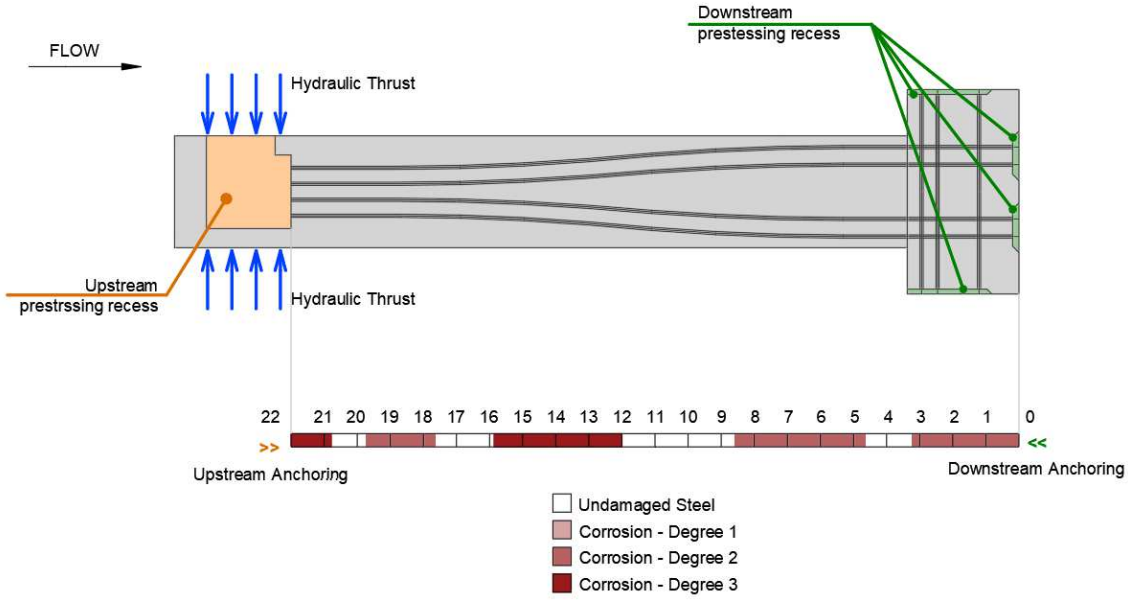

Fig. 4 – Corrosion measurements on the cables of the central trunnion girder

As shown in the figure above, the cable in question exhibits corrosion levels ranging from 1 to 3. The first corrosion level represents negligible anomalies, with no reduction in the cable's effective cross-section, but with the loss of the protective surface and the presence of very

superficial oxidation. The second level indicates minor anomalies, characterized by the formation of an oxide layer and localized oxidation with sparse corrosion points. The third level represents moderate anomalies, involving slight reduction of the effective cross-section and more significant oxidation, with greater depth and extent.

However, the test results make it evident that the corrosion process is already underway, with areas showing cross-section loss and, consequently, reduced tensile strength, which jeopardizes the integrity of the structure.

Since RIMT provides only qualitative results, it is challenging to accurately quantify the percentage of cross-section loss caused by corrosion. In the case of trunnion girders, the situation is even more critical than a typical corrosion scenario, as the strands are subjected to high tensile loads, resulting in a case of stress corrosion cracking (SCC). This condition increases the risk of sudden and brittle failure [4].

In a critical scenario, the rupture of the cables could lead to severe consequences, such as gate blockage, structural damage to the piers, interruption of the spillway's operation, or even a loss of reservoir control due to the abrupt failure of the radial gate arm support.

3. THE SOLUTION

3.1. The concept

The prestressing system of the trunnion girders typically includes an upstream prestressing niche in the pier region and another one on the downstream face of the trunnion girder. When the arms of the radial gates are positioned below the reservoir water level, it is common for the upstream niche to remain submerged, resulting in an area constantly subjected to the hydrostatic pressure of the reservoir. Therefore, two critical factors for the proper performance of this arrangement are the adequate concreting of the upstream niche and the complete filling of the prestressing ducts with cement grout.

The alkalinity of Portland cement, with a pH ≈ 12, initially protects the strands from the corrosion process through what is known as the passivation layer [5]. Passivation occurs due to the formation of a protective iron oxide film, composed of $nFe_2O_3 \cdot mH_2O$, which acts as a barrier between the corrosive environment and the steel surface. However, when concrete is exposed to corrosive agents such as CO_2 and Cl^-, it becomes less alkaline, and the passive film is damaged by reactions between oxygen, water, and Fe^{2+} ions that penetrate the concrete. At the same time, Fe_2O_3, a reddish-colored corrosion byproduct, is formed [4].

To restore the safety of the structure, a preliminary design was developed, including studies of alternatives for strengthening the affected trunnion girders. Among these, the use of external

prestressing was initially analyzed. However, this option was deemed unfeasible due to the high magnitude of stresses that would be added to the existing concrete and the limited space available between the gate arms and the pier face. Another disadvantage of this approach is the potential for the new prestressing system to also undergo corrosion, particularly since it would be external to the structure.

As a result, the concept of a prestressed buttress was developed, which proved to be the most advantageous solution for this specific case, as shown in Figure 5.

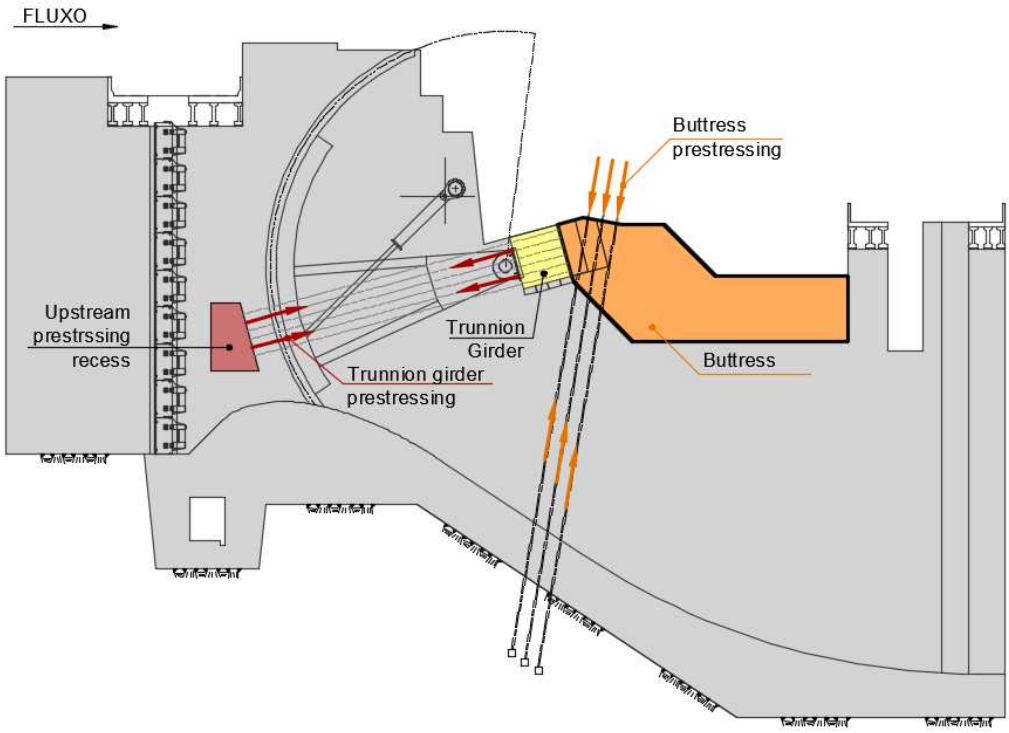

Fig. 5 – Prestressed Buttress Structural Concept

3.2. Pull-out test of the new post-tensioning system

The context of the project and the condition of the existing structure led to the development of a unique solution, requiring the use of equally specific materials. To ensure the adequate performance of the reinforcement, three pull-out tests of the new post-tensioning material were conducted by applying the full design load. The purpose of the test was to verify the parameters adopted in the executive design and to ensure that the contractor had the necessary execution methodology to implement the solution.

During the pull-out test, the pressure in the post-tensioning equipment was gradually increased, with pauses at 5 MPa intervals, except for the final increment, to record elongations and forces. All materials were marked with light chalk lines to measure elongations and detect potential slippages.

The elongations of the pistons and the corresponding hydraulic pressures in the jacks were measured and recorded in a control spreadsheet. After anchoring, the occurrence of any slippages was examined. Prior to the test, the theoretical elongations of the material were calculated, and at the end of the process, these were compared with the actual elongations observed in the field. Figure 6 illustrates the test conducted on rock similar to that of the spillway foundation.

Fig. 6 – Testing of the new prestressing system

The measured value of the immediate elongation showed a deviation of less than 5% compared to the theoretical value, and even weeks after the test, this value did not increase significantly. This indicates that the parameters adopted in the executive design were consistent. Additionally, there was no evidence of strength loss or excessive displacement of any metallic component due to the high applied loads, demonstrating that the system is correctly designed and capable of withstanding the full design load.

3.3. Analysis by the finite element method

The concrete characterization tests also supported the development of a three-dimensional finite element model (FEM), using nonlinear analysis to accurately represent the actual loading conditions to which the spillway may be subjected.

The approach included mapping the stresses of the new post-tensioning system and refining the involved geometries, ensuring effective load transfer. This step was crucial to properly design the structure, preventing excessive differential displacements that could compromise the gate's operation or cause it to jam under critical operational conditions.

The highest compressive stresses in the structure occur during the construction phase when the original post-tensioning of the trunnion girder (a scenario where the cables have not yet failed) is fully considered alongside the new reinforcement post-tensioning. However, since the new post-tensioning was allocated downstream of the existing one, the stresses are distributed without overlapping, as shown in Figure 7, making it unnecessary to reinforce the pier structure.

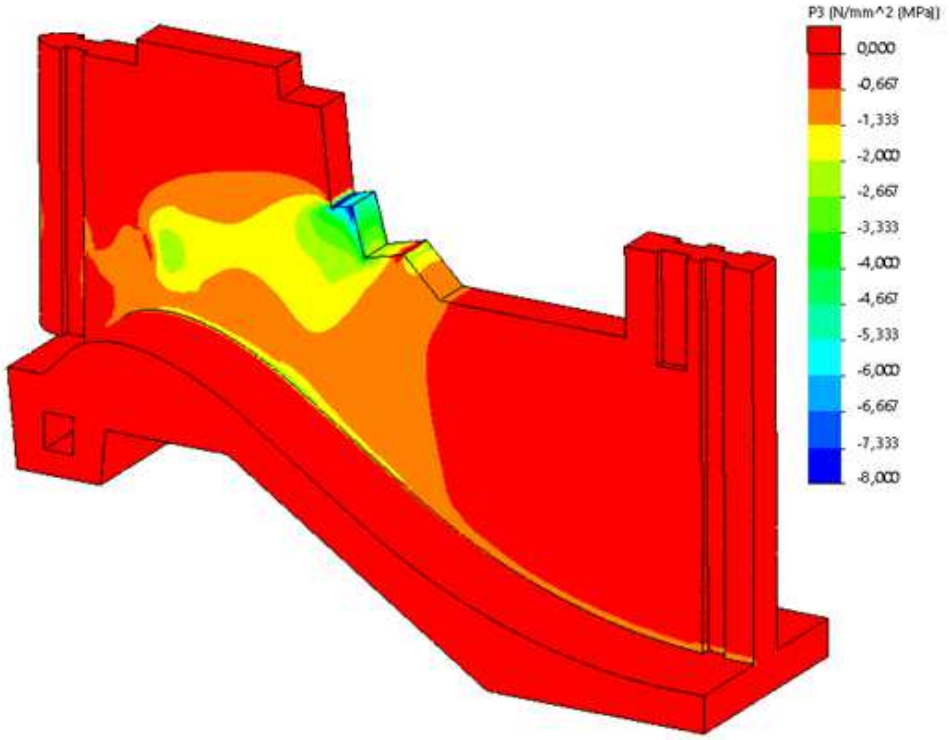

Fig. 7 – Principal compressive stress – Construction stage – [MPa] (trunnion girder and buttress hidden)

Both construction phases and final loading scenarios were analyzed. The load analysis following cable rupture aimed to study load transfer and the resulting displacements. In this process, the reinforcements of the buttress were designed to accommodate the forces transmitted through the interface with the trunnion girder, in addition to designing the connection reinforcements along the entire contact area with the existing structure.

In the trunnion girder of the central pier, post-tensioning occurs on both sides, with each side supporting half the load of a radial gate. Consequently, two main rupture scenarios for the trunnion were simulated: unilateral, in which the cables on only one side of the pier fail while those on the opposite side remain active, and bilateral, where cables on both sides fail. Among the analyzed cases, the unilateral rupture proved to be the most critical for the trunnion girder of the central pier, resulting in the greatest load imbalance and the most significant differential displacement of the gate.

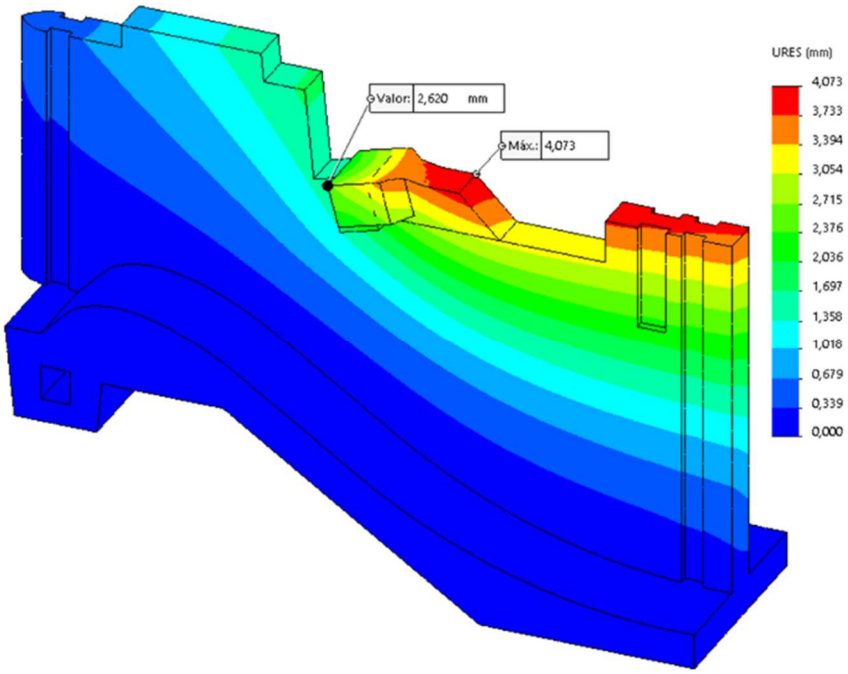

Fig. 8 – Immediate resulting displacement – Unilateral failure case – [mm]

The maximum immediate displacement obtained in the computational model at the gate bearing region was 2.6 mm (Figure 5). The estimated displacement limit for the radial gates of the spillway was 10 mm to ensure uninterrupted operation. Therefore, the adopted solution, in addition to being suitable for load transfer, also proved effective in limiting displacements.

4. CONCLUSIONS

In large dams and hydropower projects, the design of controlled spillways for flood discharge is a common practice. The gates are generally subjected to high thrust forces due to the upstream reservoir, necessitating the post-tensioning of trunnion girders to withstand such loads.

The arrangement of the spillway structure, with post-tensioning niches and trunnion girders located below the reservoir water level, combined with potential construction issues (such as improper cement grout injection), promotes water seepage along the post-tensioning cables. If this scenario occurs, the strands may be affected by oxidation, potentially losing part or all of their load-bearing cross-section.

Based on an inspection at a hydropower plant in Brazil, where signs of water seepage along the post-tensioning cables were identified, Intertechne Consultores S.A. developed a detailed study for the structural requalification of the trunnion girders. This work resulted in innovative solutions, both at the level of executive design and the specification of unconventional materials, pioneering advances in the hydropower sector and marking

significant technical progress in the structural reinforcement of controlled spillways with post-tensioning cables exposed to corrosion.

The solution, designed as a post-tensioned buttress, aims to fully transfer the load from the trunnion girder in the event of a total failure of the corroded post-tensioning cables, restricting differential displacements and effectively redistributing forces within the existing structure. Additionally, given the short period during which the spillway can remain inoperative, the solution was designed to minimize disruptions to gate operations during construction.

The spillway arrangement, featuring a significant horizontal section downstream of the trunnion girder, was critical to enabling the reinforcement solution. This free area allowed for the placement of the buttress without interfering with flood discharge flows and ensured proper stress distribution across the existing structures.

The experience gained through this solution facilitated the enhancement of methodologies and processes applied to post-tensioned structures. Consequently, technical specifications were refined, and new construction details were incorporated, ensuring greater efficiency and reliability in future projects involving post-tensioned structures.

Finally, it is important to note that the solution presented was specifically designed for the analyzed case and should not be regarded as a general approach for addressing corrosion issues in trunnion girder post-tensioning cables. Each situation requires a thorough and tailored technical analysis to determine the most appropriate solution based on the project context and its specific boundary conditions.

REFERENCES

[1] ELETROBRAS. Critérios de Projeto Civil de Usinas Hidrelétricas. October 2003.

[2] U.S. Army Corps of Engineers. EM 1110-2-2702: Design of Spillway Tainter Gates. Washington, DC, 2000.

[3] BRASIL. Agência Nacional de Energia Elétrica. Resolução nº 1.064, may 2, 2023. Available at: https://www2.aneel.gov.br/cedoc/ren20231064.pdf.

[4] Koch, Gerhardus H. "Tests for Stress-Corrosion Cracking." Advanced Materials & Processes, vol. 159, no. 8, Aug. 2001, p. 36. Gale Academic OneFile.

[5] Bureau of Reclamation. Guide to Concrete Repair. 2nd edition, August 2015.

Fifth International Dam World Conference
PORTUGAL • LISBON • LNEC • APRIL 13-17, 2025
dam world 2025

DESIGN AND CONSTRUCTION OF HARDFILL COFFERDAM ON RIVER ALLUVIAL DEPOSITS

Chongjiang Du[1]
Tractebel Engineering Ltd.

Sebastian Beck[2]
Tractebel Engineering Ltd.

Uysung Jung[3]
Nepal Water and Energy Development Company

ABSTRACT

Hardfill dam is a new type of dams and may be regarded as a dam type between CFRD and RCC gravity dams. Actually, the hardfill dam is a gravity dam and has the main characteristics similar to RCC gravity dams and CFRD. Besides other advantages, the hardfill dam can be overtopped and its requirement for foundation and for aggregate is low. This paper presents the design and construction of the hardfill cofferdam at Upper Trishuli-1 Project founded on river alluvium, because the bed rock at the project site is located at a deeper depth below the ground level. Moreover, the cofferdam has to be overtopped by monsoon floods for over three to four months every year. These are the main reasons why the hardfill dam is constructed. The river alluvium varies from sandy-clay particles to cobbles and boulders. The alluvial deposits may directly affect the stability of hardfill dam. In the design, the hydraulic conditions and abrasion of river sediment on dam concrete are described. The structural design including the layout and stability analysis for the hardfill cofferdam is then worked out. Thereafter, the mix design and production of the hardfill materials are presented, in particular, the sources and acquisition of aggregates with sizes up to 150 mm dia. are outlined. The construction of the cofferdam was uncomplicated and completed within three months. Up to date the hardfill cofferdam has operated over two years and experienced heavy flooding during two monsoon periods with no significant defect. The successful construction and operation of the hardfill cofferdam demonstrated the capacity of this dam type to suit the non-rock foundation and overtopping by floods. Although it is a cofferdam, its principle is valid for conventional hardfill dams.

Keywords: hardfill dam, cemented sand and gravel dam, roller compacted concrete dam, cofferdam, dam engineering.

[1] chongjiang.du@tractebel.engie.com, Germany
[2] sebastian.beck@tractebel.engie.com, Germany
[3] uysung.jung@nwedc.com.np, Nepal

1. INTRODUCTION

Although a cofferdam is a temporary structure, it is a dam and an important work associated with the main dam. Cofferdam failures may not only cause the construction delay, but may cause loss of life to downstream inhabitants and construction personnel and/or appreciable property damage. Most of cofferdam failures are caused by overtopping. In many cases, the cofferdam must be seated on alluvial deposits, because the bed rock is deeply buried below the riverbed. Therefore, design and construction of an overtoppable cofferdam especially founded on alluvial deposits is a challenging task to dam engineers at all times. Nonetheless, such a cofferdam has to be constructed in many cases.

For the deep alluvium foundation, a rockfill cofferdam is the common option. To protect the rockfill cofferdam from overtopping failure, a thick reinforced concrete layer must be covered on the rockfill dam body. Although this measure increases its safety, it causes significant increase in costs. To overcome the shortcoming, an innovative option with using hardfill material to construct the cofferdam at Upper Trishuli-1 hydropower project is proposed. In particular, the cofferdam is founded on alluvial deposits. The various design and construction features are described. The cofferdam has successfully survived from the long-lasting floods of two monsoon seasons with each of over three months.

2. HARDFILL DAMS AND THEIR CHARACTERISTICS

Hardfill dam concept together with roller compacted concrete (RCC) dam concept was initiated by Jerome Rafael in 1970s [1]. The concept was further developed since 1990s as “Faced Symmetrical Hardfill Dam (FSHD)” [2] and “Cemented Sand and Gravel (CSG) Dam” [3]. In a general sense, all these terms are variations of the same basic concept. Disregard the various names, we will discuss the topic hereinafter uniquely referred to as “hardfill dam” as a generally descriptive denomination for this dam type in this paper.

The hardfill dam is a new dam type with characteristics of RCC gravity dams and CFRDs (concrete face rockfill dam). The cross-section can be symmetrical or asymmetrical with upstream and downstream slope ranging from 1V:0.5H to 1V:0.8H. Same as RCC, the hardfill material is a no-slump concrete, which in its fresh stage will support heavy-duty machines while placing; and the no-slump concrete mix is transported, spread and compacted using earth/rockfill dam construction equipment [4]. The following shorthand has been adopted for the main advantages and attractions of hardfill dams:

- Reduced cement content, resulting in reduced unit costs of hardfill mix;
- No need for temperature control and internal drainage;

- Low requirement for aggregate, using as-dug river gravels and/or excavation waste;
- Minimum requirement for foundation, enable to be constructed on weak foundation or even on alluvial deposits;
- Low requirement for compressive and tensile strength;
- Excellent seismic resistance; and
- Overtoppable during construction and operation period as the conventional concrete.

With these attractive characteristics and benefits of hardfill dams, the hardfill concept becomes a dominant material and construction technology, advancing the construction of dams. It was also the advantages that we decided to apply it in the construction of cofferdam at Upper Trishuli-1.

3. UPPER TRISHULI-1 PROJECT AND ITS RIVER DIVERSION

Nepal is rich in water resources with approximately 6 000 rivers with a total length of 45 000 km. Average annual water runoff from these rivers is about 220 billion m^3. Given the perennial nature of the rivers and the steep gradients of the topography, Nepal has a significant potential for hydropower development. According to Nepal Electricity Authority (NEA) - the state-owned power utility, Nepal has the potential to harness over 72.54 GW of hydropower with economically viable potential of over 40.00 GW across 10 major river basins and their sub-basins. As of 2022, Nepal has 142 operating hydropower plants with a combined installed capacity of 2.60 GW, amounting to 96.2% of the country's total installed capacity, and a further 244 are under construction. Together the cumulative installed capacity will reach 8.76 GW.

The Trishuli River is one of Nepal's seven transboundary rivers and originates in the Trans-Himalayan Zone within Tibet Autonomous Region of the People's Republic of China, where it is known as Bhote Koshi. The catchment area of the river in Tibet is about 3 170 km^2 for a river length of 120 km. The Trishuli River extends approximately 106 km within Nepal, with high gradients in the initial 40 km and rapids along its entire length.

Upper Trishuli-1 hydropower project is a 216 MW greenfield run-of-river plant, situated on the upper reach of Trishuli River in Nepal. The dam site is about 20 km south of the international border with China and about 70 km north of the country's capital Kathmandu. The project lies within the High Mountain physiographic zone, with the project footprint located at El.1 000 m asl., so that the geomorphological characteristic affects the climate. From a climate perspective, the project is located in the sub-tropical region (up to El.1 200 m). The area has distinct wet and dry seasons. The project consists of a weir structure with a concrete gravity dam, three underground desanders, each measuring L x W x H = 143.50 x 14.25 x 26.00 m. Two intake tunnels will deliver water to a 9.8 km long headrace tunnel with a horseshoe-haped profile with a diameter of 7.2 m and a discharge capacity of 76 m^3/s. The project will also

feature a 76 m tall surge tank and a 300 m deep pressure shaft. The underground powerhouse will be equipped with three Francis units of 72 MW each. The tailrace tunnel will expend water to the Trishuli River, 10.7 km downstream of the dam.

The dam site is situated in a narrow canyon with high steep banks. Consequently, the river diversion via a tunnel is the only choice. On one hand, the monsoon floods of the Trishuli River are rather high. The monsoon seasons last about three to four months in the summer. Usually, the monsoon starts around mid-June, peaks in July and August, and winds down in early September. Thus, June to September are crucial months for the dam construction, with the discharge accounting for about 70% of the entire annual discharge. While short-term local events, particularly flash floods, cause challenging peak discharge in this season. On the other hand, the extensive underground works as mentioned above will control the construction period. As a result, it is reasonable and economic to construct the diversion facilities with a low discharge capacity for the dry seasons flow, while in the monsoon seasons the cofferdam will be overtopped by floods and the dam construction be suspended. This requires the cofferdam overtoppable. It should be noted that due to the high gradient of riverbed, only the upstream cofferdam is required, while at downstream no cofferdam is necessary.

4. DESIGN OF HARDFILL COFFERDAM

An engineering geological and geotechnical investigation indicated that the site is underlain by alluvial deposits and the depth to bedrock was estimated to be down to 34 m. Therefore, the cofferdam shall be seated on alluvial deposits from the economical point of view. The alluvial deposits primarily consist of fine and coarse fraction which can be characterised as cobber and boulders mixed sandy soil, as shown in Fig. 1. Therefore, building the overtoppable cofferdam on the alluvial deposits became a challenge for the dam engineers. Nevertheless, there are several precedents that the hardfill dams are founded on alluvial deposits [5].

Fig. 1 – Foundation of hardfill cofferdam with alluvial deposits

In the initial design, a rockfill cofferdam with a reinforced concrete cover of 1.0 to 2.0 m thickness throughout the whole length from the upstream heel to downstream toe of the cofferdam was proposed. Although it can be quickly constructed, concern was raised over its stability during the long-lasting massive monsoon flood events, by which the rockfill cofferdam may fail during its prescribed five-year service life. Moreover, the project cost would have been strongly affected. As the project has commenced, the alternatives of cofferdam were revisited, and then the hardfill dam option sprang into field of vision, particularly because its ability to be founded on alluvial deposits, overtoppable capacity and using the as-dug river gravels and/or excavation waste. A preliminary study demonstrated its feasibility and its lower construction costs.

The river channel is about 20 to 40 m wide. An asymmetrical hardfill dam section was proposed through the iterative stability analysis and economic consideration by means of the trial-and-error method. As shown in Fig. 2, the hardfill dam is 14 m high and 48.5 m long with an overtoppable crest of 6 m width at El. 1253.0 m asl. The base length (upstream to downstream) is 34 m. The dam interior is constructed with hardfill material of grade C8 mixed with the waste rock material excavated from the underground works. It should be noted that the C8 grade hardfill material is conservative, while C5 hardfill must be sufficient.

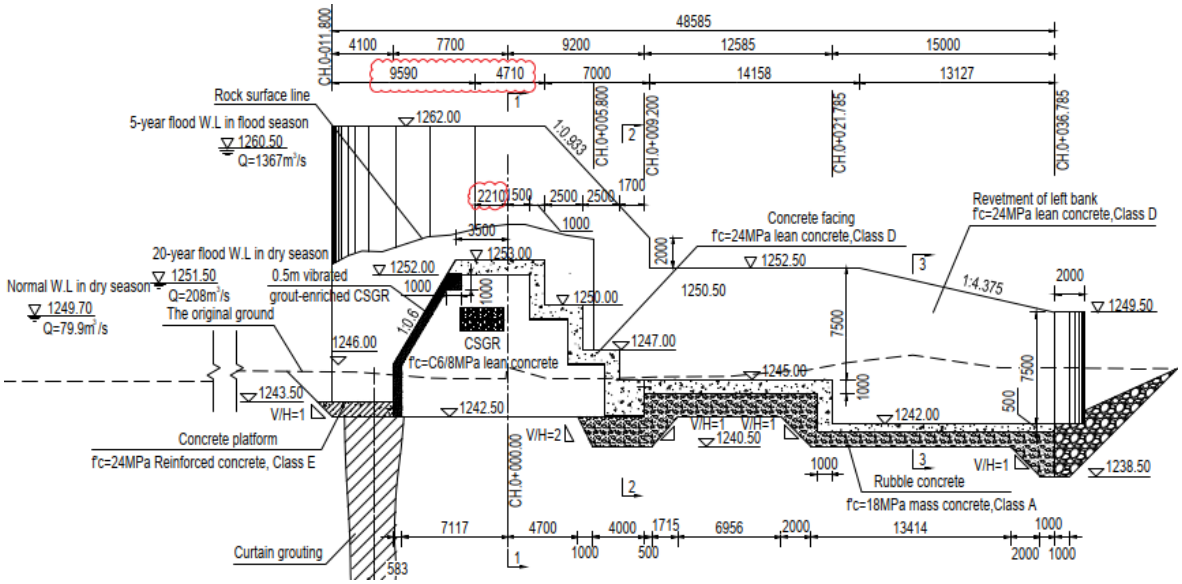

Fig. 2 – Cross Section of the hardfill dam

The upstream slope is V:H=1:0.6; the facing is constructed with the grout-enriched hardfill of 0.5 m thickness, forming an impermeable barrier. Moreover, the grout-enriched hardfill was applied at the interfaces with the rock surfaces of abutments. The crest and downstream slope are armoured with 1.0 m thick conventional concrete of grade C24 to provide the abrasion and erosion resistance to the massive discharging flow with heavy bed load sediment during the monsoon seasons. Because the short service lifespan of the hardfill cofferdam, a high-grade abrasion resistant concrete is not necessary. The downstream has a general slope of

V:H=1:0.65 and stepwise constructed to facilitate the construction besides assist in energy dissipation. In the middle area of the crest, a 1-m deep gap (El.1252.0 m) is left to divert flood flows to the central area and minimize the erosion of abutments. By minor overtopping, the flow passes only through the middle area. No contraction joint is arranged in the dam.

To reduce both leakage and uplift pressure of the dam foundation, curtain grouting was conducted in front of the dam upstream heel, for which a concrete plinth of 1.0 m thickness was constructed. Water stops are installed at the joint between the plinth and hardfill dam.

The stability analysis of the hardfill dam was carried out in accordance with the design manual of US Army Corps of Engineers EM 1110-2-2100. The maximum compressive stresses at the dam-foundation interface are far below the allowable bearing capacity of the alluvial deposits. No tensile stress develops. The minimum factors of safety against sliding on any plane are greater than the required minimum values. Therefore, the stability of the hardfill dam is ensured.

5. CONSTRUCTION OF HARDFILL COFFERDAM

As cementitious materials, Ordinary Portland Cement (OPC) and fly ash (20%) are used to produce the hardfill material. Being an EPC project, the compressive strength of hardfill was controlled by the quality control process, while the excessive content of cementitious material was not strictly controlled. The rock material excavated from the underground work was used. The maximum size of aggregate was specified to 150 mm. They do not need any treatment but screening oversized particles, thus typically lack a fixed gradation. The rock types are mainly quartzite and gneiss which are hard and blocky. Superplasticizer was applied as well.

To build the hardfill dam, a low pre-cofferdam of rockfill was constructed upstream of the hardfill dam with a prescribed service life no more than 3 to 4 months in the dry season, which serves only for the construction of the hardfill dam.

Before the construction of hardfill dam, a large-scale trial was performed in an area near the dam site in November/December 2022. From which the proposed major construction procedure and specifications were confirmed.

The hardfill material was mixed in two adjacent open-air pools, A and B. The dump trucks of 20-ton capacity transported the all-in aggregates and dumped into the pool A. After addition of cementitious materials, the materials were dry mixed with an excavator of type HE300L. After the preliminary dry mixing, the dry mix was relocated into the pool B, where it was re-mixed at least three times. Thereafter, water and chemical admixture with the specified proportion were added into the pool B, and the materials were wet mixed again for two times or more until it reached the specified uniformity. The VeBe time of hardfill mix was specified to 5 to 10s. The

prepared hardfill mix was uploaded into trucks which transported to the dam site. Prior to the dump truck entering the construction pit, its tyres were thoroughly washed and then dried to prevent contaminants and water into the construction pit.

A bulldozer was used to spread the dumped hardfill material at the placing locations into the thickness of about 45 cm. Eventual segregation of the hardfill material was improved manually. A 17-ton self-propelled steel-drum vibratory roller was used for the compaction. The compaction was started with two initial passes in the static mode without vibration, and then followed by five passes with vibration, and finally the last pass with no vibration was performed, until the layer reached the required density. The overlap was 10 to 20 cm wide for rolling strips and for hardfill interface, and 100 cm at the ends of connection. The roller was operated at a speed between 1.0 and 1.5 km/h. The total length of time from the end of mixing until the hardfill material has been placed, spread, and compacted was controlled within 1.0 hour.

To construct the grout-enriched hardfill of 0.5 m thickness at upstream face of the dam and at the interface between the hardfill dam and abutment rock, the slurry was added in two layers into the spread hardfill material, that is, a layer of the pure cement slurry at the bottom of the material and another layer at the top after the hardfill material was spread. The quantity of slurry to be added was determined by the large-scale trials according to the laboratory tests. The slurry was produced by a high-speed mixer with a mixing time of 30s. The hand-held vibrator was used for the compaction of grout-enriched hardfill material. As the watertightness is provided by the upstream grout-enriched hardfill face, the layer surfaces received a minimal treatment consisting of cleaning loose material with air jets before spreading the next layer.

The crest and downstream integrated abrasion-resistant concrete capping of 1.0 m thickness was concurrently constructed with the placement of hardfill material in the dam interior.

As curing, the lift joint was covered with a geotextile fabric and sprinkling water for at least 14 days or it covers with the next layer of hardfill material. The construction for the hardfill cofferdam with a total volume of 6300 m^3 was straightforward and completed in three months from mid-February to mid-May 2023, ahead of the originally planned construction time.

6. OPERATION OF HARDFILL COFFERDAM

Around one and a half of months after the completion of the hardfill cofferdam, the monsoon season began. The cofferdam was overtopped for over three months with sustained flood discharge through the months from June to September, as shown in Fig.3. As expected, the hardfill dam has survived from the overtopping.

Fig. 3 – Overtopping of the hardfill dam

As other mountainous rivers in Himalayan region, the Trishuli River transports both suspended sediment and bed load sediment in high concentration. Consequently, the overtopped cofferdam not only discharge water flow but also the massive sediment. Bed load sediment is transported close to the riverbed or structure bottom where particles move intermittently by rolling, sliding, or jumping, which will create cutting and impacting effects on structural surfaces besides the abrading, wearing and friction. Turbulence supports suspended load throughout the water column, and sediment is swept along at the local flow velocity. The suspended load will dominantly create the abrading, wearing and friction. The abrasion and impact of the bed load sediment may cause serious damage to the concrete faces.

Fig. 4 – Abrasion loss of concrete surface after the first monsoon (2023)

Therefore, inspection to the hardfill dam was carried out after the monsoon season. Luckily, the survey results demonstrated that the hardfill dam is stable without any movement, although

the space in front of dam is fully deposited with the river sediment. The concrete surface of the hardfill dam including the edges of steps has slightly abrasion damage (ref. Fig. 5) which is much better than the expected and not need to repair. Anyway, the surface damage can be repaired if required.

In the summer 2024, the hardfill cofferdam experienced the second overtopping period during the monsoon season from the end of June to end of September. Inspection after the monsoon floods demonstrated that the abrasion loss of concrete surface is some more intensive than the last season, but still minor and thus acceptable. Therefore, it need not to be repaired for the remaining last one monsoon season to be used.

Fig. 5 – Abrasion loss of concrete surface after the second monsoon (2024)

The observation further demonstrated that no leakage was observed in the cofferdam body during the entire operation time up to now. The watertightness of the cofferdam is given by the grout-enriched hardfill face. It is therefore concluded that the application of hardfill cofferdam at Upper Trishuli-1 project is successful.

7. CONCLUDING REMARKS

As a new dam type, the hardfill dam features essentially with a trapezoidal cross-section, low content of cementitious materials and as-dug aggregate. Moreover, the hardfill dam combines the benefits of construction simplicity and fairly broad specifications with robust structural integrity. The cofferdam at Upper Trishuli-1 is a good example of a rigid dam that could be built on alluvial deposits and overtoppable. The successful practice demonstrated the feasibility to

construct low hardfill dams on alluvial deposit foundations and the hardfill dam has many advantages. In particular, it can be founded on alluvial deposits or other weak foundation; with the integrated erosion-resistant concrete capping it is overtoppable and uses the simply processed aggregates and simplified constructive provisions, which combines the benefits of RCC dams and rockfill dams. Internal seepage gradients in foundation can be controlled with a grout curtain or a cut-off-wall. The hardfill dam offers the best solution with least risk and represents a particularly robust and cost-effective form of construction. All these will decline the project costs, speed up construction progress, and drive the rollout of this valuable technology. In fact, it becomes a competitor to rockfill dams. The successful use of the hardfill dam at Upper Trishuli-1 provides experience and can be shared to other projects. There will be an increased potential for using hardfill dams in future as the number of ideal dam sites decreases.

REFERENCES

[1] Raphael, J.M. (1970). The optimum gravity dams. *Rapid Construction of Concrete Dams*. ASCE, New York: 141-145

[2] Londe, P.; Lino, M. (1992). The faced symmetrical hardfill dam: a new concept for RCC. *International Water Power and Dam Construction* 44(2): 19-24

[3] Hirose, T.; Fujisawa, T.; Kawasaki, H.; Kondo, M.; Hirayama, D.; Sasaki, T. (2003). Design concept of trapezoid-shaped CSG dams. In Berga et al. (eds.), *Roller Compacted Concrete Dams*. Taylor & Francis Group, London: 457-464

[4] Du, C. (2023). Evaluation and selection of hardfill and roller compacted concrete dams. *Symposium "Management for Safe Dams"* - 91st Annual ICOLD Meeting held on 13-14 June 2023 in Gothenburg: 1119-1127

[5] Pawson, J.R.; Russell, E.A.P. (2014). Skhalta Dam – Design of a hardfill dam founded on deep alluvium and lacustrine deposits. In *Maintaining the Safety of our Dams and Reservoirs - Proceedings of the 18th Biennial Conference of the British Dam Society* at Queen's University, Belfast, from 3–6 September 2014, ICE Publishing: 148–160

Fifth International Dam World Conference
PORTUGAL • LISBON • LNEC • APRIL 13-17, 2025
dam world 2025

PATHOLOGY MAPPING IN CONCRETE DAMS THROUGH DIGITAL PHOTOGRAMMETRY AND IMAGE PROCESSING

Dora Roque[1]
LNEC

Maria João Henriques
LNEC

ABSTRACT

Visual inspection is a crucial task for the assessment of a dam conservation state. However, these tasks are time consuming and operator dependent, which leads to the aim of developing more objective procedures. Photographs are a way to register the conservation state of a structure at a certain epoch, providing a record that can be later reanalysed and compared to new data. Although they are already used for support of inspection activities, their capture is often limited to accessible areas of the structure, leading to large lacunae in the analysed surface. Photographs obtained from long distances can reach a larger surface area, but the achievable resolution and detail of the identifiable elements is compromised. Furthermore, the manual analysis of the photographs for pathology identification and characterization is also a tedious task.

In this study, a map of pathologies on all visible surfaces of Santa Luzia dam, in Portugal, was performed through photogrammetry and digital image processing. The dam crest, downstream wall and the emerged part of the upstream wall were thoroughly photographed through drone and terrestrial surveys, in order to achieve a digital representation of the dam. The photographs were subjected to photogrammetric procedures, in order to create orthophotographs (distortion-free images of the surfaces). Those images were used to map a set of occurrences observed on the dam surface, such as cracks, calcium carbonate deposits, biologic colonization, leakage and irregularities. The location and extension of these elements were detected in the images using digital image processing algorithms. Both the orthophotographs and the pathology outlines were imported into a spatial database, which can be explored in open-source software. As the orthophotographs and pathology outlines are geometrically corrected, it is possible to measure the dimensions of the affected regions, such as areas, lengths and widths. Furthermore, alphanumeric information can be added to the spatial database, complementing the image-based data with field observations. The initial condition assessment can be updated through new surveys, enabling the analysis of the evolution of the pathologies.

Keywords: Conservation state assessment, photogrammetry, digital image processing, spatial database.

[1]droque@lnec.pt, Portugal

1. INTRODUCTION

Many concrete dams in Portugal have been operating for several decades, demanding a thorough surveillance to ensure their safety requirements are met. Studies in distinct areas of knowledge must be performed for a complete assessment of the structure condition, such as analysing concrete properties, following the dam structural behaviour and detecting signs of damage.

Visual inspections of the dam surface are crucial for damage detection. This task is usually performed by trained experts, who characterize the visible pathologies. Registered information includes approximate location and manual crack width measurements, among others. Despite being effective, the described method is subjective, as it is operator dependent. Furthermore, when manual measurements are required, the method is limited to the accessible areas of the dam.

Visual inspections are currently supported by photographs; however, the manual image analysis for pathology delimitation is a time consuming and tedious task rarely performed. Therefore, digital image processing and machine learning methods for identifying pathologies frequently found in concrete dams have been developed. Most studies are focused on crack detection [1-5], but leakage, calcification, spalling and collapse are also considered by some authors [2][4]. Images are captured through different techniques, such as terrestrial photography [1], unmanned aerial vehicles (UAV) [2][3], closed-circuit television (CCTV) [6] or underwater remotely operated vehicles (ROV) [7]. For pathology identification, most of these studies provide a label or caption indicating the presence of a certain pathology in the image [3][4], but a few of them are capable to determine their location [1][5]. Although most studies are focused on dam emerged walls and crest, there are also some approaches for inspecting dam pathologies underwater [7] and in structure sub-surface through boreholes [6].

The Portuguese National Laboratory for Civil Engineering started studying digital image processing methods for pathology mapping in concrete dams a decade ago [8][9], but the rapid development of reality capture technology in the last years brought several improvements, by enabling high resolution image capture even in inaccessible areas of the structure. In this study, a method for pathology mapping based on photogrammetry, digital image processing and geographic information systems (GIS) is proposed. The method was applied to Santa Luzia dam, in Portugal, which was subjected to a thorough photographic survey of its visible surfaces. The achieved digital representation of the dam was used for pathology detection and delimitation. The collected information, both images and pathology limits, were integrated in a spatial database, accessible through an open-source GIS system, which forms a graphic registration of the dam conservation state.

2. CASE STUDY

Santa Luzia is a concrete dam in Pampilhosa da Serra municipality, Portugal. The dam is located in Unhais stream, a tributary of Zêzere river, and it is operating since 1943 [10]. Santa Luzia is a cylindrical arch dam, connected by an arch-gravity structure to the left bank [11] (Fig.1). It has a maximum height of 76 m and the crest length is 115 m [12].

Fig. 1 – Santa Luzia dam and its surroundings

The dam started showing signs of being affected by concrete swelling reactions of internal origin in the 1960s, but it has been decelerating since 2000. The swelling effects are more visible in the arch-gravity than in the dam main body [11].

The dam presents several pathologies in its surfaces, such as cracks, calcium carbonate deposits, leakage and biologic colonization. Other occurrences are also visible, for example temporary wet areas and irregularities corresponding to prior interventions in the dam. Furthermore, part of the downstream wall of the dam main body is covered by a mortar mixture, avoiding the visualization of the pathologies underneath.

This study is focused on the downstream wall, from both the main body and the arch-gravity (the abutment was not included), the crest and the emerged part of the entire upstream wall.

3. DAM PHOTOGRAPHIC SURVEY

The photographic survey of Santa Luzia dam was performed through terrestrial photogrammetry for the downstream walls of the main body and of the arch-gravity, while the dam crest and the upstream wall were photographed from an UAV (drone). Fig.2 presents examples of photographs from each survey.

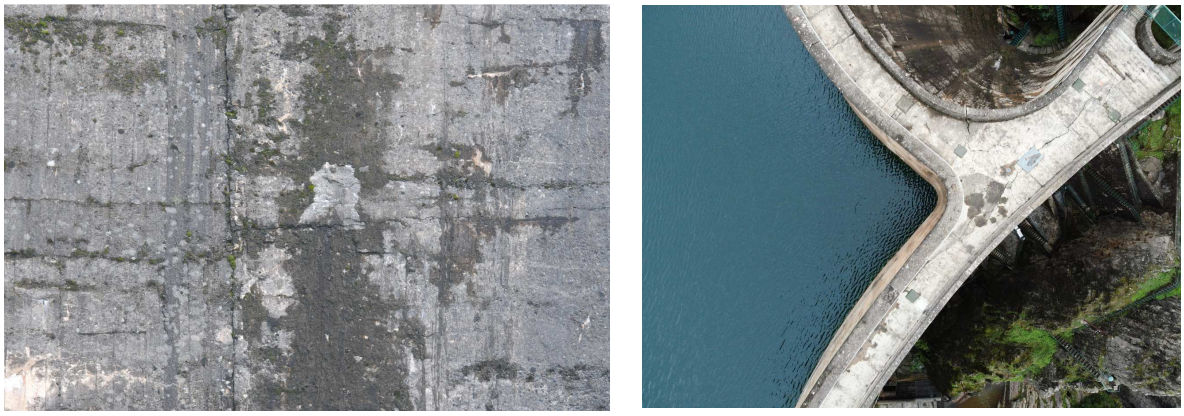

Fig. 2 – Examples of photographs from the terrestrial (left) and aerial (right) surveys

The terrestrial survey was executed from different locations in the downstream slopes, with partial areas of the dam surface being considered individually. This strategy was performed in order to achieve the best spatial resolution and the less oblique photographs possible for each location. The photographs were captured by a Nikon D200. Most of the surface was photographed using a Nikkor objective with a focal length of 180 mm, with focal lengths 50 mm and 85 mm being used sporadically. The survey took eight days to be completed and it was performed mostly in October 2022. Almost 8000 photographs were required to cover the entire surface of the downstream walls. An orthophotograph was built for each partial area, with spatial resolutions varying from 0.6 mm to 5.5 mm.

The UAV survey for the dam crest and emerged upstream wall will be described in detail in Henriques *et al*. [13]. A unique orthophotograph was built for the crest, as it is a flat surface, with a spatial resolution of 15.1 mm. As the upstream wall presents curved surfaces, several orthophotographs were built in order to minimize the distortion. Spatial resolutions varied from 13.9 mm to 16.8 mm.

Coordinates of ground control points (GCP) were determined for selected details on the dam surface, with respect to the local reference frame of the geodetic observation system. GCP were used to provide a scale and orientation to the images. All the orthophotographs, for the four considered surfaces, were flattened by corregistering them to the CAD files from the dam project. These images were geometrically corrected and free of distortions. The achieved image products were the basis for the pathology mapping.

4. PATHOLOGY MAPPING

The pathology mapping for Santa Luzia dam followed an object-based image analysis (OBIA) strategy. OBIA evaluates the similarities between neighbour pixels and aggregates them whenever they fulfil user defined criteria, forming objects. Those criteria impose a limit to the radiometric heterogeneity acceptable for each object and set the relative weights attributed to

object colour and shape. Regarding shape, compactness and smoothness object properties can be set. Hierarchical relationships between objects with different properties may also be defined.

In this study, two different approaches were followed: one for the dam walls and another one for the crest. For the walls, multiresolution segmentation algorithm from eCognition® software was used to build three object hierarchical levels. In the first level, large and compact objects were created, intending to segment the large spots on the walls, such as calcium carbonate deposits or leakage. A second level of objects, resulting from the division between those from the previous level, was used to refine the objects from the first level. Finally, a third level was set to build small non-compact objects with the goal of delimiting cracks (Fig. 3).

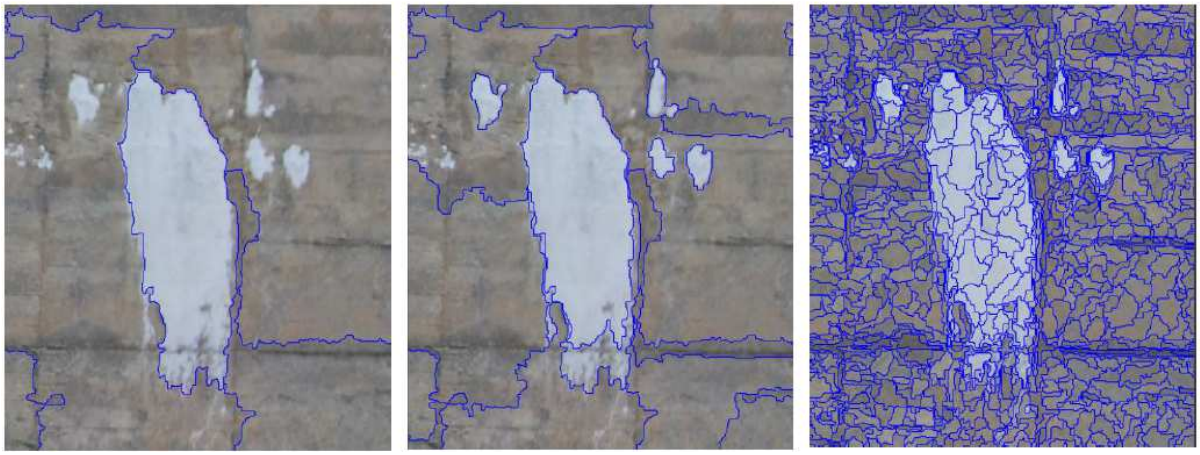

Fig. 3 – Hierarchical segmentations with increasing levels of detail

The association of a pathology class to a certain object was performed by photointerpretation, except for biological colonization in the downstream walls. In this case, the greenish colour presented by the affected areas enabled the automatic detection of the corresponding objects, through a new image built from the original one to enhance the green areas.

Regarding the dam crest, cracks were the only pathologies considered. As these elements showed high contrast to the surrounding background, the algorithm contrast-split segmentation from eCognition® was used. This strategy required a coarse crack delimitation at an initial phase, which was refined through the separation between bright and dark areas inside the initial delimitation (Fig. 4).

Pathology delimitations were exported into shapefile format, which enabled the attribution of alphanumeric information to the files. In this case, intervals of area and of crack width were associated to pathology objects.

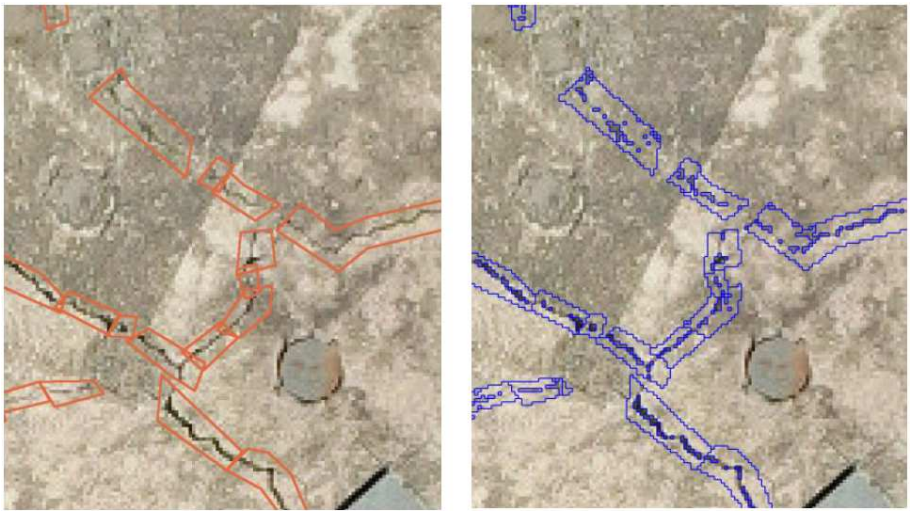

Fig. 4 – Initial crack delimitation (left) and contrast-based crack segmentation (right)

5. RESULTS

The orthophotographs, the mapped pathologies and the corresponding alphanumeric information were integrated into a spatial database that can be accessed through open-source GIS software, such as QGIS. The pathology map can be superimposed on the orthophotographs and the two datasets can be analysed together. Alphanumeric data can be easily accessed in table format or by clicking on the pathology object of interest. Fig. 5 presents the pathology maps for some of the considered dam surfaces.

The cracks with the largest widths were observed in the crest, where one of the cracks presented a width close to 100 mm. Most of the identified cracks, for the four surfaces, presented width values above 2.5 mm. However, this result was influenced by the image spatial resolution, as will be discussed in section 6. Around 60% of the main body downstream wall was covered by the mortar mixture, which did not allow the observation of the dam surface, hiding eventual pathologies. Most calcium carbonate deposits on the downstream wall covered areas below 1 dm^2. However, there were several deposits with areas larger than 1 m^2. Most leakage signs in this surface covered areas between 1 cm^2 and 1 dm^2. Areas affected by biological colonization tended to be larger in the arch-gravity (areas from 1 cm^2 to 1 dm^2) than in the main body (areas from 1 mm^2 to 1 cm^2). The upstream wall was mostly affected by calcium carbonate deposits and biological colonization. Calcium carbonate deposits had areas between 1 cm^2 and 1 m^2. Due to the water proximity, the upstream wall was wet and presented large spots of biological colonization, which, in some cases, reached more than 1 m^2.

The quality of the pathology maps was evaluated through the comparison between the map information and the ground truth achieved from photointerpretation of a set of random points. Overall accuracies are presented in Table 1. This index informs the percentage of points that were correctly mapped.

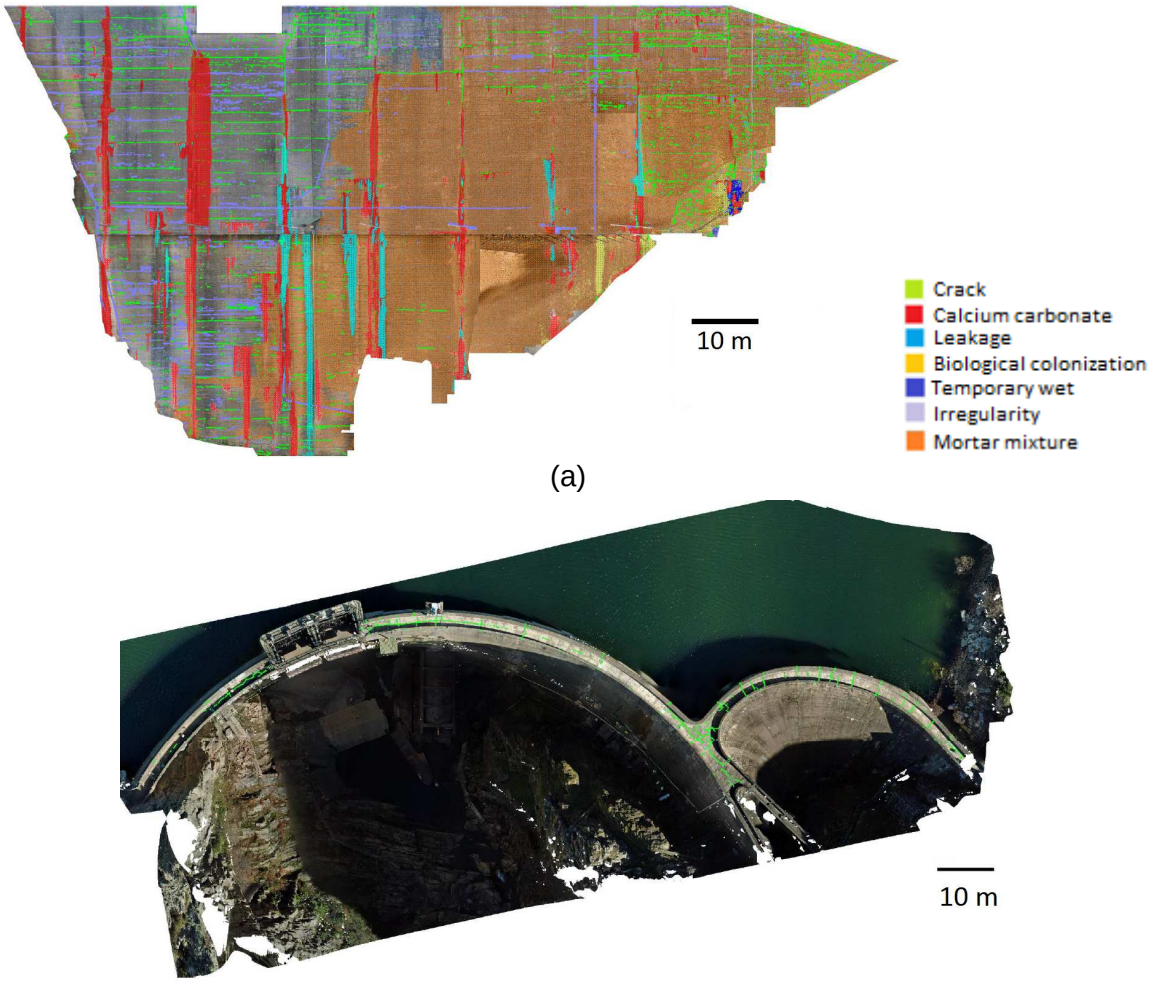

Fig. 5 – Pathology maps for the main body downstream wall (a) and the crest (b)

Table 1 – Overall accuracies for the pathology maps

Downstream wall		Upstream wall	Crest
Main body	Arch-gravity		
94.6%	85.6%	90.3%	94.7%

6. DISCUSSION

Image spatial resolution is a critical factor for the mapping quality. The usage of terrestrial photogrammetry enabled the access to higher spatial resolution images for the downstream walls than for the upstream wall and the crest, where the UAV was used. Most mapped cracks presented widths above 2.5 mm, because the image spatial resolution was not large enough to enable the detection of smaller elements. Nevertheless, when the cracks had high contrast with respect to the background, it was still possible to identify them on the orthophotographs, even when their widths were lower than the pixel size. This was verified through comparison of the pathology map with field measurements [14]. In this situation, the crack could be mapped, but its width could not be correctly determined from the image.

The organization of the downstream wall into partial orthophotographs allowed the usage of higher spatial resolution images. However, as each block of images was captured in different light conditions, it also led to light heterogeneities across the surface, which prevented the automatization of the classification procedure. As stated in the introduction, machine learning and digital image processing methods have been used to automatically map pathologies on dams. However, these studies were mostly focused on a single pathology (usually cracks) and the analysed images often presented little area of the surface besides the wanted pathology. In the present study, an area around 10000 m^2 of concrete surface was analysed, with varying spatial resolutions and light conditions, where seven types of pathologies and other occurrences were considered. Although most features were classified through photointerpretation, the usage of different object levels aided the classification task, as the largest pathologies were identified in the first object level and their delimitations only had to be refined in the other levels.

7. CONCLUSIONS

In this study, a method for pathology mapping through photogrammetry and digital image processing was proposed, with the goal of assisting in the evaluation of concrete dams' conservation state. The proposed method enabled the production of a digital representation of Santa Luzia dam, through flattened orthophotographs, which were used as the basis for the pathology mapping. The data were integrated into a spatial database that could be accessed by the dam owner through an open-source GIS software and completed with other available information. The achieved product provided a detailed testimony of the dam conservation state at the epoch of image capture, including for areas difficult to reach. Therefore, the achieved pathology maps were useful to complement the visual inspections performed by the experts, providing accurate information on pathology type, location and extension.

For future work, research on digital image processing methods to turn light uniform inside an image and between images will be performed and the capabilities of machine learning techniques to map different types of pathologies will be evaluated.

REFERENCES

[1] Valença, J. and Júlio, E. (2018). MCrack-Dam: The scale-up of a method to assess cracks on concrete dams by image processing. The case study of Itaipu Dam, at the Brazil–Paraguay border. Journal of Civil Structural Health Monitoring 8 (5): 857-866.

[2] Zhao, S., Kang, F., Li, J. and Ma, C. (2021). Structural health monitoring and inspection of dams based on UAV photogrammetry with image 3D reconstruction. Automation in Construction 130: 103832.

[3] Li, J., Lu, X., Zhang, P. and Li, Q. (2024). Weak feature crack detection in high-resolution concrete dam surface image with LarkMNet. Measurement 238: 115327.

[4] Yong, C., Yingchi, M., Yi, W., Ping, P. and Longbao, W. (2021). Keywords-based dam defect image caption generation. In 2021 IEEE Seventh International Conference on Big Data Computing Service and Applications (BigDataService), Oxford, United Kingdom, August 23-26: 214-221.

[5] Xu, G., Han, X., Zhang, Y. and Wu, C. (2022). Dam crack image detection model on feature enhancement and attention mechanism. Water 15(1): 64.

[6] Dai, Q., Ishfaque, M., Khan, S. U. R., Luo, Y. L., Lei, Y., Zhang, B. and Zhou, W. (2024). Image classification for sub-surface crack identification in concrete dam based on borehole CCTV images using deep dense hybrid model. Stochastic Environmental Research and Risk Assessment: 1-18.

[7] Shimono, S., Toyama, S. e Nishizawa, U. (2016). Development of underwater inspection system for dam inspection: Results of field tests. In OCEANS 2016 MTS/IEEE Monterey, Monterey, USA, September 19-26: pp. 1-4.

[8] LNEC (2011). Memorando sobre a inspecção visual assistida de paramentos de barragens de betão. LNEC report No. 399/2011 – DBB/NGA.

[9] LNEC (2012). Barragem do Covão do Meio: Campanha de referência para a inspeção visual assistida. LNEC report No. 351/2012 – DBB/NGA.

[10] EDP, S.A. (2024). Central Hidroelétrica de Santa Luzia. https://portugal.edp.com/pt-pt/edp-portugal/central-hidroeletrica-de-santa-luzia, acedido em novembro de 2024.

[11] Batista, A.L. (2022). Deterioration processes of dams affected by concrete swelling reactions. The Portuguese experience in monitoring and rehabilitation. In 16th International Conference on Alkali-Aggregate Reaction in Concrete, Lisbon, May 31 – June 2: 119-146.

[12] LNEC (2008). Barragem de Santa Luzia. Ensaio de vibração forçada – 2001. LNEC report No. 351/2008 – DB/NMMF.

[13] Henriques, M.J., Dias, I., Roque, D. and Gomes, A. (2025). A 3D point cloud model of Santa Luzia dam and its contribution for improving the finite element mesh. In 5th International Dam World Conference, Lisbon, April 13-17 (submetted).

[14] LNEC (2024). Barragem de Santa Luzia. Levantamento geométrico da fendilhação aparente no coroamento e numa faixa acessível do paramento de jusante. LNEC technical note No. 5/2024 – DBB/NO.

Fifth International Dam World Conference
PORTUGAL • LISBON • LNEC • APRIL 13-17, 2025
dam world 2025

SAFETY VERIFICATION BY 3D DYNAMIC ANALYSIS OF A 100-YEAR-OLD MASONRY ARCH–GRAVITY CONCRETE DAM

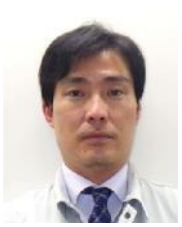

Naoki Iwata[1]
Chuden Engineering Consultants

Ryouji Kiyota[2]
Chuden Engineering Consultants

Hideaki Kawasaki[3]
Japan Dam Engineering Center

Masaharu Kurihara[4]
Onomichi City Waterworks Bureau

ABSTRACT

The Hisayamada Dam (height 22.5 m, length 75 m) was constructed in 1924 as a water intake facility (water source) to alleviate the chronic water shortages caused by the population growth in Onomichi City. It is a masonry arch–gravity concrete dam with a semicircular intake tower on the right side of the dam body. The dam is the first arch–gravity dam in Japan (excluding small dams under 15 m in height), with respect to a gravity dam it is a slender dam was theoretically designed in anticipation of arch action.

However, the design did not consider seismic forces at that time. In this study, the seismic performance of dams against large earthquakes was evaluated by applying governmental guidelines in Japan. In these guidelines, the water storage capacity of the studied dam was evaluated using dynamic finite element method (FEM) analysis to determine whether the dam's concrete can maintain its water storage capacity in the event of the largest earthquake expected to occur in the future at that location due to the extension of tensile cracks in the dam's concrete.

In general, two-dimensional dynamic FEM analysis is used for gravity dams, but because the Hisayamada Dam is an arch–gravity dam, three-dimensional (3D) FEM analysis was used for this evaluation. In the dynamic 3D FEM analysis, seismic motions created based on seismic records observed at the existing dam were input simultaneously in three directions (upstream/downstream, axial, and vertical) to a model integrating the dam, surrounding topography, and reservoir. It was found that although a small part of the upstream heel of the dam concrete failed, however no further tensile cracks extent into the dam body. It was also confirmed that sufficient stability was maintained against sliding at the dam-rock interface.

Keywords: masonry arch–gravity concrete dam, seismic performance, dynamic 3D FEM analysis, seismic stability, water storage capacity.

[1]n.iwata@cecnet.co.jp, Japan

1. INTRODUCTION

The Hisayamada Dam was built in 1924 to solve the problem of chronic water shortages caused by the population growth of Onomichi City. The dam is a masonry arch-type gravity concrete dam, and there is a semicircular water intake tower on the right bank of the dam body. The outer surface is made of stone blocks joined with mortar, and the inner core is made of concrete with large aggregates. The dam is 22.5 m high and 75 m long, with a total water storage capacity of 720,000 m^3 and a catchment area of 3.6 km^2.

This dam was designed by a famous Japanese dam engineer. The crest width is only 2 m, the overflow spillway in the center of the dam is sharp, the dam body is very thin, and the downstream slope (1:0.66) is small. It has a gentle arch shape. Excluding small dams with a height of less than 15 m, it is the first arch dam in Japan to have been designed based on theoretical assumptions about arch action. However, at that time, it was not designed with earthquake forces accounted for.

The seismic stability of arch-gravity concrete dams has been examined by ICOLD Commission in cases where static seismic forces were applied [1], although there are few cases where dynamic seismic forces were applied. In this study, the seismic performance of the dam in the event of a major earthquake was evaluated using governmental guidelines [2]. These guidelines evaluate whether the dam's water storage capacity can be maintained in the event of a maximum earthquake motion expected to occur at that location in the future (hereafter, maximum expected earthquake motion) by assessing the occurrence and development of tensile cracks in the dam's main concrete body using dynamic finite element method (FEM) analysis. Generally, two-dimensional (2D) dynamic FEM analysis is used for gravity dams. However, as Hisayamada Dam is an arch–gravity dam, three-dimensional (3D) FEM analysis was used in this evaluation for seismic stability.

2. OVERVIEW OF THE HISAYAMADA DAM

The Hisayamada Dam is a water supply facility in Onomichi City, Hiroshima Prefecture, located in western Japan, as shown in Fig. 1. It is an arch-shaped gravity concrete dam with a rough stone mortar facing, where the mortar is packed between rough stones and the surface is covered with stone cladding. There is a semicircular water intake tower on the right bank of the dam body, and the left bank side of the water intake tower is a flood spillway, with no gates and free overflow.

The unconfined compressive strength of the mortar is 30 to 48 N/mm^2, and that of the rough stone is 219 to 227 N/mm^2, which is higher than the general level. There is no significant

damage, deterioration, cracking, or leakage on the downstream face of the dam body. The results of the dam body boring and Lugeon water pressure tests also indicate no continuous cracks in the dam body. As shown by the dam body boring core, there are many rough stones of around 5 to 40 cm, but there are no cavities in the mortar, and there is no weathering at the boundary between the rough stones and the mortar. In addition, the joint surface between the dam body and the foundation bedrock is well adhered to, and there are no deteriorated areas that would cause problems for the stability of the dam body.

The foundation of the dam is made of mudstone with a uniaxial compressive strength of ~34 N/mm^2. It has a network of cracks, but these are not directional or continuous, and the permeability is low.

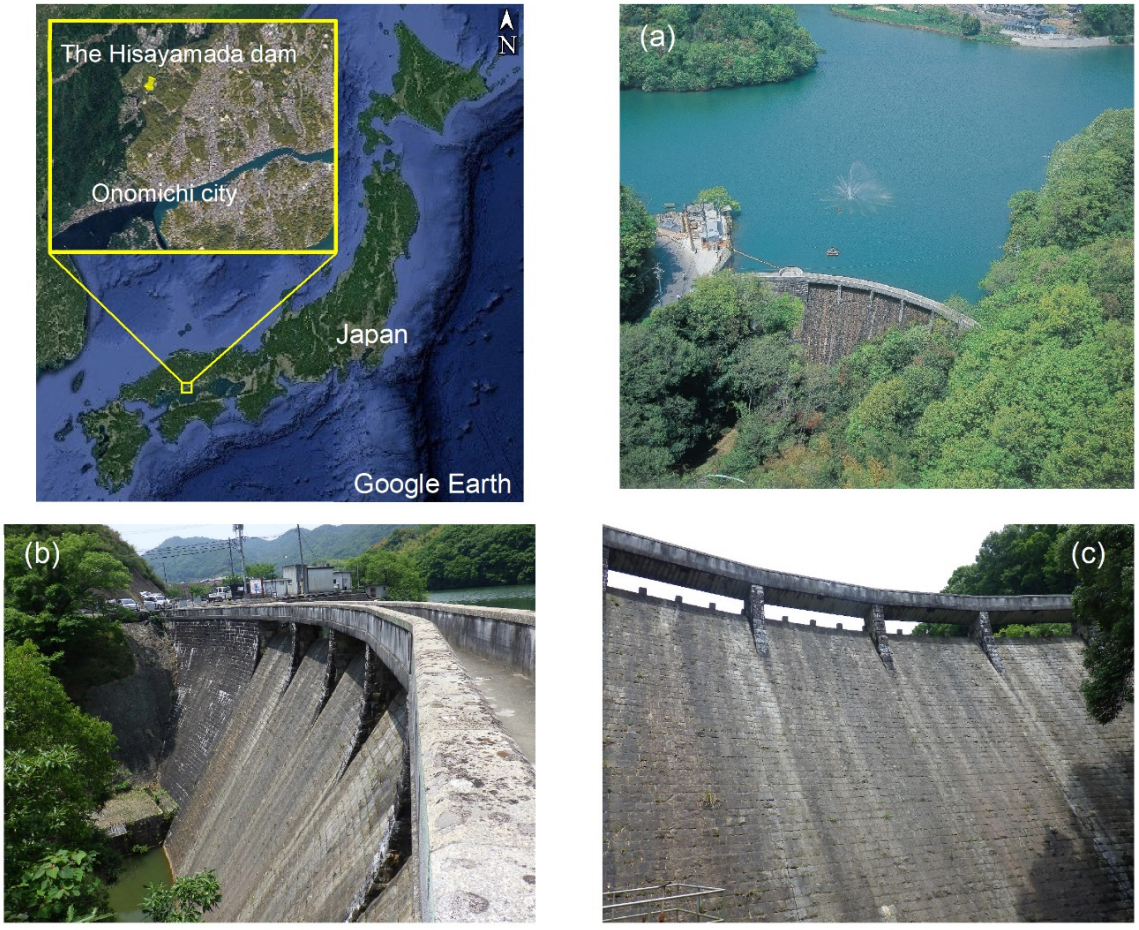

Fig. 1 – Bird's-eye view of the Hisayamada Dam and the downstream face of the dam as seen from the left and right banks.

3. SEISMIC PERFORMANCE EVALUATION METHOD

In evaluating the seismic performance of dams in the event of a major earthquake, governmental guidelines [2] are generally applied. These guidelines indicate the seismic performance that dams should satisfy in the event of the largest earthquake that can occur at

that location in the present and future (maximum expected earthquake). The seismic performance of arch-type concrete dams is investigated using 3D FEM models that include the dam body and the foundation rock because the structural behaviors of these types of concrete dams are characterized by their 3D behavior. The required seismic performance is that the tensile stress exceeding tensile strength does not cause in the dam body, that compressive or shear failure does not cause in the dam body, or even if it does, it is limited to a local area to confirm that the water storage capacity of the dam body is maintained.

As the concrete of a dam body can be treated as a linear material, the dam body is first evaluated using linear dynamic analysis, which treats it as a linear elastic body. If the results of the linear analysis indicate a risk of damage to the dam body, then nonlinear dynamic analysis is used to evaluate the damage process. The analysis in this study was conducted using the ISCEF Ver2019 Rev1.02 (Centuri Techno Co., Ltd.) software, a widely used 3D FEM program.

In this study, the maximum time history of tensile and compressive stresses in the dam body does not exceed the tensile and compressive strength of the dam body, according to the results of the 3D linear dynamic analysis. Concerning shear failure, as the shear strength of the bedrock is lower than that of the dam body, the shear force H at the bottom of the dam body is lower than the resistance R calculated from the vertical force at the bottom and the strength of the bedrock; that is, the sliding safety factor F_s ($=H/R$) is 1.0 or more. In the seismic performance evaluation, the objective is to confirm that the water storage capacity is maintained, so the evaluation is conducted for dam body elements that are below the normal water level.

4. DYNAMIC ANALYSIS CONDITIONS

4.1. Analysis Model

Fig. 2 shows the 3D FEM analysis model, which integrates the dam, surrounding terrain, and reservoir. The dam and bedrock were modeled as solid elements (three-dimensional iso-parametric elements with eight nodes or six nodes), whereas the reservoir was modeled as an incompressible fluid element. Joint elements were installed at the contact surface between the dam and the bedrock. The joint elements connect the nodes of the solid elements of the dam and bedrock in shear and vertical directions using springs. In general joint elements, sliding and separation movements at the contact surface obey shear and tensile failure criteria. However, in this study, shear and tensile failure are not considered, so the joint elements were installed to calculate the vertical and shear stress at the contact surface. The contact area between the water storage and the dam and the ground was connected by interface elements,

and dynamic water pressure due to the vibration of the water storage acted on it. The water level was set to the same height as the crest of the dam. There was a subdam downstream of the dam, but it was not included in the model because it is an independent structure. The passageway and pier at the top of the dam were also omitted because they were considered to have little effect on the seismic response of the entire dam.

The surface topography of the surrounding area was modeled using 5-m-grid digital elevation model data from the Geospatial Information Authority of Japan. The area was assumed to be uniformly covered by homogeneous bedrock. The analysis model area was set to be at least twice the dam height around the dam, and the model bottom was set to be approximately twice the dam height from the dam bottom.

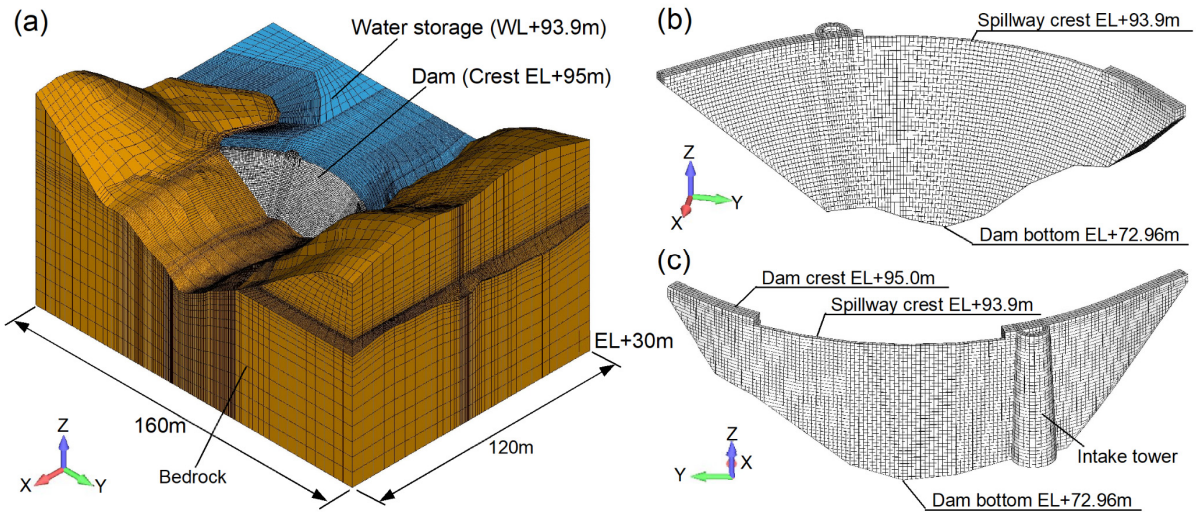

Fig. 2 – 3D FEM analysis model: (a) entire model, (b) downstream view of the dam model, and (c) upstream view of the dam model.

The analysis consisted of three steps: initial stress setting, normal stress setting, and seismic stress calculation. In the first step, the initial stress of the ground was set using the self-weight calculation method using only the ground section. In the second step, the dam was installed, the self-weight was applied, and the hydrostatic pressure acting on the dam was applied to set the normal stress state of the dam body. In the third step, the reservoir was installed and a dynamic analysis was performed by inputting seismic motion. The dynamic water pressure during an earthquake was automatically applied because the reservoir was modeled with the help of fluid elements, and seismic response analysis was performed.

For the model boundary conditions, in Steps 1 and 2, where a static load was applied, the bottom boundary was fixed and the lateral boundaries were set as vertical rollers using only the main body of the FEM model and excluding the free ground on both sides. In Step 3, when the seismic force was applied dynamically, a free ground model was installed on both sides of

the main body of the FEM model to prevent seismic motion from being reflected at the lateral boundary, and it was connected with a dashpot. The base boundary was set as a viscous boundary, and the dashpot was installed to reduce the seismic motion reflection.

4.2. Physical properties for the analysis

The physical properties for the analysis of the dam body concrete and bedrock are shown in Table 1. The compressive strength of the dam body concrete was set on the basis of the results of unconfined compression tests, and the tensile strength was set at 1/10 of the compressive strength. The elastic modulus of the dam body was that of a composite material of mortar and rough stone, so it was not easily set. Generally, microtremor observations were conducted on the dam body, and identification was done so that the natural frequency obtained was similar to the natural frequency of the FEM model. However, as microtremor observation was not conducted for this dam, the setting was made to be consistent with the dam's natural period ($T = 0.22 \times H/100$ (s): when the dam height $H = 21.5$ m is substituted, $T = 0.0473$ (s)) using a simplified formula. Other unit weights and damping constants were adopted as general values.

The mudstone rock, which had a uniaxial compressive strength of ~34 N/mm^2, was assumed to be uniformly spread throughout the model, and the elastic modulus and Poisson's ratio were set based on PS logging. Other physical properties were set according to the results of surveys of nearby dams and general values.

Table 1 – Physical properties for the analysis of the dam body concrete and bedrock.

Physical properties	Dam body concrete	Bedrock
Unit weight, γ (kN/m^3)	23.0	26.0
Poisson's ratio, v_d	0.26	0.33
Elastic modulus, E (MPa)	20,000	18,406
P-wave velocity, V_p (m/s)	—	3,183
S-wave velocity, V_s (m/s)	—	1,622
Attenuation constant, h	0.05	0.05
Compressive strength, F_c (MPa)	30.4	—
Tensile strength, F_t (MPa)	3.04	—
Shear strength, τ_0 (MPa)	—	1.46
Frictional angle, φ (°)	—	45

4.3. Input seismic motions

Two types of assumed seismic motion were set: an inland earthquake and a trench-type earthquake (Fig. 3). The inland earthquake was that of the Chojagahara–Yoshii Fault near the Hisayamada Dam (Mw 6.9; fault length, 36 km; fault width, 18 km; dip angle, 90°; depth of the top of the fault, 2 km). For the trench-type earthquake, an intraplate earthquake that extended

into the Aki-nada Sea near the dam was selected, and a fault surface with a length of 40 km and a width of 40 km (dip angle, 50°; depth at the top of the fault, 40 km) was adopted, corresponding to a moment magnitude of Mw 7.4. The location of the fault surface was set at the northeast corner of the plate shown in Fig. 3 so that it would be at the shortest distance from the dam. Using the moment magnitude Mw of the target fault, the distance from the fault, and the depth of the fault, the horizontal and vertical acceleration response spectra were calculated using the distance attenuation formula specified in governmental guidelines for evaluating the seismic performance of dams against large-scale earthquakes [3].

The seismic motion was created by adding the phase characteristics of typical strong motion records obtained from the dam foundation rock during past large-scale earthquakes. Therefore, the seismic motion created in the dam axis direction, upstream/downstream direction, and vertical direction was defined at the bottom of the dam body (EL + 72.96 m). For the phase characteristics of the Chojagahara–Yoshii Fault, the observation records of the Hitokura Dam for the 1995 Hyogo-ken Nanbu earthquake [2], an inland earthquake, were used. For the intraplate earthquake in the Aki-nada region, the observation records at the Ishite-gawa Dam from the 2001 Geiyo earthquake [4], which occurred within the same plate, were used. The phase characteristics of the strong motion records were in three directions: along the axis of the dam, upstream/downstream, and vertically. Time history acceleration waveforms in the direction of the axis of the dam and upstream/downstream were created by adding the phase characteristics of each direction to the horizontal acceleration response spectrum.

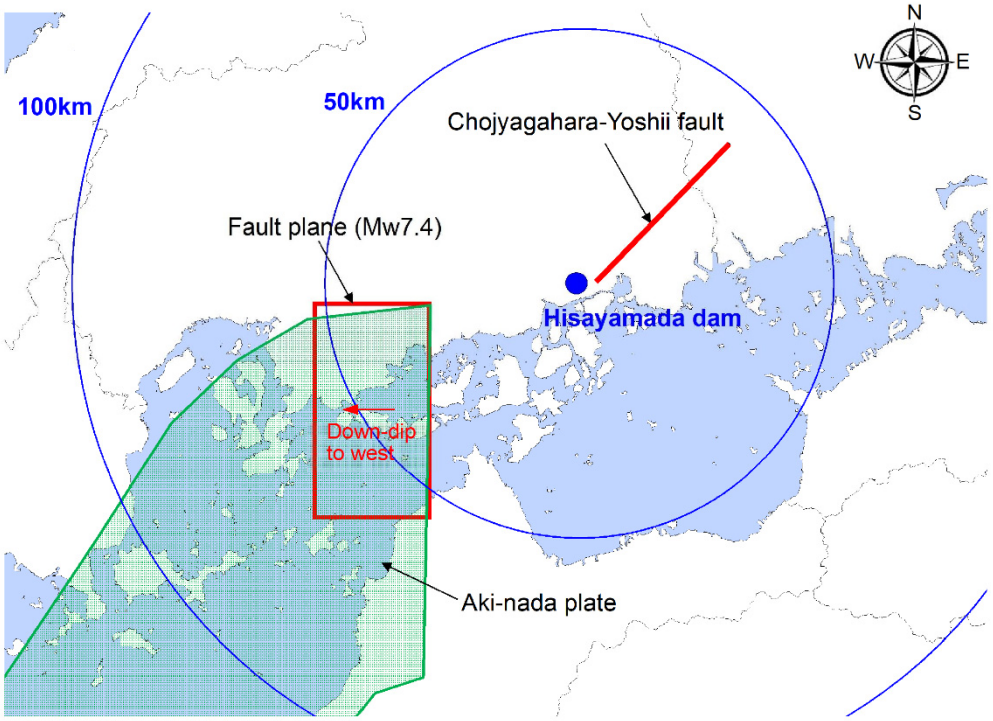

Fig. 3 – Location of the fault and Hisayamada Dam.

Fig. 4 shows the acceleration time histories and acceleration response spectra of the input seismic motion caused by the Chojagahara–Yoshii Fault earthquake (hereafter referred to as the Chojagahara earthquake) and the intraplate earthquake in the Aki-nada region (hereafter referred to as the Aki-nada earthquake), both of which were defined at the bottom of the dam body. The maximum acceleration of the Chojagahara earthquake was 182 gal in the up and downstream directions and 63 gal in the vertical direction, with a duration of 10.5 s, whereas the maximum acceleration of the Aki-nada earthquake was 596 gal in the upstream and downstream directions and 381 gal in the vertical direction, with a duration of over 20 s. According to the acceleration response spectrum, the Chojagahara earthquake was slightly larger in the 0.4 to 0.6 s range, but the Aki-nada earthquake was larger in other frequency bands. Deconvolution analysis was conducted on this seismic motion using a 3D FEM analysis model, and the seismic motion obtained at the base of the analysis model (EL + 30 m) was used to input the seismic motion in three directions simultaneously. In addition, because the acceleration waveform had a bias in the positive and negative directions, the seismic motions in the upstream/downstream directions and the dam axis direction were inverted and analyzed. Three cases were implemented:

1. CASE-1: Upstream/downstream direction only inverted.
2. CASE-2: Dam axis direction only inverted.
3. CASE-3: Upstream/downstream and dam axis direction simultaneously inverted.

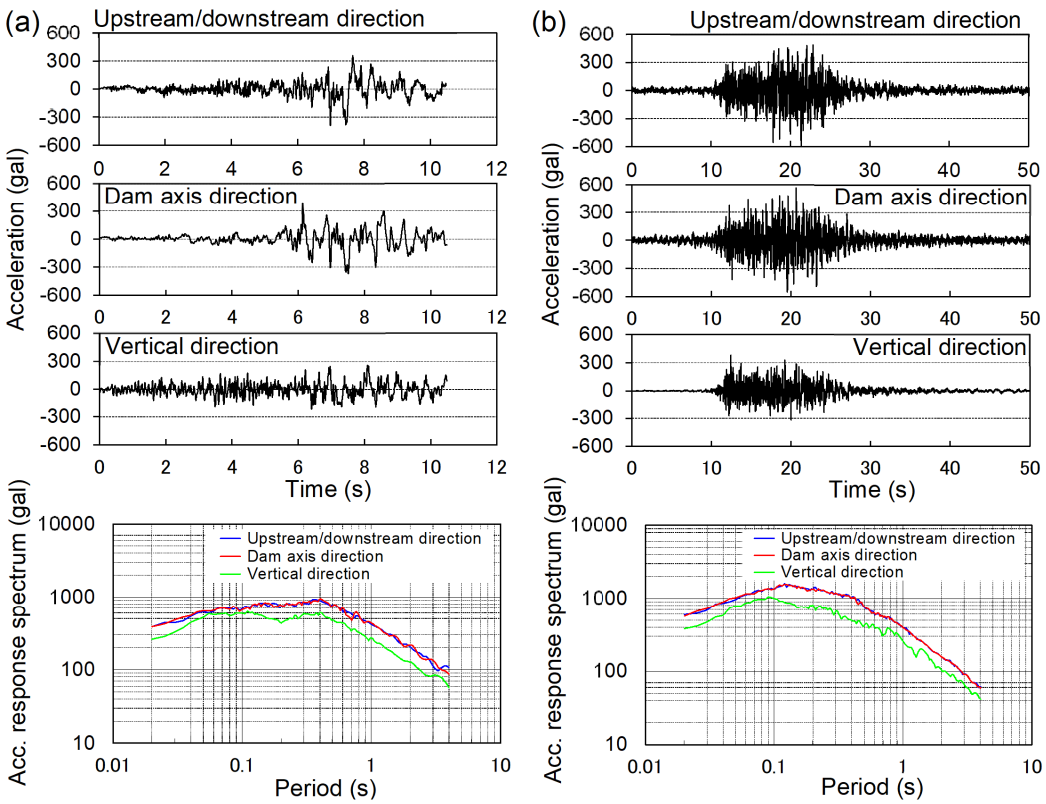

Fig. 4 – Acceleration time history and acceleration response spectrum: (a) Chojagahara earthquake and (b) Aki-nada earthquake.

5. ANALYSIS RESULTS

5.1. Eigenvalue analysis results

The first dominant period of the model coupling of the dam body and foundation ground using eigenvalue analysis was 0.2380 s, and the second was 0.0924 s. The first dominant period of the dam body alone was 0.0467 s, and the second was 0.0194 s. The first mode of the dam body and foundation and the first mode of the dam body alone are shown in Fig. 5.

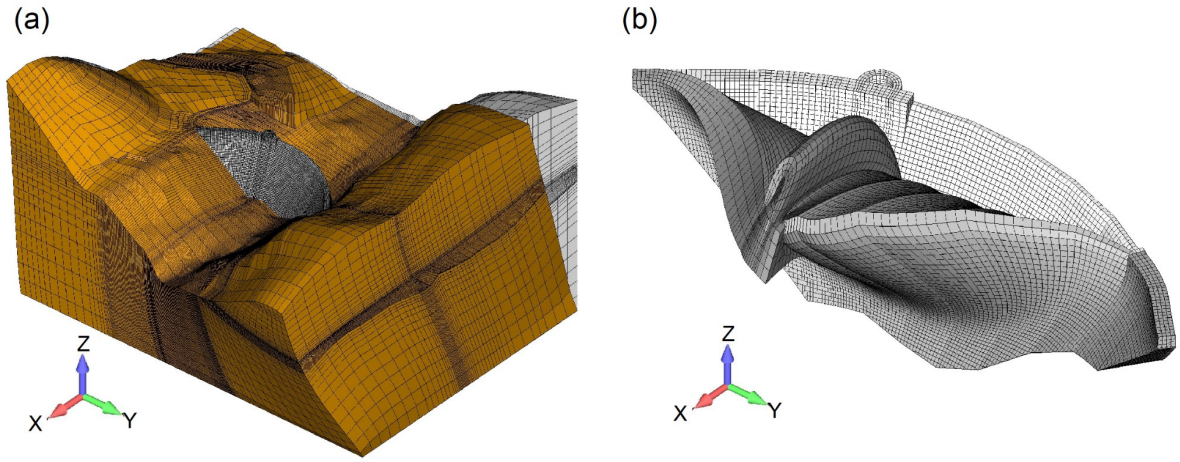

Fig. 5 – First-order mode diagrams: (a) the entire model and (b) the dam alone.

5.2. Analysis results under normal conditions

First, to verify the effect of the arch shape of the dam, the stress distribution of the dam body was examined by applying only hydrostatic pressure. Fig. 6 shows the distribution of the horizontal and vertical stresses in the dam body when only hydrostatic pressure was applied. The vertical stress increased with the dam height. However, the horizontal stress in the dam body was tensile (at ~0.2 MPa) in the side parts of the dam. It was due to the central part moving forward because of the hydrostatic pressure, and no significant compressive stress due to the arch shape could be confirmed. This showed that the dam behaved similarly to a gravity dam.

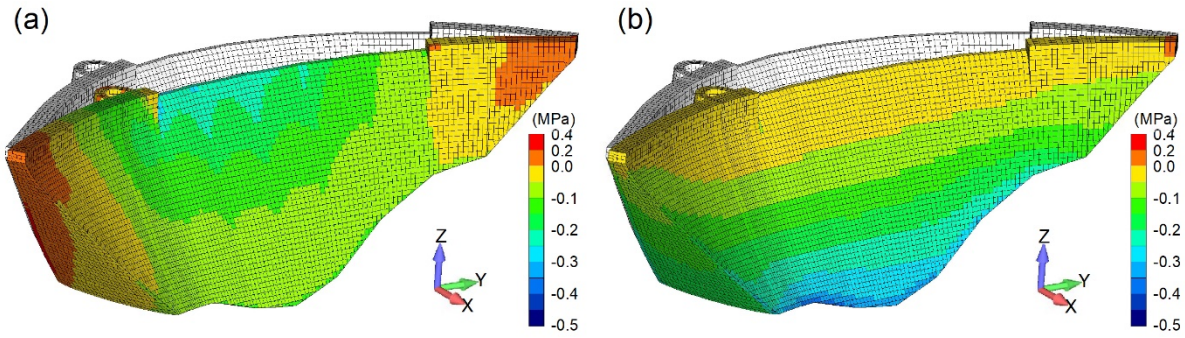

Fig. 6 – Stress distribution and deformation of the dam caused by only hydrostatic pressure: (a) horizontal direction and (b) vertical direction of the dam axis.

Fig. 7 shows the distribution of normal and shear stresses in the upstream and downstream directions at the bottom of the dam under normal conditions, as well as the stress at the bottom of the dam, which was calculated simply using a 2D cross-section in the center of the dam. The normal stress on the bottom surface of the dam in Fig. 7(c) was very small because of the tensile stress on both sides caused by the deformation of the dam, and a tensile stress exceeding 0.3 MPa occurred at the upstream end. However, the normal stress near the central part of the dam was 0.1–0.15 MPa at the upstream end and 0.55 MPa at the downstream edge; that of the central area was 0.22–0.24 MPa, which was about the same as the results of the 2D cross-section shown in Fig. 7(c). The shear stress at the bottom of the dam in Fig. 7(b) was slightly greater at the upstream and downstream edges but was around 0.1 MPa at the central part of the dam, which was slightly less than the shear stress of 0.14 MPa at the bottom of the 2D cross-section. In addition, the dam height decreased at the side parts, but the shear stress did not decrease accordingly. From these results, the arch shape was inferred as causing the shear stress at the central part of the dam to be shared by both sides.

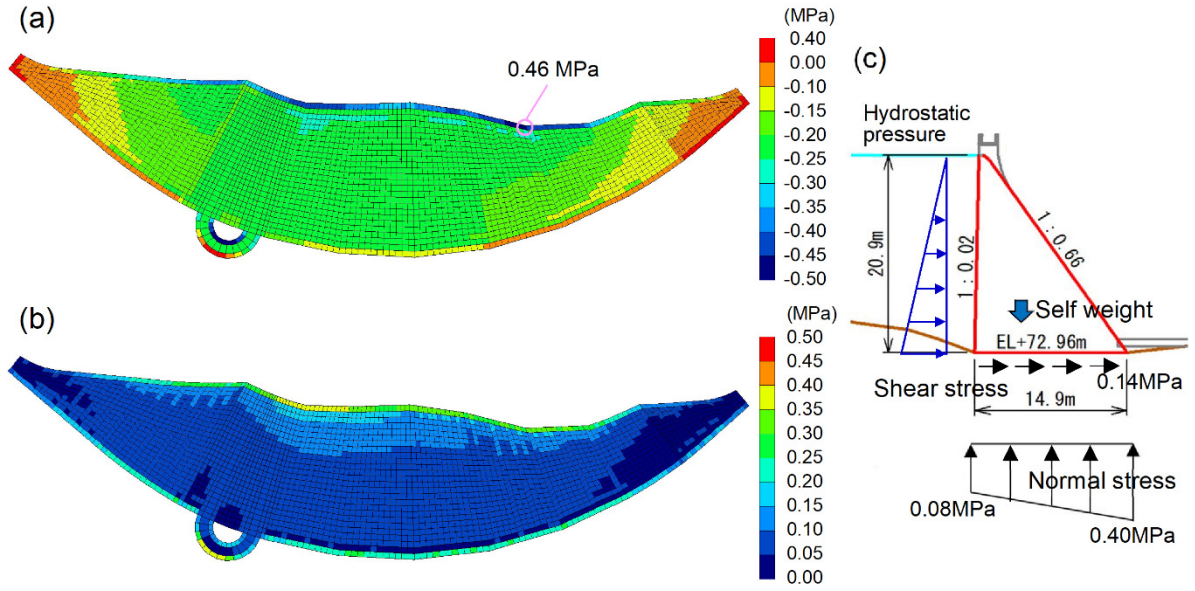

Fig. 7 Comparison of the stress at the bottom of the dam during normal conditions with the stress calculated using a simplified method for the 2D cross-section: (a) normal stress at the dam bottom, (b) shear stress at the dam bottom, and (c) stress on the dam bottom for the 2D cross-section.

Fig. 8 shows the maximum tensile stress and maximum compressive stress occurring in the dam body under normal conditions. The stress distribution is colored according to the stress at the center of each element, and while the maximum and minimum stresses depend on the element size, in this model the element size is a cube of about 0.5m, so local stresses of smaller sizes cannot be evaluated. In the vicinity of the central part of the dam body, a maximum tensile stress of around 0.1 MPa occurred in a part of the upstream edge of the dam

bottom, but no tensile stress occurred elsewhere on the dam body. Meanwhile, on both sides, a tensile stress of around 0.1 MPa occurred throughout the dam body, and a tensile stress of around 0.3 MPa occurred on the upstream edge of the dam bottom. However, the tensile strength of the dam body was 3.04 MPa or less, so this was not a concern. The maximum compressive stress was around 0.3 to 0.4 MPa at the downstream end of the bottom surface in the central part of the dam, and the compressive stress tended to be slightly higher on the downstream surface near the bottom surface in the side parts. As with the case where only hydrostatic pressure was applied, the arch shape reduced the stress near the central part of the dam and increased the stress in the side parts.

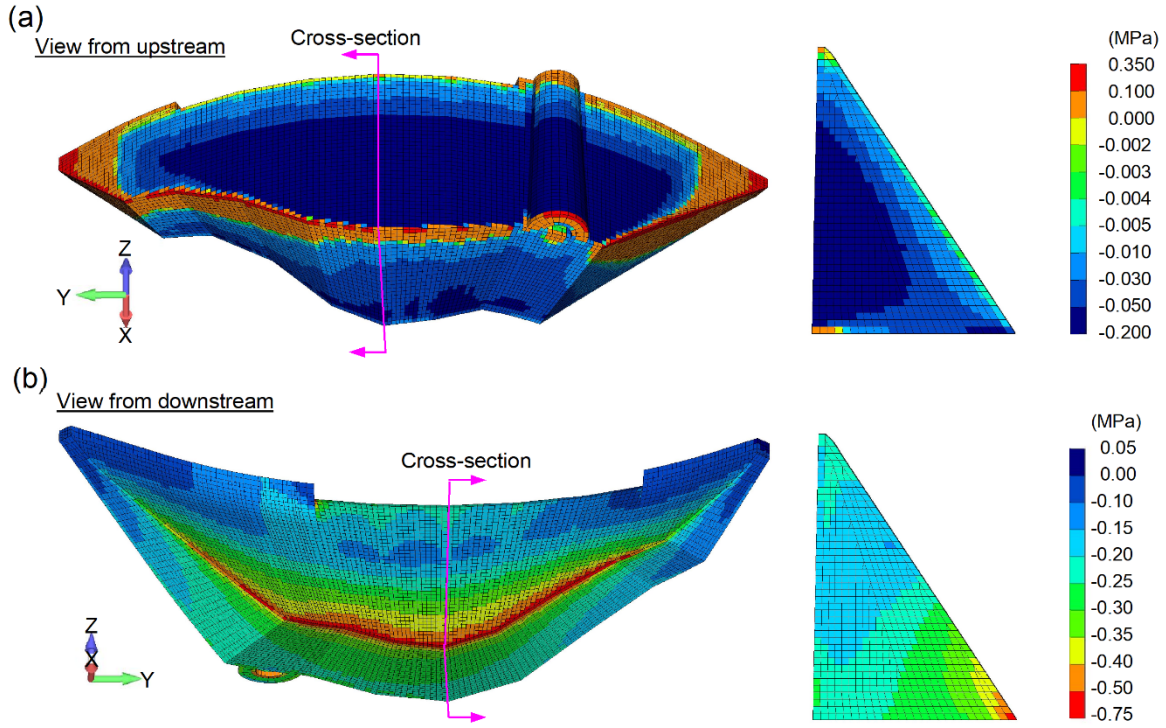

Fig. 8 – Maximum stress distribution under normal conditions: (a) maximum tensile stress and (b) maximum compressive stress.

5.3. Earthquake response analysis results

Fig. 9 shows a superimposed image of the maximum acceleration distribution in the upstream and downstream directions and the maximum deformation diagram due to the Aki-nada earthquake. The maximum acceleration was 3334 gal at the top of the dam body near the center, and the maximum displacement was 1.6 cm. The maximum acceleration at the top of the dam body was amplified 5.6 times from 596 gal at the bottom of the dam body. Meanwhile, the maximum acceleration of the Chojagahara earthquake was 1060 gal at the top of the dam body near the center, the maximum displacement was 0.8 cm, and the amplification rate of the maximum acceleration was 2.7, which was smaller than that of the Aki-nada earthquake. The

horizontal acceleration response spectrum value in Fig. 4 at the first dominant period of the dam body (0.0467 s) was around 900 gal for the Aki-nada earthquake and around 600 gal for the Chojagahara earthquake. However, because of the effects of the dynamic water pressure, the dam shape and topography, and the simultaneous application of seismic motion from three directions, the response was considerably larger than the seismic response of the dam's first mode.

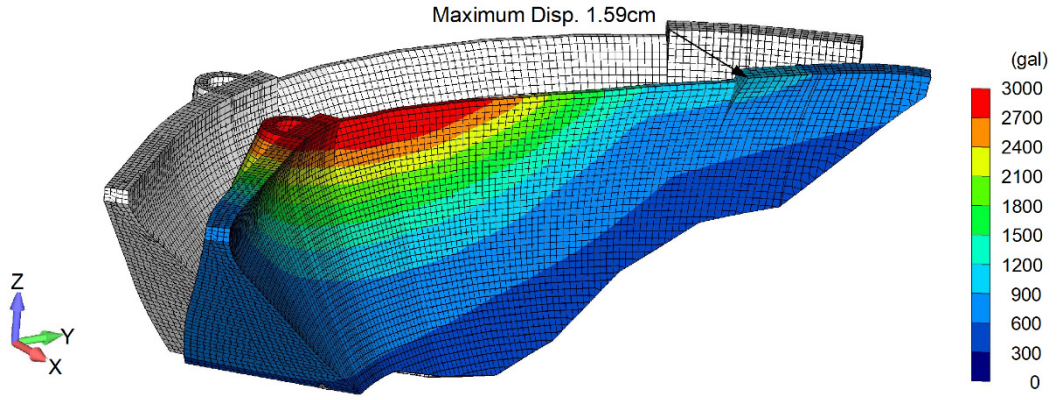

Fig. 9 – Maximum acceleration distribution and maximum deformation in the upstream and downstream directions due to the Aki-nada earthquake.

Fig. 10 shows the distribution of the maximum tensile stress and maximum compressive stress generated in the dam body due to the Aki-nada earthquake. The maximum stress indicates the stress at the center of a cube with an element size of approximately 0.5 m, so it does not evaluate the local stress of smaller sizes. The maximum tensile stress shown in Fig. 10(a) was large at the upstream and downstream heel of the dam bottom because of the earthquake force acting from the upstream and downstream sides, respectively, during the earthquake, and tensile stress was generated throughout the dam body. The maximum tensile stress was 4.26 MPa at the upstream end of the dam bottom, and the tensile stress locally exceeded the tensile strength of the dam concrete of 3.04 MPa. Meanwhile, the maximum tensile stress due to the Chojagahara earthquake was 4.12 MPa. Although the response of acceleration and displacement was smaller than that of the Aki-nada earthquake, the tensile stress was large.

As with the maximum tensile stress, the maximum compressive stress shown in Fig. 10(b) was greater at the upstream and downstream ends of the dam, with a maximum compressive stress of 3.0–3.5 MPa occurring at the upstream end of the dam. The maximum compressive stress around the central part of the dam was 4.0 MPa at the upstream end of the water intake tower, which protruded upstream. The maximum compressive stress of 4.56 MPa occurred at the left side of the dam, but as the dam height at this location was low, it was probably due to the arch

shape. In comparison, in the Chojagahara earthquake, the maximum tensile stress also occurred at the same location, but the maximum value was smaller at 2.68 MPa.

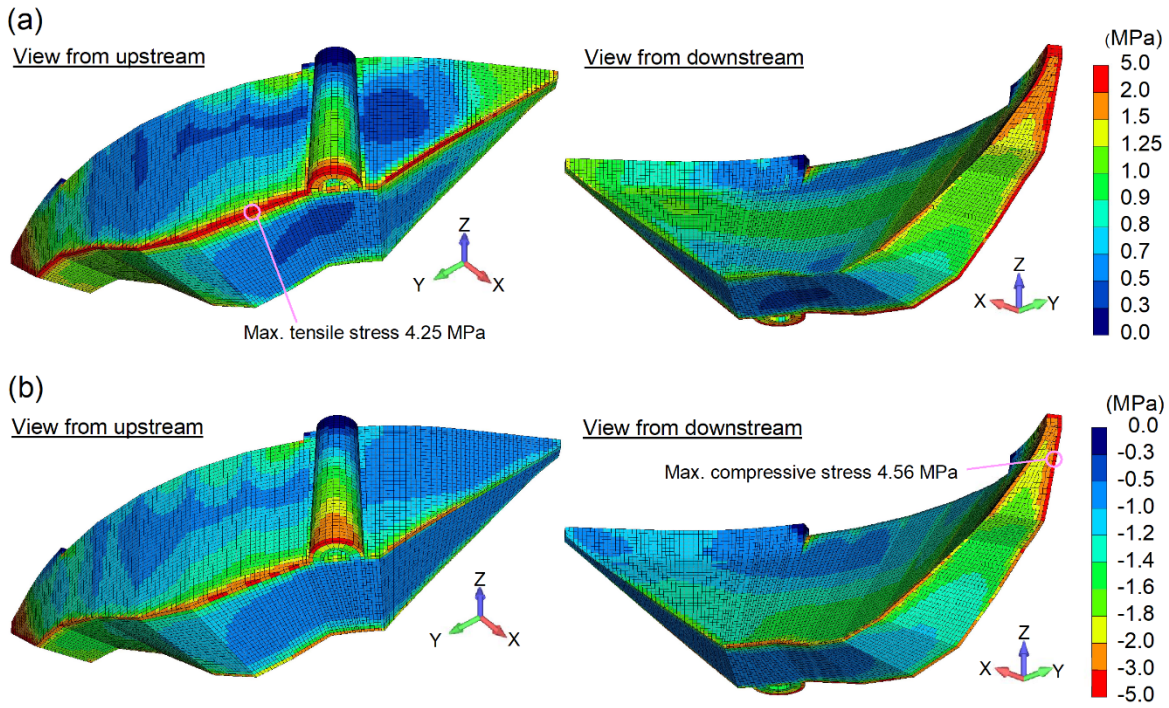

Fig. 10 – Distribution of maximum tensile stress and maximum compressive stress in the dam body due to the Aki-nada earthquake: (a) maximum tensile stress and (b) maximum compressive stress. The tensile stress is displayed as positive.

Fig. 11 shows the time history of the sliding safety factor calculated from the stress of the joint elements installed on the entire dam base at the time of the main shock of the Aki-nada earthquake and the distribution of the sliding safety factor of each element of the dam bottom at the time of the minimum sliding safety factor. The minimum sliding safety factor was 3.99, and it occurred at 17.82 s. The sliding safety factor for each element of the dam bottom at 17.82 s showed a wide distribution of elements with a sliding safety factor of less than 1.0 on the upstream side. This was because tensile stress was generated on the upstream side of the dam base. However, the sliding safety factor was 6 or more in the vicinity of the dam center, and there were no elements where the sliding safety factor became 1.0 or less due to shear failure. In addition, there were no areas where the sliding safety factor was small in continuous upstream and downstream directions. Thus, it is inferred that cracks will not penetrate and damage the water storage capacity.

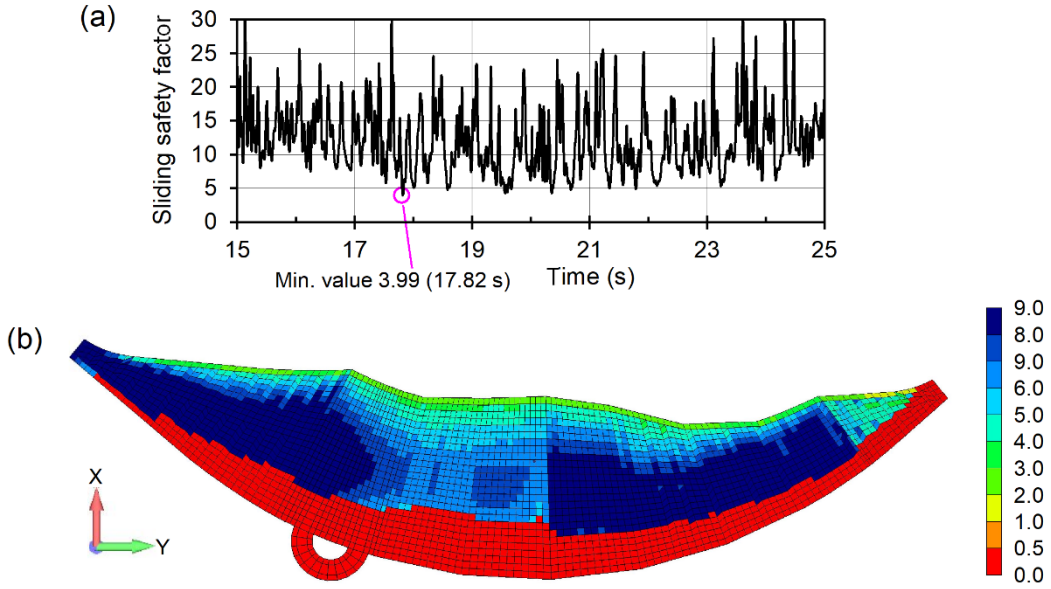

Fig. 11 – Sliding safety factor of the bottom of the dam during the Aki-nada earthquake. (a) Time history of the sliding safety factor of the entire bottom of the dam. (b) Sliding safety factor of each element at the time of the minimum sliding safety factor.

6. SEISMIC PERFORMANCE EVALUATION

For the case of the reversed input seismic motion, an analysis was performed for the Aki-nada earthquake, which caused large tensile and compressive stresses. Table 2 shows a comparison of the maximum tensile and compressive stresses, and the sliding safety factor at the dam bottom, in the case where the Chojagahara earthquake waveforms were not reversed and the Aki-nada earthquake waveforms were reversed. In all cases, the maximum tensile stress exceeded the tensile strength of the dam body concrete (3.04 MPa). However, the elements that exceeded the tensile strength were only at the bottom edge, and they were not distributed continuously in the upstream and downstream directions. In addition, this study was a linear analysis, and if a nonlinear analysis was performed, the local tensile stress would be distributed to the surrounding elements and become smaller. Therefore, tensile failure that would continue between the upstream and downstream faces was not expected to occur. Consequently, it was judged that the water storage capacity would not be lost due to tensile failure.

The maximum compressive stress was 4.91. In all cases, the compressive stress was below the compressive strength of 30.4 MPa. Thus, compressive failure was not expected to occur. The minimum sliding safety factor was 3.78, and as it satisfied a safety factor of 1.0 or more, shear failure was not expected to occur in the upstream and downstream sections.

Table 2 – Maximum tensile and compressive stresses and sliding safety factor of the dam bottom.

Earthquake	Reversed case	Max. tensile stress	Max. compressive stress	Min. sliding factor
Chojagahara	–	4.12	2.68	3.78
Aki-nada	–	4.25	4.56	3.99
ditto	CASE-1	4.10	4.91	4.13
ditto	CASE-2	4.26	3.65	4.19
ditto	CASE-3	3.96	3.43	4.07

7. CONCLUSIONS

Two types of seismic motion were set for inland-type and trench-type faults around the studied dam, and the seismic performance was evaluated using 3D dynamic FEM analysis. It was found that the maximum tensile stress during an earthquake would cause tensile failure at the heel of the dam bottom and in part of the side section. However, because the tensile stress was small and the area of failure was localized, no significant damage was expected to occur to the dam body. Meanwhile, it was found that sufficient safety was ensured in terms of compressive failure and sliding failure of the dam bottom. From these results, we confirmed that there was no significant damage to the dam body and that the water storage capacity could be maintained. However, in order to evaluate this more strictly, it is necessary to perform a nonlinear analysis using joint elements that take into account sliding and separation movements at the contact surface between the dam and the bedrock, as well as solid elements that can take into account the generation of cracks in the dam body.

The stress distribution in the dam was similar to that of a gravity dam, but the arch shape reduced the stress around the central part of the dam and increased the stress in the side parts. These trends were similar to the results of static seismic force examined by ICOLD Commission [1]. In addition, it was also found that the arch shape of the Hisayamada Dam reduced the shear and tensile stresses that occurred in the dam body around the central part of the dam due to hydrostatic pressure and seismic force.

REFERENCES

[1] Committee of Computational Aspects of Analysis and Design of Dams. (2003). Evaluation of ultimate strength of gravity dams with curved shape against sliding. ICOLD 7th Benchmark Workshops on Numerical Analysis of Dams Theme A (2003): 20-37.

[2] Water Management and Dam division, National Institute for Land and Infrastructure Management, Ministry of Land, Infrastructure and Transport. (2005). Technical note on seismic performance evaluation of dams against large earthquakes. Technical Note of

National Institute for Land and Infrastructure Management 244 (2005). (in Japanese with English abstract)

[3] Sasaki, T. Ito, T. (2016). Attenuation relationship of earthquake motion at dam foundation in consideration of Tohoku Earthquake. Journal of the Japan Association for Earthquake Engineering 16.4 (2016): 80-92. (in Japanese with English abstract)

[4] Water Management and Dam division, National Institute for Land and Infrastructure Management, Ministry of Land, Infrastructure, Transport and Tourism. (2013). Acceleration records at dams under the jurisdiction of the Ministry of Land, Infrastructure, Transport and Tourism. Technical Note of National Institute for Land and Infrastructure Management 734 (2013). (in Japanese with English abstract)

Fifth International Dam World Conference
PORTUGAL • LISBON • LNEC • APRIL 13-17, 2025
dam world 2025

CONTINUOUS AMBIENT VIBRATION MEASUREMENTS: EXPERIMENTAL SET UP AND FIRST RESULTS ON AN ARCH DAM

B. Steck[1]	E. Robbe	N. Humbert
EDF/DTG	EDF/DTG	EDF/CIH

ABSTRACT

This paper outlines a novel experiment conducted on an arch dam, with a specific focus on continuous ambient vibration monitoring.

The study covers the dam's instrumentation design, sensor placement, and initial data processing. After a year of continuous measurements, the research effectively detects the first modes, enabling the characterization of the dam's modal shapes.

The paper present two analysis methods for these data and compare a single sensor and a multi sensor approach. Hydrostatic effect is quantified over only one year measurement.

The experiment is still running to cover a larger time analysis.

Keywords: Arch dams, ambient vibration, monitoring, modal analysis.

[1] barthelemy.steck@edf.fr, France

1. INTRODUCTION

This paper presents the experimental setup and some first results of continuous ambient vibration measurements on Lanoux arch dam. Conventional mechanical monitoring of concrete dams usually relies on displacement measurements (with pendulums or planimetry) for the surveillance of the global mechanical behaviour of the structure. Nevertheless, several authors [1] [2] [3] [4] demonstrate the interest of continuous ambient vibration monitoring for the long-term monitoring of concrete dam's behaviour.

This technique involves the use of velocimeters and passive seismic methods to detect and analyse vibrations and noise naturally present in the environment. It does not require active seismic sources, making it cost-effective and non-intrusive, with the following steps :

- Data Collection: Velocimeter sensors are installed on the dam. These sensors continuously record ambient noise and vibrations of the structure.
- Data Analysis: The recorded data is processed to extract information about the natural frequencies of the dam. For concrete dams and particularly arch dams, frequencies are influenced by the reservoir level and the thermal load. On the long term, changes in frequencies can indicate structural weakness considering this parameter is somehow representative of the global stiffness of the structure, making it a promising surveillance tool.

The experiment conducted at the Lanoux arch dam aims to achieve several goals:

- Evaluation of the interest of continuous ambient vibration measurement on dams for surveillance: while EDF already uses ambient vibration measurement for the calibration of finite-element analyses under earthquake loads, the interest of this technique for surveillance has not yet been fully covered. This experiment is an excellent opportunity to test material, analyses methods and infrastructures required for long term measurements.
- Pendulums of the Lanoux arch dam showed locally and occasionally particular measurements in winter potentially linked to vertical joints movements. Continuous monitoring of the natural frequencies might provide interesting information to understand if such behavior affects the whole dam or remains local.
- Lanoux dam provides a suitable configuration fur such measurements: while located at high elevation in the Pyrénées mountain with rough winter conditions (cold, snow, remote area), the dam is protected from any human-generated or powerhouse noises and several pendulums' rooms with power supply are available at the crest to shelter the recording devices.

First, Lanoux arch dam and the experimental setup are presented. Then two methods of analysis have been carried out using the records: using a single-sensor approach with Asterion software and multi-sensor approach with an in-house software. Assumptions and initial results for each approach are presented. Finally, a synthesis of the first results is proposed with the first feedback regarding the chosen experimental setup.

2. DAM AND AMBIENT VIBRATION MEASUREMENT SET UP PRESENTATION

2.1. Dam presentation

Lanoux dam is a double curvature, 42.5 m high arch dam, which is asymmetric due to the shape of the valley. Owned by EDF, it is located in the southwest of France. It was constructed between 1957 and 1960, built in 13 blocks. In Figure 1 and Figure 2, illustrations of the dam are presented. The foundation of the dam consists of laminated metamorphic slate with a high compressive strength. However, the anisotropy of the foundation confers a higher deformability to the left bank.

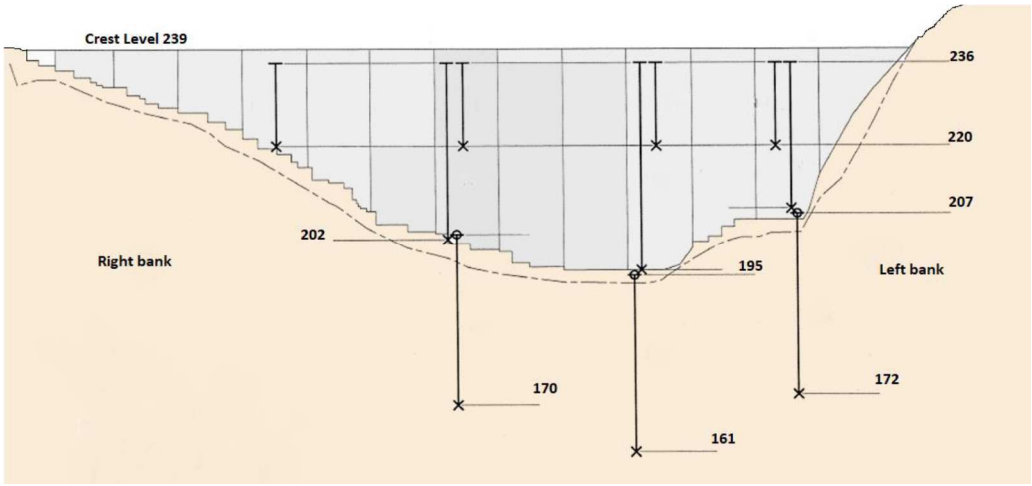

Fig. 1 - Downstream view of the dam: recording devices are located in the pendulum rooms near the crest of the dam

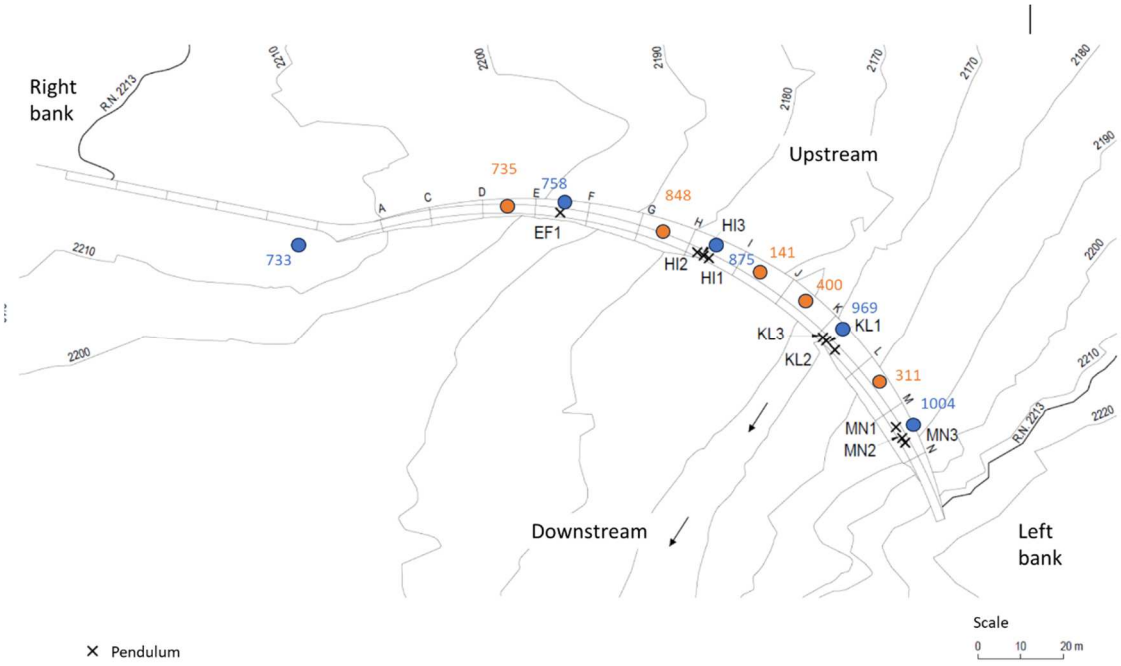

Fig. 2 - View from the top of the dam with location of the sensors

2.2. Ambient vibration measurement setup

The experimental setup consists of 5 three-dimensional velocimeters (blue circles in **Fig. *2***). The sensors are IGU-16HR 3C 5Hz from SmartSolo. Four devices are placed near the crest of the arch inside pendulum rooms as presented in **Fig. *2*** and **Fig. *3***. The last device is located on the rock at the right abutment to provide a reference measurement. These devices are independent of each other, and the GPS-synchronized timestamp allows them to be considered as a network of synchronized measurements. The measurement is performed continuously with a sample rate of 4 ms.

The raw measurements are velocities continuously recorded by three directional velocimeters. They are positioned to measure along the upstream-downstream direction of the dam, the tangential axis, and the vertical axis.

Fig. 3 - Velocimeter in a pendulum room with electric power supply

Pendulum rooms provide power supply, and the devices are equipped with around a 7 days battery in case of temporary power outage. However, due to the remote location of the dam in the mountains and the experimental nature of this instrumentation, data are stored within the sensors, requiring a manual collection of the data every 6 months.

3. DATA ANALYSES WITH SINGLE-SENSOR APPROACH

Data processing by the Astrion software [6] is done using a single-sensor approach. The results presented in this section utilize the data from the upstream-downstream axis.

3.1. Description of the data process

The data are collected in the time domain and then pre-processed by the Astrion software which performs the transformation into the frequency domain in 20-minute batches.

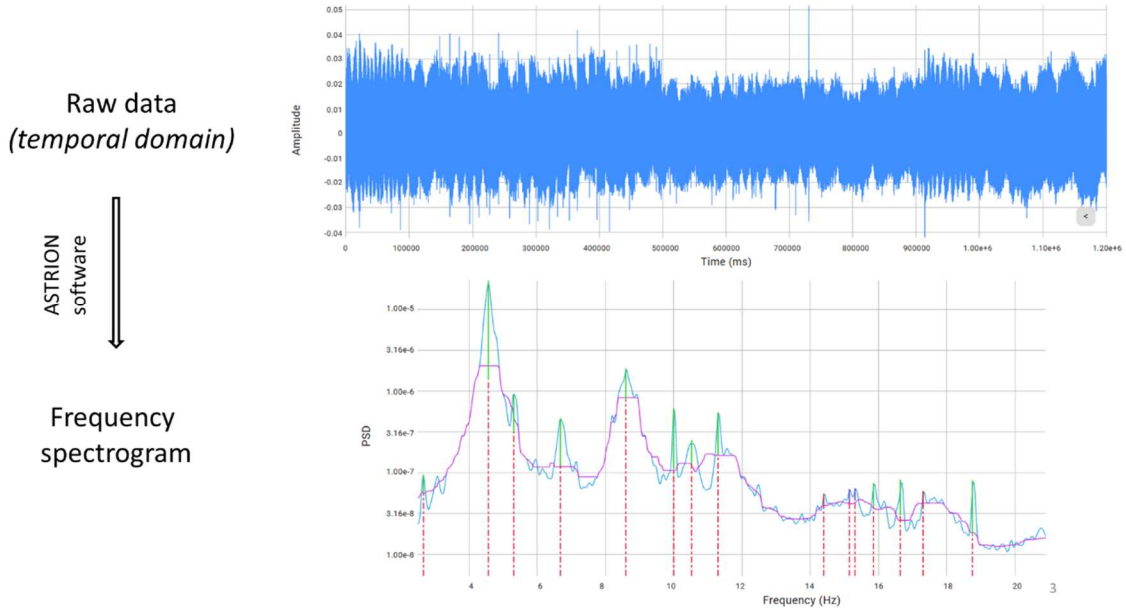

Fig. 4 - Schematic view of data processing

Next, a detection of frequency peaks is performed for each sensor, and the evolution of these peak frequencies is monitored. The analyses presented in the following sections of the article are based on the study of the evolution of these peak frequencies.

3.2. Effect of the external conditions on the measurements

Considering the measurements are sensitive to weather conditions, environmental data are available from a weather station located near the dam, within the same watershed. The available data includes temperature, precipitation, snow depth, and wind speed. Although this station is not very far from the dam, these measurements are not taken directly at the dam.

Thus, the temperature or sunlight at the dam shows an impact on the value of these frequencies. The presence of wind does not seem to have a significant impact on the frequency value but affects the amplitude of the peak. In the following section, the analyses will focus only on the frequency variations of the natural modes.

3.3. Results over one year of measurements

The evolution of the frequencies measured for the first seven natural modes, for example, by the sensor located at the central block over the course of three months with continuous measurement is plotted in **Fig. *5***.

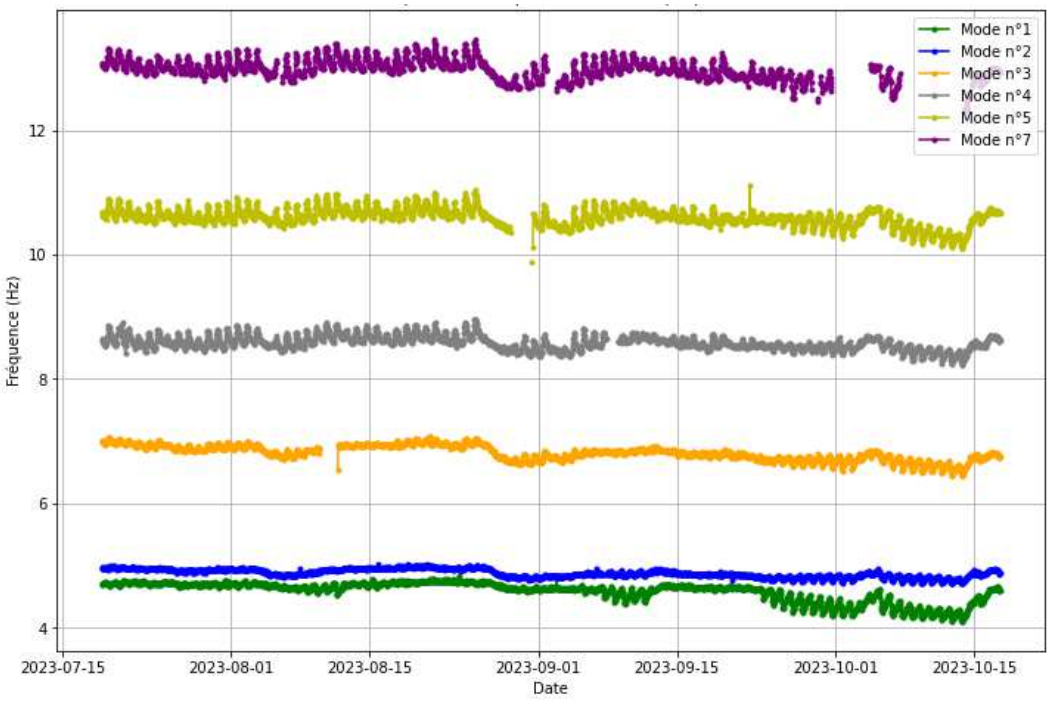

Fig. 5 - Tracking of natural modes measured by the sensor located on central block (sensor 969 in Fig. 2*)*

In this figure, we observe intraday variations across the different modes. These intraday variations seem to be linked with meteorological parameters. In particular, the variation in sunlight appears to be predominant, as shown by the intraday changes during the first months of the experiment from July to October in **Fig. *6***

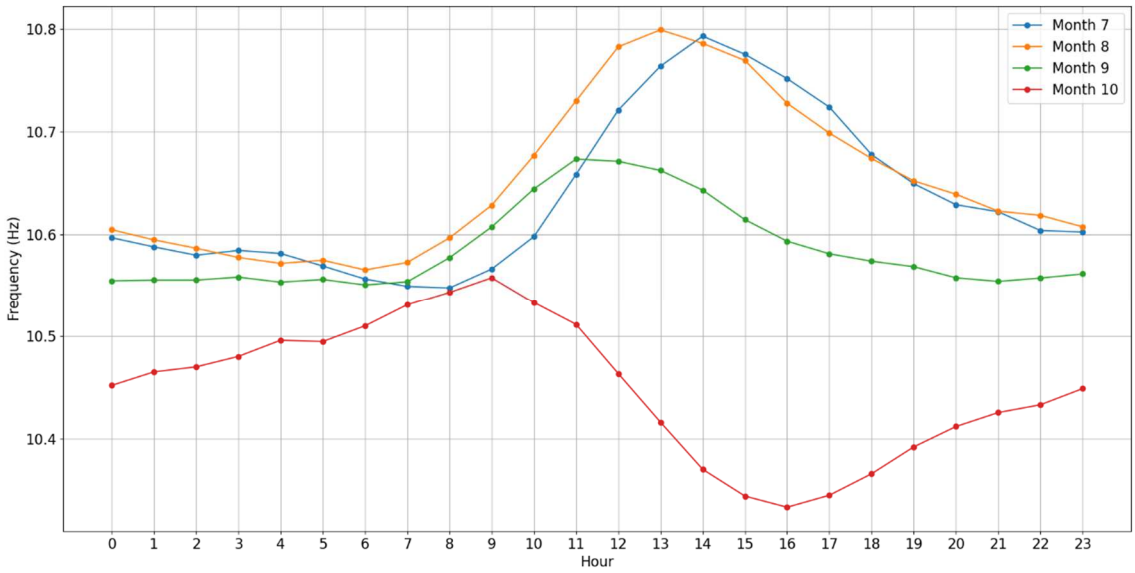

Fig. 6 - Intraday variations for the 5th natural mode

To analyse the measurements over a year and estimate the impact of hydrostatic load and temperature, the evolution of the natural modes was extracted once a day at 6 a.m. This time was chosen to minimize potential intra-daily effects.

Since we only have one year of data, a standard HST statistical analysis cannot be performed. However, we have conducted a third order polynomial calculation of the hydrostatic effect. Results are in *Fig.* **7**. Green dots represent data of the 1st natural mode frequency corrected from a seasonal effect estimated from the one-year measurement.

Within the range of tidal variations observed over the year, with a maximum level 13 meters below the normal water level, we observe an increase in frequency with the rise in level.

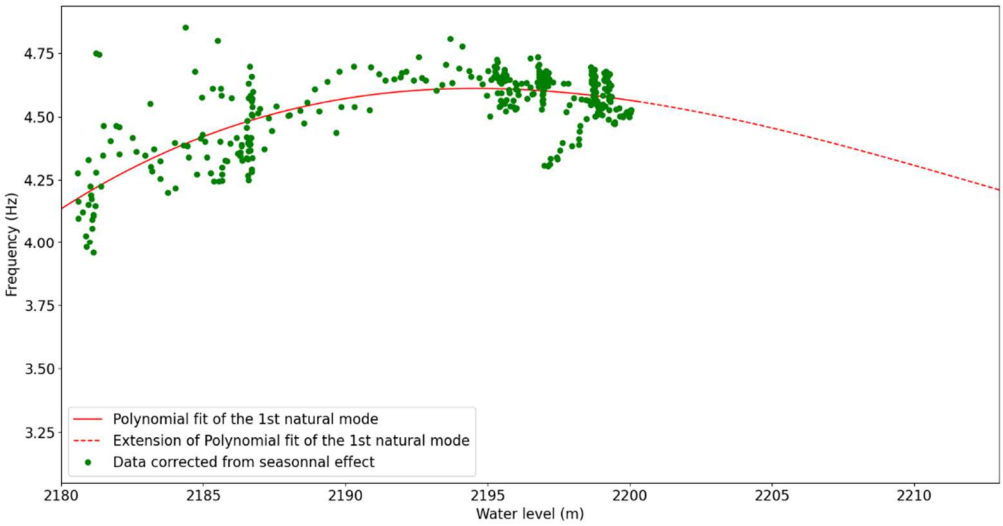

Fig. 7 - 1st natural mode frequency relation with water level

The same polynomial calculation was performed for the different eigenmodes of the dam. They are shown in **Fig. 8**, with a calculation using third-order polynomials for each mode.

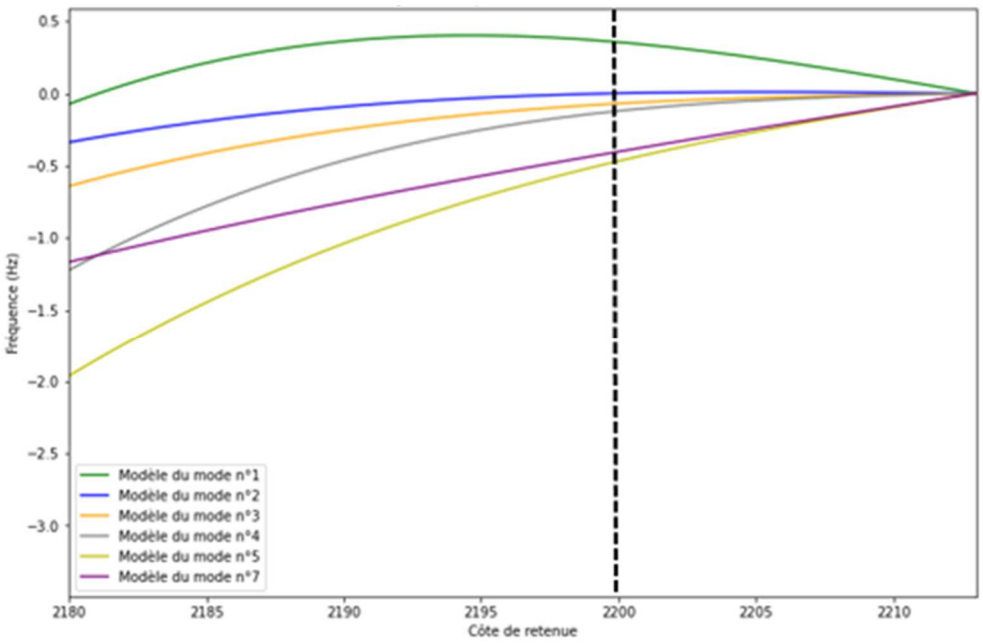

Fig. 8 - Polynomial fit of the hydrostatic effect on natural mode (extension beyond a water level of 2200 m)

The shape appears quite different depending on the modes, with a particular behaviour showing a peak in the increase of the eigenmode frequency for the first modes.

Acquiring data over several years with different tidal ranges will allow us to refine the estimation of the hydrostatic effect calculated from these initial data.

Another observation (shown in Fig. **9**) is made regarding the relationship between the variation of the frequency of the natural modes and the external temperature. Indeed, during the summer period, the two parameters seem to be in phase, with an increase in frequency corresponding to an increase in the external temperature averaged over 5 days. However, during the winter period, this relationship appears to be out of phase. There is no explanation for this observation at this stage, and data acquisition over several years will allow, once again, to verify this observation.

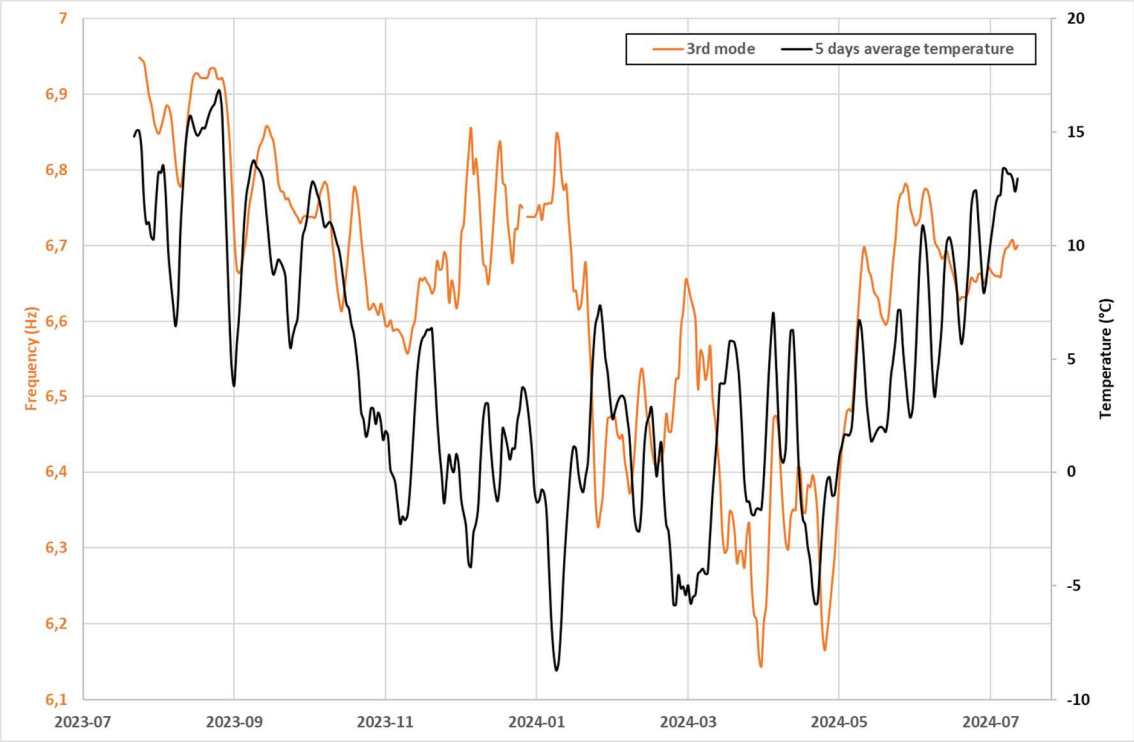

Fig. 9 - Opposition of the frequency variation compare to temperature during winter time

4. DATA ANALYSES WITH MULTI-SENSOR APPROACH

Mutli-sensor analyses using an in-house software.

4.1. Description of Data Analytics for an operational modal analysis

Data Analytics is an in-house software developed by EDF. It is a tool dedicated to vibration analysis of a structure using a multi-sensor / multi-reference approach. For this case, the operational modal analysis (OMA) tool will be used for the present study.

The OMA approach implemented by Data_Analytics largely builds upon the PolyMax algorithm: PolyMax is a frequency-domain modal parameter estimation algorithm that employs a right matrix-fraction model approach to derive clear stabilization diagrams, leading to robust pole estimations. A pole-residue model is then used to estimate the

mode shapes [8] . PolyMax is complemented by a series of methods designed to enhance the reliability and robustness of OMA. These include:

- Pole Selection via Stabilization Diagram (used to evaluate modes frequency and damping in muti-sensor configuration): The choice of the constraint leading to pole estimation from the right fraction-matrix model is based upon the PhD thesis work of B. Cauberghe [8] [9] . It improves the readability of the stabilization diagram. Moreover, in the OMA case, a preliminary band-pass filtering step is conducted to eliminate poles outside the frequency range of interest.
- Modal Shape Estimation: Once the poles are selected, Data_Analytics proposes two pole/residue models, giving the possibility to estimate either real or complex mode shapes. Different levels of optimization can be integrated to refine the initial estimation of residues, drawing upon published works by E. Balmès [10] [11] .

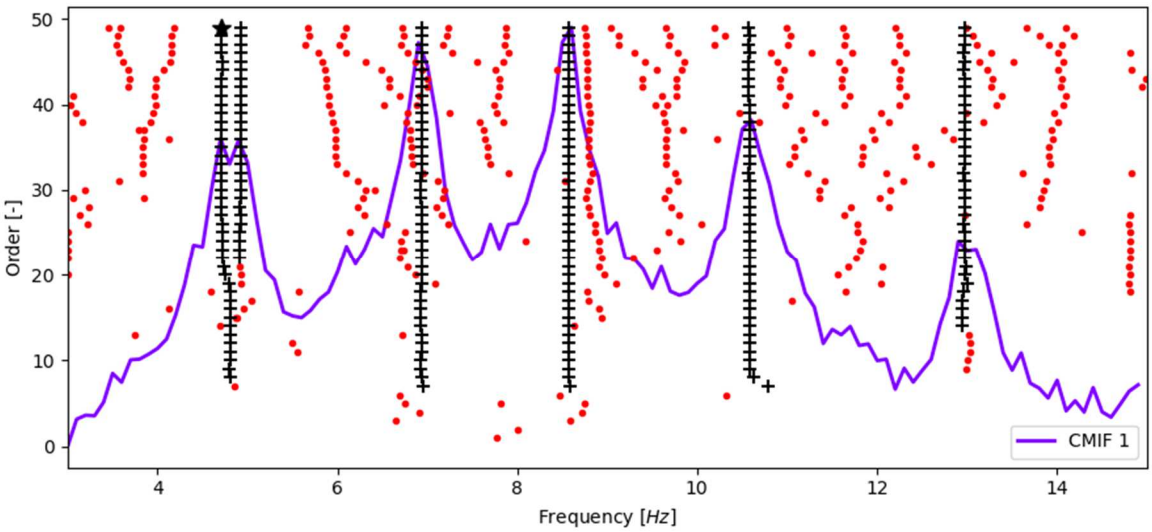

Fig. 10 - Stabilisation Diagram as it's given in Data Analytics - Stable poles correspond to black cross on the figure while instable ones are represented by red dot. The purple function seen in the figure is the Complex Modal Identification Function (CMIF).

4.2. Creation and parameterization of an automatic detection of the normal modes for the case of the Lanoux Dam

Data_Analytics is primarily designed for one-off measurement campaigns. The code has been automated to handle a large volume of measurements efficiently. The adopted approach involves extracting all stable poles within a predefined frequency range (here, between 3 Hz and 14 Hz) using the stabilization diagram.

This method used on the whole year of ambient noise recording in the Lanoux dam on the upstream-downstream component enables the identification of the first six modes (see Fig. ***11***).

However, the detection process includes some false positives and missed detections, particularly for the first two modes, whose frequencies are very close (~0.1 Hz apart).

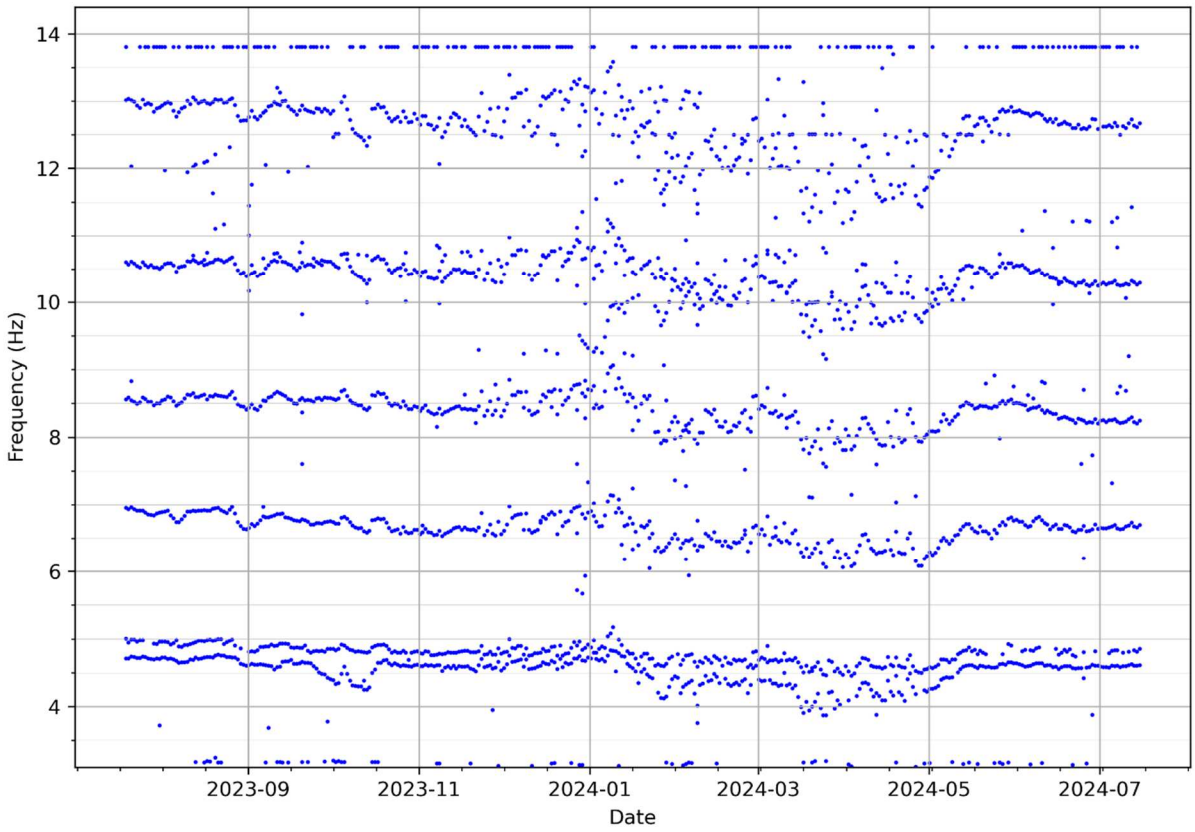

Fig. 11 - Display of the frequencies obtained after the automatic detection process with the sensor 758 as a reference and without any post treatment

To refine and enhance the robustness of this detection process, several filters are defined:

- Eliminating erroneous detections at the limits of the selected frequency range.
- Excluding modes with damping ratios that are too low, significantly below 1%.
- Use of multiple reference sensors to avoid missing a mode that present a node at the location of the reference sensor.
- Characterizing modes based on their modal shapes: The multichannel analysis conducted by Data_Analytics allows the identification of the modal shape corresponding to each stable pole. A shape recognition tool is integrated into the process, enabling the assignment of each frequency pole to a specific mode. This step is central to the multichannel approach, as it ensures that the frequency peak observed from one day to the next consistently corresponds to the same physical phenomenon

(i.e., the same mode). The result of this identification of the different normal mode is presented in the following figure :

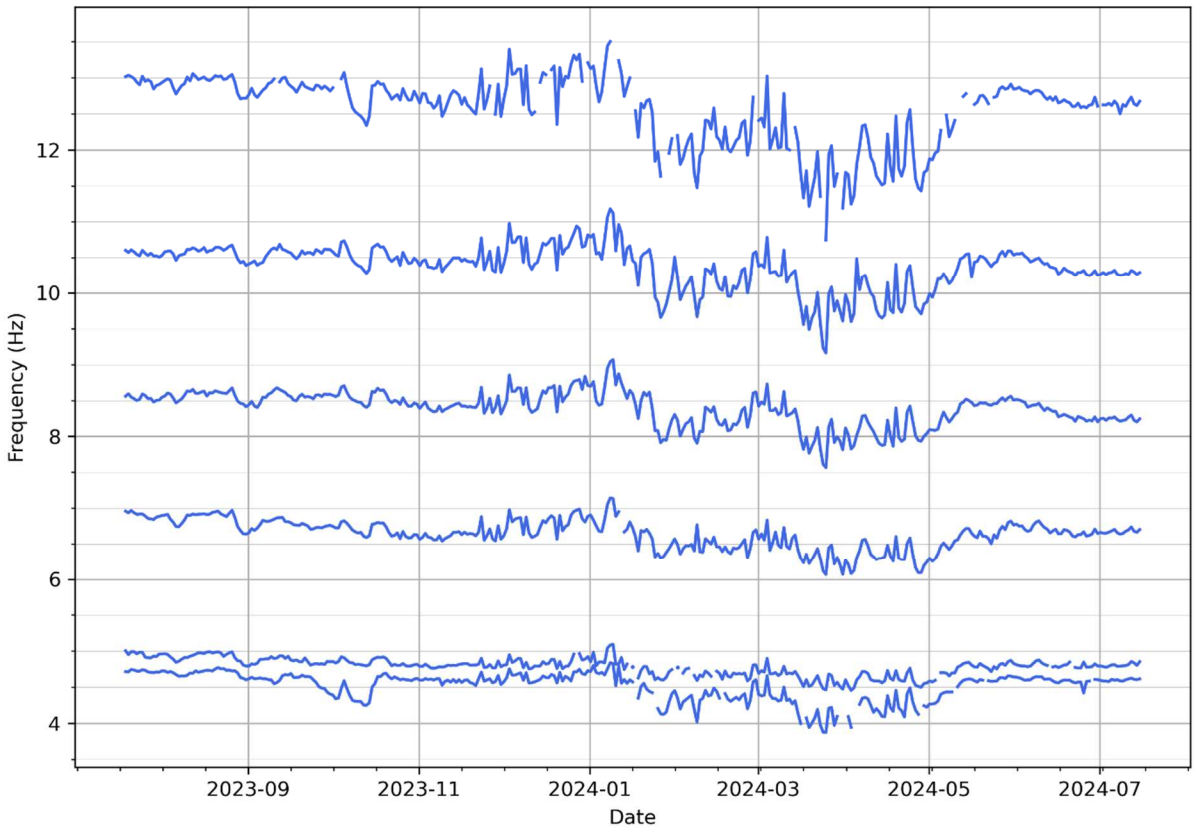

Fig. 12 - Display of the detection of normal mode using the previous post treatment and modal identification with mode shape for the combination of two detections calculated with different reference sensors (758 and 1004)

4.3. Verification of the installation's ability to represent mode shapes

In the case study of the arch dam, the presence of 4 boxes at the crest influenced the number and placement of sensors. To validate this setup, a punctual vibration measurement was conducted using 5 additional sensors (orange circles in **Fig. *2***, resulting in a total of 9 sensors on the crest of the structure and one on the rock. One hour of recording was performed in October 2024. An operational modal analysis (OMA) was conducted on this recording, identifying the first seven modes and their corresponding mode shapes. These mode shapes are compared in the following figure with those obtained from the 4 main stations.

The comparison reveals that for the first four modes, the mode shapes obtained using 4 stations are similar to those obtained with 9 sensors, although the mode shapes appear less smooth. For higher frequency modes, the mode shapes are significantly degraded when

considering only 4 stations. If these modes are of specific interest, additional stations should be added to the setup.

Finally, when significant changes in the stiffness or mass of the studied structure are anticipated, the number of stations must be increased because the mode shapes could be altered and make the chosen station locations suboptimal.

Table 1 - Modal shapes of the seven first modes - October 2024

Modal analysis with 10 velocimeters	Modal analysis with 5 velocimeters
Freq : 4.57 Hz - damp. : 1.72 % 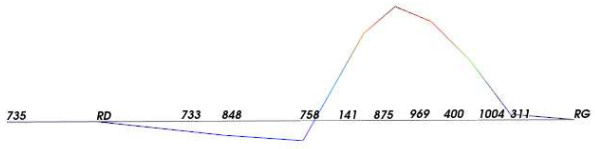	Freq : 4.54 Hz - damp. : 0.00 % 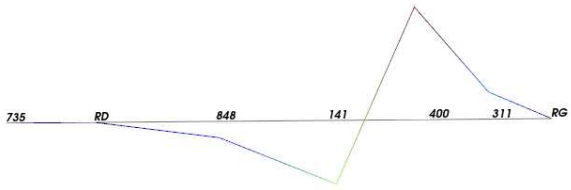
Freq : 4.76 Hz - damp. : 1.15 % 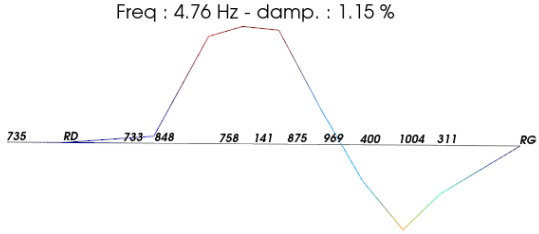	Freq : 4.76 Hz - damp. : 1.68 % 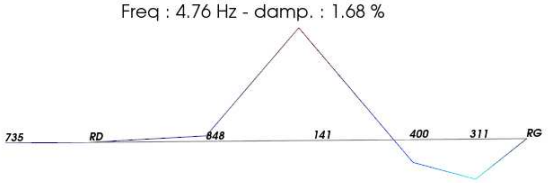
Freq : 6.64 Hz - damp. : 1.73 % 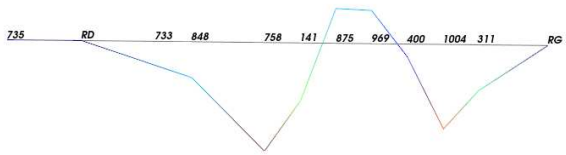	Freq : 6.65 Hz - damp. : 1.86 % 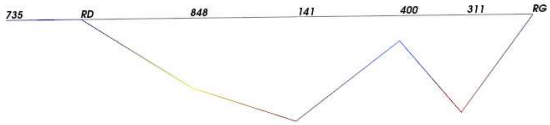
Freq : 8.41 Hz - damp. : 1.68 % 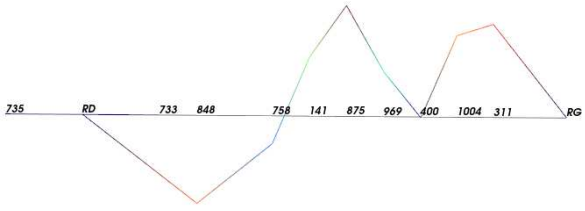	Freq : 8.37 Hz - damp. : 1.52 % 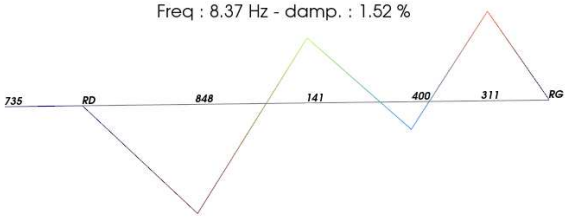
Freq : 10.48 Hz - damp. : 1.33 % 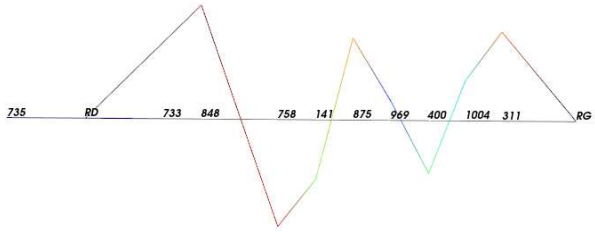	Freq : 10.43 Hz - damp. : 1.67 % 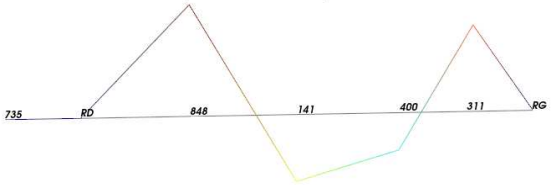

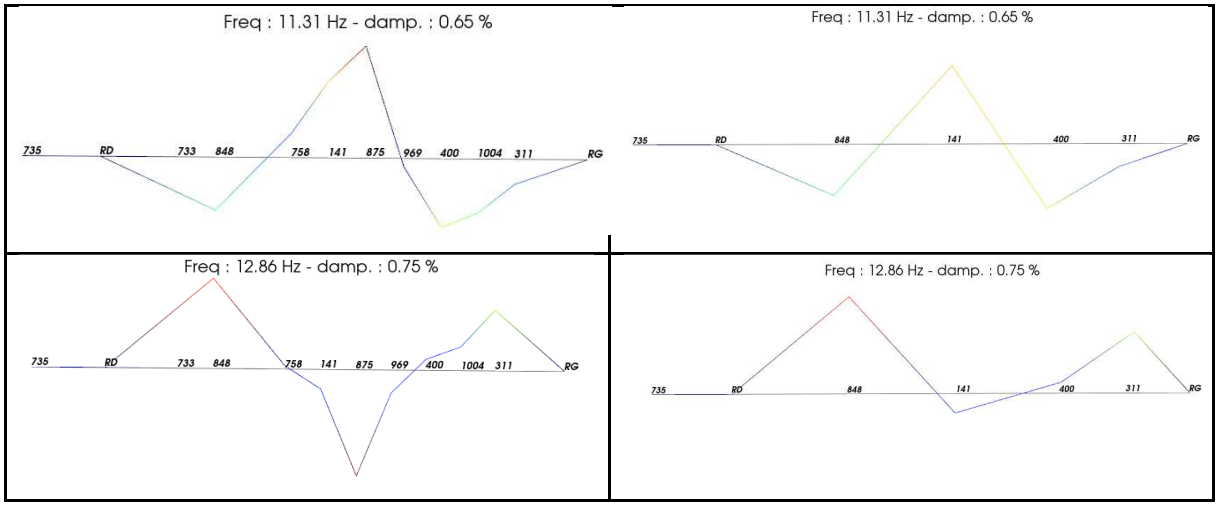

4.4. Analysis of the evolution of mode shapes with time

Although the modal shapes remain sufficiently stable during the year of measurement to enable the modal identification described in paragraph 4.2, second-order shape variations can be observed. The following figure illustrates these variations in the modal shape of the third mode, calculated daily over a four-month period between July 2023 and October 2023. A localized variation is observed on the right bank, specifically at sensors 758 and 875. These variations are likely associated with localized stiffness changes, potentially corresponding to partial openings of certain joints between cantilever blocks. This information could be used within the framework of a numerical model of the arch, providing insights into a nonlinear behaviour linked to joint openings.

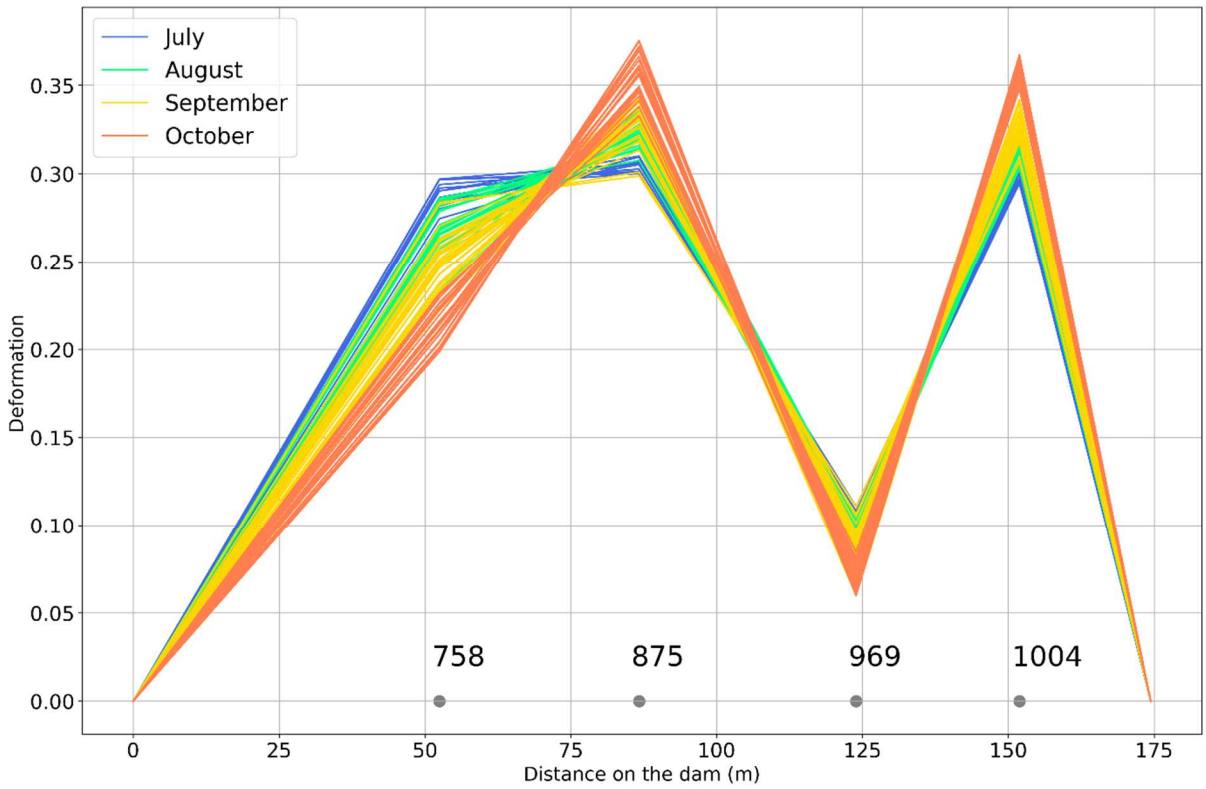

Fig. 13 - Variation of the mode shapes for the third normal mode every day between July 2023 and October 2023. The mode shapes belonging to each month is represented with a different colour.

4.5. Potential effect of the reservoir on the dam

An interesting observation can be made by looking at the data of the vertical component: another peak can be observed during the whole year, with a frequency between the fourth and the fifth mode. The following figure displays in orange the stable poles excluded from detection by the “low damping” filtering process described in Section 4.2. The pole that persists throughout the year is visible and highlighted with a gray line.

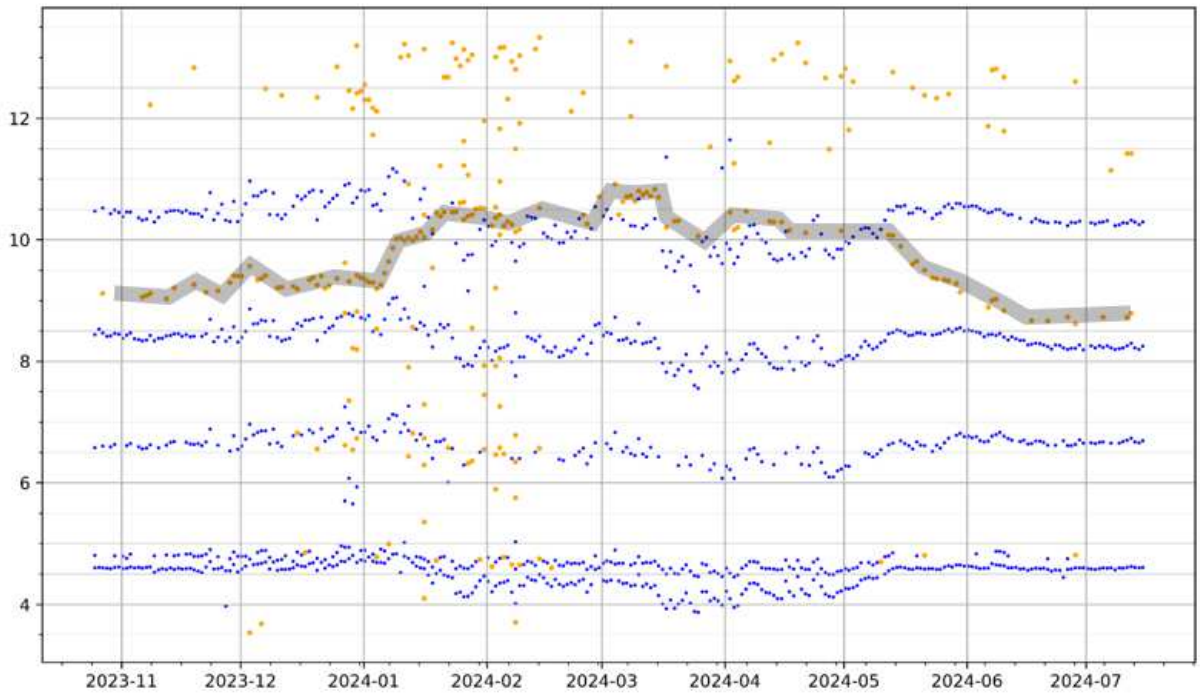

Fig. 14 - Display of the automatic detection of modes: in orange, focus on the poles eliminated by the damping filter and the modal shape filter.

This additional mode follows a very different variation than the other mode perfectly correlated with the water level of the reservoir and shows low damping, suggesting it may be driven by forced excitation (characteristic, for example, of the presence of machinery). It is likely associated with the first mode of the reservoir, whose frequency can be approximated by 1440/4H, where H is the height of the reservoir. This hypothesis could be further supported, for instance, through the use of hydrophones placed in the reservoir at the base of the structure.

5. SYNTHESIS OF THE FIRST RESULTS AND FEEDBACKS ON THE EXPERIMENT

5.1. Regarding the experimental setup

The experimental installation setup on the dam has been operating correctly for one year and continues to function. The choice of a setup with independent sensors, synchronized by GNSS, has proven to be relevant as it is simpler to implement on site while ensuring the ability to analyse data retrospectively.

However, this implementation was facilitated by the existence of protected rooms at the crest of the dam, allowing us to avoid issues related to the exposure of sensors to external conditions with power supply.

Today, automatic data retrieval has not been studied. Preliminary work will need to be done on data sampling at the appropriate level to ensure an acceptable volume for transmission. On that topic: data storage can quickly be a challenging task and the solution described in [1] to directly identify the frequencies on site might prove relevant in the long term.

A preliminary analysis, as shown by the results in section 4.3, with a higher density of sensors during a short time measurement (~1h) proves to be useful to define the position of the sensors. This allows for limiting the number of deployed sensors while maintaining a good capacity for modal analysis.

5.2. Regarding the data processing

Both approaches (single or multi sensor) provide equivalent results. Generally, data processing on that field requires dedicated software and a good mastery of the process. The multi-sensor analysis remains from the authors point of view more complex, but the visualization of the modal shapes likely allows for a better understanding of the physics of the modes and will probably be crucial for analysing the phenomena detected in winter. It should be noted that such comments are true for the Lanoux dam case but not necessarily generalizable because all modes evolve in a comparable way.

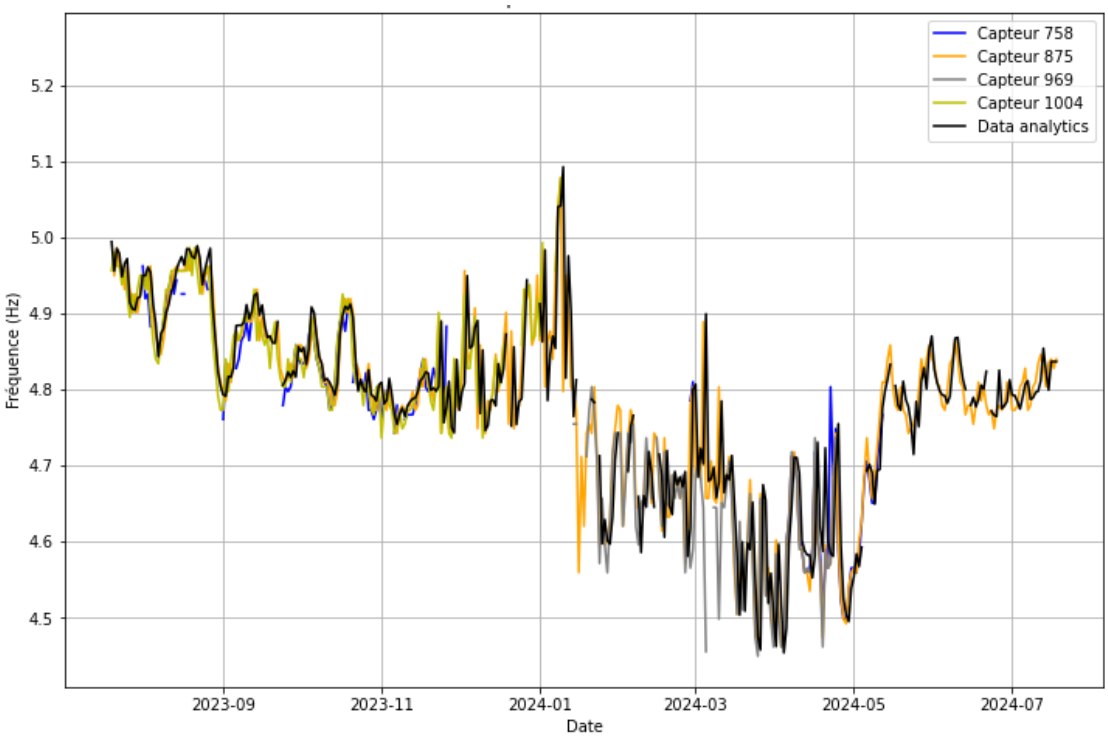

Fig. 15 - Comparison of calculation of the 2nd natural mode with Astrion for the four sensors and with multi sensor approach.

5.3. Regarding the first results

First, analyses show that windy conditions lead to higher amplitude of the records but without any consequences on the frequency results.

The effect of the hydrostatic load on the frequency is clearly shown. Water level is currently operated 13 m below the normal water level. That's probably why analyses highlight mainly an increase in frequency with the increase of water level, due to the increase in rigidity with the closing of the cantilever joints. On other dams [1] [2] [4] near maximum water level, the frequency decreases with the rise of the reservoir leading to increase added masses. This might confirm a slightly open state of the vertical joints between cantilevers (at least in the upper part), responsible for the behavior observed in winter.

Regarding the thermal effect on the frequency, the limited amount of data collected so far does not allow to numerically evaluate their influence on the frequency results. With one additional year of measurements, HST analyses of the data time-history frequency variation should allow to clearly separate hydrostatic and thermal loads:

- Regarding intraday behavior, the effect of the sunshine is clearly seen during summer and additional analyses should be carried out to evaluate the interest of such behavior.
- Looking at the evolution of the frequencies for 1 year (**Fig. *12***), there is clearly a change of behavior during wintertime from mid-November to the end of April with much more instability of the frequencies compared to the rest of the year. While frequency variation is generally in line with temperature variation during the rest of the year, this relation becomes the opposite in winter.

Additional measurements in winter 2024-2025 along with daily remote monitoring of the pendulums should allow to better understand this behavior.

REFERENCES

[1] . Oliveira, S. et al. (2024). Cahora Bassa vibrations monitoring between 2010-2022. Analysis of frequencies using HST statistical models for effects separation, Journal of Physics: Conference Series 2647.

[2] . Darbre G. et al. (2002). Continuous ambient-vibration monitoring of the arch dam of mauvoisin, Earthquake Engng Struct. Dyn. 31:475-480.

[3] . Ueshima T. et al. (2017) Structural health monitoring of an aged arch dam using long term contiuous observation of ambient vibration /seismic motion, 16th WCEE Santiago Chile

[4] . Bukenya P., Moyo P et al., Long term integrity monitoring of a concrete arch dam using continuous dynamic measurements and a multiple linear regression model, International symposium of SANCOLD, Johannesburg, 2016

[5] . Humbert, N. & Robbe E. (2023). Ambient Vibration: Feedbacks from Measurements on 20 Concrete Dams and Comparisons with Finite-Element Analyses.Focus on One Year of Recording on an Arch, Proceedings EVACES 2023.

[6] . Martin N. et al. (2021). Automated machine health monitoring at an expert level, Acoustics Australia, Special issue on Machine condition monitoring.

[7] . https://www.astriis.com/

[8] . Van der Auweraer, H., Peeters, B., et al. (2001). "PolyMAX: A Revolution in Operational Modal Analysis." Presented at the IMAC Conference on Structural Dynamics.

[9] . Bart Peeters et al. (2004). “A New Procedure for Modal Parameter Estimation” International, Leuven, Belgium

[10] . Balmes E. “Frequency domain identification of structural dynamics using the pole/residue parametrization.” International Modal Analysis Conference, Dearborn, 1996

[11] . Balmes E. “New results on the identification of normal modes from experimental complex modes” - Mechanical Systems and Signal Processing, 1997.

Fifth International
Dam World Conference
PORTUGAL • LISBON • LNEC • APRIL 13-17, 2025
dam world 2025

PREVENTIVE MAINTENANCE PROGRAM THROUGH UNDERWATER INSPECTIONS WITH ROV AND SONAR: A STRATEGIC APPROACH TO REDUCING DOWNTIME AND COSTS IN HYDRAULIC TUNNELS FAILURES

Fabio Iannotta[1]
Hibbard Inshore Brasil

David J. Malak[2]
Hibbard Inshore, LLC

ABSTRACT

Implementing a preventive maintenance program using ROV and Sonar underwater inspections in hydraulic tunnels, with recommended inspection intervals and key performance indicators such as structural integrity assessments and operational downtime metrics, can effectively prevent extended and costly downtime. This article examines the benefits and costs associated with such programs compared to emergency repairs and medium-term outages.

A real case from a few months ago illustrates this point: an ROV and Sonar inspection initially aimed at locating a lost intake trash rack discovered an unexpected collapsed crown area, significantly reducing the tunnel's operational capacity and requiring immediate corrective measures to prevent further structural degradation. This tunnel had been inspected several months prior, with data showing warning signs.

By analyzing data on collapse areas, emergency repair costs, and outage impacts, this article evaluates whether current industry practices are effective, economically viable, and socially sustainable, using evaluation criteria such as maintenance frequency, structural integrity scores, and incident response times. We assess if these practices can be improved for better service to shareholders and users.

The analysis highlights the significant advantages of preventive maintenance programs, specifically through ROV and Sonar inspections, over reactive emergency repairs. The real-world example demonstrates the effectiveness of these proactive measures in identifying potential issues before they escalate into costly and disruptive emergencies.

This approach improves the financial sustainability of preventive maintenance operations and enhances the reliability and safety of hydraulic tunnels. Furthermore, it supports better service delivery to shareholders and users by minimizing the disruption caused by unexpected failures. The proactive strategy also aligns with broader economic and social sustainability objectives.

Adopting a preventive maintenance strategy is not only cost-effective but also strategic. As industries face increasing pressures to maintain infrastructure efficiency, implementing such proactive measures becomes essential for long-term operational success and resilience. The benefits extend beyond cost savings, contributing to the overall reliability, safety, and sustainability of hydraulic tunnel operations. Therefore, a preventive maintenance program using ROV and Sonar inspections is a prudent investment for the future, ensuring ongoing operational efficiency and stability

Keywords: Hydraulic Tunnels, Preventive Maintenance, Outage Impacts, Financial Sustainability, ROV Inspections, Hydropower Generation, Water Companies.

[1] fabio@hibbardinshore.com, Brazil
[2] dave.malak@hibbardinshore.com, USA

1. INTRODUCTION

This article analyzes the implementation of a preventive maintenance program for hydraulic tunnels, aiming to enhance the operational efficiency of these critical assets. We will evaluate its economic and financial feasibility, as well as its impact on routine operations, highlighting potential benefits in terms of operational stability and reliability.

The sudden interruption of hydraulic tunnel operations, whether functioning under pressure or in open channel flow conditions, and regardless of their application for power generation or water supply, typically arises from structural failures requiring extensive repairs. These failures often result in prolonged shutdowns to perform necessary remediation, leading to significant consequences, including substantial financial losses for operators, socioeconomic challenges, reduced system reliability, and reputational damage. In a context of increasing demand for stability and operational predictability, preventive maintenance emerges as a strategic component in infrastructure asset management. It enables the identification and mitigation of risks before they escalate into critical failures that disrupt operations.

Preventive maintenance in hydraulic tunnels is essential for mitigating structural failure risks and avoiding unplanned, resource-intensive operational interruptions. These tunnels frequently lack continuous monitoring systems, and human access during operation is impractical, making it difficult to predict or detect emerging issues before they become severe. Structural collapses in hydraulic tunnels are often identified only through observable reductions in hydraulic head or flow rate, indicating that the problem has already reached an advanced stage.

Draining hydraulic tunnels solely for inspection purposes poses significant risks, as the pressure differential between the tunnel structure and the surrounding water table may induce collapses or rock detachment, particularly in geologically unstable zones, faulted regions, poorly treated areas, or formations of inferior rock quality. These factors make preventive maintenance not merely advisable but indispensable for the management of critical infrastructure systems.

The deployment of ROVs (Remotely Operated Vehicles) equipped with Sonar for underwater inspections provides an advanced solution for assessing tunnel conditions and detecting progressive detachment phenomena. This technology facilitates detailed monitoring of vulnerable areas, enabling the strategic planning of targeted interventions and enhancing overall operational safety.

Adopting a preventive approach allows for the efficient scheduling of planned maintenance shutdowns, minimizing the need for reactive measures and mitigating the financial and operational risks associated with emergency interventions. This methodology not only ensures operational continuity but also optimizes safety and predictability in critical infrastructure operations.

2. Literature Review

The studies on hydraulic tunnels analyzed for this work focus primarily on construction, structural, operational, inspection, and maintenance aspects, but they do not comprehensively integrate all the factors involved in a broad preventive maintenance program. While providing valuable guidelines, these studies exhibit a gap in addressing specific preventive maintenance practices and in analyzing the economic advantages of this approach.

This paper seeks to contribute to the existing literature by addressing preventive maintenance from both an economic and social perspective, demonstrating how the use of ROVs and Sonar can significantly improve the operational and financial sustainability of projects and systems dependent on hydraulic tunnels.

3. Implementation Methodology

The implementation of a preventive maintenance program for hydraulic tunnels requires a methodology tailored to the specific characteristics of each tunnel. A risk matrix should be developed, taking into account factors such as the geological, geotechnical, and hydrogeological conditions of the site, the type of excavation, support treatments, pressure and flow rates, the age of the structure, the extent of anthropogenic activity in the region, among other variables.

In addition to technical information, the risk matrix must include the strategic and social function of the tunnel: Does it supply water to a densely populated region, or does it contribute to power generation? Is there a contingency plan in case of interruption? If so, what are the associated costs and the timeframe required for its implementation?

The analysis of these factors enables the frequency of inspections to be adjusted precisely and efficiently, adapting the maintenance program to the specific conditions of each scenario and enhancing operational safety and predictability. This approach not only prevents structural failures but also optimizes resources proactively, ensuring that the tunnel continues to fulfill its function with minimal risk and cost

3.1. Systems for inspections

Underwater inspections in hydraulic tunnels employ ROVs specifically designed to operate efficiently at depths and pressures compatible with the tunnel's specific conditions. These devices are equipped with 2D and 3D profiling sonar, as well as high definition imaging sonar, enabling the precise identification, structural analysis, and georeferencing of anomalies. This technology provides detailed reality capture and a comprehensive view of the tunnel's internal conditions, facilitating the detection of changes or risk areas and offering a solid foundation for planning preventive interventions.

Figure 1 - This image shows the deployment of a ROV for a tunnel inspection.

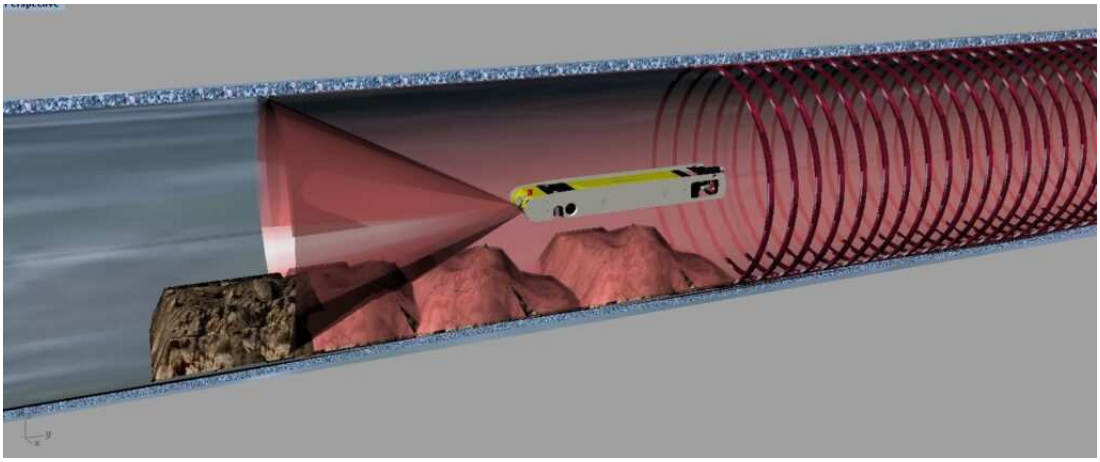

Figure 2 - This image shows a ROV conducting inspection and mapping inside a hydraulic tunnel.

3.2. Frequency e procedures

The frequency of inspections is determined based on the risk matrix. As a general recommendation, the first inspection should take place after the initial filling of the tunnel, within the contractor's warranty period. Following this initial inspection, the risk matrix must be revised

according to the results, whether they indicate anomalies or not. Subsequent inspections are scheduled according to the updated risk matrix. Whenever an inspection identifies evolving risk phenomena or confirms no changes, it is essential to update the risk matrix to reflect the latest conditions and adjust the frequency of future inspections accordingly.

3.3. Data evaluation and risk identification

The collected data, presented as reports and 2D and 3D maps, must be analyzed and interpreted by civil, geotechnical, and geological engineers specializing in underground hydraulic structures. This evaluation should include all relevant historical documentation about the tunnel, such as pre-excavation rock testing, records of geological faults, applied treatment methods, as-built plans, previous inspection reports, and operational characteristics of the tunnel. Cross-referencing design and inspection documents allow for more precise risk identification and support the development of an accurate and dependable diagnosis of the tunnel's structural condition.

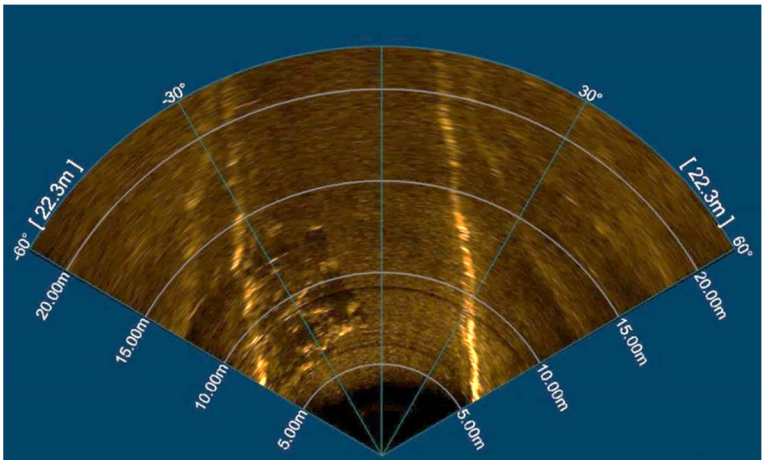

Figure 3: This figure shows the initial detachment of rock blocks on the left hydraulic wall. If not addressed through preventive treatment, this anomaly could lead to a major collapse, as illustrated in Figure 4

Figure 4 - Major collapse in a hydraulic tunnel that reduced flow capacity by 80%.

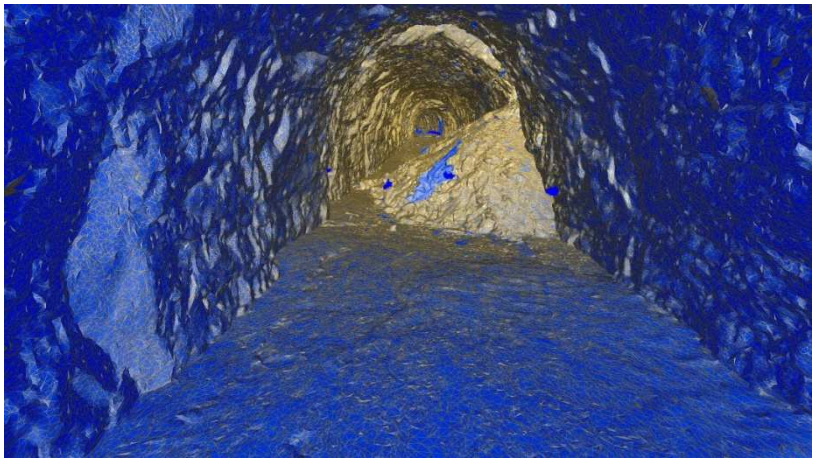

Figure 5 - 3D underwater mapping revealing a collapse in a hydraulic tunnel.

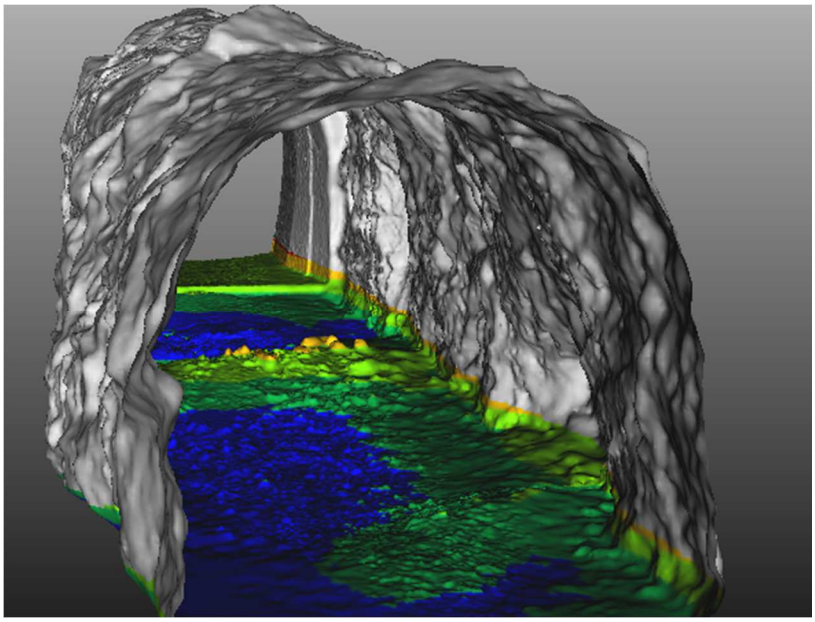

Figure 6 - 3D underwater mapping of a hydraulic tunnel showing the transition between a rock section and a reinforced concrete section.

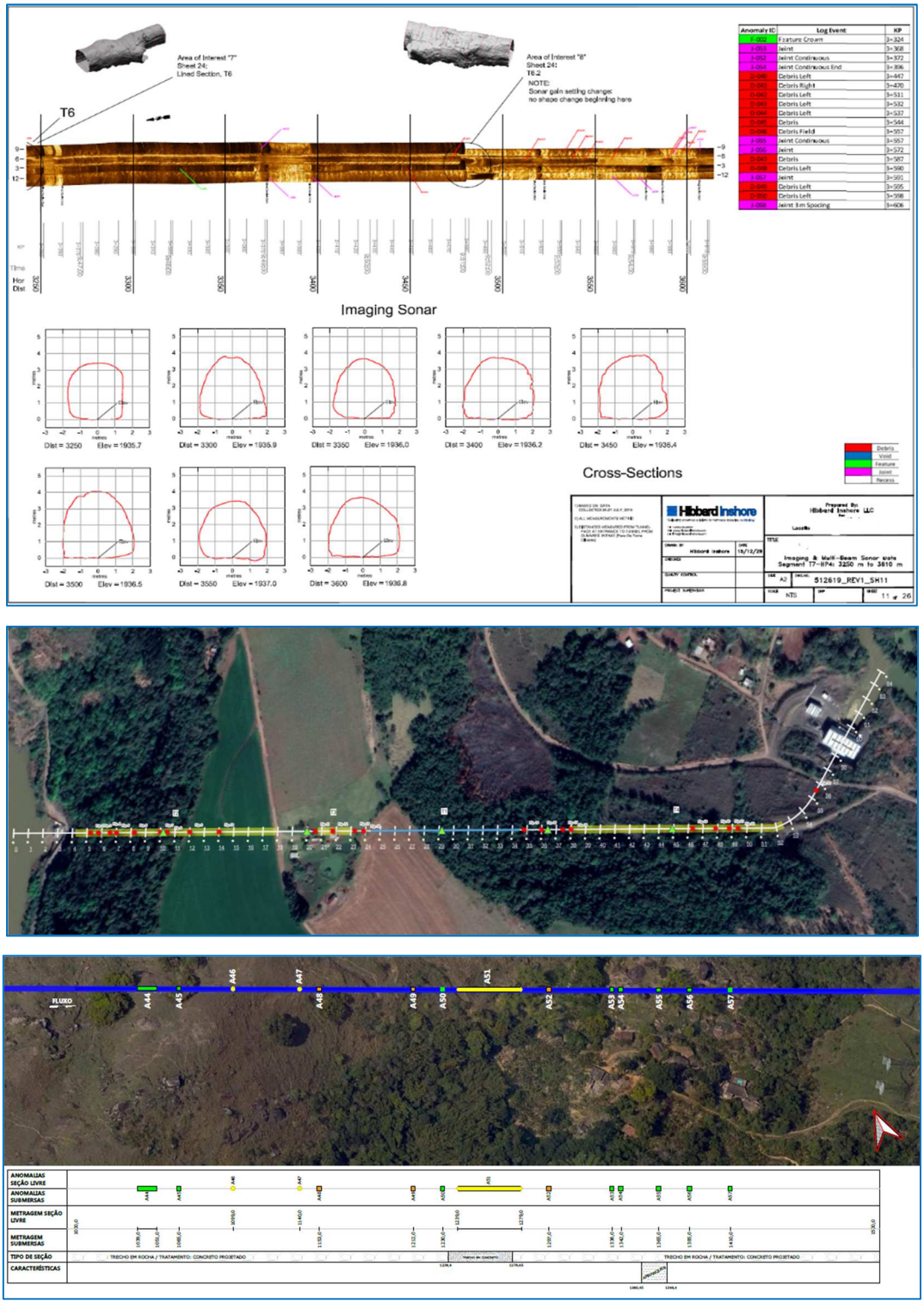

Figure 7 - The figures above illustrate three types of anomalies and feature mapping in hydraulic tunnels. This mapping should be performed in coordination with the technical report.

3.4. Operational requirements for underwater inspections

Underwater inspections in hydraulic tunnels primarily involve the operational implication of requiring zero flow (or very slow flow depending on conditions) during the inspection. As such, tunnel operations must be halted for the entire duration of the inspection. To minimize this impact, it is recommended to hire companies with proven experience and suitable equipment capable of collecting all necessary data for a comprehensive structural health analysis of the tunnel, ensuring the inspection is completed within the scheduled timeframe.

Additionally, to reduce losses associated with downtime, it is advisable to plan these inspections well in advance, aligning them with the scheduled shutdowns of the system. All hydraulic systems, whether for power generation, water supply, industrial use, or other purposes, undergo scheduled maintenance at least a few days a year. This allows underwater inspections to be integrated into the maintenance schedule with minimal operational impact.

4. CASE STUDIES

In the following sections, two cases of tunnel collapses are presented. The first case validates the analyses and recommendations outlined in inspection reports, emphasizing the importance of following data-driven technical guidelines to mitigate more severe issues. The second case, on the other hand, empirically illustrates the significant socioeconomic impacts that prolonged downtime can have on both the affected population and the enterprise, highlighting the adverse consequences of extended operational interruptions.

4.1. Case 1 – rock block detachment in a tunnel section where monitoring had been recommended

A practical example highlights the value of preventive maintenance: during an inspection conducted with ROV and Sonar in the tunnel of a Small Hydroelectric Plant in Brazil, irregularities in the tunnel’s cross-section were identified, despite no visible accumulation of debris. These irregularities resulted from the detachment of rock fragments, which, after breaking off, were partially pulverized and carried away by the water flow over time.

The inspection report advised the client to avoid draining the structure without a robust contingency plan and to maintain regular monitoring to assess the progression of the observed irregularities. Months later, during a recovery operation for a protective grate lost within the tunnel's gate shaft, a follow-up inspection revealed significant detachment of rock blocks in the previously identified irregular area, reinforcing the recommendation for continuous monitoring. This real-world case demonstrates the critical importance of preventive maintenance: with adequate monitoring, it was possible to detect early signs of deterioration before they evolved

into more severe and costly collapses. Implementing the recommended actions mitigates risks and prevents potentially more expensive and complex emergency scenarios

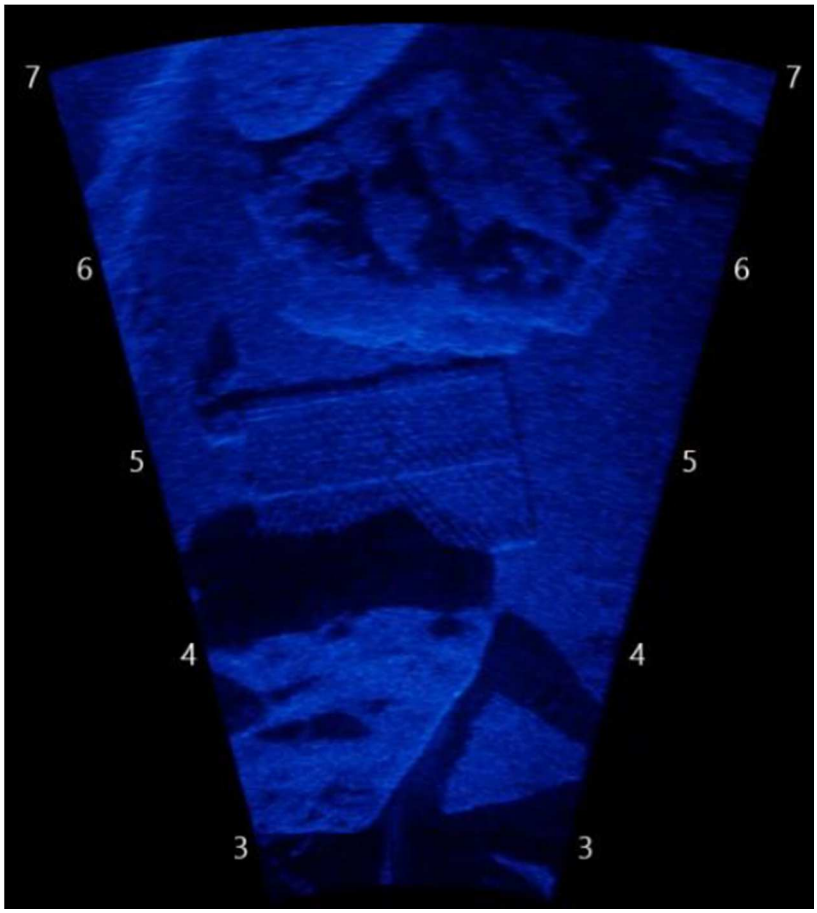

Figure 8 - In this Sonar image, the lost grate inside the tunnel is observed along with some portions of detached rock blocks.

4.2. Case 2 – Guandu-Lameirão tunnel colapse (Rio de Janeiro)

The Guandu-Lameirão tunnel is a low pressurized structure that transports treated water from the Guandu Water Treatment Plant (ETA) to the Lameirão Pumping Station, spanning approximately 11 km. Inaugurated in 1966, the tunnel suffered a significant rupture in 1967, resulting in a collapse that compromised its operation for some years.

The recovery of the affected section required large-scale works, including the reopening of shafts used during construction, the excavation of an auxiliary tunnel to facilitate debris removal, and the construction of a 5-km bypass pipeline to maintain water supply during the repair period. These interventions had considerable financial and social impacts on both the operator and the population of Rio de Janeiro, although no detailed documentation is available to estimate the exact costs.

This incident highlights the vulnerability of hydraulic structures to large-scale events and underscores the importance of implementing preventive maintenance programs. Regular

monitoring and early interventions are essential to preventing collapses, minimizing risks, and reducing financial and social impacts.

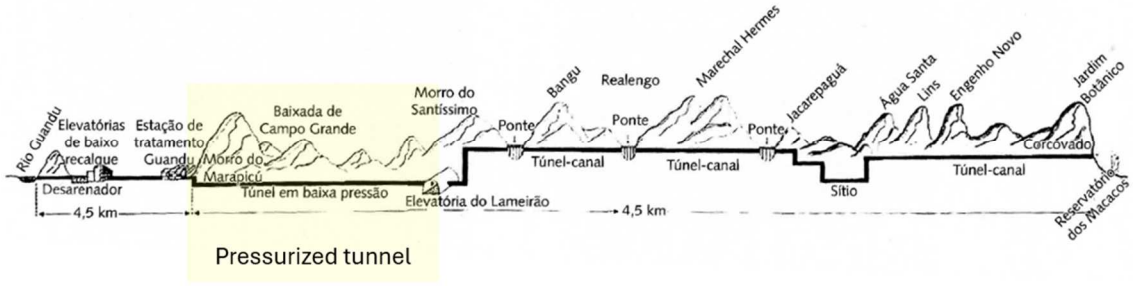

Figure 9 - Guandu System Scheme.

5. ECONOMIC ANALYSIS

Preventive maintenance in hydraulic tunnels, performed through underwater inspections with ROV and Sonar, significantly reduces long-term operational costs. This analysis outlines the costs associated with preventive maintenance compared to the financial and operational losses resulting from emergency repairs due to unexpected failures.

In the following sections, we present a cost analysis of the repairs associated with the collapse of a 6-km-long tunnel at a hydroelectric power plant with an installed capacity of 50 MW. The analysis emphasizes the importance of preventive maintenance in avoiding prolonged and costly operational interruptions

5.1. Analysis of emergency repair costs related to a collapse

When collapses occur in critical sections of a tunnel, recovery costs increase significantly due to urgency, the need for emergency contracting, and extended downtime. In a real-world scenario, the specifics of which cannot be disclosed, a hydroelectric power plant with a 50 MW capacity and an average revenue of USD 44 per MW generated faced a significant failure in its 6-km-long intake tunnel. The repair process took slightly over 10 months to complete, resulting in substantial revenue losses in addition to the additional costs associated with the recovery process, as outlined below.

- **Revenue loss due to downtime:** Revenue loss = (PMEH per MW) X (Plant Capacity in MW) X (Hours per day) X (Days of downtime).
  For this specific case: = (US$ 44MW) X (50 MW) X (24 hours) X (300 days) = **US$ 15.840.000,00**.
- **Contractual penalties and energy re-purchase:** Depending on the terms of existing contracts, the operator may face additional penalties, such as fines and the need to

purchase energy on the open market to compensate for unproduced power. These factors significantly increase the total cost of inactivity.

- **Emergency recovery costs**: In an emergency situation, the costs of personnel and equipment often rise disproportionately. Table 1 presents an estimate of these costs based on market values for Labor and specialized equipment required to repair a collapsed tunnel. The costs for works shown in Table 1 and moreover Tables are derived from an average of market prices, instead the price of a MW-generated energy is variable; in this case, the costs shown in Table 1 and moreover Tables are an average of prices from the U.S. market, derived from a report published on the Energy.gov website.

Table 1 - Estimated costs for tunnel collapse recovery

Item	Q.ty	Days	Daily cost	Total costs
Excavator	1	300	US$ 600	US$ 180.000,00
Bobcat	1	300	US$ 600	US$ 180.000,00
Dump Truck	1	300	US$ 700	US$ 210.000,00
Workers	8	300	US$ 2400	US$ 720.000,00
Confined space rescue team	1	280	US$ 5000	US$ 1.400.00,00
Consultant	2	90	US$ 3000	US$ 270.000,00
Miscellaneus equipment	1	300	US$ 1000	US$ 300.000,00
Consumable	-	-	-	US$ 100.000,00
Estimated Cost				**US$ 3.360.000,00**

Adding up all the costs described above, the total estimated loss amounts to **USD 19,200,000**, excluding any potential fines or other contractual penalties.

5.2. Analysis of costs considering the implementation of a preventive maintenance program, including only minor repairs

Preventive maintenance involves conducting periodic inspections using ROV and Sonar, as well as performing minor repairs as needed over time. The costs of maintaining a preventive maintenance program depend on the characteristics and location of the tunnels. For this analysis, we will use the same parameters as the previously mentioned 50 MW power plant.

The plant was inaugurated in 2007, and the collapse occurred in 2020, after 13 years of operation. Assuming that rocks detachments, which could indicate an imminent collapse, began approximately three years before the event, the effective operational period without structural issues would have been 10 years.

Over these 10 years, it is estimated that three preventive inspections would have been conducted: one immediately after the tunnel filling and two subsequent inspections at five-year intervals. In the event of a failure detected through preventive measures, it is assumed that draining the tunnel, repairing the fault, and resuming operations could be completed within approximately 20 consecutive days, resulting in the following costs.

In table 2, the execution of inspections during scheduled shutdowns, as recommended in this document, was not considered. Therefore, an additional cost has been included, which, in practice, could be disregarded if the inspections were properly planned to coincide with the plant's regular shutdowns. This approach would further reduce the costs associated with preventive maintenance, making it an even more economically viable and efficient alternative.

Table 2 - Estimated cost of implementation and preventive maintenance program.

Item	**Q.ty**	**Timeframe**	**Total Cost**
Inspection	3	36 hours	US$ 1.500.000,00
Downtime for Inspection		36 hours	US$ 144.000,00
Total cost			**US$ 1.644.000,00**

Table 3 - Estimated cost for minor tunnel repair

Item	**Q.ty**	**Days**	**Daily cost**	**Total cost**
Excavator	1	15	US$ 600	US$ 9.000,00
Bobcat	1	15	US$ 600	US$ 9.000,00
Dump track	1	15	US$ 700	US$ 10.500,00
Workers	8	15	US$ 2400	US$ 36.000,00
Confined space rescue team	1	15	US$ 5000	US$ 75.000,00
Consultants	2	5	US$ 3000	US$ 15.000,00
Miscellaneous Equipment	1	15	US$ 1000	US$ 15.000,00
Consumable	-	-	-	US$ 30.000,00
Total cost				**US$ 199.500,00**

In addition to the costs presented, it is necessary to include 20 days of revenue loss due to tunnel drainage and repair, which can be calculated using the formula from the previous section:

Revenue Loss = (PMEH per MW) × (Plant Capacity in MW) × (Hours per Day) × (Days of Downtime)

For this specific case:

Revenue Loss = (US$ 44MW) × (50 MW) × (24 Hours) × (20 Days) = ***US$ 1.056.000***

Considering the presented scenario, with the execution of preventive maintenance (inspections, minor repairs, and associated downtime), the tunnel in question would have practically avoided collapse. As a result, the operator would have prevented an estimated loss of **USD 19,200,000**, at a maintenance cost of **USD 2,899,500**, resulting in an **additional profit of USD 17,356,500**.

5.3. Economic feasibility analysis of implementing a preventive maintenance program in a facility with multiple tunnels

Implementing a preventive maintenance program for hydraulic tunnels in facilities with multiple critical assets requires a careful analysis of the costs and benefits associated with different management approaches. Although not all tunnels are subject to collapse, the implementation of a preventive maintenance program can be an effective strategy to ensure cost savings, structural integrity, and operational continuity, even in facilities with multiple tunnels.

This section evaluates the financial feasibility of a preventive maintenance program by comparing the costs of inspections and preventive repairs against the high costs of a potential major failure. The analysis, based on a scenario involving five tunnels, demonstrates the financial savings and the safety and predictability benefits that preventive maintenance can provide.

For this analysis, we will use the same parameters from the previously presented facility while considering that the operator owns five tunnels and that only one of them will experience a collapse after 10 years of operation

Table 4 - Summary of the economic analysis for a facility with multiple tunnels

Item	**Cost**
Cost of implementing the preventive maintenance program after 10 years and 15 inspections performed	US$ 7.500.000,00
Cost of preventive repair assuming three interventions over a 10-year period	US$ 598.500,00
Cost of generation shutdowns for the three interventions for minor repairs.	US$ 3.168.000,00
TOTAL	**US$ 11.266.500,00**
Emergency repair cost and revenue loss as per the previous analysis	US$ 19.200.000,00
Savings achieved through the preventive maintenance program	**US$ 7.933.500**

Preventive maintenance provides savings of **USD 7,933,500** over a 10-year period while significantly reducing operational and financial risks. This approach not only prevents high repair costs but also ensures operational continuity and protects the integrity of infrastructure assets, proving advantageous even when only one tunnel presents a high risk of collapse.

5.3.1. Break-even point analysis for preventive maintenance with variable downtime (depending on collapse magnitude) for hydropower generation tunnels

Based on the economic analysis, which highlights the financial impact of collapses in hydraulic tunnels, the break-even point for justifying the economic implementation of a preventive maintenance program must consider the downtime t (in months).

In the given example, a 50 MW power plant with an average revenue of **USD 44 per MW generated** experienced an estimated loss of **USD 15,840,000** for **10 months of downtime**, corresponding to loss of

Monthly loss per MW = 31.680 USD /MW

To ensure that preventive maintenance is economically viable, the minimum capacity x (in MW) required to balance the program's cost is given by the equation

$$x = \frac{1.644.000}{31.680 \times \mathrm{t}}$$

Where **USD 1.644.000,00** represents the average preventive maintenance cost per tunnel over 10 years, based on the scenario analyzed.

For different downtime durations t (in months), the minimum required capacity x (in MW) needed to justify the preventive maintenance cost is presented in table 5.

Table 5 - minimum power capacity

Downtime	Minimum MW
10 Months	$x \approx 5.18$ MW
05 Months	$x \approx 10.37$ MW
02 Months	$x \approx 25.94$ MW
01 Month	$x \approx 51.89$ MW

Based on the economic analysis, it can be observed that, to justify the cost of the preventive maintenance program, the plant's minimum capacity x must increase as the downtime t decreases. Shorter downtimes require a higher installed capacity for preventive maintenance to be economically viable, avoiding substantial revenue losses and emergency repair costs detailed in the previous analysis.

5.3.2. Break-even point analysis for preventive maintenance in facilities with hydraulic tunnels for potable water supply.

For hydraulic tunnels used for water transfer or potable water supply, preventive maintenance is economically justified in almost all cases due to high costs and significant social impact associated with service interruptions.

With the average cost of preventive maintenance comparable to the value considered in the previous section, these tunnels incur significantly higher losses than those used for hydropower generation.

Considering a tunnel with a flow rate of 30 m^3/s and a treated water value of USD 0.5/m^3, the daily interruption cost of a hydraulic tunnel is calculated as follows

Daily Interruption Cost = 30m^3/s × 3600 s/h × 24h × 0,5 USD / m^3 = 1.296.000USD / day

To simplify the analysis, a 30-day downtime for a non-severe repair intervention is assumed, referencing a non-complex recovery operation. Therefore, the total interruption cost would be:

Interruption cost = 1.296.000 × 30 = ***38.880.000 USD.***

Additionally, **USD 199.500** must be added, representing the previously determined cost for a non-complex recovery intervention.

The price has been deliberately underestimated to adopt a more conservative approach, ensuring that the estimates remain cautious and account for potential variations or unforeseen factors.

In conclusion, for potable water transport tunnels, preventive maintenance is always an economically advantageous decision. It not only minimizes the risk of severe failures but also prevents the high costs associated with prolonged downtime and emergency recovery efforts, clearly justifying the continuous implementation of a preventive maintenance program.

6. Long Term Benefits of Preventive Maintenance

In addition to direct cost savings, preventive maintenance provides several tangible and intangible benefits that increase the long-term value of the structure:

- **Asset Valuation:** Tunnels with a history of regular inspections and monitoring are more valuable, especially in the event of an asset sale, as the buyer gains access to data on structural integrity and can trust the infrastructure’s quality and durability.
- **Insurance Premium Reduction:** Insurance companies require periodic inspections before assuming risks in large-scale projects. A preventive inspection program can significantly reduce insurance premiums, as structural risks are minimized.
- **Reputation and Social Responsibility:** The practice of preventive maintenance demonstrates a commitment to safety and operational continuity, strengthening the company’s image among investors, clients, and the community.

In the long run, the preventive maintenance program also contributes to the financial sustainability of the facility, ensuring the reliability and safety of the tunnel

7. DISCUSSION

The implementation of a preventive maintenance program in hydraulic tunnels brings significant improvements in operational safety and stability. Although the primary challenge lies in shifting the organizational mindset and fostering a prevention-oriented business culture, the benefits far outweigh the initial difficulties. By outsourcing specialized service providers, enterprises can conduct periodic inspections without the need for direct investments in equipment or in-house training, facilitating the adoption of the program.

Many facilities operating tunnels also manage dams and already follow the standard practice of conducting regular inspections to ensure the safety of these critical assets. Just as it is customary to perform routine dam inspections, tunnels should be continuously monitored, as both structures often belong to the same system and are equally essential for operational continuity and enterprise safety. Establishing a culture of preventive maintenance across the entire infrastructure, including tunnels, strengthens asset reliability and operational control.

The practical example discussed validates the importance of a preventive approach in detecting early signs of anomalies before they evolve into critical events, enabling more effective resource management and enhanced structural safety. This long-term perspective supports asset preservation and operational sustainability, ensuring system integrity and service continuity over time.

8. CONCLUSION

The economic analysis and case studies confirm the financial and operational feasibility, as well as the necessity, of implementing a preventive maintenance program for hydraulic tunnels through underwater inspections with ROV and Sonar. This approach enables the early detection and mitigation of deteriorating conditions before they escalate into critical issues, minimizing costs and losses while enhancing structural and operational safety.

Additionally, the economic and financial feasibility of the preventive maintenance program is validated even in facilities with multiple tunnels, where only one tunnel may pose a potential collapse risk. This scenario demonstrates that preventive maintenance offers substantial benefits, ensuring financial sustainability, operational continuity, and long-term infrastructure asset preservation.

For tunnels used in hydropower generation, the economic analysis reveals that as plant capacity increases, implementing a preventive maintenance program becomes even more crucial. However, preventive maintenance remains relevant and justifiable even for smaller-scale enterprises due to its long-term cost-effectiveness.

Regarding hydraulic tunnels used for potable water supply, the implementation of a preventive maintenance program is even more important. In addition to significant financial losses, an unexpected water supply interruption can cause severe social impacts.

In summary, a preventive maintenance program serves as a “check-up” for hydraulic tunnels, enabling proactive interventions before minor issues escalate into serious emergencies requiring costly repairs. This practice ensures financial sustainability, operational continuity, and the long-term preservation of infrastructure asset value and integrity.

9. BIBLIOGRAPHY

Guidicini, G. Mello, F. Carvalho, N. (2022). Patologia de túneis hidráulicos: acidentes e incidentes no Brasil.

Brox, D., Dendup. T., Namgyal, D. (2023). Correlation of ROV Observations with Actual Damage in the Tala Headrace Tunnel.

Brox, D. (2020). Hydroelectric Tunnel Inspections – Recommendations for Industry Practice.

Iannotta, F. Malak, D. Kennedy, J (2017). Inspeções e trabalhos subaquáticos através de ROV, apresentação de casos de sucesso.

Iannotta, F. (2018). Inspeção de túneis adutores através de tecnologia robótica rov (veículo subaquático operado remotamente)

CEDAE. Sistema de abastecimento de água da cidade de Rio de janeiro, com ênfase com no Guandu.

Fifth International Dam World Conference
PORTUGAL • LISBON • LNEC • APRIL 13-17, 2025
dam world 2025

AUTOMATED DEFECT CHANGE DETECTION AND QUANTIFICATION FOR LARGE DAMS AND SPILLWAYS – A PATHWAY TO DETERIORATION MODELLING

Joshua Fowler
Niricson

Javier Aparicio[1]
Niricson

ABSTRACT

In response to the 2017 Oroville spillway failure, dam regulators and asset owners have intensified efforts to assess conditions and identify performance and safety risks at spillway sites. Traditional spillway assessments rely on labor-intensive and subjective methods, such as rope-access inspections to map cracks and delamination. This paper explores the application of Artificial Intelligence (AI) and Machine Learning (ML) in dam safety, particularly for condition assessments, surveillance, and monitoring. The methodology leverages datasets from visual and thermal imagery, as well as acoustic sounding data, collected via Unmanned Aerial Vehicles (UAVs) equipped with advanced sensors.

The case study details data collection, analysis, and framework development using diverse platforms and techniques. The results, presented in a collaborative Geographical Information System (GIS), enable engineers to conduct detailed condition analyses using digitized defect data in 2D and 3D formats. This approach enhances inspection, monitoring, and maintenance decision-making, supporting a comprehensive asset management strategy. Establishing a high-resolution digital baseline allows precise change detection in subsequent surveys, aiding the development of deterioration models. Peer-reviewed and deployed in over 50 global projects, this technology enhances automated condition assessments for proactive maintenance and dam safety management.

This study focuses on large concrete spillways in North America, where an improved condition survey method has been deployed. By employing this innovative method, significant changes related to failure modes and defect mapping can be identified within three years. Consequently, this suggests that spillway structures should be monitored on a 3-year cycle rather than the conventional 5-year cycle. The method combines robotics (UAVs) and computer vision to map cracks, spalls, and delamination in spillway concrete.

The study evaluates the effectiveness of this condition survey method in tracking structural changes over time and compares its performance against traditional boots-on-the-ground inspections. Following an analysis of change detection accuracy and comparisons with conventional methods, the authors will discuss how these datasets empower asset owners to make cost-efficient maintenance decisions, create long-term condition records despite staff turnover, and extend the lifespan of critical infrastructure.

Keywords: Automated Defect Detection, Proactive Maintenance, Asset Deterioration Modelling, Detailed Condition Survey, AI-enhanced Delamination Mapping with Acoustic Soundings

[1]japaricio@niricson.com, Canada

1. INTRODUCTION

Hydropower assets and dams play a critical role in power generation and water storage. However, with many concrete dams built in the mid and early 20th century in the United States and Globally, a significant percentage are approaching the design life of a typical concrete structure. In fact, according to the ICOLD database (ICOLD, 2019), approximately 75% of American large dams were built by 1974. Due to age, deterioration can accelerate, making inspections – and corresponding maintenance/rehabilitation decisions – critically important to extend the asset life critically important.

To inspect structures, civil and structural engineers traditionally complete detailed condition assessments and inspections of large civil infrastructure, often mapping and quantifying visual cracks and spalls and non-visual drummy-concrete on as-built drawings or sketches with manual notes and photos and they also perform hammer tests as needed to identify delaminated concrete. The traditional visual inspection as depicted in Figure 1. and sounding (with a hammer) are still the commonly used techniques to detect and identify surface and subsurface defects in concrete structures. This process requires physical access to the structures and occasionally significant investment towards arranging temporary scaffoldings/permanent platforms, ladders, crane and basket, and snooper trucks.

Figure 1. Traditional Visual Inspection

Dam monitoring is of great importance for dam safety. Dam failures can cause catastrophic consequences for people and infrastructure downstream. In the 2021 Infrastructure Report

Card, the American Society of Civil Engineers rated Dam Infrastructure as a “D”, citing an increase in high-hazard-potential dams, a lack of investment, and heavy seasonal rains.[1]

Due to challenges with accessibility on some structures and the associated health and safety concerns with the traditional inspection process, a detailed digital condition survey has been developed. To improve the traditional inspection procedure, an Unmanned Aerial Vehicle (UAV) assisted structural health assessment can be utilized and the application of UAVs can allow coverage of large areas in a shorter duration and can also be pre-programmed to inspect a wide variety of structures autonomously. Inspection instruments such as Optical Cameras, Thermal Cameras, and other sensors are mounted on UAVs to transmit information in real-time (or save it on the memory cards onboard) thereby facilitating inspection from the ground station. The unique benefit is that digitization of the entire monitoring activity has widened the scope for easy storage, sharing, better accessibility to end user and minimizing the potential of human error. Another advantage is that the whole inspection technique is cost-effective [2] as the entire structure could be inspected automatically using cost-effective UAV-images and other data.

However, there are also limitations to UAV-based condition assessments. For example, compared to traditional inspections, UAVs cannot operate under rain, and cannot remove debris, vegetation, or other obstructions that may block the camera’s view from inspection. In addition, weather is a significant factor, similar to traditional inspections. For example, UAVs have limitations for flying in windy conditions greater than 20km/h, meaningful thermal data requires optimal temperature fluctuations throughout the day or sufficient solar loading to pick up on delamination data, and finally, high-quality optical/visual data will be highly dependent on consistent lighting conditions (i.e. no areas with dark shadows next to very light areas)

Despite these limitations, in recent years, there has been significant progress in UAV research and application for structural health monitoring, primarily focusing on image processing and defect detection. This work includes, but is not limited to, the use of UAVs to collect images and convert them into a 3-dimensional imagery model, use of image processing to detect the surface deteriorations like cracks, discoloration, efflorescence, leaching, and spalling, and crack identification strategy by combining hybrid image processing with UAV technology.

However, there is a significant knowledge gap in terms of quantifying surface and subsurface defects accurately and practically tracking the changes over time using currently available UAV-based technique in a field environment. Additionally, the application of a UAV-based thermal and acoustic sensors in a field environment for hydropower structures is relatively unexplored. Unique software solutions paired with patented data collection technology can help asset owners not only detect defects, but also quantify those defects using those sensors.

[1] Dams 2021 Infrastructure Report Card. American Society of Civil Engineers. December 31, 2020.

The data collection technology and application described in this paper uses various advanced built- in sensors (optical, thermal, and acoustic sensors) to collect three types of primary datasets as shown in Figure 2.

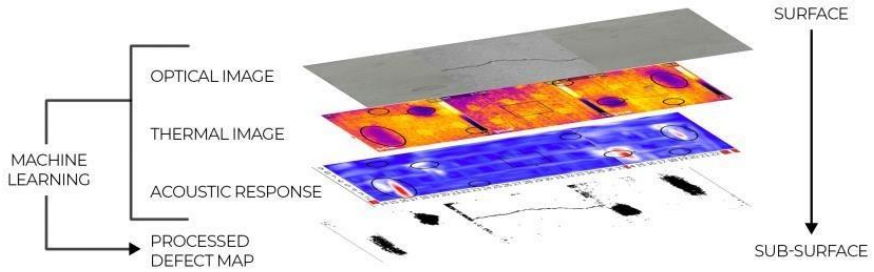

Figure 2. UAV-based Multi-layered Data Collection

In addition to these three primary datasets, the system collects positional information, camera angle, speed of the drone, acquisition distance, altitude etc. to correlate the defects not only to global positioning system but also on a local coordinate system. This additional information is stored to inspect structures on a periodic basis to detect and quantify a small change in the defects over time. The system can be mostly integrated into autonomous flights to avoid manual flight planning during the inspections and streamline the periodic inspection program for the asset.

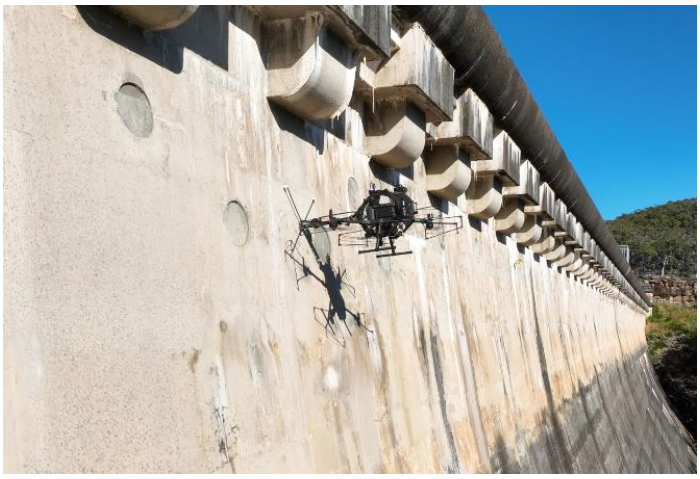

Figure 3. Utilization of DRONIC™, NCX in data collection

The optical imagery data collected is fed into a machine learning algorithm to assist in automatically mapping visual defects (i.e. cracks, spalls). Optical images allow for detection and quantification of surface defects such as cracks and spalls, and an image-based machine learning algorithm allows for automated defect identification and quantification. Infrared

sensors allow for detection of subsurface delamination, moisture ingress, surface vegetation growth etc. for up to 50 mm (requires clear sunshine) from the concrete surface. Acoustic sensors can detect and quantify delamination or voids up to 100 mm with high confidence and beyond 100 mm with low confidence. The digital condition assessment method enables the ability to build and further train a deep learning model to detect and quantify defects automatically. The model leverages a convolutional neural network (CNN)4, to train a computer using millions of images captured from concrete water control structures around the world. Following the machine's inferencing on the imagery, structural engineers manually review the inferenced data output to ensure the accuracy.5 Any false positives and negatives are properly addressed by the engineer such that defects are properly mapped on the structure up to 95% accuracy of identifying all defects as shown in Figure 4.

All data gathered via this methodology is QA/QC'd on site to ensure various teams can successfully process the data. The Collected data is reviewed and evaluated onsite and pre-project completion to minimize blurring and ensure high data accuracy and quality. These factors directly impact the creation of the 3D model. Before delivering asset's 3D Model, a QC checklist is filled out to ensure absolute accuracy is within the defined thresholds. The methodology strives to correct any image quality issues pre-emptively, therefore the Data Collection team checks collected data on-site and is willing to recollect the data when deemed necessary. Data redundancy and collection is encouraged at multiple angles to the structure of interest to gain more flexibility for processing. Additionally, an image quality score is calculated for all photos imported into photogrammetry software using methodology's data quality script.

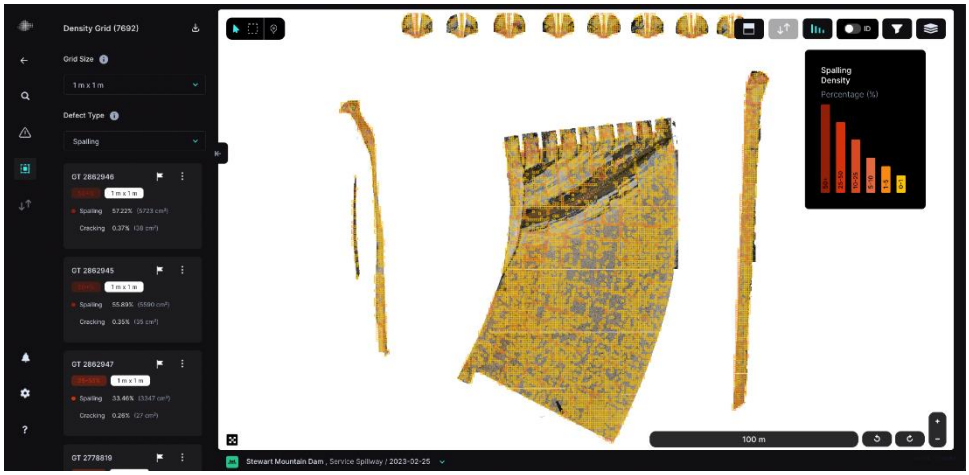

Figure 4. Digital Defect Detection and Quantification

The digital condition assessment technique is not limited to detection and quantification of defects, but also allows for tracking year over year changes automatically in order to build a

predictive deterioration model of concrete assets to provide life cycle assessment as shown in Figure 3. While many factors go into decisions for maintenance and rehabilitation of an asset, including organizational priorities as well as non-condition related factors such as failure consequence to life and economics, this predictive model can be a useful for risk analysis, maintenance or rehabilitation planning for concrete dams and appurtenant structures.

By having each defect quantified, asset owners can estimate current maintenance by deploying multiple surveys. Multiple surveys allow for a change detection and identify new quantities of defects (either increment or new) on their structures, thereby helping them understand and monitor deterioration rates. These quantities – with some level of error – can be extrapolated into the future to estimate future potential needs based on how certain quantities (crack/spall/other defects surface areas) are changing on a structure through time. Although, dam safety and dam behavior are complex areas and changing condition of different defects can't be easily predicted or extrapolated with a simple model, it may be possible to predict the growth of certain types of defects with reasonable accuracy if several years of change detection data is gathered.

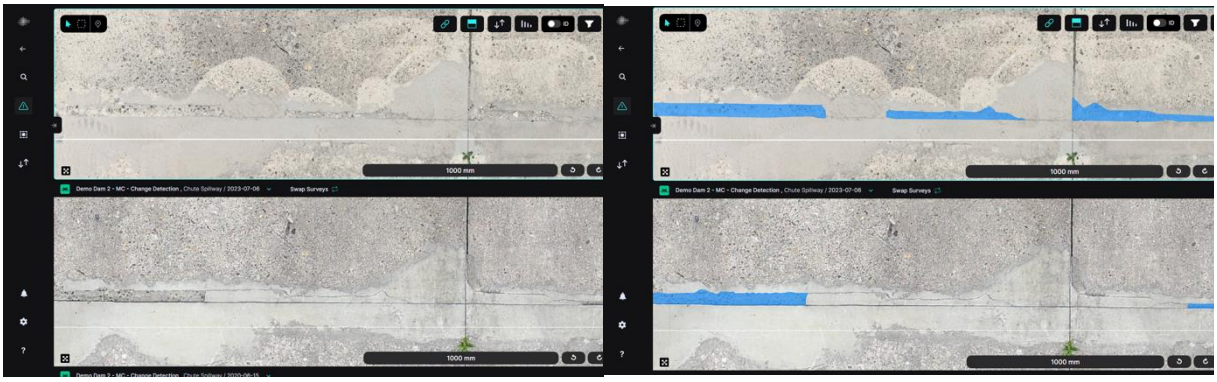

Figure 5. Change Detection from two different condition surveys (3 years apart)

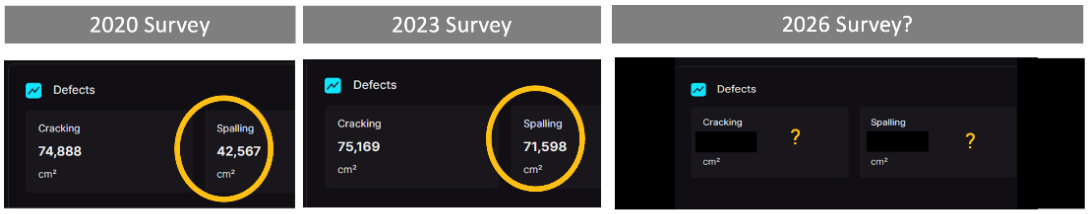

Past Cost to repair	Current Cost to repair	Deterioration Quantities	Future Cost to repair
Crack -> $11,250	Crack -> $11,280	Cracking: ~0.4% Growth	Crack~$11,325
Spall -> $138,125	Spall -> $232,700	Quantities Trajectory: Spalling: ~68.2% Growth	Spall~$391,401
=$149,375*	=$243,980*	Cost Trajectory: ~31.5%	= ~$402,726*

Figure 6. Example Prediction Model Based on Repeated Condition surveys.

2. REPEATABLE DATA COLLECTION ON LARGE SPILLWAY SITES

In Order to create a repeatable data collection workflow on large spillway sites, multiple steps are followed including choosing the appropriate UAV platform that can be pre-programmed using a flight planning software. The first step is to obtain a lower resolution- about 1cm Ground Sampling Distance (GSD) imagery for the entire site within the red boundary as shown in Figure 7.

Figure 7. High level 1 cm GSD Model of the entire site

This high level (1 cm) model allows for a pre-programmed flight planning. As can be seen in Figure 4, the visual/optical datasets are collected using preprogram flights where these green dots represent the location of where the images are taken. This way all the future UAV flights can be executed in an efficient manner without having to build the model again.

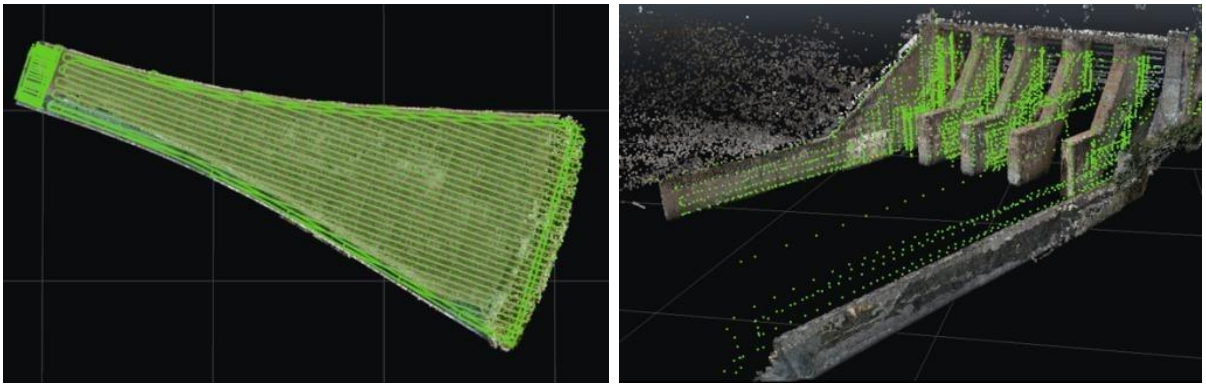

Figure 8. High Res RGB Data Collection Locations for Concrete Spillways

The second step is to collect the optical images at much higher resolution, about 1 mm GSD, using the preprogrammed flights shown in Figure 8. The spillway imagery is captured using a DJI M300 RTK with a P1 35mm camera, achieving a 1mm GSD as shown in below Figure 9.

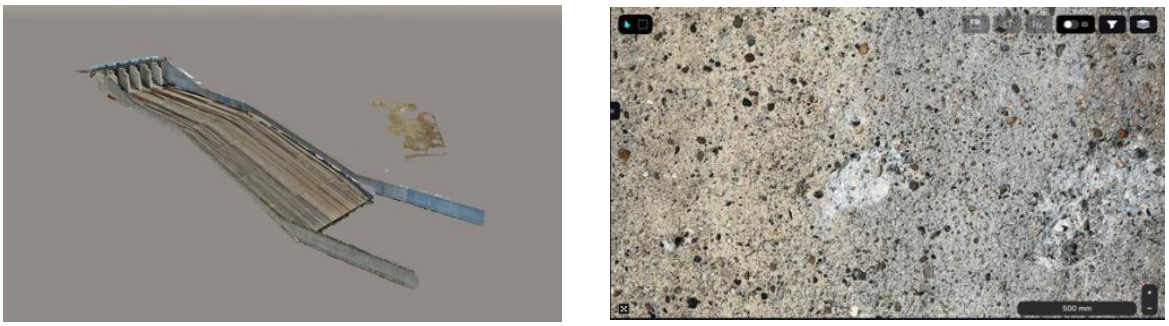

Figure 9. High resolution model (1 mm GSD) and the orthomosaic for defects detection and quantification

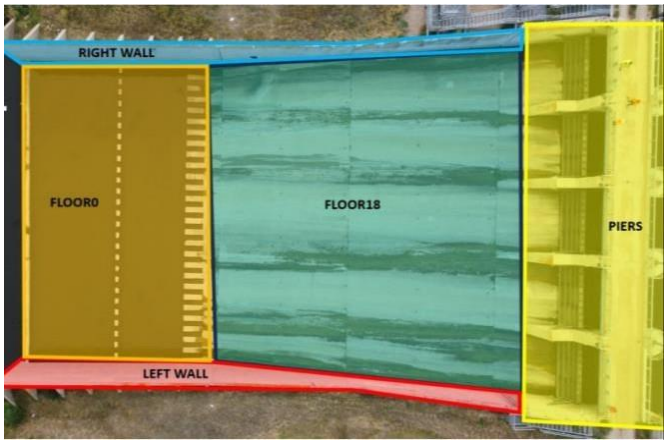

Figure 10. Labelling Spillway components for Flight planning

Different sections of the spillway are captured using various flight methods and exposure settings. In this example, FLOOR0 was captured using manual flights. Data collection was done after sunset for even lighting. Automated UgCS (flight planning software) flight paths were used for FLOOR18, as shown above in Figure 10. Data collection was performed during overcast conditions to minimize shadows.

The left wall was collected in sunny to slightly overcast conditions. Additional manual passes were flown to capture the bottom of the wall. The imagery of the floor/wall intersection was collected in sunny to slightly overcast conditions. The flight path was designed for a constant distance of 8 m from the floor/wall intersection.

Due to the Dam facing Northeast, the Right wall was always in shadow. To improve exposure, the section was flown with exposure values locked at f/5.6. Camera tilt was set to 10 degrees downward to better capture the top of the wall during higher flight passes, and to better capture

the wall/floor intersection for low flight passes. The piers were manually flown at a 0.5 mm GSD. This was because the UAV was flown tightly in between the piers to be able to collect nadir shots of the pier sides as much as possible, avoiding oblique shots angled in at the pier sides.

Image A –Approximate 10 m x 10 m view with thermal camera

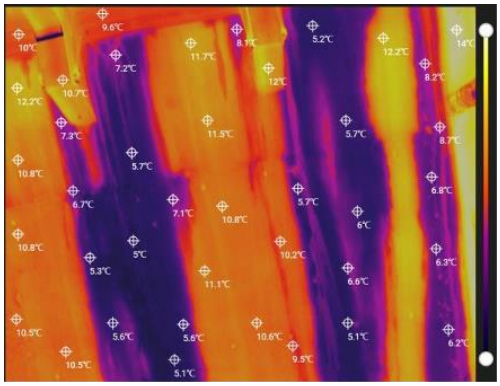

Image B – Entire view of the spillway with thermal camera

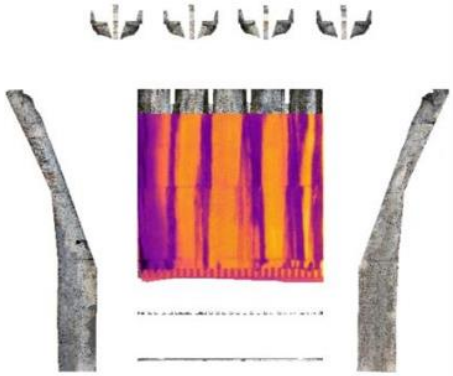

Figure 11. Thermal data collection from spillway floor slab

Thermal imagery is collected from the spillway floor section at 3cm GSD with 90/90 overlap.

Acoustic data was collected on the spillway floor (Floor27 section) using a proprietary NDX acoustic sensor. Acoustic data points were collected from the horizontal and vertical joints. In the example spillway above, there were 14 horizontal slab joints on the main floor section.

Figure 12. Acoustic data collection from spillway floor slab

3. DATA PROCESSING USING MACHINE LEARNING AND ANALYTICS

Once the high resolution optical, thermal, and acoustic layers of data are collected on site, they are then stitched and converted into 3D models and 2D projections (except the acoustic/sounding data) for further analysis. 2D projections of the structures are then imported into our machine learning platform for automated defect identification and mapping.

The results are loaded into a proprietary defect mapping platform, and overlayed on top of each other. By having distinct defect type layers, asset owners/civil engineers/inspectors can get an improved understanding of defect progression compared to only having a single layer that considers all defects as similar. Knowing the difference between a gradually widening crack and a crack that has deteriorated completely into spalling can can help asset owners perform the appropriate preventative maintenance. Each individual defect is quantified with a set of metrics and assigned a unique identifier that tracks the current state of deterioration.

The example criteria is given below,

Green: average width < a mm
Yellow: a mm <= average width <= b
mm Red: b mm < average width

Where a and b are the threshold values of the average crack width.

This allows for year-to-year comparisons following subsequent surveys. In the figure below, you can see examples of just a few of the defect layers:

Asset Dashboard Including Defect Maps **Distribution of Delamination Map**

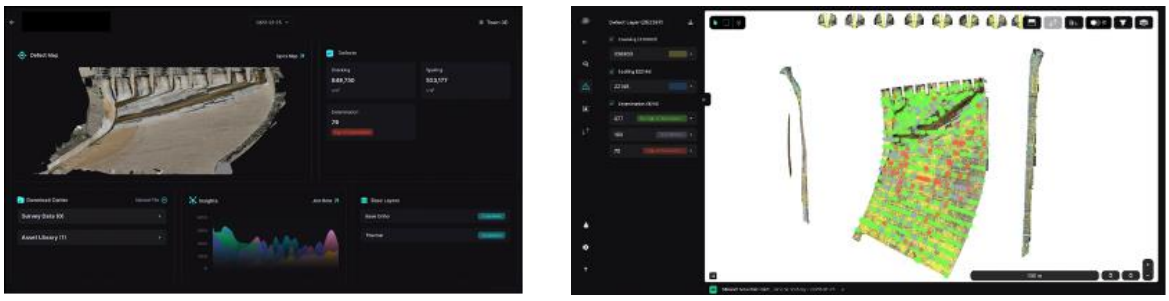

Figure 13. Example of multi-layered defects visualization along with the quantification

Figure 14. Example of processed acoustic/sounding data from a spillway floor slab

The acoustic soundings of concrete responses to the tapping with UAV mounted hammer are classified using a multi-step process which generates various feature values of the response that site staff has validated to be indicative of either delaminated or solid concrete. The results are displayed in three colors as shown in the Figure 14.

Green – Sound concrete
Yellow – Unconfirmed/monitoring suggested
Red – Delaminated

These different features can be based in the time domain, frequency domain, or 3D space that contains both. These feature values are then combined into a high- dimensional space and machine learning methods are used to produce an overall value that determines the delamination status of the concrete.

To validate our technology, we have created a still growing acoustic ground truth database. The current classification accurate rate of sound concrete is over 99%, and delamination over 60%. These values are calculated using test and train concrete responses from separate structures from our database.

4. VALIDATION OF THE RESULTS

After the UAV based scanning and data processing, two technicians were sent to access the spillway and collect ground truth data to verify the results obtained by Machine Learning and Acoustic Signal processing. As can be seen the results were in line with the traditional method.

Crack Width (Traditional Method)

Width = 2 mm

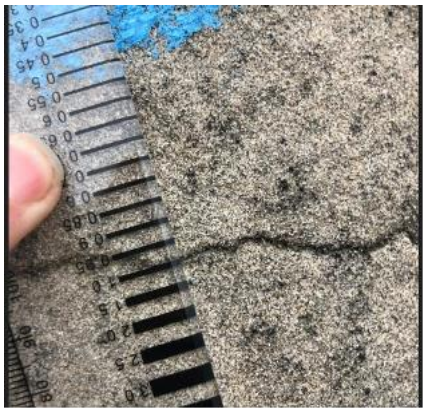

Width = 1 mm

Width = 2.5 mm

Crack width using Photogrammetry/Artificial Intelligence

Width = 1.9 mm

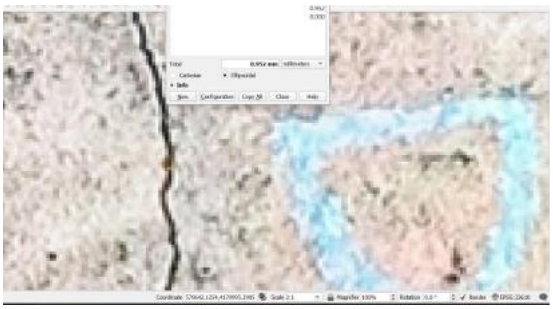

Width = 0.952 mm

Width = 2.43 mm

Figure 15. Ground Truth Data Collection and Validation for Cracks

Using the thermal dataset (Figure 11) delamination was detected (hotter area in the image) with a significant temperature difference.

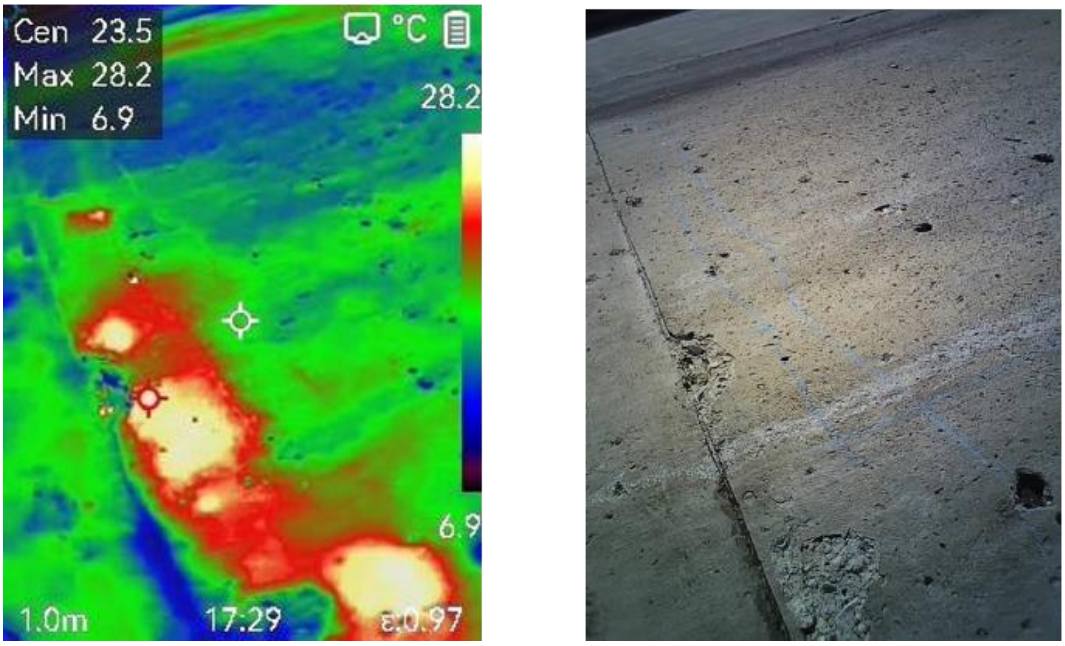

Figure 16. Ground Truth Data Collection and Validation for Delamination using Thermal

For sounding, delamination ground truth data was collected using a hammer test to approximately define the boundary between the delaminated and sound concrete. Then at least one mark was made on both sides of the boundary. When possible, this ground truth was confirmed by an external inspector which is the case for over half of the current database concrete responses for this specific project. After this, a response collection was completed with our concrete sounding devices and classification accuracy results calculated. An example of a ground truth collection location is shown in the figure below, with the delamination boundary and the marks chalked on the surface.

Figure 17. Ground Truth Data Collection and Validation for Delamination using Acoustics/sounding

5. CONCLUSIONS

The process discussed in this paper for digital condition surveys meaningfully contributes to the owners' surveillance and maintenance program, particularly in the context of aging dams where surveillance and maintenance become increasingly crucial. While not all concrete defects are important and not all dam safety concerns are concrete related, some potential failure modes and dam safety risks are associated with concrete – including spalling along joints and slab offsets. Even if known defects, such as cracks, do not currently present structural risks, susceptibility to cyclic loading, weathering and deterioration can exacerbate these defects over time, eventually posing safety concerns. Therefore, it is imperative for the owner to possess comprehensive knowledge of the current condition to inform what areas to observe and where to focus attention.

In the case of large dams like New Bullards Bar Dam, conventional manual observation methods are impractical due to limitations in both size and accessibility. However, UAVs in conjunction with AI processing enables owners to swiftly and efficiently establish baseline data for future comparisons. The high- resolution data obtained, down to the millimeter scale, empowers owners to make more informed decisions regarding their assets. The processed defects data can be utilized in the multiple applications summarized below:

- Integration with GIS and CAD for maintenance planning and structural analysis.
- Integration with CAD for Computational Fluid Dynamics (CFD) analysis.
- Integration into the owner’s dam safety surveillance and monitoring program (DSSMP) to allow dam safety professionals greater certainty when evaluating the structure.
- Utilization of data to estimate quantities for repairs which can be utilized for tendering projects as well as long term capital and maintenance planning.
- Identification of potential failure modes, such as through-cracks on piers, spillway slab offsets, or delamination/spalling along joints.
- Application as a general digital twin for integrating other data, including instrumentation data and Building Information Modeling (BIM).
- Prioritization or complementation of subsurface analyses, such as Ground- Penetrating Radar (GPR) or coring work.
- Documentation of digital baseline and enhanced year-to-year referencing for preventive maintenance.

Additionally, digitizing these defects and allowing remote collaboration will ensure owners maintain a detailed and ever-growing database on the defects and the monitoring results. Furthermore, the obtained results can serve the purpose of validating or refining asset models as many owners are often without accurate as-built records of their assets. They also offer

insights into whether correlations can be established between concentrated defect areas observed in the field and predicted outcomes.

6. REFERENCES

[1] D. Ribeiro et al, "Remote inspection of RC structures using unmanned aerial vehicles and heuristic image processing," Engineering Failure Analysis, vol. 117, pp. 104813, 2020.

[2] E. Ridolfi et al, "Accuracy Analysis of a Dam Model from Drone Surveys," Sensors (Basel, Switzerland), vol. 17, (8), pp. 1777, 2017.

[3] Sankarasrinivasan, S., Balasubramanian, E., Karthik, K., Chandrasekar, U. & Gupta, R., "Health Monitoring of Civil Structures with Integrated UAV and Image Processing System", Procedia Computer Science, vol. 54, pp. 508-515, 2015.

[4] Pragalath, H., Seshathiri, S., Rathod, H., Esakki, B., and Gupta, R., "Deterioration Assessment of Infrastructure Using Fuzzy Logic and Image Processing Algorithm", Journal of Performance of Constructed Facilities, vol. 32, no. 2, pp. 4018009, 2018.

[5] Kim, H., Lee, J., Ahn, E., Cho, S., Shin, M. & Sim, S., "Concrete Crack Identification Using a UAV Incorporating Hybrid Image Processing", Sensors (Basel, Switzerland), vol. 17, no. 9, pp. 2052, 2017.

[6] M. A. Mohammed, Z. Han and Y. Li, "Exploring the Detection Accuracy of Concrete Cracks Using Various CNN Models," Advances in Materials Science and Engineering, vol. 2021, pp. 1-11, 2021.

[7] Z. Qu et al, "Concrete surface crack detection with the improved pre-extraction and the second percolation processing methods," Plos One, vol. 13, (7), pp. e0201109-e0201109, 2018.

[8] T. Nishikawa et al, "Concrete Crack Detection by Multiple Sequential Image Filtering," Computer- Aided Civil and Infrastructure Engineering, vol. 27, (1), pp. 29- 47, 2012.

[9] J. R. Balbin et al, "Pattern recognition of concrete surface cracks and defects using integrated image processing algorithms," in 2017, DOI: 10.1117/12.2280933.

[10] K. S. Sim, Y. Y. Kho and C. P. Tso, "Application of contrast enhancement bilateral closing top-hat otsu thresholding (CEBICTOT) technique on crack images," in 2008.

[11] T. Yamaguchi and S. Hashimoto, "Fast crack detection method for large-size concrete surface images using percolation-based image processing," Machine Vision and Applications, vol. 21, (5), pp. 797-809, 2010.

Fifth International Dam World Conference
PORTUGAL • LISBON • LNEC • APRIL 13-17, 2025
dam world 2025

A STUDY ON THE INFLUENCE OF THE RESERVOIR WATER LEVEL ON THE SEISMIC PERFORMANCE OF A LARGE DOUBLE CURVATURE ARCH DAM

Sérgio Oliveira[1]	Rafael Ramos	André Alegre	Jorge Proença	Paulo Mendes	João Silva	Carlos Serra
National Laboratory for Civil Engineering (LNEC)	CERIS Instituto Superior Técnico (IST)	Kinemetrics Inc.	CERIS - Instituto Superior Técnico (IST)	Lisbon School of Engineering (ISEL-IPL)	National Laboratory for Civil Engineering (LNEC)	National Laboratory for Civil Engineering (LNEC)

ABSTRACT

This paper presents a study on the seismic performance of a large double-curvature arch dam with an horizontal crack in the downstream face, considering different reservoir scenarios to assess the effect of the water level on the non-linear seismic behaviour of the structure. The computational model of the arch dam-reservoir-foundation system is calibrated based on experimental data, including static observation and ambient vibration results, for different reservoir water levels. The computer simulations are carried out using the 3D finite element program DamDySSA5.0, developed by the authors for linear and non-linear dynamic analysis of dam-foundation-reservoir systems. In this program, the non-linear seismic response is computed in an innovative way using a time domain formulation combined with a stress-transfer technique, simultaneously considering (a) a joint constitutive model to simulate the effects due to the opening/closing and sliding of joints and cracks, and (b) a damage constitutive model for concrete with softening and two independent damage variables, to simulate tensile and compressive damage. In this study, the non-linear seismic analyses are carried out for a load combination involving the self-weight, the hydrostatic pressure and a seismic action generated to simulate a high-intensity earthquake. Results are presented for two reservoir water levels: i) full reservoir (water at the crest level of the central surface spillway) and ii) 2 m above a major horizontal crack visible at the dam downstream face (located 25 m below the central spillway crest). The seismic behaviour of the dam is analysed for two different values of the reservoir water level, comparing displacement and stress fields in the dam body. The results show the influence of the reservoir water level on the structural seismic response of large arch dams.

Keywords: Arch dams, Non-linear seismic analysis, Water level influence, Finite element model, Joint movements

[1] soliveira@lnec.pt, Portugal

1. INTRODUCTION

Large concrete dams play a vital role in the management of water resources, ensuring the supply of water to populations, the production of renewable energy and flood control. Many of the existing dams have been in operation for decades and were built in areas of medium/high seismicity, so they need a proper assessment of their seismic safety [1], taking into account their current state of deterioration and the fact that the seismic risk characterization may change over time in the dam area.

A major factor influencing dam's dynamic behaviour is the reservoir water level [1]. Even small variations in the water level can significantly affect the hydrostatic pressures in the dam body, causing changes in the dam's structural response, stress distribution and overall static and dynamic behaviour. Previous studies, on the linear seismic response of concrete arch dams considering different water levels and seismic scenarios [2,3], shown that the water level can have an impressive impact on the dam seismic response.

Dams that present signs of deterioration or evident pathologies, such as visible cracks, need a deeper insight on the effects of water level variations, to preserve their operational and seismic safety performance. Particularly in arch dams, intense seismic events can cause the existing cracks and vertical contraction joints to experience cyclic opening and closing events leading to internal stress distribution processes [4]. At the same time, exceeding the tensile strength of the materials will result in severe crack formation, as well as surpassing the compressive strength capacity will lead to localised crushing of the concrete, leading to structural collapse [5]. Consequently, these phenomena represent critical aspects that must be taken into account in the seismic performance analysis of arch dams.

This study focuses on the Bouçã dam, a 70-year-old double curvature concrete arch dam in Portugal, with small signs of swelling and a visible crack in the downstream face since the first filling [6], to investigate how reservoir water level variations affect its non-linear seismic behaviour.

Recent studies were made regarding the seismic safety verification of the Bouça dam [7,8] considering the regular water level (around 175m, Fig.2d) present in the reservoir. The present study will enhance the effect of the water level variations during a seismic event. By concentrating on the influence of the water levels in the seismic response of the Bouçã Dam, this research aims to provide valuable insights into the dam behaviour under operational conditions, to help in the monitoring and maintenance strategies, ensuring the long-term safety of the dam.

2. CASE STUDY: BOUÇÃ DAM

The Bouçã dam (Fig. 1) is a slender double-curvature arch dam located on the Zêzere river, in Pedrógão Grande (Portugal). In operation since 1955, the dam has a maximum height of 70 m above its foundation and a crest length of 175 m between embankments. The dam thickness, ranges from 7 m at the base to 2 m at the crest. The thickness of the dam varies between 7 m at the base and 2 m at the top. Structurally, the dam is composed of 17 blocks separated by vertical contraction joints [7].

The dam crest features a Creager-profile spillway designed for a nominal head of 3 m. This spillway allows water to flow efficiently over the dam's crest, away from the downstream face [6]. The crest itself is segmented into three sections, with the central section located at an elevation of 175 m, corresponding to the full reservoir level, and extending approximately 45 m in length. A significant horizontal crack has developed on the downstream face, due to thermal effects [6].

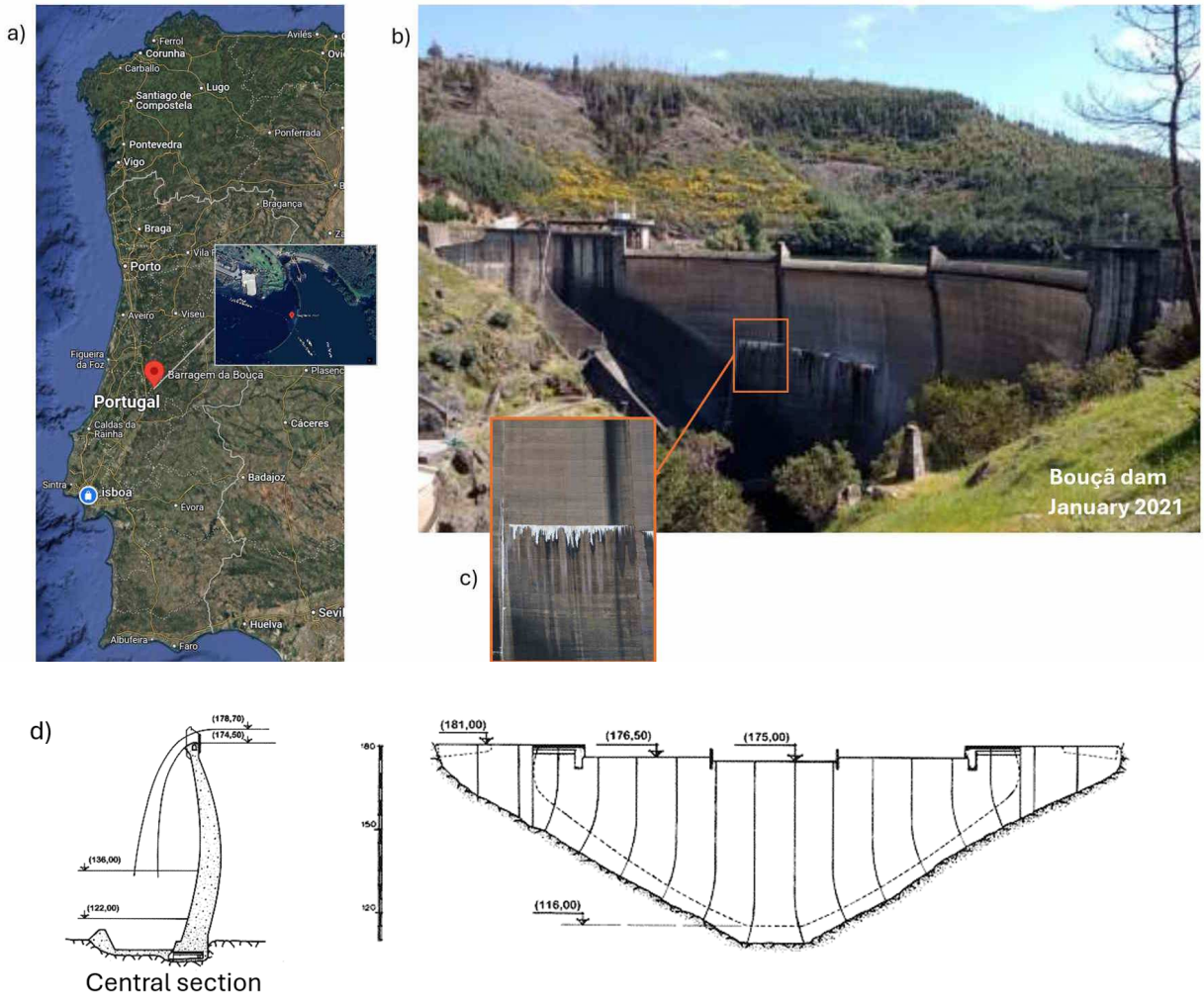

Fig. 1 – Bouçã dam. a) Dam location: Zêzere river, Pedrógão Grande, Portugal; b) Dam view from downstream; c) Horizontal crack detailed view; d) Central cantilever and front view.

2.1. Dam Monitoring System

The Bouçã dam is equipped with a classic structural monitoring system (Fig.2) designed in the construction phase. Horizontal and vertical displacements are measured using the classic geodesic method, ensuring the recording of the dam displacements over time Fig.2b.

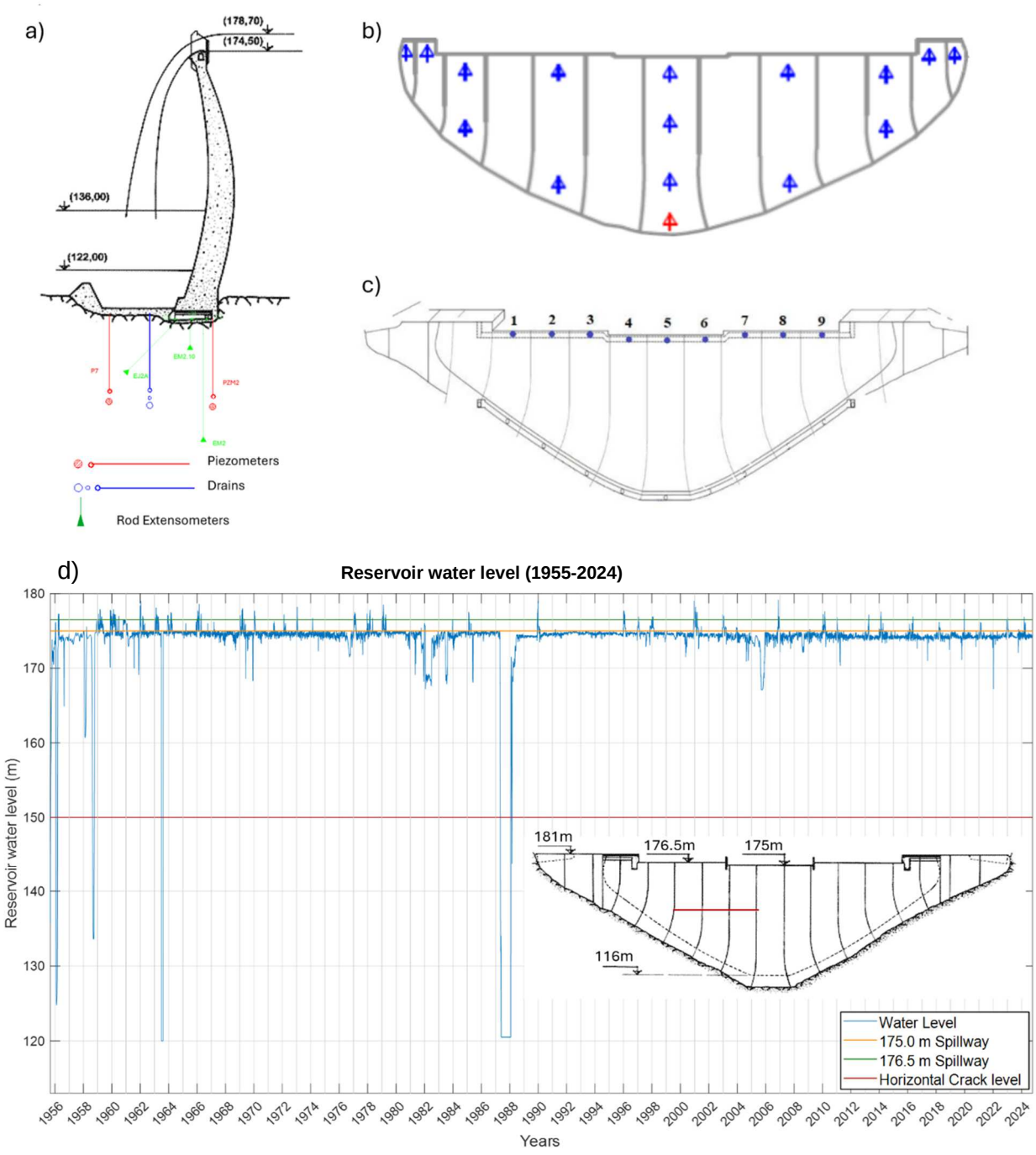

Fig. 2 – Bouçã dam monitoring system. a) Central cantilever cross section with piezometer, drains and rod extensometers; b) geodetic marks; c) Accelerometers for ambient vibration test (performed in 2018); d) Reservoir water level variation

Notably, as mentioned, a significant horizontal crack has developed on the downstream face, situated on a horizontal concreting joint. Previous reports [6,7] also state that a crack at the dam-foundation interface occurred during the first filling of the reservoir, in the upstream face, due to the water pressure, that created high vertical tensile stresses in the dam. Due to those pathologies, the dam's observation system has been improved over the years (Fig.2a and Fig.2b). Key upgrades include the addition of drainage systems, piezometers, and rod extensometers to monitor the dam-foundation's behaviour. Also, the water level is monitored from the initial stage of the first filling, as shown in Fig.2d.

The dam does not have a continuous vibration monitoring system, so an ambient vibration test was conducted on June 12th, 2018, to identify the dam's natural frequencies and corresponding vibration modes [9]. For this test, 9 uniaxial accelerometers were installed along the dam crest (Fig.2c) to measure accelerations in the radial direction, providing valuable information on the dynamic characteristics of the dam.

3. 3D FINITE ELEMENT MODEL DEFINITION

The monitoring system installed at the Bouçã dam provides valuable insight into the dam's structural behaviour. It is essential to create a 3D finite element model that reproduces the observed behaviour of the dam in order to carry out parametric studies of the dam's behaviour, computationally. This chapter will present the 3DFE model, as well as *DamDySSA5.0*, the finite element program developed by the authors to study the non-linear seismic behaviour of concrete dams.

3.1. 3DFE Model

The development of the 3D finite element model for the Bouçã Dam was based on the original design equations and drawings, as detailed in historical reports from LNEC [7, 8, 9]. The 3DFE model took into consideration key structural features such as vertical contraction joints, a visible horizontal crack on the downstream face, and the discontinuity at the dam-foundation interface. The dam mesh contains hexahedral elements with 20 nodes (serendipity) and 27 Gauss points, while interface elements with 16 nodes and 9 Gauss points are used to model the joints behaviour. In total, the dam body contains 960 elements and for the foundation it is considered 378 elements (Fig. 3). The reservoir was considered using the proposed Westergaard method of associated water masses to the dam body, with a reduction factor of 50% (CR_{MAA}=0.5) to account the curvature and flexibility of the dam.

The mechanical properties of the materials were selected to reflect the current conditions of the dam, approximately 70 years after construction [7]. For the dam's concrete body, the elasticity modulus considered was E = 37 GPa, calculated using a concrete creep function

based on the Bazant and Panula model [13]. The rock foundation was assumed to be homogeneous, with an elasticity modulus E_{found} = 15 GPa and a Poisson's ratio ν=0.2.

To account for non-linear structural behaviour, the model included detailed characterisation of the joint properties, such as normal and shear stiffness (K_N and K_T), cohesion (c), and friction angle (Φ). Additionally, the concrete's damage parameters were defined, including tensile strength (f_t), compressive strength (f_c), fracture energy (G_f), and ultimate compressive strain (ε_u). These properties ensure that the model can simulate the complex non-linear phenomena occurring in the dam during seismic events, providing a comprehensive representation of the dam's structural dynamics.

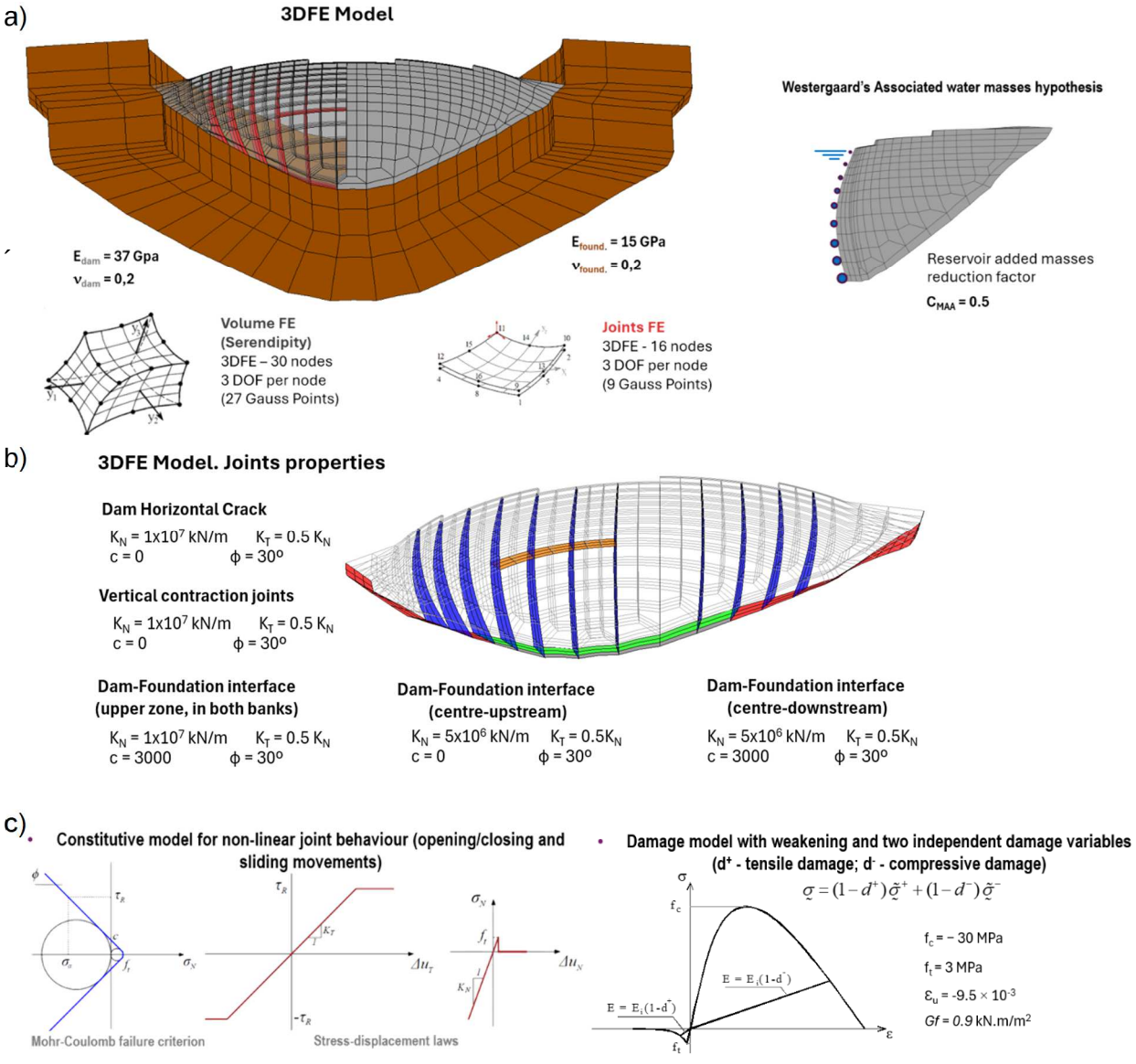

Fig. 3 – 3DFE model. a) Discretization, materials properties and FE type used; b) Joints definition by location in the 3D model; c) Constitutive models for non-linear joints behaviour and concrete damage model with two independent variables (tension and compression).

For the concrete damage model, it was used with tensile strength f_t = 3 MPa, fracture energy G_f = 0.9 kN.m/m^2, compressive strength f_c = -30 MPa, and ultimate strain ε_u = - 9.5 x 10^{-3}. For the vertical and horizontal joints, a constitutive model was adopted with a normal stiffness K_N = 1 x 10^7 kN/m, tangential stiffness K_T = 0.5 x K_N, cohesion c = 0, and a friction angle Φ = 30º. In the dam-foundation interface (upper zone and centre-downstream face) it was used a cohesion c = 3000, in order to restrain the base movements (sliding effect reduction) while the centre-upstream face considered cohesion c = 0. Also, for the central blocks of the dam (from upstream to downstream) it was considered a reduction of the normal stiffness to K_N = 5 x 10^6 kN/m, tangential stiffness K_T = 0.5 x K_N.

3.2. *DamDySSA 5.0*: 3DFE program for Linear and Non-Linear dynamic analysis

In this study, the finite element programme *DamDySSA5.0* (Fig. 4) was employed for numerical simulations. Developed over several years by the authors team [14,15], *DamDySSA5.0* is a three-dimensional finite element software designed for the static and dynamic analysis of concrete dams. It comprises modules for linear and non-linear static analysis, modal analysis, and both linear and non-linear seismic analysis.

The reservoir simulation in *DamDySSA5.0* can be approached through two methods: (i) employing the classical added water mass model, based on Westergaard's hydrodynamic pressures solution [16], which includes a reduction factor for arch dams to account for the effects of added water mass in a non-vertical and flexible face; or (ii) using pressure-based fluid finite elements for the discretisation of the reservoir, thereby enabling the simulation of dam-reservoir dynamic interaction and the propagation of pressure waves in the water[17].

The foundation is modelled as a massless system, represented by a condensed stiffness matrix and a proportional damping matrix applied at the nodes of the dam-rock interface. Seismic loading is applied directly at the base of the dam, assuming uniform ground motion.

The non-linear seismic analysis is conducted using a time integration method based on the Newmark algorithm to solve the dynamic equations describing the dam-foundation-reservoir system [15]. The non-linear simulation combines the time integration method with an iterative stress-transfer technique that consider: (i) a constitutive joint model based on the Mohr-Coulomb failure criterion, which utilises normal and shear stress-displacement laws to simulate joint opening, closing, and sliding; and (ii) an isotropic damage model with softening, characterised by two independent damage variables that describe the concrete behaviour up to failure under both tension and compression [18,19].

This methodology enables a detailed analysis of the static and dynamic responses of concrete dams under various loading conditions, including seismic events.

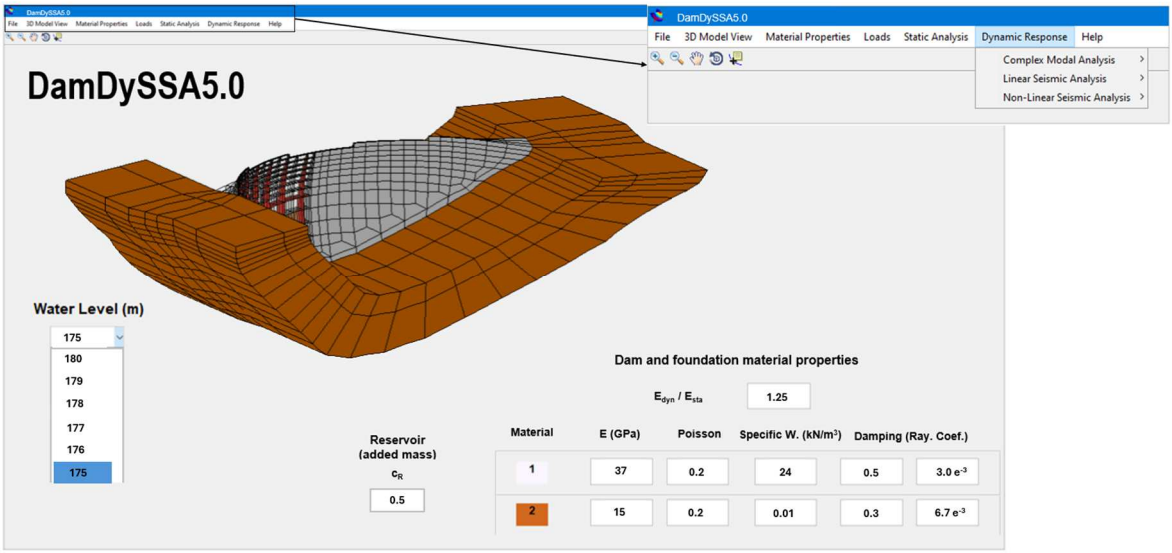

Fig. 4 – DamDySSa5.0. User interface layout

3.3. Dam behaviour under static loads. Comparison between monitoring data and FEM results

To calibrate and validate the 3D finite element model of the Bouçã Dam, the static response (Fig.5) was simulated under a load combination comprising self-weight (SW) and hydrostatic pressure (HP175) for a full reservoir scenario, with water reaching the crest of the central section at elevation 175 m. The simulation results were compared with the observed data, measured using geodetic marks (Fig2b).

The static analysis was performed using the model shown in Fig. 3, which included vertical joints, a horizontal crack, and the dam-foundation discontinuity. The results presented in Fig.5 demonstrated that the computed displacement at the central cantilever section, near elevation 170 m, was around 16 mm, matching with the observed data from geodesy, during the refilling of the reservoir after treatments made on the foundation due to high vertical stresses in the dam at the dam-foundation interface, in 1987.

It should also be noted that no vertical stresses occur upstream, near the dam-foundation interface, due to the release of stresses induced by the opening of the discontinuity at the base.

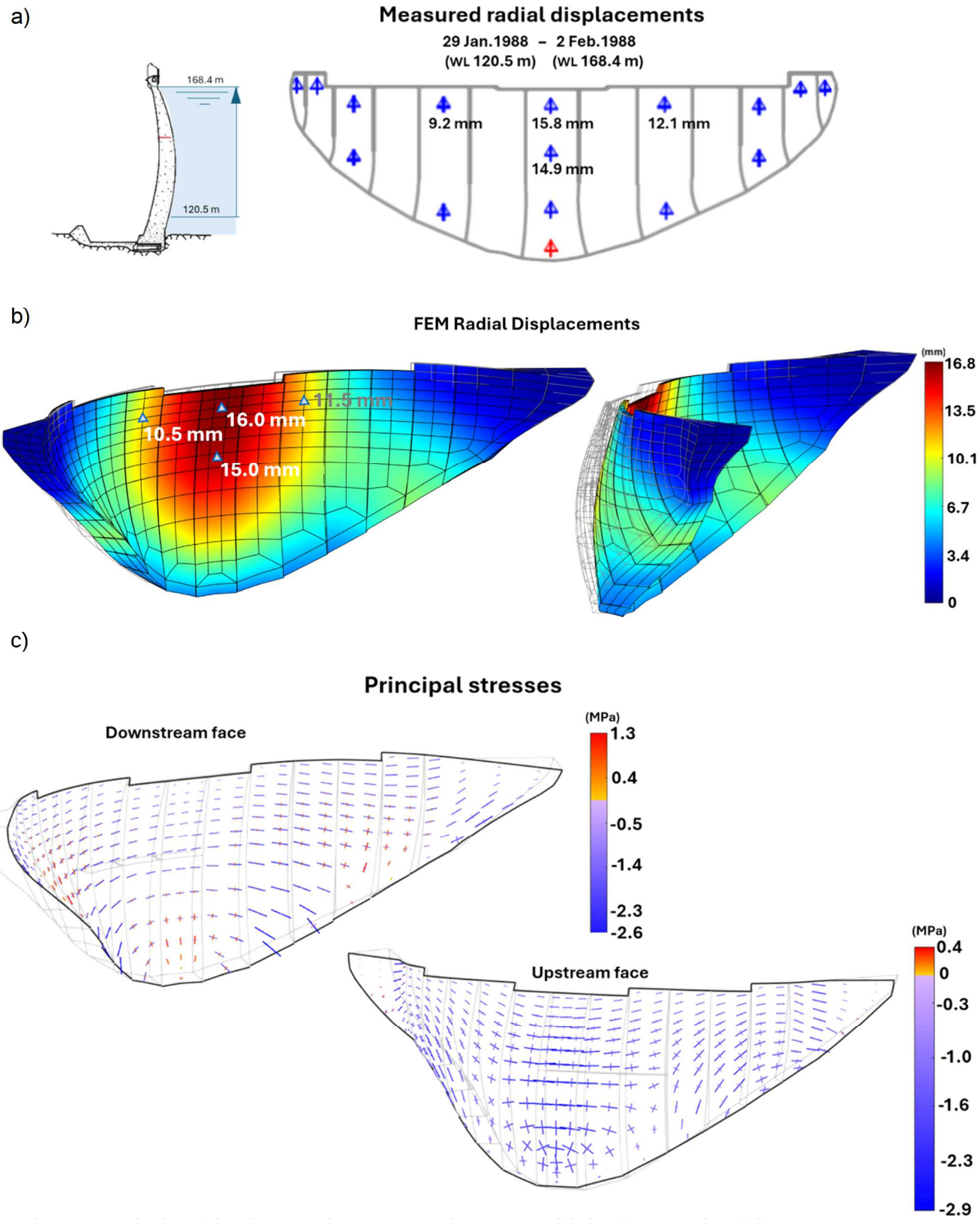

Fig. 5 – Analysis of the dam static response due to a rapid rise in water level (from 120.5 m to 164.8 m). a) Radial displacements measured by geodesy, between 29jan1988 (WL 120.5 m) and 2feb1988 (WL 168.4 m), during the refilling of the reservoir; b) Corresponding radial displacements calculated by the FEM considering dam-foundation interface and contraction joints movements (non-linear behaviour); c) Corresponding principal stresses (downstream and upstream face).

3.4. Dam dynamic behaviour. Modal parameters: comparison between measured values (ambient vibration test) and the corresponding values computed with FEM

The ambient vibration test carried out on 12th of June 2018 [9], was composed by five sets of measurements, lasting 13 minutes each, with 9 radial accelerometers installed in the area of the dam crest, as shown in Fig.2c. During this test, the reservoir was at an elevation of 174.7 metres [9]. The average power spectrum of the recordings is shown in Fig. 6b. The first frequency recorded was 3.296 Hz, corresponding to an antisymmetric mode, and the second frequency was recorded at 3.733 Hz, associated with a symmetrical mode.

The modal response was computed using the FE model, adjusting the value of the modulus elasticity to take account of the dynamic effect, E_{dyn} = 1.25 × E_{static} = 46.25 GPa, and maintaining the Westergaard's water mass reduction coefficient of 50% (Fig. 6a). The model considered the same water level of the experimental campaign, 174.7 m, in order to consider the conditions observed on the day of the test. A value of 3.312 Hz (antisymmetric mode) was obtained for the first frequency and 3.733 Hz (symmetric mode) for the second frequency. The natural frequencies calculated with this model for the first two modes show good agreement with the values of the frequencies measured during the test (Fig. 6c).

4. INFLUENCE ON THE WATER LEVEL ON NON-LINEAR SEISMIC BEHAVIOUR

The dam-reservoir interaction is one of the key factors affecting the seismic performance of arch dams during an earthquake [1]. This chapter will focus on the seismic action characterization and the water level definition for the case study and afterwards will be presented a direct comparison on the non-linear seismic response of the Bouçã dam for two different water levels.

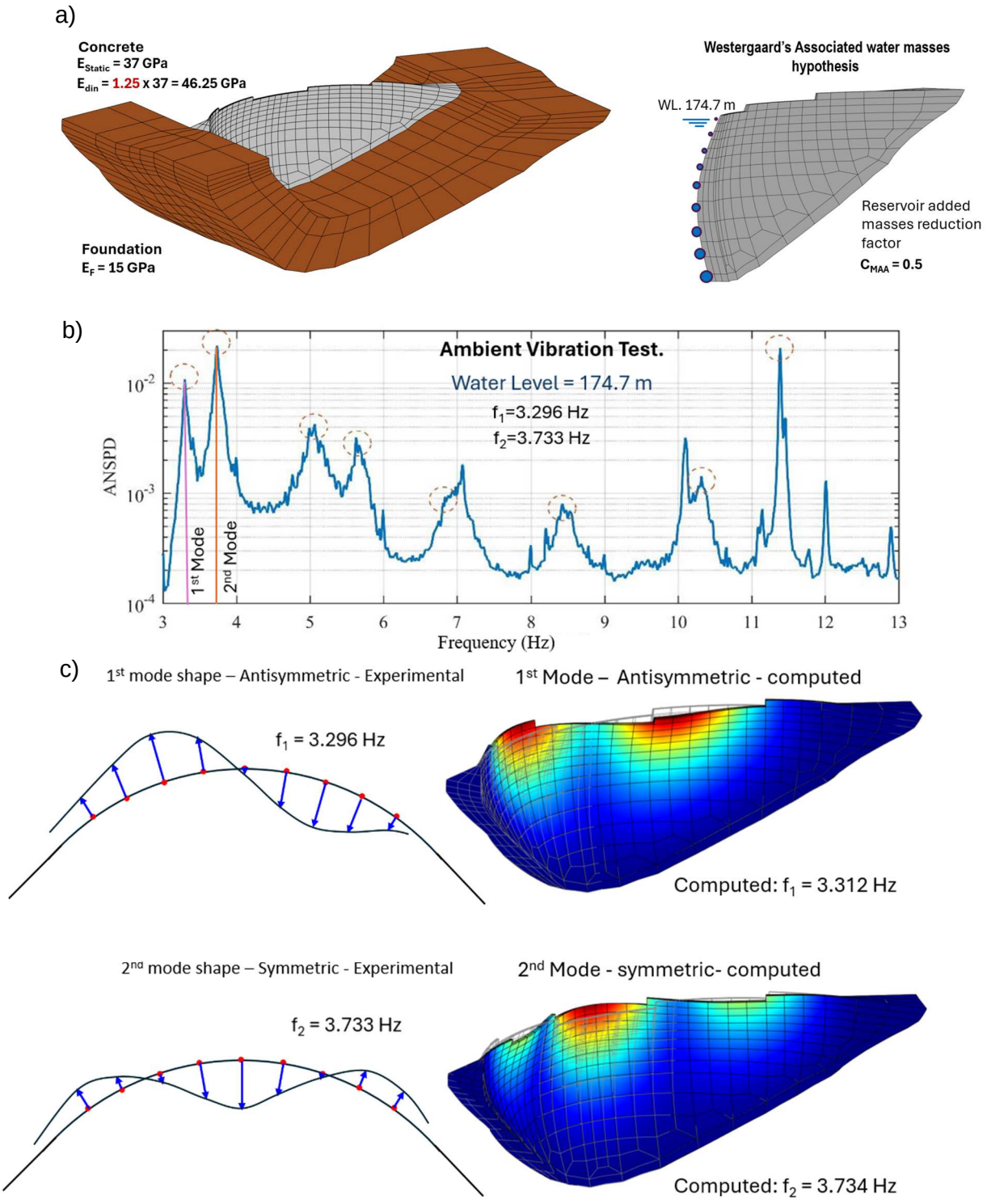

Fig. 6 – Dynamic behaviour: modal parameters. a) FEM for dynamic analysis: material properties (dam, foundation, reservoir); b) Experimental ambient vibration test results: Averaged Normalized Spectral Power Density [9]**; c) Comparison between experimental and FEM computed natural frequencies and mode shapes**

4.1. Seismic analysis considering full reservoir and the water level 2 m above the crack

The horizontal crack in the upstream face of the Bouçã dam is a concerning factor for the dam global structural behaviour. Therefore, it is important to understand how the structure perform in a scenario where the water level is lower than the normal circumstances (around 175 m). It is intended to study the dam behaviour when the water level is just 2 m above the horizontal crack, located at around el.150 m.

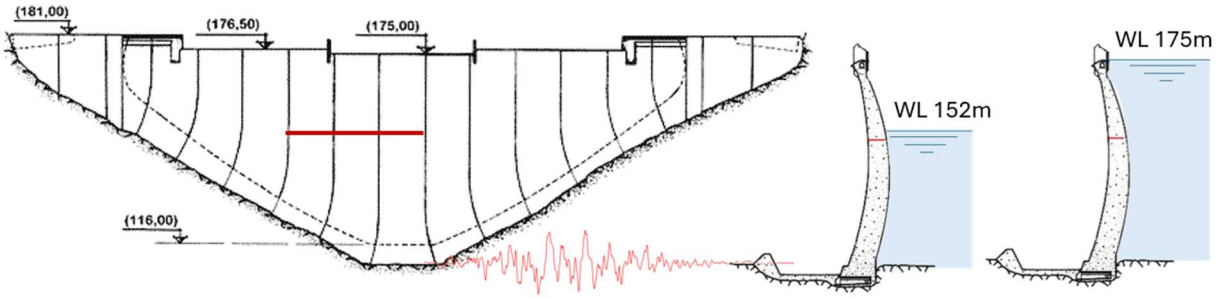

Fig. 7 – Water level values considered for the seismic behaviour study: 152 m and 175 m.

4.2. Seismic action

To perform the seismic calculations using DamDySSA5.0, a seismic accelerogram with a peak acceleration of 0.3g (PGA) was used. The accelerogram and its Fourier amplitude spectrum are shown in Fig. 8. Overlaying the Fourier amplitude spectrum are also the first two natural frequencies of the dam, considering the two different water levels as well as the Rayleigh damping law considered in the study (around 5% in the 1st vibration mode). The seismic input consists of a uniform ground motion, given by the referred seismic accelerogram [20].

The natural frequencies) were computed by *DamDySSA5.0*, for the calibrated FE model. For water level 175 m, the dam model presents a frequency $f_1^{(175m)}=3.29\ Hz$ and $f_2^{(175m)}=3.70\ Hz$, meanwhile, for water level 152 m the dam model presents a frequency $f_1^{(152m)}=4.24\ Hz$ $f_2^{(152m)}=4.89\ Hz$, showing that the water level has a great impact on the dynamic behaviour of the dam.

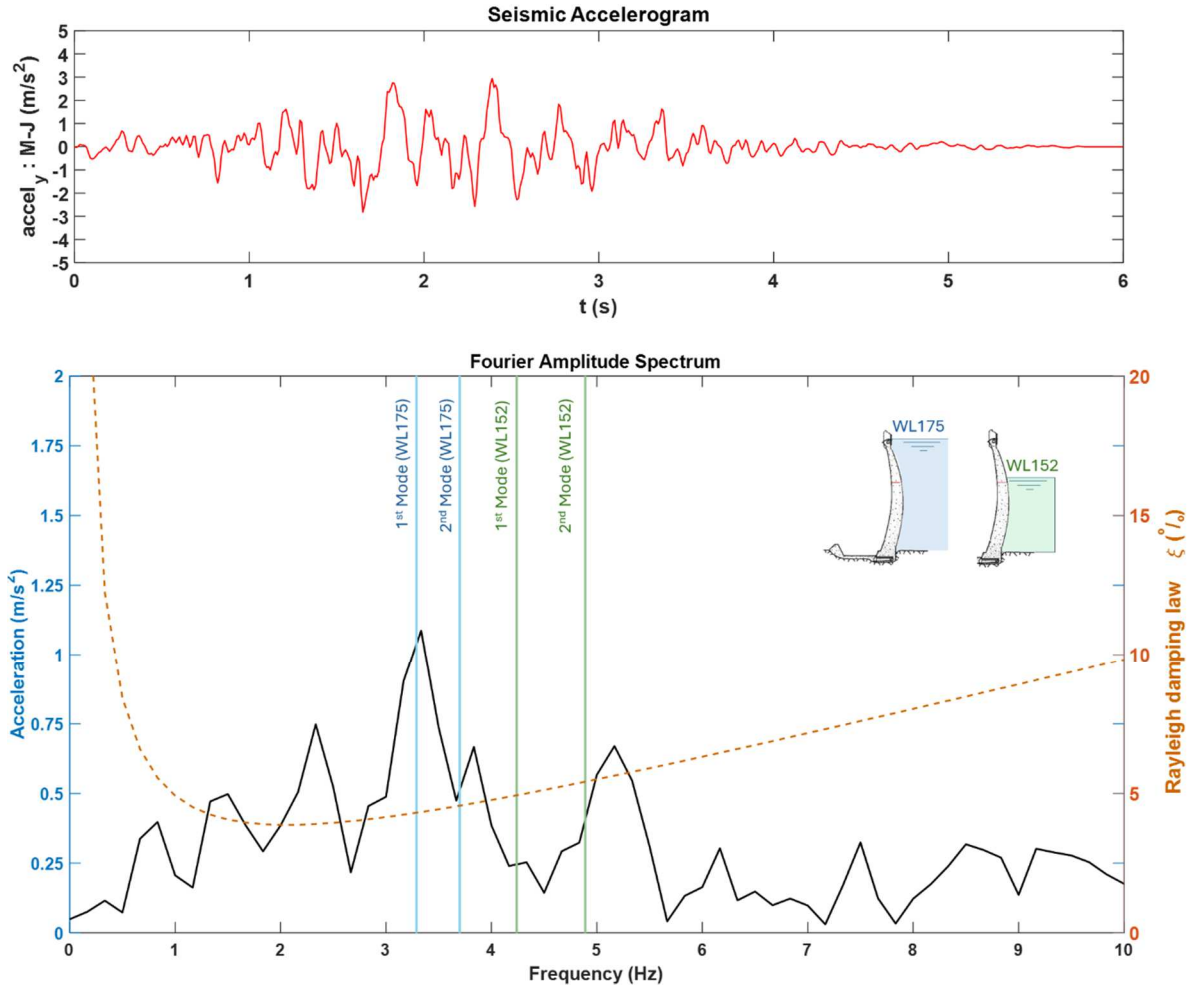

Fig. 8 – Seismic accelerogram considered (0.3g) and respective Fourier amplitude spectrum. Dam natural frequencies computed for WL 175 and WL152. Rayleigh damping law considering 5% damping around the 1st mode (WL175).

4.3. Reservoir water level influence on the seismic behaviour of the Bouçã dam

The non-linear seismic response is computed using *DamDySSA5.0*, considering the model with vertical joints, the horizontal crack, and the discontinuity at the dam-foundation interface, and considering a damage model for the concrete with two independent damage variables: tensile and compressive damage. The computed results for full reservoir (WL175 m) are presented in Fig. 9 and for WL152 m are presented in Fig. 10. The goal is to test the FE model response for each case of water level and analyse the influence of the horizontal crack in the structural movements of the blocks above the crack.

The load combination for this study includes the dam self-weight (SW), the hydrostatic pressure (HP175 and HP152, for the reservoir levels 175m and 152m respectively), and the

seismic load (Seism). As mentioned, in this case the seismic input consists of a uniform ground motion, applied at the dam base, given by a computer-generated acceleration time history for the dam area [20], with a peak acceleration of 0.3g (Fig. 8).

The results are presented in Fig. 9 and Fig. 10 for each water level, considering the instant of interest, namely the instants of maximum displacements in the upstream directions.

Fig.9a shows the history of the radial seismic displacement for the control node of the central cantilever (at the central spillway crest level) during the seismic event. There is a maximum value upstream of around 21.8 mm at time t=2.1s and a maximum displacement downstream of around 43 mm at time t=1.9s.

The results show that the dam's structural response is symmetrical, however with slightly different maximum values on each side, which is essentially due to the presence of the horizontal crack.

Fig. 9b shows that when the central cantilever reaches its maximum upstream value (around 22 mm) there is a displacement of around 32 mm upstream in the blocks above the horizontal crack, which corresponds to an opening of the horizontal joint of around 1.62 mm. This effect is particularly important when the seismic forces push the dam upstream, causing the horizontal crack to open and amplifying the movement of the upper blocks.

Fig. 9c shows the dam stress fields for the instant when the central cantilever hits the maximum displacement towards upstream, showing the tensile stresses in the central area of the upstream face. It is also notable that the horizontal crack opening (around 1.62 mm) dissipates the vertical tensile stresses in the blocks above the crack.

Considering the second case, where the water level is lower (152 m), Fig. 10a presents the non-linear seismic radial displacement of the central cantilever control node (at the central spillway crest level) during the seismic event. It is noted that the maximum value upstream is around 88 mm at t =2.8s and a maximum displacement downstream around 57 mm at t = 4.3s.

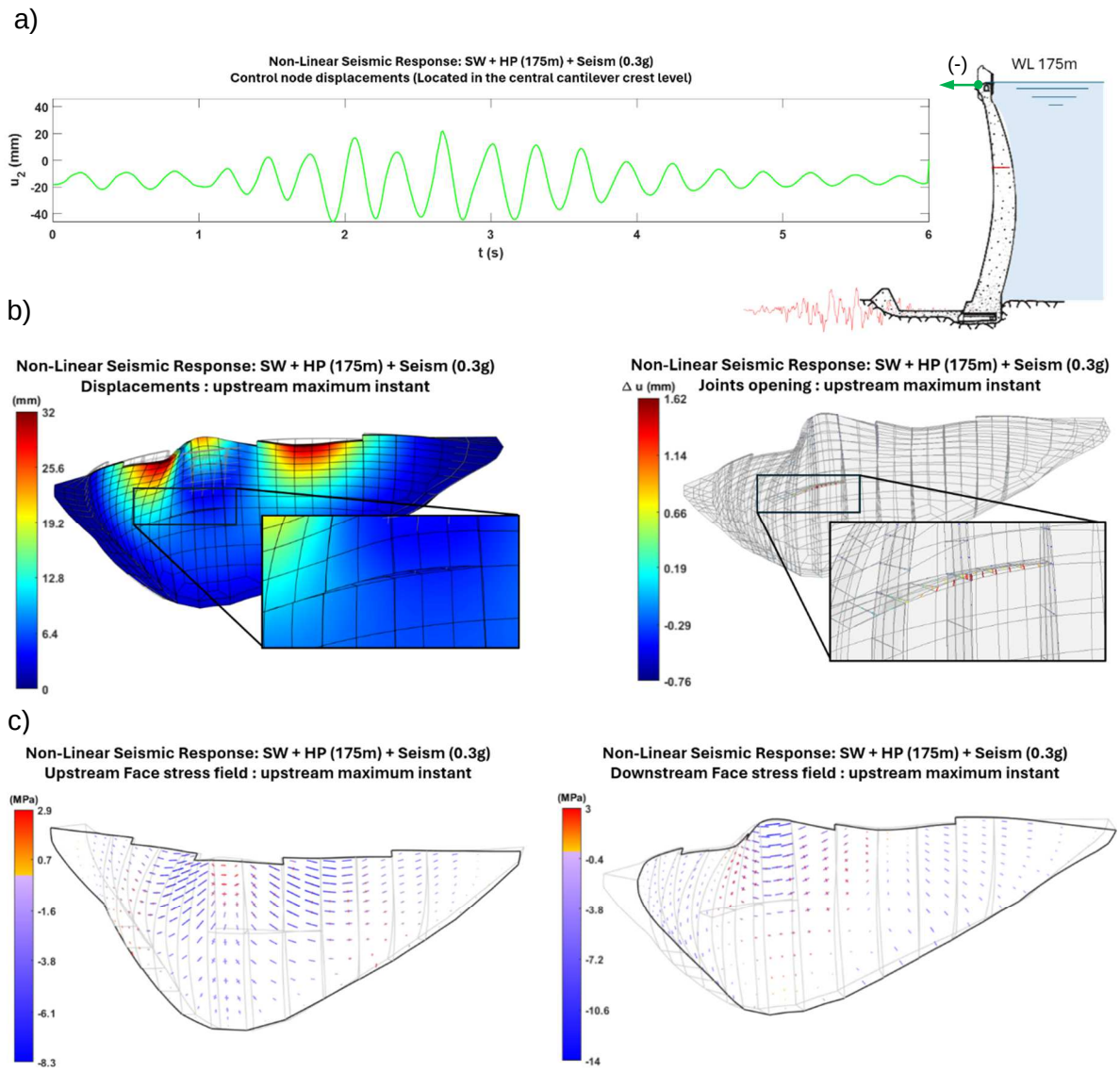

Fig. 9 – Non-Linear seismic response of the Bouçã dam, for water level 175 m, with an accelerogram of PGA=0.3g. a) Central cantilever control point displacement field throughout the seismic event; b) Displacement field and joint behaviour for maximum displacement registered towards upstream (t=2.1s); c) Stresses on the dam faces, at t=2.1s.

It is possible to see in Fig. 10b that when the central cantilever hits its maximum displacement towards upstream (causing the horizontal joint to open around 36 mm) the blocks above the horizontal crack present a total displacement of about 150 mm in the upstream direction.

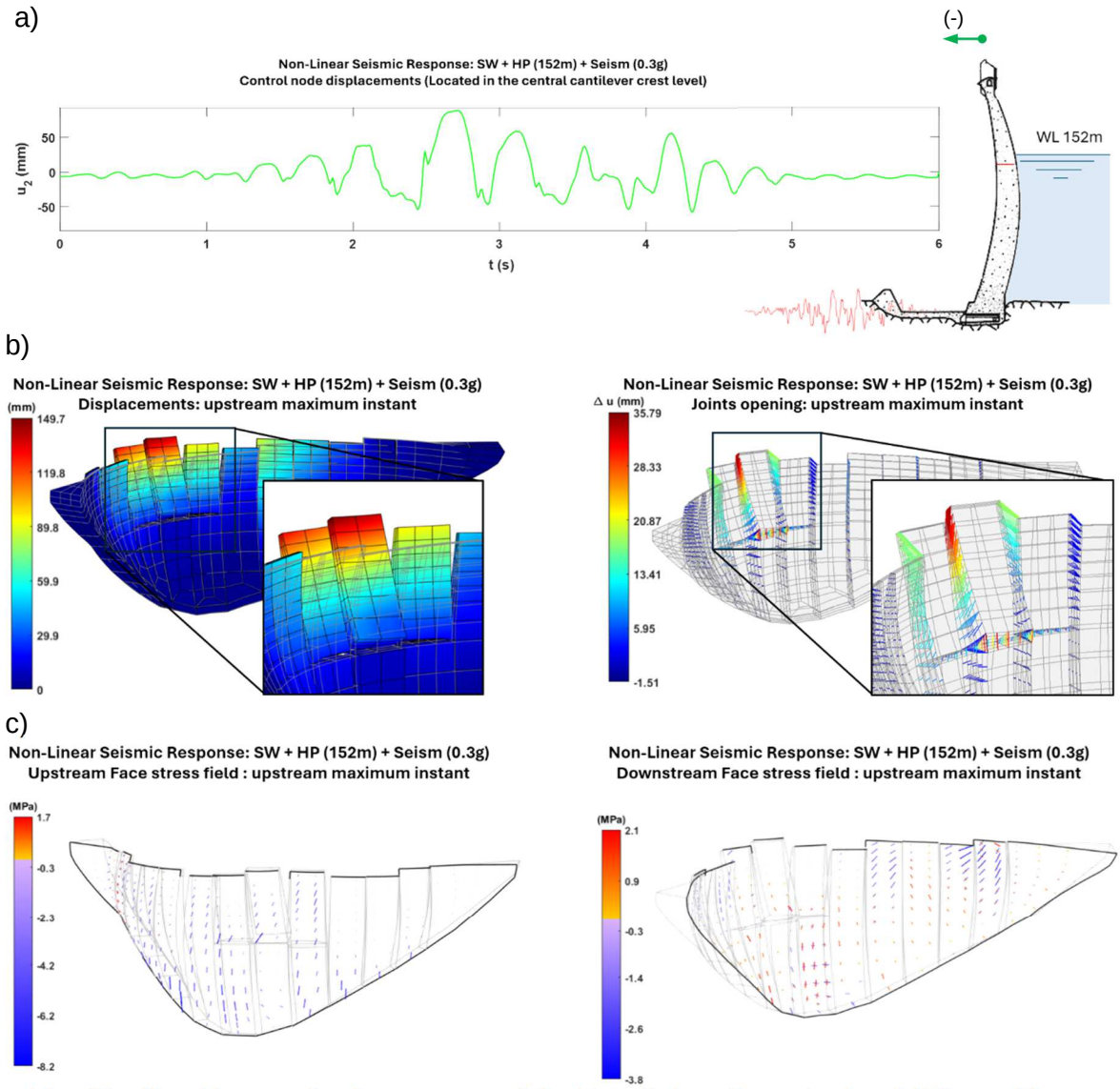

Fig. 10 – Non-Linear seismic response of the Bouçã dam, for water level 152 m, with an accelerogram of PGA=0.3g. a) Displacement field and joint behaviour for maximum displacement registered to upstream (t=2.8s); b) Displacements and joint openings; c) Principal stresses on the dam faces.

Fig. 10c shows the dam stress field for the instant when the central cantilever hits the maximum displacement value towards upstream, indicating that the horizontal crack opening, around 36 mm, dissipates the vertical tensile stresses.

4.4. Seismic Safety assessment of the Bouçã dam considering water level 2 above the horizontal crack

The non-linear seismic response is computed using *DamDySSA5.0*. With this software, the seismic performance of the dam is evaluated by controlling the evolution of the deterioration

state of the dam under the seismic excitation. The adopted seismic performance criteria were established in order to meet the requirements defined for large concrete dams under the seismic excitation levels corresponding to the Operation Base Earthquake (OBE) and the Maximum Design Earthquake (MDE) [21]. The safety criterion for the OBE states that there should be no damage such as cracking (tensile damage) or movement between blocks that could affect the integrity of the waterstops, which could compromise the proper operation of the dam. The safety criterion for the MDE states that there must be no uncontrolled reservoir water release; as such, there must be no falling blocks (towards upstream) and no concrete failure under compression (i.e. concrete crushing) in key areas of the dam structure [7,8].

The non-linear seismic behaviour was simulated using the calibrated finite element model considering the vertical joints, the horizontal crack, the discontinuity at the dam base, and considering concrete tensile and compressive damage (as presented in Fig. 3). For this safety assessment study, the load combination includes the self-weight of the dam (SW), the hydrostatic pressure for the water level 152m (HP152: water level 2 m above the horizontal crack), and the seismic load applied at the dam base. The seismic input consists of an accelerogram (presented in Fig. 8) scaled to a peak ground acceleration of 0.1g (OBE) and 0.2g (MDE).

In Fig. 11a shows the results of the seismic safety check for the OBE (0.1g) considering the water level 2 m above the horizontal crack. It is concluded that the oscillatory movements of the blocks above the crack reach a maximum value of only 8 mm and that no cracking occurs, which corresponds to the verification of the safety criterion for the OBE previously mentioned.

In Fig. 11b shows the results of the seismic safety check for the MDE (0.2g) also considering the water level 2 m above the horizontal crack. It can be concluded that the oscillatory movements of the blocks above the crack reach a maximum radial displacement of 135 mm and remain stable during the earthquake and that only superficial compression damage of less than 60% occurs, which corresponds to the verification of the safety criterion for the MDE.

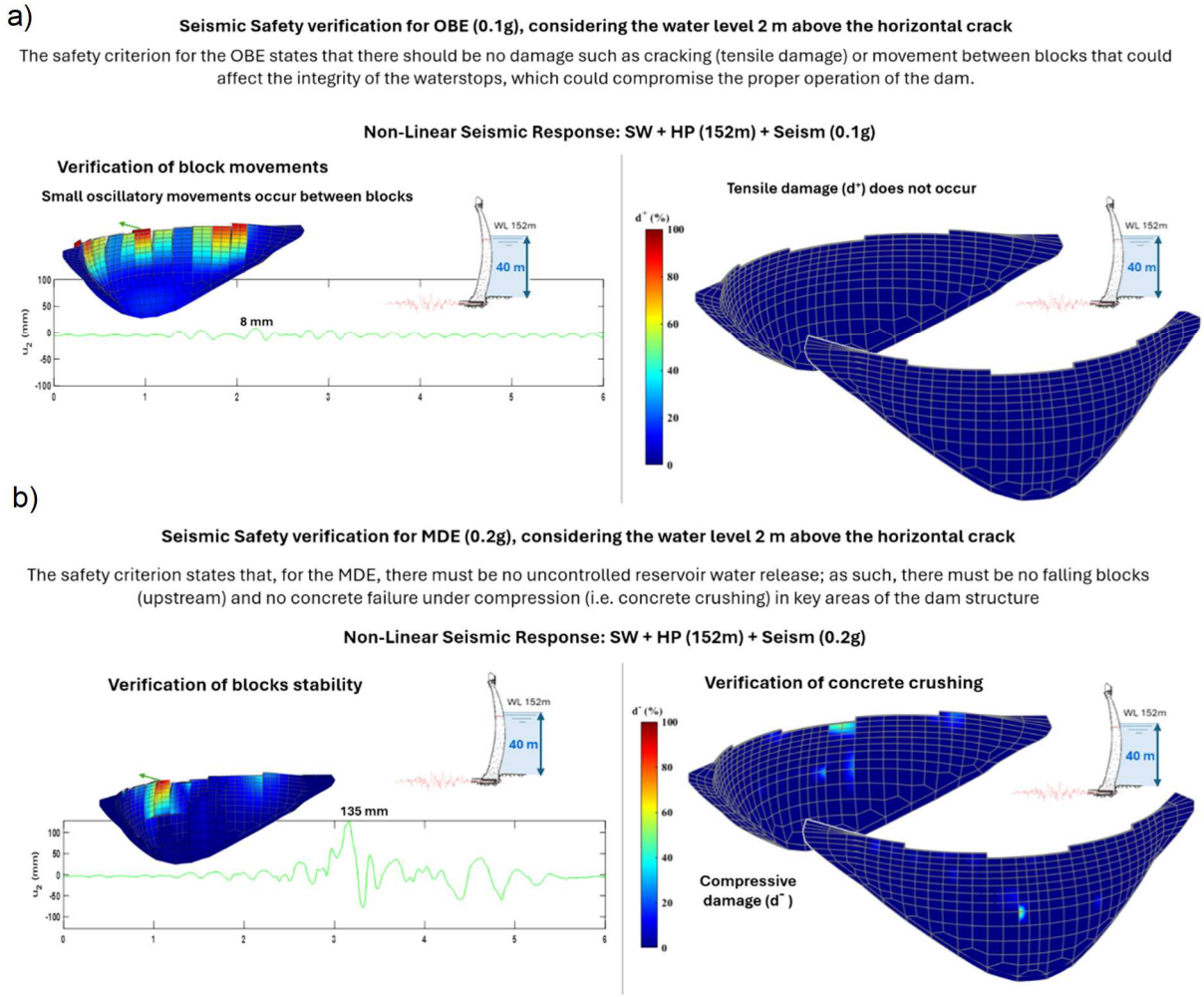

Fig. 11 – Seismic safety assessment of Bouçã dam. Seismic Safety verification considering the water level 2 m above the horizontal crack. a) Verification for OBE (0.1g): block movements and tensile damage (d^+); b) Verification for MDE (0.2g): blocks stability and concrete crushing (compressive damage d^-)

5. CONCLUSIONS

This paper presents a study of the seismic behaviour of the Bouçã dam considering two different values for the reservoir water level. Two scenarios were considered: one with the water at the maximum storage level (WL175 m) and another with the water at a significantly lower level (WL 152 m), 2 m above the horizontal crack visible in the downstream face (25 m below the crest), which extends from the central section towards the right abutment. To study the dam seismic behaviour, a 3D finite element model of the dam and foundation was developed and calibrated, considering monitoring data on the static response of the dam and on the dynamic response measured in an ambient vibration test. The numerical simulations were carried out using the DamDySSA5.0 finite element program, developed by the authors for linear and non-linear dynamic analysis of dam-reservoir-foundation

systems. Also, a non-linear seismic analysis was carried out using a seismic accelerogram with a peak acceleration of 0.3g. The results showed the importance of carrying out seismic studies for water levels below the maximum storage level. In fact, in this case, it was found that the displacements and opening/sliding movements of the horizontal crack and the contraction joints due to the seismic action are significantly higher for the lower water level situation (WL152 m, i.e. 23 m bellow the crest). These results emphasize the need to carry out seismic safety verifications not only for the full reservoir situation but also for significantly lower water level values. A study was carried out to verify the seismic safety of the dam for the situation with water level at 152 metres, 2 metres above the horizontal crack. This situation is more unfavourable for seismic safety than the full reservoir situation as higher movements between blocks can occur. The stability of the blocks was studied by analysing the possibility of blocks falling upstream without considering the favourable effect of shear keys and considering damping of only 5%. Even with these conservative assumptions, it was concluded that the dam is safe for OBE (only small movements between blocks and no tensile damage) and for MDE (stable blocks and no concrete crushing).

ACKNOWLEDGEMENTS

The authors would like to thank LNEC for the work framing support, EDP for making the data available and the Portuguese Foundation for Science and Technology (FCT) for funding the research project ‘SSHM4Dams - Seismic and Structural Integrity Monitoring of Large Concrete Dams’ (PTDC/ECI-EGC/5332/2020), the CERIS research unit funding UIDB/04625/2020 and Rafael Ramos PhD scholarship (2023.00414.BD).

REFERENCES

[1] Hariri-Ardebili, M.A., Mirzabozorg, H. and Kianoush, M.R. (2014) Structural safety of high arch dams with variable water levels based on seismic performance evaluation. Transac.of Civil Engineering.

[2] Ramos, R. (2017) Modelação do comportamento sísmico de barragens abóbada: estudo da influência da cota de água [Masters Thesis]. Instituto Superior de Engenharia de Lisboa, [Lisboa].

[3] Guo, S., Liang, H., Wu, S., Xiong, K., Li, D., Chen, H. et al. (2020) Seismic damage investigation of arch dams under different water levels based on massively parallel computation. *Soil Dynamics and Earthquake Engineering*, **129**, 105917. https://doi.org/https://doi.org/10.1016/j.soildyn.2019.105917

[4] Fenves, G., Soheil, M. and Reimer, R. (1992) Effect of Contraction Joints on Earthquake Response of an Arch Dam. *Journal of Structural Engineering*, American Society of Civil Engineers. **118**, 1039–55. https://doi.org/10.1061/(ASCE)0733-9445(1992)118:4(1039)

[5] Cervera, M., Oliver, J. and Faria, R. (1995) Seismic evaluation of concrete dams via continuum damage models. *Earthquake Engineering & Structural Dynamics*, John Wiley & Sons, Ltd. **24**, 1225–45. https://doi.org/https://doi.org/10.1002/eqe.4290240905

[6] Leitão, N. (2017) Barragem da Bouçã. Estudo do processo de fendilhação no paramento de jusante. LNEC, Lisboa.

[7] Oliveira, S., Alegre, A., Ramos, R., Proença. Jorge M., Mendes, P., Silva, J. et al. (2024) Estudo da Resposta Sísmica não-linear da barragem da Bouçã. In: Pimentel M, Faria R, Henriques AA, Sousa C, Maia L, Matos AM, et al., editors. *Encontro Nacional Do Betão Estrutural 2024 - BE2024*, Faculdade de Engenharia, Universidade do Porto, Porto. p. 271–80.

[8] Oliveira, S., Alegre, A., Ramos, R., Serra, C., Silva, J., Proença, J.M. et al. (2024) Seismic Performance Assessment of Bouçã Arch Dam. Non-Linear Analysis Considering Joint Movements and Concrete Damage Under Tension and Compression. *9th European Congress on Computational Methods in Applied Sciences and Engineering*, Lisbon.

[9] Pereira, S. (2019) Structural condition assessment of dams based on continuous dynamic monitoring. PhD Thesis, University of Porto (FEUP).

[10] LNEC. (1954) Plano de observação da barragem da Bouçã. Lisboa.

[11] LNEC. (1957) Estudo experimental da barragem da Bouçã - Relatório complementar. Lisboa.

[12] LNEC. (1955) Estudo experimental da barragem da Bouçã - Relatório Preliminar. Lisbon.

[13] Bazant, Z.P. and Panula, L. (1980) Creep and shrinkage characterization for analyzing prestressed concrete structures. *PCI Journal*, **25**, 86–122.

[14] Oliveira, S., Silvestre, A., Espada, M. and Câmara, R. (2014) Modeling the dynamic behavior of dam-reservoir-foundation systems considering generalized damping. Development of a 3DFEM state formulation. *EURODYN*, Porto, Portugal, Porto, Portugal.

[15] Alegre, A. (2021) Modelling and monitoring the dynamic behaviour of concrete dams. Modal analysis and seismic response.

[16] Westergaard, H.M. (1933) Water Pressures on Dams during Earthquakes. *Transactions of the American Society of Civil Engineers*, **98**, 418–33. https://doi.org/10.1061/TACEAT.0004496

[17] Zienkiewicz, O.C. and Bettess, P. (1978) Fluid-structure dynamic interaction and wave forces. An introduction to numerical treatment. *International Journal for Numerical Methods in Engineering*, **13**, 1–16. https://doi.org/https://doi.org/10.1002/nme.1620130102

[18] Oliveira, S. and Faria, R. (2006) Numerical simulation of collapse scenarios in reduced scale tests of arch dams. *Engineering Structures*, **28**, 1430–9. https://doi.org/10.1016/j.engstruct.2006.01.012

[19] Oliveira, S. (2000) Modelos para análise do comportamento de barragens de betão considerando a fissuração e os efeitos do tempo. Formulações de dano. PhD Thesis, University of Porto (FEUP).

[20] Carvalho, A. (2007) Modelação estocástica da acção sísmica em Portugal Continental [Stochastic modelling of the seismic action in continental Portugal]. PhD Thesis, Instituto Superior Técnico (University of Lisbon), Portugal.

[21] APA. (2018) Documentos Técnicos de Apoio ao Regulamento de Segurança de Barragens (RSB). APA.

Fifth International Dam World Conference
PORTUGAL • LISBON • LNEC • APRIL 13-17, 2025
dam world 2025

FROM SENSOR DATA TO ACTIONABLE INFORMATION WITH KMIDAM. SEISMIC EVENT REPORTING AND LONG-TERM STRUCTURAL HEALTH MONITORING OF DAMS

André Alegre[1]	Derek Skolnik	Mauricio Ciudad-Real	Mathias Franke	Mohamed El-Idrissi
Kinemetrics	Kinemetrics	Kinemetrics	Kinemetrics	Kinemetrics

ABSTRACT

This paper shares the experience gathered by Kinemetrics' engineers in the field of dynamic monitoring of dams, by providing specialized systems and services for dozens of projects around the world over the years. First, the authors present KMIDam, a complete Dam Management Platform developed for seismic and structural monitoring applications. The platform features specialized tools for system operation and control, including real-time data acquisition and equipment state of health monitoring, real-time seismic monitoring and earthquake alerts, automated event reporting, and long-term continuous ambient vibration monitoring. Emphasis is given to how KMIDam can deliver critical information to give immediate feedback on the potential impact of earthquakes on the dam and its facilities, as well as how it can produce results for long-term structural health monitoring. After that, the authors look at several examples of dam monitoring projects for which Kinemetrics has provided its products and specialized solutions. The paper covers a diverse range of real-world case studies, for single and multi-dam projects, including seismic monitoring systems and continuous vibrations monitoring systems. The goal is to show how real dam monitoring data, specifically vibrations measured with sensors based on force balance technology, can be used for earthquake monitoring, structural condition assessment, and advanced academic research.

Keywords: Dynamic monitoring systems, Sensor vibration data, Seismic event reporting, Structural health monitoring, Dam safety

[1]afa@kmi.com, United States

1. INTRODUCTION

Large dams are key infrastructures with significant social, environmental and economic impact. However, these dams are associated with high potential risks, since incidents or accidents can result in significant damage and loss to the environment and to the populations downstream. In this context, it is worth reminding that many dams are located in regions with high seismic activity, increasing the risk of exposure to strong earthquakes or, in some cases, the potential for induced seismicity phenomena, such as reservoir-triggered seismicity. These events may result in damage to the dams and their facilities, requiring the suspension of normal operations for repairs or, in more severe cases, compromising the structural integrity of the dam, with uncontrolled release of water from the reservoir [1]. In addition, dams are designed to operate for several decades, and so it is reasonable to expect them to exhibit aging effects and to experience progressive deterioration over time, potentially resulting in a gradual degradation of their structural condition [2,3].

Therefore, ensuring operational and structural safety, resilience against earthquakes, and efficient emergency response is paramount [4]. This makes it essential to invest in advanced and comprehensive monitoring systems, including seismic monitoring, for during and post-event impact assessment, and ambient vibration response monitoring, for long-term behavior analysis and structural condition assessment.

The primary objective of implementing a dynamic monitoring system on a dam is to provide reliable and actionable information to operators, engineers and decision-makers [3]. To achieve this goal, it is necessary to deploy robust and reliable high-dynamic range sensors, such as force-balance accelerometers, as well as high-end data acquisition systems, enabling to collect high-quality data on the ground motion and the structural response during earthquake events and on the dam response under ambient/operational dynamic vibrations [5]. Nevertheless, it remains indispensable to process raw data and present the results in a meaningful and easily interpretable format. Therefore, this type of system should be supported by a complete monitoring and management platform, equipped with specialized tools that allow command and control of the sensor network and for automated data analysis and report generation, in order to facilitate a continuous and effective dam behaviour assessment and to provide immediate feedback on the impact of earthquakes. Ultimately, the aim is to support informed decision-making and maximize situational awareness, reducing risk and ensuring safe and compliant operations.

This paper aims to share the experience gathered by Kinemetrics' engineers in the field of dynamic monitoring of dams. Section 2 gives a brief overview of Kinemetrics' history and addresses our approach and mission for dam monitoring projects. In section 3, the authors

present KMIDam, a complete Dam Management Platform designed for seismic and structural monitoring applications; the main core features of the platform are described, and emphasis is given to the type of information it can deliver to operators, engineers, and decision makers. Then, section 4 is dedicated to sharing several examples of dam monitoring projects from all over the world for which Kinemetrics has provided its equipment, services, and specialized solutions, covering case studies involving the implementation of seismic monitoring systems and continuous vibrations monitoring systems. Finally, section 5 provides concluding remarks.

2. KINEMETRICS AND DAM MONITORING: AN OVERVIEW

Since 1969 Kinemetrics has been designing and supplying technologies, products, and solutions for seismic networks and for seismic and structural monitoring of critical civil structures, buildings, historical monuments, and infrastructures such as dams, bridges and nuclear facilities.

For over 50 years, Kinemetrics' technicians and the engineers at the Open Systems and Services (OSS) Division have gathered extensive experience in dam monitoring, by providing specialized systems and services - comprising network design, field installation, and system integration, customization and operation - for dozens of projects around the world. Kinemetrics' portfolio of dam projects includes notable refences in North and South America, Europe, Africa and Asia. Among the earliest examples of dams instrumented with Kinemetrics equipment are the iconic Pacoima dam, in California, and Hoover Dam, located on the border of Nevada and Arizona (Fig. 1). Other examples include Aswan dam, in Egypt, El Toro Dam, in Costa Rica, and Bakun, Murum, and Batang Ai dams, in Malaysia. In addition, Kinemetrics has supplied its equipment for the two first dams in the world instrumented with continuous vibrations monitoring systems: Cabril dam, in Portugal, and Cahora Bassa dam, in Mozambique. Details on specific projects will be given in section 4 of this paper.

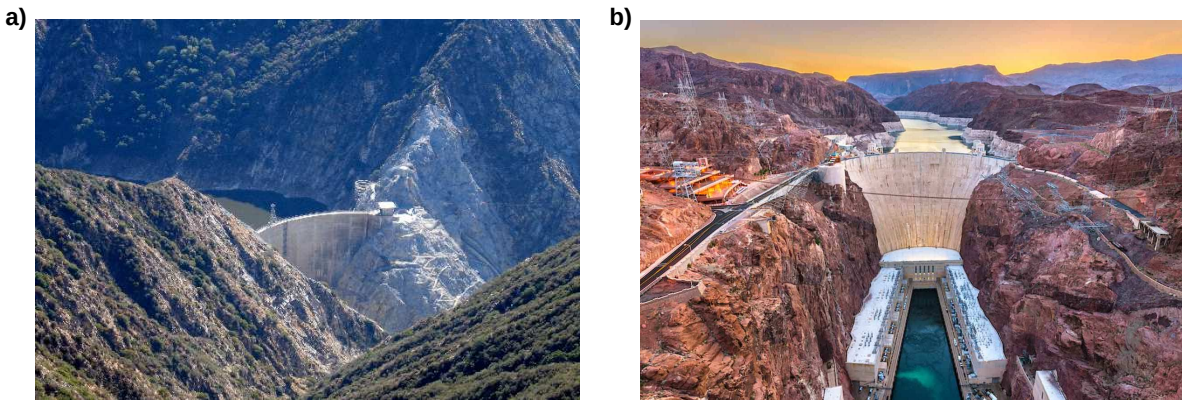

Fig. 1 - Early cases of dams in the US instrumented with Kinemetrics sensors: a) Pacoima dam, 113 m high, California; b) Hoover dam, 221 m high, Arizona-Nevada.

Kinemetrics' approach for dam monitoring projects can cover a wide range of services and customized solutions, including supplying the required equipment for data measurement and acquisition, and designing and implementing comprehensive and customized turnkey systems.

Our Infrastructure Monitoring Solution for dams is the KMIDam platform (Fig. 2), which combines the unmatched world-class Kinemetrics instrumentation, ensuring maximum data return and unmatched reliability, and high-end redundant Data Centre powered by advanced software tools, including automated processing and reporting functions, to deliver continual and reliable access to all the information required for responsible dam portfolio management during day-to-day operations and emergency events.

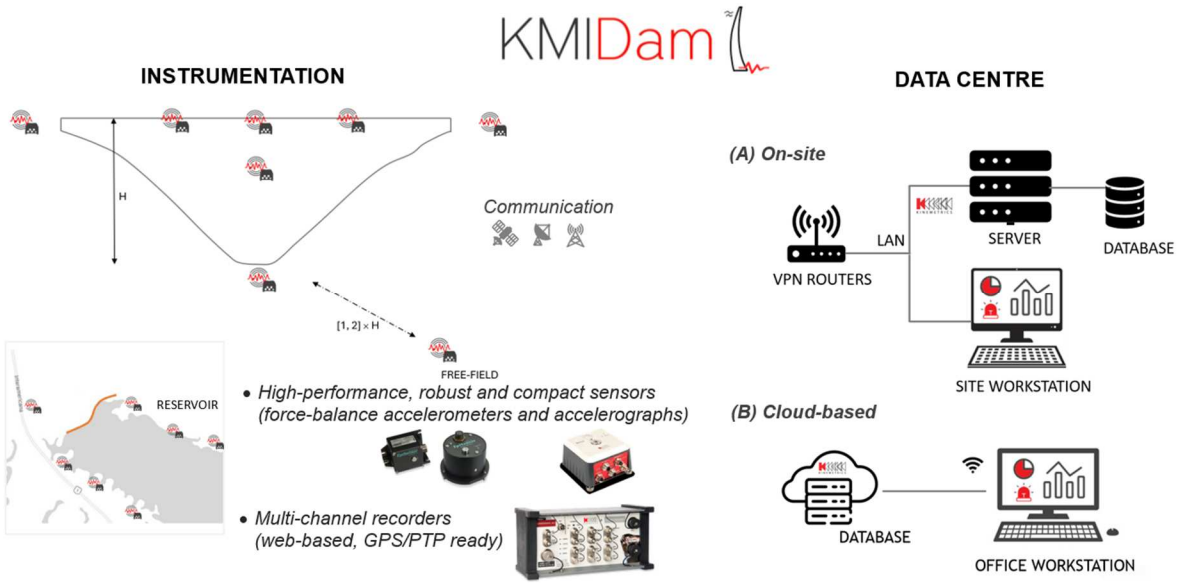

Fig. 2 - Schematic representation of KMIDam: Kinemetrics' Management of Infrastructure Solution for dams. Field equipment and Data Centre.

3. THE KMIDAM PLATFORM

KMIDam is a complete Dam Management Platform designed to deliver critical information for an immediate understanding of the impact of earthquakes on dams and to provide actionable data for long-term structural health and dam performance monitoring. The goal is to maximize situational awareness, eliminate guesswork, and enable better informed decision making, in order to ensure structural safety, compliant operations, and efficient emergency response.

This specialized technology platform is fully customizable for each unique dam monitoring project – considering the dam type, number of sensors, site constraints, project goals, etc. –, and it is also scalable, offering the capability to manage single and multi-asset projects [5].

3.1. Features and Applications

The KMIDam platform is engineered, on a first level, to manage and operate all field equipment of the seismic and structural monitoring system, and, on a second level, to deliver valuable

information and data to operators, engineers, and decision makers, for different applications. Namely, advanced tools are used for real-time seismic monitoring and earthquake alerting, as well as for automated data processing and event reporting. Additionally, KMIDam can be enhanced with vibration analysis algorithms and digital twins for long-term structural health and performance monitoring.

The main features and applications of the KMIDam platform are described next.

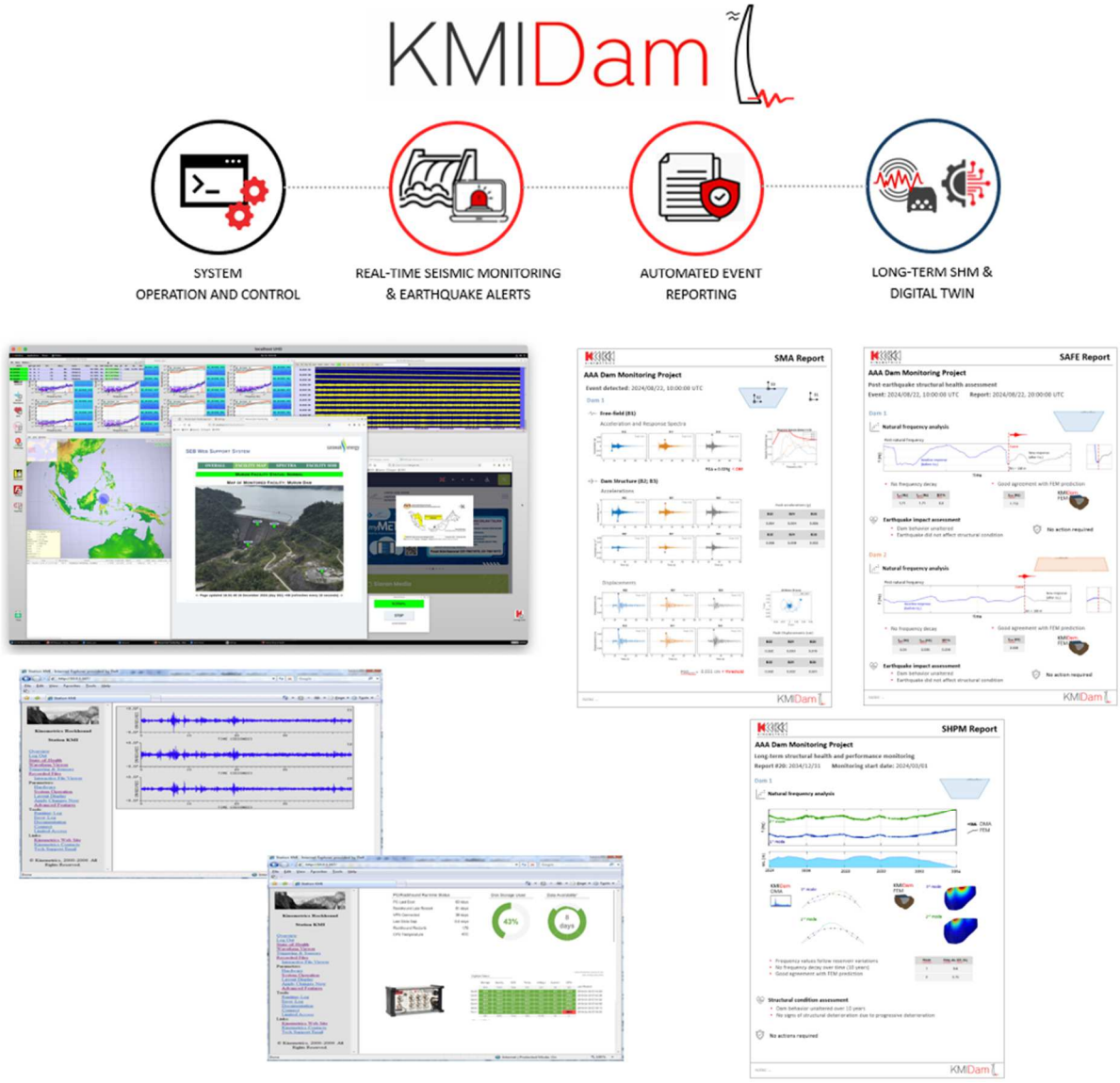

Fig. 3. KMIDam platform: main features, user interface and examples of generated reports.

System Operation and Control (SOC)

KMIDam SOC is supported by our own software applications, Rockhound and Antelope, which perform a variety of tasks that are critical to the end user, ensuring optimal functionality and continuous operation for all of Kinemetrics' field equipment and system components. These tasks comprise: real-time data acquisition from field stations (event-triggered, timed, and continuous), real-time and on-demand data visualization, and interactive control and state of

health monitoring of all deployed equipment, including sensors, recorders, servers and workstations, etc. In addition, the KMIDam platform allows remote access to the on-site Data Centre or the virtual cloud-based Data Centre, for system operation support and other recurring monitoring services.

KMIDam SOC is completely customizable according to the needs and goals of the end users, and it is scalable, meaning that it can oversee regular systems (with one or more recorders) or large networks (there is no maximum for the number of devices it can handle).

Real-Time Seismic Monitoring (RTSM) & Earthquake Alerts

KMIDam RTSM is powered by advanced tools, e.g., Rockhound and Antelope-Bighorn, used to process strong motion data and deliver critical seismic monitoring information in real-time.

During a seismic event, KMIDam RTSM issues alerts based on the exceedance of design or site-specific parameters for the Operating Basis Earthquake (OBE) or the Safety Evaluation Earthquake (SEE) (user-selectable). Essentially, this can be achieved: (a) by analyzing the ground motion acceleration time series and comparing the peak values with the design/site specific peak ground acceleration (PGA), and/or (b) through the real-time calculation of ground motion response spectra and immediate comparison with design/site-specific response spectra. KMIDam RTSM detects local or regional seismic events and delivers real-time information to understand the potential impact of earthquakes on the dams and their facilities, therefore enabling an efficient earthquake emergency response.

Furthermore, KMIDam RTSM can process data on local/regional seismic activity beneath and around the dam and reservoir, and cross-reference that information with observation data on the reservoir level variations, to provide evidence for monitoring reservoir-induced seismicity.

Automated Event Reporting (AER)

The KMIDam platform takes dam monitoring one step further with AutoPro, a specialized tool designed to automatically process data and generate and deliver technical reports after a seismic event is detected on the dam site.

As soon as a seismic event is detected, KMIDam AER reads the generated event files and prepares an SMA report, containing results on strong motion analysis from the free-field stations and the dam structure sensors. The SMA report includes: (a) figures of acceleration time series and FFTs, (b) values for PGA, PGV, CAV and the ground motion response spectra, which are compared with the design or site-specific parameters (OBE and SEE), and (c) maximum values of relevant parameters for structural response analysis.

After the earthquake event, KMIDam AER generates a SAFE report to provide additional information on the potential impact of the earthquake on the dam structure, by analyzing the

structural ambient vibration response. Specifically, Operational Modal Analysis (OMA) is used to process the ambient vibrations recorded on the dam structure for some time after the seismic event and estimate the main modal parameters. The natural frequencies are compared with reference values, and potential frequency decays are tracked to detect damage caused by the earthquake at an early stage and trigger preventive maintenance and inspection.

Long-Term Structural Health Monitoring (SHM) and Digital Twins

Dams can be equipped with permanent ambient vibrations monitoring systems (e.g., by combining Kinemetrics' force-balance EpiSensor accelerometers and Obsidian recorders), providing a reliable stream of data for continuous dynamic behavior assessment and long-term structural health monitoring (SHM). For such cases, KMIDam features a special module for automated processing and analysis of ambient vibration data measured continuously on the dam structure over time. KMIDam SHM uses Operational Modal Analysis to automatically estimate the main modal parameters of the dam, which can be correlated with reservoir level and thermal variations, operational conditions, etc., for dam performance assessment. Furthermore, special algorithms are applied to monitor the evolution of natural frequencies over time – comparison with reference values or predictive models –, in order to track a potential gradual degradation of the dam's structural condition and, if necessary, trigger preventive maintenance and inspection.

KMIDam can also feature digital twin(s) to support long-term SHM and data-driven decision making throughout the real-world dams' life cycle. These digital twins, which combine realistic 3D virtual models of the dam and its surroundings with predictive models, are continually updated using data from the long-term ambient vibration monitoring system and from the static sensors (integrated into the platform database). By leveraging this technology, KMIDam SHM delivers a new set of features, such as access to a realistic virtual replica for immersive dam visualization and inspection and to historical digital records. Moreover, simulations of the structural response for normal operating conditions, i.e., under static loads and ambient vibrations, as well as under extreme loads such as earthquakes, can be performed to characterize the expected dam behavior and to predict future behavior for different scenarios.

With KMIDam SHM, the lifespan of the structure can be better understood, and potential failure mechanisms can be identified early – discrepancies between the expected behavior and the measured performance of the physical dam may indicate damage or vulnerabilities -, enabling appropriate preventative measures to be taken.

3.2. Benefits

For dam monitoring projects, Kinemetrics supplies its world-class instrumentation, ensuring that the system will have maximum data return and unmatched reliability. In addition, the

KMIDam platform puts a set of comprehensive management and monitoring tools under the control of operators, engineers, and decision makers, ensuring a smooth and continuous operation of the system and the delivery of actionable information in the form of alerts or technical reports. Taking advantage of the proposed features and functionalities, our dam monitoring system solution may bring multiple benefits to all agents involved in system operation and dam safety management, in particular:

- Permanent control of system operation and state-of-health monitoring of field equipment
- Real-time information flow, ensuring simplified communication between operators, engineers, decision makers, etc. and streamline data access to minimize response time
- Delivery of actionable information (e.g., earthquake alerts and impact assessment reports) for a timely and precise assessment
- Enable better informed decision making and maximize situational awareness, to ensure safe and compliant operations and an efficient earthquake emergency response
- Reduce uncertainty and risk, to ensure business continuity and minimize downtime
- Increase confidence in dam safety and respond to investors and insurance companies

4. DAM MONITORING PROJECTS SUPPLIED BY KINEMETRICS

This section presents several dam monitoring projects for which Kinemetrics has provided its equipment and/or solutions and services. The real-world case studies shown here cover a diverse range of applications, for single and multi-dam projects, including seismic monitoring systems and continuous vibrations monitoring systems.

4.1. Multi-asset monitoring projects and seismic networks

Multi-Dam Project, Thailand

Kinemetrics, in collaboration with its operator representative AES, has designed and supplied a comprehensive and fully configured solution for a multi-dam seismic monitoring project in Thailand (Fig. 4). The customer was the Electricity Generating Authority of Thailand (EGAT), which is Thailand's leading state-owned power utility, under the Ministry of Energy. The largest power producer in Thailand, EGAT is responsible for power generation and transmission for the whole country, owning and operating different types of power generation facilities – including 24 hydropower plants.

In this specific project, seven EGAT dams were instrumented, namely: Srinagarind Dam (rock-fill with clay core, 140 m high), Sirikit Dam (earth-fill with clay core, 113.6 m high), Vajiralongkorn Dam (concrete face rock-fill structure, 92 m high), Rajjaprabha Dam (rock-fill with clay core, 94 m high), Bhumibol Dam (concrete arch, 154 m high), Bang Lang Dam (rock-fill with clay core, 85 m high), and Mae Chang Dam (earth-fill, 59 m high). Each dam was

equipped with (a) four short-period stations for monitoring induced seismicity, and (b) three or four Basalt accelerographs – at the crest, toe, abutment, and about 2 km downstream – for seismic and structural response monitoring. Local data acquisition is based on the Rockhound software. The centralized data acquisition is achieved in real-time using the Antelope software, installed in the Data Centre at the EGAT headquarters (Bang Kruai District, north of Bangkok).

The KMIDam system is tuned to carry out automatic location of small local seismic events near each dam and of regional earthquakes. The Antelope software performs real-time calculation of the Peak Ground Acceleration (PGA) and of the response spectra and real-time comparison with design or site-specific earthquake spectra. New events trigger the creation of event files and the automatic generation of reports containing actionable results for operators, engineers and decision makers within the organization. KMIDam also provides state-of-health monitoring for each element of the monitoring system.

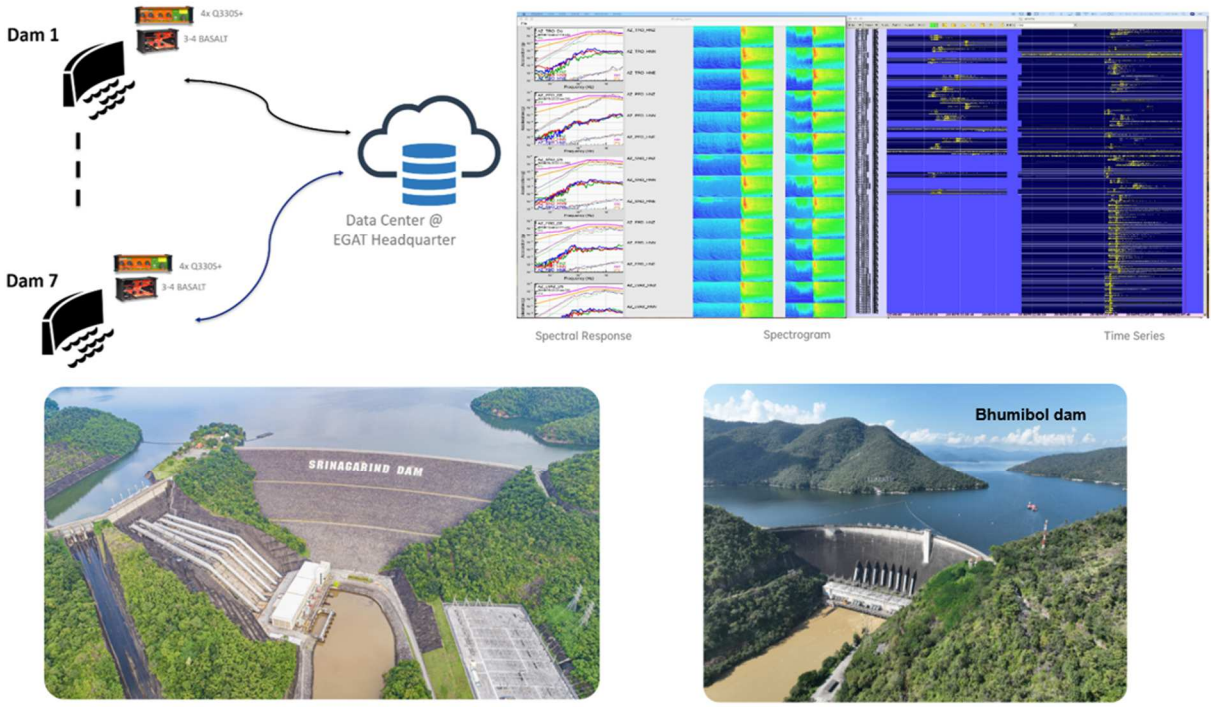

Fig. 4 - Kinemetrics' multi-dam seismic monitoring project in Thailand: implemented monitoring network (equipment for each dam and data centre) and obtained results (real-time data visualization and response spectra calculation and comparison with design spectra).

Multi-dam project in Algeria

The National Agency for Dams and Water Transfer (ANBT) manages 75 dams in Algeria, including earth-fill and rock-fill embankment dams, gravity and arch concrete dams, and RCC dams. A seismic monitoring project was undertaken and Kinemetrics designed and supplied seismic monitoring systems for five dams, including the 67 m-high Soubella embankment dam (Fig. 5). The goal of this project was to provide actionable data for real-time earthquake monitoring and impact alerting for all dams.

For each dam, a network of smart, IP-ready strong motion stations, with direct connection to the dam control room, was implemented, considering four monitoring points: three on the dam structure - crest, foundation, and abutment – and one in the free-field. Each station was equipped with the high-performance, compact, and cost effective ETNA2 accelerographs, housed in NEMA4 enclosures. The connection from the station to the control room was done by fibre optic. The ETNA2 accelerographs have built-in relays to report local alarms in case of acceleration threshold exceedance and/or to communicate state-of-health conditions.

The seismic monitoring systems at all five dams are designed to connect remotely to the ANBT Data Centre in Algiers, which is equipped with specialized KMIDam's processing tools for real-time calculation of earthquake ground motion spectra and for generating alarms in case of design spectra exceedance, as well as for automated generation of strong motion reports.

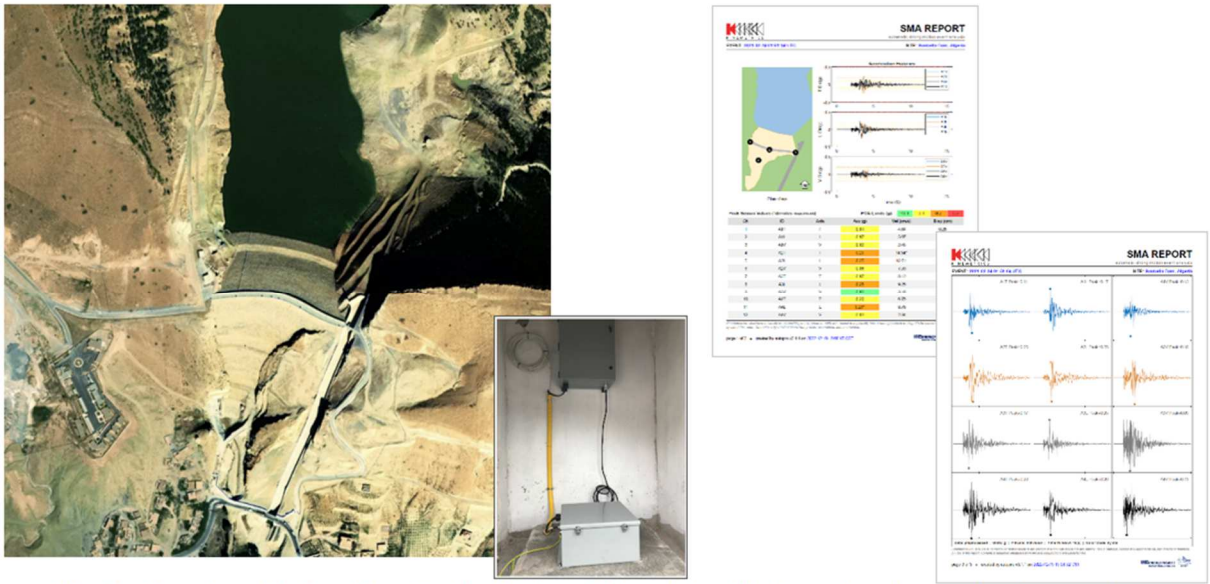

Fig. 5 - Results obtained for Soubella dam (Algeria) with the seismic monitoring system provided by Kinemetrics: delivered earthquake impact reports.

Multi-dam reservoir monitoring, Pakistan

Under the supervision of the Directorate of Seismic Studies of the Pakistan Water and Power Development Authority (WAPDA), a project for seismic monitoring of large dams was developed and implemented in Northern Pakistan, a region highly susceptible to seismic activities. The seismic monitoring system consists of 29 seismic stations, which include different types of sensors and data acquisition devices provided by Kinemetrics. All the stations are transmitting recorded seismic data through satellite links to the Central Data Centre located at the Tarbela Dam site (Fig. 6). There, all data acquisition, processing and analysis are carried out using the Antelope software.

Of these 29 stations, 10 are located around the Tarbela dam site. The Tarbela dam is an embankment dam located near the small town with the same name, in the Haripur District,

Pakistan. This earth- and rock-fill dam is over 140 m high and around 2.7 km long, making it the largest embankment dam and one of the largest dams in the world. In addition to the main embankment, there are two auxiliary embankments on the left bank, which carry two spillways. The main purpose of the Tarbela dam was to regulate water flow of the Indus River for irrigation use; other important objectives were the generation of hydroelectric power and flood control.

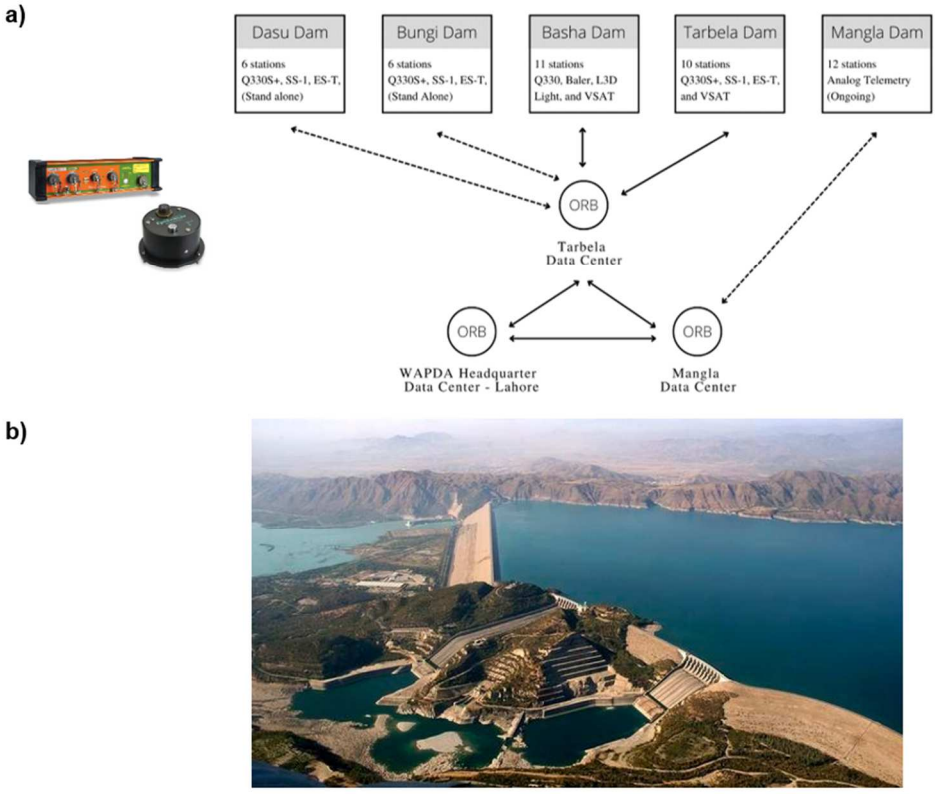

Fig. 6 - a) Layout of the multi-dam reservoir monitoring project implemented in Pakistan; b) aerial view of Tarbela dam (main embankment dam, spillway structures, and reservoir).

Peña Colorada Tailings Dams, Mexico

The Penã Colorada mine is a mining complex in Colima, Mexico, operated by the company Consorcio Peña Colorada, which is co-owned by ArcelorMittal and Ternium. The Peña Colorada iron ore deposits are the most important in Mexico, producing approximately 30% of Iron Ore used in the industry in the country. The main goal of the project was to implement a real-time seismic monitoring system for the tailings storage facilities at the Penã Colorada mining site, namely the Arrayanal and the Guásimas tailings dams (Fig. 7). The KMIDam seismic monitoring system comprised a total of 5 seismic stations, which included triaxial sensors based on force balance technology. The system was integrated with the existing geotechnical monitoring at both dams.

The KMIDam system's command-and-control centre was supported by the software applications Rockhound and AutoPro, enabling real-time alerting and automated reporting for both tailings dams. This solution provides immediate access to data and information on the

impact of the earthquake and on the structural response of these dams, enabling to support informed decision-making regarding the level of the required emergency response.

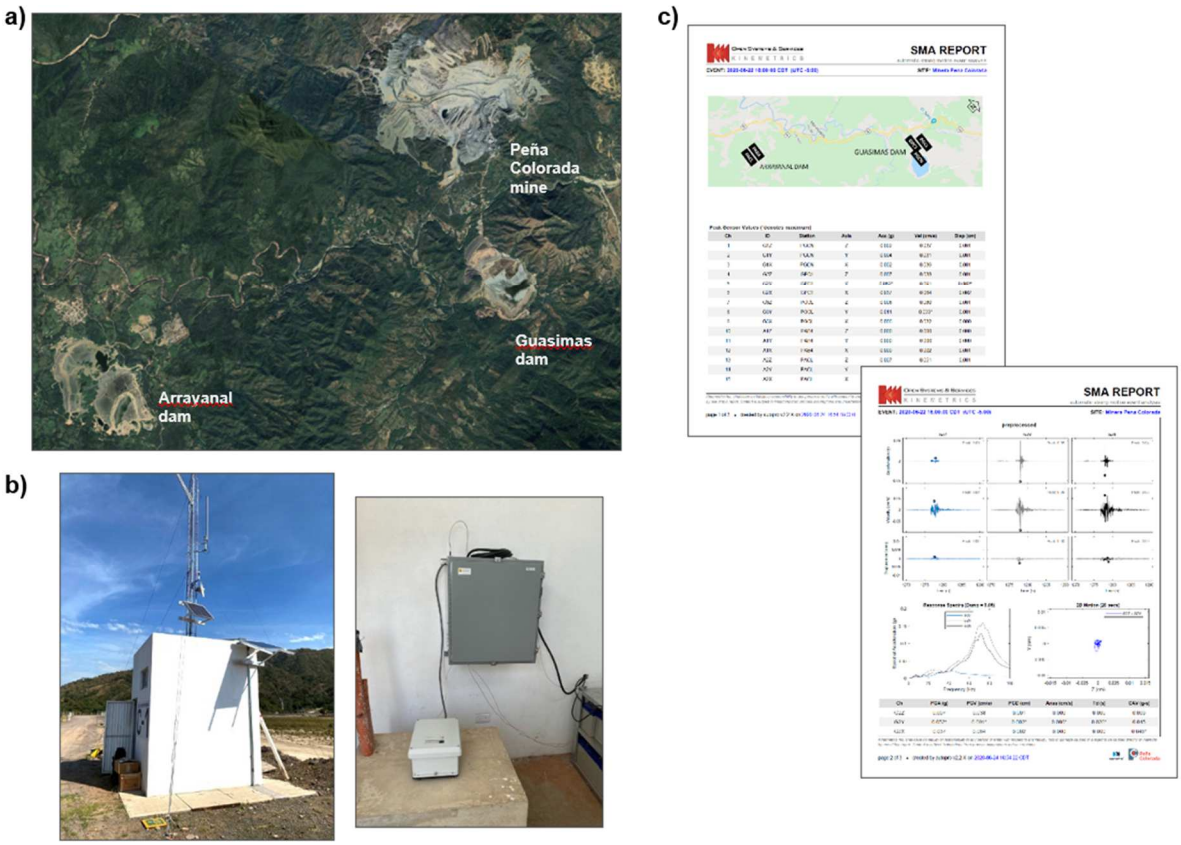

Fig. 7 - a) Penã Colorada mining site and locations of the Arrayanal and Guásimas tailings dams; b) seismic station; c) example of earthquake impact reports provided by AutoPro.

4.2. Seismic monitoring systems

Bakun Dam, Malaysia

The Bakun dam is a concrete-face rock-fill dam, in operation since 2011. The dam is 205 m high, with a 750 m long crest and a 16.93 million m^3 rockfill volume. The dam holds a reservoir with a surface area of 695km^2 and a catchment area of 14 750 km^2. Operated by Sarawak Energy, Bakun dam is the largest hydropower dam in Southeast Asia, and the Bakun Hydroelectric Plant represents the largest source of electricity generation in the Sarawak state.

Being a critical infrastructure operating in a seismic active area, the dam required seismic monitoring and an exceptional emergency alert system to ensure operational continuity and to protect the surrounding region. With that aim, a KMIDam seismic monitoring system developed and supplied by Kinemetrics was implemented at the Bakun dam (Fig. 8). In terms of equipment, the system includes three ETNA2 accelerographs (crest, base and right abutment), in order to detect on-site shaking and to monitor the structural response during seismic events. The system also integrates a management and monitoring Data Centre, located at the dam

control room. This platform is supported by KMIDam's specialized software applications not only to handle all data acquisition, but also to analyse the data and perform real-time strong-motion response calculation; this makes it possible to provide the operators at the dam with earthquake impact alerts and immediate notifications of exceedance of the design performance criteria, which for Bakun dam project are the SSE (Safe Shutdown Earthquake) and OBE (Operating Basis Earthquake). Based on the information provided by the implemented alerting and reporting tools, operators are enabled to make better emergency response decisions based on a deep understanding of earthquakes' impact to the dam site.

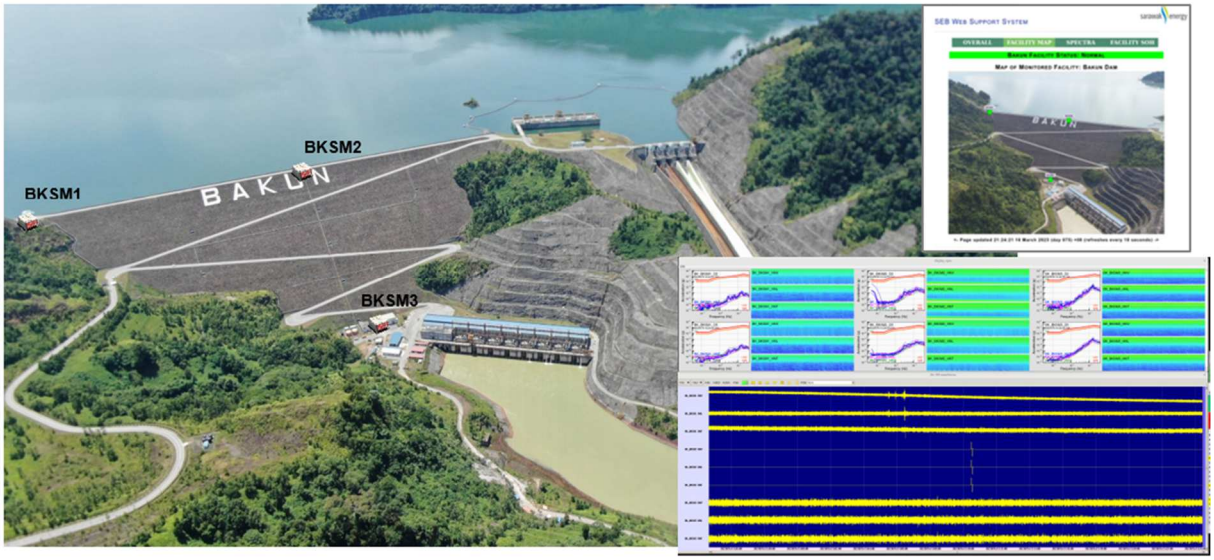

Fig. 8 - Bakun dam (downstream view), locations of installed sensors, and KMIDam interface.

Ruskin Dam, Canada

The Ruskin dam is 59.4 m high and 110 m long concrete gravity dam. Completed in 1930, on the State River in Ruskin, British Columbia, this dam was designed with the primary purpose of hydroelectric power generation. Ruskin dam is one of the 82 dams owned, operated, and maintained by BC Hydro across British Columbia. BC Hydro has a comprehensive dam safety program, which is widely recognised as one of the best in the world. This program covers all aspects of dam safety, including surveillance and monitoring, risk analysis, and regulatory compliance and reporting.

In 2017, Kinemetrics supplied and installed all equipment to implement a seismic monitoring system in Ruskin dam (Fig. 9), aiming to provide data for earthquake impact assessment and supporting earthquake emergency response. This KMIDam solution included five Obsidian recorders, as well as five triaxial accelerometers Episensor ES-T and one Shallow Borehole Episensor (SBEPI). More specifically, there are four 4-channel Obsidians, each one connected to a single ES-T, and one 8-channel Obsidian, getting the data from the fifth ES-T and from the SBEP. The sensors were installed in five locations, namely in the central upper part of the

dam (pier 4), inside a dam gallery, close to the dam base, in the right abutment, at the top of the left abutment, inside the control room, and on the ground inside the powerhouse.

Remote access, system configuration and maintenance, and real-time monitoring are made possible via the web-based user interface of the Rockhound software. The implemented KMIDam tools enable seismic event triggered data recording and alarm-notification in case of exceedance of specific PGA levels, helping operators make better and quicker informed decisions. KMIDam also allows for remote data retrieval and system state-of-health information.

Fig. 9 - a) Ruskin dam (downstream view) and locations of installed sensors; b) detail of enclosure with Obsidian recorder an ES-T accelerometer.

San Vicente Dam, US

The San Vicente dam is a concrete gravity dam located in San Vicente Creek, San Diego, California. Owned and operated by the City of San Diego, the 67 m high dam entered in operation in 1943, and its main purposes include municipal water storage and flood control. The San Vicente dam Raise Project was undertaken between 2009 and early 2014, raising the dam's height to 103 m using roller-compacted concrete, in order to increase the reservoir's original capacity; this was the largest dam raise in the United States and the largest roller-compacted concrete dam raise in the world at the time.

Being a high hazard dam located in a region of high seismic activity like California, a seismic monitoring system was designed and implemented at San Vicente dam by Kinemetrics in 2013. The KMIDam system consists of five strong motion stations installed within and around the dam (Fig. 10). Two stations were installed on the dam structure, SM-2 at the crest, to the right of the spillway, and SM-4 in the main gallery at the dam base. Station SM-5 was deployed downstream of the dam, inside the building of the control facility. Finally, SM-1 was deployed in the left abutment road and SM-3 was placed in the right abutment. The first three stations

(SM-2, SM-4, and SM-5) are networked together for common triggering and single point of access, while the other two (SM-1 and SM-3) were installed as standalone stations supplied with solar panels (since there was no AC power available).

Each station includes a 4-channel Basalt recorder, protected by a floor mountable galvanized steel NEMA4 field station enclosure, and a triaxial EpiSensor force-balance accelerometer (ES-T), inside a floor mountable NEMA4 fiberglass sensor protection box. The Basalts were configured as event recorders, with trigger and alarm thresholds to automatically create event files for dam operators and thus support informed decision making and emergency response.

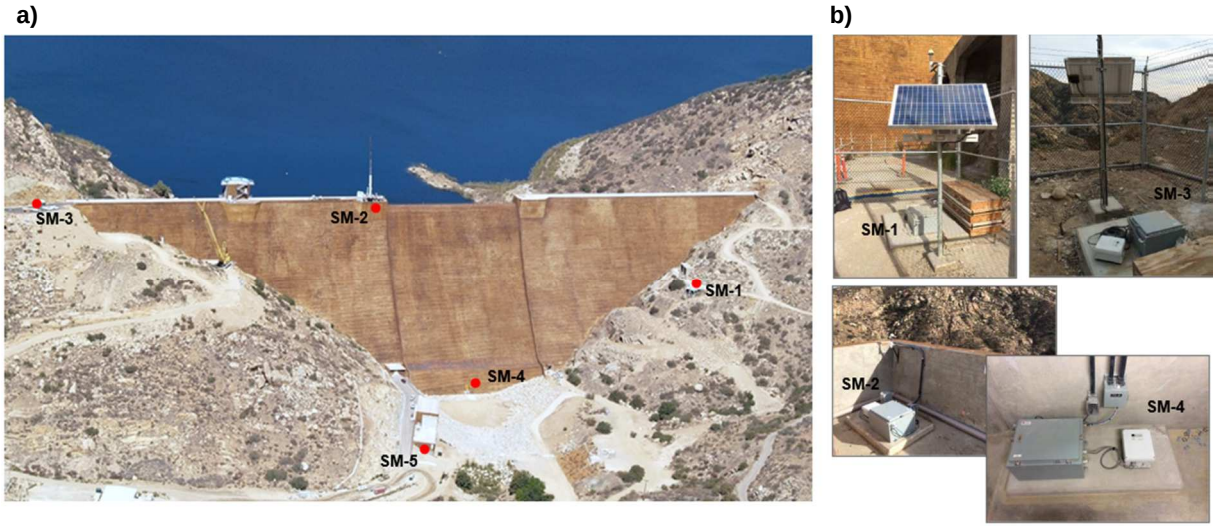

Fig. 10 - a) San Vicente dam (downstream view) and locations of sensors; b) details of the installed seismic stations.

4.3. Continuous vibrations monitoring systems for long-term SHM

Cabril dam, Portugal

The Cabril dam is a large concrete dam located on the Zêzere River, Portugal. In operation since 1954, it is a 132 m high double curvature arch structure, with a crest length of 290 m. Cabril dam is the highest dam in Portugal, and its main purposes are water supply and storage, hydropower production, and flood control. The dam is owned and operated by Energias de Portugal (EDP). Overall, the dam is in good structural condition, nevertheless, there are horizontal cracks at upper part of the downstream face, which appeared during the first filling of the reservoir, and signs of concrete swelling due to alkali-aggregate reactions were detected in the late 1990s.

With the objective of improving dam safety control, a pioneering continuous vibrations monitoring system [6] was designed in the National Laboratory for Civil Engineering (LNEC) and installed in Cabril dam in 2008, with support from EDP and the Portuguese Foundation for Science and Technology (FCT). The system was developed to continuously monitor the

dynamic behavior of the dam for long-term structural health monitoring, and to assess the response during seismic events (Fig. 11) [7,8]. This was the first permanent dynamic monitoring system installed in a large dam in the world, and Kinemetrics supplied all sensors, specifically 16 uniaxial EpiSensor force-balance accelerometers (9 placed along the crest and the other 7 in a gallery about 25 m below) and 3 triaxial EpiSensor force-balance accelerometers (1 at the crest and 2 in both abutments). The sensors have been operational for over 15 years, demonstrating the robustness and reliability of Kinemetrics' equipment for long-term vibrations monitoring solutions for dams.

The collected vibration data, which is sent to a dedicated server located on the dam control room, has allowed operators and LNEC's dam engineers to monitor the dam's response under regular operating conditions and during/after earthquake events. In addition, this data has been used to support the development and calibration of advanced FEM of the Cabril dam-reservoir-foundation system.

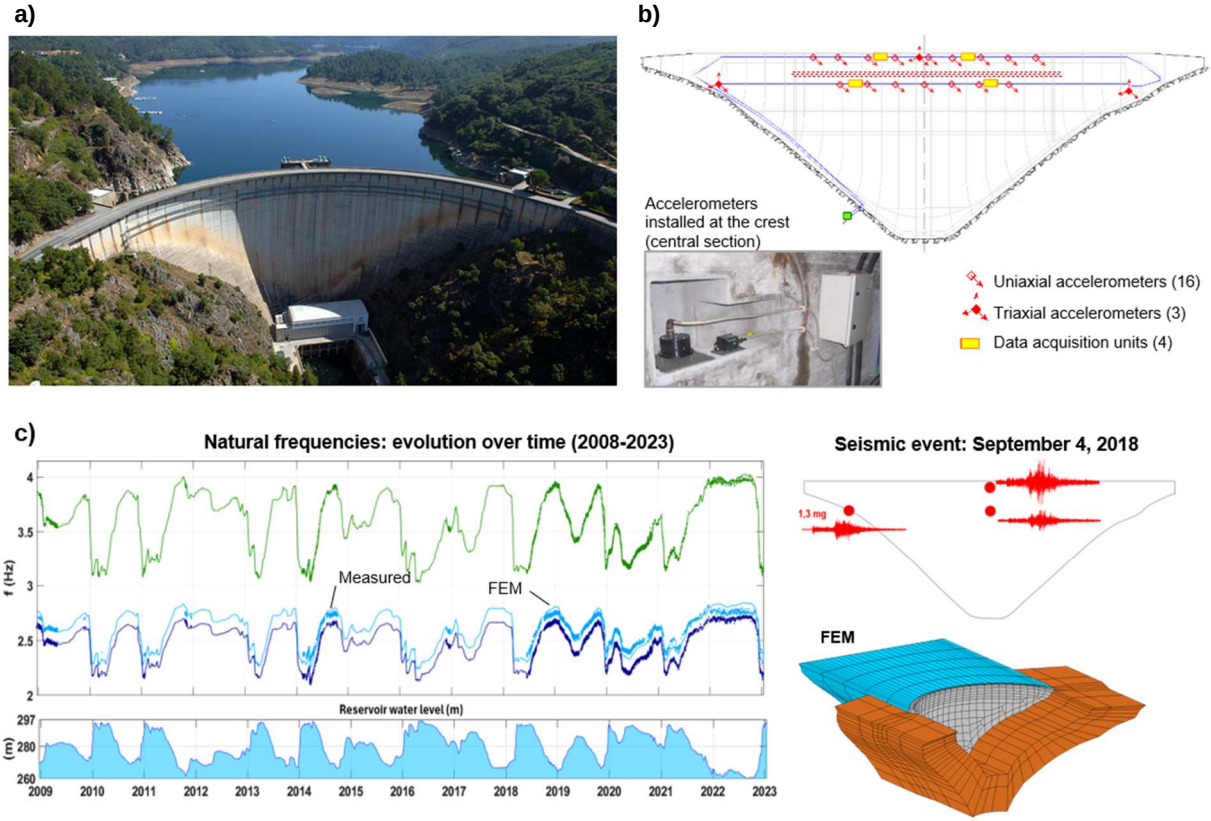

Fig. 11 - a) Cabril dam (downstream view); b) dynamic monitoring system layout, with sensor location, and installed sensor and Granite recorder; c) results [7,8]: evolution of natural frequencies over time, accelerations recorded during an earthquake event, and FEM.

Cahora Bassa dam, Mozambique

The Cahora Bassa dam, built in 1974, is a thin double curvature arch dam, standing 170 m tall with a 303 m long crest. The dam, owned and operated by Hidroelétrica de Cahora Bassa (HCB), is located on the Zambezi River, near Songo, in Western Mozambique. The

hydroelectric power station, located on the south bank of the river, is the largest hydroelectric scheme in southern Africa. In operation for over 50 years, the dam is in excellent structural condition overall; however, over time it started to exhibit signs of concrete swelling due to alkali-aggregate reactions.

In order to provide additional data and thus help support structural safety control, HCB decided to invest in the installation of a complete dynamic vibrations monitoring system [9]. This system was designed and implemented to measure vibrations in the dam structure, as well as at the base and in both abutments, with the goal of providing actionable data for seismic monitoring and for long-term structural behavior assessment and health monitoring [7,10,11] (Fig. 12).

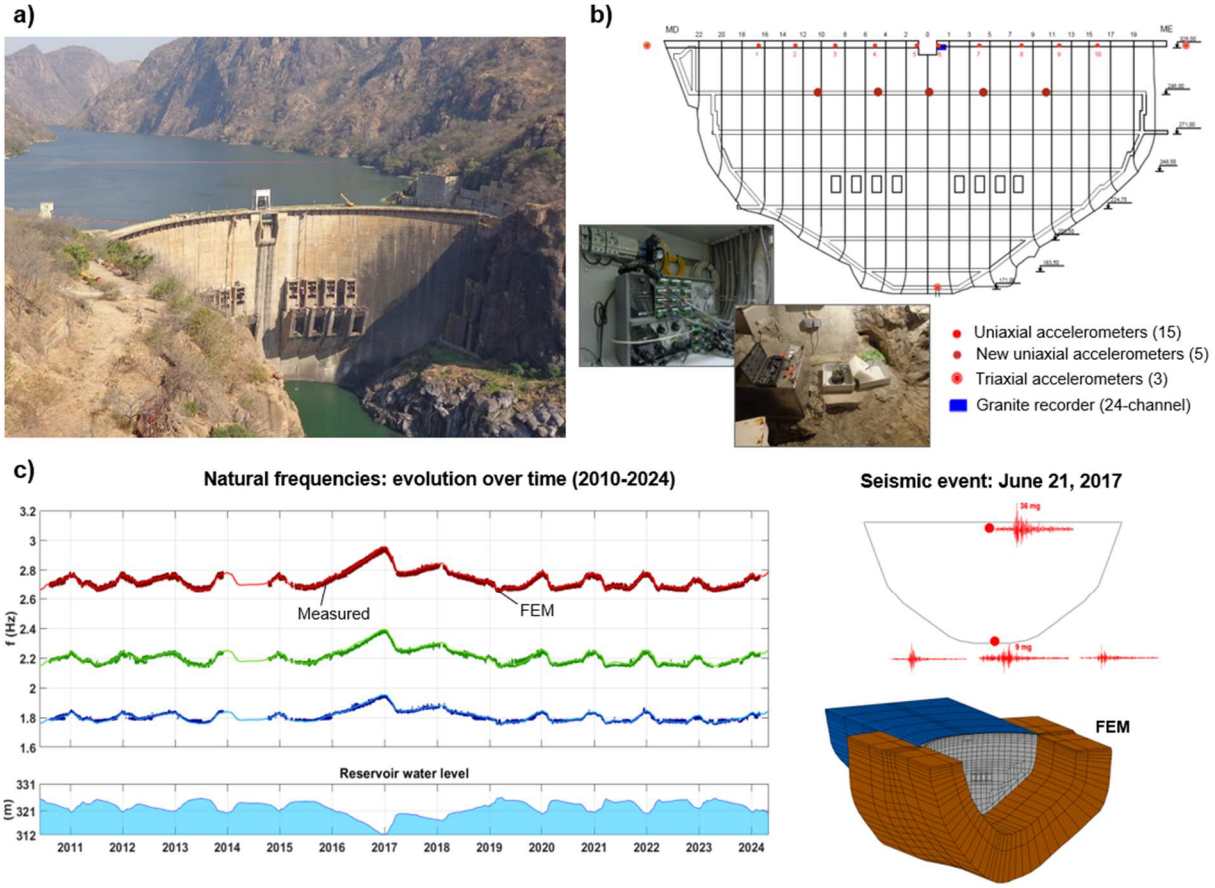

Fig. 12. a) Cahora Bassa dam (downstream view); b) dynamic monitoring system layout, with sensor location, and detail of installed sensors; c) results [7,10,11]: evolution of natural frequencies over time, accelerations recorded during an earthquake event, and FEM.

The original system, installed in 2010, was based on a turnkey solution provided by Kinemetrics, including a 24-channel Granite recorder for data acquisition and 10 EpiSensor force-balance accelerometers, specifically ten uniaxial ES-U sensors, distributed along the crest. Later, in 2013, three new accelerometers were installed, namely three ES-T triaxial sensors, one at the dam base and two in the right and left abutments. All this equipment has been fully operational since installation, showing once again the quality of Kinemetrics' equipment for long-term vibration monitoring systems for dams. Recently, in late 2024, an

upgrade to the system was proposed, and five new EpiSensor uniaxial accelerometers were installed in the dam structure and integrated into the data acquisition system.

All data files are sent to the Data Centre located in the control room at the Cahora Bassa hydropower station offices. The monitoring data gathered for over a decade has allowed operators at the dam site and dam engineers working remotely, to control the behavior of the dam during regular operations, as well as to monitor the impact of earthquake events on the dam site. Furthermore, the gathered vibration data has allowed dam engineers to develop and calibrate FEM, which are then used for predictive computations.

Foz Tua Dam, Portugal

The Foz Tua dam is a 108 m high double curvature arch structure. In operation since 2017 in the northern part of Portugal, the Foz Tua dam is one of the most recent dams in the country and it was constructed with the main purpose of hydropower generation. Originally owned by EDP, today the dam is owned and operated by Movhera, a newly created company by Engie.

A comprehensive dam monitoring project was undertaken for Foz Tua dam, entailing the installation of two main systems [12]: the seismic monitoring system and the continuous dynamic monitoring system (Fig. 13).

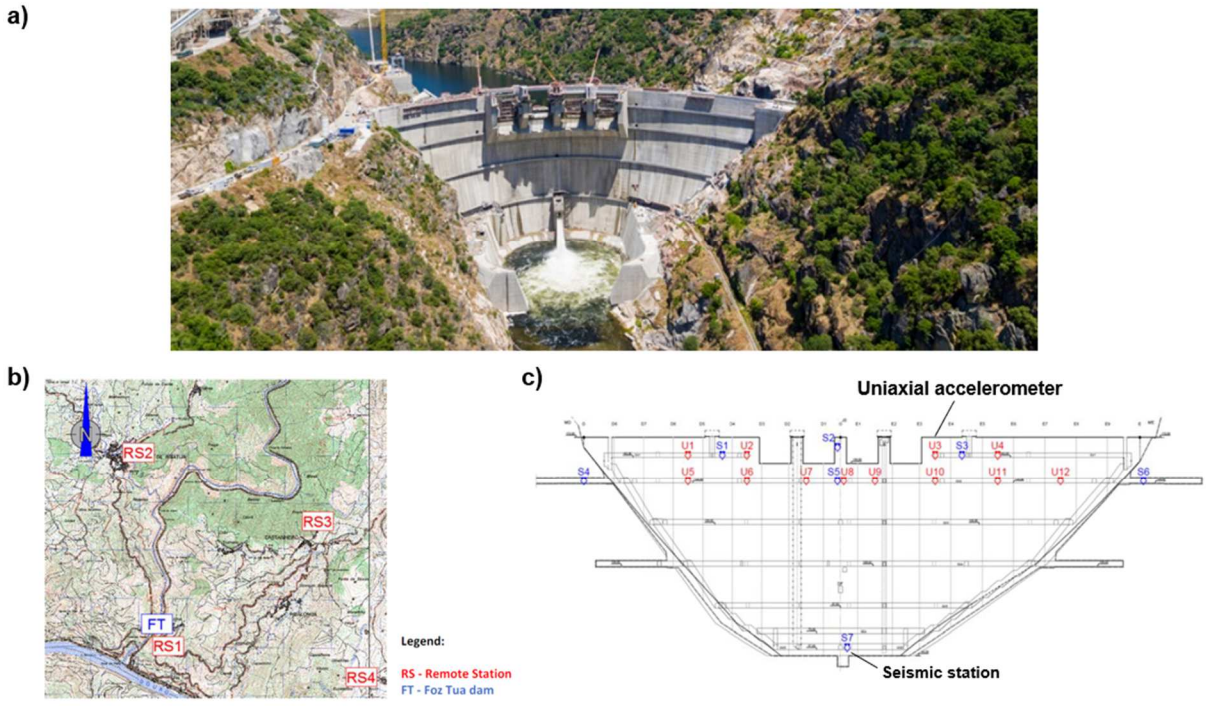

Fig. 13. a) Foz Tua dam (upstream view); b) layout of the seismic stations deployed around the dam site and reservoir [12]; c) seismic stations and accelerometer installed in the dam [12].

The first system was implemented to allow the characterization of seismic actions and to monitor the dam response during earthquakes, as well as to ensure proper characterization of the ground motion propagation and to detect and locate reservoir induced seismicity events in

the surrounding area. The second system was developed with the purpose of ensuring a reliable characterization of the dynamic behavior of the dam based on measured ambient/operational vibrations, namely by analyzing the dam's natural frequencies and mode shapes and tracking their evolution over time (considering the variation of operational conditions and possible deterioration). Kinemetrics, through its partner Quantific, in Portugal, supplied all sensors and data acquisition units for this project.

The seismic monitoring system includes four remote stations around the reservoir and seven stations installed inside the dam galleries (3 along the base and 4 in the upper part of the dam structure); in total, the data acquisition hardware included 11 ETNA2 triaxial accelerographs, configured as trigger-event. The continuous dynamic monitoring system features data acquisition devices and force-balance accelerometers, installed in the dam body. Specifically, there are three 4-channel Obsidian recorders and 12 uniaxial Episensor accelerometers, oriented in the radial direction, deployed along the upper galleries of the dam. In operation since 2019, this monitoring system has a central server to manage data acquisition and processing, as well as for sending alarms in case of detection of relevant events.

5. CONCLUSIONS

This paper offers an overview on the experience gathered by Kinemetrics' engineers and of the work carried out in the field of dynamic monitoring of dams. First, the paper presented KMIDam, a complete Dam Management Platform designed for seismic and structural monitoring applications. Essentially, this work shows how KMIDam puts a comprehensive set of management and monitoring tools under the control of operators, dam engineers and safety specialists, offering a wide range of features and benefits for dam safety management and emergency response. Next, the paper provided a comprehensive review of real-world dam monitoring projects for which Kinemetrics has provided its equipment and/or solutions and services over the past two decades, including single and multi-dam seismic monitoring systems and continuous vibrations monitoring systems. This demonstrated how real seismic and vibration monitoring data, captured with high-end sensors and recorders, and processed using advanced platform technologies, as those developed and supplied by Kinemetrics, can be used to provide valuable information to ensure informed, safe, and continued operations.

REFERENCES

[1] ICOLD (2018). Bulletin 158: Dam surveillance guide.

[2] Alegre, A., Oliveira, S., Carvalho, E., Mendes, P., Proença, J., Matsinhe, B. (2022). Continuous dynamic monitoring of large arch dams and vibration-based damage detection. HYDRO 2022, Strasbourg, France.

[3] Oliveira, S., Alegre, A., Carvalho, E., Mendes, P., Proença, J. (2022). Seismic and structural health monitoring systems for large dams: theoretical, computational and practical innovations. Bulletin of Earthquake Engineering, 20: 4483–4512.

[1] Wieland, M. (2016). Safety Aspects of Sustainable Storage Dams and Earthquake Safety of Existing Dams. Engineering, 2: 325–331.

[4] El-Idrissi, M., Saifullah, M.K., Ciudad-Real, M., Skolnik, D., Spassov, E. (2023) Operations and Dam Safety with the KMIDam Platform. EVACES 2023, Politecnico Milano, Italy.

[6] Oliveira, S., Mendes, P., Garrett, A., Oliveira Costa, C., Reis, J. (2011). Long-term dynamic monitoring systems for the safety control of large concrete dams. The case of Cabril dam, Portugal. 6th International Conference on Dam Engineering, Lisbon, Portugal.

[7] Alegre, A., Carvalho, E., Matsinhe, B., Mendes, P., Oliveira, S., Proença, J. (2019). Monitoring vibrations in large dams. HYDRO2019, Porto, Portugal.

[8] Oliveira, S., Alegre, A., Mendes, P., Proença, J., Ramos, R. (2024). Modal-Based SHM of Cabril Dam. Exploring Vibration Data Acquired Over the Last 15 Years. 10th International Operational Modal Analysis Conference (IOMAC 2024).

[9] Carvalho, E., Matsinhe, B. (2014). First steps on automatic data acquisition and analysis system in Cahora Bassa dam. HYDRO 2014, Como, Italy.

[10] Oliveira, S., Mendes, P., Rodrigues, M., Alegre, A., Proença, J., Carvalho, E., Matsinhe, B. (2023). Cahora Bassa vibrations monitoring between 2010-2022. Analysis of frequencies using HST statistical models for effects separation. XII International Conference on Structural Dynamics EURODYN 2023, TU Delft, Delft, Netherlands

[11] Carvalho, E., Matsinhe, B., Mendes, P., Oliveira, S., Alegre, A., Ciudad-Real, M., Skolnik, D., El-Idrissi, M. (2023). SSHM Systems for Dams: 12 Years' Experience in Cahora Bassa Dam. Equipment, Software, and Main Results. EVACES 2023, Politecnico Milano, Italy.

[12] Silva Matos, D., Tavares de Castro, A., Gomes, J., Faria, A., Pimentel, D., Lima, J. (2019). Static and continuous dynamic monitoring of Foz Tua arch dam. HYDRO 2019, Porto, Portugal.

Fifth International Dam World Conference
PORTUGAL • LISBON • LNEC • APRIL 13-17, 2025
dam world 2025

DYNAMIC BEHAVIOUR OF A CONCRETE DAM: DEVELOPMENT OF STATISTICAL AND MACHINE LEARNING MODELS FOR INTERPRETATION OF MONITORING DATA

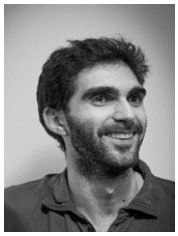

Andrés Sejas[1]
FEUP

Sérgio Pereira
FEUP / Construct-*ViBest*

Juan Mata
LNEC

Álvaro Cunha
FEUP / Construct-*ViBest*

ABSTRACT

This work focuses on the dynamic monitoring behaviour of concrete dams, with a specific emphasis on the Baixo Sabor dam as a case study. The main objective of the dynamic monitoring is to continuously observe the dam's behaviour, ensuring it remains within expected patterns and issuing alerts if deviations occur. The monitoring process relies on on-site instruments and behaviour models that use pattern recognition, thereby avoiding explicit dependence on mechanical principles.

The undertaken work aimed to develop, calibrate, and compare statistical and machine learning models to aid in interpreting the observed dynamic behaviour of a concrete dam. The methodology included several key steps: operational modal analysis of acceleration time series, characterization of the temporal evolution of observed magnitudes and influential environmental and operational variables, construction and calibration of predictive models using both statistical and machine learning methods, and the comparison of their effectiveness.

Both Multiple Linear Regression (MLR) and Multilayer Perceptron Neural Network (MLP-NN) models were developed and tested. The results showed that while both models effectively captured and predicted the dam's behaviour, the neural network slightly outperformed the regression model in prediction accuracy. However, the linear regression model is easier to interpret.

In conclusion, both methods linear regression and neural network models are suitable for the analysis and interpretation of monitored dynamic behaviour. For large-scale projects like the Baixo Sabor dam, multilayer perceptron - neural networks offer significant advantages in handling intricate data relationships, thus providing better insights into the dam's dynamic behaviour.

Keywords: Concrete Dam, Dynamic Behaviour, Machine Learning, Multiple Linear Regression, Baixo Sabor Dam.

[1]E-mail address: guzmansejasandres@gmail.com, Portugal.

1. INTRODUCTION

The behaviour of concrete dams is affected over time by environmental conditions, aging, and natural forces. Monitoring static and dynamic aspects, such as displacements, strains, and hydrostatic pressures is crucial for identifying early structural issues. This study develops statistical and machine learning models to interpret dam behaviour using continuous monitoring data. In this work, after the introduction of the HST (hydrostatic, seasonal, time) and the HTT (hydrostatic, temperature, time) approaches, a summary of the most used data-based models is presented, taking another step in its application to the analysis of data from the dynamic observation of large concrete dams. The Baixo Sabor dam was adopted as a case study, and the pattern behaviour of the natural frequencies, from 2015 to 2018, were represented through both MLR and MLP-NN models. Finally, a brief discussion about the good performance of both models is presented.

2. INTERPRETATION OF STRUCTURAL BEHAVIOUR BASED ON HST AND HTT APPROACHES

In the normal operation phase of the dam's life, the thermal effect is directly related to the air and water temperature variations. There are two main approaches for choosing the parameters that represent the thermal effect in data-based models [1]: the HST approach and the HTT approach. The HST approach is the most common for developing quick models in the field of dam engineering, being the approach adopted in this work. This approach is based on the hypothesis that the variable under study, such as horizontal displacements, depends on a combination of hydrostatic load effects, seasonal temperature variations represented in a simplified manner through the sum of sinusoidal functions with an annual period, and the effect of time [2].

This approach is only applicable if there are enough number of observations and the generated functions can model the pattern of the variable under study. The approach aims to approximate effects associated with a limited period at a specific point using the equation (1):

$$\delta(h_i, S_i, t_i) = U_h(h_i) + U_\theta(\theta_i) + U_t(t_i) + k + \varepsilon_i \quad (1)$$

where:

- $\delta(h_i, S_i, t_i)$ - The observed value of the variable under analysis in observation i, which depends on hydrostatic pressure, temperature, and the point in time when the observation is made.
- $U_h(h_i), U_\theta(\theta_i), U_t(t_i)$ - Components of the variable that correspond to the elastic effect of the water level in the reservoir, the elastic effect of seasonal temperature variations, and the effect of time in the i^{th} observation.

- k - A constant that corresponds to the difference between observed and calculated values at the beginning of the calibration period.
- ε_i - The residual of the i^{th} observation, given by the difference between the estimated value and the observed value.

The effect of the water level can be represented by a polynomial function. The approximation can be made using the following equation (2):

$$U_h(h) = a_1 * h^4 + a_2 * h^3 + a_3 * h^2 + a_4 * h \quad (2)$$

where h is the reservoir water height, and $a_1,\ a_2,\ a_3,\ a_4$ are the coefficients to be adjusted.

The temperature effects are related to variations in air and reservoir water temperatures and their influence on the thermal field of the structure. In the HST approach, the effect of temperature change can be considered as a proportional attenuation of air temperature changes, with a phase shift that depends on the depth along the analysed section. Straightforward data-based models typically do not use temperature measurements, as it is assumed that the thermal effect U_θ can be represented by a sum of sinusoidal functions with one year of period. Thus, the effect of temperature variations is defined by a linear combination of sinusoidal functions, depending only on the day of the year [3], and can be represented by:

$$U_\theta(\theta_1)^{annual} = b_1 * cos(\theta_1) + b_2 * sin(\theta_1) \quad (3)$$

with:

$$\theta_1 = \frac{2*\pi*t_d}{365} \qquad 1 \leq t_d \leq 365 \quad (4)$$

where t_d represent the number of days elapsed from the start of the year to the date of observation; and $b_1,\ b_2$ are the coefficients to adjust.

The effect of time on the structure is an irreversible component associated with the effects of inelastic actions, such as creep and/or concrete stress relaxation, as well as phenomena related to deterioration (e.g. concrete swelling) [4].

The combination of polynomial functions is often used in the context of this component, with several ways to write the equation (5), depending on the author and the phenomena under study.

$$U_t(t) = c_1 * t^3 + c_2 * t^2 c_3 * t + c_4 * ln * (1 + \frac{t}{a}) \quad (5)$$

where t represents the number of days between the observation campaign and the beginning of the monitoring; a represents the number of days between the first filling and the date of the beginning of the analysis; and $c_1, c_2, c_3, c_4$are the coefficients to be adjusted.

Based on the HTT (Hydrostatic, Temperature, Time) approach, the model represents the thermal effect through information recorded in thermometers, that can be embedded in the concrete dam body. A better performance based on the HTT models approach than HST models is usually expected. However, additional data (temperatures in the dam body) is required to perform HTT models. In this study case, as referred before, the focus was on the analysis of the performance of the HST models [5].

3. MULTIPLE LINEAR REGRESSION AND NEURAL NETWORK MODELS

3.1. The Multiple Linear Regression model

The primary goal of Multiple Linear Regression (MLR) models is to predict response values (dependent variable) based on a set of predictor data (independent variables). A model can be built initially to understand the relationship between predictors and a dependent variable, and then once this relationship is established, it can be used to produce predictions of the dependent variable based on known independent variables [6].

In the context of dam monitoring, certain loads trigger responses from the reservoir-dam-foundation system. The set of actions that stand out results from variations in environmental and operational conditions, such as the water level in the reservoir, temperature, and others.

If it can be confirmed that: i) there were no significant structural changes during the period under analysis; and ii) the structure operates with low stress levels, displaying elastic, linear, and reversible behaviour, then the principle of superposition can be considered valid. This allows for simplification in analysis by using models built with the Multiple Linear Regression method.

3.2. The Multilayer Perceptron Neural Network model

A Multilayer Perceptron Neural Network model (MLP-NN) is a type of feedforward neural network in which all nodes are interconnected across different layers. The concept of the perceptron which is a supervised learning algorithm that includes node values, activation functions, inputs, and weights to compute outputs is also a fundamental unit of an artificial neural network [7].

The MLP-NN model operates only in the forward direction, meaning each node passes its value to the next node in the forward direction only. The backpropagation algorithm is used to enhance the training model's accuracy by adjusting the weights based on the error between the predicted and actual outputs.

The general architecture of a neural network consists of three main layers: input layer, hidden layer, and the output layer. The input layer is where the network first receives data. The number

of nodes in this layer corresponds to the number of features or variables in the dataset. Each node in the input layer represents a distinct feature of the input data. The hidden layers are where the network performs its computations and learns to transform the input data. The complexity of the relationships in the input data determines the number of hidden layers required. Some models, a single hidden layer might be enough, whereas more complex models may require multiple hidden layers to effectively capture patterns in the data. Finally, the output layer provides the final prediction or classification [7].

4. CASE SUDY: THE BAIXO SABOR DAM

4.1. Introduction

The Baixo Sabor dam is an important hydroelectric infrastructure located in the Sabor River in north-eastern Portugal. This dam is part of a larger project aimed at harnessing the hydroelectric resources in the region. It is situated in the district of Bragança, within the region of Trás-os-Montes and Alto Douro, known for its mountainous landscapes and rivers. The Sabor river is one of the main tributaries of the Douro river.

The dam construction began in 2008, being the beginning of the first filling in 2015. It is a concrete double-curvature arch dam, embedded in a narrow valley zone. The dam is 123 m height and its crest, with a width of 6 m and 505 m long. The dam body has 32 blocks, separated by vertical contraction joints, which is crossed by 6 horizontal visit galleries and one general drainage gallery. Fig. 1 shows an aerial view of the representation of the dam where it is possible to see the elements that constitutes the dam [8].

Fig. 1 – Aerial view of Baixo Sabor dam

The dynamic monitoring system installed in the dam is divided into three subsystems connected by optical fiber, with 12 uniaxial force balance accelerometers at the top, and 8 other positioned in the second a third visit galleries [8]. The position of the total 20 accelerometers is characterized and showed in Fig. 2.

The dynamic monitoring system is configured to continuously record acceleration time series with a sampling rate of 50 Hz and a duration of 30 minutes at all instrumented points, thus producing 48 groups of time series per day.

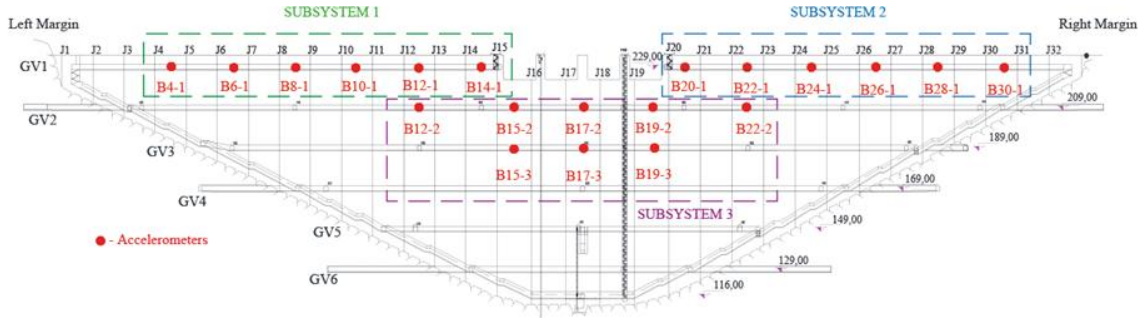

Fig. 2 – Measuring points and subsystem components of the dynamic monitoring system of the Baixo Sabor dam [8]

Fig. 3 displays the air temperature recorded during a three-year monitoring period. The variations in temperature over time offer valuable information about seasonal variations and climatic conditions in the region. Analyzing these patterns can help in assessing the impact of air temperature on various aspects of the dam's pattern behaviour.

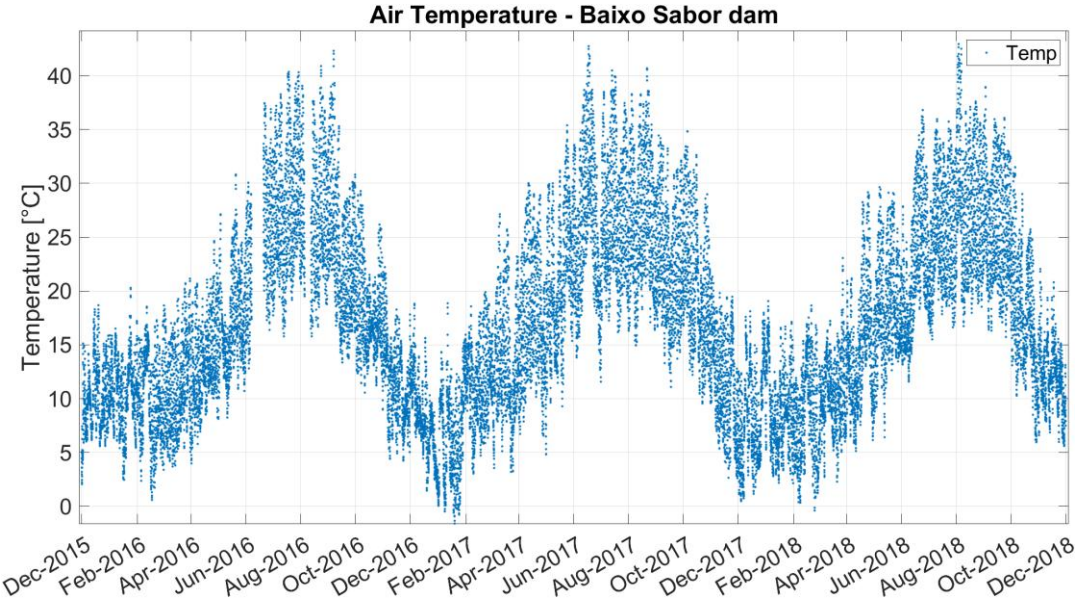

Fig. 3 – Air temperature records from 2015 to 2018

In turn, Fig. 4 illustrates the water level variation observed over a period of three years, including the last stage of the dam’s first filling. Data reveals variations in the water level over time due to the season, having more water in the reservoir during the spring and early summer,

and having less during the autumn and early winter and these fluctuations show almost the same behaviour over time, providing insights into the dynamics of the reservoir. Serving as a relevant aspect of understanding the behaviour of the dam and its surrounding environment.

Season variations affect the mass of the dam-foundation-reservoir system, as well as the stiffness of the concrete-arch, therefore leading to fluctuations in the values of modal properties, making it essential to consider these environmental factors when assessing the structural dynamic behaviour of the dam over time.

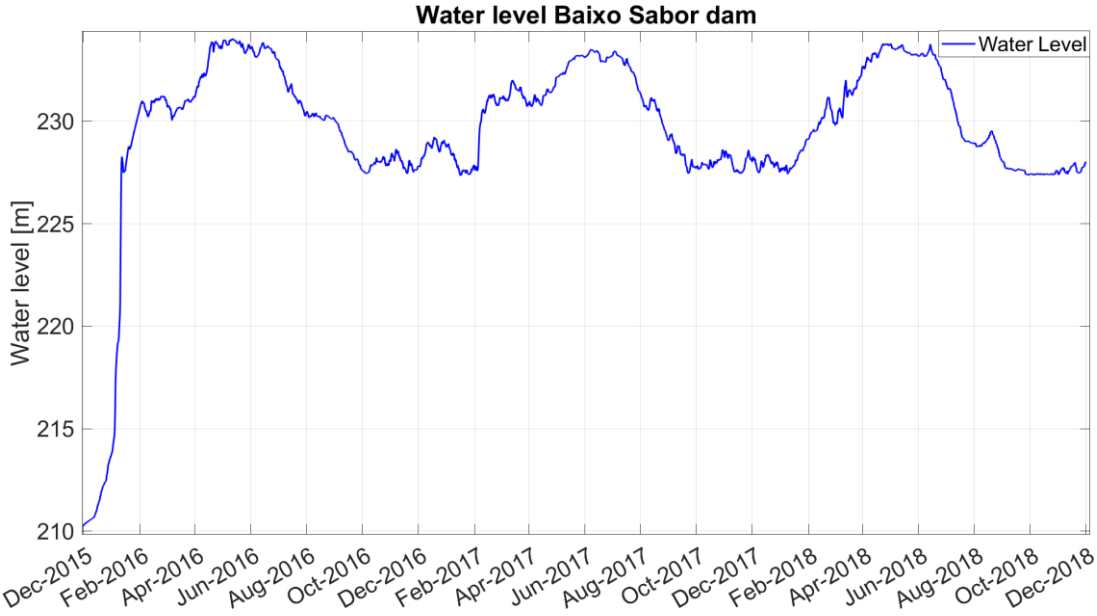

Fig. 4 – Water level records from 2015 to 2018

The continuous dynamic monitoring aims to identify and track the evolution of the dam's dynamic characteristics under various operational and environmental conditions. Fig. 5 illustrates the evolution of the natural frequencies obtained through continuous monitoring spanning three years. The dataset used for this research includes data monitored from December 1, 2015 (1/12/2015) at 00:00 hours until November 30, 2018 (30/11/2018) at 23:00 hours.

This extensive dataset allowed for the development of robust models to analyse the dam's behaviour under various conditions. The continuous monitoring provided a detailed temporal resolution, facilitating the understanding of how the natural frequencies evolved over time.

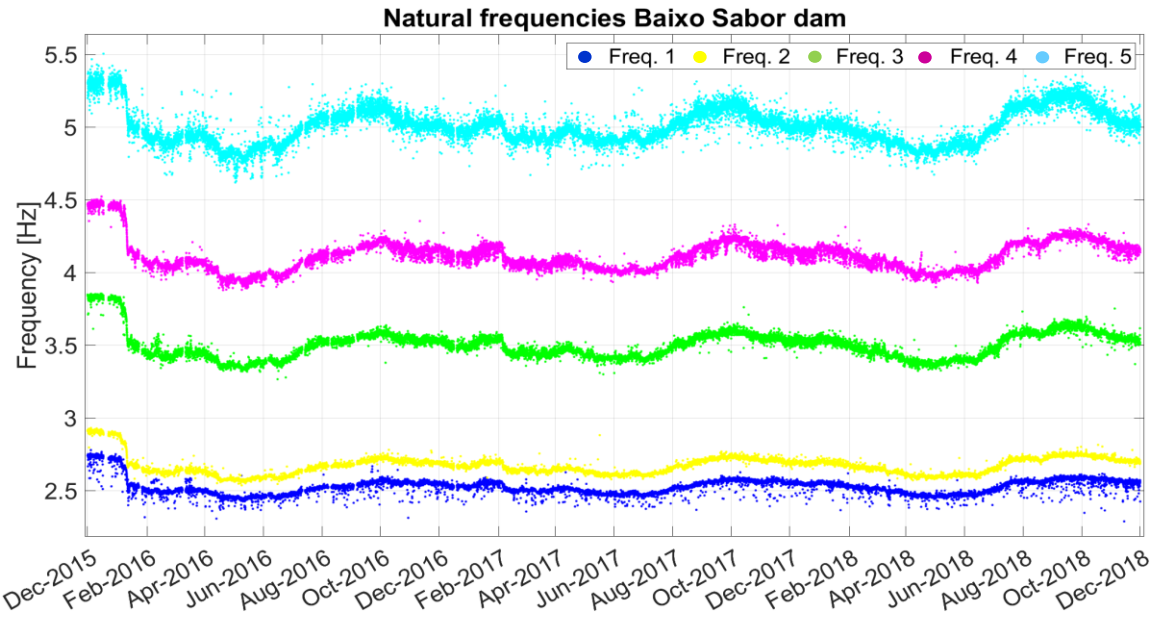

Fig. 5 – Evolution of natural frequencies through three years of monitoring

The first mode's natural frequency, ranges from approximately 2.2 to 2.8 Hz, and the first five modes can be found below 5.5 Hz.

The sudden fall of natural frequency values in January 2016 is explained by the variation in the reservoir water level. Comparing Fig. 5 and Fig. 4, it is possible to notice that an inverse proportionality occurs between natural frequency values and reservoir water level. The natural frequencies of the structure decrease considerably and continuously during the first filling of the reservoir. This phenomenon is even clearer in January, due to a sudden rise in the reservoir water level and a sudden drop in the frequency values which would be expected, given that a large amount of mass was added to the dam-foundation-reservoir system [9].

4.2. Multiple linear regression models for the characterization of the natural frequency pattern

The HST approach has primarily been used to analyse quasi-static physical quantities, such as horizontal displacements measured using the pendulum method. One of the recent innovations in this approach is the general characterization of the natural frequency pattern through data-based models, which allows the transposition of the HST approach to characterize the dynamic behaviour.

For the development of this research, the first term of the full polynomial (h^4) is considered, which represents the water level in the reservoir and is mentioned in equation (2). In addition, for the case of the sinusoidal thermal effect the use of a variable representing the day of the year is going to be used as the argument for sine and cosine functions with a period of one year.

The main terms of the model adopted in this work are presented in Equation 6:

$$\delta_{HST} = \beta_0 + \beta_1 * h^4 + \beta_2 * \sin(d) + \beta_3 * \cos(d) \quad (6)$$

The natural frequencies estimated during the three years of continuous monitoring were used. Data from the first two years of monitoring, from 01/12/2015 to 30/11/2017, was used to train and to establish the base model. Furthermore, the remaining data which refers to the third year of monitoring, from 01/12/2017 to 30/11/2018 were used to validate the quality of the forecasts provided by the regression model. Table 1 shows the results obtained from the training model based on the HST approach for the first five vibration modes. This table allows to identify the coefficients β_1, β_2, β_3, which were used to conduct testing in the third year.

Table 1 – Regression coefficients for the MLR

Vibration mode	β_0	β_1	β_2	β_3
Mode 1	2.9543	-2.2235x10^{-9}	-0.010095	-0.0040453
Mode 2	3.1742	-2.6178 x10^{-9}	-0.14286	-0.008275
Mode 3	4.2382	-3.8372 x10^{-9}	-0.026121	-0.018613
Mode 4	4.8933	-4.0449 x10^{-9}	-0.027739	-0.0081896
Mode 5	5.7554	-3.9158 x10^{-9}	-0.050674	-0.034902

The predictions obtained from the MLR model for the training and for the test sets are shown in Fig. 6 to verify the quality of the models obtained. The performance parameters are presented in Table 2.

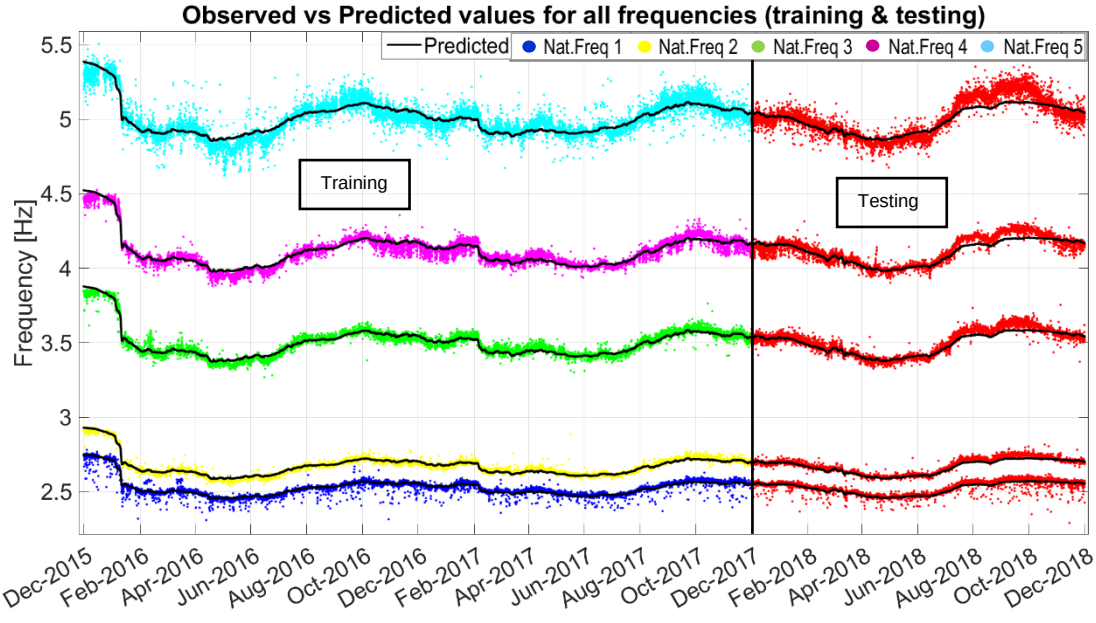

Fig. 6 – MLR predicted values and observed frequency modes values from 2015 to 2018 (training and test sets)

Table 2– Results of the training and testing set for the MLR model

Model	Frequency mode	Set	Freq. 1	Freq. 2	Freq. 3	Freq. 4	Freq. 5
MLR	Determination coefficient [%]	Training	92.4	96.9	95.3	93.5	81.6
		Testing	83.4	91.8	89.6	84.6	78.5
	Standard deviation of residuals [Hz]	Training	0.0162	0.0116	0.0212	0.0277	0.0498
		Testing	0.0163	0.0116	0.0247	0.0313	0.0550
	Max. abs. value of residuals [Hz]	Training	0.245	0.274	0.256	0.183	0.362
		Testing	0.269	0.120	0.191	0.194	0.353

The training values obtained were satisfactory, with a low decrease in the coefficients of determination from the training and testing sets for all the five vibration modes. Fig. 6 also illustrates the prediction made, which exhibits a smooth behaviour aligned with the actual values.

4.3. Multilayer perceptron neural network models

As referred before, an MLP-NN model was also adopted. The same dataset as the regression model was used. In addition, an example of the architecture of these models based on neural networks is detailed in Fig. 7. In the same way, as the multiple linear regression model was developed, the same independent variables were considered.

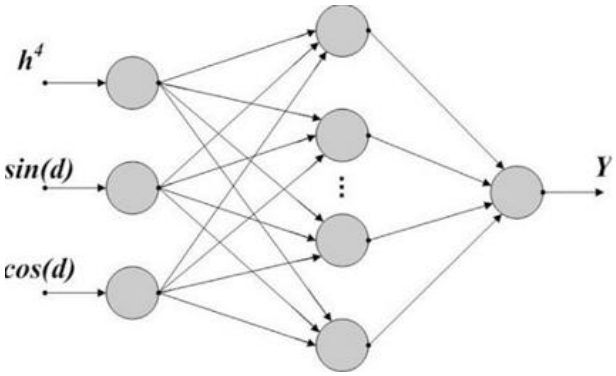

Fig. 7 – Architecture of an MLP-NN model based on the HST approach [3]

Using MATLAB software, the fitrnet [10] function was employed for training and testing the model. The model presented was determined after an iterative process that considered two hidden layers, with a range of 1 to 15 neurons per hidden layer.

In the adopted architecture, the weights are important parameters that determine the strength and direction of the influence that one neuron has on another in the neural network, the inclusion of hidden layers in the neural network allowed the model to learn more abstract and complex representations of the data. In this specific case, different configurations of hidden layers were experimented with purpose of identifying the structure that best captured the non-linear relationships present in the data, resulting in a greater ability of the model to generalize and make accurate predictions.

The predictions obtained from the MLP-NN models for the training and for the test sets are shown in Fig. 8, which allows to verify the quality of the models obtained. The performance parameters are presented in Table 3.

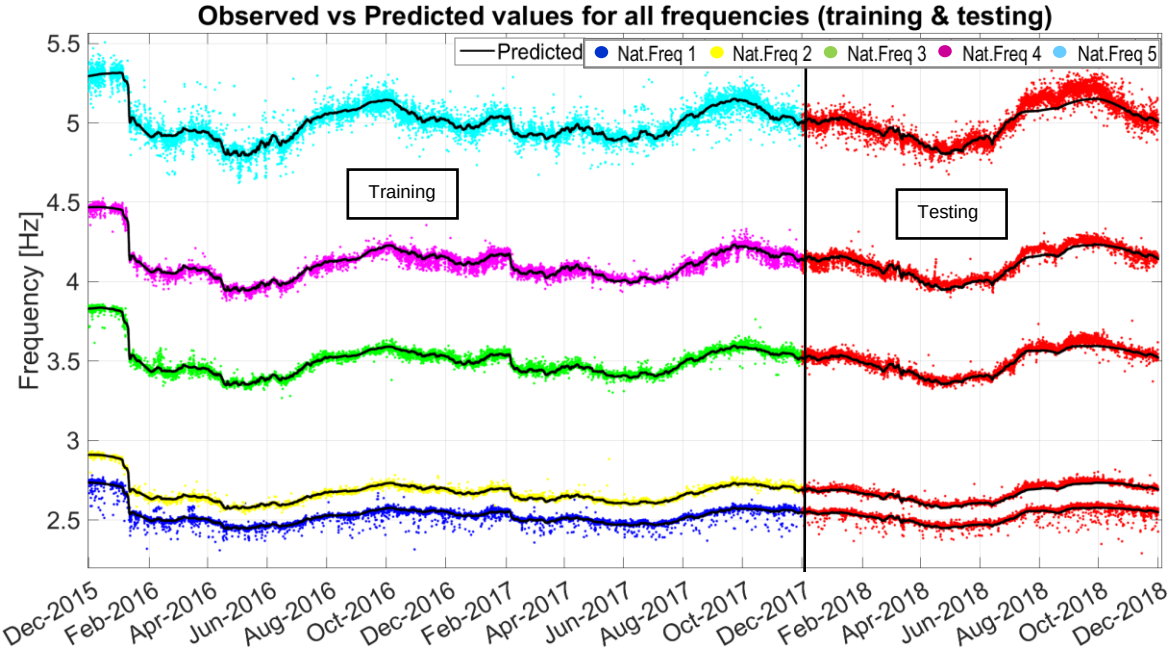

Fig. 8 – MLP-NN predicted values and observed frequency modes values from 2015 to 2018 (training and test sets)

Table 3 – Results of the training and testing set for the MLP-NN model

Model	Frequency mode	Set	Freq. 1	Freq. 2	Freq. 3	Freq. 4	Freq. 5
MLP-NN	Determination coefficient [%]	Training	93.3	98.1	97.1	97.9	90.1
		Testing	89.4	96.3	95.0	93.4	89.3
	Standard deviation of residuals [Hz]	Training	0.0152	0.00910	0.0165	0.0202	0.0386
		Testing	0.0154	0.00858	0.0177	0.0224	0.0368
	Max. abs. value of residuals [Hz]	Training	0.249	0.274	0.218	0.199	0.414
		Testing	0.269	0.123	0.196	0.188	0.316
	Number of neurons in the two hidden layers		[2 5]	[2 8]	[2 5]	[2 5]	[3 5]

It is noteworthy that Fig. 8 shows the result of a more adaptable and flexible behaviour of the MLP-NN model when compared to the MLR model, whose results were presented in Fig. 6. An indication of this is the determination coefficient, that is higher for the MLP-NN model when compared with the MLR models. Similarly, the analysis of the remaining variables shows that MLP-NN performs more effectively; however, the use of MLR remains valid, as its results are also very acceptable.

5. DISCUSSION AND FINAL REMARKS

The developed work aimed to dynamically monitor a concrete dam through MLR and MLP-NN models by tracking the evolution of its dynamic behaviour, ensuring that it stays within expected variations. This activity relies on observation through on-site instrumentation and behaviour models.

Both methods fulfilled their function of capturing and predicting information for an unseen season, with both models considered functional based on performance, although selecting an appropriate method can be complex and dependent on various factors.

For the Baixo Sabor dam case study, the following considerations can be made regarding which criterion or model is necessary:

- Overall performance: both methods performed well in predicting data, suggesting that both approaches are suitable for the problem at hand.
- Prediction accuracy: the neural network slightly outperformed the regression model in terms of prediction accuracy. This suggests that the neural network was better able to capture the relationship between input features and the target variable compared to the regression model.
- Model flexibility: the neural network can capture complex relationships between input features and the target variable, explaining its better performance on a dataset.
- Model interpretation: the linear regression model is easier to interpret than the neural network, as relationships between input features and the target variable are linear and easily interpreted. Additionally, the neural network might be considered as a black-box model by some users, making it more challenging to understand its behaviour.

In summary, both linear regression and neural network models can characterize the observed dynamic behaviour pattern based on the history of the structure's observations, which translates into a statistical relationship between key environmental variables (such as the water level in the reservoir and temperature variations), and the natural vibration frequencies.

ACKNOWLEDGMENTS

The authors acknowledge the Movhera—Hidroelétricas do Norte, S.A and Engie—Hidroelectricas do Douro, Lda that provided the data for the procedures addressed in this work.

This work was financially supported by national funds through the FCT, under the project anoMaLy: Machine Learning-based Models for Advanced Anomaly Detection in Dam Structural Health (doi.org/10.54499/2023.14874.PEX), and by Base Funding - UIDB/04708/2020 and Programmatic Funding - UIDP/04708/2020 of the CONSTRUCT - Instituto de I&D em Estruturas e Construções – also funded by national funds through the FCT/MCTES (PIDDAC).

REFERENCES

[1] Leger, P.; Leclerc, M. (2007). Hydrostatic, temperature, time-displacement model for concrete dams. J. Eng. Mech. 2007, 133, 267–277.

[2] Silva, J. A.; Mata, J.; Pereira, S.; Cunha, A. (2022). Development of HTT quantitative interpretation models using air temperature measurements Application to horizontal displacements observed in the Baixo Sabor Dam (*in Portuguese*). JPEE2022, 6ª Jornadas Portuguesas de Engenharia de Estruturas. LNEC. Lisboa.

[3] Mata, J.; Gomes, J.; Pereira, S.; Magalhães, F.; Cunha, A. (2023). Analysis and interpretation of observed dynamic behaviour of a large concrete dam aided by soft computing and machine learning techniques. Engineering Structures journal, 296 (2023) 116940. Doi: 10.1016/j.engstruct.2023.116940.

[4] Mata, J. (2007). Application of neural networks to the safety control of concrete dams (in Portuguese). Master thesis, IST.

[5] Silva, J. (2022). Development of machine learning models based on continuous monitoring data from concrete dams to interpret the observed structural behavior (in Portuguese). Master thesis, FEUP.

[6] Johnson, A.; Wichern, W. (2007). Applied Multivariate Statistical Analysis. 6th Edition, Pearson Prentice Hall, Upper Saddle River. ISBN: 978-0-13-187715-3.

[7] Banoula, M. (2023). An Overview on Multilayer Perceptron (MLP). AI & Machine Learning. Internet: < https://www.simplilearn.com/tutorials/deep-learning-tutorial/multilayer-perceptron>

[8] Pereira, S. (2019). Structural condition assessment of dams based on continuous dynamic monitoring. PhD thesis, FEUP.

[9] Pereira, S.; Magalhães, F.; Gomes, J.; Cunha, Á.; Lemos, J. (2018). Dynamic monitoring of a concrete arch dam during the first filling of the reservoir. doi.org/10.1016/j.engstruct.2018.07.076.

[10] MathWorks (2021). Train neural network regression model. Internet: <https://de.mathworks.com/help/stats/fitrnet.html>

Fifth International
Dam World Conference
PORTUGAL • LISBON • LNEC • APRIL 13-17, 2025
dam world 2025

HOW EFECTIVE IS MONITORING CONCRETE DAMS WITH GNSS IN 3D MODE?

José Nuno Lima[1]
LNEC

ABSTRACT

Since GNSS is a three-dimensional satellite positioning and navigation system, however, it is unusual to monitor dams in the altimetric component with this system, but only in the two horizontal components. Thus, the third component of three-dimensional positioning guaranteed by GNSS is wasted. There are two main reasons to justify this practice: firstly, because vertical positioning with GNSS is around two to three times less precise than horizontal positioning; and secondly, because spirit levelling allows for very precise and still very expedient vertical positioning, although it is very difficult to implement automatically.

The aim of this work is to quantify the effectiveness of GNSS in 3D monitoring of concrete dams, based on Portuguese experience of monitoring these structures with such a system.

Keywords: 3D Monitoring, Vertical uncertain, GNSS, Concrete Dams, Time Series.

[1]jnplima@lnec.pt, Portugal

1. INTRODUCTION

In so-called classical geodesy, planimetry has always been treated separately from altimetry. The reason for this separation, according to the specific literature of this science at the time (e.g., [1]), was the difficulty of correcting for the effects of atmospheric refraction, which tended to affect altimetry more than planimetry. In fact, the computations on either the ellipsoidal surface or the conformal map are inherently two-dimensional. The points are parameterised in terms of geodetic latitude and longitude or conformal mapping coordinates. Networks on the ellipsoidal surface or the conformal map have historically been labelled “horizontal networks” and treated separately from a one-dimensional “vertical network”. Such a separation was justified at a time, in addition to the justification already given, when the measurement tools could be readily separated into those that measured primarily “horizontal information” and those that yielded primarily “vertical information”. GNSS breaks this separation because it provides accurate three-dimensional positions [2]. However, the question arises: is the altimetry measured by GNSS accurate enough for monitoring the displacement of concrete dams, where the uncertainty should be of the order of one millimetre? On the other hand, spirit levelling (also known as geometric levelling or direct levelling) is very precise and still expedient, and is always a direct competitor to the altimetric monitoring obtained with GNSS.

Since 2016, some concrete dams in Portugal have been monitored with great success using continuous GNSS, but only in the horizontal component. Although GNSS provides observations in 3D mode, the altimetric component has not yet been used in this monitoring.

It is well known that the accuracy obtained with GNSS in the altimetric component is around 3 times less precise than that obtained with GNSS in the horizontal component (tests carried out on the LNEC campus also confirm this result). It is also important to note that at the scale of a civil engineering structure, i.e. locally, monitoring the altimetric component is practically equivalent to monitoring the vertical component. The altimetric component observed by GNSS is measured along to the normal to the ellipsoid, and the orthometric height is measured along to the vertical direction. However, locally the variations of these two quantities are equivalent. In the literature, orthometric height is often informally referred to as elevation.

The aim of this article is to assess the accuracy of altimetric monitoring of concrete dams as a function of the distance between the reference station and the object points and the height differences between them. Finally, it concludes on the effectiveness of GNSS in the altimetric monitoring of concrete dams.

2. GNSS DAM MONITORING SYSTEMS

This section provides a summary of the GNSS dam monitoring systems installed in four large dams in Portugal.

2.1. Baixo Sabor dam

The Baixo Sabor dam is located in north-eastern Portugal on the lower reaches of the Sabor River, a tributary of the right bank of the Douro River. The Baixo Sabor dam is a double arch dam with a height of 123 m and a total crest length of 505 m.

Four permanent GNSS stations were installed: three located on the crest of the dam, in blocks 10-11, 16-17 and 23-24 (Figure 1), and one located on the right bank, to work as a reference station.

The GNSS reference station (REFM) of the dam was installed on the right bank, on the top of a 4 m high reinforced concrete pillar. The GNSS receiver of this station was installed in a technical cabinet at the base of the pillar. The average distance between the station on the crest and the reference station is 645 m, with an average height difference of about 267 m.

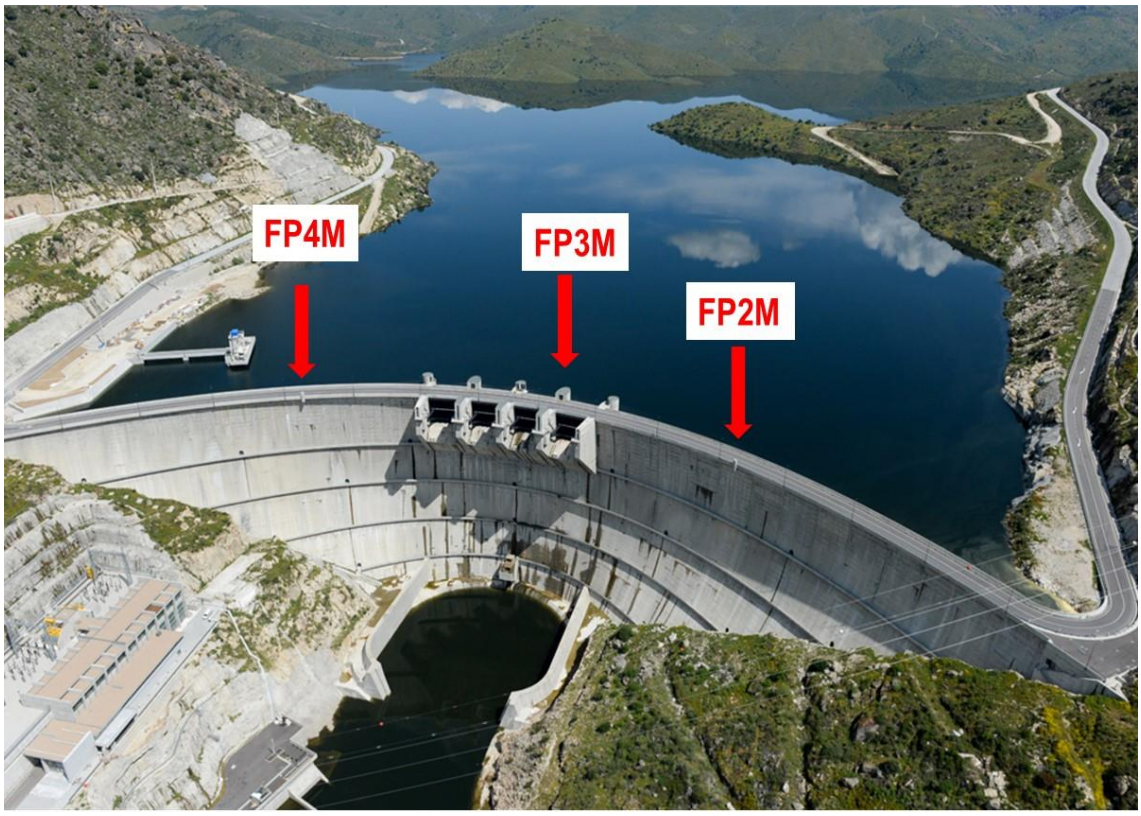

Fig. 1 – Location of GNSS stations at the Baixo Sabor dam: FP2M, FP3M, FP4M, on the dam crest

2.2. Cabril dam

The Cabril dam is located in the centre of Portugal, on the Zêzere river, which is part of the Tagus River basin. The Cabril dam is a double curvature arch dam with a maximum height above the foundation of 132 m and a total crest length of 290 m.

For the GNSS dam monitoring system two permanent GNSS stations were installed: one located on the crest of the dam, in the K-L block, and the other located on the left bank, to work as a reference station (Figure 2).

The reference GNSS station was installed on the left bank, on the top of a medium voltage pole of a deactivated power line, which was cut to a height of about 6 m. The GNSS receiver of this station is installed in a technical cabinet inside of geodetic pillar shelter, close to the former medium voltage pole. The distance between the station on the crest and the reference station is 240 m, with a height difference of 0.5 m.

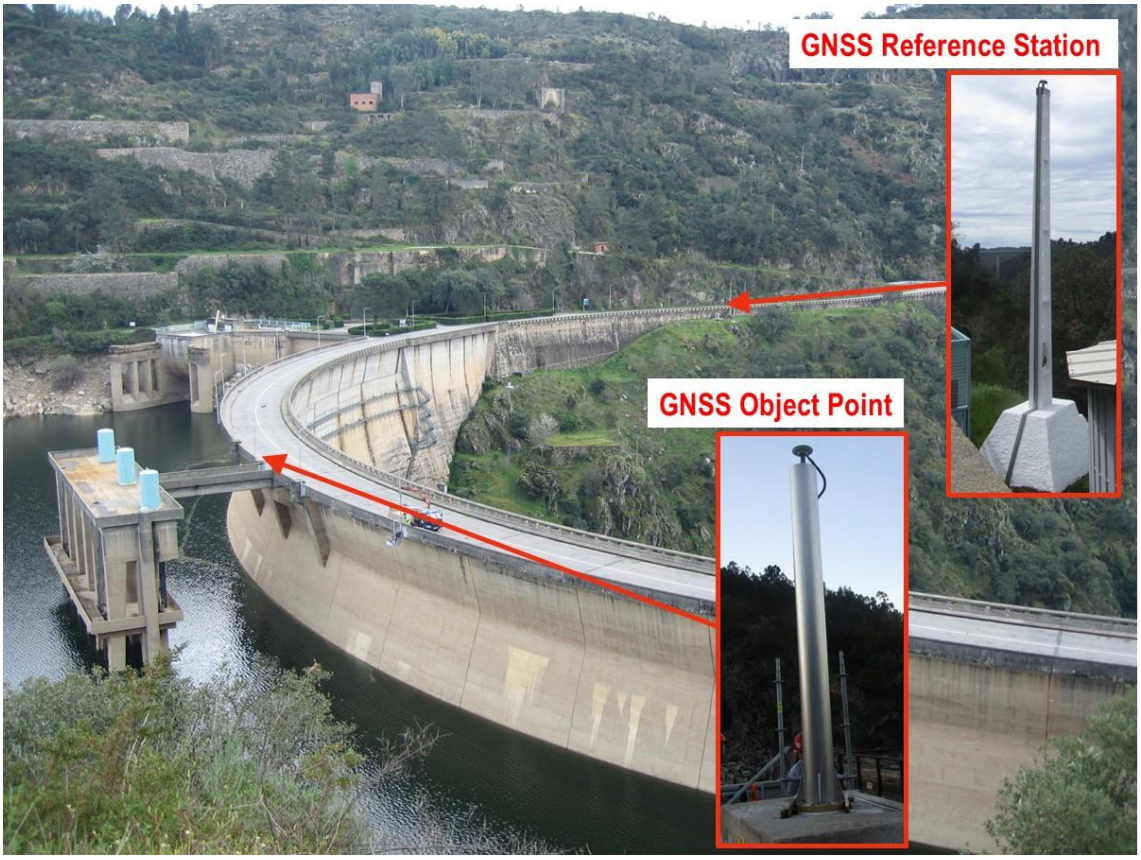

Fig. 2 – Location of GNSS stations at Cabril Dam: Reference station, left bank, and object point, crest of the dam

2.3. Feiticeiro dam

The Feiticeiro dam is located in the north-east of Portugal, on the lower reaches of the Sabor River, a tributary of the right bank of the Douro River. The Feiticeiro dam is a straight-axis concrete dam with a height of 45 m and a total crest length of 315 m.

For the GNSS dam monitoring system four permanent GNSS stations were installed: three located on the crest of the dam, in blocks 06-07, 11-12 and 16-17, and one located on the right bank, to work as a reference station (Figure 3).

The GNSS reference station (REFJ) of the dam was installed on the right bank, on top of a 3 m high reinforced concrete pillar. The GNSS receiver of this station is in a technical cabinet at the base of the pillar. The average distance between the station on the crest and the reference station is about 360 m, with an average height difference of around 60 m.

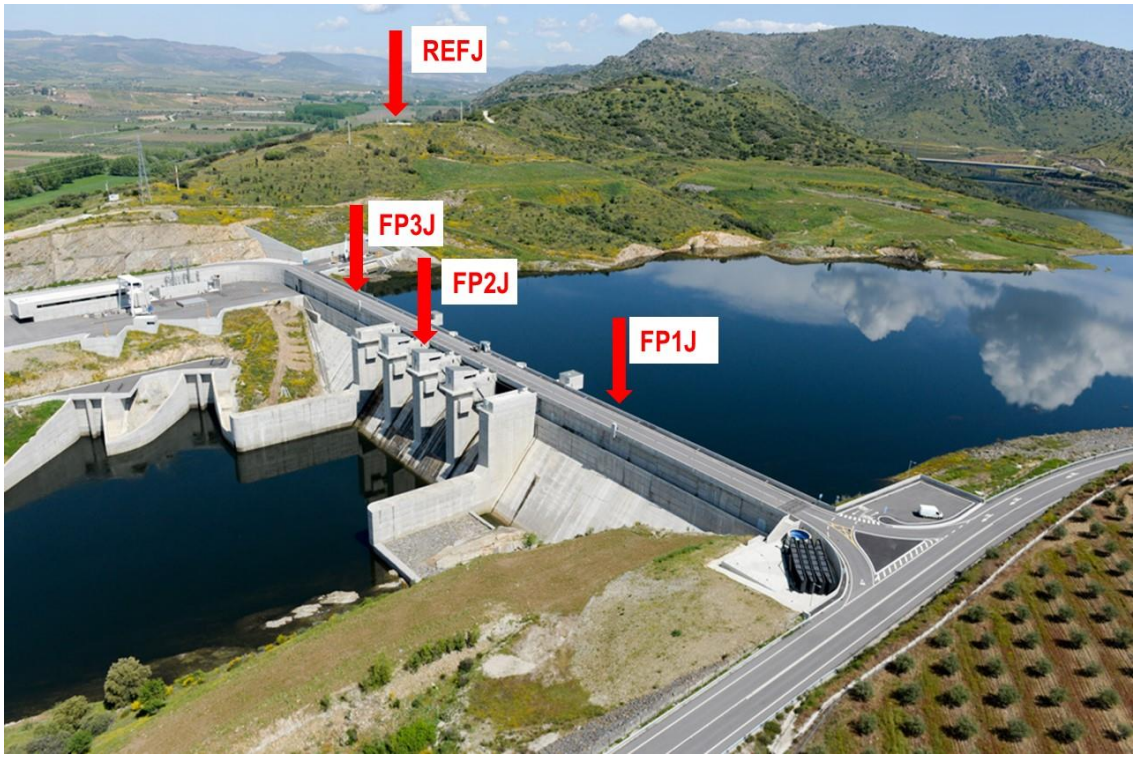

Fig. 3 – Location of the GNSS stations at the Feiticeiro dam: FP1J, FP2J, FP3J, on the dam crest, and REFJ, as a reference station, on the right bank

2.4. Foz Tua dam

The Foz Tua dam is located in the northern region of Portugal, on the Tua River, an important tributary of the Douro River, near its confluence with the Douro River. Foz Tua is a double arch dam with a height of 108 m and a total crest length of 275 m.

The GNSS dam monitoring system consists of two permanent GNSS stations: one located on the crest of the dam, in E2E1 block, and the second located on the right bank, to work as a reference station (Figure 4).

The reference GNSS station was installed on the right bank, on the top of a 2 m high reinforced concrete pillar. The GNSS receiver of this station is in a technical cabinet near by the pillar.

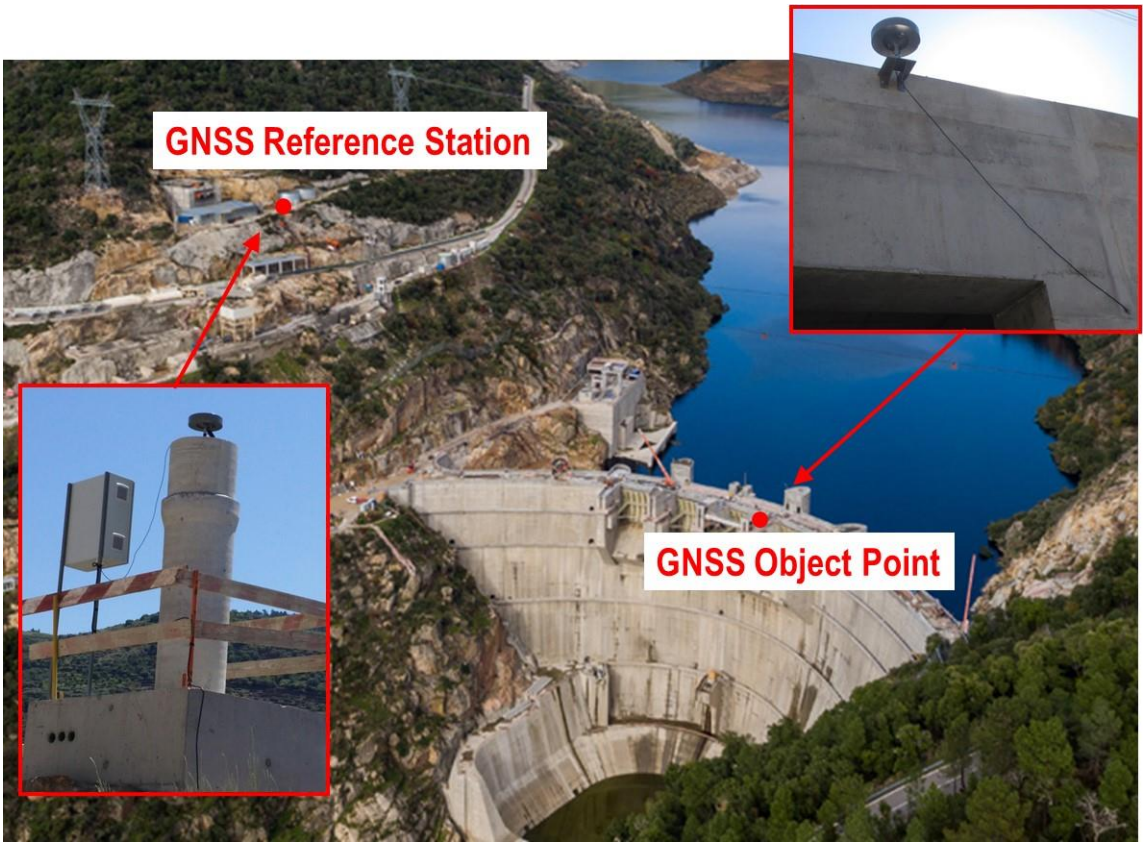

Fig. 4 – Location of GNSS stations at Foz Tua Dam: Reference station, left bank, and object point, crest of the dam

The distance between the station on the crest and the reference station is 242 m, with a height difference of 80 m.

3. LINEAR FILTER, GAIN, PHASE SHIFT AND MOVING AVERAGE

A linear combination of the terms of a time series (x_0,x_1,...,x_n):

$$y_k = \sum_{j=-q}^{r} w_j x_{k+j} \quad (k = q+1, \dots, n-r) \tag{1}$$

where the m (= q + r + 1) coefficients w_j are weights, is called linear filter of order m. If q = r and $w_j = w_{-j}$, the filter is said to be symmetric. If the weights sum up to one, the filter is called a weighted moving average. If the weights are equal and sum up to one, the filter is called a simple moving average [4].

The application of a filter to a time series (the input time series (x_0,x_1,...,x_n)) produces a new time series (the output time series (y_0,y_1,...,y_n)). The spectral characteristics of the output series are related to the spectral characteristics of the input series by means of the transfer function of the filter. The transfer function is a complex function with arguments in the frequency

domain. The modulus of the transfer function is called the gain of the filter [5]. The argument of the transfer function is called the phase shift of the filter [5].

If the gain of the filter, for a given angular frequency (ω), is greater than one, the filter amplifies the input series in that frequency. Otherwise, if the gain of the filter, for (ω), is lesser than one, the filter smooths the input series in that frequency.

Besides the change in amplitude the filter may also introduce a phase shift on the output time series depending on the frequency. Though the symmetric filters do not introduce significant phase shifts, the asymmetric ones do.

4. ANALYSIS OF VERTICAL DISPLACEMENTS OBSERVED WITH GNSS

4.1. General considerations

The estimated uncertainty for hourly solutions of the horizontal components is about 5 times greater than the estimated uncertainty for the daily solutions of the horizontal components [3]. However, hourly solutions have a higher temporal resolution than daily solutions. The application of symmetric moving averages to hourly solutions allows a significant reduction in uncertainty without compromising temporal resolution (e.g. the 25^{th} order symmetric moving average reduces de the uncertainty of the time series hourly solutions from 4 mm to 0,8 mm at the Baixo Sabor dam [3], but in horizontal components). Moving averages act as a low pass filter and are very easy to implement in time series. So now it's time to ask the following question: how will the vertical component behave in daily, hourly or even less frequent time series? It’s already known, as mentioned in the 1. Introduction, that the accuracy obtained with GNSS in the altimetric (vertical) component is about 3 times less accurate than the corresponding accuracy in the horizontal component. The explanation is that the modelling errors in the tropospheric delay are strongly correlated with the estimation errors in the (vertical) height component [6]. In addition, the altitude component is also affected by the fact that GNSS satellites are not uniformly distributed across the sky (e.g., GPS satellite orbits are inclined at 55º to the equatorial plane).

4.2. Baixo Sabor dam

The Figure 5 shows the results of the applying a 25th order symmetric moving average to the time series of observed displacements, vertical components, at the FP2M, FP3M and FP4M stations of the Baixo Sabor dam. The orange dots represent the vertical displacements observed by the GNSS at FP2M (hourly solution with the application of the 25th order symmetric moving average to the time series). The grey dots represent the vertical displacements observed by the GNSS at FP3M (idem). The light blue dots represent the

vertical displacements observed by the GNSS at FP4M (idem). The yellow dots represent the vertical displacements observed by the spirit levelling at NC1011 (benchmark near FP2M). The black dots represent the vertical displacements observed by the spirit levelling at NC1617 (benchmark near FP3M). The purple dots represent the vertical displacements observed by spirit levelling at NC2324 (benchmark near FP4M). The moving averages of order 25 applied to the time series of vertical displacements observed by GNSS are still too noisy to be analysed graphically, as can be seen in Figure 5. Increasing the order of the moving averages, for example to 168 (corresponding to a weekly average), allows the time series to be smoothed, as can be seen in Figure 6. Maintain the conventions used for the observables in Figure 5.

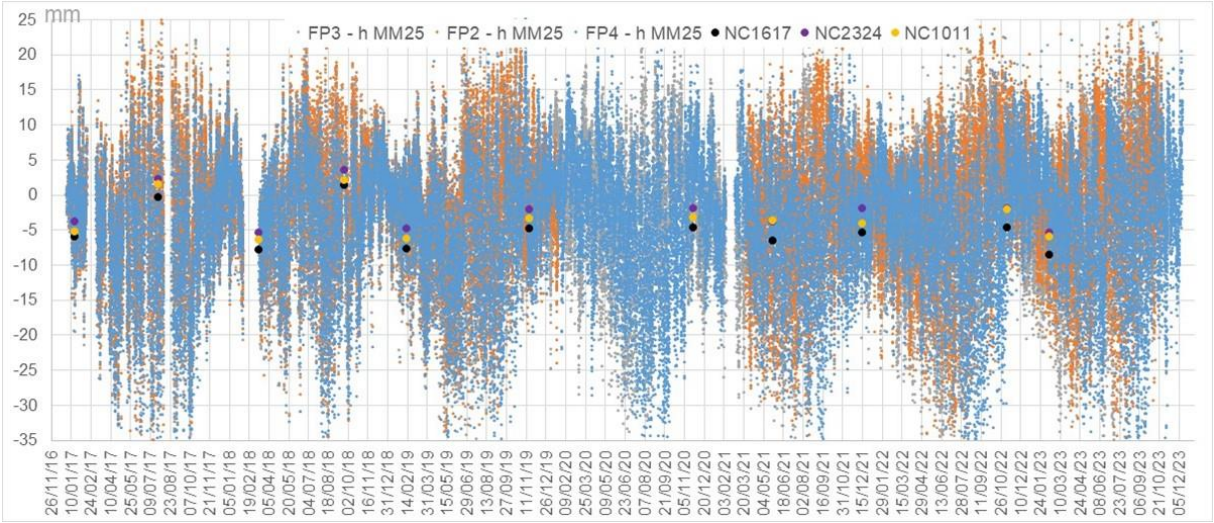

Fig. 5 – The results of the application of 25th order moving average to the time series of GNSS observed displacements, vertical components, in FP2M, FP3M e FP4M station of Baixo Sabor dam

Or by applying moving averages of order 500 (corresponding to an average of 21 days) to the time series of displacements observed by GNSS, as shown in Figure 7 (using the same conventions as in the previous figures).

Finally, by applying moving averages of order 2000 (corresponding to an average of 83 days) to the time series of displacements observed by GNSS, as shown in Figure 8 (using the same conventions as in the previous figures).

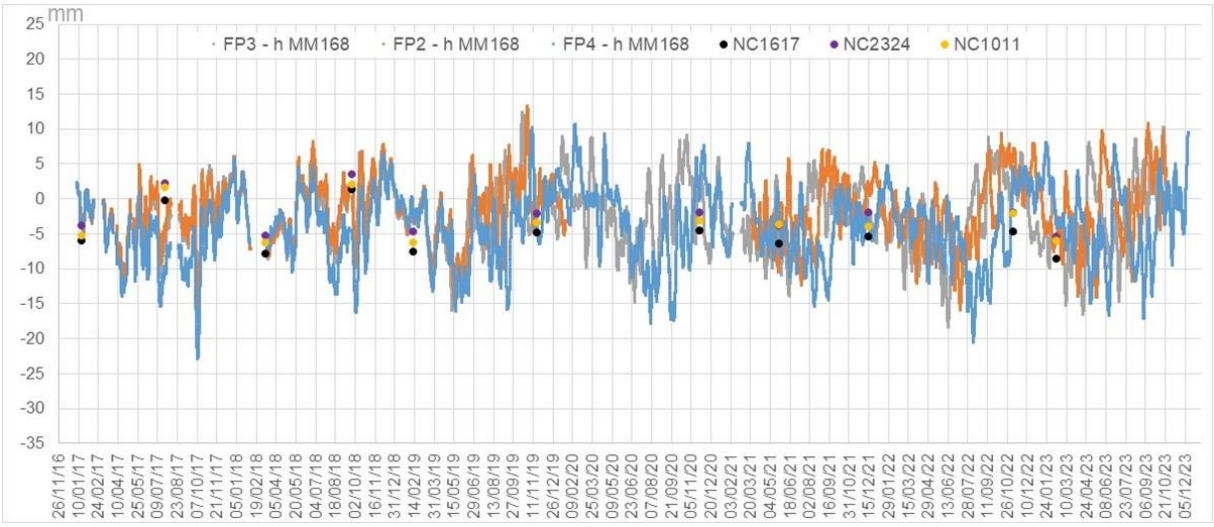

Fig. 6 – The results of the application of 168th order moving average to the time series of GNSS observed displacements, vertical components, in FP2M, FP3M e FP4M station of Baixo Sabor dam

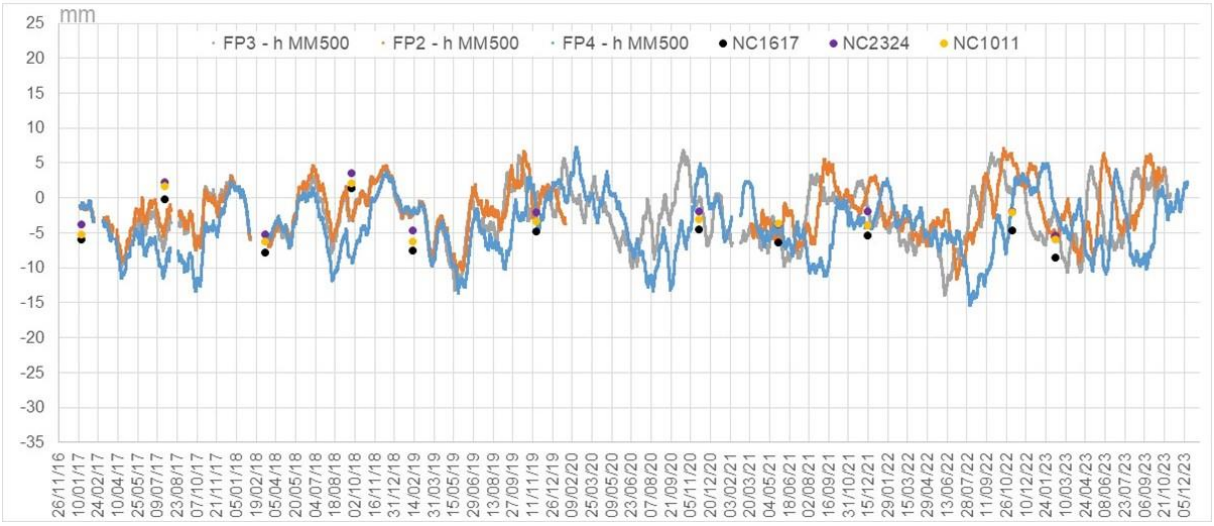

Fig. 7 – The results of the application of 500th order moving average to the time series of GNSS observed displacements, vertical components, in FP2M, FP3M e FP4M station of Baixo Sabor dam

A moving average of such a high order, as in the cases presented above, runs the risk of dissipating any significant effect caused by a large variation in reservoir level or a marked change in average temperature over one or more weeks. However, the uncertainty in the height component (vertical displacements) in this dam is greatly affected by the difference in height between the reference GNSS station and the GNSS stations on the crest, around 267 metres, more than the distance between them (the average is around 645 metres), which is nevertheless not significant in increasing the uncertainty in relative 3D positioning with GNSS.

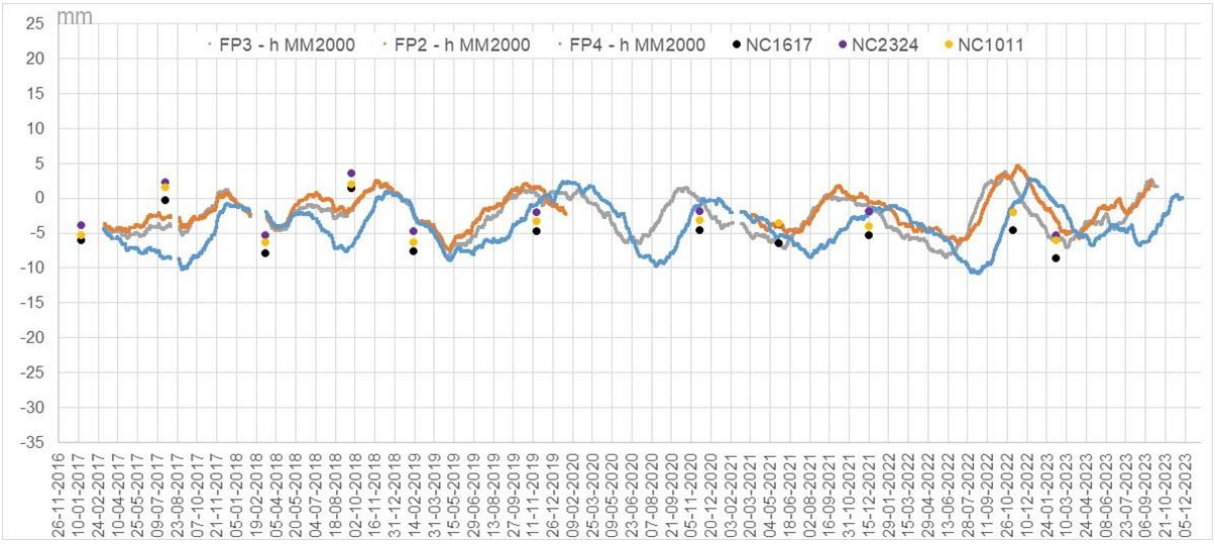

Fig. 8 – The results of the application of 2000th order moving average to the time series of GNSS observed displacements, vertical components, in FP2M, FP3M e FP4M station of Baixo Sabor dam

Figures 5 to 8 give a graphical idea of the differences between the vertical displacements observed by GNSS and those observed by spirit levelling at the benchmarks closest to the GNSS stations, but not the numerical differences, which are given in Table 1 and the values are expressed in mm. This table also shows the respective standard deviations and the average standard deviation. Due to space limitations, not all differences between the moving average of order 2000 and the spirit levelling are shown.

Table 1 – Differences in vertical displacements observed between GNSS and spirit levelling

FP2 mm25 – NC1011	FP3 mm25 – NC1617	FP4 mm25 – NC2324	FP2 mm168 – NC1011	FP3 mm168 – NC1617	FP4 mm168 – NC2324	FP2 mm500 – NC1011	FP3 mm500 – NC1617	FP4 mm500 – NC2324	FP3 mm2000 – NC1617
1.7	1.0	2.1	-3.5	-3.5	-3.4	-1.5	-1.5	-1.4	-
-11.5	-17.9	-14.6	-4.2	-10.3	-6.5	-4.6	-10.8	-6.7	-8.8
-4.8	-3.6	-2.8	-2.1	-2	-2.3	-2.5	-2.3	-2.6	-2.0
0.1	-5	-1.4	-3.3	-1.3	-4	-1	-2.7	-1.6	-0.4
-	2.7	4.6	0.7	0	2.3	-	-6.9	-6.7	-0.6
-9.3	-10.5	-11.5	-9.2	-9.1	-9	-5.4	1.9	3.2	-5.9
3.1	-0.1	2.2	6	3.2	5.1	5.8	2.9	4.9	0.5
-6.1	-5.1	-6.4	-6.3	-6	-6.7	-5.2	-5.1	-5.7	-3.0
StaDesv	StaDesv	StaDesv	StaDesv	StaDesv	StaDesv	StaDesv	StaDesv	StaDesv	StaDesv
6.47	7.72	7.44	3.68	3.79	3.92	1.90	4.69	5.49	4.19
Average StaDesv			Average StaDesv			Average StaDesv			Average StaDesv
7.21			3.80			4.03			2.75

Table 1 shows that the uncertainty in the GNSS observed vertical displacements, which in this particular case is strongly influenced by the height differences between the GNSS stations, is too high to monitor a concrete dam. Even with the application of high order moving averages, and despite the progressive smoothing of the observed time series, the corresponding standard deviations are still very high, this is still far from the 1 mm accuracy required for monitoring concrete dams.

Spirit levelling campaigns are carried out every year. For reasons of timing, these campaigns are not always carried out in the same month.

4.3. Cabril dam

In the case of the Cabril dam, in addition to the distance of only 240 metres between the GNSS reference station and the GNSS crest station, the most significant factor is the difference in height between these two stations, which is only 0.5 metres. Figure 9 shows the height variations of the GNSS station at the crest, using a 25th order moving average, and the corresponding 500th order moving average in blue and brown, respectively. The black dots represent the height variation observed by spirit levelling at the KL block benchmark, all expressed in millimetres. Finally, in red is the 168th order moving average of temperatures (corresponding to one week), expressed in degrees Celsius.

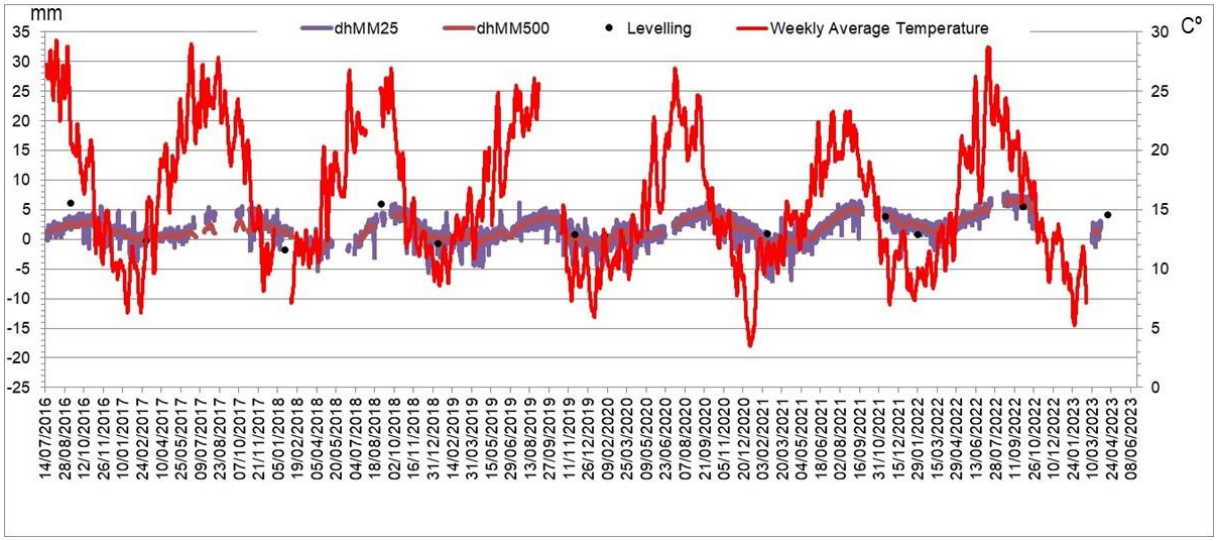

Fig. 9 – The results of the applications of 500th and 25th order moving average to the time series of GNSS observed displacements, vertical components, in block KL station of Cabril dam, plus weekly average temperature and spirit levelling

Unlike the previous case, here the 25th order moving average appears to be accurate enough to be compared with the spirit levelling time series. But let's analyse in more detail these comparisons between the 25th and 168th order moving averages of the hourly time series of dam height variation in the KL block with GNSS and compare them with geometric levelling

(Figure 10). In Figure 11, only the 168th order moving average is replaced by the 500th order moving average (using the same conventions as in the previous figures).

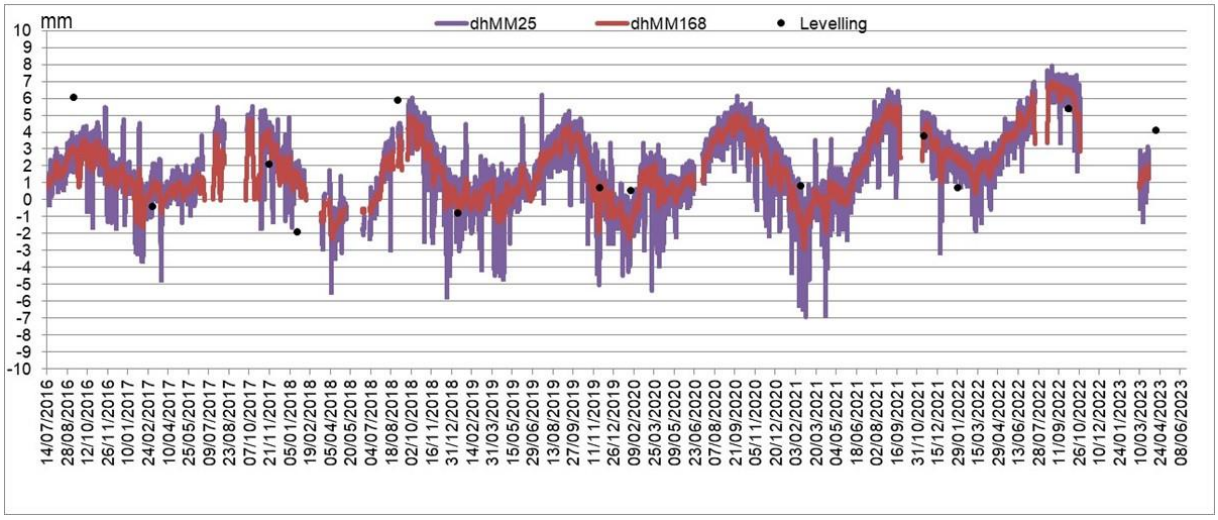

Fig. 10 – The results of the applications of 500th and 25th order moving average to the time series of GNSS observed displacements, vertical components, in block KL station of Cabril dam, plus weekly average temperature and spirit levelling

Figures 10 and 11 show that, in this case, there is no advantage in increasing the order of the moving average to improve the accuracy of the time series of the height variation of the Cabril dam observed by GNSS. Table 2 shows the numerical values observed by the two completely independent techniques, the respective differences, the mean values of the differences and the standard deviations of the differences (expressed in millimetres).

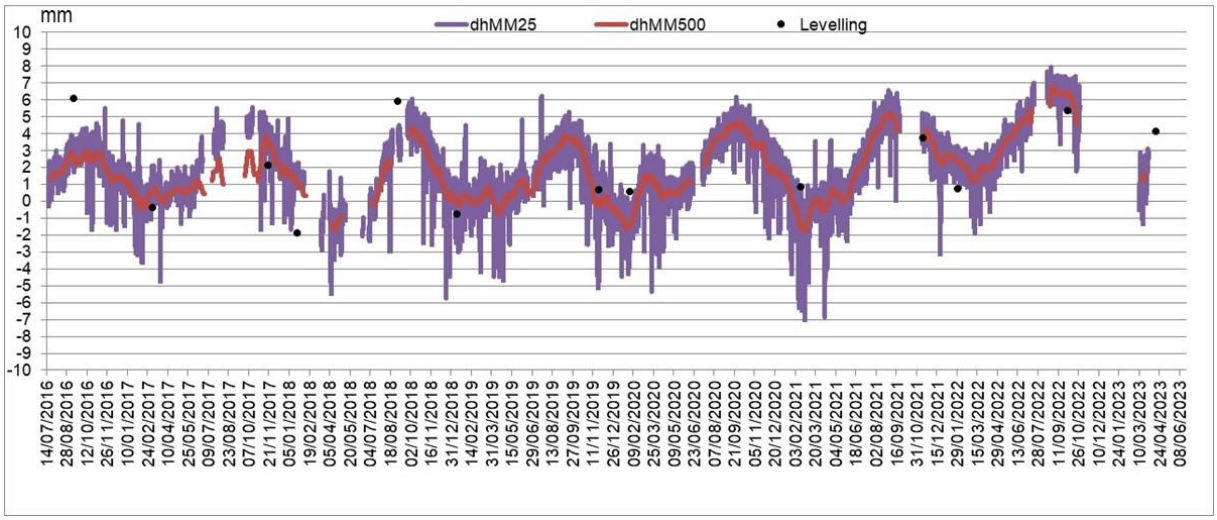

Fig. 11 – The results of the applications of 500th and 25th order moving average to the time series of GNSS observed displacements, vertical components, in block KL station of Cabril dam, plus weekly average temperature and spirit levelling

The comparison is made with the spirit levelling ‘corrected’ to make the origins of the time series in question compatible. And the numerical results in Table 2 confirm the graphical comparisons expressed in the previous figures.

Table 2 – Differences in vertical displacements observed between GNSS and spirit levelling

Campaign Data	Levelling Observed KL crest	Levelling Corrected KL crest	dh mm25 GNSS	dh mm168 GNSS	dh mm500 GNSS	Difference dhmm25 – Levelling	Difference dhmm168 – Levelling	Difference dhmm500 – Levelling
13/09/2016	12.02	6.02	2.4	2.9	2.6	-3.6	-3.1	-3.4
07/03/2017	5.6	-0.4	1.0	0.8	0.6	1.4	1.2	1.0
21/11/2017	8.07	2.07	3.8	3.6	3.4	1.7	1.5	1.3
23/01/2018	4.1	-1.9	1.6	1.5	1.0	3.5	3.4	2.9
04/09/2018	11.88	5.88	3.9	2.5		-2.0	-3.4	
14/01/2019	5.21	-0.79	0.3	-0.6	0.0	1.1	0.2	0.8
26/11/2019	6.67	0.67	-0.3	-0.9	-0.1	-1.0	-1.6	-0.8
03/02/2020	6.55	0.55	-0.5	-1.5	-1.4	-1.1	-2.1	-2.0
16/02/2021	6.82	0.82	-0.5	-1.3	-1.6	-1.3	-2.1	-2.4
16/11/2021	9.73	3.73	0.6	-0.4	-0.2	-3.1	-4.1	-3.9
31/01/2022	6.71	0.71	2.3	2.5	2.3	1.6	1.8	1.6
03/10/2022	11.34	5.34	6.7	6.4	6.4	1.4	1.1	1.1
				Average		**-0.12**	**-0.60**	**-0.35**
				Standard Desviation		**2.11**	**2.32**	**2.16**

4.4. Feiticeiro dam

The case of the Feiticeiro dam is a good example because the distance between the reference GNSS station and the GNSS stations on the top of the dam is neither too long nor too short (the average distance is around 360 metres) and, more importantly, the slope between these stations is neither too high nor too low (around 60 metres). The Figure 12 shows the results of applying a 25th order moving average to the time series of GNSS observed displacements, the vertical components, at the FP1, FP2 and FP3 GNSS stations of the Feiticeiro dam (orange, blue and grey dots, respectively) and the spirit levelling observed at the bench marks closest to the GNSS stations (NC0607, yellow dots, NC1112, dark blue dots, and NC1617, black dots).

Figure 13 is an enlargement of Figure 12. Unfortunately, there are few spirit levelling campaigns during the GNSS observation period, so it is not possible to make a good comparison between these two observing techniques, nor to correct for the different origins of the different time series.

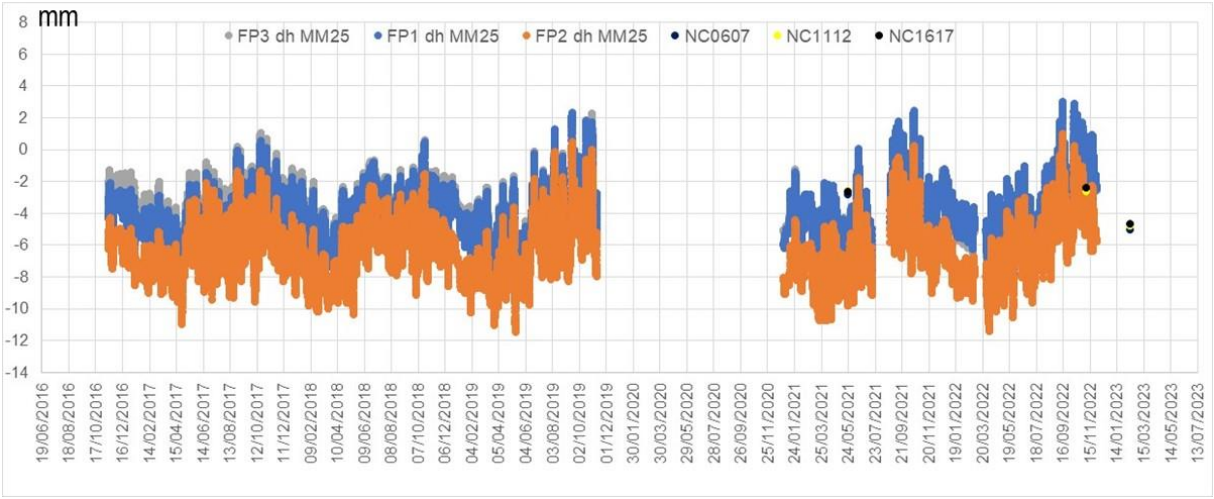

Fig. 12 – The results of applying a 25th order moving average to the time series of GNSS observed displacements, vertical components, in the FP1, FP2 and FP3 GNSS stations of the Feiticeiro dam (orange, blue and grey dots, respectively) and the spirit levelling observed at the benchmarks closest to the GNSS stations

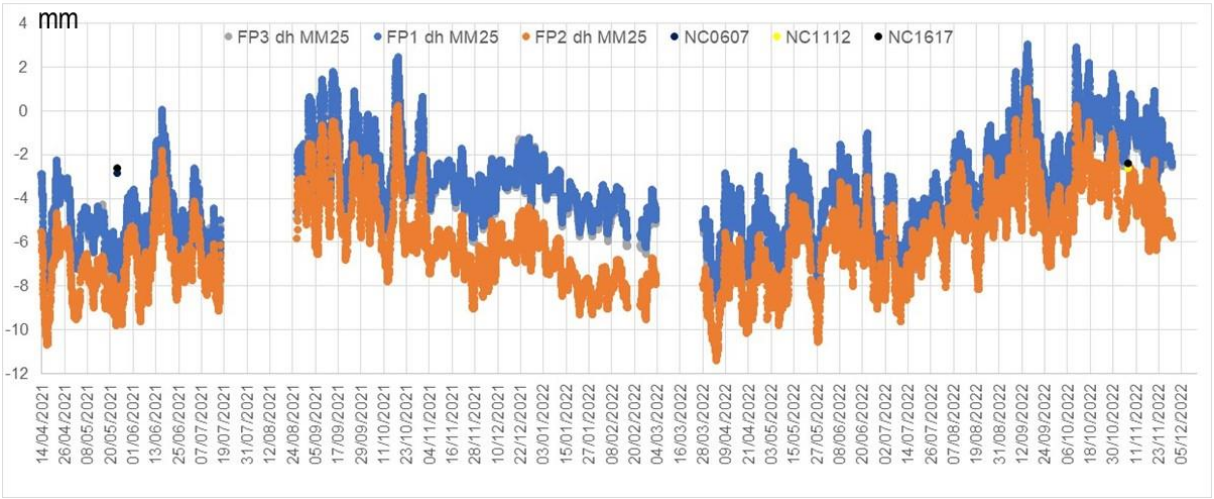

Fig. 13 – Figure 13 is an enlargement of Figure 12: The results of applying a 25th order moving average to the time series of GNSS observed displacements, vertical components, in the FP1, FP2 and FP3 GNSS stations (orange, blue and grey dots, respectively) and the spirit levelling observed at the benchmarks closest to the GNSS stations

Figures 14 and 15 are similar to Figures 12 and 13, except that the 25th order moving average is replaced by the 168th order moving average. The same conventions are used as in the previous figures.

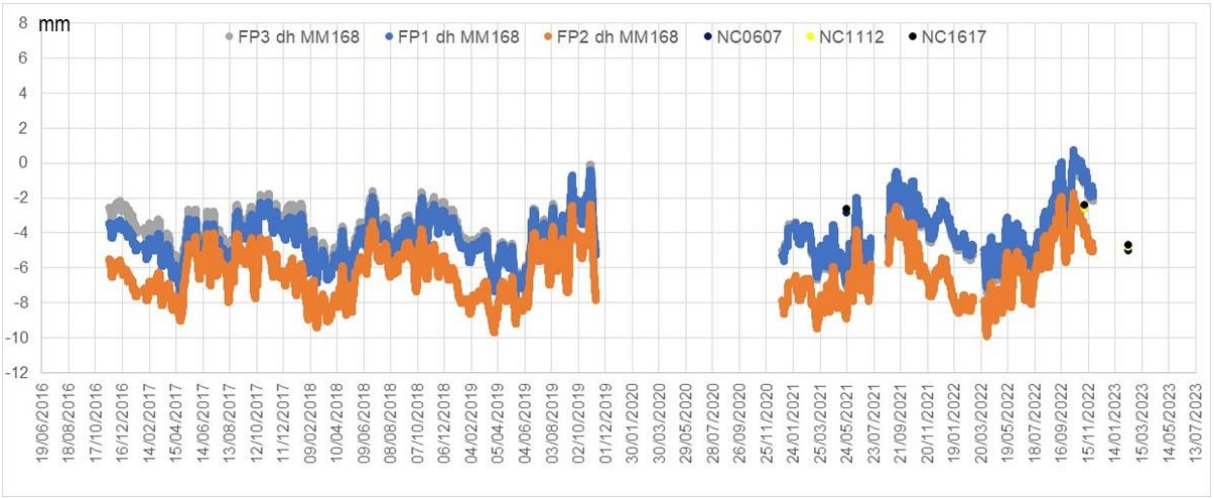

Fig. 14 – The results of applying a 168th order moving average to the time series of GNSS observed displacements, vertical components, in the FP1, FP2 and FP3 GNSS stations of the Feiticeiro dam (orange, blue and grey dots, respectively) and the spirit levelling observed at the benchmarks closest to the GNSS stations

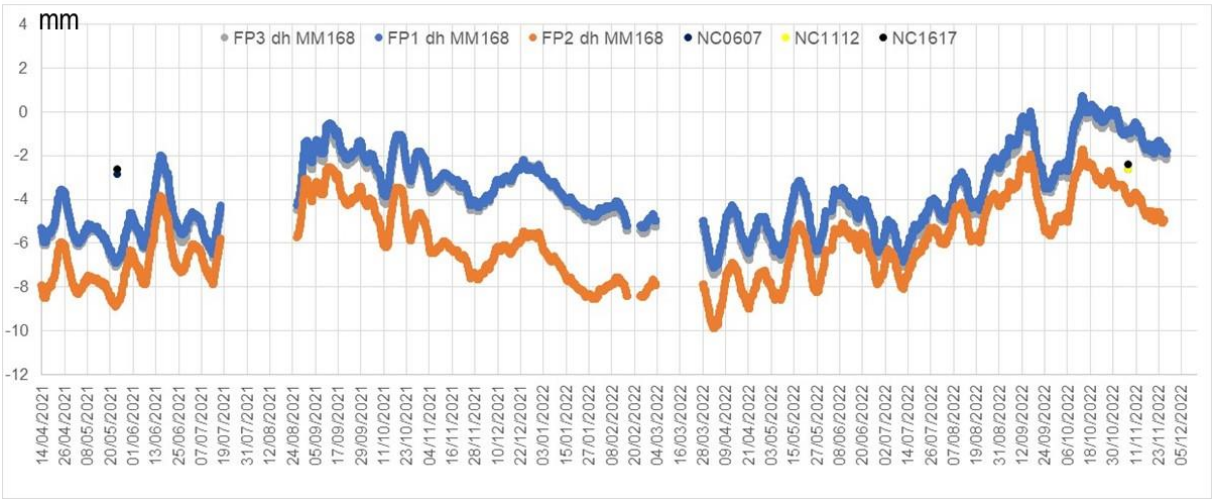

Fig. 15 – Figure 15 is an enlargement of Figure 14: The results of applying a 168th order moving average to the time series of GNSS observed displacements, vertical components, in the FP1, FP2 and FP3 GNSS stations (orange, blue and grey dots, respectively) and the spirit levelling observed at the benchmarks closest to the GNSS stations

Table 3 shows the differences between the height variations observed at the GNSS stations FP1, FP2 and FP3 and the values obtained by spirit levelling at the benchmarks closest to the GNSS stations, NC0607, NC1112 and NC1617, respectively. It should be noted, however, as already mentioned, that unfortunately there were few spirit levelling campaigns during the period under study, which did not allow a good comparison between the results of the two techniques, nor the correction of the different origins of the time series for a more accurate comparison.

Table 3 – Differences in vertical displacements observed between GNSS and spirit levelling

Campaign Data	Difference FP1 dhmm25 – Levelling Observed NC0607	Difference FP2 dhmm25 – Levelling Observed NC1112	Difference FP3 dhmm25 – Levelling Observed NC1617	Difference FP1 dhmm168 – Levelling Observed NC0607	Difference FP2 dhmm168 – Levelling Observed NC1112	Difference FP3 dhmm168 – Levelling Observed NC1617
24/05/2021	3.66	5.78	3.76	3.96	6.08	4.26
07/11/2022	-2.15	0.85	-1.83	-1.75	1.45	-1.23
13/02/2023	-	-	-	-	-	-
Standard Desviation	**4.11**	**3.49**	**3.95**	**4.04**	**3.27**	**3.88**

Figures 13 and 15 show that, in this case, there is no advantage in increasing the order of the moving average to improve the accuracy of the time series of the height variation of the Feiticeiro dam observed by GNSS. And the numerical results in Table 3 confirm the graphical comparisons expressed in the previous figures, which means that there is no advantage in increasing the order of the moving average to improve the accuracy of the time series of the height variation observed by GNSS. Due to the lack of spirit levelling campaigns during the period considered, it is not advisable to use the standard deviation of the differences as an estimate of the accuracy of the GNSS vertical component, as it would clearly be overestimated in this case. In other words, we would expect better accuracy in this component of the GNSS observations. For example, in defence of the statement in the previous sentence, note the consistency of the height variations observed at the three GNSS stations at the top of the dam.

4.5. Foz Tua dam

The Foz Tua dam was only monitored by GNSS during its first filling, between May 2016 and May 2017. During this period, there were not enough spirit levelling campaigns to validate the results of the height component observed by GNSS. The only possible comparison will be with trigonometric levelling using a robotic tacheometer installed in the dam, with hourly frequency observations for different reflector targets placed in the dam, one of which was very close to the GNSS antenna placed on the top of the dam. These comparisons will be analysed.

Like the Feiticeiro dam, the Foz Tua dam is a good example because the distance between the reference GNSS station and the GNSS station at the top of the dam is 242 metres and, more importantly, the gradient between these stations is 80 metres.

In this case there are only daily solutions, i.e. each solution corresponds to a full day of GNSS observations. Figure 16 shows the daily GNSS solution, in the altimetric component,

represented in light blue, a moving average of order 7 of this time series (corresponding to the weekly moving average), in dark blue and in red the moving average of order 24 of the hourly solutions, in the altimetric component, observed by the robotic tacheometer.

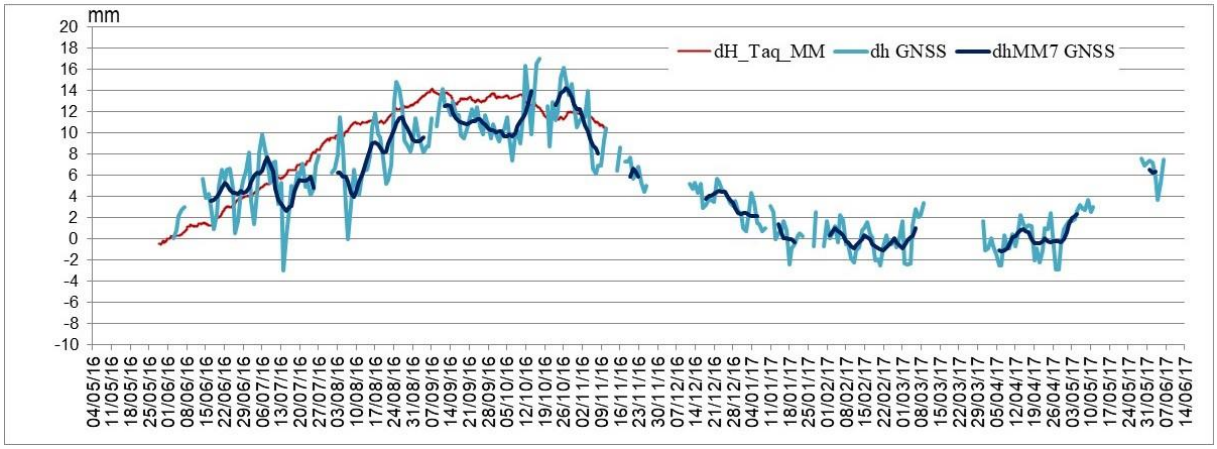

Fig. 16 – the daily GNSS solution, in the altimetric component, represented in light blue, a moving average of order 7 of this time series (corresponding to the weekly moving average), in dark blue and in red the moving average of order 24 of the hourly solutions, in the altimetric component, observed by the robotic tacheometer

The weekly moving average of the GNSS time series is much more consistent with the robotic tacheometer time series than the daily GNSS time series, with standard deviations of the differences for the latter of 3 mm and 5 mm respectively.

4.6. Discussion

The Baixo Sabor, Cabril and Feiticeiro dams are equipped with Leica GMX902 GNSS receivers, Leica AR20 antennas (choke ring antennas for the first and third dams) and Leica AS10 antennas (geodetic quality antenna for the Cabril dam). The software that manages and automatically processes the observations is also from Leica and is called Spider. The Foz Tua dam was equipped with two Topcon GB-1000 receivers with two Topcon Choke Ring antennas. The software that processed these observations was developed by Topcon and is called Pinnacle. The observations were processed manually. Both software programs are commercial and therefore have some limitations compared to scientific software, especially when it comes to processing the tropospheric delay. In other words, it would be possible to obtain better results in the height component by using scientific software, such as Bernese GNSS Software version 5.4 [6].

In general, increasing the order of the moving average in the GNSS observation time series should correspond to an increase in the accuracy of the observation time series. The other side of the coin is that the smoothing introduced may eliminate some important signals.

In the case of the Baixo Sabor dam, the large difference in altimetry between the GNSS stations is an important factor limiting the accuracy achieved in the height component. Only the weekly moving average (order 168) can reduce the uncertainty. On the other hand, for the Cabril and Feiticeiro dams, increasing the order of the time series moving average doesn't seem to bring any advantages. For the Foz Tua dam, where the difference in elevation is 80 metres, we recommend using the weekly moving average. It should be noted that there isn't much difference in the height difference between the GNSS stations at this dam and the Feiticeiro dam (80 metres versus 60 metres). It should also be noted that for the horizontal components, the results in each of these dams are very accurate, regardless of the hardware and software used [3].

5. CONCLUSIONS

High gradients between GNSS stations can significantly limit the accuracy required for dam monitoring, but only in the altimetric component. There is no problem in monitoring dams with GNSS in the horizontal component. Better results would be expected if scientific software were used to process these GNSS observations, especially software that could better model the tropospheric delay.

Table 1 shows that the uncertainty in the vertical displacements observed with GNSS at the Baixo Sabor dam, which in this particular case is strongly influenced by the height differences between the GNSS stations, is too high to monitor a concrete dam. Even with the application of high order moving averages and the progressive smoothing of the observed time series, the corresponding standard deviations are still very high, far from the 1 mm accuracy required for monitoring concrete dams. On the other hand, for the Cabril and Feiticeiro dams, increasing the order of the time series moving average doesn't seem to bring any advantages, where the 25th order moving average seems to be accurate enough to be compared with the spirit levelling time series and to be used for dam monitoring. Although there were few geometric levelling campaigns at the Feiticeiro dam during the study period, this may have affected the comparison and validation of GNSS monitoring of the vertical component.

For the Foz Tua dam, where the difference in elevation is 80 metres, we recommend using the weekly moving average.

ACNOWLEDGMENTS

Thanks are due to Engie Douro and Movhera, the former responsible for operation and the latter the concessionaire of the Baixo Sabor, Feiticeiro and Foz Tua hydroelectric plants, as well as EDP, the concessionaire of the Cabril dam, for permission to present the monitoring results.

REFERENCES

[1] Bomford, G. (1952). Geodesy. Oxford University Press, London, U.K.

[2] Leick, A. (2004). GPS Satellite Surveying. John Wiley & Sons, Inc., Hoboken, New Jersey, USA.

[3] Lima, J. N. and Casaca, J. (2018). Monitoring dam displacements with GNSS: Strategy, accuracy, and benefits. Proceedings of 3rd International Dam World Conference (Dam World 2018). Brazil, Foz do Iguaçu, 17 – 21 September 2018.

[4] S. Haykin (2002). Adaptive Filter Theory, Prentice Hall, New Jersey, USA (2002).

[5] M.B. Priestley (1981). Spectral Analysis and Time Series, Academic Press, London, UK (1981).

[6] Dach,R., Lutz, S., Walser, P. and Fridez, P. (2015). Bernese GNSS Software Version 5.2. Astronomical Institute, University of Berne, Switzerland, November 2015. ISBN: 978-3-906813-05-9.

Fifth International Dam World Conference
PORTUGAL • LISBON • LNEC • APRIL 13-17, 2025
dam world 2025

ANALYSIS OF THE DYNAMIC CHARACTERISTICS OF TRAPEZOIDAL CSG DAMS USING SEISMIC RECORDS

Nario Yasuda[1]
Eng. Division 1, Japan Dam Eng. Centre

Zengyan Cao
Eng. Dept. J-Power Business Service Corporation, Japan

Yuya Kozaki
Eng. Division 1, Japan Dam Eng. Centre

ABSTRACT

Trapezoidal cemented sand and gravel (CSG) dam is a new type of dam developed in Japan. its dynamic characteristics have not been fully understood. Therefore, in this study, seismic records of four existing trapezoidal CSG dams in Japan were analysed. It was found that the acceleration amplification factor of trapezoidal CSG dams during earthquakes is generally less than 1.5 when the maximum acceleration at the dam base was 10 cm/s^2 or greater. It is smaller than that of concrete gravity dams and rockfill dams of the same size. By analysing 30 seismic records of the Apporo Dam with an analysis method proposed by one of the authors, not only the natural frequencies of the dam, but also the mutual contributions between vibration directions in the seismic response of the dam were estimated. Furthermore, the damping ratio of CSG was quantitatively identified. The average damping ratio of the CSG is 5.5% when the maximum acceleration at the dam base is less than 30 cm/s^2. However, the damping ratio of the Apporo Dam was 8.3% during the 2018 Hokkaido Eastern Iburi Earthquake when the maximum acceleration at dam base was 450 cm/s^2. These data provide quantitative information on the dynamic characteristics of trapezoidal CSG dams. Especially, this is the first time to evaluate the damping ratio of CSG, and it is expected to be referable for the future dam design and analysis.

Keywords: trapezoidal CSG dam, dynamic characteristics, seismic record,

[1]e-mail: yasuda@jdec.or.jp, Japan

1. INTRODUCTION

Trapezoidal cemented sand and gravel (hereafter referred to as CSG) dam [1],[2] was developed in Japan and is characterized by low environmental impact, effective use of materials, and rational design and construction. As a new type of dam, earthquake monitoring at actual dams has just begun, hence, its dynamic characteristics have not been fully understood. In the countries like Japan where earthquakes occur frequently, it is extremely important to ensure the seismic performance of dams, and understanding the dynamic characteristics of dams is essential for their seismic design. Therefore, in this study the dynamic characteristics including acceleration amplification factor, natural frequency and damping ratio of such dams are investigated by analysing the seismic records of four existing dams in Japan. It is expected to present a reference material for the future dam design and analysis.

2. ACCELERATION AMPLIFICATION FACTORS

On September 6, 2018, the Hokkaido Eastern Iburi Earthquake (Mj 6.7) occurred, and the Apporo Dam, a 47.2 m-high trapezoidal CSG dam located 8.6 km away from the epicentre, was subjected to seismic motion with an intensity of 7 (Japan Meteorological Agency Seismic Intensity Class). Accelerations of up to 450 cm/s^2 were recorded in the bottom inspection gallery and 591 cm/s^2 at the dam crest, and the acceleration amplification factor of the dam body was 1.31. In contrast, at the Atsuma Dam, a 38.2 m-high rockfill dam located approximately 5 km upstream from Apporo Dam, a maximum acceleration of 297 cm/s^2 was recorded at the dam base and 1293 cm/s^2 at the crest during the same earthquake, and the acceleration amplification factor of the dam body was 4.35 [3]. Compared with the height of the Atsuma Dam, the acceleration amplification factor of the latter was less than 1/3 that of the former during the same earthquake, although the height of the Apporo Dam was greater than that of the Atsuma Dam. To clarify whether this is an individual phenomenon of the Apporo Dam or a general characteristic of trapezoidal CSG dams, seismic records of four existing trapezoidal CSG dams completed in Japan were analysed. Fig. 1 shows the locations of these existing dams named as Sanru Dam, Tobetsu Dam, Apporo Dam, and Kim Dam, and Table 1 shows their main features.

Fig. 2 shows the relationship between the maximum acceleration at the dam base and the acceleration amplification factor of the dams. Since there have been only two sets of records with a maximum acceleration of 30 cm/s^2 or greater at the dam base (the September 6, 2018 earthquake and the February 21, 2019 earthquake at the Apporo Dam), the maximum acceleration values of the lateral axes of Fig. 2 were set to 30 cm/s^2 to show the results of

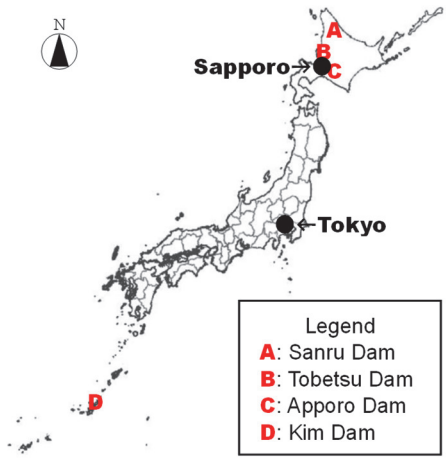

Fig. 1 – Locations of the dams

Table 1 – Main features of the dams

Name	Height (m)	Crest length (m)	Volume (10^3 m^3)
Sanru	46.0	350.0	495
Tobetsu	52.0	432.0	803
Apporo	47.2	516.0	490
Kim	39.0	461.5	339

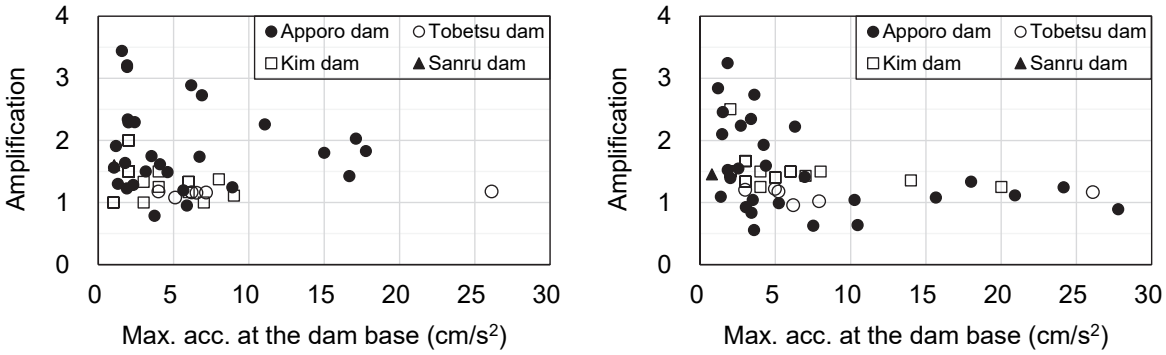

(a) Stream direction (b) Dam axis direction

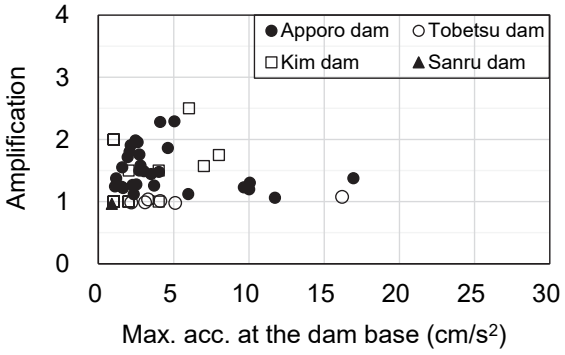

(c) Vertical direction

Fig. 2 – Relationship between the maximum acceleration at the dam base and its amplification factor of trapezoidal CSG dams

many earthquakes in detail. In Fig. 2, the acceleration amplification factors in the stream and dam axis directions tend to decrease slightly as the acceleration increases, but this is not obvious. The amplification factors for the range of maximum acceleration at the dam base above 10 cm/s^2 are less than 2.0 in the stream direction and less than 1.5 in the dam axis and

vertical directions. This is assumed because the smaller the maximum acceleration at the dam base is, the greater the variation in the amplification factor and the larger the measurement error. This trend should be examined as more seismic records are accumulated in the future.

A trapezoidal CSG dam is located between a concrete gravity dam and a rockfill dam in terms of its structural and material characteristics. Since the heights of the four trapezoidal CSG dams constructed in Japan thus far range from 39 m to 53 m, the acceleration amplification factors of the four dams are compared here with those of concrete gravity and rockfill dams of the same size (38.0 m to 55.0 m in height). The left column of Fig. 3 shows a comparison with the acceleration amplification factors obtained from the seismic records of concrete gravity

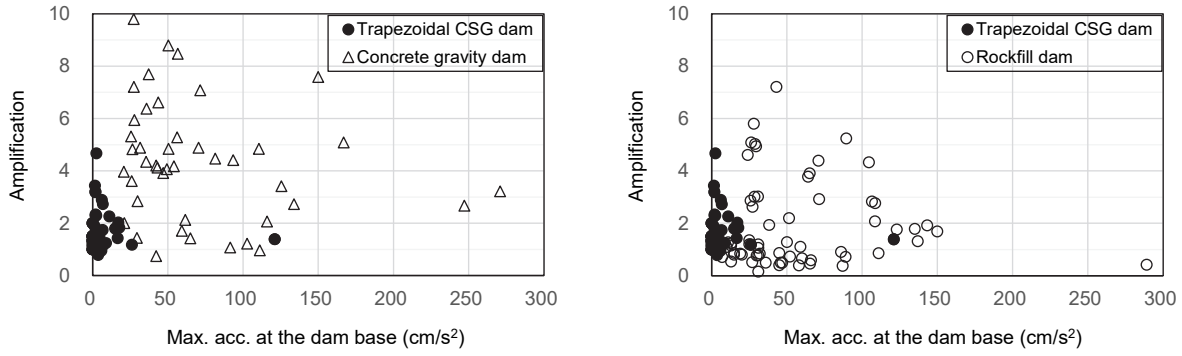

(a) Stream direction

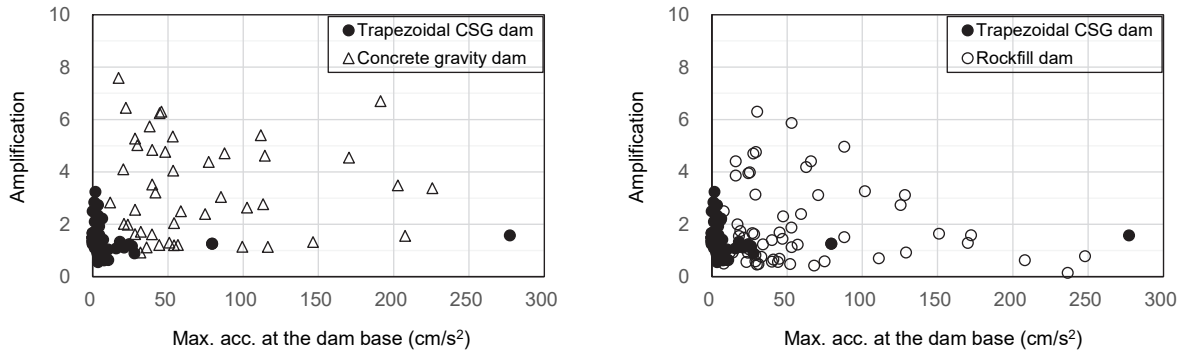

(b) Dam axis direction

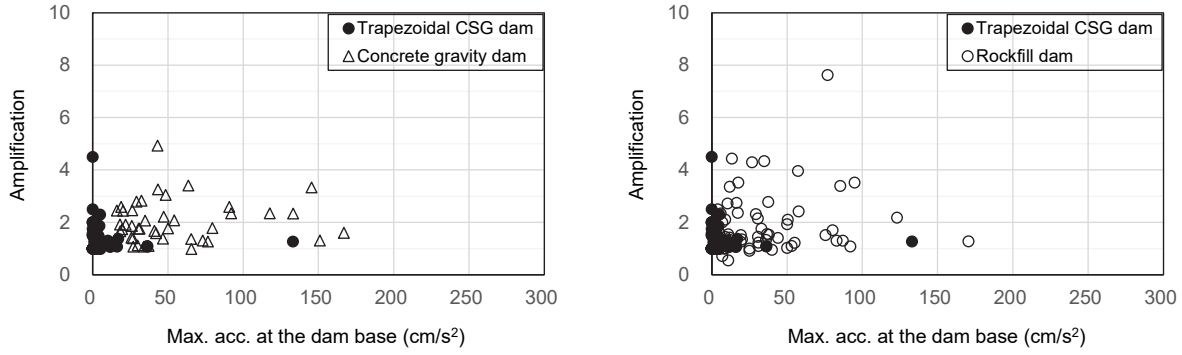

(c) Vertical direction

Fig. 3 – Comparison of the amplification factors of trapezoidal CSG dams and other types of dams

dams collected by the Japan Commission on Large Dams (JCOLD) [4]. This figure shows that, in general, the acceleration amplification factors of trapezoidal CSG dams are clearly smaller than those of concrete gravity dams of the same size. The acceleration amplification factors based on the rockfill dam data collected by JCOLD are shown in the right column of Fig. 3 and are compared with the results for trapezoidal CSG dams. This figure shows that the acceleration amplification factors of the trapezoidal CSG dams are equal to or lower than those of the rockfill dams of the same size, although there is a large variation in the acceleration amplification factor of the rockfill dam. This result indicates that the low-acceleration amplification factor of trapezoidal CSG dams is an inherent characteristic of this type of dam. The reason for the low-acceleration amplification factor of trapezoidal CSG dams may be that the natural frequency of the dam and the predominant frequency of seismic motion are generally very different. For example, Fig. 4 shows the acceleration response spectrum of the seismic ground motion measured at the dam base of the Tobetsu Dam and the natural period range of the dam. From the figure, it is generally considered difficult for the dam to resonate with seismic motions.

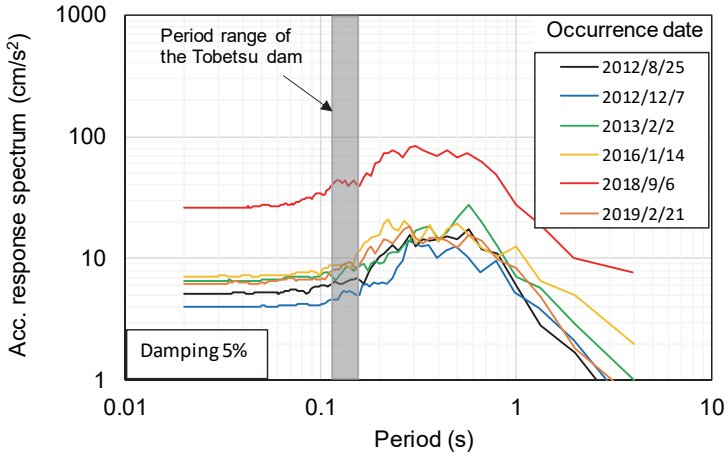

Fig. 4 – Acceleration response spectra of the seismic motions at the dam base of Tobetsu dam

3. NATURAL FREQUENCIES OF THE APPORO DAM

Of the four existing dams, Apporo dam has the most seismic records so far. Fig. 5 shows the dam and the locations of the seismographs at the dam site. The following study will focus on Apporo dam.

The transfer function of the dam was calculated based on the transfer function matrix method [5] using seismic motions at the crest and the dam base, and the natural frequencies of the dam body were investigated. In this method, a set of three seismic records are used, and the

Fig. 5 – Apporo Dam and seismographs at the dam site

transfer function can be calculated with high accuracy by decomposing the mutual interference between each direction of vibration. A total of 11 sets of data were used for the Apporo Dam (four records with relatively large acceleration were used more than once in different sets to highlight the characteristics of the transfer function). Fig. 6 shows an example of the calculated results. In this figure, each component of the transfer function matrix, T_{ij} (i, j = X, Y, and Z), is a transfer function that accounts for the mutual interference between directions; T_{ii} (i = X, Y, and Z) is a transfer function that shows the response characteristics in the i direction at the crest to the vibration in the i direction of the dam base. Each component, T_{ij} (i, j = X, Y, and Z, but $i \neq j$), is a contribution transfer function that shows the mutual interference between directions. For example, T_{XY} indicates the response characteristics of the crest in the X direction to the vibration in the Y direction at the dam base. The frequencies corresponding to the distinct peaks of the transfer functions T_{XX}, T_{YY}, and T_{ZZ} in each direction (the red lines indicate the location of the peaks, and the numbers are the frequencies corresponding to those peaks) were read as the natural frequencies of the dam according to Fig. 6. Two natural frequencies were obtained for the stream direction, one for the dam axis direction, and one for the vertical direction. These results are summarized in Table 2. The following observation were made from Fig. 6 and Table 2.

(a) The average values of the fundamental and second natural frequencies in the stream direction (T_{XX} in Fig. 6) are 7.9 Hz and 9.9 Hz, respectively. The seismograph locations are not in the largest cross-section of the dam but is heavily biased to the left bank of the dam as shown in Fig. 5. The corresponding seismograph position is close to the nodal point of the maximum value of the second natural vibration mode (antisymmetric mode) of the dam, and it is assumed that the second mode is more easily detected than the fundamental mode from seismic monitoring data at this position. As shown in Fig. 6, the

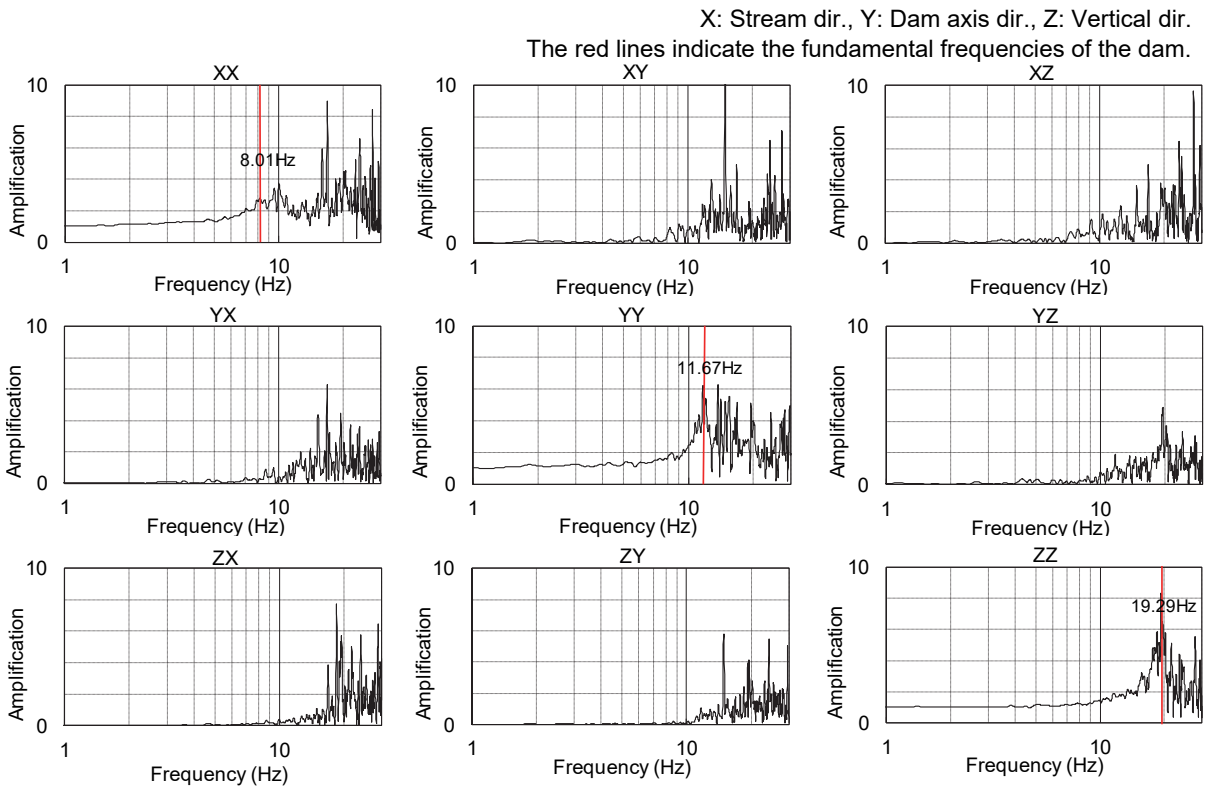

Fig. 6 – Example of the transfer function matrix of the Apporo Dam based on analysis of seismic records.

Table 2 – Natural frequencies of the dam obtained from the transfer functions of seismic records

Set No. of seismic records	Stream direction		Dam axis direction	Vertical direction
	First (Hz)	Second	First (Hz)	First (Hz)
1	8.0	9.9	11.7	19.3
2	8.0	10.0	12.9	20.3
3	8.0	9.8	12.7	20.0
4	7.5	10.2	12.0	20.2
5	8.1	9.8	12.1	19.9
6	7.6	9.5	12.1	19.3
7	8.3	10.2	13.1	19.6
8	7.8	9.9	11.9	19.7
9	7.9	10.0	12.8	20.7
10	7.8	10.0	11.7	19.6
11	7.7	9.8	12.1	19.7
Average	7.9	9.9	12.3	19.8

amplification of the secondary peak is slightly higher than the primary peak of the transfer function, which also reflects the biased installation of seismographs at the Apporo Dam. This case again demonstrates the necessity of considering the natural vibration modes of dams when installing seismographs on dams.

(b) The average values of the fundamental frequencies in the dam axis and vertical directions

of the dam are 12.3 Hz and 19.8 Hz, respectively. In the dam axis direction (T_{YY} in Fig. 6), the amplification factor remains approximately 1 up to approximately 7 Hz, indicating that the dam behaves almost rigidly in this frequency range in this direction. In the vertical direction (T_{ZZ} in Fig. 6), there is a similar tendency up to approximately 10 Hz.

(c) In the frequency range up to 10 Hz, the contribution functions T_{ij} ($i, j = X$, Y, and Z, but $i \neq j$) are almost zero, which means that the mutual interference among the stream direction, the dam axis and the vertical direction of the dam is estimated to be very small up to 10 Hz.

Moreover, it can be found the natural frequencies obtained above are much higher than those of concrete gravity and rockfill dams of the same size. This is presumably due to the shape and materials of the trapezoidal CSG dams.

4. DAMPING RATIOS OF THE APPORO DAM

Using seismic motions recorded at the crest and the dam base, the damping ratios are calculated by decomposing the vibration of the dam crest into forced and free vibrations and then applying the determination method of damping ratio to the obtained free vibration. For details of the calculation method, please refer to the related research [6]. As an example, Fig. 7(a) shows the free vibration after the peak value obtained from the acceleration waveform at the crest of the Apporo Dam during the 2018 Hokkaido Eastern Iburi Earthquake. The damping ratio obtained by applying the determination method to the approximate curve (shown in Fig. 7(b)) between the absolute the positive and negative amplitude values p_{-1}, p_{+1}, p_{-2}, ..., of this free vibration waveform and the damping ratio is 8.3% (incidentally, in the seismic design of the Apporo Dam for the MDE, the damping ratio was set to 10.0%). The relationship between the damping ratios obtained from other seismic records and the maximum acceleration at the dam base are plotted in Fig. 8. The dependence between the damping ratio and the maximum acceleration at the dam base is not clear when the maximum acceleration at the dam base is less than 30 cm/s^2, and the damping ratio varies from 3.0% to 8.0%. In comparison, the slightly larger damping ratio (8.3%) obtained from the record of the 2018 Hokkaido Eastern Iburi Earthquake suggests that minor nonlinearity of the dam body response occurred during this earthquake. There have been no published data on the damping ratios of CSG dams, and this research seems to be the first. Further studies on the damping ratio of CSG dams are needed, pending the accumulation of seismic records, especially strong-motion records.

The dynamic characteristics (acceleration amplification factor, natural frequency, and damping ratio) of the existing dams were clarified through above investigations. The results of these studies based on actual seismic records are expected to contribute to the seismic design and evaluation of the seismic performance of trapezoidal CSG dams in the future.

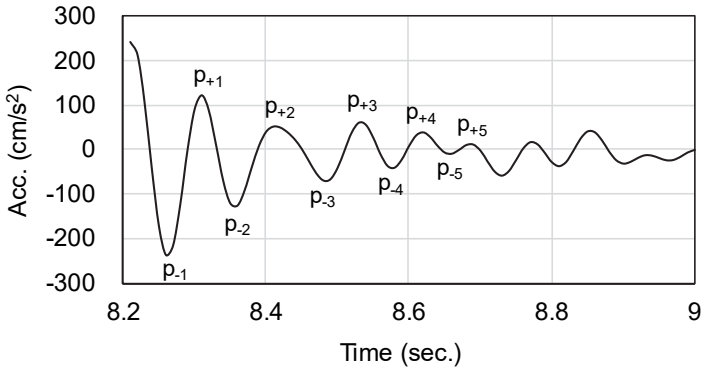

(a) Decomposed free vibration after the peak motion of the crest

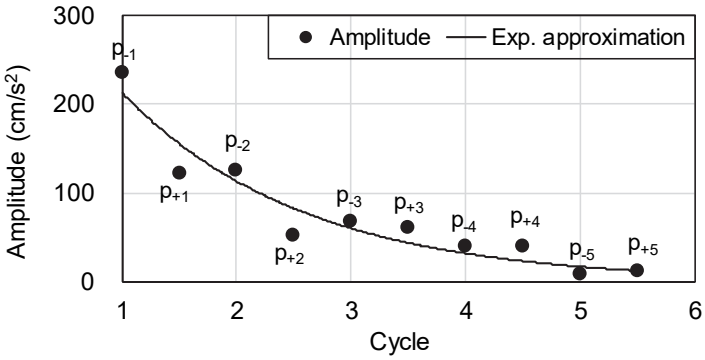

(b) Approximate curve of the amplitude and the cycle

Fig. 7 – Example of calculation of damping ratio (The 2018 Hokkaido Eastern Iburi Earthquake)

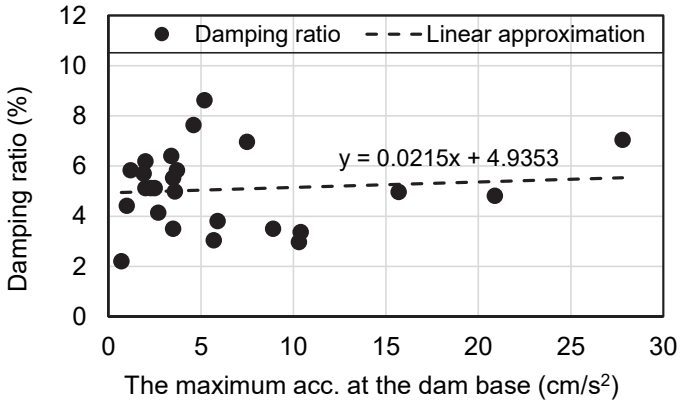

Fig. 8 – Relationship between the damping ratio and the maximum acceleration at the dam base

5. CONCLUSIONS

The conclusions of this study are summarized as follows:

(a) The acceleration amplification factors of the existing trapezoidal CSG dams were generally less than 2.0 in the stream direction and the dam axis direction, except for individual earthquakes when the maximum acceleration at the dam base was 10 cm/s^2 or smaller. The acceleration amplification factor of trapezoidal CSG dams is equal to or less than that of concrete gravity and rockfill dams of the same size.

(b) The analysis of more than 30 seismic records of the Apporo Dam clarified that the fundamental frequency of the dam is 7.9 Hz, and the second natural frequency is 9.9 Hz. They are much higher than those of concrete gravity and rockfill dams of the same size. Furthermore, the mutual contributions between vibration directions in the seismic response of the dam were estimated.

(c) The average damping ratio of the CSG is 5.5% when the maximum acceleration at the dam base is less than 30 cm/s^2. The damping ratio of the Apporo Dam was 8.3% during the 2018 Hokkaido Eastern Iburi Earthquake when the maximum acceleration at dam base was 450 cm/s^2. These data should be helpful for the future seismic design and seismic performance verification of trapezoidal CSG dams.

ACKNOWLEDGMENT

The authors are grateful to the providers of seismic records: River Management Section, Department of Public Works, Hokkaido Prefectural Government for the Tobetsu and Apporo dams, Northern Dam Integrated Control Office, Okinawa General Bureau for the Kim Dam, and Asahikawa Development Department, Hokkaido Regional Development Bureau for the Sanru Dam.

REFERENCES

[1] Fujisawa, T., Yoshida, H., Yasuda, N., Sasaki, T., Higuchi, A. and Fueta, T. (2006). Trapezoidal CSG dam. Dam Engineering, Vol. 240, 4-24, (in Japanese).

[2] Uomoto, T. (2011). Potential and issues of trapezoidal CSG dams. Dam Engineering, Vol. 21(4), 232-241, (in Japanese).

[3] Kitajima, Y., Iwata, T., and Hoshizaki, T. (2020). Damage situation and restoration details of Atsuma Dam during the 2018 Hokkaido Eastern Iburi Earthquake, Proceedings of the 66th Hokkaido Development Technology Conference, Hokkaido Regional Development Bureau, 570-575, (in Japanese).

[4] Seismic Analysis WG, Japan Commission on Large Dams (2015). Report of the subcommittee for updating the database of dam earthquake records in Japan, No.231, (in Japanese).

[5] Cao, Z., Kashiwayanagi, M., Yoshida, M. and Asaka, H. (2017). High-precision calculation method of transfer function considering interdirectional interference of vibration and its use in dam engineering. Power Civil Engineering, No. 390, 1-9, (in Japanese).

[6] Cao, Z., Kashiwayanagi, M., Yoshida, M. and Asaka, H. (2021). A new calculation method of damping ratio of structures based on earthquake records (DE/TFM). Power Civil Engineering, No. 413, 7-15, (in Japanese).

Fifth International
Dam World Conference
PORTUGAL • LISBON • LNEC • APRIL 13-17, 2025
dam world 2025

CREEP TESTS IN DAIVÕES DAM

João Conde Silva[1]
National Laboratory for Civil Engineering (LNEC)

Carlos Serra
National Laboratory for Civil Engineering (LNEC)

ABSTRACT

This paper summarises the most relevant aspects of the design and installation of the laboratory and *in-situ* setups used to determine the dam concrete deformability over time. These experimental setups aim at determining the modulus of elasticity for different ages and the creep function for the concrete used in the construction of Daivões dam. The laboratory setups have the advantage of carrying out the experimental work under relatively controlled conditions, whereas the *in-situ* setups (commonly referred to as creep cells) allow these studies to be performed under the dam actual conditions, i.e. real thermo-hygrometric conditions. The creep laboratory setup used in this work uses a rigid frame as the reaction structure and a closed hydraulic circuit which controls the applied pressure on a flat jack on the base of the concrete specimen. The strains were measured with a deflectometer, on the face of the specimens. Creep cells are composed of specimens of concrete with embedded strainmeters, installed in the body of a concrete dam (embedded in the dam concrete) during its construction, with a hydraulic flat jack underneath. During the elastic modulus and the creep tests, while the jack introduces a given compressive stress in the specimen, the embedded strain gauges measure the subsequent strains, instantly or over time, for the modulus of elasticity or creep assessment, respectively.

This paper presents the main deformability concrete test results obtained from both experimental setups, *in-situ* and laboratory, and a preliminary estimate of the creep function. Some of these results have already been used as an input to evaluate the dam structural behaviour during the first filling of the reservoir.

Keywords: Dam concrete, creep tests, semi-empirical models, laboratory, *in-situ*.

[1] jrsilva@lnec.pt, Portugal

1. INTRODUCTION

The dam-foundation-reservoir ensemble forms a complex structural system with specific characteristics conditioned by space-time circumstances, such as, for example, the properties of the rock mass foundation and the availability of raw materials for concrete production.

In the construction of large dams, it is common to use mass concrete compositions to optimize the relationship between production costs and the structural and durability requirements. For such concrete, the maximum aggregate size (often maximum aggregate size (Φ_{max}) of 150 mm) and the use of cement replacements are significantly higher than those of ordinary concrete, namely fly ash. In this context, a greater quality control (including specific laboratory testing programs) is required to characterize the concrete applied on site [1].

The larger dam concrete aggregates imply larger test specimens than usual, as well as large-capacity laboratory equipment, complicating the logistics of the tests. Due to these constraints, quality control and the characterization of dam concrete rely primarily on the results of wet-screened concrete, obtained by sieving the dam concrete (structural mass concrete) [2,3], which is the one used to embed strainmeters and used for standard-sized specimens for quality control and property characterization. Wet-screening involves removing, while fresh (wet), aggregates larger than a given diameter (typically 38 mm). Although periodic test campaigns are carried out with both types of concrete, the relationship between the properties of dam and screened concretes is still limited to instantaneous behaviour [4-9].

The phenomenon of concrete creep is particularly relevant in interpreting the behaviour of dams, as it determines the evolution of concrete deformability, contributes significantly to deformations and displacements, and induces stress redistribution over time. Since the safety control of such structures depends on modelling their behaviour, it is vital to correctly assess the creep function of the structural concrete [10,11].

This paper presents a summary of the most relevant aspects of the design and the installation of three sets of creep cells in Daivões dam and the main deformability concrete test results, obtained *in-situ* and in laboratory. The analysis of these deformability test results is also presented, including a preliminary estimate of the creep function of the creep cells concrete.

Based on the results obtained, the parameters of the basic creep law representative of the structure's long-term behaviour were estimated using the semi-empirical Double Power Law creep model, developed by Bažant and Panulla [12]. The basic creep law estimated from the experimental results has been used to estimate the viscoelastic properties of the concrete over time and to predict and interpret the structural behaviour of the dam.

2. EXPERIMENTAL WORK

2.1. Concrete composition

In the composition of the concrete for the Daivões dam, VLH IV/B (V) 22.5 cement was used, which incorporates ca. 45% of its mass in fly ash. The aggregates used in the concrete are granitic. The fine aggregates were divided into two classes, 0/1.2 mm and 1.2/5 mm, and the coarse aggregates were divided into four classes: 5/15 mm, 15/30 mm, 30/70 mm, and 70/150 mm. The admixture Muraplast FK 88i was used as a plasticizer.

The experimental work is focused on the characterization of the deformability properties of both the dam core concrete (DAM150) and the concrete wet-screened through a 38 mm sieve (SCR38), which was obtained from the previous one. Table 1 shows the values related to the particle size distribution of the aggregates used in the dam and screened concretes associated with three different groups of creep cells (GC1, GC2 and GC3). The composition of the SCR38 was estimated from the dosages of the DAM150 by removing the approximate volumes of aggregates larger than 38 mm and the volume of the surrounding mortar lost during the screening process [13].

Table 1 – Particle size distribution of the aggregates used in the dam concrete (DAM150) and in the respective screened concrete (SCR38)

Group of creep cell	Concrete type	Fine aggregate (kg/m^3)		Coarse aggregate (kg/m^3)				
		0/1.2 mm	1.2/5 mm	5/15 mm	15/30 mm	30/38 mm	38/70 mm	70/150 mm
GC1	DAM150	312.4	271.3	321.6	385.1	482.7		498.6
	SCR38†	410.9	348.4	489.4	586.0	146.7	-	-
GC2	DAM150	312.3	271.1	320.8	383.2	482.3		498.2
	SCR38†	425.7	363.1	488.0	582.8	146.5	-	-
GC3	DAM150	314.0	272.1	321.1	385.1	479.0		498.3
	SCR38†	426.4	362.8	487.7	584.9	145.3	-	-

† Estimated values

Table 2 shows the compositions of the two types of concrete and their main proportions by mass, respectively, for each of the three groups of creep cells. Note that c.a. 3/4 of the added water corresponds to ice, and the aggregates were pre-cooled.

Table 2 – Dosages of the dam concrete (DAM150) and the respective screened concrete (SCR38)

Group of creep cells	Type of concrete	Cement VLH IV B (V) (kg/m³)	Added water (kg/m³)	Aggregate water (kg/m³)	Total water (kg/m³)	Additive (Muraplast FK 88i) (kg/m³)	Fine aggregate (kg/m³)	Coarse aggregate (kg/m³)	Water-binder ratio
GC1	DAM 150	180.0	92.1	23.8	115.9	1.8	583.5	1688.0	0.64
	SCR 38†	252.7	128.9	36.2	165.0	2.5	788.8	1222.1	0.65
GC2	DAM 150	180.0	95.6	23.7	119.3	1.8	583.6	1684.5	0.66
	SCR 38†	252.7	133.7	36.1	169.8	2.5	788.3	1217.3	0.67
GC3	DAM 150	179.9	88.5	23.7	112.3	1.8	586.1	1683.5	0.62
	SCR 38†	252.2	123.6	36.0	159.6	2.5	789.3	1217.9	0.63

† Estimated value

2.2. Laboratory tests

Along with the concrete placement, for each creep cell group (GC1, GC2 and GC3), two prismatic specimens measuring 150×150×600 mm³ were moulded with the respective SCR38 for laboratory tests at LNEC, to determine the modulus of elasticity and the creep function. The screened concrete (Figure 1a)) was compacted using a vibrating table (Figure 1b)), similar to the procedure used for compacting the specimens intended for concrete characterization and quality control. These specimens were sealed with lead foil immediately after moulding (Figure 1c)). The sealed specimens were stored in a room at an ambient temperature of 20°C ± 2°C. These specimens were used to determine the modulus of elasticity according to the standards from DIN [14] and LNEC [15].

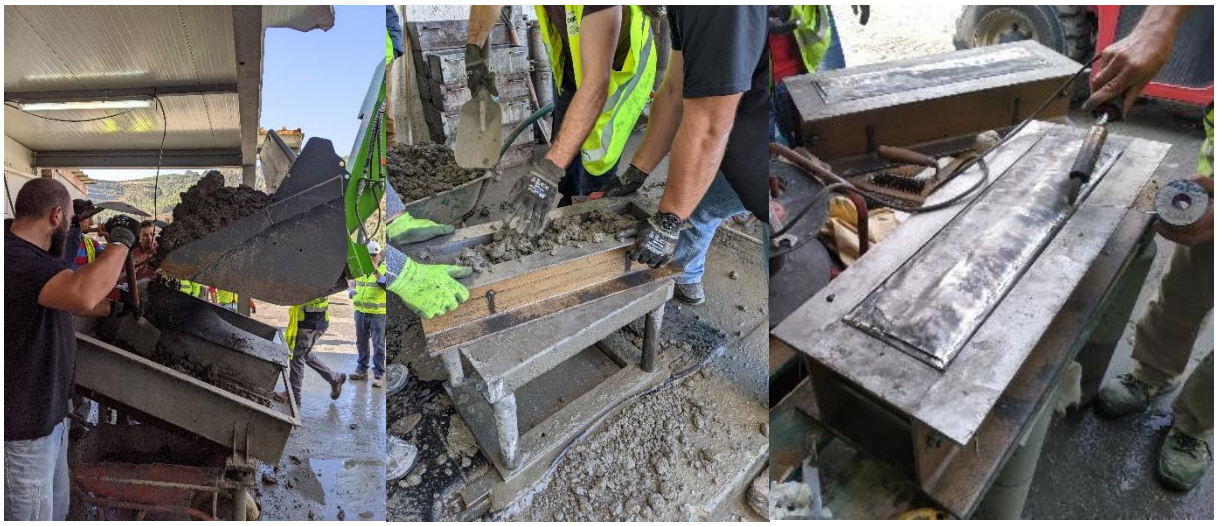

a) Screening the dam concrete

b) Moulding and compacting the concrete on a vibrating table

c) Sealing the specimens with lead foil

Figure 1 – Preparing the specimens for laboratory testing

For performing the compressive creep tests in laboratory, specific laboratory setups were used to apply the compressive stress in the vertical direction (over the longer dimension of the prism) (Figure 2a)). These setups were composed of a rigid frame as the reaction structure equipped with a pressure compensation system involving a nitrogen bottle and hydraulic oil to maintain a constant load on a flat jack on the base of the concrete specimen, which were measured with the aid of a digital manometer (Figure 2b)). The deformations were obtained by measuring the distance between two reference bases set 388 mm apart on two parallel lateral faces of each prismatic specimen with the aid of a deflectometer (Figure 2c)). These reference bases are fixed on centred rods that pass through the entire cross-section of the specimen, perpendicular to the measurement faces.

a) General overview of the specimens in the creep press

b) Pressure transducer coupled with the oil/nitrogen bottle to maintain a constant load

c) Measurement of the deformation with a deflectometer

Figure 2 – Laboratory testing for determining the creep strains

The ages in which the specimens were tested are presented in Table 3. This table shows the ages of the modulus of elasticity tests and the ages at which each specimen started to be under constant load (since the loading age, the specimen was no longer subjected to the modulus of elasticity test).

Table 3 – Ages for laboratory testing (modulus of elasticity and creep loading ages) of the screened concrete (SRC38) prismatic sealed specimens related with each creep cells group

Concrete mixture	Age (days)					
	Modulus of elasticity test					Constant loading (creep test)
GC1	8	14	32	96	-	96
GC2	8	14	33	-	-	33
GC3	7	17	28	102	797	797

2.3. *In-situ* tests

The creep cells are setups specifically designed to characterise the deformability properties of concrete under the thermo-hygrometric conditions of the site. Each cell consists of a concrete cylinder embedded in the dam body, with its longitudinal axis in the vertical direction. The dimensions of the cylinder are a function of the concrete type (Figure 3). The mould consists of an expanded polystyrene (EPS) tube, which allows the desired cylindrical shape to be obtained and creates a partition between the test specimen and the surrounding concrete (Figure 4a)). Through a flat jack with an attached load system, the cylindrical specimen is subjected to a constant stress, and the associated deformation is measured by a strainmeter embedded in the cylindrical specimen. The placement of the strainmeters is a sensitive task, because it is a challenge to ensure their centrality, verticality and integrity, especially during the placement and the vibration of the concrete.

This type of equipment allows to determine both the instantaneous and the long-term concrete deformability, using a hydraulic flat-jack capable of applying rapid load and unload cycles. In Daivões dam, three groups of creep cells were installed. Each group is composed of one cell of dam concrete (DAM150) and one cell of screened concrete with a 38 mm sieve opening (SCR38), both with loading system (active cells), paired with two other similar cells, without loading system (corrector cells). Carlson-type electrical resistance strainmeters were used, with A20 model (with a 50 cm gauge length) used for dam concrete cells and A8 model (with a 20 cm gauge length) for the screened concrete cells [16,17]. Figure 4b) shows the complete schematic of a set of creep cells (active and corrector cells), including the components of the load system embedded in the dam body (see also Figure 5a)) and the accessible equipment installed in the gallery niche (see also Figure 5b)).

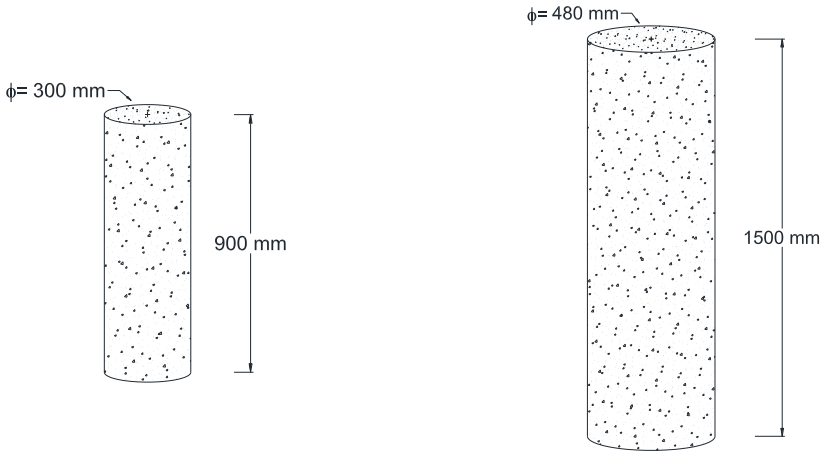

a) Specimen for screened concrete: Ø300 mm×900 mm

b) Specimen for dam concrete: Ø480 mm×1500 mm

Figure 3 – Dimensions of creep cells for each type of concrete

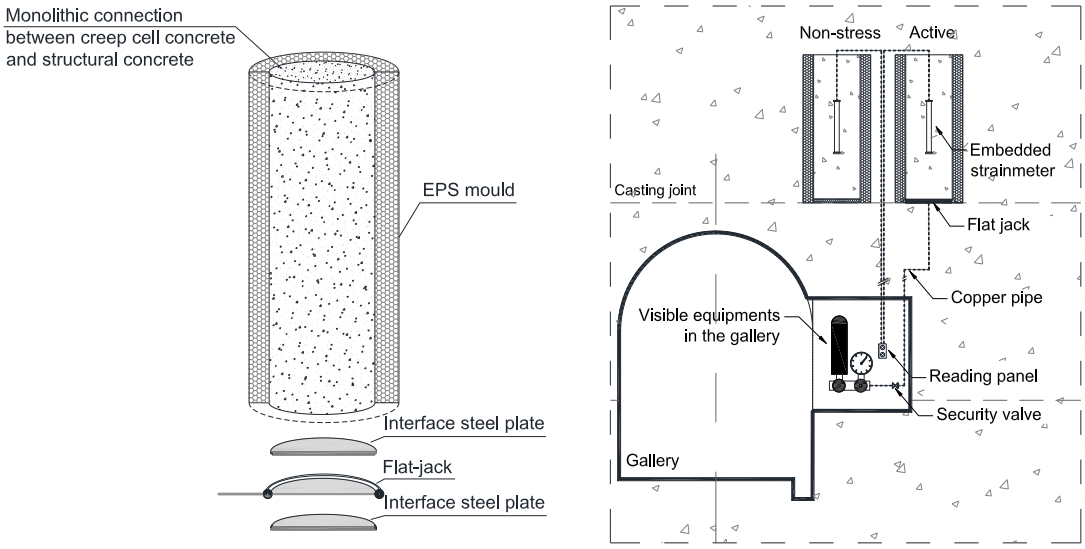

a) Active specimen

b) Embedded and accessible elements of a group of creep cells

Figure 4 – Schemes of the creep cells systems in Daivões dam

a) Installation of a group of creep cells, which were eventually embedded in the dam concrete

b) Accessible elements located in the niche of the dam gallery

Figure 5 – Images from the creep cells systems in Daivões dam

The on-site modulus of elasticity test consisted of performing three load and unload cycles in each active cell and recording the corresponding strain variations measured by the embedded strainmeters. The load variations were applied in increasing or decreasing steps of 5 and 10 bar until the upper and lower test stresses were reached. The maximum stress considered in each test corresponded to a pressure of 30 bar for younger ages and 50 bar for later ages, also depending on the system's response. The stress applied to each type of cell was calculated from the pressure applied to the load system, considering the ratio between the flat jack's diameter and the cross-sectional area of the cell's specimen. The conversion coefficients between the oil pressure in the load system (in bar) and the applied stress (in MPa) are 0.088 and 0.087 for the integral concrete cells and the screened concrete cells (with a 38 mm sieve), respectively (Table 4). The maximum test stresses were calculated based on the compressive strength test results available from similar concrete elements, with a maximum stress limit considered at each age corresponding to approximately one-third of the compressive strength obtained from cylindrical specimens at the same age, up to a maximum limit of 50 bar.

Table 4 - Conversion between oil pressure in the load system and the voltage applied to the specimen

Cell type	Maximum pressure (bar)	Contact zone diameter of the pad (m)	Pad area (m²)	Cell diameter (m)	Cell area (m²)	Conversion factor	Applied stress (MPa)
Dam concrete	50	0.450	0.159	0.480	0.181	0.088	4.4
Screened concrete	50	0.280	0.062	0.300	0.071	0.087	4.4

The loading speed sought to replicate laboratory procedures [14,15]. The tests to determine the modulus of elasticity were conducted quickly enough to avoid the influence of autogenous volume variation and concrete creep strains. For performing the creep tests, the load was maintained constant through the external hydraulic system housed in a niche within the dam's gallery (Figure 5b)). This system consists of a bottle containing pressurized oil. Each bottle is connected through a copper tube/pipe to the flat jack placed at the base of each active creep cell.

The ages in which the creep cells group were tested are presented in Table 6. This table shows the ages at which each specimen was subjected to the modulus of elasticity test and the ages at which these started to be under constant load. A few tests were not successful because the loading system was not functioning properly.

Table 6 – Ages for *in-situ* testing (modulus of elasticity and creep loading ages) of the dam and screened concrete (DAM150 and SRC38) for each group of creep cells

Concrete mixture	Age (days)					
	Modulus of elasticity test					Constant loading (creep test)
GC1	7	14	32	96	679	96
GC2	7	14	35	99	637*[1]	35
GC3	7	18	28	102	746*[2]	746*[2]

*[1] only the SCR38 cell was tested because the DAM150 cell loading system was not working
*[2] the loading system was not working for both SCR38 and DAM150 cells; thus, it wasn't possible to perform this test

3. PRESENTATION AND ANALYSIS OF RESULTS

3.1. Modulus of elasticity

In Figure 6, the average values of the modulus of elasticity obtained from sealed specimens are compared with those obtained from the average values of GC1, GC2 and GC3 creep cells. These results show that the values of the elastic modulus are higher for the *in-situ* specimens when compared with the specimens cured in the laboratory environment; that is, the development of the elasticity modulus occurs faster on-site than under controlled conditions at 20°C, especially at younger ages (7 to 28 days).

The *in-situ* results for screened concrete show higher values than those obtained in the laboratory, with the difference being more pronounced at ages up to 28 days, when the effect of temperature on binder hydration is more significant (Figure 6). Moreover, the manual

compaction of the concrete in the creep cells may have resulted in the larger aggregates to became in contact with one another, creating a rigid internal structure that leads to higher elasticity modulus values. This effect is more evident at younger ages, when the cement paste has not yet developed significant rigidity.

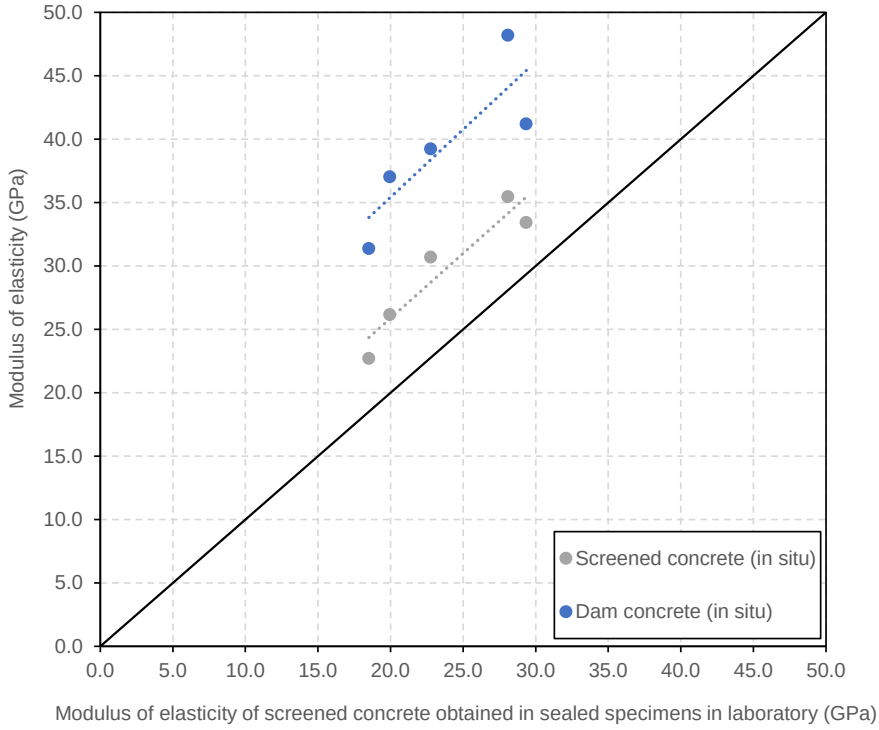

Figure 6 – Comparison of the modulus of elasticity results in laboratory (xx axis: screened concrete prisms) with the *in-situ* results (yy axis: screened concrete cells and dam concrete cells) (average values)

3.2. Creep strains

Creep corresponds to the increase in strain over time under constant stress, $\sigma(t_0)$, in conditions of constant temperature. The instantaneous strains, $\varepsilon^i(t_0)$, and creep strains, $\varepsilon^c(t, t_0)$, depend on the magnitude of the stress, with the creep function, $J(t, t_0)$, representing the total strain per unit of stress. Here, t represents the time elapsed since concreting, and t_0 represents the loading age, that is, the age of the concrete at the time of loading. Thus, we have:

$$\varepsilon(t,t_0) = \varepsilon^i(t_0) + \varepsilon^c(t,t_0) = J(t,t_0)\ \sigma(t_0) \quad (1)$$

$$J(t,t_0) = \frac{1}{E(t_0)} + \frac{\varepsilon^c(t,t_0)}{\sigma(t_0)} \quad (2)$$

In order to quantify the creep of concrete, the specific strains are calculated from the strains measured in each specimen, i.e., the strain per unit of stress from the beginning of the creep test. The strains measured in the active specimen correspond to total strains, $\varepsilon^{total}(t, t_0)$, and the free strains measured in the corrector specimen correspond to strains due to temperature variations and autogenous deformations, $\varepsilon^{corr}(t)$. The corrected total strains, $\varepsilon^{total\ corr}(t, t_0)$, and the specific total strains, $\varepsilon^{total\ spec}(t, t_0)$, are given by:

$$\varepsilon^{total\ corr}(t, t_0) = \varepsilon^{total}(t, t_0) - \varepsilon^{corr}(t) \quad (3)$$

$$\varepsilon^{total\ \ spec}(t, t_0) = \frac{\varepsilon^{total\ corr}(t, t_0)}{\sigma(t_0)} \quad (4)$$

Based on the results of each of the terms in equations (3) and (4) for the *in-situ* (creep cells) and corresponding laboratory results, a comparison between the total specific strains of screened concrete obtained in laboratory and *in-situ* is presented in Figure 7. There are no results for the GC3 creep cell group because the creep test in this group (for both SCR38 and DAM150) was unsuccessful. This creep cells group was supposed to be constantly loaded from the age of ca. 2 years old (see Table 6), but its loading system lost the ability to maintain the load. Thus, only the laboratory results are available for this loading age ($t_0 \approx 2$ y.o.). As for the other loading ages ($t_0 \approx 1$ month old for the GC2 related specimens and $t_0 \approx 3$ months old for the GC1 related specimens), Figure 7 shows that the creep values obtained in laboratory and *in-situ* are of the same order of magnitude, despite significant variations in load and temperature occurring *in-situ* throughout the tests, particularly in the screened concrete from the GC2 creep cell.

A decrease in instantaneous strains over time can be clearly observed, which is mostly explained with the increase in modulus of elasticity with time, which results in lower deformation rates over time for older loading ages.

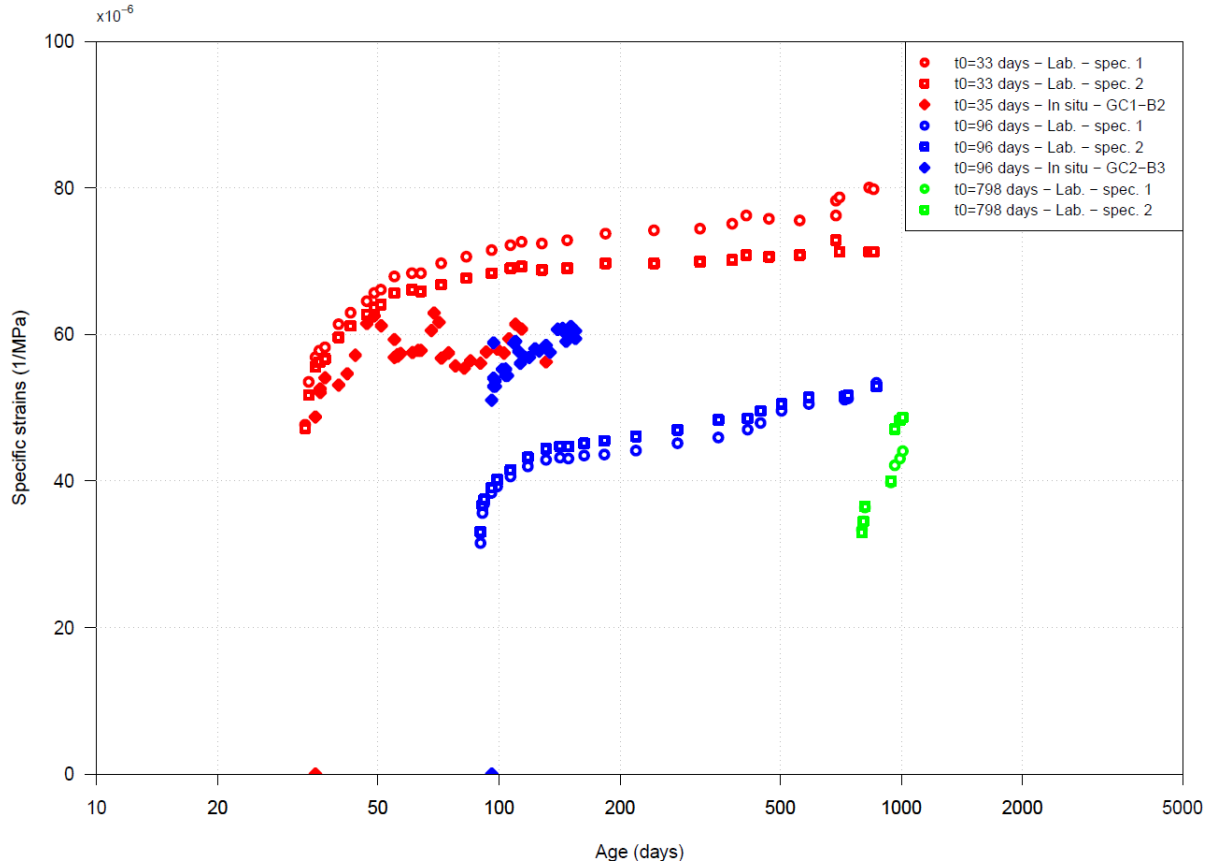

Figure 7 – Comparison between the laboratory and *in situ* (creep cells) results for the creep tests carried out on screened concrete

4. ESTIMATION OF CREEP FUNCTION

4.1. Bažant e Panula (BaP) creep function fit

Creep prediction models are associated with functions that have specific characteristics, chosen to represent the physical phenomenon of concrete creep. The parameters of these functions, typically determined from known material properties and, when available, adjusted to experimental test results, provide an estimate of creep strain values within certain assumptions.

In the Bažant and Panula (BaP) model [12], the creep function, $J(t, t_0)$, is given by the sum of the elastic component, $1/E_0$, basic creep, $C_0(t, t_0)$, and drying creep, $C_d(t, t_0,t')$.

One of the distinctive aspects of this formulation is the consideration of the concrete's maturation process in the basic creep component by multiplying a power of the age at loading, t_0, by a power of the time under load, t-t_0.

$$J(t,t_0) = \frac{1}{E_0} + C_0(t,t_0) + C_d(t,t_0,t') \quad (5)$$

$$C_0(t,t_0) = \frac{\phi_1}{E_0}(t_0^{-m} + \alpha)\ (t-t_0)^n \quad (6)$$

where E_0, φ_1, m, α e n are parameters dependent on the intrinsic characteristics of the concrete. Since, in the case of dams, the concrete does not, in practice, lose water to the outside, the drying creep component may be considered negligible compared to the basic creep values.

The prediction of the elasticity modulus over time can be obtained by considering the time under load, t-t_0, as equal to 0.1 days,

$$\frac{1}{E(t_0)} = \frac{1}{E_0} + \frac{\phi_1}{E_0} 10^{-n}(t_0^{-m} + \alpha) \quad (7)$$

It should be noted that the expressions of the BaP prediction model were calibrated based on various experimental tests available in the literature, covering different types of concrete [12].

In the absence of creep test results, the parameters of the creep law can be estimated using two distinct methods. The first method allows for estimating the creep function based on the 28-day compressive strength, $f_{c,28}$ (in MPa), and the concrete composition [12]. The second method considers only the 28-day compressive strength $f_{c,28}$ (in MPa) as the material's intrinsic characteristic [18], using expressions (8) to (11).

$$\phi_1 = 0.3 + 152.2\ {f_{c,28}}^{-1,2} \quad (8)$$

$$\alpha = 0.05 \quad (9)$$

$$m = 0.28 + 47.541\ {f_{c,28}}^{-2} \quad (10)$$

$$n = 0.115 + 0.183\ {f_{c,28}}^{3,4} \times 10^{-6} \quad (11)$$

In this work, given the specific characteristics of dam concrete and the availability of creep test results, the BaP model parameters should be adjusted considering this information. The parameters φ_1, m, n e α were adjusted by minimizing the difference between the creep calculated by the model and the experimental results of the creep function for loading ages of 35 and 96 days.

The adjustment also considered the estimate of the elasticity modulus and the experimental results obtained over time. The initial estimate of the parameters φ_1, m, n e α for the minimization process was obtained by considering, in expressions (8) to (11), the average compressive strength of the mass concrete at 90 days (24.5 MPa).

The estimate of the parameter E_0 was derived from expression (7), considering the average elasticity modulus at 680 days (48.2 GPa), to achieve a better long-term approximation.

The preliminary expression (12) represents the creep function that fits the experimental results, and it is shown graphically in Figure 8. Figure 9 shows the evolution over time of the corresponding elasticity modulus.

$$J_{BaP}(t,t_0) = \frac{1}{E_0} + \frac{\phi_1}{E_0}(t_0^{-m} + \alpha)(t-t_0)^n = \frac{1}{58.4} + \frac{4.80}{58.4}(t_0^{-0,30} + 0.01)(t-t_0)^{0.54} \quad (GPa^{-1}) \quad (12)$$

The adjusted parameter values are presented in Table 7, where it is evident that the parameters adjusted by the two methods have considerably different values. This difference is primarily due to the fact that the behavior of the concretes used to calibrate expressions (8) to (11) in the prediction method differs greatly from dam concrete, particularly the concrete used in the Daivões dam, which incorporates high content of fly ash.

Table 7 – Preliminary estimate of the parameters for the Bažant and Panula (BaP) creep function for the creep cells dam concrete

Parameter	BaP prediction model + E(t_0)	Preliminary adjustment + E(t_0)
E_0 (GPa)	67.1	58.4
φ_1	3.58	4.80
m	0.36	0.30
n	0.12	0.54
α	0.05	0.01

Figure 8 shows the specific strain values obtained in the mass concrete cells, the preliminary estimate of the creep function, $J(t, t_0)$, and the preliminary estimate of the evolution of instantaneous strains, $1/E(t_0)$, obtained by fitting to the average experimental results for loading ages of 35 and 96 days for cells GC2 and GC1, respectively. Figure 9 presents the corresponding elasticity modulus values obtained through preliminary fitting, along with a comparison to the experimental results obtained in the mass concrete creep cells.

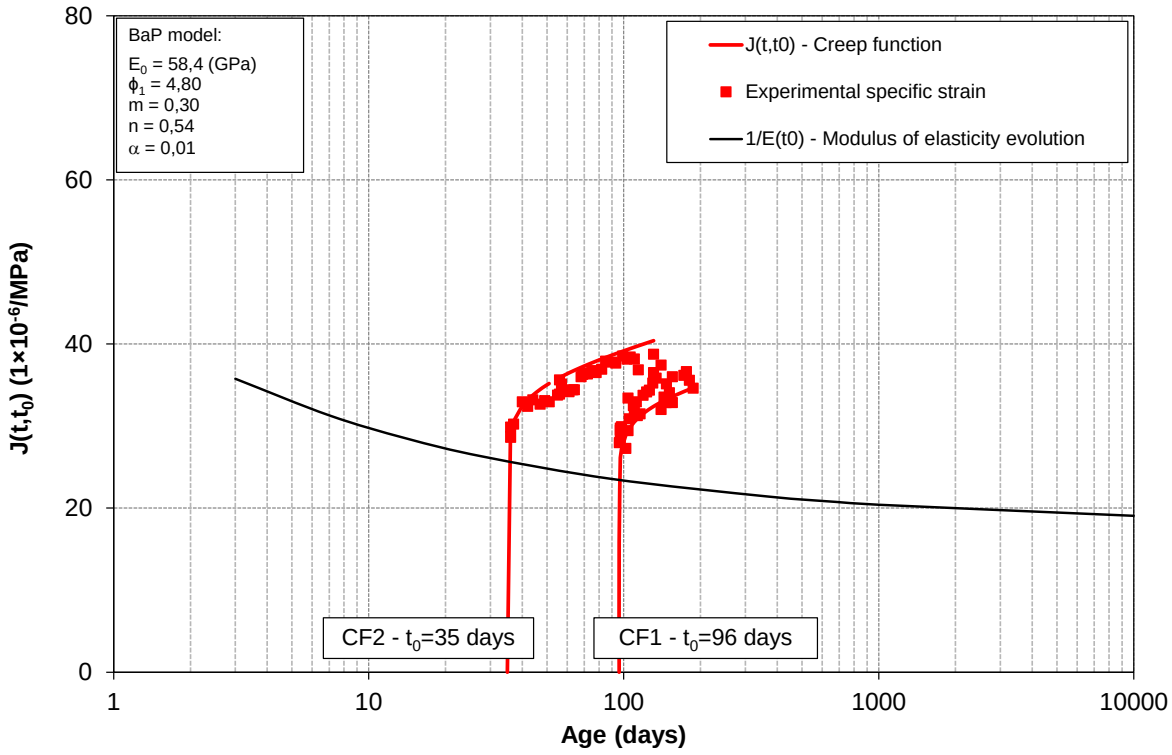

Figure 8 – Preliminary adjustment of the creep function and test results for the dam concrete creep cells

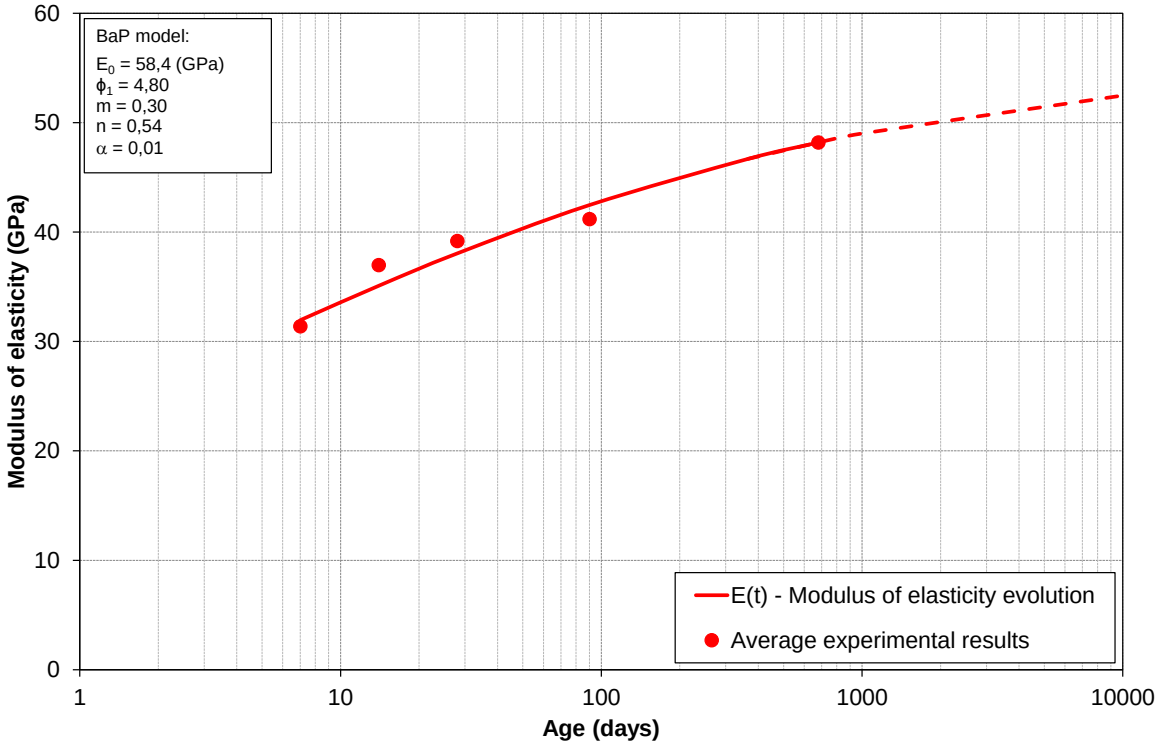

Figure 9 – Modulus of elasticity according to the preliminary adjustment of the creep function and results obtained for the dam concrete creep cells

The preliminary creep function fits well with the experimental results. The creep strains predicted by the creep function show a reasonable long-term development (Figure 8). The prediction of the elasticity modulus evolution from the creep function indicates an increase in value for ages beyond 680 days (Figure 9).

5. CONCLUSIONS

The relevant aspects of the project and installation of the three groups of creep cells at the Daivões dam and laboratory creep test setups were described. The results of the concrete deformability tests conducted *in-situ* and in laboratory are presented and briefly analysed. A preliminary estimate of the integral concrete creep function for the creep cells is also displayed.

As expected, in the creep tests, the strain increased instantaneous upon compressive load application, then gradually slowed, stabilizing over the long term. It was also concluded that the values of specific strain and the long-term creep coefficient for both integral and sieved concrete are low when compared to values calculated based on prediction models for concrete structures.

REFERENCES

[1] Serra, C.; Silva, J.C.; Vieira, M. (2022). Comportamento do betão da barragem de Daivões ao longo do tempo. Ensaios de fluência e ajuste a modelos semi-empíricos, atas 6as Jornadas Portuguesas de Engenharia de Estruturas, LNEC, Lisboa.

[2] ICOLD – ICOLD Bulletin (2008). The physical properties of hardened conventional concrete in dams. Draft for ICOLD review.

[3] USBR – Concrete manual (1988). A water resources technical publication, 8th Ed. Washington, United States Government Printing Office.

[4] Popovics, S.; Ujhelyi, J. (2008). Contribution to the concrete strength versus water-cement ratio relationship", J. Mater. Civ. Eng., 2008, vol. 20, no. 7, pp. 459–463.

[5] Elices M.; C. Rocco (2008). Effect of aggregate size on the fracture and mechanical properties of a simple concrete, Eng. Fract. Mech., 2008, vol. 75, no. 13, pp. 3839-3851.

[6] Vilardell J. et al. (1998). Estimation of the modulus of elasticity for dam concrete", Cem. Concr. Res., 1998, vol. 28, no. 1, pp. 93–101.

[7] Topçu, I. B.; Ugurlu; A. (2007). Elasticity theory of concrete and prediction of static E-modulus for dam concrete using composite models, Tek. Dergi, 2007, vol. 18, no. 1, pp. 4055– 4067.

[8] Khaloo, A. R.; Mohamadi Shooreh, M. R.; Askari, S. M. (2009). Size influence of specimens and maximum aggregate on dam concrete: Compressive strength, J. Mater. Civ. Eng., 2009, vol. 21, no. 8, pp. 349–355.

[9] Deng, Z.; Li, Q.; Fu, H. (2008). Comparison between Mechanical Properties of Dam and Sieved Concretes, J. Mater. Civ. Eng., 2008, vol. 20, no. 4, pp. 321–326.

[10] Ramos, J.M. (1985). Consideração da reologia do betão no comportamento de barragens, Laboratório Nacional de Engenharia Civil, 1985, Tese de Especialista, 223 p.

[11] Pinho, J.L. (1989). Contribuição para o estudo da deformabilidade do betão de barragens, Laboratório Nacional de Engenharia Civil, 1989, Tese de Especialista, 306 p.

[12] Bažant, Z. P.; Osman, E. (1976). Double power law for basic creep of concrete, Materials and Structures (RILEM, Paris), 1976, vol. 9, no. 49, p. 3-11.

[13] Serra, C. (2017). Prediction of dam concrete structural properties based on wet-screened test results and mesoscale modelling. Faculdade de Ciências e Tecnologia. Universidade Nova de Lisboa, 2017, PhD. thesis, 368 p.

[14] DIN (1991). Testing concrete: testing of hardened concrete (specimens prepared in mould). Part 5. Volume 1048, Berlin.

[15] LNEC (1993). Especificação LNEC E 397:1993 Betões. Determinação do módulo de elasticidade em compressão, Lisboa.

[16] Serra, C.; Silva, J.C. (2022). Barragem de Daivões - Instalação de células de fluência e ensaios de deformabilidade do betão", Relatório 229/2022, LNEC, Lisboa.

[17] Serra, C.; Conde Silva, J.; Lopes Batista, A.; Monteiro Azevedo, N. (2023). Dam Concrete in Situ Creep Tests. Experimental Setup and Results from Six Large Concrete Dams. SynerCrete 2023. RILEM Bookseries, 2023, vol 43. Springer, Cham.

[18] Neville, A.; Dilger, W.; Brooks, J. (1983). Creep of plain and structural concrete. New York: Longman Inc.

Fifth International Dam World Conference
PORTUGAL • LISBON • LNEC • APRIL 13-17, 2025
dam world 2025

LOCAL AND GLOBAL PARAMETER SENSITIVITY FOR CONCRETE HYDRAULIC STRUCTURES UNDER SEISMIC LOADING CONSIDERING STRUCTURE AND MATERIAL VARIATION

Rodrigo José de Almeida Torres Filho
Université de Sherbrooke

Rocio L. Segura[1]
Santa Clara University

Patrick Paultre
Université de Sherbrooke

ABSTRACT

The accurate analysis of hydraulic structures is crucial for ensuring their structural integrity, particularly in earthquake-prone regions. This type of analysis involves many parameters that are often challenging and expensive to define precisely, leading to significant uncertainties. In this context, sensitivity analysis is essential to identify the most influential parameters and understand their impact on system behavior. Given that the overall stability of concrete structures for water management is regulated by different failure modes, a comprehensive sensitivity assessment should include the varying sensitivity of different failure scenarios to distinct parameters. Moreover, the geometry significantly influences the structure's response to different loads, thereby affecting which parameters are most relevant to the analysis. Therefore, this study uses a nonlinear pseudo-static analysis to evaluate the response of hydraulic structures, considering material and loading variation. The effect of the structure type is considered by evaluating a gravity dam, a free-crested weir, and a gated spillway. A progressive Latin hypercube strategy is used to sample the uncertain domain to generate the experimental design matrix and identify the optimal number of simulations. The results are then used to conduct a sensitivity analysis to identify the most influential parameters for each failure mode at construction and dam-foundation joints. The adequacy of different sensitivity approaches to dam stability is investigated by comparing the more straightforward local sensitivity approach, represented by the Tornado diagram, with the more comprehensive global sensitivity method, Sobol, in terms of applicability and performance. The results offer valuable insights into the model's response given the parameters of interest and how this behavior varies depending on the structure, joint, and load case represented. Furthermore, the study enhances the understanding of how local and global sensitivity approaches influence the evaluation process for hydraulic structures.

Keywords: Local sensitivity, global sensitivity, hydraulic structures, uncertainty.

[1]rsegura@scu.edu , United States

1. INTRODUCTION

Concrete structures for retaining and water are vital infrastructures due to the costs associated with their construction and maintenance, and the severe consequences of potential failure. These structures are among the most complex engineering problems due to their unique geometries, interactions between concrete, water, and rock, and the diverse nature and magnitude of the applied loads [1]. These factors, combined with material heterogeneity and construction imperfections, introduce multiple uncertainty sources that must be addressed to ensure the safety of these structures.

The deterministic approach assumes that the relevant parameters to the analysis are known in advance [2]. However, many of these parameters are challenging or costly to characterize, often necessitating invasive field tests for material properties or relying on probabilistic inference methods for defining the seismic activity at the structure site. Consequently, deterministic analysis addresses uncertainty implicitly by focusing on extreme events with low probabilities of occurrence, often resulting in overly conservative designs [3]. To address this problem and explicitly consider the uncertainties present in the structure, the probabilistic approach is recommended [4,5]. However, given the complexity of numerical models representing concrete hydraulic structures and the significant computational effort required for their evaluation, careful selection of parameters for the analysis is essential [6]. Independently of the analysis approach selected, understanding the role of critical parameters in the structure response is essential for optimizing resource allocation and improving results.

In this context, sensitivity analysis plays a crucial role in addressing uncertainties, offering a systematic approach to evaluating how input parameter variability affects model responses. By quantifying the impact of these uncertainties, sensitivity analysis aids in identifying critical parameters, optimizing design, improving risk management, and allowing informed decision [7]. Multiple sensitivity analysis methods exist, each with distinct requirements and outputs, making it essential to select the appropriate method based on the specific objectives of the analysis. Furthermore, the different types of hydraulic structures, material properties, and loading conditions on the model sensitivity adds complexity to determining the most suitable approach. Therefore, this work compares how local and global sensitivity approaches perform when applied to hydraulic structures. To ensure the exploration of a wide range of scenarios three models — a gravity dam, a free-crested weir, and a gated spillway — are evaluated under three distinct load cases. At the same time, material and loading parameters are considered as input variables.

2. SENSITIVITY ANALYSIS

Sensitivity analysis studies how uncertainty in the model output can be attributed to different sources of uncertainty within model inputs [8] and is essential for modelling, uncertainty quantification, and risk assessment of complex systems. Within the possible approaches, local sensitivity methods examine the influence of a single input parameter at a time. For that, the parameter in question is varied while every other parameter is held constant, and the importance of the parameter is measured. Repeating this process for all input parameters allows the evaluation of the model sensitivity based on the importance of the ranked parameter. These methods are generally simple to evaluate and require a relatively small number of samples, making them straightforward and accessible for practical applications. However, they struggle to evaluate nonmonotonic input-output relationships [9], which can be limiting for hydraulic structures subjected to severe conditions.

Alternatively, global sensitivity methods study the influence of multiple input parameters on the model. Unlike local methods, all parameters can be varied simultaneously to consider the effect of the interaction between inputs. Each parameter is described by a probability distribution function (PDF), and the sampling process should consider the joint PDF to guarantee the proper representation of the uncertain domain. These methods generally require large sample sets to reach convergence, which can limit their use depending on the evaluation cost of each sample [8]. Therefore, the use of sampling techniques is recommended to minimize the necessary number of model evaluations [10].

2.1. Local sensitivity: Tornado

The tornado diagram is a straightforward method for measuring and displaying local sensitivity. The procedure starts with defining PDFs to represent each input parameter's variability. The mean value, lower limit, and upper limit are identified for each parameter considering the individual PDFs. Next, one input is selected as the target, and the model is evaluated at the upper and lower limits of this parameter while keeping the other inputs at the mean value. The difference between model responses is considered the measure of sensitivity for the target parameter. Repeating the procedure for every input parameter allows the identification of the most impactful parameters for the model [11]. Finally, the parameters are sorted from the most to the least impactful, forming a figure with a “tornado” shape.

2.2. Global sensitivity: Sobol

Sobol indices is a commonly used technique that decomposes response variance into individual contributions linked to each input or their combinations [12]. The Sobol is a variance-based method that presents characteristics that make it well-suited for diverse applications,

including compatibility with nonlinear problems and flexibility in handling parameters with varied probability distributions [13]. Sobol indices are used to quantify each input parameter's contribution to the model output's total variance. A higher Sobol index indicates a greater influence on the variability of the factor of safety relative to the other parameters. In this paper, the Sobol indices are calculated using the UQlab framework [14] available for MATLAB.

2.3. Sampling: Progressive Latin hypercube sampling technique

The Latin hypercube is a widely used method for efficient sampling as it ensures that the set of samples represents the entire range of parameters, preserving the marginal probability distribution of each simulated parameter [15]. However, once the size of the sample set is defined, it cannot be changed without losing its hypercube properties. This is a key limitation for this work as the appropriate sample size is not known beforehand. Therefore, the progressive Latin hypercube sampling technique (PLHS) was adopted [16]. In the PLHS, sets that individually contain the properties of the Latin hypercube sampling method are sampled. These samples can be progressively combined to obtain a larger set that preserves the desired distributional properties and simultaneously achieves optimum domain coverage. This property allows new samples to be progressively added to the set without requiring the procedure to return to the sampling phase.

3. CASE STUDY

Different hydraulic structures can be combined to form the system responsible for retaining and managing the water of a reservoir. Dams, spillways, weirs, intakes, outlets, and dissipators are examples of possible structure components. Each structure is designed for a specific function and must be equally capable of withstanding the system's characteristic loads. Due to their design, each type of structure reacts differently to the parameter variation, hence the importance of considering it in sensitivity studies. Therefore, in this study the considered water retaining system includes a gravity dam, a free-crested weir, and a gated spillway segment. A representative cross-section of each segment is presented in Fig. 1.

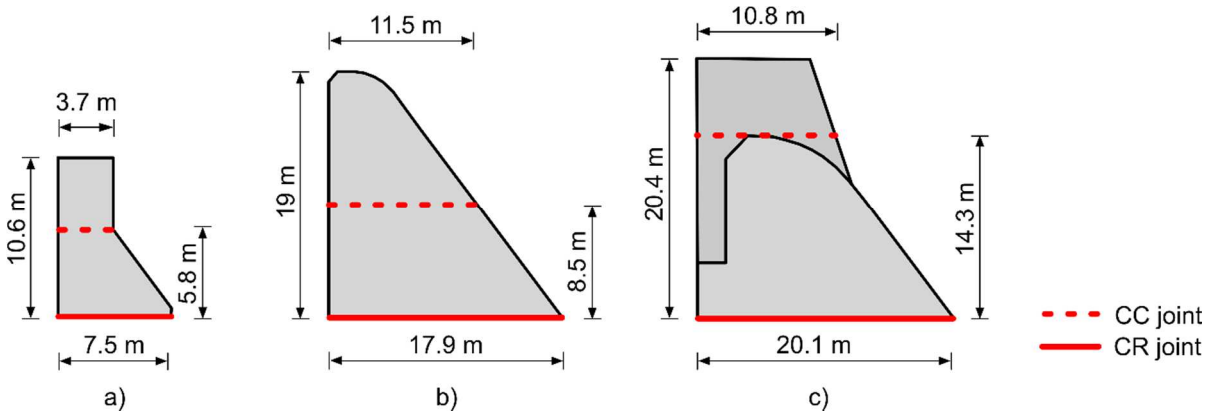

Fig. 1 - Water retaining system cross-section: (a) Gravity dam, (b) free-crested weir, and (c) gated spillway

The gravity dam (Fig. 1(a)) is designed to hold back water using its own weight to avoid sliding and overturning. The free-crested weir (Fig. 1(b)) lets the water flow freely when the reservoir reaches a certain level while the gated spillway (Fig. 1(c)) allows for controlled discharge. In this system, the gravity dam is situated near the riverbank, resulting in a reduced height compared to the other two structures, which are located in the deepest region of the river.

3.1. Numerical model

The stability analyses were performed using the gravity method, which is based on rigid body equilibrium and beam theory [17] and is recommended for preliminary analyses by different guidelines [18,19]. The agility of the method is a distinguishing feature, especially for global sensitivity analysis, which can require many analyses. All the models and analyses were generated with the software CADAM3D [20].

The structure stability response may vary significantly depending on the load combination considered. To account for the loading effect, this study considers one typical load case representing loads frequently applied to the structure, one unusual load case, and one extreme load case. These load cases are defined in Eq. 1 to 3, respectively.

$$\text{Usual} = \text{Dead load} + \text{Hydrostatic load} + \text{Uplift} + \text{Usual Ice} \quad (1)$$

$$\text{Unusual} = \text{Dead load} + \text{Hydrostatic load} + \text{Uplift} + \text{Unusual Ice} \quad (2)$$

$$\text{Extreme} = \text{Dead load} + \text{Hydrostatic load} + \text{Uplift} + \text{Usual Ice} + \text{Earthquake} \quad (3)$$

The pseudostatic method is used to evaluate the dam's response under the extreme load case. This method does not account for dynamic amplification effects due to the structure's flexibility, which becomes more significant at higher joints. Nevertheless, its efficiency makes it well-suited for the comparative analysis presented in this study. The considered water-retaining system is assumed to suffer from different aging mechanisms such as freeze-thaw cycles, alkali-aggregate reactions, and others. The effect of concrete aging is incorporated by adopting conservative assumptions during the modelling process. Uplift loads were calculated as

recommended by the United States Army Corps of Engineers [21] considering inactive drains. The stability variation through the height of the different structures is analyzed by considering two horizontal joints. The first is located at the base of the structure, defining a concrete-to-rock interface (CR). The second is positioned at a height with slope change or stress concentration chosen to represent a critical region within the structure, forming a concrete-to-concrete interface (CC). Both the CR and the CC joints are highlighted in red in Fig. 1. Nonlinear analyses considering crack opening were performed to obtain the sliding factor of safety for each joint.

3.2. Input parameters

Material and loading parameters associated with the load cases selected were considered as input variables. Therefore, they are represented by PDFs describing their variation. The uniform distribution maximized the parameter uncertainty and it is recommended when the only information known are the lower and upper limits [22]. The uniform PDF is adopted for all the parameters to represent a situation where field or laboratory tests are limited or not available. To represent the aged condition of the concrete, material parameters close to the lower limits recommended by the regulations are adopted [23]. In this study, the angle of friction is assumed to be the same in both cracked and non-cracked areas of the joint, while cohesion is considered zero in the cracked areas. Consequently, the contribution of the cracked joint section to the factor of safety depends only on the cracked joint area, vertical forces, and the angle of friction. Even though these structures have different heights, they are located at the same river cross-section. Therefore, to standardize reservoir variations across the different structures, the amplitude of fluctuation around the normal operating level was selected as an input parameter. As these structures are located in a cold region, reservoir variation is minimal. Detailed information about the parameters and respective distributions is shown in Table 1.

Table 1 – Input parameters

Parameter	Symbol	Lower limit	Upper limit	Unit
Tensile strength - CR	$f_{t\,CR}$	0	200	kPa
Tensile strength - CC	$f_{t\,CC}$	50	150	kPa
Cohesion - CR	c_{CR}	50	150	kPa
Cohesion - CC	c_{CC}	100	300	kPa
Angle of friction - CR	φ_{CR}	40	50	º
Angle of friction - CC	φ_{CC}	40	60	º
Reservoir level - upstream	h_u	-30	+30	cm
Reservoir level - downstream	h_d	-30	+30	cm

Ice – usual	i_{usual}	50	150	kN/m
Ice - unusual	$i_{unusual}$	100	200	kN/m

4. RESULTS

Evaluation of structure stability starts with deterministic analyses, generally considering conservative assumptions. This step helps identify critical joints and load cases for the sensitivity analysis. Accordingly, preliminary deterministic analyses were performed, taking the mean values of the parameters from Table 1. The sliding factor of safety (FS) is calculated considering Eq. 4.

$$FS = \frac{(\sum V)tan\emptyset + cA_c}{\sum H} \quad (4)$$

Where V are the vertical forces including uplifting and concrete inertia forces, H are the horizontal forces, including hydrodynamic and concrete inertia forces, and A_c is the area of the joint in compression.

According to the Canadian Dam Association [24] the stability criteria, considering material testing, for sliding is 2, 1.5, and 1.1 for the usual, unusual, and extreme load cases respectively. The results shown in Table 2 indicate that some scenarios are stressed to their limit. This indicates that the selected system is a good match for a sensibility analysis, as very stable structures rarely undergo exhaustive probabilistic analysis. As expected, the factor of safety decreases as the load cases advance towards the extreme case. It is noteworthy that the free-crested weir is the most affected by the seismic action, probably due to the larger concrete mass relative to the joint length. Following the deterministic analysis, the local and global sensitivity analyses were conducted for each geometry and load case.

Table 2 - Sliding factor of safety

Structure	Gravity dam		Free-crested weir		Gated spillway	
Joint	CR	CC	CR	CC	CR	CC
Usual	2.20	7.31	2.28	6.32	1.76	4.46
Unusual	2.02	2.05	2.27	6.23	1.74	3.96
Extreme	1.24	2.00	1.00	1.00	1.11	2.77

4.1. Tornado diagram

All input parameters presented in Table 1 were considered for generating the tornado diagram. As such, only 21 model evaluations were required for each structure. Additionally, the results from Table 2 were used as a benchmark for building the diagram.

Figure 2 to Figure **7** show the tornado diagrams for the three structures. Typically, input parameters in a tornado diagram are reordered from most to least important. However, in this study, the parameters are kept in the same order across all diagrams to facilitate comparisons between structures, joints, and load cases. Additionally, the section between the mean and the lower limit is depicted in blue, while the section from the mean to the upper limit is shown in red. This color scheme facilitates the identification of whether a parameter is directly or inversely proportional to the model output.

4.1.1. Gravity dam

Figure 2 and Figure 3 presents the gravity dam CR and CC joints respectively. As expected, the tornado is efficient in discarding parameters that don't influence the calculation. For example, the sliding factor of safety of the CR joint is unaffected by CC material parameters.

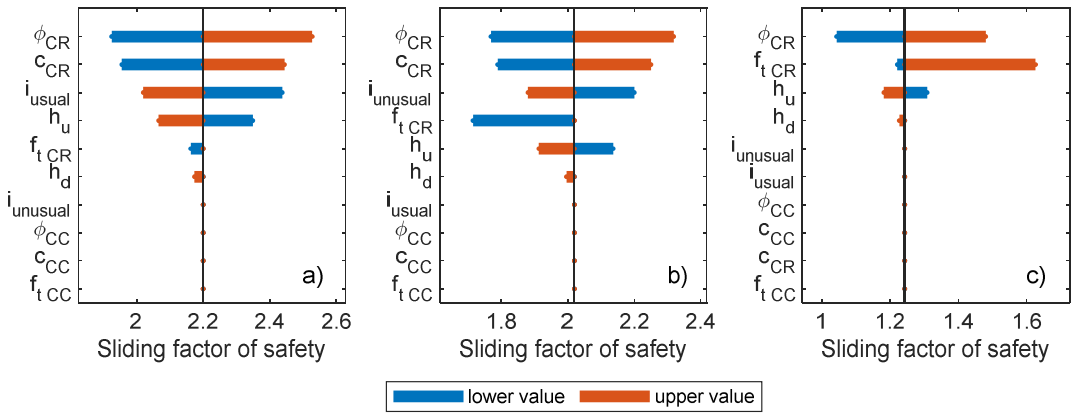

Figure 2 - Gravity dam CR joint: Tornado diagram. (a) Usual, (b) unusual, and (c) extreme load case

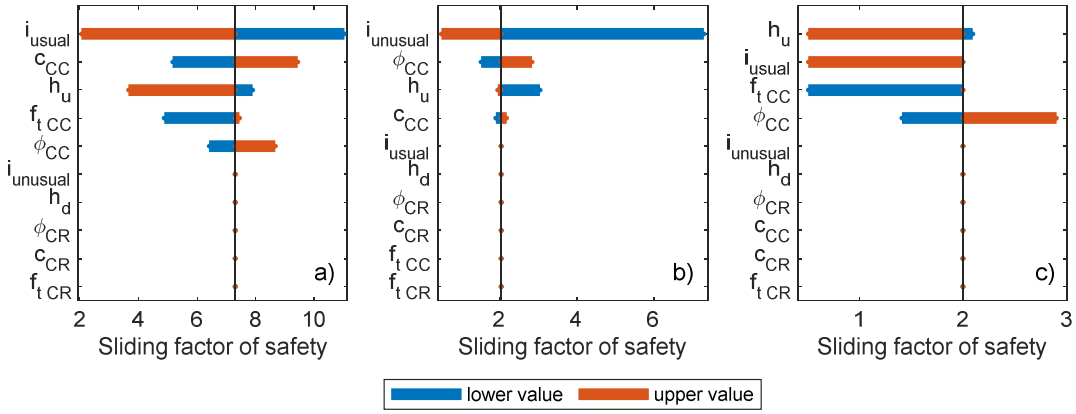

Figure 3 - Gravity dam CC joint: Tornado diagram. (a) Usual, (b) unusual, and (c) extreme load case

It is noteworthy that each one of the 6 scenarios presents a unique response, which highlights the importance of conducting sensitivity analyses that account not only for the structure itself but also for each specific scenario of interest. In the case of the gravity dam, the sudden change in the geometry at the neck drastically changes the response of the joint.

4.1.2. Free-crested weir

Figure 4 and Figure 5 presents the gravity dam CR and CC joints respectively.

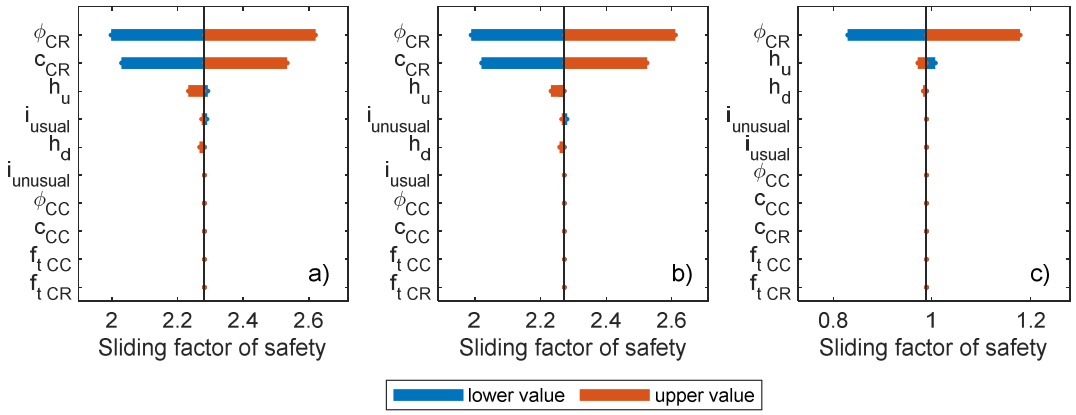

Figure 4 - Free-crested weir CR joint: Tornado diagram. (a) Usual, (b) unusual, and (c) extreme load case

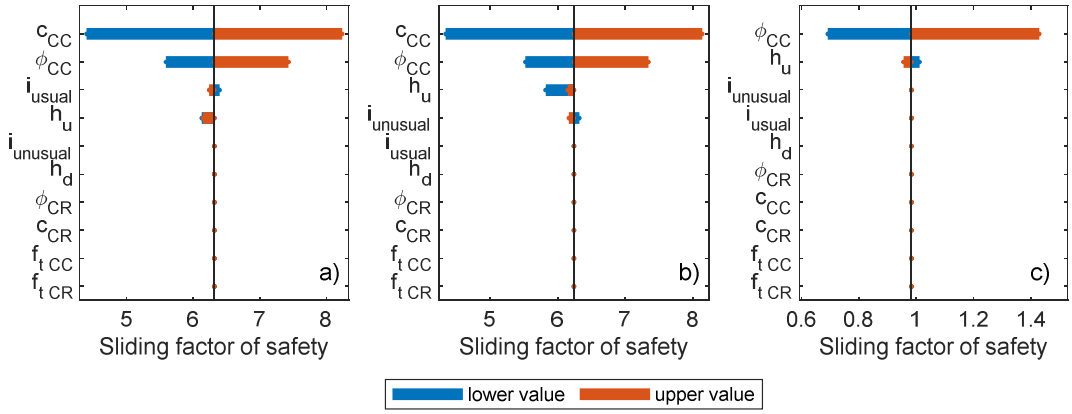

Figure 5 - Free-crested weir CC joint: Tornado diagram. (a) Usual, (b) unusual, and (c) extreme load case

In contrast to the gravity dam, the response of the free-crested weir shows lower sensitivity to variations in load parameters, indicating that material parameters play a more dominant role in determining the sliding factor of safety for this structure. This may be attributed to the slimmer design of the gravity dam, which has a base-to-height ratio of 0.77 at the base and 0.70 at the joint, compared to the free-crested weir, which exhibits ratios of 0.94 and 1.10, respectively. While the horizontal loads due to water and ice loads are associated with the height of the structure, the shear resistance, controlled by the material parameters, is largely determined by the joint length. Additionally, overtopping is permitted for this type of structure. If the reservoir height exceeds the crest level, ice loads are disregarded.

4.1.3. Gated spillway

The CR and CC diagrams for the gated spillway are presented in Figure 6 and Figure **7**.

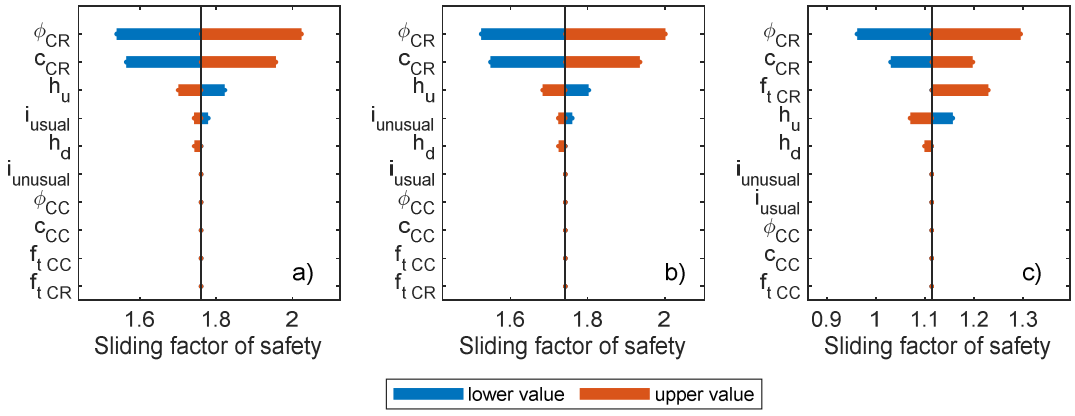

Figure 6 - Gated spillway CR joint: Tornado diagram. (a) Usual, (b) unusual, and (c) extreme load case

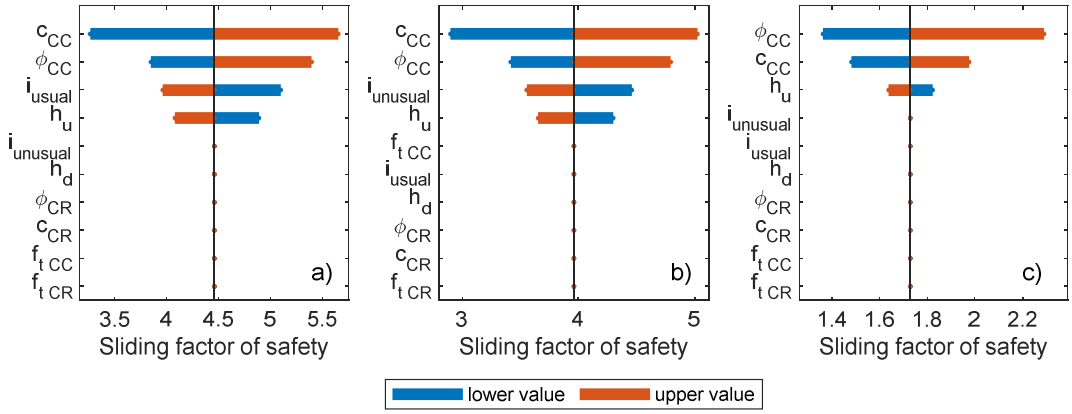

Figure 7 - Gated spillway CC joint: Tornado diagram. (a) Usual, (b) unusual, and (c) extreme load case

The gated spillway shows greater dependence on load-related parameters than the free-crested weir. Despite having high base-to-height ratios, the self-weight remains the primary stability mechanism. The presence of the gated section means that increasing the height does not significantly increase the overall weight of the structure while the water and ice-related charges keep increasing. Additionally, unlike the gravity dam and the free-crested weir, the factor of safety of the gated spillway remains sensitive to cohesion in the extreme case. This is because the joints of the first two structures were fully cracked, eliminating any cohesion at the joints. In contrast, approximately 25% of the gated spillway's joint remained uncracked, allowing cohesion to contribute to the structure's stability.

4.1.4. Inter-structure comparison

The construction of the tornado diagram requires reordering the parameters by importance, which complicates the comparison of a specific parameter's importance across different structures. To allow this comparison, the results from the tornado diagrams presented previously were centered around zero by deducting the mean value obtained for each structure. The resulting values are presented in Figure 8 and Figure **9** to compare the importance of the parameters for each retaining structure.

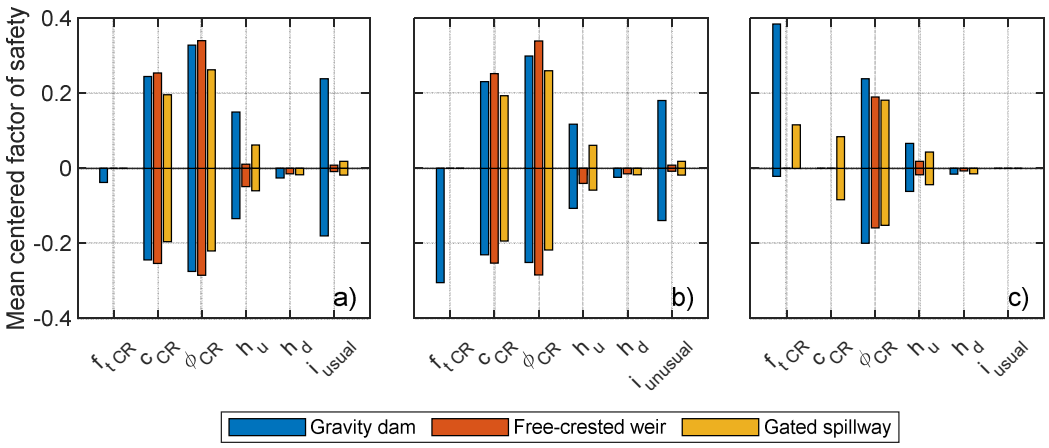

Figure 8 – Mean cantered variation at the CR joint. **(a) Usual, (b) unusual, and (c) extreme load case**

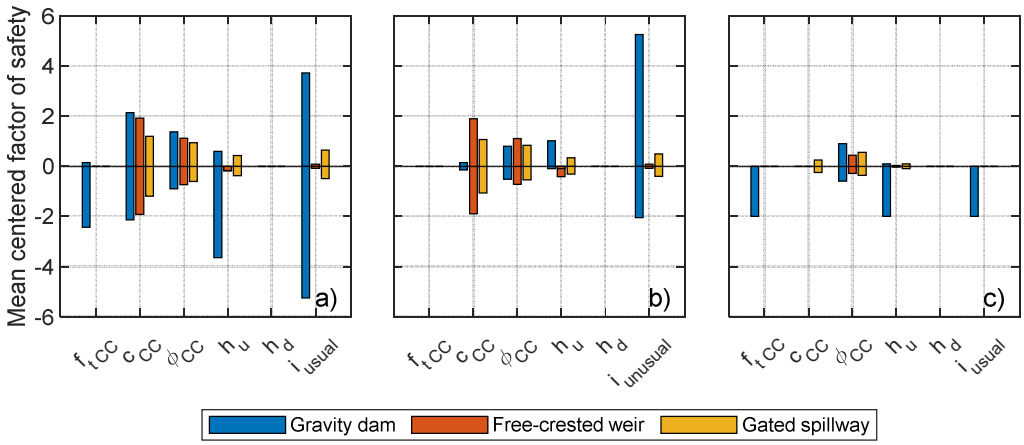

Figure 9 – Mean cantered variation at the CC joint. (a) Usual, (b) unusual, and (c) extreme load case

Notably, the angle of friction consistently emerges as one of the most critical parameters, regardless of the structure, load case, or joint. This suggests that, for the water-retaining system studied, prioritizing resources to further investigate this parameter would be beneficial. Moreover, despite the reduced reservoir variation upstream water level significantly impacted the structures response.

4.2. Sobol indices

Global methods may require hundreds of sample evaluations to identify how the interactions between input parameters influence the model output. The optimum number of samples varies according to the number of parameters, how these parameters interact, and the complexity of the model [6]. To avoid the computational burden of running an excessive number of analyses, new samples were progressively added to the set with the Sobol indices being evaluated at each new addition. In the context of the study, the number of analyses was pushed much

further than necessary, but for practical applications, the evaluations may stop as soon as the Sobol indices converge. Given the results, a tolerance of 0.05 in Sobol index variation was sufficient to ensure the accuracy of the results.

Depending on the knowledge of the model, it may be possible to discard input parameters even before starting the sensitivity analysis. It is known that CR material parameters do not influence the sliding displacement at the CC joint and vice versa. However, such information may not be known beforehand, and the inclusion of irrelevant parameters in sensitivity analyses can occur for various reasons. As demonstrated in the previous section, the tornado diagram effectively identified the irrelevance of these parameters as each one is evaluated individually. The capacity of the Sobol method to identify irrelevant parameters was assessed by analyzing the CC joint of the gravity dam under the normal loading case. The Sobol indices, calculated considering all parameters, are presented in Figure 10. It can be seen that the Sobol method is also very efficient in eliminating spurious input parameters. However, anomalies may arise when the sample size is very small. For instance, in Figure 10, φ_{CR} and $i_{unusual}$ exhibit a non-zero importance value for sample sizes smaller than 100, highlighting the need for a minimum number of samples to guarantee the performance of the Sobol method.

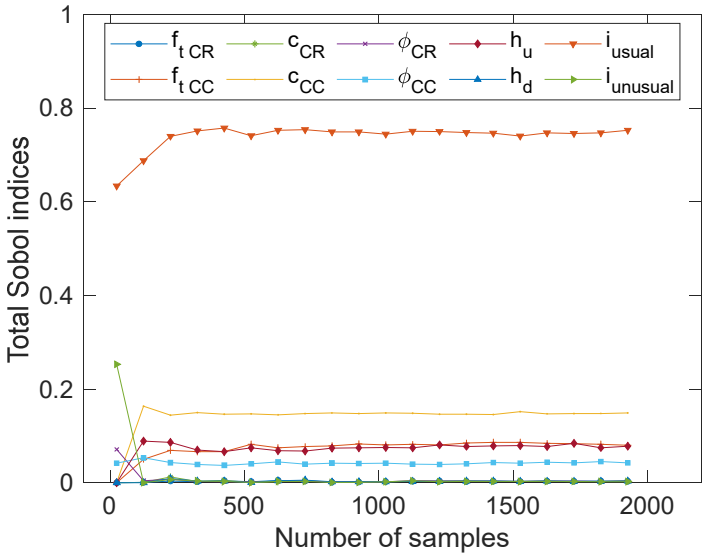

Figure 10 – Sensitivity anomalies due to parameters unrelated to the model evaluation

Removing unrelated parameters before calculating the Sobol indices is recommended whenever possible, as this reduces the likelihood of anomalous responses and results in cleaner, more interpretable outcomes. Therefore, in the following results, CR material parameters were ignored for CC analysis and vice-versa. Figure 11 to Figure 16 presents the evolution of the Sobol indices for the input parameters listed in Table 1 according to the number of samples used for the evaluation.

4.2.1. Gravity dam

The sensitivity calculated through the Sobol method for the gravity dam model given the number of samples available are presented in Figure 11 and Figure 12.

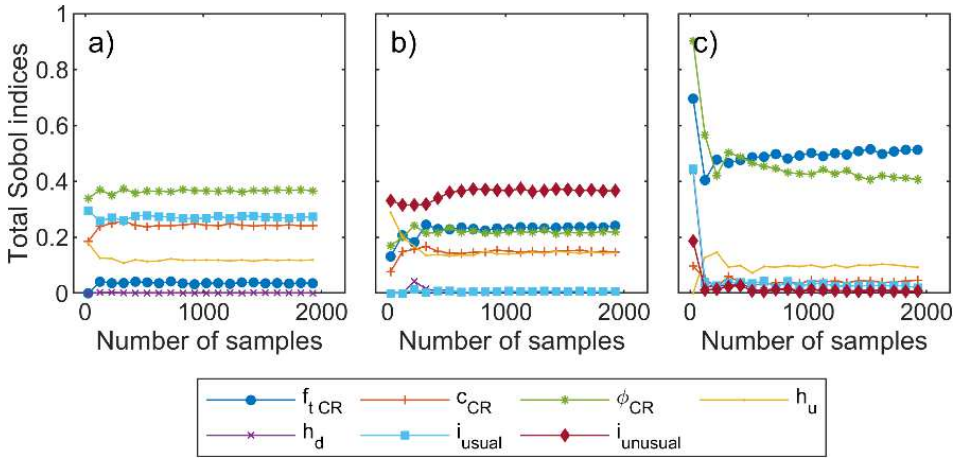

Figure 11 - Gravity dam CR joint: Number of samples vs. Sobol indices. (a) Usual, (b) unusual, and (c) extreme load case

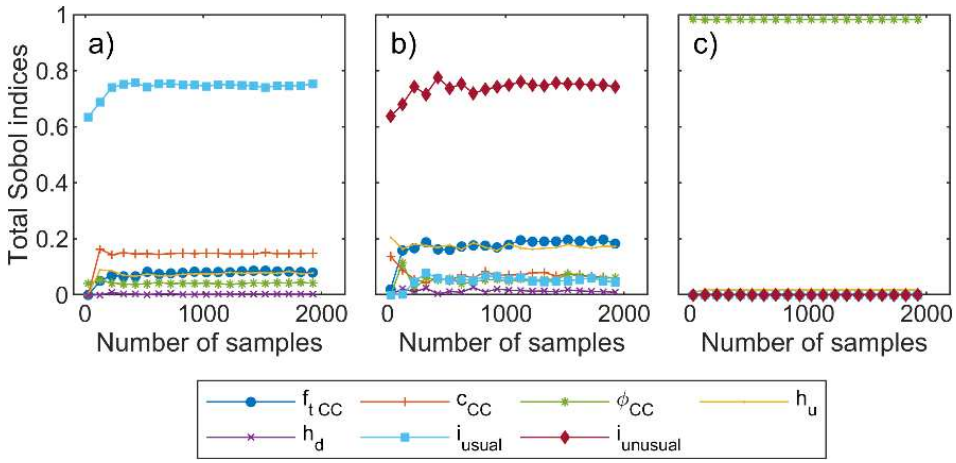

Figure 12 - Gravity dam CC joint: Number of samples vs. Sobol indices. (a) Usual, (b) unusual, and (c) extreme load case

Noticeably, the sample size required to achieve convergence varied significantly across scenarios, ranging from as few as 25 samples (Figure 12(b)) to 600 samples (Figure 11(c)), depending on the load case and joint. Even though the CR joint index convergence required progressively more samples the same was not valid for the CC joint. It can be seen in Table 2 that the gravity dam mean factor of safety at the CC joint is 2.00, meaning that the joint tends to behave linearly. The Sobol results indicate that cohesion plays a crucial role in preventing cracks at the joint, which would push it into the non-linear mode. This example shows that the number of samples required for the convergence of the Sobol indices is more dependent on the physical mechanism behind the behaviour of the model than the number of parameters or load magnitude.

4.2.2. Free-crested weir

Figure 13 and Figure 14 present the Sobol indices given the number of samples for the free-crested weir.

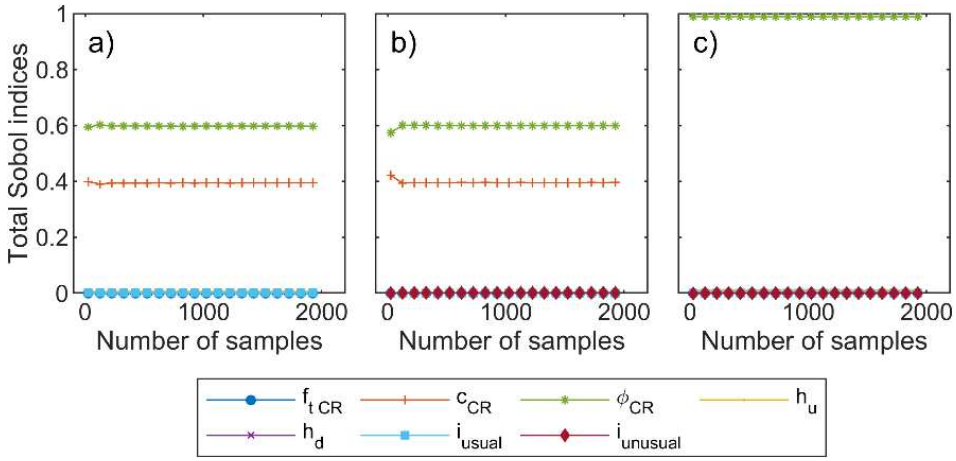

Figure 13 – Free-crested weir CR joint: Number of samples vs. Sobol indices. (a) Usual, (b) unusual, and (c) extreme load case

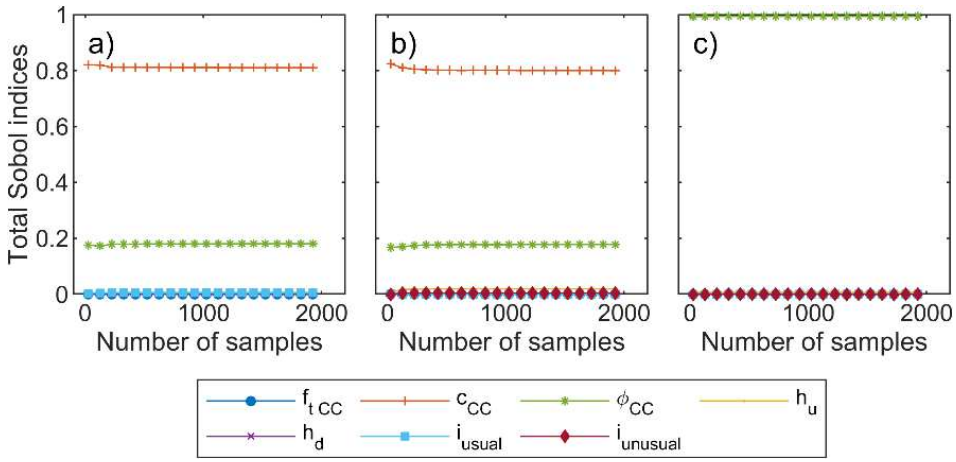

Figure 14 – Free-crested weir CC joint: Number of samples vs. Sobol indices. (a) Usual, (b) unusual, and (c) extreme load case

It is noteworthy that the free-crested weir reached the convergence for the Sobol indices much faster than the gravity dam. No more than 100 samples were required independently of the scenario. Confirming what was observed in the tornado diagrams (Figure 4 and Figure 5), material parameters play a central role in the stability of this structure, with the weight being shared between cohesion and angle of friction. The exception is the extreme load case (Figure 13(c) and Figure 14(c)), where the seismic load causes most of the joints to open, resulting in nonlinear behaviour. In this scenario, unjoined surfaces are modelled with zero cohesion, making it irrelevant to the analysis.

4.2.3. Gated spillway

Figure 15 and Figure 16 presents the Sobol indices for the gated spillway at the CR and CC joints respectively.

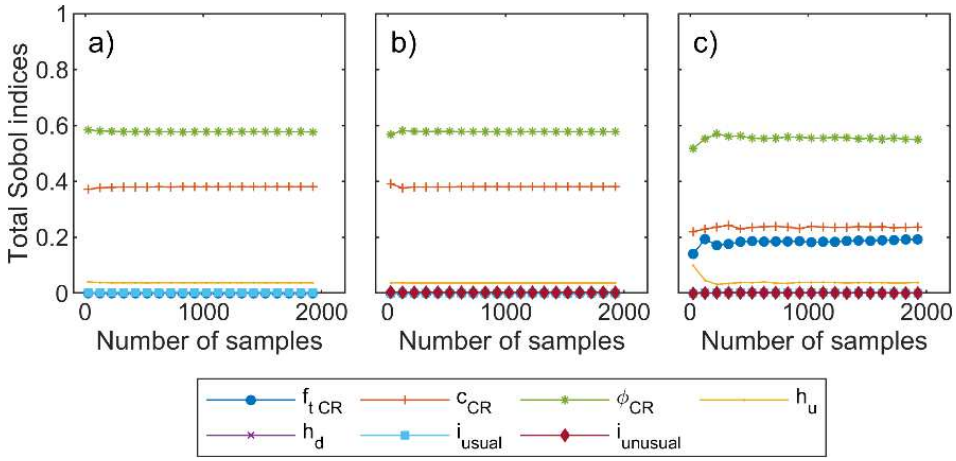

Figure 15 – Gated spillway CR joint: Number of samples vs. Sobol indices. (a) Usual, (b) unusual, and (c) extreme load case

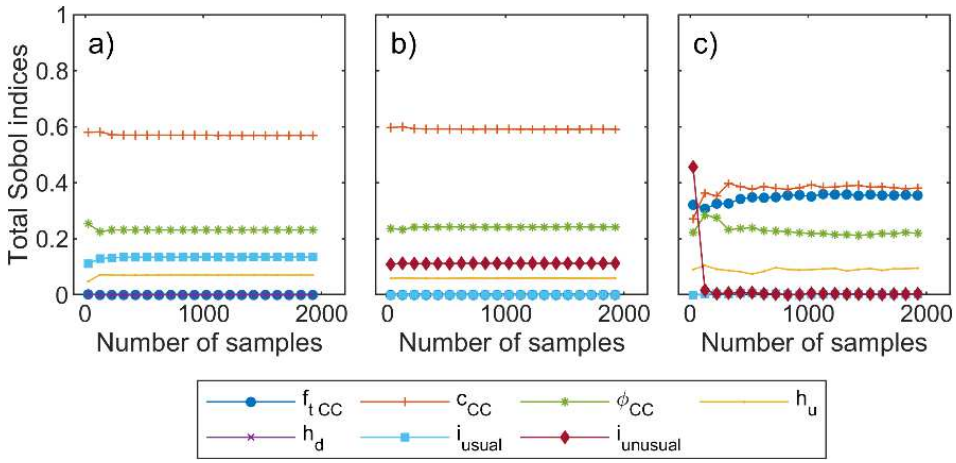

Figure 16 - Gated spillway CC joint: Number of samples vs. Sobol indices. (a) Usual, (b) unusual, and (c) extreme load case

Convergence of Sobol indices required a maximum of 500 samples for the gated spillway. When compared to the free-crested weir, the gated spillway exhibits a similar sensitivity to the cohesion and angle of friction for the usual and unusual case (Figure 15(a), (b), Figure 16(a) and (b)). However, in the extreme case, both the angle of friction, cohesion, and tensile strength are relevant to the structure response. Table 2 shows that the gated spillway exhibits higher factor of safety values compared to the free-crested weir under the extreme load case. This suggests reduced joint opening, a condition where all material parameters contribute to joint stability.

4.3. Local vs. Global Sensitivity

In this section, the CC joint of the gravity dam at the extreme load case is selected for an in-depth comparison between the local and global sensitivity analysis methods. Focusing on a single structure simplifies the presentation and enhances clarity, allowing for a more straightforward interpretation of the results.

Table 3 contrasts the lower and upper factors of safety calculated for the tornado diagram with their corresponding Sobol indices. Considering the observed in Section 4.2.1 the Sobol indices for this comparison were calculated using 600 samples. This highlights one of the key advantages of the Tornado, as it only required 21 samples for the analysis. Noticeably, for the selected load case, $f_{t\,CC}$, c_{CC}, φ_{CC}, and $i_{unusual}$ are completely irrelevant for the calculation of the factor of safety. Both methods successfully ruled out these parameters. Even though these spurious parameters present residual Sobol indices, they are small enough not to be confused with relevant parameters. Additionally, both methods identified the same parameters as presenting significative importance, the $f_{t\,CR}$, φ_{CR}, and h_u. However, Sobol identifies the $f_{t\,CR}$ as the most influential parameter while the tornado highlights φ_{CR} as causing the largest variation in the model response. This shift in the ranking of parameter importance is particularly significant, as sensitivity analysis results are expected to guide resource allocation for further investigation of the structure. This highlights the primary advantage of global sensitivity methods. By varying parameters simultaneously, they not only assess the direct impact of each parameter on the model response but also capture the interactions and combined effects of parameter variations.

Table 3 – Tornado lower and upper factor of safety vs. Sobol indices. Gravity dam, CR joint, extreme load case

Parameter	Tornado Abs(Upper – Lower)	Sobol
$f_{t\,CR}$	0.41	0.49
$f_{t\,CC}$	0	0.03
c_{CR}	0	0.04
c_{CC}	0	0.01
φ_{CR}	0.44	0.46
φ_{CC}	0	0.03
h_u	-0.13	0.09
h_d	-0.01	0.02
i_{usual}	0	0.04
$i_{unusual}$	0	0.01

5. CONCLUSIONS

The performance of local and global approaches for identifying the sensitivity of hydraulic structures to parameter uncertainty was tested. The tornado diagram and the Sobol indices were selected as the local and global methods respectively. The sensitivity to material and loading parameters were obtained for a gravity dam, a free-crested weir, and a gated spillway under usual, unusual, and extreme load combinations.

Hydraulic structures exhibit unique characteristics, and even if similar parameter variations are considered, sensitivity results are highly specific to each structure. Additionally, the position of joints and the combination of loads significantly influence the importance of input parameters in the model. Therefore, conducting individual sensitivity analyses for different type of structures is essential, as results cannot be assumed to be consistent across varying scenarios.

Results demonstrate that the tornado method is very efficient in identifying parameters unrelated to the specific scenario—for instance, CR material parameters in calculating the sliding factor of safety at the CC joint and vice-versa. Additionally, the tornado diagram provides a by-product which is a fast visual identification of critical parameters. The Sobol method is also effective in this identification; however, it requires a minimum number of samples larger than what is necessary for the tornado method. The main difference between the methods arises when the parameters of the highest importance are ranked. As the tornado varies one parameter at a time, it cannot account for the interactions between the input parameters, and depending on the scenario this may lead to suboptimal resource allocation. The global approach accounts for these interactions but requires a larger sample set, increasing the computational demand. A suitable approach would be to use a tornado to eliminate unimportant parameters and identify a limited number of parameters of interest. With this reduced set, efforts can focus on refining their PDFs to enhance prior knowledge. Subsequently, the Sobol method can be applied to perform a more comprehensive sensitivity analysis, using the refined inputs to achieve accurate results while minimizing the computational burden.

The findings emphasize the need for a tailored sensitivity analysis approach, taking into account the unique characteristics of each structure and scenario to ensure accurate and meaningful insights for decision-making and resource allocation.

REFERENCES

[1] Chopra, A.K. (2020). *Earthquake Engineering for Concrete Dams: Analysis, Design, and Evaluation*, John Wiley & Sons Ltd.

[2] McGuire, R.K. (2001). Deterministic vs. probabilistic earthquake hazards and risks. *Soil Dynamics and Earthquake Engineering*.

[3] Zentner, I. *et al.* (2017). Fragility analysis methods: Review of existing approaches and application. *Nuclear Engineering and Design*.

[4] Tekie, P.B. and Ellingwood, B.R. (2003). Seismic fragility assessment of concrete gravity dams. *Earthquake Engineering and Structural Dynamics*.

[5] Hariri-Ardebili, M.A. and Saouma, V.E. (2016). Probabilistic seismic demand model and optimal intensity measure for concrete dams. *Structural Safety*.

[6] Jeong, S.H. and Elnashai, A.S. (2007). Probabilistic fragility analysis parameterized by fundamental response quantities. *Engineering Structures*.

[7] National Research Council 2000 (2000). *Risk Analysis and Uncertainty in Flood Damage Reduction Studies*, The National Academies Press, Washington, DC.

[8] Saltelli, A. (2002). Sensitivity analysis for importance assessment. *Risk Analysis*.

[9] Hora, S.C. and Helton, J.C. (2003). A distribution-free test for the relationship between model input and output when using Latin hypercube sampling. *Reliability Engineering & System Safety*.

[10] Hariri-Ardebili, M.A. and Xu, J. (2019). Efficient seismic reliability analysis of large-scale coupled systems including epistemic and aleatory uncertainties. *Soil Dynamics and Earthquake Engineering*.

[11] Kim, J. *et al.* (2011). Sensitivity analysis of steel buildings subjected to column loss. *Engineering Structures*.

[12] Gratiet, L. Le *et al.* (2017). Metamodel-Based Sensitivity Analysis: Polynomial Chaos Expansions and Gaussian Processes. *Handbook of Uncertainty Quantification*.

[13] Saltelli, A. *et al.* (2010). Variance based sensitivity analysis of model output. Design and estimator for the total sensitivity index. *Computer Physics Communications*.

[14] Marelli, S. and Sudret, B. (2014). UQLab: A Framework for Uncertainty Quantification in Matlab. *Vulnerability, Uncertainty, and Risk*.

[15] Huntington, D.E. and Lyrintzist, C.S. (1998). Improvements to and limitations of Latin hypercube sampling. *Prob. Engng. Mech*.

[16] Sheikholeslami, R. and Razavi, S. (2017). Progressive latin hypercube sampling: an efficient approach for robust sampling-based analysis of environmental models. *Environmental Modelling and Software*.

[17] Leclerc, M. *et al.* (2003). Computer aided stability analysis of gravity dams - CADAM. *Advances in Engineering Software*.

[18] Ruggeri, G. (2004). Sliding safety of existing gravity dams - Final report. *International Commission on Large Dams*.

[19] FERC (2016). Engineering guidelines for the evaluation of hydropower projects. Chapter III: gravity dams. *Engineering Guidelines for the Evaluation of hydropower Projects*.

[20] Leclerc, M. (2020). CADAM3D User's Manual. *MLT TECHNOLOGY INC. Polytechnique Montreal*.

[21] U.S. Army Corps of Engineers (1995). Gravity dam design. *Technical Report, EM-1110-2-2200*.

[22] Ellingwood, B. and Tekie, P.B. (2001). Fragility analysis of concrete gravity dams. *Journal of Infrastructure Systems*.

[23] Deroo, L. (2019). Justification de la stabilite des barrages-poids : Pratiques actuelles. Gravity dams stability assessment : current practices. *Colloque CFBR: Justification des barrages : Etat de l'art et Perspectives*.

[24] CDA (2007). Dam safety Guidelines. *Dam Safety Recommendations Section 6.1, 6.2 and 6.3, Revised in 2013*.

Fifth International Dam World Conference
PORTUGAL • LISBON • LNEC • APRIL 13-17, 2025
dam world 2025

GIS-BASED DATABASE FOR IMPROVED DAM MANAGEMENT IN CABO VERDE

Carlos F. Correia e Silva[1]
Infraestruturas de Cabo Verde

Emanuel Tavares[2]
Infraestruturas de Cabo Verde

Adlisa Delgado[3]
Laboratório de Engenharia Civil

João N. Fernandes[4]
Laboratório Nacional de Engenharia Civil

Ivo Dias[5]
Laboratório Nacional de Engenharia Civil

ABSTRACT

The monitoring and maintenance of dams are crucial for ensuring their long-term performance and safety. In Cabo Verde, with its nine operational dams across various islands, the challenge of managing these vital infrastructures is exacerbated by the absence of a comprehensive dam management system. To address this gap, Infraestruturas de Cabo Verde (ICV) and Laboratório de Engenharia Civil from Cabo Verde, with the technical input of Laboratório Nacional de Engenharia Civil, Portugal, in the scope of the Erasmus+ VET4HYDRO project, are developing a GIS-based database specifically tailored for the dams of Cabo Verde. This database is made using open-source GIS technology and drone imagery to provide accurate and up-to-date measurements and assessments. With the integration of past historical data and current digital mapping techniques, this work aims at creating a dynamic and accessible tool for dam management. Key parameters such as reservoir level monitoring, hydrologic features, dam type, and structural monitoring indicators, including infiltration, structural deformations, and erosion data, are systematically included to ensure comprehensive characterization. The database will also include monitor dam operation metrics like flood discharge capacity and emergency response plans, providing a holistic overview needed for effective decision-making. This web-based platform, accessible at QGIS Cloud, will significantly enhance the capability for remote monitoring and real-time data access, promoting proactive maintenance and timely interventions. This initiative represents a significant advancement in dam management for Cabo Verde, providing a robust framework that aligns with global standards in dam safety and management. The integration of new technologies such as drone imagery and GIS tools not only modernizes the approach to dam management but also ensures sustainability and resilience against climatic and environmental changes. The establishment of this database marks an important step toward improving the operational efficiency, safety, and sustainability of dams in Cabo Verde, setting a benchmark for other regions with similar infrastructure challenges.

Keywords: Dam Monitoring and Instrumentation, GIS-Based Dam Management, Concrete and Masonry Dams in Cabo Verde

[1] eng.correia.silva@gmail.com, Cabo Verde
[2] emanuel.j.tavares@infraestruturas.cv , Cabo Verde
[3] adlisa.delgado@lec.gov.cv, Cabo Verde
[4] jnfernandes@lnec.pt, Portugal
[5] idias@lnec.pt, Portugal

1. INTRODUCTION

The efficient management of dams is a critical factor in ensuring the sustainable supply of water resources, particularly in arid and semi-arid regions. In Cabo Verde, an archipelago characterized by prolonged droughts and irregular rainfall, the construction of dams has been a key strategy for water capture and storage, supporting both agricultural irrigation and overall water resources management. However, the lack of an integrated monitoring and management system for these infrastructures presents a significant challenge to their operation and maintenance [1].

Currently, Cabo Verde has nine operational dams distributed across different islands, varying in construction type and storage capacity. Some of these dams face issues such as sedimentation, infiltration, and difficulties in water retention due to local geological conditions. The absence of a centralized database makes it difficult to track the structural condition of these infrastructures, compromising the efficiency of maintenance interventions and management strategies.

To address these challenges, Infraestruturas de Cabo Verde (ICV) and the Laboratório de Engenharia Civil from Cabo Verde (LEC), with the technical input of the Laboratório Nacional de Engenharia Civil from Portugal (LNEC), are developing a GIS-based geospatial database. This system integrates open-source GIS technology and drone imagery to provide accurate and up-to-date measurements. The objective is to consolidate historical and key data such as storage levels, hydrology, structural characteristics, and safety monitoring indicators.

Beyond modernizing dam management approaches, the implementation of this geospatial database allows for remote access to information via a web-based platform hosted on QGIS Cloud [2]. This enables continuous monitoring, supports strategic decision-making, and facilitates proactive maintenance planning to mitigate structural and operational risks. The introduction of this technology represents a major advancement in the management of dams in Cabo Verde, aligning with international standards for dam safety and sustainability.

This article presents the methodology adopted for the database implementation, preliminary results from its application, and an analysis of the challenges and opportunities that digital dam management offers. By sharing this initiative, we aim to contribute to the global discussion on modernizing monitoring and maintenance systems for critical infrastructures, emphasizing the importance of digital tools in ensuring the safety and operational efficiency of these structures.

2. CABO VERDE'S DAMS

Cabo Verde is an archipelago located approximately 800 km off the coast of Senegal, in the central Atlantic Ocean. The country consists of ten islands and eight islets, divided into two groups: Barlavento (windward) and Sotavento (leeward). With a total land area of 4,033 km², the islands are of volcanic origin, with a rugged topography that significantly influences hydrological dynamics and water availability. Freshwater resources in Cabo Verde originate from surface and groundwater sources, as well as desalination in maritime regions with minimal rainfall. While groundwater reserves generally provide high-quality water, they are limited due to over-extraction and increasing salinization caused by reduced rainfall and seawater intrusion [3].

The climate of Cabo Verde is classified as tropical dry, characterized by low and irregular precipitation ranging from 100 mm to 900 mm per year, strong northeast trade winds, and high temperatures averaging 25°C. The hydrological deficit is a critical challenge, making water management essential for agriculture and human consumption. Due to the scarcity of permanent rivers, the country relies heavily on rainwater harvesting, groundwater, and dam storage for water supply. Surface water resources are estimated at an average of 181 million m³ per year but remain underutilized due to insufficient storage and reservoir infrastructure. The construction of dams offers a viable method for increasing water reserves, though these systems require advanced treatment processes to ensure adequate water quality [3].

The islands' geomorphology is shaped by their volcanic origin, with steep terrains and fragile soils. The availability of arable land is limited, with only 10% of the total land area suitable for agriculture, of which 95% is rainfed and only 5% relies on irrigation. Soil degradation, mainly caused by physical factors such as erosion and aridification, poses a further challenge for sustainable land and water resource management. Given the hydroclimatic limitations, dams play a fundamental role in securing and regulating water resources, primarily for agricultural irrigation. Without effective water storage infrastructure, much of the available surface water remains unutilized, limiting its contribution to water security [3].

Currently, Cabo Verde has nine operational dams distributed across different islands, primarily in Santiago, Santo Antão, and São Nicolau. These dams vary in type, storage capacity, and operational status. While some reservoirs contain stored water, others are empty or silted due to sedimentation and infiltration issues. Figure 1 presents the location of the 9 operational dams of Cabo Verde.

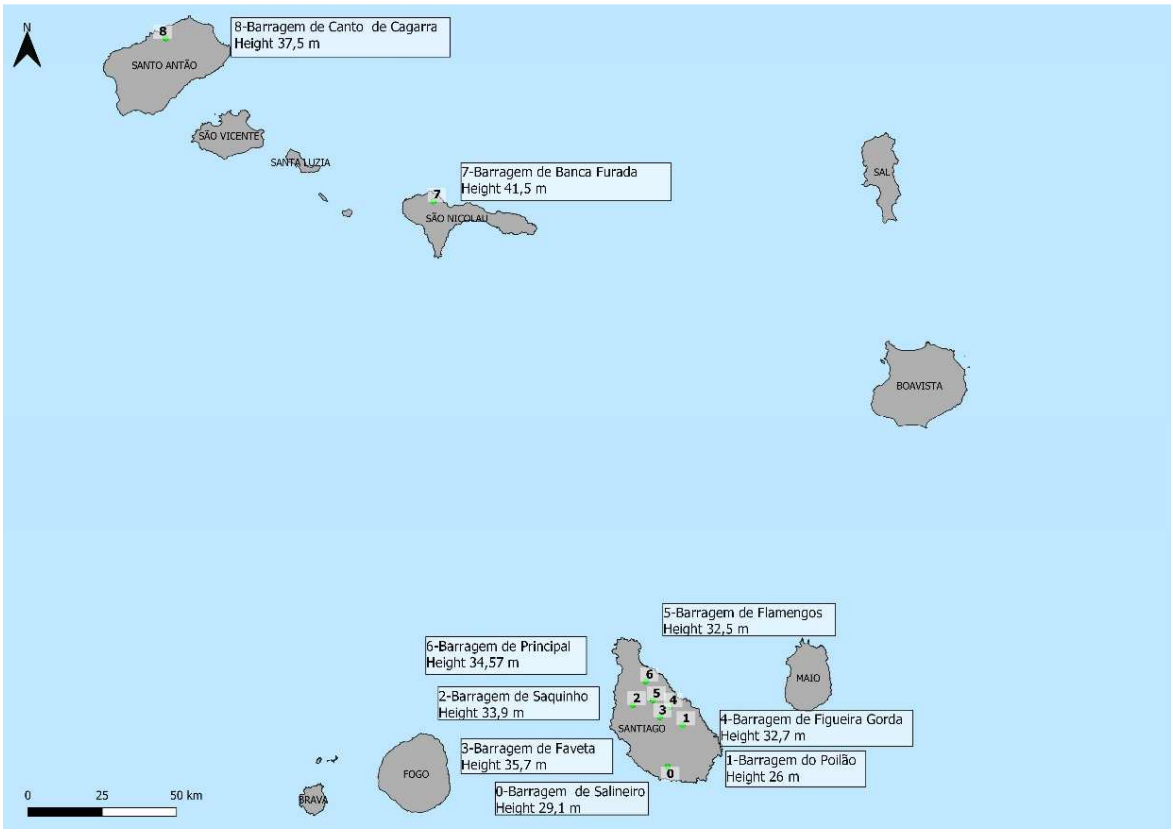

Figure 1 – Distribution of the existing Dams in Cabo Verde

Over the years, the construction of dams in Cabo Verde has been carried out in a scattered manner, without a clear regulatory framework to guide their management and operation. Despite their classification as Large Dams under ICOLD standards [4], there has been no centralized system for monitoring their structural integrity, hydrological performance, or maintenance needs. The absence of a published dam regulation has resulted in fragmented oversight, making it difficult to track key indicators such as reservoir capacity, sedimentation rates, and infiltration losses.

In this context, the lack of proper information management has hindered the development of preventive maintenance strategies, leading to sedimentation issues, reduced storage capacity, and structural concerns in several reservoirs. Without a unified database, there is no systematic tracking of hydrological changes, dam safety indicators, or operational performance, increasing the risk of unexpected failures. Given the country's arid climate, high hydrological deficit, and reliance on dam-stored water for agriculture, the need for structured and standardized management practices is particularly urgent in Cabo Verde.

The implementation of a GIS-based dam management system represents a crucial step toward overcoming these challenges by digitizing and centralizing all relevant data into an accessible platform. This system will enable to improve decision-making, and facilitate proactive maintenance planning, ensuring that dams continue to operate safely and efficiently.

Moreover, it will align Cabo Verde's dam management practices with international safety standards, supporting long-term sustainability and water security in the country.

3. METHODOLOGY

The development of a GIS-based dam management system for Cabo Verde followed a structured approach comprising three key phases: bibliographic research, database creation, and GIS platform integration. This methodology ensures that the collected data is systematically organized, easily accessible, and regularly updated to enhance dam monitoring and management.

The first stage involved an extensive bibliographic review of technical reports, design documents, and hydrological studies. The sources included construction records, project execution reports, hydrological studies, government planning documents related to the dams in Cabo Verde ([1], [5] to [13]) and also reference LNEC inspection reports ([15] to [20]). These documents provided essential information on dam specifications, watershed characteristics, storage capacities, hydraulic structures and main safety concerns. The review was crucial for establishing a consistent and standardized dataset aligned with international dam classification criteria and local operational requirements.

Based on the extracted information, a structured database was developed, encompassing key parameters categorized into general identification, hydrology, reservoir storage, structural characteristics, hydraulic features, and safety monitoring. This database was designed to accommodate additional information in the future, ensuring flexibility for further updates. The initial dataset included:

- General Identification: Dam name, island, municipality, watershed name.
- Hydrology: Watershed area, inflow and outflow calculations for a 1000-year return period.
- Reservoir Storage: Dead storage, usable storage, total storage, full supply level, and maximum flood level.
- Structural Details: Dam type, crest elevation, foundation level, maximum height, crest length.
- Hydraulic Features: Spillway type, reservoir emptying time.

Additionally, the database is prepared to integrate new data from field inspections and dam monitoring. Future updates will include:

- Monitoring & Safety: field inspection dates, main inspection results, incident records, cracks and erosion, leakage, monitoring results (reservoir level, seepage flows, uplift pressures, structural displacements, etc.) and emergency action plans.

- Installed monitoring devices: Piezometers, water level gauges, inclinometers, and other devices integrated in the observation systems of the dams.

To support the long-term monitoring of dams, a major upgrade is currently underway, incorporating yearly photographic records and measurements of the watershed area using drone technology, which enables high-resolution aerial surveys and precise topographic analysis. These updates will be compared against the maximum full storage level, helping to assess sedimentation and reservoir capacity variations over time.

To facilitate real-time access and visualization, the compiled dataset was uploaded to a GIS cloud platform, accessible at QGIS Cloud [14]. This platform enables interactive mapping, overlaying dam locations with satellite imagery and hydrological data. The system is designed to allow continuous updates, ensuring that the latest monitoring data is always available for decision-making.

Users and stakeholders can request access to the database or submit updated information by contacting Infraestruturas de Cabo Verde (ICV). This ensures that dam operators and policymakers have the most up-to-date information for infrastructure maintenance, water resource management, and safety assessments.

By integrating bibliographic research, systematic database creation, and GIS-based visualization, this methodology establishes a modern, data-driven approach to dam monitoring in Cabo Verde, ensuring long-term sustainability and resilience in water infrastructure management.

4. RESULTS AND ANALYSIS

The development of a GIS-based database for Cabo Verde’s dam infrastructure represents a transformative step in the country's water resource management. This system consolidates data from multiple sources into a centralized, accessible platform, allowing for systematic monitoring, historical analysis, and enhanced decision-making.

The primary advantages of this database include up to date monitoring, allowing engineers and policymakers to track dam conditions, reservoir levels, and structural integrity. By structuring data into a standardized format, authorities can compare dams based on storage efficiency, structural stability, and hydrological performance, facilitating comparative analysis and trend identification. Additionally, the database provides the necessary technical foundation for implementing a comprehensive regulatory framework for dam safety in Cabo Verde. Serving as a bibliographic resource for future research, the structured data supports studies on sedimentation, climate impact, and the structural resilience of dams, further enhancing decision-making and policy development.

The GIS database can be accessed through the link on [14], and it contains all the initial data, mentioned in 3., for the nine operational dams, which can be consulted by clicking on the dam point (Figure 2).

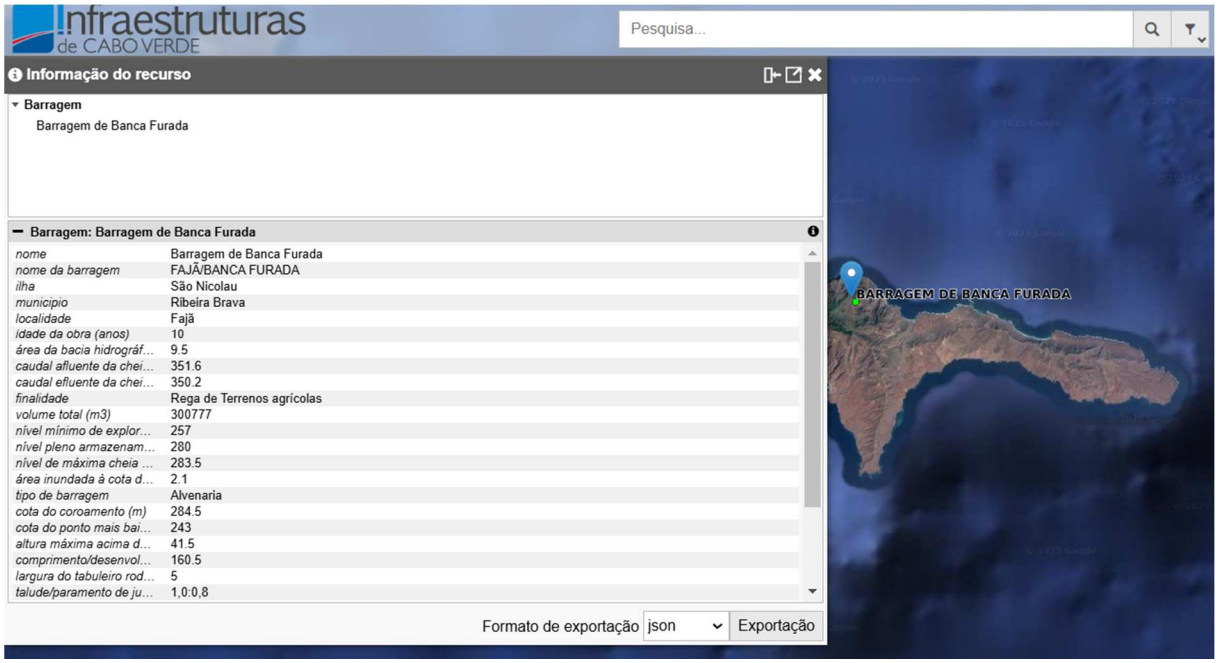

Figure 2 – Screenshot of the GIS database

With an organized GIS database, numerous analyses can be conducted to enhance dam management in Cabo Verde. One example is the assessment of dam height versus total storage capacity, illustrated in Figure 3, which provides a comprehensive picture of the country's dam profile and typology. The analysis suggests that while some moderately tall dams, such as Poilão, optimize their reservoir design to achieve high storage capacities, others with greater heights, like Fajã/Banca Furada and Canto Cagarra, may experience geological or hydrological constraints that limit their efficiency. Mid-range dams, including Salineiro and Flamengos, strike a balance between height and volume, making them valuable for regional water supply. The structured dataset not only supports maintenance prioritization but also facilitates hydrological planning and regulatory advancements, reinforcing the role of the GIS platform in evidence-based decision-making.

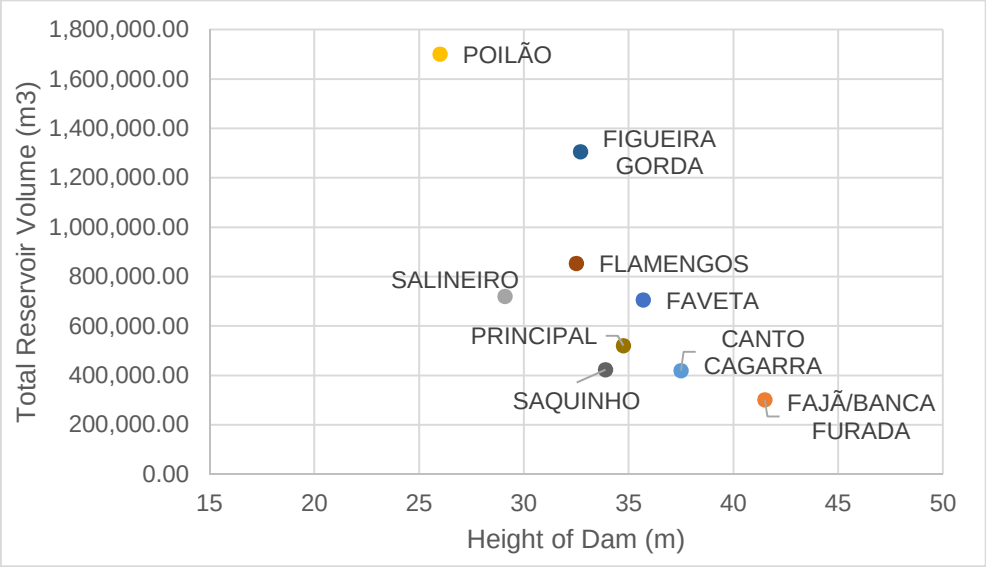

Figure 3 – Height of dam Versus Total Reservoir volume for Cabo Verde´s Dams

5. CONCLUSIONS

The study highlights the urgent need for a structured and digitalized dam management system in Cabo Verde. The absence of a centralized regulatory framework and comprehensive monitoring strategies has led to fragmented information management, impacting the ability to ensure dam safety, optimize water storage, and plan preventive maintenance. Despite being classified as Large Dams under ICOLD standards, these infrastructures have historically lacked systematic tracking of key indicators such as reservoir capacity, sedimentation rates, infiltration losses, and structural integrity. The GIS-based database developed under this study is a major step toward modernizing dam management, improving dam safety and proactive maintenance strategies.

By implementing a GIS-based monitoring system, Cabo Verde is building a digitized and accessible database that enables improved decision-making, predictive maintenance, and climate resilience planning. The next steps include regular data updates, enhanced instrumentation integration, and the development of predictive hydrological models to simulate future water availability scenarios. Establishing a national dam regulation framework will be essential in ensuring the long-term sustainability, operational efficiency, and structural safety of these critical infrastructures. This research contributes to the broader discourse on digital dam management, reinforcing the role of geospatial technologies in modernizing water infrastructure governance in arid and semi-arid regions.

ACKNOWLEDGMENTS

This work was partly supported by the project VET4Hydro - Vocational Education and Training Partnership for Hydropower, co-funded by the European Union under the scope of the Program Erasmus+ (project 101128965). Further information in https://vet4hydro.lnec.pt/.

REFERENCES

[1] Fernandes, M. M. (2024). Segurança de Barragens: Análise de Risco de Ruptura de Barragens. Livro.

[2] QGIS Cloud. (2024). QGIS Cloud - GIS Platform for Online Mapping and Data Sharing. Available at: https://qgiscloud.com/ [Accessed on: March 2025].

[3] Lei nº 28/VIII/2013. Aprova a Directiva Nacional de Ordenamento do Território, abreviadamente designada por DNOT.

[4] International Commission on Large Dams (ICOLD). (2023). Definition of Large Dams. Available at: https://www.icold-cigb.org [Accessed March 2025]

[5] Ministério do Desenvolvimento Rural - Direção Geral do Planeamento, Orçamento e Gestão. (2013). Lote 2 - Estudos e Construção da Barragem de Canto Cagarra e Rede de Adução, Ilha de Santo Antão, Cabo Verde: Volume I – Memória Descritiva e Justificativa. Norvia CV, Norvia S.A., CENOR, Armando Cunha, Construtora do Tâmega, SA. Maio 2013.

[6] Ministério do Desenvolvimento Rural - Direção Geral do Planeamento, Orçamento e Gestão. (2013). Lote 3 - Estudos e Construção da Barragem de Banca Furada e Rede de Adução, Ilha de São Nicolau, Cabo Verde: Volume I – Memória Descritiva e Justificativa. Norvia CV, Norvia S.A., CENOR, Mota-Engil Engenharia. Março 2013.

[7] Direção Geral de Agricultura, Silvicultura e Pecuária - DGASP. (2011). Construção de 3 Barragens na Ilha de Santiago - Lote 3: Barragem de Faveta e Rede de Adução. Norvia CV, Norvia S.A., CENOR, Monte Adriano. Outubro 2011.

[8] Ministério do Desenvolvimento Rural. (2013). Lote 1 - Estudos e Construção da Barragem de Figueira Gorda e Rede de Adução, Ilha de Santiago, Cabo Verde. Norvia CV, Norvia S.A., CENOR, Conduril. Janeiro 2013.

[9] Ministère du Développement Rural. (2012). Projet d'Aménagement des Bassins Versants de Ribeira de Flamengos et Ribeira Principal - Barrage Flamengos, Avant Projet Détaillé. Pan Arab Consulting Engineers (PACE). Mai 2012.

[10] Araújo, A., Hernandez, R., Fonseca, R., & Matos, J. (2014). Estimating Sedimentation Rate on Poilão Dam (Santiago Island, Cape Verde). Comunicações Geológicas, 101 (Especial II), 597-600. LNEG – Laboratório Nacional de Geologia e Energia IP. ISSN:

0873-948X, e-ISSN: 1647-581X. Available at: http://www.lneg.pt/iedt/unidades/16/paginas/26/30/185.

[11] République du Cap Vert. (2012). Projet d'Aménagement des Bassins Versants de Ribeira Flamengos et de Ribeira Principal - Barrage Principal, Avant Projet Détaillé. Pan Arab Consulting Engineers (PACE). Kuwait. Mai 2012.

[12] Direcção Geral de Agricultura, Silvicultura e Pecuária – DGASP. (2011). Construção de 3 Barragens na Ilha de Santiago - Lote 2: Barragem de Saquinho e Rede de Adução. Norvia Cabo Verde, Norvia, CENOR, Monte Adriano. Versão B - Maio 2011.

[13] Direcção Geral de Agricultura, Silvicultura e Pecuária – DGASP. (2011). Construção de 3 Barragens na Ilha de Santiago - Lote 1: Barragem de Salineiro e Rede de Adução. Norvia Cabo Verde, Norvia, CENOR, Monte Adriano. Julho 2011.

[14] Infraestruturas de Cabo Verde (ICV). (2024). *Cabo Verde Dams - GIS Cloud Database*. Available at: QGIS Cloud.

[15] LNEC (2014). Barragens de Faveta, Salineiro e Saquinho, em Cabo Verde. Inspeção às estruturas efetuada em novembro de 2013 e considerações sobre as condições de segurança das obras. Report 242/2014 – DBB/NO, LNEC, Lisboa

[16] LNEC (2019). Acompanhamento, observação e controlo de segurança de barragens em Cabo Verde. Apoio do LNEC à atividade da Agência Nacional de Água e Saneamento (ANAS) de Cabo Verde. Report 324/2019 – DBB/NO, LNEC, Lisboa

[17] LNEC (2019). Barragem de Poilão. Inspeção de referência à barragem e ao sistema de observação efetuada em fevereiro de 2019. Report 340/2019 – DBB/NO, LNEC, Lisboa

[18] LNEC (2019). Barragem de Faveta. Inspeção de referência à barragem e ao sistema de observação efetuada em fevereiro de 2019. Report 341/2019 – DBB/NO, LNEC, Lisboa

[19] LNEC (2019). Barragem de Figueira Gorda. Inspeção de referência à barragem e ao sistema de observação efetuada em fevereiro de 2019. Report 342/2019 – DBB/NO, LNEC, Lisboa

[20] LNEC (2019). Barragem de Flamengos. Inspeção de referência à barragem e ao sistema de observação efetuada em fevereiro de 2019. Report 343/2019 – DBB/NO, LNEC, Lisboa

Fifth International Dam World Conference
PORTUGAL • LISBON • LNEC • APRIL 13-17, 2025
dam world 2025

RELATIONS BETWEEN SEISMIC INPUT MOTION, DAM PATTERN, AND SEISMICALLY INDUCED SLIDING OF GRAVITY DAMS IN EUROPEAN CONTEXT

Pierre B. Labbé[1]
Ecole Spéciale des Travaux Publics

ABSTRACT

Based on a set of 100 European seismic input motions, we examine correlations between seismically induced sliding of a set of gravity dam models and input motion Intensity Measures (IMs), in view of deriving a predictive approach of seismically induced sliding.

Considered Intensity Measures are Peak Ground Acceleration (PGA), Peak Ground Velocity (PGV), Peak Ground Displacement (PGD), Arias Intensity (IA), Cumulative Absolute Velocity (CAV), and Absolute Strong motion Duration (ASD). The 100 input motions, recorded on rock sites, cover M_w magnitudes between 4.9 and 6.3 (2009 L'Aquila earthquake) and PGAs between 1,40 and 5.45 m/s².

The model of dam cross section is simply triangular with a vertical upstream face and a horizontal base. Four dam heights (30, 80, 150 & 250 m) and 3 downstream face slopes (0.6,0.8 & 1) are considered, resulting in 12 dam patterns. In addition, 6 base friction coefficients are retained for each pattern, so that 72 configurations are investigated. The dam model is a two degree of freedom system, calibrated in such a way that the first mode natural frequency and effective modal mass are those of the dam pattern under consideration, with the fluid added mass of a full reservoir.

The largest calculated final sliding is 32 cm, obtained for H=250 m under a L'Aquila earthquake input motion. The 72 configurations submitted to the 100 input motions result in 7200 sliding values, processed in a statistical viewpoint by linear regression analysis. In a first step, correlations between IMs and sliding are investigated. A major output is that dam sliding is much better correlated with PGV than it is with PGA. In a second step, correlations between dam configurations and sliding are presented. Eventually a method is introduced that enables evaluating seismically induced sliding, based on dam configuration and PGV, without running time response analyses.

Keywords: Concrete gravity dam, Seismically induced sliding, Ground motion intensity measure, Dam pattern, Linear regression analysis.

[1]pierre.labbe@estp.fr, France

1. INTRODUCTION

Sliding safety of existing gravity dams is a matter of interest for the engineering community, as witnessed by a publicly available report published by the ICOLD European Club [1]. This report is dedicated to static stability, with some references to national practices relating to the treatment of seismic loads. In current engineering practices, it is verified whether the dam stability is ensured or not under an assumed seismic load. However, in case stability criteria are not met, the only possibility to evaluate the seismically induced sliding magnitude is to run time response analyses.

A first attempt to evaluate a sliding upper bound was presented by Newmark [2]. Later, Léger & Katsouli [3] proposed an approach based on finite element analysis, with the interface between the foundation and the dam modelled by a series of friction elements, focusing on the influence of the rigidity contrast between foundation and dam materials. They obtained centimetric sliding displacements for peak ground accelerations (PGAs) of the order of 0.5 g. Chopra & Zang [4] substantiated that downstream sliding is initiated before upstream tipping, which occurs before upstream sliding. They used first a rigid body model, and second a single degree of freedom (SDOF) system with Coulomb friction element at the base. They discussed the Newmark upper bound and focused on the hydrodynamic pressure effect of the reservoir. In addition, they discussed the effect of the vertical component of the input motion. Mir & Taylor [5] carried out a series of dynamic slip tests on a concrete gravity dam model and concluded that the Newmark's approach encompasses some conservatism. More recently Basili & Nuti examined the response of dam models to many strong input motions [6]. They derived a simplified sliding evaluation applicable in situations when the PGA does not exceed the double of the sliding triggering acceleration. Mével & Robbe documented that dam models with a very limited number of degrees of freedom are sufficient to properly represent base sliding [7].

As a step forward in the wake of previous researches, the purpose of the present paper is to examine seismically induced sliding of representative dam models submitted to a series of 100 input motions presented in section 2, and to derive some statistical information about the expected base sliding. For this purpose, a set of 72 dam configurations, and some examples of time response are also presented in section 2.

Eventually a set of 7200 sliding values are available for statistical analyses that are presented in section 3. In a first step, correlations between seismically induced sliding and input motion intensity measures are investigated. In a second step correlations between sliding and dam configurations are examined. Eventually a method is introduced that enables estimating seismically induced sliding, based on dam configuration and PGV, without running time response analyses.

The considered intensity measures are peak ground acceleration (PGA), peak ground velocity (PGV), peak ground displacement (PGD), Arias intensity (AI) [12], cumulative absolute velocity (CAV) [13], and strong motion duration (SD). Regarding strong motion duration, a widely used definition is D_{5-95} the time elapsed for the Arias Intensity to increase from 5% to 95% of its final value. However, previous research gave evidence that this definition does not pertain in the present case [14]. This is because the D_{5-95} definition is based on a relative value of the input signal magnitude; indeed, multiplying a signal by a factor of 2 does not change the D_{5-95} value. Therefore, we introduce an Absolute Strong motion Duration (ASD), defined as the accumulated duration of those periods of time when the signal absolute value exceeds a given threshold, namely 0.5 m/s².

2. METHODOLOGY

2.1. Seismic input motion data

A series of 100 accelerograms, $\{a_n(t), n=1…100\}$ was extracted out of the Resorce database [8]. Resorce is an accelerometric database for the broader European area, released through successive frozen versions. The 2013 version used in this research includes 5 882 uniformly processed records from 1 814 earthquakes and 1 540 strong-motion stations.

Resorce database includes some records from large magnitude earthquakes such as those generated by the North Anatolian fault. To obtain a series of records representative of the European tectonic context, decision was made not to retain this type of input motion. In addition, we only selected input motions recorded on rock sites (category A sites in the Eurocode 8 classification). With those constrains, moment magnitudes of the selected records vary between M_w=4.9 (Kalamata earthquake aftershock, Greece, 15 Sept. 1986) recorded at a 3 km epicentral distance and M_w=6.3 (L'Aquila earthquake, Italy, 6 April 2009) recorded at 6.0 km epicentral distance. We introduce the following notations, where $a_{n,peak}$ is the PGA of $a_n(t)$:

- $a_{n,peak} = \max_t |a_n(t)|$,
- $A_{max} = \max_{n=1…100} a_{n,peak}$.

In our set of accelerograms, PGAs vary between 1,40 m/s² and A_{max}=5.45 m/s², PGVs between 0.034 and 0.52 m/s, PGDs between 1.8 mm and 13.8 cm, AIs between 0.048 and 2.04 m/s, CAVs between 0.79 and 9.10 m/s, and ASDs between 0.24 and 6.02 s. For reasons that will appear later, we make a focus on PGVs, by examining their statistical distribution. Their mean value and standard deviation are $\overline{PGV} = 0.131\ \mathrm{m}/s$ and $\sigma_{PGV} = 0.0965\ \mathrm{m}/s$. They are lognormally distributed, as illustrated in Fig. 1 where are plotted, in abscissa, anticipated

values of a standardized gaussian distribution, and in ordinate values of the standardized distribution of the 100 $\ln PGV$ values. The good fit is confirmed by the resulting coefficient of determination, given in the figure.

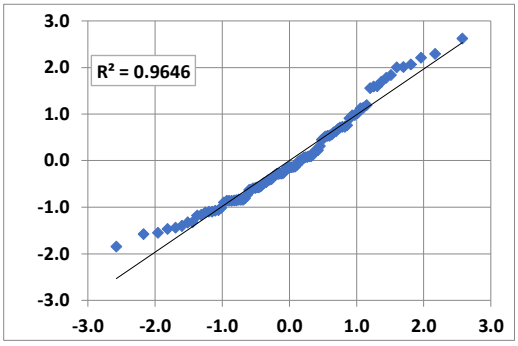

Fig. 1. Evidence of the PGVs lognormal distribution

2.2. Dam description and modelling

- *Dam patterns*

The dam cross section is simply triangular. The upstream face, of height H, is vertical and the base, of length B, is horizontal. The downstream face slope is m, where $m = B/H$, as indicated in Fig. 2, left. We select four values of H: 30, 80, 150 & 250m, and, following Schleiss & Pougatsch [9], we retain three possible slope values: $m = 0.6, 0.8 \text{ and } 1$, resulting in 12 dam patterns to be considered.

The water density is $\rho_e = 1000\ \text{kg/m}^3$. The dam is made of concrete, the density of which is taken as $\rho_b = 2400\ \text{kg/m}^3$ and the dynamic Young modulus as $E_b = 31\ \text{GPa}$. Considering a dam section of unitary thickness (one meter), we designate its mass by M, its weight norm by P and the norm of the horizontal static force resulting from water pressure by E.

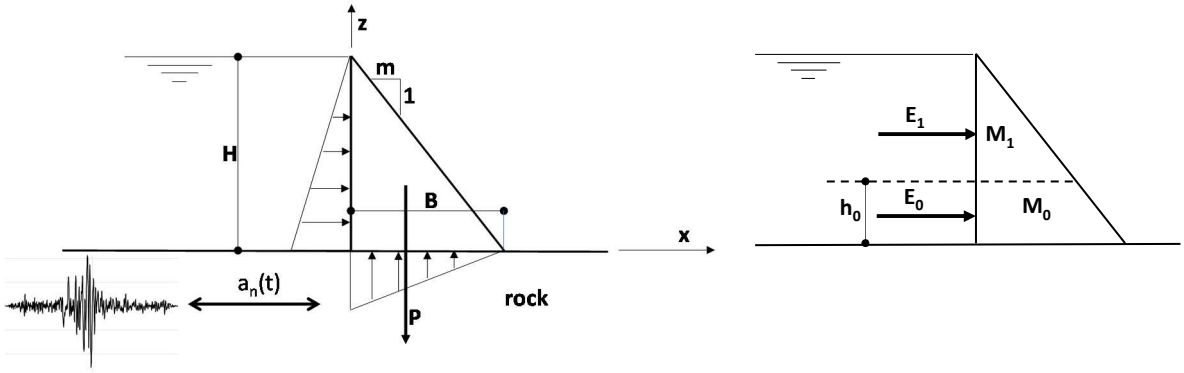

Fig. 2. Gravity dam idealization

The foundation ground is deemed to be rock, so that we may disregard soil-structure interaction effects and assume a rigid-base foundation. This base foundation is animated by horizontal input motions $a_n(t)$.

We do not introduce further refinements in description of the dam pattern, such as for instance tailwater or downstream sediments.

- *Dynamic features*

As for any structure, when dealing with the seismic response of dams, key features are eigen frequencies, as well as eigen shapes from which effective modal masses are derived. According to Schleiss & Pougatsch [9], for a full reservoir, based on Westergaard [10] approach of fluid-structure interaction between the reservoir and the dam, fundamental frequencies of gravity dams are given by Formula (1), where β is a coefficient given in Table 1. Concurrently, according to same authors, the ratio of the fundamental effective modal mass to the total mass is equal to ψ, also given in Table 1.

$$f_1 = \beta \frac{B}{H^2} \sqrt{\frac{E_b}{\rho_b}} \tag{1}$$

Table 1. β, ψ and retained ϕ values, versus *m*

m	β	ψ	ϕ					
0.6	0.13	0.41	0.72	0.75	0.80	0.85	0.90	0.95
0.8	0.12	0.43	0.55	0.60	0.65	0.70	0.75	0.80
1	0.11	0.44	0.45	0.50	0.55	0.60	0.65	0.72

- *Uplift pressure and base friction coefficients*

We assume that a Coulomb type friction resisting force takes place at the interface between the dam and the ground, and we denote φ the friction coefficient. According to Schleiss & Pougatsch [9], with due considerations paid to the type and quality of the foundation rock, φ values are comprised between 0.5 (weathered rock) and 1.7. A comprehensive review of friction conditions is presented by the ICOLD European Club [1]. No distinction is made between friction coefficient before sliding and reduced coefficient once sliding is activated.

The uplift pressure is assumed to be triangular, equal to the reservoir water pressure at the heel and to zero at the toe. Consequently, the uplift pressure effect on dam sliding stability is considered through a reduced effective friction coefficient, ϕ given by Formula (2).

$$\phi = \varphi \left(1 - \frac{\rho_e}{\rho_b}\right) = 0.58\, \varphi \tag{2}$$

Yet, the range of ϕ values retained in our analysis is calibrated as per the following rationale:

On the one hand, ϕ should not be too small, to satisfy at least static equilibrium conditions. The resulting minimum ϕ value is given by the left part of Inequation 3. On the other hand, ϕ should not be too large, otherwise sliding would be impossible. Neglecting at this stage fluid-structure interaction effects, the maximum ϕ value of interest is given by the right part of Inequation 3 (where g is gravity acceleration). However, instead of introducing A_{max} in the upper bound formula, we retain a lower value such that at least 30 input motions generate sliding for each dam pattern. For every m value, we eventually retain six ϕ values presented in Table 1. They are consistent with those that would result from application of Formula (2). Ultimately, we examine 72 sliding configurations: 12 dam patterns multiplied by 6 friction coefficients.

$$\frac{1}{m}\frac{\rho_e}{\rho_b} < \phi < \frac{1}{m}\frac{\rho_e}{\rho_b} + \frac{A_{max}}{g} \tag{3}$$

- *Two degree-of-freedom dam model*

The dam model is a two degree-of-freedom system as presented in Fig. 3. Basically, M_1 mass and k_1 stiffness are intended to represent the fundamental mode of the dam. M_0 mass is linked to the ground through k_0 stiffness. k_0 is significantly larger than k_1; it enables to obtain a representative initial displacement of M_0 under water pressure; in dynamic regime it accounts for the fact that some small deformation appears before the entire interface between the dam and the ground could be regarded as sliding. Specifically, for every dam pattern, stiffnesses and masses are calibrated in such a way that, in elastic regime:

- The total mass, $M_0 + M_1$, is equal to M;
- The first eigenfrequency is equal to f_1 given by Formula (1),
- The first effective modal mass is equal to ψM, where ψ is given in Table 1;

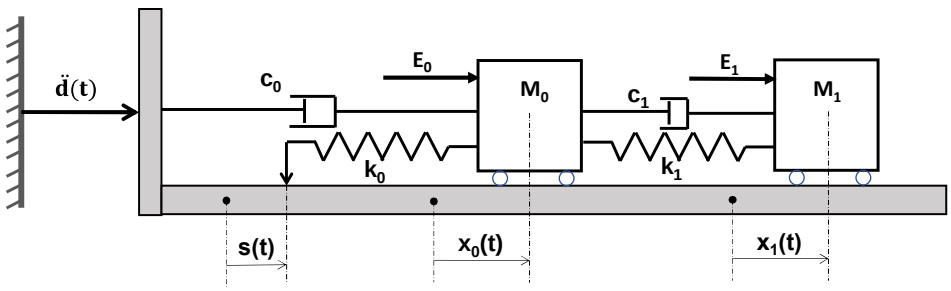

Fig. 3. Two degree-of-freedom dam model

Viscous dampers are introduced in the model, such that the modal damping value with respect to critical is equal to 5% for both eigenmodes.

The k_0 stiffness is equipped with a threshold capacity $F_e = P\phi$, corresponding to a maximum elastic elongation X_e. It results that the connection between the M_0 mass and the base exhibits

a typical elastic-perfectly plastic constitutive relationship represented in Fig. 4, where F_0 is the force carried through this connection.

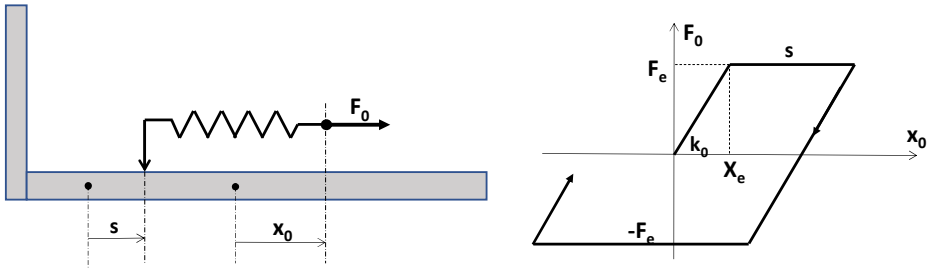

Fig. 4. Constitutive relationship of the connexion between mass M_0 and support.

The reservoir static water pressure is translated into forces E_0 and E_1 as follows (Fig. 2, right): first, h_0 is calculated as the depth of the lower part of the dam such that the mass of it is equal to M_0, then E_0 is calculated by integrating the water pressure on this lower part. And similarly, for E_1, applied on M_1, representing the water pressure on the upper part of the dam.

The support of the model is animated with a seismic input motion, acceleration of which is designated by $\ddot{d}(t)$ for the sake of homogeneity, representing any $a_n(t)$.

- *Equation of motion*

There are three possible regimes for the system, identified by a regime indicator, u, as follows:

- No sliding; $u = 0$; this is elasticity regime for which the elongation of k_0 is smaller than X_e in absolute value;
- Sliding towards downstream; $u = 1$;
- Sliding towards upstream; $u = -1$ (not observed in practice).

With these notations, the dynamic equilibrium equation reads as per Equation 4, where s is the accumulated sliding. In elasticity regime, s is unchanged. In sliding regimes, s value is updated; for instance, in a phase of downstream sliding, s is such that $s(t) = x_0(t) - X_e$.

$$\underline{\underline{M}}\,\underline{\ddot{x}} + \underline{\underline{C}}\,\underline{\dot{x}} + \underline{\underline{K}}\,\underline{x} + (1-u^2)\underline{\underline{K'}}\,\underline{x} = \underline{E} - \ddot{d}\,\underline{\underline{M}}\,\underline{\Delta} + (1-u^2)\underline{\underline{K'}}\,\underline{s} - u\underline{\underline{K'}}\,\underline{X_e}\,, \tag{4}$$

where:

$$\underline{\underline{M}} = \begin{bmatrix} m_0 & 0 \\ 0 & m_1 \end{bmatrix}, \underline{\underline{C}} = \begin{bmatrix} c_0 + c_1 & -c_1 \\ -c_1 & c_1 \end{bmatrix}, \underline{\underline{K}} = \begin{bmatrix} k_1 & -k_1 \\ -k_1 & k_1 \end{bmatrix}, \underline{\underline{K'}} = \begin{bmatrix} k_0 & 0 \\ 0 & 0 \end{bmatrix},$$
$$\underline{x} = \begin{bmatrix} x_0 \\ x_1 \end{bmatrix}, \underline{E} = \begin{bmatrix} E_0 \\ E_1 \end{bmatrix}, \underline{\Delta} = \begin{bmatrix} 1 \\ 1 \end{bmatrix}, \underline{s} = \begin{bmatrix} s \\ 0 \end{bmatrix}, \underline{X_e} = \begin{bmatrix} X_e \\ 0 \end{bmatrix}.$$

Equation 4 is resolved through a conventional Newmark integration scheme, with the initial displacement induced by the static water pressure, and zero initial velocity and acceleration.

The selected time-step is $\delta t = 0.001\text{s}$. For numerical implementation, it is necessary to calculate, once and for all, inverses of both matrices given in Equation 5.

$$\begin{aligned} \underline{\underline{Q}}_{elasticity} &= a_2\,\underline{\underline{M}} + a_1\underline{\underline{C}} + \underline{\underline{K}} + \underline{\underline{K}}' \\ \underline{\underline{Q}}_{sliding} &= a_2\,\underline{\underline{M}} + a_1\underline{\underline{C}} + \underline{\underline{K}} \end{aligned} \qquad a_1 = 2/\delta t\,, a_2 = 4/\delta t^2 \tag{5}$$

At the end of every time step, a test is performed to decide the u value for the next step. There is no need of further sophistication in the algorithm, thanks to the small δt value.

2.3. Typical time-response outputs

Time-response outputs are exemplified on the $\{H = 150\text{m}, m = 0.8, \phi = 0.6\}$ configuration, for which the dam fundamental frequency is $f_1 = 2.3\ \text{Hz}$ according to Formula (1). We illustrate in Fig. 5 the response under $a_1(t)$, the first one in our set of input motions. $a_1(t)$ is presented in Fig. 5-a, $x_0(t)$ in Fig. 5-b, $x_1(t)$ Fig. 5-c and sliding $s(t)$ in Fig. 5-d. We may observe that $x_0(0)$ and $x_1(t)$ are not equal to zero, due to the reservoir water pressure. In cases when sliding is relatively large, as presented in Fig. 6, $x_0(t)$ and $s(t)$ are not visually discernible.

We designate as situation a given dam configuration $\{H, m, \phi\}$ submitted to a given input motion. Every of the 72 configurations being submitted to the series of 100 input motion, there is a total of 7200 situations under examination. Denoting S the final sliding value obtained at the end of time-response analysis of a situation, we get a set of 7200 S values.

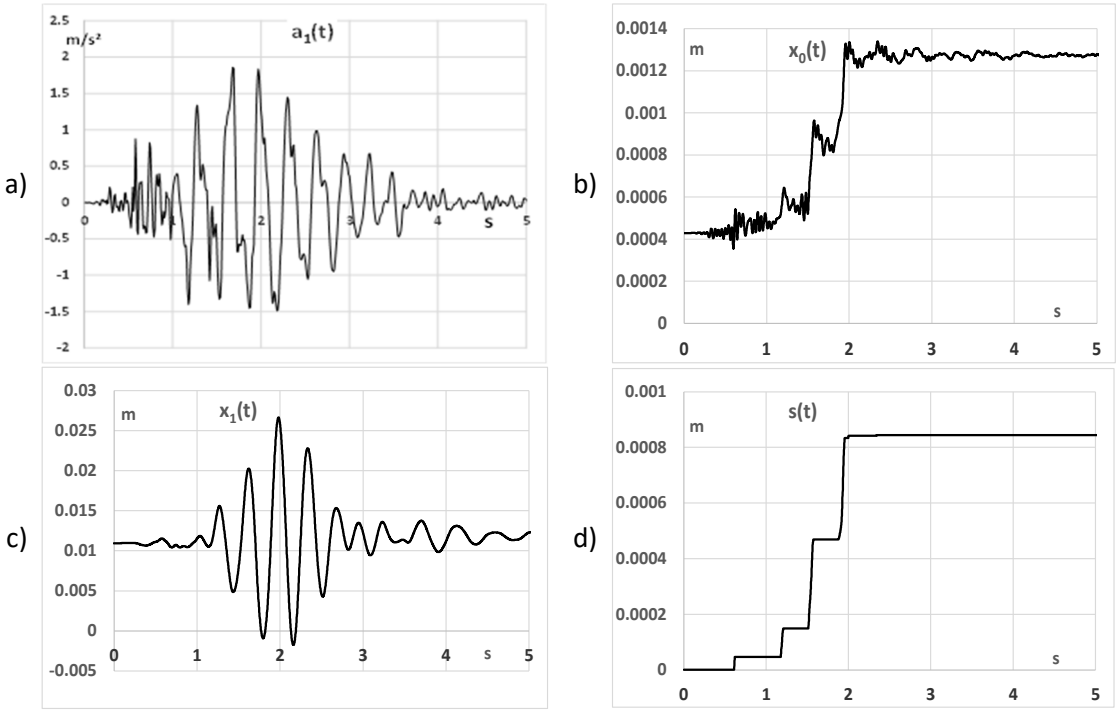

Fig. 5. Response of configuration $\{H = 150\text{m}, m = 0.8, \phi = 0.6\}$ to input motion $a_1(t)$

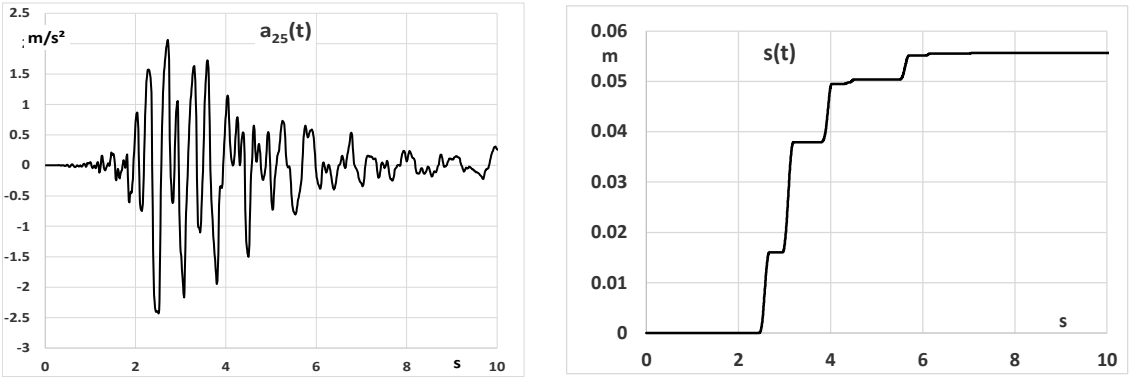

Fig. 6. Response of configuration $\{H = 150\text{m}, m = 0.8, \phi = 0.6\}$ to input motion $a_{25}(t)$

3. RESULTS

3.1. Magnitude of sliding values

In the set of 7200 sliding values, 1714 of them are zero values. Among the 5486 non-zero, 1576 are below 1 mm, 2056 between 1 mm and 1 cm, 1719 between 1 cm and 10 cm, and 135 larger than 10 cm. Such outputs are consistent with those obtained by Léger & Katsouli [3]. Not surprisingly, the largest sliding, 32 cm, is attained for the highest dam with lowest m and ϕ values, namely $\{H = 250\text{ m}, m = 0.6, \phi = 0.72\}$. This 32 cm sliding is obtained when the dam is submitted to an input motion recorded at the occasion of the M_w 6.3 L'Aquila earthquake (largest magnitude in our data set). This input motion is characterized by its PGA=3.60 m/s², PGV 0.360 m/s, PGD=13.8 cm, AI=1.22 m/s, CAV=8.15 m/s, and ASD=5.22 s. Markedly, none of these 6 intensity measure values is the maximum value in our data set, except the PGD.

In terms of dam stability, above results mean that, among 7200 situations, only 1714 would have been regarded as stable in a conventional engineering approach based on static analysis. However, if for instance a 1 cm sliding is regarded as acceptable, the number of stable situations increases to 5346. In the light of those numbers, there is a clear interest for the dam engineering community in proposing a criterion of acceptable sliding in the perspective of seismic hazard re-evaluation on dam sites.

3.2. Distribution of sliding values

For every dam configuration, we now examine the distribution of sliding values. For three representative configurations, Table 2 provides mean and standard deviation of computed sliding values, as well as the Coefficient Of Variation of them (COV=standard deviation / mean). In addition, Fig. 8, obtained by the same method as Fig. 1, illustrates that sliding value are lognormally distributed, which a key output for the following.

Table 2. Mean and standard deviation of sliding values for 3 configurations

Configuration	Mean (m)	Standard deviation (m)	COV
$H = 80, m = 0.6, \phi = 0.75$	0.0227	0.0291	1.07
$H = 150, m = 0.8, \phi = 0.60$	0.0174	0.0297	1.70
$H = 250, m = 0.8, \phi = 0.55$	0.0485	0.0612	1.26

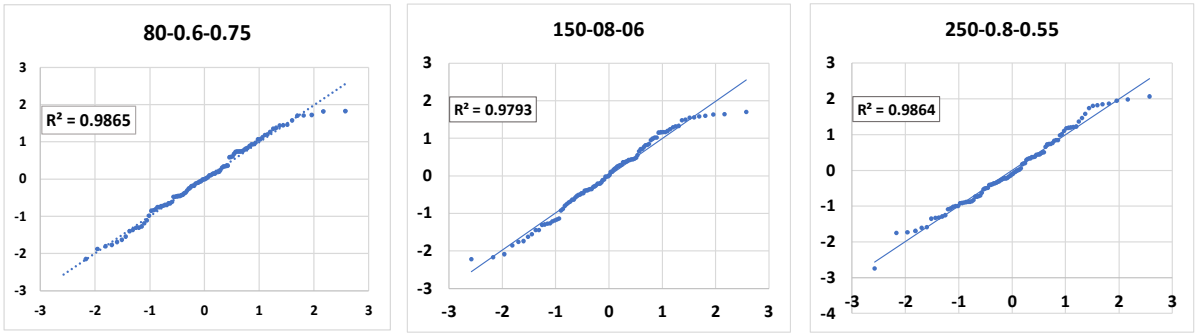

Fig. 7. Evidence, on three dam configurations, that sliding values are lognormally distributed

It may be noticed that, in every of the 3 configurations, the lognormal distribution trends to overestimate large sliding value, as compared to those that result from time-response analyses. It means that additional computations should be carried out under strong input motions to better characterize these large sliding values.

3.3. Correlation between sliding and seismic input motion intensity measures

For a specific configuration, namely $\{H = 150\ \text{m},\ m = 0.8,\ \phi = 0.6\}$, we present in Fig. 8 the 100 final sliding value, S, versus intensity measures. More precisely, figures present linear regressions between the decimal logarithm of the intensity measure and the decimal logarithm of the computed sliding. The associated coefficients of determination, R^2, are also indicated in the figure. It appears that sliding is significantly better correlated with PGV than it is with PGA or PGD. This a generic output, applicable to all investigated configurations.

Regarding correlation with AI and CAV the gap between them and the PGV trends to decrease when dealing with higher dams, so that they perform better in a few configurations. However, considering that PGV is simpler than AI or CAV, we eventually retain it as the best intensity measure of input motion, at least for analysis of seismically induced sliding. The linear regression between $\ln PGV$ and $\ln S$ is given by formula (6) where the residual r is gaussian, centred, with a 1.09 standard deviation. As mentioned in Fig. 8, the associated coefficient of determination is R^2=0.743.

$$\ln S = 1.07 + 3.03 \ln PGV + r\ ;\ \ \sigma_r = 1.09;\ \ \mathrm{R}^2 = 0.743 \tag{6}$$

It is also possible to investigate whether correlation can be improved when considering concurrently two, or more, intensity measures. As a matter of example, for the same configuration $\{H = 150\ \text{m},\ m = 0.8,\ \phi = 0.6\}$, the regression providing S versus PGV and ASD is given by Formula (7), where r is still gaussian and centred, with now a 1.05 standard deviation, and an R^2=0.761 coefficient of determination. This is not a dramatic improvement, compared to the regression obtained with the only PGV. Parenthetically, Formula (7) indicates that, may be in a contra-intuitive manner, sliding does not appear to be proportional to strong motion duration, but rather to the square root of it.

$$\ln S = -0.13 + 2.56 \ln PGV + 0.55 \ln ASD + r\ ;\ \ \sigma_r = 1.05; \mathrm{R}^2 = 0.761 \tag{7}$$

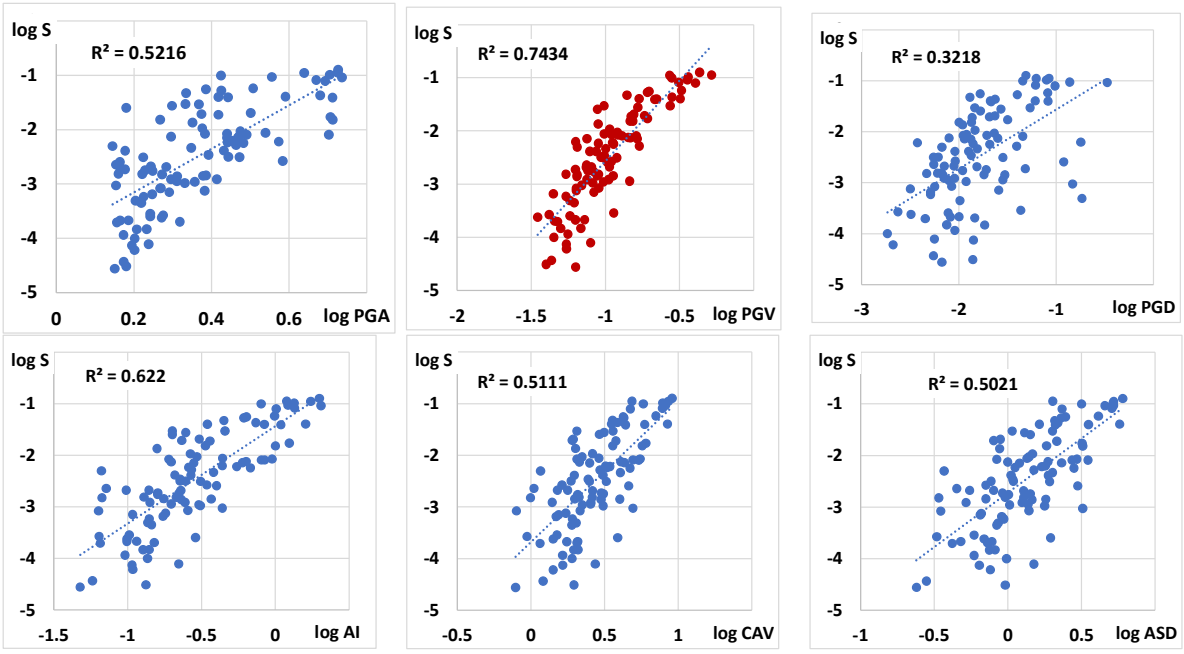

Fig. 8. Final sliding vs intensity measures, for configuration $\{H = 150\text{m},\ m = 0.8,\ \phi = 0.6\}$, in decimal logarithms

Regressions enable to calculate the probability that a given sliding value is exceeded under a seismic input motion characterized by a given intensity measure. For instance, in application of Formula (6), the median sliding value S_{50} (50% probability of non-exceedance) under a 0.2 m/s PGV is such that $\ln S_{50} = 1.07 + 3.03 \ln 0.2 = -3.807$, which gives $S_{50} = 2.22$ cm. Under the same PGV, the S value that has 84% probability of not being exceeded[1], S_{84}, is such that $\ln S = 1.07 + 3.03 \ln 0.2 + 1.09 = -2.717$, which gives $S_{84} = 6.61$ cm. Similarly, considering two standard deviations, we get $S_{97.7} = 19.7$ cm. Based on formula presented in

[1] It is reminded that for a gaussian distribution, the 84% probability of non-exceedance corresponds to $\overline{r} + \sigma_r$, while 97.7% corresponds to $\overline{r} + 2\,\sigma_r$.

appendix, it is also possible to calculate the mean sliding value $\overline{S} = 3.93\ \mathrm{cm}$. As expected for a lognormal distribution, the mean value is significantly larger than the median.

As usual, such a regression formula should be handled with care. Especially, we may observe in Fig. 8 that using it for PGV values larger than those in the database would be hazardous.

3.4. Correlation between sliding and dam configurations

In view of searching correlations between sliding and dam configurations, we first calculate for every configuration the mean, $\overline{S}$, of the 100 S values obtained for this configuration, getting a total of 72 $\overline{S}$ values. Then we apply multivariable linear regression technique between the logarithm of $\overline{S}$ and the dam configuration parameters, $\{H, m, \phi\}$.

In a first step, it was observed that the dam height, H, appears having a negligible influence on $\overline{S}$. However, i) it is obvious that the dam height influences the dam frequency, as made explicit by Formula (1), and ii) it is expected that the dam frequency plays a role in such a structural dynamics problem. Therefore, we replace H by the dam first eigenfrequency, f_1, given by Formula (1) with $B = mH$. It means that a configuration is now characterized with the three parameters $\{f_1, m, \phi\}$. With that, we get the regression Formula (8), in which the residual, r, is a zero-mean gaussian random variable of standard deviation $\sigma_r = 0.362$.

$$\ln \overline{S} = 11.85 - 0.082 f_1 - 9.17 m - 13.44 \phi + r\ ;\ \ \sigma_r = 0.362 \tag{8}$$

Similarly, we can obtain an evaluation of the sliding standard deviation, σ_S, versus $\{f_1, m, \phi\}$. We obtain it through the COV. For every configuration, we get a COV value, as exemplified in Table 2. Multi variable regression on the 72 COV values results in Formula (9), where the residual is again a zero-mean gaussian random variable.

$$\mathrm{COV} = -6.27 - 0.067 f_1 + 4.86 m + 6.66 \phi + r\ ;\ \ \sigma_r = 0.345 \tag{9}$$

It is worth observing that, in Formulas (8) and (9), the residual standard deviation carries information on uncertainty in assessment of $\overline{S}$ and σ_S. It means that selecting $r = 0$ in both (8) and (9) gives the best estimate value of $\overline{S}$ and σ_S, in the least square sense of linear regression technique.

For instance, in case of a dam characterized by $\{H = 150\ \mathrm{m},\ m = 0.8,\ \phi = 0.6\}$, we first calculate its first eigenfrequency through Formula (1), which results in $f_1 = 2.30\mathrm{Hz}$. Then we calculate the best estimate value of $\overline{S}$ through Formula (8): $\ln \overline{S} = 11.85 - 0.082 \times 2.30 - 9.17 \times 0.8 - 13.44 \times 0.6 = -3.74$, which results in $\overline{S} = 0.0238\mathrm{m}$. Eventually, we calculate the

COV through Formula (9): $\mathrm{COV} = -6.27 - 0.067 \times 2.30 + 4.86 \times 0.8 + 6.66 \times 0.6 = 1.46$, and we derive the standard deviation: $\sigma_S = \mathrm{COV} \times \overline{S} = 1.46 \times 0.0238 = 0.0348\mathrm{m}$.

Doing the same for the 2 other configurations already considered in Table 2, we obtain the mean and standard deviation presented in Table 3. To illustrate the difference between a lognormal distribution based on Table 2 and the corresponding one based on Table 3 values, we plot in Fig. 9 the two repartition functions of the three considered configurations. Even in the case $\{H = 150, m = 0.8, \phi = 0.6\}$, for which the gap between Tables 2 and 3 is the most significant, the two plots are in a reasonably good agreement: for instance, a 90% probability on non-exceedance corresponds to a 4 cm sliding when processing time response outputs (blue line), and 5 cm based on Formulas (8) and (9) (red line).

Table 3. Mean and standard deviation of sliding values obtained by linear regression from dam features for 3 configurations

Configuration	Mean (m)	Standard deviation (m)	COV
$H = 80, m = 0.6, \phi = 0.75$	0.0180	0.0252	1.205
$H = 150, m = 0.8, \phi = 0.60$	0.0238	0.0348	1.458
$H = 250, m = 0.8, \phi = 0.55$	0.0504	0.0598	1.187

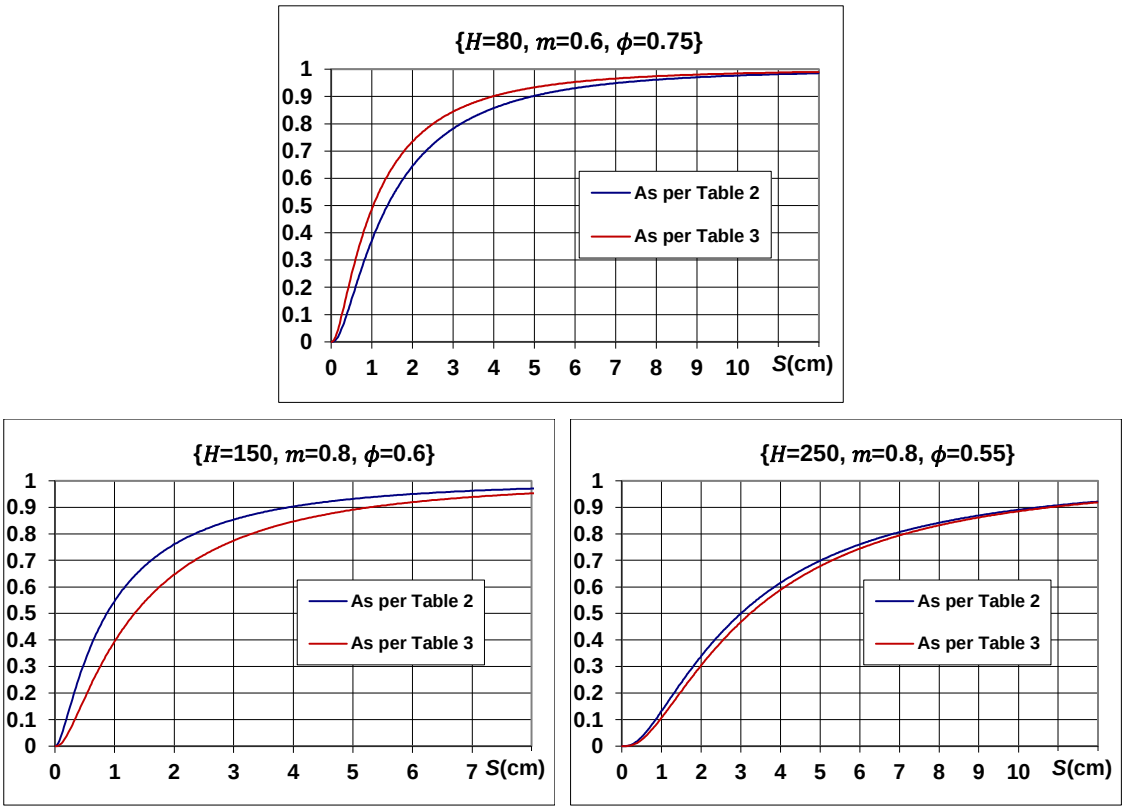

Fig. 9. Lognormal sliding repartition functions for three configurations

3.5. Predictive method of dam sliding

At this stage, we may observe that we have at our disposal, on the one hand, information that PGVs are lognormally distributed and we know their mean and standard deviation values, and; on the other hand, information that sliding values of a dam configuration are also lognormally distributed and we have an evaluation of their mean and standard deviation.

With objective of establishing a relationship between those two lognormal distributions, we introduce the following principle: A PGV and the corresponding seismically induced sliding S should be such that the percentile of S (in the set of 100 sliding values) is the same as the percentile of PGV (in the set of 100 PGVs values). For example, if the given PGV is such that 10% of PGVs are larger, the associated S should be such that 10% of sliding values are larger.

Applying the principle implies playing with some technicalities of lognormal distributions that are presented in appendix. In practice the procedure is as follows: We introduce $X = \ln PGV$ and $Y = \ln S$. Both X and Y are normally distributed. By applying formulas that are presented in the appendix, we derive

- For X: $\overline{X} = -2.2512, \sigma_X = 0.659$.
- For Y, it depends on the considered configuration. For instance, in the case $\{H = 80, m = 0.6, \phi = 0.75\}$, starting from $\overline{S} = 0.0180$ and $\sigma_S = 0.0252$ given in Table 3, we obtain $\overline{Y} = -4.560, \sigma_Y = 1.042$.

Considering the mathematical expression of the lognormal repartition function given by Formula (12) in the appendix, applying the above introduced principle implies that Equation (10) is satisfied. From this equation, we derive Y associated to a given X.

$$\frac{X - \overline{X}}{\sigma_X} = \frac{Y - \overline{Y}}{\sigma_Y} \tag{10}$$

Taking the example of the $\{H = 80, m = 0.6, \phi = 0.75\}$ dam submitted to an input motion of $PGV = 0.2\mathrm{m/s}$, we calculate $X = \ln PGV = -1.609$, we derive $Y = -3.548$ from Eq. (10), and eventually we calculate $S = \exp(Y) = 0.029\mathrm{m}$. By varying PGV value, we obtain S as a function of PGV, represented by the solid red line in Fig 8 (left). Repeating the same procedure for the two above considered other configurations, we obtain the two other solid red lines also presented in Fig. 10.

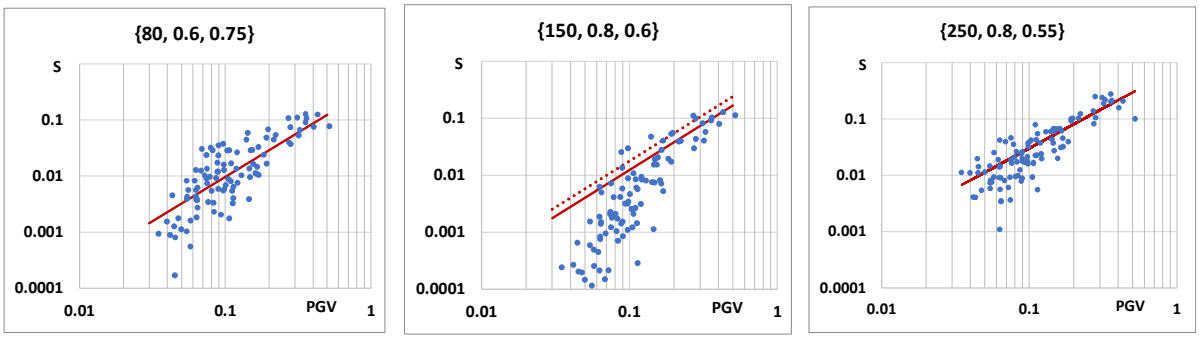

Fig. 10. Computed sliding values (blue dots) and predicted values (red lines) *vs* PGV for 3 configurations

Fig. 10 shows that the proposed predictive method performs well when dealing with relatively large sliding values, of the order of centimetres or decimetres. It trends to overestimate small sliding values, of the order of millimetres or less. Yet, such small sliding values are of little interest. To illustrate this performance, we consider again the $\{H = 150\ \text{m},\ m = 0.8,\ \phi = 0.6\}$ configuration examined in section 3.3. Under an input motion of $PGV = 0.2$ m/s, the predicted best estimate sliding value is 3.81 cm, close to the mean 3.93 cm calculated in section 3.3.

As expected, and illustrated in Fig. 10, some calculated sliding values are higher than those predicted by the proposed method. For this reason, a larger confidence of non-exceedance may be desired. A possibility for that is to play with the residual in Formula (8). For instance, the dotted red line in Fig. 10 is obtained by selecting $r = \sigma_r$ in Formula (8) instead of $r = 0$ for the solid red line.

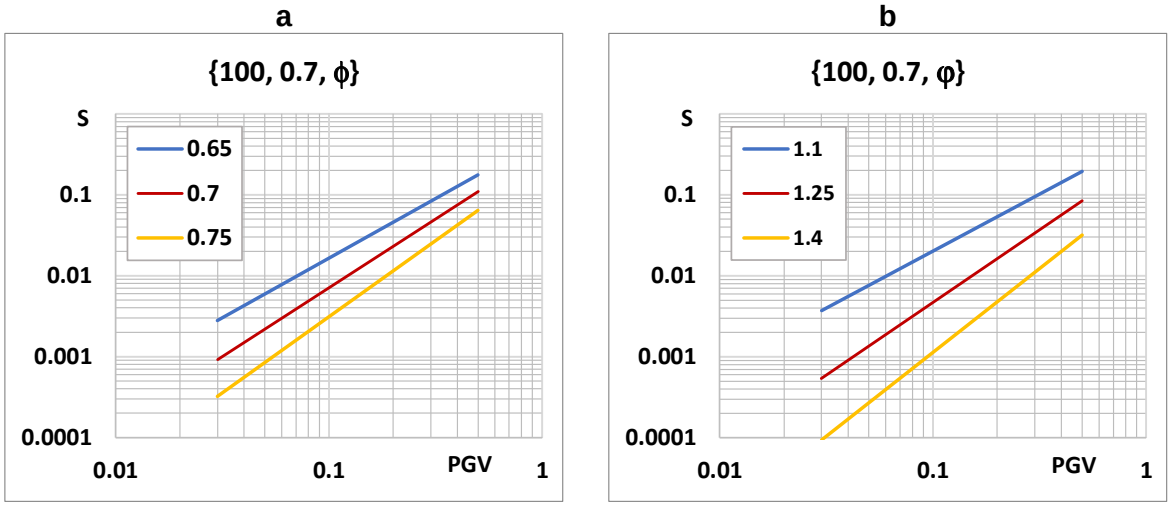

Fig. 11. Best estimate sliding *vs* PGV for $H = 100\text{m},\ m = 0.7$; a) for three ϕ values b) for 3 φ values and assuming triangular uplift pressure

Of course, not only we can repeat the procedure and get 72 figures like the 3 ones that are presented in Fig. 10, but in addition we can apply the procedure to any interpolated configuration between the 72 ones considered in this research (extrapolation would be

hazardous). For instance, we may consider a 100m heigh dam with a 0.7 downstream face slope and run a sensitivity study of sliding outputs to friction coefficient by considering three possible values of the effective friction angle ϕ: 0.65, 0.70, 0.75. The resulting best estimate S values versus PGV are presented in Fig. 11-a. Assuming a triangular uplift pressure, so that Formula (2) holds, a similar plot is presented in Fig. 11-b for three values of the φ friction angle.

4. CONCLUSIONS

The first conclusion of this research is that relatively small sliding values are obtained, consistent with those already calculated by other authors [3]. Among the 7200 situations resulting from combination of dam configurations and seismic input motions considered in this research, only 1714 would have been regarded as stable in a conventional engineering approach based on static analysis. However, if we regard for instance a 1 cm sliding as acceptable, the number of stable situations increases to 5346. It means that there is an interest for the dam community to introduce in the engineering approach a criterion of acceptable sliding in the perspective of seismic hazard re-evaluation on dam sites.

A second important output is that, when considering a large set of seismic input motions, seismically induced sliding of gravity dams is better correlated with PGVs than it is with PGAs. This output is not very surprising because, although widely used by engineers, it is recognized for decades that the PGA is a poor intensity measure of seismic input motions. This is once more confirmed. In this regard, it is worth mentioning that the PGA will not be anymore the anchoring parameter of the seismic action in the Eurocode 8 of next generation [11]. In place of it, there will be two anchoring parameters: the spectrum plateau value and the spectral acceleration at 1 Hz. This is a step forward in the direction of better physics-driven standards.

Even when selecting the PGV as intensity measure, there is still a significant dispersion of seismically induced sliding. An output of this research is that this dispersion is log-normally distributed, what enables to derive, for a given PGV, sliding values associated to a given probability of not being exceeded. For instance, for a 150 m high dam with a 0.8 downstream face slope and a 0.6 equivalent friction coefficient at the base, the sliding value with 84% probability of not being exceeded is evaluated at 6.61 cm under a 0.2 m/s input PGV. However, this result is an output of time response analysis of the dam model submitted to the set of 100 seismic input motions, out of which a mean and a standard deviation of sliding values are extracted (exemplified in Table 2).

The next step in this research is to propose a predicting method that provides evaluation of the mean and standard deviation of sliding (exemplified in Table 3), based on dam configuration features: height (converted into dam first eigenfrequency), downstream face slope, and equivalent friction coefficient at the base. This approach gives the best estimate sliding for a

given configuration and a given PGV. It is applicable to any dam configuration that interpolates among the 72 configurations considered in this research. It is also possible to increase the confidence of non-exceedance of the predicted sliding value.

Perspectives of this research are as follows:

- An effect of the European context considered so far is that we dealt with input motions that are characterized by i) relatively high frequency content resulting in relatively low PGVs, and ii) rather short strong motion durations. Enlarging the scope of the approach would require that stronger and longer seismic input motions be considered. Likely strong motion duration would play an augmented role in regression analysis.
- The effect of the vertical component of the seismic input motion has been so far disregarded. Taking it into consideration should result in increased sliding values, as already pointed by Chopra & Zhang [4].
- Although it is partly a consequence of the inherent complexity of lognormal distributions, the proposed predictive approach looks somehow convoluted. It should be possible to develop a more straightforward and easier-to-handle procedure, and to control the confidence in non-exceedance of the predicted sliding values.

REFERENCES

[1] ICOLD European Club. 2004. Working group on sliding safety of existing gravity dams. Final report. Ruggieri G. coordinator.

[2] Newmark N.M. 1965. Effects of earthquakes on dams and embankments. Fifth Rankine Lecture. Géotechnique. 15 (2): 139–160. DOI:10.1680/geot.1965.15.2.139.

[3] Léger P. & Katsouli M. (1989). Seismic stability of concrete gravity dams. Earthquake Engineering and Structural Dynamics, vol. 18, Issue 6.

[4] Chopra A.K. & Zhang L. 1991. Base sliding response of concrete gravity dams to earthquakes. Report UCB/EERC 91/05.

[5] Mir R.A. & Taylor C.A. 1996. An investigation into the base sliding response of rigid concrete gravity dams to dynamic loading. Earthquake Eng. and Structural Dynamics, vol. 25.

[6] Basili M. & Nuti C. 2011. A Simplified Procedure for Base Sliding Evaluation of Concrete Gravity Dams under Seismic Action. International Scholarly Research Network, ISRN Civil Engineering. doi:10.5402/2011/413057.

[7] Mével S. & Robbe E. 2018. Comportement au séisme des barrages en béton – Synthèse de la collaboration CFBR-JCOLD et proposition d'une méthode numérique d'évaluation simplifiée. 26th ICOLD Conference, Q101-R35, Vienna.

[8] Akkar S., Sandıkkaya M.A., Şenyurt M., Azari Sisi A., Ay B.Ö., Traversa P., Douglas J., Cotton F., Luzi L., Hernandez B., Godey S. 2013. Reference database for seismic ground-motion in Europe (RESORCE), BEE, DOI: 10.1007/s10518-013-9506-8. http://link.springer.com/article/10.1007/s10518-013-9506-8

[9] Schleiss A. & Pougatsch H. 2011. Les Barrages, du projet à la mise en service, Traité de Génie Civil. Vol.17. Lausanne: EPFL.

[10] Westergaard H.M. 1933. Water pressure on dams during earthquakes. Transactions of A.S.C.E. Vol. 98-2.

[11] Labbé P. & Paolucci R. 2022. Developments relating to seismic action in the Eurocode 8 of next generation. In Progresses in European Earthquake Engineering and Seismology, 3rd European Conf. Earthquake Eng. and Seismology – Bucharest, 2022: Springer.

[12] Arias, A. (1970). A measure of earthquake intensity. In: Seismic design for nuclear power plants, R.J. Hanson, Editor, MIT Press, Cambridge, MA , 438–489.

[13] Reed, J. W., and Kassawara, R. P., (1990). A criterion for determining exceedance of the Operating Basis Earthquake. Nucl. Eng. Des. 123, 387–396.

[14] Labbé, P., (2023). Statistical analysis of seismically induced sliding of gravity dams in European context. 91st Annual ICOLD Meeting – Gothenburg 13-14 June.

APPENDIX

a is a lognormally distributed random variable, of mean $\overline{a}$ and standard deviation σ_a. $y = \ln a$ is normally distributed, of mean $\overline{y}$ and standard deviation σ_y. Formulas (11) provide $\overline{y}$ and σ_y versus $\overline{a}$ and σ_a. In addition, the median value of a, a_0, is such that $a_0 = e^{\overline{y}}$.

$$\overline{y} = \ln \frac{\overline{a}}{\sqrt{c^2+1}};\ \sigma_y = \sqrt{\ln(c^2+1)}\ ;\text{with } c = \frac{\sigma_a}{\overline{a}} \tag{11}$$

$F_a(x)$ being the repartition function of a, it reads as per Formula (12).

$$F_a(x) = \Psi\left[\frac{\ln x - \overline{y}}{\sigma_y}\right], \text{with } \Psi(u) = \frac{1}{\sqrt{2\pi}}\int_{-\infty}^{u} e^{-\frac{t^2}{2}}\,dt \tag{12}$$

Fifth International
Dam World Conference
PORTUGAL • LISBON • LNEC • APRIL 13-17, 2025
dam world 2025

ANALYSIS AND INTERPRETATION OF THE STRUCTURAL BEHAVIOUR OF DAIVÕES DAM DURING THE FIRST FILLING OF THE RESERVOIR

Carlos Serra[1]
National Laboratory for Civil Engineering (LNEC)

Juan Mata
National Laboratory for Civil Engineering (LNEC)

ABSTRACT

This paper describes the main characteristics of Daivões dam and the construction period, presents the most relevant monitoring data and the structural behaviour interpretation of Daivões dam during the reservoir's first filling, between October 2020 and March 2022.

The safety control and the interpretation of the dam's behaviour are based on: contraction joint movements, measured in jointmeters; planimetric (radial and tangential) displacements, measured through plumbline and geodetic methods; vertical displacements, measured through geometric levelling; rock mass foundation displacements, measured with rod extensometers; seepage and leakage measured through the drainage system; uplift pressure in the rock mass foundation, measured in piezometers; and temperatures and strains in the dam's body measured with embedded electrical resistance devices.

A three-dimensional finite element model was developed for the numerical simulation of the dam structural behaviour during the first filling of the reservoir. The hydrostatic load and the measured temperature in the dam's body were considered in the model. The dam's concrete delayed behaviour was assumed to be represented by the Bažant e Panula's basic creep function, evaluated from laboratory tests.

Keywords: Daivões dam, reservoir first filling, monitoring activities, structural behaviour interpretation.

[1]cserra@lnec.pt, Portugal

1. INTRODUCTION

The failure of large dams can lead to disastrous incidents resulting in significant loss of human lives and severe economic and environmental damage. Consequently, safety monitoring for these structures is commonly governed and supervised by national organisations worldwide, typically with expert technical guidance. The safety oversight of these projects encompasses structural, hydraulic-operational, and environmental factors.

The structural safety concerns of major projects initiate during the design stage and continues until the dam is decommissioned. During and following the initial filling of the reservoir, this oversight relies on ongoing analysis and comparison between monitoring data collected from various instruments, alongside outcomes from models, typically numerical, reflecting key features of the structures like geometry and material properties.

Since the first filling of the reservoir acts as an initial load test of the structures under authentic operating conditions, safety monitoring during this phase is crucial not just for preventing accidents and incidents, but also for gaining insights into the dam's structural behaviour. The safety regulations in most developed nations stipulate distinct monitoring programs during this phase, involving both the owner and national agencies responsible for dam safety oversight, which in Portugal include the Portuguese Environment Agency (APA) and the National Laboratory for Civil Engineering (LNEC) [1].

This paper, in addition to describing the main aspects of the design and construction of the dam, with a special focus on structural safety observation and control activities, presents the assessment of the observation carried out, using the support of a numerical finite element model.

2. BRIEF DESCRIPTION OF THE PROJECT

The Daivões dam is part of the Daivões hydroelectric plant, which is located on the Tâmega River, a right-bank tributary of the Douro River, in Entre-os-Rios, between the Carrapatelo and Crestuma Lever dams. This development, which is part of the Tâmega Electric Production System, includes, in addition to the dam, two independent underground hydraulic circuits on the slope of the right bank and a semi-buried plant downstream. The dam, with abutments in the municipality of Cabeceiras de Basto, district of Braga (right bank), and in the municipality of Ribeira de Pena, district of Vila Real (left bank), is located approximately 80 km upstream of the confluence with the Douro river and approximately 3.5 km upstream from the road bridge that connects the districts of Braga and Vila Real, via the N206 national road, in the parish of

Cavez. Its reservoir extends to the municipalities of Vila Pouca de Aguiar and Boticas, with a total volume of around 55.5 hm^3, for the full storage level (FSL = 228.0 m).

The dam has a maximum height above the foundation of 77.5 m, measured between the lowest average plane of the insertion surface, at elevation 153.5 m, and the crowning floor, at elevation 231.0 m (Fig. 1). It is a conventional concrete structure, of the gravity arch type, with a vertical upstream facing and a downstream facing with a slope of 1V:0.5H up to a level of 222.25 m and vertical above this level. The crest has a width of 8.30 m and a total length of 265.0 m and 190.0 m between abutments. The geometric definition of the dam is based on circular arcs, with a reference surface having curvature radii of 140 m in the central section and 210 m in the lateral areas.

The dam is made up of 16 blocks, separated by vertical contraction joints, approximately 13.80 m to 18.30 m apart on the right bank (blocks B12 to B16), approximately 15.85 m in the central area (blocks B1 to B11) and from around 18.25 m to 18.95 m on the left bank (blocks B13 and B15). The construction of the dam took place between April 2018 and September 2020.

Fig. 1 – Daivões dam

3. MONITORING AND FIRST FILLING PLANS

Under Portuguese dam safety regulations, the monitoring plan is a binding document that supports the structural safety control of dams and rules all the activities related to safety control, including instruments and methodologies that allow the characterisation of the actions, the material properties and the structural responses.

In the case of the Daivões dam, it is recommended that the observation of most of the quantities foreseen for monitoring the actions and responses of dams be considered [2, 3]. Thus, the observation of the following quantities was planned: i) air temperature and humidity; ii) reservoir water level; iii) concrete temperatures; iv) relative displacements in contraction joints (Fig. 2); v) absolute and relative displacements (Fig. 3); vi) strains in concrete; vii) uplifts (Fig. 4); and viii) seepage and leakage (Fig. 4). Given the specificities of geodetic observation systems, a geodetic observation plan [4] was developed, which defines the characteristics of the system and the methods to be used to determine displacements.

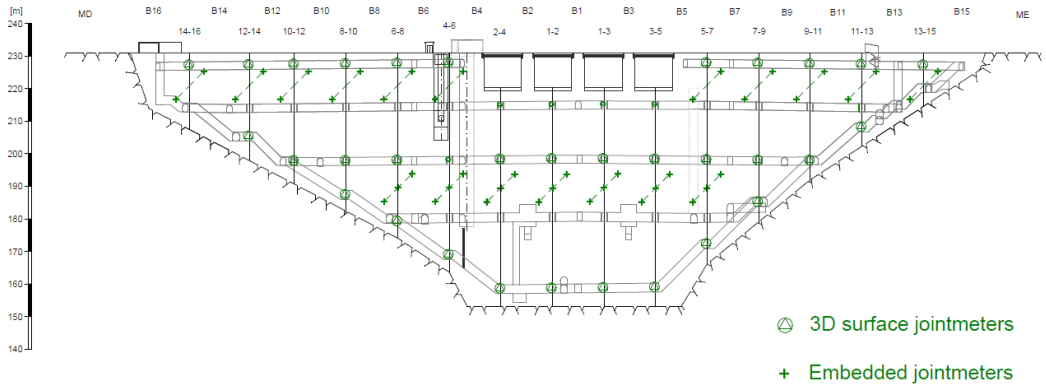

Fig. 2 – Dam monitoring system – Embedded jointmeters and 3D surface jointmeters

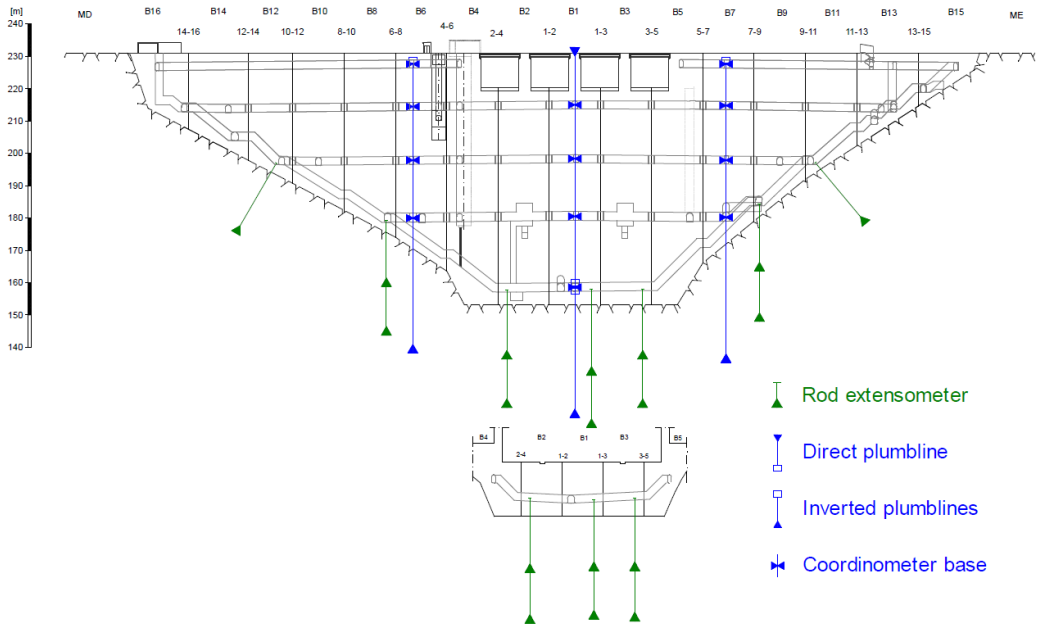

Fig. 3 – Dam monitoring system – Plumblines and rod extensometers

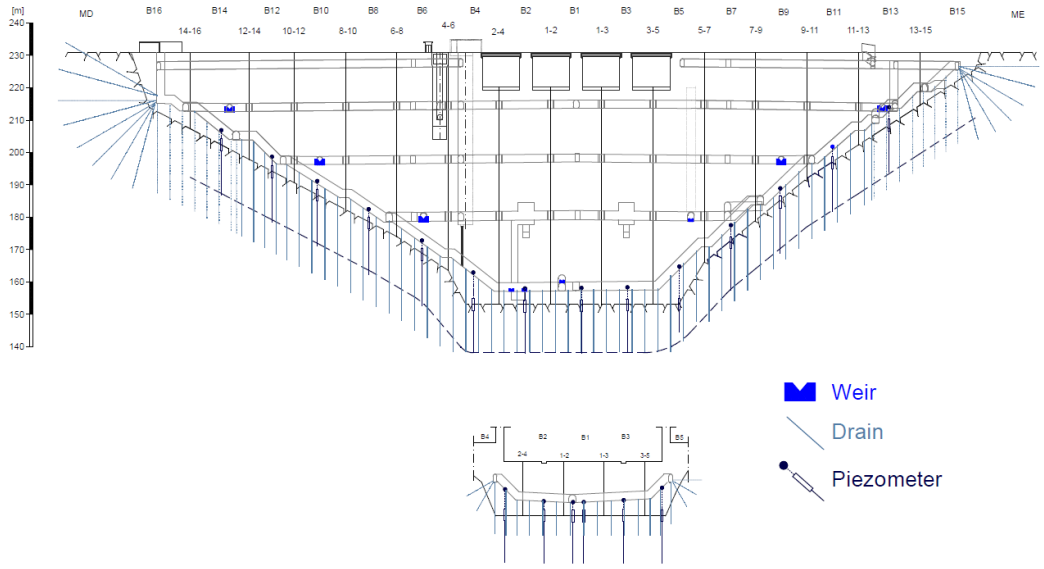

Fig. 4 – Dam monitoring system – Drainage system and piezometers

The stabilization thresholds and levels for the first filling of the Daivões dam reservoir were defined in the First Filling Plan. The plan included five observation levels (P) and a stabilization level (NE), namely, P1, P2, P3, NE1, P4 and P5-FSL, establishing that safety conditions would be assessed at the observation levels based on complete observation campaigns and visual inspections. At each of the stabilization thresholds or levels, it was established that the reservoir level would be maintained for a minimum period of 7 days, with constant hydraulic load, in order to allow the stabilization of the dam's behaviour and the execution of observation campaigns.

4. FOUNDATION AND CONCRETE PROPERTIES

4.1. Dam foundation properties

The rock mass foundation comprises two-mica granites, medium-grained and medium-to-coarse-grained. On each bank, 4 families of approximately vertical discontinuities and 2 families associated with slope decompression phenomena were identified. The rock mass foundation appears altered and fractured superficially, decreasing the degrees of alteration and fracture with depth, although differently along the insertion. Local observation, execution of surveys and field and laboratory tests were carried out to characterize the rock mass foundation, considering conventions defined by the International Society for Rock Mechanics (ISRM) [5].

Fig. 5 represents the geomechanical zoning of the foundation mass in which four zones were considered, with modulus of deformation ranging from 0.5 to 20 GPa. The rock mass presents low modules of deformability in the surface areas of the slope on the right bank and in the

upper area of the slope on the left bank. The areas with the highest modulus of deformation are the bottom of the valley and the lower and intermediate sections of the left bank slope.

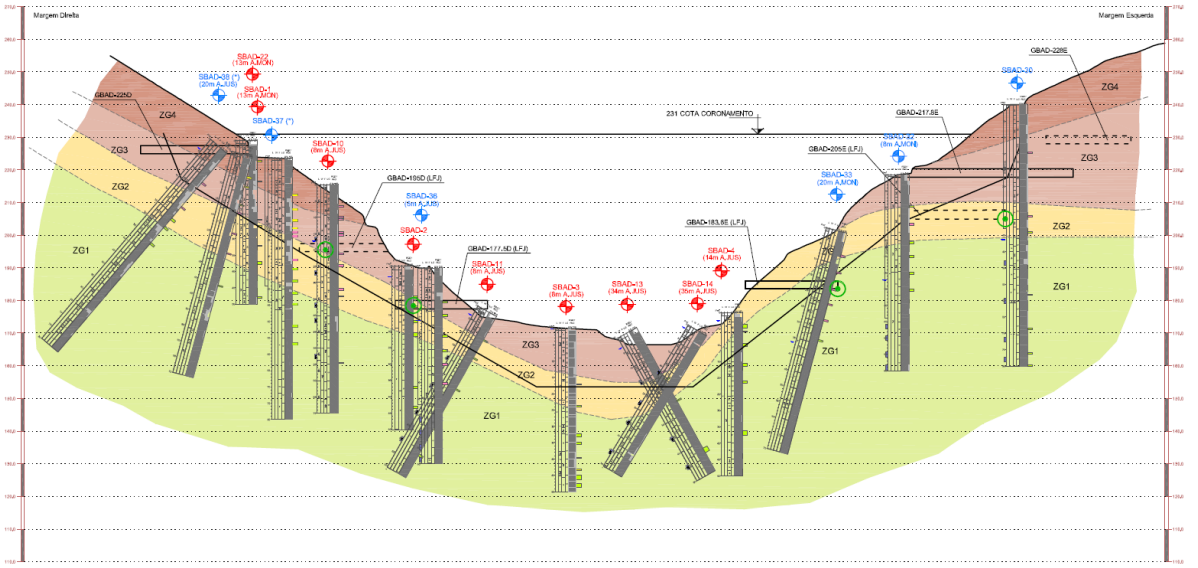

Geomechanical zoning	Meterioration degree	Fracture degree	Rock quality designation RQD (%)
ZG4	W4-5	F5	0-60
ZG3	W3-2	F3 a F4 (F5, F2)*	40-100
ZG2	W2	F2 a F1 (F4, F5)*	70-100
ZG1	W1	F1 a F2 (F4, F5)*	100 (10-90%)*

Fig. 5 – Geomechanical zoning of the foundation rock mass (view from downstream) [6]

4.2. Dam concrete properties

The concrete of Daivões dam used VLH IV/B (V) 22.5 cement, which incorporates c.a. 45% of its mass in fly ash. The aggregates used in the concrete are granitic. The fine aggregates were divided into two classes, 0/1.2 mm and 1.2/5 mm, and the coarse aggregates were divided into four classes: 5/15 mm, 15/30 mm, 30/70 mm, and 70/150 mm. The admixture Muraplast FK 88i was used as a plasticizer.

The experimental work was focused on the characterisation of the deformability properties of both the dam core concrete (DAM150) and the concrete wet-screened through a 38 mm sieve (SCR38), which was obtained from the previous one. Table 1 shows the values related to the particle size distribution of the aggregates used in the dam and screened concretes. The composition of the SCR38 was estimated from the dosages of the DAM150 by removing the approximate volumes of aggregates larger than 38 mm and the volume of the surrounding mortar lost during the screening process [7]. Table 2 shows the compositions of the two types of concrete and their main proportions by mass. Note that c.a. 3/4 of the added water corresponds to ice, and the aggregates were pre-cooled.

Table 1 – Particle size distribution of the aggregates used in the dam concrete (DAM150) and in the respective screened concrete (SCR38)

Concrete type	Fine aggregate (kg/m³)		Coarse aggregate (kg/m³)				
	0/1.2 mm	1.2/5 mm	5/15 mm	15/30 mm	30/38 mm	38/70 mm	70/150 mm
DAM150	305.3	270.2	312.1	385.3	480.1		496.9
SCR38†	423.7	367.9	495.6	611.8	152.3	-	-

† Estimated value

Table 2 – Dosages of the dam concrete (DAM150) and the respective screened concrete (SCR38)

Type of concrete	Cement VLH IV B (V) (kg/m³)	Added water (kg/m³)	Aggregate water (kg/m³)	Total water (kg/m³)	Additive (Muraplast FK 88i) (kg/m³)	Fine aggregate (kg/m³)	Coarse aggregate (kg/m³)	Water-binder ratio
DAM150	180.0	88.5	14.9	103.4	1.7	575.5	1676.1	0.57
SCR38†	251.9	127.4	23.6	151.0	2.5	790.8	1262.2	0.60

† Estimated value

The obtained values of modulus of elasticity reveal greater stiffness of the screened concrete in relation to the integral one (Fig. 6), despite the latter's higher aggregate dosages. This result may be related to the higher binder dosage in screened concrete and the better compaction conditions that screened concrete allows (Table 2). It should be mentioned that the average values of compressive strength at 90 days of age, which were 26.9 MPa and 31.5 MPa in the tests of cylindrical specimens of integral concrete ϕ30×44 cm and of cylindrical specimens of screened concrete ϕ15 ×30 cm, are greater than the characteristic value of 22 MPa defined in the project. For one-year-old concrete, these values reach 36.5 MPa and 45.3 MPa (Fig. 7).

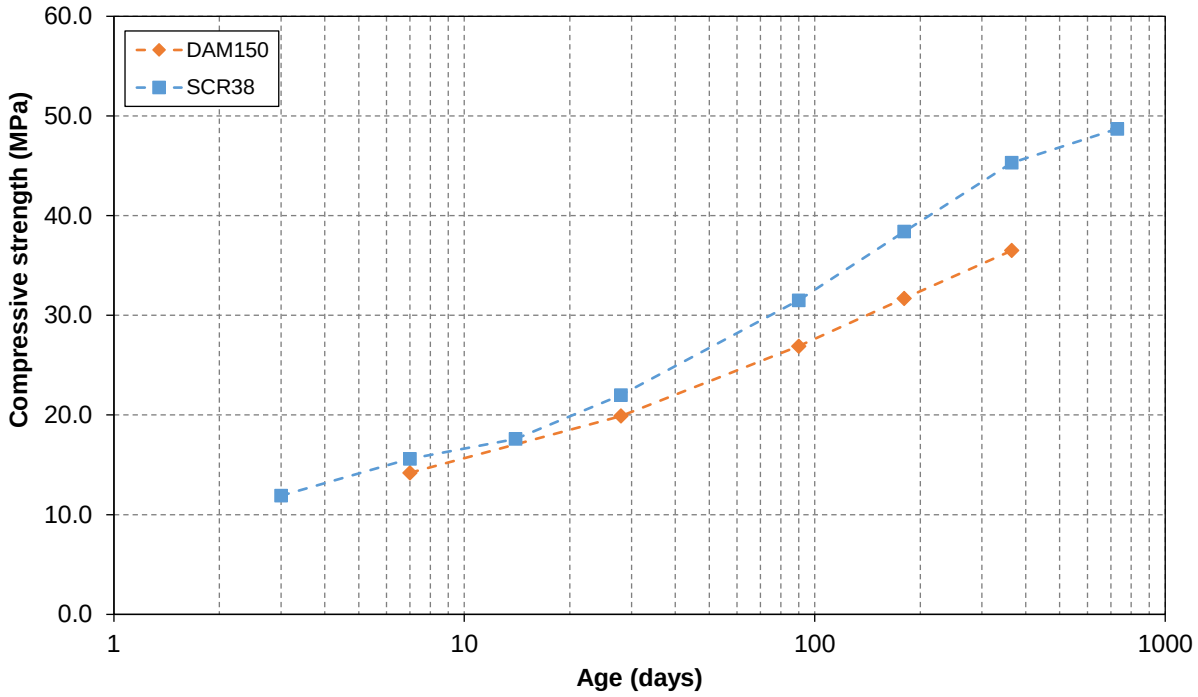

Fig. 6 – Evolution of the modulus of elasticity estimated from laboratory tests for quality control

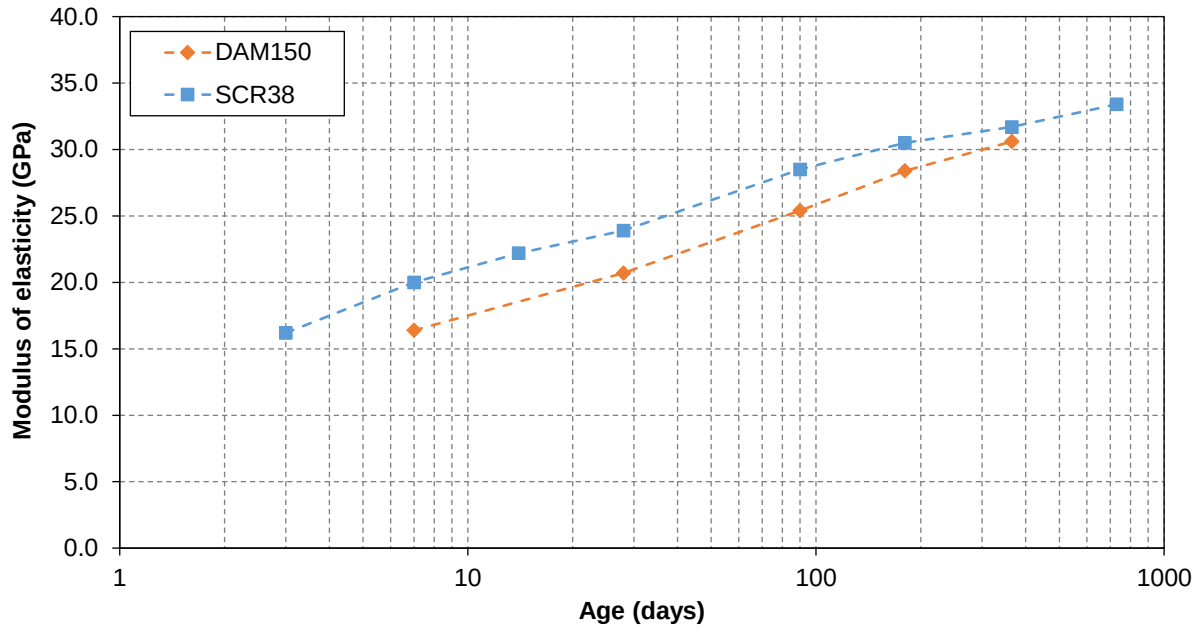

Fig. 7 – Evolution of compressive strength obtained from cylinders in the laboratory tests for quality control

5. ANALYSIS AND INTERPRETATION OF THE OBSERVED BEHAVIOUR

5.1. Structural model

The interpretation of the dam's behaviour was based on the results of a three-dimensional structural model representing the dam and its foundation (Fig. 8). The model was analysed by the finite element method, using 20-noded isoparametric brick elements with second-degree shape functions, with homogeneous and isotropic properties.

The foundation was divided into two regions of different deformability: the upper areas in both banks and the bottom of the valley and in depth. The dam was divided into several regions according to the date on which the concrete was placed, between May 2018 and January 2020.

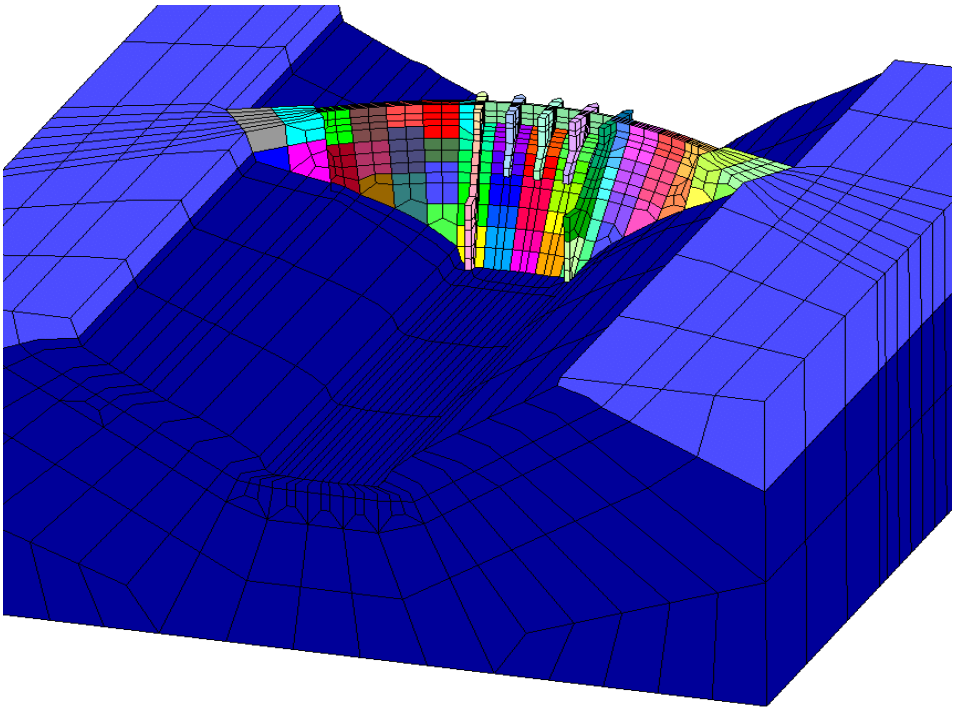

Fig. 8 – Representation of the finite element mesh of the dam-foundation set, considering the zoning of the dam and the rock mass foundation

The rock mass foundation was assumed to be an elastic behaviour and the concrete was assumed to be a viscoelastic material, whose deformability was characterised by equation 1. The main parameters considered for the material properties are presented in Table 3.

Poisson's ratio (ν) was considered equal to 0.20 for the dam concrete and the foundation mass.

Based on the temperatures and strains observed in the correcting strain gauges installed in the dam, a linear thermal expansion coefficient (α) equal to 1.0×10^{-5} $^{o}C^{-1}$ was obtained for the structural concrete.

Table 3 – Material properties considered in the finite element model

Type of material	E (GPa)	ν (-)	α (1/ºC)
Dam concrete	(Eq. 2)	0.2	1.0×10^{-5}
Superficial at elevated ground	12	0.2	0
Right bank and bottom of the valley	18		

Both the hydrostatic load on the upstream face of the dam and the time history of the observed temperatures within the dam's body were taken into account. To consider the delayed effects related to creep and relaxation, each one of these loads was discretized over time.

Regarding the boundary conditions, displacements were restrained in the outer borders of the foundation.

Creep prediction models are associated with functions that have specific characteristics, chosen to represent the physical phenomenon of concrete creep. The parameters of these functions, typically determined from known material properties and, when available, adjusted to experimental test results, provide an estimate of creep strain values within certain assumptions. In the Bažant and Panula (BaP) model [8], the creep function, $J(t, t_0)$, is given by the sum of the elastic component, $1/E_0$, basic creep, $C_0(t, t_0)$, and drying creep, $C_d(t, t_0, t')$. One of the distinctive aspects of this formulation is the consideration of the concrete's maturation process in the basic creep component by multiplying the power of the age at loading, t_0, by the power of the time under load, $t-t_0$.

The creep function coefficients were adjusted to the results of tests carried out in the laboratory with screened concrete, Equation (1). Fig. 9 and Fig. 10 present, respectively, the adjustment of the creep function to the experimental results of specific extension and the experimental results of elastic modulus obtained in the laboratory tests.

$$J(t,t_0) = \frac{1}{E_0} + \frac{\phi_1}{E_0}(t_0^{-m} + \alpha)(t - t_0)^n = \frac{1}{34.3} + \frac{4.04}{34.3}(t_0^{-0.42} + 0.00)(t - t_0)^{0.11} \quad (GPa^{-1}) \qquad (1)$$

The prediction of the elasticity modulus over time can be obtained by considering the time under load, $t-t_0$, as equal to 0.1 days,

$$\frac{1}{E(t_0)} = \frac{1}{E_0} + \frac{\phi_1}{E_0}10^{-n}(t_0^{-m} + \alpha) = \frac{1}{34.3} + \frac{4.04}{34.3}10^{-0.11}(t_0^{-0.42} + 0.00) \quad (GPa^{-1}) \qquad (2)$$

where E_0, φ_1, m, α e n are parameters dependent on the intrinsic characteristics of the concrete. Since, in the case of dams, the concrete does not, in practice, lose water to the

outside, the drying creep component may be considered negligible compared to the basic creep values.

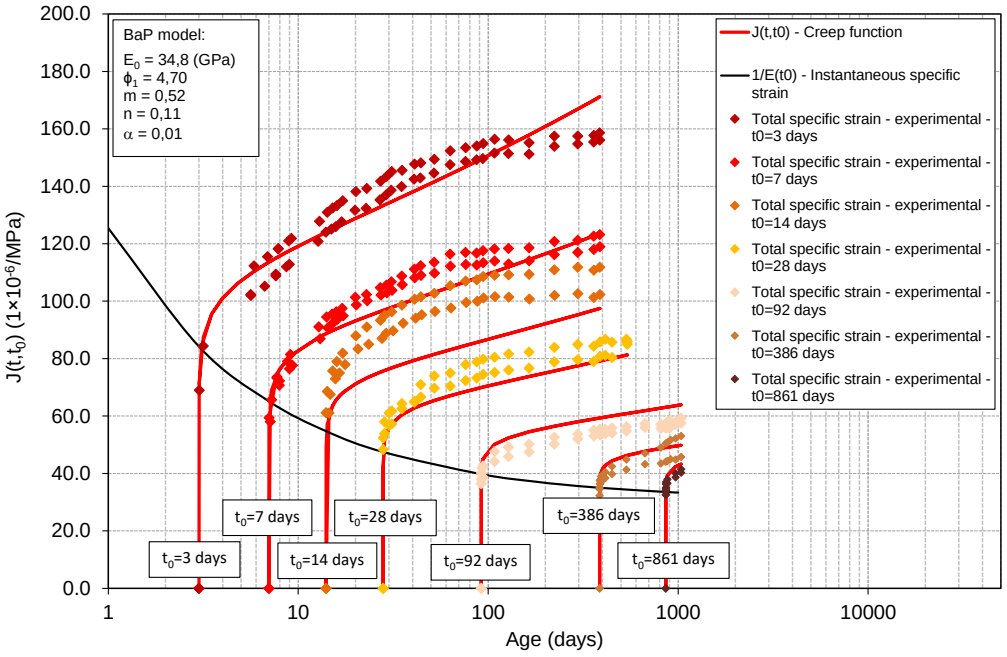

Fig. 9 – Representation of the creep function fitted from specific strains obtained experimentally for various loading ages

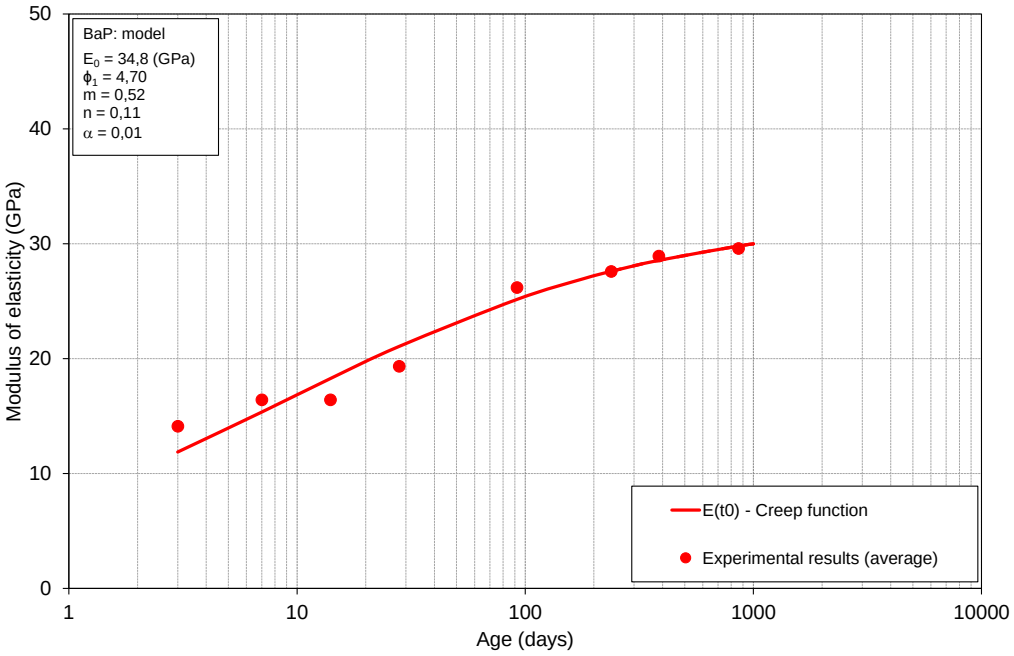

Fig. 10 – Evolution of modulus of elasticity obtained from experimental tests and from the creep function adopted

5.2. Evolution of the main actions

The main actions during the first filling of the reservoir are the hydrostatic pressure on the upstream face of the dam and the temperature variations measured within the dam's body.

Fig. 11 shows the reservoir water level evolution, as well as the daily level change rate and the accumulated daily precipitation measured at the meteorological station. The water level rose rapidly in February 2021 due to an intense period of rain. After that, the level rose gradually, considering all the predefined levels for safety control assessment, as defined in the first filling plan.

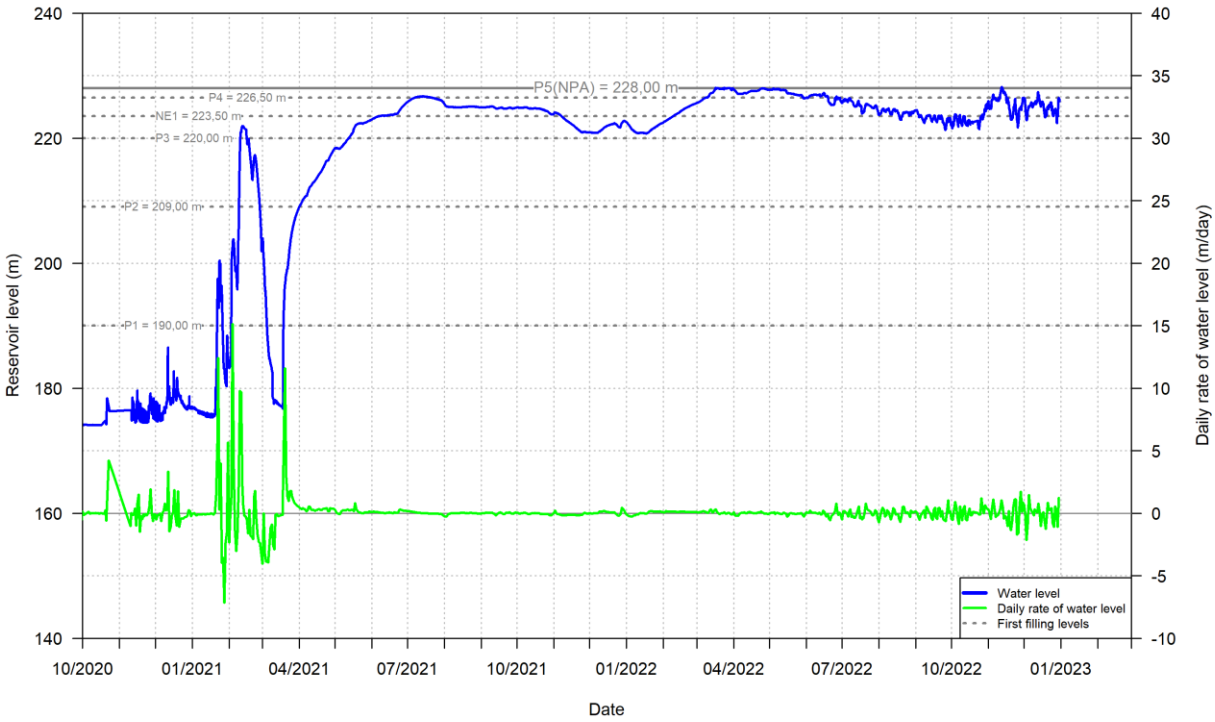

Fig. 11 – Reservoir level and daily level rate

The hydrostatic pressure on the upstream face of the dam was simulated considering a specific weight of 10 kN/m^3 for the water. The effects of uplift in the insertion between the dam and the foundation, and the hydrostatic pressure downstream, were not considered. The hydrostatic pressure in the gates was transmitted along the height of the pillars, at the intersection between the gates and the pillars in the spillway area.

The temperature variations considered in the finite element model were estimated from the temperatures observed in thermometers and electrical resistance strain gauges embedded in the dam body, considering the predominant thermal flow in the radial direction and using an interpolation method in the thickness of the dam and along reference planes. Fig. 12 shows the isothermals calculated on some key dates during the reservoir filling.

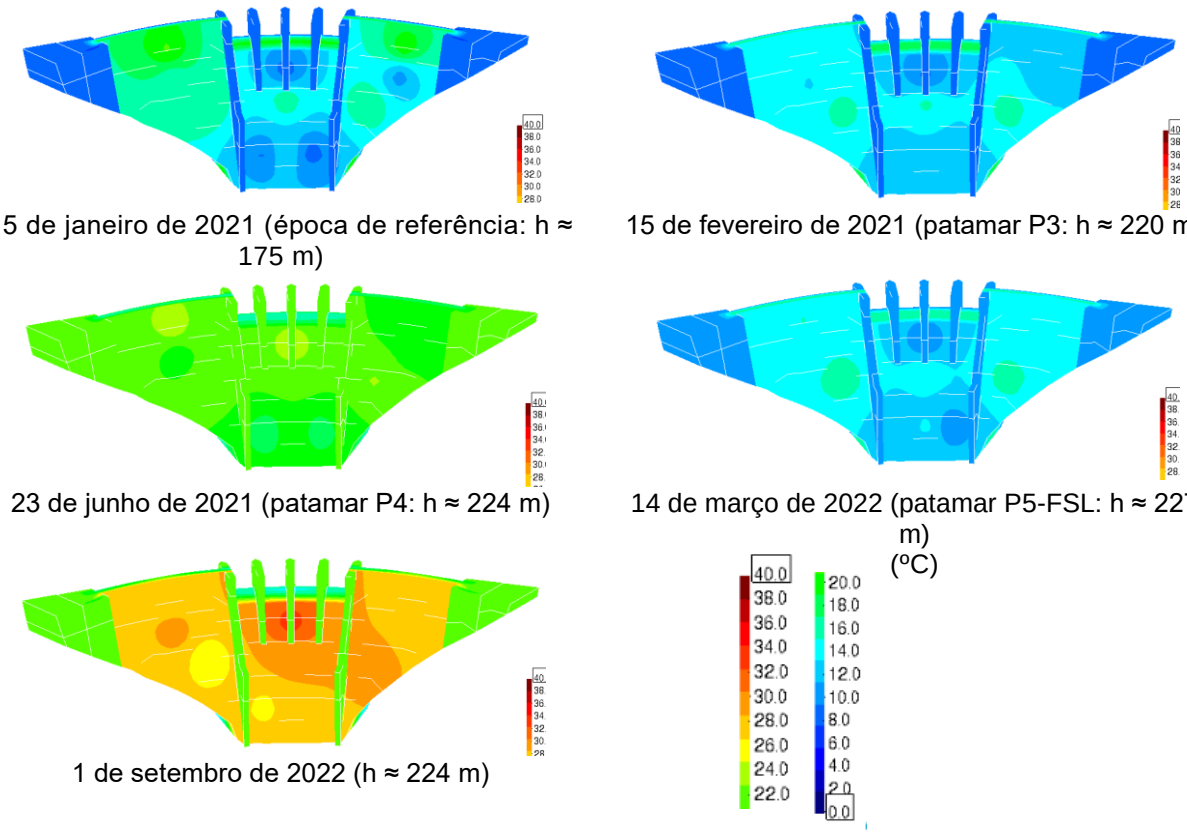

Fig. 12 – Calculated thermal field in the dam body on different dates during the first filling of the reservoir

5.3. Joint movements

Joint movements are generally small and are correlated with temperature variations in the dam body and the reservoir water level, with the greatest variations being observed in joints at higher elevations, close to the abutments. From the second half of March 2021 until the beginning of July 2021, coinciding with the refilling of the reservoir and the temperature increase of the dam body, movements were observed towards the closure of the joints. Between July 2021 and mid-January 2022, there were minor movements towards closing the joints followed by movements towards opening compatible with variations in concrete temperature. Between the second half of January and March 2022, the increase in the reservoir level up to the FSL contributed to movements towards the closure of the joints, so that the effects of level and temperature (with opposite directions) led to small movements (Fig. 13).

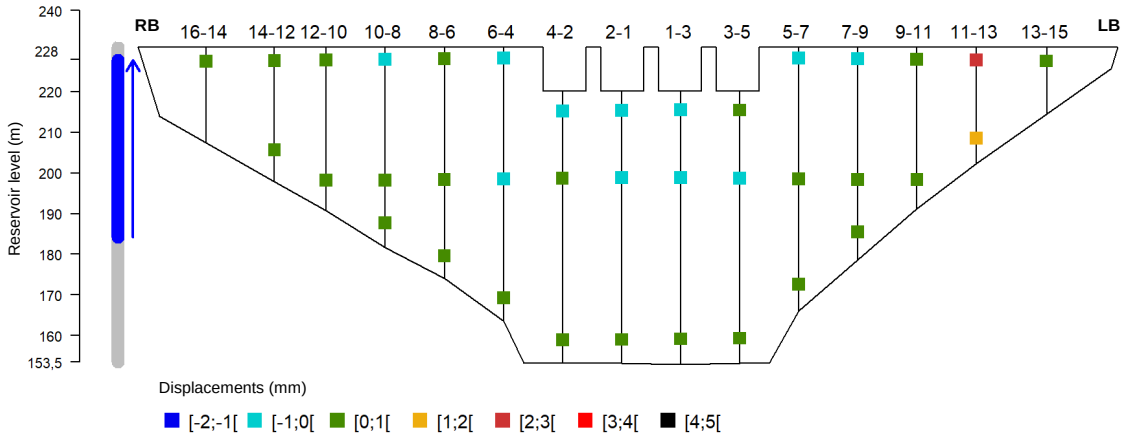

Fig. 13 – Opening and closing movements observed in 3D surface jointmeters on 03/16/2022 (P5-FSL level, h = 228 m)

5.4. Horizontal displacements

The radial and tangential displacements observed in various coordinometer bases of the central plumb line are presented (Fig. 14, the vertical dashed line corresponds to the reference date used in this analysis, January 15, 2021). The sign convention determines that positive values correspond to radial displacements towards the upstream and tangential displacements towards the left bank.

The numerical model confirms the pattern of observed behaviour, for the combined effect of the reservoir level and the temperature variations of the dam concrete. In general, the calculated results are like the results observed at the points located at the highest elevations (227 m and 231 m) and at the lowest elevations (214 m), for the plumb lines on the right bank side, central block and on the left bank side. Fig. 15 shows an example of the comparison between observed and calculated displacements at the highest elevation in the central block and the magnitude of each effect over time, namely, the hydrostatic pressure and the temperature variations.

The separation of the effects of water level and temperature highlights the magnitude of the displacements for each of these actions. At the upper level of the central zone of the dam (block B1, level 231 m), the maximum radial displacements due to the action of water upstream were around 10 mm downstream, in March 2022 with the FSL level, while the displacements Maximum radial values due to thermal action were about 10 mm upstream, estimated during the last warm season, in September 2022.

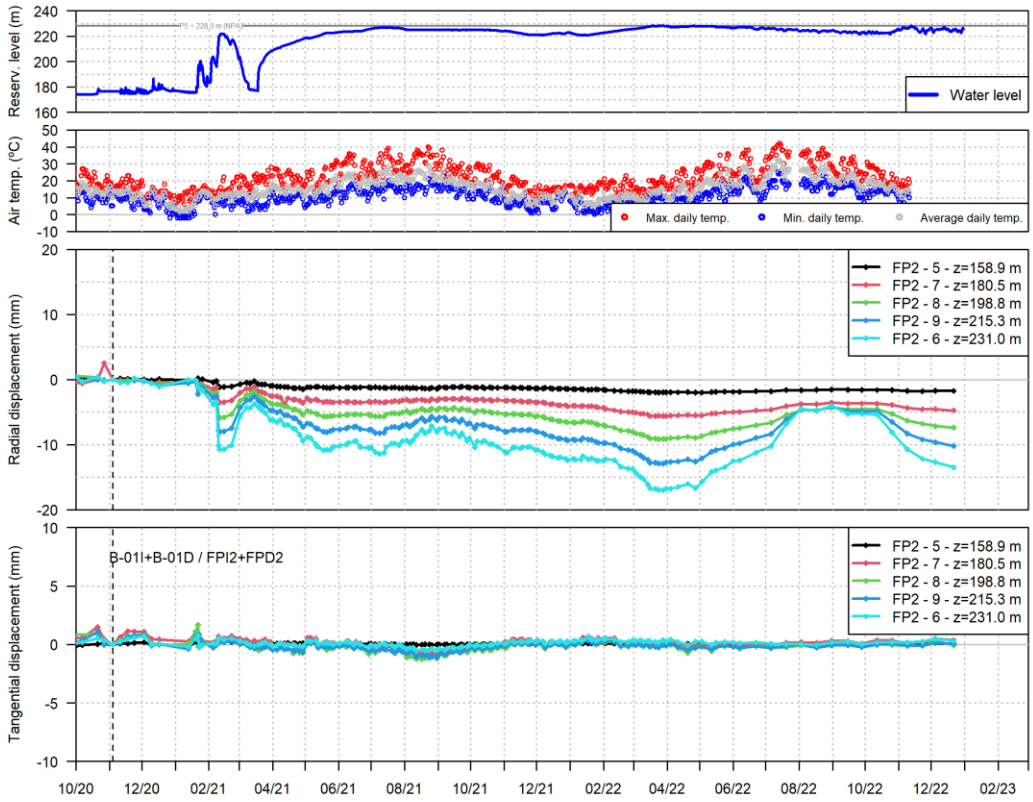

Fig. 14 – Radial and tangential displacements observed in plumb lines B-01I and B-01D / FPI2 and FPD2, located in block B1

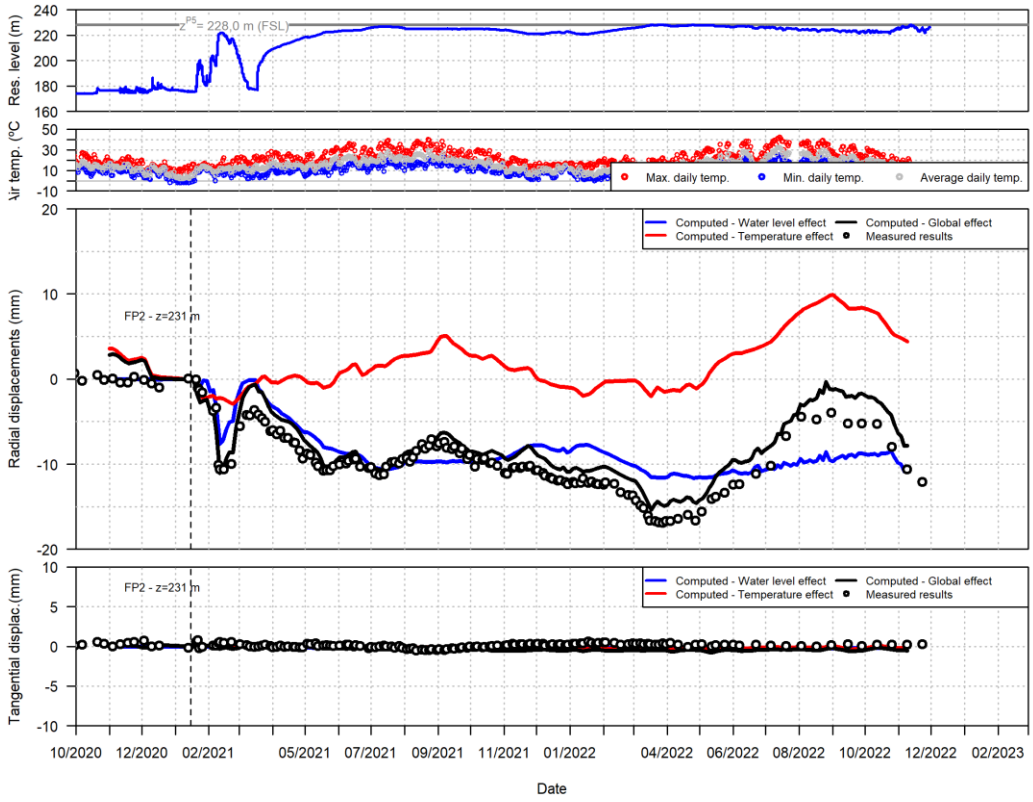

Fig. 15 – Comparison of the calculated and observed radial and tangential displacements at elevation 231 m on the FP2 plumb line, in block B1

5.5. Vertical displacements

A comparison is presented between the results obtained with the numerical model and the results of observation in rod extensometers located in the foundation, in the main drainage gallery and in the downstream gallery (Fig. 16). The sign convention determines that positive values correspond to bulging of the foundation mass and that negative values correspond to settlements of the foundation mass.

The results show a good agreement between the vertical displacements calculated with the model and the vertical displacements, considering the order of magnitude of the values (less than 1.5 mm). It is noted that the numerical model used considers the rock mass as an equivalent continuous elastic medium, and does not consider the non-linear displacements that may occur in the foundation.

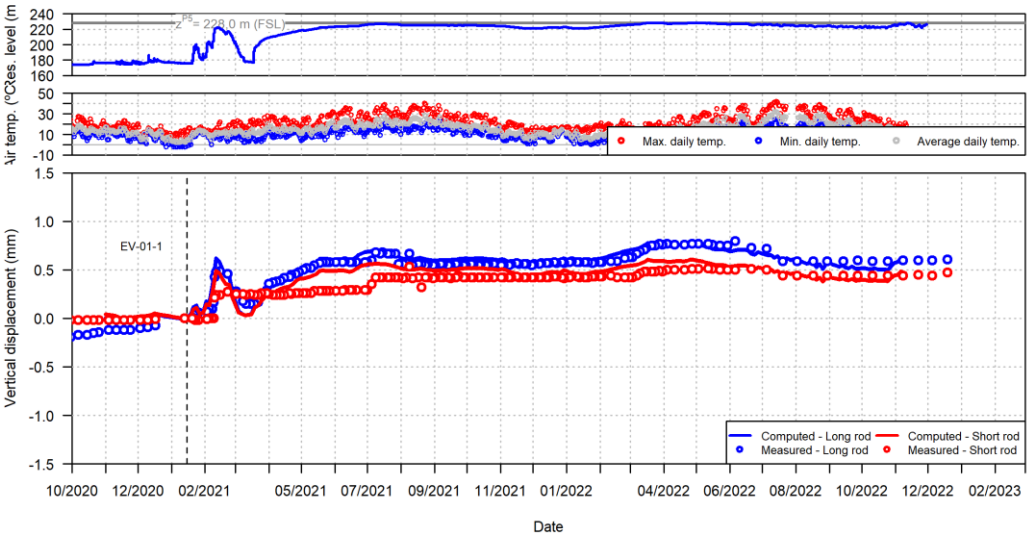

Fig. 16 – Comparison of vertical displacements calculated with the finite element model and those observed in the rod extensometer EV-01-1, located in the drainage gallery - block B1

5.6. Hydraulic behaviour of the foundation

Flows into the drainage network showed reduced values in all drains until February 2022, a date from which some drains recorded significant increases in flow, a unique situation that was monitored by increasing the frequency of measurements (Fig. 17). It was observed that a specific drain registered an increase in flow directly related to the increase in level up to the FSL, reaching a maximum of 53.9 l/min on March 18, 2022, with the level at 228 m. On this date, the average value of the drained flow in blocks B6 and B8 was 16.3 l/min and 5.9 l/min, respectively, which correspond to acceptable values for the type of dam.

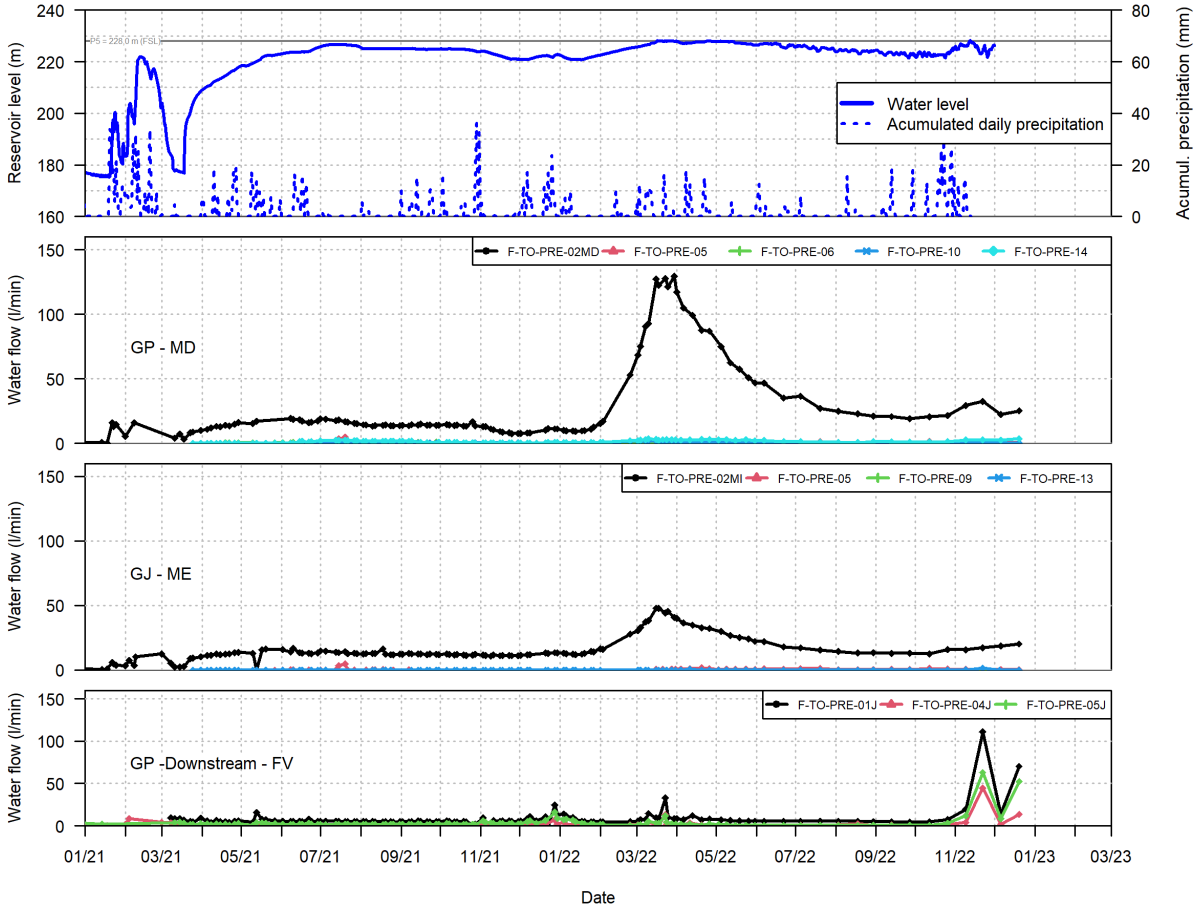

Fig. 17 – Total flows (drained and infiltrated) observed in weirs located in the drainage gallery, in the radial gallery and in the downstream gallery

Analysing globally the values of the piezometric levels observed along the drainage gallery between the months of February 2021 and March 2022, the uplifts present reduced values up to the P4 level, and from the level rise in February 2022 and with the transition to the cold season, usually associated with some decompression in the upstream area, the referred uplifts increased significantly. During the period of stabilisation of the level at the P5 level (FSL), there was stabilisation and even a slight reduction in the uplift values in the piezometers P-03-1 and P-04-1 (Fig. 18). The other piezometers showed low uplift, with percentages of hydraulic load appropriate to the type of work.

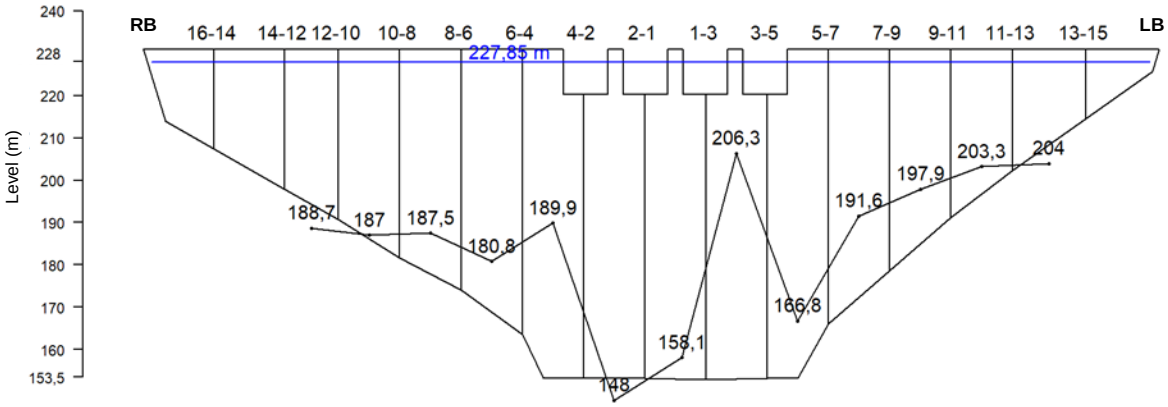

Fig. 18 – Piezometric elevations corresponding to the uplift observed in the drainage gallery on March 21, 2022, with the reservoir at approximately 228 m

6. CONCLUSIONS

The safety control of Daivões dam during the first filling of the reservoir required the installation and proper use of the instrumentation system, the complete characterisation of the main properties of the materials and the development of numerical models, whose results can validate the measured data.

In this paper, a brief description of the main results concerning the interpretation of Daivões dam behaviour during the first filling of its reservoir was presented. The numerical analysis of the structural behaviour of the dam shows that the observed response is well explained by the evolution of the main loads, considering the material's properties. Most of the devices of the monitoring system presented lower water flows and uplift pressures, indicating adequate hydraulic behaviour of the foundation. In summary, it can be concluded that the dam presented adequate structural and hydraulic behaviours.

The overall results obtained during this period represent a reference state that allows the characterisation of the dam's behaviour over time.

7. ACKNOWLEDGEMENTS

The authors acknowledge the Iberdrola, S.A. for permission to publish data relative to Daivões dam.

REFERENCES

[1] RSB (2018). Dam Safety Standard (in Portuguese). Decree-Law nº 21/2018, Diário da República. Lisbon.

[2] DTA (2018). Technical documents supporting dam safety standard (in Portuguese). Lisbon.

[3] LNEC (2011). Daivões Dam. Observation and first filling plans (in Portuguese). Report 53/2011 – NO. LNEC. Lisbon.

[4] LNEC (2020). Daivões Dam. Plan of the geodetic observation system (in Portuguese) . Report 203/2020 – DBB/NGA. LNEC. Lisbon.

[5] International Society for Rock Mechanics (1981). Basic geotechnical description of rock masses (BGD). International Journal of Rock Mechanics and Mining Sciences and Geomechanics. 18:1 (1981) 85–110.

[6] ATACI (2011). Daivões Hydroelectric Plan. Design (in Portuguese).

[7] Serra, C. (2017). Prediction of dam concrete structural properties based on wet-screened test results and mesoscale modelling. Faculdade de Ciências e Tecnologia. Universidade Nova de Lisboa, 2017, PhD Thesis, 368 p. Lisbon.

[8] Bažant, Z. P., and Osman, E. (1976). Double power law for basic creep of concrete. Materials and Structures (RILEM, Paris), 9(49), 3–11.

Fifth International Dam World Conference
PORTUGAL • LISBON • LNEC • APRIL 13-17, 2025
dam world 2025

CONTRIBUTIONS TO THE ANALYSIS OF THE EXOTHERMIC-MECHANICAL PHENOMENON IN MASS CONCRETE

Flávio Mamede P. Gomes[1]
ELETROBRAS

ABSTRACT

This paper aims to report on the advancements achieved by ELETROBRAS-FURNAS over the past 15 years in the field of mass concrete, encompassing laboratory tests, case studies of emblematic projects, and computational modeling developed within three R&D projects and during an incomplete Ph.D. at the University of Brasília (UnB).

The tests conducted by ELETROBRÁS-FURNAS, now discontinued due to the shift away from large-scale dam construction in Brazil, were part of a modernization and automation project worth reporting. Among the emblematic projects are the thermal analyses for the Santo Antônio Hydroelectric Plant (UHE Santo Antônio), which was the largest engineering project in Brazil at the time. Equally interesting and important were the thermal studies for the São Manoel Hydroelectric Plant (UHE São Manoel), Apiacás Hydroelectric Complex (CHE Apiacás), to name just the most recent ones.

In computational modeling, the state-of-the-art was achieved in thermo-chemical coupling, whether through adiabatic or isothermal formulation. The isothermal-adiabatic interconversion was introduced to support either formulation with any available calorimetric tests, whether isothermal, semi-adiabatic (Langavant), or adiabatic. Two finite element software programs (ANSYS and MULTIMECH) were customized with a viscoelastic aging model based directly on the concrete creep function, which was used to perform the mechanical analyses of these projects.

Finally, generalized analytical solutions were developed for the temperature field in typical situations such as infinite slabs/retaining walls, slabs on foundations, cylinders (test specimens and large diameter caissons), and cylinders with holes (post-cooling), considering a generic internal heat generation.

Keywords: mass concrete, viscoelasticity, aging, heat generation, calorimetry, modeling, finite elements, dams, creep.

[1] fmpgomes@eletrobras.com, Brazil

1. INTRODUCTION

The objective of this work is to report the developments achieved by Furnas in various research projects and services, encompassing laboratory testing, modeling, and monitoring of dam structures. The computational simulation behavior of mass concrete at the early-ages and the evaluation of cracking risk, particularly stress field analysis, are extremely challenging tasks. Two R&D projects (from 2012 to 2017) — one focused on modeling and optimizing mass concrete with the Federal University of Ceará (UFC), coordinated by Prof. Jorge Soares, and another about fiber-reinforced concrete, involving modeling, experimentation, and rheology with the University of São Paulo (USP), coordinated by Prof. Túlio Bittencourt — provided the context for the developments presented here. Subsequently, between 2014 and 2018, during a doctoral research project at the University of Brasília (UnB) under the supervision of Prof. Lineu José Pedroso, analytical-numerical validations of the exothermic phenomenon in concrete were achieved, enabling new insights into the problem, which will also be discussed later.

From the theoretical formulation of the thermal and mechanical problem to the finite element formulation and computational modeling of layered construction phasing, we believe we have achieved significant progress toward the state of the art. We explored two distinct but related formulations: the adiabatic and the isothermal formulations. The isothermal-adiabatic interconversion (and vice versa) was introduced to allow both formulations to be fed with experimental data from any calorimeter available, whether isothermal, semi-adiabatic (Langavant), or adiabatic. Two finite element programs (ANSYS and MULTIMECH) were customized with a viscoelastic aging model based directly on the creep function of concrete.

Among the landmark projects where the knowledge and tools developed in the R&D projects were applied, notable examples include the thermal and mechanical analyses for the Santo Antônio Hydroelectric Power Plant (UHE Santo Antônio), the largest engineering project in Brazil at the time. Equally interesting and important were the thermal studies for the São Manoel Hydroelectric Power Plant (UHE São Manoel), the Apiacás Hydroelectric Complex (CHE Apiacás), the Santa Cruz Thermoelectric Plant (UTE Santa Cruz), and the Fortim Wind Farm (EOL Fortim), to name just the most recent ones.

Experimental testing was conducted by ELETROBRÁS-FURNAS at the Goiânia Concrete Laboratory, which has been recognized for over 40 years for its excellence in civil engineering dedicated to dam construction. These efforts involved the development of numerous safety and automation improvements. Unfortunately, this activity has been discontinued due to the abandonment of large dam construction projects in Brazil.

2. FORMULATION

2.1. Thermal and Thermochemical Part

The internal heat generation rate is the source term ($\dot{\mathbb{Q}}$, [W/m³]) of the governing differential equation for the energy balance, which, for practical purposes, is presented here along with the constitutive equation for heat conduction (*Fourier's Law*), specified for isotropic materials:

$$\rho_e c_e = k\nabla^2 T + \dot{\mathbb{Q}} \tag{1}$$

where, ρ_e is the mass density of the material, c_e is the specific heat capacity, k is the thermal conductivity and T is the temperature of the material, which varies spatially and temporally. The source term can be expressed per kilogram of equivalent cement, $Q = \mathbb{Q}/C_{eq}$, or in terms of the *degree of hydration*, $\alpha = Q/Q_\infty$, where Q_∞ is the total heat per kilogram of equivalent cement. The *degree of hydration* α can be defined as a *measure of the progress of hydration*, being the rate of the degree of hydration like a function of both α itself and the temperature T.

$$\dot{\alpha} = f(\alpha) \cdot g(T) \tag{2}$$

The rate of the degree of hydration can also be described as:

$$\frac{d\alpha}{dt} = \frac{d\alpha}{dt_{eq}} \cdot \frac{dt_{eq}}{dt} \tag{3}$$

where, by comparison:, $d\alpha/dt_{eq} = f(\alpha)$ and $dt_{eq}/dt = g(T)$.

2.2. Isothermal Formulation

In an isothermal process, where $t_{eq} = t$ and $dt_{eq}/dt = 1$, it can be deduced that:

$$g(T) = \exp\left[A^T\left(\frac{1}{T} - \frac{1}{T_{ref}}\right)\right] \tag{4}$$

where A^T is known as the Thermal Activity (given in Kelvin), commonly also referred to as E_a/R, the Activation Energy divided by the universal gas constant [1].

[1] **Note:** The activation energy (E_a) has been described, interpreted, and calculated in various ways ([3], [4], [5], [6], [7]). It has been reported that different properties may have different E_a values for a given concrete, different concretes may have different E_a values for a given temperature, and different stages of development of a given property may exhibit different E_a values. Without delving into further details, we consider it appropriate to assume that E_a remains constant, invariant across different temperatures, properties, and stages of hydration development. In a multicomponent model, where the internal heat generation can be experimentally determined or "deconvoluted" through tests at different reference temperatures, it is possible to consider and calculate E_a for each reaction to represent the influence of temperature on the internal heat generation of various reactions occurring simultaneously. From an engineering standpoint, using a single E_a, said "apparent", provides sufficient accuracy to predict the temperature field in mass concrete. Furthermore, we propose abandoning the universal gas constant, which is gratuitously adopted from another context, and instead referring only to Thermal Activity (A^T). This approach acknowledges that the physical interpretation of activation energy is incompatible with the spontaneous nature of the exothermic hydration reactions.

2.3. Adiabatic Formulation

In an adiabatic process, the only difference is that T_{ref} represents the "adiabatic temperature rise curve of the process starting from an initial reference temperature":

$$g(T) = \exp\left[A^T\left(\frac{1}{T} - \frac{1}{T_{0,ref}+\alpha\cdot\Delta T_\infty^{adi}}\right)\right] \quad (5)$$

where ΔT_∞^{adi} it represents the final adiabatic temperature rise, obtained through an adiabatic temperature rise test.

Various aspects of these two formulations can be explored both conceptually and mathematically, as well as in terms of finite element modeling. However, it is not our objective to provide a detailed exposition of what was carried out. For example, if the process to which Eq. 4 is being applied is adiabatic, $T_{0,ref} + \alpha \cdot \Delta T_\infty^{adi}$ is the actual curve from the adiabatic temperature rise test. If the process is non-adiabatic, it is the curve given by the equation $T_{0,ref} + \alpha \cdot \Delta T_\infty^{adi}$ ([8]).

2.4. Viscoelastic Mechanical Formulation

The viscoelastic mechanical model with aging was derived from [1] and [2], with the results summarized in equations (6) to (11):

$$\{\Delta\varepsilon_n^{cr}\} = [\mathbb{V}]\{\Delta\sigma_n\}q_n + \{\eta_n\} \quad (6)$$

where:

$$[\mathbb{V}] = \begin{bmatrix} 1 & -\nu & -\nu & 0 & 0 & 0 \\ -\nu & 1 & -\nu & 0 & 0 & 0 \\ -\nu & -\nu & 1 & 0 & 0 & 0 \\ 0 & 0 & 0 & 2(1+\nu) & 0 & 0 \\ 0 & 0 & 0 & 0 & 2(1+\nu) & 0 \\ 0 & 0 & 0 & 0 & 0 & 2(1+\nu) \end{bmatrix} \quad (7)$$

$$q_n = \sum_{r=1}^{R} \emptyset_{r,n}^*\left(1 - \frac{1-e^{-S_r\Delta t_n}}{\Delta t_n S_r}\right) \quad (8)$$

$$\{\eta_n\} = [\mathbb{V}]\{\Delta\sigma_0\}\sum_{r=1}^{R}\emptyset_r(t_0)\, e^{-S_r(t_{n-1}-t_0)}\cdot(1-e^{-S_r\Delta t_n}) + \sum_{r=1}^{R}(1-e^{-S_r\Delta t_n})\{\omega_{r,n}\} \quad (9)$$

$$\{\omega_{r,n}\} = [\mathbb{V}]\{\Delta\sigma_{n-1}\}\emptyset_{r,n-1}^*\left(\frac{1-e^{-S_r\Delta t_{n-1}}}{\Delta t_{n-1}S_r}\right) + \{\omega_{r,n-1}\}e^{-S_r\Delta t_{n-1}} \quad (10)$$

with $\{\omega_{r,1}\} = \{\Delta\sigma_0\}D_m(t_0)$, $\emptyset_r$ and S_r are parameters of material creep function, according to $J(t-z,z) = 1/E_0(z) + \sum_{r=1}^{R}\emptyset_r(z)\left[1-e^{-S_r(t-z)}\right]$ and $\emptyset_{r,n-1}^* = \emptyset_r(t_{n-1} + \Delta t_n/2)$.

Thus, the stress increment considering aging can be calculated in a manner that depends only on the previous time step, which represents a significant computational advantage.

$$\{\Delta\sigma_n\} = \bar{E}_n[\mathbb{V}]^{-1}\left[\{\Delta\varepsilon_n^{total}\} - \{\Delta\varepsilon_n^{th}\} - \{\Delta\varepsilon_n^{aut}\} - \{\Delta\varepsilon_n^{pl}\} - \{\eta_n\}\right] \quad (11)$$

$$\bar{E}_n = \frac{E_n}{(1+E_n q_n)} \quad (12)$$

3. VALIDATIONS

3.1. Adiabatic Temperature Rise at the Concrete and Paste Scales

The purpose of this validation is to compare the isothermal and adiabatic formulations and verify the validity of their interconversion. Simulating an adiabatic situation using an internal heat generation rate derived from an adiabatic test, with the initial temperature being the initial reference temperature of the test, is straightforward. What was done here, however, was to interconvert the adiabatic temperature rise into an isothermal internal heat generation rate by fitting the adiabatic temperature rise curve as a function of the equivalent time of this adiabatic process. Subsequently, an adiabatic situation is modeled using the isothermal formulation fed with the isothermal internal heat generation rate derived. Finally, with this same formulation and internal heat generation rate, the adiabatic situation was modeled at the paste scale.

The result of the modeling using the isothermal formulation under adiabatic boundary conditions shows that the total energy generated by the cement is immediately (at each time step) stored as thermal energy. Thermal energy is calculated as the temperature change times the heat capacity: – $E_{th} = \rho_e c_e \Delta T_\infty^{adi}$. At the microscale, there is a system of inert aggregates of different sizes, voids (pores of varying sizes), and cement paste, which is the reactive component of the system. The heat generated by the cement paste first increases the paste's temperature and then, by conduction, raises the temperature of the inert parts. Figure 1 shows the simplified geometry where the proportion of aggregate to paste is the same as in the full concrete system. The paste volume relative to the total volume was set at 30%[2].

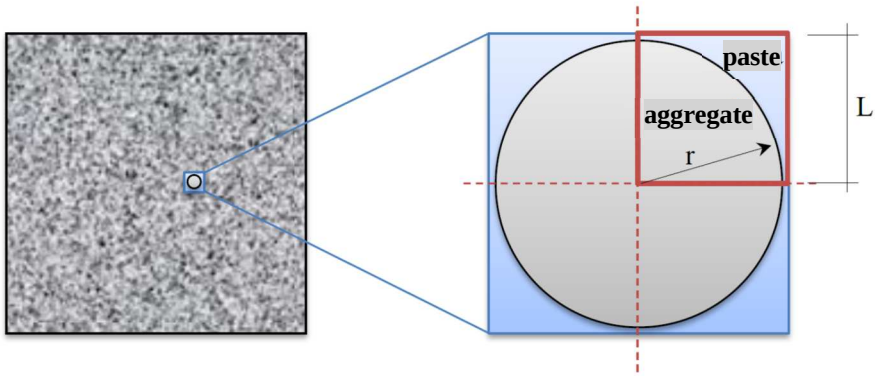

[2] This 30% paste is referred disregarding the air content

Fig. 1 – Geometry of the validation modeling at the paste scale

As a starting point, a concrete mix design with the following unit proportions was adopted:

- cement: 1.00 kg
- aggregate: 6.30 kg
- water-to-cement ratio: 0.667 kg

Additional details of the mix design can be found in Table 1.

Table 1 – Details of the concrete mix design

	cement	aggregate	w/c	total	R/L	%paste	Cpaste
weight (kg)	1	6.3	0.67	7.97	0.944		
mass dens. (kg/l)	3	2.7	1	2.39			
vol (l)	0.33	2.33	0.67	3.33			
C (kg/m³)	300					30.0%	1000

Calculation of cement consumption in full concrete:

$$C = \frac{1000}{1/\gamma_c + m/\gamma_m + w/c} = 300 \quad (13)$$

The proportion of paste relative to the total volume is:

$$\%_{paste} = \frac{1/\gamma_c + w/c}{1/\gamma_c + m/\gamma_m + w/c} = \frac{1}{3.33} = 30\% \quad (14)$$

In the case of paste of cement, where only cement and water are present, the cement consumption of the paste is:

$$C = \frac{1000}{1/\gamma_c + w/c} = 1000 \quad (15)$$

The radius of the aggregate (assumed spherical, or circular in fact) for the proposed geometry was determined based on the paste volume:

- total volume area: L^2
- aggregate area: $\pi r^2/4$
- paste area: $L^2 - \pi r^2/4$

$$\%_{paste} = 30\% = \frac{L^2 - \pi r^2/4}{L^2} \Longrightarrow r = 0.944L \quad (16)$$

The side was adopted L=0.05m as it corresponds to an aggregate size of 100 mm. In practice, the average size of coarse and fine aggregates is much smaller than this. Therefore, this represents the worst-case scenario for the purpose of the demonstration. The bondary conditions, by simetry, was considered heat flux equals zero in four sides and the period of time analysis 120 hours. Figure 2, printed from FlexPDE 7 software, shows the finite element mesh used and the temperature contour near t = 11 hours to show that there is practically no

difference between the maximum and minimum temperature points. Figure 3 shows the temperature result of the minimum and maximum temperature point, both equal to the abiabatic temperature rise. The Excel graph includes the result of modeling homogeneous concrete with C=300 kg/m3 and heterogeneous concrete with inert aggregate and cement paste with Cpasta = 1000 kg/m3.

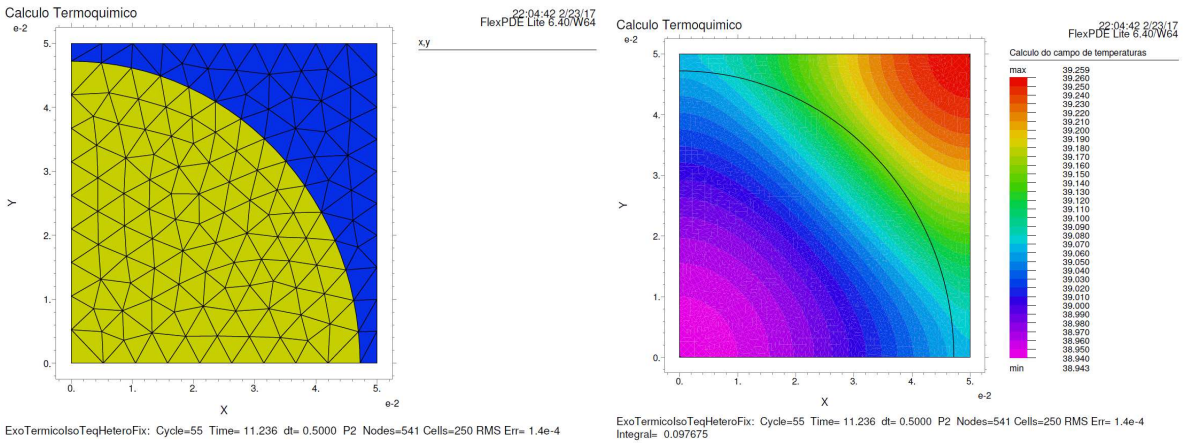

Fig. 2 – a) Left: finite elemento mesh; b) Right: temperature contour ~ uniform

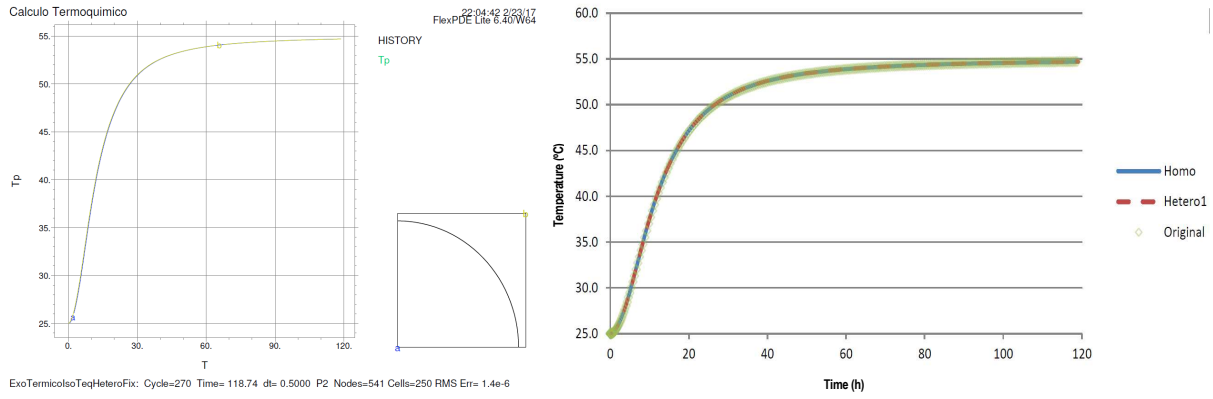

Fig. 3 – Original adiabatic curve and results for full <u>concrete</u> and at the paste scale

It's possible to conclude from this initial validation:

1) Two valid formulations were identified: the isothermal and adiabatic formulations.

2) It was indicated how to use the results from internal heat generation tests in an adiabatic process (adiabatic temperature rise test) to calculate the isothermal internal heat generation[3].

3) It was shown that for concrete, the average size of the aggregates is sufficiently small to render the temperature difference between the paste and the aggregate negligible. Even for a maximum aggregate size of 10 cm without a particle size distribution, the temperature difference between the innermost point of the paste and the innermost point of the aggregate does not exceed 0.3°C.For more typical cases, less than 0.1°C is expected.

[3] The interconversion from the isothermal to the adiabatic formulation requires the development of a numerical scheme, as the temperature in the next step is unknown and must therefore be calculated iteratively (this has already been derived and implemented).

4) Consequently, *the average thermal properties* govern heat conduction. The scope of this conclusion extends beyond the performed simulations, but was done by the author, allowing us to assert that even if the thermal properties vary with temperature, degree of hydration, or degree of saturation, heat conduction and temperature rise will still be governed by the average thermal properties of the constituent materials.

3.2. Cooling of an Infinite Slab with Internal Heat Generation

The solution to the heat equation for the case of an infinite slab was proposed and solved by the *US Bureau of Reclamation* (Bureau, 1949) for the cooling of the Hoover Dam. Initially, the equation was solved for a uniform initial temperature, with application to the Hoover Dam case, concluding that the total cooling of the dam could take over 100 years. Subsequently, it was demonstrated how to apply the principle of superposition to the case where one face is subjected to one temperature and the opposite face to another temperature. This scenario occurs after the reservoir is filled, as the water temperature imposes a different condition on one face compared to the face exposed to air.

The solution implemented in this validation involves the cooling of an infinite slab with imposed temperatures on both faces, considering internal heat generation. This heat raises the slab's temperature to a maximum value before cooling begins. The maximum temperature reached is directly proportional to the maximum tensile stress. For this reason, the maximum temperature is the general guideline for specifying dam structures. To control the maximum temperature reached, it is important to study the influential factors in this case, which, although idealized, closely corresponds to typical situations such as spillway piers, intake towers, and retaining walls. This is especially true when constructed with sliding formwork, a high-speed construction process that makes heat loss through the top surface of the layer negligible, rendering the proposed idealization equivalent to real-world conditions.

In addition to analyzing the influential factors, the analytical formulation of the infinite slab problem applied to dam pier cases allows for back-analysis using monitoring data. This can help identify deviations from predictions or confirm and determine internal heat generation. Finally, it is possible to consider the activation energy and its influence when varying the placement temperature, the significance of the structure's internal heat generation relative to laboratory test results, and whether the consideration of thermal activation is a first-order or second-order effect.

$$T(x,t) = T_\infty + 4 \sum_{m=1}^{\infty} \frac{e^{-h^2 \lambda_m^2 t} \sin \lambda_m x}{\lambda_m L} \left[(T_0 - T_\infty) + \int_0^t \frac{g(\tau)}{\rho_e c_e} e^{h^2 \lambda_m^2 t} \, d\tau \right] \quad (16)$$

This equation provides the temperature as a function of position and time for an infinite slab of height L, subject to an imposed surface temperature T_∞ and a known initial temperature T_0.

The internal heat generation is explicitly and directly included in the generic function $g(t)$. The implementation of this solution must ensure that the integral of $g(t)$ is numerically solved along with the exponential term, as described in [9].

One consideration for the generic $g(t)$ in Expression (16): it is known that, due to activation energy, the degree of hydration and equivalent time vary non-uniformly in space because the temperature history differs at each point in the domain. Therefore, no example or case study will have a valid $g(t)$ for all points. Any non-adiabatic and non-isothermal process will result in internal heat generation as a function of both position and time, $g(x,t)$. However, it is possible to adopt the internal heat generation at the point of maximum temperature as representative of the heat generation for the entire process across all points. This $g(t)$, thus considered, can be used in numerical modeling or in the analytical equation without activation energy. Starting with either an adiabatic or isothermal $g(t)$, the temperature history at the point of maximum temperature allows recalculation of a new $g(t)$ for the variable temperature process using the same adiabatic-isothermal interconversion methodology. The result of Equation (16) with this new $g(t)$ is the final result of T.

The results of this validation are presented as follows: an adiabatic internal heat generation was selected with a known A^T, along with the corresponding isothermal internal heat generation obtained through the interconversion process. Each using their own respective formulation (isotermic or adiabatic) to solve the problem of a **1m wide infinite slab** (for modeling purposes, a 1m block with zero heat flow on two opposite sides and an imposed temperature on the other two sides). Two points were chosen for comparison: one at the center of the slab and another at half the distance between that point and the edge. As described in the previous, a generic $g(t)$ without A^T was determined to be used in Equation (16). The graphs below show the comparison results of the three ways – two FEM and one by the Equation (16) – for the two points considered. Time history until 5 days.

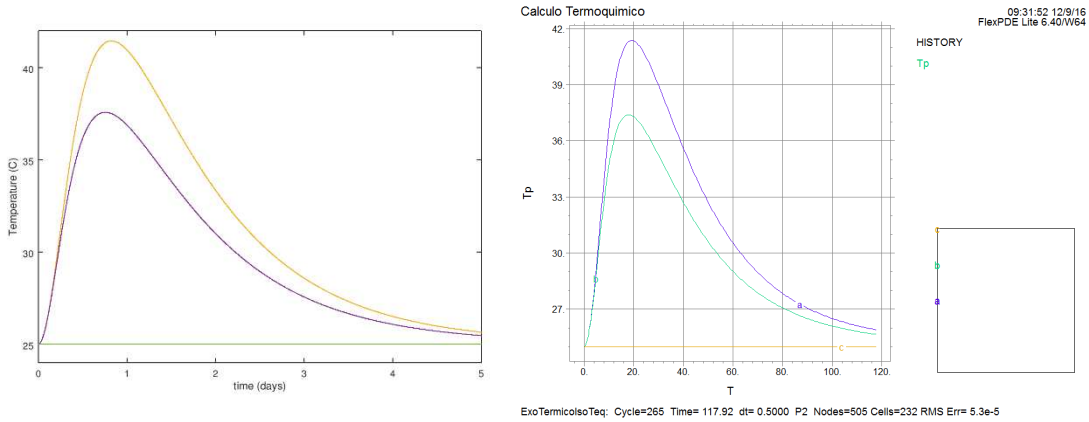

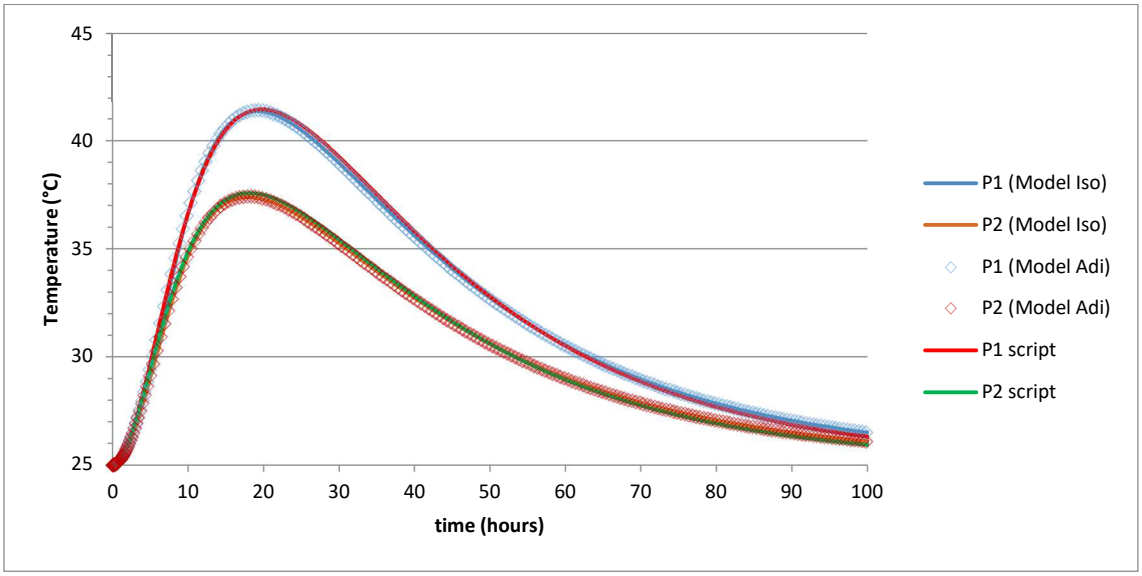

Fig. 4 – Comparison of the analytical solution with finite element modeling

To provide an account of the developments achieved, additional solutions were developed for important typical problems based on the technique used to derive the analytical solution for a generic $g(t)$. The second problem solved was that of an infinite cylinder with an imposed lateral temperature, published in [9].

Using Duhamel's theorem to derive the solution for a generic $g(t)$ from a particular $g(t)$ solution, the following problems were also addressed:

- The post-cooling problem, whose solution for a particular $g(t)$ was graphically presented in 1949 [10];
- The slab-on-rock foundation problem (with the same thermal properties as concrete), whose solution for a particular $g(t)$ was also graphically presented in 1949 [10];
- The slab-on-soil foundation problem (with thermal properties different from concrete);
- The infinite cylinder in a medium with infinite thermal properties different from concrete, simulating a caisson foundation.

The first two developments cited are described in unpublished research reports within the scope of the doctoral project at the University of Brasília (UnB). The fourth is a novel proposal based on the idea that the explicit analytical solution can be implemented as a new function in an Excel spreadsheet. This allows the parameters of internal heat generation, including the Thermal Activity (A^T), to be determined from measured temperature histories.

The slab-on-foundation case represents the most typical current application of mass concrete: the foundation blocks of tall buildings. The parameters of internal heat generation, the thermal properties of the soil, and the thermal properties of the concrete, including A^T, can be obtained from monitoring the casting process of a single caisson within a maximum of three days, a typical situation for the foundations of tall buildings. With these parameters available, it is

possible to assess the cracking risk of the most critical structural component: the foundation block of the high-rise building.

3.3. Validation of the Aging Viscoelastic Model in 1D

The viscoelastic formulation (2.4) was implemented in two finite element software platforms: Multimechanics (a multiscale software initially used for modeling asphalt concrete and polymer complex materials and now acquired by Siemens) and ANSYS (one of the most widely recognized and versatile tools in FEM).

Concrete exhibits the well-known characteristic that the Poisson's ratio is purely elastic. Therefore, the viscoelastic behavior can be validated in a single direction. During the validation phase, numerical simulations of the creep test, as well as relaxation tests at various ages, were analyzed. The creep behavior was compared to the function directly input as a property derived from tests conducted at the Furnas Concrete Laboratory in Goiânia. The relaxation behavior was compared with numerical relaxation obtained using the method proposed by Bazant (1972) and revisited by Sassone and Chiorino [11].

Table 2 - Equations for Concrete Viscoelastic Parameters for Validation Purposes

Properties	Function
Modulus of Elasticity (GPa)	$\mathrm{E(z)} = 27{,}83\,.\,\mathrm{z}^{0{,}53} / (2{,}14^{0{,}53} + \mathrm{z}^{0{,}53})$
Creep Coefficient (10^{-6}/MPa) [13]	$F_k(z) = 0{,}15 / E(z)$

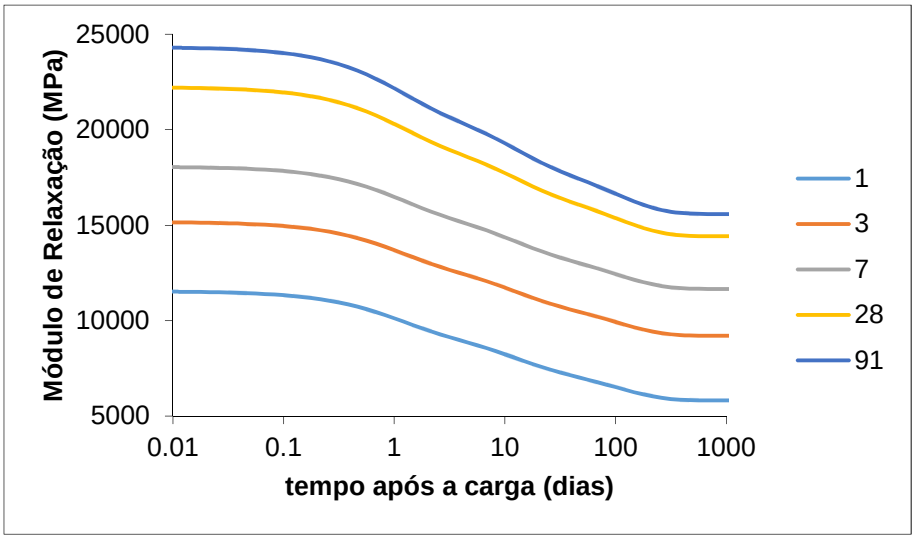

Fig. 5 – Relaxation modulus at various loading initiation ages

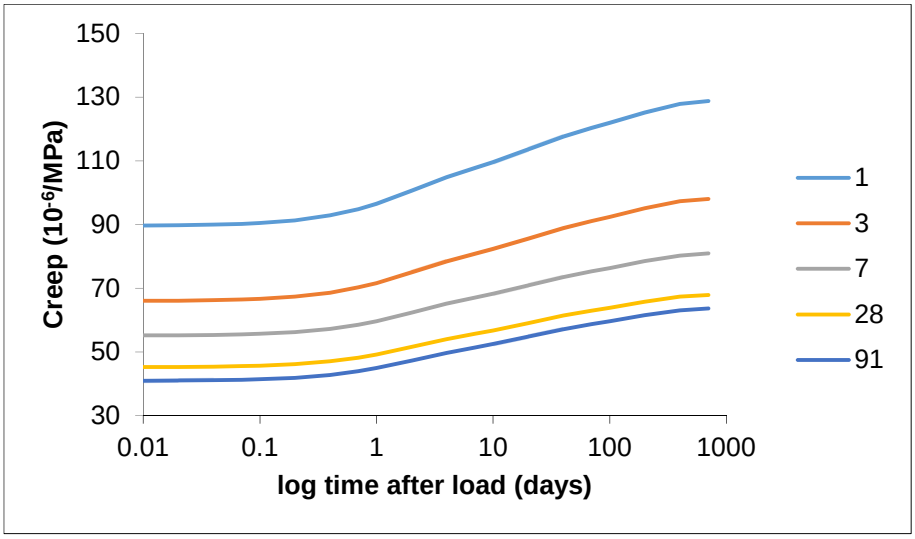

Fig. 6 – Creep modulus at various loading initiation ages

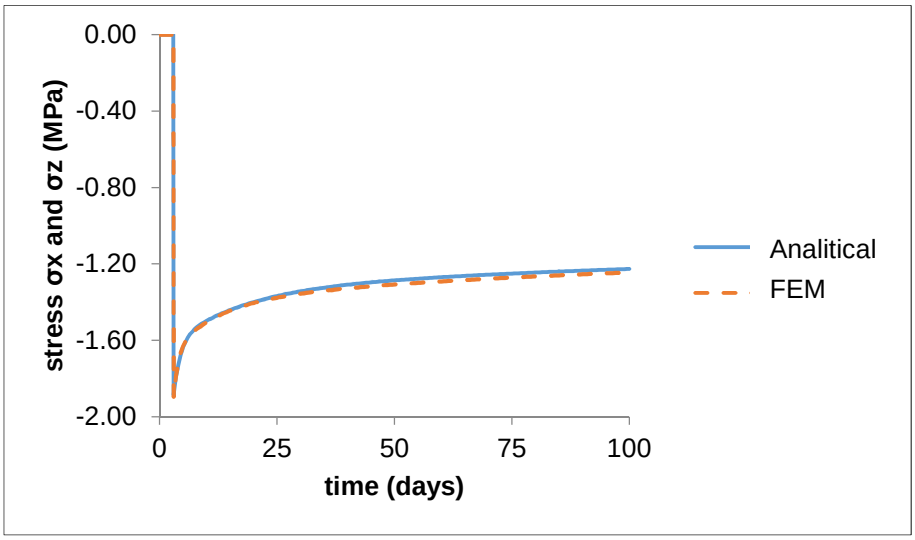

Fig. 7 – Stress results in the *x* and *z* directions after a temperature variation of 10°C at 3 days

Figure 5 shows the result of the equations presented and Figure 6 the result of the numerical interconversion, according to [11]. 1D modeling was carried out of the loading situation applied at a certain age and maintained for 90 days, as well as the relaxation situation, applying a unit deformation in one direction. In the interest of simplicity, we preferred to present only the comparative modeling of the application of a temperature gradient at a given age (3 days) and susteined for 90 days, compared to the analytical calculation based on the relaxation function obtained previously.

It is truly remarkable how complex this property is and how much has been written and studied about it. Some aspects still challenge researchers worldwide. Advances, both theoretical and technological, are frequently reported at CONCREEP conferences throughout the decades. One of the most comprehensive and up-to-date publications on this property was authored by Bazant and Jirasek [12].

In this work, some thermodynamic constraints were reported, including the restriction that negative relaxation cannot occur. Depending on the choice of the fitting model and the initial guess of the parameters, interconversion can lead to negative relaxation, not only in the early days. By refining fitting techniques, smoothing test data, and adjusting the numerous parameters of the Prony series with appropriate constraints, it is possible to ensure that no negative relaxation occurs beyond ages greater than 0.3 days[4].

4. APLICAÇÕES

4.1. UHE Batalha

The outcomes of the developments reported are the real-world applications of thermomechanical modeling carried out for energy generation projects. Initially, the goal was to undertake a pilot project where the thermal and mechanical behavior of concrete could be predicted and compared with monitoring data.

The first pilot project was at the Batalha Hydroelectric Power Plant (UHE Batalha), specifically the modeling of the spiral case. This modeling was conducted in collaboration with Prof. Miguel Azenha from the University of Minho, who served as a consultant for the project.

The results of this pilot project led to an article published in an internationally indexed journal [14] and a doctoral thesis developed at the University of Minho based on this work..

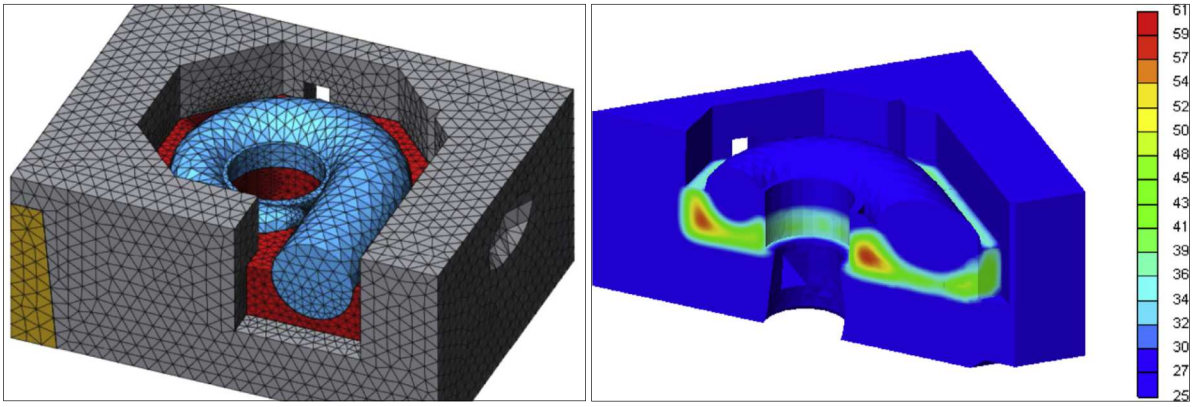

Fig. 8 – Finite Element Mesh and Temperature Field (°C) at 1.4 Days [14].

4.2. UHE Santo Antônio

In 2014, in situ monitoring of the VET (Log Overflow Spillway) structure was carried out. This special structure, a unique case to the best of our knowledge, was designed to absorb the

[4] Further validations in 2D and 3D are considered unnecessary, as they are practically equivalent to extending the 1D model to a matrix form. The software used has already been validated for other 3D material models.

impact of logs in quantities so large that they give the river its name: the Madeira River. The entire lateral and bottom surfaces of the spillway are made of high-performance fiber-reinforced concrete, with conventional mass concrete used for filling, as shown in Figs. 9 and 10.

This application involved modeling, laboratory testing, and monitoring (temperature, deformations, and stresses). It was part of two research projects coordinated by the author at the time: the “Early-ages Concrete 2” project with UFC and the “Fiber Reinforced Concrete 2” project with USP, both previously mentioned. A complete characterization including creep at 4 different ages of three concrete mixes was proposed—two for mass concrete and one for fiber-reinforced concrete.

The proposed monitoring scheme for deformations included a strain gauge rosette with six vibrating wire sensors (VW 4210 from Geokon), additional temperature sensors at critical points (middle of the layer, inside the layer, surface of the layer, and near the formwork to confirm boundary conditions), and two “no-stress” boxes with VW 4200 in different directions to account for and isolate thermal and autogenous strains. A Concrete Stress Meter was also installed to directly measure stress in one direction. The primary goal of this monitoring was to validate the aging viscoelastic behavior model for mass concrete and assess the feasibility of obtaining thermal-origin stresses “*in situ*”.

In 2014, “*in situ*” monitoring was carried out on the structure of the Special Log Spillway (VET, in portuguese). This special structure, a unique case according to our knowledge, was designed to absorb the impact of logs in such quantity that it gives its name to the river on which the project is located: the “Rio Madeira” (Wood River). The entire side and bottom surface of the spillway is made of high-performance fiber-reinforced concrete, with conventional mass concrete filling, as shown in Figs. 9 and 10. This application involved modeling, laboratory tests and monitoring (temperature, deformations and stresses). It would be used by both research projects coordinated by the author at the time: the “Early Ages Concrete 2” project with UFC, and the “Fiber Concrete 2” project with USP, mentioned above. The complete characterization of three dosages was proposed, two of mass concrete and one of fibre-reinforced concrete. The monitoring scheme proposed for the deformations was a strain gauge rosette with 6 vibrating string sensors (VW 4210 from Geokon), single temperature sensors at the points of primary interest (middle of the layer, inside the layer, surface of the layer and near the forms to confirm the boundary conditions), two “no stress boxes” in different directions, to take into account and discount the thermal and autogenous deformation plots. A Concrete Stress Meter was also inserted to measure stress directly in one direction. The main purpose of this monitoring was to validate the viscoelastic behavior model with aging of the mass concrete and to consider the feasibility of obtaining the “in situ” thermal stress.

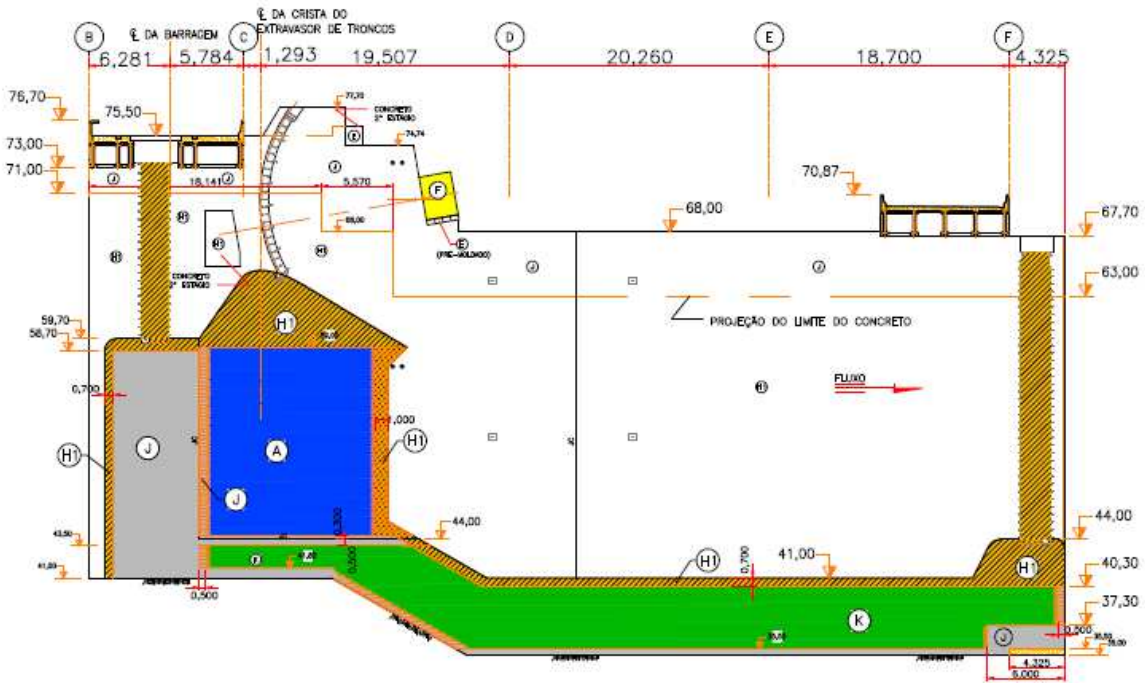

Fig. 9 – Final Design: Types of Concrete.

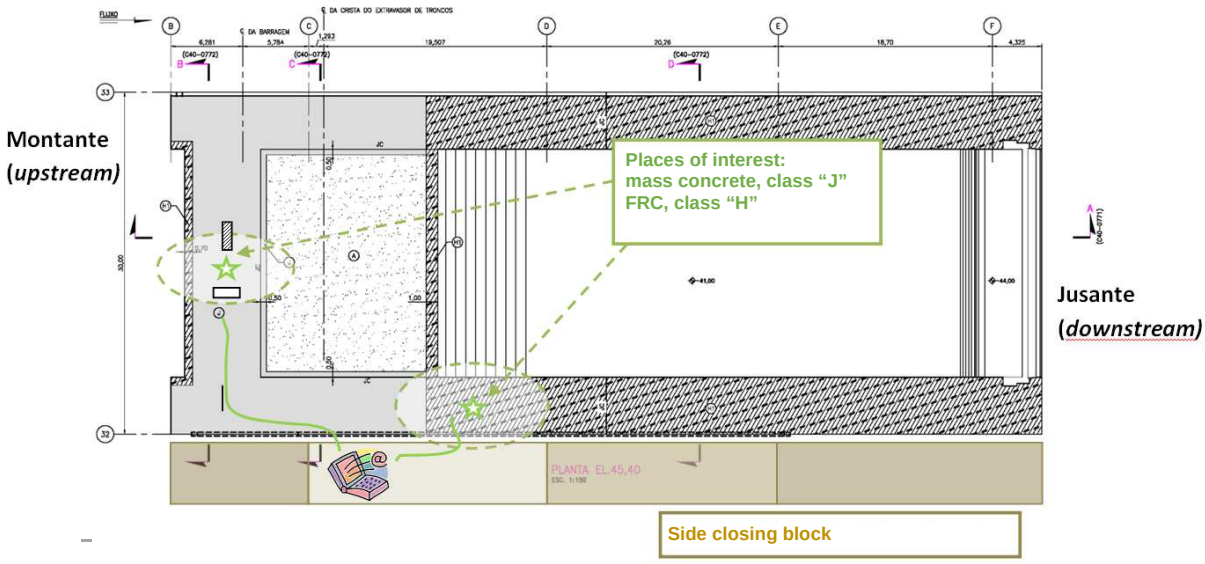

Fig. 10 – Plan View: Monitoring Locations in J and H1 Classes (HPFRC) Concrete.

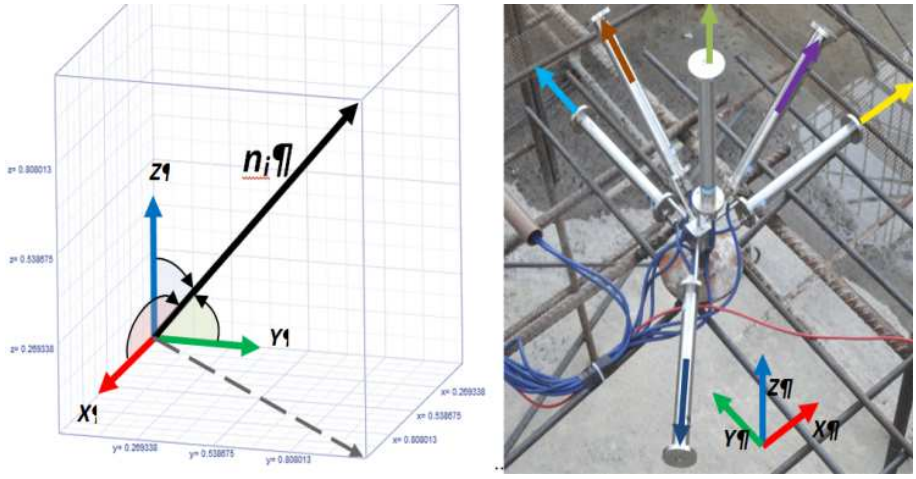

Fig. 11 – a) Position Vector and Direction Cosines; b) Rosette with 6 Sensors.

Fig. 12 – Niche: 1–Concrete Stress Meter │ 2–Strain Gauge Rosette │ 3 and 4–No-Stress Boxes.

The massive amount of monitoring data cannot be fully included in this article. However, the conclusion of this pilot project was that the efficiency of using steel fibers for crack control was successfully demonstrated through temperature and deformation instrumentation, following the methodology developed by the R&D program during the construction of the VET [16].

This efficiency is evident from the significant difference in behavior between the HPFRC and the non-fiber concrete. For instance, in the case of HPFRC (with 80 kg/m³ of steel fibers), maximum temperatures around 75°C – when exposed for approximately 10 days – resulted in cooling rates that the material could withstand. Conversely, for non-fiber concrete, this limit would be 45°C, necessitating either reduced cement content or pre-cooling of the concrete [16].

The use of HPFRC, modeled and verified *in situ*, allowed for effective control of cracking risks and the complete elimination of future interventions for repairing hydraulic surfaces [15]. This alternative reduced costs that would have been associated with installing approximately 5,000

meters of metal profiles, as well as the additional time required for their assembly and shielding, which were initially planned in the original project.

4.3. Apiacás Complex [5]

The studies conducted for this project focused on the concreting of the second-stage concrete encasement around the steel lining of the draft tube at the Salto do Apiacás Hydroelectric Plant (UHE Salto do Apiacás). Additionally, a one-dimensional parametric study was performed for the other structural components, considering various executive planning alternatives, such as layer height, placement intervals, placement temperature, and cement consumption, which are the main variables influencing cracking control due to thermal effects. The structure analyzed can be seen in Figure 9 [17].

One of the particularities of this study was the criterion for the maximum temperature to be reached at a distance of 10 cm from the cylindrical surface, which motivated the post-processing shown in Figure 15. The “maximum over time” temperature was tracked along the curved line. This term “maximum over time” was adopted from the ANSYS software to display the maximum value of the variable at each point throughout the entire time history.

[5] The *Apiacás* Hydroelectric Complex is located at the mouth of the *Apiacás* River, the main tributary of the *Teles Pires* River, on the border between the states of *Mato Grosso* and *Pará*, approximately 950 km from the capital of *Mato Grosso*. Its total installed capacity was designed to be 101.5 MW, distributed as follows: the *Cabeça de Boi* and *Fazenda* small hydroelectric plants (PCHs) with 29.0 MW each, and the *Salto do Apiacás* Hydroelectric Plant (UHE) with 43.5 MW.

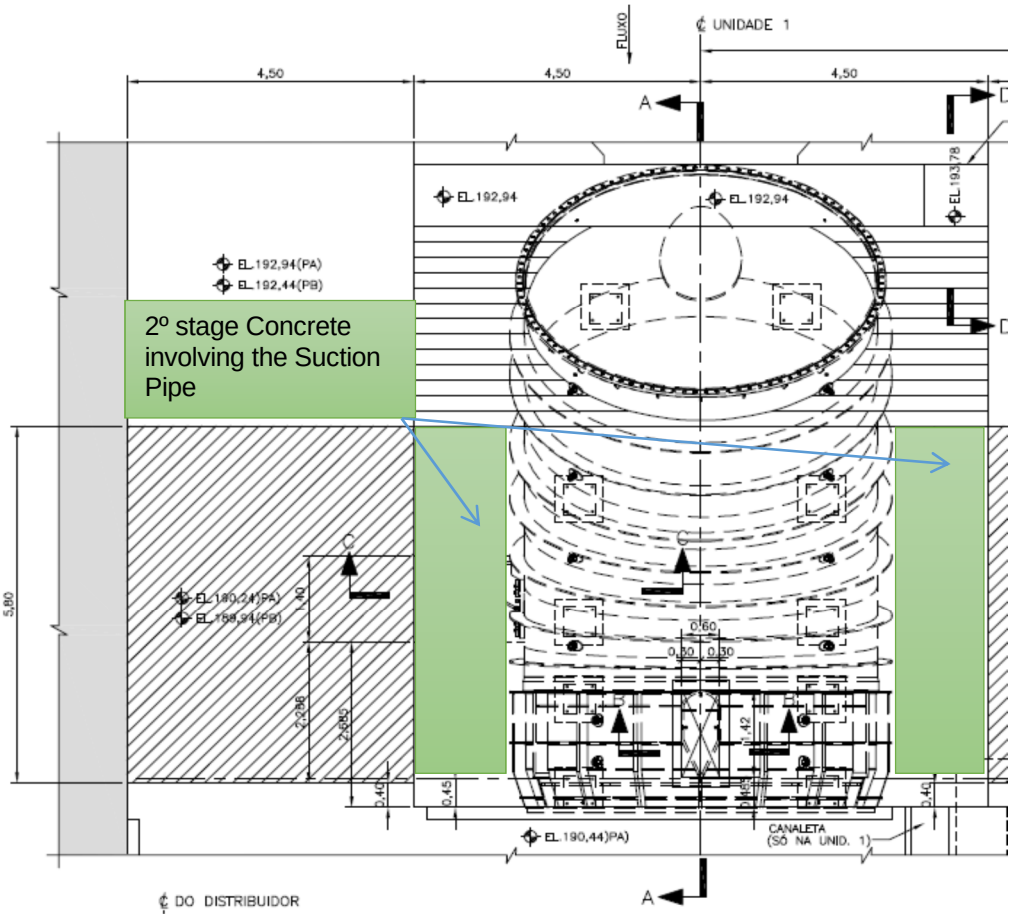

Fig. 13 – Plan View of the Draft Tube

The main results from these studies are shown in Figures 14 to 18.

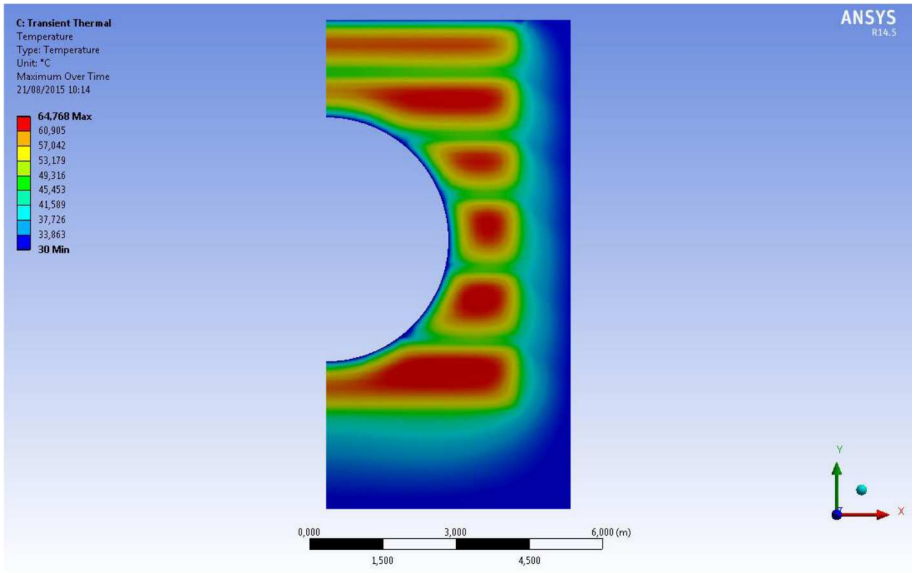

Fig. 14 – 2º stage concrete of the Draft Tube: Maximum temperature *over time* for the layers. Hipotesis "E", with 1.5m layers except the last, 1.0m, with 3 days of interval.

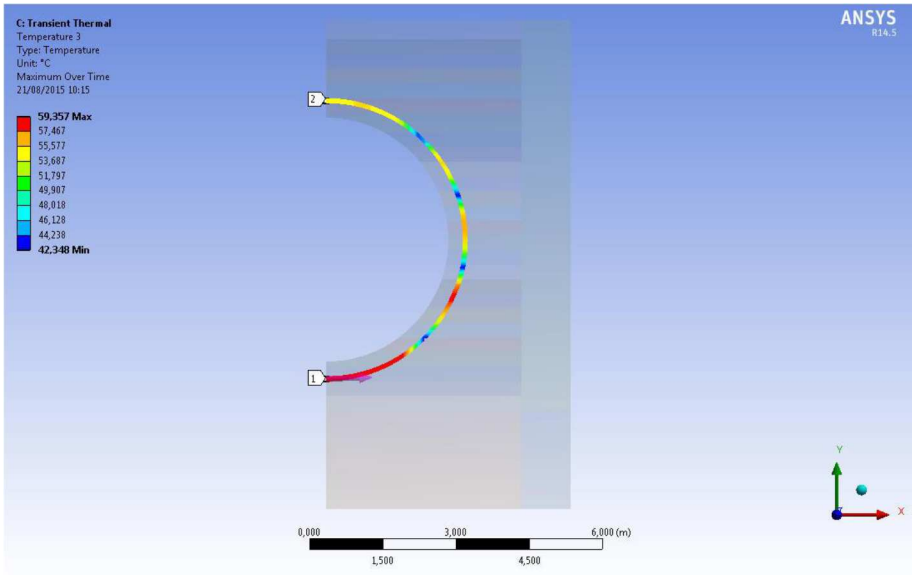

Fig. 15 – 2º stage concrete of the Draft Tube: Maximum temperature *over time* at the safety limit near the steel lining (60°C). Hipothesis "E".

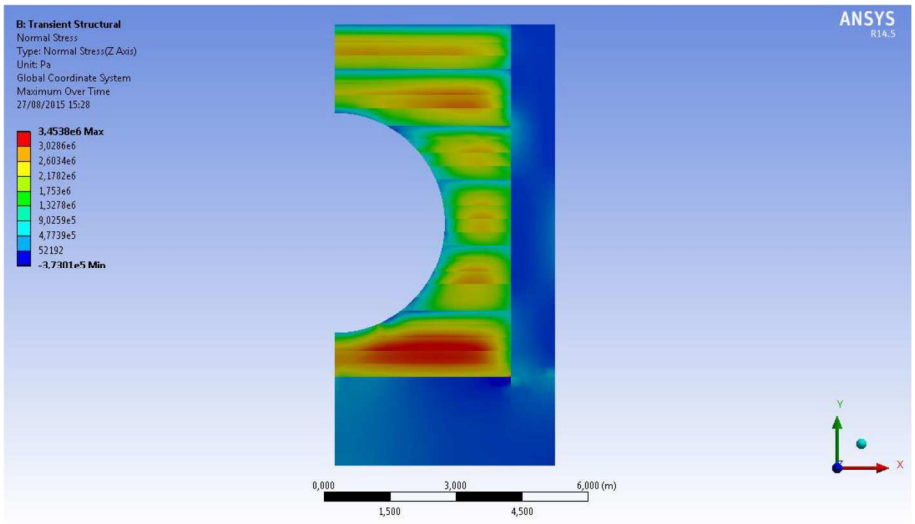

Fig. 16 – 2º stage concrete of the Draft Tube: Maximum principal stress over time. Idem.

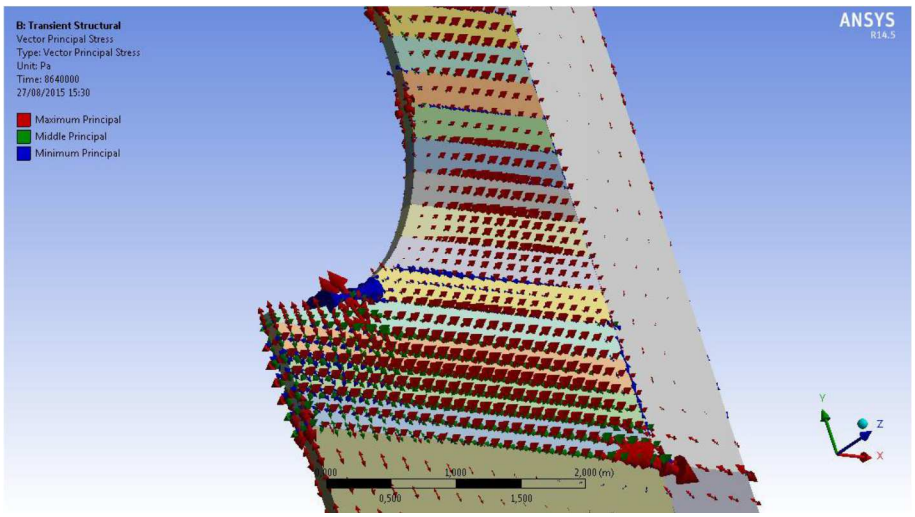

Fig. 17 – 2º stage concrete of the Draft Tube: Directions of principal stresses *over time*. Idem.

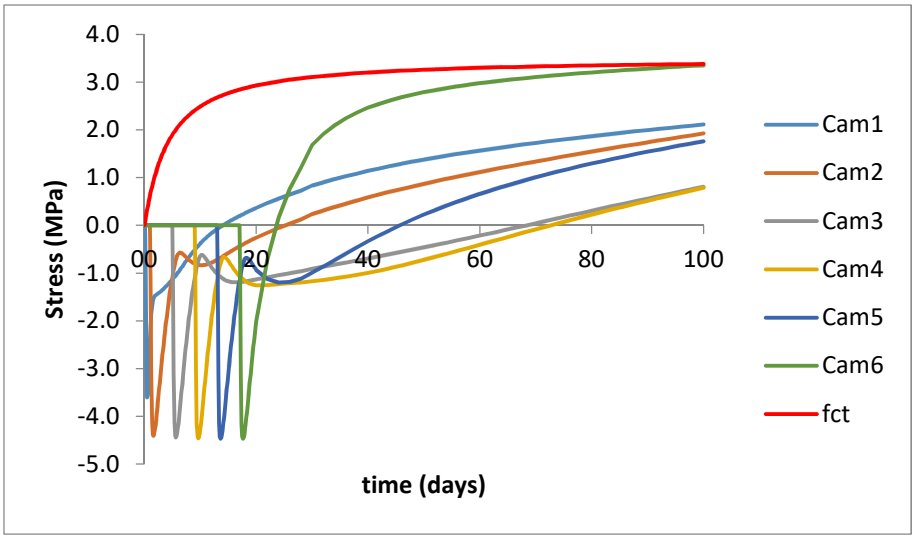

Fig. 18 – Temperature history of various layers and tensile strength.

Results achieved from these studies, one can list:

One-Dimensional Parametric Analysis

The one-dimensional parametric analysis revealed the following:

a) The maximum temperature reached depends on the placement temperature and cement consumption, as follows:

i) The placement temperature shifts the curve upward or downward, where a 1°C variation in the former results the same variation in the maximum temperature.

ii) Cement consumption is directly proportional to the difference between the maximum temperature and the placement temperature.

b) The maximum tensile stress is directly proportional to the difference between the maximum temperature and the placement temperature, and therefore directly proportional to cement consumption. Additionally:

i) In the specific case of the one-dimensional analysis and within the range of placement intervals studied (1 to 4 days), the maximum tensile stress is practically independent of the placement interval.

ii) It is slightly influenced by the placement temperature (an increase of 5% or 0.15 MPa in the final stress when the placement temperature increases from 30°C to 36°C).

c) Beyond these analyzed factors, it is worth noting that stresses are always directly proportional to the coefficient of thermal expansion and the modulus of elasticity and inversely proportional to the creep coefficient [8].

Two-Dimensional Parametric Analysis of the Draft Tube

In this bidirectional study, the assumptions for continuous placement—whether with a placement temperature of 30°C or 36°C, or cement consumption of 310 kg/m³ or 328 kg/m³—showed a high risk of cracking. However, the placement hypothesis with shorter placement intervals presented an adequate safety level for layers 2 to 6.

Layer 1 could be adjusted by executing the placement in two smaller layers—60 cm and 90 cm—with a 3-day placement interval between them and the next layer.

Thus, the concreting schedule for the structures on the project's critical path was established and carried out without significant issues related to cracking risk, in accordance with international recommendations [17].

4.4. UHE São Manoel[6]

The studies conducted for the São Manoel Hydroelectric Plant (UHE São Manoel) included 3D analysis of the temperature and stress fields for the discharge area, intake structures, spillway ogee, spillway pier, and trunnion girder. Additionally, a 1D parametric study was performed, considering executive planning alternatives such as placement intervals, placement temperature, and cement consumption, which are the main variables for controlling cracking due to thermal effects.

Water Intake Structure

The first study for this project considered a cement consumption of 250 kg/m³ and estimated thermal properties. Later, after confirming the thermal properties, no revisions to the conclusions were necessary. The main conclusion of this report was that the cracking risk could be controlled with pre-cooling. Key conclusions from the first report:

a) Experience has shown that it is not advisable to let a layer cool by more than 20°C before it reaches 28 days of age (a conservative conclusion later revised). It was estimated that a layer height of 2 m, with a 3-day placement interval and a placement temperature of 30°C, presented a high risk of cracking (Figure 15).

[6] The UHE *São Manoel* is located on the *Teles Pires* River, at the border of the *Mato Grosso* and *Pará* states, 950 km from the capital city of Cuiabá/MT and 125 km from *Paranaíta*/MT. The UHE *São Manoel* was designed with an installed capacity of 700 MW.

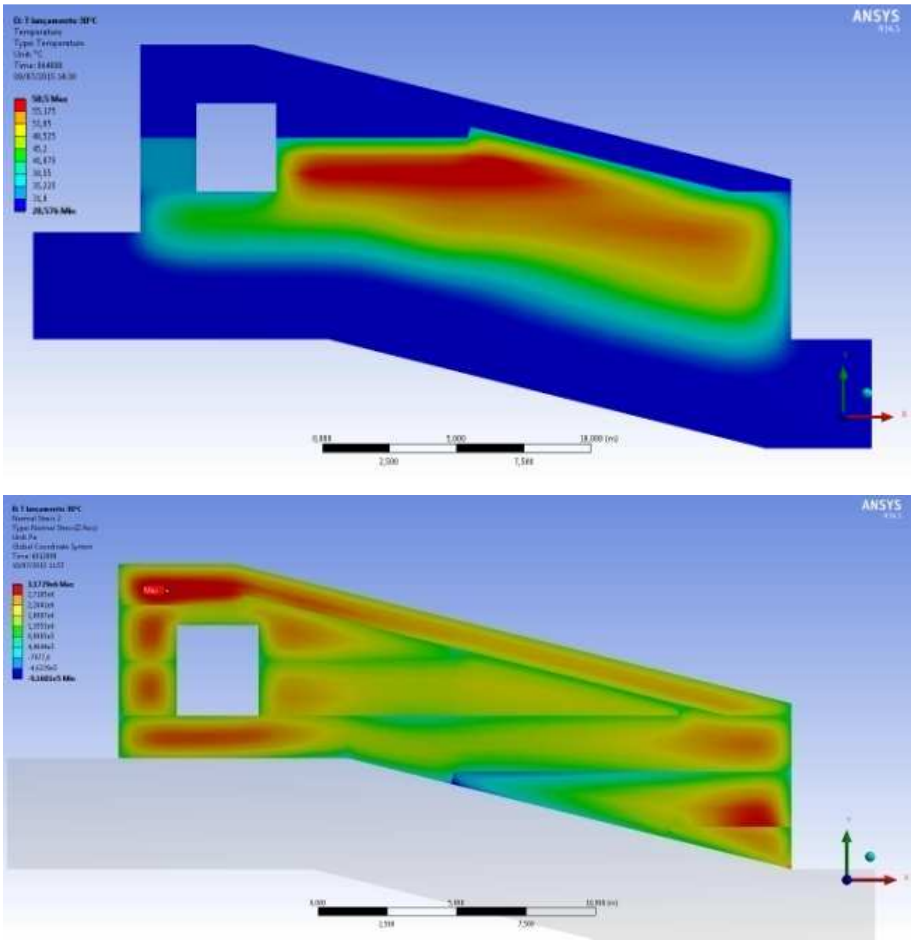

Fig. 19 – a) Layer 5 | t = 10 days | Max temperature: 58.5°C; b) t = 80 days | Max σ_z 3.17 MPa.

However, a placement temperature of 25°C (-5°C below the ambient average) showed an acceptable cracking risk, not according to the project's maximum temperature specification but according to the criterion of maximum stress, which was 1.9 MPa in the layer. This finding is significant and is purely a result of the research project: the ability to specify a particular hypothesis based on stress calculations and cracking risk, which can often be less conservative than relying solely on the temperature field, as per conventional specifications.

Another conclusion from this study was that, if cracks are found in undesirable numbers or widths, it is recommended to lower the placement temperature to below 25°C and verify the effectiveness of this control measure on-site. If cracking cannot be controlled solely with this measure, reducing the layer height to 1 m is advised until further analyses can be performed. The first layer above the leveling course should ideally be kept at 0.5 m.

Spillway Pier

The analysis of the spillway pier aimed to simulate as executed. The reported cement consumption was 347 kg/m³, and the average placement temperature was 23°C. The placement was performed using sliding formwork. Data from five thermometers confirmed the adiabatic temperature rise and the thermal properties used in the analyses. The maximum

temperature reached at various points exceeded 70°C. The conclusion of this study was that the execution conditions led to an undesirable cracking risk.

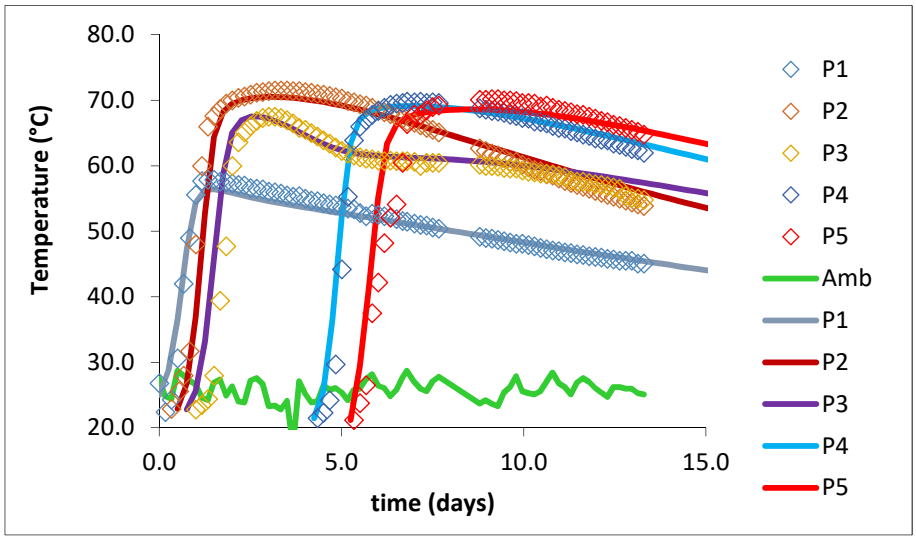

Fig. 20 – Monitoring results of the spillway pier compared to computational modeling

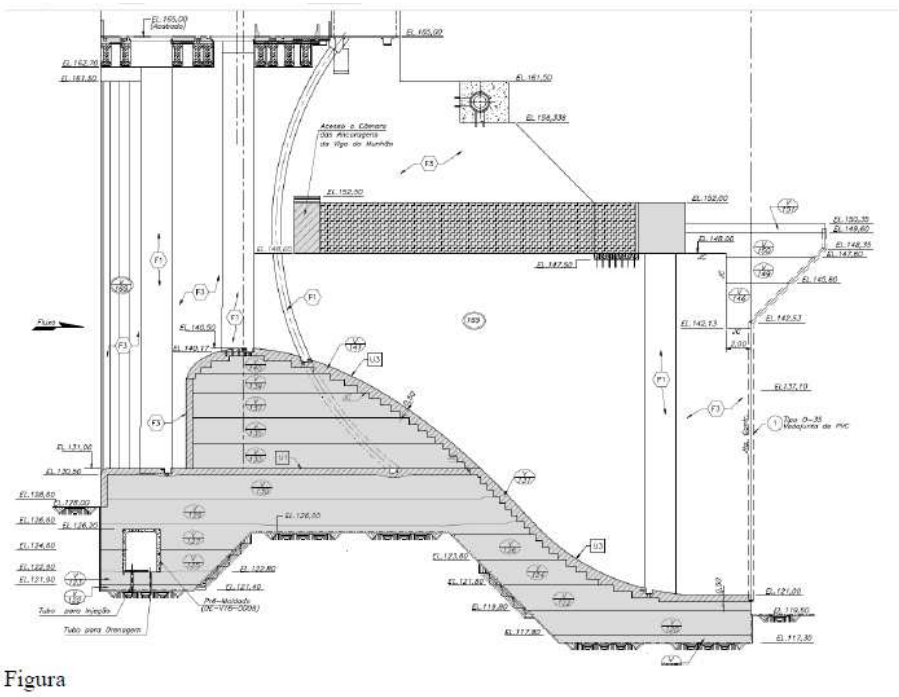

Fig. 21 – UHE São Manoel – Spillway Design – Cross-section

Spillway Ogee

The analysis of the spillway ogee (Figure 17) aimed to optimize the overall placement timeline while meeting the technical specification for maximum temperature as a function of relative height (up to 10%, 10–30%, and above 30%). It was concluded that, above the first layer, a layer height of 1 m is feasible up to 30% of the height, and 1.5 m for heights above 30%. To summarize multiple hypotheses, a single hypothesis encompassing various layer heights was formulated.

This study corroborates the findings of the one-dimensional parametric study, highlighting the correlation between maximum temperature and layer height and between maximum tensile stress and layer height.

The key point of this study was to demonstrate the nonlinearity between the restraint coefficient and relative height. In the case of a plane strain state, restraint is only slightly reduced with relative height. However, based on the maximum admissible stress criterion, temperatures above the specified value for a certain relative height may be permissible in certain cases.

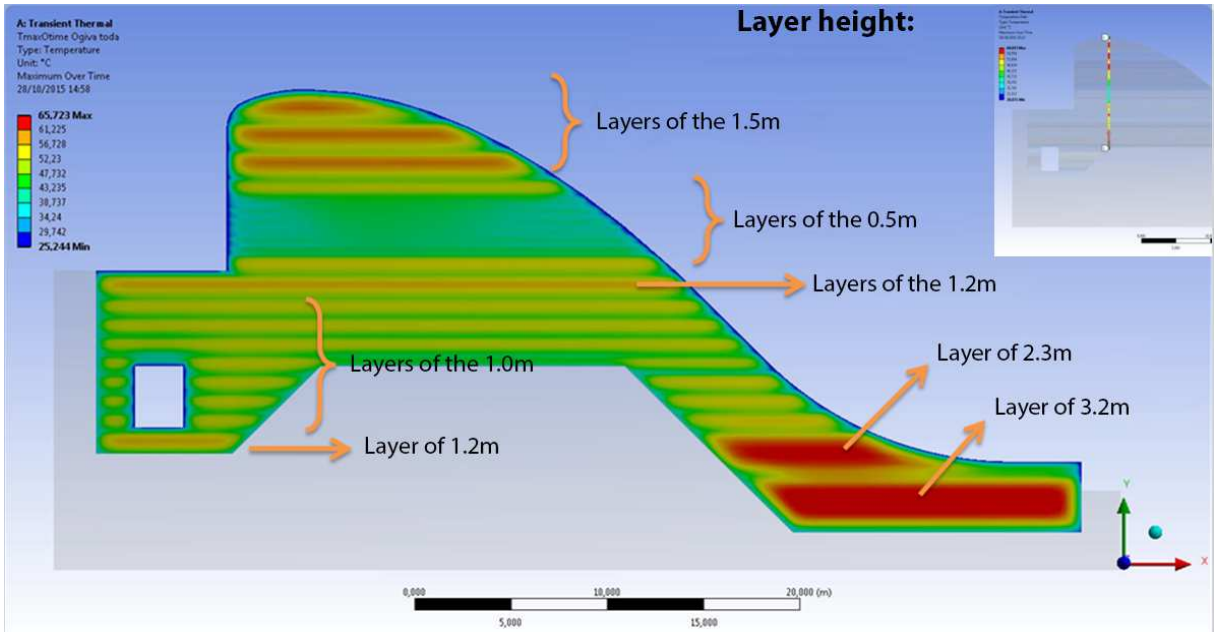

Fig. 22 – Maximum *over time* temperature contours

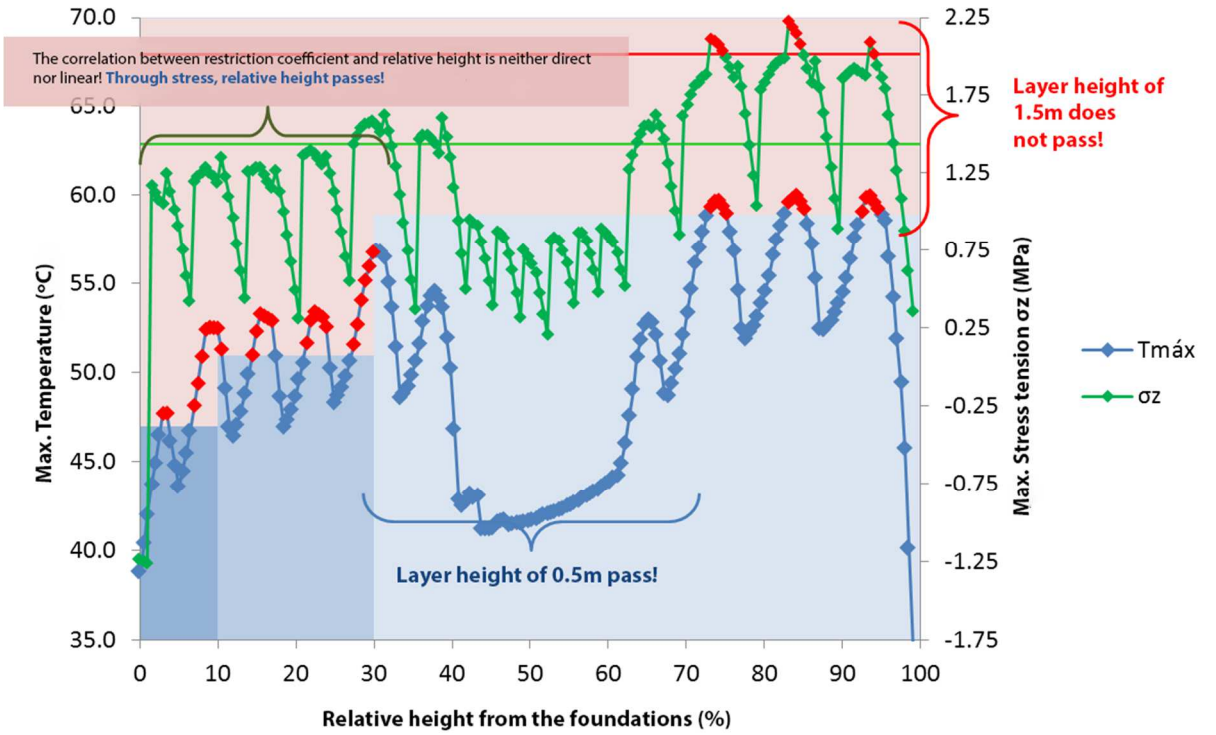

Fig. 23 – Maximum temperatures and stresses *versus* relative height

5. CONCLUSIONS

This article has shown how Furnas has possibly reached the state of the art in thermomechanical modeling and applied the available tools to practical use in various dam projects.

In addition to enhancing the safety of the projects by analyzing thermally induced stresses, this studies allowed Furnas to offer more accurate analyses for construction alternatives, like wind tower foudations, optimizing costs and timelines while maintaining the required safety levels, such as wind power foundation towers and foundation slabs for thermoelectric and nuclear power plants.

Suggestions for future research include:

a) Extending the proposed computational model to a multiscale model (including the size, shape, orientation, and distribution of aggregates, as well as the thermomechanical properties of aggregates and cement paste);

b) Applying the developed computational models (and multiscale modeling) to analyze dams with asphalt concrete cores or new materials such as fiber-reinforced concrete (steel, glass, and/or carbon) or sustainable concrete with low carbon and cement content;

c) Modeling dam structures subject to dynamic loads, such as structural components housing hydroelectric turbines;

d) Structural analysis and optimization of wind turbine towers, including multiscale modeling of composite-reinforced components.

From an academic perspective, the significance of each application discussed here may be debatable. While each case study is unique and unrepeatable, the theoretical thermal and mechanical framework has been developed by various authors over decades. The aging viscoelastic model has been well established since the 1970s. What has been proposed and implemented here is neither the state of the art in mechanics nor in finite element techniques. There are no large deformations, discontinuities, continuous-discontinuous transitions, multiscale approaches, nonlinearity, fracture mechanics, or anisotropy. Even though I worked with researchers at the forefront of various fields—Flávio Souza, David Allen, Jorge Soares, Miguel Azenha, Túlio Bittencourt, Oswaldo Manzoli, Antônio Figueiredo, Rafael Pileggi, Eduardo Fairbairn, Romildo Toledo, among others—the objective was to report what was achieved. There are many more applications and developments than those presented in this work, like UTE Santa Cruz, EOL Fortim and some tal buildings foundations. We tried to push as far as possible within the limitations and toward what I believed could be effectively utilized.

REFERENCES

[1] Wu, S. et al. Estimation of cracking risk of concrete at early age based on thermal stress analysis. Journal of Thermal Analysis and Calorimetry. 2011; v. 105, n. 1, p.171-186.

[2] Zocher M.A., Groves S.E., Allen D.H. A three-dimensional finite element formulation for thermoviscoelastic orthotropic media. International Journal for Numerical Methods in Engineering, 1997; 40(12), 2267–2288.

[3] De Schutter G (2004) Applicability of degree of hydration concept and maturity method for thermo-visco-elastic behaviour of early age concreten. Cement and Concrete Composites 26(5):437–443

[4] Fairbairn EMR, Toledo RD, Ribeiro FLB, et al (2007) Modelagem do concreto a poucas idades com aplicações em barragens: Novos paradigmas e novas soluções. Relatório final de P&D, COPPETEC.

[5] D'Aloia L, Chanvillard G (2002) Determining the "apparent" activation energy of concrete: Ea - Numerical simulations of the heat of hydration of cement. Cement and Concrete Research 32(8):1277–1289. https://doi.org/10.1016/S0008-8846(02) 00791-3

[6] Jieying Zhang JJB (2005) A Discussion of the paper "Application of degree of hydration concept and maturity method for thermovisco-elastic behaviour of early age concrete" by Geert De Schutter. Cement and Concrete Composites 27(6):734–735. https://doi.org/10.1016/j.cemconcomp.2004.12.001

[7] Zhang J, Cusson D, Monteiro P, et al (2008) New perspectives of maturity method and innovative approach for high performance concrete applications. Cement and Concrete Research 38(12):1438–1446.

[8] Cervera M, Faria R, Oliver J, et al (1999) Macroscopic Modelling of Concrete Aging Regarding Hydration and Temperature Effects. Publication CIMNE (170):25

[9] Gomes, F. M. P. et. al. Uma solução analítico-numérica para a difusividade do calor em um cilindro com e sem geração de calor. Proceedings of the XXXVII Iberian Latin-American Congress on Computational Methods in Engineering Suzana Moreira Ávila (Editor), ABMEC, Brasília, DF, Brazil, November 6-9, 2016.

[10] US Bureau of Reclamation (1949). Boulder Canyon Project: Final Reports. Cement and concrete investigations. Cooling of concrete dams, Part VII.

[11] Sassone, M.; Chiorino, M. A., 2005. Design aids for the evaluation of creep induced structural effects. In: Gardner, D. J.; Weiss, J. (Ed.). SP-227: Shrinkage and Creep of Concrete. American Concrete Institute. Special Publication 11, p. 239-259.

[12] Bažant, Z. P., & Jirásek, M. (2018). Creep and hygrothermal effects in concrete structures (Vol. 225). Dordrecht, The Netherlands: Springer.

[13] Gomes F.M.P., “Estudo da Fluência do Concreto Massa - Hidrelétricas mais Seguras e Sustentáveis”. Anais do 54º Congresso Brasileiro do Concreto, IBRACON, Gramado - Brasil, 2013.

[14] Conceição J., Faria R., Azenha M.D., Gomes F.M.P., Souza F.V., Early-age behaviour of the concrete surrounding a turbine spiral case: Monitoring and thermo-mechanical modelling, Engineering Structures, vol. 81, pp. 327–340, Out. 2014.

[15] Chieregato A.C.; Guerra E.A.; Gomes F.M.P.; Traboulsi M.A.; Silva R.R. da; Santana W.G. (2017). Propriedades do CRFA Utilizado na Construção do Vertedouro Extravasor de Troncos da UHE Santo Antônio. Revista Concreto & Construções. Nº 88, p. 68. Out- Dez de 2017.

[16] Gomes F.M.P., Pedroso L.J. “Monitoramento da UHE Santo Antônio - Vertedouro Extravasor de Troncos: Execução e Resultados”. RTP-FMPG-03/2015. Not published.

[17] Gomes F.M.P. “Estudos térmicos e tensionais unidimensional e bidirecional do concreto de 2º estágio da blindagem do tubo de sucção para a UHE Salto do Apiacás”. Relatório GST.E.051.2015-R0. Agosto, 2015. Not published.

Fifth International Dam World Conference
PORTUGAL • LISBON • LNEC • APRIL 13-17, 2025
dam world 2025

EVALUATION METHOD FOR SAFETY OF CONCRETE SLAB STRESS BASED ON MULTI-AXIAL STRENGTH CRITERION

Zhankuan Mi
Nanjing Hydraulic Research Institute

Kuangmin Wei
Nanjing Hydraulic Research Institute

Fang Wang[1]
Nanjing Hydraulic Research Institute

ABSTRACT

The concrete-faced rockfill dams (CFRDs) rely on the key impermeable structures, such as concrete slabs, for their safe operation. Ensuring the safety of the concrete slabs is of the utmost importance. The current evaluation method, which utilizes uniaxial strength, overlooks the influences of slab stress on their strength and may lead to unreasonable judgments regarding the damage zone. To address this issue, a method is proposed for evaluating the stress in the concrete slabs based on the multi-axial strength criterion. The safety of the slabs is assessed by determining the strength adjustment coefficient of concrete and the stress level index of multi-axial strength. A refined stress distribution analysis of the slabs is conducted using the cross-scale fine simulation method based on the multi-point constraint. The improved viscoelastic method is employed to comprehensively simulate the impact of dynamic and permanent deformations on the slab stress. This approach accurately depicts the progression of slab damage during an earthquake. To illustrate the effectiveness of the proposed multi-axial strength method, a 240 m-high concrete-faced rockfill dam located in a narrow valley within a seismic zone is taken as an example for comparison with the current uniaxial strength method. The results demonstrate that during the operational period, the material strength at both sides of the dam abutment is reduced, while it is enhanced on the riverbed, particularly at the bottom. Both methods yield similar conclusions regarding the tensile damage zones, but there are significant disparities in the compressive damage zones. During an earthquake, the multi-axial strength method indicates slightly smaller tensile damage zones, whereas the location and extent of the compressive damage zones differ significantly between the two methods. Considering the limitations of the uniaxial strength method in considering the influences of slab stress on their strength, it is suggested to adopt the multi-axial strength criterion as a guide for designing and constructing concrete slabs in extra-high CFRDs.

Keywords: CFRD, strength criterion, dynamic analysis, safety evaluation, refinement method.

[1]wangfang@nhri.cn, China

1. INTRODUCTION

Concrete-faced rockfill dams have a strong ability to adapt to foundation deformation, are economical and environmentally friendly, and have mature technology, making them highly competitive among many dam types. With the growing energy demand of society, the height and size of dams are increasing, and the construction and operation are facing important problems such as deformation control [1-2], infiltration safety [3], and structural earthquake resistance [4-5]. The concrete slab represents the principal seepage control structure of the CFRDs, and its stress safety is directly correlated with the overall safety. However, there is currently a lack of stress safety evaluation method for concrete slab in the specifications that are currently in place. The 'Design specification for hydraulic concrete structures' [6] is the most commonly referenced document in this regard, as it is used to assess the strength safety of concrete based on its uniaxial compressive and tensile strength [7]. Empirical evidence indicates that the impact of stress state on concrete strength is relatively insignificant for CFRDs with a height of 100 meters. The application of the uniaxial strength index to assess the slab stress safety is, in principle, a viable approach. However, for CFRDs with a height of 200 m or those with inadequate foundation conditions, the overall stress on the slab is likely to be more pronounced.It is imperative to consider the impact of stress on slab strength when assessing the safety of the slab, as failure to do so may result in erroneous conclusions. A similar issue arises in the assessment of dynamic damage to slabs during strong earthquakes. The extant evaluation criteria are unable to reflect the dynamic alteration in the strength of slabs resulting from intricate stresses during seismic events. It is therefore untenable to utilise the outcome of superposition of static and dynamic stress envelopes that exceed the uniaxial ultimate strength as the benchmark for assessing dynamic damage[8-9].

In conclusion, this paper presents a methodology for assessing the deterioration of slabs by integrating the principles of multiaxial strength in concrete with the refinement simulation techniques.The main features of this method include: a) adopting the uncoordinated grid calculation technology [10] to achieve the refined simulation of the slab structures, avoiding the problem of reduced simulation accuracy caused by the ‘averaging effect’; b) adopting the improved viscoelasticity method [11] to comprehensively consider the effects of dynamic displacement and permanent deformation on the dynamic stress of the slab, which can truly reflect the damage development process of the slab in the process of earthquake; c) combining the stress state of the slab with the multiaxial strength criterion of concrete, proposing the multiaxial stress level of concrete as an indicator of the safety evaluation of the slab. The paper takes a 240m concrete-faced rockfill dam as an example. and compares the difference between the uniaxial strength method and the multiaxial strength method in evaluating the

stress safety of concrete slabs. The conclusions of this study can provide technical support for the evaluation of slab damage criteria in CFRDs.

2. METHODS FOR REFINEMENT SIMULATION OF SLAB STRESSES

2.1. Uncoordinated Grid Computing Methods

In the numerical simulation of CFRDs, the accuracy of the slab stress simulation may be reduced due to the 'averaging effect' of the sparse mesh. In this paper, an uncoordinated mesh calculation technique for CFRDs based on the displacement multipoint constraint method can realize the refinement simulation of slabs by matrix transformation, which improves the computational efficiency because it does not need to introduce the penalty function and iterative solving.

The basic principle of the displacement multipoint constraint method is shown in Fig. 1, where e1 and e2 are sparse meshes and e3 is a dense mesh, then the displacements of nodes o', p', q', and r' can be expressed by the node displacements of e1 and e2. Taking node o' as an example, its displacement can be expressed by the displacement of node i, j, m, and n if the interpolation method of equivariant mesh is used:

$$\begin{aligned} u_{o'} &= N_1 u_i + N_2 u_j + N_3 u_m + N_4 u_n \\ v_{o'} &= N_1 v_i + N_2 v_j + N_3 v_m + N_4 v_n \\ w_{o'} &= N_1 w_i + N_2 w_j + N_3 w_m + N_4 w_n \end{aligned} \tag{1}$$

where: N_1~N_4 are the shape functions in i, j, m, n plane local coordinates. At this time, the degrees of freedom of the mesh nodes o', p', q', r' are all 'slave degrees of freedom', and the degrees of freedom of the nodes i, j, m, n, l, k are the 'master degrees of freedom'.

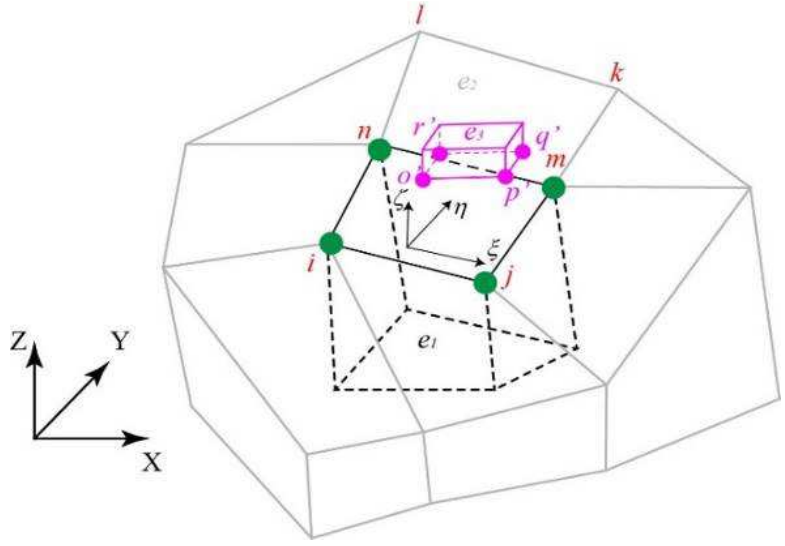

Fig. 1 – 3D example of the multi-point constraint refinement

The stiffness matrix and load matrix of dense mesh e3 can be assembled to the overall stiffness matrix and load column matrix by conversion matrix condensation operation, and after solving the equilibrium equations, the displacements of nodes i, j, m, and n are obtained, and then the displacements of node o' are inverted according to Eq. (1).

2.2. Improved dynamic viscoelastic analysis method

The conventional viscoelastic method is built on the basis of soil hysteresis curves, using the soil dynamic shear modulus and damping ratio as variables to describe the hysteresis law of the cyclic strain component of the soil material [12], and expresses the plastic residual deformation as a function of the dynamic shear strain, stress level, and number of vibrations. The improved dynamic viscoelastic method adopted in this paper can unify the effects of dynamic displacement and permanent deformation on the dynamic stresses of slabs and the actual dam damage process [11]. In the computational analysis, the “actual displacement” of the node at each moment is the sum of the dynamic cyclic displacement and the cumulative permanent displacement. The stresses and strains of the element are calculated from the ‘actual displacements’. The improved method can more realistically reflect the impact of the dam deformation on the slab.

3. METHOD AND APPLICATION OF STRESS EVALUATION BASED ON MULTI-AXIAL STRENGTH CRITERION

3.1. Guidelines for multi-axial strength of concrete

Concrete slabs are in a typical triaxial stress state during the operation period, and the Code for the Design of Hydraulic Concrete Structures [6] stipulates that the concrete strength under the triaxial stress state should be satisfied:

$$|\sigma_i| \leq |f_i| \tag{2}$$

where: σ_i represents the main stress value, $\sigma_1 \geq \sigma_2 \geq \sigma_3$; f_i represents the concrete strength multiaxial strength representative value, $f_1 \geq f_2 \geq f_3$. In this paper, the stress sign is negative in tension and positive in compression.

Concrete is in triaxial stress state, the value of f_i which needs to be adjusted on the basis of uniaxial strength, the degree of strength adjustment varies according to different combinations of stresses, and there are three main stress states, namely triaxial tensile, triaxial tensile-pressure and triaxial compression. The specification provides that the tensile strength is 0.9 times the uniaxial tensile strength in the case of triaxial tension, and also gives the adjustment factor for the compressive strength in the triaxial tension and triaxial compression condition,

see Fig. 2. However, the rule governing the change in concrete strength under tension and compression is more intricate than that governing only compression or only tension. Consequently, it is challenging to accurately assess the damage state of the slab by solely relying on compressive strength as the evaluation criterion. Therefore, when determining the ultimate strength, it is essential first to ascertain the potential damage state of the slab in accordance with the prevailing stress conditions and subsequently perform a damage assessment.

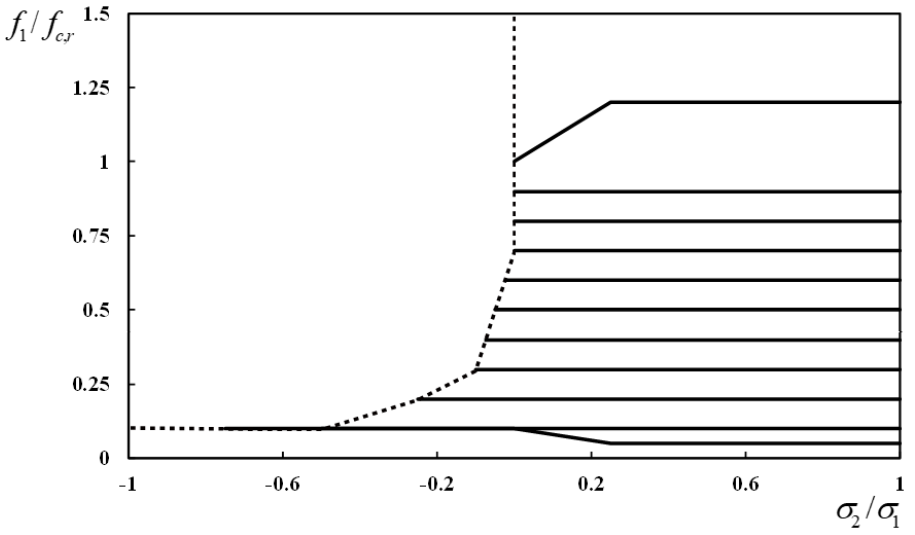

(a) Triaxial tensile-compressive stress state

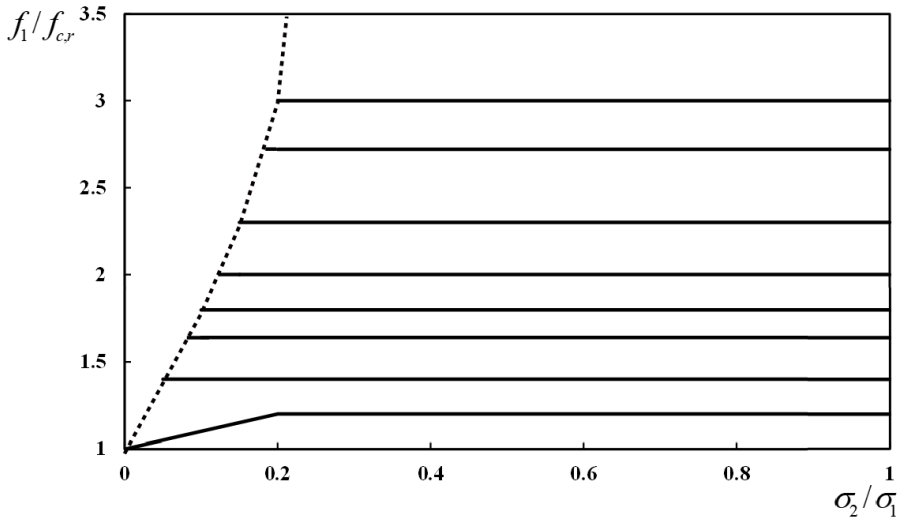

(b) Triaxial compressive stress state

Fig. 2 – Ultimate strength of concrete under triaxial stress state

Guo et al [13-14] have carried out a large number of experimental studies on the strength of concrete under multiaxial stress, which showed that the typical damage patterns of concrete

specimens under multiaxial stress include tensile breakage, columnar compression, lamellar splitting, diagonal shear damage, and extruded flow. At the same time, the range of the stress state and control stress of the above five typical damages are given through the statistical experimental data, which are shown in Table 1. Concrete under triaxial tension and compression is dominated by pull-off, columnar crushing and sheet splitting damage, of which the latter two damage forms have compressive stress as the dominant stress. In this paper, the computational analysis adopts the research results of Guo[13-14], and the stress state range given in Table 1 is used as a supplementary condition to make a preliminary judgment on the damage forms of slabs under tension and compression and to determine the dominant stress. The value of compressive strength adjustment factor has been clearly defined in the specification. The test results have shown [15], due to the presence of compressive stress leads to a significant reduction in tensile strength, about 0.3 ~ 0.95, mainly concentrated in the 0.3 ~ 0.6. Due to the adjustment coefficient fluctuation interval is large, respectively, take 0.3, 0.4, 0.5, 0.6 as the adjustment coefficient for testing. According to the test results, its adjustment coefficient has less influence on the results of panel damage judgment, so this paper adopts 0.5 as the adjustment coefficient of tensile strength of the panel after pulling bad under tension and compression state.

Table 1 – Division of the typical failure mode of concrete samples[13]

	Typical failure mode	Pull off	Columnar fracture	Sheet splitting	Shear destruction	Squeeze flow
	Dominant stress	σ_3	σ_2	σ_1,σ_2	σ_1,σ_3	σ_1,σ_3
Stress state	tensile/tensile/tensile	$0 > \sigma_1 > \sigma_2 > \sigma_3$	-	-	-	-
	compression/tensile /tensile	$\left\|\frac{\sigma_3}{\sigma_2}\right\|, \left\|\frac{\sigma_2}{\sigma_1}\right\| \geq 0.1$	$\left\|\frac{\sigma_3}{\sigma_2}\right\|, \left\|\frac{\sigma_2}{\sigma_1}\right\| < 0.1$	-	-	-
	compression /compression/tensile	$\left\|\frac{\sigma_3}{\sigma_1}\right\| \geq 0.1$	-	$\left\|\frac{\sigma_3}{\sigma_1}\right\| < 0.1$	-	-
	compression/compression /compression	-	$\left\|\frac{\sigma_3}{\sigma_1}\right\|, \left\|\frac{\sigma_2}{\sigma_1}\right\| \leq 0.15$	$\left\|\frac{\sigma_3}{\sigma_1}\right\| \leq 0.15$, $\left\|\frac{\sigma_2}{\sigma_1}\right\| > 0.15$	$\left\|\frac{\sigma_3}{\sigma_1}\right\| =$ 0.15~0.2 , $\left\|\frac{\sigma_2}{\sigma_1}\right\| > 0.15$	$\left\|\frac{\sigma_3}{\sigma_1}\right\|, \left\|\frac{\sigma_2}{\sigma_1}\right\| > 0.15$

3.2. Method of stress evaluation based on multi-axial strength criterion

Based on the computational simulation technique for CFRDs in Section 1 and the concrete multiaxial strength criterion in Section 2.1, the stress safety evaluation process for concrete

slabs based on multiaxial strength proposed in this paper is shown in Fig. 3, with the following steps:

(1) Conduct static analysis to calculate the static stress state of slabs under the action of construction, impoundment, operational rheology, etc. ;

(2) Perform dynamic calculations to calculate the dynamic stress, dynamic strain, and cumulative plastic strain of the mesh based on the acceleration, velocity, and displacement of the node at the current moment i ;

(3) Based on the results of the slab stresses at different moments during the static and seismic processes, the damage pattern of the mesh is determined according to the damage pattern criteria given in Table 1. ;

(4) Determine the concrete strength adjustment factor $f_1/f_{c,r}$、$f_2/f_{t.r}$ based on the typical failure mode and Fig. 2 ;

(5) Calculation of multi-axis stress level, and output the judgment result.

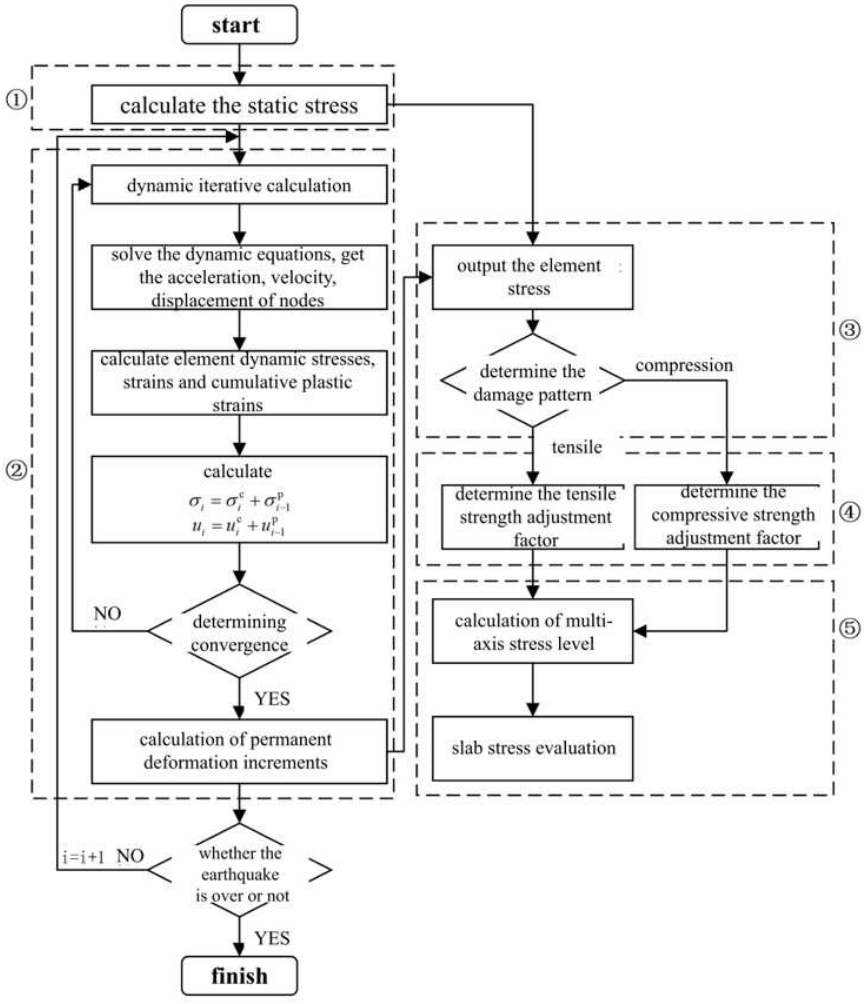

Fig.3 – Flow chart of concrete slab stress evaluation based on multi-axial strength criterion

4. FINITE ELEMENT MODEL AND CALCULATION PARAMETERS

4.1. Finite element model

This paper takes a proposed 240m-high CFRD as an example to carry out a slab safety evaluation study, the typical section of the dam is shown in Fig. 4. The upstream slope of the dam is 1:1.5, with a cross-seam at the slab elevation of 2232m. The downstream slope of the dam has a combined slope ratio of 1:1.763 above the elevation of 2230m, and a combined slope ratio of 1:2.2~1:2.5 below the elevation of 2230m. The dam body is mainly divided into cushion zone, transition zone, main rockfill zone, strengthen zone, downstream rockfill zone, and pressing slope zone. The 3D model established according to the actual topography is shown in Fig. 5. The seismic design intensity of the dam is VIII degree, taking the base period of 100 years beyond the probability of 2% as the design earthquake, and the peak acceleration of horizontal ground vibration is 305 gal, which belongs to the strong seismic zone of the narrow valley of the CFRDs.

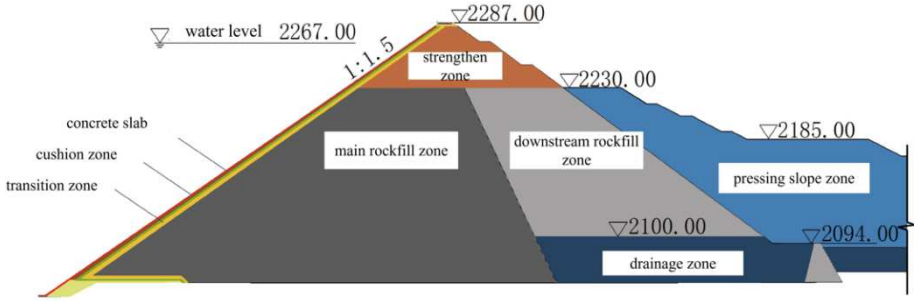

Fig. 4 – Material zoning of the typical section

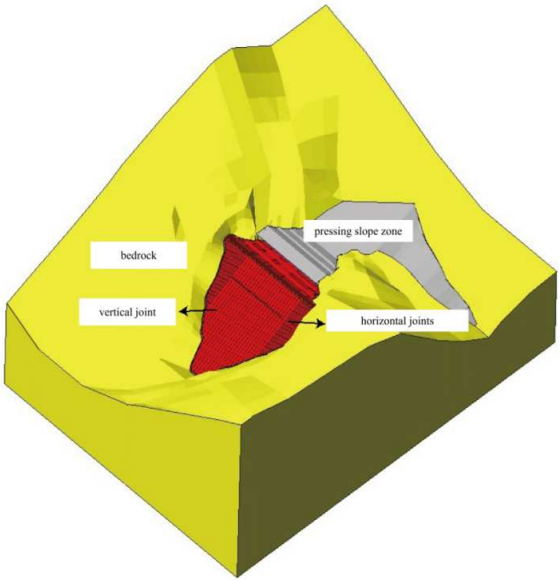

Fig. 5 – 3D FEM model

In order to realize the slab refinement simulation, the slabs are encrypted by non-coordinated grid calculation technique, as shown in Fig. 6, the maximum size of the concrete slab mesh is 1.0~2.0m, the slab is divided into 3 layers along the thickness direction, and the model summarizes about 270,000 nodes and the total number of mesh is about 200,000 meshes.

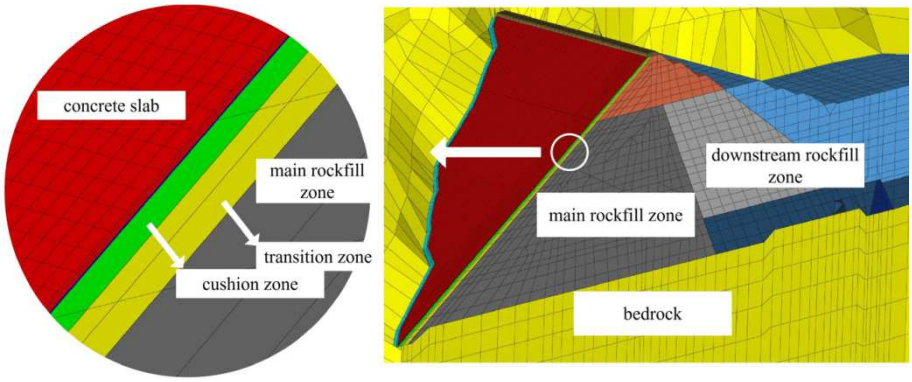

Fig. 6 – Detailed view of mesh refinement

4.2. Constitutive model and parameters

The static calculation is based on the 'Nanshui' model [16], and the rheological calculation is based on the 7-parameter rheological model [17], with the parameters determined according to the indoor tests, as shown in Tables 2 and 3. The dynamic model is based on the Shen's Dynamic Model [12], with the values of the parameters shown in Table 4. The Goodman mesh was used to simulate the contact between the slab and the bedding. Vertical and perimeter joints are simulated using seam mesh. The slabs were made of C30 concrete, calculated by linear elastic model, with elastic modulus of 31.5 GPa, Poisson's ratio of 0.167, standard compressive strength of 20.1 MPa and standard tensile strength of 2.01 MPa. The slabs are poured in two phases, and the total length of the construction period is 54 months, which is simulated up to 20 years of operation.

Table 2 – Parameters of the "NHRI" model

Zone	ρ(g/cm^3)	φ_o(°)	$\Delta\varphi$(°)	K	n	R_f	c_d(%)	n_d	R_d
cushion zone	2.324	54.2	10.3	1515	0.33	0.8	0.002	0.54	0.707
transition zone	2.296	55.0	11.1	1186	0.32	0.8	0.004	0.654	0.697
main rockfill zone	2.268	54.1	11.1	1519	0.29	0.83	0.004	0.594	0.735
strengthen zone	2.296	54.4	11.1	1750	0.29	0.83	0.003	0.613	0.723
downstream rockfill zone	2.260	57.3	13.5	1494	0.32	0.81	0.005	0.533	0.703
drainage zone	2.240	57.3	13.5	1296	0.32	0.81	0.005	0.533	0.703
pressing slope zone	2.010	44.5	6.8	450	0.35	0.63	0.008	0.578	0.583

Table 3 – Parameters of the creep model

Zone	α	b/%	c/%	d/%	m_1	m_2	m_3
Drainage zone	0.002	0.1014	0.046	0.1480	0.462	0.567	0.893
Others	0.002	0.0806	0.019	0.1272	0.425	0.541	0.801

Table 4 – Parameters of Shen's dynamic model

Zone	k_2	n	k_1	λmax	c_1(%)	c_2	c_4(%)	c_5
cushion zone	3618	0.45	40.0	0.17	0.64	0.97	6.33	0.69
transition zone	4007	0.42	55.5	0.24	0.61	1.26	6.12	0.88
main rockfill zone	4589	0.49	62.7	0.23	0.56	1.23	5.80	0.79
strengthen zone	4718	0.49	62.7	0.23	0.60	1.23	5.92	0.79
downstream rockfill zone	4030	0.56	54.1	0.24	0.58	1.26	5.89	0.88
drainage zone	3917	0.55	54.1	0.24	0.60	1.26	5.90	0.88
pressing slope zone	500	0.35	20.0	0.28	0.62	1.23	6.17	0.80

4.3. Ground motion input

Using the non-coherent ground vibration input method with artificial viscoelastic boundaries combined with boundary equivalent nodal loads [18], the dam axial, down-river, and vertical acceleration time courses are shown in Fig. 7.

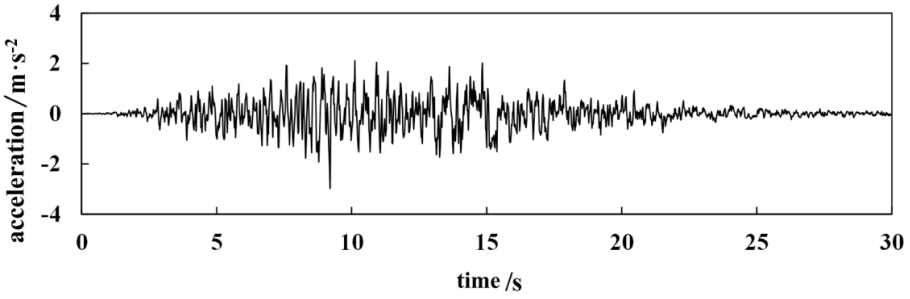

(a) axial direction

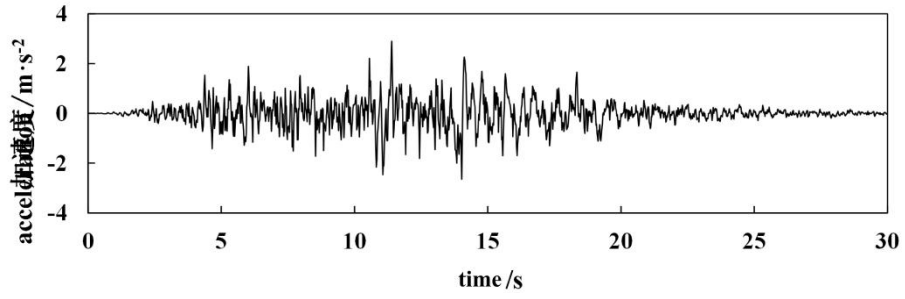

(b) river-oriented

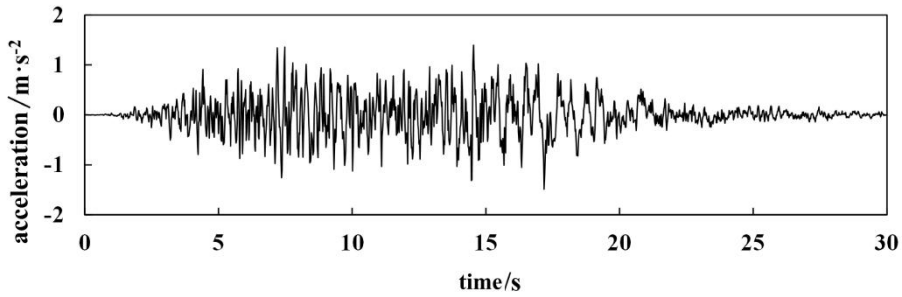

(c) vertical

Fig. 7 – Input acceleration time history

5. RESULT AND DISCUSSION

5.1. Safety evaluation of slab stresses during the operation period

In order to reasonably reflect the stress security state of the slab, the multiaxial strength evaluation method proposed in this paper and the uniaxial strength evaluation method using the uniaxial standard strength as the evaluation index were used to judge the damage area of the concrete slab in this project respectively. Fig. 8 shows the area of compressive damage and tensile damage obtained by the two methods respectively. According to the simulation, the maximum axial compressive and tensile stresses were 22.47 MPa and 2.52 MPa respectively. Affected by the dam deformation from banks to the riverbed, the axial compressive stress was mainly concentrated in the middle of the riverbed and the local edge of the vertical joints. Taking the uniaxial standard strength as the slab stress evaluation index, the compressive damage zone appeared in the same area, while the tensile damage zone appeared on both sides of the bank. The stress along slope was basically compressive, with the maximum compressive stress of 20.73 MPa, and a compressive damage zone occurs in the middle and lower part of the phase 1 slab.

Comparison can be seen that the two methods of slab tensile damage area was basically the same. However, for the compression damage area, there was differences in the judgment results of the two methods. The difference was mainly in the uniaxial strength method where a large extent of extrusion damage occurred in the middle of the riverbed slabs, whereas the multiaxial strength method resulted in only a small extent of localized damage in the low elevation area of the right bank. The reason for the above differences is that the multi-axial strength takes into account the effect of the stress state on the concrete strength. The slab compressive strength adjustments were given in Fig. 9, and it can be seen that, except for the reduction of the compressive strength on the banks of the river ($f_1/f_{c,r}$<1), the compressive strengths of the slabs in the remaining areas have been improved (Zone I: $f_1/f_{c,r}$ >2, Zone II:

2 > $f_1/f_{c,r}$ > 1). Especially for the slabs in the middle and lower part of the riverbed, the multi-axial strength had been increased by more than 2 times, while for the tensile strength, the stress state had less influence on it as described in Section 2.1.

Adjustment coefficients for compressive and tensile strengths of each mesh can be derived from the stress state (see Fig. 9). As most area of the middle of the slab was in the state of triaxial pressure, the compressive strength were in different degrees of enhancement, especially the riverbed section of the slab near the bottom of the part of the extrusion effect was stronger, the compressive strength increased to the uniaxial standard strength of more than two times. Due to the presence of tensile stresses, the compressive and tensile strength of the slabs on both banks and localized at the top of the CFRDs had been significantly reduced, and the safety of the 'strength reduction zone' of the slabs should be emphasized.

Therefore, the use of uniaxial criteria for evaluating the safety state of the slabs underestimates the compressive strength of the compression zone and overestimates the compressive strength of the tension zone, thus misjudging the actual safety of the slabs.

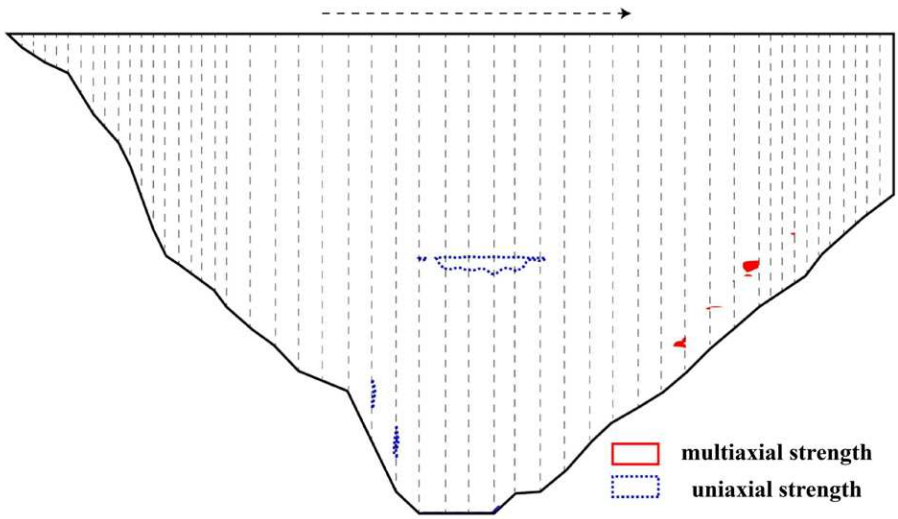

（a）comparison of the damage area of slabs under compression

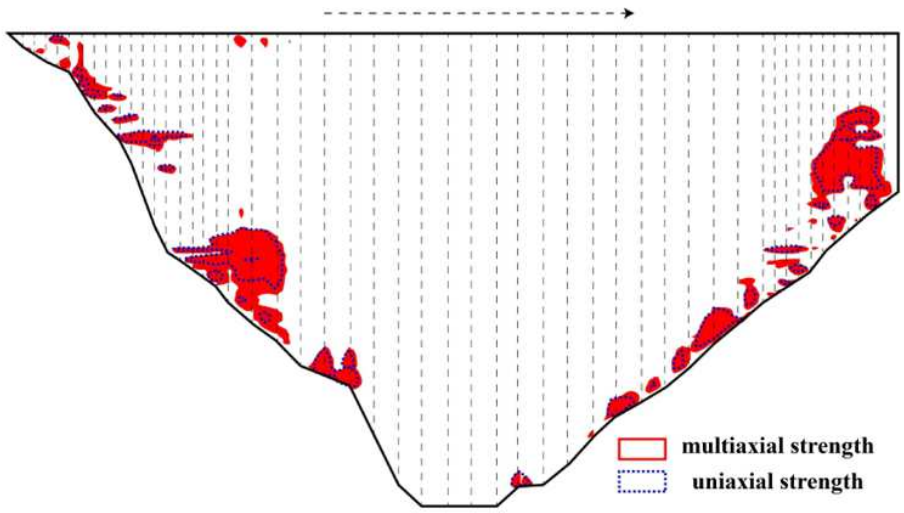

（b）comparison of the damage area of slabs under tensile

Fig. 8 – Damage zone on concrete slab after 20 years

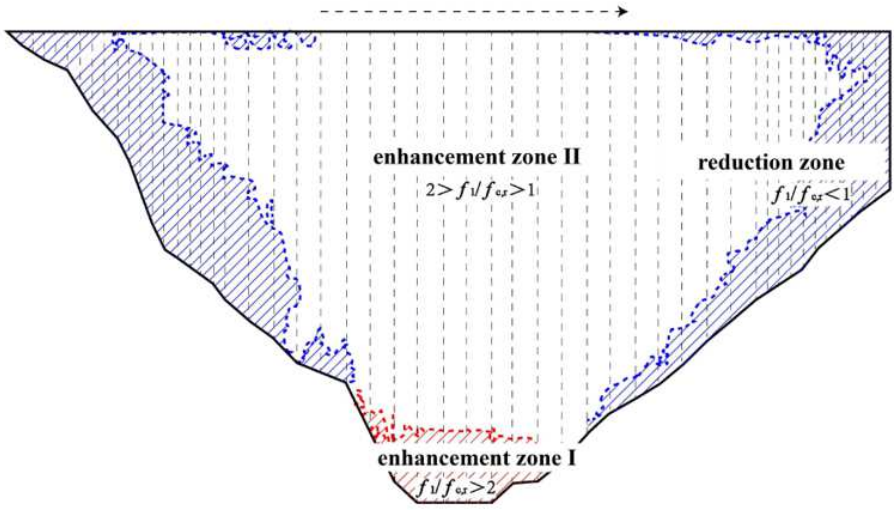

Fig. 9 – Compressive strength adjustment of slab during the operation period

5.2. Safety evaluation of stresses in slabs during the earthquake

5.2.1 Dam dynamic damage process

Fig. 10 shows the displacement curves of the sample nodes at the top of the dam. The dam during the seismic process had produced irrecoverable deformation. Most of the deformation was generated in the early stage of the earthquake, and the maximum settlement of the top of the dam caused by the earthquake was 63.28 cm. After the earthquake, the top of the dam was deformed downstream, and the maximum settlement was 29.12 cm.

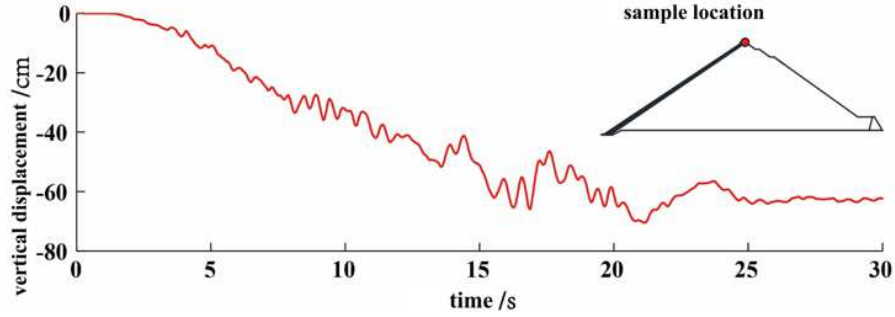

（a）vertical

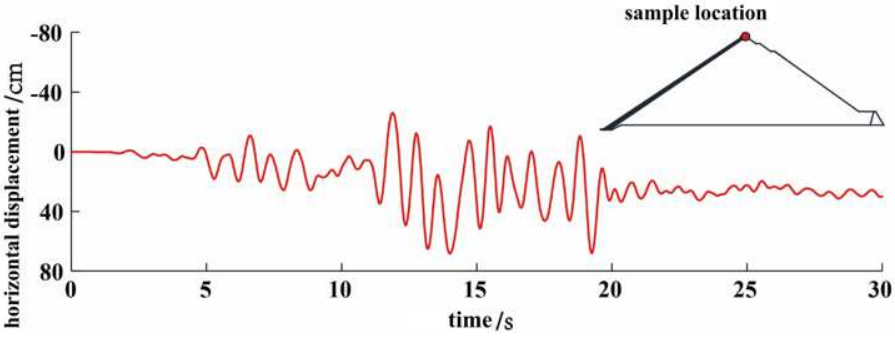

（b）horizontal

Fig. 10 – Displacement time history of the sample node at the dam crest

Fig. 11 shows the development process of the damage area of the slabs judged by the multi-axial strength method, and it can be seen that the damage of the slabs is mainly concentrated in the pre-earthquake period[19-20]. The damage area of the slabs in the late stage of the earthquake would not show a substantial increase, and the damage in the late stage was mainly compression damage.

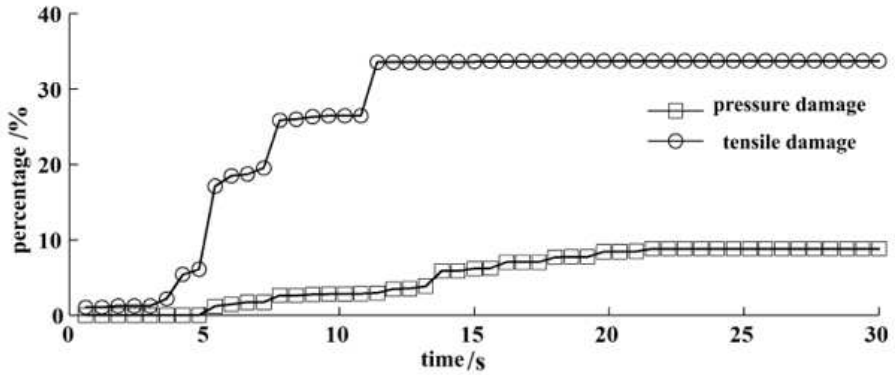

Fig. 11 – Percentages of damaged zone on concrete slab

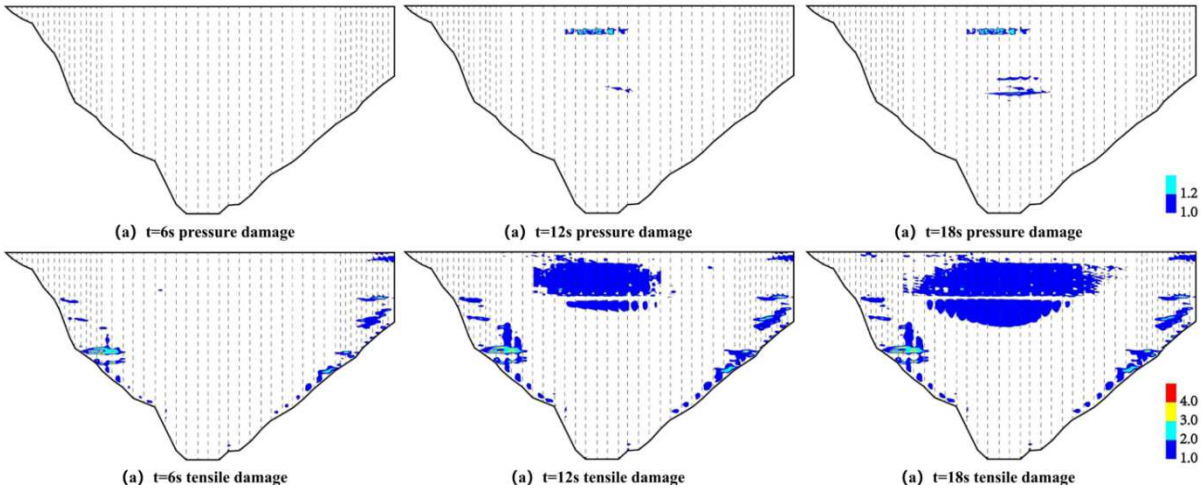

Fig. 12 – The development of the concrete slab's damage zone at different moment

5.2.2 Comparative analysis of the dynamic damage area

Fig. 13 compares the damage area of slabs judged by uniaxial strength method and multiaxial strength method. It can be seen that the compression damage area of slabs under multiaxial strength method was obviously reduced compared with that of uniaxial strength method, and the distribution pattern of tensile damage was basically the same but with a reduced area. Considering that the multi-axial stress intensity had a great influence on the judgment of the compressive damage area of the slabs under dynamic state, the uniaxial intensity method used in this project overestimated the compressive damage area of the slabs.In order to investigate the reason for this difference, the time-range curves of stress levels of two sample points located at 0.4H and 0.9H elevations of the middle slab of the riverbed were selected for comparison. The stress time curve of the sample point of the slab at the elevation of 0.4H is given in Fig. 15, which was in the middle of the slab and was always compressed during the seismic process, and the stress along slope is obviously higher than that in the axial direction. The stress along slope in this point shows an increasing trend and exceeds 1.0% at 11.92s. With the use of the multi-axial strength method, the multi-axial stress level in this point was consistently below 0.6, which shows that the use of the uniaxial strength method significantly underestimated the compressive capacity of the slab at this location. Fig. 15 gives the time-range curves of the compressive and tensile stress levels of the sample point in the middle of the slab at 0.9H elevation, respectively. From Fig. 16(a), it can be seen that the maximum compressive stress level in this area did not exceed 0.7 if judged by the uniaxial strength method. After considering the multi-axial strength, its multi-axial compressive stress level reaches 1.0 at 11.96 s, which is due to the reduction effect of the stress along slope tensile stress on its compressive strength. Fig. 15(b) shows the development of the tensile stress level of the point, and it can be seen that the stress along slope and the multi-axial tensile stress level exceeded 1.0 at 11.32s and 6.20s, respectively, and tensile damage occurred.

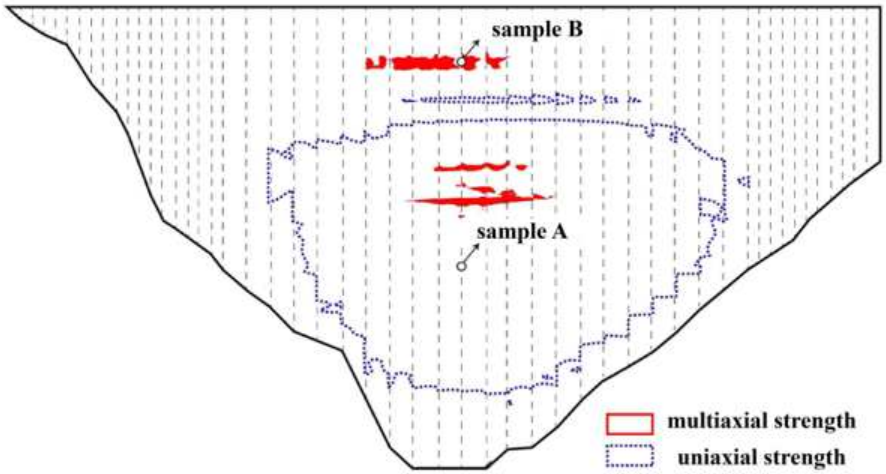

（a）comparison of the damage area of slabs under under compression after the earthquake

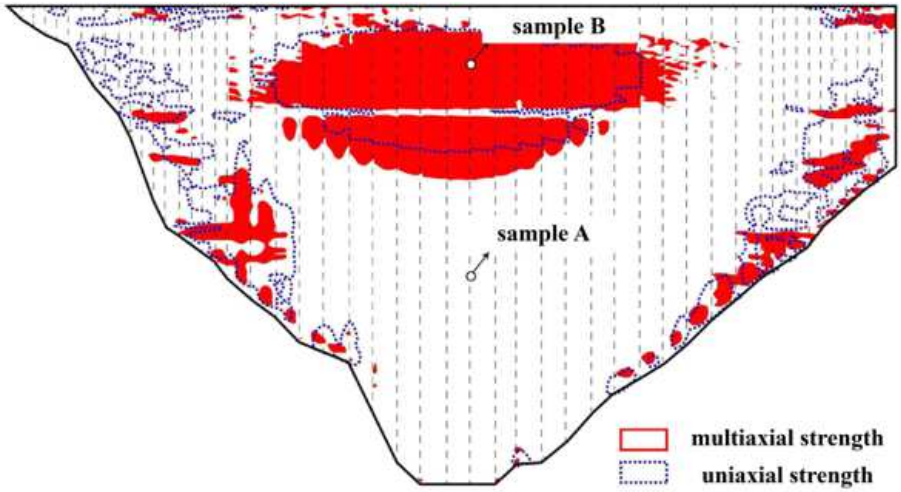

（b）comparison of the damage area of slabs under tensile after the earthquake

Fig. 13 – Damage zone on concrete slab at the end of earthquake

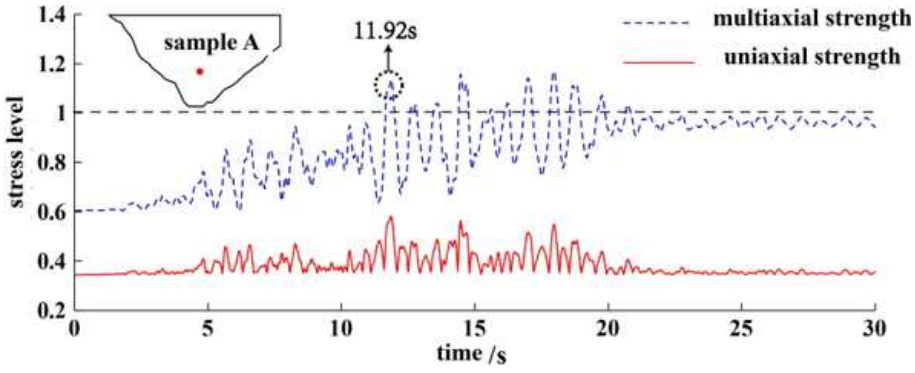

Fig. 14 – Stress level time history of the typical element at 0.4H

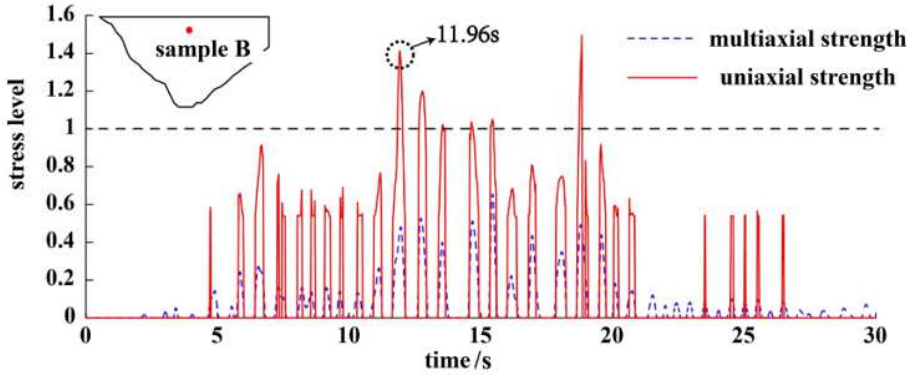

(a) compressive stress level

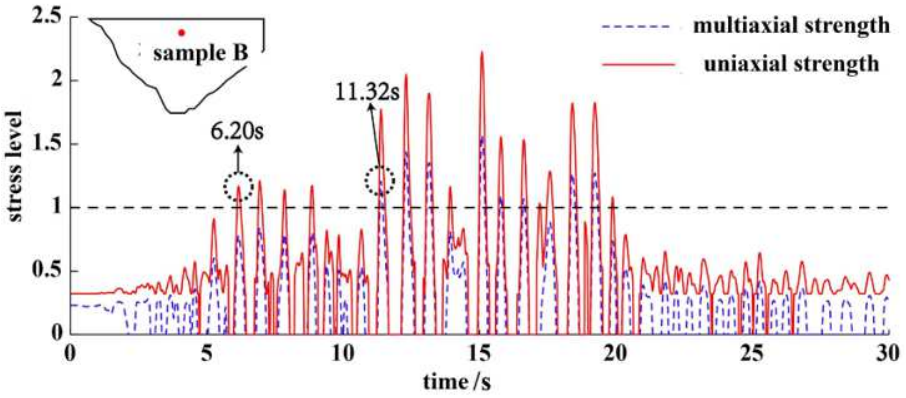

（b）tensile stress level

Fig. 15 – Stress level time history of the typical element at 0.9H

6. CONCLUSIONS

This paper proposes a stress safety evaluation method based on multiaxial strength criterion for the concrete slab, and analyzed the difference between the traditional uniaxial strength criterion and the above method by comparing with the 240m-high CFRD, and the main conclusions obtained are as follows:

(1) Under the static state, the concrete slabs basically take the dam banks as the ‘compressive strength reduction zone’, and the other parts as the ‘compressive strength enhancement zone’. The corresponding area of the strength of the concrete material is enhanced or weakened to different degrees. The traditional uniaxial strength method underestimates the compressive strength of the slabs under compression. There is a big difference between the two methods in judging the damage area of the slab under compression.

(2) Under the earthquake, the area of tensile damage derived from the multi-axial strength method is basically the same as the evaluation results of the uniaxial strength method, but there is a large difference in the pattern and range of dynamic compression damage. The multi-axial strength method can reflect the increase in compressive strength of the slabs due to compressive stresses and the decrease in compressive strength due to tensile stresses.

(3) Since the uniaxial strength method is unable to take into account the effect of slab stress on its strength and the possible misdiagnosis of slab damage area, it is recommended that a multi-axial strength criterion be used to guide the design and construction of extra-high CFRDs.

In this paper, a 240m-high CFRD is taken as the main research object to verify the rationality of the slab safety evaluation method proposed. However, it should be noted that due to the influence of various factors such as dam height and terrain, the comparison results of different evaluation methods may be different, so it is necessary to demonstrate and compare.

ACKNOWLEDGEMENTS

This study is supported by National Key Research and Development Program of China (2024YFF1700702), Key Research and Development Program of Shaanxi Province(2024GX-YBXM-470) and National Natural Science Foundation of China (52350393). We thank the anonymous reviewers and the editor for their valuable comments and suggestions, which significantly improved the manuscript.

REFERENCES

[1] ZHAN Zheng-gang, ZHANG He-zuo, CHENG Rui-lin, et al. Application of methods for life-cycle deformation control of high concrete-faced rockfill dams[J]. Chinese Journal of Geotechnical Engineering, 2022, 44(6): 1141-1147.

[2]XU Ze-ping, LU Xi, ZAI Ying-chun, et al. Study on stress and deformation and engineering measures for concrete faced rockfill dam built in narrow valley[J]. Journal of Hydraulic Engineering, 2022, 53(12): 1397-1409.

[3]XU Ze-ping. Research progresses and key technologies of CFRD construction[J]. Journal of Hydraulic Engineering, 2019, 50(1): 62-74.

[4]Zou De-gao, Kong Xian-jing, Liu Jing-mao, et al. Criteria for ultimate aseismic capacity of high rockfill dam. Sci Sin Tech, 2022, 52(12): 1831–1838.

[5]CHEN Sheng-shui, LI Guo-ying, FU Zhong-zhi. Safety criteria and limit resistance capacity of high earth-rock dams subjected to earthquakes[J]. Chinese Journal of Geotechnical Engineering, 2013, 35(1): 59–65

[6]National Energy Administration. Code for Design of Concrete Face Rockfill Dams[S]. Beijing: China Water & Power Press, 2022.

[7]DANG Fa-ning, CHEN Jing-jing, GAO Tian-qing, et al. Study on the influence of seismic wave input angle on dynamic response of high face slab pumped storage dam[J]. Journal of China Institute of Water Resources and Hydropower Research, 2022, 20(5): 402-410+421.

[8]Federal Emergency Management Agency. Federal Guidelines for Dam Safety: Earthquake Analyses and Design of Dams ,2005,FEMA P-65.

[9]USACE. (2003). Time-History Dynamic Analysis of Concrete Hydraulic Structures (EM 1110-2-6051). Headquarters, US Army Corps of Engineers.

[10]WEI Kuang-min, CHEN Sheng-shui, LI Guo-ying, et a1. Application of displacement multi-point constraint refinement method in simulation of concrete-faced rockfill dams[J]. Chinese Journal of Geotechnical Engineering, 2020, 42(4): 616-623.

[11]WEI Kuang-min, CHEN Sheng-shui, MA Hong-yu, et al. A necessary improvement of the viscoelastic method for calculating the dynamic behaviors of the concrete faced rockfill dams[J]. Rock and Soil Mechanics, 2021, 42(12): 3475-3484.

[12]SHEN Zhu-jiang, XU Gang. Deformation behavior of rock materials under cyclic loading[J]. Hydro-science and Engineering, 1996, (2): 143-150.

[13]Guo Zhen-hai, Wang Chuan-zhi. Investigation of strength and failure criterion of concrete under multi-axial stresses[J]. China Civil Engineering Journal, 1991, 24(3): 1-14.

[14]Wang Chuan-zhi, Guo Zhen-hai, Zhang Xiu-qin. Strength tests for biaxial and triaxial compression concrete[J]. Chinese Journal of Civil Engineering, 1987, (1): 15-27.

[15]YANG Jian-hui. Research on static tensile and tensile fatigue properties of concrete under lateral compression[D]. Dalian: Dalian University of Technology, 2003.

[16]Zhu Bai-li, Shen Zhu-jiang. Computational Soil Mechanics [M]. Shanghai: Shanghai Science and Technology Press, 1990.

[17]LI Guo-ying, ZHAO Kui-zhi, MI Zhan-kuan. Influence of rheological behaviors of rockfills on stress-strain behaviors in concrete faced rockfill dam[J]. Rock and Soil Mechanics, 2005, 26(Suppl.1): 117-120.

[18]WEI Kuang-min, CHEN Sheng-shui, LI Guo-yin, et al. Application of Earthquake Wave Motion Input Method to High Earth-Rock Dam Dynamic Analysis[J]. Journal of China Three Gorges University (Natural Sciences), 2019, 41(1): 17-23.

[19]Xu Bin, Zou De-gao, Kong Xian-jing, et al. Dynamic damage evaluation on the slabs of the concrete faced rockfill dam with the plastic-damage model[J]. Computers & Geotechnics, 2015, 65(apr.): 258-265.

[20] Cen W J , Wen L S , Zhang Z Q ,et al.Numerical simulation of seismic damage and cracking of concrete slabs of high concrete face rockfill dams[J].Water Science and Engineering, 2016,9(3),205-211.

Fifth International Dam World Conference
PORTUGAL • LISBON • LNEC • APRIL 13-17, 2025
dam world 2025

ADAPTIVE WARNING THRESHOLDS IN DAM SAFETY USING KERNEL DENSITY ESTIMATION

Nathalia Silva-Cancino[1]
International Centre for Numerical Methods in Engineering (CIMNE)

Joaquín Irazábal
International Centre for Numerical Methods in Engineering (CIMNE)

Fernando Salazar
International Centre for Numerical Methods in Engineering (CIMNE)

Juan Mata
Laboratório Nacional de Engenharia Civil (LNEC)

ABSTRACT

This study presents a novel adaptive warning threshold approach for dam safety monitoring, employing Kernel Density Estimation (KDE), a statistical method for estimating the probability density function of continuous random variables. This technique adjusts thresholds based on data density and residual variability. Traditional fixed-threshold methods often fail to account for variability caused by environmental and operational changes. The proposed approach addresses these limitations by enhancing sensitivity in high-density regions and providing flexibility in sparse data areas. It operates on the premise that test set points in low-density regions indicate higher model error —not due to abnormal measurements of operational variables, but because external variables, such as reservoir levels or temperatures, fall outside the range of the training set—.

The methodology integrates a Boosted Regression Tree (BRT) model for predictive analysis, identifying key factors such as reservoir levels and temperatures. KDE is employed to estimate data density, enabling dynamic threshold calibration. In low-density regions, where prediction uncertainty is higher, thresholds are widened, while high-density regions maintain stricter thresholds to ensure precision.

This framework was applied to monitoring data from a double-curvature arch dam, utilizing reservoir levels and temperatures over multi-scale moving averages. Results demonstrated a substantial reduction in false alarms while retaining robust anomaly detection. The adaptive thresholds improved reliability by accommodating deviations caused by external factors not captured in the predictive model, such as extreme environmental conditions.

By leveraging KDE, this approach offers an interpretable, scalable solution for modern dam safety monitoring, particularly under varying load conditions. It enhances the detection of structural anomalies without excessive false positives, making it a practical advancement in early warning systems. This study underscores the importance of adaptive methodologies in addressing the complex and evolving challenges of dam safety.

Keywords: Warning thresholds, dam safety, kernel density estimation (KDE), anomaly detection, Boosted Regression Tree (BRT).

[1] nsilva@cimne.upc.edu, Spain.

1. INTRODUCTION

Dams are critical components of global water management, supporting essential activities like water supply, irrigation, industrial use, flood control, and energy production. Ensuring their safety is increasingly vital as many dams near the end of their service life, raise concerns about structural integrity [1]. The growing number of recorded dam failures underscores the importance of robust safety monitoring and control practices [2].

The behaviour of dams is influenced by numerous physical and environmental factors, including reservoir levels, air temperature, and dam age, which determine structural responses like deformation and seepage [3], [4]. Data on these variables is collected by instruments located on or within the dam structure, forming a critical part of ongoing safety assessments [1].

Modern approaches to predictive modelling for dam safety include numerical techniques like the Finite Element Method (FEM) [5] and Machine Learning (ML) methods [6], [7]. These models are often paired with safety thresholds, comparing the measured values and predictions, which act as triggers for identifying abnormal conditions.

However, establishing effective thresholds presents challenges, particularly under extreme load conditions, due to limitations in model accuracy. Usually, warning thresholds are set by considering load values and estimating prediction error, establishing acceptable ranges by adding a confidence interval —typically based on the standard deviation of residuals— to model predictions [8], [9], [10], [11].

The confidence interval method relies on statistical parameters, assuming that the residual errors follow a normal distribution. Equation 1 defines the warning threshold commonly adopted using confidence intervals, where $\hat{y}_i$ is the predicted value, σ_ϵ is the standard deviation of the residuals, and k is a scaling factor determining the threshold width. Commonly, $k=2$ corresponds to a confidence interval capturing approximately 95% of expected values, while $k=3$ corresponds to a 99% confidence interval.

$$WT = \hat{y}_i \pm k * \sigma_\epsilon \quad (1)$$

However, using a constant threshold for dam safety warnings presents several limitations, particularly given the complex and variable nature of dam behaviour. A fixed threshold may not account appropriately for fluctuations in external factors such as seasonal changes in water levels, temperature variations, or extreme weather events, all of which can significantly affect the behaviour of a dam.

In this context, we proposed an adaptive warning threshold approach for identifying abnormal behaviour in dams, addressing limitations associated with constant thresholds and methods that are unable to account for extreme load variables. By combining Kernel Density Estimation (KDE) with residual analysis, the methodology dynamically adjusts thresholds based on data density, providing greater sensitivity to underrepresented conditions and improving anomaly detection in dam monitoring systems.

2. METHODOLOGY

The methodology involves the following steps: 1) Constructing a model to predict dam behaviour using Boosted Regression Trees (BRT), 2) Evaluating the importance of the BRT model's features and categorizing input parameters into two groups —water level and temperature— to identify the most influential variables, 3) Computing the KDE area over the training set using the most influential variables identified in the BRT model to derive the KDE for the test set, and 4) Calculating a density factor for each sample based on its KDE and establishing the adaptive warning threshold accordingly.

2.1 Data

We analysed monitoring data from a pendulum (P1DR1) installed in a double-curvature arch dam with a crest length of 302 meters and a height of 102 meters from its foundation. The dataset includes external variables such as the reservoir level (m.a.s.l.) and the daily average temperature (°C). The data covers the period from January 1991 to December 1997 as the training set and from January 1998 to December 1999 as the test set.

Considering that the behaviour of concrete dams is influenced by not only instantaneous water pressure and temperature but also by their long-term variations, we incorporate moving averages of these factors into the analysis. For the reservoir level, we include moving averages over periods of 1, 7, 14, 30, 60, and 90 days, while for temperature, we consider periods of 1,7, 14, 30, 60, 90, 120, 150, and 180 days.

The data utilized in this study is believed to be accurate, with no anomalies present during collection. This assumption ensures that the analysis reflects normal dam behaviour without interference from erroneous readings or sensor malfunctions, providing a reliable basis for model development and validation.

2.2 Model development

A Boosted Regression Tree (BRT) model was developed to predict the pendulum’s readings. The model was developed using SOLDIER [12], a user-friendly application for building machine-learning-based predictive models.

We used the default parameters provided in SOLDIER to train the model, which are n.trees = 500, interaction.depth = 2, n.minobsinnode = 5, shrinkage = 0.01, and bag.fraction = 0.5. The input data corresponds to the external variables and their derivatives, and the output is the displacement of the pendulum.

2.3 Feature importance analysis

In a BRT model, feature importance analysis determines which variables most influence predictions by assessing how often and effectively each feature splits the data across all trees. Each feature is assigned a score between 0 and 1, with higher scores indicating greater significance [13].

The input parameters were categorized into two groups: reservoir water level and ambient temperature. The total importance of each group was computed: Imp_L for reservoir levels and Imp_T for temperatures, using Equations 2 and 3, where Imp_{Li} and Imp_{Ti} are the importance scores of the individual features. Additionally, the most significant variable within each group was identified as the one with the highest importance value in that group (Top_Imp_L, Top_Imp_T).

$$Imp_L = \sum_{i=1}^{n} Imp_{Li} \tag{2}$$

$$Imp_T = \sum_{i=1}^{n} Imp_{Ti} \tag{3}$$

2.4 KDE area calculation

Kernel Density Estimation (KDE), also known as Parzen's window [14], is a nonparametric method to estimate the probability density function of a continuous variable by smoothing the data histogram. Each data point contributes a kernel, typically Gaussian, with the bandwidth controlling the smoothing level. In Equation 4, KDE is defined for a matrix with *n* variables and *m* samples, where *H* is the bandwidth matrix and *K* represents the Gaussian kernel function [15].

$$\hat{f}(\mathrm{x},\mathrm{H}) = \frac{1}{m}\frac{1}{|H|^{\frac{n+1}{2}}}\sum_{i=1}^{n} K[H^{\frac{1}{2}}(x - x_i)\,H^{-\frac{1}{2}}] \tag{4}$$

KDE was computed using the training data using Top_Imp_L and Top_Imp_T as axes, normalized from 0 to 1. This process was done using the Min-Max Scaler technique, which subtracts the minimum value of a feature and then divides it by its range, defined as the difference between its maximum and minimum values.

Bandwidths were adjusted according to variable importance (Imp_L and Imp_T) to reflect the influence of variables in the KDE domain. Specifically, the bandwidths were modified based on the relative importance levels of both groups, ensuring that features with higher importance receive finer resolution.

Equations 5 and 6 define the bandwidth for each axis, with a base bandwidth h_b of 0.15, chosen to capture relevant details and avoid overfitting, As the importance approaches 1, the h_b is reduced, and as the importance approaches 0, the bandwidth tends to h_b.

$$h_x = h_b(1 - Imp_L) \quad (5)$$

$$h_y = h_b(1 - Imp_T) \quad (6)$$

2.5 Density factor and Adaptive warning threshold

We developed an adaptive warning threshold based on the Kernel Density Estimate (KDE). For high KDE values (≥ 0.9), a threshold of $2\sigma_\epsilon$ is used. As KDE decreases, the threshold increases: $3\sigma_\epsilon$ for KDE of 0.5 and $6\sigma_\epsilon$ for KDE of 0.2 (Fig. 1).

This adaptive approach ensures greater sensitivity in dense regions and more flexibility in sparser areas. The relationship between KDE and threshold was modelled with a polynomial function, as shown in Equation 7, with an determination coefficient (R^2) value of 0.999, enabling dynamic adjustment of the warning threshold. Once the factor is calculated for each sample, the warning threshold is determined by multiplying the standard deviation by the factor (as shown in Equation 8).

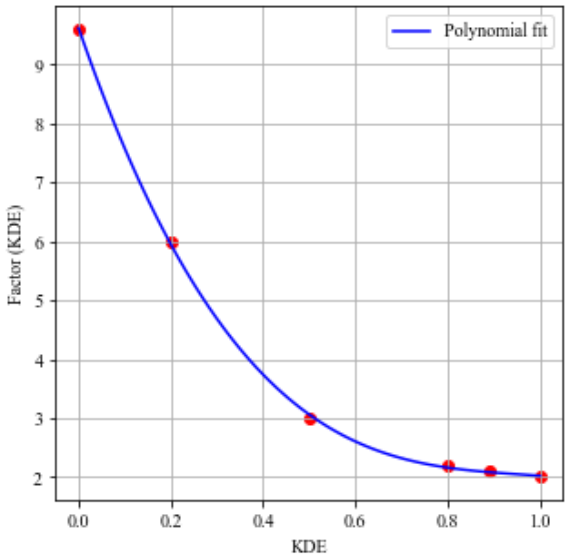

Fig. 1 – Adaptive factor as a function of the KDE. The red dots are the threshold-defining points and the blue curve shows the polynomial fit to the data

$$\text{Factor(KDE)} = -8.699\text{KDE}^3 + 23.787\text{KDE}^2 - 22.732\text{KDE} + 9.615 \quad (7)$$

$$WT_{KDE} = \hat{y}_i \pm Factor(\text{KDE}) * \sigma_\epsilon \quad (8)$$

3. RESULTS AND DISCUSSION

3.1. BRT model

Fig. 2 presents the time series of water level and air temperature from 1991 to 1999, illustrating the separation between the training and testing sets. Notably, water levels in the test set are lower than those in the training set, while the temperature range exhibits periodic behaviour consistently throughout the time series.

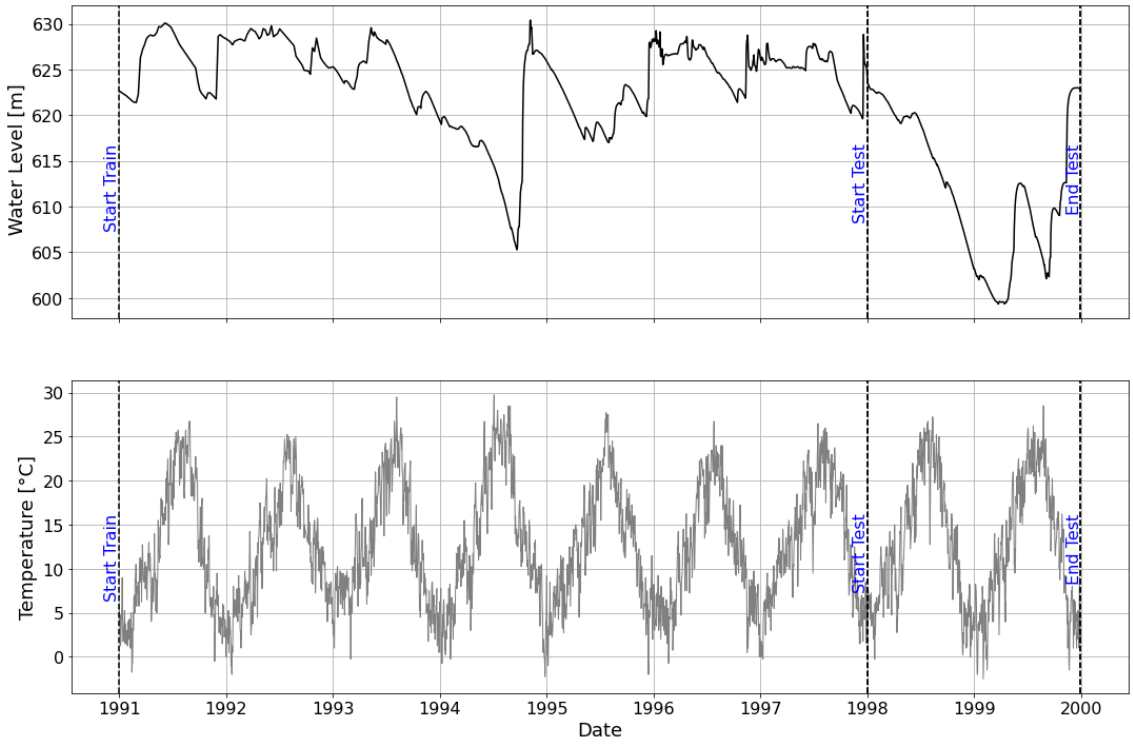

Fig. 2 – Evolution of the reservoir water level and ambient temperature between 1991 and 1999

The BRT model was fitted to predict the pendulum response using level, temperature, and their derived variables as inputs (Fig. 3). The observed and predicted values from each BRT were used to calculate the residuals (predicted minus observed value).

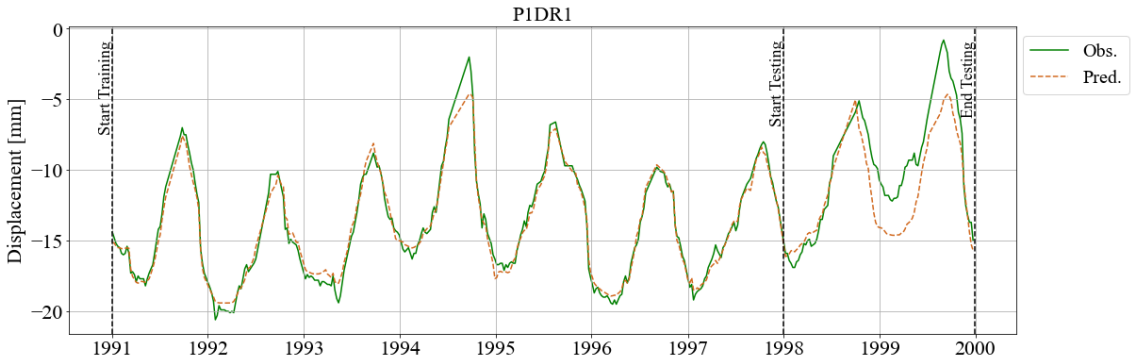

Fig. 3 – Observed and predicted displacement of P1DR1.

Based on the importance analysis, it was found that the most important variable for reservoir water level group (Top_Imp_L) is the daily water level (*Level_001D*), while for ambient temperature group (Top_Imp_T) is the 90-day moving average of ambient temperature (*Tair_090D)*. The calculated group importance values are Imp_L = 0.253 and Imp_T=0.737.

3.2. KDE area

Fig. 4 presents the KDE area calculated using the training set, computed with the normalized Top_Imp_L and Top_Imp_T, and the bandwith based on Equations 5 and 6. The effect of the bandwidths can be observed in the shape of the contour curves of density. Since the y-axis variable has greater importance, its corresponding bandwidth is smaller, resulting in more noticeable variation in the space.

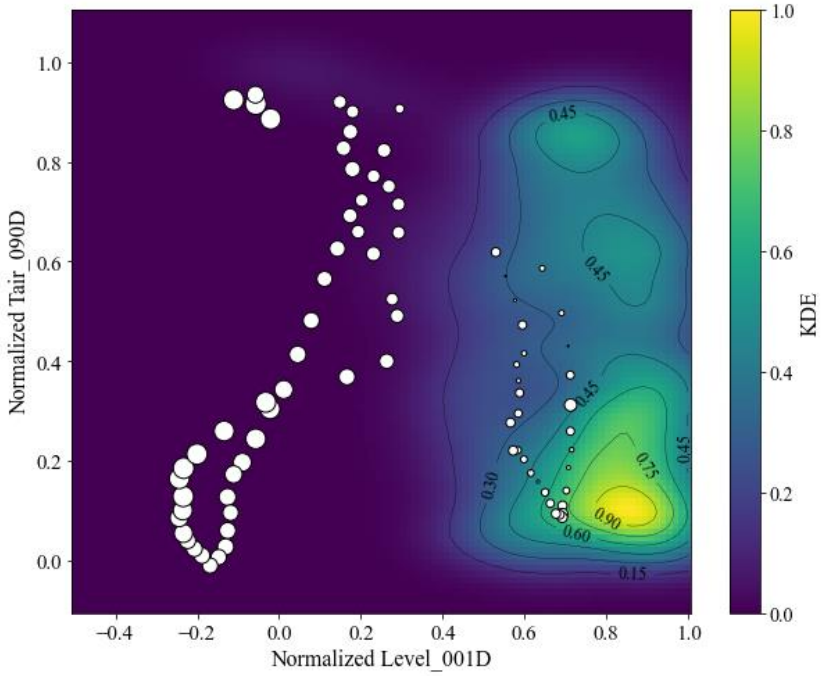

Fig. 4 – KDE area for PD1R1 for the training set. White circles are the test samples and their size is related to the residual

The white circles represent testing set samples, with their size proportional to the residual. Negative values on the Level axis correspond to unseen data points outside the training set's range. Residuals are larger in areas with low KDE density, indicating that the BRT model is less reliable in regions underrepresented in the training set.

3.3. Adaptive warning threshold

The KDE values for each sample in the test set were extracted from the data shown in Fig. 4 and the adaptive warning threshold was calculated for each sample with Equations 5 and 6. Fig. 5 presents the observed and predicted data, the residual, the KDE value and the adaptive warning threshold for P1DR1. It can be observed that as the KDE decreases, the WT(KDE) increases and for samples where the KDE is close to 1, the WT(KDE) is maintained at $2\sigma_\epsilon$. When applying the adaptive threshold, no anomalies were detected in the testing sets, despite the residuals in the test sets being larger than those in the training set.

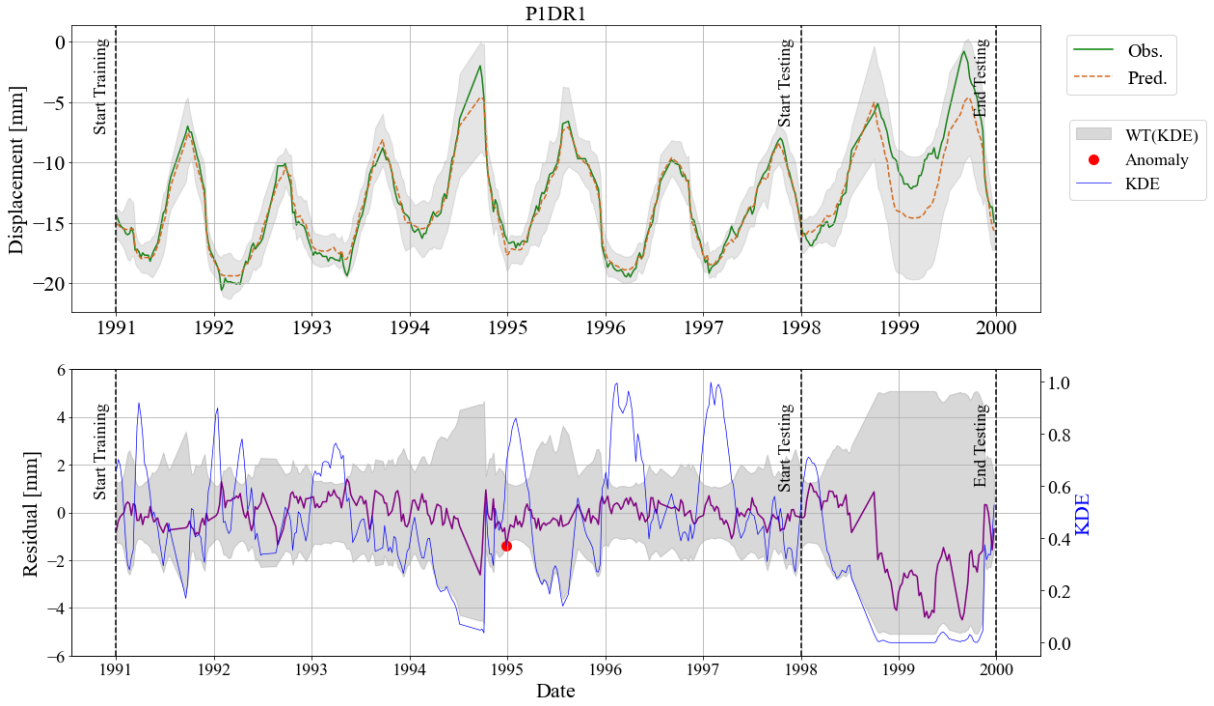

Fig. 5 – Observed and predict data, adaptive warning threshold and KDE for each sample

Fig. 6 shows the anomalies detected for P1DR1 using fixed thresholds of $2\sigma_\epsilon$ and $3\sigma_\epsilon$. It was observed that the use of fixed thresholds significantly increases the number of detected anomalies, particularly in the test set, where the residuals are larger. With a threshold of $3\sigma_\epsilon$, 59% of the test set is classified as anomalies, while with $2\sigma_\epsilon$, 64% are classified as anomalies.

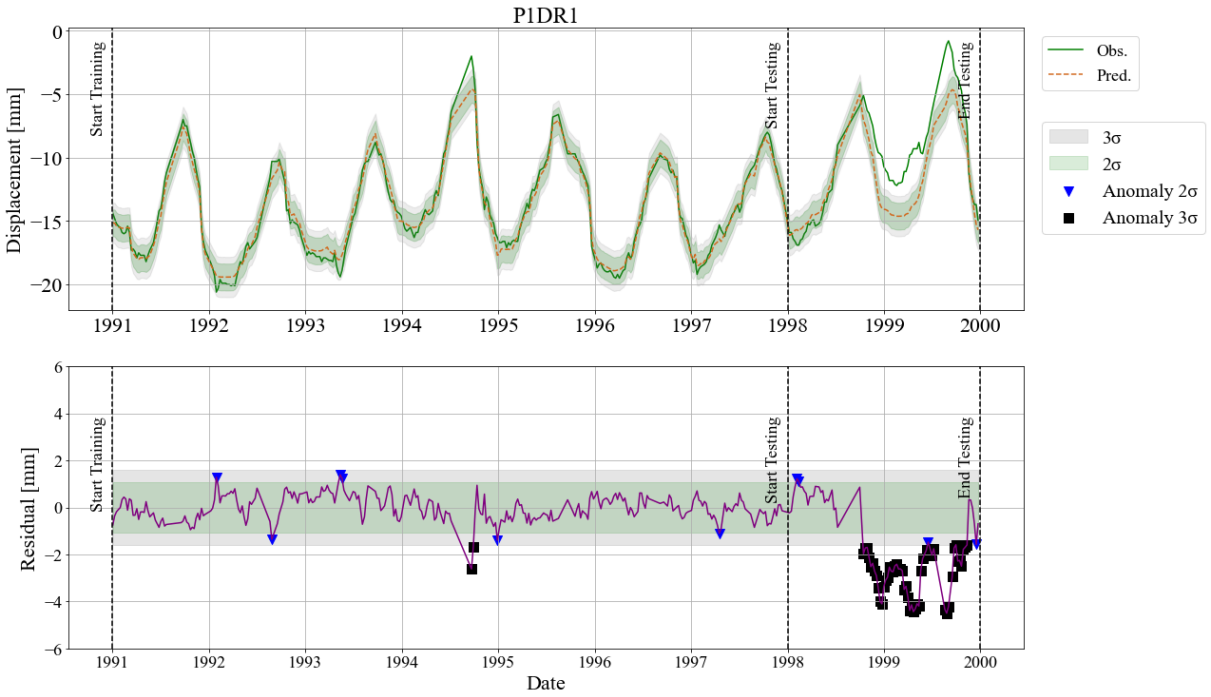

Fig. 6 – Observed and predicted data, fixed thresholds based on standard deviations

4. CONCLUSIONS

This study presented a novel approach for defining adaptive warning thresholds for dam safety using Kernel Density Estimation (KDE). The results demonstrate that adaptive thresholds offer greater sensitivity in areas with high data density and increased flexibility in underrepresented regions. Compared to static thresholds, the KDE-based approach adapts more effectively to environmental and operational variations. This adaptability is especially critical during significant changes in load conditions.

The proposed approach accounts for variations in load variables, such as reservoir levels and ambient temperatures, which significantly influence the performance of predictive dam behaviour models. By considering that deviations between observed and predicted values might result from changes in loads not captured by the model —rather than anomalous dam behaviour— the KDE method enhances interpretability. This methodology demonstrated notable capabilities in reducing false alarms and improving the detection of structural anomalies, particularly under extreme load conditions.

REFERENCES

[1] D. Perera, V. Smakhtin, S. Williams, T. North, and R. Curry, Ageing Water Storage Infrastructure: An Emerging Global Risk 11. 2021. doi: 10.13140/RG.2.2.29149.44003.

[2] (International Commission on Large Dams) ICOLD, 'ICOLD Incident Database Bulletin 99 Update: Statistical Analysis of Dam Failures'. 2019.

[3] F. Salazar, M. Á. Toledo, J. M. González, and E. Oñate, 'Early detection of anomalies in dam performance: A methodology based on boosted regression trees', Structural Control and Health Monitoring, vol. 24, no. 11, p. e2012, 2017, doi: 10.1002/stc.2012.

[4] S. C. on Dams, 'Methods of analysis for the prediction and the verification of dam behaviour', ICOLD, 2003.

[5] G. Willm and N. Beaujoint, 'Les méthodes de surveillance des barrages au service de la production hydraulique d'Electricité de France-Problèmes ancients et solutions nouvelles', in 9th ICOLD Congres, 1967, pp. 529–550.

[6] F. Salazar, A. Conde, J. Irazábal, and D. J. Vicente, 'Anomaly Detection in Dam Behaviour with Machine Learning Classification Models', Water, vol. 13, no. 17, Art. no. 17, Jan. 2021, doi: 10.3390/w13172387.

[7] H. Su, Z. Chen, and Z. Wen, 'Performance improvement method of support vector machine-based model monitoring dam safety', Structural Control and Health Monitoring, vol. 23, Jun. 2015, doi: 10.1002/stc.1767.

[8] R. Hellgren, R. Malm, and A. Ansell, 'Performance of data-based models for early detection of damage in concrete dams', Structure and Infrastructure Engineering, vol. 17, no. 2, pp. 275–289, Feb. 2021, doi: 10.1080/15732479.2020.1737146.

[9] E. Oñate, M. A. Celigueta, S. R. Idelsohn, F. Salazar, and B. Suárez, 'Possibilities of the particle finite element method for fluid–soil–structure interaction problems', Computational Mechanics, vol. 48, no. 3, pp. 307–318, 2011.

[10] F. Li, Z. Wang, and G. Liu, 'Towards an Error Correction Model for dam monitoring data analysis based on Cointegration Theory', Structural Safety, vol. 43, pp. 12–20, 2013.

[11] J. Mata, A. Tavares de Castro, J. Sá da Costa, J. Barateiro, and P. Miranda, 'Threshold Definition for Internal Early Warning Systems for Structural Safety Control of Dams. Application to a Large Concrete Dam', presented at the 54th Congresso Brasileiro do Concreto, 2012. Accessed: Mar. 06, 2024. [Online]. Available: https://scholar.tecnico.ulisboa.pt/records/b9b8964c-2307-4e1e-b06e-65d00d346a30

[12] F. Salazar, J. Irazábal, and A. Conde, 'SOLDIER: SOLution for Dam behavior Interpretation and safety Evaluation with boosted Regression trees', SoftwareX, vol. 25, p. 101598, Feb. 2024, doi: 10.1016/j.softx.2023.101598.

[13] A. C. Müller and S. Guido, Introduction to Machine Learning with Python: A guide for data scientists. USA: O`reilly Media, 2017.

[14] E. Parzen, ‘On Estimation of a Probability Density Function and Mode’, The Annals of Mathematical Statistics, vol. 33, no. 3, pp. 1065–1076, 1962.

[15] L. Xiong, J. Liang, and J. Qian, ‘Multivariate Statistical Process Monitoring of an Industrial Polypropylene Catalyzer Reactor with Component Analysis and Kernel Density Estimation1’, Chinese Journal of Chemical Engineering, vol. 15, no. 4, pp. 524–532, Aug. 2007, doi: 10.1016/S1004-9541(07)60119-0.

Fifth International Dam World Conference
PORTUGAL • LISBON • LNEC • APRIL 13-17, 2025
dam world 2025

REHABILITATION OF SORDO DAM

André Costa[1]
Águas do Norte

José Cordeiro[2]
Águas do Norte

José Vale[3]
MVC
(Machado do Vale Consulting)

Luís Nicolau[4]
Águas do Norte

Sofia Gonçalves[5]
Águas do Norte

ABSTRACT

Sordo Dam is located on the Sordo River, southwest of Vila Real, tributary of Corgo and Douro Rivers. The main propose of this infrastructure was to create a reservoir to supply drinking water to the populations of the municipalities of Vila Real and Santa Marta de Penaguião. The project started in 1991 and entered service in 1997.

The dam is a concrete gravity structure with a slight curvature in plan, standing 36 meters high with a crest length of 108 meters at an elevation of 527 meters. The reservoir has a capacity of approximately 1 hm³ at Full Storage Level (FSL). The spillway, located at the dam's central section, is a free-flow structure with three bays, a total width of 21 meters, and a WES-type crest at 522.5 meters, designed to discharge up to 200 m³/s.

The use is for multiple purposes, water supply and energy production, with a hydroelectric plant away from the dam, with 2 Pelton turbines, 10 MW total power.

As the entity responsible for the dam, Águas do Norte has identified several critical needs for the efficient management of the facility. These include the inoperability of equipment associated with the bottom outlet and the presence of significant pathologies related to concrete permeability, as well as in the construction joints, particularly at the bottom outlet valve chamber and at the stoplog shaft.

A series of interventions have been implemented to mitigate the identified issues. These included waterproofing the concrete by injecting cement grout into the internal construction joints, and applying an external waterproof coating, which required underwater work. Regarding the bottom outlet system, operational components were replaced, and the stoplog and slide roller gates were rehabilitated, along with the rehabilitation of the hydraulic circuit steel lining.

Given the specificity of the interventions, it was decided to hire specialized companies directly, planning and integrating the works sequency. Due to the multipurpose nature of the facility, there were significant constraints on the normal progress of the work, particularly in controlling the reservoir water level, which were aggravated by the inoperability of the bottom outlet.

Keywords: Rehabilitation, Concrete permeability, Waterproofing Interventions, Bottom Outlet System, Construction Joints

[1]andre.costa@adp.pt, Portugal
[2]j.cordeiro@adp.pt, Portugal
[3]jlmv09@icloud.com, Portugal
[4]l.nicolau@adp.pt, Portugal
[5]s.goncalves@adp.pt, Portugal

1. INTRODUCTION

Águas do Norte manages the multimunicipal water supply system in northern Portugal, ensuring water availability for 1.06 million people. Among its 16 operational dams, seven were built by the company, while the remaining nine were integrated from municipal entities. These dams vary in typology, comprising seven concrete dams, two rockfill dams with upstream concrete faces, and seven embankment dams.

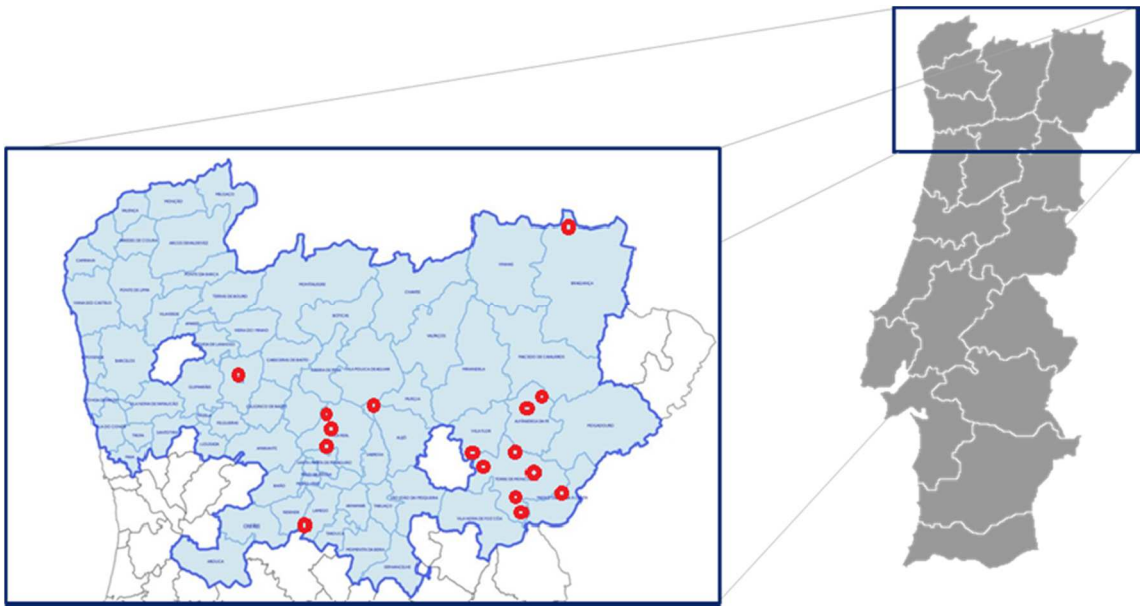

Fig. 1 - Location of Águas do Norte dams

As the owner, Águas do Norte is responsible for monitoring, maintaining, and rehabilitating these infrastructures to ensure their safe and efficient operation. Over the years, several dams, Salgueiral, Palameiro, Valtorno, Vale Ferreiros, Camba, Queimadela, and, more recently, Sordo, have undergone significant interventions.

Designed in 1991 [1] and completed in 1997 [2], the Sordo Dam is located on the Sordo River, a tributary of the Corgo and Douro Rivers, southwest of Vila Real. Although its primary function is to supply water to Vila Real and Santa Marta de Penaguião, it is a multipurpose infrastructure, also contributing to hydroelectric power generation.

A detailed assessment identified multiple structural and operational deficiencies, leading to a comprehensive rehabilitation project [3] covering civil works, hydromechanical systems, and monitoring equipment. However, to maximize impact and address the most pressing issues, the most urgent and technically complex interventions were prioritized in this phase, executed through two specialized contracts.

This document focuses on these key interventions, specifically:

- Correction of concrete permeability issues, particularly in the bottom outlet valve shaft, chamber, and stoplog gate shaft;
- Rehabilitation of hydromechanical components, ensuring the full operational restoration of the bottom outlet system.

All interventions were executed under rigorous planning, ensuring continuous water supply and adequate reservoir levels, despite limitations imposed by the bottom outlet's inoperability.

Meanwhile, non-urgent rehabilitation works, including the restoration of ancillary structures, electrical system upgrades, and further modernization of monitoring instruments are planned for a subsequent phase.

2. SORDO DAM

The Sordo Dam (Fig. 2) is a multipurpose infrastructure, serving both public water supply and hydroelectric power generation. Initially promoted and owned by the Vila Real Municipal Council (CMVR) through the Municipalised Water and Sanitation Services (SMAS-VR), the dam’s management was transferred in 2004 to the Vila Real Municipal Water and Waste Company (EMAR-VR) and later, in 2019, to Águas do Norte (AdN).

The hydroelectric concession was originally operated by HidroCorgo before being transferred to Pebble Hydro. In 2008, Pebble Hydro was acquired by the EDP group, which later sold the operation to Aquila Capital. Since 2018, the facility has been operated by Águia Enlica, a subsidiary of Aquila Capital.

Designed by Tecnopor in 1991, the dam was constructed by Conduril and completed in 1997, with initial reservoir filling occurring between March and November of that year.

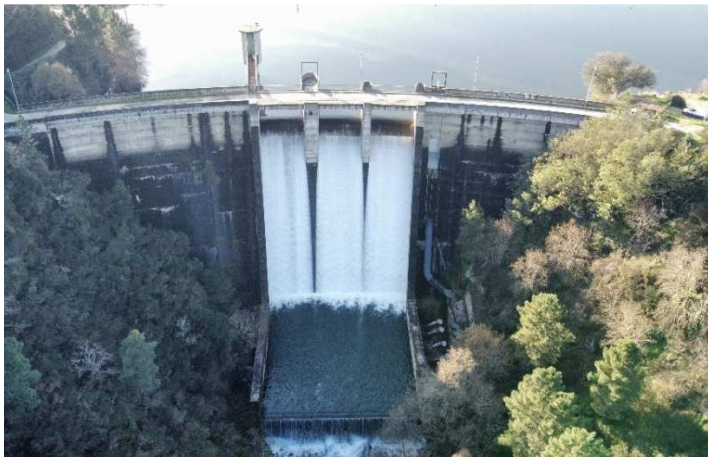

Fig. 2 - Sordo Dam - Aerial frontal view

This is a massive concrete gravity dam with a slight curvature in plan, featuring a maximum height of 36.0 meters above the foundation and a total crest length of 108.0 meters, situated at an elevation of 527.0 meters.

The dam structure is divided by six transverse joints: D1, D2, and D3 on the right bank, and E1, E2, and E3 on the left bank, spaced approximately 15 meters apart. The bottom outlet structure is integrated into the central section of the dam, between joints D1 and E1, as illustrated in Fig. 3.

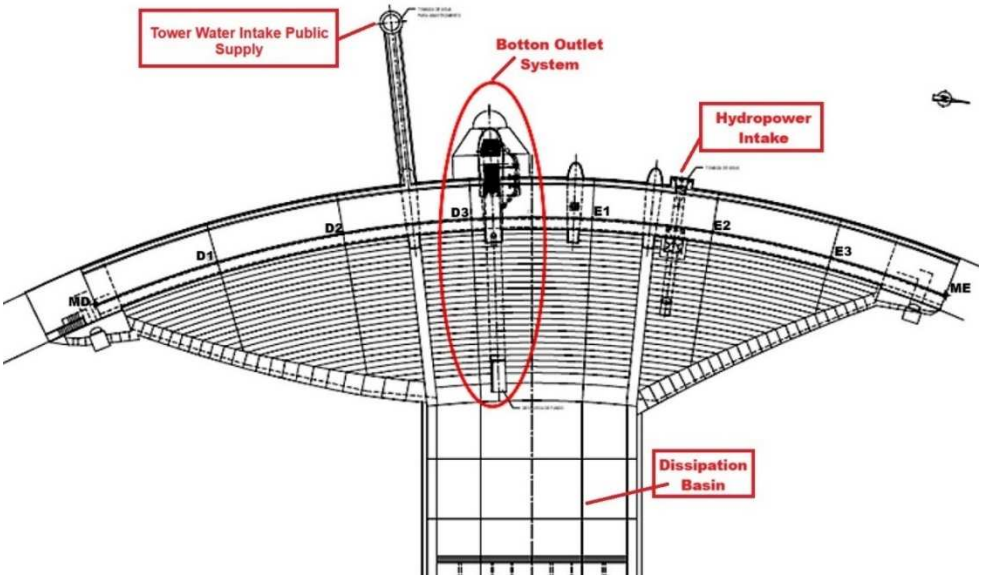

Fig. 3 - Sordo Dam – Plan View [3]

The water intake for public supply is made through a tower upstream, on the right bank, connected by a walkway to the crest. The conduit crosses the crest beneath the downstream walkway slabs, extending to the left bank, where it connects to the Sordo Water Treatment Plant.

The hydropower intake is located on the upstream side of the dam, on the left bank, and consists of a steel pipe accessible from within the dam through a dedicated chamber on the downstream side. The hydroelectric facility is equipped with two Pelton turbine units, with a total installed capacity of 10 MW.

The dam includes three main galleries (Fig. 4):

- General drainage gallery, runs along the upstream interface between the dam and the foundation (GF1 in the upper left and right abutments, corresponding to blocks E3-ME and D3-MD; and GF from blocks E3-E2 to D2-D3);
- Downstream drainage gallery, positioned at the lowest point of the valley (GFJ at elevation 491.7 meters);

- Inspection gallery, positioned at approximately mid-height within the dam body, at elevation 508.0 meters.

The spillway consists of three bays located in the central section of the dam, with a total length of 21 meters. It features a WES-type crest, followed by a dissipation basin, and is designed for a maximum discharge capacity of 200 m³/s. The spillway crest is at an elevation 522.5 metres, corresponding to full reservoir level (FRL), while the maximum flood level (MFL) is set at 525.5 metres [3].

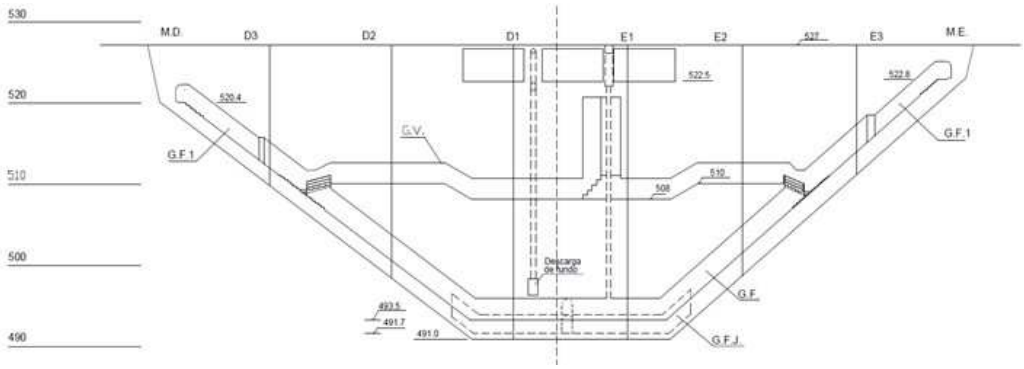

Fig. 4 - Sordo Dam – Section through the reference surface [2]

The bottom outlet system consists of a rectangular-section conduit (1.50 × 2.00 m), extending through the dam. It enables water discharge through a sequence of hydraulic elements, ensuring both operational efficiency and safety (Fig. 5).

At full reservoir level (FRL), the reservoir has a useful capacity of approximately 1.0 hm³ and covers an area of 8.4 ha.

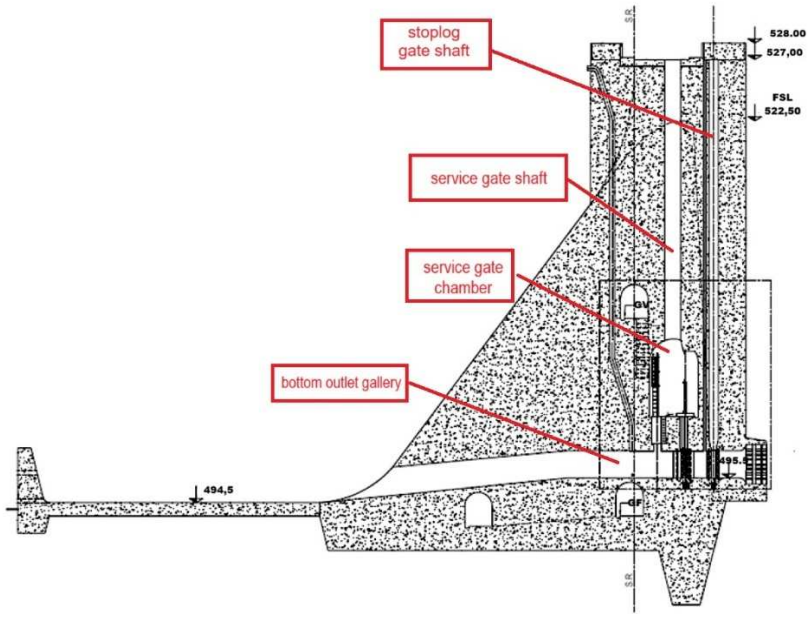

Fig. 5 - Sordo Dam – Section through Block E1-D1 [3]

2.1. Structure of the Bottom Outlet Chamber and Shaft

The bottom outlet system of the Sordo Dam includes two main shafts (Fig. 5): the stoplog gate shaft and the service gate shaft. These shafts are integral to the structural layout of the bottom outlet and are separated by a 1.25 m thick reinforced concrete septum. Additionally, the service gate shaft is isolated from the reservoir by a 0.75 m thick reinforced concrete wall, extending from the dam crest (527.00 m) down to elevation 509.00 m (Fig. 6).

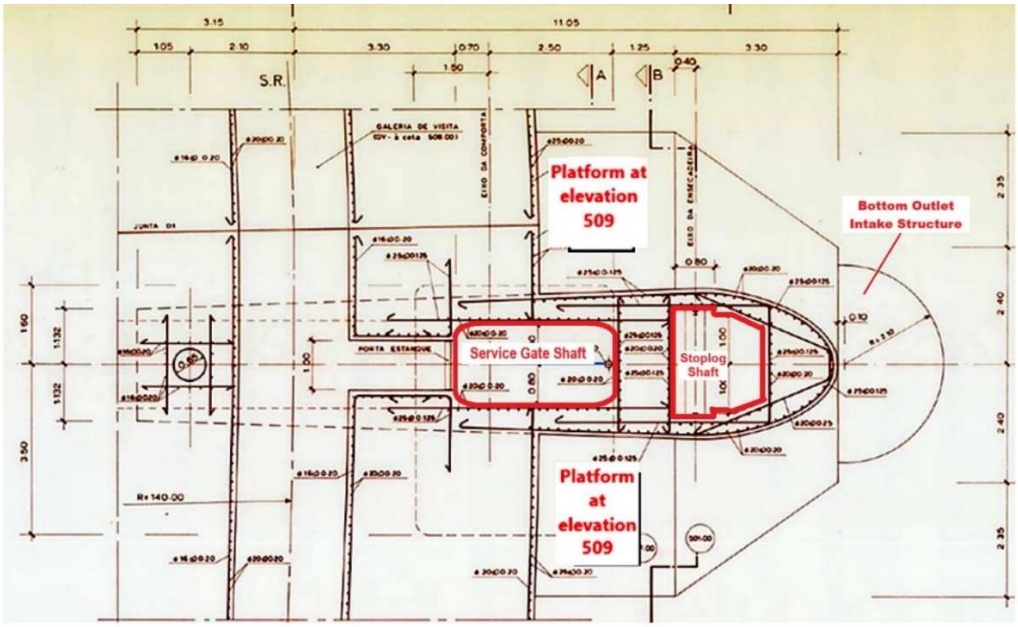

Fig. 6 - Bottom Outlet – Section at elevation 509.00 – Reinforcements (not to scale) [1]

Between elevations 509.00 m and 501.00 m, the geometry of the surrounding structure changes, particularly along the lateral faces of the service gate shaft, due to the thickening of the platform at elevation 509.00 m. However, the 1.25 m thick upstream septum remains unchanged, ensuring separation from the stoplog gate shaft.

At elevation 503.00 m, the bottom outlet valve chamber is located, with internal dimensions of 5.55 m × 4.25 m (Fig. 7). The stoplog gate shaft extends from elevation 501.00 m to the dam crest (527.00 m), with an in situ measured width of 2.45 m and an upstream-downstream dimension of 1.80 m.

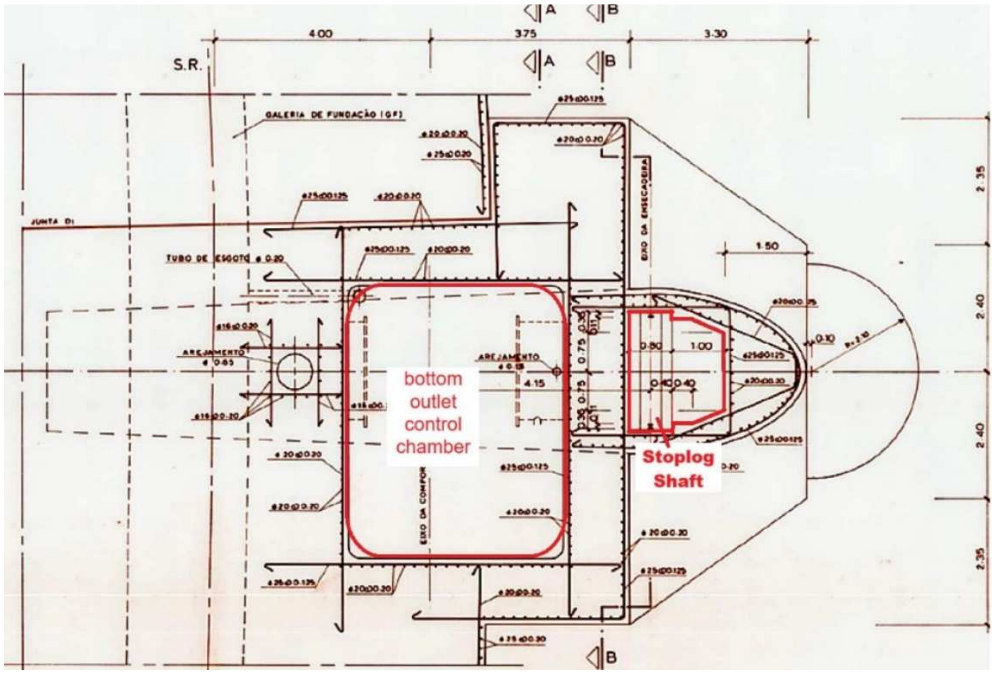

Fig. 7 - Bottom Outlet – Section at elevation 503.00 – Reinforcements (not to scale) [1]

2.1.1 Concrete Pathologies

Since the first filling of the reservoir in 2003, significant seepage has been observed in the bottom outlet control chamber, particularly through the upstream walls and sidewalls [4] . Reports indicate that this seepage is linked to the construction phase, likely due to poor concrete permeability, improper placement and compaction, or inadequate treatment of construction joints [5].

In 2016, polyurethane resins were injected to seal specific seepage areas, covering not only the chamber and valve shaft but also joints between dam blocks. This intervention significantly reduced seepage, from approximately 70 l/min to 20 l/min [6]. However, some localized seepage areas remained, particularly in cracks and construction joints within the bottom outlet chamber and valve shaf (Fig. 8).

Fig. 8 - General view of the interior walls of the Bottom Outlet Well and Chamber (2021)

To assess the extent of concrete degradation, Águas do Norte conducted core extractions in 2021, obtaining eight samples from two seepage levels in the upstream and sidewalls (Fig. 9). Laboratory tests revealed high porosity and voids, with compressive strength values varying significantly. As shown in Table 1, the results exhibited a standard deviation of 8.10 MPa, indicating heterogeneous deterioration of the concrete due to prolonged water infiltration. The extracted cores confirmed that the samples taken from the construction joint plane showed higher porosity compared to the other cores, reinforcing the hypothesis that inadequate joint treatment contributed to seepage issues.

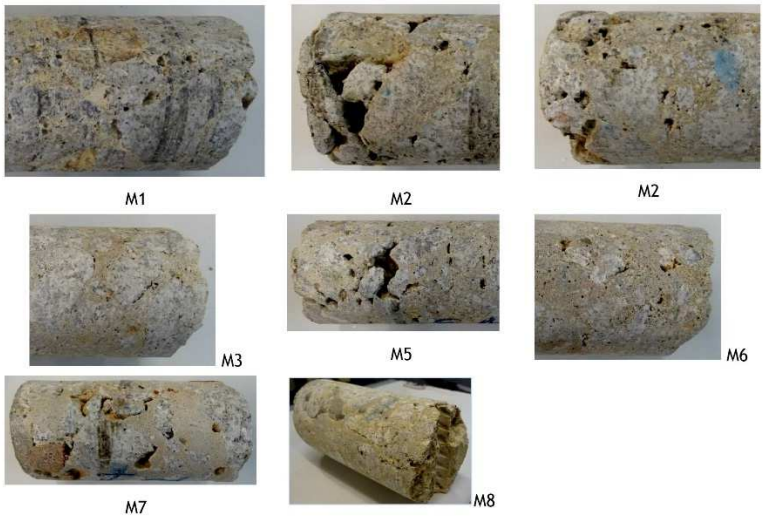

Fig. 9 - General view of cores taken from the walls of the Bottom Outlet Control Chamber [7]

The carbonation process, driven by continuous water seepage through the joints, was visibly compromising the concrete's durability. Without further intervention, this degradation could threaten the long-term structural integrity, accelerating reinforcement corrosion due to the leaching of cement compounds. The progressive dissolution of portlandite results in the breakdown of the protective passive layer around the reinforcement, increasing its susceptibility to corrosion and, in the medium term, jeopardizing the structural integrity [5].

Table 1- Compressive strength values of the laboratory-molded concrete specimens [7]

Identification of cores	Test date	Maximum breaking load (kN)	Height/diameter ratio	Compressive strength (MPa)
M1	17.11.2021	117	1,0	26,5
M2		177	1,0	40,1
M3		122	1,0	27,6
M4		191	1,0	43,2

M5/E1	129	1,0	29,2
M6/E2	134	1,0	30,3
M7-D1	81	1,0	18,3
M8-D2	109	1,0	24,7

2.1.2 Proposed Treatment

Ferreira Lemos Engenharia Lda. was selected to prepare a technical note [5] defining a treatment strategy for waterproofing the concrete in the chamber and shafts of the bottom outlet. The intervention was designed to address three key aspects: structural protection, waterproofing, and functionality.

Structural protection focuses on preserving the service life of the structure, particularly by reducing the degradation of construction joints and protecting the internal reinforcement. Finally, functionality ensures that the interior of the shaft remains accessible and provides suitable working conditions for periodic inspections, maintenance activities, and the proper operation of installed equipment.

The proposed solution includes both internal and external interventions, all aimed at ensuring the effective waterproofing of the service gate chamber and shaft. The internal treatment consists of low-pressure cement grout injections applied within the service gate chamber and shaft, targeting construction joints and areas affected by seepage (Fig. 10).

The drilling process is carried out at two inclinations, 31º and 45º, to ensure full penetration along the joint plane, with a maximum spacing of 0.33 m between boreholes. The injection system scheme, detailing the drilling points and injection collectors, is illustrated Fig. 11.

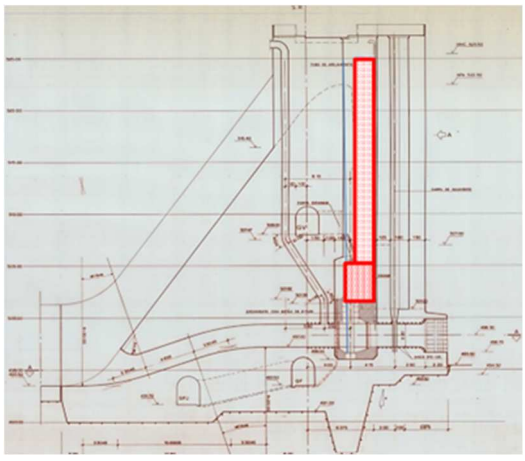

Fig. 10 Bottom Outlet – Vertical Section through the Bottom Outlet axis, highlighting the interior area to be treated (not to scale)

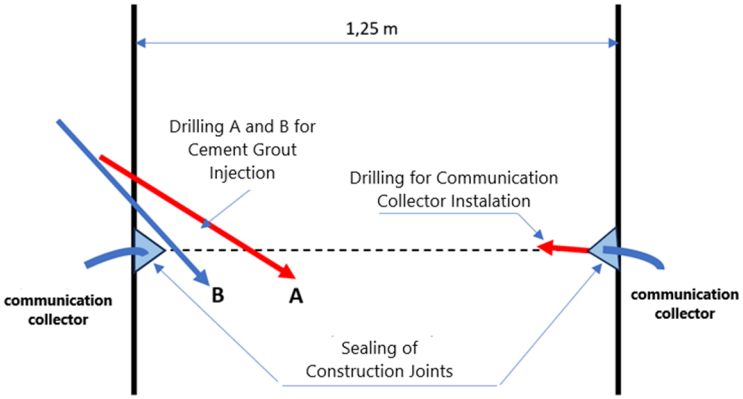

Fig. 11 - Injection system scheme for construction joints [5]

The injection process follows a systematic progression from elevation 501.00 m upwards, treating one joint at a time. Injection begins at the deepest borehole (hole A) using grout FC4, maintaining pressures up to 2.0 bar. If no communication occurs, or if leakage is detected through collectors, they are immediately sealed. The process then moves to hole B, continuing with grout FC4. If communication is observed at hole B, grout FC3 is used until the pressure stabilizes at 2.0 bar for 10 minutes. If leakage to adjacent joints is detected, the injection shifts to the next communicated hole, adapting accordingly.

The cement grouts used for concrete waterproofing injections were selected based on laboratory tests conducted at FEUP in 2022, ensuring low viscosity (7.8 to 13.0 seconds) while maintaining a low water-to-cement ratio. Table 2 summarizes the composition of the planned grout formulations.

Table 2 - Cement Grouts Used for Concrete Waterproofing Injections

Planned Cement Grouts			
Designation	Mix Ratio (by weight) Cement : Water	Theoretical Density (kg/dm3)	Viscosity EN 445 (s)
FC1	2,3 : 1,0	1,890	13,0
FC2	2,15 : 1,0	1,856	10,3
FC3	2,0 : 1,0	1,820	8,9
FC4	1,85 : 1,0	1,781	7,8

The external waterproofing treatment targets the surrounding concrete, including the interior of the stoplog gate shaft and the exterior surfaces of both the stoplog gate shaft and the service gate chamber (Fig. 12).

The process involves applying an epoxy coating, specifically selected based on exposure conditions. In submerged areas, a water-compatible epoxy resin (Alocit 28.15) is applied in two coats using a specialized painting device, with divers executing the application sequentially. In emerged areas, a single 200-micron coat is applied after surface preparation with a zinc primer (Alocit Systems). Before application, all surfaces undergo high-pressure water jet cleaning to remove disaggregated concrete and surface irregularities. Additionally, emerged areas are treated with an air and water jet, while submerged sections are cleaned exclusively with high-pressure water. Surface irregularities are corrected using epoxy mortar in emerged areas and epoxy paste in submerged regions.

The exterior collectors are secured with epoxy resin during the sealing of construction joints. In submerged areas, each collector includes a temporary extension in transparent tubing, ensuring that the upper end remains above the reservoir level to prevent water ingress into the concrete mass until injection is completed. Additionally, the drill holes for sealing the submerged communication collectors, both on the reservoir side and in the stoplog gate shaft, are immediately sealed after drilling, with the shutter closed to prevent water seepage along the concrete walls.

To optimize waterproofing efficiency, a waiting period was established between the application of the external epoxy coating and the start of internal cement grout injections. This delay allows residual water in submerged concrete to drain, enhancing the treatment’s effectiveness and ensuring long-term durability.

These combined interventions ensure the long-term integrity of the bottom outlet system, minimizing water infiltration and preserving the structural performance of the dam.

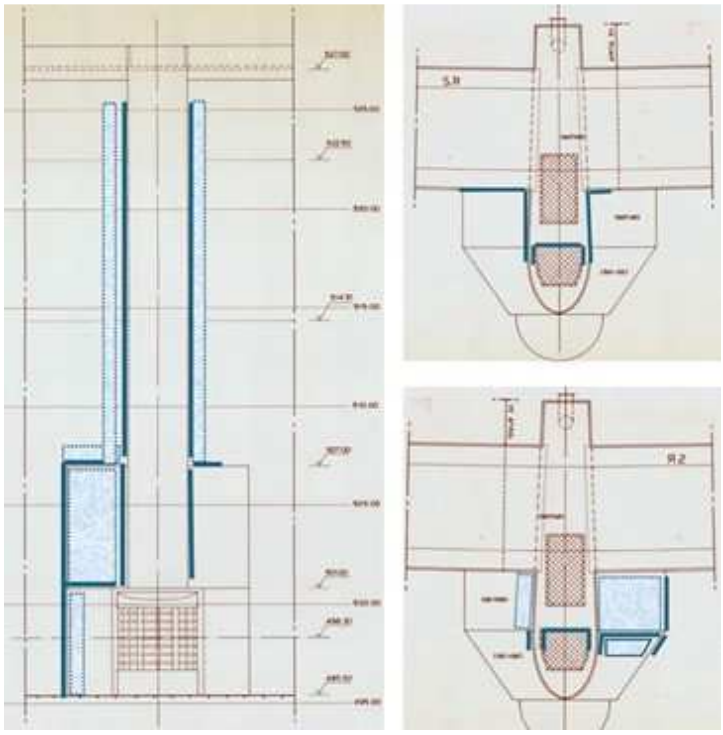

Fig. 12 - Identification of treatment areas on the upstream face between elevations 495.50 and 525.50 [5]

2.2. Bottom Outlet Equipment

The Bottom Outlet System of the Sordo Dam consists of a series of hydraulic and mechanical components, arranged from upstream to downstream, as illustrated in Fig. 13. The system includes a concrete intake grille, installed at the upstream face to prevent debris entry, followed by a steel-lined gallery measuring 1.80 × 2.20 × 15.00 m (WxHxL). At the upstream end, a sliding stoplog gate (1.80 × 2.20 m) is installed to provide hydraulic isolation when necessary. This gate is operated via suspension bars and a winch mounted on a gantry at the dam crest.

Downstream of the stoplog gate, the service gate is housed in a watertight structure and consists of a wagon-type slide roller gate (1.80 × 2.20 m). This gate is operated by an oil-hydraulic servomotor, controlled through a Hydraulic Unit and Electrical Control Panel. To prevent cavitation and ensure smooth operation, an aeration pipe is positioned downstream of the service gate.

Despite being designed for controlled water discharge, the bottom outlet system has remained inoperable since the construction of the dam. The stoplog gate has never been operated and remains permanently open inside the shaft, while the service gate is closed and appears watertight.

The ecological flow circuit, which is designed to ensure a minimum environmental discharge, does not operate under a predefined regime but can be activated via a DN200 pipe that draws water from the bottom outlet gallery, upstream of the stoplog gate. The circuit crosses the Bottom Outlet Control Chamber and discharges into a tapping point downstream of the service gate. Inside the chamber, the ecological flow system is controlled by two manually operated elastic wedge-type valves: a guard valve and a regulation valve, as illustrated in Fig. 14.

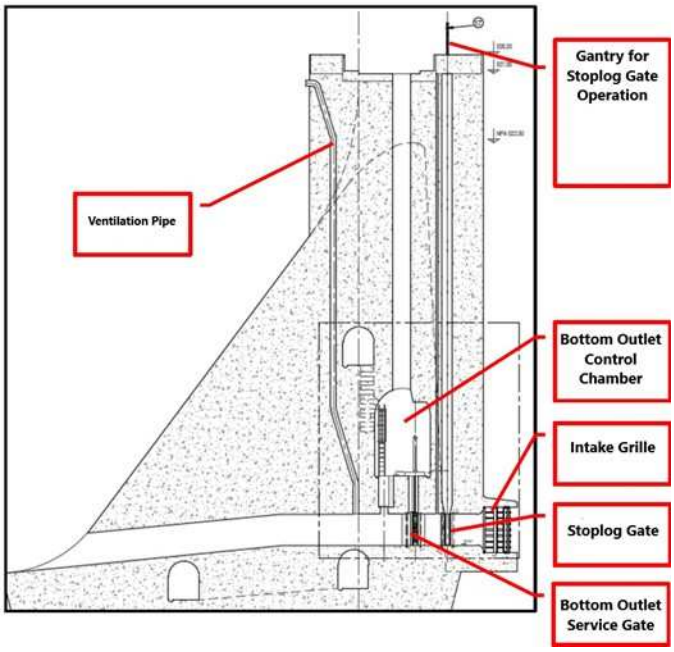

Fig. 13 - Bottom Outlet – Vertical Section through the Bottom Outlet axis (not to scale) [3]

Fig. 14 - Ecological Flow Circuit inside the Bottom Outlet Control Chamber - Before the proposed intervention

2.2.1 Current Condition of Components

Due to prolonged inactivity, an inspection was conducted to evaluate the operational condition of the bottom outlet components. The findings are summarized as follows:

- The stoplog gate and suspension bars remain in good condition;

- The servomotor is in poor condition, requiring further evaluation and workshop inspection (Fig. 15);
- The service gate operating mechanisms are inoperable, with severe damage observed in the Control Station, Electrical Panel, pipes, and cables (Fig. 16);
- The downstream side of the service gate appears to be in reasonable condition, but a detailed assessment of the seals, wheels, and upstream face can only be performed after removal and workshop inspection;
- The steel lining of the bottom outlet gallery downstream of the service gate appears to be in reasonable condition; however, a detailed inspection will be required following thorough cleaning.

Fig. 15 - General condition of the Service Gate Servomotor Base and Watertight Box – Before the proposed intervention

Fig. 16 - General condition of the Service Gate Control Station – Before the proposed intervention

2.2.2 Proposed Interventions

The proposed interventions for the Bottom Outlet system aim to achieve two primary objectives:

- Rehabilitate and restore the system to full operational condition, ensuring that all components function as intended;
- Automate the Ecological Flow release, integrating a motorized valve with a dedicated control and command system.

Stoplog Gate

Based on available records, the stoplog gate was originally coated in the 1990s with Intertol Poxitar, a tar-based paint, and has not undergone any maintenance or recoating since its installation. A preliminary visual inspection indicated that the anticorrosive protection (PAC) remains in reasonable to good condition, though some localized areas exhibit paint peeling and degradation.

The proposed intervention consists of workshop-based treatment, following **Scheme A**, which involves applying a new PAC layer over the existing coating without abrasive blasting. The process includes:

- High-pressure water jet cleaning (250 bar) for degreasing;
- Sanding with a medium-grain disc and needle scaler to roughen the existing paint;
- Application of two coats of epoxy resin-based paint (Hempadur 45141) on degraded areas, extending 20 to 50 mm onto adjacent intact surfaces (minimum dry film thickness: 2 × 75 µm);
- Application of two general coats of Hempadur 45141 across the entire surface (minimum dry film thickness: 2 × 100 µm).

Additionally, the balancing valve and gate seals will be refurbished, including the replacement of bolts.

Service Gate

The complete repair process for the service gate will only be finalized after transportation to the workshop, where a detailed inspection of all components will be conducted. However, based on preliminary on-site assessments, the restoration of the anticorrosive protection is planned, following the same Scheme A treatment as for the stoplog gate.

Watertight Box and Servomotor of the Service Gate

For the servomotor and watertight box, the proposed intervention includes:

- Replacement of seals and bolts to restore functionality;
- Application of PAC Scheme B to the servomotor body, which consists of:
    - Abrasive blasting to "Sa 2½" grade (ISO 8501-1)

- Application of one coat of zinc-rich epoxy primer (minimum dry film thickness: 1 × 50 µm);
- Application of two coats of solvent-free epoxy resin-based paint (minimum dry film thickness: 2 × 225 µm).

Bottom Outlet Gallery Lining

The initial assessment of the gallery lining revealed that it remains in good condition, requiring only cleaning and localized surface repairs. The proposed intervention includes:

- Surface preparation to grade St3, using hand and power tools;
- Application of two touch-up coats of Hempadur 4514 (minimum dry film thickness: 2 × 75 µm);
- Sanding to ensure adhesion;
- Application of two general coats of Hempadur 4514 (minimum dry film thickness: 2 × 100 µm).

Hydraulic Unit and Electrical Control Panel for the Service Gate

For the hydraulic and electrical control systems, the proposed intervention includes:

- Installation of a new hydraulic unit and electrical control panel, ensuring a fully operational power supply and control system.
- Replacement of oil-hydraulic pipes, cables, cable trays, and accessories.
- Redesign and recalculation of the oil-hydraulic system, as no prior information on operating forces and motor power was available.

Ecological Flow Circuit

The ecological flow release system was designed to operate within a flow range of 100 to 350 l/s, under upstream pressures between 27 mca and 30 mca. The objective is to automate the ecological flow regulation, ensuring precise control over discharge conditions.

The proposed intervention includes the supply and installation of:

- 1 electrically actuated flow regulation valve for automated control;
- 1 electromagnetic flow meter to monitor discharge conditions;
- 1 power and control panel, fully integrated with the Service Gate control system.

3. INTERVENTIONS – PLANNING AND EXECUTION

This chapter presents the rehabilitation of the hydromechanical equipment and concrete structures of the Sordo Dam bottom outlet. As a multipurpose infrastructure, ensuring water supply to the Vila Real district and contributing to hydroelectric power generation, the project involved complex technical and operational challenges.

The primary objective was to restore the operability of critical safety components and mitigate structural pathologies in the concrete, ensuring the long-term efficiency and durability of the dam. The works were carried out within an elevation range of 501 m to 525.5 m (maximum flood level), focusing on the rehabilitation of hydromechanical equipment and waterproofing of concrete structures, particularly in submerged and emerged areas.

The interventions were strategically planned for winter, the most suitable period for concrete treatments, considering operational constraints related to water supply and hydroelectric production. To minimize the complexity of submerged operations, the works were scheduled for periods when the reservoir was at its lowest feasible level, reducing the need for specialized diving operations. Emerged areas were treated using suspended scaffolding from the dam crest, ensuring both accessibility and operational safety.

Hydroelectric production was maintained whenever possible, with the water intake at elevation 506.60 m operating at a maximum turbine flow of 3.30 m^3/s. However, reservoir management posed significant challenges due to highly variable inflows, ranging from 5.83 m^3/s in February to 0.06 m^3/s in August [1], compounded by adverse weather conditions during the rehabilitation period.

The rehabilitation was executed in two structured phases:

- Phase 1 – Hydromechanical Equipment Rehabilitation
    - Dismantling and refurbishment of the stoplog gate, service gate, servomotor, and watertight box cover.
    - Cleaning and inspection of the steel lining downstream of the stoplog gate.
- Phase 2 – Concrete Rehabilitation and Final Integration
    - Grout injections and structural repairs in submerged and emerged areas.
    - Temporary removal of the stoplog gate, preventing potential damage during injections.
    - Installation of new electrical and mechanical systems, integrating all rehabilitated components.
    - Final testing of the hydromechanical, oil-hydraulic, and electrical systems, ensuring safety and operational efficiency.

The following subchapters provide detailed descriptions of each intervention, including methodologies and technical challenges encountered during execution.

3.1. Removal, Repair, and Reinstallation of the Stoplog Gate

In September 2023, the stoplog gate was removed and transported to a specialized workshop for detailed inspection and rehabilitation.

Upon arrival, the gate underwent initial cleaning, including high-pressure washing and degreasing, followed by mechanical cleaning (ST3) and sanding. During this process, localized corrosion and coating irregularities were identified [8]. A preliminary Corrosion Action Plan (PAC) Scheme A was tested, which involved localized treatment without complete blasting. However, unexpected chemical reactions with existing coatings made it unfeasible. Consequently, Scheme B (which included full surface blasting and repainting) was adopted to ensure durability and prevent future incompatibilities. This adjustment required additional material procurement and schedule revisions. The selection criteria and methodology for Schemes A and B were previously detailed in Section 2.2.2.

The balancing valve seals were replaced, rehabilitated, and tested, ensuring restored performance. Additionally, all critical gate components, including lateral and top seals, guide rollers, suspension bars, pins, and calibration beam—were inspected, repaired, and tested to ensure structural and operational integrity.

Before returning the gate to the dam, a comprehensive inspection was performed, including visual assessment, thickness measurement, pull-off tests, and porosity (Holiday) testing to verify the coating quality and rehabilitation effectiveness. The assembly of seals and replacement of bolts were confirmed to ensure watertightness.

The reinstallation commenced in January 2024, requiring preliminary underwater work:

- Cutting horizontal bars from the concrete intake grille to facilitate diver access;
- Removing accumulated sediment from the gallery floor to inspect and position the stoplog gate;
- Cleaning the service gate groove and pumping out sediment to ensure correct placement and function.

Following the removal of the horizontal grille bar, a new stainless-steel replacement bar was fabricated and installed, designed to minimize operational vibrations and enhance structural reliability.

A general view of the rehabilitated stoplog gate (upstream face) is shown in Fig. 17, illustrating the final condition after the application of anticorrosive protection and full reassembly.

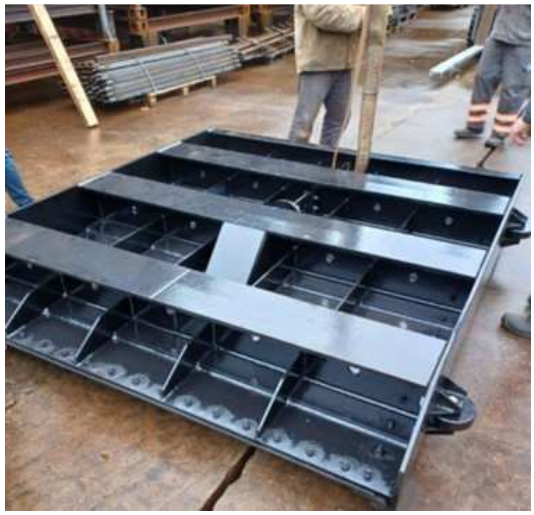

Fig. 17 - General view of the rehabilitated stoplog gate, upstream face

3.2. Removal, Repair, and Reinstallation of the Service Gate

The removal of the service gate took place in mid-January, after the successful installation of the stoplog gate. A mobile crane positioned on the dam crest was used for extraction, as shown in Fig. 18. The gate panel, weighing 2.7 tons, along with the watertight cover, was transported to Prozinco for rehabilitation, while the servomotor was sent to Navipa.

Fig. 18 - Servomotor - General Appearance - Removal with crane truck

At the Prozinco workshop, the gate was cleaned, disassembled, and inspected [9], revealing localized deep corrosion and steel thickness loss. The wheels exhibited significant loss of protective coating and surface irregularities, requiring weld filling and leveling, as shown in Fig. 19.

Fig. 19 -Wheels with corrosion/thickness loss

Before rehabilitation, PAC Scheme A was tested on the watertight box cover and sealing clamp bars. Since this method involved localized treatment without full blasting, it was ultimately considered unsuitable due to surface irregularities and adhesion issues with the existing coating. Consequently, Scheme B (which included full abrasive blasting and primer application) was adopted to ensure long-term durability.

The rehabilitation process included complete abrasive blasting of the watertight box cover, wheel surfaces, and sealing clamp bars, followed by primer application. Weld filling was performed at corroded areas and gate wheels, and all rubber seals were replaced to restore watertightness. After these interventions (Fig. 20), a yard inspection was carried out, verifying coating thickness, adhesion, and porosity (Holiday) testing.

Fig. 20 - Downstream face of the service gate. Sealing bolts with primer application only

At Navipa, the servomotor and its components were inspected, with no unexpected corrosion or mechanical defects found. The interventions performed on the servomotor, hydraulic system, and associated components are summarized in Table 3.

Table 3 - Summary of Inspection and Rehabilitation Interventions on the Servomotor and Hydraulic System

Components	Tasks to Perform
Servomotor Fasteners	Replacement of all fasteners (does not include bolts for fixation in the dam's strongbox)
Servomotor Rod	Cleaning and light polishing
Cylinder	Cleaning
Seal	Complete replacement of the seal
	Modification of the housing to accommodate the scraper
Position Indicator Rod	Cleaning and light polishing
Servomotor Body and Position Indicator	New anticorrosive protection treatment
Remaining Components	Cleaning

The final reception tests of the oil-hydraulic system were conducted in the workshop to confirm compliance with design requirements. These included visual inspections for correct assembly, dimensional checks, pressure tests for safety valves and limiters, and functional tests evaluating the servomotor's opening/closing times under no-load conditions and confirming the absence of oil leaks.

The rehabilitated servomotor and new hydraulic unit successfully met all technical and operational requirements, ensuring reliable performance.

3.3. Inspection of the Lining of the Tunnel Downstream of the Stoplog Gate

The cleaning and inspection of the bottom outlet gallery lining began immediately after the installation of the stoplog gate, conducted simultaneously with the rehabilitation of the service gate in the workshop.

Due to the confined nature of the gallery, maintaining specific environmental conditions was essential for both paint application, requiring temperature and humidity control, and worker safety, ensuring adequate ventilation.

Initially, high-pressure jet cleaning was performed on the side walls, ceiling, and floor, covering the section from the downstream face of the stoplog gate to the transition to concrete. This process revealed several corrosion points that had been concealed by dirt, with the highest incidence on the floor of the gallery lining.

Following the removal of the service gate, previously inaccessible areas, such as the interior of the service gate slot, were inspected. Significant coating defects were observed, especially on previously submerged surfaces.

The inspection report identified the following key issues [10]:

- Downstream wall of the stoplog gate, where localized corrosion was detected on both sides.
- Service gate slot, where the protective coating was completely removed (Fig. 21).
- Welded joints in the steel lining, where the coating was missing, revealing inconsistencies between the on-site applied scheme and the general protective scheme (Fig. 22).
- Stainless steel and carbon steel transitions in the service gate fixed parts, which were in generally poor condition.
- Upstream section of the front crossbeam of the service gate, where severe coating deterioration and corrosion were observed on the interior face of the service gate slot, both upstream and downstream.
- Lining floor, where corrosion was widespread (Fig. 22).
- Lower side walls (left and right banks) downstream of the service gate, which exhibited generalized corrosion (Fig. 22).
- Steel/concrete transition at the end of the gallery lining, where localized corrosion and surface irregularities were present in the adjacent concrete.
- Voids in the gallery floor lining, identified in 40% of the total area, extending from the stoplog gate to the steel/concrete transition.

Fig. 21 - Areas of the service gate slot with total removal of the protective coating

Fig. 22 - Defects in the PAC Scheme of the bottom outlet gallery – sides, floor, and weld areas

The inspection revealed that 57% of the total gallery lining area exhibited corrosion or coating loss, requiring extensive treatment beyond the initial scope. Given the newly identified issues, it was decided to maintain the previously defined treatment scheme, but with additional corrective actions, including:

- Surface preparation to grade ST3, treating all areas affected by corrosion or coating failures.
- Full abrasive blasting inside the watertight box, including paint removal on stainless steel surfaces.
- Treatment of assembly welds, removing the incompatible coating scheme and applying the general protective scheme.
- Injection of voids in the lower lining with low-viscosity polyurethane resin (MC Bauchemie 2700 L), suitable for damp substrates.

The execution of these treatments faced significant constraints due to external factors, primarily adverse environmental and weather conditions. The bottom outlet gallery, accessible only via the dissipation basin, was frequently submerged whenever the reservoir reached the Full Storage Level (FSL) and discharged through the surface spillway.

Additionally, there was no possibility of lowering the reservoir level beyond the hydroelectric plant’s turbine capacity, which further complicated the work schedule. Between January and February 2024, the dam reached FSL multiple times, with 22 days of spillway discharge, making it impossible to establish a safe operational window.

This led to temporary work suspensions and adjustments in planning, waiting for favorable weather conditions and a decrease in reservoir level to ensure both worker safety and the quality of the lining treatment.

The gallery lining treatment was completed in early May 2024 (Fig. 23). Following this, the project was temporarily suspended to coordinate with the concrete waterproofing interventions, minimizing interference, particularly in the service gate valve chamber. The remaining works related to the gates resumed only after the completion of the waterproofing project.

Fig. 23 - Service gate slot and gallery lining after treatment

3.4. Concrete Rehabilitation Works

The concrete waterproofing interventions were focused on the bottom outlet control valve shaft, covering elevations 501 m to 525.5 m (MFL). The interventions began in March, with submerged activities conducted by specialized divers, while the emerged areas were treated using suspended scaffolding from the dam crest (Fig. 24).

To ensure safe underwater operations, stainless steel vertical safety cables were installed, fixed at both the crest and the base of the upstream face, with a maximum spacing of 4.0 m. These cables enabled constant diver attachment via carabiners, ensuring operational safety.

Additionally, a fine mesh was installed in the submerged area at the bottom of the stoplog gate shaft to prevent debris from causing damage to the gate or the bottom outlet gallery lining.

The first phase of the intervention involved water jet cleaning of the upstream face. Surfaces intended for epoxy resin treatment were cleaned using pressures between 350-400 bar for emerged areas and 350-500 bar for submerged areas, as specified in the project. However,

during execution, these pressures contributed to concrete disaggregation in some areas. To mitigate this, adjusted pressures between 220-250 bar were adopted, ensuring effective residue removal without compromising concrete integrity.

Fig. 24 - Cleaning works on the upstream face using a suspended platform

Once the cleaning of emerged and submerged areas was completed, the sealing of construction joints on the reservoir side commenced. This included the right and left lateral faces of the upstream face in submerged areas.

The sealing process utilized specialized equipment to create irregularities in the joint faces, forming a chamfered profile, which significantly improved adhesion of epoxy resins in submerged conditions. The entire process was video-recorded, revealing several joints in severe degradation (Fig. 25). The cleaning and sealing of upstream joints were completed in less than a month.

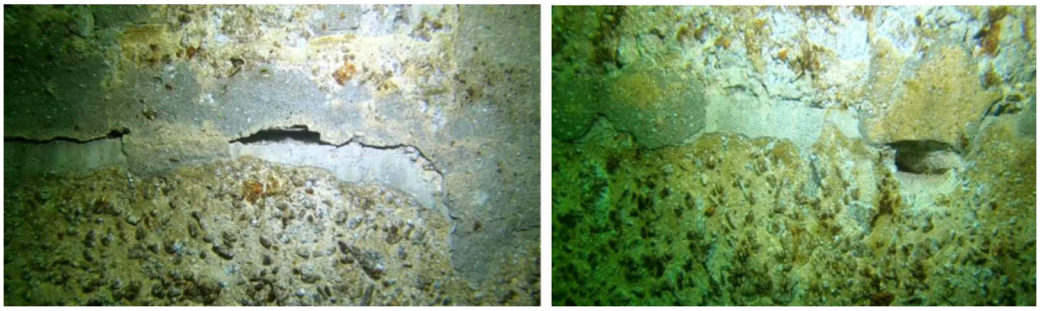

Fig. 25 - Construction joints in a submerged area in a noticeable state of degradation

Following joint sealing, drilling was carried out on the upstream face, in direct contact with reservoir water, for the installation of communication collectors and application of EPICOL-T epoxy resin.

For the submerged collectors on the reservoir side and in the stoplog gate shaft, immediate sealing was applied after drilling to prevent water seepage into the concrete walls (Fig. 26). Subsequently, a crystal tube extension was installed in these collectors, extending to the water surface to avoid water flow through the drilled holes (Fig. 27).

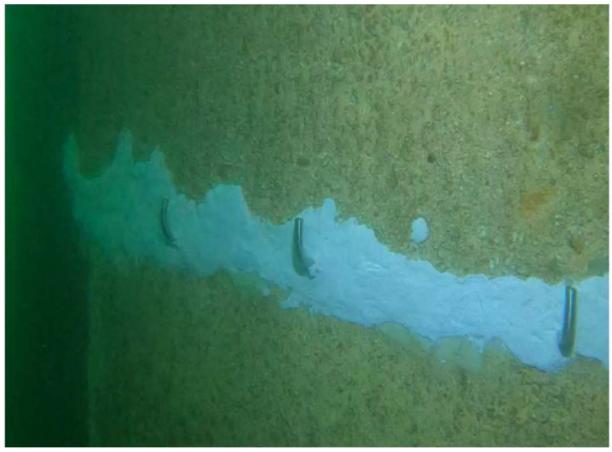

Fig. 26 - Application of communication collectors and joint treated with EPICOL-T epoxy in the submerged area

Fig. 27 - Application of communication collectors and joint treated with EPICOL-T epoxy – emerged area

Simultaneously, tests were carried out to assess the technical compliance of resins for external applications, specifically on the upstream plane and the stoplog gate shaft. The products Alocit 28.14 and 28.15 were applied to 10 concrete blocks (0.30 × 0.25 m² each) (Fig. 28), with five blocks painted under submerged conditions and the remaining five in emerged conditions.

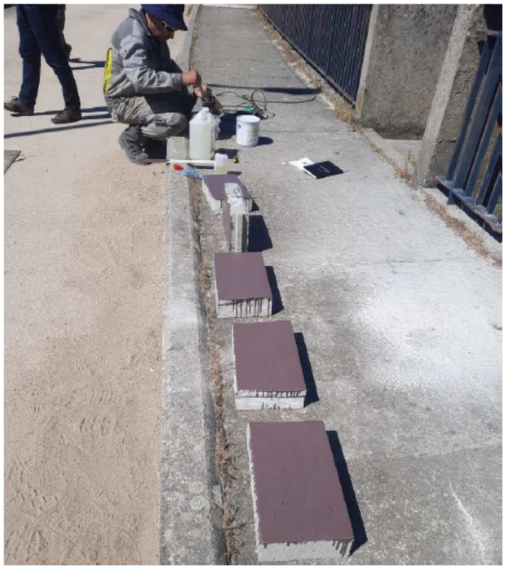

Fig. 28 - Painting of concrete blocks for testing

The first coat of paint on the emerged blocks showed better quality, whereas the submerged blocks exhibited uneven coverage, leaving visible uncoated areas (Fig. 29). Despite this, a second coat was applied to all blocks.

Fig. 29 - General appearance of a submerged concrete blocks after the first coat

Tests on these blocks included Barcol hardness measurements (on-site, Fig. 30), paint thickness assessment, and pull-off adhesion tests (laboratory analysis). The tests, conducted by the Portuguese Institute for Welding and Quality (ISQ), revealed that submerged applications exhibited adhesion and drying difficulties compared to those applied in atmospheric conditions.

Fig. 30 - Blocks after the second coat

Regarding yield, paint consumption doubled compared to the technical specifications due to the irregular surface conditions and losses during application, particularly in submerged environments. Given these limitations, the designer recommended restricting the application of Alocit 28.15 to submerged areas between elevations 501 m and 509 m, corresponding to the top of the bottom outlet chamber, to optimize yield and minimize waste.

Fig. 31 - General appearance of submerged painting application with Alocit 28.15 – upstream face and surroundings of the bottom outlet chamber

While the resin application was ongoing on the upstream plane, the construction joints inside the bottom outlet valve chamber were enlarged. Once this process was completed, drilling at points A and B for cement grout injection commenced, followed by the installation of the corresponding injection tubes inside the structure (Fig. 32).

Fig. 32 – Joint treated with Sikadur 31+ and installed cement grout injection piping – Bottom Outlet Chamber

For construction joint filling, Sikadur 31+ epoxy mortar was applied, ensuring high sealing capacity and resistance to injection pressure. In areas with active water leaks, Sika-4a Fast Mortar was used to provide rapid waterproofing.

A total of approximately 325 type A and B drill holes were executed, treating 216 meters of joints inside the chamber and shaft, and 161 meters on the upstream side (Stoplog Gate Shaft and upstream faces).

The total grout injection volume amounted to 732 liters, of which approximately 55 liters corresponded to injection hole filling. Thus, the effective grout volume used in the joints was approximately 677 liters.

In the final phase, an integral crystalline waterproofing agent (Penetron Standard) was applied to all treated surfaces (Fig. 33). This served as a surface carbonation catalyst, reducing moisture retention in the chamber walls and enhancing long-term durability.

Fig. 33 - General view of the bottom outlet chamber: on the left, the condition before the intervention; on the right, the chamber after rehabilitation

3.5. Installation of the Control Station, Electrical Panel, Piping, and Cabling Associated with the Bottom Outlet and Ecological Flow System

The new hydraulic unit was installed and tested only after the completion of all civil works related to concrete waterproofing. This sequencing ensured that hydromechanical interventions remained compatible with structural operations, minimizing interferences between teams and providing optimal conditions for installation and final testing.

To enhance operational efficiency, the new oil-hydraulic control station was strategically placed in the access gallery of the bottom outlet control chamber, approximately 20 meters from the servomotor (Fig. 34). This relocation brought several advantages, including removing the control panel from the humid environment of the chamber, thus improving operational conditions and long-term equipment reliability. Additionally, this repositioning eliminated the need for frequent descents to the chamber level, facilitating system operation and maintenance.

During the final phase of the intervention, the assembly of the new control station and its components was completed, including the installation of key elements of the ecological flow system, such as valves, a flow meter, and connecting piping sections (Fig. 35).

Additionally, the stoplog gate, which had been temporarily removed to facilitate well rehabilitation and prevent structural damage, was retrieved and prepared for installation. The placement process was supported by an ROV (Remotely Operated Vehicle) and a diving team, who ensured proper cleaning of the seating surface to prevent damage to the gate or its new seals during operation.

Simultaneously, Navipa, the company responsible for the oil-hydraulic system, handled the transportation and setup of the Hydraulic Unit, connecting it to the servomotor to maintain the bottom outlet's operability throughout the final assembly process.

Fig. 34 - New control station for the Service Gate and ecological flow

Fig. 35 - New ecological flow circuit installed

3.6. Testing of Hydromechanical, Oil-Hydraulic, and Electrical Equipment

The hydromechanical, oil-hydraulic, and electrical equipment underwent rigorous testing protocols, performed both at the factory and on-site, in full compliance with project specifications. These tests assessed functionality, performance, and safety, ensuring that all components met the defined technical and operational requirements.

The primary objective of these tests was to validate the integrated operation of all components, including the gates, the new hydraulic unit, the electrical systems, and the ecological flow system. Validation procedures involved leak-tightness and sealing performance tests, flow regulation assessments, and functional evaluations under simulated operating conditions.

A detailed analysis of the tests and results will be presented in the results chapter, highlighting key performance metrics and reliability assessments of the rehabilitated systems.

4. RESULTS

To monitor infiltration volumes inside the bottom outlet chamber and shaft, a flow measurement system was implemented during project execution. This included the installation of a collection spout at the base of the bottom outlet valve chamber, enabling continuous flow monitoring. Measurements were recorded at least weekly, and the collected data is presented in (Fig. 36).

For a more accurate interpretation of the graph, it is important to note that injection procedures were completed on June 28, and the final coat of Penetron was applied on July 10. As shown, infiltration values ranged between 3.14 L/min and 0.07 L/min. The maximum value was associated with a joint inside the bottom outlet valve chamber that exhibited significant leakage, requiring the application of Epicol-T epoxy resin to mitigate water seepage. This joint corresponded to the last injection hole completed.

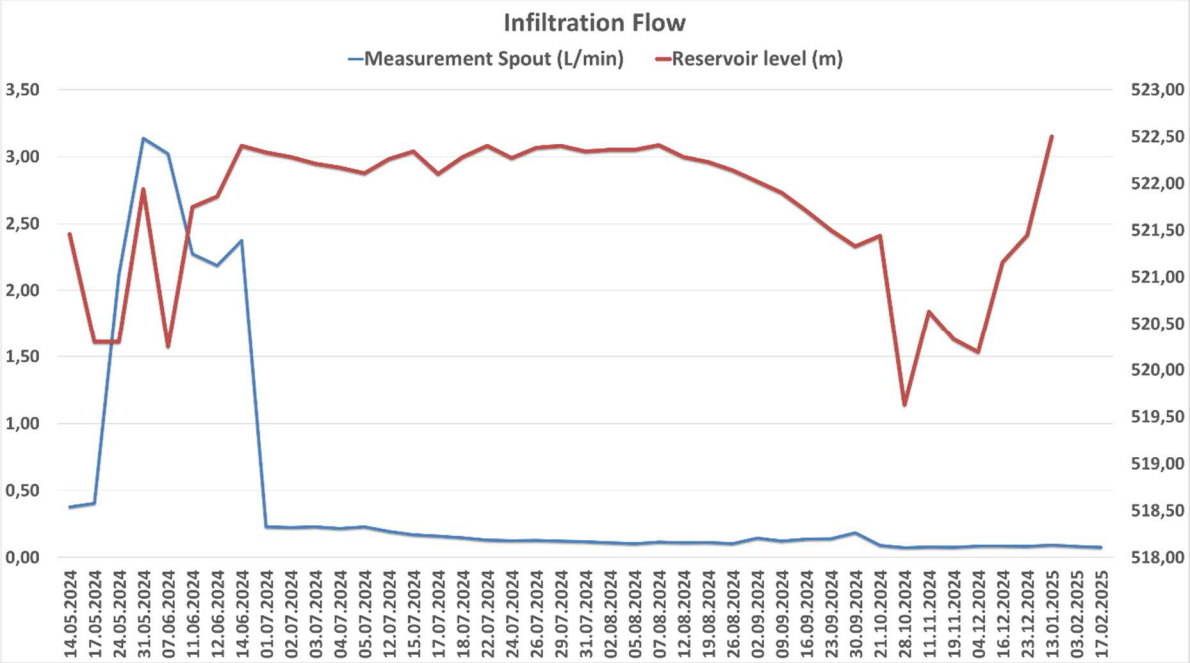

Fig. 36 - Graph of infiltrated flow measured at the spout at the base of the bottom outlet chamber as a function of the reservoir water level

The minimum recorded value of 0.07 L/min, corresponding to the most recent measurement in February 2025, confirms the absence of visible infiltration from the construction joints. The initial infiltration rate, recorded on May 14, 2024, was 0.38 L/min, decreasing to 0.23 L/min following the completion of joint treatment on July 1, 2024—representing an initial reduction of approximately 40%. From that point onward, infiltration rates stabilized at around 0.07 L/min, resulting in a total reduction of approximately 82%, even as reservoir levels fluctuated, including periods at FSL. These results highlight the effectiveness and long-term reliability of the interventions, demonstrating their resilience to variations in reservoir conditions.

The relationship between infiltration flow and water temperature variations is presented in Fig. 37. As shown, values have remained consistently low (~10°C) since August, yet no significant impact on infiltration has been observed. Although thermal contraction of the concrete could theoretically increase seepage by creating new percolation paths, measured infiltration rates have remained stable despite fluctuations in reservoir level. This consistency further reinforces the conclusion that the structural and waterproofing measures implemented were effective in minimizing long-term infiltration.

Although the results are still preliminary, evidence suggests that the observed stability may be linked to increased carbonation in previously identified infiltration zones.

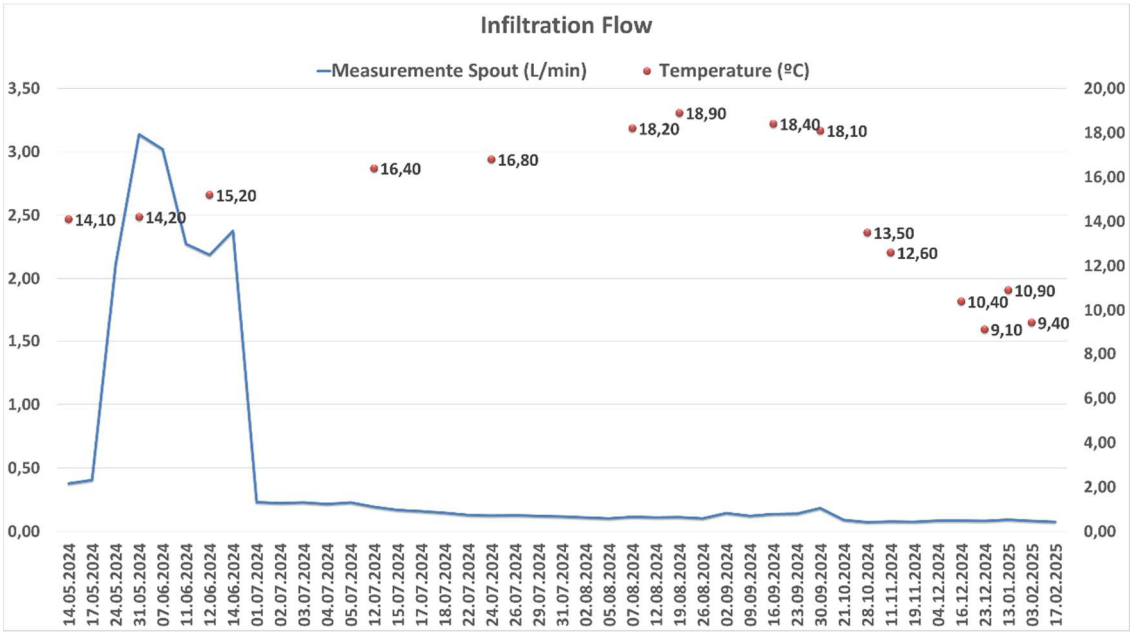

Fig. 37 - Graph of infiltrated flow measured at the spout at the base of the bottom outlet chamber as a function of water temperature

The service gate and ecological flow system were tested to validate their operability and compliance with project specifications. For the service gate, tests included functionality checks and watertightness evaluations.

During the functional tests, the system underwent opening and closing command verifications, failure simulations (such as filter clogging, oil shortages, electrical failures, and communication disruptions), and end-of-stroke response assessments. The watertightness tests, conducted under hydrostatic pressure, confirmed that the service gate was fully operational, with no detected leaks.

The stoplog gate also underwent watertightness testing. Once properly seated on the sill, the structure was verified to provide effective sealing, confirming its full functionality without leaks. These results demonstrate that all rehabilitated structures and systems are fully operational, meeting the project's objectives and ensuring both dam safety and operational efficiency.

For the ecological flow system, tests focused on the regulation valve and flowmeter, evaluating their performance in both local and remote control modes. The test procedures involved verifying manual opening and closing commands, calibrating the valve for various flow levels, and conducting failure simulations, such as flowmeter disconnection. Calibration defined a maximum valve opening limit of 70%, corresponding to a flow rate of 130 L/s. This setting effectively prevented excessive vibrations and cavitation while ensuring compliance with regulatory flow requirements. The system demonstrated robustness and precise control, effectively managing ecological flow discharge under demanding operational conditions.

5. CONCLUSIONS

The rehabilitation of the Sordo Dam was a highly complex project, involving critical structural and functional interventions to ensure the safety and operational reliability of this multipurpose infrastructure. The primary objectives were the restoration of the bottom outlet's hydromechanical equipment and the correction of structural pathologies in the concrete, ensuring the dam's operational efficiency and long-term durability.

A phased and meticulously planned approach was crucial in overcoming significant operational and environmental constraints. The recorded improvements, particularly the 82% reduction in infiltrations in the bottom outlet valve chamber and shaft, confirm the effectiveness of the implemented solutions.

The use of cement grout injections for concrete treatment proved to be highly effective, ensuring strong integration with the existing structure. This method suggests further long-term improvements, as the injected material continues to interact with the surrounding environment.

Waterproofing efforts posed notable challenges, particularly with the Alocit 28.14 and 28.15 resins. While they partially fulfilled their intended purpose, limitations in adhesion and yield were observed, especially under submerged conditions.

The application of a surface carbonation catalyst (Penetron Standard) to the interior of the shaft proved to be a successful strategy, effectively reducing moisture levels and creating a more suitable environment for the newly rehabilitated equipment to operate efficiently.

The rehabilitation of the stoplog and service gates was a key milestone, restoring the full functionality and reliability of the bottom outlet system. Rigorous testing confirmed that the gates met all safety and performance standards, with no leaks or operational failures detected.

The ecological flow system demonstrated efficiency and reliability, ensuring precise regulation of programmed flows while fully complying with regulatory requirements. Its robust operation, both locally and remotely, guarantees effective and sustainable management of ecological releases.

Despite some challenges encountered during the project, the results indicate that the primary objectives were fully achieved. The rehabilitated bottom outlet system is now fully operational and compliant with the safety standards established by the Dam Safety Regulation. These enhancements significantly improve the dam's efficiency and safety, reinforcing its critical role in water supply and hydroelectric power generation.

REFERENCES

[1] Tecnopor, *SMVR (Serviços Municipalizados de Vila Real) - Barragem do Sordo. Projecto Estrutural. Memória Descritiva e Justificativa,* Porto: Tecnopor, Consultores Técnicos, Lda, 1991.

[2] LNEC, *Barragem do Sordo. Inspecção à Estrutura e Diagnóstico do Sistema de Observação efectuados em abril de 2012,* Lisboa: LNEC, 2012.

[3] A. E. e. Ambiente, *Projeto de Reabilitação da Barragem do Sordo - Vila Real,* Lisboa: AQUALOGOS, 2019.

[4] LNEC, “Barragem do Sordo - Analise do comportamento observado durante o primeiro enchimento da albufeira e o primeiro período de exploração,” LNEC, Lisboa, 2005.

[5] Ferreira Lemos Engenharia, “Elaboração de Especificações Técnicas para a Impermeabilização de Betões na Barragem do Sordo,” Ferreira Lemos Engenharia, Porto, 2023.

[6] LNEC, “Barragem do Sordo - Atualização do plano de observação,” LNEC, Lisboa, 2023.

[7] FEUP, “Determinação da resistência à compressão de carotes de betão - Barragem do Sordo,” FEUP, Porto, 2021.

[8] LTU Engenharia, “BARRAGEM DO SORDO - RELATÓRIO DE INSPECÇÃO DA COMPORTA ENSECADEIRA,” Lisboa, 2023.

[9] LTU Engenharia, “BARRAGEM DO SORDO - RELATÓRIO DE INSPECÇÃO E REABILITAÇÃO DA COMPORTA DE SERVIÇO,” LTU Engenharia, Lisboa, 2023.

[10] LTU Engenharia, “Barragem do Sordo - Relatório de Inspeção e Reabilitação da Blindagem do Túnel,” Lisboa, 2023.

[11] Laboratório Nacional de Engenharia Civil, “Apreciações do estudo de avaliação da conformidade com o RSB e do plano de observação,” LNEC, 2014.

Fifth International Dam World Conference
PORTUGAL • LISBON • LNEC • APRIL 13-17, 2025
dam world 2025

INFLUENCE OF FINE MATERIALS ADDITION ON THE COEFFICIENT OF THERMAL EXPANSION OF REPAIR MORTARS

R. G. G. OLIVEIRA	L. REGINATO[1]	E. F. de FARIA	F. L. WILLRICH	A. C. P dos SANTOS
Itaipu Parquetec	Itaipu Parquetec	Itaipu Binacional	Itaipu Binacional	Universidade Federal da Integração Latino-Americana (UNILA)

ABSTRACT

The compatibility of the coefficient of thermal expansion (CTE) between the substrate and the repair material, as well as the precise determination of the CTE of cementitious materials, is essential to ensure the effectiveness of repairs performed on concrete structures. Incompatibilities between the CTEs can lead to additional stresses at the substrate/repair interface, resulting in cracks and/or delamination of the repair material due to significant thermal variations. The CTE of aggregates directly influences the CTE of the cementitious material containing that aggregate; the higher the CTE of the aggregate, the higher the CTE of the cementitious material. The magnitude of this influence also depends on the amount of aggregate and the proportion of all components in the mixture, including paste, aggregates, and admixtures. Thus, this study investigated the CTE of ten different repair mortars with sand replaced by fine materials of quartz, calcitic limestone, and dolomitic limestone, in addition to a reference mortar, for application in concrete dam structure repairs. The fine materials were added in four different proportions: 0%, 5%, 15%, and 30%. The determination of the CTE was carried out following a methodology which considers factors that influence the analysis of CTE and the variability of results, using equipment available in concrete laboratories in Brazil. The results showed that the CTE of aggregates influences the resulting coefficient of the mixture. An increase in the CTE was observed with the replacement of sand by pure quartz and a reduction in the CTE with the replacement of sand by the other fines, with a more pronounced reduction in the case of calcite compared to dolomite. Additionally, the greater the replacement of sand by these materials, the more significant the observed influence on the increase or reduction of the CTE. This indicates that it is possible to adjust the CTE of the repair mortar by mineralogical substitution of the aggregates, allowing the production of a mortar with a thermal expansion coefficient compatible with that of the substrate where the repair material is intended to be applied.

Keywords: Repair mortar, Coefficient of thermal expansion (CTE), Thermal compatibility, Fine materials

[1] luan.reginato@itaipuparquetec.org.br, Brazil

1. INTRODUCTION

The Coefficient of Thermal Expansion (CTE) is defined as a unit strain per unit temperature change. Material deformation due to temperature variation depends on its CTE. When the temperature increases, the material undergoes expansion, and when it decreases, the material undergoes volumetric contraction. The magnitude of volumetric variation is directly proportional to the CTE value.

Therefore, matching the substrate's CTE with that of the repair material and determining the CTE of materials through a precise testing methodology is essential for ensuring reliable stress analysis. Incompatibilities between the CTE of the repair material and the substrate can lead to increased stresses at the substrate/repair interface, potentially causing cracking and/or delamination of the repair material due to thermal variations [1, 2].

The CTE of the aggregate influences the CTE of the cementitious material containing this aggregate, with higher aggregate CTE leading to higher CTE in the cementitious material. However, the magnitude will also depend on the amount of aggregate and the proportion of all mix components, such as paste, fine aggregate, and additives [1].

The CTE of aggregates varies according to the parent rock, with values typically ranging from 0.9 to 16×10^{-6}/°C, and most common values between 5 and 13×10^{-6}/°C [1]. Table 1 presents the CTE values for each type of aggregate and the concrete containing the respective aggregates.

Table 1 – CTE of concretes with different aggregates [1, 3, 4]

ROCK	CTE (10^{-6}/°C)	
	Aggregate	Concrete
Granite	1.8 - 11.9	7.7 - 9.5
Basalt, diabase	3.6 - 9.7	7
Quatzite	11.0 - 12.0	11.7 - 12.8
Sandstone	4.3 - 13.9	8.6 - 11.7
Limestone	0.9 - 12.2	5.9 - 7.4
Dolomite	6.7 - 8.6	-

Given the extent of aggregate influence on the CTE of mortars, the material's CTE can be estimated through the weighted average of its components' CTEs [3]. This suggests that this property could be adjusted by using mineral additions with different mineralogical origins.

The methodology proposed by Reginato et al. [5] enables the measurement of repair mortar CTE while accounting for factors that affect its analysis. This includes elements that may influence result variability, such as moisture, testing cycles, specimen geometry, and quantity, using standard equipment commonly available in concrete laboratories in Brazil.

Various standards and methodologies exist for determining CTE, including ABNT NBR 12815 [6], AASHTO T 336 [7], and TI-B 101:1994 [8] for general use and concrete; Nenevê [9] for pre-mixed mortars produced on-site or in laboratories; and NT BUILD 367 [10] and Reginato et al. [5] for repair mortars.

In this context, this project aimed to investigate the CTE of nine different repair mortars, containing 5%, 15%, and 30% additions of quartz fines, calcitic limestone, and dolomitic limestone, as well as a reference mortar, for application in concrete dam structure repairs. The thermal expansion coefficient test was conducted using the methodology developed by Reginato et al. [5].

2. MATERIALS AND EXPERIMENTAL PROGRAM

The materials used to produce the mortars were Portland cement CP V (PC), natural sand (NS), silica fume (SF), superplasticizer additive (SP), and fillers of quartz (QZ), calcitic limestone (CL), and dolomitic limestone (DL).

For particle size characterization of the cement, silica fume, and fine materials, laser granulometry testing was performed according to ISO 13220 [11], and for sand, particle size distribution was assessed through mechanical sieving per ABNT NBR 17054 [12]. Additionally, the specific gravity of sand was tested following ASTM C128 [13], the BET surface area according to ISO 9277 [14], and the specific gravity of fine powders per ABNT NBR 16605 [15], as shown in Figure 1 and Table 2.

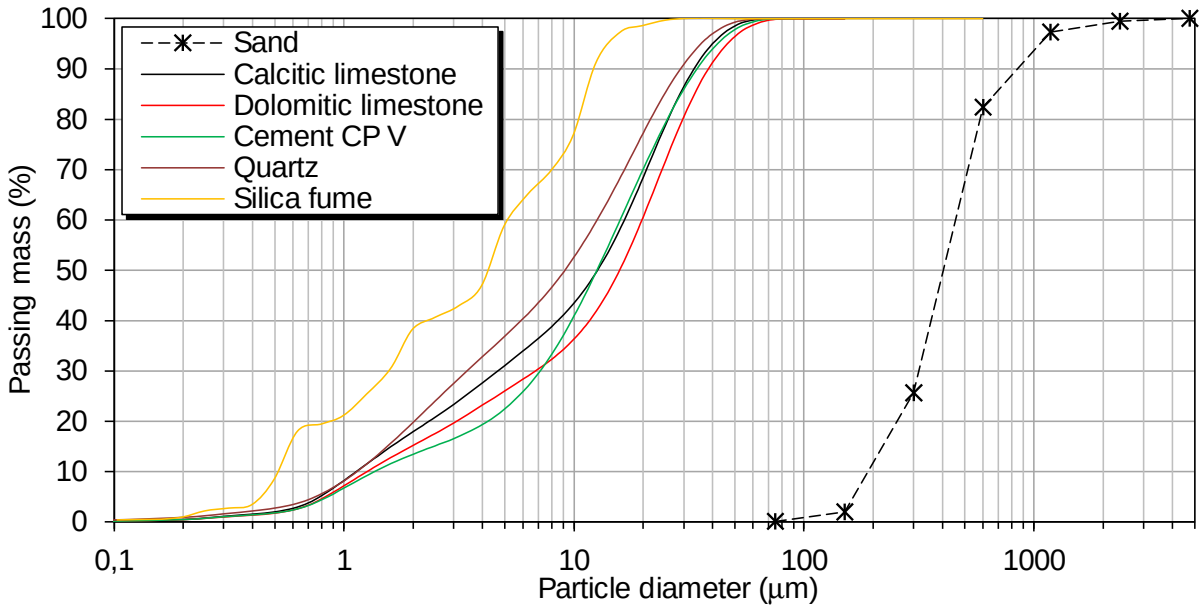

Fig. 1 – Particle size distribution curve of fine materials

Table 2 – Results of the physical characterization tests of the materials

Properties	PC	SF	QZ	CL	DL	NS
Maximum diameter (mm)	-	-	-	-	-	1.18
Fineness modulus	-	-	-	-	-	1.93
Cumulative diameter 10% (µm)	1.36	0.52	1.14	1.13	1.26	-
Cumulative diameter 50% (µm)	12.57	19.85	9.13	12.65	15.77	-
Cumulative diameter 90% (µm)	34.31	12.4	29.12	33.26	38.38	-
Specific gravity (g/cm³)	3.06	2.25	2.71	2.77	2.86	2.64
Specific surface area (m²/g)	2.834	17.3	2.42	2.014	1.72	-

Ten repair mortar mixes were produced by replacing part of the sand mass with 5%, 15%, and 30% fine/pulverulent materials, along with a reference mix. The nomenclature used for each mixture corresponds to REF (reference mix), Q (Quartz), C (Calcitic Limestone), D (Dolomitic Limestone), 05 (5%), 15 (15%), and 30 (30%). The mix proportions of the repair mortars are presented in Table 3.

Table 3 – Mixes

Name	Cement kg/m³	Silica fume kg/m³	Sand kg/m³	Filer type kg/m³		Water kg/m³	water/binder	Superplasticizer %
REF	595	60	1381	0	-	256	0.39	0.5
Q05	595	60	1312	71	Quartz	256	0.39	0.7
Q15	595	60	1174	213		256	0.39	0.8
Q30	595	60	967	425		256	0.39	1.15
C05	595	60	1312	72	Calcitic limestone	256	0.39	0.8
C15	595	60	1174	217		256	0.39	0.9
C30	595	60	967	435		256	0.39	1
D05	595	60	1312	75	Dolomitic limestone	256	0.39	0.8
D15	595	60	1174	224		256	0.39	0.9
D30	595	60	967	449		256	0.39	1

For each mix, three prismatic specimens (25x25x285 mm) were cast, with stainless steel pins (ϕ6x22.5 mm) attached to the ends, as per ASTM C490 [16]. After demolding, which was carried out 24 hours after casting, the samples were identified and subjected to curing in saturated lime water for 48 hours. They were then placed on shelves for air curing in a controlled environment (22 ± 2ºC) with monitored humidity for 260 days. The laboratory humidity conditions during all tests ranged between 55 and 65%.

After the curing period, the specimens were placed in a climatic chamber with a temperature of 80ºC and a relative humidity of 50% for 72 hours to achieve thermal-hydric equilibrium. Before starting the test, the dial gauge must be calibrated to zero using the standard bar. After the 72-hour period, the specimen is removed from the climatic chamber using a high-temperature

protective glove, weighed, and placed on the dial gauge, as shown in Figure 2. This handling takes approximately 20 seconds.

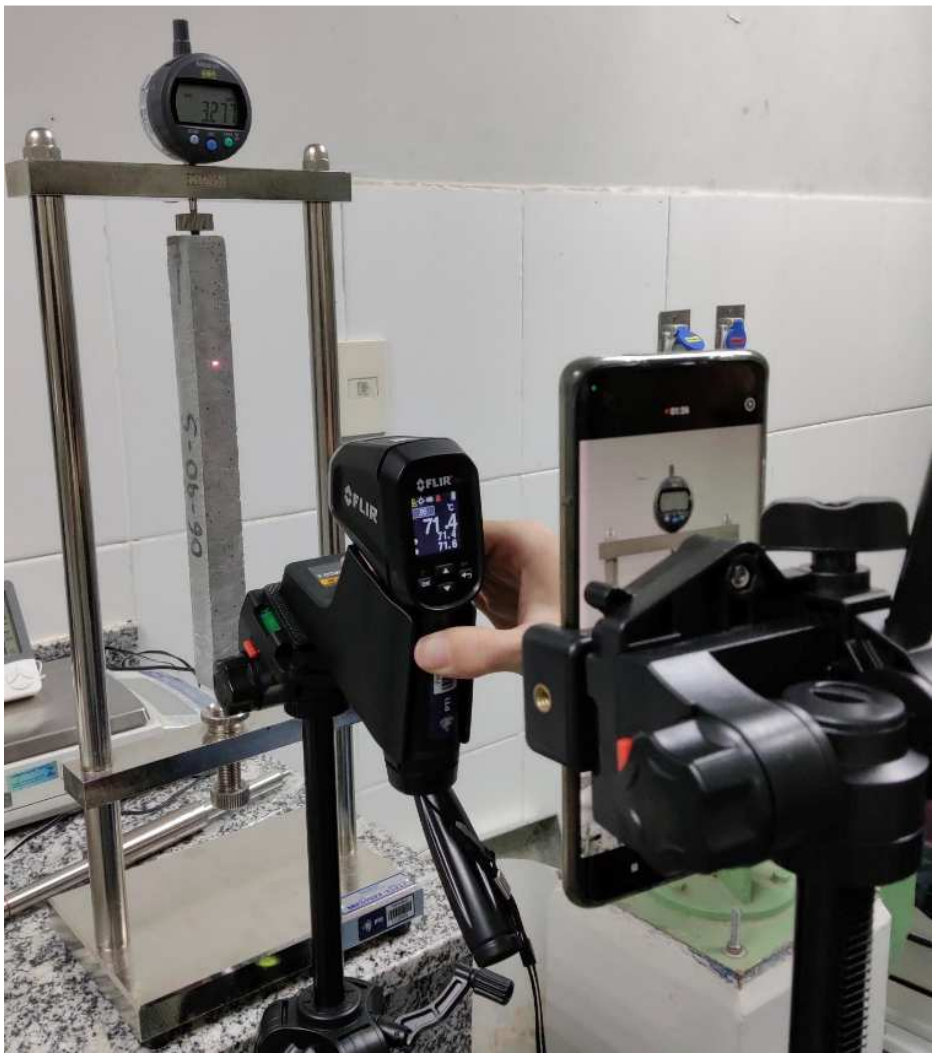

Fig. 2 – a) Specimens in the climatic chamber; b) CTE testing

As the specimen cools, the length is recorded using the dial gauge, and the temperature is measured two-thirds of the way up the specimen with the laser thermometer. The frequency of these recordings is presented in Table 4. At the end of the temperature and length measurements, the specimen is weighed again to obtain the final mass.

With the data records, Table 4 can be constructed using the expressions from Table 5 [5]. It is noted that the deformation calculation excludes the expansion of the reference pin, based on the known coefficient of the pin material.

Using the accumulated deformation ($\varepsilon_{accum,n}$) and accumulated temperature change ($\Delta T_{accum,n}$), a graph is constructed with deformation on the y-axis and temperature on the x-axis. With these data, linear regression is performed, and the tangent of the angle with the x-axis (slope) of the fitted line corresponds to the thermal expansion coefficient [5].

Table 4 – Distribution of readings over time during the test and variables for recording [5]

Reading	Time (min)	Temperature (ºC) - T_n	Length (mm) - L_n	Strain (10^{-6}) - ε_n	Temperature Variation (ºC) - ΔT_n	ε Accumulated (10^{-6}) - $\varepsilon_{accum.n}$	ΔT Accumulated (ºC) - $\Delta T_{accum.n}$
0	0	T_0	L_0	-	-	-	-
1	0.5	T_1	L_1	ε_1	ΔT_1	$\varepsilon_{accum.1}$	$\Delta T_{accum.1}$
2	1	T_2	L_2	ε_2	ΔT_2	$\varepsilon_{accum.2}$	$\Delta T_{accum.2}$
⋮	⋮	⋮	⋮	⋮	⋮	⋮	⋮
6	3	T_6	L_6	ε_6	ΔT_6	$\varepsilon_{accum.6}$	$\Delta T_{accum.6}$
7	3.5	T_7	L_7	ε_7	ΔT_7	$\varepsilon_{accum.7}$	$\Delta T_{accum.7}$
8	4	T_8	L_8	ε_8	ΔT_8	$\varepsilon_{accum.8}$	$\Delta T_{accum.8}$
9	5	T_9	L_9	ε_9	ΔT_9	$\varepsilon_{accum.9}$	$\Delta T_{accum.9}$
10	6	T_{10}	L_{10}	ε_{10}	ΔT_{10}	$\varepsilon_{accum.10}$	$\Delta T_{accum.10}$
⋮	⋮	⋮	⋮	⋮	⋮	⋮	⋮
22	18	T_{22}	L_{22}	ε_{22}	ΔT_{22}	$\varepsilon_{accum.22}$	$\Delta T_{accum.22}$
23	19	T_{23}	L_{23}	ε_{23}	ΔT_{23}	$\varepsilon_{accum.23}$	$\Delta T_{accum.23}$
24	20	T_{24}	L_{24}	ε_{24}	ΔT_{24}	$\varepsilon_{accum.24}$	$\Delta T_{accum.24}$
25	22	T_{25}	L_{25}	ε_{25}	ΔT_{25}	$\varepsilon_{accum.25}$	$\Delta T_{accum.25}$
⋮	⋮	⋮	⋮	⋮	⋮	⋮	⋮
28	28	T_{28}	L_{28}	ε_{28}	ΔT_{28}	$\varepsilon_{accum.28}$	$\Delta T_{accum.28}$
29	30	T_{29}	L_{29}	ε_{29}	ΔT_{29}	$\varepsilon_{accum.29}$	$\Delta T_{accum.29}$

Table 5 – Equations for calculating strain, temperature variation, respective accumulative values, and mass variation [5]

Variable	Equations
Strain (ε_n)	$$\varepsilon_n = \frac{L_{n-1} - L_n - \Delta L_{dil.stud.n}}{L_{bar} + L_0 - 2 \times L_{stud}}$$ Where: L_{bar} the length of reference bar (295 mm); L_{stud} the length of the stud (22,5 mm); $\Delta L_{dil.stud.n}$ the estimated expansion of the studs, as follows: $$\Delta L_{dil.stud.n} = 2 \times L_{stud} \times \alpha_{stud} \times \Delta T_n$$ Where: α_{stud} the CTE of studs, where: Stainless steel: $\alpha_{stainless} = 17{,}5 \times 10^{-6}/°C$; Nickel alloy: $\alpha_{nickel} = 4{,}0 \times 10^{-6}/°C$;
Temperature variation (ºC) (ΔT_n)	$\Delta T_n = T_{n-1} - T_n$
ε Accumulated ($\varepsilon_{accum.n}$)	$\varepsilon_{accum.n} = \varepsilon_{accum.n-1} + \varepsilon_n$
ΔT Accumulated (ºC) ($\Delta T_{accum.n}$)	$\Delta T_{accum.n} = \Delta T_{accum.n-1} + \Delta T_n$
Mass variation (%) (Δm)	$$\Delta m = \frac{m_f - m_i}{m_i} \times 100$$

3. RESULTS AND DISCUSSIONS

As an example, Figures 3a and 3b show the deformation and temperature variation of the C05 mortar samples, respectively. It can be observed that the behavior is nonlinear, as the difference between the specimen temperature and the environment decreases, since the rate of heat exchange between the media decreases as the temperature difference becomes

smaller. Figure 3c presents the CTE results for each tested sample, with values of 11.48, 11.37, and 11.38×10^{-6}/°C, resulting in an average of approximately 11.4×10^{-6}/°C, a standard deviation of 0.06×10^{-6}/°C, and a coefficient of variation of 0.56%.

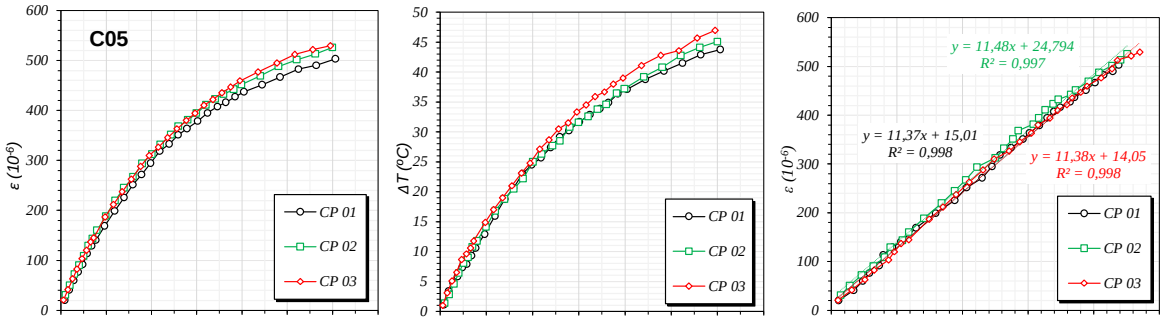

Fig. 3 – a) Deformation and b) Temperature over time; c) Strain vs. temperature and fitted curves

The results of the average CTE for all the mortars are presented in Figure 4. It can be observed that the CTE increases, compared to the reference mortar (0%), as the inclusion of quartz powder increases, with a rise of up to 7.1% when 30% is replaced. For the limestone types, however, there was a reduction in the CTE, with decreases of 4.2% and 9.6% for dolomitic and calcitic limestone, respectively, when 30% substitution was used.

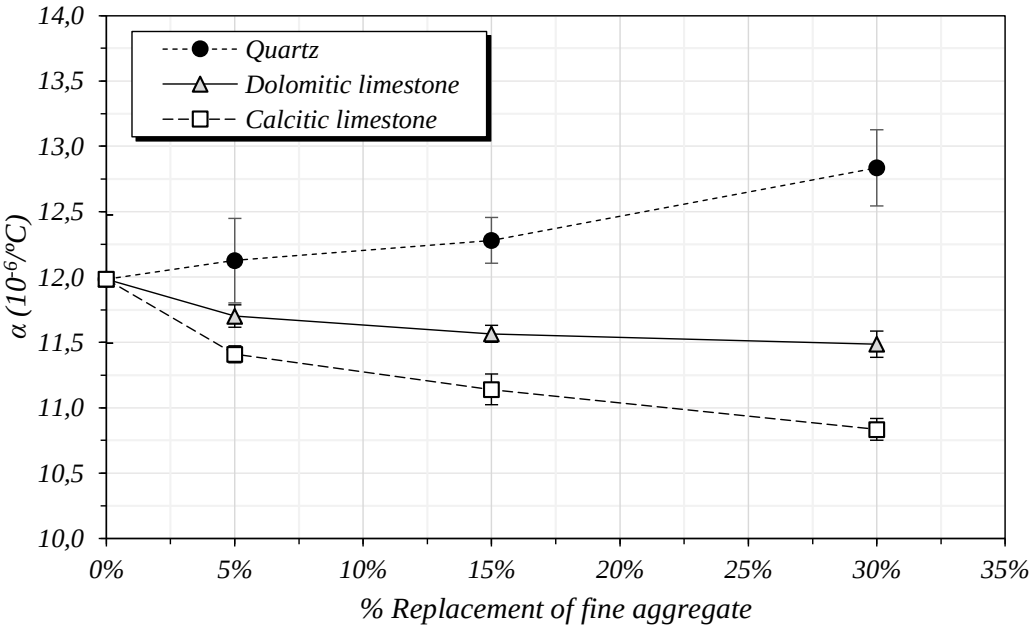

Fig. 4 – Coefficient of thermal expansion for mortars with substitutions of quartz powder, dolomitic limestone, and calcitic limestone

4. CONCLUSIONS

The highest values of the thermal expansion coefficient (CTE) were observed in the mortars with added quartz, followed by those containing dolomitic limestone, and finally, those with

calcitic limestone. This pattern suggests that the CTE of the minerals present in the fine aggregates directly impacts the CTE of the cementitious material. In other words, the higher the CTE of the mineral, the higher the CTE of the cementitious material, and vice versa. This behavior reflects the influence of the mineralogical characteristics of the components on the thermal behavior of the mortars.

An increase in the CTE of the mortars was observed as higher amounts of quartz fines were incorporated. On the other hand, a decrease in the CTE was noted for mortars with increased additions of calcitic and dolomitic limestone fines when compared to the reference mix. This suggests that the minerals in limestone aggregates have a lower CTE than quartz, resulting in a reduction in the thermal expansion of the material.

In general, the CTE of the mortar can be considered as the weighted average of the CTE of its constituents. This means that as the amount of substitution of the aggregates increases, the effect of this addition on the CTE of the cementitious material becomes more pronounced. For instance, the progressive substitution of sand (mainly composed of quartz but with the presence of other minerals) by calcitic and dolomitic limestone, whose minerals have a lower CTE than quartz, leads to a decrease in the CTE of the mortars. In contrast, when sand is replaced by pure quartz, an increase in CTE occurs due to the high thermal expansion of quartz.

This behavior highlights the possibility of adjusting the CTE of repair mortars through mineralogical substitution of aggregates. Modulating the CTE of the mortars is crucial as it allows for alignment with the CTE of the substrate where the material will be applied, ensuring better thermal compatibility and reducing the risk of thermal stresses, cracks, and detachment. This process of adapting the mortar to the substrate is essential in repair applications, particularly in structures exposed to significant thermal variations, such as concrete dams and other large-scale works.

REFERENCES

[1] A. M. Neville, *Propriedades do Concreto*, 5o ed. 2015.

[2] A. M. Vaysburd, B. Bissonnette, e K. F. von Fay, “Compatibility Issues in Design and Implementation of Concrete Repairs and Overlays”, *Bureau of Reclamation. U.S. Department of the Interior*, vol. Report, no MERL-2014-87, p. 134, 2014.

[3] P. K. Mehta e P. J. M. Monteiro, “Concreto - Microestrutura, propriedades e materiais”, *IBRACON*, vol. 2 ed., p. 751, 2014.

[4] Azo Materials, “Magnesia – “Magnesium Oxide (MgO) Properties & Applications”. [Online]. Disponível em: www.azom.com/properties.aspx?ArticleID=54

[5] L. Reginato, R. G. G. Oliveira, e F. L. Willrich, “Coefficient of thermal expansion of cementitious mortars : new testing methodology”, *Revista IBRACON de Estruturas e Materiais*, vol. 18, no 1, p. 1–18, 2025, doi: https://doi.org/10.1590/S1983-41952025000800009.

[6] ABNT NBR 12815, “Concreto endurecido — Determinação do coeficiente de dilatação térmica linear — Método de ensaio”, 2012.

[7] AASHTO T 336-15, “Coefficient of Thermal Expansion of Hydraulic Cement Concrete”, 2019.

[8] TI-B 101, “Test method expansion coefficient of concrete”, *Danish Technological Institute*, vol. 101, no 94, p. 1–5, 1994.

[9] B. L. Nenevê, “Proposta de ensaio para verificação do comportamento de argamassas de revestimento vertical externo expostas à ação de calor e choque térmico”, *Pós-Graduação em Engenharia de Construção Civil. Universidade Federal do Paraná*, p. 192, 2020.

[10] NT BUILD 367, “Concrete, repair materials: coefficient of thermal expansion”, *Nordtest Method*, 1991.

[11] ISO13320, “Particle size analysis - Laser diffraction methods”, Genebra, 2020.

[12] ABNT NBR 17054, “Agregados — Determinação da composição granulométrica — Método de ensaio”, 2022.

[13] ASTM C128 − 15, “Standard Test Method for Relative Density (Specific Gravity) and Absorption of Fine Aggregate”, 2015, doi: 10.1520/C0128-15.2.

[14] ISO 9277, “Determination of the specific surface area of solids by gas adsorption - BET method”, Genebra, 2010.

[15] ABNT NBR 16605, “Cimento Portland e outros materiais em pó — Determinação da massa específica”, 2017.

[16] ASTM C 490, “Standard practice for use of apparatus for the determination of length change of hardened cement paste, mortar, and concrete”, *ASTM International*, p. 1–5, 2017, doi: 10.1520/C0490.

Fifth International Dam World Conference
PORTUGAL • LISBON • LNEC • APRIL 13-17, 2025
dam world 2025

DEVELOPMENT OF IMPROVEMENTS IN FLOW METER DEVICES FOR DAM MONITORING

Luis Antonio Sucapuca[1]	Bruno João Arenhardt[2]	Ricardo Miranda Rojas[3]	Diego Liska Darli[4]	Luan Reginato[5]
Itaipu Parquetec	Itaipu Parquetec	Itaipu Binacional	Itaipu Binacional	Itaipu Parquetec

ABSTRACT

The study focuses on the development of prototypes for water level measurement in flow monitoring instruments for dams, following a systematic methodology structured into five stages: initiation, proposal development, fabrication, laboratory testing, and field validation. In the initial phase, internal discussions and field visits were conducted to gather information on the actual conditions of the dam, complemented by market research and patent analysis to align the project with existing technological solutions. The proposal development stage involved conceptual and technical modeling, adjusted based on site-specific requirements. During fabrication, 3D modeling (SolidWorks) was employed for prototyping using accessible materials such as PVC and PLA, ensuring technical and economic feasibility. In the laboratory testing phase, the prototypes were evaluated for stability, sensitivity to flow variations, and ease of operation. After necessary adjustments, the devices underwent field testing to validate their functionality under real operational conditions, refining the measurement frequency as needed. This methodology highlights the importance of customized and cost-effective solutions to enhance safety and efficiency in dam flow monitoring.

Keywords: water level gauge, **flow meter, alternative solutions, prototypes, dams**.

[1]luis.aracayo@itaipuparquetec.org.br, Brazil
[2]bruno.arenhardt@itaipuparquetec.org.br, Brazil
[3]ricardem@itaipu.gov.py, Paraguay
[4]liska@itaipu.gov.br, Brazil
[5]luan.reginato@itaipuparquetec.org.br, Brazil

1. INTRODUCTION

Dams serve the function of retaining or controlling the flow of water in watercourses, creating reservoirs for various purposes, such as hydroelectric power generation, irrigation, and potable water supply. Flow monitoring in dams is essential to ensure structural safety, prevent accidents, and effectively manage available water resources. For the proper operation of a dam, it is crucial to control the volume of water infiltrating through the structures and foundation, which is achieved through flow monitoring.

This monitoring is carried out through the installation of equipment such as weirs, flow gauges, limnigraphs, level sensors, and rain gauges, which record information on the amount of infiltration water. These data enable the tracking of water levels in the reservoir, the detection of variations, and the implementation of preventive measures to ensure the structural safety of the dam.

Additionally, monitoring internal flows in critical areas, such as between concrete blocks, concrete-rock interfaces, changes in geometry, foundations, and material transitions, enables the detection of potential anomalies and water level variations that may compromise structural stability. According to ICOLD Bulletin No. 109 [1], internal erosion (piping) and exceptional floods cause 90% of embankment failures, which are associated with the dam's characteristics, as well as the time and location of its construction. Among these cases, 45% are attributed to failures due to internal erosion.

The high rate of failures in earthfill or rockfill dams due to internal erosion highlights the importance of measuring drainage flows, both during the initial reservoir filling and throughout its operation. This study aims to enhance flow monitoring technologies to improve dam safety.

In this context, this study explores different water level measurement methods to indirectly determine flow rates, analyzing the advantages and disadvantages of each technology. Low-cost solutions tested in a laboratory environment are also presented, considering variables such as water flow rate, filling velocity and response time, among others. The study describes the design, fabrication, and validation of three water level measurement prototypes, using accessible and durable materials such as PVC and incorporating modern technologies, including laser rangefinders and ultrasonic sensors. These prototypes were designed to meet operational requirements, enabling a scalable and cost-effective approach suitable for real field conditions. The methodology and results obtained are presented below, highlighting contributions to the advancement of dam monitoring technologies.

2. FUNDAMENTALS

In dams, there are three types of flow meters based on the weir plate method: the V-notch weir, the rectangular weir, and the Cipolletti (trapezoidal) weir. According to [2], triangular (V-notch) weirs offer higher accuracy for flow rates below 30 L/s and are simpler to install compared to other types. For estimated flow rates between 30 L/s and 300 L/s, both triangular and rectangular weirs provide similar accuracy. For flow rates above 300 L/s, rectangular weirs are more suitable due to their well-defined discharge coefficients.

The height of the overflow sheet should be measured approximately 1.0 m upstream of the weir to account for the depletion of flow near the measuring device. Figure 1 illustrates some criteria recommended in the literature. If the upstream flow is not uniform, it is advisable to install a flow stabilizer, such as a gravel box, perforated curtains, screens, or other devices. Downstream, it is essential to prevent the weir from being submerged by the water level, ensuring it always remains below its crest.

In earthfill or rockfill dams, the accumulation of sediments upstream of these measuring devices can become an issue, necessitating frequent cleaning and maintenance operations. Particularly during the rainy season, the transport of loose material and sediments can affect the accuracy of measurements, while during the summer, there is an increase in the proliferation of aquatic plants.

The components of the flow meters include the weir, made of 5-6 mm stainless steel sheet with a 45º chamfered edge, whose shape varies according to the flow rate to be measured. The meter box, constructed from masonry or concrete, is approximately 2.5 m in length, 1.0-1.2 m in width, and up to 1.2 m in height, and is waterproofed to prevent infiltration. Inside the box, the turbulence stabilizer consists of two steel mesh panels and stabilizes the water flow before the weir. A 20 mm diameter PVC pipe connects the interior of the box to the external reading hose, while a 6 mm diameter transparent glass hose or tube measures the water column height. The graduated stainless steel ruler, calibrated by aligning with the crest or base of the weir, is fixed alongside the hose or glass tube. Finally, the bottom discharge pipe consists of PVC pipes installed at the bottom of the box, with screw caps or valves for draining during cleaning or maintenance.

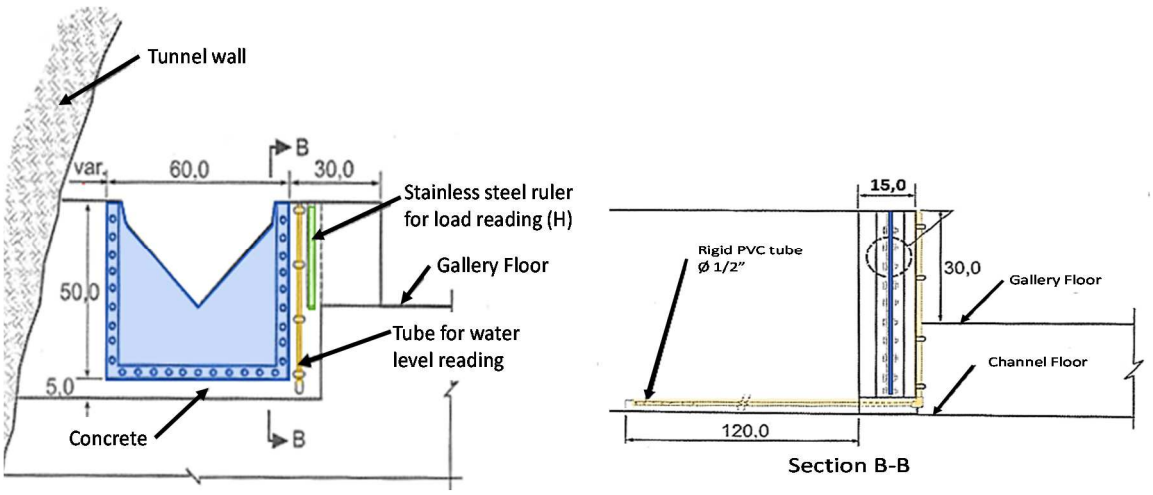

Figure 1 – Bolted metal profile on the plate (units in cm). Adapted from [3].

In practice, operational challenges may compromise the accuracy of measurements. Typically, the water column level in the hose or in the graduated ruler is located in areas that are difficult to access or in positions that hinder precise readings. The need to align the line of sight horizontally with the water level increases susceptibility to uncertainties and random errors, as well as complicating visualization, as illustrated in Figure 2.

Figure 2 – Difficulties in reading V-Notch Weirs.

Therefore, it is necessary to develop solutions that transmit the water level to a more suitable position, ensuring accuracy and efficiency in the measurement. The methodology adopted for the development of these solutions is presented below.

3. METHODOLOGY

To obtain a suitable solution according to the site characteristics (Figure 3) and aiming to make the readings of flow meters easier and more reliable, a process consisting of five steps was carried out: initiation, proposal development, fabrication, laboratory testing, and delivery for field testing (Figure 4).

Step 01 begins with internal discussions to align expectations, followed by a field visit to collect information on the actual conditions of the instruments. In parallel, a market and patent search is conducted to ensure the project is aligned with existing solutions and technological trends.

Figure 3 – Field data collection.

Step 02, based on the collected information, involves the development of technical and conceptual proposals. This phase may include adjustments after a follow-up field visit, ensuring that the project meets the specific needs of the site.

Step 03, based on the defined proposal, involves 3D geometric modeling using three-dimensional models developed in SolidWorks software, allowing for a detailed and precise representation of the prototype. After modeling, the prototype fabrication process begins, using available and low-cost materials to ensure economic feasibility during this initial phase.

Step 04, the prototype is subjected to laboratory testing, where key aspects are evaluated, such as the stability of components under sudden increases and decreases in water flow, the measurement sensitivity for different scenarios, and the ease of operator change, ensuring

that the device is functional and adaptable to operational needs. After testing, necessary adjustments are made to improve or correct the prototype's performance.

Finally, in Step 05, the adjusted prototype is delivered for field testing, where it is evaluated under real operational conditions. During this stage, an appropriate measurement frequency is defined to understand the behavior, validating the device's performance and making final adjustments if necessary. This phase concludes the process, allowing the integration of the prototype into the operational environment.

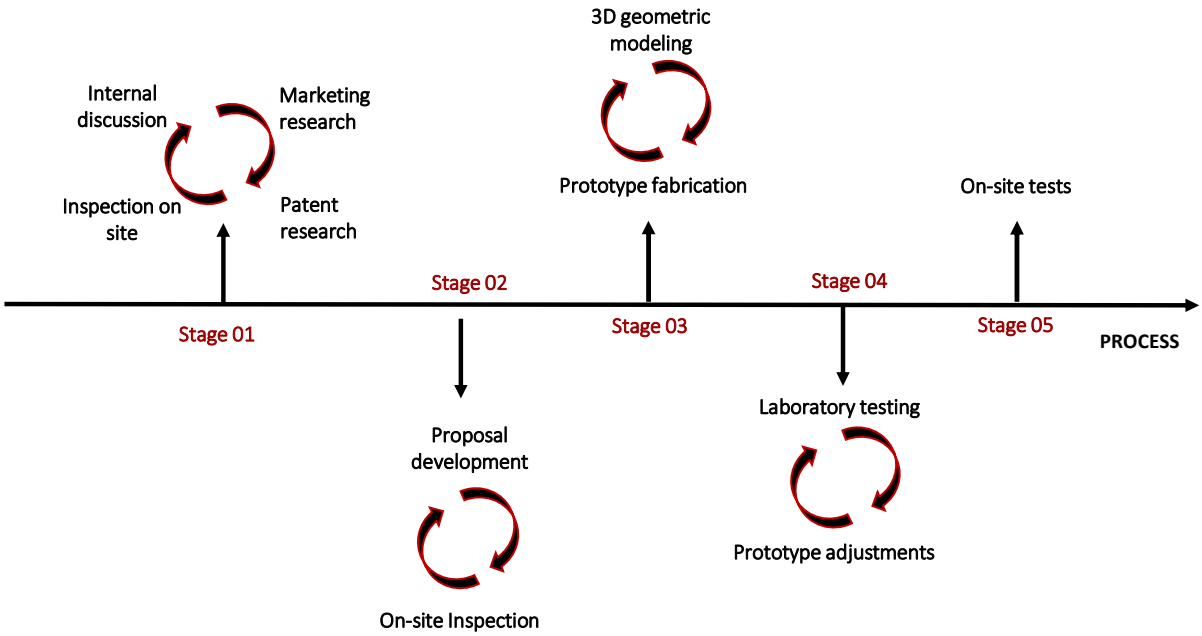

Figure 4 – Prototype creation and integration process.

3.1. Market technologies

To improve the measurement process, market technologies from different fields of expertise were explored, which are activated only on-site, using fixed-position instruments. This enables technicians to efficiently detect structural anomalies or equipment failures. These improvements are essential to ensure greater accuracy and reliability in measurements, as well as to allow a quick and precise response to potential equipment failures. Within the scope of this article, remote or automated flow or liquid level measurement technologies were not explored

The combination of technological innovations and field validation is what ensures the success of implementing increasingly effective measurement systems. There are several technologies available for level measurement, each with its own characteristics, advantages, and limitations.

Level sensors are essential devices for monitoring and controlling fluids in reservoirs and industrial processes. Among the available technologies, float sensors operate through mechanical, magnetic, or hydraulic actuation, providing direct level indication, but with limited

accuracy due to variations in the fluid. Metallic reference electrodes, widely used in pump automation, perform discrete measurements upon contact with the liquid. Pressure-based level sensors, such as piezoresistive and capacitive sensors, offer high accuracy and repeatability, but are influenced by the fluid's density.

Capacitive, vibratory, and optical methods are also employed in level measurement. Capacitive sensors measure the variation in capacitance between the probe and the reservoir, ensuring high accuracy but are sensitive to the dielectric constant of the material. Vibratory sensors use piezoelectric rods to detect the presence of the material through changes in vibration, making them useful for powders or low-density materials. Optical sensors, on the other hand, employ light refraction and reflection to detect liquids, offering efficiency but being susceptible to optical interferences.

Advanced technologies, such as ultrasonic, radar, radiometric and flow sensors, expand the possibilities for measurement. Ultrasonic and laser sensors determine the level by the reflection of waves, being fast and accurate, but sensitive to environmental conditions. Radar sensors, including guided models (TDR), provide precise and robust measurements for both liquids and solids. Radiometric methods, which use ionizing radiation, are employed in extreme conditions. Flow sensors based on the angular velocity of the liquid allow for accurate flow monitoring, being applicable to various industrial processes.

3.2. Development of proposals

The development of proposals is the stage of creating technical solutions. In this phase, the specific characteristics and conditions of the installation site are analyzed, as well as the operational requirements of the flow measurement system. This approach aims to ensure that the designed prototypes meet the practical, technical, and economic demands of the project, considering factors such as available space, the prevailing measurement technique, the flow meter dimensions, basin depth, the presence of solids in the water, the measurement device's time and weight, and the materials to be used. Based on these parameters, three distinct prototypes were conceived, each with configurations and functionalities adapted to the context.

Prototype 01 features an inverted "U" shape, fixed to the bottom of the structure. It consists of two parallel pipes with internal floaters that move via two pulleys, connected by a wire. This wire transfers the water level displacement from one floater to the other. The water level is directly read from a scale positioned at the top of the pipe not connected to the water, as illustrated in Figure 5.

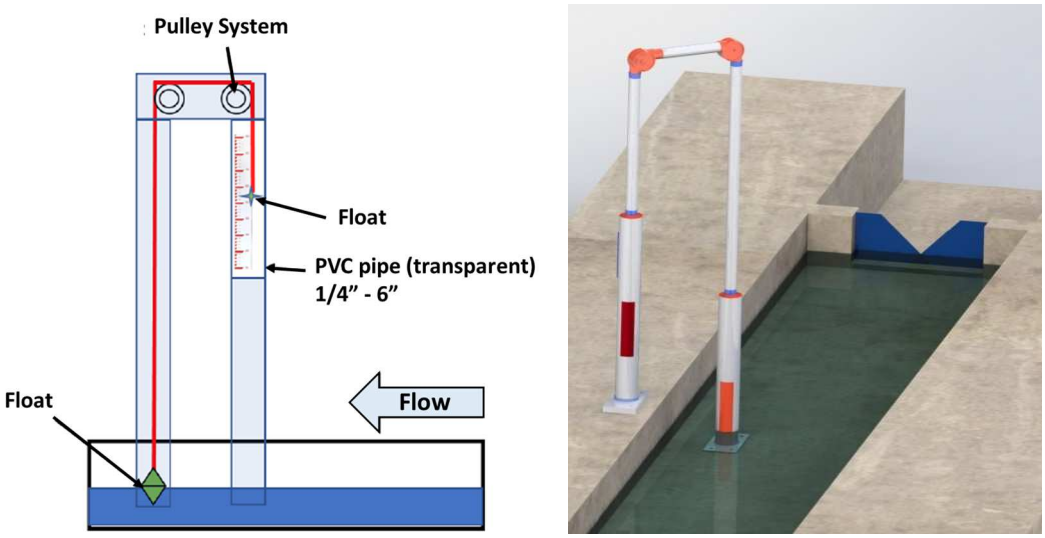

Figure 5 – Prototype 01

Prototype 02 features a tubular shape fixed vertically to the side of the basin wall, consisting of four main components: (1) a triangular or trapezoidal weir, which regulates the water flow; (2) a measurement device, such as a laser tape or ultrasonic sensor, positioned at the top of the prototype; (3) a tubular support with a fixed base, designed to ensure the stability and proper positioning of the measurement device; and (4) an internal float or target, which follows the variations in the water level, allowing for precise measurements of changes in the reservoir.

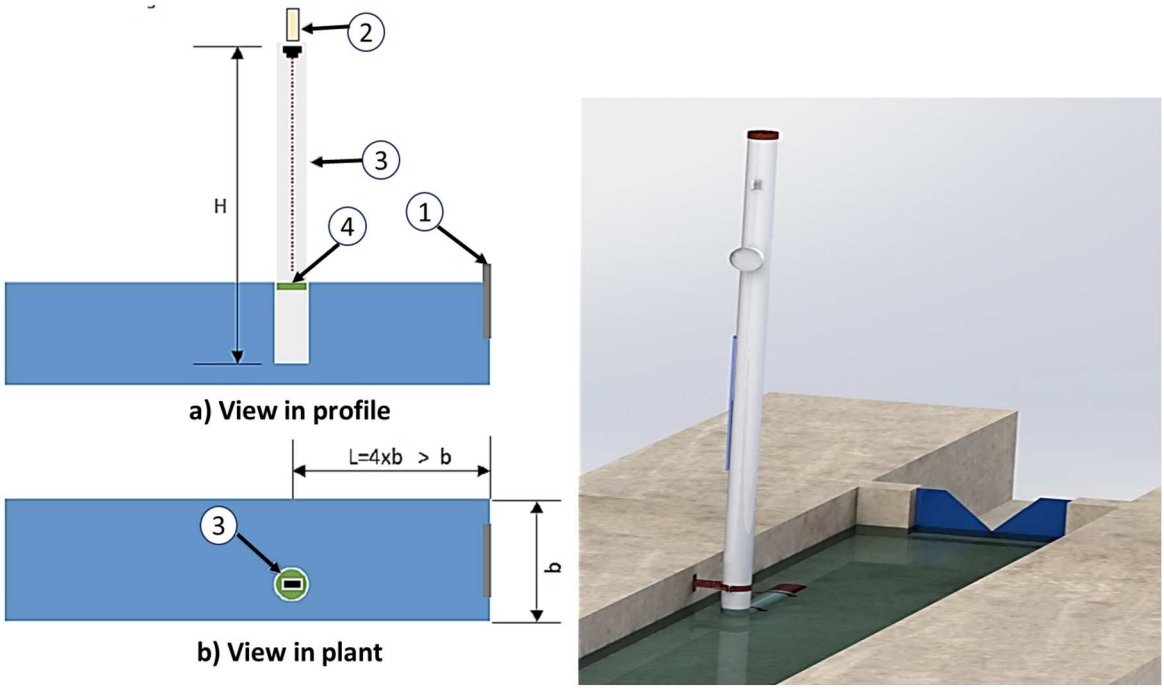

Figure 6 – Prototype 02

Prototype 03 is similar to Prototype 02. It also has a tubular shape fixed to the side of the basin wall, mounted vertically with an internal float or target. The difference lies in the inclusion of a

measuring ruler located on the side of the tube, where the reading is taken, as shown in Figure 7.

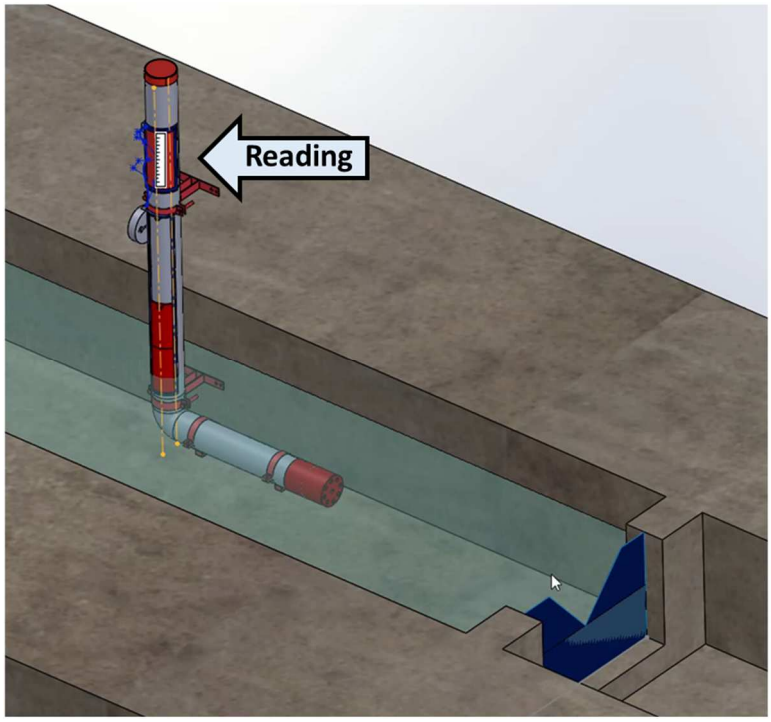

Figure 7 – Prototype 03.

3.3. Fabricated devices

During the fabrication and geometric modeling phase, the three distinct prototypes were planned and assembled using low-cost materials such as PVC, PLA, acrylic, iron sheets, waterproofing agents, sealing silicone, and hydraulic fittings. These materials were selected to make the project feasible in technical, financial, and logistical terms, allowing for assembly, disassembly, and transport to the installation site, as shown in Figure 8. The strategic choice of materials ensured lightweight, durable, and adaptable structures for different operational conditions and installation environments.

The materials used include PVC pipes, fittings, and flanges, custom parts fabricated with a 3D printer using PLA material, iron sheet clamps (Figure 8a), acrylic scales, carbon fiber rods, and multifilament fishing line. In total, 43 custom parts were printed, with 27 different designs, totaling 351 hours of printing and consuming 2.97 kg of filament (Figure 8d). This approach allowed for the development of functional and optimized prototypes, designed to meet the specific conditions of the system.

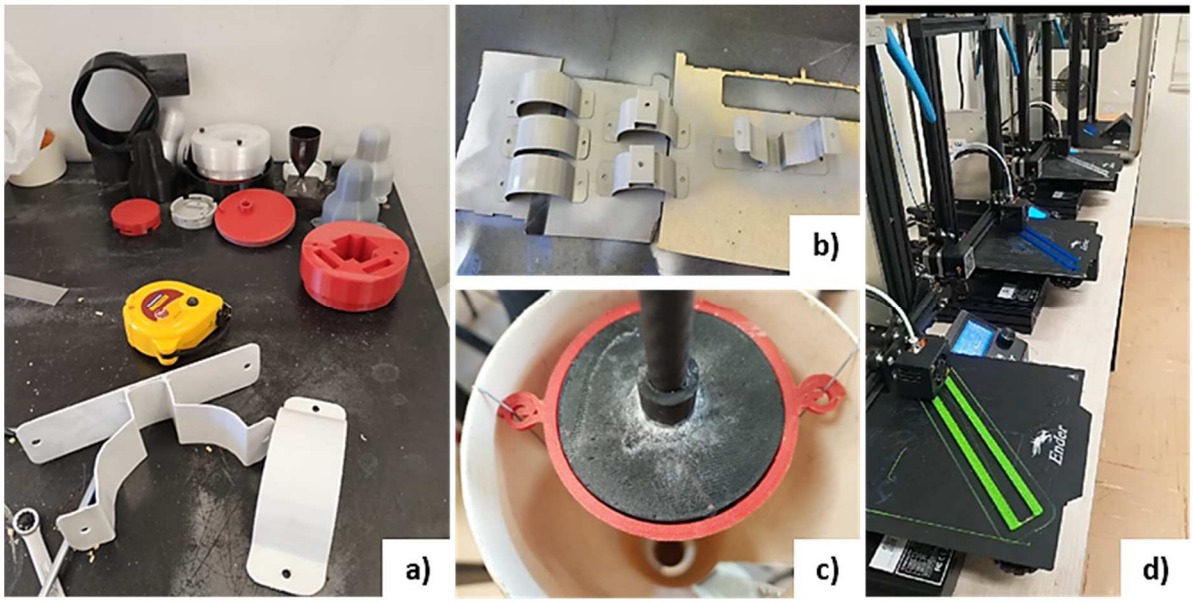

Figure 8 – a) fabrication of the parts, b) clamps, c) float, d) printers in operation.

From the proposal phase to fabrication, the prototypes were improved and adjusted to enable their installation in the field. The fabricated prototypes are described below and shown in Figure 9.

Prototype 1, presented in Figure 9a, features a tubular structure composed of two floaters (1), two pulleys (2), two mounting supports (3), tube connections (4), a graduated scale (5), and two maintenance windows — one for each floater. Additionally, it includes a fishing line guide, holes at the bottom to facilitate water entry, base mounting screws, and filters at both lower ends to prevent solid ingress, avoiding sediment accumulation and ensuring the proper functioning of the measurement system.

Its main advantage is operational simplicity, allowing direct measurement of the water level through the graduated scale, without the need for electronic devices. The key advantages observed are: ease of maintenance, with practical access windows; low manufacturing cost; direct reading; and suitability for level transfer over long distances. However, the dependency on the pulley system makes it susceptible to obstructions, such as dirt or wear, and installation may be more complex due to the number of components involved.

Prototype 2 employs a technological approach, utilizing high-accuracy devices such as laser tapes or ultrasonic sensors to enable precise water level measurements. The entire device structure was designed and developed to reduce random visual uncertainties, converting them into more controllable systematic uncertainties.

The structure of the prototype and the components used for its assembly are shown in Figure 9b, numbered from 1 to 5. Inside the tubular structure, there is a float or target (1), essential for precise measurement (Figure 8c), and a maintenance window (2), which facilitates secure

access for inspections and adjustments. Additionally, filters are positioned at the lower end (3) to prevent the entry of sediments and debris. The support for positioning the measuring device (4) provides stability and precision during operations (Figure 10a). Furthermore, two clamps (5) ensure a firm attachment, while the level bubbles at the top ensure the horizontal alignment of the support, optimizing the alignment for reliable measurements. This combination of features provides the prototype with versatility and good performance in environments with significant water level variation.

Prototype 3, also shown in Figure 9b, follows a traditional approach, utilizing a tubular structure consisting of a float or target (1), maintenance window (2), filter (3), and graduated scale (6) — laser tape or ultrasonic sensor. Additionally, it includes two clamps (5) and a level bubble at the top to ensure the horizontal alignment of the prototype.

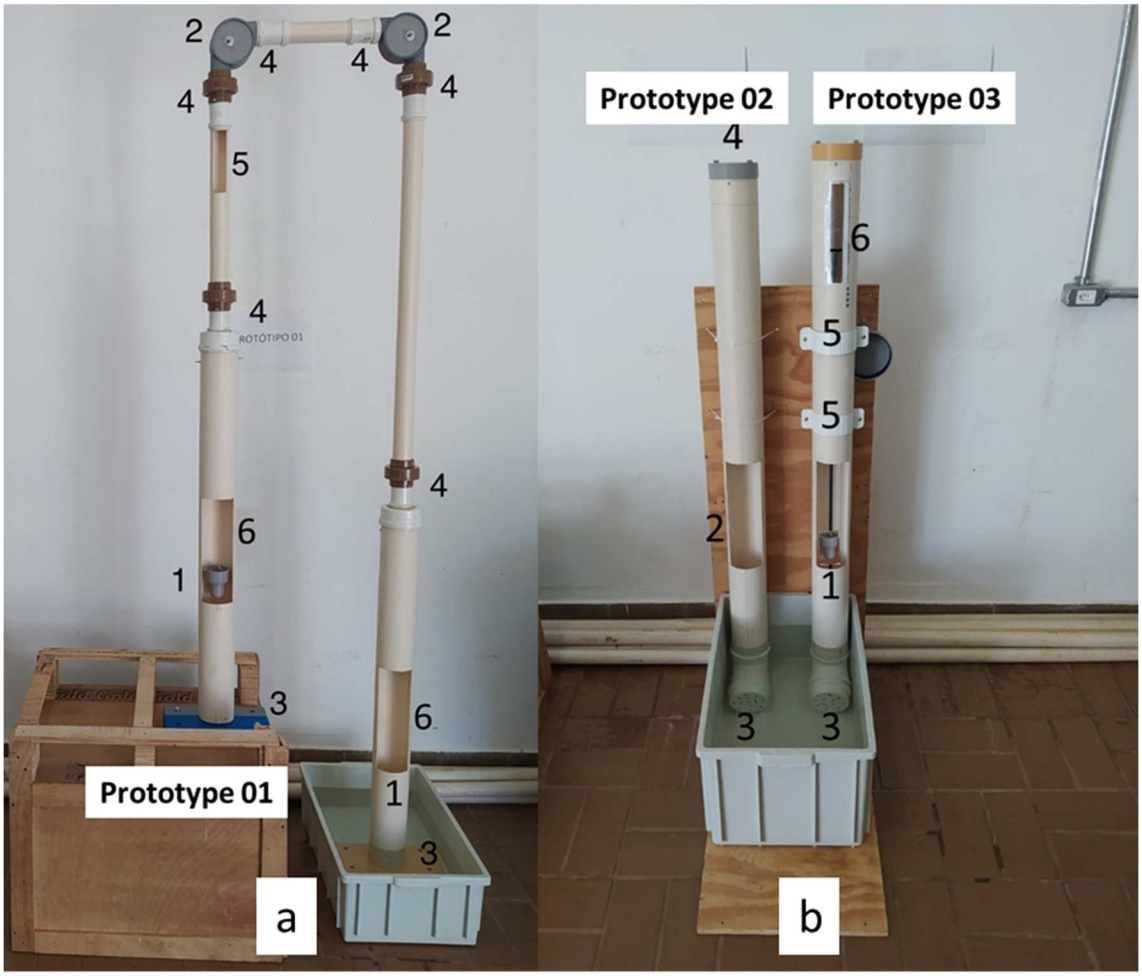

Figure 9 – Presentation of the three fabricated prototypes.

Figure 10 – a) Base for measuring the tape of prototype 2, b) internal filters, c) disc with graduated scale of prototype 3.

3.4. Laboratory and Fiel Testing

To ensure the functionality and precision of the prototypes developed during an exceptional event, specific laboratory tests were conducted. Each test aimed to evaluate a critical aspect of the equipment's performance, considering the field operational conditions. Below, the tests are described in technical detail:

Float stability test - Designed to analyze the behavior of the float in response to rapid changes in water level. It involved abruptly lowering and raising the water level while observing the time required for the float to stabilize after each change. The results indicated that the float took approximately 7 seconds to stabilize after a sudden rise in water level and 20 seconds after a rapid decrease. These values reflect the dynamic response of the system and are useful for maintenance planning, such as determining the time needed to perform a measurement.

Repeatability test - Evaluates the equipment's ability to provide consistent measurements under repetitive conditions. Multiple readings were taken under the same operational conditions, analyzing the accuracy and reliability of the system.

Operator variation test - To verify if different operators influence the reading of the results. Variables such as visual alignment, reading method, and adjustments to the device were analyzed. The results demonstrated the need for standardization in operator training and validation of visual indicators to minimize discrepancies.

Float Sealing Test - To validate the integrity of the float under prolonged operational conditions in direct contact with water. The equipment was subjected to pressure tests and continuous immersion to assess the sealing provided by the silicone and materials used. No leakage was detected, confirming the efficiency of the materials and the sealing process applied.

All tests provided essential data for the validation of the prototypes, ensuring reliability, accuracy, and durability for installation and field operation. Following the laboratory verification, the installation was carried out in the field for testing under real operational conditions, with the initial measurement frequency determined to be weekly. It is intended, in the future, to present the results once sufficient data is collected.

4. CONCLUSIONS

It can be stated that the methodology presented in section 3.2 is effective for the fabrication of prototypes, serving as a viable process for generating solutions in the measurement of water level in open channels. This method allows, indirectly, the determination of water flow rate.

The laboratory tests provided relevant data for the validation of the prototypes, ensuring reliability, accuracy, and durability for installation and use in the field. Although PVC is a durable and functional material, it requires maintenance. Therefore, it is recommended to fabricate the final model in a more resistant material, such as stainless steel, once the final design is defined.

The results, as well as the analysis of measurements in the laboratory and in the field, will be presented in another article, in order to provide a greater amount of detailed information and contribute to the development of engineering prototypes for dams.

5. REFERENCES

[1] ICOLD – International Commission on Large Dams. (1998). Dams Less than 30 m High – Cost Savings and Safety Improvements. Bulletin 109. Paris: ICOLD.

[2] ABNT – Associação Brasileira de Normas Técnicas. (1995). NBR 13403: Medição de vazão em efluentes líquidos e corpos receptores – Escoamento livre. Rio de Janeiro: ABNT.

[3] Silveira, J. F. A. (2006). Instrumentação e segurança de barragens de terra e enrocamento. São Paulo: Oficina de Textos.

Fifth International Dam World Conference
PORTUGAL • LISBON • LNEC • APRIL 13-17, 2025
dam world 2025

HYDROLOGICAL RISK OF FLOODING AND COLLAPSE DUE TO THE OVERTOPPING OF THE RIBEIRA DE PRINCIPAL DAM ON SANTIAGO ISLAND, CAPE VERDE

Manuel M. Fernandes[1]
Hidropórtico

Francisco Osny E. Silva I
UFC-CE

ABSTRACT

In the Ribeira Principal Dam project located in the Ribeira de Principal watershed area of 7.3 km² on the island of Santiago in Cape Verde [1], the time of concentration was adopted and estimated in comparison with that calculated for the Faveta Dam in the Ribeira dos Picos catchment area of 7.92 km². The time of concentration adopted was 1 hour, without a more precise verification based on the physiographic characteristics of the watershed itself.

According to the results of recent research on hydrological risk analysis of several dams in Cape Verde, [2], [3], the Kirpich formula presented good results for small watershed and proved to be well suited to small watershed with rugged topography, such as the topography of the Ribeira de Principal watershed on Santiago Island, in Cape Verde.

The Kirpich formula applied to the Principal Dam watershed estimates the time of concentration to be around 35% of the value adopted in the project, which implies a possible underestimation of the peak discharge of the design flood.

The main objective of this work is to analyze the hydrological risk of rupture of the Principal Dam due to the underestimation of the design flood considering the local hydrological parameters, as well as to evaluate the downstream impacts resulting from the rupture of the dam for different scenarios.

Keywords: Principal Dam. Time of concentration. Hydrological risk. Overtopping. Dam collapse.

[1]nunoadelio@outlook.com, Cabo Verde
[2]osny@deha.ufc.br, Brazil

1. INTRODUTION AND OBJECTIVE

The risks associated with dam failure, which result in the possibility of loss of human life and the significant material, economic, social and environmental damage, require the definition of a regulatory framework in which numerous factors linked to the quality of the design, the safety requirements of the work, the observation and inspection of the execution of the works, and the operational management of the dams must be taken into account.

On the other hand, according to recent estimates by various researchers, a general increase in the Earth's surface temperature of between 1.5ºC and 4.5ºC is expected by the year 2100. The greater amount of energy stored in the atmosphere as a result of global warming will inevitably lead to an intensification of the hydrological cycle and, consequently, to significant spatial and temporal asymmetries in rainfall in different regions of the world. These are global forecasts, but it is clear that the seasonal distribution of rainfall in Cape Verde has also undergone profound changes in recent years. There are places where rainfall has decreased, however there are others where it has increased. Similarly, hydrological cycles have also undergone significant changes.

Records of risks, failures and incidents were the subject of treaties by several international public bodies and organizations responsible for dam safety, especially ICOLD (International Committee on Large Dams) [4] and USCOLD (United States Committee on Large Dams) [5], CMB (World Commission on Dams) [6], decrees and laws were created in several countries, such as Federal Law No. 12,334/2010 (Brazil, 2010) [7].

Silva (2017) [8], states that hydrological risk is the main factor addressed in the study and was verified based on three basic conditions that directly affect the sizing of dam spillways:

• the lack of fluviometric stations to study the flows drained in the watershed;

• the short length of the historical series of maximum daily rainfall, usually less than 30 years of data for most of the rainfall stations on Santiago Island (according to rainfall data from INMG, 2017) [9];

• the diversity of formulas used to calculate the time of concentration in the watershed under study when designing dams.

There is still no specific legislation on dam safety in Cape Verde, although there is a proposal (Fernandes, MM 2020) [10].

One of the objectives of the underlying research that gave rise to this work is to define criteria and principles for dam design for the islands of Cape Verde that can contribute

to the formation of a dam safety culture adapted to local conditions of hydrological information, topography, land use and riverbanks conditions downstream.

The main objective of this work is to analyze the hydrological risk of rupture of the Principal Dam due to the underestimation of the design flood considering the local hydrological parameters, as well as to evaluate the downstream impacts resulting from the rupture of the dam for different scenarios. This work also analyzes the hydrological design methodologies adopted by the design company when selecting design parameters that impact the dam's safety risk analysis.

2. LOCATION AND CHARACTERIZATION OF THE STUDY ÁREA

The Principal Dam is located in the Ribeira de Principal watershed, in the municipality of São Miguel, Santiago Island in Cape Verde, as shown in Figure 1, whose characteristics of the respective watershed are found in Table 1.

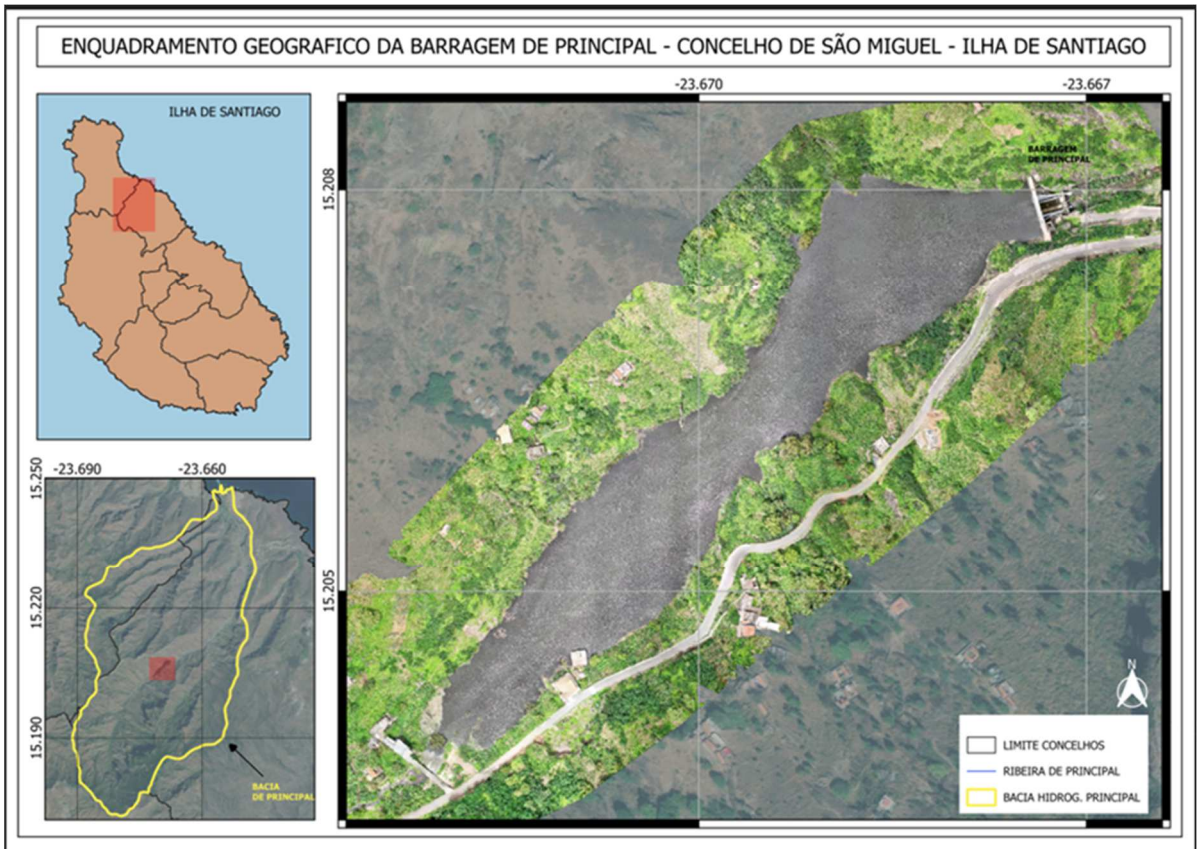

Figure 1 – Geographic location of Santiago Island and the Principal dam and the respective watershed.

Table 1 – River watershed characteristics

Total area (km²)	Perimeter (km)	Main waterline (km)	Minimum altitude (m)	Maximum altitude (m)	Average altitude (m)	Mean slope of the main waterline (m/m)	Slope between 10 and 85% of the main waterline lenght (m/km)
7,3	11,8	5,2	135	1100	465	0,166	185

The Principal Dam, built in 2017, in the absence of specific legislation on dam safety, a gravity dam constructed with mortared, in mortar stone masonry, whose purpose is irrigation, has the following characteristics are found in Table 2.

Table 2 – Ribeira Principal Dam characteristics

Dam	Watershed (km²)	Fundation elevation (m)	Minimum Level (m)	Full Storage Level (m)	Maximum Full Level (m)	Crowning Elevation (m)	Height (m)	Lenght (m)	Volume reservoir (m³)	Area reservoir (m²)
R. Principal	7,3	106,8	133	146	149	147,4	34,75	64	700000	7,95

3. METHODOLOGY

3.1. Hydrological Studies (using HEC HMS)

To carry out this hydrological study, the National Institute of Meteorology and Geophysics of Cape Verde (INMG), Praia delegation, was asked for records of maximum daily annual precipitation over the last 30 years at the rain gauge stations closest to the respective watersheds under study.

The nearest rainfall station to the Ribeira of Principal watershed with records of the above-mentioned rainfall is the Serra da Malagueta station located immediately upstream of the dam.

Table 3 below shows the positions used for the Ribeira Principal dam, as well as their respective locations and precipitation for a return period of 1,000-year.

A return period of 1,000-year was chosen for the design flow of the flood spillway for this hydrological study. This is also the return period recommended by the Portuguese Dam Safety Regulations for concrete (or masonry) dams with more than 100,000 m3 of storage and a maximum height above the foundation of between 15 and 50 m, as is the case with these dams under study. [14].

Table 3 shows the location of the rainfall station and the 24-hour rainfall for a 1,000-year return period and in the Table 4 a) and b), presents the historical composition with maximum annual precipitation.

Table 3. Location of the rainfall station and rainfall lasting 24 hour for a 1000-year return period.

Post	Location	Precipitation 24h, in mm for TR 1,000-year	Designation	Coordenates		Altitude (M)
				Latitude (° N)	Longitude (° W)	
Serra da Malagueta	Santa Catarina/S. Miguel	420.33	806082	15° 11’	23 °42’	850

Table 4 a) and b) presents the historical composition with maximum annual precipitation.

a)

Years	1987	1988	1989	1990	1991	1992	1993	1994	1995	1996	1997	1998	1999	2000	2001	2002
Pmáx, mm	122	104,4	87,5	67,6	207,5	76,6	85,7	51,7	47,0	22,0	38,9	61,0	163,7	129,6	89,0	86,5
LN(Pmax)	4,80402	4,64823	4,47164	4,21361	5,33513	4,3386	4,45085	3,94546	3,85015	3,09104	3,66099	4,11087	5,09804	4,86445	4,48864	4,46014

b)

2003	2004	2005	2006	2007	2008	2009	2010	2011	2012	2013	media	desvio padrão
125,0	75,5	67,0	93,0	113,0	107,0	103,0	137,0	61,0	162,0	101,0	95,7481	41,4042
4,82831	4,32413	4,20469	4,5326	4,72739	4,67283	4,63473	4,91998	4,11087	5,0876	4,61512	4,4626	0,47882

Once the rainfall station with information available for the hydrological study had been identified, three statistical laws were adjusted to the annual maximum daily rainfall records, namely the Gamma, Gumbel and Log-normal laws described in the respective equations below.

3.2 Statistical distribution and Chi-Square Test

Gamma Distribution

This distribution is considered equivalent to the log-normal distribution and it applies to the same hydrological variables as log-normal distribution. The gamma probability density function is developed from the gamma mathematical function and has the following equation:

$$f(x) = \frac{x^{\alpha-1}.e^{-x/\beta}}{\beta^{\alpha}.\Gamma(\alpha)} \quad (1)$$

Where α e β are the shape and scale parameters of the distribution and Γ(α) represents the gamma function. Using the method of moments, the parameters of the function can be calculated using the following equations:

$$\mu = \alpha\beta \; e \; x\sigma^2 = \alpha\beta^2 \quad (2)$$

Gumbel Distribution

In the Gumbel distribution, the cumulative probability density function (F) is the most widely used and is represented by the following equation:

$$F(y) = 1 - e^{-e^{y}} \quad (3)$$

Where y represents the reduced Gumbel variable and is calculated by the following equation:

$$y_i = \alpha(x_i - \beta) \quad (4)$$

With α being the concentration parameter and β being the distribution parameter. The values of α and β are estimated by the method of moments using the equations:

$$\alpha = \frac{1.2825}{\sigma} \text{ e } \beta = \mu - 0.450\sigma \quad (5)$$

Being μ and σ, respectively, the mean and standard deviation obtained in the sample.

Lognormal Distribution

In the Lognormal distribution, the probability density function is represented by the following equation:

$$f(x) = \frac{1}{\sqrt{2\pi}\sigma} \; e^{-\frac{(x-\mu)^2}{2\sigma^2}} \quad (6)$$

Where x represents the random variable under analysis, μ and σ are the distribution parameters, the mean and standard deviation in the logarithm domain.

The Chi-Square test

The chi-square test (χ^2) is a procedure for evaluating the goodness-of-fit of a random sample and a given population characterized by its probability density function with its respective calculation parameters, which is simplified using Excel spreadsheets. Samples were divided into k intervals, in this case six intervals. Once the intervals had been divided, the number of expected values was estimated for each one and the number of observed values was counted. The value of χ^2 was calculated using the following equation:

$$\chi^2 = \sum_1^k \frac{(o_i - e_i)^2}{e_i} \quad (7)$$

Where χ^2 represents the test statistic; o_i denotes the number of observed values in interval i and e_i represents the number of expected values in interval i. The critical value of χ^2 is obtained from the statistics table of the inverse chi-squared distribution and is a function of the number of degrees of freedom (η) and the significance level of the test (α). $o\ valor\ de\quad \eta = k - m - 1.$

The results of the calculations of the statistical methods used and the respective chi-squared test are shown in Table 5 a) e b).

Table 5 a) and b)- Comparative study between project and current situations a) and Chi-Square Test b) of the Ribeira de Principal dam.

a)

TR	S.Malag.	S.Malag., current	Δ, %	S.Malag., current	Δ, %
	Project	Gumbel		Gamma	
5	------	157.068	-16.395	159.876	-14.900
10	80	187.025	-17.460	188.724	-16.710
20	90	215.760	-17.005	214.914	-17.331
100	114	280.828	-13.843	270.009	-17.162
1000	-------	372.927	-11.277	341.344	-18.791
10000	--------	407.912		476.13	

b)

Chi - Square test			
Distribution	Assomada	S. Malagueta	Obs
Gamma	1.4	4.25	Best adjustment.
Gumbel	1.4	6.25	
LogNormal	4.2	2.75	

In the rainfall-runoff modeling of the project, as well as in the hydrological analysis of the present work, the SCS unit hydrograph was adopted, which is characterized by the delay time (“lag time”) given by equation 8:

$$tp = \ 0{,}6t_c \quad (8)$$

Where:

t_p – lag time in min.

t_c – time of concentration in min.

The runoff number (N) for return periods of 100, 1000, and 10000 years was determined to be 92, taking into account the CN (Curve Number) used in the projects and similar watershed, taking into account the type of soil and its occupation, as the soil was considered to be saturated at the start of the project's rainfall (AMC III situation in the SCS classification).

Time of Concentration

Many methods have been developed to determine the time of concentration value, however, they were generated from the observation of watershed in different parts of the world and adjusted according to the physical and hydrological characteristics of the observation sites, which makes them very particular and limits their applicability, although the Kirpich method (1940) [13] is one of the most frequently found in the literature and widely used in the construction of Brazilian dams (Melo, 2018) [11].

In the original executive project for the Principal Dam, a time of concentration of 1 hour was adopted, based on the similarity of the watershed with the Faveta dam, without taking into account the characteristic parameters of the Principal Dam watershed itself.

The time of concentration calculated in the present analysis was based on the Kirpich method. Kirpich's formula is well suited to small watersheds with rugged terrain, such as the terrain of Santiago Island in Cape Verde. It follows that this fact should also be taken into consideration when selecting the time of concentration for preparing hydrological studies of dams. Applying equation 9, the calculated value Tc = 28 minutes.

Chow/Kirpich:

$$Tc = 57(L^3/H)^{0,385} \quad (9)$$

where:

T_c – time of concentration in min.

L – length of the main waterline (km).

H – difference in level between the highest and lowest points of the pelvis (m).

The flood hydrograph over each spillway was calculated according to the design hydrograph of a 1,000-year flood re-evaluated on the basis of the shortest time of

concentration and calculated directly by the HEC-HMS model, as well as for the simulation of the design flood (100-year and 1,000-year floods), considering:

a) Flow rates (for return periods Tr = 100-years and 1,000-year) calculated with the time of concentration adopted for the project: t_c = 1 hour;

b) Flow rates (for return periods, Tr = 100-year and 1,000-year) calculated with time of concentration given by the Kirpich equation, Tc = 28 minutes.

c) Propagation of design flows in the dam lake with the dimensions designed for the spillway and verification of the overflow condition.

For the hydrological analysis of this project, the rainfall equation for Cape Verde, known as the Fernandes-Osny equation, 2022, was applied.

3.2 Hydraulic Studies (using HEC RAS)

The HEC RAS software was used to analyze the hydraulic studies and to simulate the dam break in the event of overflow over the spillway. The HEC RAS software [12], was also used to simulate the propagation of the dam break hydrograph into the downstream valley, as well as estimating the loss of human life and the flood area with the dam break downstream.

4. RESULTS

The results of the hydrological and hydraulic analysis of the Ribeira de Principal dam can be found in the following tables and figures.

a)

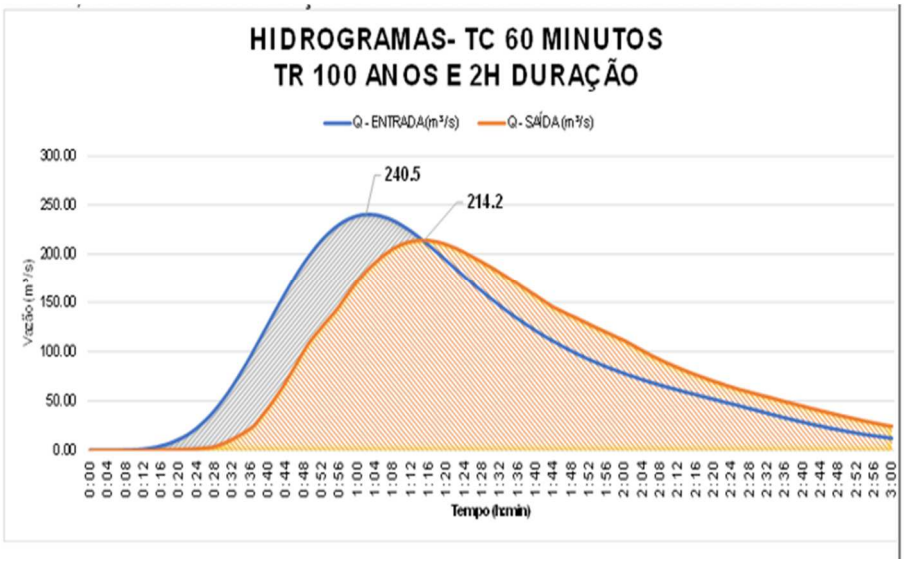

b)

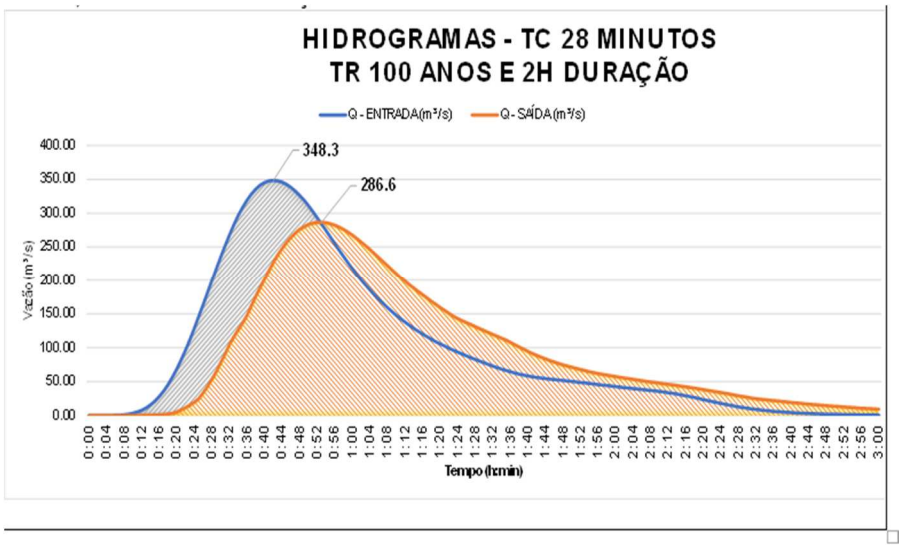

Figure 2 - Hydrograph for return period (Tr) 100-year and time of concentration (Tc) = 60 minutes a) and 28 minutes b) and respective table with inflows and outflows.

a)

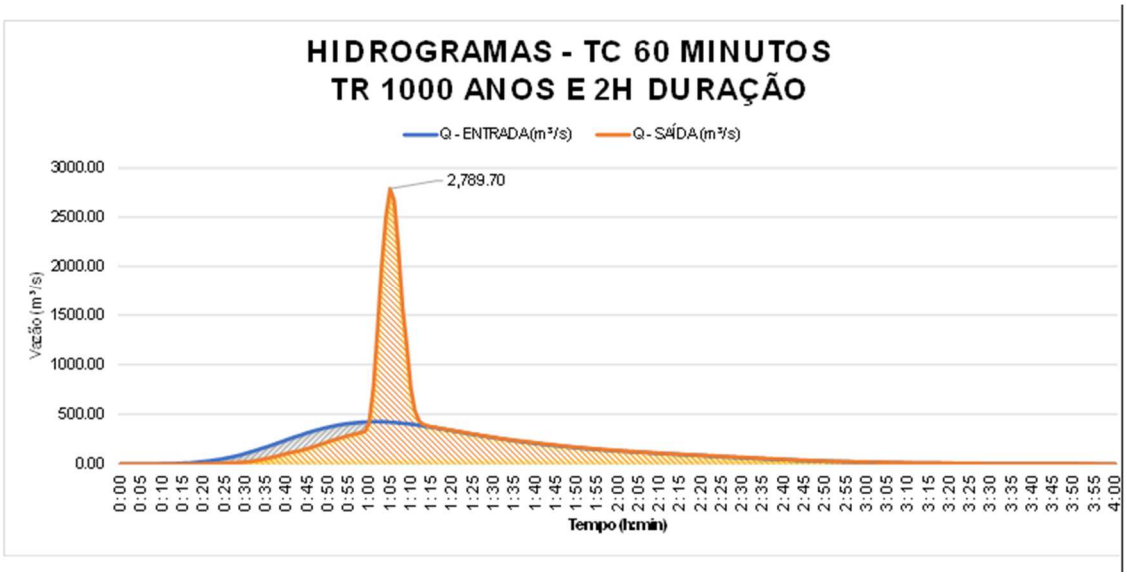

b)

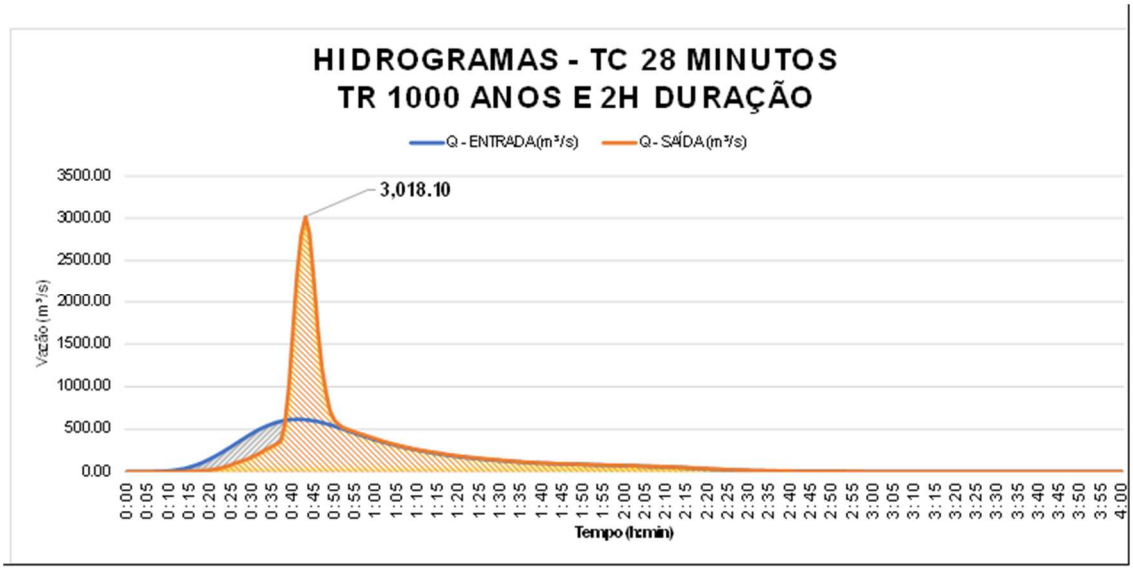

Figure 3 - Hydrograph for Tr =1,000-year, with Tc= 60 minutes, a) and with Tc=28 minutes, b).

Table 6 – Inlet, dam break and outlet flows.

	Tr = 100 - years		Tr = 1,000 - years	
	Tc = 1h	Tc = 28 min.	Tc = 1 h	Tc = 28 min.
Q inflow (m³/s)	240,5	348,3	426,5	616,6
Q outflow (m³/s)	214,2	286,6	2789,7	3018,1
Elevation (m)	148,65	149,26	149,65	149,89
Volume maximum (m³)	78130	835000	864860	883220

a) Tr = 1,000-year, Tc = 60 minutes

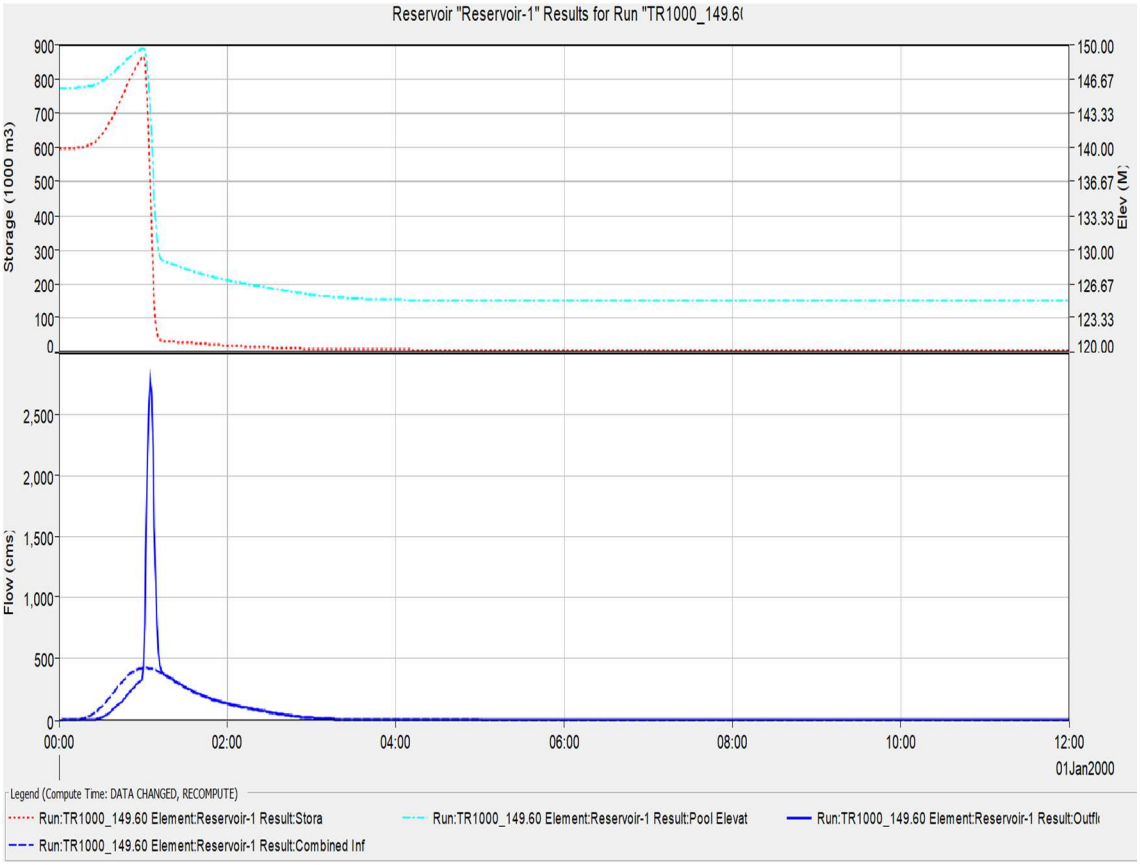

b) Tr = 1,000 - yeras, Tc = 28 minutes

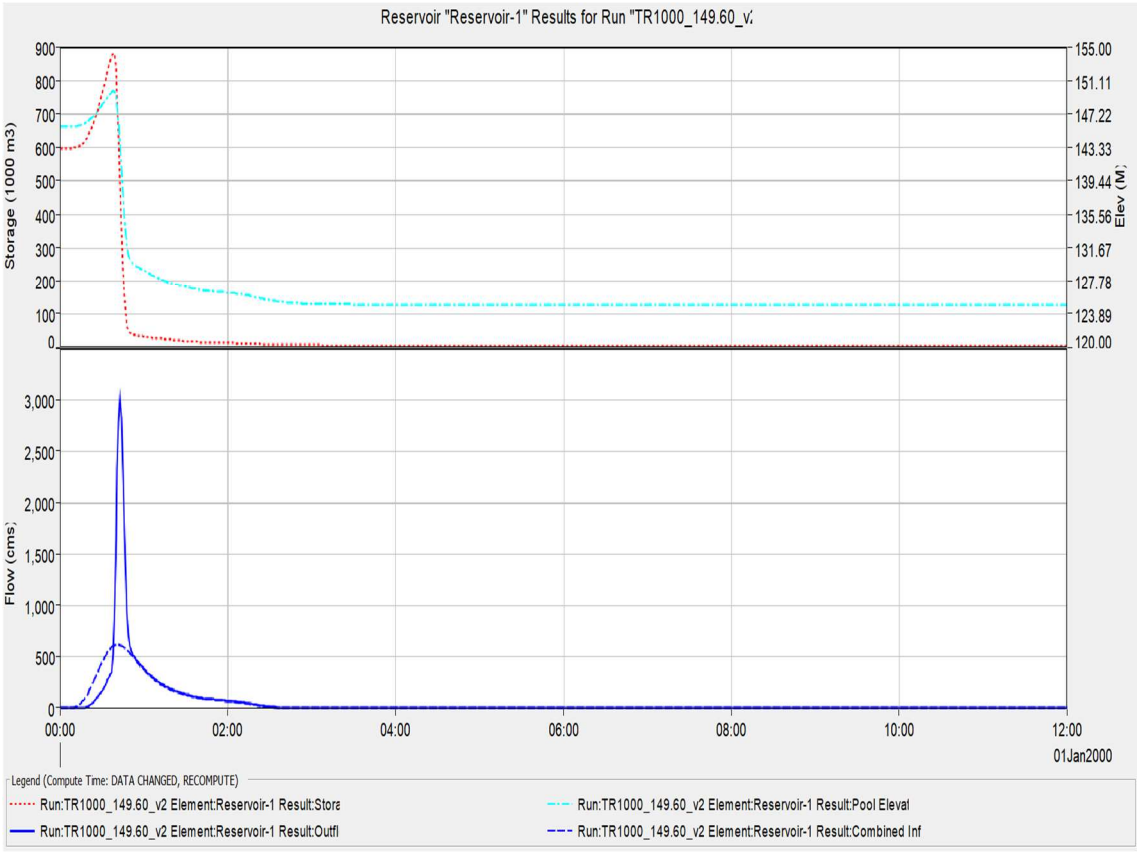

Figure 4 - Rupture hydrogram for Tr = 1,000-year, with Tc = 1 hour a) and Tc = 28 minutes b).

a) Arrival time.

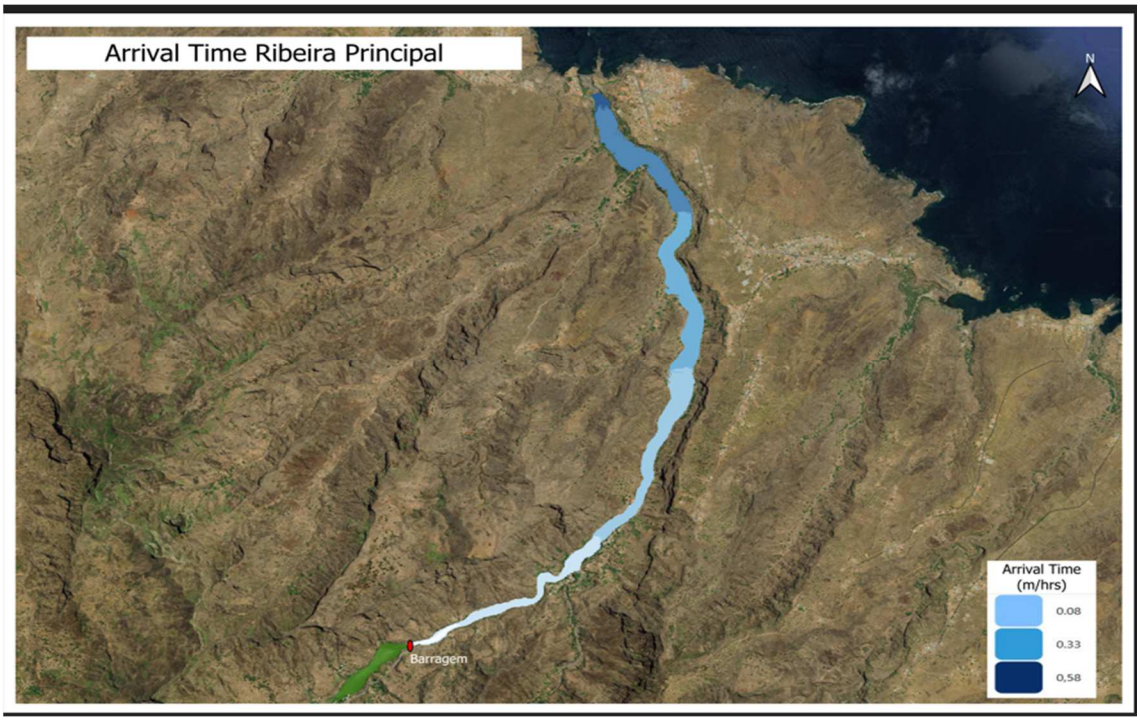

b) Velocity.

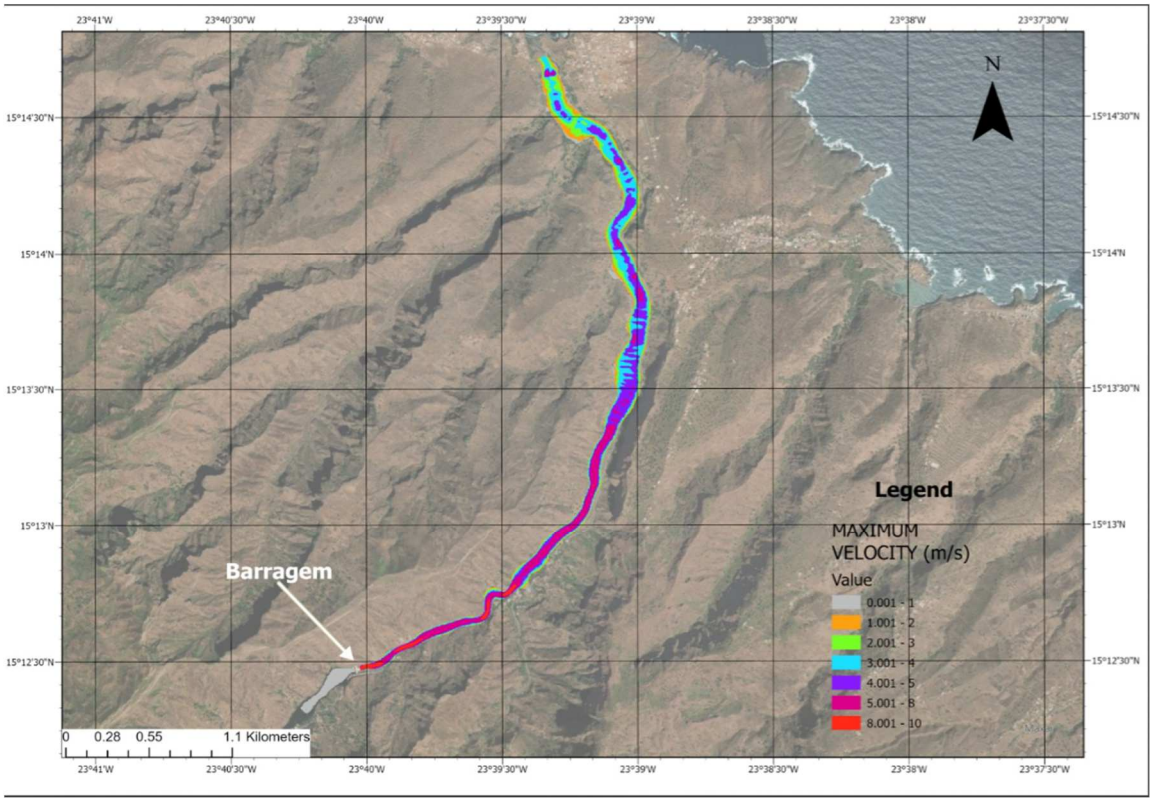

Figure 5 - Simulation of hydrograph propagation of dam failure in the downstream valley for Tr = 100-year and Tr = 1,000-year with Tc = 1 hour and Tc = 28 minutes.

5. CONCLUSION

Basedon the results presented, the dam failure would only occur for the 1,000-year flood and would not occur for the 100-year flood.

The time of concentration that was used in the hydrological studies for the executive project with which the Principal Dam was built was mistakenly adopted on the basis of a time of concentration determined for another watershed with similar physiographic characteristics, but different from the Principal Dam watershed. Thus, the time of concentration was much longer (1 hour) than what should in fact have been determined by the Kirpich equation (28 minutes), resulting in an underestimation of the peak flow of the hydrographs for 100-year and 1,000-year floods. This mistake increased the hydrological risk associated with the preparation of the executive project.

The analyses carried out in this article demonstrated that the hydrological risk for a 1,000-year flood at the Principal Dam, based on the studies conducted in the preparation of its executive project, is high and could lead to the collapse of the dam in the event of a 1,000-year flood, bringing tragic consequences for the population located downstream of the Principal Dam, in terms of loss of human lives and damage to goods and properties.

This study assesses the hydrological risk associated with the Principal Dam on Santiago Island, Cape Verde, emphasizing the potential for dam failure due to the underestimation of peak flood flows in the original design. By applying the Kirpich formula, the study demonstrates that the adopted concentration time (60 minutes) significantly overestimates actual conditions (28 minutes), leading to an underestimation of design flood peaks. Using numerical hydraulic models (HEC-HMS and HEC-RAS), the study evaluates dam failure scenarios, concluding that while the structure would withstand a 100-year flood, it is at risk of collapse under a 1000-year flood event. The findings highlight the critical impact of accurate hydrological parameter selection on dam safety and provide a cautionary example for dam design and water resource management in Cape Verde, particularly in the context of climate change-driven shifts in extreme precipitation events.

This article, which used a hydrological and hydraulic modeling methodology, simulating the "dam breach" of the Principal Dam based on the use of computational packages

internationally recognized for their performance (HEC HMS and HEC RAS), had the objective of alerting the community of dam designers and public agents in Cape Verde related to water resource management and dam safety to the fact that a simple mistake in the adoption of an easily-determined hydrological parameter (time of concentration) can greatly affect the hydrological risk for dam works that may have an impact on the safety of communities in the future.

A number of studies conducted by the international academic community have shown that climate change is bringing forward millennia floods to occur in periods still within the useful life of hydraulic works such as dams, which are based dimensionally on the prediction of hydrological phenomena.

REFERENCES

[1] Pan arab consulting engineers-pace. Projet d'Aménagement des Bassins Versants de Ribeira de Flamengos et Ribeira Principal, PABVFLAPRI, 2012.

[2] Silva, F.O.E., Fernandes, M.M., Mello, M.R. (2019). Hydrological Risk Associated with uncertainties in determining the concentration time - Case study: Dams on the Island of Santiago-Cape Verde. APRH, 14º SILUSBA, Cidade da Praia, Setembro de 2019.

[3] Silva, F.O.E DA., Fernandes, M. M. (2020). Hydrological analysis for dams on Santiago Island, Cape Verde, West Africa, DAE Magazine, February. Available at www.revistadae.com.br/approved articles.

[4] Icold, (1998). Dam break flood analysis: review and recommendations. Bulletin 111. Paris: International Commission of Large Dams, 301 p.

[5] United State Committee on large dam - USCOLD. Lessons from dam incidents, USA II. Committee on Dam Safety of the United States Committee on Large Dams (USCOLD). American Society of Civil Engineering, New York, 1988.

[6] Comissão Mundial de Barragens - CMB, (WCD). (World Commission on Dams). Dams and Development. A new framework for decision-making. Earthscan Publications. Londres, 2000, 404 p. Disponível em http://www.dams.org/report/contents.html. Acesso em Fevereiro de 2018.

[7] Brazil, L. S. S. (2010). Federal Law No. 12,334, Brasilia, 20 September 2010.

[8] Silva da, O. E., Curso de hidrologia para dimensionamento de barragens e análise de riscos em barragens, Cidade da Praia, Cape Verde, Julho de 2017.

[9] Silva, F.O.E DA., Fernandes, M. M. (2022). Equação de chuva para Cape Verde. Studies in Multidisciplinary Review, Curitiba, v.3, n.4, p. 891-908, oct./dec., 2022.

[10] Silva, F.O.E DA., Fernandes, M. M. (2020). Simulation of Salineiro dam rupture using HEC-RAS. Fourth International Dam World Conference. Portugal • Lisbon • LNEC • September 21-25, 2020.

[11] Melo, M. R., Dissertação de Mestrado. Risco hidrológico associado às incertezas na determinação do tempo de concentração: Caso de estudo: Barragens na Ilha de Santiago - Cape Verde. Fortaleza, UFC, 2018.

[12] USACE - U.S. Army Corps of Engineers, Washington DC 20314-1000, Department of the army, May 2016.

[13] Kirpich, Z. P. (1940) Time of concentration of small agricultural watersheds. Journal of Civil Engineering, 40 (6).

[14] Fernandes, M.M., Análise de Risco de Ruptura de Barragens: Estudo de caso de seis barragens na Ilha de Santiago em Cape Verde, África.Tese (doutorado) – Universidade Federal do Ceará, Centro de Tecnologia, Programa de Pós-Graduação em Engenharia Civil: Recursos Hídricos, PhD Thesis, UFC-CE,Fortaleza, 2020.

Fifth International Dam World Conference
PORTUGAL • LISBON • LNEC • APRIL 13-17, 2025
dam world 2025

DETERIORATION DUE TO SIMULTANEOUS EXPANSIVE REACTIONS IN DAM CONCRETE: EVALUATIONS ON PROTOTYPES

Eduardo I. Funahashi Jr. [1]	Nicole P. Hasparyk [2]	Patrícia G. Gambale [3]	Edna Possan[4]	Selmo C. Kuperman[5]
UNILA	Eletrobras	UNILA	UNILA	Desek

ABSTRACT

Concrete structures of dams and hydroelectric power plants affected by internal expansive reactions is a reality in the world. Depending on the materials used in concrete, the environment and the constructive conditions, internal expansive chemical reactions may occur, with an early reduction in concrete durability due to progressive cracking. Concrete deterioration may occur individually due to the alkali-silica reaction (ASR) and to internal sulfate attack, such as DEF (Delayed Ettringite Formation). Recently, cases of combined attacks (DEF/ASR) by these two types of deleterious reactions have been diagnosed in Brazilian dams, resulting in additional costs to owners due to periodic monitoring, maintenance and repair that were not initially foreseen. In view of the above, an experimental program was developed to understand the behavior of concrete from cubic prototypes with 80 cm edges exposed to the natural environment and monitored for a period of 4 years. To this end, a multilevel investigation of the expansive reactions due to the conjugate attack was implemented, involving an extensive program of visual and drone inspections, evaluation of instrumentation data obtained by strain gauges, mechanical tests and microstructural analyses. In addition, thermal studies were carried out using 3D mathematical modeling to assess the risk of thermal cracking. Based on the studies carried out, the occurrence of a combined attack by DEF/ASR in the prototypes and their negative consequences on the mechanical properties due to the intense cracking of the concrete were proven.

Keywords: concrete, prototypes, expansive reactions, alkali-aggregate reaction (ASR), delayed ettringite formation (DEF).

[1]eduardo.funahashi@desek.com.br, Brazil
[2]nicolepha@gmail.com, Brazil
[3]patricia.gambale@gmail.com, Brazil
[4]edna.possan@unila.edu.br, Brazil
[5]selmo@desek.com.br, Brazil

1. INTRODUCTION

The construction of infrastructure works, such as dams, hydroelectric power plants, nuclear, thermoelectric and wind farms, for example, requires significant volumes of concrete. The durability of these structures can be compromised due to expansive reactions, depending on the materials used and the environmental conditions during their useful life. Thus, the careful choice of materials and planning of the appropriate construction techniques in the project's initial phase is essential to prevent its deterioration. At the beginning of the twentieth century, many dams and power plants were built without technical standards and control of the composition of materials, resulting in problems such as differential displacements and operational locks of some structures. These problems, often associated with expansive reactions such as alkali-silica reaction (ASR) and sulfate attack (e.g., DEF – Delayed Ettringite Formation), generate excessive costs of monitoring, maintenance, and recovery. Corrosion of reinforcement can also generate significant expansion. Such reactions, often combined, result from chemical interactions that are deleterious to the concrete. In Brazil, the alkali-aggregate reaction (AAR) is widely documented with standards [1] and technical guides [2], which indicate a risk assessment, preventive measures and mitigation. On the other hand, DEF, although known since 1980 [3] apud [4], still lacks technical standardization in the country and in the world, being identified by specific laboratory tests, due to the difficulty of visual diagnosis and the possibility of confusion with AAR. The Brazilian Technical Instruction [5], which evaluates the potential occurrence of DEF, is still little used due to the long execution time of the test and the lack of standardization. Attack by sulphates of internal origin, as in DEF, occurs in concretes subjected to temperatures above 60-65°C. DEF depends on factors such as the type of cement, the concrete mix design, and the environmental conditions during the service life [6, 7]. Thermal studies are essential to prevent thermal cracking in mass concrete structures, such as hydroelectric power plants [8, 9]. The occurrence of DEF affects the mechanical properties of concrete, such as compressive strength, tensile strength, and modulus of elasticity [10-13]. DEF can be aggravated depending on the increased availability of sulphates, high alkali content, and the presence of moisture. Studies show that this reaction can coexist with AAR under favorable conditions, as seen in concrete mass of pillars and walls of spillways of dams and hydroelectric power plants [14, 15, 16, 17]. The interaction between the two reactions is facilitated by the formation of cracks in the concrete, which allow moisture to enter, accelerating the expansive processes. High levels of alkalis will increase the long-term expansion of ASR, while any alkali consumption (from leaching or gel formation) will favour ettringite precipitation, called DEF. Thus, the combined attack (DEF/ASR) may promote earlier expansions compared to isolated attack of DEF or ASR. Furthermore, higher levels of expansion can be achieved depending on the concrete materials and moisture conditions

[4,18]. In one study [19], AAR showed expansions after about 1 year, while DEF manifested itself in 6 months and, in the case of combined attack (DEF/ASR), in only 3 months, resulting in greater damage to the mechanical properties of the concrete. It is possible to avoid expansive reactions through adequate prior studies of materials and assertive action in construction procedures [20]. Advances in diagnostic and testing techniques have allowed the identification of these phenomena with greater precision, highlighting the importance of the correct choice of mix design as well as the adoption of preventive practices to ensure the durability and safety of concrete structures. To reduce the risk of the combined attack from DEF and ASR, strict control of the temperature increase inside the concrete must be carried out by means of pre-cooling or post-cooling of the concrete mass, as well as the use of cements with low SO_3/Al_2O_3 ratio, low alkali content and low heat of hydration, associated with a reduction of cement consumption in the concrete mix and the use of higher contents of pozzolanic mineral admixtures [21].

2. EXPERIMENTAL PROGRAM

2.1. Research overview

This research is part of an ELETROBRAS-FURNAS / ANEEL R&D Project that included the initial study of concrete samples cast in the laboratory, followed by multilevel investigations over time in cubic prototypes of unreinforced mass concrete with 80 cm edge. Conducted by Eletrobras-Furnas, a Brazilian energy company, an extensive laboratory study was carried out to evaluate the effect of different materials on the combined attack due to DEF and ASR in cement pastes, mortars and concrete. The studies include the following evaluations: visual inspection; deformation and temperature measurements; length measurements to measure expansion, humidity and temperature recording; coring of concrete from the prototypes; mechanical tests and microstructural analyses of the cores extracted from the blocks. Part of these studies will compose two doctoral theses, and this article addresses an initial part of what is being processed in terms of analysis of the data obtained. Some blocks were subjected to the induction of elevated temperatures to simulate the cement hydration process in attempt to promote DEF in an isolated way, with fine and coarse aggregates considered non-reactive. For the study of ASR and combined attack (DEF/ASR), a reactive coarse aggregate and a non-reactive fine aggregate were used, in addition to a CP V-ARI type cement with high initial strength (without potential to mitigate ASR), and a pozzolanic cement, CP IV-32, with the addition of fly ash, usually used in mass concrete of Brazilian structures. The prototypes were exposed in two environments, one of them in the South of Brazil (Curitiba/PR), where the climate is cold, and the other in the Midwest region (Aparecida de Goiânia/GO), which has a hot climate almost all year round. A contextualization of the first part of this research was

presented at the International Conference on Alkali-Aggregate Reaction Proceedings Alkali-Aggregate (ICAAR) in 2022 [22].

The present work specifically addresses the prototypes in the aging field of the Midwest region of Brazil. Each prototype was instrumented with one embedded rod extensometer, two embedded Carlson strain meter, and embedded thermocouples. The thermal studies by 3D calculations using the b4cast software showed that temperatures would reach values above 85ºC, making it possible to induce DEF. For the reference prototype REF. (with CP V cement), without deterioration, the temperatures inside were limited to 60°C to prevent DEF, adopting a pre-cooling system (with ice in partial replacement of mixture water), as well as a concrete post-cooling system (through the installation of pipes inside the forms for the circulation of water pre-cooled with ice). In this block, forms with expanded polystyrene were not used. After reaching the peak temperature of each block, the forms were removed. Table 1 shows a general information about the prototypes presented in this article.

Table 1 – Prototypes exposed to the natural environment – Midwest Brazil

Type of attack	Field of aging	Aggregates	Type of cement	Addition mineral	Pre-cooling with ice
Reference	Aparecida de Goiânia, state of Goiás (Brazil Midwest Region)	Non-reactive	CP V-ARI (2)	-	Yes (1)
DEF/ASR		Reactive			No
DEF/ASR		Reactive	CP IV-32 (3)	Fly ash	

Note: (1) A concrete after-cooling system with chilled water at 15°C was used; (2) Similar to [24] type III or CEM I of [25]; (3) Similar to the IP type of [24] or CEM IV of [25] with 26% pozzolan (fly ash).

Figure 1 shows details of the aging field (A) during the concrete coring operations and the post-coring samples (B).

Fig. 1 – Coring and classification of the concrete cores of the prototypes (at Eletrobras-Furnas)

2.2. Materials and concretes used

The materials used in the concrete prototypes were carefully selected based on their physicochemical characteristics for the intended objectives in relation to the manifestation not

of the expansive reactions in time, according to [20]. The concretes were designed for a characteristic strength (f_{ck}) close to 40 MPa. Two prototypes used granite coarse aggregate ($D_{máx}$ of 19 mm and fineness modulus of 6.32) from the Brazilian northeast region (Recife/PE). It was classified as potentially innocuous for ASR according to the test on mortar prescribed in [1] and petrographic analysis. The aggregate consists of alkaline feldspar, quartz, plagioclase, and mica biotite. The average expansion detected from accelerated mortar bar test (AMBT) reached 0.07% at 30 days, below the maximum Brazilian limit of 0.19%. It is known that some granite-gneisses may be harmful in service, considering that this type of rock presents slower reactivity, giving false negative results from AMBT. On the other hand, due to the abundant presence of silica, isolated petrographic and mineralogic analysis presents some limitation when evaluating the reactivity of some rock in relation to ASR. In this case, it is essential to proceed with concrete investigations. For the prototype evaluated in the combined attack (DEF/ASR), a coarse aggregate potentially reactive for ASR, of granitic origin (19 mm and a fineness modulus equal to 6.60), coming from the same region, was used. This has a content of more than 5% of deformed quartz as well as more than 15% of microgranular quartz, according to petrographic analysis. Expansions reached 0.39% at the 30-day trial age. The fine aggregate used in all concrete blocks is from natural pit and was considered potentially innocuous for ASR. Its origin is the Midwest Brazil Region (Cristalina/GO). The sand is composed of quartz, with low undulating extinction angle. The expansions in the mortar bar test were below the limit of 0.09% at 30 days. Two cements were used in the research, one without additions (Brazilian standard CP V ARI - similar to type III of [24] or CEM I of [25]) and one pozzolanic cement, composed with fly ash (Brazilian standard CP IV-32 - similar to type IP of [24] or CEM IV of [25]). A polyfunctional viscosity modifier chemical admixture based on polycarboxylates was used to maintain the workability of the mixtures in the range of 200± 20 mm (slump test).Table 2 and Table 3 present the physical and chemical composition of the cements. Table 4 shows the mechanical properties of the cements used in concrete.

Table 2 – Physical composition of CP V-ARI and CP IV-32 cements

Parameter	Unit	CP V-ARI(1)	NBR 16697 [23]	CP IV-32(2)	NBR 16697 [23]
Specific mass	g/cm³	3.08	-	2.82	-
Hot Expandability	Mm	0	≤ 5	0	≤ 5
Cement setting time	H:mm	3:20	≥ 0:60	04:20	≥ 0:60
Cement final setting time	Hour:minute	5:25	≤ 10:00	5:40	≤ 12:00
Normal consistency	%	29.90	-	31.20	
Blaine Fineness	cm²/g	4720	-	4280	

Note: (1) Similar to [25] type III or CEM I of [26]; (2) Similar to the IP type of [25] or CEM IV of [26] with 26% pozzolan (fly ash).

Table 3 – Chemical composition of CP V-ARI and CP IV-32 cements

Parameter	Unit	CP V-ARI(2)	NBR 16697 [20]	CP IV-32(3)	NBR 16697 [20]
Al_2O_3	%	4.50	-	8.40	-
SiO_2	%	19.10	-	27.00	-
Fe_2O_3	%	2.90	-	3.50	-
CaO	%	61.30	-	48.20	-
MgO	%	2.80 (1)	≤ 6.50 %	2.50 (1)	-
SO_3	%	3.50 (2)	≤ 4.50 %	2.50 (2)	≤ 4.50 %
K_2O	%	0.70	-	1.10	-
Na_2O	%	0.20	-	0.30	-
Loss on ingnition	%	4.03 (3)	≤ 6.50 %	3.60 (3)	≤ 6.50 %
Free lime	%	0.79		0.67	
Insoluble residue	%	0.984 (4)	≤ 3.50 %	26.07	-
$Na_2O_{eq.}$ = 0.658.K_2O+Na2O	%	0.66	-	1.02	-
Heat of hydration (41 hours)	J/g	376	(1)	272	
SO_3/Al_2O_3	-	0.78		0.30	
$(SO_3)^2/Al2O_3$	-	2.72		0.74	
SO_3 in concrete (kg/m³)	-	16.5		11.8	
Alkali content in concrete (kg/m³)	-	3.11		4.80	

Note: (1) Low heat of hydration ≤ 270 J/g [23]; (2) Similar to [24] type III or CEM I of [25]; (3) Similar to the IP type of [24] or CEM IV of [25] with 26% pozzolan (fly ash).

Table 4 – Mechanical properties of CP V-ARI and CP IV-32 cements

Parameter	Age (days)	Unit	CP V-ARI(1)	NBR 16697 [23]	CP IV-32(2)	NBR 16697 [23]
Compressive strength	1	MPa	27.2	≥ 14	-	-
	3		32.2	≥ 24	24.9	≥ 10
	7		40.5	≥ 34	28.1	≥ 20
	28		-	-	41.6	≥ 32

Note: (1) Similar to [24] type III or CEM I of [25]; (2) Similar to the IP type of [24] or CEM IV of [25] with 26% pozzolan (fly ash).

The plasticizer admixture used has a pH of 5.41, a solids content of 43.97%, and a density of 1.187 g/cm3. To define the characteristics of the concrete mix design, cement content (kg/m^3) and water/cement ratio (w/c), the work of [19] was taken as a basis. Table 5 shows the mix design adopted in this study, and a mixture of 1:1.6:1.8:0.46 (cement ratio: fine aggregate: coarse aggregate: water-cement ratio) was considered.

Table 5 – Concrete mix designs of the prototypes adapted from [19]

Material	Unit	REF. (CP V)	ASR/DEF (CP V)	ASR/DEF (CP IV)
Type of attack	-	Reference	Reactive coarse aggregate	Reactive coarse aggregate
Type of cement	-	CP V-ARI (1)	CP V-ARI (1)	CP IV-32 (2)
Cement	kg/m³		471	
Fine aggregate	kg/m³		754	
Coarse aggregate	kg/m³		838	
Water	kg/m³		217	
Plasticizer additive	kg/m³		0.659	
Consistency	millimeters		200 ± 20	
w/c ratio	-		0.46	

Note: (1) Similar to [24] type III or CEM I of [25]; (2) Similar to the IP type of [24] or CEM IV of [25] with 26% pozzolan (fly ash).

The mix design were based on a real concrete structure affected by DEF in Brazil. It was a pumped concrete used in trunnion beams of a hydroelectric power plant.

2.3. Test method

- Thermal studies by 3D mathematical modelling

To evaluate the thermal behavior of the three prototypes REF. (CP V), DEF/ASR (CP V) and DEF/ASR (CP IV), four thermometers (thermocouple type) were also inserted at fixed points to measure the blocks internal temperatures. From the monitoring data of the thermocouples, thermal and mechanical properties of the concretes and the environmental conditions, computer simulations were performed by mathematical modeling of finite elements in 3D. The maximum temperatures reached by the mathematical model were evaluated and compared with the field monitoring in the prototype, in addition to the thermal stresses resulting in the structures due to the shrinkage of the material when dissipating the heat from its interior. The mix designs adopted in the modeling are shown in Table 5. The values of the evolution of compressive strength and modulus of elasticity used in the thermal calculation were estimated based on laboratory tests carried out by [19]. Table 6 shows the concrete mechanical

characteristics. The thermal characteristics of the concrete (thermal conductivity and specific heat) were estimated (table 7) based on the mix design, type of cement and lithology of the aggregates according to [26]. The coefficient of thermal expansion was calculated as 12.1x10^{-6}/°C. The evolution of the hydration heat of the two cements was estimated from tests carried out by [19] and based on the thermal monitoring carried out using the embedded thermocouples in the prototypes..

Table 6 – Estimated mechanical characteristics for concretes [19]

Type of attack	REF.	DEF/ASR	DEF/ASR
Type of cement	CP V	CP V	CP IV
f_{ck} (MPa)	40	40	40
Compressive strength (MPa)			
28 days (1)	47.2	40.2	39.7
91 days (1)	46.7	41.8	42.0
Tensile strength (MPa)			
28 days (1)	3.9	3.6	3.2
91 days (1)	4.4	4.3	3.2
Static modulus of elasticity (GPa)			
28 days (1)	28.0	25.6	30.0
91 days (1)	28.9	23.7	30.9
Note: (1) Test data [19]			

Table 7 – Estimated thermal properties

Prototype	REF.	DEF/ASR (CP V)	DEF/ASR (CP IV)
Specific heat	1.16 kJ/kg°C		
Thermal conductivity	9.6 kJ/m.h.°C		
Coefficient of thermal expansion	12.1x10^{-6}/°C.		

The adiabatic rise of the concrete was calculated using the equation of Rastrup [26].

$$\Delta T = \frac{C \cdot (heat\ of\ hydration)}{\gamma \cdot c} \quad (1)$$

Where: ΔT = Adiabatic temperature rise (°C); γ = Specific mass of concrete (kg/m³); c = Specific heat of concrete (kJ/kg °C); C= Cement content (kg/m³).

Based on the thermal retroanalysis, the adiabatic rise for the concrete of the prototypes REF. (CP V) and DEF/ASR (CP V) was estimated as 69°C. Based on retroactive thermal analyses performed for the prototype cast with CP V cement, an increase in hydration heat of 3% was

adopted between the ages of 41 hours [19] and 168 hours. For the concrete of the DEF/ASR prototype (CP IV) with CP IV-32 cement, the adiabatic rise of 66.1°C was estimated based on the retroactive calculation. For the concrete of the DEF/ASR prototype (CP IV), an increase in hydration heat of 22 % was considered at the age of 41 hours in relation to the test data presented by [19], in addition to the increase of 10 % up to the age of 168 hours. The higher degree of hydration, verified in the prototypes, especially for CP IV cement, is related to the higher hydration kinetics for the high temperatures reached in concrete. The average ambient temperature and wind speed were considered according to data from the National Institute of Meteorology (INMET) of a station in Goiania/GO, approximately 20 km from the aging field where the prototypes are exposed.

- Field Evaluations

To assess the evolution of the cracking, an inspection was carried out using a drone, followed by image treatment, where it was possible to assess the evolution of the cracks in the prototypes by inspections carried out in September 2022 and 2023. To monitor the evolution of temperatures and expansion in the prototypes, two embedded Carlson type extensometers, four embedded thermocouples, and a one embedded rod extensometer were installed (figure 2). The Carlson-type instrument measures deformations and temperatures, and the rod extensometer allows the monitoring of vertical displacements in the centre of the prototypes. The rod extensometer was adjusted and positioned on top of the blocks to record the first measurements..

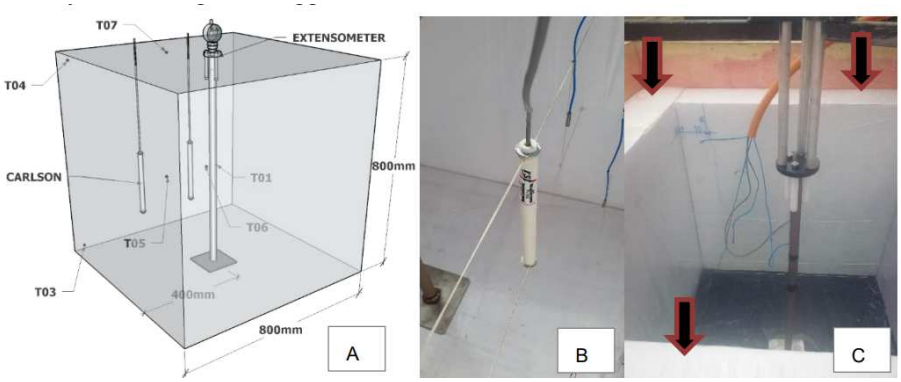

Fig. 2 – (A) Instrumentation design; (B) Carlson type extensometer; (C) Rod extensometer. Note expanded polystyrene formwork [22]

- Laboratory tests and analyses

To evaluate the mechanical properties of the concrete of the prototypes, concrete cores with a diameter of 75 mm were extracted for compressive and tensile strength tests. In addition, SDT (Stiffness Damage Test), was carried out to quantify the damage to concrete derived from expansive reactions such as AAR and DEF, obtaining two indices – SDI and PDI, according to [27] and [28-30]. In this work, the data of compressive strength ($f_{c,\,ext}$) and tensile strength

($f_{t,\ ext}$) and dynamic modulus of elasticity (E_d) of the concretes cores will be presented. The concrete deterioration index or DRI (Damage Rating Index*)* was also determined according to the Brazilian technical instruction [31], by means of a stereoscopic microscope with 16x magnification. This index aims to quantify the damage caused to concrete by the presence of expansive reactions [32] and [33].

3. RESULTS

3.1. Thermal studies by 3D mathematical modeling

The evolution of temperatures and stresses (figure 3A) that would occur in a three-dimensional finite element model in the most critical sections of the structure of the analyzed prototypes was simulated. The finite element mesh is automatically formed by tetrahedral elements as shown in figure 3 (B).

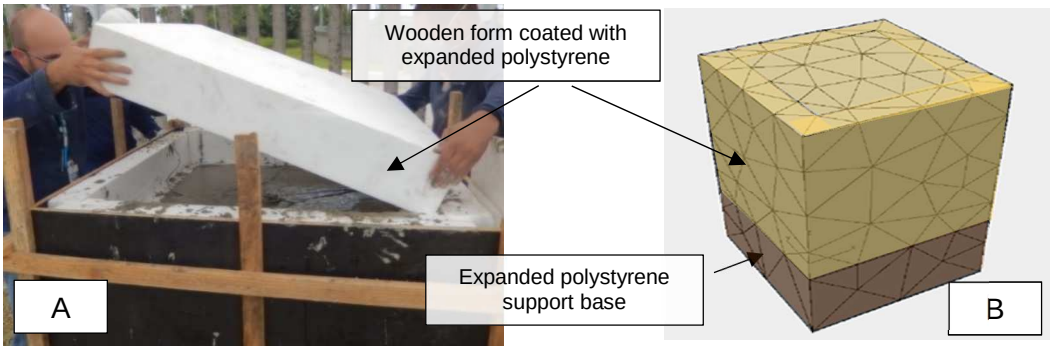

Fig. 3 – Detail of the execution of the cubic prototype and FEM used in the thermal calculations

Figure 4 presents the isotherms referring to the maximum temperatures in the analyzed prototypes and a comparison between the temperatures monitored by the embedded thermocouples and the thermal calculations performed by mathematical modeling.

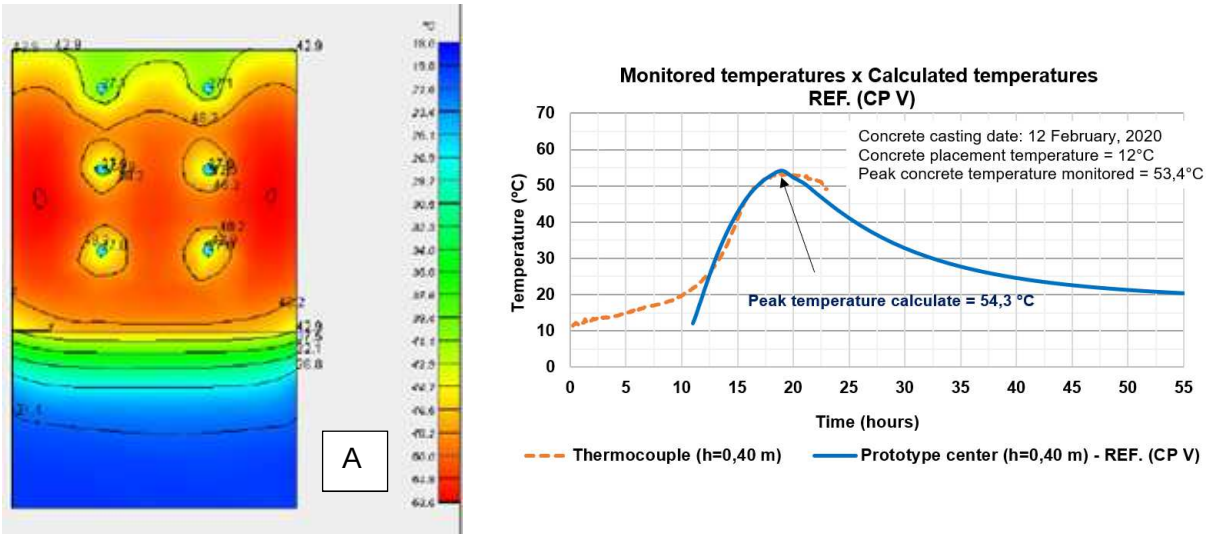

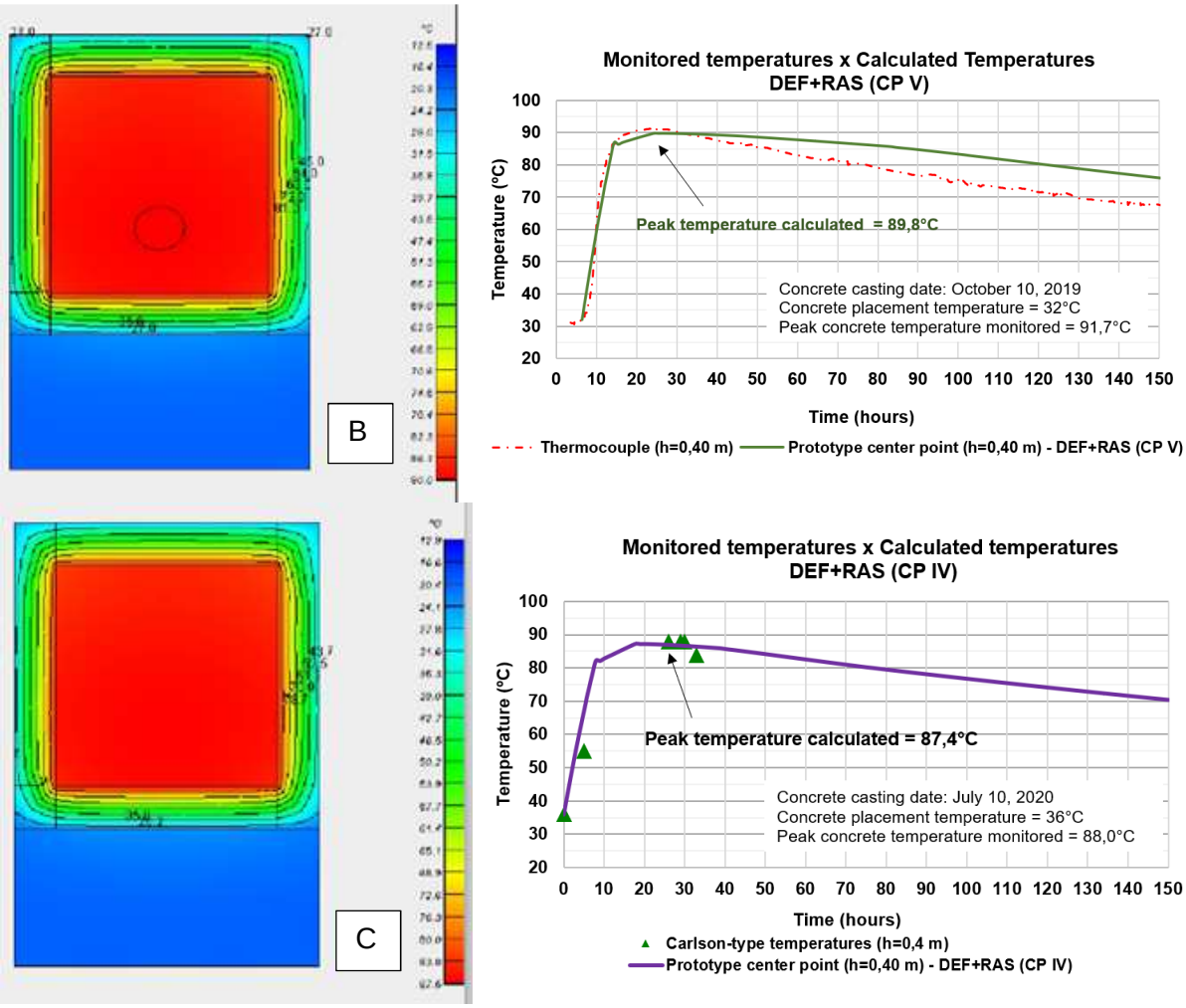

Fig. 4 - Isotherms of the prototypes and comparison between the results of the mathematical calculation and thermal monitoring by the thermocouples

From the isotherms and isostresses, the most critical regions of the prototypes and with the highest probability of thermal cracking were studied. Based on the calculated and monitored temperatures, it was confirmed that concrete temperatures above 85°C were reached, which made it possible to induce DEF in the concretes studied with both cements (CP V and CP IV), with maximum temperatures equal to 91.7°C and 88.0°C, respectively (> 65°C). The maximum temperature inside the prototype REF. (CP V) was 53.4°C (below < 60°C), which reduces the risks of DEF formation in the future. Based on the analysis of the maximum thermal stress it was found that these are lower than the tensile strength of the concrete of the analyzed prototypes. The calculated major principal stress was less than 1 MPa for the analyzed prototypes. The use of expanded polystyrene at the base of the DEF/ASR (CP V) and DEF/ASR (CP IV) blocks and smaller concrete dimensions reduces the restraint on its movement. The formwork coated with expanded polystyrene on its lateral faces made it possible to dissipate heat more slowly, contributing to the reduction of the risk of thermal stress cracks

3.2. Field evaluations

For the investigation of the cracks of the prototypes affected by the expansive reactions in the field, an unprecedented classification of the cracks was carried out from images obtained by drone inspections, and the expansions were calculated from monitoring and data obtained by embedded rod extensometer.

- Drone inspection

In this stage of the cracking investigation, the R&D project acquired georeferenced images, through RPAS/DRONE, for the elaboration of a three-dimensional model of each concrete prototype and mapping/monitoring of the anomalies existing in its 5 faces exposed to the environment (Brazil Midwest Region). The work protocol was divided into three main stages: 1. Flight and acquisition parameters; 2. Post-processing and anomaly detection; 3. Comparison with previous data as shown by [34].

Figure 5 shows the orthomosaics of the tops of the blocks processed from the last inspections conducted in 2023. Visually, when compared to the year 2022, it was observed an evolution of the fissuratory framework of the prototypes, a region subjected to a higher incidence of sun and rain.

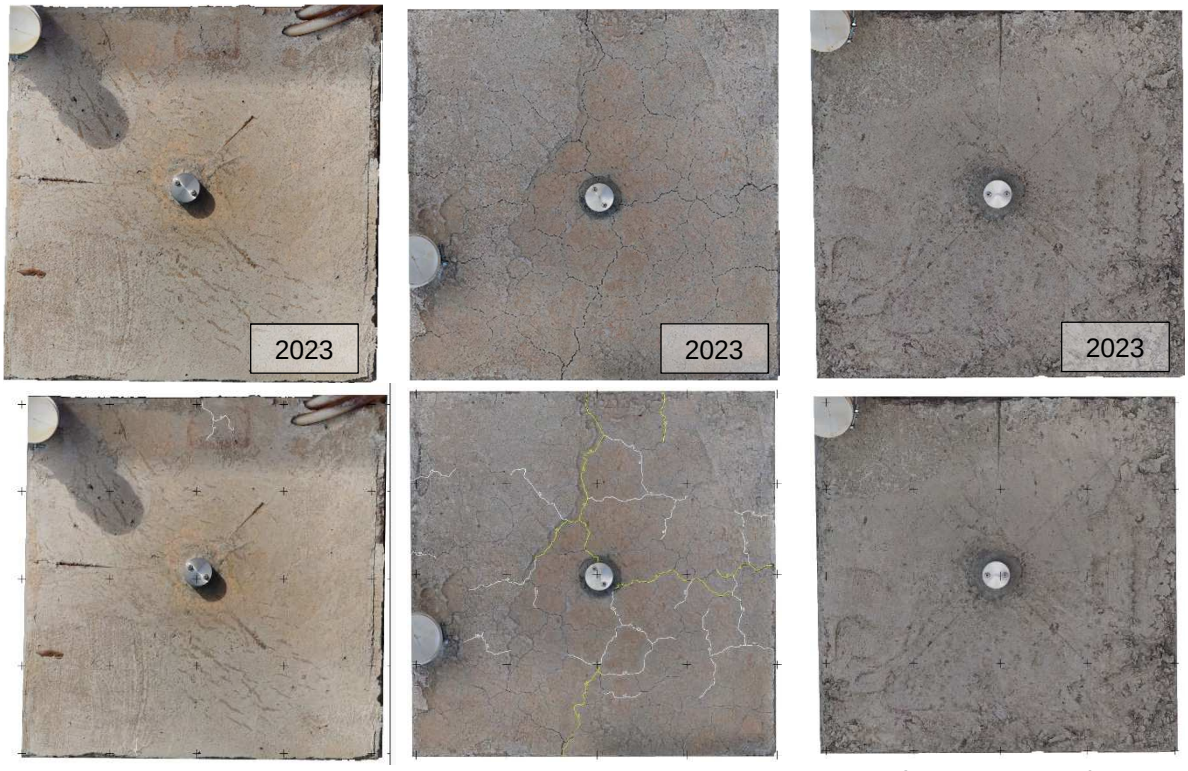

a) REF. CP V b) CP V-DEF/ASR) c) CP IV-DEF/ASR

Fig. 5 – Orthomosaics – Top of the prototypes – Inspections in 2023 (at Furnas).

The cracks were classified according to the dimensions of their mean opening, as shown in Table 8.

Table 8 – Classification of cracks according to their average opening.

Type of anomaly (Cracks)	Opening width	Colour
F1	0.2 to 1 mm	White
F2	1 to 2 mm	Yellow
F3	> 2 mm	Red

After the measurements of the length of the cracks existing in the prototypes, the data were pooled, and all 5 exposed faces of the prototypes were considered in the final calculation for each crack opening range. Then, a comparative analysis was made between the values found in 2022 and 2023. Figure 6 shows the quantification of the cracks on the five faces. Based on this first analysis, longer crack lengths F1, F2 and F3 were observed in the prototype with DEF. There was an increase in the total crack length in the three prototypes analyzed in the period of 1 year. This increase was equal to 214%, 146%, and 60% for those with DEF, ASR, and REF, respectively. The prototype with DEF/ASR (CP V) showed F1 and F2 cracks with a 62% increase in F1 cracks, in addition to the appearance of new F2 and F3 cracks in the following year. No F2 and F3 cracks were quantified in the prototype of REF. (CP V) in the year 2022. The following year, in the REF prototype, few F1 cracks were observed. For the prototype with DEF/ASR (CP IV), F1 cracks were observed in the inspections carried out in 2022 and 2023, with the appearance of F2 cracks in 2023. Between 2022 and 2023, this prototype had a 60% increase in F1 cracks. Based on the results of the visual inspections and the use of the drone with image processing, it was possible to evaluate a good correlation between them for the period analyzed..

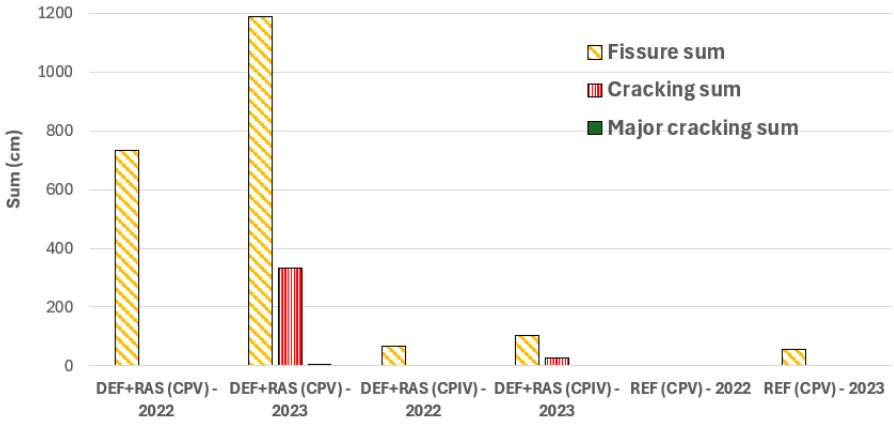

Fig. 6 – Classification and sum of prototype cracks

Periodically, visual inspections are conducted to evaluate any evolution of existing cracks or the appearance of new cracks. Based on inspections conducted in 2024, a visual increase in cracks was observed compared to the inspection carried out by a drone in 2023. It has not yet been possible to observe an increase in F2 cracks or the appearance of F3 cracks in the DEF/ASR (CP IV) prototype. Figure 7 shows details of the top of these blocks from visual

inspection using a manual camera, where it is possible to visually evaluate the evolution of the fissuratory chart of the DEF/ASR (CP V) blocks.

Fig. 7 – Current photographic record (2024): visual inspection of the prototypes.

3.2.1. Expansion monitoring by extensometry

The record of the rod extensometer data (Figure 6) indicates very high calculated expansions for the prototype containing cement without additions (CP V), reaching 0.10% at the age of 3 years. This level of expansion is considered high, according to a global analysis executed by [35] in the DEF study, with important negative effects on mechanical properties, especially on the modulus of elasticity (drops of around 45%) and on strengths (to traction and compression), above 20%. The behavior observed for this cement (figure 8) follows a sigmoidal model, as presented and previously discussed in the literature by [36]. As for the prototype made with pozzolanic cement, also induced to DEF/ASR, up to the measured age no expansions have yet been observed, although by microscopic analyses and DRI data, symptoms related to expansive reactions have already been observed as well as an increase - over time - in the cracking index during inspections carried out by drone and data processing. In the accelerated laboratory studies presented by [35] for DEF, the same type of pozzolanic cement also showed minor damage when compared to cement without addition.

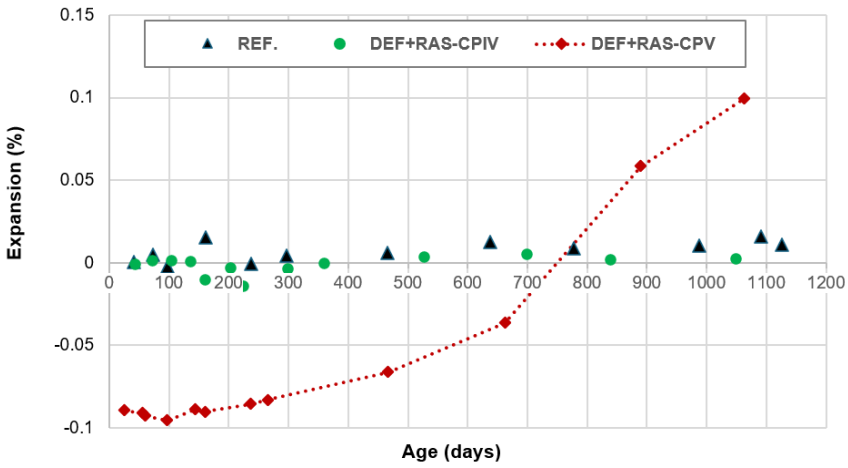

Fig. 8 – Evolution of expansions monitored by rod extensometer

The reference, without any induction of the ASR and DEF, does not show expansion, as expected. What can be said in relation to the behaviors observed (in the induction of the combined attack) is that, in general, there is a lag between the onset of symptoms as well as expansions when comparing two different cements, especially CP V with those combined with pozzolanic mineral additions, according to the literature [7]. Based on the laboratory studies carried out by [19] in mortars and concretes with the same materials up to the age of 360 days, there was expansion for samples submitted to heat treatment with a maximum temperature of 85°C and according to protocol [5]. The mortar and concrete specimens undergone thermal cycle showed expansions of 0.30% and 0.43% at the age of 360 days. At the age of 88 days, an expansion of 0.04% was observed. Mortar and concrete made with CP IV cement showed an expansion of 0.01% and 0.03% at the age of 360 days. In the studies presented by [19], these differences are shown between exactly these two types of cement used in the present study, but in tests performed in the laboratory, with molded specimens. It should be noted that the present study simulates prototypes under field conditions, which are more similar to the behavior of real concrete structures in service.

3.3. Laboratory tests

3.3.1. Mechanical tests

Table 9 shows the results of the specimens drilled from the prototypes at the approximate age of 3 years.

Table 9 – Average results of compressive strengths (fc) and tensile strengths and modulus of elasticity of the cast and extracted concrete

Prototype	Compressive strength (MPa)	Tensile Strength (MPa)	Modulus of elasticity (GPa)
REF. (CP V)	71.5	5.3	40.8
DEF/ASR (CP V)	50,5	n.a.	21.9
DEF/ASR (CP IV)	57.2	3.7	44.9

Note: n.a.: not available.

The results of compressive strength show divergences between the reference (without attack by DEF/ASR) and the concrete cores (induced to combined attack by DEF/ASR) due to the different temperatures reached inside the concrete of the blocks, cements and the development of chemical reactions. In the presence of CP V, the drop was approximately 30%; with CP IV, the difference was smaller, in the order of 20%. In terms of tensile strength, the behaviors follow that of compression and represented in the order of 7%. Taking as reference the expected modulus of elasticity for the strengths reached at the evaluated age of the

concrete cores, it is observed that the REF. is close to the expected as well as the concrete containing the pozzolanic cement. On the other hand, the combined attack in the presence of CP V registers a drop of approximately 50% for the modulus of elasticity due to deterioration by the expansive reactions. Considering the nature of these expansive phenomena, a decrease in compressive strength without a decrease in the modulus of elasticity observed for fly ash concrete (CP IV) is not clear understood, thus cannot be attributed to expansions due to combined attack at this age of the present study.

3.3.2. Semi-quantitative analysis (DRI)

The results of the DRI (figure 7) show evolution over time regarding the symptoms of the expansive reactions for the two blocks in which DEF and ASR were induced together, for both cements tested. The DRI value obtained for concrete made with CP V cement, without additions, is much higher (DRI = 547) than that with pozzolanic cement, CP IV (DRI = 212). The reference block presented a very low DRI value (24), as expected.

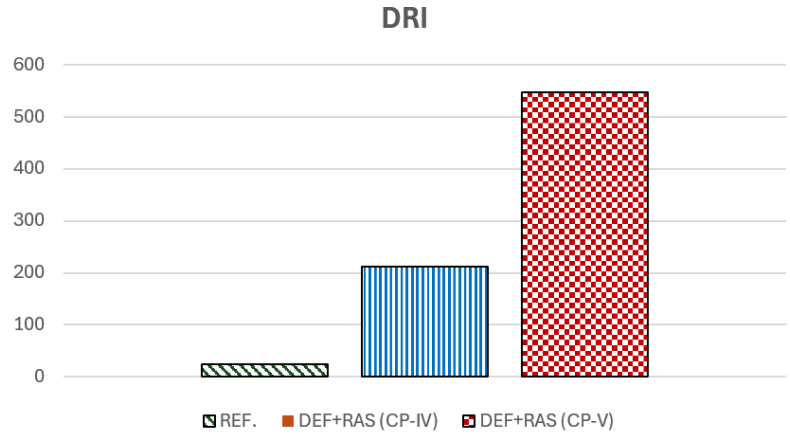

Fig. 9 – Concrete Deterioration Index (ID) or DRI (Damage Rate Index)

It is worth noting that, in the study of [37], the references of concretes with little deterioration due to expansive reactions analyzed presented DRI ranging from 25 to 68, different from the two blocks induced to the combined attack of the present study, which presented much higher DRI values, and above 200. These data indicate that concretes are deteriorated by expansive reactions, but at different stages. The prototype containing cement without addition (CP V) represents an DRI 158% higher than that containing pozzolanic cement.

The most intense symptoms observed in the analyses, in general, were cracks filled or not by reaction products in the coarse aggregate and edges with products around the aggregates (table 9 and figure 10).

Table 9 – The DRI weinghting factors associated with ISR damage [38] and [31]

	Distress feature	Acronym	Weighting factor
1	Closed crack in aggregate	CCA	0,25
2	Opened crack in aggregate	HOLLOW	2
3	Opened crack in aggregate with reaction product	OCA-RP	2
4	Disaggregated/corroded aggregate particle	DAP	2
5	Crack in the cement paste	CCP	3
6	Crack in the cement paste with reaction product	CCP-RP	3
7	Coarse aggregate debonding	CAD	3
8	Reaction product around the aggregate	RPA	0,25
9	Lined or filled voids in the cement paste	LFVCP	0,25

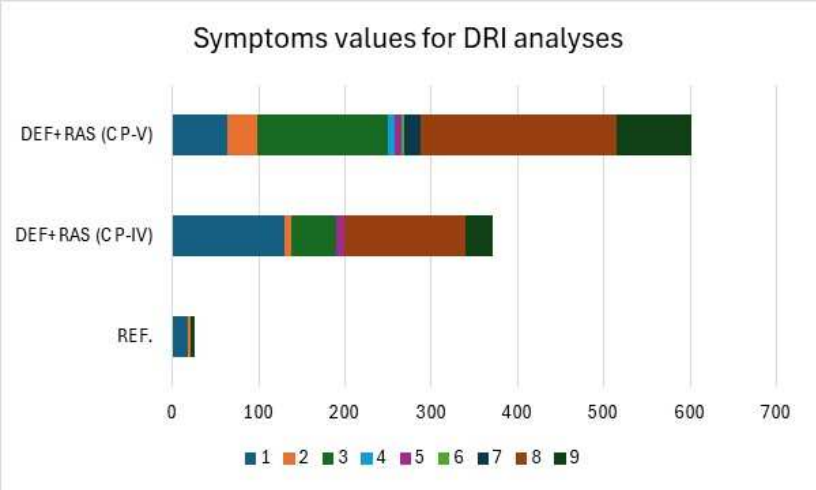

Fig. 10 – Symptoms verified in the semi-quantitative analysis (DRI)

According to a study carried out by [34] for concretes affected by different types of expansive reactions of internal origin, the DRI allows to accurately quantify the extent of the damage, correlating it with the loss of mechanical properties due to the presence of internal cracks and respective levels of expansion. In addition, it has been shown to be effective in distinguishing between different deterioration mechanisms, being a valuable technique for the investigation of structures affected by ISR (Internal Sulfate Attack).

3.4. Global discussion of the results

The studies show significant differences in thermal, mechanical and durability behaviour between the concrete samples prepared with different types of cement (CPV and CP IV), considering the combined phenomena of DEF and ASR.

The concrete prototypes produced with CP V and CP IV, purposely reached maximum temperatures of 91.7°C and 88°C, respectively, and above the critical limit of 60-65°C that prevents occurrence of DEF. On the other hand, the reference concrete prototype made with CP V and without induction of reactions, cast with innocuous aggregates, achieved a maximum

temperature of 53.4°C, which minimized the risk of the emergence of these types of expansive reactions. It is known that some granite-gneisses may be harmful in service, considering that this type of rock presents slower reactivity, giving false negative results from AMBT. In this case, it is essential to proceed with concrete investigations. Despite the high temperatures in the induced prototypes, the thermal origin stresses calculated by mathematical modeling remained below 1 MPa, thus mitigating the risk of thermal cracking caused by restraints. The prototypes with DEF/ASR (CP V and CP IV) showed higher cracking degrees than the reference prototype (REF.). For the DEF/ASR (CP V) prototype, there was an increase in F2 and F3 cracks between 2022 and 2023, proving the progressive expansion and deterioration of this structure. For the block containing pozzolanic cement (CP IV), there was a 60% increase in F1 cracks, in those without F3 cracks, indicating lower severity. The REF. (CP V) showed only a few small F1 cracks that emerged in 2023.

Rod extensometers indicated expansion of 0.10% in concrete with CP V, while CP IV did not show significant expansions up to 3 years. This prototype with DEF+ASR and CP V shows a reduction in compressive strength and modulus of elasticity, and the one with CP IV only in compression so far. The REF. (CP V) is within expectations.

The DRI values were significantly higher in the prototypes induced to DEF/ASR, with CP V, presenting an index 158% higher than CP IV (547 against 212). These data show the greater susceptibility of CP V to damage caused by expansive reactions for the period evaluated. On the other hand, although concrete with CP IV has shown lower intensity of symptoms, such as cracks and reaction products in the aggregates and paste, a value above 200 of DRI already indicates internal damage.

The results indicate that, although both cements are susceptible to DEF and ASR under critical conditions of curing temperature, CP IV cement type showed better overall performance up to the age evaluated, however, already in the initial stage of deterioration at the microstructural level. However, CP V cement type is more vulnerable, as well as more pronounced deterioration over time. These results reinforce the importance of carefully choosing the appropriate materials to mitigate the effects of expansive reactions in concrete structures at more advanced ages of the structures.

4. CONCLUSIONS

Based on the studies and investigations conducted over the years, it is believed that additional expansions and cracks will still occur in prototypes prone to combined reactions (ASR and DEF). Embedded instruments are expected to record stresses and volumetric changes before new cracks appear. At the same time, non-destructive tests and microstructural

complementary analyses to the study presented herein will be carried out to verify the evolution of chemical reactions.

This publication aimed to show the association of investigative techniques in the monitoring of concrete structures affected by combined expansive reactions (DEF/ASR). The use of drones during inspections is unprecedented in the field and proves to be a very attractive practice, because, in addition to allowing agility in obtaining images and characteristic symptoms, it allows access to locations that cannot be visually inspected by a specialist and gives important quantitative data. Differences in behavior were also observed between the two types of cement analyzed in the face of a combined attack, based on the techniques evaluated, indicating for the Brazilian standard cement CP V ARI a faster and at the same time an intense deleterious process, based on the development of cracking pattern. For the prototype with pozzolanic cement, based on the evaluation period, the development of reactions was slower up to the age of 3.5 years, with fewer symptoms. For the reference sample, without induced reactions and cracking, no symptom was observed, as expected. These practices of analysis and laboratory tests, associated with inspections and instrumentation in the field contribute to the evaluation of the evolution of expansive reactions and, consequently, in the taking of actions, corrective measures and any interventions that may be necessary.

ACKNOWLEDGMENTS

ELETROBRAS-FURNAS/ANEEL supported financially and the infrastructure of this research through FURNAS ANEEL R&D project of code PD 0394-1504-2015, entitled "Evaluation of the interdependent reaction mechanisms of late ettringite formation and alkali-aggregate reaction in concretes and mortars and the effect of nanomaterials for mitigation". The work also had technical and some financial support from UNILA (Latin American University) as well as technical support from the company DESEK. The DRI analyses were carried out with technical and infrastructure support from the ABCP (Brazilian Association of Portland Cement).

REFERENCES

[1] ASSOCIAÇÃO BRASILEIRA DE NORMAS TÉCNICAS. ABNT. (2018) - NBR 15577: Agregados - Reatividade álcali- agregado, Rio de Janeiro.
[2] SBRIGHI, C. N. et al. (2018). Guia da prevenção da reação álcali-agregado. Prática recomendada Ibracon. Comitê 201 Ibracon, 32p. São Paulo, SP.
[3] HEINZ D. & LUDWIG U. (1987). Mechanism of secondary ettringite formation in concrete subject to heat treatment. Concrete Durability SP 100, ACI vol.2 pp. 2059 -2072.
[4] GODART, B. & WOOD, J. (2022). Interaction of DEF and ARR, a review. In proceeding of 16th International Conference on Alkali Aggregate Reaction in Concrete – 16th ICAAR, Ed. LNEC, v. 1, p. 97-106. Lisbon, Portugal.
[5] HASPARYK, N.P. et al. (2020). Instrução Técnica GSTE004R0 - Método de ensaio para a avaliação do potencial de ocorrência da etringita tardia (DEF) em concreto, Furnas, Goiânia, GO.

[6] BAUER, S. et al. (2006). Alkali-Silica Reaction and Delayed Ettringite Formation in concrete: A Literature Review. CTR Technical Report, Report n. FHWA/TX-06/0-4085-1. Center for Transportation Research, Texas.

[7] FUNAHASHI JR, E.I. et al. (2021). Influência do metacaulim na elevação da temperatura e na formação de etringita tardia em compósitos cimentícios. Revista Matéria, Rio de Janeiro, RJ.

[8] FUNAHASHI JR, E.I. & KUPERMAN, S.C. (2010). Estudos de tensões térmicas em vertedouro de pequena central hidrelétrica, VII Simpósio de Pequenas e Medias Centrais Hidrelétricas, São Paulo, SP.

[9] FUNAHASHI JR, E.I. et al. (2018). Belo Monte hydropower plant – Temperatures and thermal stresses analysis of the intake. In: Third International Dam World Conference, pp. 17–21, Foz do Iguaçu, PR.

[10] GU, Y. et al. (2019). Pore size analyses of cement paste exposed to external sulfate attack and delayed ettringite formation, Cement and Concrete Research, vol. 123, pp. 105766.

[11] SCHOVANZ, D. et al. (2021). Evaluation of delayed ettringite formation through physical, mechanical, and microstructural assays. ACI Materials Journal, v.118, n. 1, pp. 101‑109.

[12] PORTELLA, K.F. et al. (2021). Multiple techniques of micro- structural characterization of DEF: Case of study with high early strength Portland cement composite. Construction and Building Materials, v. 311, 125341.

[13] HASPARYK, N. P. et al. (2022). Global analysis of DEF damage to concretes with and without fly-ash. Ibracon. Journal of Structures and Materials, São Paulo, SP.

[14] FUNAHASHI JR, E.I. et al. (2023). Deterioração do concreto de barragens e usinas hidrelétricas devido ao ataque combinado de RAA/DEF ‑ Estudos de casos. XXXIV Seminário Nacional de Grandes Barragens. Tema 129. CBDB (Comite Brasileiro de Barragens). Foz do Iguaçu, PR.

[15] HASPARYK, N. P. et al. (2016). Combined attack from ASR and DEF in the foundation. In: Proceeding of 15º International Conference on Alkali Aggregate Reaction in Concrete – 15th ICAAR, Ed. Bernardes, H.; Hasparyk, N.P. São Paulo, SP.

[16] MARTIN, R-P. et al. (2017). Evaluation of different techniques for the diagnosis & prognosis of Internal Swelling Reaction (ISR) mechanisms in concrete. Construction and Building Materials, v. 156, p. 956-964.

[17] ZHANG, Z. et al. (2017). Influence of the initial moist curing time on the sulfate attack resistance of concretes with different binders. Construction and Building Materials, v. 144, p. 541-551.

[18] MARTIN et al. Alkali aggregate reaction and delayed ettringite formation: common features and differences. 14th International conference on alkali aggregate reaction ICAAR14, May 2012, France. 10 p. hal-00852367.

[19] BRONHOLO, J.L. (2020). Estudo do ataque individual e misto de DEF e RAA e de seus efeitos deletérios nas propriedades físico-químicas e mecânicas de concretos e argamassas de cimento Portland pozolânico e de alta resistência. Dissertação (Mestrado). Instituto de Engenharia do Paraná, Curitiba, PR.

[20] HASPARYK, N. P.&KUPERMAN, S. C. (2021). Reações expansivas deletérias no concreto. Revista Concreto & Construções, vol. 102, pp. 60-66, São Paulo, SP.

[21] HASPARYK, N., P.; KUPERMAN, S., C.; FUNAHASHI JR, E. I; VICENTE, G. R.; GAMBALE, E. A. Recomendações técnicas para a prevenção da DEF e da fissuração térmica do concreto. 1st edition. São Paulo. 2023.

[22] HASPARYK, N. P. (2022). Concrete block sites in Brazil for assessing ASR, ISA and coupled attack over time. 16th International Conference Alkali-Aggregate Reaction in concrete. Lisboa, Portugal.

[23] ASSOCIACÃO BRASILEIRA DE NORMAS TÉCNICAS (ABNT). (2018). NBR 16697. Cimento Portland – Requisitos. ABNT. Rio de Janeiro, 2018.
[24] ASTM C150/C150M-22 (2024). Standard Specification for Portland Cement.
[25] BS EN 197-1 (2011). Cement Part 1: Composition, Specifications and Conformity Criteria for Common Cements. British Standard Institute, London.
[26] FURNAS CENTRAIS ELETRICAS S.A (1997). Equipe Furnas. Editor Walton Pacelli de Andrade, Concretos: Massa, Estrutural, projetado e compactado com Rolo - Ensaios e Propriedades - Ed. Pini, São Paulo-SP, 1997.
[27] FURNAS CENTRAIS ELÉTRICAS S.A (2021). Instrução Técnica ITDSBE001 – SDT - Método de ensaio para a determinação do índice de dano de rigidez (SDI) e índice de deformação plástica (PDI) em Concretos", 1ª Edição, Goiânia, GO.
[28] GIANNINI, E., R. et al. (2018). Characterization of concrete affected by delayed ettringite formation using the stiffness damage test. Construction and Building Materials, vol. 162, pp. 253-264.
[29] SANCHEZ, L.F.M. et al. (2017). Overall assessment of Alkali-Aggregate Reaction (AAR) in concretes presenting different strengths and incorporating a wide range of reactive aggregate types and natures. Cement and Concrete Research. 93, p. 17–31.
[30] SANCHEZ, L.F.M. et al. (2018). Comprehensive damage assessment in concrete affected by different internal swelling reaction (ISR) mechanisms. Cement and Concrete Research, 107, p. 284-303.
[31] HASPARYK, N.P. (2022). Instrução Técnica n. DSBE002 - Método de análise para a determinação do índice de deterioração (ID) do concreto por reações expansivas. 1ªedição. Ed. FURNAS, Goiânia. GO.
[32] GRATTAN–BELLEW, P.E.; DANAY, A. (1992). Comparison of Laboratory and Field Evaluation of Alkali –Silica Reaction in Large Dams. Proceedings of the International Conference on Concrete Alkali-Aggregate Reactions in Hydraulic Plants and Dams. Fredericton, Canada.
[33] GRATTAN–BELLEW, P.E.; MITCHELL, L. D. (2006). Quantitative Petrographic Analysis of Concrete – The Damage Rating Index (DRI) Method, A Review. M.A. Bérubé Symposium on Alkali-Aggregate Reactivity in Concrete-8th CANMET/ACI Int. Conf. on Recent Advances in Concrete Technology, Montréal, Canada.
[34] FUNAHASHI JR., E. I. et al. (2024). Inspeção de estruturas de concreto afetadas por reações expansivas com o uso de drone. Revista Concreto & Construção. Ed. 114;
[35] HASPARYK, N.P. et al. (2022). Global analysis of DEF damage to concretes with and without fly-ash. Ibracon. Structures and Materials Journal, v. 15, n.3, p. 1-19;
[36] BRAGANÇA, M.D.G.P. et al. (2021) Electrochemical impedance spectroscopy and ultrasound for monitoring expansive reactions and their interactions on cement composites. Construction and Building Materials 305. 124726;
[37] SILVA, P.N. (2007) Reação Álcali-agregado nas usinas hidrelétricas do complexo Paulo Afonso/CHESF, influência da reação nas propriedades do concreto. Dissertação de Mestrado. Escola Politécnica da Universidade de São Paulo. São Paulo;
[38] SANCHEZ, L.F.M. et al. (2020). Assessing the condition of concrete affected by internal swelling reactions (ISR) through the Damage Rating Index (DRI). Cement, v.1-2, p.100001.

Fifth International Dam World Conference
PORTUGAL • LISBON • LNEC • APRIL 13-17, 2025
dam world 2025

YES, THERE APPEAR TO BE OPTIONS TO STOP OR CONTROL ASR IN SOME DAMS!

Robin Charlwood[1]
Independent Consultant

Bruno Godart[2]
Gustave Eiffel University

Etienne Grimal[3]
EDF CIH

Burkan Isgor[4]
Oregon State University

ABSTRACT

Many dam owners around the world have been faced with swelling concrete issues at their dams and hydro projects for the past 70 years or more. Several different management strategies have been adopted to allow continued operation, although the options so far appear limited and no technologies to stop or limit the reactions have been successfully implemented. In some cases, alkali-silica reactions (ASR) and its associated expansion appear to have diminished after 30 or so years, while in many other cases it continues with more or less vigour. In such cases the potential role of releasable alkalis from aggregates and recycling needs to be considered in order to reliably forecast future behaviour and develop a long-term management plan.

In cases where the ASR continues, given the very long required service life of dams, a hundred years and more, there is a clear need to seek to identify some practical solutions to limit the ASR and its effects in these long-term cases. In such cases the roles of the key ingredients to the reactions, silica, alkalis and water must be clearly understood.

Recent simulations by the authors have shown that, given the increasingly long required service lives of dams, and often the slow rate of expansion, some very long-term solutions, such as draining and drying the concrete to reduce the expansion rates in some parts of dams and associated structures, may be possible and worth considering in some cases.

This paper reviews the issues involved in such notions and suggests some scenarios and technical solutions where very long-term sealing, draining and drying may be effective in existing dams with continuing ASR. In addition, we note that in some extreme cases of new dams or rehabilitation of existing dams where there is persistent uncertainty in performance testing of mix designs for ASR prevention, consideration could be given to applying such techniques immediately as a backup in case ASR occurs despite the testing.

We suggest some practical options to achieve these objectives and identify issues that would need to be addressed to confirm their feasibility and practicability.

Keywords: Concrete dams, alkali-silica reactions (ASR), sustainable long-term management of dams, control options, drainage and drying of concrete.

[1]robincharlwood@gmail.com ,USA
[2]godart.br@orange.fr, France
[3]etienne.grimal@edf.fr, France
[4]Burkan.Isgor@oregonstate.edu, USA

1. INTRODUCTION

1.1. ASR Issues in Concrete Dams

Alkali-Silica Reaction (ASR) is a pathology that along with Delayed Ettringite Formation (DEF), affects between 20% and 40% of older existing concrete dams in many countries around the world. Swelling generally appears after several years and, in many cases, shows little or no decrease even after very long periods. This phenomenon induces irreversible displacements and significant stresses. In such situations, it is essential for dam owners to reliably predict future behaviour and develop a long-term management plan. Comprehensive reviews of these challenges are provided in ICOLD Bulletin 184 [1] and DSC2017 [2] and specific issues are discussed in ICAAR 2022 [3] and ICAAR2024 [4]. At the present time there are no proven methods to limit or stop the ASR and its effects in existing dams.

In many cases, alkali release and/or recycling may be causative factors in cases where the ASR is continuing with little sign of abatement. The nature of these processes and tests to identify and address these factors are not discussed in this paper, but we note that such cases are likely the ones most in need of control.

Consequently, there is an urgent need to find practical methods to control or limit ASR in many existing dams, especially recognizing the increasing need to extent the service life of dams into the future to provide sustainable green energy options to help moderate climate change.

1.2. The Purpose of this Paper

This paper is a follow-up to the paper presented at ICAAR 2024 where the basic question “Are there options to stop or control ASR in existing dams?” was asked [5]. It was shown that the time frames to significantly reduce moisture content and at least significantly slow and thereby extend the life of some modest sized dams with ongoing ASR is perhaps 50 years or so with just sealing and drainage but could be reduced to less than 20 years if evaporative drying were applied to the surface. It was noted that the drying time is roughly proportional to the square of the length of the drying pathway, so size would be a limiting factor.

This paper reviews the issues involved, presents some simulations of generalized dam cases and suggests some scenarios and technical solutions where very long-term sealing, draining and drying may be effective in existing dams with continuing ASR. The work reported in this paper was partly triggered by independent observations of the experience at Pracana Dam where the ASR slowed in the central parts of the buttress dam after the reservoir was drained for 12 years and the dam was exposed to dry atmospheric conditions [6].

We suggest some practical options to achieve these objectives and identify issues that would need to be addressed to confirm their feasibility and practicability.

2. BACKGROUND

2.1. The Challenge of Life Extension of Dams

In cases where the ASR continues essentially indefinitely, given the very long required service life of dams, a hundred years and more, there is a clear need to seek to identify some practical solutions to limit the ASR and its effects in these long-term cases. In considering options to address long lasting ASR, it is important to recognize that the time scales are very long: the service life of dams may be hundreds of years, the ASR phenomena is very slow and so a control measure that takes several decades may be worthwhile for some dams and related structures that have long lasting ASR.

2.2. The Options to Control or Stop ASR in Concrete Dams

Basically, there are three principal ingredients for ASR: silica, alkalis and water. Possible options to control long-term ASR are addressed in terms of these key ingredients.

For existing dams, it is impossible to remove the silica from aggregates embedded in the cementitious paste.

The primary source of alkalis has in the past been considered to be from the cement. However, it is now recognized that in some cases, alkalis will be released from the aggregates and/or resupplied by recycling thereby extending the reaction. In such cases, the ASR may continue essentially indefinitely and thereby exacerbates the challenge to the long-term service life of some dams.

There is sufficient water in the mass concrete after hydration to feed the ASR for a long time. Unsealed concrete dams will absorb more water with time. If it could be achieved, it appears that sealing, draining and drying to reduce the degree of saturation below the ASR threshold might work but would depend on the size of the concrete masses and would take a very long time.

Furthermore, the reduction in the degree of saturation, even if it does not reach the triggering threshold of the reaction, will be beneficial in reducing the kinetics and amplitude of long-term swelling. As noted above, the time scales are very long, but nevertheless, a control measure seeking to address the water content that takes several decades may be worthwhile for dams that have long lasting ASR. This possibility is explored in the following sections.

3. MOISTURE CONDITIONS IN LARGE CONCRETE DAMS

In large structures like dams, sufficient moisture is present after hydration of cement to initiate, and in many cases maintain the ASR and facilitate on-going expansion, even after 50 years of service life. To ensure the workability, there is always more water than necessary for the complete hydration of cement (for pouring concrete), and a supplementary supply of moisture, extraneous to the concrete itself, is not necessary to sustain the ASR.

Figure 1 shows an illustrative example, based on the composition of a mortar in a concrete with a compressive strength of about 30 MPa and a water-to-cement ratio (W/C) of 0.5, the volumetric composition would be approximately 40 % of cement and 60 % of water in the mortar. The changes in volume are illustrated in Figure 1. After a complete hydration of cement, 12 % of the original water remains as free water in the porosity of the cement paste and can participate in the ASR.

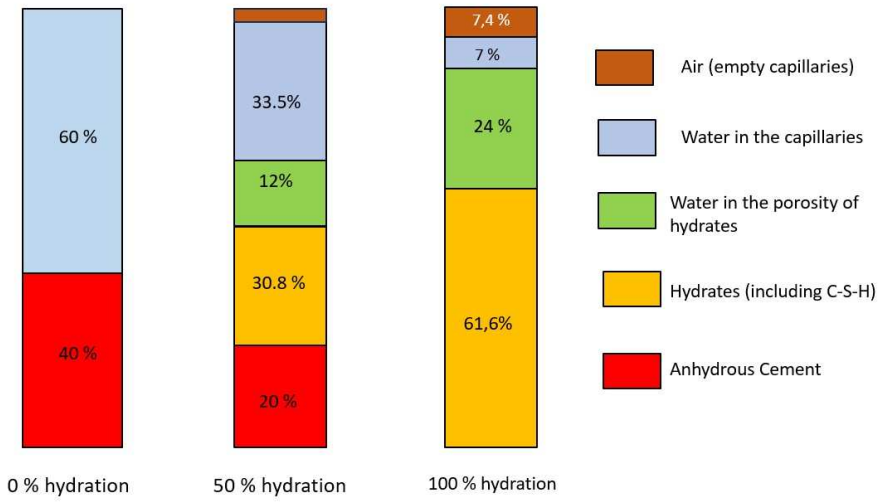

Figure 1 - Composition of a cement paste with a W/C ratio of 0.5 (from Acker [7])

It is accepted that ASR swelling rate decreases with water content measured as degree of saturation Sr (or relative humidity, RH) and it appears that below a threshold value Sr^0, of approximately 0.60 (approximately equivalent to an “80%-RH threshold” for a concrete environment) it becomes low but not nil [8].

In this paper, we adopt the saturation degree Sr ($Sr = \frac{Evaporable\ water\ volume}{Void\ volume}$) as an indicator of water volume and an indicator of the extent of drying. The relationship in equation (1) was employed to calculate the effect of water on the reaction kinetics by Grimal et al in [9].

$$\frac{\partial A}{\partial t} = \alpha_0 . \exp\left[\frac{Ea}{R}\left(\frac{1}{T_{ref}} - \frac{1}{T}\right)\right] \frac{(Sr - Sr^0)^+}{(1 - Sr^0)} (Sr - A)^+ \quad (1)$$

α_0 is a relevant parameter for the kinetics, $\exp\left[\frac{Ea}{R}\left(\frac{1}{T_{ref}}-\frac{1}{T}\right)\right]$ is the thermal influence on kinetics, $\frac{(Sr-Sr^0)^+}{(1-Sr^0)}$ represents the influence of the water saturation degree on kinetics, Sr^0 is a threshold saturation below which the kinetics are close to zero, and $(Sr-A)^+$ is the influence of water on total chemical expansion.

It is important to note the dependence of the kinetics on Sr which allows estimates to be made of the benefit of partial drying in terms of reduced expansion rates throughout a dam body.

It also follows from the above relationship that reducing the temperature would have a beneficial effect of slowing the reaction. Typical dam concrete is quite sensitive to temperature. Reducing the temperature by 10 degrees Celsius would approximately halve the reaction rate. However, although physically possible, such a strategy would be extremely energy intensive and only work as long as the temperature is held down, and consequently, it is difficult to envisage the practicality of such a cooling strategy at this time.

Moisture transport in concrete dams is a multiphase (liquid and vapor) process that takes place in a porous media, where the degree of saturation varies as a function of the relative distance from the upstream (wetting) and downstream (drying) faces. Concrete that is close to the upstream face could reach nearly full saturation due to the hydrostatic pressure of the reservoir, while the relative humidity of the pores in the downstream face might be in equilibrium with the ambient air. Typically, there is an equilibrium between the liquid and vapor phases in each pore, where the equilibrium conditions depend on pore size and temperature, and vary based on whether the pore is being wetted (liquid water is filling the pore) or drying (liquid water is leaving the pore). The liquid water movement is driven by a liquid pressure gradient, which is a combination of hydraulic pressure driven process such as Darcian flow and capillary pressure (suction) that depends on the vapor pressure and the geometry of the pore. Vapor movement in the phases are driven by the vapor pressure gradient. Some of the water/vapor may also be adsorbed on the walls of the channel or react chemically with compounds in the pore walls. Some pores are so isolated and difficult to reach by the water that they are only filled with water after a long exposure period depending on the proximity to the upstream face.

The moisture conditions within a concrete dam body will change progressively after construction and be affected by the concrete surface conditions, the presence of reservoir water and atmospheric conditions on the various exposed surfaces. Moisture transfer at unsealed concrete external surfaces will vary throughout the year and depend on the geographic location and orientation of the dam, the humidity in the air in contact with it and which in summer may be dryer than the interior pores, and in wet winters the opposite.

4 SOME EXAMPLE DRAINAGE AND DRYING OPPORTUNITIES TO RELIEVE ASR IMPACTS IN EXISTING CONCRETE DAMS

4.1 Objectives of the Modelling

Representative examples similar to some existing gravity dams and arch dams have been modelled to illustrate the water saturation processes and suggest where and how upstream membrane seals, drainage and ventilation drying could help slow or limit the ASR by modifying the degree of saturation Sr.

The basis of the simulation results presented is described in detail in the forthcoming companion paper [10] for the medium size gravity dam and the arch dams and in the reference documentation [11] for the Chambon Dam simulations.

These simulations included both vapor diffusion and “Darcian flow” moisture transport mechanisms within the concrete and used reasonably representative estimates of properties and boundary conditions to demonstrate drainage and drying principles. Additional investigations will be required to confirm boundary condition assumptions, particularly behind a membrane seal, and identify case specific moisture transport parameters.

4.2 Concrete Gravity Dams

Expansion effects have caused concern in some gravity dams particularly at changes of geometry; for instance, at the change from a straight section to a smaller curved abutment section where the longitudinal thrust from ASR is having adverse effects on stability and also around galleries creating local cracks. The examples used were taken from curved dams, but the results for these examples may apply to others.

4.2.1 Example 1: A medium size, curved gravity dam

A generalized model of a medium size gravity dam was used in these simulations and is shown in Figure 2. The geometry chosen is similar to that of an existing dam, but the results should not be considered to apply or infer any conditions or options for any specific existing dam.

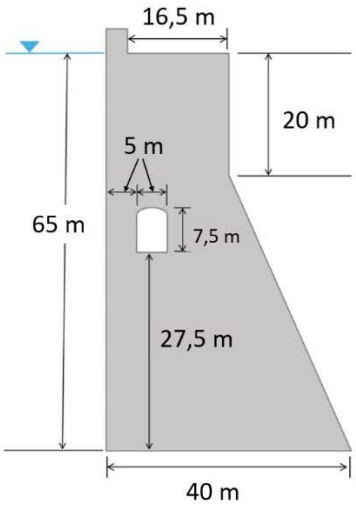

Figure 2 - Dimensions of the medium size gravity dam example

A typical evolution of the moisture conditions in a medium size gravity dam is shown in Figure 3 with wetting from the reservoir on the upstream face starting at t = 0 and natural atmospheric conditions, assumed as 75% RH, on all other exposed surfaces, and no water coming from the foundation. Concrete was assumed to have a W/C of 0.40 and porosity of 0.22. Moisture transport properties (e.g., transport coefficients, wetting/drying isotherm properties, etc.) were assumed to represent such concrete but are not provided here for brevity. Further details could be found in [9].

The initial Sr^{i} was assumed to be uniformly 0.88 after hydration, well above the ASR threshold of Sr^{o} = 0.60. The reservoir water can be seen to steadily progressing into the dam body creating a significant moisture gradient after 30 years or so and an increased ASR rate near the upstream face and a lower rate near the downstream face.

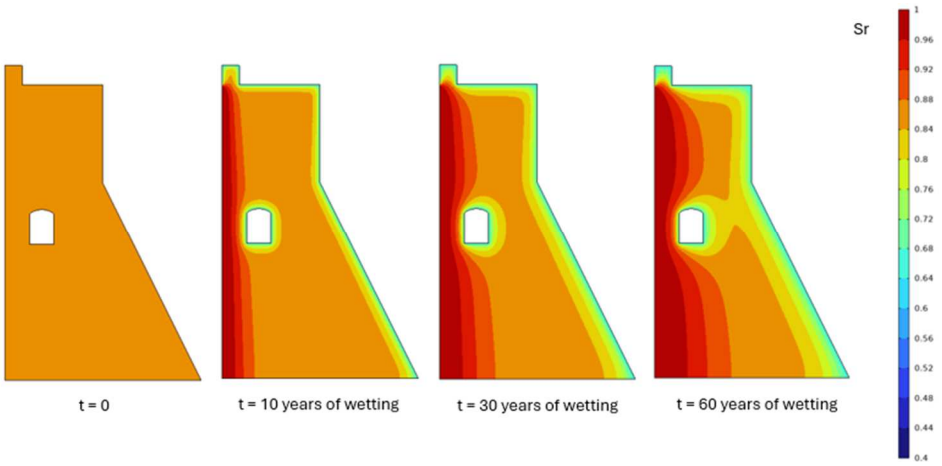

Figure 3 - Natural evolution of wetting in a medium size gravity dam

Figure 4 shows results for this medium size gravity dam with a seal, drainage and actively ventilated drying (50% RH) applied on the upstream face after 60 years of reservoir water contact; with 75% RH on all other exposed surfaces (including gallery).

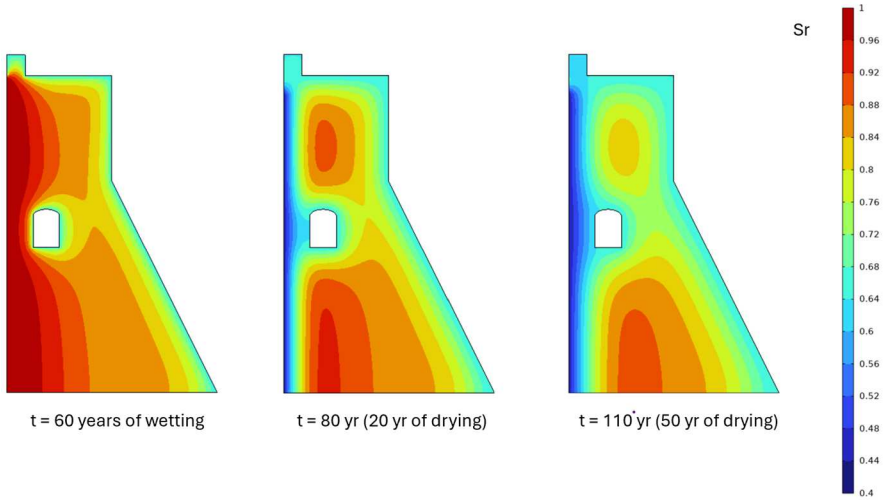

Figure 4 - A medium size gravity dam with upstream face drainage and drying starting at age 60 years

Figure 4 shows that the combination of drainage and drying has an appreciable effect on ASR after 20 years and significantly reduces it after 50 years. It also shows that just maintaining natural atmospheric conditions in the gallery has a beneficial effect on the dam body.

Figure 5 shows effects if a seal, drainage, drying (50% RH) on the upstream face and in the access gallery after 60 years of wetting; 75% RH on all other exposed surfaces.

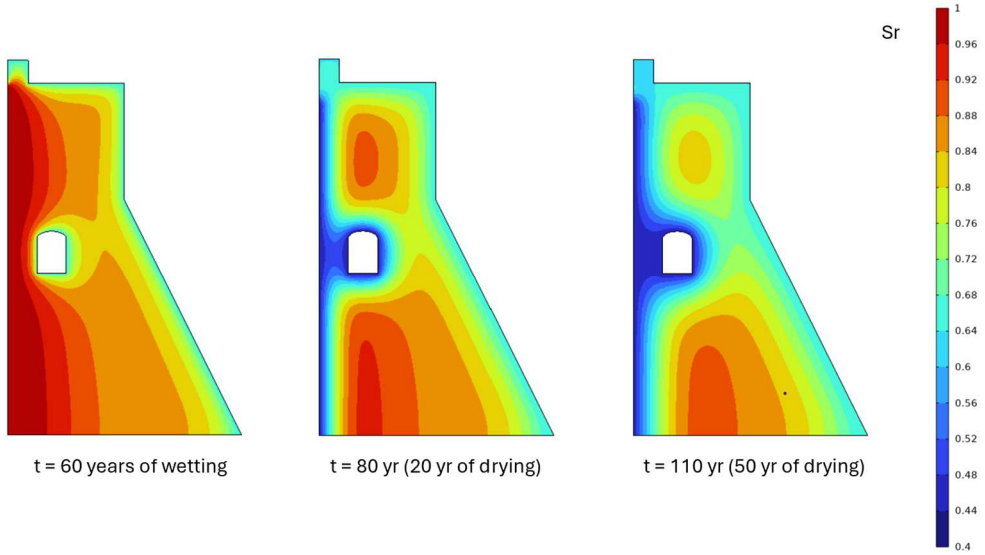

Figure 5 - A medium size gravity dam with upstream face and gallery drainage and drying starting at age 60 years

It can be seen that applying ventilation drying in the access gallery has only a modest additional effect in reducing the extent of the ASR in the dam body.

4.2.2 Example 2: A larger sized gravity dam

These results are from independent studies of drying of Chambon Dam, a larger sized curved gravity dam which is subject to ASR, and do not necessarily reflect the official opinion of the owner. Figure 6 shows the assumed geometry. The initial saturation degree Sr^i in these simulations is assumed to be 0.85. The water content for Sr=1 is 220 l/m³. In each case, a membrane is installed 50 years after construction in the upper part (30 m height) of the dam. The assumption of water saturation of the concrete on the faces in contact with water is taken into account (220 l/m^3 water content).

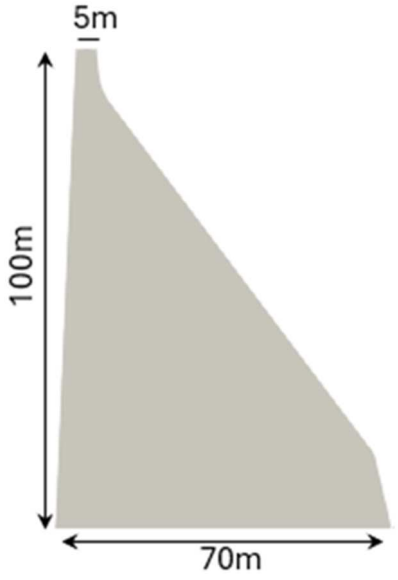

Figure 6 - Geometry of Chambon Dam

In a first case, Figure 7 shows the evolution of the degree of saturation over time, considering the absence of exchange on the downstream face of the structure. It illustrates the penetration of water over time through the upstream face and the foundation. The influence of the membrane on the degree of saturation is difficult to quantify. It is likely that the air between the membrane and the concrete became saturated; therefore, the simulations assume a 100% RH against the facing. The entire structure is highly saturated, allowing significant swelling throughout the structure.

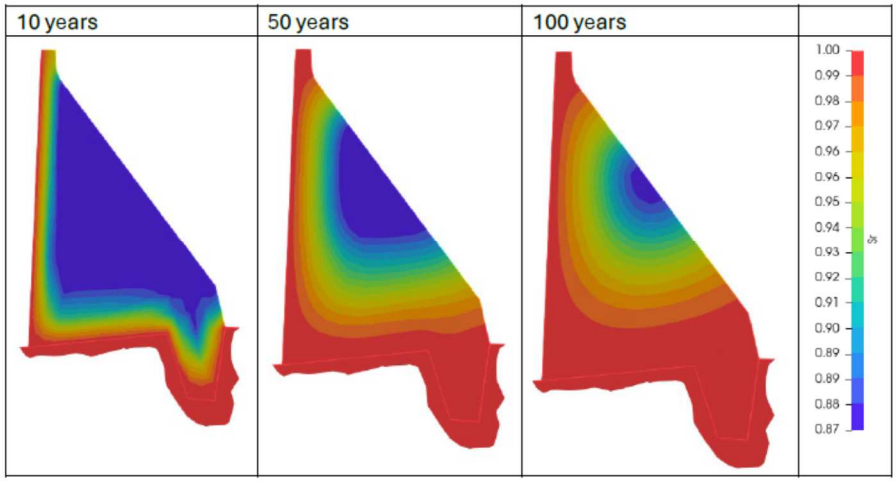

Figure 7 – A larger sized gravity dam with zero flux on the downstream face, 100% RH between the membrane and the concrete

In the second case, Figure 8 shows the evolution of the degree of saturation over time, considering the drying of the dam through the downstream face (natural atmospheric flux at 60% RH). The air between the membrane and the concrete is again assumed to be at 100% RH. A swelling gradient between the upstream and downstream sides will be more pronounced, but the drying of the concrete remains localized to the downstream side.

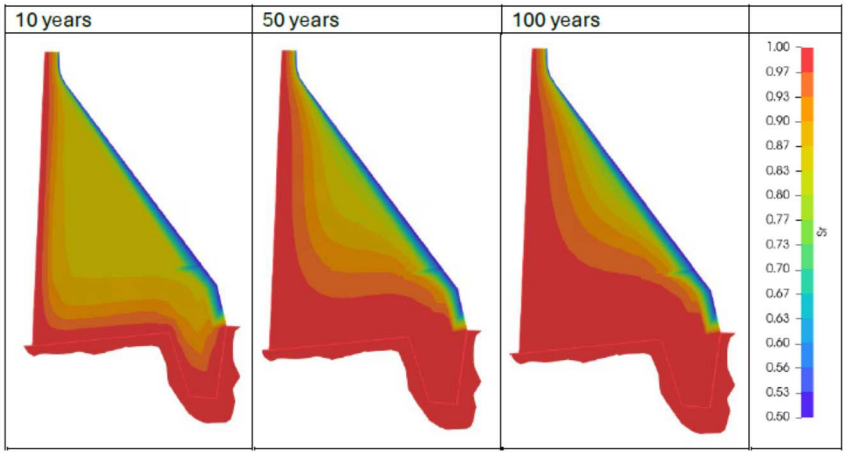

Figure 8 - A larger sized gravity dam with an initial Sr=0.85, 100% RH between the membrane and the concrete and 60% RH on the downstream face

In the third case, Figure 9 takes into account the same assumptions as the second case, with a membrane and ventilation drying applied to the upper part of the upstream face, at 60% RH between the membrane and the concrete. The influence of the membrane is more pronounced, with a global drying effect in the upper part of the structure, which will have a long-term beneficial effect in reducing swelling.

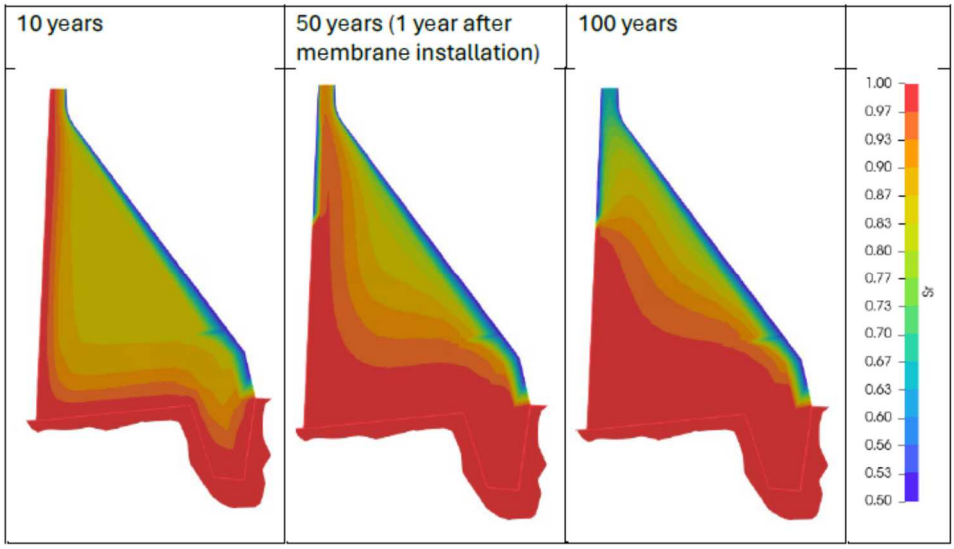

Figure 9 - A larger sized gravity dam with an initial Sr=0.85, a ventilated membrane with 60% RH between the membrane and the concrete and 60% RH on the downstream face.

The following figures show some of the effects of limiting the degree of saturation on the displacement of the structure.

Figure 10 shows a comparison of the displacements obtained with or without a ventilated membrane placed on the upper part of the structure.

A reduction in swelling is observed, associated with the decrease in the saturation profile. The decrease in vertical displacements clearly shows the effect of drying the upper part of the structure, with a gain of about twenty years in this case. The reduction in upstream/downstream displacements is even more significant and would help reduce the upstream/downstream swelling gradient and the associated shear stresses.

Figure 11 illustrates a comparison of the vertical displacements obtained with a ventilated membrane or not, placed on the upper part of the structure or covering the entire upstream face. This figure also shows that an identical displacement is reached at 90 years without ventilation, at 108 years with a ventilated membrane, and at 120 years with a ventilated membrane covering the entire face. Limiting swelling would also have the effect of reducing stresses in the longitudinal (bank to bank) direction.

These results are very encouraging and demonstrate that drying the concrete helps to limit the long-term swelling and it’s structural effects. Numerical calculations could help optimize the

positioning of the membrane, taking into account safety issues as well as the cost associated with the work.

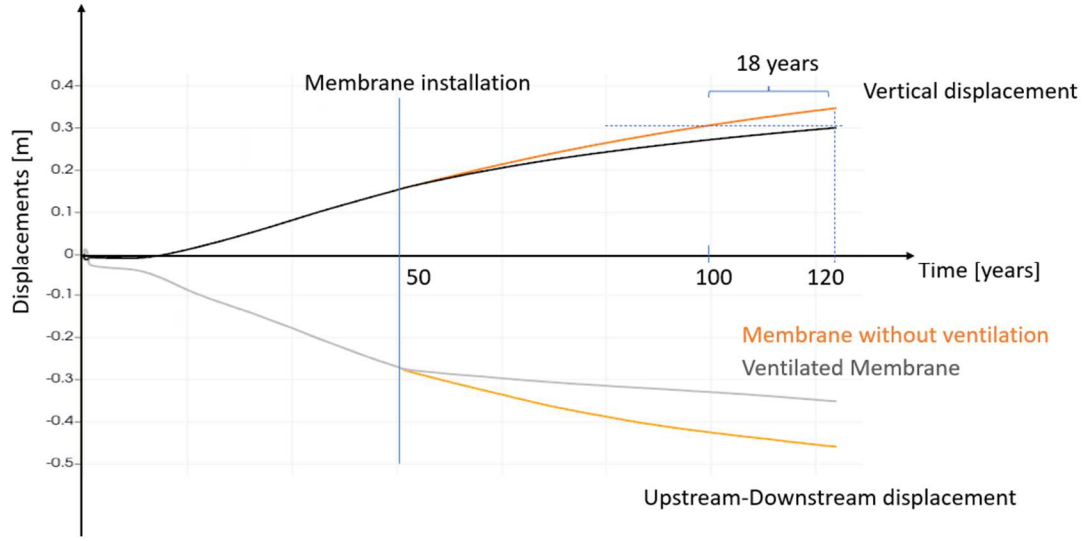

Figure 10 - The influence of a ventilated membrane placed in the upper part of the larger gravity dam on AAR swelling.

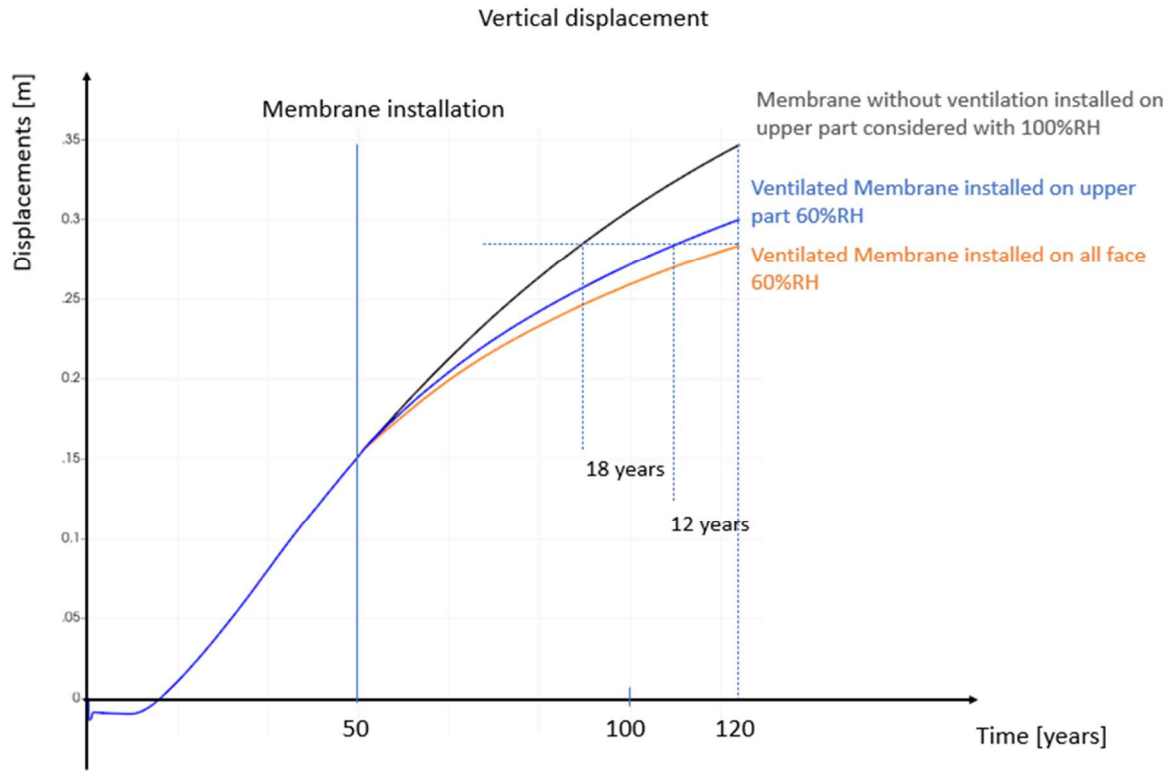

Figure 11 - Comparison of the effect of a ventilated membrane installed on upper part versus across the entire upstream face in a larger gravity dam

4.3 Concrete Arch Dams

Key mechanisms of concern for arch dams affected by ASR include increase of horizontal arch stresses near the crown, upstream movement causing upstream/downstream shear stresses on horizontal lift joints of the upper arches and build-up of adverse shear stresses close to the upper parts of the abutments. To reduce the ASR contributions to horizontal arch stresses and shear stresses on horizontal lift joints it may be sufficient to focus the moisture reduction on the upper arches. However, to address the shear stresses close to the upper parts of the abutments it would probably be necessary to achieve moisture reduction over most of the arch dam body since these shear stresses are caused by the expansion of the entire body of the arch dam tending to lift the upper arches of the abutments.

4.3.1 Example 3: A small arch dam

The assumed geometry used in these simulations is shown in Figure 12 and is similar to that of an existing dam. However, the simulation results are presented as a generic illustration and are not intended to apply to any specific dam. Concrete properties used in this case are similar to those of Example 1.

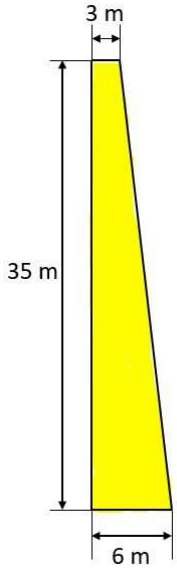

Figure 12 - Assumed dimensions of a small thin arch dam

A typical evolution of the moisture conditions in a small arch dam is shown in Figure 13 with wetting on the upstream face from t = 0 and 75% RH on all other exposed surfaces.

Figure 13 shows that the reservoir water infiltrates most of the dam body within 30 years.

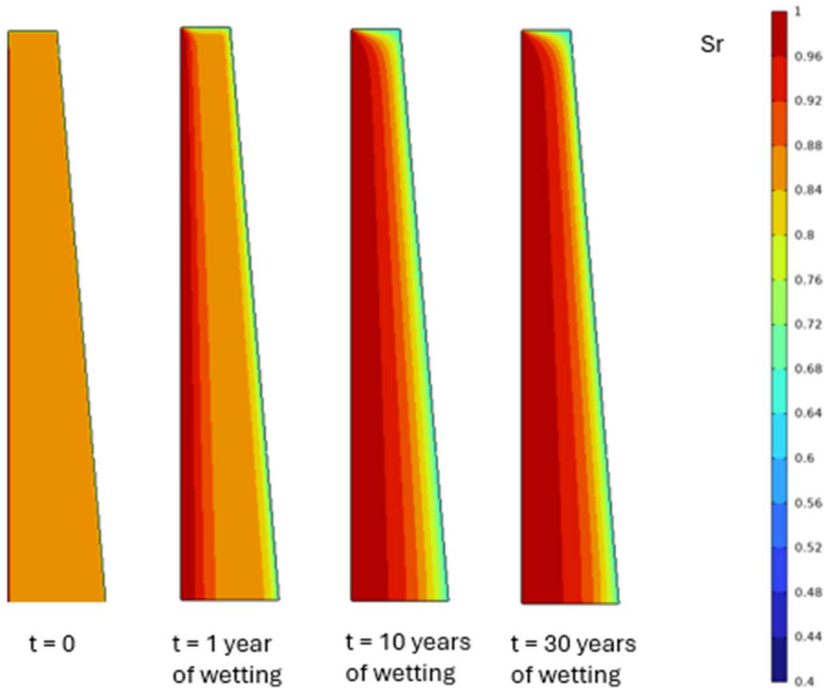

Figure 13 - Natural evolution of wetting in a small arch dam

Figure 14 shows the Sr evolution with an upstream seal and drainage (no drying) applied on the upstream face after 30 years of exposure to the reservoir water; 75% RH on all other exposed surfaces.

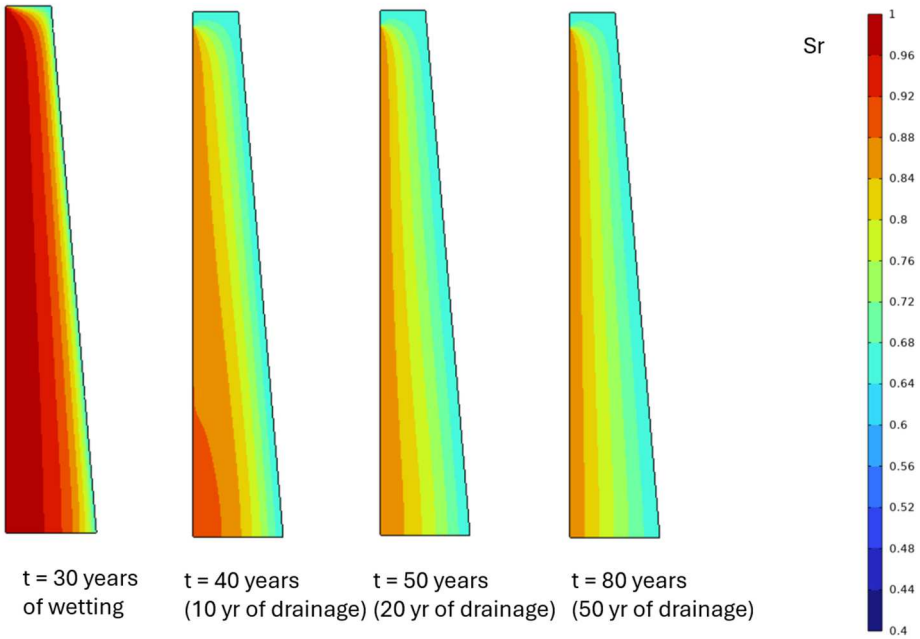

Figure 14 - A small arch dam with upstream face drainage starting at age 30 years

Figure 14 shows that a membrane with drainage substantially reduces the Sr and associated ASR within 10 to 20 years after installation on a fully saturated small arch dam. This would significantly reduce the reaction rate.

Figure 15 shows the Sr evolution with sealing, drainage and drying (50% RH) on the upstream face; 75% RH on all other exposed surfaces.

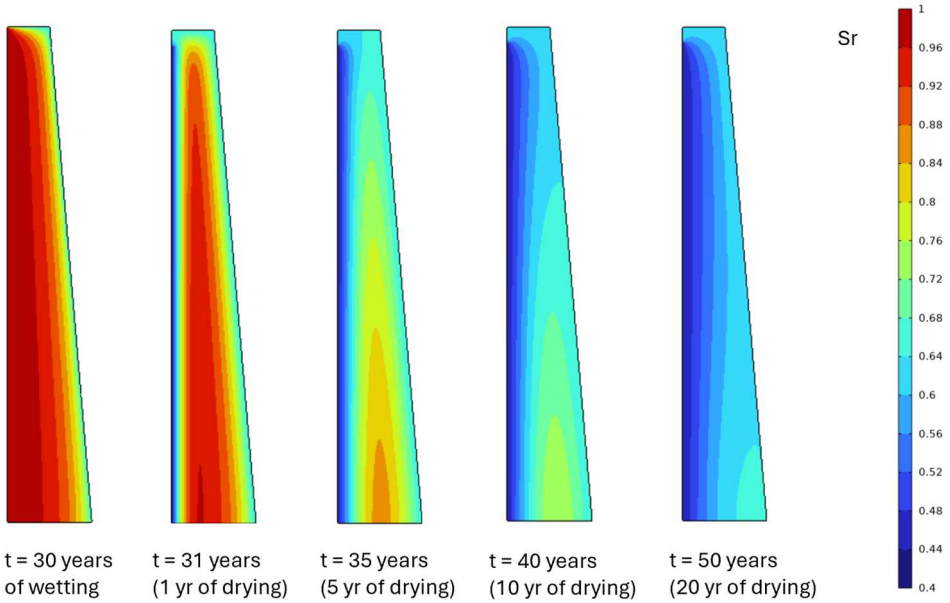

Figure 15 - A small arch dam with upstream face drainage and drying starting at age 30 years

Figure 15 shows that an upstream seal with drainage and drying substantially reduces the Sr and associated ASR within 5 to 10 years after installation on a fully saturated small arch dam. This would significantly reduce the reaction rate.

In order to avoid the diagonal cracks near the upper abutments, it is probably necessary to dry the entire height of the arch dam body. This could be achieved within about 10 years with combined drainage and drying.

4.3.2 Example 4: A larger arch dam

Example 4 considers the same shape as in Example 3 but increased in height to 100 m with increase in thickness to show time scales for a bigger dam. Concrete properties are the same as Example 3.

Figure 16 shows the dimensions of the larger arch dam example.

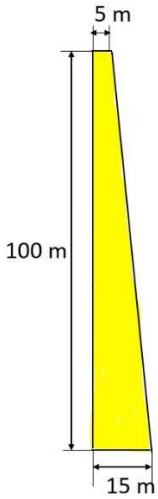

Figure 16 - Assumed dimensions of a larger arch dam

A typical evolution of the moisture conditions in a larger arch dam is shown in Figure 17 with wetting on the upstream face and 75% RH on all other exposed surfaces. This figure shows that the reservoir water infiltration in this thicker arch dam is also extensive after 30 years.

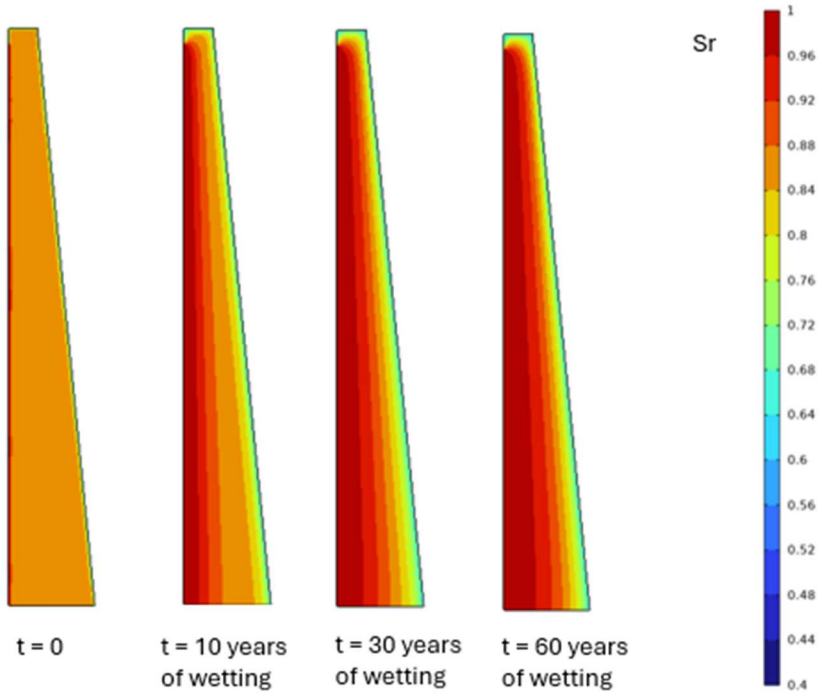

Figure 17 - Natural evolution of wetting in a larger arch dam

Figure 18 shows the Sr evolution with an upstream seal and drainage (no drying) applied on the upstream face after 60 years of exposure to the reservoir water; 75% RH on all other exposed surfaces. This figure shows that for a thicker arch dam, drainage alone takes considerably more than 20 years to be effective.

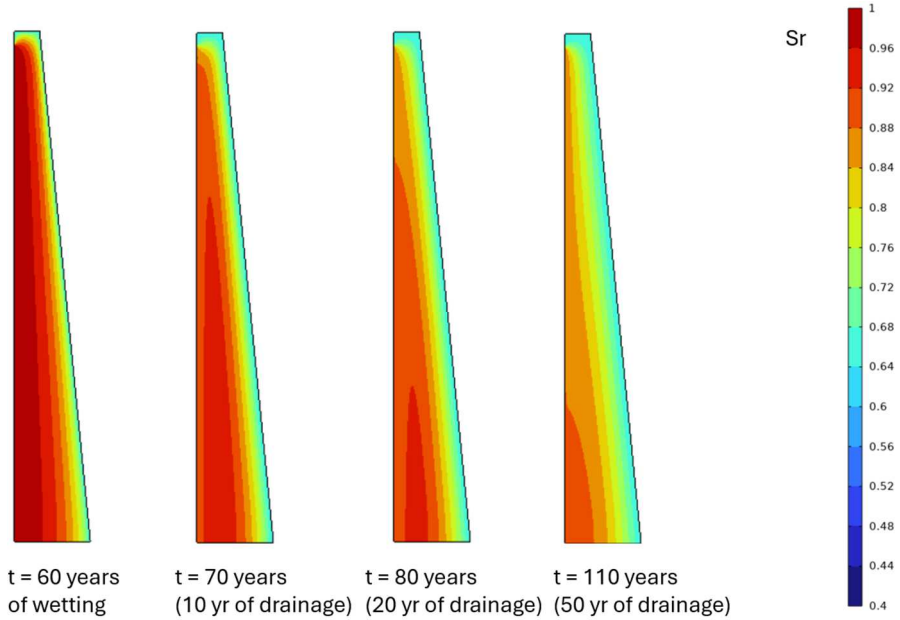

Figure 18 - A larger arch dam with upstream face drainage starting at age 60 years

Figure 19 shows Sr evolution with a seal, drainage and drying (50% RH) applied on the upstream face after 60 years of exposure to the reservoir water; 75% RH on all other exposed surfaces.

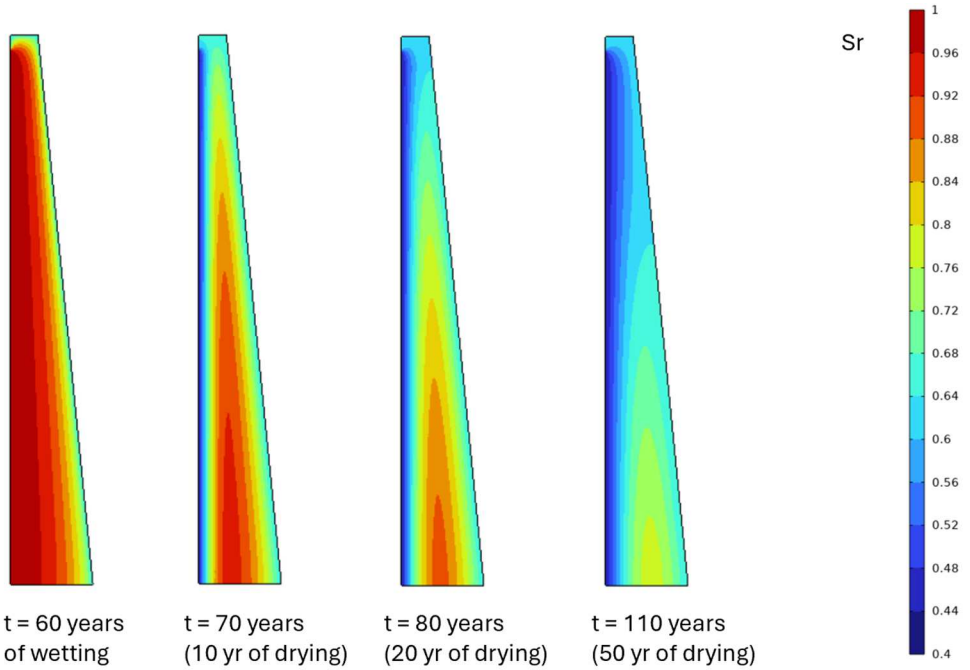

Figure 19 - A larger arch dam with upstream face drainage and drying starting at age 60 years

Figure 19 shows that for a thicker arch dam, 20 years of drainage and drying is effective in significantly reducing ASR in the upper parts of the dam body.

The most severely stressed areas may be the upper horizontal lift joints subjected to shear be due to differential expansion and upstream movement of the upper arches. To reduce these shear stresses, it may be sufficient to only dry the upper portions of the dam. The other issue of concern in arch dams is often the diagonal shear stresses in the “shoulders” of the dam near the upper parts of the abutments. To reduce these ASR added stresses it may be necessary to dry most of the dam body although if moisture reduction in the upper arches slows vertical ASR in that area, then the ASR expansion rate reduction due to the higher vertical compressive stresses at lower elevations in the lower parts of the central vertical cantilevers may be sufficient to sufficiently limit the uplifting effect of these on the diagonal shear stresses at the abutments. The effectiveness of various extents of drying could be established by FEA modelling.

5. SOME PRACTICAL ASPECTS OF DRAINING AND DRYING CONCRETE DAMS

The aim of this paragraph is to suggest some technical principles to install seals, drainage and drying systems on a dam.

A sealing and drainage system combining a PVC sealing geomembrane thermo-laminated to a geotextile with a geogrid serving as a draining layer as described in the ICOLD Bulletin 135 [12] could be an effective option. In such systems, a geo-composite is fixed on the concrete upstream dam face by stainless anchors and profiles. The purpose of such drainage layers is:

- to collect and drain any water which may infiltrate through the geomembrane, thus preventing hydrostatic pressure acting against the dam face and allowing pressure balance of the geomembrane in the event of a rapid draw down of the reservoir,
- to relieve vapour pressure behind the sealing layer caused by the humidity of the dam body,
- to balance air pressure behind the sealing layer in the event of sudden changes in the atmospheric pressure,
- to allow the monitoring of the watertightness of the geomembrane sealing layer.

The water that may flow by gravity in the spaces between the seal and the dam face is then collected at the base into a collector which discharges into the inspection gallery or directly downstream.

To accelerate the Sr reduction in the dam body, the drainage system could be enhanced by adding a drying system to such a seal and draining layer by injecting dry air through it so that the whole upstream face of the dam is exposed to this air. Various technical solutions are possible. Such concepts could consist of bringing dry air into the drainage collector installed at the bottom of a drainage geogrid, and then to distribute this air along the collector through perforated pipes installed along the collector. This dry air would go up through the geogrid until the upper face of the membrane. In order to enhance the air distribution, the system may be improved by also injecting air directly through the perforated anchorage profiles forming a vertical drainage duct, or through added horizontal perforated anchorage profiles at various heights.

In the upper part of the sealing device, at the level of the crest, the covering could be finalized by a mechanical fixing made by a stainless-steel perforated profile anchored by mechanical dowels and allowing the air to escape. On the left and right sides of the sealing device, the fixings should be watertight in order to avoid air leaks.

Of course, a control of the air pressure into the drainage system is necessary to avoid damages to the sealing membrane.

The quantity of air volume injected as well as its pressure, its temperature and its humidity are parameters that need to be determined by a model of the dam where it is necessary to define

the saturation ratio or relative humidity that is targeted inside the dam with time. Warm air should not be used as this would accelerate the reaction. The determination of these parameters would then determine the dehumidification system design. The location of the system could be external to the dam or possibly in a gallery of the dam.

It is noted in passing that applying a seal to the upstream face of a new dam before reservoir filling has been done to reduce leakage rates and eliminate uplift pressures, thereby contributing to safety. Sometimes they are installed at the construction phase as a sealing barrier. If ASR remained a possibility after all other precautions were taken, then the addition of a drainage system, with or without drying ventilation, could be considered and would only need to reduce the Sr from the initial post hydration level down towards the threshold level.

6. DEHUMIDIFICATION OF SOME OTHER CIVIL ENGINEERING STRUCTURES

In civil engineering, the injection of dry air for the dehumidification of structures has already been used. It is the case for about 60 years for box girders and anchor chambers of suspension bridges, and for 26 years for the main cables of suspension bridges.

In this latter case, the objective is to keep the atmosphere inside the cables so dry that corrosion cannot occur, and this technique was developed by the Japanese for the Akashi-Kaikyo bridge in 1998, and then applied by the Danish to the Little Belt Bridge in 2003 and applied in France for the first time on the main cables of the Aquitaine bridge in 2003.

It has been proven by experience that corrosion does not take place if RH in the vicinity of a steel structure is kept below 40 %, and that the corrosion is very low when RH is kept between 40 % and 60 %. This is the basic concept upon which corrosion protection by dehumidification is based.

There are two principal methods of dehumidification: condensation and sorption. The active sorption is generally applied with excellent results [13]. The dehumidification system produces dry air and blows it through sections of the main cables; it assures an overpressure inside the sealed cable system. The dehumidification system is made up of the following main components: dehumidification plants, several injection points along the cables and exhaust points.

For the Aquitaine bridge, there is about 200 m between each injection and exhaust point. The RH, temperature and pressure within the cables are monitored at some intermediate points, and when HR < 25% the dehumidifiers stop, and when HR > 35% they restart. After 20 years of operation, the system has been performing well, with the respect of the 40 % RH target level on an annual basis, with some brief peaks of up to 50% RH allowed on a daily basis.

For the Little Belt bridge, the total electrical consumption of the entire system is around 20,000 kWh per year [14].

The lessons learned on bridges could be applied to dams, based on an "active sorption" with a forced ventilation introducing dry air, with an overpressure. The main difference is the greater volume of air to be injected, and therefore the sizing of the machinery and the higher energy cost.... However, we do not see insurmountable obstacles to apply this technique validated on bridge cables to dams.

7. CONCLUSIONS

There is an urgent need for methods to slow or limit ASR in many existing dams, and the only practical approach that appears to have potential is reduction of the moisture content of the mass concrete. For dams with indefinitely continuing ASR, upstream face membrane seal and drainage schemes, possibly augmented by ventilation drying appear to be worth considering.

The simulation results presented herein for generalized examples of existing gravity dams and arch dams demonstrate the theoretical feasibility of effective swelling control by sealing, drainage and /or drying in certain situations within reasonable such a time frames. For smaller existing structures, installing an upstream membrane seal with drainage may be sufficient to significantly reduce the ASR rate within 20 years or so. For larger existing structures the addition of an air ventilation system significantly accelerates the drying process and has an appreciable effect after 20 years and may significantly reduce the ASR rate within 50 years.

These analyses illustrate important phases in the evolution of moisture and ASR throughout the life of concrete dams:

1. After hydration Sr will likely be sufficient to initiate ASR throughout the dam body in reactive situations.
2. After a number of years of operation with reservoir water in direct contact with the upstream face, moisture will permeate progressively into the dam body from the upstream face causing an increase in Sr and the associated ASR rate.
3. Application of a membrane seal with a drainage system after a number of years of operation will stop the direct permeation of reservoir water into the concrete face. Then, depending on the drainage system and the RH in the space between the seal and the concrete, some moisture loss from the concrete face will take place thereby reducing the Sr and its associated ASR rate.

4. The addition of a ventilation system passing dry air though the space between the membrane seal and the concrete face would enhance moisture loss from the concrete and significantly accelerate the rate of reduction of Sr and associated ASR rate.
5. It is noted that any reduction in Sr will cause a reduction in the rate of ASR. Ideally, it would be best to reduce the Sr to below the “threshold level” and stop the ASR, but significant benefits can be achieved by partial drying and reducing the ASR rate.
6. It is also noted, in passing, that the amount of moisture to be removed increases with time after initial filling of the reservoir. Consequently, the sooner a drainage and drying system is installed, the better!

Clearly, these simulation results are very dependent on the ability of the upstream face boundary condition assumptions to properly represent the effects of a membrane seal and drainage system and need further assessment and correlation with field cases before firm conclusions are drawn regarding the relative benefits of drainage behind an upstream face seal and drainage with or without dry air ventilation.

These simulations addressed changes in degree of saturation Sr which will affect reaction rates and expansion effects. Temperature dependency and gradient effects were not considered. In interpreting the potential effects of the indicated gradients in Sr on expansion rates and deformations of the dam, it will be important to note that temperature gradient effects will likely also be present and modify the resulting overall behaviour. To correlate theoretical deformation predictions with actual behaviour, both Sr and temperature effects will need to be considered.

These conclusions are based on theoretical models and will need to be validated by laboratory and field tests and might be different for specific cases. Each case should be investigated separately.

Systems are available for sealing and draining the upstream face of dams, and they could be adapted to add air ventilation drying.

Using cement with a sufficiently reduced content of alkalis and suitable SCM is the best way to mitigate ASR for new dams, but the sealing and drying concepts discussed herein could possibly be used as a backup if there are uncertainties related to the reactivity of the concrete composition and if the dam has highly critical importance.

The conclusions in this paper have been related to ASR. However, similar benefits are to be expected with DEF affected dams.

REFERENCES

[1] ICOLD, Management of expansive chemical reactions in concrete dams & hydroelectric projects, ICOLD Bulletin Preprint – 184, 2017

[2] DSC2017 Swelling in Dams and Hydraulic structures, Chambery, 2017 ISTE/Wiley

[3] ICAAR 2022, Proceedings of the 16th International Conference on Alkali-Aggregate Reaction in Concrete, Volumes I & 2, LNEC, May 2022

[4] ICAAR2024, Proceedings of the 17th International Conference on Alkali-Aggregate Reaction in Concrete, Volumes I & 2, University of Ottawa, May 2024, RILEM Bookseries Volume 49

[5] Charlwood, R. Godart, B. and Grimal, E. (2024). Are there options to stop or control ASR in existing dams? ICAAR 2024, Ottawa, Canada

[6] Gomes J., Matos, D., Batista A. Ferreira J., Structural behavior of Pracana dam 30 years after the large rehabilitation due to severe ISR-ASR damage. Proceedings of the 16th International Conference on Alkali-Aggregate Reaction in Concrete, Volume I, LNEC, May 2022, pp. 1425-1436.

[7] Acker, P., "Comportement mécanique du béton - Apports de l'approche physico-chimique", LCPC, rapport de recherche LPC n° 152, 1988 (In French).

[8] AFNOR, FD P18-464, Béton - Dispositions pour prévenir les phénomènes d'alcali-réaction, juin 2021. (In French, Provisions for preventing alkali-aggregate reaction phenomena)

[9] Grimal, E., Morenon, P., Sellier, A., Multon, S., Bourdarot, E., AAR and DEF structural effects modelling, Swelling in Dams and Hydraulic structures, 2017

[10] Isgor, B. and Charlwood, R. (2025). Computational proof of concept of controlling ASR and DEF in concrete dams through sealing and drying technologies. Submitted for publication

[11] Code_Aster, Modeling of thermohydration, the drying and the shrinking of the concrete, https://code-aster.org/doc/default/en/man_r/r7/r7.01.12.pdf

[12] ICOLD Bulletin 135, Geomembrane sealings systems for Dams, ICOLD, 2010

[13] Bloomstine, M., Sørensen O. - State-of-the-Art Main Cable Corrosion Protection by Dehumidification, 3rd New York City Bridge Conference, 2005.

[14] Bloomstine, M., Sørensen, O. - Prevention of main cable corrosion by dehumidification. Chapter of “Advances in Cable-Supported Bridges”, 1st Edition, 2006, CRC Press.

Fifth International Dam World Conference
PORTUGAL • LISBON • LNEC • APRIL 13-17, 2025
dam world 2025

A 3D POINT CLOUD MODEL OF SANTA LUZIA DAM AND ITS CONTRIBUTION FOR IMPROVING THE FINITE ELEMENT MESH

Maria Joao Henriques[1]
LNEC

Ivo Dias
LNEC

Dora Roque
LNEC

Alexandre Gomes
EDP Produção

ABSTRACT

The analysis and interpretation of the structural behavior of concrete dams is usually performed by using finite element models of the dam and its rock mass foundation. The finite element mesh of the dam must accurately represent the real geometry of the structure being traditionally created from the design drawings.

Currently, techniques from geospatial sciences (laser scanning and photogrammetry) allow the creation of very rigorous 3D models of objects, based on point clouds of surfaces. The improved knowledge of dam geometry can be useful for creating more realistic meshes of the structure, thus increasing the accuracy of the numerical modeling. The paper presents a use case of data generated from a drone photogrammetric survey of a concrete arch dam.

The Santa Luzia dam is the first arch dam built in Portugal (it was completed in 1943). The concrete of this dam is subject to a deterioration process due to expansive reactions of internal origin. A very comprehensive study of the structure was recently carried out, which included the mapping of pathologies in the faces and crest of the dam and the analysis and interpretation of the dam behavior. The mapping of pathologies was carried out using digital image processing techniques, based on orthomosaics generated from photographs obtained from ground and aerial surveys, using photogrammetric software. When generating orthomosaics, point clouds were created which were used to obtain data on the dam's geometry and to improve the finite element mesh created many years ago, based on the dam design drawings.

The paper includes a description of the aerial survey and the presentation of the most important phases for obtaining the dam geometry and for preparing the finite element mesh.

Keywords: Photogrammetry, point cloud, 3D model, drone, FEM

[1]mjoao@lnec.pt, Portugal

1. INTRODUCTION

Finite element models play a crucial role in the study and analysis of dams, serving as essential tools for interpreting its behaviour and for the safety assessment of these large critical infrastructures.

The correct definition of the dam's geometry through an appropriate finite element mesh ensures that the model accurately represents the actual structure of the dam, which is fundamental for achieving accurate results.

The finite element meshes are usually created from the information of the design drawings. Nevertheless, in some cases, particularly with dams built many years ago, only the design drawings are available and the final drawings after construction are not accessible, therefore any changes made to the dam geometry during construction are not documented. This issue can introduce miss representations in the finite element mesh if only the design drawings were considered.

In this context point cloud models can be useful either to check the dam design geometry or to improve the finite element mesh if differences are found.

Actually, the structural analysis of Santa Luzia dam is being updated, as it is affected by swelling reactions. Since the faces and crest of the dam show significant cracking the updated model considers the tensile nonlinear behaviour of the concrete, by using a damage viscoelastic model. This type of non-linear finite element model requires the use of more refined meshes and therefore the finite element mesh used in previous studies [1,2] had also to be updated.

The geometries of the Santa Luzia dam, as provided by the project drawings, were initially verified using the point cloud model. Then, the finite element mesh was developed, considering the improved knowledge of the dam geometries, provided by the point cloud model.

2. SANTA LUZIA DAM

Santa Luzia dam is in a natural gorge excavated by the Unhais stream in a quartzite outcrop, in a mountain region of the centre of Portugal, near Coimbra. It was designed by André Coyne and built between 1939 and 1943 [3].

The dam (Fig. 1) consists of two arch structures. The main structure is a thin cylindrical arch, 75 m high, with thickness ranging from 13.0 m at the bottom and 2.5 m, while the secondary structure is gravity arch, about 27 m high, that closes the upper section of the left bank. Between these two arches exists a concrete structure (V shaped buttress) functioning as an abutment. The crest of the dam is 115 m long.

Fig. 1 – Santa Luzia dam

In 1966, after some geodetic observation campaigns and site inspections, it was confirmed the existence of progressive upward displacements at the dam crest [4]. Cracking survey and site inspection, performed in 1991 [5], showed the existence of subhorizontal cracks at mid-height of the main arch, parallel to the insertion surface, close to the foundation. In 1995, three vertical cores were drilled from the dam and used to carry out different laboratories tests which identified subproducts of the alkali silica reactions, as well ettringite resulting from internal sulphate reactions [6]. In the 2000s a finite element analysis of the structural effects of the swelling reactions was performed, by using a visco-elastic model for the concrete [1,2]. The finite element mesh used in those simulations was elaborated from the dam project drawings and had a total of 155 20-node hexahedral elements and 1114 nodal points (Fig. 2).

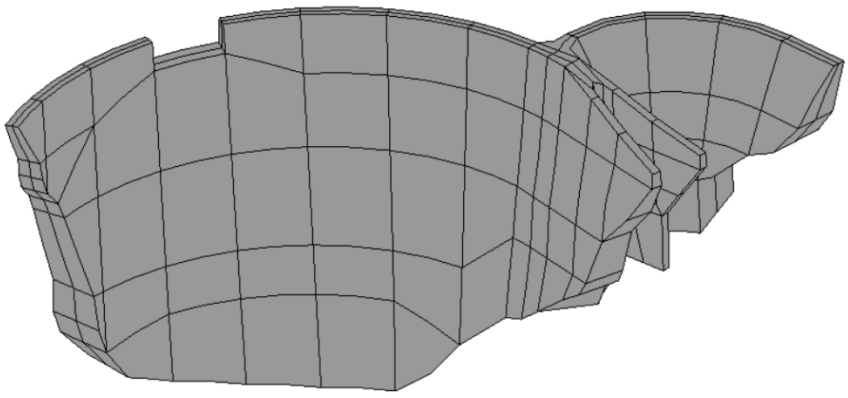

Fig. 2 – 3D finite element mesh used in the studies developed in de 2000s [1,2]

More recently, a mapping of pathologies (Fig. 3) was carried out in 2022/2023, through the identification and mapping of anomalies (cracks, calcium carbonate deposits, etc.) on orthomosaics of the faces and crest [7] using digital image processing techniques.

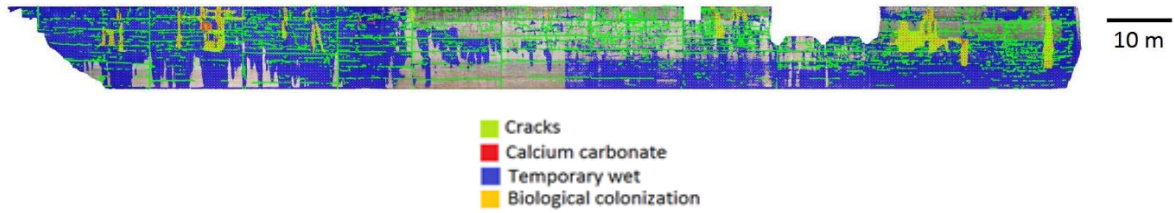

Fig. 3 – Mapping of the most important occurrences on the orthomosaic of the upstream side

The Orthomosaics were generated using photogrammetric software (Metashape) with photographs taken in the fall of 2022.

Photographs of the crest and upstream face were taken with a camera mounted on a UAV (drone) DJI M300 RTK (Fig. 4). The UAV had to take off from the upstream side, about 350 m away from the dam, because there are no safe places near the dam. Independent flights were carried out to photograph the two areas. On the upstream face (Fig. 5), only the upper 11 meters were visible due to the reservoir level. The flights over the crest (Fig. 6) were carried out with the camera oriented in the direction of the nadir, while those towards the upstream face were performed with the camera tilted 45º. The flights were programmed so that the photos had an overlap of 80% (both longitudinal and transversal). Four flights were carried out and the total flight time was 40 minutes. A total of 567 photographs were taken.

The photographs of the downstream face were taken from the ground (a terrestrial camera with zoom lenses) as the narrow valley on the downstream side does not allow flights to be carried out safely.

To connect the different surveys, points on the three surfaces were coordinated using topographic methods based on a local reference frame (the one used in the geodetic monitoring of the dam). These points must be visible in the photographs and can be artificial, like arrows painted specifically on the crest for the photo survey, or natural, like the targets placed on the downstream face of the main arch or other features with contrast (Fig. 7). Usually, these points are called ground control points (GCP).

Fig. 4 – Drone taking off

Fig. 5– Aerial photo of the upstream face of the gravity arch

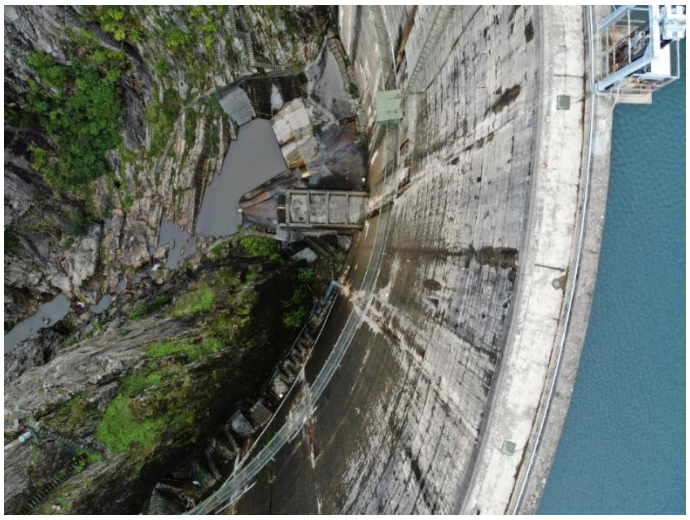

Fig. 6 – Aerial photo of the crest

Fig. 7 – Target (the rectangular) used as GCP (on the left); Corner of an access cover used as GCP (on the right)

3. POINT CLOUD OF SANTA LUZIA DAM

The processing of the photos to generate an orthomosaic, includes, always, the creation of a point cloud. In the case of the aerial surveys made at Santa Luzia, as the photographs are taken at different points (see Fig. 8), the clouds of the crest and of the upstream face model these two surfaces well. In Figure 8 each dot indicates the location of the drone when a photograph was taken. In the case of the terrestrial photo surveys, given the difficulty of accessing the slopes (Fig. 9), the requirements for a photogrammetric survey, such as capturing a block of photographs with parallel optical axes from different locations, could not be met. For this reason, the clouds of the downstream face don't model this face well enough.

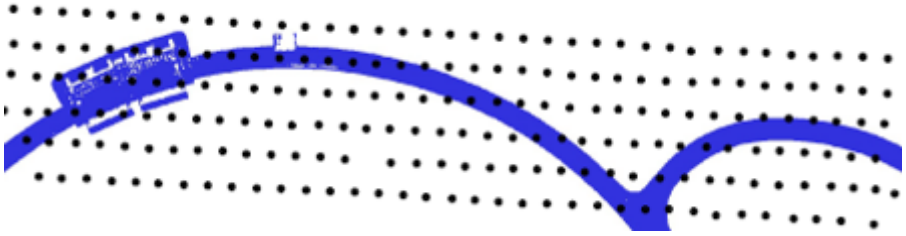

Fig. 8 – Camera locations during the photo survey of the crest (partial image of one of the flights over the crest)

Fig. 9 Santa Luzia dam; right bank (on the left) and left bank (on the right)

When analysing the two clouds obtained from the aerial photographs it was found that not only the crest and upstream face were, as expected, well modelled, but also the downstream face (Fig. 10) was sufficiently covered by points. The exception was an area at mid-high, because it is under a walkway.

Fig. 11 shows the cloud of the downstream face, with some horizontal sections coloured with plain colours by the authors. This type of sectioning was carried out in all arches. The X,Y coordinates of the points from the referred sections were included in the two scatter plots presented in Fig. 12. The points were coloured using the colours of the cloud (white points were not included in the plots). In the graph of the downstream face, the black line represents a joint (the joint I).

It was thus verified that the distribution of points corresponded globally to that presented in the dam project. The information that can be extracted from the point cloud is more accurate because it corresponds to the real structure, not to the one of the drawings of the project phase. For this reason, it was decided to use the coordinates of the points in the cloud to determine the geometries of the dam, this is, to determine the coefficients of the equations that described the distribution of points on the dam walls at different elevations.

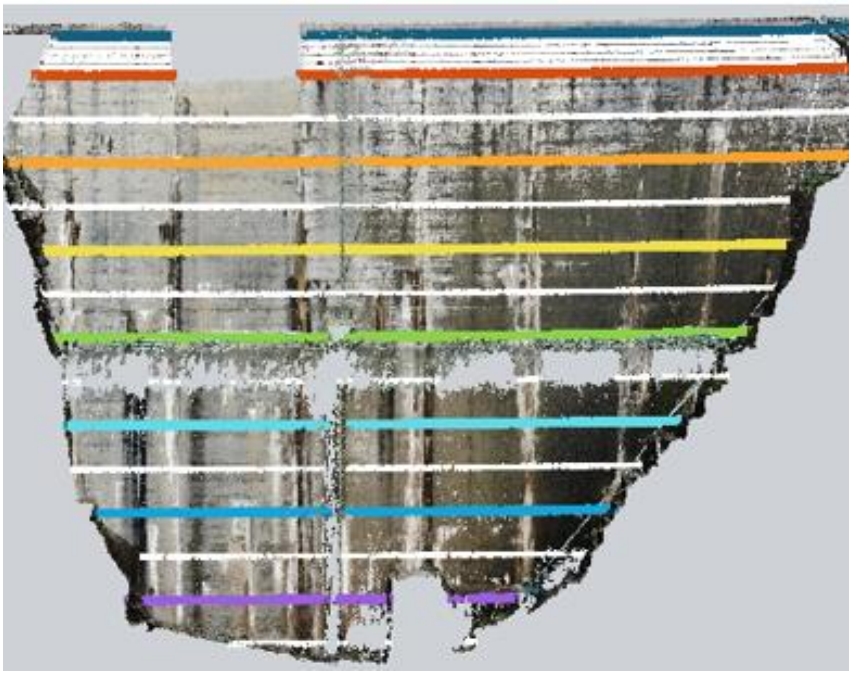

Fig. 10 – Point cloud of the downstream face of the main body with some points artificially coloured

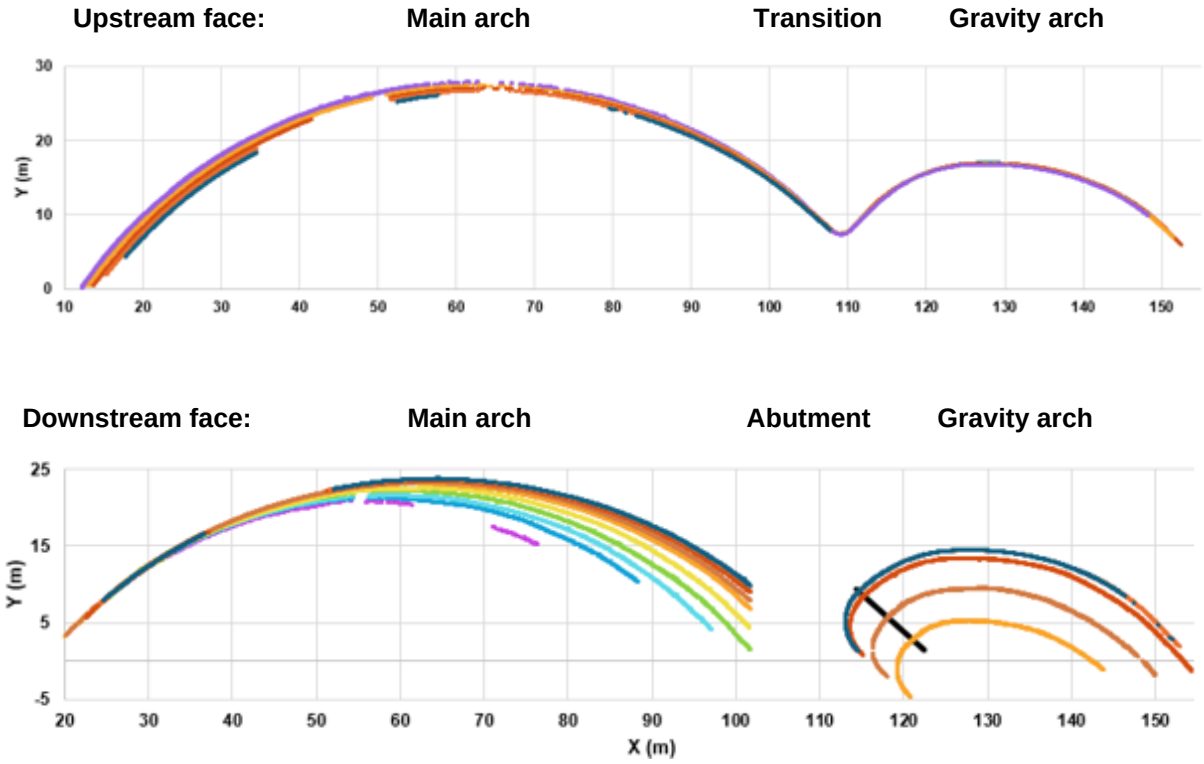

Fig. 11 – Points extracted from horizontal sections of the arches displayed in scatter plots, upstream face and downstream face respectively

4. THE GEOMETRIES OF SANTA LUZIA DAM

Analysing each set of points presented in Figure 10, it was concluded that the vertical surfaces of Santa Luzia dam were described by three types of lines: circle arcs, cubic lines arcs and vertical plane sections. The vertical plane sections are only on the abutment which was not included in the analysis that will be presented.

The two types of equation referred are presented below, along with the information of the areas where they can be found:

$$\textbf{Circles: } (x-x_0)^2 + (y-y_0)^2 = r^2 \quad (1)$$

Areas: Main arch: upstream and downstream faces
Gravity arch: a section of the downstream face between the abutment and joint I
Transition between the arches of the upstream face

$$\textbf{Cubic lines: } y = ax^3 + bx^2 + cx + d \quad (2)$$

Areas: Gravity arch: upstream face and a section of the downstream face between joint I and the abutment

With the coordinates of the points of each coloured section, and using software developed by the authors that applies the least squares method [8], the values for the unknowns of equations (1) and (2) were obtained. The unknowns are x0, y0, r, a, b, c, and d.

Table 1 presents the values obtained for some sections of the gravity arch. The elevations (z) of these sections are also included in the table. In Table 2 are presented the values obtained for the sections considered in the main arch downstream face.

Table 1 – Examples of the unknown values obtained for the gravity arch

Upstream face				Downstream face between joint I and abutment				
z (m)	x_0 (m)	y_0 (m)	r (m)	z (m)	a	b	c	d (m)
147.40	129.78	-9.26	26.40	147.40	0.00014	-0.076	12.795	-661.59
144.60	129.90	-9.85	26.96	145.60	-0.00001	-0.018	5.271	-340.50
141.80	129.97	-10.24	27.29	143.80	-0.00004	-0.007	3.809	-274.47
139.00	129.87	-10.25	27.23	137.90	0.00006	-0.051	10.019	-569.93
136.20	129.69	-9.35	26.30	127.90	0.00534	-2.111	278.065	-12198.80

Table 2 – Examples of the unknown values obtained for the main arch downstream face

z (m)	x_0 (m)	y_0 (m)	r (m)	z (m)	x_0 (m)	y_0 (m)	r (m)
147,40	64,30	-33,69	57,42	122,90	61,57	-31,03	53,59
146,50	64,19	-33,61	57,29	117,90	60,90	-30,34	52,75
145,60	64,12	-33,61	57,25	112,90	60,21	-29,53	51,71
144,70	64,03	-33,54	57,12	107,90	59,80	-29,04	50,92
143,80	63,92	-33,30	56,86	102,90	59,10	-28,32	49,96
142,90	63,85	-33,17	56,71	97,90	58,54	-27,72	49,18
137,90	63,20	-32,77	56,08	92,90	57,90	-26,70	47,97
132,90	62,65	-32,34	55,42	87,90	57,32	-26,24	47,22
127,90	61,98	-31,54	54,39	82,90	55,65	-20,76	41,44

The values obtained for the unknowns have a linear variation along the elevation, consistent with the project definition. As an example, for the downstream face, the values of x0, y0 and r are presented in scatter plots (Fig. 12 and Fig. 13), as function of the elevation (z).

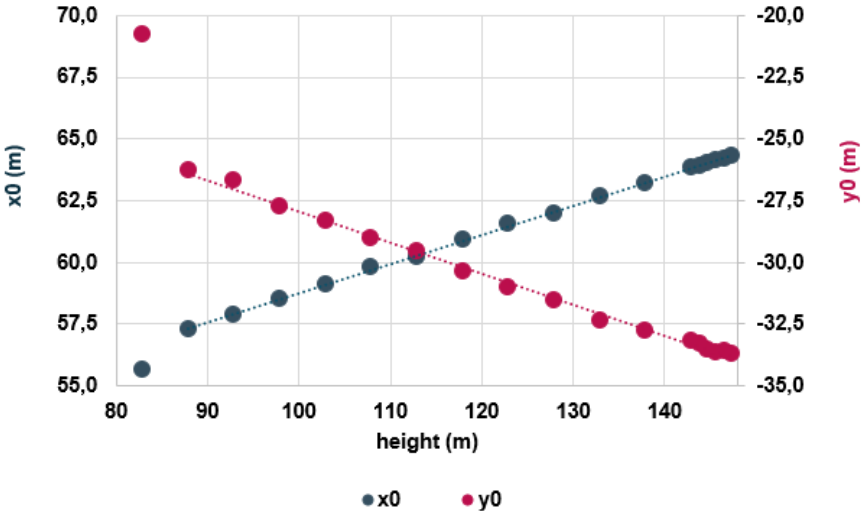

Fig. 12 – Scatter plot of x0 and y0 for the main arch downstream face

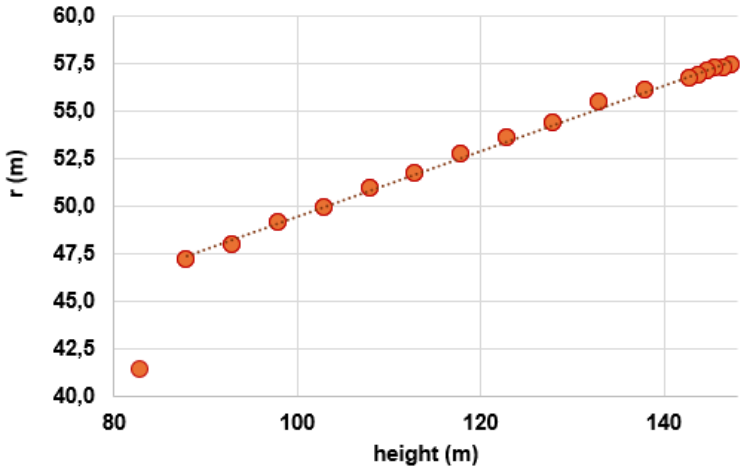

Fig. 13 – Scatter plot of r (radius) for the main arch downstream face

Except for the lower points (corresponding to the elevation 82.9 m) the others have near linear distributions. The straight segments are also included in the graphics, represented by dot lines. The equations of these lines were also determined and are included in Table 3. The abnormal values related to the lower elevation (82.9 m) may result from the fact that the cloud is quite sparse in this zone, with some areas without points.

Table 3 – Equation of the lines that model the distribution of x0, y0 and r as function of the elevation (z) for the main arch downstream face

$x_0 = 0.1174\ z + 47.03$	(3)
$y_0 = -0.1257\ z + 15.34$	
$r = 0.1717\ z + 32.30$	

At this point only one element is missing for a correct use of the equations presented in (1) and (2). The equations referred are of circles and cubic lines. The surfaces analysed are described by arches (of circles and cubic lines). So, it is necessary to determine the limits of the arches (their beginning and endings, that is, their borders) in the transition between surfaces with different characteristics. The analysis here presented doesn't include the borders at the abutment sides.

To better demonstrate this idea of the borders between surfaces, it was chosen the transition between the main arch and the gravity arch on the upstream side. The distribution of the points in a scatter graph was presented before, in Fig. 11, and is included again in Fig. 14. In this figure the area of interest is marked with a rectangle outlined in red, and the corresponding enlargement is included in the lower area of the same Figure. The three black arrows indicate the direction of the normals to the surface at three points. One of the points is in the main arch; the second in the transition arch; the third in the gravity arch.

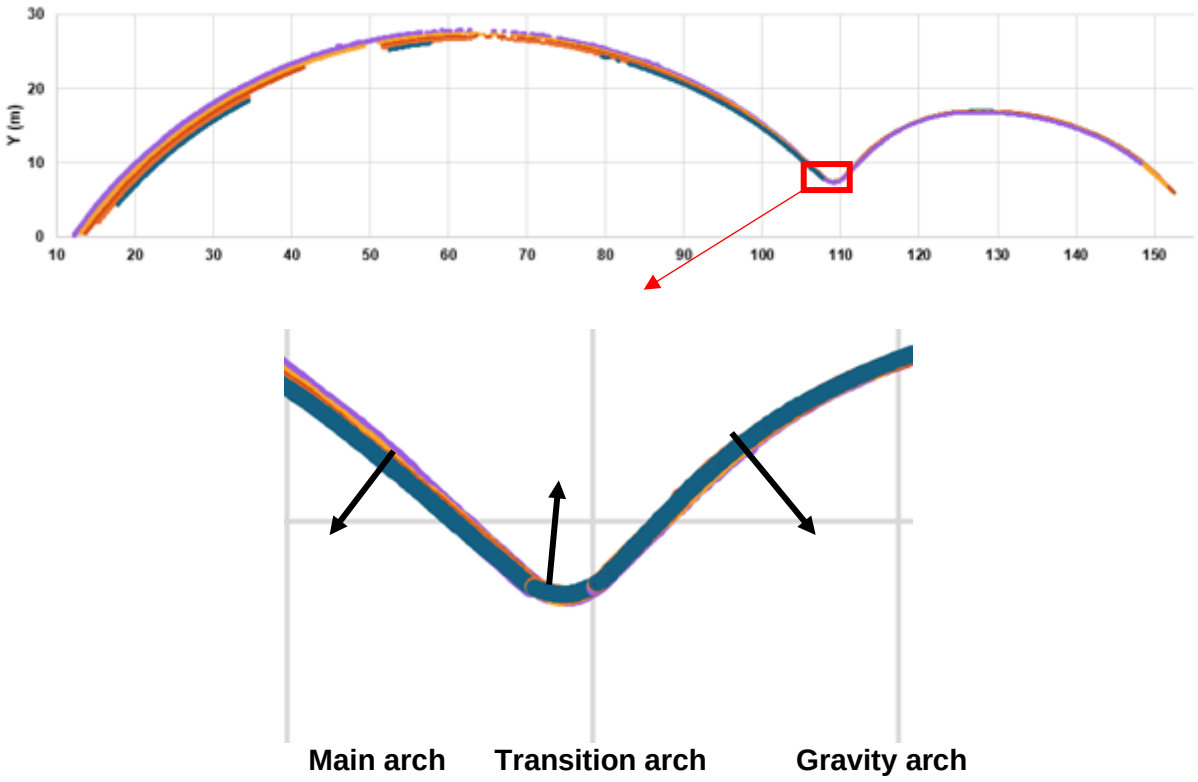

Fig. 14 – A detail of sections of the clouds of the upstream face where the black arrows represent the normals to the surfaces in three points

The borders of the transition arc are, in relation to the curvature, inflection zones. The point cloud can contribute to determine their locations, using the data of the unit vector normal to the surface in each point. This data can be included in the point cloud, as one can see in Fig. 15, that presents the information associated with two points of the transition arch. Each point

of the cloud contains the following information: X, Y, Z coordinates in meters (with three decimal places), the colour of the point (integer value for each of the channels Red, Green, Blue) and the three components of the unit normal vector.

```
109.021 7.469 146.497 63 55 52 -0.025523 0.999486 -0.019398
109.022 7.468 146.529 72 64 60 -0.058565 0.997738 -0.033009
```

Fig. 15 – Data relative to two points of the cloud

Fig. 16 presents the point cloud of the transition arch and surrounding areas, without the crest and guards, seen slightly from above so one can notice the curvature of this arch.

Gravity arch **Transition arch** **Main arch**

Fig. 16– Point cloud of the transition arch and surrounding areas

Fig. 17 presents the point cloud of the transition arch and surrounding areas seen from upstream. The colour of each point is artificial and related to the components of the unit normal vector. The pallet used emphasises the transition arch (in red). This one is limited by two thin yellow areas, which are the borders between this arch and the main and the gravity arches. In the figure, one can notice in the main arch, a narrow area in red, which corresponds to an irregularity of the surface.

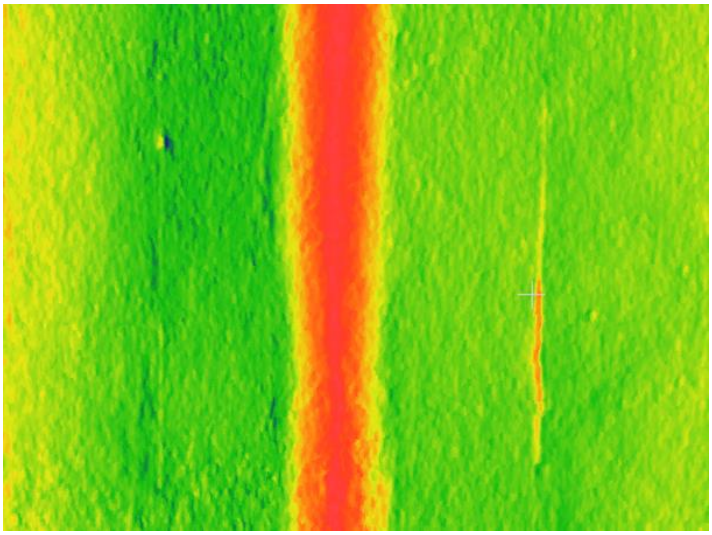

Fig. 17 – Point cloud artificially coloured using data of the unit normal vector

The unit normal vector was used to detect the borders listed in Table 3. This table also includes the equations of the vertical border planes.

Table 3 – Vertical planes equations of the frontiers

Wall	Border between…	Vertical plane equation
Upstream	Main arch – Transition arch	X = 108,06 m
	Transition arch – Gravity arch	X = 110,08 m
Downstream	Main arch – Abutment	X = 101,07 m
	Abutment – Gravity arch	Y = -0,95 X + 110,43 m
	Joint I	Y = -0,97 X + 20,16 m

5. FINITE ELEMENT MESH

To elaborate the new finite element mesh, first a 3D CAD model of the geometry was created (right side of Fig. 18) from the point cloud model (left side of Fig. 18) and from the project drawings.

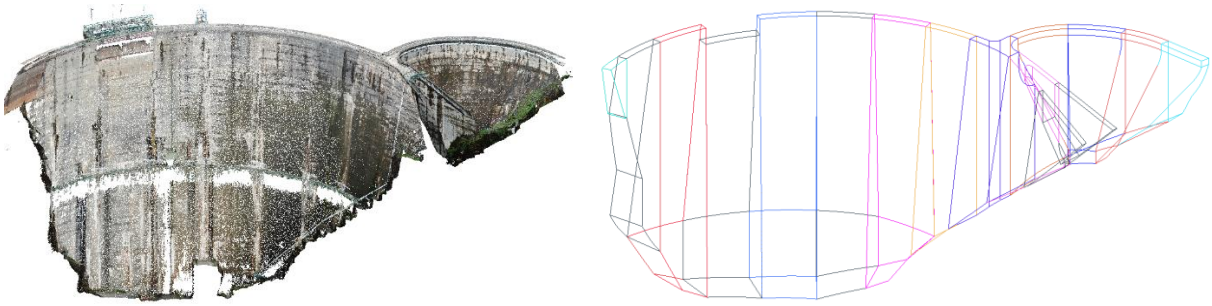

Fig. 18 – Point cloud model (on the left) and 3D CAD geometry model (on the right)

Fig. 19 shows a superposition of both models. It can be observed that the CAD model approaches well the point cloud model. As it was mentioned before it was found that the equations determined in section 4 from the cloud point model match quite well the project face equations.

The main differences found between the cloud model and the project drawings lie in the location of the construction joints. The original dam design specified construction joints with a thickness of 1.1 meters, but this plan was modified during the dam's construction, and the joints were built without thickness. As a result, the final position of the joints remained unknown due to the absence of final drawings of the completed dam. The cloud model helped to overcome this issue allowing to localize accurately the joint positions in the dam.

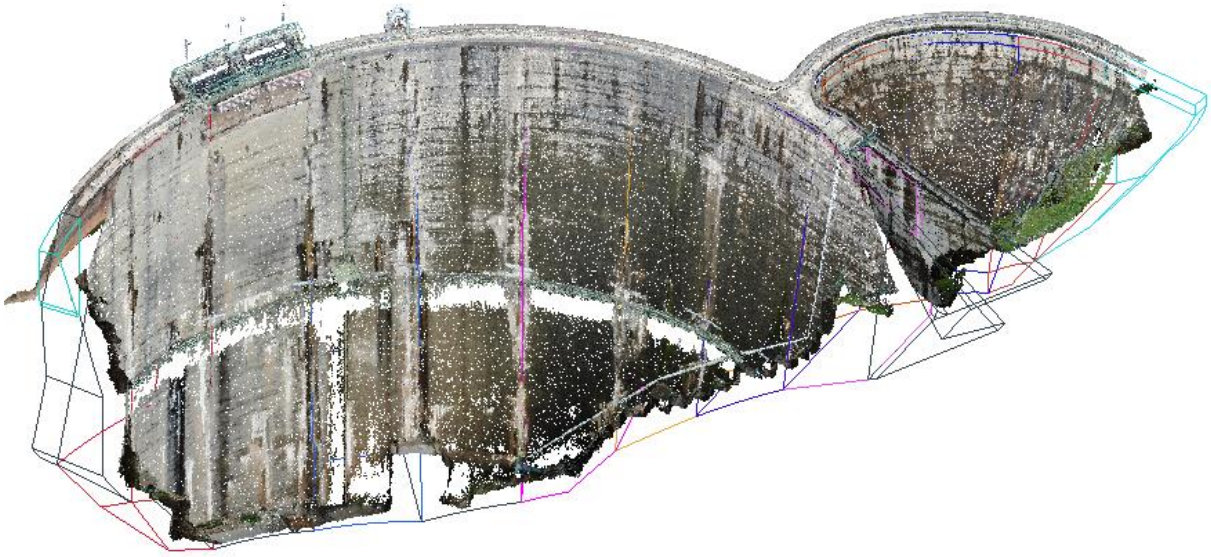

Fig. 19 – Superposition of the point cloud model with the 3D CAD geometry model

Due to the complexity of the geometries, particularly in the zones where the main arch connects to the gravity arch and to the abutment, a macro dam mesh of hexahedral elements was manually drawn using CAD (Fig. 19 on the left). Afterwards each macro element was automatically subdivided in 8 finite elements to obtain a refined mesh of the dam, consisting of 2368 20-node hexahedral finite elements and 10152 nodal points (Fig. 20 on the right).

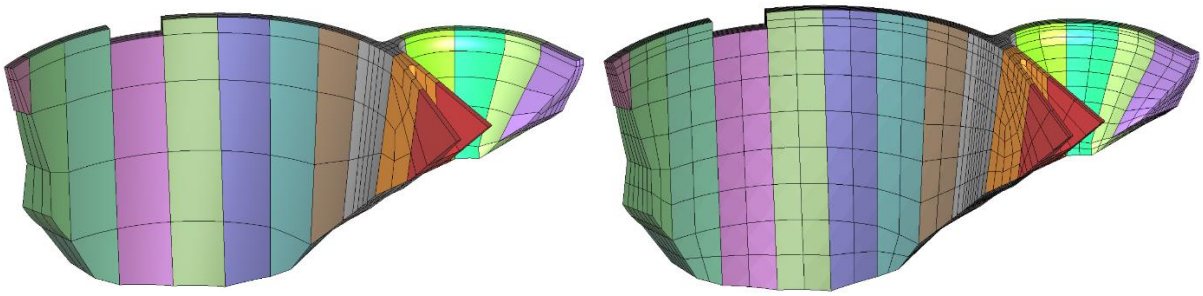

Fig. 20 – Coarse (on the left) and fine (on the right) finite element meshes

Finally, the mass rock foundation was generated from the dam-foundation interface.

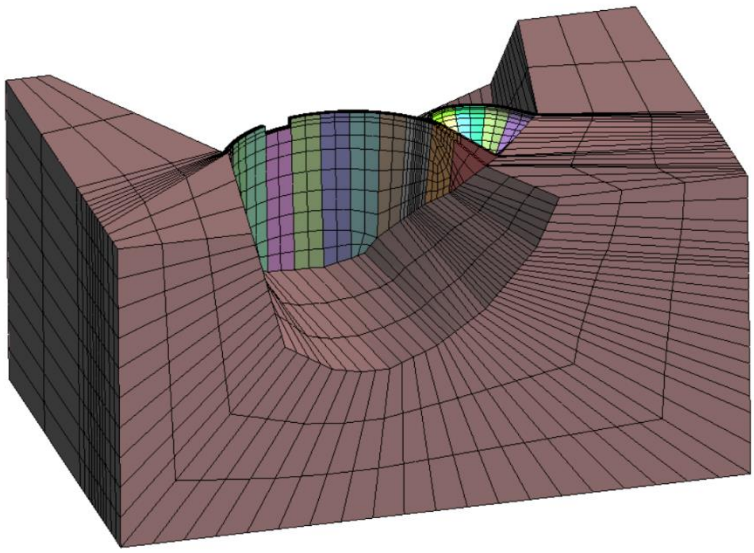

Fig. 21 – Finite element mesh of the dam and rock mass foundation

6. CONCLUSIONS

A point cloud is a set of data that includes 3D coordinates of points of a surface. The cloud can also include, for each point, its colour and, not so usually, the three components of the unit normal vector. The analysis of spatial distribution of the points and other information included in the point cloud can lead to clues about the real shape of the surface modelled by the point cloud and, in the case of regular surfaces, it can be used to determine the geometry(ies) of the surfaces.

This paper presents the methods used to derive the geometries of the three main structures of Santa Luzia dam: two arches and an abutment. The geometry of the arches is modelled by simple equations of arcs of circle or of cubic lines while the faces of the abutment are modelled by vertical planes. The surface geometries were determined using the coordinates of the cloud points while the boundaries between different surfaces were determined based on the information from the unit normal vector at each cloud point.

Comparing the geometries of the different elements of Santa Luzia dam with the ones presented in the project, it was found that the differences are generally small. The main differences between the original dam design and the constructed dam lied on the position of the construction joints. The improved knowledge about the joint location was represented in the new mesh.

In the example included in this paper, the point cloud was generated from a photogrammetric survey, done with an UAV. The survey took 40 minutes. Another option could have been to use a laser scanner to make the survey. Laser scanner is more accurate, and the post processing of the data is faster than the post processing of a photogrammetric survey. In the case of Santa Luzia dam, the survey with a laser scanner would certainly take many hours due to the difficulty in accessing the banks.

REFERENCES

[1] Piteira Gomes, J. (2007). Structural behaviour modelling of concrete dams subject to swelling reactions (in Portuguese), PhD thesis, Faculdade de Ciências e Tecnologia, Universidade Nova de Lisboa, Lisboa, Portugal.

[2] Piteira Gomes. J.; Batista. A.L. and Oliveira S. (2004). Analysis of concrete dams under swelling process. Proceedings of 12th International Conference on AAR in Concrete. Lisboa. Portugal.

[3] Piteira Gomes. J.; Cunha. J.; Batista. A.L. and Almeida, F. (2022). Monitoring and assessment of the structural effects due to ASR in Santa Luzia dam (Portugal). Proceedings of 16th International Conference on AAR in Concrete. Lisboa. Portugal.

[4] LNEC (1966). Geodesic surveys of Santa Luzia dam in February 1996 (in Portuguese). Report, LNEC, Lisboa.

[5] LNEC (1991). Visual inspection of Santa Luzia dam. Cracks and leakage (in Portuguese). Report, LNEC, Lisboa.

[6] LNEC (1996). Santa Luzia dam. Observation and analysis of concrete samples (in Portuguese). Report, LNEC, Lisboa.

[7] Roque. D.; Henriques, M.J. (2025). Pathology mapping in concrete dams through digital photogrammetry and image processing. Proceedings of 5th International Dam World Conference. Lisboa. Portugal. (submitted)

[8] Strang, G. and Borre, K. (1997). Linear algebra, geodesy, and GPS. Wellesley-Cambridge Press.

Fifth International Dam World Conference
PORTUGAL • LISBON • LNEC • APRIL 13-17, 2025
dam world 2025

APPLICATIONS OF GNSS TECHNOLOGY IN DAM MONITORING: A SYSTEMATIC LITERATURE REVIEW

Hanna B. de A. F. Moreira[1]
Federal University of Pernambuco (UFPE)

Roberto Q. Coutinho[2*]
UFPE

Jailson S. Alves[3]
UFPE

Wilson R. Aragão Júnior[4]
UFPE

ABSTRACT

Dams are crucial for socioeconomic development due to their ability to store water, irrigate large agricultural areas, control floods, and produce hydroelectric power. However, the potential for dam failures poses significant risks to people, infrastructure, and the environment. Therefore, monitoring the structural integrity of dams to detect anomalies that may indicate potential failures is essential. This monitoring enables early warnings and the adoption of appropriate predictive actions. Since the 20th century, displacement monitoring has relied on geodetic control networks using classical techniques such as precision triangulation and geometric levelling. With technological advancements, the Global Navigation Satellite System (GNSS) has become essential for monitoring surface displacements in large structures. GNSS, a service based on satellite signals, enables high-precision positioning and navigation, operating continuously and autonomously regardless of environmental conditions. This study aims to analyze the fundamentals and applications of GNSS technology in dam monitoring. The research was conducted through the review of recent scientific publications from 2018 to 2022, using a hybrid model of bibliometric and systematic analysis. The bibliometric analysis involved the quantitative and qualitative evaluation of publications on applying GNSS for dam monitoring, obtained from the Scopus database. This phase identified the involved institutions, participating countries, and the most relevant journals, among other factors. The systematic analysis discussed these applications, highlighting that GNSS positioning allows for determining surface displacements in three directions remotely, in real time, and with high precision. This phase provides parameters for the confirmation and improvement of mathematical displacement prediction models. Furthermore, this technology can be integrated with other instruments (rain gauges, seismographs, inclinometers, robotic total stations, InSAR – Interferometric Synthetic Aperture Radar, etc.), enhancing the understanding of surface movement mechanisms and potentially composing risk control and alert systems.

Keywords: GNSS, monitoring, geotechnics, dam, risk control systems.

[1]hanna.bfalcao@ufpe.br, Brazil
[2*]roberto.coutinho@ufpe.br, Brazil
[3]jailson.alves@ufpe.br, Brazil
[4]wilson.ramos@ufpe.br, Brazil

1 INTRODUCTION

Data analyses regarding the movement of slopes, embankments, subsidence areas, and dams demand rigorous monitoring of displacements, both vertical and horizontal. Dam structures are considered sensitive elements, as failures can cause significant damage to the environment, economy, and society [1]. Therefore, monitoring dam movements plays an essential role in ensuring public safety.

In the early 20th century, geotechnical displacement was conducted using classical techniques, such as precision triangulation and geometric leveling. These methods have been complemented or even replaced by advanced technologies like Global Navigation Satellite System (GNSS), particularly for monitoring surface displacements in large structures [2, 3].

GNSS can be described as a high-precision positioning and navigation service based on satellite signals. Over the years, this technique has been enhanced to become fully operational with multiple satellite constellations, capable of performing measurements throughout the day, regardless of environmental conditions, delivering high-precision information autonomously and continuously.

The ability to record high-precision data with high temporal resolution, combined with real-time data provision, allows GNSS receivers to be integral components of monitoring systems. These systems can detect displacements on the order of millimeters per year, making them particularly suitable for applications in control and early warning systems aimed at disaster prevention [4].

In this context, the objective of this article is to evaluate the potential and limitations of GNSS for displacement monitoring of dams through recent technical-scientific literature. Scientific publications (2018 to 2022) that address the application of GNSS for dam monitoring were utilized.

This study, based on the PRISMA method and the Scopus database, conducted a bibliometric and systematic analysis of GNSS use in displacement monitoring. The bibliometric analysis quantitatively and qualitatively evaluated the publications, highlighting scientific production, institutions, countries, and journals involved. The systematic analysis explored case studies, discussing challenges, positioning methods, and contributions, with an emphasis on applications in dams.

2 METHODOLOGY

Bibliographic research aims to identify the available knowledge on a specific topic and assist in understanding the problem, developing insights, and supporting the construction of

hypotheses through the critical analysis of published documents [5, 6]. According to [7], this is a fundamental step in scientific work, as it provides the theoretical foundation for future research.

Thus, the importance of systematic bibliographic reviews becomes evident, as they aim to refine and update knowledge through the scientific investigation of published works. In this context, a hybrid research and analysis model were applied, combining quantitative and qualitative techniques of literature review and bibliometric analysis, following the guidelines of [8], to investigate GNSS applications in the monitoring of dam structures.

The work was divided into three phases (Fig. 1): (1) Database search; (2) Bibliometric analysis; and (3) Systematic analysis. Details of the methodological procedures used in each phase of this study are presented below.

2.1 Phase 1: Database search

This study utilized the Scopus database, recognized as a platform with broad scientific coverage, accessed through the Coordenação de Aperfeiçoamento de Pessoal de Nível Superior (CAPES) portal, to identify studies published on the application of GNSS in dam monitoring.

To define the scientific articles relevant to the research context, the methodology known as Preferred Reporting Items for Systematic Reviews and Meta-Analyses (PRISMA) was applied, which is divided into four stages [9] (Fig. 2): (1) Identification; (2) Selection; (3) Eligibility; and (4) Inclusion.

According to [10], the use of the PRISMA method helps authors enhance systematic reviews and meta-analyses. As noted by [11], the PRISMA methodology is widely utilized for analyzing studies published across various scientific disciplines.

2.1.1 Identification stage

The first stage, Identification, involves searching for relevant articles related to the use of GNSS positioning applied to dam monitoring. This search is performed by applying keywords in the Scopus database, one of the largest repositories of peer-reviewed scientific publications, providing a comprehensive overview of global technical and scientific production.

A set of English keywords was applied in Scopus, combined using the boolean operator "AND" to restrict the search to publications addressing the topic. The search included articles published up to December 2022, using keywords that must appear in the title, abstract, or author-provided keywords of each scientific document. The keywords used were "monitoring" and "GNSS," combined with "dam." This search strategy identified 90 scientific articles.

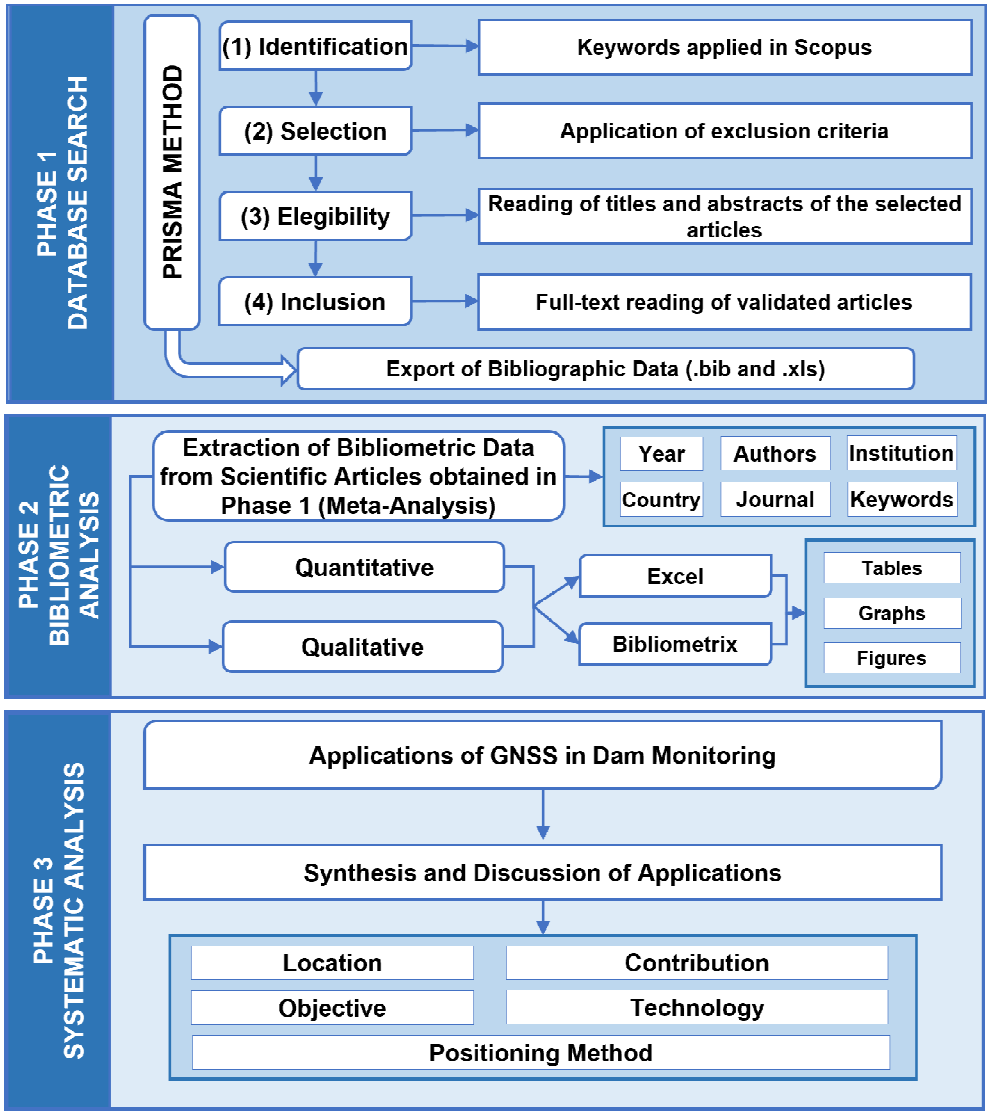

Fig. 1 – Systematic flow chart of the research

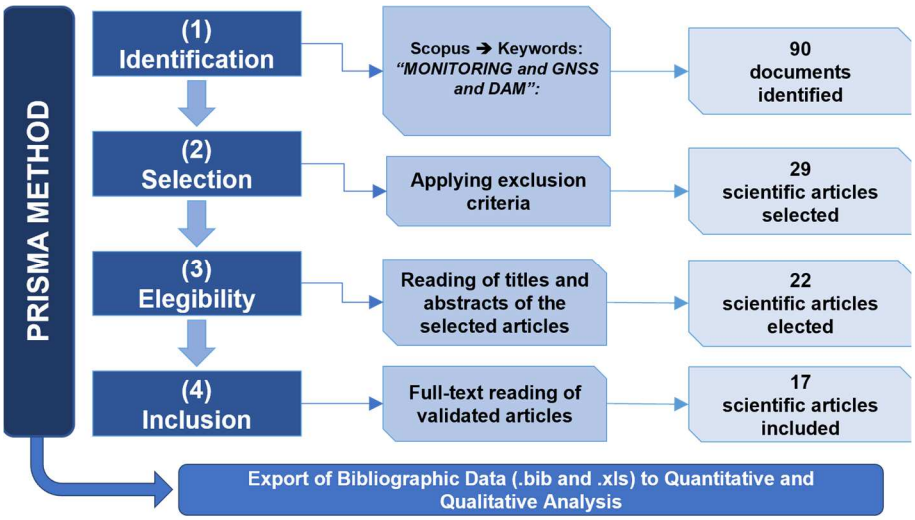

Fig. 2 – Systematic flow chart of the PRISMA methodology employed

2.1.2 Selection stage

The Selection stage involves applying exclusion criteria to the initial sample to refine it and align it more closely with the study's objectives. The following filters were applied: publication period (2018-2022), document type (scientific articles), publication stage (final version), source type (journal), and language (English). Through the application of these criteria, articles not aligned with the research objectives were excluded. As a result, 61 articles were excluded, leaving 29 articles relevant to the study.

2.1.3 Elegibility stage

The third stage, Eligibility, involves reviewing the titles, abstracts, and keywords of the selected works to ensure their alignment with the central theme of the study, thereby refining the sample for the main objective. During this stage, 12 articles were excluded because they did not adequately address the problem under analysis. Consequently, 17 articles were identified whose central theme focused on presenting GNSS positioning as a monitoring tool for dam structures. Articles that exclusively discussed mathematical and/or statistical tools for verifying GNSS data or those using the technology solely to validate results from other instruments were not considered.

2.1.4 Inclusion stage

In the fourth and final stage, Inclusion, the selected articles were read in full to identify any potential inconsistencies with the study's theme. Through this initial reading, it was confirmed that the selected articles were appropriately aligned with the research objectives. The article information was exported from Scopus in .bib and .csv formats to be processed by bibliometric software, R Studio (Bibliometrix package) and Microsoft Office Excel. From these data, the bibliometric, quantitative, and qualitative analyses were generated.

2.2 Phase 2: Bibliometric analysis

Bibliometric analysis is related to the quantitative evaluation of specific parameters within a set of articles. This analysis aims to map the structure of knowledge in a particular scientific field through a quantitative and statistical assessment of various bibliographic data [12, 13]. Thus, the bibliometric analyses of the article groups obtained in Phase 1 were conducted, utilizing the files exported from Scopus for the meta-analysis, with the assistance of R Studio (Bibliometrix package) and Microsoft Office Excel.

Descriptive statistics were used to create graphical elements (tables, graphs, and figures) to support both the quantitative and qualitative analyses. The bibliometric data of the publications examined in Phase 2 – Bibliometric Analysis – included the following items: year of publication; authors; authors' institutions; authors' country of origin; number of citations and average

citations per year; journal of publication; and words from the title, abstract, and keywords provided by both the authors and the journal.

2.3 Phase 3: Systematic analysis

The systematic analysis aims to identify the knowledge produced on a specific topic and evaluate the main research trends related to it. In this context, the systematic analysis in this study sought to understand the application of GNSS in displacement monitoring, particularly in dam structures.

For this phase the articles selected in the previous phase were used, allowing for their synthesis and discussion based on case studies. These studies highlighted, where applicable, the investigation location, research objectives, applied technologies, main contributions to the state of the art, and the positioning method employed.

3 RESULTS

The applications of GNSS in the geotechnical field are related to the monitoring of displacements resulting from local surface movements, such as landslides, subsidence (due to mining, groundwater extraction, or load on soft soils), dam construction and operation, and settlement in buildings.

GNSS positioning can also be applied in the monitoring of engineering projects and works, such as tunnel construction, bridges, highways, canals, and buried pipeline systems. Furthermore, [14] states that GNSS can be used to monitor areas during and after excavation in both open-pit and underground mines.

Regarding dams, these structures play a key role in the socioeconomic development of a region. By storing water, they ensure a reliable supply for human consumption, agricultural irrigation, flood control, and electricity generation.

Due to the large volumes of water stored in these structures, there is an increased risk of failure and damage. Therefore, monitoring is crucial to identify anomalies that may indicate potential failures, enabling early warnings for appropriate corrective actions [15].

Dam monitoring takes place at various parts of the structure, such as embankments, abutments, foundations, the soil-structure interface, auxiliary works (such as cofferdams, spillways, etc.), or along the reservoir area. To achieve this, different instruments can be used to measure the wide range of variables involved, including deformation and displacement, temperature, infiltration rate, and piezometric level [15].

For monitoring dam movements, it is common to use control points established at areas of interest, such as the crest, downstream banks, and lateral junctions, to evaluate the overall behavior of the entire structure [16].

In this context, GNSS is integrated into monitoring systems, often used in combination with geotechnical, hydraulic, and structural instrumentation. This enables real-time displacement monitoring with high precision, in a remote and autonomous manner [17].

3.1 Bibliometric results and analysis

The analysis conducted on the Scopus database for the period from 2018 to 2022 showed a certain stabilization in the number of articles published on the topic of dam monitoring using GNSS, as illustrated in Fig. 3. The year with the highest number of publications was 2018, with five articles, followed by a decline in 2019, which led to a steady number of publications starting from 2020.

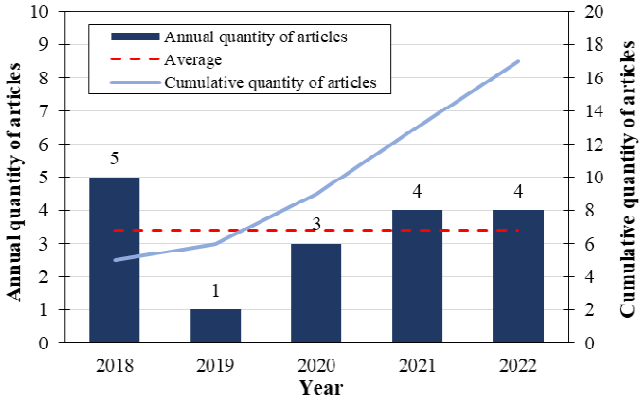

Fig. 3 – Evolution of the number of publications in the Scopus database from 2018 to 2022

It was also possible to identify that three institutions account for the majority of publications, with each responsible for two articles (Table 1). These institutions are located in China and Italy, collectively totaling six articles, which represents 35% of the total publication sample.

Table 1 – Main institutions with publications on the application of GNSS in dams

Institutions	Country	Quantity of articles	Reference
Wuhan University	China	2	[3]; [27]
Politecnico di Milano	Italy	2	[16]; [21]
Università degli Studi di Palermo	Italy	2	[22]; [17]

The information in the Scopus database indicates that, for the selected articles, the total number of citations was 211. However, only ten articles account for the majority of the citations, as shown in Fig. 4a. Among the ten articles with the highest citation averages per publication time (Fig. 4b), most also appear in the list of those with the highest citation counts (Fig. 4a), highlighting their relevance to the topic.

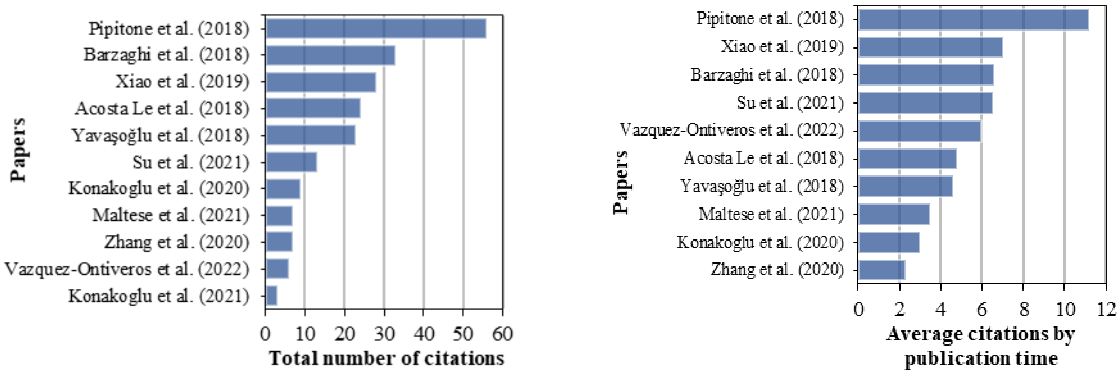

(a) (b)

Fig. 4 – Analysis of citations of articles on the application of GNSS in dams: (a) 10 highest number of citations, 10 articles; (b) 10 highest average number of citations by publication time, 10 articles

Among the analyzed articles, [17] stands out with the highest total number of citations and the highest average citations per publication time. The work of [15], despite being from the most recent year, is well-positioned in terms of the average citations per publication time, which suggests its relevance in the academic field.

Regarding the journals to which the publications are linked, four journals account for the majority of the articles, as shown in Table 2. The journal with the highest contribution was Sensors, representing 17% of the articles. These journals have strong impact factors, which enhances the influence of the published works.

Table 2 – Main journals with their respective impact metrics

	Journals	Distribution of articles		Impact metrics	
		Quantity	Contribution	CiteScore 2021	Journal Citation Reports (JCR) 2021
1	Sensors (Switzerland)	3	17.65%	6.4	3.847
2	Geomatics, Natural Hazards and Risk	2	11.76%	5.8	3.922
3	IEEE Access	2	11.76%	6.7	3.476
4	Remote Sensing	2	11.76%	7.4	5.349
	Total	9	52.93%	–	–

3.2 Cases in the literature on dam monitoring

Large-scale works, such as dams, require monitoring to control anomalous situations, establish forecasts, and create early warning systems. In this context, GNSS can be used as part of the project's instrumentation.

Below are cases from the literature on dam monitoring with GNSS: earth dams [18, 17]; and concrete dams [19, 20].

3.2.1 Application of GNSS in earth dam monitoring

There are several cases in the literature that demonstrate the application of GNSS as part of the instrumentation for earth dams, with these elements being responsible for monitoring the surface displacements of the structures. In this regard, the work of [18] details the use of GNSS positioning in monitoring horizontal displacements in an earth dam in Spain through seven surveying campaigns between 2008 and 2016, utilizing relative static positioning.

The surveys were based on control points, which were placed along four sections of the dam body, which has a height of 80 ms and a crest length of 1480 m. The measurements were taken between February and July 2008, March to July 2013, March 2014 to September 2015, and March 2013 to September 2016.

Vertical displacements were obtained using leveling techniques and analyzed in conjunction with GNSS data. Regarding accumulated vertical displacements, it was observed that the rate of the movements decreased over time, confirming the idea that the dam tends to stabilize.

The authors found that the maximum horizontal displacement occurred at the crest, around 4 cm in 2008, but this was reduced to millimeter scale in subsequent surveys. The region with the largest horizontal displacements coincided with the area exhibiting the most intense vertical displacements. These displacements were observed to trend downstream, due to the buoyant force caused by the stored water. In the lateral zones, a similar behavior to the crest was noted, but with a smaller magnitude.

Additionally, the monitoring results showed a good correlation with predictions made using finite element methods (FEM) analysis. Despite small differences between the measured and estimated values—due to simplifications and approximations made in estimating the values — the trends observed in the data were similar. This reinforces the feasibility of using GNSS as a dam monitoring tool, measuring surface displacements and providing confirmation and enhancement parameters for potential mathematical models predicting displacements.

Thus, the authors concluded that the results demonstrate the viability of using GNSS as a tool for earth dam monitoring, measuring surface displacement, and providing parameters for the confirmation and improvement of potential predictive mathematical models of displacements.

The study by [17] demonstrates the relationship between GNSS-measured displacements and the water level in the reservoir. During the study, conducted at an earth dam in Italy, it was observed that the maximum displacement measured at the dam occurred when the water level was at its minimum.

The monitoring was based on GPS and GLONASS constellation data, with optical and SAR images used to check the water surface, and consequently, the reservoir level. For the GNSS

survey, a permanent continuous base station was employed, with data acquisition from April 8, 2011, to May 13, 2013.

The results confirmed the relationship between the water level and the measured displacements, with the maximum displacement identified when the reservoir was at its minimum level. However, the water level alone was not sufficient to fully explain the displacement behavior, and the authors also highlighted the influence of the average air temperature and surface temperature.

The authors noted that the analyzed time series was relatively short, which could result in a high standard deviation or an inability to identify clear relationships between the water level and the measured displacements. Despite these limitations, the results emphasize the utility of GNSS, combined with other methods, in monitoring earth dams and analyzing their interactions with environmental factors.

3.2.2 Application of GNSS in concrete dam monitoring

Regarding concrete dams, the article published by [19] discusses the use of GNSS for displacement monitoring. The authors monitored the horizontal displacements of the Deriner arch concrete dam in Turkey through GNSS positioning campaigns using the relative static method. Seven verification points were distributed along the crest and the downstream face, with 12 reference stations installed near the structure in stable areas.

Measurements from GPS and GLONASS constellations were conducted in May and November 2016 and in May and August 2017. A statistical method was applied to identify significant displacements, confirming that the greatest measured displacements occurred in the central section of the crest and decreased toward the abutments.

This study confirmed that the GNSS technique could be efficiently used for precise monitoring of horizontal displacements in an arch dam. Furthermore, the results revealed that horizontal displacements were influenced by the reservoir water level.

For the same dam, the work by [20] delved deeper into the analysis of displacements identified during the GNSS campaigns, employing three deformation models: static, kinematic, and dynamic. The static model determines displacements independently of time and external factors. The kinematic model incorporates variables such as position, velocity, and acceleration but does not consider external forces. The dynamic model integrates geometric parameters, time-dependent factors, and external forces causing deformation.

All three deformation models produced similar results for horizontal displacements, with the largest displacement occurring at the central part of the dam crest, moving downstream.

However, the dynamic model proved more effective, revealing a strong correlation between variations in water level and horizontal displacements at the dam crest.

Vertical displacements showed greater variability, likely due to precision limitations in environments such as narrow valleys. Despite these limitations in vertical accuracy, the authors confirmed GNSS as a viable tool and a complement to other geotechnical techniques in dam monitoring.

4 CONCLUSIONS

This article aimed to evaluate GNSS technology in the displacement monitoring of dams based on a comprehensive review of recent literature. The study analyzed publications from 2018 to 2022, adopting a hybrid model combining bibliometric and systematic analyses.

The bibliometric review identified key countries, institutions, and journals contributing to research on GNSS in dams, highlighting the prominence of studies conducted in China and Italy. The systematic analysis presented case studies where GNSS was used to monitor horizontal and vertical displacements in earth and concrete dams.

From the analyzed articles, it was evident that GNSS is a standout tool for displacement monitoring. Furthermore, the integration of GNSS with other technologies and instruments, such as SAR imagery and water level gauges, enhances the understanding of observed movements, facilitating the evaluation of displacement behavior and associated factors. The autonomous and continuous operation capability of GNSS also makes it highly efficient for early warning systems.

Thus, GNSS proves to be a valuable tool for detecting and monitoring displacements in dams and other geotechnical structures.

REFERENCES

[1] Scaioni, M., Marsella, M., Crosetto, M., Tornatore, V., Wang, J. (2018). Geodetic and Remote–Sensing Sensors for Dam Deformation Monitoring. Sensors, 18(11), 3682. doi: https://doi.org/10.3390/s18113682

[2] De Lacy, M. C., Ramos, M. I, Gil, A. J., Franco, O. D., Herrera, A.M., Avilés, M., Domínguez, A., Chica, J.C. (2017). Monitoring of vertical deformations by means high–precision geodetic levelling. Test case: The Arenoso dam (South of Spain). Journal of Applied Geodesy, 11(1), 31–41. doi: https://doi.org/10.1515/jag-2016-0034

[3] Jiang, W., Chen, Y., Chen, Q., Chen, H., Pan, Y., Liu, X., Liu, T. (2022). High precision deformation monitoring with integrated GNSS and ground range observations in harsh

environment. Measurement, 204, 112179. doi: doi.org/10.1016/j.measurement.2022.112179

[4] Sharifi, S., Hendry, M.T., Macciotta, R., Evans, T. (2022). Evaluation of filtering methods for use on high–frequency measurements of landslide displacements. Natural Hazards and Earth System Sciences, 22(2), 411–430. doi: doi.org/10.5194/nhess-22-411-2022

[5] Gil, A. C. (2002). Como elaborar projetos de pesquisa. São Paulo, SP: Atlas.

[6] Boccato, V. R. C. (2006). Metodologia da pesquisa bibliográfica na área odontológica e o artigo científico como forma de comunicação. Rev. Odontol. Univ. Cidade São Paulo, São Paulo, 18(3), 265–274. doi: https://doi.org/10.1590/S0103–65132013005000078.

[7] Amaral, J. J. F. (2007). Como fazer uma pesquisa bibliográfica. Fortaleza, CE: Universidade Federal do Ceará.

[8] Page, M. J., Mckenzie, J. E., Bossuyt, P. M., Boutron, I., Hoffmann, T. C., Mulrow, C. D., Moher, D. (2021). The PRISMA 2020 statement: an updated guideline for reporting systematic reviews. BMJ, 71. doi: 10.1136/bmj.n71.

[9] Moher, D., Liberati, A., Tetzlaff, J., Altman, D. G. (2009). Preferred reporting items for systematic reviews and meta–analyses: The PRISMA statement. International Journal of Surgery, 8, 336–341. doi: https://doi.org/10.1016/j.ijsu.2010.02.007.

[10] Galvão, T. F., Pansani, T. de S. A., Harrad, D. (2015). Principais itens para relatar Revisões sistemáticas e Meta–análises: A recomendação PRISMA. Epidemiologia e Serviços de Saúde, 24(2), p. 335–342. doi: https://doi.org/10.5123/S1679–49742015000200017.

[11] Pacheco, R. L., Silva, L. D. G. M. da., Melo, S. M. M. de, Riera, R. (2018). Guidelines para publicação de estudos científicos. Parte 4: como publicar revisões sistemáticas. Diagn. Tratamento, 23(1), 19–23.

[12] Vanti, N. (2002). Da bibliometria à webometria: uma exploração conceitual dos mecanismos utilizados para medir o registro da informação e a difusão do conhecimento. Ciência da Informação, 31(2), p. 152–162, doi: https://doi.org/10.1590/S0100–19652002000200016.

[13] Lacerda, R. T. O., Ensslin, L., Ensslin, S. R. Uma análise bibliométrica da literatura sobre estratégia e avaliação de desempenho. Gestão & Produção, 19(1), p. 59–78. 2012. doi: https://doi.org/10.1590/S0104–530X2012000100005.

[14] Seeber, G. Satellite Geodesy. 2003.

[15] Vazquez-Ontiveros, J. R., Martinez-Felix, C.A., Vazquez-Becerra, G.E., Gaxiola-Camacho, J.R., Melgarejo-Morales, A., Padilla-Velazco, J. (2022). Monitoring of local deformations and reservoir water level for a gravity type dam based on GPS

observations. Advances in Space Research, 6(1), p. 319–330. doi: //doi.org/10.1016/j.asr.2021.09.018

[16] Reguzzoni, M., Rossi, L., De Gaetani, C.I., Caldera, S., Barzaghi, R. (2022). GNSS–Based Dam Monitoring: The Application of a Statistical Approach for Time Series Analysis to a Case Study. Applied Sciences, 12(19), p. 9981. doi: doi.org/10.3390/app12199981

[17] Pipitone, C., Maltese, A., Dardanelli, G., Lo Brutto, M., La Loggia, G. (2018). Monitoring Water Surface and Level of a Reservoir Using Different Remote Sensing Approaches and Comparison with Dam Displacements Evaluated via GNSS. Remote Sensing, 10(1), p 71. doi: doi.org/10.3390/rs10010071

[18] Acosta, L. E., De Lacy, M.C., Ramos, M.I., Cano, J.P., Herrera, A.M., Avilés, M., Gil, A.J. (2018). Displacements Study of an Earth Fill Dam Based on High Precision Geodetic Monitoring and Numerical Modeling. Sensors, 2018, 18(5), p 1369. doi: https://doi.org/10.3390/s18051369.

[19] Konakoglu, B., Cakir, L., Yilmaz, V. (2020). Monitoring the deformation of a concrete dam: a case study on the Deriner Dam, Artvin, Turkey. 11(1), p. 160–177. Doi: doi.org/10.1080/19475705.2020.1714755

[20] Konakoglu, B. (2021). Deformation Analysis Using Static, Kinematic and Dynamic Geodetic Deformation Models with GNSS: Deriner Dam, Artvin, Turkey. 45(1), p. 645-660. doi: doi.org/10.1007/s40799-020-00435-z.

[21] Barzaghi, R., Cazzaniga, N., Pinto, L., & Tornatore, V. (2018). Estimating and Comparing Dam Deformation Using Classical and GNSS Techniques. Sensors, 18(3), 756. doi: 10.3390/s18030756

[22] Maltese, A., Pipitone, C., Dardanelli, G., Capodici, F., & Muller, J.-P. (2021). Toward a Comprehensive Dam Monitoring: On-Site and Remote-Retrieved Forcing Factors and Resulting Displacements (GNSS and PS–InSAR). Remote Sensing, 13(8), 1543. doi: 10.3390/rs13081543

[23] Su, Weng, K., Lin, C., & Zheng, Z. (2021). An Improved Random Forest Model for the Prediction of Dam Displacement. IEEE Access, 9, 9142–9153. doi: 10.1109/ACCESS.2021.3049578

[24] Xiao, R., Shi, H., He, X., Li, Z., Jia, D., & Yang, Z. (2019). Deformation Monitoring of Reservoir Dams using GNSS: An Application to South-to-North Water Diversion Project, China. IEEE Access, 1–1. doi: 10.1109/ACCESS.2019.2912143

[25] Yavaşoğlu, H. H., Kalkan, Y., Tiryakioğlu, İ., Yigit, C. . O., Özbey, V., Alkan, M. N., … Alkan, R. M. (2017). Monitoring the deformation and strain analysis on the Ataturk Dam, Turkey. Geomatics, Natural Hazards and Risk, 9(1), 94–107. doi: 10.1080/19475705.2017.1411400

[26] Zhang, C., Zhan, Q., Wang, Q., Wu, H., He, T., & An, Y. (2020). Autonomous Dam Surveillance Robot System Based on Multi-Sensor Fusion. Sensors, 20(4), 1097. doi: 10.3390/s20041097

[27] R. Xi, Y. Qin, W. Jiang, X. Zhou, D. Xu and X. Fan, "Water Level Retrieval Using a posteriori Residual of GNSS Pseudorange and Carrier-Phase Observations," in *IEEE Transactions on Geoscience and Remote Sensing*, vol. 60, pp. 1-13, 2022, Art no. 5803713, doi: 10.1109/TGRS.2022.3188332.

Fifth International Dam World Conference
PORTUGAL • LISBON • LNEC • APRIL 13-17, 2025
dam world 2025

DAM SAFETY: HOW A GOOD CONTRACTUAL DESIGN AND A THOROUGH PROJECT EXECUTION MANAGEMENT CAN CONTRIBUTE TO IT

Bettina Geisseler[1]

ABSTRACT

The papers presents the essential success factors of a dam construction contract:

- A clear-cut description of the Scope of Works avoiding any ambiguities in the wording together with clearly defined Technical Specifications (Employer's Requirements)
- A project-adapted interface management in line with the chosen contractual set-up and cooperation duties of the Employer
- An allocation of risks for unforeseen events, which should be already defined in the contract in case the risks materialise during the project execution
- An appropriate Quality Assurance program and monitoring system
- An efficient project organisation as well as a suitable reporting system

The paper additionally discusses, in how far an external expert resp. DSPoE (Dam Safety Panel of Experts) accompanying the project from the beginning could contribute to an improved dam safety. In this context the role, tasks and obligations of such a DSPoE will be discussed – in particular regarding its relation towards all stakeholders and the adequacy and possibility to impose his/ her recommendations.

Keywords: Scope of Works, Interface Management, Quality Assurance, Dam Safety

[1] geisseler@geisseler-law.com, Germany

1. DESCRIPTION OF THE SCOPE OF WORKS AND CONTRACTOR'S OBLIGATION TO DELIVER THE WORKS IN THE REQUESTED QUALITY

The definition of the Scope of Works, is the core clause of a dam construction contract. Experience shows, that from a lawyer's point of view – contrary to what non-lawyers might imagine - it is not the liability clause that is the most important clause in a plant construction contract, but the Scope of Works clause. Uncertainties among the contractual partners regarding the Scope of Works/ limits of supply, and in particular the quality, in which the Contractor must deliver his Scope of Works, might cause major problems to the project execution resulting in quality problems, cost overruns and delays. Even in turnkey contracts, where the risk of incomplete supplies is much lower than in a multi-contracting structure, a precise definition of the Scope of Works together with the limits of supply is of utmost importance.

The Scope of Works – including the quality requirements and a clear definition of the requested technical parameters – is the reference for evaluating whether the delivered plant has deficiencies or not. And, it is the benchmark in disputes between the "Employer" (future Owner and Operator of the dam) [1] and the Contractor if the latter asserts a claim for "EOT" (extension of time) and compensation of additional costs, alleging that works requested by the Employer are "Extra Work" requiring a so-called "Change Order".

There are different approaches to define the Scope of Works. In countries with a long-standing experience in coordinating and supervising dam – and if applicable: hydropower plant - projects, state utilities seem to prefer to specify their requirements for the whole plant down to the smallest detail in their "Employer's Requirements", e.g. down to the properties of the construction material (e.g. the composition of the concrete) to be used, whereas in World- or other Development Bank financed projects Employers seem to prefer a more functional description of the plant to be delivered, leaving it up to the Contractor how to achieve this. Employers should be aware of the fact that an Employer stipulating detailed specifications risks bearing the responsibility that the specified parameters are "fit for the intended purpose." In those cases, a Contractor might be released from his responsibility for the functioning of the works if he fully complies with the requested specifications.

As far as the contract does not explicitly provides for specific Employer's Requirements, the following applies: requirements resulting from public law provisions applicable at the place of the project execution are compulsory and always have to be complied with [2]. The same applies for the "state of the art" requirement. But it is obvious, that Employers are free to define additional requirements. If this is done by reference to Guidelines/ Recommendations [3], edited by private norming associations, the contractual wording should clearly express which

edition (including the year of edition) is referred to and to which extent the Employer expects the Contractor to strictly follow these Guidelines, even if the Guidelines are “only” recommendations, or only to consider them and take them into account during the construction and erection.

The wording has to be clear-cut (*see fig.1*). While drafting the Scope of Works clause and setting up the Employer’s Requirements, the Parties need to avoid ambiguous expressions such as “of superior quality”, which can be interpreted in many ways. Other expressions like “state of the art” have – among experts – a clear meaning and can thus be used.

The Technical Guarantees such as resistance against floods, density, stability and permitted allowances for (smallest) deviations have to be clearly defined.

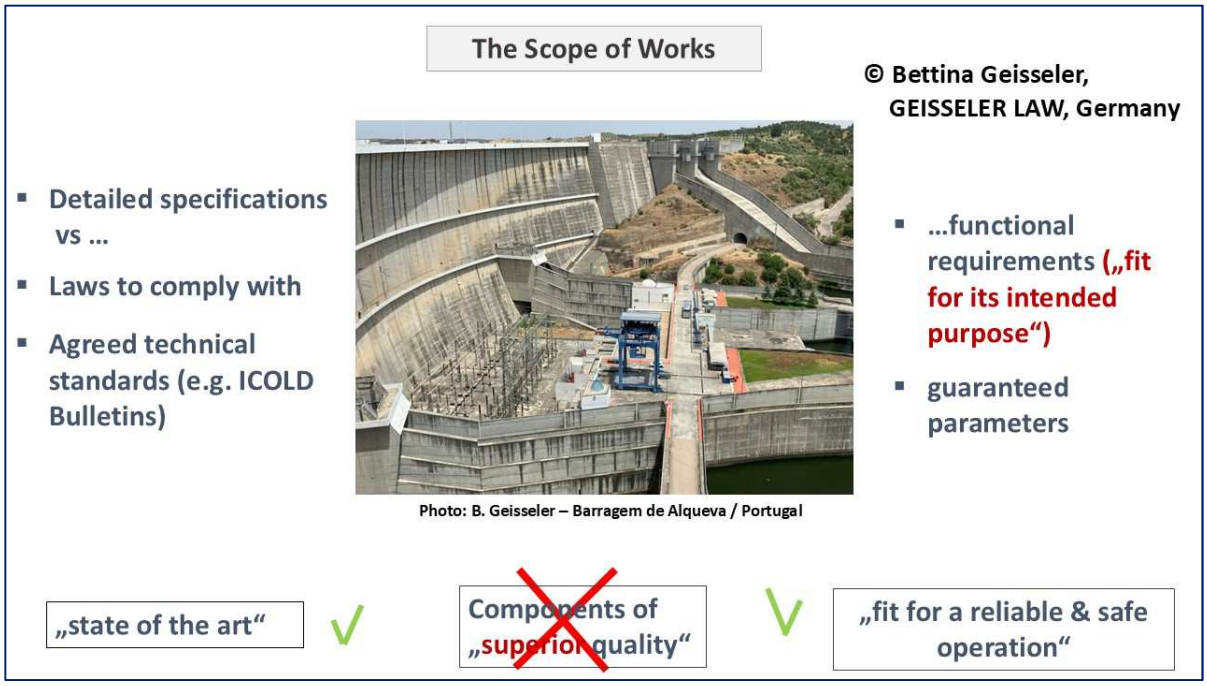

Fig.1 – The Scope of Works Clause

The contractual parties should be reminded that the agreement between them will be submitted to one national law (the applicable law of the contract), either (preferable) chosen by them or determined in line with international conventions. Knowledge of this law is essential as the so-called private law of the applicable law – often codified in Civil Codes/ Codes of Obligations - usually stipulates at least basic obligations of the parties to a construction contract. But as those provisions are often not suitable for the construction of large infrastructure projects, the contractual parties are well advised to stipulate in detail their own intentions adapted to the project. They can and should , if suitable, deviate from the applicable (private law, not public law, see above) law, as far as the provisions concerned are not compulsory and resulting from the “ordre public”, which is rather seldom the case. [4]

2. INTERFACES AND COOPERATION DUTIES OF THE EMPLOYER

Another challenging issue is the interface management.

2.1. In General

Even though in dam construction projects the number of lots might be less than in the contract regarding the erection of a (if any) connected hydropower plant ("HPP")and even though in most cases there will be one General Contractor to build the main dam, this one will often – depending on the type of the dam – subcontract a part of the works to subcontractors. In this case the General Contractor has the role of an Employer vis-à-vis his subcontractors.

The role of the contract is to clearly attribute the respective responsibilities and to define the mutual obligations regarding the interfaces and the interface *management*. Besides the definition of the Scope of Works the interface *management* is one of the most critical success factors of the project execution. While the Scope of Works determines the limits of supply, and thus determines which works around the interfaces fall within the Contractor's responsibility, the interface management relates to the question which party is responsible for coordinating the different lots. The parties need to decide who shoulders the risk if one lot upon which another lot is dependent is performed poorly or delivered too late. This risk cannot be underestimated.

Coping with interfaces first of all requires both from a technical point of view as well as from a contractual point of view to identify the interfaces.

In most cases the Employer will be in the best position to manage the interfaces, as the other stakeholders to the project (e.g. various subcontractors) do not have a contractual relationship with each other. Helpful will be an Interface Matrix. Sometimes, not to say often, Employers anyhow try to pass on this obligation to all their subcontractors. First, I doubt whether this will be an efficient solution. Further, this requests a more than detailed contractual set-up granting or imposing on each of the stakeholders/ contractors concerned explicit rights and obligations towards the other stakeholders/ contractors, as there will be no direct contractual relationship (*see fig. 2*) between them. In case – what I recommend – the interface management lies entirely with the Employer this one has to take into account while calculating his potential damage and determining the amount of Liquidated Damages for delay the potential compensation for damages the Employer has to pay to one of its contractors (Contractor A) if another contractor (Contractor B), on which the Contractor A is dependent for the execution of his works, is late and cannot perform, but has to wait and keep personnel and equipment available at the construction site.

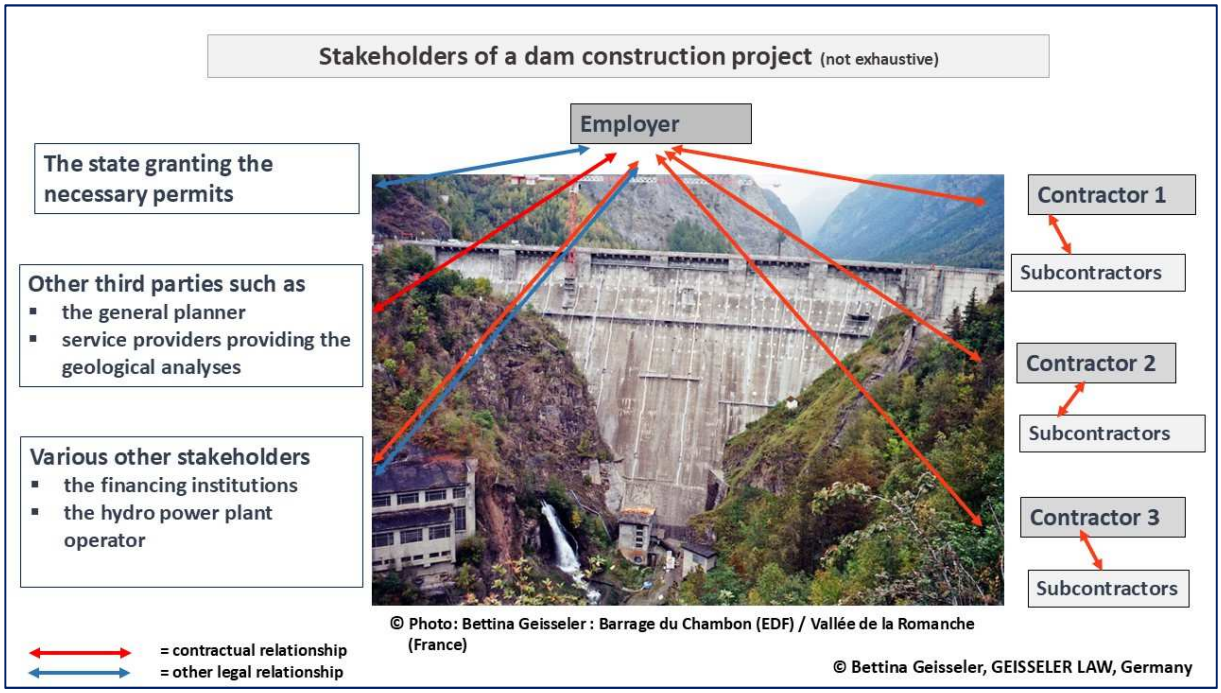

Fig. 2 – Interfaces and contractual relationships

2.2. Interface Employer - Contractor and Employer's cooperation duties

A special "interface" interface is the one between Employer – Contractor considering the Employer's duties, in particular cooperation duties. Usually the Employer has to inform the Contractor on already known site specifica and he must assure that the Contractor gets access to the site. Normally it is the Employer being responsible for – to the extent necessary – the concession or construction permit. In case that the contract is concluded and the concession not yet granted the contractual parties will agree on conditions precedent for the contract to come into force with a deadline, within this has to happen.

Further to the above, the Employer usually reserves the right to approve the detail design and the engagement of subcontractors for either critical works/ components or a work volume above a certain value. The contract should clearly state the conditions under which the Employer can withhold his approval and how the Contractor will be compensated if the approval is not granted within the agreed deadlines without the contractor being responsible for this.

2.3. The triangle relationship Employer – General Contractor – Subcontractor

In case the (General) Contractor A subcontracts part of the works which he has to perform under a Main Contract with Employer A, it is common practice that Contractor A makes the Main Contract between the Employer A = Final Client and himself an integral part of the Subcontract with his Subcontractor. One particularly critical issue are the provisions regarding the approval of works performed by the Subcontractor, be it partial approvals after the

achievement of milestones during the construction/ erection time, be it the final approval before/ after impounding of the reservoir.

The interests of Contractor A and his Subcontractor might be diametrically opposed to each other and the contractual parties to the Subcontract have to find a way to balance them. If the Subcontractor insists on an approval by his Employer = Contractor A that is independent from the approval by the Final Client, this might bring the (General) Contractor A into a difficult position if his Client/ Employer refuses for (sometimes perhaps not justified reasons) the approval of the works, performed (instead of being performed by Contractor A) by the Subcontractor. If on the other hand the parties agree on a provision that Contractor A will only then approve the works performed by his Subcontractor, when the Final Client has approved them, the Subcontractor is in a very difficult situation, if the final Client refuses for non-justified reasons the approval, as the Subcontractor has no contractual means to claim the approval from the Final Client (no contractual relationship). The only possible legal way would then be to claim against his Employer = Contractor A to initiate legal proceedings against the Final Client.

3. ALLOCATION OF RISKS IN CASE OF UNFORESEEN EVENTS

There are typical risks in dam construction projects – or to put it differently: unforeseen conditions, where the risk that they materialise is considerable high. The materialisation of these risks might lead to considerable delays and in consequence considerably higher costs (*see fig. 3*).

The contractual parties should identify and discuss in detail the major and typical project-related risks. In dam construction projects these will be the geological/ subsurface and hydrological risks such as flooding during and after construction.

The contractual parties should carefully evaluate these risks and then find a balanced , adapted to the project and the parties, solution for the question who assumes the consequences if such a risk materialises. Today it seems to be international common practice to establish a so-called Geotechnical and/ or Hydrological Baseline Report (GHBR). This report reflecting the common assumptions should be made an integral part of the Contract. In consequence: deviations in the conditions are the risks which have to be dealt with in the Contract. This can be the allocation of that specific risk to one of the parties. Often people in negotiations say: to that party which is in the best position to evaluate the probability of the materialisation of the risk or in the best position to handle the consequence; but this should be carefully considered. Or, the parties can share the consequences, when the risk occurs, at least above a certain threshold. Today, one often finds so-called Alliance Agreements, where both contractual

parties share more or less the consequences, as incentive for both parties to minimise impacts on the construction time and the costs/ price.

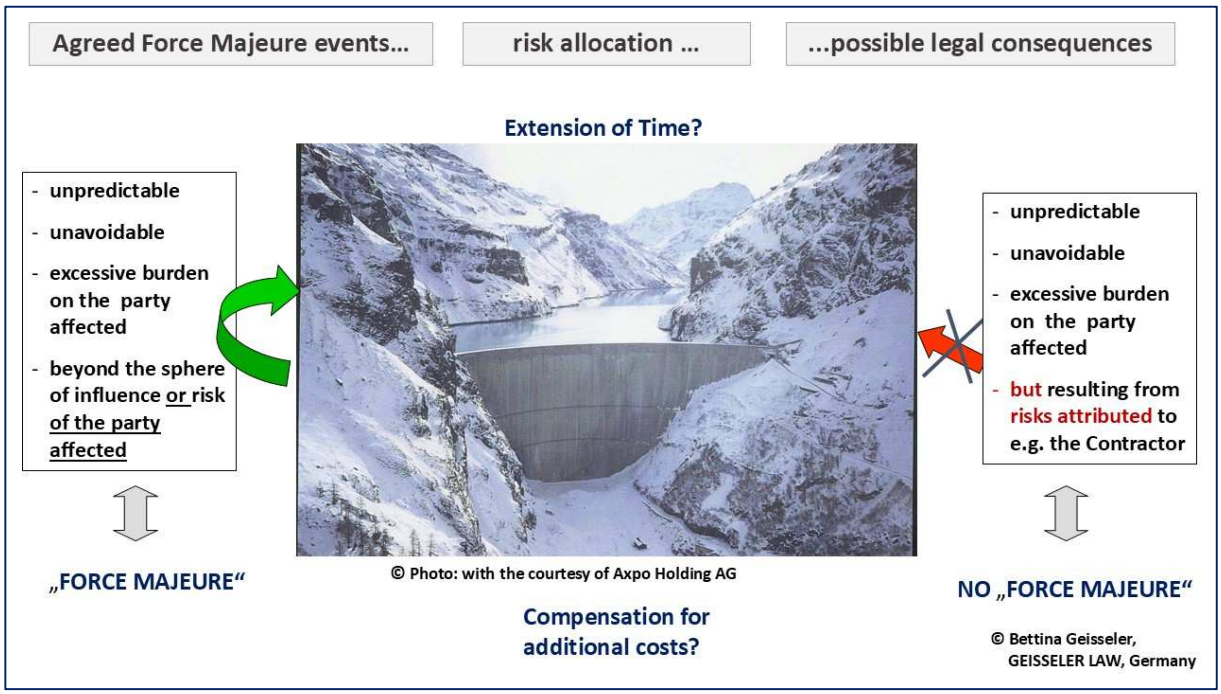

Fig. 3 – Unforeseen events – risk allocation

4. QUALITY ASSURANCE – PROJECT ORGANISATION – REPORTING OBLIGATIONS

Experience shows how important an appropriate project organisation, Contractors with skilled workforces, regular meetings as well as an adapted Quality Assurance Program are and last, but not at all least, the Contractor's obligation to report truthfully and regularly or, in case of sudden events having an impact e.g. on the compliance with the milestones or the price, on an ad hoc basis to the Employer on the progress of the works performed by him. Only such a regular reporting will enable the Employer to monitor the whole project in an appropriate way.

5. THE ROLE OF AN INDEPENDENT DAM EXPERT ACCOMPAGNYING THE PROJECT

It has become good practice in the past decades that dam construction projects are accompanied by a Dam Expert respectively a Dam Safety Panel of Experts (DSPoE), consisting usually of a dam specialist, a geological/ geotechnical expert and a hydrologist [5]. This practice has been to a large extent triggered by the requirements of the World Bank and other International Financial Institutions (IFI).

The crucial question in this context will be not only the independency of the experts, in particular from the mandating party (Employer e.g.), but to which extent the Expert's role is not only an advising one giving recommendations, but issuing binding instructions which have to be complied with by the Contractor even if the Employer does not consider it necessary and/ or appropriate. There is a current discussion around this question in the dam world community, in particular within ICOLD (International Commission on Large Dams), with still quite a number of consequential questions to be resolved. Such as question will be: who bears the additional costs if the solution instructed by the DSPoE is not within the originally agreed Scope of Works as defined in the Construction Contract.

6. CONCLUSIONS

A carefully drafted contract with balanced and project adapted solutions considering the above mentioned critical success factors can help to minimise the project–related risks of huge infrastructure projects like a dam construction project.

REFERENCES / REMARKS

[1] According to accepted drafting standards for international contracts, the specific commonly used expressions such as Employer – Contractor (as the contractual parties) are used and written with capital letters.

[2] Otherwise the Owner risks the withdrawal of the construction & operation permit

[3] E.g. ICOLD Bulletins or the JSCE Guidelines

[4] An example is Art. 1792-4-1 of the French Code Civil providing mandatorily for a ten years' defects' liability period for certain civil works contracts, from which the parties cannot deviate in the construction contract

[5] Lino, Canale, Giraud & Geisseler: " Enhancing dam safety through contractual strategies", published in Hydropower & Dams, issue 2, 2023

Fifth International Dam World Conference
PORTUGAL • LISBON • LNEC • APRIL 13-17, 2025
dam world 2025

CACULO CABAÇA HYDROPOWER PROJECT - EVALUATION OF THE SUSCEPTIBILITY OF AGGREGATES FOR PARTICIPATION IN EXPANSIVE ALKALI-SILICA REACTION

João Custódio[1] LNEC
A. Bettencourt Ribeiro LNEC
Augusto Chico GAMEK
Cristina Costa COBA
Gonçalo Mateus COBA
Wen Liu CGGC

ABSTRACT

It is worldwide recognised that alkali-silica-reaction (ASR) may cause premature deterioration of concrete dams. GAMEK as the representative of MINEA – Energy and Water Ministry of Angola, owner of Caculo Cabaça Hydropower Project (HPP), and its consultant COBA, were concerned with this phenomenon and the problems that it may cause in the future, during the operation stage, namely in the structures' integrity and the adequate functioning of the equipment, especially the gates integrated in the dam and the waterways of the powerhouses. For that purpose, in the tender specifications, it was requested that the Contractor CGGC carry out a set of laboratory tests in the design stage to evaluate the potential for the development of ASR in the concrete to be used. The assessment also involves the evaluation of the efficiency of preventive measures, such as the use of mineral additions with pozzolanic characteristics. This paper presents and discusses the results from the tests carried out at LNEC to assess the susceptibility of aggregates and combinations of aggregates with pozzolan for participation in expansive alkali-silica reaction (ASR). The results obtained can then be used to establish the dosages of mineral additions that allow mitigating expansive reactions in the concrete, thus guaranteeing the operation of the hydropower project without constraints due to this phenomenon.

Keywords: Concrete, Aggregates, Alkali-Silica Reaction, Prevention, Supplementary Cementitious Materials

[1] jcustodio@lnec.pt, Portugal

1. INTRODUCTION

It is worldwide recognised that alkali-silica-reaction (ASR) may cause premature deterioration of concrete dams [1-3]. For instance, in Portugal, the Alto Ceira dam was decommissioned and partially demolished in 2014 due to severe damage as a result of ASR and a new dam was built in a downstream zone near the demolished dam [4]. The Alto Ceira dam was built between 1940 and 1949, with the first impounding of the reservoir occurring in March 1950. The main structure was a thin arch defined by circular arches of constant thickness with a maximum height of 37.0 m, a crest development of 120.0 m, and a thickness varying from 1.5 m at the crest to 4.5 m at the bottom. The coarser aggregates used in the concrete were obtained from crushing the quartzite blocks extracted during the excavation of the adduction tunnel of Santa Luzia dam. The finer aggregates were obtained from alluvial areas of the riverbeds in the region, namely the river Alva.

GAMEK - Gabinete do Médio Kwanza, as the representative of Angola Ministry of Energy and Water (MINEA), owner of Caculo Cabaça Hydropower Project (HPP), and its consultant COBA, were concerned with this phenomenon and the problems that it may cause in the future, during the operation stage, namely in the structures' integrity and the adequate functioning of the equipment, especially the gates integrated in the dam and the waterways of the powerhouses. As it is usually the case of aggregates for dams, for Caculo Cabaça HPP, it was also necessary, for economic and environmental reasons, to use local materials, i.e., from the bedrock removed for the HPP construction. This means that there was not a history of use of the rock as aggregate for concrete. Hence, effective long-term testing became particularly important. For that purpose, in the tender specifications, it was requested that the Contractor China Gezhouba Group Corporation (CGGC) carry out a set of laboratory tests in the design stage to evaluate the potential for the development of ASR in the concrete to be used. The aggregate to be used in the concrete to be produced from the bedrock removed for the HPP construction is mainly gneiss with plagioclase amphibolite and cataclasite. This rock type is known to be potentially alkali-reactive [5] and it is believed that it may also release alkalis and contribute to the concrete pore solution alkalinity. The alkalinity of the pore solution in the concrete can be kept to a level where damaging reaction with silica in aggregates is unlikely by limiting the alkali content of the concrete mix, or by inclusion in the concrete of a sufficient proportion of a low-lime fly ash, or other pozzolan demonstrated to be effective, or ground granulated blast furnace slag. Therefore, the assessment also involved the evaluation of the efficiency of preventive measures, such as the use of mineral additions with pozzolanic characteristics. In the present case, fly ash and silica fume were considered.

This paper presents and discusses the results from the tests carried out at LNEC to assess the susceptibility of aggregates and combinations of aggregates with pozzolan for participation in expansive alkali-silica reaction (ASR). The results obtained were used to establish the dosages of mineral additions that allow mitigating expansive reactions in the concrete, thus guaranteeing the operation of the Caculo Cabaça HPP without constraints due to this phenomenon.

2. CACULO CABAÇA HYDROPOWER PROJECT

The Caculo Cabaça Hydropower Project (HPP) in Angola has a nominal capacity of 2,172 MW and is the third stage of the cascade development along the Kwanza River. It is located 19 km downstream from Laúca HPP, 70 km upstream from Cambambe HPP, and 260 km southeast of Luanda. The project covers a watershed area of 112,663 km^2 with an average flow rate of 587 m^3/s. It includes a main dam, two saddle dams, an underground waterway, a powerhouse, and an additional ecological flow powerhouse on the left side of the spillway (Fig. 1).

Fig. 1 – Aerial overview of the Caculo Cabaça Hydropower Project.

During the construction design phase, the layout of the Caculo Cabaça dam was adjusted based on new bathymetric and topographic surveys and geological and geotechnical studies. The final layout consists of a 116 m-high roller compacted concrete (RCC) gravity dam 533 m-long at the crest at elevation (633). The bedrock is mainly gneiss with plagioclase amphibolite and cataclasite band parallel to the river developed between low elevation of right bank and right side of the riverbed blocks. The dam's cross-section was optimized with a downstream face slope change from 0.85h/1v to 0.80h/1v and a vertical upstream face above elevation (560), sloping 0.20h/1v below that point. The adoption of this cross-section allows a reduction in the concrete volume of the dam of about 60,000 m^3, using as a reference the dam foundation surface defined in the Tender Design (Fig. 2). At full supply level (elevation 630), the reservoir holds 436 hm^3 and covers 16.6 km^2.

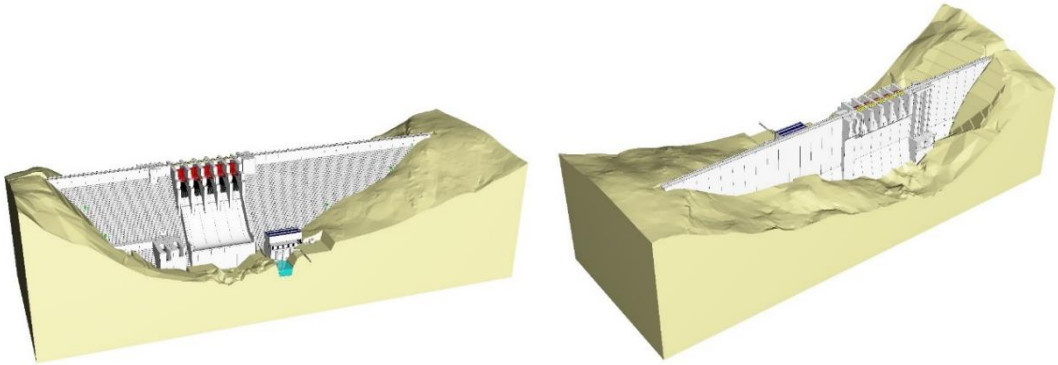

Fig. 2 – Caculo Cabaça dam overview

A frontal overflow spillway with a design flood capacity of 10,020 m^3/s is in the central blocks of the dam, aligned with the main riverbed. The spillway is divided into five bays, with its crest at elevation (612.5) and it is controlled by radial gates, each one 12.4 m-wide by 19.3 m-high. The flow is guided along the downstream surface of the dam onto a flip-bucket that directs the water into an excavated plunge pool.

The right side of the spillway houses a double bottom outlet with a maximum discharge flow of 1,489 m^3/s at FSWL. Each bottom outlet includes a 6 m-wide by 7.5 m-high fixed-wheel safety gate, a 6 m diameter steel liner, and a 5 m-wide by 5.1 m-high radial gate for flow regulation. A numerical model study recommended and led to the adoption of a jet deflection structure at the exit of the bottom outlets to prevent scouring on the right bank, which might cause slope instability.

In the construction design phase, an alternative solution for the waterway system ecological flow powerhouse was chosen over the solution of the Tender Design. This new approach features a water intake structure within the dam, raising the inlet sill from elevation (566) to (612) which connects to a penstock embedded in the dam's concrete, aligned parallel to the downstream face of the dam (Fig. 3).

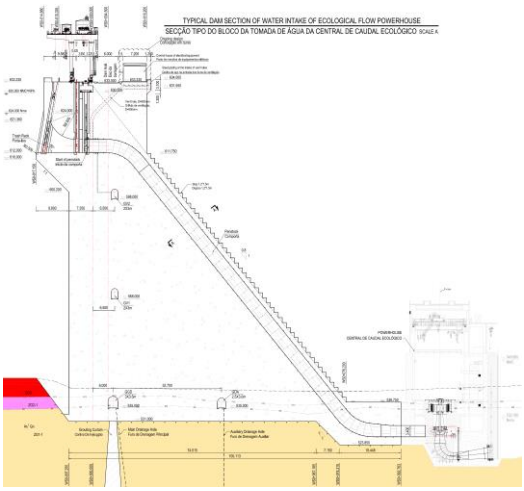

Fig. 3 – Cross-section of the water intake for the ecological flow powerhouse

Two saddle dams on the left bank are essential to close the reservoir at full supply and maximum water levels. These dams, featuring an RCC gravity profile, will have a maximum height of 39.5 m and a total crest length of 714 m.

The dam construction will be protected by two rockfill cofferdams for seepage control, a clayey core on the upstream cofferdam, 30 m-high and 212 m-long and a clay blanket on the downstream cofferdam, 14 m-high and 149 m-long. A symmetrical cross section with slopes of 1.5h:1v was adopted with an 8 m-wide crest. Two tunnels on the right bank, surrounding the area limited by the cofferdams, about 357 m and 415 m long with a horseshoe cross section with 14.4 m maximum width and height (Fig. 4), divert the river. The tunnels' inlet includes a 28.5 m-long reinforced concrete structure that holds 6 stoplogs and a fixed-wheel gate.

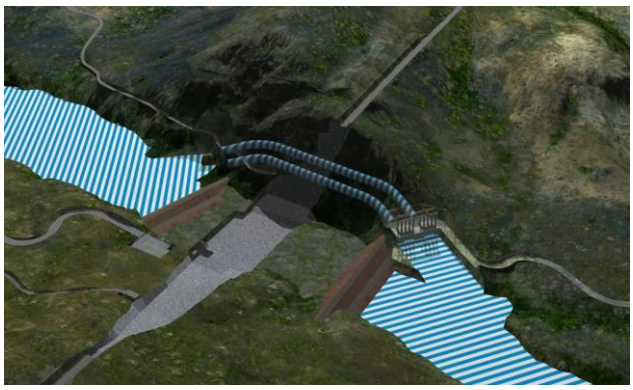

Fig. 4 – Diversion tunnels on the right bank and cofferdams

The waterway system of the main powerhouse on the left bank is entirely underground and designed for a water discharge of 1,100 m^3/s. The water intake structure, located 2.4 km upstream from the dam's left abutment, conveys the flow to four reinforced concrete-lined vertical pressure shafts with 9 m diameter, involving a vertical drop of 190 m (Fig. 5 and Fig. 6).

Fig. 5 – Water intake structure in the reservoir and switchyard (behind)

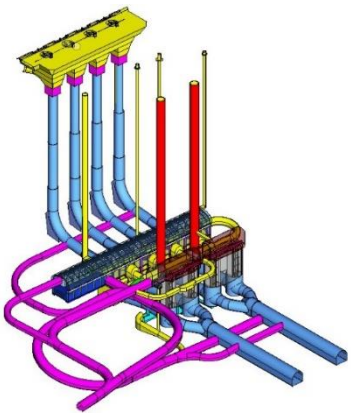

Fig. 6 – Underground waterway system and powerhouse

Four steel-lined headrace tunnels, 60 m long and 6.5-m in diameter, lead to the underground powerhouse. The cavern housing the powerhouse is 26.5 m-wide and 221 m-long, with a height of 68 m in the turbine-generator area and 28 m in the equipment assembly hall.

The underground powerhouse is equipped with four Francis vertical axis turbines with a nominal capacity of 530 MW, coupled to a 590 MVA generator, operating at a nominal net head of 209 m.

The connection to the transformers located on the surface is established through 21 kV isolated busbars installed in two shafts, each with a diameter of 9 m and height of 243 m (Fig. 6). The switchyard is located beside the transformers on a platform (Fig. 5).

The powerhouse has two double girder overhead cranes with a 550-t capacity for equipment assembly, disassembly, and maintenance (Fig. 7Figure 7). The average annual energy generation is around 8,120 GWh.

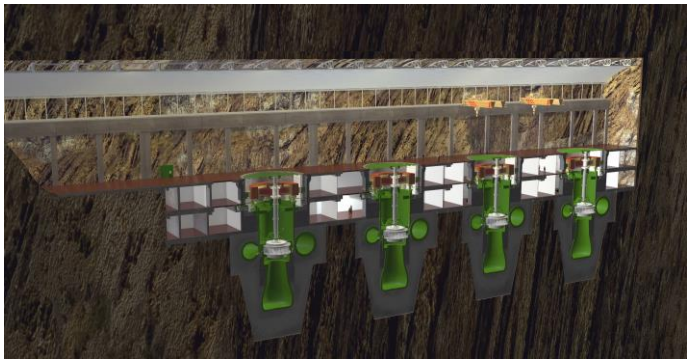

Fig. 7 – Longitudinal section of the underground powerhouse

Two pressurized tailrace tunnels, each about 5,200 m-long with a 0.4% upslope, carry out the water from the powerhouse to the Kwanza River. The unlined tunnels have an arch-rectangle cross-section, 16 m-wide and 16 m-high. At their ends, a U-shaped reinforced concrete canal (70x50 m^2 in plan, 24 m-high) accommodates two stoplogs for dewatering the tunnels.

The mass oscillation system, designed for transient pressures and to maintain the stability of the hydraulic circuit, comprises two surge chambers, located 79 m downstream of the powerhouse, each one with an area of approximately 1,000 m^2 and 65.5 m-high, capped with a semi-cylindrical dome measuring 24 m in diameter (Fig. 6).

To utilize the 60 m^3/s ecological flow required between the dam and the main waterway's outlet, a small powerhouse will be built. This powerhouse, located at the dam’s toe on the left side of the spillway, is partially buried, is equipped with a 52 MW Francis vertical axis turbine for a 94.6 m net head, connected to a 57 MVA generator and transformer via busbars.

The Caculo Cabaça HPP includes approximately 19 km of access roads, with a 9.0 m wide platform. Access to the main powerhouse includes a bridge over the Kwanza River (230 m-long and 20 m-high) and a 1.5 km tunnel with a 9.5 m wide and 8.75 m high arch rectangular cross-section.

Fig. 8 – Overview of the bridge over the Kwanza River

3. MATERIALS AND METHODS

The test campaign performed to evaluate the potential alkali-silica reactivity of the aggregates and the effectiveness of fly ash and silica fume in preventing deleterious development of ASR in the concrete, made with the potentially alkali-reactive aggregates, comprised the assessment of the fly ashes activity index, the determination of the fly ashes alkali content, and carrying out expansion tests on concrete prisms.

3.1. Fly ash activity index

The activity index at 28 days was assessed according to the standard EN 450-1:2012 [6]. The activity index is the ratio (in per cent) of the compressive strength of standard mortar bars, prepared with 75% test cement plus 25% fly ash by mass, to the compressive strength of standard mortar bars prepared with 100% test cement, when tested at the same age. Section 5.3.2 of the standard EN 450-1:2012 [6] mentions that the preparation of mortar bars and the determination of the compressive strength shall be carried out by the standard EN 196-1:2005 [7]. The test cement used was Portland cement of type CEM I, strength class 42,5 R, conforming to EN 197-1:2011 [8]. The additional required characteristics for the test cement are presented in Table 1. Two fly ashes were assessed, one from South Africa (DuraPozz® - AshResources Afrimat) and one from India (Jaycee Buildcorp LLP).

Table 1 – Test cement: fineness and contents of tricalcium aluminate and alkalis

Property	Reference cement used	Requirement EN 450-1
Fineness (Blaine)	342 m^2/kg	≥300 m^2/kg
Content of tricalcium aluminate	10 %	≥6 %; ≤12 %
Total content of alkalis (Na_2O_{eq})	1.01 %	≥0.5 %; ≤1.2 %

Note: The properties of the cement presented in the above table represent the arithmetic mean of the respective property values determined by the cement manufacturer from 10/09/2019 to 10/09/2019, i.e., the period that preceded its use in the test campaign.

3.2. Fly ash alkali content

As required by section 5.2.9 of the standard EN 450-1:2012 [6], the total content of alkalis was determined following EN 196-2:2013 [9]. The fly ash samples from South Africa and India were taken from the same packages as those used in the activity index tests.

3.3. Assessment of alkali-silica potential reactivity

The standard ASTM C1293 [10] provides a test method to evaluate the potential of an aggregate, either coarse or fine, to expand deleteriously due to the alkali-silica reaction. It is generally recognized that, from the several tests available, the concrete prism test, CPT, provides the more reliable indication of the potential for deleterious expansion of an aggregate in concrete. Thus, the expansion tests, conducted to assess the susceptibility of the aggregates for participation in expansive alkali-silica reaction, were performed according to the above-mentioned method.

The test period to assess the aggregates' ASR susceptibility was set to 1 year, as established in the standard; nevertheless, the test was extended beyond that period to better understand the long-term behaviour of the aggregates. Two types of aggregates were tested, a granodiorite and a gneiss, the latter having two varieties, a lighter one and a darker one. The aggregates came from the excavations carried out for the works of the boreholes of the geological survey.

In the ASTM C1293 test method, concrete test prisms, 75x75x285 mm^3, are prepared from the aggregate under assessment and are stored in warm, 38°C, and humid conditions, with relative humidity higher than 95%, for at least 12 months to promote any alkali-aggregate reaction. Length change measurements are made at periodic intervals to determine whether any expansion has occurred. To promote further any potential for reaction, the prisms are made with a relatively high content of Portland cement with a high alkali content, such that the alkali level in the concrete is 5.25 kg sodium oxide equivalent per cubic metre of concrete. Sodium hydroxide is added to the mix to enhance the alkali level and thus further promote ASR. To identify the effect of specific aggregate combinations, the coarse and fine aggregates are tested in combination with a non-reactive aggregate. The non-reactive aggregate used was crushed limestone. The limestone potential alkali-silica reactivity was assessed according to the accelerated mortar bar test method ASTM C1260 [11]. Since the average expansion attained was 0.003%, at the end of the test period, the limestone aggregate is classified as nonreactive aggregate.

As described in Table 2, the determination of the susceptibility of the aggregates for participation in the expansive alkali-silica reaction was performed on eight concrete mixes, all using the same cement, a CEM I 42.5 R, supplied by CIMPOR and produced at the Alhandra

Cement Plant. Observations by scanning electron microscopy with energy dispersive X-ray analysis (SEM/EDS) were made to the specimens that have expanded the most during the tests, to confirm that the prevailing expansion mechanism was ASR.

Table 2 – Samples received at LNEC, and tests performed to assess the potential alkali-reactivity of the aggregate

Material	Sample assessed	Comment	Test	Test period	Test code
Granodiorite	Coarse aggregate	The rock was crushed at LNEC to the sieve sizes specified in ASTM C1293.	ASTM C1293	1 year	GD/1/G
Granodiorite	Fine aggregate	The rock was crushed at LNEC to the sieve sizes specified in ASTM C1293.			GD/1/F
Gneiss (lighter colour)	Coarse aggregate	The rock was crushed at LNEC to the sieve sizes specified in ASTM C1293.			GN/1/G
Gneiss (lighter colour)	Fine aggregate	The rock was crushed at LNEC to the sieve sizes specified in ASTM C1293.			GN/1/F
Gneiss (25 % lighter colour + 75 % darker colour)	Coarse aggregate	The rock was crushed at LNEC to the sieve sizes specified in ASTM C1293.			GN/25-75G
Gneiss (25 % lighter colour + 75 % darker colour)	Fine aggregate	The rock was crushed at LNEC to the sieve sizes specified in ASTM C1293.			GN/25-75F
Gneiss (darker colour)	Coarse aggregate	The rock was crushed at LNEC to the sieve sizes specified in ASTM C1293.			GN/100G
Gneiss (darker colour)	Fine aggregate	The rock was crushed at LNEC to the sieve sizes specified in ASTM C1293.			GN/100F

3.4. Evaluation of mitigation measures

The standard test method ASTM C1293 [10] can also be sued to evaluate the potential of an aggregate, either coarse or fine, with pozzolan to expand deleteriously due to the alkali-silica reaction. Hence, the feasibility of using fly ash (Jaycee Buildcorp LLP) and silica fume to mitigate the deleterious development of ASR, in a concrete produced with the aggregates mentioned in the previous section, was evaluated with the test method defined in ASTM C1293 [10]. The test period to assess the pozzolans ASR mitigation capability was set to 2 years, as established in the standard; nevertheless, the test was extended beyond that period to better understand the long-term behaviour of the combination of aggregate with pozzolan. The aggregates tested were the same as in the previous section.

As described in Table 3 and Table 4, the determination of the susceptibility of the combinations of aggregates with pozzolan for participation in expansive alkali-silica reaction was performed to twenty concrete mixes, all using the same cement, a CEM I 42.5 R, supplied by CIMPOR and produced at the Alhandra Cement Plant.

Table 3 – Samples received at LNEC, and tests performed to determine the susceptibility of a combination of an aggregate with fly ash for participation in expansive ASR

Rock material	Rock sample assessed	SCM sample assessed	Comment	Test	Test period	Test code
Gneiss (lighter colour)	Coarse aggregate	Fly ash 20 %	The rock was crushed at LNEC to the sieve sizes specified in ASTM C1293.	ASTM C1293	2 Years	GN/CV20/G
Gneiss (lighter colour)	Fine aggregate	Fly ash 20 %	The rock was crushed at LNEC to the sieve sizes specified in ASTM C1293.			GN/CV20/F
Gneiss (lighter colour)	Coarse aggregate	Fly ash 30 %	The rock was crushed at LNEC to the sieve sizes specified in ASTM C1293.			GN/CV30/G
Gneiss (lighter colour)	Fine aggregate	Fly ash 30 %	The rock was crushed at LNEC to the sieve sizes specified in ASTM C1293.			GN/CV30/F
Gneiss (lighter colour)	Coarse aggregate	Fly ash 50 %	The rock was crushed at LNEC to the sieve sizes specified in ASTM C1293.			GN/CV50/G
Gneiss (lighter colour)	Fine aggregate	Fly ash 50 %	The rock was crushed at LNEC to the sieve sizes specified in ASTM C1293.			GN/CV50/F
Granodiorite	Coarse aggregate	Fly ash 20 %	The rock was crushed at LNEC to the sieve sizes specified in ASTM C1293.			GD/CV20/G
Granodiorite	Fine aggregate	Fly ash 20 %	The rock was crushed at LNEC to the sieve sizes specified in ASTM C1293.			GD/CV20/F
Granodiorite	Coarse aggregate	Fly ash 30 %	The rock was crushed at LNEC to the sieve sizes specified in ASTM C1293.			GD/CV30/G
Granodiorite	Fine aggregate	Fly ash 30 %	The rock was crushed at LNEC to the sieve sizes specified in ASTM C1293.			GD/CV30/F
Granodiorite	Coarse aggregate	Fly ash 50 %	The rock was crushed at LNEC to the sieve sizes specified in ASTM C1293.			GD/CV50/G
Granodiorite	Fine aggregate	Fly ash 50 %	The rock was crushed at LNEC to the sieve sizes specified in ASTM C1293.			GD/CV50/F

Note: SCM stands for supplementary cementitious material.

Table 4 – Samples received at LNEC, and tests performed to determine the susceptibility of a combination of an aggregate with silica fume for participation in expansive ASR

Rock material	Rock sample assessed	SCM sample assessed	Comment	Test	Test period	Test code
Gneiss (lighter colour)	Coarse aggregate	Silica fume 5 %	The rock was crushed at LNEC to the sieve sizes specified in ASTM C1293.	ASTM C1293	2 Years	GN/SF5/G
Gneiss (lighter colour)	Fine aggregate	Silica fume 5 %	The rock was crushed at LNEC to the sieve sizes specified in ASTM C1293.			GN/SF5/F
Gneiss (lighter colour)	Coarse aggregate	Silica fume 10 %	The rock was crushed at LNEC to the sieve sizes specified in ASTM C1293.			GN/SF10/G
Gneiss (lighter colour)	Fine aggregate	Silica fume 10 %	The rock was crushed at LNEC to the sieve sizes specified in ASTM C1293.			GN/SF10/F
Granodiorite	Coarse aggregate	Silica fume 5 %	The rock was crushed at LNEC to the sieve sizes specified in ASTM C1293.			GD/SF5/G
Granodiorite	Fine aggregate	Silica fume 5 %	The rock was crushed at LNEC to the sieve sizes specified in ASTM C1293.			GD/SF5/F
Granodiorite	Coarse aggregate	Silica fume 10 %	The rock was crushed at LNEC to the sieve sizes specified in ASTM C1293.			GD/SF10/G
Granodiorite	Fine aggregate	Silica fume 10 %	The rock was crushed at LNEC to the sieve sizes specified in ASTM C1293.			GD/SF10/F

Note: SCM stands for supplementary cementitious material.

4. RESULTS AND DISCUSSION

4.1. Fly ash activity index

The results of the activity index are presented in Table 5. Table 6 compares the activity index of the tested samples with the limit values required by the standard EN 450-1:2012. It is observed that both fly ashes comply with the single result limit value specified in EN 450-1:2012 for this property.

Table 5 – Activity index

Fly ash source	Age (days)	Compressive strength (MPa)	Activity index (%)
No fly ash (reference)	28	56.3	-
South Africa		48.6	86
India		43.7	78

Table 6 – Activity Index at 28 days and limit values

Fly ash source	Activity index (%)	EN 450-1:2012 Minimum characteristic value (%)	EN 450-1:2012 Limit value for single result (%)
South Africa	86	75	70
India	78		

4.2. Fly ash alkali content

The results of the alkali content determinations are presented in Table 7. Table 8 compares the total content of alkalis of the tested samples with the limit values required by the standard EN 450-1:2012 for fly ash obtained from the combustion of pulverised coal. The total content of alkalis, calculated as Na_2O_{eq}, of both fly ashes comply with the single result limit value specified in EN 450-1:2012 for this property.

Table 7 – Total content of alkalis

Fly ash source	Total content of alkalis		
	Na_2O (%)	K_2O (%)	Na_2O_{eq} (%)
South Africa	0.23	0.60	0.62
India	0.81	1.29	1.66

Table 8 – Total content of alkalis and limit values

Fly ash source	Total content of alkalis, $Na_2O_{eq.}$ (%)	EN 450-1:2012 Characteristic value limit (%)	EN 450-1:2012 Upper limit value for single result (%)
South Africa	0.62	5.0	5.5
India	1.66		

4.3. Assessment of alkali-silica potential reactivity

The results obtained in the laboratory test campaign, made on specimens produced with the concrete mixtures detailed in Table 2.2, are presented in Table 9 and Table 2.4, and also in Fig. 9 to Fig. 12. Observation by scanning electron microscopy, with energy dispersive X-ray analysis (SEM/EDS), was made to the specimens that expanded the most during the tests, and it showed that the expansion was due to ASR.

According to the standard test method ASTM C1293 [10], an aggregate might reasonably be classified as potentially deleteriously reactive if the average expansion of three concrete specimens is equal to or greater than 0.04% at one year.

Therefore, from the results presented in Table 9, it can be considered that the tested granodiorite coarse aggregate (Fig. 9), the gneiss coarse aggregate (100 % lighter colour) (Fig. 10), the gneiss coarse aggregate (25 % lighter colour + 75 % darker colour) (Fig. 11), and the gneiss coarse aggregate (100 % darker colour) (Fig. 12) are potentially deleteriously alkali-reactive, as they exhibited an average expansion of 0.04% or 0.05% in the test period assessed.

However, from the results presented in Table 9, it can be considered that the tested granodiorite fine aggregate (Fig. 9), the gneiss fine aggregate (100 % lighter colour) (Fig. 10), the gneiss fine aggregate (25 % lighter colour + 75 % darker colour) (Fig. 11), and the gneiss fine aggregate (100 % darker colour) (Fig. 12) are not potentially deleteriously alkali-silica reactive, as they exhibited an average expansion below 0.04% in the test period assessed.

Henceforth, preventive measures, which minimize the risk of deleterious development of ASR in concrete using the above-mentioned aggregates, should be assessed and adopted in the dams' concrete. Because of this, tests to determine the susceptibility of a combination of those aggregates with fly ash or silica fume for participation in expansive ASR were executed.

The SEM/EDS observations (not reported in the present paper), made to identify the presence of products from internal expansive chemical reactions, confirmed that the expansion observed in the test has indeed resulted from ASR.

From the results presented in Fig. 9 to Fig. 12, it can be seen that the concrete prism test specimens produced with the coarse aggregates (granodiorite; gneiss - 100 % lighter colour; gneiss - 25 % lighter colour & 75 % darker colour; gneiss - 100 % darker colour) continued to expand beyond the regular test period of 364 days. In the case of granodiorite and gneiss 100 % lighter colour coarse aggregates, there was distinct expanding behaviour between the two test specimens, after roughly two years of testing, with one of the specimens expanding much more than the other; even though the mass variation was similar for both specimens. This behaviour was not observed when testing the fine aggregates, with both test specimens

showing a similar expansion trend. After 1800 days of testing, all the tested fine aggregates exhibited an expansion lower than 0.04%. The expansion increasing trend after the regular test period of 364 days suggests that the tested aggregates might be alkali-releasers.

Table 9 – Length change obtained in the tests performed to determine the susceptibility of an aggregate for participation in expansive ASR

Concrete	Test specimen	Average length change (%) at the age of							
		1 d	7 d	28 d	56 d	91 d	182 d	273 d	364 d
Cement + nonreactive fine aggregate + granodiorite coarse aggregate	GD/1/G-1	0	0.007	0.013	0.016	0.017	0.025	0.030	0.035
	GD/1/G-2	0	0.008	0.014	0.016	0.019	0.025	0.030	0.033
	GD/1/G-3	0	0.009	0.015	0.017	0.019	0.026	0.033	0.041
	Average†	0	0.01	0.01	0.02	0.02	0.03	0.03	**0.04**
Cement + granodiorite fine aggregate + nonreactive coarse aggregate	GD/1/F-1	0	0.005	0.009	0.011	0.013	0.016	0.018	0.019
	GD/1/F-2	0	0.006	0.011	0.012	0.014	0.017	0.019	0.022
	GD/1/F-3	0	0.006	0.011	0.013	0.015	0.018	0.020	0.022
	Average†	0	0.01	0.01	0.01	0.01	0.02	0.02	**0.02**
Cement + nonreactive fine aggregate + gneiss coarse aggregate (100 % lighter colour)	GN/1/G-1	0	0.007	0.014	0.017	0.022	0.034	0.044	0.052
	GN/1/G-2	0	0.007	0.014	0.017	0.022	0.037	0.049	0.057
	GN/1/G-3	0	0.007	0.013	0.016	0.021	0.034	0.044	0.048
	Average†	0	0.01	0.01	0.02	0.02	0.04	0.05	**0.05**
Cement + gneiss fine aggregate (100 % lighter colour) + nonreactive coarse aggregate	GN/1/F-1	0	0.005	0.009	0.010	0.013	0.015	0.013	0.020
	GN/1/F-2	0	0.004	0.009	0.010	0.013	0.016	0.018	0.020
	GN/1/F-3	0	0.005	0.009	0.011	0.014	0.016	0.017	0.022
	Average†	0	0.00	0.01	0.01	0.01	0.02	0.02	**0.02**
Cement + nonreactive fine aggregate + gneiss coarse aggregate (25 % lighter colour + 75 % darker colour)	GN/25-75G-1	0	0.004	0.011	0.014	0.015	0.029	0.035	0.037
	GN/25-75G-2	0	0.004	0.011	0.014	0.017	0.028	0.032	0.036
	GN/25-75G-3	0	0.004	0.012	0.015	0.018	0.029	0.034	0.038
	Average†	0	0.00	0.01	0.01	0.02	0.03	0.03	**0.04**
Cement + gneiss fine aggregate (25 % lighter colour + 75 % darker colour) + nonreactive coarse aggregate	GN/25-75F-1	0	0.006	0.011	0.013	0.014	0.017	0.018	0.019
	GN/25-75F-2	0	0.004	0.009	0.011	0.013	0.017	0.018	0.018
	GN/25-75F-3	0	0.003	0.011	0.012	0.010	0.018	0.019	0.022
	Average†	0	0.00	0.01	0.01	0.01	0.02	0.02	**0.02**
Cement + nonreactive fine aggregate + gneiss coarse aggregate (100 % darker colour)	GN/100/G-1	0	0.005	0.013	0.017	0.020	0.022	0.036	0.039
	GN/100/G-2	0	0.007	0.014	0.017	0.022	0.033	0.040	0.042
	GN/100/G-3	0	0.006	0.013	0.016	0.020	0.028	0.034	0.037
	Average†	0	0.01	0.01	0.02	0.02	0.03	0.04	**0.04**
Cement + gneiss fine aggregate (100 % darker colour) + nonreactive coarse aggregate	GN/100/F-1	0	0.005	0.012	0.014	0.016	0.018	0.022	0.023
	GN/100/F-1	0	0.005	0.011	0.014	0.016	0.019	0.021	0.021
	GN/100/F-1	0	0.007	0.012	0.014	0.016	0.018	0.020	0.020
	Average†	0	0.01	0.01	0.01	0.02	0.02	0.02	**0.02**

NOTE: † Arithmetic mean of the individual values, rounded down to two decimal places as required by the American Standard ASTM C 1293 [10]; the rounding of the arithmetic mean number to two decimal places was performed according to ISO 80000-1 [12] and NIST Special Publication 811 [13].

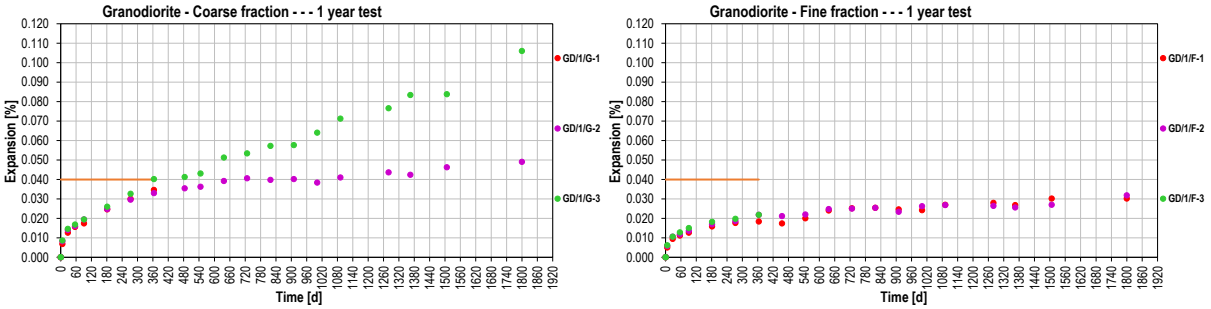

Fig. 9 – Length change of the concrete prisms, observed in the ASTM C1293 test, for the concrete mixtures GD/1/G and GD/1/F.

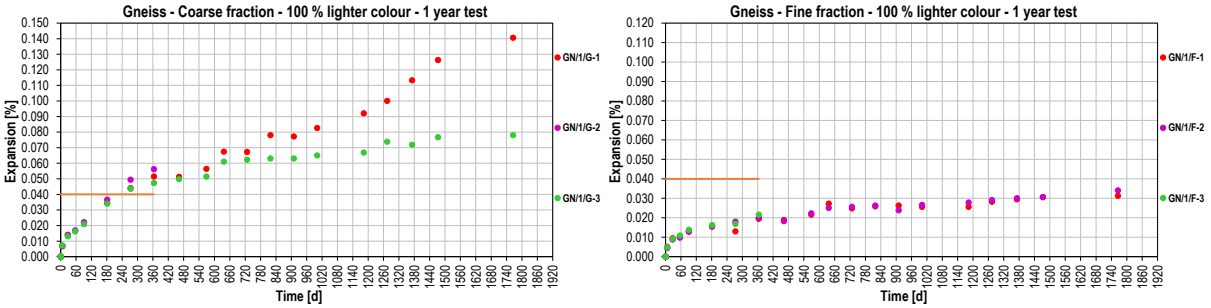

Fig. 10 – Length change of the concrete prisms, observed in the ASTM C1293 test, for the concrete mixtures GN/1/G and GN/1/F.

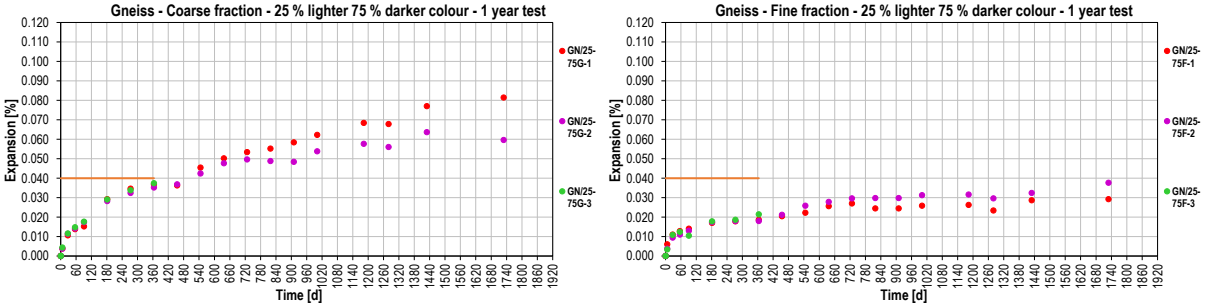

Fig. 11 – Length change of the concrete prisms, observed in the ASTM C1293 test, for the concrete mixtures GN/25-75G and GN/25-75F.

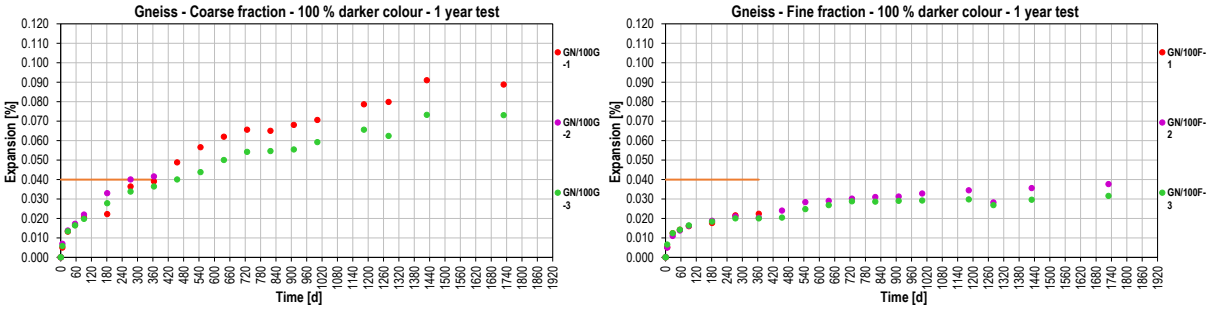

Fig. 12 – Length change of the concrete prisms, observed in the ASTM C1293 test, for the concrete mixtures GN/100G and GN/100F.

4.4. Evaluation of mitigation measures

The results obtained in the laboratory test campaign, made on specimens produced with the concrete mixtures detailed in Table 3 and Table 4, are presented in Table 10 to Table 13, and also in Fig. 13 to Fig. 22. Observation by scanning electron microscopy, with energy dispersive X-ray analysis (SEM/EDS), was made to the specimens that expanded the most during the tests, and it showed that the expansion was due to ASR.

Table 10 – Length change obtained in the tests performed to determine the susceptibility of a combination of an aggregate with fly ash for participation in expansive ASR (1/2)

Concrete	Test specimen	Average length change (%) at the age of											
		2 d	7 d	28 d	56 d	91 d	182 d	273 d	364 d	455 d	546 d	637 d	728 d
Cement + nonreactive fine aggregate + gneiss coarse aggregate (100 % lighter colour) + fly ash 20 %	**GN/CV20/G-1**	0.000	0.007	0.010	0.010	0.013	0.018	0.022	0.025	0.027	0.035	0.039	0.042
	GN/CV20/G-2	0.000	0.007	0.011	0.011	0.015	0.019	0.024	0.027	0.030	0.037	0.042	0.046
	GN/CV20/G-3	0.000	0.007	0.009	0.010	0.013	0.018	0.023	0.026	0.029	0.037	0.039	0.044
	Average†	0.00	0.01	0.01	0.01	0.01	0.02	0.02	0.03	0.03	0.04	0.04	**0.04**
Cement + gneiss fine aggregate (100 % lighter colour) + nonreactive coarse aggregate + fly ash 20 %	**GN/CV20/F-1**	0.000	0.005	0.007	0.007	0.008	0.010	0.013	0.014	0.014	0.020	0.022	0.024
	GN/CV20/F-2	0.000	0.005	0.007	0.007	0.009	0.010	0.014	0.014	0.014	0.020	0.023	0.025
	GN/CV20/F-3	0.000	0.005	0.006	0.006	0.009	0.010	0.013	0.013	0.013	0.019	0.022	0.024
	Average†	0.00	0.00	0.01	0.01	0.01	0.01	0.01	0.01	0.01	0.02	0.02	**0.02**
Cement + nonreactive fine aggregate + gneiss coarse aggregate (100 % lighter colour) + fly ash 30 %	**GN/CV30/G-1**	0.000	0.004	0.008	0.008	0.009	0.012	0.015	0.017	0.019	0.025	0.029	0.032
	GN/CV30/G-2	0.000	0.006	0.009	0.009	0.011	0.013	0.015	0.017	0.020	0.026	0.028	0.031
	GN/CV30/G-3	0.000	0.004	0.007	0.008	0.010	0.012	0.015	0.016	0.018	0.026	0.029	0.032
	Average†	0.00	0.00	0.01	0.01	0.01	0.01	0.01	0.02	0.02	0.03	0.03	**0.03**
Cement + gneiss fine aggregate (100 % lighter colour) + nonreactive coarse aggregate + fly ash 30 %	**GN/CV30/F-1**	0.000	0.005	0.005	0.006	0.007	0.008	0.009	0.009	0.010	0.014	0.016	0.018
	GN/CV30/F-2	0.000	0.005	0.006	0.007	0.007	0.009	0.010	0.010	0.011	0.015	0.016	0.018
	GN/CV30/F-3	0.000	0.005	0.007	0.006	0.007	0.008	0.008	0.009	0.010	0.015	0.017	0.019
	Average†	0.00	0.01	0.01	0.01	0.01	0.01	0.01	0.01	0.01	0.01	0.02	**0.02**
Cement + nonreactive fine aggregate + gneiss coarse aggregate (100 % lighter colour) + fly ash 50 %	**GN/CV50/G-1**	0.000	0.004	0.006	0.006	0.007	0.008	0.009	0.011	0.012	0.015	0.018	0.020
	GN/CV50/G-2	0.000	0.004	0.005	0.006	0.006	0.007	0.008	0.009	0.011	0.014	0.018	0.019
	GN/CV50/G-3	0.000	0.004	0.005	0.006	0.006	0.008	0.009	0.011	0.011	0.015	0.018	0.019
	Average†	0.00	0.00	0.01	0.01	0.01	0.01	0.01	0.01	0.01	0.01	0.02	**0.02**
Cement + gneiss fine aggregate (100 % lighter colour) + nonreactive coarse aggregate + fly ash 50 %	**GN/CV50/F-1**	0.000	0.005	0.004	0.005	0.005	0.005	0.006	0.008	0.009	0.012	0.015	0.016
	GN/CV50/F-2	0.000	0.005	0.004	0.005	0.005	0.006	0.007	0.008	0.009	0.011	0.015	0.017
	GN/CV50/F-3	0.000	0.005	0.005	0.005	0.005	0.006	0.007	0.009	0.009	0.012	0.015	0.017
	Average†	0.00	0.01	0.00	0.00	0.00	0.01	0.01	0.01	0.01	0.01	0.02	**0.02**

NOTE: † Arithmetic mean of the individual values, rounded down to two decimal places as required by the American Standard ASTM C 1293 [10]; the rounding of the arithmetic mean number to two decimal places was performed according to ISO 80000-1 [12] and NIST Special Publication 811 [13].

Table 11 – Length change obtained in the tests performed to determine the susceptibility of a combination of an aggregate with fly ash for participation in expansive ASR (2/2)

Concrete	Test specimen	Average length change (%) at the age of											
		2 d	7 d	28 d	56 d	91 d	182 d	273 d	364 d	455 d	546 d	637 d	728 d
Cement + nonreactive fine aggregate + granodiorite coarse aggregate + fly ash 20 %	**GD/CV20/G-1**	0.000	0.006	0.009	0.010	0.012	0.015	0.018	0.018	0.023	0.027	0.034	0.031
	GD/CV20/G-2	0.000	0.006	0.009	0.010	0.012	0.015	0.016	0.017	0.022	0.025	0.029	0.031
	GD/CV20/G-3	0.000	0.006	0.008	0.010	0.011	0.013	0.016	0.017	0.022	0.025	0.029	0.030
	Average†	0.00	0.01	0.01	0.01	0.01	0.01	0.02	0.02	0.02	0.03	0.03	**0.03**
Cement + granodiorite fine aggregate + nonreactive coarse aggregate + fly ash 20 %	**GD/CV20/F-1**	0.000	0.005	0.007	0.007	0.009	0.010	0.012	0.012	0.017	0.018	0.022	0.023
	GD/CV20/F-2	0.000	0.004	0.006	0.007	0.009	0.009	0.011	0.011	0.015	0.018	0.022	0.020
	GD/CV20/F-3	0.000	0.005	0.007	0.008	0.009	0.011	0.012	0.012	0.016	0.017	0.021	0.021
	Average†	0.00	0.00	0.01	0.01	0.01	0.01	0.01	0.01	0.02	0.02	0.02	**0.02**
Cement + nonreactive fine aggregate + granodiorite coarse aggregate + fly ash 30 %	**GD/CV30/G-1**	0.000	0.004	0.008	0.008	0.008	0.010	0.012	0.013	0.015	0.018	0.019	0.021
	GD/CV30/G-2	0.000	0.006	0.008	0.009	0.010	0.011	0.013	0.014	0.016	0.019	0.020	0.023
	GD/CV30/G-3	0.000	0.006	0.008	0.009	0.010	0.013	0.014	0.015	0.017	0.021	0.024	0.021
	Average†	0.00	0.01	0.01	0.01	0.01	0.01	0.01	0.01	0.02	0.02	0.02	**0.02**
Cement + granodiorite fine aggregate + nonreactive coarse aggregate + fly ash 30 %	**GD/CV30/F-1**	0.000	0.003	0.005	0.005	0.005	0.006	0.010	0.010	0.012	0.013	0.016	0.018
	GD/CV30/F-2	0.000	0.003	0.006	0.005	0.006	0.008	0.009	0.010	0.011	0.013	0.018	0.016
	GD/CV30/F-3	0.000	0.006	0.006	0.005	0.006	0.007	0.009	0.011	0.012	0.014	0.018	0.015
	Average†	0.00	0.00	0.01	0.00	0.01	0.01	0.01	0.01	0.01	0.01	0.02	**0.02**
Cement + nonreactive fine aggregate + granodiorite coarse aggregate + fly ash 50 %	**GD/CV50/G-1**	0.000	0.006	0.007	0.005	0.006	0.008	0.008	0.010	0.011	0.014	0.017	0.017
	GD/CV50/G-2	0.000	0.005	0.005	0.004	0.005	0.006	0.008	0.008	0.008	0.011	0.013	0.014
	GD/CV50/G-3	0.000	0.006	0.006	0.005	0.006	0.007	0.009	0.009	0.010	0.013	0.016	0.017
	Average†	0.00	0.01	0.01	0.00	0.01	0.01	0.01	0.01	0.01	0.01	0.02	**0.02**
Cement + granodiorite fine aggregate + nonreactive coarse aggregate + fly ash 50 %	**GD/CV50/F-1**	0.000	0.004	0.004	0.003	0.004	0.006	0.006	0.007	0.007	0.010	0.014	0.015
	GD/CV50/F-2	0.000	0.005	0.004	0.003	0.004	0.005	0.005	0.006	0.008	0.011	0.014	0.014
	GD/CV50/F-3	0.000	0.006	0.006	0.004	0.005	0.007	0.007	0.009	0.009	0.013	0.016	0.017
	Average†	0.00	0.00	0.00	0.00	0.00	0.01	0.01	0.01	0.01	0.01	0.01	**0.02**

NOTE: † Arithmetic mean of the individual values, rounded down to two decimal places as required by the American Standard ASTM C 1293 [10]; the rounding of the arithmetic mean number to two decimal places was performed according to ISO 80000-1 [12] and NIST Special Publication 811 [13].

Table 12 – Length change obtained in the tests performed to determine the susceptibility of a combination of an aggregate with silica fume for participation in expansive ASR (1/2)

Concrete	Test specimen	Average length change (%) at the age of											
		2 d	7 d	28 d	56 d	91 d	182 d	273 d	364 d	455 d	546 d	637 d	728 d
Cement + nonreactive fine aggregate + gneiss coarse aggregate (100 % lighter colour) + silica fume 5 %	**GN/SF5/G-1**	0.000	0.000	0.009	0.012	0.017	0.025	0.029	0.042	0.049	0.052	0.054	0.058
	GN/SF5/G-2	0.000	0.000	0.008	0.011	0.017	0.025	0.028	0.042	0.049	0.052	0.058	0.063
	GN/SF5/G-3	0.000	0.001	0.009	0.012	0.018	0.024	0.031	0.046	0.055	0.059	0.064	0.069
	Average†	0.00	0.00	0.01	0.01	0.02	0.02	0.03	0.04	0.05	0.05	0.06	**0.06**
Cement + gneiss fine aggregate (100 % lighter colour) + nonreactive coarse aggregate + silica fume 5 %	**GN/SF5/F-1**	0.000	0.002	0.007	0.009	0.011	0.014	0.015	0.022	0.021	0.025	0.026	0.027
	GN/SF5/F-2	0.000	-0.002	0.005	0.006	0.008	0.011	0.011	0.018	0.018	0.021	0.021	0.021
	GN/SF5/F-3	0.000	0.002	0.007	0.010	0.011	0.014	0.014	0.021	0.024	0.026	0.025	0.024
	Average†	0.00	0.00	0.01	0.01	0.01	0.01	0.01	0.02	0.02	0.02	0.02	**0.02**
Cement + nonreactive fine aggregate + gneiss coarse aggregate (100 % lighter colour) + silica fume 10 %	**GN/SF10/G-1**	0.000	0.002	0.007	0.008	0.008	0.013	0.018	0.025	0.028	0.030	0.031	0.030
	GN/SF10/G-2	0.000	0.002	0.008	0.009	0.011	0.014	0.018	0.026	0.029	0.031	0.031	0.033
	GN/SF10/G-3	0.000	0.003	0.008	0.009	0.010	0.014	0.019	0.027	0.031	0.034	0.035	0.034
	Average†	0.00	0.00	0.01	0.01	0.01	0.01	0.02	0.03	0.03	0.03	0.03	**0.03**
Cement + gneiss fine aggregate (100 % lighter colour) + nonreactive coarse aggregate + silica fume 10 %	**GN/SF10/F-1**	0.000	0.002	0.006	0.007	0.008	0.009	0.011	0.016	0.020	0.022	0.022	0.021
	GN/SF10/F-2	0.000	0.001	0.006	0.007	0.008	0.010	0.012	0.018	0.021	0.020	0.020	0.021
	GN/SF10/F-3	0.000	0.002	0.007	0.008	0.009	0.011	0.012	0.018	0.021	0.022	0.021	0.022
	Average†	0.00	0.00	0.01	0.01	0.01	0.01	0.01	0.02	0.02	0.02	0.02	**0.02**

NOTE: † Arithmetic mean of the individual values, rounded down to two decimal places as required by the American Standard ASTM C 1293 [10]; the rounding of the arithmetic mean number to two decimal places was performed according to ISO 80000-1 [12] and NIST Special Publication 811 [13].

Table 13 – Length change obtained in the tests performed to determine the susceptibility of a combination of an aggregate with silica fume for participation in expansive ASR (2/2)

Concrete	Test specimen	Average length change (%) at the age of											
		2 d	7 d	28 d	56 d	91 d	182 d	273 d	364 d	455 d	546 d	637 d	728 d
Cement + nonreactive fine aggregate + granodiorite coarse aggregate + silica fume 5 %	**GD/SF5/G-1**	0.000	0.000	0.009	0.010	0.013	0.016	0.021	0.014	0.028	0.030	0.029	0.025
	GD/SF5/G-2	0.000	0.000	0.009	0.011	0.013	0.014	0.021	0.027	0.026	0.031	0.028	0.033
	GD/SF5/G-3	0.000	0.003	0.010	0.011	0.014	0.016	0.019	0.026	0.027	0.030	0.032	0.028
	Average†	0.00	0.00	0.01	0.01	0.01	0.02	0.02	0.02	0.03	0.03	0.03	**0.03**
Cement + granodiorite fine aggregate + nonreactive coarse aggregate + silica fume 5 %	**GD/SF5/F-1**	0.000	0.003	0.009	0.009	0.011	0.003	0.013	0.016	0.021	0.022	0.023	0.022
	GD/SF5/F-2	0.000	0.004	0.009	0.010	0.012	0.003	0.016	0.016	0.019	0.023	0.020	0.022
	GD/SF5/F-3	0.000	0.004	0.008	0.010	0.011	0.012	0.015	0.012	0.017	0.019	0.020	0.021
	Average†	0.00	0.00	0.01	0.01	0.01	0.01	0.02	0.01	0.02	0.02	0.02	**0.02**
Cement + nonreactive fine aggregate + granodiorite coarse aggregate + silica fume 10 %	**GD/SF10/G-1**	0.000	0.004	0.008	0.009	0.011	0.014	0.017	0.023	0.023	0.023	0.024	0.025
	GD/SF10/G-2	0.000	0.003	0.007	0.008	0.010	0.011	0.016	0.021	0.022	0.021	0.023	0.025
	GD/SF10/G-3	0.000	0.004	0.007	0.009	0.010	0.012	0.016	0.016	0.021	0.022	0.024	0.024
	Average†	0.00	0.00	0.01	0.01	0.01	0.01	0.02	0.02	0.02	0.02	0.02	**0.02**
Cement + granodiorite fine aggregate + nonreactive coarse aggregate + silica fume 10 %	**GD/SF10/F-1**	0.000	0.003	0.006	0.007	0.009	0.010	0.013	0.018	0.018	0.019	0.019	0.020
	GD/SF10/F-2	0.000	0.001	0.005	0.007	0.009	0.009	0.013	0.010	0.017	0.018	0.019	0.020
	GD/SF10/F-3	0.000	0.004	0.007	0.008	0.010	0.012	0.015	0.015	0.019	0.020	0.020	0.021
	Average†	0.00	0.00	0.01	0.01	0.01	0.01	0.01	0.01	0.02	0.02	0.02	**0.02**

NOTE: † Arithmetic mean of the individual values, rounded down to two decimal places as required by the American Standard ASTM C 1293 [10]; the rounding of the arithmetic mean number to two decimal places was performed according to ISO 80000-1 [12] and NIST Special Publication 811 [13].

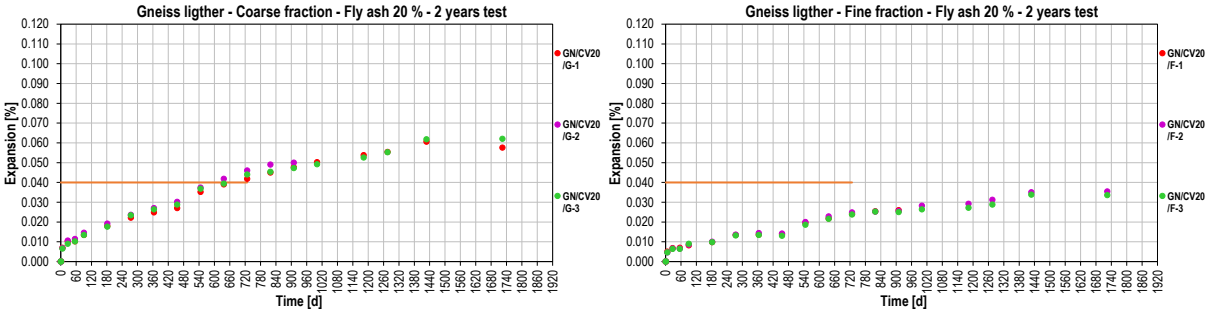

Fig. 13 – Length change of the concrete prisms, observed in the ASTM C1293 test, for the concrete mixtures GN/CV20/G and GN/CV20/F.

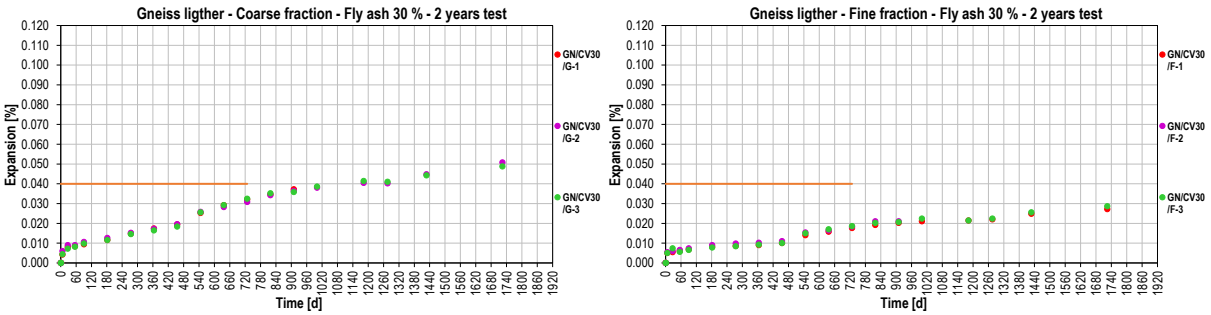

Fig. 14 – Length change of the concrete prisms, observed in the ASTM C1293 test, for the concrete mixtures GN/CV30/G and GN/CV30/F.

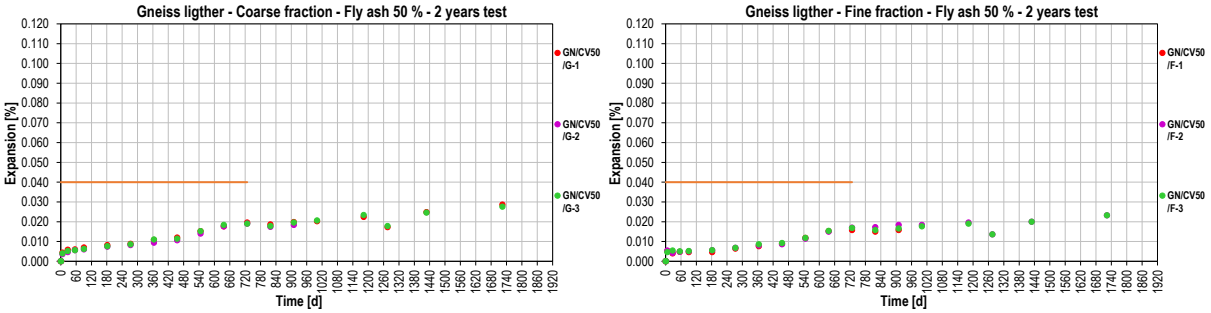

Fig. 15 – Length change of the concrete prisms, observed in the ASTM C1293 test, for the concrete mixtures GN/CV50/G and GN/CV50/F.

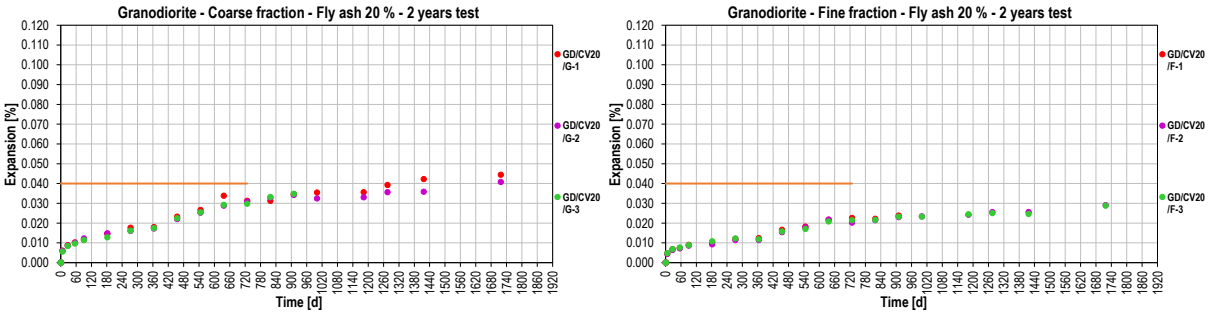

Fig. 16 – Length change of the concrete prisms, observed in the ASTM C1293 test, for the concrete mixtures GD/CV20/G and GD/CV20/F.

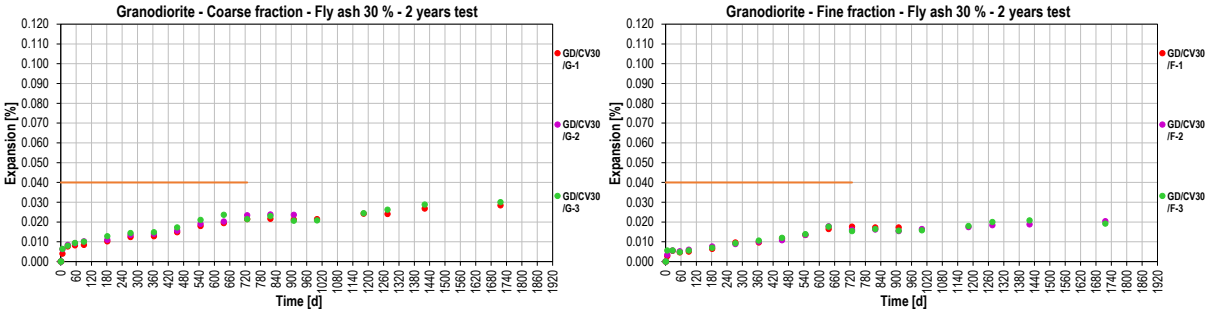

Fig. 17 – Length change of the concrete prisms, observed in the ASTM C1293 test, for the concrete mixtures GD/CV30/G and GD/CV30/F.

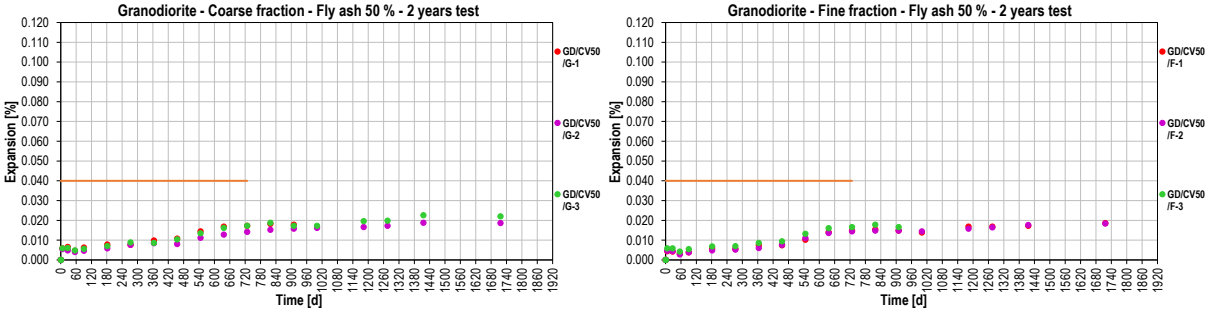

Fig. 18 – Length change of the concrete prisms, observed in the ASTM C1293 test, for the concrete mixtures GD/CV50/G and GD/CV50/F.

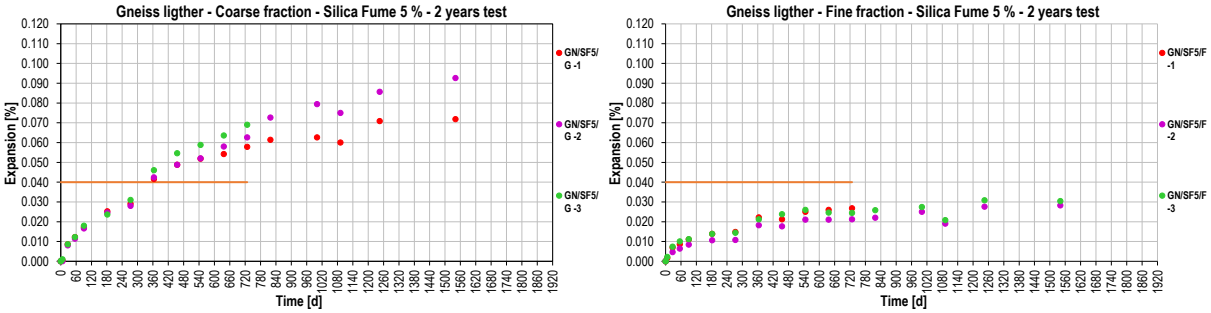

Fig. 19 – Length change of the concrete prisms, observed in the ASTM C1293 test, for the concrete mixtures GN/SF5/G and GN/SF5/F.

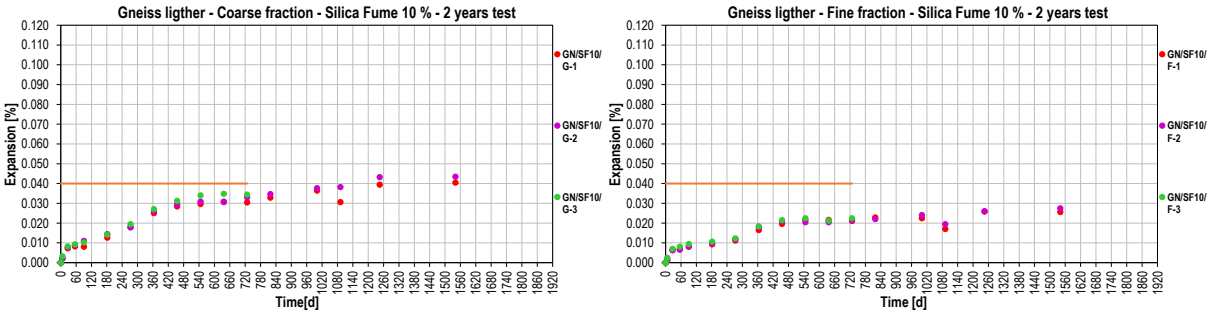

Fig. 20 – Length change of the concrete prisms, observed in the ASTM C1293 test, for the concrete mixtures GN/SF10/G and GN/SF10/F.

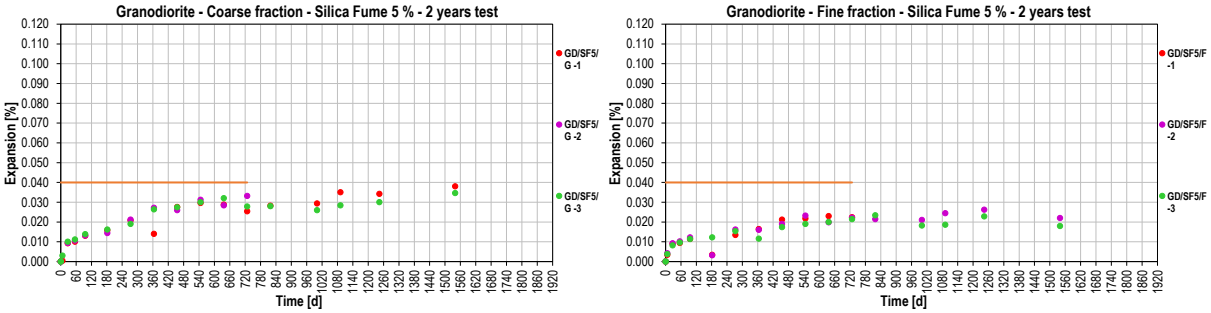

Fig. 21 – Length change of the concrete prisms, observed in the ASTM C1293 test, for the concrete mixtures GD/SF5/G and GD/SF5/F.

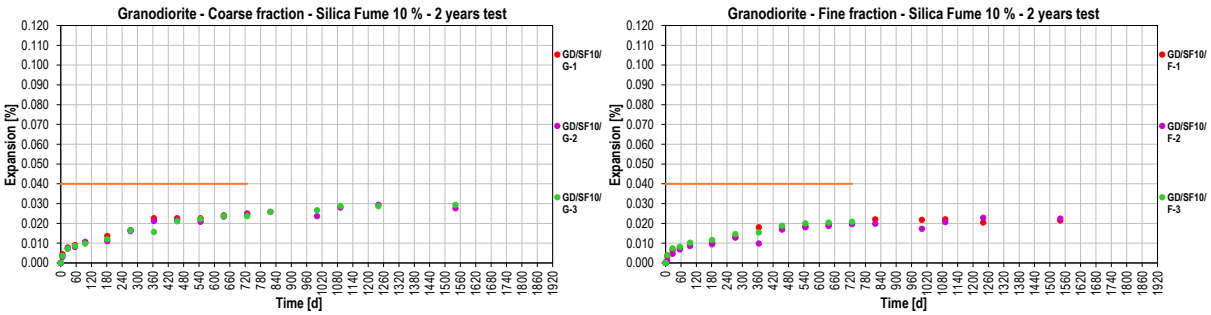

Fig. 22 – Length change of the concrete prisms, observed in the ASTM C1293 test, for the concrete mixtures GD/SF10/G and GD/SF10/F.

According to the standard test method ASTM C1293 [10], it is reasonable to conclude that the amount of pozzolan or slag used in combination with an aggregate is at least the minimum needed to prevent excessive expansion in field concrete if the average expansion, of three concrete specimens, is less than 0.04% at two years. ASTM C1778 [14] states that if expansions are <0.04% at two years on the ASTM C1293 test, the combination of pozzolan and reactive aggregate is considered suitable for use in concrete construction. It also refers that the expansion of concrete prisms produced with Portland cement (Specification C150/C150M Type I) with the alkali content raised to 1.25% Na_2O_{eq} provides a reliable prediction of the field expansion of concrete produced with portland cements with alkali contents up to 1.00% Na_2O_{eq}. If the cement to be used in the field has an alkali content above 1.00% Na_2O_{eq}, this same cement should be used for the concrete prism test and the alkali content should be raised by 0.25% Na_2O_{eq} by the addition of NaOH to the mix water.

From the results presented in Table 10, it can be observed that the tested combinations of gneiss aggregate (100 % lighter colour) with fly ash (used at cement replacement levels of 20%, 30% and 50%, in mass) exhibited an average expansion of less than 0.04% in the 2 years test period; the only exception was the combination of the gneiss coarse aggregate (100 % lighter colour) with 20% fly ash, which presented an expansion of 0.04%. Therefore, it is possible to conclude from these tests that:

(i) fly ash in an amount of 20% (by mass of cement), in combination with the gneiss fine aggregate (100 % lighter colour) - Fig. 13 - is likely to be sufficient to prevent excessive

expansion in field concrete (produced with the gneiss fine aggregate, 100 % lighter colour, and the fly ash in the mentioned cement replacement level); and

(ii) fly ash in an amount of 30% (by mass of cement), in combination with the gneiss coarse aggregate (100 % lighter colour) - Fig. 14 - is likely to be sufficient to prevent excessive expansion in field concrete (produced with the gneiss coarse aggregate, 100 % lighter colour, and the fly ash in the mentioned cement replacement level).

From the results presented in Table 12, it can be observed that the tested combinations of gneiss aggregate (100 % lighter colour) with silica fume (used at cement replacement levels of 5% and 10%, in mass) exhibited an average expansion of less than 0.04% in the 2 years test period; the only exception was the combination of the gneiss coarse aggregate (100 % lighter colour) with 5% silica fume, which presented an expansion of 0.06%. Therefore, it is possible to conclude from these tests that:

(i) silica fume in an amount of 5% (by mass of cement), in combination with the gneiss fine aggregate (100 % lighter colour) - Fig. 19 - is likely to be sufficient to prevent excessive expansion in field concrete (produced with the gneiss fine aggregate, 100 % lighter colour, and the silica fume in the mentioned cement replacement level); and

(ii) silica fume in an amount of 10% (by mass of cement), in combination with the gneiss coarse aggregate (100 % lighter colour) - Fig. 20 - is likely to be sufficient to prevent excessive expansion in field concrete (produced with the gneiss coarse aggregate, 100 % lighter colour, and the silica fume in the mentioned cement replacement level).

From the results presented in Table 11, it can be observed that all tested combinations of granodiorite aggregate with fly ash (used at cement replacement levels of 20%, 30% and 50%, in mass) exhibited an average expansion of less than 0.04% in the 2 years test period. Therefore, it is possible to conclude that fly ash in an amount of 20% (by mass of cement), in combination with the granodiorite aggregate - Fig. 16, Fig. 17, Fig. 18 - is likely to be sufficient to prevent excessive expansion in field concrete (using the granodiorite as either fine or coarse aggregate and the fly ash in the mentioned cement replacement level).

From the results presented in Table 13, it can be observed that all tested combinations of granodiorite aggregate with silica fume (used at cement replacement levels of 5% and 10%, in mass) exhibited an average expansion of less than 0.04% in the 2 years test period. Therefore, it is possible to conclude that silica fume in an amount of 5% (by mass of cement), in combination with the granodiorite aggregate - Fig. 21, Fig. 22 - is likely to be sufficient to prevent excessive expansion in field concrete (using the granodiorite as either fine or coarse aggregate and the silica fume in the mentioned cement replacement level).

The SEM/EDS observations (not reported in the present paper), made to identify the presence of products from internal expansive chemical reactions, confirm that the expansion observed in the tests has indeed resulted from ASR.

It should be mentioned that the considerations made here are only valid for aggregates, fly ash and silica fume of the same nature, and having the same chemical and physical characteristics, as those tested in the present study. If deviations in the materials are envisaged or detected, e.g., aggregate or pozzolan from new sources, tests shall be performed to those materials to verify their behaviour towards ASR.

5. CONCLUSIONS

This paper presented the laboratory test campaign performed to aggregates intended to be used in concrete for Caculo Cabaça HPP. The aggregates were obtained locally from the bedrock removed during the geological survey performed before HPP construction. Since, the main rock type (gneiss with plagioclase amphibolite and cataclasite) of the bedrock is known to be potentially alkali-reactive, the main existing varieties were collected and assessed in terms of their potential alkali-silica reactivity. The rocks were categorised into three varieties: granodiorite, gneiss lighter colour, gneiss darker colour. Furthermore, the efficacy of pozzolans (fly ash and silica fume) in mitigating the deleterious development of alkali-silica reaction (ASR) in concrete produced with them was also assessed.

The assessments, done according to the standard test method ASTM C1293, allowed to characterise the alkali-silica reactivity of the aggregate varieties collected from the HHP construction site and determine the amount of pozzolan need to control ASR in concrete produced with them; thus, allowing for the definition of the concrete mixtures to be used in the Caculo Cabaça HPP.

Considering the (i) results obtained in the present study; (ii) observed ASR reactivity potential of the aggregates; (iii) possibility of the aggregates to contribute with alkalis to ASR; (iv) uncertainty existing in the scientific community in respect to the expansion limits that must be fulfilled by this type of aggregates; (v) long-term expansion profile observed in the laboratory reactivity tests; (vi) current concerns in the scientific community that some concrete compositions containing SCMs may actually suffer the same ultimate expansion level as the compositions without the SCMs, but in a delayed and slowly progressive way, so that the final effect on the concrete would be similar to that observed in compositions without SCMs, although at a much later age of the structure; it would be interesting, from a scientific perspective, to complement the already performed test campaign with the production of concrete blocks, with selected concrete mixtures, to assess their long-term field performance.

It would also be useful to determine the aggregates alkali-release potential, and to perform expansion tests with the concrete(s) mixture(s) to be used in the structure.

REFERENCES

[1] Swamy, R. N., "The Alkali-Silica Reaction in Concrete", 1st ed., Blackie and Son Ltd.: Glasgow and London, 1992.

[2] Sims, I. & Poole, A., "Alkali-Aggregate Reaction in Concrete. A World Review". CRC Press: London, UK, 2017.

[3] Sims, I. & Poole, A., "Despite Stanton: AAR from denial to remedy in the UK, Europe & the World", in 16th International Conference on Alkali-Aggregate Reaction – ICAAR 2020-2022. Lisbon, Portugal. 2022.

[4] Custódio, J.; Silva, A. S.; Costa, D. & Miquithaio, Â., "Diagnosis and Prognosis of Internal Swelling Reactions in Cahora Bassa Dam – A Case Study", in *Proceedings of the 17th International Conference on Alkali-Aggregate Reaction in Concrete*, Sanchez, L. F. M. & Trottier, C. (Eds.). Springer Nature Switzerland: Cham, 2024. https://doi.org/10.1007/978-3-031-59349-9_41

[5] Nixon, P. J. & Sims, I., "RILEM Recommendations for the prevention of damage by alkali-aggregate reactions in new concrete structures (State-of-the-Art Report of the RILEM Technical Committee 219-ACS)", in *RILEM State-of-the-Art Reports*. Springer: Dordrecht, NL, 2016. https://doi.org/10.1007/978-94-017-7252-5

[6] CEN, "EN 450-1:2012 Fly ash for concrete. Definition, specifications and conformity criteria". European Committee for Standardization (CEN): Brussels, 2012.

[7] CEN, "EN 196-1:2005 Method of testing cement. Part 1: Determination of strength". European Committee for Standardization (CEN): Brussels, Belgium, 2005.

[8] CEN, "EN 197-1:2011 Cement. Composition, specifications and conformity criteria for common cements". European Committee for Standardization (CEN): Brussels, Belgium, 2011.

[9] CEN, "EN 196-2:2013 Method of testing cement. Part 2: Chemical analysis of cement". European Committee for Standardization (CEN): Brussels, Belgium, 2013.

[10] ASTM, "ASTM C1293-08b (Reapproved 2015) Standard Test Method for determination of length change of concrete due to alkali-silica reaction". ASTM International: West Conshohocken, PA, 2015.

[11] ASTM, "ASTM C1260-14 Standard Test Method for Potential Alkali Reactivity of Aggregates (Mortar-Bar Method)". ASTM International: West Conshohocken, PA, 2014.

[12] ISO, "ISO 80000-1:2009 Quantities and units. Part 1: General". International Organization for Standardization (ISO): Geneva, 2009.

[13] Thompson, A. & Taylor, B. N., "NIST Special Publication 811. Guide for the Use of the International System of Units (SI)". National Institute of Standards and Technology (NIST), U.S. Department of Commerce: Gaithersburg, MD, USA, 2008.

[14] ASTM, "ASTM C1778-23 Standard Guide for Reducing the Risk of Deleterious Alkali-Aggregate Reaction in Concrete". ASTM International: West Conshohocken, PA, 2023.

Fifth International Dam World Conference
PORTUGAL • LISBON • LNEC • APRIL 13-17, 2025
dam world 2025

RIVER DIVERSION OF THE CACULO CABAÇA HYDROPOWER PROJECT

Cristina Costa[1]	Gonçalo Mateus[2]	António Amador[3]	António Morgado[4]	Augusto Chico[5]	Xiong Zebin[6]	Liu Wen[7]
COBA	COBA	COBA	COBA	GAMEK	CSPDR	CGGC

ABSTRACT

The Caculo Cabaça Hydropower Project, located in the Kwanza River in Angola, with a 112 663 km^2 watershed and 587 m^3/s average flow, features a nominal capacity of 2 172 MW. The scheme includes a dam, two saddle dams, a main powerhouse with an underground waterway and an ecological powerhouse on the left bank side of the spillway, at the dam's toe.

The Caculo Cabaça dam is a 116 m-high RCC gravity dam with a crest length of 533 m. The dam includes a frontal spillway, controlled by five radial gates, for a design flood of 10 020 m^3/s, a double bottom outlet with 1 489 m^3/s design flow and the water intake of the ecological powerhouse.

The dam's construction included a river diversion design for a maximum flow of 3 400 m^3/s, with a 25-year return period. To dry the dam's riverbed foundation, two rockfill cofferdams were used adopting for seepage control a clayey core and a clay blanket respectively on the upstream and downstream cofferdams. The river was diverted through two tunnels, on the right bank, surrounding the area limited by the cofferdams, each with a horseshoe cross section measuring 14.4m in width and height, and extending about 357 m and 415 m. A canal with 60m-wide and 220 m-long connects the river to the tunnels' inlet, where is located a 28.5 m-long reinforced concrete structure which accommodates 6 stoplogs and a fixed wheel gate.

Currently this HPP in under construction by CGGC through an EPC contract in which CSPDR is responsible for the development of the Civil Construction Design and COBA, author of the Detailed Design, is responsible for its review and approval also providing technical assistance to the Owner (GAMEK).

This paper presents the main features of the Caculo Cabaça river diversion and addresses the constraints imposed to the construction design by the geological and geotechnical features of the rock mass and the results of the hydraulic physical model tests performed to verify the flow discharge capacity, water levels and flow conditions of the diversion tunnels and to assist in the design of the river closure.

Keywords: Caculo Cabaça, Hydropower, River Diversion, Cofferdams

[1] c.costa@cobagroup.com, Portugal
[2] g.mateus@cobagroup.com, Portugal
[3] a.amador@cobagroup.com, Portugal
[4] a.morgado@cobagroup.com, Portugal
[5] augusto.chico@gamek.gov.ao, Angola
[6] xiongzebin@cjwsjy.com.cn, China
[7] liuwen@cggcintl.com, China

1. INTRODUCTION

Angola is developing several major hydropower projects under the national Energy Development Program to meet growing electricity demand and promote social and economic development.

The Caculo Cabaça Hydropower Project (HPP) in Angola is the third scheme of a seven-step cascade development on the middle Kwanza River, downstream Capanda and Laúca HPP.

With a total drainage area of 151 250 km^2, the Kwanza River has its source in the Maçamba and Malange plateaus, near the city of Huambo, at elevation (1 500). It crosses the provinces of Huambo, Bié, Cuanza Sul, Cuanza Norte, Bengo and Luanda, covering a distance of 1 000 km before reaching the Atlantic Ocean, about 60 km south of Luanda.

The river basin and network are divided into three main units: Upper, Middle, and Lower Kwanza (Fig. 1). The Middle Kwanza spans about 23 000 km^2 and 200 km in length, located between the Cangandala bridge and Cambambe following an East-West direction (Fig. 1). This river section features major falls and rapids, making it ideal for hydropower development.

Fig. 1 – The Kwanza River basin

The Kwanza Basin has a tropical climate, with a winter dry season. Average annual rainfall ranges from 1 400 mm in the center to 600 mm near the coast, averaging around 1 200 mm across the whole basin.

Given the significant hydropower potential of the Kwanza River's middle course, large flows, available heads, and proximity to Luanda, a cascade development of 7 schemes has long been planned (Fig. 2).

By around 2030, the existing hydropower projects under operation - Capanda, Laúca (2 069 MW), Cambambe 1 Power upgrade (266 MW), Cambambe 2 (714 MW), together with Caculo Cabaça (2 172 MW) - will provide a reliable supply of electricity to both the region and the entire country. One of the primary objectives of the Angolan government is now to construct transmission lines that will ensure the efficient distribution of energy to all provinces.

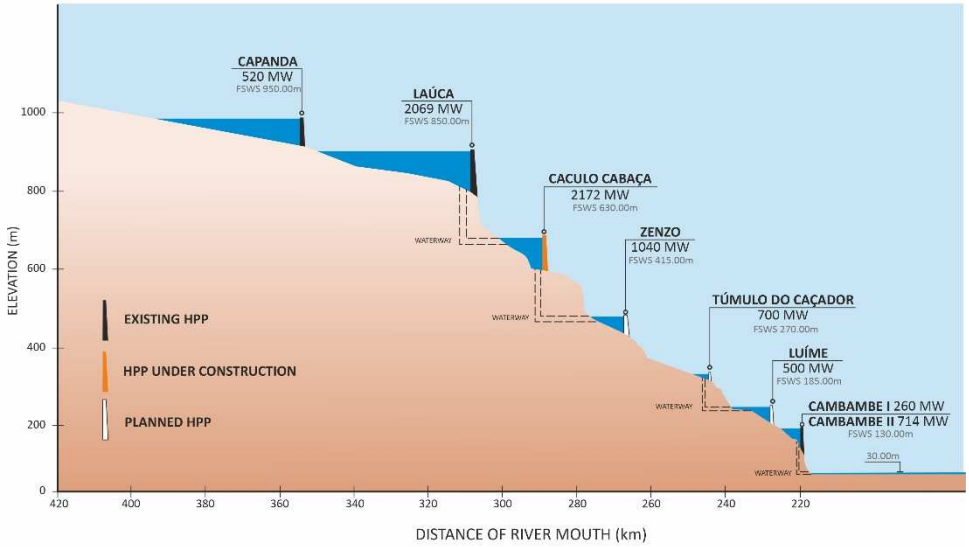

Fig. 2 - Existing, under construction and planned hydropower schemes in the Kwanza River

2. OVERVIEW OF CACULO CABAÇA HYDROPOWER PROJECT

The Caculo Cabaça Hydropower Project (HPP) in Angola has a nominal capacity of 2172 MW and is the third stage of the cascade development along the Kwanza River. It is located 19 km downstream from Laúca HPP, 70 km upstream from Cambambe HPP, and 260 km southeast of Luanda. The project covers a watershed area of 112 663 km^2 with an average flow rate of 587 m^3/s. It includes a main dam, two saddle dams, an underground waterway, and a powerhouse, and an additional ecological flow powerhouse on the left side of the spillway (Fig. 3).

Fig. 3 - Aerial overview of the Caculo Cabaça Hydropower Project

During the construction design phase, the layout of the Caculo Cabaça dam was adjusted based on new bathymetric and topographic surveys and geological and geotechnical studies, based on the comprehensive survey undertaken at this stage. The final layout consists of a

116 m-high RCC gravity dam 533 m-long at the crest at elevation (633). The bedrock is mainly gneiss with plagioclase amphibolite and cataclasite band parallel to the river developed between low elevation of right bank and right side of the riverbed blocks. The dam's cross section was optimized with a downstream face slope change from 0.85h/1v to 0.80h/1v and a vertical upstream face above elevation (560), sloping 0.20h/1v below that point. The adoption of this cross section allows a reduction in the concrete volume of the dam of about 60 000 m^3, using as reference the dam foundation surface defined in the Tender Design (Fig. 4). At full supply level (elevation 630), the reservoir holds 436 hm^3 and covers 16.6 km^2.

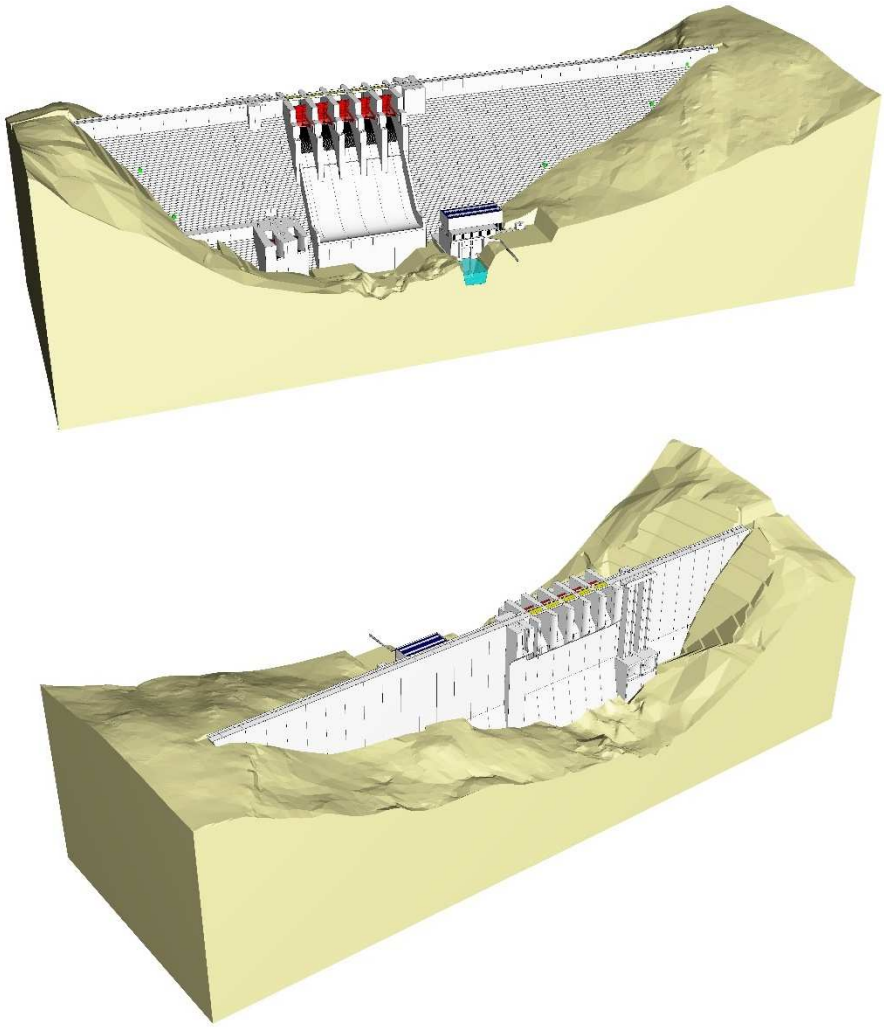

Fig. 4 - Caculo Cabaça dam overview

A frontal overflow spillway with a design flood capacity of 10 020 m^3/s is in the central blocks of the dam, aligned with the main riverbed. The spillway is divided into five bays, with its crest at elevation (612.5) and it is controlled by radial gates, each one 12.4 m-wide by 19.3 m-high. The flow is guided along the downstream surface of the dam onto a flip-bucket that directs the water into an excavated plunge pool.

The right side of the spillway houses a double bottom outlet with a maximum discharge flow of 1 489 m^3/s at FSWL. Each bottom outlet includes a 6 m-wide by 7.5 m-high fixed-wheel safety

gate, a 6 m diameter steel liner, and a 5 m-wide by 5.1 m-high radial gate for flow regulation. A numerical model study recommended and led to the adoption of a jet deflection structure at the exit of the bottom outlets to prevent scouring on the right bank, which might cause slope instability.

In the construction design phase, an alternative solution for the waterway system ecological flow powerhouse was chosen over the solution of the Tender Design. This new approach features a water intake structure within the dam, raising the inlet sill from elevation (566) to (612) which connects to a penstock embedded in the dam's concrete, aligned parallel to the downstream face of the dam (Fig. 5).

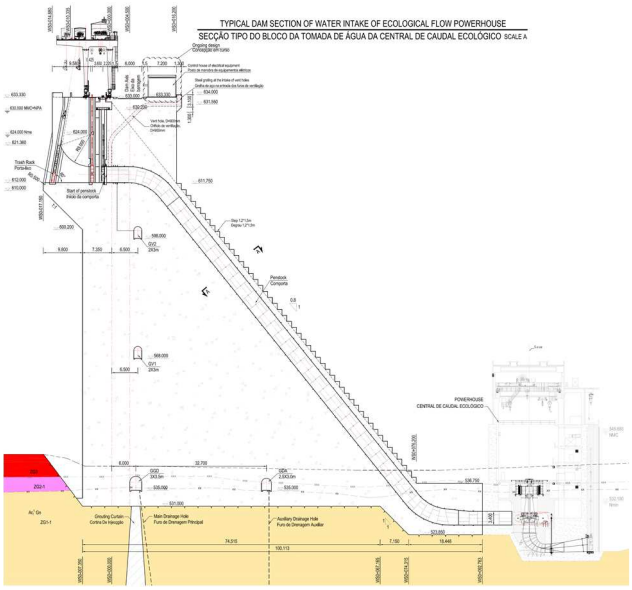

Fig. 5 - Cross-section of the water intake for the ecological flow powerhouse

Two saddle dams on the left bank are essential to close the reservoir at full supply and maximum water levels. These dams, featuring an RCC gravity profile, will have a maximum height of 39.5 m and a total crest length of 714 m.

The waterway system of the main powerhouse on the left bank is entirely underground and designed for a water discharge of 1 100 m^3/s. The water intake structure, located 2.4 km upstream from the dam's left abutment, conveys the flow to four reinforced concrete-lined vertical pressure shafts with 9 m diameter, involving a vertical drop of 190 m (Fig. 6 and Fig. 7).

Fig. 6 - Water intake structure in the reservoir and switchyard (behind)

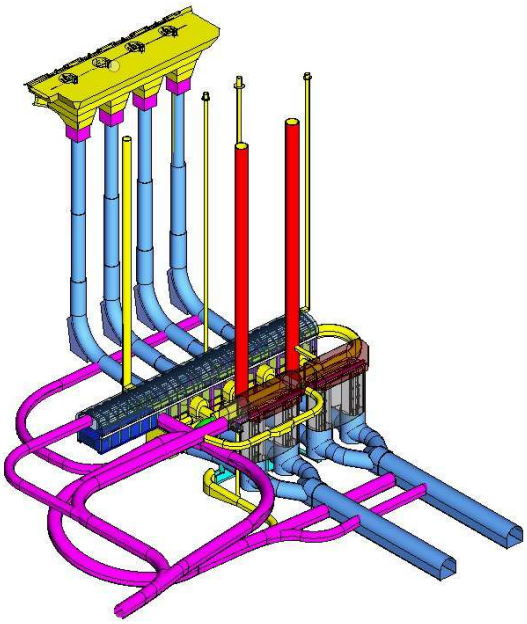

Fig. 7 - Underground waterway system and powerhouse

Four steel-lined headrace tunnels, 60 m long and 6.5-m in diameter, lead to the underground powerhouse. The cavern housing the powerhouse is 26.5 m-wide and 221 m-long, with a height of 68 m in the turbine-generator area and 28 m in the equipment assembly hall.

The underground powerhouse is equipped with four Francis vertical axis turbines with a nominal capacity of 530 MW, coupled to a 590 MVA generator, operating at a nominal net head of 209 m.

The connection to the transformers located on the surface is established through 21 kV isolated busbars installed in two shafts, each with a diameter of 9 m and heights of 243 m (Fig. 7). The switchyard is located beside the transformers on a platform (Fig. 6).

The powerhouse has two double girder overhead cranes with a 550-t capacity for equipment assembly, disassembly, and maintenance (Fig. 8). The average annual energy generation is around 8 120 GWh.

Fig. 8 - Longitudinal section of the underground powerhouse

Two pressurized tailrace tunnels, each about 5 200 m-long with a 0.4% upslope, carry out the water from the powerhouse to the Kwanza River. The unlined tunnels have an arch-rectangle cross-section, 16 m-wide and 16 m-high. At their ends, a U-shaped reinforced concrete canal (70x50m^2 in plan, 24 m-high) accommodates two stoplogs for dewatering the tunnels.

The mass oscillation system, designed for transient pressures and to maintain the stability of the hydraulic circuit, comprises two surge chambers, located 79 m downstream of the powerhouse, each one with an area of approximately 1 000 m^2 and 65.5 m-high, capped with a semi-cylindrical dome measuring 24 m in diameter (Fig. 7).

To utilize the 60 m^3/s ecological flow required between the dam and the main waterway's outlet, a small powerhouse will be built. This powerhouse, located at the dam's toe on the left side of the spillway, is partially buried, is equipped with a 52 MW Francis vertical axis turbine for a 94.6 m net head, connected to a 57 MVA generator and transformer via busbars.

The Caculo Cabaça HPP includes approximately 19 km of access roads, with a 9.0 m wide platform. Access to the main powerhouse includes a bridge over the Kwanza River (230 m-long and 20 m-high) and a 1.5 km tunnel with a 9.5 m wide and 8.75 m high arch rectangular cross section.

Fig. 9 - Overview of the bridge over the Kwanza River

3. GENERAL DESCRIPTION OF THE RIVER DIVERSION

3.1. Overall design

The dam construction is protected by an upstream and a downstream rockfill cofferdams, drying the riverbed in an extension of about 200 m, and the river was diverted through two tunnels, located into the right bank, surrounding the area limited by the cofferdams (Fig. 10).

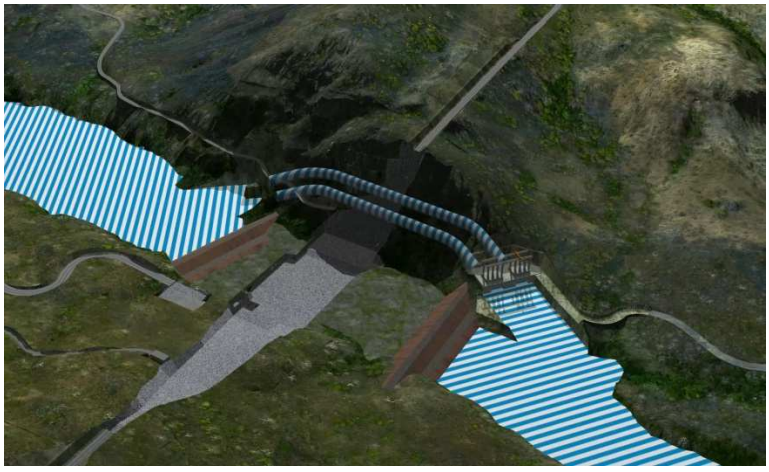

Fig. 10 - Diversion tunnels on the right bank and cofferdams

The river diversion was designed for a maximum flow of 3 400m^3/s associated to a 25 years' return period and a freeboard of about 2 m was guaranteed in the upstream and downstream cofferdams.

An entrance channel, 60 m-wide and 240 m medium extension, connects the river to the tunnels' inlet and an outlet channel, with equivalent width and an extension of 100 m, returns the water from the tunnels to the riverbed. These entrance and outlet channels were built using natural cofferdams, remained in place until the diversion tunnels became operational (Fig. 11 and Fig. 12).

To allow the closure of the diversion tunnels, a reinforced concrete tunnels' inlet structure was built in order to execute this closure with gates. Since this structure will be inaccessible after the reservoir is filled, and subject to about 100 mWC pressure, the tunnels will be permanently sealed with concrete plugs.

Fig. 11 – Aerial view of the layout of diversion tunnels: left-side during construction and right-side during operation

3.2. Diversion Tunnels

The diversion tunnels present a horseshoe cross section with 14.4 m maximum width and height and extensions of about 357 m and 415 m. In the longitudinal profile, after the initial flat section, the tunnels present an inclination of about 0.5% until the exit mouth, and an axis distance in plan of 36 m between them (Fig. 12).

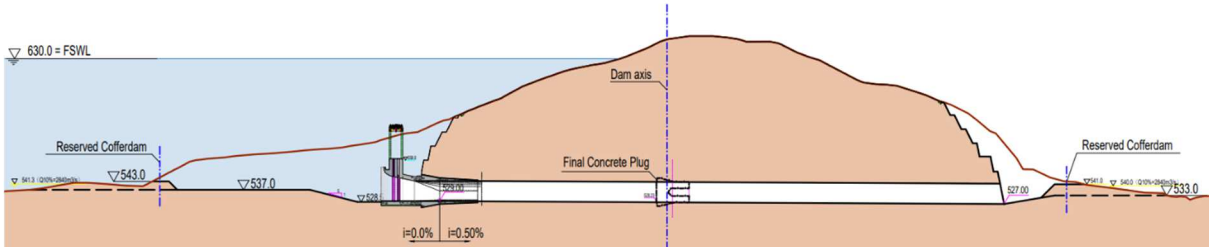

Fig. 12 – Longitudinal Profile of Diversion Tunnel 1

Considering that the stoplog gates placed at the tunnels inlet structure will be definitively inaccessible, the tunnels will be permanently sealed with reinforced concrete (RC) plugs placed at the crossing of dam's axis (Fig. 12), where the rock cover is higher and, if necessary, a specific grout curtain can be executed in the alignment of the grout curtain of the dam to cut-off seepage.

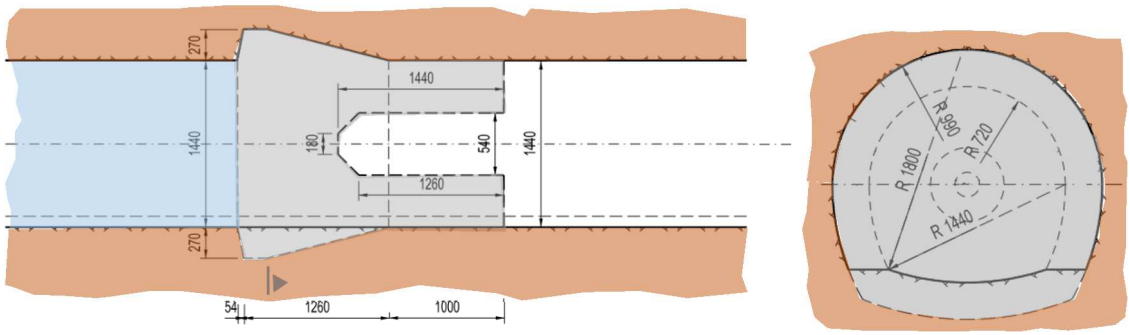

Fig. 13 – Tunnel's RC plug: longitudinal section (left) and cross section (right) (dimensions in centimetres)

Generally, the tunnels are lined with shotcrete, reinforced with steel fibres, with a thickness varying from 5 cm (Q≥10) to 15 cm (Q<0.09), depending on the quality of the rock mass. At the tunnels' portals, and at the crossing of fault zones, the shotcrete lining is reinforced with steel profiles TH29 or rebar lattice girders. The initial branch of the tunnels is lined with reinforced concrete (Fig. 14) in an extension compatible with the hydraulic gradient that the rock-mass can bear during the provisional phase where the stoplogs are placed at the inlet structure, the reservoir is full, and the concrete plugging of the tunnels are not yet executed.

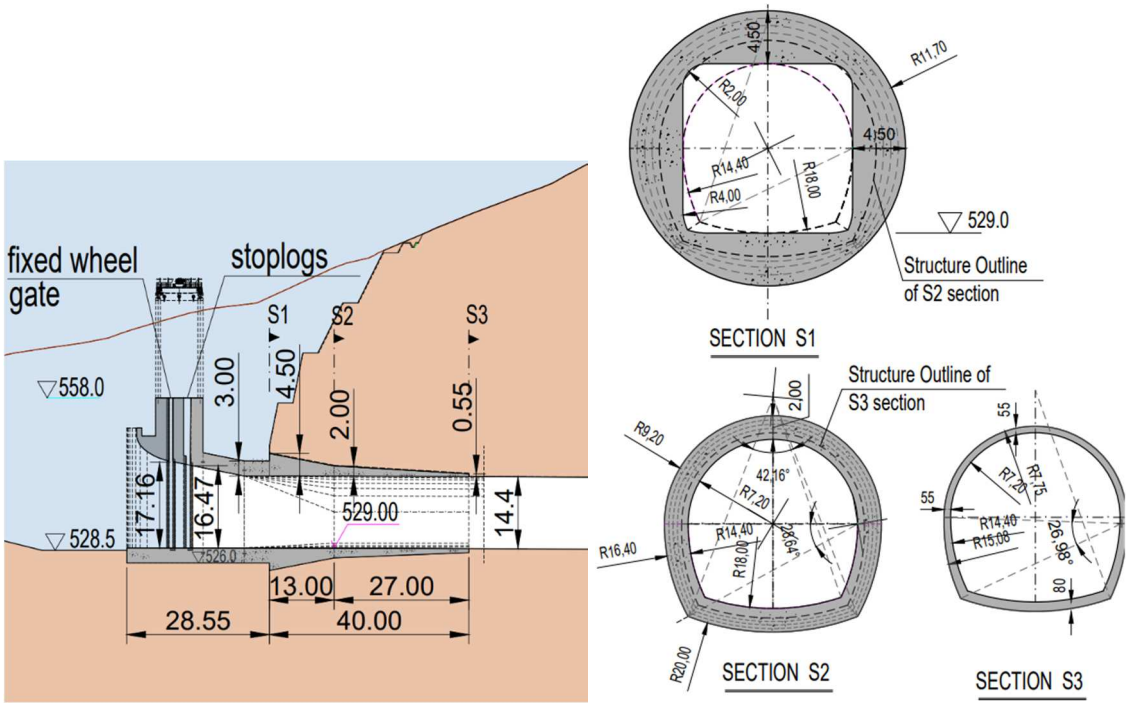

Fig. 14 – Tunnels' RC lining at initial stretch

Fig. 15 – Tunnels' inlet (before the execution of the RC lining) (left) and tunnels' outlet (right)

3.3. Inlet Structure

The inlet structure of the diversion tunnels is a 28.5 m-long, 33.0 m-high reinforced concrete structure designed to accommodate the gates for the closure of the tunnels withstanding a hydraulic pressure with the reservoir at full supply level. Considering the dimensions of each inlet and the hydraulic pressure of about 100 mWC, the total width of each inlet was divided by 3 spans of 3.70 m (Fig. 16).

Two gate slots were planned: one upstream for the fixed wheel gate to control water closure, and one downstream for stoplogs to retain water until tunnels plugs are built (Fig. 14). A 100-ton overhead crane supported by a concrete frame structure is foreseen to operate the gates. Six stoplogs (three per tunnel), 3.70 m-wide and 17.16 m-high, and one fixed wheel gate, 3.70 m-wide and 16.47 m-high, which will be used to cut the water flow in each span to allow the placement of the stoplogs, have been planned.

Fig. 16 – Inlet structure of the diversion tunnels: external view (left) and internal view (right)

3.4. Cofferdams

The construction of the dam is currently being executed with the protection provided by upstream and downstream cofferdams, which have approximate heights of 30 m and 18 m, and crest lengths of 212 m and 149 m, respectively. A trapezoidal cross-sectional profile with a slope ratio of 1:1.5 (V:H) has been adopted, with the upstream cofferdam featuring a crest width of 8 m, and the downstream cofferdam a crest width of 14 m, facilitating vehicular access (Fig. 17 and **Fig. 18**).

The upstream cofferdam, located about 120 m upstream of the dam axis, is designed with a clay-core wall for seepage control, while the downstream cofferdam employs an inclined clay wall, constructed through surface dumping, for seepage mitigation. Additionally, two pre-cofferdams have been established at the upstream and downstream toes of the main cofferdams, each comprising inclined clay walls, dumped from the outer faces, to prevent seepage. Both cofferdams considered the use of released rockfill material for the pre-cofferdam and compacted rockfill for the outer shells, obtained from the diversion tunnels' excavations. Filter and transition layers were adopted between the clay material and the rockfill.

Both the upstream and downstream cofferdams were constructed on a dry foundation.

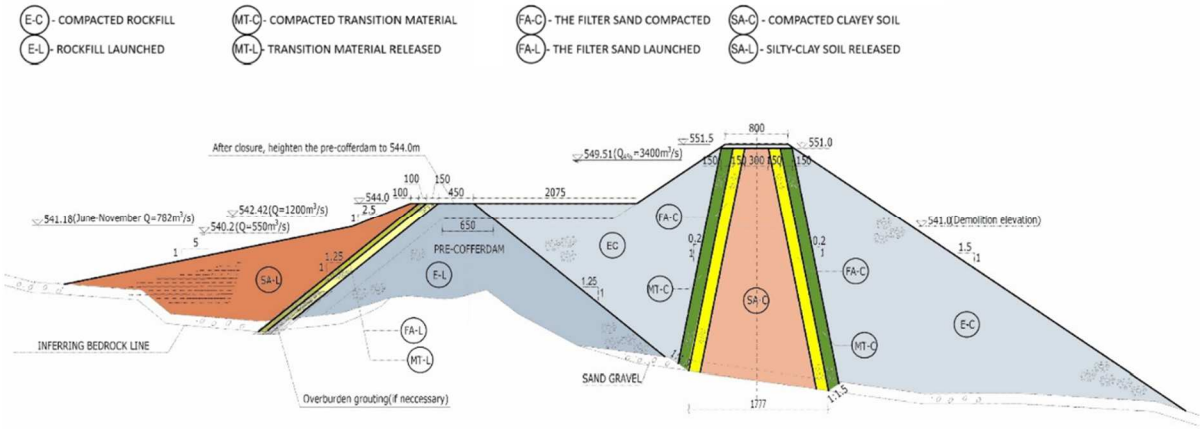

Fig. 17 - Upstream cofferdam typical profile

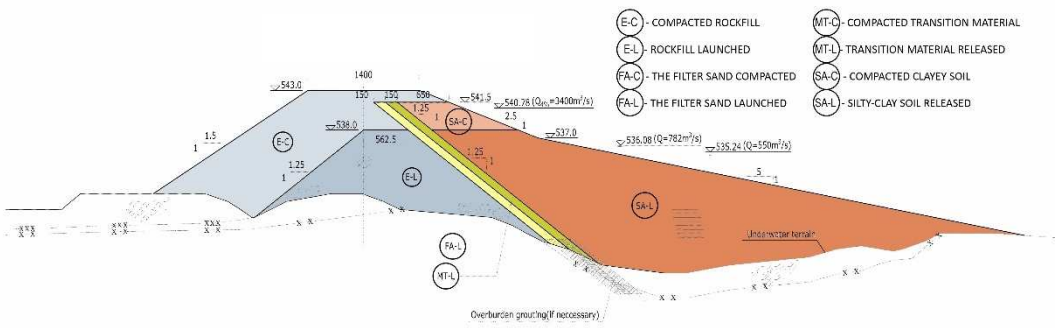

Fig. 18 - Downstream cofferdam typical profile

In terms of construction phasing, both cofferdams started with the installation of a pre-cofferdam to close off the river, using the embankment toe method, which involved the placement of appropriately sized rockfill, starting from the ends near the riverbanks and progressing towards the center until the river is fully closed. To ensure impermeability of the pre-cofferdams, a transition granular material and clayey soil were placed on the water side of the rockfill. Under the protection of the pre-cofferdams, the main cofferdams could be constructed in dry conditions using compacted layers.

In case the seepage flow through the cofferdams' foundation would be considered significative, eventual grouting injections with cementitious material were foreseen to be carried out at the interface between the dumped clay material and the transition material.

4. MAJOR DESIGN ASPECTS AND CONSTRAINTS FACED DURING THE DEVELOPMENT OF THE CONSTRUCTION DESIGN

4.1. Geological and Geotechnical setting

From a lithological perspective, the Caculo Cabaça Hydropower Project (HPP) region, is primarily composed of gneisses, with occasional intercalations of migmatites and amphibolites from the Base Complex, dating from the Lower Proterozoic.

Geotechnical data gathered during early investigations, including borehole samples, seismic refraction profiles, and electrical resistivity measurements, revealed a rock mass predominantly made up of compact crystalline rocks exhibiting good geomechanical conditions.

On the right bank, the geomorphological characteristics of the slope, which has an angle of 35° from the riverbed to intermediate elevations and 50° higher up, uncovered a weaker geotechnical zone. This zone, associated with a significant cataclastic band, extends up to 150 m - wide along the dam axis. Geotechnical site investigations performed during the design phase exposed the presence of a poor-quality rock mass, heavily weathered and decomposed (W4-W5), and intensely jointed (F4-F5), extending up to depths of 24 m in tunnel 1's inlet zone and 16 meters in tunnel 2's inlet zone. This condition represented a major geotechnical constraint for construction, as the poor-quality rock mass extended approximately 5 m below the roof of tunnel 1 and around 7 m above the roof of tunnel 2.

Further analysis of the geotechnical data revealed that the poor-quality rock mass generally followed the slope's topography, becoming thicker towards the river and decreasing inland. As a result, several design modifications were implemented: tunnel 1 was relocated inland to align with the original tunnel 2 position, and tunnel 2 was shifted 36 m into the right bank. The distance between the two diversion tunnels was maintained (Fig. 19). Additionally, the

portals'positions were optimized, moving slightly downstream from their original locations, ensuring better geotechnical conditions at both tunnels' entrances.

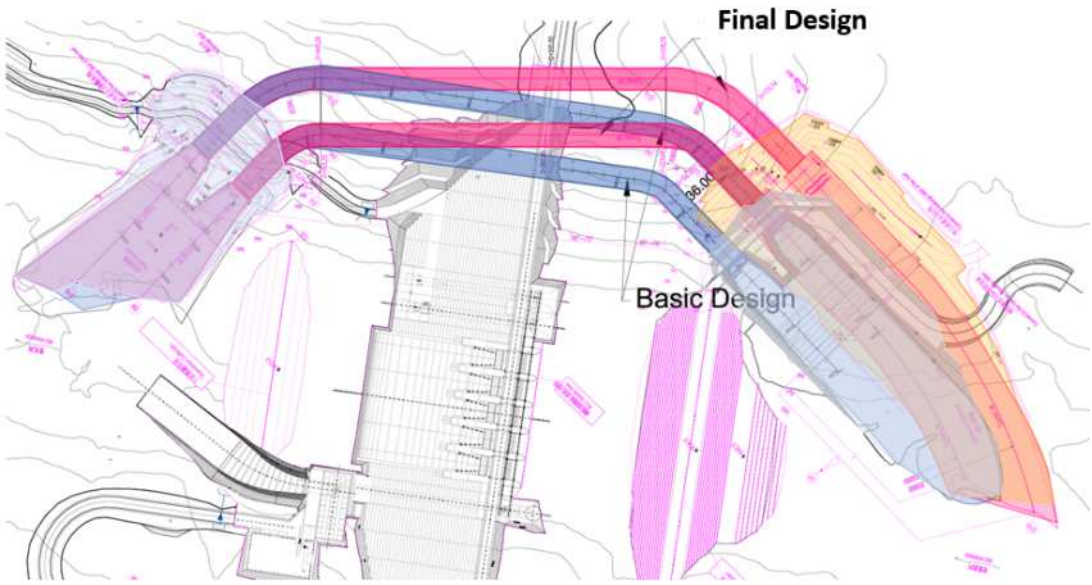

Fig. 19 - Diversion Tunnels' layout adjustment due to geotechnical constraints (Blue: Basic Design, Magenta: Final Design)

These design adjustments successfully addressed the challenging excavation conditions identified during the construction design phase, eliminating the need for extensive ground treatment and support. Fig. 20 shows tunnel 1's inlet zone was excavated in a rock mass with fair quality.

Fig. 20 - Detail of tunnel 1's inlet zone, on the left, excavated in medium weathered (W3) and intensely jointed (F4-5) rock mass

4.2. Hydraulic design supported by model tests

The following design criteria was considered for the hydraulic design of the diversion tunnels:

- The maximum average flow velocity for design flow, Q=3400 m^3/s (return period of 25 years), is limited to 10 m/s;
- During operation inexistence of blocked air pockets inside the tunnels.

The hydraulic conditions in the river diversion tunnels were studied in 1:100 physical scale model constructed in Changjiang River Scientific Research Institute.

The hydraulic model tests allowed to study the discharge capacity of the diversion tunnels; the flow conditions inside the tunnels for different discharges; time average pressures inside the diversion tunnels and flow velocity distributions at tunnel outlet and downstream canal.

The hydraulic design criteria in the Basic Design of the diversion tunnels considered pressurized flow for the design flow (Q=3400 m^3/s).

The hydraulic model tests performed with the Basic Design scheme did not confirm the expected flow conditions in the tunnels diversion. When flow is between 2 472 m^3/s and 3 406 m^3/s occurs alternate free surface/pressure flow inside the tunnels and associated pressure fluctuations on top of the tunnels which are prejudicial for the safety and stability of tunnels operation.

The Construction Design considered the following main modifications in relation to the Basic Design layout:

- Reducing the bottom slope gradient, raising 3 m the outlet tunnel invert, from elevation (524.0) to elevation (527.0);
- Different arrangement of the tunnel inlet structure, with the bellmouth entrance composed by double circular arcs and 18 m transition from the rectangular section downstream gates to the horseshoe section of the tunnels;
- Reduction of outlet plane spreading angle from 17º to 10º.

The hydraulic model tests showed that the diversion tunnels meet the requirements of discharge capacity, with the upstream water level more than 4 m below the crest of upstream cofferdam for the design flow (3400 m^3/s).

According to the Hydraulic Model Tests results it was noted an improvement of the hydraulic conditions in the diversion tunnels for the Construction Design layout. The less favourable hydraulic conditions observed in the Construction Design (for flows higher than 2 600~2 698 m^3/s) are associated to flood events with low probability of occurrence hence representing a low risk for diversion tunnels stability and operation during their lifetime.

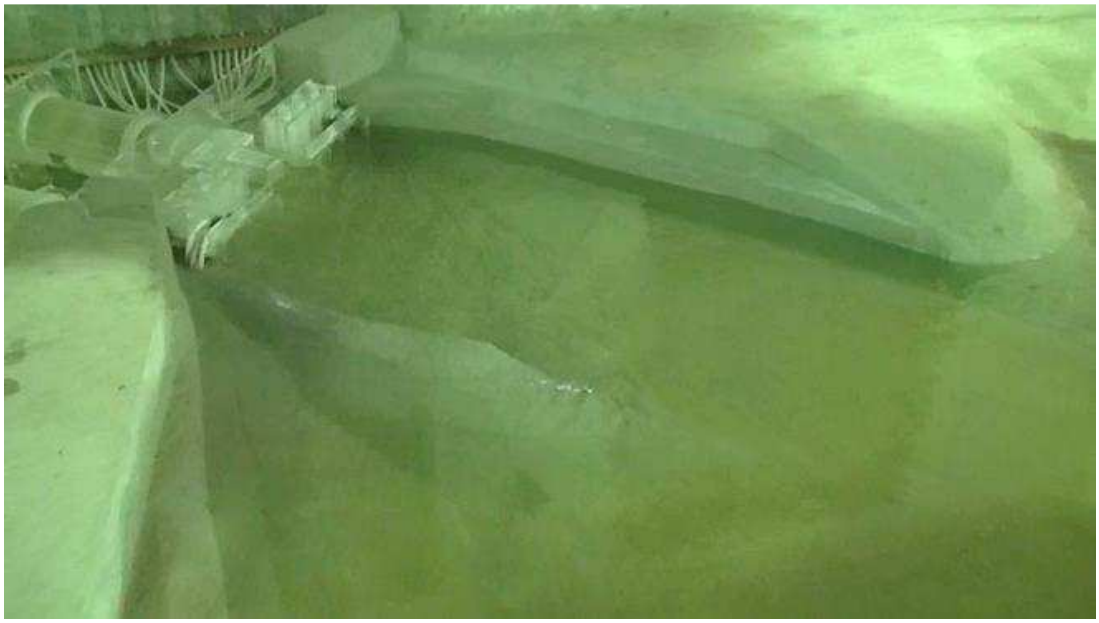

Fig. 21 - Flow conditions at tunnels inlet (Q=3 400 m³/s)

4.3. River closure design supported by model tests

The river closure scheme involves a single pre-cofferdam and horizontal closure with a design discharge of 550 m³/s (corresponding to half of the nominal flow capacity of Laúca HPP situated upstream). During the closure period, two diversion tunnels on the right bank are used for flow diversion.

Hydraulic model tests were conducted using a 1:70 physical scale model to observe the diversion capacity, hydraulic parameters, and the feasibility of the proposed river closure scheme and to investigate possible optimizations.

The pre-cofferdam crest is set at elevation (542.0). The typical cross-section of the pre-cofferdam is composed by a 6.5 m width crest, a 1:1.25 upstream and downstream temporary slopes.

The river closure is divided in two phases: the first phase is the pre-advancing (or advancing of non-gap segment) corresponding to reduction of gap width from 117 m (natural conditions) to 77 m. A second phase named advancing in gap segment where the gap width advances from 77 m to 0 m.

In the pre-advancing phase, pre-cofferdam advances 30 m from left bank and 10 m from right bank. Medium-small stones[1] are used during this phase for a design discharge of 550 m³/s.

[1] Rocks with diameter between 300 and 700 mm and single weight between 40 and 480 kg, and average density of 2.75 x 10^3 kg/m³. 50% of rock content shall have a diameter bigger than 400 mm and a weight exceeding 170 kg.

No loss of dumping materials or collapse of pre-cofferdam head is noted for discharge up to 800 m^3/s.

For the phase of advancing in gap segment multiple schemes (five) were tested to decide on the optimized way for the river closure.

The tests were performed for design discharge (550 m^3/s) and a smaller discharge (310 m^3/s). The one-way and bi-directional advancing were evaluated as well as different sizes of materials during the river closure.

The results of the different schemes tested lead to an optimized solution: one-way advancing with medium-small stones in non-difficult segment (gap width between 77~30 m) and a combination of big stones[2] and medium-small stones in difficult segment (gap width 30~10 m).

Fig. 22 - One way advancing. Q=310 m^3/s. Gap width=30 m

The test results of the different closure schemes indicate that the loss amount of dumping materials range between 8.7% and 2.3%. The dumping intensity envisaged was 720 m^3/hr for non-difficult segments and 840 m^3/hr for difficult segments.

The hydraulic tests results provided scientific support for the Designer to develop a safe and economical scheme for river closure.

4.4. Structural design of the inlet structure

The key aspects of the structural design of the inlet structure of the diversion tunnels included:

- Using a watertight reinforced concrete lining capable of withstanding the high hydrostatic pressure after gate closure, during the plug construction period.
- Limiting the hydraulic gradient near the tunnels' portals to:
  - Prevent hydraulic erosion that could cause progressive instability of blocks around the tunnels' perimeter;

[2] Rocks with diameter between 700 and 1300 mm, and single weight between 480 and 3000 kg, and average density of 2.64 x 10^3 kg/m^3

- Prevent hydrofracturing in the joints of the surrounding rock mass that could lead to unacceptable leakage;
- Minimize pumping needs after gate closure;
- Given the medium quality rock mass at the tunnels' inlet, a hydraulic gradient between 2 and 3 was considered suitable, resulting in a reinforced concrete lining extending 40 m from the beginning of the tunnels (Fig. 14 above). With this extension, the reinforced concrete lining was implemented until a satisfactory rock mass condition was encountered, where only drained shotcrete lining was required.

- For the initial stretch lined with reinforced concrete, an entrance cross-section with a circular shape into the rock mass was implemented. This design efficiently resists to high hydrostatic pressures, reduces the span and volume of excavation needed, and facilitates its support.
- Adopting tunnels' plugs with a shape that favors the transfer of the hydrostatic force to the rock mass mainly with normal stresses (Fig. 13 above).

4.5. Cofferdams

In accordance with the Basic Design, 64 000 m^3 of anti-seepage clayey soil were sourced from a borrow area approximately 28 km upstream of Caculo Cabaça (HPP), near the right bank of Laúca Dam. The 216 000 m^3 of rockfill material, along with transition and filter materials, were derived from the excavation of the diversion tunnels and associated portals. This material primarily consists of high-quality gneissic and cataclastic rock.

Regarding the cofferdam foundation, the Quaternary overburden, with a maximum thickness ranging from 3 to 8 m, is mainly composed of alluvial and colluvial deposits. Lugeon test results revealed high water permeability, exceeding 10LU. Additionally, the uppermost layers of the rock mass, which are more weathered and fractured, exhibited absorption values ranging from 5LU to 11LU to a depth of 11 m. In the main river fault zone, the ≥10LU zone extended from 6 to 12 m in depth, while the ≥5LU zone reached 16 to 40 m.

To address potential leakage through the cofferdam foundations, several design measures were incorporated:

- A thick anti-seepage wall, made of dumped clay, was placed on the water side;
- The clay core of the upstream cofferdam was embedded at least 1.5 m into the foundation rock mass, following the removal of the alluvial material in the riverbed area;
- An injection grouting curtain was planned at the base of the dumped clay, at the interface with the dumped rockfill, to prevent seepage through the overburden layer (Fig. 17 and Fig. 18).

The injection grouting was specifically carried out on the right and left banks of the downstream cofferdam to reduce seepage in the upper foundation layers, which corresponded to the very weathered to decomposed (W4-5) rock mass. Grouting holes were spaced 1.5 m apart and were drilled from the top of the cofferdam, extending 3 m into the medium weathered rock mass; the injection reached up to 1 m into the clay anti-seepage body. These grouting measures proved effective, as seepage flow was reduced to acceptable levels, with a final rate of about 25 m^3/h.

The anti-seepage design for the cofferdams was successfully adapted to the site's geological and geotechnical conditions. Only minor adjustments were made to the downstream cofferdam's rockfill geometry, particularly at the top, to ensure better compaction of the clay on the water side.

5. FINAL REMARKS

The Detailed Design of Caculo Cabaça HPP was developed by COBA for the tender of the Civil Construction and Equipment Supply, under an EPC contract. The established contractual framework foresees that the Contractor is responsible for the development of the Construction Design, which must embrace all the adjustments needed to cope with the possible new geological and geotechnical features revealed by the complementary surveys and during the excavation work, as well as the test results from the hydraulic physical models, mandatory to be executed to validate the tender design solutions and the technical features of the selected equipment.

The construction of the Caculo Cabaça HPP began in August 2017. Despite various constraints, the river diversion was completed on May 20, 2023, with the President of the Republic of Angola attending the ceremony. Currently, the HPP’s full commercial operation is planned for mid-2029. When in operation, the Caculo Cabaça hydropower scheme will be, in terms of installed capacity, the biggest hydropower scheme in Angola, playing a key role in the power system of the region.

The Design Review and the close and continuous Technical Assistance of the Owner’s Engineer, in cooperation with the Site Supervision and Contractor’s Designers, has proved to be an effective way to guarantee that good practice international standards are followed through the Construction Design and that fitted engineering solutions are applied to all the geotechnical, hydraulic and structural constraints revealed during the construction works. It is also worth mentioning the importance of the engineering conception solutions adopted at early design stages, which were as flexible as possible to accommodate unforeseen situations later discovered during the construction work, without compromising the overall project conception and the work schedule.

REFERENCES

[1] COBA, “Detailed Design for the Tender of the Caculo Cabaça Hydropower Project”, Lisbon, 2015.

[2] CSPDR, “Experiment Results of Hydraulic Integrated Model about River Diversion”, Construction Design of Diversion Tunnels of Caculo Cabaça HPP, Wuhan, 2017.

[3] CSPDR, “Test outline for the hydraulic model of river closure”, Construction Design of Caculo Cabaça HPP, document AHCC-PE-CC-DEV-HID-NT-002-EE-0 and videos AHCC-PE-CC-DEV-HID-IA-001-EE-0, Wuhan, 2019.

[4] CSPDR, Diversion Tunnels Construction Design of Caculo Cabaça HPP, Wuhan, 2019.

[5] CIRIA, C683 “The Rock Manual. The use of rock in hydraulic engineering (second edition)”, London, 2007.

Fifth International Dam World Conference
PORTUGAL • LISBON • LNEC • APRIL 13-17, 2025
dam world 2025

LNEC SUPPORT TO THE DESIGN ADAPTATION OF ALTO TÂMEGA DAM DUE TO THE ROCKSLIDE ON THE RIGHT BANK SLOPE

José Muralha	**António Batista**	**Luís Lamas**	**Juan Mata**	**Carlos Serra**
National Laboratory for Civil Engineering (LNEC)	National Laboratory for Civil Engineering (LNEC)	National Laboratory for Civil Engineering (LNEC)	National Laboratory for Civil Engineering (LNEC)	National Laboratory for Civil Engineering (LNEC)

ABSTRACT

During the excavations for the Alto Tâmega dam, a rockslide occurred on the right bank slope immediately downstream from the dam insertion surface, involving a volume of about 23,000 m^3, which led to the complete stop of the works. To resume construction, design adaptations had to be introduced to stabilize the downstream slope and ensure adequate safety conditions during dam construction, first filling and operation.

The main measures adopted were the following: i) construction of a concrete structure anchored to the rock mass, to replace the volume of rock mass that was affected by the landslide; ii) adjustment of the insertion surface by deepening and widening the excavation of several dam blocks; iii) extension of a gallery in the foundation to monitor two faults and to increase the drainage of the rock mass; and iv) relocating, symmetrically, the dam's bottom discharge from the right side of the river bed to its left side.

Additionally, a series of procedures related to the monitoring plan aimed at guaranteeing adequate safety conditions for the work execution and, mainly, to ensure that the project adaptations yielded the intended effects were implemented.

This paper presents a brief description of the events preceding the slope failure, a description of the countermeasures that were implemented to ensure dam safety and some results of the monitoring of the right bank during dam construction and the first filling of the reservoir.

Keywords: Alto Tâmega dam, construction, rockslide, design adaptation, safety control.

[1]jmuralha@lnec.pt, Portugal

1. INTRODUCTION

The Alto Tâmega dam, located on the Tâmega River - a right-bank tributary of the Douro River in northern Portugal - forms a crucial part of the Tâmega Electrical Production System (SET), owned by Iberdrola Generación. The dam is a double-curvature concrete arch structure founded on a metamorphic rock mass predominantly composed of mica schists, with the powerhouse located at the downstream toe (Fig. 1 and Fig. 2).

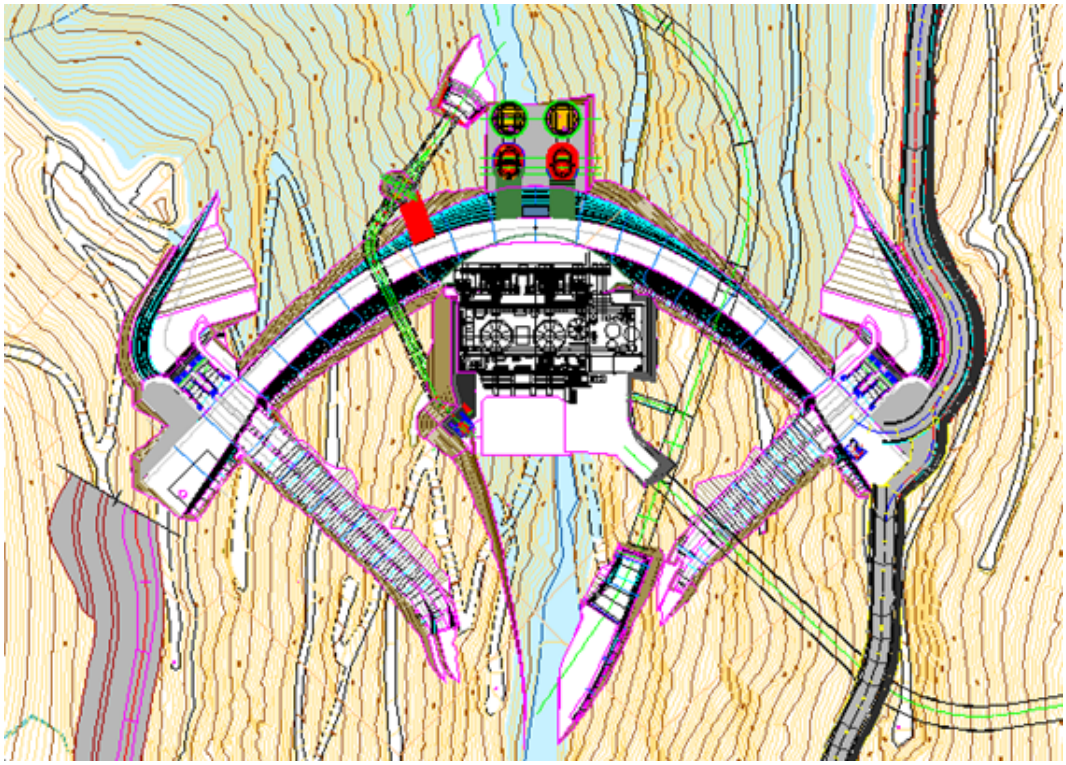

Fig. 1 – General plan of the dam as designed in 2017 [3]

Fig. 2 – Downstream view of the Alto Tâmega dam after the first filling of the reservoir, in 2024

From a preliminary design [1,2], the final design was entrusted to Granell Ingenieros Consultores [3,4]. LNEC (National Laboratory for Civil Engineering, in Lisbon) provided technical support to the owner during the design, construction, first filling of the reservoir, and operational phases. This included safety control activities and studies related to rock mechanics, hydraulics, and structural engineering. During construction, LNEC was involved in the definition of the monitoring plan [5,6] and overseeing the installation of the monitoring instrumentation.

The dam has a maximum height of 104.50 m, measured between the crest at elevation 318.00 m and the average lower surface of its foundation at elevation 213.50 m. Its geometric definition comprises parabolic arches with increasing thicknesses towards the abutments, based on the central cantilever and reference surface. The total crest length, including the abutments, is 332 m, with a chord length between abutments of 210 m, resulting in a chord-to-height ratio of 2.01. The dam's thickness is 5.00 m at the crest and 17.46 m at the foundation of the central cantilever, reaching a maximum of 22.61 m at mid-height near the banks, where the stresses are most significant. The average excavation depths in the valley floor and slopes were 12 m and 16 m, respectively. The total concrete volume of the dam amounts to approximately 223,000 m^3.

The structure is divided into 21 blocks. On the right bank, blocks are numbered evenly from B2 to B22, while on the left bank, they are designated by odd numbers from B1 to B19. The terminal blocks — B17 and B19 on the left bank, and B18, B20, and B22 on the right bank — have gravity-type profiles and house the intake structures for the spillway channels (Fig. 3). Contraction joints are oriented perpendicular to the upstream face and foundation, forming arched surfaces. In the lower sections, these joints follow curvatures defined by parabolic functions in the profile based on the reference cylinder.

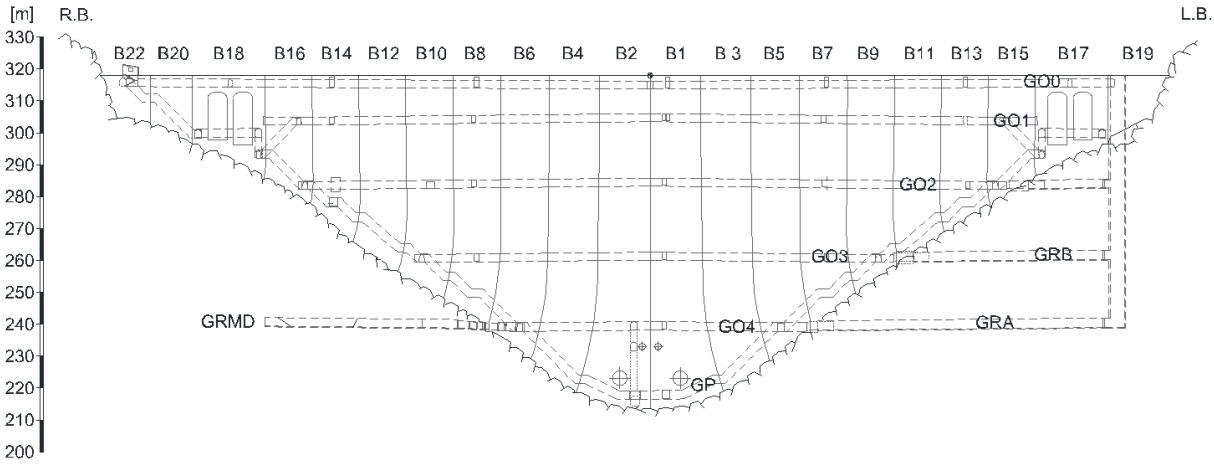

Fig. 3 – Alto Tâmega dam planned downstream elevation

The dam contains a set of galleries. The perimeter gallery (GP), located upstream, is the drainage gallery. Horizontal galleries (GO0 to GO4), which are inspection galleries, are near the mid-thickness of the arch at elevations 313.70 m, 303.50 m, 283.30 m, 260.10 m, and 238.17 m, respectively. These intersect all blocks, extend to the perimeter gallery, and connect to additional galleries in the rock mass foundation (GO2, GRB, GRA, and GRMD). On the left bank, galleries GO2, GRB, and GRA link to an elevator shaft located vertically beneath block B19. On the right bank, only gallery GO4 extends into the rock mass foundation (GRMD).

The dam is located within a near-straight 500 m stretch of the Tâmega River, oriented approximately N35°E. The valley bed, with a width ranging from 10 to 30 m, lies at an elevation of 225.0 m. This section of the valley is nearly symmetrical, with the right bank slope averaging an inclination of 34° and the left bank slope averaging 44° up to elevation 247.0 m, reducing to 34° above this height.

From a lithological perspective, the dam site is predominantly composed of mica schists, intersected by subhorizontal aplite-pegmatite veins on both banks. The rock mass is characterised by two main discontinuity sets [2,4]. One set is parallel to several subvertical faults, with average orientations of 71°/089° (dip/dip direction) on the left bank and 76°/084° on the right bank. The second set (named D5) displays an average orientation of 54°/145°. Schistosity of the mica schists (set D6) has average orientations of 24°/136° on the left bank and 24°/149° on the right bank.

Fig. 4 illustrates the geomechanical zoning of the rock mass foundation, identifying four zones based on deformability. Dry-state deformability moduli range between 3 and 34 GPa, while saturated-state values range from 2 to 27 GPa. Areas with lower deformability moduli are found in the superficial regions of both slopes, while the valley floor exhibits the highest deformability. The upper reaches of the right bank slope represent the zone with the poorest geotechnical quality.

2. DESCRIPTION OF THE RIGHT BANK SLOPE FAILURE

The excavations of the Alto Tâmega dam foundation started in January 2018. By March 2019, during the final stages of the excavations of the right bank, near the powerhouse location, anomalous increases in rock mass displacements were observed at the base of the right bank slope. Work was immediately suspended, and displacement evolution was closely monitored. Displacements showed no signs of stabilisation, with significant increases recorded during rainy periods. On 2 May 2019, a major landslide occurred on the right bank slope, immediately downstream of the dam's insertion surface, involving an estimated rock volume of approximately 23,000 m^3.

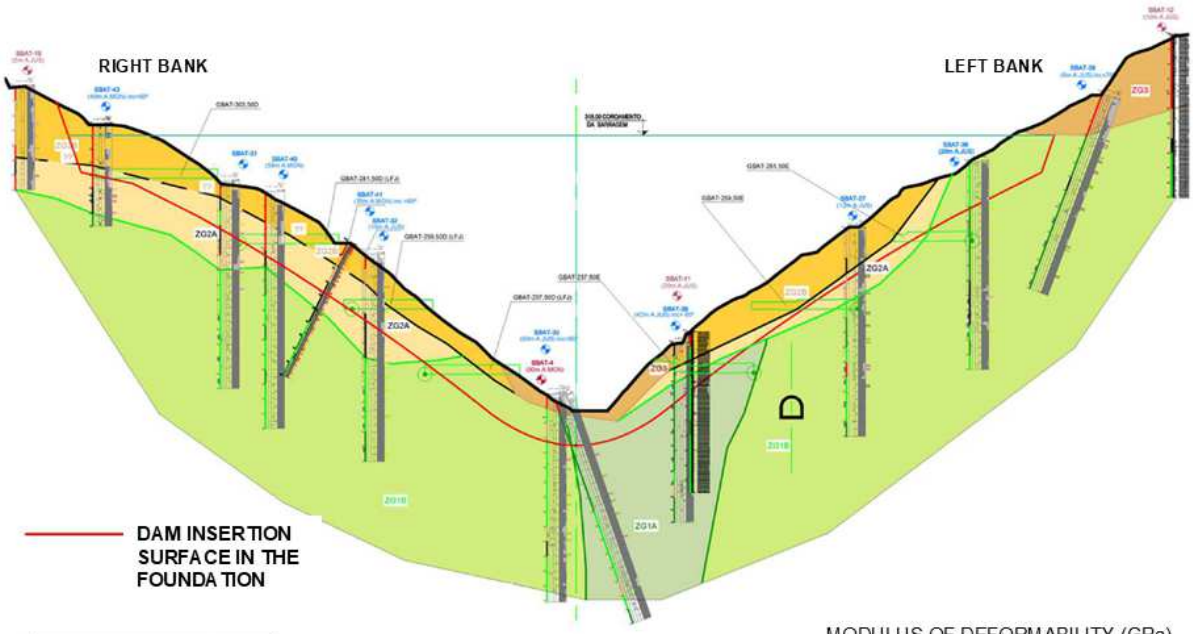

GEOMECHANICAL ZONING		RMR
ZGT-3	[ZG3B]	<55
	[ZG3A]	
ZGT-2	[ZG2B]	55-60
	[ZG2A]	60-75
ZGT-1	[ZG1B]	65-75
	[ZG1A]	70-80

GEOMECHANICAL ZONING

GEOMECHANICAL ZONING		WEATHERING	FRACTURE INTERCEPT	RQD (%)	REC (%)
ZG3	[ZG3B]	W4 - W5	F4 e F5	0 - 30	13 - 60
	[ZG3A]	W3	F3 e F4	0 - 50	30 - 60
ZG2	[ZG2B]	W3 (W2)*	F3 a F4 (F5-2)*	50 - 100	60 - 100
	[ZG2A]	W2 (W3-W1-2)*	F2 a F3 (F4-5)*	70 - 100	100(50)*
ZG1	[ZG1B]	W1 - W2	F1 - F2	100	100
	[ZG1A]	W1	F1 - F2	100	100

MODULUS OF DEFORMABILITY (GPa)

ZONE	DRY	SATURATED
ZG2B	3.2* - 5.7* 4.9 - 8.3	2.4* - 4.3* 3.7 - 6.2
ZG2A	9-16* 13-20	7-12* 10-16
ZG1B	14-20* 20-26	9-13* 13-17
ZG1A	21-27* 28-34	17-22* 23-27

Fig. 4 – Geomechanical zoning of the Alto Tâmega dam rock mass foundation

At the start of the right bank excavations for the dam foundation, powerhouse, and spillway channels, three key geological structures were identified downstream of the dam's insertion surface (Fig. 5):

- **Fault F33** – Orientation: 66°/078° (dip/dip direction), previously identified during geotechnical surveys in the design phase.
- **Probable faults FP36 and FP13** – Persistent discontinuities detected only during excavation, with orientations approximately parallel to joint set D5 (average orientation 54°/145°).

By December 2018, during early excavation stages, surface mapping revealed that fault FP36 appeared on the powerhouse excavation slope. This necessitated reinforcement of the originally designed rock mass support system — shotcrete and rock bolts — with 23 Gewi/Dywidag-type anchors (50 mm diameter, 12 m length). Slope monitoring was enhanced by installing additional prismatic targets for geodetic monitoring (Fig. 6), load cells in selected anchors, and conducting daily visual inspections.

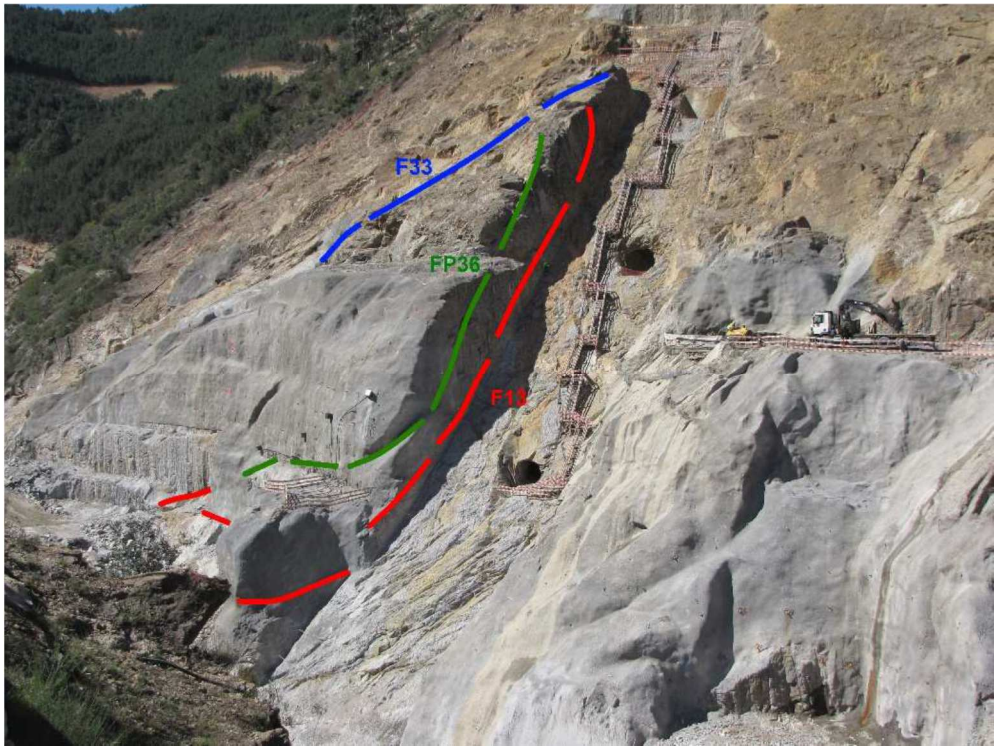

Fig. 5 – Right bank slope view with reference to the relevant discontinuities

Fig. 6 – Location of the slope zone with larger displacements and of the set of geodetic prisms on the slope surface

By late January 2019, further excavations on the powerhouse slope revealed a significant variation in the orientation of fault FP36, making it unfavourably inclined. This required additional reinforcement, increasing the number of anchors to 41. In March 2019, excavations reached an elevation of 226 m, uncovering a discontinuity that was later identified as fault FP13. The orientation of FP13, previously mapped along the downstream slope of the dam's insertion, indicated its extension below the riverbed. However, as excavation progressed,

FP13 exhibited a tilt in its orientation, causing it to daylight on the powerhouse excavation slope. At lower elevations, fault FP13 was found to contain crushed material fillings and emerging water, leading to its reclassification as fault F13.

On 21 March, significant displacements exceeding 10 mm were detected in prismatic targets, alongside substantial increases in forces recorded by load cells in the anchors. Widespread cracking in the shotcrete near fault F33 and subsidence around anchor plates were also observed. Consequently, work on the right bank was suspended, and slope displacement monitoring was intensified. This included:

- installation of a robotic total station for hourly readings;
- increased reading frequency of conventional geodetic stations;
- placement of additional prismatic targets above and below fault FP36;
- installation of plaster tell-tales on fault traces and shotcrete cracks;
- expansion of visual inspection areas using escalated access.

The slope movements were attributed to fault F13, prompting actions to accurately define the movement mechanism, fault geometry, and the volume of rock mass involved. These actions included:

- plotting target displacement data in a 3D geometric model (Fig. 7) and stereographic projections to identify involved discontinuities;
- performing back-analysis calculations;
- conducting tests to characterise the filling material of fault F13 to inform rock mass support requirements.

Subsequent monitoring indicated some stabilisation, confirming that displacements were limited to a rock mass volume bounded by faults F13 and F33 (Fig. 5). Movements were more pronounced downstream compared to areas near the dam insertion.

In the early hours of 2 May 2019, a rock mass volume of approximately 23,000 m^3 slid, leading to a year-and-a-half-long suspension of works. Post-failure analysis identified a wedge failure mechanism involving faults F13, F33, and FP36. The primary cause was the dip variation of fault F13. Following the landslide, the displaced rock material was removed, and extensive slope stabilisation measures were implemented to safely resume construction.

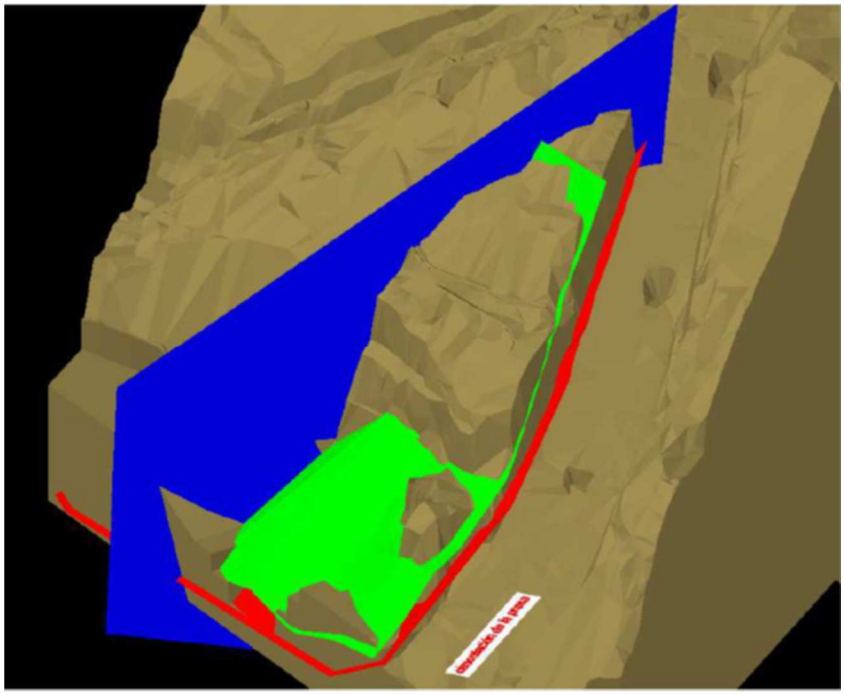

Fig. 7 – Three-dimensional representation of the failure mechanism, with faults F13 in red, F33 in blue, and FP36 in green [7]

3. SYNTHESIS OF THE DESIGN ADAPTATION OF THE DAM

3.1. Structure and foundation adaptations

In October 2020, works resumed after the design adaptations to address the new conditions. Stabilisation measures were defined [7, 8] to enhance safety during dam construction, first filling, and operation. The main measures implemented included:

- construction of a new concrete structure anchored to the rock mass to replace the volume of rock mass affected by the slope failure (Fig. 8 and Fig. 9);
- adjustment of the insertion surface by deepening and widening the excavation of blocks B10, B12, and B14 (Fig. 10, Fig. 11 and Fig. 12);
- extension of the foundation gallery at elevation 237.5 m to monitor faults F13 and F20 and enhance drainage of the rock mass foundation (Fig. 13);
- relocation of the dam's bottom discharge from the right side of the riverbed to its left side, symmetrically.

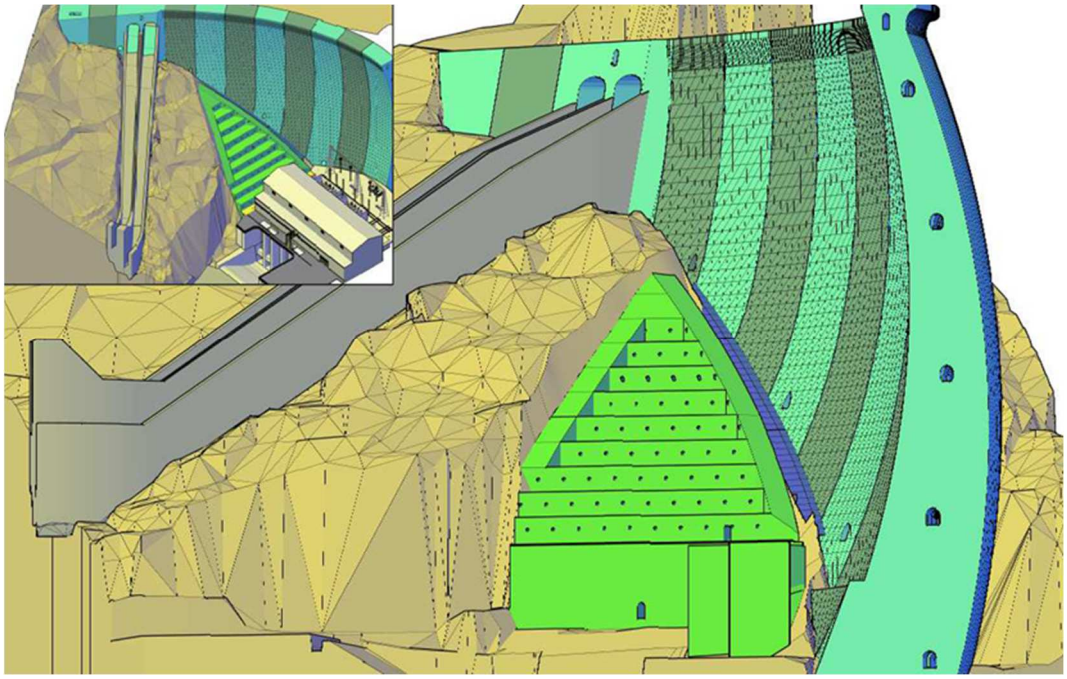

Fig. 8 - Schematic view of the new concrete structure on the right bank slope [7]

Fig. 9 - Downstream view of the Alto Tâmega dam during construction, in October 2021

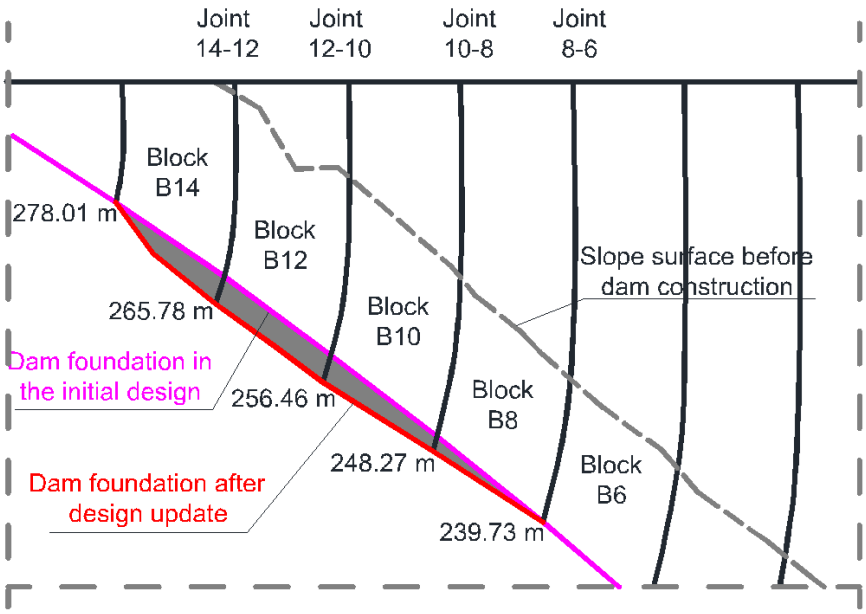

Fig. 10 - Schematic view of the deepened dam insertion surface (adapted from [7])

Fig. 11 – General view of the enlargement of the foundation surface on the right bank

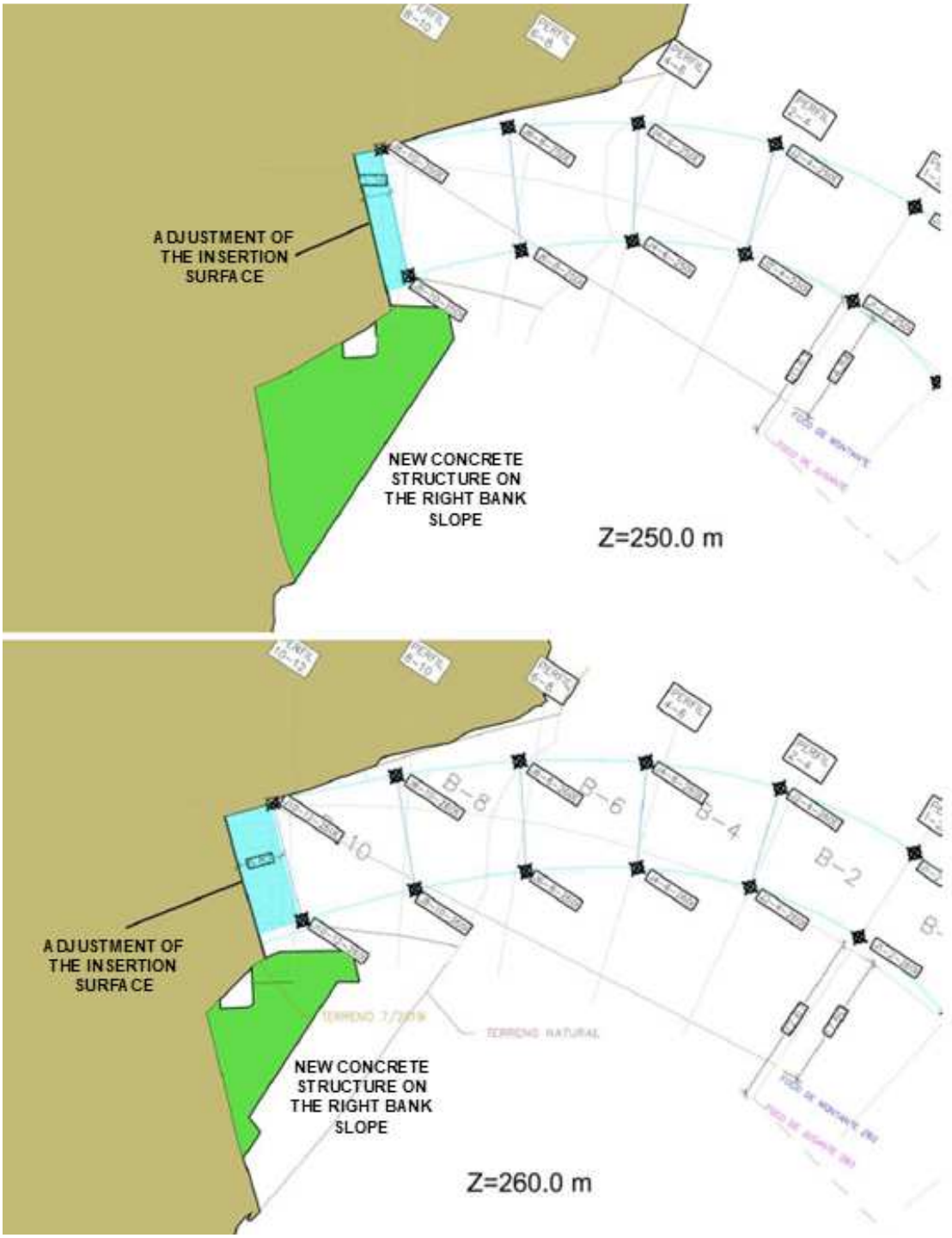

Fig. 12 – Horizontal cross-sections of the adjusted dam insertion surface, including the new concrete structure to fill the right bank gap (adapted from [7])

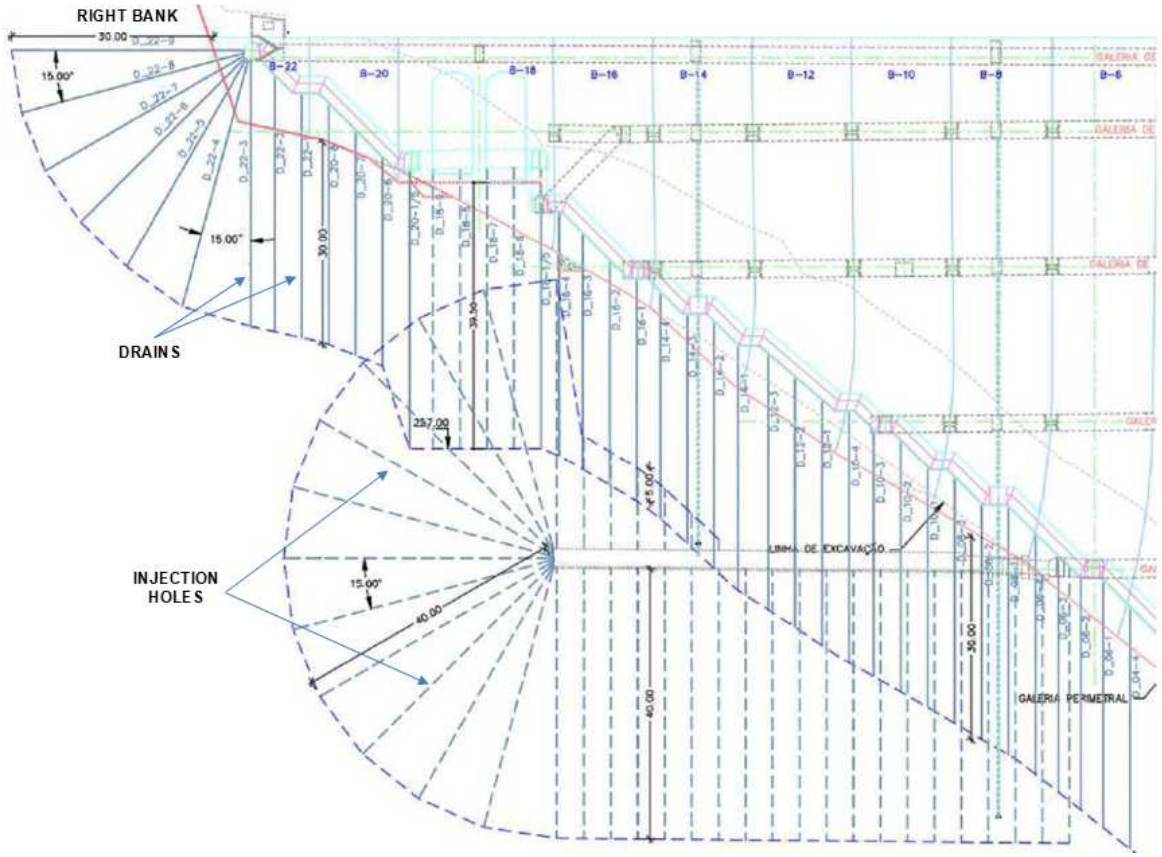

Fig. 13 – Extension of the right bank foundation gallery at elevation 237.5 m, to monitor faults F13 and F20 and enhance drainage of the rock mass foundation (adapted from [7])

3.2. Monitoring plan and safety control procedures adaptations

Numerical modelling for structural calculations of the dam, incorporating the new geometry of the insertion surface, demonstrated marginal changes in stress fields within the dam body. Consequently, the following potential risk scenarios were identified:

- detachment and failure of rock mass blocks on the downstream slope of the dam foundation due to dam loads;
- global failure caused by discontinuities in the dam foundation;
- modifications to the dam thrust on the right bank foundation;

Comprehensive studies conducted by the designer, reviewed by the owner with LNEC's support, confirmed that general safety requirements remained met.

In accordance with the revised design, the monitoring plan for the right bank was enhanced with the following equipment installations:

- levelling marks on the right bank foundation gallery, to monitor vertical displacements;
- prismatic targets for geodetic observation of displacements in the new concrete structure;

- piezometers for measuring water pressure in the rock mass under the new concrete structure;
- weirs for measuring seepage and leakage flows within the new concrete structure;
- load cells in the anchors of the new concrete structure;
- rod extensometers and inclinometers for measuring displacements in the rock mass;
- three-dimensional joint meters for measuring relative displacements in fault traces (within the rock mass foundation gallery, GRMD);
- thermometers to monitor temperature variations in the new concrete structure during construction.

The locations of the rod extensometers installed in the dam body and immediately downstream on the right side are shown in Fig. 14.

Acknowledging that the landslide and subsequent measures altered the characteristics of the rock mass near the most stressed area of the right bank, actions were implemented to ensure the adaptations achieved the intended effects for dam and foundation behaviour. These actions included:

- construction of dam blocks on the right bank commenced only after completing the new concrete structure to an elevation higher than the blocks' foundations;
- installation and operational readiness of essential monitoring equipment before concreting block B6;
- intense monitoring during activities involving rock mass drilling on the right bank foundation (e.g., for rock mass consolidation, installation of bolts and anchors on fault F13, and waterproofing and drainage curtains);
- immediate availability of monitoring results on a digital platform for all entities involved in safety control;
- interpretation of monitoring results using a numerical model of the dam-foundation system, including the downstream concrete structure and its connection to the rock mass foundation;
- development of contingency plans defining actions and responsibilities for effective work monitoring, especially in response to anomalies;
- appropriate planning for the first filling of the reservoir, ensuring a slow and gradual process with readiness for contingency measures if needed.

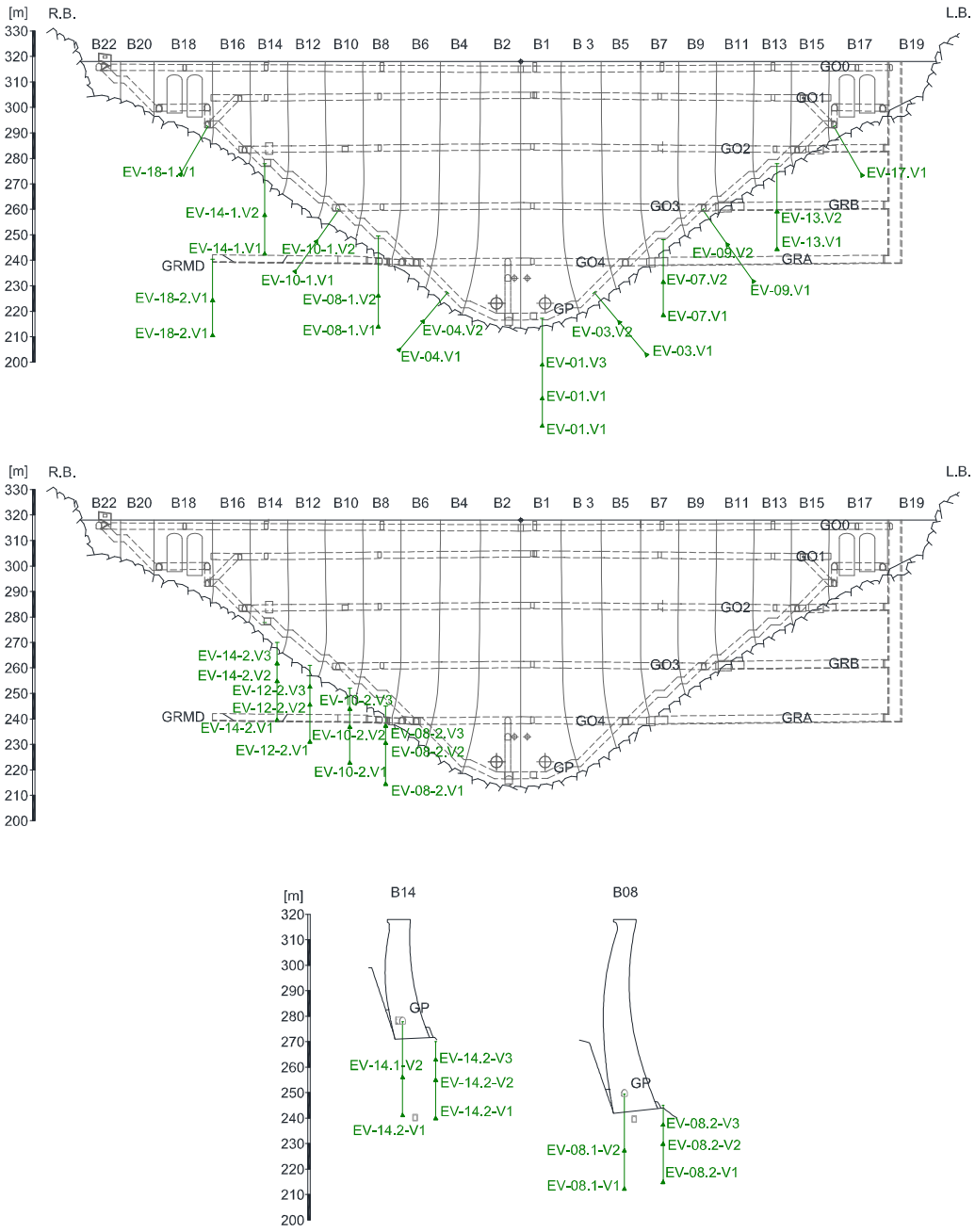

Fig. 14 - Locations of select rod extensometers in the updated monitoring plan

4. SAFETY CONTROL DURING CONSTRUCTION AND FIRST FILLING OF THE RESERVOIR

The behaviour of the reservoir-dam-foundation system was carefully monitored during construction and reservoir first filling phases. In early July 2023, the river diversion was closed, while the proper filling began in November 2023 and concluded in February 2024. The predefined temporary halt stages, as specified in the reservoir's first filling plan, were generally adhered to.

Monitoring efforts during the construction phase focused predominantly on data provided by rod extensometers, drains and weirs, and piezometers. Visual inspections were also carried out regularly. Displacement measurements from rod extensometers located downstream, near the new concrete structure on the right bank, are presented in Fig. 15. Fig. 16 shows the small water flows collected in the weirs of the foundation gallery of the right bank (F-TO-PRE-GRMD) and of the bottom gallery on the interface between the new concrete structure and the foundation (F-TO-PRE-REF-R1). The construction works, during 2021 and 2022, proceeded without significant events.

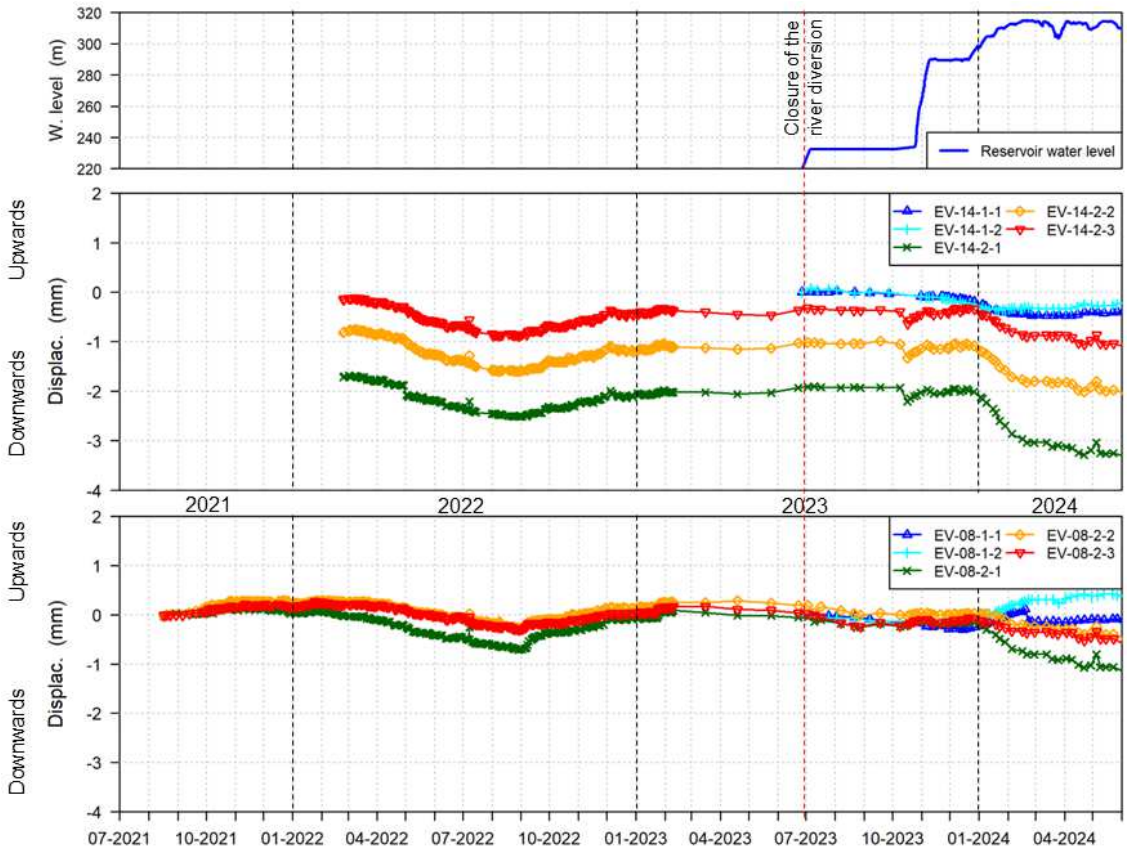

Fig. 15 - Displacements measured during dam construction, first filling of the reservoir and following months in rod extensometers located downstream of the dam, close to the new concrete structure, on the right bank

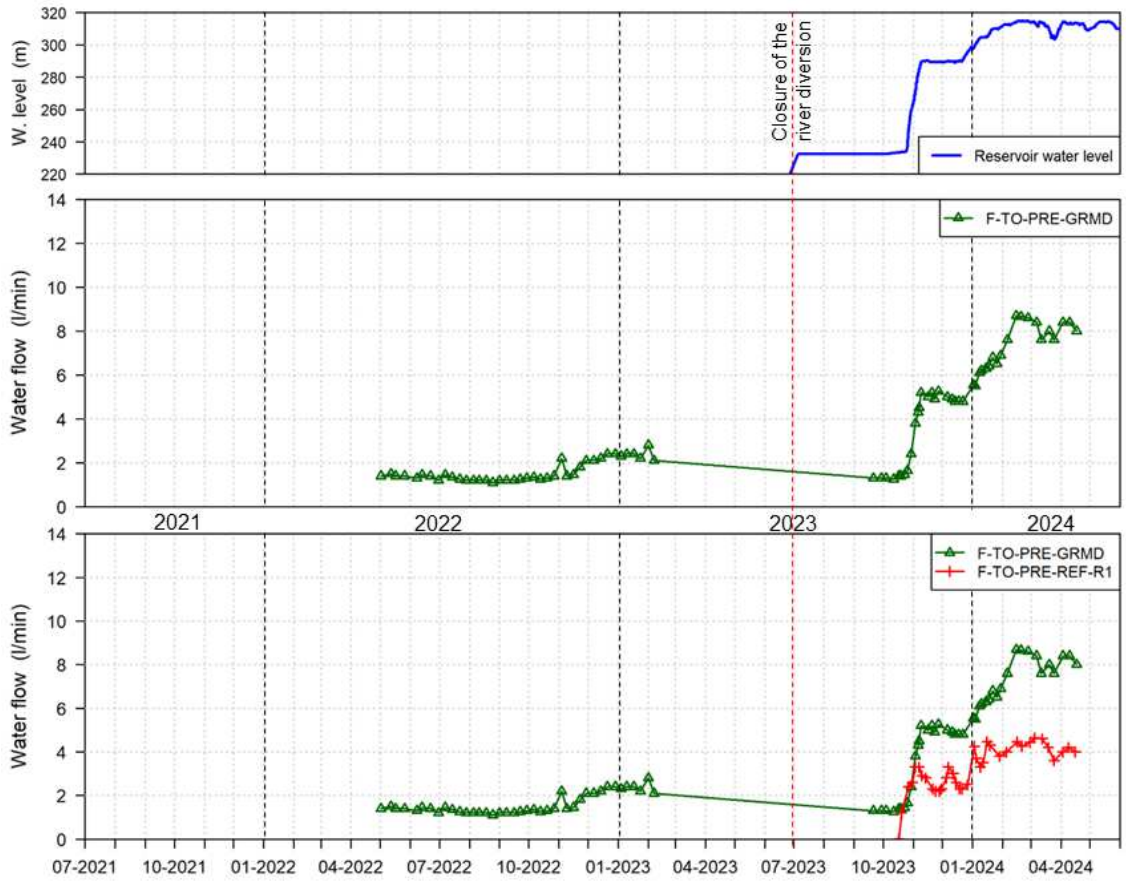

Fig. 16 – Water flows collected during dam construction, first filling of the reservoir and following months in the weirs of the foundation gallery of the right bank (F-TO-PRE-GRMD) and of the bottom gallery on the interface between the new concrete structure and the foundation (F-TO-PRE-REF-R1)

Key observations and relevant findings during the first filling of the reservoir are summarised below:

- the first filling of the reservoir, spanning approximately eight months, commenced during the hot season and concluded during the cold season;
- movements in the dam's contraction joints were minimal and consistent with variations in primary loads, as verified through embedded jointmeters and three-dimensional jointmeters;
- radial and tangential displacements recorded by pendulums (Fig. 17) and vertical displacements observed in rod extensometers (Fig. 15) were consistent with the dam's structural type and scale. These measurements were compared with independent numerical finite element models developed by Iberdrola and LNEC;

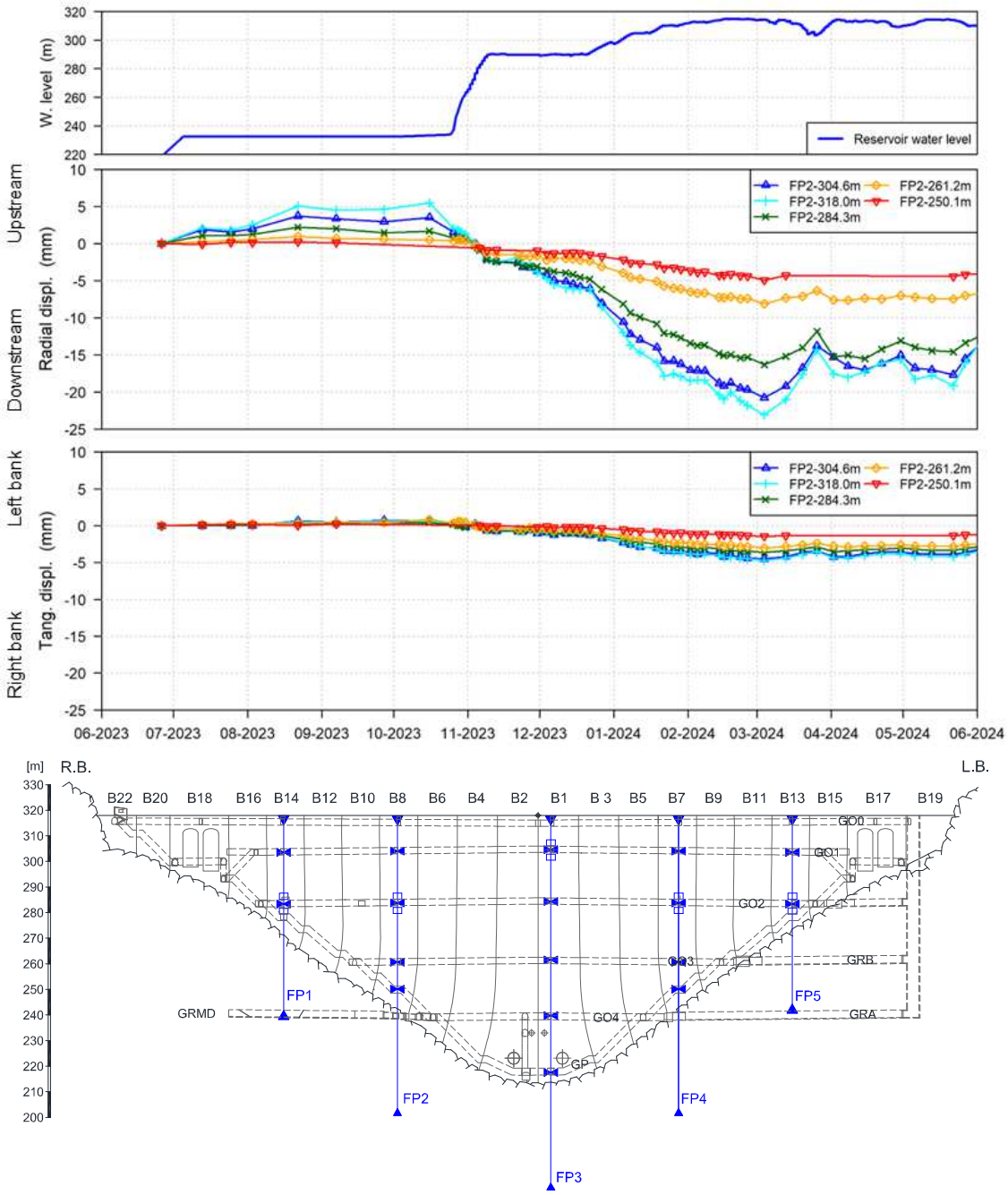

Fig. 17 - Horizontal displacements measured in the pendulum FP2 (above), located over the adjusted zone of the foundation (below), during the first filling of the reservoir and the following months

– seepage and leakage through the drainage system were generally small or non-existent, namely in the foundation gallery of the right bank and in the bottom gallery on the interface between the new concrete structure and the foundation (Fig. 16). Notable exceptions included seepage values from drains D-01-1 and D-01-2 within the central zone, which measured approximately 27 l/min and 64 l/min, respectively, at the retention water level (RWL);

- resurgences were observed in January 2023 within the rock gallery in the left bank (GRA). These were promptly rerouted, and no additional resurgences were identified thereafter;
- uplift pressures in the interface between the dam and rock mass foundation recorded in piezometers were generally low, except in the central zone and at low elevation in the left bank, for piezometers P-01 (block B1), P-05 (block B5), and P-02 (block B2), which measured uplift pressures up to 70%, 80%, and 60% of the hydraulic load, respectively;
- other measurements from weirs and piezometers in the monitoring system of the new concrete structure reported negligible or reduced values;
- anchor load cell readings remained largely stable throughout the monitoring period;
- no anomalies were identified during visual inspections conducted during the construction period and throughout the reservoir's first filling.

5. FINAL REMARKS

The Alto Tâmega dam, a double-curvature concrete arch structure on the Tâmega River in northern Portugal, went through design adaptations, mitigation measures and adaptive engineering solutions to ensure structural stability, operational safety, and compliance with international standards, following a major rockslide on the right bank slope during excavation. In fact, in the first semester of 2019, the excavations exposed unforeseen, complex rock mass characteristics, namely changes in fault and discontinuity orientations, that led to the sliding of a large rock wedge on the right bank slope.

The adaptations introduced in the dam's design, to face the consequences of the rockslide that occurred on the slope of the right bank, considered five main components:

- resurfacing of the insertion surface of blocks B8, B10, B12 and B14 to ensure better conditions for supporting and transmitting stress to the rock mass foundation;
- construction of a new concrete structure, to partially restore the geometry and the loading conditions of the rock mass existing before the rockslide;
- extension of the rock mass foundation gallery in the right bank, at elevation 237.5 m, to survey the foundation in depth and promote waterproofing and drainage under the affected area;
- updating of the monitoring plan, including the definition of additional instrumentation to be installed in the new concrete structure, as well as adjustments to monitor the foundation area on the right bank;
- moving the location of the dam's bottom discharge to the left bank.

These measures were implemented on site without major difficulties. Construction works took place normally, following well-defined planning and strict safety control. The first filling of the reservoir occurred as planned.

The phases of construction and of the first filling of the reservoir showed the robustness of the design adjustments. Monitoring data revealed adequate behavior of the dam structure and of the rock mass foundation, namely concerned with small absolute and relative displacements, stable seepage and uplift pressures, and consistent anchor loads, all of which align with the safety requirements established during design and construction phases. The dam has been in operation since February 2024, with very good performance.

The comprehensive safety monitoring plan, supported by continuous data analysis, has proven critical in verifying the dam's behaviour during construction and under reservoir filling conditions. The numerical models developed by Iberdrola and LNEC provided valuable contributions to evaluate the effectiveness of the implemented measures.

In summary, the Alto Tâmega dam may be seen as a successful collaboration between designers, contractors, authorities, and monitoring teams in overcoming complex geotechnical and structural challenges. This collaborative approach, reinforced by rigorous monitoring and advanced modelling, ensured the safe and successful completion of this complex project. Insights gained will serve as a valuable reference for future infrastructure projects, particularly those involving challenging geotechnical conditions.

ACKNOWLEDGEMENTS

The authors acknowledge Iberdrola for provided the data and information for this work and allowing it to be published.

REFERENCES

[1] ATACI (Aqualogus-Cenor-Iberinsa), 2011 – H.E. Alto Tâmega. Design. General memory. Annex 8 – Stability, dimensioning and structural safety (in Portuguese). Volume 1 – Dam. January 2011.

[2] ATACI (Aqualogus-Cenor-Iberinsa), 2011a – H.E. Alto Tâmega. Design. Annex 2. Geological and geotecnical studies (in Spanish), January 2011.

[3] GRANELL INGENIEROS CONSULTORES, 2017 – H.E. Alto Tâmega. Execution project. Dam (in Portuguese). Ref. 1862/11/121001, rev0, February 2017.

[4] GRANELL INGENIEROS CONSULTORES, 2013 – H.E. Alto Tâmega. Dam. Review of geology and rock mass parameters. Ref. 1862/OA/211001, Rev1, November 2013.

[5] LNEC, 2011 – Alto Tâmega dam. Monitoring plan and specific monitoring plan during the first filling of the reservoir (in Portuguese). Report 52/2011, February 2011.

[6] LNEC, 2017 – Alto Tâmega dam. Adaptation of the monitoring plan to the dam to be built (second geometry definition) (in Portuguese). Report 346/2017, October 2017.

[7] GRANELL INGENIEROS CONSULTORES, 2020 – H.E. Alto Tâmega. Integrated memory of the Alto Tâmega project review (in Portuguese). Ref. 1862-INFT-00072, Rev0, February 2020.

[8] LNEC, 2020 - Alto Tâmega dam. Opinion on the design adaptation, due to the landslide in the right bank slope (in Portuguese). Report 143/2020. April 2020.

Fifth International Dam World Conference
Portugal • Lisbon • LNEC • 13-17 April, 2025
dam world 2025

FIRST INFILLING OF THE UNDERGROUND STRUCTURES OF THE GOUVÃES HYDROELECTRIC SCHEME – MONITORING AND OBSERVED BEHAVIOUR

Renato Pereira[1]
LNEC

José Muralha
LNEC

Luís Lamas
LNEC

ABSTRACT

The Gouvães pump-storage hydroelectric scheme includes a 7800m-long underground power conduit connecting the Gouvães and the Daivões reservoirs, with a hydraulic head of 657 m and a 49 m-high underground powerhouse located at the depth of 300 m. To monitor the behaviour of the main caverns during the construction stages, a monitoring plan was developed and implemented. For the first infilling of the power conduit, a detailed plan was prepared, and the monitoring plan was upgraded to account for the hydraulic actions and the water flow in the rock mass.

This paper describes the main structures of this scheme, presents the main geological and geotechnical information and introduces the main aspects of the monitoring system used for the construction stage of the underground structures. The paper outlines and justifies the proposed sequence and schedule for the first infilling phase, as well as the upgrades made to the monitoring system for this stage. It examines the observed behaviour during infilling, such as flow rates and water pressures, and how these factors influenced adjustments to the original infilling plan. Finally, it reviews the condition of the underground structures at the start of their service life.

Keywords: Gouvães hydroelectric scheme, Underground structures, Monitoring, Construction, First infilling

[1]rpereira@lnec.pt, Portugal

1. INTRODUCTION

The first infilling corresponds to a critical phase of the life of an underground hydroelectric scheme, since it constitutes the first loading of the underground structures, with water pressures in the hydraulic tunnels, which influences the rock mass hydraulic conditions. Water inflow in the rock mass, originated from the hydraulic tunnels, introduces internal hydrostatic pressures, which are proportional to the hydraulic head. Such pressures, together with the hydromechanical properties of the rock mass and the existing confining conditions, influence the flow pattern in the rock mass.

During the first infilling of the power conduit, not only the internal water pressure is introduced but also temperature variations, due to the water flowing, from the reservoir, at lower temperatures than the tunnel. In addition, the first infilling initiates a process of groundwater level rise, as water flows into the rock mass, particularly through unlined or concrete-lined sections. This influences the external water pressure on the linings of the underground openings and may induce leakage into them.

It should be emphasised that concrete-lined sections considerably reduce the exchange of water with the rock mass but cannot be considered impervious because concrete inevitably fissures under the action of the internal pressure and of the temperature variations imposed by the water flow. In addition, external water pressure may be present which deserve control measures. Steel-lined sections, adopted in high-pressure zones and transition zones, can be considered impervious.

For these reasons, first infilling of the Gouvães reversible hydroelectric scheme required the definition of a detailed plan [1], which includes an upgrade of the monitoring system used for the construction phase, providing adequate information for assessing the safety throughout the infilling process and identifying potential risk situations in a timely manner.

This paper presents, in section 2, a summary of the main aspects of the Gouvães underground works structures, the geological and geotechnical aspects, the schedule of the construction phase and the monitoring plan implemented for observation of the behaviour of the main underground caverns and tunnels. Section 3 presents the aspects related to the first infilling of the power conduit, namely the necessary upgrade of the monitoring system, the first infilling plan and the main occurrences registered during this period. At the end, some conclusions on the benefit of developing a detailed plan and on its application to the Gouvães power conduit are presented.

2. PROJECT DESCRIPTION

2.1. Underground structures

The Gouvães reversible hydroelectric power scheme is intended for energy production, utilizing a gross head of 657.0 m, and enabling the pumping of water from the upper reaches of the Daivões dam reservoir on the Tâmega River to the Gouvães dam reservoir in the Torno River, a right bank tributary of the previous.

This scheme consists of a 34 m high concrete gravity dam (Gouvães dam), located on the Torno River, creating a reservoir with a storage capacity of 13.7 hm^3 at the full supply level (FSL) of 885.0 m. The power conduit is located on the right bank of this river, with a total length of approximately 7800 m, and discharges into the Daivões reservoir on the Tâmega River. The underground powerhouse, located in a cavern at a depth of 300 m, is equipped with four Francis reversible pump-turbines with a total power of 880 MW, upstream of the transformers cavern.

The power conduit of the Gouvães hydroelectric power scheme has the following main elements:

- Upper water intake structure at the Gouvães reservoir, with a water level at elevation 885.0 m.
- Headrace tunnel, relatively shallow, with a gradient of less than 1%, a 7 m diameter circular cross-section and a length of 4770 m.
- Upper surge shaft.
- Penstock between the upper surge shaft and the upper manifold, approximately 1710 m in length, with circular cross-sections of 6.0 m and 5.4 m in diameter, consisting of an initial underground section, an intermediate section in a trench, followed by another underground section.
- Penstock between the upper manifold and the powerhouse cavern, including two vertical shafts with a circular cross-section of 3.6 m in diameter and a length of 65 m, at the end of which are located two lower manifolds that lead to the four turbines.
- Powerhouse complex and its associated underground structures comprising the main cavern, the transformers cavern, the lower surge chamber, several access adits and the access tunnel.
- Tailrace tunnel, with a circular cross-section of 7 m in diameter and 800 m in length.
- Lower water outlet structure in the Daivões reservoir, with a water level at elevation 228.0 m.

The underground powerhouse complex lies around 300 m below the surface. It includes two large caverns and several tunnels, adits and shafts for hydraulic and access purposes. The powerhouse cavern, with approximate dimensions of 20 m in width, 48 m in height, and 121 m in length, is oriented approximately N35ºE. The transformers cavern is parallel to the powerhouse cavern, located downstream of it, and has approximate dimensions of 18 m in width, 18 m in height and 81 m in length. The horizontal distance between these two caverns is about 29 m.

Connecting these two caverns are four busbar galleries, approximately 8 m wide and 8 m high. The four draft galleries have a diameter of about 4.5 m and a slope of 15%, ending at the draft tube tunnel. Figs. 1 and 2 present a perspective view and a plan view of the powerhouse cavern complex.

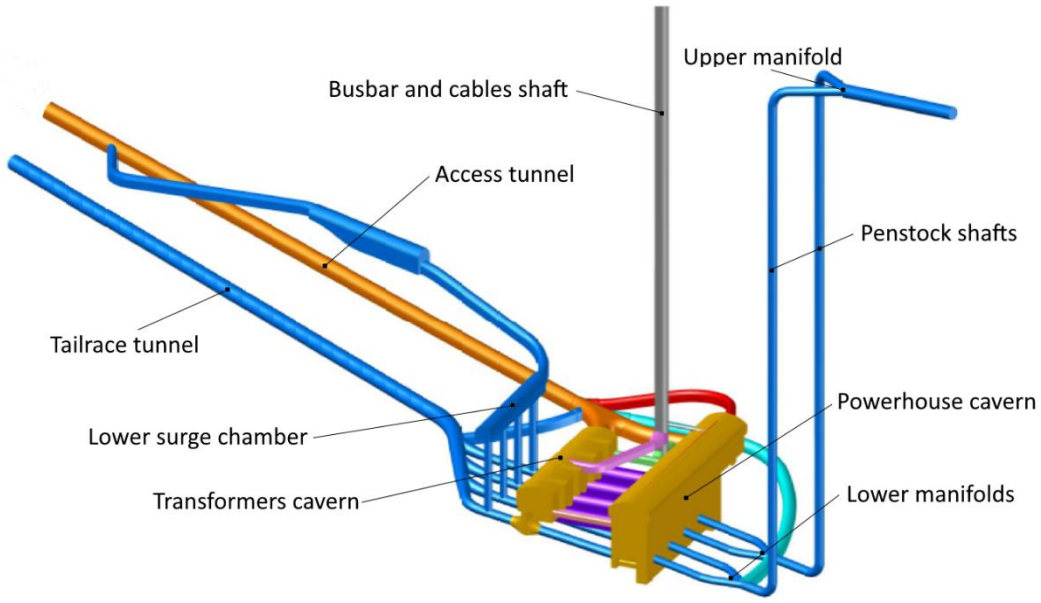

Fig. 1 – Perspective view of the underground powerhouse complex

2.2. Geological and geotechnical aspects

Three different geologic units occur in the zone of interest of the Gouvães hydroelectric power scheme. At the Gouvães dam site and along the upper third of the headrace tunnel, granite formations are of primary interest, referred to as the syntectonic granite massif of Santa Marta do Alvão (unit G1), which can generally be described as medium- to coarse-grained, porphyroid, two-mica granites. The remaining hydraulic circuit is developed within the schist formations of the Fragas Negras unit (unit X1). These formations are composed of fine-grained mica-schists and schists, as well as quarzitic and biotitic schists.

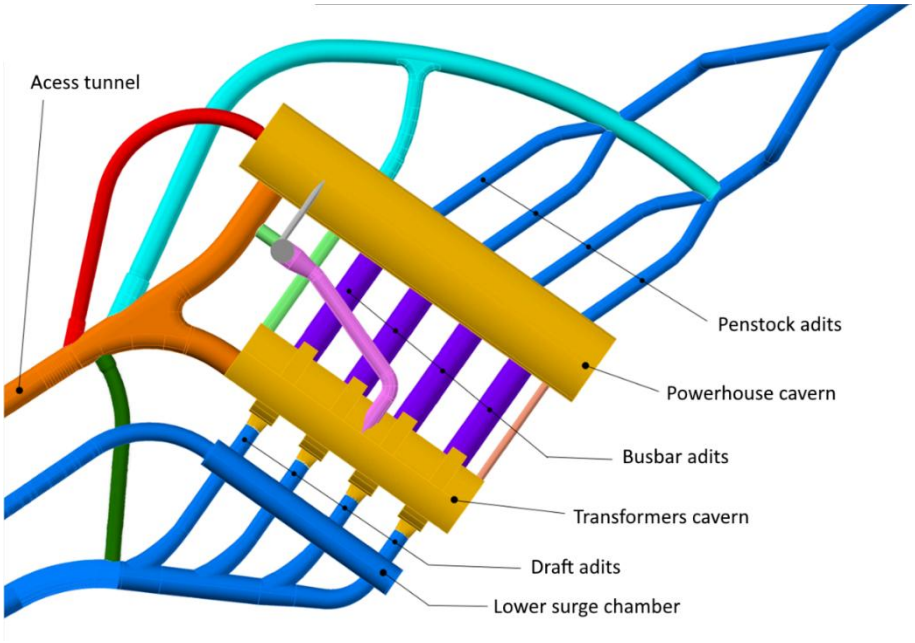

Fig. 2 – Plan view of the underground powerhouse complex

Two different rock lithologies with an undulating, sub-horizontal contact occurs in the rock mass surrounding the powerhouse complex: the intrusive, gray-colored, medium- to coarse-grained two-mica granites (unit G2), and the overlying fine-grained mica schists with frequent occurrences of exudation quartz (unit X1). The contact between these two lithologies is gradual and includes intercalations of aplites, dolerites, and pegmatites (Fig. 3). Although this contact between the two lithologies (granites and mica-schists) is welded and even in general difficult to ascertain, during the excavation of the access galleries, particularly the exploratory adit in the crown of the powerhouse cavern, the occurrence of faults and the presence of water in the rock mass were observed.

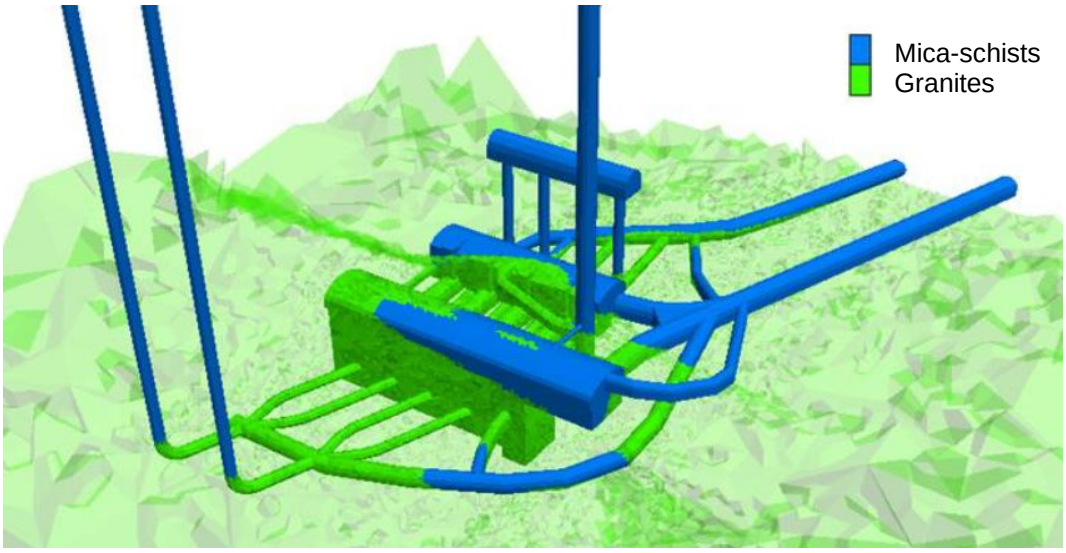

Fig. 3 – Perspective view of the contact between the mica schist and the granites

In the design phase, the designers consisting of Eptisa, Granell Ingenieros Consultores, and Intecsa Industrial carried out a study [2] of the characteristics of the geological units crossed along the hydraulic circuit alignment (units X1, G1, G2), classifying them according to the degree of weathering (W) and fracturing (F) and the values of Rock Quality Designation (RQD) and Rock Mass Rating (RMR). Table 1 summarizes the geomechanical properties of the rocks in each geological unit, specifically the unit weight, porosity, compressional wave propagation velocity (V_P), uniaxial compressive strength (UCS), Young's modulus, and Poisson's ratio.

Table 1 – Geomecahnical properties for the intact rock of the geological units

Geologic unit	Unit weight (kN/m^3)	Porosity (%)	V_P (m/s)	UCS (MPa)	Young's modulus (GPa)	Poisson's ratio (-)
Granite G1	24.5–26.5	0.5–1.5	4200–5000 (W1–W2) 2500–3500 (W3–W4)	70–100 (W1–W2) 35–60 (W2/3-W3) 5–15 (W4)	40–55 (W1–W2) 25–35 (W2/3–W3) 5–20 (W4)	0,15–0,3
Mica-schist X1	27.5–28.2	0.2–0.9	3900–4500 (W1) 3000–4000 (W2)	15–25 (W1–W2) 3–5 (W2/3–W4)	20–30 (W1–W2) 10 (W2/3–W4)	0.2–0.25 (W1–W2) 0.25–0.3 (W2/3–W4)
Granite G2	26.0–27.0	0.3–0.6	4500–5500	70–85 (W1–W2) 40–50 (W3-W4)	40–60 (W1–W2) 25–40 (W3-W4)	0,2–0,3

It is relevant to note that the values presented in Table 1 are for intact rock. Estimates for rock mass values, based on results from *in situ* tests and considering the Hoek-Brown failure criterion and the GSI classification system, revealed that the mica schist is two times more deformable than the granite.

2.3. Construction

The construction works of the Gouvães hydroelectric power scheme started with a contract for the excavation of the access adits to the underground power complex, which ran from December 2015 to August 2016. It comprised the excavation of several access tunnels, namely the main access tunnel starting close to the location of the water outlet structure near the Daivões reservoir and reaching the confluence of several other shorter access adits. One of them, the access adit to the crown of the vault, running along the whole length of the powerhouse cavern, was used for geotechnical surveys, in particular to establish the contact between the granite and the mica-schist formations. The general contract for the civil works

followed shortly, as it started in January 2017 and ended in October 2021, and the commissioning of the power units took place between March and June 2022.

The period between the contract for the access adits and the main contract was used to carry out *in situ* overcoring and flat jack tests for the estimation of the *in situ* stress field and other geotechnical surveys [3], which were needed for the design of the underground structures.

2.4. Monitoring plan

The monitoring plan for the underground works of the Gouvães hydroelectric scheme [4] was established considering the geotechnical and geological characteristics of the surrounding rock masses, the specific conditions of the designed structures, and their construction processes. The plan included monitoring of the actions, characterization of the material properties and observation of the structural, hydraulic and thermal response of the structures and the surrounding rock mass.

It comprised a set of measurement instruments that were installed primarily for monitoring the excavation and construction stages. They remained in place during the first filling and operation stages and were supplemented by additional instruments specifically for the monitoring of these stages of the project lifecycle.

Details on the monitoring of the structural behaviour and actions during the excavation and construction of the underground works, as well as during the first infilling of the power conduit are presented in Table 2.

Table 2 –Monitoring equipment

Physical quantity	Equipment	Location	Quantity
Relative displacement	Rod extensometer	Powerhouse cavern Transformers cavern	18 12
Force on anchors	Load cell	Powerhouse cavern	3
Hydrostatic pressure	Piezometer	Powerhouse cavern	2
Ambient temperature	Thermometer	Powerhouse cavern	1
Water temperature	Thermometer	Gouvães and Daivões reservoirs	2
Internal hydraulic pressure	Pressure transducer	Draft gates	1
Inflow discharge	Weir	Access tunnel to the powerhouse Cables shaft Busbar adits Powerhouse cavern	5 2 2 6

Additionally, displacements of the excavated surfaces, both in the underground caverns and tunnels, and on slopes at the ground surface, were measured all around the various working faces using topographic equipment during the construction stage.

Monitoring of the behaviour of the rock caverns during constructions relied strongly on the measurement of displacements inside the rock mass provided by the rod extensometers installed in the powerhouse and transformers caverns. This equipment measures relative displacement between the anchoring points and the head at the surface of the excavation. In this case, triple extensometers were used with anchoring points located approximately at depths of 3 m, 6 m and 25 m inside the rock mass, with the exception of the extensometers installed in the rock mass between the two caverns, where they are located approximately at depths of 3 m, 6 m and 15 meters.

The extensometers were installed in the crown, at the springing points of the arch and in the sidewalls, at four cross-sections of the powerhouse cavern (at 8 m, 32 m, 75 m and 102 m along the longitudinal axis) and at four cross-sections of the transformers cavern (at 8 m, 42 m, 52 m and 77 m along the longitudinal axis). Figs. 4 and 5 show, respectively, the locations of the rod extensometers in the powerhouse and the transformers caverns.

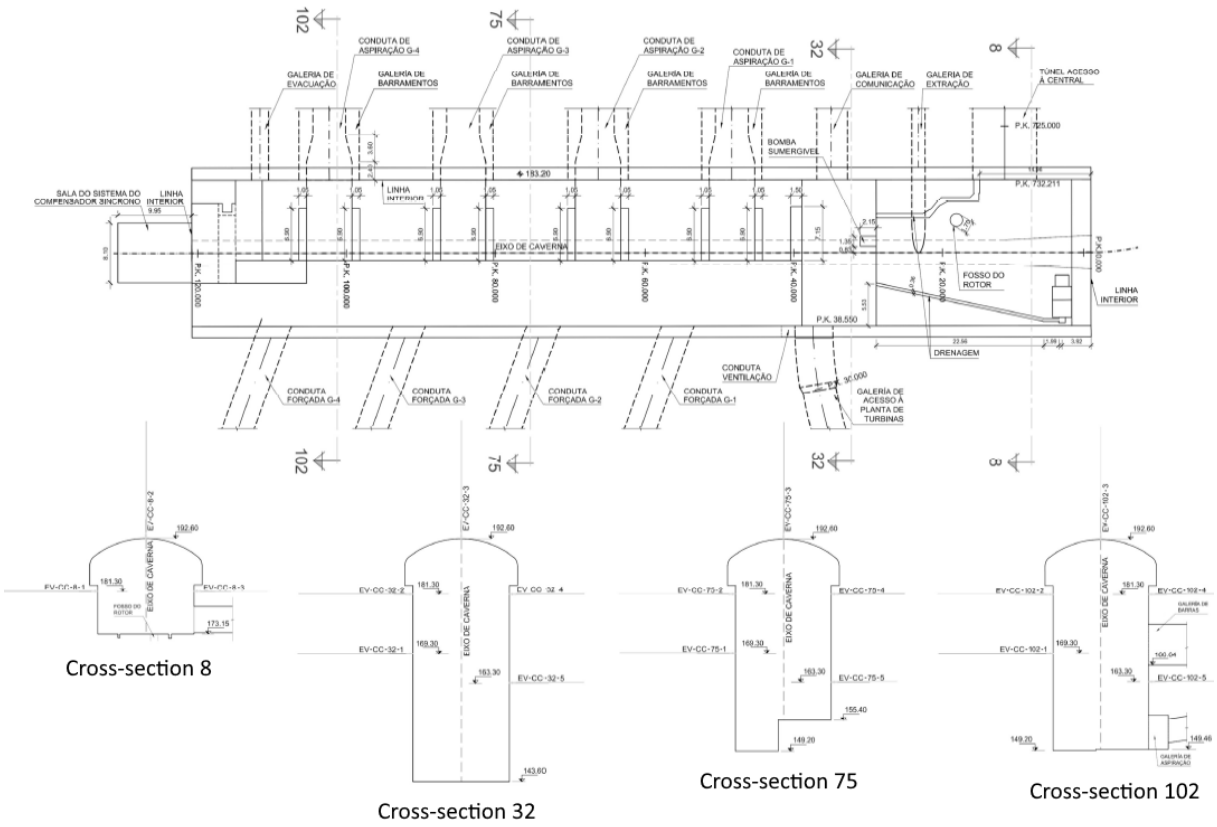

Fig. 4 – Extensometers in the powerhouse cavern

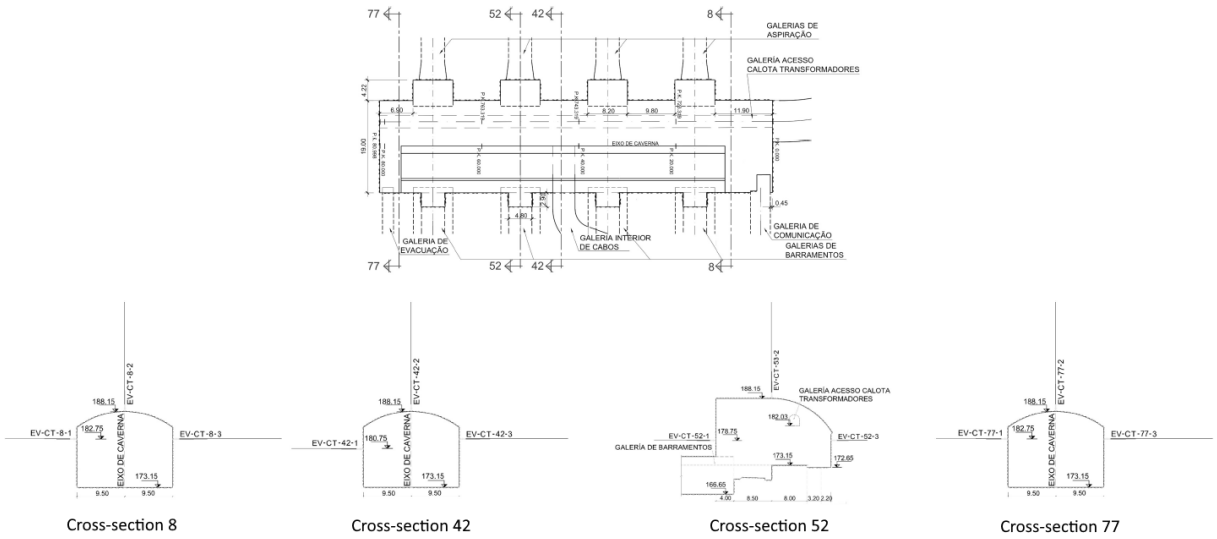

Fig. 5 – Extensometers in the transformers cavern

3. FIRST INFILLING OF THE POWER CONDUIT

3.1. Upgraded monitoring system

The monitoring system, initially designed to monitor the structural behaviour during construction, considered for the geological-geotechnical characteristics of the site and the construction sequence. It included a set of instruments, presented in Table 2, that remained functional during the first infilling but needed to be supplemented by additional instruments, specifically designed for this phase of the project. Therefore, in addition to the thermometer installed in the powerhouse cavern, and the rod extensometers and load cells installed in the powerhouse and transformers caverns, a set of piezometers and flow weirs, were included to measure hydrostatic pressures and flow rates in underground tunnels, adits and caverns, respectively, as well as a pressure transducer to measure the internal pressures in the circuit.

The two piezometers, PZ170 and PZ192, were installed close to power units G2 and G3, respectively (Fig. 6). Although providing only localized information regarding the hydrostatic pressures installed in the rock mass surrounding the main caverns, this setup allowed to evaluate the impact of the infilling of the power conduit onto the water flowing through the rock mass.

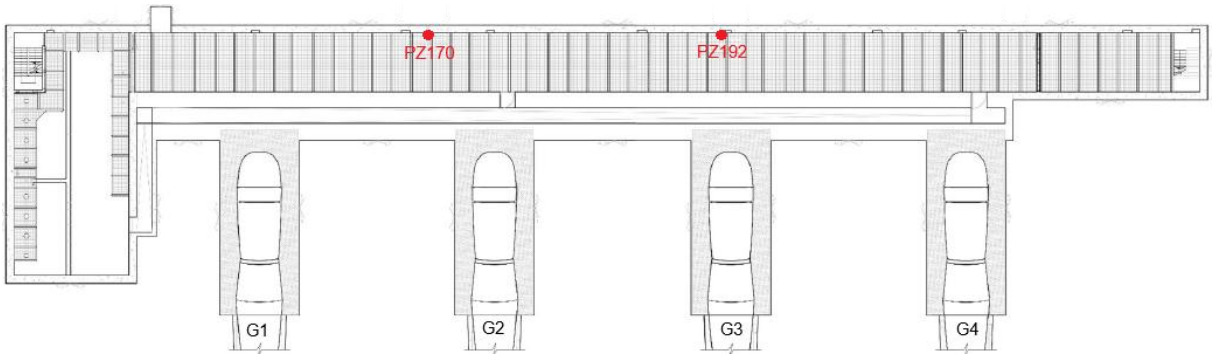

Fig. 6 – Spatial disposition of the piezometers

Initially, five flow weirs were located in pre-defined locations to isolate different portions of the access tunnels, namely water coming from the entrance of the access tunnel (flow weirs F-TO-CEN-01 and F-TO-CEN-03), water flowing to the access adit to the lower surge shaft (F-TO-CEN-02), water coming from the cables shaft (F-CEN-01) and a totalizing weir at the entrance of the powerhouse cavern (F-TO-CEN-04), which could isolate the volume of water flowing to the powerhouse cavern, based on the total water volume pumped from the pumping shaft. However, after the infilling began, this setup needed to be expanded and a total of 15 flow weirs were installed. Additional flow weirs were located in the cables shaft (F-CEN-02), at the entrance of the powerhouse cavern (F-TO-CEN-05), at the powerhouse cavern to isolate water coming from each rod extensometer (F-TO-CEN-06 to F-TO-CEN-11) and at the busbar adit (F-TO-CEN-12 and F-TO-CEN-13). Fig. 7 shows the spatial distribution of flow weirs.

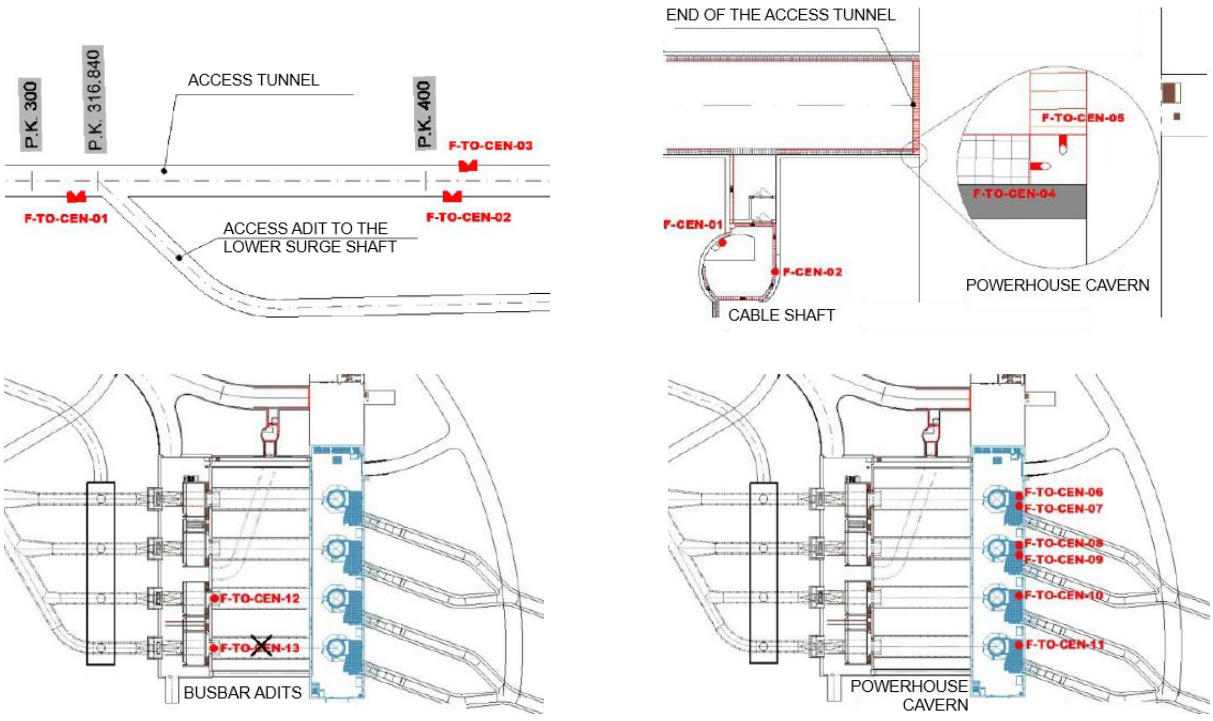

Fig. 7 – Spatial disposition of the flow weirs

3.2. First infilling plan

The “First infilling plan” [1] establishes the safety control measures to be carried out with the aim of:

a) preventing accidents or incidents, or minimizing their significance and effects;
b) ensuring the structural capability of withstanding service loads and the operationality of the equipment;
c) assessing the effectiveness of the monitoring system. It accounts for the specific characteristics of the Gouvães power conduit, namely the magnitude of internal pressures, type of linings adopted, geological-geotechnical conditions and the dimension of underground works.

The plan defines a cautious approach, based on LNEC’s experience and technical recommendations [5, 6, 7], characterized by a staged infilling procedure, where the inflow is interrupted at pre-defined levels. Furthermore, it ensures a slow infilling procedure, specially in the case of unlined or concrete-lined elements, avoiding a transient flow state and any damage that may occur, mainly around the powerhouse and the upper and lower plug sections. In those cases, a maximum increase in elevation of the water level of 5.0 m/h was adopted. This is particularly relevant for the tailrace tunnel, but also for the headrace tunnel, where the still-lined penstock is the most loaded structure of the power conduit but is considered impervious.

The first infilling plan establishes that it should begin by the tailrace tunnel. The water inflow was controlled by managing the balancing valves in the sluice gate at the lower water outlet. Five infilling stages were prescribed, specifically when the water level in the tailrace tunnel reached elevations of 166.0 m, 193.0 m and the Daivões reservoir level, followed by opening the draft gates, filling the draft adits and, finally, the spherical valves of the power units, filling the portion of the penstock below the Daivões reservoir level. Between each stage, a stoppage period of 24 to 48 hours is prescribed, to assess pressure losses in the circuit and to detect any resurgence in underground tunnels, galleries and caverns. Fig. 8 illustrates this process.

The filling of the lower portion of the penstock creates a water cushion that allows the infilling of the headrace circuit to take place, while protecting the spherical valves. The infilling of the headrace can be initiated after this condition be met and the plan prescribes eight infilling stages, achieved by opening and closing the sluice gate at the upper water intake. The first five stages regard the filling of the penstock which, due to its steel-lining, can be carried out very fast. The stoppages between each of these stages are short, allowing for a short inspection. In a second phase, the upper surge shaft and headrace tunnel are filled, with 24-hour stops at elevations 831.5 m, 865.6 m and the Gouvães reservoir level. The structural

behaviour during this phase is assessed by measuring the water level drop in the upper surge shaft.

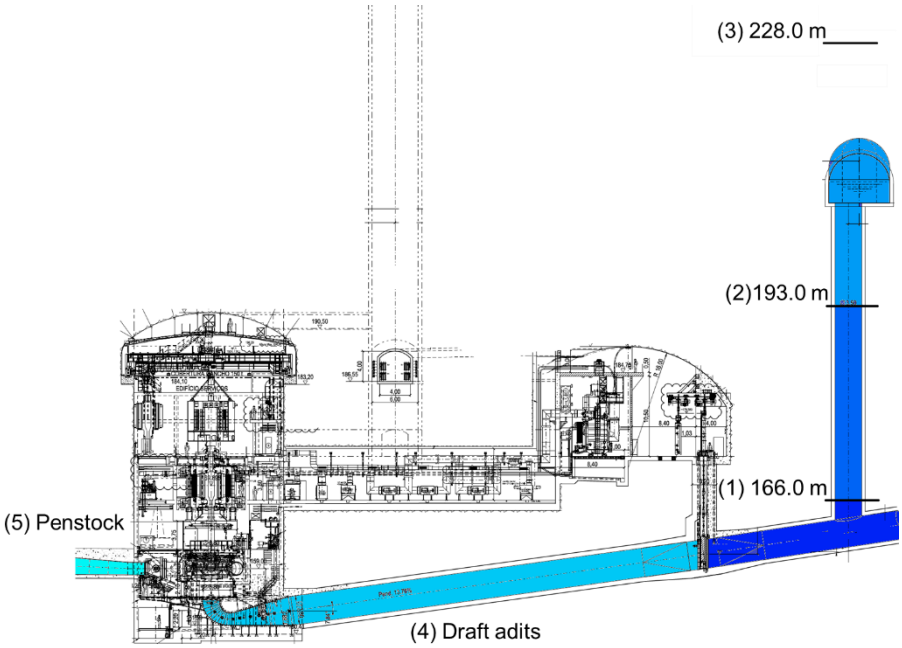

Fig. 8 – Infilling stages of the tailrace tunnel

The plan also indicates the observations that should be performed during the infilling, as well as their frequency, and the visual inspection details. It distinguishes six different observation periods. The first three correspond to the infilling of the tailrace tunnel, starting from one month prior to the infilling, during the infilling and during one month after. The other three for the infilling of the headrace circuit with the same rationale. Finally, the plan also includes a list of possible risk scenarios and the corresponding contingency and mitigation measures.

3.3. Occurrences during the first infilling

The predicted duration of the first infilling was one week for the tailrace circuit and five days for the headrace circuit. However, several constraints and delays made the first infilling of the underground structures of the Gouvães hydroelectric scheme take longer than expected.

A new stop at 178.0 m was included in the infilling procedure of the tailrace tunnel, as requested by the owner. This way the security of the underground works could be assessed before opening the draft gate of power unit G4, allowing testing the operation of the respective turbine under pressures smaller than planned. Afterwards, the infilling would proceed, as planned, with the infilling of the draft adits of power units G3, G2 and G1 after the tailrace tunnel reached a pressure corresponding to the elevation of the Daivões reservoir. This adaptation would make the infilling of the tailrace circuit to take two weeks.

However, the planned sequential procedure could not be fulfilled because, on one hand, delays in the installation of mechanical equipment occurred, making it impossible to perform tests on the turbines. This way the stop at 178.0 m would not be needed. On the other hand, the balancing valves in the sluice gate at the lower water outlet could not be managed properly after the first stop (166.0 m), making it impossible to completely stop the inflow. This way, the infilling of the tailrace tunnel had to proceed continuously, without stops, but at a lower rate (0.2 m/h), until the elevation of the Daivões reservoir was reached. From this point, the infilling of the draft adits was conditioned on the installation of the mechanical equipment in each power unit.

The infilling started on 7 June 2021 and an internal pressure corresponding to the Daivões reservoir elevation was reached, in the tailrace tunnel, on 16 June. The infilling of the draft adits took place on 21 June, 17 July, 4 August and 15 October for power units G4, G3, G2 and G1, respectively. During the infilling the observation schedule was fulfilled. The most important occurrences to be mentioned are the water inflow through some of the rod extensometers installed, which may have intersected flow paths, namely conductive discontinuities, the seepage through the floor slab of the transformer cavern (Fig. 9), and the infiltration through the lower plug (Fig. 10). These situations were promptly mitigated by installing new drains and carrying out waterproofing works and monitored by installing new flow weirs. The observation system performed appropriately, except the pressure transducer which lost functionality during the procedure and, therefore, could not track the evolution of the internal pressure.

Fig. 9 – Floor slab of the transformers cavern before (left) and after (right) waterproofing works and collecting water

Fig. 10 – Lower plug before (left) and after (right) pumping the inflow water to the access tunnel

After the infilling of power units G4 and G2, it was possible, by opening the respective spherical valves, to fill the lower portion of the penstock, ensuring this way the creation of a water cushion that protect the spherical valves. The infilling of the headrace circuit started on 9 August and ended, following the plan, on 16 August. Seepage through the upper plug and fissures in the concrete blocks surrounding the penstock close to the upper and lower bifurcation were observed. No significant changes were observed in the access tunnel to the powerhouse cavern. A detailed account of the first infilling was presented in a specific report [8].

4. CONCLUSIONS

The Gouvães reversible hydroelectric scheme has very large and deep underground structures—caverns, tunnels and shafts—most of them with a concrete lining. The most important ones, namely all the large caverns and most adits and shafts, are located downstream of the powerhouse. Having in mind the importance of these underground structures and the impact that the increase in the water pressures may have on the leakage that may occur into them, the first infilling of the power conduit is usually done in a planned way, in steps, and relatively slowly so that the flow in the rock mass can be established and stabilised.

The paper presented the first infilling plan and the upgraded monitoring system, and demonstrated the importance of performing the first infilling of the Gouvães power conduit in accordance with a plan, which was agreed beforehand between the LNEC, the owner and the

designer. The established procedure proved to be very useful to understand the hydraulic behaviour of the rock mass around the underground structures, to detect unforeseen occurrences, namely leakage into the openings, and to implement the necessary corrective measures.

REFERENCES

[1] LNEC (2021). Gouvães Hydroelectric Scheme – Plan for the first filling and start of operation of the power conduit (in Portuguese). Report 138/2021.

[2] Eptisa, Granell, Intecsa (2011). Tâmega project. Gouvães Hydroeletric Scheme – General document. Annex 2 – Geological and geotechnical study (in Spanish).

[3] LNEC (2016). Underground works for the Gouvãs powerhouse – Determination of initial stress state (in Portuguese). Report 277/2016.

[4] Iberdrola (2016). Monitoring plan for the powerhouse and transformers caverns of Gouvães Hydroeletric Scheme (in Spanish). Informe 1860/INTF-00026.

[5] Benson, P. B. (1989). Design of unlined pressure tunnels. Tunneling and Underground Space Technology, 4(2): 155-170.

[6] NFF (2013). Norwegian Hydropower Tunnelling II. Publication no. 22, Norwegian Tunnelling Society.

[7] Schleiss, A. and Johannesson, P. (1991). First Filling of Pervious Pressure Tunnels and Shafts (in German). Proceedings of the 7th ISRM Congress: 1345-1350, Aachen, Germany.

[8] LNEC (2024). Gouvães Hydroelectric Scheme – Final report of the first filling of the power conduit (in Portuguese). Report 119/2024.

Fifth International Dam World Conference
PORTUGAL • LISBON • LNEC • APRIL 13-17, 2025
dam world 2025

ASSESSMENT OF CONCRETE DAM FOUNDATION DISCHARGES FOR DIFFERENT RESERVOIR LEVELS FOLLOWING A HYDROMECHANICAL DISCRETE MODEL

M.L. Braga Farinha[1] LNEC
N. Monteiro Azevedo LNEC
Sérgio Oliveira LNEC

ABSTRACT

The ability to anticipate and avoid failures in concrete dams necessarily includes a detailed analysis of the mechanical/hydraulic properties and monitoring data relating to the dam-foundation system, an in-depth analysis of the geometry of the foundation rock mass, complex numerical analysis of dam behaviour and quantitative interpretation models. This ability to assess the safety of the dam-foundation system in an integrated way still needs to be improved, namely by incorporating coupled models that consider the significant interdependence between the mechanical and hydraulic behaviour. In addition, the models for interpreting hydraulic quantities are based on methodologies developed for the interpretation of the mechanical model, which, as a rule, do not fit the observed behaviour and do not consider the coupled behaviour. Coupled hydromechanical analysis of the water flow through the foundation rock mass of a concrete dam is carried using a 2D numerical model that allows seepage through the block interfaces and considers the influence of both grout and drainage curtains. Numerical predictions obtained during cycles of filling and emptying the reservoir are used to establish the influence lines of the hydrostatic pressure on recorded discharges. Two different dam heights and two different foundation geometries are evaluated. Also, two different behaviour scenarios are assessed: i) linear elastic and ii) non-linear behaviour at the concrete/rock and rock/rock interfaces. A series of different polynomial curves are adjusted to the numerical predictions using the least square method to find the best fit equation which can later be adopted in the development of more accurate quantitative interpretation methodologies of recorded data.

Keywords: concrete dams, rock foundations, hydromechanical behaviour, drain discharges.

[1]lbraga@lnec.pt, Portugal

1. INTRODUCTION

As mentioned by Enzell et al. [1] dam failure is a complex and highly dynamic process influenced by numerous factors, such as irregular geometries, nonlinear material behaviour, dynamic effects of water release, dam structural movement, and erosion of rock and soil. Anticipating and preventing failures in concrete dams requires a comprehensive approach that includes detailed analysis of the mechanical and hydraulic properties, along with monitoring data related to the dam-foundation system. It also involves an in-depth study of the foundation rock mass geometry, complex numerical modelling of dam behaviour, and the development of quantitative interpretation models.

Monitoring plays a vital role in understanding dam behaviour and preventing failures. Monitoring systems are usually fitted with alarm thresholds that allow the dam owner to detect issues early and take necessary corrective measures. Foundation monitoring results include foundation movement, water pressures and seepage. It is not easy to study the hydromechanical behaviour of dam foundations as this behaviour is non-linear, due to the influence of stress on permeability and to the possible time gap between the variation in the main loads and the variation in the measurement data [2].

The complex coupled hydromechanical behaviour of the foundation rock masses, which has a great influence on foundation seepage behaviour was the subject of several studies in the late 60s and early 70s of the last century [3-5], but still needs to be further studied in situ and adequately analysed using numerical models [6]. In addition, the bond mechanism and the crack development under hydrostatic pressure at the dam/foundation interface add complexity to the dam foundation behaviour and may have an influence on the durability of a dam and/or modify the failure mechanism of a concrete dam on a rock foundation [7, 8].

Regarding modelling of the complex hydromechanical behaviour of fractured dam foundations, equivalent continuum models can be used [9], but more advanced analysis is carried out with fracture flow models in which the discontinuities are explicitly represented [10-12]

In this study, fully coupled hydromechanical analysis of the water flow through the foundation rock mass of concrete gravity dams is carried using a 2D numerical model that allows seepage through the block interfaces and considers the influence of both grout and drainage curtains [11, 12]. Two hypothetical gravity dams of two different heights (15 m and 30 m) are considered. The analysis was conducted under two different behaviour scenarios: i) linear elastic and ii) non-linear behaviour at the concrete/rock and rock/rock interfaces. Numerical predictions obtained during cycles of filling and emptying the reservoir are used to establish the influence lines of the hydrostatic pressure on recorded discharges.

2. HYDROMECHANICAL DISCRETE MODEL

2.1. Fluid flow analysis with Parmac2D-Fflow

The hydromechanical model used in this study, Parmac2D-Fflow, is part of the Parmac2D computational framework [13] and enables the study of the interaction between hydraulic and mechanical behaviours in a fully coupled manner.

The model utilizes interface elements between the mechanical domain blocks and seepage channels (SC) in the hydraulic domain, with these channels aligned along the midplane of the interface elements. The interaction between the blocks, which represent both the rock mass foundation and the dam, occurs always edge to edge. The apertures of foundation discontinuities and water pressures are updated at each timestep, as outlined in [11] and [12]. The rock blocks are assumed to be impervious, with water flow occurring exclusively through the interconnected discontinuities. Water pressures are assigned to the hydraulic nodes (HN), which coincide with the mechanical nodes, and flow rates are computed within the SC.

Flow is modelled using the parallel plate model [4], with the flow rate per unit width of the model expressed by the cubic law. The flow rate [$(m^3/s)\cdot m^{-1}$] in each seepage channel is given by:

$$Q_{SC} = \frac{1}{12\,\mu}\, a_{h.SC}^3\, \rho_w\, g\, \frac{\Delta H_{SC}}{L} = k_{SC} \rho_w\, g\, \Delta H_{SC} \quad (1)$$

where $1/(12\,\mu)$ = theoretical value of a joint permeability factor (also called joint permeability constant), being μ the dynamic viscosity of the fluid; a = hydraulic aperture of the seepage channel; ρ_w = water density; g = acceleration of gravity; and ΔH = difference in piezometric head between both ends of the discontinuity; and L = length of the SC.

The hydraulic aperture to be used in Equation 1 is given by:

$$a_{h.SC} = a_{h.SC} + \Delta u_n \quad (2)$$

where $a_{h.SC}$ = hydraulic aperture at nominal zero normal stress and Δu_n = joint normal displacement taken as positive in opening. A maximum aperture, a_{max}, is assumed, and a minimum value, a_{min}, below which mechanical closure does not affect the contact permeability (Figure 1).

Each model block is subdivided into a mesh of linear triangular elements to account for its deformability. The flow is influenced by the stress state within the foundation.

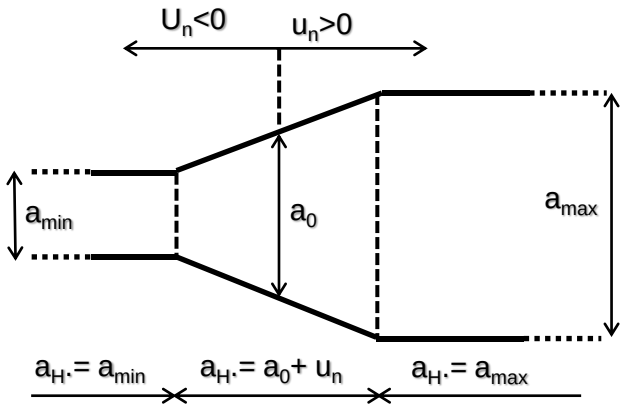

Fig. 1 – Hydraulic aperture

2.2. Model geometry

Two gravity dams of different heights, (15 m and 30 m) are assessed adopting two foundation fracture geometries. Figure 2 shows the schematically geometry of the models and Table 1 shows all the required geometric parameters.

The foundation rock masses were represented with two families of discontinuities. One model, called "reg", was considered, with a family of continuous horizontal discontinuities with a spacing of 5.0 m and a family formed by vertical discontinuities with an average spacing of 5.0 m and a standard deviation of 1.0 m. Another model was considered, called "dip", with families of continuous orthogonal discontinuities that make angles of 15º and 105º with the horizontal. In the latter case, the orientation, and the fact that the families of discontinuities are continuous and flat favours the formation of failure mechanisms, with the formation of wedges that can slide under the dam. In concrete, a set of horizontal continuous discontinuities located 3.0 m apart in the 15 m dam height model and 6.0 m apart in the 30 m dam height model were assumed to simulate dam lift joints.

Table 2 shows the number of mechanical and hydraulic elements used in the four different models. In the gravity dam 15 m high models, Dam 15-reg and Dam 15-dip, the adopted average size of the edges of the triangular elements is 0.5 m, whereas in the gravity dam 30 m high models, Dam 30-reg and Dam 30-dip, the adopted average size of the edges of the triangular elements is 1.0 m.

Figure 3 shows the hydromechanical discontinuum models that were developed for the dam 15 m high, Dam 15-reg and Dam 15-dip. In Figure 3 c) and d) each block is discretized using triangular plane finite elements and interact with others through joint elements. Regarding the hydraulic model, Figure 3 e) and f), the hydraulic head is assumed on the rock mass surface upstream and downstream from the dam (light blue dots); at the drainage system (dark blue

dots); at the hydraulic channels (red dots). Impervious lateral and bottom model boundaries are represented by black dots.

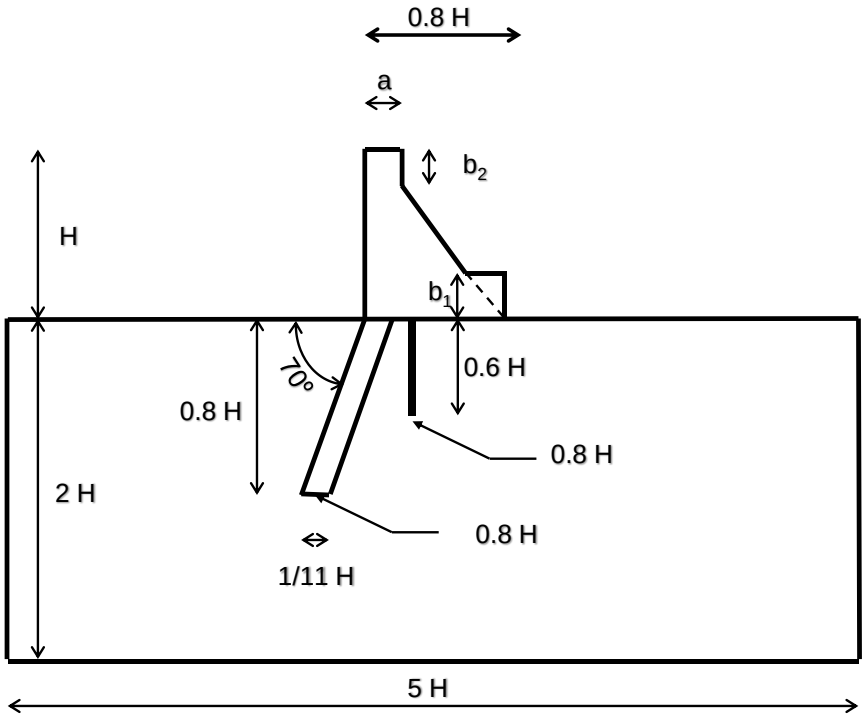

Fig. 2 – Model geometry

Table 1 – Geometry model parameters

Dam model	H (m)	a (m)	b_1 (m)	b_2 (m)
Dam 15	15	4.0	3.0	5.0
Dam 30	30	7.5	6.0	9.0

Table 2 – Information about the hydro-mechanical discontinuum models

Dam height (m)	Foundation type	Mechanical model				Hydraulic model	
		Blocks	FE triangular elements	FE joint elements	Nodes	Seepage channels	Hydraulic nodes
15	reg	375	15395	3503	11803	3442	3151
15	dip	403	15052	3632	11788	3568	3249
30	reg	387	15425	3659	11974	3446	3155
30	dip	417	15174	3761	11981	3549	3239

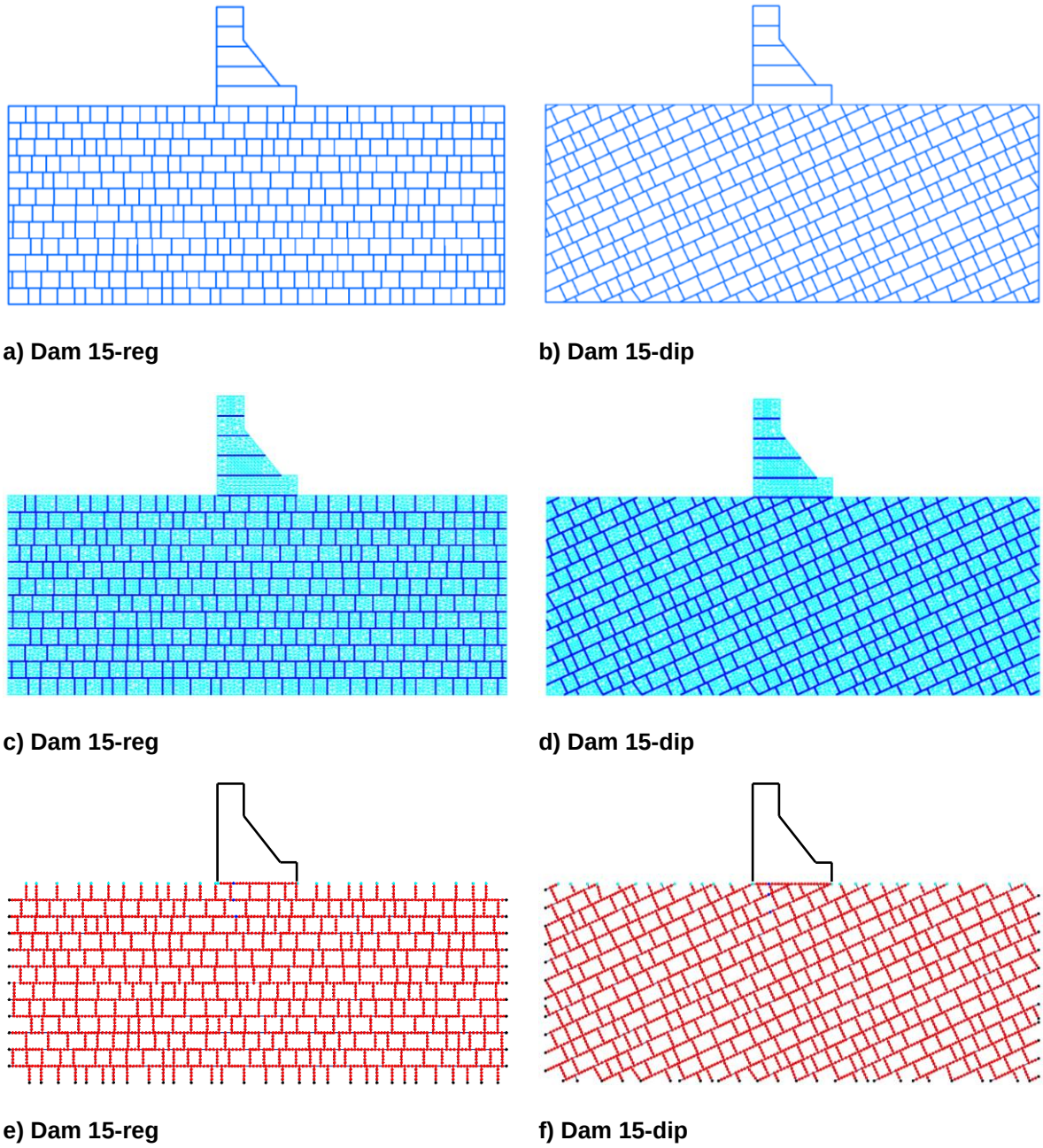

a) Dam 15-reg b) Dam 15-dip

c) Dam 15-reg d) Dam 15-dip

e) Dam 15-reg f) Dam 15-dip

Fig. 3 – Hydromechanical discontinuum model of the dam/foundation system of Dam 15-reg (a) and Dam 15-dip (b). Dam and foundation discrete blocks mechanical model ((c) and (d)). Hydraulic model ((e) and (f)). Hydraulic head assumed on the rock mass surface upstream and downstream from the dam (light blue dots); hydraulic head assumed at the drainage system (dark blue dots); hydraulic channels (red dots); impervious lateral and bottom model boundaries (black dots)

2.3. Mechanical and hydraulic parameters

Both dam concrete and rock mass blocks are assumed to follow elastic linear behaviour, with the properties shown in Table 3. A ratio of 0.5 is assumed between normal and shear stiffnesses. Table 3b) also shows the interface contact strength model parameters adopted for the concrete/concrete and concrete/rock interfaces that follow a bilinear softening model. Also shown are the rock-rock interface properties when a nonlinear foundation model is adopted.

The following hydraulic apertures were considered: a_0 = 0.1668 mm, $a_{res} = \frac{1}{3} a_0$ and $a_{max} = 5\ a_0$. It was assumed that the permeability of the dam/foundation interface was half that of the discontinuities in the foundation. The grout curtain permeability is 2.5 times lower than that of the rock mass. The dam construction joints are impervious.

Table 3 – Mechanical properties

a) Volume FE elements

Material	G (GPa)	v (-)	ρ (kg/m^3)
Dam concrete	30.3	0.24	2.4
Rock mass	64.4	0.2	2.7

b) Joint FE elements

Interface	k_n (GPa/m)	k_s (GPa/m)	σ_t (MPa)	C (MPa)	μ (-)	G_I (Nm/m^2)	G_{II} (Nm/m^2)
Concrete/Concrete	60.6	24.2	2.88	5.76	1.0	87.0	435.0
Concrete/Rock	120.8	51.5	1.37	2.74	1.0	24.7	123.3
Rock/Rock[1]	120.8	51.5	0.0	0.0	1.0	-	-

[1] In the rock mass discontinuities, when non-linear behaviour is considered, zero cohesion and traction and a friction coefficient of 1.0 are assumed.

2.4. Boundary conditions

For the mechanical models, both horizontal and vertical displacements at the base of the models, as well as horizontal displacements perpendicular to the lateral boundaries, were restricted. A pressure corresponding to the hydrostatic pressure was applied at the bottom of the reservoir and on the upstream face of the dam in each model.

Regarding the hydraulic boundary conditions, the dam body and the lateral and bottom boundaries of the model were considered impermeable. It was assumed that there was no water downstream of the dam, and the reservoir was at the same level as the crest of the dam, resulting in a constant pressure at the bottom of the reservoir corresponding to the water height. The drainage system was modelled by applying a water pressure along the drain axis equal to one-third of the hydraulic head upstream of the dam.

2.5. Analysis sequence

The mechanical effect of gravity loads with the reservoir empty is initially applied to the model. Following a hydromechanical analysis is carried out applying successive increments of water head at the reservoir bottom and of hydrostatic pressure at the upstream face of the dam to simulate the rising of water in the reservoir, followed by lowering the water level until the reservoir is emptied.

For the two different dam heights and the two different foundation geometries, two different foundation behaviour scenarios are assessed regarding the rock/rock interfaces: i) linear elastic and ii) non-linear behaviour. At the dam foundation interface a non-liner behaviour is always assumed. For the 15 m high dam models a water increment of 2.5 m is adopted whereas for the 30 m high models a 5.0 m water level increment is adopted.

3. RESULTS ANALYSIS

3.1. Fluid flow analysis

Results of the hydromechanical fluid flow analysis, with the reservoir at the same level as the crest of the dam are shown in Figures 4 and 5 for each adopted dam height. The pseudo-equipotentials of piezometric head in the foundation of each dam are presented, in Figures 4 and 5, using percentages of hydraulic head contours within the dam foundation that represent the ratio of the water head measured at a given level, expressed in metres of height of water, to the height of water in the reservoir above that level. Note that, the term pseudo-equipotentials [10] is used due to the discrete nature of the flow, which takes place along the rock mass foundation discontinuities.

Both figures show that the loss of hydraulic head is concentrated below the heel of the dam, at the drainage and grout curtain’s area. It is also shown that when a nonlinear model is adopted for the rock foundation mass, the contour that represents a 77.8% water head percentage tends to be located at a higher rock mass depth.

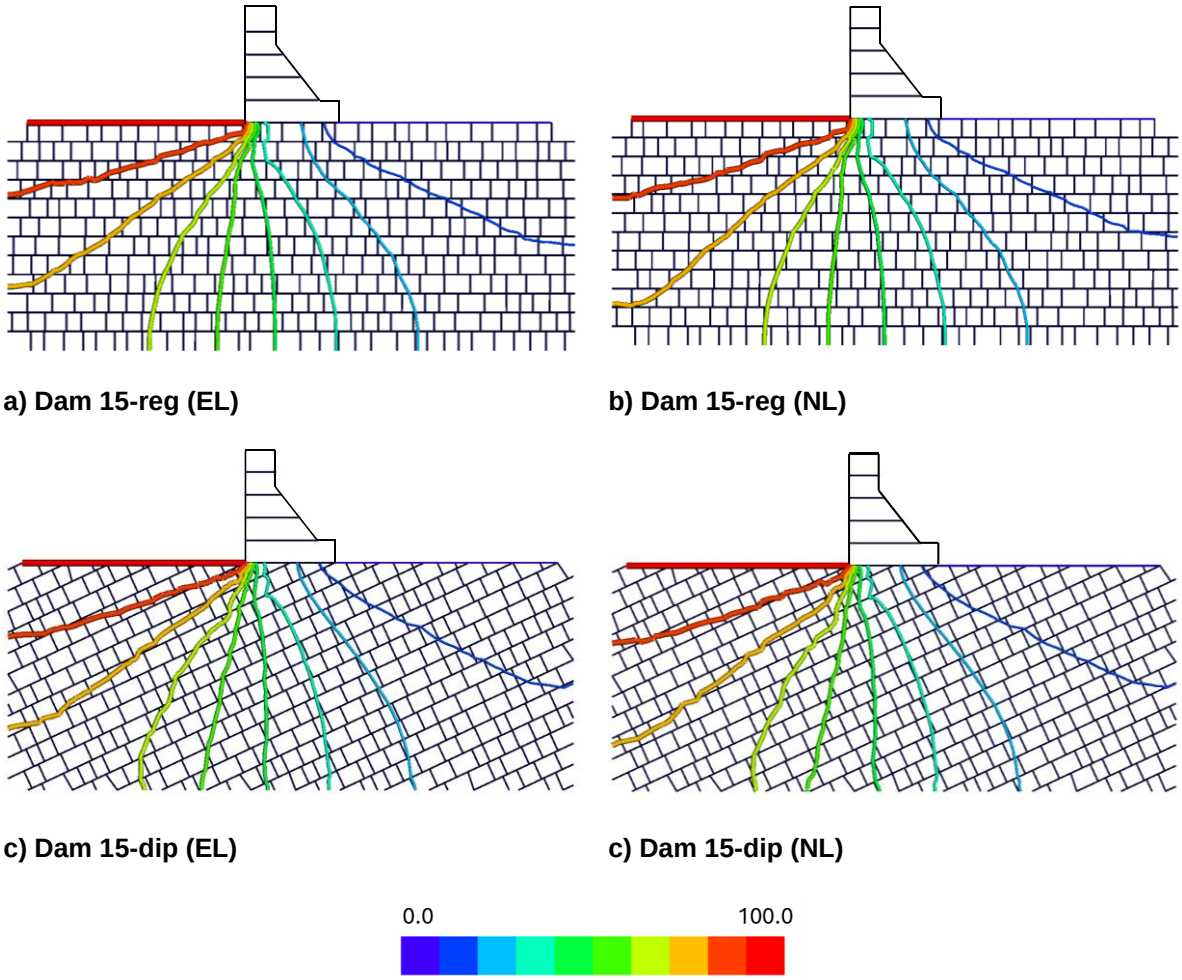

Fig. 4 – Percentage of hydraulic head for full reservoir for the 15 m high dam assuming a rock mass elastic model (EL) and a nonlinear rock mass model (NL)

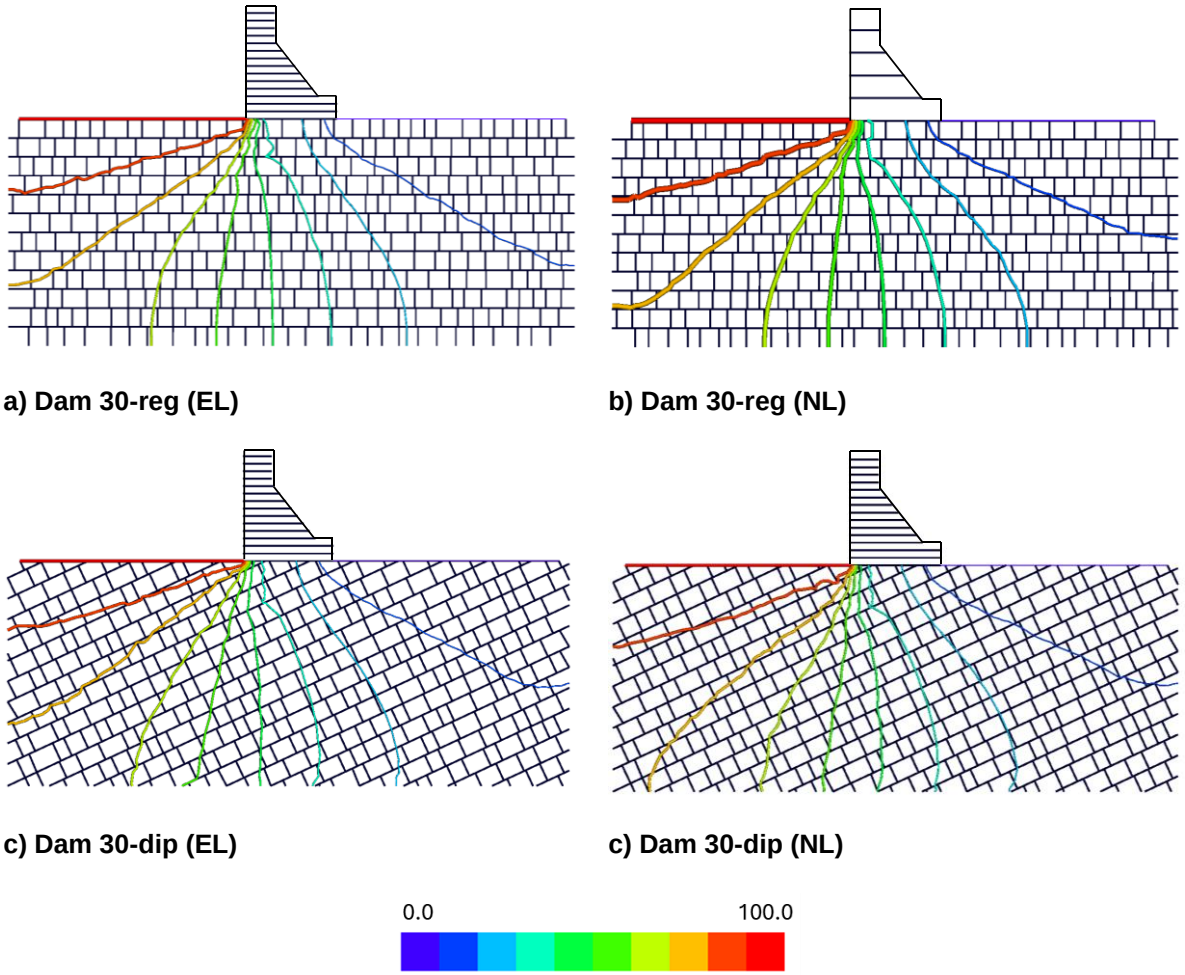

Fig. 5 – Percentage of hydraulic head for full reservoir for the 30 m high dam assuming a rock mass elastic model (EL) and a nonlinear rock mass model (NL)

3.2. Variations in discharges due to variations in reservoir level

Due to the hydromechanical behaviour of rock masses, the permeability depends on the state of stress and strain within the foundation and, consequently, discharges vary with variations in the reservoir level and resulting changes in rock mass permeability.

For the two different dams, for the two dam geometries and for the two adopted foundation behaviours, a load path, carried out applying successive increments of water head at the reservoir bottom and of hydrostatic pressure at the upstream face of the dam, was followed by an unload path, simulating the filling and a subsequent emptying of the reservoir.

Figure 6 shows the drain discharges for the studied examples. For the dam 30 m high and for the nonlinear foundation behaviour the loading and unloading paths do not match which is due to cracking that occurs at the concrete/rock foundation as the water level rises. This behaviour is more noticeable for the Dam 30-dip model.

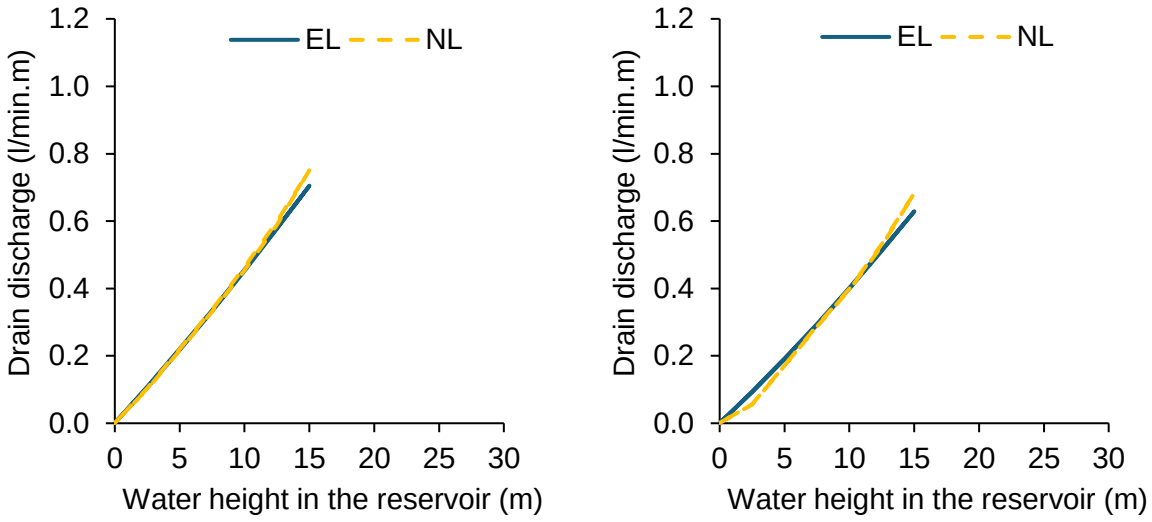

a) Dam 15-reg **b) Dam 15-dip**

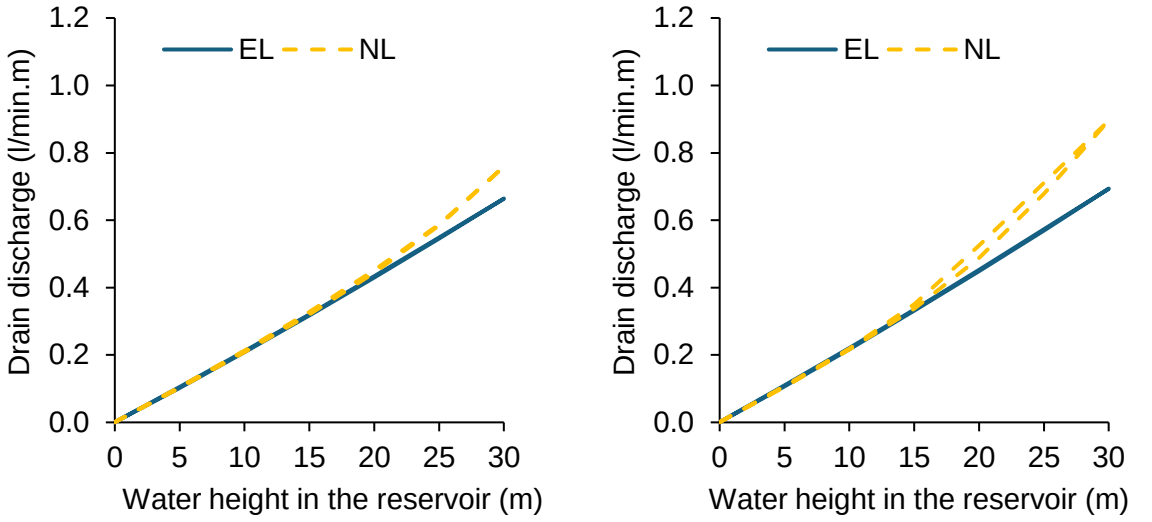

c) Dam 30-reg **d) Dam 30-dip**

Fig. 6 – Calculated drain discharges at different reservoir levels for the two different dam heights, two different foundation geometries and for the two different foundation behaviour scenarios

3.3. Adjustment of polynomial curves

A series of different polynomial curves was adjusted to those shown in Figure 6, regarding the dam 30 m high, using the least square method, to define the functions that better fit the numerical results. Eight polynomial functions were adjusted to the calculated drain discharges. Table 4 shows the different polynomial functions and the correlation coefficients that were obtained, where the best fits are highlighted in bold.

Table 4 – Correlation coefficients of the prediction functions

Polynomial function	Model			
	30-reg (EL)	30-reg (NL)	30-dip (EL)	30-dip (NL)
h^4	0.303085	0.467299	0.305463	0.580904
h^3	0.558291	0.682296	0.560148	0.767186
h^2	0.835983	0.901082	0.837044	0.924246
$h^4 + h$	0.999908	**0.999985**	0.999902	0.999484
$h^3 + h$	0.999963	0.999873	0.99996	**0.999922**
$h^2 + h$	**0.999999**	0.999203	**0.999999**	0.999093
$h^4 + h^2$	0.961773	0.968812	0.962037	0.98035
$h^3 + h^2$	0.975402	0.978243	0.975577	0.98571

Table 4 analysis leads to the conclusion that a function of the type q = f (h^2, h) would accurately fit the numerical results for both the 30-reg and 30-dip models, assuming linear elastic behaviour of the dam foundation. Assuming a non-linear behaviour both at the concrete/rock and rock/rock interfaces, a function of the type q = f (h^4, h) would better fit the numerical results for the 30-reg foundation, and a function of the type q = f (h^3, h) would better fit the numerical results for the 30-dip foundation.

Equations 3 to 6 are the functions that better fit the numerical results, for the four different models, respectively, 30-reg (EL), 30-reg (NL), 30-dip (NL) and 30-dip (NL):

$$q = 6.40\text{x}10^{-5}\, h^2 + 0.020215\, h \quad (3)$$

$$q = 1.68\text{x}10^{-4}\, h^4 + 0.020784\, h \quad (4)$$

$$q = 6.91\text{x}10^{-5}\, h^2 + 0.021048\, h \quad (5)$$

$$q = 1.07\text{x}10^{-5}\, h^3 + 0.020274\, h \quad (6)$$

The comparison between numerical results and those obtained with the adjusted polynomial curves that better fit the results is presented in Figure 7. Figure analysis clearly shows that the graphs of the adjusted curves follow adequately the curves which represent the variation in discharges due to variations in reservoir level.

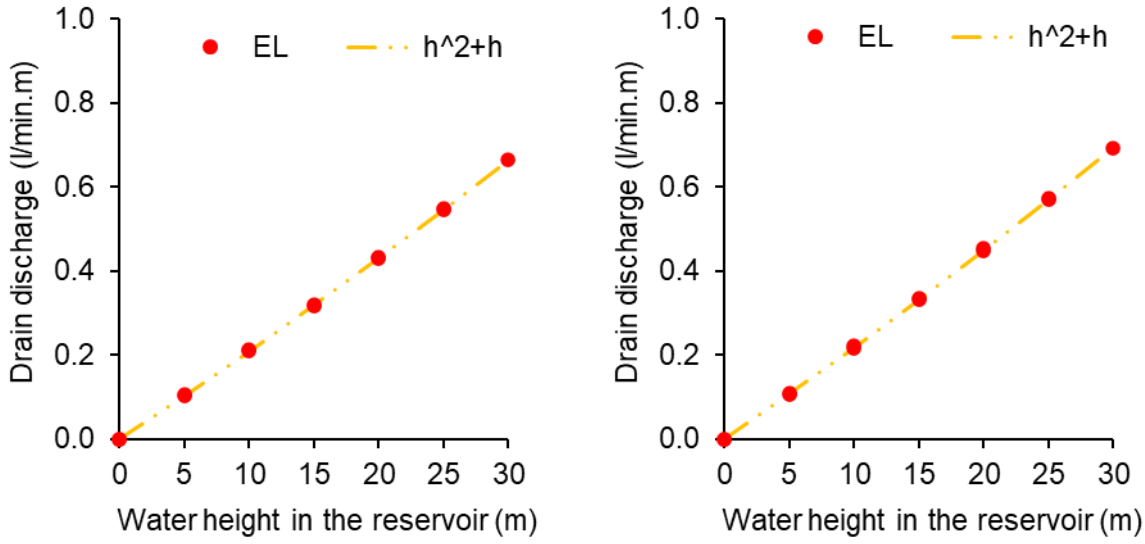

a) Dam 30-reg (EL) **b) Dam 30-dip (EL)**

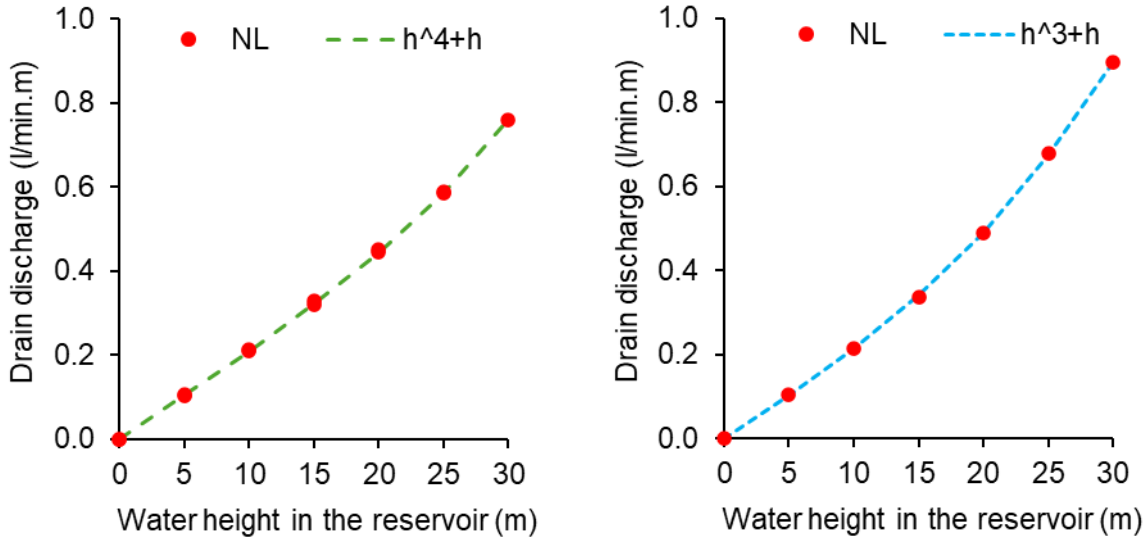

c) Dam 30-reg (NL) **d) Dam 30-dip (NL)**

Fig. 7 – Calculated drain discharges at different reservoir levels for the 30 m dam height, for the different foundation behaviours, and functions that better fit the numerical results

It must be highlighted that, in practice, the comparison of recorded discharges with those calculated using such functions may allow anomalous foundation behaviour to be identified.

4. CONCLUSIONS

This paper presents a study on seepage through gravity dam foundations using discontinuum models. The analysis focused on two hypothetical gravity dams of two different heights (15 m and 30 m), and, for each height, two different foundation geometries. A two-dimensional model, Parmac2D Flow, was used, which considers the coupled hydromechanical behaviour of rock masses. For each dam, the study examined the distribution of hydraulic head within the foundation and the amount of water flowing through the models under different scenarios involving foundation discontinuity pattern and foundation behavioural assumptions.

The results demonstrate the significant impact of the grout curtain and drainage system on the distribution of water pressures. The volume of water flowing through the dam foundations was found to be greater, for the highest reservoir levels, when a non-linear behaviour is assumed, compared to the results from linear elastic analysis.

The study also allowed the determination of the hydrostatic pressure influence line on discharges for each dam height, and polynomial functions were developed to accurately represent the shape of these lines.

Ongoing research is focused on studying the influence of the aperture of the foundation discontinuities on numerical discharges and establishing a unified polynomial function that incorporates both the calculated discharge values and the dam height. Similar studies are also going to be carried out using the 3D version of the Parmac2D code (Parmac3D-Fflow), that allows the three-dimensional behaviour of dams to be considered.

ACKNOWLEDGMENTS

The study presented here is part of the research project StepDam: A step forward for the ability to anticipate and prevent failures of concrete dam foundations (Proc. 0403/1102/24145, included in LNEC´s Research and Innovation Plan 2021-2027. The authors express their gratitude to the Portuguese Foundation for Science and Technology (FCT) for funding the research project Seismic Monitoring and Structural Health of Large Concrete Dams (SSHM4Dams) - PTDC/ECI-EGC/5332/2020.

REFERENCES

[1] Enzell, J., Nordström, E., Sjölander, A., Ansell, A., & Malm, R. (2023). Physical model tests of concrete buttress dams with failure imposed by hydrostatic water pressure. Water, 15(20), 3627. https://doi.org/10.3390/w15203627.

[2] Farinha M.L.B (2010). Hydromechanical behaviour of concrete dam foundations. In situ tests and numerical modelling. PhD Thesis, Instituto Superior Técnico, Lisbon.

[3] Londe, P. & Sabarly, F. 1966. La distribution des perméabilités dans la fondation des barrages voûtes en fonction du champ de contraint. In Proc. of the 1st Intern. Congr. on Rock Mechanics. 25 September - 1 October 1966, Lisboa, Portugal, Vol.II, pp 517-522.

[4] Louis C. 1969. A study of groundwater flow in jointed rock and its influence on the stability of rock masses. PhD Dis-sertation, University of Karlsruhe (in German), English translation, Imperial College Rock Mechanics Research Report nº10, London.

[5] Louis, C. & Maini, Y.N. 1970. Determination of in situ hydraulic parameters in jointed rock. In Proc. of the 2nd Intern. Congr. on Rock Mechanics, 21-26 September 1970, Bel-grade, USA, Vol.I, pp 235-245.

[6] Farinha, M. L. B., Azevedo, N. M., Schclar Leitão, N. A., Rocha de Almeida, J., & Oliveira, S. (2022). Sliding stability assessment of concrete dams using a 3D discontinuum hydromechanical model following a discrete crack approach. Geotechnics, 2(1), 133-157. https://doi.org/10.3390/geotechnics2010006.

[7] Dong, W., Wu, Z., and Zhou, X. (2016). Fracture mechanisms of rock-concrete interface: experimental and numerical. ASCE, Journal of Engineering Mechanics, 142(7): 04016040, DOI: 10.1061/(ASCE)EM.1943-7889.0001099.

[8] Dong W., Wu, Z, Zhou, X, Wang, N., Kastiukas G. (2017). An experimental study on crack propagation at rock-concrete interface using digital image correlation technique. Engineering Fracture Mechanics, 15 (February 2017): 50-63.

[9] Erban, P. & Gell, K. (1988). Consideration of the interaction between dam and bedrock in a coupled mechanic-hydraulic FE-program. Rock Mechanics Rock Enginering 21(2):99-117.

[10] Kafritsas J.C. (1987). Coupled flow/deformation analysis of jointed rock with the distinct element method. PhD Thesis, Massachusetts Institute of Technology, Cambridge.

[11] Azevedo N.M. & Farinha, M.L.B. (2015). A hydromechanical model for the analysis of concrete gravity dam foundations. Geotecnia - Journal of the Portuguese Society for Geotechnical Engineering 133(March 2015):5-33 (in Portuguese).

[12] Farinha, M.L.B., Azevedo, N.M. & Candeias, M. (2017). Small displacement coupled analysis of concrete gravity dam foundations: Static and Dynamic Conditions. Rock Mechanics Rock Engineering 50(2):439-464.

[13] Azevedo N.M. (2003). A rigid particle discrete element model for the fracture analysis of plane and reinforced concrete. PhD Thesis, Heriot-Watt University, Scotland.

Fifth International Dam World Conference
PORTUGAL • LISBON • LNEC • APRIL 13-17, 2025
dam world 2025

STABILITY ANALYSIS OF CONCRETE DAM FOUNDATIONS FOLLOWING A HYBRID DISCRETE ELEMENT/FINITE ELEMENT APPROACH

N. Monteiro Azevedo[1] LNEC
M.L. Braga Farinha LNEC
S. Oliveira LNEC

ABSTRACT

In concrete dam foundations, failure mechanisms are primarily influenced by natural rock discontinuities, the dam-foundation interface, or weaker strata. Instability can manifest beneath the dam, within the abutments, or along adjacent slopes. For arch dam foundations, particular attention is required for failure scenarios involving sliding along weaker surfaces in areas where the arches are supported (along the valley sides and abutments), as well as issues related to seepage at the valley bottom, that may lead to the discontinuities erosion. Sophisticated analyses employ discrete element models, which capture well the discontinuous nature of rock and can incorporate fluid flow through these discontinuities. In stability analyses of concrete dam foundations, interface models whether based on discrete element or finite element techniques typically use planar joint formulations, such as point-to-point, point-to-surface, and edge-to-edge contacts. This paper introduces a new hybrid discrete element/finite element approach. When large displacement may occur, the rock blocks outer surfaces are discretized with spherical particles, allowing interactions to be modelled through particle-to-triangular surface interactions which are known to be computationally robust. Whenever possible, the contact interaction is defined in small displacements using finite element joint elements. A simplified gravity dam equilibrium example is presented to validate the proposed hybrid model. Stability analysis of an idealized arch dam foundation is also performed. The presented results are shown to closely match those obtained with a more complex polyhedral-based discrete element model.

Keywords: concrete dams, rock foundations, stability analysis, contact interaction, hybrid model.

[1]nazevedo@lnec.pt, Portugal

1. INTRODUCTION

The foundation rock mass of concrete dams is a crucial element in the safety of this type of construction, as most failures occur due to problems in the foundation. The behavior of the rock mass is influenced by the load transfer mechanism from the dam body to the foundation. In concrete dams, failure mechanisms usually involve discontinuities in the foundation rock mass, the dam/foundation contact surface or layers of rock mass with lower resistance. Instability can occur under the dam, at the abutments or on the adjacent slopes.

In the case of arch dam foundations, special consideration must be given to failure scenarios involving sliding along surfaces of lower strength located in the arch support zone, particularly at abutments and mid-slope areas, and those involving percolation in the valley bottom zone, which leads to the erosion of discontinuities [1, 2]. The safety of this type of structures requires the use of three-dimensional models and the consideration of water pressures in the foundation discontinuities [3].

Stability assessments have been carried out in recent years using three-dimensional discrete element models, in which the blocks of the rock mass are represented by deformable polyhedral blocks, discretized with an internal mesh of uniformly stressed tetrahedral finite elements. Simplified pressure fields are usually assumed, determined considering the water level in the reservoir, the existence of the drainage curtain, and a phreatic surface downstream of the work compatible with the slope inclination. In [1] these pressures are obtained by performing hydraulic calculations with equivalent continuous medium models and in [3, 4] a 3D discontinuum hydromechanical model is used that performs a fully coupled hydromechanical analysis, where fracture conductivity is dependent on mechanical deformation.

This paper proposes a new hybrid discrete element/finite element approach. When large displacement may occur, the rock blocks outer surfaces are discretized with spherical particles, allowing interactions to be modelled through particle-to-triangular surface interactions which are known to be computationally robust. For this purpose, the interior domain of each block is discretized with spherical particles that interact with the triangular surfaces adopted in the discretization of the neighboring blocks. In [5] a similar algorithm for interaction between deformable blocks is proposed, in which the contact surfaces of each block are approximated by spherical particles. Whenever possible, the contact interaction is defined in small displacements using finite element joint elements. A similar contact rounding scheme that adopts inscribed spheres at the block vertexes and inscribed cylinders at the block edges has been proposed for contact recognition in discontinuous deformation analysis (DDA) [6, 7].

The 3D large displacement contact scheme is based on the 2D circular particle/side interaction model proposed in [8, 9]. In [10] it is also proposed a particle-particle interaction model for particle systems, which defines the unit normal of the contact as a function of the joint plane to which the contact belongs, thus reducing the influence of the roughness of the particle-particle contact. This particle-particle interaction algorithm has been applied to 3D slope stability analysis [11].

The proposed approach for large displacement interaction that adopts spherical particle/spherical particle or spherical particle/triangular surface interactions is not only simpler but also more computationally robust than models based on the actual geometry of each block [7, 8].

A simplified gravity dam equilibrium example is presented to validate the proposed hybrid model and to highlight the relevance of adopting a large displacement contact model when evaluating the associated safety factor. The stability analysis of an idealized arch dam foundation is also performed, the presented results are shown to closely match those obtained with a more complex polyhedral-based discrete element model.

2. 3D HYBRID DISCRETE ELEMENT/FINITE ELEMENT MODELLING

2.1. General formulation

The mechanical model adopted is a discrete model that uses an explicit solution algorithm based on the central difference method [14]. Each block of the model is internally discretized with a mesh of tetrahedral or 2nd degree hexahedral finite elements, to take its deformability into account. Figure 1 shows the calculation cycle of the explicit mechanical model adopted.

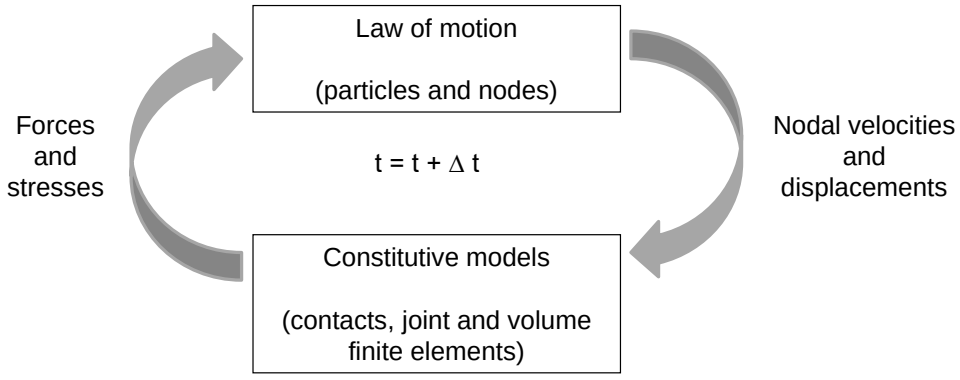

Fig. 1 – Mechanical model calculation cycle

For a given nodal point or spherical particle, the equations of motion are given by:

$$\mathrm{m}\,\ddot{u}_i(\mathrm{t}) + \mathrm{c}\,\dot{u}_i(\mathrm{t}) = F_i(t) + m\,g_i \quad (1)$$

where $\dot{u}_i(\mathrm{t})$ is the velocity, $\ddot{u}_i(\mathrm{t})$ is the acceleration, c is the damping constant, m is the nodal mass, g_i is the acceleration due to gravity and $F_i(t)$ are the nodal forces acting at a given instant defined by three terms:

$$F_i(t)=F_i^e(t) + F_i^c(t) + F_i^l(t) \quad (2)$$

where $F_i^e(t)$ are the external forces applied at the nodal point, $F_i^c(t)$ are the external forces due to contact with neighboring blocks that only exist at the nodal points on the block boundary, and $F_i^l(t)$ are the internal forces due to the deformation of the associated plane finite elements. Equation 1 is integrated using the central difference method, which is conditionally stable. The definition of the calculation step and the solution scheme to be adopted when only the static solution of the problem is required can be found in [14].

The interaction between deformable blocks can be carried out using discrete element techniques, which make it possible to analyze large displacements. In 3D there are 6 different types of contact, defined according to the elements used to represent the surface of the block: vertices (V), edges (A) and faces (F). There are two fundamental types of interaction that need to be modelled and which allow the correct definition of the various types of contact: vertex-face interaction (VF) and edge-edge interaction (AA) [15].

Joint finite elements [16, 17] require the finite element meshes of each block to be compatible, and are generally suitable for analysis at small displacements. This type of formulation has the advantage of allowing perfect compatibility of the displacement field along the interfaces between elements of the same degree. Thus, for similar discretizations, a more accurate representation of the stress distribution along the interfaces is obtained than with traditional discrete element models. However, this formulation requires more robust generation schemes to ensure that the interactions in 3D are only of the face/face type [3], or in 2D of the edge/edge type [8].

2.2. Large displacement contact model

Spherical particle/triangular surface interface model

The spherical particle/triangular surface interface model between deformable blocks is based on the particle/wall contact model traditionally adopted for contact between rigid elements [14]. The interface model considers the deformability of each block, since it considers the influence of the mesh, tetrahedral finite elements or hexahedral finite elements adopted in the discretization of each block, in the definition of the relative contact velocity and the distribution of the contact force.

Thus, as in the rigid model, the contact between the spherical particle belonging to a given block and the triangular surface of the neighboring block presents, at each instant, a normal

given as a function of the area of the triangular surface that interacts with the spherical particle (Figure 2a). The overlap between the spherical particle and the triangular surface at the point of contact and the location of the point of contact is given by:

$$U^n = R^{[B]} - d \tag{3}$$

$$x_i^{[c]} = x_i^{[B]} + (R^{[B]} - \frac{1}{2}U^n)\, n_i \tag{4}$$

The contact point velocity is given by the relative velocity of each entity at the contact point, thus:

$$\dot{x}_i^{[c]} = \dot{x}_i^{[ST.C]} - \dot{x}_i^{[B.C]} \tag{5}$$

where the velocity of the triangular surface $\dot{x}_i^{[ST.C]}$ and the velocity of the particle $\dot{x}_i^{[B.C]}$ are defined as a function of the value of the shape functions at the contact point of the tetrahedral element or hexahedral element associated with each entity, and their nodal velocities. For the case of a spherical particle (*B*) associated with a tetrahedron of nodes *i,j,k,l* (Figure 2 b), the velocity at the point of contact is given by:

$$\dot{x}_i^{[B.C]} = N^i \dot{x}_i^i + N^j \dot{x}_i^j + N^k \dot{x}_i^k + N^l \dot{x}_i^l \tag{6}$$

For a given tetrahedron the shape function associated with node ^{i} is defined as a function of the volumes of the following tetrahedrons:

$$N^i = \frac{Vol\ \Delta\ (j.l.k.x^{[c]})}{Vol\ \Delta\ (i.j.k.l)} \tag{7}$$

The proposed model assumes that the spherical particles used in the internal discretization of each block are rigidly connected to the finite element (s) that intersect their center of gravity. The shape functions associated with each spherical particle are therefore defined at the start of the calculation, and these shape function values are constant throughout the simulation. These values are used to define the new positions of the spherical particles needed to define the contact point.

The displacement increment of each local contact point, associated with the interval $\Delta\, t$ in the normal, $\Delta\, x_n^{[c]}$, and shear components, $\Delta\, x_{s,i}^{[c]}$, is determined using the following expressions:

$$\Delta\, x_n^{[c]} = (\dot{x}_i^{[c]} \Delta\, t) n_i \tag{8}$$

$$\Delta\, x_{s,i}^{[c]} = \dot{x}_i^{[c]} \Delta\, t - \Delta\, x_n^{[c]}\, n_i \tag{9}$$

In the adopted formulation, the normal component of the displacement of the local contact point corresponds to a scalar quantity and the tangential component corresponds to a vector quantity. The increments of normal force, $\Delta\, F_n^{[c]}$, and shear force, $\Delta\, F_{s,i}^{[c]}$, at each local contact point are determined according to a linear force-displacement relationship as a function of the

normal stiffness, k_n, and shear stiffness, k_s, associated with the local contact and the relative displacement:

$$\Delta F_n^{[c]} = -k_n \Delta x_n^{[c]} \tag{10}$$

$$\Delta F_{s,i}^{[c]} = -k_s \Delta x_{s,i}^{[c]} \tag{11}$$

It should be noted that the normal and shear stiffnesses are defined as a function of the particle's diameter. At a given moment, the resultant force at the point of contact is given by the sum of the normal component and the shear component using the following expression:

$$F_i^{[c]} = F_n^{[c]} n_i + F_{s.i}^{[c]} \tag{12}$$

The contact force is transferred to the nodal points of the finite element associated with the spherical particle and to the nodal points of the finite element associated with the triangular surface. Thus, for the nodal point *i* of the tetrahedron *ijkl* associated with the particle *B*, the internal force of the nodal point is updated given the value of the shape function associated with the nodal point to:

$$F_i^{[i]} = F_i^{[i]} - F_i^{[c]} N^i \tag{13}$$

For the nodal point *m* of the *mnop* tetrahedron associated with the triangular surface, the internal force of the nodal point is updated given the value of the shape function associated with the nodal point using the following expression:

$$F_i^{[m]} = F_i^{[m]} + F_i^{[c]} N^m \tag{14}$$

The mass scaling technique can be adopted if only a static solution is required [14] that increases the algorithm's convergence rate by reducing the ratio between the system's minimum and maximum frequencies. In this case, the mass of each nodal point is changed at each calculation step to guarantee the stability of the algorithm for a unit time increment. The normalized mass is determined using the following expression:

$$m_{escalada} = 0.25\, K_t \tag{15}$$

The translation stiffness, K_t, of each nodal point must consider the contribution of all contacts and all associated finite elements. An upper limit on the contribution of a given contact to nodal point i, not considering the orientation of the contact plane, is given by:

$$K_t = \sum_{c=1}^{N} 2\,(k_n + k_s) \tag{16}$$

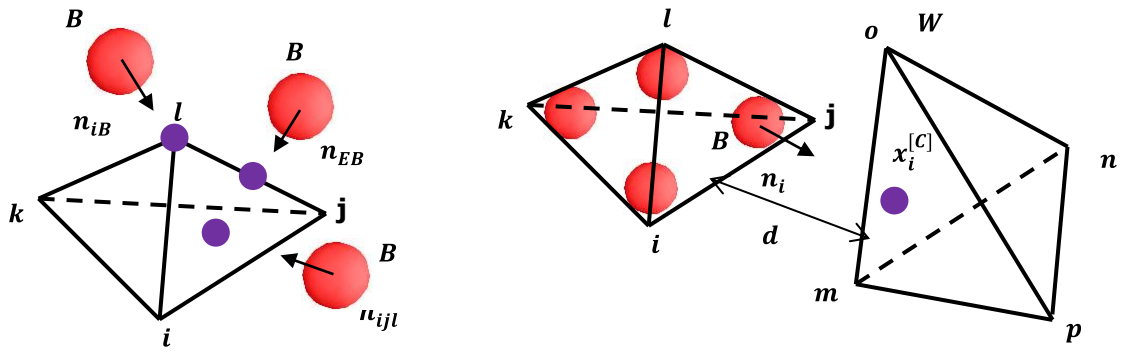

a) Contact normal direction depends on the location of the particle/block contact point

b) Geometry of the contact between a particle (*B*) inside a block and the outer triangular *mno* surface (*W*) of another block

Fig. 2 – Point contact spherical particle (*B*)/triangular surface (*W*)

Internal discretization of a given block

In the proposed contact model, it is necessary to previously discretize each block with a particle system, adopting the models proposed in [14]. After defining a compact particle system, the interior particles that are not in contact with the block exterior surfaces are discarded. Finally, the particles, which come to represent the outer geometry of the block, are classified according to their position, as shown in Figure 3. The radius of the particles representing the outer geometry of the block are then redefined to bring the sum of the areas associated with the spherical particles as close as possible to the area corresponding to the outer surface they represent. The contact stiffness values are determined considering these new particle radius values.

It is necessary to classify the particles according to their positioning, as the unit normal of the contact must be corrected to ensure that the roughness of the outer surface of the particle system does not influence the interaction between blocks, avoiding the appearance of artificial entanglements. Figure 4 shows the corrective measures to be adopted when redefining the contact normal depending on the classification of the particle and the positioning of the contact on the triangular surface.

With this approach, the level of discretization of the contact is independent of the internal finite element mesh used to represent the deformability of the block and is given as a function of the particle size used in the discretization of each block.

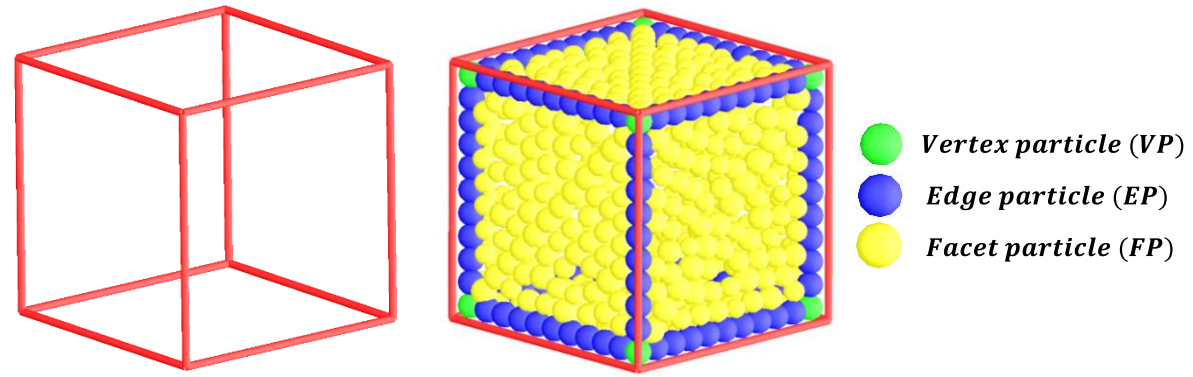

a) Block without particles

b) Block with the classification of particles that represent the exterior surface

Fig. 3 – Internal discretization of a block by a system of particles

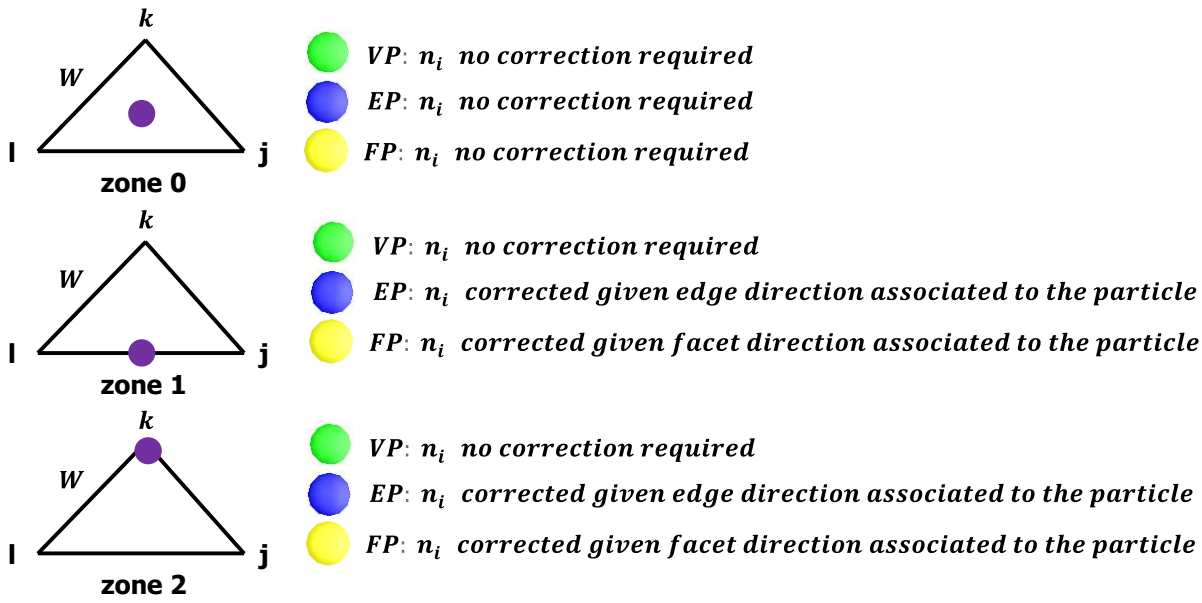

Fig. 3 – Correction of the unit normal of the contact depending on the location of the contact in relation to the triangular surface (*W*) and the classification of the spherical particle

With this approach, the level of discretization of the contact is independent of the internal finite element mesh used to represent the deformability of the block and is given as a function of the particle size used in the discretization of each block.

3. CASE STUDIES

3.1. Gravity dam stability analysis

The stability of a 30 m high gravity dam is assessed. The geometry of the gravity dam model is shown in Figure 5. As shown, several discontinuities were considered in the rock foundation. Three numerical modes were developed. In the first model the block interaction was carried out using only interface joint elements suitable for small displacements, FE-SD, in the second model an internal discretization with particles with 0.50 m radius in the areas where large displacements are expected to occur was adopted, PM-LD, and in the third model an internal discretization with particles with 0.50 m radius in the areas where large displacements are expected to occur was adopted, but the interaction between the fracture media and the foundation base is carried out using joint finite elements, Hybrid-FE&PM.

In all developed models, 8 node hexahedra elements are adopted in the volume discretization, 57 finite elements are adopted in the dam, 84 finite elements are adopted in the fracture media and 288 finite elements are adopted in the base, Figure 6a). In the FE-SD model joint finite elements are adopted for block interaction purposes, 57 joint elements represent the dam/fracture media interface, 84 joint elements represent the fracture media/fracture media interfaces and 96 joint elements represent the fracture media/base interface, Figure 6b). In the PM-LD a total of 6625 particles are adopted in the inner discretization of the outer boundary of the blocks that belong to the fractured media, Figure 6c). In the PM-LD the block interaction is represented by 2699 spherical particle/triangular surface contacts. In the Hybrid-FE&PM given that the interaction of the fracture media with the foundation base is carried out using joint finite elements only 1856 spherical particle/triangular surface contacts are required.

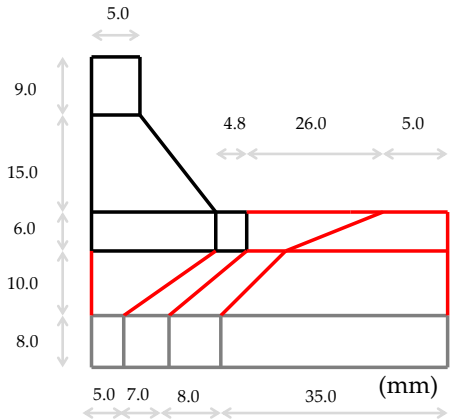

Fig. 4 – Gravity dam geometry

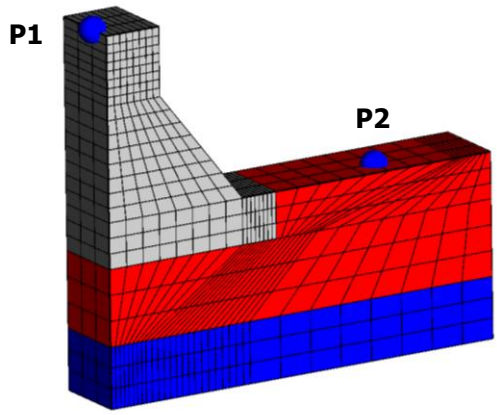

a) 8 node Hexahedra finite elements

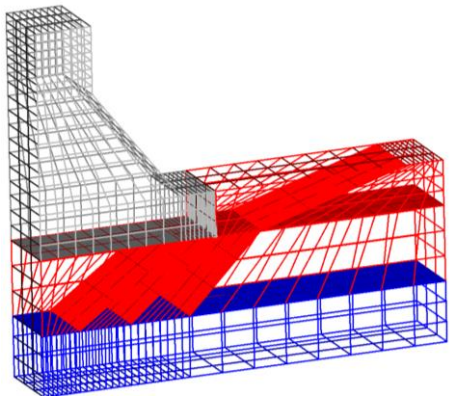

b) 4 node Joint finite elements

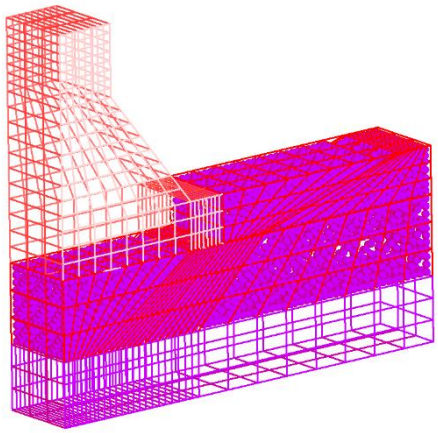

c) Fracture media discretized with spherical particles for interaction purposes

Fig. 5 – Gravity dam numerical modes

The mechanical properties adopted for the concrete and the rock foundation, and the elastic properties adopted for the contacts are presented in Table 3. The analysis was carried out in two phases, first the dam and rock mass weight were considered along with the hydrostatic pressure applied to the upstream section, assuming the level of the reservoir of 30.0 m. In this initial phase, linear elastic behaviour was considered in all interfaces. The calculations assumed that at the foundation base, zero displacement field is imposed in all directions. Following, a stability analysis was carried out by increasing the water pressure at the upstream face of the dam with an amplification factor (λ). In each cycle an increment in λ equal to 0.2 was adopted. In the stability analysis all interfaces had a zero cohesion and tensile strength and a friction angle of 35.0º.

Table 1 – Mechanical properties

a) Volume FE elements

Material	G (GPa)	v (-)	ρ (kg/m^3)
Dam concrete	20.0	0.20	2.4
Rock mass	20.0	0.20	2.75

b) Joint FE elements

Interface	k_n (GPa/m)	k_s (GPa/m)
Concrete/Concrete	20.0	10.0
Concrete/Rock	20.0	10.0
Rock/Rock	20.0	10.0

Figure 7 shows the variation of the displacement in the upstream/downstream direction of points P1 and P2, see Figure 6a), with the hydrostatic amplification factor up to failure. As shown, a large displacement formulation predicts the initiation of a change in behaviour for lower amplification factors, whereas a small displacement formulation predicts less pronounced displacement variations up to failure. Figure 7 also shows that the response predicted with a Hybrid-FE&PM-LD is very similar to the response predicted with the model PM-LD that demands higher computational costs.

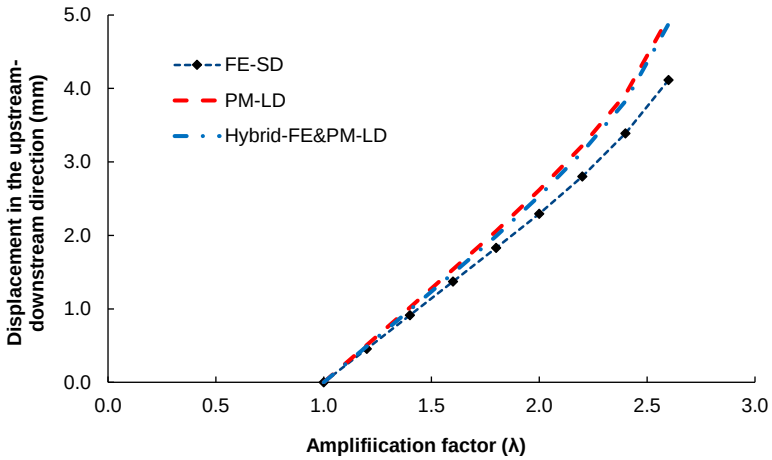

a) Point P1

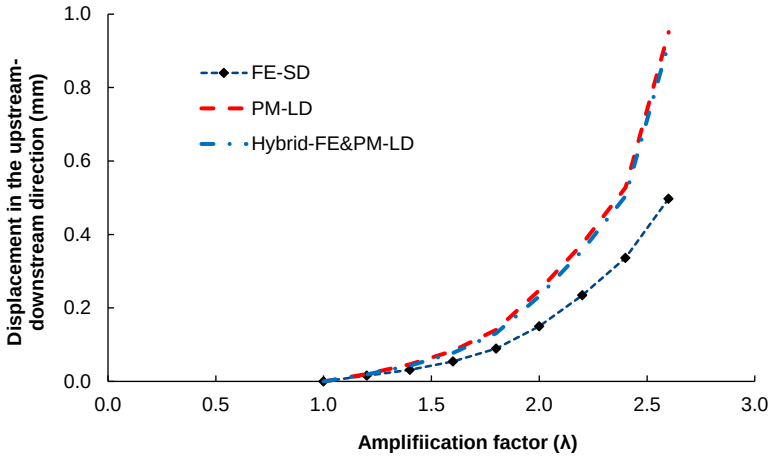

b) Point P2

Fig. 6 – Variation of the displacement in the upstream/downstream direction with the amplification factor - Points P1 and P2 (see Figure 6a))

Figure 8 presents the predicted failure modes for the FE-SD and the PM-LD models, as shown the predicted failure modes are similar, but at the onset of failure the FE-SD model based on small displacements does not guarantee that the correct final failure mode is obtained, whereas with a large displacement model, it is always assured that the failure mechanism is mechanically acceptable.

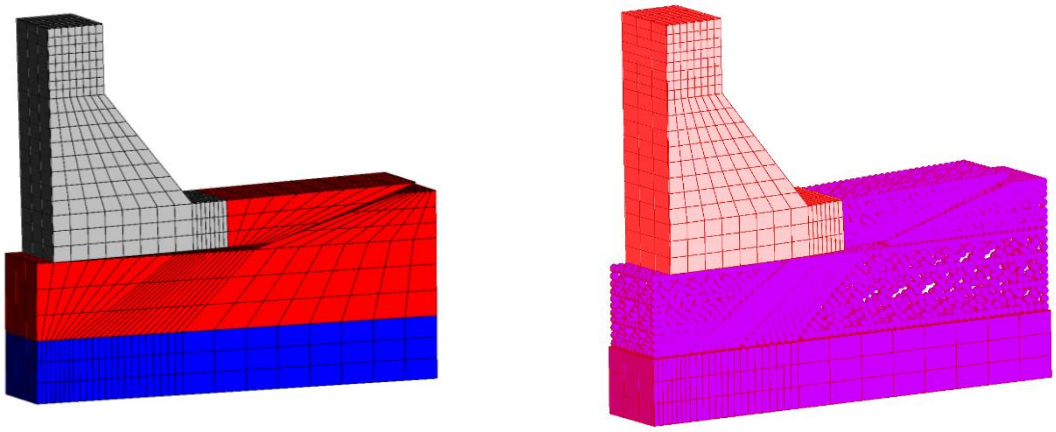

a) FE-SD **b) PM-LD**

Fig. 7 – Failure modes

3.2. Arch dam stability analysis

In this section stability of a hypothetical foundation of an arch dam is assessed. The geometric characteristics of the Talvacchia dam, located in Italy, were considered. The dam has a maximum height above the foundation of 77.0 m and the crown development is around 225.8 m. In the dam model shown in Figure 9, five dam contraction joints, the dam's insertion surface in the foundation, and two discontinuities in the foundation that define a hypothetical wedge in the rock mass on the right bank side, which provide a foundation failure mechanism. The three-dimensional finite element mesh used to represent the arch dam has two hexahedral 20 nodes finite elements on its thickness. Elements of the 1st degree tetrahedron type are used to discretize the foundation. The foundation model was generated in the 3DEC program [18].

With the proposed hybrid model two analyses were carried out: Hybrid-FE&PM (R=0.375), that adopts an internal discretization with particles with 0.375 m radius in the areas where large displacements are expected to occur, and Hybrid-FE&PM (R=0.75) which adopts an internal discretization with particles with 0.75 m in the areas where large displacements are expected to occur. Whenever possible, triangular joint elements were used in both models at the rock/rock and concrete/rock interfaces to reduce computational costs, in the other interfaces it adopts an internal discretization with particles at the vertices of the blocks. It should be noted that the 3DEC program's generation system does not guarantee perfect compatibility between the faces of the blocks, otherwise the analysis with the hybrid model could have been carried out using only triangular joint elements.

In the Hybrid-FE&PM (R=0.375) model all the blocks in the wedge zone are discretized with spherical particles with a 0.375 radius, Figure 10. A total of 75,509 particles are used in this zone. In the remaining zones, around 6493 spherical particles are used at the vertices of each block. In the Hybrid-FE&PM (R=0.375) model, around 4542 triangular joint elements and 66

2nd degree quadrangular joint elements (concrete/concrete interface) are adopted. In this model, around 61034 points of spherical particle/triangular surface contact are identified in the initial phase of the simulation. Figure 10 presents the interaction models, joint interface elements and triangular surfaces, adopted in the Hybrid-FE&PM (R=0.375) model.

In the Hybrid-FE&PM (R=0.75) model all the blocks in the wedge zone are discretized with spherical particles with a 0.75 radius. A total of 15755 particles are used in this zone. In this model, around 21274 points of spherical particle/triangular surface contact are identified in the initial phase of the simulation.

An analysis was also carried out using the 3DEC program with a similar mechanical model, in which the interactions between blocks follow the principles usually adopted in the interaction between polyhedral elements, considering the real geometry of the blocks. The model consists of 339 blocks (6 of which are the dam) with 9738 nodal points and the interaction between blocks is represented through 4441 contact points. The average size of the tetrahedral finite elements in the foundation is 25 m, except for the block at the base of the model where an average size of 40 m was adopted. The finite volume elements, 1st order tetrahedra and 20 node hexahedra elements, and the nodal points used to discretize the blocks are identical in the three models (Hybrid-FE&PM (R=0.375), Hybrid-FE&PM (R=0.750) and 3DEC).

The mechanical properties adopted for the concrete and the foundation rock mass and the elastic properties adopted for the contacts are similar to the previous example, Table 3. The same calculation procedure was followed for the three mechanical models adopted. The analysis was carried out in two phases, first the initial stress installed in the rock mass without the presence of the dam is considered, following the mechanical effect of the weight of the dam considering a model of independent cantilevers in the body of the dam is considered and finally the hydrostatic pressure to the upstream section is applied, assuming the level of the reservoir 5.0 m below the top of the dam. In this initial phase, linear elastic behaviour was considered in the various existing contacts. The calculations assumed that the rock mass has the following mechanical boundary conditions: zero displacement normal to the outer surface at the lateral boundaries and zero displacement in all directions at the outer surface corresponding to the base of the model.

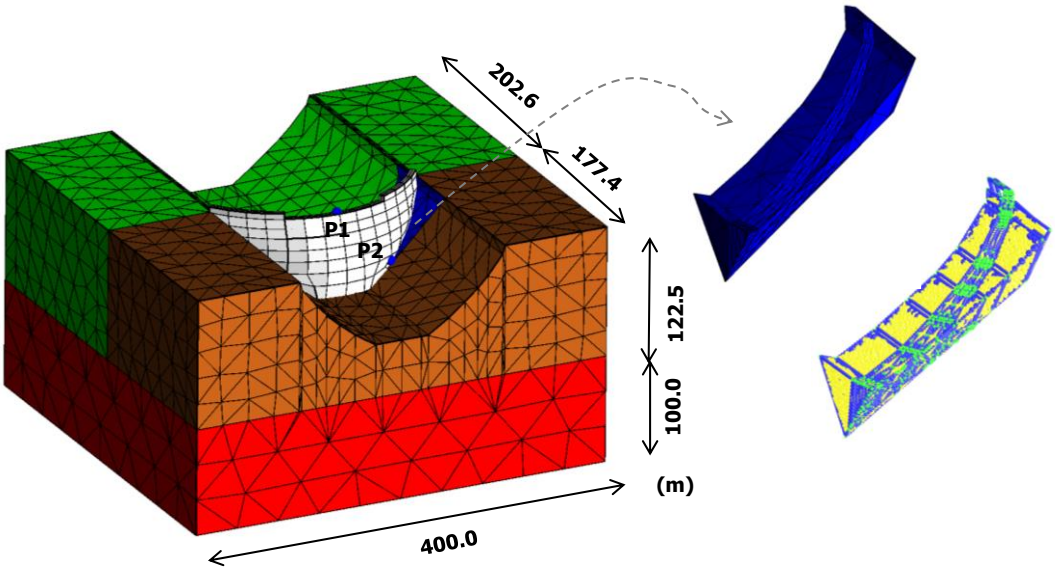

Fig. 8 – Numerical model of the Talvacchia Dam including the rock mass and the internal discretization by a particle system of the zone where large displacements are expected to occur

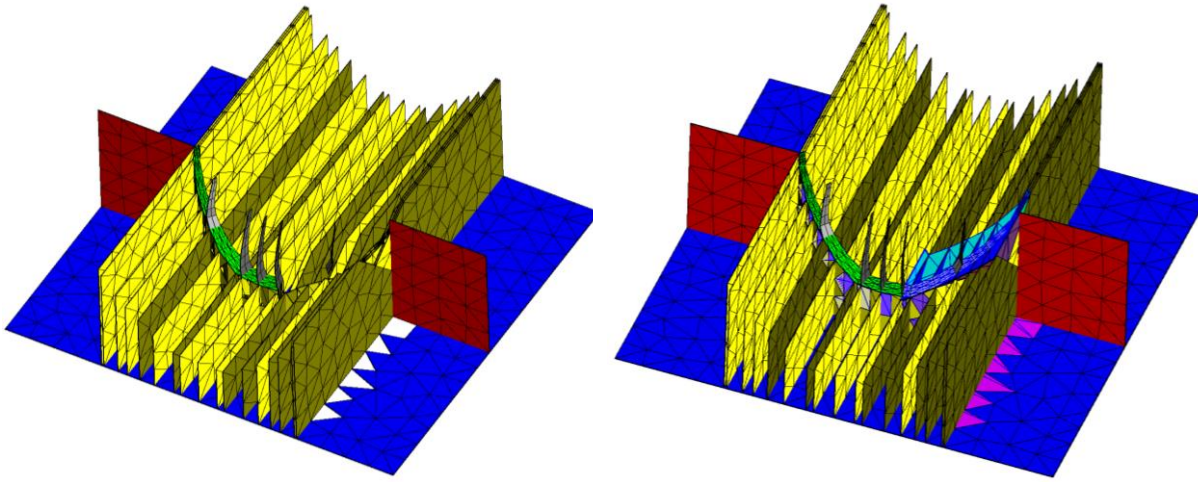

a) Triangular joint elements and 2nd degree quadrangular joint elements

b) Interactions between blocks including spherical particle/triangular surface contacts

Fig. 9 – Interaction models - Hybrid-FE&PM (R=0.375)

The stability analysis was carried out using the strength reduction method typically used in foundation design. The calculation process in the three models was similar. An initial friction angle of 35° was assumed in the discontinuities of the rock mass in the volume of influence of the wedge, with zero cohesion and tensile stress. A linear elastic contact model was adopted for the concrete/rock, concrete/concrete and other rock/rock joints outside the wedge's zone of influence.

In the stability analysis, a local damping model with a value of 0.70 was adopted for all the models [14]. The effect of water pressure on the discontinuities in the rock mass was not

considered in the calculations, nor was the hydromechanical behaviour of the foundation rock mass. Figure 11 shows the displacement in the upstream/downstream direction evolution with the reduction in the friction angle in the discontinuities associated with the failure mode analyzed, Figure 10.

There is reasonable agreement between the proposed hybrid models and the 3DEC model. It can also be seen that for a value of zero friction angle, all models predict stable behaviour. The results presented in Figure 11 also show the relevance of adopting a higher outer boundary discretization, Hybrid-FE&PM (R=0.375), for which a more stable equilibrium configuration with lower displacements was predicted for a zero friction angle.

It should be noted that although the hybrid models and the 3DEC model reach a stable equilibrium configuration for a for zero friction angle values, the displacements recorded are already quite significant and the behaviour of the dam body is already quite far removed from that obtained for static initial loads. For this equilibrium position, the displacements both in the dam body and in the concrete/rock mass interfaces are already quite significant, and this position cannot be considered acceptable from a safety point of view. For friction angle values below 22º there is a clear change in the dam-foundation system behaviour, Figure 11, and the predicted displacements may compromise the dam safety.

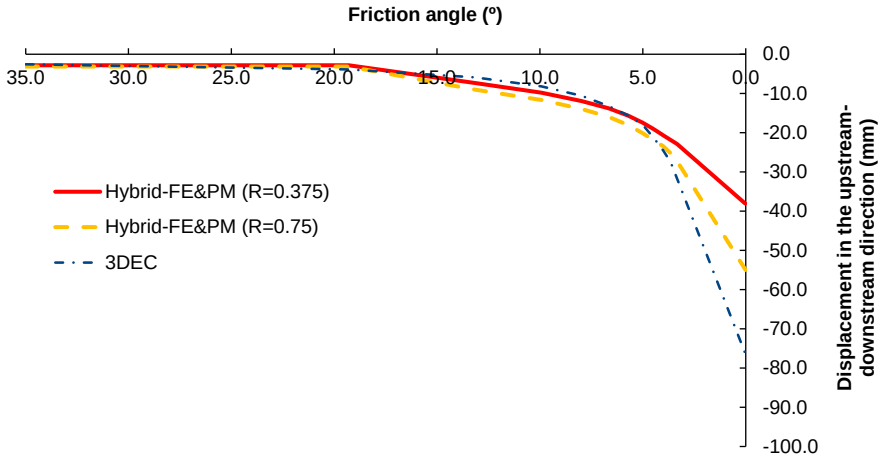

a) Point P1

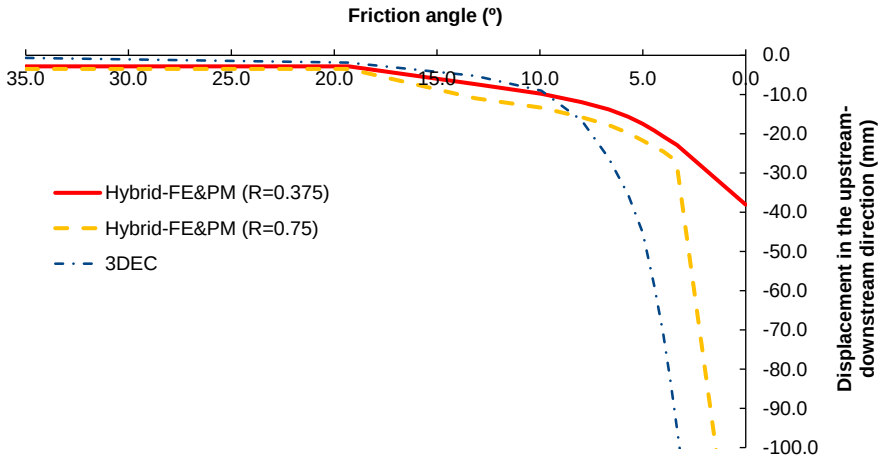

b) Point P2

Fig. 10 – Displacement variation in the upstream/downstream direction with the reduction of the friction angle in the discontinuities associated with analysed failure mode - Points P1 and P2 (see Figure 10)

Figure 12 shows the final deformation of the model obtained for a zero friction angle with a magnification factor of 10. A similar displacement field is obtained with the 3DEC model. Some of the independent blocks in the wedge zone show significant displacements and that, especially on the right bank, the support of the dam body on the rock mass is compromised, which is only possible because a linear elastic behaviour was considered in the vertical joints of the dam body.

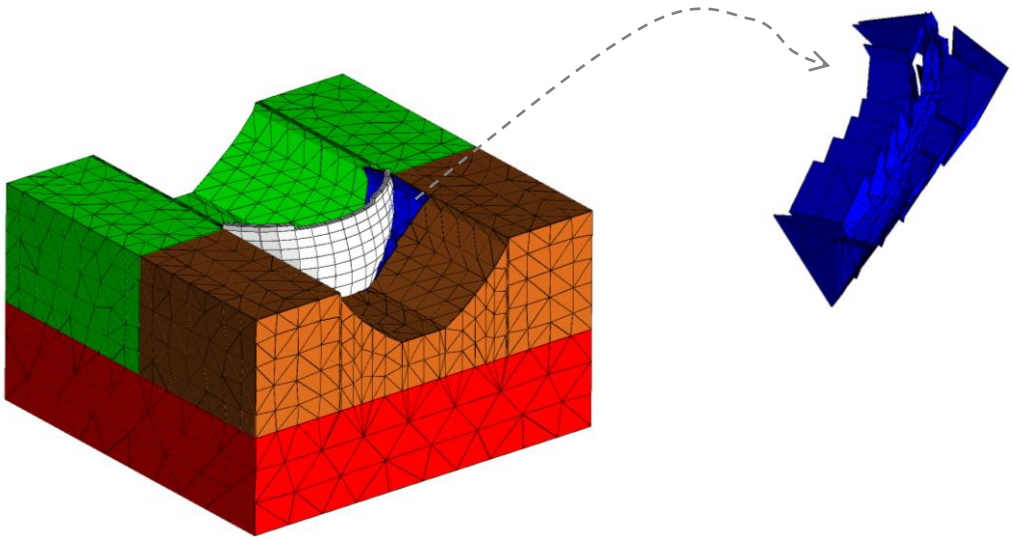

Fig. 11 – Final deformation - 10x amplified displacement - Hybrid-FE&PM (R=0.375).

4. CONCLUSIONS

This paper presents a new hybrid discrete element/finite element approach. Under large displacements, an interaction algorithm between neighbouring deformable blocks of the spherical particle/triangular surface type is adopted. The interior domain of each block is discretized with spherical particles that interact with the triangular surfaces adopted in the discretization of the neighbouring blocks, minimizing the effect of possible artificial entanglements.

The contact interaction scheme proposed for large displacement leads to an increase in computational requirements compared to other calculation schemes that consider the actual geometry of the block surface, as it requires the consideration of a greater number of contacts. However, the treatment of each contact is simpler, particularly when it comes to defining: i) the area of influence of each contact (particle diameter); ii) the normal of each contact (normal to the triangular facet); iii) the transition from a vertex/vertex contact to a vertex/face or vertex/edge contact and iv) the transition from an edge/edge contact to an edge/face contact. In order to reduce the associated computational costs, whenever possible, the contact interaction is defined in small displacements using finite element joint elements.

The proposed large displacement interaction scheme leads to a significant increase in the number of contacts, but it is a simpler and more computationally robust model than other schemes that take into account the actual geometry of the surface of the blocks. It should also be noted that with this approach the level of contact discretization is independent of the internal finite element mesh used to represent the block's deformability, and is given as a function of the particle size to be used in the discretization of each block.

The gravity dam shows that the proposed hybrid algorithm predicts a response closer to the response obtained with a full interaction model in large displacements. Note that a large displacement contact model is essential to obtain the correct failure mode. The presented arch dam foundation example shows that the proposed hybrid model for contact interaction predicts a response close to that obtained with discrete polyhedral elements based on more complex interaction models.

ACKNOWLEDGMENTS

The study presented here is part of the research project StepDam: A step forward for the ability to anticipate and prevent failures of concrete dam foundations (Proc. 0403/1102/24145, included in LNEC´s Research and Innovation Plan 2021-2027. The authors express their gratitude to the Portuguese Foundation for Science and Technology (FCT) for funding the research project Seismic Monitoring and Structural Health of Large Concrete Dams (SSHM4Dams) - PTDC/ECI-EGC/5332/2020.

REFERENCES

[1] Farinha, M.L.B., Lemos, J.; Maranha das Neves, E. (2012). Analysis of foundation sliding of an arch dam considering the hydromechanical behaviour, Frontiers of Structural Civil Engineering, vol. 6(1), pp 35–43

[2] Farinha, M.L.B., Lemos, J.; Maranha das Neves, E. (2012). Modelação tridimensional das pressões da água na fundação da barragem de Alqueva. Proceedings do 13º Congresso Nacional de Geotecnia, LNEC, Lisboa.

[3] Farinha, M.L.B., Monteiro Azevedo, N., Schclar Leitão, N.; Rocha de Almeida, J.; Oliveira, S. (2022). Sliding Stability Assessment of Concrete Dams Using a 3D Discontinuum Hydromechanical Model Following a Discrete Crack Approach. Geotechnics 2022, 2, pp 133-157.

[4] Monteiro Azevedo, N.; Farinha, L. (2015). Um modelo hidromecânico para a análise de fundações de barragens gravidade em betão, Geotecnia, 2015, 133, pp 5-33 (in Portuguese).

[5] Belytschko, T. e O' Neal, M. (1991). Contact-impact by the pinball algorithm with penalty and lagrangian methods, International Journal for Numerical Methods in Engineering, vol. 31(3), pp 547–572.

[6] Ahn, T. Y., Ryu, S., Song, J. J. & Lee, C, (2009). A New Contact Method using Inscribed Sphere for 3D Discontinuous Deformation Analysis. Analysis of Discontinuous Deformation: New Developments and Applications. 127-134.

[7] Ahn, T. Y., Song, J. J. (2012). New Contact Resolution Algorithm using Two-stage Contact Definition and Rounding Scheme in 3D DDA. In Proceedings of the 10th International Conference on Analysis of Discontinuous Deformation, Advances in Discontinuous Numerical Methods and Applications in Geomechanics and Geoengineering Editors. pages 101-106.

[8] Farinha, M.L B., Monteiro Azevedo, N., Candeias, M. (2017). Small Displacement Coupled Analysis of Concrete Gravity Dam Foundations: Static and Dynamic Conditions, Rock mechanics & Rock Engineering, , Vol 50 (2), pp 439-464.

[9] Monteiro Azevedo, N.; Lemos, J. (2022). A Hybrid Particle/Finite Element Model with Surface Roughness for Stone Masonry Analysis. Applied Mechanics, 3, pp 608–627.

[10] Ivars, D., Pierce, M., Darcel, C., Montes, J., Potyondy, D., Young, R. e Cundall, P. (2011). The synthetic rock mass approach for jointed rock mass modelling, International Journal of Rock Mechanics & Mining Sciences, vol. 48 (2), pp 219-244.

[11] Scholtes, L. e Donzé, F. (2012). Modelling progressive failure in fractured rock masses using a 3D discrete element method, International Journal of Rock Mechanics & Mining Sciences, vol. 52, pp 18-30.

[12] Pulatsu, B., Erdogmus, E., Lourenço, P.B. et al. (2021). Numerical modeling of the tension stiffening in reinforced concrete members via discontinuum models. Comp. Part. Mech. 8, 423–436. https://doi.org/10.1007/s40571-020-00342-5

[13] Ghazvinian, E.; Diederichs, M.; Quey, R. (2014). 3D Random Voronoi grain-based models for simulation of brittle rock damage and fabric-guided micro-fracturing. J. Rock Mech. Geotech. Eng., 6, 506–521.

[14] Azevedo, N. (2003). A rigid particle discrete element model for the fracture analysis of plane and reinforced concrete. PhD Thesis, Heriot-Watt University, Scotland

[15] Lemos, J. (1995). Metodologias para deteção e atualização de contactos em modelos de elementos discretos. Proceedings do IV Encontro Nacional de Mecânica Computacional, Lisboa, pp. 61-72 (in Portuguese).

[16] Goodman, R. e Taylor, R.; Brekke, T. (1968). A model for the mechanics of jointed rock, Journal of the Soil Mechanics and Foundations Division (ASCE), vol. 94(SM3), pp 637-659.

[17] Hohberg, J. (1992). A joint element for the nonlinear dynamic analysis of arch dams. PhD Thesis. Institute of Structural Engineering, ETH, Zurich, Switzerland.

[18] Itasca (2013). 3DEC - 3-Dimensional Distinct Element Code, Version 5.0, User's Manual. Itasca Consulting Group, Minneapolis, USA.

Fifth International Dam World Conference
PORTUGAL • LISBON • LNEC • APRIL 13-17, 2025
dam world 2025

IMPLEMENTATION OF 3D THERMAL MODELS IN THE CONSTRUCTION OF THE ALTO TÂMEGA DAM

Luís Capinha
IBERDROLA

Rafael Chacón
IBERDROLA

Alicia Sigüenza[1]
IBERDROLA

Luis de la Torre
IBERDROLA

Emilio José Vinagre
IBERDROLA

ABSTRACT

The Alto Tâmega dam is a 104.5-meter-high vault dam that is part of the hydroelectric complex developed by Iberdrola in northern Portugal in the Tâmega river basin. The filling of the reservoir was completed in February 2024, and the dam is currently operating normally. The dam was constructed using the most advanced cooled concrete techniques, in which Iberdrola has extensive experience. During the dam construction, cooling concrete is essential to prevent thermal cracking and ensure its structural integrity. Therefore, it is crucial to control the entire process by means of numerical models. For this reason, various 2D and 3D finite element numerical models were carried out in different project stages, with different scopes and objectives. These numerical models include thermal models simulating the construction of the dam and the moment of injection of the joints between blocks, as well as coupled mechanical models simulating the different behaviour of the dam for the loads applied before and after the injection and during the filling phase.

Once the dam was put into service, with new data available, these models were integrated and calibrated with the values provided by the monitoring to achieve a better approximation of the future behaviour of the dam. In conclusion, the Alto Tâmega dam serves as a representative case study for the successful application of this innovative tool in large scale projects, effectively controlling the entire process from design to construction.

Keywords: Cooling Concrete, Thermal Finite Element Models.

[1] asiguenza@iberdrola.es

1. INTRODUCTION

The Tâmega Complex is a hydroelectric project that IBERDROLA recently built and commissioned in northern Portugal, on the Tâmega River. It consists of three power plants with their corresponding dams in cascade: Gouvães, Daivões, and Alto Tâmega. The total installed capacity of these power stations is 1158 MW, which means an annual energy production of 1766 GWh and 40 GWh of storage, enough to satisfy the daily electricity demand of 11 million people. Since the end of 2024, it has been fully operational.

Focusing on Alto Tâmega HPP, the facility is located at the downstream dam toe and consists of two groups of vertical-axis Francis turbines, each designed for a flow rate of 100 m^3/s, with a total installed capacity of 160 MW.

Regarding the reservoir, its storage total capacity is 131.7 hm^3, with a maximum upstream level of 315 meters above sea level. The geology of the foundation mainly consists of mica schists, and the highest excavation depths for the foundation reaches up to 16 meters.

The dam has a double-curvature arch geometry. It stands 104.50 meters high and has a total crest length of 332 meters, including the abutments. It has a variable thickness, with 5.00 meters at the crest and a maximum of 22.61 meters in the central foundation area. It is divided into 21 blocks, with contraction joints injected with cement grout and provided with four horizontal galleries at different levels and a perimeter gallery that serves to carry out foundation treatments.

The low heat hydration concrete used had a characteristic strength equal to 22 MPa, composed by granite aggregates and Portland cement with a 42% mixed of fly ashes. The aggregates were extracted from a quarry located in the Gouvães basin, totaling 223,000 m^3. Thanks to IBERDROLA's technical knowledge accumulated from previous experiences in the hydroelectric energy business, the cooling concrete technique was chosen for the construction of the dam.

2. COOLING CONCRETE TECHNIQUES

2.1. Cooling Technology

Concrete cooling involves lowering the temperature of freshly poured concrete to a specific level. This process ensures the concrete's quality and allows construction to proceed smoothly.

Small batches of concrete can be easily handled: mixing, pouring, and waiting for it to harden. However, applying the same process to large quantities can compromise quality. Heat is generated during the hardening of concrete, and if not controlled, it can negatively affect the

durability of the structure. Additionally, temperature control during curing is essential to prevent thermal cracking and ensure long-lasting structures.

Concrete cooling is primarily used in warm climates and in projects that require huge volumes of concrete, like large dams. It is also employed in projects where significant temperature variations occur during concrete use.

2.2. Cooling Systems

Chilled Water:

Water cooling is a common and cost-effective method in concrete cooling systems. It involves directly adding chilled water to the concrete mix. Concrete batch plants typically have a thermal water tank that can be cooled in summer or heated in winter.

By adding chilled water to the mix, the heat energy in the concrete is absorbed, lowering its temperature. Water cooling is effective for moderate temperature control and is often used in projects where the maximum concrete pour temperature is not excessively high.

Ice:

In this method, ice flakes are added to the concrete mix. As the ice melts, it absorbs latent heat, significantly reducing the mixture's temperature.

When substituting water with ice, the mixing method and type of batch plant must be considered. Since water is present in the aggregates' moisture, this amount needs to be accounted for when adding ice. Therefore, there is always a limit to the amount of ice that can be added to a concrete batch, directly related to the aggregates' moisture content.

Nevertheless, using ice is particularly efficient and beneficial in hot climates or when a faster cooling rate is required.

Aggregates:

The aggregates are submerged in cooled water before adding them to the concrete mix. It is required to dry the aggregates after being submerged in water, in order to avoid adding additional moisture to the concrete mix.

3. CONSTRUCTION STAGES

3.1. Concrete of the dam: requirements and characteristics

The dam crest has a development in plan of 350 meters and its width is 9 meters. It is composed of 21 blocks: 16 body blocks (1-16), 3 right bank blocks (18, 20 and 22) and 2 left bank blocks (17 and 19).

IBERDROLA defined the technical parameters for the desired concrete characteristics for the dam. The concrete is applied at low temperatures, between 8°C and 10°C. This temperature is achieved during manufacturing by cooling the aggregates, using cold water and applying ice flakes if necessary.

The types of concrete defined in the execution project are as follows:

The types of concrete defined for the execution of the project were classified based on the maximum aggregate size into Type I (150 mm, C25/30), Type II (70 mm, C25/30), Type III (30 mm, C25/30 or C30/37), and Type IV (15 mm, C30/37).

3.2. Concrete plant

The technical requirements for the design of manufacturing factories and plants were:

- Concrete Manufacturing Plant: with a capacity of 200 m³/h, it had six aggregate compartments with a total capacity of 700 tons. Cement silos at the plant had a capacity of 100 tons.
- Aggregate Cooling Installation: One silo for chilled water at 1°C for cooling mixed granulometries in the dosing proportions and three silos for aggregate immersion with a capacity of 170 m³ of aggregates or 1 hour of concrete production.
- Ice Flake Manufacturing Plant: Generators for a production of 80 tons/day of ice flakes with dimensions of 30 mm in length by 2 mm in width, at a temperature between -1°C and -2°C, and an ice flake storage tank with a net capacity of 50 tons.
- Mixing Water Cooling plant at 1°C for dimensioned a concrete production of 200 m³/h.

Fig. 1 – Manufacturing plants

3.3. Executive methodology

The concrete buckets were fed at the plant's bucket dock by 2 self-propelled 9 m³ silobuses on track and then were placed in the dam using buckets moved by 2 parallel blondins with a volume of approximately 9 m³.

When the concrete was on the block, it was spread with a bulldozer type D4 and vibrated with sets of six oil-hydraulic vibrators with 150 mm needles.

The elevation gain of the blocks aims to be as uniform as possible to avoid thermal imbalances between them. Due to the slope of the embankments, each block must rest on the previous one. The concrete blocks were executed with a maximum layer height of 2 meters.

The dam concreting started from the central blocks (from lower levels), in parallel with the execution of the blocks located on the right (B18, B20, B22) and on the left abutment (B17, B19).

Fig. 2 – Construction - three phases (central, right and left abutment)

3.4. Joint injection

The injection works carried out at Alto Tâmega dam, aimed at achieving a final monolithic structure, were performed from the galleries using the injection system that was implemented as the work progressed.

The cement used was type CEM II/B-V 42.5 N, and different dosages were planned, depending on the project sequence. The work started with more fluid grouts (water / cement = 2/1), and it finished with denser grouts (water / cement = 1/ 2,5).

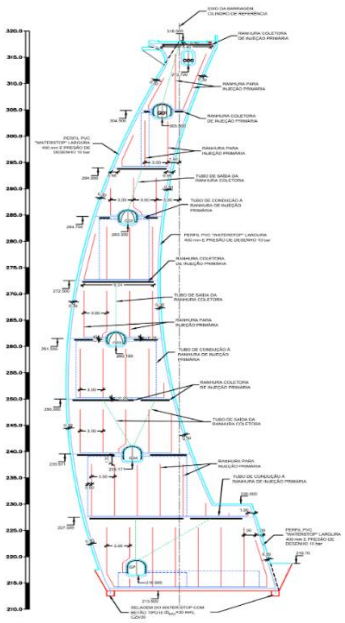

Fig. 3 – Cross-section of a typical joint

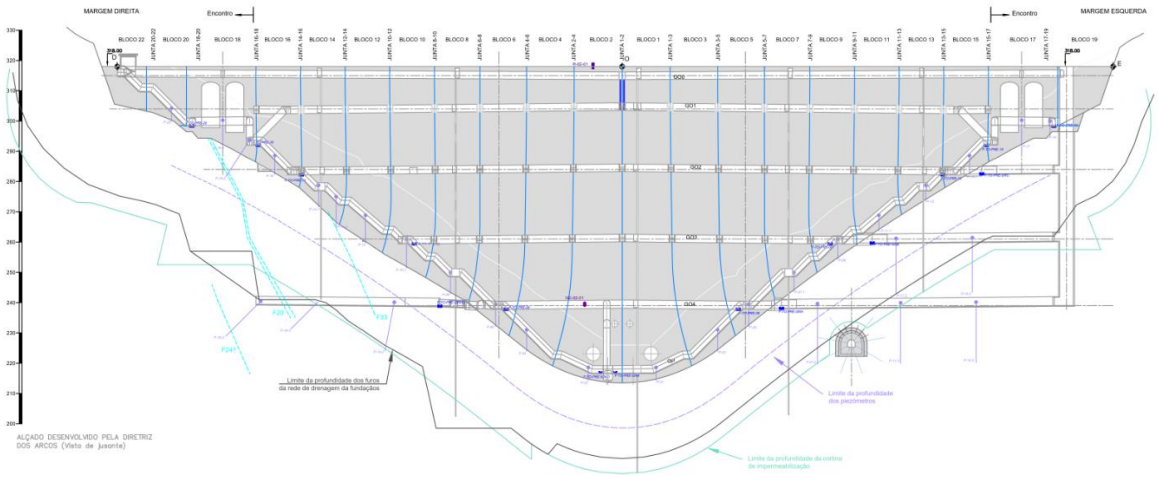

Fig. 4 – Joints of the Alto Tâmega Dam

The execution of the joint injection activities of a dam involves the implementation of a set of auxiliary works and necessary equipment, such as identification of the pipes at the front of each compartment, water supply in the galleries, installation of a cement grout manufacturing plant, installation of cement grout injection equipment, and a grout manufacturing plant with an automated system for recording injection parameters.

3.5. Execution and planning methodology of the joints

Methodology – preliminary tests and injection.

Before starting any injection activity, an inspection was carried out in the different compartments to ensure they were properly working. Subsequently, water tests were carried

out in all primary compartments to verify the circuits; generally, these were tested at a maximum pressure of 2 bars.

For a pressure P in a compartment, pressures P/2 should be ensured in the adjacent enclosures located in the same compartment. The water tests allowed cleaning the enclosures, verifying the circuits. The tests were considered valid when the water injection pressure could be maintained for several hours to identify possible leaks through walls, galleries, or holes.

Also, during the water tests, the opening of the dam joints was monitored with the instrumentation installed in the dam.

Following the preliminary tests, the consecutive injection of cement grouts was carried out, with progressively higher cement contents, according to the dosages defined in the project, continuing with increasing density ratios until reaching, whenever possible, the W/C ratio of 1 / 2,5. The average closing pressure reached was 3.5 bars, with the maximum injection pressure not exceeding 4.5 bars. The pressure is measured at the inlet and outlet using manometers in each of the compartments.

Before starting the grout injection, the compartment to be injected had to be saturated. Then, it was emptied, and the grout injection began. When the density of the grout being injected is equal to the density of the grout coming out of the collector pipe, the change to a denser grout could be made, and so on, until the last grout.

The injection was considered complete when the last grout remains in the joint for a minimum period, with all circuits closed. Finally, to verify that the cement mixture present in the enclosure is adequate, the collectors were opened, recharging them with grout.

Executed planning.

The baseline work program contractually provided for the execution of the joint injection of the Alto Tâmega dam consisted of a single campaign, from January to May 2023. The compartments to be injected were a total of 100 units, divided into 9 levels between the lowest foundation levels and the dam crest. During construction, it was decided to divide the injection into 2 campaigns, with a first injection campaign of 13 compartments in May 2022, and the second and final campaign of 77 compartments between February and May 2023.

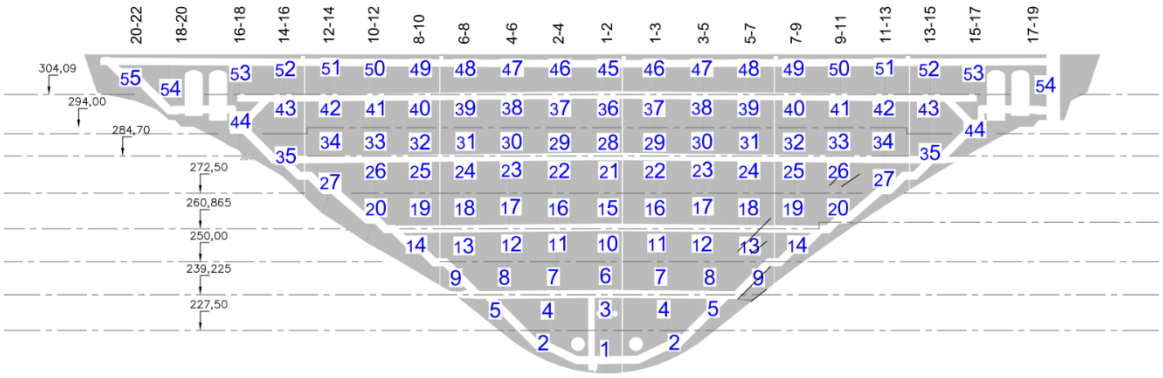

Fig. 5 – Injection sequence defined in the project - from the foundation with injection symmetry between the banks - 100 compartments

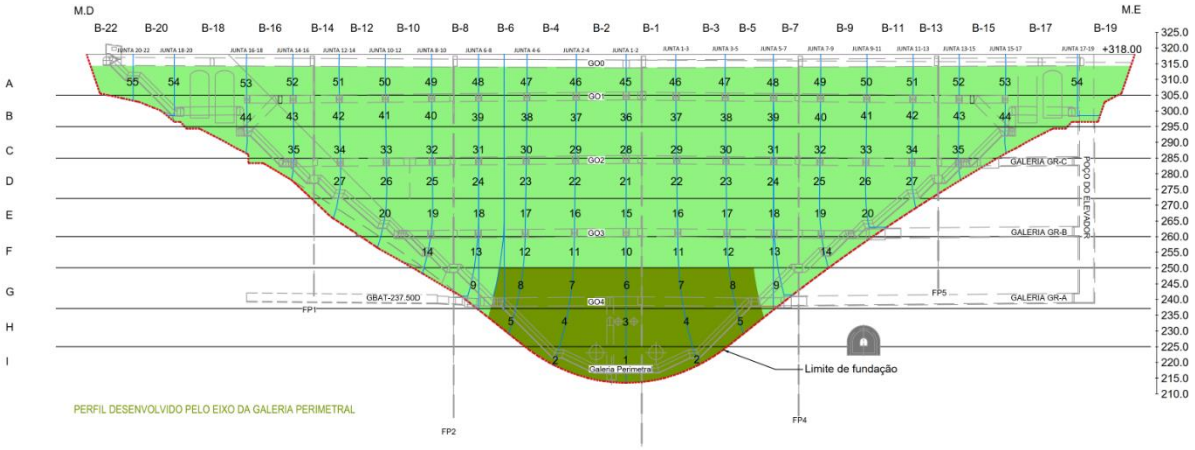

Fig. 6 – 1st campaign in 2024 and 2nd campaign in 2023 - 77 compartments

4. THERMAL FINITE ELEMENT MODELS

4.1. Heat transfer theory

In the construction of concrete structures, an exothermic reaction occurs, resulting in the release of heat. This phenomenon becomes more significant in large-scale projects that require very high volumes of concrete, such as dams. Therefore, during the construction phase, a constant thermal analysis of the concrete's state must be carried out, considering the thermal data of the material, the heat curve of the cement-ash mixture, environmental factors, and the construction schedule. The equation governing heat transfer in continuous media follows Fourier's law:

$$\left[\frac{\delta}{\delta x}\left(kxx\frac{\partial T}{\partial x}\right)+\frac{\delta}{\delta y}\left(kyy\frac{\partial T}{\partial y}\right)+\frac{\delta}{\delta z}\left(kzz\frac{\partial T}{\partial z}\right)\right]+q(x,y,z\,|t)=\rho c\frac{\partial T}{\partial t}$$

Given:

- *Kxx*,*Kyy*,*Kzz* Thermal conductivities [J/(h·m·K)]

- ρ Density [kg/m³]
- c Specific heat [J/kg·K]
- q Heat generated within the material [J]

For dams, boundary conditions associated with insolation, radiation, convection, and evaporation on their free surfaces must be added, as they are exposed to the open air; in this way, thermal exchange with the environment is considered. Additionally, an extra boundary condition must be added to fix the temperature at the terrain edge.

Similarly, an initial thermal state condition is set in the model. To do so, a starting state with an imposed temperature at all the nodes that make up the model has been considered.

The parameters used for modeling the concrete and the foundation are as follows:

Table 1 – 3D Model Parameters

PARAMETERS	Concrete	Foundation (*)
Density [kg/m³]	2420	2803
Conductivity [W/m·K]	2.6	2.45
Specific heat capacity [kJ/kg·K]	1.207	0.86
Insolation absorption coefficient (dimensionless)	0.75	0.5
Convection coefficient h for walls [W/m³·ºC]	12 (initial and calibrated)	
Convection coefficient h for galleries [W/m³·ºC]	7 (initial); 5 (calibrated)	

(*) The ground where the dam is founded is composed of mica schists.

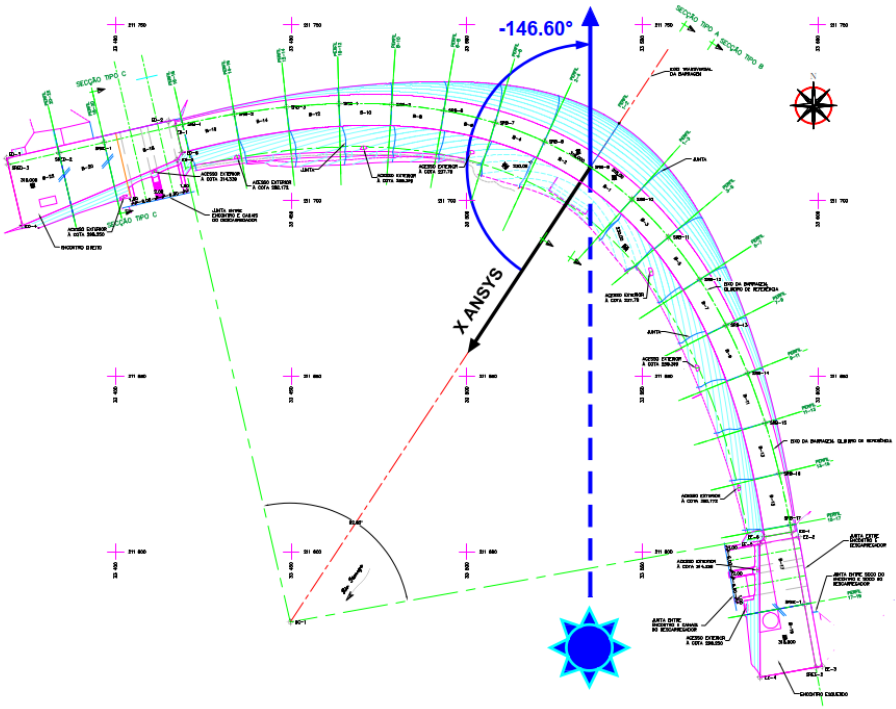

Fig. 7 – Layout of thermal variables with the dam. Plan view

4.2. Model Analysis Methodology

The thermal and structural analysis of the dam to verify the stress behaviour after joint injection was carried out using 2D and 3D thermo-mechanical models, with the ANSYS software.

2D Thermal Model

Initially, a two-dimensional finite element model was used to perform quick calculations and thus draw conclusions about a large number of parameters and hypotheses that needed to be established for the subsequent design phases. It consisted of a 2D model representing the central blocks of the dam, including a sufficient portion of the ground to represent heat dissipation in the lower layers, as shown in the following diagram. The lateral and lower boundaries of the ground are adiabatic.

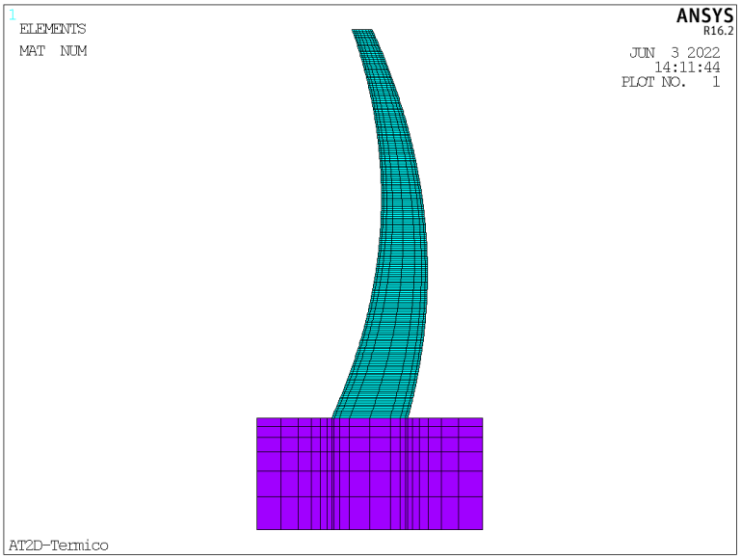

Fig. 8 – 2D FEM Alto Tâmega dam

In this model, various parameters were included and calibrated during the initial phases of analysis. On one hand, tests were conducted to establish the mechanical properties of the materials, and characteristic values of these materials were also adopted from existing literature. Since the model is fully parameterized, it is easy to analyse the response obtained by altering any of them. Comparative analyses were carried out between thermal tests of concrete using adiabatic boxes and finite element models for the calibration of materials to be introduced into the dam models, particularly the heat of hydration law to be used.

Among these parameters adjusted with the 2D model are those related to the characteristics of the materials (heat of hydration of cement at 28 days, specific heat, conductivity, dosage, density) and construction-specific parameters, for which various possibilities were also analysed (layer height, placement time between layers, construction start date, concrete placement temperature).

This model was subjected to a transient thermal calculation that considered the heat generation of the concrete and the natural cooling through heat exchange with the environment (atmospheric air and reservoir water).

In this analysis, three phases have been established:

- Phase I (Excavation Phase): This is the pre-construction phase where the model is subjected to a certain period with the excavation open, exposed to ambient temperature variations. The objective is to determine the initial conditions of the foundation at the time of excavation to simulate heat transfer with the first layers of the dam.
- Phase II (Construction Phase): The thermal evolution is analysed as the dam is being constructed, considering ambient temperature, concrete placement temperature, concrete dosage, construction start dates, and the time between layers.
- Phase III (Cooling Phase): Once construction is completed, the entire model is subjected to ambient temperature. The cooling phase includes an initial stage with the reservoir empty and a second stage where the reservoir is full, considering its influence on temperature evolution.

The main objective of the 2D model was to select the construction start time, adjusting both material and construction parameters, to achieve a final construction state with the lowest possible temperatures.

The results anticipated by the 2D FEM model were compared with data obtained from temperature monitoring system in various locations of the dam.

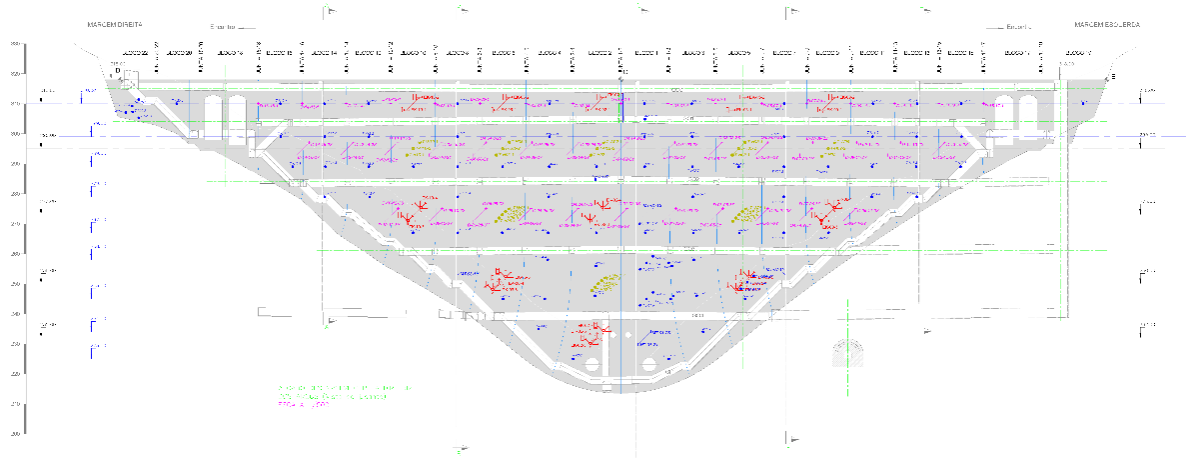

Fig. 9 – Thermal monitoring dam system

2D Model were calibrated during the construction phase, and the reviewed results closely matched the data collected by the monitoring system of the dam.

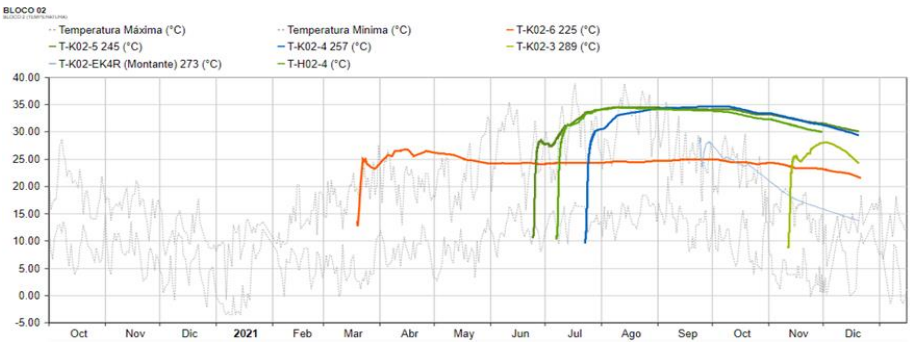

(a)

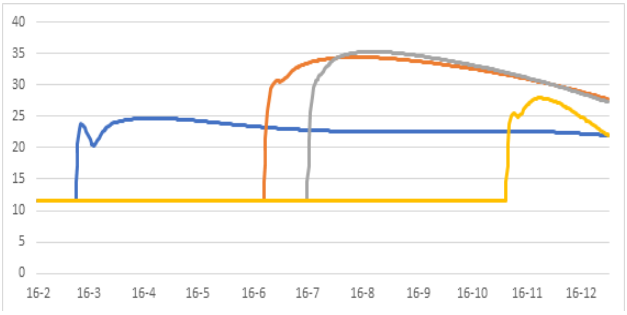

(b)

Fig. 10 – Block 2. (a): Monitoring system data. (b): 2D FEM results at different levels.

3D thermal Model

The model was designed based on the Finite Elements Model (FEM) methodology using the structural analysis software ANSYS.

The modeled elements are composed of ten or twenty nodes, depending on the meshing needs. In total, the model consists of 977,766 elements, 367,483 nodes, and 2,440 load steps.

The coordinate system is the rectangular Cartesian system, with the origin at the axis of the dam, the OX axis being horizontal following the direction of the river and positive downstream; and the OY axis being horizontal and perpendicular to the OX, with a positive direction towards the left bank. Thus, the OXYZ trihedron is right-handed.

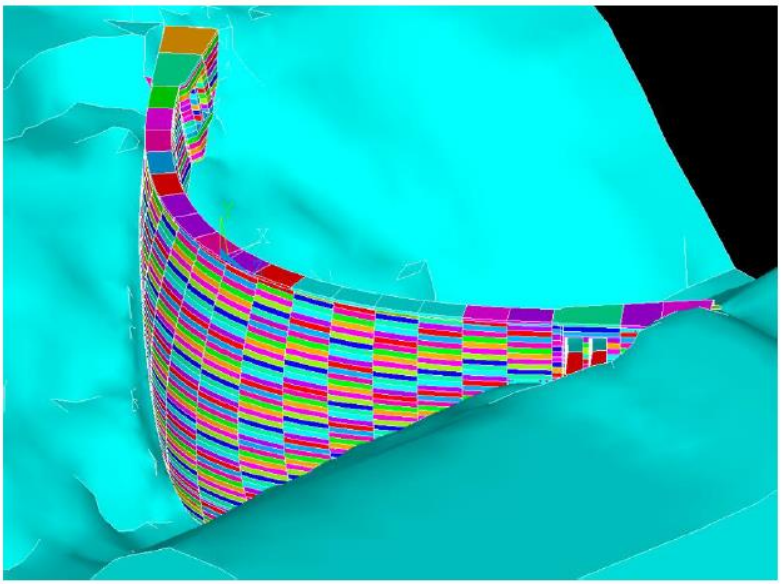

Fig. 11 – 3D Model. Diagram of the dam's concrete layers

The geometry of the terrain, dam and galleries was imported to ensure that the model accurately reflects reality, providing a precise and detailed representation of the physical characteristics of the dam infrastructure under study. Then, the dam blocks were divided into lifts of variable height, with the dimensions fixed in the construction plan.

For the generation of contacts, the mesh between lifts of the same block was made continuous, unlike between terrain and lifts, as well as between blocks. The continuity of the medium was generated with contact elements with the birth and death property, necessary for the evolutionary simulation of the process.

The calculation was planned in an evolutionary manner, with the aim of reflecting the construction phases of the dam, with the continuous placement of concrete layers.

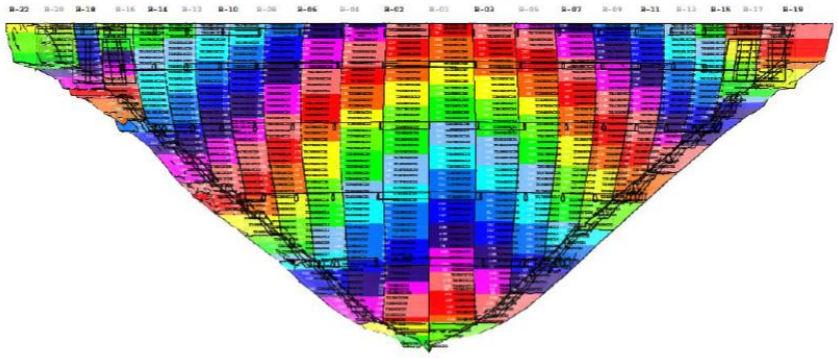

Fig. 12 – Construction schedule

The model calibration was carried out using data from the thermometers. The following graph shows information about the results in one thermometer after the calibration process.

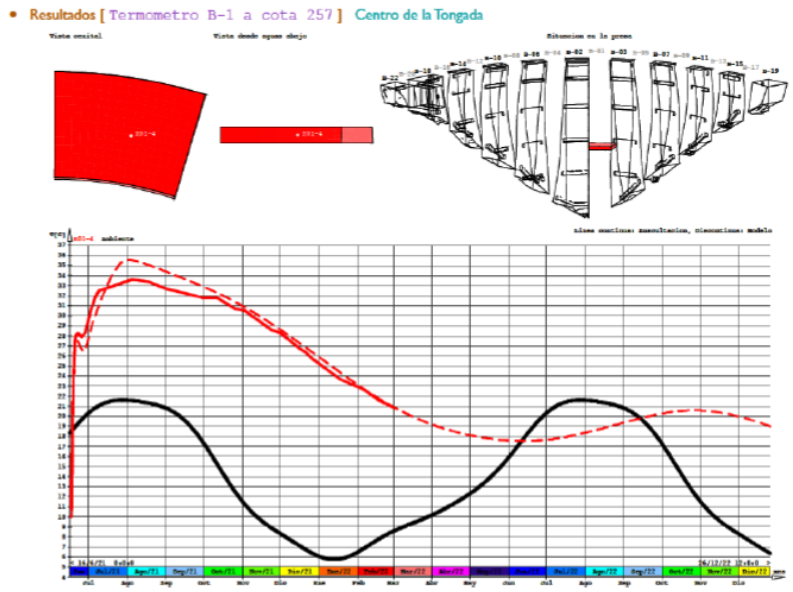

Fig. 13 – Thermometer K01-4. Thermometer position, Ambient temperature curve, Temperature curve measured by the monitoring and Calibrated model temperature curve.

During the construction of the dam, a thorough analysis was conducted comparing thermometer data with the model results. As an example, images of the results obtained from the model, are shown.

The following graphs represent the temperature evolution in different concrete layers (from the day the block construction began until December 26, 2022) and the temperature distribution in the dam on a given day.

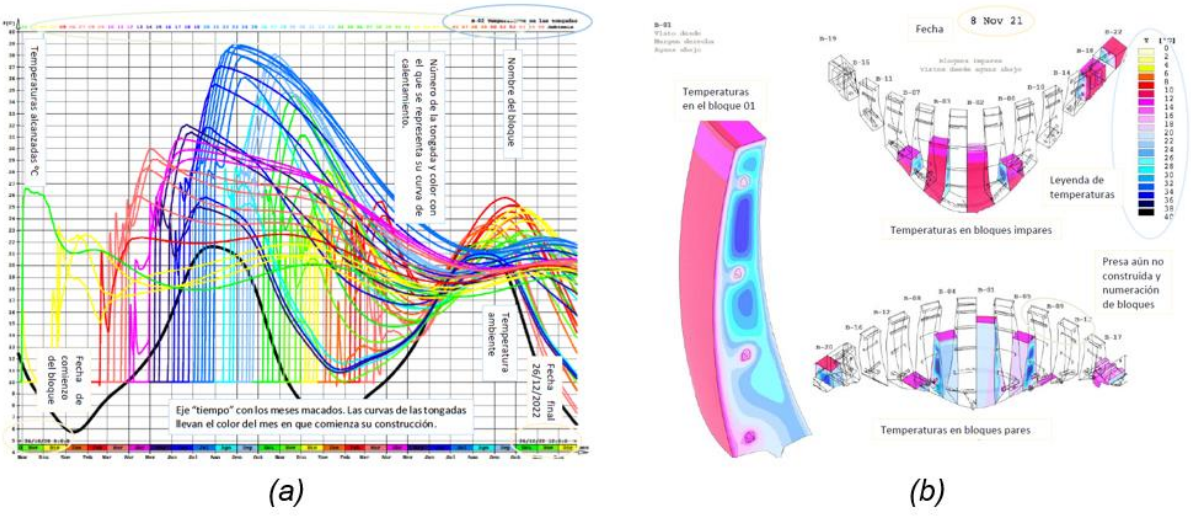

Fig. 14 – (a): Temporal graphs. Temperature results. (b): Temperature distribution.

The 3D FE Model was not only created to perform a thermal analysis but also to develop a structural analysis. A sequentially coupled thermo-structural analysis consists of two separate analyses: first, a heat transfer simulation to determine the temperature history; second, a

stress analysis that incorporates the temperature history as part of the loading. Both models share geometry and meshing to ensure the most accurate results.

4.3. Calibration and results

As indicated, the thermal models have two primary objectives:

1) Selecting the optimal time to perform injection work between blocks. This is the moment when the dam begins to function as a single solid element.

2) To determine the thermal load cases to be introduced into the Mechanical Model and then combined with the other loads.

The model calibration was initially performed on the 2D model and was later verified with the more accurate 3D model, which allowed for checking results at all points of the dam where thermometers had been installed for monitoring.

Regarding the injection works between blocks, it was initially planned to be completed in a single campaign from January to May 2023.

It is important to note that this activity requires strict temperature control, as the optimal time for joint injection is when the temperature inside the dam is low. Otherwise, the injected joints may reopen.

Having such an accurate 3D model that integrates real-time temperature and time data during construction, enabled precise control of the dam's thermal behaviour, allowing the joint injection campaign to be partially advanced by one year.

The first phase was carried out from March to May 2022. The blocks below the level 250 were injected, leaving those areas with high temperatures for the following year.

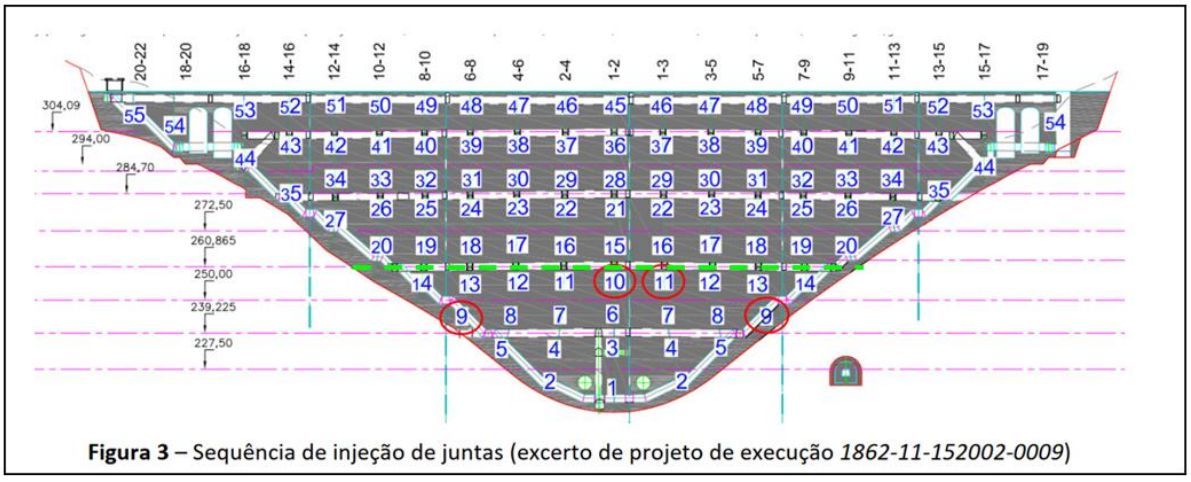

Figura 3 – Sequência de injeção de juntas (excerto de projeto de execução *1862-11-152002-0009*)

Fig. 15 – Joint Injection Sequence between Blocks

One of the observed factors was that the temperature inside the dam, due to thermal inertia, required delaying the start of the injection campaign to March-April, as temperatures in January were still high.

The following graphs illustrate the main results in the block 1.

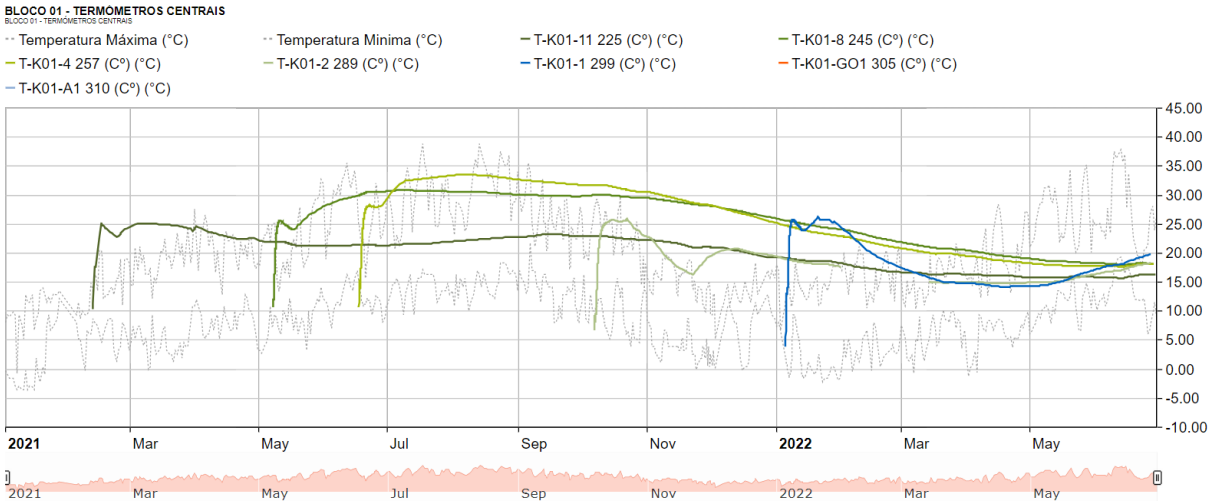

Fig. 16 – Block 1. Monitoring system data.

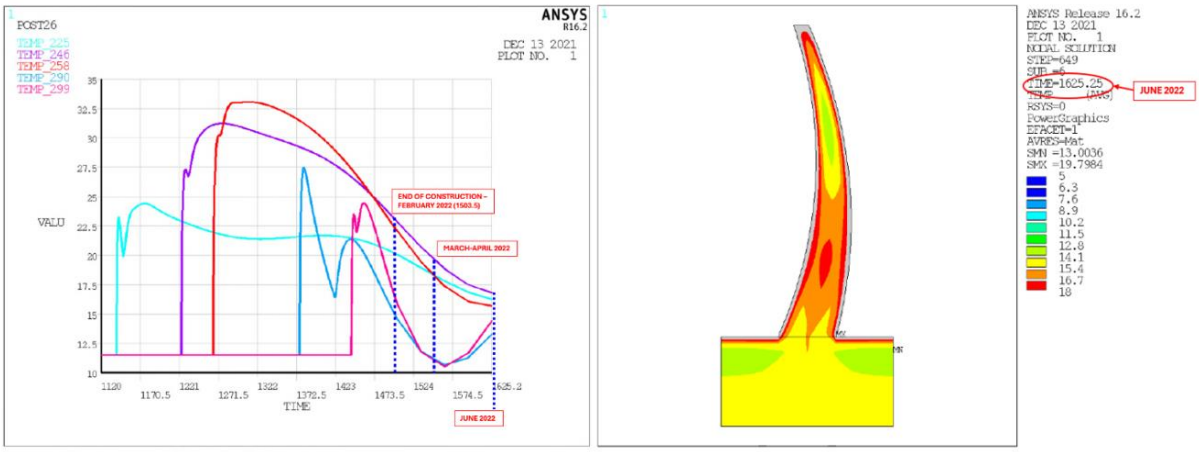

(a) *(b)*

Fig. 17 – Block 1. (a): FE Model results at different levels. (b): FE Model temperatures at June 2022

The second phase started in March 2023 and thermal control allowed the injection work to be extended until the first half of June 2023.

The following graph shows the results until June 2023. It was observed that until that date, the temperatures in block centers remained below 17 degrees.

SET	TIME/FREQ	LOAD STEP	SUBSTEP	CUMULATIVE	DATE
2440	94133000	2440	4	2885	26/12/2022
2441	94997000	2441	3	2888	05/01/2023
2442	95861000	2442	2	2890	15/01/2023
2443	96725000	2443	3	2893	25/01/2023
2444	97589000	2444	3	2896	04/02/2023
2445	98453000	2445	2	2898	14/02/2023
2446	99317000	2446	3	2901	24/02/2023
2447	100180000	2447	3	2904	05/03/2023
2448	101040000	2448	2	2906	15/03/2023
2449	101910000	2449	3	2909	26/03/2023
2450	102770000	2450	3	2912	04/04/2023
2451	103640000	2451	2	2914	15/04/2023
2452	104500000	2452	3	2917	24/04/2023
2453	105360000	2453	3	2920	04/05/2023
2454	106230000	2454	2	2922	15/05/2023
2455	107090000	2455	3	2925	24/05/2023
2456	107960000	2456	3	2928	04/06/2023
2457	108820000	2457	2	2930	13/06/2023
2458	109680000	2458	3	2933	23/06/2023

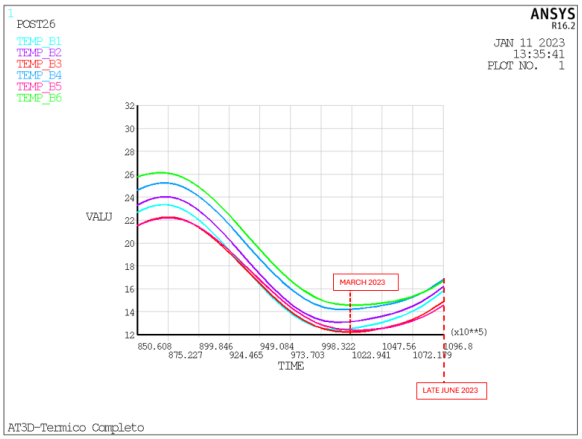

Fig. 18 – Model date equivalences and results

As an example, a comparative analysis was performed on block 2, between the actual data and the model results.

The model result at the end of December shows that the temperature in the block center area was between 18 and 20 degrees and the actual record on December 29th (thermometer T-K02-3) was 19.7 degrees.

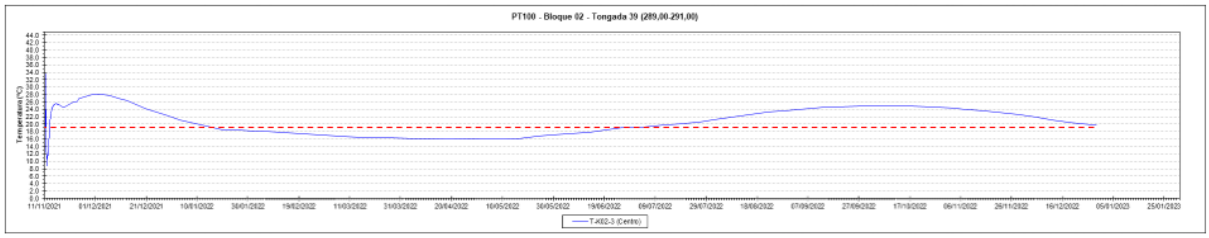

(*a*)

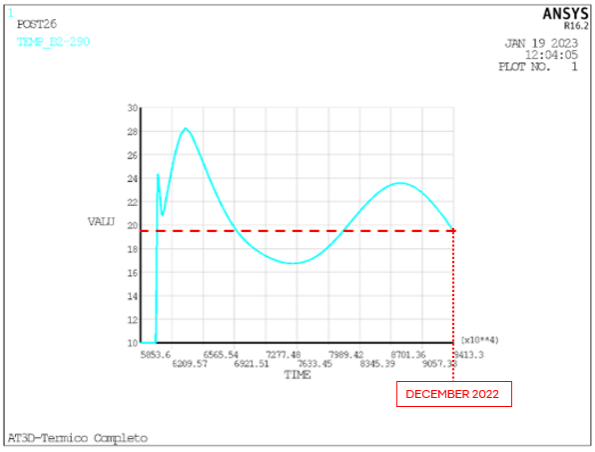

(*b*)

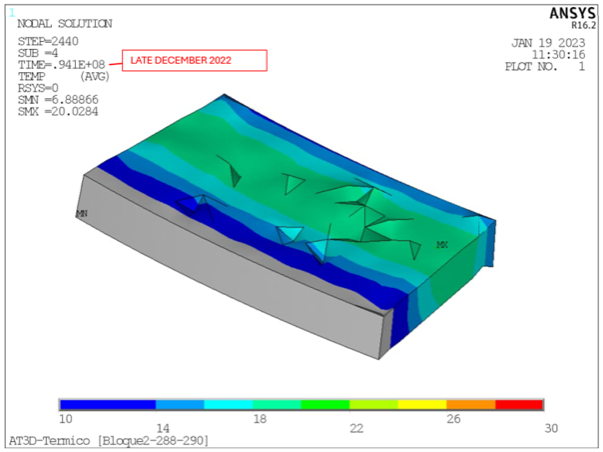

(*c*)

Fig. 19 – Block 2. Level 290- (a): Monitoring system data (Thermometer T-K02-3). (b): 3D Model results. (c): Temperatures results December 2022.

As can be observed, the behaviour of both graphs was very similar, even during the first winter and following warming in the summer of 2022. Therefore, the forecasts until the summer of 2023 were considered reliable.

4.4. First filling control process

As mentioned, another fundamental objective of the Thermal Model was to determine the thermal load cases to be introduced into the Mechanical Model, that proved to be crucial for monitoring during the first filling of the reservoir.

This moment is a critical phase in the dam project, so it is vital to maintain control over the process, allowing sufficient time to analyse all the data recorded by the monitoring system.

The first filling plan of the Alto Tâmega dam included seven stages, aligning them with different levels of hydrostatic load and other construction constraints. Within these seven stages, stops were established to evaluate the structure's behaviour, and a stabilization level where the reservoir level was simply maintained constant.

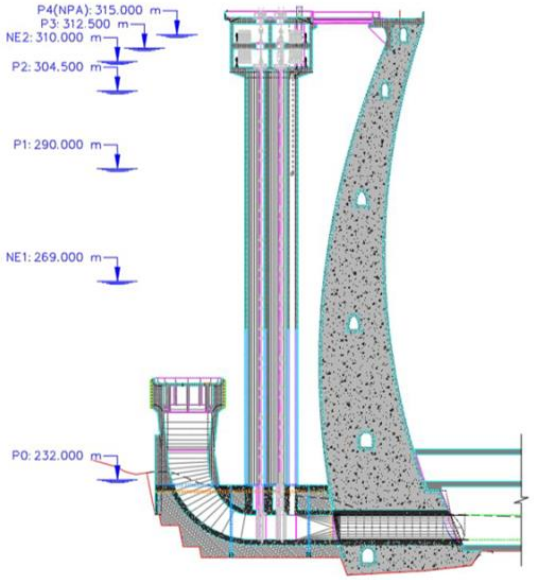

Fig. 20 – First Filling. Stabilization levels.

In the Mechanical Model, the load cases for each stabilization level and the thermal load corresponding to the actual temperatures measured.

The analysis developed was carried out using as a reference the moment when the central pendulum was installed and began providing results, at the end of June 2023. The thermal cases were obtained using the thermal state at that date as the reference temperature.

The following results were compared during the filling process, demonstrating an exceptionally similar behaviour between the measurements obtained from the monitoring system and those provided by the model.

Key points to highlight:

- The installation of the central pendulum was completed at the end of June 2023 (beginning of summer). Throughout the summer, the dam experienced heating, which

in double curvature dams causes upstream movement. During this period the reservoir was empty, so there was no effect causing downstream displacement.

- At the end of summer 2023, a change in trend was observed with a decrease in upstream displacements.
- In November 2023, the filling of the reservoir started. At that time, both hydrostatic load and thermal cooling, cause downstream displacement.

This behaviour is reflected in the following graph, which shows the records at different bases of the central pendulum from the moment of installation until the date of the last control level.

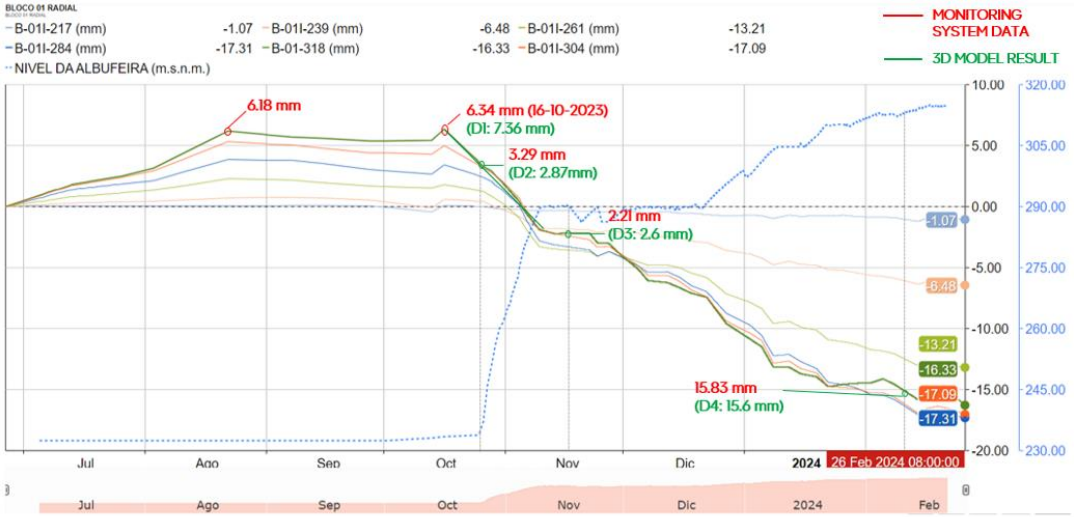

Fig. 21 – Block 1- Monitoring system data. Displacements and reservoir water level.

The following images show the 3D Model results of the main stages of the process.

<u>Displacement Analysis in the 3D-Model:</u>

- Summer 2023 (D1). Displacement at B-01-318 position 7,36 mm (upstream displacement). The actual displacement recorded at the end of summer 2023 exceeded 6 mm, reaching its peak in October (6.34 mm), due to an extraordinarily warm autumn.

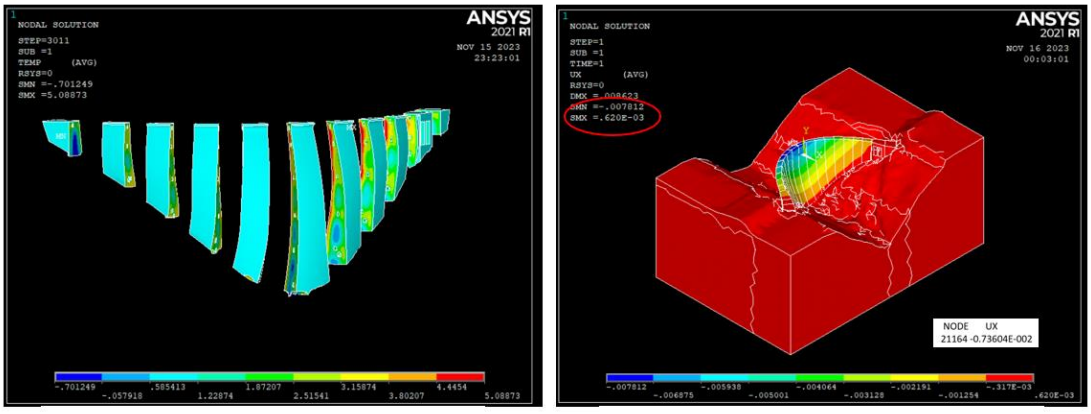

(a) *(b)*

Fig. 22 – Temperature load and displacements. Late summer 2023.

- October 2023 (D2). Displacements were only generated by thermal loads. The displacement at B-01-318 position was 2,87 mm (upstream displacement). The displacements registered before the begging of the filling by the monitoring system was 3,29 mm.

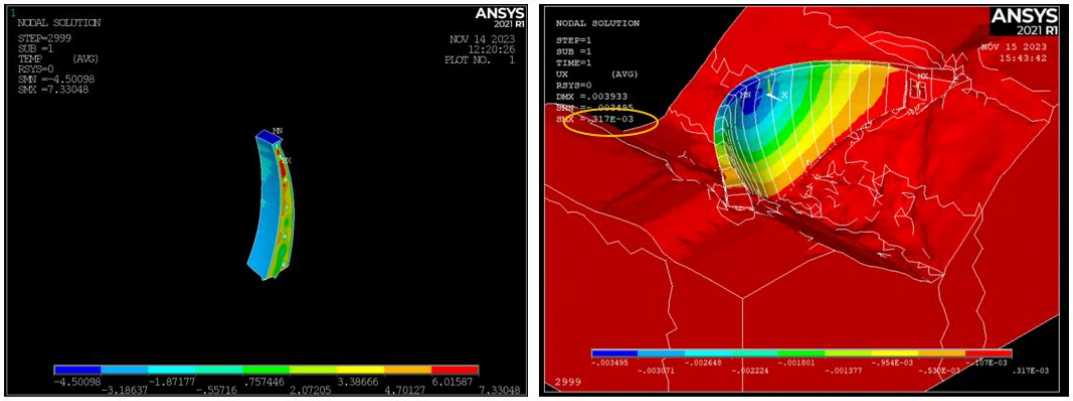

(a) *(b)*

Fig. 23 – Temperature load and displacements. October 2023.

- November 2023 (D3). Initial reservoir filling. Reservoir level 290 m.a.s.l.

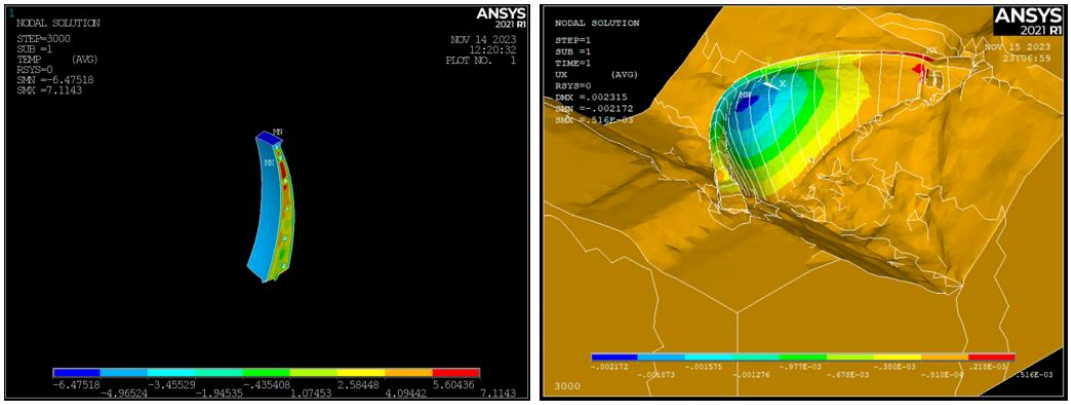

(a) *(b)*

Fig. 24 – Temperature load and displacements. November 2023.

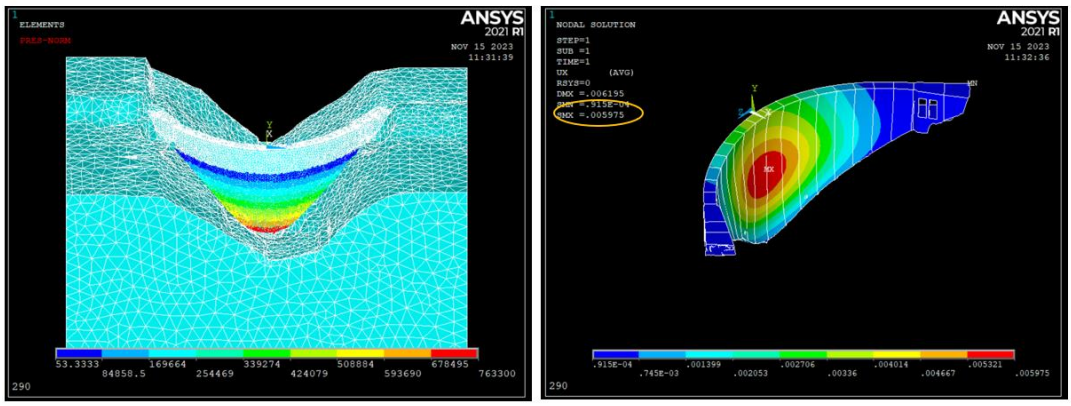

(a) *(b)*

Fig. 25 – Hydrostatic load and displacements. Level 290 m.a.s.l.

- The total displacement at the pendulum node B-01-318 was 2.6 mm (upstream displacement), calculated as the sum of 3.32 mm (downstream displacement) and 0.72 mm (upstream displacement). The displacement recorded by monitoring system in November was 2.21 mm.
- January 2024 (D4). Reservoir level 315 m.a.s.l.

  Finally, the analysis for January-February 2023 is presented, when the maximum reservoir level was reached.

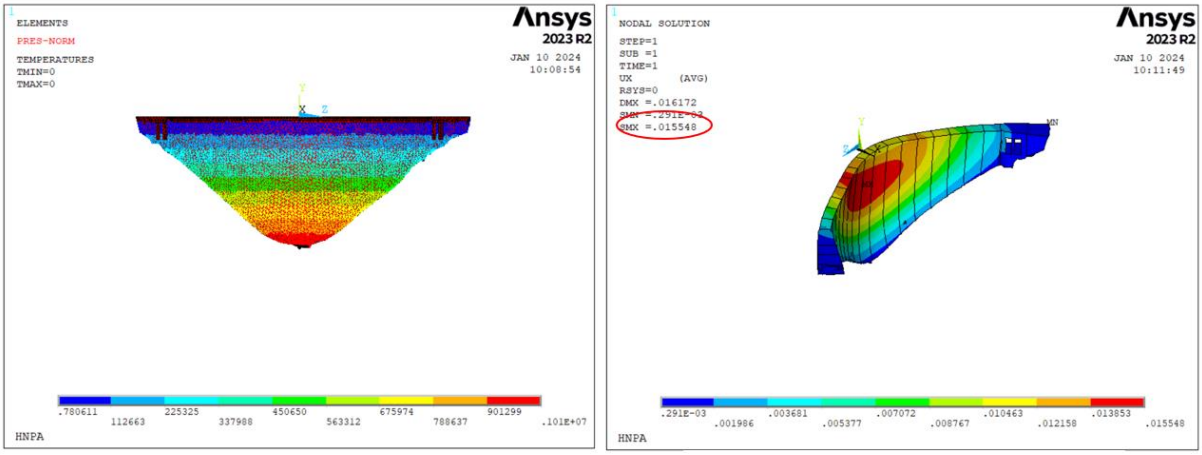

(a) *(b)*

Fig. 26 – Hydrostatic load and total displacements. Level 315 m.a.s.l

The total displacement at the pendulum node B-01-318 was 15.6 mm (upstream displacement). The displacement recorded by the monitoring system when the 315 m.a.s.l. level was reached was 15.83 mm.

It is observed that the maximum range of displacements in the selected scenarios is 15.6 mm, with an error of 0.23 mm (1.45%). In scenarios with smaller displacements, the relative error increases due to the reduced magnitude.

It is important to consider that displacements induced by thermal loads are calculated in the model using an ambient temperature law obtained from historical records. However, there may be a variation with the registered temperatures on those dates, which could slightly influence the results. For example, the autumn of 2023 was significantly warmer than usual.

Therefore, the overall behaviour of the model shows a fairly precise adjustment.

5. CONCLUSIONS

Concrete cooling techniques have proven to be highly appropriate for achieving an optimal high-quality concrete at the Alto Tâmega dam, which results in greater safety for the hydraulic infrastructure and lower operating and maintenance costs, by minimizing concrete cracking and therefore, leakage.

For the correct application of this technique, it is considered essential to have highly experienced construction teams who, together with the appropriate technology, have ensured the success of Iberdrola in the application of cold concrete techniques at the Alto Tâmega dam.

Additionally, it has been necessary to have the fundamental support of expertise engineers who are able to create very sophisticated thermal, three-dimensional, non-linear and multiparametric numerical models, which have allowed detailed knowledge of the structure's behavior, optimizing the construction program. These models, calibrated and validated by the dam's monitoring systems, will be also used as a fundamental tool during the operation of the plant.

ACKNOWLEDGMENTS

The authors acknowledge the LABORATÓRIO NACIONAL DE ENGENHARIA CIVIL (LNEC), GRANELL INGENIEROS CONSULTORES and TECOPY for their outstanding work and exemplary professionalism, which was fundamental in the successful completion of this project.

REFERENCES

[1] TECOPYSA (2023). Structural analysis of the Alto Tâmega dam (in Spanish).

[2] TECOPYSA (2022). Thermal 3D analysis of the construction of the Alto Tâmega dam (in Spanish).

[3] IBERDROLA (2021). Integration of thermal and mechanical models for the design of Daivões dam (in Spanish). Spancold Congress – Gran Canaria 2021.

[4] GRANELL INGENIEROS CONSULTORES, (2017). H.E. Alto Tâmega. Execution project. Dam (in Portuguese). Ref. 1862/11/121001, rev0.

[5] LNEC (2011). Alto Tâmega dam. Monitoring plan and specific monitoring plan during the first filling of the reservoir (in Portuguese). Report 52/2011.

Fifth International
Dam World Conference
PORTUGAL • LISBON • LNEC • APRIL 13-17, 2025
dam world 2025

PREDICTION MODELS FOR THE HYDRAULIC BEHAVIOUR OF IRAPÉ DAM

João Marcelino[1]
LNEC

Paula Luciana Divino
CEMIG

Diego Balbi
CEMIG

ABSTRACT

The Irapé dam, situated in the northeastern region of the State of Minas Gerais, Brazil, is renowned as the tallest rockfill dam in the country. This rockfill dam incorporates a central clay core, serving as the primary sealing element. It is located in the Jequitinhonha river, it was constructed between 2002 and 2005, and inaugurated in June 2006, marking the initiation of operations for the associated power plant.

The dam has a crest length of 530 meters, while its maximum height is around 210 meters. The downstream slope has a gradient of 1V:1.3H, whereas the upstream slope attains a maximum gradient of 1V:1.5H.

CEMIG, a state-owned company, undertakes the management and operation of both the power plant and the dam. They also bear the responsibility of monitoring and ensuring the safety of the entire structure.

This paper presents an overview of the comprehensive monitoring system employed for the Irapé dam. Taking advantage of the extensive database available, the paper proposes models capable of predicting and understanding the dam's hydraulic behavior in the central clay core. These models serve as a foundation for forecasting the dam response for the near future, and their validity is subsequently discussed. By examining the monitoring system and utilizing the database, this study aims to enhance the understanding of the Irapé dam's performance and behavior. The proposed models contribute to the development of predictive capabilities, enabling timely assessments of potential risks and facilitating effective decision-making regarding dam management and safety control.

Keywords: Irapé da, Rockfill dam,clay core, monitoring, behaviour prediction.

[1]marcelino@lnec.pt, Portugal

1. INTRODUCTION

Dams play a pivotal role in meeting the escalating demand for energy, particularly in the context of surging global energy needs. Among their multifaceted functions, dams stand out as crucial components for clean power generation, providing a reliable and sustainable source of electricity. This significance becomes even more pronounced in the face of increasing energy requirements worldwide. In Brazil, the importance of dams, especially in the energy sector, is underscored by the country's rich hydroelectric resources. However, as the demand for energy continues to rise, so does the imperative for robust safety measures and regulations governing dam construction and operation. Brazilian legislation on dam safety is modern and comprehensive, emphasizing the need for stringent safety controls and monitoring mechanisms to ensure the structural integrity of dams.

Under the scope of a contract between CEMIG and LNEC, the analysis of the Irapé dam monitoring data collected was carried out. During the analysis it was found that the database is comprehensive and therefore suitable to establish statistical based behavior models. These models allow for a more objective and rational analysis of the dam behavior playing a crucial role in the safety assessment and furthermore permit a performance prediction for the coming years.

This paper presents the main characteristics of Irapé dam and, briefly, describes its monitoring system. Following, a general approach on statistical models is presented and applied to Irapé monitoring database allowing to obtain a deeper understanding of the seepage in the impervious core.

2. IRAPÉ DAM BRIEF DESCRIPTION

The Irapé Hydroelectric Power Plant (HPP) is located on the Jequitinhonha River, whose source is in the Espinhaço Mountain Range in the northeastern state of Minas Gerais, at an altitude of approximately 1,300 meters. The river runs for about 1,090 kilometers, mostly in an eastward direction, and flows into the Atlantic Ocean in Belmonte, in the state of Bahia. The Irapé dam, constructed between 2002 and 2005, was inaugurated in June 2006. The HPP is located approximately 578 kilometers from the mouth of the Jequitinhonha River, dominating a hydrographic basin of about 16,200 km² [1].

In Fig. 1, an aerial view of the dam body from downstream shows both, the exit from the spillway and the outlets located in the left abutment. Additionally, the power plant building is visible at the bottom of the image. The overall layout of the hydropower scheme is depicted in Fig. 2.

Fig. 1 - Aerial view of Irapé dam

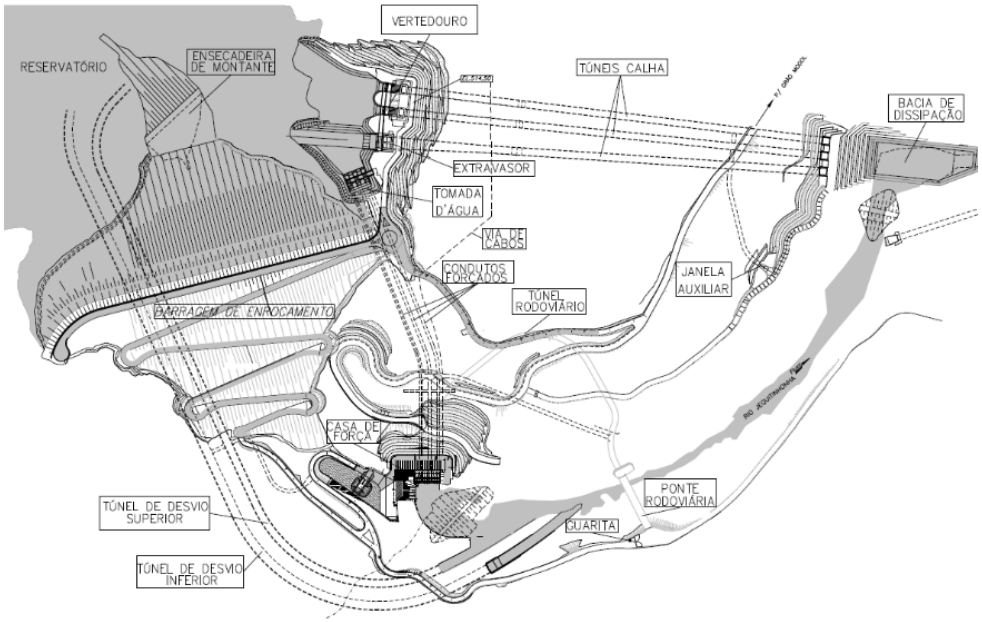

Fig. 2 - Layout of Irapé hydropower scheme

Structurally, Irapé Dam is a rockfill embankment with a central clay core as the water tightness element (Fig. 3). The dam crest is 13 meters wide and 530 meters long, following a nearly straight line (Figs. 1 and 2). Additionally, its maximum height reaches approximately 210 m. The downstream slope has a gradient of 1V:1.3H, whereas the upstream slope attains a maximum gradient of 1V:1.5H. Access to the downstream area of the dam can be achieved via a road descending along the downstream slope or through a road on the left abutment originating from the downstream region. Both roads provide access to the power plant.

Irapé´s dam seepage is controlled by a filter/drain system composed by a multilayer filter immediately after the core and a sub horizontal drain that helps conducting the flow to

downstream. The multilayer filter comprises a 2 m thick sand layer and two transition layers composed progressively of coarser materials [1].

In the design and construction, specific measures were adopted to prevent or minimize the problems or issues regarding stress transfer between the embankment and the abutments of the dam. This is very important to avoid the possibility of hydraulic fracturing in the core due to low effective stresses. Additionally, specific instrumentation was installed to assess total and effective stresses, thereby monitoring this phenomenon. Another important aspect at the

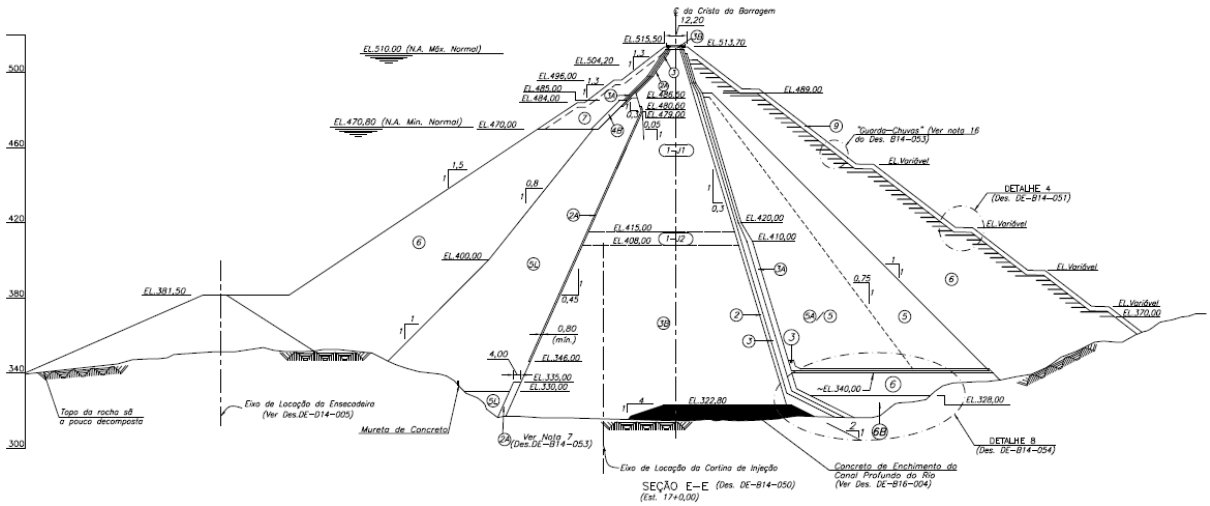

Fig. 3 - Typical Irapé dam cross-section

Irapé dam, that was subjected to specific studies, is related to the presence of sulphides in the rock masses, a factor that was crucial in the design of the civil concrete structures [1] and was extensively studied [2]. The dam design considered the use of the construction materials available on-site, some with a high content of sulfides and others with a low sulfide content that were placed in selected locations such as the clay core, filters and drains.

However, there are several less common occurrences in the dam that may be related to this factor. For example, high temperatures were noticed in the inclinometer tubes (around 70°C), and frequent obstructions of drainage systems due to the formation of iron bacteria.

The foundation treatment project for the Irapé dam included the implementation of waterproofing grout injections, carried out in 3 mandatory borehole lines up to the 3rd order and 2 occasional lines with depths between 40.0 and 60.0m. These injections involved the use of cement and/or mortar grout, starting from the excavation surface. Additionally, consolidation injections were occasionally performed in areas with excessive fracturing, aiming to enhance the mechanical properties of the rock mass prior to the curtain injections.

3. MONITORING OF THE DAM

3.1. Monitoring system

In order to monitor the behavior of the dam, access its safety conditions and comply with the best practices in dam monitoring, a comprehensive monitoring system was installed. Most of the instruments were installed during the construction while others were placed at the end of this phase. These instruments are primarily concentrated in five cross sections (Fig. 4), which were considered representative of the dam's behavior and are therefore relevant to the safety assessment. The monitored parameters include, besides the upstream and downstream water level, displacements (both external and internal), pore pressures, total stresses and flow. While these quantities are commonly monitored for an embankment dam [3], the installation of different types of devices was necessary for some of these parameters in the case of the Irapé Dam.

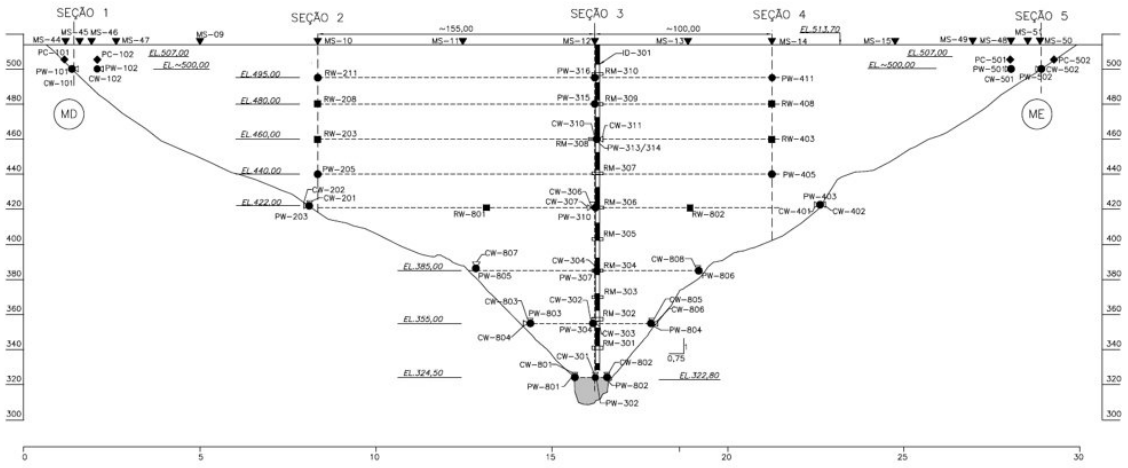

Fig. 4 - Longitudinal section highlighting the five cross sections and its monitoring devices

For monitoring internal displacements of the dam, several instruments are utilized, including inclinometers, magnetic settlement gauges within the inclinometer tubes, vibrating wire gauges, and hydraulic settlement gauges. Surface displacements, on the other hand, are measured using topography in external settlement targets. Total stresses are monitored through vibrating wire total stress cells, while pore pressures are measured using vibrating wire cells and standpipe piezometers. These instruments provide valuable data for assessing the behavior and safety of the dam. The data is validated and stored in CEMIG internal dam safety database being available to periodic studies performed either by CEMIG's internal technical team or by external specialists. The dam behavior has been followed and accessed since the beginning of the construction by comparing the instrumentation data with pre-established threshold limit values defined by the dam designer that are updated when necessary.

Sometimes, due to the complexity of the dam, special studies are performed, for example using 3D finite elements modelling, giving support to update threshold limit values.

3.2. Statistical models

Statistical models are extensively employed in LNEC's practice to analyze and interpret the behavior of embankments and embankment dams [4, 5, 6, 7] or concrete dams [8, 9]. These models rely on historical measurements and utilize mathematical expressions to effectively capture and represent the observed data.

This paper aims to apply statistical modeling approaches to Irapé data particularly to study the pore pressures at the dam's core and extract valuable information with these models.

Depending on the type of expression employed two situations may occur. The first, where the mathematical expressions yield additional insights, such as estimating permeability or elasticity modulus and the second where the expressions purely serve as a data-fitting tool without direct physical significance. Alternative methods can be explored, including the application of Artificial Intelligence (AI) techniques like neural networks. In such instances, the model's response is not constrained by specific mathematical expressions, as it adapts to the data. However, it is important to note that employing AI, being more of a black-box type, may lead to a diminished level of interpretability and understanding compared to traditional (statistical model) approaches.

Examples of common statistical models are:

$$Q_{i,t} = \sum_j k_j V_{j,t} \tag{1}$$

$$Q_{i,t} = \sum_j k_j f\left(V_{j,t}\right) \tag{2}$$

In the first case, the independent variables $V_{j,t}$ (where t stands for the time), are combined linearly to derive the dependent variable $Q_{i,t}$. On the other hand, in the second scenario, an additional function $f\left(V_{j,t}\right)$ may be applied to the independent variable before the linear combination takes place. The parameters k_j of the model are obtained through an adjustment fit technique, such as the least squares method, to optimize the fit between the model predictions and the actual (observed) data.

The following example may be used to fit the flow (F) measured as a function of the water level (WL):

$$F = k_1 WL_t^2 + k_2 WL_t + k_3 \tag{3}$$

Sometimes there may be a temporal variation in the observed quantity, for example, due to the obstruction of a drain. In such cases, it can be advantageous to include a term that accounts for the time. The following expression may therefore be considered:

$$F = k_1 WL_t^2 + k_2 WL_t + k_3 (T - T_0) + k_4 \quad (4)$$

In equation 4, an additional term is included to permit the analysis of a possible variation over time. Of course, in these cases the expressions relate the flow polynomially dependent on WL and a linear variation over time. While more intricate equations, such as higher-degree polynomials, may provide a more precise fit to the data, the preference for simplicity underscores the importance of selecting the most straightforward expression that adequately captures the data's essence, promoting clarity, interpretability, and generalizability in the modeling process. Furthermore the interpretation is simpler.

3.3. Application to Irapé pore water pressure measurements

In Irapé there are five cross-sections instrumented with vibrating wire piezometers (PW). These are all located in the clay core and are essential instruments to follow the behavior of the dam and control its safety. A model suitable to the piezometric data is:

$$P_{WL}(t) = k_1 WL(t) + k_2 T + k_3 \quad (5)$$

where P_{WL} stands for the piezometric water level (pore pressure), T the time in days after an arbitrary reference date and k_i the model parameters to be adjusted to fit the data. Eq. (5) provides the most straightforward representation of the correlation between the piezometric water level and the reservoir level, considering the potential influence of time.

Applying Eq (5) to all PW cells in cross-section 3, allows to obtain the models for each individual PW. Fig. 5 shows, the example plot for the results obtained for the instruments located at El. 355 m. From the plots it is clear that the model fits well the data, and the dissipation of the pore pressure from upstream to downstream is also noticeable but besides, it is also clear that the quality of the model decreases from upstream to downstream. Moreover, the piezometric water level exhibits minimal variations over time (negligible k_2 values), indicating the consistent and stable performance of the clayey core.

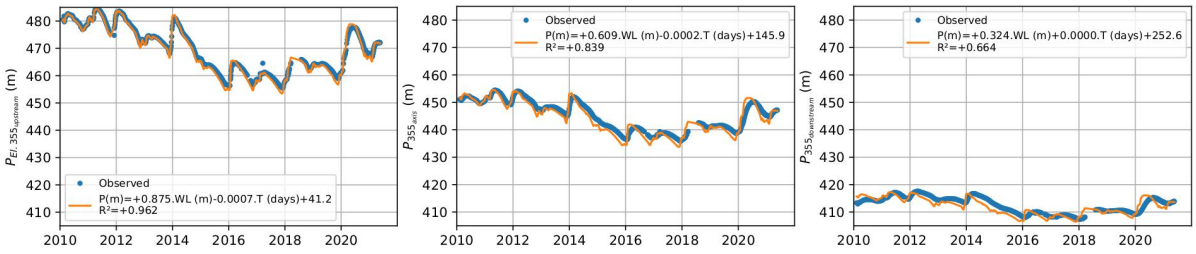

Fig. 5 - Data and model results for piezometers located at elevation 355 m

Analyzing the plots it is clear that there is a delay in the response of the PW cells located more on the downstream side, being an expected behavior. This is the obvious observation that downstream piezometers take longer to reflect variations in the upstream water level. It is therefore reasonable to study the delay between the level in the reservoir and the response of the cell. To achieve, this Equation (5) may be modified to

$$P_{WL}(t) = k_1 WL_{(T-n)} + k_2 T + k_3 \tag{6}$$

where $WL_{(T-n)}$ stands for the water level in the reservoir at date T minus n days, to account for the delay in the response due to the time the water takes to travel from upstream face of the core to each piezometer. To identify the optimal number of days '*n*' for each piezometer, one can make a translation in the model to overlap it to the data. This will provide a rough estimate for the time gap.

Another way that was adopted here, is to apply the model using different delay options for the WL, for example, within the range of 0 (no delay) to 150 days. The quality of the adjustment is then evaluated according to the determination coefficient R². The results are summarized in Fig. 7. According to the optimization of the time delay it was found that each PW in elevation 355 m has a delay of 10, 25 and 75 days (from upstream to downstream) to achieve a better model fit.

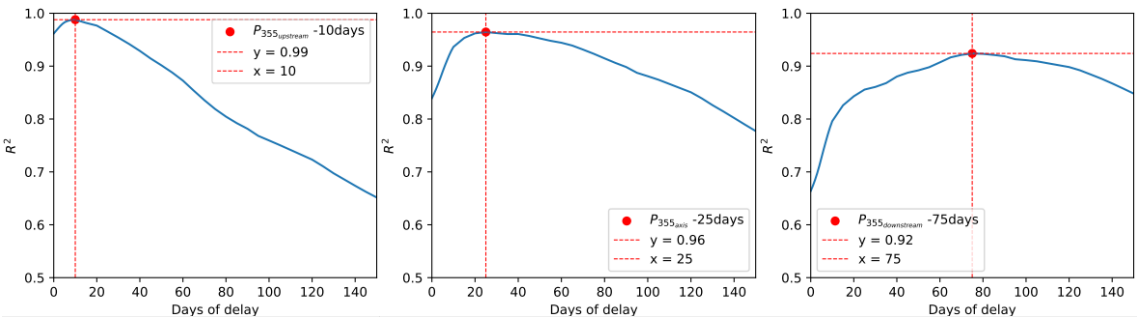

Fig. 6 - Evaluation of optimal delay for piezometers at El. 355 m

This result provides a very reliable and accurate model to fit the data. In this case:

$$P_{WL(upstream)}(T) = 0{,}799\, WL_{(T-10)} - 0{,}0009\, T + 80{,}2\,(m) \tag{7}$$

$$P_{WL(axis)}(T) = 0{,}569\, WL_{(t-25)} - 0{,}0003\, T + 166{,}3\,(m) \tag{8}$$

$$P_{WL(downstream)}(T) = 0{,}280\, WL_{(t-75)} - 0{,}0001\, T + 275{,}0\,(m) \tag{9}$$

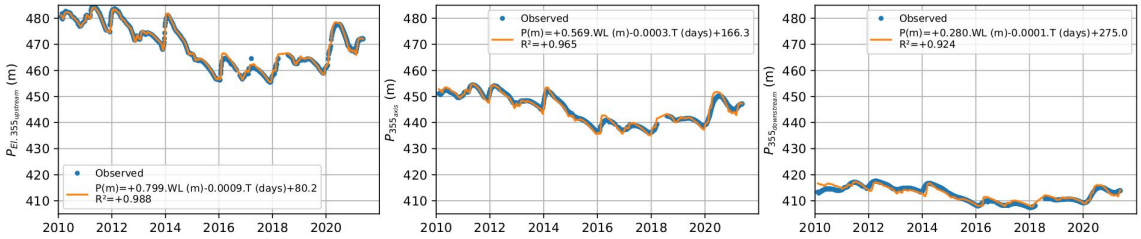

Fig. 7 - Data and optimized model results for piezometers at elevation 355 m

The same procedure can easily be applied to all the piezometers in the cross section and the delay results are presented in Fig. 8.

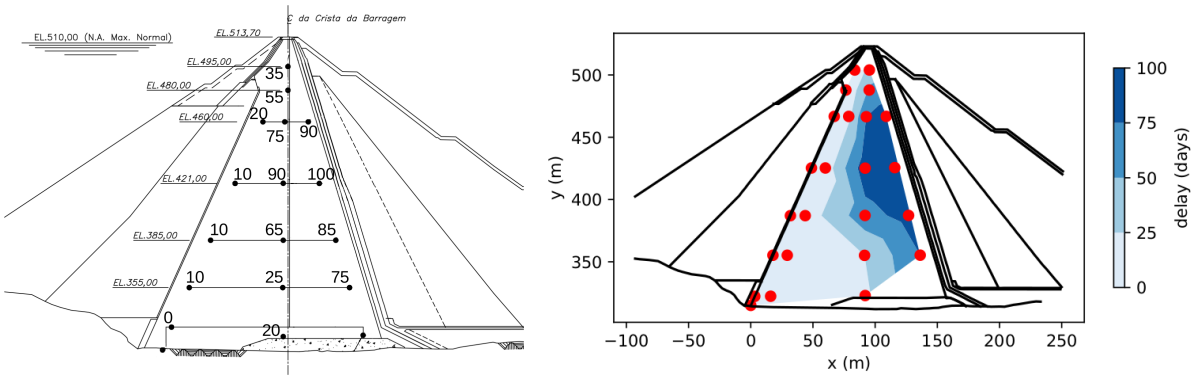

Fig. 8 - Time delay in days for all piezometers in cross-section 3

It becomes clear that a pattern may be derived. The delay increases from upstream to downstream, which is expected, and also increases from the bottom to the middle of the dam, and then decreases again. Low delay values are found at the bottom of the core. This can be the result of multiple factors but most likely the piezometers in this area may be affected by the pressures coming from the foundation.

Another possible and more likely reason for this pattern is the placement of a coarser material up to elevation 408 m. This was a design option in order to use a more resistant material in the lower layers where higher stresses are expected.

These results can also be used to estimate the permeability of the core materials. In fact, considering some degree of simplification one can regard that the flow in the core is mainly horizontal or approximately perpendicular to the upstream boundary of the core. Admitting laminar flow, and according to the Darcy's law:

$$v = k\,.\,i \Leftrightarrow \frac{d}{\Delta t} = k\frac{\Delta H}{d} \Rightarrow k = \frac{d^2}{\Delta t\,.\,\Delta H} \tag{10}$$

where d stands for the distance between two sampling points, ΔH for head difference between these points and Δt is the time delay determined before, which means the time to the pressure travels the distance d. The permeability coefficient evaluated from Equation (10), will be mostly related to the horizontal direction (k_x).

Using Eq.(10) it is possible to estimate the horizontal permeability as shown in Fig. 9. It is clear from the picture that a more permeable material occurs in the lower part of the core where it is ten times higher than in the upper part.

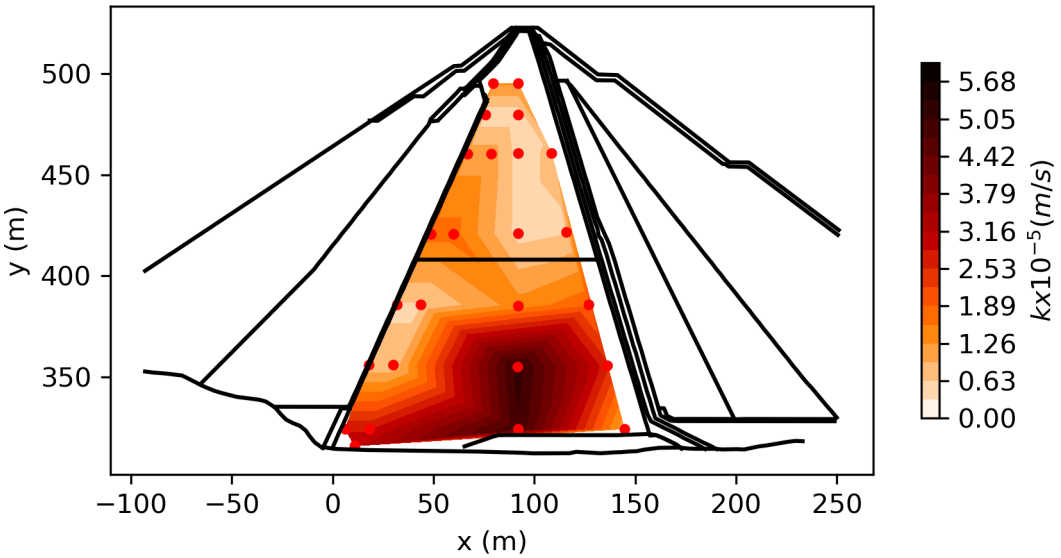

Fig. 9 - Horizontal permeability in cross section 3

This is probably related to the material 3B used in the lower part of the core as shown in Fig. 1 [1,10]. Using the same procedure the other cross sections may also be analyzed as shown in Fig. 9 and Fig. 11.

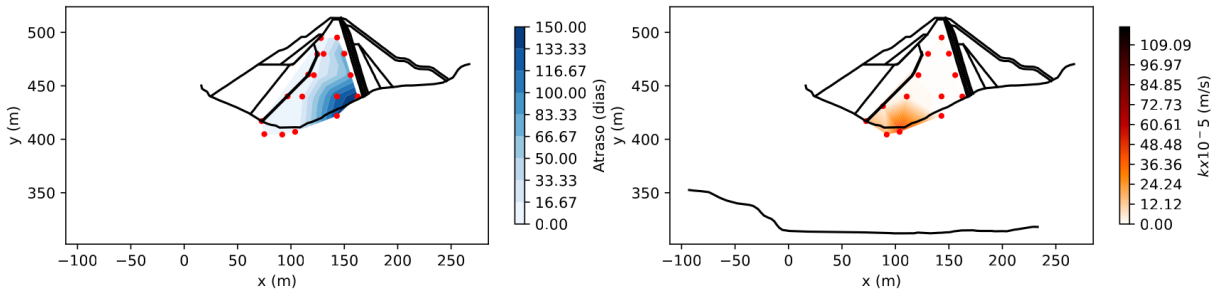

Fig. 10 - Cross section 2 - time delay and horizontal permeability

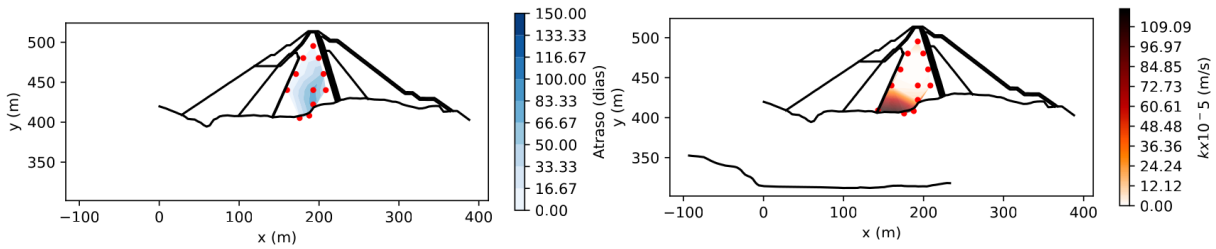

Fig. 11 - Cross section 4 - time delay and horizontal permeability

4. FINAL REMARKS AND CONCLUSIONS

Dams play a crucial role in water resource management, serving as vital infrastructure for both human consumption and power production. For human consumption, dams act as reservoirs, storing large volumes of water that can be strategically released during periods of drought or increased demand. This ensures a consistent and reliable water supply for agricultural, industrial, and domestic use, contributing to water security and mitigating the impact of water scarcity on communities. Moreover, dams are integrated to power generation, harnessing the potential energy of stored water to produce electricity through hydropower. This renewable energy source is environmentally friendly, providing a sustainable and efficient means of meeting the ever-growing global demand for electricity.

However, the construction and operation of dams come with inherent risks and challenges. The impoundment of large water bodies behind dams creates a significant risk due to the large amount of stored energy which if released without control can lead to devastating downstream flooding. The potential for such failures necessitates rigorous engineering, monitoring, and maintenance practices to ensure the structural integrity of the dam over its lifespan.

The monitoring of dams is essential for ensuring their safety. It is a mandatory activity and is even stipulated in dam regulations in most countries. In some cases, guidelines are provided regarding the parameters to be observed and the minimum observation frequencies. Beyond safety control, observation allows inferences about the characteristics and behaviour of the materials used in dam construction. To achieve this, it is crucial to have a robust database with high-quality and quantity data. This is the case with the Irapé dam, where the richness of available data allows a detailed study of the flow through its impermeable core. In this study, quantitative analysis models (statistical models) are applied to describe the flow through the core. It is observed that the models can be enhanced by explicitly considering the delay in the piezometer response to variations in the water level in the reservoir, and based on this, an attempt is made to estimate the core permeability.

This paper allows verifying the importance of a comprehensive, well-maintained, and thoroughly explored observation system, not only to effectively control safety, as is the case, but also to enable the acquisition of data regarding the behaviour of the observed structures.

REFERENCES

[1] CEMIG. (2019). PLANO DE SEGURANÇA DA BARRAGEM UHE IRAPÉ - 2022.

[2] Duarte, Marcelo; Leite, Adilson; Gomes, Romero (2013) - ENSAIOS DE ALTERABILIDADE PARA A PREVISÃO DA DRENAGEM ÁCIDA NA BARRAGEM DE IRAPÉ, BRASIL. Geotecnia n.o 128 – Julho 13 – pp. 49-66

[3] Pinto, P. S. S. e. (1982). Observação de barragens de aterro. Laboratório Nacional de Engenharia Civil.

[4] Marcelino, J., Sibia, Ó. J., & Figueiredo, L. (2018). Barragem de Massingir em Moçambique. Historial e Cenários Futuros. Congresso Luso-Brasileiro de Geotecnia, Salvador Da Bahia.

[5] Marcelino, J., & Portugal, J. (2012). Modelos de comportamento da barragem de Massingir em Moçambique. XIII Congresso Nacional de Geotecnia, Lisboa Abril.

[6] Portugal, J., & Marcelino, J. (2012a). Modelos de comportamento da barragem de Corumana em Moçambique. XIII Congresso Nacional de Geotecnia, Lisboa, Abril.

[7] Portugal, J., & Marcelino, J. (2012b). Modelos de comportamento da barragem dos Pequenos Libombos em Moçambique. XIII Congresso Nacional de Geotecnia, Lisboa Abril.

[8] Oliveira, S. B. (2000). Modelos para a análise do comportamento de barragens de betão considerando a fissuração e os efeitos do tempo. Formulações de dano. Tese de Doutoramento. FEUP.

[9] Ramos, M. (2004). Observação do comportamento estrutural de barragens de betão. Aspetos práticos. LNEC.

[10] Aires, Alexandre (2006). ESTUDO TENSÃO-DEFORMAÇÃO DA BARRAGEM DE IRAPÉ. Dissertação apresentada ao Programa de Pós- Graduação do Núcleo de Geotecnia da Escola de Minas da Universidade Federal de Ouro Preto.

Fifth International Dam World Conference
PORTUGAL • LISBON • LNEC • APRIL 13-17, 2025
dam world 2025

NOTES ON THE APPLICATION OF NEW ZEALAND'S 2022 NSHM IN SLOPE STABILITY

Tarik Dirikolu, Elena Zabolotnii[1], Siva Sivathayalan, John Read, Julian Venter

ABSTRACT

The use of pseudo-static analysis for the seismic stability assessment of open pits and earthen dams is legislated in a number of countries such as Chile, Brazil and Italy, ensuring the continued use of the method. This paper responds to a question posed by the practitioners, whether the three-dimensional formulation of the method can be used to meet the regulatory requirements. This paper discusses the interpretation of pseudo-static outputs and demonstrates that three-dimensional seismic coefficients cannot be used interchangeably with their two-dimensional counterparts. The authors present the case for developing the correct equivalencies and/or the expanded use of displacement-based deformation analysis. The case study of Wall 375 recovery design in the aftermath of the 2016 Kaikōura earthquake is used to illustrate this issue, especially in the context of the updated 2022 National Hazard Seismic Maps from New Zealand's Institute of Geological and Nuclear Sciences.

Keywords: Pseudo-static slope stability analysis, selection of seismic k-coefficient, design acceptance criteria in seismic analysis, the Kaikōura earthquake.

[1] elenazabolotnii@cunet.carleton.ca, Canada

1. INTRODUCTION

Pseudo-static analysis belongs to the class of slope stability solutions known collectively as “limit equilibrium methods” (LEM). While more advanced methods for seismic analysis have been advanced since its formulation, the authors recognize that its legislated or otherwise mandated use in many jurisdictions (e.g., Chile, Brazil, Italy) ensures its continued application by practitioners, regardless of the objections voiced by researchers regarding its reliability and accuracy [37].

Recent advancements in computational geomechanics have rendered three-dimensional pseudo-static slope stability analysis feasible for routine applications in the operational practice, and all commercial LE software known to the authors includes it. Two- and three-dimensional pseudo-static outputs are different, the latter typically predicting higher stability levels under equivalent seismic loads as approximated by the seismic k-coefficient. Existing guidance on pseudo-static analysis does not differentiate between its two- and three-dimensional formulation [1], [26], [28], [37].

As it is the case with the parent LE analyses, an argument has been made that the two-dimensional pseudo-static analysis is conservative owing to the omission of “sidewall resistance” from the calculations, resulting in some overlooked strength that renders the slope more stable than it presents. In consequence, the question was posed whether it is appropriate and safe to use three-dimensional pseudo-static analysis as an alternative to the two-dimensional solution in order to meet the mandated requirements.

The authors recognize that in view of the increased use (and potential for use) of the three-dimensional pseudo-static analysis, there is an urgent need and responsibility to provide the practitioners with guidance regarding its applicability. This paper addresses this question and presents an argument that using two- and three-dimensional pseudo-static analyses interchangeably to meet recommended seismic k-coefficient values is not only incorrect but potentially unsafe.

1.1. Overview of case study

New Zealand is highly susceptible to risks associated with natural hazards such as earthquakes [26]. A 2012 study by London’s Centre for Economics and Business Research indicates that, of the assessed countries, New Zealand is predicted to incur the third highest yearly losses attributable to natural disasters [8]. The destruction brought about by the 2016 Kaikōura earthquake, including above all the loss of life but also the extensive damage to the infrastructure and the resulting disruptions to essential services underscored the need for

updated guidance for seismic-resilient infrastructure design [34]. In 2022, New Zealand's

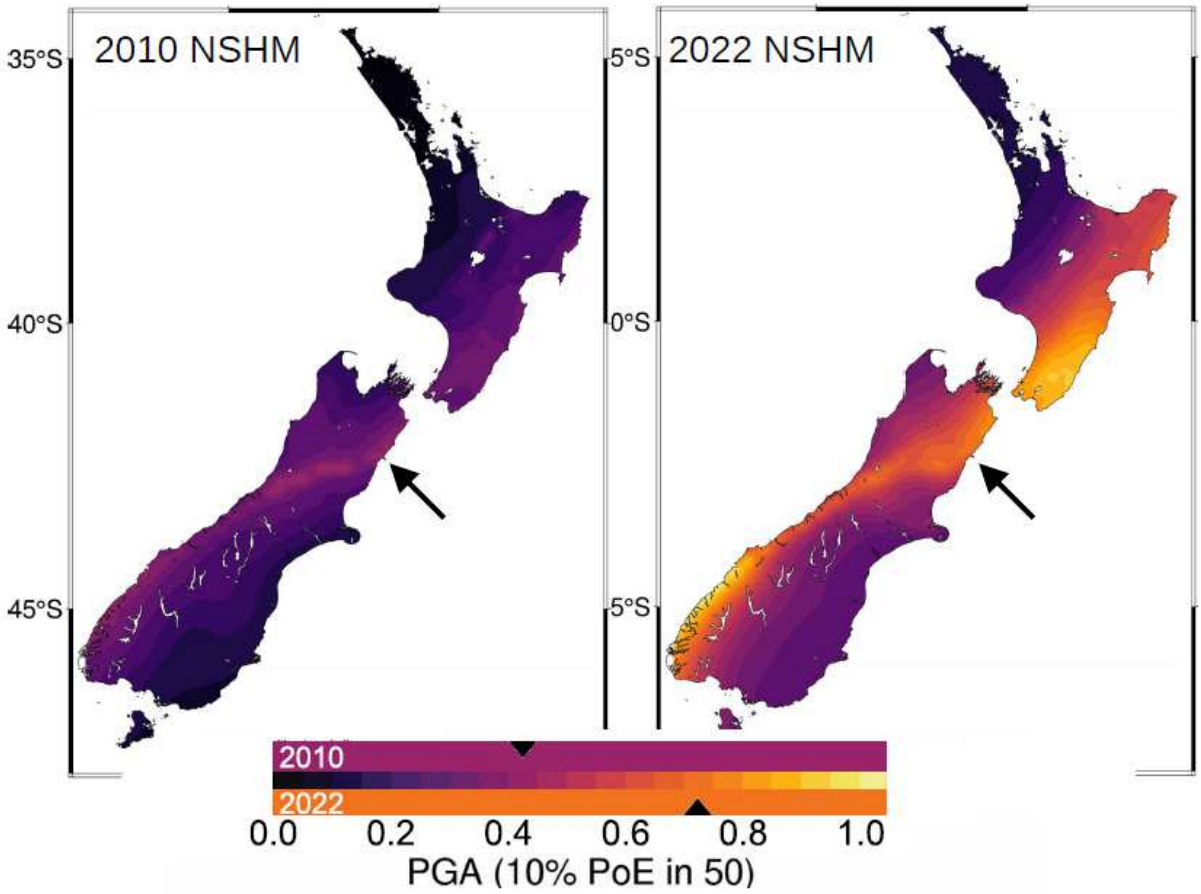

Fig. 1 – 2010 and 2022 NSHM maps (adapted from GNS 2022 and modified to add labels) showing colour-coded PGA values with PoE=10% in 50 years. The arrows point to a location near Kaikōura; and the solid colour bars with triangle arrows identify the forecast PGAs along the colour-code bar.

Geological and Nuclear Sciences (GNS) issued updated maps of expected seismic hazards, to be used by professionals as inputs for their design checks to ensure seismic resilience. Shortly thereafter, the nation's Geotechnical Society produced a set of guidelines on slope stability that addresses, among other things, seismic slope stability analysis methods and associated design acceptance criteria.

Even with this guidance, questions remain regarding good practices in seismic slope stability analysis. This paper was triggered by one such question posed by Dr. Ian Brown [7] regarding the selection of inputs (and indirectly, of the design acceptance criteria or DAC) for pseudo-static slope stability analysis. Following the publication of the slope stability guidance by the NZGS [26], the authors identified several other areas of concern. The authors address these issues to the extent possible and pose the questions to the practice hoping to generate a conversation on the subject. The case study of the recovery design of Wall 375 along State Highway No. 1 originally presented by Kendal-Riches [16] is used to illustrate these issues.

1.2. The National Seismic Hazard Model (NSHM)

New Zealand's Institute of Geological and Nuclear Sciences (GNS) prepares the National Seismic Hazard Model (NSHM), which among other things, provides maps of forecast shaking hazards with some specified probability of exceedance (PoE) over some time window into the future [11]. At the time of the Kaikōura earthquake, the GNS-issued 2010 NSHM was in force. In 2022, a revised model was released which saw an increase in the magnitude of the expected seismic events of 50% on average and up to 100% in places [11].

The NSHM is used by practitioners to evaluate the seismic risks of infrastructure designs and/or existing structures at project-specific locations. GNS does not mandate seismic design standards or seismic design acceptance criteria; instead, engineering practitioners are expected to use professional judgment along with project-specific criteria and methods accepted in their fields to determine the acceptable risk and produce designs that would meet these requirements.

1.3. New Zealand's guidelines for evaluating seismic slope stability

Pseudo-static analysis and dynamic numerical modelling are two common methods for assessing a slope's seismic resilience. The former is a variant of limit equilibrium analysis; its formulation and some limitations are briefly explored in the next section. While more advanced tools for seismic analysis have been proposed since its introduction in mid-20th Century, the authors recognize its current extensive use by the practice, and consequently the need for appropriate guidance. The latter is a sophisticated approach that is often recommended for larger slopes or locations with significant consequences [26] and can capture progressive and deformation-dependent failure; this method is not discussed here.

In pseudo-static analysis, the design seismic k-coefficient is the input that correlates the NSHM with the slope stability analysis and is often seen as a measure of either PGA, MHA, or seismic deformation. Values recommended by literature can range significantly. As the k-value is a sensitive input, its selection can impact considerably the design and project costs.

The NZGS [26] offers guidance on the selection of this value as follows. The document indicates the seismic k-coefficient is a "seismic load" but that its selection must be based on threshold displacements that would reduce the slope to its limiting equilibrium [26]. The displacement-based selection of k is consistent with the modern view of seismic problems being deformation-controlled. The guide lists the Newmark [25] block-sliding method which assumes that some minimum ground acceleration is needed to induce rigid-body translational displacement; and equates the cumulative displacements to the double integral the portion of the ground acceleration that exceeds this critical value vs. the time record. Several procedures for assessing slope displacement are listed: by Jibson [15], Anderson et al [2], Rathje and

Antonakos [29], Bray and Macedo [6] and Macedo et al [17]. The guidance provides additional notes regarding the interpretation of the k-coefficient in terms of MHA (described as the ceiling k-value), PGA (described as generally greater than the k-value) and acceptable deformation levels in conjunction with target factors of safety.

In seeking clarity on how the NHSM and NZGS guidance might be used by slope stability practitioners to design earthquake-resilient slopes (using pseudo-static analysis), the authors assembled the flowchart in Fig. 2 that reflects their best interpretation of the current process.

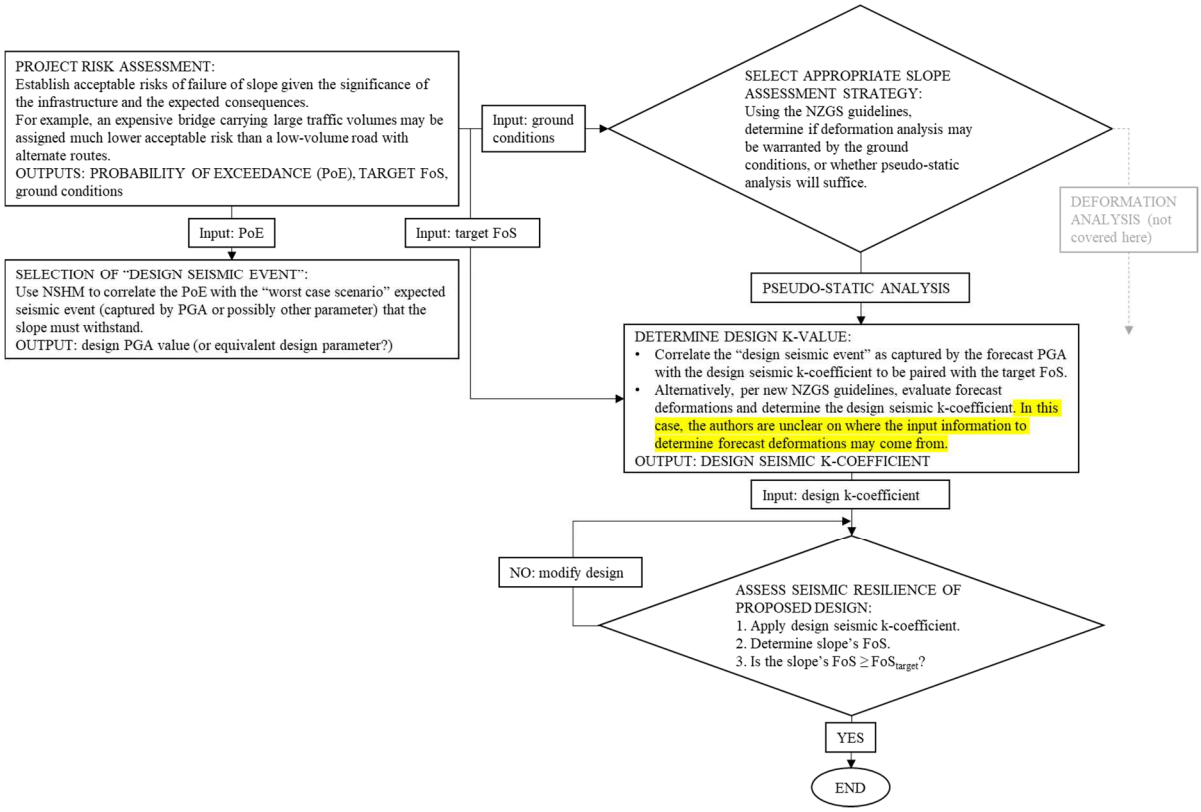

Fig. 2 Flowchart represents the authors' best interpretation of the current process in New Zealand with regard to the use of pseudo-static analysis in earthquake-resilient slope design.

2. THEORY

Pseudo-static analysis is a method for evaluating the seismic resilience of slopes. It belongs to the class of limit equilibrium methods (LEM), where the effect of seismicity is approximated through the application of a force F over and above the weight of the sliding soil mass, acting in the outward direction to the slope face at some angle. This force is expressed as a fraction of the slide's weight, with the scaling coefficients k_h and k_v being the proportion of the gravitational acceleration g acting along the vertical and horizontal directions [39]:

$$F = kW \tag{1}$$

$$F_h = k_h W \tag{2}$$

$$F_v = k_v W \tag{3}$$

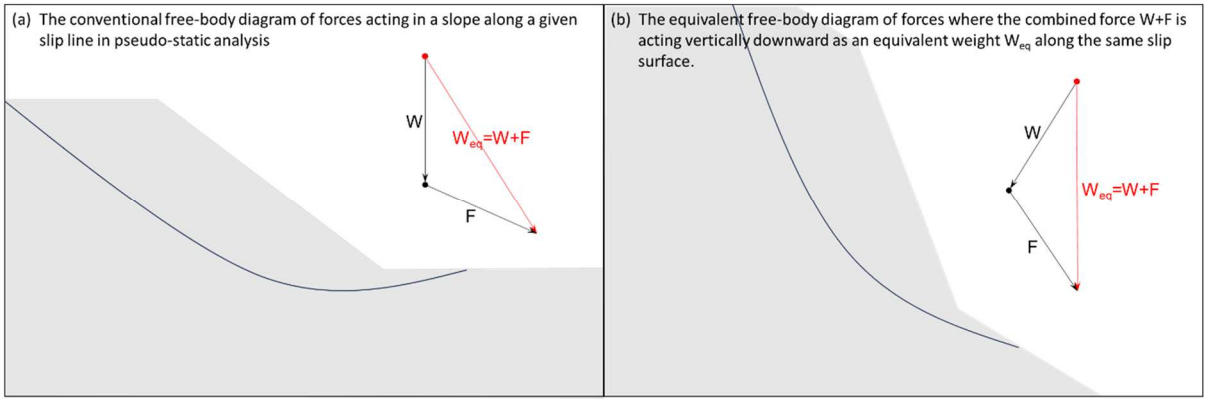

Fig. 3. The conventional and equivalent free-body diagrams of forces acting along some slip surface owing to gravity and earthquake-induced acceleration.

The effect of such an approximation of earthquake impact on a slope's stability can be thought of as being equivalent to rotating the slide so that the combined force vector W+F is acting vertically; this steepens the outer face as well as increases the equivalent "weight" acting along the critical slip surface, decreasing the slope's stability. This equivalency is illustrated in Fig. 3, showcasing the simplifying assumptions underlying the method's formulation, characterized by Seed [30] as "inaccurate, to say the least" in how they capture an earthquake's effects. Nevertheless, since at least the 1930-40s, this method was a standard approach for evaluating the seismic stability of earth dams [30] and is recommended by NZGS [26] for seismic stability assessments of slopes made of non-liquefiable soils or where liquefaction would not bring the system to its limiting equilibrium. One common simplification is to ignore the vertical component of the seismic-induced force [30], [26]; this approach is used herein.

2.1. Interpretation of the pseudo-static k-coefficient

In the formulation of the pseudo-static analysis, the effect of an earthquake on slope stability is said to be equivalent to some force caused by seismic ground acceleration acting on the soil or rock mass. Therefore, the seismic k-coefficient is rationalized as some direct measure of said ground acceleration which, when multiplied by the weight of the soil mass above the slip line, is equal to that force.

In literature, this interpretation is commonly accepted without additional interrogation, and the only outstanding question is that of determining the correct value such that its effect on slope stability in pseudo-static calculations is equivalent to the destabilizing effect on the actual slope of the earthquake of some given magnitude. According to Seed [30], the earliest documentation of the pseudo-static method is found in Terzaghi [35] that also lists approximate

k-values at 0.1 for “severe” earthquakes, 0.25 for “violent, destructive” earthquakes, and 0.5 for “catastrophic” earthquakes, based on “independent estimates” by Freeman in 1932. The US Corps of Engineers [36] provides a lower range of recommended values, between 0.1 and 0.15 for “major” and “great” earthquakes, respectively. Seed [30] proposes values of 0.1-0.2, which conservatively reduce the slope to a FoS≥1.15 (as opposed to the US Corps of Engineers 1982 values that reduce the slope to its limiting equilibrium). Such values suggest that, for example, great earthquakes have the equivalent effect on a slope of imposing a lateral acceleration of 0.15g, 0.2g and 0.5g respectively, depending on the source of choice and on the interpretation of earthquake magnitude in qualified terms. Given that the k-coefficient is a sensitive parameter that greatly affects the outputs, it is unclear how such widely different values can produce equivalent or at least similar results.

In practical terms, establishing the equivalency between an earthquake’s effect and the seismic k-coefficient is not straightforward. For example, ground acceleration during seismic events is nonuniform. Peak and mean accelerations (e.g., PGA, MHA) can be computed and neither is directly equated to the k-coefficient. Instead, some researchers propose relationships where k is equated to a fraction of these measures: ⅓ to ½ of PGA per Marcuson et al [18], or ½ of PGA per Hynes-Griffin et al [14]. Further complicating these matters, Newmark [25] highlights the deformation-driven nature of seismic impact on slopes and proposes to evaluate this value as a function of ground acceleration histories, where accelerations exceeding some threshold value are assumed to produce velocity and displacement; in this approach, the k-coefficient can differ for events with the same PGA and MHA values but with different durations.

The above illustrates that albeit the formulation of pseudo-static analysis suggests that k-values are measures of horizontal acceleration, the connection to actual ground acceleration measurements is indirect. The selection of the “equivalent values” appears to be done by means of calibration against field data, i.e. it is empirically determined from back-analyses, at least in the cases where this process is documented [30], [14]. With the advent of dynamic analysis using numerical methods, an alternative approach to determining the appropriate seismic k-coefficients was introduced. For example, Melo and Sarma [19] compare 2D dynamic with pseudo-static parametric analysis to establish an equivalent response, and then correlate the ground acceleration record applied in the former with the seismic k-coefficient used in the latter. Their findings suggest that literature-recommended k-values in terms of PGA tend to be on the lower end of the range, i.e. underestimations.

2.2. The rational vs. empirical interpretation of the k-coefficient

The question of whether the seismic k-coefficient is a rational measure of earthquake-induced ground acceleration and force or an empirical scaling parameter that produces the expected response, is not an idle one. In the first case, it can be asserted that the method directly accounts for the earthquake-generated force acting in a slope along with the soil weight to destabilize it; then, to assess a slope's seismic stability, one may compute the shear strength and the maximum resisting force to counter the former. In the second case, the pseudo-static method is semi-empirical and thus the k-coefficients are scalar values specific to the method used to determine them. While not immediately obvious, this issue is at the heart of the question posed by Brown [7] on whether three-dimensional pseudo-static analysis can be used to meet the recommended seismic k-coefficients to produce earthquake-resilient slope designs, and merits examination. Zabolotnii et al [39] discuss this issue at length; a summary is provided here.

Based on our analysis of literature and discussions with practitioners, we conclude that the notion that the k-coefficient can be directly correlated with the earthquake-generated force is traceable to the erroneous interpretation of the LEM factor of safety in terms of available strength – an interpretation that persists even today, despite sustained attempts in geotechnical literature to correct it.

The original definition of the FoS proposed by Fellenius [9] was patterned after the traditional formulations used in other fields of engineering where it is commonly expressed as the ratio of maximum stabilizing to acting destabilizing forces/stresses. Fellenius defines it as the ratio of maximum resisting force to the driving shear force along the slip line. This definition was modified by Bishop [4] and re-interpreted by Morgenstern and Price [21] as discussed by Zabolotnii et al [39] but retained the fundamental form of a ratio where the shear strength calculations are in the numerator and the acting stress is the denominator. It is therefore unsurprising that practitioners sometimes interpret a slope's factor of safety as a measure of "available" or "reserve" strength: i.e. a slope with a FoS=2 has "twice the strength than its current loads/driving stresses". It will be shown further here that this is inaccurate.

The FoS definition by Fellenius was recognized as lacking early on, especially with the introduction the "method of slices" and the incorporation of the Mohr-Coulomb strength model into the calculation, as variations of the factors of safety for individual slices meant inadmissible stress states for individual slices with FoS below unity (i.e. either plotting above the strength envelope or suggesting a non-zero inertia *ma* along the slice base). The issue of the so-called "zones of overstress" was addressed by subsequent LEM formulations by introducing the assumption of a uniform factor of safety along the entire slip surface [4] – one implication of this assumption will be addressed later in the paper. However, as pointed out by Barron [3],

the LEM FoS definitions and formulations rely, in their determination of "available shear strength", on the current normal stress acting along the slip surface and do not accommodate any changes to the latter as the slope follows a stress path to failure. On a $\sigma'_n - \tau$ plot, the strength of the soil τ_f used for FoS calculations is located directly above the current normal stress σ'_n, whereas, depending on the particular stress path that a soil element follows toward the yield surface, any strength along it might apply. For example, an element experiencing "undrained failure", or "liquefaction" would have a shear strength at failure somewhere to the left of the vertical. From the above we conclude that the interpretation of the factor of safety as either a ratio of resisting to acting force or as "excess" resistance, is inaccurate.

Morgenstern and Price [21] recognized this limitation and redefined the FoS as "the factor by which the shear strength parameters may be reduced in order to bring the slope into a state of limiting equilibrium along a given slip surface". This provided a mathematically precise definition of the FoS. However, its interpretation in real-life terms is also problematic. Consider the aforementioned slope with the FoS=2. Suppose that the slope is made of gravel with c'=0 and $\varphi'=45^o$. Per the above, this slope would be reduced to its limit equilibrium (FoS=1, i.e., failure) when its shear strength parameter $\tan(45^o) =1$ is reduced by 1/FoS=1/2; this suggests that the slope would fail when $\tan\varphi'=0.5$ and $\varphi'\approx27^o$, i.e. when gravel behaves more like silt, an obviously illogical pathway to failure. This limitation of the FoS interpretation is highlighted by Morgenstern and Sangrey [22] and Morgenstern [23],[24] and illustrated in the Alameda dam case study [27].

So, if the interpretation of the factor of safety in terms of resisting and driving forces is incorrect and its interpretation in terms of strength reduction is illogical, what is the actual meaning of the LEM FoS?

Morgenstern [23] elucidates this issue. He notes that the meaning of the factor of safety was established through its extensive use as (a) a "factor of ignorance" and (b) as an empirical indicator of desired performance. The latter describes the calibration process whereby the historic performance of structures informs the target factor of safety values used in subsequent designs. For example, dams are typically designed to FoS minimum values of 1.5 because, based on a body of experience with prior dam designs, this is the value that limits deformations to acceptable levels, preventing dam core cracking and other performance issues.

In other words, in interpreting the LEM FoS, we do not rely on the rational basis used by the original proponents to derive it (however reasonable it may sound) but ground it in our interpretation in the historic performance of slopes.

As illustrated in Fig. 23, pseudo-static analysis is equivalent to a traditional LEM analysis whereby the slope is rotated to realign the driving forces W+F vertically. Therefore, the

conclusions reached herein about the LEM FoS can be extended to the k-coefficients. We conclude that, as the LEM calculations should not be interpreted as a measure of resisting and driving forces, so the k-coefficient should not be viewed as a rational measure of earthquake-generated forces. Instead, the meaning of the seismic k-coefficient is derived empirically from our experience of studying slopes' response to earthquakes.

If the above conclusion stands, it raises two additional issues: that of three-dimensional stability effects and that of validation and/or calibration.

2.3. Three-dimensional slope stability effects

It is well-established that three-dimensional LEM FoS are greater than their two-dimensional equivalents, by ~30% [38]. The same holds true for seismic k-coefficients: geotechnical publications show that three-dimensional k-coefficients are greater than their two-dimensional equivalents by ~45-60% [7], [19]. The arguments in the Theory elucidate that the two phenomena are not independent but underlain by a common cause: sidewall effects. Zabolotnii et al [39] offers an algebraic argument for this common causality in addition to the graphic one presented here.

This difference, referred to as "three-dimensional slope stability effects", is the reason why some practitioners may argue that the 2D LEM FoS and k-values are "conservative," i.e. lower than actual, and that 3D LEM FoS and k-values can be used instead as a more accurate measure of the slope's stability as they represent a more accurate account of acting and resisting forces along the slip surface. This reasoning, grounded in the "available strength" based interpretation of the LEM outputs as per our earlier discussion, may lead one to believe that it can be appropriate to use three-dimensional FoS and k-values to meet design targets.

It has been demonstrated here that interpreting LEM outputs in this manner is incorrect. Now, we will demonstrate the effect on slope performance of such substitutions using the earlier example of the dam built to a recommended FoS_{2D}=1.5, thus ensuring that deformations are not sufficiently large to cause core cracking. This structure would have a FoS_{3D} that is 30% higher, so ~1.9. In following with the argument. above, this dam's design can be altered (by steepening its face, for example) to reduce its FoS_{3D} to the recommended value. However, the new design with a steeper face is likely to deform more than the 2D design, i.e. it would not meet the target performance. We therefore argue that the FoS (and k) values that are recommended for slope designs are two-dimensional, having been empirically determined substantively from two-dimensional analysis. The three-dimensional values cannot be directly substituted for these. The case study of Wall 375 illustrates this issue for pseudo-static analysis.

New Zealand's recently published slope stability guidelines [26] to not explicitly differentiate between the seismic k-coefficients obtained from two- and three-dimensional analysis. The guidelines discuss three-dimensional slope stability effects, recognizing that (a) three-dimensional factors of safety are greater than their two-dimensional equivalents and that (b) where three-dimensional analyses are warranted over two-dimensional ones, the strength inputs are calibrated from three-dimensional back-analyses of failures. The latter statement recognizes the semi-empirical nature of slope stability analysis, where calibration against observation is an essential component of proper analysis. We submit that the seismic k-coefficients, like strength parameters and recommended FoS values, are calibrated parameters, therefore method-dependent; they are not transferrable as 1:1 equivalents between two- and three-dimensional analyses.

3. DISCUSSION

3.1. The case study of Wall 375 recovery design

The 2016 Kaikōura earthquake was a magnitude 7.8M_w seismic event with an epicentre offshore the South Island of New Zealand along the Alpine fault and south of the Hikurangi plateau, both located at the boundary of the Australian and Pacific plates. The event caused, among other things, widespread damage to the transportation network and triggered an estimated 80,000-100,000 landslides [9]. Large sections of New Zealand's State Highway No. 1 along the Southern Island's eastern coastline were severely damaged and were subjected to emergency repairs. One such repair at a section identified as "Wall 375" was reported by Kendal-Riches [16], where a temporary recovery design consisting of an anchored retaining wall was implemented.

The design's seismic resilience was evaluated using two-dimensional pseudo-static analysis and inputs based on 2010 NSHM maps of expected seismic activity in the area. At the location, the 2010 NSHM PGA maps forecast a PGA value of ~0.4 (PoE=10% in 50 years). Kendal-Riches [16] tests the proposed design's seismic resilience using two-dimensional pseudo-static analysis. She demonstrates that a k-value of 0.4 reduces the slope to a FoS value of 1.2; the justification for the choice of k and FoS is not discussed. If the author bases her choice on the PGA maps with PoE of 10% in 50 years, then this choice appears to be conservative; whereas for a lower PoE this value may appear better aligned with those recommended by literature [20], [35].

Under the 2022 NSHM, the PGA value at the same location is 0.70-0.73, a ~70% increase (Fig. 1). Brown [7] poses the question about the effect of such an increase on the recommended seismic k-coefficients. If the increase is proportional (i.e., also 70%), then the

design of Wall 375 by Kendall-Riches [16] may not meet the new recommendations and may need to be altered.

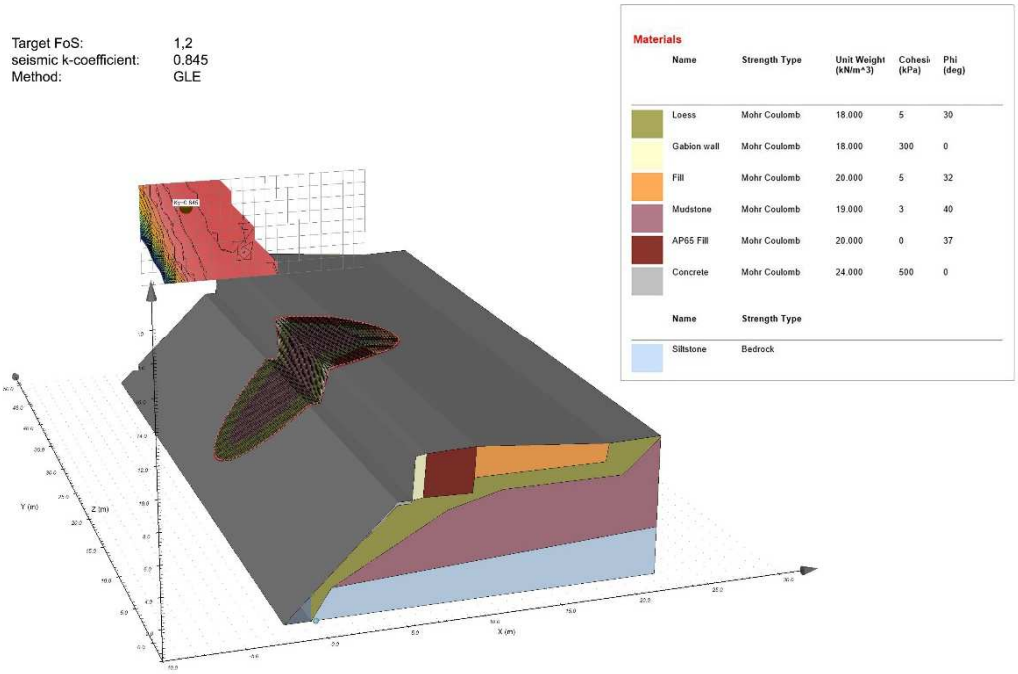

Fig. 4 A three-dimensional pseudo-static analysis of Wall 375 using Bentley's Plaxis LE.

Brown [7] demonstrates that if three-dimensional slope stability effects are considered, the Wall 375 design proposed by Kendall-Riches [16] is more earthquake-resilient than suggested by two-dimensional analysis. He reports that when using three-dimensional pseudo-static analysis, the k_{3D}-coefficient of 0.4 reduces the slope to $FoS_{3D}\approx2$, much higher than the target FoS=1.2; and that the slope is reduced to a limit equilibrium ($FoS_{3D}=1$) when $k_{3D}=0.81$.

In other words, if three-dimensional slope stability effects are considered, the design for Wall 375 may meet the new, higher standards without alteration. Brown [7] uses this case study to pose a question to the practice regarding the applicability of three-dimensional slope stability effects in such analyses.

Our own analysis shows that, to reduce this slope to a $FoS_{3D}=1.2$, a seismic k_{3D}-coefficient as high as 0.85 must be applied (Fig. 4), i.e. much higher than the presumed new value of k=0.7. Our analyses [39] mirror Brown's findings that the ultimate k-coefficients (i.e., the values that reduce the slope to a limiting equilibrium) are ~0.5 in 2D and 0.8-0.9 in 3D, depending on software.

If we take the view that the k-coefficients are a direct measure of the earthquake-generated force and the method merely accounts for driving and resisting forces along the three-dimensional slip surface, then these results appear to suggest that, when three-dimensional stability effects are factored in, the slope meets or even exceeds the new standards.

If, however, one accepts the view presented in this paper, that the recommended values have been determined empirically against experience to ensure some target performance (i.e., resilience against some seismic event with given PGA, MHA or deformation levels), then it becomes very important to establish whether this number was determined in 2D or in 3D. If, as we argue here, the previously recommended values (i.e. k=0.4) were established based on a body of case studies back-analysed using two-dimensional analysis, and as a result of the Kaikoura earthquake were deemed insufficient based on observed performance, then the argument that those same slopes may have been more earthquake-resilient (and could withstand a higher k-value owing to overlooked sidewall resistance) does not withstand scrutiny.

3.2. Validation and calibration

The interpretation of the seismic k-coefficient is further complicated by the difficulties associated with validating and/or calibrating the pseudo-static method. The two-dimensional limit equilibrium methods were extensively evaluated against case studies of failures [5], [12], [13], [32], [33]. These evaluations were undertaken for validation purposes in following with the scientific method as it was recognized that in an applied field such as slope stability, the proof of validity is empirical in the form of observed performance, regardless of the rational basis for a method's formulation. In retrospect, the efforts to establish the validity of the limit equilibrium methods were hampered by the variability of sensitive modelling inputs (e.g., strength parameters estimated from laboratory tests) or gaps in knowledge (e.g., pore pressure distributions at failure or mechanical properties). As a result, today, these methods are seen by many researchers to have been calibrated[1], rather than validated, as to yield the correct results. Furthermore, the accumulating experience with the performance of slopes was continuously used to calibrate the recommended values for the factors of safety associated with target performance.

It is of interest to determine whether similar efforts to validate the pseudo-static method have been undertaken; this need is highlighted by Seed [30] who notes a lack of such studies. If the same general process as described above would be followed, this would entail the back-analysis of slopes that failed as a result of seismic events. Seed discusses several case studies where the observed performance of the structures during seismic events was not as expected based on prior or post-failure analysis. For example, the failure of the San Fernando dam during the 1971 earthquake was unexpected as this structure was subjected to rigorous seismic analysis five years prior and deemed safe; a back-analysis using k=0.15, a value on the upper end of recommended range at the time, yields FoS=2-2.5. The back-analysis of the

[1] With the evaluation conducted using cases of slope failures under the assumption that the failure equates to FoS=1, the two-dimensional limit equilibrium method is considered to yield the best results for slopes with factors of safety close to unity.

Sheffield Dam failure by Seed et al [31] demonstrates that the pseudo-static analysis would have not predicted it; a back-analysis using k=0.15 yields FoS=1.3. The 1964 Alaska earthquake also caused a number of failures in slopes that “proved difficult to predict using the pseudo-static approach” [30]. The 1978 tailings dam failure in Oshima, Japan, was also back-analysed, yielding FoS=1.3 for k=0.2. Seed also discussed the case of the 1906 San Francisco 8.25 magnitude earthquake that subjected 33 nearby dams to peak ground accelerations equal to 0.25g and possibly as high as 0.6g over a prolonged period of 1 minute; the lack of significant damage underscores the role of foundation soils (non-liquefiable clays in this case) in earthquake-resilient design.

Based on the review of current geotechnical literature, the evidence that would demonstrate the validity and the predictive power of the pseudo-static method is still lacking. While the common response to this state of knowledge is to either increase the recommended k-values or to modify the manner in which they are calculated based on rational arguments (e.g. using displacements as per NZGS [26]), these modifications in themselves do not constitute validation for the method.

Finally, we wish to broach the subject of consistency. The authors evaluated the case study of Wall 375 using three software packages: the results varied by over by 10-15% for the same slip surface [39]. One software package uses a modification of the pseudo-static method which appears to produce larger k-values. This is a considerable variation which warrants evaluation.

4. CONCLUSIONS

This paper reviews the pseudo-static method and its underpinnings. The authors discuss the interpretation of the pseudo-static outputs and present their case that the recommended seismic k-coefficient values were empirically established from case histories using by and large two-dimensional pseudo-static analysis. Owing to the complexities of the factor of safety interpretation in slope stability, the outputs of this analysis should not be seen as capturing the ratio of driving to resisting forces. In consequence, seismic k-coefficients derived from three-dimensional pseudo-static analysis should not be used as 1:1 substitutes for recommended k-coefficients that have been established on the basis of two-dimensional analysis. The authors note that, unlike for two-dimensional limit equilibrium analysis, the body of work to validate and/or calibrate the seismic k-coefficients is not compelling.

From the discussions with practitioners, it would be of value to develop recommendations on the applicability of three-dimensional slope stability effects using pseudo-static analysis. From the current state of research, doing so would require additional calibration studies of known histories. Finally, the authors suggest that a formal effort to validate or calibrate the pseudo-static method is undertaken in accordance with the scientific method, as to confirm, correct or

expand the existing guidance. The use of three-dimensional pseudo-static analysis to meet recommended or mandated seismic k-coefficients may lead to nonconservative, i.e. unsafe, design, a practice that could have considerable impact on dam and mining operations.

At this time, the authors have teamed up with Dr. Ian Brown to advance some of this work as the available data permits.

ACKNOWLEDGMENTS

The authors would like to acknowledge Dr. Ian Brown for having raised the question on how slope stability practitioners should be applying the 2022 NSHM, and for providing the authors with the site data and TAGA's TSlope software, thus enabling them to carry this discussion forward. This study was funded by the National Science and Engineering Research Council of Canada (NSERC) through its Discovery Grant. The authors acknowledge Bentley® for providing software Plaxis LE to complete research presented herein.

ABBREVIATIONS AND NOTATION

DAC	Design Acceptance Criteria
FoS	Factor of Safety
GNS	New Zealand's Institute of Geological and Nuclear Sciences
LE	Limit Equilibrium
LEM	Limit Equilibrium Method
MHA	Maximum (Average) Horizontal Acceleration
NSHM	National Seismic Hazard Model
NZGS	New Zealand Geotechnical Society
PGA	Peak Ground Acceleration
PoE	Probability of Exceedance

REFERENCES

[1]. Associação Brasileira de Normas Técnicas (ABNT). Mining Elaboration and presentation of dam projects for tailings disposal, sediment containment and water reservation – Requirements. Report, Ref. No. ABNT NBR 13028. 2017, 16 p. ISBN 978-85-07-07286-7.

[2]. Anderson, D.G., Martin, G.R., Lam, I., Wang, J.N. (2008) Seismic Analysis and Design of Retaining Walls, Buried Structures, Slopes and Embankments. NCHRP Report 611, Transportation Research Board, Washington, DC (2 volumes).

[3]. Barron, R.A. (1964). Correspondence. Géotechnique, 14(4): 360-61.

[4]. Bishop, A.W. (1955). The use of the slip circle in the stability analysis of earth slopes. Géotechnique 5(1): 7-17.

[5]. Bjerrum, L. and B. Kjaernsli (1957). Analysis of the stability of some Norwegian natural clay slopes. Géotechnique 7(1): 1-16.

[6]. Bray, J.D., and Macedo, J. (2023) “Performance-Based Seismic Assessment of Slope Systems,” Soil Dynamics and Earthquake Engineering J., V. 168, 10.1016/j.soildyn.2023.107835.

[7]. Brown, I. Slope stability analysis and the new National Seismic Hazard Model. NZ Geomechanics News, December 2022.

[8]. Centre for Economics and Business Research (Cebr). Lloyd’s global underinsurance report. October 2012, 90 p.

[9]. Davies, JD, V. Sadashiva, M. Aghababaei, D. Barnhill, SB Costello, B Fanslow, D Headifen, M Hughes, R Kotze, J Mackie, P Ranjitkar, J Thompson, DR Troitino, T Wilson, S Woods, L Wotherspoon (2017). Transportation infrastructure performance and management in the South Island of New Zealand, during the first 100 days following the 2016 Mw 7.8 “Kaikōura” earthquake. Bulletin of the NZ Society for Earthquake Engineering 50(2): pp. 271-95.

[10]. Fellenius, W. (1936). Calculation of the stability of earth dams. In Proceedings of the 2nd Intl. Congress on Large Dams, Washington, D.C. 4: 445.

[11]. GNS (NZ’s Institute of Geological and Nuclear Sciences Limited). National Seismic Hazard Model, Rev. 2022. https://www.gns.cri.nz/research-projects/national-seismic-hazard-model/ accessed 2024.

[12]. Golder, H.Q., and D.J. Palmer (1955). Investigation of a bank failure at Scrapsgate, Isle of Sheppey, Kent. Géotechnique 5(1): 55-73.

[13]. Henkel, D.J. and A.W. Skempton (1955). A landslide at Jackfield, Shropshire, in a heavily over-consolidated clay. Géotechnique, 5(2): 131-137.

[14]. Hynes-Griffin ME, Franklin AG. Rationalizing the seismic coefficient method. U.S. Army Corps of Engineers Waterways Experiment Station, Vicksburg, Mississippi, 1984, Miscellaneous Paper GL-84-13, 21 p.

[15]. Jibson RW. Regression models for estimating co-seismic landslide displacement. Eng Geo 2007;91(2–4):209–18. https://doi.org/10.1016/j.engeo.2007.01.013. Wyllie D. C., Mah C.W (2004). Rock Slope Engineering, Civil and Mining. 4th Ed (2004).

[16]. Kendal-Riches, L. (2018). The design of ground anchors and soil nails in the repair of State Highway 1. NZ Geomechanics News 96: 70 – 81.

[17]. Macedo, J., Bray, J.D., and Liu, C. (2023). Seismic Slope Displacement Procedure for Interface and Intraslab Subduction Zone Earthquakes. J. Geot. GeoEnv Eng. 149(11).

[18]. Marcuson WF, Franklin AG. Seismic Design, Analysis, and Remedial Measures to Improve the Stability of Existing Earth Dams - Corps of Engineers Approach. in Seismic Design of Embankments and Caverns, T.R. Howard, Ed., New York, ASCE, 1983.

[19]. McPherson, I. Assessment of earthquake induced lateral displacements at Transpower Hayward HVDC Link Pole 3 upgrade. In Proc., 1st GeoMEast Intl. Congress and Exhibition, Sham El-Sheikh, 2017.

[20]. Melo, C. and S. Sarma. Seismic coefficients for pseudostatic slope analysis. In proc., 13th World Conf. on Earthquake Engg., Vancouver, BC, Canada, August 1-6, 2004.

[21]. Morgenstern, N.R., and Price, V.E. (1965). The analysis of the stability of general slip surfaces. Géotechnique, 15(1): 79–93.

[22]. Morgenstern, NR and Sangrey, DA. Methods of Stability Analysis. In: Landslides: Analysis and Control, RL Schuster and RJ Krizek (eds.), Special Report No. 176, Transportation Research Board, National Academy of Sciences, Washington, DC, pp. 155-71.

[23]. Morgenstern, NR. Keynote paper: The role of analysis in evaluation of slope stability. Landslides, Bell (ed.) © 1995 Balkema, Rotterdam, ISBN 90 5410 032 X.

[24]. Morgenstern, N.R. The evaluation of slope stability: a further 25-year perspective. Distinguished Lectures, Hong Kong Institution of Engineers, 12 December 2017.

[25]. Newmark, N.M. (1965) Fifth Rankine Lecture: Effects of Earthquakes on Dams and Embankments. Géotechnique 15: 139-160.

[26]. New Zealand Geotechnical Society (NZGS). Slope Stability Geotechnical Guidance Series: Unit 1 – General Guidance. December 2023, Report, 157 p., www.nzgs.org

[27]. Quinn, Joseph, Bill Chin, Mark Pernito and Jody Scammell (2014). Geotechnical assessment of Alameda Dam. In proceedings of GeoRegina 2014.

[28]. Rampello, S., Fargnoli, P. and Callisto, L. (2008): Evaluation of Seismic Coefficients for Slope Stability Analysis Using a Displacement-Based Approach, Panel lecture for International Conference MERCEA08 (in print).

[29]. Rathje EM, Antonakos G. (2011). A unified model for predicting earthquake-induced sliding displacements of rigid and flexible slopes. Eng Geol. 122(1–2): 51–60.

[30]. Seed, B. (1979). 19th Rankine Lecture: Considerations in the earthquake-resistant design of earth and rockfill dams. Géotechnique 29(3): 215-263.

[31]. Seed, H. B., Lee, K. L. & Idriss, I. M. (1969). Analysis of Sheffield Dam failure. J. Soil Mech. Fdn Diu., Am. Soc. Civ. Engrs 9.5, No. SM6, Proceedings Paper 6906, 1453-1490.

[32]. Sevaldson, R.A. (1956). The slide in Lodalen, October 6, 1954. Géotechnique, 6(4): 167-182.

[33]. Skempton, A.W. and J.D. Brown (1961). A landslide in boulder clay at Selset, Yorkshire. Géotechnique, 11(4): 280-293.

[34]. Stevenson JR, Becker J, Cradock-Henry N, Johal S, Johnston D, Orchiston C and Seville E (2017). Economic and social reconnaissance: Kaikōura Earthquake 2016. Bulletin of the New Zealand Society for Earthquake Engineering, 50(2): 346-355.

[35]. Terzaghi K. Mechanisms of Landslides. Engineering Geology (Berkeley) Volume, Geological Society of America, 1950.

[36]. US Corps of Engineers. “Slope Stability Manual EM-1110-2-1902.” Washington, D. C.: Department of the Army, Office of the Chief of Engineers, 1982.

[37]. Williams, D., R. Davidson, D. Blowes and S. Barrera. Independent technical review board BHP Escondida Laguna Seca TSF – Commentary on design basis. Report, September 2023, ITRB Escondida, 11 p.

[38]. Zabolotnii, E. 2020. Three-dimensional slope stability effects in the failure at the Mount Polley Tailings Storage Facility. Ph.D. thesis, University of Alberta, Edmonton, Alta., Canada.

[39]. Zabolotnii, E., Dirikolu, T., Kumar, J.S., Venter, J. and J. Read. The applicability of 3D effects to pseudo-static design acceptance criteria: the recovery design for Wall 375. In review 2024, Bulletin NZ Soc. Earthq. Engg.

Fifth International
Dam World Conference
PORTUGAL • LISBON • LNEC • APRIL 13-17, 2025
dam world 2025

TROPICAL LATERITIC AND SAPROLITIC SOILS –THE BRAZILIAN EXPERIENCE

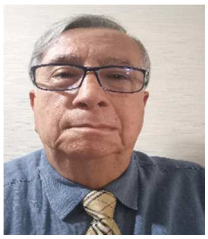

Manoel S. Freitas Jr[1]
Consultant Engineer

Eraldo L. Pastore [2]
PhD, Director WRC
Consultoria E.

ABSTRACT

Tropical soils are the result of chemical disintegrating acting on rocks, forming horizons represented in typically weathering profiles. The main horizons of a tropical profile are colluvial lateritic soil, residual lateritic soil, saprolitic soil (always residual), and weathered rock. This paper addresses geotechnical aspects of the lateritic and saprolitic horizons in undisturbed state and in compacted states for "homogeneous" fills and impervious core in high rockfill dams. There is frequently a misunderstanding with the term saprolite regarding saprolitic soil. Saprolite is not a soil horizon. It is a horizon intermediary between the saprolitic soil and weathered rock with values of Nspt > 40 until the impenetrable SPT, while saprolitic soils have 15 < Nspt < 40, typically a soil horizon. Traditional geotechnical concept and routine methods of sampling preparation, test control at site or laboratory based on standard laboratory tests, cannot afford a direct use to the tropical soils and have induced many mistakes in classification and restricted as construction material.

A special aspect of the lateritic and saprolitic soils is the occurrence of "canaliculi" formed by the organic action (termitic origin). These "canaliculi" are tubular holes found in many dam foundations in Amazon Brazil region always demanding treatment with grout injection.

Keywords: Lateritic,Saprolitic,Weathering,Canaliculi,Tubular

[1] msousafreitas@uol.com.br, São Paulo, Brazil
[2] elpastore@uol.com.br, São Paulo, Brazil

1. INTRODUCTION

Saprolitic soils are the final product of the weathering processes. In engineering terms residual soils (saprolitic soils are always a residual soil) are described in the Earth Manual- Bureau of Reclamation (1963) as: *"weathering action on rock progress, the rock fragments are gradually reduced in size until the total material assumes the characteristics of soil." According to the ICOLD bulletin No. 151 "Residual soils as Dam Foundation and Fill Material for Dams"* (2017), physical-chemical factors affecting weathering are more readily present at the surface, the extent of weathering usually decreases with depth. Several authors [1], [2], [3], [4], [5], [6], [7] have proposed typical weathering profiles. For engineering practical purposes four horizons should be considered: i) Lateritic superficial porous that can be residual or coluvionar, characterized by the enrichment of oxides and concretionary hardened materials (horizon B, [1], [2], [3]); ii) Saprolitic soils with relic structure, easily excavated mechanically without any blasting, and the resulting product being a typically soil; iii) saprolite, a mixture of fines and weathered rock blocks; iv) weathered rock, high to low over the sound rock substratum.

Saprolitic soils (which preserves the relict rock texture) as a construction material, become a very attractive alternative for embankment zoning, when the available in dam site from the required excavations (power house, spillway). Geologically, saprolitic soils are conceptualized as a low resistance, easily excavated without blasting, compact and very sensitive to changes in natural weather, (weathering dependence). Fig. 1 presents weathering profile, showing the different horizons.

Fig. 1 - Weathering profile, showing the different horizons of the saprolitic soil

2. CHARACTERISTICS OF SAPROLITIC SOILS

Data of saprolitic soils relating to granulometric composition, mineralogy, permeability, and compressibility of natural soil free from possible interference from veins and discontinuities commonly preserved in the massifs, are related.

It should be noted that recent studies have clearly shown that the usual procedures for sedimentary soil mechanics are not at all suitable for tropical soils. Several authors [8] and [9], [10] have in depth on this issue especially in relation to geotechnical identification, stress state and analysis of properties of shear and compressibility of these soils.

2.1. Granulometric composition

Granulometric composition of soils are intimately related to texture and mineralogy of the original rock and weathering. The results of granulometry depend on the energy used in the test due to presence in the coarse fraction of grains of weathered feldspar [10]. Furthermore, and considering that the rocks have fine to coarse grains, and that on wait for saprolitic soils granulometry, of them derivate, be very variable. Despite this, it can be said based on results of granulometric tests, that for soils derived from migmatites, granites and gneisses, they are composed predominantly of silty sands and sandy silts. Soils derived from fine grained rocks such as basalts and some types of granitoids are composed predominantly by clayey silts and silty clays.

2.2. Mineralogy

Saprolitic soils present in the sandy fraction a complex mineralogy containing several minerals like quartz, kaolinite and mica in different degrees of change. In the silt fraction mainly kaolinite, mica and quartz and in clay fraction kaolinite, halloysite, nontronite, vermiculite and attapulgite.

2.3. Permeability

The permeability of saprolitic soils is in general quite variable, depending on their intrinsic heterogeneity. This fact was attested [11] who showed the great variation in the values obtained in tests carried out in laboratory. According to this author, the values of permeability coefficient K can cover a wide range of values, from 10^{-3} cm/s to 10^{-7} cm/s. On the other hand, [12] the author presents results of laboratory tests carried out on micaceous silty sand and sandy silt soils in the parallel direction (Kpl) and perpendicular (Kpp) to the band of the original rock. The values found [12], in cm/s, are 1×10^{-4} to 5×10^{-4} (Kpl) and 0.5×10^{-4} to 2.0×10^{-4} (Kpp) for silty sand, 0.2×10^{-4} to 2×10^{-4} (Kpl) and 0.1×10^{-4} to 0.5×10^{-4} (Kpp) for sandy silt.

2.4. Compressibility

Some authors [13] present in Table 1 many laboratory test results of compressibility for saprolitic soils.

Table 1 – Example of a table

Saprolitic soil	Cv coefficient of Compressibility (cm^2/seg)	Cc compression index	Eoed deformability modulus (MPa)
From gneiss	$1.0.10^{-1}$ to $1.0.10^{-3}$	0.05 – 0.25	22 - 33
From basalt	--	0.5 - 0.8	3 - 14
From granite	$2.5.10^{-1}$ to $2.0.10^{-2}$	0.23	10 - 25

3. CHARACTERISTICS OF RELICT FEATURES

Relict features include all the joints such as foliations, fractures, and faults in the rock mass that have been preserved in the saprolitic soil mass. Their influence on several geotechnical parameters is of great importance. Triaxial laboratory tests carried out with a saprolitic soil derived from gneiss containing relict joints with slickensides [7] (**Fig. 2**). The position of the relict planes in relation to mean stress axis was variable between 0 to 90 degrees in the tests.

Fig. 2 - Relict joint preserved in saprolitic soil of gneiss with slickensides.

The results are shown in Fig. **3** where it is possible conclude that there is a perceptible fall in the soil shear strength in the range of 30-40 degrees due to relict joint.

4. CHARACTERISTICS OF SAPROLITIC MASS

The characteristics of saprolitic soil masses are understood to be the parameters obtained in situ through tests and investigations that reflect the behavior of the entire soil material, relict joints and other complex features that may be present in the terrain. The characteristics most determined in the field are the resistance to penetration, through the SPT test, the permeability coefficients, through infiltration and/or pumping tests, and compressibility, through plate tests and pressure gauges.

4.1. Standard penetration tests index (Nspt)

Analyzing profiles of several SPT boreholes carried out in saprolitic migmatite soil, it turns out that the values of N behave in three ways different with increasing depth, as illustrated in **Figure 3** . In case a) N increases or varies little with the depth. In case b) one or more cases presents values more elevated than the others, due to presence of veins of quartz or cores of rock less weathered. In case c) in general, a higher value appears close to the water level.

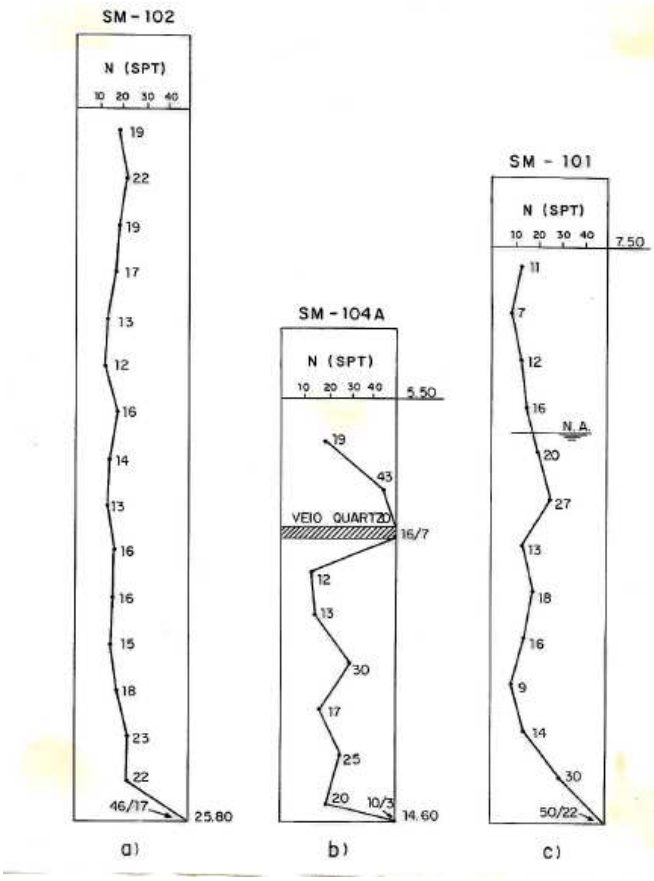

Fig. 3 - Profiles of SPT boreholes

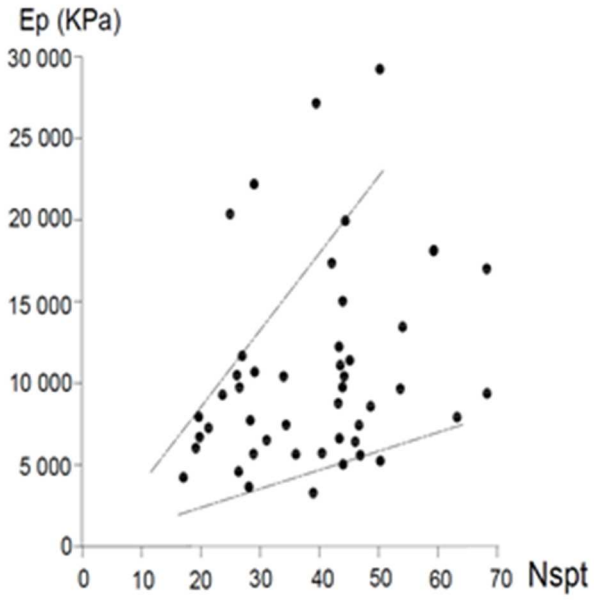

Fig. 4 - Correlation between Nspt and Ep (KPa)

Nspt values in boreholes carried out in Caconde, Passauna and Mogi-Guaçu Dams showed a large dispersion. More recently, the experience with a hundred of soil nailing and retaining wall cut slope design in Brazil, show that the values of Nspt saprolitic mass range between 15 and 40.

4.2. Permeability

Several authors [14] present values of K obtained in field testing. From the results, it is observed great variation in values of K in case of basalts and migmatites. Considering infiltration tests carried out in migmatite saprolitic mass foundation of Caconde Dam, the highest frequency of K lies in the range of 1×10^{-5} to 5×10^{-5} cm/s.

4.3. Compressibility

A correlation between N values (SPT) with deformability values Ep obtained through pressuremeter tests on gneiss saprolitic mass, as shown in **Fig. 4**. [15]

5. CANALICULI PHENOMENON

Canaliculi phenomenon has been mentioned largely during the hydroelectric plants of tropical environment construction at Brazil's Amazon Region. The first recorded occurrence of tubular cavities in soils occurred on 1957s, during the Vereda Grande dam (Piauí State). Subsequently, canaliculi presence were largely divulgated since 1978s at Tucuruí dam (Pará State, 1984), Samuel (Rondônia State, 1989), Balbina (Amazonas State, 1989), and Belo Monte Complex (Pará State, 2020), in different types of soils. From the construction periods

mentioned up to now, canaliculus has been monitored in these dams by the Owner ELETRONORTE S.A and Norte Energia (Belo Monte Hydro Complex). The presence of canaliculus in dam foundations directly influences percolation and seepages at downstream areas. Nevertheless, any case of rupture by piping phenomenon or dam slopes instability have not been recorded in Brazil, in view canaliculi presence, so far.

At Belo Monte Hydro Complex on the Xingu River (Pará State), residual soils of migmatites predominant lithology are present on the foundations of almost a main embankment material for the construction of the dams and the dikes [16], [17]. During the excavation of the first foundation areas, the presence of a great concentration of tubular cavities (canaliculi) of sub centimetric to decimetric diameters was found in the foundation of the dikes as shown in Fig. **5** and Fig. **6.**

Fig. 5 - Macro-canaliculi at Dike19 [16]

Fig. 6 - Macro-canaliculi at Dike19 [16]

Fig. 7 - Exploratory Trench

According to some authors [16], canaliculus present sub-vertical development reaching more than 6m depth and lateral interconnections, promoting a significant increase of the permeability of the dike's foundation. The infiltration tests in the wells indicated permeability values of the order of 10^{-4} cm/s for the saprolitic soil of migmatite.

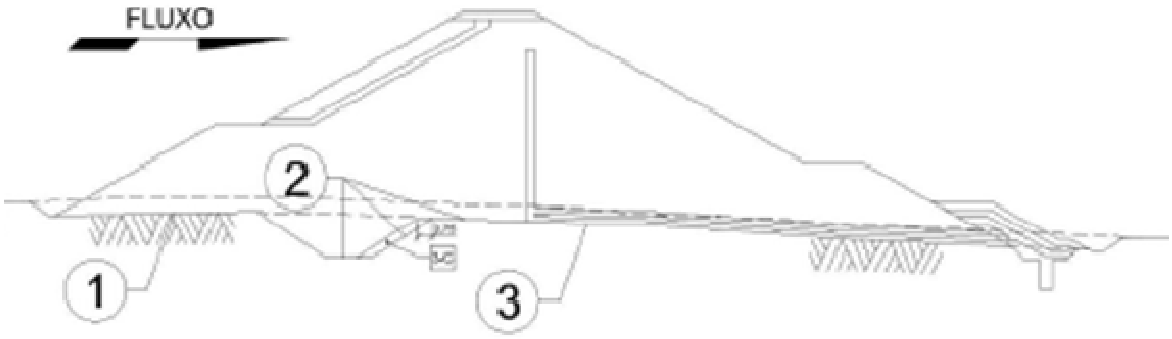

Fig. 8 - Schematic section of the canaliculus treatments in the foundation of the Dams and Dikes [16].

The following measures were adopted in the treatments of the Belo Monte dykes canaliculus:

- Exploratory trench, depth of 3m, air jet cleaning execution to check the presence of micro-canaliculus (millimetric diameter) and macro-canaliculus (centimetric to decimetric diameter);
- Trench excavation 3 m up to 6 m depth at foundation areas; (**Figs**.**7** and Fig. **8**)
- In Fig. regions of points 2 and 3 indicated, the canaliculus with a diameter ≥20 mm was obturated, with a cement grout (factor of 0.7: 1.0, w:c);

- In point 2, sand filter was executed, 0.75 m wide (horizontal), compacted with DR (Relative Density) ≥ 65%, in contact with the downstream wall of the trench, to control eventual high gradients;

After the reservoir filling most of the dikes, up to 60 m in height, were observed high seepages at the downstream areas and cases of artesianism, particularly in the region of the abutments of some dikes. The piezometer readings revealed a normal behavior and pore pressures lower than the design predictions.

At Tucuruí Hydro dam, in metabasic and diabase decomposed soils zone, subverticals 5 to 30cm diameters canaliculus were recorded, permeability ranging from 10^{-5} to > 10^{-3} cm/s and various tests showing total absorption [17]. In laterized metasediments foundation area canalículus recorded during years 79/80 flood, where many springs were observed with random característics, 1 to 2 cm diameters and maximum water absorption 1,900 liters/minute em 10 m^2 square area. At mature residual soils areas subvertical cavities of 20 cm diameter were recorded. Exploratory trench, cement grouting, increasing up to 6m depth, Bidim OP 60 applied over sand layer 2 m over a sand-clayed gravel layer of 5m [17], [18].

At Balbina Hydro dam, located 170 km north of Manaus city, high occurrence of cavities canaliculus were recorded in saprolitic soil foundation area with low natural dry density ranging from 5 to 10 kN/m^3, diameters by 2 cm and 10 cm exceptionally. [20]. The permeability recorded ranged from 10^{-4} to 10^{-1} cm/s, intercommunicating and with an erratic geometric pattern. They were detected in most trenches, with a frequency, which would vary grossly between one or two per square meter for the largest diameters, and one per square decimeter (100 per m^2) for the canaliculi of 2 mm diameter. According to the author [19], this frequency varies along the foundation, and some trenches did not detect any canaliculus at all, [20]; [21] .These canaliculus were interpreted as being generated by intense termite activity linked with the last glacial period quaternary era (12,000 to 18,000 years ago), when the Amazon region had relatively dry climatic conditions, decisive for the existence of vegetation formations for the proliferation of termites. Many different alternatives were evaluated prior to the definition of the foundation treatment to be used in the dam [22], including conventional cut-offs, use of diaphragm walls to implement a cut-off, use of impervious blankets, etc. Grouting of the saprolitic soils at high pressures, generating hydraulic fracturing using the tube a manchette technique and thus intercepting the net of canaliculi was proved to be the best cost-effective alternative. The foundation by grouting pressure treatment was focused on to create by soil fracturing a zone under dam area in which all localized permeability singularities were eliminated [23]. After treatment an analysis of this data demonstrated the success considering the elimination of high permeability (> 5 x 10^{-3} cm/s) at saprolitic soil foundation zones [19].

At Samuel Hydro dam, sub verticals and e sub-horizontals canaliculus were founded in alluvial excavation soils, diameters 1 to 2 cm, in max depth 4 meters. These canaliculi are named “minhocussu” [21]. In residual and colluvial soils, canaliculus recorded 0,2 to 30 cm diameters. In Samuel dam the canaliculus don´t seem to communicate with each other, the flat region demanded but low height earth dam and no special treatment was performed. Several authors present hypotheses for canaliculi phenomenon source [24]. However, from the mentioned several authors there are not a consensus of source formation, shapes and directions so far. Exploratory trench’s cement grouting, conventional cut-offs, use of diaphragm walls to implement a cut-off, use of impervious blankets, were applied by several designers and consultants. Besides high seepages at the downstream areas and artesianism, particularly, any case of rupture by piping phenomenon or dam slopes instability have been recorded in Brazil, in view canaliculus presence, so far.

At People´s Republic of Laos, the Xe-Pian Xe-Namnoy Project, failure of Saddle Dam *the highest section* occurrence was commented [25], *according to* Report of Independent Expert Panel (IEP). *The site visits, as well as the results of geotechnical investigations, the IEP considers that the root cause of the incident is related to the high permeability of the foundation favored by the presence of canaliculus interconnected path having high sensitivity to erosion.*

6. COMPACTED SAPROLITIC AND LATERITIC SOILS - ENGINEERING PROPERTIES

Based on many authors [1], [2], [3], [4], [26} the compacted soils and peculiar structure were divided in four groups according to their similarity of behavior :

i. Group I lateritic clayey soils, in some occasions have been called residual mature soils, and/or residual soils, correspond the first layer of weathering profile are porous, homogenous, low natural density, high porosity, low degree of saturation, and a natural water content close to standard Proctor Optimum. The Workability is quite good for water content up to +2% wopt above;
ii. Group II – Saprolitic soil soils, sometimes called young residual soils, not affected by laterization, the second layer of the weathering profile. They are denser heterogeneous, more silty, higher natural water contents. Good workability, higher levels of moisture content and more heterogenous after compaction;
iii. Group III – Lateritic sandy soils, in these soils the transport is usually larger than in Group I, and it is common to find mixtures of soils. Originating from weathering of sandstones, but containing a clay fraction from basaltic soils that occur in the area. Are homogenous porous, or low density, and have a water content close to Proctor Optimum. The workability is good for moisture contents close to Plastic Limit;

iv. Group IV – Transported soils, sometimes named colluvium soils. Depending on the origin they may be more or less clayey, silty or sandy materials and more or less affected by laterization. The workability depends very much on their natural conditions of density and water content. These soils have been used with high productivity in Brazilian dams. In the Northeastern Area of Brazil with an arid climate, the weathering is less intensive and depths of soils in the borrow areas are quite small. The soil is also very dry in its natural condition, which requires much more intensive work for the proper wetting of the soils prior to compaction. A important question the use of the optimum water contents for saprolitic soils once they have been handled and compacted at site to water contents 8 to 5% above the nominal optimum water content (Standard Proctor) in the field, which would be practically impossible for soils of the group I (lateritic clayey soils). Some authors [27] present the concept of "workability water content" for the saprolitic soils, to replace the conventional optimum water content. Figure 7 shows the correlation of IP, Plasticity Index with the friction angle Ø'c, including Brazilian soils and data [28], according to **Fig. 9**.

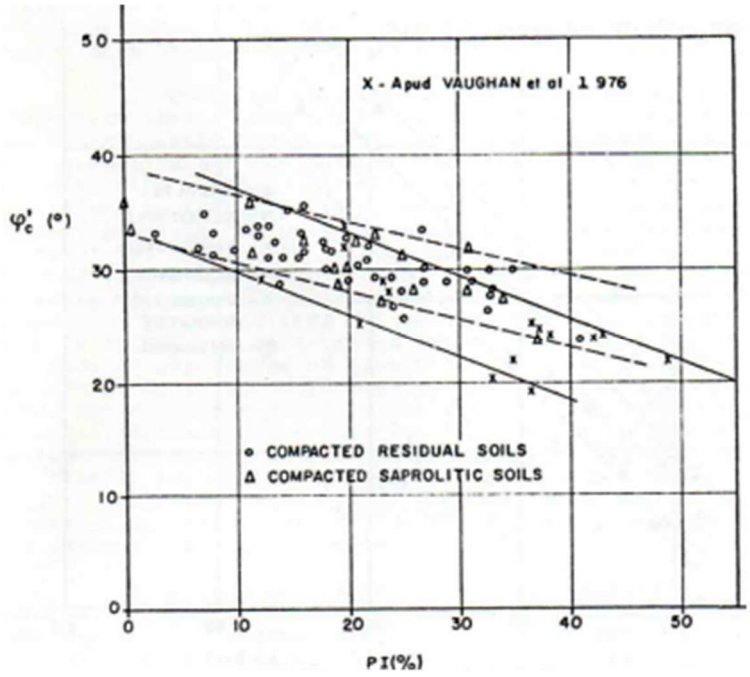

Fig. 9 - Characteristic Ø'c versus Plasticity Index modified [28]

Saprolitic and lateritic soils, as referred to in this paper, correspond whose characteristics are the remaining relict rock structure and their heterogeneous visual aspects. A distinguishing feature of this material is that workability during construction appreciably reduces the grain size which makes it difficult to predict its performance by standard laboratory tests (Standard Proctor, HILF Control Method at site).

However, saprolitic and lateritic soils have relevant geotechnical properties which have been observed during design studies and during construction in many important dams in Brazil, such as: basalt and gneiss saprolitic soils from the South-Central part and granite saprolitic soils from the North, North-East and Central regions in Brazil.

Saprolitic soils as construction material has been handled and test controlled at site in wrong way traditional standard specifications for moisture content and compaction degree similar to what is commonly used for colluvial, mature residual and alluvial soils. Non appropriate and mistake procedures for dealing with compacted saprolitic soils are the intense preliminary scarifying operations at site an attempt to lower the apparently high-water content. The concept of minimum disturbing preparation and “high band of moisture content “for a saprolitic soil from basalt compacted “in a body of an earthfill dam was adopted in the Nova Avanhandava dam, in Southern Brazil [29]. This concept of placement and compaction of saprolitic soil was applied at Itaipu dam (basalt saprolitic soil), Armando de Salles Oliveira and Euclides da Cunha dams -CESP (gneiss saprolitic soils), Itaparica dam – ELETROBRÁS FURNAS (impervious core of gneiss saprolitic soil), Corumbá I dam (micaschist saprolitic soil) and Manso dam – ELETROBRÁS FURNAS (metasiltstone/metasandstone).

Although standard laboratory tests for soils classification are not adequate for saprolitic soils due to the destruction of the original soil structure, they are still being used for identification purposes. In addition, several authors [30], [31], have shown the conflicts of “conventional” classification systems in a remolded and dry state sample, breaking inherited relic structures for residual soils. A basic principle in geotechnical testing is to reproduce in-situ conditions in the laboratory to anticipate the behavior of soils for design purposes. This fundamental requirement for useful and successful testing is usually not satisfied for residual soils. Lateritic soils are considered easy to sample, because of their relative homogeneity and less sensitivity to disturbance. (Ref. Icold Bulletin 151 2017). **Fig. 10** presents the Plasticity Chart for saprolite soils of basalt, gneiss and granite, comparatively [32].

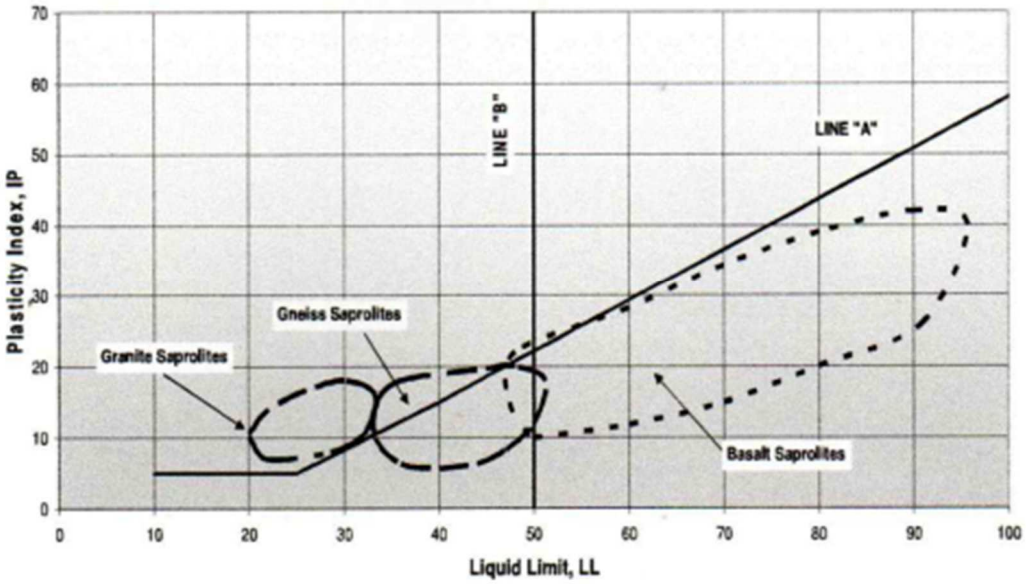

Fig. 10 - Saprolitic soils – Plasticity Chart.

Basalt saprolitic soils are very clayey while gneiss and granite saprolitic soils are sandy and less plastic. Compacted saprolitic soils present as their main geotechnical characteristics a relict structure heritage from the original rock. Its heterogeneous appearance is strictly related to the original rock. The natural water content of the saprolitic soils at the borrow areas is very often quite higher than the Standard Proctor optimum water content, but it is closer to the Plastic Limit (PL) both on its wet and dry side. The natural water content reaches values of 20% above the optimum, mainly basalt and gneiss saprolitic soils from the South-Central regions of Brazil where precipitations in the rainy season are sometimes intense. The specifications for saprolitic soil compaction should allow the water content well above optimum water content of the Standard Proctor test, provided there is no waving of the compacted layer. Sometimes, this characteristic is a strong reason for refusing this type of soil by designers and owners during the construction. He states that degree of saturation of saprolitic soils well above optimum moisture content may be sufficient to ensure no waving of the layer under compaction.

7. BASALT SAPROLITIC SOILS PROPERTIES

Basaltic saprolitic soils have been used in earth dams since the 70s in South areas in the main basins of the Paraná, Uruguay and Iguassu rivers at Brazil. Soil materials with high moisture content at borrow areas or from required excavations areas have been applied by handling his moisture content at site by means of tractor blade plowing which accelerates the drying of the materials in earthfill areas. This usual practice should be handled carefully in order not “break” its “relic weathered rock fragments”, which means its original grain size because this process can change the material characteristics.

7.1. Control at site

Compaction control evolved from the methodologies used in compaction of gravelly materials, called “weighted density method”, which consists of comparing the apparent density of the sample material with its “in situ” density. The determination of the control point, which has the maximum apparent density, is obtained by separating the material from the sampling pit into three fractions by using the 2” and 3/8 “mesh sieves. The sieving is done manually in order not to crush the sample. This process was used in Salto Santiago dam (South areas) [33].

7.2. Strength and compressibility

According to one dimensional consolidation tests and triaxial undrained tests results on undisturbed samples from compacted basaltic saprolitic soils of and gneiss have shown less influence of water content in compressibility parameters in comparison to the lateritic residual or colluvial clayey soils from the same origin. In addition, the deformability modulus of compacted saprolitic soils present a smaller range of variation than the homogeneous clay. This behavior has been observed in other materials such as the micaschit saprolitic soils at the Corumbá I Dam core zone [34],[35]. The small variation of the compressibility of compacted basalt saprolitic soils for a large range of water contents has been shown to be desirable to improve the uniformity of the compacted embankment structure. The resistance of the compacted saprolitic soils is governed by the intact “soft rock” particles which remain in the compacted layers. They keep their original structure and its intrinsic hardness, in spite of the higher water content. The water existing in the voids of the “soft rock” fragments does not affect the soil behavior. The field compacted saprolitic soil is expected to present still higher shearing resistance than that measured at the laboratory compacted sample, because the content of intact blocks would be higher and their size larger.

7.3. Permeability

Although the compacted saprolitic soil presents intact “soft rock” particles, the permeability of the whole compacted mass is still low and appropriate for an impervious zone of the dam. The completely destroyed particles and the resulting disturbed fraction surround the fragments and the permeability is more like that for the homogeneous clayey soil than that of “dirty rockfill”. The in-situ saprolitic soil at borrow areas have a coefficient of permeability of 10^{-4} cm/s. For compacted basalt saprolitic soils from Monday Dam and Nova Avanhandava Dam the coefficient of permeability measured in laboratory compacted samples varies between 2.8 x 10^{-6} to 2.2 x 10^{-7} cm/s [32].

8. GNEISS AND GRANITE SAPROLITIC SOILS PROPERTIES

Saprolitic soil soils from extremely micaceous granite-gneiss have been used at the Paraibuna and Paraitinga Dams (94 m and 105 m high, respectively) construction in the 70s in São Paulo State, Southern Brazil. A saprolitic soil micaceous material had its use quite restricted as core impervious material. At the Paraitinga and Paraibuna Dams this material from borrow areas located close to the dams brought a significant costs reduction due to shorter transportation distances [36], [37].

8.1. Strength

An interesting results of residual parameters for from compacted block samples of gneiss saprolitic soils (silty sand soil, 5 a 12% clay percentage) from the Paraitinga and Paraibuna dams, with high percentage of mica. [38] Ring shear tests carried at Vicksburg laboratory (USA) shown residual parameters such as $\phi r = 28^o$ (Paraibuna Dam) and $\phi r = 30^o$ (Paraitinga Dam). According to the author, soils from granites, basalts and mudstones are comparatively more uniform. Soils from metamorphic rocks have their heterogeneous characteristics associated with schistosity and foliation of the “mother rock” such as limestones and gneisses. Results from drained tests [32] show the internal friction angle ϕ' results from drained tests (assuming $C' = 0$) varying from 29^o ~ 32^o for gneiss saprolitic soils to 38^o ~ $40{,}5^o$ for granite saprolitic soils.

8.2 Compressibility

An interesting comparison [35] between saprolitic and lateritic residual schist and colluvial soils, compressibility (modulus of deformability), $E_{1\%}$ remained almost constant for a large range of water content $-3{,}5\% < w_{opt} < +5{,}0\%$. ($w_{opt}$ – optimum water content). This behavior has been observed by the authors as related to stress strength. The range of water content is less influential in stress strength than colluvial soils. As the water content increases, the colluvial deformability drops at the same time and the residual modulus keeps the same value. For practical purposes, the Corumbá I dam’s experiences shown:

a) The smooth vibratory metallic roller presented the best performance for the saprolitic soil.
b) Micaschist saprolitic soil could be compacted in a higher range of water content than the colluvial and alluvial soils.
c) After rainy periods, compaction works could be restarted more quickly than those using colluvial soil. Some authors [38] present an interesting experience of random material from metasiltstones and metasandstones excavated from required excavations (spillway and main structures) at the Manso dam without using blasting methods (D8

CAT blade). A “fine” random was adopted at the core central zone and a “coarse” random material at the upstream and downstream dam zones. Fine random material from required excavation areas were used at cofferdams placing and compacting 45 cm thick layers which resulted in substantial advantages in costs and time savings.

9. RETROSPECTIVE & PRACTICAL RECOMMENDATIONS

In view of the saprolitic soils heterogeneous aspects and high-water content, laboratory tests and sample preparation standard methods for characterization tests should be handled carefully and not in standards way. Samples from borrow areas should be broken and crumbled in readiness for sieving, as is usually done for colluvial soils. For saprolitic soil these proceedings must be carefully handled in order to prevent the undue breakdown of the particles that may result in gradation changes and parameters changing, due to the breakdown of the real soil or saprolitic soil structure from the “mother rock”. The tamping vibrating roller (pad roller), whose high speed is 25 km/h, was used in the Sossego dam works of using granite saprolitic soil compacted at a high content degree and was successfully used in the Paraibuna and Paraitinga Dams (CESP, São Paulo State). At the Salto Santiago Dam (in South Brazil) compacted basalt saprolitic soil “fines” were compacted with type Hyster C- 410A roller, completing 8 to 10 passes on a 30 cm thick layer. Coarse saprolitic soil (weathered rock fragments) on 50 cm thick layers received 8 to 10 passes of a smooth vibratory roller (Dynapac CA 25 D) [34].

10. QUALITY CONTROL AND SAMPLING SUGGESTIONS

- the use of tractor blade plowing should be limited and controlled. A good workability of the saprolitic soil/residual soils is directly influenced by the preservation of the “relic fragments from the mother rock”;
- water content control at borrows areas should always be implemented;
- thick layer control and number of passes of the roller control;
- Standard Proctor tests without drying and sieving the material in order to preserve the characteristics of the saprolitic soil;
- no drying or sieving proceedings for the LL, PL and grain size tests;
- the smooth drum vibratory roller, 10 ton (model CA 25) for silty soils can be used successfully;
- the tamping vibratory rollers also presented good results;
- test fills are necessary to be implemented during the design phase or during the construction.

11. CONCLUSIONS

During the bidding process a thorough deep investigation of the geological horizons at the dam foundation areas, mainly at the abutments and borrow areas, must be implemented. Lithology, the identification of different saprolitic soils that are available, and the determination of their depth must be defined correctly. Inspection pits must be excavated, and samples be collected to determine the construction material's geotechnical characteristics. Significant volumes of saprolitic soil (fine and coarse) from the main excavations areas were sometimes rejected because of their heterogeneous visual appearance. Standards tests such as grain size and Atterberg Limits for testing preparation at borrow areas might include substantial mistakes in view of the partially weathered and heterogeneous aspect of many saprolitic soil horizons. So, test fills are quite fundamental in testing these saprolitic soil materials. Equipment and compaction proceedings compactor rollers should be tested particularly because of the nature of the saprolitic soil materials. Intense preliminary scarifying operations at site, breaking relic structure by as routine an attempt to lower and correct high water content must be avoided.

Brazilian experiences accumulated in the last 50 years in saprolitic soil (fines and coarses) construction data are available for the Southern and Central parts of Brazil. Sampling for testing of many engineering properties (permeability, strength) requires large specimens to ensure structure and relitic features representative of the mass. Regarding undisturbed sampling full recovery can be performance by SONIC drilling process for saprolitic soil investigation and sampling in view typical anisotropy, heterogeneity and variability of tropical residual soils at site. SONIC drilling (Horizonte Mineiro) method can recover integrally some bedrock formations, with bigger sample size, with recovery and even dry, without usage of drilling fluid. Typically softer, weathered shale, sandstone, limestone, basalt, sand, and others soft rocks or fractured rocks using single OR dual wall core barrel. Geotechnical investigation is also possible when using SONIC drilling in combination with Standard Penetration Test and Cone Penetration Test.

12. REFERENCES

[1] Vargas, M. (1969) - "Residual Soil Sampling " - VII International Conference on Soil Mechanics and Foundation Engineering – Special Session.

[2] Vargas, M. (1974), - "Engineering properties of residual soils from South-central region of Brazil", Brazil. Proceedings of the II Int. Cong. Of the International. Assoc. of Engineering Geology, São Paulo, Brazil, Vol. 1, B.

[3] Deere, D. U., Patton, F.D. (1971) "Slope Stability in Residual Soils. State of the Art Report. Proceed. On Int. IV Panamerican Conference on Soils Mechanics and Foundation Engineering, Puerto Rico, vol. I.

[4] De Mello, V.F. B. (1972) “Thoughts on soil engineering applicable to residual soils. Proc. Of the 3rd Southeast Asian Conference on Soil Engineering.

[5] Mori, R. T. Leme , C. R. de M., Abreu, F. L. R. de, Pan, Y. F. (1978) (Portuguese) “Saprólitos de basalto –um estudo de comportamento geotécnico em maciços compactados “(Portuguese) .Anais do VI Congresso Brasileiro de Mecânica dos Solos e Engenharia de Fundações (Portuguese), Rio de Janeiro, ,ABMS.

[6] Wolle, C. M. (1985) , (Portuguese) Resistência de Contatos Solo-Rocha.Seminário da Escola Politécnica (Portuguese) ,USP.

[7] Pastore, E. L. (1992). (Portuguese) Maciços de Solos Saprolíticos como Fundação de Barragens de Concreto Gravidade (Portuguese). Tese de Doutoramento, Escola de Engenharia de São Carlos, USP.

[8] Vaughan, P.R., Kwan, C.W. (1984). Weathering, structure and in situ stress in residual soils. Geotechnique, v. 34, n. 1, p. 43.

[9] Vaughan, P.R. (1985). Mechanical and hydraulic properties of tropical lateritic and saprolitic soils, particularly as related to their structure and mineral components. In: International Conference On Geomechanics Tropical Soils, 1, 1985. Proceedings Brasilia: ABMS, V. 3, P. 231-263 (General Report).

[10] Vaughan, P. R. (1990). Keynote Paper: Characterinsing The Mechanical Properties Of In-Situ Residual Soils. Internat Conference On Geomechanics Tropical Soils, Singapore, Rotterdam: A.A. Balkema. P. 469 - 487.

[11] Lumb, P. (1962). The properties of decomposed granite. Geotechnique, v. 12, n. 3, p. 226.

[12] Sowers, G. F. (1963). Engineering properties of residual soils derived from igneous and metamorphic rocks. In: Panamerican Conference On Soil Mechanics And Foundation Engineering, 2, 1963, São Paulo, Proceedings… São Paulo: ISRM: ABMS. V. 1.

[13] Lacerda, W. A. et al. (Coord) (1985). Mechanical and hydraulic properties of tropical lateritic and saprolitic soils: compressibility properties. In: Committee On Tropical Soils Fo The International Society Of Soil Mechanics And Foundation Engineering. Progress Report, 1982-1985. São Paulo: ABMS. Theme 2, topic 2.4, p. 85-113.

[14] Costa, L. M., Vargas, E. A. (Coord) (1985). Mechanical and hydraulic properties of tropical lateritic and saprolitic soils: hydraulic properties. In: Committee On Tropical Soils Fo The International Society Of Soil Mechanics And Foundation Engineering. Progress Report, 1982-1985. São Paulo: ABMS. Theme 2, topic 2.3, p. 67 - 84.

[15] Sandroni, S. S., Brandt, J. R. T. (1983). (Portuguese) Ensaios pressiométricos em solos residuais gnáissicos jovens. Solos e Rochas, v. 6, n. 1, p. 3.

[16] Bandeira O. M., Daniel T. L. et. al. (2018) Analysis of the Treatments of Foundation of the Dams of Belo Monte HPP, Norte Energia S. A. - Dam World Conference, Foz do Iguaçu, PR, Brazil.

[17] Buosi, M. A., Cadmam, J. D. (1984) (Portuguese) Sobre a ocorrência de cavidades tubulares em solos lateríticos na região amazônica. Associação Brasileira de Geologia e Engenharia Ambiental (ABGE), 4, B.H, MG, v. 3, p. 10-24.

[18] Adriana E. L., A.E.; Boaventura, et al (2023); (Portuguese) " Ocorrência de canalículos em fundação de Barragem da Região Amazônica – Estado da Arte - Brazilian Committee on Dams, XXXIV Seminar on Large Dams, Foz do Iguaçu, PR, Brazil, August 2023.

[19] De Mello, L. G. (2018) – "Some Case Histories with Lessons to Learn in Dam Engineering". 2nd Prof. Victor de Mello Goa Lecture, Indian Geotechnical Society, Goa Chapter.

[20] De Mello, L. G., et al. (1987). The Foundation Treatment of Residual Soils Conditioned by Canaliculae: A Case History. Anais da Conferencia Ibero-Americana sobre Aproveitamentos Hidráulicos.

[21] Machado, A.B. (1983). The contribution of termites to the formation of laterites. II International Seminar on Lateritisation Process, São Paulo. 1983.

[22] Remy, J. P.P. et. al. (1985). Choice of the Foundation Treatment of Balbina Earth Dam. 15th International Conference on Large Dams. 1985.

[23] De Mello V.F.B. (1977). Reflections on design decisions of practical significance to embankment dams. XVII Rankine Lecture / Geotechnique. 27, 1977, Vol. 3.

[24] Jury, W. J., Paraguassú, A. B. (1990) – (Portuguese) "Considerações sobre a ocorrência de canalículos em locais de barragem na Região Amazônica". Anais do 6. Congresso Bras.de Geologia de Engenharia e IX Congresso de Mecânica dos Solos e Engenharia de Fundações, v. 1. p. 511-517.

[25] Xe-Pian Xe –(2019) Namnoy Project, Failure of Saddle Dam Report of Independent Expert Panel (IEP)-Final Report. . People's Republic of Laos.

[26] Cruz, P. T. (1985). Peculiarities of Tropical Soils used as construction material – Progress Report - First International Conference on Geomechanics in Tropical lateritic and Saprolitic soils - TROPICALS' 1985. – ABMS- CESP.`

[27] Mori, R.T.,(1983) (Portuguese) "Solos Lateríticos e Saprolíticos como materiais de construção de barragens – Encontro Técnico Solos Tropicais ABMS – CESP

[28] Cruz, P.T., Maiolino A. L. G. (1983) (Portuguese) Materiais de construção Anais do Simpósio sobre a Geotecnia da Bacia do Alto Paraná (portuguese) , São Paulo ABMS/ ABGE/CBMR .

[29] Mori, R. T.(1983) (Portuguese) “Propriedades de Engenharia de Solos Saprolíticos. Anais do Simpósio sobre a Geotecnia da Bacia do Alto Paraná , São Paulo, (Portuguese), ABMS/ABGE/CBMR, V. IA.

[30] Wesley, L.D. (1988) Engineering Classification of Residual Soils. Proceed. 2nd International Conf. Geomechanics of Tropical Soils, Singapore, A.A. Balkema Rotterdam.

[31] Fooks, P.G, (1997), Tropical Residual Soils.Geol. Soc. Handbook, London, UK

[32] Mori, R.T. (1979). Engineering properties of compacted basalt saprolitic soils. Proceedings of the 6th Panamerican Conference on Soil Mechanics and Foundation Engineering, (1979), Lima, Peru. V.II.

[33} Sardinha, A.E., Ludwig, N.G., et al (1985) . “ Design construction and behavior of saprolite dam” First International Conference on Geomechanics in Tropical Lateritic and Saprolitic Soils , ISSMFE, Brasilia., Brazil , Vol. 2

[34] Caproni, Jr. N., Palocci, A., Shimabukuro, M. Ribas, J. B. M., Mori, R. T. (1994). (Portuguese) Propriedades Geotécnicas dos Solos Coluvionares e Residuais da AHE Corumbá, XXI Seminário Nac de Grandes Barragens, Recife,PE.

[35] Mori, R. T, et al (1993). “Peculiarities of the design of Corumbá 1 earth core rockfill dam “Proceedings International Symposium on High Earth-rockfill dams, Vol. II, Beijing, China.

[36] Oliveira, H. G., Bordeaux, G., Celeri, R., Pacheco, I. B. (1976) (Portuguese) Comportamento Geotécnico das Barragens e Diques de Jaguari, Paraibuna e Paraitinga – Anais do XI Seminário Nac. de Grandes Barragens, Fortaleza, CE.

[37] Cruz, P. T. (1996) 100 Barragens Brasileiras : Caso históricos, materiais de construção e projeto, Oficina de Textos, (Portuguese), São Paulo, SP, Brazil.

[38] Monti, H. C. (1999), Aproveitamento Múltiplo de Manso – Aplicação de Materiais não Convencionais (Portuguese), XXIII Seminário Nacional de Grandes Barragens, , Belo Horizonte, Brasil.

Fifth International
Dam World Conference
PORTUGAL • LISBON • LNEC • APRIL 13-17, 2025
dam world 2025

MICRO SEISMIC RESONANCE (MSR) - A HELPFUL AND COMPLIMENTARY TOOL FOR MAPPING SEEPAGE THROUGH, BENEATH AND AROUND DAMS, EMBANKMENTS & LEVEES

Dr Andy K Hughes[1]
Reservoirs & Dams Ltd

Ryan Blanchard
Willowstick Technologies

ABSTRACT

In recent years, innovative geophysical techniques have been developed to provide a more detailed understanding of water flow and identify potential sources of pollution and leakage. One such technique is Micro Seismic Resonance (MSR), which can identify locations of geologic, lithologic, and structural anomalies as well as stratigraphic units; assisting in the holistic understanding of a dam structure and its foundation. MSR works by detecting structural weakness in rocks by measuring the resonance intensity and thus can also locate weak or fractured zones of high permeability. Another technique, Willowstick magneto-metric resistivity, is able to map and model groundwater flow paths and patterns through dams in three dimensions.

In our work, we have employed these innovative techniques in many countries around the world but in this paper we present two case studies in Canada and the USA to assess groundwater conditions in dams. The results of these studies have provided valuable insights into how and where water preferentially infiltrates the dam. By combining the results of the MSR and Willowstick techniques, the engineering consultant is able to help owners identify locations of potential leakage/seepage and develop a comprehensive model of groundwater flow through, under and around the dam. Holistic modelling and interpretation allow for the implementation of targeted remediation measures and the rehabilitation of the site.

The use of innovative geophysical techniques has significant implications for the management of dams. By providing a more accurate and comprehensive understanding of these systems, operators and consultants can take targeted remediation efforts to reduce the long-term costs of the operation of a dam. Our work is an example of the potential of these techniques to improve the management of dams and reduce their impact on the environment.

Keywords: Seepage, Mapping, Dams, Safety, Remediation.

[1]andy.hughes@damsandreservoirs.co.uk, UK

1. INTRODUCTION

Willowstick has successfully employed a new Micro Seismic Resonance (MSR) method to improve seepage characterisation through, beneath, and around dams. MSR is a passive seismic method that detects zones of higher permeability in the foundation and fill materials of a dam. Just as the ocean has tides, the earth's crust experiences daily "Earth Tides" and is constantly in motion. Continual motion produces resonance signals that can be measured, interpreted, and modelled to identify zones of higher permeability within a dam and its foundation. The MSR results are analysed in conjunction with the traditional "Willowstick" method to better characterise seepage flow paths and patterns trough, beneath, or around a dam in three dimensions. When both methodologies, which use entirely different scientific principles, identify the same anomalous feature, a higher degree of confidence is gained in the results of the investigation. Willowstick has effectively utilised the MSR method on many successful dam seepage investigations. The two geophysical techniques when used in parallel have yielded complementary results, with both methods providing beneficial information about seepage locations. Location of seepage locations allows targeted remedial works. This paper will detail seepage flow paths identified using both Willowstick and MSR methods for two case study dams in Canada and the United States, and refer its use in Uzbekistan, and when trying to identify the source of waters which threatened to wash out fill beneath a high speed rail track in Scotland.

2. BACKGROUND

Since 2004, Willowstick has specialised in identifying, mapping and modelling preferential groundwater and seepage flow paths and patterns through, beneath and around dams and other sites. Willowstick has completed nearly 500 groundwater/seepage investigations worldwide. The name "Willowstick" is synonymous with mapping and characterising groundwater. In times past, dowsers often used "willow sticks" to locate groundwater. Although there is no scientific basis behind dowsing, the name "Willowstick" was selected to describe the business's focus on groundwater and seepage characterisation

2.1. Willowstick Method

Willowstick's flagship tool, used mainly for seepage investigations of earthfill and concrete dams, called the "Willowstick" method, is explained in a peer-reviewed article in Geophysical Journal International (see Jessop et al., 2018)[1], also in patents (Kofoed et al., 2017[2] and Jessop et al., 2014[3]), as well as in many other publications with case studies exhibiting its successful application. The technology is a quick and non-intrusive imaging methodology

specifically designed to identify, map and model preferential seepage flow paths and patterns through, beneath and around dams. Similar to an angiogram, which uses radioactive dye as a contrast agent to image and visualise the flow of blood through the human body, the Willowstick technology uses a signature electric current as a contrast agent to image and visualise the flow of seepage and can quickly and accurately render 2-dimensional ("2D") maps and/or 3-dimensional ("3D") models of seepage flow paths and patterns through and beneath dams. The application of the technology is based on the principle that seepage generally increases the conductivity of earthfill materials through which it flows. As a signature electric current flows between strategically placed electrodes (located on either side of the dam), it concentrates in the more conductive zones (i.e., in hydrated areas of highest permeability) where seepage preferentially leaves the reservoir. Magnetic fields generated by the flow of the signature electric current are measured and modelled to identify preferential electric current flow paths and patterns. The electric current flow paths and patterns are then modelled and interpreted to characterise seepage flow paths and patterns.

2.2. Micro Seismic Resonance (MSR)

Willowstick has dedicated a significant amount of effort to research and development (R&D) to prove and establish the scientific basis upon which the Willowstick flagship technology is founded. Most recently, Willowstick has made remarkable progress in several key areas, one of which is the application of a new and emerging technology called Micro Seismic Resonance (MSR), which is a passive seismic method that compliments the Willowstick Method in providing further insight as to how and where seepage develops through, beneath and around dams. Willowstick has effectively utilised the MSR method on many highly successful seepage investigations at dam sites and also on a project involving artesian water under a railway line.

The MSR method detects structural weaknesses in soil and rock and is excellent at locating zones of higher permeability caused by fissures and fractures. The constant cycle of tidal motion that affects the oceans, resulting in high and low tides twice a day, is common knowledge. It is a well-established fact that the moon and sun drive these ocean-tidal events. A lesser-known fact is that there are tidal movements in the earth's crust as a result of these same gravitation forces. Earth tides fluctuate between 15 cm (6 inches) and 45 cm (18 inches) a day depending on the location on the earth's surface and the position of the sun, moon and earth in relation to one another. As a result, it is now an established fact the ground below our feet is constantly in motion—rising and falling on a continuous 12-hour cycle. Although we cannot feel the earth's movement (other than during relatively large seismic events—i.e., earthquakes and tremors), it is only detectable with sophisticated and sensitive equipment. Movement of 15 to 45 cm (6 to 18 inches) a day may seem minor in comparison to the earth's diameter; nevertheless, when considering there are hundreds of metres (thousands of feet) of

rock and soil beneath our feet in constant motion, we can start to appreciate the magnitude of this geologic fact. Over time, stresses build in the earth's crust from the repeated rising and falling of the earth's crust until stress release points or zones are established along faults and fractures in rock formations and along zones of secondary permeability in soil formations. As the earth moves, frictional grinding takes place. This grinding creates a resonance signal. The movement and grinding of the earth's crust, in conjunction with water naturally collecting in these areas, produce resonance signals that can be measured and modelled to identify zones of higher permeability in the rock and soil matrix. High frequency MSR measurements (within the resonance frequency domain) indicate that the stress relief point is near the surface. Lower resonance frequencies (within the resonance frequency domain) indicate a deeper anomalous zone. As a result, the zones of highest structural weaknesses within the soil and rock matrix that make up a dam can be identified—more specifically, where and how weaknesses reflect through the foundation and into the embankment of a dam and where and how these weaknesses align with the results of a traditional Willowstick investigation.

3. CASE STUDY 1 (CANADIAN DAM)

3.1. Background and Site Conditions

A close-up aerial photograph of an earthfill dam with a grout curtain is shown in Fig. 1.

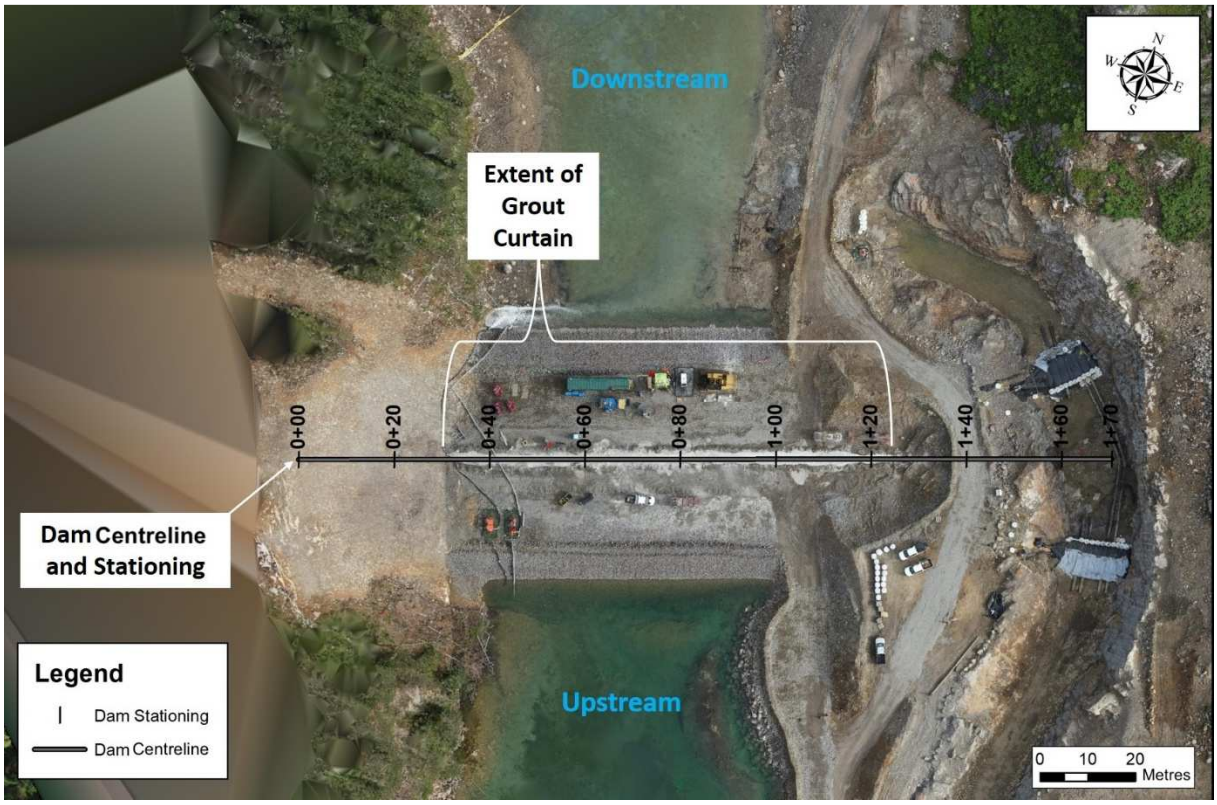

Fig. 1 – Site Map

Fig. 2 presents a cross-sectional view of the dam's general construction.

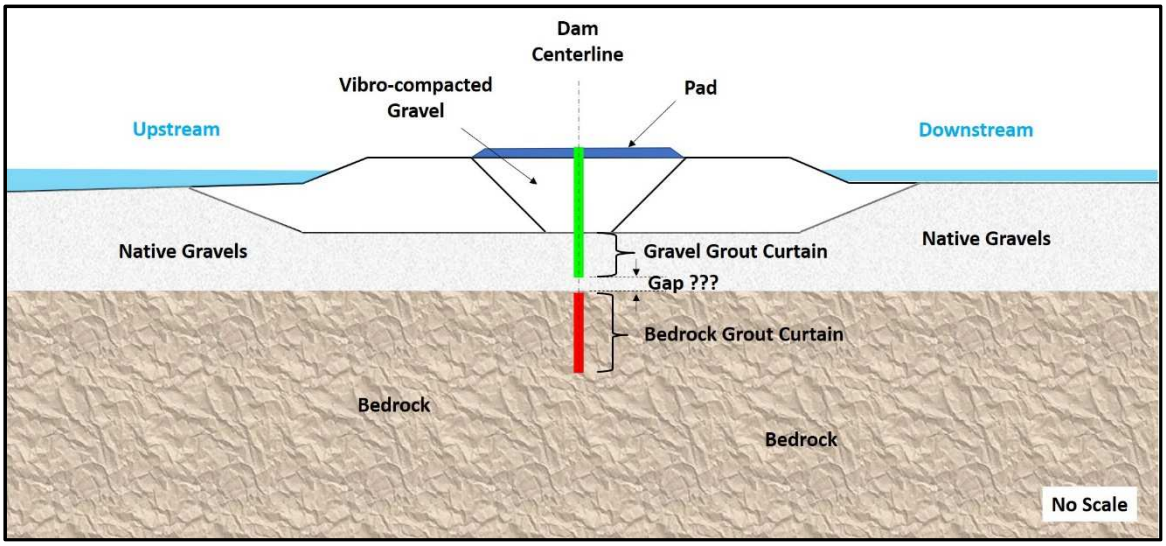

Fig. 2 – Dam Cross-Sectional View (looking west)

The dam was under construction at the time of the investigation. The dam consisted of a bedrock grout curtain (see red vertical line), a cement-bentonite (CB) slurry wall (see the green vertical line), with vibro-compacted gravel zones on both sides of the grout curtain on top of native gravels. It should be mentioned that the CB slurry wall (green vertical line) failed to reach bedrock in some locations due to very dense gravelly material, leaving a gap between the red and green lines.

A longitudinal profile drawing of the dam's grout curtain is shown in Fig. 3. The drawing represents the completion of the grout curtain prior to the investigation. The brown line identifies the top of bedrock. The blue line identifies the top of native gravels.

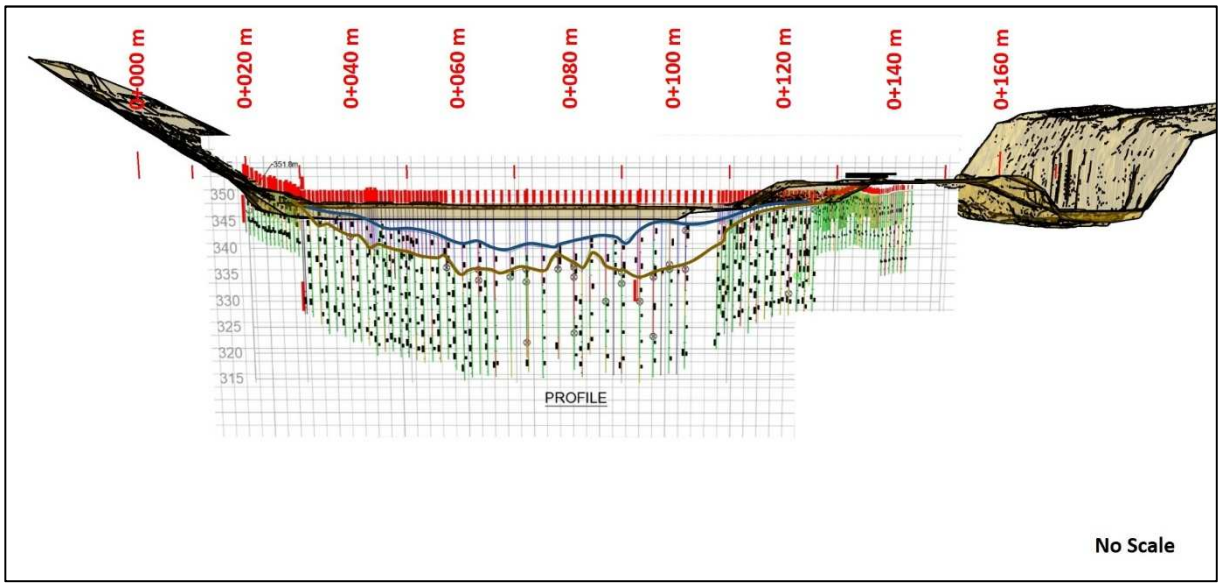

Fig. 3 – Longitudinal Profile As-built Drawing of Grout Curtain
(looking downstream through the grout curtain and unfinished embankment)

While constructing the grout curtain, higher than expected grout takes occurred - more specifically in the centre area of the grout curtain. Before completing grout work (which was nearing completion), the owner wanted to identify any potential weaknesses where seepage could occur either beneath or around the grout curtain. Therefore, the purpose of the investigation was to identify, map and model preferential electric current flow paths and patterns that indicate high-probability pathways for seepage to follow as electric current was biased to flow through, beneath and around the grout curtain (i.e., the Willowstick Method). The investigation also included a MSR survey to detect structural weaknesses in the soil/rock matrix to identify any potential weaknesses or fractured zones of high permeability through the fill and foundation materials. Therefore, the overall intent of the investigation was to identify areas that warrant additional grouting while the grouting contractor was still on site.

3.2. Results

The Willowstick Method identified two preferential electric current flow paths through the dam's grout curtain (see Fig. 4).

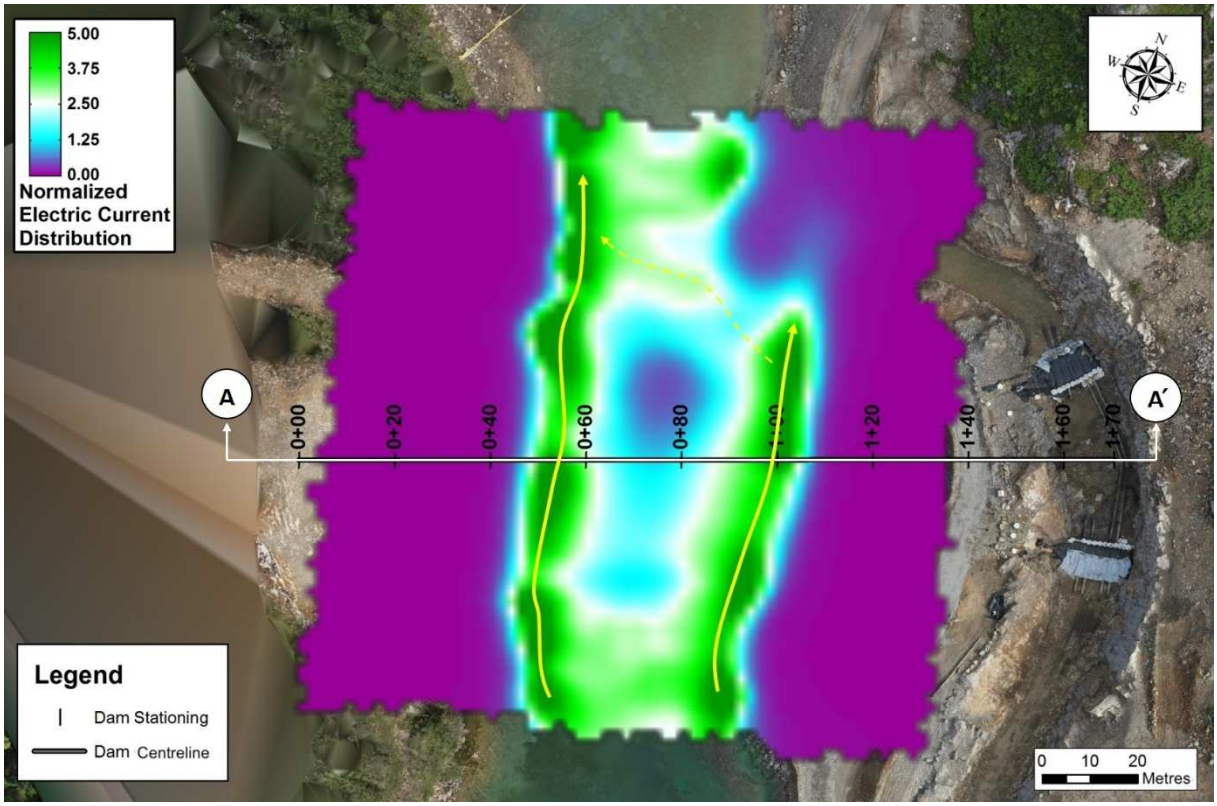

Fig. 4 – Willowstick Method Results (Plan View)

In Fig. 4, the green shading represents areas where the signature electric current density is more concentrated than expected. On the other end of the scale, the dark-purple shading identifies areas where electric current is less concentrated. The yellow arrows highlight the

more intense locations where the signature electric current preferentially concentrates as it leaves the impoundment - interpreted as following along preferential seepage flow paths.

To describe the depths of the seepage flow paths, Fig. 5 (Section A-A′) presents a longitudinal profile slice of the electric current distribution model taken directly beneath the centre line of the dam - looking downstream through the embankment and grout curtain.

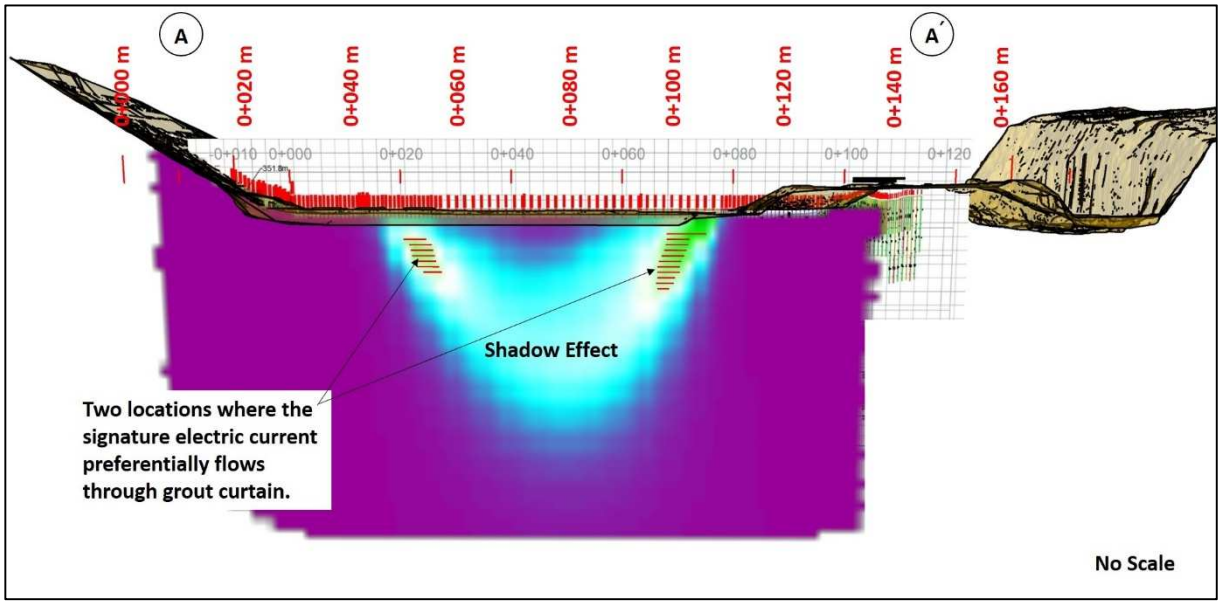

Fig. 5 – ECD Model Slice Section A-A′

In Fig. 5, the green shading (hatched with red horizontal lines) is interpreted as the horizontal and vertical position of the preferential flow of electric current - interpreted as following preferential seepage through the grout curtain. Note how the white to green shaded areas spread downward in Fig. 5 from the two anomalous seepage flow paths (forming a white to blue parabola shape anomaly). This spreading effect is referred to as the “shadow effect”. A good analogy for explaining the shadow effect is to think of the survey data as shining a flashlight downward from above (because measurements can only be taken from above). If there is a solid object (a flow path or some conductive pathway), the top will be illuminated, but a shadow will be cast below the object, as shown in Fig. 5.

To further describe the location of the electrically conductive flow paths, Fig. 6 presents Section A-A′ (i.e., the same view as shown in Fig. 5, but with the ECD model slice turned “off”). The red hatched horizontal lines remain to show the position of the preferential flow of electric current in relation to the grout curtain, bedrock surface, native gravels and earthfill embankment interface.

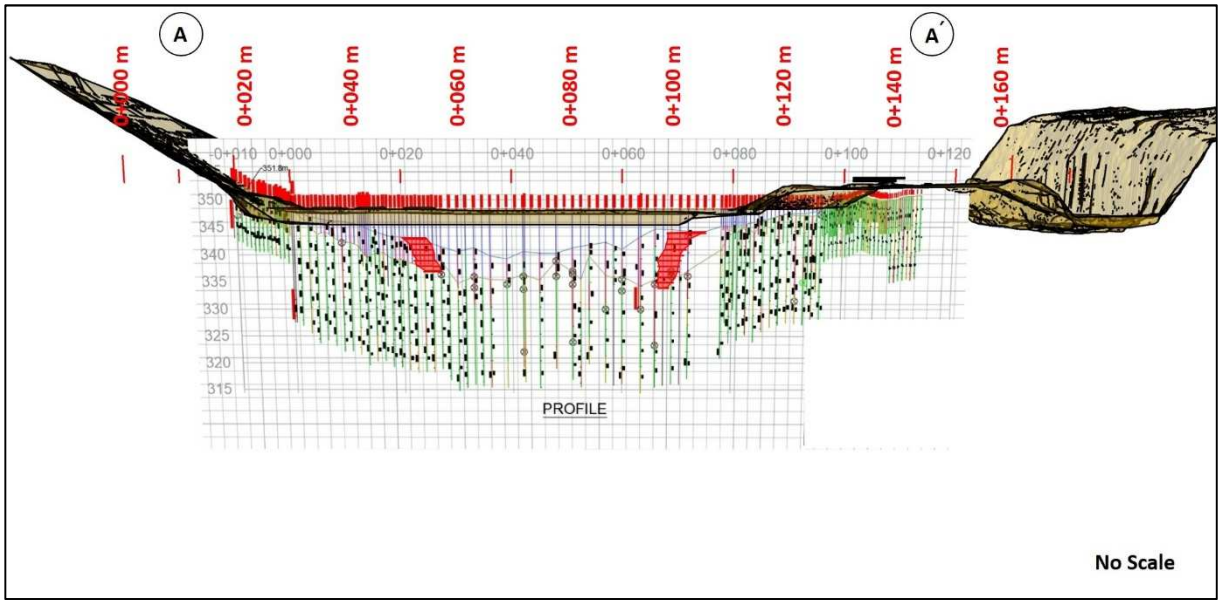

Fig. 6 – Flow Path Positions in Relation to Grout Curtains, Bedrock Surface, Native Gravels, and Earthfill Embankment Interface

As mentioned, the brown line identifies the top of the bedrock. The blue line identifies the top of native gravels. The preferential flow of electric current (red hatched area) is located above the bedrock surface in native gravels and below the embankment fill.

The MSR results revealed several weak areas at or just below the bedrock surface with a few deeper anomalous features noted (i.e., representing possible fracture or faulted zones - see Fig. 7). Please know that the MSR line shown in Fig. 7 is taken upstream of Section A-A´ (centre line of dam roughly 4 metres).

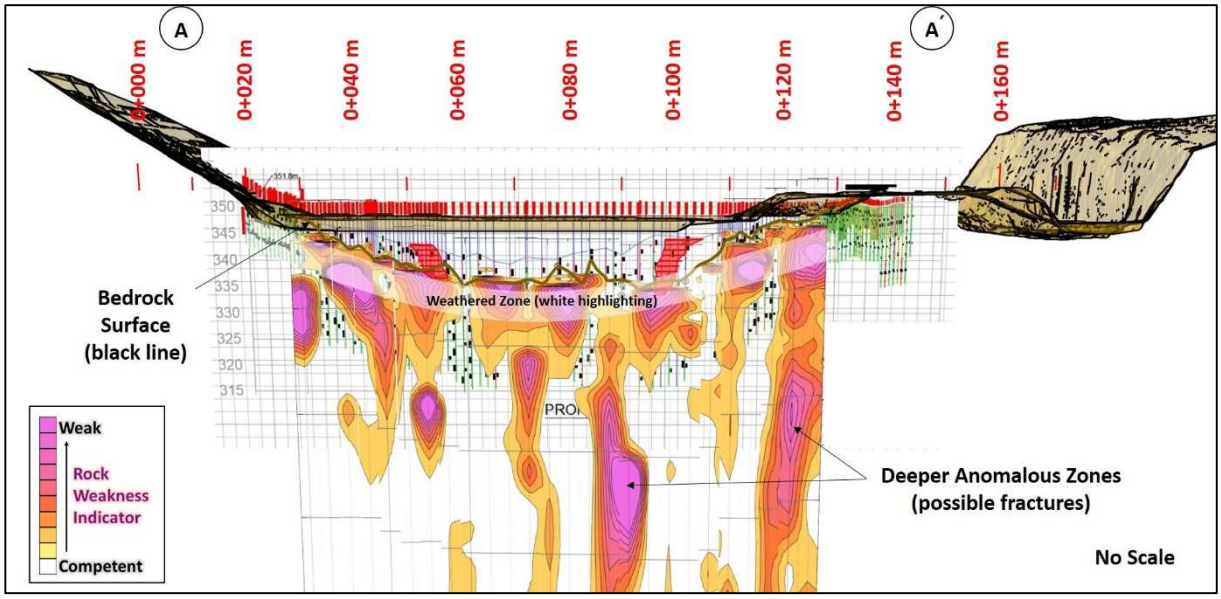

Fig. 7 - MSR Line 1

In Fig. 8, the white shaded areas on the MSR profile indicates competent soil and rock. The yellow to orange to pink shading, going up the scale, represents higher degrees of soil/rock weakness - strong pink shading representing the weakest, most highly fractured or weathered and permeable zones. The transparent white parabola identifies what is interpreted as a weathered zone located in the upper reaches of the bedrock formation. The anomalous vertical features identify what is interpreted as deeper fractures. The bedrock grout curtain appears to extend down through the weathered zone. We did not see any evidence from the Willowstick method suggesting that electric current preferentially flows at depth through the deeper vertical anomalous features observed in the MSR profile.

During a conference call with the owner and grout contractor, wherein the preliminary results of the investigation were presented, the grouting contractor revealed that larger than expected grout takes occurred in the centre of the grout curtain. Figs. 8 and 9 present two views of the 3D site model with an electric current distribution iso-surface embedded in the model. Fig. 8 shows a view of the iso-surface from above looking downstream through the grout curtain, whereas Fig. 9 shows a view of the iso-surface from above looking upstream through the grout curtain. The views clearly show that the signature electric current preferentially bifurcates and skirts around the centre area of the dam where grout takes were more than expected.

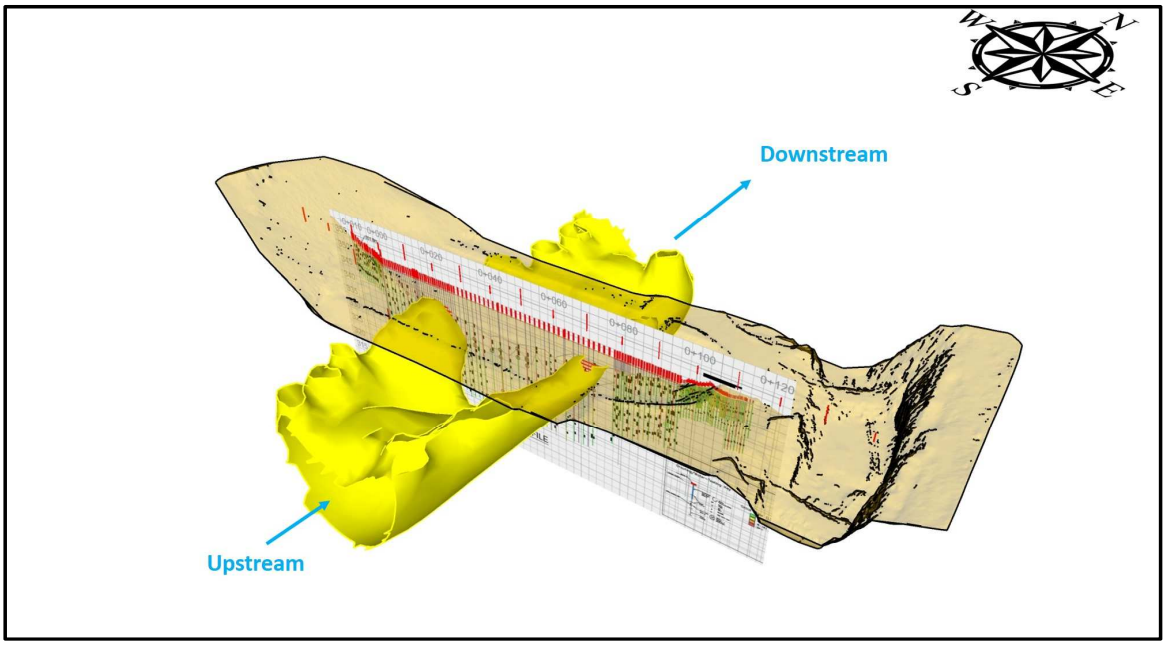

Fig. 8 - View of Iso-surface (looking downstream from above)

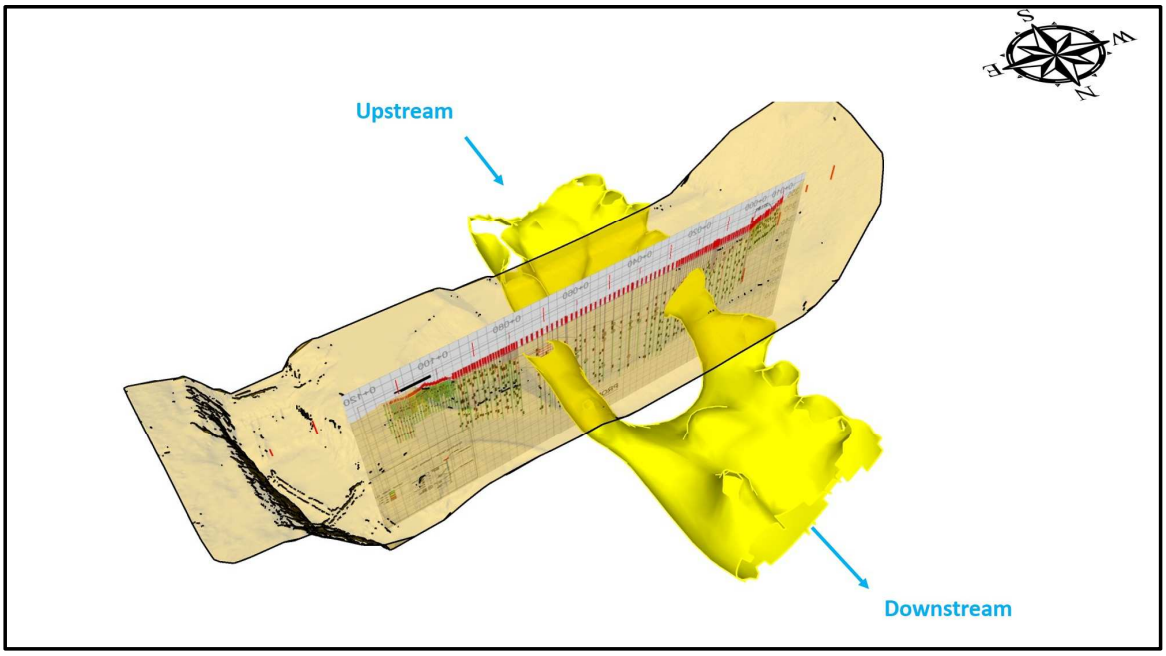

Fig. 9 - View of Iso-surface (looking upstream from above)

Based on the results of the Willowstick and MSR methodologies in conjunction with known grout takes, weaknesses were found in the native gravel layer on either side of the centre area of the grout curtain. Target locations were recommended for additional grout work to reduce potential seepage out of the reservoir. These locations are represented by the pink rectangular windows shown in Fig. 10.

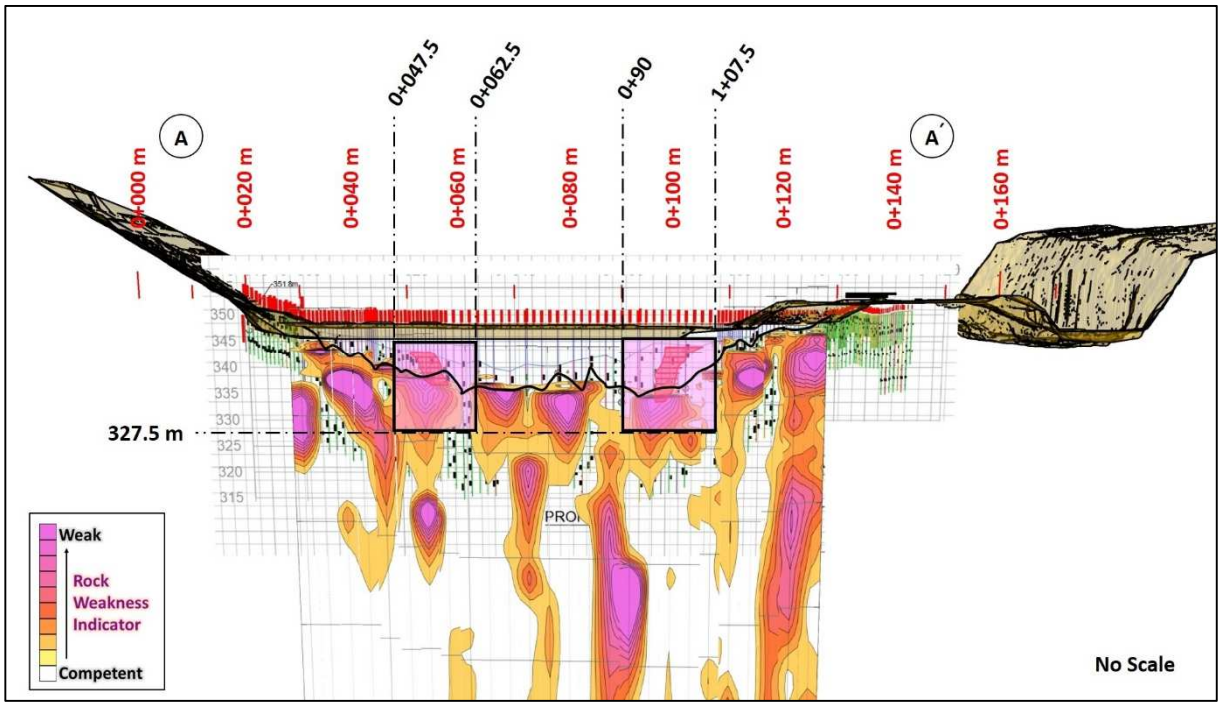

Fig. 10 - Target Windows to Reinforce Grout Curtain

The investigation identified two electrically conductive flow paths located in the native gravel layer on top of the weathered bedrock zone. The preferential flow of electric current along these flow paths was interpreted as highly probable pathways for seepage to follow as seepage escapes the impoundment. Seepage does not appear to preferentially flow through, beneath or around the grout curtain in any location other than that described.

The MSR resonance signal measures structural weaknesses in the dam's embankment and foundation where fractured and weathered rock or secondary porosity in permeable soils exists that can facilitate hydraulic conductivity through the grout curtain. It appears that in the area where grout takes were reported to be more than expected (i.e., centre area of the grout curtain), it's highly probable that the grout has filled voids in the weathered bedrock and porous zones in the native gravel layer; however, on either side of this area, it appears more grout was needed to minimise seepage. The fact that both methodologies identified common anomalous features and patterns (which use entirely different scientific principles) provides a great deal of confidence in the results of the investigation. As a result, the seepage investigation revealed highly probable electric current pathways and porous zones where seepage preferentially concentrates to leave the impoundment. The entire seepage investigation (fieldwork, data reduction, modelling and interpretation) was completed in roughly a week while the grouting contractor was on standby.

4. CASE STUDY 2 (U.S. DAM)

4.1 Background and Site Conditions

Following the completion of a modification to a dam and after filling the reservoir to its new high-water level, flow rates in the dam's seepage collection system increased, but stabilised and never exceeded threshold or action levels. However, two new wet spots appeared downstream of the right abutment on the hillside (outside the footprint of the dam's seepage collection system). It is reported that when the reservoir was at a high or a low water level, seepage was apparent in the seepage collection system. However, only when the reservoir is at a high-water level does seepage manifest in the wet areas observed downstream of the right abutment (at SW-5 and SW-6). The owner of the dam installed Weirs SW-5 and SW-6 to monitor seepage from these wet spots (see seepage locations in Fig. 11 - Site Map).

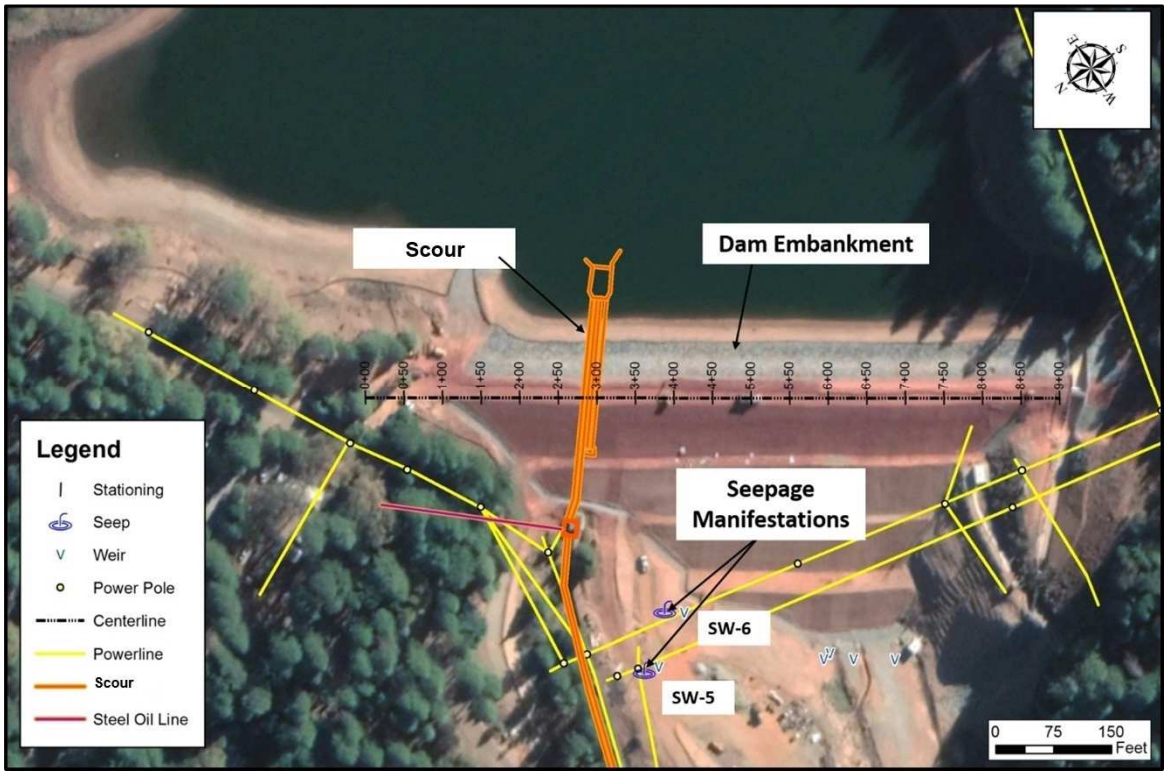

Fig. 11 – Site Map

The purpose of the geophysical investigation was to identify, map, and model the horizontal and vertical positions of seepage flow paths through, beneath, and around the dam, influencing the new wet areas observed downstream of the right abutment as well as identify the origin of seepage infiltrating the seepage collection system. A secondary purpose was to provide information on whether to and how to reduce seepage.

4.2 Results

The investigation first used the Willowstick Method to identify seepage flow paths. Only one common seepage flow path was identified beneath the dam contributing to seepage observed downstream of the embankment in both the wet areas and the seepage collection system (see Fig. 12).

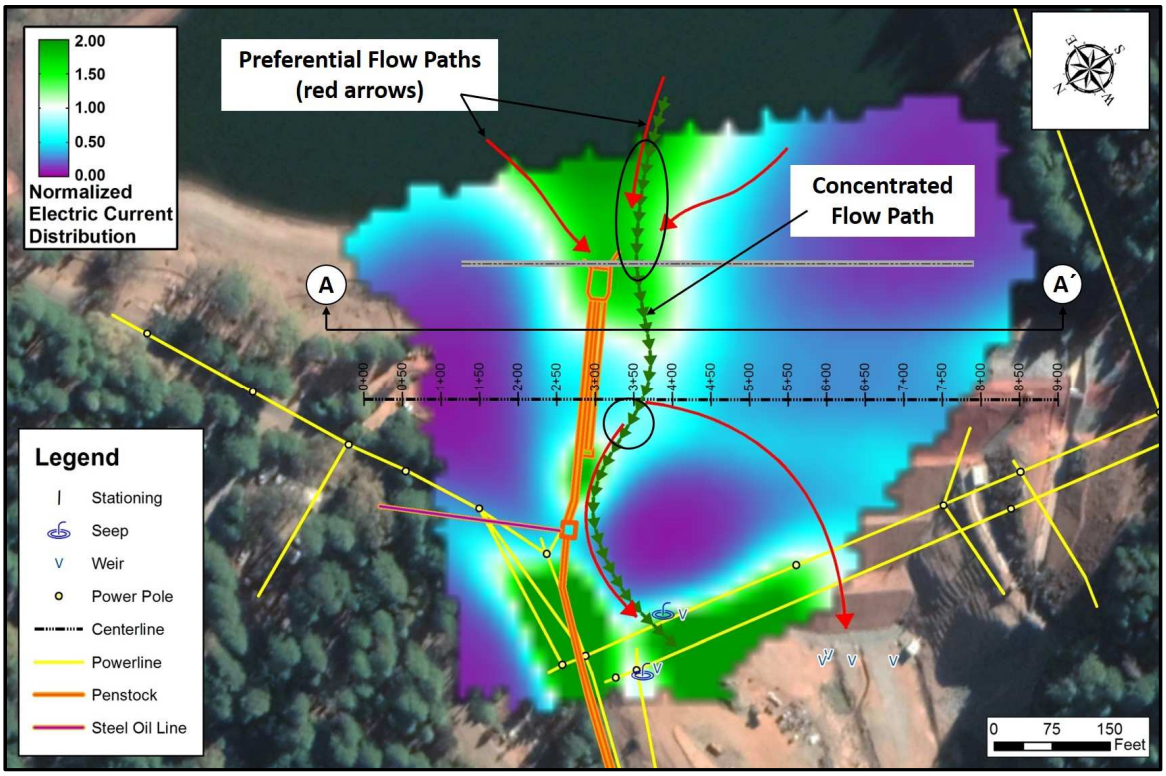

Fig. 12 - Summary of Willowstick Method Findings

Fig. 12 presents an Electric Current Distribution (ECD) model slice of the Willowstick method with interpretive markings taken at elevation 3,675 feet (1120 metres) - which is a good representative slice to begin a discussion about the preferential flow of electric current beneath the dam. For reference, the lowest elevation of the original dam's earthfill embankment is roughly elevation 3,700 feet (1127 metres). As such, this elevation slice is taken very close to the interface between the dam's homogeneous earthfill embankment and its underlying rock foundation.

In Fig. 12, the green shading represents areas where the signature electric current density is more concentrated than expected. On the other end of the scale, the dark-purple shading identifies areas where electric current is less concentrated. The red arrows highlight the more intense locations where the signature electric current preferentially concentrates as it leaves the reservoir and appears central downstream of the dam - interpreted as following along a preferential seepage flow path out of the reservoir. The grey-highlighted black dashed line upstream of the crest identifies the approximate upstream toe of the embankment. The dark green line with recurrent arrowheads identifies a seepage flow path zone in what will be shown as a highly weathered and/or fractured bedrock zone that crosses beneath the dam (having a northwest/southeast orientation). The black ellipse positioned upstream of the dam crest identifies where electric current is most concentrated as it infiltrates beneath the upstream toe (i.e., see converging thin red arrows upstream of the crest). The black circle located downstream of the crest identifies where electric current appears to well-up toward the

seepage collection system as it flows beneath the embankment under reservoir head pressure (see thick red arrows downstream of the crest).

To further describe seepage flow beneath the dam, Fig. 13 (Section A-A′) presents a longitudinal profile slice of the ECD model taken 50 feet (15 metres) upstream of the centre axis of the dam.

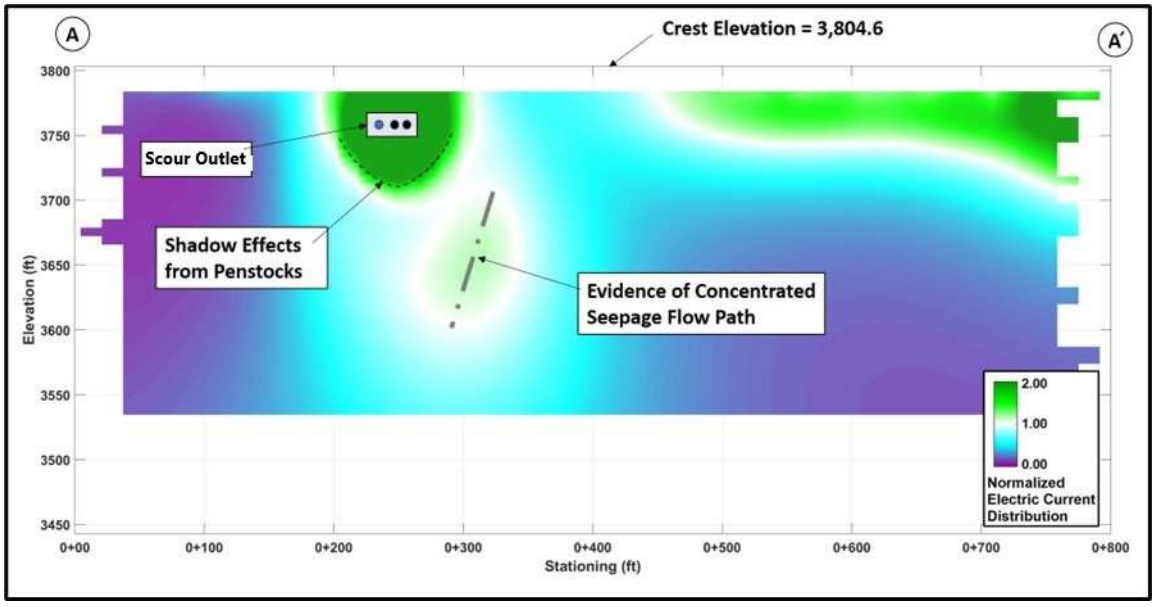

Fig. 13 - ECD Model Slice Section A-A' (looking upstream)

In Fig. 13, a long narrow anomalous feature was identified beneath and to the southwest side of the scour outlet. We anticipated that some of the signature electric current would concentrate on the relatively conductive scour outlet. At first, we were concerned that the conductivity of the scour might blind or hide any evidence of seepage through this area of the dam. However, there was no other area along the upstream face of the dam where electric current preferentially concentrated as the signature electric current left the reservoir. After having inverted the data, an anomalous electric current flow path emerged from the data set identifying the primary seepage flow path influencing seepage observed downstream of the dam. Since we observed only the one electric current flow path in front of the dam, it became apparent that seepage concentrated in this one flow path infiltrating and increasing flow into the seepage collection system as the reservoir level rises. The route of the seepage path was found to be under the original embankment. As the reservoir level increased, it became apparent that seepage was not all collected in the seepage collection system, with most seepage (up to 11 litres/second) infiltrating and discharging through the seepage collection system. However, some seepage (less than 0.38 litres/second total) follows along a flow path when under higher reservoir elevation pressure and eventually manifests downstream of the embankment as evidenced by the wet areas at SW-5 and SW-6 (see thin red arrow downstream of the crest and adjacent to the scour).

To further confirm and characterise the presence of an apparent weathered or fractured zone beneath the dam that seepage follows, we utilised the MSR method specifically designed to detect and characterise highly weathered and/or fractured zones. MSR measurements were taken at 16 foot (5 metre) intervals along the downstream edge of the crest and on Bench 1 (the upstream-most bench) over the suspect weathered/fractured area. MSR measurements cannot be taken over water or where the surface has a protective riprap blanket. Therefore, the crest and Bench 1 were the most accessible areas to gather MSR measurements crossing over the suspect seepage zone.

Fig. 14 presents the results of MSR survey line 1 (taken along the downstream edge of the crest and looking upstream). For reference, the elevation of the crest is 3804.6 feet (1160 metres) and the scour invert is at El 3748.9 feet (1142 metres).

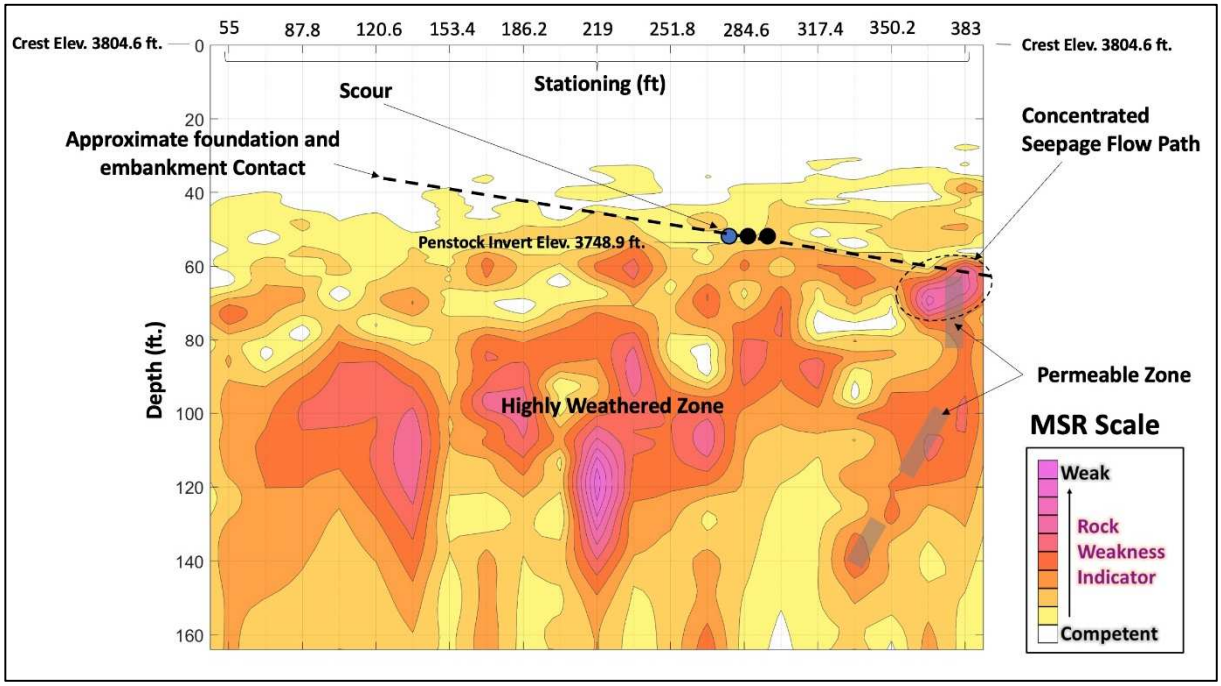

Fig. 14 - Dam Crest MSR Line 1 (Cross Section Looking Upstream)

Fig. 15 presents the results of MSR survey line 2 (taken along Bench 1).

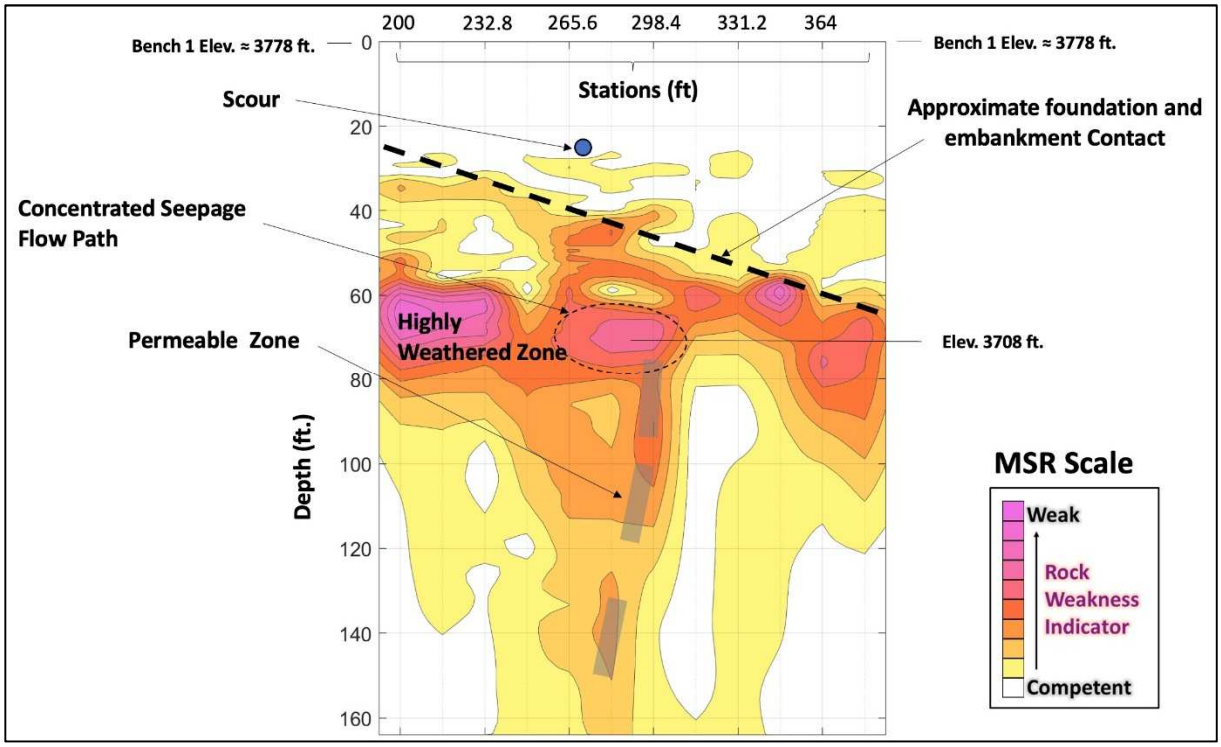

Fig. 15 - Bench 1 MSR Line 2 (Cross Section Looking Upstream)

In Figs.14 and 15, the white colour indicates competent soil and rock. The yellow to orange to pink colours, going up the scale, represent higher degrees of soil/rock weakness - strong pink shading representing the weakest, most highly fractured or weathered and permeable zones. The thick dashed black sloping line approximates the northeast abutting hillside (i.e., right embankment-foundation abutment contact). The blue dot identifies the approximate location of the scour. The thick dashed grey line (almost vertical) identifies what is interpreted as a permeable zone beneath the dam. This anomalous zone aligns with the nearly vertical anomaly observed in Willowstick method. The MSR and Willowstick survey data sets appear to corroborate the presence of a highly weathered and/or fractured zone in this location (see Figure 16).

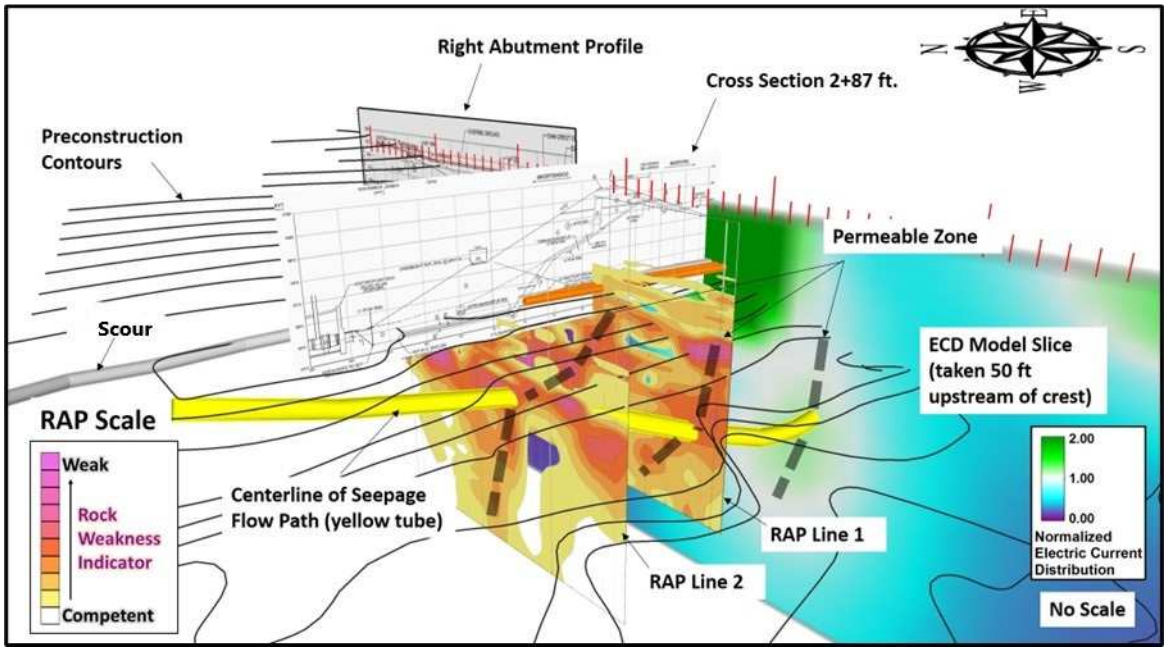

Fig. 16 - 3D Model View of Concentrated Seepage Flow Path (Looking Upstream and from Left to Right Abutment)

In Figure 16, the yellow tube represents the centreline of the more concentrated flow of electric current beneath the crest and downstream face of the dam. An ECD model profile slice is turned “on” in the figure, which is positioned 50 feet (15 metres) upstream of the crest showing the approximate depth and location of the preferential flow of electric current. Both MSR lines 1 (dam crest) and 2 (upper bench) are also turned “on” in the model view for comparison with the ECD model slice. The yellow tube and thick grey almost vertical dashed lines identify where electric current and seepage is concentrated, and where the foundation rock is most pervious. It appears that seepage infiltrating the drainage collection system and manifesting downstream of the right abutment originates from the reservoir along a common seepage flow path (left of, and below the scour) which originates beneath the embankment, influencing seepage observed in the seepage drainage system during low water events and in both the seepage collection system and wet areas during high water events.

The fact that both methodologies, which use entirely different physical and scientific principles, identified the same anomalous features and patterns, provided a great deal of confidence in the results of the investigation. As a result, the seepage investigation revealed highly probable locations where seepage leaves the reservoir and gets into the seepage collection system and wet areas downstream of the dam.

5. CONCLUSIONS

Willowstick has effectively utilised the MSR method in conjunction with the traditional Willowstick Method on many highly successful seepage investigations at dam sites. The

geophysical techniques have yielded complimentary results, with both methods providing beneficial information about seepage locations. The traditional Willowstick Method tracks the preferential flow of electric current through, around or beneath dams, which is interpreted as highly probable pathways for seepage to follow as electric current preferentially leaves the reservoir. The MSR signal measures structural weaknesses (having secondary porosity and permeable zones) in the dam's fill and bedrock foundation that can facilitate hydraulic conductivity through, around or beneath the dam. Both methodologies, which use entirely different scientific principles, have identified similar anomalous features and patterns providing a great deal of confidence in the results of these investigations.

REFERENCES

[1] Jessop, M., Jardani, A., Revil, A., and Kofoed, V (2018). Magnetometric resistivity: A new approach to the detection of preferential flow paths in mine waste rock dumps, in press in Geophysical Journal International, https://doi.org/10.1093/gji/ggy275.

[2] Kofoed, V.O., Montgomery, J.R., Jeffery, R.N., Montgomery, N.R., Jessop, M.L., Wallace, M.J., Christensen, B.A., inventors (2017). "System for detecting a location of a subsurface channel". U.S. Patent 9,588,247.

[3] Jessop, M. L., Wallace, M. J., Qian, W., Montgomery, J. R., Jeffery, R., Kofoed, V. O., inventors (2014). "Subsurface hydrogeologic system modelling". U.S. Patent 8,688,423.

Fifth International
Dam World Conference
PORTUGAL • LISBON • LNEC • APRIL 13-17, 2025
dam world 2025

THE USE OF LEAKAGE DETECTION SYSTEMS TO IMPROVE RESERVOIR SAFETY AND DIRECT REMEDIAL WORKS

Dr Andy K Hughes[1]
Reservoirs & Dams Ltd

ABSTRACT

If you own a dam, then one of the biggest worries faced must be is it leaking, and even more worrying is it leaking undetected?

Most dams leak to some extent – in many cases it is a steady state situation, and we just monitor the flows. In other cases, we have to implement fixes/remedial works to stem the leakage.

When doing risk assessments, particularly for embankment dams, usually the highest contribution to the total probability of failure relates to internal erosion, and yet we often don't know if there are any leaks, and whether the flows are through, around or under the structure.

If one is able to identify whether there are leakage paths through, under or around a dam then you can look at reducing the levels of uncertainty in trying to predict the probability of failure. After predicting the probability of failure, a prioritised programme of capital works can be developed.

The use of leakage detection systems enables an owner to be more confident about the safety of the structure. If a leakage path can be plotted in both plan and elevation, then targeted remedial works can be put in place. Thus, the total level of probability of failure can be markedly reduced and allow the more effective use of capital monies.

This paper will describe a number of case studies, and how the results have allowed owners to better manage their portfolio of dams but also their capital expenditure and programme by the use of leakage detection methods.

Keywords: Leakage, Remedial, Detection, Probability

[1]andy.hughes@damsandreservoirs.co.uk, UK

1. INTRODUCTION

As anyone who owns a dam knows, a dam, as a piece of infrastructure, can be a liability as well as an asset. When the water contained within a reservoir is used, whether it is for hydropower production, water supply or the reservoir is used for amenity use, river regulation, or flood attenuation, then the owner is willing to expend monies to try to ensure the safety and integrity of their structure. However, if the reservoir is no longer used for the purpose for which it has been built, and it has not been 're-purposed' then there is often a reluctance to spend money on the structure. However, in many cases, the owners' legal responsibilities have not changed, and should a failure occur then the repercussions would often be the same, whether the reservoir is put to beneficial use or not.

Thus, an owner with a portfolio of dams and reservoirs will also be facing a demand, and often a conflicting demand, on their resources. Those resources can be manpower but more often or not it is money. The difficult question that the owner faces with limited resources, is "what should be my priority – what should I do first?". Many of the larger water companies and power generating companies in the UK and overseas have portfolios in excess of 100 dams and thus the problem of prioritisation of works with limited resources becomes a significant problem.

In terms of liabilities which a company faces clearly if a failure occurs, there are the liabilities associated with the failure of that structure and the resulting consequences of the failure. This could lead to legal actions for the losses suffered by those affected downstream and these actions will be particularly uncomfortable if there is loss of life. It is likely that legal challenges could be made of those directors, engineers etc within an organisation or indeed outside the organisation who are deemed to be part of the group who try to ensure the safety of the structure.

When discussing the levels of risk that a company is taking at any point in time, I often say to directors that lack of investment in reservoir safety, should a failure occur, could result in the company losing its operating licence, whether or not there has been loss of life. Indeed, the reputational loss and reduction in share price could cause the collapse of the business.

Attempts will be made in any action to prove negligence which could be very uncomfortable for all involved. Thus, an owner will and should strive to bring their reservoirs up to the best standard and use their best endeavours to ensure safety. My advice is always to do enough to defend oneself in a court of law, particularly if you could be compared with other owners with a similar stock of dams. In addition, one must question whether you could have done more and used the most up to date means to try to ensure dam safety; if the answer is no then you may have no defence or certainly limit your defence.

2. DRIVERS

The ‘drivers’ to carry out works at a reservoir, can come from a number of sources, mainly associated with the UK’s legal framework associated with reservoirs. These include:

- The owners’ own expertise can drive investigations and schemes either across the whole portfolio or at a particular site where they detect a change in condition or may just be worried about the consequence of failure;
- The Supervising Engineer can call for an inspection by an independent Inspecting Engineer (IE) if he is worried about the deterioration or the condition of the dam;
- The Inspecting Engineer (IE) in his statutory inspection make recommendations in the interests of safety (MITIOS) that must be carried out which might include a review of dam performance with respect to leakage and perhaps are follow-on remedial works.

Currently there is no legal requirement to carry out formal qualitative or quantitative risk assessment within the UK legislative framework, but some companies do carry out quality risk analyses.

The author has been involved in risk assessments, leakage detection and the design and implementation of remedial plans, using in particular the Willowstick process, for nearly 40 years. He describes the use of the techniques in one of three ways:

(1) **Reactive** – the dam springs a leak, or a leak gets worse and it is almost an emergency situation.
(2) **Proactive** – a company is worried about leaks is not sure whether they are present or not, or if there is a leak does it threaten the safety of the dam.
(3) **Asset Management** – where an owner with a large portfolio of dams wants to prioritise remedial works and reduce the overall risk to the company.

3. THE WILLOWSTICK TECHNIQUE

What is Willowstick? – well it is the most useful leakage detection system the author has found. Willowstick is a Micro Seismic Resonance (MSR) technology, utilising a 380H_z signal to maximise the coil magnetometer sensitivity whilst avoiding all harmonics of traditional 60 or 50 H_z power sources.

In simple terms, an electrode is placed upstream and another downstream of the zone of interest (e.g. a dam) and a ‘signature’ electric current is applied between the electrodes. This electric current sets up magnetic fields between the electrodes producing a uniform magnetic field. If there is a leak the water is a better conductor than the earthfill and so the magnetic

field is altered by the flow of water and the magnetic field is modified. If the intensity of the magnetic field is measured, on a grid basis, then those areas of disturbance can be plotted, in plan, and an algorithm is used to find the depth of the flow path. Measurements can be taken all over the dam, on to the abutments, and on the water. It is a high speed, accurate, non-invasive system of tracking individual leakage paths. In summary, it is a non-intrusive technique which enables individual leakage paths both in plan and elevation.

The technique allows individual flow paths to be identified through, under and around a dam which then allows targeted remedial works. The author has successfully used the technique to more than 200 metres below the foundation of a dam and on more than 100 sites.

4. APPROACHES

In carrying out risk assessments one Water Company was the first to use the methodologies developed in the United States. Later the methodologies were adapted for use in the United Kingdom – some 15-20 years ago as an asset management tool. This enabled them to focus on failure mode assessments and to make attempts to identify those reservoirs with the highest risk of failure. That was used to understand the ‘total risk’ profile carried by the company and where the resources could be best targeted to achieve the biggest reduction in ‘risk’ which the country tolerates.

In Fig. 1, this shows the total risk profile for a portfolio of a significant number of dams.

Each step in the risk profile for the company shows the effect of capital investment to reduce the probability of failure of an individual dam. The company may have an ambition to achieve a lower level of risk than a ‘standard’ level of risk.

The blue line shows a strategy where capital is invested in those dams where the risk reduction is largest.

Clearly the ‘blue’ strategy is better than the ‘red’ strategy because the risk is reduced quickly and also the capital expenditure may be less.

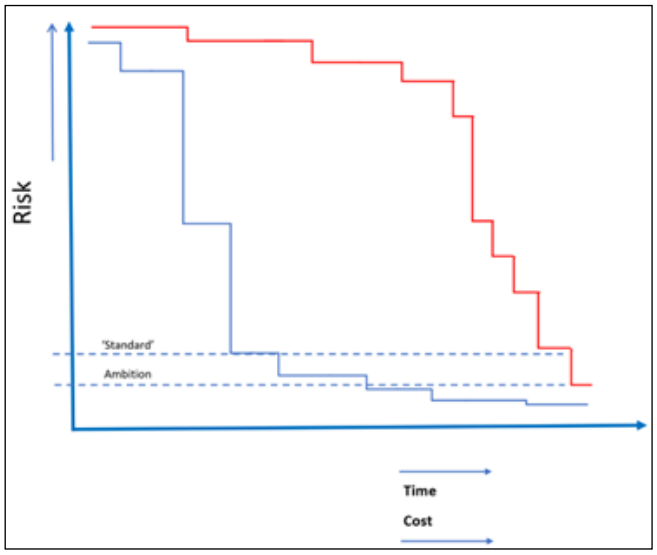

Fig. 1 – Total Risk Profile (Risk v Time & Cost)

In the scenario described, it is possible to prioritise works in different ways:

- perhaps in terms of the probability of failure – the highest probability site to be fixed first.
- perhaps in terms of consequence of failure – fixing the dam first where the consequence of failure, whether cost or lives lost, or both are highest.
- perhaps when the dam was the only water supply to the area and the loss of supply would be very difficult to replace or manage.

What is apparent in this exercise was that the system is very dependent on data and information. Lack of information can result in a lack of consistency in application and thus lack of applicability. Clearly the use of risk assessment across a portfolio is a dynamic situation in as much as data will be lacking, new data will be received all the time, and the results of previous analysis will have to be revisited. In my opinion, risk assessment techniques must be applied via a staged approach. As you move from a qualitative to a quantitative or even semi-quantitative analysis you need much more consistent and accurate information and also trained practitioners in risk assessment. In many cases, at least initially, it is not necessary to generate a ‘number’ and the process can be used as a ‘comparative exercise’ in order to rank reservoirs/dams in terms of the highest risk of failure. Again, in my opinion, the most important element of any risk assessment is sitting down and thinking about the structure and identifying all of the potential failure modes and evaluating a Failure Modes and Effects Analysis (FMEA).

In assessing the modes of failure, it is common certainly where most of the dams are embankment dams, for the three main modes of failure for embankment dams to be overtopping as a result of inadequate spillway capacity, instability, or seepage/leakage/piping failure. In many cases it is the seepage/leakage element which is the largest driver of the

probability, and this is because many spillways have been constructed in the UK following the publication of a means of assessing floods – the Flood Studies Report of 1974[2] and the Flood Estimation Handbook (1999)[3] - stability can be assessed by tried and tested analytical techniques supported by perhaps some limited site investigation, and signs of instability can be seen. However, leakage and piping may not be seen and the probability of failure due to seepage can be difficult to calculate. If a leakage survey system indicates no or little evidence of piping the overall probability of failure can be reduced.

5. OWNER 1

One owner, whose stock of some 50+ dams are very different to others in the UK. They have thin clay cores, but they also have shoulders constructed from sands and gravels and they sit on a foundation of sands and gravels, has adopted an approach which is rather different to others. In this situation any leakage which might be passing through the core or the cut-off might not be seen as it is unlikely to surface on the embankment or the toe and more likely to 'disappear' into the foundation via the shoulder.

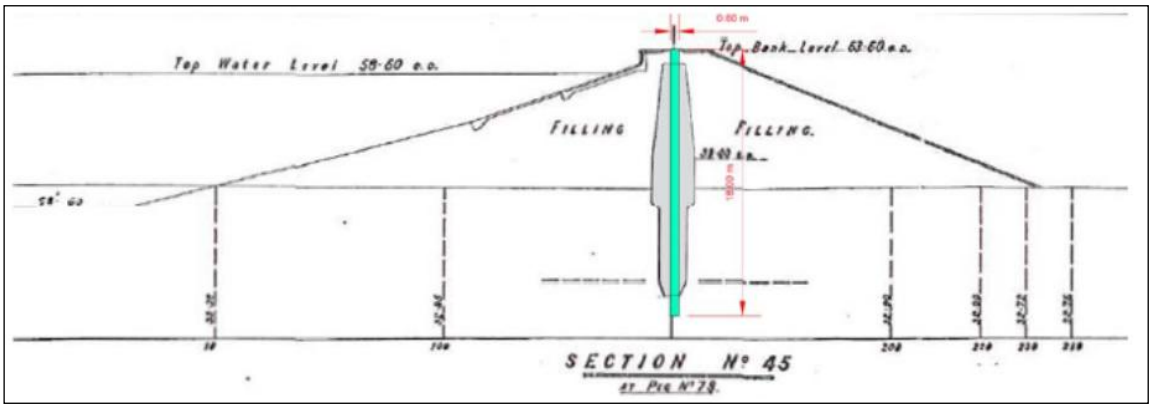

Fig. 2 – Cross Section including proposed diaphragm wall

Fig. 2 shows a cross-section common to dams in the portfolio. The dams have a very thin clay core taken down to a clay foundation about 15 metres below. The shoulders and the foundation are sands and gravels.

The cross-section also shows the typical 'fix' when it is found that the core is compromised. The remedial works involve either the installation of a sheet piled cut-off wall or a cement bentonite wall – but in both cases just over the length where the defect has been noted.

The owner has a very frequent monitoring and surveillance system involving a walkover at least every 48 hours and he has also initiated a programme of leakage surveys of every structure in the portfolio. This is a large undertaking particularly when some of the embankments have crest lengths in excess of 8 kilometres.

5.1 Results

Thus, if the uncertainty associated with leakage/seepage can be reduced and the probability of that element occurring evaluated, then the overall probability of failure can be reduced. Internal erosion is often the largest proportion of the total probability and so the reduction often results in a structure plotted on a fN chart, in the 'inacceptable zone' being moved to the 'tolerable zone'

BEFORE WILLOWSTICK

Name of Dam	Internal Erosion	Slope Stability	Foundation Failure	Total Probability
Dam 1	7.58E-04	2.80E-06	3.40E-06	7.64E-04

AFTER WILLOWSTICK

Name of Dam	Internal Erosion	Slope Stability	Foundation Failure	Total Probability
Dam 1	2.12E-06	2.80E-06	3.40E-06	8.32E-06

Fig. 3 – Risk Reduction

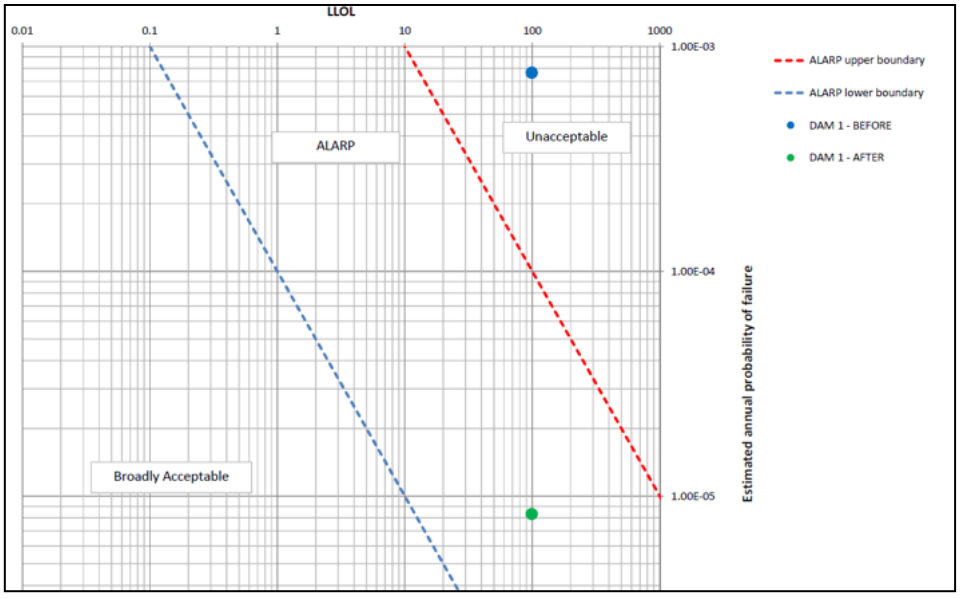

Fig. 4 - fN Chart – showing the benefit of a reduction in probability of failure after a Willowstick survey

Fig. 4 shows the benefit of reducing the uncertainty associated with the probability of failure, moving the element from the unacceptable zone to the ALARP zone. Leakage surveys[4] are being carried out on the complete stock over a period of some 5 years. As the surveys have been carried out a number of leaks have been discovered not known previously. Some have existed at the point at which the core enters the original ground, some at where the cut-off is

socketed into the underlying clay, and some where the original stream channels have not been cut off.

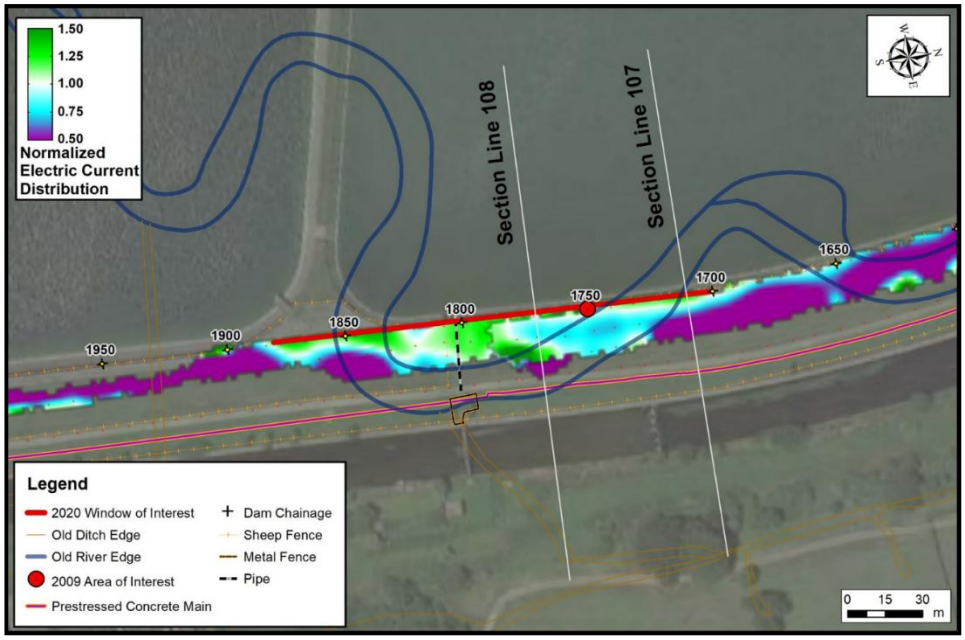

Fig. 5 - Leakage zone between Chainages 1750 and 1850

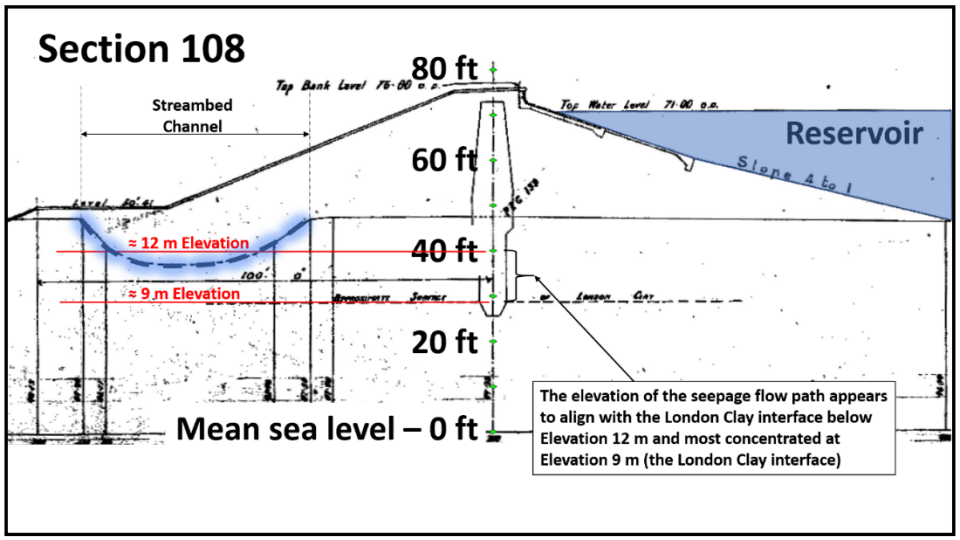

Fig. 6 - Cross Section of reservoir at Chainage 1700

Figs. 5 and 6 show the position of the original stream channel and the green shading in Fig. 5 shows the position of leakage.

In following a very responsible approach to reservoir safety and recognising the failure mode considered could progress quickly, unseen with this type of dam, this owner instigated a series of remedial works contracts to cut off the leaks. The chosen method, in most cases, was to drive sheet piles through the core into the underlying foundation.

Fig. 7 - Installation of piles in the clay core.

As the leakage detection system targets the individual seepage paths, both in plan and elevation, the piles were only installed where the leakage paths were seen. Once the piles had been installed, and the working area reinstated the leakage survey was repeated to confirm the leakage paths had been cut off. By repeating the leakage survey every 5 years the company is able to detect any deterioration of the structure. They believe they have used the best techniques available to them and can demonstrate that their best endeavours have been used to ensure reservoir safety for reservoirs where the speed of failure, if the warning signs are not detected or recognised, could be very fast and the consequences of failure is in the billions of pounds – the highest 'consequence' dams in the UK.

6. OWNER 2

Owner 2 has a much larger, older portfolio of dams and has been more active in using risk assessment and associated techniques to assist in their risk evaluation and capital programme.

The figures which follow (Figs. 8, 9 and 10) illustrate the process adopted, and which after a high level screening exercise, reviews the possible failure mechanisms for the dam. Again, it is the norm that piping failure/leakage contributes most to the total for the probability of failure. The USBR seepage toolbox (New South Wales Assessment Method)[5], adapted to be applicable to UK dams, is used, usually in a 2 day expert elicitation type workshop to evaluate the probability of failure for some of the 29 failure modes within the methodology, as illustrated in Figs. 8 and 9.

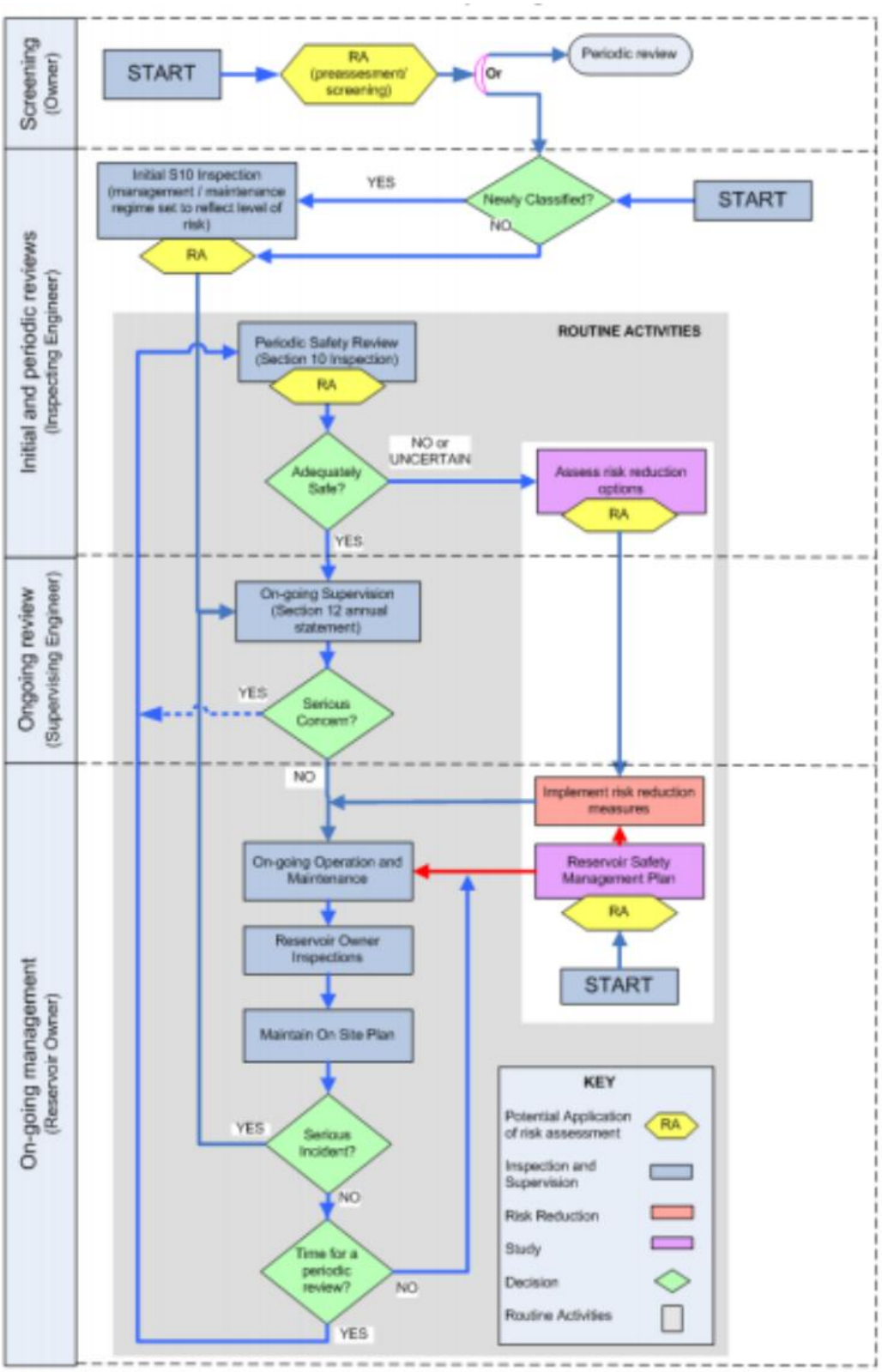

Fig. 8 - UK reservoir safety management process illustrating the potential role of risk assessment in decision making

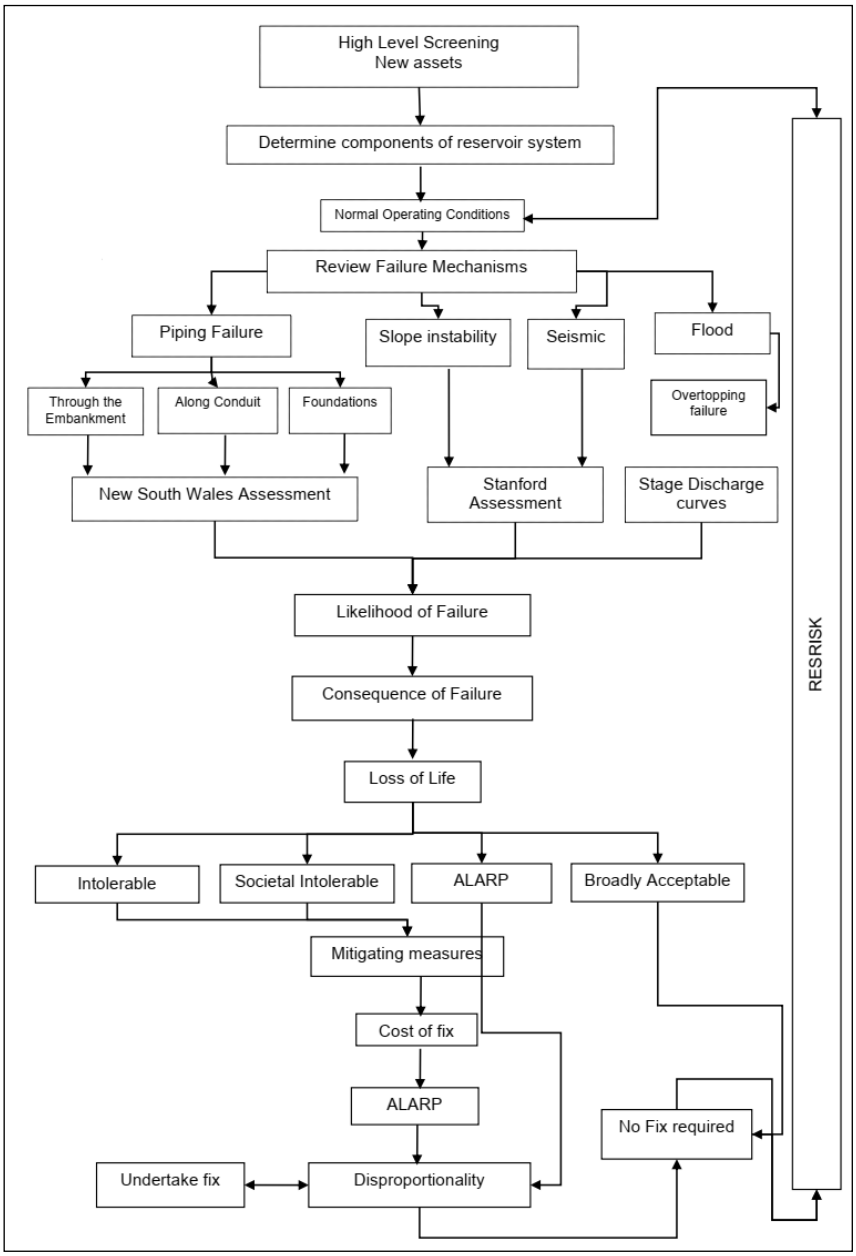

Fig. 9 - Portfolio Risk Assessment Process – Open Reservoirs

Having established the relevant failure modes, the company identifies any additional site investigation required to support the analyses and carries out a leakage survey to be able to confirm or otherwise whether the failure modes identified are active.

Potential solutions are then identified if the leaks are deemed in need of remediation (and not all are) and the associated risk reductions are evaluated as below in Fig. 10.

Solutions include piling, grouting, diaphragm walls and again the leakage survey allows the introduction of targeted solutions and repeat surveys can confirm the success of the solution chosen. Discontinuance, or the reduction of the top water level can also be used as a solution.

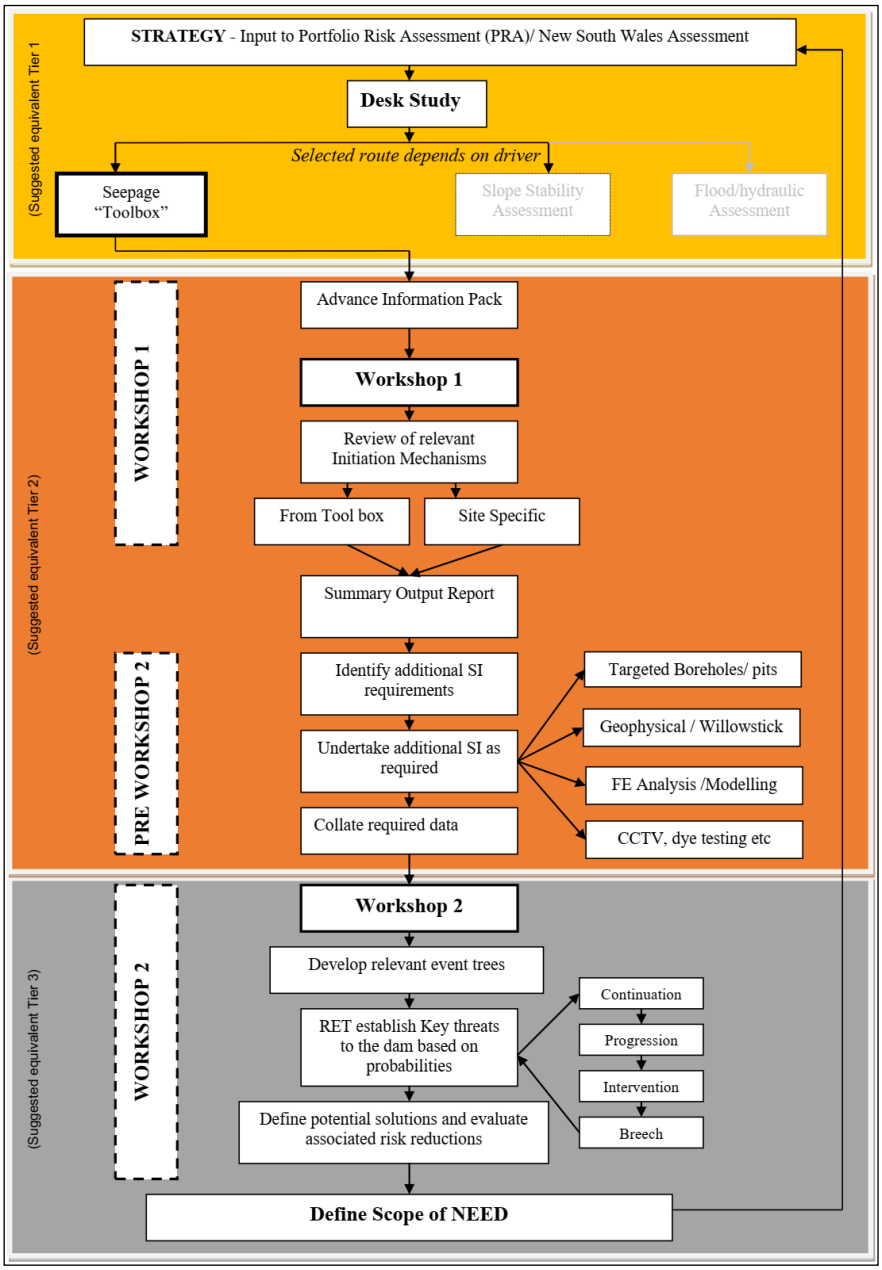

Fig. 10 - Seepage Toolbox Assessment Process

7. CONCLUSION

The paper illustrates two different approaches by two of the large water supply companies in the UK who own significant numbers of reservoirs. Each approach, although different in the level of analysis, identified the largest contribution to the total probability of failure was due to leakage/piping and by using the best available techniques to track individual seepage paths both in plan and elevation has allowed the companies to progress targeted remedial works if deemed necessary.

REFERENCES

[1] “Reservoirs Act 1975”, HMSO

[2] Flood Studies Report, (1974) NERC, HMSO, UK.

[3] Flood Estimation Handbook (1999) Centre for Ecology & Hydrology

[4] Willowstick Surveys for the owners’ reservoirs – recent surveys

[5] “Risk Analysis for Dam Safety (2008) – A United Method for Estimating Probabilities of Failure of Embankment Dams” USBR

Fifth International Dam World Conference
PORTUGAL • LISBON • LNEC • APRIL 13-17, 2025
dam world 2025

SELECTION OF THE CRITICAL STATE PARAMETER M FOR DEFORMATION ANALYSIS UNDER GENERALIZED STRESS PATHS

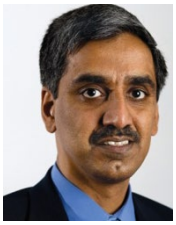

Aravind Murali
Klohn Crippen Berger

Vinayak Bangera
Carleton University

Elena Zabolotnii[1]
Carleton University

Siva Sivathayalan
Carleton University

ABSTRACT

The effect of the intermediate principal stress on the shear strength of granular materials has been long established experimentally. In critical state theory, its impact on the ultimate state is quantified through the critical stress ratio M=q/p, a variable that assumes different values depending on the intermediate stress (and consequently the Lode angle θ, or intermediate principal stress parameter b_σ). This paper examines the relationship between the angle of internal friction (a material property defining the Mohr-Coulomb failure criterion), the Lode angle, and the critical stress ratio M under the conditions of simple shear. Three literature-reported expressions and the exact derivation, all defining M as a function of these two variables (M=f(φ,θ)) are evaluated in this study. The findings have implications for the selection of inputs for critical theory based constitutive models (e.g., Cam-Clay, Modified Cam-Clay) for the deformation modelling of structures following stress paths other than triaxial compression and extension, e.g. natural slopes and manmade earthen embankments. The authors posit that, rather than specifying the M-value as a constant input, this parameter may be evaluated as a function of the evolving stresses. The implications for two-dimensional analysis are also discussed.

Keywords: Critical state theory, modified Cam-Clay, critical stress ratio, finite element slope analysis

[1]elenazabolotnii@cunet.carleton.ca, Canada

1. INTRODUCTION

1.1. Use of three-dimensional FEM analysis for embankment stability

In the past two decades, the geotechnical practitioners have faced growing challenges related to the mechanical stability of earthen embankments such as tailings storage facilities [1,2,3]. One solution advanced by the practice is known as “performance-based design”, the technique that consists of coupling advanced FEM analyses with monitoring data in order to achieve a better understanding of the mechanical behaviour of these structures over the duration of their construction and operation, improving our forecasting power [4,5].

There is a general agreement that three-dimensional FEM analyses are more accurate than their two-dimensional equivalents, in that they better capture the geometry of the problem as well as account for stabilizing effects overlooked in 2D [6]. Three-dimensional stress states and their effects on the stability of embankments are less explored, albeit researchers have long established that these have an impact on the soil’s response [9,13,15]. As the use of three-dimensional FEM analysis at operational scale is significantly more challenging compared to the 2D formulation owing to higher computational demands, it is of interest to establish the full range of 3D effects that may impact stability assessments, including those related to stresses as determined by 2D and 3D solutions, so that practical decisions can be made. This paper focuses on one such aspect of FEM solutions.

1.2. Objectives

The concept that a soil undergoing shearing eventually reaches and maintains indefinitely a constant state of stress and strain is foundational to critical state theory. This critical state is described through the “critical stress ratio” denoted by *M*, defined as the ratio of deviatoric to spherical stress components:

$$M = \frac{\mathrm{q}}{\mathrm{p}} = \frac{\sqrt{3J_2}}{I_1} \tag{1}$$

The three-dimensionality of this criterion, evident from Eq. 1, was recognized early on and firmly established from experimentation [9,13,15], thus demonstrating its dependence on the intermediate stress σ_2. For the simpler cases of triaxial extension ((σ_2=σ_1) and triaxial compression (σ_2=σ_3), [13] introduce equations for deriving M using the material property φ, angle of internal friction:

$$M_{TE} = \frac{6\sin\varphi}{3+\sin\varphi} \tag{2}$$

$$M_{TC} = \frac{6\sin\varphi}{3-\sin\varphi} \tag{3}$$

However, a general relationship correlating σ_2 and M is not offered by the proponents of the critical state theory [11,12,13]. Throughout most of 20th Century, finite element modelling, which offers the means for evaluating constitutive models based in critical state theory, was largely two-dimensional and thus did not provide for a σ_2 calculation. In consequence, the implementation of such constitutive models (e.g., CamClay, Modified CamClay) necessitated assumptions to be made regarding σ_2 and the value of M. The authors note that the implementations of these models in software typically require the input of a constant M value. This may be adequate for simulating controlled stress states (such as simple laboratory tests); however, the complexity of stress paths in slopes may not be adequately captured by such simplification.

This paper presents an evaluation of several relationships establishing the value of the critical stress ratio M as a function of the intermediate stress σ_2 and the internal angle of friction φ, in three-dimensional simulations involving generalized stress states (e.g., $\sigma_2 \neq \sigma_1$ and $\sigma_2 \neq \sigma_3$) using the Modified CamClay model. The implications for practitioners of geotechnical engineering using this or similar constitutive models to evaluate structures are then presented.

2. THEORY

An examination of the geotechnical literature yields several published relationships relating the critical stress ratio M to the three-dimensional stress state. [16] introduce Eq. 4 below:

$$M = \frac{2\alpha M_{TC}}{1+\alpha-(1-\alpha)\sin 3\theta} \tag{4}$$

where Lode angle $\theta = \tan^{-1}\left[\frac{1-2b_\sigma}{\sqrt{3}}\right]$, $b_\sigma = \frac{\sigma_2-\sigma_3}{\sigma_1-\sigma_2}$ and $\alpha = \frac{3-\sin\varphi'}{3+\sin\varphi'}$. The justification for this relationship is somewhat unclear from the paper, but it produces a yield surface that is reasonably close to the well-known Morh-Coulomb "hexagonal cone" in the principal stress state while also being continuous and convex at all points (i.e., differentiable) for φ values <22˚, a computational advantage over the Mohr-Coulomb criterion which at the vertices corresponding to triaxial compression and extension has a discontinuous derivative. Noting that for φ values >22˚, the surface becomes concave, [14] proposes a modification to Eq. 4 which remains convex for φ<49˚, a range that is more appropriate for application in soils:

$$M = M_{TC}\left[\frac{2\alpha^4}{1+\alpha^4-(1-\alpha^4)\sin 3\theta}\right]^{1/4} \tag{5}$$

Another relationship is reported by [8]:

$$M = M_{TC}\left[1 - \frac{M_{TC}}{3 + M_{TC}}\cos\left\{\frac{3\theta}{2} + \frac{\pi}{4}\right\}\right] \quad (6)$$

It can be shown through algebraic transformations of Eq. 1 and using identities herein for b_σ and Θ that the exact relationship between σ_2, φ and M for cohesionless Mohr-Coulomb soils can be expressed through Eq. 7 below:

$$M = \frac{3\ \sin\varphi'}{\cos\theta\ (\sqrt{3} -\ \sin\varphi' \tan\theta)} \quad (7)$$

For the triaxial compression (b_σ=0 or $\theta = +30°$) and extension (b_σ=1 or $\theta = -30°$) conditions, the expressions in Eqs. 4-7 all simplify to match Eqs. 2 and 3 respectively. It is also worth noting for the range of b_σ values corresponding to simple shear (b_σ=0.35…0.40), Eqs. 4-6 yield close values (Fig. 1). In consequence, all these expressions could be used to simulate these three tests without expecting much differentiation; yet it is unclear how well any or all of these expressions capture the real behaviour of soils under complex stress paths.

2.1. Method

To evaluate the four expressions for M, a series of numerical simulations were conducted in Itasca's FLAC3D using its implementation of the constitutive model Modified CamClay along with some custom code.

Multi-element simulations of soil under direct simple shear

The code by [10] simulating the direct simple shear (DSS) test was used to evaluate the response of Modified CamClay using initial consolidation pressures of 100 and 400 kPa combined with an overconsolidation ratio OCR=1. The code provides for realistic geometry and boundary conditions (e.g., unrestricted internal drainage with no-drainage boundaries) and is a multi-element simulation, allowing for the development of 3D stresses (in contrast with single-element simulations whereby plane strain conditions along the sides would preclude a true 3D response).

FLAC3D's implementation of Modified CamClay provides for the input of a constant M value and the manual advises determining it by carrying out a series of triaxial tests to large strains.

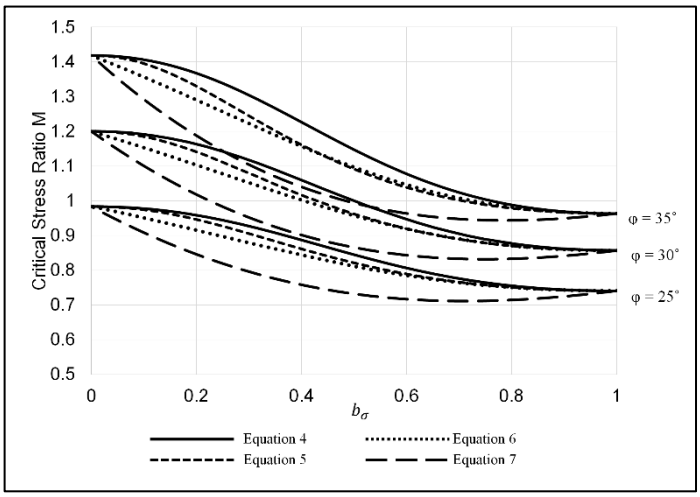

Fig. 1 Plots of the critical stress ratio M as a function of b_σ calculated using Eqs. 4-7.

In these tests, the b_σ values are different from those of soils under simple shear; this suggests that using M values based on Eqs. 1 or 2 may not be appropriate in simulations of DSS tests. From the literature, soils subjected to simple shearing experience, at critical state, stress conditions corresponding to b_σ=0.25…0.4 [7] and in FLAC3D, the steady-state b_σ value is 0.5. Therefore, simulations were completed to compare the response using updated M values with the base case of constant M value set using either the assumption of triaxial compression condition or calculated using Eq. 7, thus allowing for an evaluation the expressions for M but also of the impact of the stress path on the response.

Parametric slope

In laboratory tests, steady state stress states (and, in consequence, M values) are known; this is not so with in-situ structures such as natural slopes or dams. These structures follow generalized stress paths, and the M values vary throughout the domain both in time and in space. Therefore, specifying a constant M input using any of the expressions discussed here or elsewhere in literature would not be ideal; and the approach of updating M spatially as the stress states evolve might be a more appropriate approach, at least in theory.

To evaluate the effect of parameter M in simulations of such conditions, a parametric study of a generic slope was conducted using (i) Eq. 7, (ii) $M_{const}=M_{DSS}$ and (iii) $M_{const}=M_{TC}$. The analysis geometry is illustrated in Fig. 2; an angle of internal friction φ=30˚ was used for all three cases.

3. RESULTS

3.1. DSS test simulations

Eleven simulations of the DSS test were completed: six with an initial vertical consolidation stress σ_{cv} of 100 kPa and another five with a σ_{cv} value of 400 kPa; all use an overconsolidation ratio OCR=1 and an angle of internal friction φ=30˚. Aside from the initial consolidation stresses, these simulations are differentiated by how the critical stress ratio M is applied: 8 simulations use Eqs. 4-7 respectively to continuously update this value throughout the domain as a function of evolving stresses, and the other three apply a constant M value.

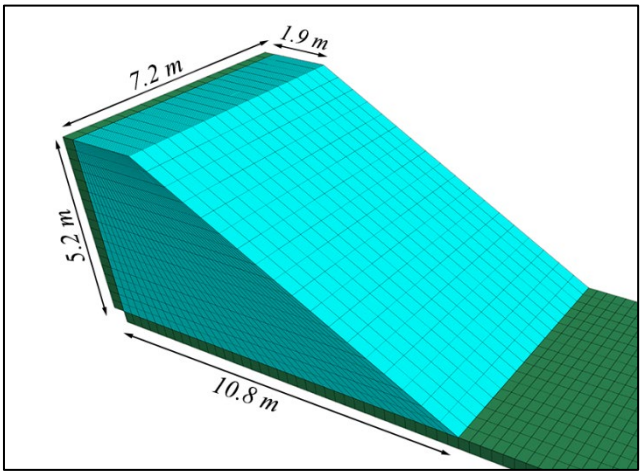

Fig. 2 Parametric slope geometry.

Fig. 3 illustrates the p-q and τ_{xz}-γ_{xz} responses of these simulations. These data represent averages from twelve points distributed uniformly throughout the domain. These results exhibit a notable

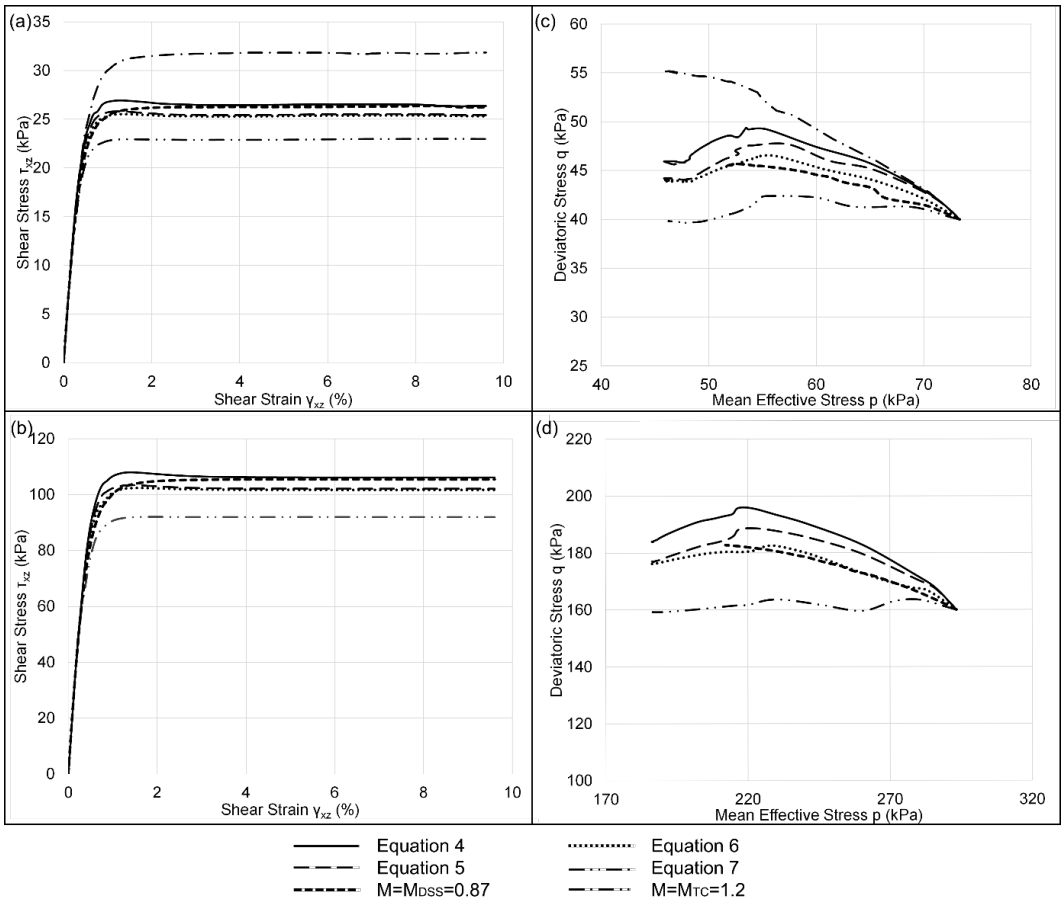

Fig. 3 (a,c) Simulation responses for initial consolidation stress σ_{cv}=100 kPa and OCR=1. (b,d) Simulation responses for initial consolidation stress σ_{cv}=400 kPa and OCR=1.

differentiation of responses. This can be further assessed from Table 1 reporting peak shear resistance in the direction of shearing and deviatoric stresses at critical state, along with the differences from the base values obtained in the M_{DSS} simulations.

The simulation #6, using a constant M value calculated per Eq. 3 (e.g. the value of the critical stress ratio under triaxial compression conditions) predicts the strongest material of all assessed scenarios, with a peak shear resistance τ_{xz} of 31.7 kPa and a deviatoric stress at steady state $q_{10\%}$=55.1 kPa. These values are 21-22% above those recorded in simulation #5 using a constant M value reflective of simple shearing conditions, and 38-41% above those recorded in simulation #4 employing Eq. 7.

Of the three idealizations for the M expressions, Eq. 4 [16] in simulations #1 and #7, yields the highest peak shear resistance τ_{xz} of 26.9 and 45.7 kPa, respectively; while also exhibiting the closest τ_{xz}-γ_{xz} response to the baseline simulations #5 and #11 using a constant M=0.87 (his critical state ratio value is obtained from Eq. 7 using a b_σ=0.5, the latter corresponding to the q/p ratio observed in all simulations of the DSS tests at steady state). However, in the p-q space, the stress path of this simulation diverges substantively from the baseline.

The simulations #3 and #9 using Eq. 6 [8] produce the most similar stress path to the baseline simulations; however, the steady-state p and q values vary diverge considerably.

The responses of simulations #2 and #8 using Eq. 5 [14] fall roughly between the ones using Eqs. 4 and 6. Finally, the Eq. 7 (e.g., the exact relationship) in simulations # 5 and #11 yields the lowest shear resistance τ_{xz} (with peak values of 22.5 and 91.8 kPa, representing a marked decrease from the baseline of -13.5 and -12.2% respectively) as well as the lowest stress path lines in the p-q space.

Table 1 Differentiation of select DSS simulation responses

Test (OCR=1, φ=30˚)	$\tau_{xz,max}$ kPa	γ_{xz} @ $\tau_{xz,max}$ %	$\%\Delta\tau_{max}$ from M_{DSS}, %	$\%\Delta\tau_{max}$ from Eq. 7	$q_{10\%}$ kPa	$\%\Delta q_{10\%}$ from M_{DSS}, %	$\%\Delta q_{10\%}$ from Eq. 7
1: 100 kPa, Eq. 4	26.9	1.25	3.5	19.6	45.7	0.7	14.8
2: 100 kPa, Eq. 5	25.8	1.06	-0.8	14.7	44.0	-3.0	10.6
3: 100 kPa, Eq. 6	25.5	1.34	-1.9	13.3	43.9	-3.3	10.3
4: 100 kPa, Eq. 7	22.5	1.25	-13.5	-	39.8	-12.3	-
5: 100 kPa, $M_{const.}=M_{DSS,Eq.7}=0.87$	26.0	1.53	-	15.6	45.4	-	14.1
6. 100 kPa, $M_{const.}=M_{TC}=1.2$	31.7	2.88	21.9	40.9	55.1	21.4	38.4
7: 400 kPa, Eq. 4	108.0	1.34	3.3	17.6	183.9	0.7	15.4
8: 400 kPa, Eq. 5	103.4	1.34	-1.1	12.6	176.9	-3.2	11.0
9: 400 kPa, Eq. 6	102.3	1.44	-2.2	11.4	176.1	-3.6	10.5
10: 400 kPa, Eq. 7	91.8	1.34	-12.2	-	159.3	-12.8	-
11: 400 kPa, $M_{const.}=M_{DSS,Eq.7}=0.87$	104.6	1.82	-	13.9	182.7	-	14.7

Lastly, the somewhat “wobbly” response noted in the Fig. 3 plots is attributable to two effects: (1) the averaging of the response across 12 points in the domain which probably captures some of the edge effects and (2) the downward adjustment, in the variable M simulations, of the M value as shearing proceeds. The latter takes place because at the start of shearing, the stress state in the domain reflects the triaxial compression condition: $\sigma_{zz}=\sigma_1$, $\sigma_{yy}=\sigma_{xx}=\sigma_2=\sigma_3$, corresponding to M=1.2; and as shearing proceeds, the M-value reduces, ultimately reading the values determined by Eqs. 4-7 and a b_σ=0.5, the principal stress ratio value at the end of simple shearing in these simulations.

3.2. Parametric slope

The three simulations of the parametric slope in Fig. 2 using (i) $M_{const.}=M_{DSS,\varphi=30^{\circ}}=0.87$, (ii) $M_{const.}=M_{TC,\varphi=30^{\circ}}=1.20$ and (iii) $M_{variable}$= f(Eq. 7, $\varphi=30^{\circ}$) produce differentiated responses as illustrated in Fig. 4.

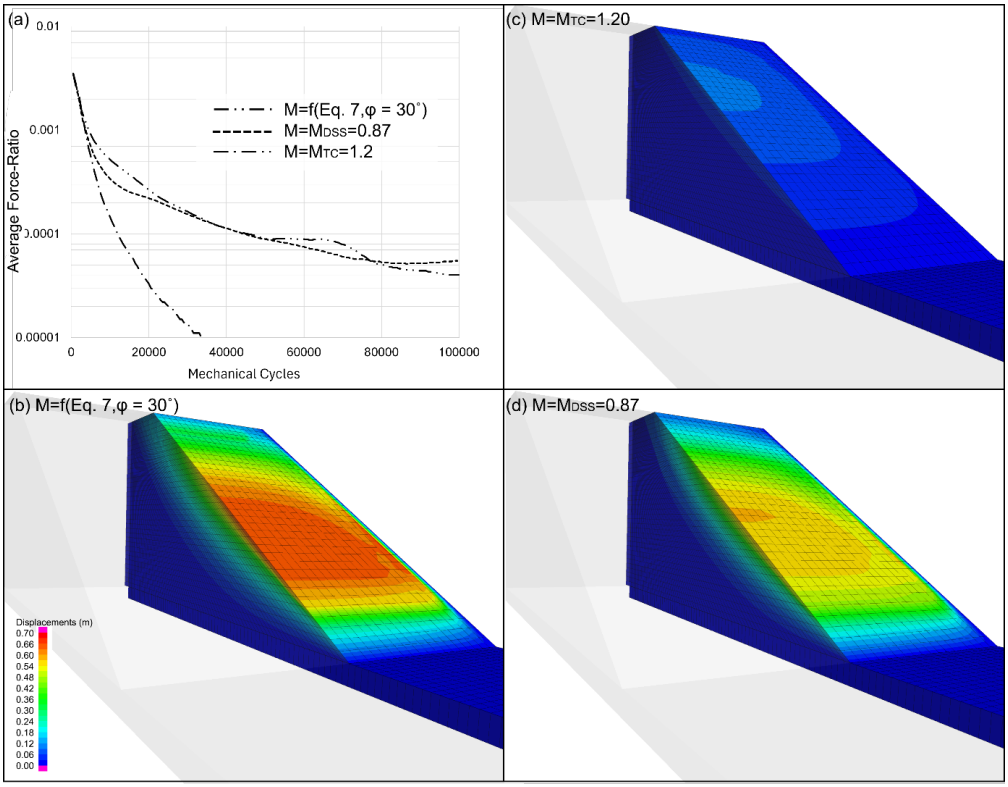

Fig. 4 (a) Average force-ratios. (b,c,d) Total displacements at 30,000 mechanical cycles into the simulations of the slope response. The slope is shown in a cross-sectional view through the middle of the soil mass.

The simulation using a constant critical stress ratio M calculated under triaxial compression conditions M_{TC}=1.20 predicts a stable slope with deformation levels <0.01m; the two other simulations predict an unstable slope, with the plots of the average force-ratios (a measure of the soil mass translational inertia ma) indicating continuing deformation at the end of simulation (Fig. 4a). Of the latter two, the simulation using a constant critical stress ratio M=0.87 estimated from Eq. 7 under simple shear conditions predicts lower deformation levels at equivalent simulation points: for example, at 30,000 mechanical cycles, displacements at face do not exceed 0.55m, compared to 0.70m in the simulation using variable M calculated using Eq. 7. These results suggest that M_{TC} predicts stronger material response and M= f (Eq. 7) produces the weakest; this matches the observations in the DSS simulations.

4. DISCUSSION

4.1. Response comparison

The responses of the two DSS simulations using $M_{constant}$=0.87 can be regarded as “baseline”: this is the response of the model when the default implementation of the Modified Cam-Clay model is used while selecting the input M-value with knowledge of steady state stress conditions under direct simple shear and without adopting any idealizations of M such as those in Eqs. 4-6. From plots in Fig. 3 one may assert that the use of these idealizations impacts the response to a variable extent, affecting both peak shear resistance as well as stresses at critical state.

The simulation responses under simple shear conditions using Eqs. 4-6 also diverge amongst themselves, with the idealization proposed by [16], (Eq. 4) predicting the strongest material both at peak and critical state; while the expression by [8], (Eq. 6) predicting the weakest, albeit by a small margin. All three idealizations predict considerably stronger materials than the exact expression (Eq. 7), with differences of peak shear resistance τ_{xz} varying between 11 and 20%, and with q values at critical state varying between 10 and 15% (Table 1).

Such variation of response invites the question, which of these idealizations, if any, would be best used in the design or analysis of slopes whose behaviour is approximated with constitutive models based in critical state theory. We pose this question to the geotechnical community and posit that satisfactory answers may be obtained by back-analysing known slope failures. Conversely, these idealizations could be assessed against full testing datasets, i.e. where the same soil specimen is subjected to triaxial extension, compression simple shearing and perhaps other stress paths.

4.2. Stress path effects

In many laboratory tests, the stress state at critical state is known, as are the principal stress ratio b_σ and Lode angle Θ. It can also be argued that these values are known beforehand in some slope problems. It is then worth asking what the value of updating M continuously might be, considering the computational demands associated with this operation.

The DSS simulation results herein allow us to observe the effect of the stress path on the response by comparing the simulations with $M_{constant}$=$M_{DSS,Eq.7}$ against simulations with M using Eq. 7 (e.g., 4, 5, 10 and 11 in Table 1). Fig. 5 illustrates the plots from simulations 10 and 11, the former updating M per Eq. 7 and the latter using a constant value corresponding to simple shear conditions at critical state. Albeit both simulations produce the same critical state ratio M=0.87, the stress states at the same point diverge substantially, with the $M_{variable}$ simulation predicting a much weaker response ($\Delta\tau_{xz}$=-12.2% and $\Delta q_{10\%}$=-12.8% for σ_{cv}=400kPa).

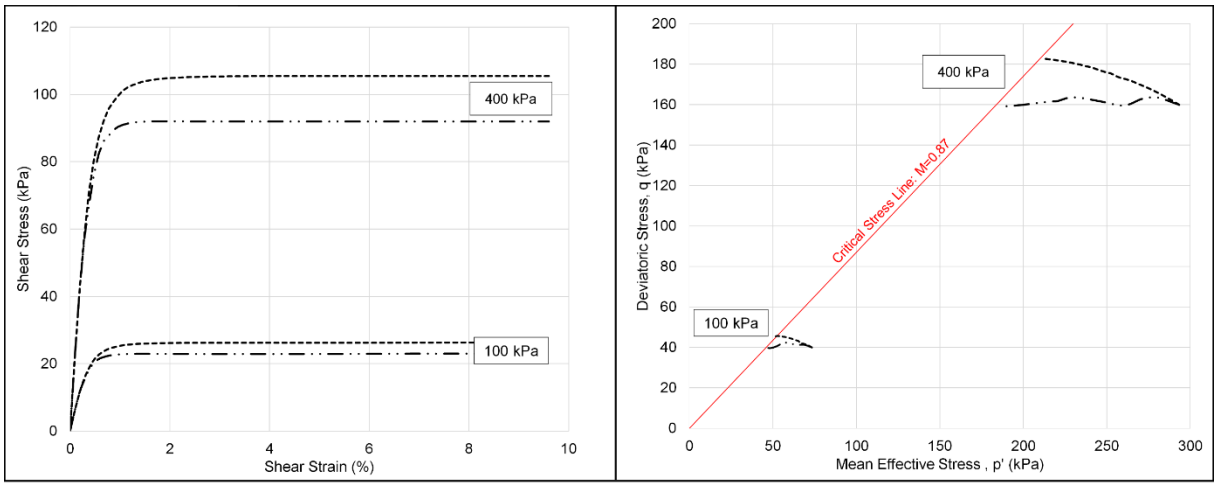

Fig. 5 Comparison of Eq. 7 response: constant vs. variable in the DSS simulations using initial overburden pressures of 100 and 400 kPa.

In the parametric slope simulations, stress path effects are noted from the plot of average force-ratios (Fig. 4a) and the displacement plots taken at equivalent simulation points (Fig. 4b,d). In the simulation using $M_{variable}$=f (Eq. 7), as the simulation proceeds, the value of M in the failure zone appears to trend toward a value of 0.87 or thereabout (Fig. 6d). Despite this similarity with the simulation using M_{DSS}=0.87, the two models respond differently (Fig. 4a,b,d).

This suggests that stress path effects might be significant and could qualitatively affect the conclusions about designs or forecasts. This finding also supports the conclusion that the use of a constant M value based on a known b_σ at critical state may be insufficient for accurate predictions.

This finding has implications for two-dimensional analysis employing constitutive models based in critical state theory. Since two-dimensional analysis does not evaluate the intermediate principal stresses, the stress path effects noted here would be overlooked.

4.3. Evolution of M-value in slope failure

The evolution of the critical stress parameter M in the parametric slope simulation is illustrated in Fig. 6. As the shearing processes go on, the M-values decrease throughout the domain from an initial value of 1.2. In the region of failure, the M-values decrease to 0.85-0.87, suggesting at-failure conditions similar to those under simple shear. Outside the failing soil mass, the M-value remains higher, ranging from ~0.97 to ~1.10.

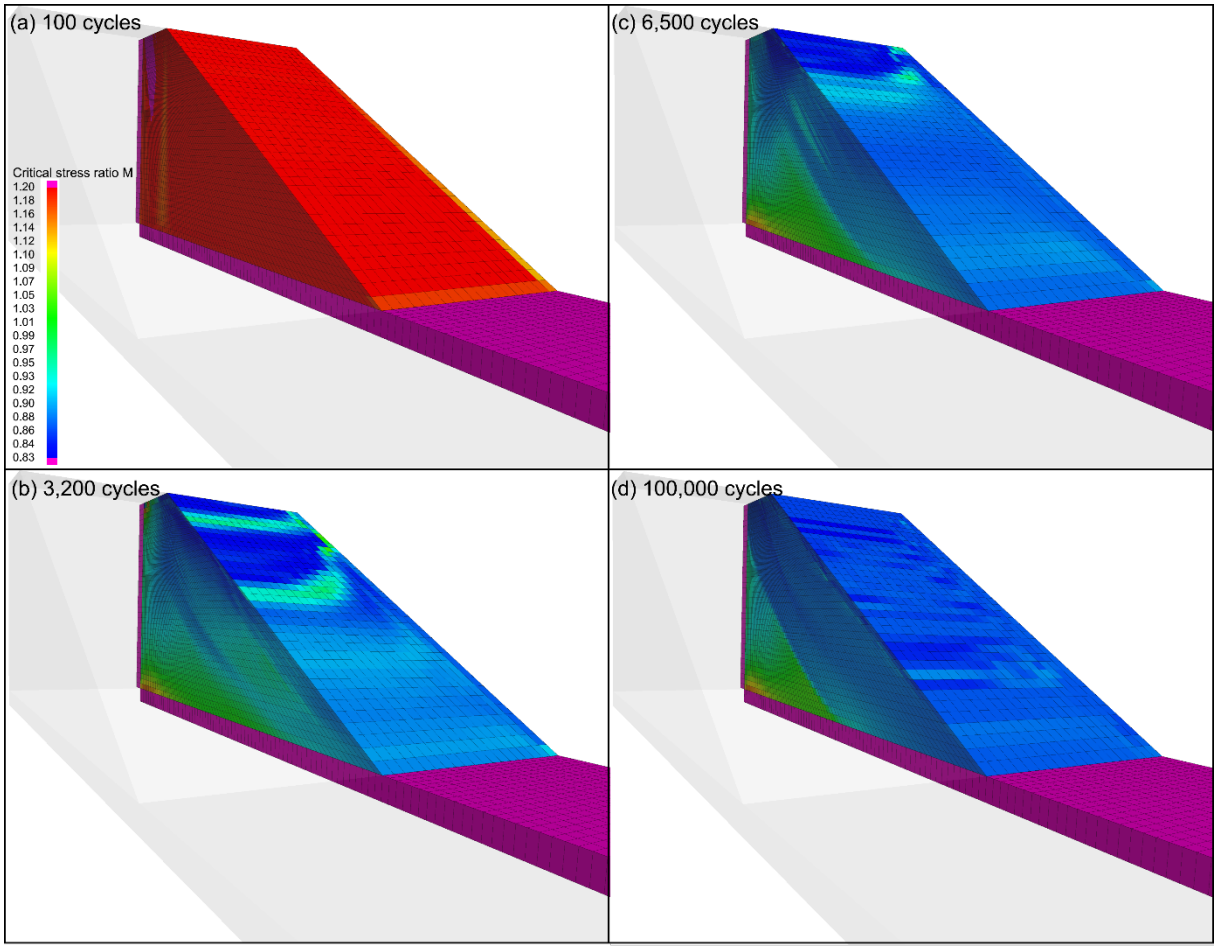

Fig. 6 Critical stress ratio M in the parametric slope simulation using Eq. 7

It is worth noting that the evolution of the M value in the slope appears to be interlinked with the progression of the failure processes: in Fig. 6, the variations of the M parameter appear to clearly indicate the locations of shearing.

One may also note localization effects and the development of multiple sub-parallel shear zones, an effect also noted in real spoon-shaped landslides in clayey soil.

This finding underscores the role that the three-dimensional stress state, as captured through the M parameter, has on the predicted strength behaviour, and the potential that the implementation of variable M calculations may have on forecasting accuracy.

4.4. Three-dimensional effects

The simulations of simple shearing and of the parametric slope that use some constant value of the M parameters do not fully take advantage of the three-dimensional solution. Conversely, the simulations employing idealizations in Eq. 4-7 relating the M-parameter to the intermediate principal stress can be interpreted as being fully three-dimensional. In consequence, the differentiation between the former and the latter constitutes a three-dimensional effect. From

the results presented here, one may conclude that these effects are present and can be substantive.

5. CONCLUSIONS

On the use of the MTC value in problems involving generalized stress paths

In this study, simulations of simple shear using M_{TC} values produce peak shear resistance estimates that are considerably higher than any other scenarios, including constant M values evaluated under simple shear conditions, idealizations captured by Eqs. 4-6 and the exact solution in Eq. 7. In the parametric slope exercise, the use of M_{TC} also produced a more stable configuration than other simulations. This invites the conclusion that the use of critical stress ratio values evaluated under triaxial compression in simulations of problems following other stress paths (e.g., slope failures in clays; simple shearing) may produce nonconservative predictions.

Stress path effects and the three-dimensional aspect

The stress path to failure appears to have a substantive impact on the predicted strength behaviour, with simulations accounting for the evolution of stresses (including the intermediate principal stress) producing lower estimates. This finding has implications for two-dimensional deformation analysis using constitutive models based in critical state theory, as the predictions may diverge and be potentially nonconservative.

Implications for slope design and forecasting

The three idealizations of the M value (in Eqs. 4-6) and the exact derivation (Eq. 7) offer divergent predictions of material behaviour, with differences of peak shear resistance of up to 20% as well as significant variations of critical stress states (Table 1). Furthermore, the stress path to failure appears to have considerable impact on the peak and critical state responses.

This suggests that the careful selection of the appropriate idealization is required prior to conducting slope simulations. This is achievable by way of calibrating the constitutive model(s) using such idealizations against observed responses under a variety of stress paths, including but not limited to triaxial extension/compression and simple shear.

Furthermore, the results herein indicate the presence of three-dimensional effects in slopes, which can be substantive. Therefore, the use of idealizations such as in Eqs. 4-7 may be preferrable to the use of constant M inputs, so long that their capacity to reasonably capture real behaviour has been established through calibration or other means.

ACKNOWLEDGMENTS

This study was supported by the Government of Canada Funding in the form of NSERC’s Discovery Grant, and through the Kochar Family Scholarship awarded to Author 1.

ABBREVIATIONS AND NOTATION

2D, 3D	Two-dimensional, three-dimensional
DSS	Direct Simple Shear
FEM	Finite Element Method
OCR	overconsolidation ratio
M	critical stress ratio
$M_{TC/TE}$	critical stress ratio under triaxial compression/extension
b_σ	principal stress ratio

REFERENCES

[1] Independent Expert Engineering Investigation and Review Panel (IRP). Report on Mount Polley Tailings Storage Facility Breach. Government of British Columbia, January 30, 2015. 147 pages.

[2] Morgenstern, N.R., S.G. Vick, C.B. Viotti and B.D. Watts. Report on the immediate causes of the failure of the Fundão dam. August 25, 2016, Report, 76 p.

[3] Robertson, P.K., L. de Melo, D.J. Williams and G.W. Wilson. *Report of the expert panel on the technical causes of the failure of Feijão Dam I. December 12, 2019.* http://www.b1technicalinvestigation.com/ accessed December 2019.

[4] ANCOLD. Guidelines on Tailings Dams—Planning, Design, Construction, Operation and Closure; Revision 1; Australian National Committee on Large Dams: Hobart, Australia, 2019.

[5] Zabolotnii, E., N.R. Morgenstern, G.W. Wilson and P. Simms. Pre-failure stability of the Mount Polley TSF embankment: Conventional vs. performance-based evaluations. In Proc. Tailings and Mine Waste, Nov. 6-10, 2022, Denver CO.

[6] Zabolotnii, E., N.R. Morgenstern, and G.W. Wilson (2022). *Mechanism of failure of the Mount Polley Tailings Storage Facility.* Can. Geot. J. 59(8). DOI: 10.1139/cgj-2021-0036.

[7] Ishihara, K. (1997). Terzaghi oration: Geotechnical aspects of the 1995 Kobe earthquake. Proc., Intl. Conf. Soil Mech. and Found. Engg.-Intl. Soc. Soil Mech. and Found. Engg. Vol. 4: 2047-2074.

[8] Jefferies, M. G., and Shuttle, D. A. (2011). On the operating critical friction ratio in general stress states. Géotechnique 61(8): 709-713.

[9] Matsuoka, H. and Nakai, T. (1974). Stress-deformation and strength characteristics of soil under three different principal stresses. Proc. JSCE 232: 59–70.

[10] Murali, A. (2024) Three-dimensional simulations of the behaviour of layered soils under simple shear. MSc Thesis, Carleton University, Ottawa CA.

[11] Roscoe, KH and Burland, JB (1968) On the Generalized Stress-Strain Behavior of Wet Clay. In: Heyman, J. and Leckie, F., Eds., Engg. Plasticity, Cambridge University Press, Cambridge, 535-609.

[12] Roscoe, KH, AN Schofield and A Thurairajah (1968). Yielding of clays in states wetter than critical. Geotechnique 13: 12-38.

[13] Schofield AN and Wroth CP (1968). Critical state soil mechanics. New York: McGraw-Hill.

[14] Sheng, D, SW Sloan and HS Yu (2000). Aspects of finite element implementation of critical state models. Computational Mech. 26: 185-196.

[15] Shibuya S and DW Hight. Predictions of pore pressure under undrained cyclic principal stress rotation. Proc. 12th Intl. Conf. Soil Mech. Found. Engg. (Rio de Janeiro 1989).

[16] Zienkiewicz OC and GN Pande (1977). Some useful forms of isotropic yield surfaces for soil and rock mechanics. In: Gudehus G (Ed) Finite Elements in Geomechanics, Ch. 5:179-198.

Fifth International
Dam World Conference
PORTUGAL • LISBON • LNEC • APRIL 13-17, 2025
dam world 2025

ADVANCED GEOMEMBRANE SYSTEMS FOR DAMS AND RESERVOIRS OF NEW PUMPED HYDRO STORAGE SCHEMES

G. Vaschetti
Carpi Tech

A. Jackson
Carpi Tech

A. Blanco[1]
Carpi Tech

ABSTRACT

The first applications of geomembranes in pumped storage schemes date back to the beginning of the 1990ies, and aimed to restore the watertightness of ageing dams forming one of the reservoirs. A few of such projects were discussed at the 2015 Dam World conference.

Construction of pumped storage schemes is now booming thanks to the acceleration towards clean energies: pumped hydro storage is the “clean battery” that can balance the alternating energy shortage and surplus characteristic of wind and solar sources. In pumped hydro storage schemes, watertightness of the upper and lower reservoirs is important not only for structural safety, but also to minimise maintenance, which often involves outage and heavy revenue losses. Therefore, in the middle of the 2010ies geomembranes started to be used also in new construction, to waterproof the dams forming the reservoirs, or to waterproof the entire reservoirs, as effective alternative to conventional facings such as concrete or bituminous concrete, which are less effective in accepting settlements and differential displacements, and in sealing joints at boundaries, and are more sensitive to temperature variations, with subsequent frequent need for maintenance. Advanced geomembrane systems, based on the experience acquired in applications in embankment dams and reservoirs, were developed to meet the requirements of these demanding schemes. Portugal, with the Pico da Urze reservoir, part of the Calheta pumped storage schemes, was a pioneer in these applications.

The paper amplifies what discussed in the 2015 conference, outlining the characteristics and design of advanced geomembrane systems in dams and reservoirs of new pumped storage schemes, discussing their advantages, and presenting the solutions adopted in three projects: Pico da Urze in Portugal and Pinnapuram in India, with an exposed flexible geomembrane lining respectively the upper reservoir and the dams forming both reservoirs, and Abdelmoumen in Morocco, where both reservoirs are lined with a lacquered exposed flexible geomembrane to enhance durability in an environment with particularly high UV radiation.

Keywords: Pumped storage, waterproofing, geomembrane, settlements, differential displacements, Co-Energy.

[1]alejandro.blanco@carpitech.com, Spain

1. INTRODUCTION

Geomembranes have a successful history of more than 60 years of waterproofing large dams. In pumped hydro storage schemes, the oldest projects are now 30 years old; until about one decade ago, in such schemes the geomembranes were basically used to restore watertightness to ageing dams forming one of the reservoirs.

With growing awareness of the urgency of changing our energy sources to reduce CO2 emissions, the construction of wind and solar plants has been booming in many countries in the world. Such sources however are intermittent and cannot grant grid stability: there are times when excess energy is produced that cannot be absorbed by the grid, and there are times of low wind speed, or absence of wind or sun, when little to no energy is produced. Wind and solar therefore need energy storage technologies, which can be of the gravitational type (pumped hydro storage), chemical (batteries), mechanical (compressed air), or thermal (molten salt). The latest of these techniques are in an initial state of technological development; battery storage is a mature technology, which however is too costly for grid size electricity storage, provides less storage time, has shorter life if compared to gravitational storage, and the disposal of batteries also poses a non-negligible environmental issue. Pumped hydro, a well-established technology available on a large scale, stores gravitational energy in form of a large mass of water pumped into an upper reservoir during hours of low demand, using also the excess energy produced in wind or solar plants; when there is shortage in the grid, water can be released almost instantaneously down to a lower reservoir, generating the power needed to feed the grid. The revenues of the schemes come from selling more energy at peak demand, when costs of energy are the highest, while low-cost off-peak energy is used to run the pumps. Pumped hydro storage is a giant water battery, clean, reliable, renewable, and sustainable.

Pumped hydro storage schemes (PHSS) can be built using existing lakes and dams, or building one or two new reservoirs, or using the ocean as lower reservoir and building the upper reservoir up above the coastline. To the knowledge of the authors, although potential sites for this last option have been identified (e.g., Chile, California, South Africa, Australia, & some sites in Europe), the only real example has so far been the Okinawa scheme, a pilot plant completed in 1999 and having the upper reservoir lined with an exposed geomembrane, never put into practical use because the demand for electric power in Okinawa did not grow as predicted and the plant was not profitable; eventually in 2016 the plant was dismantled.

To ensure that, apart from conversion losses, evaporation losses, and losses due climate change, a PHSS is maintained in total safety and at maximum efficiency, all components

of the scheme, and in particular the two storage reservoirs, must be kept watertight, because water leakage decreases the efficiency of the system, and in the long-term may affect its structural safety. Unless excavated in low-permeability soils, the reservoirs are generally lined with an impervious liner. Traditional linings have been concrete and bituminous concrete, which however have shown some drawbacks, as discussed in a previous Dam World conference [1]. The drawbacks are mainly related to their poor ability to resist settlements and differential displacements occurring in the reservoirs' embankments and bottom, to the difficulties in achieving an effective sealing at boundaries, to the susceptibility to temperature variations, and to the frequent need for maintenance, which is expensive and generally requires outage periods involving heavy revenue losses.

A PHSS is a complex infrastructure where minimising outages is critical, and a liner not needing routine maintenance is an asset. The tensile characteristics of geomembranes, and in particular of the Sibelon® composite geomembranes used since 1976 on large dams, make them the only liner capable of resisting the movements associated with the repeated loading and unloading conditions of these schemes. The connections of the liner to the concrete structures have been part of the design of many embankment dams and reservoirs, showing an outstanding capability of accepting large displacements, also along the peripheral joints of rockfill dams, and large openings, as can be experienced in existing cracks at the concrete linings of pressure tunnels that are part of the schemes. Using geomembrane systems also for reservoirs and dams of new schemes came as a logical consequence, and in the middle of the 2010s, at the new Panama Canal, an exposed geomembrane system was used to line > 595,000 m^2 at the 18 Water Saving Basins for the navigation locks on the Atlantic and on the Pacific side. This project can be compared to a particularly challenging PHSS, since the basins are filled and emptied 5/6 times a day.

2. GEOMEMBRANES IN NEW PUMPED HYDRO STORAGE SCHEMES

2.1. Assets and applicability

The Sibelon® liner used in all such schemes is a prefabricated composite material (Fig. 1 at left) consisting of a flexible polyvinylchloride (PVC) geomembrane providing watertightness, heat-bonded during manufacture to a nonwoven needle punched geotextile providing essential anti-puncture protection, increased thermal stability and drainage. The thickness of the geomembrane is generally not inferior to 2-2.5 mm, the mass per unit area of the geotextile is typically 500/700 g/m^2. While the thickness of the geomembrane and the mass per unit area of the geotextile are site-specific, the elongation capabilities of the liner always largely exceed 230% elongation. No routine maintenance is needed for a geomembrane system using these high quality thick geomembranes. Maintenance is limited

to the exceptional event of accidental damage. In almost all limited cases of reported accidental damage, the cause was the fall of sharp heavy objects upon the geomembrane. In a PHSS this event is unlikely to occur due to the generally remote location and the inaccessibility of the reservoirs to the public. Accidental damage can be repaired during the low-level phase in a few minutes even by the owner's personnel properly trained, or underwater by specialised divers, without outage of the scheme.

Fig. 1 – At left, detail of the composite liner discussed: in grey the watertight geomembrane, in white the backing anti-puncture geotextile. At right, the liner being deployed with the geotextile in contact with the upstream face of the embankment

All components of the geomembrane systems are prefabricated in a factory, under controlled and documented conditions, ensuring constant quality & compliance with specifications. All components of the systems have light weight and small volume, and only small tools and light equipment (ropes, scaffolding, travelling platforms) are needed for placement (Fig. 1 at right), so that the environmental impact, in terms of site organisation and traffic, is substantially lower than with other systems such as concrete and asphalt.

These geomembranes can be installed on very steep slopes and on vertical faces of structures, in much shorter times than traditional liners, allowing earlier power generation; installation can be carried out in all climates and practically in all conditions, the watertightness of the system (watertightness of the geomembrane, of the junctions, of the perimeter seals) is controlled 100% with standard methods, so that the final quality of the works is not affected by meteorological conditions. Construction of a concrete or bituminous concrete liner on the contrary involves heavy equipment, very high impact on the environment with possible stronger opposition from local population, longer construction times, and difficult control of the final quality. Globally, the carbon footprint of concrete or bituminous concrete liners can be 4 to 6 times higher than that of an exposed geomembrane liner.

The expected durability of geomembranes is a function of their thickness. A 2.5 mm thick geomembrane has a durability largely in excess of 30 years in the area always over the water, where watertightness in fact is not even required, and in the fluctuation zone, and much longer in the area always submerged by water. Geomembranes with higher thickness have much longer durability.

What are the potential limits and drawbacks of such liners and of such systems? Concerning the liner, if the thickness of the geomembrane and the mass per unit area of the geotextile are not selected in function of the subgrade and of the expected loads, with adequate factor of safety, the liner may not be able of accommodating the maximum loads, or may not have the expected durability. Concerning the geomembrane system in its entirety, design and installation are the driving factors. Selecting the wrong type of geomembrane, or using insufficient safety factors, or inadequate details for face anchorage and perimeter seals, are crucial. Finally, bad installation and insufficient quality control can undermine a potentially adequate design. Experience of the designer and of the installer are essential for the good performance of the project.

The geomembrane systems discussed above are applicable and have been used for all components of a PHSS: upper and lower reservoirs, embankment or RCC dams forming the reservoirs, headrace tunnels, tailrace tunnels/channels, pressure shafts, surge shafts/tanks. In some cases, they have substituted a traditional lining system planned in the original design, while in other cases they have been included in the design since the initial stage. This paper deals with geomembrane systems as linings for new reservoirs and for embankment dams forming new reservoirs.

2.2. Geomembrane system to line an upper reservoir: Pico da Urze, Portugal 2019

Pico da Urze is part of a project aiming to increase the share of renewable energy sources used in the production of electricity in the island of Madeira, with much of the plant's output replacing thermal energy. The Calheta PHSS will optimise the operation of the grid, combining wind generation with hydro generation. The new upper reservoir is formed by Pico da Urze dam and by an excavated reservoir, with a total volume of 1,000,000 m^3, while the lower reservoir, formed by the Calheta dam, has a volume of 73,750 m^3. The scheme includes a 3.6 km high pressure penstock (70 bar) to the Calheta III powerhouse (2 turbines, 15 MW each), and a pumping station (3 pumps, 5 MW each, and a maximum head of 750 m).

The Pico da Urze dam, 31 m high above the foundation, crest elevation at 1354 m and bottom at elevation 1329 m, consists of a compacted rockfill embankment with extensive grading and with an upstream face inclination 1V:1.4 H. A side spillway, 85 m long, a bottom outlet, Ø 800 mm, and an intake tower complete the scheme. Due to a very permeable soil, an impervious liner was needed as water barrier on the upstream face of the dam and on the entire reservoir, and since the dam is founded on deformable foundations having variable characteristics, large settlements were foreseen, and it was decided that an exposed geomembrane liner was the most suitable solution. The Tender design foresaw a 2.5 mm thick high-density polyethylene (HDPE) geomembrane installed over a 1000 g/m^2 anti-puncture geotextile, the two resting on

a 4 m wide granular transition zone. Although a fine graded layer, maximum diameter 20 mm, with no fines less than 0.075 mm, was specified, it was clear that this condition would be difficult to achieve in construction with a 1V:1.4H slope. Irregularities in the subgrade were to be expected in the rockfill dam and in the excavated surfaces of the reservoir. A more flexible geomembrane, with a low Young's modulus, would exhibit a better puncture and burst resistance than a high-modulus HDPE geomembrane, because it would better adapt to an irregular subgrade distributing the load exerted by water and reducing the risk of damage due to concentrated loads at protrusions (puncture) and cavities (burst). A flexible geomembrane bonded to an anti-puncture geotextile would require less surface preparation than an HDPE geomembrane placed on a separate geotextile, and would have higher friction angle on the slopes. A low-modulus and low thermal expansion geocomposite would reduce the forces transferred to the anchorage lines, and would not form large wrinkles [2], which result in higher susceptibility to wind uplift and damage and may form very wide channels for water infiltration in case of puncture. Large wrinkles can amplify the tensile and displacement effect caused by the dynamic action of water and wind uplift, increase the risk of stress cracking and the formation of sharp edges that are detrimental under the pressure of water; if the geomembrane is not adequately laid flat, proper execution of seams will be affected, and failure of the seams due to stress concentration may occur.

The maximum estimated settlements were 0.67 m at construction, 0.054 m for the first phase of reservoir filling, and a settlement at crest of about 0.50 m for the exploitation phase. In presence of such large settlements and of differential displacements at the connections between the deformable embankments and rigid concrete appurtenances, an HDPE geomembrane would be less performing than a PVC geomembrane, which has a lower Young's modulus, is more flexible, and has a tension-strain curve increasing monotonically. To evaluate the response of a geomembrane to differential displacements, the concept of Co-Energy developed by Giroud and Soderman [3] was considered: the Co-Energy is the area between the tension-strain curve of a geomembrane and the tension axis (i.e., the vertical axis), where only the continuously increasing portion of the tension-strain curve can be used. The authors showed that an appropriate way to evaluate and compare the abilities of geomembranes to withstand differential settlements is through the Co-Energy concept. The use of the concept was illustrated with a numerical example comparing the abilities of several common geomembrane types to withstand differential displacements. A geomembrane with high Co-Energy has a much higher capacity of deformation and flexibility in relation to the settlements of the support. Fig. 2 compares the Co-Energy of an HDPE geomembrane to that of a SIBELON® PVC composite geomembrane. The areas showing the respective capability to accept the displacements evidently favour the use of a PVC liner.

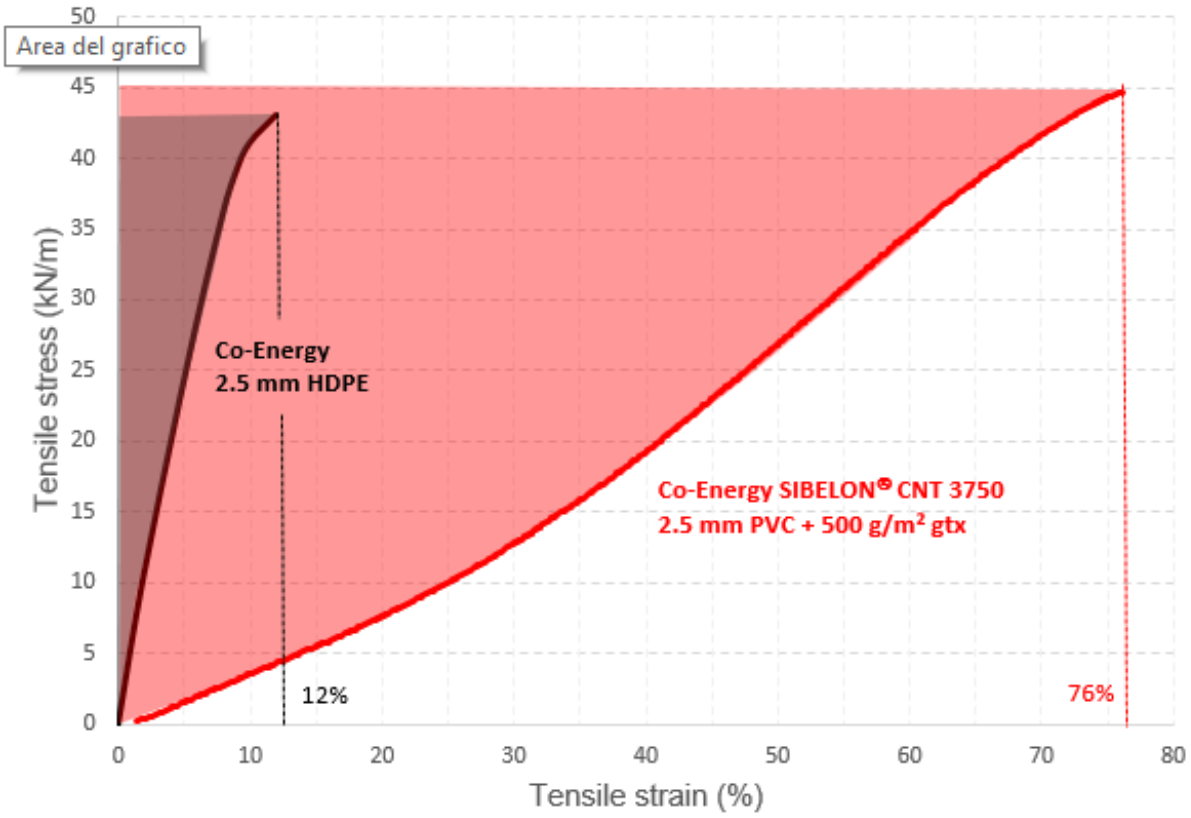

Fig. 2 – Co-energy of a composite SIBELON®PVC geomembrane 2.5 mm thick (red/orange area) and of a 2.5 mm thick HDPE geomembrane (grey area)

The HDPE geomembrane + 1000 g/m^2 geotextile of the original design were substituted by a geomembrane with higher Co-Energy, the composite Sibelon® CNT 3950, consisting of a 2.5 mm thick flexible PVC geomembrane heat-bonded during fabrication to a 700 g/m^2 polypropylene geotextile. The 1V:1.4H dam slope was covered by two 50 mm thick shotcrete layers, reinforced at the interface by a geogrid. The shotcrete was covered by a 1000 g/m^2 anti-puncture geotextile having the main purpose of increasing the drainage capacity between the shotcrete and the geomembrane liner. At the excavated reservoir, the same geotextile was placed at the most irregular zones (about 40% of the excavation).

The face anchorage system was based on a persistent wind of 90 km/h and on wind gusts of 150 km/h. The primary face anchorage is made by longitudinal trenches where the waterproofing liner is placed and ballasted by concrete. The trenches are positioned along the crest of the dam (marked 1 in Fig. 3), the crest of the reservoir (2 and 3), the intermediate and peripheral berms (4 and 5), the toe of the slopes (6), and the centre of the bottom of the reservoir (7), serving also as traffic paths. A concrete platform ballasts the waterproofing liner at the spillway, at the feeding canal, and at the concave corner. The complementary face anchorage is made by vertical trenches at 10 m spacing (8) filled with concrete, placed on the upper part of the excavated slopes, where the geomembrane liner is fastened onto the concrete by 60x4 mm stainless-steel flat profiles secured to the concrete with anchor rods

embedded in chemical anchors. At the dam, the complementary face anchorage is placed on a supporting shotcrete layer and consists of 50x3 mm stainless-steel flat profiles at 8 m spacing (9a and 9B), secured with mechanical anchors.

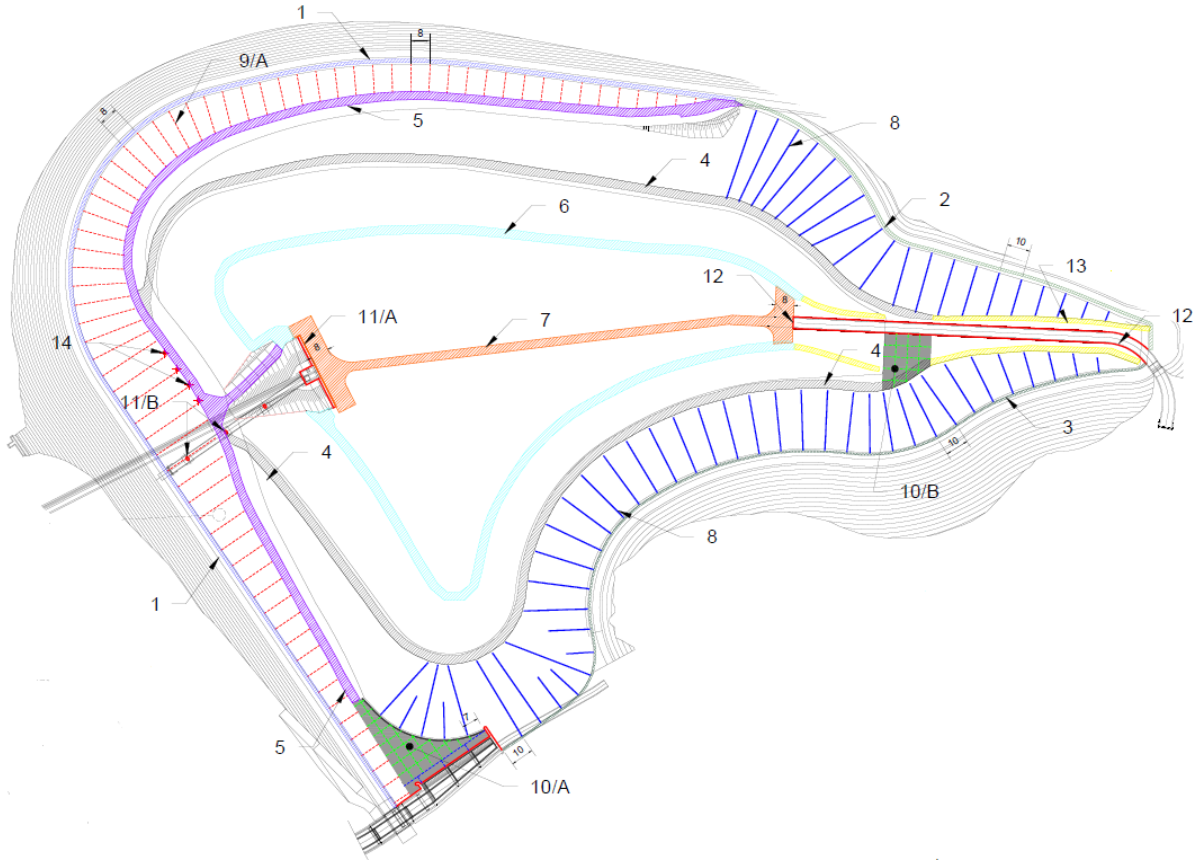

Fig. 3 – Pico da Urze: face anchorage system layout. Main components are the trenches at the crest of the dam (1) and of the reservoir (2, 3), the intermediate and peripheral trenches (4, 5), the toe trench (6), the bottom trench (7), and the mechanical fastenings on the vertical trenches (8) and on the shotcrete at the dam (9a and 9b)

The face anchorage system allows gravitational flow of water that should be present behind the geomembrane towards the drainage system of the reservoir, avoiding bulges caused by unbalanced water pressure when the water level drops. At the contact between the embankments and the concrete structures (feeding canal and intake tower), the geomembrane is sealed with a watertight mechanical seal, an 80x8 mm stainless-steel flat profile secured to the concrete with anchor rods embedded in chemical anchors at 0.15 m spacing. To resist the expected differential displacements between the embankments and the concrete structures, the seal has been provided with a settlement slot, to avoid the stress that a large displacement could create in the geomembrane.

The contract foresaw 104 days for installation including 14 days of allowance for bad weather. Waterproofing works started on July 8, 2019, and were completed on October 23, 2019. In

total 78 days for installation and 21 days for bad weather for a surface of about 82,400 m^2. Using a geomembrane system allowed such a fast installation.

Fig. 4 – Pico da Urze. At left, the dam with the shotcreted slope, and the geocomposite under installation over the vertical and longitudinal anchor trenches at the excavated reservoir. At middle, view from the crest: the geomembrane anchored by a vertical flat profile and ballasted by concrete at the intermediate berm. At right, the reservoir impounding in 2020

2.3. Geomembrane systems to line the dams forming the two reservoirs: Pinnapuram, India, under completion

The Pinnapuram Integrated Renewable Energy pumped storage project, which includes 1000 MW solar, 550 MW wind and 1680 MW of standalone pumped storage capacities, is under completion in India. The scheme is a first-of-its-kind PHSS developed by Greenko, an independent power producer in India, whose second PHSS, Gandhi Sagar, has started in fall 2024. At Pinnapuram, a 6.5 km long continuous rockfill dam, maximum height about 40 m, forms an upper reservoir having a nearly rectangular shape. The lower reservoir is formed by three separate rockfill dams, with a total crest length of about 3.3 km and maximum height of about 46 m, connecting existing natural slopes. Fig. 5 at left shows a cross section of Embankment 1. The plinth is cast on the rock foundation, and the geomembrane is connected to the plinth by a watertight mechanical seal designed to withstand movements at the contact embankment/plinth (Fig. 5 at right).

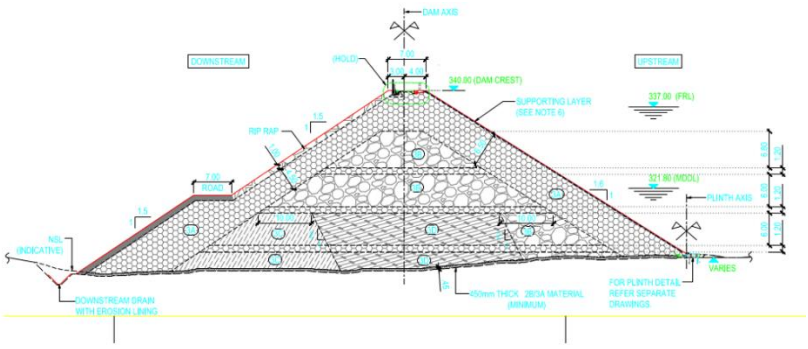

Fig. 5 – Pinnapuram lower reservoir Embankment 1. Cross section and detail at plinth

Pinnapuram is an example of a geomembrane liner substituting the traditional liner foreseen in the original design. At this site, the need for a waterproof liner at the rockfill dams was of particular importance: both reservoirs are located away from existing natural water systems and have no/negligible catchment area. Water will be withdrawn only once from the existing Gorakallu Reservoir irrigation system, will be stored in the Pinnapuram reservoirs, and then used cyclically for energy storage and production. Evaporation losses, if any, will be recouped periodically.

Due to these operational constraints, for the Pinnapuram scheme avoiding/minimising water losses is evidently critical. Consequently, a bituminous concrete facing had been planned as a waterproof barrier for all dams forming the reservoirs. After further technical and economic assessments, the bituminous concrete facing was eventually replaced by an exposed geomembrane facing. The geomembrane liner selected for all dams is the same material used at Pico da Urze, but with higher geomembrane thickness (3 mm instead of 2.5 mm) and lower geotextile mass (500 g/m^2 instead of 700 g/m^2).

At Pinnapuram dams, the owner required placing an optical fibre cables leak location system under the geomembrane liner. A plain cement concrete layer was placed over the transition layer of rockfill material 3A-US/2B, to form a confinement layer and enable the optical fibre cable to detect the leakage flowing in the drainage layer under the geomembrane liner.

The face anchorage for the geomembrane liner is made along vertical trenches created in the abovementioned concrete layer and in the superposed porous concrete layer acting as bedding and drainage layer (Fig. 6 at left), where geomembrane anchor bands are embedded and ballasted, partly protruding from the trench to form vertical anchorage bands for the geomembrane liner (Fig. 6 at right). The regular spacing between the trenches, calculated based on the wind force, the resulting uplift, the water drawing cycles, is 16 m.

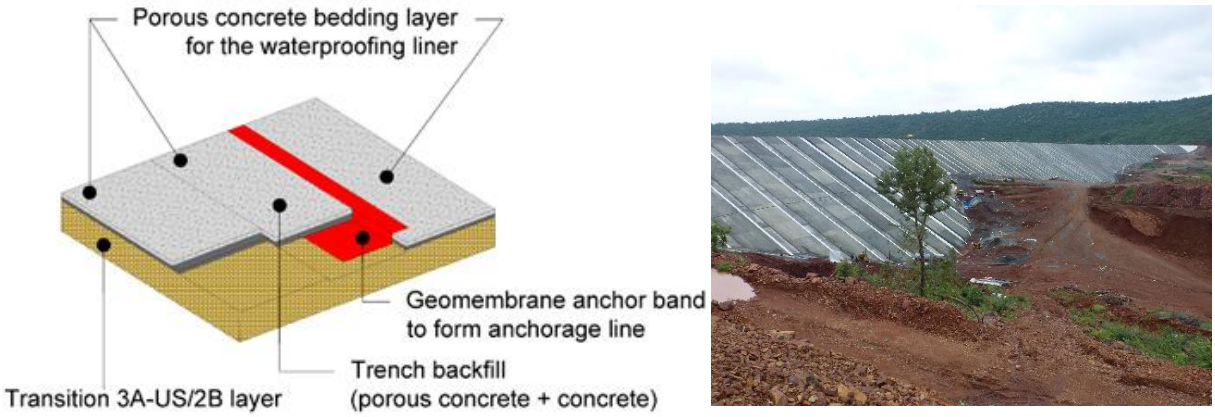

Fig. 6 – Pinnapuram dams: vertical geomembrane anchor bands embedded and protruding from the trenches

The geomembrane liner is then deployed from the crest over the drainage layer, and anchored by heat-seaming it to the protruding geomembrane bands. The waterproofing works can proceed in a sequential manner, following the civil works: earth works for the construction of the embankments, placement of the concrete and of the porous concrete layers, discontinuing them every 16 m to form the anchor trenches, installation and ballast of the geomembrane anchor bands in the trenches, deployment of the geomembrane liner and fastening to the anchor bands by heat-seaming (Fig. 7 at left). At the upper reservoir, to expedite works at the > 6 km long dam, the porous concrete bedding/drainage layer was substituted with a synthetic drainage layer (Fig. 7 at right).

Fig. 7 – Pinnapuram: installation of the geomembrane upon porous concrete drainage layer at lower reservoir dams (left) and on geosynthetic drainage layer at upper reservoir dam (right)

The geomembrane system adopted at the upper reservoir dam was selected to substitute also the bituminous concrete facing planned for the tailrace channel connecting the two reservoirs. At present, works have been completed at the lower reservoir dams (Fig. 8 at left was taken before completion) and at the tailrace channel, with a surface covered by the exposed geomembrane liner respectively of 178,169 m^2 and 231,993 m^2. At the upper reservoir (Fig. 8 at right), works are about 60 % completed, and the total lined surface will be 244,000 m^2 .

Fig. 8 – Pinnapuram: lower reservoir dams (left), with the waterproofing system of the third embankment in the background not yet completed, and upper reservoir dam (right), with installation of the waterproofing system ongoing

2.4. Geomembrane systems to line the two reservoirs: Abdelmoumen, Morocco 2023

Abdelmoumen is a PHSS on the River Issen, in the Taroudant Province of Morocco. The scheme is composed of two reservoirs, of an approximately 2.9 km long waterway, essentially consisting of a single external penstock of diameter varying between 3.6 m and 4.8 m over a length of 2 km, which connects the two basins and supplies the power plant, of underground waterways (shafts, high- and low-pressure tunnels, penstocks), and of a power plant hosting two reversible pump-turbines with generators of 175 MW each. The plant is designed to operate in turbine mode when electricity is needed by exploiting the 500 m head between the two reservoirs, and in pumping mode when surplus electricity is available. Each reservoir can store 1.3 million m^3 of water, displaced in either operational mode, which can be switched up to 20 times in a day. The reservoirs are formed by compacted earth fill embankments; maximum height on foundations are 33 m for the upper embankment, and 21 m for the lower embankment. In both reservoirs the inclination of the slopes is 2:1 (H:V), while the fluctuation of water is 20 m.

The geological investigations ascertained a high permeability in the soil of both reservoirs, and a waterproofing lining was therefore foreseen over their entire surface to prevent any loss of water. Based on technical and economic considerations, the owner ONEE (National Agency for Electricity and Potable Water) and its consultants selected and included in the tender design an exposed geomembrane lining. The specified geomembrane was a composite consisting of a PVC geomembrane, minimum thickness 2.5 mm, and of a bonded geotextile.

Apart from the usual requirements for a geomembrane lining in a PHSS, i. e., the capability to withstand the environmental attacks, the uplift by wind, the stresses generated by continuous fill/empty cycles, two additional issues had to be considered: due to the geographic location, a particularly intense UV radiation, and due to the poor subgrade material and the rather steep embankments, the potential for significant settlements on the slopes and/or for slope stability under the effect of repeated hydraulic loading/unloading. Therefore, the slopes had to be properly compacted, and the placement of the geomembrane should have no impact on the slope stability and vice versa – the waterproofing liner should not be adversely affected by the settlement of the slope.

To address the issue of intense UV radiation, a material specifically tailored for the reservoirs' location was selected, Sibelon® CNT 4400 L, a 3.0 mm thick PVC geomembrane heat-bonded to a 500 g/m^2 non-woven polypropylene geotextile, and treated with a surface lacquered treatment (L) designed to increase the service life of the liner. Accelerated and specific weathering tests have shown that this treatment enhances the life of the material under intense UV radiation as compared to a non-treated liner of the same thickness, while keeping the remarkable flexibility and excellent tensile response of the standard Sibelon® PVC liners. To

assess the effect of cycling loading on the geocomposite and on a heat-seam, a real-scale testing campaign was carried out in the laboratory, simulating the conditions at Abdelmoumen. The simulation parameters included the Abdelmoumen subgrade material, the geomembrane liner, water pressure corresponding to the expected daily fluctuations, and number of fill/empty cycles compatible with the expected operation of the plant: with water pressure fluctuating between 0 and 2 bar during each cycle, cycling loading at the rate of 144 cycles per day was performed for 127 days in a row (Fig. 9). This procedure corresponds to 25 years of operation of a pumped storage scheme with 2 fill/empty cycles per day, or 50 years of operation of a scheme with 1 fill/empty cycle per day. The tested sample and seam were then evaluated and compared with a virgin sample of the same material and seam by an independent laboratory in Germany, evaluating the change in thickness, tension/elongation, and seam resistance to shear and peel. The test results showed that the tested geomembrane had withstood cycling loading with no quantifiable evidence of fatigue, showing no sign of damage or loss of watertightness, and variation of the mechanical properties inferior to 3% as compared to the ex-work samples.

Fig. 9 – Test for resistance to cyclic loading for Abdelmoumen PHSS: 0-2 bar, 2 cycles/day for 127 days, corresponding to 50 years operation of a 1 cycle/day PHSS. No quantifiable evidence of fatigue in the geomembrane

To address the issue of providing stable slopes with a good compaction and a sound face anchorage for the geomembrane liner, it was decided not to adopt an anchorage based on geomembrane bands embedded in trenches, and to embed instead geomembrane anchor strips directly in the embankments as they were being raised, with a specific procedure allowing to adequately compact the final subgrade on which the geomembaren liner would be installed. The result is a stable slope of well compacted granular material, and an effective robust confinement of the anchor strips. After the strips had been embedded, a continuous geomembrane band was heat-seamed to their part protruding from the subgrade, creating a continuous vertical anchorage line, which distributes the stresses at placement and during

operation (Fig. 10 at left). The geomembrane liner is then secured to the embankment by heat-seaming it to the vertical anchor bands (Fig. 10 at right).

Fig. 10 – Abdelmoumen. At left, the geomembrane anchor strips embedded in the embankment, and the geomembrane anchor band heat-seamed onto them. At right, the geomembrane liner under installation on the slopes

The design wind velocity was about 90 km/h for both reservoirs, with a safety factor of at least 2. The resulting spacing of the vertical anchorage lines on the slopes is 8.0 m, measured along the crest. Considering the possibility of a complete emptying of the reservoirs, a specific anchorage system is provided in the bottom, consisting of trenches backfilled with concrete at 16 meters spacing.

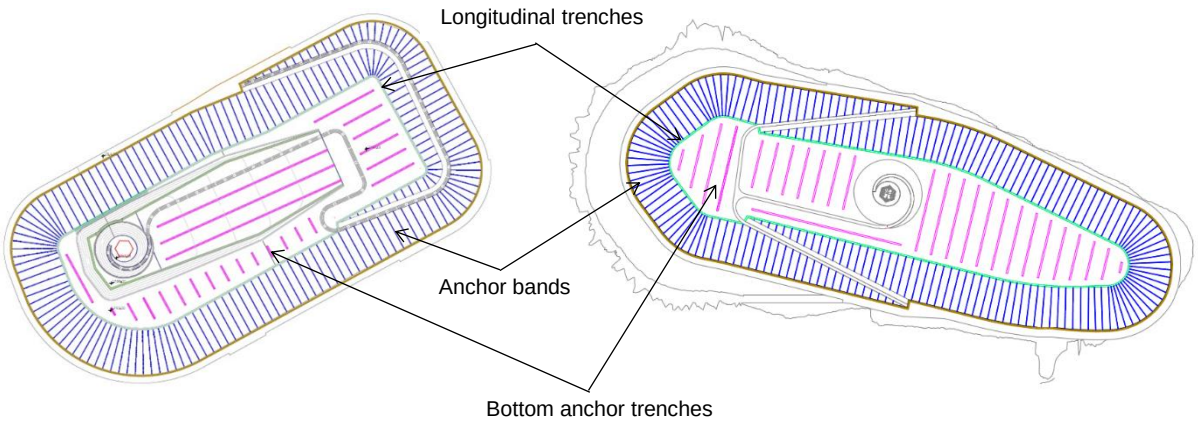

Fig. 11 – Abdelmoumen face anchorage system. At left, the upper reservoir, at right, the lower reservoir

Compaction of the embankments and installation of the geomembrane anchor strips started at the lower reservoir in April 2021, and the geomembrane system was completed in August 2022. At the upper reservoir, installation of the geomembrane anchor strips started in May 2022, and the geomembrane system was completed in January 2023. About 195,500 m^2 of exposed geomembrane liner have been installed. Additional anchorage lines consisting of

ballasting prefabricated concrete blocks were placed at some top locations of the upper reservoir where wind gusts stronger than expected were experienced (Fig. 12 at left). Impounding of both reservoirs for scheme testing is ongoing (Fig. 12 at right).

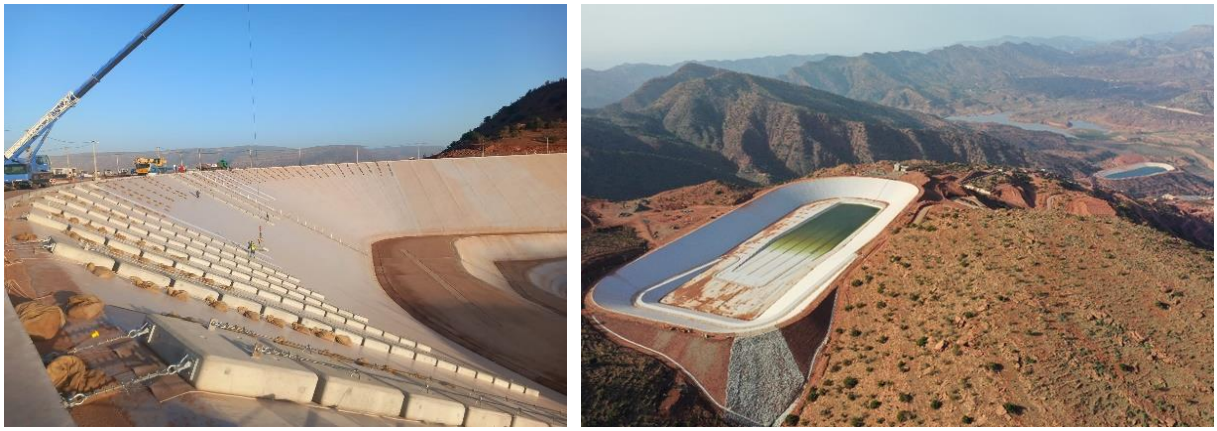

Fig. 12 – Abdelmoumen. At left, additional top anchorage in a section of the upper reservoir. At right, both reservoirs impounding

3. CONCLUSIONS

Carpi experience in existing and new pumped hydro storage schemes now accounts for 23 projects, with two additional projects, one started in 2024 and one starting in 2025. Experience has shown that geomembrane liners prevent water losses and resist settlements and differential movements, granting safety and efficiency of the schemes. They are a sustainable technology, which reducing construction time and costs, and allowing earlier generation, is also financially effective.

REFERENCES

[1] Scuero, A., Vaschetti, G., and Lilliu, G. (2015). Geomembrane systems in pumped storage schemes: Carpi experience. Second International Dam World Conference.

[2] Giroud, J.P. (2005). Quantification of geosynthetic behaviour. Geosynthetics International, Volume 12, No. 1.

[3] Giroud, J.P. and Soderman, K.L. (1995). Comparison of Geomembranes Subjected to Differential Settlement". Geosynthetics International, Volume 2, No. 6.

Fifth International Dam World Conference
PORTUGAL • LISBON • LNEC • APRIL 13-17, 2025
dam world 2025

EXPERIMENTAL INVESTIGATION OF SEDIMENT PROPAGATION IN CASE OF HOMOGENEOUS EARTH-FILL DAM BREAK BY PIPING

Zehra Büyüker[1]
İzmir Kâtip Çelebi University

Ebru Taşkaya

Gökçen Bombar
İzmir Kâtip Çelebi University

Gökmen Tayfur
İzmir Institute of Technology

ABSTRACT

During the earth-fill dam break, the water in the reservoir moves to the downstream region together with the sediment of the dam body. Considering the size of the dams, the resulting destruction can be huge. Hence, flood propagation is an important topic in terms of detecting and preventing risks that may occur after the dam break in the residential areas at downstream region. This experimental study was carried out in a concrete channel of 18 m long, 2 m wide and 0.88 m high in the Hydraulics Laboratory of İzmir Kâtip Çelebi University to define the sediment propagation during dam failure by piping. The dam body was constructed in the main channel; 2 m wide, 2.02 m long, and 0.6 m high. The upstream and downstream slopes of the dam were constructed to be 32˚ (1:1.6). After the water reached a certain level in the reservoir, the pump was turned off and the test period was initiated. During the experiment, the water levels were measured with metal rulers attached to the left of the channel and using the ULS-40D device; time-dependent precise level measurements were made with the sensors. Two cameras were placed on the channel in order to observe the propagation of sediments of the dam body. At the end the dam break, sediment height profile was obtained by using the sensor of the ULS40-D device. Firstly, the downstream edge of the dam was eroded before the sediment in the dam body propagated downstream. At the end of the experiment, approximately 50 cm of the dam body from the left bank was completely eroded, and the rest was partially transported. The fact that the flood wave came from the left bank caused the flow to be faster on this axis, and as a result, it caused the sediment to accumulate more on the right side.

Keywords: Earth-fill dam failure, sediment transport, piping.

[1]zehra.buyuker@ikcu.edu.tr, Türkiye

1. INTRODUCTION

A dam is a structure built across rivers, streams, or other water bodies to regulate water flow, thereby forming an upstream reservoir that stores water for several purposes [1,2]. Serving as a critical infrastructure, dams are engineered for a range of essential functions, including water supply management, flood control, and agricultural irrigation, and transportation purposes [3,4]. Additionally, many dams support renewable energy generation through hydroelectric facilities, contributing to sustainable energy needs.

Dams are structures that, in addition to their wide-ranging applications, can be systematically classified in various ways; with the most common classification based on their construction materials and aligning with specific environmental, geographical, and operational requirements. According to the body material of the existing dams by the ICOLD (International Commission on Large Dams); earth-fill (embankment) dams, rock-fill dams, gravity dams, buttress dams, barrages, arch dams and multiple arch dams [5]. Earth-fill dams are classified into three main types based on their internal structure and use of materials: homogeneous earth-fill dams, zoned earth-fill dams and diaphragm earth-fill dams as shown in Figure 1 [6]. In the construction of homogeneous earth-fill dams, a single type of material, usually well-compacted earth, is used. Zoned earth-fill dams are built using more than one material. The core zone, typically composed of low-permeability material like clay, acting as a barrier to prevent water seepage.

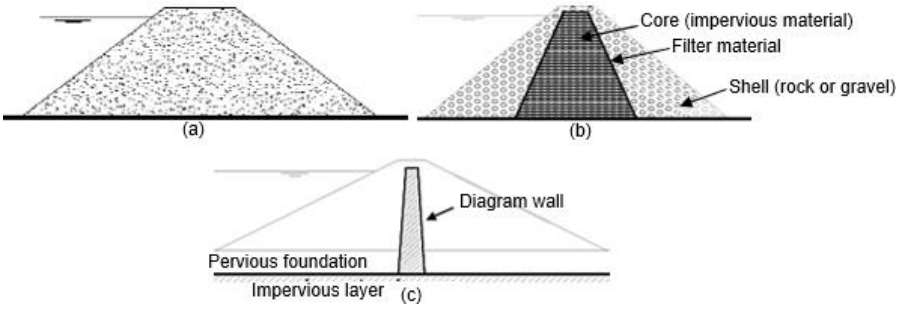

Fig. 1 – Different types of earth-fill dams (a) homogenous, (a) zoned (a) diaphragm [7]

According to ICOLD's 2023 data, a significant majority, about 67%, of the world's existing dams are classified as earth-fill dams [8,9]. In Turkiye, they constitute about 75% of large dams [10]. This distribution reflects a preference for fill-type dams due to their adaptability and cost-

effectiveness in local terrain and construction conditions. Since the filling material is natural materials that occur in nature, the material costs are minimal. Labor is very less compared to other types of dams. Most of the dam construction is completed with machinery [11].

Despite their many advantages, embankment dams have historically been prone to collapses and they account for 64% of all dam failures worldwide [12]. Their reliance on natural materials, such as soil and rock, makes them vulnerable to erosion, seepage, and structural weaknesses. Additionally, environmental factors like heavy rainfall, earthquakes, and changes in upstream water flow increase these vulnerabilities, leading to potential failures [6,13].

Most frequent causes of dam failures are overtopping, piping, foundation defects, materials used in dam construction and inadequate maintenance [14]. According to the Ağıralioğlu's study [15], 38% of earth- and rockfill dam breaks are caused by piping which occurs when water seeps through the embankment body, carrying away small particles of dam material and gradually enlarging the breach [4], 35% insufficient spillway capacity, 21% by ill-foundation, and 6% by other reasons mentioned above. Observations of real embankment failures, supported by laboratory experiments, indicate that piping erosion is particularly dominant in water structures composed of non-cohesive materials lacking a cohesive core. Teton Dam in the USA serves as a notable example of earth-fill dam failure caused by piping. During the initial filling of the reservoir, seepage was detected in the dam's right abutment. This seepage facilitated the removal of fine soil particles from the dam’s core, resulting in the formation of internal voids and the progressive enlargement of the seepage path. As the flow intensified, the erosion accelerated, ultimately leading to a critical loss of structural integrity and an uncontrollable breach. The failure of the Teton Dam resulted in the release of approximately 300 million cubic meters of water, causing catastrophic downstream impacts. The disaster led to the loss of 14 lives and extensive destruction of infrastructure, residential areas, and agricultural lands. Additionally, severe scouring and sediment deposition significantly altered the downstream landscape.

As a result, due to the dam break, large volumes of water stored in the reservoir exceeds the dam body and this uncontrolled water moves to the downstream region. Failures of earth-fill dams have shown that such events result in not only the uncontrolled flow of water but also the movement of sediment [16]. The resulting flood poses significant risks to residential areas and infrastructure located in the downstream region. Therefore, understanding these break mechanisms is important for predicting flood movement for assessing potential risks, implementing measures to protect downstream areas and reduce the impact of such catastrophic events.

Numerous experimental studies have been carried out to simulate the dam break phenomena. For example, Güney et al. [17] conducted an experimental study to simulate flood-wave propagation by constructing a three-dimensional scaled physical model of the Ürkmez Dam, with vertical and horizontal scales of 1/30 and 1/150, respectively. The model incorporated critical features such as the upstream reservoir, dam body, and a topographical representation of the downstream area, including the town, the highway, and the creek. Although their study was the first to reflect such detailed and large-scale components of a real dam system, the dam body was designed as a movable metal gate, a common approach in experimental studies on dam breaks. This approach is commonly utilized to simplify the modeling process while allowing for the analysis of flood-wave dynamics and associated impacts [18, 19, 20, 21, 22]. Dumlu [23] conducted 12 experiments to investigate piping-induced failure mechanisms in dam bodies. Piping was initiated by placing horizontal pipes of varying lengths at different locations within the dam body. The results revealed four distinct stages of the destruction process: the formation of wet areas in the downstream region, the initiation and progression of erosion in this region, the development of breaches, and the subsequent collapse of the structure. Also, Sharif et al. [24] investigated the piping process using cohesive earthen embankments in a laboratory flume.

Not only the experimental but also the numerical model simulations were done to understand the flood wave propagation. Okeke et al. [25], investigated the formation of pipes and breaches caused by piping in earth-fill dams. Analyses revealed that piping typically initiated in the downstream region and progressed toward the upstream. Kemaloğlu et al. [26] carried out 1-dimensional (1D) analysis of dam break of the Rahmanlar Dam, to determine whether or not the flood wave occurred as a result of dam break would reach the three villages located at the downstream of the dam. Elçi et al. [27] conducted an analysis of flood-wave propagation in the downstream regions resulting from the failures of the Porsuk and Alibey dams. They determined the maximum flow depths and velocities that could occur due to the dam breaks. Countless numerical studies were done to determine the propagation of flood wave [28, 29].

The existing literature indicates that most experimental studies have modeled dam bodies using movable metal gates, focusing primarily on flood-wave movement. While some studies have constructed earth-fill dam bodies, concentrating mostly on breaching and piping processes resulting from seepage. A significant knowledge gap exists in the literature

regarding the earth-fill dam body failure and resulting water and sediment transport at the downstream area in three dimensions. The objective of this study is to address this knowledge gap by conducting piping-induced earth-fill dam break experiment.

2. EXPERIMENTAL STUDY

This experimental study was carried out in the Hydraulics Laboratory of İzmir Kâtip Çelebi University to investigate the sediment propagation in case of homogeneous earth-fill dam break by piping.

2.1. Experimental Set-up

The experimental set-up consisted of two rectangular tributary channels merging into a rectangular, wider, downstream main channel (see Figure 2). Tributaries were connected at a 45° angle symmetrically to the sides of the main channel. Both tributaries were 4.9 m long and 1.00 m wide, whereas the main channel was 6.5 m long and 2.00 m wide. The lateral walls of these channels being 0.88 m high.

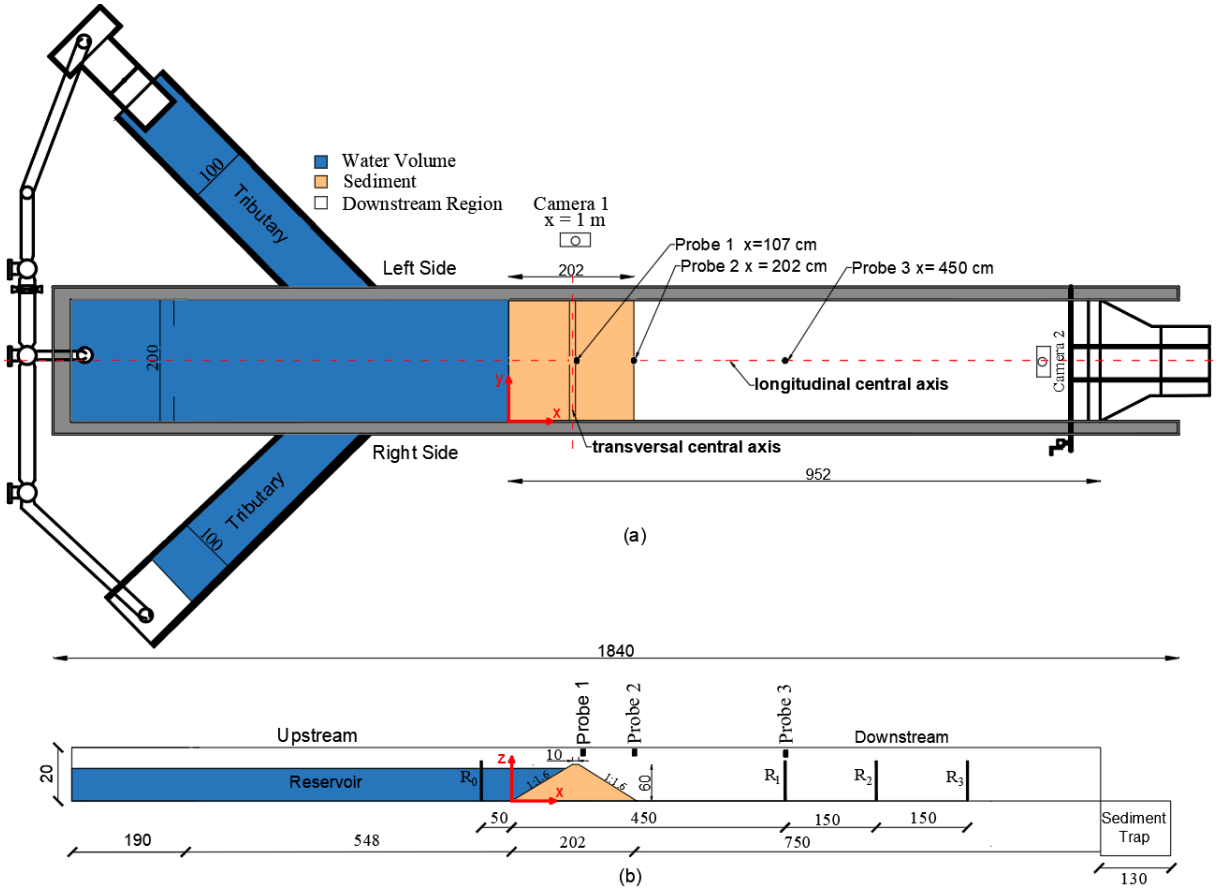

Fig. 2 – Experimental setup (a) plan, (b) view (all units are in cm)

The experimental set-up included a water reservoir placed underneath the laboratory floor. The dam reservoir which is shown in blue color in Figure 2, was filled with the transferred water from this tank to the system by the help of a pump.

The dam body consists of 6 layers with a height of 10 cm. The upstream and downstream slopes of the dam were constructed to be 32˚ (1:1.6) (see Figure 2-3).

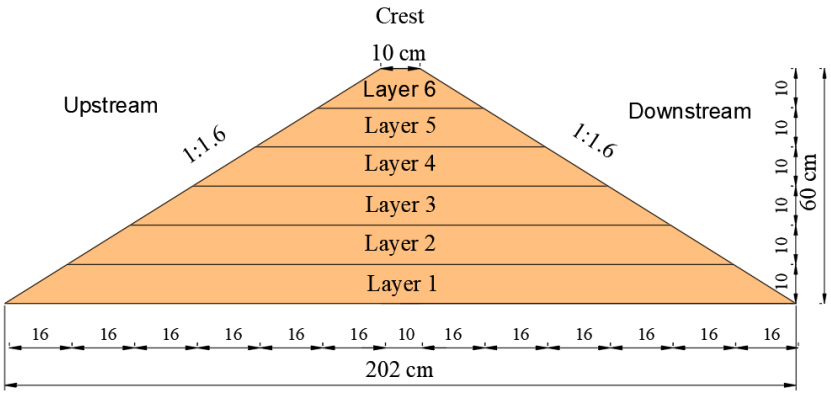

Fig. 3 – Dam body longitudinal section

4 rulers (R_0, R_1, R_2, R_3) were attached to the left wall of the main channel to measure the water level at x = -0.5 m, x = 4.5 m, x = 6 m, and x =7.5 m, respectively, such that one of them was in the upstream, the others were in the downstream region of the dam. (see Figure 2.b).

The sensors of the ULS-40D (Ultra-lab Level System) device were positioned at 3 different points of the channel longitudinal central axis to obtain the time-dependent precise water level measurement during the experiment (Figure 2). One of these sensors (Probe 1) was at x = 1.07 m which was just downstream of the crest level. Probe 2 was placed at x = 2.02 m, at the end of the downstream edge of the dam body. Probe 3 was positioned at x = 4.5 m (Figure 2). The ULS-40D sensor is widely utilized for measuring water surfaces in hydraulic laboratories and physical model simulation facilities. This sensor is an easy-to-use ultrasonic measurement system capable of quickly and accurately measuring water levels. The ULS-40D probes allow distance measurement ranging from 30 mm to 3.4 m and provide sub-millimeter resolution. The key feature of this device is its ability to perform measurements without disturbing the flow (non-intrusive).

Two cameras were used to monitor the sediment propagation from the dam body at two different points. Camera 1 (GoPro Hero 5) was placed at x = 1 m transversal central axis, in a

position to show the change in the dam body exactly. The camera 2 (Bood action camera) was positioned at the end of the main channel, at x = 9.5 m, along to longitudinal central axis so that it can see the downstream face of the dam.

The ULS-40D probe, installed on a rigid frame that could be placed at different x positions along the channels, was used to obtained the sediment depth profile variation at the end of the experiment. Also colored lines were drawn at 50 cm intervals downstream of the dam to determine the rate of progression of the sediment and water mixture along the channel.

2.2. Experimental Procedure

The homogeneous earth-fill dam body was constructed between x = 0 m and x = 2.02 m of the main channel, 2 m wide, by using uniform sediment with a median grain diameter (d_{50}) of 0.441 mm, at a height of 60 cm in 6 layers with a slope of 1:1.6 (Figure 2-3).

If an analogy were to be drawn with a real-world scenario, using the Froude similarity law and a distorted physical model with a distortion ratio of 5 [17], with a 1/30 vertical scale and a 1/150 horizontal scale, the dimensions of the experimental dam body in this study would correspond to a prototype with an 18 m height, a 300 m crest length, and a 1200 m distance from the downstream face edge of the dam body to the end of the downstream area.

The construction of the dam includes laying and compaction from 1st to the 6th layer (Figure 4-5).

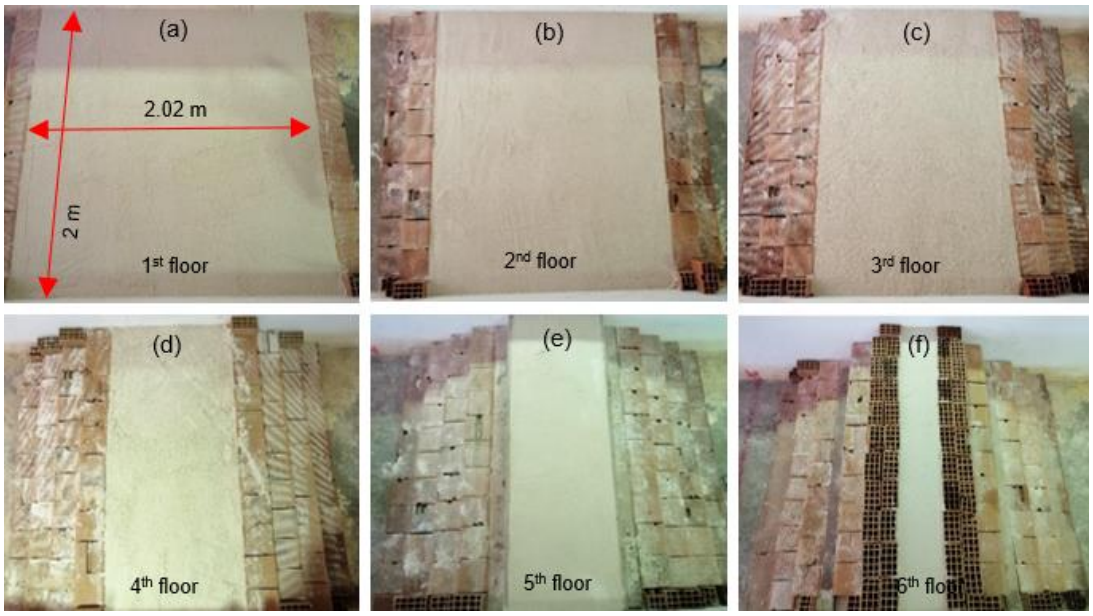

Fig. 4 – Construction steps of the dam body uncompressed a) 1st floor, b) 2nd floor, c) 3rd floor, d) 4th floor, e) 5th floor, f) 6th floor

The bricks were placed 2 m wide and 2.02 m long, as in Figure 3 a, and the sediment was laid to construct first layer of the dam body. Each layer of the dam body was formed as 10 cm thickness.

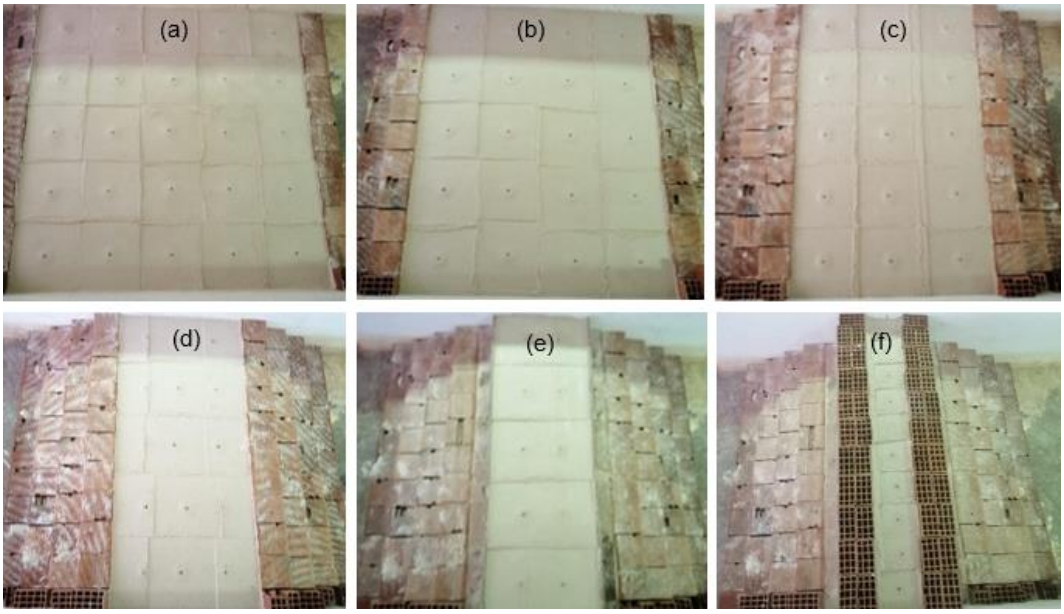

Fig. 5 – Construction steps of the dam body compressed a) 1st floor, b) 2nd floor, c) 3rd floor, d) 4th floor, e) 5th floor, f) 6th floor

While constructing the dam, standard compression methods were used (ASTM-D1557). Accordingly, an iron weight of 4.5 kg was dropped 10 times on a 40 cm × 40 cm plate from a height of 46 cm (Figure 6). The same procedure was performed on the 2nd floor to 5th floor, while the 20 cm × 20 cm plate was used when compressing the 6th floor.

Fig. 6 – Compaction materials

After the compression process was completed, the bricks placed the both face of the dam were removed and the slope of the upstream and downstream face were controlled with the help of a digital protractor so that the downstream and upstream face slope of the dam was retained as 32˚(1:1.6).

Figure 7 illustrates the final state of the constructed dam body, featuring a crest width of 10 cm, a height of 60 cm, a longitudinal base width of 202 cm, and a transverse base width of 200 cm, as well as the smooth downstream area and the probes, rulers and cameras. The plastic cover was placed at the upstream face of the dam body to prevent the dam any damage to the dam while filling the reservoir of the dam body with water (Figure 7).

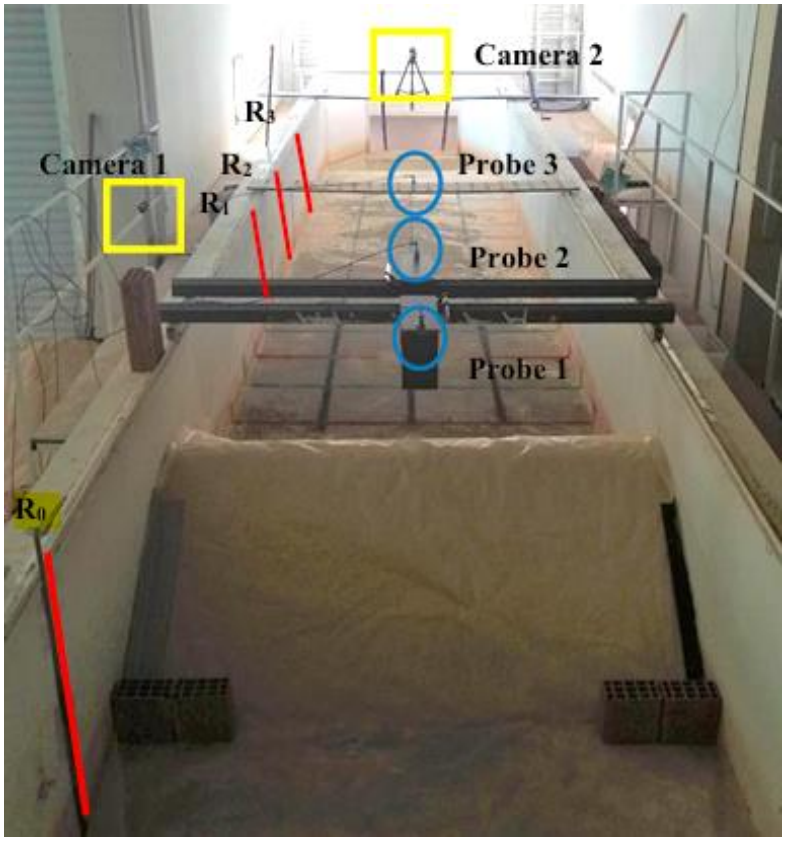

Fig. 7 – The final form of the dam body and measurement devices [3]

The reservoir volume was gradually filled over approximately 9 minutes prior to initiating the dam break. Once the water in the dam reservoir reached a certain level, the pump was turned off, and the plastic cover was removed from the upstream side without disturbing the reservoir water surface or the upstream face of the dam body and the test period was initiated. For the sake of simplicity, this timing is noted as t=0 s herein.

The filling of the reservoir was completed in 9 minutes and 19 seconds. The water level reached 53 cm in the reservoir. The volume of the reservoir was 11.64 m^3.

During the experiment, the water level was measured at 4 different points with metal rulers attached to the left wall of the main channel. In addition, time-dependent precise level measurement was made by using the sensors of the ULS-40D (Ultra-lab Level System) device at 3 different points of the channel longitudinal central axis during the experiment (Figure 2-7). With the help of these sensors, 100 data per second was obtained and depth changes were made with precise measurements. Experiment was recorded with cameras at 2 different points in order to observe the propagation of the sediments from the dam body. At the end of the experiment, the sediment depth profile variation was obtained with using the ULS-40D probe. Sediment height measurement was made at 10 cm intervals on the x and y axes and Surfer Software [30] was used to develop the topographical maps.

3. EXPERIMENTAL RESULTS AND DISCUSSION

The results obtained from the experimental study and conducted within the scope of this research examine the failure of a homogeneous earth-fill dam with smooth downstream conditions due to piping.

Figure 8 presents simultaneous images of the propagation of the flood wave captured by camera 2 (left column) and camera 1 (right column) at 137 s, 283 s, 297 s, 329 s, 347 s, and 427 s. The downstream face of the dam began to slide after 81 seconds, with nearly half of it eroded by 137 seconds (Figure 8 a-b). Erosion of the dam body continued up to the crest level until the 283rd second, the dam crest continued to be thinned and the water in the reservoir overflowed from the left bank over the crest (Figure 8 c-d). The breach widened rapidly from the left bank to the middle of the channel within 64 seconds, as shown in Figures 8 e-f, Figures 8 g-h, Figures 8 i-j. Due to the initial high kinetic energy of the flood wave, gradually propagated sediment along the main channel formed a threshold at 6.5 m distance from the downstream edge of the dam body in the left part. This buildup led to a noticeable water swell in this region, accompanied by a sudden increase in water depth, and this swell widened towards side walls (Figure 8 g-h, Figure 8 i-j, the blue arrows show the water swell). After 427 seconds, no further visible changes in sediment distribution were observed (Figure 8 k-l).

Fig. 8 – Flow and sediment propagation (Camera 2) and stages of breach formation (Camera 2) at a-b) 137 s, c-d) 283 s, e-f) 297 s, g-h) 329 s, I-j) 347 s, k-l) 427 s [3]

Figure 9 illustrates the sediment distribution at the downstream area at the end of the experiment. As shown, the right part of the dam body remained standing still, approximately

50 cm of the dam body from the left side has been washed away and sediment between 50 cm and 100 cm has been partially transported. The sediment moved to the downstream end, with a shallower sediment depth near the left side due to the high velocity of water flow. Higher sediment accumulation was observed near the right wall, between x=5 m and x=9 m.

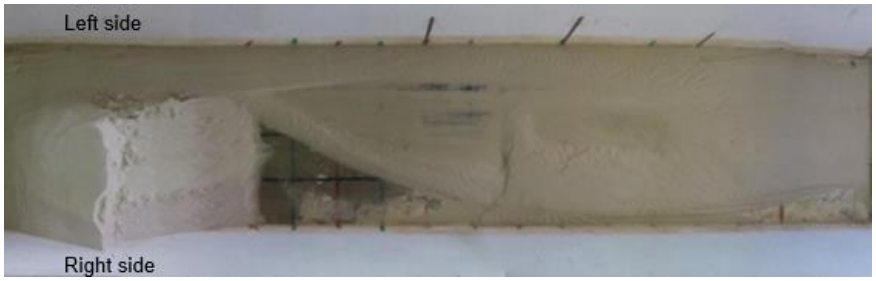

Fig. 9 – Picture of sediment distribution at the end of the experiment

At the end of the experiment, the sediment height readings were taken using the ULS-40D probe at 10 cm intervals along the x- and y-axes, and the three-dimensional contour map were created by using the Surfer Software as illustrated in Figure 10. It should be noted that these sediment depths were measured at the end of the experiment.

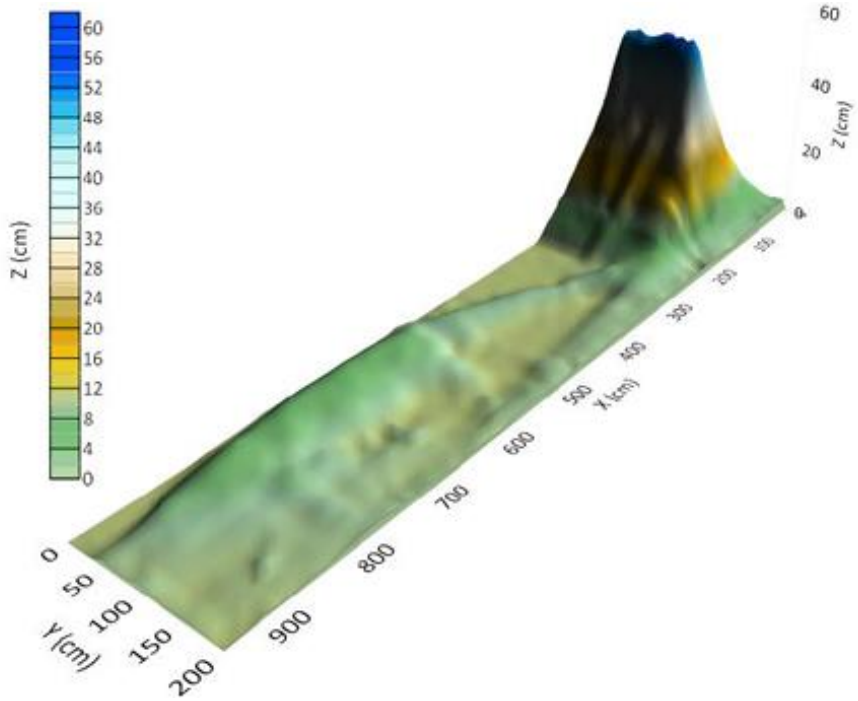

Fig. 10 – Three-dimensional contour map of sediment distribution at the end of experiment

As seen, sediment heights at a distance between 5 m and 9 m from the dam body varied

around 5 cm along the right side of the channel (y=0 cm to y=75 cm) The sediment depth would correspond to 1.5 m a distance between 750 m and 1350 m from the dam body in the prototype, based on the above-mentioned distorted model (the 1/30 vertical scale and 1/150 horizontal scale).

Figure 11 shows the longitudinal sediment height profiles (from x = 0 to 9.5 m) along the channel length. Here, y=0 cm and y=200 cm corresponds to the right and the left side, respectively. According to Figure 11a-b, the maximum sediment height in the dam body was approximately 49.1 cm at y=0 cm while it was measured at 4.2 cm at y=200 cm due to the dam failure occurring from the left side. The sediment height at x=2.02 m is 13.8 cm at y=0 cm and 2.2 cm at y = 200 cm. Along the streamwise direction, sediment height measured 0.2 cm and 1.8 cm at x=4 m; 0.8 cm and 0.5 cm at x=6 m; 0.4 cm and 1.7 cm at x=8 m for the y=0 cm and y=200 cm, respectively.

The maximum sediment height in the dam body is 49.8 cm and 4.7 cm for y=25 cm and y=175 cm, respectively. The sediment height at x=2.02 m is 13.9 cm at y = 25 cm and 3.1 cm at y=175 cm. Along the streamwise direction, sediment height measured 0.1 cm and 1.9 cm at x=4 m; 5.5 cm and 0.6 cm at x=6 m; 4.4 cm and 1.9 cm at x = 8 m for the y=25 cm and y=175 cm, respectively.

The maximum sediment height in the dam body is 50.1 cm and 13.2 cm for y=43.75 cm and y=156.25 cm, respectively. The sediment height at x=2.02 m is 14.1 cm at y=43.75 cm and 9 cm at y=156.25 cm. Along the streamwise direction, sediment height measured 0.7 cm and 0.9 cm at x=4 m; 5.2 cm and 0.0 cm at x=6 m; 5.5 cm and 2.2 cm at x=8 m for the y=43.75 cm and y=156.25 cm, respectively.

The maximum sediment height in the dam body is 52.6 cm and 25.8 cm for y=62.5 cm and y=137.5 cm, respectively. The sediment height at x=2.02 m is 13.7 cm at y=62.5 cm and 13.7 cm at y=137.5 cm. Along the streamwise direction, sediment height measured 2.8 cm and 0.2 cm at x=4 m; 4.3 cm and 0.1 cm at x=6 m; 4.9 cm and 2.1 cm at x=8 m for the y=62.5 cm and y=137.5 cm, respectively.

The maximum sediment height in the dam body is 53.7 cm and 38.8 cm for y=81.25 cm and y=118.75 cm, respectively. The sediment height at x=2.02 m is 14.7 cm at y=81.25 cm and 14 cm at y=118.75 cm. Along the streamwise direction, sediment height measured 2.3 cm and 0.2 cm at x=4 m; 2.7 cm and 0.0 cm at x=6 m; 4.3 cm and 2.9 cm at x=8 m for the y=81.25 cm and y=118.75 cm, respectively.

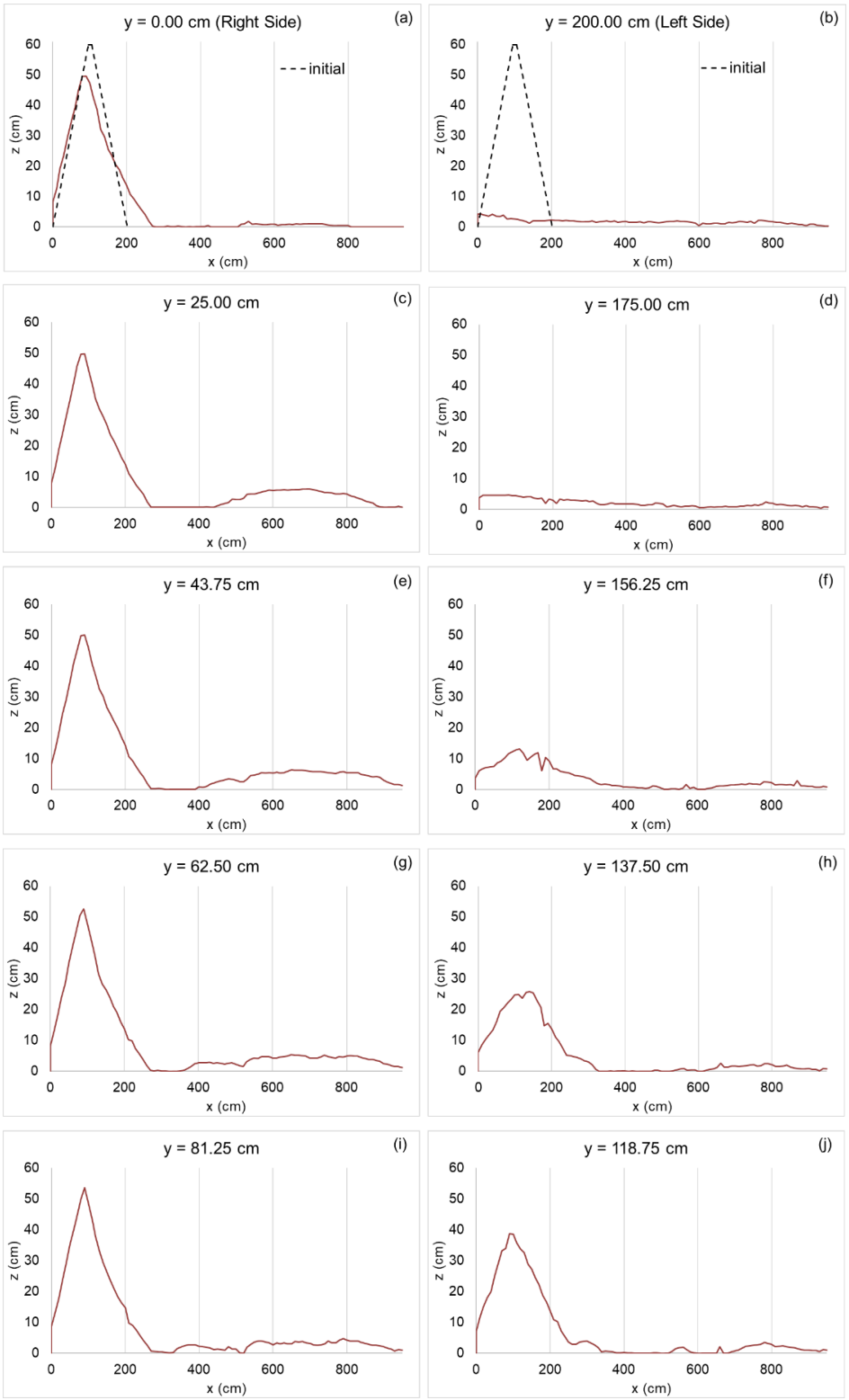

Fig. 11 – a-j) Longitudinal sediment height profiles measured along the channel width

Additionally, sediment on the downstream edge of the dam body shifted from 200 cm to 270 cm in the sections between y=0 cm and approximately y=100 cm.

The final topography obtained at the transversal central axis of the dam body that corresponds to the crest is depicted in Figure 12. As shown, the right part of the dam body remained standing still, approximately 50 cm of the dam body from the left side has been washed away and sediment between 50 cm and 100 cm has been partially transported.

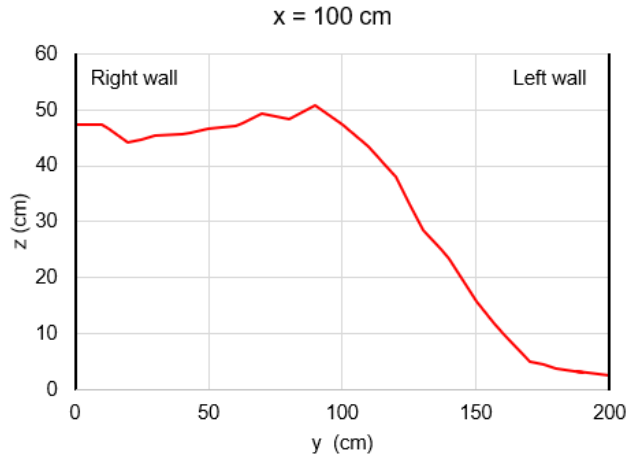

Fig. 12 – Transversal crest section of the dam body

Figure 13 shows the sedimentary water levels measured by Probe 1, Probe 2, and Probe 3 sensors and R_0, R_1, R_2, R_3 rulers, during the experiment. Probe 1 and R_0 were placed at the upstream part of the dam body, while the remaining sensors and rulers were placed at the downstream part of the dam body.

Figure 13a illustrates the levels measured by Probe 1 (sensor) and R_0 (ruler). R_0 indicates the change in water level within the reservoir (x = -0.5 m), while Probe 1 shows the level changes at the dam body location (x = 1.07 m). As observed in R_0, the water level began to decrease at the 285th second, corresponding to the moment when water in the reservoir overflowed from the left bank over the crest as in Fig 8 c-d. After that point, the water level decreased from 53 cm to 8 cm at the end of 800 seconds. As seen in Probe 1, due to the right portion of the dam body remained standing, no significant change was observed in the dam body.

Figure 13b shows the levels measured by Probe 2 sensor. Probe 2 shows the change in the level at the end of the dam body (x=2.02 m). The water in the reservoir passed through the gaps in the dam body and the sediment in the dam body started to be transported to the downstream region after 81 seconds. It was observed that the height of the transported sediment increased up to 6.5 cm (t= 277 s).

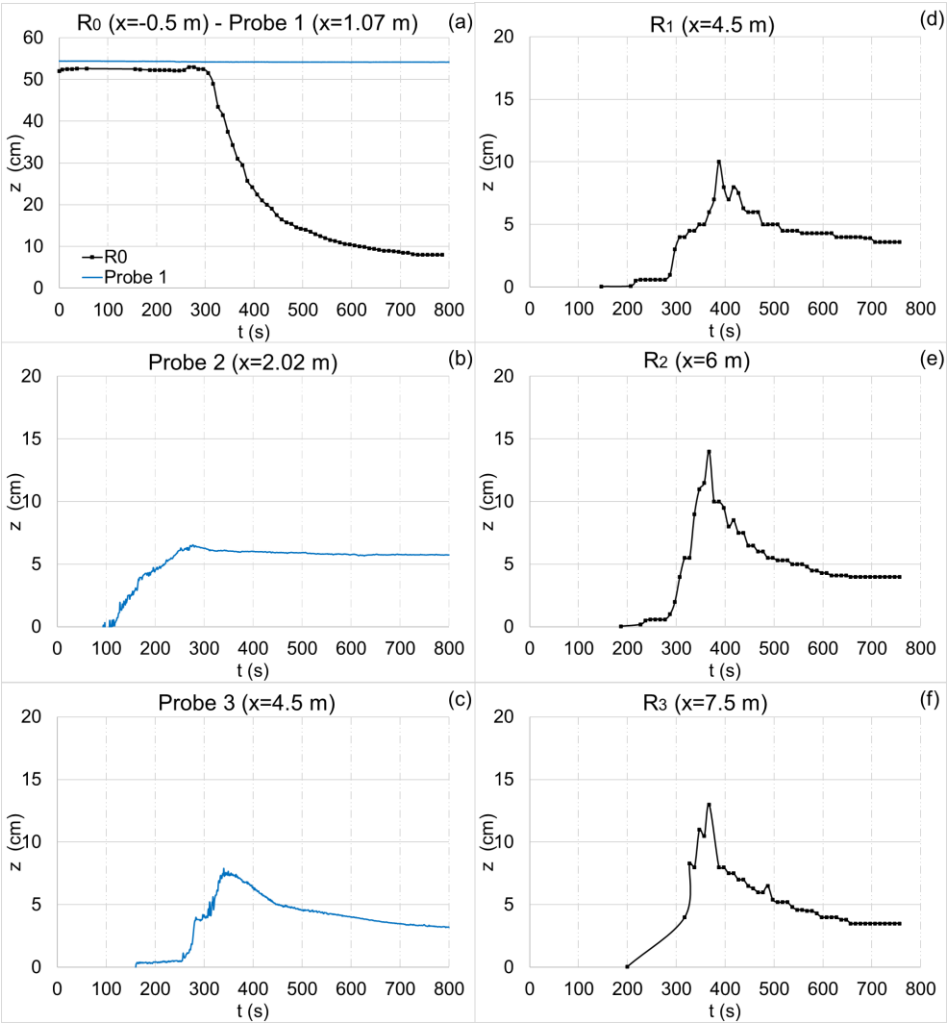

Fig. 13 – Measured levels by the sensors and rulers during the experiment

Figure 13 c-d show the levels measured by Probe 3 (sensor) and R_1 (ruler). While the sensor was positioned at the channel longitudinal central axis, R_1 was placed to the left wall of the main channel. Both measurements capture the level change in the channel at the x=4.5 m section. The water reached Probe 1 and R_1 at 161 seconds and 147 seconds, respectively. The maximum level recorded by Probe 3 was 7.9 cm at 340 seconds, while the maximum level of R_1 was 10 cm at 387 seconds.

Figures 13 e-f show the levels measured by the R_2 and R_3 rulers positioned at x=6.0 m and x=7.5 m, respectively, along the main channel. The water reached R_2 at 187 seconds and R_3 at 200 seconds. The maximum level of R_2 was 14 cm, while R_3's was 13 cm at 367 seconds.

During the experiment, while the dam break is in progress, the sedimentary water levels can reach 14 cm at 4 m distance from the downstream face edge of the dam body (R_3), which corresponds to 4.2 m level at about 600 m distance in the prototype according to the above-mentioned distorted model. This result indicates that, during the dam break, the flood flow could reach a height comparable to that of a 2-floor building. These findings can be considered compatible with those observed during the dam failure in Jakarta, Indonesia, where a 16-meter-high earth-fill dam broke in 2009 due to heavy rainfall. Reports included that a surge of water and debris several meters high inundated the town of Cirendeu, washing away cars, homes, and a brick-built bridge. The flood caused standing water with the 2.5 m depth, submerging approximately 400 homes [3]. Also, the failure of the Kelly Barnes Dam in 1977, caused by heavy rainfall over several days, resulted in a catastrophic flood wave that surged down the valley, inundating the surrounding areas, including Toccoa Falls College causing the deaths of 39 people [31].

4. CONCLUSIONS

This study was carried out in a concrete channel of 18 m long, 2 m wide and 0.88 m deep in the Hydraulics Laboratory of İzmir Kâtip Çelebi University to define the sediment propagation during earth-fill dam break by piping. The homogeneous dam body was constructed in the main channel, 2 m wide, 2.02 m long, by using uniform sediment with a median grain diameter (d_{50}) of 0.441 mm, at a height of 60 cm in 6 layers with a slope of 1:1.6. The stages of dam breach, along with associated flow and sediment movements, were closely monitored throughout the failure process. During the experiment, water levels were measured with metal rulers attached to the left side of the channel, while the ULS-40D device provided precise time-dependent measurements through its sensors. Two cameras were positioned along the channel to observe sediment propagation from the dam body. After the dam break, the sediment distribution map was obtained using the ULS-40D probe.

The results show that, initially, the sediment in the dam body started to be transported to the downstream region as the water in the reservoir passed through the breaches in the dam body and the downstream skirt of the dam is eroded. After the dam broke, subsequently, a water-sediment mixture propagated downstream. By the end of the experiment, approximately 50 cm of the dam body from the left side had been washed away, while the sediment between 50 cm and 100 cm had been partially transported. The flood wave originated from the left bank, resulted in a faster flow along this axis and caused an increased sediment accumulation along the right wall.

While the most experiments designed the dam body as a movable gate in literature, in this study, the whole dam body was constructed using actual sediment, providing experimental data that can serve as a robust foundation for developing numerical models that could later be applied to simulate such catastrophic events at larger scales. The experimental data can facilitate the identification of risky and affected areas that may emerge during the collapse of existing dams and contribute to the necessary planning.

Actual earth-fill dams have a clay core. Therefore, constructing this clay region and conducting experiments may be recommended for future studies to enable numerical models to accurately simulate real dams and calibrate the related numerical models.

ACKNOWLEDGEMENTS

This study is financially supported by Turkish Science and Technological Research Council (TUBITAK) through Project No: 119M959. We deeply thank TUBITAK.

REFERENCES

[1] Urzica, A., Pintilie, A. M., Stoleriu, C. C., Cîmpianu, C. I., Hutanu, E., Pricop, C. I., Grozavu A. (2020). Using 2D HEC-RAS modelling and embankment dam break scenario for assessing the flood control capacity of a multi-reservoir system (NE Romania). Water 13.1 (2020): 57.

[2] Büyüker, Z., Taşkaya, E., Bombar, G., Tayfur, G. (2024). Mansap pürüzlülüğünün toprak dolgu barajın üstten aşma ile yıkılması durumunda taşkın dalgası ve sediment yayılımına etkisinin deneysel olarak incelenmesi. Fırat Üniversitesi Mühendislik. Bilimleri Dergisi 36.1 (2024): 341-356.

[3] Taşkaya, E. (2023). Experimental investigation of propagation of sediment due to earth-fill dam break, Master's Thesis, İzmir Kâtip Çelebi University.

[4] Najar, M. (2021). Production and assessment of hazard maps for dam-break connected floods in the case of embankment dams through GIS and mathematical models, PhD Thesis, Dokuz Eylül University.

[5] International Commission on Large Dams, Deterioration of Dams and Reservoirs, Examples and Their Analysis, 1983. http://www.icold-cigb.org

[6] Yardımcı, E. (2019). Toprak dolgu barajların tasarım esasları: Boğazköy Barajı örneği, Master's Thesis, İstanbul University.

[7] Kirra M. S. A. (2015). Combined seepage and slope stability analysis of reservoir earth dams, Master's Thesis, Tanta University.

[8] International Commission on Large Dams, General Synthesis, 2023, https://www.icold-cigb.org/article/GB/world_register/general_synthesis/general-synthesis

[9] Foster, M., Fell, R., Spannagle, M. (2000). Statistics of embankment dam failures and accidents. Canadian Geotechnical Journal 37.5 (2000): 1000–1024.

[10] Saraylı, S. (2024). Baraj güvenliği ve dolgu barajlarda sayısal analiz: İkizdere Barajı örneği, Master's Thesis, Sakarya University.

[11] Coşkun, H. (2021). Dolgu barajlarda gövde stabilitesi ve Çukurca Barajı örneği, Master's Thesis, Karabük University.

[12] Yanmaz, A. M., Beser, M. R. (2005). On the reliability-based safety analysis of the Porsuk dam. Turkish Journal of Engineering and Environmental Sciences 29.5 (2005): 309–320.

[13] Tilav E. S. (2021). Baraj yıkılması sonucu oluşan taşkının incelenmesi: Darlık Barajı örneği, Master's Thesis, İstanbul University.

[14] International Commission on Large Dams, Dams' safety is at the very origin of the foundation of ICOLD, https://www.icold-cigb.org/GB/dams/dams_safety.asp

[15] Ağıralioğlu, N. (2011). Baraj güvenliği. Beta Basım Yayım Dağıtım A.Ş.

[16] Taşkaya, E., Bombar, G., Tayfur, G. (2023). Experimental investigation of sediment movement as a result of homogeneous earth-fill dam overtopping break over a simplified urban area. Journal of Hydrology 617(B) (2023).

[17] Güney, M. S., Tayfur, G., Bombar, G., Elçi, Ş. (2014). Distorted physical model to study sudden partial dam break flows in an urban area. Journal of Hydraulic Engineering 140.11 (2014).

[18] Kocaman, S., Güzel, H. (2011). Baraj yıkılması taşkın dalgası yayılmasının 3-boyutlu deneysel ve nümerik karşılaştırılması. Engineering Sciences 6.1 (2011): 406-414.

[19] Kocaman, S., Çagatay, H. O. (2015). Investigation of dam-break induced shock waves impact on a vertical wall. Journal of Hydrology 525 (2015): 1:12.

[20] Liu, W., Wang, B., Guo, Y., Zhang, J., Chen, Y. (2020). Experimental investigation on the effects of bed slope and tailwater on dam breakflows. Journal of Hydrology 590 (2020).

[21] Wang, B., Liu, W., Wang, W., Zhang, J., Chen, Y., Peng, Y., Liu, X., Yang, S. (2020). Experimental and numerical investigations of similarity for dam-break flows on wet bed. Journal of Hydrology 583 (2020).

[22] Bahmanpouri, F., Daliri, M., Khoshkonesh, A., Namin, M.M., Buccino, M. (2021). Bed compaction effect on dam break flow over erodible bed; experimental and numerical modeling. Journal of Hydrology 594 (2021).

[23] Dumlu, E. (2022). Experimental and numerical investigation of the evolution of piping and resulting breach in earth-fill dams, Master's Thesis, İzmir Institute of Technology.

[24] Sharif, Y. A., Elkholy, M., Chaudhry, M. H., Imran, J. (2015). Experimental study on the piping erosion process in earthen embankments, Journal of Hydraulic Engineering ASCE 141.7 (2015).

[25] Okeke, A. C., Wang, F., Sonoyama, T., Mitani, Y. (2012). Laboratory experiments on landslide dam failure due to piping: An evaluation of 2011 typhoon-induced landslide and landslide dam in Western Japan. Environmental Science and Engineering (2012): 525-545.

[26] Kemaloğlu, N. P., Koçyiğit, M. B., Akay, H. (2019). Baraj yıkılması taşkın dalgası yayılımınım 1-boyutlu sayısal simülasyonlarla incelenmesi: Rahmanlar Baraj örneği. Gazi University Journal of Science Part C: Design and Technology 7.1 (2019): 97-111.

[27] Elçi Ş., Tayfur G., Haltas İ., Kocaman B. (2017). Baraj yıkılması sonrası iki boyutlu taşkın yayılımının yerleşim bölgeleri için modellenmesi. Teknik Dergi 28.3(2017): 7955-7975.

[28] Nsom, B., Debiane, K., Piau, J.M. (2000). Bed slope effect on the dam-break problem. Journal of Hydraulic Research 38.6 (2000): 459-464.

[29] Macchione, F. (2008). Model for predicting floods due to earthen dam breaching. I. Formulation and Evaluation. Journal of Hydraulic Engineering 134.12 (2008): 1688-1696.

[30] Surfer (2022). "Surfer® Quick Start Guide, Contouring and 3D Surface Mapping for Scientists and Engineers" Golden Software, LLC, www.GoldenSoftware.com, https://downloads.goldensoftware.com/guides/SurferQSG.pdf.

[31] Sowers, G.F. (1978). Reconnaissance report on the failure of Kelly Barnes Lake, Toccoa Falls, Georgia. National Research Council.

Fifth International Dam World Conference
PORTUGAL • LISBON • LNEC • APRIL 13-17, 2025
dam world 2025

EMBANKMENT DAM MONITORING USING ELECTRICAL RESISTIVITY TOMOGRAPHY FOR ABNORMAL SEEPAGE ANALISYS

Altan Abdulamit
Technical University of Civil Engineering, Bucharest, Romania

Tudor Pisculidis[1]
Someș-Tisa Regional Water Administration, Cluj-Napoca, Romania

Răzvan Obreja
Mureș Regional Water Administration, Târgu Mureș, Romania

ABSTRACT

Earthfill dams represents the most common type of dams, but also having most of the accidents occurred at these structures. However, the percentage of failed earthfill dams from the total dams of this type is below 1% [1]. One of the main reasons of structural failures is associated with abnormal seepage that can trigger an internal erosion process. Dam structural monitoring is a regularly technical inspection which includes visual inspection and measurement using geotechnical instrumentation. After 50-60 years in operation, embankment dams' instruments started to display some abnormal values that need verification by using alternative investigation, such as the non-destructive ones. One of the main geophysical methods with the potential to detecting seepage and structural failure associated with dams is the electrical resistivity tomography (ERT) or imaging (ERI). ERT consists in research of interrelation between soil structure and resistivity distribution, measured on the ground surface. ERT represents the modern adaptation of the classical resistivity method in continuous current. High water level in open standpipe piezometers at the crest of the Calinesti embankment dam were compared to 2D and 3D ERT results. Induced polarization and 2D ERT were conducted throughout the length of dam's crest and 3D models were built for each standpipe piezometer. At the Suplacu de Barcau embankment dam, ERT method was used in conjunction with a thermal camera for detecting possible leakage on the downstream face of the dam. Because the dam was not instrumented for seepage monitoring, a non invasive and rapid acquisition method was preferred, as a preliminary investigation. At the Taul Mare historical dam, built in the 17th century, the development of an internal erosion process within the dam body was detected using geophysical methods. ERT equipment was used in order to locate hollow zones in the embankment and to adopt counter measures to prevent any subsequent structural failure.

Keywords: embankment dam, seepage detection, structural failure, resistivity tomography, internal erosion.

[1]tudor_pisculidis@yahoo.com, Romania

1. INTRODUCTION

Statistic data (ICOLD 1995) shows that most accidents occur on dams having reduced crest height (H< 30 m). Meanwhile, tall dams (over 100 m) have low damage frequency. This aspect is due to a superior care for implementing biggest projects of large dams (extensive field studies, design and execution by superior competent personnel, rigorous monitoring etc).

The extensive needs of water for diverse services, the capitalization of hydroelectric potential and demands for flood risk management have determined the accomplishment of over 2000 dams in Romania, of which 246 are considered large dams, according to ICOLD criteria [2]. Most dams were built between 1950s to 1980s.

Embankment dams record quite great accident frequency compared to other types of dams, excepting buttress dams. The reasons for these situations are diverse. Embankment dams are built using natural materials having geomechnical parameters with rather broad dispersions, foundations and materials for dam bodies have lower strength characteristics. Also, embankment dams are more vulnerable to overtopping and seepage.

When seepage increases in an earthfill dam, internal erosion may occur, resulting in the formation of piping. This can lead to sinkholes underneath the crest or sideslopes [3]. The result may be the sudden collapse of the dam.

Hence, practical methods for seepage monitoring and internal erosion detection are well appreciated. Surveillance of dams that are in service for over 50 years, has shown that existing methods are sometimes insufficient.[4] Therefore, is a worldwide need for diverse and improved monitoring. The most frequent types of earthfill dam failures include overtopping and internal erosion through dam body and/or foundation. [5]

Nominal processes for internal erosion emergence include seepage and pore pressure measurements, water turbidity and visual inspections.

Abnormal seepage, both elevated and concentrated, may result in dam failure. The mechanism of structural damage may take place during the first impoundment of the reservoir, but also after may years of uncovered seepage. [6]

Geophysical methods for investigating dams are commonly used when a disturbance appear during the monitoring process. Geoelectrical tomography has shown the capability to detect and locate preferential flowpaths through dams and their foundations.

2. DESCRIPTION OF THE GEOPHYSICAL METHOD

2.1. Electrical resistivity tomography

Geoelectrical investigation studies the behaviour of the natural or induced (artificial) electric field of rocks. Natural electric field or electromagnetic is created by earthly currents, polarization of deposits or metallic ore. Induced electric fields may be obtained using DC or AC sources coupled with soil surface through electrodes.

Decisive factors that influence the rock resistivity includes the nature and concentration of solid mineralogical components, geometric configuration of pores, saturation of pores, composition and concentration of electrolyte inside of pores, soil temperatures, soil pressures, soil texture, structure and geologic age.

Electrical resistivity imaging is a combination of electric profiling and vertical electric sounding (VES). ERT (ERI) method consists of determining of resistivity along the profile of observation, with successive measurement devices, with regards to the needed depth of investigation.

Recent improvements in resistivity equipment, inversion software and computer technology have enabled labs, institutions and companies to use ERT method for many purposes : finding optimal location for groundwater wells, finding caves, voids and sinkholes, depth of bedrock, natural slope monitoring, finding and monitoring pollution plumes, marine 2D and 3D surveys, lithology, finding mineral deposits, exploring archaeological sites, time-lapse (4D) monitoring etc.

3D resistivity surveys are used to solve complex problems where 2D are inadequate. The most common method for 3D acquisition data is parallel 2D line surveys (sometimes called 2.5D). 2D and 3D methods use depend on the available equipment, topographic conditions, cost and time constrains. [7]

In field investigation, for different geologic site various configurations of electrode arrangements can be used.

a) Wenner array, where the four electrodes are placed in a line with equal spacing, with the outer electrodes are the current electrodes (A, B) and the two inner ones (M, N) are potential electrodes.

b) Schlumberger array, where the two outer electrodes (A, B) are current electrodes and and two inner electrodes (M, N) placed close together in the middle are potential electrodes.

c) Dipole-dipole array, where both the current electrodes (A, B) and the potential electrodes (M, N) are placed together as dipoles, with the distance typically larger that the dipole size.

The most common configurations are presented in Fig 1:

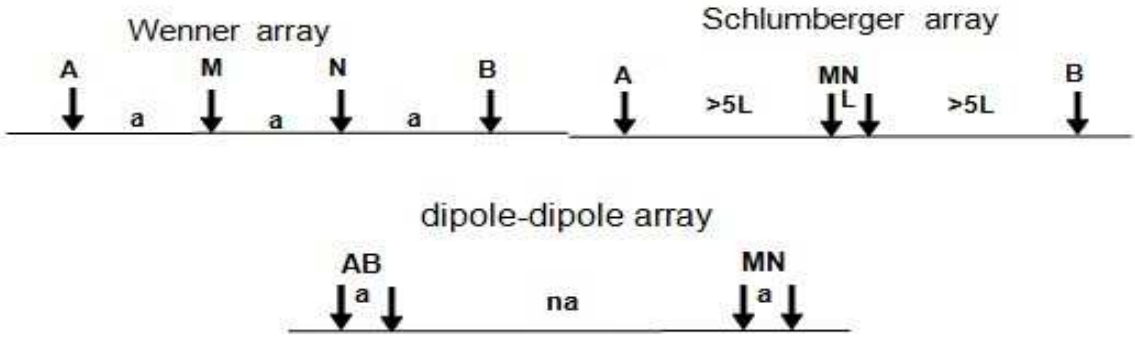

Fig. 1 – Wenner, Schlumberger and dipole-dipole arrays for field investigation

3. SUPLACU DE BARCĂU DAM

3.1. Description of the test site

Suplacu de Barcau is an earthfill dam that impounds a reservoir of 17,86 hm^3, of which 6,02 hm^3 represents the normal (useful) storage capacity. The dam has a maximum height of 11 m and a crest length of 1725 m. The crest is at an elevation of 174,50 maSL with 6 m in width. The upstream face has 3:1 slope and the downstream face has 2,5:1 slope. The upstream face has a concrete lining consisting of reinforced concrete with thickness of 15 cm, while the foundation was sealed using a "Kelly" slurry wall reaching to depths of max. 8 m with 60 cm thickness.

The dam has spillways consisting of 3 openings (3x12 m total width). The maximum discharge capacity of the spillways is 359 m^3/sec. An intake tower contains two concrete galleries of 2,00x2,50 m section each, representing the bottom outlets.

The reservoir was designed for water supply and flood control.

3.2. Abnormal seep

In the design phase of the dam, it was planned to use earthen materials with low permeability characteristics, hence it was not considered necessary to install devices for seepage monitoring and analysis.

In April 2013 and later, in March 2017, a seep has been observed at the downstream toe, followed by extensive inspections of the dam. The events occurred with the reservoir filled

near the normal water elevation. After the inspections a decision was made to install standpipe piezometers at the downstream toe of dam, to measure seepage discharge and extend the levelling topographic measurements.

3.3. Geoelectric study - phase 2013

The purpose of the ERT investigation was to identify seepage zones in the dam structure. The study was conducted in May 2013 using a Wenner-Schlumberger method with 64 electrodes.

Fig. 2 – Location of geoelectric sections at the Suplacu de Barcau Dam.
FPi – location of the analysed cross sections

During the study, two longitudinal and eight cross sections were studied, as presented in Fig. 2. The location of each section was chosen empirical, based on the expert judgement and taking into account quite equal distances between the successive sections.

Geoelectric investigation data results showed 3 sections with clear seepage traces, presented in Fig. 3.

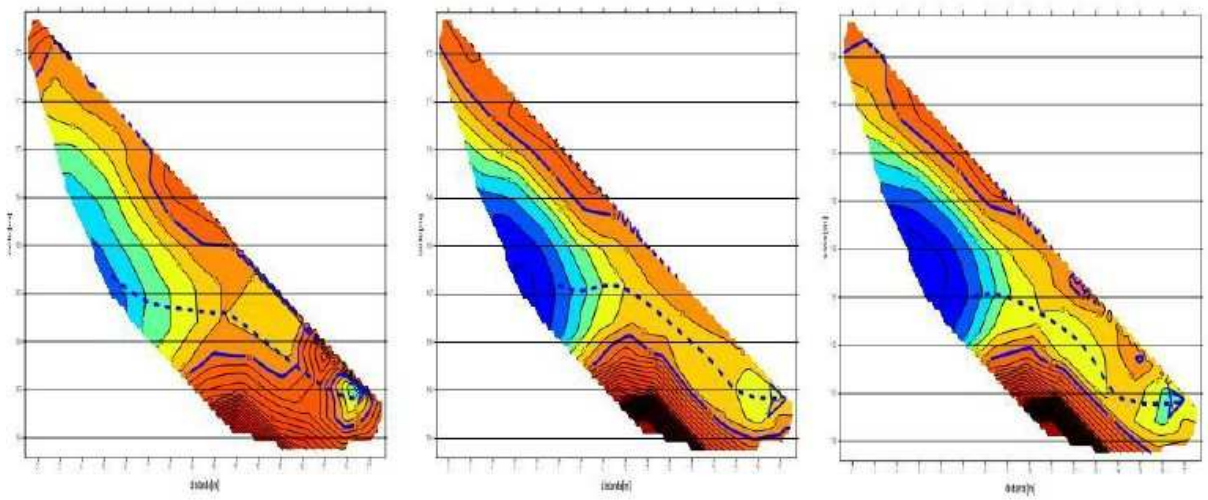

Fig. 3 – Geoelectric cross sections, abnormal zones marked, possible seepage line detected (blue dotted line) at Suplacu de Barcau Dam, 2013 campaign

The lithology was composed of cohesive materials (clay and marl - bedrock) and non cohesive materials (sand and gravel). The dam was built as a homogeneous mixture of both materials, and the seepage line was detected at 25 Ohm*m threshold, which divides clay from sand and gravel.

ERT study showed multiple anomalous areas of potential seepage origin. Further studies were considered necessary, in order to clarify the situation. Longitudinal profiles were to be executed from the crest beyond the toe of the downstream face, with space of 2-3 m, while cross sections were to be created throughout the length of the dam, including both upstream and downstream slopes.

3.4. Geoelectric study - phase 2020

A second study was conducted in August 2020 and consisted of 3 2D sections measured at the crest of dam. The maximum depth of the investigations was set at 45 m.

On the first section - SB1 (Fig. 4), there is a spur that extends beyond the depth of 45 m (orange - red colour - at 115 m). Also, at the 75-85 m disposition of the electrodes, the area was characterized by low Ohm*m values, between 1 - 30 Ohm*m, with predominant values at 10 Ohm*m, associated to the paleo-stream of the river Barcau. The area is represented by divisions of sand, gravel and clay, associated to the old river meadows. A possible origin for seepage in the SB1 section might be the influence of this paleo-stream, but also the presence of some local aquifers.

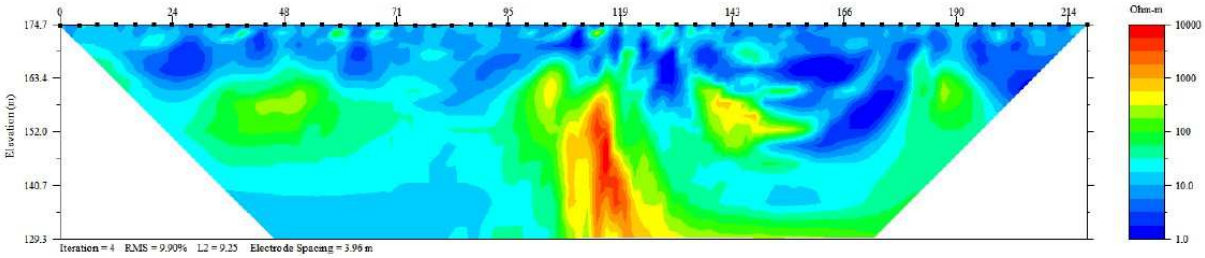

Fig. 4 – Electric resistivity tomography - SB1 section at Suplacu de Barcau Dam, 2020 campaign

To conclude, the dam consists of various areas with materials of different resistivity, prevailing lower values. The bedrock is presented with higher values, as normal, with different gap areas representing the paleo-streams of the river Barcau.

3.5. Thermography non-destructive testing

A thermography study was conducted in order to identify imperfections within the dam / embankment structures, related to seepage. In the first phase, field measurements were

performed on the areas of the downstream face that were considered normal. These areas were chosen, where possible, near the piezometric sections, in order to analyze and compare seepage lines. Thus, the reference measurement is obtained.

Further measurements were performed all along the downstream face of the dam, in order to detect abnormal data in relation with the reference value. The basic condition is to have all the measurements taken on the same circumstances (atmospheric temperatures, rainfall, reservoir elevation). Deflection values report impervious or drainage faults.

Independently performed or in sequence with other NDTs, IR tomography of the downstream face represents a convenient, efficient and relatively inexpensive method to detect, through NTDs, early imperfections and dissimilar behaviour that may cause severe structural failures, if left unchecked. Investigations using IR tomography method were performed on the downstream face of the dam, close to the right sideslope, where anomalous behaviour was reported. The ditch at the toe of the dam, separates it from the natural site. The ditch is located below the top surface, at the base of the drainage system of the dam.

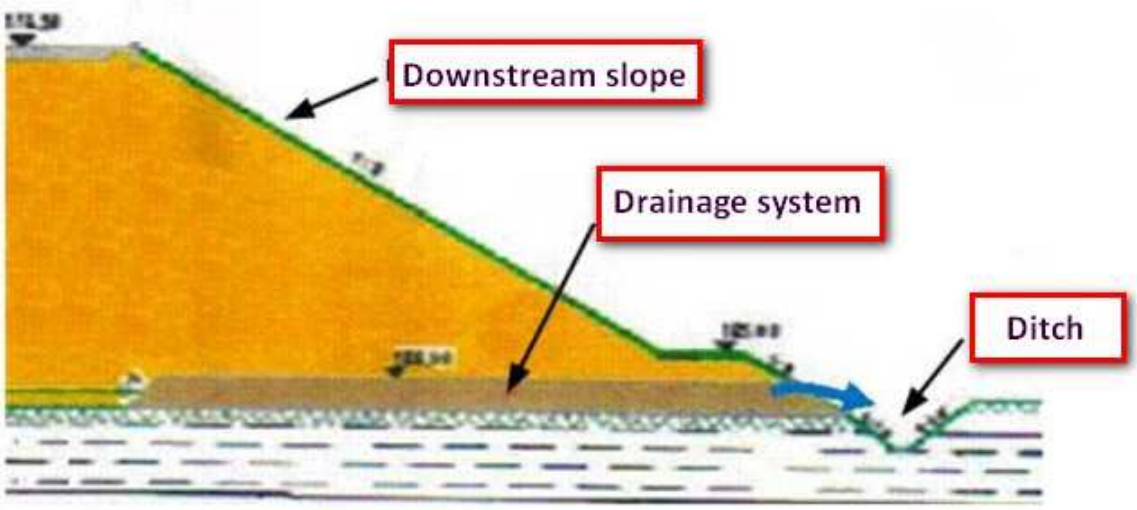

Fig. 5 – Drainage system at the toe of the dam, Suplacu de Barcau Dam

The conditions were considered quasi monotonous, thus local aquifer seemed unlikely.

During the second phase, the investigations were concentrated on the area of interest. Previous recordings suggested the seepage line may be detected at 1/3 of the height of dam near the downstream slope.

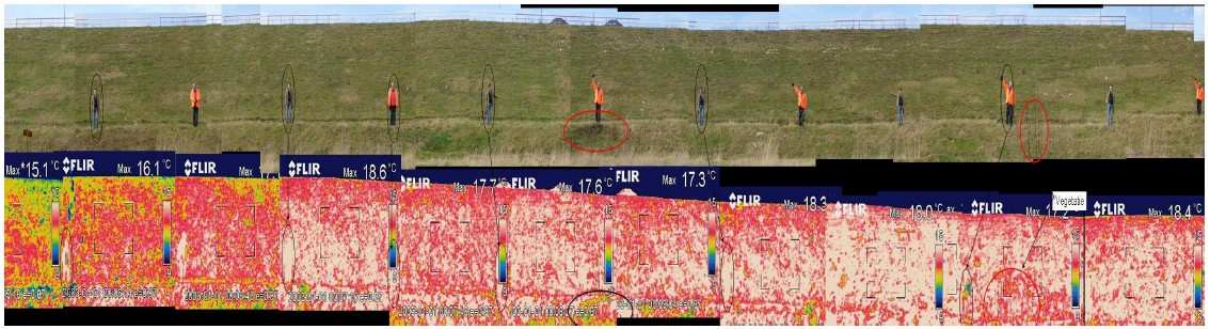

Fig. 6 – Suplacu de Barcau Dam. IR tomography of the downstream slope of dam, with lower temperature values recorded on the marked zones on the downstream face

The infrared camera records the infrared radiation of an object. The radiation is temperature dependent, therefore it can present variations of the temperature in the structure. In order to measure the temperature with accuracy, it is necessary to differentiate the effects of the other radiation sources. This can be achieved if presented information regarding structure emissivity, apparent temperature, distance between camera and the structure and relative humidity.

After a careful inspection, the area of interest is represented by lower values at 13^0C, compared to 17^0-22^0C average values recorded on the downstream face. Compared to water temperature in the reservoir, it rises by a few degrees. While the area of interest is of narrow amplitude, the seepage is obvious. The outflow has a small discharge, thus integrated along the slope and unloaded into the ditch.

4. CĂLINEȘTI DAM

4.1. Description of the test site

The field site is an earthfill dam that impounds a reservoir of 29,21 hm^3, of which 7,56 hm^3 constitutes the normal (useful) storage capacity. The reservoir was designed for hydro-electricity, irrigation, fish farming and flood control. The dam has a maximum height of 13,20 m and a crest length of 797 m. The upstream face has a 3.5:1 slope, while the downstream face has a 3:1 slope. The upstream face is protected by a concrete lining from toe to maximum water elevation with a thickness of 15 cm. The dam has an open channel spillway and an intake tower with 3 concrete bottom outlet galleries, the spillways and the bottom outlets capable of transiting the 1000 yrs. return period flood (F1000 = 510 m^3/sec).

Fig. 7 – Călinești dam and reservoir (red line - 2D measurements at the crest)

4.2. Abnormal seep

The piezometric head values measured at the crest of the dam are constantly higher than the reservoir elevation. The average difference is circa 2-3 m and is related to reservoir elevation variation and rainfalls (Fig. 8).

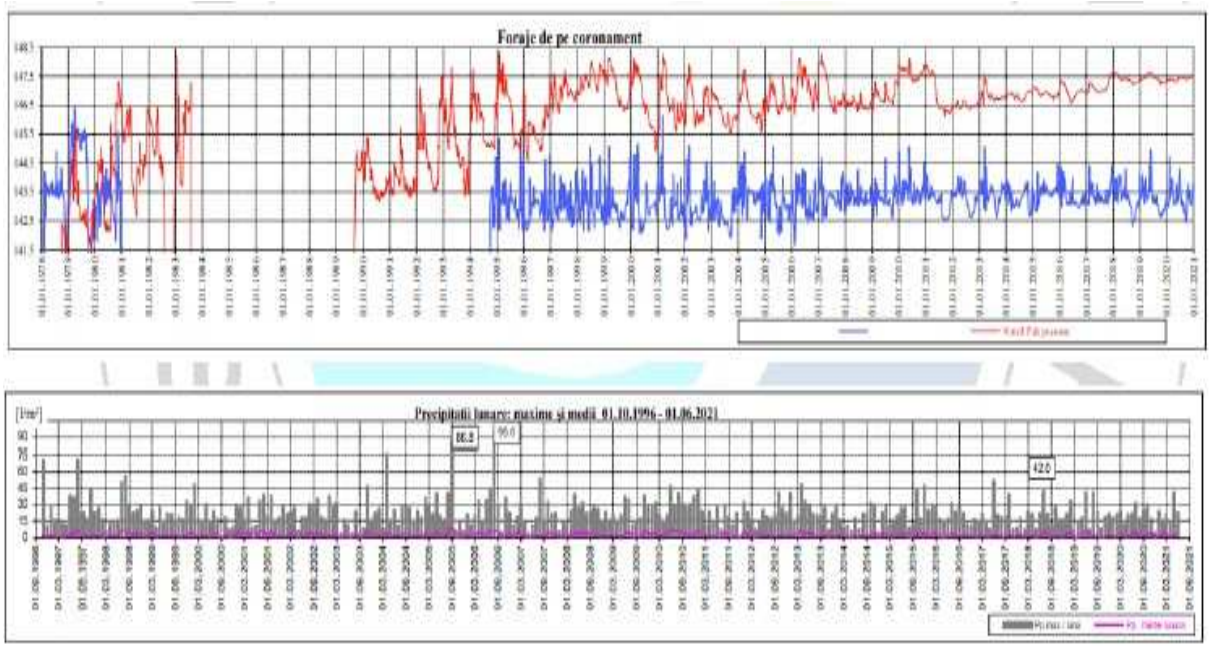

Fig. 8 – Reservoir elevations (blue), piezometric head variation at dam crest (red), rainfall variation (grey) from 1978-2021, Călinești dam

Seepage related data are a concern for many years, given the high values recorded in the standpipe piezometers all across the length of the crest. In addition, a swampy area was detected at the contact between the left sideslope and the toe of the downstream face.

Starting with 2012, there is a clear change of amplitude variation of the piezometric head, aspect that was attributed to drainage defaults around each standpipe piezometer. Therefore, it was considered necessary to perform 3D ERT survey around each of the 5 piezometers at the crest of dam and one 2D ERT measurement, resulting in a longitudinal profile at the crest.

4.3. Electric resistivity tomography study – 2021 campaign

The survey was performed in December 2021. Longitudinal profile was executed using 2 m spacing between electrodes, composed of 9 separate sections of 110 meters each. The total length of the profile was 766 m, starting from the limit of the open channel spillway up to the left sideslope. The depth of the survey was 20 meters, thus taking 7-8 meters of bedrock.

Of great interest were the sections BC1 (close to the right sideslope) where the main channel of the river Tur was located and BC9 (close to the left sideslope) where and old paleo-stream was identified, as presented on the geologic map created by the Romanian Geologic Institute (Fig. 9).

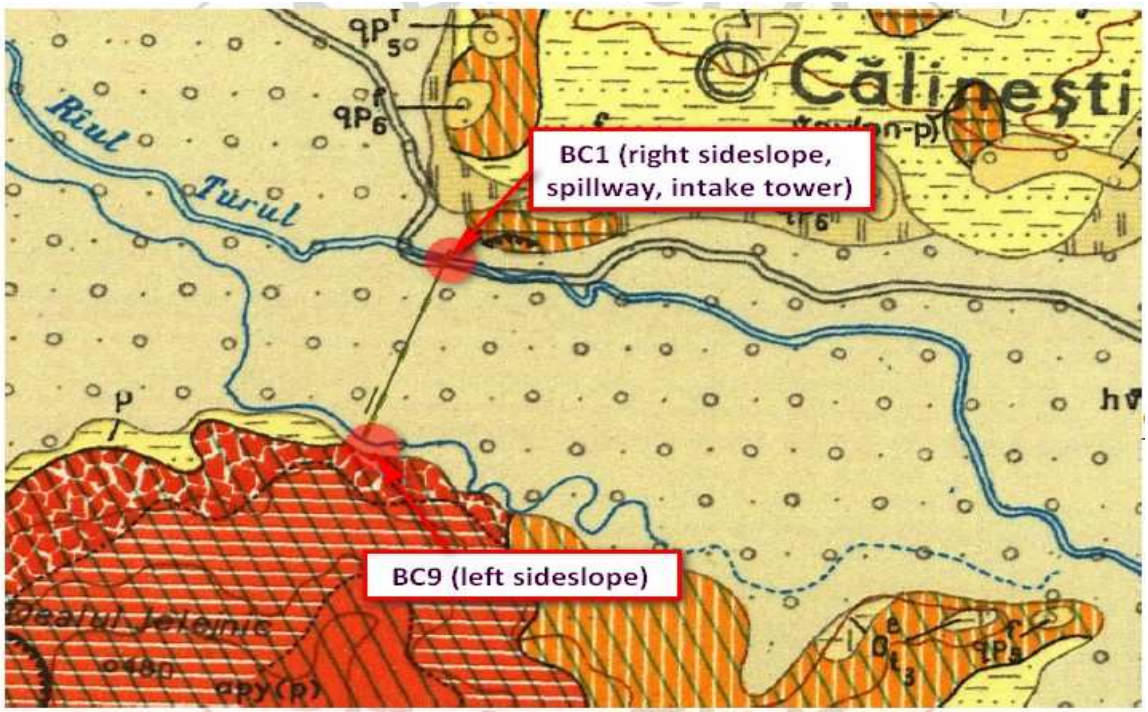

Fig. 9 – Geologic map of the dam with location of BC1 and BC9 sections of interest, that overlaps the main channel and stream of the river Tur, Călinești dam

BC1 section starts at the limit of the concrete open channel spillway and continues for 110 m over the tunnels of the intake tower (Fig. 10). The depth of measurements was 19 m and the distance between the electrodes was 2 m.

Fig. 10 – Călinești dam plan view, right side. BC1 section, with regards to the spillway and the intake tower

Field variation for the measured values of resistivity are between 12-52 Ohm*m (Fig. 11). The minimum values of resistivity are located between 141-146 maSL, corresponding to the normal water level in the reservoir (143,60 maSL). The presence of the main channel of the river is revealed in the geoelectric section by severe disturbance of minimum values that goes beyond the depth of the survey. Next, the tunnels of the intake tower, while executed of reinforced concrete, present low values that show the tunnels are not sealed. The resistivity values of 30-52 Ohm*m (shown in orange - red) reflect the presence of the gravel and small blocks.

BC9 section intersects the F5 piezometric alignment, continuing to the left sideslope, and is the last of the 2D sections at the crest (Fig. 12).

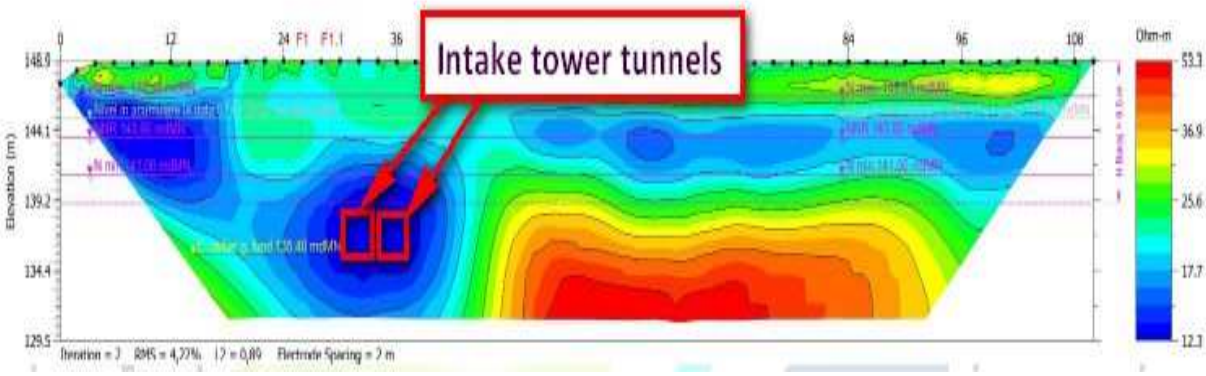

Fig. 11 – Călinești dam. BC1 ERT section, with regards to the intake tower tunnels

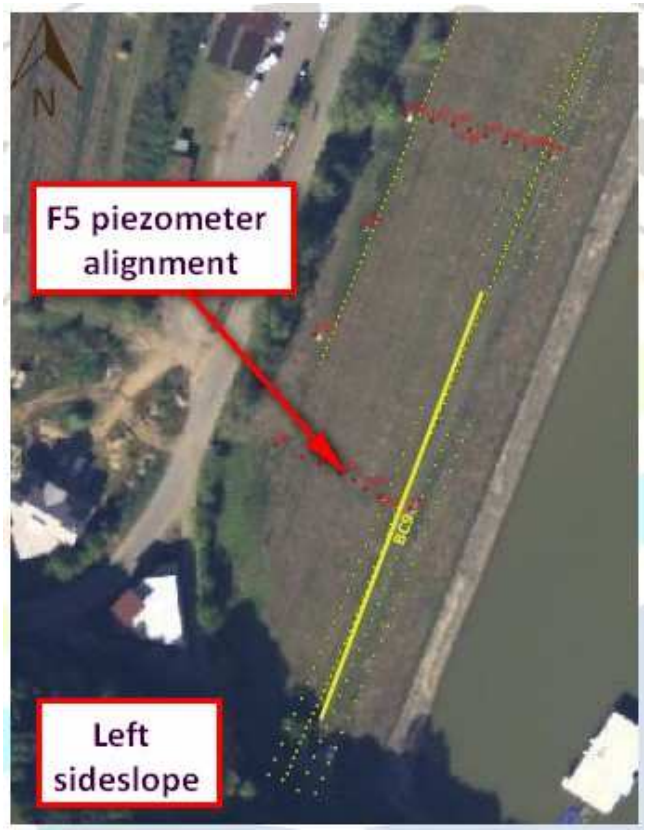

Fig. 12 – Călinești dam. BC9 section, which crosses the F5 piezometric alignment

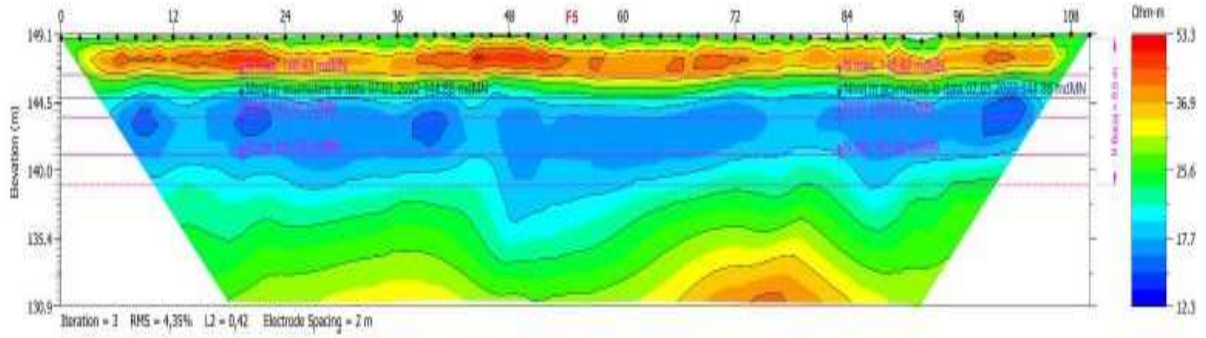

Fig. 13 – Călinești dam. BC9 ERT section, above the paleo stream of the river

The interval of lowest resistivity values, under 13 Ohm*m, is situated between 139-145 maSL, corresponding to normal reservoir elevation (143,60 maSL). The values measured indicate soil pores filled with water (saturated), at crest distance between 18-40 m and 84-102 m, the last one close to the left sideslope. The blue colour, that represents lower resistivity values, at the crest distance 46-60 m, descends to 135 maSL, explained by the paleo-stream of the river Tur.

Călinești Dam was built using local natural materials extracted from the river meadow, consisting of dusty clays and sandy clays. The lithology structure is irregular, therefore a 2D ERT cross section - BC1M was executed (Fig. 14), next to the F5 piezometer alignment. The gap between two electrodes was reduced to only 1 m, therefore the accomplished depth was reported as 8 m.

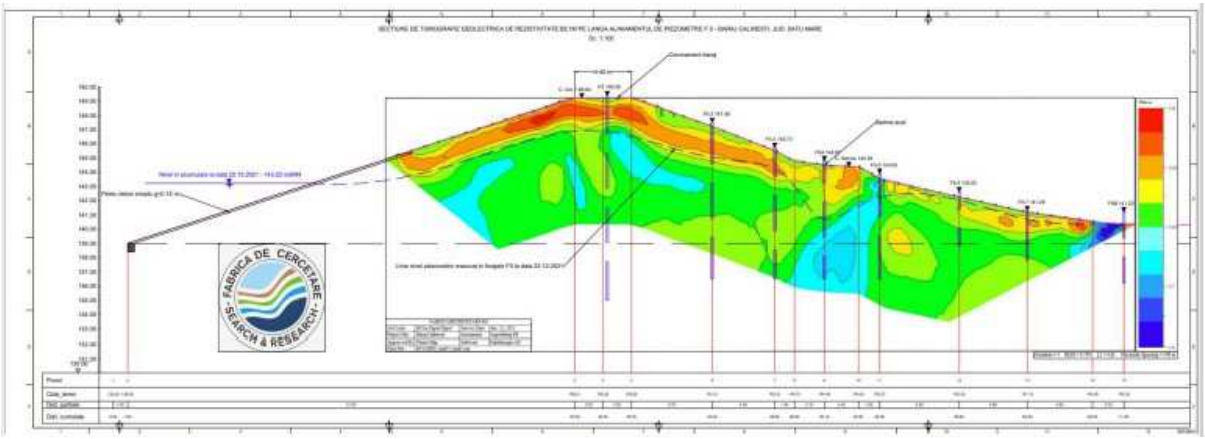

Fig. 14 – Călinești dam. BC1M ERT cross section, in the piezometric alignment

The seepage in the dam, represented in the resistivity cross section by light blue colour, that correspond to values of less than 13,9 Ohm*m, follows the seepage line (dotted gray) that was built using measurement at the piezometric head in the F5 alignment, dated 20 December 2021. The anomaly of minimum resistivity suggests an area that connects to the paleo-stream of the river. At the toe of the dam the terrain is saturated and continues up to the road ditch.

In order to determine the spatial distribution of resistivity at the piezometers located at the crest, 3D measurements were performed, consisting of 4 parallel lines spaced at 4 m, using14 electrodes for each measurement. The depth of survey was 13 m, equalling the height of the dam (Fig. 15).

3DF5 was built around the F5 piezometer (Fig. 16). Values measured at 13 Ohm*m, represented by light blue colour, suggests the presence of water in the solid structure (embankment). The values are located between the elevations 138-145 maSL, with minimum around 140 maSL. It has a parabolic shape, with a more prominent distribution on the

downstream slope. The measured values are similar to the ones taken from de 2D longitudinal section, plus the flow through the structure.

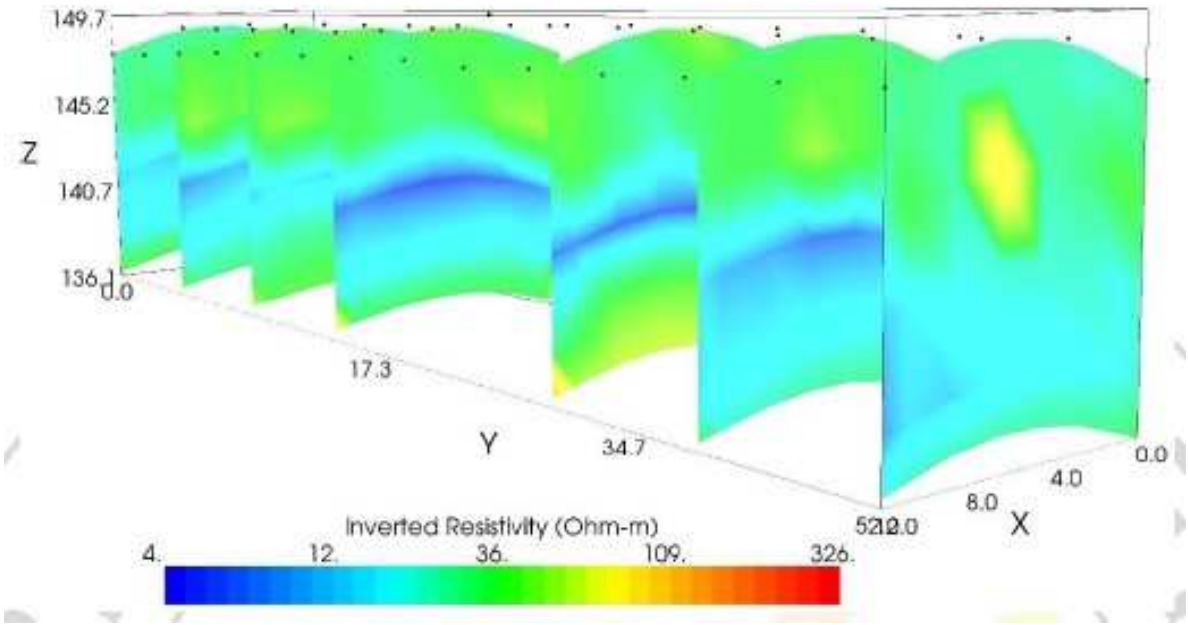

Fig. 15 – Călinești dam. ERT vertical cross section

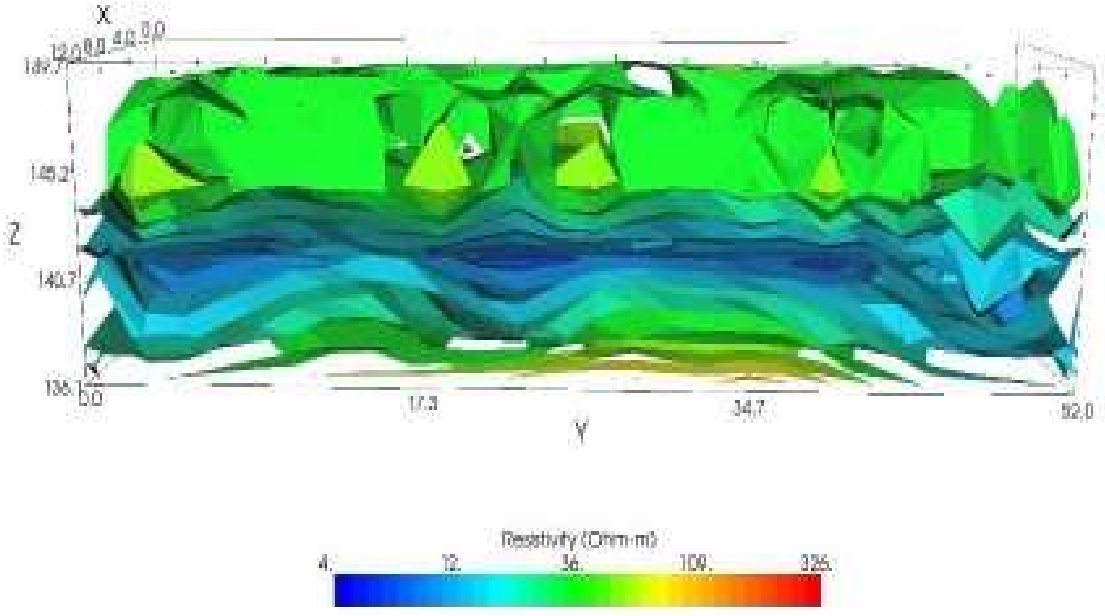

Fig. 16 – Călinești dam. 3D of izosurfaces at the 3DF5 (right)

5. TĂUL MARE DAM

5.1. Description of the test site

The hydraulic structure is a mixture of earth and rockfill dam, creating a maximum storage reservoir of 0,30 hm^3, of which 0,27 hm^3represents the normal (useful) storage capacity. The oldest documents refer to a dam built in the 17th century. The dam was rebuilt in the 18th century, as a small pond for mining in the Apuseni Mountains. The dam has a maximum height of 18 m with a total length at the crest of 160 m. The upstream and downstream faces have 2:1 slopes. The dam has an open channel spillway, with a maximum outflow capacity of 20 m^3/sec, an intake tower with a bottom outlet of iron pipeline of 500 mm in diameter. Currently, the reservoir is mainly used for leisure activities.

5.2. Abnormalsituation

On the 1 October 2022, representatives of the dam owners, the Roșia Montană village, observed that part of the gallery that stores the metal pipeline is damaged (Fig. 17).

Fig. 17 – Taul Mare dam. Damaged gallery containing the bottom outlet of the dam

On the surface, an apparent sinkhole was reported at the dam crest having a depth of some 1,5 m (Fig. 18). After careful inspection, the dam owner asked for the evacuation of population living downstream (some 261 persons).

During the next 10 days, the reservoir elevation was continuously decreased by 6,35 m, using mobile pumps.

Topo-bathymetric surveys were performed.

Fig. 18 – Apparent sinkhole on top of the Taul Mare dam

5.3. Electric resistivity tomography study - phase 2022

During this time, an ERT study was performed, with the aim to identify other voids / eroded hollows within the dam body. The ERT team selected a longitudinal section using 24 electrodes with gaps of 7 meters. The objective of the survey was to present relevant data regarding the geological structure of the area, but also to provide information regarding the apparent sinkhole. Given the fact that the void had the diameter less than 1 m, a shorter space between electrodes was considered ideal for this survey. It was expected that the void would appear as a positive anomaly, with high resistivity value.

Due to topographic conditions, the profile was not created in a straight line, neither the electrodes placed at the same elevation. The GPS data could not be integrated.

The profile was constructed using Wenner - Schlumberger methodology.

The results were somewhat ambiguous and could not show clear origins of the sinkhole. More ERT surveys were needed in order to address all questions, using a smaller space between the electrodes. The second aspect regards the need for 2-3 parallel longitudinal profiles, close to each other (around 0,5 m) with electrode spaces of maximum 1 m, which

could help understand the lateral and vertical extension of the erosion funnel and speed up data reading.

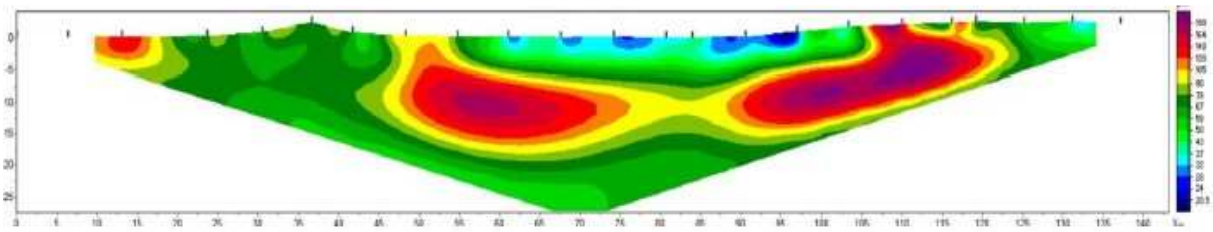

Fig. 19 – Taul Mare dam. Inversion model of the dam - no voids were identified

During the technical inspection, no occurrence of structural discontinuity of the dam was found. It was concluded that no abnormal strains in the structure or foundation were present. In addition, the seepage on the downstream face did not increase.

The values of maximum resistivity, presented in red colour, at the depth of 5-10 m from the crest, with the length of 20-30 m, were not considered as voids. The dam consists of a mixed earth and rockfill structure, without clear separation. The funnel at the crest had a diameter of 60 cm, with an estimated depth of 1,5 m. Therefore, the size of the funnel was too small to be detected using ERT with 7 meter spacing electrodes. The values of maximum resistivity could be interpreted as rock filling in the earthen structure.

Additional geophysical investigations using electrical resistivity imaging (ERI) were performed to verify the dam body integrity. The results presented in Fig.20 have shown that there were no other cavities within the earthfill mass [8].

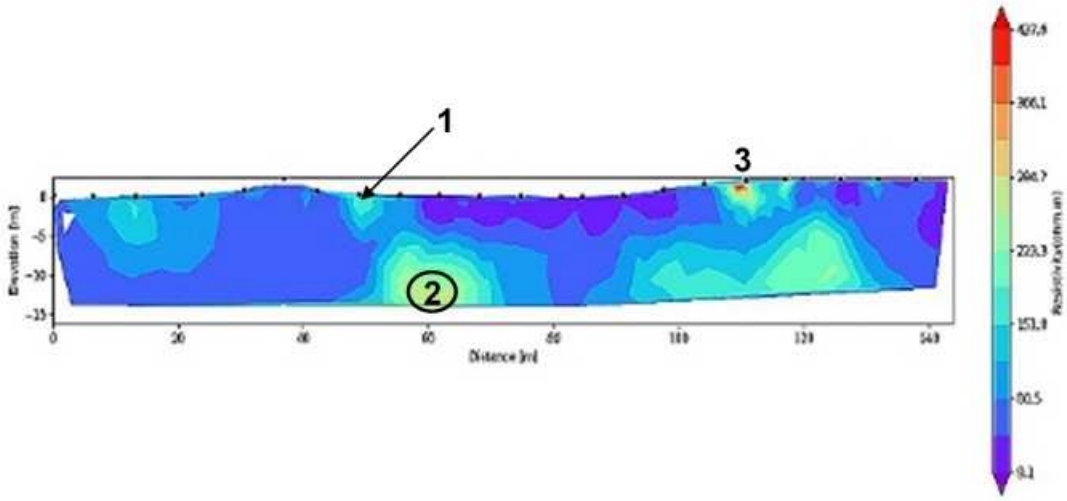

Fig.20 –Taul Mare dam. Electrical resistivity imaging (ERI) investigations interpretation; 1 – approx. location of crest sinkhole; 2 – bottom outlet gallery; 3 – rock abutment [8]

Subsequent investigations will allow for a possible relocation of the bottom outlet intake elevation, due to the thick layer of sediments in the reservoir. Obviously, the dam needs post

analyses to assess the safety status, both structural and related to the capacity of flood routing according to present day's conditions. Since the dam is included in the list of UNESCO world inheritance sites, the technical solutions will have to preserve the type, materials and appearance of the ancient structure [8].

6. CONCLUSIONS

Electrical resistivity tomography measurements showed great potential in addressing different problems related to earthfill dams. When done properly, as it happened with the Călinești dam survey, it showed the values of minimum resistivity considered anomalies that must be taken into consideration. Even though the physical and mechanic properties of soils and rocks were not known, the results provided quite clear answers. The recommendation was to perform a geotechnical investigation and take soil samples in order to correlate information and to update the survey's reading of data. The existing standpipe piezometers were considered obsolete, thus new piezometers with automated data recording were recommended. The recommendations included the necessity to perform another ERT study during the summer months, on all 5 piezometric cross sections in order to better understand seep anomalies.

At the Suplacu de Barcău dam, electrical resistivity tomography measurements coupled with IR tomography, showed less satisfactory results. The recommendation to endow the dam with diverse dam monitoring equipments was made based more on the systematic visual observations. ERT measurements need to answer the question of finding the best locations to install the monitoring equipment.

Regarding the situation presented at the Tăul Mare dam, the initial measurements could not provide reliable data in order to locate the sinkhole. Additional ERT measurements were needed to solve the situation. Subsequent investigations will allow for a possible relocation of the bottom outlet intake elevation, due to the thick layer of sediments in the reservoir. Since the dam is included in the list of UNESCO world inheritance sites, the technical solutions will have to preserve the type, materials and appearance of the ancient structure.

Generally, geophysical methods play a key role in dams and embankments monitoring in order to detect potential hazard in the area of interest. There are different restrictions in using all geophysical methods, but coupling results from various methods offers, in general, a better overall picture.

6.1. Acknowledgements

The authors would like to thank Mr. Filip Florin of the Fabrica de Cercetare Company, Ms. Alexandra Gerea and Mr. Andrei Mihai of the Romanian Geologic Institute, for support in data acquisition and interpretation.

7. REFERENCES

[1] International Commission on Large Dams (ICOLD), Technical Committee on Dam Safety (2019). ICOLD Incident database. Bulletin 99 update;

[2] Stematiu, D., Ionescu, Ș., Abdulamit, A. (2010). Dam safety and risk management (2010): p30-33;

[3] Icard, S.J., Revil, A., Schmutz, M., Karaoulis, M., Jardani, A., Mooney, M., (2014). Characterization of focused seepage through an earthfill dam using geoelectrical methods (2014);

[4] Sjodahl, P., Dahlin, T., Johansson, S., (2010). Using the resistivity method for leakage detection in a blind test at the Rossvatn embankment dam test facility in Norway;

[5] Sjodahl, P., Dahlin, T., Zhou, B., (2015). 2.5D resistivity modelling of embankment dams to assess influence from geometry and material properties;

[6] Icard, S.J., Rittgers, J., Revil, A., Mooney, M.A. (2015). Geophysical investigation of seepage beneath an earthen dam;

[7] Jones, G., Zielinski, M., Sentenac, P., (2012). Mapping desiccation fissures using 3D electrical resistivity tomography;

[8] Abdulamit, A., Stematiu, D., Sârghiuţă, R. Safety of Historical Dams in Romania, Proc. International Symposium “Management for Safe Dams”, 91st Annual ICOLD Meeting, Gothenburg, Sweden, 13 – 14 June, 2023, pp. 12-21.

Fifth International Dam World Conference
PORTUGAL • LISBON • LNEC • APRIL 13-17, 2025
dam world 2025

INTEGRATION AND CHALLENGES IN THE SLOPE HEALTH MONITORING SYSTEM (SHMS)

Samuel Carneiro[1]	Filipe Guimarães[2]	Iggor Penha[3]	Silvia Faria[4]
Vale S.A.	Vale S.A.	Progen S.A.	Progen S.A.

Flavio Thimotio[5]	Camila Souza[6]	Vinicius Pereira[7]
Vale S.A.	Vale S.A.	Vale S.A.

Abstract

This abstract addresses the topic of the Slope Health Monitoring System (SHMS), focusing on the integration of various sensors and the inherent challenges of this process. The SHMS is a technology that allows for remote and real-time/near-real-time monitoring of the structural integrity of a structure. The integration of various sensors in the SHMS allows for the collection of comprehensive data, which is essential for an accurate assessment of structural health.

However, the integration of various sensors presents several challenges. These include sensor compatibility, synchronization of collected data, and effective management of the large volumes of data generated. In addition, the creation of a robust database and the implementation of an event/ failure tree are crucial for the effective operation of the SHMS.

This work explores these challenges and discusses possible solutions, intending to improve the effectiveness of the SHMS and, ultimately, ensure the safety and longevity of the monitored structures.

Keywords: SHMS, integration, challenges, monitoring.

[1] samuel.carneiro@vale.com, Brasil
[2] filipe.guimaraes@vale.com, Brasil
[3] c0664489@vale.com, Brasil
[4] c0645962@vale.com, Brasil
[5] flavio.thimotio@vale.com, Brasil
[6] camila.souza@vale.com, Brasil
[7] vinicius.campos.pereira@vale.com, Brasil

1. INTRODUCTION

SHMS: Slope Health Monitoring System

The occurrence of various soil mass landslides on natural and artificial inclined surfaces since the 19th century motivated studies on slope stability in the early 20th century worldwide [1]. These studies led to the development of the Limit Equilibrium Method, which calculates a Factor of Safety (FS) for the structure. This method was created by Swedish researchers after observing the landslide of the Gothenburg Wharf in 1916 [2]. An initial and globally recognized result was published by [3]. Following this, various hypotheses and improvements to the Limit Equilibrium Method emerged, leading to different calculation methods for the Factor of Safety, including those by [4-9]. According to [10], the values of the variables involved in the FS calculation are subject to variability. These values are obtained from geotechnical tests that simulate field conditions, and their variability is attributed to several factors, including different interpretations during test execution, human errors in testing, and the inherent spatial variability of soil properties, as samples are collected from different locations. To manage this variability and ensure the safety and effectiveness of engineering projects, continuous geotechnical monitoring is essential. It involves the observation and measurement of soil and structural conditions over time, either in situ or using remote monitoring systems. For this reason, VALE utilizes the Slope Health Monitoring System (SHMS) to conduct geotechnical monitoring of all its dams and other structures.

The SHMS is adaptable to the general geotechnical workflow, and its digital transformation can be segmented into six distinct stages. These stages include data-driven modeling during site investigation, point cloud representation of ground modeling, automatic geotechnical modeling, visualization of analysis outputs, design decision-making, and the use of a lot of data collection and machine learning throughout construction, operation, and maintenance [11].

IntellTech's SHMS (Figure 1) is a sensor-agnostic software platform that provides structured, contextualized, and standardized integration of spatiotemporal data, supported by a data center acquired by Vale S.A. This system focuses on integrating various sensors and addressing the inherent challenges of this process. The SHMS enables remote and real-time or near-real-time monitoring of structural integrity. Integrating multiple sensors allows for comprehensive data collection, essential for accurate structural health assessments. Geotechnical monitoring is a critical tool to ensure safety and stability in mining operations [12], such as open pits, waste dumps, and dams.

The SHMS offers dynamic dashboards, artificial intelligence (AI), advanced analyses, automated notifications, business intelligence (BI), customizable automated reports, and other features (Figure 2).

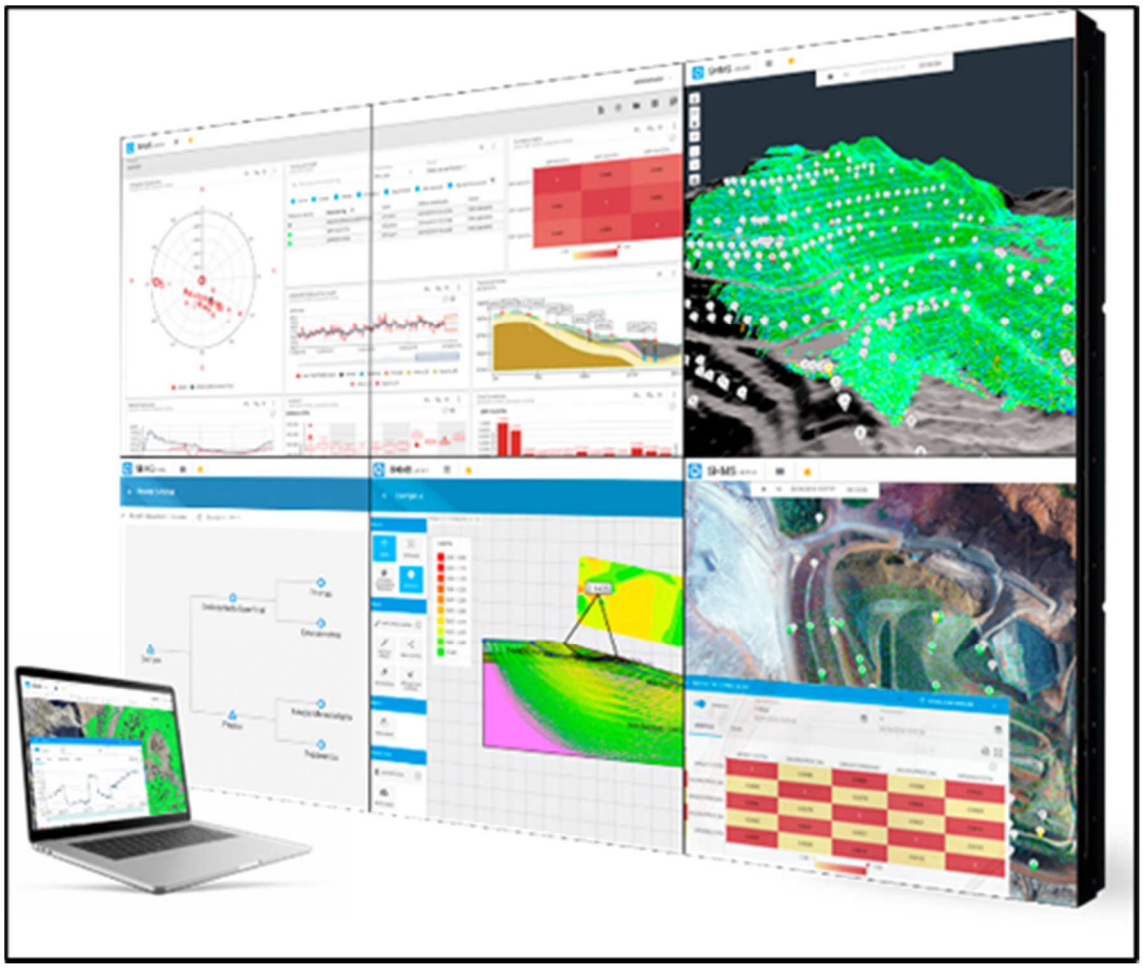

Figure 1 - SHMS Platform.

The SHMS utilizes communication interfaces to ensure precise integration with any instrument using standard OPC (OLE for Process Control) networks, automated data loggers, SQL databases, FTP directories, CSV files, and more. Manual instrument readings can be accessed directly from the field via third-party applications through a database or manual entry into the SHMS platform.

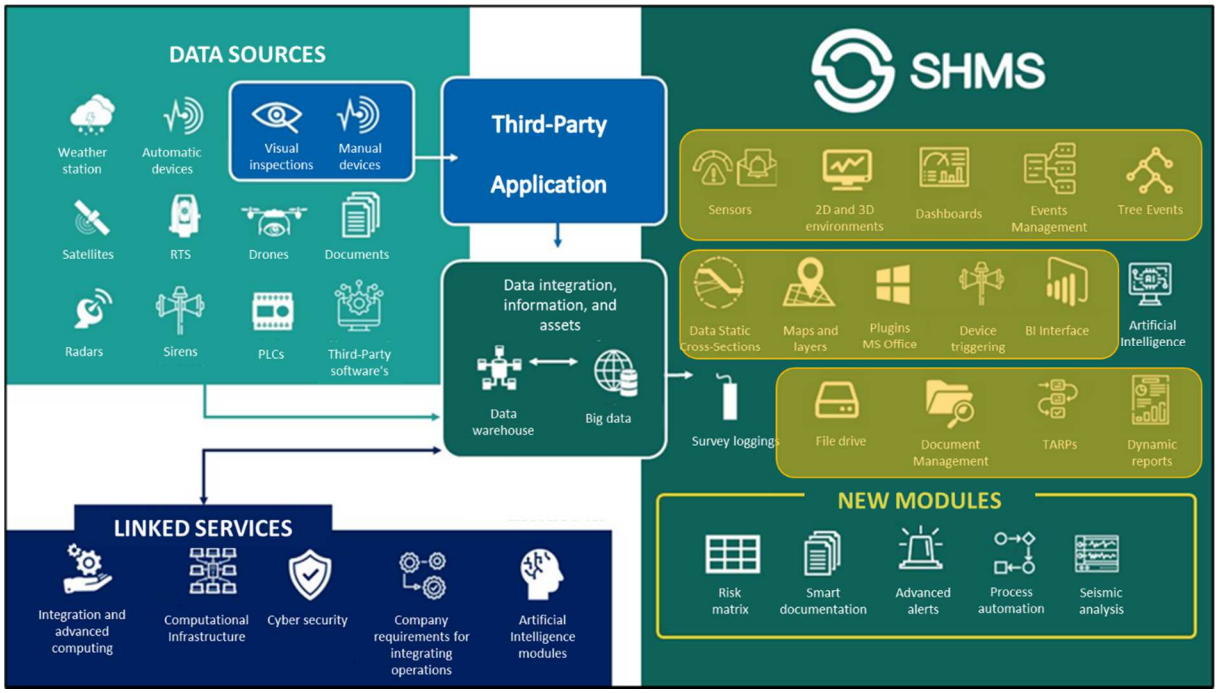

Figure 2 - Overview of the complete SHMS solution. In yellow are the tools used by the Geotechnical team at Vale S.A.

The SHMS can also integrate data from other databases, such as Plant Information Management Systems (PIMS) and similar information systems. All stored and managed data within SHMS is auditable, allowing full traceability of technical information, including dates, original values, registered values, and responsible persons.

2. GENERAL INFRASTRUCTURE

The general infrastructure required to support the SHMS platform varies. The ideal solution is cloud-based hosting, offering performance, scalability, and flexibility. However, Vale S.A. has implemented SHMS on a physical server within a closed network. Typical hosting options:

- Client Hosting: where the client manages the infrastructure.
    - Physical server installation.
    - Client's cloud.

Successful data integration within SHMS requires four main interconnected components:

1. Communication interfaces with instrumentation.
2. Data storage.
3. Database integration with third-party applications.
4. Software modules.

2.1. Communication Interface

Due to the variety of sensors in the market, a generic interface must be designed to work with available instruments for the mining industry once a globally adopted data exchange standard is established. To ensure compatibility, the supplier develops specific communication interfaces for Vale S.A. personalized to the instrumentation or databases used in a project. This ensures that all instruments connect correctly and automatically with the data storage center. Users can manage connections by adding new instruments of the same type and configuring the necessary communication interfaces for automatic data synchronization.

SHMS can collect data from the following sources:

- Automatic Instruments;
- Manual Instruments;
- Dataloggers & Gateways;
- Databases;
- APIs.

2.2. Data Warehouse

The data warehouse serves as an automated database or central repository with standardized and contextualized information. It ensures fast and efficient access through well-defined rules, specific requirements, and protocols established by the project.

2.3. Integration of Databases and Third-Party Applications

SHMS supports integration with specialized third-party systems, including:

- PIMS (Plant Information System);
- AD (Active Directory);
- SAP (Systems Applications and Products);
- Third-Party applications.

As SHMS communication interfaces are developed for instrumentation, they can also be adapted to any data source connected to an accessible network.

3. SHMS MODULES

The SHMS provides a comprehensive and flexible range of interconnected modules, offering users various tools for leveraging integrated information and ensuring operational safety. The

supplier continuously develops new modules based on client demands and industry standards. Key SHMS modules used at Vale S.A. are summarized in Table 1.

Table 1 - SHMS Modules.

SHMS Modules	
Instrumentation	Data Static Cross-Sections
Dynamic Stability Analysis	Risk Maps and Layers
2D Environment (2D Monitoring)	File Drive
3D Environment (3D Monitoring	BI Interface
Event/ Fault Trees	Document Management
Predictive Analysis and Big Data	

Each module contributes to a robust monitoring and analysis strategy, ensuring comprehensive operational support. The SHMS is built with a modular architecture that includes standard modules and additional advanced modules personalized to specific needs.

3.1. Instrumentation

This module manages the interface with all connected instruments and sensors. Once an instrument is geolocated and integrated, primary tags are created for each sensor, recording direct measurements with timestamps.

3.2. Dynamic Stability Analysis

This module incorporates advanced tools for slope stability analysis using limit equilibrium and finite element method models, offering insights into potential failure mechanisms.

3.3. 2D Environment (2D Monitoring)

The 2D Environment module allows users to visualize geolocated data, including instrument positions and monitoring areas, overlaid on 2D maps for straightforward monitoring and analysis.

3.4. 3D Environment (3D Monitoring)

This module allows users to visualize instruments, terrain models, and monitoring data within a 3D space, providing a comprehensive view of site conditions and changes over time.

3.5. Event/ Fault Trees

This module facilitates the creation and analysis of event and fault trees, helping users understand potential chain reactions and causes leading to critical slope stability failures.

3.6. Predictive Analysis and Big Data

The Predictive Analysis and Big Data module enables real-time decision-making through machine learning algorithms, helping predict possible future outcomes and aiding in proactive risk management.

3.7. Static Cross-Sections

This module allows users to generate and analyze cross-sections of monitored slopes or geological structures, supporting detailed surface and subsurface data evaluation.

3.8. Risk Maps and Layers

This module provides spatial representations of hazard levels, creating visual overlays on maps to highlight risk-prone areas while integrating multiple data sources.

3.9. File Drive

The File Drive module acts as a document repository with version control, allowing users to store, manage, and link documents to specific instruments or project areas within SHMS.

3.10. BI Interface

The Business Intelligence (BI) Interface module delivers advanced data visualization and analytics, enabling users to create customizable dashboards and reports for deeper insights into monitoring data.

3.11. Document Management

This module streamlines document management by supporting version tracking, tagging, and notifications, ensuring users stay informed of updates or relevant changes to critical documents.

4. ANALYSIS

The SHMS incorporates several types of components and similar information systems to help users extract significant insights from raw data stored in the data warehouse. Analyses are accessible through the 2D Environment module and Dashboard.

4.1. Temporal Analyses

Temporal analyses display data points over time. Since most collected data has time stamps, visualizing data over a set or dynamic period is useful for investigating measurement changes and behaviors to identify trends.

Temporal Analysis Properties displays the relative or absolute value of a measurement over a specified period. Series can be shown on a single graph multiple times. Scales can be defined automatically or manually with different options, such as absolute, relative, or logarithmic. Temporal series can be enabled or disabled. Axes can be adjusted automatically or manually. Alert profiles can be shown in graphs as color-coded lines. Marker lines can indicate a significant level without triggering an alert status.

4.2. Special Analyses

Special analyses enable the visualization of data in more complex forms. Data sets can be shown as combined lines and bars in the same graph (Figure 3).

For example, daily precipitation can be shown as bars next to piezometer readings displayed as lines.

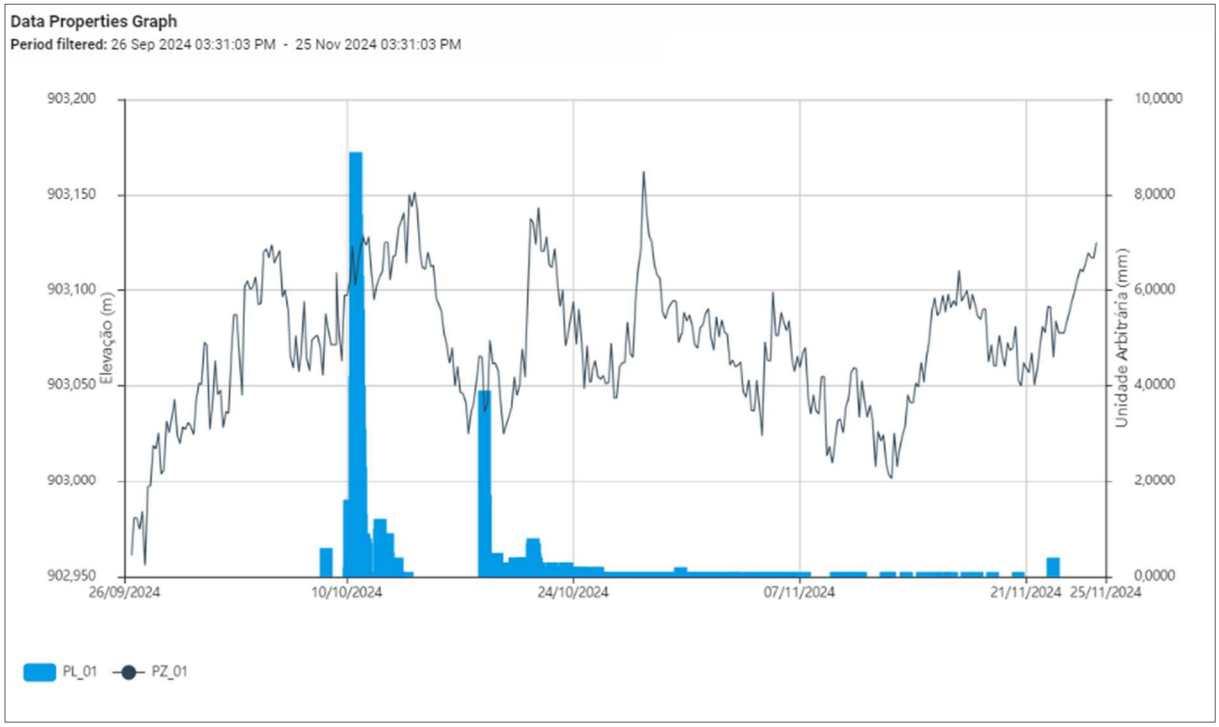

Figure 3 - Data properties graph showing a line chart of a piezometric reading (black line) and a bar chart in blue of daily precipitation from a weather station.

We can do quick statistical transformations, including:

Measurement, Difference between measurements, Velocity, Average velocity, Acceleration, Average acceleration, Mean, Frequency, Period difference, and Cumulative sum of measurements.

Robotic Total Station (RTS) displacement can be plotted as a line next to the average monthly velocity (blue bars) and acceleration displayed as bars in red (Figure 4).

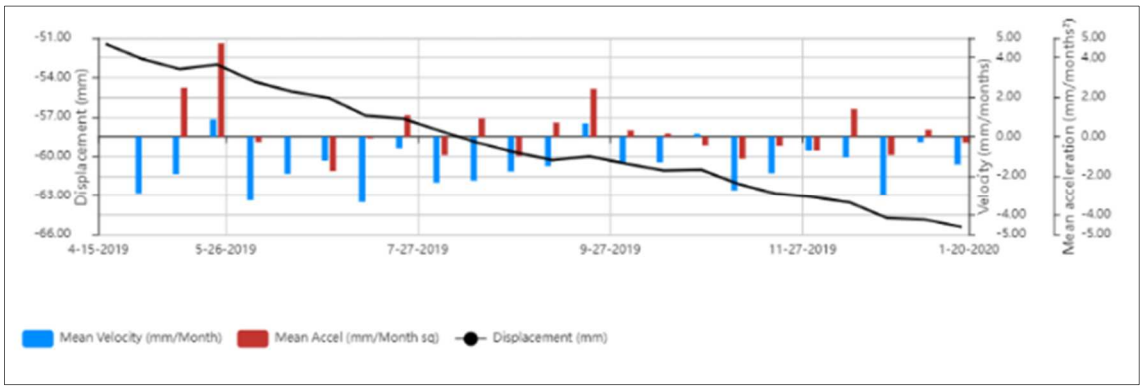

Figure 4 – Example of data properties graph with RTS data showing the average displacement of an area (black line) alongside the average monthly speed (blue bars) and the average monthly acceleration (red bars).

4.3. Comparative Analyses

Comparative analyses enable data comparison over time and between instruments to evaluate the relationship between measurements within the observed context.

Figure 5 shows statistical comparisons of multiple instrument measurements across two dates. When non-consecutive dates are selected, users can choose the statistical analysis to perform, including:

Maximum, Minimum, Median, Mean, Last measurement, Highest, Lowest, 1st quartile, and 3rd quartile.

Selected calculations are performed using all measurements within a single day for each specified date, with the variation displayed in a bar chart for each instrument.

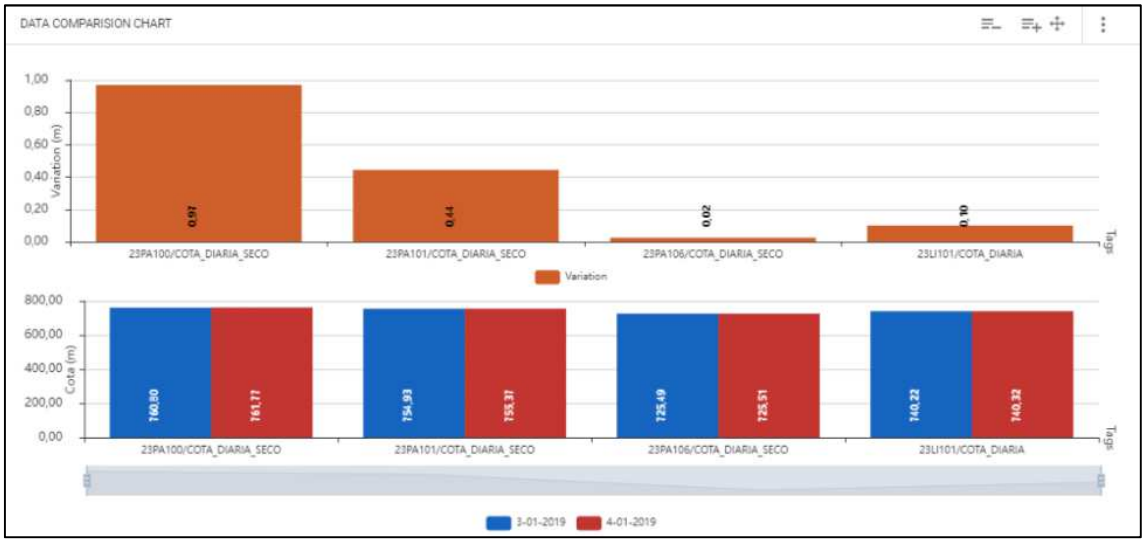

Figure 5 - This data comparison graph shows data from four piezometers on two different days (blue and red). The upper graph shows the variation in the chosen statistical calculation. In this case, we see the variation in the daily mean.

4.4. Forecasting Analyses

Forecasting analyses project expected trends based on algorithms that calculate behavior tendencies with specific parameters.

Types of Forecasting Analyses:

Displacement (Measurements), Velocity (1st derivative), and Acceleration (2nd derivative).

Each forecasting analysis (Figure 6) provides:

Data: Direct measurements or calculated derivatives.

Model: The best-fit polynomial model calculated by the algorithm.

Trend: General data movement without noise and cyclical/seasonal effects using Singular Spectrum Analysis (SSA).

Forecast: Expected series values for the selected horizon.

Confidence Intervals: Calculated with 95% and 80% confidence levels.

Model fit errors: Including MAE, MAPE, R, R^2, RMSE.

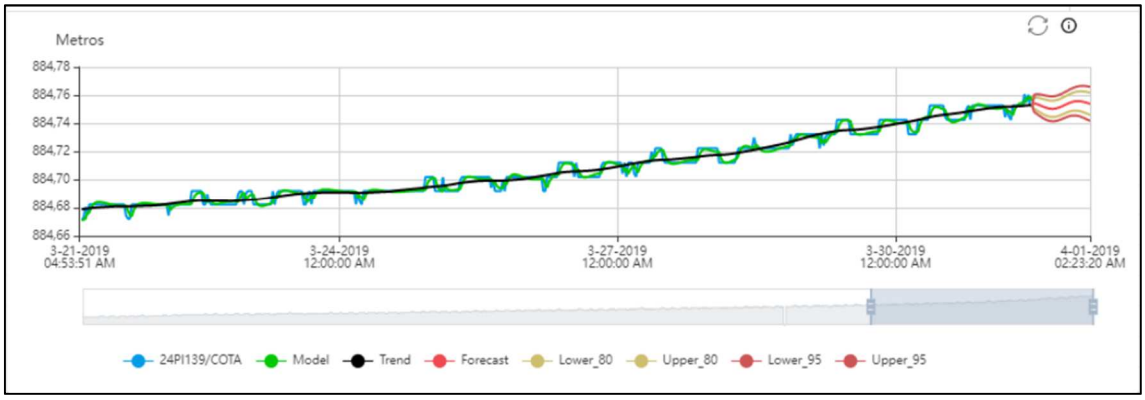

Figure 6 – Example of forecast analysis for displacement data.

The graph shows the time series of measurements (blue), the best-fitted polynomial model (green), and the SSA trend analysis. The projected calculated results are displayed as a forecast (light red), as well as the 80% confidence intervals (yellow) and 95% confidence intervals (dark red).

4.5. Statistical Analyses

Statistical analyses provide metrics on selected data portions, primarily used to characterize general trends and behaviors over time.

Box Plot Analysis (Figure 7) displays temporal data across multiple periods, highlighting:

Median, Quartiles, Whiskers, Upper and lower bounds, and Outliers.

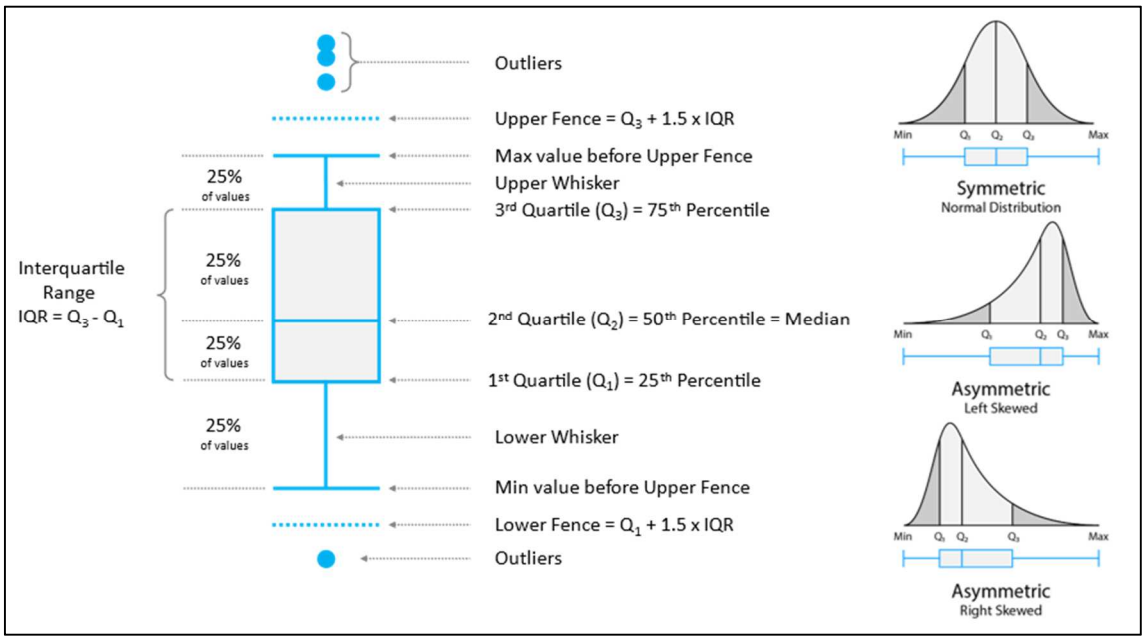

Figure 7 - Features of a box plot.

5. MONITORING TOOLS & TABLES

Monitoring tools in SHMS include tables that display information on dashboards, such as:

Tag value tables. Show current status, last recorded values, and operational state alerts.

6. CHALLENGES

The integration of various sensors into complex systems is a process that offers numerous advantages but also presents significant challenges. These include sensor compatibility, synchronization of collected data, and effective management of the large volumes of data generated. In addition, the creation of a robust database and the implementation of an event/ failure tree are crucial for the effective operation of the SHMS.

Below, detail some of these challenges and important considerations:

6.1. Sensor Compatibility

Sensors are often manufactured by different companies and may operate on various platforms and protocols. Ensuring that all sensors are compatible with the system in which they will be integrated may require hardware and software adaptations. Tools such as protocol converters, specific middleware, and interface standardization are essential to overcome these obstacles.

6.2. Synchronization of Collected Data

The synchronization of collected data is crucial to ensure the accuracy and consistency of information obtained from different sensors. Challenges include the need for fast response times and the coordination of data collection schedules. Methods such as precise timestamps, the use of time servers, and synchronization algorithms are common strategies to solve synchronization problems.

6.3. Managing Large Volumes of Data

With the integration of multiple sensors, the amount of data generated can be extremely large. Effective management of these data volumes is a significant challenge involving storage, processing, and analysis. Using big data solutions such as distributed databases, data compression techniques, and real-time data analysis tools can help manage these volumes efficiently.

6.4. Technological Solutions

1. **Middleware and Integration Platforms**: Using specific middleware to facilitate communication between different sensors and systems.

2. **Cloud Services**: Leveraging cloud services for scalable storage and analysis of large volumes of data.
3. **Artificial Intelligence and Machine Learning**: Implementing AI algorithms to analyze data in real-time, detect patterns, and identify anomalies.

7. CONCLUSION

Sensor integration is a growing field that promises to enhance the accuracy and utility of collected data for a variety of applications. However, overcoming challenges related to compatibility, synchronization, and data management is essential to achieve successful integration and take advantage of the benefits offered by these complex systems.

REFERENCES

[1] Terzaghi, K. (1950). Mechanism of landslides. In: Application of Geology to Engineering Practice (Berkey Volume), Geological Society of America, pp. 83-123.

[2] Cheng, Y. M., & Lau, C. K. (2008). Slope Stability Analysis and Stabilization: New Methods and Insight. CRC Press.

[3] Fellenius, W. (1936). Calculation of the stability of earth dams. Transactions of the 2nd Congress on Large Dams, Washington, DC, 4, pp. 445-462.

[4] Bishop, A. W. (1955). The use of the slip circle in the stability analysis of slopes. Géotechnique, 5(1), pp. 7-17.

[5] Lowe, J., & Karafiath, L. (1960). Stability of earth dams upon drawdown. Proceedings of the 1st Pan-American Conference on Soil Mechanics and Foundation Engineering, Mexico City, 3, pp. 537-552.

[6] Morgenstern, N. R., & Price, V. E. (1965). The analysis of the stability of general slip surfaces. Géotechnique, 15(1), pp. 79-93.

[7] Spencer, E. (1967). A method of analysis of the stability of embankments assuming parallel inter-slice forces. Géotechnique, 17(1), pp. 11-26.

[8] Janbu, N. (1973). Slope stability computations. In: Embankment-Dam Engineering, Casagrande Volume, John Wiley & Sons, pp. 47-86.

[9] Sarma, S. K. (1973). Stability analysis of embankments and slopes. Géotechnique, 23(3), pp. 423-433.

[10] El-Ramly, H., Morgenstern, N. R., & Cruden, D. M. (2002). Probabilistic slope stability analysis for practice. Canadian Geotechnical Journal, 39(3), pp. 665-683.

[11] Wang, Y., & Tian, H. M. (2023). Digital geotechnics: from data-driven site characterisation towards digital transformation and intelligence in geotechnical engineering. Georisk: Assessment and Management of Risk for Engineered Systems and Geohazards, 18(1), 8–32. https://doi.org/10.1080/17499518.2023.2278136

[12] Bezerra, C. O., Carneiro. S., Gaio, G., Junior, L. A. T., Faria, A. (2024, April). Enhancing Geotechnical Monitoring Productivity with SHMS. Paper presented at the Slope Stability 2024, Belo Horizonte, Brazil.

Fifth International
Dam World Conference
PORTUGAL • LISBON • LNEC • APRIL 13-17, 2025
dam world 2025

CODEGUA, A COMPENDIUM OF THE CHILEAN EXPERIENCE IN CFRD DAMS

Luis San Martin[1]
SMI Ingenieros

Bayardo Materon[2]
Independent assessor

ABSTRACT

The document reviews the evolution and development of Concrete Face Rockfill Dams (CFRD) in Chile, a process that began in the 1930s and has significantly progressed over time. Several emblematic cases of dams in Chile are highlighted, including Caritaya, Cogotí, Conchi, Santa Juana, Ancoa, Chironta, and the Codegua reservoir currently in design. The experience gained from these projects has allowed for improvements in rockfill compaction techniques, plinth design, and handling of river materials, which have increased the stability and safety of these structures in a highly seismic country.

The Codegua reservoir synthesizes this accumulated experience by proposing a mixed solution between CFRD and Concrete Face Gravel Dam (CFGD) due to the insufficiency of river materials, like the Bollenar project. The "Design as You Go" approach, adapted from previous projects such as Ancoa, is discussed, and the necessary geotechnical and structural considerations for the foundation and plinth design are examined. The document concludes by highlighting the importance of learning from the past and accumulated experience to maintain innovation and safety in dam construction, particularly in seismic zones.

Keywords: CFRD, CFGD, Plinth, Foundation

[1]smart@smi-chile.cl, Chile
[2]bayardo.materon@terra.com.br,Brazil

1. INTRODUCTION

Chile, one of the most seismic countries of the world, has developed experience in the engineering and subsequent construction of Concrete Face Rockfill Dams (CFRD) since the 1930s, a period during which these projects have advanced by absorbing both local experience and knowledge from other countries. Initially, these dams were conceived as rockfill structures extracted from quarries and simply dumped without any compaction process, with a reticulated concrete face and a precarious structure that served as the plinth. Since then, the development of reservoir projects, mainly for irrigation purposes and designed with CFRD-type walls, has seen continuous advancement in Chile, with some periods of "silence" in these projects primarily due to regional and global economic factors, but with other periods of great productivity and advances in this type of wall construction.

Below, we present a brief "journey" through the development of projects in Chile, attempting to show the progress in the science of these projects and how each one has contributed to the current state of the art of these works, and how not only materials but also structures and particular solutions are being incorporated based on the specific characteristics of each site.

2. HISTORICAL CASES

2.1. 1935 CARITAYA

The Caritaya Dam, constructed between 1930 and 1935, is a precursor of this type of works. Its main characteristics are [1]:

Uncompacted CFRD wall: Wall volume 350,000 m³

Slopes: 1.5:1 on both sides

Height: 40 m

Crest width: 5 m

Crest length: 156 m

Fig. 1 - Reticulate Concrete Face

Fig. 1 shows the reticulated concrete face, and **Fig. 2** shows the structure that served as the plinth, which was exposed during an inspection of the work.

Fig. 2 - Concrete cord that is in the plinth area

Given the history of this dam, almost 100 years old and located in a highly seismic country, it is possible to observe how the lack of compaction in the fills led to significant settlements, as shown in **Fig. 3**, highlighting that this is a dam with a maximum height of 40 m.

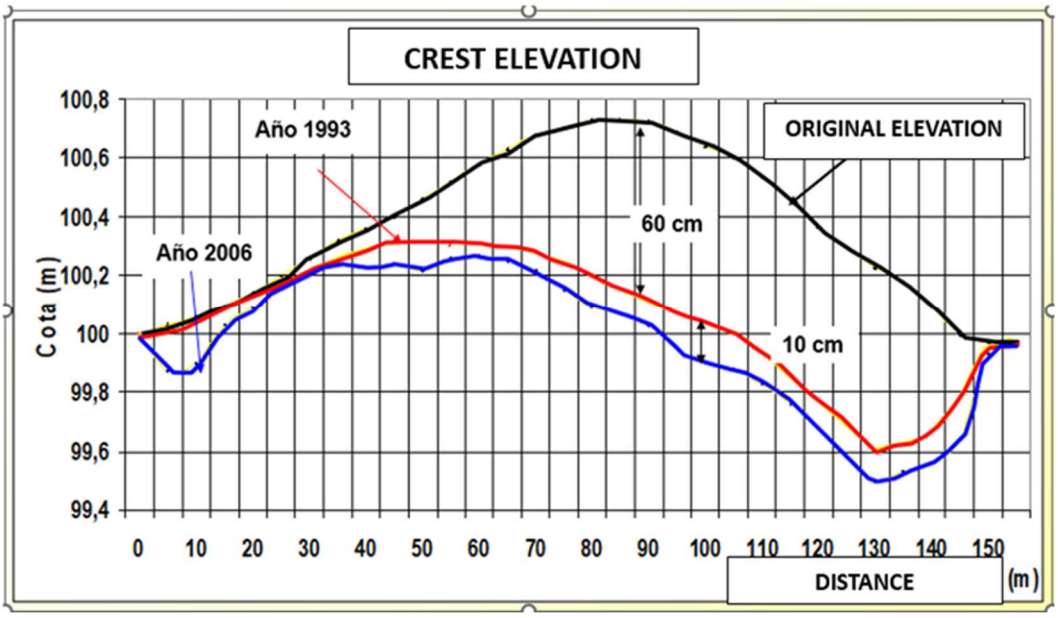

Fig. 3 - CARITAYA Historic settlement

2.2. 1938 Cogotí

Another example from that same era is the Cogotí reservoir, completed in 1938. It was also built under the concept of dumped, uncompacted rockfill and features a reticulated concrete face with a rather primitive plinth.

In **Fig. 4**, a photo of the concrete face is shown, along with a historical photo from the time when the concrete face was being poured. [2]

Fig. 4 - Current state of the COGOTI dam and historical photo of the construction of the reticulated concrete face

The main characteristics of this dam are:

Uncompacted CFRD wall: Wall volume 774,000 m³

Slopes: 1.6:1 Downstream, 14:1 Upstream

Height: 83 m

Crest width: 8 m

Crest length: 160 m

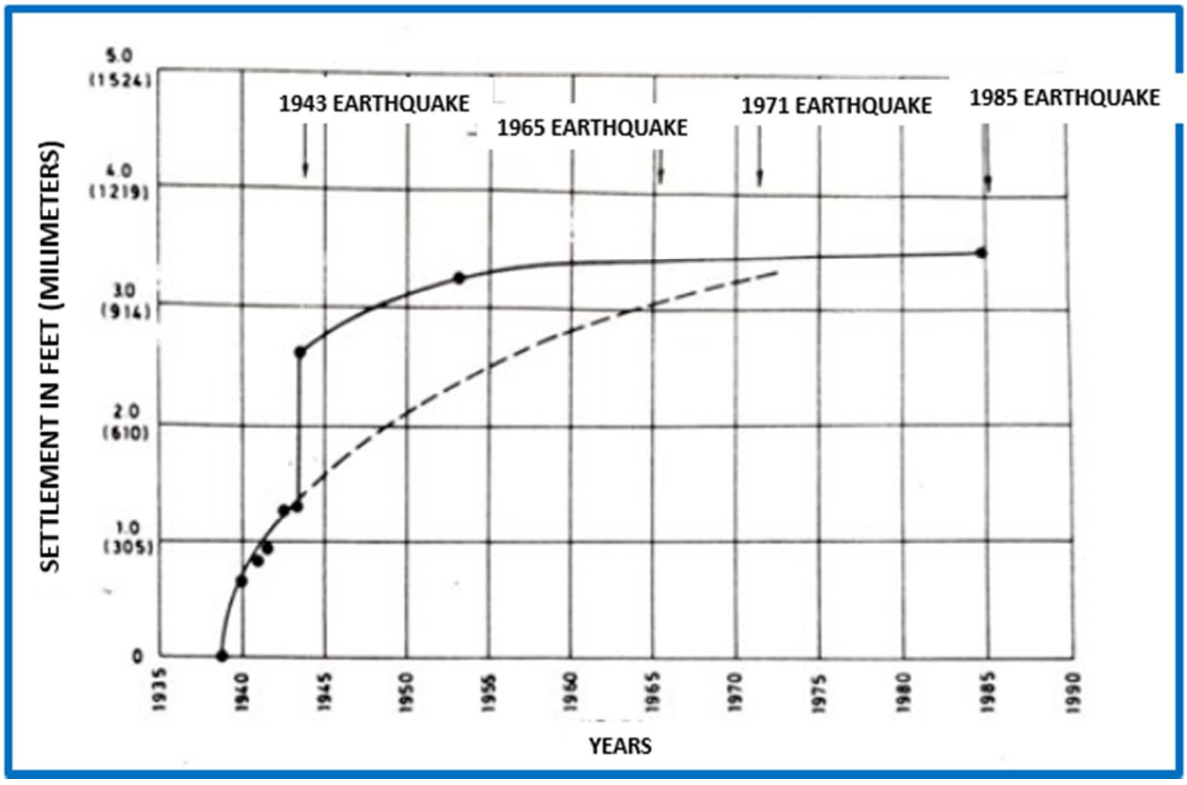

Fig 4a – Cogotí crest settlement curve

Fig 4a represents crest settlement behavior during the following earthquakes.

Epicenter Location (Year)	Richter Magnitude	Radial Distance to Epicenter (km)
Illapel (1943)	7,9	95
La Ligua (1965)	7,1	165
Papudo (1971)	7,5	176
Llo lleo (1985	7,7	281

It is noted that the 1943 Illapel earthquake produced an instantaneous settlement of 40 cm, approximately equal to the total settlement experienced to that date since dam completion 4.5 years earlier. [2]

2.3. 1976 Conchi

Forty years later, in 1976, the construction of the Conchi reservoir was undertaken, where the concept of compacted rockfill was introduced, which was a significant step forward, but still maintained the concept of a simple or basic plinth, meaning it did not include the impermeabilization and elasticity precautions of modern designs. Additionally, the concept of a reticulated slab with transverse joints was still in use at that time.

The main characteristics are:

Compacted CFRD wall: Wall volume 500,000 m³

Slopes: 1.5:1 Downstream, 1.5:1 Upstream

Height: 66 m

Crest width: 6 m

Crest length: 167 m

Fig. 5 - shows a current photo of the Conchi reservoir

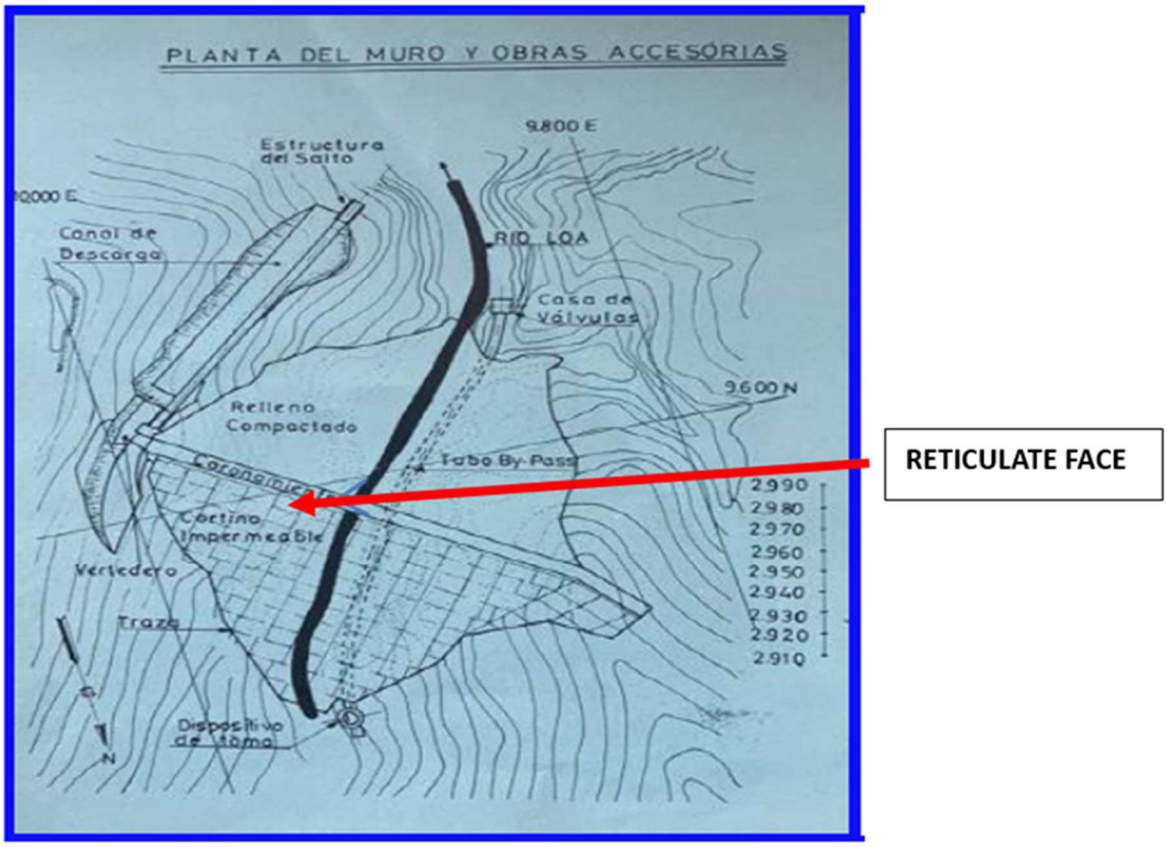

Fig. 6 - presents a plan of one of the project drawings showing the reticulated slabs.

2.4. 1995 SANTA JUANA

Almost 20 years after the construction of the Conchi reservoir, the Santa Juana reservoir was completed, incorporating several modifications in its design, and introducing, on a global level, a solution to optimize the design of the plinth in the riverbed foundation area.

The main characteristics are:

Compacted CFGD* wall: Wall volume 2,700,000 m³
Slopes: 1.6:1 Downstream, 1.5:1 Upstream
Height: 113 m
Crest width: 6 m
Crest length: 390 m
(*) Concrete Face Gravel Dam

One of the noteworthy features of this dam is the use of riverbed material, consisting of high-quality andesitic gravels, for the fills. Regarding the following geotechnical parameters, we can say the following:

Compressibility: Gravel compressibility, in general, is much lower than rockfill compressibility. [6]

Internal Friction Angle: Quarry rockfill also presents a higher internal friction angle due to its angularity, making it more effective for applications requiring high slip resistance and stability.

This situation led to a slight reduction in slopes compared to rockfill dams, with the slopes used in Santa Juana being 1.5:1 upstream and 1.6:1 downstream, eliminating the 3A layer since the fills were sourced from the existing riverbed material, which did not require a filter between the 2B and 3B materials. Also, in this case, it is used an external plinth, as show on **Fig.** 8

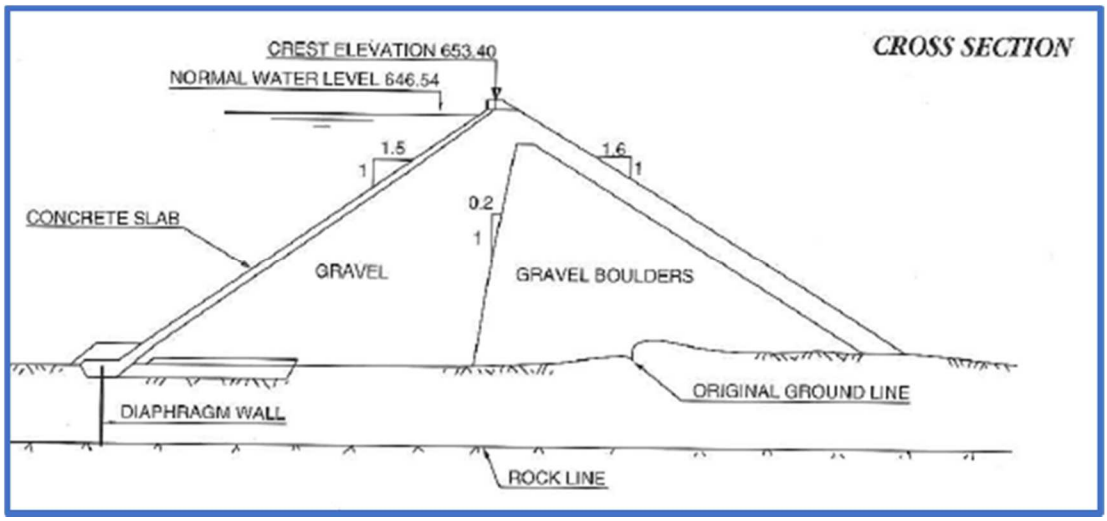

Fig. 7 - shows a typical section of the Santa Juana reservoir

There is no doubt that compaction and the use of gravel, instead rockfill, when that is possible, have several advantages under the settlement point of view, as we can see in point 10.9 of reference [6]

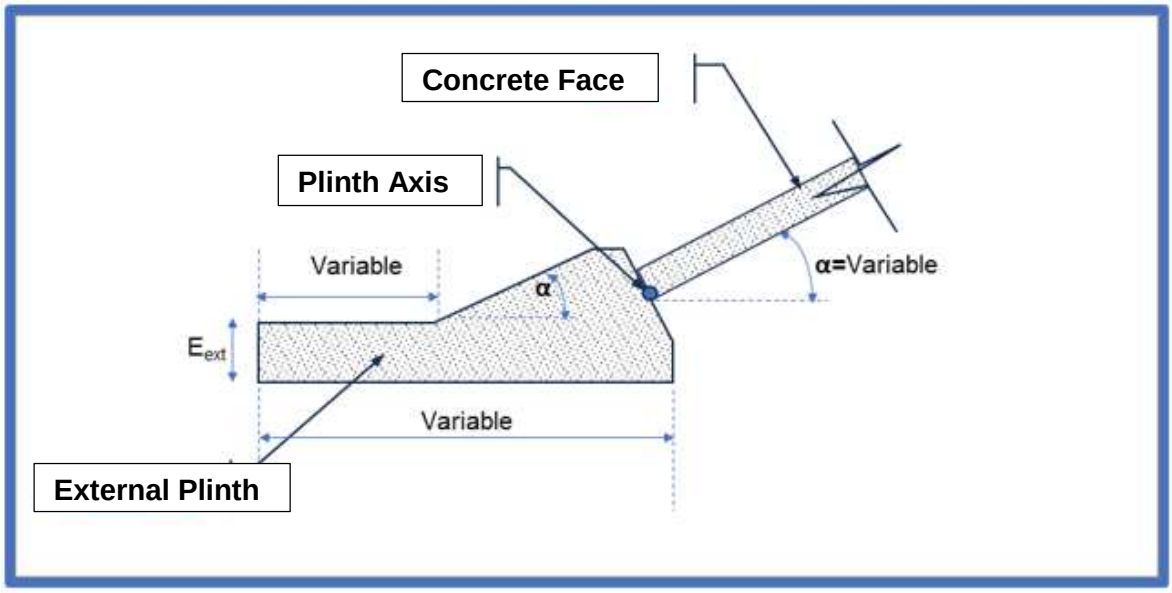

Fig. 8 - depicts the external plinth, which is located upstream of the concrete face.

Given that the thickness of the river material in the bed is more than 30m, a diaphragm wall was incorporated at the upstream foot to ensure the watertightness of the system, designing a horizontal plinth or tri-articulated valley plinth, which in addition to granting a greater degree of freedom for differential movements provided a space of 6 meters that allowed the work of placing fillers simultaneously with the construction of the molded wall, as shown in **FIG.** 9

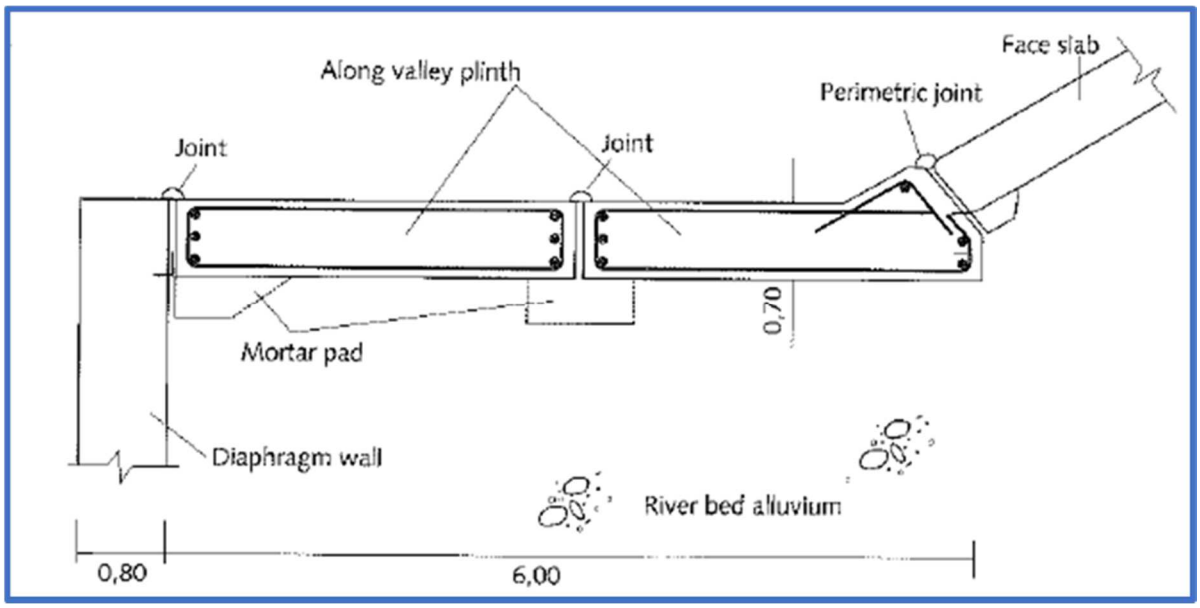

Fig. 9 - Santa Juana HORIZONTAL PLINTH

[3], [4], [5], [6]

2.5. 1999 Corrales

The Corrales Dam, like Santa Juana, was constructed using fills sourced from the riverbed, without the need for a diaphragm wall, since the thickness or depth of the riverbed at the site was minimal, with shallow bedrock.

Compacted CFGD wall: Wall volume 2,700,000 m³
Slopes: 1.6:1 Downstream, 1.5:1 Upstream
Height: 113 m
Crest width: 6 m
Crest length: 390 m
(*) Concrete Face Gravel Dam

However, geologically, the site is composed of decomposed granite in situ, which, due to its incompressible characteristic, was left in place instead of being removed as originally planned, which would have involved removing about 20 meters of material. Special precautions had to be taken with the injections to avoid fracturing the weak granite matrix, controlling the pressure, and confining them with footings or slabs as shown in **Fig. 10**. [7]

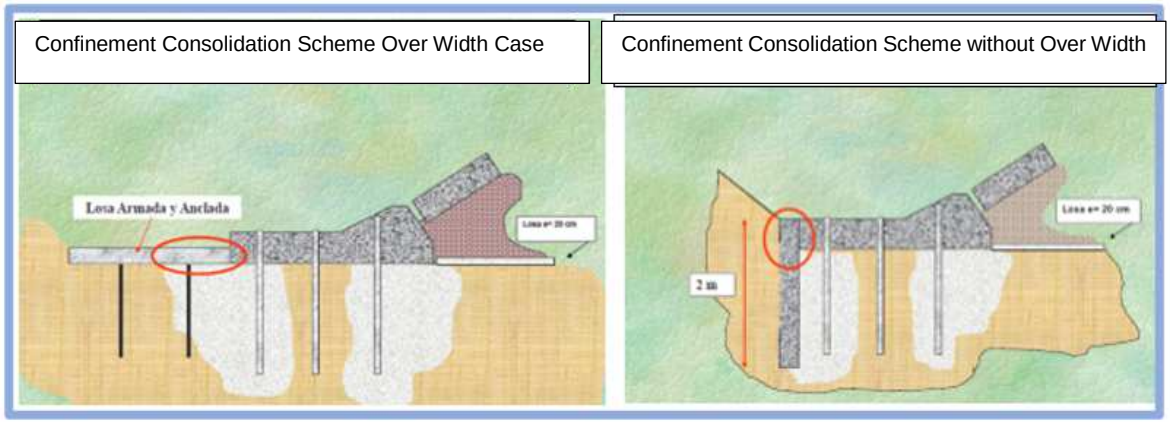

Fig. 10 - Confinement schemes for injections in areas with Decomposed Granite

2011 Ancoa

The Ancoa Reservoir also has a dam composed of gravels located in the riverbed, but it is characterized by the steep verticality of the valley on the right abutment, making access practically impossible and, therefore, any type of prospecting. Additionally, due to its verticality, proposing a traditional plinth would have resulted in a large excavation volume.

Compacted CFGD wall: Wall volume 3,700,000 m³
Slopes: 1.6:1 Downstream, 1.5:1 Upstream

Height: 136 m

Crest width: 10 m

Crest length: 370 m

(*) Concrete Face Gravel Dam

Fig. 11 - shows the right abutment of Ancoa, highlighting its verticality.

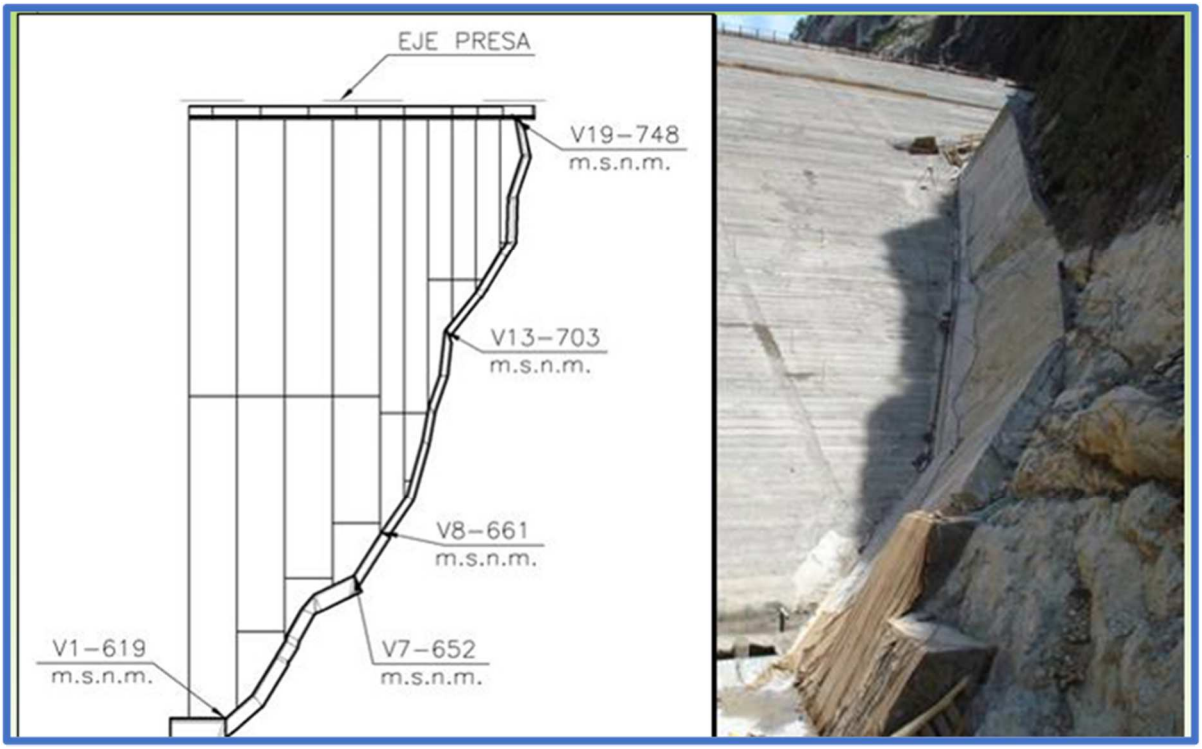

Fig. 12 - provides details of the right plinth that was constructed under the "Design as You Go" approach.

It is noteworthy that the slab width on the right side was reduced to 7.5 m instead of 15 m to provide greater freedom of movement for differential settlements.

For the foundation of the dam, especially in the area corresponding to the valley or horizontal plinth, it was decided to excavate to a depth of 20 meters until reaching the basal rock to close off the seepage under the dam. Cost studies demonstrated that a diaphragm wall of that depth in the characteristics of the valley was more expensive than the excavation. The final closure of the foundation in the valley plinth area was achieved with an underwater concrete footing, as shown in **Fig. 13**. [8]

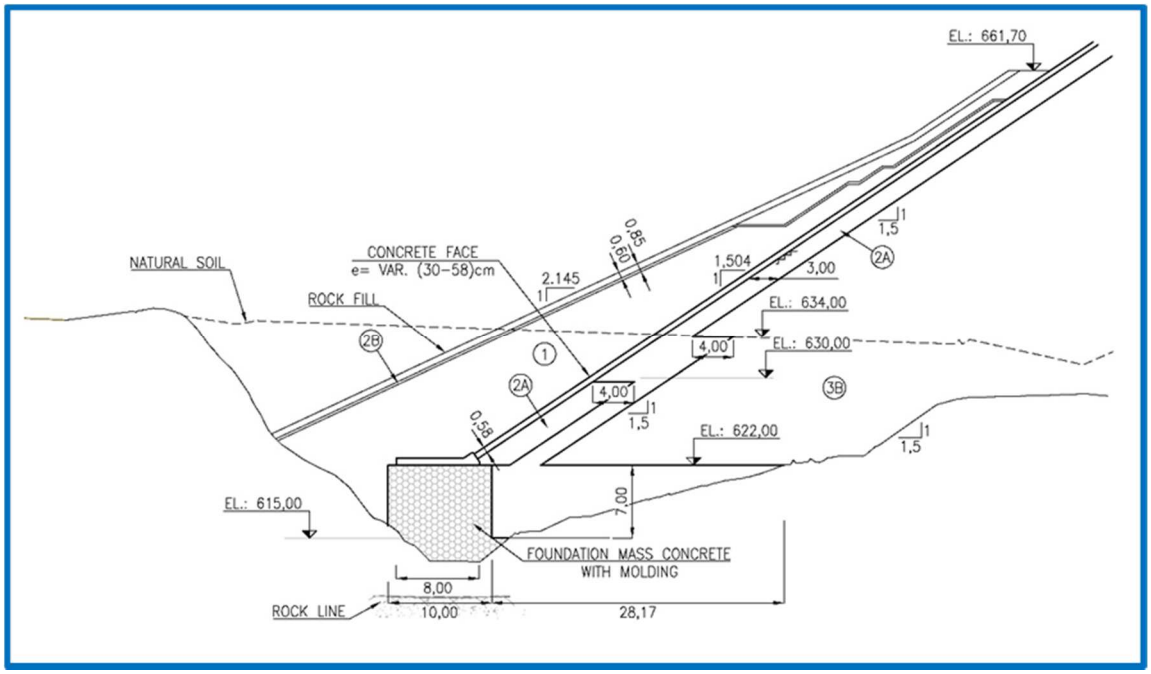

Fig. 13 - Valley Plinth of ANCOA with massive concrete on the bottom

2.6. 2021 Chironta

This reservoir, located in the far north of Chile, has the following characteristics:

Compacted CFGD wall: Wall volume 2,300,000 m³
Slopes: 1.6:1 Downstream, 1.5:1 Upstream
Height: 136 m
Crest width: 10 m
Crest length: 300 m
(*) Concrete Face Gravel Dam

As in the case of Ancoa, the foundation in the riverbed area involved excavating 25 meters below the riverbed elevation, leaving very little space between the bottom of the planned excavation and the downstream toe of the cofferdam, as shown in **Fig. 14.**

Fig. 14 - Cofferdam and upstream toe of the dam

During construction, it was found that the bedrock was located 7 meters deeper than initially assumed, requiring further excavation and the construction of a nearly vertical concrete block footing to seal the riverbed, as shown in **Fig. 15**. This task was complex due to the proximity of the cofferdam, requiring continuous pumping and underwater concrete placement.

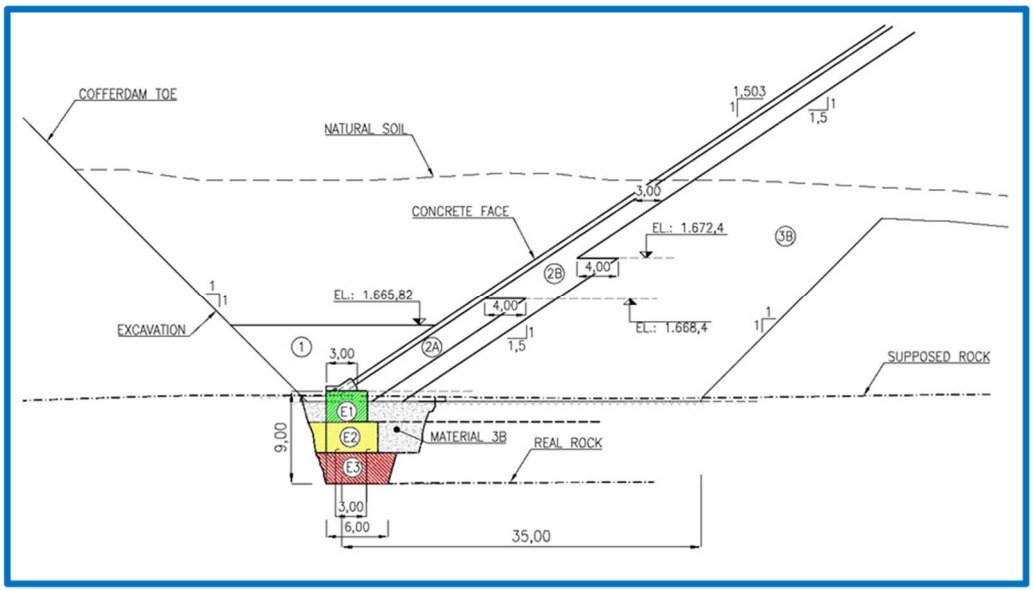

Fig. 15 - scheme of blocks that were placed to seal against the basal rock

However, the experience gained from Ancoa and Chironta allows us to conclude that when the thickness of the riverbed material on which the dam will be founded is less than 25 meters, excavation rather than a diaphragm wall is an attractive alternative to close or minimize the flow under the dam. For greater depths, up to approximately 30 meters, detailed analysis is necessary.

This dam also used the concept of an internal plinth, maintaining a single type for the upstream part of the concrete face, optimizing the excavations, and varying the part under the fills according to the determined RMR (Rock Mass Rating), as shown in **Fig. 16**.

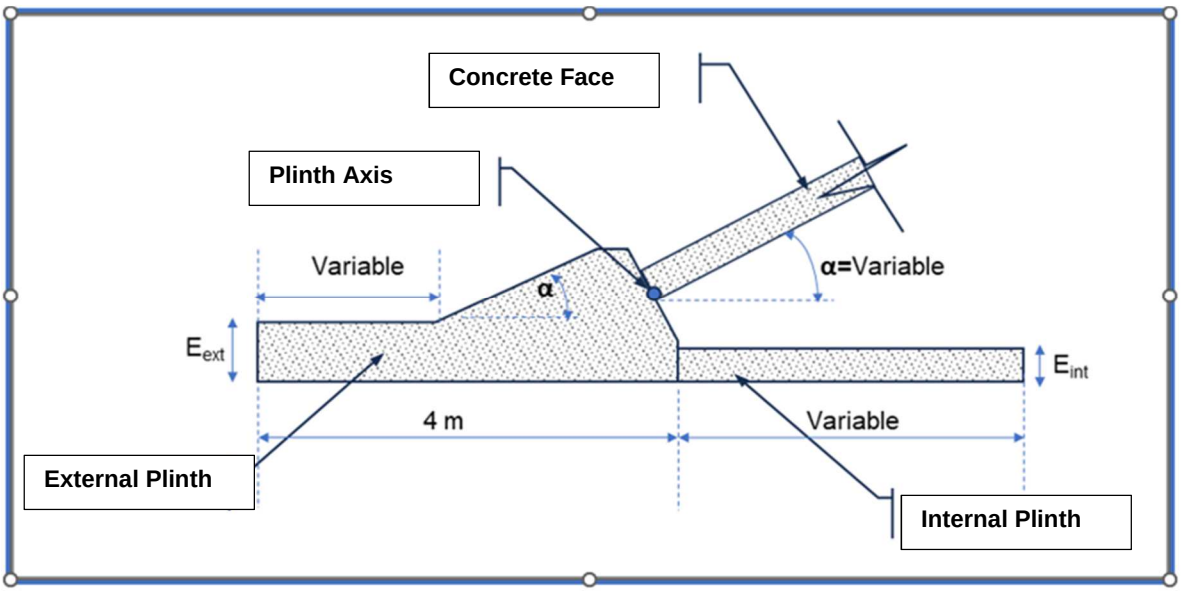

Fig. 16 - External and internal plinth assembly diagram

2.7. 2024 Bollenar

Bollenar is a mixed-type concrete face dam, with fills sourced from riverbed gravels and quarry rockfill, as the available gravels are insufficient to meet the total volume required. It is currently awaiting bidding for its construction.

The main characteristics of this dam are as follows:
Mixed Gravel and Rockfill Dam
Compacted CFGD volume: 2,260,000 m³
Compacted CFRD volume: 2,450,000 m³
Total volume: 4,700,000 m³
Variable slopes: See **Fig. 17**
Height: 110 m
Crest width: 9 m
Crest length: 720 m

Given that it is a mixed dam, the materials were placed as shown in Fig. 17, with the indicated slopes, taking full advantage of their geomechanics characteristics.

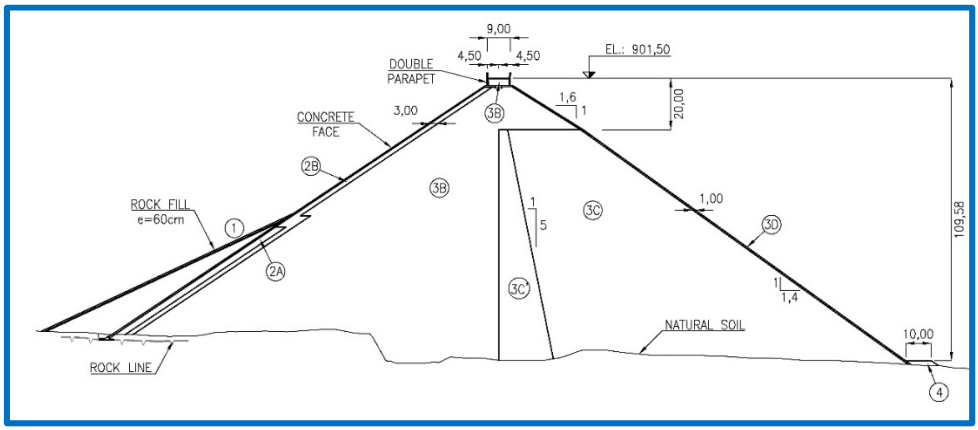

• Zone **1**	Non-cohesive fines
• Zone **2A**	Non-cohesive fines ≤ 1 ½''
• Zone **2B**	Gravel maximum size 3''
• Zone **3B**	Gravel maximum size 22''
• Zone **3C**	Rockfill maximum size 32''
• Zone **3C'**	Mix of gravel and quarry rockfill
• Zone **3D**	Rockfill size > 3''
• Zone **4**	Protective riprap

Fig. 17- Bollenar cross section

It is noteworthy that the slope in the upper section of the downstream face was changed to take advantage of the better internal friction angle of the rockfill. It is also worth mentioning the placement of riverbed materials, mainly on the upstream face, i.e., in the concrete face area, to leverage the compressibility modulus of these materials and minimize settlements.

Another important aspect of the Bollenar project is that, being a dam with a significant volume of quarry rockfill, and with a right abutment with geotechnical quality suitable for extracting this material, a frontal spillway was proposed, given that the excavation volume on that side will be used entirely for the rockfill fills, which are preferably placed on the downstream face, next to the spillway, resulting in significant savings in transportation and placement. The configuration of this work is shown in **Fig. 18.**

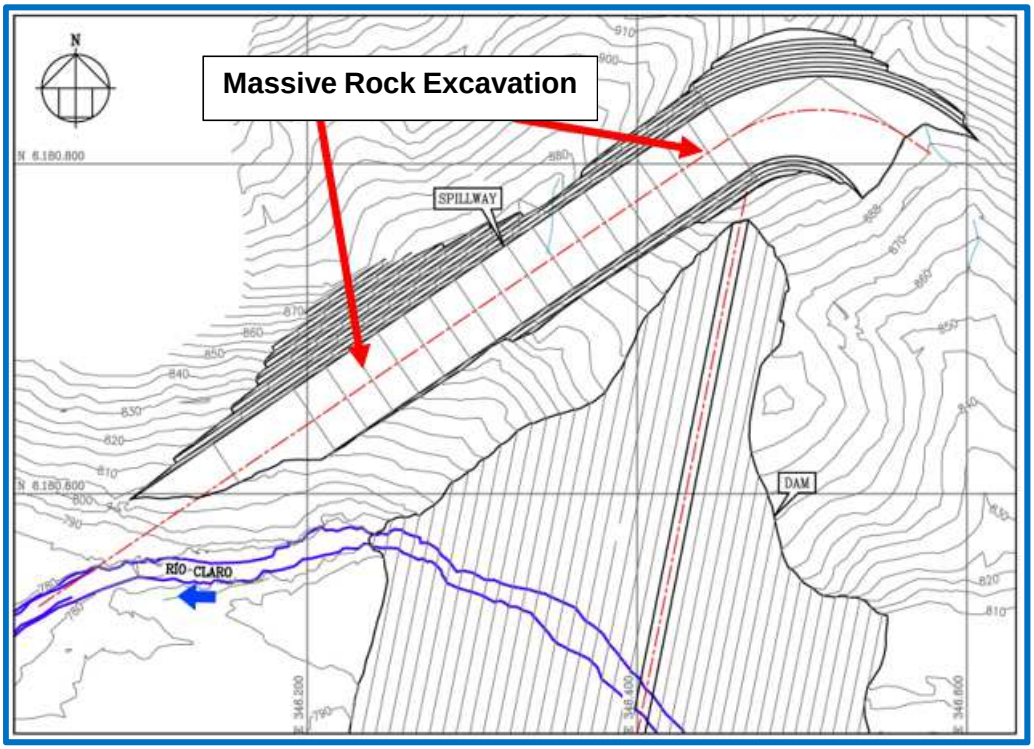

Fig. 18 - Frontal spillway scheme to take advantage of the excavation rockfills

3. CODEGUA IN DESIGN STAGE AS A COMPENDIUM OF THE DESCRIBED EXPERIENCE

Given the previously presented information, it is now time to configurate. the layout of the Codegua reservoir based on the accumulated experience, not only from Chile but also from international projects. Below, we present, in general terms, the main components and concepts incorporated into this design:

3.1. Type of dam

The experience gained over nearly 100 years, combined with the geological and geotechnical characteristics of the site, allows us to select a CFRD-type dam.

3.2. Placement of fills

The fills must be compacted due to the performance of the fills under these conditions, considering the addition of water to the fills has become a common practice for high dams.

This is typically at a minimum rate of 200 liters per cubic meter. [6]

3.3. Source of fills

In this case, the situation is like that of the Bollenar project, where, despite the presence of riverbed materials, their volume is insufficient to meet the total required volume. Therefore, a mixed CFRD and CFGD dam was chosen.

The characteristics of this dam are as follows:

Mixed Gravel and Rockfill Dam
Compacted CFGD volume: 384,000 m³
Compacted CFRD volume: 3,158,000 m³
Total volume: 3,542,000 m³
Variable slopes: See Fig. 20
Height: 110 m
Crest width: 8 m
Crest length: 503 m

It has been decided that the gravels will be used in zones 2A, 2B, and 3A, creating a zone called 2-3 BA with a width of 6 m, placed between the extruded curb and the 3B material sourced from quarry rockfill. This design was presented at the Chengdu Congress in China.

[9]

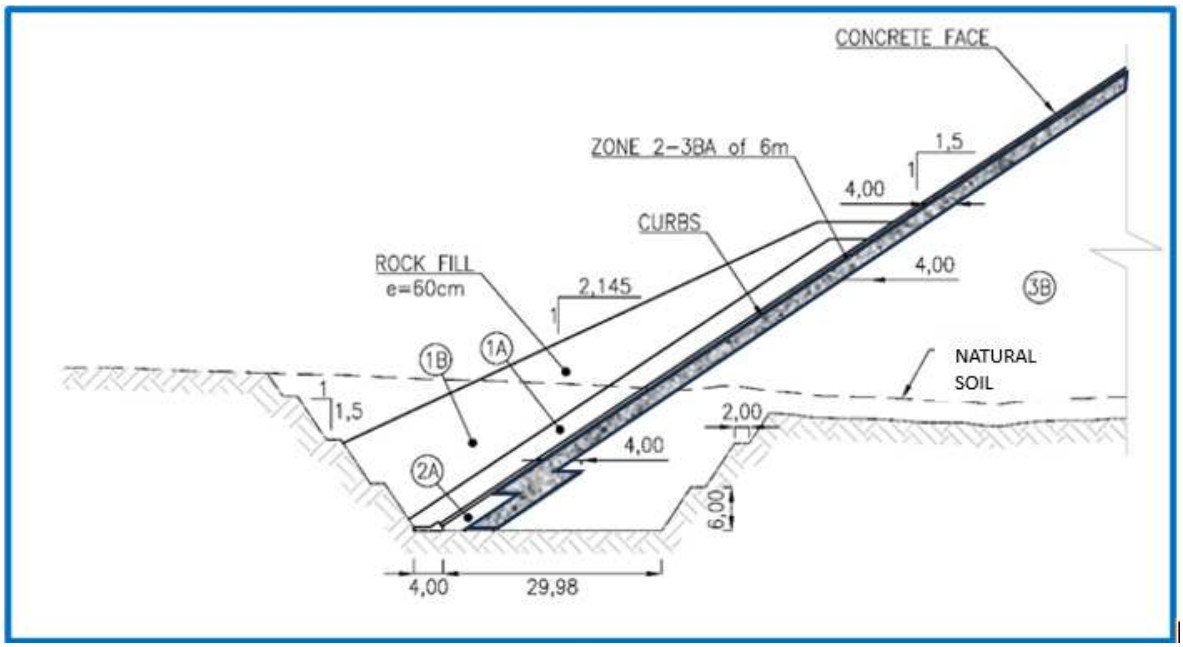

Fig. 19 - shows the detail of this area adjacent to the concrete face, optimizing the 2-3 BA Zone by leveraging the curb.

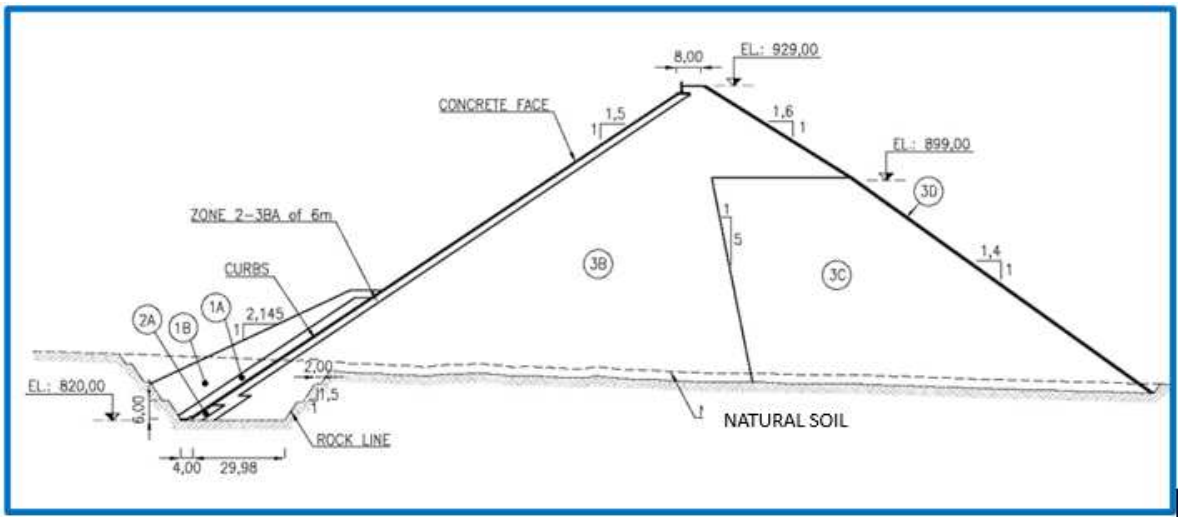

Fig. 20 - shows the typical cross-section of the dam with the slope change on the downstream face, as adopted in the Bollenar project.

3.4. Site characteristics

As seen in **Fig. 21**, the right abutment is very similar to that of the Ancoa reservoir, where a vertical plinth was adopted.

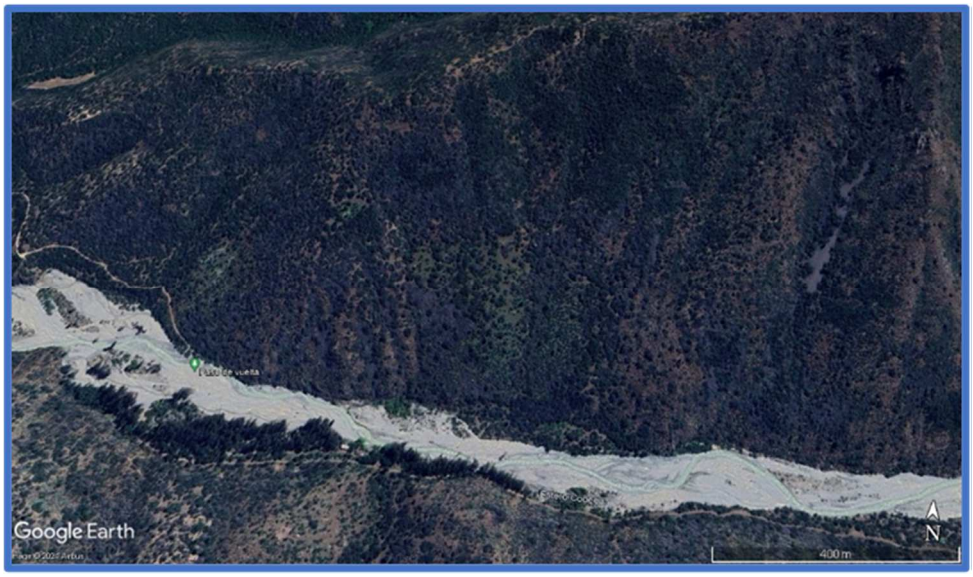

Fig. 21 - Vertical right abutment

Given that the site is very similar in terms of topography to the Ancoa reservoir, with a nearly vertical right abutment that necessitates a vertical plinth solution on that side, the same solution was adopted, based on a "Design as You Go" approach, as shown in Fig. 22.

Fig. 22 - Vertical plinth adopted

3.5. Foundation in the riverbed

The thickness of the riverbed material in the valley or horizontal plinth area suggests that an excavation of approximately 22 meters will be adopted to avoid using a diaphragm, wall, as shown in **Fig. 19.**

3.6. Final configuration

The final configuration of the Codegua reservoir, representing a true compendium of the development of concrete-faced dam engineering in Chile and worldwide, is shown in **Fig. 23**. The design adapts to the current state of the art while considering the unique characteristics of each site.

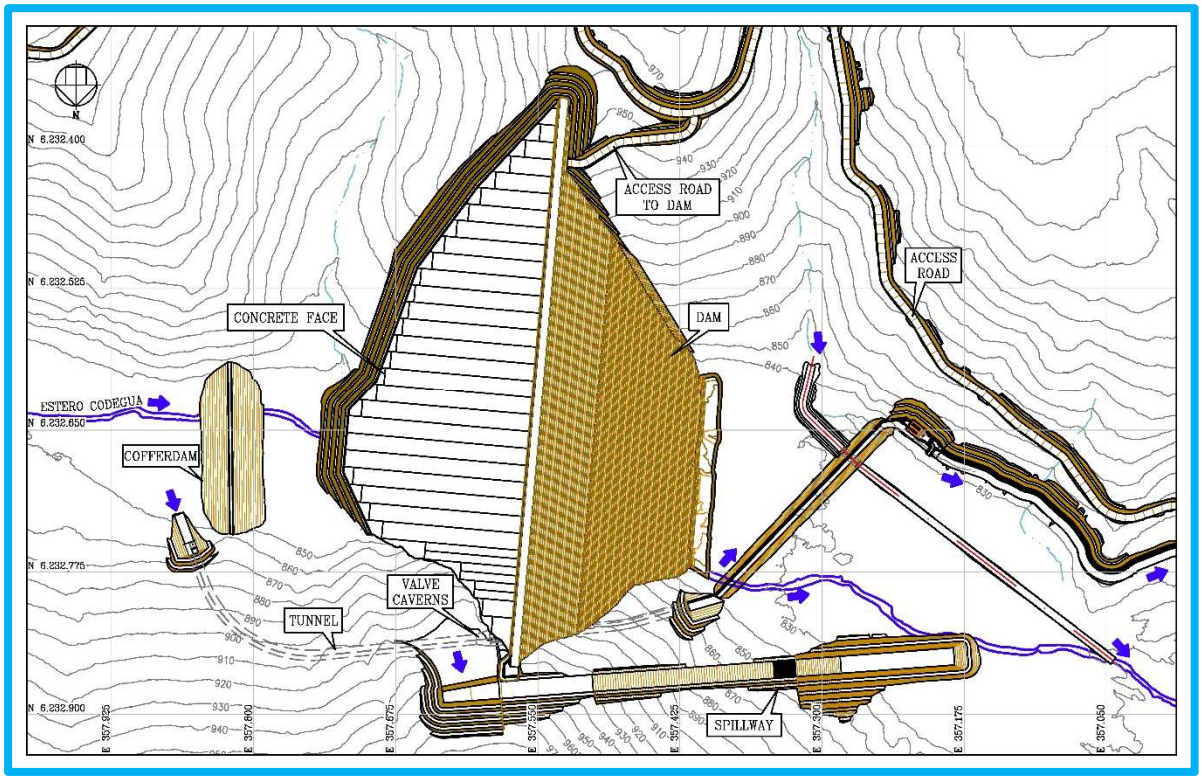

Fig. 23 - General layout of Codegua

4. CONCLUSIONS

There is no denying the global progress made in the design and, consequently, the adoption of concrete-faced dams. Each day, driven by new equipment and technology, as well as the constant demand and need to regulate water for purposes such as power generation, irrigation, or industrial processes, these dams continue to be relevant. Therefore, to maintain this progress uninterrupted, it is essential to keep an eye on our historical past. Undoubtedly, history will help us embrace changes and innovations, if they are supported by experience, knowledge, and, above all, understanding and comprehension, specially taken from a highly seismic country, as it is Chile.

REFERENCES

[1] Quezada M.; San Martin L. (2007) Caritaya Reservoir - III Symposium on CFRD – Florianopolis, Brazil.

[2] Arrau L.; EA (1985) Performance of Cogotí Dan Under Seismic Loading – Concrete Face Rockfill Dams – Design, Construction and Performance – J Barry Cooke and James Sherard

[3] San Martin L.; EA (1992) The Santa Juana CFRD for irrigation in northern Chile – Waterpower & Dam Construction

[4] San Martín L. (1993) Santa Juana Project, A Concrete Panel Wall Solution – International Symposium on High Earth – Rockfill Dams – Beijing, CHINA

[5] San Martin L.; EA (2000) CFRD Constructed on Deep Alluvium – J Barry Cooke Volume

[6] Materon B.; EA (2009) Santa Juana (Chile 1995) – CONCRETE FACE ROCKFILL DAMS

[7] San Martin L. (1999) Plinto en Granito Descompuesto y su Materialización en Corrales – II SIMPOSIO SOBRE BARRAGENS DE ENROCAMENTO CON FACE DE CONCRETO – Florianópolis, BRAZIL

[8] San Martin L.; EA (2011) Vertical Plinth ANCOA DAM – Second International Symposium on Rockfill Dams – Rio de Janeiro, BRAZIL

[9] Materon B.; San Martin L. (2025) CFRD Dam Zoning with Extruded Curb – Creation of Zone 2-3 BA – CODEGUA CASE – CHENGDU, CH

Fifth International
Dam World Conference
PORTUGAL • LISBON • LNEC • APRIL 13-17, 2025
dam world 2025

DEVELOPMENT OF AN INTEGRATED SYSTEM FOR RISK MANAGEMENT AND DECISION-MAKING: AN FMEA/FMECA AND PFMA-BASED APPROACH

Daniel E Mendes[1]
Cemig Geração e Transmissão S.A.

ABSTRACT

Risk analysis methodologies, such as FMEA/FMECA and PFMA, have been commonly used as risk assessment tools in dams, supporting the stages of identification and evaluation of risks and the definition of control measures to reduce the probability of failure. In this paper, the use of these risk analysis methodologies is proposed for structuring a computational tool applied to risk management and decision-making, focusing on the response to situations that could lead to dam failure.

The proposed tool consists of a computational system, integrated with a relational database management system (RDBMS), which allows the documentation and management of relevant information about the dam structure, including technical documents and information regarding possible failure modes identified during the risk analysis. Through a simple and intuitive interface, the system offers quick access to information about the risks, categorized by structure and by abnormal situations related to each documented failure mechanism. This functionality provides managers and technical teams with a comprehensive view of the risks, facilitating the identification of the root causes of problems and supporting decision-making for timely response during critical scenarios.

The proposed tool contributes to risk management in dams, in addition to providing structure knowledge management, such as construction particularities and possible weaknesses, ensuring a faster response to abnormal situations. Additionally, the system is customizable and can be adapted and expanded to meet the specific needs of different types of structures and risk scenarios.

Keywords: FMEA/FMECA, PFMA, RIDM, Risk Assessment, Risk Analysis.

[1]daniel.mendes@cemig.com.br, Brazil

1. INTRODUCTION

Risk analysis methodologies have been increasingly applied to dams as a tool for identifying and controlling risks that could compromise the safety of both the structure and the surrounding population. These analyses typically involve a multidisciplinary team focused on identifying and evaluating risks, often resulting in a substantial volume of documentation. This process culminates in a report outlining measures necessary to mitigate the identified risks. However, a significant portion of the knowledge acquired during these risk analyses remains restricted to the multidisciplinary team that conducted the evaluation. This is because the risk analysis report is typically concise and objective, aiming to streamline the process of characterization and implementation of controls.

The **Integrated System for Risk Management and Decision Making (IS-RMDM)**, proposed in this article, seeks to address this limitation by facilitating knowledge management and tracking changes over the lifecycle of the structures. The system ensures that risks identified during the risk analysis phase are stored on a platform that is easily accessible to all managers and working teams. The information and documents generated during these analyses are made available in a structured format, promoting efficient knowledge management and supporting risk-informed decision-making.

Moreover, the platform enables dynamic risk management, allowing information to be added and updated as needed, transforming the tool into a living document. This dynamic capability ensures that risk management evolves during the structure’s life, enhancing the overall effectiveness of the decision-making process.

2. RISK ANALYSIS

Risk analysis applied to dams involves the adoption of specific methodologies to identify, analyze, and assess potential risks, considering the various hazards to which the structure may be exposed. Numerous methodologies for risk analysis are available in the literature, encompassing qualitative, quantitative, and semi-quantitative approaches, depending on the inclusion of indexes or numerical values for ranking identified risks.

Among the existing methodologies, Failure Mode and Effect Analysis (FMEA) and Potential Failure Modes Analysis (PFMA) were adopted for the development of the methodology applied in the Integrated System for Risk Management and Decision Making (IS-RMDM). While FMEA enables the evaluation of systems and individual components, ranking risks based on indexes such as Likelihood, Severity, and Detectability, PFMA, although less structured, provides a detailed examination of the failure mechanism's development. PFMA also identifies the factors

that influence the likelihood of occurrence, supporting more accurate risk classification and evaluation.

2.1. Failure Mode and Effect Analysis (FMEA/FMECA)

According to [1], FMEA is a systematic method for evaluating an item or process to identify potential failure modes, assess their effects on the performance of the item or process, and evaluate their impact on the surrounding environment and personnel. This methodology supports decision-making to reduce the likelihood of failures and mitigate their effects.

The prioritization of identified potential failure modes is typically based on a combination of likelihood, severity and detection indexes. When failure modes are prioritized, the process is referred to as Failure Modes, Effects, and Criticality Analysis (FMECA). International Standard IEC [1] outlines the basic steps for performing FMEA/FMECA analysis, which can be summarized as follows:

- Sub-divide systems or processes into components / elements, identifying functions and performance standards for each one;
- Identify failure modes and their causes;
- Identify detection methods and existing controls;
- Identify local and final effects of failure modes;
- Determine the severity of the final failure effects, estimate the likelihood of failure modes, and assess other criticality parameters;
- Identify actions to reduce or mitigate residual risks.

The elements identified during the FMEA process are typically presented in a table, organized by their functions and the corresponding failure modes. There is no standardized layout for presenting this table; the format should be determined by the risk assessment team to best suit the specific evaluation.

Fig. 1 provides an example of a table illustrating the application of the FMEA methodology.

SUBSYSTEM										
COMPONENT	FUNCTION	FAILURE MODE	CAUSES	LOCAL EFFECT	FINAL EFFECT	EXISTING CONTROLS	LIKELIHOOD	SEVERITY	DETECTION	ACTIONS

Fig. 1 – Example of FMECA spreadsheet

The identified failure modes are usually assessed based on criticality prioritization. The most common approach involves representing the Criticality Number, obtained by multiplying the likelihood and severity indices, or other metrics such as the Risk Priority Number (RPN), calculated by multiplying the indexes of likelihood, severity, and detectability. Another common representation method is through Criticality Matrix, where the likelihood and severity indexes are displayed in matrix form, and risks are evaluated based on the tolerability class defined within the matrix.

There is no single guideline for defining risk tolerability categories; they must be adapted to align with the specific objectives of each organization.

Fig. 2 illustrates the risk matrix adopted in the IS-RMDM, which defines four levels of tolerability: Acceptable risks (green); Tolerable risks (yellow); Undesirable risks within the ALARP principle ("As Low As Reasonably Practicable") (orange); and Unacceptable risks (red).

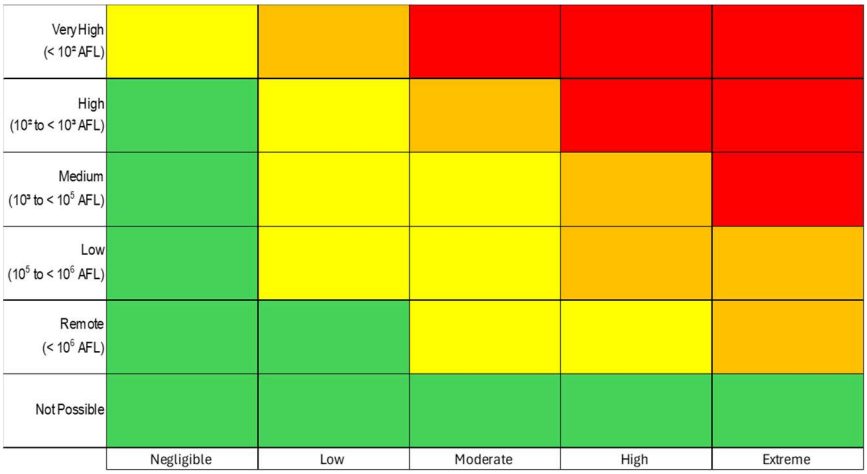

Fig. 2 – Example of Criticality or Risk Matrix

2.2. Potential Failure Modes Analysis (PFMA)

According to the methodology described in [2], a Potential Failure Mode (PFM) is the unique and specific chain of events that can lead an element to failure. The sequence of events associated with each PFM must be based on a comprehensive understanding of the structure's entire history of design, construction, operation, and maintenance, as well as occurrences that may indicate points of vulnerability. After conducting an in-depth study of the dam's aspects, a detailed definition of each step is developed, highlighting three key elements: the initiating event (or trigger), the development or progression of the failure mechanism leading to its final effect, and the impacts or consequences of partial or total failure.

The level of detail in the description of each PFM should be as thorough as possible to ensure the failure mode is well understood by the entire team. Once the team has fully described a potential failure mode, it is evaluated by listing the adverse factors that increase the likelihood of the failure mode and the positive factors that decrease it. After completing this step, each PFM is assessed to determine its potential contribution to the overall risk.

3. INTEGRATED SYSTEM FOR RISK MANAGEMENT AND DECISION MAKING (IS-RMDM)

The Risk Management and Decision-Making System (IS-RMDM) was developed to standardize the storage of knowledge obtained during the stages of risk identification, analysis, and assessment, enabling proper information management.

The system's structure was designed with the development of a Relational Database Management System (RDBMS) for storing data related to the risk analysis process, based on the FMEA/FMECA and PFMA methods. This database is supported by a Graphical User Interface (GUI) that facilitates data entry, modification, query, and analysis.

3.1. Database

According to [3], a Database Management System (DBMS) is a data storage system where each record represents information or an aspect of the real world. Through a DBMS, users can perform various operations involving stored data, such as adding, deleting, or modifying records, following a defined set of rules. There is a wide range of DBMS software available, each with distinct characteristics. For the development of the IS-RMDM database, Microsoft SQL Server and SQL Server Management Studio were adopted.

Conceptual data models consist of **entities**, **attributes**, and **relationships**, where an entity represents a real-world object or concept, an attribute corresponds to a property of interest that helps describe an entity, and a relationship indicates an association between two or more entities in the database.

In the relational database model (RDBMS), adopted for this project, there is a collection of relations, with relationships potentially constrained by rules that limit the combinations of entities that can participate in each relationship set. The cardinality ratio for a binary relationship specifies the maximum number of relationship instances in which an entity can participate.

For IS-RMDM, the primary database entity is STRUCTURE, representing the system and its subsystems or elements as divided in the FMEA. Each STRUCTURE was populated with the

attributes “Structure Name” and “Structure Description,” as well as a “Parent_ID” attribute, used to define a recursive relationship linking structures with a cardinality ratio of 1:0 (each STRUCTURE can be related to only one or no other STRUCTURE), thereby forming the components of a chain of structures within each system.

The same data association model is adopted to other tables relationship. Data related to potential failure modes, for example, are stored in the FAILURE MECHANISM entity, with attributes for “Title” and “Failure Mechanism Description.” This entity was designed to detail the trigger, initiation, progression, and failure/consequence of each PFM, enabling each PFM defined in FAILURE MECHANISM to be associated with both a FMEA and a PFMA entity, each with a one-to-one (1:1) cardinality ratio.

All other information that comprises a risk analysis based on FMEA and PFMA methodologies was directly linked to their respective entities to enable the structured storage of information and facilitate multi-criteria queries during the risk management phase in IS-RMDM.

The complete database structure for IS-RMDM includes 35 entity tables and 20 auxiliary relationship tables, with an average of 35 records entered by the user for each identified failure mechanism. A simplified version of the database structure developed for this project is presented in Fig. 3.

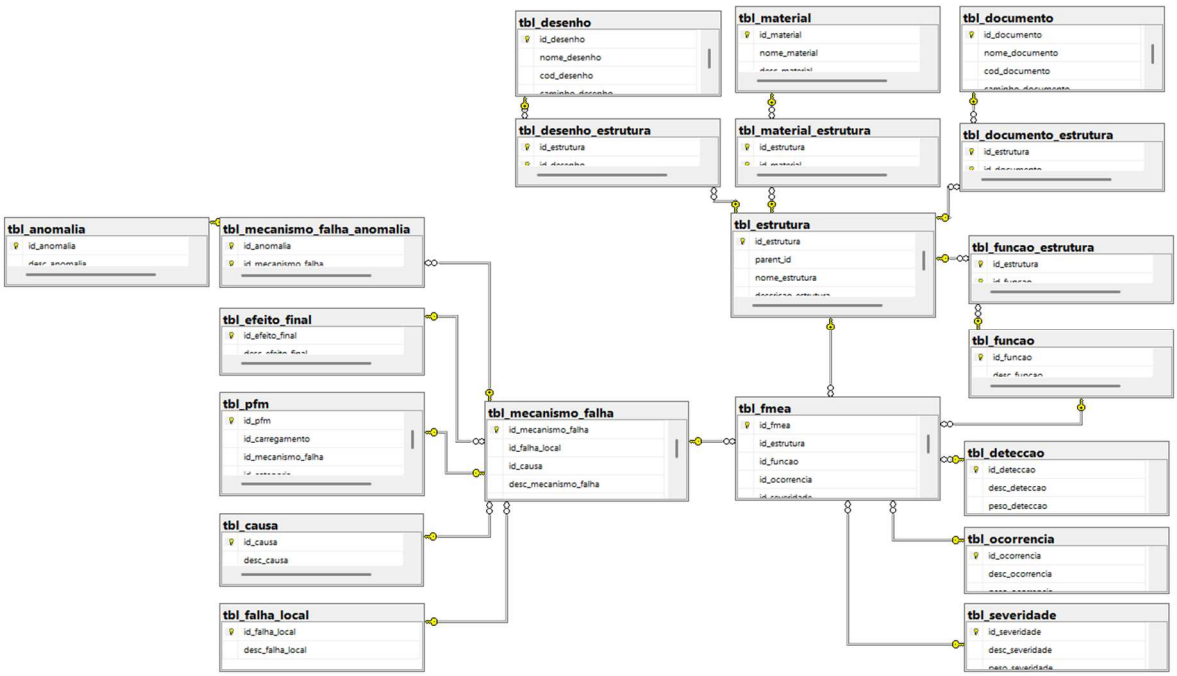

Fig. 3 – Example of the database structure of the IS-RMDM

3.2. Graphic User Interface (GUI)

On RDBMS, the Structured Query Language (SQL) is the programming language used to query and manipulate the database. To simplify data entry and manipulation for users, two

Graphical User Interfaces (GUIs) were developed: The Data Entry Interface, responsible for the structured inclusion of data; and The Risk Management and Decision-Making Interface, designed for analyzing, interpreting and presenting stored data.

Both interfaces were programmed in Python, using the PySimpleGUI library for graphical interface creation. Additionally, the system leverages the following libraries: PyODBC for database connectivity, Matplotlib for plotting graphs, Pandas for data analysis and manipulation, and NumPy for processing large, multidimensional arrays and matrices.

- **Data Entry Interface**

The Data Entry Interface of the IS-RMDM was designed to facilitate the inclusion and manipulation of data related to structures and associated Potential Failure Modes. The initial screen displays editable fields for registering a new structure, followed by a list of already registered structures.

Registered structures can either be a System or be related to an existing structure (via a Parent ID) as a Subsystem or Component. Once registered, the structure is added to the list of structures, with a hierarchical representation relative to its immediate parent component, subsystem, or system.

Within the Structure Data tab (Fig. 4), users can input information about construction materials and drawings/documents using specific forms. These details can later be linked to the corresponding structures and accessed via the platform.

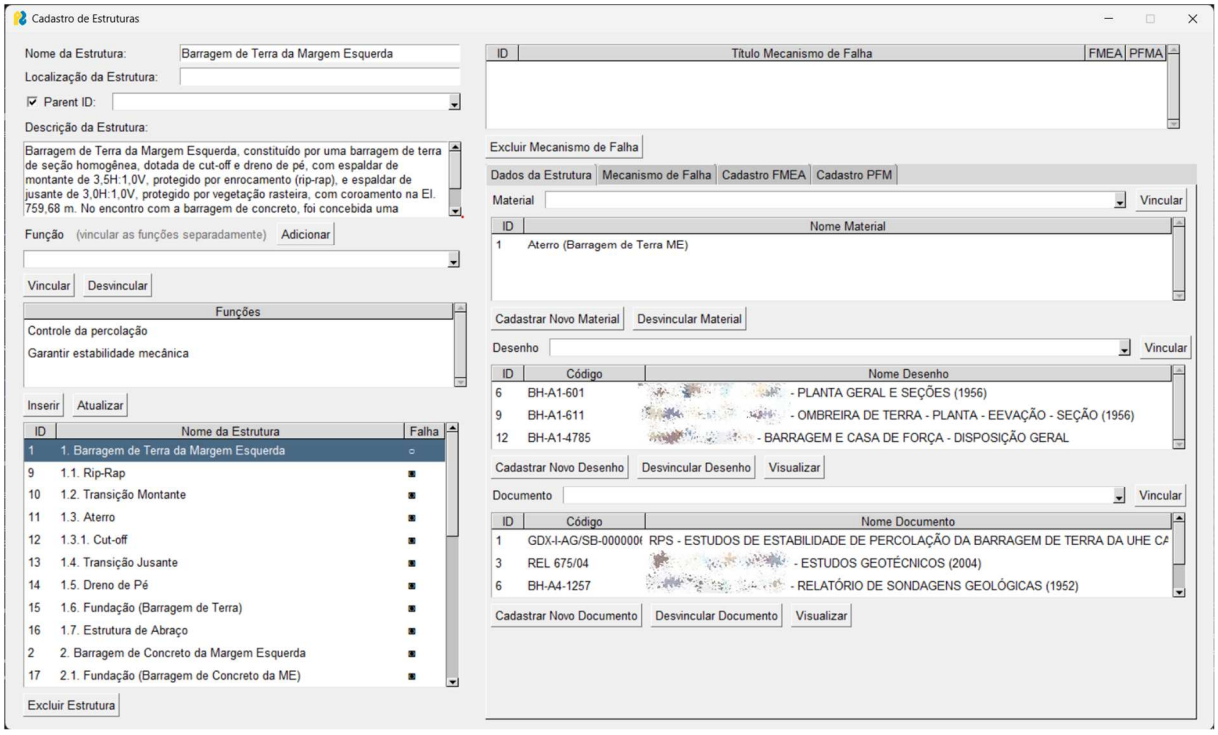

Fig. 4 – Structure Data tab of the Data Entry Interface

In the table of registered structures, the column titled “Failure” indicates structures that do not yet have any associated failure mechanisms. Once failure mechanisms are registered, they are displayed on the failure mechanism table, located at the top of the window.

The “Failure Mechanism” tab (Fig. 5) provides a form for entering information related to failure mechanisms. Most of the form's fields are categorized, enabling the identification of common elements across different PFM and structures.

After registration, the “Failure” column in the structure table is updated, indicating that the structure has at least one associated PFM. The PFM Title is then added to the upper table, with the columns “FMEA” and “PFMA” showing pending entries for the evaluation data associated with the failure mechanism.

The key data to be entered in the PFMA registration tab are Loading, Category (FERC Class), Positive Factors / Documentation, Adverse Factors / Documentation and Unknown Factors / Documentation. In the FMEA registration tab, the key data to be entered are Likelihood Index / Confidence of Likelihood Index, Severity Index / Confidence of Severity Index, Failure Mode Development Time, Existing Controls / Control Efficiency, Detectability Index, Detection Methods / Detection Time Interval and Anomalies and Visual Evidences.

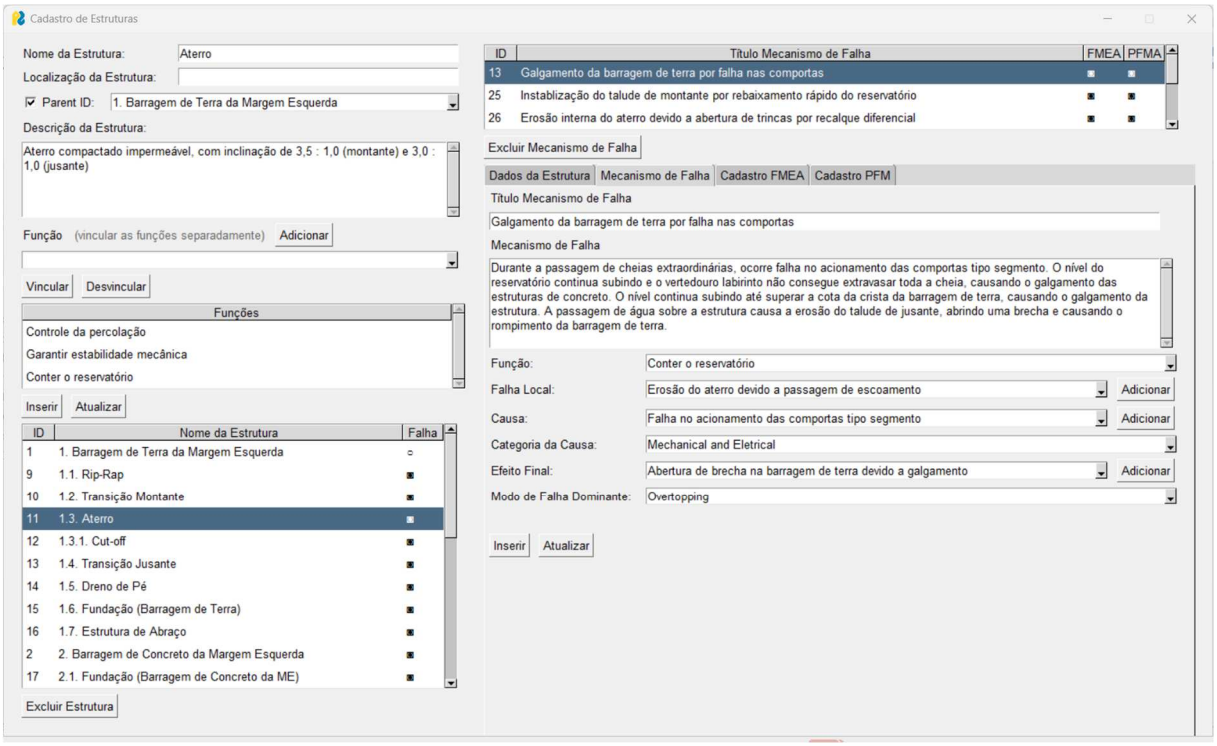

Fig. 5 – Failure Mechanism tab of the Data Entry Interface

In addition to the drawings and documents associated with the structures, each Positive Factor, Adverse Factor, or Unknown Factor can be linked to drawings and documents that

represent the existing condition. In this way, each failure mechanism is tied to documentation that supports the assessment of the actual conditions for likelihood, severity, and detectability.

All registration and linking operations performed through the Data Entry Interface are automatically added to the database, updating the entities and relationships without requiring the user to have knowledge of SQL for data manipulation. The recorded information is then made available for consultation through the Risk Management and Decision-Making Interface.

- **Risk Management and Decision-Making Interface**

The Risk Management and Decision-Making Interface was designed to access the data stored in the database. The initial screen presents an overview of all the registered PFM, sorted in descending order based on Criticality (Likelihood Index x Severity Index), also displaying the classification based on the Risk Prioritization Number (RPN) and risk tolerability, as defined by the Risk Matrix. Several filters have been developed to allow customized access to specific failure mechanisms, either by selecting the structure or through filters based on attributes related to each PFM.

When a registered structure is selected, the system automatically updates the list of failure mechanisms, displaying only those related to the selected structure or its associated components. This enables access to all failure mechanisms inherent to a given structure, facilitating an overview of the failure modes for each system. The system also allows access to and viewing of the documentation linked to the selected structure, as well as the information on construction materials associated with it.

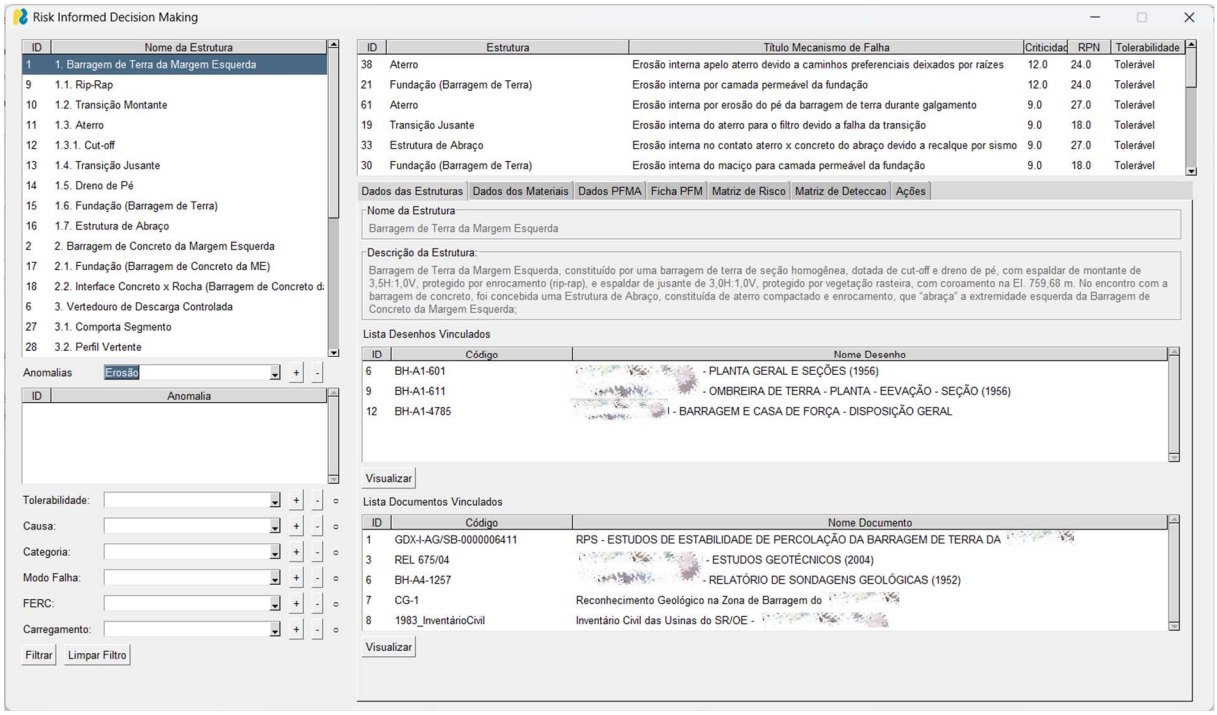

Fig. 6 – Initial screen of the Risk Management and Decision-Making Interface

Quick access to the structural characteristics of the system enables the decision-maker to make a more accurate assessment of the necessary preventive or corrective measures during emergency situations. This interface also facilitates knowledge management, allowing even teams without advanced knowledge of the structure to access important information in a structured and centralized manner.

After selecting the structure, the failure mechanisms are presented in the upper list, also sorted by Criticality. The failure mechanisms can be viewed through the Criticality Matrix tab, where each failure mechanism is represented in a risk matrix, with the Likelihood Index represented on the Y-axis and the Severity Index represented on the X-axis. In the matrix, error bars are also plotted, representing the uncertainties of each classification, determined by the confidence levels of the Likelihood and Severity classifications.

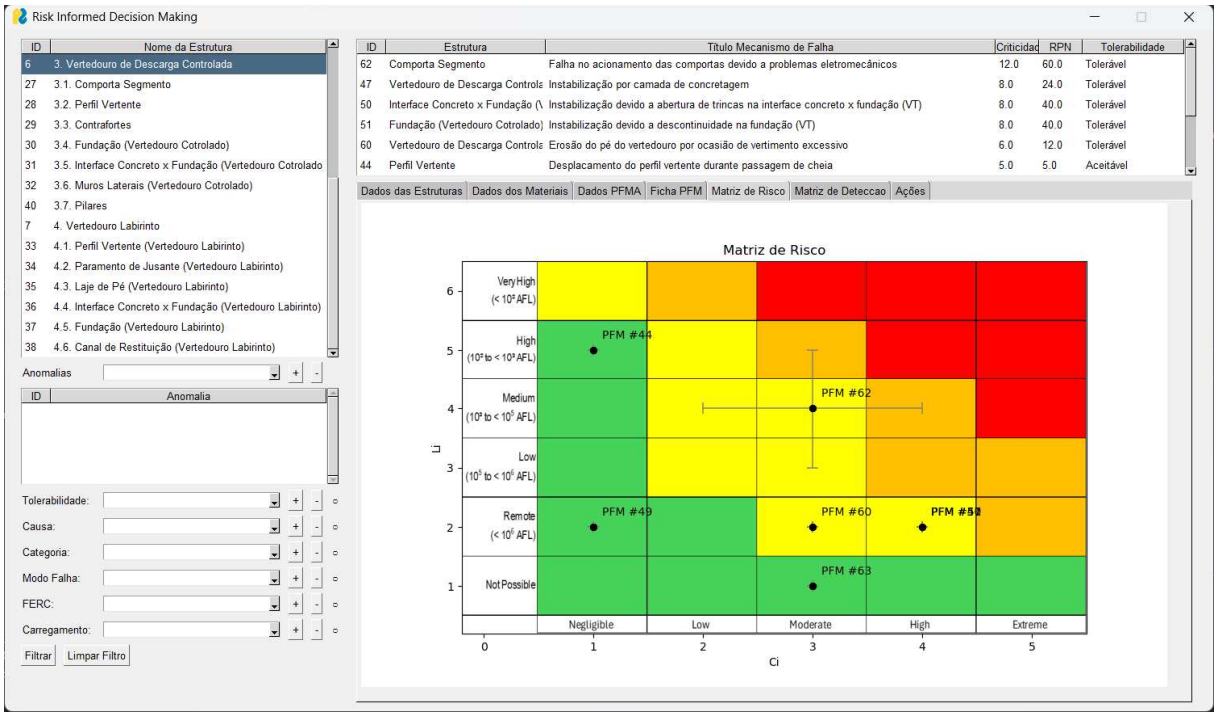

Fig. 7 – Criticality Matrix tab of the Risk Management and Decision-Making Interface, with error bars representing uncertainties on PFM #62

In the "Controls" tab, controls linked to the selected failure mechanism are displayed, allowing the management of their effectiveness. The loss of control effectiveness may affect the residual risk of the PFM, impacting its Criticality.

In the "Detection Matrix" tab, the PFMs are represented according to their Criticality and the likelihood of detection, defined by the Detectability Index, which classifies the probability of identifying the failure mechanism before its development. Ideally, PFMs with higher Criticality should have more efficient detection methods, particularly if the associated controls involve

corrective measures after the failure development has been identified (e.g., structural measures to stop the development of the failure or evacuation actions for the population).

In addition to the general view of the registered mechanisms, when a specific PFM is selected from the upper list, the "PFM Record" tab provides an overview of all the information related to that particular issue. Selecting the PFM also changes the representation of the Risk and Detection matrix, where the PFM is plotted individually. In the "PFMA Data" tab, the mitigating, aggravating, and unknown factors are displayed, along with the documents and drawings linked to each factor, which can be viewed from the management interface.

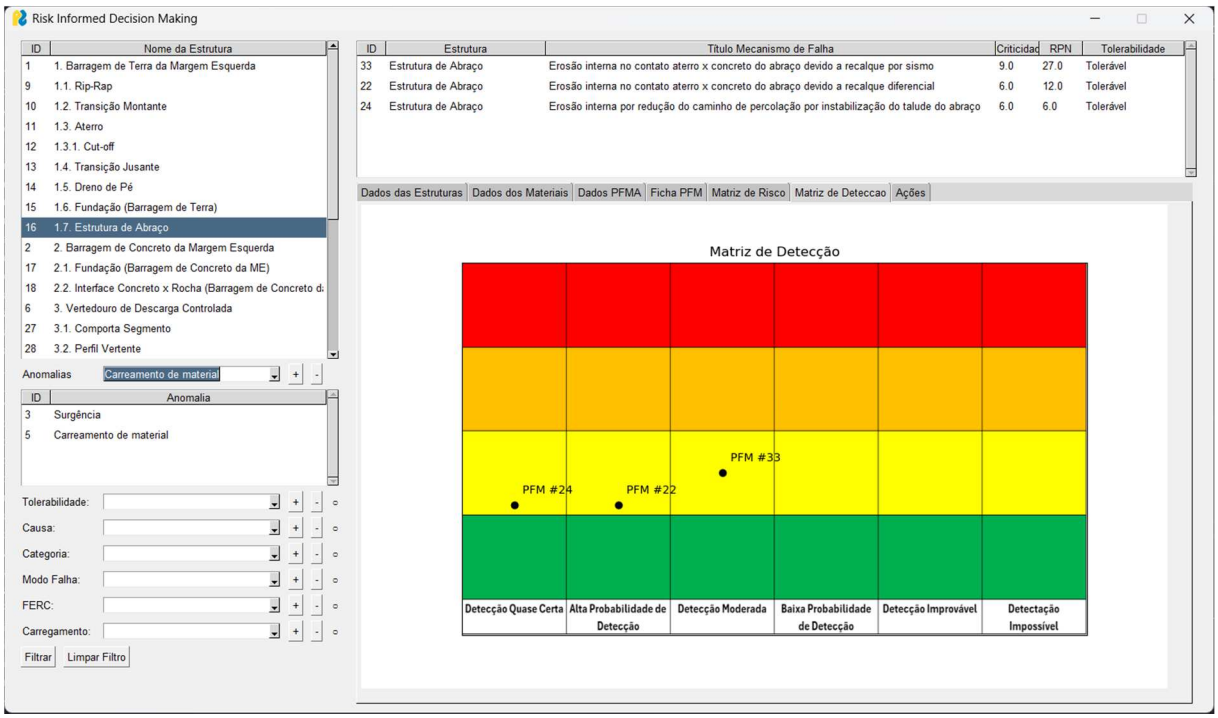

Fig. 8 – Detection Matrix tab of the Risk Management and Decision-Making Interface

The Risk Management and Decision-Making Interface allows filtering the PFMs by the Failure Causes registered in the Data Entry Interface. Due to the composition of the database, it is possible to identify PFMs that share a common cause, enabling the manager to conduct risk management much more efficiently.

The Anomalies or Visual Evidence filter was designed to assist in decision-making when facing unusual situations that have been identified. This filter allows one or more anomalies or visual evidence to be selected, and the PFMs related to these evidences will be displayed in the upper list, facilitating the identification of the potential failure mechanism in development. By selecting the structure where the alteration was identified, the filter becomes even more restrictive, helping to pinpoint these potential failure modes.

3.3. The IS-RMDM Methodology

The IS-RMDM was structured to allow risk assessment related to dams, based on the FMEA/FMECA and PFMA risk analysis methodologies. Both methodologies have qualities that, when combined, complement the risk assessment process. In addition to improving the identification process of failures and mechanisms, adopting both methodologies has a positive impact on the quality of the records generated during the risk analysis, as the process of identifying risks and classifying indexes can be better characterized and documented for future reference.

The methodology adopted for the IS-RMDM is described in the following items:

- **Division into Systems and Subsystems/Components**

The division of structures into Systems and Subsystems/Components follows the FMEA/FMECA methodology, with 4 levels of hierarchy defined for this project. The first level (system) divides macro-structures such as earth dams, concrete dams, spillways, etc. This is the primary division and will be adopted in the visualization of all risks mapped in the lower hierarchical levels.

The second level (subsystems) defines structures related to the first hierarchical level that make up and detail the system. In the other hierarchical levels (components), specific structures of the subsystem or other characteristics of interest for analysis may be detailed.

Despite these guidelines, there is no clear rule for dividing the structures, which must be done in accordance with the scope and limits established for risk assessment. Specific systems and subsystems, such as electromechanical components of controlled gates, may require additional hierarchical levels, and the team responsible for the analysis will assess the study boundaries.

Components such as instrumentation should only be considered as part of the structure when they present hazards that physically affect the system or subsystem, such as the possibility of internal erosion near buried instrumentation pipes. Failures related to data reading and acquisition should be considered under control measures, detection, and positive/adverse factors.

- **Definition of Potential Failure Mode (PFM)**

The Potential Failure Mode (PFM) is the foundation of the IS-RMDM methodology, from which all risk analysis and evaluation will be conducted.

In the adopted methodology, it is recommended to begin evaluating the PFMs from the lower hierarchical levels, as the failure mechanisms identified in these layers can cause the failure of structures in higher hierarchical levels, avoiding the registration of redundant failure

mechanisms. Generally, PFM should only be registered when their failure mechanism starts at the structure's hierarchical level to avoid repetition in different components.

The PFM description should cover the full sequence of events from initiation to the failure condition. Just like in the PFMA methodology, each PFM describes a unique sequence of events leading to failure, covering all necessary elements for proper characterization. When any step in the sequence of events is changed, it should be created a new PFM, which may have different elements to be evaluated during the risk assessment stage. It is up to the team responsible for registration to judge whether it is necessary to represent very similar PFMs, as there is a risk of making the process tedious and repetitive. It’s important to represent similar PFMs when they are caused by different factors, progress through distinct structures, or have impacts on different components or systems.

During the PFM registration, other elements related to the description of the failure mechanism are also recorded, as described below:

1. **Function**: the failure mechanism must be linked to one of the functions registered for the structure, reflecting the loss of the structure's capacity to fulfill that functionality;
2. **Cause**: these are the events or circumstances that led the component to fail, which can be external hazards (floods, earthquakes) or inherent characteristics of the component (filter sizing failure, construction defects). Several PFMs can share the same cause, and it is recommended to define the causes in a more general way, leaving the specifics for the PFM description;
3. **Local Effect**: represents the failure or effect in the component or subsystem analyzed, without considering its impact on higher hierarchical levels;
4. **Final Effect**: represents the effects of the failure on the respective Systems, reflecting the greatest impact of that PFM;
5. **Cause Category / Dominant Failure Mode**: pre-defined categories representing the cause and failure mode, based on the categories adopted by ASDSO in "Lessons Learned From Dam Incidents and Failures" (https://damfailures.org/) for classifying incidents and accidents. In IS-RMDM, it is used only for categorization and as filtering criteria.

Since the description of the PFM is free text field, the system can be used to identify different categories of failure, including those of electromechanical origin and those resulting from operation or human error. The classification of the Cause Category / Dominant Failure Mode aims to categorize the various registered failure types entered by the user, facilitating future queries.

- **PFMA Assessment**

Once the PFM description has been made, the risk evaluation in terms of PFMA Assessment is performed by classifying the loading conditions associated with the failure, as well as identifying positive and adverse factors and classifying the PFM category. It is recommended to start the classification with the PFMA elements, as these will support the classification of the FMEA/FMECA indexes.

The Load Condition classification refers to the external loading required to initiate the PFM, without which failure would not occur.

Positive and adverse factors should be registered based on the team's understanding of the facility, considering the available documents that reflect characteristics that make the PFM more or less likely to occur. Previously identified conditions, specific studies, and other information related to design, implementation, and operation phases can be informed to help define the failure's probability or consequences. Additionally, IS-RMDM has a field for unknown factors, which represent uncertainties regarding the likelihood of the PFM, which should be investigated to improve the understanding of the actual risk associated with the PFM.

Each positive / adverse / unknown factor is classified based on its impact on the failure probability or consequence or only as a condition already established in the structure. After identifying the positive and adverse factors, the PFMA is classified based on one of the categories defined in [2] regarding its relevance for defining mitigation actions.

- **FMEA/FMECA Assessment**

Considering FMEA methodology, almost all elements of the spreadsheet, except for existing controls and actions, have already been filled in during other IS-RMDM stages, including: “Component”, “Function”, “Failure Mode”, “Cause”, “Local Effect”, and “Final Effect”. Therefore, there are the tables with the verbal descriptors and index weights adopted for ranking and prioritizing the PFMs identified, based on FMECA.

Likelihood: The Likelihood Index should represent the probability of failure, considering the possibility of PFM initiation due to the identified cause, its progression, the loss of existing controls, and environmental conditions necessary for its occurrence. The classification of this index should consider only the residual risk related to the probability of occurrence, with the existing controls. Table 1, adapted from [4], presents the verbal descriptors adopted in IS-RMDM and their respective ratings.

Table 1 – Likelihood Classification

Descriptor	Definition of Likelihood	Likelihood Rating
Very High (< 10^2 AFL)	There is direct evidence or substantial indirect evidence to suggest the failure has initiated or is very likely to occur.	6
High (10^2 to < 10^3 AFL)	The fundamental condition or defect is known to exist; indirect evidence suggests it is plausible; and key evidence is weighted more heavily towards “mora likely” than “less likely”.	5
Medium (10^3 to < 10^5 AFL)	The fundamental condition or defect is known to exist; indirect evidence suggests it is plausible; and key evidence is weighted more heavily towards “less likely” than “more likely”.	4
Low (10^5 to < 10^6 AFL)	The possibility cannot be ruled out, the fundamental condition or defect is postulated. Evidence indicates it is very unlikely.	3
Remote (< 10^6 AFL)	Several events must occur concurrently or in series to cause failure, and most, if not all, have negligible likelihood such that failure likelihood Is negligible.	2
Not Possible		1

The uncertainty associated to the Likelihood verbal descriptor is characterized by the Uncertainty Index, which represents “unknowns” or any relevant aspect that should be investigated so that the index could be more accurately represented. The representation of reliability in the risk matrix is given by error bars, indicating the uncertainty in the classification. Unknown factors that hinder the correct classification of the index should be recorded in the unknown factors section of the PFMA.

Severity: The Severity Index represents the severity of the consequence arising from the development of the failure mechanism and reflects the impacts on the population in the affected areas, as well as socio-environmental and economic impacts. The classification should consider only the impacts related to residual risk, as defined previously. The existence of warning systems and sufficient time for the evacuation of at-risk populations are controls that, once properly implemented and tested, can be considered at the Severity classification stage, reducing the affected population by removing people from the risk zone. Table 2 presents the verbal descriptors and ratings adopted in IS-RMDM.

The uncertainty regarding the Severity verbal descriptor is also characterized by an Uncertainty Index, with this index represented in the risk matrix by error bars, just as is done for the Likelihood Index.

In addition to the Severity Index, the failure mechanism development duration should be defined, to describe the available time for action after identifying the development of the failure mechanism. This index is compared with the frequency of the detection method to assess its efficiency in controlling the risk.

Table 2 – Severity classification

Severity Category	Description	Severity Rating
Extreme	Probable loss of life and major environmental and infrastructure losses (loss of life is expected due to limited warning time, large population and/or limited evacuation routes) (Restauration impossible)	5
High	Potential loss of life and significant environmental and infrastructure losses (although life-threatening releases occur, direct loss of life is unlikely due to severity or location of the flooding, or effective detection and evacuation) (Restauration probable)	4
Moderate	Without loss of life No significant environmental and infrastructure losses Loss of generation (need to stop generation or to lower the reservoir to carry out repairs).	3
Low	No loss of life or environmental damages. Damage to infrastructure restricted to the industrial area	2
Negligible	Loss of components of easy restauration or maintenance	1

Detectability: The Detectability Index represents the ability to identify the development of a failure mechanism in an efficient and timely manner, considering all existing detection methods. Table 3 presents the verbal descriptors and ratings adopted in IS-RMDM.

Table 3 – Detectability classification

Detectability Category	Description	Detectability Rating
Almost Certain Detection	Failure is almost certain to be observed or detected well in advance, allowing enough time for preventive action.	1
High Probability of Detection	Failure has a good chance of being detected before worsening, but there may be cases where the alert is not immediate.	2
Moderate Detection	Failure may be detected before it occurs, but with some uncertainty or delay, making a quick response difficult.	3
Low Probability of Detection	Failure detection is unlikely until it reaches an advanced or critical stage, leaving little time for preventive action.	4
Unlikely Detection	Failure is very unlikely to be detected in advance, being visible only at an imminent stage or when already in development.	5
Impossible Detection	Failure cannot be detected in advance in a practical or predictable way. It occurs without visible or measurable signs until the damage is already established.	6

Each existing detection method related to the identification of a specific PFM is individually recorded, along with its approximate frequency. The frequency of detection methods is compared with the failure mechanism development time to assess their efficiency in identifying the development of the failure mechanism in a timely manner.

Controls: All existing controls, which, as defined in [1] are "the arrangements used to prevent or reduce the likelihood of the failure mode or mitigate its effects" should be listed. Only existing

and implemented measures can be considered controls. Any activities necessary for risk mitigation that are planned for future implementation should be recorded as "actions" and not included in the controls. Detection methods, recorded earlier, can be considered controls, as long as they allow for proper identification of the risk (detection frequency aligned with failure mechanism development duration) and there is sufficient response time after detection.

The control field is a free text field, allowing the user to register any type of control, each of which is stored in a single table, creating a collection of controls that can later be accessed and linked to other PFM, generating a unique set of controls.

Each control is classified based on its impact on reducing the likelihood of failure or mitigating the effects of the consequence, allowing the identification of the impact of losing control on the residual risk of the structure.

Actions: Actions are preventive or corrective measures, not yet implemented, that must be carried out to meet the risk tolerability levels. If the analysis shows that the identified controls are deemed insufficient or inadequate, and the associated residual risks are considered undesirable or unacceptable according to the Criticality Matrix, actions should be defined to reduce the residual risk to acceptable levels. In this case, each proposed action is also classified based on its impact on reducing the probability of occurrence, mitigating the consequences, or improving detection procedures.

Like the control registration, the action field is a free text field, allowing the user to register any type of action that can later be accessed and linked to other PFMs, generating a unique set of actions.

3.4. Preliminary Application Tests

Since the IS-RMDM is still under development, a preliminary and non-exhaustive application was conducted to illustrate its functionalities in the context of risk identification for a hydroelectric dam. The selected case study consists of an earth dam, a concrete dam, a gated spillway, and a labyrinth spillway. Two application cases were analyzed, as presented below:

- **Case 1:** Prioritization of Identified Risks

In this scenario, the objective was to prioritize risks to define appropriate risk reduction measures. A total of forty-three PFMs were identified, and prioritization was performed based on Criticality and RPN. According to the Criticality criterion, three PFMs stand out with a score of 12: **ID62** (Radial Gate | *Failure in gate operation due to electromechanical issues*), **ID21** (Earth Dam Foundation | *Internal erosion caused by a permeable foundation layer*), and **ID38** (Earth Dam Embankment | *Internal erosion in the embankment due to preferential seepage paths left by roots*). When prioritizing by RPN, the most critical failure modes include **ID62**, with

RPN = 60, and **ID40** (Concrete Dam | *Instability due to crack formation at the concrete-rock interface*), with RPN = 48.

All identified risks are also mapped onto the risk matrix to classify them within the risk tolerance categories. Due to the presence of effective control and detection measures, the residual risks of all registered PFMs fall within the Acceptable and Tolerable categories, as shown in Fig. 9.

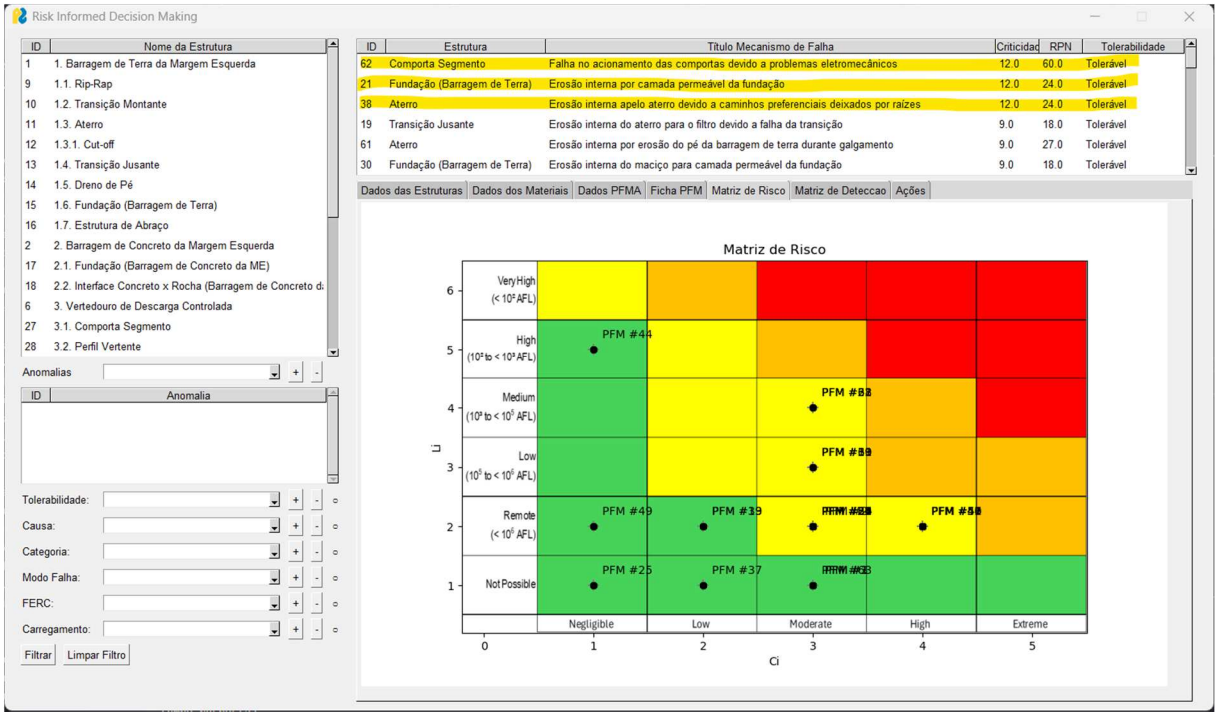

Fig. 9 – Use of IS-RMDM for Risk Prioritization and Risk Matrix

In this example, the user could implement risk reduction measures by enhancing the redundancy of gate operation components, thereby reducing the probability of occurrence of ID62. Additionally, structural measures such as installing filters and transition zones downstream of the earth dam could help mitigate the likelihood of internal erosion, both from the more permeable foundation layer (ID21) and from preferential seepage paths left by roots (ID38).

- **Case 2**: Support on Decision-Making

In this scenario, it is hypothetically assumed that water seepage with material transport has been detected at the base of the Earth Dam. In response, the user could filter all registered PFMs related to the Earth Dam that include anomalies or evidence of 'seepage' or 'material transport.' These filtered PFMs can be easily identified, with their associated documentation readily accessible within the system.

In the example shown in Fig. 10, the user identifies that one of the potential aggravating factors contributing to seepage with material transport is the presence of a more permeable layer in the foundation. The documentation related to the PFM is readily accessible, allowing for easy

consultation of the geotechnical survey that identified this layer. Based on this information, the user can define remediation measures for the detected anomaly, leveraging the risk analysis to enable more timely and effective responses.

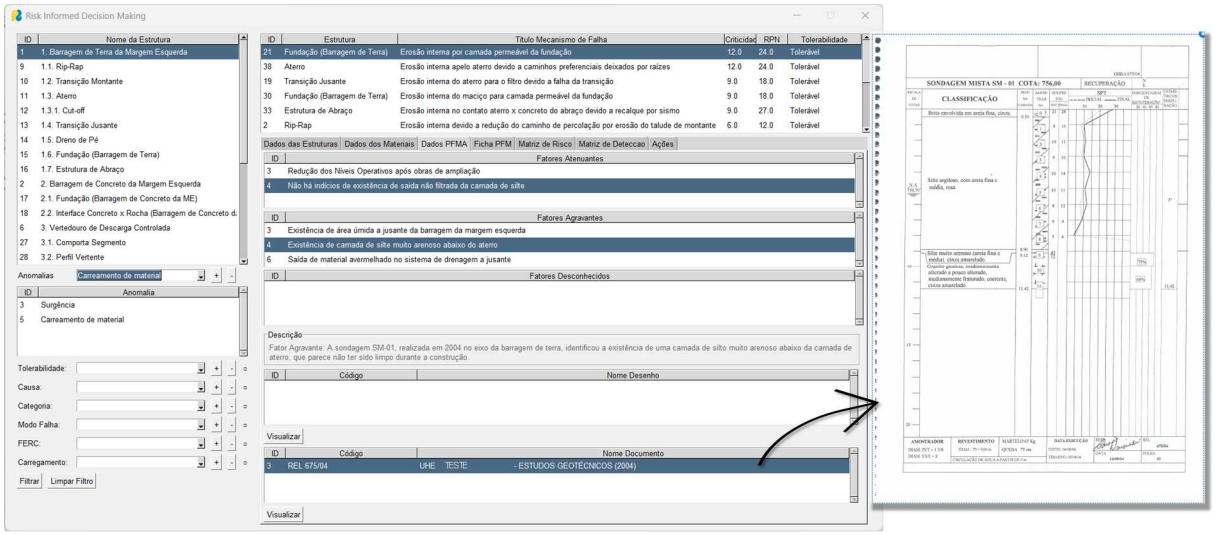

Fig. 10 – Use of IS-RMDM on Decision-Making support

4. CONCLUSIONS

The IS-RMDM was developed by integrating the FMEA/FMECA and PFMA methodologies into a system that offers the key advantage of improving the assessment of dam safety risks in a structured manner, combining the main strengths of each method. The system employs a relational database for information storage, enabling quick access to the identified potential failure modes by structure, thereby supporting risk management and risk-informed decision-making.

Preliminary application tests of the system were conducted on a water storage dam for hydropower generation, adjusting the weights and matrices to ensure that the identified risk outcomes accurately reflected the concerns specific to that dam.

Despite the tools employed for the system's design and presented in this article, a significant advantage of the IS-RMDM methodology is its flexibility, allowing it to be easily adapted and adjusted to the specific context of each company by employing different systems and software for information storage and management.

Although the methodology focuses on the individual assessment of risks for components within the same facility, it also allows for portfolio-level prioritization. This can be achieved by listing the most relevant actions for the dam owner, provided that a consistent rating system is maintained across evaluations.Furthermore, the use of tools such as criticality matrix and indexes for the classification of potential failure modes enables a detailed and

dynamic risk analysis, allowing real-time adjustments as new data and information are collected, making the system a living mechanism.

REFERENCES

[1] IEC 60812-2018. Failure modes and effects analysis (FMEA and FMECA)

[2] FEDERAL ENERGY REGULATORY COMMISSION (FERC), 2021. Engineering Guidelines for the Evaluation of Hydropower Projects - Chapter 17 – Potential Failure Mode Analysis. December 16, 2021.

[3] ELMASRI, R.; NAVATHE, S. B. Fundamentals of Database Systems. 2006.

[4] Alberta Environment and Parks (2022). PFMEA Tool for Risk-informed Dam Safety Prioritization. CDA Bulletin Spring 2022

Fifth International Dam World Conference
PORTUGAL • LISBON • LNEC • APRIL 13-17, 2025
dam world 2025

SIMPLIFIED ANALYTICAL SOLUTIONS OF FREE SURFACE MIGRATION WITHIN ORIGINALLY DRY, COARSE GRAIN SIZED, EMBANKMENT DAM MATERIALS

Francesco Federico[1]
University of Rome Tor Vergata, Italy

Chiara Cesali[2]
University of Rome Tor Vergata, Italy

ABSTRACT

Tightness of homogeneous embankment dams is often ensured by means of upstream water barriers, as bituminous concrete facings, concrete slabs, shotcrete membranes, metallic sheets, geomembranes, earth and soil cement blankets.

The stability analyses of these dams, especially in areas with high seismicity, must include the hydraulic and mechanical effects resulting from an extensive cracking of the impervious facing.

Referring to the unsteady seepage flow potentially induced by these kind of failures, it is therefore necessary to estimate the position of the exit point on the downstream slope of the dam, the maximum height of the saturation front at the downstream face, the evolution of the discharge flow, up to its maximum value, the time necessary by the saturation front to reach the downstream face, or to raise the saturation front to a height close to the final one.

The variables depend in turn on: geometry of the dam, transversal and main longitudinal sections, according the valley shape, homogeneity or heterogeneity of the materials of the dam body, permeability coefficient of the dam material (partial or full saturation condition), resistance law to describe the seepage flow motion (Darcy's law, or non-linear laws).

The high number of factors, especially for design problems, prevents the development of extensive 3D FEM analyses, computationally heavy, especially if partial saturation conditions and nonlinear relationships to describe the seepage law, are taken into account.

Conversely, it is very practical to apply closed form analytical solutions that, although approximate, could allow to define the role of the various factors and their interaction, to quickly desume the main design indications, these last ones to be refined with further advanced FEM analyses.

In the paper, based on the Dupuit and Forcheimmer assumptions, parabolic 1D Boussinesq equation and Baremblatt's solutions, simple, original, analytical solutions are proposed.

By this way, the preliminary answers to the above mentioned questions are firstly reported; the time evolution progress of the free surface and of the saturated mass within a homogeneous dam body, after a hypothesized sudden lack of the watertightness of its upstream facing, are expressed, and applied referring to some practical applications.

Keywords: Massive failure of impervious facing, Seepage flow, Simplified solutions of Boussinesq Equation, Exit point, Saturation front at the downstream face.

[1] fdrfnc@gmail.com, Italy
[2] cesali@ing.uniroma2.it, Italy

1. INTRODUCTION

Under post-earthquake conditions or extensive lacerations of the facing and complete loss of tightness, a massive seepage flow could occur in dry, coarse grain sized, embankment dam materials, governed by Darcy's law and Laplace's equation or, alternatively, by non-linear relationships between the permeability coefficient and the piezometric head ([1], [2]).

The seepage flow is modulated by the progressive saturation of the dam body, due to the advancement of the free surface towards the downstream facing, through the different cross-section of the dam. Flow velocity and saturation depend on *(i)* the height of the dam, *(ii)* the upstream hydraulic head, *(iii)* the corresponding extensions of the different cross-sections at the base of the dam: they vary along the longitudinal axis ([3], [4], [5], [6]).

Therefore, potential release of water from the dam body is analysed under the simplifying hypotheses below listed:

- seepage flow mainly occurs along each cross sections of the dam (2D flow for each cross section, i.e. by neglecting the longitudinal components of the flow velocity);
- flow rates are in accordance with a Darcy laminar flow;
- in case of non-laminar flows may by applying specific laws for coarse materials (e.g., Forchheimer relationship, [7], [8], [9]), describing seepage flows in a granular material initially dry and progressively saturated, with variable water depth in space and time.

At the same time, it must be checked that, under the hypothesis of seepage, the dam material essentially maintains its granulometric stability, in the presence of the dragging water actions generated by the seepage flow ([10], [11]).

In other words, the facing and the drainage system behind it guarantee the safety of the dam under ordinary conditions, preventing, even in the case of ordinary deterioration of the facing, that the leaks give rise to seepage flow from the reservoir through the embankment.

In extreme conditions, e.g. after a very strong earthquake, the absence of uncontrolled release of water from the reservoir must be checked. The corresponding seepage analyses must start from the hypothesis that the sudden breakage and inefficiency - local or global - of the upstream facing occurs; consequently, a seepage flow would start through the dam body.

The progressive saturation of the dam materials, coupled with the evolution of the free surface, will be governed by the hydrodynamic resistance to the seepage flow through the dry material. This phenomenon may be also accompanied by possible dragging, suffusion, particle migration of incoherent materials. In this last case, potential self-healing and self-protection characteristics of the saturated materials must be checked too (e.g. [12]).

The outflow is ensured by the downstream draining face; initially, the free surface lies entirely within the dam body and it progressively moves towards the downstream face, that is reached after a critical time *t*;* after *t*,* the free surface progressively rises and the water seeps through the downstream face.

This second phase of the unsteady seepage flow is very important, owing to the problems possibly related to the discharge rates that should be safely collected and conveyed far from the dam as well as to the possible limit states related to particle migration phenomena.

The need to study these particular *Limit States*, in addition to specific requirements reported in national laws and safety standards, derives from the analysis of documented cases of failures of dams composed by coarse-grained materials and/or rockfill, even in the recent past (e.g., [13], [14], [15]).

2. THE BOUSSINESQ EQUATION IN THE CASE OF SIMPLIFIED 1D GEOMETRIC SCHEMES

2.1. General setting

Despite the basic simplifying assumptions (i.e., constant porosity of the material; Dupuit's hypothesis; Darcy's law; horizontal impervious base boundary; incompressible water and solid skeleton soil), the well-known Boussinesq equation:

$$\frac{1}{2}\frac{\partial^2 h^2}{\partial x^2} = \frac{n_s}{K}\frac{\partial h}{\partial t} - \frac{\varepsilon}{K} \tag{1}$$

being x = main flow (spatial) direction; t = time; n_s = porosity of material; K = permeability coefficient; ε = growth coefficient; h = water table, can be solved analytically only in some particular cases.

A solution can be obtained by separating the variables *x* and *t,* expressing the function *h(x; t)* as the product of two functions, one dependent only on *x* and the other only on *t*, as originally applied by Boussinesq (1904).

Another method, proposed to solve the Boussinesq equation, consists in combining the variables *x* and *t* in a parameter *α*, in which the relationship between *x* and *t* is known a priori. This method was used by ([1], [16], [17]) in the form:

$$h_{(x,t)} = f(\alpha) \tag{2}$$

being

$$\alpha = c\frac{x}{t^{1/2}}$$

to determine the flow rate through the initial vertical section (where the free surface of the upstream water and the free surface of the seepage water are in contact), when the upstream free surface rises, or falls, instantaneously from a level H_1 to a level H_2.

The result of this method provides the seepage flow rate (q) as a function of the geometric and physical (K, n_s) parameters of the soil and the time:

$$q = \pm H_2 \sqrt{H_1 K \frac{n_s}{2t}} \tag{3}$$

More advanced, recently proposed (e.g., [17]) procedures allow to consider some general case. Following a similar procedure, the propagation of the free surface can be analytically modeled by assuming that *(i)* the initial level of the free surface coincides with the impermeable base boundary and *(ii)* following the sudden rise of the free surface, the seepage flow occurs through a homogeneous dry soil.

The propagation maximum distance of the free surface, along its base, in this case, is expressed by the following relation (e.g., [18], [19]):

$$x_0(t) = 1.62 \sqrt{\frac{tKH}{n_s}} \tag{4}$$

To confirm the reliability of this result, let us first consider the advancement $x_0(t)$ in the lowest position of the saturation front, i.e. at the contact with the impermeable base surface, where the fluid threads can advance only horizontally, as if the permeability in the vertical direction were null.

At the generic time t, the saturation front has reached the position $x(t)$ and continues to advance due to the piezometric head $(H_m - H_v) / x(t)$, decreasing in space and time, as t increases: H_m is the level of the water reservoir, measured from the base of the dam; H_v (= *0*) is the piezometric head at the base of the saturation front (i.e., *z=0*; interstitial pressure=0).

By recalling the continuity equation:

$$q\, dt = dV_w \tag{5}$$

from which:

$$K \cdot i(t) \cdot 1 \cdot\ dt = 1 \cdot n_s\, dx_0 \tag{6}$$

$$K \cdot \frac{H_m}{x_0(t)} dt = n_s\, dx_0 \tag{7}$$

being n_s = volumetric porosity. By separating the variables and integrating the eq. (7):

$$x_0(t) = 1.414\sqrt{\frac{t \cdot K \cdot H_m}{n_s}} \tag{8}$$

The eq. (8) is entirely comparable with the previous eq. (4). By imposing that x_0 is equal to the length L of the dam base, the time t^* necessary for the saturation front to reach the downstream foot of the dam, in the highest portion of the dam (maximum height of the cross section) can be obtained:

$$t^* = \frac{n_s \cdot L^2}{2 \cdot K \cdot H_m} \tag{9}$$

It is interesting to rewrite the same continuity equation (5) by assuming a non-linear relationship between flow velocity and piezometric gradient, such as (e.g., [7], [14]):

$$v = K \cdot i(t)^{1/2} \tag{10}$$

Thus,

$$K \cdot \left(\frac{H_m}{x_0(t)}\right)^{1/2} dt = n_s \, dx_0 \tag{11}$$

By separating the variables and integrating the eq. (11):

$$x_0(t) = 1.31 \cdot \left(\frac{t \cdot K}{n_s}\right)^{2/3} (H_m)^{1/3} \tag{12}$$

The time t^* needed for the saturation front to reach the downstream foot of the dam is:

$$t^* = \frac{2}{3}\frac{n_s \cdot L^{3/2}}{K \cdot (H_m)^{1/2}} \tag{13}$$

As shown in the following figure, the results obtained with the two distinct relationships between velocity and piezometric gradient (i.e., eq. (9) and eq. (13)), by assuming $L=60m$, $H_m=32m$, $n_s=0.38$, appear comparable.

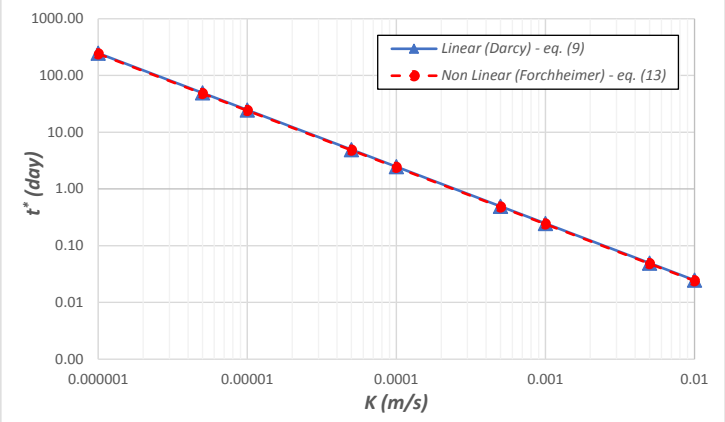

Fig. 1 – Time *t necessary for the saturation front to reach the downstream foot of the dam vs permeability *K*: comparison between eq. (9) and eq. (13)**

In conclusion, it can be deduced that, for preliminary qualitative and quantitative evaluations of the characteristics of the seepage motion, laminar motion regimes (permanent and various), according to Darcy's law, can be applied.

2.2. 2D Solutions for "real" dam body

Based on the previous general considerations, to model the advancement of the free surface referred to a real geometry of a dam, a simplified solution can be developed by admitting the validity of Dupuit's hypothesis (the vertical component of the seepage flow is neglected, i.e. k_z (vertical permeability) << k_x (horizontal permeability) is assumed) and adopting the technique of successive stationary states to model the unsteady state.

It is worth noting that, under the assumed hypotheses, the flow lines are practically horizontal; the flow motion advances, at any elevation "*z*", in a horizontal direction, regardless of the evolution of the motion at elevations different from the one considered.

Following this line of thoughts, the previous eq. (8) can be rewritten for this case as follows:

$$x_0(z,t) = \sqrt{2\frac{t \cdot K \cdot (H_m - z)}{n_s}} \tag{14}$$

At each time instant *t*, under the assumed hypotheses, in the case of a vertical upstream face, the free surface (curve *z(x)*) is a parabola.

To take into account the inclination of the upstream face (angle θ with respect to the horizontal plane), to the path *x(z,t)* it is necessary to add the length $x_0(z)$ of the initial position of the upstream face with respect to *x=0*, which depends on the elevation *z* (see also Fig. 2):

$$x_0(z) = \frac{z}{tan\ \theta} \tag{15}$$

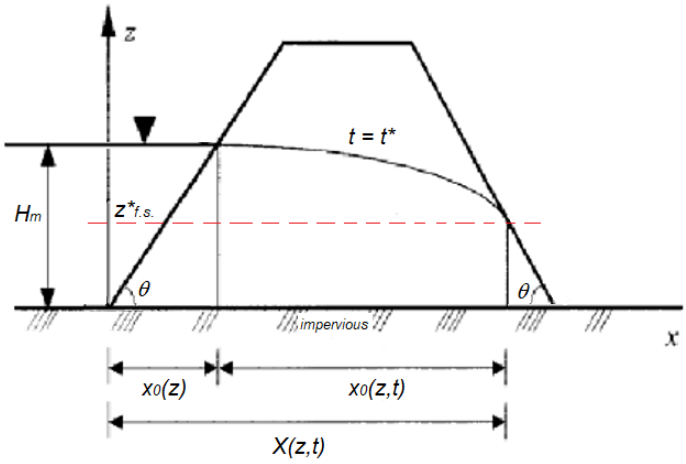

Fig. 2 – Simplified scheme of cross section of a homogeneous dam, with upstream facing: definition of variables $x_0(z,t)$, $X(z,t)$, $z^*_{f.s.}$

Definitively, at time *t* and for the elevation *z*, the saturation front reaches the position *X(z,t)*

$$X(z,t) = x_0(z,t) + x_0(z) \tag{16}$$

Thus,

$$X(z,t) = \sqrt{2\frac{t \cdot K \cdot (H_m - z)}{n_s}} + \frac{z}{tan\,\theta} \tag{17}$$

The position *X(z,t)* therefore also depends on the slope (θ) of the upstream face. Furthermore, the free surface always intersects the upstream face at the reservoir level $z = H_m$, for any time instant *t*.

For *z=0*, the downstream foot of the dam (path equal to the length *L* of the base of the dam) is reached even after the time *t* (z=0),* independent of the angle θ (equal to the previous eq. (9)):

$$t^*(z=0) = \frac{n_s \cdot L^2}{2 \cdot K \cdot H_m} \tag{9.bis}$$

For *z > 0*, the downstream face is reached after a path dependent on the elevation *z*:

$$t^*(z>0) = \frac{n_s}{2 \cdot K \cdot \tan^2\theta} \cdot \frac{(L \cdot \tan\theta - 2z)^2}{(H_m - z)} \tag{18}$$

To estimate the minimum time required for the free surface *X(z,t)* to reach the downstream face and, correspondingly, determine its related elevation $z^*_{f.s.}$, the first derivative *dt*/dz* equal to zero must be imposed. Thus,

$$z^*_{f.s.} = H_m - \left(H_m^2 - H_m L \tan\theta + \frac{L^2 \tan^2\theta}{4}\right)^{\frac{1}{2}} \tag{19}$$

Based on the expression of $z^*_{f.s.}$, the minimum time *t** for which the saturation front reaches the downstream face (corresponding to the elevation $z^*_{f.s.}$) can be obtained. Following this procedure, it is obtained:

$$t^*\left(z = z^*_{f.s.}\right) = \frac{n_s}{2 \cdot K \cdot \tan^2\theta} \cdot \frac{\left(L \cdot \tan\theta - 2z^*_{f.s.}\right)^2}{\left(H_m - z^*_{f.s.}\right)} \tag{20}$$

As expected, the minimum time *t** depends on H_m, *L*, θ, as well as on the permeability K and porosity n_s.

Through eq. (19), the graph shown in Fig. 3 ($z^*_{f.s.}/L$ *vs* H_m/L) can be obtained. It defines the field of admissible (resulting) values for $z^*_{f.s.}$, for different values of θ.

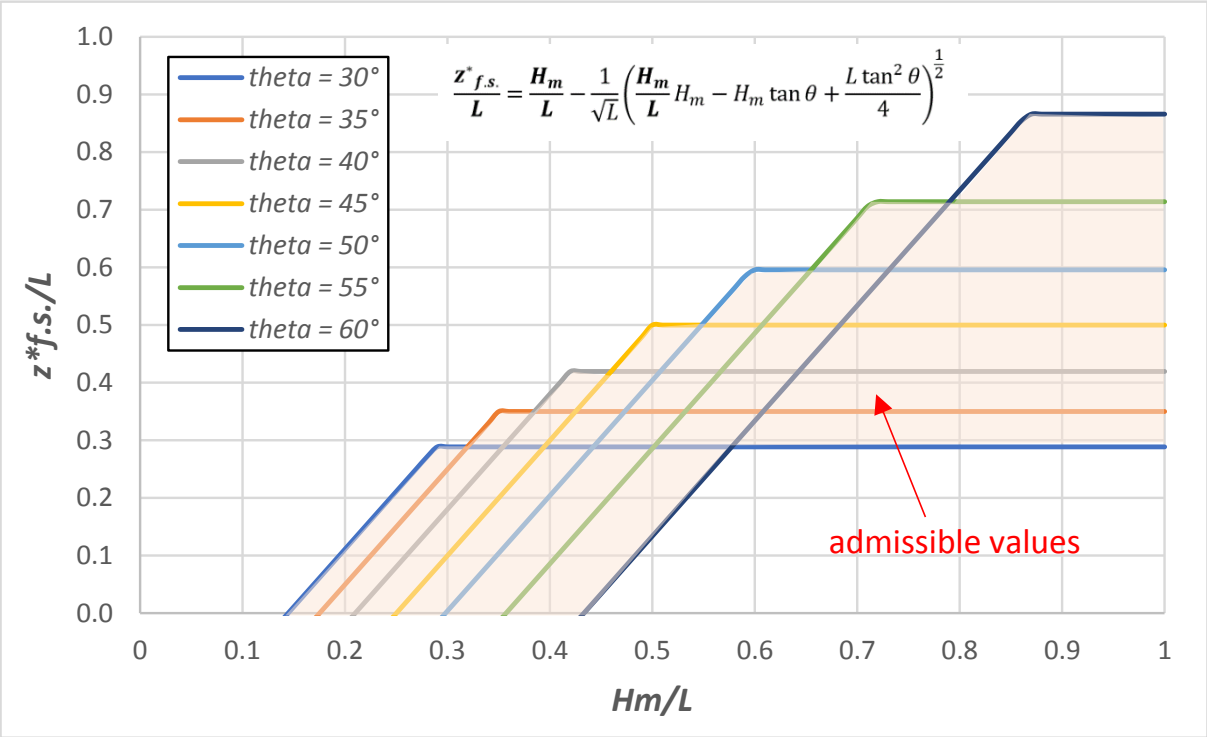

Fig. 3 – $z^*_{f.s.}/L$ *vs* H_m/L, for different values of θ (according to eq. (19))

Specifically, $z^*_{f.s.}/L$ *vs* H_m/L assumes a bilinear evolution: once a particular value of H_m (depending on θ) has been exceeded, $z^*_{f.s.}$ becomes independent on H_m itself because it is geometrically "*limited/defined*" by the length of the dam base, *L*.

Through the eq. (20), in the following figures (Fig. 4 and Fig. 5), the influence of n_s (fixed θ) and θ (fixed n_s) on $t^*(z = z^*_{f.s.})$ *vs K*, for different values of H_m/L, is investigated: if n_s increases, $t^*(z = z^*_{f.s.})$ increases, although in a less appreciable way; $t^*(z = z^*_{f.s.})$ tends to reduce if H_m/L increases.

Even if θ increases, $t^*(z = z^*_{f.s.})$ increases; then, $t^*(z = z^*_{f.s.})$ tends to reduce if H_m/L increases, enough significantly for lower values of θ.

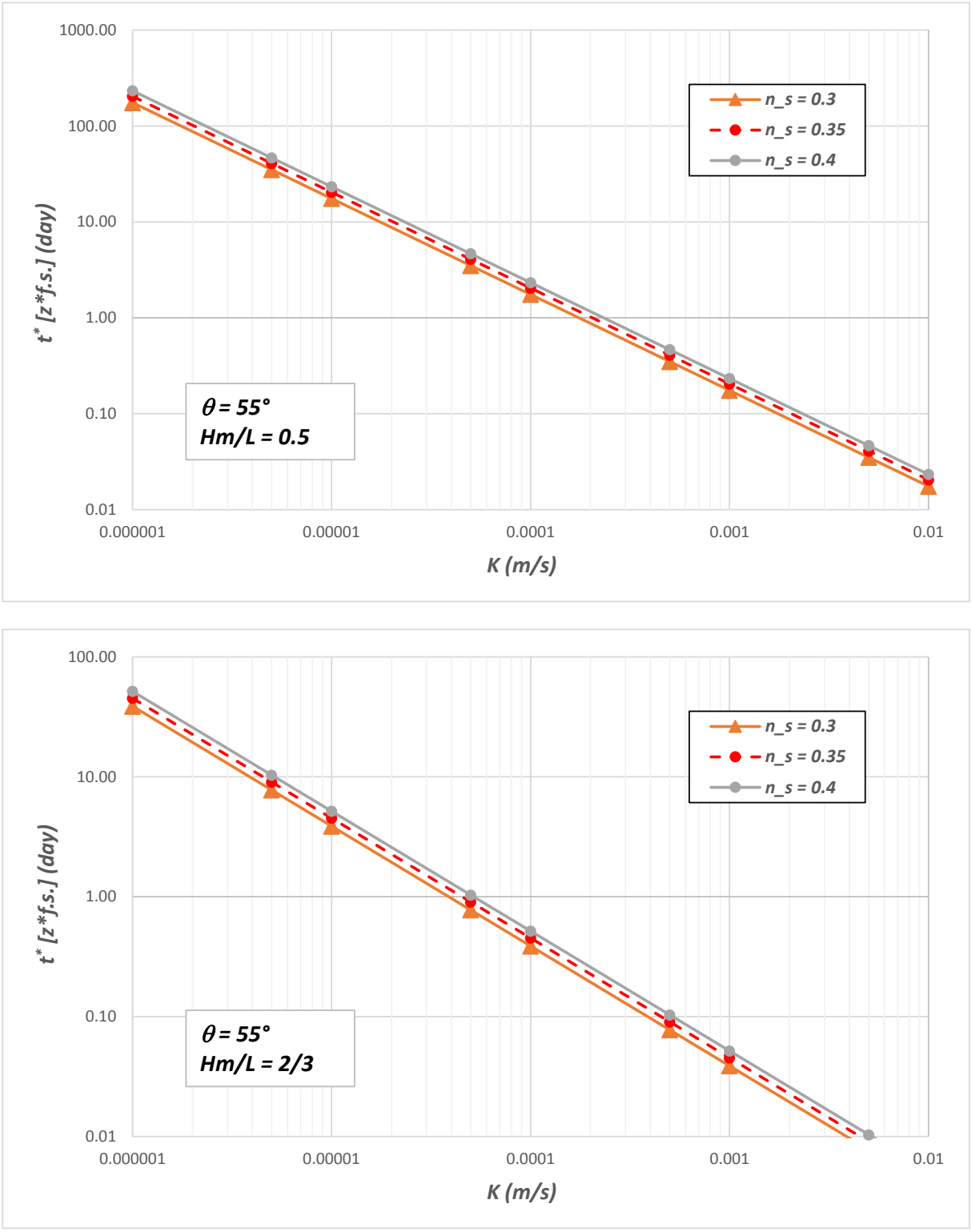

Fig. 4 – $t^*(z = z^*_{f.s.})$ *vs K*, for different values of n_s and H_m/L (according to eq. (20))

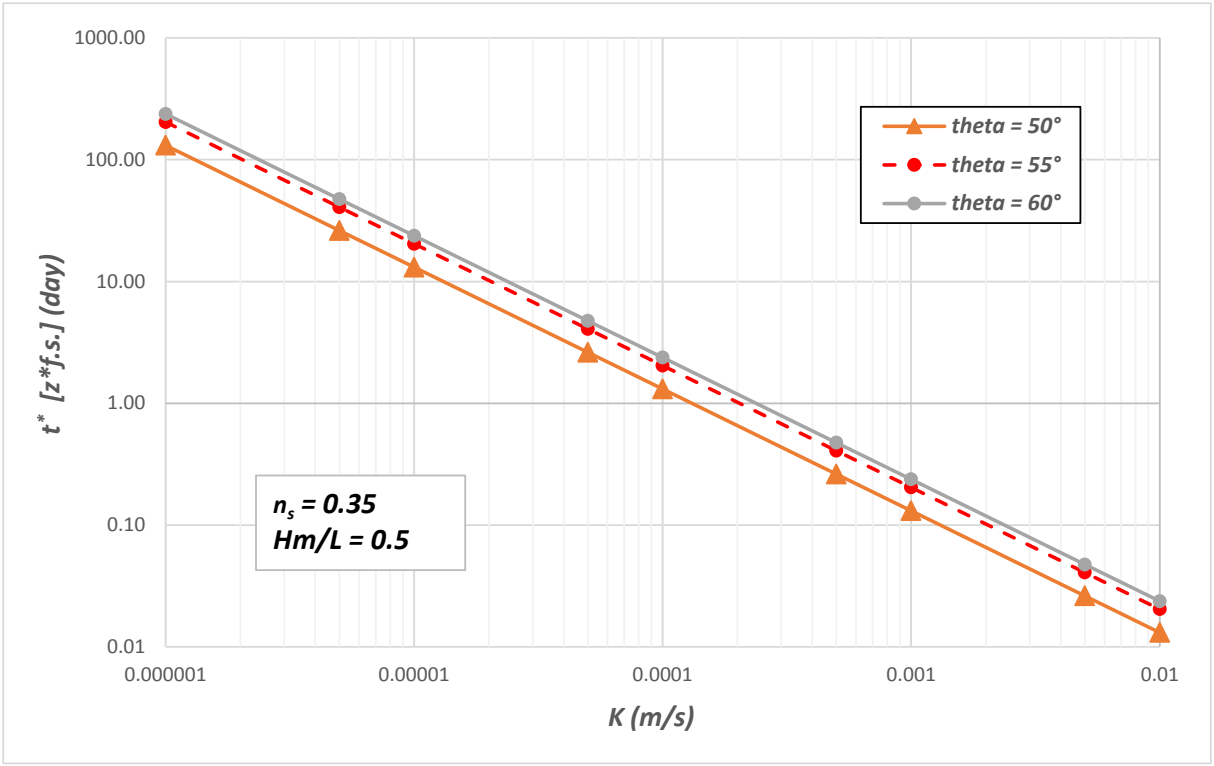

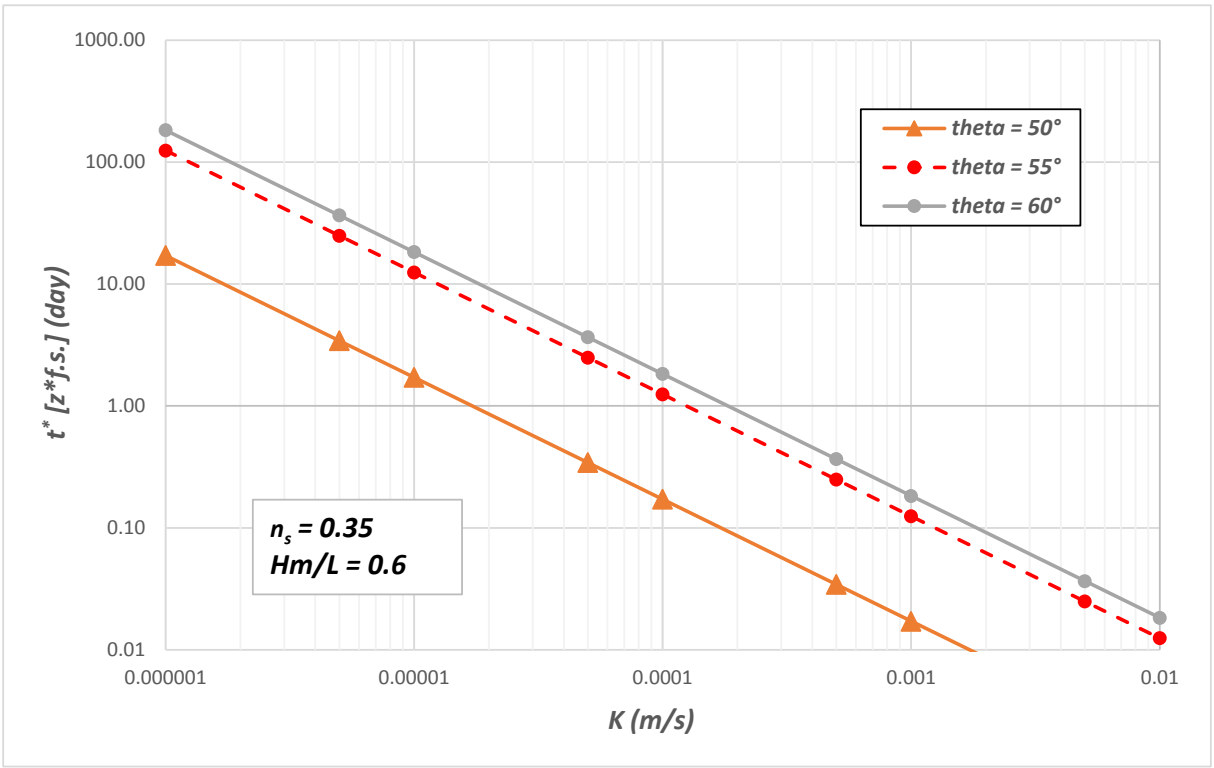

Fig. 5 – $t^*(z = z^*_{f.s.})$ *vs K*, for different values of θ and H_m/L (according to eq. (20))

For completeness, assigned the parameters $H_m/L = 0.5$, $n_s = 0.35$ and $\theta = 50°$, the following figure shows the comparison between $t^*(z = z^*_{f.s.})$ and $t^*(z = 0)$.

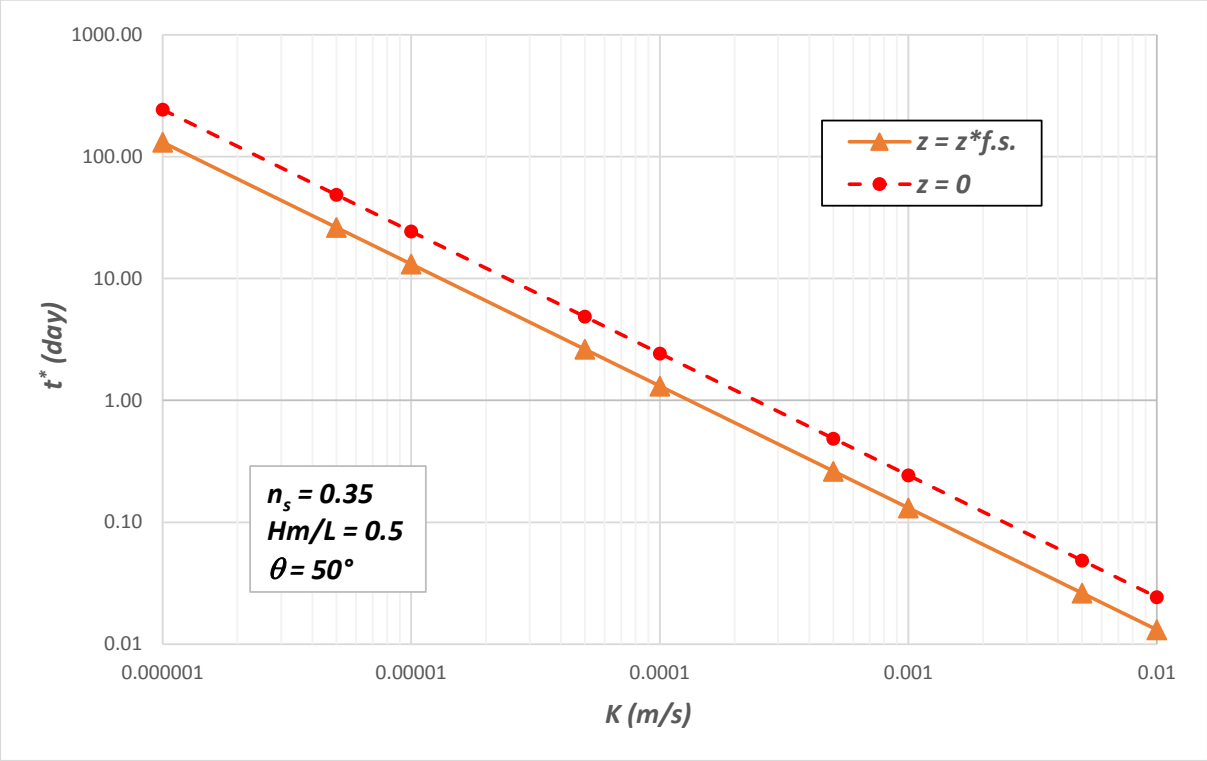

Fig. 6 – Comparison between $t^*(z = z^*_{f.s.})$ *vs K* and $t^*(z = 0)$ *vs K*

It is therefore confirmed that the saturation front reaches the downstream face more quickly for "*intermediate-high*" positions.

2.3. 3D Simplified solutions

To qualitative forecast the dynamics of the seepage flow within the entire dam body, it is further necessary to rewrite the previous equations as a function of the longitudinal coordinate "*y*", too; the origin (*y = 0*) corresponds to the position of the cross section of maximum height (see Fig. 7).

Specifically, by recalling the equations previously obtained and introducing the longitudinal coordinate "*y*", the previous equations (9), (17) are generalized as follows:

$$X(y,z,t) = \sqrt{2\frac{t \cdot K \cdot (H_m(y) - z)}{n_s}} + \frac{z}{tan\,\theta} \tag{21}$$

$$t^*(y, z = 0) = \frac{n_s \cdot B(y)^2}{2 \cdot K \cdot H_m} \tag{22}$$

being *B(y)* = length of the dam along the transversal direction, variable along the *y*-coordinate (*B(y=0)* = *L*, as previously defined). Thus, it is obtained;

$$z^*_{f.s.}(y) = H_m(y) - \left[\left(H_m(y)\right)^2 - H_m(y)B(y)\tan\theta + \frac{B(y)^2\tan^2\theta}{4} \right]^{1/2} \quad (23)$$

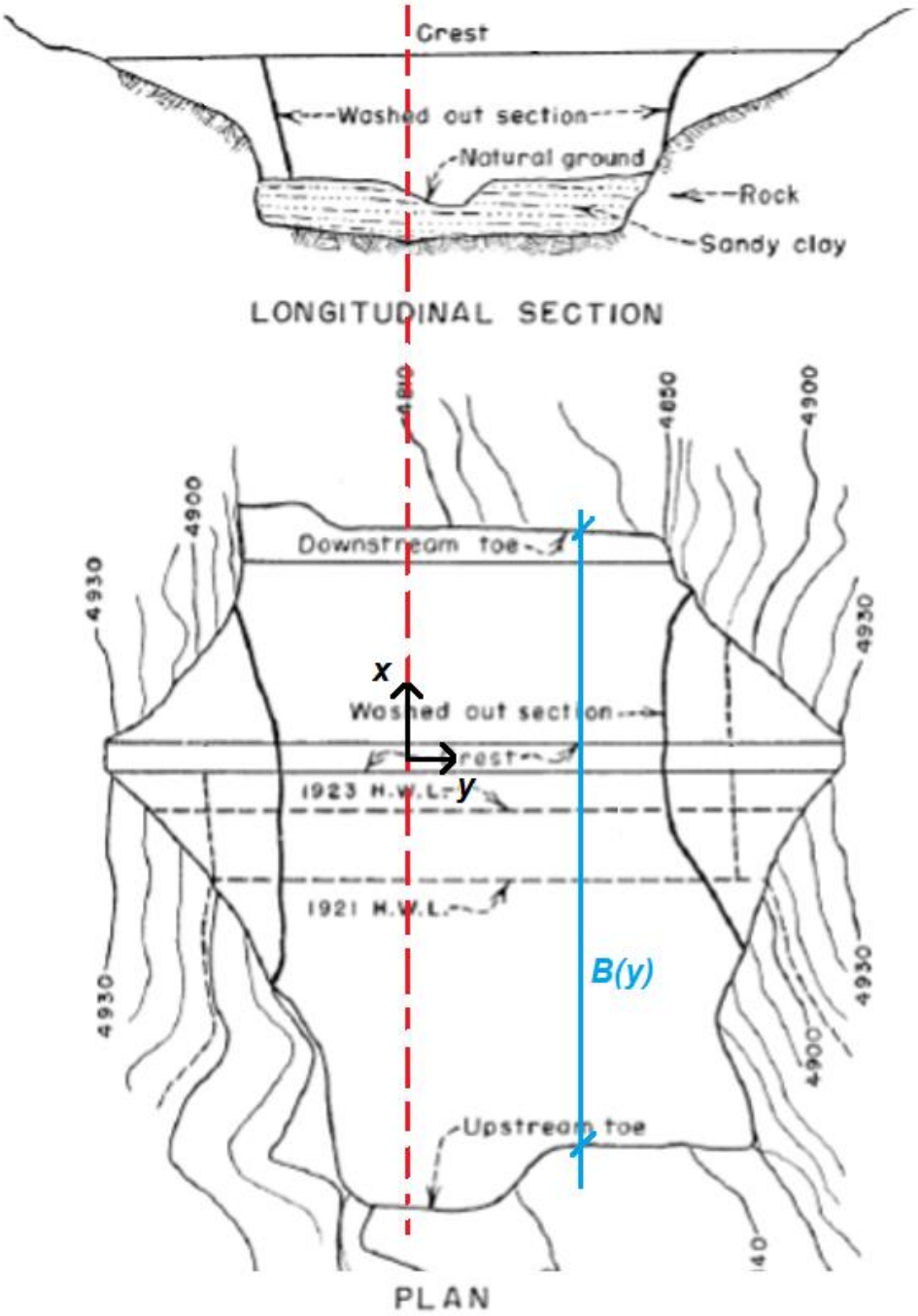

Fig. 7 – Definition of reference system for 3D simplified analytical solutions: coordinate "*y*" along the longitudinal section of a dam

Eq. (21) highlights that if *y* increases (fixed *z* and *t*), the length *X(y,z,t)* of the saturation front decreases, due to the reduction of the piezometric head.

Furthermore, "*z*" must be understood as "local" coordinate, from the base of the cross section of the dam corresponding to "*y*".

In order to refer the results to the base plane of the dam with minimum elevation (*z=0*), the following relationship must be introduced:

$$z(y) = z'(y) + r(y) = z'(y) + y\ tan\beta \tag{24}$$

being β = the angle formed by the valley bank with the horizontal plane (along the longitudinal axis of the dam). The above equations (for 3D cases) are applied to a specific case: $H_m(y = 0)$ = 32 m; $B(y = 0) = 60$ m, θ = 53,13°, β = 10,08°, n_s = 0.38, $K = 10^{-4}$ m/s, characterized by the following geometric relationships:

$$H_m(y) = 0.178 \cdot (180 - y)$$

$$B(y) = 12 + 0.267 \cdot (180 - y)$$

Main results in terms of *t** (see eq. (22)) for ***z'*** = 0 and *y* = 0, 60 m, 120 m and 150 m, are reported in the following table.

Table 1 – 3D case: results in terms of *t for the considered case**

z' (m)	***y (m)***	***Hm (y)***	***B (y)***	***r (y)***	***t* (h)***
0	0	32	60	0.0	59.42
	60	21	44	10.7	47.92
	120	11	28	21.3	38.80
	150	5	20	26.7	39.57

The reaching the downstream face (for *z'=0*) occurs more rapidly as *y* increases due to the shorter distance to travel. The reaching the downstream face occurs earlier than in the central portions of the dam, which are higher and much wider.

Therefore, as also indicated in the 3D FE analyses by [20], [21], the leakage of the reservoir water might occur first at the abutments of the dam and subsequently in the highest (and widest) part of the dam. The same condition happens for $t^*(z'^*_{f.s.})$.

3. COMPARISON BETWEEN ANALYTICAL SIMPLIFIED SOLUTIONS AND NUMERICAL SIMULATIONS

To test and validate the simplified solutions of Boussinesq equations previously obtained and described, reference is made to a typical cross section of a rockfill dam whose tightness is ensured by an impervious upstream facing, initially perfectly efficient (cross section scheme reported in Fig. 8).

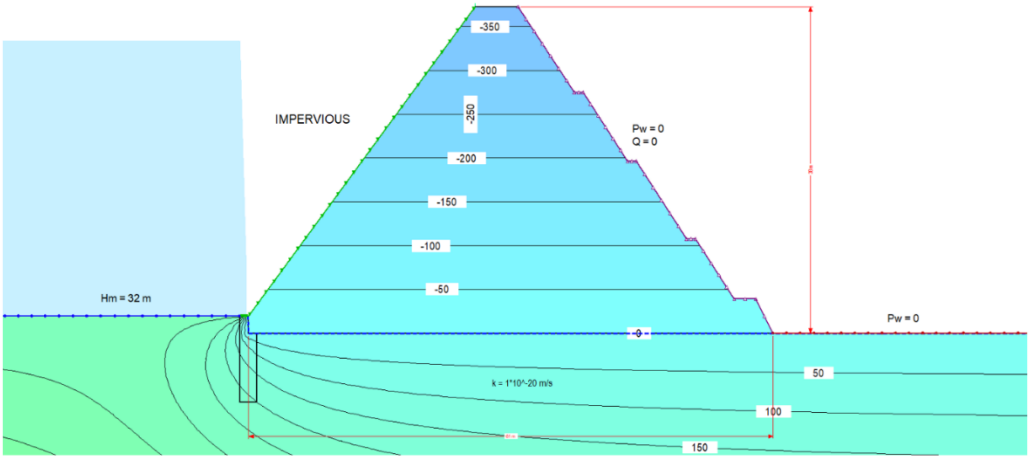

Fig. 8 – 2D FEM simulations: scheme of the examined dam at the initial condition, before the facing failure, and related boundary conditions (*Pw = interstitial pressure; Q = flow discharge*)

Numerical 2D FEM simulations of seepage flow through the dam body, through SEEP/W code, following an instantaneous, widely extended failure of the upstream facing, under unsteady state conditions, for different values of K (10^{-4}, 10^{-3}, 10^{-5} m/s), are carried out.

The results of the 2D FEM simulations, in terms of temporal and spatial progression of the saturation front as well as raising the free surface once the dam foot is reached, are shown in the following figures.

Fig. 12 summarizes the obtained main results.

In Table 2, the comparison between the results obtained from 2D FEM simulations and simplified analytical solutions (eqs. (19), (20)) is shown.

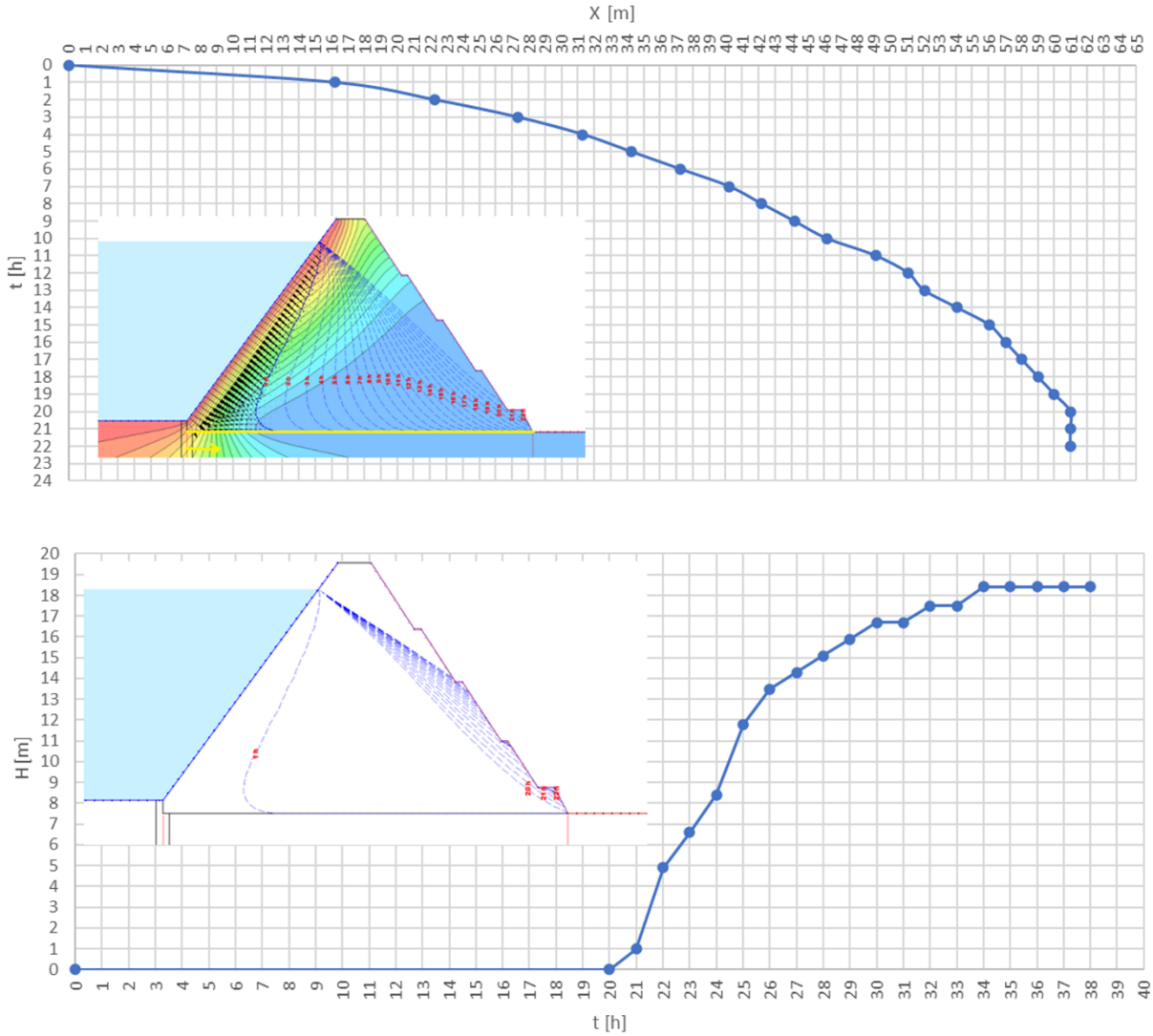

Fig. 9 – 2D FEM simulations: *X(t),* temporal progression of the saturation front (above) and *H(t),* raising the free surface within the dam body (below), for K = 10^{-4} m/s

The maximum height of the saturation front falls in the range 18-21 m, compliant with the values (i.e., 24 m) determined through the simplified 2D analytical solutions.

The time required for the saturation front to reach this maximum height, obtained through the 2D FEM numerical simulations as well as through the simplified analytical solutions, previously determined, are favourably comparable.

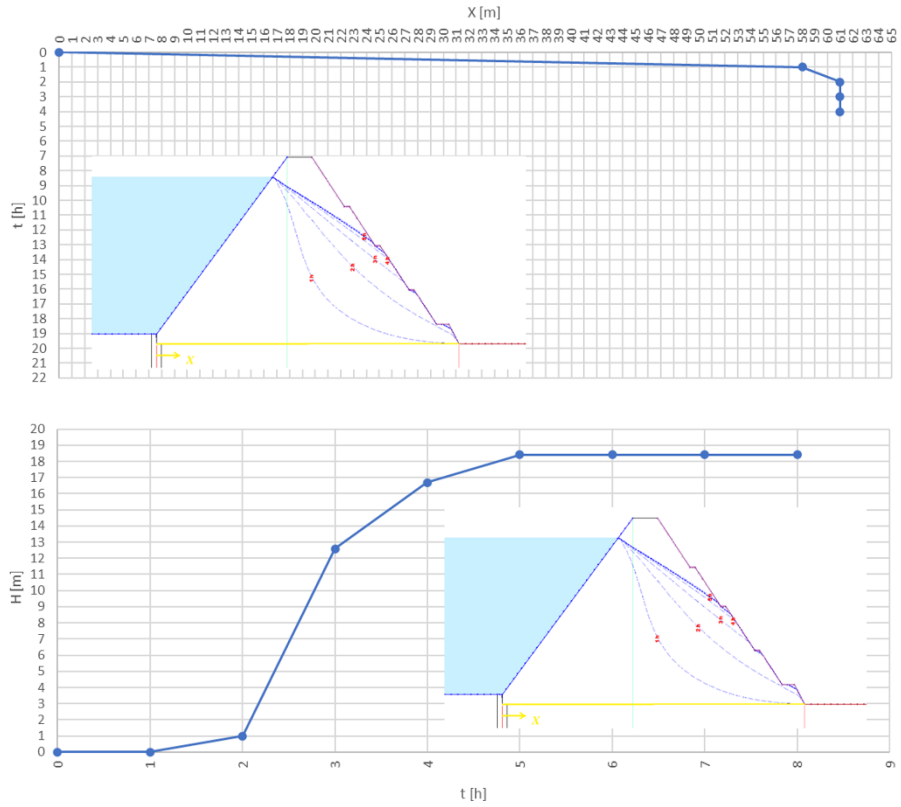

Fig. 10 – 2D FEM simulations: *X(t)*, temporal progression of the saturation front (above) and *H(t)*, raising the free surface within the dam body (below), for K = 10^{-3} m/s

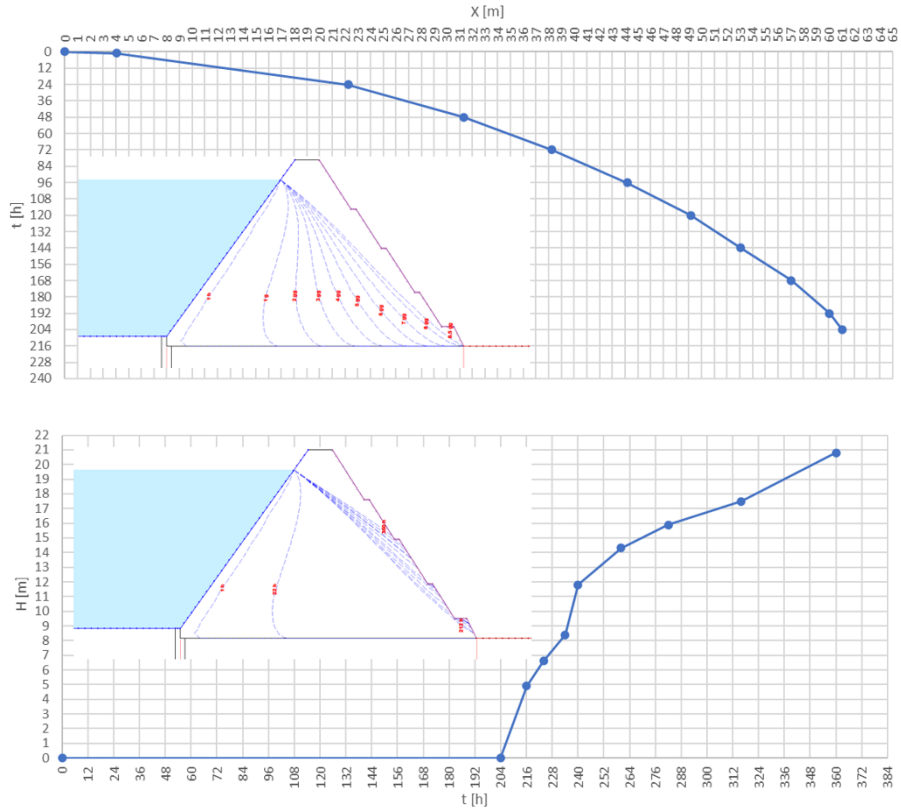

Fig. 11 – 2D FEM simulations: *X(t)*, temporal progression of the saturation front (above) and *H(t)*, raising the free surface within the dam body (below), for K = 10^{-5} m/s

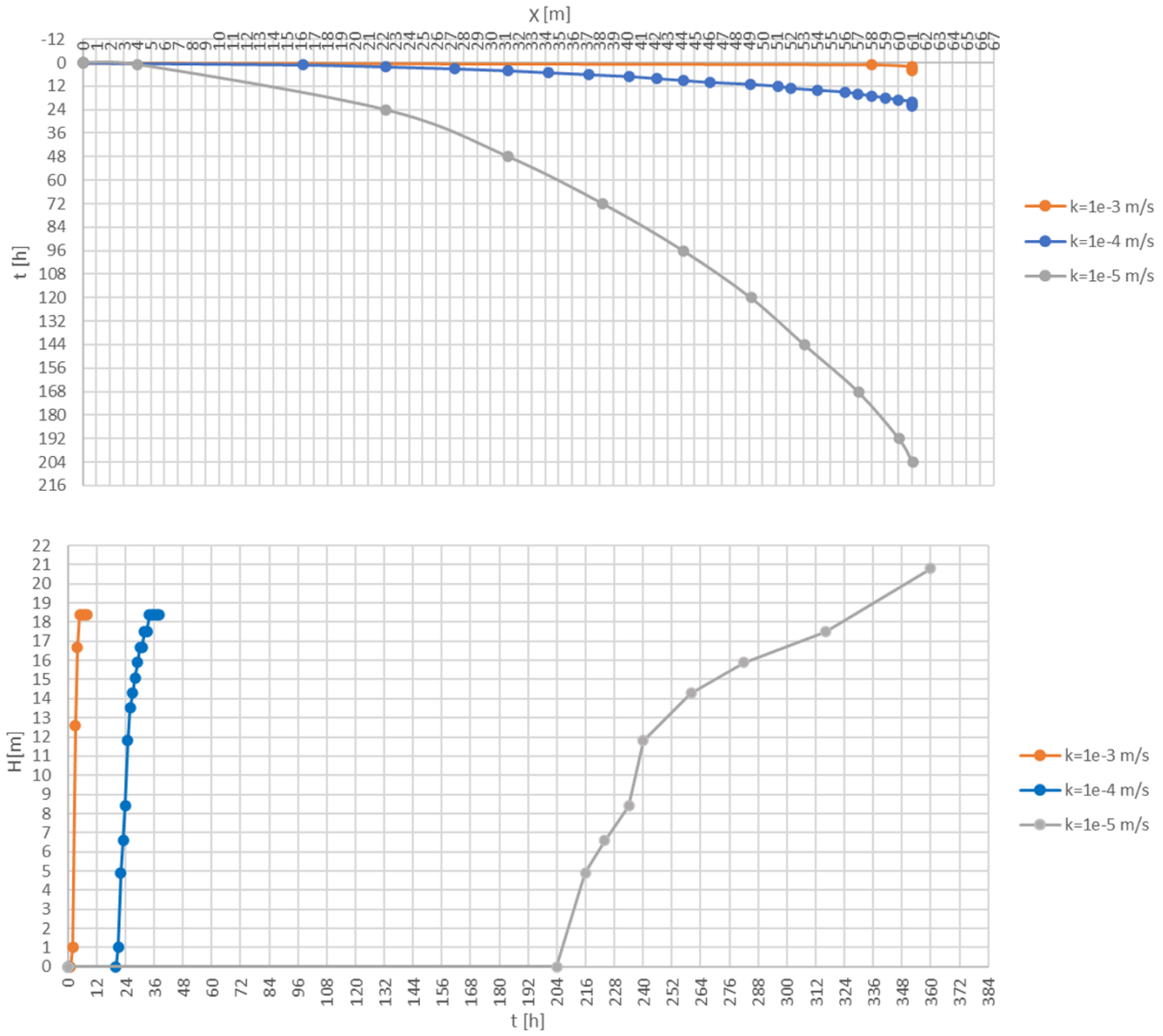

Fig. 12 – 2D FEM simulations: *X(t)*, temporal progression of the saturation front (above) and *H(t)*, raising the free surface within the dam body (below), for different values of K

Table 2 – Comparison between results from 2D FEM simulations and 2D simplified solutions

	2D FEM	2D simplified solutions
K = 1E-04 m/s		
$z^*_{f.s.}$ *[m]*	18.5	24
t (z=z*$_{f.s.}$) [h]*	34	38
K = 1E-03 m/s		
$z^*_{f.s.}$ *[m]*	18.5	24
t (z=z*$_{f.s.}$) [h]*	5	4
K = 1E-05 m/s		
$z^*_{f.s.}$ *[m]*	21	24
t (z=z*$_{f.s.}$) [h]*	360	380

4. CONCLUDING REMARKS

Simple, original, analytical solutions, based on the Boussinesq's equation, are proposed to assess the seepage flow progression within dry, coarse grain sized, embankment dam materials, following an instantaneous very large loss of tightness of its impervious upstream facing.

2D FEM simulations through SEEP/W code are developed in order to test and validate the proposed simplified solutions, by referring to a specific case.

The main results obtained by the proposed analytical solutions and the 2D FEM numerical analyses can be summarized as follows:

- it is confirmed that, independently of the hypotheses at the basis of the respective developments (*analytical solutions*: negligibility of the vertical component of the seepage flow velocity, application of the method of successive stationary states; *FEM solutions*: partial saturation and, therefore, suction, in the portions not reached by the seepage flow), both developed analyses are sufficiently reliable;
- the results obtained through the two, analytical and numerical, procedures, are favourably compared, both from qualitative and quantitative points of view;
- it is highlighted the appreciable dependence of the obtained results on the permeability coefficient (in saturated condition) of the dry material;
- in particular, the saturation front would reach the downstream foot in about 2 hours, 18 hours or, again, in about 7.5 days, for values of the permeability coefficient K (saturated condition, dry material) equal to 10^{-3} m/s, 10^{-4} m/s, 10^{-5} m/s respectively.
- as also indicated in the 3D FE analyses by [21], the leakage of the reservoir water occurs first at the abutments of the dam and subsequently in the highest (and widest) part of the dam. The same condition happens for $t^*(z'^*_{f.s.})$.

Finally, it is worth observing that the issues above described and analysed are prevented in the case of non-homogeneous dams, equipped by a clay core, coupled with an efficient filter and drainage system, against the migration of phreatic line and internal erosion phenomena.

REFERENCES

[1] Aravin, V.I., Numerov, S.N., (1953). Theory of Fluid Flow in Undeformable Porous Media. Gostekhizdat, Moscow (in Russian). English Translation: Israel Program for Scientific Translation, Jerusalem, 1965.

[2] Casagrande, A., (1937). Seepage through dams. J. New England Water Works 51, pp. 295–336.

[3] Federico F., Jappelli R., Musso A., (1996). Analysis of seepage limit states in embankment dams. XVI Int. Conf. on Large Dams, Q. 73, Florence, 1996.

[4] Federico F., Calzoletti F., Montanaro A., (2010). Steady state seepage flow through zoned earth structures affected by permeability defects. NUMGE 2010, 7th European Conf. on Numerical Methods in Geotechnical Engineering, June 2-4, Trondheim, Norway.

[5] Federico F., Cesali C., Jappelli R., (2018). Geotechnical design of large central draining cores in embankment dams - 3th Int. Conf. “DAM WORLD 2018”, Brazil, September.

[6] Federico F., Cesali C., Jappelli R., (2019). Design of draining cores to control seepage through embankment dams. XVII ECSMGE Geotechnical Engineering foundation of the future. ISBN 978-9935-9436-1-3, Reykjavik.

[7] Cedergren, H.R., (1989). Seepage, Drainage and Flow Nets. Wiley, New York. Chahar, Bhagu R., 2004. Determination of length of a horizontal drain in homogeneous.

[8] Chapuis, Robert P., Aubertin, Michel, (2002). A simplified method to estimate saturated and unsaturated seepage through dikes under steady-state conditions. Can. Geotech. J. 38 (6), 1321–1328.

[9] Jafari, N. H., Cadigan, Jack A., Stark, Timothy D., Woodward, Mark L., (2019). Phreatic surface migration through an unsaturated levee embankment. J. Geotech. Geoenviron. Eng. 145 (11), 05019010. https://doi.org/10.1061/(ASCE)GT.1943- 5606.0002139.

[10] De Mello, V.F.B., 1977. Reflections on design decisions of practical significance to embankment dams. Geotechnique, 27 (3), 281–355.

[11] Charles, J. A. (1998): Internal erosion in European embankment dams-progress report of working group on internal erosion in embankment dams, Dam Safety (ed. by Berga, L.), A. A. Balkema, Rotterdam, Netherlands, 2, 1567-1576.

[12] Jappelli R., Federico F. et al., (1988). Impervious facing and large central drain for the embankment dams of a pumped-storage plant. XVI Int. Congress on Large Dams, Q. 61, Vol. II, pp. 465 - 492, S. Francisco.

[13] Chen, Q., Zhang L.M. (2006). Three-dimensional stability analysis of bank slopes with reservoir drawdown based on rigorous limit equilibrium method. Canadian Geotechnical Journal, May, (43), 449-461, doi:10.1139/T06-011.

[14] Zhang L.M., Chen, Q. (2006). Seepage failure mechanism of the Gouhou rockfill dam during reservoir water infiltration. Soils and Foundations, Vol. 46, No. 5, 557-568, Oct. 2006.

[15] ICOLD (2017). Bulletin 164: Internal erosion of existing dams, levees and dikes, and their foundations. Volume 1: Internal erosion processes and engineering assessment. Volume 2: Case histories, investigations, testing, remediation and surveillance.

International Commission on Large Dams, Paris. (Publication of final preprint in English and French, from: http://www.icold-cigb.org).

[16] Polubarinova-Kochina, P.Ya., (1962). Theory of Ground Water Movement. Princeton University Press, Princeton.

[17] Kacimov A. R., Simunek, J. (2021). Analytical traveling-wave solutions and HYDRUS modeling of wet wedges propagating into dry soils: Barenblatt's regime for Boussinesq's equation generalized. Journal of Hydrology, 598, https://doi.org/10.1016/j.jhydrol.2021.126413.

[18] Jaswal, M., Sinha, R. K., Sen, Phalguni, (2020). Delineation of phreatic surface in soil type slope—A comparative study using physical and numerical modeling. J. Min. Sci. 56 (3), 494–504. Jia, G.W., Zhan, Tony L.T., Chen, Y.M., Fredlund,

[19] Liggett, J. A., Liu, P. L. F., (1979). Unsteady interzonal free surface flow in porous media. Water Resour. Res. 15 (2), 240–246.

[20] Masciopinto, C., Passarella, G., Vurro, M., Castellano, L., (1994). Numerical simulations for the evaluation of the free surface history in porous media. Comparison between two different approaches. Adv. Eng. Softw. 21 (3), 149–157.

[21] Zhou, X.P., Wei, X., Liu, C., Cheng, H., (2020). Three-dimensional stability analysis of bank slopes with reservoir drawdown based on rigorous limit equilibrium method. Int. J. Geomech., ASCE 20 (12), 04020229.

Fifth International Dam World Conference
PORTUGAL • LISBON • LNEC • APRIL 13-17, 2025
dam world 2025

ADVANCED LIMIT EQUILIBRIUM 2D ANALYSES TO ASSESS GLOBAL SLIDING SAFETY OF EMBANKMENT DAMS UNDER SEISMIC ACTIONS

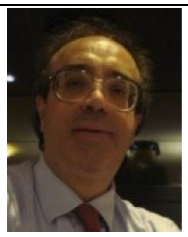

Francesco Federico[1]
University of Rome Tor Vergata, Italy

Chiara Cesali[2]
University of Rome Tor Vergata, Italy

Herald Caushi
Civil Engineer
Rome, Italy

ABSTRACT

The conventional 2D limit equilibrium method could be not correctly applied to evaluate the safety sliding factor, especially in case of dams whose different parts may vary significantly their heights (narrow valley dams) as well as dams whose upstream and downstream slopes are steep.

An advanced 2D limit equilibrium method to assess the sliding safety factor along horizontal planes at the base of embankment dams, subjected to hydrostatic loads, hydrodynamic and seismic forces, resting on sloped rock/soils foundation along the longitudinal direction, is presented.

After an arbitrary, initial, subdivision of the dam in N blocks by means of (N-1) cross sections, the general set of equilibrium equations is decoupled into two distinct set of equations, analytically describing, respectively the equilibrium of the blocks along the longitudinal direction of the dam as well as along the cross sections.

Both sets of equations must be solved by taking into account the external pressures and the massive, applied forces. The classical Mohr–Coulomb model was considered to compute the shear strength mobilized along the dam foundation interface, as well as at the interfaces between the blocks that compose the dam. The solution of the first system of equilibrium equations allows to estimate a global safety factor FOS_{long} referred to the potential sliding along the longitudinal direction as well as the normal and shear forces mobilized at the interfaces along the cross sections. The obtained FOS_{long} assumes in general high values: therefore, the mobilized shear forces acting at the base of each block, along the longitudinal direction, are small (often, almost negligible, if compared to the other shear forces). On the base of these results, by assuming some simplifying hypotheses, the second system of equilibrium equations is then solved; by this way, the local safety factor ($FOS_{cross,i}$) of each block (i = 1,2, ...N), referred to the potential sliding along the cross direction, is evaluated.

The proposed procedure is applied to analyze the sliding responses of different embankment dams, leading to the computation of the minimum value of the sliding local safety factors ($FOS_{cross,\ min}$) that characterize the considered dam.

Keywords: Global sliding safety of embankment dams, Seismic actions, Limit Equilibrium Methos (LEM), Cracks Formation.

[1] fdrfnc@gmail.com, Italy
[2] cesali@ing.uniroma2.it, Italy

1. INTRODUCTION

The conventional 2D limit equilibrium method could be not correctly applied to evaluate the safety sliding factor, especially in case of:

- dams whose different parts may vary significantly their heights (dams in narrow valleys),
- dams whose upstream and downstream slopes are steep,

as well as to properly identify the conditions (i.e., geometrical, stress-strain, contact foundation-dam, ...) that could induce transverse cracks (e.g. [1],[2],[3]).

In the paper, limit equilibrium method is firstly applied to assess the distribution of longitudinal forces, orthogonally acting on the cross sections of the dam, and of shear forces along the same cross sections. A first set of parametric analyses puts into evidence the role of the shape of the valley, of discontinuities of the foundation profile, of heterogeneity of rock/soil foundation.

On the base of these results, two different analyses are then developed:

- the estimate of the sliding safety factor along horizontal planes at the base of embankment dams, subjected to hydrostatic loads, hydrodynamic and seismic forces, resting on sloped rock/soils foundation along the longitudinal direction;
- the evaluation of the potential conditions that could favour the formation of transverse cracking in the dam body.

The obtained results are favourably compared with results reported in technical literature.

2. DIFFERENT 2D LIMIT EQUILIBRIUM ANALYSES

After an arbitrary, initial, subdivision of the dam in N blocks by means of (N-1) cross sections, the general set of equilibrium equations is decoupled into two distinct set of equations ([1]), analytically describing, respectively:

- the equilibrium of the blocks along the longitudinal direction of the dam;
- the equilibrium of each block, along the cross sections.

Both sets of equations must be solved by taking into account the external pressures and the massive (gravity, seismic) applied forces, previously defined.

The classical no-tension Mohr–Coulomb model was considered to determine the shear strength mobilized along the dam foundation interface, as well as at the interfaces between the *N* blocks ([1], [2]).

The solution of the first system of equilibrium equations allows to estimate *(i)* a global safety factor $\boldsymbol{FOS_{long}}$ referred to the potential sliding along the longitudinal direction as well as *(ii)* the

normal and *(iii)* the shear forces mobilized at the interfaces along the cross sections. The obtained FOS_{long} assumes in general high values: therefore, the mobilized shear forces acting at the base of each block, along the longitudinal direction, are small (often, almost negligible, if compared to the other shear forces).

On the base of these results, by assuming some simplifying hypotheses, the second system of equilibrium equations is then solved; by this way, the *local* safety factor ($FOS_{cross,i}$) of each block (i = 1, 2, ...N), referred to the potential sliding along the cross direction, is then evaluated.

The proposed procedure is applied to analyze the sliding responses of different embankment dams, leading to the computation of the minimum value of the sliding local safety factors ($FOS_{cross,\,min}$) that characterize the considered dam.

2.1. Potential sliding along the longitudinal direction (FOS_{long})

2.1.1 "Three macro-blocks" scheme of a dam

To simply explain the "strategy" of the proposed procedure, first of all, the analysis of the equilibrium of a dam along the longitudinal direction is developed according to a "*three macro-blocks*" scheme, as shown in the following figure.

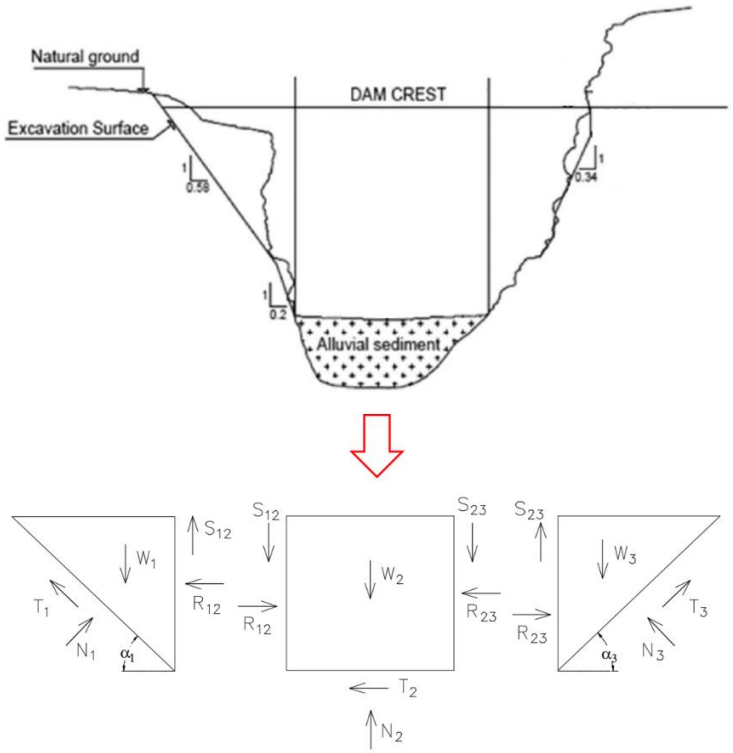

Fig. 1 – General longitudinal cross-section of a dam (above) and the related "*three macro-blocks*" scheme (below) and acting forces.

For each block (*i = 1,2,3*), by referring to the previous figure, the corresponding equilibrium equation can be written as follows:

Block n. 1 (left side)

$$W_1 - N_1 cos\alpha_1 - T_1 \sin\alpha_1 - S_{12} = 0 \quad (1)$$

$$N_1 sin\ \alpha_1 - T_1 \cos\alpha_1 - R_{12} = 0 \quad (2)$$

Block n. 2 (central)

$$W_2 + S_{12} + S_{23} - N_2 = 0 \quad (3)$$

$$R_{12} - T_2 - R_{23} = 0 \quad (4)$$

Block n. 3 (right side)

$$W_3 - N_3 cos\alpha_3 - T_3 \sin\alpha_3 - S_{23} = 0 \quad (5)$$

$$N_3 sin\ \alpha_3 - T_3 \cos\alpha_3 - R_{23} = 0 \quad (6)$$

being W_i = force associated to own weight; N_i = force normally acting to the sliding surface; T_i = shear force along the sliding surface; R_i = force normally acting to the block (vertical) interfaces; S_i = shear force along the block (vertical) interfaces; α_i = angle between the sliding surface and the horizontal plane, for the *i-th* block.

According to Mohr Coulomb law, the forces T_i, S_i, at the equilibrium, assume the following expressions:

$$T_i = \frac{N_i tan\varphi'_i + c' \cdot B_i}{\eta_L};\ C_i = \frac{c' \cdot B_i}{\eta_L};\ S_i = \frac{R_i \cdot tan\varphi'_n}{\eta_L} \quad (7)$$

being φ'_i = friction/shear resistance angle along the sliding surface for *i-th* block; φ'_n = friction/shear resistance angle along the block interfaces; η_L = global safety factor (***FOS$_{long}$***) referred to the potential sliding along the longitudinal direction; B_i = width of the *i-th* block; ***c'*** = cohesion coefficient. Thus, from the system of eqs. (1), (2), (3), (4), (5), (6), the following resolving expressions are obtained:

$$N_1 = \frac{W_1 - C_1\left(\sin\alpha_1 - \frac{\cos\alpha_1 \cdot tan\varphi'_n}{\eta_L}\right)}{\left[cos\alpha_1 + \frac{tan\varphi'_1}{\eta_L}\sin\alpha_1\right]\left(1 + \frac{\left(\left[sin\ \alpha_1 - \frac{tan\varphi'_1}{\eta_L}\cos\alpha_1\right]\right)\cdot tan\varphi'_n}{\eta_L\left[cos\alpha_1 + \frac{tan\varphi'_1}{\eta_L}\sin\alpha_1\right]}\right)} \quad (8)$$

$$N_3 = \frac{W_3 - C_3\left(\sin\alpha_3 - \frac{\cos\alpha_3 \cdot tan\varphi'_n}{\eta_L}\right)}{\left[cos\alpha_3 + \frac{tan\varphi'_3}{\eta_L}\sin\alpha_3\right]\left(1 + \frac{\left(\left[sin\ \alpha_3 - \frac{tan\varphi'_3}{\eta_L}\cos\alpha_3\right]\right)\cdot tan\varphi'_n}{\eta_L\left[cos\alpha_3 + \frac{tan\varphi'_3}{\eta_L}\sin\alpha_3\right]}\right)} \quad (9)$$

$$R_{12} = N_1 \left[sin\ \alpha_1 - \frac{tan\varphi'_1}{\eta_L} \cos \alpha_1 \right] - C_1 \cos \alpha_1 \quad (10)$$

$$R_{23} = N_3 \left[sin\ \alpha_3 - \frac{tan\varphi'_3}{\eta_L} \cos \alpha_3 \right] - C_3 \cos \alpha_3 \quad (11)$$

By way of example, in the following table, the results in terms of η_L obtained by applying the previous equations, by assigning specific values to W_i and repeating the calculations by exchanging them, are shown.

Table 1 – "Three macro-blocks" scheme analysis: results in terms of η_L.

Case		***c'=0*** ***$\varphi'_n = 0$***	***c'≠ 0*** ***$\varphi'_n \neq 0$***
W_1 = 213728 kN W_2 = 706244 kN W_3 = 1388962 kN	(left side) (central) (right side)	$\eta_L = +48.2$	η_L=complex solution
W_1 = 1388962 kN W_2 = 706244 kN W_3 = 213728 kN	(right side) (central) (left side)	η_L=complex solution	$\eta_L = -56.3$

The obtained values for η_L highlight the dependence of the solution on the assignment of the verses initially attributed to the forces, in imposing the equilibrium condition of each block.

2.1.2 "N-blocks" scheme of a dam

A stability analysis was developed, based on the limit equilibrium method (LEM), admitting the subdivision of the dam into *"N"* blocks, along the longitudinal direction, each with longitudinal extension Δx ([1],[2]). The blocks transmit each other normal and tangential actions, both at the base and along the vertical interfaces. The solution of the vertical and horizontal equilibrium equations (along the longitudinal direction) of the internal blocks, together with the equilibrium equations of the two blocks at the ends of the dam, allows the determination of the sliding safety coefficient η_L and the determination of the normal longitudinal (as well as tangential) stresses R_i and the corresponding longitudinal tangential stresses (S_i).

Following the previous considerations on the results obtained through the simply "*three blocks macro-blocks*" scheme, in developing the equilibrium equations according to a "*N-blocks"* scheme, the change of direction (towards the left side or towards the right side) of the shear actions at the base of the blocks, in correspondence with an element, with a priori unknown position, inside the central portion of the dam, is taken into account. Specifically, it is important to note that, a priori, the directions (towards the left side or towards the right side) of the shear forces at the base of each block cannot be defined unambiguously.

In the following table, limit equilibrium equations and related solutions for "*N-blocks*" scheme analysis, are shown.

Table 2 – *"N-blocks"* scheme analysis: limit equilibrium equations and solutions.

Case/block	*Limit equilibrium equations*	*Solutions*
Left side (internal) blocks 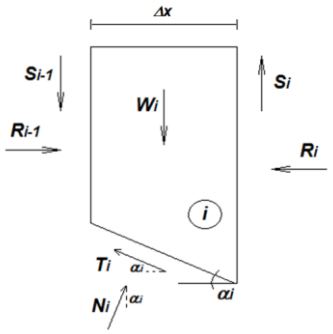	$W_i + S_{i-1} = N_i cos\alpha_i + T_i \sin\alpha_i + S_i$ $R_{i-1} + N_i sin\,\alpha_i - T_i \cos\alpha_i - R_i = 0$ (2 x N) available equations (4N – 2) unknown variables	$\sum_{i=2}^{Z} \frac{W_i \frac{F_{1,i}}{F_{2,i}} - C_i\left[\frac{F_{1,i}}{F_{2,i}}\sin\alpha_i - \cos\alpha_i\right]}{\left[1 - \frac{tan\varphi'_n}{\eta_L}\frac{F_{1,i}}{F_{2,i}}\right]} = R_1 - R_Z$ being: $F_{1,i} = \left(\frac{tan\varphi'_i}{\eta_L}\cos\alpha_i - sin\,\alpha_i\right)$ $F_{2,i} = \left(cos\alpha_i + \frac{tan\varphi'_i}{\eta_L}\sin\alpha_i\right)$ The "Z" index identifies the element of the central portion of the dam from which it is intended to assume the inversion of the shear actions at the base of the blocks.
Right side (internal) blocks (direction/versus of shear forces at the base of the blocks in agreement between right and left sides) 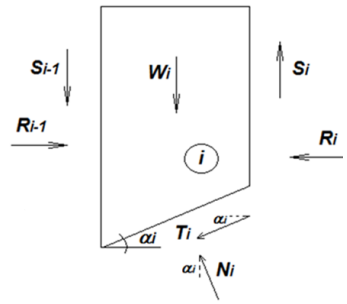	$W_i + S_{i-1} + T_i \sin\alpha_i = N_i cos\alpha_i + S_i$ $R_{i-1} - N_i sin\,\alpha_i - T_i \cos\alpha_i - R_i = 0$	$\sum_{i=2}^{Z} \frac{W_i \frac{F_{1,i}}{F_{2,i}} - C_i\left[\frac{F_{1,i}}{F_{2,i}}\sin\alpha_i - \cos\alpha_i\right]}{\left[1 - \frac{tan\varphi'_n}{\eta_L}\frac{F_{1,i}}{F_{2,i}}\right]} + \sum_{i=Z+1}^{N-1} \frac{W_i \frac{F_{1,i}}{F_{2,i}} + C_i\left[\cos\alpha_i + \frac{F_{1,i}}{F_{2,i}}\sin\alpha_i\right]}{\left[1 - \frac{tan\varphi'_n}{\eta_L}\frac{F_{1,i}}{F_{2,i}}\right]} = R_1 - R_{N-1}$ being: $F_{1,i} = \left(\frac{tan\varphi'_i}{\eta_L}\cos\alpha_i + sin\,\alpha_i\right)$ $F_{2,i} = \left(cos\alpha_i - \frac{tan\varphi'_i}{\eta_L}\sin\alpha_i\right)$
Right side (internal) blocks (direction/versus of shear forces at the base of the blocks opposite between right and left sides) 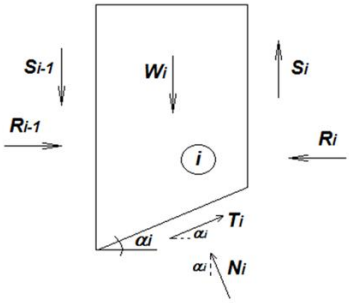	$W_i + S_{i-1} - T_i \sin\alpha_i = N_i cos\alpha_i + S_i$ $R_{i-1} - N_i sin\,\alpha_i + T_i \cos\alpha_i - R_i = 0$	$\sum_{i=2}^{Z} \frac{W_i \frac{F_{1,i}}{F_{2,i}} - C_i\left[\frac{F_{1,i}}{F_{2,i}}\sin\alpha_i - \cos\alpha_i\right]}{\left[1 - \frac{tan\varphi'_n}{\eta_L}\frac{F_{1,i}}{F_{2,i}}\right]} + \sum_{i=Z+1}^{N-1} \frac{W_i \frac{F_{1,i}}{F_{2,i}} - C_i\left[\cos\alpha_i + \frac{F_{1,i}}{F_{2,i}}\sin\alpha_i\right]}{\left[1 - \frac{tan\varphi'_n}{\eta_L}\frac{F_{1,i}}{F_{2,i}}\right]} = R_1 - R_{N-1}$ being: $F_{1,i} = \left(sin\,\alpha_i - \frac{tan\varphi'_i}{\eta_L}cos\,\alpha_i\right)$ $F_{2,i} = \left(cos\alpha_i + \frac{tan\varphi'_i}{\eta_L}sin\,\alpha_i\right)$
Extremal (border) blocks 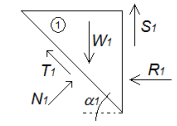 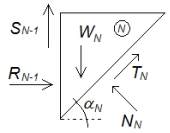	***i = 1*** $W_1 - S_1 - T_1 \sin\alpha_1 - N_1 cos\alpha_1 = 0$ $R_1 - N_1 sin\,\alpha_1 + T_1 \cos\alpha_1 = 0$ ***i = N*** $W_N - S_{N-1} - T_N \sin\alpha_N - N_N cos\alpha_N = 0$ $R_{N-1} - N_N sin\,\alpha_N + T_N \cos\alpha_N = 0$	$N_1 = \frac{W_1}{\left[sin\,\alpha_1\left(\frac{tan\varphi'_n + tan\varphi'_1}{\eta_L} + C_1\right) - \cos\alpha_1\left(\frac{tan\varphi'_n tan\varphi'_1}{\eta_L} - 1 + C_1\frac{tan\varphi'_n}{\eta_L}\right)\right]}$ $R_1 = N_1 sin\,\alpha_1 - \frac{N_1 tan\varphi'_1 + c' \cdot B_1}{\eta_L}\cos\alpha_1$ $T_1 = \frac{N_1 tan\varphi'_1 + c' \cdot B_1}{\eta_L};\ S_1 = \frac{R_1 \cdot tan\varphi'_n}{\eta_L}$ $N_N = \frac{W_N}{\left[sin\,\alpha_N\left(\frac{tan\varphi'_n + tan\varphi'_N}{\eta_L} + C_N\right) - \cos\alpha_N\left(\frac{tan\varphi'_n tan\varphi'_N}{\eta_L} - 1 + C_N\frac{tan\varphi'_n}{\eta_L}\right)\right]}$ $R_{N-1} = N_N\left(sin\,\alpha_N - \frac{tan\varphi'_N}{\eta_L}\cos\alpha_N\right) - C_N\cos\alpha_N$ $T_N = \frac{N_N tan\varphi'_N + c' \cdot B_N}{\eta_L};\ S_{N-1} = \frac{R_{N-1} \cdot tan\varphi'_n}{\eta_L}$

The above equations are implemented and solved by means of a specific code, written according to the *Matlab* language. The calculations are repeated by assuming different distributions of these directions. Specifically, the following 4 distributions were considered:

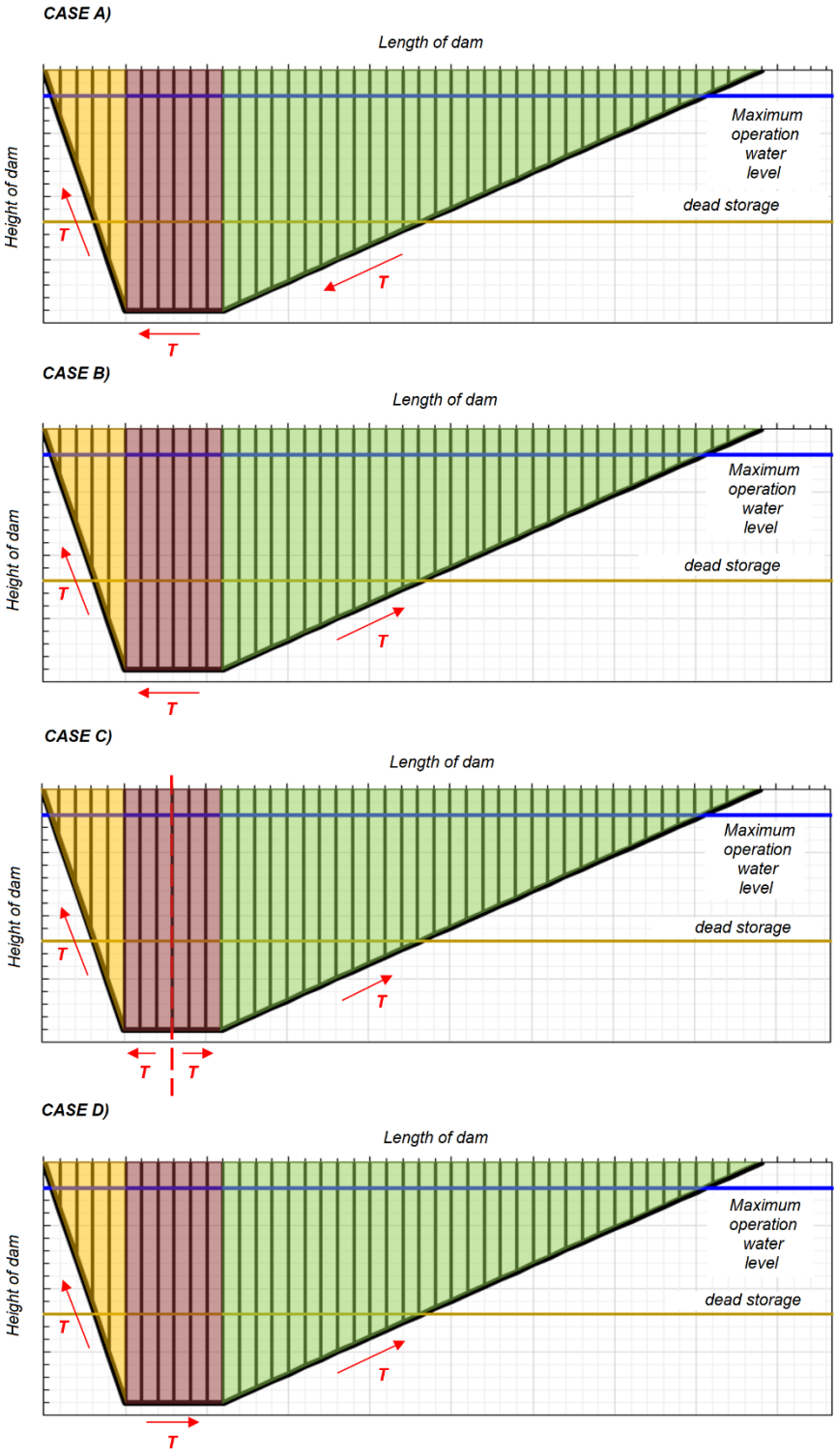

Fig. 2 – Different possible verses configurations of basal shear forces along the sliding surface of blocks composing the dam.

In Table 2, the values of η_L obtained by applying the previous (*N-blocks*) equations, and by assigning the following parameters: Δx = 6 m; φ' = 45° and c' = 0 (left side); φ' = 24° and c' = 35 kPa (central and right side); φ'_n = 45°; γ_p = 1.66 t/m^3 (specific weight of the dam material); L_l =30 m (length of the left side); L_c =36 m (length of the central part); L_r =198 m (length of the right side); H = 38 m (height of the dam), α_s = 51.7°; α_c = 0; α_d = 10.9°, are shown.

Table 2 – "*N-blocks*" scheme analysis: results in terms of η_L.

Case	η_L
A	(-) 498
B	(-) 158
C	(-) 74.8
D	(+) 36.5

As previously specified, η_L always assumes very high values, as expected due to the specific cinematic conditions; the negative sign ("-") means that the verses of the shear forces, in the central part of the dam (i.e. maximum height) are opposite to those initially hypothesized.

In the following figure, the results in terms of distribution of values of forces R_i along the longitudinal direction of the dam are shown.

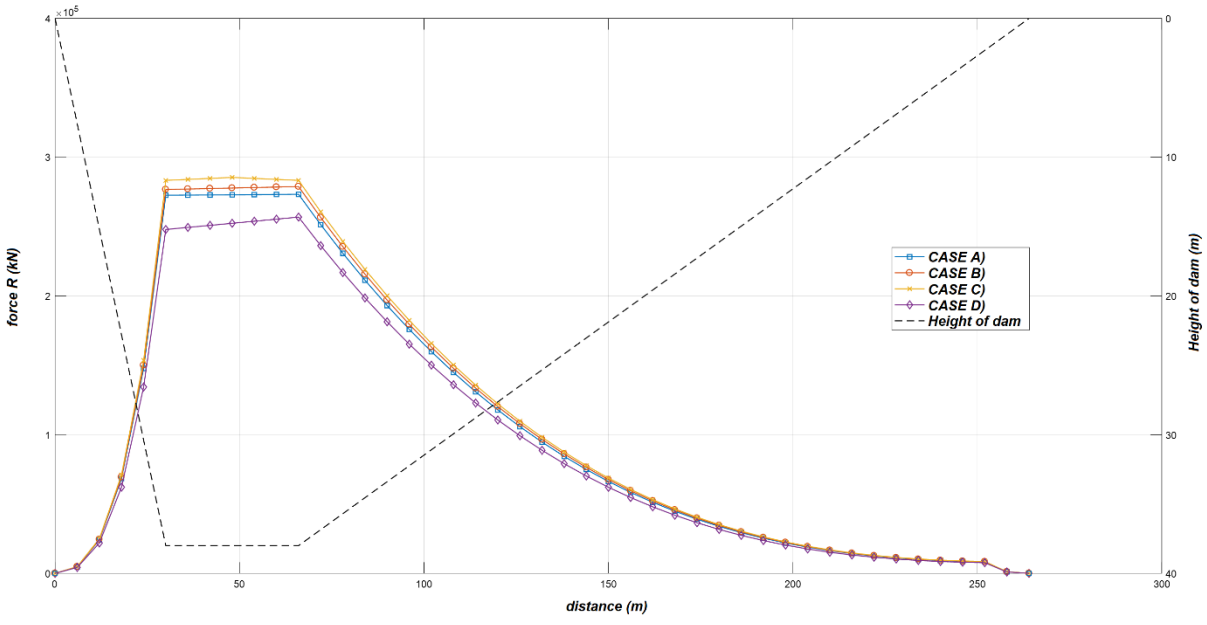

Fig. 3 – "*N-blocks*" scheme analysis: results in terms of R_i vs (longitudinal) length of dam.

In any case, due to the small width of each block and the high calculated value (positive or negative) of the η_L coefficient, the distributions of the value of the normal forces R_i acting in

the longitudinal direction are very similar and differ by a few percentage points, also in the central part of the dam (i.e. for blocks of maximum height).

A ***Δx*** sensitivity analysis was carried out on the values of *R* (for the case B previously defined). The corresponding results are shown in Fig. 4.

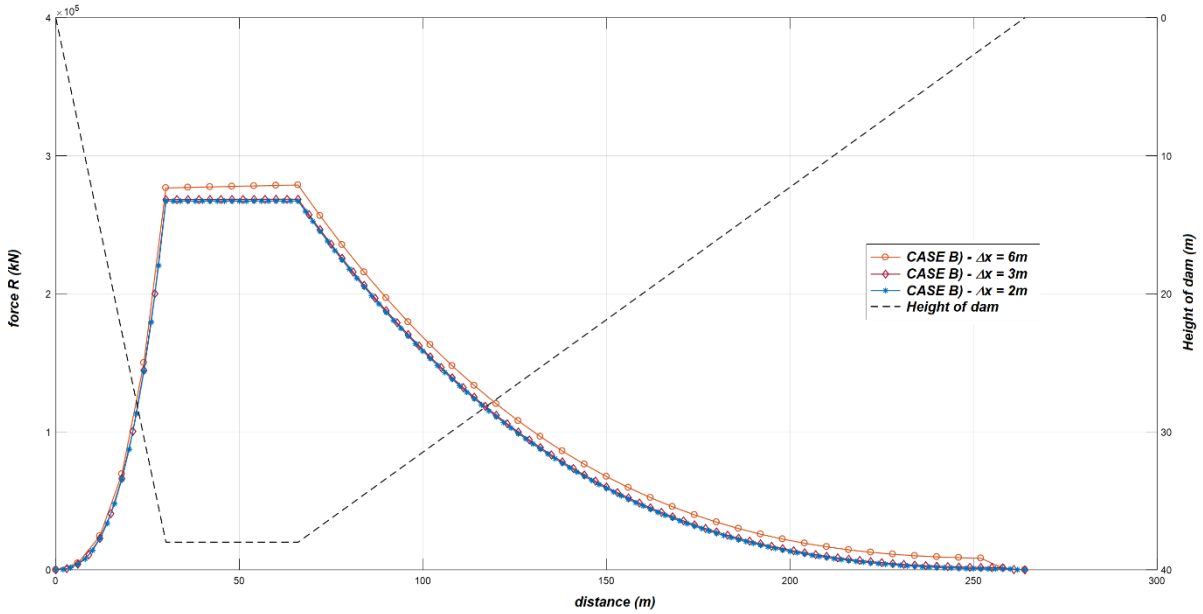

Fig. 4 – "*N-blocks*" scheme analysis: results in terms of R_i vs (longitudinal) length of dam, case B, for different values of *Δx*.

Definitively, the influence on the safety coefficient η_L is observed both of the "direction" assumed for the shear forces at the base of the blocks representing the portions of the dam on the left and right sides and of the "direction" assumed for the shear forces at the base of the blocks representing the central portion of the dam, consistent with those of the blocks of the portion of the dam on the left or right side.

The maximum value of R_i, in the central portion, falls between (minimum) 25700 tons and (maximum) 28500 tons. In the case of "opposite directions" and "*central block + left block*" (i.e., case B), the effects of the size of the blocks, i.e., the spatial discretization of the dam (Δx), on the R_i include a slight reduction in the maximum value is observed (from 27900 tons for Δx = 6m to 26720 tons for Δx = 2m) in correspondence with the central portion.

For each distribution of the shear stresses at the base in the longitudinal direction, related to the assignment of the inversion point ("R_z") or to the change of direction of the shear stresses themselves, a balanced admissible distribution is obtained by imposing the equilibrium.

The values obtained for R_i are very similar to each other; the actions $R_{n,i}$ exhibit extremely limited variations.

Due to the high values of η_L, the role of the shear stresses at the base, along the longitudinal direction, as well as those in the vertical direction, appears negligible, as expected.

Therefore, the error related to the "a priori" choice of the position of the inversion point ("R_z") is negligible too, in the verification model exclusively in the longitudinal direction or for stability control with potential kinematics in the longitudinal direction.

The limitations of the model lie in the evaluation of the potential sliding only in the longitudinal direction (safety factor η_L) in a completely analogous way to the usual choice of limiting the verification of potential sliding only in the transverse direction (upstream-downstream).

A complete analysis aimed at the coupled determination of both safety factors in the potential sliding in the two directions (longitudinal, upstream-downstream) would provide more correct results. Therefore, the results obtained with the *"LEM scheme*" (*N-blocks*) must fundamentally be aimed at determining the order of magnitude of the actions R_i.

2.1.3 2D FEM analyses: scope and results

To validate the previous analyses and estimate some main parameters for the successive LEM analyses, devoted to estimate the safety of the blocks referred to potential sliding along the *cross* direction of the dam, 2D FEM simulations are firstly carried out. Reference is made to a general *longitudinal* vertical section of the dam, through the dam crest axis (see scheme in Fig. 5). The physical and mechanical parameters, previously selected, are maintained.

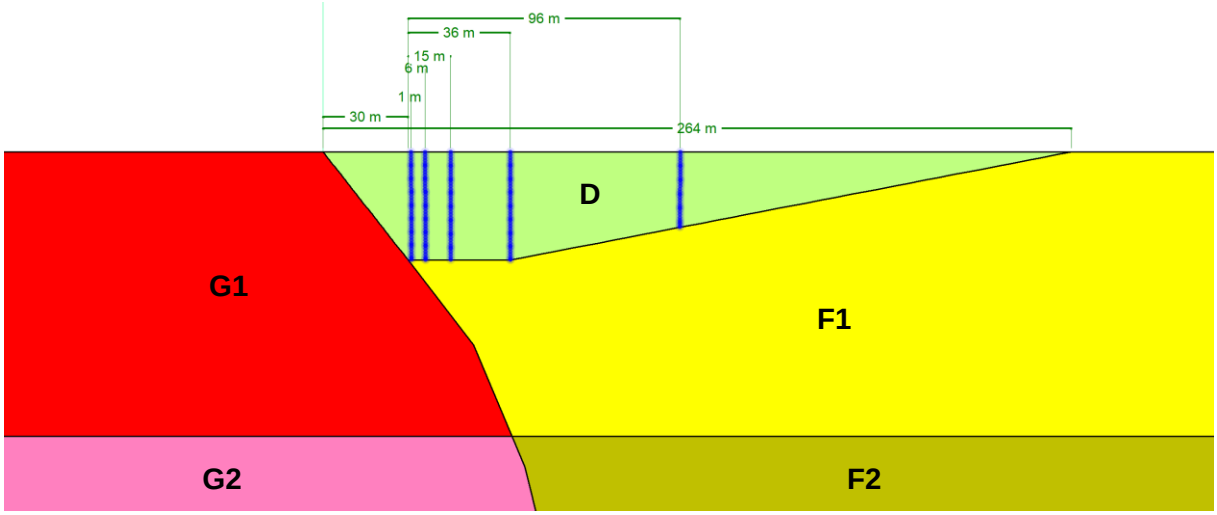

Fig. 5 – 2D FEM simulations: scheme of a general *longitudinal* vertical section of the dam, through the center of the dam crest.

For the different materials, as shown in previous figure, the following values of the Young Modulus (E) are assigned: *E (D) = 800 MPa; E (G1, H=100m) = 250 MPa; E (G2, H=900m) = 750 MPa; E (F1, H=100m) = 300 MPa; E (F2, H=900m) = 900 MPa.*

The analyses aim to investigate the distributions of vertical, horizontal and shear stresses at the base of the dam; the same analyses allowed to estimate the mean values of the ratio k_0 between horizontal and vertical stresses, along the longitudinal abscissa of the dam (Fig. 6), as well as to evaluate the role of the deformability and heterogeneity of the foundation soils/rocks, even at depth.

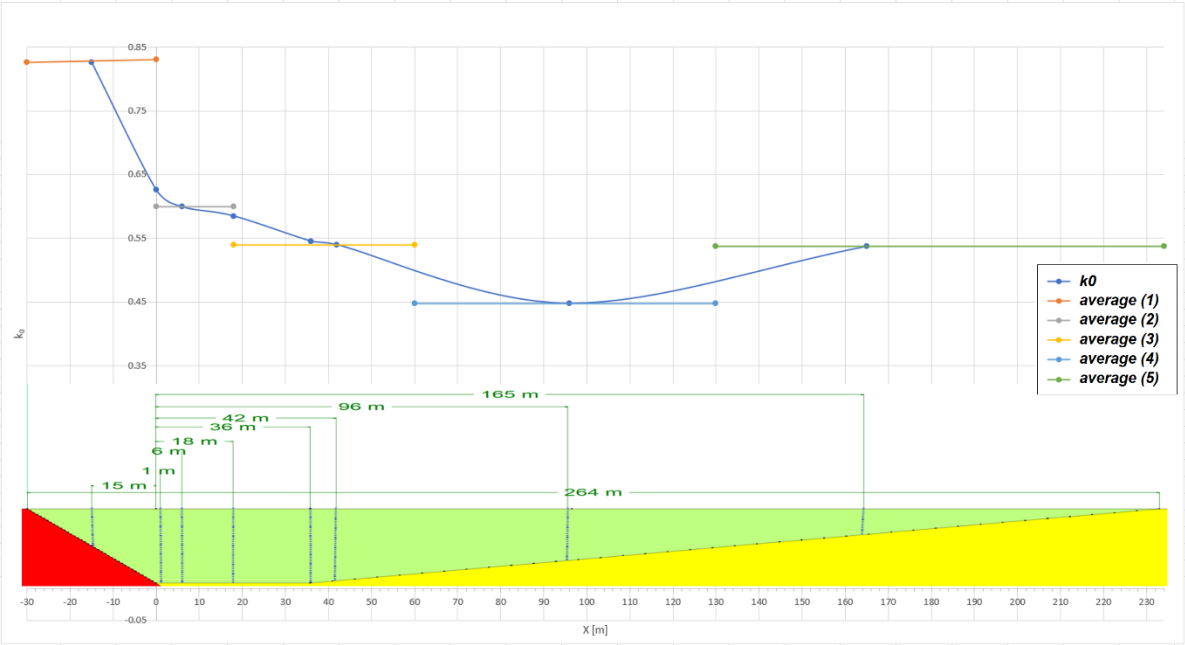

Fig. 6 – 2D FEM simulations: k_0 vs x (longitudinal abscissa of the dam).

It is particularly significant the comparison between the values of the horizontal internal reaction $R_{analytical,i}$ calculated for each cross section between two adjacent blocks, *(a)* by considering the average values of the coefficient k_0 deduced from the above 2D FEM analyses, estimated as (with b = crest width; L_i = transversal length of the dam for the *i-th* block):

$$R_{anal,i} = \frac{k_0 \cdot \gamma_p \cdot (3 \cdot b + 2 \cdot L_i)}{6} \tag{8}$$

and *(b)* the analogous values previously determined exclusively on the basis of the LEM equations (Table 2).

The R_i values obtained with the two different calculation procedures, shown and compared in Fig. 7, exhibit an appreciable correspondance, especially if the marked differences between the reference analytical models and the calculation procedure are taken into account.

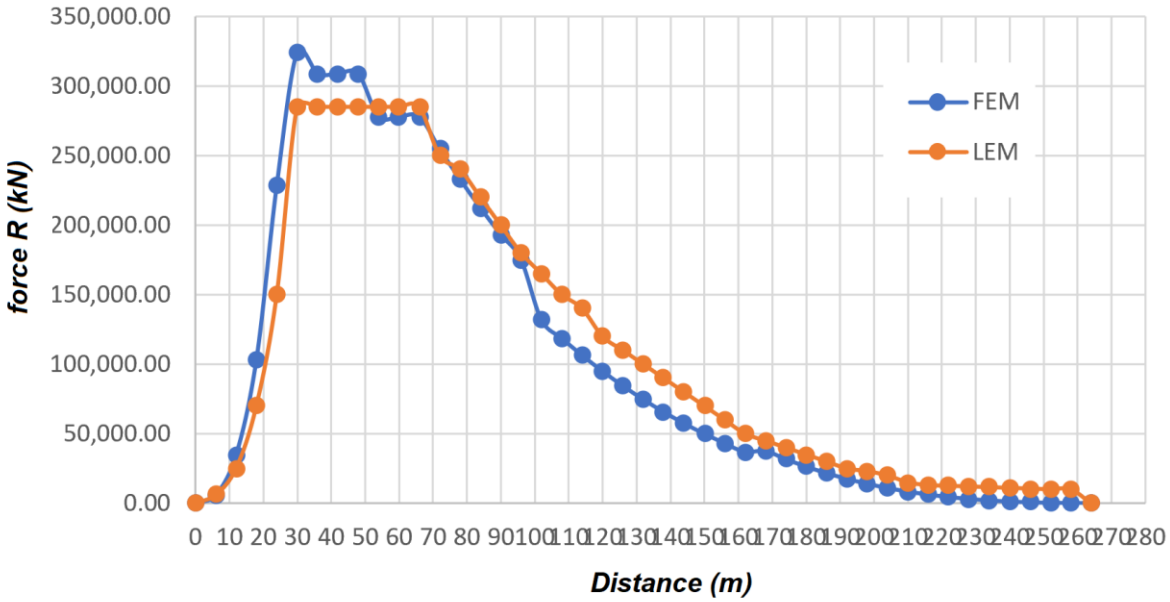

Fig. 7 – 2D FEM simulations vs LEM results: R_i vs *abscissa x* (longitudinal length of the dam).

2.2. Potential sliding along the cross direction ($FOS_{cross,I}$, $FOS_{cross,\ min}$)

For each block, the following acting forces are determined:

- *horizontal forces (upstream-downstream)*

$$O_h = \left(S_{w,h} + S_{wd,h} + S_{int,h} + k_h \cdot W\right) \cdot \Delta x \tag{9}$$

being $S_{w,h}$= hydrostatic force; $S_{wd,h}$ = hydrodynamic force; $S_{int,h}$ = force related to the dead storage volume of the dam; $k_h \cdot W$ = seismic force (k_h = horizontal maximum earthquake acceleration).

- *vertical forces*

$$V_{max} = \left(\left(W \cdot (1 - k_v)\right) + S_{w,v} + S_{wd,v} + S_{int,v}\right) \cdot \Delta x \tag{9}$$

being $S_{w,v} = 0.7 \cdot S_{w,h}$ (vertical component of hydrostatic force); $S_{wd,v}$ (vertical component of hydro dynamic force); $S_{int,v} = 0.7 \cdot S_{int,h}$ (vertical component of the force related to the dead storage volume of the dam); $W \cdot (1 - k_v)$ = vertical component of the seismic force (k_v = vertical maximum earthquake acceleration).

- *Maximum shear resistance basal force*

$$T_{res,base} = (c' \cdot B + V_{max} \cdot \tan \varphi') \cdot \Delta x \tag{10}$$

- *maximum shear resistance lateral force*

$$T_{max,lat} = \left(R_{anal,sx} + R_{anal,dx}\right) \cdot \tan \varphi'_n \quad (11)$$

- *<u>total</u> maximum shear resistance force*

$$T_{global} = T_{res,base} + T_{max,lat} \quad (12)$$

Thus, by considering the upstream-dowstream direction, the following simplified expression for the safety factor SF can be obtained:

$$SF = \frac{T_{global}}{O_h} = \frac{(c' \cdot B + V_{max} \cdot \tan \varphi') \cdot \Delta x + \left(R_{analytical,sx} + R_{analytical,dx}\right) \cdot \tan \varphi'_n}{O_h} \quad (13)$$

The above equations are numerically implemented for each block in which the dam is subdivided.

Referring to the same geometrical, physical and mechanical parameters assumed above (for different values of *∆x = 6, 18, 36, 42 m*), in the Table 3 the main obtained results are shown.

Table 3 – Potential sliding along the transversal direction: results in terms of *SF* (for different values of *∆x*).

∆x (m)	$T_{max,lat}$ (kN)	T_{global} (kN)	SF (-)
6	633735,1	748435,5	8,96
18	626281,9	899092,5	3,59
36	605775,1	1115751,1	2,23
42	594244,5	1181253,6	2,02

As expected, the role of interslices longitudinal forces R_i on the *Safety Factor FS* becomes more and more valuable if the width of each block becomes smaller (massive forces become progressively less significant).

For the examined case, the values thus obtained of *SF* for upstream-downstream sliding of portions of blocks of different longitudinal extension Δx, of maximum height or of considerable height, are always higher than the minimum value of 2.0 (value corresponding to a longitudinal extension of 42 m, which includes the entire central portion of the dam, of maximum height and a further 6 m on the right side).

In general, the most appropriate longitudinal extension Δx must be selected according a careful examination of the longitudinal profile of the base of the dam.

2.3 Conditions for transverse crack formation

The proposed procedure, through a careful subdivision of the blocks (equal or different width), allows to analyze the conditions for which a transverse crack can develop, as often occurs in correspondence with sudden variations of the slope of the base plane of the dam, in the longitudinal direction. An example is shown in Fig. 7: a strong reduction of the interslices longitudinal forces R_i is observed, by both FEM and LEM analyses, at the change from the horizontal base plane (central part, of maximum height) to the sloped bases of lateral blocks. The decrease of R_i is very rapid for steeper abutments.

Some cases, reported in technical literature, are shown in the following figures 8 and 9. Some documented cases, in figures 10, 11.

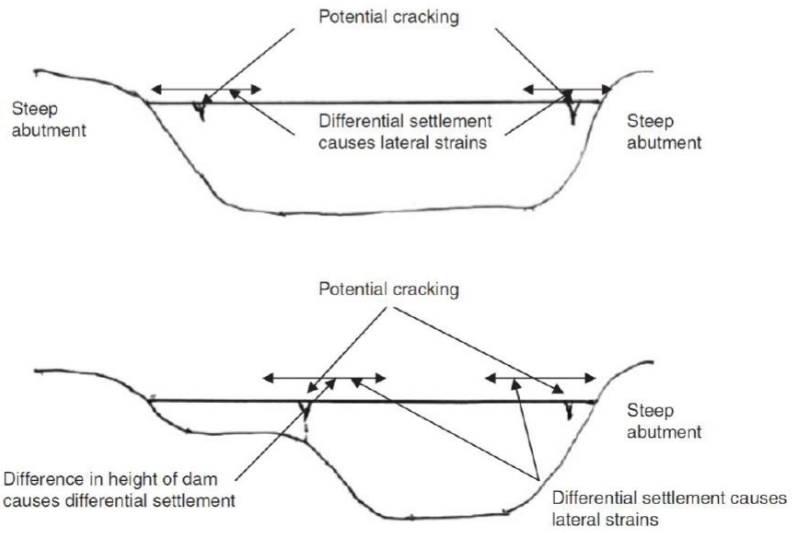

Fig. 8 – Situations in which cross valley differential settlement may lead to cracking or lateral strain and low stress zones subject to hydraulic fracture (adapted from [5],[6]).

Embankments with a step in the abutment profile appear susceptible to cracking over or adjacent the step; e.g. Matahina, Buffalo, Round Butte, East Branch ([4]).

For all the above reported cases, the cracks occur in correspondence with a marked step in the abutment profile. Particular interesting is the case of the Woodcrest Dam: although the same materials compose the whole dam and the same placement and compaction procedure have been applied for these materials, the crack developed only in correspondence with the steepest abutments of the dam with a high inclination, where a marked reduction in the longitudinal normal internal forces is evident.

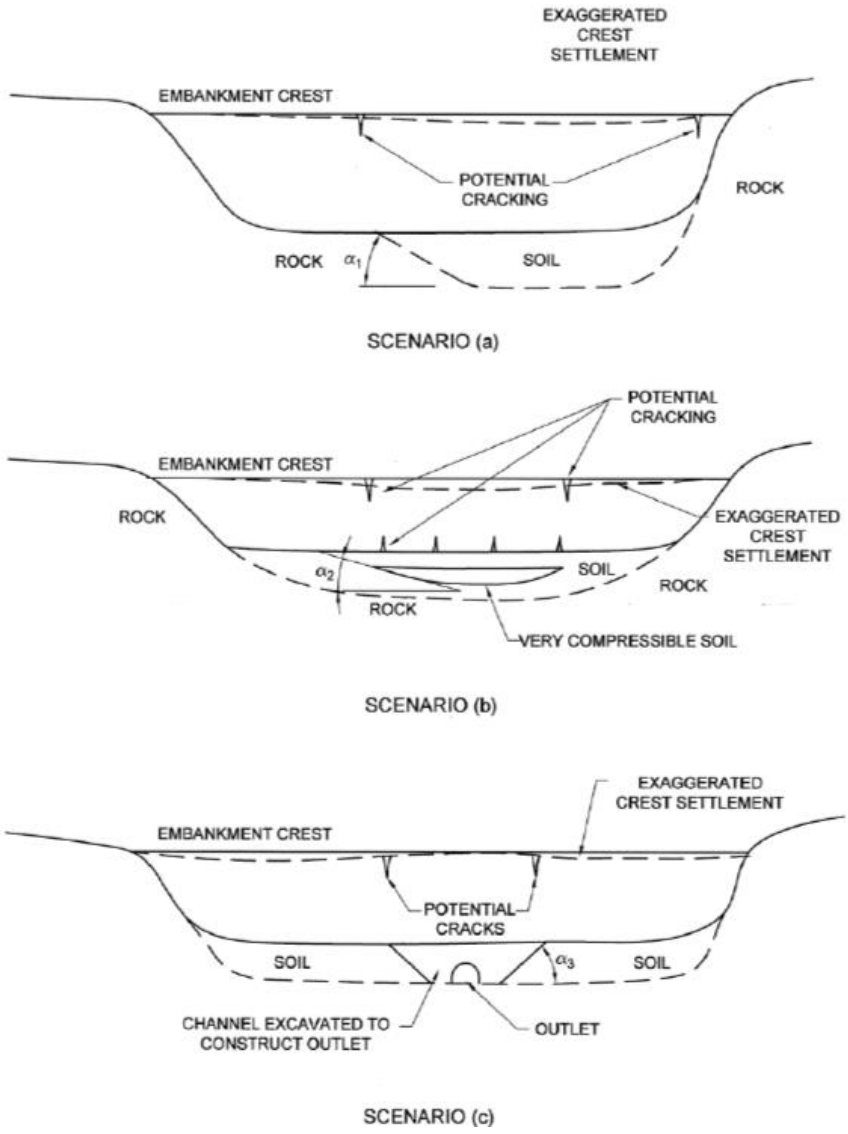

Fig. 9 –Situations which may cause differential settlement in the foundation of dams leading to horizontal strains and low stress zones potentially subject to cracking and hydraulic fracture (adapted from [5], [6], [7]).

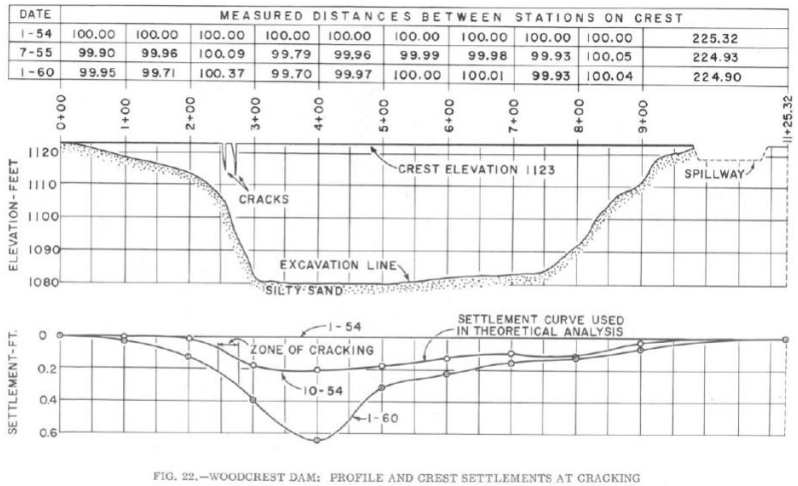

FIG. 22.—WOODCREST DAM: PROFILE AND CREST SETTLEMENTS AT CRACKING

Fig. 10 – Woodcrest Dam: Profile and crest settlement at cracking (adapted from [5], [6], [7]).

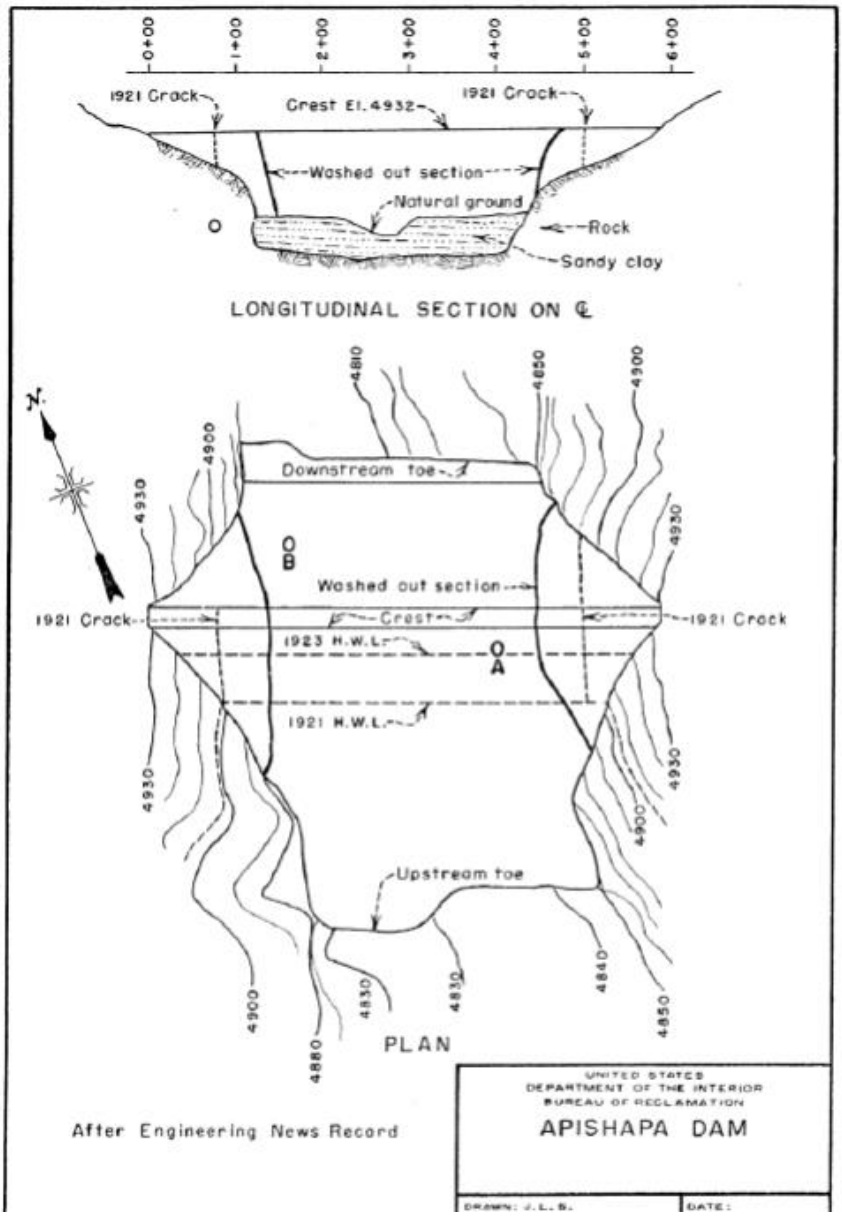

Fig. 11 – Apishapa Dam: Profile and crest location of cracks (adapted from [5], [6], [7]).

3. CONCLUDING REMARKS

The main conclusions of this study can be summarized as follows:

- the 2D analysis of isolated potentially sliding blocks, developed by neglecting the interslice forces (as individual potentially sliding parts), especially for dams characterized by appreciable slenderness (dam with steep upstream and downstream slopes), could be not reliable, because a significant rate of the shear forces mobilized against the forces that could induce the sliding, is neglected; the corresponding minimum safety factor might result less than unity;

- the proposed method, developed through a sequence of successive limit equilibrium analyses, firstly along the longitudinal, secondly along the transversal direction, may be easily implemented;
- the comparisons with results from FEM 2D numerical analyses indicate that the proposed procedure get reliable results and allow to perform several preliminary analyses, before more advanced 3D numerical analyses are carried out.

Specifically, obtained results from proposed 2D LEM may be applied:

- to investigate the influence of dam geometry, mainly the height and the valley shape, on the longitudinal normal forces distribution acting along the vertical cross sections;
- to better estimate, in turn, the safety referred to potential sliding of parts of the dam along their bases, due to seismic action, manly in case of cross sections characterized by appreciably sloped abutments (high height and limited base length);
- to define an additional valley shape factor, beyond other useful factors (e.g. [8]), aiming to detect possible critical conditions related to the geometry of the dam, especially in presence of narrow canyons or discontinuities of the longitudinal base profile.

The AA. wish to thank F. Forti (ENEL, Italy), F. Fornari (ENEL, Italy; ITCOLD), R. Caruana (ENEL, Italy; ITCOLD), G. Gatto (SPERI-Rome, Italy), E. Costantini (SPERI-Rome, Italy) for their precious suggestions.

REFERENCES

[1] Bretas, E. M., Léger, P., Lemos, J.V. 2012. 3D stability analysis of gravity dams on sloped rock foundations using the limit equilibrium method. Computers and Geotechnics 44 (2012) pp. 147–156.

[2] Bretas, E.M., Lemos, J.V., Lourenço, P.B. (2014). Numerical modelling of masonry gravity dams considering the internal structure of the material. 9th International Masonry Conference 2014 in Guimarães.

[3] Lombardi, G. (2007). 3-D analysis of gravity dams. Hydropower & Dams.

[4] He, K., Fell, R., Chongmin, S. (2017). Stresses and strains in embankment dams resulting from differential settlements. NICIV Report No. R-466, UNSW SYDNEY 2052 AUSTRALIA, ISBN: 978-0-7334-3773-1.

[5] Fell, R., Foster, M., Davidson, R., Cyganiewicz, J., Sills, G. and Vroman, N. (2008). A Unified Method for Estimating Probabilities of Failure of Embankment Dams by Internal Erosion and Piping. UNICIV Report R 446, The School of Civil and Environmental

Engineering, University of New South Wales, Sydney, Australia 2052.ISBN:85841 413 9. www.engineering.unsw.edu.au/civil-engineering/uniciv-reports.

[6] Fell, R., MacGregor; P, Stapledon, D., Bell, G, and Foster, M. (2014). Geotechnical Engineering of Dams, Second edition. Taylor Francis Group, London.

[7] Sherard, J.L., Woodward, R.J., Gizienski, S.F. and Clevenger, W.A. (1963). Earth and earth rock dams. John Wiley and Sons.

[8] Sukkarak, R., Jongpradist, P. and Pramthawee, P. (2019). A modified valley shape factor for the estimation of rockfill dam settlement. Computers and Geotechnics, 108, pp. 244–256, https://doi.org/10.1016/j.compgeo.2019.01.001.

Fifth International Dam World Conference
PORTUGAL • LISBON • LNEC • APRIL 13-17, 2025
dam world 2025

IN-SITU ESTIMATION OF BREACH OUTFLOW HYDROGRAPHS FROM FLUVIAL DIKE FAILURES: A METHODOLOGY INTEGRATING REAL-TIME MONITORING AND PHYSICAL MODELLING

Ricardo Jónatas[1]
Laboratório Nacional de Engenharia Civil (LNEC)

Sílvia Amaral[2]
Laboratório Nacional de Engenharia Civil (LNEC)

Rui Aleixo
Institute of Hydro-Engineering of Polish Academy of Sciences (IBW PAN)

João Serra
Laboratório Nacional de Engenharia Civil (LNEC)

Rui Ferreira
Instituto Superior Técnico (IST)

ABSTRACT

Embankment structures in civil engineering, such as earth dams and fluvial dikes, have a crucial role in society. these structures, often used for water storage and mining tailings containment, are cost-effective due to their reliance on locally sourced materials. While the failure of concrete structures is not so frequent but often lead to severe consequences, embankment structure, particularly fluvial dikes, are more prone to breach and the consequences vary between mild to catastrophic, depending on the proximity to human populations. Worldwide, some fluvial dike failures resulted in catastrophic outcomes for human lives, local economy and environment.

This paper aims to develop a methodology to calculate in-situ breach outflow hydrographs, resorting to real-time, non-intrusive and friendly-access technology. The goal is to provide a practical platform for developing and testing integrated systems applicable to prototype failure cases. An accurate, real-time hydrograph estimation capacity improves the risk assessment.

The proposed methodology deploys, in medium-scale experimental facility, common technology and data processing techniques to characterize the evolution of a fluvial dike failure. The morphodynamic and hydrodynamic components influencing the in-situ breach outflow hydrograph were assessed by characterizing, in real-time, the breach morphology, at the surface and underwater, the surface velocity maps and its corresponding cartesian coordinates.

Keywords: Fluvial dike failure; breach outflow hydrograph; real-time monitoring; Physical modelling; non-intrusive measurement techniques.

[1] rjonatas@lnec.pt, Portugal
[2] samaral@lnec.pt, Portugal

1. INTRODUCTION

Embankment structures, like all civil engineering constructions, inherently carry the risk of failure a phenomenon that can lead to significant downstream damage, including property destruction, loss of human life and ecological disasters. Historical records of embankment failures around the world feature the universal vulnerability of these structures to various hazards. A particularly notable instance occurred in 2005 with the failure of the fluvial dike system in New Orleans, which was triggered by Hurricane Katrina. This catastrophic event resulted in the flooding of approximately 85% of the metropolitan area, causing an estimated $75 billion in property damage and directly leading to hundreds of fatalities [1].

In some Mediterranean basins there have been some notable embankment failure events. For example, the Tous Dam in Spain failed due to overtopping on 20 October 1982, flooding the downstream city of Sumacárcel [2]. In Italy, the Val di Stava dam collapsed on 19 July 1985, unleashing a devastating mudflow that ravaged the downstream valley [3]. Similarly, on 27 March 2016, Greece experienced the failure of Sparmos Dam due to internal erosion, which resulted in significant flooding [4]. In Portugal, embankment failures are also quite frequent such as the failure of two fluvial dikes in the Mondego dikes system on 22 December 2019 due to overtopping [5]. These recurrent incidents, coupled with their destructive potential, highlight the importance of continued research in embankment failures.

The accurate forecasting of breach outflow hydrographs during such failure events is critical for effectively allocating resources and implementing strategies to mitigate both the evolution of the breach and its potential consequences. Take as example the mitigation actions undertaken during a fluvial dike failure in 2024 in South China where 2300 workers were deployed to rescue 5700 residents and establish an additional line of defence across 226 metres of the dike [6]. In such scenarios, real-time forecasting of the breach outflow hydrograph can be an invaluable tool in decision-making and risk management.

At the Portuguese National Laboratory for Civil Engineering, research has been ongoing to better understand embankment failure mechanisms, with a particular focus on embankment dams and fluvial dikes [7]. This research aims not only to characterise the physical processes that underlie embankment failures but also to develop integrated monitoring systems for medium-scale laboratory tests.

A comprehensive understanding of the breach evolution process necessitates the integration of physical model experiments, numerical modelling, and real-world monitoring data. In the future, this multi-disciplinary approach will enable the live forecasting of breach outflow hydrographs by extracting data from calibrated numerical models and applying it to real-world

failure scenarios. Given the hazardous nature of embankment failures, local data collection during such events is inherently challenging. However, the development of technologies such as Light Detection and Ranging (LiDAR) [8], [9], Particle Tracking Velocimetry (PTV) and Large-Scale Particle Image Velocimetry (PIV) [10], [11] when combined with remotely operated Unmanned Aerial Vehicles [12], provides a promising solution for overcoming these challenges.

These technologies allow for the in-situ collection of vital data, which can then be processed to estimate the breach outflow hydrograph with high accuracy. Recent advancements in data processing techniques have enabled the extension of direct methods—traditionally confined to laboratory settings—into real-world applications, thus improving the accuracy of risk assessments for areas downstream of embankments.

The present study focuses on the in-situ estimation of the breach outflow hydrograph as a direct consequence of breach morphodynamics and the hydrodynamics of the approaching flow. Experiments were conducted in a medium-scale experimental facility designed to vary hydraulic and geotechnical parameters. These experiments analysed key factors, including the Froude number (Fr) of the approach flow, embankment soil characteristics, dry density (γ_d), and water content (ω%) as determined through the standard Proctor test.

This paper is structured as follows: after this introduction, Section 2 describes the experimental setup, including the facility, monitoring instruments, and embankment characteristics. Section 3 details the methodology for estimating the in-situ breach outflow hydrograph (ISBOH), outlining the techniques used for breach geometry assessment and velocity field measurements. Sections 4 and 5 present and analyse the experimental results, respectively. Section 6 evaluates the accuracy and consistency of the ISBOH methodology by comparing it with conventional estimation techniques. Finally, Section 7 summarises the key findings and discusses potential applications and future research directions.

2. EXPERIMENTAL SETUP AND TEST PROTOCOLS

2.1. Experimental facility and monitoring instruments

The dike failure experimental facility, located at the Portuguese National Civil Engineering Laboratory (LNEC), operates in a closed-circuit system, with the flow following a defined path. Initially, water is pumped from an underground reservoir to an upper reservoir. Under the influence of gravity, the water then flows down into the facility, passing through the main channel before being redirected to the underground reservoir through a system of gutters positioned at the outlet.

As shown in Fig. 1a, the facility consists of a 1.40 m wide, 19.15 m long channel, designed to simulate a river flow. It allows testing dikes with a maximum height of 0.50 m and length of 2.00 m. The water level upstream the dike is controlled by a motorized gate downstream. Both the dike and the main channel are located on an elevated platform and a sediment basin (4.50 m wide by 2.25 m long) collects the eroded soil during dike failure tests. A mixed V-notch rectangular weir at the end of the sediment basin is used to estimate breach outflow discharge by water level correlation. Additionally, the flow rate of the main channel outflow is measured by comparing water levels above the downstream rectangular weir's crest with its flow rating curve. The main channel is also equipped with a modular, non-erodible dike section, allowing for the construction of an erodible dike at the desired location.

The experimental setup is specifically designed to replicate the failure of a typical fluvial dike on a river's left bank. The flow in the main channel runs parallel to the dike crest, simulating real-world flow conditions. Structural boundaries, such as the downstream gate and non-erodible dike section, help contain the failure zone and replicate prototype-scale fluvial conditions.

For live, non-intrusive data collection, the facility is equipped with various monitoring tools, as illustrated in Fig. 1a):

- An upstream **electromagnetic flowmeter** (Krohne Optiflux) for inflow measurement.
- **Seven ultrasonic probes** (Baummer U500) for water level measurement (four over the main channel, two over the sediment basin and one downstream);
- A **medium-speed camera** (GoPro Hero 8), capable of capturing 240 fps at 1080p resolution for water surface velocity and surrounding parameter estimation;
- Two synchronously **LiDARs** (Microsoft Azure Kinect), each capable of capturing five-point clouds per second, for 3D characterization of the dike and water surface.

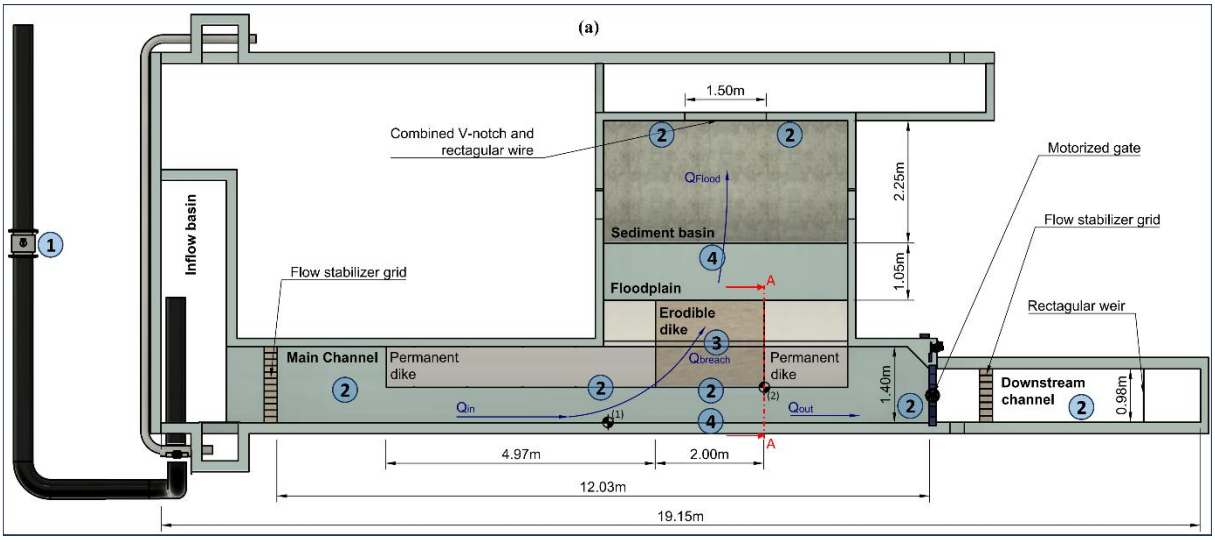

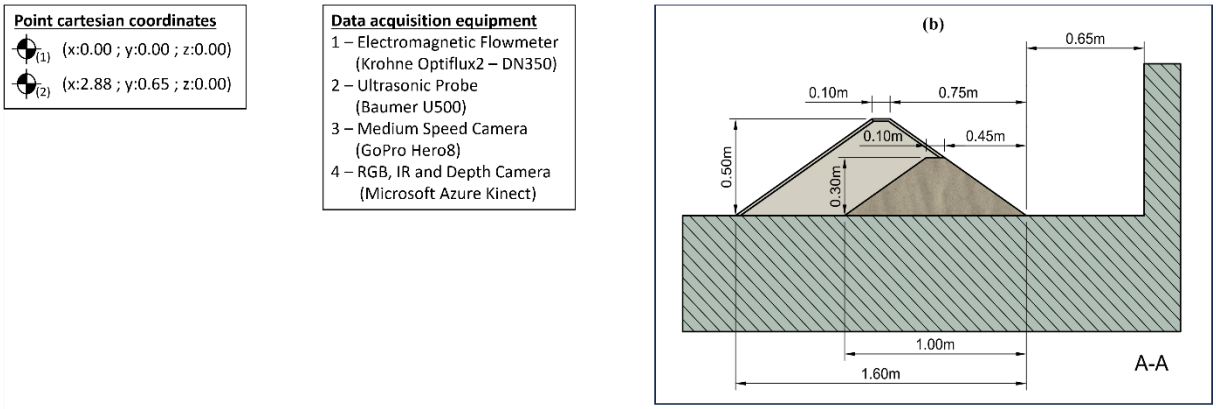

Fig. 1 – Experimental setup for dike failure experiments. a) Plan view and monitoring equipment's b) transversal section

2.2. Soil characterization for erodible dike construction

The erodible dike is placed 4.97 m from the upstream end of the permanent dike to account for inflow deflection. It has a height ranging from 0.50 m to 0.30 m, a fixed length of 2.00 m, side slopes of 1:1.5 and a crest width of 0.10 m (Fig. 1b).

Experimental tests in this study considered two soil grain-size distributions (Fig. 2). Dikes were constructed using a multi-lift system (0.05m lifts) compacted by vibration with a compaction plate, following the reference values from the Standard Proctor Compaction test (LNEC E197-1966). Throughout the construction of the embankment subjected to failure, soil samples were taken during construction to measure the water content (ω%) % and dry unit weight (γ_d).

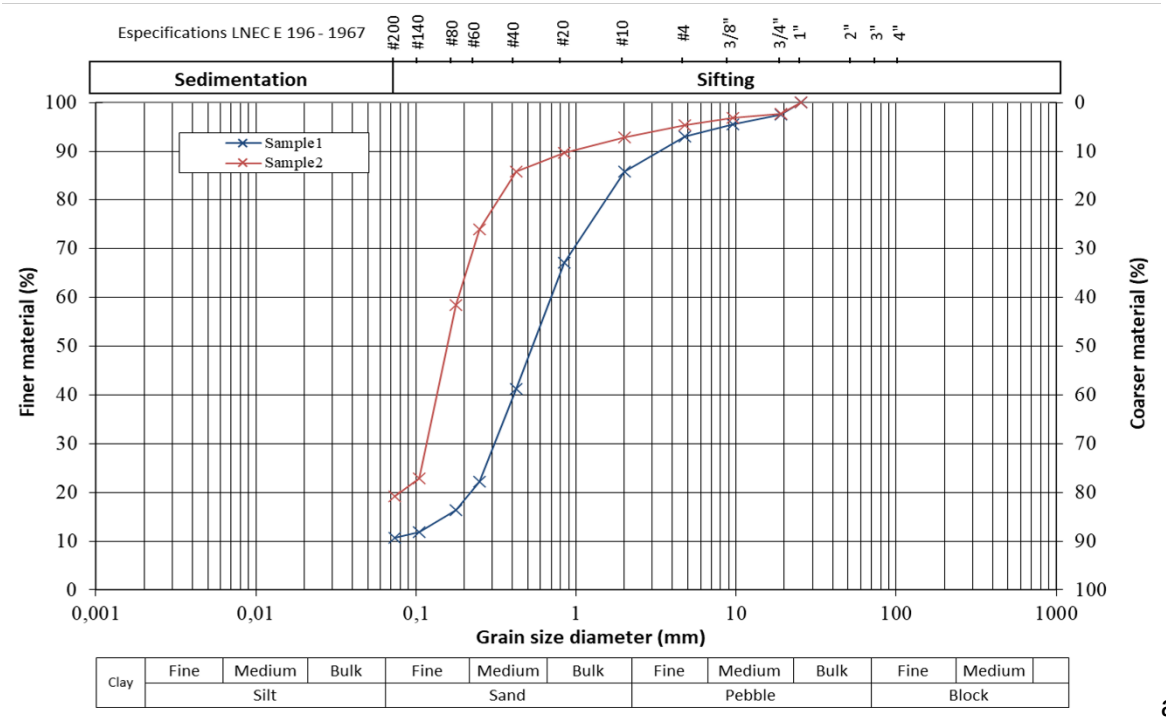

a)

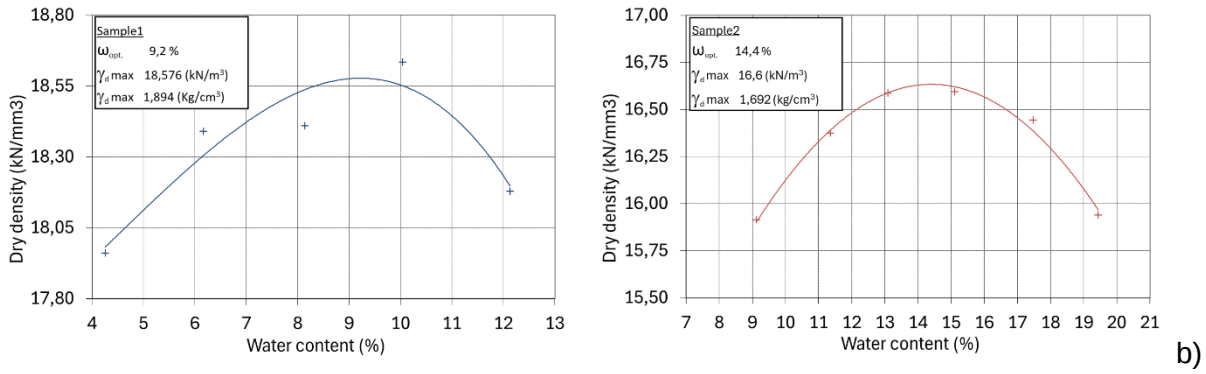

Fig. 2 – Soil samples 1 and 2 a) Soils grain-size distribution curves. b) compaction curves of the samples – Standard Proctor compaction

To replicate real dike material variability, both soils were non-cohesive sandy soils, with varying silt content and particle size distribution. Sample 1 (S1) had an average particle diameter (d_{50}) of 0.60 mm and 10% silt content, with an optimal ω% of 9.2% and a maximum dry unit weight (γ_d^{max}) of 18.6 kN/m^3. Sample 2 (S2) had d_{50} of 0.16 mm and 20% silt content, with an optimal ω% of 14.4% and a γ_d^{max} of 16.6 kN/m^3.

2.3. Experimental protocols for dike failure testing

Table 1 presents the set of dike failure experiments conducted to evaluate if the in-situ breach outflow hydrographs (ISBOH) estimates could be applied to a varying scenario of not-controlled variables (chaotic environment) and controlled variables (Table. 1).

Table. 1 – Experimental conditions during each test

Dike Failure Test (S#T#)	Set variables	Crest height (m)	ΔQ_{in} (m^3/s)	$h_{MChannel}$ (m)	Fr (-)	ω% (%)	CD (%)
S1T1	Not controlled	0.50	0.047-0.160	0.30- 0.50	0.1- 0.4	7.3 (-1.9)	95.4
S1T2	Controlled	0.50	0.080	0.48	0.1	10.4 (+1.2)	99.8
S2T1	Controlled	0.50	0.080	0.47	0.1	13.4 (-1.1)	93.7
S2T2	Controlled	0.30	0.075	0.28	0.2	13.0 (-1.5)	96.6
S2T3	Controlled	0.30	0.075	0.28	0.2	12.1 (-2.4)	95.1

- **Variable conditions (not-controlled variables)**

Before the test, the downstream and sediment basins were filled to the minimum levels corresponding to their respective weirs crest. An initial breach, measuring 0.1 m in width, 0.1 m in length, and 0.02 m in depth, was prepared at the crest of the erodible dike, precisely 0.3 m from the transition between the non-erodible and erodible sections. This setup ensured consistent and controlled breach initiation coordinates.

The test began when water fully passed through the initial breach and reached the embankment's floodplain. The endpoint was defined at the moment the sediment basin's weir

no longer provided reliable data. During the test, inflow rates were increased while the downstream gate, initially closed, was progressively opened to maintain the water level in the main channel.

A chaotic environment was created by intermittently halting the downstream gate's movement and irregularly varying the inflow (Table. 1 first row). These actions resulted in fluctuations in the upstream Froude number (Fr) and modified the flow-embankment interaction dynamics. Consequently, various erosion patterns were observed, including constant hydraulic erosion and mass detachment due to undercutting.

- **Controlled conditions**

For subsequent tests (Table. 1, last four rows), the initial state of the downstream gate was fully open, and the inflow conditions were stabilized before water passed through the breach. . At this point, the gate's operation was automated to maintain a constant water level in the main channel throughout breach evolution. The test concluded when the flow no longer exhibited characteristics of fluvial behaviour.

3. BREACH OUTFLOW HYDROGRAPH ESTIMATION

To simplify the ISBOH methodology exposition, all regarded data refers to S1T1 test (Soil 1, Test 1). This test was also used as a baseline case for evaluating the ISBOH methodology within a chaotic environment characterized by an increasing number of interacting variables, including inflow, outflow, water level, upstream Froude number and breach erosion behaviour.

3.1. Indirect estimation (non-local)

The breach effluent hydrograph can be indirectly estimated through two distinct methods that are detailed below:

i. **Spillway's discharge rating curve:** The use of spillways is a hydraulic standard procedure to estimate flow rates. In this study, a spillway positioned downstream of the sediment basin allows to indirectly calculate the breach outflow. By correlating the continuously measured water level in the sediment basin with the pre-calibrated spillway discharge curve, the breach outflow could be determined with precision;

ii. **Mass balance principles:** The breach outflow was alternatively estimated through the application of the continuity equation within the reservoir. The later encompasses the equilibrium between the inflow (Q_{in}), the volume variations within the main channel $\left(Q_v = \frac{\mathrm{dV}}{dt}\right)$ and the outflow (Q_{out}): in this case, the later

corresponding to the outflow from the spillway located in the downstream side of the main channel ($Q_{spillway}$) and from the breach (Q_{breach})

$$\frac{\mathrm{dV}}{dt} = Q_{in} - Q_{out} = Q_{in} - Q_{breach} - Q_{spillway} \quad (1)$$

$$Q_{breach} = Q_{in} - \left(\frac{\mathrm{dV}}{dt} + Q_{spillway}\right) \quad (2)$$

3.2. Direct estimation *('in-situ')*

The ISBOH method involves advances data extraction techniques to capture detailed flow and structural characteristics during breach tests. A medium-speed camera recording 1080p video at 240 fps enabled Particle Tracking Velocimetry (PTV) to compute 2D flow vectors, including velocity magnitude and direction. Additionally, a LiDAR system, with an RGB camera, a depth sensor, and an IR emitter provided 3D point clouds, capturing the breach structure above and below the water surface., both over and underwater.

To define the flow transition line, the ISBOH method used the water level Cartesian coordinates F(z)=hf(z)=h. This line marks changes in water surface geometry and, in turn, defines the vertical intersection with the breach structure, forming the flow transition cone. The breach outflow, Q_{breach}ISBOH, was then calculated as:

$$Q_{breach}ISBOH = A_{BC} \times \left(\frac{\sum_{i=1}^{n} V_{BL}}{n}\right) \quad (3)$$

where $\mathbf{A_{BC}}$ is the breach cone area, $\mathbf{V_{BL}}$ is the velocity vectors magnitude and **n** is the number of vectors considered.

In the following subsections, the procedures for determining the breach geometry and flow transition cone, as well as the surface velocity fields, essential for implementing the ISBOH method, are presented in detail

a. Determination of breach geometry and flow transition cone

Homogeneous dike embankment failure tests pose significant challenges due to the unpredictability of mass detachments from the dike main structure. This dynamic nature complicates the morphodynamic characterization. Laboratory-controlled conditions, often fall short of replicating the embankment structure without influencing breach erosion patterns. [13], [14].

To overcome these limitations, real-time LiDAR equipment applying Time-of-Flight (ToF) principles was employed. This approach allowed for continuous, non-intrusive monitoring of breach morphology, while preserving the natural instability of the embankment. while extracting 3D cartesian data.

The LiDAR system measured round-trip times of IR light pulses, with distance data (d) derived by means of a single pulse or by phase, respectively determined by equations (4) and (5):

$$d = \frac{ct}{2} \tag{4}$$

$$d = \frac{c}{4\pi f}\varphi = \frac{c}{4\pi f}\tan^{-1}\left(\frac{C_3 - C_1}{C_0 - C_2}\right) \tag{5}$$

where **d** is the distance between the object and the equipment, **c** is the speed of light, **φ** is the phase difference and **f** is the signal frequency [8], [15].

Two Microsoft Azure Kinect LiDAR units, integrating high resolution RGB camera, infra-red sensors (IR) and depth sensors, captured five-point clouds per second with a resolution of up to one million points per points per frame. Post-processing corrected for the refraction indices and shadow effects.

The processed point clouds enabled volumetric characterization of the breach at intervals of 0.2 seconds. Fig. 3 outlines the steps for defining the flow transition cone geometry, while Table 2 summarises key geometrical data for the Q_{breach}ISBOH estimation.

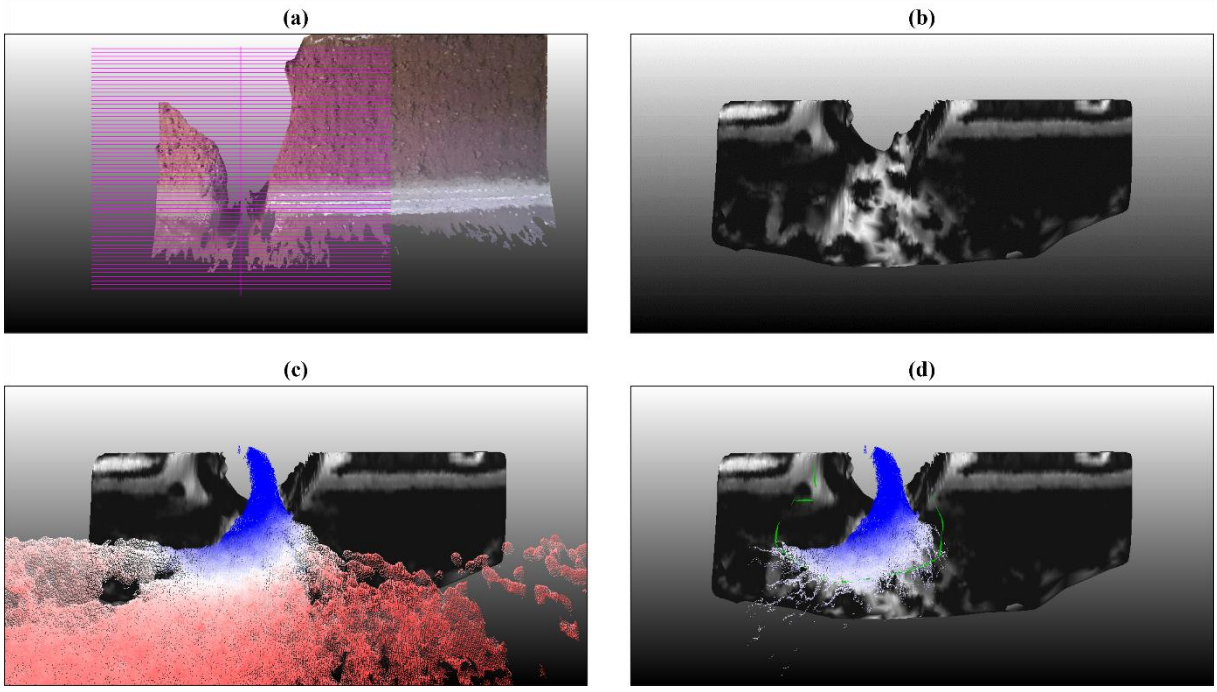

Fig. 3 – Flow Transition Cone Geometry Steps in Cloud Compare (S1T1): (a) Point cloud converted to mesh (b) Mesh curvature gradient; (c) Main channel water level as z-coordinate gradient; (d) Water surface flow transition line (green).

Table. 2 – Dike breach geometric data extracted from the point cloud processing in S1T1

Event	t (s)	Breach cone area (m^2)	Flow transition line length (m)	Distance between breach banks (m)
E2	200	0.003	0.195	0.155
E3	255	0.017	0.376	0.161
E4	275	0.043	0.571	0.221
E5	291	0.047	0.595	0.248
E6	296	0.064	0.676	0.260
E7	301	0.083	0.711	0.246
E8	328	0.071	0.635	0.287
E9	332	0.076	0.597	0.339
E10	358	0.165	1.140	0.625

The distance between banks is defined using the horizontal water level upstream the breach. The flow transition line (Fig. 3c, d), is established by mapping the water surface in a point cloud, integrating Cartesian coordinate data with continuously measured water surface data from ultrasonic probes. This integration delineates the flow transition line, representing the water surface z-coordinate just below the main channel water level (Fig. 3d, green line). The flow transition cone area is then calculated by vertically intersecting this line with the dike structure.

The flow transition cone represents the region where hydraulic flow velocity shifts from conventional fluvial flow (upstream-downstream) to the breach-derived flow (upstream-breach). At the dike breach facility, this transition cone typically forms where the main channel water surface shows a sudden decrease in the coordinate z. Accurate determination of the cone boundary and area is critical for estimating the ISBOH, especially since planar velocimetry methods are limited to two-dimensional (2D) analysis.

b. Determination of surface velocity fields

Styrofoam particles were dispersed across the water surface to measure velocity fields. An action camera captured footage at 240 fps, offering advantages such as high memory capacity and affordability. On the other hand, barrel distortion from the camera's fish-eye lens, required pre-processing corrections.

The footage was processed using Particle Tracking Velocimetry (PTV), which involves identifying particles, matching them between consecutive frames and computing the velocity vectors [16].

The Voronoï PTV algorithm was used to track the particles [17], [18]. It consists in drawing the Voronoi diagrams around the detected particles (Fig. 4b) and uses the resulting Voronoï stars for matching between frames (Fig. 4c) which is achieved by minimising the distance between Voronoï stars: The same procedure is applied for the following images - t=t+dt (Fig. 4d).

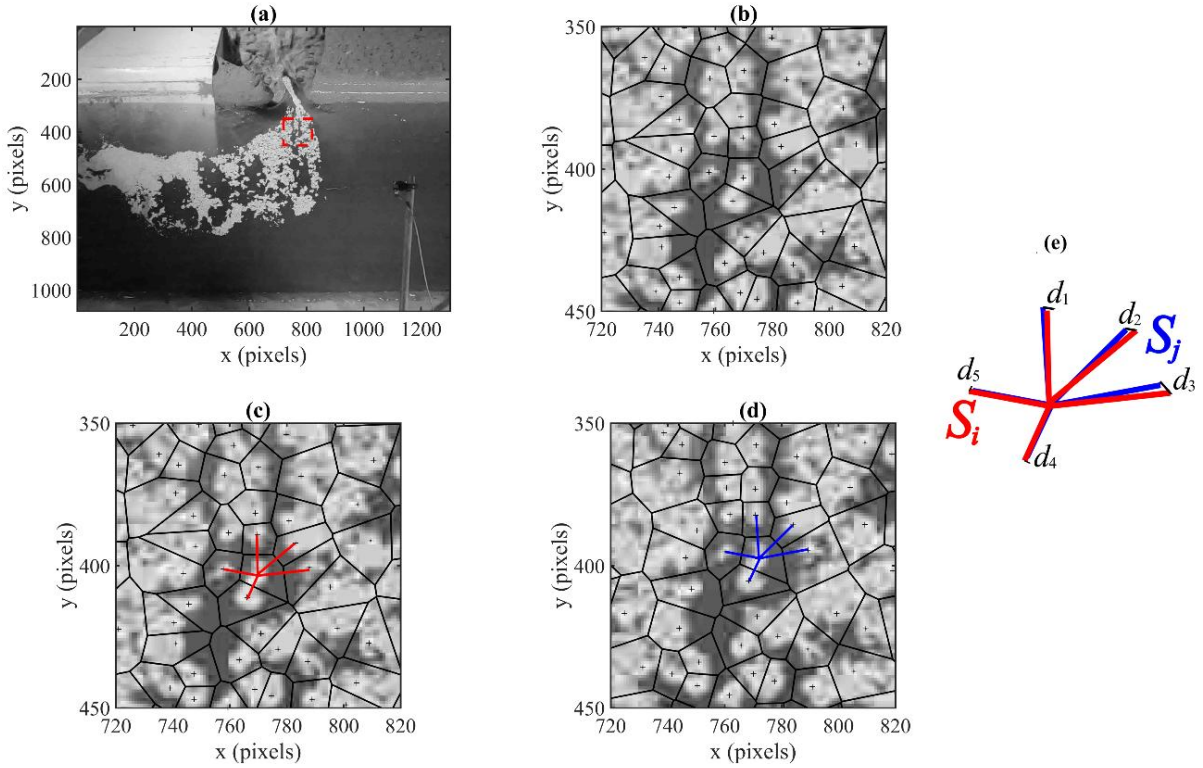

Fig. 4 – Voronoï PTV algorithm steps (a) Flow image from S1T1 test at *t* = 328 *s* indicating the area of analysis. (b) Voronoï diagram at t (c) Voronoï diagram and star at t. (d) Voronoï diagram and star at *t+Δt*. (e) matching determination by overlapping the two stars

This star pattern will be used as matching template, and a matching between particle i and particle j occurs if the distance between the extremities of the two stars $\mathbf{S_i}$ and $\mathbf{S_j}$ is a minimum:

$$\text{match}(P_i, P_j) = \min\left(dist(S_i, S_j)\right) \tag{6}$$

The distance between the extremities is given by:

$$\text{dist}(S_i, S_j) = \text{median}\ (d_1, d_2, \ldots, d_n) \tag{7}$$

where $\mathbf{d_i}$ (i = 1, 2, …, n) is the Euclidean distance between each extremity. The velocity of particle i is given by:

$$\mathbf{v} = \frac{dist(S_i, S_j)}{dt} \tag{8}$$

where **dt** is the time interval between consecutive frames. This procedure is then extended to all detected particles.

Using the median in equation (7) ensures robustness against high gradients and missing particles, making this method particularly effective for transient flows such as those in dike breach scenarios [17], [18].

4. ISBOH METHOD DATA PROCESSING

All extracted data was post-processed to define the breach geometry, breach transition cone and average magnitude velocity of the water surface.

4.1. 3D Breach geometry reconstruction:

Fig. 5 depicts the evolution of the breaching process at three-time instants of the laboratory test, which lasted 406 s. The breaching process evolves quite rapidly and is characterized by two primary erosive processes. The first, referred as continuous erosion, due to the hydraulic flow's action on the dike's surface. The second, described as a discrete erosive process, due to the detachment and consequent falling of masses of soil from the dike body.

The data extracted by the LiDAR equipment allowed to assess detailed 3D information of the breaching process. The top images from Fig. 5 capture visual breaching stages at three time-instants while the bottom ones display the corresponding point cloud reconstructions, revealing the 3D geometry of over- and underwater dike structures.

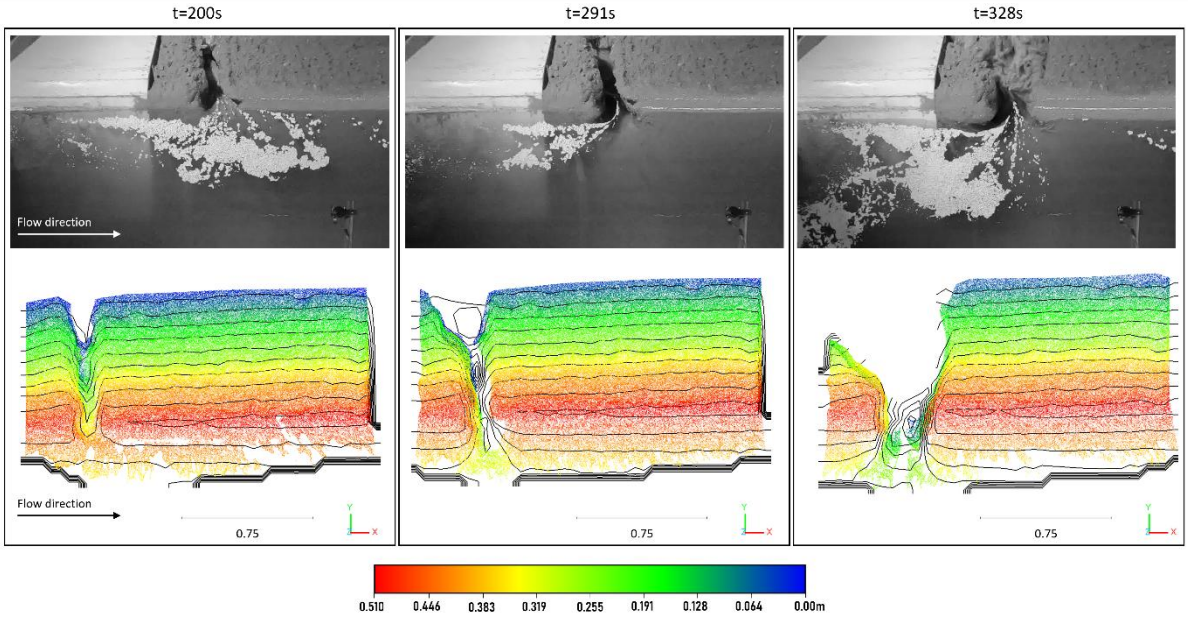

Fig. 5 –Breach evolution at three-time instants (S1T1). Top: Plain images (GoPro camera images) Bottom: 3D reconstruction of the dike structure (point clouds)

4.2. Flow transition cone area definition:

The flow transition cone, critical for ISBOH calculations, is derived by vertically intersecting the flow transition line (mapped from water surface coordinates) with the dike structure. Point cloud data (10-second intervals) was processed using an RGB noise filter to address floating tracer noise (Fig. 3c, d). The cone's geometry reflects hydraulic flow changes from the main channel to the breach, with the cone area evolving as erosion progresses.

4.3. Surface velocity field measurements:

With the PTV algorithm the direction and magnitude velocity of the dispersed tracers in the main channel water free surface was computed at 240 fps. Fig. 6 depicts the gradient of velocity at different time-instants, matching the instants used to characterize the breach geometry.

The velocity gradients near the breach (Fig. 6) reveal flow acceleration toward the breach and its role as a flow attractor, pulling the seeding from farther regions into the breach (t = 328 s). Binning techniques structured the velocity data, allowing a detailed view of breach influence on upstream flow dynamics.

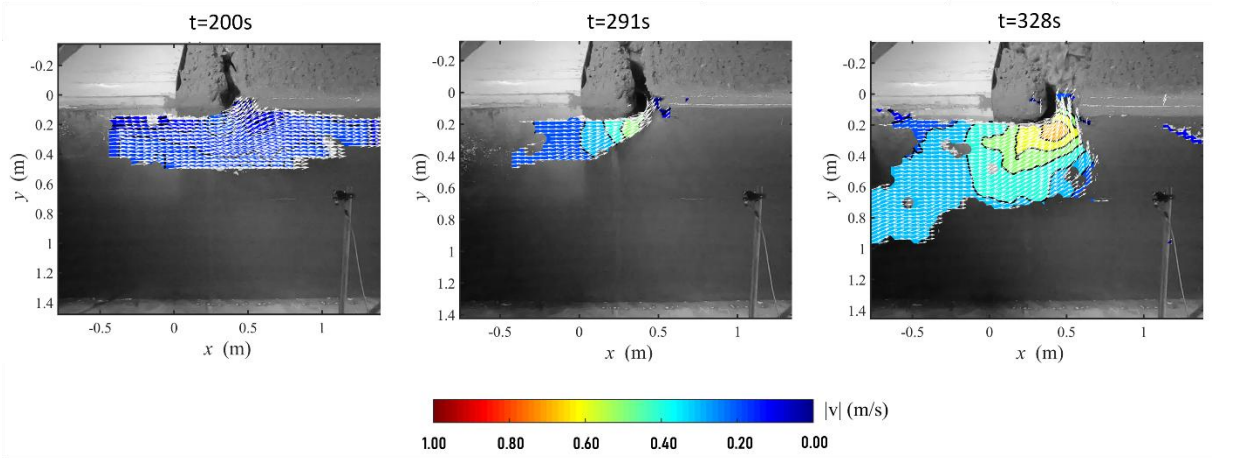

Fig. 6 – Example of the application of PTV to obtain the surface velocity map at the breach vicinity in the fluvial dike failure S1T1 at different time instants

Fig. 7 illustrates the intersection between the water surface velocity field and the flow transition line at the specified time instants. The data used to estimate the breach outflow using the ISBOH method is summarized in Table 3.

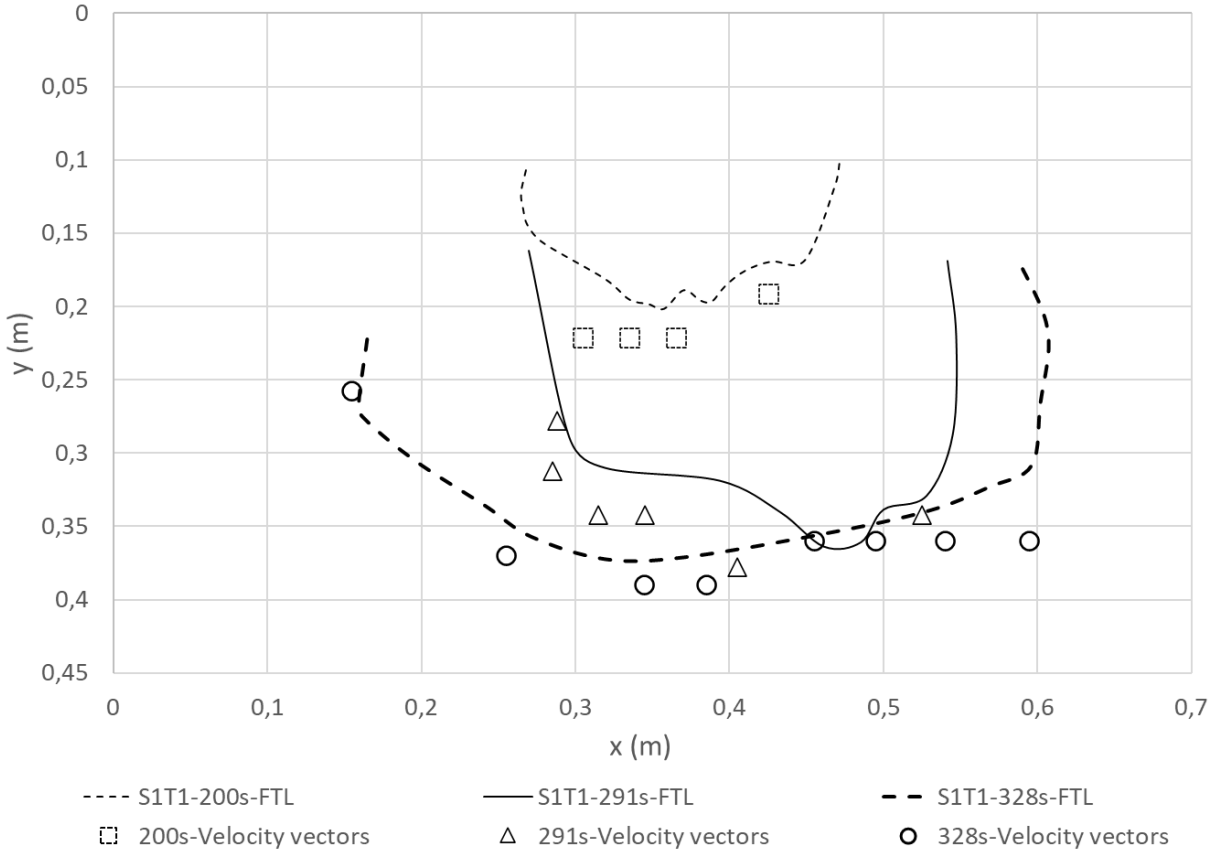

Fig. 7 – Cartesian coordinates of Flow Transition Line (FTL) and velocity vectors considered at the considered time-instants t=200s; t=291s; t=328s (S1T1 experimental data)

Table. 3 – Geometric and velocity data considered to estimate the breach outflow at the presented given instant (S1T1 experimental data)

S1T1 - 200s Cone area (m^2) = 0.003				S1T1 - 291s Cone area (m^2) = 0.047				S1T1 - 328s Cone area (m^2) = 0.071			
x (m)	y (m)	u (m/s)	v (m/s)	x (m)	y (m/s)	u (m)	v (m/s)	x (m)	y (m)	u (m/s)	v (m/s)
0.305	0.221	0.108	-0.096	0.288	0.278	0.456	-0.167	0.155	0.258	0.556	-0.019
0.335	0.221	0.086	-0.077	0.285	0.312	0.487	-0.263	0.255	0.37	0.338	-0.006
0.365	0.221	0.055	-0.010	0.315	0.342	0.610	-0.502	0.345	0.39	0.512	-0.225
0.425	0.191	0.030	-0.039	0.345	0.342	0.224	-0.267	0.385	0.39	0.688	-0.560
				0.405	0.378	0.109	-0.278	0.455	0.36	0.333	-0.469
				0.525	0.342	0.001	-0.257	0.495	0.36	0.176	-0.456
								0.54	0.36	0.318	-0.552
								0.595	0.36	-0.036	-0.527

4.4. Breach outflow hydrographs

Breach outflows (Q_{breach}) were indirectly estimated using spillways rating curves and mass balance methods and directly via ISBOH.

Fig. 8 depicts the measured or indirectly estimated flow rates associated with the S1T1 test. Upstream inflow (Q_{in}) was measured with an electromagnetic flowmeter placed at the facility's entrance. Downstream outflow (Q_{out}) from the main channel downstream spillway was estimated with two different approaches, depending on the water level control conditions. If the downstream gate maintains a stable water level, Q_{out} is estimated by the discharge rating curve of the downstream channel spillway. If the downstream gate is stopped and the water level fluctuates, Q_{out} is estimated using equation (10), where **μ** is the flow coefficient, **b** is the height of the gate opening, and **l** is the width of the gate opening.

$$Q = \mu b l \sqrt{2gh} \tag{10}$$

The breach outflows depicted in Fig. 8 (from test S1T1) were indirectly estimated through two different techniques. The Q_{breach}SBWeir correspond to the estimate based on the spillway's discharge rating curve of the Sediment Basin, and the Q_{breach}MB corresponds to the Mass Balance estimate calculated with the water level data acquired in the main channel.

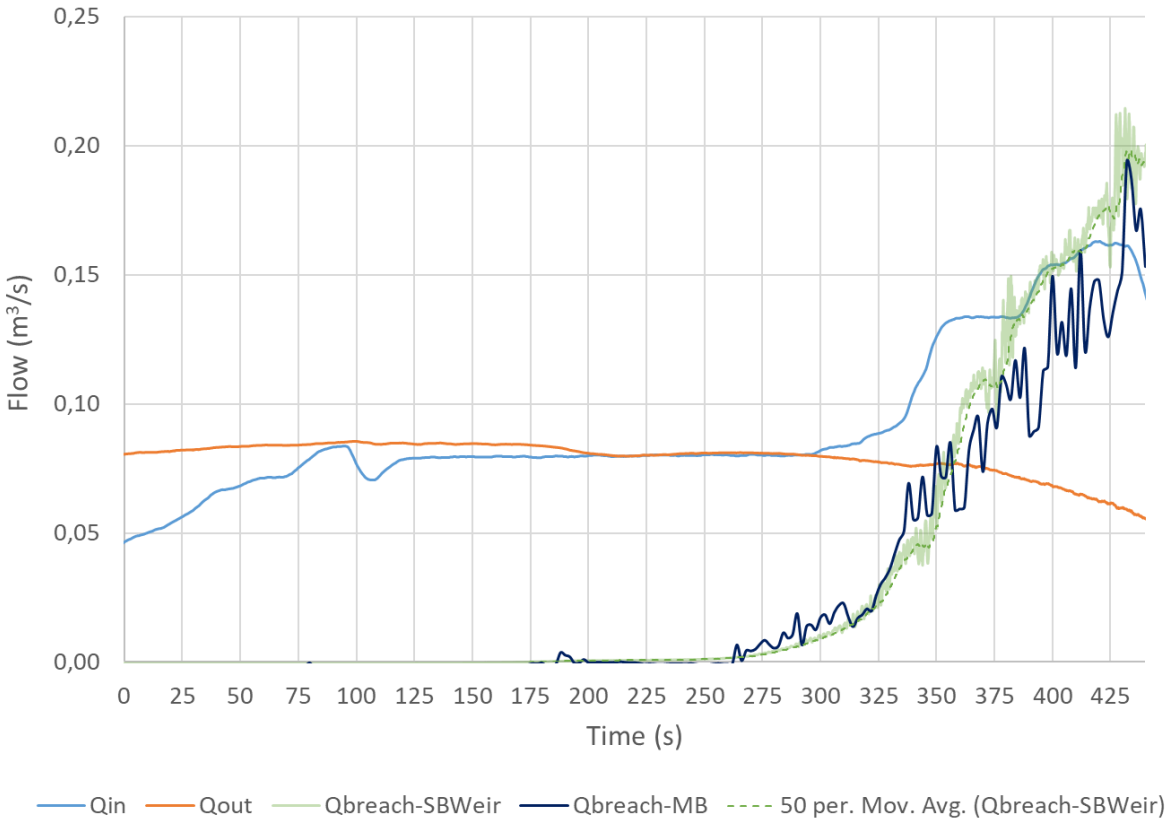

Fig. 8 – Flow rates estimates for Dike breach test (S1T1). Upstream inflow and effluent flows (downstream spillway outflow, sediment basin outflow and breach outflow hydrograph estimated by mass balance)

Fig. 9 focuses on the breach outflow hydrographs estimated using both indirect methods and the direct ISBOH method (Q_{breach}ISBOH). The ISBOH method combines velocimetry data, breach geometry, and the flow transition cone area by multiplying the cone area with the average velocity of vectors intersecting the flow transition line (Fig.7 and Table 3). The figure also highlights the time instants used for direct breach outflow estimation, as shown in Figures 5 and 6. Despite the chaotic test conditions, the ISBOH method closely matched the magnitudes and evolution of breach outflows estimated by conventional indirect methods, particularly for the higher flows

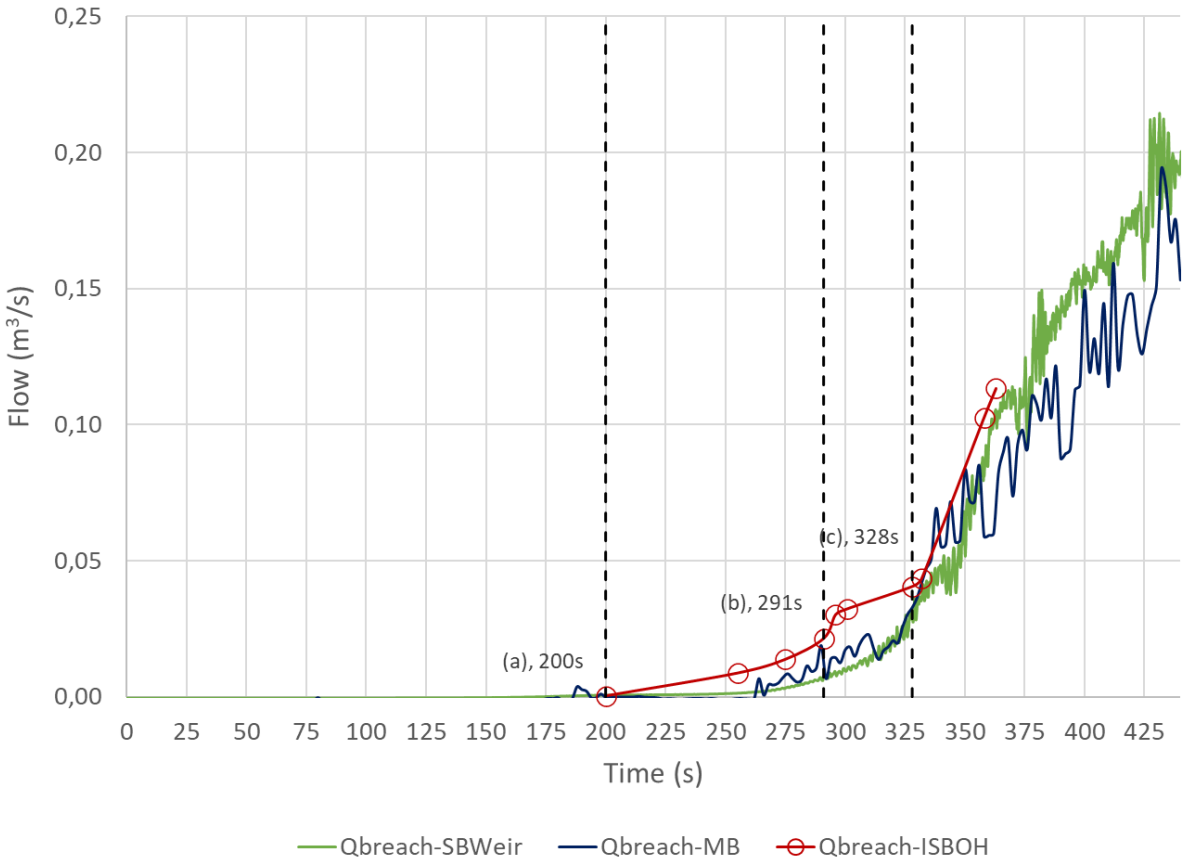

5. ISBOH ESTIMATION TECHNIQUE CONSISTENCY AND ACCURACY

The ISBOH method entail the fusion of LiDAR-driven data (resulting in the determination of the breach geometry and flow transition cone area) and the PTV technique (resulting in the surface velocity field determination). The output data consistency of the method was evaluated by comparing 5 experimental tests, encapsulating different upstream hydraulic conditions (constant and variable Fr), and water contents for 2 grain sized soils (denoted as S#T#).

To validate the ISBOH method, it is essential to benchmark it against more commonly applied breach outflow estimation methodologies. Such comparisons provide critical assessment into the accuracy of the ISBOH methodology. This section outlines both direct (Q_{breach}ISBOH) and indirect (Q_{breach}SBWeir and Q_{breach}MB) methodologies for breach outflow calculation.

5.1. ISBOH consistency

In the context of ISBOH method, the use of multiple data processing tools implies a specific experimental protocol of intermittent seeding deployment on the water surface for the following goals:

- calculating water surface velocity fields calculations and defining the flow transition cone;
- reproducing the breach geometry without seeding.

Although the seeding protocol is essential for the ISBOH estimation process, its implementation poses the following challenges:

- Time misalignment between the reproduced breach geometry and the velocimetry or flow transition cone data;
- Inconsistent seeding particle orientation due to flow directions parallel to the dike crest, leading to velocity vectors not being always perpendicular to the flow transition line.

Despite these challenges, the ISBOH method produced breach outflow estimates with magnitudes and temporal evolution comparable to those derived from indirect and more conventional methods (Fig. 9, a). The complete integration of data used for ISBOH estimation, highlighting the vectors considered for calculating average flow velocity, is illustrated in Fig. 10, b).

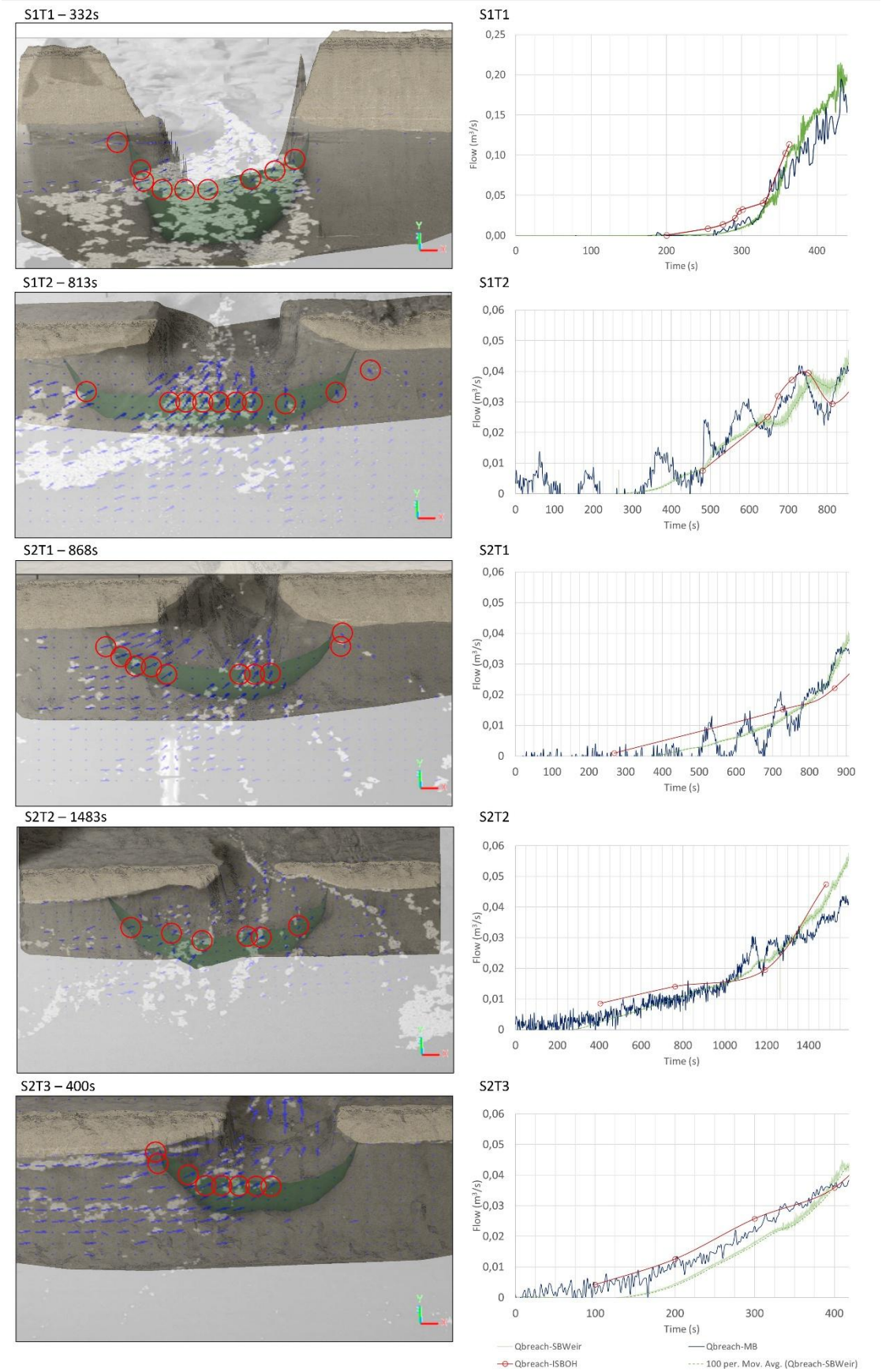

Fig. 9 – Dike breach tests at different stages a) Breach geometry, flow transition cone (green structure) and water surface velocity. Red circles indicate velocity vectors considered for average flow velocity calculations; b) Estimated breach outflows

5.2. ISBOH accuracy

The ISBOH method was tested in both chaotic environments (constantly changing) and controlled experimental environments. constants and established variables (controlled environment). Intermittent seeding deployment, added a time-lag between processed data, further challenging the method's accuracy.

All experimental tests were compared at the same time-instants using ISBOH, SBWeir, and MB methods for breach outflow hydrograph estimation. Despite differences in test environments, Fig. 10 illustrates that breach outflow hydrographs from the three methods exhibit similar magnitudes and temporal evolution.

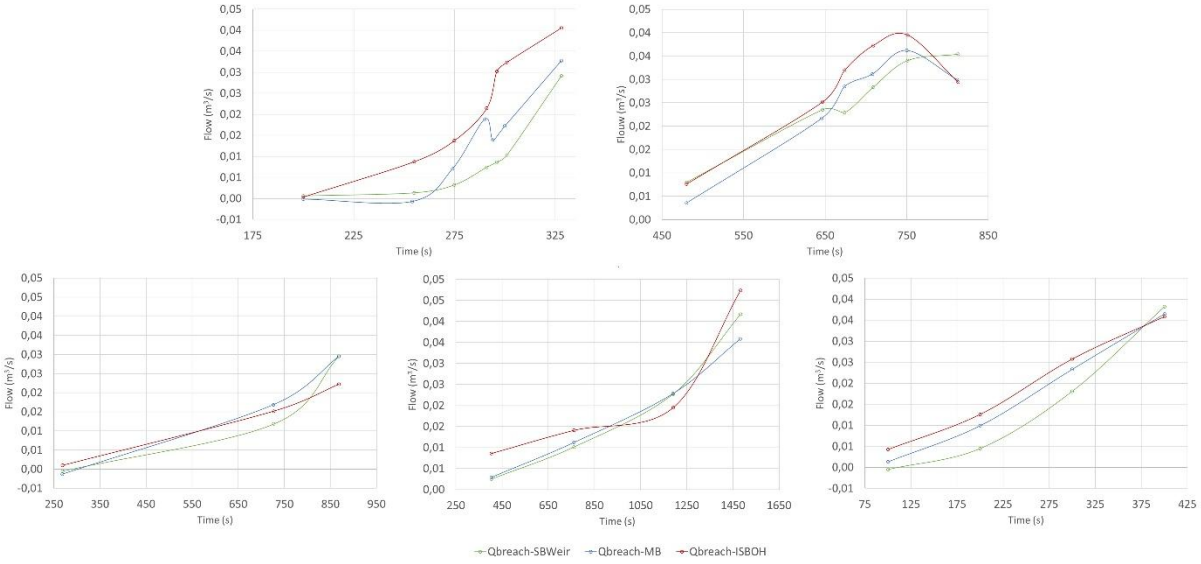

Fig. 10 – Breach outflow hydrograph magnitudes and time-step evolution for all methods

Fig. 11 depicts the average differences ($\bar{d}$) and standard deviation (σ) of the breach outflow estimates from each experimental test, between ISBOH and the benchmark methods (SBWeir and MB). A global analysis shows minor differences between the ISBOH and the MB methods ($\bar{d}$ ≈ 5.0x10^{-3} m^{3}s^{-1} and σ = 1.6x10^{3} m^{3}s^{-1}) compared to the differences between the ISBOH and the SBWeir methods ($\bar{d}$ ≈ 7.0x10^{3} m^{3}s^{-1} and σ = 2.0x10^{-3} m^{3}s^{-1}).

Fig. 11 also evidences the impact of chaotic tests, showing that S1T1 Test, which lacked intermittent seeding, presented higher global differences that affected the accuracy of the data processing for breach geometry reproduction.

When isolating the tests executed in a controlled environment, differences between the methods: i) ISBOH and MB reduced to $\bar{d}$ ≈ 4.0x10^{-3} m^{3}s^{-1} and σ = 0.9x10^{-3} m^3/s); and ii) ISBOH and SBWeir reduced 1.5x10^{-3} m^{3}s^{-1} to $\bar{d}$ ≈ 5.0x10^{-3} m^{3}s^{-1} and σ = 0.8x10^{-3} m^{3}s^{-1}.

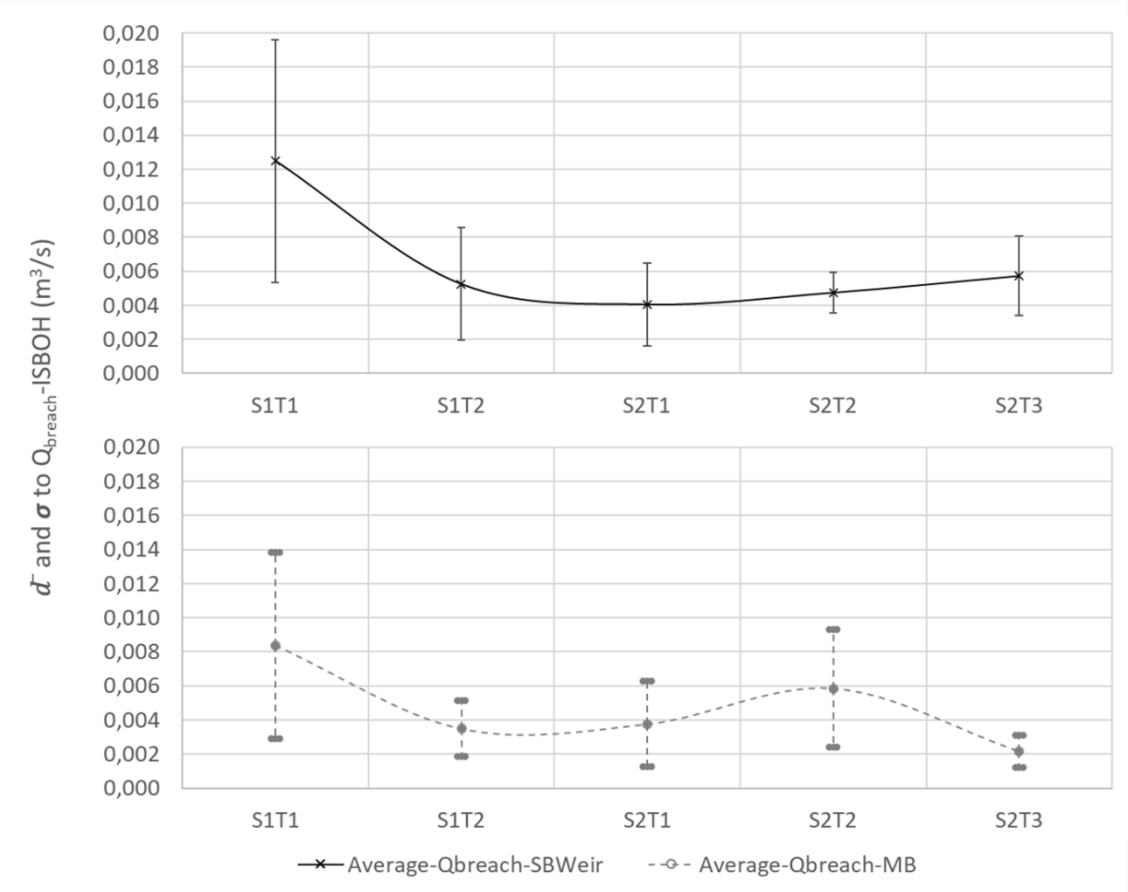

Fig. 11 – ISBOH method estimation compared to estimated breach outflows by Flood Basin weir's rating curve (Q_{breach}-FBWeir) and Mass Balance (Q_{breach}-MB). Average flow difference and standard deviation in each presented test

6. CONCLUSIONS AND FUTURE WORKS

6.1. Key findings

A step-up approach for directly estimating embankment breach outflows was developed, integrating various technologies and techniques to measure key variables such as water levels, velocity maps and 3D breach characterization. The results validated the experimental method (ISBOH) and its monitoring layout, providing a comprehensive understanding of the breaching process.

The key findings of the present work were:

1) **Live 3D Breach Modelling**: The methodology enables real-time 3D monitoring of breach evolution during failure, allowing geometric data extraction for parametric dike failure forecasts.
2) **Optimized Camera Placement**: Strategic camera positioning captured the complete breaching process, with action cameras proving viable for velocity measurement when

paired with tracer particles. This suggests potential Unmanned Aerial Vehicle (UAV) applications for monitoring natural channels and rivers.

3) **Seeding Importance in Velocity Measurements:** Adequate seeding distribution on the free surface is crucial for accurate velocity field assessment. Increased particle density would enhance coverage and accuracy.
4) **Hydrograph Estimation:** The *in-situ* method demonstrated promising results, aligning closely with indirect breach outflow estimations.
5) **Seeding Deployment Intermittency:** This approach improved breach geometry data quality and refined breach outflow estimations.

Tests revealed that breach outflow estimations conducted near the breach site exhibited lower discrepancies compared to those derived indirectly through sediment basin spillway calculations. The ISBOH method enhanced direct estimation techniques by introducing the concept of a flow transition line and defining the flow transition cone area. Unlike previous methods, ISBOH offers applicability not only to fluvial dikes but also to other embankment structures, such as earth and tailing dams. However, modelling tailing dams in laboratory settings remains complex due to their non-Newtonian behaviour.

6.2. Practical applications and future developments

Drones and remote sensing offer potential for field applications, both in pre-failure monitoring and post-failure flood propagation assessment. Accurate estimates of the breach hydrograph are critical for risk assessment, as they are inputs for flood models that help mapping the flood impacts. The ISBOH methodology has proved to be successful across various fluvial dike breach scenarios, aligning well with indirect flow estimates.

The methodology has enabled the determination of crucial hydraulic variables, particularly breach hydrograph, breach geometry and surface velocity field, demonstrating its viability for real-time monitoring. Although velocity measurements at the free surface are valuable, incorporating velocity profiling methods at depth (e.g. acoustic velocity profilers) would allow for a better understanding.

Point cloud data from LiDAR technology has proved effective in reproducing breach topography of the breach and the coordinates of the free surface, both above and below the water. This capacity is key to define the flow transition line and estimating the area of the flow transition cone. Given its potential, LiDAR could be extended to real-time monitoring and prediction of tailing dam breaches.

Ongoing research aims to refine breach flow estimates using aerial drones and to develop a simplified forecasting model correlating breach width with outflow. Experimental tests must

continue under varying inflow conditions and embankment compositions to effectively calibrate the numerical models.

The ISBOH method is yet to be fully automated. To achieve reliable forecasting of the breach outflow, data from real events must be complemented with results from numerical models, enabling integration into flood mapping software for use by Civil Protection Authorities.

ACKNOWLEDGMENTS

The authors acknowledge DikesFPro Project PTDC/ECI-EGC/7739/2020 and the PhD scholarship 2021.07337.BD both supported by the Portuguese Foundation for Science and Technology (FCT).

REFERENCES

[1] I. H. Katrina *et al.*, “Investigation of the Performance of the New Orleans Flood Protection Systems Volume I: Main Text and Executive Summary,” 2005. [Online]. Available: www.noaa.gov

[2] F. Alcrudo and J. Mulet, “Description of the Tous Dam break case study (Spain),” *Journal of Hydraulic Research*, vol. 45, no. sup1, pp. 45–57, Dec. 2007, doi: 10.1080/00221686.2007.9521832.

[3] A. David, *Natural Disasters*, 1st ed. New York: Routledge, 1993.

[4] G. T. Dounais and M. E. Bardanis, “The failure of homogeneous dams by internal erosion–The case of Sparmos Dam, Greece,” in *Sustainable and Safe Dams Around the World*, JP Tournier, T. Bennett, and J. Bibeau, 2019.

[5] A. Nunes, A. Amaro, A. Vieira, F. Velez de Castro, and F. Félix, *Geografia, Riscos e Proteção Civil. Homenagem ao Professor Doutor Luciano Lourenço. Volume 1*, vol. 1. RISCOS - Associação Portuguesa de Riscos, Prevenção e Segurança, 2021. doi: 10.34037/978-989-9053-04-5_1.1.

[6] S. Gangadharan, “In China, Over 5000 People Evacuated After Floodwaters Breach A Dike,” Start News Global.

[7] S. Amaral, L. Caldeira, T. Viseu, and R. M. L. Ferreira, “Designing Experiments to Study Dam Breach Hydraulic Phenomena,” *Journal of Hydraulic Engineering*, vol. 146, no. 4, Apr. 2020, doi: 10.1061/(asce)hy.1943-7900.0001678.

[8] R. Horaud, M. Hansard, G. Evangelidis, and C. Ménier, “An overview of depth cameras and range scanners based on time-of-flight technologies,” *Mach Vis Appl*, vol. 27, no. 7, pp. 1005–1020, Oct. 2016, doi: 10.1007/s00138-016-0784-4.

[9] G. Kurillo, E. Hemingway, M.-L. Cheng, and L. Cheng, “Evaluating the Accuracy of the Azure Kinect and Kinect v2,” *Sensors*, vol. 22, no. 7, p. 2469, Mar. 2022, doi: 10.3390/s22072469.

[10] R. Aleixo, E. Carvalho, M. M. C. L. Lima, and R. M. L. Ferreira, “Determinação dos campos de velocidades de escoamentos bifásicos usando PIV-PTV,” *Revista Recursos Hídricos*, vol. 41, no. 1, pp. 9–15, Jan. 2020, doi: 10.5894/rh41n1-cti1.

[11] A. M. Bento, S. Amaral, T. Viseu, R. Cardoso, and R. M. L. Ferreira, “Direct Estimate of the Breach Hydrograph of an Overtopped Earth Dam,” *Journal of Hydraulic Engineering*, vol. 143, no. 6, Jun. 2017, doi: 10.1061/(asce)hy.1943-7900.0001294.

[12] J. Yoon and J. Doh, “Optimal PID control for hovering stabilization of quadcopter using long short term memory,” *Advanced Engineering Informatics*, vol. 53, p. 101679, Aug. 2022, doi: 10.1016/j.aei.2022.101679.

[13] T. Alvarez, R. Aleixo, S. , V. Mendes, S. Amaral, T. Viseu, and R. , M. , L. Ferreira, “Frozen in time: Continuous measurements in a dam breach flow,” in *River Flow 2022*, 2024.

[14] I. Rifai *et al.*, “Continuous Monitoring of Fluvial Dike Breaching by a Laser Profilometry Technique,” *Water Resour Res*, vol. 56, no. 10, Oct. 2020, doi: 10.1029/2019WR026941.

[15] K. Kim and J. Kim, “Dynamic displacement measurement of a vibratory object using a terrestrial laser scanner,” *Meas Sci Technol*, vol. 26, no. 4, Apr. 2015, doi: 10.1088/0957-0233/26/4/045002.

[16] R. Aleixo *et al.*, “Challenges of Surface Image Velocimetry - The dam-breach example,” in *Proceedings of the 39th IAHR World Congress*, Spain: International Association for Hydro-Environment Engineering and Research (IAHR), 2022, pp. 5150–5155. doi: 10.3850/IAHR-39WC2521711920221156.

[17] H. Capart, D. L. Young, and Y. Zech, “Voronoi imaging methods for the measurement of granular flows,” *Exp Fluids*, vol. 32, pp. 121–135, 2001, doi: 10.1007/s003480100351.

[18] R. Aleixo, S. Soares-Frazão, and Y. Zech, “Velocity-field measurements in a dam-break flow using a PTV Voronoï imaging technique,” *Exp Fluids*, vol. 50, no. 6, pp. 1633–1649, Jun. 2011, doi: 10.1007/s00348-010-1021-y.

[19] T. Lei, J. Wang, X. Li, W. Wang, C. Shao, and B. Liu, “Flood Disaster Monitoring and Emergency Assessment Based on Multi-Source Remote Sensing Observations,” *Water (Basel)*, vol. 14, no. 14, p. 2207, Jul. 2022, doi: 10.3390/w14142207.

[20] I. Rifai *et al.*, “Overtopping induced failure of noncohesive, homogeneous fluvial dikes,” *Water Resour Res*, vol. 53, no. 4, pp. 3373–3386, Apr. 2017, doi: 10.1002/2016WR020053.

Fifth International Dam World Conference
PORTUGAL • LISBON • LNEC • APRIL 13-17, 2025
dam world 2025

LIME TREATMENT FOR HYDRAULIC STRUCTURES: BENEFITS, CHALLENGES, AND LONG-TERM PERFORMANCE

Federica Bertola[1]	Sylvie Nicaise	Lucile Saussaye	Kristof Verelst	Henk van Hemert
Lhoist R&D	INRAE	Cerema	Flanders Hydraulics	Rijkswaterstaat

ABSTRACT

Soil treatment with lime is a well-established technique that is safe, economical, and allows to reuse mediocre soils in transport infrastructure construction. By reducing landfill disposal and construction times, lime treatment offers significant advantages. Despite the extensive experience, the use of lime treatment in hydraulic structures is still far from its maturity. In addition to common requirements for traditional embankments, such as workability and stability, hydraulic structures require specific functionalities. Among these, the most relevant include watertightness (low permeability to prevent seepage), internal erosion resistance (resistance to piping, contact erosion, suffusion, regressive erosion), surface protection (resistance to external erosion), and resistance to high water flows.

Over the past fifteen years, numerous studies, investigations, and full-scale projects have demonstrated the multiple benefits associated with the use of lime treatment for the construction of hydraulic structures. For instance, treating the soil with lime allows the valorization of locally available soils, and the simplification of the typical design cross section while also resulting in improved mechanical properties, higher erosion resistance, reduced overall costs, and material transport.

However, durability concerns still limit a widespread implementation of lime treatment for hydraulic structures. Being a relatively recent technology, there is limited documented feedback on its long-term performance and the effects of prolonged exposure to weathering, particularly concerning its specific functional requirements in hydraulic structures. It is essential to prove that lime treated hydraulic structures are not only efficient and sustainable but also long-term solutions.

This paper compiles and presents previous experiences with the aim of sharing the knowledge acquired during the construction and monitoring of full-scale structures. Dikes built in France, Belgium, and the Netherlands using lime treated soils are described. Their construction details, properties measured shortly after their construction, and results from monitoring campaigns conducted several years later, are discussed leading to valuable conclusions.

Keywords: lime treatment, soil improvement and stabilization, hydraulic structures, durability

[1]federica.bertola@lhoist.com, Belgium

1. INTRODUCTION

Lime treatment is a well-known and widely used technique for soil improvement and stabilization in the construction of roads, highways, railways, and airfields [1].

Several benefits can be obtained thanks to lime treatment in transport infrastructures, together with allowing the use of locally available soils; the most significant effects are related to workability and stability. The physio-chemical reactions between soil and lime quickly enhance the material workability, facilitating easier placement (short term effect). Subsequently, pozzolanic reactions between lime and soil components increase cohesion and stability of the entire structure, both under its own weight, and against mechanical stresses (medium-long term effect).

The use of lime in stabilizing hydraulic structures like levee and embankment is relatively less common, especially in Europe, compared to its application for transport infrastructures. It is crucial to consider that in a dam or levee, each component or part of the structure plays a specific role in contributing to the overall water retaining capacity. The design of a hydraulic structure depends on the local practice and on its destination, but in general:

- the slopes must provide resistance against erosion caused by wave attack (waterside) and overflow (crest and landside).
- the waterside surface layers and/or the core should provide impermeability.
- drain constructions or surface layers on the land side should remain permeable.
- the fill (and subsoil) should provide shear resistance.
- the berms on the landside contribute to stability, mainly by their weight.

Besides the simplest form of an earthen levee, all kinds of composite levees occur [2]. Lime treated soils may be applied for different components of a levee, to contribute to either the erosion resistance or shear strength and stability. In case of reconstructions, the application of lime treated soils could reduce the need for a revetment or other protective techniques from wave attack, increase the allowable overtopping discharge thus reducing or preventing heightening of the crest and decrease the dimensions of required stability berm. Optimizing the required dimensions of the levee reduces the volume of construction material needed. It also facilitates embedding a levee reconstruction in its environment, often already used by other functions as well.

In this context, besides workability and stability, some other functionalities are required due to the possible contact of the structure with water that can lead to risk of leaching, erosion, decrease of strength, and compromise the long-term durability of lime treated structures. For application in hydraulic structures the main additional functionalities are watertightness, resistance to internal erosion, superficial erosion, and resistance to high water flows.

When designing a hydraulic structure, depending on its final application and purpose, one or several functionalities needs to be guaranteed. For each functionality lime treated soil must fill a certain role and ensure certain parameters, which must be guaranteed soon after the construction, but also over the years of service of the structure. Table 1 is the result of an analysis carried out over the years on treated soils and their performance [3]. Results of both general applications for infrastructure as for hydraulic structures are included.

Several examples of the use of this technique can be found since the 1970s around the world, mostly in the United States, South Africa, Asia, and Australia. In many cases, the treatment of soil with lime was reported to solve problems due to dispersive soils and internal erosion, to prevent swelling-shrinkage phenomena linked to heavy plastic soils, and to stabilize the slopes [4, 5, 6, 7].

Table 1 – Functionalities and specific parameters to ensure

Functionalities	Role of lime treated soil	Specific parameters to study	
Workability	Ease of placement of wet soils and/or clayey soils	Bearing capacity	Compaction
Stability	Stability under own weight and possibly under seismic loading	Shear strength (cohesion)	Tensile or compressive strength
Watertightness	Watertightness	Homogeneity	Permeability
Internal erosion resistance	Resistance to internal erosion	Homogeneity	Resistance to Hole Erosion Test (HET)
Surface erosion resistance	Resistance to external erosion	Homogeneity	Resistance to surface erosion (waves action, runoff) and in case of overflow Jet Erosion Test (JET) Mobile Jet Erosion Test (MoJET)
Overspill water	Resistance to high-velocity flows (channels, etc.)	Homogeneity	Resistance to surface erosion resistance for a spillway JET, MoJET

Despite substantial knowledge in the field of infrastructural works, some open questions regarding the application for hydraulic structures remain and need to be answered. With this purpose, since 2005, multiple research projects were conducted in Europe, starting from a laboratory approach, and then extending to the design and construction of multiple dikes in different European countries. Over the years the lime treatment technique has proven to be effective in hydraulic structure construction providing that specific procedures for implementation are used. In fact, it was proved that lime treatment preserves low permeability levels like those of original untreated materials controlling the mixing and compaction

conditions [8, 9, 10]. Conventional jobsite equipment can be used but with an appropriate procedure for the treatment and placement of materials, the moisture content of treated soils needs to be adjusted above the optimum moisture content (OMC) and the compaction by kneading using sheep foot compactors.

This paper was written with the intention of collecting experiences from fifteen years of applied research on hydraulic structures constructed using the lime treatment technique. It summarizes and presents the results of construction and monitoring activities on real-scale structures over the years, highlighting the unique aspects of each project.

2. DIKES

Each project was realized with the aim of proving different functionalities and at the same time following/adapting to the local practices in dike construction. In fact, three dikes were built in France with the purpose of validating the implementation process; in these cases, the entire structure was built of lime treated soil and the compaction was performed horizontally in consequent layers. Differently the Belgian and the Dutch demonstrators were built only treating the shell cover and using two different processes representative of the local practice: for the Belgian dike the compaction was done in the direction of the slopes, while for the Dutch case a staircase profile was adopted and compact in horizontal layers.

2.1. DOFEAS project

The first experimental structure was constructed in the CER (Experimental and Research Center) of Cerema in Rouen, France, in September 2011. The structure consisted of two full-scale experimental dry dikes; the first one built with 2.5% lime treated silty soil and the other built using the untreated soil as reference. Only limited and well-defined sections were covered with topsoil, the rest was directly exposed to the environment. Table 2 collects the construction details of the part of the structure built with lime treatment, while Figure 1 presents views of the dikes soon after the construction and after seven years [11]. The main objectives of this project were to validate the use of soil treatment in the application of hydraulic structures, checking that the implementation conditions can guarantee the required performance of mechanical properties, permeability, and erosion resistance.

Multiple monitoring activities [12, 13] have been conducted during the years following the construction and have shown that lime treatment allows to:

- increase the mechanical performance: 1 month after construction, the bearing capacity increased from 5 to 30 times, and the cohesion was found to be 7 to 12 times that of the untreated soil. After 7 years the unconfined compressive strength was 3 MPa.

- preserve a low hydraulic permeability level comparable with that of the untreated soil: values of the order of 10^{-9} m/s were measured through Nasberg in-situ test and triaxial cells on core samples after one month, six months and one year from the construction.
- improve the erosion resistance: after only 1 month the values measured thanks to the HET were improved of 7 orders of magnitude compared to the untreated soil, and the same trend was also found through the in situ MoJet.

Table 2 – Construction details DOFEAS dike

Type of soil	-	Silty soil
Plasticity index PI	%	11
Height	m	2
Slope	-	Asymmetric 3H/2V and 2H/1V
Dosage of quicklime	%	2.5
Process of treatment	-	Mobile treatment facility
Design	-	Entire embankment treated
$\rho_d/\rho_{d,OPN}$	%	96.7

Fig. 1 – DOFEAS dike (2011 left and 2018 right)

After 7 years the pozzolanic reaction products were found to be stable, and the pH was maintained high in the backfill (higher than 11). Reduced pH values were found just in a surface thickness limited to 10 cm, proving that lime actions were still ongoing and that the aging of the structure is rather limited [1].

An additional experimental campaign will be conducted in 2025 (14 years after the construction) to continue the monitoring of performance.

2.2. DigueELITE project

An experimental earth fill dike was built in the framework of the French R&D program DigueELITE in July 2015. Located in the commune of Aimargues (Gard, France) along the Vidourle river, the demonstrator comprises a section untreated, as reference, and a section treated with lime, and was part of the rehabilitation works of the dike network along the Vidourle river [14, 15]. The soil used for the construction was a silty soil locally available. The slopes of

the dike were not covered with topsoil, so directly exposed to the environment, to wide temperature variations; the dike is not in direct contact with the Vidourle river. Table 3 collects the construction details of the lime treated dike, while Figure 2 shows two views of the dike, one soon after the construction in 2015, the other taken in 2023.

It is important to highlight that during the construction superficial cracks appeared, probably due to the very high summer temperature during the activities and the not enough care in protecting the structure from excessive evaporation [16].

The main objectives were the validation of the construction methodology and the achievement of certain mechanical performance, permeability, resistance to internal and surface erosion. The project was also run with the final goal of developing a new concept for river dikes; in this regard, some important uptakes allow to develop a viable technique to measure erosion resistance: an overflow simulator for large scale experiments.

Table 3 – Construction details DigueELITE dike

Type of soil	-	Silty soil
Plasticity index PI	%	5
Height	m	3.5
Slope	-	3H/2V
Dosage of quicklime	%	2
Process of treatment	-	Mobile treatment facility
Design	-	Entire embankment treated
$\rho_d/\rho_{d,OPN}$	%	95

Fig. 2 – DigueELITE dike (2015 left and 2023 right)

Also in this case, several monitoring campaigns have been conducted during the years [17, 18, 19] allowing to draw the following conclusions:

- increase and maintenance of mechanical performance were proven, after 6 years the unconfined compressive strength was measured in the range of 0.8 - 2.4 MPa (0.2 MPa in the case of untreated soil), while the cohesion obtained thanks to the treatment was measured as 12 to 20 times that of the untreated soil.

- the permeability measured was consistently low, 10^{-8} to 10^{-10} m/s in triaxial cells on core samples.
- an increased resistance to internal erosion, measured through HET, surface erosion was assessed thanks to overflow tests and onsite JET. The experiments demonstrate that lime treated soil is 2 to 100 times more resistant after 6 years from the construction, depending on the area of fill under consideration and its exposure to the environment.

During the last monitoring (6 years after the construction), the impact of the environmental exposure was found to be limited to the first 15 cm, the carbonation rate of the lime decreases below this depth, while the measured pH and available lime beyond 15 cm proved that lime is still present in sufficient quantities for reactions to continue.

An additional monitoring campaign was performed at the end of 2024 after 9 years from the construction to continue with the collection of results.

2.3. SYMADREM dike

In November 2017, SYMADREM (interregional mixed union for the management of the levees of the Rhône Delta and the Sea) commissioned the construction of experimental embankments in the commune of Salin de Giraud (Bouches du Rhône, France) to test erosion-resistant dike solutions. Two embankments were built using the locally available soil: one with untreated soil as reference, and one treating the soil in-place with 2% of lime. The slope of the lime-treated structure faces south, and 30 cm of topsoil was applied as protection in half of the structure. The slope of the untreated embankment faces north, consequently being less exposed than the treated one to temperature variations, 30 cm of topsoil were applied also in this case. The embankments are not in direct contact with the Rhône River; however, the water table is close to the embankments and in wet periods its rise affects the platform. It is important to note that the Rhône water table is slightly salty in this area; the salt concentrations are of the order of 12 $g.l^{-1}$. Table 4 presents the construction details of the treated embankment, while Figure 3 shows two views of the dikes, one during the construction in 2017, the other in 2023.

Table 4 – Construction details SYMADREM dike

Type of soil	-	Silty soil + clay
Plasticity index PI	%	9 (average)
Height	m	2
Slope	-	2.5H/1V
Dosage of quicklime	%	2
Process of treatment	-	Treatment on the platform
Design	-	Entire embankment treated
$\rho_d/\rho_{d,OPN}$	%	95

Fig. 3 – SYMADREM dike (2017 left and 2023 right)

Immediately after the construction and then after 5 years, numerous investigations have been conducted and the following feedback on the performance of the lime treated dike can be listed [17, 18]:

- values of unconfined compressive strength and shear strength were found significantly higher than those of the untreated soil, also highlighting a tendency to improve with depth.
- a low permeability was measured, 10^{-9} to 10^{-10} m/s in triaxial cells on core samples.
- high resistance to internal erosion was measured by means of HET, as well as a significant surface erosion through JET and overflow tests, proving little to no erosion compared to breakdown of untreated soil.

2.4. Vlassenbroek dike

In the context of the Sigma Plan, a plan to protect Flanders from flooding from the Scheldt River and its tributaries, a Flood Control Area was built in Vlassenbroek. On the ring dike of this Flood Control Area a test section was dedicated to experimental purposes [20]. The ring dike was built according to the Flemish practice with a sandy core to ensure stability and a clay cover layer (PI > 15%) to guarantee water tightness. In a part of this test section in 2019 the clay cover was constructed using a silty soil treated with 2% lime while the other part, considered as a reference, with untreated clay. The lime treated soil cover was compacted in four consecutive layers (total thickness of 1.10 m) in the direction of the slope. Details of the construction are reported in Table 5, while Figure 4 shows the design of the dike (above) and views of the dike during the construction and after 5 years (bottom). In addition, to study the influence of lime treatment on the vegetation development, different mixes of vegetation were seeded. The treated section was divided in sub-sections with different seed mixtures seeded on the lime treated soil with and without application of topsoil.

In this specific case the main purpose was the validation of the different design and compaction process adapted according to the local practice and to study the influence of lime treatment on the vegetation development.

Table 5 – Construction details Vlassenbroek dike

Type of soil	-	Silty soil
Plasticity index PI	%	8-10
Height	m	6.5
Slope	-	3H/1V
Dosage of quicklime	%	2
Process of treatment	-	Treatment on the platform
Design	-	Reinforced protective cover
$\rho_d/\rho_{d,OPN}$	%	95

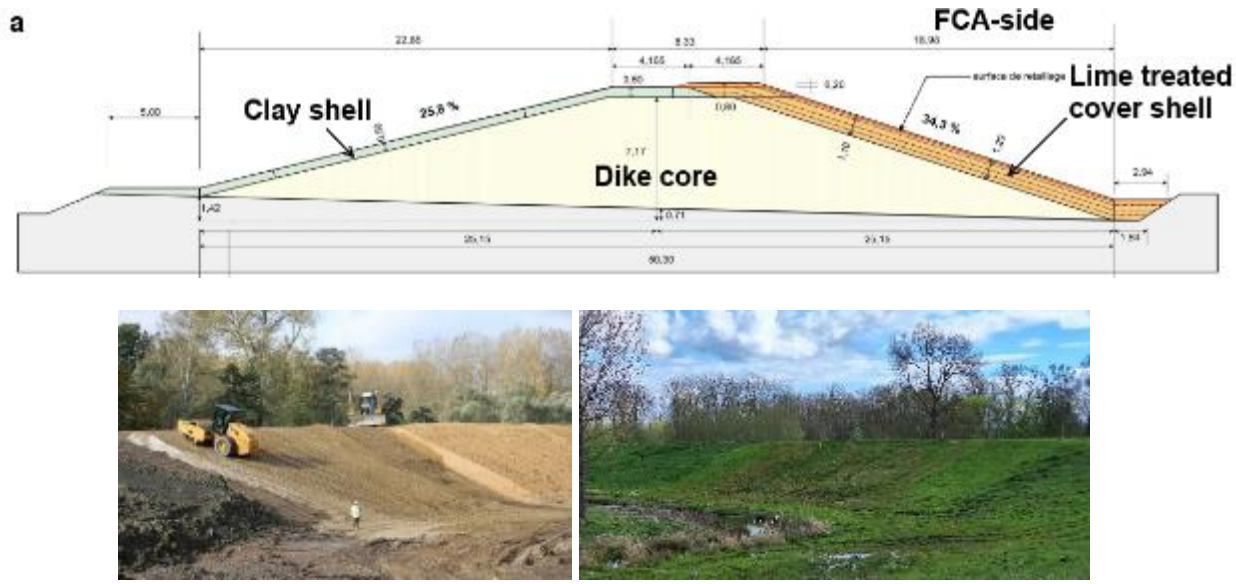

Fig. 4 – Vlassenbroek dike: design (above), view during the construction in 2019 (bottom left) and view in 2024 (bottom right)

Monitoring and follow up of the test section started in February 2020 and are still ongoing with the final monitoring campaign planned for winter 2025/26, including large scale wave impact tests. The main findings collected so far can be summarized as:

- the mechanical resistance of the treated soil was measured using a dynamic penetrometer and found, already after 1 year from the construction, higher than the device measurement range.
- a more extensive study of permeability and its evolution over time is needed.
- very high surface erosion resistance was measured through JET after 1 year and 3 years.
- a gradual improvement in the vegetation growth was measured, showing that after application of topsoil the vegetation coverage and the root development are comparable to these measured in the untreated section. Without application of topsoil

the vegetation coverage is 40 to 50 % less than in the untreated section and the root penetration is rather limited (less than 7.5 cm).

More conclusions will be drawn at the end of the project.

2.5. Hedwigepolder dike

The depoldering of Hedwige-Prosperpolder, located near the river Scheldt at the border between Netherlands and Belgium, offered the opportunity to prove the potential of Dutch clays treated with lime for their use in levee reinforcement. In November 2021, three experimental test sections were built on the inner slope of the already existing levee within the Polder2C Living Lab (funded by the Dutch Flood Protection Program). Three months after the construction wave overtopping tests were performed. Each section was built using a clayey soil improved by adding lime, one section using a good quality clay (PI of 47%) imported from elsewhere, while two sections using two poor quality clays (PI of 22-24%) extracted from the surrounding area, one of them having marine origin. As this application targets dike reinforcement, the design consists in a protective shell built with a staircase profile, the standard design in The Netherlands for this specific application, as it is presumed to increase resistance of the cover layer against sliding down the slope. Table 6 presents the construction details of the project, while in Figure 5 the staircase profile is visible in the design of the dike and a phase of overtopping tests is shown.

The main objectives were proving the effectiveness of lime treatment in valorizing locally available clay enhancing their erosion resistance, testing the erosion resistance at weak points around obstacles (representing the presence of housing) on the inner slope, and demonstrating that lime treated clays can be used at transitions or near encroachments, where generally a good grass cover is hard to maintain [21].

Table 6 – Construction details Hedwigepolder dike

Type of soil	-	Clayey soil
Plasticity index PI	%	20-45
Height	m	8
Slope	-	2.5H/1V
Dosage of quicklime	%	4-5
Process of treatment	-	Treatment on the platform
Design	-	Reinforced protective shell (staircase profile)
$\rho_d/\rho_{d,OPN}$	%	96.4 – 102.4

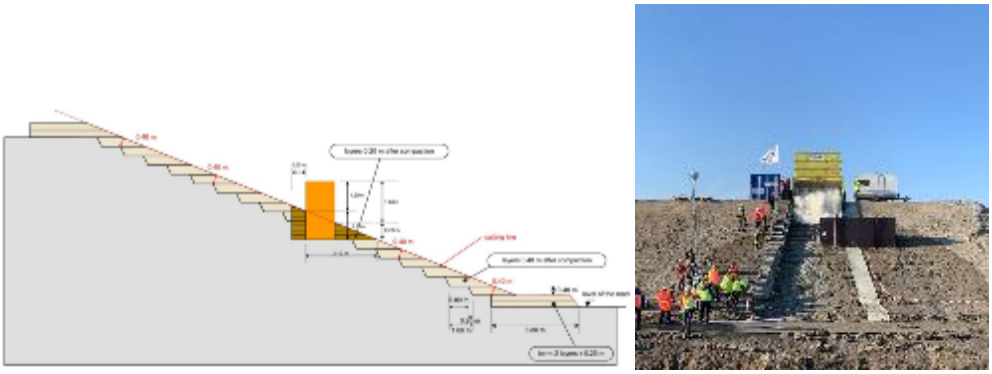

Fig. 5 – Hedwigepolder dike: design according to the staircase profile (left), views of the dike during the overtopping tests (right)

In this last case monitoring studies were not conducted due to the limited duration of the project. But this is the only case among the several cited where overtopping tests were conducted. It is important to highlight that the tests were conducted after only 3 months from the construction of the dike with curing time in quite adverse conditions for the development of the pozzolanic reactions (winter season). Objects were placed on the slope of the dike to simulate the presence of houses or other constructions. Such transitions form weak points concerning erosion, due to the concentration of the flow around such obstacles.

In every test section, five different scenarios of storm events were reproduced, the first four based on typical testing conditions for river dikes, while the fifth was a representative condition for sea dikes. Erosion measurements were conducted by means of photogrammetry. During some tests, additional solicitations were applied on the layer already damaged, to further test the resilience of the lime treated clay layer.

The observations gained during the overtopping tests allow to conclude that:

- the lime treated clay cover never failed at any point, but the slope profile in stair steps was revealed where the material was not properly compacted.
- some weak points with more pronounced erosion were identified: in a specific part of the crest where intense rainy conditions occurred during the construction, around the first obstacle due to the inexperience in compaction after its placement (the same result was not observed in the case of the two objects placed successively), and at the bottom of the slope where groundwater seepage hindered the compaction.

Thanks to this project lime treatment was proven to improve the characteristics of clays, regardless of their original quality, and ensure good resistance to external erosion, including around obstacles, when the implementation conditions are properly conducted and after a short curing period in adverse conditions.

3. DURABILITY

As mentioned, lime treatment improves the performance of local soils. This performance, considered in the design of a hydraulic structures, must be maintained throughout the lifetime of the structure. The functions that the structure must fulfil are thus ensured, and the need for maintenance and repairs limited.

Durability must be assessed at two different levels. The first is the treated material one: maintenance of performance are assessed based on sample-scale tests. At present, there is no specific laboratory protocol that allows to age treated samples in a way that is representative of actual conditions, as for concrete. This is why in this paper we propose measurements carried out on materials exposed to the environment in real structures as feedback on the durability of the performance of treated soil at the material scale. The results of the extensive investigations conducted over the years on the previously described dikes allow to state with confidence that the improved properties of the treated soils are maintained over time beyond the performance retained for the design.

The second level pertains to the structure itself. In this case durability must be examined considering the overall structure. The degradation mechanisms that can deteriorate the functions of the structure must be considered; the environmental conditions at which the structure is exposed, such as alternating periods of rainy and dryness, frost, and carbonation, can alter the long-term performance. The evaluation of these second level is complicated and requires years of exposure and consequent studies on real structures to allow to draw conclusions. To complete the direct experiences described above, it is necessary to add the cases listed in the literature that can serve as additional references.

With this in mind, one of the aspects to which attention should be directed is definitely the appearance of cracks. Among the experiences considered in this paper, crack formation was noticed only in the case of the demonstrator built in the framework of the DigueELITE project. No other structures were affected by the same problem, and the appearance of the cracks can be explained by difficulties encountered during implementation, while no changes in the number or position of the cracks were noticed over the years. The case of DigueELITE remarks the need for a strong control of the implementation process and an initial protection of the treated material in the case of adverse climatic conditions.

In all the cases, the high mechanical performance of the lime treated material represents a limit for the root penetration, highlighting the need of a layer of topsoil. Besides allowing the grass cover growth the topsoil layer will also protect the treated layer from weathering agents (carbonation, freeze-thaw, wet and dry cycles) reducing the superficial degraded layer and helping the durability of the hole structure.

It must be remarked that the improved mechanical resistance and cohesion of the lime treated material, in addition to help the stability of the structure and the erosion resistance, is also

helping to prevent burrowing animals to excavate in the cover layer creating weak point for erosion. This last advantage is based on observations; tunnels dug by animals have never been noticed in any of the lime-treated dike, only limited attempts.

To add some more elements to the reflection, it is important to consider the most famous example of the durability of a hydraulic structure reinforced with lime: the Friant-Kern irrigation canal built in California (US) in the 1940's. Since its construction, and due to the use of highly plastic clayey soils, the canal suffered periodic disorders and maintenance issues. In the early 1970's lime treatment was used to control the progressive deterioration of the structure restoring approximately 8.5 km of damaged sections using lime treatment (3 to 4% quicklime) [22]. The site experiences severe environmental exposure conditions: significant temperature variations (ranging from -7°C and +41°C), repetitions of freeze and thaw cycles (cumulative freezing period ranging from 0 to 45 days per year), dry and wet cycles (dry conditions mainly during cleaning processes for canal maintenance) [23].

The performance of this renovated sections of the canal have been monitored periodically since the construction showing no new slides and little or no maintenance needed. A massive study was performed in 2010, 40 years from the rehabilitation operations proving the long-term durability of lime treatment [24]. As main findings, a permanent reduction of the plastic behaviour of the treated clays was confirmed, the pH was found to be still higher than the pH of the native soil (8.90 compared to 6.30), the geo-mechanical stability of the structure was guaranteed thanks to the improved compressive strength, the enhanced erosion resistance and the reduced swelling and shrinkage potential. Therefore, the obtained results showed that lime treatment was appropriate to ensure a long-lasting effect after 40 years of permanent contact with water. Figure 6 shows a view of the canal in 2012 in which the traces of the sheep foot roller used for its renovation are still very evident, as well as the water level line, proving that soil treated with lime experienced very limited erosion after 40 years of service life in permanent or temporary contact with water.

Fig. 6 – Friant Kern Channel, view of 2012

4. CONCLUSIONS

In conclusions, the experiences presented in this paper prove that, when good conception and good implementation are carried out, lime treatment allows to obtain interesting performance when used in the field of hydraulic structure construction. It was in fact highlighted that, in addition to ensure the improvement of the immediate properties for the reuse of wet or unsuitable materials extending the possibility to reuse soils that are locally available, lime treatment helps to produce cohesive and erosion resistant materials without increasing of the permeability properties of the soil.

The Bulletin 195 “Cemented Soil Dams” published by the International Commission of Large Dams [23] considered all these elements, and it broadly extends the use of treated soils to applications other than upstream slope protection, notably to homogeneous medium-height dams (up to 30 m high, and exceptionally up to 50 m), zoned dams and levees. It provides useful recommendations for the design, construction and repair of dams and levees using treated soils.

As clearly demonstrated using lime treatment for the rehabilitation of the Friant Kern canal, the technique allows to build structures capable of resisting hydraulic solicitations with guarantees on durability and advantages on maintenance over traditional structures.

Over the years, deployment methodologies have been developed, such as by extending the practice to the in-place treatment (common practice considered only the in-plant treatment). Findings related to the maintaining of the different functionalities during the years and the exposure to weathering are successfully presented in this paper, highlighting the need of continue collecting information as the exposure time progresses.

REFERENCES

[1] Little, D.L. (1995). Handbook for Stabilization of Pavement Subgrades and Base Courses with Lime, Dubuque (Iowa). Published by Kendall/Hunt Publishing Company

[2] Sharp M., Wallis M., Deniaud F., Hersch-Burdick R., Tourment R., et al. (2013). The International Levee Handbook. CIRIA, pp.1349, 978-0-86017-734-0. ⟨hal-02598878⟩

[3] Puiatti D., Herrier G., Nerincx N., Bonelli S., Fry J.-J. (2018). The use of lime treated soils in water retaining structures. IV International Seminar on Earthworks in Europe, April 19-20, Madrid (Spain)

[4] Fleming, R., Sills, G., Stewart, E. (1992). Lime Stabilization of Levee Slopes. Proceedings of the second interagency symposium on stabilization of soils and other materials, LA, pp. 5-15 to 5-22

[5] Garver, L.L. (1987). Canal Repair Techniques Using Lime-Stabilized Soil, Lime for Environmental Uses. ASTM STP931, pp.115-120

[6] Gutschick, K.A. (1978). Lime stabilization under hydraulic conditions. 4th lime congress, Hershey, PA, pp 1-20

[7] Belgian Research Road Center. Code of good practice R103 (2021). Soil treatment with lime – European experiences for soil improvement and soil stabilisation. State of the art. Brussels (BE), pp. 88-93

[8] Das G., Razakamanantsoa A., Herrier G., Deneele D. (2021). Compressive strength and microstructure evolution of lime-treated silty soil subjected to kneading action. Transport Geotechnics, vol. 29, July 2021, 100568

[9] Das G., Razakamanantsoa A., Herrier G., Deneele D. (2022). Hydromechanical and Pore-Structure evolution in lime-treated kneading compacted soil. Geo-Congress 2022. DOI: 10.1061/9780784484012.026

[10] Cuisinier O. and Le Borgne T. (2008). Relationship between microstructure and hydraulic conductivity in compacted lime-treated soils. Advances in Transportation Geotechnics, p.643.

[11] Charles I., Herrier G., Chevalier C., Durand E. (2012). An experimental full-scale hydraulic earthen structure in lime treated soil. Proceedings of the Sixth International Conference on Scour and Erosion, Paris (F), Aug. 2012: 181–188

[12] Makki-Szymkiewicz L., Hibouche A., Taibi S., Herrier G., Lesueur D., Fleureau J.-M. (2015). Evolution of the properties of lime-treated silty soil in a small experimental embankment. Engineering Geology, 191, pp. 8-22

[13] Das G., Razakamanantsoa A., Herrier G., Saussaye L., Lesueur D. Deneele D. (2021). Evaluation of the long-term effect of lime treatment on a silty seven years of atmospheric exposure: Mechanical, physicochemical, and microstructural studies. Engineering Geology 281(6)

[14] Nerincx N., Bonelli S., Puiatti D., Herrier G., Fry J.-J., Tourment R., Nicaise S. (2016). Impact of lime treated soils performance on design of earthfill dikes. FLOODrisk 2016 - 3rd European Conference on Flood Risk Management, E3S Web of Conferences 7, 14004

[15] Nerincx N., Bonelli S., Nicaise S., Herrier G., Lesueurs D., Tachker P., Puiatti D., Cornacchioli F. (2018). The DigueELITE project: lessons learned and impact on the design of levees with lime treated soils. Hydropower and Dams, vol. 25, issue 6

[16] Poncelet N., François B. (2019). Desiccation crack in lime-treated silty clay: Experimental evaluation and constitutive interpretation. E3S Web of Conferences 92, 11002

[17] Nicaise S., Klotz F., Bertola F., Byron F., Chaouch N., Grémeaux Y., Aubriet J., Ozturk T., Doghmane A., Bonelli S. (2024). Evolution des performances de digues traitées à la chaux en climat méditerranéen. Digue 2024, 27-29 March 2024, Aix-en-Provence (F)

[18] Bertola F., Klotz F., Nicaise S., François B., Gerard P. (2024). Digues en limons traites à la chaux : évolution des matériaux 6 ans après la mise en œuvre. Journées Nationales de Géotechnique et de Géologie de l'Ingénieur, 25-28 June 2024, Poitiers (F)

[19] Bertola F., Klotz F., Gerard P. François B. (2024). Evaluation of the geomechanical properties of lime-treated silt samples extracted from an experimental levee 6 years after the construction. XVIII ECSMGE 24, 26-30 August 2024, Lisbon (P)

[20] Herrier G., Bonelli S., Nerincx N., Tachker P., Peeters P., and Puiatti D. (2020). Improving dams and dikes strength and resistance to erosion by means of lime treatment. Proceedings of the Fourth International Dam World Conference, Portugal, Lisbon, LNEC, September 21-25,2020, pp. 1-19

[21] Konstadinou M., Herrier G., Stoutjesdijk T., Losma F., Zwanenburg C., Dobbe R. (2023). Lime treatment: Evaluation for use in dike applications in the Netherlands. Journal of Materials in Civil Engineering, 35(3): 04022465

[22] Howard A.K., Bara J.P. (1976). Lime stabilization on Friant-Kern Canal. US Bureau of Reclamation, Report No. REC-ERC-76-20, Denver, CO (US), pp. 53-61

[23] Bulletin 195 (2022). Cemented Material Dams: Design and Practice. CEMENTED SOIL DAMS. CIGB

[24] Akula P., Hariharan N., Little D., Lesueur D., Herrier G. (2020). Evaluating the Long-Term Durability of Lime Treatment in Hydraulic Structures: Case Study on the Friant-Kern Canal. Transportation Research Record 036119812-0919404

Fifth International Dam World Conference
PORTUGAL • LISBON • LNEC • APRIL 13-17, 2025
dam world 2025

BRIEF INSIGHTS: IN-SITU PERMEABILITY TEST IN WEATHERED AND POORLY-GRADED ROCKFILL

Laina-Gómez, Carlos[1]	Escudero-Merino, Diego	Asanza-Izquierdo, Enrique	Díez-Torres, Juan Antonio
CEDEX	CEDEX	CEDEX	CEDEX

ABSTRACT

Rockfills safeguard the core of engineered earth structures, enhancing strength and mitigating pore pressure accumulation. Factors such as significant thermal oscillations, severe frost/thaw, wetting/drying cycles, and shifts in rainfall patterns are likely to speed up the weathering of in-place rockfill particles. Throughout the past decade, investigations at CEDEX have revealed signs of particle alteration, including potential crumbling in aged dams, harbours, and embankments. These alterations result in significant changes in particle size distributions, consequently leading to a decline in drainage efficiency and overall structural strength. While large-scale laboratory tests such as permeameter, triaxial tests, or Rowe's cell, are able to assess the permeability of coarse-grained soils, in-situ tests performed on a larger scale appear to yield even more reliable results. These tests replicate natural conditions, including porosity, compaction, true grain-size distribution, and boundary conditions. This paper presents a case study on the in-situ measurement of permeability in a weathered, poorly-graded rockfill, providing valuable insights into real-world conditions.

Keywords: In-situ, measurement, permeability, trench, weathered, rockfill.

[1]carlos.laina@cedex.es, CEDEX Geotechnics Laboratory, Spain.

1. INTRODUCTION

This communication presents a singular in-situ test carried out by CEDEX Geotechnics Laboratory, whose purpose was to assess how much the weathering and breakdown of the rockfill particles of an earth structure reduces its permeability. The rockfill basically consists of cobbles and gravels from a nearby quarry in a dolomite rock with sugary (saccharoidal) texture, yet partially dedolomitized into a somehow sandstone-like.

The study of the degradation of its particles, that had been addressed by CEDEX in the past, did not lead to sound conclusions regarding frost/thaw and wetting/drying cycles; however, those laboratory test that entailed direct mechanical stresses, showed that the particles were highly prone to crumble (into sugary sand). It was apparent that the mere rough mechanical handling at the lab led to fine production. For instance, dropping a particle onto the concrete floor might cause its crumbling.

After four decades as the upstream slope that protected the clay core of a large dam, a keen eye could recognize certain weathering features in the rockfill (bulgy profile, dying dusty, sandy patches). Since an expert assessment after on-site inspection had stated that the current bulk permeability of the rockfill could be as low as k≈0.01cm/s and that, therefore, the upstream slope stability during a rapid drawdown might be at risk due to excess pore pressures, CEDEX Geotechnics Laboratory engineered a full-scale test aimed at measuring the permeability on site.

2. THEORETICAL FRAMEWORK

2.1. About permeability

Darcy's law (1856) (Equation 1) relates the discharge rate of a water flow through a permeable media with the hydraulic gradient by the permeability coefficient.

$$v = k \cdot i \tag{1}$$

where: *v*, is the discharge rate [$L \cdot T^{-1}$]; k, the permeability coefficient [$L \cdot T^{-1}$]; and *i*, the hydraulic gradient [-].

On the other hand, departing from Poiseuille's law (1839) and assuming a Newtonian fluid in laminar flow Taylor (1948) (Equation 2) broke down the formulae to account for the nature of the fluid and the soil fabric:

$$k = \frac{\gamma}{\mu} \cdot C \frac{e^3}{1+e} \cdot {D_s}^2 \tag{2}$$

where: k, is the permeability coefficient [$L \cdot T^{-1}$]; γ, the specific weight of the fluid [$M \cdot L^{-3}$]; μ, the dynamic viscosity of the fluid [$M \cdot L^{-1} \cdot T^{-1}$], C a shape factor [-], e the void ratio [-], and D_s, the effective diameter of particles with a specific surface S [L].

Much in the manner of the Equation 2 above, the recognized Kozeny-Carman's relationship (1927, 1937 and 1956) states that permeability is twofold, as it depends on both the fluid properties and the features of the porous media, through its grain size distribution and its void ratio.

2.2. On the laminar flow

An elementary assumption in conventional soil permeability tests is that the fluid flows in laminar regime. The Reynolds number (*Re*) (Equation 3) is used to determine whether a flow is laminar (viscous forces prevail) or turbulent (inertial forces prevail).

$$R_e = \frac{D \cdot v}{\nu} \tag{3}$$

where: D, is the equivalent diameter of the porous media [L]; v, is the flow rate [$L \cdot T^{-1}$]; and ν, is the cinematic viscosity of the fluid [$L^2 \cdot T^{-1}$] (at 20ºC $\nu_{water} \sim 1 \cdot 10^{-6}$ m^2/s).

In classical Hydraulics, where the flow is conveyed along straight outlines within simple geometries (canals and pipes), the threshold between laminar and turbulent flow is *Re*~2000.

However, in porous media, where bottleneck effect and tortuosity have to be accounted for, it is accepted that laminar flow is attained for *Re*<1 (Bear, 2018). By default, laminar regime is assumed even in coarse gravelly sands to high hydraulic gradients.

The present study aims to determine the permeability of a coarse soil (rockfill, in fact), with D_{min}~20mm and D_{50}~60mm (gravels and cobbles). In addition, the in-situ test arrangement, designed as a percolation process (shown below), entails a gradient of i~1. Note that in this case sand fraction produced by crumbling is likely to be washed downwards and to eventually get clogged in the shape of pouches within the skeleton.

Although judgment based on Equation 3 leads to believe that the flow in the rockfill at i~1 is clearly turbulent, for the sake of simplicity, laminar flow is assumed; moreover, such assumption would be on the side of safety (the true permeability would be higher than that derived from the test, as inertial loses are neglected).

2.3. On the in-situ measurement of permeability

Some formulations and tables the compute permeability based on non-comprehensive soil features (grain size and size distribution) can be found in the literature, such as the classical equations of Hazen (1911 and 1930) or Sherard (1984). Note that many of them neglect the

degree of soil packing (void ratio), thereby the permeability of a shallow normally consolidated soil would erroneously remain constant until its maximum dry density.

Thus, such desk appraisal fails to take into account in-situ conditions (dry density, particle degradation and boundary conditions). Unfortunately, laboratory permeability tests with coarse soils fail again to reproduce the in-situ conditions, not to mention the drawbacks concerning the maximum grain size (a few inches) to meet standards. Soil resampling would force the coarse fraction to be excluded, changing the natural soil structure and, therefore, its porosity, which is a key issue in this study.

On the contrary, in-situ tests hardly disturb the natural conditions and allow a large mass of material to be tested, so its representativeness is much more reliable. In-situ measurements of permeability can be divided into two groups: tests carried out inside a borehole (Gilg-Gavard, Lugeon and Lefranc tests) and percolation tests on the surface through a trench in the soil (Haefeli and Matsuo tests).

In-situ measurements of the permeability inside a borehole were discarded, due to the major difficulties of placing a drilling machine on a steep slope and drilling into a coarse granular material. Additionally, a standard drilling diameter is not large enough in relation to the pore size of the rockfill skeleton. Furthermore, taking into account that the particles are prone to crumble, drilling works would likely produce an undesired amount of fines.

According to Fell et al. (2015), drilling works in such materials tend to cause the soil pore structure to close and become clogged, leading to highly biased permeability results, one or two orders of magnitude lower than that of the original soil.

2.4. Vedernikov´s solution (1934)

The percolation tests carried out on the surface through a trench seem to be an appropriate alternative when it comes to coarse materials. The State of the Art on percolation tests refers to several geometry arrangements of the trench or pit, but all of them assume a deep impermeable layer, are based on the Vedernikov's solution (1934), a 2D percolation model (q) from trapezoidal canal, given by Equation 4:

$$q = k \cdot (W + A \cdot y) \tag{4}$$

where: q, is the flow rate [$L^2 \cdot T^{-1}$]; k, the permeability coefficient [$L \cdot T^{-1}$]; W, the width of the free water surface (L); y, the height of the trench from the discharge level; and A, a parameter that accounts for the maximum widening experienced by the downward flow [-].

As the close-form solution for the parameter A is rather complex, Vedernikov presented a chart for a wide range of shapes of trapezoidal canal (Fig. 1).

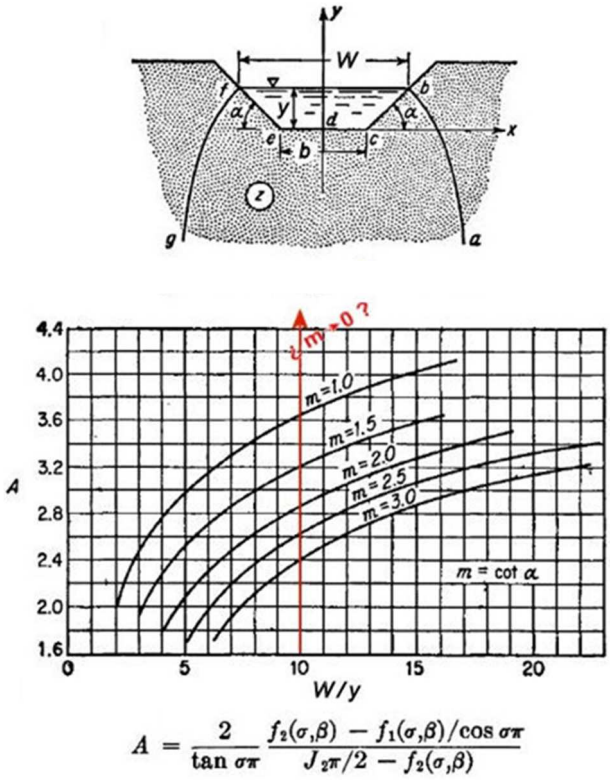

$$A = \frac{2}{\tan \sigma\pi} \frac{f_2(\sigma,\beta) - f_1(\sigma,\beta)/\cos \sigma\pi}{J_2\pi/2 - f_2(\sigma,\beta)}$$

Fig. 1 – Percolation from a trapezoidal canal, Vedernikov's model (Harr, 1990).

However, this chart falls short to solve upper or lower bound cases, thereby vertical face (m=0), perhaps the simplest, the geometry selected by the CEDEX Geotechnics Laboratory. For this reason, the article by Chahar (2001) has been used, which extends this abacus for extreme geometries (Fig. 2).

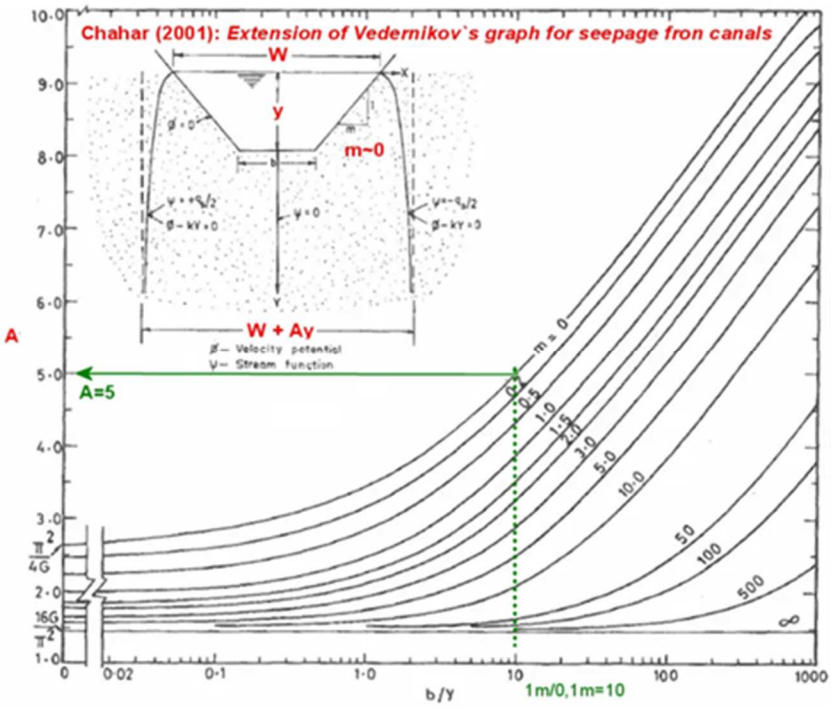

Fig. 2 – Chahar's chart (2001); generalization of Vedernikov's chart for obtaining *A*.

3. IN-SITU MEASUREMENT OF THE PERMEABILITY

3.1. Definition and scope

Fig. 3 is a general layout of the in-situ permeability test that the Laboratory drew up. The aim was to measure the permeability of a large mass of the rockfill in the upstream slope, preferably in a zone with clear evidence of crumbling a weathering.

Vedernikov's model was taken on as the reference theoretical framework. In fact, it has been proven that percolation tests are in close agreement with theory as long as *H>3W*.

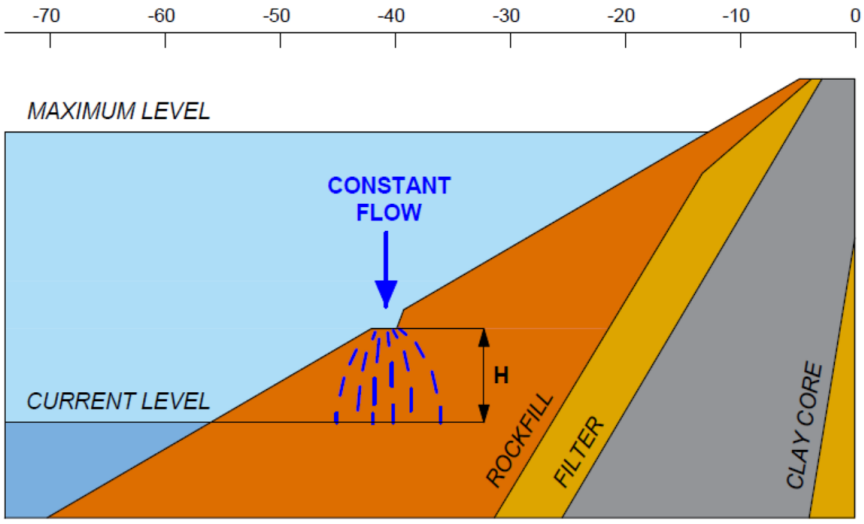

Fig. 3 – Layout of in-situ measurement of the permeability.

In this case, CEDEX set the base of the trench 3m above the discharge level, considering a trench width of *W*=1, due to constrains by the limited number and capacity of the available pumps. It is worth pointing out that in-situ tests long enough (*L>>W*) to meet 2D conditions turn out impractical for many other reasons. Thus, CEDEX concluded that even a square shallow pit would result cost-effective, regardless of minor fitting to match a 2D model with a 3D.

Bearing in mind the available pumps, pressure losses and preliminary judgement on the permeability expected, the in-situ test carried out by CEDEX was based on digging a shallow trench (*W*=1m, *y*=10cm), reaching total area between 1 and 3m².

3.2. Equipment calibration and mock test at CEH Laboratory

Due to the novelty of the test design, the large volume and flow rates of water and the specific devices (4 pumps operating in parallel, electronic flowmeters and connecting elements), the calibration, setting up and even a mock permeability test were carried out at CEDEX Hydraulics Laboratory (CEH), with ample resources and expertise in this field (Fig. 4).

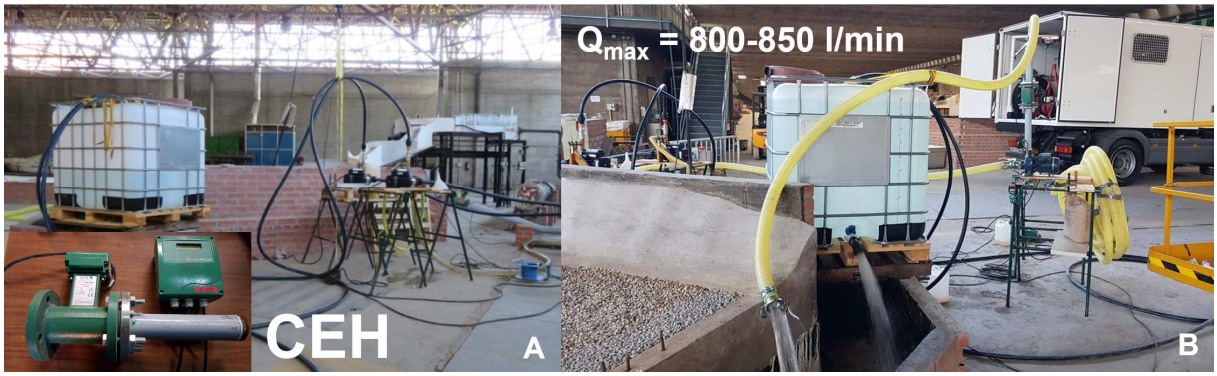

Fig. 4 – Equipment calibration in CEH Laboratory.

3.3. Description, details, and results of the in-situ test

The first preliminary works consisted of clearing and levelling a trail through the upstream slope with a backhoe to the approved testing spot. Next, CEDEX technicians contoured and prepared manually the trench. Finally, they proceeded to fix the pumps and the hoses, with special care with the intake from the reservoir, as well as the rest of the elements (Fig. 5).

A)

B)

C)

D)

E)

F)

Fig. 5 – Stages of testing; A) access road into the rockfill; B) installation of the 4 hydraulic pumps; C) preparation of the trench of 3m x 1m; D) preparation of the trench of 1m x 1m; E) detail of the trench of 1m x 1m; F) Trench of 1m x 1m with the level of water stabilized in 10cm.

The design included the trench be lined with a macro-perforated sheet, in order to avoid potential erosion from the water squirting from the hose without loss of percolation capacity.

First test: Trench 1m x 3m in size.

A rectangular trench was meant to reduce somehow the 3D effect. Thus, the principle of the test was to adjust a flow of water just capable of maintaining a target height of water (10cm) in the trench.

However, it was soon recognized that with a size of 3m² the array of pumps at its maximum water flow rate ~13.6 l/s (~820 l/min) failed to fill the trench at all.

In any case, the percolation capacity (permeability) in those 3m² exceeded 820 l/min. These results made possible to set a lower bound of the permeability of the rockfill (it was an order of magnitude higher than assumed, of k=0.01cm/s), and therefore, dissipating all the doubts raised about the hypothetical loss of permeability due to the material "sanded".

Second and final test: Trench of 1m x 1m.

The technicians of the CEDEX Geotechnics Laboratory dissatisfied with the results, decided to repeat the test in a smaller trench (1m x 1m), even though this geometry maximized the three-dimensional effect.

Finally, following a very similar methodology this test was completed successfully. The main advantage was to obtain the order of magnitude flow rate associated with a steady height of water, which was maintained for several minutes in the trench.

The final flow rate of water, using three of the four available pumps, was 8.7 l/s (520 l/min).

4. ANALYSIS RESULTS

4.1. Approach

The difference in level between the trench and the water surface of the reservoir (about 3m) is sufficient to accept that the widening of the percolating flow is very close to its asymptotic value; in other words, the flow is almost vertical when it reaches the reservoir level.

The flow rate required to obtain a steady percolation flow in the trench of 1m x 1m was about 520 l/min. It is a three-dimensional flow and very similar to the case of an axil-symmetric problem (assuming a circular surface of area 1m²).

An approximation with the two-dimensional flow model could also be accepted, understanding that the asymptotic border does not influence whether it is a square trench or one of infinite length of equal width.

4.2. In-situ measurement

If there were a two-dimensional flow in a trench with vertical faces (m=0), width (W) of 1m and water depth (y) of 0.1m, the flow would widen to an asymptotic value ($L_{asymptote}$) of:

$$L_{asymptote} = W + A \cdot y = 1m + A \cdot 0.1m \quad (5)$$

As seen in the above Fig. 2, the present case it results that A = 5. Then:

$$L_{asymptote} = W + A \cdot y = 1m + 5 \cdot 0.1m = 1.5m \quad (6)$$

It can be accepted that the flow is already practically vertical once it has descended the 3m difference between the trench and the reservoir's water surface, with a width equal to its asymptotic value.

As it is a square trench, three assumptions can be made about the dimensions and shape of the flow section when it intersects the level of the reservoir. The three options are represented in Fig. 6.

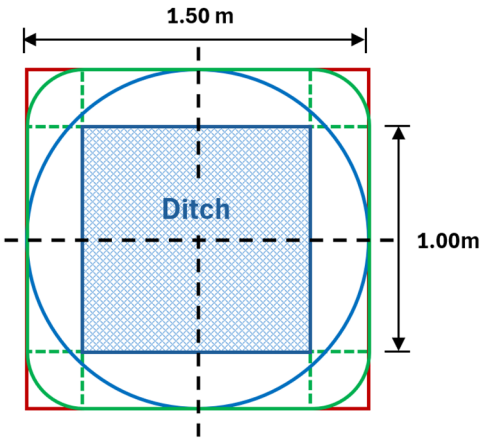

Fig. 6 – Possible sections formed by the flow when it intercepts the reservoir level.

Hypothesis 1: (upper bound) it is a square section with side $L_{asymptote}$=1.5m.

$$S_{max} = (1.5m)^2 = 2.25m^2 \quad (7)$$

Then, the apparent speed for 520 l/min flow is:

$$v = \frac{0.52m^3/min}{2.25m^2} = 0.39\,cm/s \quad (8)$$

Hypothesis 2: (intermediate bound) it is a square section with side $L_{asymptote}$=1.5m and the corners rounded.

$$S_{max} = (1.5m)^2 - 4 \cdot (0.25m)^2 + \pi \cdot (0.25m)^2 = 2.20m^2 \quad (9)$$

Then, the apparent speed for the same flow is:

$$v = \frac{0.52m^3/min}{2.20m^2} = 0.39\,cm/s \quad (10)$$

Hypothesis 3: (lower bound) it is a circle section with a diameter of $L_{asymptote}$=1.5m.

$$S_{max} = 0.25 \cdot \pi \cdot (1.5m)^2 = 1.77m^2 \quad (11)$$

Then, the apparent speed for the same flow is:

$$v = \frac{0.52m^3/min}{1.77m^2} = 0.49\,cm/s \quad (12)$$

It can be accepted with reasonable approximation that the area of the flow, when it reaches the level of the reservoir, will be that of the intermediate value between the different hypotheses raised. Therefore, it can be considered valid to approximate the apparent velocity to 0.4cm/s.

As the gradient in this percolation problem is i=1, according to Darcy's law (Equation 1), permeability is equal to the flow rate: k ~0.4cm/s.

5. CONCLUSIONS

The CEDEX Geotechnics Laboratory suggested this purpose-built permeability test in the poorly-graded weathered rockfill at upstream slope of the earthfill dam, since an expert assessment had stated that its current permeability could be as low as k ~0.01cm/s.

For this purpose, the Laboratory took the Vedernikov solution, described by Harr (1990). In these “percolation" problems the gradient reaches i ~1 and the seepage turns soon downwards and tends to a constant "seepage area".

The setting up of this novelty model needed prior levelling and pumps capable of supplying a flow rate that would maintain the water level at the ditch. This calibration was carried out at CEDEX Hydraulics Laboratory under the support of its staff.

Although, an attempt was made to carry out the test as planned: a 3x1m² ditch, it was soon recognized that the array of pumps at its maximum water flow rate failed to fill the trench at all.

Finally, test was completed successful in a smaller trench of 1x1m² with a final flow rate of water of 520 l/min.

As a conclusion and assuming a laminar flow (the true permeability would be higher than that derived from the test, as inertial loses are neglected), permeability equals the flow rate results: *k* ~0.4cm/s, and accordingly all the doubts raised about the hypothetical loss of permeability due to the material "sanded" were dissipated.

REFERENCES

[1] Bear, J. (2018). Modelling phenomena of flow and transport in porous media (Vol. 31). Springer.

[2] Carman, P. C. (1937). Fluid flow through granular beds. Transactions of the Institution of Chemical Engineers, 15, 150-166.

[3] Carman, P. C. (1956). Flow of gases through porous media. Butterworths.

[4] Chahar, B. R. (2001). Extension of Vedernikov's graph for seepage from canals. Groundwater, 39, 272-275.

[5] Darcy, H. (1856). Les fontaines publiques de la ville de Dijon. Dalmont.

[6] Fell, R., MacGregor, P., Stapledon, D., Bell, G., & Foster, M. (2015). Geotechnical engineering of dams. CRC Press.

[7] Gilg, B., & Gavard, M. (1957). Calcul de la perméabilité par des essais d'eau dans les sondages en alluvions. Bulletin technique de la Suisse romande.

[8] González de Vallejo, L., Ferrer, M., Ortuño, L., & Oteo, C. (2002). Ingeniería geológica. Prentice Hall.

[9] Harr, M. (1990). Groundwater and seepage. Dover Publications.

[10] Hazen, A. (1911). Discussion on dams on sand foundations. Transactions of the American Society of Civil Engineers, 73, 199.

[11] Hazen, A. (1930). Water supply. In American Civil Engineers Handbook (Wiley).

[12] Kozeny, J. (1927). Über Grundwasserbewegung. Wasserkraft und Wasserwirtschaft, 22.

[13] Matsuo, S., Hanmachi, S., & Akai, K. (1953). A field determination of permeability. In Proceedings of the 3rd ICSMFE (Vol. 1, pp. 268-271). Zurich.

[14] Poiseuille, J. L. M. (1840). Recherches expérimentales sur le mouvement des liquides dans les tubes de très petits diamètres: 1. Influence de la pression sur la quantité de liquide qui traverse les tubes de très petits diamètres. Comptes Rendus de l'Académie des Sciences, 11, 961-967.

[15] Sherard, J. L., Dunnigan, L. P., & Talbot, J. R. (1984). Filters for silts and clays. Journal of Geotechnical Engineering, 110(6), 701-718.

[16] Taylor, D. W. (1948). Fundamentals of soil mechanics. John Wiley & Sons.

Fifth International
Dam World Conference
PORTUGAL • LISBON • LNEC • APRIL 13-17, 2025
dam world 2025

THE DESIGN AND CONSTRUCTION OF 71 NDÚE DAM – ANGOLA

Rui Costa[1]
LCW, Engenharia de Estruturas/Geovia, Consultores de Geotecnia

Jorge Sousa Cruz[2]
LCW, Engenharia de Estruturas/Geovia, Consultores de Geotecnia

Nuno A. Henriques[3]
Prospectiva - Projectos, Serviços e Estudos, SA

ABSTRACT

The commonsense saying: “the design of a dam takes place during its construction” rings especially true in the case of the 71 Ndúe dam.

This 27m high and 1,4Km long dam on the Caundo river (Cuvelai river watershed; Cuvelai municipality of the Cunene district, Angola) was a unique project for our design team. Although not a design-build delivery method project “per se”, construction work progressed almost simultaneously with the design, with the two sometimes overlapping at various stages.

Thus, it was possible, to reevaluate in real time the design assumptions and solutions against the backdrop of the actual geotechnical constraints and conditions that emerged from the field works as they progressed. This was particularly relevant for decisions concerning the dam’s positioning in relation to tectonic activity, the cross-section design and embankment long-term behaviour, the design of the filter/drain, the foundation treatment towards water seepage control due to thick stretches of decomposed rock and the placement of the spillway and water intake tower.

This paper describes the most important technical aspects of the dam design, focusing on the ongoing adaptations in response to fieldwork findings. It presents key features of the works, design approaches, and detailed analyses carried out to define the typical dam cross-section and drainage system, based on seepage, stability, and settlement conditions, as well as the grouting works and water intake tower and side-channel spillway design.

Project closure and delivery to the owner are scheduled for September 2024, with the dam and hydraulic scheme set to begin operations in early 2025.

Keywords: Ndué, Dam, Embankment, Design, Construction.

[1] rcosta@geovia.pt, Portugal
[2] jcruz@geovia.pt, Portugal
[3] nunohenriques@prospectiva.pt, Portugal

1. INTRODUCTION

The 71 Ndúe Dam is part of the Program of Structuring Actions to Combat the Effects of Drought in Cunene Province, promoted by the Ministry of Energy and Water (MINEA) through the National Institute of Water Resources (INRH) of Angola. Its objectives include ensuring water supply and establishing a district irrigation system to support local-scale agriculture.

The dam is located in the administrative region of Cunene, on the Caundo River, one of the tributaries of the expansive Cuvelai River basin. This basin spans approximately 160,000 km², with 32.7% of its area in Angola and 67.3% in Namibia.

The chosen location for the dam lies in an area where the Caundo River valley narrows, likely due to tectonic activity and the presence of a shallow rock layer beneath the alluvial deposits at the valley's bottom.

The valley's cross-section along the dam axis reveals a slightly entrenched, single-thread channel, with asymmetrical, gently sloping abutments and a flattened central stream channel about 170 meters wide, making it suitable for an embankment dam. The geotechnical quality of the subsoil and bedrock, the thickness of the alluvium and colluvium, and the availability of suitable materials within the reservoir area all contributed to the decision to implement an earth-filled dam. Other factors, such as the favourable placement of the spillway and outlet works, as well as better integration with the surrounding landscape, further supported the choice of an embankment dam.

The dam spans a 1.4 Km width of valley and is 27 m high above the foundation. Typical cross-section is of an earth embankment zoned dam with:

- Symmetrical central impervious core (1V:0,3H), made from selected residual fine-graded soils from the weathering of schists and phyllites inside the reservoir (Material 1);
- Upstream and downstream faces (1V:2,5-3H) made from coarse-grained residual soils of granodiorite rocks (Materials 2A and 2B) inside the reservoir and from excavation surplus;
- Upstream cofferdam with a zoned earthen dams cross-section (Mat. 1: impervious core; Mat. 2B: upstream and downstream faces) and a slurry cut-off wall (slurry trench) at the foundation level for groundwater flow management;
- Quarry sourced drainage system consisting of a sand sloped chimney filter (Mat. 4), associated with a horizontal gravel drain (Mat. 5) at the base, connected to draining blankets;

- Quarry sourced filtering sand blanket in contact with the downstream stabilizing mass and the foundation (Mat. 4);
- Quarry sourced rip-rap for upstream slope protection (Mat. 7E1);
- Quarry sourced or selected alluvium coarse-grained layer with characteristics of transition material (Mat. 7E2) protecting the downstream slope;
- Downstream toe protection made of quarry sourced rockfill (Mat. 6).

The thick cover of Quaternary soils, the heavily weathered granodiorite foundation, and the presence of tectonic findings at the bottom of the valley determined the need to minimize seepage through the permeable layers of the foundation. The heavy weathering of the foundation was also a key factor in the decision to use consolidation grouting at the concrete-rock interface at the side channel spillway approach channel.

The provisional river diversion will be made through a concrete gallery with a 4.5x4.5 m square internal section and a length of 136 m, which will be converted in the second phase into a bottom outlet and inlet. Appurtenant hydraulic structures include a side-channel spillway on the left riverbank, an 1800 mm intake pipe, and a 1600 mm bottom outlet pipe, all of which will be installed in the first-phase provisional diversion gallery. The water intake tower will also be installed on the left riverbank. (Fig. 1).

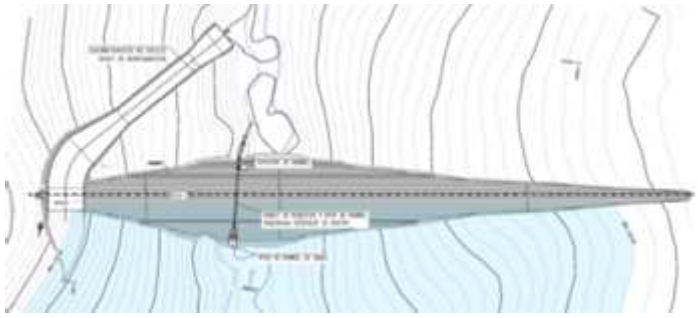

Fig. 1 - Plan view of the 71 Ndué dam and appurtenant hydraulic structures

The following chapters further address, in addition to the geological and geotechnical characterizations, the most relevant geotechnical constraints, the role of the geological and geotechnical studies during the design phase, and the ongoing design adaptations in response to fieldwork findings, particularly regarding:

- The dam cross-section and its drainage system, in response to the type and availability of soils within the reservoir, and their behaviour towards seepage, stability, and settlement;

- Seepage control on the foundation, considering the thick weathering mantle with less-than-ideal conditions for the use of standard grout curtains; and
- Appurtenant hydraulic structures, considering the findings of heavily weathered tectonic-related foundation grounds with poor geotechnical characteristics.

2. GEOLOGICAL AND GEOTECHNICAL ASPECTS AND CONSTRAINTS DURING DESIGN AND THROUGH FIELDWORK FINDINGS

2.1. Geology

The geology of the dam site and appurtenant hydraulic structures is relatively simple and monotonous, and, according to the nomenclature adopted by the Geological Map of Angola (1:1,000,000, sheets 3 and 4), issued by the Geological Institute of Angola (1992) [1] the occurring formations correspond to the Quaternary alluvial deposits in the Caundo river valley floor (Q-ed), the Tertiary deposits belonging to the Kalahari Group - "Areias Ocres" Formation (N1-N2^{1}*kl2*) both covering the slopes of the abutments, and the post-Lower Proterozoic crystalline bedrock belonging to the “Granitos da Quibala” unit (γPR_1) that intruded totally or partially the existing ancient basement rocks of the “Grupo Bale” unit (PR_1*bl*), leading to the formation of migmatites and hornfels type rocks.

The Quaternary Caundo alluvium consists of silty sands and silty-sandy clays, generally topped locally by a finer, clayey or silty horizon. It also locally contains a more or less thick layer of gravel at the base, which is limited to the minor riverbed area. The thickness of these deposits’ ranges from 2.5 to 9.7 m, but is typically between 4.2 and 6.1 m.

Tertiary deposits are composed of fine, wind-blown sands rich in reddish iron, river sands, silty and/or sandy clays, and occasional gravels. These occur on both abutments, with varying thicknesses between 0.9 and 7.0 m on the right bank slope and between 2.5 and 5.5 m on the left bank slope.

The crystalline bedrock, belonging to the Quibala Granites unit (γPR_1), consists mainly of biotite porphyroblastic granites, leucocratic granites, and granodiorites. It also includes migmatites and hornfels, formed due to contact or thermal metamorphism and tectonics.

This bedrock is affected by fault sets, one of which, with an NNW-SSE trend and a 70-80º west dip, crosses the valley floor at the dam site. This fault is filled with 2.4 m of fine and brecciated materials, where secondary minerals in gray-green and olive-green colours can be observed in the site drillings.

Particularly on the right bank slope, due to the presence of this fault inclined towards that sector, the granodioritic bedrock is significantly degraded. As a result, the weathering mantle is deep, reaching depths up to 33 m.

Fig. 2 – General view of the dam site and its foundation. Top photo: Quaternary and tertiary deposits on the river channel and abutments; bottom photo: residuals soils from the "Granitos da Quibala" unit

Groundwater levels in the boreholes suggest the presence of a free/unconfined aquifer that spans both the Quaternary-Tertiary cover and the granodiorite residual soils. In this aquifer, the water table is located either at the top of the residual soils or at the interface between the Tertiary sediments and residual soils, with depths ranging from 11 m to 3 m on the right abutment, and from 7 m to 6.6 m on the left abutment. The water table is underlain by highly to slightly weathered rock of lower permeability. At the bottom of the valley, groundwater levels are found at the base of the alluvium, between depths of 3 m and 5 m, and are influenced by the flow regime of the Caundo River.

2.2. Geotechnics

The geotechnical characteristics of the dam foundation and associated hydraulic structures were investigated in two phases: the first phase took place during the early stages of the design, and the second phase occurred during construction, as it was required to the Contractor to carry out a confirmation investigation campaign due to the lack of robustness of the previous campaign.

The scope of both investigation campaigns included core drillings, SPT testing, in-situ permeability tests (Lefranc and Lugeon tests), undisturbed sampling and laboratory testing,

geo-electrical methods (apparent resistivity pseudosections), trial pits, and dynamic probe testing with the dynamic probe super heavy (DPSH).

The information gathered from these investigation works highlighted the following key aspects of the foundation:

- The Quaternary and Tertiary cover has poor geotechnical characteristics, ranging from loose to medium-dense (N_{SPT} = 4-30), and is generally of low thickness;
- The granodioritic bedrock is significantly degraded, with a deep weathering mantle on both abutments;
- The weathering profile of the granodiorite at both abutments consists of a top layer of medium-dense (N_{SPT} = 10-30) residual soil (W_6 – ISRM [2]), composed of silt-sandy soils (SM – USCS [3]). This is followed at depth by a thick layer of heavily weathered rock (W_5 to W_{4-5} – ISRM), exhibiting soil-like behaviour and very dense (N_{SPT} > 60). The basement rock occurs at depths ranging from 16 to 22m on the right abutment and 17 to 33m on the left abutment. The rock quality at the top is poor to medium, heavily weathered to medium-heavy weathered (W_4 to W_{3-4} – ISRM), with very close to close spaced fracturing (F_5 to F_4 – ISRM). Below this layer, the granodiorite basement rock is of good to excellent geotechnical quality, generally moderately to slightly weathered (W_3-W_2 – ISRM), resistant to very resistant, and fracture spacing is highly variable, ranging from wide spaced (F2) to very close to moderately close spaced (F3-F4);
- Although affected by tectonics, the valley's bottom shows a general decrease in the thickness of the weathering mantle, with basement rock of good to excellent geotechnical quality (W_3-W_2 – ISRM) found at depths between 9 and 10m. In the vicinity of the NNW-SSE trending fault, the weathering thickness increases and can reach depths of up to 17 m;
- The weathering mantle, reaching depths of up to 33 m, has moderate to low permeability (10^{-5} to 10^{-6} m/s). However, permeability may be higher due to the type of soils present. The basement rock itself has low permeability, as indicated by the Lugeon tests, which showed water absorption consistently below 2-1 µL. Near the fault zone at the valley's bottom, permeability increases significantly, resulting in a moderate to high permeability interface ($K < 10^{-4}$ m/s).

For design purposes, a geotechnical zoning of the dam foundation and hydraulic structures was developed, defining seven distinct zones (Fig. 3). The mechanical properties of each zone were initially interpreted based on the drilling log observations, considering factors such as the degree of weathering (W), discontinuity spacing (F), core recovery percentages, and RQD. After this first analysis, these properties were further assessed using results from SPT and

DPSH tests, along with data from apparent resistivity pseudosections and laboratory testing results.

The hydraulic and hydrogeological zoning of the dam foundation was determined from the results of Lefranc and Lugeon permeability tests (Fig. 4).

Table 1 and Table 2 below show the defined geotechnical and hydrogeological/hydraulic zoning for both the dam and the appurtenant hydraulic structures. Table 3 shows the geotechnical parameters for the foundations.

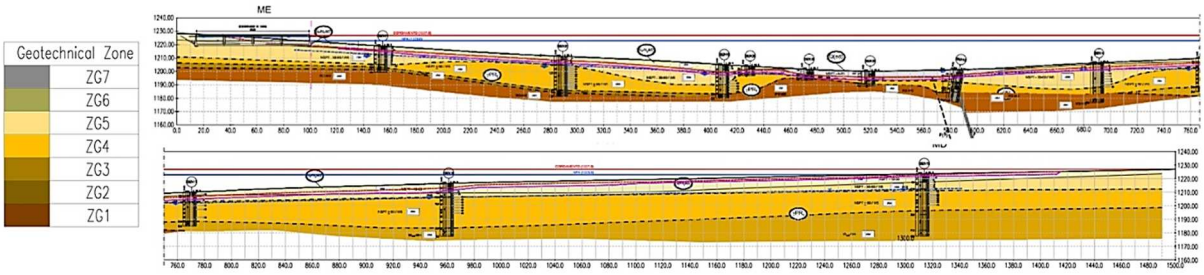

Fig. 3 – Geotechnical zoning of the dam foundation

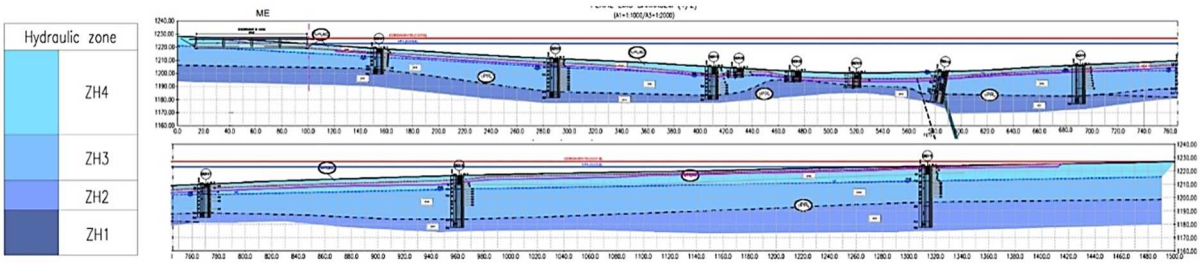

Fig. 4 – Hydrogeological/hydraulic of the dam foundation

Table 1 – Geotechnical zoning for both dam and appurtenant hydraulic structures foundations

Geotechnical Zone	N_{SPT}	W (ISRM, 1980)	F (ISRM, 1980)	RQD (Deere, 1964) [4]	RMR (Bieniawski, 1989) [5]	GSI (Hooke, Brown, 2018) [6]
ZG7	4-15	Cover soils		-	-	-
ZG6	10-30			-	-	-
ZG5	30-60	W6	-	-	-	-
ZG4	≥60	W5	-	-	-	-
ZG3	-	W4-5-W4	F5	0-15	<20-37 (25)	≥20
ZG2	-	W3-4	F4-5-F4	15-30	50-55	38-44
ZG1	-	W3-W2	F3-F4 <F3-2, F2>	30-100	58-85 (70)	47-78 (65)

Table 2 – Hydrogeological/hydraulic zoning for the dam foundation

Hydrogeological/hydraulic Zone	uL	K (m/s)	Hydrogeological/Hydraulic function
ZH4		$1x10^{-8}$-$2x10^{-5}$ ($5x10^{-7}$)	Porous medium – vadose zone, unsaturated to sub-saturated, subject to the percolation of rainwater and runoff and to evapotranspiration phenomena
ZH3		$1x10^{-6}$-$5x10^{-5}$ ($2x10^{-6}$)	Porous medium, saturated, limited at the top by the water table
ZH2	≤ 2		Fractured-type medium, sub-saturated
ZH1	≤ 1-2		Fractured-type mass, impermeable to low permeability

Table 3 – Geotechnical parameters of the foundation

Geotechnical zone	γ sat	c'	ϕ'	E'	ν	kh	kv
	kN/m³	kPa	º	MPa	-	m/s	m/s
ZG7	19	10	30	10	0.3	5E-05	1E-05
ZG6	20	11	29	20	0.3	5E-06	1E-06
ZG5	20	20	33	50	0.3	1E-05	4E-06
ZG4	21	30	35	70	0.3	1E-05	4E-06
ZG3	22	70	41	80	0.28	2E-07	2E-07
ZG2	25	220	69	4500	0.28	2E-07	2E-07
ZG1	28	1000	72	≥25000	0.26	1E-07	1E-07

The territory of Angola is a craton, meaning it is a stable interior portion of a continent. Seismic activity is therefore of low prevalence throughout the entire territory. The region of the hydraulic scheme has very low to low seismicity, so this aspect was not considered a constraint in the design development.

2.3. Quarry and borrow areas

The characterization study of borrow materials aimed to maximize the utilization of the land within the perimeter of the reservoir. This approach sought to minimize negative environmental impacts, reduce transportation distances, and increase the reservoir's storage capacity.

Geotechnical investigations revealed that suitable materials for the dam body are available within the reservoir, specifically residual soils from schists and granodiorites. Schist residual soils from the unit “Grupo Bale (PR1*bl*)”, found on the slopes of the reservoir, were deemed suitable for an impervious core. Residual soils from the unit “Granitos da Quibala (γPR1)” obtainable on the reservoir slopes and site excavation surplus, were deemed suitable for the upstream and downstream faces.

Schist residual soils for the impervious core are characterized as follows:

- USCS: SC and CL;
- #200 (ASTM) = 39-68%;

- W_L = 19-33%; W_P = 10-19%; IP = 10-16;
- $\gamma_{dmáx}$ = 16.7-18.7 kN/m^3; $W_{ópt}$ = 11-22%;
- E_{oed_ref} = 9-23 MPa;
- K_v = 1.4x10^{-8}-1.8x10^{-8} m/s;
- ϕ = 23-37º; ϕ' = 30-31º; c = 10-33kPa; c' = 16-18kPa.

Granodiorite residual soils for upstream and downstream faces are characterized as follows:

- USCS: SM-SC;
- #200 (ASTM) = 6-19%;
- W_L = 15-24%; W_P = 9-15%; IP = NP to 5-10;
- $\gamma_{dmáx}$ = 20.0-20.9 kN/m^3; $W_{ópt}$ = 10-14%;
- E_{oed_ref} = 27-37 MPa;
- K_v = 1.2x10^{-8}-2.7x10^{-8} m/s;
- ϕ' = 33-34º; c' = 0kPa.

Both aggregates for concrete, as well as for drains and riprap (Materials 4 to 7), will be sourced from the excavation of a granodiorite quarry located approximately 5.5 km from the dam site. The geotechnical characteristics and excavation methodology of the quarry were assessed through mechanical drilling with continuous core sampling and laboratory testing of the rock cores.

3. DAM CROSS-SECTION

3.1. Cross-section definition based on the type and availability of soils

The cross-section of the dam was defined based on the morphological characteristics of the valley and the geotechnical properties of the residual soils from the schists and granodiorites present in the reservoir or from excavation surplus, with conditions that allow them to be exploited under technically and economically suitable conditions (Fig. 5).

Materials for the upstream and downstream faces (Mat. 2) from residual soils of the granodiorites were found to lack fine content (6-19%) and, as a result, had higher expected permeabilities than those typically recommended (although laboratory testing showed permeabilities that contradict this assessment). This finding prompted the consideration of a transition zone (Mat. 2A) upstream of the core, consisting of more weathered gravel with a higher percentage of fines. The purpose of this zone was to optimize the thickness of the core, providing clear economic and environmental advantages. Soils with lower fine content (Mat. 2B) were then considered for the remaining upstream face sections.

Residual soils from the schists exhibited significant variation in fine content, due to differences in weathering degree and lateral variations of this property observed in the borrow pits and also higher permeabilities than those typically recommended.

This finding led to the imposition of a highly restricted granulometric range for placement and the adoption of a wide core geometry, which, when combined with the placement of material 2A upstream of the core, enhances its effectiveness in controlling percolation.

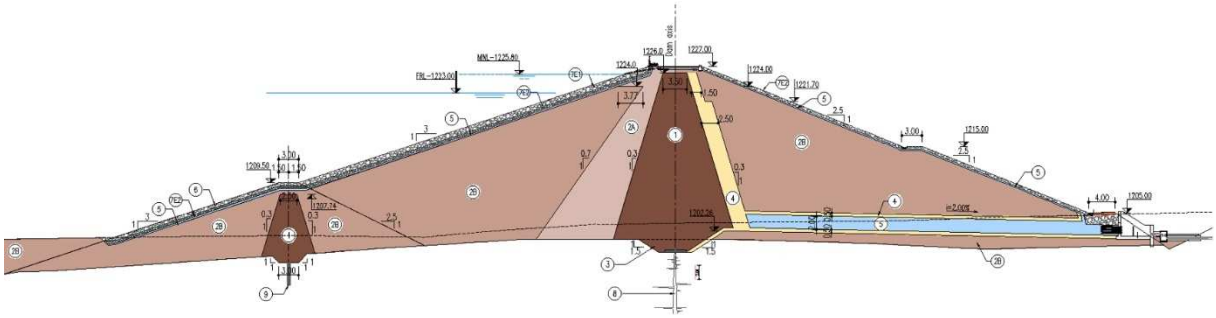

Fig. 5 – Typical dam cross-section (river channel)

3.2. Seepage, stability and settlement security checks

Investigation works on the borrow areas was conducted in different phases of the design, leading to continuous adjustments to the cross-section design and security checks.

During construction, the Contractor was required to carry out a new confirmation investigation campaign due to the lack of robustness in the previous campaigns, particularly regarding the mechanical and hydraulic properties of materials of types 1, 2A, and 2B. The confirmation campaign revealed mechanical properties of the materials that were lower than those considered during design, necessitating a revision of the geotechnical calculation parameters and an update of the stability and settlement checks during the construction phase of the first embankments. Table 4 presents a comparison of the geotechnical parameters of the fill materials during the design and construction phases.

Revised seepage safety checks performed on PLAXIS 2D indicated that the overall balance of seepage through the dam body, using the permeability coefficients from the construction phase compared to the design phase, is positive. Generally, all simulations showed a reduction in the percolated flow, although the magnitudes were considered minimal.

Stability safety checks performed using PLAXIS 2D with the Hardening-Soil rheological model for the fill and residual soil foundation, and the Mohr-Coulomb rheological model for the weathered rock foundation, indicated that, across all phases of construction and operation, the revised safety factors were slightly lower than those of the initial design, without compromising

the stability of the fill. The global safety factors remain above the minimum required by regulatory standards, despite the slight reductions in these factors - ranging from 4 to 5% during the construction phase, from 3 to 7% during the normal operation phase, and 10% during the rapid drawdown phase.

Table 4 – Comparison of the geotechnical parameters of the fill materials during the design and construction phases

Material		Location on dam	γsat	c'	ϕ'	Dilatancy	Mohr-Coloumb		Hardening-soil				ν	kh	kv
							E'	E_{eod}	E_{50}^{ref}	E_{eod}^{ref}	E_{ur}^{ref}	m			
			kN/m³	kPa	º	º	MPa	MPa	MPa	MPa	MPa	-	-	m/s	m/s
Design phase															
Mat. 1		Core	20.5	1	32	-	35	-	23	16	70	1	0.3	1E-07	5E-08
Mat. 2	a	Upstream and downstream faces	21.0	10	33	3	35	-	23	31	70	0.5	0.3	1E-06	5E-07
	b		21.5	1	35	5	45	-	30	40	90	0.5	0.3	5E-06	2.5E-06
Construction phase															
Mat. 1		Core	20.5	17	30	-	35	-	27	18	82	1	0.3	3E-08	1.5E-08
Mat. 2	a	Upstream and downstream faces	21.0	1	33	3	35	-	23	31	70	0.5	0.3	4E-08	2E-08
	b		21.5	1	33	3	35	-	21	28	63	0.5	0.3	3E-08	1.5E-08

Settlement safety checks, also performed using PLAXIS 2D, showed that the results obtained with the revised parameters, compared to the design parameters, are essentially identical across the various phases of construction and operation of the project. The maximum estimated variations are on the order of, or less than, -2 cm for both vertical and horizontal displacements. In relative terms, the differences between different areas of the dam body, reflecting the internal performance of the embankment - particularly in the core - are very small.

3.3. Internal drainage system

Since the design safety checks regarding seepage showed very small gradients, it was decided to suppress the horizontal drainage blanket on the abutments, as this suppression resulted in economic savings and reduced construction time.

During the construction phase, a change was made to the originally designed foundation treatment. The initially proposed deep grout curtain was replaced with a combined jet-grouted seepage cut-off wall at the upper levels of the foundation, and a conventional grouted seepage cut-off wall below. Concerns raised by both the reviewers and our design team about a potentially inefficient connection between the upper jet-grouted columns and the lower grout

curtain led to design changes in the internal drainage system, specifically addressing the suppression of the filter blanket on the abutments.

It was then decided that changes should be made to the downstream toe to enhance its catchment and drainage efficiency.

In the sections of the dam body where the downstream toe had already been constructed, a trench drain was installed downstream of the toe (Fig. 6).

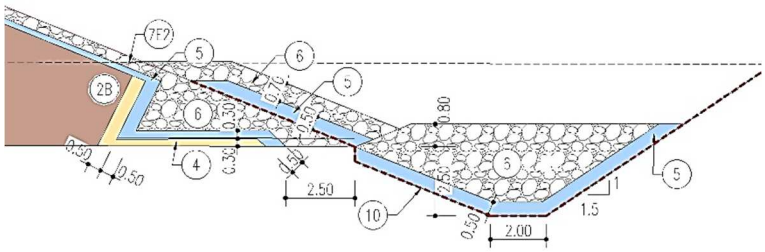

Fig. 6 – Reinforcement of downstream toe drainage in sections where the toe has already been constructed

In the newer sections, the toe geometry was modified by deepening it below the natural ground level to function as a wellpoint (Fig. 7).

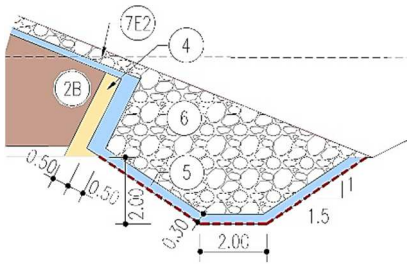

Fig. 7 – Deepening of downstream toe in new sections

4. FOUNDATION TREATMENT

4.1. Design adaptations in light of field findings and suitability to grouting

Design foundation treatment consisted of a monolayer deep grout curtain with primarily vertical holes, varying in length between 8 and 23 meters. The goal was to penetrate at least 3.0 meters into slightly permeable rock (≤ 3 uL), or, if this was not possible, to a maximum depth of one and a half times the maximum hydraulic load at the foundation.

Excavation works during construction and construction phase supplementary drillings along the proposed deep grout curtain alignment raised concerns about the foundation's suitability for grouting.

Field observations revealed a greater prevalence of heavily weathered rock with soil-like behaviour than originally anticipated. In contrast, the design phase had anticipated a predominance of highly weathered and fractured rock mass, which is more suitable for common grout procedures.

Design adaptations of the previously proposed foundation seepage control system was ensued finally settling, as suggested by the Contractor, and due to the resources available to him on site, for the construction of a jet-grouted seepage cut-off wall spanning the whole foundation unsuitable to grouting and embedded in the basement rock and a conventional grouting seepage cut-off wall in the fractured rock basement bellow the jet-grouted columns.

In the central part of the valley in the vicinity of the NNW-SSE trending fault, reinforcement grouting was planned with 60º grouting holes with variable length.

The jet-grouted cut-off wall consisted of double fluid jet grouting 0.8-1.0 m diameter columns with an overlap between columns of 0.10-0.13 m (Fig. 8). Core drillings of the jet-grouted columns were performed and samples were taken. The three-day unconfined compressive strength of the jet-grouted columns was 4 MPa, as reported by the field laboratory.

Fig. 8 – Jet-grouted columns on the right and left abutments, respectively

Grouting curtain comprised primary (P), secondary (P) and reinforcement/tertiary (R/T) holes.

5. APPURTENANT HYDRAULIC STRUCTURES

5.1. Water intake tower

In the early stages of the design, the water intake tower was placed on the right riverbank due to its better integration, offering clear construction benefits (shorter length, nearly linear development) and hydraulic advantages.

During the construction phase, and following additional drillings performed by the contractor, it was discovered that the tectonized zone associated with the NNW-SSE trending fault crossing the valley floor was more extensive than originally thought. This zone exhibited significant deterioration of the rock mass, extending to the area where the water intake tower was to be installed.

Based on these findings, it was decided to relocate the water intake tower to the right riverbank, thus avoiding the sector of the valley where the foundation proved to be complex due to the high degree of tectonization, which could have resulted in challenging and costly technical feasibility works (Fig. 9).

Fig. 9 – Bird's-eye view of the construction of the water intake tower in the left riverbank

5.2. Side-channel spillway

Given that the geological and geotechnical characteristics along the axis of the side-channel spillway were very similar on both riverbanks, the decision to place this hydraulic structure on the left riverbank was primarily driven by economic reasons, as the length on this bank was significantly shorter than on the opposite bank (Fig. 10).

This led to dealing with the geological constraints on a case-by-case basis, depending on the defined alignment, instead of adapting the placement of the spillway based on these constraints.

Major geotechnical constraints were identified at the locations of the overflow entrance, along the chute, and in the stilling basin. These constraints were primarily related to the significant depth of the weathering profile and the poor geotechnical characteristics of the ground.

At the overflow entrance, consolidation grouting was planned and carried out using 10-meter-long vertical holes, arranged in a quincunx pattern within a rectangular grid of 3.0 x 3.0 m^2. Geotechnical issues along the chute were easily addressed through overexcavation followed by concrete filling. In the stilling basin, Ø32 mm rock bolts were installed, sealed in 10-meter-long holes.

Fig. 10 – Bird's-eye views of the construction of the side-channel spillway

6. CONCLUSIONS

This paper details an uncommon situation where construction work for the dam and appurtenant structures progressed almost simultaneously with the design, with the two occasionally overlapping at various stages.

This situation offered the benefit of real-time revaluation of design assumptions and solutions based on the actual geotechnical constraints and conditions that emerged from the fieldwork as it progressed. However, it also had its drawbacks, introducing challenges in managing the evolving design and construction processes within a limited timeframe and the fast pace of the contractor's work.

This paper also aims to highlight the need for a robust investigation campaign during the appropriate phase of the project, that is, at the beginning of the design, to avoid the need to revise the completed designs, sometimes requiring significant changes. This situation becomes even more critical when a significant part of the construction work has already been

completed due to the fast pace set by the Contractor and Project Owner, as previously mentioned.

A final point worth noting about the project is that major constraints in developing the geological and geotechnical studies, and subsequently the design, were closely linked to working abroad with a non-English-speaking contractor. These challenges were further compounded by differences in work methodologies, classification and design criteria, as well as ongoing difficulties in monitoring the investigation work.

REFERENCES

[1] Araújo, A.G., Guimarães, F. (1992). Geologia de Angola. Notícia Explicativa da Carta Geológica à escala 1:1.000.000. Serviços Geológicos de Angola, Luanda, 137 p.

[2] ISMR, Basic Geotechnical Description of Rock Masses, Int. Jour. Rock Mech. Min. Sci. & Geomech. Abstr., Vol. 18, pp. 85-110, Pergamon Press Ltd (1981).

[3] ASTM D2482. Standard classification of soils for engineering purposes (unified soil classification system). American Society for Testing and Materials, Philadelphia, USA

[4] Deere, D.U. and Deere, D.W. (1988). The rock quality designation (RQD) index in practice. In Rock classification systems for engineering purposes, (ed. L. Kirkaldie), ASTM Special Publication 984, 91-101. Philadelphia: Am. Soc. Test. Mat.

[5] Bieniawski, Z. T. (1989). Engineering Rock Mass Classification. New York, 251 p.

[6] Hoek, E. and Brown, E.T. (2019). The Hoek-Brown Failure Criterion and GSI - 2018 Edition. Journal of Rock Mechanics and Geotechnical Engineering, 11, 445-463

Fifth International Dam World Conference
PORTUGAL • LISBON • LNEC • APRIL 13-17, 2025
dam world 2025

MAIN FAILURE MODES IN EMBANKMENT DAMS, MAPPABLE WITH DRONE SURVEYS

Daniel Leite[1]	João Marcelino	Nuno Guerra	João Manso	Ricardo Sardinha
COBA	LNEC	NOVA/FCT	LNEC	COBA

ABSTRACT

Dams play a crucial role in water management, serving to store water for purposes, such as human consumption, agricultural irrigation, flood control, and hydroelectric power generation. Due to their importance, dam safety is fundamental to preventing disasters that can cause loss of human lives, environmental damage, and significant economic losses. Regular maintenance and rigorous inspections are essential components of an appropriate dam safety policy, minimizing the risks associated with potential failures. However, with technological advances, new technologies have been demonstrated to be promising in order to complement the traditional procedures used in dam safety.

In this sense, drones can be used as a complementary tool to dam safety. They enable the accurate visual inspection and the generation of spatial models, that can be used to detect settlements, potentially identifying anomalies in embankment dams and contributing to the early detection of potential failure modes. These devices offer an innovative and efficient approach, allowing fast and secure access to inaccessible areas and capturing detailed images to identify anomalies. Furthermore, the creation of a digital model of the geometry, from drone images, makes it possible to create a digital record, with dimensional quality of the state of the work at the time of the inspection, and to compare with previous records.

This article presents fourteen failure modes that can be mapped with drones by detecting anomalies such as cracks, slippage, resurgences, settlements, uplift, deformation, sinkholes, heave, turbid water, wetlands, among others, which manifest on the surface of the dam, foundations, and/or abutments. A briefcase study is also presented, along with an analysis of the use of open-source software for processing data obtained from drones, such as WebODM and CloudCompare. This analysis highlights the flexibility and control these software programs offer in analyzing. Additionally, the GCP Finder software, developed by LNEC in collaboration with Universidade Nova de Lisboa, is presented. This program optimizes the processing of ground control points, improving dam monitoring and maintenance activities.

Finally, this article demonstrates how the early identification of these anomalies, through routine drone inspections, allows the implementation of mitigation strategies in a timely manner, preventing embankment dam failures.

Keywords: drones, embankment dams, anomalies, failure modes, dam safety, visual inspection, survey.

[1] d.leite@cobagroup.com, Portugal

1. INTRODUCTION

Dam safety is a multidisciplinary subject, involving various fields of study. In Portuguese legislation, dam safety is defined in terms of the structure's ability to meet behavioral requirements in four main aspects of safety: structural, hydraulic, operational and environmental [1].

In order to prevent stability issues arising from construction activities and operational actions throughout the structure's useful life, it's essential to ensure the structural aspects of dam safety, which involves appropriate design with suitable technical criteria, meticulous construction with adequate materials. With regard to the hydraulic aspects, it is crucial to ensure accurate design, including the proper calculation of free board and wave effects, as well as the correct design of waterproofing, filtration and drainage systems. From an operational point of view, it is essential to manage the dam efficiently, complying with applicable safety standards and implementing robust operation and maintenance programs. Finally, environmental aspects require efforts to minimize social and economic impacts, with priority given to protecting and preserving the environment [2].

However, for an embankment dam to perform, the main aspects to take into consideration are the structural hydraulic. According to Cruz [3], in order to guarantee adequate performance of dams, in terms of structural hydraulic, it is essential that they fulfil three fundamental requirements: controlled flow, stability, and compatibility in deformations. Dams are essentially structures designed to retain and store water or waste. To say that a dam is hydraulically and structurally safe means that seepage through the dam and foundation is controlled, and the mechanical stability of the system is maintained for the service and design loads.

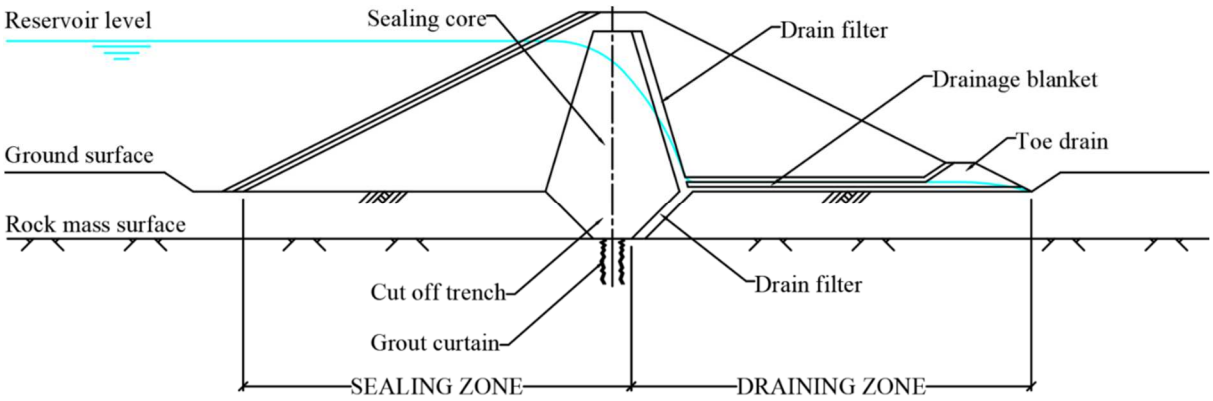

Fig. 1 – Example of hydraulic-structural performance in an embankment dam

Figure 1 illustrates the proper performance of an embankment dam in terms of percolation, the saturation limit (phreatic line) schematically represented by the blue line. The core, cut-off

trench, and injection curtain act as flow barriers or retainers, while the filters, drainage blanket, and toe drain serve to convey flows downstream in a controlled manner.

However, if a dam does not perform adequately in terms of flow control, stability and/or deformation compatibility, anomalies may develop in the embankment and/or foundations, which, if not corrected in a timely manner, may evolute to a failure mode and ultimately result in the failure of the structure.

2. THE ADVANTAGES OF DRONES FOR INSPECTION OF DAMS

Concerning the detection of anomalies in dams, regular monitoring plays a crucial role in ensuring their safety and preventing potential catastrophic failures. Portuguese legislation [1] establishes specific guidelines for the parameters to be monitored, the equipment to be used and the frequency of their measurements, as well as guidelines for routine visual inspections and special inspections, with the purpose of early detection of anomalies that could lead to a possible failure mode.

Normally, when monitoring the hydraulic-structural performance of embankment dams, deformations, percolated flows and piezometric levels inside the dam body, and in its foundation are monitored. Deformations are often monitored using surface markers, inclinometers and extensometer, while flows are controlled using flowmeters, in conjunction with piezometers, to monitor water pressures within the structure and in the foundation. In addition, dam safety includes visual inspections to assess the condition of the structure and to identify possible anomalies, such as seepage, settlement, cracking, subsidence, among others [4, 5, 6, 7].

Fig. 2 – High risk inspection of piping at the Pampulha Dam in Belo Horizonte [8]

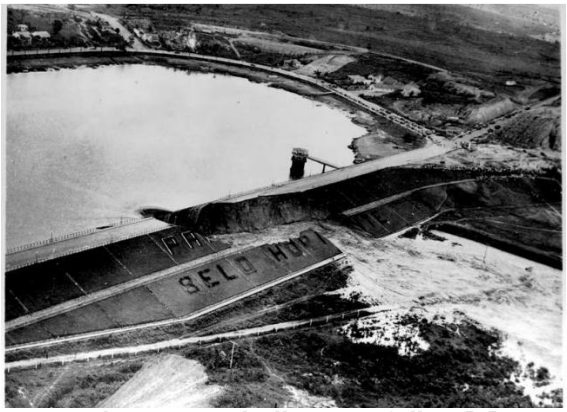

Fig. 3 – Pambulha Dam failure[8] on (04/20/54)

However, although visual inspections are essential, they may be inefficient due to access difficulties and, in some cases, can expose technicians and inspectors to risks, especially in emergency situations. An

example of this is the case of the Pampulha [8] dam collapse (Brazil, 20 April 1954), where an inadequate drainage system resulted in high gradients that led to piping. Fig. 2 shows a risk inspection carried out by the Brazilian authorities a few hours before the failure, which occurred about 48 hours after the anomaly was detected (Fig. 3).

In this context, Unmanned Aerial Vehicles (UAVs), popularly known as drones, offer a number of advantages that can be combined with traditional observation systems to complement dam monitoring. Firstly, they can reach hard-to-reach areas quickly and safely, eliminating, for example, the need to expose workers to potential hazards.

Figure 4 shows an example of a slope about 40 m high, where cracks and slips have been identified. This image was taken from a 3D model obtained from a point cloud generated by processing images taken by a drone. It was possible to identify and map the anomalies in approximately 40 minutes, without putting the inspectors at risk, with the advantage of obtaining an accurate description of the geometry and characteristics of the anomalies.

Fig. 4 - Inspection of a risk area carried out with a drone (image extracted from a textured 3D model, generated from images captured by the drone).

In addition, these devices may be equipped with high-resolution cameras and advanced sensors, including multispectral cameras, radar, LiDAR, infrared, magnetic sensors, among others. This enables the capture of detailed and precise images of the structures, which can facilitate the identification of potential issues at an earlier stage.

Regarding visual inspections, drones offer the advantage of covering extensive areas and detecting anomalies such as deformations, settlements, cracks, seepages and wet zones, among others. When aerophotogrammetric processes are conducted, they produce orthophotos and spatial models, which can provide important information into the current condition of the dam and surrounding areas. Additionally, they allow precise comparisons of the evolution of settlements, development of cracks, wet zones and other anomalies over time.

It should be noted that images captured by digital cameras, or even cell phones, can be used in the photogrammetry process to improve the resolution of orthophotos in areas affected by anomalies. This approach can improve the efficiency of traditional visual inspection, allowing

a more comprehensive and precise analysis of the structural condition. Nevertheless, in order to identify a potential failure mode, it is essential to conduct a comprehensive analysis of the anomalies in question, correlating the information from visual inspection, available instrumentation data, design and construction features. This correlation will allow the identification of the failure mode that is most consistent with the observed anomalies. In addition, the advantage of creating an accurate three-dimensional model of the dam and associated structures should be emphasised, as this provides a series of visualization and analysis possibilities that would otherwise not be achievable.

3. FOURTEEN FAILURE MODES MAPPABLE WITH DRONES

Most anomalies in embankment dams typically appear on the surface of the dam, abutments, and adjacent areas, and they may be linked to potential failure modes. Is crucial to accurately identify the failure mode developing in an embankment dam in an early stage, to allow for effective mitigation measures to address the issue and prevent more severe consequences. To categorize anomalies into a potential failure mode, they should be analysed collectively and, whenever possible, associated with monitoring devices. Combining these findings with visual inspections is important to identify the failure mode most consistent with the observed anomalies.

In this context, Figures 5 to 18 schematically present anomalies related to fourteen failure modes manifesting themselves on the surface, in the foundations, and/or in the dam abutments, which can be mapped using drones. These anomalies include cracks, slumping, seepage, settlements, uplifts, deformations, sinkholes, heaving, muddy water, wet zones, and others. It is essential to examine these together in order to correctly assess the failure mode developing in the embankment dam.

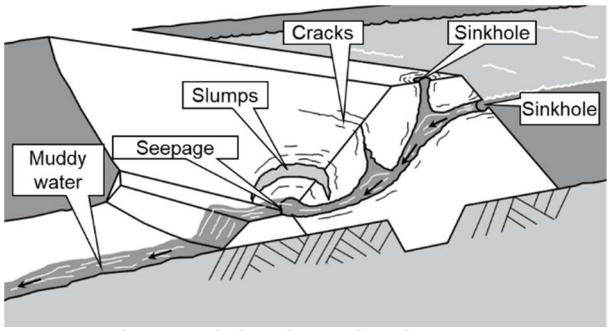

Fig. 5 - Piping in embankments

Internal erosion or piping in embankments can be identified through seepages with muddy water, slumps, and arch cracks, as well as the presence of sinkholes [8, 9, 10].

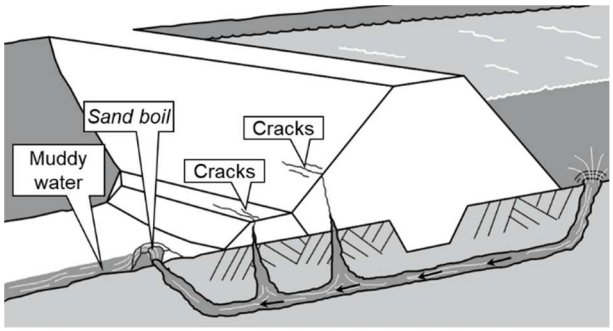

Fig. 6 - Piping in foundations

In foundations, the piping can manifest itself through downstream seepages with the presence of turbid water or the dragging of fines from the foundation, sand boils, and cracks on the embankment [11].

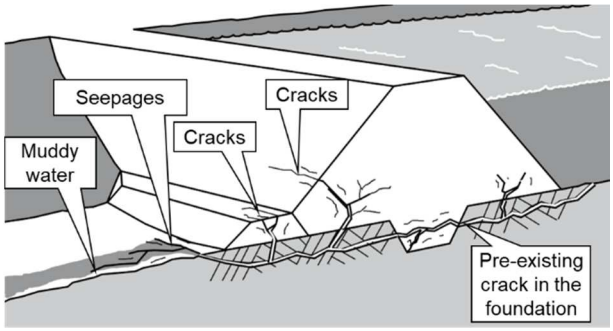

Fig. 7 - Piping into pre-existing fractures

Pre-existing fractures in the foundations can facilitate the occurrence of piping, which is initially manifested by cracks, seepages with muddy water, and/or fines from the foundation [12].

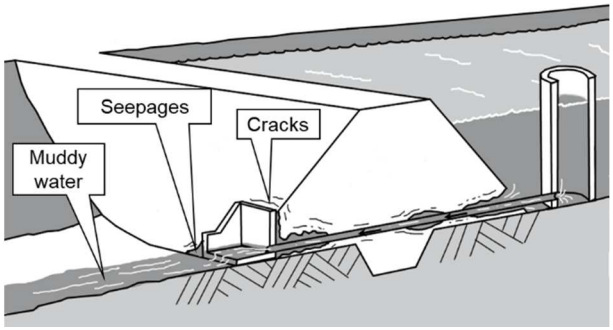

Fig. 8 - Piping on contact between soil and structure

Piping can occur at the interface between the soil and the structure, initially manifesting itself through cracks, seepages of muddy water and with the presence of fines from the foundation in the zone downstream of the dam [13, 14].

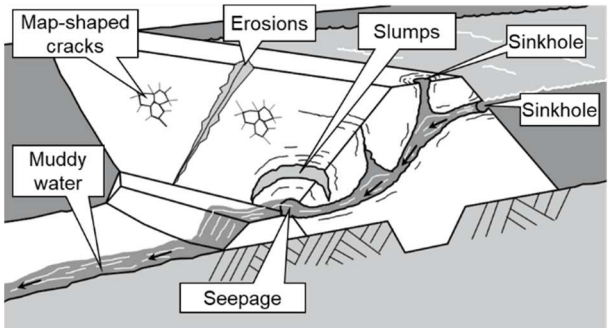

Fig. 9 - Piping in dispersive soils

Dispersive soils are susceptible to piping, which can be manifested by map-shaped cracks, erosions, as well as seepages, slides, sinkholes, and the presence of muddy water [15, 16, 17, 18].

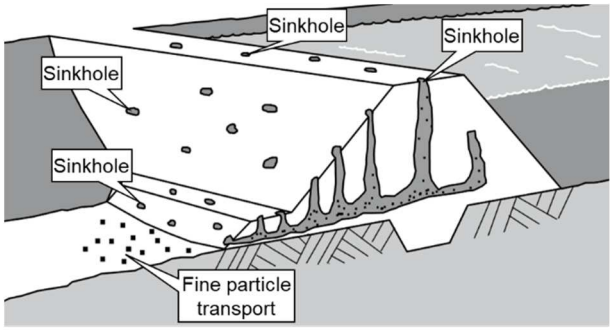

Fig. 10 - Piping by suffusion

Poorly graded soils, which allow for the migration of fines, can result in the suffusion process, which is typically evidenced by the formation of numerous sinkholes and the presence of fines in the downstream slope [19, 20].

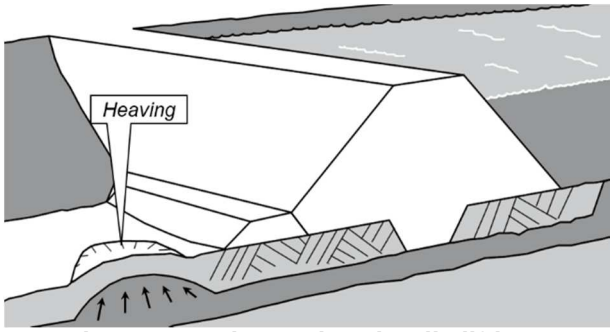

Fig. 11- Heaving and Hydraulic lifting

The aerophotogrammetry process allows the comparative analysis of point clouds, facilitating the identification of anomalies, such as heaving, caused by excessive underpressure [21, 22].

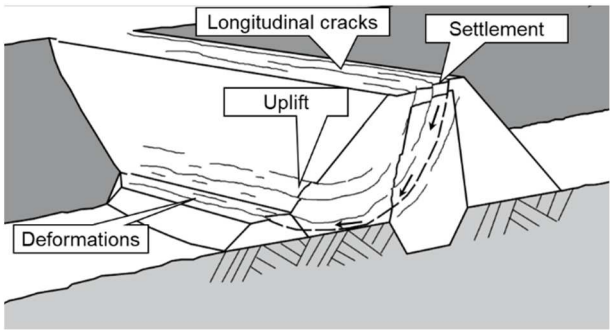

Fig. 12 - Excess pore pressure

When the loads applied to soils increase rapidly and the pore water pressures are not allowed to dissipate, a loss of shear strength may occur, leading to the occurrence of longitudinal cracking and settlement [23, 24].

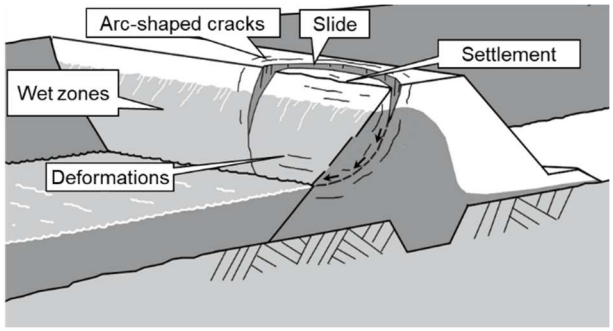

Fig. 13 - Rapid drawdown failure

The rapid drawdown of the reservoir can cause instability in the upstream slopes, increasing the probability of slides, settlements, and arch cracks [25, 26].

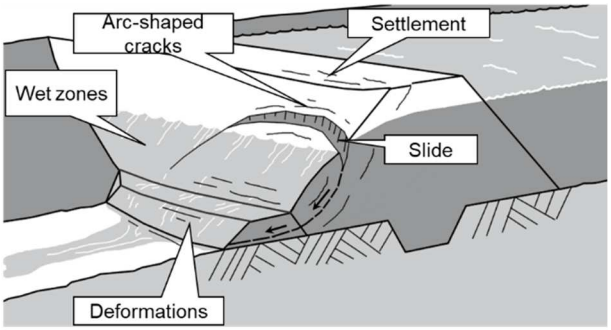

Fig. 14 Faulty drainage system

Deficiencies in the internal drainage system have the potential to elevate the water level within the embankment, favouring the formation of wet zones, settlements, cracks in the arches, deformations, and slides [27].

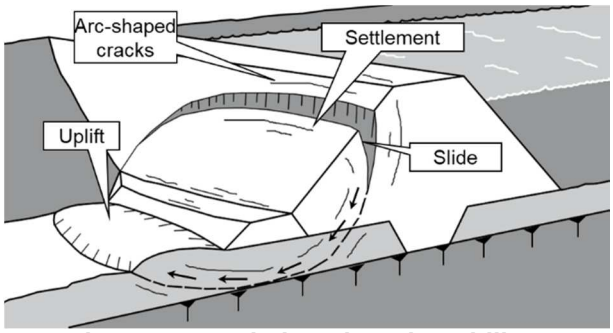

Fig. 15 - Foundation shear instability

In the presence of soft soils in the foundation with insufficient load-bearing capacity, there is a greater propensity for sliding, settlement, uplift, and arch cracks [28].

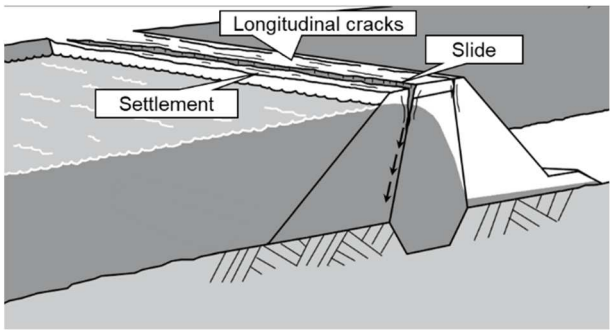

Fig. 16 - Freeboard loss failure

Rockfill dams or dams with collapsible material can experience excessive settlement due to wetting, especially during the first filling of the reservoir, resulting in longitudinal cracks, sliding, and deformations [29].

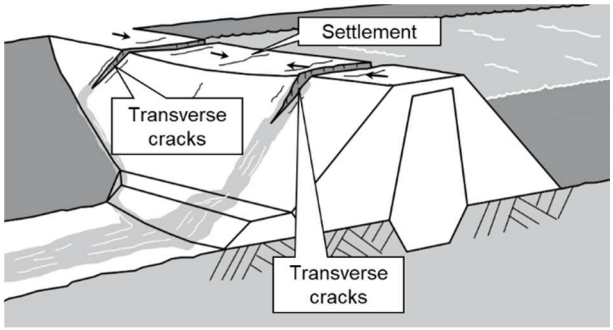

Fig. 17 - Freeboard loss due to cracks

Differential settlements in the foundation and embankment can cause transverse cracks, resulting in a loss of freeboard and allowing the opening of a breach in the dam [30, 31].

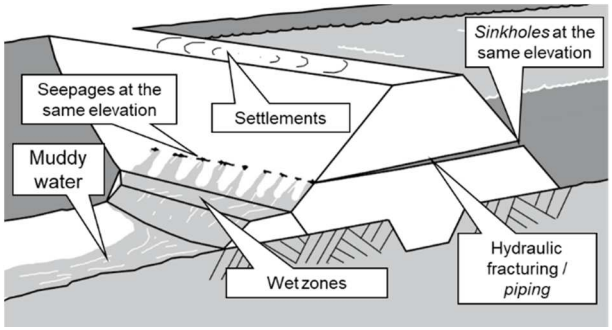

Fig. 18 - Hydraulic fracturing

Construction problems between joints or layers in embankments, as well as differential settlements, can lead to hydraulic fracturing and seepage at the same level, as well as sinkholes, and settlements [32].

As shown in the figures, the different failure modes can show signs of anomalies both on the surface of the structures and in adjacent areas. These anomalies can be detected through conventional visual inspections, and/or using drones to carry out aerial mapping of the dam [33, 34]. The use of drones also makes it possible to view the entire dam, and adjacent areas, from perspectives that would not be possible with traditional inspections, as well as to record

images with dimensional accuracy (as presented in Section 5). By combining the expertise of dam inspectors with sophisticated monitoring technologies, it is possible to identify anomalies associated with the aforementioned failure modes at an early stage. This enables the implementation of preventive measures to guarantee the security of dams.

4. OPEN-SOURCE SOFTWARE FOR PROCESSING AND ANALYSING 3D MODELS

Nowadays, aerial surveys can be conducted in an efficient and cost-effective manner using drones. In this work, the surveys were conducted using a DJI Phantom 4 Pro drone. By applying the technique of aerophotogrammetry, using images captured by drones, it is possible to generate a range of spatial models, including Digital Surface Models (DSM), Digital Terrain Models (DTM), orthophotos, elevation maps, contour lines, and other by-products. These models are of significant value in the context of dam safety, as will be discussed in further detail later on.

While the initial cost of purchasing drones is relatively low, the processing of images in commercial software to generate these models can represent a significant investment. Nevertheless, open-source software (OSS) can provide high-quality results, at zero cost.

4.1. WebODM

In the context of ongoing research at LNEC, data obtained through the use of drones has been processed using the OSS platform. This approach aims not only to optimise financial resources, but also to facilitate the development of new applications from existing ones and avoid dependence on specific suppliers. While the functionalities available in OSS may lack the intuitiveness of those commercial products, which are designed to yield results rapidly, this choice offers greater flexibility and control over data analysis processes. Furthermore, it facilitates the dissemination of results [33, 34, 35, 36, 37, 38].

In order to achieve this objective, this study used the Open Drone Map (ODM) software in its web interface version (WebODM). This tool, available at https://www.opendronemap.org/webodm/, enables the processing of drone data to generate point clouds, orthophotos, and three-dimensional models. The selection of WebODM reflects the prioritisation of OSS in aerial data processing, offering an accessible and flexible solution for analysing information obtained from aerial drone surveys.

4.2. The GCP finder tool

In order to improve the precision and accuracy of aerial mapping carried out with drones, the use of Ground Control Points (GCPs) is essential. These points are essential for correcting

errors and distortions that may occur during image processing, as well as serving as tools for verifying the topographical errors involved in the surveys. Finally, GCPs allow the quality of the results obtained to be assessed.

However, processing GCPs usually requires the arduous task of locating these points on each image taken with a drone (there can be hundreds of images) and assigning the reference coordinate to these images. Nonetheless, as part of its work, LNEC, in partnership with Nova University Lisbon, has developed a tool called GCP finder [39] to optimise the processing of GCPs.

In cases where georeferencing is in place, substantial errors can nevertheless be made in determining the camera's position. Factors such as the size of the image, the pixel, the quality of the optics or small variations during the flight of the drone greatly influence the errors made. This is where GCPs are used.

Any object with a visible and identifiable shape at a certain altitude can be considered a GCP, but there are objects with shapes and patterns that are easily recognised regardless of the environment in which they are placed. A good GCP should be identifiable at a high altitude, have a shape or colours that differentiate it from the environment in which it is placed, and have a well-defined point where the GPS can be placed [40]. Regardless of the shape of the GCP used, they should have a matt/matte finish, because if they are shiny, depending on the angle at which the photos are taken, they can reflect the light and make it difficult to identify them in the images [41]. Figure 19 shows an example of GCPs locatable with the GCP Finder software.

Fig. 19 - Example of ground control points identifiable with the GCP Finder

The process of creating the list of coordinates for each photograph, done manually, is relatively simple for a small number of photographs (10, for example), but is very time-consuming and error-prone in the case of a large number of photographs, as happens in any real survey. Therefore, the algorithm developed is essential for the identification phase of the points in the

photos taken with drones, as it allows an exhaustive list of the coordinates of the GCP in each image to be obtained automatically and with good quality.

The algorithm developed is available for free use on the GitHub platform at https://github.com/octaviojardim/GCP_Finder (in the console version) and on the web interface for installation on servers, at https://github.com/octaviojardim/Web-Interface-GCP-Finder. The platform includes the source code, installation instructions and an example application.

4.3. CloudCompare

The CloudCompare program stands out as an essential tool in the context of point cloud comparison, helping to identify surface changes between different surveys. Developed as an open-source project, CloudCompare is designed for visualizing, editing, and processing 3D data, with a focus on point cloud and mesh analysis. Its latest version, 2.14. alpha, Kharkiv, released on September 29, 2024, is governed by the GNU General Public License (GPL), allowing its use for various purposes, including commercial and educational applications [42]. CloudCompare supports several features, such as change detection, and can compare two different point clouds, proving useful in detecting settlements, heaving, and other deformations related to mass movements in dams and adjacent areas.

5. CASE STUDY

To illustrate the benefits of drones in dam inspection, a case study is presented, based on surveys conducted as part of safety inspections by LNEC at the Lapa Dam. Lapa is an earthfill dam with a maximum height of 24 m and crest elevation of 174.0 m, as shown in the cross-section in Figure 20. The normal water level (NWL) is 170.0 m, the maximum water level (MWL) is 171.92 m, and the minimum operating level (MOL) is 162.2 m. The reservoir at MWL has a relatively small volume (0.64 hm^3), with a flooded area of 9.5 ha. The upstream and downstream slopes have inclinations of 1:3.25 (V:H) and 1:2.5 (V:H), respectively. The downstream face features a berm, 2.5 m wide, located at 164.0 m elevation.

For the analysis of this dam, aerial surveys were carried out using a DJI Phantom 4 Pro drone, with the support of 10 GCPs, georeferenced with a Geodetic GPS. These surveys were conducted on two separate occasions, on 07/20/2021 and 05/19//2022, aiming to identify possible settlements and other anomalies.

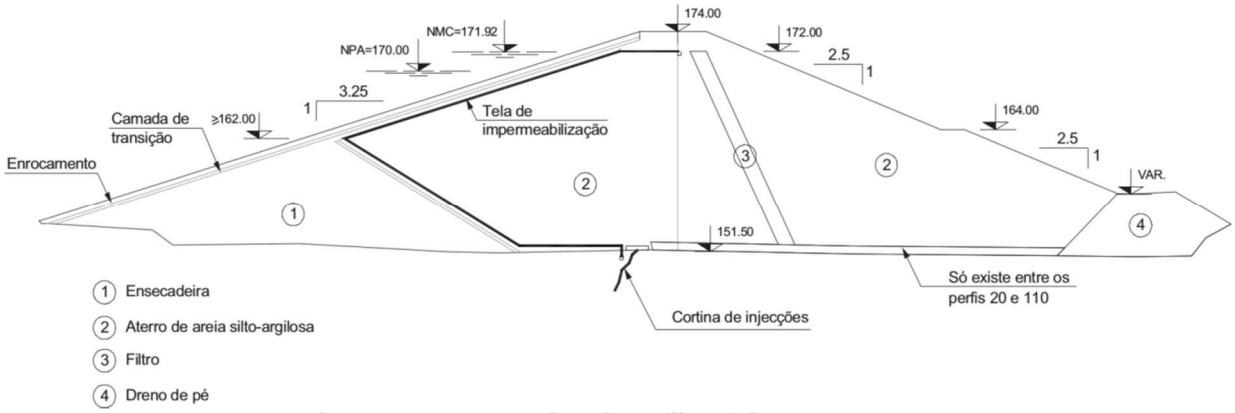

Fig. 20 - Cross-sectional profile of the Lapa Dam

As shown in Figure 21, processing the images using OSS software allows the generation of textured 3D models. It also enables the creation of DTM and DSM, such as the one illustrated in Figure 22, and contour lines associated with orthophotos (Figure 23). This results in a set of accurate data on the geometry and condition of the structure, highly useful for dam safety. These models faithfully represent the condition of all areas of the dam and surrounding regions.

Fig. 21 - Textured model of the Lapa Dam (WebODM)

As illustrated in Figure 23, this survey enabled the detection of an area of old settlement in the central region of the dam, indicating a loss of freeboard, mass movement, landslides, and cracks in the embankment and/or foundation. In detail, Figure 24 shows the cracks in the area where the settlements occurred.

Figures 25 and 26 show a comparison of two orthophotos generated in WebODM, from surveys carried out over a period of approximately 10 months, whose differences in vegetation can be easily observed.

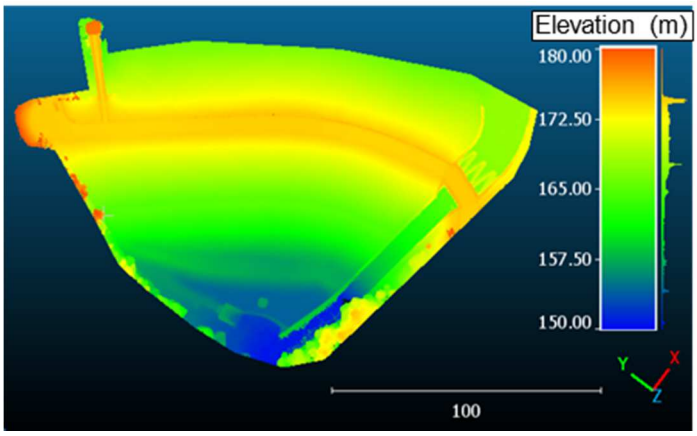

Fig. 22 - Digital Surface Model (CloudCompare)

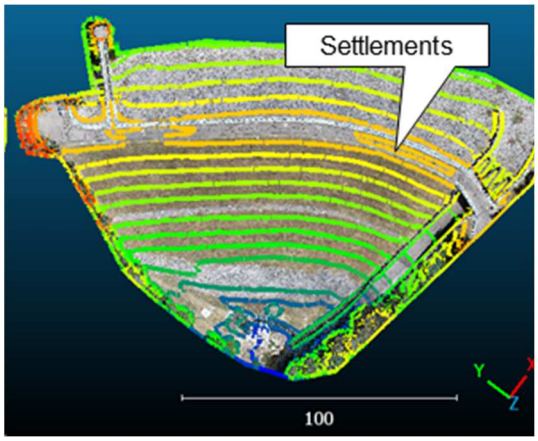

Fig. 23 - Contour lines (every 2.0 m)

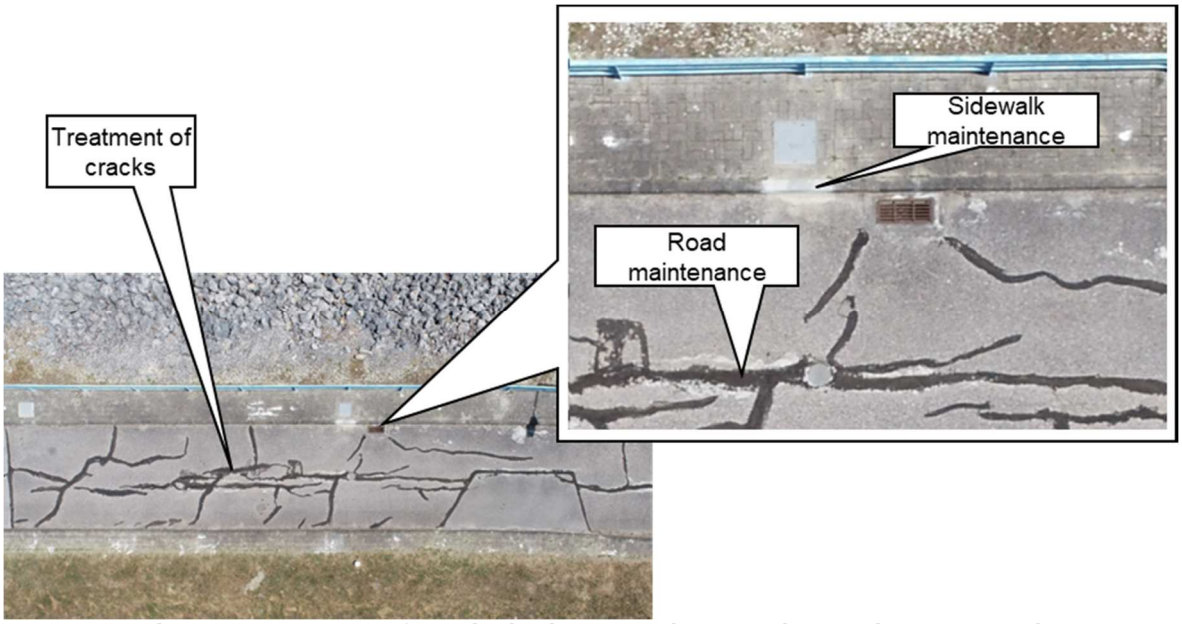

Fig. 24 - Treatment of cracks in the area where settlement has occurred

Fig. 25 - Survey carried out on 07/20/21

Fig. 26 - Survey carried out on 05/19/22

For a comparative analysis of deformations over a specific period, the use of CloudCompare software is recommended. This program allows for examining discrepancies between point

clouds generated from images captured by drones, as shown in Figure 27. The areas highlighted in red represent differences greater than 1 m, indicating the removal of shrub vegetation during dam maintenance. The green and yellow areas denote changes of about 0.5 m, associated with the removal of ground vegetation. By analysing the colour patches and comparing them with the orthophotos (Figures 25 and 26), it is possible to distinguish between the deformations in vegetation and minor deformations in areas of interest, such as the crest and upstream rock protection. However, no significant deformations were observed in the body of the dam (blue patch), indicating that no substantial deformations occurred between the two surveys.

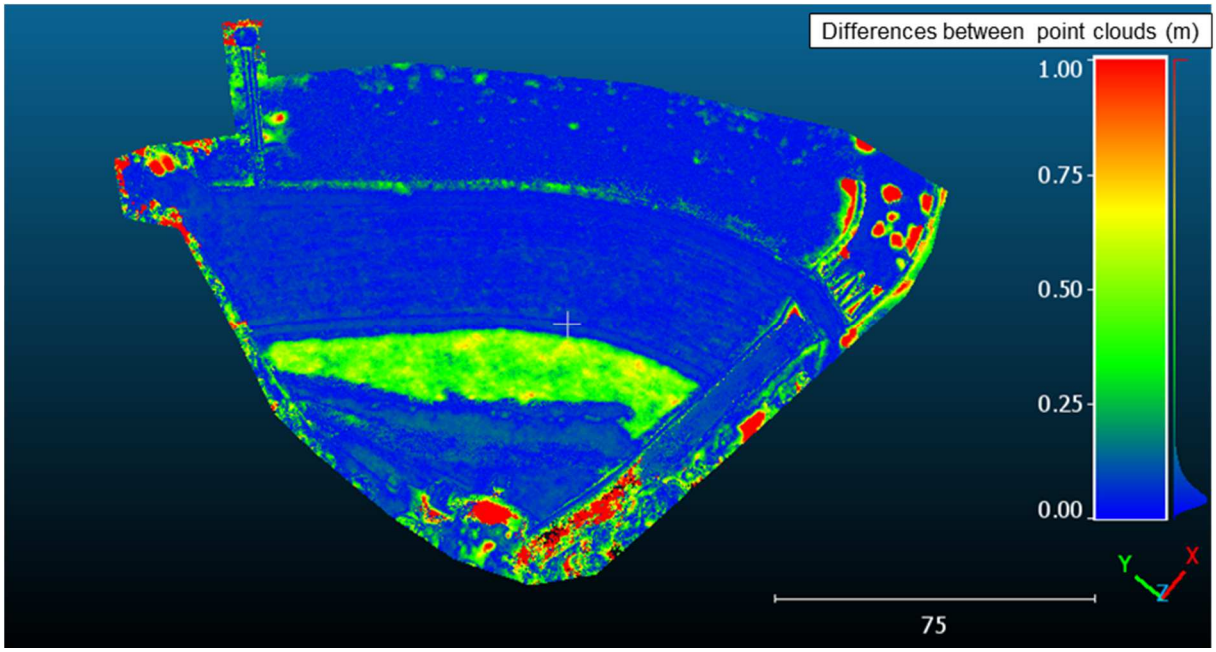

Fig. 27 - Point cloud comparison (CloudCompare))

6. CONCLUSION

As shown above, when it comes to detecting anomalies in embankment dams, the use of drones and photogrammetry is proving to be an effective tool to complement traditional visual inspections. By capturing high-resolution aerial images, these methods allow for a detailed analysis of the surface of slopes, abutments and areas downstream of the dam. This technology makes it possible to map cracks, settlements and other anomalies associated with possible failure modes in embankment dams, aiding preventive maintenance and the mitigation of potential safety risks.

Furthermore, by integrating drone inspections with the performance analysis of conventional instrumentation, it is possible to obtain a comprehensive view of the state of the dam. Combining these techniques allows for a more complete understanding of the structure's behaviour over time, making it possible to implement corrective and preventive measures more

efficiently. Thus, the joint application of traditional visual inspections and advanced monitoring technologies becomes a powerful strategy for assuring the safety and integrity of dams.

The use of drones to support the recording of construction inspections has become increasingly important, both because of the reduction in the cost associated with the necessary equipment and because of the ever-increasing capabilities of the equipment and post-processing programmes.

With regard to the programmes available for post-processing, the use of Open Source software is proving to be efficient, offering good tools for spatial modelling and the detection of changes, indicating, for example, the occurrence of mass movements on dam surfaces.

The quality of the surveys and the models obtained through post-processing depend greatly on various factors, such as the quality of the optics, the resolution of the images, the ambient light at the time of photography, and also the existence of GCPs with known coordinates that allow the reconstructed model to be improved. In this sense, the GCP Finder tool can help optimise the processing and automatic recognition of GCPs used in surveys.

With regard to the case study of the anomalies observed with drones at the Lapa dam, there were old settlements on the dam crest, with the presence of sharp cracks in the longitudinal direction of the dam axis, possibly associated with the failure mode related to localised settlement and reduction in the freeboard, shown in Figure 16. However, in the 10-month period, no evolution of the settlements was observed. It should be noted that the dam is currently operating under conditions, with water level limitations during the wet season.

REFERENCES

[1] Decreto-Lei nº 21/2018 - Regulamento de Segurança de Barragens (RSB), de 28 de março. Diário da República nº 63/2018, Série I de 2018-03-28, Portugal.

[2] Quintela, A. C., Pinheiro, A. D. N., Gomes, A. S., Afonso, J. R., Almeida, J. M., & Cordeiro, M. S. (2001). Curso de exploração e segurança de barragens. Instituto da Água, Lisboa.

[3] Cruz, P. T. D. (1996). 100 barragens brasileiras: casos históricos, materiais de construção, projeto. Oficina de Texto, São Paulo.

[4] Ministério da Integração Nacional (2002). Manual de Segurança e Inspeção de Barragens. Brasília, DF.

[5] Groenier, J. S. (2012). Pocket safety guide for dams and impoundments. U.S. Department of Homeland Security, Federal Emergency Management Agency and National Dam Safety Program, USA.

[6] Department of Environmental and Natural Resources, Division of Land Resources, Land Quality Section (2007). Dam Operation, Maintenance, and Inspection Manual, 1985, revised, North Carolina.

[7] Silveira, J. F. A. (2006). Instrumentação e segurança de barragens de terra e enrocamento. Oficina de Textos, São Paulo.

[8] Guidicini, G., Sandroni, S. S., & Mello, F. M. (2021). Lições aprendidas com acidentes e incidentes em barragem e obras anexas no Brasil [livro eletrônico]. Comitê Brasileiro de Barragens. Rio de Janeiro.

[9] USBR (2019). Best Practices in Dam and Levee Safety Risk Analysis, Internal Erosion Risks for Embankments and Foundations, USA.

[10] Government of British Columbia. (2020, March 3). Module 3: Common Issues. B.C. Dam Safety Self Directed Learning. [https://www2.gov.bc.ca/gov/content/environment/air-land-water/water/drought-flooding-dikes-dams/dam-safety/11965/12021/module-3-common-issues].

[11] FEMA. (2023). A.V. Watkins Dam Backward Erosion Piping Incident Update. In National Dam Safety Program Technical Seminar.

[12] Mejia, L.H. (2013). Analysis and design of embankment dams for foundation fault rupture. Em Proceedings of 19th symposium of the New Zealand Geotechnical Society, Queenstown, Nova Zelândia.

[13] Silveira, J.F.A. (2019). Ruptura de barragens de terra-enrocamento. SBB Engenharia.

[14] Medeiros, C.H. (2015). Segurança de barragens e avaliação de riscos. XXX Seminário Nacional de Grandes Barragens, Painel: Lei da Segurança de Barragens e Avaliação de Riscos (Tema 113), 41.

[15] United States Department of Agriculture. (2006). Chapter 45 Filter Diaphragms. Part 628 Dams National Engineering Handbook.

[16] Tosun, H., & Kılbıyık, M. (2006). Internal erosion resulted from dispersive soils in earthfill dams and a case study. Em ASDSO National Dam Safety Conference. Setembro (pp. 10-14).

[17] Hardie, M., Doyle, R., Cotching, B., Duckett, T., & Zund, P. (2009). Dispersive soils and their management. Technical Reference Manual, Sustainable Land Use Department of Primary Industries and Water.

[18] Cruz, S.I.C. da. (2008). Caracterização e utilização de solos dispersivos nos aterros compactados da barragem de Sobradinho. Dissertação de mestrado, Programa de Pós-Graduação em Engenharia Geotécnica, Núcleo de Geotecnia.

[19] Richards, K., Doerge, B., Pabst, M., Hanneman, D., & O'Leary, T. (2015). Evaluation and monitoring of seepage and internal erosion. Em S. Leffel (Ed.), Washington, DC: FEMA (pp. A1 91-95).

[20] USACE. (2022, novembro). DLS208 M11 Brodhead Dam Case History (Internal Instability) [Vídeo]. USACE Risk Management Center. Recuperado de https://youtu.be/gM5X2q3O9aw?si=LjZwTO3S7CuGL8bZ.

[21] Robbins, B.A., Sharp, M.K., & Corcoran, M.K. (2015). Laboratory Tests for Backward Erosion Piping. In Geotechnical Safety and Risk V (pp. 849-854). IOS Press.

[22] Bandeira, O., Carvalho, R., Leite, D., & Hitaka, J. (2018). Intervention carried out in the Left Side Dam of the Pimental site of the Belo Monte HPP during the filling of the reservoir. Dam World.

[23] Souza, A.N. de. (2017). Análise do comportamento da barragem engenheiro Armando Ribeiro Gonçalves-Açu/RN-durante sua construção, primeiro enchimento e operação do reservatório [Mestrado, Brasil].

[24] De Mello. (1982). A case history of a major construction period dam failure.

[25] Narita, K. (2000). Design and construction of embankment dams. Dept. of Civil Eng., Aichi Institute of Technology.

[26] Federal Energy. (1978). Walter Bouldin Dam failure and reconstruction.

[27] de Mello, V. F. Da importância de resgatar o passado, no caso de incidentes em barragens; O exemplo de Santa Branca.

[28] Vu, B.T., Van Pham, M., Nguyen, D.Q., Phan, D.C., & outros. (2023). Understanding downstream slope failure in earth dams: Causes and remedies-A case study of Trieu Thuong No. 2 Dam, Quang Tri, Vietnam. GEOMATE Journal, 25(108), 163-171.

[29] Silva, J.M.M. da. (1996). Modelação do colapso e da fluência em aterros [Tese de doutorado, Universidade do Porto].

[30] He, K., Song, C., & Fell, R. (2021). Numerical modelling of transverse cracking in embankment dams. Computers and Geotechnics, 132, 104028. https://doi.org/10.1016/j.compgeo.2021.104028

[31] Fell, R. (2015). Geotechnical engineering of dams. CRC Press.

[32] Sherard, J. L. (1986). Hydraulic fracturing in embankment dams. Journal of Geotechnical Engineering, 112(10), 905-927. https://doi.org/10.1061/(ASCE)0733-9410(1986)112:10(905)

[33] Leite, D., Marcelino, J., & Gonçalves. (2020). Application of drones and OSS for mapping and visual inspection of embankment dams. In Proceedings of the Fourth International DAM WORLD Conference (Vol. 1, pp. 527-532). LNEC-Laboratório Nacional de Engenharia Civil.

[34] Leite, D., Marcelino, J., & Gonçalves. (2020). Presentation on application of drones and OSS for mapping and visual inspection of embankment dams. In Proceedings of the Fourth International DAM WORLD Conference. LNEC-Laboratório Nacional de Engenharia Civil.

[35] Leite, D., Marcelino, J., Manso, J. (2024). Drones como Ferramenta de Inovação e Segurança na Observação de Barragens de Aterro. In Proceedings of the 12º Congresso Luso-Brasileiro de Geotecnia e 8as Jornadas Luso-Espanholas de Geotecnia, Lisboa.

[36] Leite, D., Marcelino, J., Manso, J. (2024). Presentation on “Drones como Ferramenta de Inovação e Segurança na Observação de Barragens de Aterro”. 12º Congresso Luso-Brasileiro de Geotecnia e 8as Jornadas Luso-Espanholas de Geotecnia, Lisboa.

[37] Marcelino, J., Manso, J., Leite, D., Marques, N. C., Freire, O. (2024). Structural health monitoring and inspection of dams based on Unmanned Aerial Vehicles photogrammetry with image 3D reconstruction. Proceedings of the XVIII ECSMGE 2024: Geotechnical Engineering Challenges to Meet Current and Emerging Needs of Society. Taylor & Francis. ISBN 978-1-032-54816-6. DOI 10.1201/9781003431749-337.

[38] Marcelino, J., Manso, J., Leite, D., Marques, N. C., Freire, O. (2024). Presentation on Structural health monitoring and inspection of dams based on Unmanned Aerial Vehicles photogrammetry with image 3D reconstruction. XVIII European Conference on Soil Mechanics and Geotechnical Engineering (ECSMGE 2024), Lisboa.

[39] Freire, O (2022) – Autonomização de software open source (webodm) para modelação e mapeamento de barragens com drone, Universidade Nova, Lisboa.

[40] P. Aero – “Things To Know About Ground Control in Drone Surveying”, Last accessed 4 May 2021. Dez. de 2016. u r l: www.propelleraero.com/blog/things-to-know-about-ground-control-in-dronesurveying (p. 15).

[41] J. Kuze – “Ground Control Points (GCPs) for aerial photography”. Last accessed 17 May 2021. Fev. de 2015. url: https://diydrones.com/profiles/blogs/ground-control-points-gcps-for-aerial-photography (p. 15).

[42] CloudCompare (version 2.13) [GPL software]. (2024). Retrieved from http://www.cloudcompare.org/

Fifth International Dam World Conference
PORTUGAL • LISBON • LNEC • APRIL 13-17, 2025
dam world 2025

CONSTRUCTION OF AN ASPHALT CORE DAM IN A SEISMIC ZONE

Newton Goulart Graça[1]
CONSAG ENGENHARIA

José Flauzino Moreira[2]
CONSAG ENGENHARIA

Bruno Cesar Oliveira Carleto[3]
CONSAG ENGENHARIA

Tarcísio Araújo Pantoja[4]
CONSAG ENGENHARIA

ABSTRACT

The Montegrande Dam was built in an area of high seismicity, in the Dominican Republic.

The project, built on the Yaque del Sur River and owned by INDRHI – Instituto Nacional de Recursos Hidraulicos, a Dominican government agency, has multiple objectives such as the containment of extreme floods, which can occur due to hurricanes, water reservation, irrigation and power generation.

The dam has a maximum height of 57m and a total length of 1,447m, with a total volume of 4,250,000m³ of rockfill.

On the abutments, the dam is seated on a soft rock mass and on the riverbed on alluvial gravel, with the seal being through a plastic diaphragm wall.

The aim of this paper is to present the care taken during construction, including the recommendations of Prof. Dr. Kaare Hoeg and his assistant Vahid Afsari Rad, as well as the results obtained during the execution and quality control.

Keywords: Dam, Asphalt Core, Seismic, Quality Control, Tests

[1]newton.graca@agnet.com.br, Brazil
[2]jose.moreira@agnet.com.br, Brazil
[3]bruno.carleto@agnet.com.br, Brazil
[4] tarcisio.pantoja@agnet.com.br, Brazil

1. INTRODUCTION

The Montegrande Dam is a rock fill dam with asphalt core 1,447m long, 57m high with a total volume of 4.25 million m³ of materials, built from 2018 to 2022 in Dominican Republic, in an Caribbean island, as it showed in Figure 1.

Fig. 1 – Montegrande Dam Location

The purposes of this project are flood control, prevention against hurricanes and several storms, irrigation, water supply and power generation.

The zone of this construction present a very complicated seismic pattern as it shows in Figure 2. In 2010, a severe earthquake in Haiti, in the same island of Dominican Republic cause 210.000 dead.

I other occasions, other floods caused by hurricanes David and Federico (1979) and George (1998) caused more than 2.000 dead.

Fig. 2 – Geology of the island and surroundings

2. GENERAL LAY OUT

The Montegrande Project includes from the left to the righ abutment: Rockfill Asphalt Core Dam, Diversion Channels and Tunnel, Concrete Wall, Bottom Spillway, Concrete Wall, Service Spillway, Concrete Wall and Homogeneous Dam.

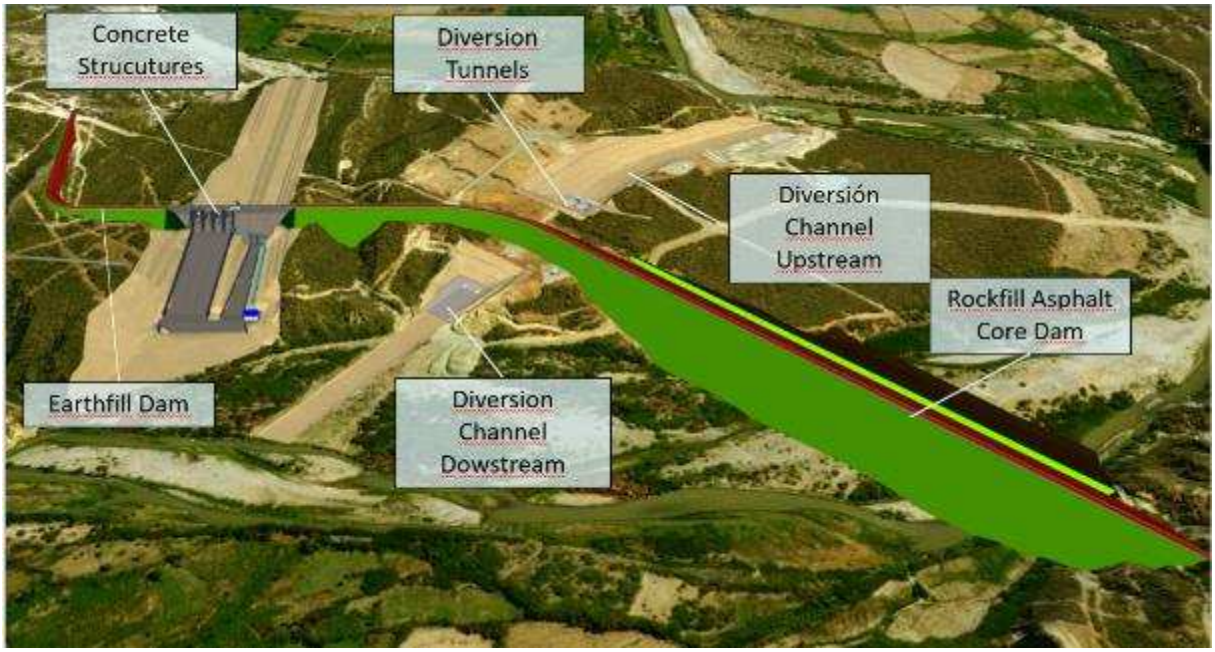

Fig. 3 – Montegrande General lay out

DAM PLAN VIEW AND CROSS SECTION

The Main Dam is 1447m long and 57m high, and is composed by diaphragm wall crossing the alluvium, from the sound rock to the plinth where the asphalt core began, rockfill and transitions. The first rockfill was placed on May, 10th 2019 and finished on November, 3rd 2022.

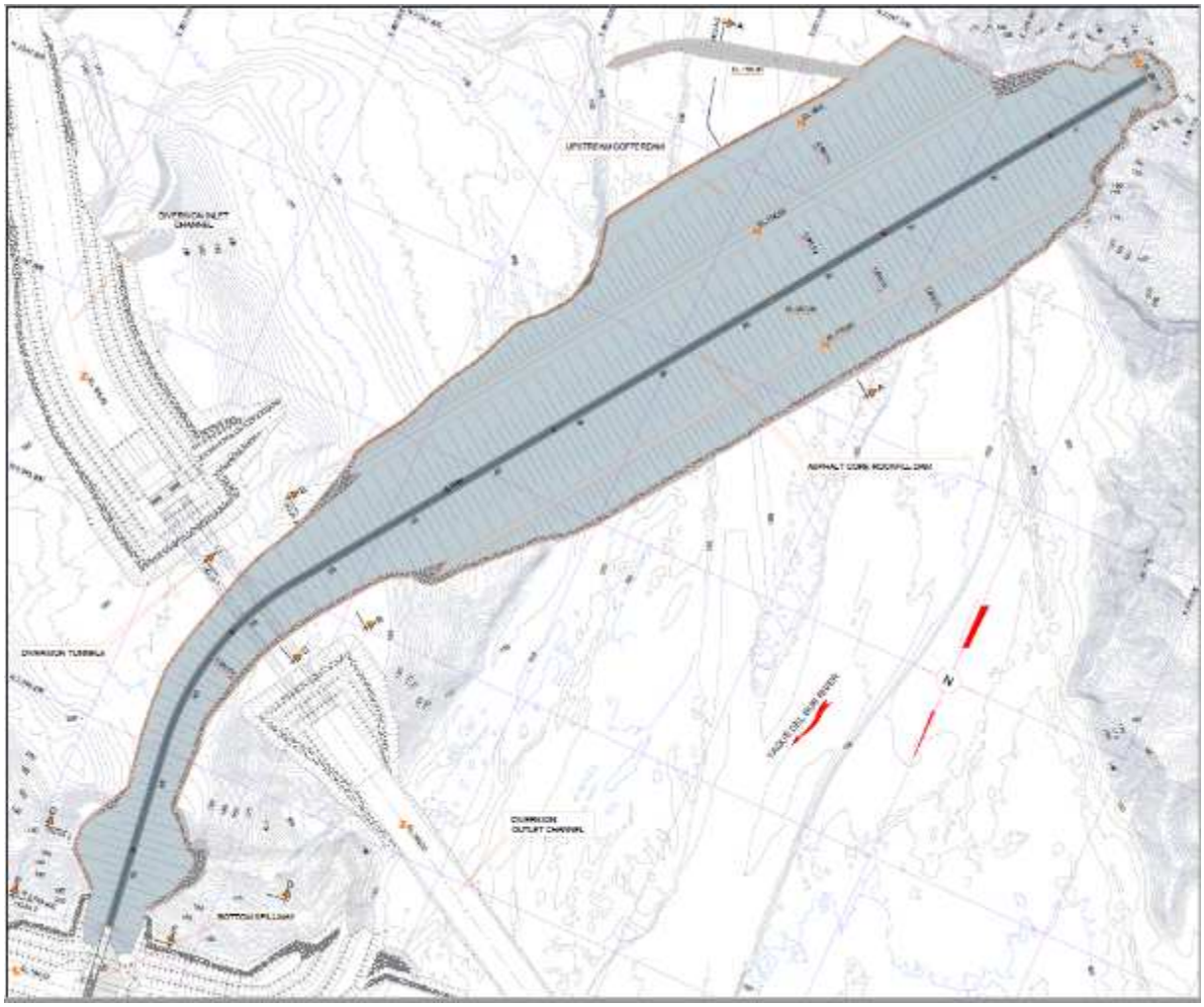

Fig. 4 – Dam Plan View

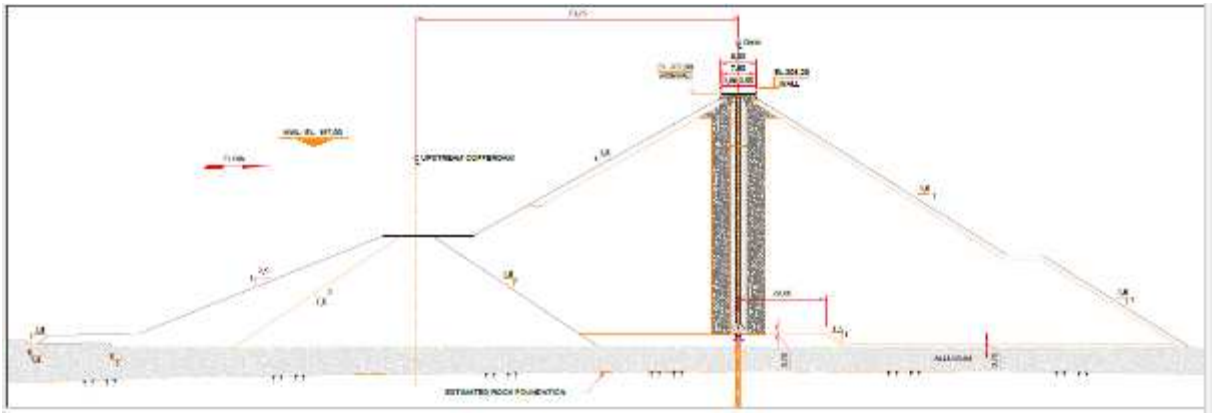

Fig. 5 – Dam Cross Section

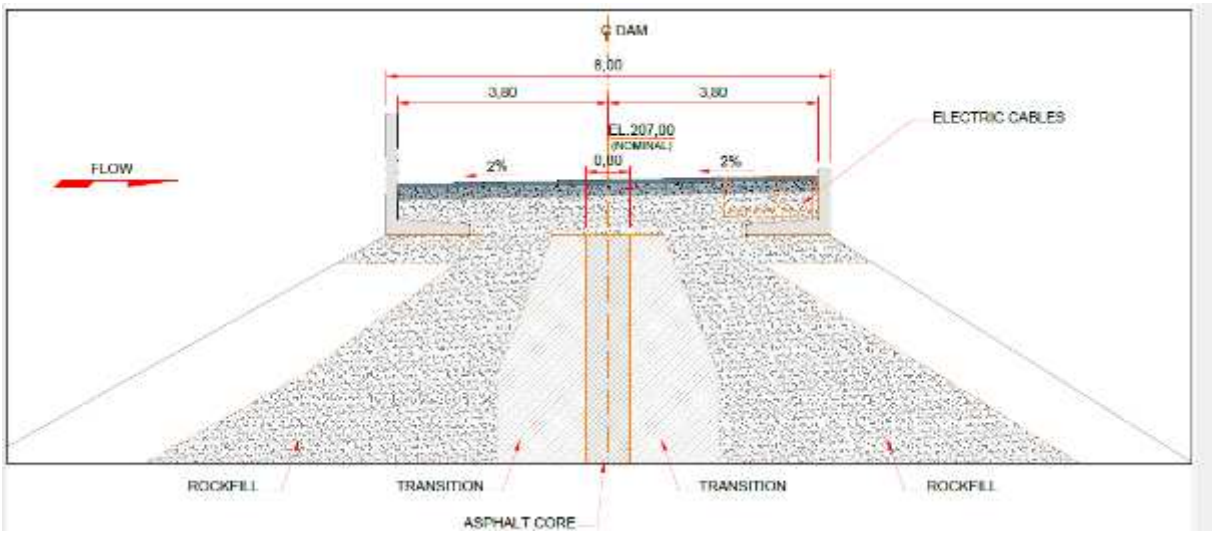

Fig. 6 – Dam Cross Section – Crest Detail

3. PRELIMINARY TESTS ANS FULL SCALE TRIAL

3.1. Preliminary Tests

The initial mix was done in Norway, in Veiteknisk Laboratory and the triaxial tests in NGI Laboratory, and follow it is presented the comments and recommendations of Dr Kaare Hoeg:

“AsphaltCoreDams AS contracted NGI to perform triaxial tests on a trial laboratory mix of asphalt concrete for use in the core of the Monte Grande Dam, Dominican Republic. Three triaxial specimens were prepared by Veiteknisk Institutt, Oslo and delivered to NGI. Only two specimens should be tested unless the two first specimens gave very different stress-strain-strength results.

Triaxial specimens and test conditions

Specimen size: 100 mm in diameter and 200 mm high

Bitumen type: Penetration value B 160-220

Bitumen content: 5.9% (of total specimen weight)

Filler content: 14%

Specimen was built up in 6 layers of approx. 50 mm height and each layer was compacted by 30 blows of a Marshall hammer. The resulting air void content (air porosity) was about 1.5% for both specimens

The triaxial tests were run as axial compression tests (strain-controlled) with an axial strain rate of 2%/hour.

Radial confining stress on specimen: 500 kPa (kept constant throughout the test)

The described test conditions follow standard procedures used by NGI for triaxial testing of the trial mix for asphalt core embankment dams (ACED). By following standard procedures, one may directly compare the results with the results from other ACED projects.

For the Monte Grande Dam the testing temperature was specified by the Client to be 10^0C.

Test results

The stress-strain-strength results from the two triaxial tests are shown in Figure 1.

The peak strength from the two tests are very similar with a peak deviator stress of about 2500 kPa. The axial strain at peak deviator stress is about 8 %, and the reduction in deviator stress after peak is reached is small. Both specimens show ductile (as opposed to brittle) behaviour with only modest strain-weakening. This is a very positive characteristic for asphalt concrete to be used as dam core material.

Test No. 1 (black curve in Fig.1) shows a fairly stiff behaviour at small strains. Test No. 2 (blue curve) exhibits a more flexible behaviour and has a lower compression modulus, E. Usually the secant modulus up to 1 % axial strain is used as a quantitative measure of the stiffness, and for the two tests the values are about 145 MPa and 105 MPa for Tests No.1 and 2, respectively.

The magnitude of volumetric strain as function of axial strain is plotted in Fig. 1 for both tests. Test No. 1 shows somewhat more volumetric expansion (dilation) than Test No. 2. Increased dilation causes increased permeability with shearing. The average value for dilation shown as negative volumetric strain in Fig.1, is only about 0.5% for axial strain of 4% and 1.5% for axial strain of 8 % at peak stress level. These low volumetric expansion values only lead to very minor increases in permeability. With the low bitumen content (5.9%), the degree of dilation was expected to be higher and the strain-weakening to be more pronounced.

Conclusions and recommendation

The Monte Grande asphalt core rockfill dam is to be built at a site with high seismicity. Furthermore, the dam foundation may cause some differential settlements under the dam, and unless all susceptible foundation material is excavated, there is a potential for some foundation liquefaction and resulting displacements and dam distortions.

The core and asphalt concrete mix must be designed to accommodate the dam shell and foundation distortions both for static and earthquake loading without undergoing detrimental cracking. Therefore, the core should exhibit both flexible and ductile behaviour. This is partly achieved by the specification of a bitumen with high penetration value, B 160-220. Higher flexibility and improved cracking resistance may be achieved by increasing the bitumen content

of the mix above the content (5.9%) used in the preliminary trial mix. Furthermore, if cracks should develop in the core during severe earthquake lading, a richer asphalt concrete mix will selfheal better and faster than a leaner mix.

Recommendation: Supplementary testing, including triaxial tests, should be performed with a bitumen (B 160-220) content of about 6.8% to investigate the performance of a richer mix. Field experience and measurements show that one must be prepared for +/- 0.3 percentage points deviation from the design value. That deviation is also allowed according to the Technical Specifications for the Monte Grande asphalt core.”

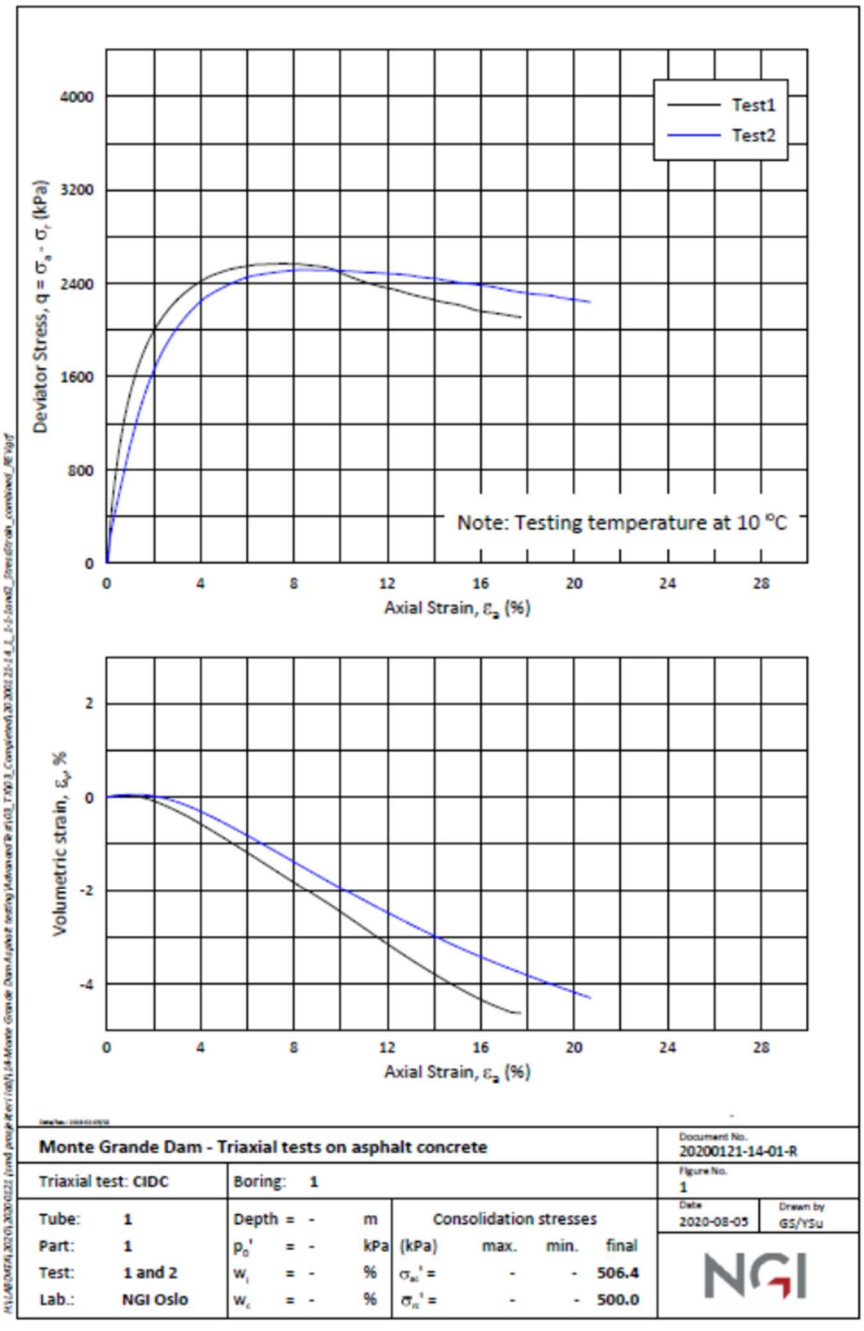

Fig. 7 – Figure 1 referred by Dr Hoeg

3.2. Full Scale Trial

According to the standard procedures for asphalt core dams, prior to commencement of asphalt works at the dam, the Contractor shall carry out a Panel Test /Trial.

The objective of the Panel Test is to demonstrate that the personnel and the machinery are able to perform the required various tasks based on Consultant's construction method with his guidelines.

Furthermore, the asphalt mix workability shall be evaluated during the Panel Test performance. Asphalt mix properties in respect to bitumen content, grain size distribution and its air void content shall meet the technical specifications requirements.

The Trial shall be conducted over a minimum length of 25 m – 30 m. The Trial shall include:

A. Construction of a concrete slab 30 m long, 3.0 m wide and 0.2 m thick (see Fig. 8 below).

F

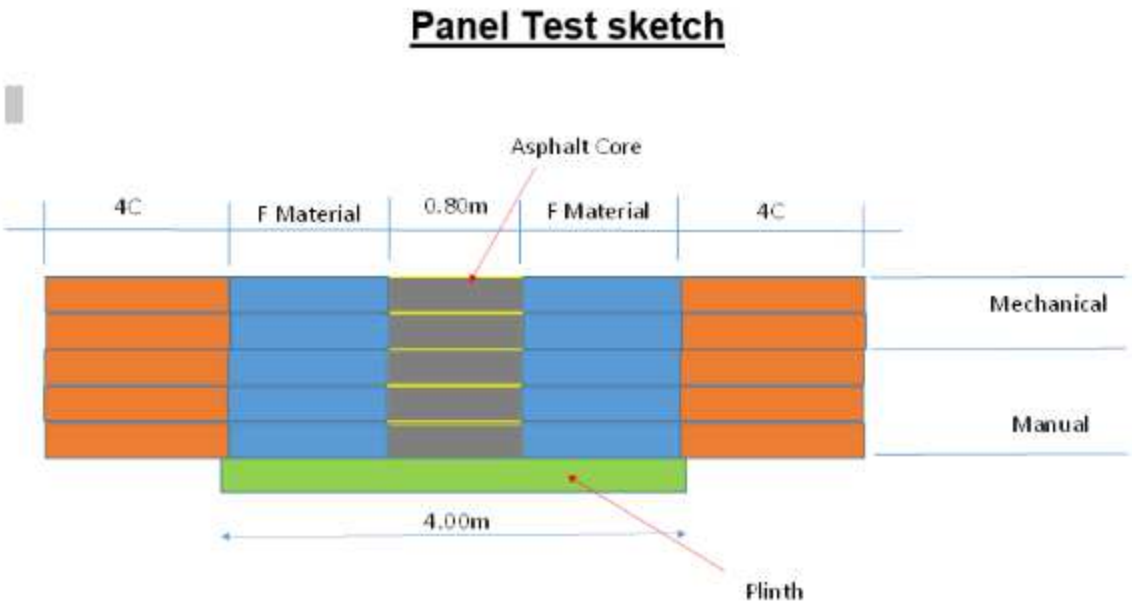

Fig. 8 – Pannel Test Sketch

B. Demonstration of the method proposed to clean and dry the concrete slab.

C. Application of mastic over 30 m length with a width of 1.3 m.

D. Asphalt temperature shall be controlled for each delivery to jobsite and prior to compaction.

E. Manual construction of 3 layers of asphalt core equal 0.80 m width and the transition zones (Zone 2) by excavator and wheel loader over the full 30 m.

F. Representative asphalt mix samples shall be collected at the Panel Test location

G. After a sufficient cooling period (approx. 3 – 7 days), minimum 6 cores to be drilled through all 3 asphalt core layers. Minimum 2 cores to be drilled through the concrete slab.

H. After cutting off approx. 3.0 cm on top and at bottom of the cores, the cores shall be cut into slices approx. 5.0-6.0 cm. The core's slices to be dried and then controlled for air void content. Each of the core's slices shall be marked with numbers with identifications A1, A2, A3, …..from top to down!

I. The surveyor shall measure the average thickness and width of the cores for each layer.

Fig. 9 – Asphalt Core Filling at the Full Scale Trial

Fig. 10 – Asphalt core and transitions compaction at the Full Scale Trial

The final result was achieved in the extracted cores, taken from the trial as is showed in the scheme below, distributed in 6 different places as showed in Figures 11 and 12.

Provision for cutting samples for testing

Core Drilled A			Core Drilled B			Core Drilled C		
		3cm - Discard			3cm - Discard			3cm - Discard
56 cm	A 1	20cm Axial Compressive Strength	56 cm	B 1	15cm Permeabilty	56 cm	C 1	20cm Axial Compressive Strength
	A 2	5cm Void Content		B 2	6cm Void Content		C 2	5cm Void Content
	A 3	20cm Traixial Test		B 3	20cm Traixial Test		C 3	20cm Traixial Test
	A 4	5cm Void Content		B 4	5cm Void Content		C 4	5cm Void Content
	A 5	6cm Void Content		B 5	6cm Void Content		C 5	6cm Void Content
		3cm - Discard			3cm - Discard			3cm - Discard

Core Drilled D			Core Drilled E			Core Drilled F		
		3cm - Discard			3cm - Discard			3cm - Discard
56 cm	D 1	20cm Traixial Test	56 cm	E 1	15cm Permeabilty	56 cm	F 1	20cm Traixial Test
	D 2	6cm Void Content		E 2	6cm Void Content		F 2	6cm Void Content
	D 3	20cm Axial Compressive Strength		E 3	20cm Traixial Test		F 3	15cm Permeabilty
	D 4	6cm Void Content		E 4	6cm Void Content		F 4	6cm Void Content
	D 5	6cm Void Content		E 5	6cm Void Content		F 5	6cm Void Content
		3cm - Discard			3cm - Discard			

Void Content includes also bitumen content and grain size analysis

Fig. 11 – Plan of Extracted Cores at the Full Scale Trial

Fig. 12 – Asphalt core and transitions compaction at the Full Scale Trial

The extracted cores were tested as the planed and the results are according to the specifications.

4. CONSTRUCTION

4.1. Equipment

An dedicated crusher and sieving plant was installed to produce the aggregates for the asphalt concrete: 16mm-11mm; 11mm-8mm, 8mm-4.8mm and less than 4.8mm.

The transitions were produced in the normal crushed and sieving plant, were the aggregates for the conventional concrete were produced, too.

To produce the asphalt concrete, a gravimetric plant LINTEC CSD 1510 was bought by the Contractor to assure the required very low void index, below than 3%. The Contractor's experience with asphalt volumetric plant related to voids index is between 3 to 5%. Fig. 13 show the asphalt concrete plant.

Fig. 13 – Asphalt concrete plant

To produce the mastic used as a bonding applied at the plinth concrete surface before the first concrete asphalt placement and special mixer was fabricated in the site as showed at Fig. 14.

Fig. 14 – Asphalt mastic production

For concrete asphalt placement a paver machine was bought by the Contractor from Geometri an Asphalt Core Dam ACDR X-4 as showed below at Figs. 15 and 16 and placed both asphalt concrete and transitions.

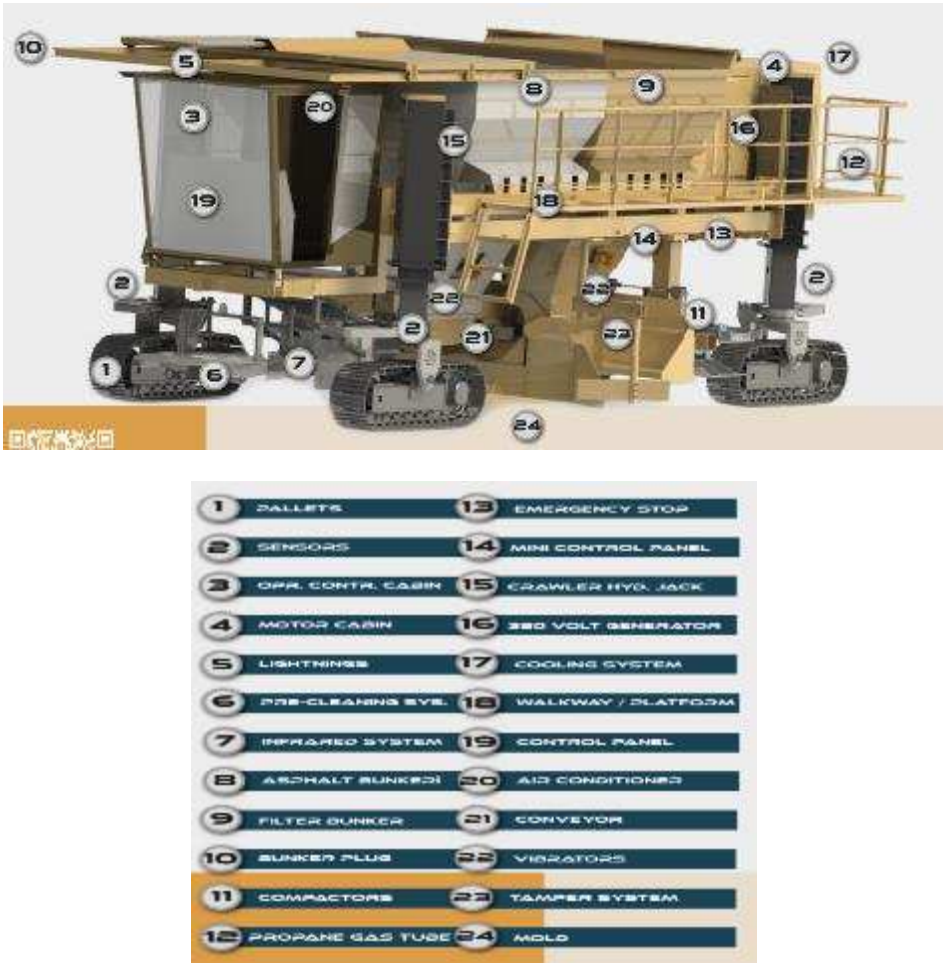

Fig. 15 – Asphalt core machine

Fig. 16 – Asphalt core and transitions compaction at the Full Scale Trial

4.2. Quality Control Results

Tables 1 and 2 show the statistic control of the filters F and F', Table 3 the statistic control of the transition 4C and Table 4 the statistic control of the rockfill 5A (gravel from riverbed)

Table 1 – Statistic Control of Filter F

Filter F	Laboratory Tests		Determinación IN SITU					Grain Size Analisys									
	Maximum Density (g/cm³)	Minimum Density (g/cm³)	Wet Density (g/cm³)	In Situ Moisture(%)	Dry Density (g/cm³)	Compaction Degree (%)	Relative Compacity (%)	Sieves in mm (% Passing)									
								63,0	50,00	31,50	25,00	19,00	9,50	4,75	2,00	0,425	0,075
Samples	583	583	583	583	583	583	583	581	581	581	581	581	581	581	581	581	581
Average	2,146	1,698	2,097	2,83	2,039	95,00	80,05	100,00	99,99	91,45	78,50	63,03	33,46	16,47	9,34	3,88	1,57
Maximum	2,231	1,781	2,364	9,12	2,191	98,71	92,76	100,00	100,00	98,88	93,11	83,58	50,28	29,39	18,41	6,82	4,47
Minimum	1,877	1,628	1,857	0,55	1,839	92,71	69,62	100,00	95,62	80,84	57,67	40,50	14,19	2,46	1,43	0,51	0,09
Standard Deviation (SD)	0,071	0,056	0,088	1,47	0,065	1,02	3,44	0,00	0,18	3,37	5,36	6,31	6,21	5,01	3,21	1,41	0,59
Average + SD	2,218	1,754	2,185	4,30	2,104	96,02	83,50	100,00	100,17	94,82	83,86	69,34	39,67	21,48	12,54	5,29	2,16
Average - SD	2,075	1,643	2,009	1,36	1,974	93,98	76,61	100,00	99,81	88,07	73,14	56,72	27,25	11,46	6,13	2,47	0,98
Coefficient of Variation	0,033	0,033	0,042	0,52	0,032	0,01	0,04	0,00	0,00	0,04	0,07	0,10	0,19	0,30	0,34	0,36	0,38

Table 2 – Statistic Control of Filter F'

Filter F'	Laboratory Tests		Determinación IN SITU					Grain Size Analisys									
	Maximum Density (g/cm³)	Minimum Density (g/cm³)	Wet Density (g/cm³)	In Situ Moisture(%)	Dry Density (g/cm³)	Compaction Degree (%)	Relative Compacity (%)	Sieves in mm (% Passing)									
								63,0	50,00	31,50	25,00	19,00	9,50	4,75	2,00	0,425	0,075
Samples	337	337	337	337	337	337	337	337	337	337	337	337	337	337	337	337	337
Average	2,095	1,515	2,124	9,02	1,949	93,01	80,33	100,00	98,45	84,70	78,42	64,57	61,17	57,16	22,09	7,73	3,54
Maximum	2,095	1,515	2,325	15,86	2,034	97,07	92,12	100,00	100,00	99,79	86,11	73,13	70,64	67,11	34,82	13,31	4,98
Minimum	2,095	1,515	1,996	3,70	1,900	90,71	73,24	100,00	93,06	75,06	66,38	49,96	46,86	42,75	13,68	2,99	1,22
Standard Deviation (SD)	0,000	0,000	0,043	1,92	0,024	1,13	3,39	0,00	1,23	3,07	3,65	4,48	5,22	5,49	3,94	1,44	0,70
Average + SD	2,095	1,515	2,167	10,94	1,972	94,14	83,71	100,00	99,68	87,77	82,08	69,05	66,39	62,65	26,03	9,16	4,23
Average - SD	2,095	1,515	2,081	7,10	1,925	91,88	76,94	100,00	97,23	81,63	74,77	60,08	55,96	51,67	18,14	6,29	2,84
Coefficient of Variation	0,000	0,000	0,020	0,21	0,012	0,01	0,04	0,00	0,01	0,04	0,05	0,07	0,09	0,10	0,18	0,19	0,20

Table 3 – Statistic Control of Transition 4C

Transition 4C	Wet Density (g/cm³)	In Situ Moisture(%)	Dry Density (g/cm³)	Grain Size Analisys Sieves in mm (% Passing)								
				203,2	75,0	19,00	9,50	4,75	2,00	0,600	0,150	0,075
Samples	549	549	549	548	548	548	548	548	548	548	548	548
Average	2,244	5,08	2,135	100,00	88,37	55,56	40,77	29,80	21,52	12,56	4,96	3,46
Maximum	2,558	9,98	2,391	100,00	100,00	69,85	56,38	43,80	31,95	21,67	9,94	8,07
Minimum	2,019	2,15	1,905	100,00	75,88	42,83	30,19	17,11	10,50	5,02	1,95	0,48
Standard Deviation (SD)	0,059	1,23	0,053	0,00	4,39	5,10	4,76	4,73	3,71	2,93	1,45	1,41
Average + SD	2,303	6,31	2,188	100,00	92,75	60,67	45,53	34,53	25,23	15,49	6,40	4,87
Average - SD	2,184	3,86	2,082	100,00	83,98	50,46	36,02	25,07	17,81	9,63	3,51	2,05
Coefficient of Variation	0,026	0,24	0,025	0,00	0,05	0,09	0,12	0,16	0,17	0,23	0,29	0,41

Table 4 – Statistic Control of Rockfill 5A

Rockfill 5A	Wet Density (g/cm³)	In Situ Moisture(%)	Dry Density (g/cm³)	Grain Size Analysis Sieves in mm (% Passing)															
				457,2	355,6	304,8	254,0	203,2	152,4	100,0	75,0	50,00	37,50	25,00	12,50	9,50	4,75	2,00	0,425	0,075
Samples	882	882	882	883	883	883	883	883	883	883	883	883	883	883	883	883	883	883	883	883
Average	2,471	4,86	2,356	100,00	99,98	99,90	99,65	98,46	94,23	85,31	77,96	67,70	59,85	49,87	35,69	31,68	24,55	18,32	9,63	4,03
Maximum	2,634	9,31	2,537	100,00	100,00	100,00	100,00	100,00	100,00	100,00	97,28	89,61	83,01	70,84	56,62	52,12	41,37	31,73	19,28	9,36
Minimum	2,291	1,82	2,174	100,00	83,63	83,63	83,43	75,66	67,49	58,04	46,50	37,71	23,63	19,76	15,05	13,07	8,45	3,37	0,71	0,00
Standard Deviation (SD)	0,045	1,15	0,040	0,00	0,55	1,19	2,04	4,29	7,12	8,23	8,79	9,28	9,25	8,59	7,14	6,74	5,83	4,81	3,10	1,78
Average + SD	2,516	6,01	2,396	100,00	100,53	101,08	101,69	102,75	101,35	93,54	86,76	76,98	69,10	58,46	42,83	38,41	30,38	23,13	12,73	5,81
Average - SD	2,426	3,71	2,317	100,00	99,43	98,71	97,62	94,16	87,11	77,09	69,17	58,42	50,60	41,28	28,55	24,94	18,72	13,50	6,53	2,25
Coefficient of Variation	0,018	0,24	0,017	0,00	0,01	0,01	0,02	0,04	0,08	0,10	0,11	0,14	0,15	0,17	0,20	0,21	0,24	0,26	0,32	0,44

During the construction 4 asphalt concrete mixes were used due to changing materials and asphalt suppliers. For fines, a filer by-product of cement and cement itself were used and for asphalt, European and American cements were used. The Tables 5 to 8 show statistic control of asphalt concrete during the production and the Fig. 17 to 20 the respective grain size analysis of the aggregates that made up the mixes.

Table 5 – Statistic Control of Mix 1 (European Cement and Filer by-product of cement)

Asphalt Concrete Mix MPG 001	Asphalt Concrete Characteritics				Marshall Characteristics - Speciments molded in Laboratory					
	Asphalt Content (%) Rice	Maximum Theorical Density (g/cm³)	Real Density Combinated Aggregates (g/cm³)	Filer/Asphalt Relation	Bulk Density (g/cm³)	Compaction Degree (%)	Voids (%)	B.V.R. (%)	V.M.A. (%)	V.F.A. (%)
Samples	229	230	229	229	1456	1456	1446	1456	1456	1456
Average	6,93	2,485	2,786	1,88	2,473	99,52	0,48	97,26	17,40	16,93
Minimum	6,63	2,464	2,764	1,64	2,432	98,21	0,00	90,79	16,54	16,21
Maximum	7,39	2,499	2,810	2,32	2,491	100,77	1,80	104,74	19,99	18,33
Standard Deviation (SD)	0,12	0,006	0,007	0,09	0,007	0,19	0,18	1,06	0,30	0,24
Coefficient of Variation	1,70	0,24	0,25	4,99	0,26	0,19	36,50	1,09	1,72	1,45
				V.F.A.	Voids full of asphalt		V.M.A = Voids of Mineral Aggregate			
				B.V.R.	Bitumen Void Ratio					

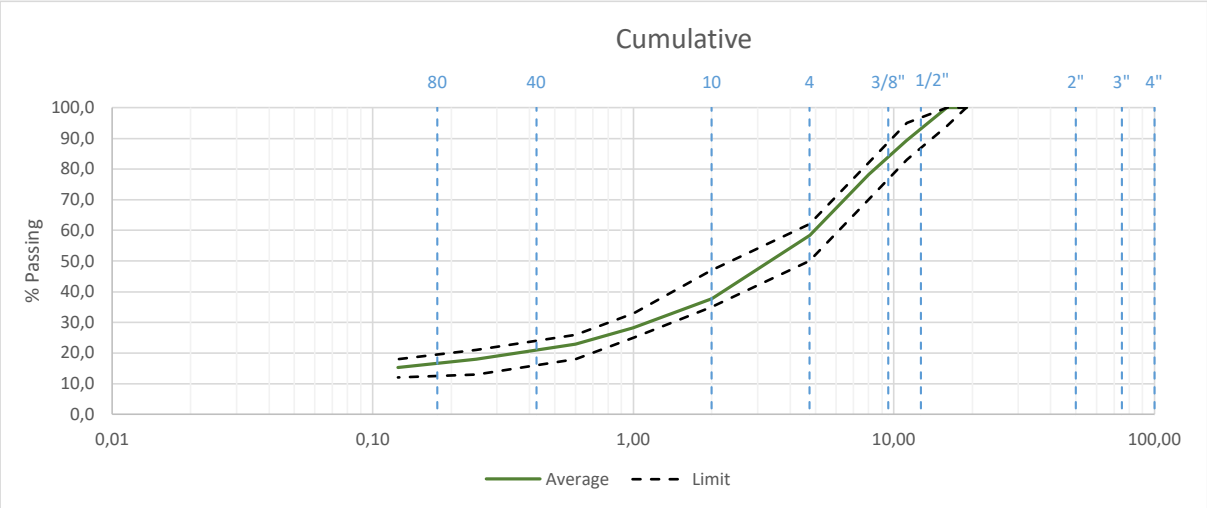

Fig 17 – Average Grain Size Analysis of Mix 1

Table 6 – Statistic Control of Mix 2 (European Asphalt and Cement)

Asphalt Concrete Mix MPG 002	Asphalt Concrete Characteritics					Marshall Characteristics - Speciments molded in Laboratory					
	Asphalt Content		Maximum Theorical Density	Real Density Combinated Aggregates	Filer/Asphalt Relation	Bulk Density (g/cm³)	Compaction Degree (%)	Voids (%)	B.V.R. (%)	V.M.A. (%)	V.F.A. (%)
	NCAT Oven / Rotarex	Rice									
Samples	102	102	102	102	102	576	576	572	576	576	576
Average	6,89	6,94	2,484	2,785	1,89	2,474	99,59	0,41	97,64	17,21	16,81
Minimum	6,59	6,74	2,475	2,772	1,75	2,457	99,07	0,00	94,85	16,49	16,05
Maximum	7,08	7,24	2,494	2,807	2,05	2,492	100,35	0,90	102,41	17,96	17,32
Standard Deviation	0,10	0,08	0,003	0,005	0,06	0,005	0,17	0,17	0,98	0,27	0,23
Coefficient of Variation	1,40	1,21	0,14	0,17	3,28	0,21	0,17	40,03	1,00	1,56	1,39
	V.F.A.	Voids full of asphalt		V.M.A = Voids of Mineral Aggregate							
	B.V.R.	Bitumen Void Ratio									

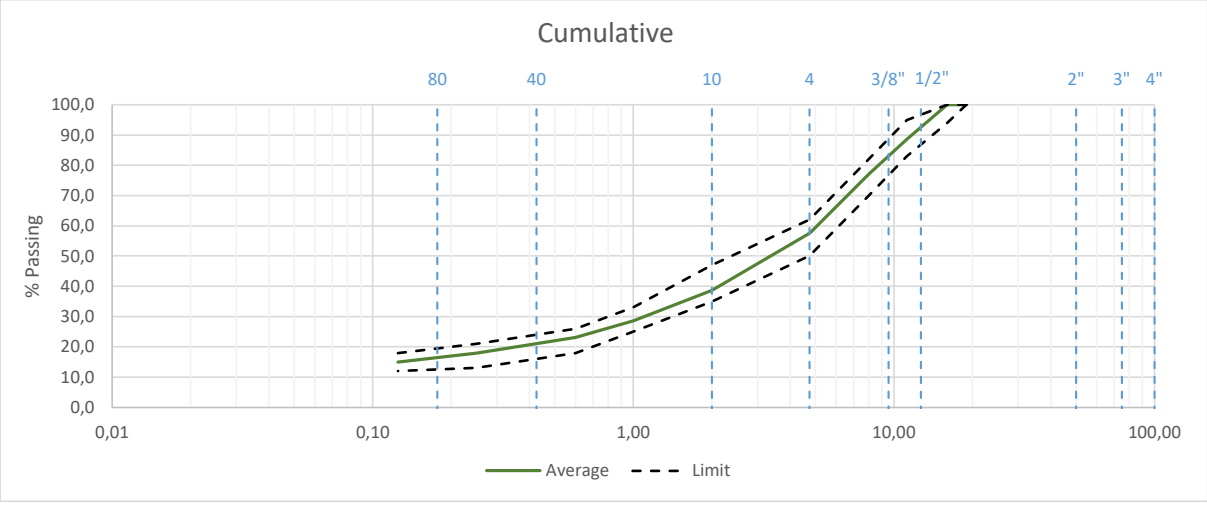

Fig 18 – Average Grain Size Analysis of Mix 2

Table 7 – Statistic Control of Mix 3 (American Cement and Filer by-product of cement)

Asphalt Concrete Mix MPG 003	Asphalt Concrete Characteritics					Marshall Characteristics - Speciments molded in Laboratory					
	Asphalt Content (%)		Maximum Theorical Density (g/cm³)	Real Density Combinated Aggregates (g/cm³)	Filer/Asphalt Relation	Bulk Density (g/cm³)	Compaction Degree (%)	Voids (%)	B.V.R. (%)	V.M.A. (%)	V.F.A. (%)
	Forno NCAT / Rotarex	Rice									
Samples	12	12	12	12	12	72	72	67	72	72	72
Average	6,89	6,92	2,485	2,785	1,87	2,474	99,59	0,45	97,69	17,21	16,81
Minimum	6,76	6,75	2,477	2,779	1,77	2,463	99,17	0,00	95,42	16,65	16,46
Maximum	7,03	7,14	2,488	2,790	1,99	2,495	100,30	0,80	101,80	17,88	17,17
Standard Deviation	0,07	0,09	0,003	0,003	0,06	0,006	0,25	0,20	1,44	0,28	0,18
Coefficient of Variation	1,07	1,35	0,11	0,10	3,41	0,26	0,25	44,03	1,48	1,65	1,07
V.F.A. Voids full of asphalt V.M.A = Voids of Mineral Aggregate											
B.V.R. Bitumen Void Ratio											

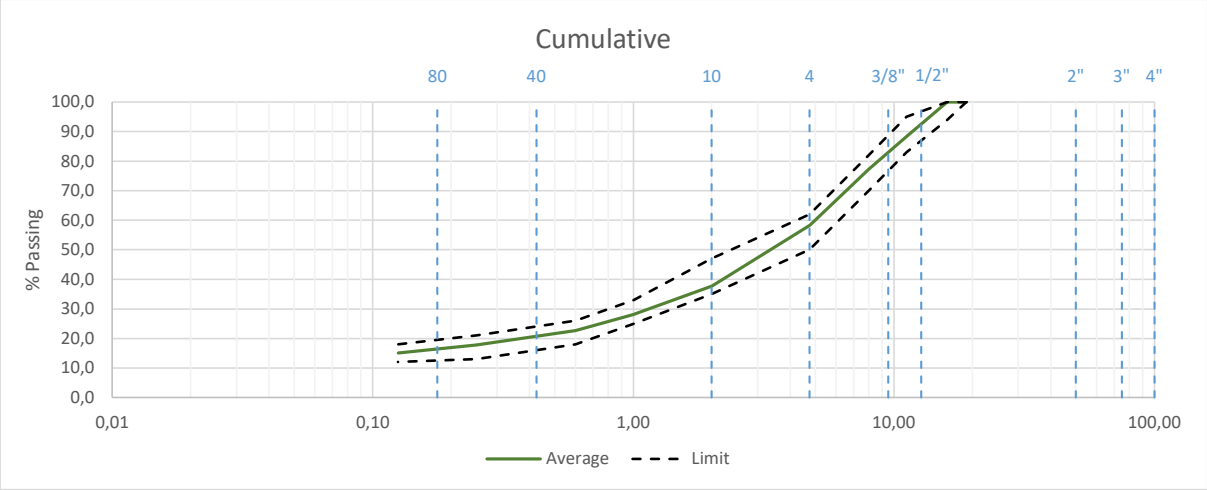

Fig 19 – Average Grain Size Analysis of Mix 3

Table 8 – Statistic Control of Mix 4 (American Asphalt and Cement)

Asphalt Concrete Mix MPG 004	Asphalt Concrete Characteritics					Marshall Characteristics - Speciments molded in Laboratory					
	Asphalt Content		Maximum Theorical Density (g/cm³)	Real Density Combinated Aggregates (g/cm³)	Filer/Asphalt Relation	Bulk Density (g/cm³)	Compaction Degree (%)	Voids (%)	B.V.R. (%)	V.M.A. (%)	V.F.A. (%)
	NCAT Oven / Rotarex	Rice									
Samples	61	61	61	61	61	345	345	345	345	345	345
Average	6,86	6,91	2,486	2,786	1,85	2,475	99,55	0,44	97,42	17,18	16,74
Minimum	6,57	6,65	2,481	2,772	1,71	2,460	98,99	0,00	94,28	16,37	15,99
Maximum	7,05	7,14	2,490	2,796	2,06	2,488	99,95	1,00	100,00	17,84	17,22
Standard Deviation	0,10	0,08	0,002	0,004	0,08	0,005	0,19	0,19	1,07	0,29	0,23
Coefficient of Variation	1,45	1,19	0,07	0,14	4,43	0,20	0,19	42,69	1,10	1,66	1,39
V.F.A. Voids full of asphalt V.M.A = Voids of Mineral Aggregate											
B.V.R. Bitumen Void Ratio											

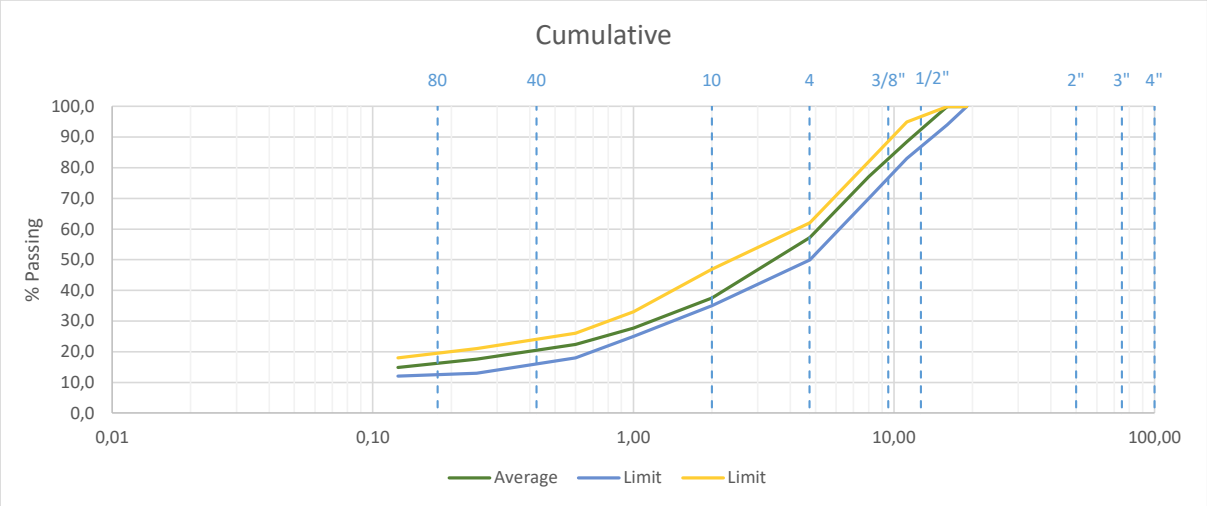

Fig 20 – Average Grain Size Analysis of Mix 4

Table 9 shows the statistic control done during the placement and compaction of the asphalt concrete. The density control was done using a non nuclear densometer Troxler.

Statistic Control		Maximum Theeoretical Density (g/cm³)	Placement Temperature (ºC)	Compaction Temperature (ºC)	Bulk Density (g/cm³)	Compaction Degree (%)	Voids Index (%)
Cumulative	Numder os tests	359	359	359	7741	7741	7741
	Average	2,485	204,98	148,50	2,471	99,47%	0,54%
	Standard Deviation (SD)	0,005	829,42	9,20	0,030	0,37%	0,34%
	Coefficient of Variation	0,20%	404,64%	6,19%	1,23%	0,37%	63,72%
	Average +1 SD	2,490	1034,39	157,70	2,502	99,83%	0,89%
	Average -1 SD	2,480	-624,44	139,31	2,441	99,10%	0,20%

5. CONCLUSIONS

The main measures taken by the Contractor for the success of the construction were:

a) Purchase of a gravimetric asphalt plant to assure low voids in the asphalt concrete and Lintec is one of the best;
b) Set up a specific sieve plant to produce the aggregates for asphalt concrete;
c) Purchase a specific paver for asphalt concrete and filter placement;
d) Support of Dr Kaare Hoeg and his assistant Vahid Afsari Rad from Asphalt Concrete Dams – ACD, as Consultant both for design and construction, Veitenisk Laboratory and NGI for special tests and analysis;
e) Carry out a very good technical specification by the designer Intertechne and the job site good management by eng. Eduardo Roque;
f) Create a Training Model (UDC) to qualify the labors during the trial for the construction;
g) Carry out very strict quality control.

REFERENCES

[1] INTERTECHNE - 1802- MG-8-BA-B00-00-C-12-ET-0003 – Presa - Núcleo de Asfalto – Especificación Técnica – Março, 2020 – Dam – Asphat Core – Technical Specification – March, 2020.

[2] Andrade Gutierrez Engenharia – UDC Núcleo de Asfalto – Created by Newton Goulart Graça , São Paulo, 2020.

[3] GUIMARÃES, R.C. (2012). Barragens com Núcleo de Concreto Asfáltico – Análise do Comportamento Mecânico e Hidráulico. Tese de Doutorado, Publicação G.TD – 076/12, Departamento de Engenharia Civil e Ambiental, Universidade de Brasília, Brasília, DF, 189 p..

[4] Norwegian Geotechnical Institute (NGI) – Technical Note - Results from preliminary triaxial tests on asphalt concrete for Monte Grande Dam Core, by Dr Kaare Hoeg, August, 2020.

Fifth International Dam World Conference
PORTUGAL • LISBON • LNEC • APRIL 13-17, 2025
dam world 2025

GEOLOGICAL AND GEOTECHNICAL STUDIES IN DAMS DESIGN. FOUNDATION, RESERVOIR AND CONSTRUCTION MATERIALS

Roque, M.[1]
COBA

ABSTRACT

This paper reflects on the critical role of geological and geotechnical studies during the design of a dam, emphasizing their importance in ensuring safety, functionality, and cost-effectiveness. Geological and geotechnical studies provide valuable insights concerning foundation conditions, reservoir slopes stability and construction materials availability and characteristics. Historical dam failures, such as Vajont, Malpasset, and Teton, underscore the devastating consequences of unsuitable geological and geotechnical investigations, serving as stark reminders of their importance. This article present case studies that demonstrate the value of site investigations before construction, including to relocate dam axes due to unfavourable site conditions, to design adequate impermeable barriers to control seepage issues, and to optimise solutions when construction materials are scarce. Examples from Portugal, Algeria, Tunisia, and Mozambique illustrate how comprehensive geological and geotechnical assessments improve decision-making and enhance the sustainability of dam design. The role of adequate approaches to conduct geological and geotechnical studies as part of integrated risk management strategies is also emphasized in this paper.

Keywords: Geological studies, geotechnical investigations, dam design, foundation, construction materials

[1]m.roque@cobagroup.com, Portugal

1. INTRODUCTION

The design and construction of dams require a comprehensive understanding of the subsurface and surrounding environment to ensure stability, safety, and economic feasibility. At the core of this process are geological and geotechnical studies, which provide invaluable insights during the design phase. These studies are fundamental to identify potential risks, to specify appropriate design parameters, and to select suitable construction materials. Without these investigations, dam projects are vulnerable to unforeseen challenges that can lead to costly delays or even structural failures.

We can recall several historically dam failures linked to geological and geotechnical problems, such as St. Francis dam (USA, 1928), Malpasset dam (France, 1959), Vajont dam (Italy, 1963) or Teton dam (USA, 1976). These case studies remain as some of the most emblematic dam failures worldwide, where the geological and geotechnical were not fully understood prior to construction [1] [2].

Malpasset Dam was a 66,5 m high concrete arch dam in Southern France, constructed over fractured gneisses. The rock's foliation pattern along with increased uplift pressures during reservoir filling, combined with a fault in the left riverside, caused the dam failure. This ultimately led to more than 400 deaths. The investigations at the time felt that the geology under the dam was not adequately studied and accounted for [2] [3] [4].

The Vajont Dam disaster, in 1963, in Italy, serves as a stark reminder of the importance of extend geological and geotechnical studies beyond the dam side, including the reservoir area, which can pose significant risks such as landslides. The Vajont Dam, an arch dam, was designed and constructed with massive attention to its foundation, however, a tragic event was caused by a massive landslide within the reservoir area, which was not adequately assessed during design phase. This landslide caused a catastrophic wave to surge over the dam, resulting in the deaths of over 2 000 people and widespread destruction in the downstream valley. This disaster underscores the importance of evaluating the stability of the reservoir slopes, to identify potential risks such as landslides or slope failures. [1] [4].

The Teton Dam failure, in 1976, in USA, illustrates the significance of the behaviour and control of construction materials during the construction process. The Teton Dam is an earthfill embankment with about 93 m high assembled on a foundation of fractured volcanic rock. Seepage through the porous foundation materials initiated internal erosion, which progressed into piping as the foundation's lack of impermeability allowed increasing amounts of water to

flow through. As seepage increased, it caused progressive erosion of the material beneath the dam, ultimately resulting in the catastrophic failure of the structure [5].

Today, an increasing number of regulations and standards are being implemented worldwide to ensure that adequate geological and geotechnical studies are conducted during dam's design. This is the case of those provided by the International Commission on Large Dams (ICOLD), the Federal Energy Regulatory Commission from United States (FERC), the Canadian Dam Association (CDA), the Australian National Committee on Large Dams (ANCOLD), or those from the European Union, namely European Standard EN 1997 (Eurocode 7), which is being introduced and adapted in different European countries.

In the following sections, key issues that geological and geotechnical studies should address will be discussed and illustrated through examples from both Portuguese and international cases. Additionally, aspects related to site investigations and laboratory tests for characterizing foundation or construction materials from borrow areas will be further discussed.

2. UNDERSTANDING FOUNDATIONS CHARACTERISTICS

The foundation of a dam is of paramount importance in ensuring the stability, safety, and functionality of the overall structure. A robust foundation must provide adequate bearing capacity to support the weight of the dam and any additional loads it may encounter over its lifespan. Moreover, it should have acceptable levels of deformation to prevent excessive settlement or movement that could compromise the dam's integrity. Additionally, low permeability is crucial to minimize seepages, which can lead to storage capacity reduction, internal erosion phenomena and other failure types.

To meet these stringent requirements, conducting a comprehensive geological and geotechnical survey is essential. This survey provides critical insights into the site's geological composition, including soil types, rock mass characteristics, groundwater conditions, etc. These efforts support informed decision-making regarding foundation levels, waterproofing and/or consolidation treatment needs, excavation slopes geometry and their eventually reinforcement solutions requirements and so forth.

A dam site in a Western African country provides an illustrative example of the complexities of foundation levels assessment. This dam is being planned to be constructed in an asymmetric valley, which apparently offers suitable geotechnical conditions, either for a concrete or an earthfill dam. However, *in situ* investigations have shown significant disparities between the subsurface conditions of the two banks, which led to significant excavation and stabilization challenges.

On the left bank, the rock mass consists of volcanic and igneous rocks with reasonable geotechnical properties, covered by a thin layer of loose sandy soils (Fig. 1).

In contrast, the right bank has significantly less favourable conditions, with the competent rock mass appearing only at depths of about 15–20 m. It is covered by a thick layer low-strength materials (sandy and clayey soils mixed with rock boulders) (Fig. 1).

To ensure a suitable foundation for the dam, particularly if a concrete solution is chosen, all overburden and loose sandy soils must be excavated. This approach entails significant excavation volumes, leading to large quantities of material requiring disposal. Additionally, the process will result in high slopes requiring stabilization measures, including specialized treatments and reinforcement solutions.

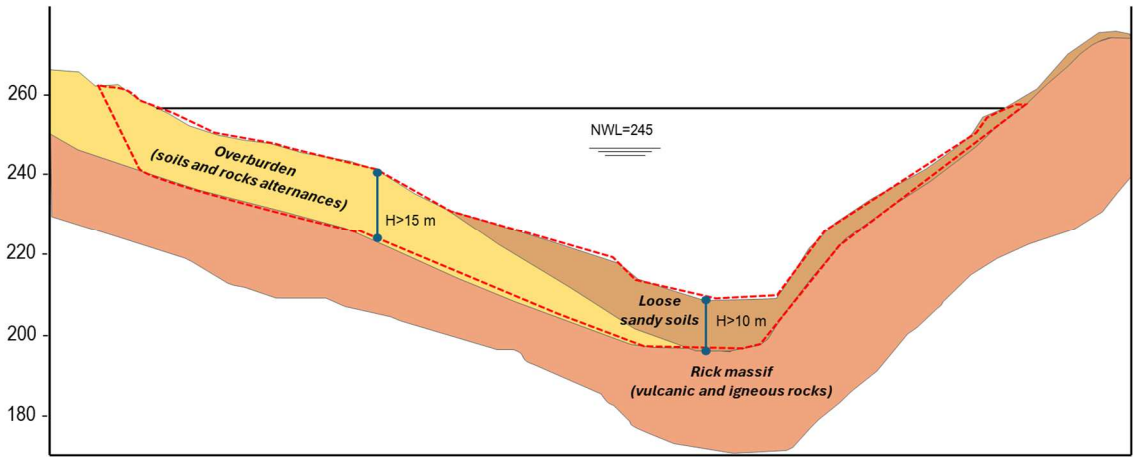

Fig. 1 – Foundation with differential conditions. Example of dam in a western African country.

Concerning waterproofing treatment requirements, two case studies that led to different final solutions will be further showcased.

The first example is the Furta Galinhas Dam, located in Moura, Portugal (Fig. 2). This dam stands 19 meters high and spans 810 meters at the Brenhas stream. Its location was shifted several times due to the presence of high-permeability Palaeozoic carbonate formations, including marbles and calcareous schists. After a detailed geological survey, an optimal site for the dam was identified, where there are a thick low-permeability Cenozoic soils, reaching up more than 15 m, at the centre of the valley. The composition and the thickness of these soils supported the decision to dispense waterproofing treatments. [6] [7] [8].

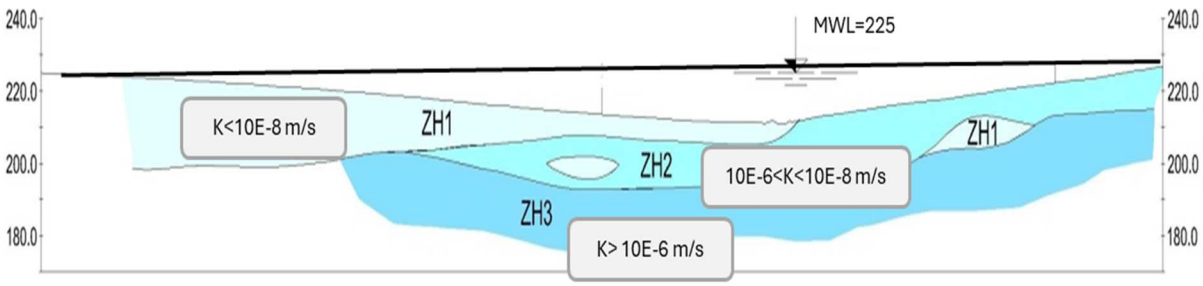

Fig. 2 – Furta Galinhas dam (Moura, Portugal). Example of a dam without waterproofing system [7].

Another example is the Saïda Dam, in Tunisia, a zoned-earthfall embankment with a maximum height of 48 meters and a span of approximately 2 500 meters. The foundation consists of alternating sandy and clayey deposits from a fluvio-deltaic Pliocene sequence, dipping about 15-20º NE (*i.e.*, dipping to the right bank and downstream) (Fig. 3). The sandy layers, with variable permeability coefficients (sometimes greater than exceed 1×10^{-5} m/s) are prone to upstream-downstream water loss and piping.

A detailed site investigation revealed significant differences between the base and the top of the fluvio-deltaic sequence. The basal strata (Raf Raf unit), which outcrops within the reservoir area, contains less frequent and less permeable sandy layers compared to those at the top (Porto Farina unit), which, in turn, outcrops outside the reservoir area, inkling on site initaily proposed to the dam's axis. These findings led to relocating the dam and designing a diaphragm wall, with more than 1 400 m long and 35 m of maximum depth, to reduce piping phenomena and water losses [9] [10] [11].

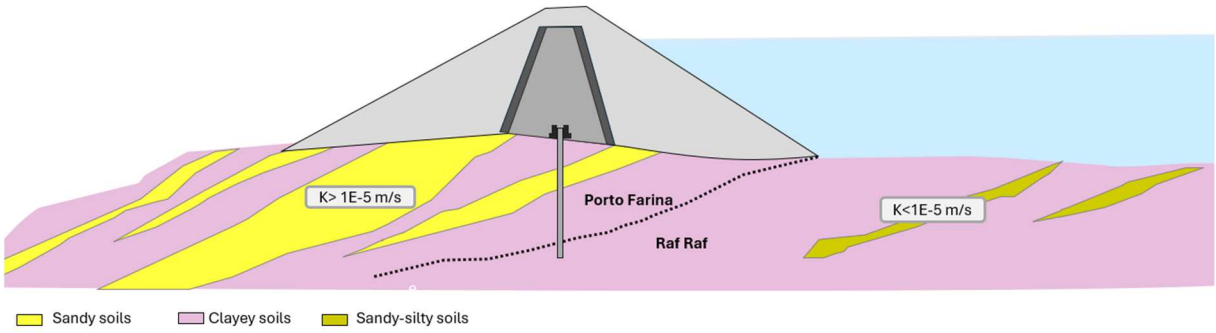

Fig. 3 – Saïda dam (Tunis, Tunisa). Example of dam with a diagram wall.

3. UNDERSTANDING RESERVOIR CHARACTERISTICS

The thorough study of the reservoir area is essential in dam design, particularly for assessing slope stability and watertightness conditions of the future reservoir, and even for searching construction materials.

Slope stability

Slope stability analysis is crucial to prevent landslides, which may compromise the dam integrity and downstream population safety, as seen in historical failures such as the Vajont Dam disaster. Assessing the stability conditions of adjacent reservoir area aids to identify potential hazards and subsequently guides decisions regarding dam relocation alternatives and/or slope reinforcement solutions.

Fig. 4 illustrates a dam case in Algeria, where geotechnical assessments revealed rock slope instabilities on both sides of the watercourse slopes. It arose concerns about the structure

stability due to the risk of large-scale landslides that could lead to its failure by overtopping. Based on these findings, axes 3 and 4 were chosen as the most suitable locations for the dam construction, as the upstream area of the reservoir features more stable and lower slopes.

Fig. 4 – An Algerian dam. An example of how slopes stability of the reservoir influences the dam positioning in relation to landslide risk.

Watertightness conditions

Additionally, understanding the hydrogeology of the reservoir basin, including its permeability and groundwater flow patterns is necessary to prevent water losses.

The Ouziert dam, in Mascara province, in Algerie, is an emblematic example of water losses through the reservoir banks, which compromises the functionality of the overall facility. It is an earthfill dam with about 60 m high, constructed in 1986. Since the first filling, the designed NWL has never been reached, due to water losses through the left bank of the reservoir, which reached up 1 300 l/s. On the left bank, there are thick detrital deposits from Miocene, as known as *puddings*, which are composed by well-rounded conglomerates, sometimes bounded by a clayey a carbonate or a siliceous cement, but many other times without any type of cement. Detailed site investigations shown that the *puddings* permeabilities are highly variable, occasionally reaching up to $8x10^{-4}$ m/s. To enhance the reservoir's capacity to meet the NWL, a grout curtain was designed along the left bank, with heights ranging from 40 to 80 meters over a length of 1 340 meters (Fig. 5). [12] [13] [14] [15].

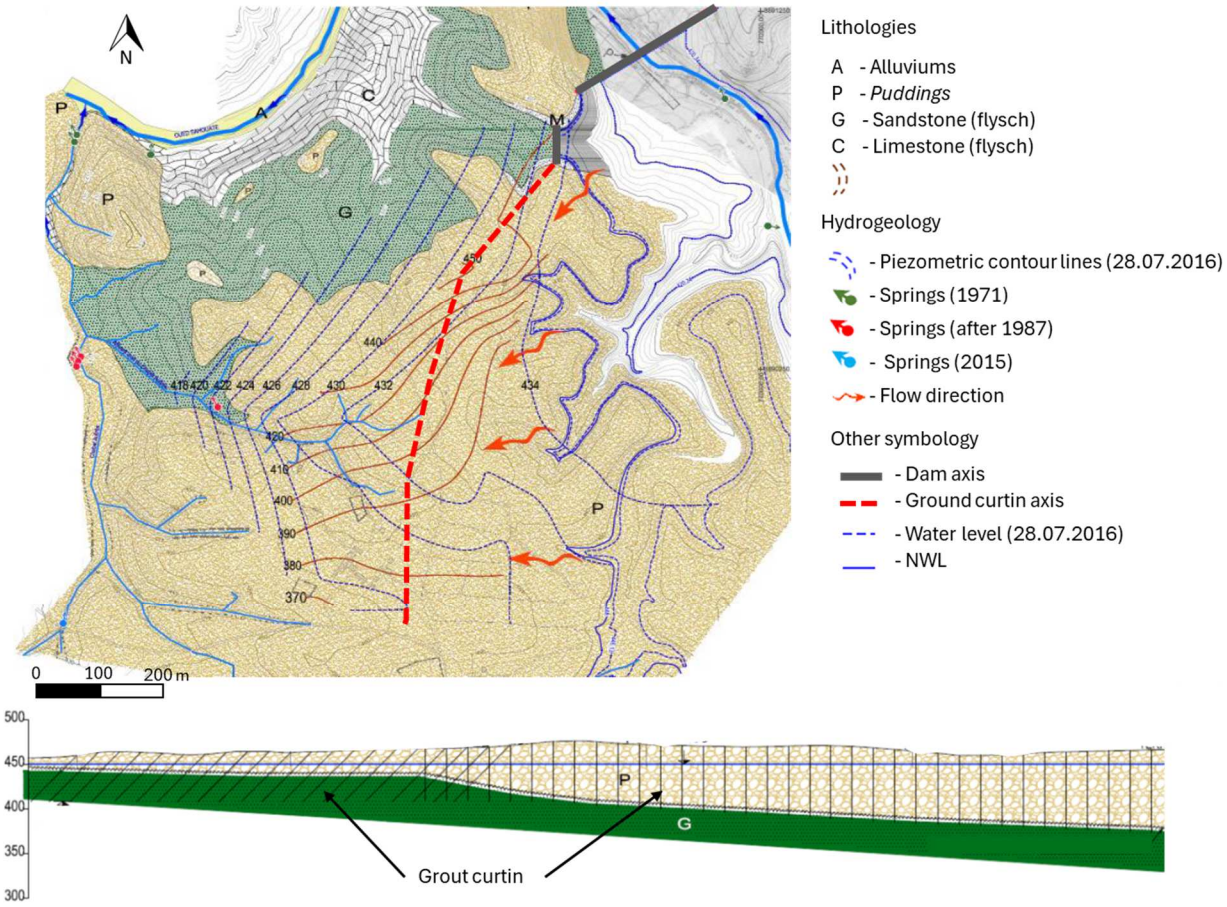

Fig. 5 – Ouzert Dam (Mascara, Algeria). An example of how ground permeability in the reservoir area affects dam functionality due to water losses.

Construction materials sources

Since part of the feasibility of construction is related with the availability of raw materials to construction nearby, the future reservoir area offers an opportunity to search for suitable materials, such as fine-grained soils for embankment cores or even for homogenous solutions; or durable rocks for concrete aggregates or for rockfill embankment.

The reservoir is, in fact, conveniently close to the dam site, which provides logistic benefits, reducing the dependency on external supply chains and transportation costs, enhancing both economic efficiency and project sustainability.

Moreover, since the future reservoir area will ultimately be submerged, it would otherwise become an unusable space. Therefore, extracting raw materials from this zone further mitigates environmental impacts compared to sourcing from untouched areas outside the reservoir footprint.

Therefore, the geotechnical studies within the reservoir area not only enhances dam safety and functionality but also optimize resource use and reduce construction costs.

4. IDENTIFYING AND SELECTING CONSTRUCTION MATERIALS

The selection of the type of dam (earthfill, rockfill, concrete, etc.) is closely linked to the availability and quality of construction materials in the surrounding areas, as previously said. It not only influences costs related to exploitation and transport, but also influences the dam's overall design and construction method. For example, earthfill dams require large amounts of suitable soils, especially clayey soils (low permeability), while rockfill dams or concreate dams rely on the availability of resistant and durable rocks.

In cases where suitable construction materials are scarce, innovative solutions, such as the use of asphaltic cores, have been successfully employed. In Northern Europe, the scarcity of clayey soils for ensuring dam impermeability led to the construction of many dams with bituminous concrete cores, also known as asphaltic cores, since from the 1950s. The Valcros Dam, in France (1957) and the Rørvikfossen Dam, in Norway (1960) are considered successful examples of earthfill dams utilizing this technique.

In Portugal, this solution is not very common, as most dams are: i) concrete dams, such as Carrapatelo, Crestuma-Lever, Bemposta and Pocinho (gravity solutions) or Picote, Alqueva, Daivões e Alto Tâmega (arch-gravity); ii) homogeneous earthfill embankments, like Burgo, Palemeireiro, Sabugeiro and Santa Maria de Aguiar; iii) zoned earthfill embankments with clayey cores, such as Odelouca, Camba, Azibo, Alijo or Sabugal; iv) rockfill embankments, like Vilar and Paradela; or v) soil-rock embankments, such Rego do Milho.

Fig. **6** shows some examples of Portuguese dams.

Carrapatelo dam
(gravity)
Source: https://cnpgb.apambiente.pt/content/carrapatelo

Alqueva dam
(arch)
Source: https://cnpgb.apambiente.pt/content/alqueva

Odelouca dam
(zoned earthfill embankment)
Source: https://cnpgb.apambiente.pt/content/odelouca

Santa Maria de Aguiar dam
(homogeneous embankment)
Source: https://cnpgb.apambiente.pt/content/santa-maria-de-aguiar

Paradela dam
(rockfill embakment)
Source https://cnpgb.apambiente.pt/content/paradela

Rego do Milho
(soil-rock misture embakment)
Source: https://cnpgb.apambiente.pt/content/rego-do-milho

Fig. 6 – Examples of Portugues dams

Due to the insufficiency of clayey soils, two dams with asphaltic cores have been recently designed in Portugal, both in the northeastern region of the country: the Redonda das Olgas dam, in Vila Flor, which is an earthfill embankment, with 26 m high and 482 m long, with a bituminous concrete core (Fig. 7) [16]; and the Gebelim dam, in Alfândega da Fé, a soil-rock

embankment, with 44 m high and almost 200 m long, also featuring a bituminous concrete core [17].

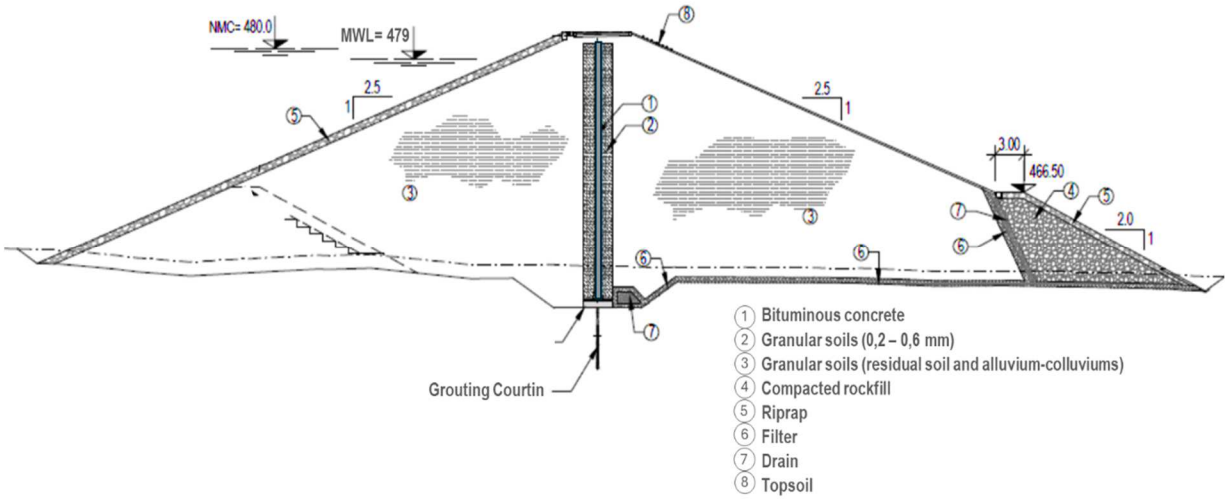

Fig. 7 – Redonda das Olgas dam (Vila Flor, Portugal). Example an earthfill embankments dam with asphaltic core [16].

After this, is clear that understanding the availability of construction materials early in the project is essential for selecting the appropriate dam type and ensuring a cost-effective, sustainable construction process.

5. GEOLOGICAL AND GEOTECHNICAL STUDIES APPROACHES

The importance of establishing a strategic approach to maximize the efficiency of geological and geotechnical studies during the design phase is evident. Such approaches inherently involve bibliographic research, site visits for geological and geotechnical surveys and laboratory tests.

As discussed in previous sections, these studies should simultaneously be focus on the dam site characterisation, including foundation and reservoir; and on the searching for construction materials, preferentially within the future reservoir zone.

Investigations at the dam site and its nearby

The first step is gaining a comprehensive understanding of the regional and site geology, since they are predictive of subsurface material types and their expectable geo-mechanical and hydraulic characteristics.

Drawing from both bibliographic sources and field geological surveys, a detailed mapping of the site is the first key outcome (Fig. 8). It should represent the geographic distribution of main rock and soil types; special constrains, such as weak grounds, swelling rocks or slope instability situations; geological structures (faults, folds, etc); and rock mass characteristics,

such as discontinuities patterns (spacing, orientation, filling, roughness), etc. It also may include the identification of potential borrow areas, either within or outside the reservoir area.

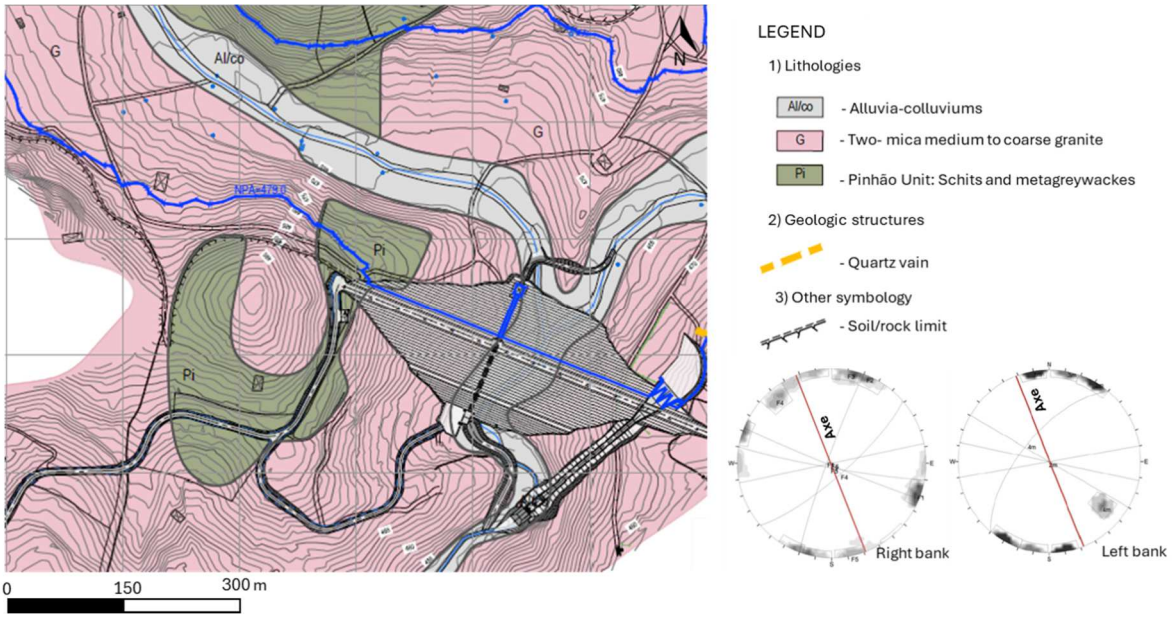

Fig. 8 – A dam in Northwestern Portugal. Example of geologic survey.

Based on this initial study, it becomes possible to decide where site investigation efforts should be prioritized. Key examples are areas with suspected geological faults, karstic zones, geomorphological anomalies, etc.

This prior conscience of the site helps to better optimize field survey strategies, managing the available human and materials resources, reducing costs and saving time.

Megarruma dam, in Mozambique, is a great example of this optimized strategy. The suspension of a geological fault at the bottom of the valley led to a concentrated effort in that area, using both geophysics and crossed boreholes [18] [19] (Fig. 9).

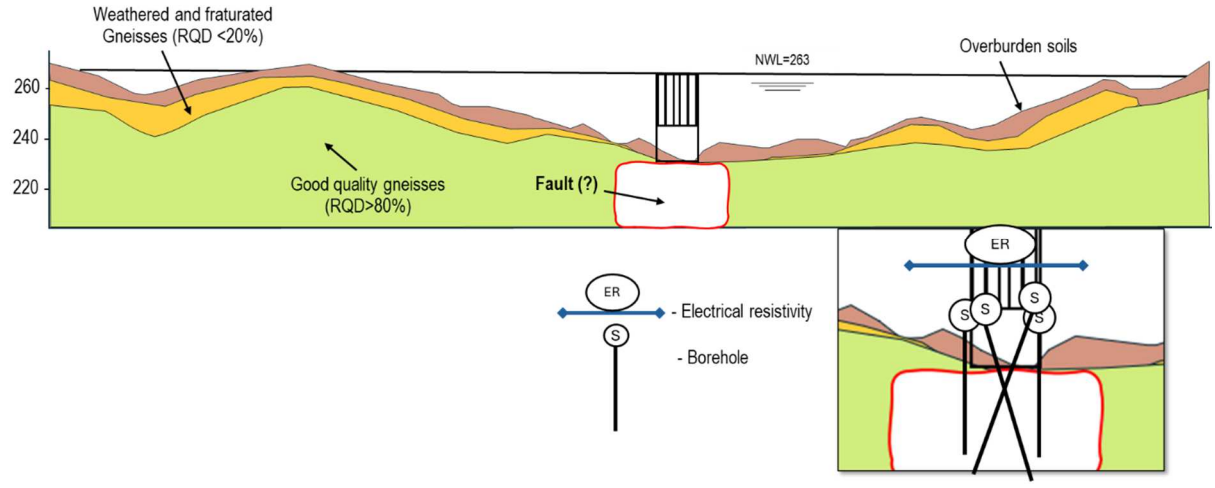

Fig. 9 – Megarruma dam (Pemba, Mozambique). Example of field investigations plan.

Therefore, the original site investigation plan needed to be revised, relocating boreholes and adjusting *in situ* tests, to ensure the investigation requirements were met without exceeding the budget.

The same way, this initial survey will be the basis for preparing a targeted site investigation for searching for construction materials and to their characterisation.

Foundations characterisation

When concentrating on dam's foundation, the assessment aims to estimate its bearing capacity, deformability and watertightness. Depending on the local geology, there are a few available field surveys, *in situ* tests and laboratory tests. Fig. 10 intend to illustrate some of the most common ones.

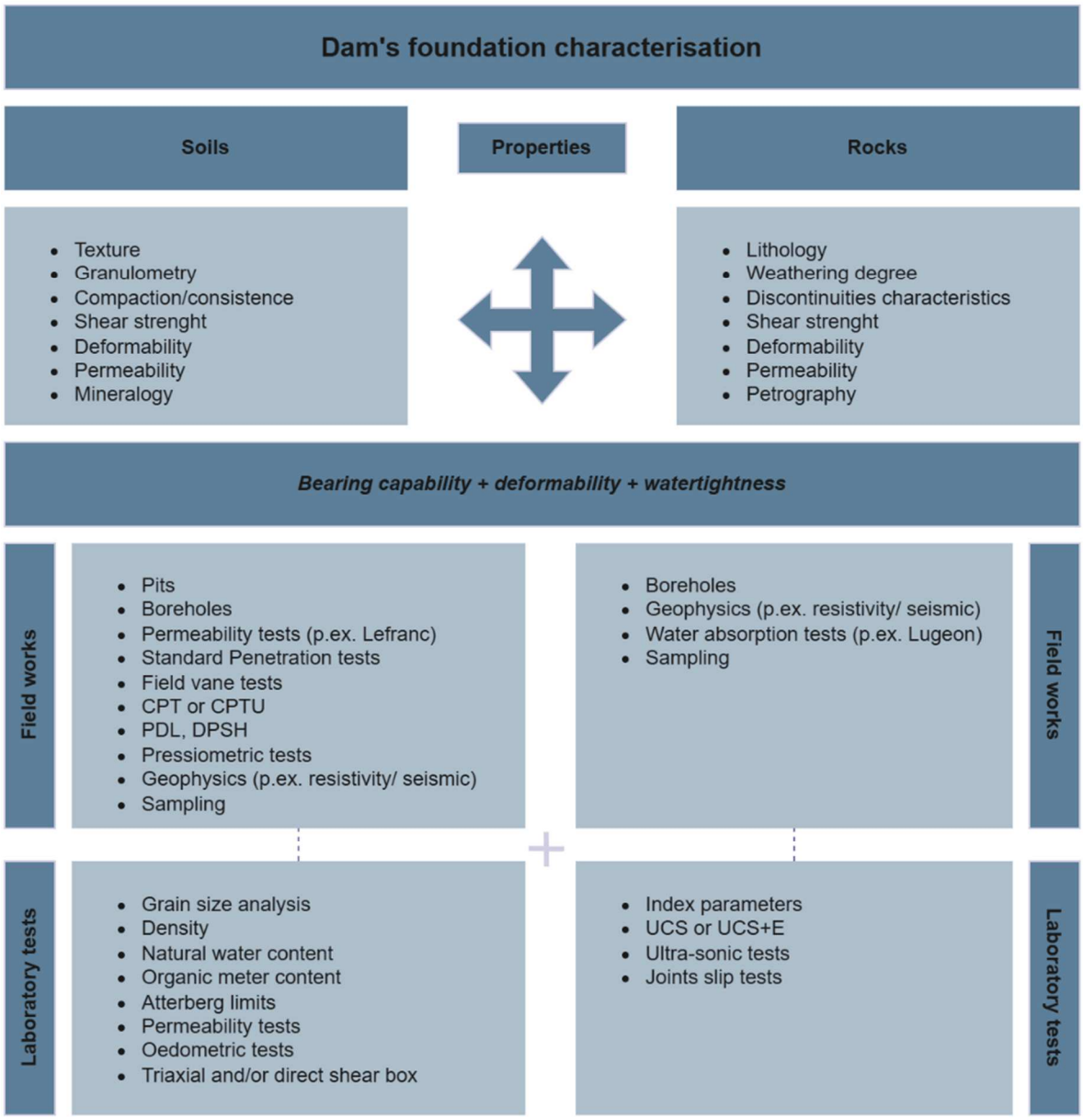

Fig. 10 – Site investigation to dam's foundations. Common field works and laboratory tests.

Construction materials

The study of construction materials begins by identifying potential borrow areas as close to the dam site as possible to minimize transportation and environmental impacts. Ideally, borrow areas within the future reservoir zone offer an optimal solution, as they are conveniently located near the dam site, as previously discussed.

This process starts with an overall field survey, focus on i) main geologic aspects, such as soils and rock types and its characteristics, ground water level position, etc; and ii) exploration conditions, such as accessibilities to the dam's site, potential environmental impacts, safety, etc.

Subsequently, after defining potential borrow areas, a site investigation programme has place. Different *in situ* surveys and laboratory tests are chosen depending on the type of materials to be characterised, because different materials have different functions within the dam's body. For instance, fine-grained soils, commonly used in the cores of earthfill embankments, provide waterproofing and deformability control. Coarse-grained soils, employed in the shoulders of earthfill dams, have strength and deformability control functions. Rocks, typically utilized in rockfill dams, primarily ensure strength and durability.

Fig. 11 shows some common field surveys and laboratory test to characterize different construction materials, taking in account their requirements and function within a dam's body.

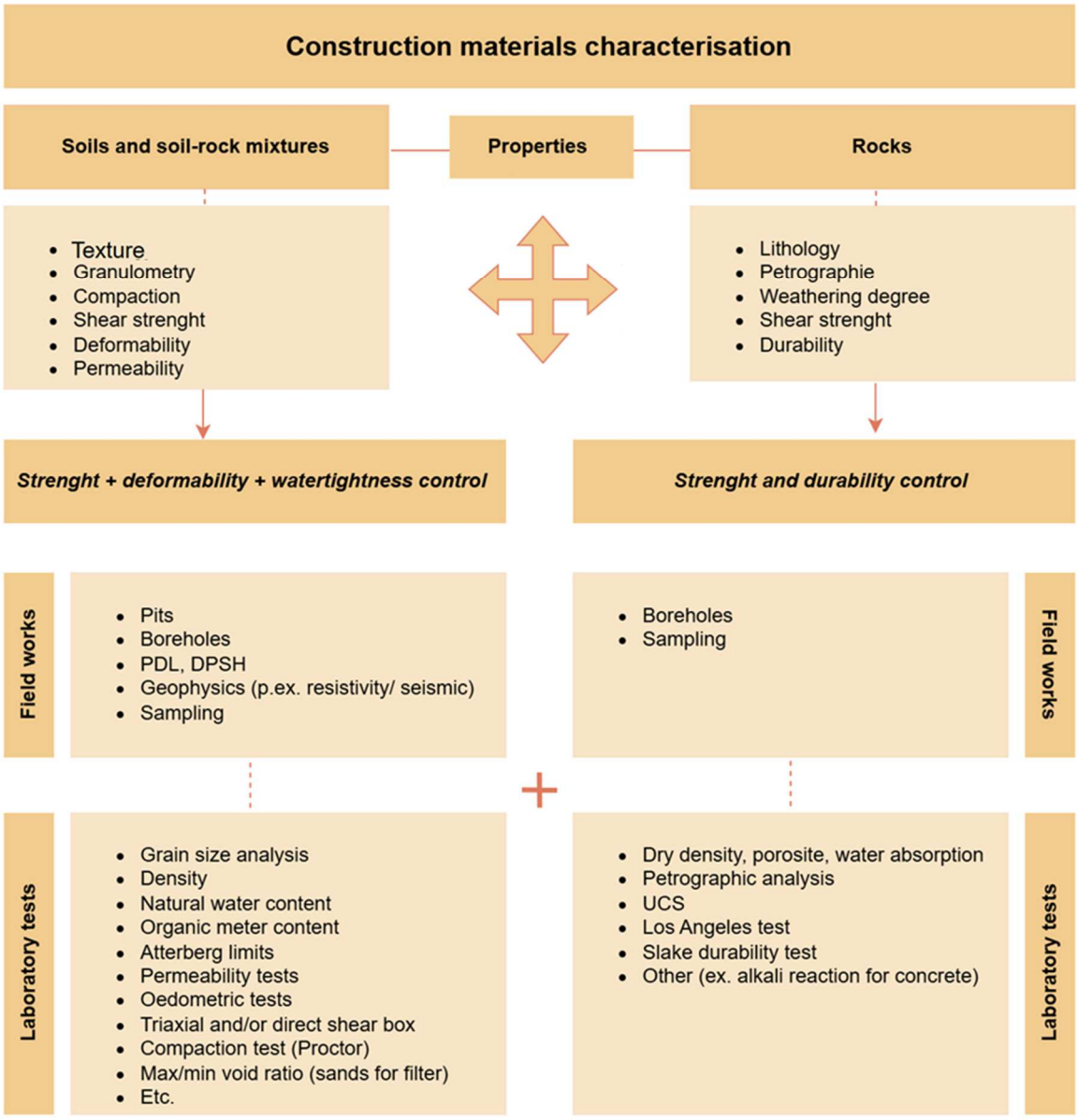

Fig. 11 – Site investigation to dam's foundations. Common field works and laboratory tests.

6. CONCLUSIONS

The design and construction of dams is a complex process that relies on many challenging requirements, including on efficient geological and geotechnical studies. These studies underpin the understanding of critical factors such as foundation characteristics, reservoir behaviour, and the availability of construction materials nearby. Historical case studies, such as Malpasset, Vajont, and Teton Dam failures starkly illustrate the catastrophic consequences of insufficient assessments, underscoring the need for a strategic and integrated approach to these studies to ensure structural integrity, safety and project sustainability.

Thorough adequate and timely site investigations, naturally coupled with adaptative solutions, modern dam engineering can successfully address complex challenges. These challenges rely

on dam's foundations issues, namely its bearing capacity, deformability and permeability; on the reservoir area conditions, that must ensure slope stability; and on the characteristics of available construction materials.

From understanding asymmetric valley conditions in southwestern Africa to the design of impermeable solutions for dams in Tunisia and Portugal or to the design of adaptive solution due to scarcity of fine-grained soils in Northwest Portugal, this paper shows the positive impact of suitable geological and geotechnical studies under the scope of the design phase of a dam.

It's clear that geological and geotechnical investigations are not merely technical requirements, instead they are essential investments in the safety, resilience, and longevity of dam projects. By continuing to refine these processes and integrating them into early project phases, the industry can better mitigate risks and enhance the socio-economic benefits of water resource management infrastructure worldwide.

REFERENCES

[1] Nasrat Adamo, N. A.A. (2020). Dams Safety and Geology. Journal of Earth Sciences and Geotechnical Engineering. Vol. 10, No. 6 (2020):133-189 pp.

[2] Brown, E. (2017). Reducing risks in the Investigation, Design and Construction of Large Concrete Dams. Journal of Rock Mechanics and Geotechnical Engineering. Vol. 9, Issue 2. 197-209 pp. Golder Associates Pty. Ltd., Brisbane, Australia.

[3] Duffaut, P. (2013). The Traps Behind the Failure of Malpasset Arch Dam, France, in 1959. Journal of Rock Mechanics and Geotechnical. CSRME.

[4] P.G., P. S. (s.d.). Turning Geologic Data into Knowledge: A summary of Dam Failure Case Histories. US Army Corps of Engineers.

[5] – Seed, H. B.; Duncan, J.M. (1987). The failure of Teton Dam. Engineering Geology. Volume 24, Issues 1-4: 173-205 pp.

[6] Roque, M.; Nazareth, A.; Ferreira, P.; Cabral, M. (2012). Contributo dos Estudos Geológico-geotécnicos do Aproveitamento Hidroagrícola de Caliços-Machados para o Conhecimento do Contexto Hidrogeológico da Região. XIII Congresso Nacional de Geotecnia. LNEC (Lisboa, Portugal). 16 p.

[7] Pimenta, L.; Faustino, V.; Roque, M.; Cabral, M. (2012). Concepção e Projecto Geotécnico das Infra-estruturas Primárias do Aproveitamento Hidroagrícola de Caliços-Machados. XIII Congresso Nacional de Geotecnia. LNEC (Lisboa, Portugal). 19 p.

[8] Nazareth, A.; Roque, M.; Reis, F.; Ferreira, P. (2011). Estudo de Impacte Ambiental nos Recursos Hídricos Subterrâneos a partir de um Aproveitamento Hidroagrícola Caliços-Machados. 8.º Seminário Águas Subterrâneas. FCUL (Lisboa, Portugal). 4 p.

[9] Roque, M., Rosa, A., Antunes, J., Pimenta, L. (2021). Atualização do Modelo Geológico-Geotécnico e do Projeto Geotécnico da Barragem de Saïda, na Tunísia. 17.º Congresso Nacional de Geotecnia. LNEC (Lisboa, Portugal). 10 p.

[10] Antunes, J., Pimenta, L., Roque, M., Sardinha, R., Rosa, A. (2018). Barragem de Saïda. Revisão e Atualização do Projeto. XIX Congresso Brasileiro de Mecânica dos Solos e Engenharia Geotécnica. (Salvador, Bahia, Brasil). 10 p.

[11] Antunes, J., Pimenta, L., Sardinha, R., Roque, M., Rosa, A. (2018). Revisão e Atualização do Projeto Geotécnico da Barragem de Saïda. 16.º Congresso Nacional de Geotecnia. Universidade de Ponta Delgada (Ponta Delgada, Portugal). 10 p.

[12] Sardinha, R., Pimenta, L., Roque, M., Rosa, A., Ferhat, H., (2018). Reabilitação da Barragem de Ouizert. Projeto do Tratamento de Impermeabilização da Margem Esquerda - XIX Congresso Brasileiro de Mecânica dos Solos e Engenharia Geotécnica. (Salvador, Bahia, Brasil). 10 p.

[13] Rosa, A., Roque, M., Pimenta, L., Sardinha, R., Ferhat, H. (2018). Perdas de Água Pela Albufeira da Barragem de Ouizert. Solução de Reabilitação Preconizada. 16.º Congresso Nacional de Geotecnia. Universidade de Ponta Delgada, (Ponta Delgada, Portugal). 10 p.

[14] Roque, M., Pimenta, L., Sardinha, R., Martins Carvalho, Rosa, A., J., Ferhat, H., (2018). Perdas de Água pela Albufeira da Barragem de Ouizert. Atualização da Situação de Referência. 16.º Congresso Nacional de Geotecnia. Universidade de Ponta Delgada (Ponta Delgada, Portugal). 10 p.

[15] Pimenta, L., Roque, M.; Sardinha, R.; Martins Carvalho, J.; Djir, K. (2016). Perdas de Água pela Albufeira da Barragem de Ouizert. Estudos de Diagnóstico e de Reabilitação. 15.º Congresso Nacional de Geotecnia. Universidade do Porto (Porto, Portugal).12 p.

[16] Aqualogus (2021) – Projeto de execução e estudo de impacte ambiental da barragem Redonda das Olgas. Estudo de Impacte Ambiental. Volume I – Peças escritas, Tomo 1 – Capítulos introdutórios.

[17] Engirecursos (2020). Projeto de execução da barragem de Gebelim e caminho de acesso ao coroamento. Estudo de Impacte Ambiental. Volume II – Relatório síntese.

[18] Sardinha, R., Pimenta, L., Rosa, A., Roque, M. (2018). Projeto Geotécnico da Barragem de Megarruma, 16.º Congresso Nacional de Geotecnia. Universidade de Ponta Delgada (Ponta Delgada, Portugal). 10 p.

[19] Roque, M., Pimenta, L., Sardinha, R. (2018). Estudo Geológico-geotécnico da Barragem de Megarruma, 16.º Congresso Nacional de Geotecnia. Universidade de Ponta Delgada (Ponta Delgada, Portugal).10 p.

Fifth International
Dam World Conference
PORTUGAL • LISBON • LNEC • APRIL 13-17, 2025
dam world 2025

APPLICATION OF A COST-EFFECTIVE IN-PLACE INCLINOMETER SYSTEM ON A ZONED EARTH DAM

João Palma
FCT-UNL

R Correia dos Santos[1]
LNEC

João Marcelino
LNEC

Nuno Marques
FCT-UNL – NOVA.ID

ABSTRACT

Monitoring in embankment dams is crucial for ensuring structural integrity and preventing potential failures. Traditional inclinometer data collection methods are time-consuming, labour-intensive, and lack support for automatic real-time or remote monitoring. Existing In-Place Inclinometer (IPI) systems are often prohibitively expensive, particularly when multiple sensors are required, limiting their adoption in resource-constrained settings. To address these limitations, a cost-effective IPI prototype using MEMS (Micro-Electro-Mechanical Systems) accelerometers was developed alongside a web application for automated data collection and visualization.

This paper focuses on the application of the developed system in the Azibo Dam, a zoned embankment dam in northern Portugal. Inclinometer monitoring data, collected over several decades using traditional methods, were used to evaluate the system's capabilities. A web application is being developed to enable users to visualize both historical and real-time data directly, providing tools for trend analysis and pattern recognition. A key feature is the ability to define "Monitoring Profiles," which spatially visualize data from multiple inclinometers within a cross-section or top-down view, enhancing the understanding of dam behaviour over time. Advanced filtering options, such as interval selection and customizable reference points, further support detailed analysis.

The case study demonstrates the effectiveness of proposed visualizations in streamlining data interpretation and improving decision-making for dam safety management. By offering a user-friendly, open-source, and cost-effective solution, the proposed solution addresses critical monitoring challenges, particularly for dams in financially constrained environments.

Keywords: Earth dam, Monitoring, In-place-inclinometer (IPI), Data visualization.

[1]ricardos@lnec.pt, Portugal

1. INTRODUCTION

Inclinometer monitoring is an important geotechnical technique used typically to measure and track changes of internal horizontal displacements in embankment dams and other geotechnical structures over time [1]. This method typically involves installing a metal or plastic pipe (casing) with inner grooves in two orthogonal directions into a borehole drilled within the dam body. By regularly measuring the inclinations of the casing at specific depths, engineers and geotechnical experts can determine the lateral deformations in two directions and assess the behaviour and stability of the dam [2].

This technique provides valuable data on ground movements, enabling the early detection of potential issues and allowing for timely remedial actions to prevent accidents or damage to the dam. Inclinometers are essential for monitoring the stability of embankment dams, where ground movement can be critical to the overall structural integrity [3].

The traditional traversing inclinometer probe, introduced in the late 1960s, uses servo-accelerometer sensors known for their precision and durability [4]. These probes measure the casing shape through manual measurements at intervals (typically 50 cm), yielding a profile in two orthogonal directions. However, the use of a traversing inclinometer probe makes automatic and remote measurements difficult to implement. Also, servo accelerometers are costly and sensitive to temperature variations, making them unsuitable for In-Place Inclinometer (IPI) solutions, as the large number of sensors required would result in prohibitively high costs for such applications [5].

IPI systems involve the installation of multiple sensors at discrete depths along the tube casing. This approach is particularly useful when regular monitoring of ground movement is essential or when site accessibility is limited. IPI systems save time by eliminating the need for manual measurements and enable the seamless collection of regular data through automated data acquisition equipment [6].

To address the economic challenges associated with commercial IPI systems, cost-effective integrated systems using microelectromechanical systems (MEMS) technology are being developed [7 – 8]. These systems aim to enhance access to inclinometer technology, enabling more widespread deployment with consistent sensor spacing.

Managing the large amounts of data generated by multiple IPI systems in real-time is a significant challenge. To address this issue, specialized visualizations are explored using Dam collected data. A web application is being developed to facilitate real-time monitoring, remote accessibility, and user-friendly visualization of historical data. This application will serve as a dashboard for structural health monitoring of embankment dams, integrating real-time data

and providing key metrics such as average angle variation and maximum deviation. The interactive visualizations will allow users to drill down on each sensor and its relations for specific dates, aiding in informed decision-making regarding the structural integrity and safety of the dam.

The primary objective is to demonstrate a use case scenario of the visualization dashboard through its application to the Azibo dam. By utilizing decades of historical inclinometer data from Azibo, the system showcases its ability to provide actionable insights, uncover historical trends, and support effective decision-making and risk management.

2. IN-PLACE INCLINOMETER SYSTEM UNDER DEVELOPMENT

2.1. Need for a New Affordable Inclinometer Solution

A new inclinometer system is being developed at Laboratório Nacional de Engenharia Civil (LNEC) with the cooperation of the Department of Computer Science of NOVA School of Science and Technology as a cost-effective alternative to the expensive commercial In-Place Inclinometer (IPI) systems currently available. These systems, offered by established companies such as *GeoSense* [9], *Measurand* [10], *SignalQuest* [11], *SisGeo* [12], and *Soil Instruments* [13], are renowned for their reliability but are often unaffordable for some dam owners.

The developed system addresses the need for a precise yet affordable inclinometer solution, focusing on reducing costs without compromising accuracy. The system employs advanced MEMS sensor technology to deliver highly precise lateral displacement measurements. It also integrates wireless data transmission, automated data logging, and an intuitive web interface, creating a comprehensive and user-friendly monitoring solution.

By balancing performance and affordability, the proposed inclinometer aims to make high-quality monitoring accessible to a broader range of dam owners.

2.2. System Architecture

Fig. 1 provides an overview of the proposed system that is under development, illustrating the data flow from the inclinometer readings on a specific dam to their visualization in a web application, as defined in [14].

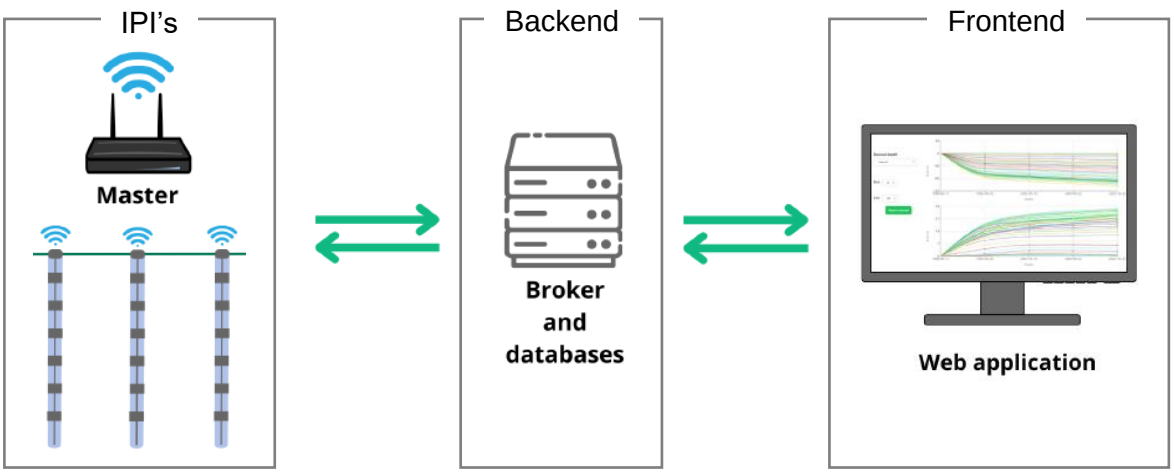

Fig. 1 – IPI system architecture: from acceleration sensors to web application (adapted from [14])

The system architecture of the inclinometer monitoring system is composed of three primary components:

- *The physical in-place inclinometers (IPI's)*: Each in-place inclinometer is composed of several sensors, placed along an inclinometer casing with regular spacings, that collect data on the inclination of the embankment dam body. These sensors are equipped with low-cost accelerometers and microcontrollers that wirelessly transmit data measured in sensor nodes to a master node that in turn transmit that info to the backend server.
- *The backend infrastructure*: The backend infrastructure acts as a broker to manage the sensors data coming from the master node of each in-place inclinometer and deals with the databases, ensuring the seamless storage and processing of the collected data; and
- *The frontend user interface*: The frontend is responsible for user interaction through a web interface. This web application serves as the primary interface for users to interact with the system, providing a user-friendly and intuitive way to visualize and analyze the data results.

2.3. Features and Requirements

In addition to its cost-effectiveness, the system is being designed to offer some unique features that make it a robust and efficient solution for monitoring the inclination of embankment dams. These features include:

1. *Bidirectional communication and interactive capabilities*: The system facilitates bidirectional communication, enabling users to both read data from the inclinometer sensors and interact with their master nodes. This feature allows adjustments to the

frequency of readings and data storage, ensuring efficient data management and preventing the accumulation of unnecessary data.

2. *Wireless communication*: The system utilizes wireless communication between the sensors and their master node, with wires used only for power delivery. Data is also sent to the backend wirelessly using standard transmission protocols. This design minimizes the need for extensive wiring, reducing even further assembling costs and enhancing ease of installation and use.
3. *Real-time and remote monitoring*: It offers real-time monitoring capabilities, enabling immediate detection of movements and providing early warning systems to protect life and valuable assets.
4. *Adaptive reading and record frequency*: A unique feature under development is the ability to adjust the frequency of readings based on previous data, leveraging artificial intelligence and machine learning. This dynamic adjustment ensures that critical changes are captured accurately while reducing unnecessary data points.
5. *Monitoring groups and profiles*: It introduces 'Monitoring Groups,' allowing users to aggregate data from selected inclinometers at each dam site. The unique 'Monitoring Profiles' feature is a powerful visualization tool that presents the results from all inclinometers along a specified dam profile, whether transverse or longitudinal. Users will be able to overlay these results onto an image of the cross-section, offering a clear and intuitive representation of the data within its structural context.
6. *Geological layer visualization*: The system allows users to visualize soil layers in each inclinometer casing, defined by the user based on survey data. This feature helps in identifying abnormal movements on different materials in the embankment, such as, for example, the core or the shell.
7. *Advanced filter capabilities*: It features advanced filter capabilities, allowing for highly customized and precise data filtering. It can filter data by specific dates or date intervals, reading types (absolute/relative/cumulative displacements, casing distortions, sensor temperatures, etc.) and enables filtering by depth, allowing for the examination of data within a specific depth interval. This is particularly useful for analysing the behaviour of different layers within the embankment dam, such as the core or the shell, and identifying any anomalies or movements specific to those depths.
8. *Specific datum as reference date*: The system is also designed to allow users to set a specific datum as the reference date for calculations, enabling the calculation of differential deformations over a selected time interval. For example, users can compute deformations occurring during the first five years of operation while excluding displacements from the initial filling phase. This feature is essential for providing

precise analysis and enabling accurate comparisons of structural movements over time.

Once fully implemented, these features position the proposed system as a robust, interactive, and highly customizable solution for inclinometer monitoring in embankment dams, providing relevant advantages over traditional methods and established IPI commercial systems.

The following sections highlight the main components of the proposed system infrastructure. After presenting the IPI requirements and capabilities a special focus is given to the frontend web application components for visualization and user interaction.

3. PROTOTYPE OF THE PHYSICAL IPI

At this stage, the proposed in-place inclinometer (IPI) exists as a functional prototype (Fig. 2). The prototype consists of four sensor nodes and a master node. Each sensor node captures angle data from its accelerometer and wirelessly transmits it to the master node. The master node, in turn, relays this data to a web-based time-series database at predefined intervals, ensuring efficient and organized data storage for analysis.

3.1. IPI prototype components

Each sensor node consists of an accelerometer board (HW-86C) and a microcontroller (ESP8266 D1 mini R2) [15], both of which are readily available at affordable prices (less than 3 euros per unit) from online marketplaces. A custom-designed PCB manages power distribution and facilitates seamless communication between the microcontroller and the accelerometer. The main components of each sensor node are shown in Fig. 2 (a).

The sensor board features an ADXL345 [16], a consumer-grade, triple-axis MEMS accelerometer with 10-bit digital output, offering a broad measurement range and low power consumption.

The electronic components are housed within a stainless-steel probe, with an outer diameter of about 30 mm and a length of 10 mm. Each node is powered by a 5V parallel circuit source, drawing approximately 50 mA when active and peaking at 300 mA during wireless transmission (lasting between 1 to 5 milliseconds). To avoid current overload, wireless transmission occurs in a staggered sequence, with each sensor transmitting at 100-millisecond intervals.

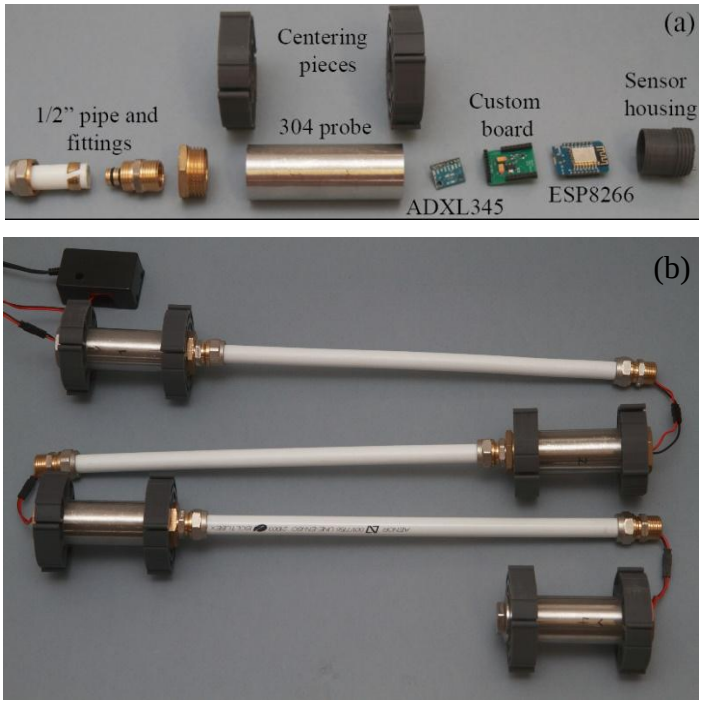

Fig. 2 – In-place Inclinometer physical prototype unassembled [17]

The connection between each sensor probe is established using multi-layer ½ inch pipes and compression pipe fittings typically used in fluid applications. Fig. 2 (b) shows the prototype setup prior assembly with the four node sensors.

Unlike other solutions that rely on costly flexible joints (e.g., [11 – 13, 18]), the proposed IPI prototype uses flexible pipes connecting each sensor node. These pipes provide a cost-effective alternative, allowing the system to accommodate large movements within the inclinometer casings without compromising functionality. This design significantly reduces overall costs while maintaining the flexibility required for accurate displacement monitoring.

3.2. Interaction between Sensors and Master Nodes

Each sensor node in the prototype is equipped with a microcontroller programmed in C++ using the Arduino IDE [19]. The system is designed to perform the following tasks:

1. *Retrieve gravitational data*: Gravitational forces along the X, Y and Z axes (gX, gY and gZ) are measured using the accelerometer. These values represent the acceleration due to gravity experienced by the sensor along each axis. Temperature readings are also obtained to account for any sensor drift caused by temperature variations. Communication with the accelerometer is performed using the I2C protocol, which allows efficient data transfer.
2. *Compute angles*: The angles aX and aY are computed based on the gravitational forces measured along the respective axes. The accelerometer measures the

components of the gravitational vector in three dimension. The angles aX and aY are derived using trigonometric relationships (1) and (2).

$$aX = arctan\left(\frac{gX}{\sqrt{gY^2+gZ^2}}\right) \quad (1)$$

$$aY = arctan\left(\frac{gY}{\sqrt{gX^2+gZ^2}}\right) \quad (2)$$

The calculated angles represent the inclination of the accelerometer along the X and Y axes, allowing for precise monitoring of the sensor's orientation relative to gravity.

3. *Enhance accuracy*: A low-pass filter was applied to the accelerogram data, effectively smoothing the measurements by averaging multiple values. This approach reduces high-frequency noise, ensuring a more accurate representation of the overall signal while preserving its essential characteristics.
4. *Wireless data transmission*: Send the processed data wirelessly to the master node using the ESP-NOW protocol [20]. Each ESP device features a unique MAC address for identification purposes. Data transmission occurs at regular intervals, configurable through a user-defined variable. During laboratory tests, data was transmitted every 10 seconds.

The master node employs two ESP8266 microcontrollers to manage both ESP-NOW communication and Wi-Fi connectivity (Fig. 3), as these protocols cannot run reliably on a single device simultaneously. ESP-NOW ensures real-time, low-latency data transfer from the sensor nodes, while a dedicated microcontroller handles the Wi-Fi connection for internet-based data transmission. Separating these tasks avoids protocol conflicts and resource overload, ensuring stable and efficient operation.

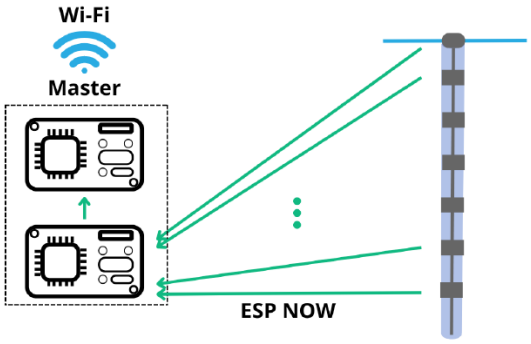

Fig. 3 – Communication between sensor's inclinometer and its master [14]

Each microcontroller has distinct roles:

1. *First Microcontroller*
   - Receives data wirelessly from the sensor nodes.

- Aggregates the readings into an array.
- Transmits the aggregated data in JSON format via Serial communication at regular intervals (set to 30 seconds in lab tests).
- Incorporates a timeout mechanism to ensure timely data transmission, even if some sensors fail to provide readings within the specified timeframe.

2. *Second Microcontroller*
   - Establishes a secure Wi-Fi connection.
   - Receives JSON-formatted data from the Serial port containing all sensor measurements.
   - Functions as an MQTT (Message Queuing Telemetry Transport) client, utilizing a lightweight, publisher/subscriber messaging model widely used in IoT applications for efficient and reliable communication. In this model, data is published under specific identifiers, known as topics, and can be received by subscribers to those topics. The client forwards data to a remote backend broker via the MQTT protocol [21].
   - Publishes the received data under a unique topic, identified by the inclinometer's specific code.

Santos and Marcelino [17] conducted laboratory tests to validate the prototype, demonstrating its potential for applications such as slope stability assessments, excavation safety, and foundation integrity evaluations. The results indicate that the system is suitable for low-risk scenarios, where total errors of approximately 0.4° are acceptable. However, its use is not yet recommended for high-risk projects requiring highly precise inclinometer monitoring.

Ongoing research aims to integrate an optimal commercial MEMS accelerometer into the prototype to achieve the best price-to-quality ratio, further enhancing the system's reliability and applicability.

4. SERVER COMMUNICATION AND DATABASES

Fig. 4 illustrates the interactions and communications occurring in the backend, facilitating communication between the IPIs and the web application's frontend.

An MQTT broker has been set up using HiveMQ's cloud service [22] on its free tier. The MQTT broker acts as a server that receives messages from clients and routes them to the appropriate destination. Specifically, it manages, and aggregates messages published by the master node of each inclinometer and forwards them via Telegraf—a plugin-driven open-source agent for collecting and reporting time-series data [23]. Telegraf then sends this data to InfluxDB, a time-series database optimized for high write throughput and low-latency queries [24].

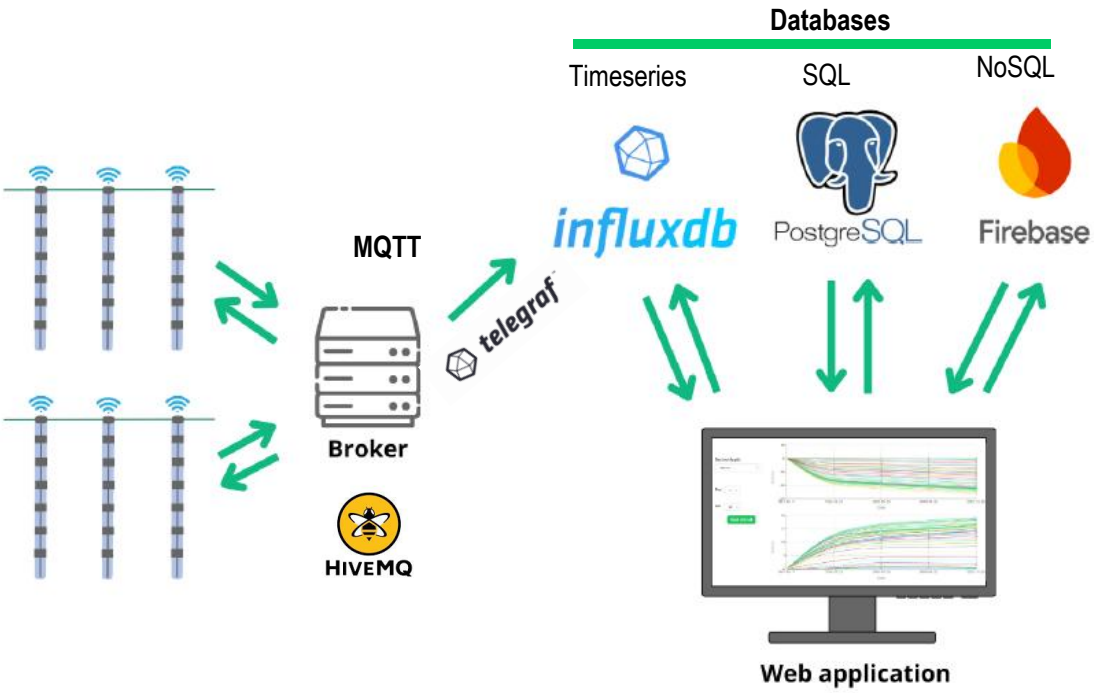

Fig. 4 – Communication between sensor's inclinometer and its master (adapted from [14])

A local server has been configured with Telegraf and InfluxDB running in Docker containers. InfluxDB stores data with timestamps, enabling efficient real-time tracking and analysis of time-series information. This setup provides a reliable and scalable backend for data collection, storage, and analysis.

The raw data in the time-series database (InfluxDB) is structured to support detailed analysis of inclinometer readings over time. Each data point includes several key fields to provide context and meaning.

For instance, the 'Field' parameter specifies the property being measured, such as inclination angles ('aX', 'aY') or temperature ('temp'), while the 'Value' field contains the corresponding numerical measurement. The 'Host' and 'Structure' fields identify the worksite, such as the Azibo Dam, where the data was collected, ensuring traceability. Additionally, each reading is associated with a 'SensorID' and an 'Inclinometer', indicating the specific device and its location within the dam. A timestamp field records the exact time the measurement was taken, enabling precise time-series analysis. This structured format ensures the data is comprehensive, making it suitable for in-depth monitoring and evaluation of dam stability over time.

A relational database, implemented in PostgreSQL [25], is responsible for storing distinct types of data, such as, inclinometer data (excluding the readings), user information, and database connections parameters. This database ensures that all the needed information is well-organized and accessible, allowing for efficient data access and retrieval.

In order to facilitate the design and development of the application, an Entity-Relationship Diagram (ERD) of the complete schema was developed, which is a visual representation that illustrates the relationships among entities within a database.

The complete ERD, as developed and published in [14], includes the following main entities:

1. *Inclinometer*: A collection of sensors installed within the same borehole.
2. *Sensor*: The individual sensor of an inclinometer, which collects the actual data.
3. *InfluxDB*: Contains the connection parameters for the InfluxDB time-series database, essential for establishing a connection to retrieve data measured in the sensors.
4. *Structure*: A work site associated with a group of inclinometers.
5. *Monitoring Group*: A set of inclinometers associated with a specific structure being monitored.
6. *Monitoring Profile*: A set of inclinometers defined by the user to view their results simultaneously.
7. *Monitoring Profile Group*: A collection of monitoring profiles grouped together to assist in evaluating different views of the same structure.
8. *Soil and Water Layers Set*: A collection of soil and water layers at the location of the inclinometer.
9. *Layer*: An individual layer found along the length of an inclinometer.

Additionally, the system integrates a cloud database using Firebase, which includes a NoSQL database (Firebase [25]) for storing user-uploaded images, such as cross-section drawings and top-down plan views of the dam. These base images serve as visual references for displaying inclinometer data, which can be overlaid onto the relevant images in the web app.

This integration also serves as a proof of concept for a future cloud-based infrastructure, showcasing the system's ability to handle cloud data and providing a solid foundation for expanding to a fully cloud-based implementation.

5. WEB INTERFACE

The frontend is built around a web interface developed using the *React* framework [26], an open-source JavaScript library renowned for creating dynamic user interfaces. Despite its relatively recent emergence, *React* has proven to be a powerful tool for this project.

The web interface was designed with a user-centered approach, focusing on ease of use, clarity, and smooth alignment with the intended workflow. Initial sketches mapped out the layout and navigation flow, ensuring that core features were intuitive and easily accessible.

Through multiple iterations, the design was refined to address usability challenges and improve the overall user experience. The final goal was to create a visually appealing, user-friendly

interface that enables users to interact seamlessly with the data, navigate effortlessly, and conduct swift, accurate analyses.

Depicted in Fig. 5 is the layout and the navigation sidebar of the web application.

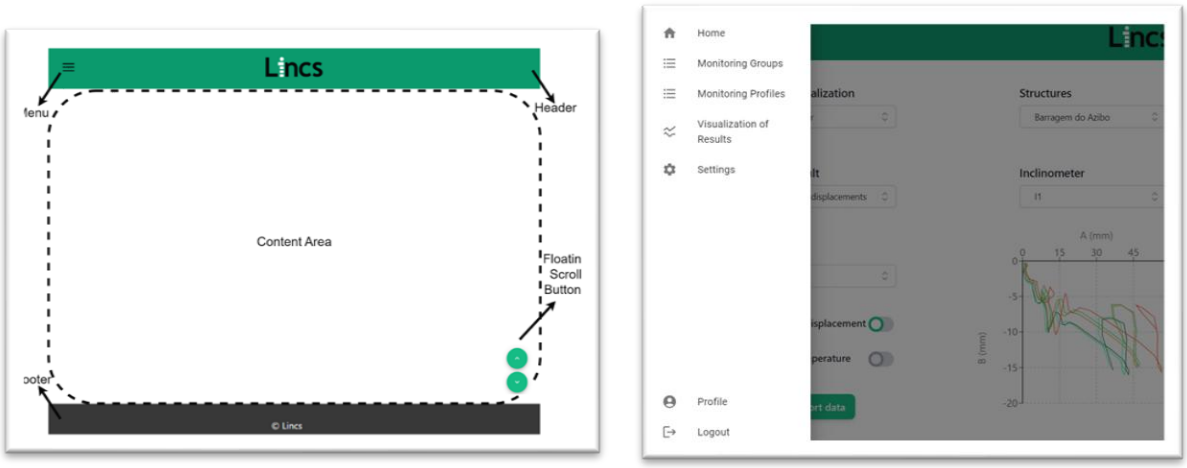

Fig. 5 – Web-app interface layout (left) and navigation sidebar (right) [14]

The web application allows users to assign inclinometers into Monitoring Groups and manage detailed information for each one, including sensor spacing, casing azimuth, geographic coordinates of the borehole, and associated soil layers.

The application also enables Monitoring Profiles that interlink inclinometers to visual representations, enabling a richer analysis environment and easier correlation between real-world structures and collected data. The system supports two distinct types of position corrections depending on the profile type, namely by:

- *Plan view*: type of position corrections allows users to place a dot marker on the plan representing the relative position of each inclinometer. Once the positions are adjusted, the plan can be viewed with the dots, providing a clear visual representation of where each inclinometer is located; and
- *Cross-sectional view*: it involves placing a line to represent each inclinometer along its length. Users can select the top and bottom points of the inclinometer, and the interface automatically draws and adjusts the line to match these points. This approach ensures that the inclinometer position is accurately represented in relation to its depth on the image.

5.1. Visualization of Results from individual inclinometers

The web application's fundamental feature for result visualization is its ability to plot various outcomes derived from sensor readings and calculations for a single inclinometer. This

capability provides users with clear and intuitive insights into the data, enabling effective analysis and interpretation.

Fig. 6 illustrates the initial webpage for selecting the inclinometer the user wishes to analyze, along with various filtering options. These filters allow users to specify the desired period to inspect, select a reference (datum date), and choose the type of result to view, including cumulative or relative displacement, distortion, or angles.

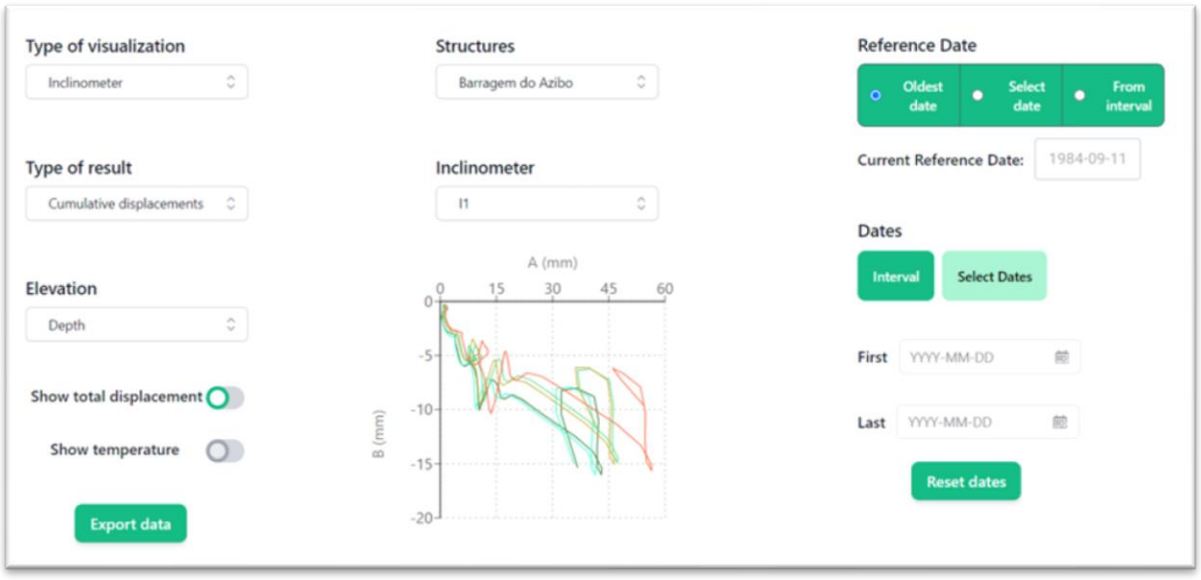

Fig. 6 – Visualization of Results page [14]

As an example of the interface's visualization capabilities, Fig. 7 and Fig. 8 showcase plot results generated from a selected inclinometer.

Fig. 7 depicts cumulative displacements, measured in millimetres, for two orthogonal directions (A and B) as a function of casing depth across various dates. Four dates were selected for representation, with the reference date clearly highlighted. Users can interact with the graph to obtain detailed information about displacement values at specific depths for each date, enabling an in-depth and interactive analysis. Additionally, the graph can be adjusted to display data based on sensor levels instead of depth, offering precise values for each sensor location.

Fig. 8 illustrates the interface's ability to display additional data views, such as total values and temperature values at different depths for angles A and B. A slider is integrated into the interface, allowing users to adjust the depth range displayed and limit the representation of the monitoring data across different dates. This interactive functionality enhances the user experience by providing tailored and precise visualizations of the monitoring data.

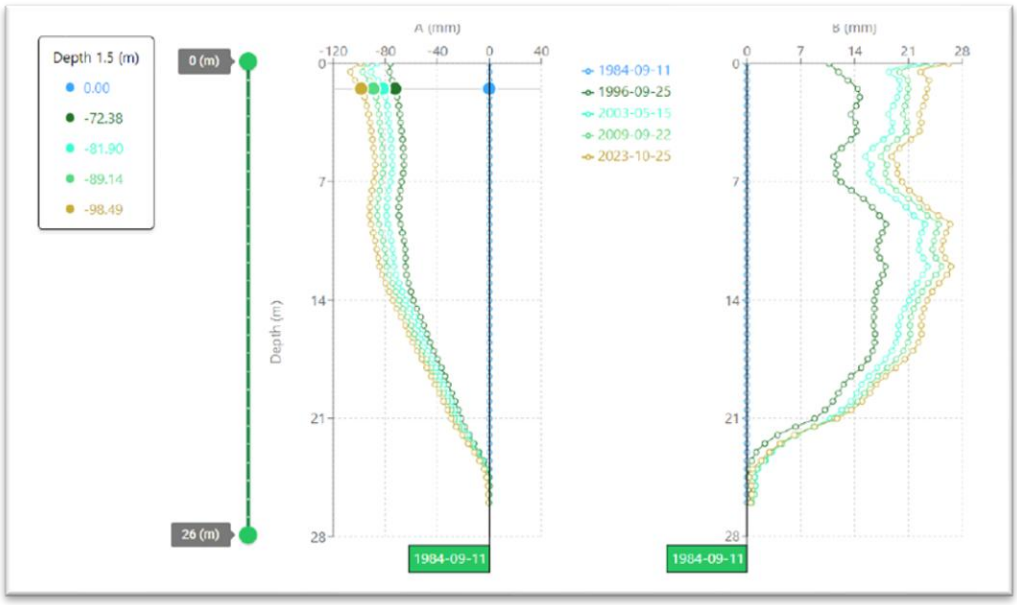

Fig. 7 – Charts with A/Depth and B/Depth of an inclinometer [27]

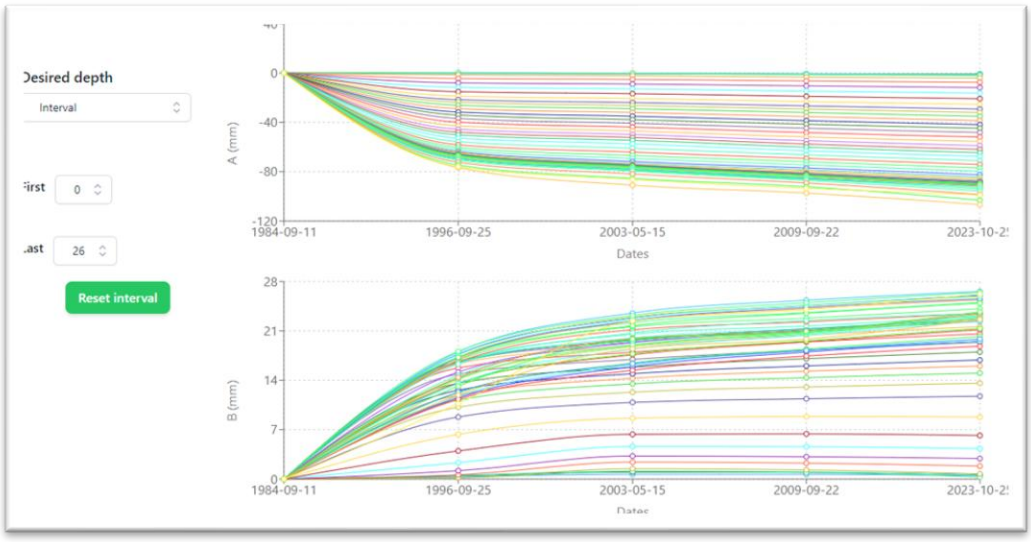

Fig. 8 – Visualization of cumulative displacements in a particular inclinometer and corresponding soil layers along the casing borehole [27]

5.2. Visualization of Results from inclinometers in a Monitoring Profile

This option combines graphical data with geographic and image-based visualizations for a comprehensive analysis.

A specialized view was designed to facilitate the comparison of multiple inclinometers within a Monitoring Profile. This feature enables the simultaneous display of data from different inclinometers, with charts carefully scaled to ensure consistency and accuracy. The scaling accounts for elevation, displacement values, and the depths at which the inclinometers are

installed, providing a relative representation of their lengths and positions within the Monitoring Profile.

As with the individual inclinometer visualization, this comparative view includes filters that allow users to refine their analysis by selecting specific time periods, reference dates, or result types. This functionality enhances the ability to perform detailed comparisons between multiple inclinometers, supporting a more comprehensive interpretation of the data.

Fig. 9 demonstrates this feature by presenting a monitoring profile containing two inclinometers, I6 and I9. These inclinometers are positioned 30 meters apart horizontally and have depths of 51 meters and 20.5 meters, respectively. This visualization highlights the effectiveness of the comparative view in analysing spatially distributed monitoring data. Future enhancements will include the ability to overlay these plots on top of user-uploaded images, further improving the integration of graphical data with visual context.

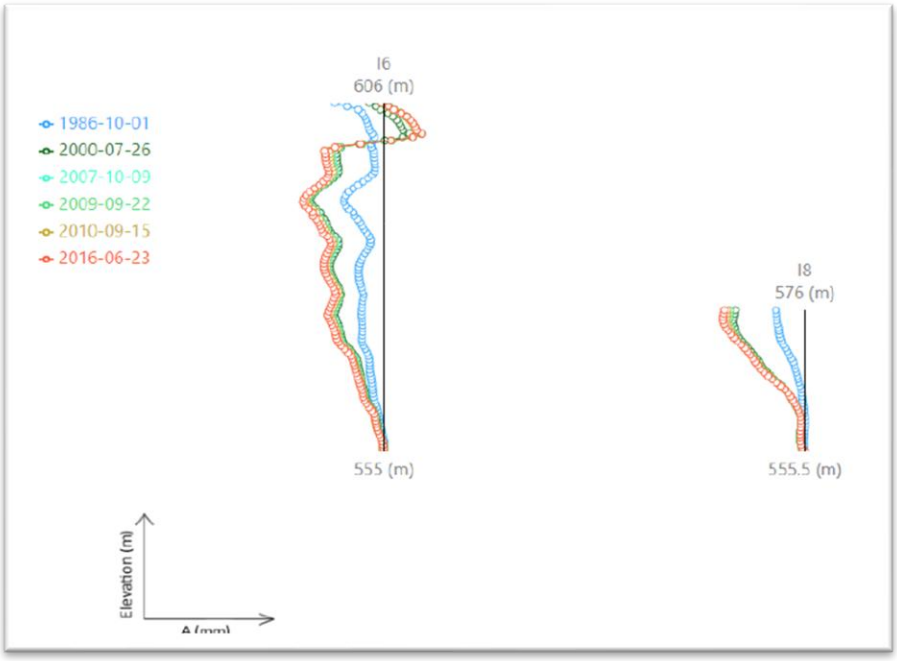

Fig. 9 – Visualization of cumulative displacements in a particular Monitoring Profile [14]

6. CASE STUDY OF AN EARTH DAM AS PROF-OF-CONCEPT

This case study demonstrates the practical application of the developed system using historical data from the Azibo dam, located in Portugal. The data, collected through traditional inclinometer methods, was digitized and uploaded into the time-series database used by the interface. This integration allowed the legacy data to be seamlessly incorporated into the modern visualization and analysis tools of the system. By utilizing this historical information, the case study showcases the system's ability to effectively manage and analyze real-world

geotechnical data, offering valuable insights and a user-friendly experience for monitoring and evaluating inclinometers in earth dam applications.

6.1. Azibo dam

The structure used as a case study is a zoned earth dam, constructed in 1984, with a maximum height of 56 meters above its foundation, and a reservoir with a total capacity of 54.5 hm^3 (Fig. 10). The dam's crest, with a total length of 551 meters and a width of 10 meters, is located at an elevation of 606.00 m. The full storage level (FSL) is at 602.00 m, while the maximum water level (MWL) occurs at 603.65 m. The minimum operating level (MOL) is at 575.00 m.

The dam has 9 operational inclinometer casings distributed across four cross-sectional profiles (P5, P7, P9, and P13). The inclinometer casings were installed in vertical boreholes, anchored to the foundation rock.

The dataset stored in the time-series database (InfluxDB) includes inclinometer data collected quarterly over several years, comprising a total of 44,920 entries.

Fig. 10 – Aerial view of Azibo dam (photo by [28])

6.2. Visualization of results on inclinometers of Azibo dam

In addition to the traditional analysis of plots displaying displacement versus depth and displacement versus time in both transverse and longitudinal directions, the web app offers additional plots that provide enhanced insights, supporting a more comprehensive analysis for dam engineers.

In particular, Fig. 11 presents a plot generated by the interface, illustrating the cumulative displacement at the top of the inclinometers (i.e., at surface level), with scaled arrows and a color range reflecting the value magnitude. Additionally, users can choose to display the maximum displacement at each inclinometer, showing the depth where it occurs, instead of the surface-level value.

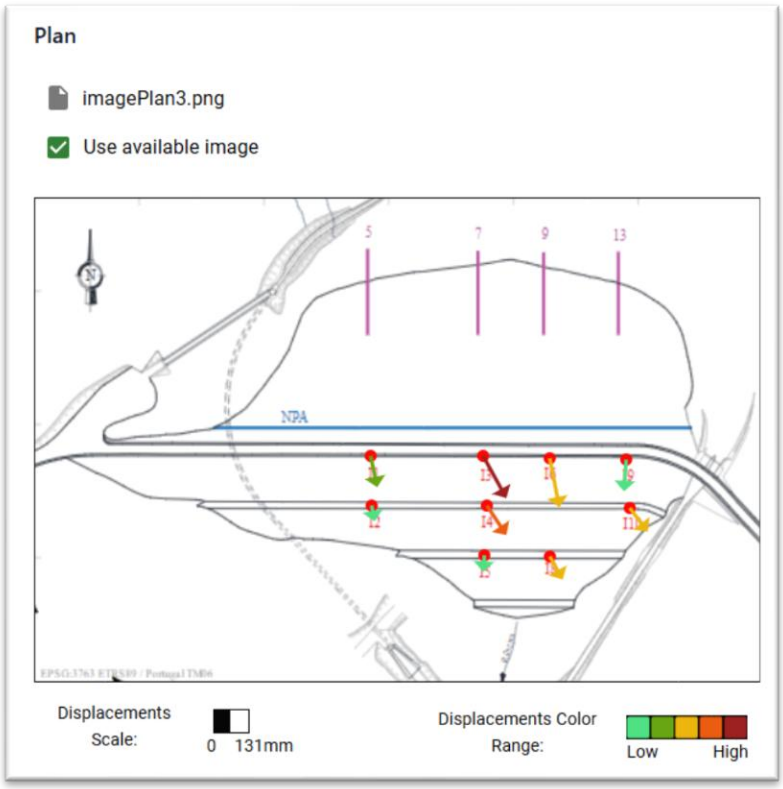

Fig. 11 – Cumulative displacement arrows in each inclinometer at its surface level with color range [14]

This representation allows dam engineers to quickly identify that the displacements tend to be greater at the crest of the dam and at the center of the valley where the embankment is higher. Such a pattern is consistent with typical dam behaviour, where the tallest sections often experience the most significant deformation due to the increased load and pressure. The plot's ability to show maximum displacement at various depths through corresponding arrows adds another layer of insight, enabling engineers and analysts to assess the structure's behaviour throughout its entire profile. This comprehensive view is crucial for monitoring the dam's stability, identifying potential weak points, and informing maintenance decisions. Moreover, the visual nature of the plot makes it an effective tool for communicating complex geotechnical data to both technical and non-technical stakeholders, facilitating informed discussions about the dam's performance and safety measures.

To achieve a realistic visualization, a composition can be created by combining an image of the profile being studied with its scaled displacements, as shown in Fig. 12. In this plot, the initial position of the inclinometers in the profile is marked in red, and the cumulative displacement lines at depth for the specified date (as indicated in the image legend) are shown in blue. This compositing technique provides a realistic view of the displacement, allowing users to compare the effects of different soil layers on the inclinometer casing position.

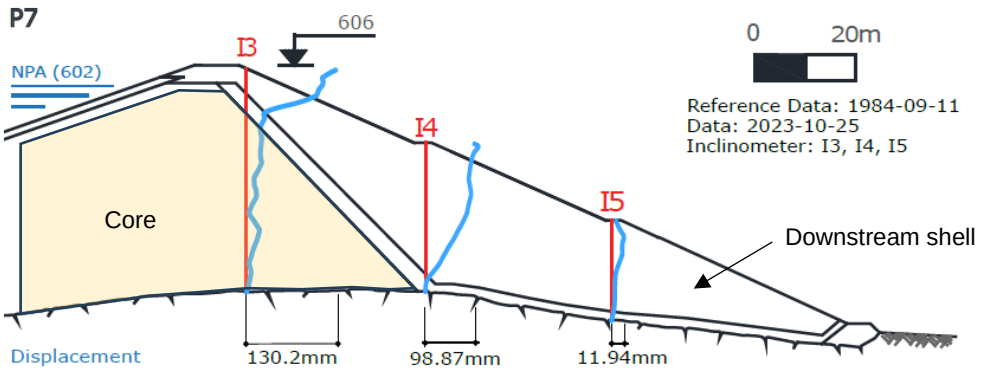

Fig. 12 – Overlay of displacement measurements taken on 2023-10-25 of inclinometers I3, I4 and I5 on profile P7 of Azibo dam [27]

This plot shows the cross-sectional profile P7 of Azibo dam, including inclinometers I3, I4, and I5. It has proven to be particularly useful for observing that the material from the downstream shell appears to be less stiff than the material from the core, as indicated by the greater displacements observed in the downstream material. Inclinometer I3, for example, shows significantly more deformation in the area where it crosses the downstream shell compared to the zone of the core.

7. CONCLUSIONS

This paper presents the development of a cost-effective In-Place Inclinometer (IPI) system, addressing the challenges of traditional inclinometer data collection methods and the high costs of existing commercial IPI systems. The Azibo dam case study provided a real-world context to evaluate the system's performance and demonstrate its practical application in dam monitoring.

Key conclusions from this article include:

1. *Cost-effectiveness*: The system offers a viable and affordable alternative to expensive commercial IPI systems, as demonstrated through its application to the Azibo dam. This affordability enables dam owners in resource-limited settings to adopt advanced monitoring technologies.
2. *Practical applicability*: Using historical inclinometer data from the Azibo dam, the system proved its capacity to handle and visualize real-world data effectively, validating its usefulness for dam safety management.
3. *Enhanced visualization*: The developed web application enabled the creation of monitoring profiles for the Azibo dam, allowing spatial visualization of inclinometer data on cross-sections and plan views. This feature provided valuable insights into the dam's behaviour over time.

4. *Comprehensive software solution*: The web application facilitated real-time monitoring and analysis of Azibo dam data, with features such as customizable monitoring profiles and advanced filtering options, enhancing user capability to interpret and act on the information.
5. *Scalability and integration*: The system architecture demonstrated its scalability during the Azibo dam case study, highlighting the potential for integrating multiple IPIs into a unified monitoring solution.
6. *Future potential*: The system design, validated through the Azibo dam study, allows for future enhancements, such as integrating more precise sensors or AI-driven adaptive reading frequencies, further improving its monitoring capabilities.

In conclusion, the Azibo dam case study highlights the effectiveness of a proposed system that can provide a cost-effective, user-friendly, and comprehensive tool for dam safety management. We argue that the ability to analyse real-time monitoring, data visualization offers significant potential for improving dam safety practices, enabling more proactive and informed decision-making in embankment dam management. The successful application of these visualizations to the Azibo dam highlights the system's practical value and potential for improving dam safety practices in similar settings.

REFERENCES

[1] Marr, W. A. and Standing, J. (2023). Principles of geotechnical monitoring. In: 2nd ed. Vol. 2. Emerald Publishing Limited.

[2] Li, B., Yang, J. and Hu, D. (2020). Dam monitoring data analysis methods: A literature review. In: Structural Control and Health Monitoring 27.

[3] Stark, T. D., and Choi, H. (2008). Slope inclinometers for landslides. Landslides, n. 5, 339–350.

[4] Green, G. E., and Mikkelsen, P. E. (2008). Deformation Measurements with Inclinometers. Transportation Research Record, n. 1169.

[5] Uhlemann, S., Smith, A., Chambers, J., Dixon, N., Dijkstra, T., Haslam, E., Meldrum, P., Merritt, A., Gunn, D., and Mackay, J. (2016). Assessment of ground-based monitoring techniques applied to landslide investigations. Geomorphology, 253, 438–451.

[6] Allasia, P., Godone, D., Giordan, D., Guenzi, D., and Lollino, G. (2020). Advances on Measuring Deep-Seated Ground Deformations Using Robotized Inclinometer System. Sensors, 20(13), 3769.

[7] Li, C., Fernandes-Steeger, T. M., Link, J. A., May, M., and Azzam, R. (2014). Use of MEMS accelerometers/inclinometers as a geotechnical monitoring method for ground subsidence. Acta Geodynamica et Geomaterialia, 337–349.

[8] Niu, W., Fang, L., Xu, L., Li, X., Huo, R., Guo, D., and Qi, Z. (2018). Summary of Research Status and Application of MEMS Accelerometers. Journal of Computer and Communications, 06(12), 215–221.

[9] GeoSense. (2025). www.geosense.co.uk (available on 2025-01-04).

[10] Measurand. (2025). www.measurand.com (available on 2025-01-04).

[11] SignalQuest. (2025). www.signalquest.com (available on 2025-01-04).

[12] SisGeo. (2025). www.sisgeo.com (available on 2025-01-04).

[13] Soil Instruments (2025). www.soilinstruments.com (available on 2025-01-04)

[14] Palma, J. (2024). Development of a web interface for an inclinometer monitoring system. Master thesis in Computer Science and Engineering. FCT-UNL, Caparica, Portugal, September.

[15] Mesquita, J., Guimarães, D., Pereira, P, Santos, F., Almeida, L. (2018). Assessing the ESP8266 Wi-Fi module for the Internet of Things. 2018 IEEE 23rd international conference on emerging technologies and factory automation (ETFA), Vol 1, pp784-791.

[16] Su, Y.; Gong, M.; An, B.; Zhang, J.; Zhao, X. (2014). Design of a tilt angle measurement system based on ADXL345 sensor. Journal of Measurement Science & Instrumentation, 2014, Vol 5, Issue 2, p19.

[17] Santos R., Marcelino, J. (2024). Development and laboratory testing of a low-cost wireless in-place inclinometer prototype. In: Proceedings of the XVIII ECSMGE 2024. Geotechnical Engineering Challengers to Meet Current Emerging Needs of Society. Ed. by SPG. ISSMGE.

[18] Freddi, F., Mingazzi, L., Pozzi, E., and Aresi, N. (2023). Laboratory Assessment of an In-Place Inclinometer Chain for Structural and Geotechnical Monitoring. Sensors, 23(20), 8379.

[19] Amestica, O. E., Melin, P.E., Duran-Faundez, C.R., Lagos, G.R. (2019). An Experimental Comparison of Arduino IDE Compatible Platforms for Digital Control and Data Acquisition Applications. 2019 IEEE CHILEAN Conference on Electrical, Electronics Engineering, Information and Communication Technologies (CHILECON). 13-27 November 2019. Valparaiso, Chile.

[20] Wicaksono, M., Rahmatya, M. (2022). IoT for Residential Monitoring Using ESP8266 and ESP-NOW Protocol. Jurnal Ilmiah Teknik Elektro Komputer dan Informatika 8(1).

[21] Bender, M., Kirdan, E., Pahl, M., Carle, G. (2021). Open-Source MQTT Evaluation. 2021 IEEE 18th CCNC. 09-12 January 2021. Las Vegas, NV, USA.

[22] HiveMQ (2025). www.hivemq.com (available on 2025-01-04).

[23] Telegraf (2025). www.influxdata.com/time-series-platform/telegraf/ (available: 2025-1-4).

[24] InfluxDB (2025). www.influxdata.com/products/influxdb/ (available on 2025-01-04).

[25] Denira, F., Azizah, F. (2023). SQL Interface For CRUD Operations on Cloud Firestore. 2023 IEEE International Conference on Data and Software Engineering (ICoDSE). 07-08 September 2023. Toba, Indonesia.

[26] React (2025). https://react.dev/ (available on 2025-01-04)

[27] Palma, J., Marques, N., Santos, R. (2024). BI-Enabled Web Visualization of In-Place Inclinometer Data for Geotechnical Applications. Progress on Artificial Intelligence. EPIA2024. Lecture Notes in Computer Science (LNAI, volume 14969 pp 176–187). Doi 10.1007/978-3-031-73503-5_15.

[28] A Terceira Dimensão (2025). http://portugalfotografiaaerea.blogspot.com (in 2025-1-5).

Fifth International
Dam World Conference
PORTUGAL • LISBON • LNEC • APRIL 13-17, 2025
dam world 2025

SETTING AN EARTHQUAKE MAGNITUDE THRESHOLD AND EVALUATING ITS IMPACT ON A ROCKFILL DAM

Binaya Raj Pandey[1]
Institute of Hydraulic Engineering and Water Resources Management, TUGraz, Austria

Gerald Zenz[2]
Institute of Hydraulic Engineering and Water Resources Management, TUGraz, Austria

ABSTRACT

This study examines how to categorize seismic events better to ensure rockfill dam safety considering the Kulekhani earthen dam of Nepal, focusing on Peak Ground Acceleration (PGA) as a key measure for defining earthquake thresholds. The earthquakes were classified into three levels: Safety Evaluation Earthquake (SEE), Design Basis Earthquake (DBE), and Operating Basis Earthquake (OBE), each linked to PGA values and their expected frequency. Finite Element Method (FEM) was used to analyze the dam's response to the 2015 Nepal earthquake with time series of horizontal accelerations. The findings show that a classified DBE- "Moderate to high for seismic region" earthquake with a PGA of 0.60g led to a vertical crest settlement of 9.1 cm, while an extreme event with a PGA of 2.95g (SEE) could result in 27 cm of vertical crest settlement. Slope stability tests using the Newmark sliding block method revealed that the downstream slope, in particular, is more prone to permanent displacement. The downstream slope's maximum permanent displacement was 0.72m in response to the 2015 Nepal earthquake and 1.65m with adopted 2.95g (SEE). This highlights the critical importance of reinforcing dam structures and implementing real-time monitoring to reduce seismic risks. To enhance dam stability, it is recommended to strengthen the downstream slope with deep soil nails, improve drainage, and install monitoring systems for early detection of seismic effects. These strategies are essential to ensure the dam's resilience and safety under both frequent and extreme seismic events.

Keywords: Dam displacement, Newmark method, Equivalent linear model, Thresholds, SEE, DBE, OBE.

[1]binaya.pandey@tugraz.at, Austria

1. INTRODUCTION

In highly seismic active zones like Nepal, classifying earthquakes into different levels such as the Safety Evaluation Earthquake (SEE), Design Basis Earthquake (DBE), and Operating Basis Earthquake (OBE) have become a necessity for ensuring the safety and functionality of dam structures. These classifications enable engineers to assess impact and design dams based on varying earthquake magnitudes and frequencies. Wieland [1,2,3] has carried out several studies on large dams to classify earthquakes as SEE, DBE, and OBE. SEE addresses the most extreme, rare events that a dam must withstand without catastrophic failure, protecting lives and downstream infrastructure. The DBE accounts for probable seismic events with limited, repairable damage, while the OBE focuses on frequent, lower-magnitude events that ensure uninterrupted dam operation. By categorizing these seismic events, engineers can tailor the dam's design to balance safety, resilience, and operational continuity, making it vital for reducing risks in earthquake-prone regions.

Over the past decade, the application of the Finite Element Method (FEM) for seismic evaluation has been grooming for the prediction of possible displacement, adopting different magnitude scenarios. Durmaz [4] applied finite element-based dynamic analysis of Concrete-faced rockfill dams (CFRDs) under real earthquake records, followed by Newmark's sliding block approach to estimate permanent displacements. The proposed procedure reliably predicts earthquake-induced displacements, offering engineers a practical tool for the preliminary seismic design of CFRDs. Sunbul [5] used finite element analysis to evaluate the static and dynamic behavior of a clay core rock-fill (CCR) dam, considering both construction stages and reservoir impoundment under static conditions and seismic response under real earthquake data with 0.4 g Peak Ground Acceleration (PGA). Results have shown a gradual increase in vertical displacements during the static phase, with significantly larger displacements observed when subjected to seismic loading, highlighting the importance of earthquake resistance in CCR dams. Fu [6] proposed a modified strain-potential method for predicting earthquake-induced permanent deformation in concrete face rockfill dams (CFRDs), using a strain-decomposition concept that separates viscoelastic and plastic strains during dynamic loading. The method, which can be implemented in an equivalent linear analysis program, was validated through numerical tests and a successful application in a high CFRD, proving its effectiveness in predicting permanent deformation without complex constitutive models. Han [7] simulated the seismic response of the Yele rockfill dam using a dynamic hydro-mechanically coupled finite element method, validated against monitoring data from before and during the Wenchuan earthquake (2008). Results have shown that the predicted seismic deformations align with field observations, confirming the dam's safety, while parametric

studies highlight the influence of material permeability and vertical ground motion on the dam's seismic behavior. Chen [8] studied the seismic response of the Zipingpu concrete face rockfill dam using the finite element method, with rockfill materials modeled through a viscoelastic and empirical permanent strain model. Results show significant acceleration amplification near the top of the dam, leading to over 90 cm of settlement at the crest, which caused gaps beneath the concrete slabs and failure of horizontal construction joints due to slab rotation and tensile cracking. The effectiveness and limitations of the equivalent linear method were also evaluated.

Several studies have been made in the past but the range of threshold magnitude based upon its impact on structure especially in rockfill-dam has not been classified. This paper studies historical events and post-field observation to set the threshold value, considering the Peak Ground Acceleration (PGA) based upon its impact on the Rockfill dam. After all, the classified threshold of SEE, DBE, and OBE was used to distinguish the earthquake event of 2015 in the Kulekhani reservoir rockfill dam of Nepal, Figure 1. The following clear objectives were carried out during the study through Geo-studio:

- Distinguishing the 2015 earthquake events and comparing FEM results with post-event field observations.
- Predicting maximum displacement through the possible highest peak considering the most likelihood extreme case.

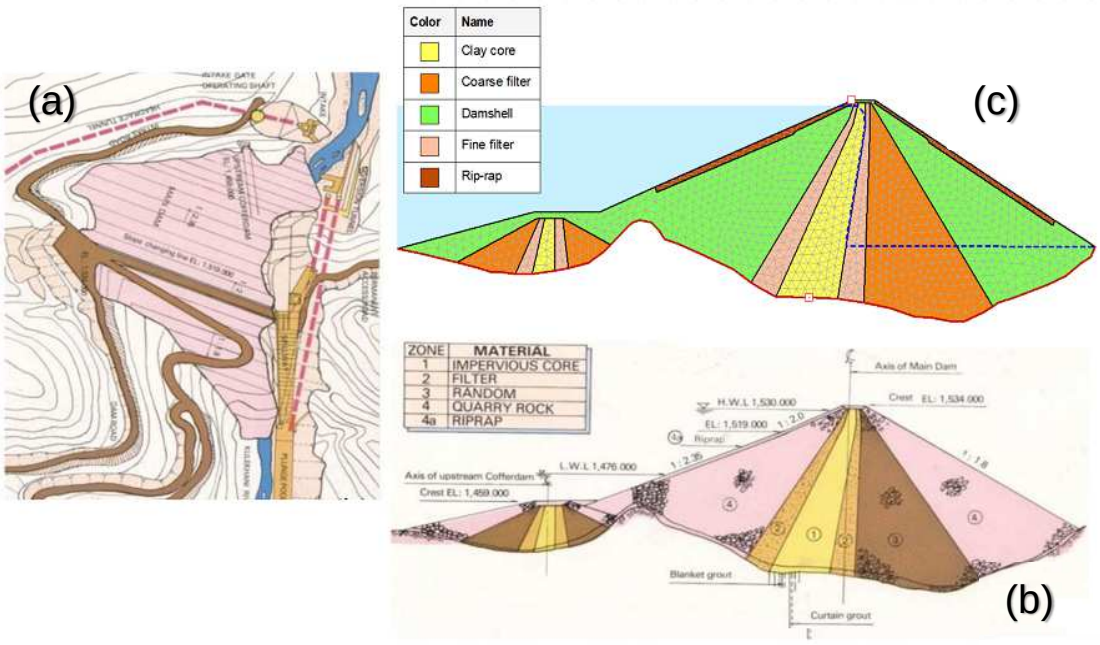

Figure 1:Rock-fill Dam, Kulekhani Reservoir plan view (a), In-built design cross-section (b) [9], and FEM cross-section (c).

2. METHODOLOGY

2.1. Magnitude Threshold and Impact

The classification and earthquake magnitude thresholds were set considering the Peak Ground Acceleration (PGA) value based on the historical time series events as follows:

$$\mathrm{PGA} = \max\left(|a(t)|\right) \tag{1}$$

Where,

$a(t)$ is the acceleration at time t, and $|a(t)|$ is the absolute value of the acceleration.

Wieland [10], Lin [11], Irinyemi [12], and Dost [13] have carried out studies to some extent for defining PGA(g). This paper investigates defining thresholds based on the structural impact with the magnitude and classifies the earthquake. Yamada [14] mentioned the largest peak ground motion of 4.27g ever recorded in the 2008 Iwate-Miyagi earthquake, Japan. The statistical analysis with available recorded data of Nepal for frequency analysis was carried out with the range of 0.25 to 0.7g, including the earthquake major events of 1934, 1988 and 2015. Several available historical seismic events and post-field observations were studied to set the magnitude threshold value range, based on the degree of impact in the rock-fill dam. The likelihood of extreme events with return period (T) was obtained through the following relation:

$$\mathrm{T} = \frac{\mathrm{n}+1}{\mathrm{m}} \tag{2}$$

Where, **T** is the return period, **n** is the total number of years recorded, and **m** is the peak rank.

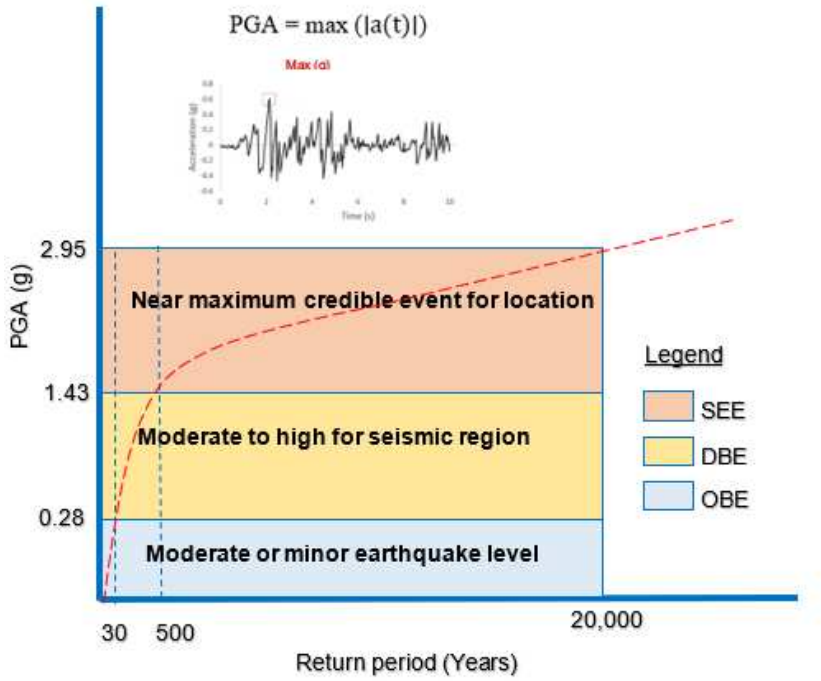

Figure 2:Carried-out classification based on the impact.

The obtained relation of PGA(g) and the likelihood of extreme events with return period (T) shows the non-linear log behavior, which leads to the following relations:

$$PGA\ (g) = a * \log(T) + b \quad (3)$$

Where, constants; a = 0.941 and b = -1.106

Figure 2 details three earthquake levels critical to seismic design: Safety Evaluation Earthquake (SEE), Design Basis Earthquake (DBE), and Operating Basis Earthquake (OBE), each defined by purpose, frequency, and ground acceleration (PGA) values. The SEE represents the highest-intensity, rarest events (return periods of 20,000 years) with a PGA range of 1.43g to 2.95g. It evaluates the ultimate resilience of dams to withstand extreme seismic activity. The DBE targets safety and functionality during strong but expected earthquakes (500-years return period) with PGA values from 0.28g to 1.43g. This level applies to dams, ensuring they can handle significant seismic loads. Lastly, the OBE covers moderate, more frequent events (return periods of 30 years) with a lower PGA range of up to 0.28g, verifying that structures can continue operation during these minor quakes without significant damage. Together, these levels ensure that structures are equipped to balance operational continuity, durability, and safety across varying seismic events, with increasing stringency as seismic intensity and rarity grow.

2.2. Model Material Properties

The material properties used in the study have been listed in tabular form in Table 1.

Table 1: Material Properties, Pandey [9,15].

Materials	k_s (m/s)	W.C	Res. W.C	m_v (kPa^{-1})	γ (kN/m^3)	ϕ	c (kPa)	E (MPa)	v
Clay core	1×10^{-8}	0.50	0.050	3.3×10^{-5}	16	25	10	30	0.45
Dam Shell	1×10^{-4}	0.40	0.040	2×10^{-5}	20	30	8	50	0.3
Fine Filter	1×10^{-3}	0.30	0.030	4×10^{-5}	18	32	2	25	0.25
Coarse Filter	1×10^{-2}	0.25	0.025	1.6×10^{-5}	22	35	1	60	0.3
Rip-rap	1×10^{-1}	0.20	0.020	1×10^{-5}	27	37	0.5	95(GPa)	0.35

Where symbol defines; permeability (k_s), unit weight (γ), the volume of water content (w.c), residual water content (res. w.c) (10% WC),s cohesion (c), compressibility coefficient (m_v), frictional angle (ϕ), Modulus of elasticity (E) and Poisson's ratio (v)

Dynamic material properties

The dominating factors in the seismic evaluation are the dynamic shear modulus (G) and damping ratio (ξ) as a function of the cyclic shear strain. The relation is obtained from the dynamic triaxial test. For this study well-known validated empirical relation defined by Ishibashi and Zhang (1993) through Geo-studio, detailed has been coverd by Pandey [9]. The implemented relation of dynamic shear modulus (G) and damping ratio (ξ) during the simulation has been shown in Figure 3.

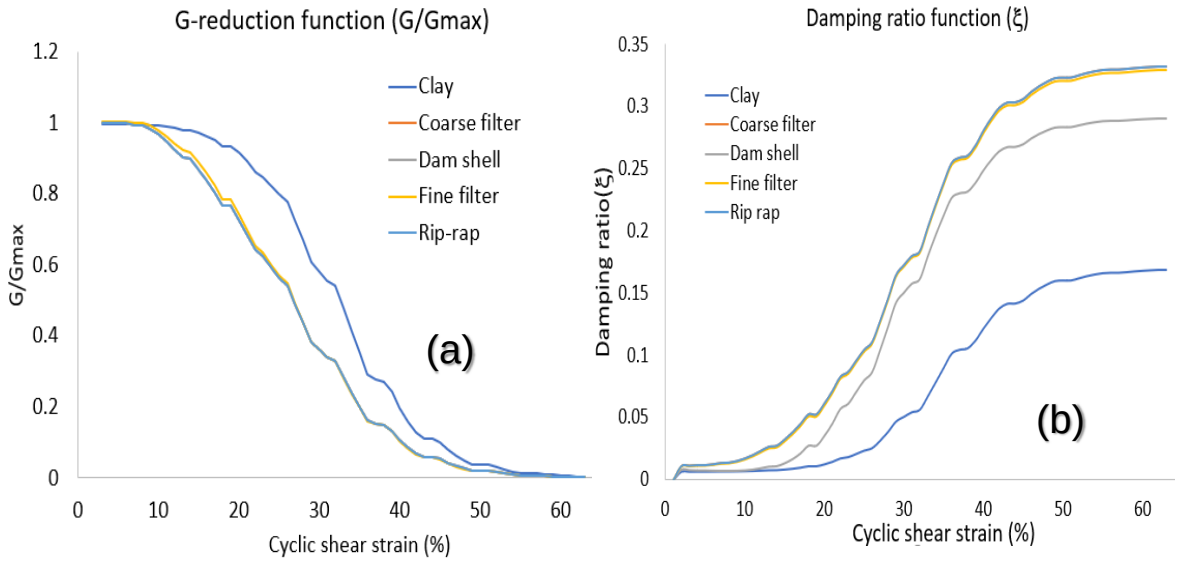

Figure 3: G-reduction function (a), Damping ratio (b) plot for different materials, Pandey [9].

For a rockfill dam shell, shear strains above 20% are quite large and may not be typical under normal loading conditions. However, such high strains could occur in extreme cases like strong earthquakes or progressive failure scenarios, the plot was obtained from empirical relation defined by Ishibashi and Zhang (1993) through Geo-studio [9].

2.3. Numerical Schemes

An Equivalent Linear Model (ELM) is applied which simplifies the nonlinear behavior of soils during seismic events by iteratively adjusting soil properties like shear modulus and damping ratio based on strain levels, providing a computationally efficient approach for geotechnical seismic evaluation. It uses predefined modulus reduction and damping curves by adjusting soil stiffness and damping until convergence within a set tolerance is achieved. The earthquake analysis was performed using the equivalent linear method, originally developed by H.B. Seed and colleagues. This approach is widely recognized as the standard practice for earthquake analysis and the design of embankment dams, Wieland (2002) [16].

The applied Newmark sliding method on the other hand calculates permanent displacement of sliding masses during seismic loading by integrating average acceleration over time, though it is limited in cases involving excess pore-water pressure, structural collapse, or liquefaction. The method has been widely used due to its simplification and effectiveness. The sliding slip surface of mass is defined by the evaluating the critical slip circle.

The average acceleration relation for a sliding mass [17]:

$$a_{ave} = \frac{\sum S_m - \sum S_{m(static)}}{\sum W} \quad (4)$$

Where, S_m is the current and $S_{(m(static))}$ is the initial (static) mobilized shear force, and W is the slice weight.

Time-velocity distribution is obtained by time integration of the area above yield acceleration with the following relation, considering the FOS is less than 1 [17]:

$$V = \int_t^{t+dt} (a_{ave} - a_y)\, dt \quad (5)$$

Further time integration leads to a permanent displacement [17]:

$$d = \int_t^{t+dt} V\, dt \quad (6)$$

2.4. Classified ground motions

As per the US Geological Survey [18] (USGS National Earthquake Information Center, KTP Station), horizontal ground motion (2015) near the Kulekhani Dam area felt with maximum peak ground acceleration (PGA) of 0.60g for a fraction of seconds, as shown in Figure 4 (a), which is classified as **"Moderate to high for seismic region"** and fall in DBE with the possible return period of 65-years, defined by equation (3).

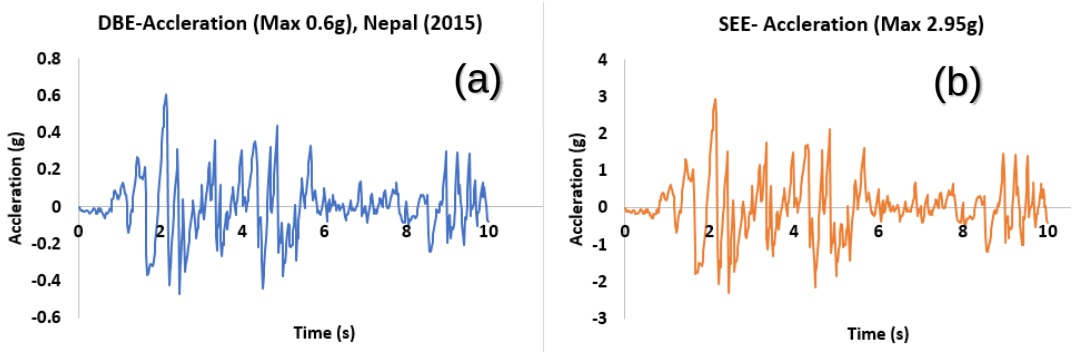

Figure 4: Nepal earthquake (2015) (a), and Amplified to SEE (b).

Figure 4 (b) shows amplified ground motion with PGA 2.95g adopting **SEE – "Near maximum credible event for location"** for a 20,000-year return period, adopting as a Probable Maximum Earthquake Event, which peak response stayed nearly unchanged despite a significant increase in return period. Both ground motions were tested to evaluate the extreme impact on the dam.

3. RESULT AND DISCUSSIONS

The crest settlements, and upstream - downstream slope instabilities were tested considering two different adopted time series of accelerations.

Crest Settlements

The crest settlements were evaluated for both types of ground motion. Post-field observations after the earthquake confirmed the simulation results. This shows the dam's vulnerability to seismic forces as shown in Figure 5. For a peak horizontal ground acceleration of 0.6g (DBE), the simulation showed a maximum displacement of 9.1 cm at the crest. This closely matched the observed post-event displacement of about 10 cm. This agreement reinforces the model's accuracy, suggesting that even minor movements could lead to cracking in the crest. When the acceleration increased to 2.95g (SEE), the predicted displacement surged to 27 cm. This showed a far more severe response. Such large displacements would exceed the dam's tolerance for deformation, likely resulting in significant cracking, structural weakening, and an increased risk of failure. Therefore, these observations and simulation data emphasize the urgent need to reinforce the dam's structure to withstand high-intensity seismic events.

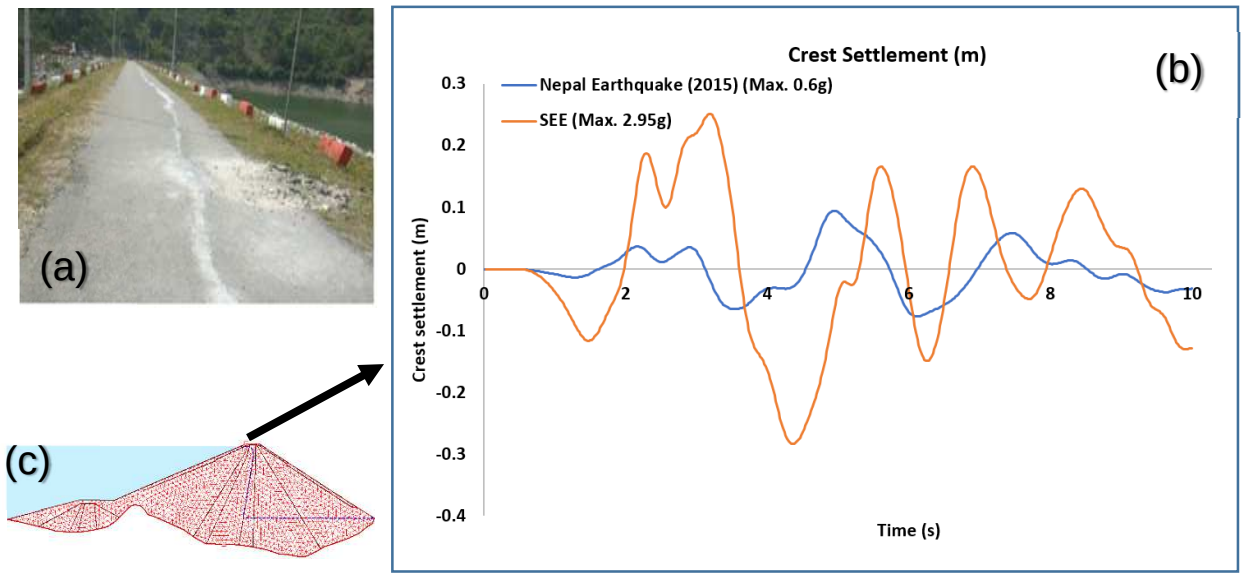

Figure 5: Post field observed crack- Earthquake 2015 (a), Simulated vertical settlements (b) FEM dam cross-section (c)

Slope Instability

Furthermore, a comprehensive study was conducted on the expected risk of permanent slope displacement using the Newmark method across the downstream and upstream slopes of the dam. Table 2 provides the summary of the simulated results of different displacements, considering different sensors of horizontal accelerations.

Table 2: Simulated dam displacements summary for horizontal accelerations.

	Vertical crest Settlement	Upstream slope displacement	Downstream slope displacement
Nepal Earthquake, 2015 (0.6g)	0.09m	0.15m	0.72m
Adopted SEE (2.95g)	0.27m	0.87m	1.65m

In the initial simulation considering earthquake- Nepal (2015) with a peak ground acceleration (PGA) of 0.6g, yield accelerations of 0.05g for the downstream slope and 0.12g for the upstream slope were obtained. This was based on a factor of safety (FOS) of less than 1, indicating a likelihood of sliding. The results showed a permanent displacement of 0.72m on the downstream side and 0.15m on the upstream side. These findings as shown in Figures 6 (a) and 7 (a), indicated that the downstream slope was more prone to displacement compared to the upstream, as a result of reduced movement due to reservoir water load on the upstream slope. Post-event field observations show the overestimation of sliding with simulation results, where only noticeable movement of the rip-rap was seen during field observation.

For a subsequent simulation considering SEE, the PGA was amplified to 2.95g with a return period of 20,000 years. The yield accelerations of 0.07g for the downstream slope and 0.13g for the upstream slope were obtained, based on a factor of safety (FOS) of less than 1, indicating a likelihood of sliding. These findings as shown in Figures 6 (b) and 7 (b) illustrate the increase in PGA led to displacements of 1.65m on the downstream slope and 0.87m on the upstream slope, highlighting a significant escalation in displacement with the higher ground acceleration. The results demonstrated that, under intensified seismic conditions, both slopes are more prone to sliding, although the downstream slope exhibited a greater increase in displacement.

To strengthen the dam's stability for robust design, reinforcing the downstream slope with deep soil nails and improving drainage can help prevent excessive displacement during seismic events. Real-time monitoring systems, such as seismic sensors and displacement gauges should be implemented for early detection of potential risks. These combined measures will

ensure better preparedness and reduce the likelihood of failure under extreme seismic conditions.

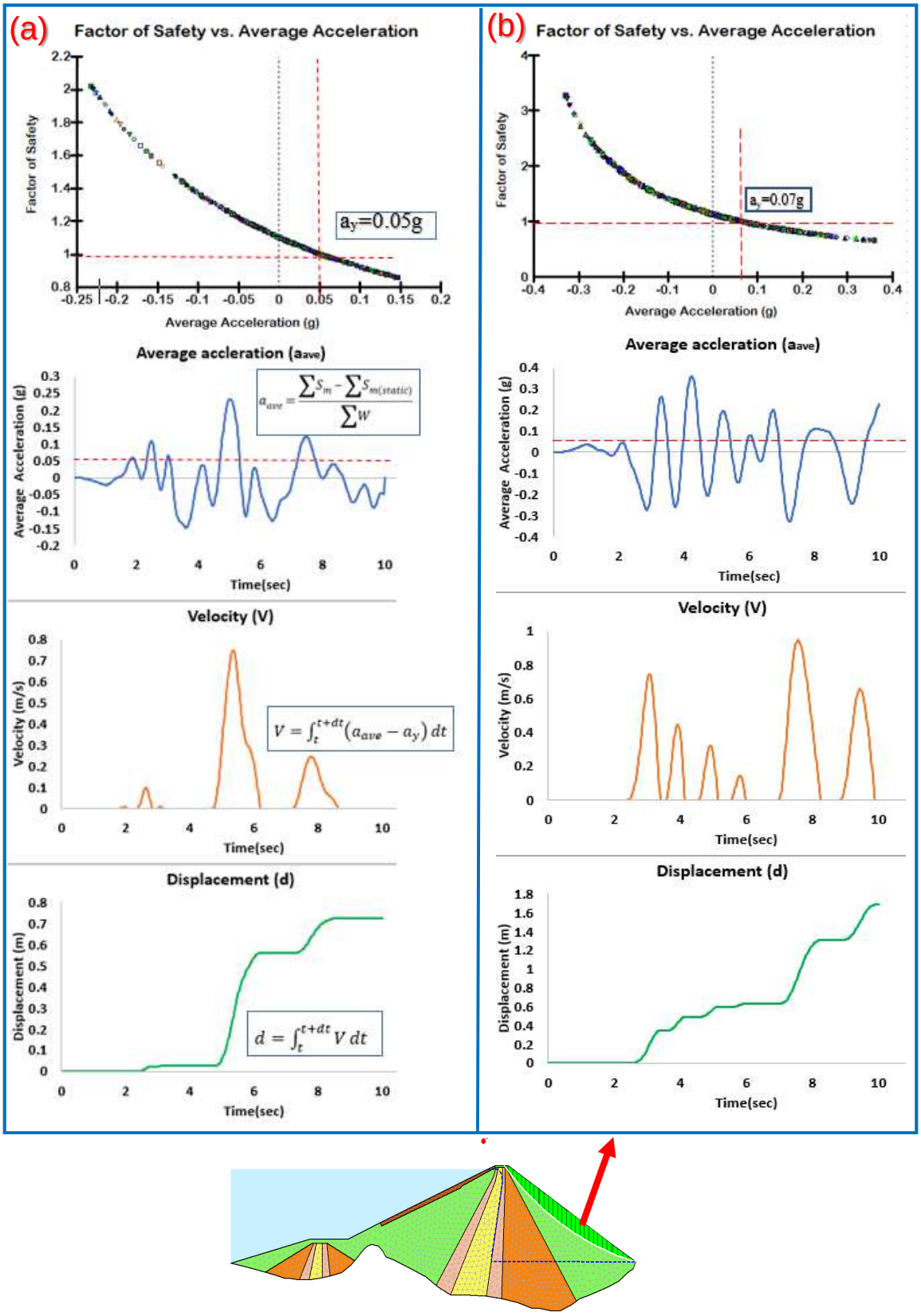

Figure 6: Downstream slope stability with 2015- Nepal earthquake (a) and SEE (b)

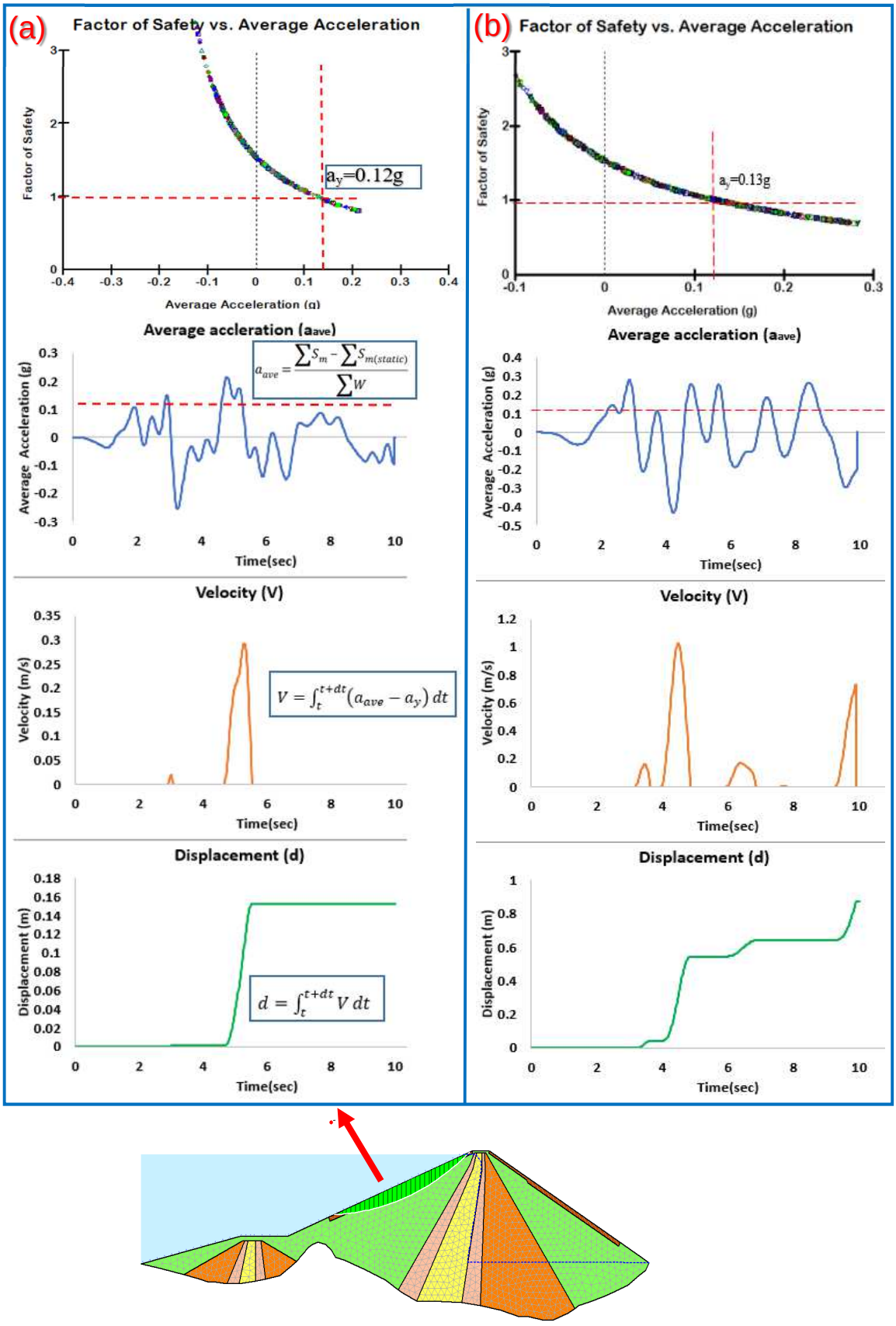

Figure 7: Upstream slope stability with 2015- Nepal earthquake (a) and SEE (b)

4. CONCLUSIONS

The carried out seismic evaluation study draws the following specific conclusions:

- The research establishes thresholds for SEE, DBE, and OBE using Peak Ground Acceleration (PGA) values based on historical earthquake data and their return periods, enabling more accurate dam safety design. The 2015 earthquake event in Nepal was classified as DBE with a return period of 65 years.
- Finite Element Method (FEM) simulations effectively model dam displacements during seismic events with results aligning closely to post-2015 earthquake field observations, supporting the reliability of the FEM approach.
- The results emphasize the need for robust infrastructure design in seismic regions, as a moderate earthquake in Nepal, 2015 (DBE, PGA 0.60g) resulted in vertical crest settlement of 9.1 cm and a downstream slope displacement of 0.72 m, whereas an extreme event (SEE, PGA 2.95g) led to a vertical crest settlement of 27 cm and a downstream slope displacement of 1.65 m, highlighting the significant impact of higher seismic intensities.
- Slope stability is particularly vulnerable on the downstream side of the dam, with the Newmark sliding block method showing significant displacements under high PGA levels, although slight movement of boulder rip-rap was observed in the post-field observation after the 2015 earthquake on the dam side. This indicates a model overestimation of the slope displacement with the Newmark Method of block sliding due to complex geotechnical parameters.
- Rehabilitation efforts should prioritize reinforcing the downstream slope with deep soil nails, enhancing drainage, and integrating real-time monitoring systems to prevent excessive displacement and ensure rapid risk detection for significantly reducing the likelihood of dam failure under extreme seismic conditions.

REFERENCES

1. Wieland, M. (2016). Safety aspects of sustainable storage dams and earthquake safety of existing dams. Engineering, 2(3), 325-331.
2. Wieland, M. (2019). Models of earthquake ground shaking used in seismic design and safety checks of large dams. International Journal of Civil Engineering, 17(4), 515-522.
3. Wieland, M. (2014). Seismic hazard and seismic design and safety aspects of large dam projects. Perspectives on European Earthquake engineering and seismology, 1, 627-650.

4. Durmaz, S., & Ülgen, D. (2021). Prediction of earthquake-induced permanent deformations for concrete-faced rockfill dams. Natural Hazards, 105(1), 587-610.
5. Sunbul, A. B., Mungan, H., Sünbül, F., & Kartal, M. E. (2018). Investigation of seismic behavior of a clay core rockfill dam using finite element method. Eurasian Journal of Civil Engineering and Architecture, 2(1), 7-16.
6. Fu, Z., Chen, S., & Wang, T. (2017). Predicting the earthquake-induced permanent deformation of concrete face rockfill dams using the strain-potential concept in the finite-element method. International Journal of Geomechanics, 17(11), 04017100.
7. Han, B., Zdravkovic, L., Kontoe, S., & Taborda, D. M. (2016). Numerical investigation of the response of the Yele rockfill dam during the 2008 Wenchuan earthquake. Soil Dynamics and Earthquake Engineering, 88, 124-142.
8. Chen, S. S., Fu, Z. Z., Wei, K. M., & Han, H. Q. (2016). Seismic responses of high concrete face rockfill dams: A case study. Water Science and Engineering, 9(3), 195-204.
9. Pandey, B. R., & Zenz, G. (2024). Seismic Displacement Analysis in Kulekhani Rockfill Dam. In Wasserbau_Symposium_2024 (pp. 77-86). Article A10 Hydraulic Engineering Symposium Graz 2024.
10. Wieland, M. (2006). Earthquake safety of existing dams.
11. Lin, L., & Adams, J. (2008). Seismic vulnerability and prioritization ranking of dams in Canada. In Proceedings of the 14th world conference on earthquake engineering, Beijing, China.
12. Irinyemi, S. A., Lombardi, D., & Ahmad, S. M. (2022). Seismic risk analysis for large dams in West Coast basin, southern Ghana. Journal of Seismology, 1-16.
13. Dost, B., Caccavale, M., van Eck, T., & Kraaijpoel, D. (2013). Report on the expected PGV and PGA values for induced earthquakes in the Groningen area. Report KNMI (Koninklijk Nederlands Meteorologisch Instituut).
14. Yamada, M., Yamada, M., Hada, K., Ohmi, S., & Nagao, T. (2010). Spatially dense velocity structure exploration in the source region of the Iwate-Miyagi Nairiku earthquake. Seismological Research Letters, 81(4), 597-604.
15. Pandey BR, Knoblauch H, Zenz G. Slope Stability Evaluation Due to Reservoir Draw-Down Using LEM and Stress-Based FEM along with Mohr–Coulomb Criteria. Water. 2023; 15(22):4022. https://doi.org/10.3390/w15224022
16. Wieland, M., & Malla, S. (2002, September). Seismic safety evaluation of a 117 m high embankment dam resting on a thick soil layer. In 12th European Conference on Earthquake Engineering (Vol. 3, pp. 836-843).

17. Geostudio. (2024). QUAKE/W theory manual. Retrieved from [https://www.seequent.com/products-solutions/geostudio-2d/]

18. US Geological Survey. (2015). An earthquake with peak ground acceleration near Kulekhani Dam. Retrieved from [https://www.usgs.gov]

Fifth International Dam World Conference
PORTUGAL • LISBON • LNEC • APRIL 13-17, 2025
dam world 2025

OCCURRENCE OF CANALICULI AND TREATMENTS IN THE FOUNDATIONS OF THE BELO MONTE HYDROELECTRIC COMPLEX DURING CONSTRUCTION AND OPERATION

Marcelo B. Boaventura [1]
Norte Energia S.A.

Joaquim P. de Ávila [2]
Pimenta de Ávila Consultoria Ltda.

Ricardo A. Abrahão [3]
Ricardo Abrahão Geociências S/S.

Wady C. Junior [4]
Norte Energia S.A.

Wagner L. dos Santos [5]
Norte Energia S.A.

Erlene D. Krajewski [6]
Norte Energia S.A.

Leandro C. Lima [7]
Norte Energia S.A.

ABSTRACT

During the initial excavations in the foundations of Belo Monte Hydroelectric Complex dikes and dams, the largest entirely Brazilian hydroelectric powerplant, areas with large concentrations of tubular cavities, known as canaliculi, were found. This geotechnical phenomenon occurs in tropical Amazon region residual soils. The presence of canaliculi in dam foundations developed preferential flow paths through the foundation. To mitigate these consequences, special foundation treatments were carried out during construction. The treatments included deepening cut off trench in sections where canaliculi are present, sealing them with cement grout injections, filling with sand and building filters. The main objective of these treatments was to avoid possible preferential flows and eventual internal erosions in the foundations. However, due to the construction difficulties to fulfill all design concepts, some seepage through canaliculi was expected in the downstream area after reservoir impoundment. Thus, during the construction design of the dams reverse filters in the downstream areas were included. During the initial phase of operation and maintenance, new resurgences and canaliculi were observed and mapped downstream of some structures, in regions not previously treated. These phenomena are being monitored by the dam safety technical teams, based on three fundamental pillars: visual inspection, instrumentation analysis and topographic surveys. Due to the evolutionary behavior of the canaliculi, the occurrences are treated by complementary interventions, which consist of reverse filters and draining trenches. Over the years of operation, methodologies with geometric variations were tested and evaluated regarding implementation costs and treatment efficiency. The results of these methodologies proved to be consistent, according to field monitoring and instrumentation data of the structures.

Keywords: canaliculi, foundation treatment, tropical soils, preferential percolation, dam safety

[1] marceloboaventura@norteenergiasa.com.br, Brazil
[2] joaquim.pimenta@pimentadeavila.com.br, Brazil
[3] ricardo@rageociencias.com.br, Brazil
[4] wadycharone@norteenergiasa.com.br, Brazil
[5] wagnerlsantos@norteenergiasa.com.br, Brazil
[6] erlenekrajewski@norteenergiasa.com.br, Brazil
[7] leandrolima@norteenergiasa.com.br, Brazil

1. INTRODUCTION

The Belo Monte Hydroelectric Complex comprises six earth fill and rockfill dams, 30 dikes, a diversion canal, two powerhouse units, and a spillway with a discharge capacity of 62,000 m³/s. With a nominal installed capacity of 11,233.1 MW, distributed among 18 Francis-type turbines, each with 611.1 MW, in the Main Powerhouse, and 6 Bulb-type turbines, each with 38.85 MW, in the Complementary Powerhouse, Belo Monte it is not only the largest entirely Brazilian power plant but also a landmark in large-scale engineering projects in tropical regions. Located in the heart of the Amazon, along the Xingu River, the project presented a unique set of geological-geotechnical and environmental challenges that demanded equally innovative solutions. Among the most complex geotechnical phenomena encountered were canaliculi—tubular cavities typical of the residual soils in the Amazon region [1].

Various hypotheses have been proposed regarding their origin, including root systems, pseudo karst mechanisms of internal erosion, leaching associated with laterization, and termite activity [2] [3]. The presence of this phenomenon in dam foundation terrains can lead to significant consequences, such as the development of direct and preferential flow paths through the foundation, eventually reaching the downstream area. This progression can result in the transport of fine particles and potentially initiate regressive erosion processes [4].

Addressing this phenomenon required the development and application of various geotechnical treatments. These included exploratory trenches, grout injections, and the installation of drainage filters, each technique tailored to the specific characteristics of Amazonian soils. Despite these efforts, the dynamic evolution of canaliculi continued to necessitate new interventions, highlighting the ongoing nature of this challenge.

This article presents the treatments employed, technical advancements achieved, lessons learned, and challenges that remain. The objective is to provide a comprehensive perspective on the management of canaliculi and their importance for dam safety in Brazil and globally.

1.1. Occurrence of Canaliculi in Dams in the Amazon Region

The first occurrence of canaliculi in foundation terrains in Brazil was observed around 1957, during the construction of the Vereda Grande Dam, in the state of Piauí [4] [5]. Subsequently, these tubular cavity phenomena were reported in the foundations of the Tucurui Dam (Fig. 1), in Pará, in 1974; at the Samuel HPP, in Rondônia, in 1982; at the Balbina Dam, in Amazonas, in 1985 [6]; and during the construction and operation of the Belo Monte HPP, in Pará, in 2015 [7].

Fig. 1 – Canaliculi found in the UHE Tucurui region.

1.2. Occurrence of Canaliculi in Dams at the Belo Monte HPP

At Belo Monte, canaliculi were observed in residual soils derived from migmatites, predominantly in the foundations of dams and dikes [7]. These channels, with dimensions ranging from sub-centimetric to decimetric scales, exhibit varied geometries, including sub-horizontal trajectories and complex vertical branching, with potential interconnections.

The occurrences and evolution of canaliculi were extensively mapped and monitored during both the construction and operation phases of the structures, highlighting the dynamic and unpredictable nature of canaliculi in tropical soils.

Additionally, field evaluations revealed that canaliculi exhibit dynamic behavior, characterized by the progressive enlargement of their diameters due to erosion of their walls. This behavior underscores the need for continuous monitoring and adaptive geotechnical treatment strategies, such as those implemented at Belo Monte.

2. TREATMENT OF CANALICULI DURING CONSTRUCTION

During the construction of the Belo Monte Hydroelectric Complex, various treatment techniques were employed [8]. One of the standard procedures established during the investigation phase was the excavation of exploratory trenches (Fig. 2) in the foundations of the dikes to identify and treat canaliculi.

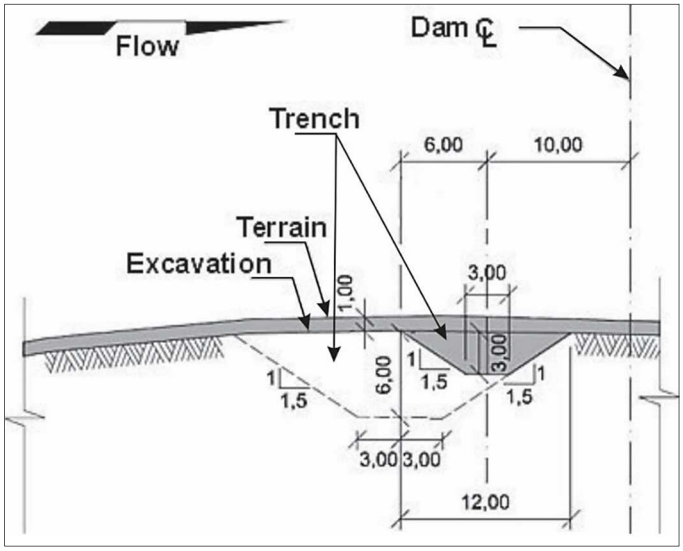

Fig. 2 – Schematic drawing of the exploratory trench at the Left Closure Dam (BFE).

Exploratory trenches were initially excavated with dimensions of 3 meters in depth and width, which could be extended to up to 6 meters in areas where the concentration of canaliculi was more significant. After excavation, the internal surfaces of the trenches were cleaned using compressed air jets (Fig. 3), enabling the detection of microcanaliculi (millimeter-scale diameter) and macrocanaliculi (centimeter to decimeter-scale diameter).

Fig. 3 – Internal surface of the trench – cleaning with compressed air jets.

In locations where canaliculi were confirmed, cut-off trenches were implemented to disrupt preferential water flows. These trenches were filled with compacted clayey soil, carefully selected and prepared to meet stringent low-permeability criteria.

When canaliculi with diameters exceeding 20 mm were encountered, the adopted procedure involved grouting the cavities with cement slurry (Fig. 4). The grouting criterion entailed injecting up to 300 kg of slurry with a water-to-cement ratio (w/c) of 0.7:1.0 into the cavity. If the canaliculus was not fully sealed, the ratio was adjusted to 0.5:1.0 (w/c) until grout refusal occurred.

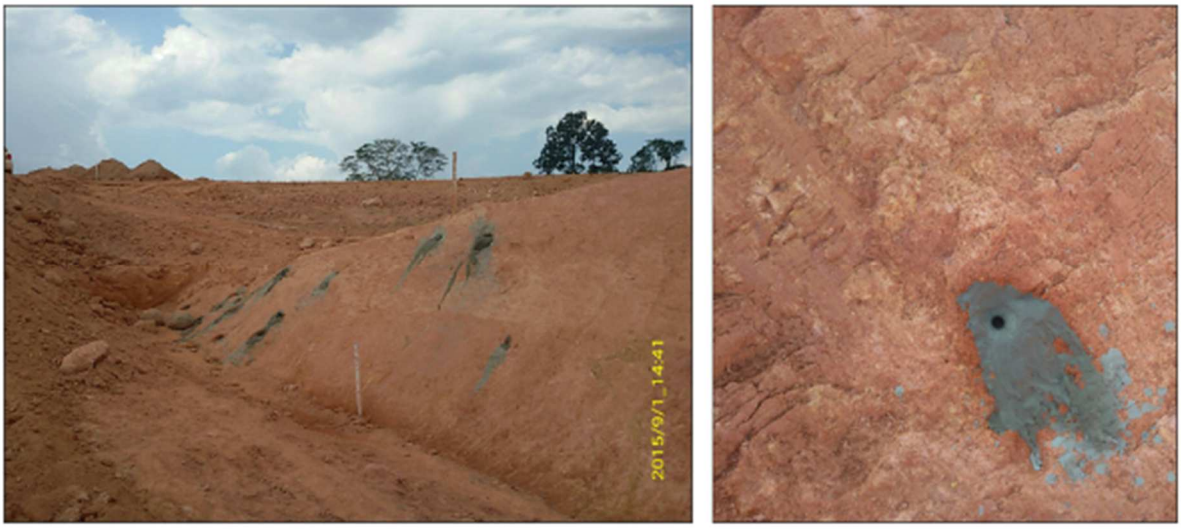

Fig. 4 – Upstream area: cement grout injections in the cavities.

Additionally, blind drains were installed on the downstream slope of the exploratory trenches to address smaller canaliculi with diameters less than 20 mm.

The technique involved applying a filter layer of specifically graded sand, compacted to a minimum Relative Density (RD) of 55%, and, in some cases, exceeding 65%. The width of this layer ranged between 0.75 m and 1.00 m.

In specific situations, such as areas beneath the horizontal filter, canaliculi with larger diameters (≥5 cm) were pre-filled with sand, using running water to enhance material fluidity, prior to the application of the blind drain

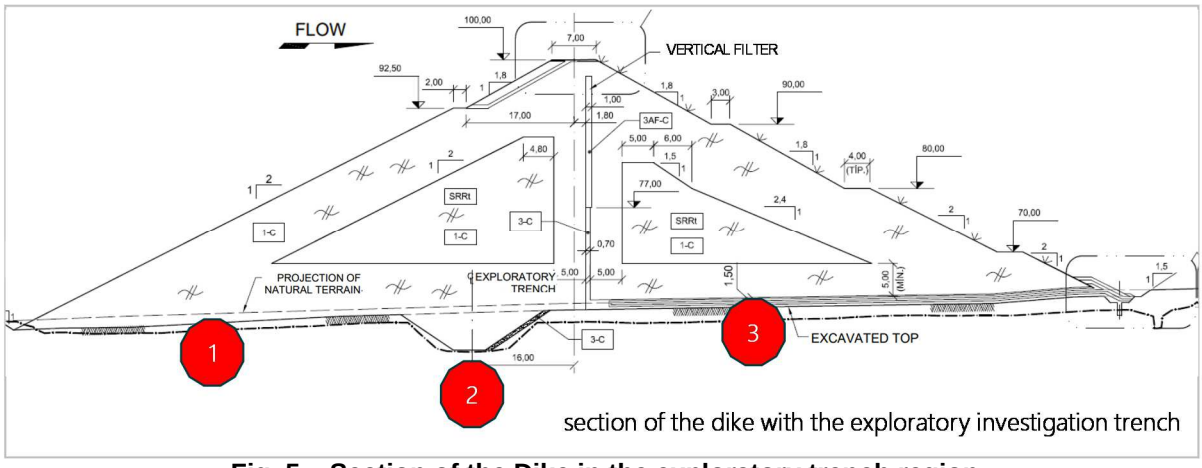

Fig. 5 – Section of the Dike in the exploratory trench region.

Fig. 5 illustrates the foundation treatment areas. In **Area 1**, located upstream of the exploratory trench, the soil was prepared, and a compacted embankment layer was placed for stabilization. In **Area 2**, encompassing the downstream slope and bottom of the exploratory trench, canaliculi with diameters greater than 20 mm were sealed with cement grout, while smaller canaliculi (less than 20 mm) were treated with blind sand drains. In **Area 3**, beneath the

horizontal filter, canaliculi with diameters equal to or greater than 5 cm were pre-filled with sand.

To control water seepage in critical areas downstream of the structures, reverse filters were installed (Fig. 6). These filters consisted of alternating layers of sand and gravel, with a total thickness of two meters (Table 1).

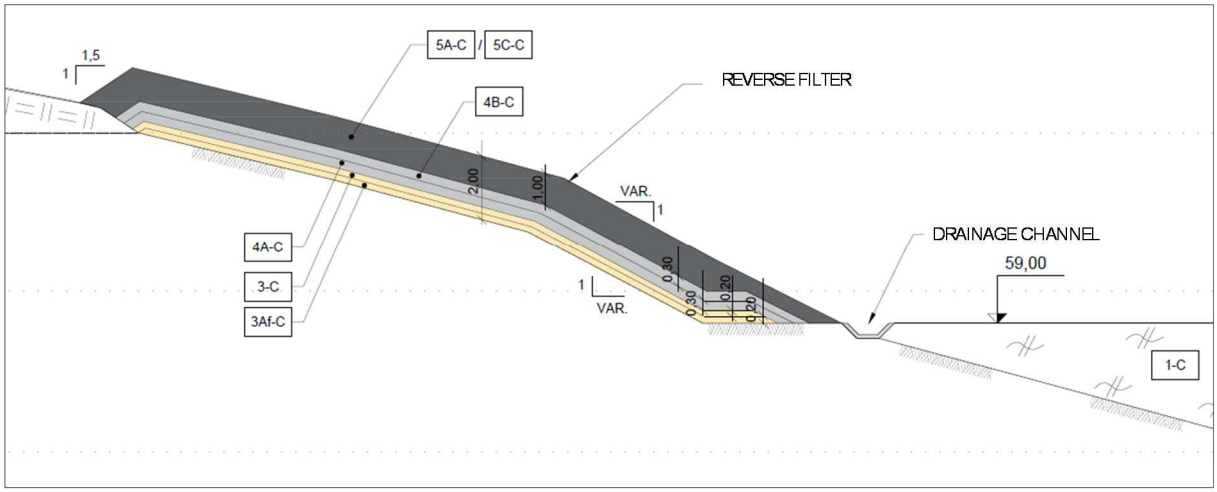

Fig. 6 – Schematic Drawing of the Reverse Filter.

Table 1 – Construction Period – Materials and Thicknesses Applied in the Reverse Filters.

PROTECTIVE LAYERS	
Material	Thickness (m)
3AF-C	0.20
3-C	0.20
4A-C	0.30
4B-C	0.30
5A-C / 5C-C	1.00

3. DRAINAGE TRENCHES AS A TREATMENT ALTERNATIVE

During the reservoir filling phase, water seepage was observed in the downstream areas of the dams and dikes, influenced by the dynamics of canaliculi present in the foundations. The pressurization induced by the reservoir filling process resulted in increased connectivity between canaliculi and an intensification of percolation flows, exacerbating hydraulic gradients in the affected areas.

Initially, to mitigate the effects of water seepage, conventional solutions such as reverse filters were implemented. While the efficacy of reverse filters in regulating subterranean flows and interrupting soil particle migration is widely acknowledged, their application posed significant challenges. This method required extensive vegetation clearance and removal of the topsoil layer, generating large volumes of excavation. Furthermore, it involved the intensive use of

materials, such as sand and gravel aggregates, for filter construction, leading to high implementation costs. Another critical issue was the limited effectiveness of this method in dissipating pore pressures, which compromised its performance in certain contexts.

The technical team from Norte Energia S.A.'s dam safety division faced the challenge of developing an alternative water seepage treatment method that would minimize environmental impacts and reduce financial costs, without compromising the solution's effectiveness and safety. Within this context, the development of drainage trenches emerged as an innovative response, aiming to optimize the treatment of seepages associated with canaliculi while offering a more sustainable and efficient approach.

3.1. Santo Antônio Slope Dam (BVSA)

The development of drainage trenches as an innovative solution is directly linked to inspections conducted between 2018 and 2020 at the Santo Antônio Slope Dam (BVSA). These inspections confirmed the persistence of water seepage downstream, associated with the presence of canaliculi (Fig. 7 and 8).

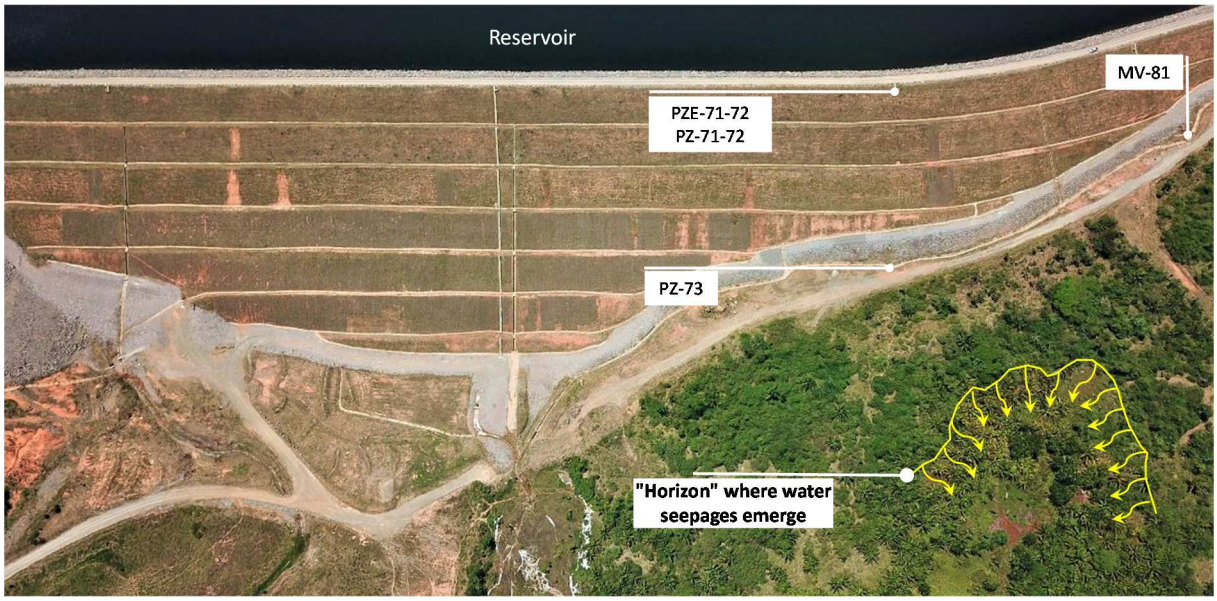

Fig. 7 – BVSA: Indicative area of water seepage on the left abutment.

These seepages exhibited a gradual increase in both water flow and canaliculi diameters (Fig. 9). Among the various monitored points, one canaliculus stood out, with its diameter expanding from 8 cm in 2018 to 28 cm in 2020, highlighting the progressive nature of the phenomenon. Although the observed water flow appeared visually clear, detailed inspections conducted with a borescope confirmed the presence of fine particle transport—a slow and imperceptible erosive process that could potentially compromise the integrity of the foundation structures.

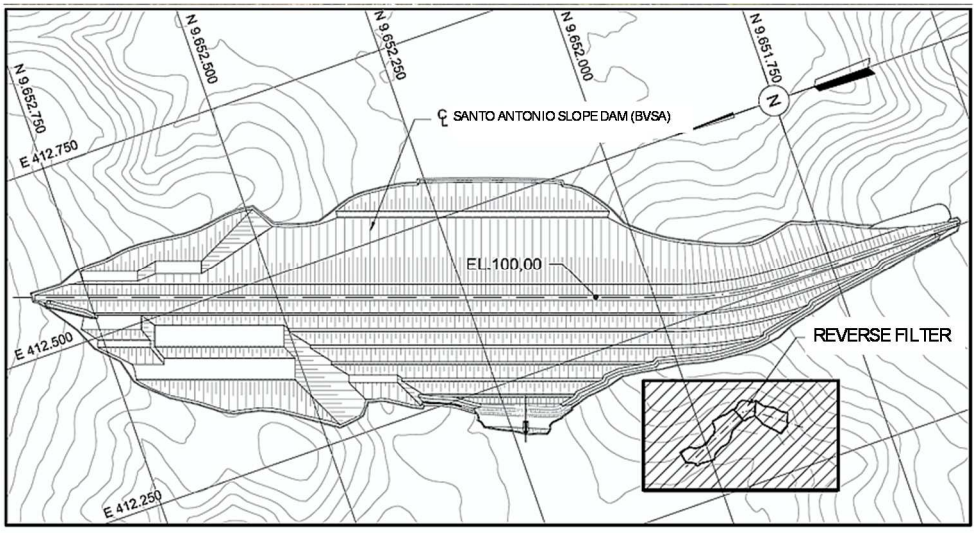

Fig. 8 – BVSA - Indicative area with water seepage occurrence.

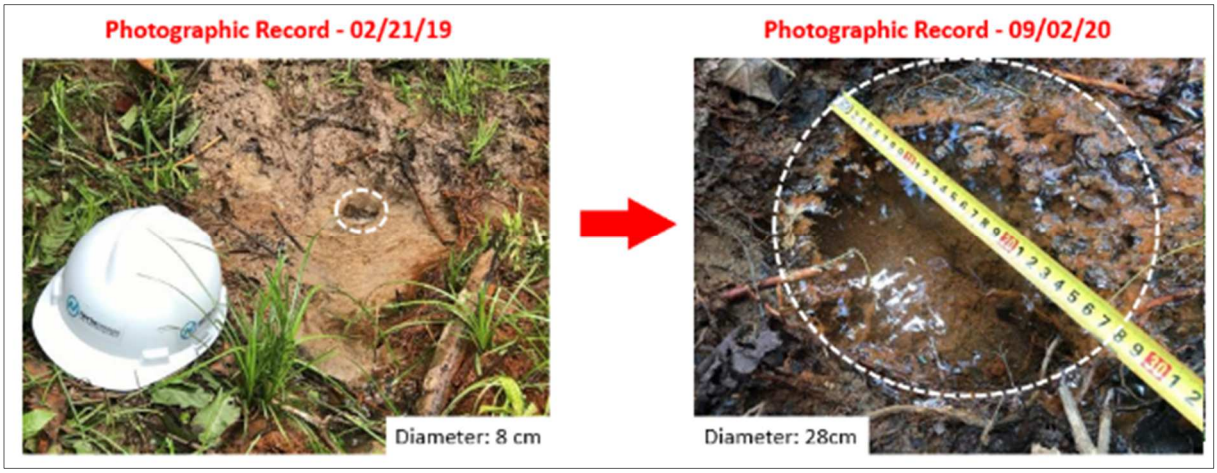

Fig. 9 – BVSA: Gradual increase in both water flow and canaliculi diameters.

Field observations also revealed that water seepages tended to manifest within a clearly defined "horizon" downstream of the dam, typically aligned with an increased presence of boulders in the natural terrain. The field technical team interpreted this correlation as indicative of the proximity of the younger residual soil layer, characterized by higher permeability. Overlying this younger residual soil layer is a mature residual soil layer with significantly lower permeability. This stratigraphy contributes to conditions of hydraulic pressurization within the subsurface flow, as the mature soil acts as a natural barrier, hindering the relief of induced pressures.

This permeability differential between the layers promotes the accumulation and pressurization of subsurface flows within the younger soil layer. As the flow migrates downstream, it seeks relief through the canaliculi present in the mature soil. Upon encountering these cavities, the canaliculi act as preferential conduits, facilitating the bypass of the mature soil barrier and culminating in seepages in the natural terrain downstream. This interaction generates elevated

hydraulic gradients and increases the risk of particle transport, particularly in areas where the mature soil layer is thinner.

In 2020, at the request of Norte Energia S.A., geotechnical engineer Alex Martins Calcina, a member of the technical team from the engineering firm Intertechne, conducted an on-site inspection of the affected areas. During the inspection, the technical team presented their field observations, including the conditioning factors and hypotheses regarding the mechanisms related to the water seepages. Additionally, the team proposed a pioneering solution: the construction of a drainage trench aligned with the "horizon" where seepages were occurring.

The specialist validated the technical basis of the proposal and recommended the adoption of a trapezoidal geometry for the trench, thereby consolidating the scope of the initial experiment. Designed to intercept subsurface flows, possibly located within the more permeable layer of younger residual soil, the trench aimed to redistribute these flows in a controlled manner and mitigate the risks associated with water seepages. Although based on a hypothesis derived from field observations, the implementation represented an innovative approach in the absence of prior guarantees of efficacy.

With a maximum depth of 2 meters, the trench was initially filled with sand to ensure drainage efficiency. It was then complemented with rock materials, such as granular transitions and riprap, providing geotechnical stability and protection against surface erosion processes (Fig. 10 and 11).

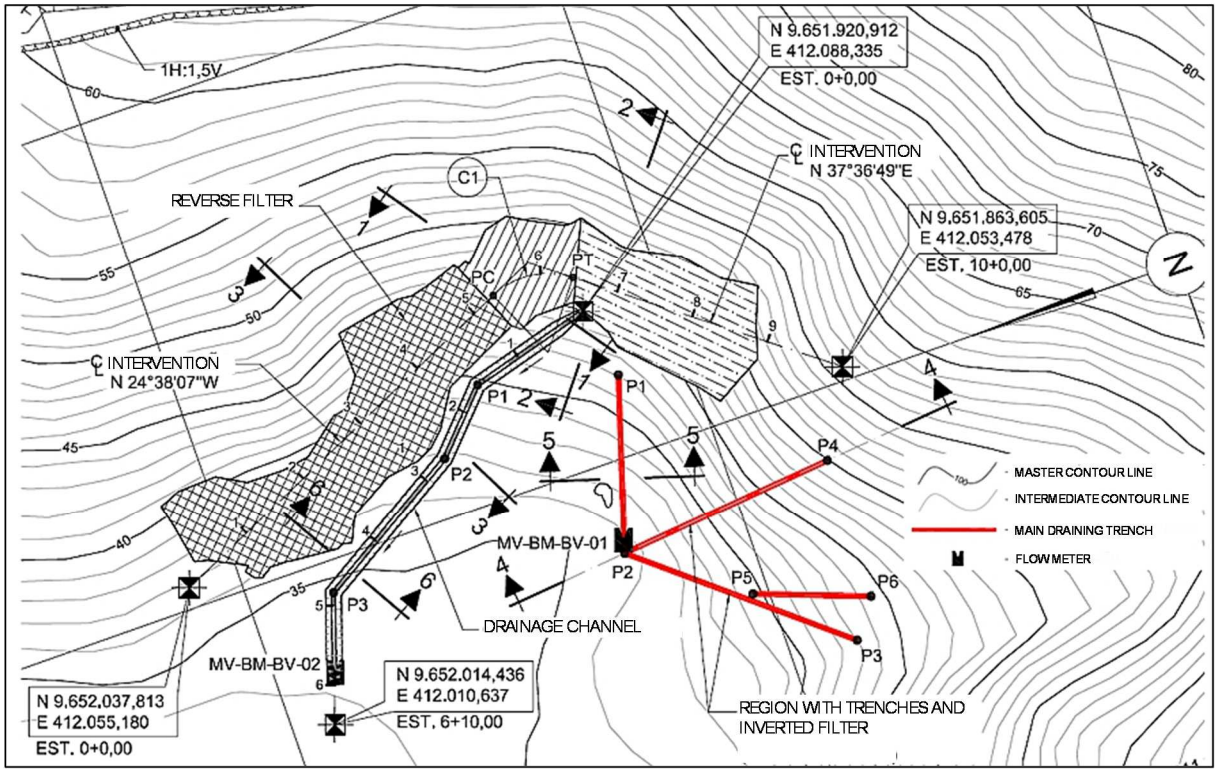

Fig. 10 – BVSA: Intervention design – Plan view (edited from BM4-BV00-ITT-CTG-DE-0010).

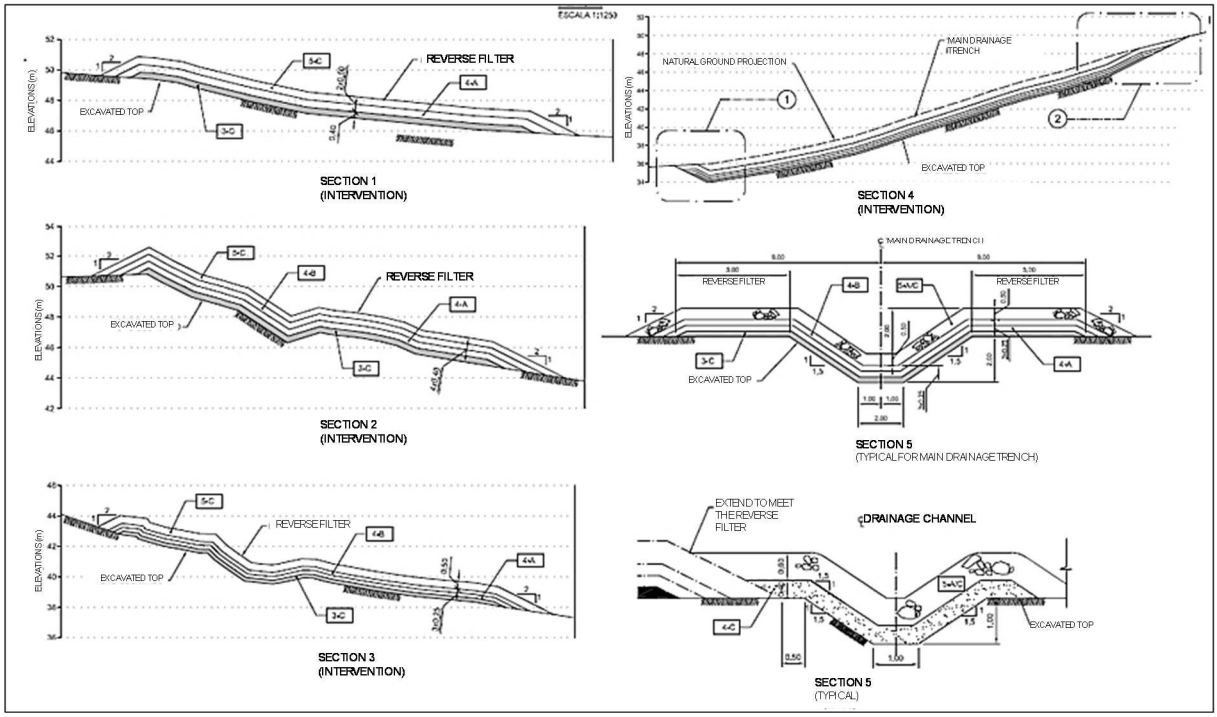

Fig. 11 – BVSA: Intervention Design – Sections (edited from BM4-BV00-ITT-CTG-DE-0010)..

At the end of 2021, the Geotechnical and Geological Consulting Board of Norte Energia, comprising Joaquim Pimenta and Ricardo Abrahão, conducted on-site inspections at Belo Monte to evaluate the results of the treatments applied to address the water seepages at BVSA (Fig. 12).

Fig. 12 – BVSA: Execution of the trapezoidal trench (record from the November 2021 board).

During the visit, the Board validated the effectiveness of the implemented drainage trenches, highlighting their efficiency in drying adjacent areas, regulating water flows, and preventing soil

transport through the canaliculi. Despite the solution's success, the Board noted that the interventions could be optimized, suggesting the potential to achieve the same results with a less robust and more cost-effective approach.

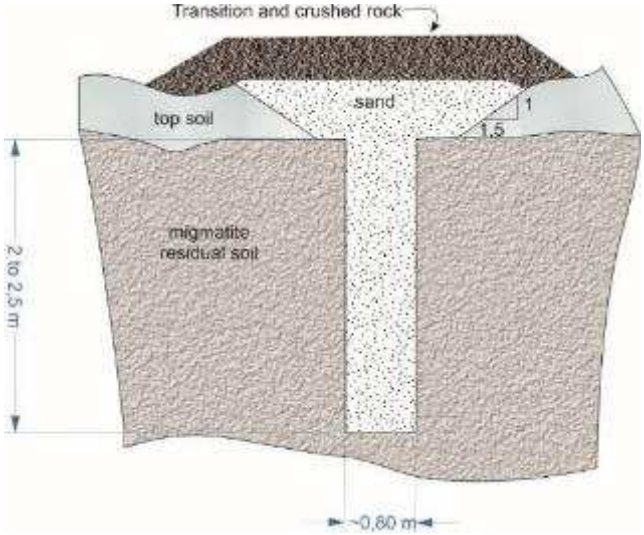

Fig. 13 – Proposal for a vertical trench by the Board of Consultants.

Based on this analysis, the Board recommended replacing the trapezoidal trenches with vertical trenches, excavated with the minimum width required to accommodate the available hydraulic excavator bucket [9]. The proposal included sequentially filling the trenches with sand, complemented by layers of granular transition and fine riprap at the top. For greater operational efficiency, it was recommended to execute the trenches in 5-meter segments, allowing for the filling and stabilization of each segment before progressing to the next (Fig. 13). This methodology was subsequently successfully implemented for addressing water seepage downstream of Dike 11.

Drawing on the observations and reports from Norte Energia S.A.'s field technicians, the Board developed a simplified modeling of the canaliculi at the Belo Monte HPP (Fig. 14).

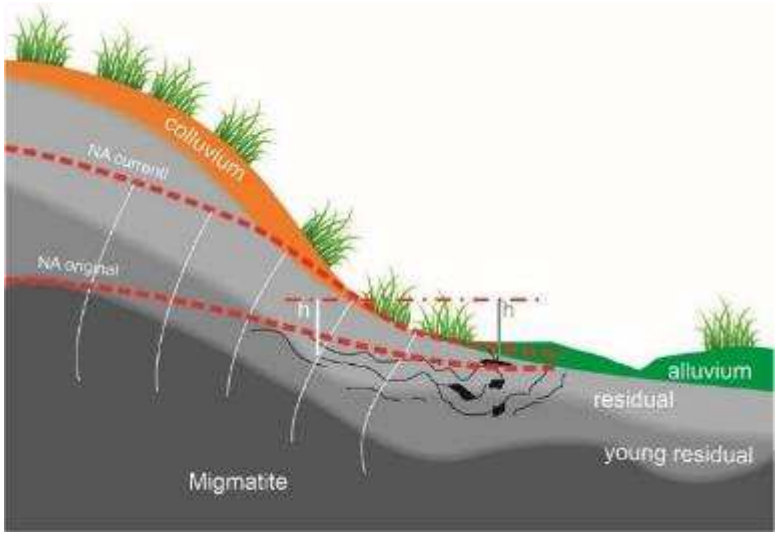

Fig. 14 – Simplified idealization of the canaliculi arrangement.

3.2. Dike 11

After the completion of the Reservoir's filling in 2016, water seepage was identified downstream of Dike 11. In 2018, the Construction Consortium carried out interventions using reverse filters near the base of the structure. However, areas of moisture and water seepage continued to emerge, being regularly monitored during field inspections. Between 2018 and 2021, a progressive increase in the extent of the areas affected by seepage was observed (Fig. 15 and 16).

Fig. 15 – Dike 11: Start of reservoir filling - absence of water seepages (2016).

Fig. 16 – Dike 11: Operation phase - presence of water seepages (2022).

At the end of 2021, following inspections conducted by Norte Energia's Board of Consultants, complementary instrumentation was installed in the downstream area of Dike 11 (Fig. 17), prior to the implementation of the drainage trenches. This instrumentation aimed primarily to monitor specific parameters, such as pore pressures and subsurface flows, to establish a baseline for evaluating the effectiveness of the trenches after their implementation.

Fig. 17 – Dike 11: Complementary instrumentation for downstream monitoring.

The implementation of the drainage trenches was carried out in six stages, as detailed in Fig. 18. The collected data demonstrated a significant reduction in pore pressures and water levels in almost all monitored instruments, as shown in Table 2.

It is worth noting that a flow meter, identified as MV-D011-03, was installed downstream of the intervention area to measure the seepage flow through the Dike 11 drainage system. The recorded flow is approximately 0.06 m³/s, a loss considered insignificant, given that the turbine flow rate of each generating unit at its nominal capacity is approximately 750 m³/s.

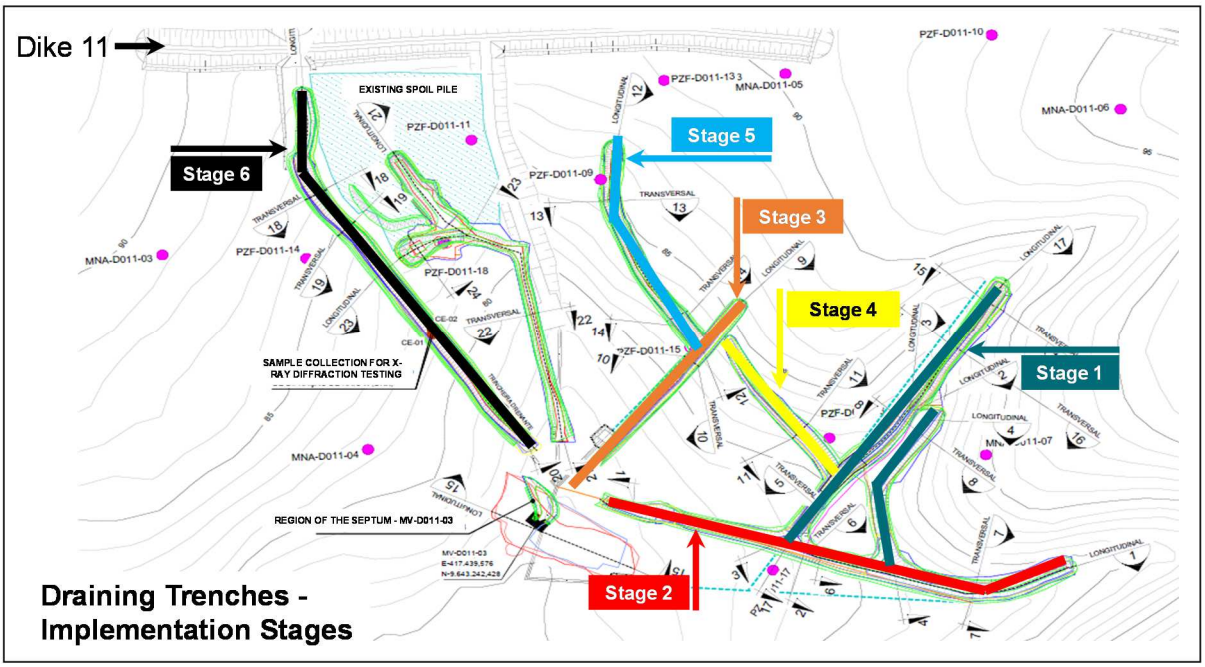

Fig. 18 – Dike 11: Sketch of the implementation of drainage trenches in six sequential stages.

Table 2 – Dike 11 - Instrument Reading Results

Stages	Instrument	Distance from the dike axis (m)	Reduction (m)
1	MNA-D011-07	78.72	2.51
1	MNA-D011-08	94.56	3.44
1	MNA-D011-09	47.31	0.82
1	PZF-D011-17	11.70	1.43
3	PZF-D011-15	3.75	0.98
3	PZF-D011-10	129.8	1.69
4	PZF-D011-16	6.22	1.81
6	MNA-D011-01	211.2	1.20
6	MNA-D011-02	130.87	1.38
6	MNA-D011-03	52.77	1.53
6	MNA-D011-04	39.5	0.25
6	PZF-D011-18	20.53	1.15
6	PZF-D011-11	46.67	0.61
6	PZF-D011-14	14.36	0.75

Fig. 19, featuring a comparative aerial image, highlights the impact of the intervention, showing that previously waterlogged areas were completely dried after the trench implementation, thereby confirming the effectiveness of the solution.

Fig. 19 – Aerial photo of Dike 11 – Before and after the implementation of the draining trenches.

4. CONCLUSIONS

The experience of the Belo Monte Hydroelectric Complex in addressing canaliculi phenomena in foundations has provided fundamental insights into the dynamics and persistence of this challenge in tropical residual soils. The evolution of these cavities, evidenced by changes in flow rates and dimensions, necessitated innovative interventions and continuous monitoring. The implementation of drainage trenches represented a significant technical advancement, demonstrating superiority over conventional methods. This solution effectively reduced pore pressures, managed subterranean flows, mitigated particle transport, and stabilized the treated areas, all while delivering lower costs and reduced environmental impact. Instrumentation data

and visual inspections confirmed the methodology's efficacy and safety. By aligning technical innovation with operational efficiency, Belo Monte has set a benchmark that can guide future interventions in similar geotechnical contexts, contributing to the advancement of dam safety and sustainable management within the sector.

5. REFERENCES

[1] Jury, W. J.; Paraguassú, A. B. (1990). Considerations on the Occurrence of Canaliculi in Dam Sites in the Amazon Region. Proceedings of the 6th Brazilian Congress of Engineering Geology and 9th Congress of Soil Mechanics and Foundations Engineering, 1990. Vol. 1, pp. 511–517.

[2] Andrade Gutierrez (1987) – “Technique used in injection reduces the permeability of residual soil”. CONSTRUTORA ANDRADE GUTIERREZ Magazine, Year 7 – nº 15 – September/December 1987, p. 19-22.

[3] Limberger, A. E.; Boaventura, M., Marcelo B.; Rodrigues, R. L.; Costantin Filho, M.; Fernandes, D. O.; Krajewski, E. D.; Lima, L. C. (2023). Occurrence of Canaliculi in Dam Foundations in the Amazon Region - State of the Art. Proceedings of the XXXIV National Seminar on Large Dams, Brazilian Committee on Dams.

[4] Barradas, S. S. (1985). Initiation and Propagation of Fractures Induced by Injections in Clayey Soils with Canaliculi – Application to the Treatment of Residual Soil in the Foundation of the Earth Dam of the Balbina Hydroelectric Plant. Thesis submitted to the Graduate Program in Engineering at the Federal University of Rio de Janeiro (UFRJ), Rio de Janeiro, RJ, March 1985.

[5] Sathler, G.; Mesquita, J. B. (1985). Canaliculi: Suggestions for Classification and Field Investigation Methodologies. Proceedings of the Brazilian Congress of Engineering Geology, ABGE, Vol. 3–4, pp. 407–414, Belo Horizonte.

[6] Buosi, M. A.; Cadmam, J. D. (1984). On the Occurrence of Tubular Cavities in Lateritic Soils in the Amazon Region. Brazilian Association of Geology and Environmental Engineering (ABGE), Vol. 4, Belo Horizonte, 1984, São Paulo, ABGE, 1984. Vol. 3, pp. 10–24.

[7] Bandeira, O. M.; Silveira, J. F.; Leite, D. T. (2017). Dam Safety at the Belo Monte Hydroelectric Plant – Authors: Oscar Machado Bandeira. Brazilian Journal of Dam Engineering, Year IV, No. 04, May 2017.

[8] Belo Monte – Design Consortium (2014). Work Instruction. RI3-D011-GER-CGT-IT-0001-00.

[9] Belo Monte – Board of Consultants (2021). 23rd Report of the Sectoral Board of Geology and Geotechnics of the Belo Monte Hydroelectric Plant.

Fifth International Dam World Conference
PORTUGAL • LISBON • LNEC • APRIL 13-17, 2025
dam world 2025

DEVELOPING A REMOTE SENSING TOOL FOR RESERVOIR VOLUME EVALUATION

João Pimenta
National Laboratory for Civil Engineering

João N. Fernandes[1]
National Laboratory for Civil Engineering

Alberto Azevedo
National Laboratory for Civil Engineering

ABSTRACT

The efficient management of water reservoirs is crucial for ensuring water security, flood control, and hydroelectric power generation. Accurate reservoir volume measurements are essential for optimizing these functions. Traditional methods, which rely on in-situ measurements and physical surveys, are often time-consuming, resource-intensive, and impractical in many countries due to financial constraints or complex environmental conditions. To address these challenges, this research presents the development of a novel remote sensing tool that offers an effective and globally accessible method for evaluating reservoir volumes.

This study explores the integration of satellite imagery and advanced geospatial analysis techniques to estimate reservoir volumes. Using high-resolution imagery from Sentinel-2, along with storage capacity data from official repositories and the GLOBAthy dataset, the tool automatically calculates surface area and water volume at varying water levels over a user-defined time period. The tool features an intuitive interface that allows users to easily select reservoirs, date ranges, and cloud cover percentages, generating time-series data on volume. A key aspect lies in the use of machine learning algorithms, which enhance the accuracy of water surface delineation and volume estimation, even in the presence of built structures like bridges or challenging environmental conditions such as cloud cover.

The tool was tested across reservoirs of varying sizes and topographies in Portugal and California, USA. Comparative analyses showed a high degree of accuracy, with a mean absolute percentage error of 5.4% and a correlation coefficient (R^2) of 0.9 in comparison to official measurements. This cost-effective, scalable, and timely alternative offers significant improvements for reservoir volume evaluation, particularly in remote or hard-to-access regions. Ultimately, this research makes a substantial contribution to global water resource management by enhancing the resilience and sustainability of dam operations worldwide.

Keywords: Remote sensing, Reservoir volume, Satellite imagery, Machine learning, Water resources management.

[1]jnfernandes@lnec.pt, Portugal

1. INTRODUCTION

Water stress is becoming a major national security issue, impacting quality of life, food and energy production, and political stability. Monitoring water levels is crucial for managing demand, flood control, and dam safety. Reservoirs have been vital since ancient times and over the centuries, dam construction and water management have advanced, with reservoirs playing key roles in flood control, hydropower, and irrigation. However, the impact of dams on rivers and water distribution is significant, with two-thirds of the world's long rivers affected by dams.

Despite extensive documentation of large dams, monitoring reservoir storage is still mostly limited to developed countries. This lack of data contributes to global water issues, as 2.2 billion people lack access to clean drinking water, and 3.5 billion lack proper sanitation, as highlighted in the 'UN World Water Development Report 2024' [1]. To address this, better monitoring and data-driven approaches are needed for efficient and sustainable water management.

The goal of this study is to develop a web-based tool that monitors the volume of reservoirs globally, especially in regions lacking data. The tool will analyse satellite images and provide information to help improve water management. By improving access to reservoir storage data, the tool aims to mitigate the effects of water stress and enhance global water security.

2. METHODOLOGY

2.1. Workflow

The tool employs a multi-stage workflow to calculate reservoir volumes. First, users define the Region of Interest (ROI) and a date range. The platform retrieves satellite images, then applies an unsupervised learning method to apply a threshold to the Normalized Difference Water Index (NDWI) to detect water pixels, excluding non-water features like bridges, which are detected using Google Places API and removed through morphological operations, such as dilation and erosion. If the images have a high percentage of cloud-coveraged areas, the cloud pixels areas are filtered out, and the reservoir shape is reconstructed using bathymetry data.

After determining the area, if an Area-Volume (A-V) relationship is available in the database, it is used for volume calculation. Otherwise, the user can either input the relationship or a Digital Elevation Model (DEM), and if the second option is chosen the code will use that file to estimate the A-V relationship. If none of these options are selected, global database – GLOBAthy – is used ([2]). The final step interpolates the calculated surface area to generate

a time-series of reservoir volumes. Figure 1 presents a flowchart addressing all the stages mentioned and how they are connected.

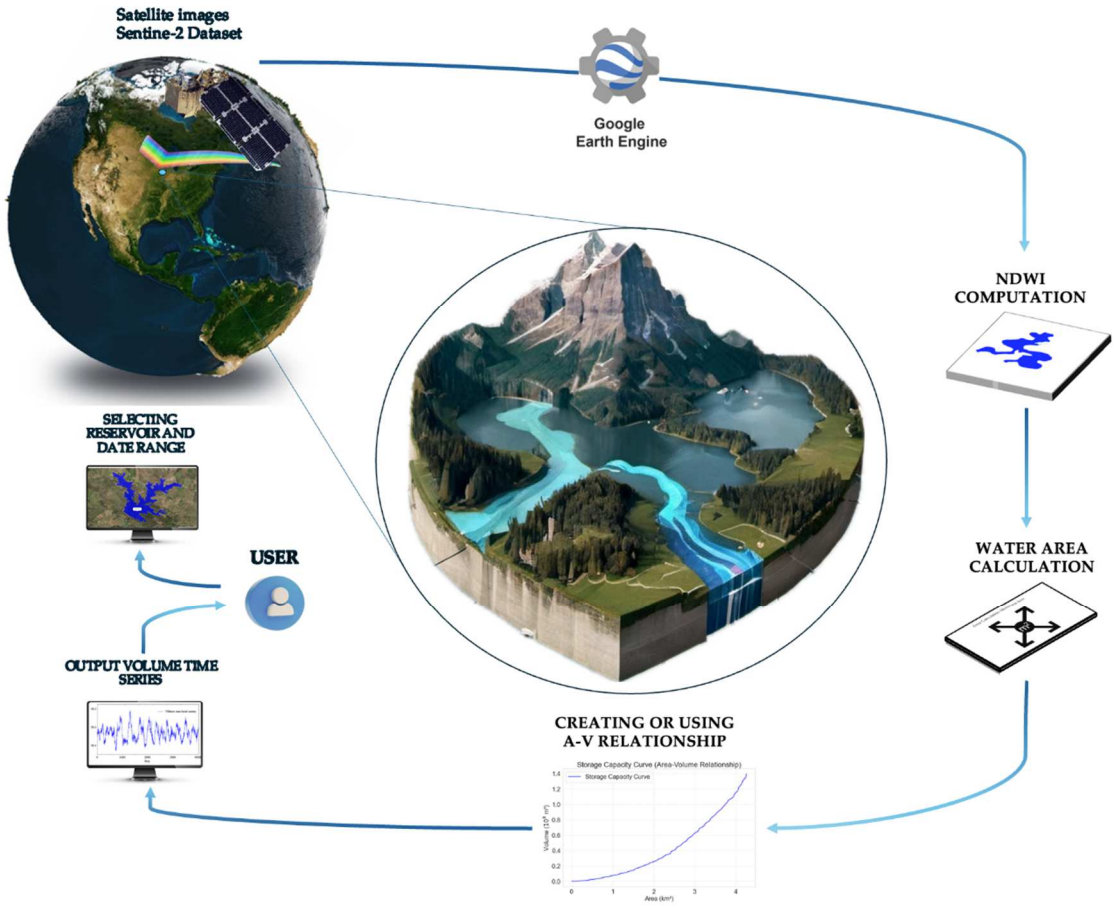

Fig. 1 — Workflow of the Tool

2.2. Google Earth Engine Platform

Google Earth Engine (GEE) is central to this study, providing an accessible platform for satellite data and computational resources. It allows for remote sensing data acquisition and processing via its Python API ([3]). Sentinel-2 imagery was chosen for its global coverage, high spatial resolution (10 m), and 5-day revisit time, making it ideal for water resources management (S2 Mission, [4]). The platform enables access to imagery based on region and cloud coverage criteria, ensuring only high-quality images are processed.

2.3. Calculating Water Area

The process begins by retrieving satellite images based on the user-defined date range and region of interest. Next, a binary mask of the NDWI is generated using a clustering algorithm. The tool then filters out unwanted features, such as environmental interferences like clouds and shadows, as well as man-made structures like bridges. Once these elements are removed,

the reservoir's water area is calculated by determining the pixel area of the regions classified as water in the NDWI binary image. Depending on the image resolution and projection system, this area is then converted to square meters using the reducer function in GEE.

2.4. Volume Estimation

The final stage involves calculating the reservoir's volume by interpolating the inundated water area using established relationships between surface area and stored water volume. This volume can be derived through several methodologies, depending on available data and the reservoir's characteristics. The approach employs a multi-source strategy to obtain the necessary Area-Volume (A-V) relationships. If the selected reservoir does not have the relationship in the platform's database, a selection box is presented to the user to choose other options (Fig. 2).

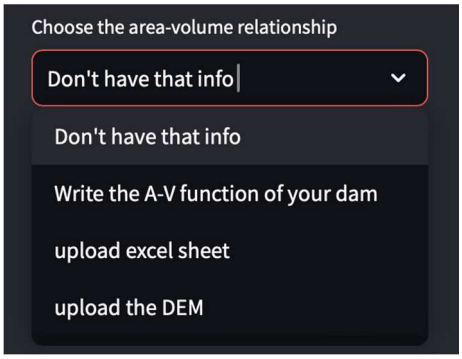

Fig. 2 – Select box to choose how to obtain the area-volume relationship

The storage capacity curve, also known as the area-storage or capacity-elevation curve, describes the relationship between the volume of water in a reservoir and its surface area or elevation. This curve is typically derived from detailed bathymetric surveys or elevation data, often maintained by local authorities. Two primary datasets for A-V relationships are the Portuguese Water Resources Information System (SNIRH) and the Global Reservoir and Dam Database (GRanD, [5]). The SNIRH provides historical hydrological data for reservoirs in Portugal, while GRanD offers a comprehensive global dataset, incorporating detailed information on reservoirs and their capacity relationships, managed by McGill University, in collaboration with several key institutions ([6]). The software retrieves these relationships and applies linear interpolation to estimate volume based on the calculated water area.

Estimating with Bathymetric Information of the Reservoir

If users have a Digital Elevation Model (DEM) (Fig. 3) but no existing A-V relationships, the tool can generate custom relationships using the DEM. This involves calculating the area and

volume at various elevation levels, providing a tailored estimate of the reservoir's storage characteristics. This method enables the software to create a specific A-V relationship for reservoirs lacking standard data. The code divides the model into different and equal elevation slices, by masking the pixels that have a specific elevation for that step, after which it defines two functions. The first function, computes the volume below a specified elevation by determining the water height above each cell and summing these values, multiplied by the cell area. The second function, creates a mask to identify inundated cells, counts them, and multiplies by the cell area to get the total inundated area. Lastly, a dictionary is initialized and created to store these calculated volumes and areas. This process systematically computes and logs the volume and area for a range of elevation levels (cf. Fig. 4), providing a comprehensive dataset for creating an Area-Volume dictionary, which will also be delivered as part of the output.

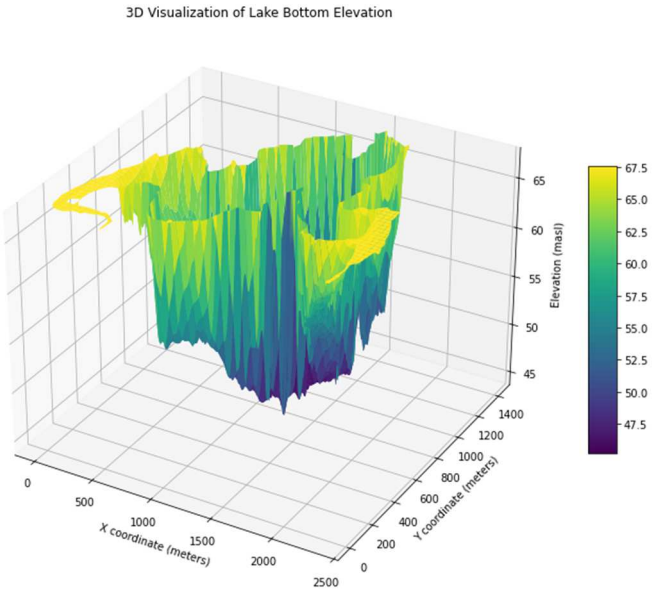

Fig. 3 – Lake bottom Elevation of the lake Patillas, Porto Rico

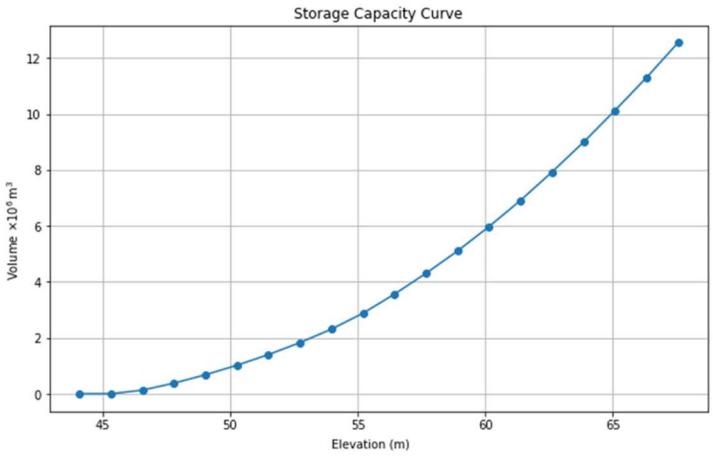

Fig. 4 – Storage capacity curve created of the lago Patillas, Puerto Rico

Using GLOBathy Data

In scenarios where neither A-V relationships nor DEM data are available, the tool defaults to the GLOBathy dataset. This comprehensive global bathymetric dataset covers over 1.4 million water bodies and integrates maximum depth estimates with water body characteristics ([2]). The GLOBathy dataset includes derived head-Area-Volume (h-A-V) relationships, ensuring that even without local data, accurate volume estimations can still be achieved by utilizing global standards.

3. RESULTS

A series of validation tests were conducted to assess the performance of the tool across its main algorithms. The objective of these tests was to verify the accuracy and reliability of the tool in processing remote sensing data for reservoir volume estimation.

The tests validated the tool's core functionality – accurate volume calculation – by establishing area-volume relationships derived from satellite imagery and comparing these estimates against measured data from various reservoirs. To comprehensively evaluate the tool's capabilities, data were used from multiple reservoirs of varying sizes and characteristics, incorporating both localized datasets, such as SNIRH and GLOBathy. Through this comparison, the accuracy of the tool is tested across different contexts, with the aim of improving its generalizability and applicability in diverse water resource management scenarios.

The diverse selection of reservoirs was chosen for testing across a minimum date range of five years. The selection criteria for these reservoirs were primarily based on the availability of publicly accessible historical data, which allowed for direct comparison between the observed

values and the volume estimates computed by the software for the same time periods. The reservoirs selected span two distinct regions: Portugal and the state of California in the United States (Fig. 5). Both regions were chosen due to their extensive networks of water bodies and the availability of high-quality historical data. In Portugal, data was sourced from the SNIRH, the national water resources information system, which provides detailed records of hydrological metrics across the country's numerous reservoirs.

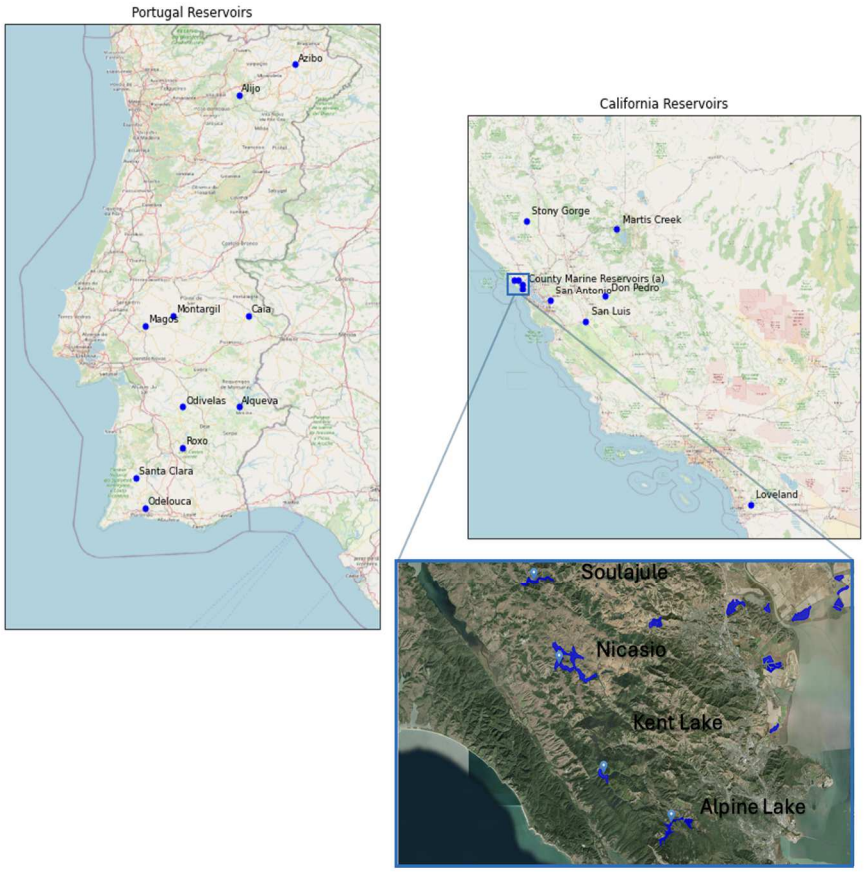

Fig. 5 – Location of the reservoirs tested

In California, data was retrieved from the California Data Exchange Center (CDEC), a centralized repository for hydrological and meteorological information in the state. This validation not only tests the software's performance across different geographical and hydrological conditions but also demonstrates its versatility in using data from different sources and environments. These reservoirs vary in type, use, geometry, and bathymetry together and represent a significant amount of water storage corresponding to a total volume of 13 402 hm^3 and an inundated water area of 141 744 ha.

The tool prioritizes relationships stored in its internal database, giving preference to official repositories due to their higher reliability and accuracy. Then, to ensure a thorough evaluation, its performance was tested under default conditions, simulating its typical operation by comparing strictly its output with the official data for each reservoir. Figure 6 illustrates this

process, where the red line in each chart represents the platform's automatic output for six of the reservoirs tested, adapting dynamically to the available data source, whether from SNIRH or GLOBathy.

Ultimately, the accuracy and reliability of the software in calculating reservoir volumes are quantitatively assessed using key performance metrics, including the Coefficient of Determination (R^2), Mean Absolute Percentage Error (MAPE), and Mean Bias Deviation (Bias). These metrics provide a robust evaluation of the software's effectiveness under different scenarios and are presented in Table 1, offering a detailed assessment of its performance.

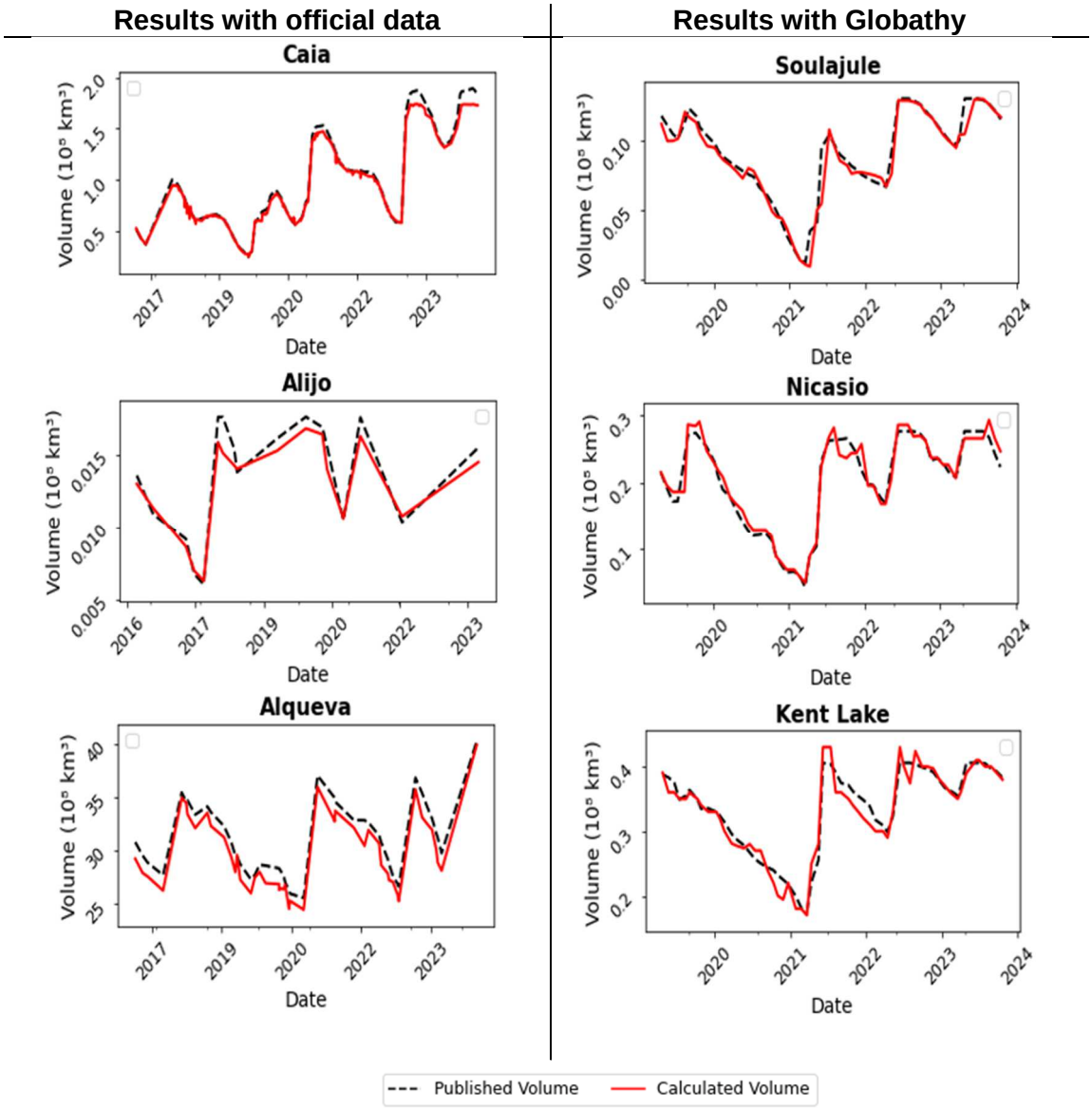

Fig. 6 – Actual vs Predicted volume for 6 reservoirs in Portugal and California, USA

The performance metrics indicate a strong predictive capability of the model. The tests yield an average Mean Absolute Percentage Error (MAPE) of 5.1%, an average Coefficient of Determination (R^2) of 0.9, and a Bias of 0.0. The low MAPE reflects that the model's predictions, on average, deviate by only 5.11% from the observed values, suggesting a high

level of accuracy in the estimations. The R^2 value of 0.9 indicates that 90% of the variance in the observed data is explained by the model, demonstrating its robustness and reliability in capturing the underlying data patterns.

Moreover, the Bias of 0.0 suggests the absence of systematic errors in the model's predictions, implying that the model neither consistently overestimates nor underestimates the actual values. This balance is crucial for ensuring the credibility and generalizability of the model's outputs across different datasets.

Table 1 – Summary table of the tools' performance towards the reservoirs tested

Reservoir	Maximum Area (ha)	Maximum Volume (10^3 hm^3)	A-V relationship source	Date range tested	Performance Metrics		
					R^2	MAPE	BIAS
Caia	1 970	203 000	SNIRH	8 years	0,988	2,404	-0,002
Alijó	18	1 760	SNIRH	8 years	0,924	5,546	0,000
Alqueva	25 000	4 150 000	SNIRH	8 years	0,833	4,081	-0,124
Kent Lake	350	40 582	GLOBAthy	5 years	0,943	3,917	0,000
Soulajule Reservoir	730	13 198	GLOBAthy	5 years	0,932	4,5	0,079
Nicasio Reservoir	3 170	85 800	GLOBAthy	5 years	0,957	5,112	0,000

4. CONCLUSIONS

This research successfully developed a remote sensing tool that significantly improves reservoir volume evaluation, addressing key challenges in water resource management. By utilizing Sentinel-2 satellite imagery and machine learning algorithms, the tool offers a cost-effective alternative to traditional methods, providing accurate calculations of reservoir surface area and volume. Tested across reservoirs in Portugal and California, the tool demonstrated a mean absolute percentage error of 5.1% and a strong correlation coefficient of 0.9 compared to conventional measurements.

Although the prototype shows promising results, areas for improvement remain. These include updating storage capacity curves, improving satellite image resolution, and expanding the database with more local reservoir data. Future enhancements may incorporate additional data sources, such as radar imagery and telemetry, and improve the tool's adaptability to handle complex environmental factors like sedimentation. Machine learning capabilities could also enhance forecasting of reservoir volumes under various climate scenarios, providing greater value for water management stakeholders.

In conclusion, this software represents a significant advancement in remote sensing for water resource management, with the potential to greatly enhance the sustainability and resilience of global reservoir operations. Continued refinement and integration of new data sources will be crucial for maximizing its utility and accuracy.

The tool is available in https://github.com/joao862/BLU.

5. REFERENCES

[1] Nations, U. (2024). The United Nations World Water Development Report 2024: Water for Prosperity and Peace. UN. Available at: https://www.unwater.org/publications/un-world-water-development-report-2024

[2] Khazaei, B.; Read, L. K.; Casali, M.; Sampson K. M.; Yates D. N. (2022) GLOBathy, the global lakes bathymetry dataset. Scientific Data, 9(36)

[3] https://developers.google.com/earth-engine/tutorials/community/intro-to-python-api - An Intro to the Earth Engine Python API | Google Earth Engine. Google Developers.

[4] https://www.esa.int/Enabling_Support/Operations/Sentinel-2_operations - Sentinel-2 operations, European Space Agency.

[5] Lehner, B.; Liermann, C.; Revenga, C.; Vörösmarty, C.; Fekete, B.; Crouzet, P.; Döll, P.; Endejan, M.; Frenken, K.; Magome, J.; Nilsson, C.; Robertson, J. ;Rodel, R.; Sindorf, N.; Wisser, D. (2011). High-Resolution Mapping of the World's Reservoirs and Dams for Sustainable River-Flow Management. Frontiers in Ecology and the Environment 9 (9): 494-502.

[6] Messager, M. L.; Lehner, B.; Grill, G.; Nedeva, I.; Schmitt, O. (2016). Estimating the volume and age of water stored in global lakes using a geo-statistical approach. Nature Communications,7, article number 13603.

Fifth International Dam World Conference
PORTUGAL • LISBON • LNEC • APRIL 13-17, 2025
dam world 2025

OPTIMIZING SEISMIC INTENSITY MEASURES FOR FRAGILITY ANALYSIS OF EARTH DAMS: A COMPREHENSIVE EVALUATION INCORPORATING FUNCTIONALITY METRICS

Rocio L. Segura[1]
Santa Clara University,
Santa Clara, CA, USA.

Guillaume Veylon
INRAE, RECOVER,
Aix-en-Provence, France

ABSTRACT

Most existing earth dams were designed according to outdated standards that often incorporated the effects of earthquakes in a simplified manner. As a result, the seismic re-evaluation of these structures has become increasingly important for dam owners. In line with modern goals for a sustainable and resilient society, there is a growing need for reliable and efficient assessments of these dams. Probabilistic-based approaches, such as fragility analysis, offer an innovative framework that shifts away from rigid safety standards toward risk-informed decision-making. One critical prerequisite for seismic fragility analysis is determining the optimal earthquake intensity measure (IM).

Although several studies have performed seismic fragility analyses of earth dams, they have not thoroughly examined the optimal seismic IM with respect to metrics such as correlation, practicality, efficiency, and proficiency—especially in the context of crest settlement performance levels. Furthermore, the optimal IMs identified in the literature often involve intermediate steps, such as analysing the frequency and energy content of input motions, which may not be straightforward to apply.

In this paper, we analyse 16 intensity measures using 186 records and introduce a new qualitative metric called the "functionality metric" to assess the ease of use of the IM by obtaining them in a more straightforward manner, based on code standards and readily available seismic intensity measures. Additionally, we propose an importance factor to weight these metrics and select the optimal IM based on correlation, practicality, efficiency, proficiency, and functionality. Our findings indicate that the Weighted Total Power is the most efficient IM for predicting crest settlement when functionality metrics are not considered, while Peak Ground Velocity (PGV) emerges as the optimal IM when functionality metrics are included.

Keywords: Earth dams, fragility, seismic intensity measures, functionality.

[1]RSegura@scu.edu, France

1. INTRODUCTION

Earth dams are critical infrastructure systems that support community resilience by serving diverse functions, such as water storage, flood control, and hydropower generation. Their significance has increased in recent years due to the growing challenges of climate change, including prolonged drought periods that strain water resources [1-2]. Consequently, ensuring the serviceability, stability, and safety of dams has become a priority for engineers and policymakers alike, particularly in seismic-prone regions [3].

Earthquakes pose a significant risk to earth dams, potentially compromising their stability and triggering catastrophic dam-break waves that endanger lives and property [4]. This risk is heightened by the fact that most existing embankment dams were constructed shortly after the Second World War, under design standards that often inadequately addressed seismic actions [5]. These older design codes typically relied on simplified methods for considering earthquake effects, leaving many dams vulnerable to modern seismic challenges [6]. As a result, the seismic re-evaluation of existing earth dams has emerged as a critical area of research and practice for dam owners and regulators [7].

Seismic re-evaluations require advanced methodologies that incorporate site-specific, hazard-consistent ground motions and robust probabilistic metrics to assess dam vulnerability comprehensively. Analytical fragility functions are widely used to quantify seismic vulnerability by linking ground motion intensity measures (IMs) to various damage mechanisms. However, selecting appropriate seismic IMs is crucial to accurately capturing the seismic response of earth dams [8-9]. Optimal IMs should exhibit strong correlations with structural response metrics while being practical, efficient, and readily available for use in engineering applications [10-12].

Although several studies have explored seismic fragility analyses of earth dams considering different intensity measures (IMs) [6,13-18], the selection of "optimal" IMs often prioritizes metrics such as correlation, practicality, efficiency, and proficiency while neglecting considerations of ease of application in industry practices. While these studies provide valuable insights, the IMs identified are frequently derived using intermediate steps, such as analyzing the frequency or energy content of ground motions, which may not align with the straightforward needs of dam industry professionals.

This study sheds light on this gap by emphasizing the importance of ease of use and ease of obtaining IMs, particularly in the context of crest settlement performance levels—a critical indicator of dam damage level and functionality. By incorporating both traditional metrics and a focus on practical applicability, this research aims to bridge the gap between theoretical analyses and industry implementation.

This paper addresses these gaps by evaluating the efficiency and predictability of 16 intensity measures using 186 ground motion records. Additionally, we introduce a novel qualitative metric called the "functionality metric" to assess the ease of use of IMs based on code standards and readily available seismic parameters. To provide a holistic assessment, an importance factor that weighs these metrics and selects the optimal IMs based on correlation, practicality, efficiency, proficiency, and functionality is proposed. This approach offers a streamlined and practical framework for assessing the seismic vulnerability of earth dams, contributing to safer and more resilient infrastructure systems.

2. CASE-STUDY

The methodology proposed in this study and presented in the following sections was applied to a case-study earth dam to demonstrate its practical implementation. The selected structure is a 25 m high zoned embankment dam with a central clay core flanked by upstream and downstream rockfill shells (Figure 1). The downstream slope features two berms and an average slope of 2.4H/1V, while the upstream slope has a single berm at its base and an average slope of 2.2H/1V.

The dam rests on a foundation of clay material, with its weathering degree decreasing progressively with depth. At approximately 20 m below the surface, the foundation transitions into a rock-like material, characterized by shear wave velocity values indicative of a rock foundation (V_S = 1000 m/s).

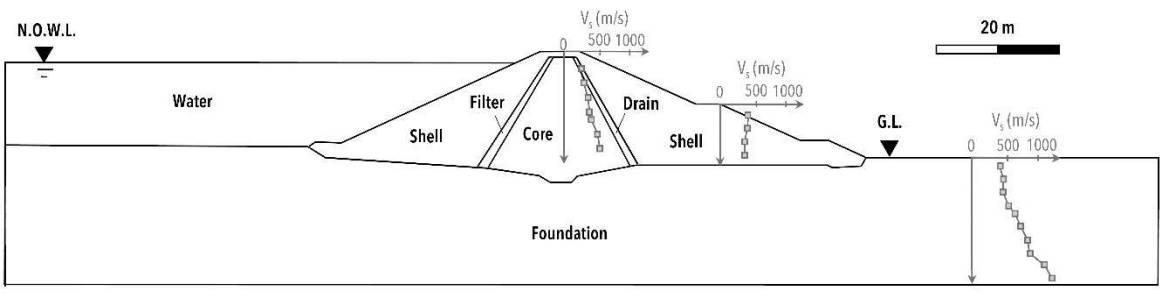

Fig. 1 – Case-study dam cross-section

3. METHODOLOGY

Evaluating the dynamic response of earth dams involves numerous uncertainties, including the spatial variability of soil-rock properties, heterogeneity of dam-body materials, and the unpredictable characteristics of bedrock ground motions. Traditional deterministic analyses often fall short in addressing these uncertainties, limiting their ability to predict the system's performance accurately. To overcome these limitations, performance-based earthquake engineering (PBEE) [19] provides a robust framework for seismic risk assessment. PBEE incorporates various sources of uncertainty and presents the results in a format that is accessible to both engineers and stakeholders [8].

A critical component of PBEE is the probabilistic seismic demand model (PSDM), which defines the relationship between the engineering demand parameter (EDP) and the ground motion IM. The present study identifies the most effective IMs through a comprehensive evaluation based on five criteria: (i) correlation (R^2), (ii) efficiency (σ), (iii) practicality (k), (iv) proficiency, and (ε) (v) a newly introduced functionality metric ($\mathcal{F}$) that evaluates the ease of use.

The selected IMs are then used to construct seismic fragility curves, offering a probabilistic assessment of the dam's performance under seismic loading. Figure 2 outlines the stepwise process for identifying optimal IMs, incorporating these criteria to enhance practical application in seismic risk evaluation. The following sections describe each one of these steps.

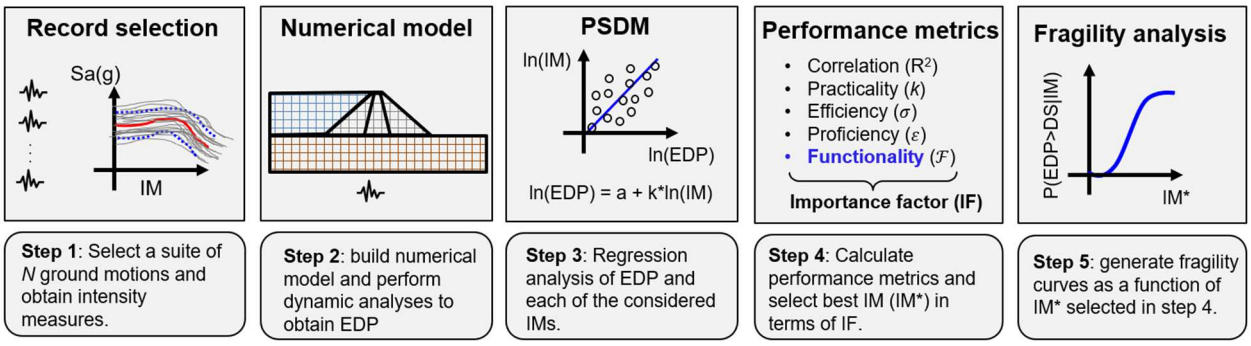

Fig. 2 – Flowchart of the framework to identify the best IMs and generate fragility functions

3.1. Record Selection

The characterization of ground motion is a critical source of uncertainty in seismic performance assessment analyses [20]. To address this, a database comprising triplets of ground motion records was utilized. These accelerograms were sourced from the Engineering Strong Motion Database [21], the RESORCE 2018 database [22], and the KiK-net database [23]. Given that the base of the model exhibits mechanical properties

of a rocky substratum, only ground motions recorded at sites classified as Eurocode 8 class A (V_{S30} > 800 m/s) [24] were included.

The selection of ground motions ensured a balanced representation of events across a range of local magnitudes (M_w), peak ground accelerations (PGA), and peak ground velocities (PGV). A minimum magnitude of M_w = 5.0 was applied to exclude very small events, reducing the over-representation of low-intensity records while maintaining diversity in the IM values. For this study, recordings from 186 events were analyzed, ensuring a comprehensive dataset. Figure 3 illustrates the distribution of magnitudes, focal depths, and epicentral distances, providing an overview of the variability in the selected records.

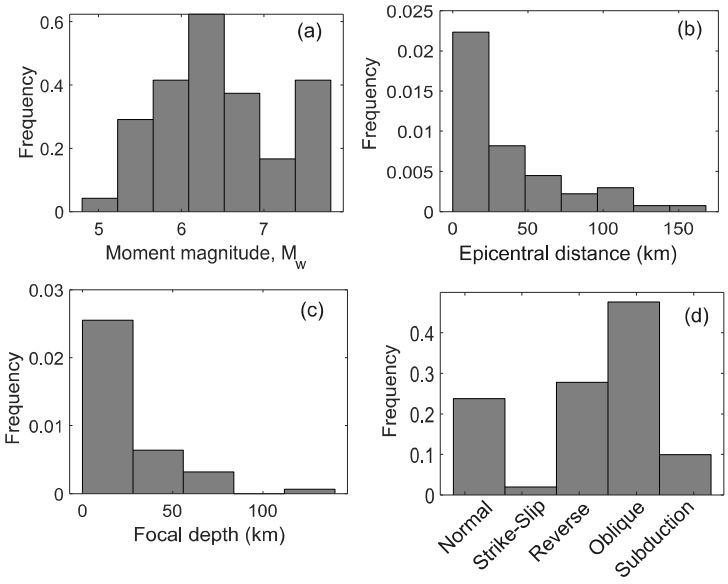

Fig. 3 – Ground motion records characteristics: (a) moment magnitude, (b) epicentral distance, (c) focal depth and (d) dominant focal mechanism

3.2. Numerical Model

The 2D numerical model represents the tallest cross-section of the dam, situated at its central part. The horizontal extent of the model is three times the dam height on both sides of the embankment base, while the rock foundation extends vertically to a depth equal to three times the height of the dam. This configuration ensures the inclusion of sufficient domain for accurate analysis of the dam's response. The boundary-value problem is solved using a finite difference code based on an explicit integration scheme. The dam construction process is explicitly modeled in layers, replicating the real-world construction sequence. To prevent artificial reflections of seismic waves at the model boundaries, absorbent, non-viscous boundaries are applied. The mesh size is optimized to capture the vibrational behavior of the dam accurately (Figure 4).

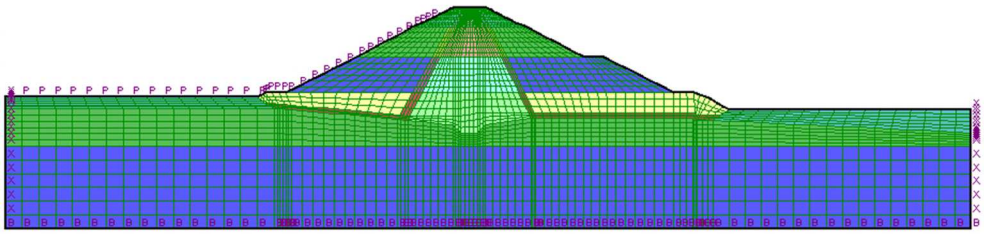

Fig. 4 – Numerical model of the dam with boundary conditions.

Specifically, the domain discretization ensures that the largest element size (ΔL) satisfies the condition $\Delta L \leq V_{S30}/10f_c$, where f_c is the cut-off frequency of the ground motion records, set to 20 Hz in this study. This criterion ensures adequate resolution of the dynamic response without introducing numerical dispersion. The filling phase, up to the normal operating water level, is also modeled using a transient flow calculation to simulate the progressive saturation of the embankment and the stabilization of the phreatic line. Seismic loading is introduced as a time series of shear and normal stresses applied along the lower boundary of the model, representing the input ground motion. The material properties considered in the numerical model are shown in Table 1.

Table 1 – Material properties considered in the numerical model

Model element	Dry density (t/m^3)	Young modulus (MPa)	Poisson's ratio	Angle of friction (^{o})	Cohesion (kPa)
Foundation	1.70	500-4000*	0.20	32	8.0
Shell	2.00	800	0.25	43	5.0
Core	1.30	120-400*	0.20	32	1.0
Drain/Filter	1.55	190	0.25	38	0.0

* Linear variation increasing with depth

3.3. Probabilistic Seismic Demand Model

The seismic demand model predicts the median of the EDP as a function of the ground motion intensity. For the development of the demand model, the numerical model is subjected to a suite of *N* ground motions, and the mean peak value of the EDP for each motion is often assumed to follow a power law function in terms of the IM [25], which can be expressed as:

$$\mu_{EDP} = a \cdot IM^k \quad (1)$$

For simplicity, the power-law function can be rearranged to natural logarithmic space as shown in Eq. 2, where $\ln a$ and k are the vertical intercept and the slope factor, respectively.

$$\mu_{\ln EDP} = \ln(\mu_{EDP}) = \ln a + k \cdot \ln IM \quad (2)$$

This functional form assumes that the EDP follows a lognormal distribution, with the mean $\mu_{\ln EDP}$ given by Eq. 2 and the standard deviation ($\sigma_{\ln EDP}$) computed with Eq. 3.

$$\sigma_{\ln EDP} = \sqrt{\frac{\sum_{i=1}^{N}\left(\ln EDP_i - \mu_{\ln EDP,i}\right)^2}{N-2}} \quad (3)$$

where EDP_i is the recorded maximum value of the EDP for input motion *i*, $\mu_{\ln EDP,i}$, is the natural log of the EDP predicted from Eq. 2 for the IM of motion *i*, and *N* is the number of input motions. In this study, the EDP of interest is the settlement of the crest of the dam (U_z) which can be assumed as a reliable index of seismic performance in that it is representative of the overall response of the dam and is suitable for the evaluation of the level of damage induced by earthquake loading [6].

3.4. Performance Metrics

Four performance metrics, which have been typically utilized in the literature for different engineering structures [10,13,18,26], and a new qualitative metric to assess the ease of use are adopted to identify the most convenient IMs in this study. Each of these metrics will be briefly explained below.

3.4.1 Correlation: The correlation criterion reflects the goodness of the empirical regression model of Eq. 2. The correlation of an IM can be measured by the adjusted coefficient of determination R^2. A larger R^2 value can strongly imply a better correction between the specified EDP and the given IM.

3.4.2 Practicality: In conventional linear regression, the practicality of the regression model shown in Eq. 2 can be assessed by the absolute value of the slope factor $|k|$. A regression model for an intensity measure with a higher absolute value of k indicates that the IM is significantly dependent on EDP. Consequently, such an IM is considered more practical.

3.4.3 Efficiency: The efficiency of an IM determines the level of variability or dispersion of the calculated seismic responses around the regression model for a given IM. For this study, the standard deviation obtained from Eq. 3 is used to quantify the efficiency of a candidate IM. A more efficient IM would lead to a lower value of $\sigma_{\ln EDP}$ and indicates less dispersion around the predicted values from Eq. 2.

3.4.4 Proficiency: This compound indicator measures the simultaneous effect of both efficiency and practicality. The proficiency index is the ratio between the efficiency and

practicality and metrics, as shown in Eq. 4. In general, a lower ε value indicates a more proficient IM.

$$\varepsilon = \frac{\sigma_{\ln EDP}}{|k|} \tag{4}$$

3.4.4 Functionality: This new qualitative metric, is introduced to evaluate the ease of use of ground motion IMs. This metric is designed to prioritize IMs that can be obtained or computed straightforwardly, reflecting their practicality in engineering applications. One of the key advantages of this qualitative approach is its flexibility; the metric can be tailored to the specific characteristics of each analysis and the ease with which the required data can be obtained. Table 2 outlines the criteria for assigning functionality score to various IMs based on their computational and data requirements. IMs that are readily available in code standards or provided directly with recorded ground motions are assigned $\mathcal{F} = 1$, indicating the highest level of ease. IMs that require the estimation of structure-dependent parameters, such as the fundamental period of vibration, are assigned $\mathcal{F} = 2$. If the computation involves integrating the acceleration, velocity, or displacement time histories or analyzing the energy content of the ground motions, $\mathcal{F} = 3$ is assigned. Finally, IMs that necessitate a detailed analysis of the frequency content of input ground motions are assigned $\mathcal{F} = 4$, reflecting the highest computational complexity.

Table 2 – Functionality metric criteria for IMs

Functionality score	Criteria	Examples
$\mathcal{F} = 1$	Readily available in code standards or directly provided with recorded ground motions.	Peak Ground Acceleration (PGA), Peak Ground Velocity (PGV).
$\mathcal{F} = 2$	Requires estimation of structure-dependent parameters.	Spectral Acceleration ($Sa(T_1)$), where T_1 is the fundamental period.
$\mathcal{F} = 3$	Requires integration of acceleration-velocity-displacement time history or analysis of energy content.	Cumulative Absolute Velocity (CAV), Arias Intensity.
$\mathcal{F} = 4$	Requires analysis of the frequency content of input ground motions.	Mean period (T_m), weighted total power (I_F), damage intensity (I_D)

3.5. Fragility Analysis

Within the PBEE framework, the seismic performance is addressed using fragility functions which, for any given level of a ground motion intensity, provide the probability that the EDP reaches (or exceeds) a certain damage state (DS). Based on the linear

relationship between the logarithmic value of EDP and IM shown in Eq. 2 and the lognormally distribution assumption, seismic fragility functions can be derived according to a lognormal distribution as shown in Eq. 5,

$$P(EDP \geq DS_i|IM) = \Phi\left(\frac{\mu_{\ln EDP} - \ln DS_i}{\sigma_{\ln EDP}}\right) \quad (5)$$

where $P(EDP \geq DS_i|IM)$ represents the seismic fragility estimate, and $\Phi(\cdot)$ is the standard normal cumulative distribution function. To evaluate seismic fragility across various damage states, it is necessary to define threshold values of the EDP corresponding to each damage state. In this study, damage states are characterized by the maximum relative crest settlement, defined as the ratio between the crest settlement, U_z, and the height of the dam, H, as shown in Table 3.

Table 3 – Damage level thresholds based on Pells and Fell (2003) [27]

Damage state	Description	U_z/H (%)
DS1	Minor	0.05
DS2	Moderate	0.2
DS3	Major	0.5
DS4	Severe	1.5
DS5	Collapse	5

4. RESULTS AND DISCUSSION

4.1. Performance Metrics for Maximum Relative Crest Settlement

From the 186 records analyzed, 16 IM were derived, as listed in Table 4. Thirteen of these are commonly used in the literature [10,13,18,26], while three additional IMs were included for their strong predictive capabilities in assessing earth dam's performance. These additional measures include the non-dimensional displacement, $U^* = f\left(k_y, Sa(T_1), PGA^{-1}\right)$, which is a function of the yield coefficient (k_y) obtained through pseudo-static limit equilibrium, spectral acceleration at the fundamental period and peak ground acceleration, proposed by Veylon et al. (2017) [28]. The weighted total power (I_F) and the damage intensity (I_D), proposed by Nardo et al. (2024) [6], are also included and described in Eqs. 6 and 7, respectively.

$$I_F = I_A \times T_m \quad (6)$$

$$I_D = \frac{I_A \times T_m}{\sqrt{PGV}} = \frac{I_F}{\sqrt{PGV}} \quad (7)$$

In these equations, I_A is arias intensity and T_m is the mean period proposed by Rathje et al. (1998) [29]. The weighted total power represents an integral seismic parameter calculated as the area of a weighted power spectrum, where greater emphasis is given to lower frequencies by using the inverse of the circular frequency as the weighting factor. Similarly, the damage intensity combines the products I_F and $PGV^{-0.5}$ to account for energy demand across lower and intermediate frequencies, which are particularly relevant for geotechnical systems like dams and embankments. This approach leverages PGV, directly correlated with earthquake intensity and energy demand, making I_D a robust measure for assessing seismic performance [6].

When multiple IMs are used in seismic analyses, their correlations must be considered, as they often reflect overlapping aspects of ground motion characteristics. Neglecting these correlations can lead to inaccuracies in risk assessment [30]. Figure 5 illustrates the correlation matrix for the 16 IMs. The results show that SED, T_m, T_p, PGA, I_A, CAV, and U* exhibit a weak correlation with each other. Additionally, D595 correlates poorly with most IMs. In contrast, Sa(1s), Sa(T_1), Sa(1.5T_1), Sa(2T_1), I_F, I_D, U*, PGA, PGV, CAV and I_A demonstrate strong correlation.

Figure 6 and Table 3 summarize the results of the EDP-IM regression analysis and the performance metrics for each considered IM, respectively. The analysis shows that I_F performs best in terms of correlation, while PGA ranks highest in practicality. For efficiency, I_A exhibits the least dispersion, CAV emerges as the most proficient, and PGA and PGV are the easiest to implement based on functionality.

4.2. Best Performing Intensity Measure

Since no single IM outperforms across all metrics, an importance factor (IF) was introduced to combine the five performance metrics. This factor is calculated using Eq. 8, where PM_i represents a given performance metric, $PM_{i,\min}$ and $PM_{i,\max}$ are its minimum and maximum values across all IMs, and w_i is the relative weight assigned to each metric.

$$IF = \sum_{i=1}^{5} w_i \left(\frac{PM_i - PM_{i,\min}}{PM_{i,\max} - PM_{i,\min}} \right) \tag{8}$$

Two cases were analyzed: one including the functionality metric and another excluding it. In the first case, the functionality metric was assigned a weight of 0.4, while the remaining metrics were each assigned a weight of 0.15. In the second case, all metrics were weighted equally at 0.25. The final importance factors for both cases are presented in the last two columns of Table 3. In the first case, PGV emerged as the

best-performing IM with IF=0.799, followed by PGA with IF=0.762. This outcome aligns with expectations, as the functionality metric carried a significant weight, and according to the criteria defined in this study, PGA and PGV are the most functional IMs. In the second case, I_F was the top-performing IM with IF=0.750, closely followed by I_A with IF=0.747. These findings are consistent with results reported in the literature for earth dams [4][17] [18].

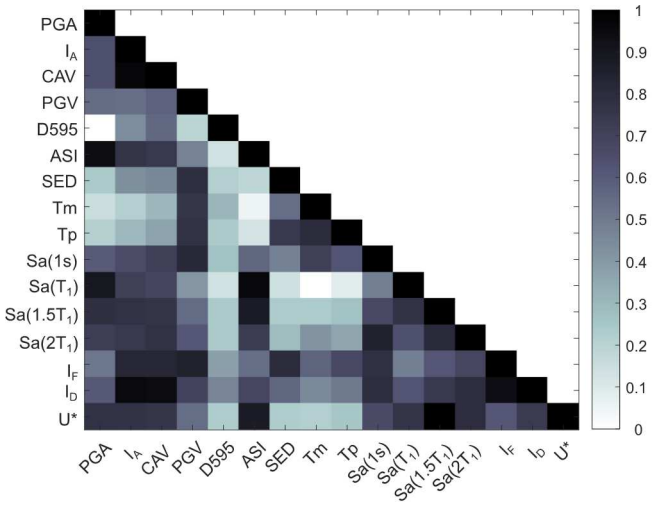

Fig. 5 – Correlation among considered IMs

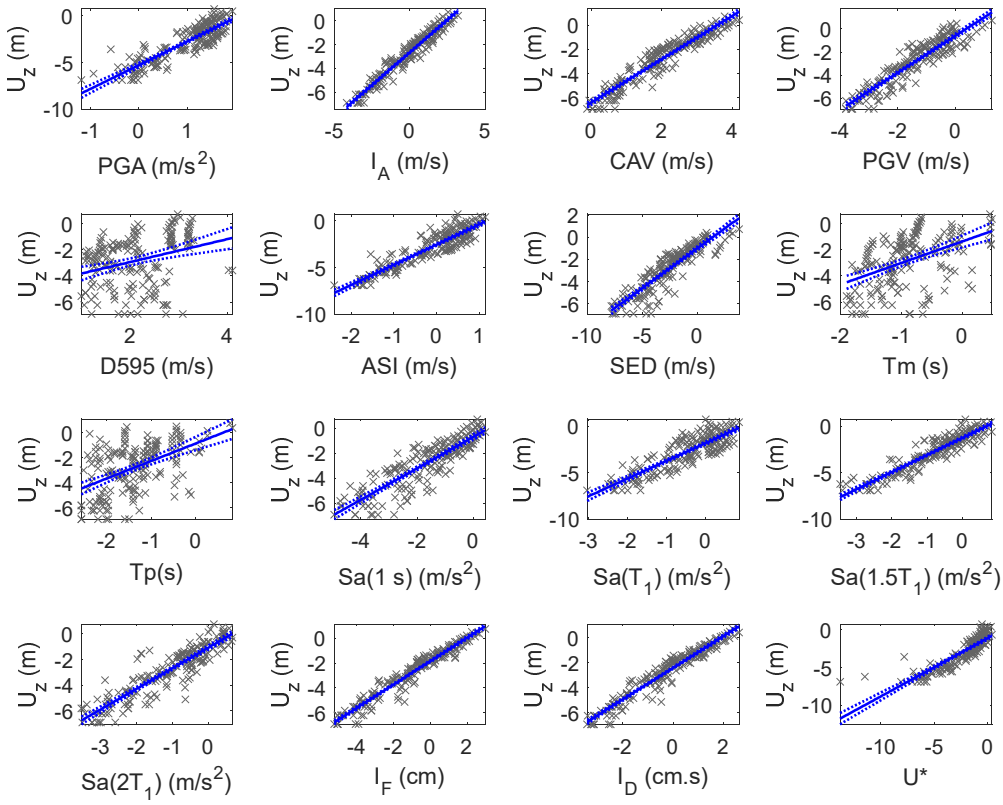

Fig. 6 – Regression analysis between U_z and each of the considered IMs (logarithmic scale)

Table 4 – Performance metrics of considered IMs

IM	Symbol	R^2	k	$\sigma_{\ln EDP}$	ε	$\mathcal{F}$	IF**	IF*
Peak ground acceleration	PGA	0.753	**2.550**	0.970	0.380	**1.0**	0.762	0.603
Arias intensity	I_A	0.944	1.100	**0.461**	0.419	3.0	0.583	0.747
Cumulative absolute velocity	CAV	0.894	1.790	0.637	**0.356**	3.0	0.556	0.704
Peak ground velocity	PGV	0.844	1.606	0.771	0.480	**1.0**	**0.799**	0.665
Effective duration	D595	0.092	0.873	1.859	2.128	3.0	0.283	0.250
Acceleration spectrum intensity	ASI	0.826	2.171	0.814	0.375	3.0	0.525	0.652
Specific energy density	SED	0.794	0.723	0.885	1.223	3.0	0.511	0.630
Mean period [29]	T_m	0.229	1.651	1.713	1.037	4.0	0.190	0.316
Predominant period	T_p	0.261	1.398	1.677	1.200	2.0	0.466	0.332
Spectral acceleration at T=1s	Sa(1s)	0.757	1.261	0.961	0.763	2.0	0.630	0.606
Spectral acceleration at $T=T_1$	$Sa(T_1)$	0.743	1.908	0.989	0.518	3.0	0.491	0.596
Spectral acceleration at $T=1.5T_1$	$Sa(1.5T_1)$	0.862	1.842	0.726	0.394	3.0	0.540	0.678
Spectral acceleration at $T=2T_1$	$Sa(2T_1)$	0.820	1.606	0.827	0.515	3.0	0.522	0.648
Weighted total power [4]	I_F	**0.945**	0.941	0.474	0.504	4.0	0.448	**0.750**
Damage intensity [4]	I_D	0.933	1.266	0.506	0.400	4.0	0.443	0.739
Non-dimensional displacement [15]	U*	0.759	0.774	0.958	1.238	2.0	0.631	0.607

IF**: Importance factor including all metrics.

IF*: Importance factor without the functionality metric.

4.3. Fragility Curves

For the best-performing IMs in both cases, when functionality is considered and when it is not, Fragility curves were generated. These curves were developed using Eq. 5, with the assumption of lognormality verified for IM and EDP as shown in Figure 7. The verification covered the range of I_F, PGV and U_z values obtained from the simulations using the 186 records.

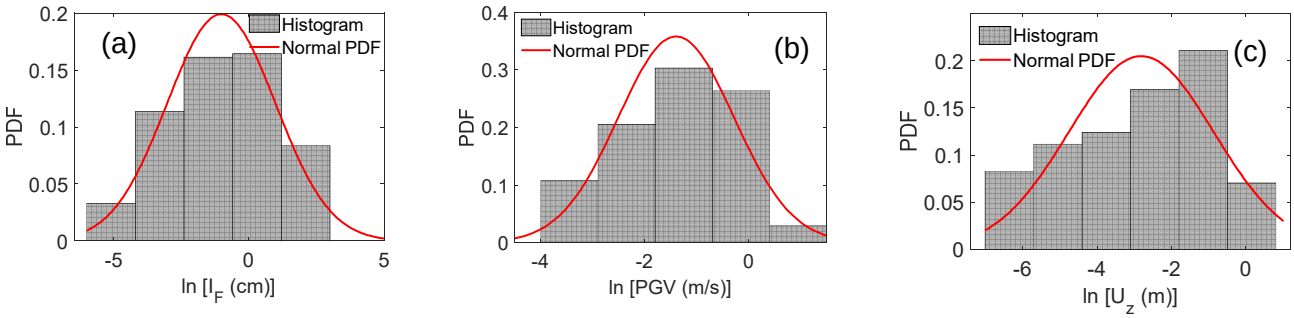

Fig. 7 – Probability density function (PDF) for: (a) IM=I_F, (b) IM=PGV and (c) EDP=U_z

Fragility curves were obtained for IM=PGV using Eq. 9 and for IM=I_F using Eq. 10, with the damage states defined in Table 2. The resulting fragility curves for both cases are presented in Figure 8.

$$P(U_z \geq DS_i|PGV) = \Phi\left[\frac{(-0.569 + 1.605 \cdot \ln PGV) - \ln DS_i}{0.771}\right] \quad (9)$$

$$P(U_z \geq DS_i|I_F) = \Phi\left[\frac{(-1.852 + 0.941 \cdot \ln I_F) - \ln DS_i}{0.474}\right] \quad (10)$$

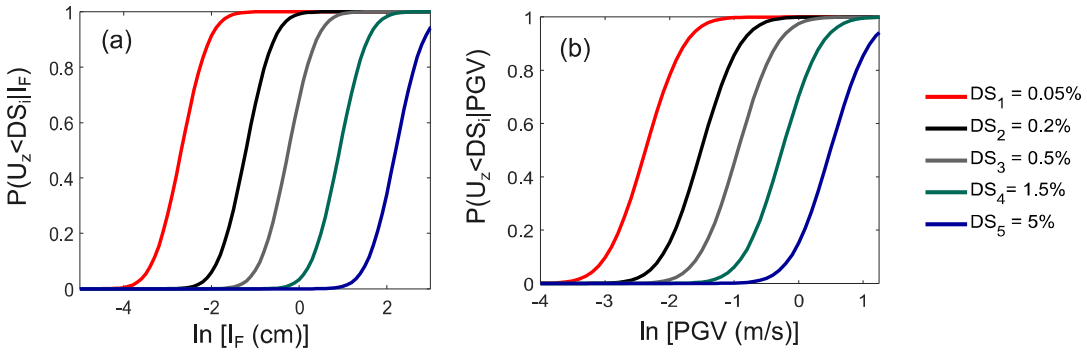

Fig. 8 – Fragility curves as a function of: (a) IM=I_F and (b) IM=PGV.

4.4. Impact of IMs in the Fragility Estimates

To evaluate the impact of the conditioning IM on fragility estimates, the logarithmic standard deviations of the fragility curves provide a useful quantitative comparison. From Eqs. 9 and 10, the logarithmic standard deviations are found to be 0.771 for PGV and 0.474 for I_F. This indicates that I_F is associated with lower uncertainty and provides a more accurate seismic fragility evaluation.

To better visualize the differences between the IMs, the fragility curves for PGV and I_F were normalized, allowing for direct comparison. As shown in Figure 9, the fragility

curves exhibit similar overall shapes and tendencies. However, the PGV-based fragility curves are more conservative across most of the value range, particularly for severe and collapse damage states. For instance, at a normalized IM value of 0.7, the fragility estimates for severe damage are 0.26 for I_F and 0.41 for PGV, while for collapse, the estimates are 0.002 for I_F and 0.07 for PGV. These differences highlight that while both IMs produce comparable trends, PGV tends to yield more conservative estimates in higher damage states.

5. CONCLUSIONS

This study presented a flexible framework for seismic fragility assessment, applied to a case-study earth dam, to identify the optimal intensity measure based on stakeholder priorities and available resources. Sixteen IMs were evaluated using 186 ground motion records, incorporating a new qualitative metric, the functionality metric, to account for the ease of obtaining and using IMs in practice. Additionally, an importance factor was introduced to weigh five performance criteria—correlation, practicality, efficiency, proficiency, and functionality—ensuring a balanced assessment.

The results showed that the Weighted Total Power is the most efficient IM for predicting crest settlement when functionality is excluded, while Peak Ground Velocity emerges as the optimal IM when functionality is considered. Fragility curves generated for both IMs reveal similar shapes and trends, but PGV-based curves are more conservative, especially for severe and collapse damage states. It is important to note that only uncertainties related to seismic loading were considered in this study. Other factors, such as uncertainties in the dam-foundation-reservoir system, were not included. This conservatism makes PGV suitable for safety-critical applications, where slightly higher estimates of fragility provide an added margin of safety.

The proposed methodology’s adaptability is one of its key strengths. By allowing practitioners to tailor functionality values and adjust the weights of performance metrics, the framework bridges the gap between theoretical research and practical engineering needs. This flexibility enables better resource allocation and control over parameters in fragility analyses, expanding the usability of performance-based earthquake engineering frameworks within the dam industry. Ultimately, this approach equips engineers with a practical tool to balance accuracy and resource availability, enhancing the robustness of fragility assessments and supporting more informed decision-making for dam safety evaluations.

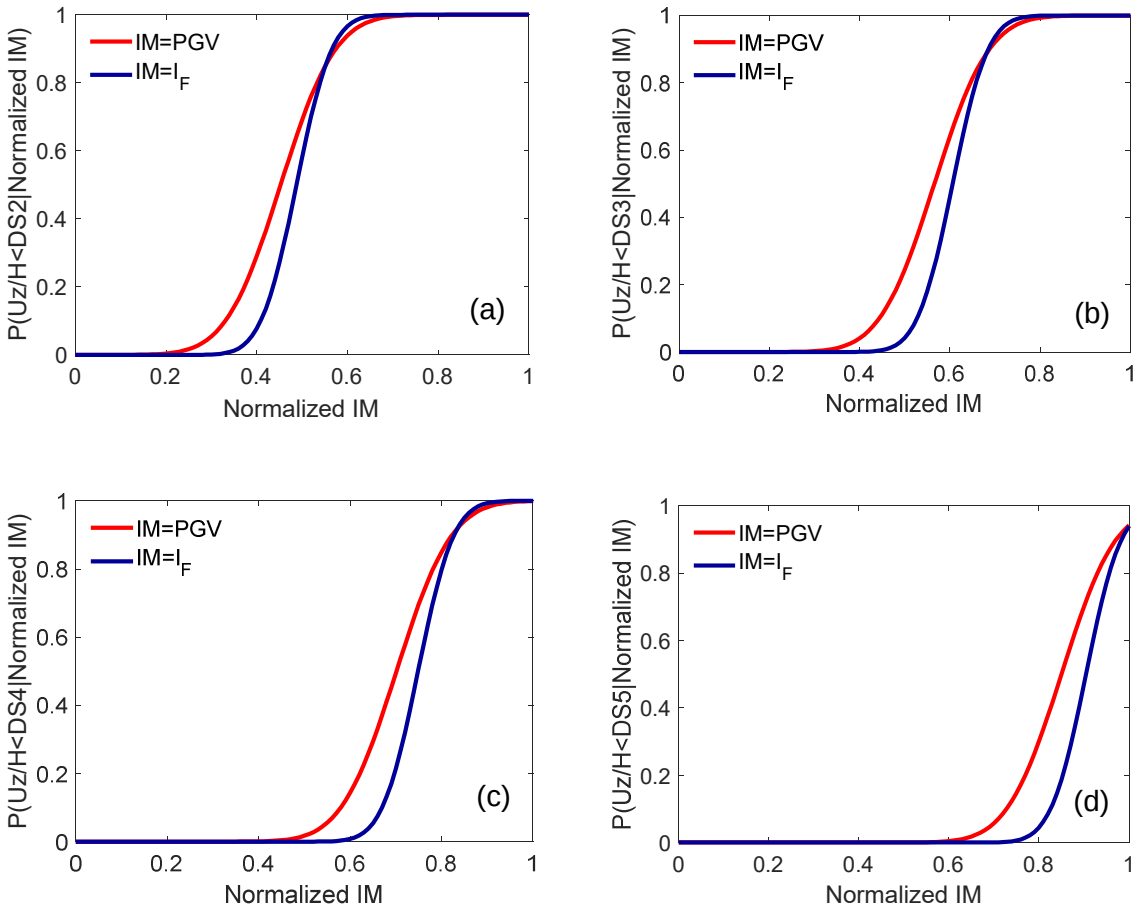

Fig. 9 – Fragility curves conditioned on normalized IMs: (a) moderate, (b) major, (c) severe and (d) collapse damage states.

REFERENCES

[1] Intergovernmental Panel on Climate Change, “Climate Change 2023: Synthesis Report. Contribution of Working Groups I, II and III to the Sixth Assessment Report of the Intergovernmental Panel on Climate Change,” Geneva, Switzerland, Jul. 2023. doi: 10.59327/IPCC/AR6-9789291691647.

[2] P. Concha Larrauri, U. Lall, and M. A. Hariri-Ardebili, “Needs for Portfolio Risk Assessment of Aging Dams in the United States,” J Water Resour Plan Manag, vol. 149, no. 3, Mar. 2023, doi: 10.1061/jwrmd5.wreng-5673.

[3] R. Segura, C. Bernier, R. Monteiro, and P. Paultre, “On the seismic fragility assessment of concrete gravity dams in eastern Canada,” Earthquake Spectra, vol. 55, no. 1, pp. 211–231, Feb. 2019, doi: 10.1193/012418EQS024M.

[4] M. Wieland, “Seismic Hazard and Seismic Design and Safety Aspects of Large Dam Projects,” in Perspectives on European Earthquake Engineering and Seismology, vol. 34, A. Ansal, Ed., Springer, 2014, ch. 20, pp. 627–650. doi: 10.1007/978-3-319-07118-3_20.

[5] S. Schmutz and O. Moog, “Dams: Ecological Impacts and Management,” in Riverine Ecosystem Management: Science for Governing Towards a Sustainable Future, S. Schmutz and J. Sendzimir, Eds., Cham: Springer International Publishing, 2018, pp. 111–127. doi: 10.1007/978-3-319-73250-3_6.

[6] A. Nardo, G. Biondi, O. Casablanca, G. Di Filippo, and E. Cascone, “Seismic intensity measures and predictive equations for the evaluation of earthquake—induced crest settlements of earth dams,” Earthquake Engineering and Structural Dynamics , vol. 53, no. 9, pp. 2680–2709, Jul. 2024, doi: 10.1002/eqe.4135.

[7] R. L. Segura, B. Miquel, P. Paultre, and J. E. Padgett, “Accounting for uncertainties in the safety assessment of concrete gravity dams: A probabilistic approach with sample optimization,” Water (Switzerland), vol. 13, no. 6, Mar. 2021, doi: 10.3390/w13060855.

[8] M. A. Hariri-Ardebili and S. Rezaeian, “Utilization of stochastic ground motion simulations for scenario-based performance assessment of geo-structures,” Reliab Eng Syst Saf, vol. 251, Nov. 2024, doi: 10.1016/j.ress.2024.110375.

[9] M. A. Hariri-Ardebili and V. E. Saouma, “Probabilistic seismic demand model and optimal intensity measure for concrete dams,” Structural Safety, vol. 59, pp. 67–85, 2016, doi: 10.1016/j.strusafe.2015.12.001.

[10] H. Hu and Y. Bao, “Seismic fragility functions for earthquake-induced landslide risk assessment using identified optimal earthquake intensity measures,” Catena (Amst), vol. 234, Jan. 2024, doi: 10.1016/j.catena.2023.107589.

[11] M. I. Khalid, J. Fei, and X. Chen, “Optimal earthquake intensity measures for seismic vulnerability assessment of concrete-faced rockfill dams,” in IOP Conference Series: Earth and Environmental Science, Institute of Physics, 2024. doi: 10.1088/1755-1315/1334/1/012034.

[12] A. R. Tidke and S. Adhikary, “Optimal intensity measure selection and probabilistic seismic demand models for dam-reservoir-layered foundation system,” Structures, vol. 37, pp. 318–337, Mar. 2022, doi: 10.1016/j.istruc.2022.01.005.

[13] J. He and E. M. Rathje, “Seismic capacity models for earth dams and their use in developing fragility curves,” Earthquake Spectra, 2024, doi: 10.1177/87552930241243067.

[14] H. Hu, ; Gang Gan, ; Linyong Cui, T. Xia, L. Wang, and X. Han, “Nonparametric Representation for Seismic Fragility Assessment of Earth Dams with Spatially Variable Soil Properties,” 2023, doi: 10.1061/IJGNAI.G.

[15] C. Jin and S. Chi, “Seismic Fragility Analysis of High Earth-Rockfill Dams considering the Number of Ground Motion Records,” Math Probl Eng, vol. 2019, 2019, doi: 10.1155/2019/6958643.

[16] T. Ahmed, M. N. A. Alel, M. A. A. Kadir, A. Rahim, and M. I. Shahrin, “Seismic fragility assessment of embankment: A displacement-based approach using dynamic finite element model analysis,” in IOP Conference Series: Earth and Environmental Science, Institute of Physics, 2024. doi: 10.1088/1755-1315/1369/1/012009.

[17] E. M. Rathje and J. He, “A Seismic Fragility Framework for Earth Dams,” in Lifelines 2022, Reston, VA: American Society of Civil Engineers, Nov. 2022, pp. 405–415. doi: 10.1061/9780784484432.036.

[18] G. Regina, P. Zimmaro, K. Ziotopoulou, and R. Cairo, “Evaluation of the optimal ground motion intensity measure in the prediction of the seismic vulnerability of earth dams,” Earthquake Spectra, vol. 39, no. 4, pp. 2352–2378, Nov. 2023, doi: 10.1177/87552930231170894.

[19] R. D. Bertero and V. V. Bertero, “Performance-based seismic engineering: The need for a reliable conceptual comprehensive approach,” Earthq Eng Struct Dyn, vol. 31, no. 3, pp. 627–652, 2002, doi: 10.1002/eqe.146.

[20] J. D. Bray and T. Travasarou, “Simplified Procedure for Estimating Earthquake-Induced Deviatoric Slope Displacements,” Journal of Geotechnical and Geoenvironmental Engineering, vol. 133, no. 4, pp. 381–392, 2007, doi: 10.1061/ASCE1090-02412007133:4381.

[21] National Institute of Geophysics and Volcanology (Italy), “Engineering Strong-Motion Database,” https://esm-db.eu/#/home.

[22] S. Akkar et al., “Reference database for seismic ground-motion in Europe (RESORCE),” Bulletin of Earthquake Engineering, vol. 12, no. 1, pp. 311–339, Feb. 2014, doi: 10.1007/s10518-013-9506-8.

[23] National Research Institute for Earth Science and Disaster Resilience (NIED), “NIED K-NET, KiK-net Database.”

[24] European Committee for Standardzation, “Eurocode 8: Design of structures for earthquake resistance,” 2004.

[25] C. A. Cornell, F. Jalayer, R. O. Hamburger, and D. Foutch, “Probabilistic Basis for 2000 SAC Federal Emergency Management Agency Steel Moment Frame Guidelines,” Journal of Structural Engineering, pp. 526–533, 2002.

[26] W. Che, P. Chang, and W. Wang, “Optimal Intensity Measures for Probabilistic Seismic Stability Assessment of Large Open-Pit Mine Slopes under Different Mining Depths,” Shock and Vibration, vol. 2023, 2023, doi: 10.1155/2023/8851565.

[27] S. Pells and R. Fell, “Damage and Cracking of Embankment Dams by Earthquake and the Implications for Internal Erosion and Piping,” in 21st Congress on Large Dams, Montreal, Jun. 2003, pp. 259–274. [Online]. Available: https://www.researchgate.net/publication/290248185

[28] G. Veylon et al., “A simplified method for estimating Newmark displacements of mountain reservoirs,” Soil Dynamics and Earthquake Engineering, vol. 100, pp. 518–528, Sep. 2017, doi: 10.1016/j.soildyn.2017.07.003.

[29] E. M. Rathje, N. A. Abrahamson, and J. D. Bray, “Simplified Frequency Content Estimates of Earthquake Ground Motions,” Journal of Geotechnical and Geoenvironmental Engineering, vol. 124, no. 2, pp. 150–59, Feb. 1998.

[30] M. R. Zolfaghari and M. Forghani, “Spatial correlation assessment of multiple earthquake intensity measures using physics-based simulated ground motions,” Sci Rep, vol. 14, no. 1, Dec. 2024, doi: 10.1038/s41598-024-72241-1.

Fifth International Dam World Conference
PORTUGAL • LISBON • LNEC • APRIL 13-17, 2025
dam world 2025

GEOSTATISTICAL SPATIAL PREDICTION MODELS OF RESURGENCE AND CANALICULUS IN THE DIKES SURROUNDING THE INTERMEDIATE RESERVOIR OF THE BELO MONTE HYDROELECTRIC PLANT

Edivaldo J. SILVA Junior[1] Itaipu Parquetec	**Débora de O. Fernandes**[2] Itaipu Parquetec	**Adriana E. Limberger**[3] Itaipu Parquetec	**Rodrigo de L. Rodrigues**[4] Itaipu Parquetec
Luan Reginato[5] Itaipu Parquetec	**Candy G. D. Concepción**[6] UNILA	**Erlene D. Krajewski** [7] Norte Energia S.A.	**Marcelo B. Boaventura**[8] Norte Energia S.A.

Leandro C. Lima[9]
Norte Energia S.A.

ABSTRACT

The Belo Monte Hydroelectric Complex, located on the Xingu River bend in the city of Altamira-PA, Brazil, includes the Pimental hydropower plant, constructed in the river's natural bed, and Belo Monte, whose water comes from an intermediate reservoir surrounded by over 30 containment dikes. These topographic closure structures were built mostly on migmatite residual soils. During the investigation phase, areas with concentrations of tubular cavities, known as canaliculus were found, with dimensions varying from millimetric to centimetric. During construction, geotechnical impermeabilization techniques were applied to mitigate risks associated with these canaliculi in the foundation. Since 2016, the operational period of the hydropower plant, the dam safety team has been monitoring and controlling the resurgence and the evolution of canaliculus downstream of the intermediate reservoir dikes. The interest to understand these phenomena gave rise to the ANEEL Research and Development Project 07427-0322/2022, financed by Norte Energia S.A. company, which encompasses field investigation, laboratory testing, and the development of resurgence and canaliculus spatial prediction models using geostatistical methods. During the initial modeling tests of the phenomena, positive results were obtained, validating the hypothesis created by the dam safety team, which relates the resurgence location to the outcropping contact between two soil layers, referred to in this work as surface soil and young residual soil. The spatial prediction model was developed using the ordinary kriging method and overlaying the digital terrain model.

Keywords: dam safety, geoprocessing, kriging, spatial prediction, resurgence, canaliculus

[1]edivaldo.junior@itaipuparquetec.org.br, Brazil
[2]deboraof@itaipuparquetec.org.br, Brazil
[3]adriana.limberger@itaipuparquetec.org.br, Brazil
[4]rodrigo.lr@itaipuparquetec.org.br, Brazil
[5]luan.reginato@itaipuparquetec.org.br, Brazil
[6]candy.dc@itaipuparquetec.org.br, Brazil
[7]erlene.krajewski@norteenergiasa.com.b, Brazil
[8]marcelo.boaventura@norteenergiasa.com.br, Brazil
[9]leandrolima@norteenergiasa.com.br, Brazil

1. INTRODUCTION

The Belo Monte Hydroelectric Complex is composed of 36 dams, two powerhouses, and a spillway. The Complex's structures were built on different types foundations, such as migmatite residual soils and rock masses. During the excavation of the first exploration, areas with high concentrations of tubular cavities, known as canaliculus, were found, with dimensions ranging from millimetric to decametric [1]. This phenomenon is relatively common in soils of northern of Brazil, and has been identified during the construction of the Vereda Grande, Tucuruí, Samuel, Balbina, and Belo Monte dams [2]. International studies also report this phenomenon in soils from the African and Asian continents. Some examples are the Saddle Dam (in Laos) and Comoe Dam (Burkina Faso), that failure and had interventions to control seepage, respectively. Hypotheses about canaliculus origin have been researched, however, the genesis of the canaliculus on the soil foundations has yet to be defined [3].

1.1. History of Canaliculus Presence in Dam Constructions

The tubular cavities that occur in residual soils of the Amazon region are generically referred as canaliculi [4]. The presence of this phenomenon in dam foundation can cause significant consequences, such as the development of preferential flow paths to downstream areas through the foundation, increasing the probability of transport fines and regressive erosion process [5].

The first occurrence of canaliculi in foundation of dams in Brazil was observed around 1957, during the construction of the Vereda Grande Dam in the Piauí state [6]. In 1974, at the Tucuruí Dam, occurrences of these tubular cavities were reported in weathered metabasite and diabase soils, with degrees of laterization.

Then, in 1982, at the Samuel Hydroelectric Plant in Rondônia state, canaliculi were found in recent alluvial deposits and residual soils. In the alluvium, the canaliculus showed subvertical and sub horizontal orientation, with diameters of 1 to 2 cm and a maximum depth of up to 4 m [7]. In the residual and colluvial soils, the canaliculus diameters ranging from 0,2 to 30 cm, with shapes varying from irregular, anastomosed, to circular. The cavities were empty or partially filled with pulverulent or organic material [8].

In 1985, during the construction of the Balbina Dam in low-density saprolitic soil in Amazonas, a high incidence of canaliculus was found, with typical diameters from a few millimeters to 10 cm in exceptional cases.

Finally, during the construction of Belo Monte Hydroelectric Plant in the state of Pará in 2015, the presence of canaliculus was reported in migmatite residual soils. These canaliculi

appeared in high concentrations, with centimetrics diameters (Figure 1), with subvertical shapes and depth greater than 6 meters, with lateral interconnections, promoting high permeability in the foundation [1].

Fig. 1 –Exploratory excavation for construction of dikes

1.2. The Studies About Canaliculus Genesis

About the origin, several hypotheses have been discussed, which are: intrinsic characteristic of the material, biological action and vegetal action.

The first hypothesis, related to the material's characteristics, attributes the formation of canaliculi to pedo-karstic erosion, a physical erosive process that occurred due dissolution of small rock bodies on the intersection of minor joints, forming the initial cavities. Another hypothesis considers the origin of the cavities as a consequence of intense soil laterization. The leaching of soluble soil elements would facilitate water infiltration [8].

The hypothesis associated with a biological origin considers the formation of canaliculi through termite activity, which involves complex biological systems containing species with various feeding and nesting behaviors. These animals, along with earthworms, are the main invertebrates responsible for the ingestion and manipulation of organic and mineral matter [9]. In Balbina Dam, the hypothesis that termites contributed to canaliculi formation through root ingestion was widely accepted. Microscopic examinations of undisturbed samples from that dam, as well as from Samuel and Tucuruí, revealed traces of organic remains from these animals [10].

Another hypothesis considers the life cycle of vegetation. Tree roots undergo chemical and structural changes over time. When a tree dies, the cells in its roots begin to decompose through the process of autolysis. At the same time, bacteria and fungi break down the components of plant cells, creating voids in the soil [11].

1.3. Impacts Mitigation of Canaliculi at Belo Monte and Empirical analyses

After to discovery the canaliculi in various dams in the Amazon region, some treatment alternatives have been investigated. In the Belo Monte complex, treatment was carried out in exploratory excavations, where canaliculi were found [1]. To enhance the exposure of canaliculi on the walls and bottom, compressed air blasting was performed over the entire area. Canaliculi with diameters greater than 20 mm were waterproofed by injecting a cement grout, as shown in Figure 2 [12].

Fig. 2 –Treatments carried out in excavations with canaliculi.

After construction and filling of the reservoir, some instruments installed in the foundations of the dikes and dams had a short time response. Additionally, resurgence and evolution of canaliculi were observed, particularly downstream of some dikes. The solution initially adopted by the designers was the implementation of an inverted filter [1]. Currently, when necessary, the solution involves the construction of trenches.

During the excavation of trenches to drain resurgence in various dikes at different times, field observation revealed a pattern in the water flow associated to region lithology. In many cases, the resurgence areas coincided with a reduction in the depth of contact between the surface

soil and the young residual soil (YRS), like an outcrop contact region. This information was verified during the development of the geological model for the foundation of Dike 11 to conduct flow simulations and analyze the efficiency of the constructed trenches. This observation was crucial in developing the spatial prediction methodology for resurgence and canaliculi evolution, using the available data for modelling and validation of the results.

2. METHODOLOGY FOR SPATIAL PREDICTION OF RESURGENCE AND CANALICULI AT THE BELO MONTE HYDROELECTRIC PLANT

Some of the more than 30 dikes that surround the intermediate reservoir, despite having undergone canaliculi treatment in their foundations, it's presented infiltration and evolution of canaliculi downstream after filling the reservoir and during the operation period. Figure 3 shows the location of the dikes around the intermediate reservoir.

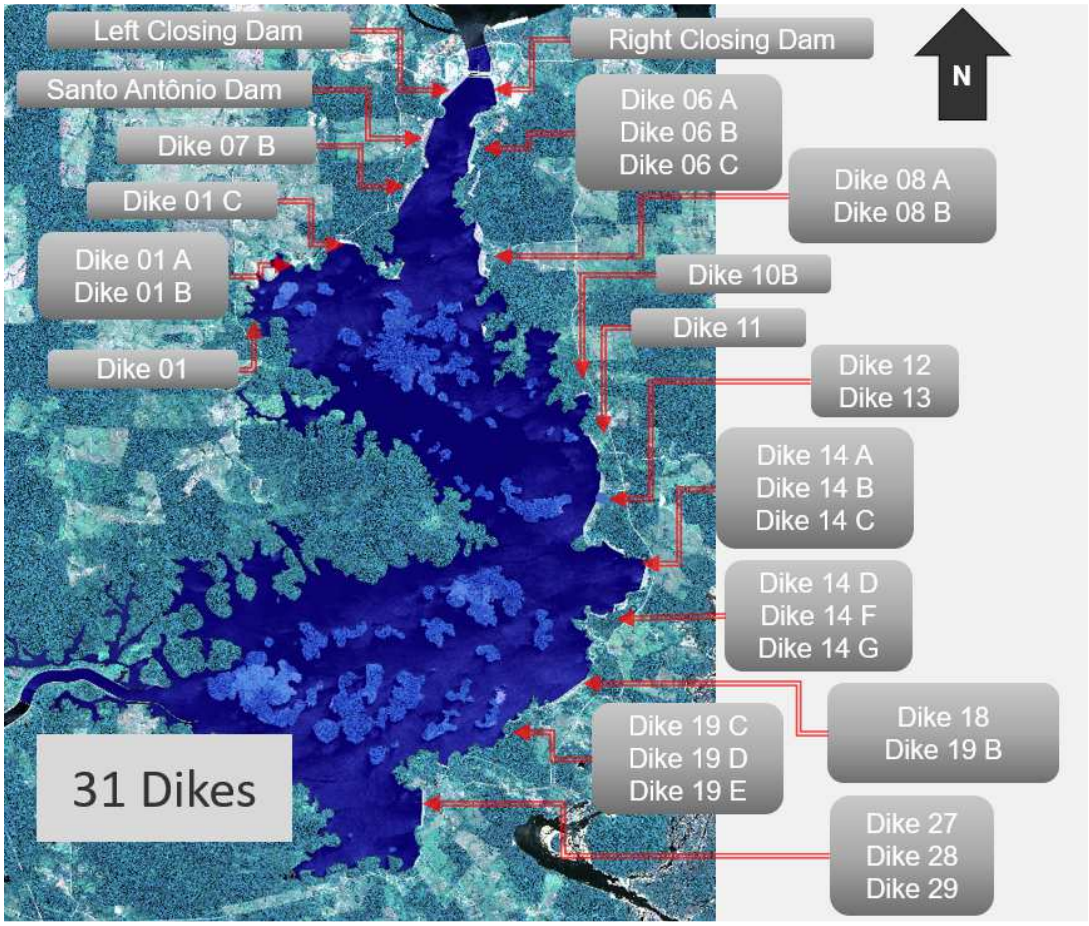

Fig. 3 – Location of dikes around the intermediate reservoir

To determine patterns related to the resurgence and canaliculi phenomena and the distribution of physical properties and lithological characteristics of the foundation, the borehole data from investigation period was compiled to create foundation soil models.

Due to the high variability of surface soil types, they were standardized as Superficial Soil (SS), followed by Young Residual Soil of Migmatite (YRS), as illustrated in Figure 4.

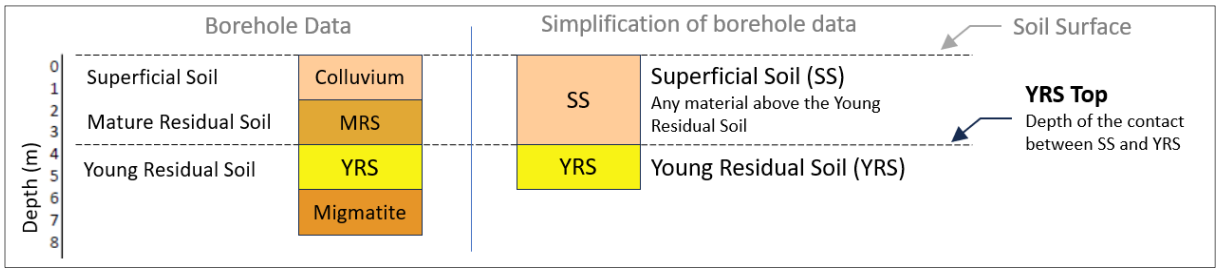

Fig. 4 – Standardization of the lithological profile from borehole data

Simultaneously, inspection data were obtained from 2020 to 2023, detailing the location and date where resurgences and canaliculi were detected downstream of these dikes, was compiled to validate the spatial prediction model.

The sampling data was used to develop the digital elevation model of the contact between the surface soil and the young residual soil (YRS) using the ordinary Kriging method (Figure 5.b).

To use the Ordinary Kriging methods, the Smartmap Plugin was used in the QGIS Software. Geostatistical interpolation by kriging is a regression method that allows for the interpolation of soil data (property, characteristic, concentration, etc.), using spatial correlation between boreholes, through the adjustment of an isotropic theoretical variogram model [13].

In addition, considering the empirical analysis (areas where the contact of YRS is closer to the surface, there is a higher incidence of resurgence and canaliculi), another data used in this work to complete the prediction methodology was the Digital Elevation Model (Figure 5.a).

In this way, combining the two digital models from Equation 1, contact and topographic surface, was possible to predict the outcrop regions (Figure 5.c)., and validate the perceptions about correlation between resurgences, canaliculi and YRS outcrop location (Figure 5.d).

$$\begin{aligned} &\boldsymbol{IF}\ (Elevation_{YRS\ Model\ x,y} \leq Elevation_{DEM\ x,y}) \\ &\quad Elevation_{MDC\ SRJ\ x,y} \\ &\boldsymbol{Otherwise}, location\ (x,y) = 0\ or\ NULL \end{aligned} \tag{1}$$

Where x and y are the UTM North and East georeferenced coordinates of the models, $Elevation_{YRS\ Model\ x,y}$ is the elevation of the contact of the young residual soil, and $Elevation_{DEM\ x,y}$is the elevation of the topographic surface of the digital elevation model.

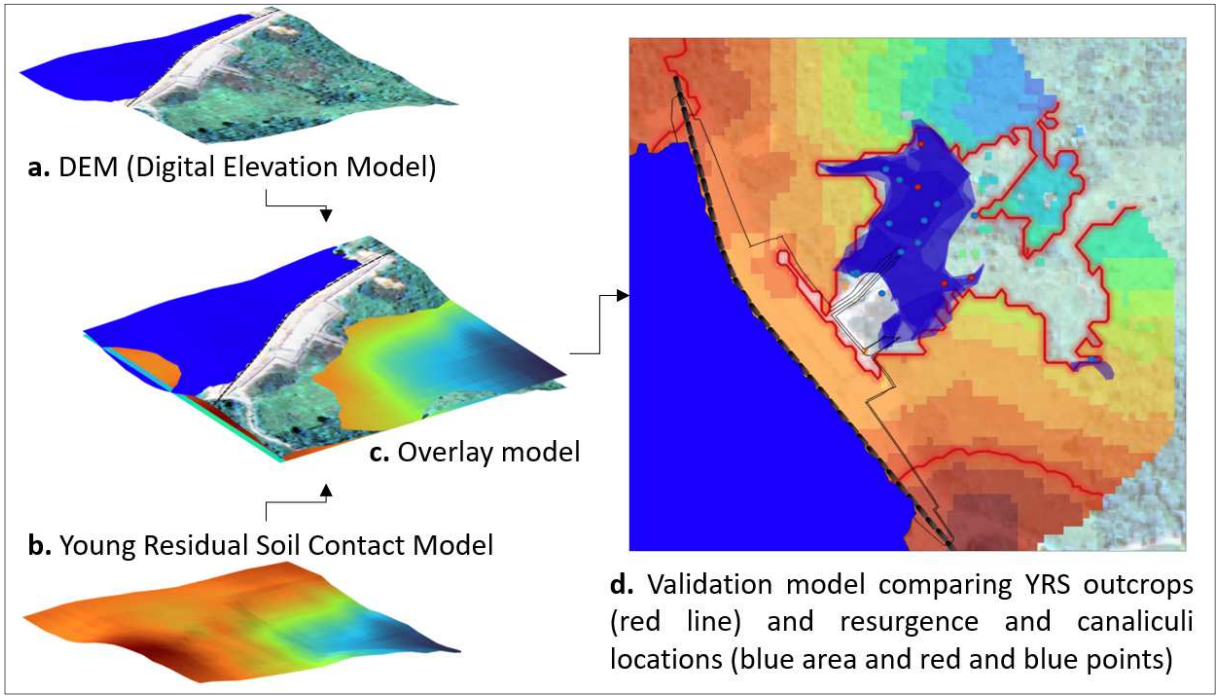

Fig. 5 – Models Overlay illustrations

The same procedure was applied to all dikes with resurgence and canaliculi location detected in the same borehole area, validating the methodology presented in Figure 6. In cases where inspection data are far from boreholes data, a new approach will be studied.

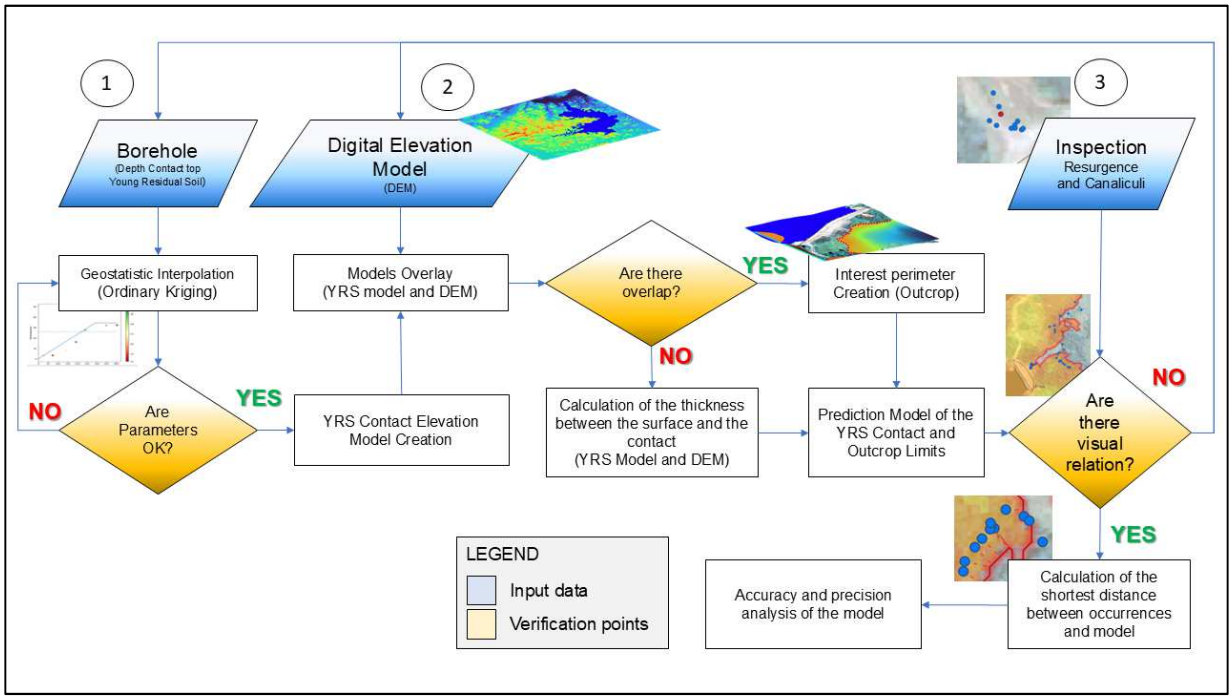

Fig. 6 – Flowchart of the methodology developed for predicting resurgence and canaliculi based on the prediction of the SRJ contact outcrop

As presented in Figure 6, the methodology involves three types of input data: borehole data, digital elevation model (DEM), and the inspection data (resurgence and canaliculi location). Borehole data is used to create the digital contact model of the young residual soil (YRS Model)

through interpolation using the geostatistical method of Ordinary Kriging (OK). The next step is to apply geoprocessing methods to combine YRS Model and DEM to identify the contact outcrop areas and determine the boundary of the model (YRS Model boundary). Finally, inspection data are used to validate the prediction of resurgence and canaliculi through the prediction model of YRS contact outcrop. To quantitatively assess the model's effectiveness, a Python algorithm was developed to calculate automatically the shortest distance between resurgence and canaliculi points and the vectorized YRS Model boundary line. Lastly, the average shortest distance for each dike and the standard deviation are calculated.

3. STUDY CASE AND RESULTS

Considering the spatial distribution of the boreholes and inspection data, the ordinary kriging method was applied to three dikes to obtain the contact outcrop model:

- Santo Antônio Dam (BVSA);
- Dike 11 and;
- Dike 13

Figure 7 shows the spatial distributions of the boreholes and occurrences in each dike (not to scale).

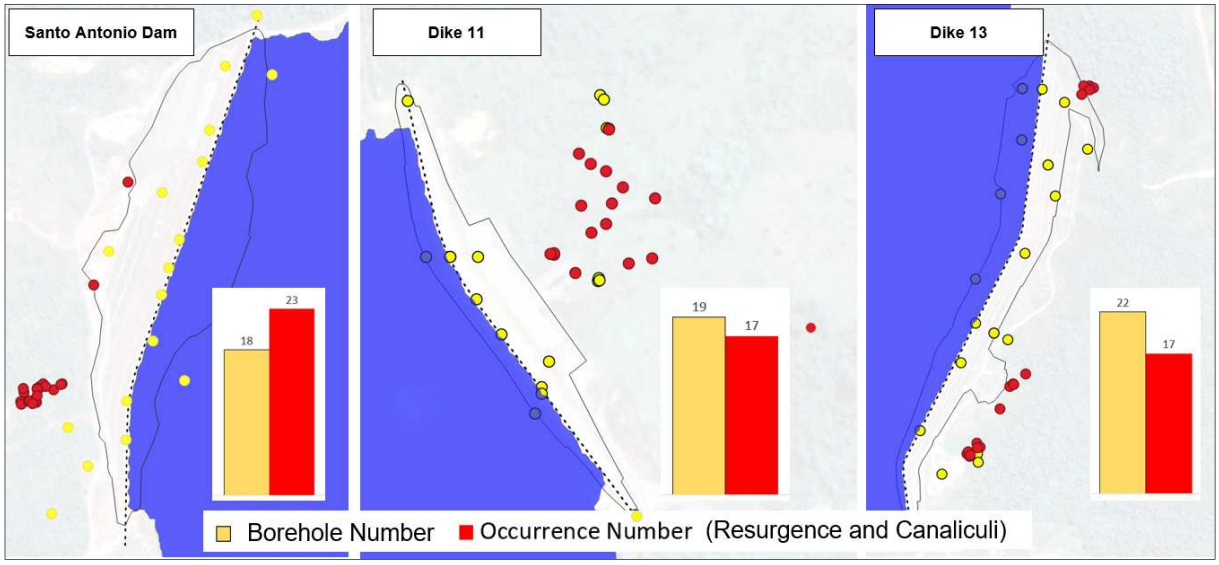

Fig. 7 – Spatial distribution of the samples and occurrences

Table 1 presents the location of the boreholes (column 2), the fitted variogram used in the modeling (column 3), and the digital model of the young residual soil (column 4).

Table 1 – Borehole Locations, Variogram and Contact Digital Model

Dike	Borehole and Moran Index	Variogram (OK)	YRS Contac Digital Model
BVSA	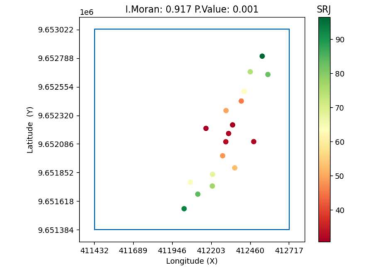	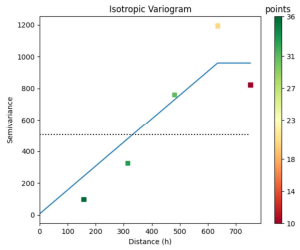	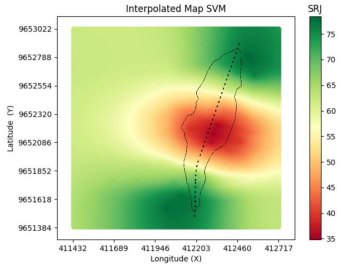
11	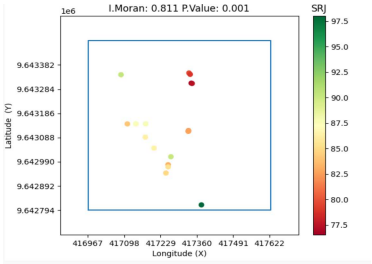	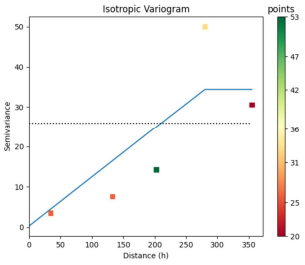	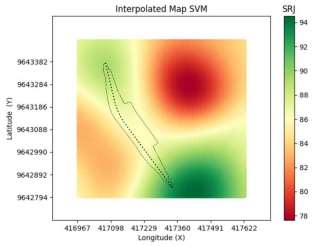
13	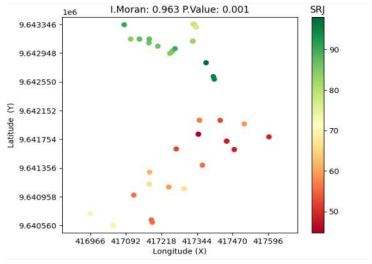	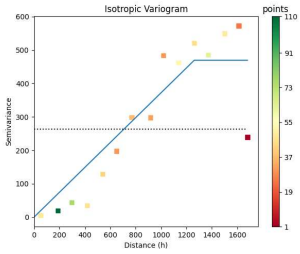	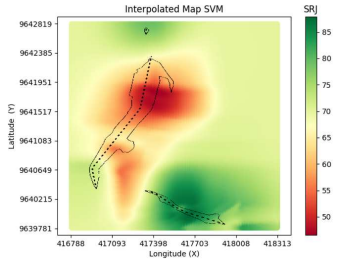

After the development of the YRS contact digital elevation models (column 4 of Table 1), the overlay processing between the contact models and the digital elevation model (DEM) was performed. The DEM was obtained through laser scanning in the intermediate reservoir area during the site investigation phase, referred to in this work as the Lidar DEM.

Following the methodology presented in Figure 6, georeferenced vectors were generated representing the boundary of the YRS contact model, indicating an outcrop area of the contact. By overlaying the YRS contact Boundary with the inspection data (location of resurgence and canaliculi), a concordance in the spatial distribution of both phenomena (YRS contact outcrop and the location of occurrences) was observed, as illustrated in Figures 9 to 11.

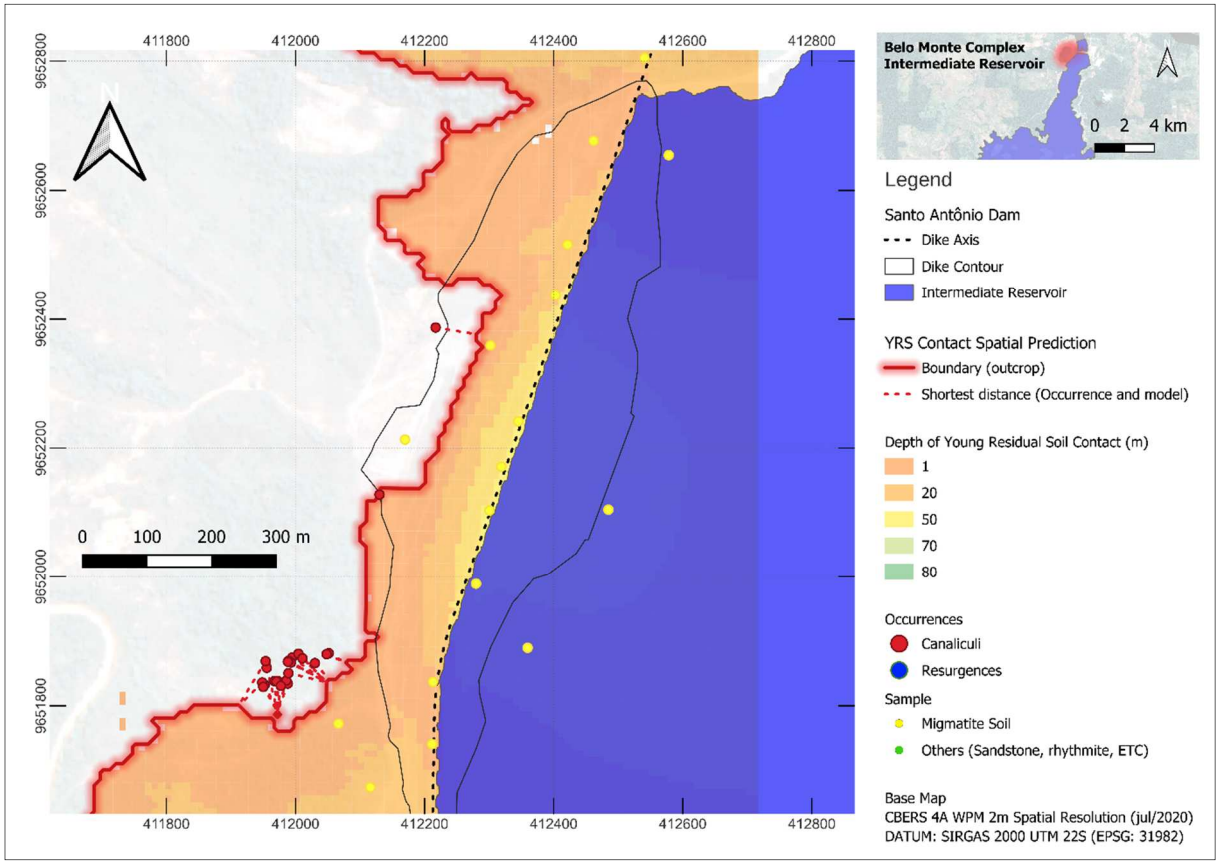

Fig. 9 – Santo Antonio Dam (Spatial Prediction Model)

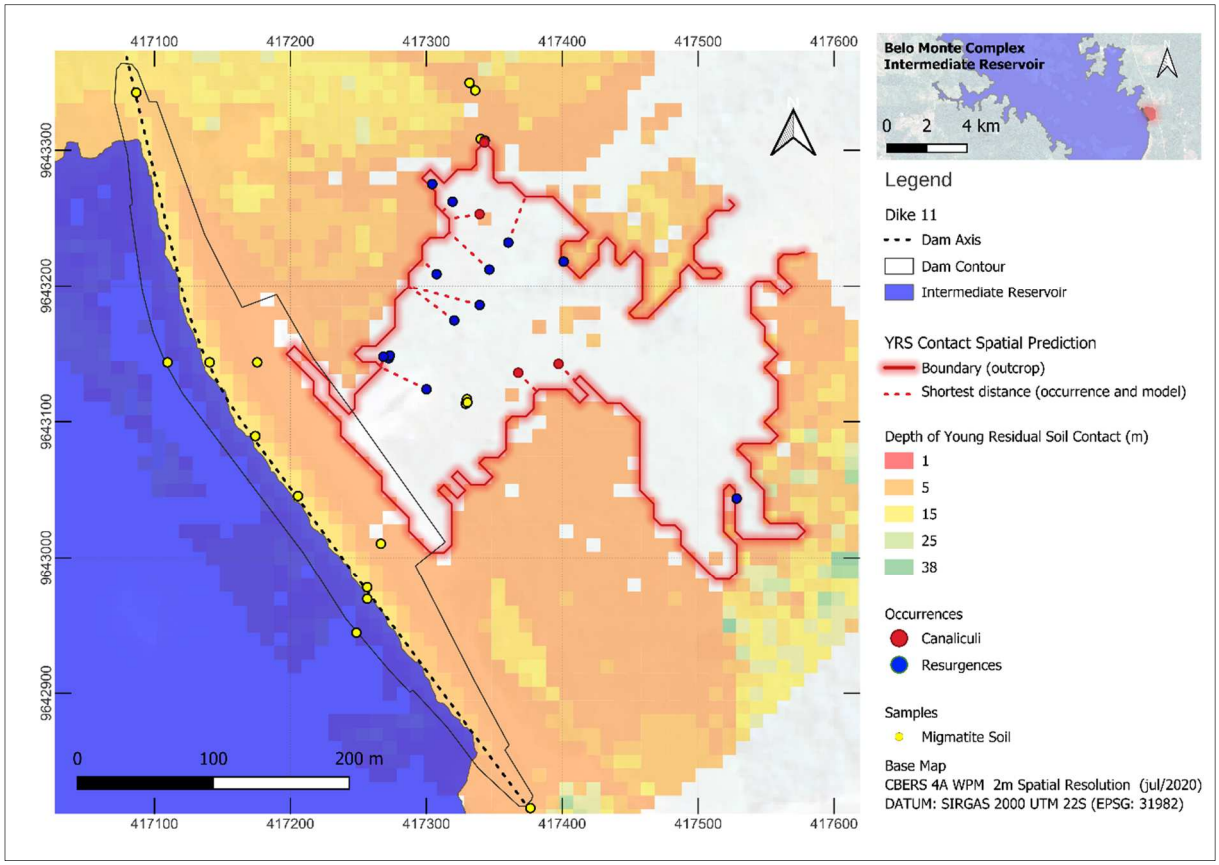

Fig. 10 – Dike 11 (Spatial Prediction Model)

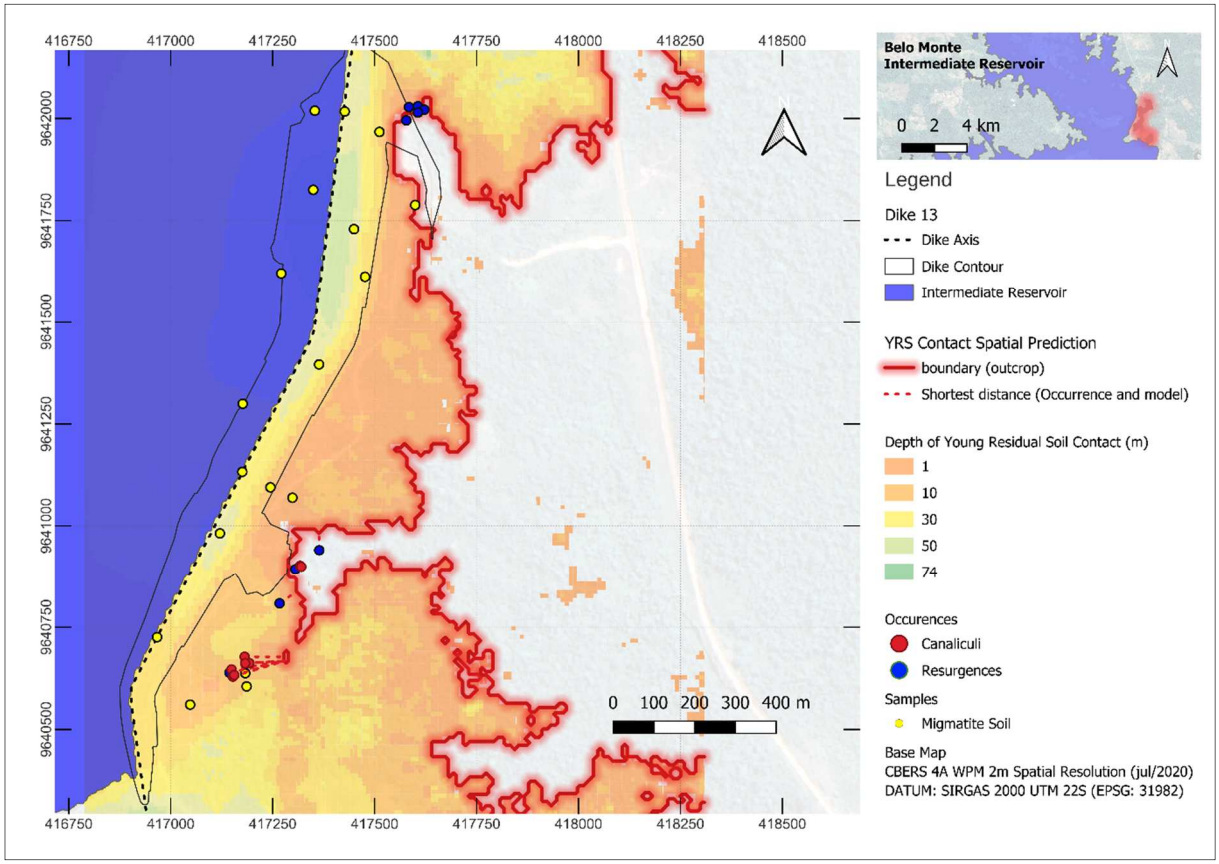

Fig. 11 – Dike 13 (Spatial Prediction Model)

To quantify how close the YRS Boundary line is to the resurgence and canaliculi points, a Python algorithm was developed to calculate the shortest distance between the points and the line. Subsequently, the averages of these distances were calculated for each dike, referred to as the Mean Shortest Distance (MSD), and their respective standard deviations (Table 2).

Table 2 – Statistical indicators of the Dikes Spatial Prediction

DIKE	Mean Shortest Distance (MSD) [m]	Standard Deviations [m]
BVSA	50,63	16,94
11	19,04	16,91
13	59,93	50,83

4. CONCLUSIONS

One of the objectives in the initial proposal of the project was to use mathematical methods to understand the spatial distribution and predict the behavior of resurgence and canaliculi development in the downstream areas of the dikes of the intermediate reservoir of the Belo Monte hydroelectric complex. The concentration of the boreholes along the dam axis and the lack data downstream made the modeling process difficult. Thus, the development of the solution required a better geological and geotechnical understanding of the resurgence and canaliculi phenomena. Analyzing the borehole data, the lithological distribution was the only

information available in all boreholes. After discussions with the Belo Monte dam safety team, it was possible to obtain empirical information about the lithology in areas where resurgence and canaliculi were detected. This is because, upon detecting the phenomenon, the team intervenes by excavating trenches to drain the water. Then, they fill the trenches with drainage material to prevent the transport of the fine particles. The team's perception, after multiple interventions over the years, is that the outcrop of the young residual migmatite soil (YRS) contact is involved. As a result, a modeling methodology was established, validated with inspection data from most of the dikes. The Ordinary Kriging geostatistical interpolation method was used to create soils contact model. To validate the field insights, geoprocessing was conducted between the topographic digital elevation model (Lidar) and the YRS contact digital model. In areas where the elevation (altimetry) of both models intersected, it was considered a potential outcrop region of the contact, creating the resulting model, the YRS Contact Boundary. This model showed a strong similarity in the spatial distribution of resurgence and canaliculi found during inspections in most dikes, which validated the empirical perception of Belo Monte and created a spatial prediction model that can help and optimize inspection work, reducing the time spent searching for new resurgence and canaliculi. The statistical indicators, mean shortest distance and standard deviation, allow to create an inspection corridor based on the YRS Boundary model line, with the width defined by the smallest average value. The standard deviation, on the other hand, provides an idea of the spatial distribution similarity between the model and the real phenomenon.

REFERENCES

[1] Bandeira, O.M.; Silveira. J. F.; Leite, D. T. Segurança de Barragens da UHE Belo Monte - Autores: Oscar Machado Bandeira. Revista Brasileira de Engenharia de Barragens, Ano IV n° 04, maio de 2017.

[2] Limberger, A. E.; Boaventura, M., Marcelo B., Rodrigues, R. L.; Costantin Filho, M; Fernandes, D. O.; Krajewski, E. D.; Lima, L. C. Ocorrência de Canalículos em Fundações de Barragens da Região Amazônica - Estado Da Arte. XXXIV Seminário Nacional de Grandes Barragens. Comitê Brasileiro de Barragens, 2024.

[3] Chraibi, A.F., Schleiss, A.J., Tournier, JP. (2020). Failure of Saddle Dam, Xe-Pian Xe-Namnoy Project: Executive Summary. In: Zhang, JM., Zhang, L., Wang, R. (eds) Dam Breach Modelling and Risk Disposal. ICED 2020. Springer Series in Geomechanics and Geoengineering. Springer, Cham. https://doi.org/10.1007/978-3-030-46351-9_2.

[4] Sathler, G.; Mesquita, J.B. Canalículos. Sugestões de classificação e metodologia de investigações de campo. Anais. Congr. Bras. Geol. Eng., ABGE, v.3, 4, p.407-414, Belo Horizonte.

[5] Sandroni, S. S.; Guidicini, G. Barragens de terra e enroncamento. São Paulo: Oficina de Textos, 2021.

[6] Barradas, S. S. Iniciação e Propagação de Fraturas Induzidas por injeções em solos argilosos com canalículos – Aplicação ao tratamento do solo residual da fundação da barragem de terra da UHE Balbina. Tese submetida ao programa de pós-graduação de engenharia da Universidade Federal do Rio de Janeiro (UFRJ), Rio de Janeiro RJ, março de 1985.

[7] Buosi, M. A.; Cadmam, J. D. Sobre a ocorrência de cavidades tubulares em solos lateríticos na região amazônica. Associação Brasileira de Geologia e Engenharia Ambiental (ABGE), 4, Belo Horizonte, 1984, São Paulo, ABGE, 1984. v. 3, p. 10-24.

[8] Jury, W. J.; Paraguassú, A. B. Considerações Sobre A Ocorrência de Canalículos Em Locais de Barragem Na Região Amazônica. Anais do 6. Congresso Brasileiro de Geologia de Engenharia E Ix Congresso de Mecânica dos Solos E Engenharia de Fundações, 1990. V. 1. P. 511-517.

[9] Bignell, D E; Eggleton, P. Termites in the ecosystem. Termites: Evolution, Sociality, Symbioses, Ecology, p. 363–387, 2000.

[10] Andrade Gutierrez (1987) – “Técnica usada na injeção reduz a permeabilidade do solo residual”. Revista da CONSTRUTORA ANDRADE GUTIERREZ, Ano 7 – nº 15 – Setembro/Dezembro de 1987, p. 19-22.

[11] Saha, S. et al. Fine root decomposition in forest ecosystems: an ecological perspective. Frontiers in Plant Science, v. 14, 27 out. 2023.

[12] Belo Monte – Consórcio Projetista (2014) – Instrução de trabalho. RI3-D011-GER-CGT-IT-0001-00.

[13] Pereira, G.W.; Valente, D.S.M.; Queiroz, D.M.D.; Coelho, A.L.D.F.; Costa, M.M.; Grift, T. Smart-Map: An Open-Source QGIS Plugin for Digital Mapping Using Machine Learning Techniques and Ordinary Kriging.Agronomy 2022, 12, 1350.

Fifth International Dam World Conference
PORTUGAL • LISBON • LNEC • APRIL 13-17, 2025
dam world 2025

THE EFFECTS OF HYPOTHETICAL OCHRE CLOGGING OF DRAINAGE SYSTEM ON SLOPE STABILITY OF THE ITUMBIARA DAM, BRAZIL

Marcos B. Mendonça[1]
Universidade Federal do Rio de Janeiro

Maria C. R. Cavalcanti
Universidade Federal do Rio de Janeiro

Gabriela W. Machado
Universidade Federal do Rio de Janeiro

ABSTRACT

Clogging reduces the pore spaces available for the water flow within a material and, consequently, its permeability. The ochre formation is one of the causes of clogging and involves physical, chemical, and microbiological processes. This type of clogging was observed in the internal drainage systems of several dams worldwide, including several cases in Brazil. In earth dams, drainage systems aim to control water seepage, reducing the magnitude of pore pressures and hydraulic gradients that could compromise the stability of the structure's downstream slope, preventing piping, among other problems. This work presents the simulation of ochre clogging hypothetical scenarios in the blanket drain and vertical filter of the Itumbiara earth dam located in the Parnaiba River, in Minas Gerais State, Brazil. It was built between 1974 and 1981 and has a total length of approximately 6,800 m and a maximum height of 110 m. Nine scenarios of clogging of the dam's drainage system (blanket and vertical filter) were represented in the analysis, varying the clogged region and the intensity of permeability reduction. The effects on water flow in the dam massif and its consequences on the downstream slope stability were evaluated using the RocScience software (Slide2), considering the different scenarios of progressive clogging, with reductions of 10 to 200 times in the permeability. The paper presents the variation of piezometric levels in the earth massif and their effects on the downstream slope stability as the severity of the clogging scenario increases. A slight effect of clogging on the position of the phreatic line and the downstream slope stability is observed until the scenario in which clogging reaches 40% of the drainage blanket length. When it reaches 70% of the blanket length, there is a sharp drop in the safety factor, and a failure situation is verified at 80%. The simulation results contribute to the dam's safety management and decision-making by providing the expected piezometric values if significant clogging occurs in its drainage system.

Keywords: Ochre, Clogging, Seepage, Slope Stability, Numerical Modelling

[1]mbm@poli.ufrj.br, Brazil

1. INTRODUCTION

Dams bring many benefits to the population, but at the same time, they can represent a threat to society due to the potential consequences of a dam failure. Therefore, the design and monitoring of a dam deserves special attention to guarantee a low level of hazard throughout its useful life. One of the requirements of a dam project is the design of the internal drainage system, which aims to control the water seepage in the embankment and foundations to keep pore pressures below a certain level and prevent piping.

It is well known that one of the hazardous phenomena that can occur during the useful life of a dam is clogging, which means the reduction in drain void spaces available for water seepage provoked by the accumulation of some materials, thus resulting in clogging.

One of the types of clogging is caused by the accumulation of a rust-coloured, gelatinous material composed of microorganisms, secreted polymers, and iron oxyhydroxides called ochre [1]. The growth of microorganisms, the secretion of polymeric substances, and the precipitation of iron minerals lead to the formation of a biofilm that coats the solid surfaces of drainage systems, reducing the voids available for water seepage. As a result, clogging occurs, compromising the operating efficiency of the drainage system [1], [2], [3], [4], [5], [6]. Koerner and Koerner [7] cited ochre as the primary threat to the proper performance of filters and drainage systems.

The main route to the precipitation of iron oxides in nature occurs when dissolved Fe(II) from anoxic environments finds conditions favorable for oxidation to Fe(III), leading to precipitation. The oxidation state of iron in the environment depends on several factors, including dissolved oxygen (DO), pH, chemicals such as hydrogen sulfide, and microorganisms. When there is a near-neutral to alkaline pH and saturated DO, dissolved Fe(II) is quickly oxidized to Fe(III), which readily precipitates as Fe(III) oxyhydroxides. The DO is the main parameter determining the fate of iron. Because O2 dissolves poorly in water, its concentration depends on both sources and sinks. The main DO sources for aquatic environments and wet soils are the atmosphere and photosynthesis. The surface layer of water is usually saturated with O2 due to transference from the air. Thus, ochre formation is more intense at the air-water interface due to the greater availability of oxygen, as demonstrated by Mendonça et al. [5] and Correia et al. [8]. As expected, any air-water interface in the dam's internal drainage system components (vertical filter, drainage blanket, relief well, trench drain, and toe drain) are susceptible to ochre clogging phenomena.

Many cases related to ochre clogging in earth dams in Brazil and other countries around the world were reported in the literature [9], [10], [11], [12], [13], [14], [15], [16], [17], [18], [19], [20].

Despite the severity and high incidence of the problem, there are several gaps in the understanding of the phenomenon in dams, and scientific studies are still scarce.

To contribute to the understanding of the possible effects of ochre clogging in a real dam, this paper presents the development of numerical simulations of different hypothetical clogging scenarios in the Itumbiara earth dam in Brazil.

2. METHOD

2.1. Itumbiara Dam

Itumbiara dam is located in the Parnaiba River, in Minas Gerais State, Brazil. This is a homogeneous earth dam built between 1974 and 1981. It is the ninth-largest dam in Brazil in terms of installed capacity, with 2,082 MW. The dam comprises two earthen massifs divided by concrete structures (Fig. 1). Its total length is approximately 6,800 meters, and its maximum height is 110 meters, with the crest located at an elevation of 523 meters above mean sea level. The volume of compacted embankment is around 36 million cubic meters, composed mostly of homogeneous soil. The downstream slopes were protected with grass, and the upstream slopes were covered with a layer of rockfill.

The Paranaíba River flows through a region of metamorphic rocks from the Precambrian era. Further away from the river banks, it is possible to find outcrops of basaltic rocks. Approximately 75% of the dam site consists of metamorphic rocks [21].

It should be noted that although this dam was chosen as a case study, no records of ochre occurrence in this dam were found in the literature.

The data on Itumbiara Dam was obtained from the work of Vilhena et al. [22]. Figure 2 shows the typical section of the dam at stake 35+50 that will be used in the development of this work. The permeability parameters were taken from Vilhena et al. [22], with some adaptations, as well as the hydraulic conductivity anisotropy (kh/kv) of 5, 10, 20, and 50, increasing with depth, as suggested by Cruz [23]. The adaptation of hydraulic conductivity values of the materials resulted from the seepage backanalysis considering the piezometric measurements of July 2003 (piezometers G4, G6, G9, G10 e G14), presented by Vilhena et al. [22].

The dam body was divided into four layers of approximately 21 m, to which these anisotropy values were assigned. Table 1 shows the hydraulic and shear strength parameters considered in the analyses carried out in this work.

Fig. 1 – General view of Itumbiara Dam. Fonte: Furnas.

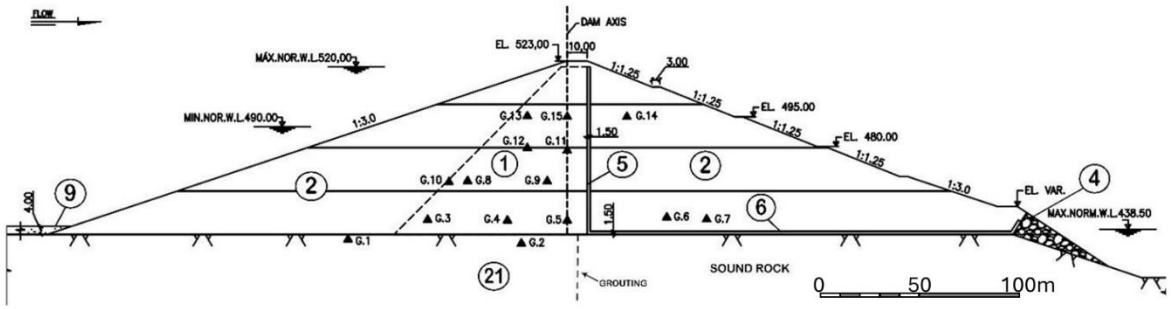

Materials:
1 and 2: compacted soil: silty-sandy clay, plastic, dark reddish colour; residual soil of basaltic rocks
4: Downstream toe drain: crushed stone (gneiss rockfill)
6: horizontal blanket: uniform coarse sand ,
5: vertical filter: uniform sand;
21: Foundation: metamorphic rocks, with grouted fractures.

Fig. 2 – Typical cross section of Itumbiara Dam (stake 35+50) – [22] modified.

Table 1 Properties of the constituent materials of the Itumbiara dam

	Color	Material	Specific weight (kN/m³)	Hydraulic conductivity k (m/s)	Cohesion (kPa)	Friction angle (°)
Compacted fill		silty-sandy clay	16.29	7.0E-09	20	33
Horizontal blanket		Coarse sand	14.83	3.8E-05	0	35
Vertical filter		sand	14.83	3.8E-06	0	30
Toe drain		Crushed stone	19.26	5E-01	0	53

2.2. Numerical Analysis

To evaluate the effect of ochre clogging, the simulation of nine hypothetical scenarios was carried out considering clogging concomitantly in the blanket drain and vertical filter of the Itumbiara earth dam.

Progressive clogging from downstream to upstream was considered in the horizontal blanket from the toe drain, as the formation of ochre generally occurs in areas with higher amounts of available oxygen, i.e., near the outlet of the drains. In addition, the simultaneous occurrence of ochre clogging in the vertical filter was considered. Both drainage devices were divided into ten longitudinal sessions and three transverse sessions, named according to Figure 3. Reduction factors ($k_{virgin}/k_{clogged}$) of 10, 50, 100, 200 for the drainage blanket and 10 to 100 for the vertical filter were considered. The range of values adopted was based on tests carried out on soil samples from Ilha Solteira, in which an average 28-fold reduction in the permeability coefficient was observed over 550 days [14]. The authors of this study extrapolated these results to 50 years, which resulted in a 219-fold reduction in permeability.

Then, nine scenarios of clogging (Figure 3) of the dam's drainage system (blanket and vertical filter) were represented in the analysis, varying the clogged region and the intensity of permeability reduction. The effects on water flow in the dam massif and its consequences on the downstream slope stability (Morgenstern-Price method) were evaluated using the RocScience software (Slide2), considering the different scenarios of progressive clogging.

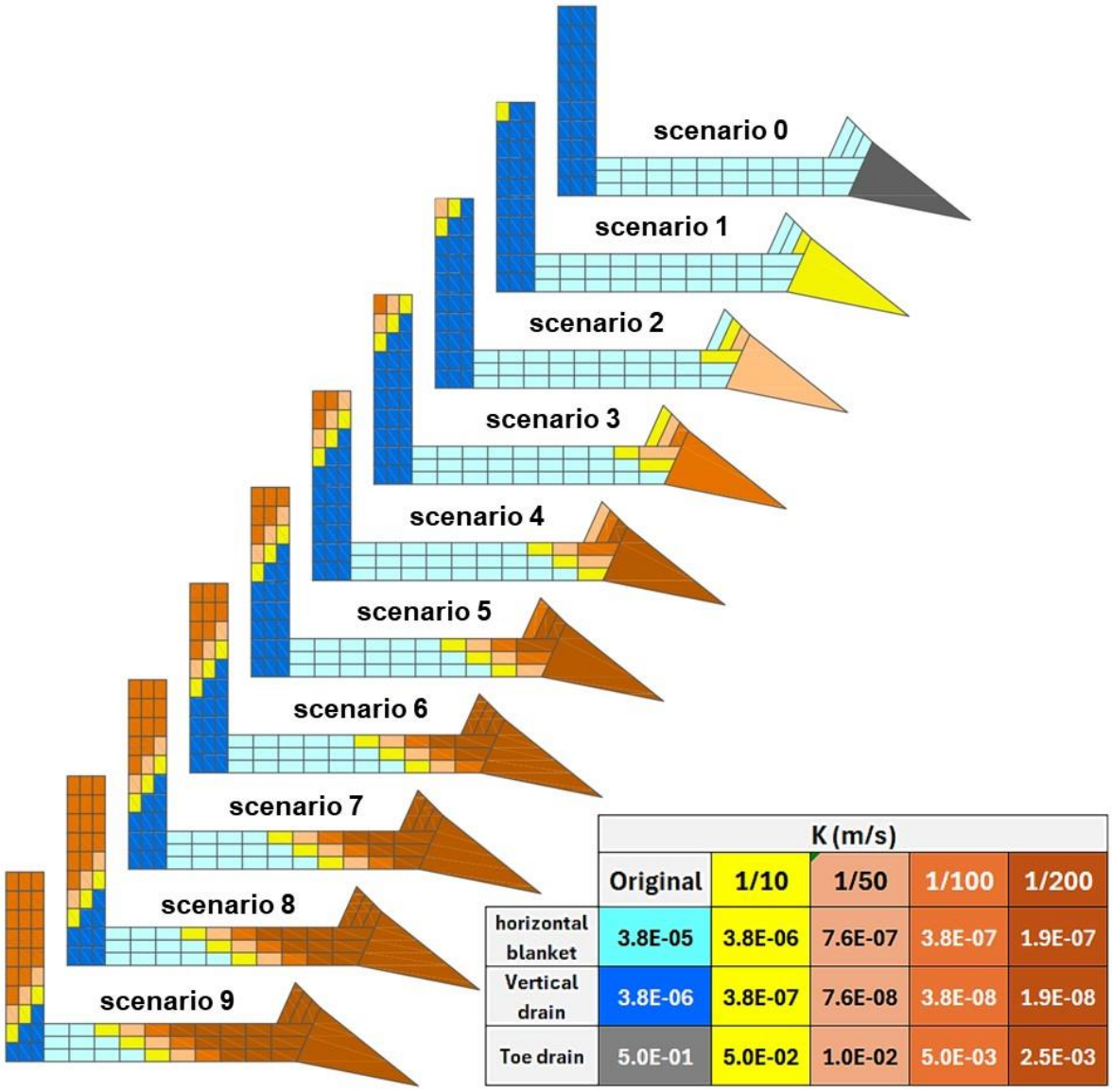

	K (m/s)				
	Original	1/10	1/50	1/100	1/200
horizontal blanket	3.8E-05	3.8E-06	7.6E-07	3.8E-07	1.9E-07
Vertical drain	3.8E-06	3.8E-07	7.6E-08	3.8E-08	1.9E-08
Toe drain	5.0E-01	5.0E-02	1.0E-02	5.0E-03	2.5E-03

Fig. 3 – Schematic representation of horizontal mat and vertical filter clogging scenarios (out of scale).

3. RESULTS AND DISCUSSION

The numerical model was validated before analyzing the flow under the nine clogging scenarios. For this purpose, the piezometric head results estimated by the model were compared with the values measured in the field considering steady-state flow with the reservoir at maximum level (84.5m, in July 2003) at piezometers G4, G6, G9, and G10 (see Fig. 2), which are presented by Vilhena et al. [22]. There was good agreement between the values estimated by the model and those measured at piezometers G4, G6, and G9, while the result at G10 was discrepant. Therefore, only the first three piezometers were considered when assessing the effect of clogging on the dam's piezometric load.

After validation, the drainage system clogging was progressively simulated into nine scenarios, as indicated in the previous section. The effects on the downstream pressure head, shown in Fig. 4, and slope stability, using the Morgenstern-Price method, are shown in Fig. 5.

The results of the numerical simulations of the progressive ochre clogging scenarios in the drainage blanket and vertical filter (Figs. 4 e 5) and the piezometry values in instruments G4, G6, and G9 (Figure 6) indicated that:

- clogging did not cause significant effects until scenario 4;

- from scenario six onwards, there is a significant increase in the piezometric heads in the three piezometers;

- in scenario 9, where clogging reaches an average of 80% of the vertical filter height, the phreatic line tends to behave as if there were no drainage system, forcing the flow to the downstream slope;

- the downstream slope stability safety factor only starts to drop considerably from scenario six onwards, with the rupture (FS=1) occurring in the transition between scenarios 8 and 9, consistent with the piezometry results.

Fig. 7 shows the spatial distribution of the degree of clogging in the horizontal mat and vertical filter in scenarios 6 and 9 when significant changes in the dam's behavior were observed.

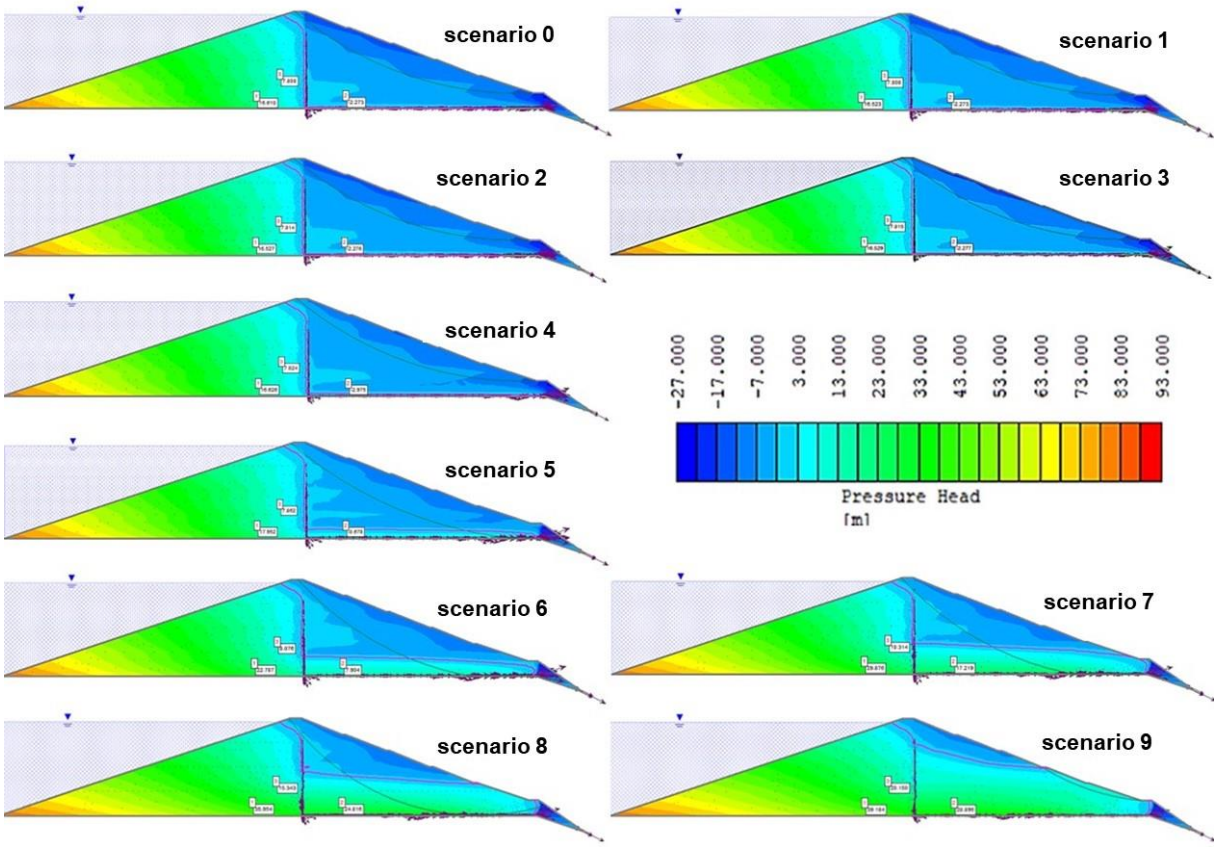

Fig. 4 - Results of total head by the numerical model for the scenarios of the drainage blanket and vertical filter clogging (progression from scenario 1 to 9)

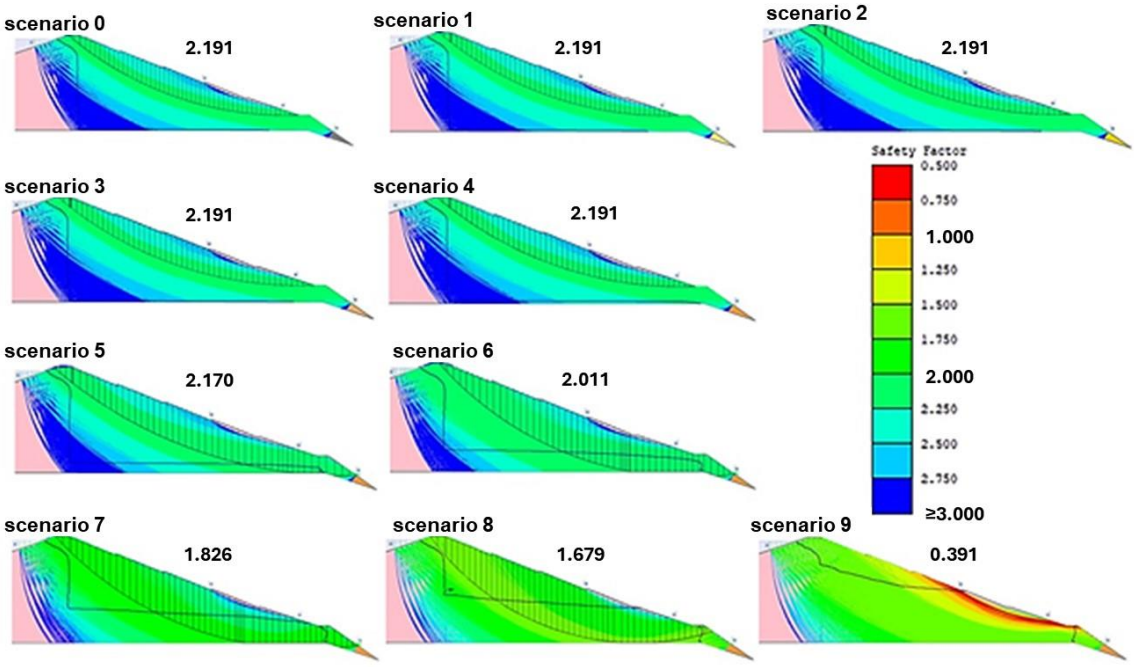

Fig. 5 - Results of slope stability safety factor by Morgenstern-Price Method for the scenarios of the drainage blanket and vertical filter clogging (progression from scenario 1 to 9).

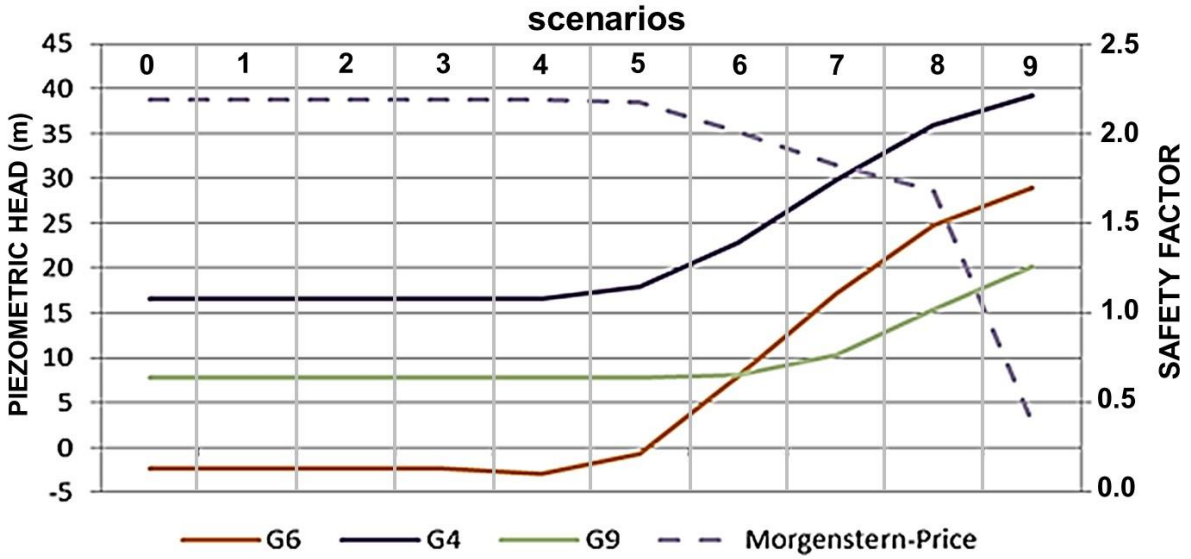

Fig. 6 - Evolution of the piezometric head and downstream slope stability safety factor (Morgenstern-Price method) with progressive clogging of the horizontal blanket and vertical filter.

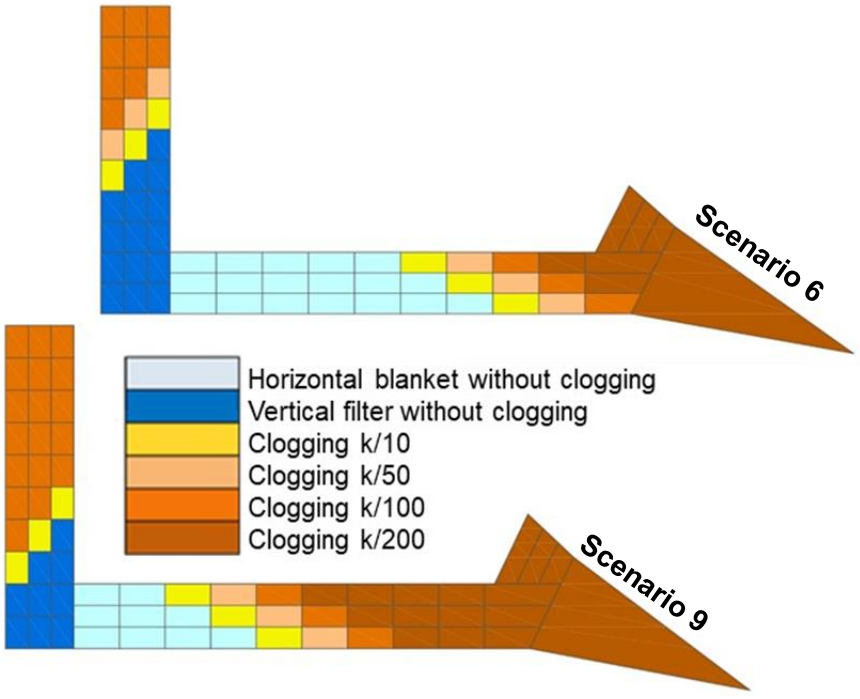

Fig. 3 - Detail of spatial distribution of the degree of ochre clogging in the horizontal blanket and vertical filter of scenarios 6 and 9.

4. CONCLUSIONS

Even though a hypothetical case study, the work demonstrates that it is possible to quantitatively assess the effects of various ochre clogging scenarios on a real dam, considering conditions for the ochre formation and degrees of clogging reported in the literature.

The results indicate that, for the case studied, even with the occurrence of ochre formation, the effects on pore pressures would only be noticed by the instrumentation after an advanced degree of clogging of the internal drainage system. This observation highlights the importance of two actions involved in a dam's safety plan: visual inspections to previously verify the occurrence of ochre formation even if the piezometers do not indicate anomalies and the assessment of the evolution of the problem and its consequences through piezometric monitoring.

It should be noted that the scarcity of records and more in-depth analyses of cases of clogging in geotechnical works, especially dams, means that the observations presented in this study may be limited.

Although the occurrence of ochre in dam drainage systems is common, there are still many doubts about the spatial distribution and evolution of the degree of clogging of the constituent elements of a dam's drainage system and the efficiency of mitigating measures. To advance this line of research, investment should be made in research into real cases of clogging to better understand the process, and the support of entrepreneurs and consultants is essential.

This research was partially funded by the National Council for Scientific and Technological Development (CNPq) and the Foundation for Research Support of the State of Rio de Janeiro (Faperj).

REFERENCES

[1] Kuntze, H. (1982). Iron clogging in soils and pipes, analysis and treatment, in: German Assoc. for Water Resources and Land Improvement, Bulletin 10, Pitman.

[2] Ford, H. W. (1979). Biological clogging of synthetic drain envelopes, in: Proc. 2nd Int. Drainage Workshop. Washington, D.C.

[3] Puig, J., Gouy, J.L., Labroue, L. (1986). Ferric clogging of drains. in: Proc.3rd Int. Conf. on Geotextiles, v.4, pp. 1179–1184, Vienna, Austria.

[4] Mendonca, M.B., Ehrlich, M., Camarota, M.C. (2003). Conditioning factors of iron ochre formation on geotextile filters. Can. Geotech. J. (ISSN: 0008-3674), 40(6), 1225–1234.

[5] Mendonca, M.B., Ehrlich, M. (2006). Column test studies of ochre biofilm formation in geotextile filters. J. Geotech. Geoenviron. Eng. 132, 1284–1292.

[6] Fannin, R.J. (2010). On the clogging of geotextile filters, in: 9th Int. Conf. on Geosynthetics, Guarujá, Brazil. 401–412.

[7] Koerner, R.M., Koerner, G.R. (2015). Lessons learned from geotextile filter failures under challenging field conditions. J. Geotext. Geomembr. 43(1), 272–281.

[8] Correia, L.G.C.S., Ehrlich, M., Mendonca, M.B. and Keim, C.N. (2023). Laboratory studies on ochre formation and removal from geotextile filters. Canadian Geotechnical Journal. 60(1): 31-43. https://doi.org/10.1139/cgj-2022-0084

[9] Terzaghi, K. and Leps, T.M. (1958). Design and Performance of Vermilion Dam, California. Journal of Soil Mechanics and Foundations Engineering Division, ASCE, 84(3):1728.1 - 1728.30.

[10] Infanti Jr., N. and Kanji, M.A. (1974). Preliminary considerations on geochemical factors affecting the safety of earth dams. In Proceedings of the 2nd International Congress of the International Association of Engineering Geology, São Paulo, Brazil. pp. 33.1-33.11.

[11] Xu, J. K., Guo, B. J. and Chen, D. C. (1976). Experience in using residual soils for earth dam construction in Guandong Province, China. Proc., 12th Congrès Int. des Grands Barrages, 821—838.

[12] Guerra, M.O. (1980). Ação química e biológica na colmatação de filtros e drenos. Implicações na Barragem do Rio Grande, In Anais do XIII Seminário Nacional de Grandes Barragens, V.II, pp.257-289, Rio de Janeiro.

[13] Lindquist, L.N. and Bonsegno, M.C. (1981). Análise de sistemas drenantes de nove barragens de terra da CESP, através da instrumentação instalada. In Anais do XIV Seminário Nacional de Grandes Barragens, Recife, Brazil, pp.267-290.

[14] Kanji, M.A., Ferreira, R.C., Guerra, M.O. and Infanti Jr., N. (1981). Geoquímica do ferro nas obras de engenharia em solos topicais: breve histórico do conhecimento. In: Anais do Simpósio Brasileiro de Solos Tropicais em Engenharia, Rio de Janeiro, Brazil. Vol. 2., Rio de Janeiro. pp.146-158.

[15] Vaughan, D., Ord, B. G. (1994). Influence of dissolved humic substances on the deposition of iron in field drains. The Science of the Total Enviroment, v. 152, pp. 73-80.

[16] Geibel, N. M. (2004). Rehabilitation of a biofouled pressure-relief well network, Garrison Dam, North Dakota. Environmental and Engineering Geoscience, v. 10, n. 2, pp. 175-183.

[17] Sterpejkowicz-Wersocki, W. (2014). Problem of Clogging in Drainage Systems in the Examples of the Żur and Podgaje Dams. Archives of Hydro-Engineering and Environmental Mechanics, v. 61, n. 3–4 (Dez), pp. 183-192.

[18] Strozberg, I.; Valerio, E.; Nascimento, J. W. (2019).Evaluation of Interference of Iron Bacteria in Geotechnical Works in the State of Ceara-Brazil. XVI Pan-American Conference on Soil Mechanics and Geotechnical Engineering (XVI PCSMGE), Cancun.

[19] Godoi, C. S., Correa J. F., Sola, M. C. et al. (2019). Análise de Materiais Provenientes do Sistema de Drenagem Interna da Barragem de Terra Da UHE São Salvador. Revista Brasileira de Engenharia de Barragens, ano 5, n. 7 (Fev), pp. 26-32.

[20] Li, S., Wang, Y., and Feng, D. (2023). Chemical clogging of synthetic filters in tailings ponds caused by ferrous iron ions. Environmental Geotechnics,10:8, 529-538

[21] Ávila, J. P. D.; Bicudo, R. I.; Pierre, L. F. (1982). Main Brazilian Dams, Design, Construction and Performance. [S.l.]: Brazilian Committee on Large Dams.

[22] Vilhena, R. M., Schliewe, M.S., Alves, R.D., Gitirana Jr., G. (2018). Seepage Analysis of Itumbiara Dam Considering Soil-Atmosphere Interactions. Third International Dam World Conference. Foz do Iguaçu: Laboratory of the Division of Technology in Civil Engineering of FURNAS.

[23] Cruz, P. T. (1996) 100 barragens brasileiras: casos históricos, materiais de construção, projeto. São Paulo, Oficina de Textos.

Fifth International
Dam World Conference
PORTUGAL • LISBON • LNEC • APRIL 13-17, 2025
dam world 2025

LET'S TALK ABOUT FMEA

Teresa C Fusaro[1]
Fusaro Engenharia e Consultoria Ltda

Alexandre V Melo[2]
Cemig Geração e Transmissão S.A.

Daniel E Mendes[3]
Cemig Geração e Transmissão S.A.

ABSTRACT

Risk-informed decision-making approaches are increasingly being used by many dam owners around the world, aiming to provide a transparent and defendable method of presenting the rational for dam safety prioritization to decision makers. This movement can also be seen in Brazil, after the recent failure of two large tailings dams in the state of Minas Gerais.

Failure Modes and Effects Analysis – FMEA has been the most used method in Brazil, both for mining and hydro dams. In the hydroelectric sector, this can be justified by the previous use in Reliability Centred Maintenance (RCM), employed by many owners to define the strategy for electrical-mechanical equipment maintenance.

Nevertheless, experiences in Brazil have shown some difficulties as well as fragilities in the use of FMEA. The difficulties vary from terminology to the scales used to provide guidance for ranking potential failure modes, including different simplifications and adaptations made to the process. Additionally, Brazilian legislation for hydropower generation dams requires that all recommendations from inspections must be prioritized and met according to their gravity, urgency and tendency, leading to attempts to include this information in the criticality analysis.

This article will discuss such points and some possible improvements in the application of FMEA, considering the experience of the authors, that could help to enhance the efficiency of this tool in identifying risks and defining action strategies related to dam safety.

Keywords: Risk analysis, FMEA, FMECA.

[1]tcfusaro@gmail.com, Brazil
[2]alexandre.melo@cemig.com.br, Brazil
[3]daniel.mendes@cemig.com.br, Brazil

1. INTRODUCTION

"*Safety in a societal context is understood to mean protection of a community from harm*" [1], and, concerning dam safety, approaches such as engineering standards, codes of practices, good practices and procedures have evolved to achieve this goal.

However, accidents can still occur, even when a system is well designed and is being maintained and operated adequately. Variability and uncertainty are inherent factors that justify this question, as there will always be some residual uncertainty and associated risk that must be managed during a dam's lifespan.

ICOLD's Bulletin 191 [1] offers a Safety Management Framework, incorporating legislative and administrative arrangements in conjunction with engineering and management activities to reach dam safety and reinforces that "*the dam owner is responsible for ensuring that there is an effective and transparent process for making decisions about the need for risk reduction measures when it is found that a dam or its operation does not meet the safety goals*".

This framework (Fig. 1) shows that dam safety is founded on governance, responsible ownership and diligent engineering, considering that governments and dam owners both have essential roles in providing assurance of the safety of dams under their control.

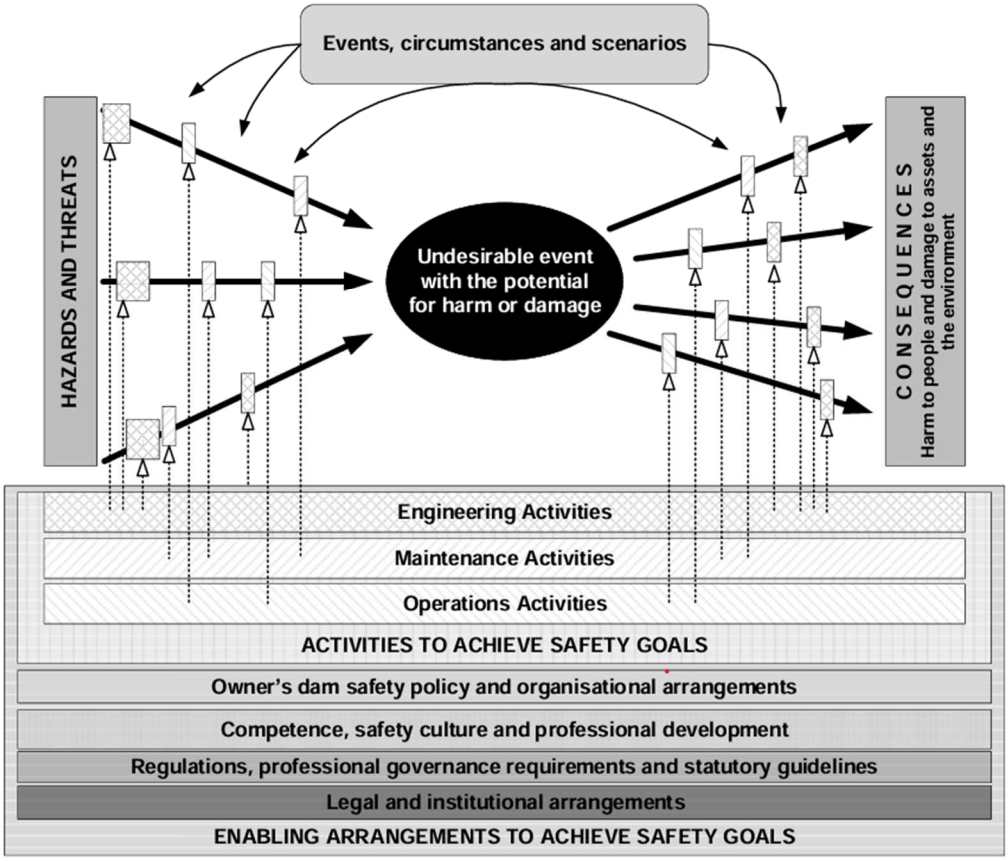

Fig. 1 – Safety Management Framework. Source: [1].

It demonstrates that “Dam Safety” is an integrated set of activities and highlights the focus that must be given to potential failure modes (undesirable events with the potential for harm or damage), linking their causes (hazards and threats) and effects (consequences), and incorporating barriers established to help to reduce the likelihood of occurrence or mitigate the impact of the consequences of failures.

This emphasizes the need for risk assessments, to provide a more systematic approach to understanding and controlling the effects of variability and uncertainty, and to document decisions concerning these risks in a more transparent way.

There are many different methods for risk analysis. This article will discuss the application of Failure Modes and Effects Analysis (FMEA/FMECA), widely used in various industries and for dams. Although being the most used method in Brazil, its application rarely results in new discoveries or are used to justify recommendations concerning dam safety.

Limitations are rooted in part in lack of knowledge of the methodology, shortcomings used to make it simpler and faster and, maybe, lack of specific standards for dams, that will be discussed following the steps of FMEA methodology.

2. FMEA

Application of FMEA/FMECA follows, in general terms, the International Standard IEC 60812 [2] on Failure Modes and Effects Analysis (FMEA and FMECA). It should be noted that this standard is only a general guide. It can be adapted and applied in different ways depending on the intended objectives, keeping the basic structure proposed, that is, breaking the systems down into subsystems and components to identify potential failure modes and existing controls, to allow the establishment of response measures.

The first step on FMEA analysis is to set the objectives to be achieved. Unfortunately, a written purpose statement defining the reasons for the analysis is not a common practice in Brazil.

3. SYSTEM DEFINITION AND DIVISION IN COMPONENTS

The analysis starts with the definition of the boundaries of the studies, that usually includes all civil structures built to contain the reservoir. The system is then divided in subsystems and components, in a level of detail that allows to easily understand their functions. Generally, components whose failure does not initiate a sequence of events that may lead to dam breach are not covered in the analysis. Electromechanical equipment is also not usually detailed, only its direct impact on dam safety being considered. This can be justified by the fact that the dam and electromechanical components are assessed by distinct teams, and these teams conduct their analysis separately.

Many times, there is a tendency for simplification, and the analysis is conducted only at a subsystem level or is very superficial and would be better considered a PRA (Preliminary Risk Analysis). Even simplified functional block diagrams, built to allow a better understanding of the interrelationships of component functionalities and framing the sequential functionality of a particular subsystem, may be forgotten.

Block diagrams can be easily drawn, as an example as the ones proposed by Santos et al. [3] and may include a description of each component function as shown in Fig. 2.

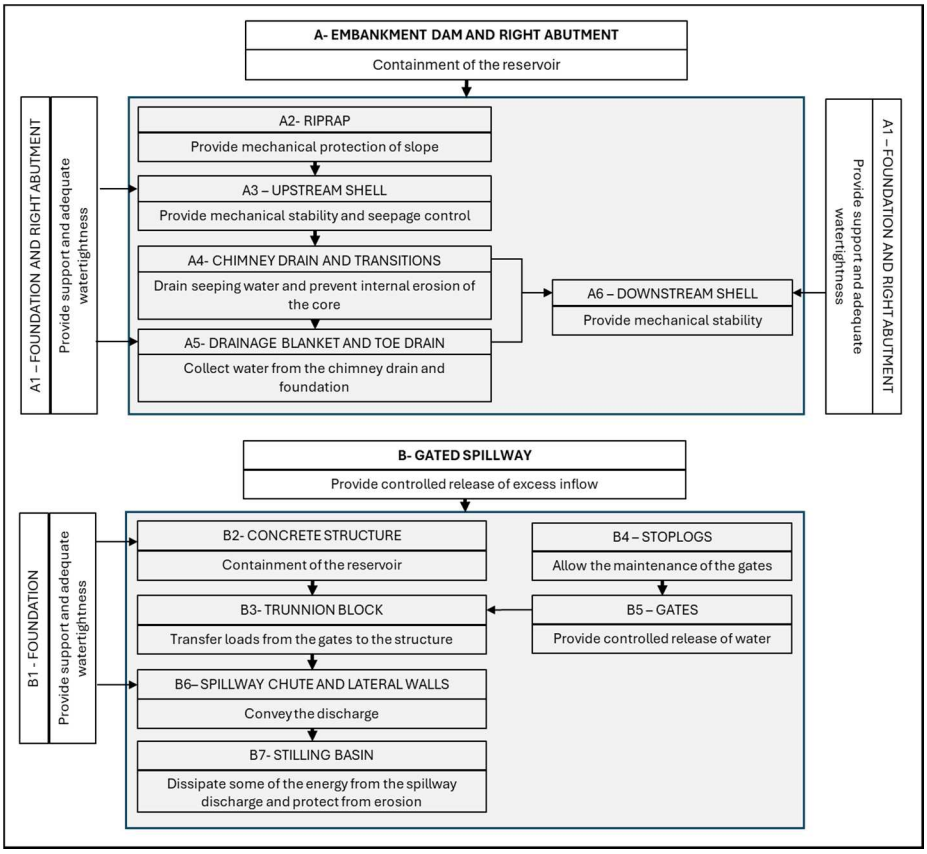

Fig. 2 – Functional block diagrams for a hypothetical dam (adapted from [3])

In some cases, surveillance processes or instrumentation processes are analysed separately (Process FMEA), to give focus to the processes involved and to avoid repetition. In this case, the starting point is the process flow diagram. The function of each step or its intended outcome is defined and the ways in which the process function could fail are listed as failure modes in the process FMEA. Failure causes may involve both human and hardware features.

Although for a complex system such as a dam, it seems logical to subdivide it into subsystems and components, one point of discussion is whether to perform FMEA analysis at all hierarchical levels: system, subsystems and components. Would risks be adequately identified if the analysis was carried out only at the lower level? When applying a bottom-up approach, it is worth remembering that a component's failure mode is a cause in a higher-level subsystem.

4. IDENTIFICATION OF FAILURE MODES, THEIR CAUSES AND EFFECTS

The identification of failure modes of components and subsystems, their causes and effects constitute the essence of FMEA methodology. Nevertheless, it is not a simple task, especially for complex systems such as dams, where conflicts in the definitions of these terms are still quite common.

Santos [4] reports that, to obtain consistent and substantial results from the method, it is important to maintain a disciplined approach in "cause-effect" reasoning. Otherwise, the analysis may become difficult and unmanageable, leading to confusion about the distinction between failure mode, cause, and effect in different system components.

Typically, failure mode is defined as "*the way or manner in which a failure occurs*". However, this definition receives diverse interpretation in different uses and different areas of knowledge, many times being defined as the cause or the failure itself. There is also confusion regarding the term PFM (Potential Failure Mode) from PFMA methodology and defined by FERC [5] as a "*chain of events leading to failure*", which would be the most appropriate definition for failure mechanism [6].

The authors consider more appropriate, in the context of dams, the following definitions, most of them given by CDA [6]:

Table 1– Terms and definitions

Term	Definition
Failure	Loss of function. Inability of a component or a subsystem to perform as intended, including incorrect operation [6].
Failure mode	*What can go wrong?* State or condition of loss of function (non-functional states), or a specific manner or way by which a failure occurs in an element/component or overall system, causing loss of function [6].
(Failure) Cause	*Why would the failure mode occur?* Event or circumstances leading to failure, that is, why the failure occurred.
(Failure) Effect	Failure consequence within or beyond the boundary of the failed item [2].

Even with this guidance, it may be tricky to list failure modes, causes and effects across the subsystems and components and the following questions can help to verify the correct cause-effect relationship [7]:

- a component's failure mode may be a cause in a higher-level subsystem;
- a subsystem's failure mode may be the effect of a failure mode at a lower-level component.

Fig. 3 illustrates the time-based relationship between the three terms for a specific subsystem or component. When we are focusing on the present, we use 'failure mode'. In turn, 'failure cause' explains why a failure occurred (looking back), and 'failure effect' focuses on the results of a failure, looking forward.

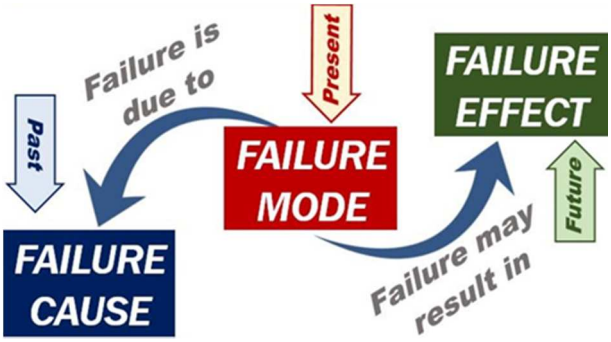

Fig. 3 – Cause-failure-effect relationship. Extracted from [8]

In practical terms, there is a finite number of **failure modes** for each component of the system, but identifying these failure modes is not always straightforward and can be subjective. Brainstorming can provide an initial framework for this task, by screening credible failure modes. The Hazards and Failure Modes Matrix (HFMM) [6], provides a structure for reasoning about the potential vulnerabilities of dams and the conditions that could negatively impact these vulnerabilities, considering both external and internal hazards.

GLOBAL FAILURE MODES		ELEMENT AND/OR ELEMENT FUNCTION	MOST BASIC FUNCTIONAL FAILURE CHARACTERISTICS	External Hazards			Internal Hazards (Design, Construction, Maintenance, Operation)			
				Meteorological	Seismic	Reservoir Environment	Water barrier	Hydraulic struct.	Mech/elec	Infrastructure & Plans
DAM COLLAPSE BY OVERTOPPING (erosion or overturning)	Water elevation too high	Inadequate installed discharge capacity	Meteorological inflow > buffer + outflow capacity							
		Inadequate available discharge capacity	Inadequate reservoir operation (rules not followed)							
			Random functional failure on demand							
			Discharge capability not maintained or retained							
		Inadequate freeboard	Excessive elevation due to landslide or U/S dam							
			Wind-wave dissipation inadequate							
	Management System Failure	Safeguards fail to provide timely detection and correction	Operation, maintenance and surveillance fail to detect/prevent hydraulic adequacy							
			Operation, maintenance and surveillance fail to detect poor dam performance							
DAM COLLAPSE BY LOSS OF STRENGTH (External or internal structural failure and weakening)	Crest elevation too low	Stability under applied loads	Mass movement (external stability:- displacement, tilting, seismic resistance)							
			Loss of support (foundation or abutment failure)							
		Watertightness	Seepage around interfaces (abutments, foundation, water stops)							
			Through dam seepage control failure (filters, drains, pumps)							
		Durability/cracking	Structural weakening (internal erosion, AAR, crushing, gradual strength loss)							
			Instantaneous change of state (static liquefaction, hydraulic fracture, seismic cracking)							

Fig. 4 – A generic HFMM - Hazards and Failure Modes Matrix [6]

The same matrix guides the determination of the root **causes** of a failure mode. Failing to determine the root cause may lead to poor results in criticality evaluation (FMECA) and FMEA steps do not include a method for a full causal analysis [2]. According to [4], root causes can

originate from natural phenomena (rainfall, temperature, earthquakes); internal physical, chemical, or biological processes; design flaws; defects in material quality; operational failures or human actions (errors, sabotage, etc).

Regarding the **consequences** of failure modes, it is possible to consider local, intermediate (or in other elements), and final effects. Although there is a tendency to simplify the analysis by focusing on final effects, the authors believe it is very important to consider local effects, since the combination of both piece of information (local effects with final effects) helps to understand the failure mechanism and, therefore, useful for registering the "rationale" of the risk analysis for future reviews, possibly by different working groups.

Considering all these aspects, it can be concluded that the development of FMEA, especially for dams, is not a simple task, and sometimes the failure will not fit perfectly into the proposed definitions (failure mode, cause, and effect). However, the important thing is to assure that the relevant failure modes are considered, so that the necessary actions can be taken to mitigate or eliminate it, as defined in the following item.

5. DETECTION METHODS, EXISTING CONTROLS AND ACTIONS

As shown in the Safety Management Framework [1], barriers must be established to reduce the likelihood of occurrence or mitigate the consequences of dam failure. Within the context of FMEA, these barriers can be understood as controls, defined as "*design features, or other existing provisions, that have the ability to prevent or reduce the likelihood of the failure mode or modify its effect*" [2].

Thus, controls are any preventive or corrective actions duly implemented to detect, control or mitigate the effects of a failure mode, with the objective to reduce the residual risk of failure.

Controls can be implemented during the design/construction or operational phases of the structure. Design/construction controls refer to aspects of design for safety, including hydraulic, structural, and operational capacities, as well as other aspects related to construction quality control. Operational controls are related to operational procedures, performance monitoring, maintenance and testing, and emergency preparedness. When a detection method allows for early identification of a failure mode, providing enough time to act in a way that reduces the likelihood of the occurrence or enables a more efficient response to mitigate the consequences, it can be considered a control.

Given the broad range of controls, in the author's opinion, their assessment should be analysed depending on the life phase of the dam. If FMEA is conducted during the design and construction stage, design/construction features could be included as controls. Nevertheless, if the analysis is conducted in the operational phase, the suggestion is to consider design and

construction features as “positive or adverse factors”, as proposed in item 6, and only existing measures to detect, cease the evolution or mitigate the effects of a failure mode as controls. These measures to cease the evolution of the failure mechanism may include routine surveillance, tests and monitoring, maintenance activities, and actions *promptly accessible at the dam site* (given that the materials and equipment are available). This suggestion is to reduce the list of controls, leaving only those that must be dealt with during operation.

Naturally, if the analysis shows that the controls identified are deemed insufficient or inadequate, and the associated residual risks are considered high or intolerable according to the acceptability criteria, actions should be listed and may include new controls, investigation or studies to reduce uncertainties, structural improvement, rehabilitation, or even mitigation actions to protect the valley downstream.

6. IDEAS FOR IMPROVING THE LIKELIHOOD AND CONSEQUENCE RATINGS

The results of a risk analysis are dependent on the quality of the information and the knowledge and experience of the team members. “*The process relies on engineering judgment to subjectively determine the relevance of the various failure modes. When a failure mode is ruled out in large part because of a single factor, such as the interpretation of the geology, the assessment of the supporting information for that factor needs to be diligent*” [9].

This can be an issue, but, even with an experienced team and rich discussions, one weakness of the method may be the lack of formal register of the discussions and analyses that led to the Occurrence and Severity ratings. This detailed information should be part of FMEA report, but as a rule, most of the information regarding the analyses are the ones found in FMEA/FMECA spreadsheets. These spreadsheets are tailored to each specific use, but in Brazil it is not usual to include columns to register this information.

SUBSYSTEM											
COMPONENT	FUCTION	FAILURE MODE	ID	CAUSES	LOCAL EFFECT	FINAL EFFECT	EXISTING CONTROLS	OCURRENCE	SEVERITY	DETECTION	ACTIONS

Fig. 5 – Example of FMECA spreadsheet

A possibility could be to include two new columns, “Adverse and Positive Factors” (evidence that make the possible failure mode more /less likely to occur), as done in PFMA methodology, to assist in assessing the likelihood (occurrence) as well as ensuring the traceability of information that justifies the assessment given.

This insertion has shown to be an interesting tool to get the group to look for evidence and evaluate issues in more detail. The inclusion of a column for rating uncertainties can also be a

possibility, or this information can be included in the adverse/positive factors as “Uncertainties” or “Unknowns”, as shown in Fig. 6.

SUBSYSTEM												
COMPONENT	FUCTION	FAILURE MODE	ID	CAUSES	LOCAL EFFECT	FINAL EFFECT	ADVERSE FACTORS (that make the PFM more likely to occur)	POSITIVE FACTORS (that make the PFM less likely to occur)	EXISTING CONTROLS	OCURRENCE	SEVERITY	DETECTION	ACTIONS

Fig. 6 – FMECA spreadsheet including the register of Adverse and Positive factors that make the failure mode more or less likely to occur

The risk qualitatively assessed is usually the Residual Risk, that is, the risk after considering the existing control measures. Thus, the ability to detect and intervene (perform repairs) before the failure mode materializes should be taken into consideration in the qualitative definition of occurrence and severity.

The efficiency of these control measures depends on their capability of timely implementation to become effective in the short term. So, to support their evaluation, guidance tables can be used, as shown in Table 2. Naturally, this table is not supposed to be used directly, and it is up to the team members to conclude on the possibility of detecting a potential problem in advance and carrying on interventions and/or issuing alerts downstream in a timely manner.

Table 2 – Guidance for checking Control Efficiency ([10] apud Thompson et al.2015)

Response Time	***Duration***	***Example Failure Step***	***Ability to monitor and detect before occurrence***	***Response options to address PFM***
Class A No time do respond	Minutes (Seconds to hours)	Earthquake liquefaction	No	**Limited Response** – Little or no ability to respond due to rapidity of failure
	Hours (Minutes to days)	Dam overtopping	Yes	
Class B Short time do respond	Days (Hours to weeks)	Flood	*Yes*	**Reactive Responses** – Visual inspection, monitoring existing instruments and implementing protection systems as required. Some intervention options are possible such as lowering the reservoir.
	Weeks (Days to months)	Slope saturation	*Yes*	
Class C Long time do respond	Months (Weeks to years)	Regressive erosion piping	Yes	**Proactive Responses** – Inspecting critical features, monitoring existing instruments, analyzing dam performance and enhancing monitoring system are possible with options to implement physical remediation or other interventions.
	Years (Months to decades)	Fines Migration	Yes	
	Decades (Years to centuries)	Corrosion	Yes	

One should note that, in some types of dams, some slowly evolving failure modes may be difficult (e.g. internal erosion of the clay core in rockfill dams) or even impossible to detect early and the effectiveness of controls should be assessed carefully.

Given the information gathered (failure modes, causes, adverse and positive factors and efficiency of controls), the next step is to evaluate the criticality of the risks, either using the *Risk Priority Number or a Criticality Matrix*.

7. RISK PRIORITISATION USING RPN AND GUT

The Risk Priority Number (RPN) is a semi-quantitative measure of criticality, obtained by multiplying ratings on a numerical scale for severity (failure consequence), occurrence (likelihood), and detection (in other words, higher priority if failure is difficult to detect).

RPN is subject to inherent limitations of defining and using subjective risk scales. The broad nature of RPN scales, commonly ranging from 1 to 10, can contribute to subjective interpretations and imprecise classifications, as noted by the authors. Therefore, scales should be clearly defined to facilitate consensus during classification.

IEC standards [6] also draw attention to certain limitations of RPN: the scale is not continuous; numerical ratios between values have no specific meaning and RPN can be sensitive to small changes in the value of one parameter.

Ideally, the scales must reflect the range of risks expected for dams and must be very well described, to facilitate reaching a consensus during the classification process (but this is not what is seen in several tables used). Table 3 below has been frequently used in Brazil, with the occurrence index being more suitable for electrical or mechanical equipment.

Table 3 – Severity (Si), Occurrence (Oi) and Detection indexes (Di) - (adapted from [11])

Severity index (Si)		Occurrence index (Oi)		Detection index (Di)	
Si	**Effect**	**Oi**	**Probability**	**Di**	**Detection**
1	Very low	1	Improbable (0.1%)	1	Almost right
2 3	Low	2 3	Remote (0.1 to 1%)	2	Very high
4 5	Medium	4 5 6	Occasional (1 to 10%)	3	High
6 7 8	Severe	7 8 9	Probable (10 to 20%)	4	Moderately high
9	Very severe	10	Frequent (> 20%)	5	Moderate
10	Catastrophic			6	Low
				7	Very low
				8	Remote
				9	Very remote
				10	Almost impossible

In Brazil, legislation for hydro dams (for hydropower generation) [12] requires that all *recommendations and requirements from inspections and dam safety reviews must be met within the deadlines indicated in the respective reports, according to their gravity, urgency and tendency.*

This requirement led to the use of a management tool known as GUT Matrix for this objective. In this method, each issue being analysed is evaluated according to its gravity, urgency and tendency and the scores are multiplied to calculate a GUT score. The issue with the highest GUT score is given the highest priority. This method offers the advantage of simplicity. However, it also requires clear definitions of the various levels of gravity, urgency, and tendency. Obviously, there is an inherent level of subjectivity in the classification process.

Table 4 – Example of a GUT matrix scale

Score	Gravity	Urgency	Tendency
5	Extremely severe	Needs immediate action	It will get worse fast
4	High severity	Very urgent	It will get worse in the short term
3	Severe	As soon as possible	It will get worse in the medium term
2	Low severity	Not very urgent	It will get worse in the long term
1	Not severe	Can wait	It will probably not get worse / It will stay stable

In general, the same limitations described for RPN are found in GUT methodology. It is important to note that in both methodologies, due to the use of three parameters, different sets of scores may produce the same value but with completely different risk implications.

Gravity here usually do not mean severity of the consequences, but if the problem is directly associated to a global failure mode of the structure. An extra issue for GUT matrices is that urgency many times is directly related to tendency and even to severity. For example, if “it can wait”, it is because it is “not serious” or “it will not change”. Thus, scoring the tendency and urgency may eventually lead to deviations in the classification. Attention should also be given to important design issues that will not get worse with time (e.g. insufficient spillway capacity).

In an attempt to aggregate processes and meet legal compliance, several Brazilian companies have been trying to use GUT Matrix to replace RPN in risk assessment using FMEA. However, the topic is quite controversial, as GUT is a tool primarily designed for prioritizing issues, not for quantifying risk in a context of formal risk assessment.

In any case, good practice for using RPN or GUT involves a comprehensive review of the values before forming an opinion about the criticality assessment and determining treatment actions. Furthermore, the authors recommend applying the Criticality Matrix for a better visualization of the risks and understanding the acceptability criteria.

8. CRITICALITY MATRIX

The Criticality Matrix is a form of representation that combines two or more indexes, typically representing Consequence scales on the horizontal axis and Likelihood scales on the vertical

axis. It is usually used for representing results of qualitative and semi-quantitative methods, where scales are not represented by continuous values. The Criticality Matrix allows a good visualisation and understanding of the risks, and an easier definition of their category. It offers the advantage of facilitating risk management, highlighting the failure modes that require preventive or corrective actions.

There are no standard scales to be followed when assessing likelihood and consequence indexes, and, many times, scales developed for electromechanical equipment are used. Table 5 presents a suggestion of Likelihood scale for dams, adapted from [10] and [13], considering the annualized probability of occurrence.

Table 5 – Estimating Likelihood (adapted from [10] and [13])

Descriptor	Definition of Likelihood	Quantitative Interpretation	Annualized Probability of Occurrence
Expected (E)	There is direct evidence or substantial indirect evidence to suggest the failure has initiated or is very likely to occur.	• Undesired result almost certain to happen • Higher than 10% probability in a year	$p > 0,1$ $p > 10^{-1}$
High (H)	The fundamental condition or defect is known to exist; indirect evidence suggests it is plausible; and key evidence is weighted more heavily towards “more likely” than “less likely”.	• Undesired result happens more than once in 10 years or more • Higher than 10% probability in 10 years	$p > 0,001$ $10^{-3} < p \leq 10^{-1}$
Moderate (M)	The fundamental condition or defect is known to exist; indirect evidence suggests it is plausible; and key evidence is weighted more heavily towards “less likely” than “more likely”.	• Undesired result happens once in 100 years or more • Less than 1% probability in 10 years	$p \leq 0,001$ $10^{-4} < p \leq 10^{-3}$
Low (L)	The possibility cannot be ruled out, the fundamental condition or defect is postulated. Evidence indicates it is very unlikely.	• Undesired result happens once in 10.000 years or more • Less than 1% probability in 100 years	$p \leq 0,0001$ $10^{-5} < p \leq 10^{-4}$
Remote (NL)	Several events must occur concurrently or in series to cause failure, and most, if not all, have negligible likelihood such that failure likelihood Is negligible.	• Undesired result happens once in 100.000 years or more • Less than 1% probability in 1.000 years	$p \leq 0,00001$ $p < 10^{-5}$
Virtually impossible	Failure mode ruled out because physical possibility does not exist, or information came to light which eliminates the concern that had generated the development of the failure mode; or the required load and subsequent structural response is considered so remote as to be non-credible or not reasonable to postulate.		Close to non-credible

The same problem of no standards or the use of scales from other areas of knowledge happens to Consequences evaluation, aggravated by the difficulty of how to evaluate the potential of life loss due to the failure. It’s important to consider, during the classification process, all the control measures that could mitigate the severity of the consequences, such as alarm systems or evacuation procedures.

For failure modes that evolve over months, years or decades or for those with high capacity of detection and intervention, it is usual to consider that the effects/impacts can be

mitigated/controlled, and neither loss of life nor damage to the downstream valley will occur (no residual risks).

Table 6 presents a suggestion of scale for estimating Consequence, which evaluates Impact considering life loss, financial and environmental damages. EXTREME consequence is considered when loss of life is expected due to limited warning time or large populations to be evacuated. Despite the release of life-threatening flow, HIGH consequence is considered when direct loss of life is unlikely due to the location of the flooded areas (therefore dam break studies should consider different scenarios and different failure modes) and/or the possibility of effective detection and evacuation.

Table 6 – Estimating Consequences

Consequence Category	Description
Extreme (E)	• Probable loss of life and major environmental and infrastructure losses (loss of life is expected due to limited warning time, large population and/or limited evacuation routes) *(Restauration impossible)*
High (H)	• Potential loss of life and significant environmental and infrastructure losses (although life-threatening releases occur, direct loss of life is unlikely due to severity or location of the flooding, or effective detection and evacuation) *(Restauration probable)*
Moderate (M)	• Without loss of life • No significant environmental and infrastructure losses • Loss of generation (need to stop generation or to lower the reservoir to carry out repairs).
Low (L)	• No loss of life or environmental damages. • Damage to infrastructure restricted to the industrial area
Negligible (N)	• Loss of components of easy restauration or maintenance

The Criticality Matrix allows the definition of risk categories, that would guide decision-making. These categories are usually adapted to each company's policy for establishing risk acceptability / tolerability criteria or to regulatory requirements in different countries, varying in terms of number of classes and acceptance of risks.

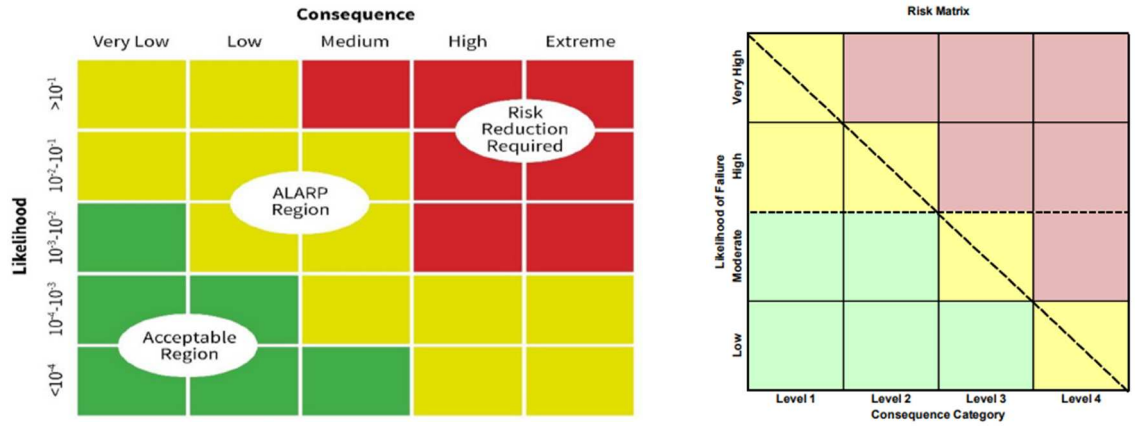

Fig. 7 – Example of Qualitative Risk Matrix, according to [14] and [15], respectively.

Usually, as shown in Fig. 7, three or four risk categories are considered. As an example, Schafer et al. [13] indicate that 4 zones could be delimited: acceptable risks, tolerable risks with control, undesirable risks ALARP (risks should be "As Low As Reasonably Practicable") and intolerable risks.

Tolerable risk is defined by ICOLD [16] as "*a risk within a range that people are prepared to tolerate in order to secure benefits, in the expectation that:*

a. *the nature and level of the risks are properly assessed and the results used properly to determine control measures;*
b. *the residual risks are not unduly high and kept as low as reasonably practicable (ALARP Principle); and*
c. *the risks are periodically reviewed to ensure that they still meet ALARP criteria."*

According to [17], a key principle in achieving Tolerable Risk would be "reducing risks as low as reasonably practicable" (ALARP), that is, to reduce risks to a point where additional risk reduction would "cost disproportionally" more than the risk reduction benefit achieved. A prerequisite for estimating and evaluating whether ALARP has been met is the identification of any "physically possible" structural or non-structural options for further risk reduction.

This concept is consistent with the common law legal system, which does not prescribe reasonable practice in any field, but not for other legal systems. Decisions on tolerable risks are a very sensitive issue, as "*there is a lack of a widely recognised and accepted methodology for determining tolerable risks, particularly for life safe risks* "[16].

This way, the concept of risk acceptability or tolerability, as well of ALARP, is not widespread or fully understood in Brazil. Following the recent failures of two large tailings dams, there has been a societal demand for zero-risk dams. This highlights the significant challenge of effectively communicating risks, as risk matrix could be misinterpreted with the misconception that identified risks should invariably be eliminated.

Further regarding the criticality matrix, [2] suggests that the number of classes should be compatible with the likelihood and consequence classes adopted in the risk assessment and should be calibrated to ensure that failure modes of similar significance have similar criticality and tolerability classification. This way, when analysing processes (as monitoring process, for example) compatible scales should be used.

Considering this suggestion, Fig. 8 proposes a Criticality Matrix for dam safety purpose, with the lower line for unacceptable risks defined as the probability of 10^{-4} (spillway design criteria = 10,000 years flood) and moderate damage (only material damage and no loss of production/generation if a hydroelectrical power plant).

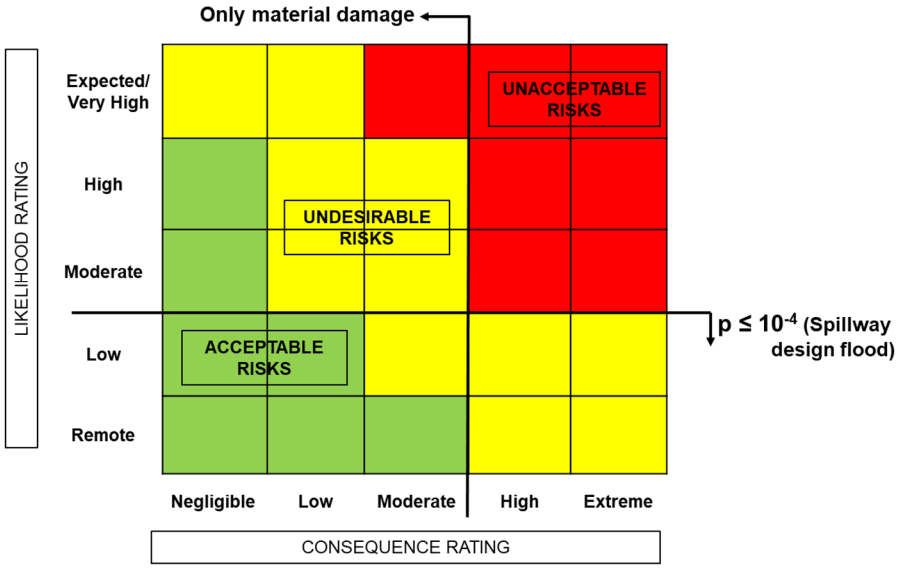

Fig. 8 – Example of Criticality Matrix for risks associated to Dam Safety

9. CONCLUSIONS

The purpose of performing FMEA is to support decisions and reduce the likelihood of failures and their effects. Nevertheless, the complex interdependencies within systems and failure modes, especially for dams, and the dependence on the quality of the information, knowledge and experience of the participants impose restrictions on the final quality of the analysis.

This may lead to not capturing or ruling out possible failure modes and, on the other hand, may result in overlooking the impact of shared control measures and risk reduction opportunities. "*However, when used as a decision support tool in conjunction with standards-based assessments and sound engineering judgement, they provide a transparent and scientifically defendable risk informed approach to decision making that allows for better informed dam safety prioritization that better accounts for the hazards that a dam can present* [14]".

Risk analysis should improve the understanding of the dam performance and its safety, over and above simple regulatory requirements. Unfortunately, sometimes the exact opposite is observed. There may be a fear of exposing risks to regulatory agencies and shortcomings are used in dam safety practice, resulting in very superficial and ineffective analyses.

Another important obstacle to risk analysis in Brazil is the challenge to communicate risks to the stakeholders, and, sometimes, even to the owner's high administration. Risk acceptability is not a current concept in people's mind, who tend to believe that dams should offer no risks at all.

Qualitative risk analysis, using methods like FMEA, have the value of being simple enough, so as to assure that the value of the discussions and improvement in understanding the dam

performance is not lost. The development of the application of this method can certainly help with the prioritization of actions and budget allocation, in favor of safer dams.

REFERENCES

[1] ICOLD (2021). Bulletin 191. Dam Safety Concepts, Principles and Framework. Preprint.

[2] IEC 60812-2018. Failure modes and effects analysis (FMEA and FMECA)

[3] Santos, R.N.C., Caldeira, L.M.S, Serra, J.P.B. (2011). FMEA of a Tailings Dam. Georisk 2011. Lisbon, Portugal.

[4] Santos, R.N.C. (2006). Enquadramento das Análises de Riscos em Geotecnia, Master Thesis, FCT-UNL.

[5] Federal Energy Regulatory Commission. (2005). Dam Safety Performance Monitoring Program. Chapter 14. Washington, DC: Federal Energy Regulatory Commission.

[6] Canadian Dam Association (2021). Functions, failure Modes and Failure Mechanisms. Dam Safety Committee Working Group Report – progress as of July 2021. Accessed 11 November 2024. <https://www.cdabulletin-digital.com/cdaq/0421_fall_2021>.

[7] Chrysler Corporation, Ford Motor Company, General Motors Corporation (1995). Potential Failure Mode and Effects Analysis (FMEA): Reference Manual.

[8] MBN (2024) What is failure mode. Accessed 17 November 2024, <https://marketbusinessnews.com/financial-glossary/failure-mode/>

[9] Independent Forensic Team (2018). Oroville Dams Spillway Incident. ASDSO

[10] Alberta Environment and Parks (2022). PFMEA Tool for Risk-informed Dam Safety Prioritization. CDA Bulletin Spring 2022.

[11] Espósito, T., Palmier, L.R. Application of risk analysis methods on tailing dams. Soils and Rocks 2013. Brazil, São Paulo.

[12] ANELL (2023). Resolução Normativa ANEEL Nº 1.064, de 2 de maio de 2023.

[13] Schafer, H.L.; Beier, N.A.; Macciotta, R. (2021) A Failure Modes and Effects Analysis Framework for Assessing Geotechnical Risks of Tailings Dam Closure. Minerals 2021, 11, 1234. https://doi.org/10.3390/min11111234

[14] Donnely, C.R. (2020). A Discussion on the Evolution and Application of Quantitative Risk Informed Dam Safety Decision Making. (DOI: 10.1007/978-981-15-1971-0_52)

[15] FERC (2015). Federal Guidelines for Dam Safety Risk Management. FEMA P-1025/January 2015.

[16] ICOLD (2005). Bulletin 130. Risk Assessment in Dam Safety Management: A reconnaissance of benefits, methods and current applications.

[17] Bowles, D.S. (2003) ALARP Evaluation: Using Cost Effectiveness and Disproportionality to justify risk reduction. ANCOLD 2003 Conference on Dams

Fifth International Dam World Conference
PORTUGAL • LISBON • LNEC • APRIL 13-17, 2025
dam world 2025

QUXUE DAM 2D FEM ANALYSIS - ASPHALT CORE DISPLACEMENTS COMPARISON WITH SIMILAR STRUCTURES

Maria do Carmo Reis Cavalcanti[1]
Universidade Federal do Rio de Janeiro

Marcos Barreto de Mendonça[2]
Universidade Federal do Rio de Janeiro

Fernanda Silva Drumond[3]
Geocoba Projetos de Engenharia

ABSTRACT

Asphalt concrete mixtures have been used as waterproofing core elements for dams since the middle of the 20th century, avoiding the need for impervious material borrow areas and enabling construction even during the rainy season. In Brazil, the construction of rockfill dams with asphalt cores is recent; only two such structures have been built so far. Some aspects of asphalt core dams' behavior still deserve further investigation, such as the stresses and displacements along the interface fine transitions/asphalt core due to the deformability contrast between the materials. The present work presents Finite Element Method flow and stress-strain analyses of the Quxue dam, an asphalt core rockfill dam 174m high in China, simulating the construction sequence and reservoir impounding. The study focused on the core horizontal and vertical displacements and their comparison with the behavior of similar structures from different parts of the world. The plane strain analysis results have shown good agreement with the ones from broad valleys dams but not with the data from the instrumentation of the Quxue dam itself. This discrepancy, as explained by Qiu et al. [1], may come from the valley's narrowness, a little wider (200m) than the Quxue dam height (174m), which compromises the plane strain conditions and its results, leading to potential implications for the design and construction of similar structures.

Keywords: Dams, Asphalt core, Finite Element Method (FEM), Stress x strain 2D analysis.

[1]carminhacavalcanti@poli.ufrj.br
[2]mbm@poli.ufrj.br
[3]fsilvadrumond@gmail.com

1. INTRODUCTION

Asphalt mixtures started to be used as waterproofing elements on the upstream face of dams. According to Falcão [2], Germany is one of the pioneer countries in this construction technique; from 1930 onwards, the first dams with asphalt mixtures on the upstream side were built in the country.

The development of dams with an asphalt core began in 1948 with the Vale do Gaio dam in Portugal. In this dam, a layer of bituminous mastic was used over the masonry core, with a thickness varying from 0.10 m to 0.20m and a slope of 1.0V:0.8H (ICOLD, [3]). In this case, the bituminous material was used only as an additional safety measure for sealing.

According to Micheluzzi [4], the first dam with a central asphalt core as the only waterproofing element was built in Germany in 1962. According to Guimarães [5], it was built exclusively with dense asphalt concrete, known in the literature as the DACC (Dense Asphaltic Concrete Core) methodology, which here in Brazil is known as hot machined bituminous concrete (CBUQ).

This innovation led to an increase in the number of dams of this type of dams, mainly in Germany and Norway, where the speed and safety of the construction process were verified (Guimarães, [5]), being used in Norway, according to Höeg [6] since 1978.

The evolution of technology has enabled the construction of dams with great heights, such as the Zarema dam in Ethiopia, 153 m high, completed in 2017; the Moglicë dam in Albania, 167 m high, in 2019; and the Quxue dam, 174 m high, in 2017 (Feng et al., [7]).

This construction technique is relatively new in Brazil. It was first used in 2010 in the Hydroelectric Power Plant (HPP) Foz de Chapecó dam, located on the border between the States of Santa Catarina and Rio Grande do Sul. Later 2012, it was also applied in the HPP of Jirau, located in the State of Rondônia.

According to Guimarães [5], this type of dam can reduce costs compared to other solutions due to its fast construction and few limitations due to meteorological conditions. This technique also eliminates the need to explore extensive borrow areas for the impervious core material compared to rockfill dams with a clay core.

2. BEHAVIOR OF ASPHALT CORE

According to Höeg [6], the main function of the asphalt core in a rockfill dam is to maintain low permeability without any significant increase in permeability due to fractures or cracks. Furthermore, if cracks occur, the asphalt mixture must be able to self-heal due to its viscoelastic-plastic behavior.

Additionally, according to Wang and Höeg [8], the asphalt core mixture must be sufficiently malleable to accommodate the deformations imposed by the dam, foundation, and reservoir during construction, filling, and operation. Laboratory tests indicate that the Young modulus of asphalt mixture used in dam cores is smaller than those used in pavements due to the higher content and lower viscosity of the binder used (Guimarães, [5]; Souza Neto et al., [9].

According to ICOLD [3], as the deformability modulus of the asphalt mixture is much lower than that of the rockfill and transition by its sides, there may be a “hanging” of the asphalt core over the most rigid regions of the dam, with a reduction in the vertical stresses in the dam core.

2.1. Vertical and Horizontal Displacements

This item discusses the behavior of vertical and horizontal displacements of the asphalt core for the highest section of some asphalt core rockfill dams present in the literature at the end of construction and reservoir impounding.

The numerical analysis results of the Aikou (Fang and Liu [10]), 72m high, and Foz do Chapecó dams (Pereira [11] and Peña [12]), 47.5m, and instrumentation records of the Quxue (Qiu et al. [1]) and Megget (Gallacher [13]), 56m high, dams are presented.

According to Law (1975 apud Peña [12]), vertical displacements at the end of the construction of an asphalt core dam can be approximated by a parabolic curve, where the most significant displacement occurs at the dam´s mid-height.

However, according to Pagano et al. [14], the approach to approximate vertical displacements as a parabola is based on a one-dimensional analysis, which does not consider the geometry and the effects of the confining stress variation with the embankment height increase; thus, many earth dams present maximum displacements above or below the average height.

Figure 1 shows the normalized vertical displacements in relation to the height of the dam at the end of construction and reservoir impounding, measured for the Megget dam and calculated for the Aikou and Foz do Chapecó dams (Pena [12] and Pereira [11]). There is no data on vertical displacement measurements for the asphalt core of the Quxue dam.

The vertical displacements at the end of construction (in orange) from the numerical analyses and those measured at the Megget dam showed similar behavior, describing parabolas of the second degree as proposed by Law in 1975. However, in terms of magnitude, the measured displacements were lower than those calculated, with the maximum value at approximately at one-third of the dam height. In contrast, the calculated ones occurred at half height.

Regarding the vertical displacements during the reservoir impounding, the numerical curves showed behaviors that differ significantly from each other and those recorded at the Megget

dam. Among the numerical analyses, Pereira [11] presents normalized values very close to those measured in the Megget dam.

The small values of measured vertical displacements reflect the fact that, at this stage, the forces acting on the asphalt core are eminently in the horizontal direction.

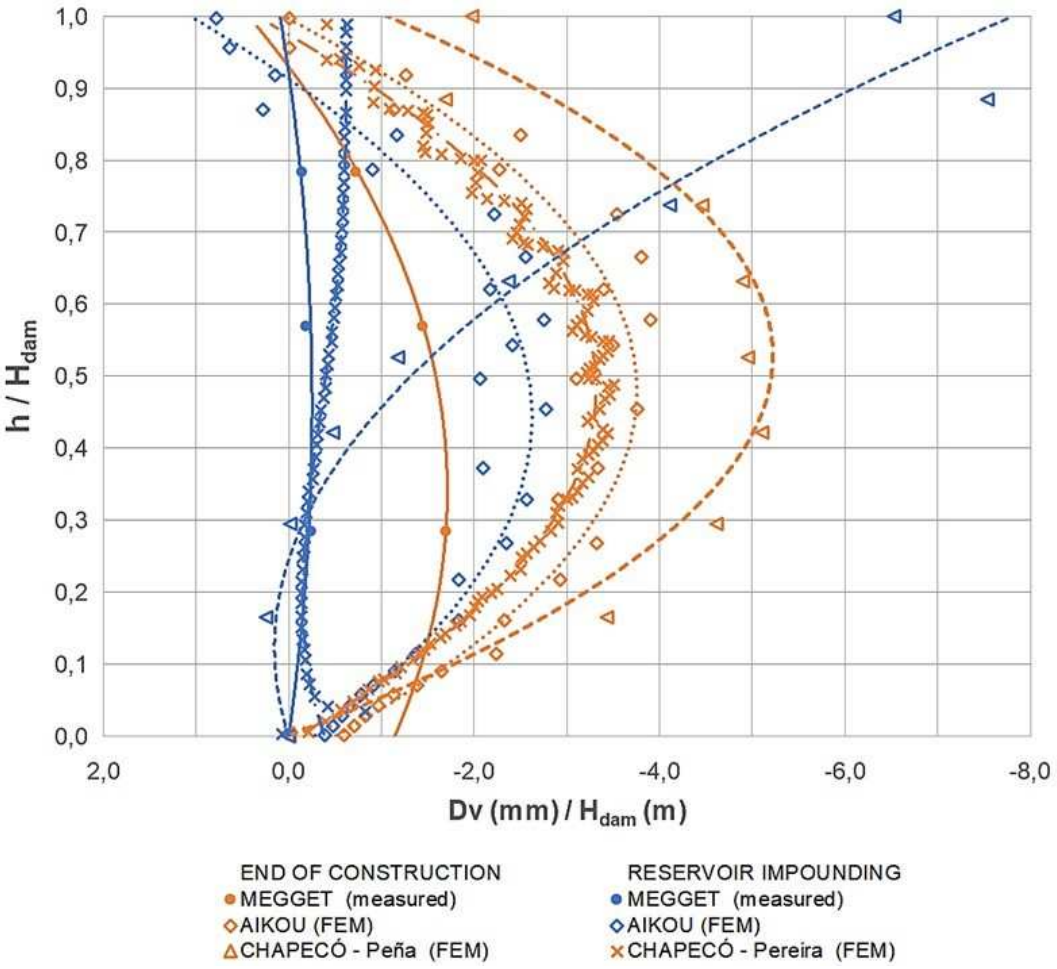

Fig. 1 – Vertical normalized displacements at the end of construction and reservoir impounding

Figure 2 shows the normalized horizontal displacements at the end of construction and reservoir impounding, registered by the instrumentation of the Megget dam and estimated in numerical analyses for the Aikou and Foz do Chapecó dams (Peña [12] and Pereira [11]). It also includes the horizontal displacements measured at the Quxue dam only during the reservoir filling.

The measured values and the numerical analysis results for the horizontal displacements at the end of the construction are very small, which is justified by the fact that during the construction phase, the efforts in the asphalt core are predominantly vertical.

After the reservoir impounding, when horizontal efforts predominate, the normalized displacements of the numerical analyses show much superior values than those measured in the Megget and Quxue dams, which are very similar.

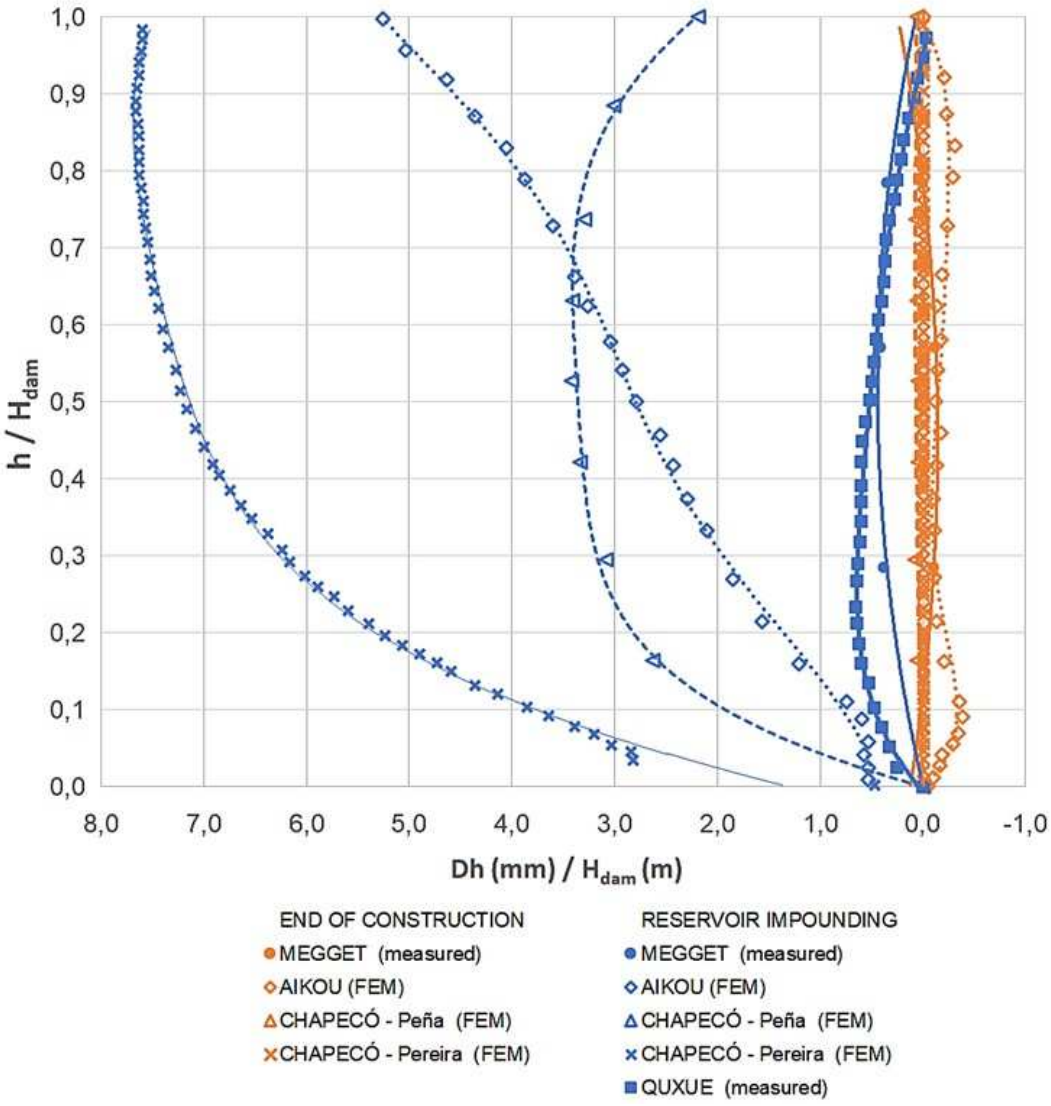

Fig. 2 – Horizontal normalized displacements at the end of construction and reservoir impounding

The numerical analyses considered different constitutive models for the dams' asphalt core under discussion, as shown in Table 1. Although such constitutive models can approximately reflect the behavior of the asphalt core at the end of construction, the results for the reservoir filling do not show the same representativeness.

Table 1 – Constitutive models used in modeling the core asphalt of dams are under discussion

Dam	Asphalt core constitutive model
Aikou Fang and Liu (2011)	Hyperbolic
Foz do Chapecó - Pereira (2010)	Elastoplastic Mohr Coulomb
Foz do Chapecó – Peña (2010)	Hardening soil
Dam	Asphalt core constitutive model

3. CASE STUDY - QUXUE DAM

3.1. Quxue Dam

Quxue Dam was built in a mountainous area with narrow valleys that experience significant seismic movements. According to Qiu et al. [1], by 2021, it was the tallest asphalt-core rockfill dam ever built in the world.

According to Feng et al. [7], the dam has a height of 174 m and a crest length of 220 m. Due to the region's seismicity, the dam was designed with an upstream slope of 1V:1.9H and an average downstream slope of 1V:1.84H. Additionally, as a protection measure against earthquakes, polypropylene geogrids were installed in the upper 30 m of the dam, vertically spaced at each 2.40 m. Figure 3 shows the cross-section of the dam.

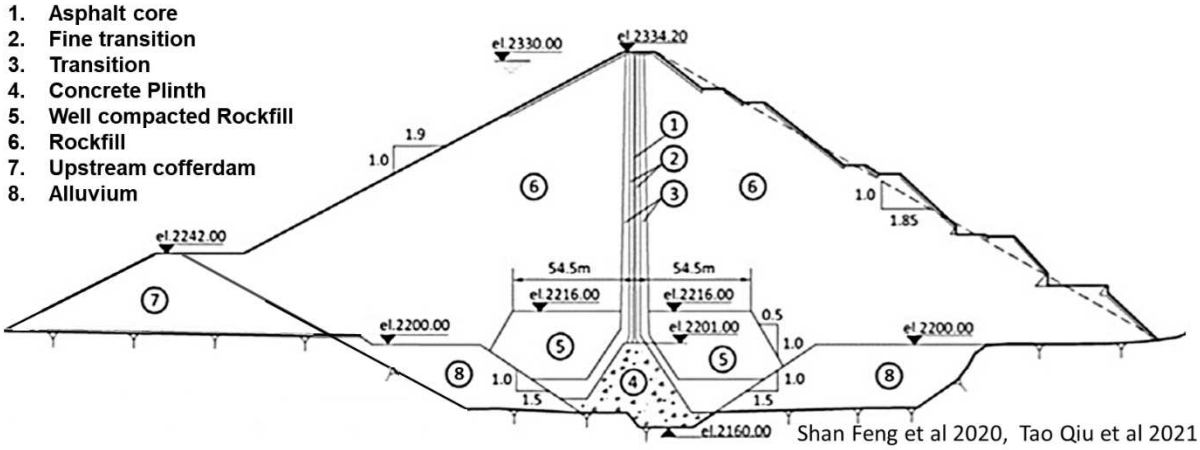

Fig. 3 – Cross section of Quxue Dam (modified from Feng et al. [7])

The asphalt core is 132 m high and is located 2.0 m upstream of the dam center line, 1.50 m wide at the bottom and 0.60 m wide at the top. The fine transition zones, upstream and downstream, adjacent to the core are 2 m wide, while the coarse transition zones are 4 m wide at the bottom and 2 m wide at the top. To minimize rockfill settlement in the central part of the dam, a well-compacted rockfill was placed adjacent to the thick upstream and downstream transitions up to the 2216m level. (Feng et al. [7]).

3.2. Methodology

To evaluate the impact of the asphalt core constitutive models on the results of horizontal displacements during reservoir filling, two-dimensional finite element analyses of the Quxue dam were carried out, simulating the entire sequence of embankment construction and reservoir filling.

Qiu et al. [1] carried out two-dimensional and three-dimensional numerical analyses of the Quxue dam, and their results will be compared to those of the present study.

Except for the asphalt core material, the shear strength and deformability parameters of the other materials were kept as defined by Qiu et al. [1]. In contrast, for the asphalt core, two constitutive models were assigned, the elastoplastic Mohr-Coulomb and the nonlinear elastoplastic model proposed by Wang and Höeg [8].

In the present study, steady-state flow analyses were performed for the different NAs of the reservoir during its filling.

The finite element software RS2, developed by RocScience©, was used for the bidimensional stress x strain and flow numerical analyses.

Plane strain analyses were carried out considering steady-state pore pressures. The construction process and reservoir impounding were simulated in 24 stages. The embankment construction was divided into approximately 15-meter-thick layers. The initial water level was considered at 2201 m, and the level at the end of filling the reservoir was 2330 m; this way, the filling of 129 meters of water column was simulated in 13 stages, as depicted in Figure 4 flowchart.

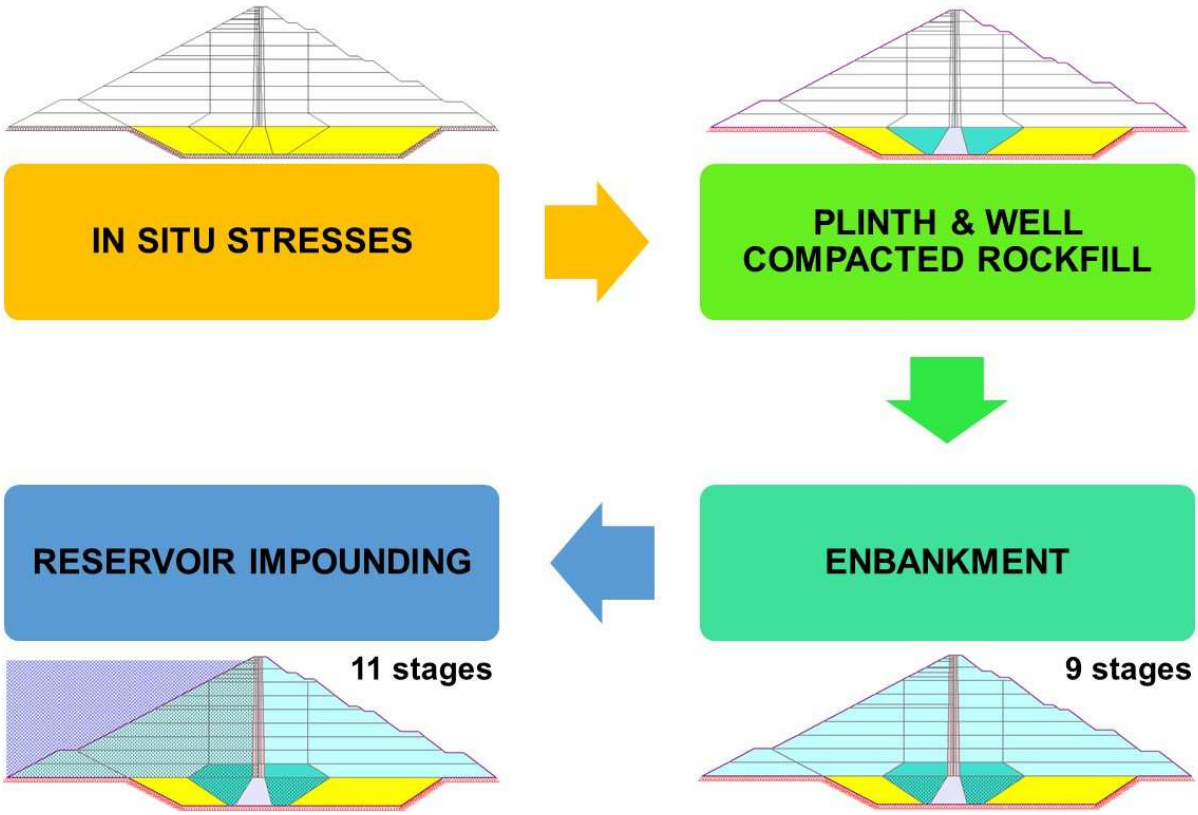

Fig. 4 – Simulation Sequence

The dam was discretized into 5,767 elements of 4 nodes, as shown in Figure 5, which also indicates the applied boundary conditions, material discretization, and final water level in the reservoir.

The steady-state flow analysis considered the reservoir “Total Head (H)” as the boundary condition for the upstream slope, while for the lower part of the downstream slope, the boundary condition “Unknow (?) (P=0 or Q=0)” was applied, satisfying the conditions of zero flow or zero pore pressure. The reservoir water weight was simulated by a triangular load applied to the upstream face of the dam.

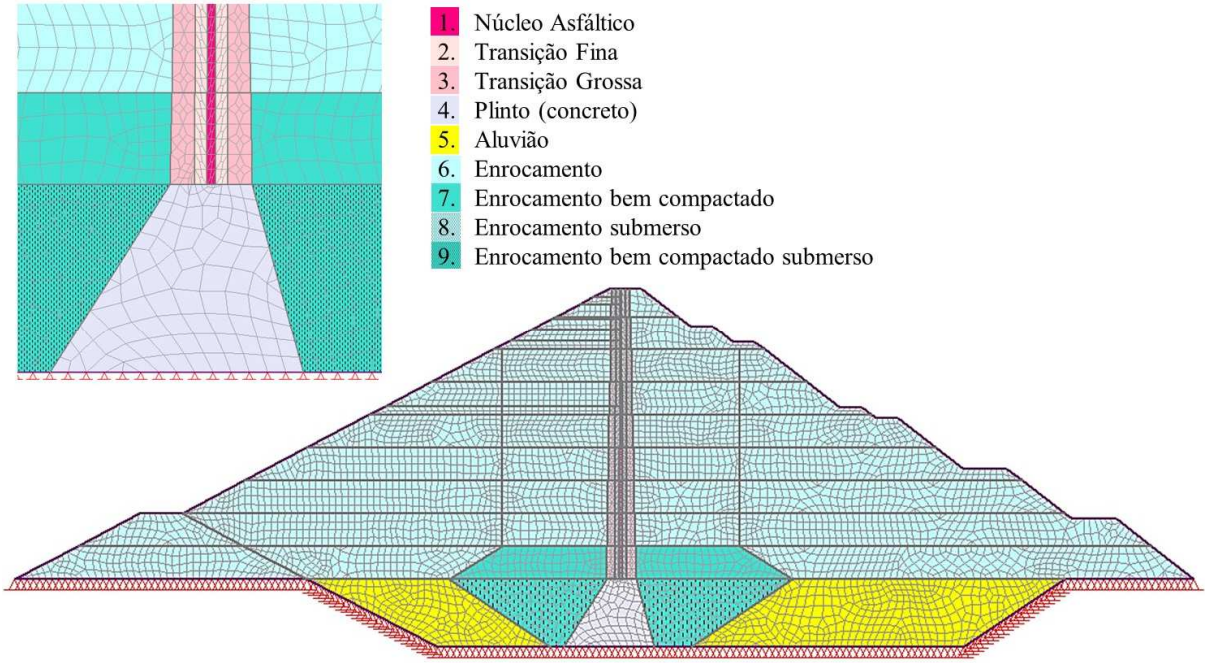

Fig. 5 – Finite Element Mesh, materials distribution, and boundary conditions

3.3. Deformability and Permeability Parameters

The deformability parameters, presented in Table 2, were obtained from the article by Qiu et al. [1], in which the hyperbolic model of Duncan and Chang [15] was used for the alluvium and embankment materials. For the reservoir filling phase, the rockfill K parameters were reduced by 30% to simulate the effect of submersion, as done by Qiu et al. [1].

Table 2 – Hyperbolic parameters used in the analysis (Qiu et al. [1])

Material	γ (tf/m³)	c´ (MPa)	ϕ´ (º)	Δϕ´ (º)	K	n	R_f	K_b	m
Fine Transition	2.35	0	51	8	901	0.30	0.67	359	0.23
Transition	2.32	0	50	8	981	0.27	0.69	561	0.05
Well compacted Rockfill	2.38	0	52	9	1080	0.47	0.73	580	0.30
Rockfill	2.38	0	52	9	980	0.51	0.69	398	0.40
Submerged well-compacted Rockfill	2.38	0	52	9	756	0.47	0.73	580	0.30
Submerged Rockfill	2.38	0	52	9	686	0.51	0.69	398	0.40
Alluvium	2.10	0	44	4	400	0.45	0.75	250	0.10

For the asphalt core, the analyzes were carried out with two constitutive models, the Mohr-Coulomb elastoplastic and the nonlinear elastoplastic model proposed by Wang and Höeg [8], the latter defined by the formulation presented in Equation 1.

$$E_t = \frac{E_{cs}}{(1-\alpha)^2}\left[1 - \frac{(\sigma_1-\sigma_3)(1-\sin\varphi)}{2\sigma_3 \sin\varphi + 2c\cos\varphi}\right]^2 \quad (1)$$

Where E_{cs} represents the stable creep state modulus, α is defined by the ratio between the maximum elastic deviatoric stresses and the yield deviatoric stress, c = cohesive intercept; φ = friction angle; σ_1 and σ_3 are the largest and smallest principal effective stresses.

Once the constitutive model proposed by Wang and Höeg [8] is very similar to the hyperbolic formulation of Duncan and Chang [15], which is expressed by Equation 2.

$$E_t = KP_{atm}\left(\frac{\sigma_3}{P_{atm}}\right)^n \left[1 - R_f \frac{(\sigma_1-\sigma_3)(1-\sin\varphi)}{2\sigma_3 \sin\varphi + 2c\cos\varphi}\right]^2 \quad (2)$$

Where K = dimensionless modulus; P_{atm} = Atmospheric pressure (~101.325 kPa); n = exponent that reflects the influence of the confining stress on the initial modulus; R_f = failure ratio; c = cohesive intercept; φ = friction angle; σ_1 and σ_3 are the largest and smallest principal effective stresses.

With some adjustments to the constants, K, n, and Rf of Duncan and Chang's [15] formulation, the constitutive model of Wang and Hoeg's (2016) can be represented as demonstrated below in Equation 3.

$$E_t = \overbrace{K.P_{atm}}^{K.P_{atm}=\frac{E_{cs}}{(1-\propto)^2}} \underbrace{\left(\frac{\sigma_3}{P_{atm}}\right)^{\hat{n}}}_{=1\ for\ n=0}^{n=0} \left[1 - \underbrace{R_f}_{=1} \frac{(\sigma_1-\sigma_3)(1-\sin\varphi)}{2\sigma_3 \sin\varphi + 2c\cos\varphi}\right]^2 \quad (3)$$

Therefore, reproducing the Wang and Hoeg constitutive model used by Qiu et al. [1] to simulate the behavior of the asphalt core can be done by considering the values of K = 270, n=0, and Rf=1 in a hyperbolic constitutive model. The parameters considered for the asphalt core are presented in Table 3.

Table 3 – Asphalt core parameters

Constitutive Model	γ (tf/m³)	c´ (MPa)	ϕ´ (º)	Δϕ´ (º)	E_t (MPa)	K	n	R_f
Mohr Coulomb elastoplastic	2.47	0.12	51	10.5	-	-	-	0.46
Wang and Hoeg	2.47	0.12	44	-	270	0	1	0.46

For the steady-state flow analysis, the permeability coefficient of the asphalt core came from a study carried out by Falcão [2] for an asphalt concrete with Limestone aggregate CBUQ and 5.5% binder like the one used in the Quxue dam. The permeabilities of the other materials were obtained from USBR [16] based on the unified classification of each material. Table 4 presents the permeability coefficients used in this study.

Table 4 – Asphalt core permeability parameters

Material	k (m/s)	kh/kv
Asfaltic Core (Falcão - 2007)	1.0 E-11	1
Fine Transition - SC	1.0 E-06	1
Gross Transition - SM	1.0 E-05	1
Well-compacted Rockfill - GW	1.0 E-03	1
Rockfill - GW	1.0 E-00	1
Alluvium - SP, medium	1.0 E-05	1

4. ANALYSIS RESULTS AND DISCUSSION

Figures 6 and 7 show, in colors, the horizontal and vertical displacements, respectively, at the end of construction and filling of the reservoir considering for the asphalt core the Mohr-Coulomb elastoplastic model and Wang and Hoeg nonlinear constitutive model along with the results obtained by Qiu et al. in their 2D and 3D analyses.

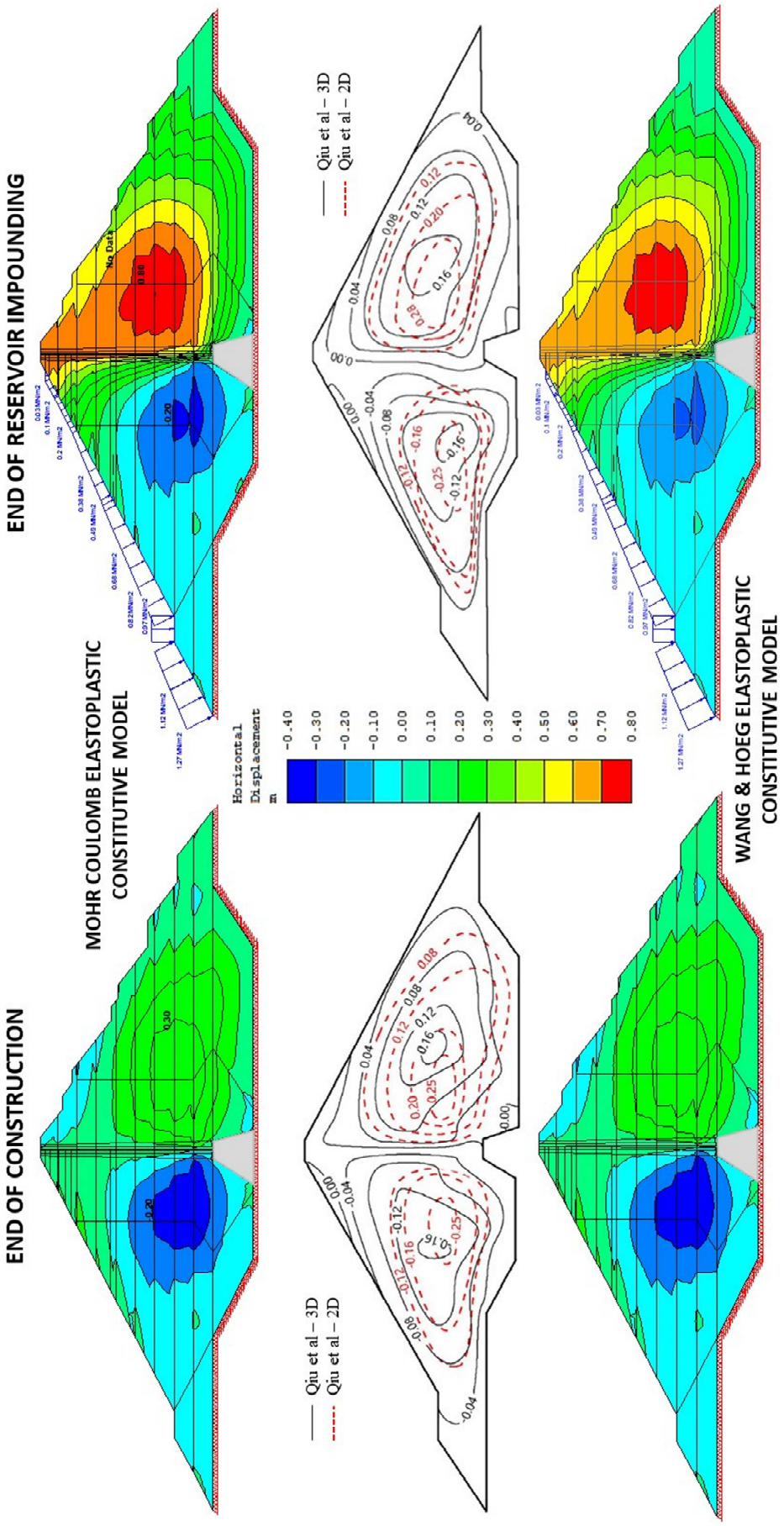

Fig. 6 – Horizontal Displacements

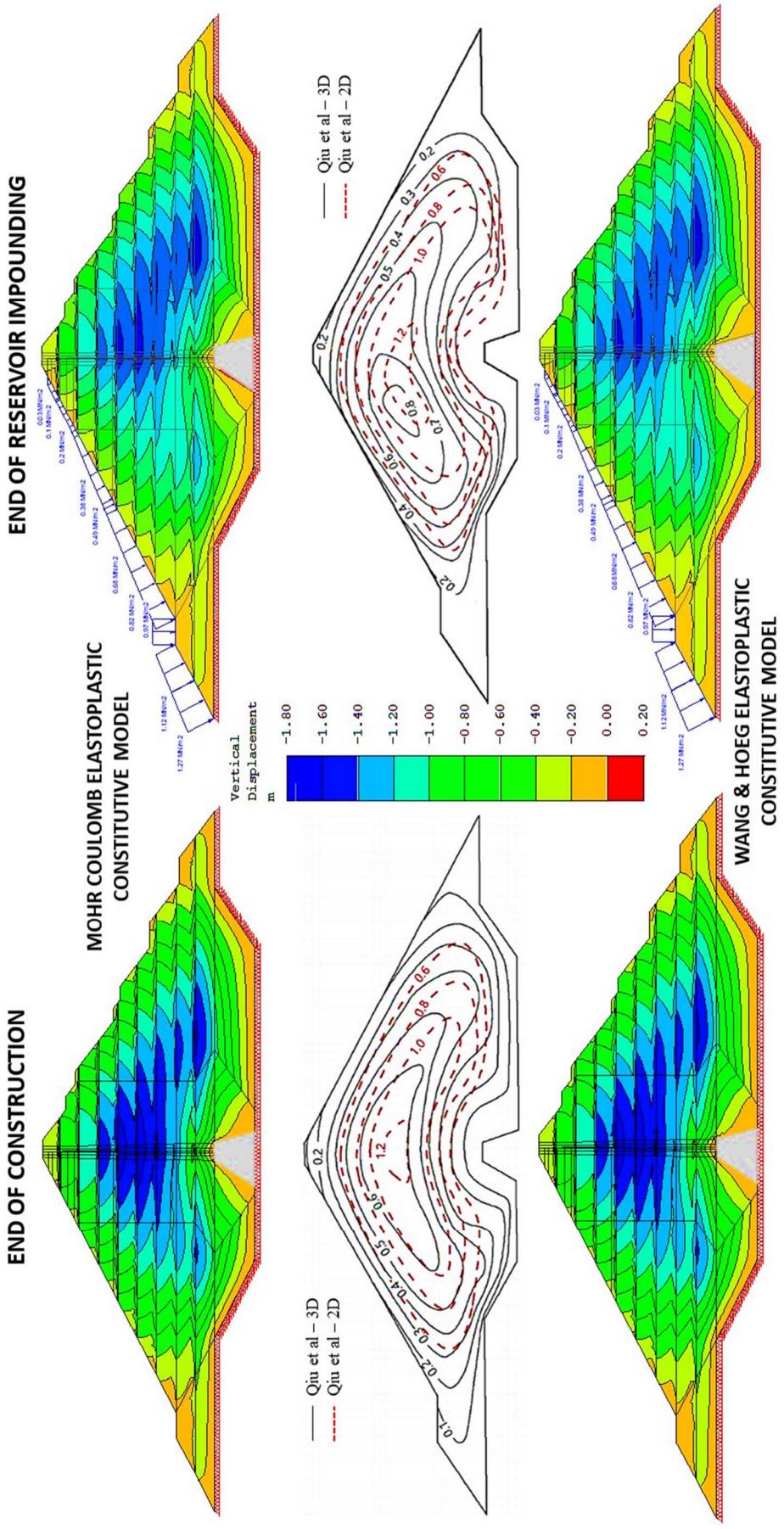

Fig. 7 – Vertical Displacements

The horizontal displacement values obtained at the end of the construction are quite similar to those from the 2D (dashed red lines) analysis by Qiu et al. Nevertheless, the values obtained at the end of the reservoir filling are quite different for both constitutive models evaluated in this study.

Analogous behavior is observed for the vertical displacements after the reservoir impounding, with greater displacements on the downstream slope, while Qiu et al.'s analysis showed the opposite tendency.

Due to various unfortunate circumstances, only a very limited number of vertical displacement measurements were recorded; therefore, a comparison was not possible. Nevertheless, an extensive field instrumentation was installed on the downstream face of the asphalt to measure asphalt core horizontal displacements during impounding and operation. To protect the SAA (Shape-Accel-Array) type inclinometers from the construction high temperatures in the core (around 150º C), casings for the inclinometers were installed on the downstream face of the core during dam construction, and the SAA sensors were introduced into the casings from the dam top after dam construction.

The measured horizontal displacements and the results from the present study, as well as Qiu et al. [1] 2D and 3D analyses, are presented in Figure 8

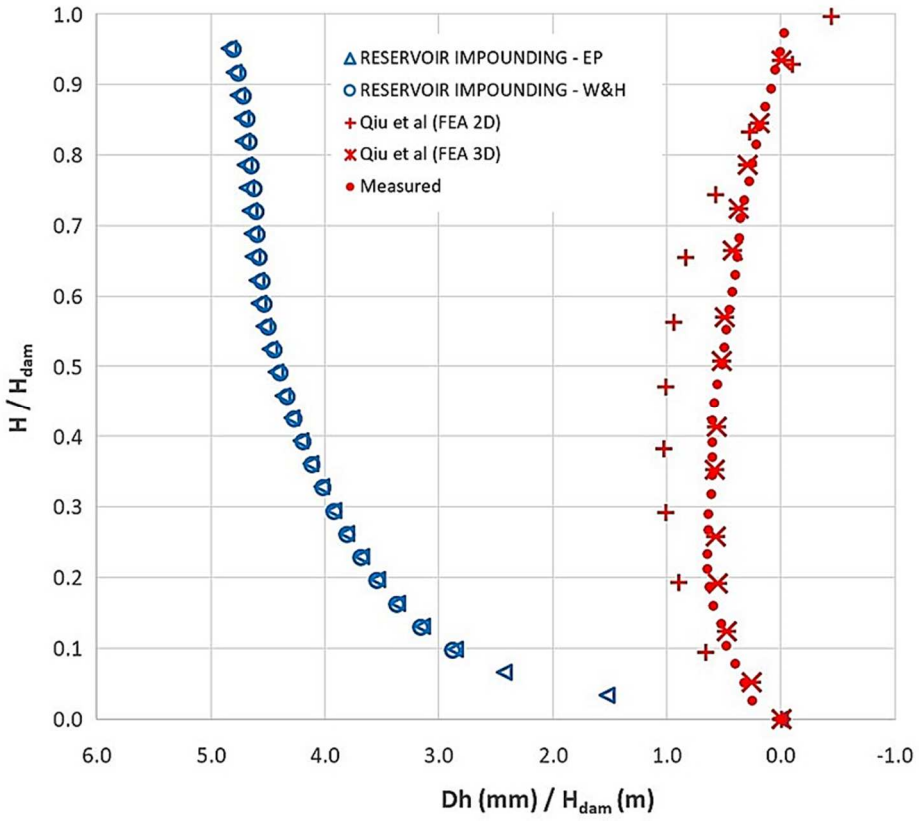

Fig. 8 – Horizontal Displacements – Measured x Numerical Analyses

The horizontal displacements for both asphalt core constitutive models studied are very similar, but much different from the measured values and the analyses presented by Qiu et al. [1]; such discrepancies between the measured and numerical simulation of reservoir impounding have already been registered in Figure 2, comparing different dams.

5. CONCLUSIONS

Although the horizontal displacements after the reservoir's impounding show a discrepancy between Qiu et al.'s [1] numerical results and measured values, the displacements at the end of the construction are similar to those from numerical analyses.

Once the same geometry and parameters have been used, the discrepancies may be attributed to the loading procedure adopted by Qiu et al. [1] during the reservoir filling, which applies water pressure directly on the upstream face of the asphalt core and buoyancy in the submerged upstream rockfill. Additionally, according to Qiu et al. [1], the lower values of the 3D analysis compared to their 2D results were closer to those measured due to the narrowness of the valley in which the Quxue dam was located.

The present study demonstrates that both software users and developers must reevaluate the numerical simulation of the effect of reservoir filling on asphalt core dams.

REFERENCES

[1] Qiu, T., Wang, W., Höeg, K., Feng, S., Zhao, R. (2021). 3D analysis of the 174 m high Quxue asphalt core rockfill dam in a narrow canyon. Soils and Foundations 61 (2021), ScienceDirect.

[2] Falcão, P.R.F. (2007). Estudo das Propriedades Mecânica e Hidráulicas de Concreto Asfáltico para Aplicação em Barragens. DSc Thesis, Departamento de Engenharia Civil e Ambiental, Universidade de Brasília, DF.

[3] ICOLD. (1982). Bituminous Cores for Earth and RockFill. Dams International Commission on Large Dams, Bulletin 42, Paris. ICOLD. 1988. Bituminous Cores For Fill Dams, State of the Art. 16th Congress of the International Commission on Large Dams -San Francisco.

[4] Micheluzzi, A. G. (2016). Controle de qualidade de uma barragem de enrocamento com núcleo asfáltico caso UHE Jirau. Dissertação (MSc) - Universidade Federal de Ouro Preto-Escola de Minas. Ouro Preto, MG.

[5] Guimarães, R.C. (2012). Barragens com núcleo de concreto asfáltico – Análise do comportamento mecânico e hidráulico do núcleo. Tese de Doutorado, Departamento de Engenharia Civil e Ambiental, Universidade de Brasília, Distrito Federal.

[6] Höeg, K. (1993), Asphaltic Concrete Cores for Embankment Dams: Experience and practice. Noruega, StikkaTrykk.

[7] Feng, S., Wang W., Hu W., Deng Y., Yang J., Wu S., Zhang C., Höeg K. (2020). Design and performance of the Quxue asphalt-core rockfill dam. Soils and Foundations 60 (2020), ScienceDirect.

[8] Wang, W., Höeg, K. (2016). Simplified material model for analysis of asphalt core in embankment dams. Construction and Building Materials 124 (2016), ScienceDirect.

[9] Souza Neto, F. A. D. D., Motta, L.M.G., Mendonça, M. B. (2014). Concreto Asfáltico para Uso em Núcleo de Barragem Um estudo de caso. In: Anais dod 21 Encontro de Asfalto, Rio de Janeiro.

[10] Fang, C., Liu, Z. (2011). Stress-strain analysis of Aikou rockfill dam with asphalt-concrete core. Journal of Rock Mechanics and Geotechnical Engineering 2011.

[11] Pereira, F. A. (2010). Análise numérica de uma barragem de enrocamento com núcleo asfáltico. Dissertação MSc, Universidade Estadual do Norte Fluminense Darcy Ribeiro - UENF Campos dos Goytacazes, RJ.

[12] Peña, A. H. V. (2012). Comportamento de Barragem de Enrocamento com Núcleo Asfáltico. Dissertação (Mestrado) - Pontifícia Universidade Católica do Rio de Janeiro, Departamento de Engenharia Civil, Rio de Janeiro.

[13] Gallacher, D. (1988). Asphaltic Central Core at the Megget Dam. 16th Congress on Large Dams, San Francisco.

[14] Pagano, L., Desideri, A., Vinale, F. (1998). Interpreting settlement profiles of earth dams. Journal of Geotechnical and Geoenvironmental Engineering (October 1998).

[15] Duncan, J. M., & Chang, C. Y. (1970). Nonlinear analysis of stress and strain in soils. Journal of Soil Mechanics & Foundations Div.

[16] USBR. (2018). Design Standards No. 13 Embankment Dams, Chapter 8 U.S. Department of the Interior.

Fifth International Dam World Conference
PORTUGAL • LISBON • LNEC • APRIL 13-17, 2025
dam world 2025

NUMERICAL SIMULATION OF DAM BEHAVIOR DURING THE RESERVOIR FILING UNTIL REACHING STEADY-STATE CONDITIONS

Pablo H da C.R.Moreira[1]
Elera Renovavéis

Maria do C. R. Cavalcanti[2]
COPPE/UFRJ

Marcos B. Mendonça
COPPE/UFRJ

ABSTRACT

This paper presents the compared results of numerical models and data coming from monitoring systems during the filling of a 75 m high embankment dam. It compares the pore pressure and vertical displacement records from the instrumentation installed in the dam with the results from finite element numerical modeling using the Mohr-Coulomb elastoplastic constitutive model and, through back-analysis, assess the need for possible adjustments in parameters related to permeability, strength, and deformability of the materials. A transient flow analysis was performed to simulate the reservoir filling and the advancement of the saturation front until a steady-state condition was reached. Parameter adjustments were made to align the numerical analysis results more closely with the piezometric values measured in the field. Using these results, the displacements were verified with pore pressures coupled in the back-analysis, varying over time. The results indicated discrepancies in the originally adopted parameters, both in terms of permeability coefficient values and in relation to anisotropy, elasticity modulus, and material strength parameters. It is noteworthy that the saturation speed recorded in the foundation by the instruments was higher than those estimated during the executive design, and the same was observed for the vertical displacements occurring in the abutments. It is noteworthy that significant increases in settlement were observed in regions with colluvium soil foundations on different dates. The transient flow analysis demonstrated that saturation of the foundation material occurred at about the same time, suggesting a relationship between the increase in displacement and saturation. It was possible to recreate such behavior in the numerical analysis by eliminating the colluvium cohesion after saturation.

Keywords: Dams, Finite Element Method (FEM), Stress x strain 2D analysis, Transient Flow, Back-analyses.

[1]pablo.moreira@elera.com, Brail

1. INTRODUCTION

In recent decades, there has been an increase in concern about dam safety in Brazil and around the world. The importance of dams for the socioeconomic development of a region is evident; however, these structures pose risks to society and the environment due to the potential impacts in case of accidents [1].

To better understand and predict the behavior of a dam structure under the demands it will face throughout its useful life, back analyses are a valuable tool. They compare the projected results with those that occurred in the structure through instrumentation [2,3]. Back analysis allows for the verification/evaluation of the projected, executed, and actual behavior of the structure based on instrumentation readings during the construction and operation phases. This helps validate and adjust, if necessary, both the calculation models and the parameters considered in the design phase to better represent the current behavior and predict its future behavior [4].

The objective of this work is to study the transient behavior of flow and stress/deformation of a saddle dam, with a mixed section and 72 meters in height, in response to the rise in water level during the reservoir filling. Based on the data from the instrumentation installed in the structure, the aim is to obtain adjusted parameters and information on the dam's behavior, which can support future analyses of this and other similar structures.

2. CASE OF STUDY

The object of study will be a saddle dam, part of the hydraulic circuit for power generation at a hydroelectric plant, which is shown in Fig. 1.

Fig. 1 - Aerial view of the dam structure under study

The dam has a maximum height of approximately 75.00 meters, a crest length of 255 meters, and a width of 7.00 meters. It is composed of an upstream slope made of compacted soil, a downstream slope made of compacted soil and rockfill, and a central core made of soil with a high clay fraction. The upstream slope incorporates a compacted soil cofferdam with a crest elevation of 209.00 meters, which was used for river diversion during the excavation, embankment, and foundation grouting phases. The upper section of the upstream slope also features rockfill protection against wave action in the reservoir.

The dam's foundation, within a strip of approximately 75 meters in the creek bed, is in rock. The left abutment has the central core foundation and upstream and downstream slopes in residual soil, with 3.0 meters of the most superficial foundation soil removed upstream of the central core and 6.0 meters downstream and beneath it. The right abutment has the foundation in residual soil, with part of the superficial foundation soil removed to a thickness of 3.0 meters. To monitor and evaluate the dam's behavior, piezometers were installed in the embankment and foundation, surface markers along the crest and berms, a flow meter at the toe of the downstream slope to measure seepage through the dam and foundation (at the abutments), and water level gauges at the abutments.

3. METHODOLOGY

3.1. SUMMARY

The methodology of this study is summarized in the topics below:

- Data consolidation: Instrumentation, projects, geotechnical parameters, and reservoir filling data.
- Model creation: Geometry/regions, materials, finite element mesh, instruments position.
- Numerical modeling of transient flow: Initial saturated and unsaturated permeability parameters, flow back analysis with instrumentation, and permeability parameter adjustments.
- Numerical stress-deformation modeling: Initial deformability and strength parameters, plane strain state analysis, deformation back analysis with instrumentation, and deformability parameter adjustments.
- Discussion of the geomechanical behavior of the dam: Evaluation of piezometric behavior and evaluation of displacement behavior in response to changes in pore water pressure during filling.

3.2. RESERVOIR FILLING DATA

After the completion of part of the embankment, the closure of the diversion gallery initiated the partial filling of the reservoir, which remained for approximately 3 years. To recreate the actual flow conditions at the start of filling, a steady-state flow analysis was performed with the level corresponding to an elevation of 225.00 meters. In the simulation of the reservoir filling, the water levels recorded by the limnigraphs were used, starting from an elevation of 225 meters until reaching the normal maximum level of 251.30 meters. (Fig.2)

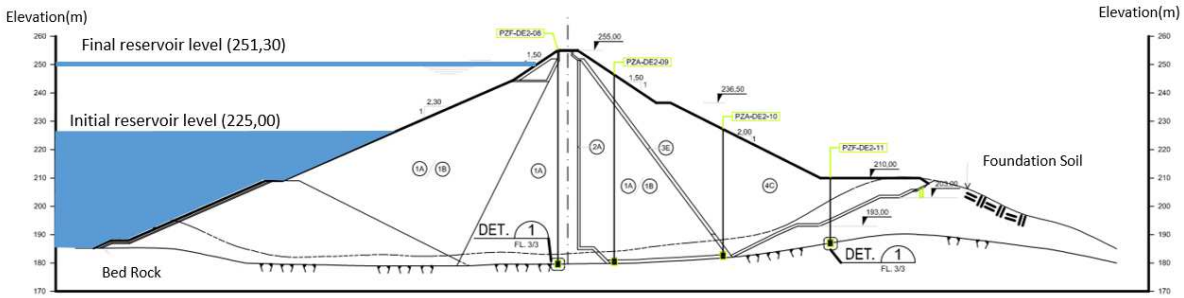

Fig. 2 – Reservoir levels at the analyses

The boundary conditions considered in both analyses were the hydraulic head corresponding to the reservoir's water level (variable over time) on the upstream slope, zero pore pressure at the end of the horizontal drainage blanket downstream of the dam where the flow is free, the groundwater level before filling at the downstream end of the model, and a variable boundary condition where there is a drain condition when pore pressure > 0 or impermeable when pore pressure < 0 on part of the downstream slope of the dam.

A transient analysis was conducted over a duration of 3 years to ensure that by the end of the transient analysis, the flow regime had reached a steady-state condition. The temporal discretization of the analysis steps was defined exponentially, allowing for greater detail at the beginning of the analysis. This reflects the monitoring process of the structure, which starts with closely spaced readings during filling and whose intervals are increased after confirming the good performance of the structure through instrument readings.

3.3. Sections and numerical model

The design of this dam includes 4 instrumented cross-sections, with piezometers for measuring pore pressure and surface markers for vertical displacement. The piezometers were predominantly installed in three regions: in the drainage blanket, in the soil foundation, and in the upstream embankment.

The 4 instrumented sections were analyzed, even though they were not in a perfect plane strain state. For the discretization of the problem, 1.0 meter elements were used in the embankment materials, except for the filter where the element size was reduced to 0.5 meters

to achieve better pore pressure distribution in the filter. In the foundation, 3.0 meter elements were used to optimize mach.

The sections with materials, instruments, and the finite element mesh are presented in the following Figure 3.

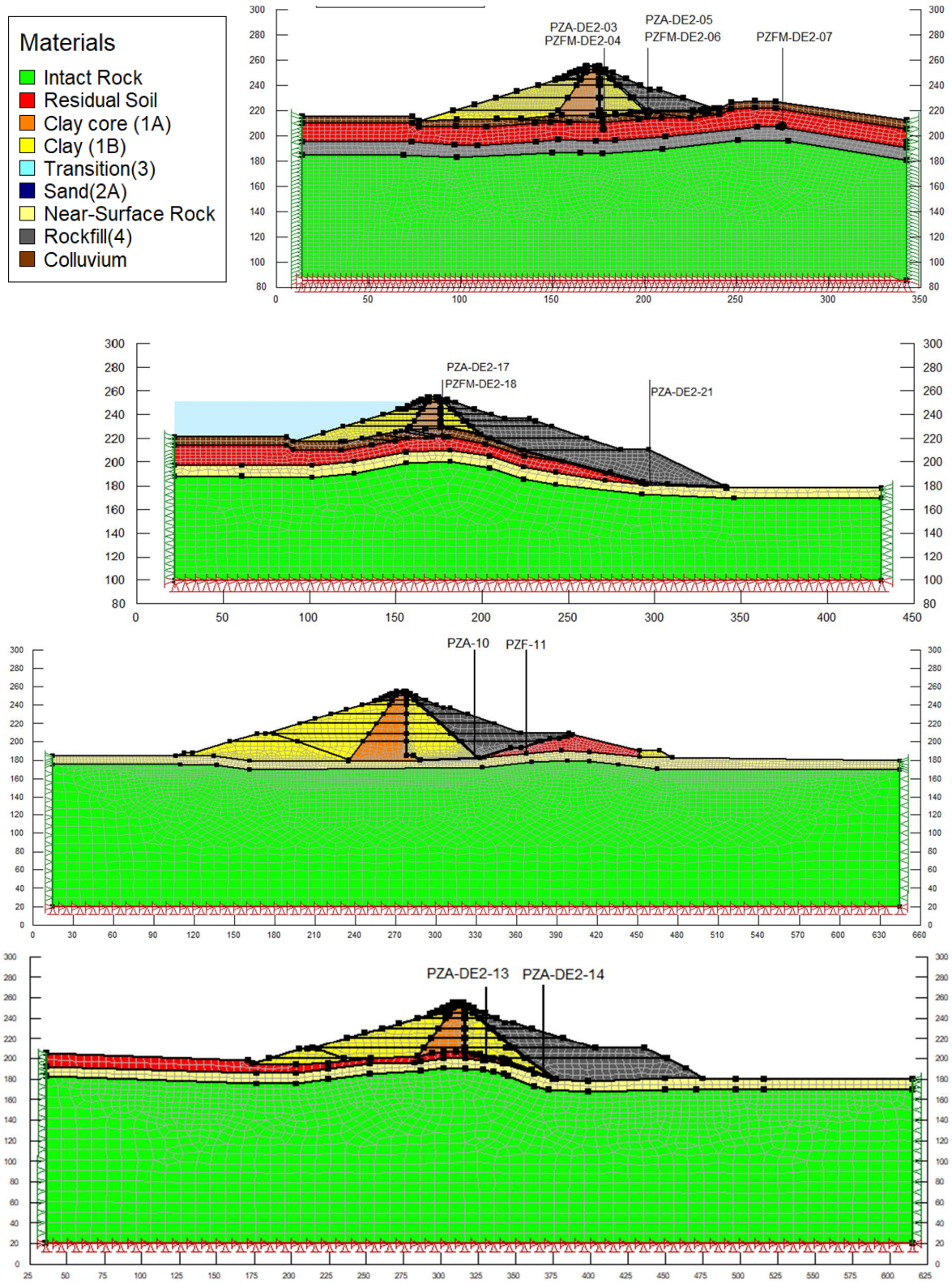

Fig. 3 – Section B, E, C e D, respectively

3.4. Material properties

For the initial flow and stress/strain analyses, the parameters of saturated permeability, deformability, strength, and the hydraulic conductivity and volumetric moisture content curves of the dike materials were considered, with the adopted values presented in Table 1

Table 1 – Material properties of the studied Dam

Material	Constitutive models	γ (kN/m³)	c' (kPa)	ϕ (°)	E(kPa)	k_x (cm/s)	k_y/k_x (cm/s)
Colluvium	Elasto-perfectly plastic	18	15	23	9500	1,00E-04	1
Residual soil	Elasto-perfectly plastic	18	10	29	29580	1,00E-03	1
Clay(1B)	Elasto-perfectly plastic	18	10	26	9500	4,00E-05	4
Clay core (1A)	Elasto-perfectly plastic	18	13	27	11730	4,00E-06	4
Transition (3)	Elasto-perfectly plastic	20	0	35	25000	1,00E+00	1
Sand (2A)	Elasto-perfectly plastic	17	0	33	20000	1,00E-02	1
Rockfill (4)	Elasto-perfectly plastic	23	0	45	60000	1,00E+01	1
(*) Near-surface Rock	Linear elastic	24	-	-	6000	1,00E-04	1
Intact rock	Linear elastic	24	-	-	30000	1,00E-05	1

(*) For the near-surface rock, a reduction in the modulus of elasticity relative to sound rock was used, as proposed by [5], adopting a factor of 0.3 due to its low quality (A2C3F3).

4. RESULTS

4.1. Transient analysis

In all instrumented sections, the piezometers installed immediately above the drainage blanket did not register any variation with the filling of the reservoir, demonstrating the effectiveness of the internal drainage system. Since sections C and D had only instruments without variations during the filling of the reservoir, these sections were not used in this phase of the back-analysis. Thus, to evaluate the permeability parameters and verify the compatibility of the numerical model with the field instrumentation, the transient flow analyses considered the data from piezometers PZFM-DE2-04 and 06 in section B and PZFM-DE2-18 in section E.

To verify the compatibility of the model with the field instrumentation, three analyses were performed with changes in the permeability parameters, as shown in Table 2, where the parameters altered in each analysis are highlighted in bold.

In the initial flow back-analysis (F1), the original project parameters were used without any changes, while in F2, the permeability value of the foundation colluvium was increased by an order of magnitude, and in F3, the kx/ky ratio of embankments 1A and 1B was altered, increasing the horizontal permeability of the embankment from 4 to 10 times the vertical permeability, according to [6].

Table 2 - Saturated permeability parameters used in the flow back-analysis

Material	F1		F2		F3	
	Ky (cm/s)	Kx/Ky	Ky (cm/s)	Kx/Ky	Ky (cm/s)	Kx/Ky
Clay(1B)	4,00E-06	4	4,00E-06	4	4,00E-06	**10**
Clay core (1A)	4,00E-05	4	4,00E-05	4	4,00E-05	**10**
Rockfill (4)	10	1	10	1	10	1
Transition (3)	1	1	1	1	1	1
Sand (2A)	1,00E-02	1	1,00E-02	1	1,00E-02	1
Colluvium	1,00E-04	1	**1,00E-03**	1	1,00E-04	1
Residual soil	1,00E-03	1	1,00E-03	1	1,00E-03	1
(*) Near-surface Rock	1,00E-04	1	1,00E-04	1	1,00E-04	1
Intact rock	1,00E-05	1	1,00E-05	1	1,00E-05	1

Figure 4 presents the results of the piezometric levels of PZFM-DE2-04 for each back-analysis performed, where it is possible to verify that the three analyses show slopes close to those demonstrated by the instrumentation readings, differing, however, in terms of the magnitude of the readings and saturation dates. In this case, the closest result was F1 with the project parameters, but all analyses closely represent the measured instrumentation.

For PZFM-DE2-06, the analyses showed quite divergent behavior, as shown in the results presented in Figure 5, with the saturation rate criterion being considered of greater importance in the evaluation. In F2, where the colluvium is considered more permeable, the instrument showed better results in terms of the saturation front speed; however, due to the higher permeability, it did not develop pore pressures compatible with the measurements, reaching a maximum value of 2 mca compared to the 4 mca recorded by the instrument. Considering the saturation rate and pore pressures, the best compatibility was F3, despite the delay of about 15 days for the start of saturation and the instrument data not being available from 03/20/2013.

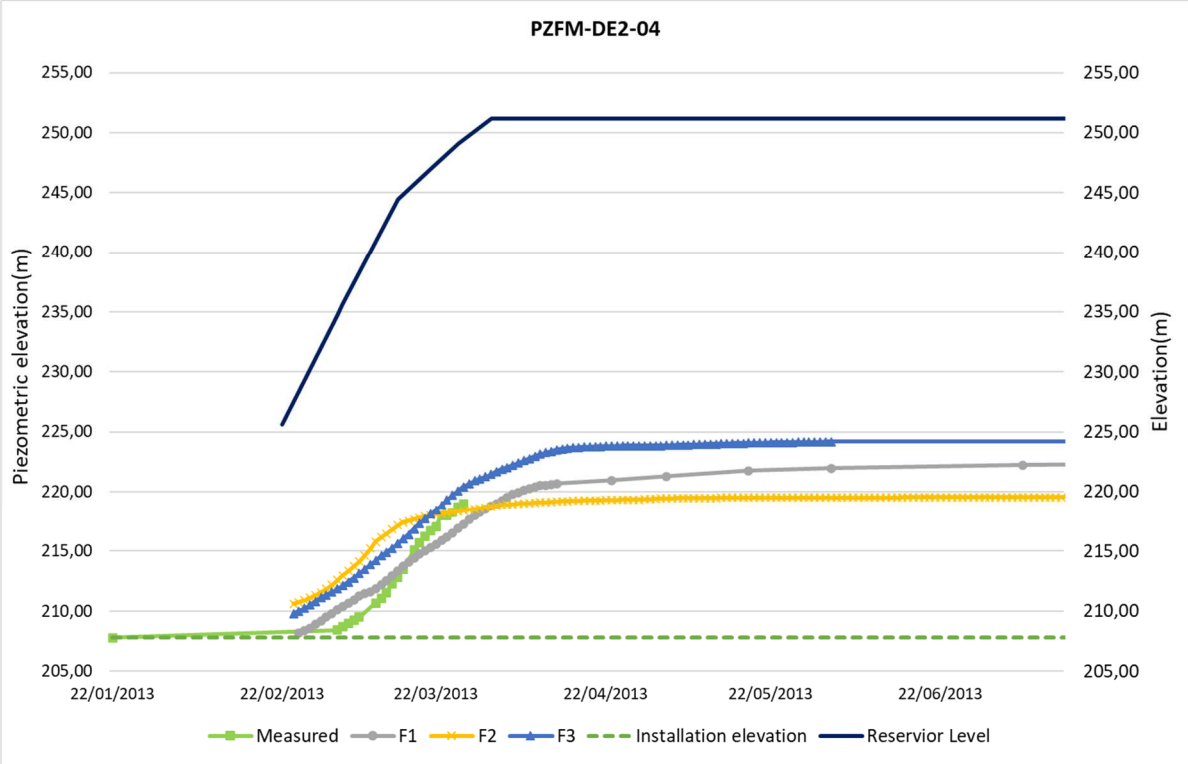

Fig. 4 – Comparison of flow analyses and piezometric elevation PZFM-DE2-04

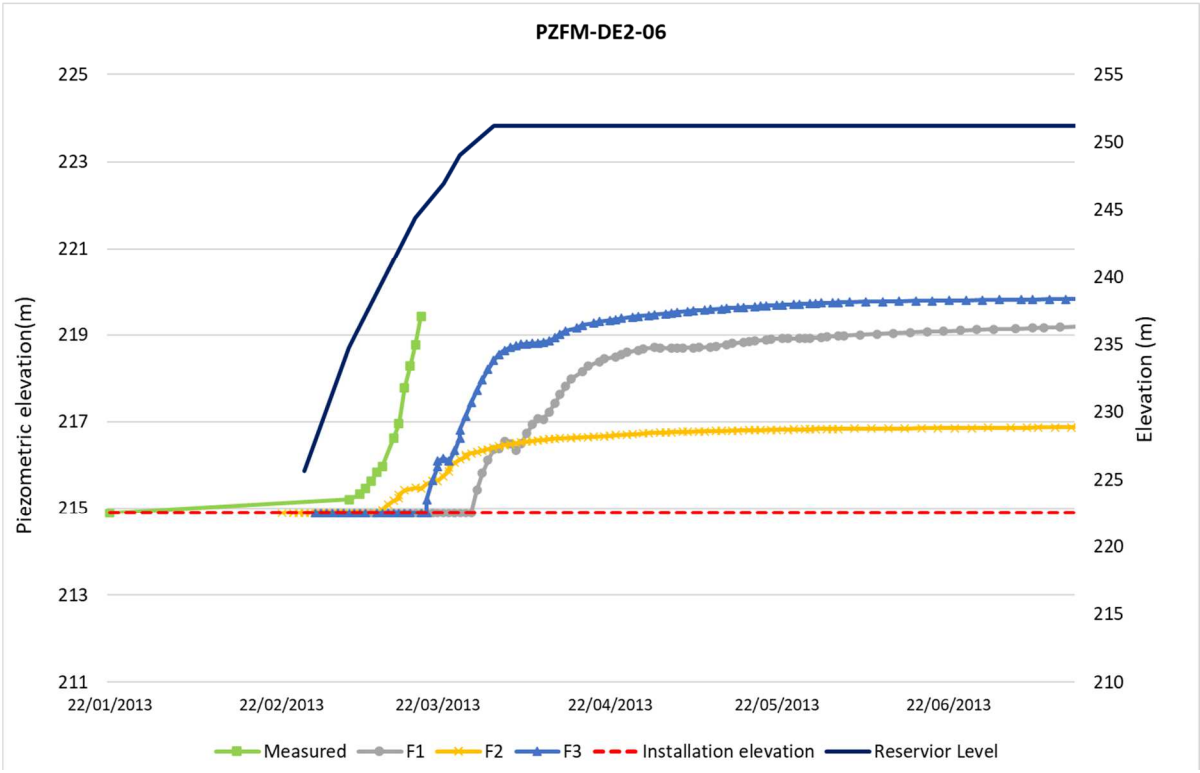

Fig. 5 - Comparison of flow analyses and piezometric elevation PZFM-DE2-06

The behavior of the PZFM-DE2-06 instrument shows a certain anomaly since it does not present a head loss compared to PZFM-DE2-04 upstream, which would be expected given the 25 meters that separate them, suggesting a geological-geotechnical condition not found during

the investigation. It is worth noting that both instruments showed defects after a period of operation, which may have occurred for various reasons not appearing in the instrumentation records. However, in summary, back-analysis 3 showed greater compatibility between the numerical model and the field instrumentation for section B.

In section E, PZFM-DE2-18 showed variations that allowed the comparison of its behavior and saturation rate with the results of the transient flow numerical modeling. The results of the measured and generated piezometric levels in the three analyses are presented in Figure 6, along with the variation of the reservoir water level.

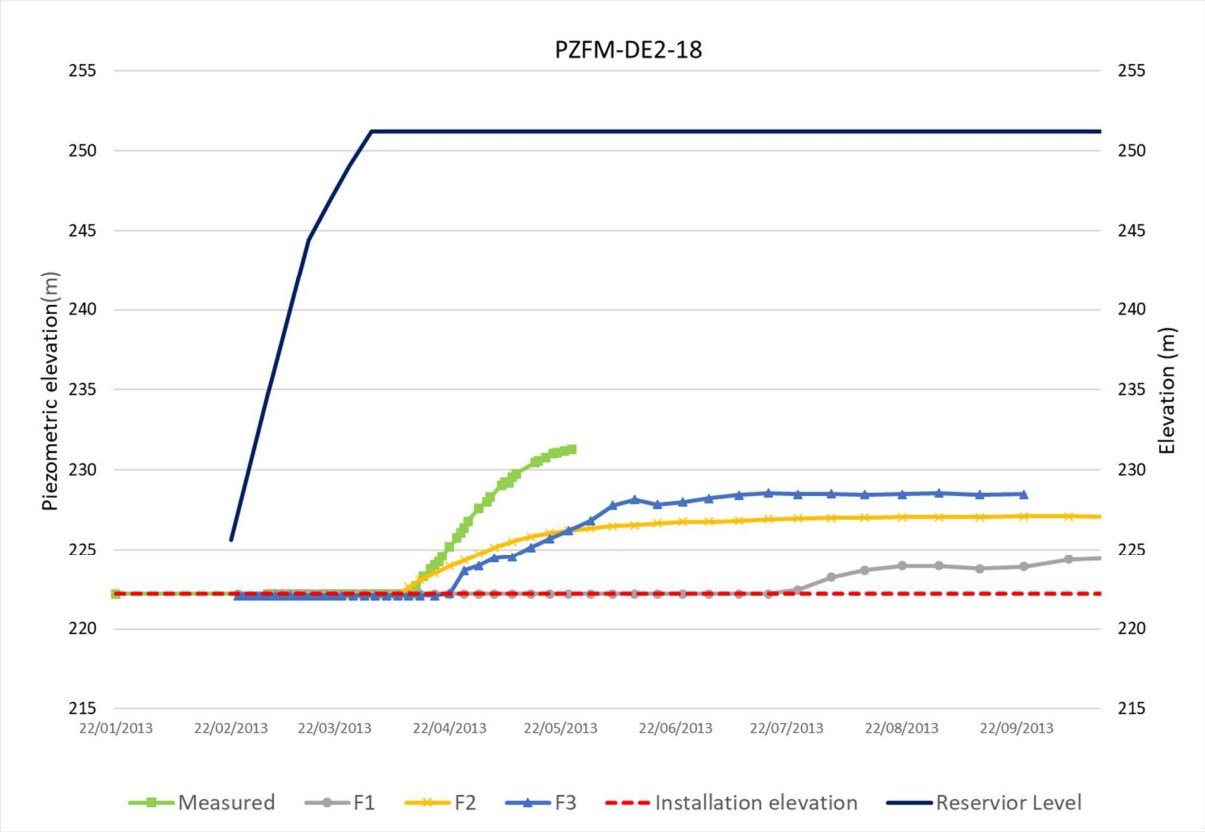

Fig. 6 - Comparison of flow analyses and piezometric elevation PZFM-DE2-18

It is found that the results of F1, with the project data, diverge greatly from the behavior of the field instrumentation, taking about 100 days to start the saturation process of the instrument installation region. For F2, the saturation rate results are compatible, even indicating slightly anticipated saturation; however, the pore pressures of the numerical model were much lower than the instrument readings, reaching a maximum value of 5 mca. Analysis F3, in turn, presented a close saturation date with a delay of about 3 days compared to the field instrumentation, but showed more compatible pore pressures, reaching 6.5 mca.

Even with the three results, it is perceived that the model cannot completely reflect the instrumentation records; however, F3 showed about 70% compatibility in terms of pore pressures and only a small delay in the foundation saturation date. For this reason, in

subsequent analyses, for all instrumented sections, the permeability parameters of analysis 3 will be considered, as it also showed compatibility with the instruments installed in section B.

Figures 7 present the phreatic lines for section E, as an example, for the days corresponding to the dates of the leveling campaigns of the crest surface benchmarks, starting on 03/04/2013, whose pore pressure data were considered in the stress and deformation analyses for comparative evaluation with the vertical displacements of the model.

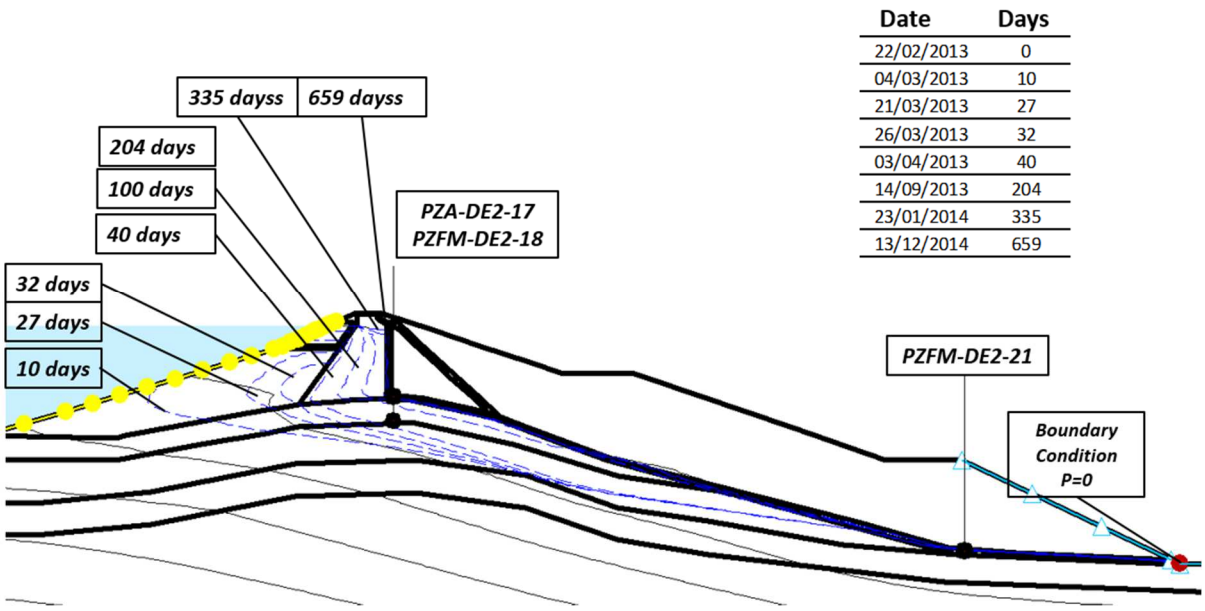

Fig. 7 - Variation over time of phreatic lines in section E

4.2. Stress-strain analyses

The stress-strain analyses were developed in two stages due to the differentiated characteristics of the foundation type. The back-analysis began with sections D and C, on the riverbed resting on rock, to adjust the deformability parameters of the upstream clay embankment/central core, and subsequently, sections B and E, on the abutments with soil foundation, to adjust the deformability parameters of the foundation materials.

Three analyses were performed, varying the values of the modulus of elasticity for the embankment material, while keeping the project resistance parameters unchanged. The first alternative (D1) considered the modulus of elasticity estimated based on oedometer tests, the second (D2) with the modulus of elasticity of embankments 1A and 1B increased by 25%, and the last analysis (D3) increased by 50% (Table 3).

Table 3 – Deformability parameters

Material	D1 E (MPa)	D2 E (MPa)	D3 E (MPa)
Clay(1B)	11,73	14,66	17,60
Clay core (1A)	9,50	11,88	14,25
Rockfill(4)	60,00	60,00	60,00
Transition (3)	25,00	25,00	25,00
Sand (2A)	20,00	20,00	20,00
Colluvium	9,50	9,50	**9,50**
Residual soil	30,00	30,00	30,00
(*) Near-surface Rock	3500,00	3500,00	3500,00
Intact rock	35000,00	35000,00	35000,00

Figure 8 presents the results of the vertical displacements recorded at the surface benchmark MS-DE2-06 by topography and those obtained in the three analyses. The results reflect the effect of the reservoir filling load and the pore pressures generated by the advance of the saturation front, altering the stress state existing at the end of construction.

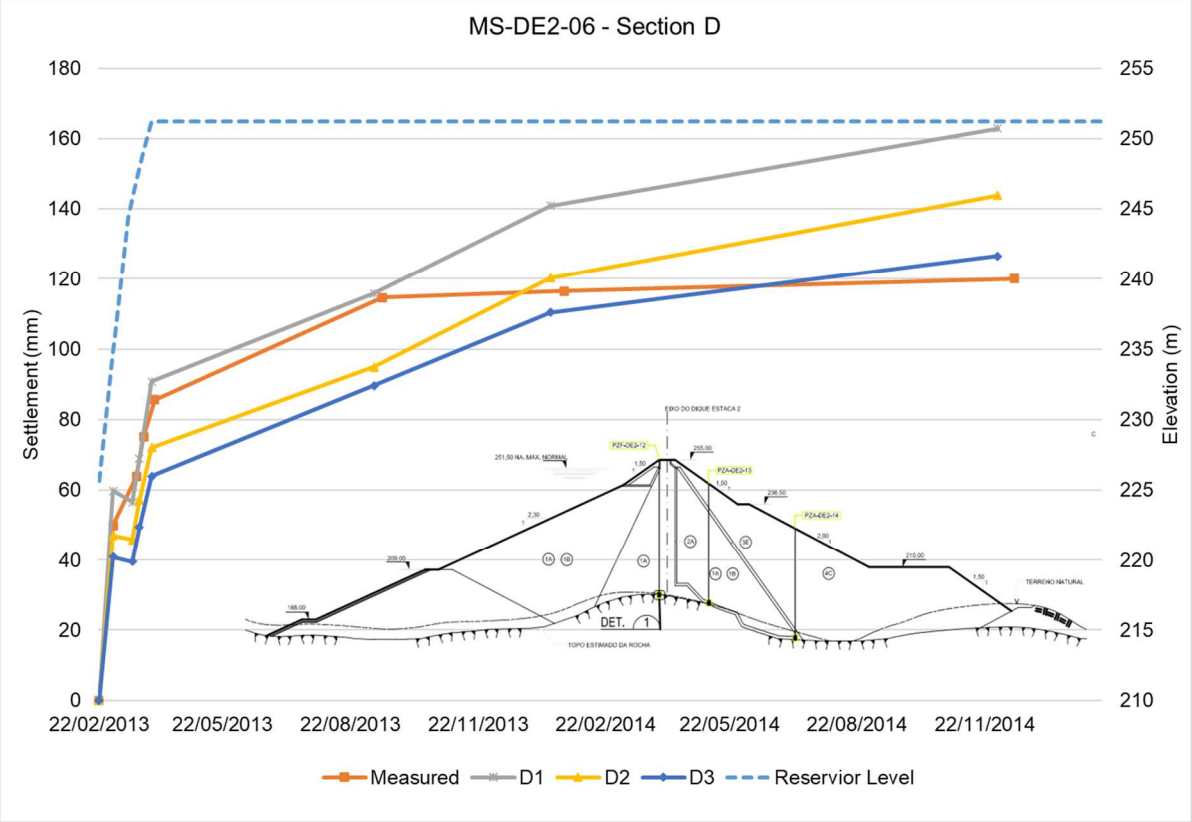

Fig. 8 - Comparison of deformation analyses and settlement measured by MS-DE2-06

For MS-DE2-06 in section D, the initial analysis (D1) showed final displacements much higher than those measured, exceeding them by about 1/3, demonstrating that the initial estimate of deformability parameters from the oedometer test resulted in a modulus of elasticity value

lower than that obtained in embankments 1A and 1B. The best fit between the measured and calculated final displacement values was obtained for a modulus of elasticity of the clay material increased by 50% (D3). However, in this analysis, a time lag was observed in relation to the measurement dates after the reservoir filling, presenting a deformation rate in the first month after filling of about half of that recorded by the instrumentation.

Since pore pressures are an important factor in displacement behavior at this stage, and as it was not possible to measure the permeability parameters in the clay material due to a lack of instrumentation data, the observed delay could be attributed to a lag in the advance of the saturation front. Additionally, there is uncertainty about the plane strain state, with possible influence from the longitudinal displacements of the abutments generating greater confinement in the riverbed region.

For section C, the same procedure adopted for section D was repeated, with the settlements recorded at the surface benchmark MS-DE2-03 and the modeling results presented in Figure 9. The results obtained for section C were very similar to those observed for section D, where back-analysis D1 showed the most divergent behavior and D3 the most compatible. The displacement rate of the analyses also showed some delay compared to the values recorded by the instrumentation.

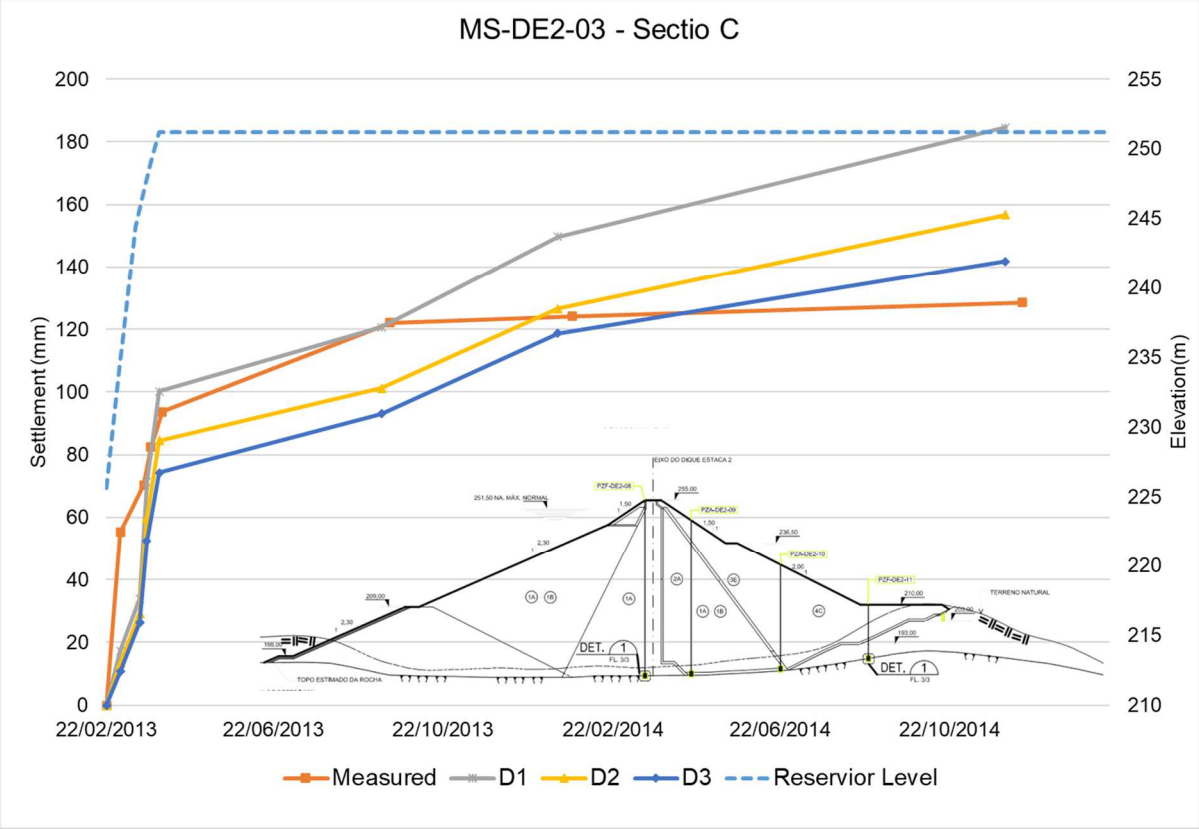

Fig. 9 - Comparison of deformation analyses and settlement measured by MS-DE2-03

However, despite the differences in geometries and embankment height, sections C and D showed displacement results close to those measured when using the deformability parameters from back-analysis D3, which will be adopted for the clay embankment in the analyses of sections B and E, which have a soil foundation.

In sections B and E, located respectively on the right and left abutments, both with soil foundation, the surface benchmarks MS-DE2-01 and MS-DE2-10 are installed to monitor vertical displacements. To evaluate the deformability of the foundation soils, analyses were performed using the estimated parameters as presented in Table 3. The displacement results obtained from the analyse D3 and recorded by the instrumentation are shown in Fig.10, along with the evolution of the reservoir water level.

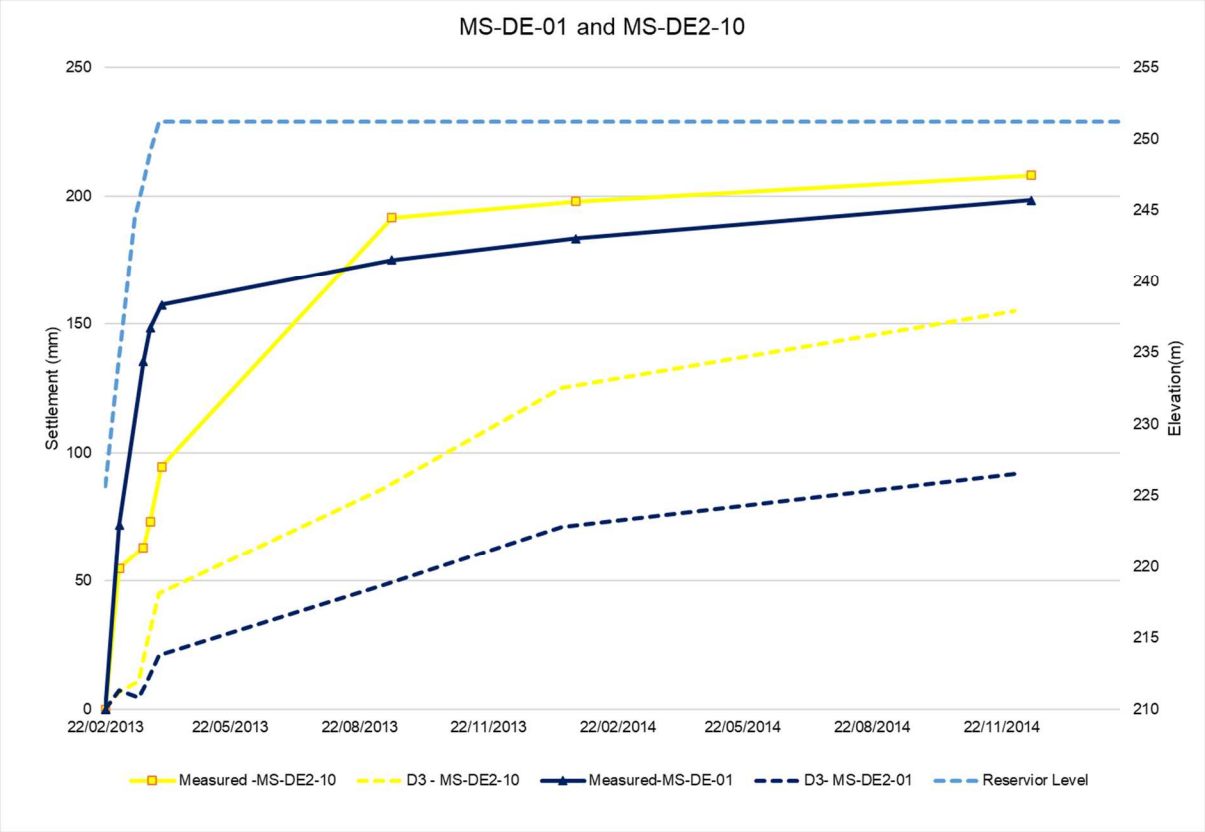

Fig. 10 - Comparison of deformation analyses D3 and settlement measured by MS-DE2-01 and 10

The results of the analyses for both sections showed displacements much lower than those recorded by the surface benchmarks, and despite the difference in embankment heights between the sections, discrepancies between the measured and calculated displacements were of the same order of magnitude, between 100 to 150 mm.

It was also observed that there was a sudden acceleration of deformations in MS-01 almost immediately after the start of filling, while for benchmarks MS-07 and MS-10, a similar

phenomenon was recorded about 180 days after the start of filling, which was not observed for the other benchmarks.

This pronounced displacement behavior over a short period occurred only in the sections resting on colluvium in the abutments. Given this, assuming that this soil was naturally unsaturated before the dam and had not undergone compaction like the embankment materials, it was hypothesized that such high vertical deformations over a short period were due to the saturation of the foundation with the reservoir filling.

According to [7], it is a characteristic of unsaturated soils to exhibit a tendency for volumetric changes when moisture varies, even without stress variation. Volume reduction can occur with increased moisture content, which commonly happens in low-density soils. Additionally, in these soils, there can be a decrease in interparticle contact strength and a structural rearrangement conditioned by the new saturation level. In [8] the author cites a similar case in dam foundation soils due to the increase in soil saturation degree from reservoir filling.

The response of the piezometers to the reservoir filling shows that the moments when the greatest displacement variations occur correspond to the piezometric record indicating material saturation in both instrumented sections in the abutments, as shown in Figure 11. Thus, it is plausible to consider a correlation between the saturation of the foundation colluvium and the high displacement rate occurring in specific periods.

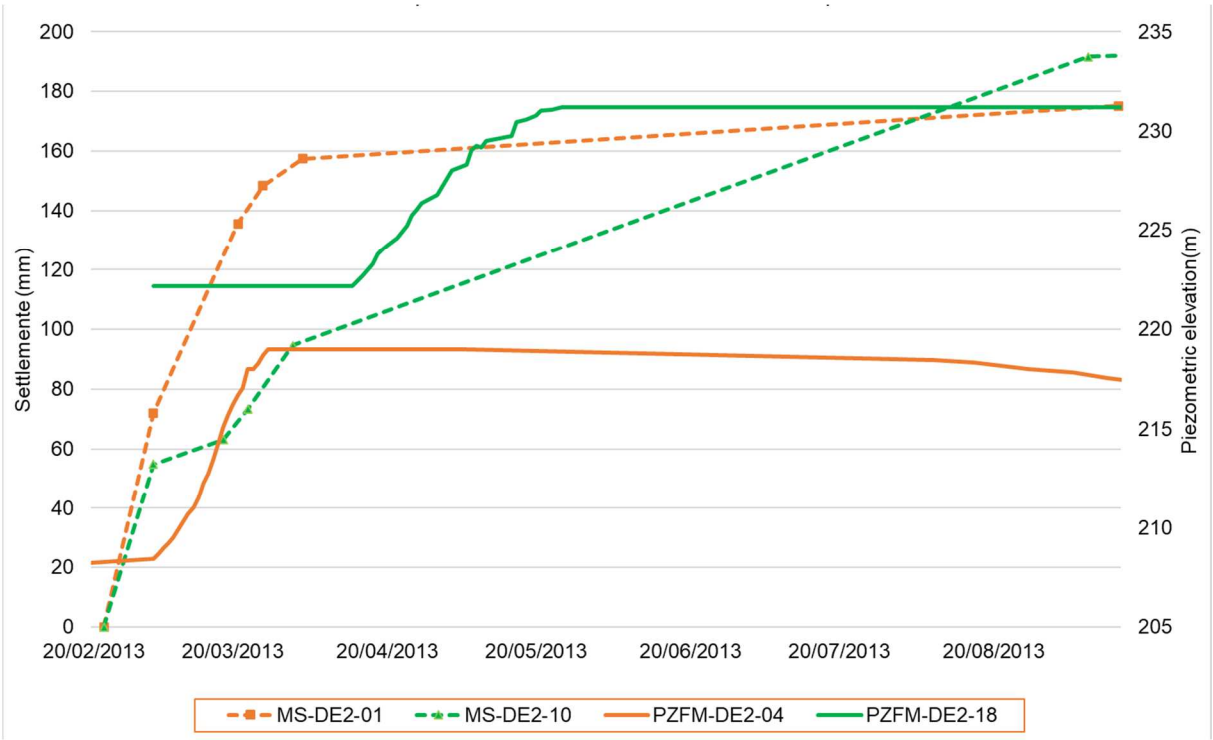

Fig. 11 – Relationship between settlement and saturation in section B and E

Triaxial tests performed by [9], on samples with different suction values demonstrated a small variation in the friction angle but a large variation in cohesion with the reduction of suction. A direct correlation between matric suction and the total cohesion intercept was observed, which decreases as saturation increases.

Based in the possibility to this type of behavior, it was decided to verify the validity of the hypothesis by performing a numerical simulation eliminating the cohesion of the foundation soils when the soil is saturated, according to the results of the transient flow analysis. The simulation of the saturation effect in this study was carried out by replacing the foundation material with a material of the same characteristics but without cohesion at the stage when the saturation front reaches it.

With the reduction in cohesion and, consequently, the strength of the foundation colluvium, there was an increase in displacements due to the material's plasticization, according to the Mohr-Coulomb constitutive model, as shown in Figure 12 in the section B, which compares the measured displacements with and without the reduction in cohesion. Despite the increase in total displacements with the elimination of cohesion, the displacement rate measured during the initial readings remained quite different, demonstrating that the numerical model still needs adjustments to better reflect field behavior.

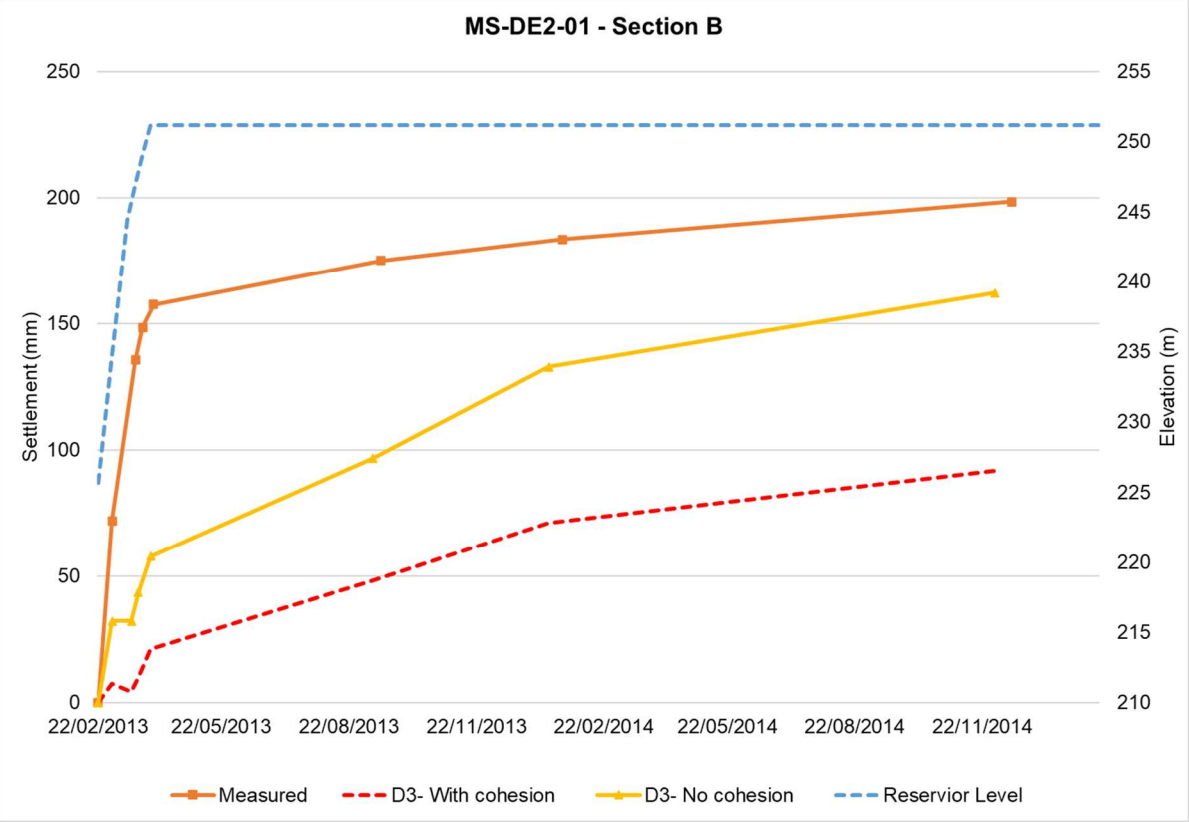

Fig. 12 – Comparison of deformation analyses D3 with cohesion, D3- no cohesion and settlement measured by MS-DE2-01

Following the same methodology for section B, the colluvium had its cohesion reduced to zero at the moment the transient analysis indicated saturation of the material in section E. The displacement results of the analyses with and without cohesion reduction for section E, along with the measured values and the variation of the reservoir water level, are presented in Figure13 .

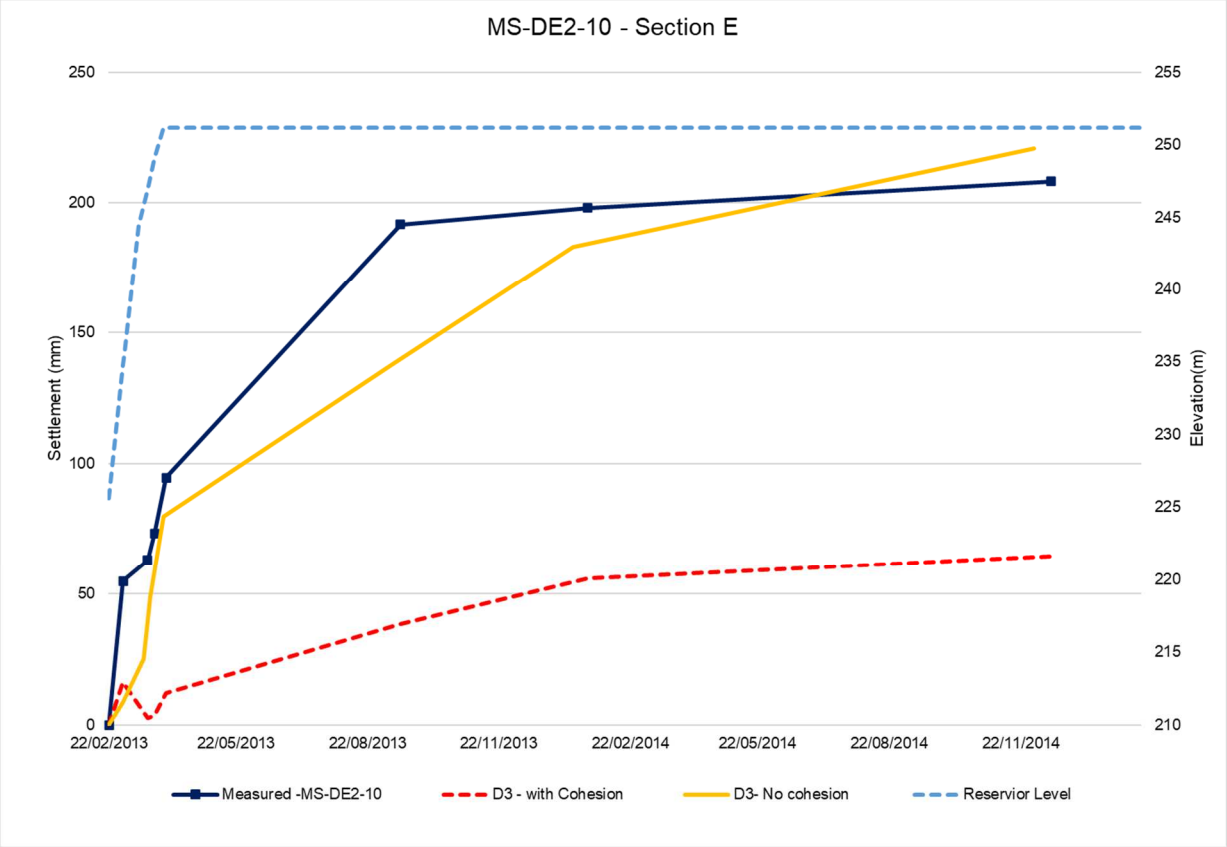

Fig. 13 - Comparison of deformation analyses D3 with cohesion, D3- no cohesion and settlement measured by MS-DE2-10

When the full foundation saturation occurs between the fourth and fifth displacement measurement campaigns, the analysis with cohesion reduction showed an acceleration in displacements, like that observed in the measured displacements. With the removal of cohesion in the foundation colluvium as the material is saturated, the model presented more compatible results, although at the end of the simulation it showed a displacement value slightly higher than the measured one, already showing a stabilization trend.

5. RESULTS DISCUSSION

Despite the parameter changes, it was not possible to achieve 100% compatibility with the records; however, the values found can simulate the approximate behavior of the dam's flow, showing the structure's performance during the reservoir filling, which is a critical phase for the dam.

For the stress/strain analysis with the reservoir filling loads associated with the pore pressures from the transient analysis, it was possible to perform a temporal analysis of the settlements, verifying not only the magnitude but also the speed and acceleration of the displacements, making the stress state at the time of the surface benchmark readings more realistic and consequently the displacements resulting from the change in the stress state.

For sections B and E, resting on colluvial and residual soils, the numerical model's displacements showed values much lower than those measured, suggesting that the foundation material characteristics did not match the project expectations. The time distribution of displacements along the crest of the structure indicated significant displacement increases only in the abutments and at different dates in just one of the reading campaigns. Based on the literature, it was hypothesized that such behavior could be due to the loss of cohesion from the saturation of the foundation colluvium due to the reservoir filling.

Figure 14 presents the vertical displacements obtained in the model compared to those measured in the field for all analyzed sections, where it is possible to verify the discrepancy between the displacements of section C (MS-03) and D (MS-06) with rock foundation and the displacements of section B (MS-01) and E (MS-10). In general, the initial displacements determined in the model were lower than those measured, but over time the displacements equalize, showing very close values, evidencing the compatibility between the model and the measured data.

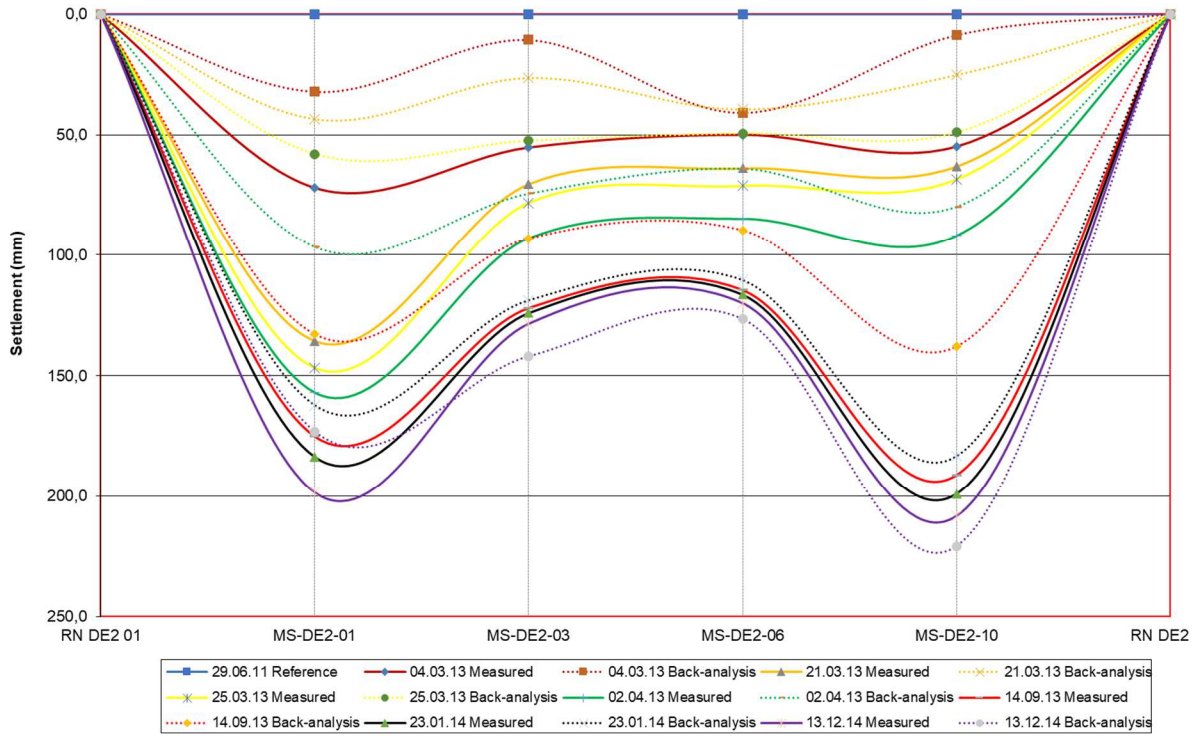

Fig. 14 - Graph of the vertical displacements of all sections comparing the back-analyses with the measured values

6. CONCLUSIONS

The study allowed, based on the actual performance of the structure, to make adjustments to the geotechnical parameters of the materials, demonstrating that numerical analysis is a highly useful tool to support decision-making, corrective and preventive actions, and to simulate the behavior of the structure in the face of unforeseen behavior in the project, determining the values that the instrumentation should assume at each loading stage of the structure.

It is noteworthy that in the modeling of the flow and the behavior of the saturation front, it was demonstrated that the transition from the transient regime to the steady-state regime occurs almost two years after the reservoir is fully filled. The results show that the compaction of the embankment can generate greater anisotropy than expected in the project, where horizontal permeability was estimated to be 4 times higher than vertical, but the anisotropy result was around 10 times.

For the region resting on colluvial and residual soil, the measured displacements were higher than those of the higher sections, demonstrating that the foundation soils account for a large portion of this displacement. However, despite the estimated modulus of elasticity, the initially modeled values were much lower than those measured for this region, and in this, the modeling considering the loss of strength due to material saturation [9] showed greater compatibility.

It is highlighted that there were significant punctual increases in settlement observed on different dates in both regions with colluvial foundation soil, and the transient flow analysis demonstrated the saturation of the foundation material at the same time as this occurrence, corroborating that there is a relationship between the increase in displacement and saturation.

The results of the displacement varying over time bring important relevance to monitoring, as during filling it is necessary to know what the acceptable magnitude of displacements for the earth structure is. Without this analysis, monitoring does not have a parameter to evaluate what normal behavior is and what would be anomalous behavior.

REFERENCES

[1] HWANG, R.N. (2016). Back Analyses in Forensic Geotechnical Engineering. In: Rao, V., Sivakumar Babu, G. (eds) Forensic Geotechnical Engineering. Developments in Geotechnical Engineering. Springer, New Delhi.

[2] DESCHAMPS R., YANKEY G. (2006). Limitations in the back-analysis of strength from failures. Journal of Geotechnical and Geoenvironmental Engineering v.132, n.4, pp. 532–536.

[3] FARIVAR, A. R.; MIRGHASEMI, A. A.; MAHIN ROOSTA, R. (2012). Back analysis of Tabarak Abad dam behavior during construction.” In: Proceedings. of the int. symp. on

dams for a changing world—80th annual meeting. and 24th congress. of ICOLD. pp. 13-18. Kyoto, Japan.

[4] ICOLD. (2019). Dam failures statistical analyses- Bulletin 99 Update. Bullentin 18.pp. 65.

[5] VALLEJO, L. L., FERRER, M., ORTUÑO, L., & OTEO, C. (2002). Ingeniería Geológica. Prentice Hall, Espanha.

[6] CRUZ, P. T. Da.(2004) 100 Barragens brasileiras. 2. ed. São Paulo. Oficina de textos.

[7] BISHOP, A.W.; ALPAN, I.; BLIGHT, G.E. & DONALD, I.B. (1960). Factors controlling the strength of partially saturated cohesive soils. In: Proceedings. Research Conference on Shear Strength of cohesive Soils, pp 500-532, United States.

[8] SILVA FILHO, F. C. DA.(1998) Análise Numérica de Problemas em Solos Não Saturados, Tese de Doutorado , Universidade Federal do Rio de Janeiro/COPPE, Rio de Janeiro, Brasil.

[9] SCHELLMANN R., RAHARDJO H., SCHNEIDER H.R. (2013). Unsaturated shear strength of a silty sand, Engineering Geology, v.162, pp. 88-96.

Fifth International
Dam World Conference
PORTUGAL • LISBON • LNEC • APRIL 13-17, 2025
dam world 2025

ARCHING EFFECT INDUCED BY A CONCRETE GALLERY INSIDE TULLAROOP DAM - THREE-DIMENSIONAL FINITE ELEMENT ANALYSIS

Gabriel Nogueira Rodrigues[1]
COPPE-UFRJ

Maria do Carmo Reis Cavalcanti[2]
UFRJ-Universidade Federal do Rio de Janeiro

Marcos Barreto de Mendonça[3]
UFRJ-Universidade Federal do Rio de Janeiro

ABSTRACT

The presence of rigid concrete structures inside compacted embankments induces an arch effect in their surroundings, concentrating stresses at the top of the structure and relieving stresses on their sides. Such concentration of stresses, if not considered in the design, can lead to the structure collapse, and the stress relief on the sides can promote hydraulic fracturing, risking total or partial collapse of the dam structure. Two-dimensional analyses of a dam cross-section cannot capture the arching effect, and a longitudinal analysis along the axis of the dam would only allow for its evaluation for the highest section but not along the whole length of the gallery. This work presents a three-dimensional stress-strain analysis of the Tullaroop Dam in Australia, which counts with a morning glory spillway associated with a concrete gallery inside its embankment. It explores aspects of the stress distribution around rigid structures inside compacted embankments. The 3D analyses simulated the construction phase in 7 stages using RS2 and RS3 finite element softwares from the RocScience package. A comparative evaluation was carried out between the numerical analyses normal stresses and the instrumentation records from stress cells installed in the interface concrete/soil at seven sections along the gallery length, demonstrating the establishment of the arc effect.

Keywords: Embankment Dams, Stress and Strain Analysis, Finite Element Method, Arching Effect.

[1]gabriel.rodrigues@coc.ufrj.br
[2]carminhacavalcanti@poli.ufrj.br
[3]mbm@poli.ufrj.br

1. INTRODUCTION

Due to the contrasts in deformability between materials, the arching effect on embankment dams has been observed on earth and rockfill dams when the impervious material is more compressible than transition and rockfill [1] [2]. Such phenomena may result in undesirable fissures on the impervious core, leading to piping failure, such as what was observed at Bidvaz Dam seven and a half years after the first reservoir impounding [3].

Analogous behavior is also observed around rigid structures within earth dams, such as river diversion, water intake, or spillway conduits [4] [5] [6]. The arching effect concentrates the earth load on the top of the conduit, which may cause damage and excessive deformation if not considered in the structural design. It also reduces the confining stresses laterally, which, if associated with poor compaction, may also lead to piping.

Conduits through dams are difficult to build properly and represent a risk if problems develop after construction once they are challenging to repair due to their location within the earthfill, requiring extensive excavation.

There are many reports of dam failure because of piping around conduits, as shown in the following images of Figure 1.

Fig. 1 – Dam failures due to piping around buried conduits (FEMA-2005)

The present study presents 2D and 3D stress-strain analyses carried out using the Finite Element software RS2 and RS3 from RocScience to explore the stress distribution around the morning glory spillway of Tullaroop dam, built in 1959, which has several total stress cells installed on the concrete/embankment interface.

2. TULLAROOP DAM CHARACTERISTICS

Tullaroop Dam [7], shown in the Google Earth satellite photo of Figure 2, is a 45m high and 415m long rockfill dam with a clay core built to store water for irrigation and domestic/industrial use in Australia. It was constructed over highly resistant sedimentary rocks, which provided a solid and stable base for the structure.

Fig. 2 – Tullaroop dam (From: Google Earth, 2023)

The dam comprises downstream and upstream rockfill slopes, granulometric transition, a clay core, and a Morning Glory spillway, which includes a reinforced concrete gallery, 6 m high and 6.4 m wide with a wall thickness of 0.5 meters, that crosses the dam embankment from upstream to downstream on the right abutment.

The cross-section of this Gallery is shown in Figure 3; pressure cells were installed at eight points along the length of the Gallery, identified as M, N, S, T, P, U, Q, and R, shown in Figure 4, along with the earth fill material distribution; some of the sections have instruments only at the top of the structure.

Cross-sections S, T, and U have five pressure cells: 1 and 5 record the horizontal stresses, cell number 3 registers the vertical stress, and cells numbers 2 and 4 measure the normal stresses on a 45º plane.

Daily readings were carried out from January 1959 to November 1962 throughout the construction period and the next three months. Then, readings were taken every two weeks during the last 12 months of records.

The behavior recorded by the cells during the construction period was consistent with raising the dam. At the end of construction, vertical stresses at the top of the Gallery ranged from 1.5 to 2.9 times the earth's weight before the reservoir impounding.

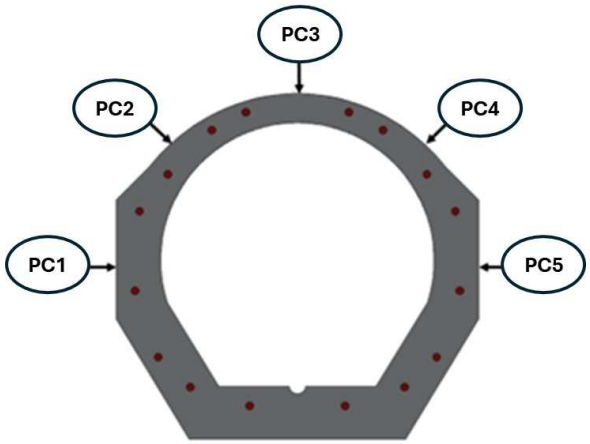

Fig. 3 –Cross section of Tullaroop Dam's concrete Gallery indicating the position of the installed pressure cells around the structure.

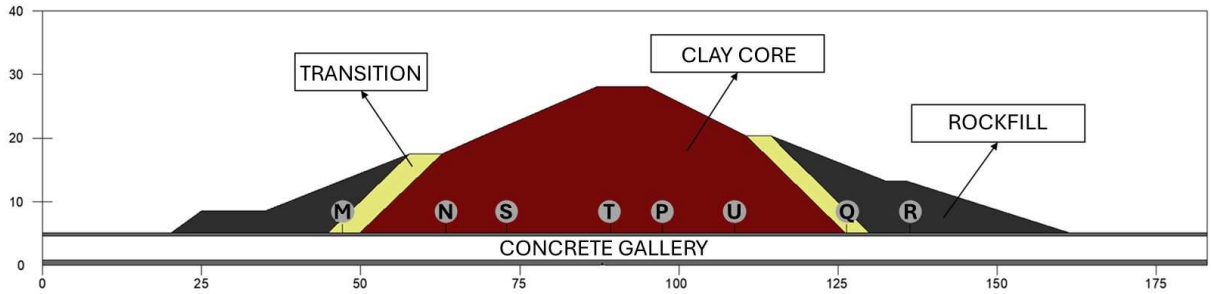

Fig. 4 – Cross section of Tullaroop Dam's concrete Gallery indicating the installed pressure cells' position along the structure length and earth fill material distribution.

3. METHODOLOGY

The study focused on the construction period and contemplated 2D and 3D analyses developed for Mohr-Coulomb elastoplastic constitutive models.

Initially, a simplified approach was adopted to evaluate the stresses around the Gallery. A longitudinal plane strain analysis was carried out, simulating the earth fill construction in 20 stages, discretized in 16,544 triangular elements, as shown in Figure 5.

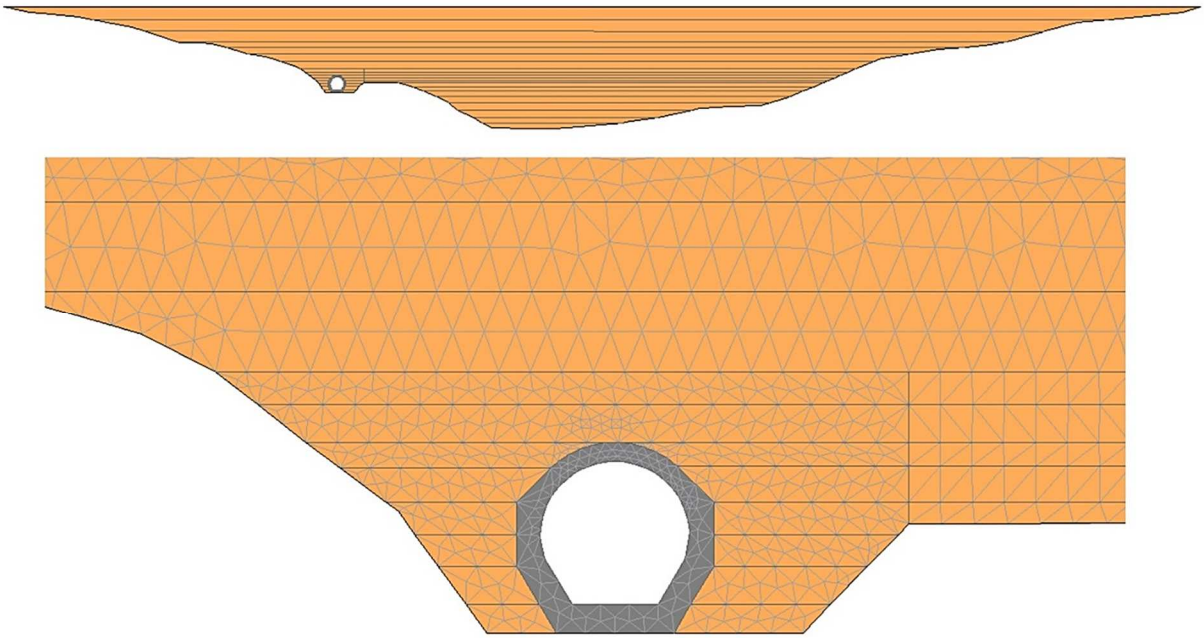

Fig. 5 – Longitudinal analysis stages and discretization around the Gallery.

Additionally, a 2D transversal analysis was performed to evaluate the vertical stress distribution along the top of the Gallery; the model consisted of 692 four-node quadrilateral elements and 11 construction stages, detailed in Figure 6.

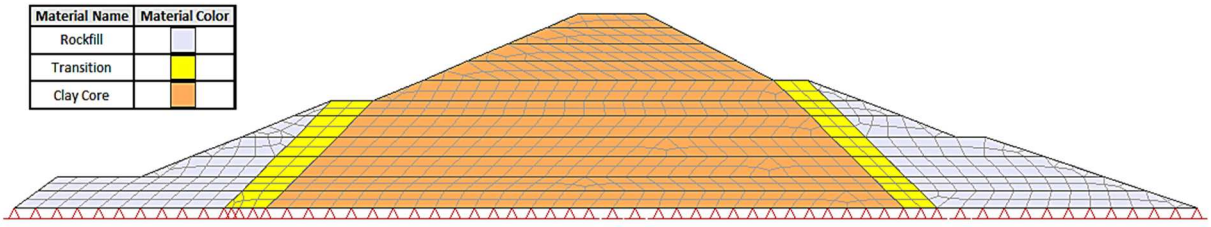

Fig. 6 – Transversal analysis stages and discretization above the Gallery.

The 3D model demanded topographic data from the contour map creator tool provided by Google Earth, as shown in Figure 7; underneath the embankment and below water level, the longitudinal cross-section geometry was replicated, resulting in the 3D model presented in Figure 8.

Fig. 7 – Contour map of the dam site.

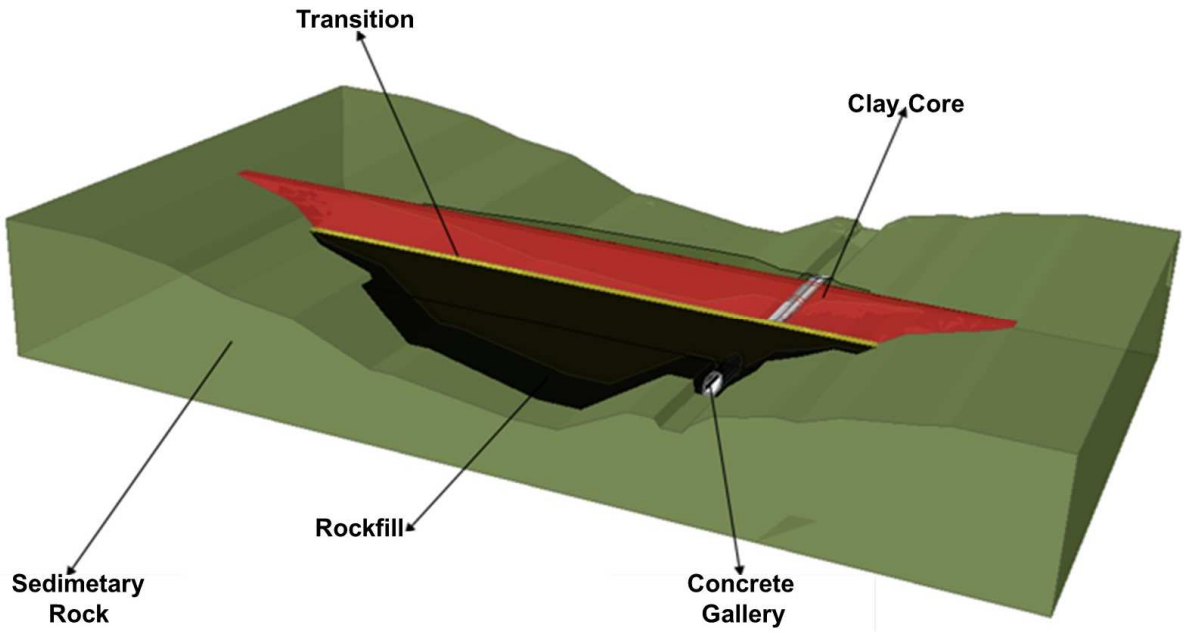

Fig. 8 – 3D model.

The software automatically generated the finite element mesh using tetrahedral four-node elements, which were adequately refined around the Gallery, as seen in Figure 9. The 3D analyses considered the dam foundation nondeformable, and the construction was simulated in 7 stages, as depicted in Figure 10.

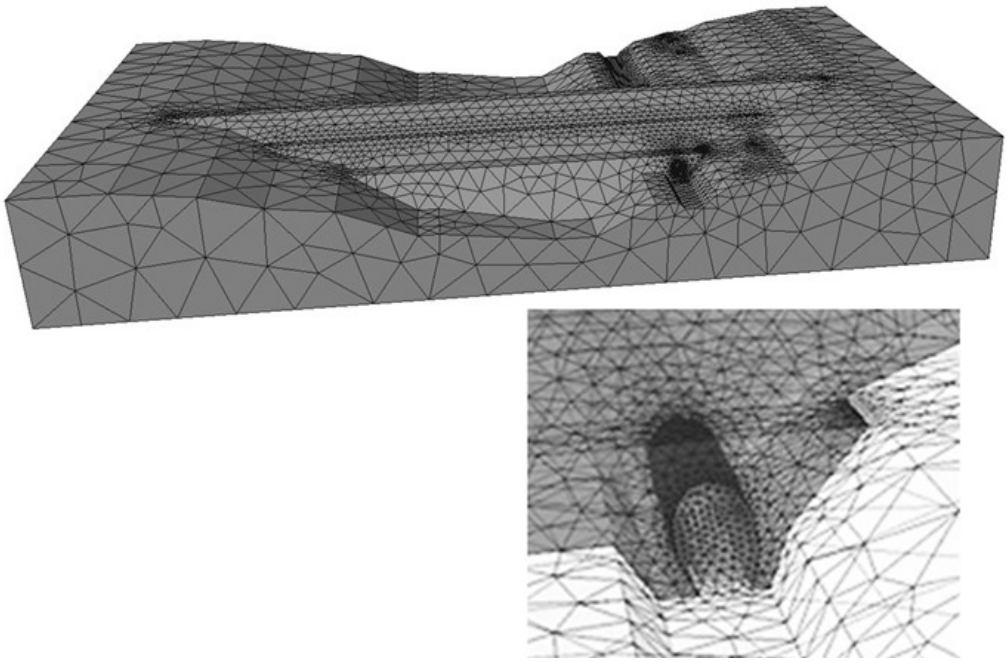

Fig. 9 – 3D model mesh.

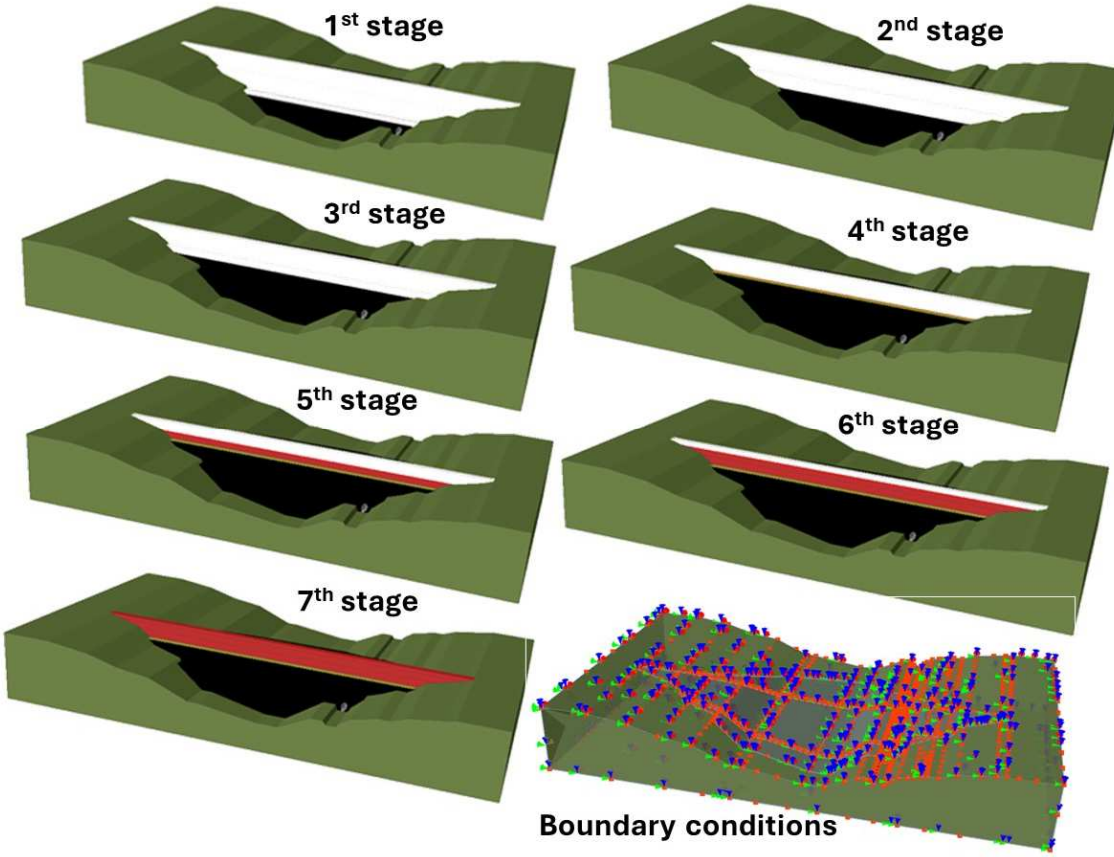

Fig. 10 – 3D model construction sequence simulation and boundary conditions.

The total stress data around the Gallery on positions 1, 2, 3, 4, and 5 contemplate only cross-sections S, T, and U within the clay core. Therefore, sections were created in the 3D model to

obtain the normal stresses acting on the structure from the numerical analysis, adding six additional points indicated in red lowercase letters in Figure 11 to get a better stress distribution around the Gallery.

Pressure cells at points 1 and 5 record the horizontal stresses, cell number 3 registers the vertical stress, and cells numbers 2 and 4 measure the normal stresses on a 45º plane. In this case, it is necessary to estimate the normal (σ_n) stress from the horizontal (σ_{yy}), vertical (σ_{zz}), and shear (σ_{yz}) stresses in the point, according to Equation 1, where θ is the angle of the plane normal vector with the vertical direction in the longitudinal plane.

$$\sigma_n = \sigma_{YY} \cdot \sin^2\theta + \sigma_{ZZ} \cdot cos^2\theta - \sigma_{YZ} \cdot \sin 2\theta \quad (1)$$

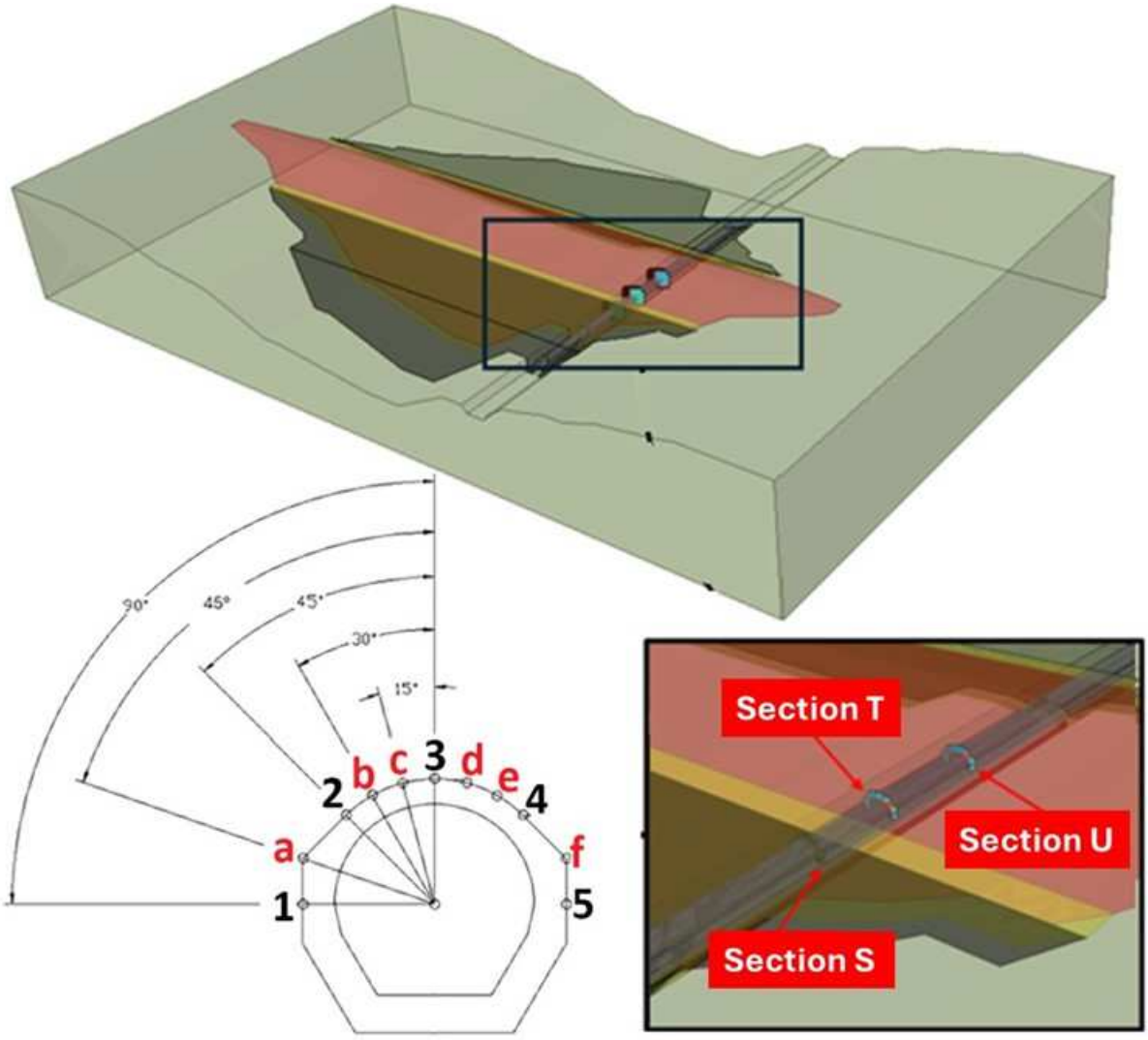

Fig. 11 – Instrumented cross-sections S, T, and U and numerical analysis data points.

Although Trollope, Speedie & Lee [7] provided many details about instrumentation and geometry, the materials' parameters were not mentioned, except for the excellent quality of the rock foundation wich, along with the external surface of the concrete galery, had

displacements restricted in all directions. A set of parameters was defined based on the most used dam materials from the literature [2]; the adopted parameters are presented in Table 1.

Table 1 – Material Parameters

Material	γ (kN/m³)	c' (kPa)	ϕ' (º)	E (kPa)	Poisson (ν)	Ko
Clay Core	20.5	19.2	33	20,000	0.2	0.5
Rockfill	22	0	36	30,000	0.2	0.5
Transition	23	0	39	45,000	0.2	0.5

4. RESULTS

4.1. 2D plane strain analyses

The 2D longitudinal analysis simulating the construction in 20 stages has shown the arching effect as illustrated in Figure 12, where it can be observed the rotation of the principal stresses axis toward the Gallery and the terrain surface as well as the concentration of σ_1 on top of the structure and its values decrease on the laterals, reaching values close to zero near the bottom of the concrete structure.

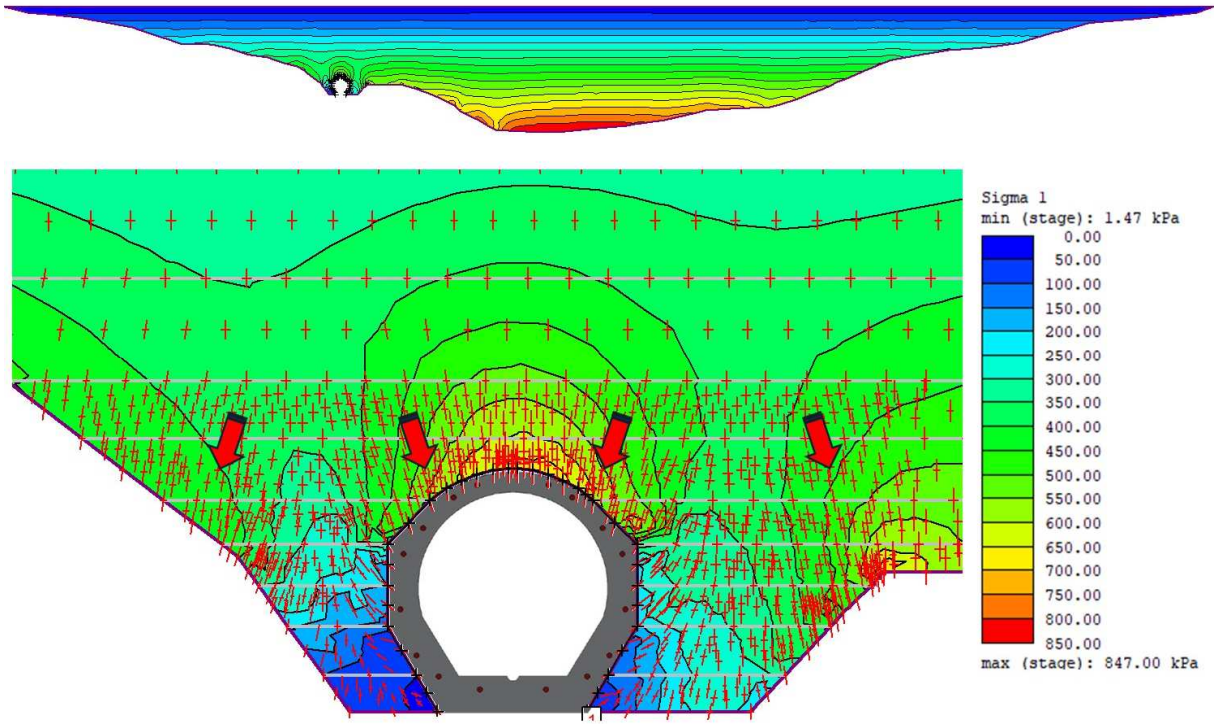

Fig. 12 – Longitudinal 2D analysis – σ_1 distribution and principal stresses axis

The longitudinal analysis is aligned with the "T" instrumented section; therefore, comparing the results around the Gallery with the registered values was possible. Figure 13 shows the measured and calculated normal stresses acting on the concrete Gallery along with the

embankment weight at the top of the Gallery and the results of a 2D analysis along the axis of the gallery.

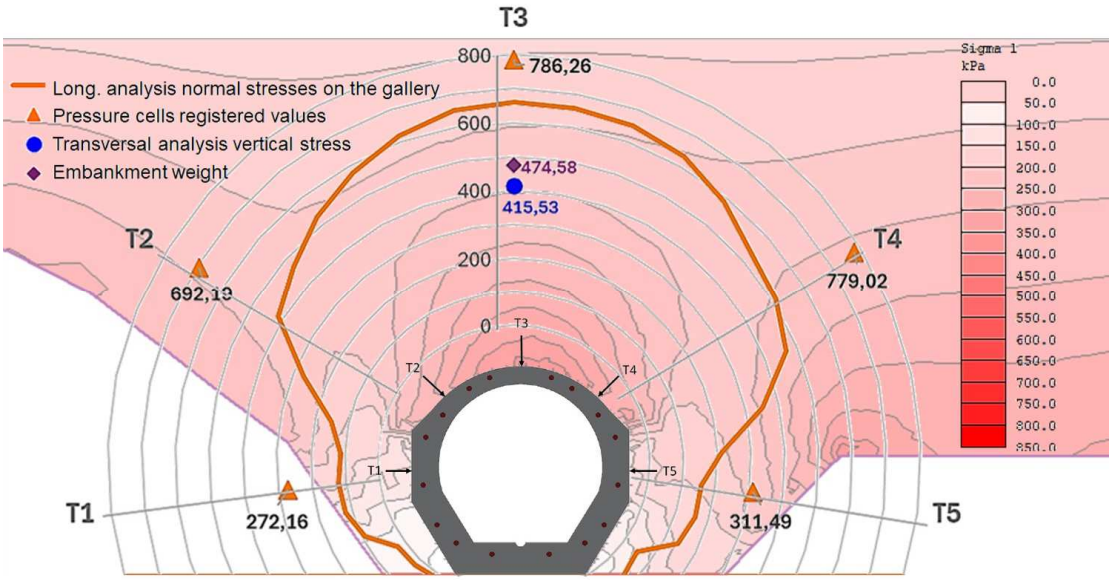

Fig. 13 – Normal stresses around the concrete Gallery

It can be observed that the normal stress distribution displays a behavior similar to the one registered by the pressure cells, while the transversal analysis and embankment weight do not reflect the arching effect.

As expected, the transversal analysis along the gallery axis did not show the arching effect. Nevertheless, a correction of its vertical stresses along the top of the gallery, based on the ratio between the values at the common point of the longitudinal and transversal analyses, as suggested by Cavalcanti [8], resulted in a more compatible vertical stress distribution, as seen in Figure 14.

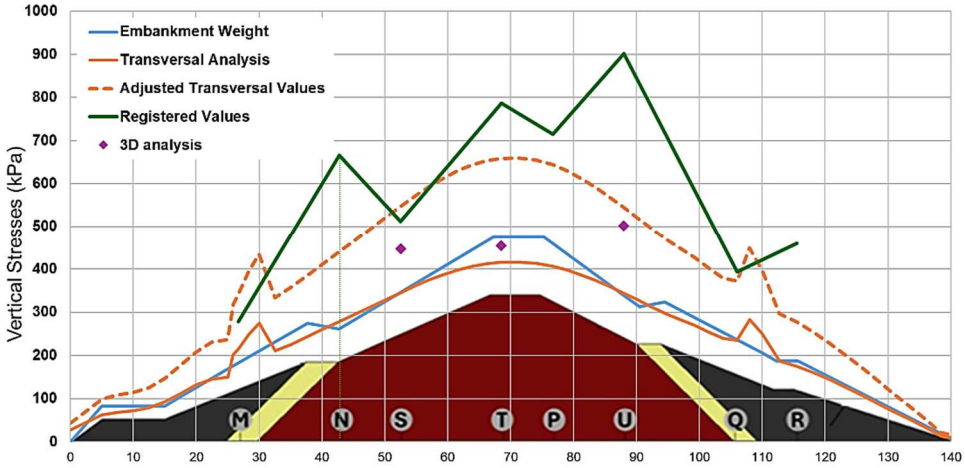

Fig. 14 – Vertical stresses along the top of the concrete gallery

4.2. 3D analysis

The 3D analysis also indicated the arching effect around the concrete Gallery, as seen in the vertical stresses distribution of Figure 15, with an increase of stresses on the top of the Gallery and a relief on the lateral of the structure.

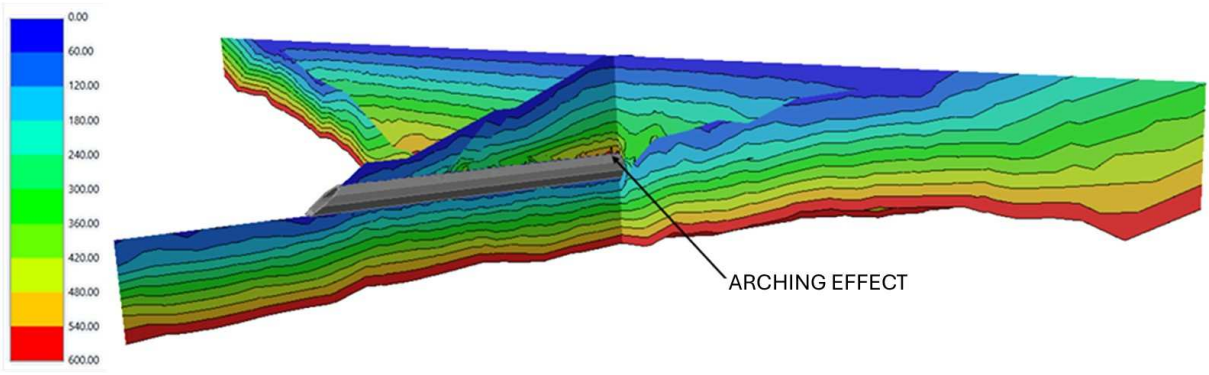

Fig. 15 – Vertical stresses at the end of construction based on 3D analysis

The normal stresses around the concrete Gallery at each instrumented section within the clay core are shown in Figures 16, 17, and 18, respectively, for sections S, T, and U at each stage of construction simulated.

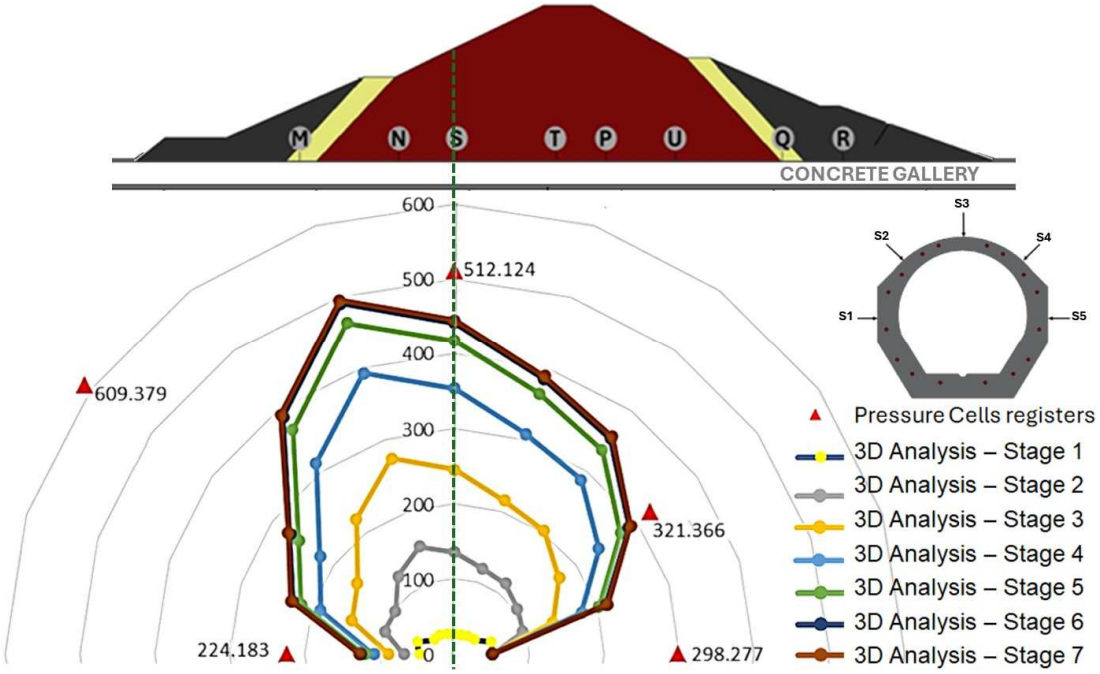

Fig. 17 – Normal stresses on the Gallery at the end of construction based on 3D analysis – Section "S"

Section "S" results of the 3D analysis are similar to what has been registered by the pressure cells, indicating the distribution asymmetry; nevertheless, the values on points 1 and 5 are much inferior.

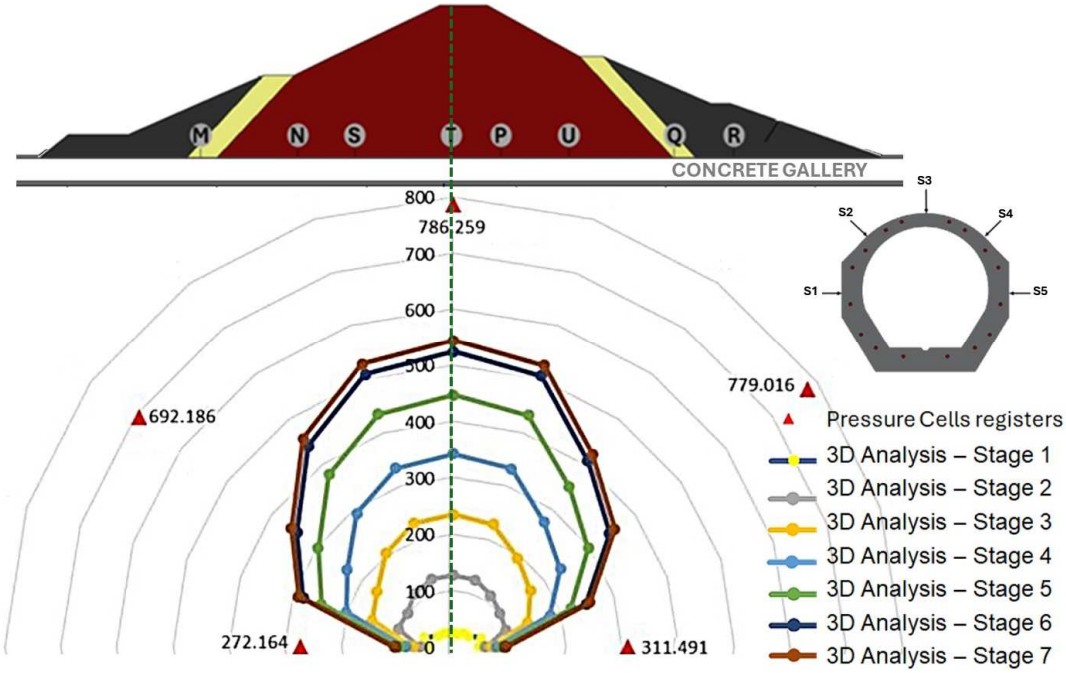

Fig. 18 – Normal stresses on the Gallery at the end of construction based on 3D analysis – Section "T"

Section "T" results of the 3D analysis distribution, although geometrically similar, present inferior values of stresses.

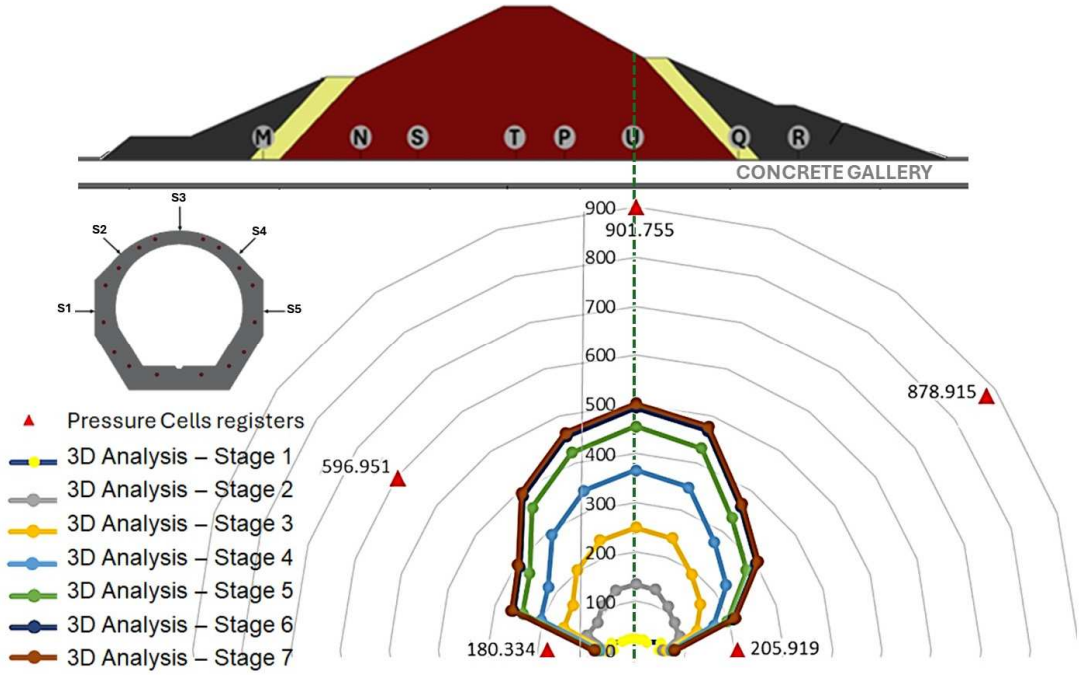

Fig. 19 – Normal stresses on the Gallery at the end of construction based on 3D analysis – Section "U"

The values from the 3D analysis on section U are much inferior to the registered values on the upper part of the Gallery, top, and 45 degrees. However, at the lateral, they show more consistency with the observed values.

The results from the longitudinal 2D analysis and those from the tridimensional analysis for section "T" seem more compatible with the values registered by the pressure cells, as shown in Figure 20.

Nevertheless, it must be taken into account that the material parameters and terrain geometry may not reflect the real characteristics of the problem besides that no embankment compaction reduction around the structure was simulated.

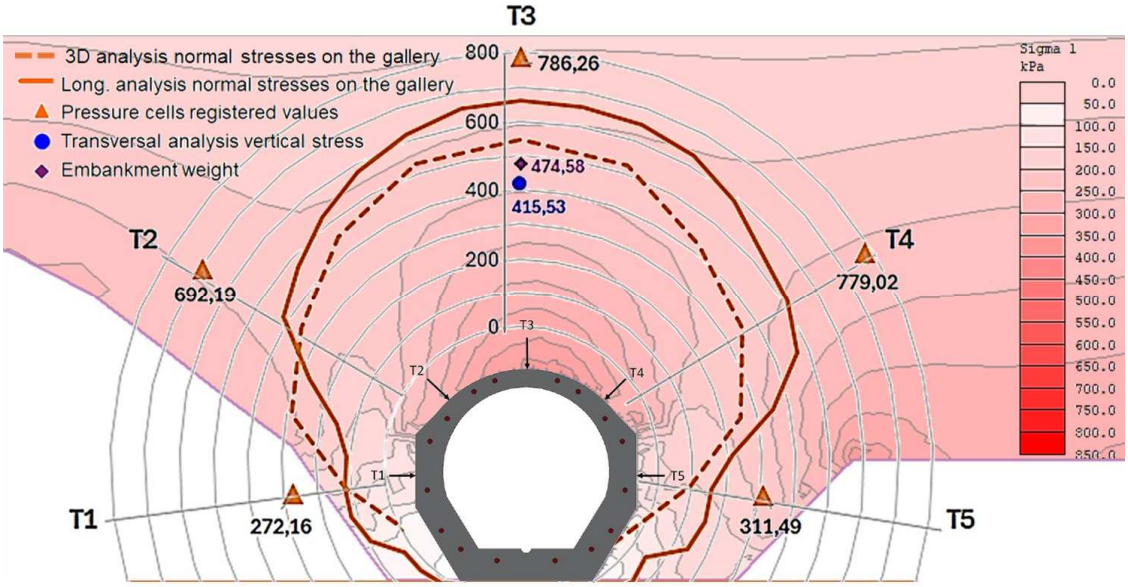

Fig. 20 – Normal stresses on the Gallery at the end of construction – Section "T"

Table 2 summarizes the stresses on the concrete Gallery from the numerical analyses and their percentage of registered values. The values highlighted in red correspond to the values from the plane strain transversal analysis adjusted based on the result of the longitudinal analysis on the common point between them.

Table 2 – Vertical stresses measured and calculated

Section	Pressure Cell	Embankment weight (kPa)		Numerical Analyses Normal Stresses (kPa)						Measured Values (kPa)
				Transversal 2D		Longitudinal 2D		3D		
S	1	-	-	-	-	-	-	124.12	55%	224.18
	2	-	-	-	-	-	-	274.80	45%	609.38
	3	346.22	68%	344.96	67%	546.45	107%	446.39	87%	512.12
	4	-	-	-	-	-	-	291.91	91%	321.37

Section	Pressure Cell	Embankment weight (kPa)		Numerical Analyses Normal Stresses (kPa)						Measured Values (kPa)
				Transversal 2D		Longitudinal 2D		3D		
	5	-	-	-	-	-	-	49.85	17%	298.28
T	1	-	-	-	-	121.50	45%	120.28	44%	272.16
	2	-	-	-	-	437.24	63%	356.17	51%	692.19
	3	474.58	60%	415.53	53%	658.23	84%	454.21	58%	786.26
	4	-	-	-	-	631.58	81%	335.78	43%	779.02
	5	-	-	-	-	449.73	144%	94.9	30%	311.49
U	1	-	-	-	-	-	-	85.71	42%	205.92
	2	-	-	-	-	-	-	279.11	34%	878.91
	3	399.17	38%	343.57	38%	544.23	60%	502.04	56%	901.76
	4	-	-	-	-	-	-	307.70	52%	596.95
	5	-	-	-	-	-	-	80.32	45%	180.33

5. CONCLUSIONS

Accounting for the inevitable deformability contrasts in engineering works is an often neglected aspect that deserves close attention, both in the design phase and the monitoring interpretation.

The present study demonstrated that rigid concrete structures inside compacted embankments induce an arching effect in their surroundings, concentrating stresses at the top of the structure and relieving stresses on their sides. Such concentration of stresses, if not considered in the structure design, can lead to its collapse, and the stress relief on the sides, especially if associated with poor compaction, can promote hydraulic fracturing, risking total or partial collapse of the dam structure.

Tridimensional numerical analyses, besides rigid structures within deformable embankments, are also useful in evaluating the arching effect due to the contrast in deformability among embankment materials and irregularities on the terrain. Nevertheless, 3D analysis demands much more modeling time and computational effort for processing and data interpretation.

The 2D longitudinal analysis through the embankment axis captured the arching effect, with results similar to the ones from the 3D analysis and the instrumentation measured values. The correction of a 2D transversal analysis based on the longitudinal analysis also presented compatible results. Therefore, such a scheme may be useful in evaluating the arching effect on embankments once used carefully and aware of its limitations.

REFERENCES

[1] Massad, F., 2010, Obras de Terra: Curso Básico de Geotecnia, 2. Ed., Oficina de Textos, São Paulo, p. 63-65.

[2] CRUZ, P. T., 1996, Cem Grandes Barragens Brasileiras: Casos Históricos, Materiais de Construção e Projetos. Oficina dos Textos, São Paulo, Brasil.

[3] Morteza Salari, Ali Akhtarpour & Amin Ekramifard (2018): Hydraulic fracturing: a main cause of initiating internal erosion in a high earth-rock fill dam, International Journal of Geotechnical Engineering, DOI: 10.1080/19386362.2018.1500122

[4] Federal Emergency Management Agency (FEMA), 2005. Technical Manual: Conduits through Embankment Dams, Best Practices for Design, Construction, Problem Identification and Evaluation, Inspection, Maintenance, Renovation, and Repair.

[5] SANDRONI, S. S.; MELLO, F. M; GUIDICINI, G., Lições aprendidas com acidentes e incidentes em barragens e obras anexas no Brasil, Rio de Janeiro: Comitê Brasileiro de Barragens, 2021.

[6] SANDRONI, S. S, GUIDICINI, G., Barragens de Terra e Enrocamento, Oficina de Textos, Rio de Janeiro, 2022.

[7] Trollope, D. H.; Speedie, M. G.; Lee, L. K., (1963). Pressure Measurements on Tullaroop Dam Culvert, Proceedings of the Fourth Australian New Zealand Conference on Soil Mechanics and Foundation Engineering, p. 81-92.

[8] Cavalcanti, M. C. R. (1990). Estudos Pseudo-Tridimensionais das Tensões em Galerias no Interior de Barragens de Terra Utilizando o Método dos Elementos Finitos. Tese de mestrado, Coordenação dos Programas de Pós-Graduação de Engenharia (COPPE), Universidade Federal do Rio de Janeiro.

Fifth International Dam World Conference
PORTUGAL • LISBON • LNEC • APRIL 13-17, 2025
dam world 2025

INSAR MONITORING AND FEM MODELING OF THE VADOMOJÓN EARTHFILL DAM (CÓRDOBA, SPAIN)

Elías Esteban Mateos
Universidad Politécnica de Madrid

Ignacio González Tejada[1]
Universidad Politécnica de Madrid

Francisco Lamas-Fernández
Universidad de Granada

Miguel Marchamalo-Sacristán
Universidad Politécnica de Madrid

Antonio Ruiz-Armenteros
Universidad de Jaén

Rubén Martínez Marín
Universidad Politécnica de Madrid

Candela Sancho
Detektia

Alfredo Fernández-Landa
Detektia

Alfredo Granados
Universidad Politécnica de Madrid

Isabel Granados
Universidad Politécnica de Madrid

Luis Jordá
Universidad Politécnica de Madrid

ABSTRACT

Embankment dams require consistent and reliable monitoring. Interferometric Synthetic Aperture Radar (InSAR) is a microwave remote sensing technique that can be used for continuous deformation monitoring of embankment dams. Satellite signals are processed to provide timely settlement measurements at high spatial resolution. This information may enhance the safety of dams, especially in the cases of limited or damaged monitoring systems, thanks to a continuous assessment of the dam settlement and deformation patterns. We illustrate the capabilities of InSAR monitoring by studying the behaviour of Vadomojón Dam, a 75 m zoned earth dam in the Guadajoz river, southern Spain, which is in service since 1997. We compare the deformations collected from InSAR with those obtained from conventional monitoring and from a physics-based numerical model of the dam. Many control points were established over and around the area of the dam, and the measurements of their displacements took place during several periods. We pay particular attention to the variability in time of the measurements of the settlements on the crest, using the reservoir levels record as primary input for the model. We present the details on the analysis of the variability of data collected from InSAR and present the strategy for the FEM model in the light of the intervening physical phenomena. This strategy can be helpful to establish coupled InSAR-FEM models for other situations of less available information on the actual behaviour of the embankment dam.

Keywords: InSAR, Remote sensing, embankment dams, numerical modelling, digital twins.

[1]ignacio.gtejada@upm.es, Spain

1. INTRODUCTION

Embankment dams play a crucial role in water resource management, flood control, and irrigation and according to recent statistics from the International Commission on Large Dams (ICOLD), earthfill dams constitute approximately 70% of all large dams worldwide [1]. Internal erosion is one of the leading causes of failure [2] but sometimes it initiates and progresses while remains unrevealed. Although there is evidence from failure statistics that since the improvement of filter design and construction methods there was a reduction of the percentage of failures due to internal erosion, ageing affects may still cause undetected internal erosion [3]. Recent examples of failures due to internal erosion include the Oroville Dam incident in California (2017) or the Toddbrook Reservoir dam in the UK (2019), where internal erosion was identified as a contributing factor to the failure of the dams' spillways. In small embankments and dikes, sometimes without adequate filter protection, internal erosion is also a significant cause for failure. All these examples underscore the importance of robust and continuous monitoring and maintenance practices to detect and mitigate internal erosion in embankment dams, ensuring their long-term safety and functionality.

An essential aspect of dam health monitoring is the detection of anomalies in dam behaviour, which can indicate potential structural issues or failures. Traditionally, point measurements obtained from conventional surveying, piezometers, water flowmeters, inclinometers, etc. are compared to reservoir levels to find signs for anomalies. There are two main shortcomings of this approach. On one hand, traditional monitoring methods, while effective, often face limitations in spatial coverage and frequency of data collection. On the second hand, the detection of anomalies is usually based on human analysis and many times it is just based on the analysis of crossed correlations between the measurements. The combination of Interferometric Synthetic Aperture Radar (InSAR) with numerical models is a powerful tool to overcome these constraints as it provides continuous monitoring, and the measurements can be continuously compared to the estimations coming from advanced numerical methods. In fact, the integration of InSAR with other remote sensing techniques and data-driven of physics-based virtual models, in the framework of Digital Twins, can further enhance the predictive capabilities and continuous monitoring of these critical infrastructures [10-14].

Regarding the scarcity of data, InSAR has emerged as a powerful remote sensing technique that provides high-resolution, continuous deformation monitoring of large structures such as embankment dams [4-6]. InSAR utilizes satellite-based radar signals to detect ground movements with millimetre-level precision, making it an invaluable tool for monitoring the settlement and deformation patterns of dams. This technique is particularly beneficial in

scenarios where conventional monitoring systems are limited or damaged, offering a robust alternative for continuous assessment.

Regarding the identification of anomalies, as much more and more continuous information is available, this makes it possible to perform advanced analysis. The added value is that more information makes it possible to find out whether the observations correspond to expected deformation patterns or are actually unravelling a hidden process that may end with a dam failure. So far, crossed correlations between the measurements (e.g. settlement vs reservoir levels) are often used for anomaly detection. The patterns are identified as usual when the fluctuations of the data seem to be coupled, and they maintain the correlation patterns within a given range. Unusual patterns are understood as signs for an anomaly, which is sought through additional investigation. In contrast to this visual analysis, numerical models can be used to better understand the observations. Physics-based models (e.g. Finite Element Methos) solve boundary values problems and provide estimations that can be compared to real measurements. The higher the complexity the model, the higher accuracy and precision of the estimations. Nevertheless, the complexity usually is limited by computational, calibration and training costs. In the last years, data-driven numerical models, such as those based on machine learning and artificial intelligence, have been increasingly applied to analyse the data obtained from monitoring and identify unusual patterns. For example, in [15] temperature sensing is used for the fast detection of anomalies based on temperature sensing. However, data-driven approaches need large data sets for a proper training, which, in addition, must be a representative selection of the several stages occurring during the life of an embankment dam. The time scales for primary and secondary consolidation processes, the construction process, the impounding and operation plans (in turn affected by climate fluctuations and trends), eventual reinforcements, ground improvements or later dam raising, etc. introduce significant differences along the life of an embankment dam, and the training from data can be difficult or misleading as the data are not always gathered in similar conditions. Therefore, data-driven approaches blindfolded applied may fail to predict the future behaviour of the dam.

In this research we present an approach to combine InSAR remote sensing with Finite Element Modelling. The purpose of the FEM model is to better explain the fluctuations observed with the remote monitoring to separate the main trends from the fluctuations (which could be associated to secondary phenomena, stochastic noise or unveil signs for anomalies). The approach is applied to the Vadomojón dam, located in the Guadajoz river basin in southern Spain, serves as an exemplary case study for demonstrating the capabilities of InSAR monitoring. This is a 75-meter zoned embankment dam that has been subject to various monitoring efforts to ensure its stability and performance.

The structure of this work is organized as follows: First, we provide a brief description of the Vadomojón dam. Second, we outline the process of collecting data. Third, we describe the observed behaviour of the dam so far. Fourth, we present the methodology for using FEM models combined with InSAR. Finally, we conclude with some remarks on the findings and implications of the research.

2. THE VADOMOJON DAM

The Vadomojón dam is a zoned rockfill dam with vertical clay core and curved shape built between 1995 and 1997 in South Spain. The capacity of the reservoir is of 163.2 hm^3 at normal operation levels, covering an area of 788 hectares. The geology of the reservoir is mostly marly limestone. The maximum height of the dam is 75 meters above the foundation and 60 meters above the riverbed. The crest length is of 427 meters, with a width of 7 meters. The upstream shoulder slope has a horizontal to vertical ratio of 2 and includes a 5-meter-wide berm. The downstream shoulder slope is also with a horizontal to vertical ratio of 2 but includes three 5-meter-wide berms. An image of a representative section of the dam is shown in Fig. 1.

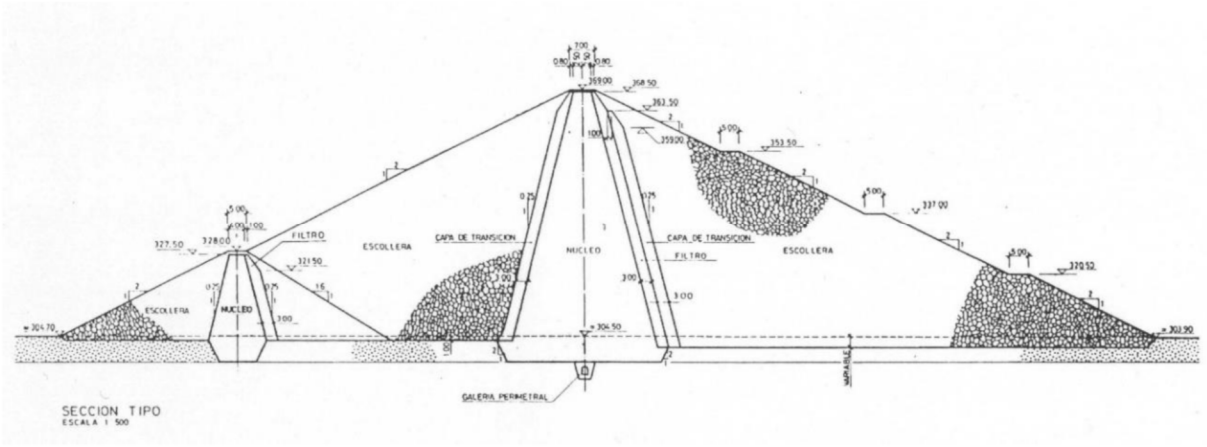

Fig. 1: Section of the Vadomojon zoned rockfill dam.

The dam includes several sensors for conventional monitoring of both the water seepage and the deformation and settlements. It includes piezometers, drains and water level meters, inclinometers, total pressure cells, settlement systems, etc.

3. DAM MONITORING

Surveying is based on 19 survey markers placed over the crest and over the downstream berms.

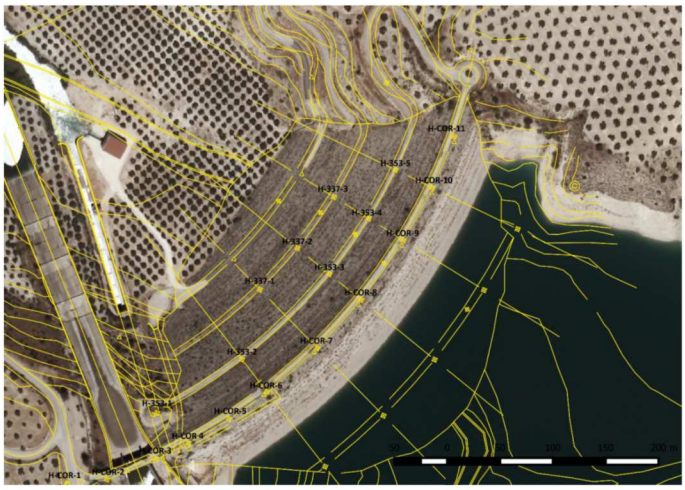

Fig. 2. Location of survey marks over the dam.

In the case of InSAR remote sensing, a dense network of points has been randomly generated that control the entire surface of the infrastructure and its surroundings to monitor subsidence. The number of control points whose coherence is greater than 70% is more than 550. The control points include areas upstream of the dam, although if these points are covered by water they will give erroneous readings and points that allow us to know the behaviour and evolution of the abutments.

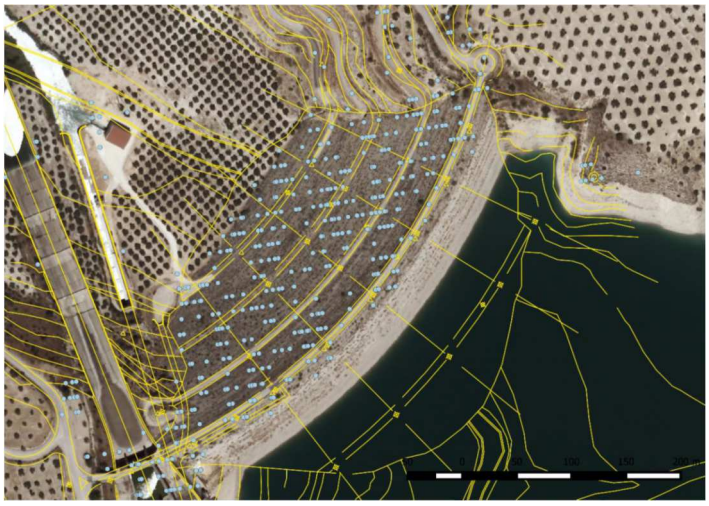

Fig. 3. Cloud of InSAR points over the Vadomojon Dam

The InSAR points are compared with the survey marks, after imposing the following conditions: distance between the InSAR points and the land marks (within a buffer of 15 meters radius with the center of the landmark, 20 m in a few cases), coherence greater than 0.85 and reading considered as reasonable after overview.

4. DAM BEHAVIOR

In Fig. 4, the evolution in time of the reservoir levels and the settlements at the crest of the dam since its commissioning are shown. The first filling of the reservoir happened in Nov. 1997. Since then, the operating levels of the reservoir have been oscillating. Three periods of low water levels, which are associated to prolonged drought years, are identifiable: 2006-2009, 2015-2017 and 2019-2023.

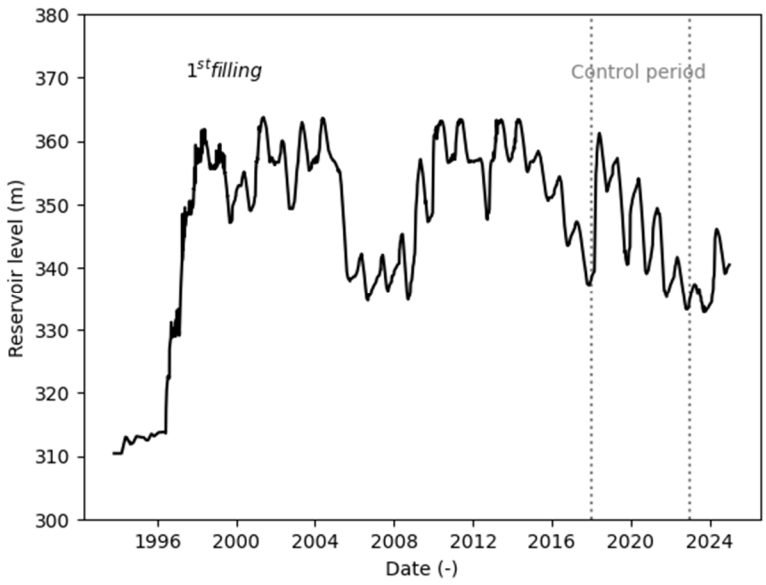

Fig. 4. Evolution in time of reservoir levels

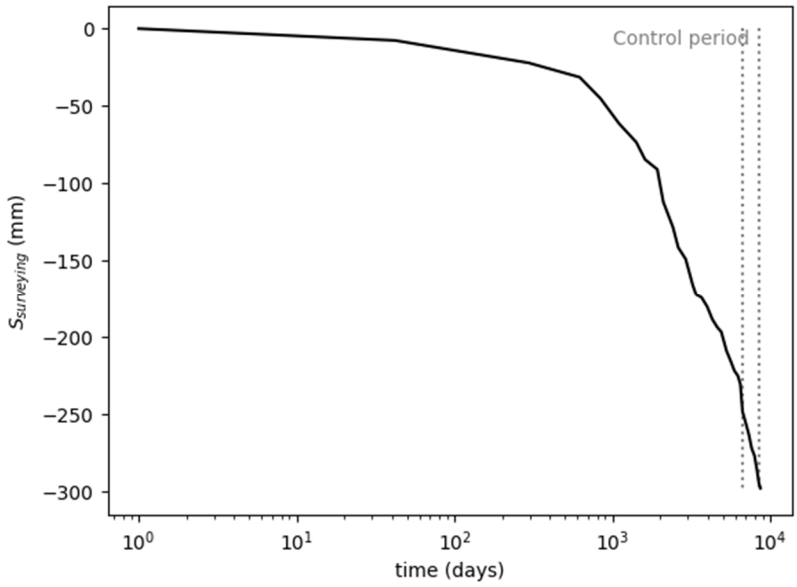

Fig. 5. Evolution in time of the settlement measured at the crest of the dam with surveying marks.

Conventional surveying has shown a settlement of the crest dam that in the last years has grown with the logarithm of time (Fig. 5). This trend together with the features and dimensions of the dam and foundation suggests that a secondary consolidation process is going on.

A period of 5 years, between 2018 and 2022 has been chosen as control period for this research. This period is large enough to provide over 300 InSAR measurements and starts around 20 years after the first filling, at a time in which the settlement grows with logarithm of time in a stable fashion.

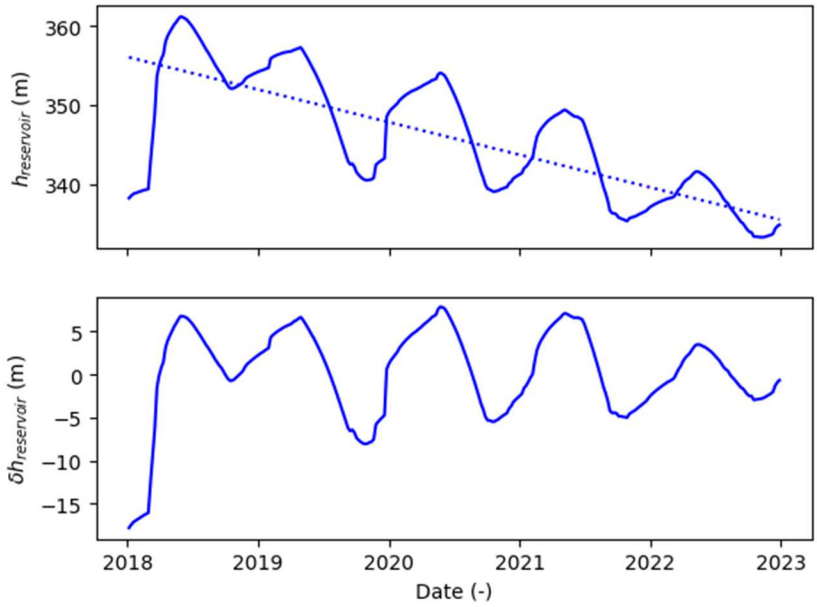

Fig. 6. Evolution in time of the reservoir levels.

During the control period the reservoir levels, $h_{reservoir}$ (m), decreased following an oscillating pattern. This pattern was simplified by decomposing the data into two components (Fig. 6): the main trend, $\bar{h}_{reservoir}$ (m), which was fitted to a linear expression during the control period:

$$\bar{h}_{reservoir} = h_0 - A.t,$$

(being h_0 (m) and A (m/day), the fitting parameters), and the fluctuation around the main trend, $\delta h_{reservoir}$ (m), which is defined as:

$$\delta h_{reservoir} = h_{reservoir} - \bar{h}_{reservoir}.$$

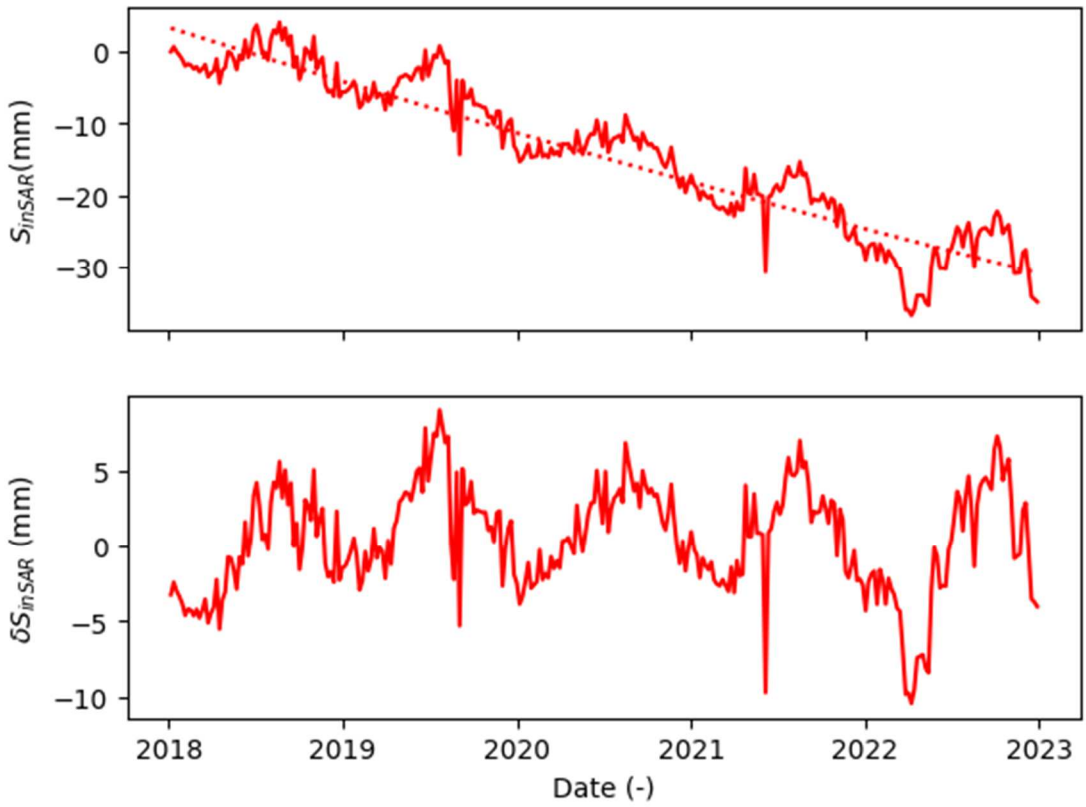

Fig. 7. Evolution of the settlements measured with InSAR during the control period.

During the control period the settlements measured with InSAR, S_{InSAR} (mm), increased also following an oscillating pattern. This pattern was simplified by decomposing it into two components (Fig 7): the main trend, $\bar{S}_{InSAR}$ (mm), which was fitted to a logarithmic expression during this period, as it is expected to be caused by a secondary consolidation process:

$$\bar{S}_{InSAR} = -C_\alpha \ln\left(\frac{t}{t_0}\right),$$

(being, C_α (mm) a fitting constant and t_0 the reference time at which the settlement would be zero) and the fluctuation around the main trend, δS_{InSAR} (mm), which is defined as:

$$\delta S_{InSAR} = S_{InSAR} - \bar{S}_{InSAR}.$$

The fluctuation of the InSAR settlements around the mean trend is associated to secondary phenomena, which add to the main phenomenon (secondary consolidation). These secondary phenomena could be explained to some extent by the continuous variation of the effective stress occurring during the transient seepage pattern produced by the reservoir levels. The variation of effective stress affects both the fully saturated and partially saturated regions of the dam core and shoulders and may entail both elastic and plastic deformations. Additional ageing effects could contribute to the secondary phenomena.

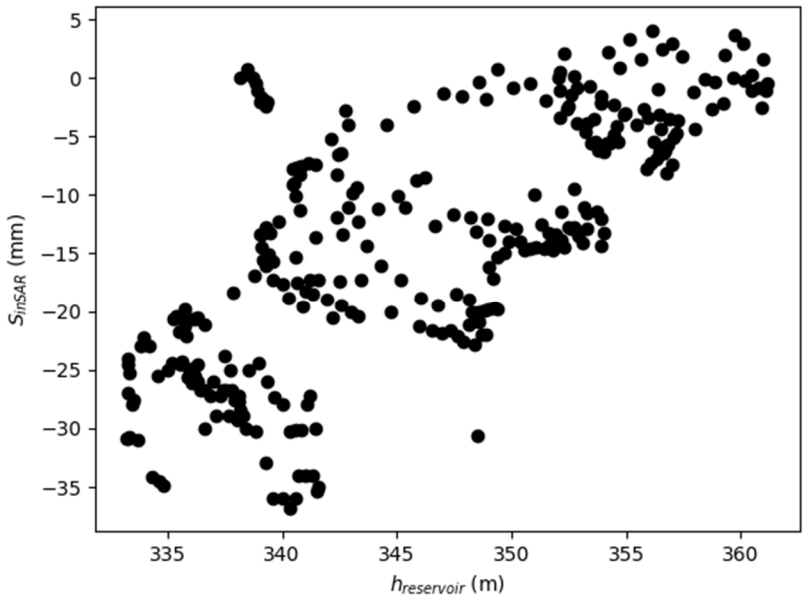

Fig. 8. Comparison of the settlements measured with InSAR with the reservoir levels during the control period.

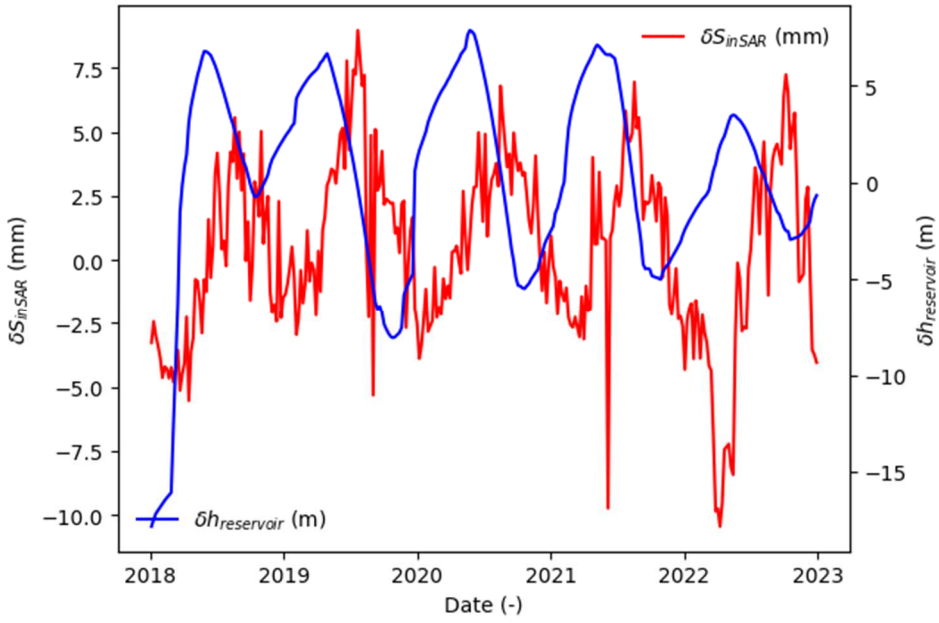

Fig. 9. Evolution with time of the fluctuations of the reservoir levels and those of the settlements measured with InSAR during the control period.

Indeed, if the settlements measured with InSAR are directly compared to the reservoir levels (Fig. 8) the correlation is not very clear. However when the fluctuations around the mean values of both the reservoir levels and the settlements measured with InSAR are plotted against time, the correlation between the 1st order fluctuations of reservoir levels and the InSAR measurements is much clearer (Fig. 9). Although there is a time offset between them, it seems

that the variation of the reservoir levels could explain the variation in the settlements measured with InSAR. Fig. 9 also shows that there is a fluctuation of higher order in the case of InSAR measurements, which could be statistical noise or could be due to a more complex phenomenon. The proposed approach is to progressively explain the fluctuations with numerical models of increasing complexity. If the fluctuations are properly reproduced by a relatively simple model, unusual patterns in the behaviour of the dam can be more easily identified.

5. FEM MODELING

Physics-based numerical models are very useful to exploit the effectiveness of InSAR as a tool for continuous and accurate monitoring. These models may help to understand the real cause for the variability at different time scales.

A 2D FEM model of the highest section of the Vadomojón Dam has been developed. The software used to create the model was MIDAS GTS-NX and a fully coupled hydro-mechanical analysis was performed. The hydraulic problem was solved during a significant part of the control period in transient regime and the reservoir levels changed with time according to the real data. The entire control period was not fully covered due to computational constraints.

The constitutive relationship used for the core of the dam was the so-called hardening soil model. This model completes the hyperbolic Duncan-Chang model [16], which reproduces the yielding upon deviatoric compression, with a cap-yielding surface to account for more isotropic compression stress paths. The model was calibrated from the tests included in the construction project. The foundation and rockfill shoulder were modelled through linear elastic constitutive equations with a Mohr-Coulomb yielding surface. None of these models consider time-dependent parameters or other approaches that could reproduce secondary consolidation processes. This is not a problem since the objective is not to reproduce the absolute value of the settlements but to explain their fluctuations around the mean trend according to the changes of effective stress caused by the transient seepage. The analysis did not include the effect of suction on effective stress within the partially saturated zone.

The model shows that the main trend of the settlement during the control period is to that it remains almost stationary, with a very small increase with time. This is reasonable as the model cannot reproduce secondary consolidation.

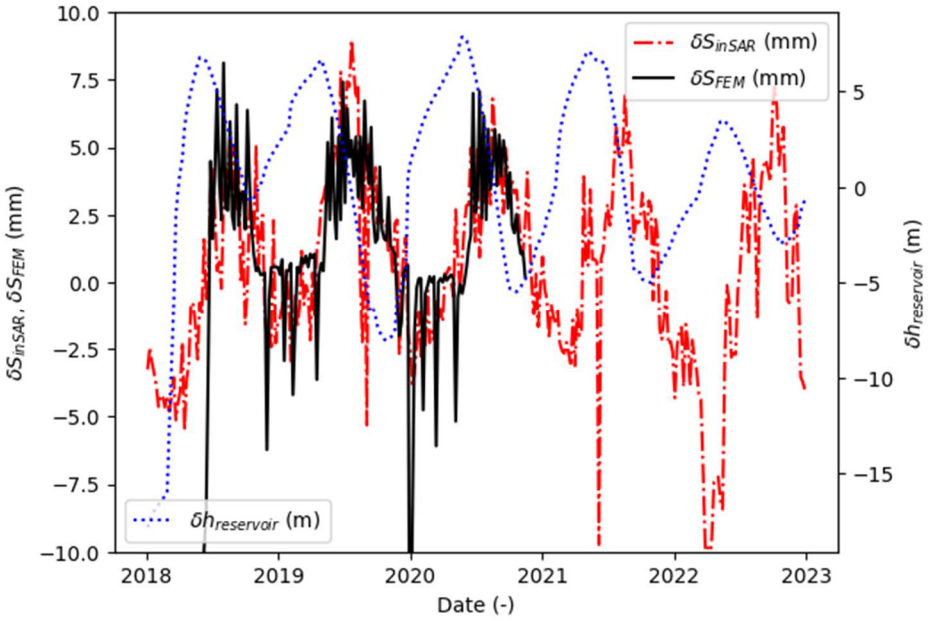

Fig. 10. Evolution with time of the fluctuations of the reservoir levels and those of the settlements measured with InSAR and simulates with FEM during the control period.

In Fig. 10 the evolution with time of the fluctuations of the settlements predicted by FEM model is shown in comparison to InSAR measurements and reservoir levels. Interestingly, both InSAR measurements and the FEM model show 1st order fluctuations that follow those of the reservoir levels and with the same offset. However a fluctuation of higher order is also observed in the predictions of the FEM model. More research is needed to explain if this is a numerical noise (or artifact), or it has a physical meaning that is also observed through InSAR. Again, more complex advanced models (e.g. considering suction in the partially saturated zone) could be useful to better understand the physics behind the observations.

6. CONCLUDING REMARKS

InSAR is a powerful tool for continuous monitoring of embankment dams with the purpose of detecting eventual anomalies. Its value is particularly interesting in the framework of digital twins: Huge amounts of data can be collected with time continuity can be collected from satellite and this can be used to feed models that may anticipate anomalies. However simplistic correlations between the collected data and other parameters, such as reservoir levels, not always provide valuable insights into the behaviour of the dam. Numerical models, data-driven or physics-based, can be used to go further with the understanding of the dam, but there are still some important limitations: The training of data-driven models must take into account that the embankment dam goes through several stages (construction, first filling, consolidation, improvements, raising, drought years, etc.), what

can make it difficult to train the model (and in some cases can lead to misleading results). Regarding physics-based models, the capability for reproducing the fluctuations on multiple scales is linked to the complexity of the model (and hence the cost of computation, calibration and user training). A solution can come from combinations of physics-based numerical models of (which reproduce general trends) with data-driven models (which explain the fluctuations). The higher the complexity of physics-based numerical models, the higher the achieved prediction an accuracy. We are exploring the capacity of FEM to explain the behaviour of a zoned embankment dam in operation since 1997, monitored with both conventional techniques and InSAR remote sensing. A simple 2D model with basic constitutive relationships was able to explain the 1st order fluctuations of the InSAR measurements, which are caused by the variations of the reservoir level and the induced seepage. Higher order fluctuations are observed in both the InSAR measurements and FEM model predictions. More complex physics-based or data-driven numerical models can be used to explain these fluctuations and eventually detect anomalies.

ACKNOWLEDMENT

This work is supported by: a) the SIAGUA research project PID2021-128123OB-C21 and PID2021-128123OB-C22 funded by MCIN/AEI/10.13039/501100011033/FEDER, EU and b) the Industrial Doctorate Program of the Community of Madrid (IND2020/TIC-17528; IND2023/TIC-28743). The authors express their gratitude for the support received from Confederación Hidrográfica del Guadalquivir.

REFERENCES

[1] International Commission on Large Dams (ICOLD). General Synthesis.

[2] Caldeira, L. (2019). Internal erosion in dams: studies and rehabilitation. International Journal of Civil Engineering, 17, 457-471.

[3] Slimani, N., Boukhemacha, M. A., & Marouf, N. (2023). Surface and Internal Erosion in Embankment Dams: A Comparative Review. Selected Studies in Geotechnics, Geo-informatics and Remote Sensing.

[4] Milillo, P., Perissin, D., Lundgren, P., & Lanari, R. (2016). Monitoring dam structural health with InSAR and GPS: A case study of Mosul Dam, Iraq. Journal of Geophysical Research: Solid Earth, 121(6), 4765-4780. https://doi.org/10.1002/2016JB013071 .

[5] Zhang, L., Ding, X., Lu, Z., & Jung, H. S. (2014). Application of InSAR technology for monitoring the deformation of the Three Gorges Dam. Remote Sensing of Environment, 152, 26-38. https://doi.org/10.1016/j.rse.2014.05.015 .

[6] Hu, J., Li, Z., Ding, X., Zhu, J., & Sun, Q. (2013). InSAR monitoring of the Xiaolangdi Dam on the Yellow River. IEEE Transactions on Geoscience and Remote Sensing, 51(1), 225-232. https://doi.org/10.1109/TGRS.2012.2194158.

[7] Marchamalo Sacristán, M., Ruiz Armenteros, A. M., Lamas Fernández, F., González Rodrigo, B., Martínez Marín, R., Delgado Blasco, J. M., Bakon, M., Lazecky, M., Perissin, D., Papco, J., & Sousa, J. J. (2023). MT-InSAR and Dam Modeling for the Comprehensive Monitoring of an Earth-Fill Dam: The Case of the Benínar Dam (Almería, Spain). Remote Sensing, 15(11), 2802. https://doi.org/10.3390/rs15112802.

[8] Zhou, W., Li, S., Zhou, Z., & Chang, X. (2016). InSAR Observation and Numerical Modeling of the Earth-Dam Displacement of Shuibuya Dam (China). Remote Sensing, 8(10), 877. https://doi.org/10.3390/rs8100877

[9] Fetel, R.H. Comparison of Finite Element Methods and Satellite InSAR for Monitoring Deformations of a Large Tailings Dam. PhD Thesis

[10] Smith, J. A., & Brown, L. M. (2023). Digital Twin for Dam Safety: Integrating Real-Time Monitoring and Numerical Modeling. Water Resources Research, 59(4), e2023WR032456. https://doi.org/10.1029/2023WR032456.

[11] Johnson, P. R., & Lee, H. K. (2024). A Digital Twin Framework for Earthfill Dams: Enhancing Predictive Maintenance and Risk Management. Journal of Hydraulic Engineering, 150(2), 04023045. https://doi.org/10.1061/(ASCE)HY.1943-7900.0002001HY.1943-7900.0002001).

[12] Wang, X., & Zhang, Y. (2023). Application of Digital Twin Technology in the Monitoring and Management of Earthfill Dams. Computers and Geotechnics, 151, 104923. https://doi.org/10.1016/j.compgeo.2023.104923

[13] Huerta, A. (2022). Hybridized methods for compressible and incompressible flows within computational engineering-based digital twins strategies. CIMNE.

[14] Noureddine, M. A., De Martin, F., El Meouche, R., Sammuneh, M. A., Ababsa, F., & Beaufils, M. (2024). Seismic Digital Twin of the Dumanoir Earth Dam. Innovations in Smart Cities Applications Volume 7.

[15] Bekele, B. M., Song, C. R., Eun, J., & Kim, S. (2022). Fast Detection of Anomalies in A Model Earth Dam Based on A Distributed Temperature Sensing Data Integrated with Artificial Intelligence. *ACEM22 Proceedings*. http://www.i-asem.org/publication_conf/acem22/2.%20GE/1.GE217/3.%20GE2177_7305A.pdf.

[16] Duncan, J.M., Chang, C. Y. (1970). *Nonlinear analysis of stress and strain in soils*. J Soil Mech Found Div 96 (5), 1629–1653. https://ascelibrary.org/doi/abs/10.1061/JSFEAQ.0001458

Fifth International Dam World Conference
PORTUGAL • LISBON • LNEC • APRIL 13-17, 2025
dam world 2025

A CFD ACCOUNT OF THE MEAN FLOW AND TURBULENCE OVER BREACHED EMBANKMENT DAM

Rui M.L. Ferreira[1]
CERIS - Instituto Superior Técnico - Universidade de Lisboa

Nuno M Martins
CERIS - Instituto Superior Técnico - Universidade de Lisboa,

Teresa Alvarez
CERIS - Instituto Superior Técnico - Universidade de Lisboa

Teresa Viseu
Laboratório Nacional de Engenharia Civil

ABSTRACT

We measure and compute the flow over a breached dam, identifying the main topological features of the mean flow (separation and stagnation surfaces, attached vortexes), secondary currents and boundary layer development.

The Navier-Stokes solver is based on the RANS with a k-ω SST closure model and a rough-wall correction, implemented in OpenFoam.

The geometry of the breached dam corresponds to a fixed instant of a model dam tested at LNEC. It depicts a homogeneous dam at the transition between the first and second erosion stages (the breach has started to deepen). Validation data is provided by PIV measurements obtained at IST.

We show that the development of the boundary layer over the crest is unlikely to be described by the Kármán momentum integral, as it is influenced by the breach crest wall curvature, secondary currents and strong lateral flow convergence.

Three-dimension separation is observed in the plunging pool. Two different attached vortices develop at the interface between the dam body and horizontal fixed wall. The first is associated to an adverse pressure gradient at the lower end of the boundary layer. The second seems originated by the flow that spreads outward from the stagnation point of the plunging flow. The attached vortices rotate in opposite directions but may both contribute to underscoring. Strong turbulence production is observed in the plunging pool. A counter rotating vortex pair is observed in the flow exiting the dam breach channel.

We discuss the significance of these structures for hydraulic erosion and underscoring. We also provide recommendations for CFM modelling of dam breaching.

Keywords: CFD, k-omega, dam-breach, 3D-separation.

[1]ruimferreira@tecnico.ulisboa.pt, Portugal

1. INTRODUCTION

Earth dams and dikes are prone to breaching following overtopping. Water flowing over the crest results in an erosion process that may lead to a significant or complete destruction of the dam. Erosion process is a complex process, with a strong transient character. It includes hydraulic erosion (Amaral et al. 2020) and the detachment of earth blocks that will add another layer of complexity to the process. Experimental techniques are needed to collect evidence of the relation between flow hydrodynamics and erosion processes. The characterization of the flow field, in particular, is paramount.

Velocity measurements in dam breach flows are not trivial due to lack of optical access and the impossibility to deploy intrusive instrumentation. Imaging-based techniques are mostly used to measure velocity fields on the free surface (Bento et al. 2017, Aleixo et al. 2022). Due to these limitations and the transient character of the flow, it is often impossible to experimentally investigate in detail the different phenomena acting during the breaching process.

To address this problem, we propose CFD modelling as a means to generate the 3D flow field over the breached dam and within the erosion cavity. The CFD model must, however, be shown to reproduce the actual flow field, which leads to the problem of validating the code for a flow for which there is no available detailed velocimetry data.

This paper provides a possible solution. We developed and employed a simplified experimental facility, which replicates the fundamental hydrodynamic characteristics of the phenomenon while maintaining control over critical variables. The facility generates velocimetry data sets, used to confront a Reynolds-Averaged Navier-Stokes (RANS) based Computational Fluid Dynamics (CFD) model, implemented in OpenFoam.

The simplified experimental facility features a scaled breached dam model, that preserves the shape of a live overtopped erodible dam at a specific instant (Alvarez et al. 2022). The fixed bed model allows for optical access and for a comprehensive experimental characterization of the flow field for that specific instant. The key aims of this paper are thus to compare the computational solution with the experimental data and to use the CFD results to highlight the flow structures that may influence the erosion process.

2. EXPERIMENTAL APPROACH

2.1. The fixed dam model

A dam with 0.45 m height and 1.2 m wide was constructed in a facility at the Portuguese Laboratório Nacional de Engenharia Civil (LNEC), as a part of an experimental setup detailed in Amaral et al. (2019) or Amaral et al. (2023). It was tested in overtopping conditions, under an approximately constant hydraulic head. In the transition between the initial and second erosion stages, the test was interrupted in an almost instantaneous way. This allowed for breach characterization with a Kinect sensor for Xbox One from Microsoft. Kinect is a depth sensing device composed by two internal cameras (RGB and IR-camera) that allows simultaneously to acquire colored and depth images. The post-processing of the acquired data allowed the creation of points clouds, which, led to 3D reconstructions of the embankment. The interruption is required because the water flow over the breach is turbid, due to suspended sediments, and this low transparency disturb the Kinect acquisitions (Alvarez et al. 2019).

The post processing of the depth images was performed with the software CloudCompare. It included the point cloud alignment to the same coordinate system; removal of all points that are not the breach dam (e.g., channel walls); merging of the point clouds and noise removal and smoothing of the final cloud. This procedure allowed for the reconstruction of the breach surfaces and 3D characterization of the erosion cavities (Figure 2).

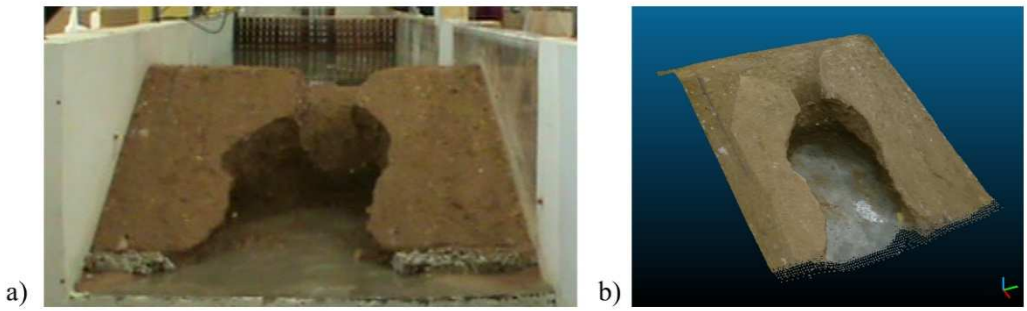

Fig. 1 – a) Downstream view of the live breached dam. b) Perspective of the 3D model.

The surface data depicting the 3D geometry of the breached dam was then converted in a solid mesh to be 3D-printed, to obtain a non-erodible scaled model (Figure 2). This scaled model as used in a smaller flume at Instituto Superior Técnico, under controlled flow conditions and susceptible to be studied in detail with optical access and without the constraints associated with transient flows. To allow the optical flow for Particle Image Velocimetry (PIV) having observed that the flow was essentially symmetric, only half of the dam was printed. The cut section was selected considering the thalweg of the breach channel (Figure 2).

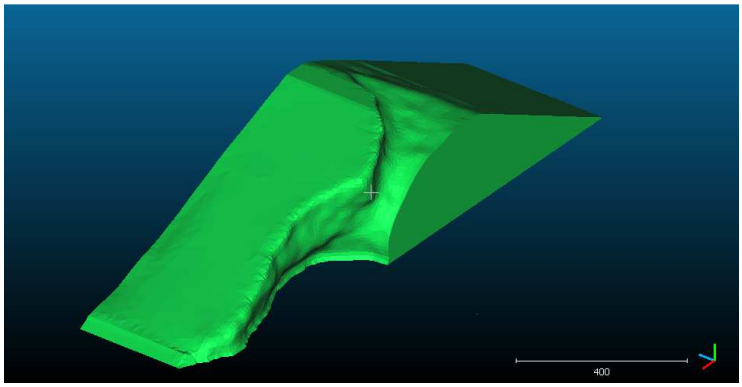

Fig. 2 – View of the printable 3D model.

2.2. Experimental facility and PIV instrumentation

The measurements were carried in a close circuit flume of the Hydraulics Laboratory of Instituto Superior Técnico. The flume is 5.8 m long, 0.395 m wide and 0.40 m height. The channel can be divided into 3 sections: 1) settling chamber, 2) test section and 3) exit section. The settling chamber has a length of 1.230 m. and the transition for the test section is made by a honeycomb like structure to break the large turbulence eddies and to allow a more stable flow. The test section has a length of 3.630 m and the glass walls allow the optical access to the flume. Finally, the exit section has a length of 0.94 m. The water was evacuated from the channel by means of two orifices in the channel exit section. These orifices are connected to the flume's reservoir by means of two independent flexibles pipes, each one having a valve allowing to adjust the water level in the channel. The bottom of the channel in the test section is made of Perspex allowing optical access to the flume from the bottom, whereas in both settling chamber and exit section, the bottom is made of PVC. Water from a reservoir placed under the channel was pumped by a frequency-controlled pump, allowing a fine tuning of the flow rate. The flow rate was measured by means of an electromagnetic flowmeter placed in the channel feeding circuit and it was set at $Q = 2.75$ l/s. Figure 3 depicts the flume section used in the experiments with the PIV laser light sheet positioned above the channel and the camera placed parallel to the channel window.

To measure velocity field, a Particle Image Velocimetry (PIV) system by Dantec was used. This system consisted in a Solo pulsed laser, a camera with a resolution of 1600 × 1200 pixels and timer box to synchronize the laser and the camera. The camera was equipped with a Nikon 60 mm/f2.8 lens. The system was controlled by the Dantec's software DynamicStudio 7.3. The laser was placed above the channel attached to a moving frame (Figure 3), allowing to sweep the channel in the x and y directions (details on the PIV system of the IST Hydraulics lab can be found in Ferreira et al. 2011). The water was seeded with polyamide particles with 50 µm of diameter.

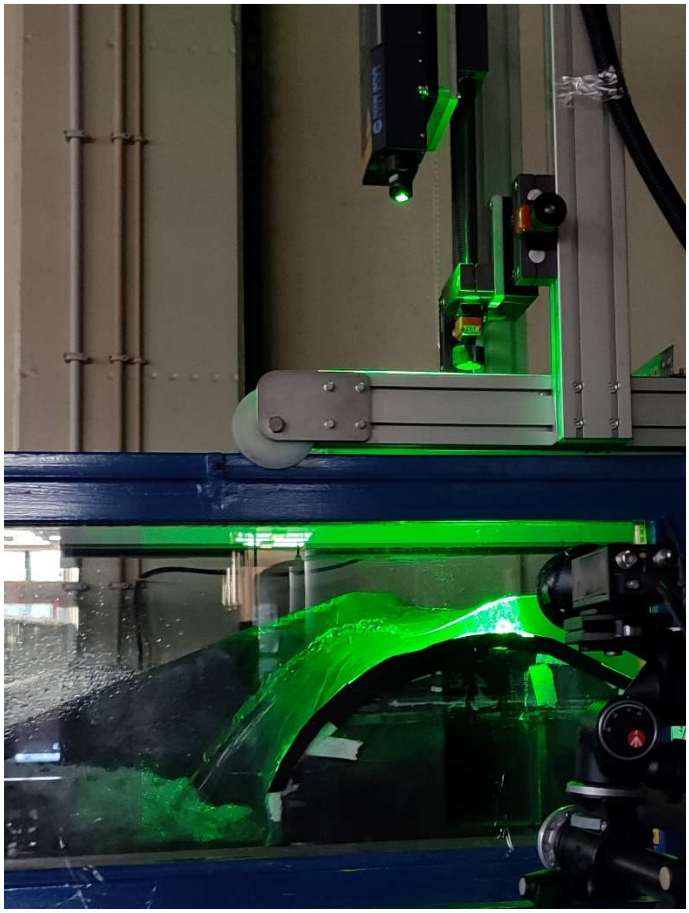

Fig. 3 – Flume and dam breach model used in the experiments. Above the channel, the laser source is place in a rigid frame on a moving chariot.

2.3. Data acquisition procedure

It was not possible to observe all the region of interest (ROI) in the camera as this would make it impossible to resolve appropriately the seeding particles, resulting in peak-locking. Therefore, the region of interest was divided into smaller regions, hereafter referred as sample regions, and the system laser+camera was moved accordingly to sweep all the ROI. An overlap of at least 10% of the image areas was considered between adjacent sample regions. Figure 4 depicts the scheme used to cover the ROI above the crest of the dam.

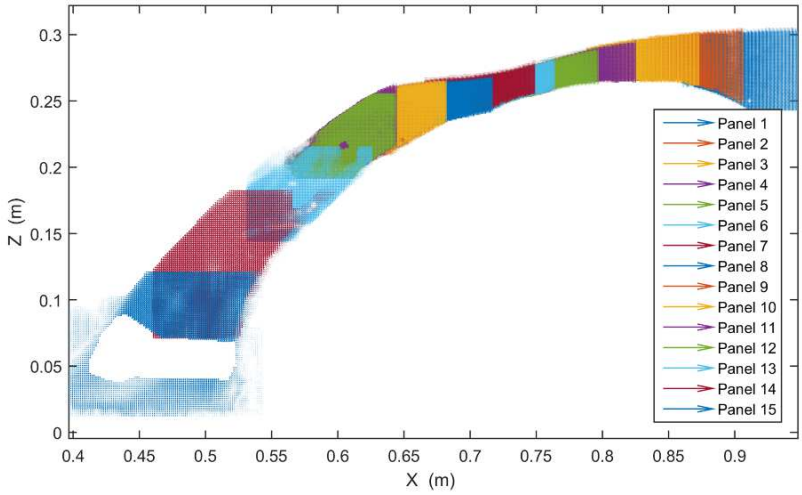

Fig. 4 – Segmentation of the ROI in sample regions and respective measurements.

The final interrogation window size was 16 × 16 pix corresponding to a spatial resolution between 0.6 and 1.5 mm. Each PIV acquisition was made with at least 4500 images pairs and repeated 3 times. PIV is nowadays an established technique described in detail in the literature, as in Adrian and Westerweel (2011) and references therein

Image calibration was performed using a checkerboard, with 2×2 mm squares (Figure 5). Since the distortion observed in the images was negligible, a linear conversion algorithm was applied to obtain the final velocity fields in metric units.

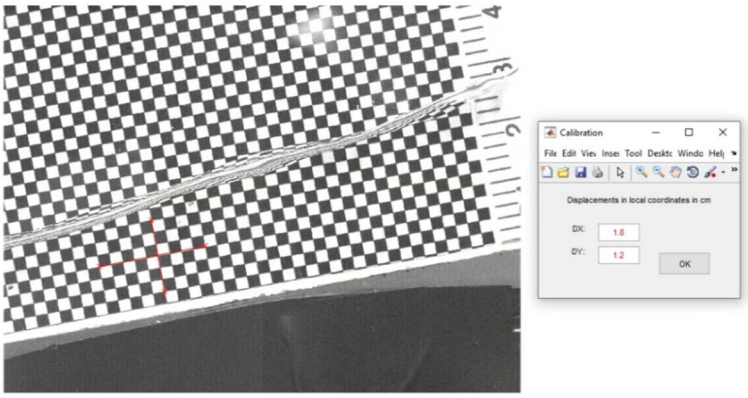

Fig. 5 – Example of calibration image over the breached dam crest.

After image calibration, masks were applied with the two following goals: (i) to restrict the analysis to the ROI, thus reducing the processing time; and (ii) to remove areas where the velocity measurements could not be trusted due to the excessive aeriation and turbulence of the jet. In particular, near the plunging jet impact area, the air bubbles block the visibility of the seeding particles (Figure 6).

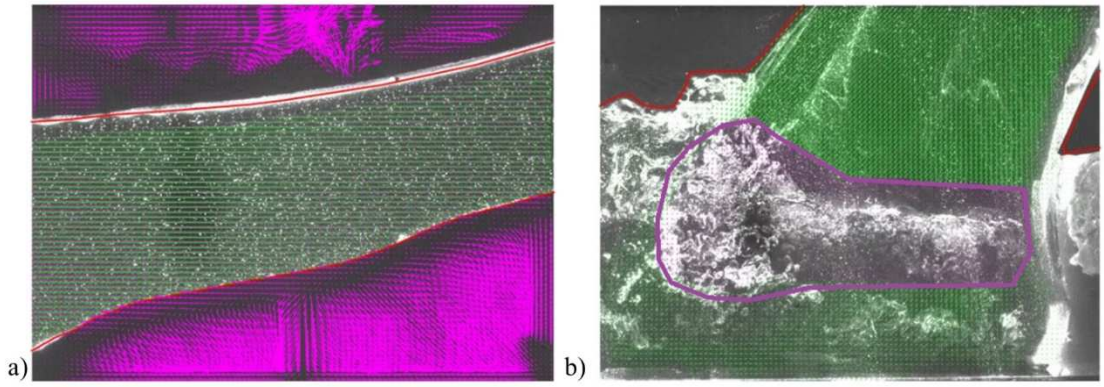

Fig. 6 – Flume and dam breach model used in the experiments. Above the channel, the laser source is place in a rigid frame on a moving chariot.

For the jet impact area, panel 15, the Reynolds shear stresses were computed as

$$\tau_{xz} = -\rho\overline{u'_z u'_x} \tag{1}$$

were ρ is the water density, u'_i velocity fluctuations in x and z directions.

3. THE CFD APPROACH

3.1. Conservation and closure equations

Our approach is based on Reynolds-Averaged Navier-Stokes (RANS) equations, as a widely used solution for simulating turbulent flows. The Reynolds stresses require modelling of turbulent stresses to close the system of equations. We opted for the $k-\omega$ Shear Stress Transport (SST) turbulence model, a two-equation eddy-viscosity model that combines the robustness of the $k-\omega$ model near walls with the free-stream independence of the $k-$ò model. Its hybrid nature makes it particularly suitable for flows with adverse pressure gradients and separation, as envisaged in this application.

The governing RANS equations can be written as:

$$\frac{\partial \rho}{\partial t} + \frac{\partial(\rho u_i)}{\partial x_i} = 0\,, \tag{1}$$

$$\frac{\partial(\rho u_i)}{\partial t} + \frac{\partial(\rho u_i u_j)}{\partial x_j} = -\frac{\partial p}{\partial x_i} + \frac{\partial}{\partial x_j}\left[\mu\left(\frac{\partial u_i}{\partial x_j} + \frac{\partial u_j}{\partial x_i}\right)\right] - \frac{\partial \tau_{ij}}{\partial x_j}\,, \tag{2}$$

where ρ is the fluid density, u_i are the velocity components in a cartesian frame $\{x, y, z\}$, where z is the vertical coordinate, against the gravity vector, p is the pressure, μ is the dynamic viscosity, and $\tau_{ij} = -\rho\overline{u'_i u'_j}$ represents the Reynolds stresses.

The $k-\omega$ SST model introduces two transport equations for the turbulent kinetic energy k and the specific dissipation rate ω:

$$\frac{\partial(\rho k)}{\partial t}+\frac{\partial(\rho u_j k)}{\partial x_j}=P_k-\beta^*\rho k\omega+\frac{\partial}{\partial x_j}\left[(\mu+\sigma_k\mu_t)\frac{\partial k}{\partial x_j}\right] \quad (3)$$

$$\frac{\partial(\rho\omega)}{\partial t}+\frac{\partial(\rho u_j \omega)}{\partial x_j}=\alpha\frac{\omega}{k}P_k-\beta\rho\omega^2+\frac{\partial}{\partial x_j}\left[(\mu+\sigma_\omega\mu_t)\frac{\partial\omega}{\partial x_j}\right]+2(1-F_1)\rho\sigma_{\omega 2}\frac{1}{\omega}\frac{\partial k}{\partial x_j}\frac{\partial\omega}{\partial x_j}, \quad (4)$$

where P_k is the production of turbulent kinetic energy, and $\mu_t=\dfrac{\rho k}{\omega}$ is the turbulent viscosity.

The blending function F_1 ensures a smooth transition between the $k-\omega$ and $k-$ò formulations. It is formulated as

$$F_1=\tanh\left(\min\left[\max\left(\frac{\sqrt{k}}{\beta^*\omega y},\frac{500\nu}{y^2\omega}\right),\frac{4\rho\sigma_\omega k}{CD_{k\omega}y^2}\right]^4\right). \quad (5)$$

The $k-\omega$ SST model is implemented in OpenFOAM using the RAS turbulence modelling framework. Having been subjected to extensive validation, $k-\omega$ SST approach has been shown to provide credible solutions in 3D flows with separation, recirculation, and wall-bounded turbulence.

3.2. Considerations on discretization and numerical solution

The discretization of the governing equations is performed using a finite volume method (FVM) on a computational grid composed of structured hexahedral elements. Hexahedral meshes, implemented in OpenFOAM, are preferred due to their higher numerical accuracy, efficiency, and robustness in resolving flow fields. This is particularly important in flows with strong gradients, such as boundary layers and recirculation zones, expected in the flow in the erosion cavity of the dam.

In the finite volume framework, the computational domain is divided into discrete hexahedral control volumes, and the governing equations are integrated over each volume. Fluxes of mass, momentum, and energy are evaluated at the faces of the control volumes using appropriate interpolation schemes, such as linear upwind or central differencing. The face-normal gradients are computed using second-order accurate schemes to ensure consistency and accuracy. Hexahedral grids also facilitate structured alignment with the flow direction, minimizing numerical dissipation and improving the resolution of anisotropic turbulence structures.

The numerical mesh is built around the digital model of half the dam, to mimic the experimental conditions (Figure 7).

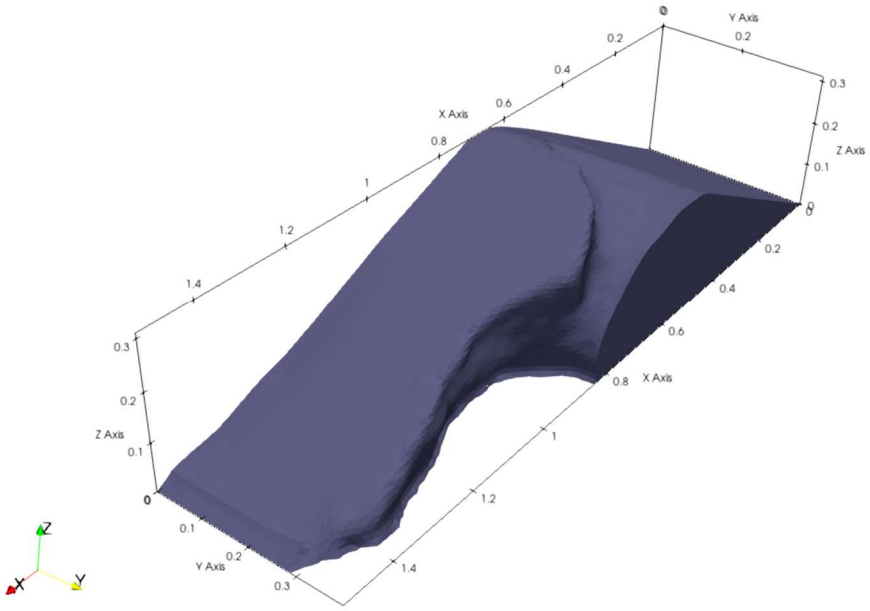

Fig. 7 – Digital model of the breached dam.

OpenFoam includes a combination of interpolation techniques, robust time-stepping methods, and boundary conditions while ensuring the numerical stability and accuracy required to resolve complex hydrodynamic phenomena.

Interpolation and differentiation schemes determine the accuracy and stability of the numerical solution. For convective fluxes, we employed linear upwind differencing (LUD) to balance accuracy and stability, particularly in regions with steep gradients. It uses flux-limiting functions to prevent spurious oscillations near discontinuities. For diffusive fluxes, central differencing as employed, providing second-order accuracy by averaging values at cell faces. Cell-face values are reconstructed using appropriate linear or non-linear interpolation techniques.

Time-stepping is handled using a semi-implicit scheme based on the backward Euler method and the second-order implicit Crank-Nicholson scheme, unconditionally stable and well-suited for (URANS) transient simulations. The time step was adjusted to ensure numerical stability.

The boundary treatment is critical to ensuring the accuracy of the numerical solution and maintaining physical fidelity. An inner region wall function was employed with near-wall grid refinement. For the inlet, we prescribe the water flux as well as turbulence quantities (e.g., k and ω). A zero-gradient Neumann boundary condition is used to allow free outflow. Cyclic boundary conditions are applied when the flow geometry or physical configuration allows, reducing computational cost and ensuring consistent treatment of periodic domains.

4. EXPERIMENTAL DATA AND NUMERCAL RESULTS

The mean velocity field over the dam crest, measured with PIV is shown in Figure 8. Dimensionless velocity profiles along the crest are plotted in Figure 8a) showing the development of the boundary layer. Figure 8 shows that: i) the thickness of the flow layer increases from upstream to downstream (right to left in Figure 8b); ii) the mean velocity increases from upstream to downstream; and iii) the thickness of the boundary layer increases along the breach channel.

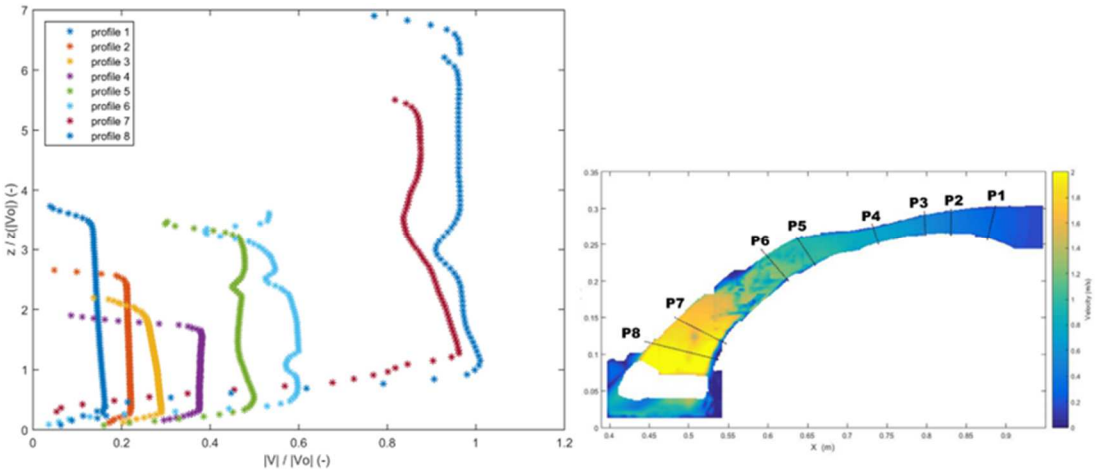

Fig. 8 – a) Mean velocity field along the breach channel; b) velocity profiles in the 7 cross-sections identified in the left panel.

As the flow depth increases, the pressure gradient becomes adverse, eventually past the threshold of separation. The last two profiles in Figure 8a) already show a curvature indicating that the flow is near the onset of separation. Separation eventually takes place near the end of the breach channel and comes to occupy a region adjacent to the bottom of the flume. Figure 9 reveals the existence of an anti-clockwise rotational structure inside the separated region (note that the flow is from the right to the left in Figure 9).

The flow in Figure 9 corresponds to the plunging jet impact area. The central part has been masked out since air entrainment would reduce the quality of the velocity data. Below the region where air entrainment is the dominant feature, the flow encounters the bottom, generating a stagnation point. The flow curls clockwise downstream (to the left in the figure), to exit the dam cavity. Upstream the stagnation point (to the right, in the figure), the flow circulates in the separated region.

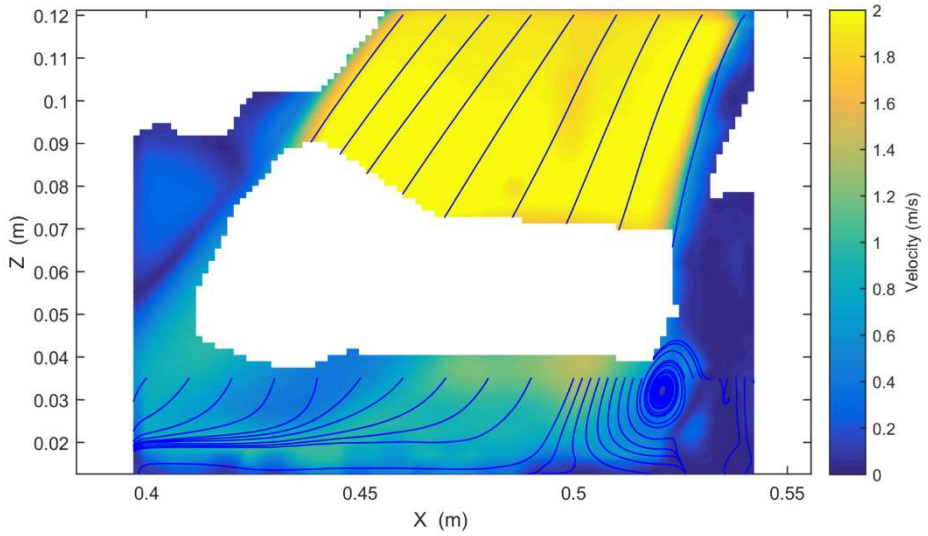

Fig. 9 – Mean velocity and stream lines at Panel 15, at the impact area of the plunging jet. Note vorticial structure inside the separated region and the stagnation point at $x \approx 0.5$ m.

Reynolds shear stresses in this region are shown in Figure 10. High values of shear stresses are found on the separated region an in the developing boundary layer downstream the stagnation point. Around the locus of the stagnation point turbulence is strongly supressed, as the pressure gradients are very high, rendering the lowest values of the Reynolds shear stresses.

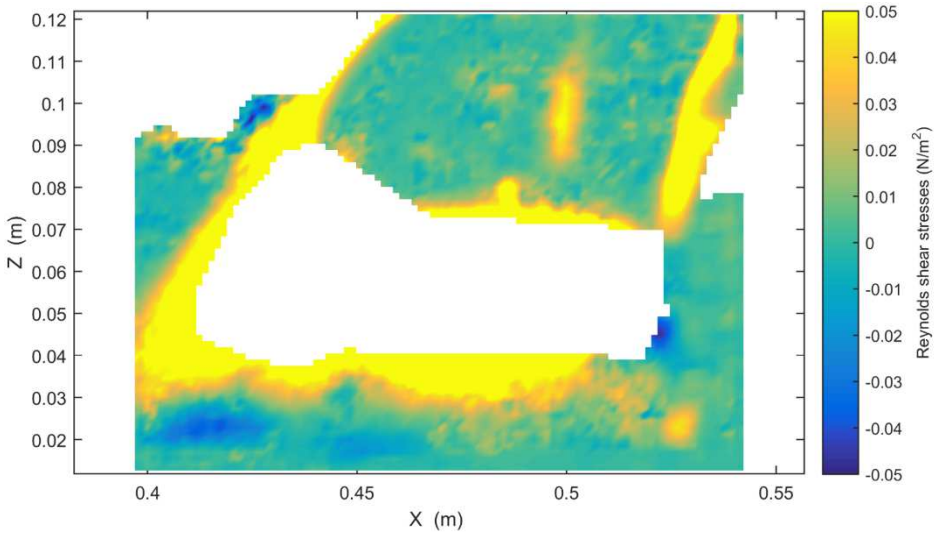

Fig. 10 –Reynolds shear stresses in the plunging jet impact area.

We compared the results of the CFD numerical simulations with the experimental results in order to assess the potential of the unsteady RANS solution to describe the dam-breach flow.

Complete verification and validation, with mesh sensitivity analysis or mesh convergence, and analysis of spatial error distribution is out of the scope of this work.

An overview of the solution is depicted in Figure 11. The simulation correctly captures the convergent flow into the breach, including the increase of flow depth. The latter feature is revealed to be the consequence of the diversion of a substantial part of the discharge in the from the breach wall to the centre of the breach. The laterally diverted flow pushes upwards the flow in the centre of the breach (represented in the simulation as the symmetry no-friction wall).

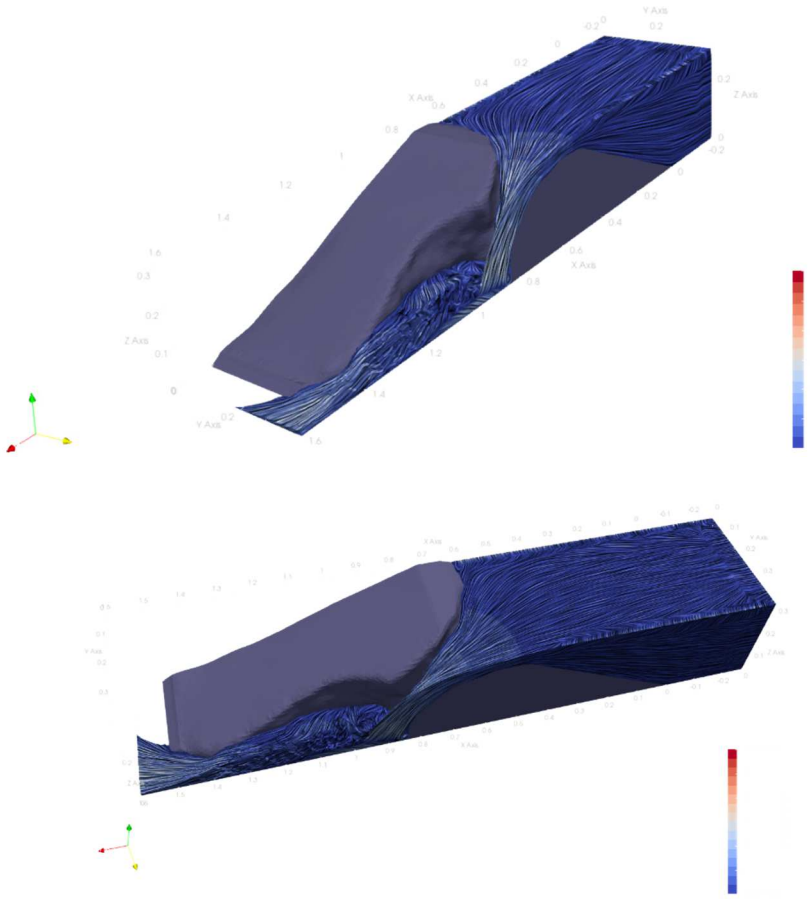

Fig. 11 – General aspect of the velocity field obtained with the RANS-based CFD solution (velocity magnitude and streaklines)

A closer look at the structure of the flow in the breach channel, for instance in the cross-section depicted in Figure 12, reveals that the lateral diversion of the flow creates a complex topology. The detailed flow is shown in Figure 13. The lateral diverted flow curls to the channel wall to form an attached vortex but is also directed upwards to the free-surface. This is the result of the interaction with the flow nearest to the symmetry wall, that develops similar structures. The result is saddle point topological structure that separates the flow adjacent to the cavity wall and adjacent to the symmetry wall and forms a stagnation surface between the upward and

downward flow, encompassing the later separated cells. This topological structure has not been confirmed by observations.

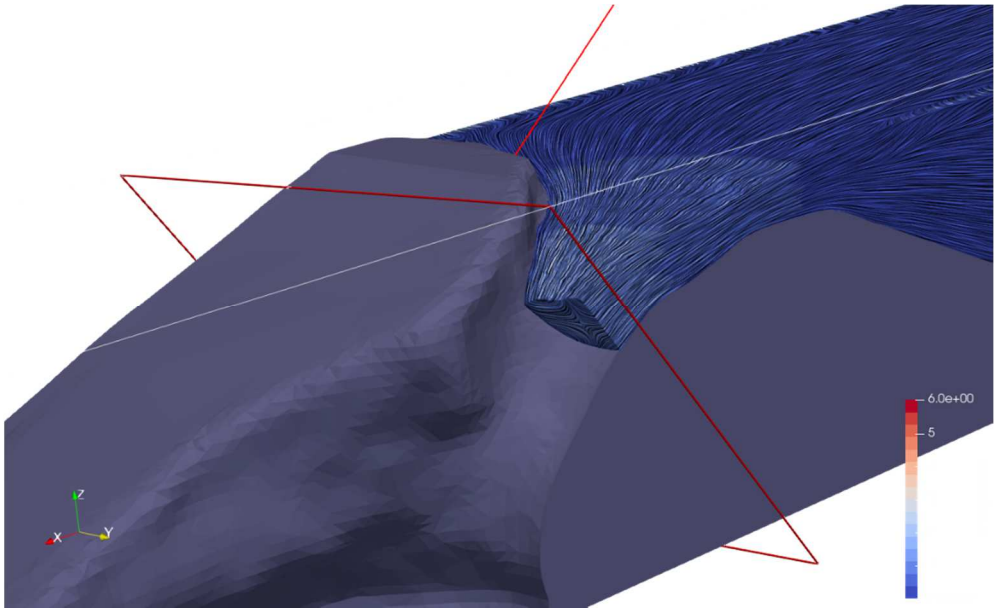

Fig. 12 – Cross-section in the flow in the breach channel

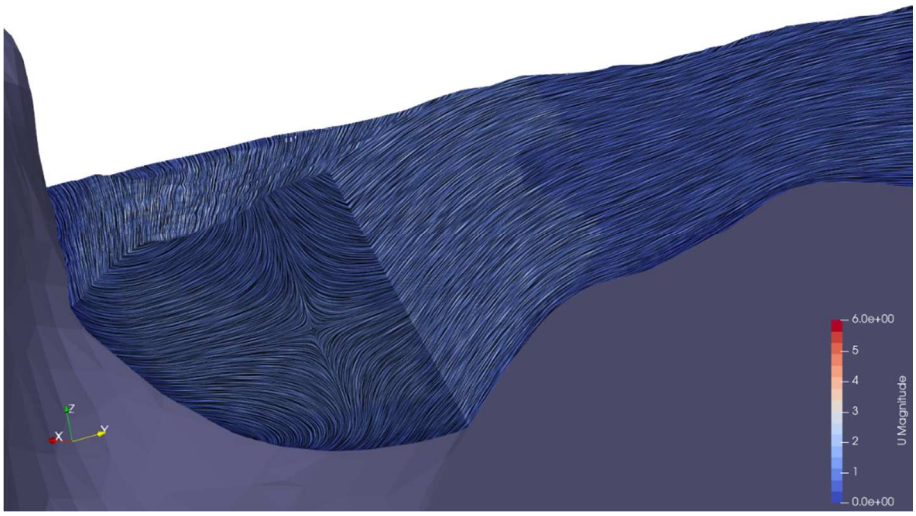

Fig. 13 – Detail of the cross-sectional flow in the breach channel. Note the formation of a saddle point.

As a result of the complex topological structure, the development of the boundary layer over the crest is unlikely to obey to the Kármán momentum integral, as it is influenced by the breach crest wall curvature, secondary currents and strong lateral flow convergence.

The plunging jet is, as seen, concentrated around the centre of the breach channel. As it hits the channel bottom wall, it spreads laterally, downstream and upstream. There is thus a stagnation point, associated to a maximum of pressure in the bottom wall. The stagnation point in the numerical solution can be seen in Figure 14.

Above the stagnation point, the flow topology features a saddle point, not confirmed in the PIV measurements. It should be noticed that the saddle point occurs at the symmetry wall while the PIV measurements were taken at 3 mm from the physical channel glass wall.

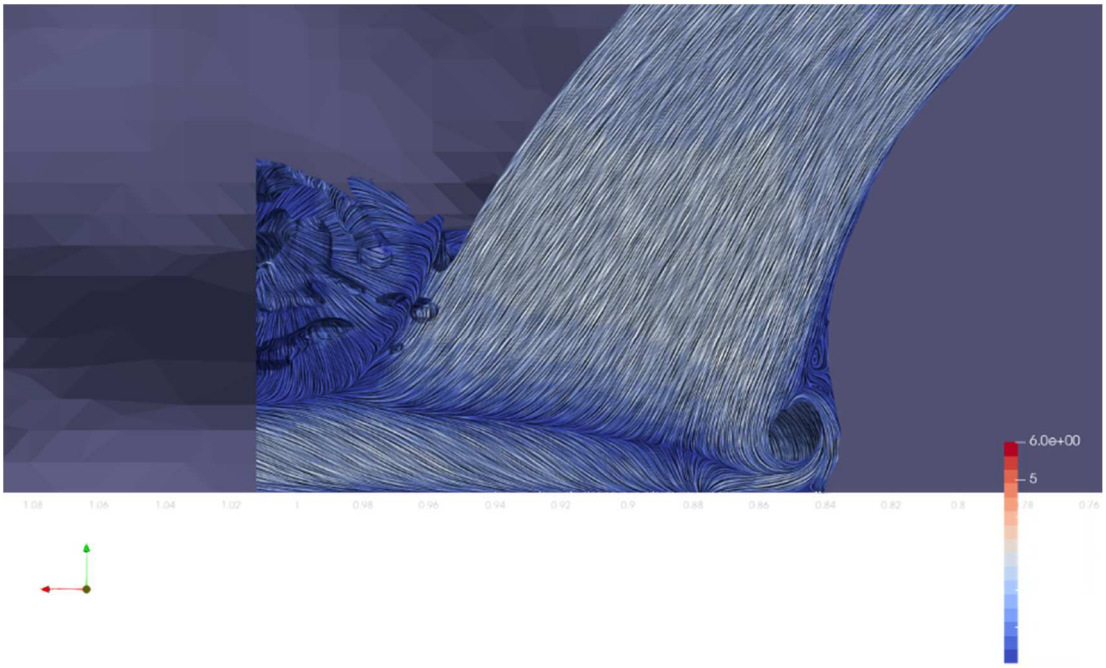

Fig. 14 – Separated region and stagnation point in the CFD solution for the plunging jet region.

In the upstream direction, the flow curls into a separated region, the same observed experimentally, as seen in Figure 14. The separation of the boundary layer along the breach channel is resolved with great detail. The numerical solution suggests that the separated zone is populated by three vortical structures. From upstream to downstream, the flow separates and forms a small counter-clockwise rotating cell, followed by a compatibility cell (clockwise rotating). Lastly, adjacent to the channel bottom, the large counter-clockwise rotating cell occupies most of the separated region.

Downstream the stagnation point, there is evidence of a longitudinal of a helical cell (the streaklines detach from the bottom wall to attach to the separation line issued from the saddle point), presumably a part of counter-rotating vortex pair conducting flow out of the erosion cavity. The experimental rests confirm the formation of a helical cell, since the stream lines seem to converge to a separation line (Figure 9). The helical cell seems less strong in the measurements though.

Figure 15 shows a cross-section of the flow in the erosion cavity. A detailed depiction of the cross-section is shown in Figure 16.

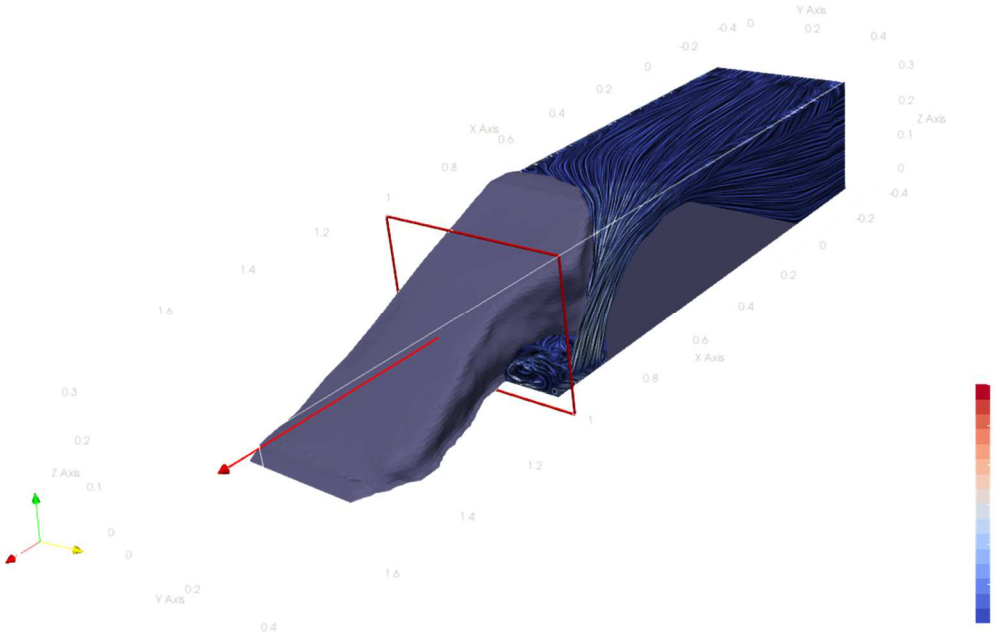

Fig. 15 – General aspect of the flow and cross-section to show the flow in the erosion cavity.

Figure 16 shows that the left half of counter-rotating vortex pair is clearly visible attached to the symmetry wall. The main trend of the flow is from the symmetry wall to the dam cavity wall. As it hits the cavity wall, the flow curls back and forms a large counter-clockwise rotation flow, driving the flow out of the cavity.

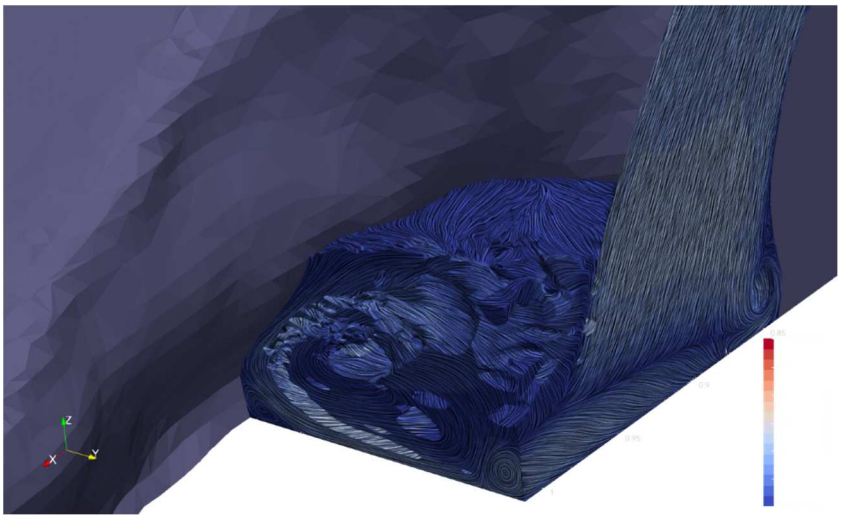

Fig. 16 – Flow in the erosion cavity. Notice the main helical cell generated by the curling back of the lateral flow, cell attached to the symmetry wall the and the separated cell around the rim of the cavity.

However, Figure 16 also reveals that the later flow separates before reaching the cavity wall. There is apparently a separated region running along the rim of the erosion cavity with clockwise rotating cell. This structure is unlikely to have been originated in the boundary layer separation cell at the end of the breach channel, since the rotation is opposite.

This jet impinging on the plunging pool generates a complex flow pattern of vortices with a strong air-water emulsion. This complex flow pattern is the responsible for the erosion of the dam's downstream bank. The simulation results suggest that erosion is mostly driven by the separation structures at the end of the breach channel and around the cavity, both contributing to undercutting and upstream and lateral progression of the erosion cavity. The lateral flow towards the cavity walls should also be responsible for significant erosion in the cavity walls.

5. CONCLUSIONS

We have used CFD simulation results to identify structures that may be relevant to influence the erosion process of the overtopped dams. Measuring live dam breach flows is currently beyond technical capacities, hence the need for CFD approach. But the need to validate the CFD simulation tool still remains. We thus used a simplified 3D printed model of a breach dam to generate a stationary flow representing one instant of the transient flow over the breach crest. We performed long-duration measurements using PIV allowing to determine the mean velocity field and the Reynolds stresses. We employed the results to compare with the numerical simulations.

Overall the agreement between the observations and the results of the numerical simulations is good. We further used the simulation results to highlight the complexity of the flow dynamics in the breach channel and erosion cavity. We showed that the flow in the breach interacts with the symmetry wall, forming complex topological structures, including saddle points and attached vortices. The strong lateral gradients in the breach channel, influenced by boundary curvature and attached cells should defy classical models like the Kármán momentum integral to describe the evolution of the boundary layer.

The boundary layer along the breach cannel separates as it reaches the bottom wall. The plunging jet impacts the bottom wall of the breach channel, creating a pressure maximum, in the stagnation point, that drives lateral and longitudinal flow, upstream and downstream. In the erosion cavity, the flow topology becomes increasingly intricate, with helical cells and counter-rotating vortices. The flow from the symmetry wall curls towards the cavity wall, forming large counter-clockwise rotations and a detached cell along the cavity rim. These structures contribute significantly to the erosion process. The simulation suggests that erosion is predominantly influenced by the separation structures at the end of the breach channel and around the cavity, emphasizing the role of lateral flow in undercutting and cavity wall erosion.

These findings underline the interplay between flow dynamics and non-hydraulic erosion mechanisms in overtopped dams.

ACKNOWLEDGEMENTS

This work was partially supported by national funds through Portuguese Foundation for Science and Technology (FCT), project DikesFPro PTDC/ECI- EGC/7739/2020, strategic funding UIDB/04625/2020 for the research unit CERIS (DOI: 10.54499/UIDB/04625/2020) and the Doctoral Grant PD/BD/127801/2016.

REFERENCES

[1] Adrian, R.J. & Westerweel, J. (2011). Particle Image Velocimetry, Cambridge: Cambridge University Press.

[2] Aleixo, R. Amaral, S., Mendes, S.V., Viseu, M.T., Alvarez, T., Fraga Filho, C.A. & Ferreira, R.M.L. (2022). Challenges of Surface Image Velocimetry - The dam-breach example. 39th IAHR World Congress, Granada, 19-24 June 2022.

[3] Alvarez, T., Valente, S., Amaral, S., Viseu, T., & Ferreira, R. M. L. (2019). Sensitivity analysis to initial conditions in dam breach by overtopping. 38th IARH World Congress – Water Connecting the World, Panama, 1-6 September 2019.

[4] Amaral, S.; Caldeira, L.; Viseu, L. and Ferreira, R.M.L. (2020) Designing Experiments to study Dam Breach Hydraulic Phenomena. Journal of Hydraulic Engineering. 145(4):: 04020014-1-04020014-17 https://ascelibrary.org/doi/10.1061/(ASCE)HY.1943-7900.0001678

[5] Amaral, S.; Viseu, T. and Ferreira, R.M.L. (2019) Experimental methods for local-scale characterization of hydro-morphodynamic dam breach processes. Breach detection, 3D reconstruction, flow kinematics and spacial surface velocimetry. Journal of Flow Measurement and Instrumentation. Volume 70, December 2019, Article number 101658. https://doi.org/10.1016/j.flowmeasinst.2019.101658

[6] Amaral, S., Viseu, T., Zhao, G., Ferreira, R.M.L. (2023). Recent Advances in Instrumentation and Monitoring Techniques Applied to Dam Breach Experiments. In: Chastre, C., Neves, J., Ribeiro, D., Neves, M.G., Faria, P. (eds) Advances on Testing and Experimentation in Civil Engineering, pp. 299–324. Springer Tracts in Civil Engineering, Online ISBN 978-3-031-05875-2. Springer, Cham. https://doi.org/10.1007/978-3-031-05875-2_13

[7] Bento, A.M.; Amaral, S.; Viseu, T.; Cardoso, R. & Ferreira, R.M.L. (2017) Direct Estimate of the Breach Hydrograph of an Overtopped Earth Dam. Journal of Hydraulic

Engineering. 143(6), 06017004-1: 06017004-13, http://dx.doi.org/10.1061/(ASCE)HY.1943-7900.0001294#sthash.UWJRuUjg.dpuf

[8] Ferreira, R.M.L. (2011) Turbulent flow hydrodynamics and sediment transport. Laboratory research with LDA and PIV. In Pawel Rowinski, editor, “Experimental Methods in Hydraulic Research”, GeoPlanet-Earth and Planetary Sciences, Polish Acad Sci, Inst Geophys. pp. 67-111. ISBN: 978-3-642-17474-2, DOI: 10.1007/978-3-642-17475-9_4.

Fifth International Dam World Conference
Portugal • Lisbon • LNEC • 13-17 April, 2025
dam world 2025

CRITICAL ASPECTS OF USING VIBRATING WIRE PIEZOMETERS IN GEOTECHNICAL MONITORING OF DAMS: HOW TO MEET BASIC OPERATING PRINCIPLES OF THE DEVICES AND AVOID COMMON ERRORS THAT COMPROMISE MONITORING

Bastos, Wellerson[1]	Pimenta Filho, Marcos[2]	Almeida, Luiza[3]	Ferreira, Marina[4]	Santos Junior, Mauro[5]
Pimenta de Ávila	Pimenta de Ávila	Pimenta de Ávila	Pimenta de Ávila	Pimenta de Ávila

ABSTRACT

This paper presents a discussion on critical aspects related to the operating principles of vibrating wire piezometers for geotechnical monitoring in dams, aiming to provide dam professionals, including both designers and operators, with a practical understanding of these instruments and their reading devices, in order to avoid errors and optimize the use of these tools. Unlike commonly published content on these instruments, which typically address general aspects related to objectives, advantages, limitations and installation methods, this paper presents the operating principles, basic requirements and precautions during preparation and post-installation configuration, including those related to verification parameters and correlation equations used by manufacturers. Additionally, it discusses the importance of initial readings and the saturation process of the porous stone and offers a detailed view of the reading devices, including their operating principles and the key parameters of the electrical signals of vibrating wire instruments. Finally, real cases of common errors are presented, along with the necessary actions to avoid them, ensuring the accuracy and reliability of the collected data and enhancing the performance of dam safety monitoring.

Keywords: Vibrating Wire Piezometers, Geotechnical Monitoring, Dam Safety, Correlation Equations, Reading Devices, Electrical Signal Parameters, Measurement Accuracy.

[1]wellerson.bastos@pimentadeavila.com.br, Brazil

1. INTRODUCTION

Geotechnical monitoring of dams is a key component of risk management, aiding in the early identification and prevention of structural failures that could lead to catastrophic events. According to ICOLD Bulletin 158 [1], a comprehensive monitoring plan must encompass three primary pillars: instrumentation-based monitoring, visual inspections, and electromechanical equipment testing. Instrumentation-based monitoring relies on devices such as vibrating wire piezometers (VW piezometers) to measure critical parameters, including pore pressures, displacements, and water levels. Visual inspections detect physical anomalies that are observable by sight, while electromechanical tests ensure the proper function of critical components, such as reservoir gates and valves.

Effective monitoring requires an understanding of the primary failure modes to which dams are susceptible, as outlined by [2] and [3]. These modes include overtopping (caused by excessive reservoir levels), internal erosion (loss of material due to seepage), liquefaction (loss of soil strength due to increased pore pressures), and slope instability (sliding of soil masses driven by elevated pore pressures). Piezometric monitoring is directly associated with slope instability, where measurements indicate increased interstitial pressures that could compromise slope stability. It is also indirectly linked to liquefaction detection and the identification of hydraulic gradients that signal internal erosion.

VW piezometers are recognized for their robustness, precision, and long-term durability, making them indispensable in dam monitoring, particularly in conditions where manual readings are impractical or where structures experience high dynamic loads. Their ability to transmit data over long cables without significant signal degradation further enhances their utility in remote or large-scale installations.

However, the accuracy and reliability of VW piezometer readings depend on adherence to best practices during installation, operation, and maintenance, as recommended by manufacturers such as Geokon [4], Encardio Rite [5], RST Instruments [6], Geosense [7], Soil Instruments [8]. The "fully grouted" installation method, highlighted by [9], has gained prominence for enabling the placement of multiple sensors along a single borehole, thereby enhancing spatial data resolution, particularly in low-permeability soils.

Beyond installation, several technical procedures are critical for obtaining accurate measurements. These include verifying sensor condition, ensuring proper saturation of the porous stone, inspecting electrical parameters, and correctly applying frequency-to-pressure conversion formulas. Initial zero readings, taken after the sensor reaches thermal equilibrium, provide a baseline for subsequent data and must be recorded before the final installation at

the monitoring point. Additionally, correcting for environmental variables, such as temperature and barometric pressure changes, is essential to avoid misinterpretation of data due to frequency deviations [10].

Given the complexities involved in both operating and interpreting VW piezometer data, this article aims to systematize the key technical aspects and highlight best practices. The structure follows a logical and didactic progression: it begins with the physical principles underlying VW piezometer operation, a description of essential components, and their influence on performance. It then addresses sensor preparation steps, such as porous stone saturation and initial zero readings, before discussing manufacturer-specific correction equations and their adaptation in automated and manual data acquisition systems. Lastly, diagnostic tools for identifying errors and optimizing monitoring system performance are presented.

By integrating these considerations, the article seeks to provide a comprehensive understanding of the operational nuances of VW piezometers, aiming to mitigate common errors and enhance the reliability of geotechnical monitoring programs for dam safety.

2. OPERATION OF VIBRATING WIRE PIEZOMETERS

2.1. Physical Principles, Components and Operation

The operating principle of vibrating wire piezometers can be understood in a manner analogous to the functioning of a tuning fork. According to [11], frequency measurement in a vibrating wire transducer involves two main stages: wire excitation and the measurement of the vibratory response over time, with the aim of determining its vibration frequency.

Vibrating wire sensors consist of a steel wire stretched between two anchoring points fixed to the structure being monitored, as illustrated in Fig. 1. A coil positioned near the wire generates an electrical impulse that excites the wire and subsequently captures its vibration frequency. This frequency varies according to the tension applied to the wire, which, in turn, is related to the relative displacements of the anchoring points [12].

[1]wellerson.bastos@pimentadeavila.com.br, Brazil

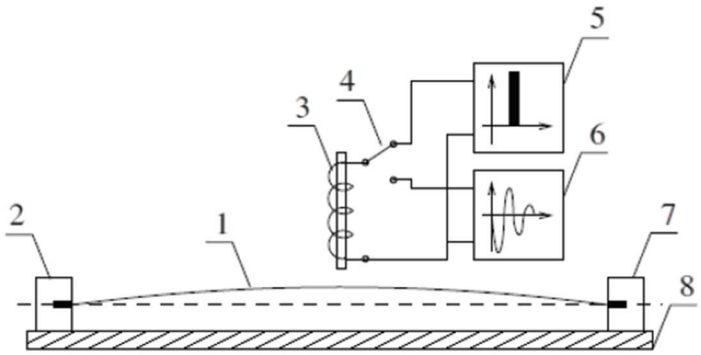

Fig. 1 – Simplified Model of a Vibrating Wire Sensor

Note: 1 – Wire; 2 – Anchoring Points; 3 – Coil; 4 – Selector Switch; 5 – Input Signal; 6 – Damped Sensor Response Signal.

Source: Adapted from [12]

The excitation dynamics of the wire are analogous to the classical experiment involving two tuning forks. When one tuning fork is struck, it emits vibrations at its resonance frequency. If a second tuning fork with the same frequency is placed nearby, it also begins to vibrate, even without direct contact (Fig. 2). However, if the tuning forks have different frequencies, resonance does not occur.

Fig. 2 – Classical Experiment Using Tuning Forks

Similarly, in a vibrating wire piezometer, when the wire is excited at its resonance frequency, the reflected signal reaches its highest amplitude at that specific frequency, enabling precise measurement. This allows for the subsequent application of correlation formulate to calculate the pressure and, consequently, determine the height of the water column at the monitored point.

In addition to the vibrating wire and diaphragm, the piezometer includes other essential components, as illustrated in Fig. 3. The porous filter, located at the sensor's tip, allows water

to pass through while preventing fine particles from entering the device, protecting the diaphragm from clogging. The excitation and reading coils are responsible for generating and detecting the vibration signal, while the thermistor measures the temperature, enabling pressure values to be corrected for thermal variations. The instrumentation cable transmits the signal, ensuring both the electrical excitation of the wire and the collection of data for analysis.

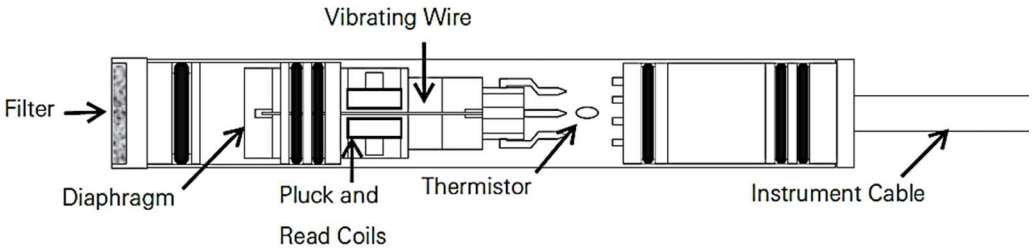

Fig. 3 – Schematic of the Vibrating Wire Piezometer and its Main Components

Source: Adapted from [4].

To ensure the reliable operation of the sensors, certain procedures are essential, such as the proper saturation of the porous filter and the execution of the initial reference reading (known as the "zero" reading), which is detailed in sections 2.2 and 2.3, respectively. Proper saturation prevents air from entering the sensor chamber, a factor that can compromise measurement accuracy.

Another crucial aspect is the ability of the reading and excitation equipment to generate electrical signals that match the sensor's frequency range. The signal captured by the readout or datalogger must have an appropriate amplitude, a good signal-to-noise ratio and remain within the sensor's operational range. Parameters such as the electrical resistance of the coils and the thermistor can directly influence the accuracy of the measurements and, therefore, should be verified according to the manufacturers' technical specifications.

With advancements in technology and the standardization of monitoring procedures, it has become possible to systematically verify whether the sensor's electrical signal meets the manufacturers' specifications, ensuring proper instrument functioning and data reliability. Section 4 of this article presents the main technologies and recommended practices for the performance verification and fault diagnosis of vibrating wire piezometers.

[1]wellerson.bastos@pimentadeavila.com.br, Brazil

2.2. Filter Saturation Process and Importance for Precision

The filters of vibrating wire piezometers play a crucial role in accurately measuring pore pressures in soils, acting as an interface that allows water to pass through while blocking fine particles, thereby protecting the sensor's diaphragm. For the filter to function properly, it must be fully saturated, without any air bubbles present. As highlighted by [13], the introduction of air into the system can dampen the vibration of the wire and cause deviations in readings, a phenomenon known as "zero drift," where the pressure reading gradually shifts over time.

Fig. 4 presents the three possible filter saturation conditions: unsaturated, where the chamber is completely filled with air; partially saturated, containing both water and air; and fully saturated, where the chamber is filled only with water. These conditions clearly illustrate how the level of saturation can influence the sensor's response.

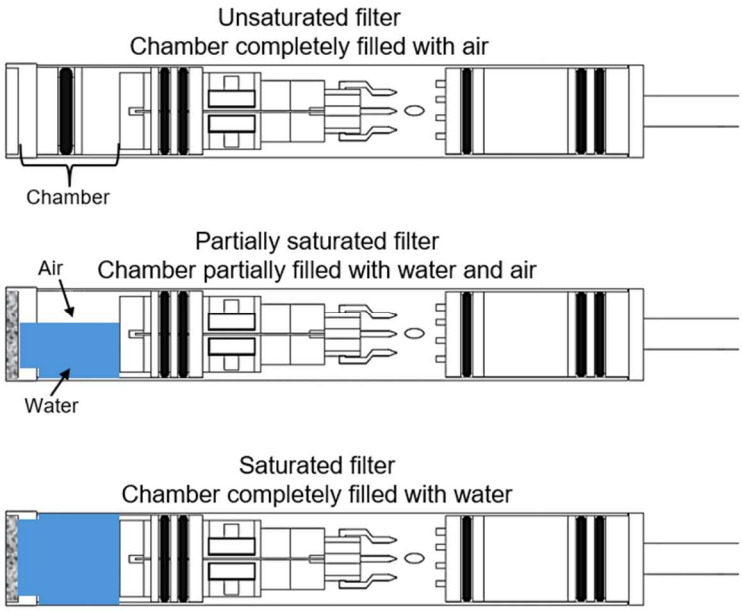

Fig. 4 – Representation of Saturation Conditions for a Vibrating Wire Piezometer Filter

Source: Adapted from [4].

Vibrating wire piezometer filters can be classified into two main types based on their air entry capacity. **Low Air Entry (LAE)** filters have air entry values (AEV) ranging between 5 and 10 kPa and are widely used in soils with varying permeability [7] and [15]. Although these filters may temporarily desaturate when the soil water level drops, they tend to resaturate quickly once the water level rises again. However, they are not suitable for suction measurements, as they cannot register significant negative pressures. On the other hand, **High Air Entry (HAE)** filters have AEVs exceeding 100 kPa and are designed to remain saturated even in partially

saturated soil conditions [7] and [15]. Nevertheless, maintaining their saturation requires meticulous care, especially in clayey soils, where their efficiency can be compromised due to the difficulty of fully removing air bubbles.

To ensure adequate saturation, various methods are recommended, as indicated in the manuals from different manufacturers. The **boiling method** [13], for instance, involves submerging the filter in deaerated boiling water for 15 to 30 minutes, followed by slow cooling in a sealed container, allowing complete expulsion of air from the filter interior. This method is often cited as effective for HAE filters, which demand complete and uniform saturation.

Another commonly used technique is the **vacuum chamber method**, where the dry filter is placed in a low-pressure environment before introducing deaerated water, ensuring the removal of trapped air. Alternatively, in field conditions, a manual vacuum pump can be used to extract air from the filter while it is submerged in deaerated water, enabling effective saturation in hard-to-reach locations.

For LAE filters, the simple immersion method involves carefully removing the filter, filling the chamber with deaerated water and gently reinstalling the filter before performing the zero reading with the readout equipment. This procedure, as illustrated in Fig. 5, is widely employed due to its simplicity in field applications and its effectiveness for most use cases of these instruments.

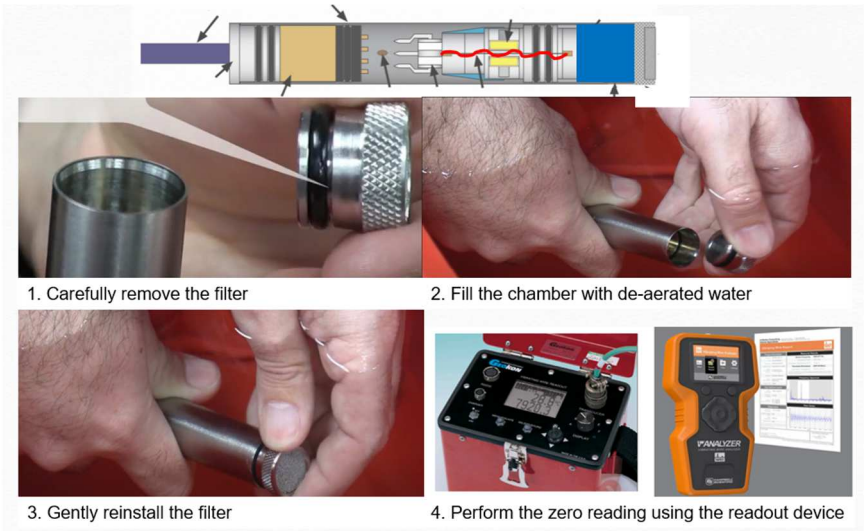

Fig. 5 – Schematic of the Simple Immersion Saturation Method for LAE Filters

Source: [6], [14] and [20]

[1]wellerson.bastos@pimentadeavila.com.br, Brazil

2.3. Field Zero Reading Procedures

The initial zero reading is an essential step in the installation of vibrating wire piezometers, as it establishes the reference point for all subsequent pressure measurements. The accuracy of these measurements depends directly on a correct initial reading, as errors in this phase can introduce systematic deviations, compromising the monitoring analysis and leading to incorrect decisions in geotechnical engineering projects [13]. This procedure is particularly relevant for avoiding misinterpretations of pressure variations caused by phenomena such as the desaturation of the porous stone.

During the zero-reading process, it is crucial that the piezometer is properly prepared. The porous stone filter must be saturated with deaerated water to eliminate air bubbles that can interfere with the accurate transmission of water pressure to the sensor [15]. Inadequate saturation can result in the phenomenon known as "zero drift ", where the sensor provides inaccurate readings due to the presence of air in the internal chamber. This phenomenon can be observed when the readings in do not correspond to the actual applied pressure, as seen in cases where the porous stone loses saturation after installation, generating negative or inconsistent readings.

Another critical aspect is the thermal equilibrium of the sensor before the reading. Manufacturer manuals, such as those from GEOKON and DGSI, recommend a stabilization period of 15 to 30 minutes, especially in environments with significant temperature variations [4], [16]. During this period, the piezometer should be placed in an area where only atmospheric pressure acts on the sensor, free from external loads or water column pressure. This ensures that the initial reading exclusively reflects zero pressure and not external factors.

The zero reading is recorded in terms of digits ($Hz^2/1000$) and temperature (°C). Comparing this reading to the calibration values of the sensor is essential to validate the accuracy of the equipment. For example, the RST Instruments manual recommends that the difference between the zero reading and the reference value in the calibration report should not exceed 0.5% of the sensor's full scale. If this difference is greater, the procedure should be repeated or re-evaluated to verify potential issues, such as filter desaturation, thermal changes, or sensor defects [21].

The validation process may also include performing consecutive readings, as suggested by the ENCARDIO-RITE and Soil Instruments manuals. These additional readings help verify consistency and discard isolated anomalies [5] and [8]. Additionally, the readouts or dataloggers used must be configured to operate within the sensor's specific frequency range, ensuring an adequate signal-to-noise ratio and avoiding interpretation errors.

Fig. 5 illustrates the zero-reading procedure, detailing the steps that involve removing the filter, filling the chamber with deaerated water, reinstalling the filter, and taking the reading with the readout equipment. This process ensures that the sensor is free from external influences and helps detect potential problems, such as filter desaturation after installation.

Proper execution of the initial zero reading is a key component in ensuring the accuracy of measurements throughout geotechnical monitoring. When performed according to the best practices recommended by manufacturers, the risk of errors is reduced and subsequent readings are more representative of actual field conditions. This strengthens the reliability of safety and stability analyses for dams, preventing incorrect diagnoses that could compromise decision-making in critical situations [13].

3. CORRELATION EQUATIONS

3.1. Frequency and Temperature Conversion to Pressure

The conversion of frequency and temperature into pressure in vibrating wire piezometers is an essential process to ensure accurate pore pressure readings. The equations used for this calculation vary between manufacturers and equipment models, but all are based on frequency readings and calibration factors that convert the data into engineering units.

DGSI VW [16] piezometers use a polynomial equation (Equation 3.1) that incorporates linear, quadratic and cross terms, considering frequency (Hz^2), temperature (T^2) and the interaction between them (Hz × T). This approach provides greater accuracy in scenarios with significant thermal variations:

$$P = C0 + (C1 \times Hz) + (C2 \times T) + (C3 \times Hz^2) + (C4 \times Hz \times T) + (C5 \times T^2) \quad (3.1)$$

Where:

- C0 to C5: calibration coefficients provided in the sensor's calibration certificate;
- Hz: frequency reading in hertz squared; and
- T: temperature in degrees Celsius.

This approach requires that the coefficients are correctly entered into the dataloggers and readouts, as default configurations using linear equations can lead to measurement errors.

On the other hand, piezometers such as those from Geosense [7], GEOKON 4500 [4], Encardio-Rite [5] and RST VW2100 [17] use more common linear equations because they are practical and provide acceptable error margins. It is important to note that Equation 3.2 is presented according to the terms used by GEOKON but is also valid for other instruments, with only the variable names differing.

[1]wellerson.bastos@pimentadeavila.com.br, Brazil

GEOKON, Encardio-Rite and Geosense (Equation 3.2):

$$P = G \times (R1 - R0) + K \times (T1 - T0) \quad (3.2)$$

Where:

- G: linear calibration factor (e.g., kPa/digit);
- R1: subsequent frequency readings taken in the field (in digits or Hz²/1000);
- R0: zero reading taken during installation (in digits or Hz²/1000);
- K: thermal correction coefficient (e.g., °C/digit).
- T1: current sensor temperature (°C); and
- T0: initial reference temperature (°C);

The linear approach simplifies field operations by reducing the complexity of data input, making the process more efficient compared to polynomial equations, which require more constants for pressure calculation. This simplification facilitates sensor calibration and integration with monitoring systems without significantly compromising instrument accuracy in most applications.

However, using instruments from different manufacturers with shared dataloggers or readout devices requires adjusting the variable nomenclature and conversion factors to match the calibration settings of each piezometer model.

The following equations (3.3 to 3.6) present the transformations between different piezometers, highlighting variations in the positioning of factors and the addition and subtraction operations adopted by different manufacturers.

Soil Instruments (Equation 3.3) [8]:

$$P = G \times (L0 - L) + Tk \times (T1 - T0) \quad (3.3)$$

Where:

- G: linear calibration factor (e.g., kPa/digit);
- L0: zero reading taken during installation (in digits or Hz²/1000);
- L: subsequent frequency readings taken in the field (in digits or Hz²/1000);
- Tk: thermal correction coefficient (e.g., °C/digit).
- T1: current sensor temperature (°C); and
- T0: initial reference temperature (°C);

RST Instruments (Equation 3.4) [17]:

$$P = CF \times (L0 - L) - Tk \times (T0 - T) \quad (3.4)$$

Where:

- CF: linear calibration factor (e.g., kPa/digit);
- L0: zero reading taken during installation (in digits or Hz²/1000);
- L: subsequent frequency readings taken in the field (in digits or Hz²/1000);
- Tk: thermal correction coefficient (e.g., °C/digit).
- T0: initial reference temperature (°C); and
- T1: current sensor temperature (°C);

Roctest (Equation 3.5) [15]:

$$P = Cf \times (L - L0) - Ct \times (T1 - T0) \quad (3.5)$$

Where:

- CF: linear calibration factor (e.g., kPa/digit);
- L: subsequent frequency readings taken in the field (in digits or Hz²/1000);
- L0: zero reading taken during installation (in digits or Hz²/1000);
- Ct: thermal correction coefficient (e.g., °C/digit).
- T1: current sensor temperature (°C); and
- T0: initial reference temperature (°C);

The Roctest PW piezometer [15] uses a linear equation similar to most of the instruments discussed. However, to convert frequency readings in Hz to a unit similar to "digit," referred to as Linear Unit (L), the calculation is performed using Equation 3.6:

$$L = K * \frac{F^2}{1000} \quad (3.6)$$

Where:

- L: Reading in linear units;
- K: Piezometer constant (1.0156); and
- F: Frequency (Hz).

[1]wellerson.bastos@pimentadeavila.com.br, Brazil

Although these equations share similar structures, the arrangement of terms and the signs used vary. For example, if a datalogger configured with the RST Instruments equation is used with a GEOKON or Encardio-Rite piezometer, the result will be incorrect even if the frequency readings are the same.

This issue can be avoided by properly configuring the dataloggers and accurately entering the calibration parameters. Some readouts, such as the Encardio-Rite EDI-54V [18], RST Instruments VW2106 [6] and Geosense VWR1 [19], come with default settings that may not be compatible with all piezometers unless adjusted. Furthermore, devices that use VSPECT technology, such as CampbellSCI's VW Analyzer [20] and Geokon's GK-406 [21], apply Fourier transforms to identify resonant frequencies and eliminate noise. However, even with this advanced technology, it is essential to correctly input the thermal coefficients and calibration factors.

The use of the correct equations for converting frequency and temperature into pressure is crucial to avoid errors in pore pressure readings. Calibration certificates provide the necessary conversion coefficients and must be followed rigorously. Additionally, the monitoring team must be aware of operating conditions, such as temperature and atmospheric pressure, to ensure that readings reflect real field conditions. Implementing a continuous verification program ensures the reliability of the geotechnical monitoring system.

3.2. Correction Factors for Environmental Variations

The readings of vibrating wire piezometers are susceptible to environmental factors such as temperature and barometric pressure, which can compromise the accuracy of pore pressure measurements. To ensure that the data accurately reflects field conditions, it is crucial to apply the appropriate corrections consistently.

Temperature is one of the main factors affecting piezometer readings. The vibrating wire, made of steel, expands or contracts with thermal variations, altering its vibration frequency. All analyzed manufacturers, including DGSI, GEOKON, Soil Instruments, Encardio-Rite, Roctest and RST Instruments, incorporate thermistors in their sensors to monitor internal temperature and allow real-time corrections.

In addition to thermal correction, barometric pressure also impacts readings, especially in absolute piezometers, which measure total pressure (the sum of pore pressure and atmospheric pressure). Barometric correction is essential for sensors installed in areas exposed to significant atmospheric variations, such as mountainous regions, dams and deep

ventilated boreholes. To correct this effect, many dataloggers and readouts offer options to record barometric pressure using embedded or external sensors.

In the case of absolute piezometers, such as those from GEOKON, RST Instruments and Encardio-Rite, it is recommended that the reference reading be taken using a barometer located near the installation point. The difference between the atmospheric pressure recorded on-site and that recorded during factory calibration can be applied using a linear correction factor.

The barometric correction equation can be represented as Equation 3.7:

$$\mathrm{Pcorr} = \mathrm{Pmeasured} - (\mathrm{Bsite} - \mathrm{Bcalib}) \tag{3.5}$$

Where:

- Pcorr: corrected pressure;
- Pmeasured: uncorrected sensor reading;
- Bsite: barometric pressure measured at the site; and
- Bcalib: barometric pressure recorded during calibration.

Devices such as the Geosense VWR1 and the RST Instruments VW2106 feature configurable modes that automatically perform barometric correction. However, dataloggers with default configurations, without the inclusion of Bsite and Bcalib, may produce discrepancies in readings, especially during abrupt atmospheric pressure changes due to weather fluctuations.

In addition to thermal and barometric corrections, electromagnetic interference can impact readings. Modern equipment, such as the VWAAnalyzer with VSPECT technology, applies Fourier transforms to separate frequencies of interest from noise signals, providing accurate readings even in high-interference environments, such as dam galleries near power transmission lines.

To ensure reliable measurements, the use of shielded cables and routing away from noise sources is recommended. The signal-to-noise ratio (SNR) [20] should be monitored regularly, with ideal values above 10 and preferably above 50.

In addition to correction factors and installation practices, periodic verification of electrical resistance and sensor continuity helps identify physical issues, such as damage to connectors and cables. The installation inspection should also confirm that thermal and barometric correction coefficients are up to date in the datalogger or readout to avoid systematic errors.

Finally, the correct application of correction factors and the validation of conversion equations ensure that vibrating wire piezometers provide precise and representative measurements.

[1]wellerson.bastos@pimentadeavila.com.br, Brazil

Adopting best practices and advanced signal analysis technologies reinforces the reliability of the monitoring system, enabling safe and effective tracking of geotechnical structures.

4. VERIFICATION RESOURCES AND PARAMETERS

4.1. Available Reading and Diagnostic Technologies

The accuracy of measurements obtained from vibrating wire piezometers directly depends on the reading technologies and diagnostic resources of field devices. These devices convert the resonant frequency of the vibrating wire into engineering units, such as pressure or displacement, and are essential for identifying anomalies that could compromise data reliability. With technological advancements, modern devices offer tools not only for reading but also for detailed signal quality analysis, ensuring reliable measurements in geotechnical monitoring campaigns.

One of the key monitored parameters is the analysis of the vibrating wire's frequency. The traditional approach consists of time-domain analysis, where the frequency is calculated based on zero-crossings within a given time interval. Devices such as the VW2106 and the GK-404 use this method, which, despite its efficiency, is susceptible to low and medium-frequency noise from external sources, such as power grids and engines.

To mitigate these effects, more advanced equipment, such as the GK-406 and VWAnalyzer, uses VSPECT™ technology, which applies Fourier transforms to convert the signal into a frequency spectrum, enabling precise identification of the dominant frequency even in environments with high electromagnetic interference.

In Fig. 6, two examples of signals in the time domain and frequency spectrum are presented, illustrating the differences between a clean signal and one with interference:

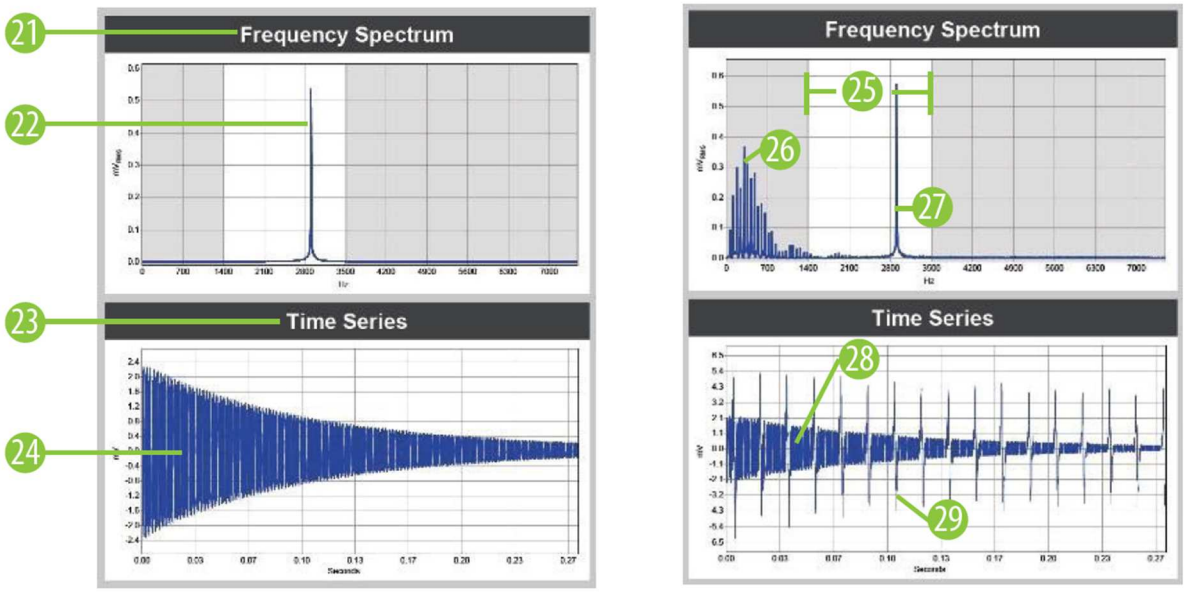

Fig. 6 – Graphical representation of signals in vibrating wire piezometers

***Source*: [*20*]**

Fig. 6 highlights that, in an ideal signal, the frequency spectrum presents a clear and isolated peak (an indicator of an accurate reading), while a signal with interference shows multiple peaks (markers 25 to 27), indicating the presence of noise. In the time domain, a clean signal decays gradually (marker 28), whereas a contaminated signal exhibits irregular oscillations (marker 29), making it difficult to accurately identify the resonant frequency.

Another important parameter is the signal-to-noise ratio (SNR), defined as the ratio between the sensor's signal amplitude and the highest detected noise amplitude. SNR values above 10 indicate a reliable reading, while values below 3 suggest significant interference. Devices such as the EDI-54V and VW Data Recorder allow adjustments to the sensor's excitation level to improve the SNR by increasing the power of the signal applied to the vibrating wire [18] and [22].

The signal decay rate is another critical indicator, representing the time it takes for the signal to reach its resting state after excitation. Equipment such as the VWR1 and VWnote records the decay curve, enabling the identification of issues such as misalignment of the vibrating wire or excessive tension [19] and [8]. Rapid signal decay may indicate structural failures or wire rupture, while prolonged vibrations are generally normal for sensors installed at greater depths.

Additionally, verifying the electrical resistance of the sensor's coils and integrated thermistors is essential. Readings outside the recommended ranges—such as extremely high values or

[1]wellerson.bastos@pimentadeavila.com.br, Brazil

near-zero resistance—may indicate short circuits or broken cables. Devices like the GK-404 and VWR1 perform this verification automatically, displaying results on-screen to facilitate problem identification [23] and [6].

The data export capabilities vary by model but play an essential role in improving field monitoring efficiency. The EDI-54V, for example, uses Bluetooth connectivity for synchronization with Android smartphones, allowing real-time data visualization and export. The VWnote offers USB export, simplifying data collection without requiring external computers [18] and [8]. The GK-406 includes features such as integrated GPS georeferencing, making it ideal for large-scale distributed monitoring [21].

Finally, the portability and durability of reading devices are crucial for operations in harsh environments. Devices such as the VWR1 and GK-404 have enclosures resistant to dust and water splashes and are lightweight and easy to transport. Battery life is another relevant factor, with devices like the EDI-54V and VW Data Recorder offering up to 100 hours of continuous operation on a single charge [22].

The appropriate choice of equipment should consider the nature of the project and operating conditions, ensuring measurement accuracy and efficiency in geotechnical monitoring activities. Devices equipped with spectral analysis and noise correction tools, such as VSPECT™ technology, are recommended for environments with high interference levels. In contrast, portable models with easy data export are ideal for projects in remote locations, where mobility is crucial.

4.2. Methods for Verification and Fault Diagnostics

4.3. Initial Sensor Verification

Before installation, the piezometer must undergo checks to ensure its integrity and functionality:

- **Visual inspection:** Examine the piezometer body, cables and connections to detect damage such as deformations, cracks, or signs of oxidation. Corroded connectors or frayed cables can compromise readings [4].
- **Comparison with the calibration sheet:** Confirm that the initial reading matches the value specified in the calibration sheet. Differences greater than 0.5% of the full scale may indicate issues. GEOKON allows a tolerance of up to 50 $Hz^2/100$, while Geosense permits up to 100 $Hz^2/100$ [4], [7] and [17].

- **Electrical resistance test:** Measure the resistance of the coils and thermistor. The coil resistance should be 180Ω ± 10Ω and the thermistor resistance should be approximately 3,000Ω. Infinite readings suggest broken cables, while very low values indicate short circuits [7] and [17].

Fig. 7 presents a reference resistance table from the GEOKON 4500S manual, along with an example of a multimeter used for these measurements.

Vibrating Wire Sensor Lead Grid - SAMPLE VALUES					
	Red	Black	White	Green	Shield
Red					
Black	≅180Ω				
White	Infinite	Infinite			
Green	Infinite	Infinite	3000Ω at 25°C		
Shield	Infinite	Infinite	Infinite	Infinite	

Fig. 7 – Reference Table for Resistance Measurements Between Components of a Vibrating Wire Piezometer

Source: Adapted from [4].

These steps are essential to ensure that the sensor is in optimal condition before installation. Identifying faults during the initial verification prevents future issues and ensures that the measurements are reliable and consistent with actual field conditions.

The initial verification confirms that the sensor is in good working order before being installed, thereby avoiding potential issues that could compromise readings shortly after installation.

4.4. Procedures During Installation

The proper installation of the piezometer is essential to ensure accurate and interference-free measurements:

- **Parameter Configuration in Dataloggers or Readouts:** Before installation, it is necessary to check whether the pressure (G) and temperature (K) correction coefficients are configured according to the values provided by the manufacturer. Dataloggers with default parameters may show significant deviations if not correctly adjusted [7]. When the piezometer is connected to a datalogger especially plug-and-play models, such as those from RST Instruments, Worldsensing and Geokon, which come with default equations it is crucial to verify the compatibility between the pre-

[1]wellerson.bastos@pimentadeavila.com.br, Brazil

configured equation and the conversion equation of the instrument. For example, RST Instruments dataloggers are pre-set with the default equation for RST instruments, as indicated in their manual.

- **Adjustment of Initial Reading:** During installation, the piezometer must be positioned in an environment where only atmospheric pressure acts on the sensor to set the initial reference reading. This reference point is essential for subsequent measurements.
- **Noise Verification:** Real-time signal analysis can help identify noise sources near the installation point. High-voltage equipment or electromagnetic sources can introduce detectable interference in both time-domain and frequency-domain graphs [20] and [21].

4.5. Verification of Sensor Performance During Operation

Once the sensor is installed and operational, periodic verifications are necessary to ensure reliable readings:

- Signal-to-Noise Ratio (SNR) Monitoring: The SNR measures the ratio between the signal amplitude from the sensor and the highest detected noise amplitude. Values above 10 indicate a good-quality signal, while values close to 1 suggest significant noise interference, which can compromise the readings [20] and [21].
- Signal Decay Analysis: The time required for the vibration signal to return to its resting state is an indicator of the sensor's mechanical integrity. Rapid decays may indicate structural issues with the vibrating wire, while prolonged vibrations are common in sensors installed at greater depths or in clayey soils [20] and [21].
- Evaluation of Multi-Frequency Noise: In environments with high levels of interference, such as dam galleries or areas near high-voltage power lines, noise may appear across different frequency bands. VSPECT technology can distinguish the sensor's resonant frequency and filter characteristic noise, such as 50 Hz or 60 Hz signals from the power grid [20] and [21].
- Electrical Resistance Testing: The resistance of the sensor's coils and thermistor should be regularly measured and compared to the reference values in the calibration certificate. Readings around 180Ω ± 10Ω for the coil and approximately 3,000Ω for the thermistor indicate that the sensor is functioning within the recommended standards [4].

Conducting these field tests helps detect and correct potential anomalies, such as signal loss or increased noise due to external interference. Additionally, regular analysis ensures measurement accuracy and extends the sensor's service life, enhancing the overall reliability of the geotechnical monitoring system.

4.6. Preventive Maintenance and Corrective Actions

In addition to the previously mentioned verifications, preventive maintenance is crucial to prevent failures:

- **Replacement of Cables and Connectors:** Worn or oxidized components should be replaced to avoid the amplification of external noise. The use of shielded twisted-pair cables and protected connectors is recommended to minimize interference [23].
- **Protection Against Noise Sources:** Whenever possible, sensors should be installed at a safe distance from motors, generators and other sources of electromagnetic interference [4].
- **Reconfiguration of Dataloggers:** After interventions or environmental changes at the monitoring site, dataloggers should be reconfigured to ensure that correction parameters are updated and aligned with the current field conditions [4].
- **Electrical Resistance Testing:** The resistance of the sensor's coils and thermistor should be measured and compared to the reference values in the calibration certificate. For instance, the coil resistance should be around 180Ω ± 10Ω, while the thermistor resistance should be approximately 3,000Ω [4].

The systematic application of these verification and fault diagnostic methods ensures that the data obtained is accurate and reliable, supporting robust geotechnical analyses and safe decision-making in large-scale engineering projects. The adoption of advanced technologies, such as VSPECT spectral analysis, strengthens this approach by facilitating the rapid identification of issues and the implementation of corrective measures efficiently.

5. CONCLUSIONS

This paper presented an in-depth exploration of vibrating wire piezometers (VW piezometers), covering their operational principles, key considerations for installation, and the interpretation of readings to ensure precise geotechnical monitoring of dams. The study highlighted how these instruments contribute to monitoring pore pressures, a critical parameter for assessing dam stability and detecting failure modes such as slope instability and internal erosion.

[1]wellerson.bastos@pimentadeavila.com.br, Brazil

In summary, the article emphasized the importance of proper configuration and maintenance practices to achieve reliable data. The analysis of manufacturer-specific conversion equations underscored significant differences in calculation methodologies. While some manufacturers, such as DGSI, employ complex polynomial equations to enhance accuracy in varying environmental conditions, others, like Roctest and Soil Instruments, use simpler linear corrections for ease of implementation. This reinforces the need to align the device configuration with the calibration specifications provided by the manufacturer to prevent data inconsistencies.

Key Findings:

1. **Environmental Influence:** Temperature fluctuations and barometric pressure significantly impact VW piezometer readings. Instruments such as those by GEOKON have integrated compensation mechanisms to mitigate these effects, ensuring stable readings even in environments prone to abrupt changes.
2. **Signal Integrity:** Advanced signal processing technologies like VSPECT can effectively separate noise from relevant signals, proving valuable in areas affected by electromagnetic interference.
3. **Maintenance Protocols:** Regular maintenance, including resistance checks, connector inspections, and verification of calibration coefficients, is essential to avoid sensor drift, short circuits, and inaccurate measurements.
4. **Data Logger Configuration:** It is crucial to verify that the frequency-to-pressure conversion formulas and correction coefficients in the dataloggers are consistent with the calibration certificates of the installed sensors. Misconfigured systems can lead to errors that compromise the monitoring system's reliability.

Practical Recommendations:

- **Initial Calibration:** Before installation, ensure the piezometer is calibrated, and the correction coefficients are accurately set in the datalogger.
- **Zero Readings:** Perform baseline readings under controlled conditions after thermal equilibrium to establish reference values for accurate comparisons.
- **Inspection and Maintenance:** Periodically inspect sensor components, including cables and connections, and perform electrical resistance checks to identify potential issues early.

- **Noise Mitigation:** Use shielded cables and place sensors away from interference sources. In high-noise environments, apply spectral analysis tools to improve data accuracy.
- **Deaerated Water Use:** When filling the piezometer, use deaerated water to prevent air bubbles, which can affect pressure readings, particularly in saturated soils.

By following these best practices, industry professionals can ensure the precision, consistency, and longevity of VW piezometers, reinforcing the safety and effectiveness of geotechnical monitoring programs. This integration of proper installation, calibration, and diagnostic techniques enhances the overall performance of dam safety instrumentation systems and aids in preventing critical structural failures.

6. REFERENCES

[1] International Commission on Large Dams (ICOLD). (2018). *Bulletin 158: Dam Surveillance Guide, Chapter 9*. Paris: ICOLD.

[2] Marinaro, R. A. (2022). *Methodology Proposal for Defining Instrumentation Control Levels Associated with Failure Modes: A Case Study in a Tailings Dam* (Master's Thesis). Graduate Program in Geotechnical Engineering, Federal University of Ouro Preto.

[3] Penna, D., Marinaro, R., Lopes, M., & Carmo, A. (2017). *Risk Map as a Tool for Dam Safety Management*. Belo Horizonte, pp. 1–15.

[4] GEOKON. (n.d.). *Model 4500 Series Vibrating Wire Piezometer*. Retrieved from https://www.geokon.com/4500Series

[5] Encardio-Rite. (n.d.). *Users' Manual: Vibrating Wire Piezometer EPP-30V, EPP-40V, EPP-50V*. Retrieved from [insert URL if available].

[6] RST Instruments Ltd. (2020). *VW2106 Vibrating Wire Readout Manual (ELM0042M)*. Coquitlam, BC, Canada: RST Instruments Ltd.

[7] Geosense. (n.d.). *Piezometers Indepth V10*.

[8] Soil Instruments. (n.d.). *VWnote User Manual (Man230 VWnote – MN1114 – Rev1.2.0)*. United Kingdom: Soil Instruments Limited.

[9] Mikkelsen, P. E., & Green, G. E. (2003). *Pore Pressure Monitoring with Fully Grouted Vibrating Wire Piezometers*. *Canadian Geotechnical Journal*.

[1]wellerson.bastos@pimentadeavila.com.br, Brazil

[10] U.S. Army Corps of Engineers (USACE). (2014). *Engineer Manual: Design and Construction of Levees (EM 1110-2-1908)*. Washington, DC: U.S. Army Corps of Engineers. Retrieved from https://www.publications.usace.army.mil

[11] Pop, S., Ciascai, I., Bande, V., & Pitica, D. (2013). High Accuracy Method for Measurement of Vibrating Wire Transducer. Paper presented at the ISSE 2013 - 36th International Spring Seminar on Electronics Technology. doi:10.1109/ISSE.2013.6648273

[12] Cieplok, G., Karwowski, W., & Bednarski, Ł. (2018). Influence of Cable Length on the Vibrating Wire Sensors Dynamic Measurements. *Archives of Civil Engineering, 64*(4), 65–76. https://doi.org/10.2478/ace-2018-0063

[13] Simonsen, T. R., & Sorensen, K. K. (2018). *Performance of Vibrating Wire Piezometers in Very Low Permeable Clay*. Geo and Aarhus University, Aarhus, Denmark.

[14] Geokon. (2024). *Instruction Manual: Model GK-404 Vibrating Wire Readout (Document Rev. P.1)*. Lebanon, NH, USA: Geokon Inc.

[15] Roctest. (2013). *Equipment Manual E1100D (Roctest E1100D20240408)*. Saint-Lambert, QC, Canada.

[16] VW Piezometer. (2023). *VW Piezometer Manual (DGSI VWPiezometerManual20231)*.

[17] RST Instruments Ltd. (2023). *VW2100 Vibrating Wire Piezometer Instruction Manual (ELM005U)*. Retrieved from https://www.rstinstruments.com

[18] Encardio-Rite Electronics Pvt. Ltd. (2019). *Users' Manual: EDI-54V Vibrating Wire Indicator (Doc. # WI 6002.135 R01)*. Lucknow, India: Encardio-Rite.

[19] Geosense Ltd. (2016). *Instruction Manual: VWR1 Vibrating Wire Sensor Readout (Version 1.1)*. Suffolk, United Kingdom: Geosense.

[20] Campbell Scientific. (2017). *VWAnalyzer: Vibrating Wire Analyzer User Manual (Manual No. 31913)*. Retrieved from https://s.campbellsci.com/documents/eu/manuals/vw_analyzer.pdf

[21] Campbell Scientific. (2020). *GK-406 Vibrating Wire Analyzer User Manual*. Logan, Utah, USA: Campbell Scientific Inc.

[22] Durham Geo-Enterprises. (2023). *VW Data Recorder Manual*. Tucker, GA, USA: Durham Geo-Enterprises Inc.

[23] Roctest. (2018). *Instruction Manual: MB-3TL Vibrating Wire Data Recorder*. Saint-Lambert, QC, Canada: Roctest Limited.

Fifth International Dam World Conference
PORTUGAL • LISBON • LNEC • APRIL 13-17, 2025
dam world 2025

REINFORCEMENT OF THE FOUNDATION WATERPROOFING OF THE ALVORNINHA DAM

Romeiro, Manuel
TPF, Portugal

Candeias Portugal, João[2]
LNEC, Portugal

ABSTRACT

The paper describes the work methodologies to reinforce the waterproofing curtain of the Alvorninha dam foundation.

Excessive seepage was recorded during the first filling of the reservoir, mainly due to poor waterproofing of the dam foundation, particularly on the left bank. As a result, the operation of the reservoir was restricted by Authority and the construction of a new one-line grouting curtain was required to reinforce the waterproofing at the downstream of the existing curtain. The work carried out was aimed to ensure the correct functioning and so that to minimise percolation through the foundation, reducing the flow rate to commonly accepted values, while also avoiding possible erosion phenomena associated with the friable sandstone layers and old percolation paths. This reinforcement covered the existing waterproofing curtain, although focused on the left abutment and under the spillway channel. The remedial grouting of the foundation considered the data on previous treatments, the results of the preliminary geological investigations (deep boreholes) and the ongoing grouting. The reinforcement treatment was based on a study interpreting percolation, which included: i) water loss while drilling; ii) water levels; iii) stability of the holes; iv) water pressure tests (Lugeon tests) on the curtain to verify the effectiveness of the previous works and the reference situation and; v) choose the injection methodologies most appropriate for to the specific characteristics of foundation (layers of different hardness and permeabilities). The proposed solution took in consideration the existing embankment dam conditioning the work, particularly regarding drilling operations and grout pressures/volume takes criteria.

The paper describes all aspects relating to the execution of injection holes, methodology for defining the effective drilling length, injection equipment and grout used, maximum injection pressures, injection methodology, grout control and groutability tests.

Keywords: Grouting, grout curtain, embankment dam, foundations, efficacy, efficiency, sleeve port grout pipe (tube-à-manchette)

[2]portugal@lnec.pt, Portugal

1. INTRODUCTION

The dam is located near the village of Alvorninha, in the center-west of Portugal, at 9 km of Caldas da Rainha. It consists of a homogeneous earthfill dam with chimney and blanket drains and rock downstream toe. The top of dam is at 106,50 m above sea level (ASL), the crest length about 180 m and the maximum height above the foundations of 24 m.

The appurtenant structures are a concrete-lined uncontrolled spillway in the left abutment and a bottom outlet structure for releasing stored water and irrigation. It comprises the gated intake tower, the HDPE conduit with 700 mm of diameter under the dam embedded in reinforced concrete beam placed in a trench excavated on the bedrock. and a box chamber valve assembled to impact dissipation basin.

The original grout curtain was placed 10 m upstream of the axis of dam. The holes were inclined 80º to downstream and drilled in a linear pattern from the bottom unconsolidated and shallow cutoff. The collapse of the holes, surface leaks and communications were frequent and the final hole spacing was 1,5 m (quaternary holes).

The waterproofing reinforcement project consisted of the construction of a new continuous single-line grout curtain with a total length of 180 m for remedial the seepage deficiencies in left abutment and the risks of piping in the rock foundation of embankment dam. Fig. 1 shows the site where the new curtain was built and the site of the grout production batch plant.

Fig. 1 – General view of the site where the curtain was built from the right side of the dam

The project included a geological and hydrogeological investigation campaign with boreholes and permeability and groutability tests to be carried out at the beginning of the injections of the

new curtain, to adjust the construction procedures to the actual geotechnical conditions of the foundation.

2. GEOLOGICAL AND HYDROGEOLOGICAL INVESTIGATIONS

2.1. Desk study and reconnaissance survey

Before starting the exploratory boring investigations program, a detailed study was carried out involving the collection and evaluation of available data on the execution of the original grout curtain and subsequent work to reinforce the waterproofing of the rock mass. At the same time, a geological characterization of the rocky outcrops and springs around the dam was carried out.

2.2. Boring investigations

For geological and hydrogeological investigations of the bedrock, before the execution of the new curtain for waterproofing reinforcement, the project provided 7 exploratory, vertical cored boreholes: SE8, SE24, SE36; SE60, SE84, SE120 and SE156. However, it was decided to make the borehole in the left abutment, inclined at 60º for detailed investigation of the bedrock at the end of grout curtain and under the spillway channel. The drilling in the bedrock varied between 24,7 and 44,2 meters, with a total of 223,8 meters.

Up to about 30 meters below the top of the dam, the altered sandstones layers (GD) are of very poor quality, easily disintegrated, and the collapse of the holes were frequent. Below that depth the collapses were rare. For this reason, the holes were cased and the entire test program of permeability by water pressure tests and groutability was changed.

2.3. Permeability tests

The permeability of the altered rock mass was assessed by Lefranc tests, water level and water losses while drilling [1] [2]. Only 58% of the total drilled boreholes length was tested by WPT, most in unaltered rock mass, with a permeability of less than 3 lugeons.

According to these permeability studies, it was considered that the top of the relatively impervious stratum, where the grout holes should end, was located at a depth of around 30 metres. Later, it was found that the impervious massif was higher up on the right abutment, which made it possible to lighten the waterproofing work.

2.4. Groutability tests

Groutability tests were conducted using the downstage method in 4 holes of the curtain, located at the left and right abutments. In each test, several grouting and redrilling attempts

were made always resulting in the collapse of the holes. The grout did not penetrate the rock mass, and the cement was removed during the re-drilling of the holes.

Based on these results, it was decided to apply the multi-port sleeve pipe (“tube à manchette”) system in the grout curtain construction [3] [4].

3. GEOLOGY OF THE SITE

3.1. Lithostratigraphy

The dam is founded on a detrital sedimentary and flat lying sequence of the Upper Jurassic. The rock mass consists of very thick layers of sandstones and siltstones and thin intercalations of weak claystones and marls. The layers dip steady 5º westly direction (to left abutment).

The outcrops rock mass exposures are mainly medium to coarse sandstone, moderately altered and slightly friable, in very thick layers with rare fractures (Fig. 2). The silt-clay layers are very fissured, altered, and decompressed. The structure of the massif is dominated by bedding joints filled with clay and marl beds. The thickness of these interlayers is irregular, varying between centimetres and several decimetres.

Fig. 2 – Outcrop of a slightly fractured, altered and friable sandstone, near the right abutment of dam

This bedded rock mass comprises the alternances of layers of two different lithological and geotechnical formations (Fig. 3):

- MAS – Bedded, fine grained and argillaceous layers, that assemble fine and thigh rocks, comprising layers and intercalations of fine sandstones and thin to thickly bedded, weak, friable or fissile claystones, siltstones and marls.

– C – Massive and thickly, arenaceous layers composed by medium to coarse sandstones with soluble cement.

  These arenaceous rocks are fresh, moderately altered or intensely altered, depending on the degree of cement dissolution, which is related to the intensity of percolation during geological times [5]. These sandstone formations have therefore been subdivided into 3 geotechnical units:

  GC – fresh, hard, very stiff and consolidated sandstones.

  GPC – moderately altered, stiff and medium to weak sandstones.

  GD – intensely altered, disaggregated and unconsolidated sandstones.

The MAS formations are medium to hard, lightly weathered rocks, sometimes with intraformational shear and crushing zones.

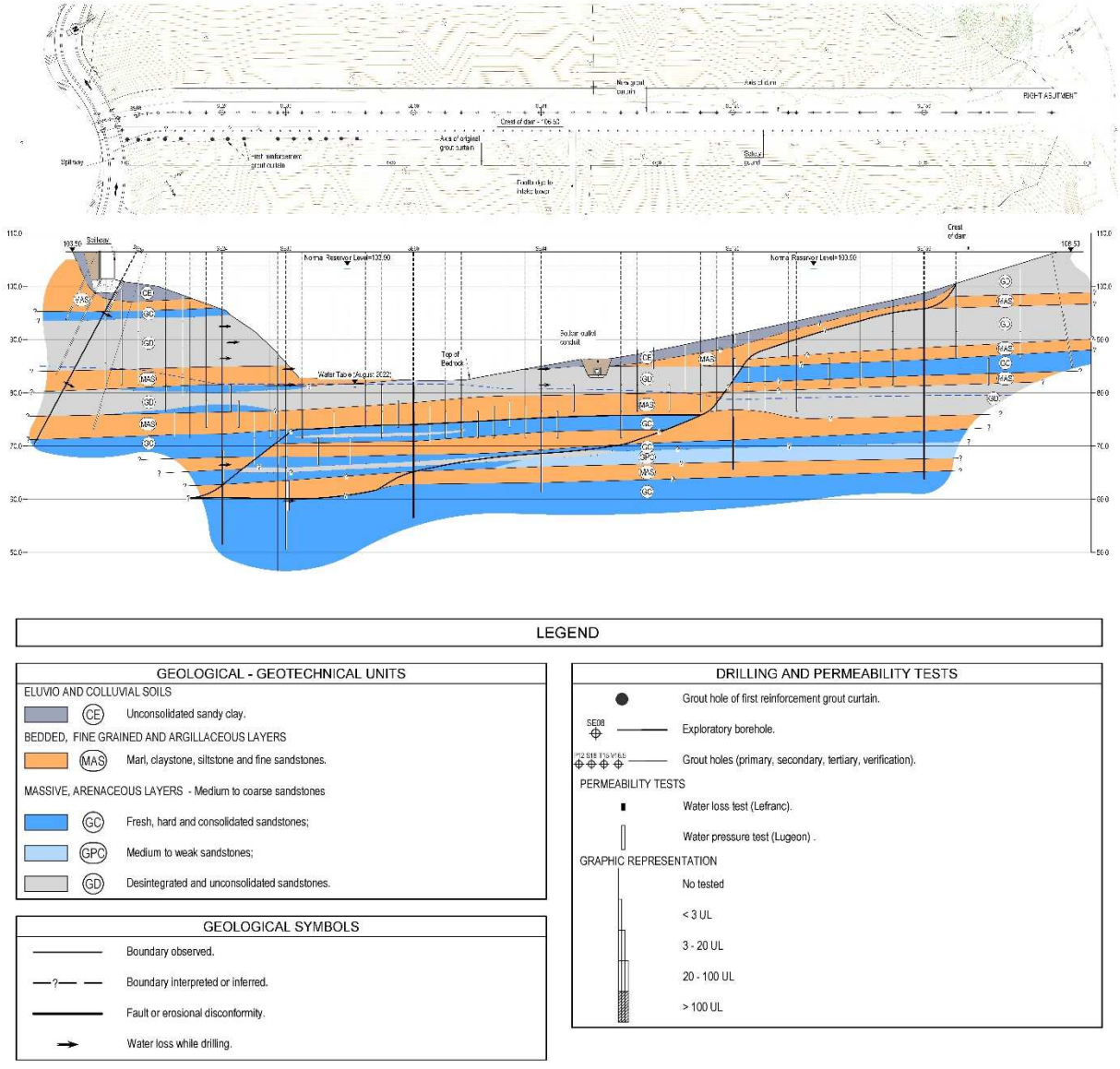

Fig. 3 – Plan and geological section along of grout curtain

3.2. Geological structure

The structure of the bedrock is dominated by the alternance of thick and lightly fractured layers of fresh to completely altered and friable sandstones and fissile argillaceous beds.No fault zones were found. Some open bedding joints at the bottom of thick sandstones layers are filled by soft and erodible gouge material, as shown in the Fig.4.

Two geological unconformities along the longitudinal profile of the curtain were revealed by the exploratory boreholes. These unconformities are of the type of disconformity and represent periods of active erosion of strata with different conditions of percolation and consequent dissolution of the sandstone cement. The geological section along of grout curtain, shown in the Fig. 3, indicates the inferred position of these disconformities. In the rare outcrops in the dam area, these unconformity surfaces are associated with crushed beds.

Fig. 4 – Vue of a major bedding joint, very permeable, in the reservoir

3.3. Hydrogeology

According to the general characteristics of the bedrock described above, where it is emphasized that the massif is generally slightly fractured, the percolation of water through the dam foundation is mainly through the open bedding joints and in the layers of highly altered and disaggregated sandstone (GD). These are old percolation paths formed during phases of intense erosion.

These open joints are usually located at the contact between the impermeable clay layers and the overlying sandstone, as shown in Fig. 4. The opening resulted from the removal of the soft filler materials and the dissolution of the cement carbonates in the rocks (high susceptibility to internal erosion of dam foundation) [6].

3.4. Interface bed rock embankment

The conditions of the embankment-foundation interface along the new grout curtain are very variable, both because of the irregularity of the profile and because the surface has not been adequately prepared for the new treatment [1].

On the left abutment, the surface is very sloping and not very favourable for injection with vertical holes. At the top of the sloping surface, the bedrock is overlayed by unconsolidated sandy clayed eluvial or colluvial cover soils and fill materials (CE). This soft material was difficult to inject.

At the bottom of the valley the surface has been well cleaned. On the other hand, on the right bank with a slightly sloping surface, the removal of the decompressed soil layer was insufficient for the insertion of the curtain. On the right abutment, at the end of the curtain, the bedrock surface presented good conditions for inserting the grout curtain.

4. GROUT MIXES

4.1. Materials

The materials used for grouting and sealing were:

- Water of the reservoir (W)
- Portland Type IV Cement (C)
- Sica ViscoCrete 3003 Super-Plasticizer (SP)
- Sodium bentonite (BT).

4.2. Grouting and sealing mixtures

An extensive laboratory trial tests for the mixes formulations was performed before installing PVC standpipes casing and starting grouting the holes of the curtain.

The grouting mixtures formulations included water, cement and a small amount of super plasticizer. Three grout mixtures were selected, which are shown in Table 1.

Table 1 – Grouting mixtures

Grout mixes	Formulations		Marsh funnel	Unity weight	USC (28 days)
	W/C	SP (%C)	(s)	(g/cm^3)	(MPa)
Mix A	1/1	0,5	≤30	1,42	12,3
Mix B	1/1,5	0,5	33	1,49	22,9
Mix C	1/2	0,5	37	1,67	-

The pipe sealing mixes formulations comprised water, cement and hydrated bentonite. Two sealing mixtures were selected, as shown in Table 2.

Table 2 – Sealing pipes mixtures

Grout mixes	Formulations		Marsh funnel	Unity weight	USC (28 days)
	W/C	BT (%C)	(s)	(g/cm3)	(MPa)
Standpipe	1/1,5	0,2	-	1,63	-
Sleeved pipe	1/1	2,0	75	1,49	5,9

5. GROUT CURTAIN CONSTRUCTION PROCEDURES

5.1. Grout curtain geometry

The grout curtain was constructed using a single line, split spacing method. The primary holes were placed on 12,0 meters centers, with spacings progressively smaller through tertiary holes on 3 meters centers (Fig. 5) [1].

The grout curtain was achieved by 72 holes for a total of 1094,5 meters of drilling in the bedrock. These included 7 exploratory boring holes, 13 primary holes, 15 secondary holes, 25 tertiary holes, 8 verification grout holes and 4 consolidation holes under the spillway.

For the treatment of the foundation in the left abutment 509,0 meters were drilled in the rock (about 46,5% of the total drilling length).

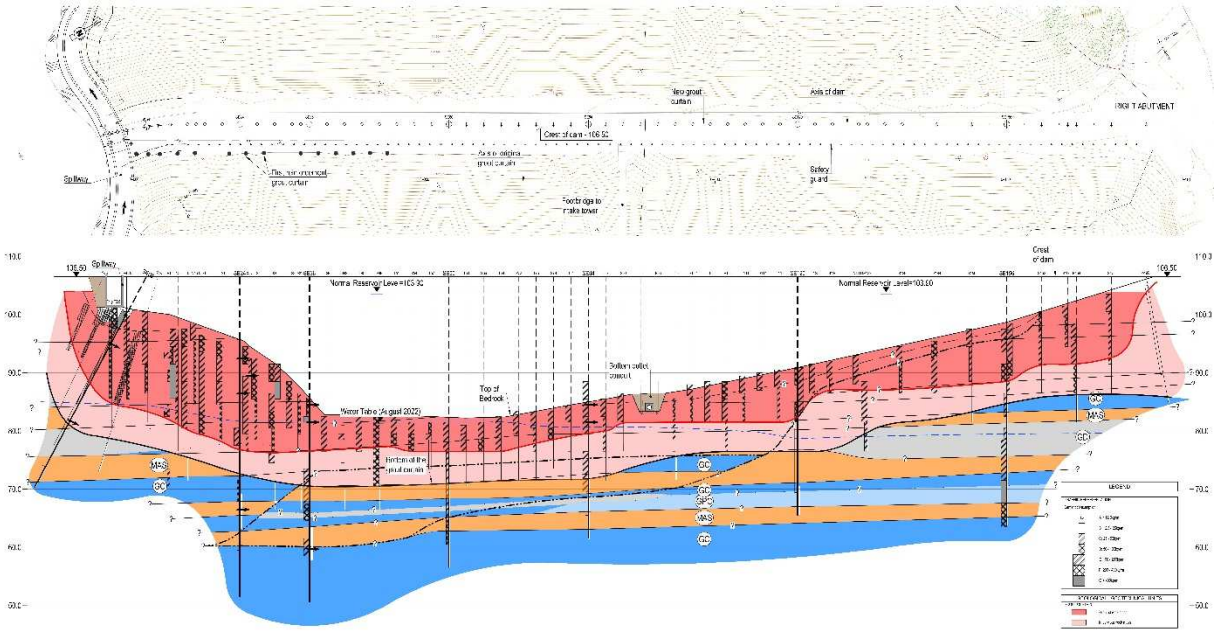

Fig. 5 – Plan and profile of the new grout curtain

5.2. Drilling

The holes were drilled through of the embankment and socketed a minimum 0,20 m into underlying soft bedrock with hollow-stem auger DN200 mm from the crest of the dam. All holes were cased with PVC standpipes DN125 mm and the annulus was sealed upward with cement grout [6].

The holes were extended through the underlying rock foundation by rotary drag bit drilling method DN76mm, cased and widened to DN86 mm and washed with water to remove cutting. The water pressure test was carried out in the last 3 meters. Then, the casing was removed and the multi-port sleeve tube placed and sealed with cement grout.

Afterwards, the multi-port sleeve tube was placed, and, at the same time, the casing was removed and the tube sealed with cement grout.

5.3. Hole grouting principles

The mixtures were produced in a principal, fixed batch plant, placed in the right abutment of the dam. It consisted of a high-speed colloidal mixer with balance attached, an agitator tank and a pump. The grout was produced as required and pumped through hoses to a mobile “Unigrout grouting platform – Unigrout Flex” equipped with a Pumpac grout pump of single cylinder, double acting piston. This mobile platform was placed near the grout hole. The flow rate has been set at 7 to 8 l/min.

The gaskets were opened one by one with water injection using double packer at a maximum pressure of 20 bar, followed by removal of the water in the pipe. The cement mixtures were injected using the ascending method at intervals of 4, 3, 2 and 1 m, as shown in the following table. The injection of each stage was suspended once the grouting pressure or cement weight (cement take) had reached the maximum limits previously established, in accordance with the distance to the embankment/foundation interface (depth) and the geotechnical conditions of the bedrock. The grouting pressures and cement take maximum limits are shown in Table 3.

Table 3 – Maximum grouting pressures and cement take

Depth	Stage length	Maximum pressure	Stop criteria
(m)	(m)	(bar)	-
0 - 3	1,0	1,5	Pressure and volume
3 - 8	2,0	2,0	Pressure
8 - 25	3,0	5,0	Pressure
> 25	4,0	8,0	Pressure

Near the interface the stop criteria were the pressure and volume due to embankment sensitivity and the poor quality of the material at the top of the bedrock. Below the interface zone the stop criterion was the pressure specified by the project. If the pressure was not reached, the stage was washed and injected again 4 hours later.

Below the interface zone, the stop criterion was the pressure specified by the project. If the limit pressure was not reached with the maximum cement take, the hole was washed and re-injected. The cement maximum takes by stage are shown in Table 4.

Table 4 – Maximum cement takes by stage

Depth	Stage length	Maximum cement takes
(m)	(m)	(kg)
0 -1	1,0	100
1 - 2	1,0	200
2 - 3	1,0	300
3 - 8	2,0	400
> 8	3,0 - 4,0	500

The grout mixes were progressively changed when the injection pressure levels were below 50% of the maximum pressure at the depth of the stage.

5.4. Treatment under the spillway

Under the spillway, very unfavourable geological conditions were found for the construction of a grout curtain above elevation 97 meters (about 8 meters below the normal level of the reservoir). These conditions lead to high gradients under the spillway foundation, when the water level in the reservoir rises to close to the normal level.

On the other hand, the data obtained in borehole SE8 revealed that the soils had been replaced by coarser materials, including remains of concrete (Fig. 6). Despite the 10 grout holes drilled in this area and the extremely high cement consumption, it is suspected that the treatment was not totally effective. Thus, there may still be water passages under the spillway, which will increase the percolation flows measured at the downstream toe of the dam.

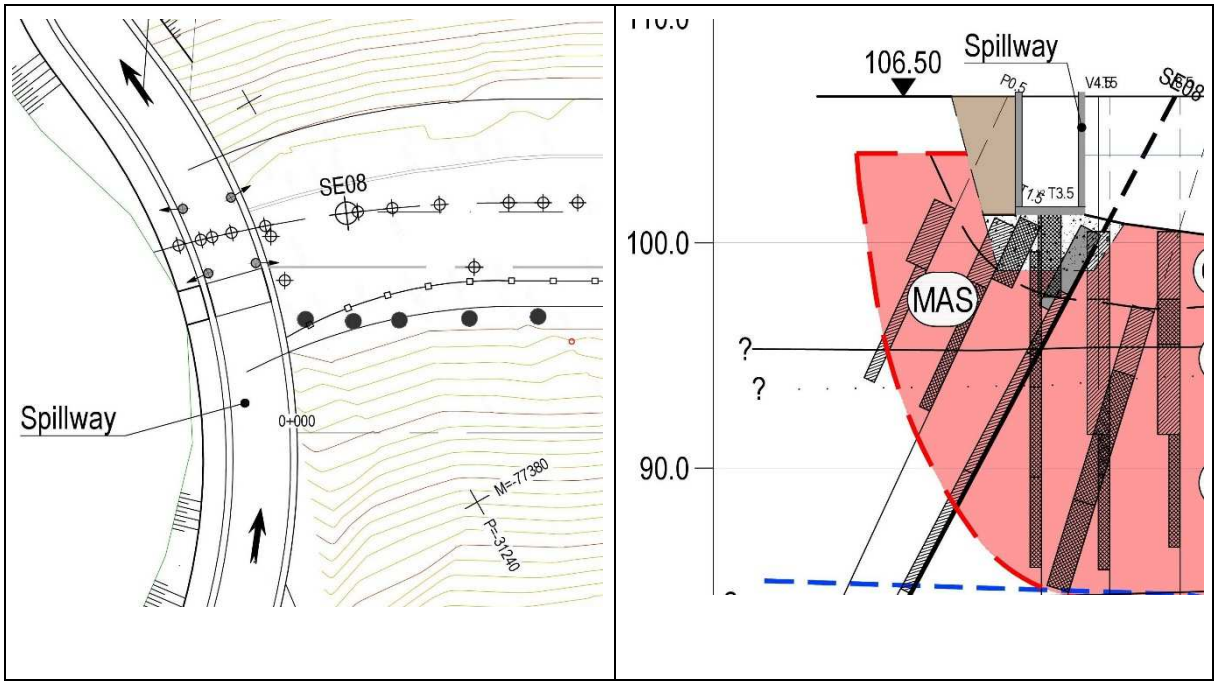

Fig. 6 – Plan and profile of the left abutment and spillway

6. GROUT TAKES

6.1. Cement consummation

A total of some 79 465 kg of cement were injected into a total of 1019 m of grout hole. Almost all the cement (75,890 kg) was injected into the foundation's waterproofing curtain, with an area of 1,700 m^2, using the sleeve pipe method, in down stage groutability tests and to seal some water leaks that appeared during drilling. A reduced amount of cement (3575 kg) was injected into the impermeable underlying rock mass, on average 5 m high.

The cement absorption per section along each hole is graphically represented in the longitudinal profile of the new grout curtain (Fig. 5). The representation of cement consumption per linear meter and per section (kg/m) followed the classes proposed by D. Deere [8].

6.2. Zoning of grout curtain and average cement takes

The grout curtain was divided into 4 different zones as follows:

- Zone A, corresponds to the left abutment up to borehole T39, with an area of 660 m^2;
- Zone B corresponds to the valley floor, considering the boundary next to borehole T75, with an area of 200 m^2;
- Zone C refers to the section of the curtain between boreholes T75 and SE120/T123, with an area of 320 m^2;
- Zone D, concerning the right abutment of the dam, past T123, with an area of 520m^2.

A summary of average cement takes by zones is presented in Table 5.

Table 5 – Average cement takes by zone (kg/m)

ZONE	Impermeable underlying rock foundation (< 3 lugeon)	Permeable and weathered rock foundation (> 3 lugeon)
A	8,1	138,9
B	9,4	146,5
C	8,1	124,7
D	7,7	97,8
Total	**8,2**	**129,7**

The average cement takes by grout holes sequence was as follows:

- P+S grout holes: 122,2 kg/m;
- T grout holes: 119,3 kg/m ;
- V grout holes: 88,9 kg/m.

Despite the very restrictive stop criteria for grouting pressures and cement takes, it can be concluded that the progressive reduction in average cement take by the successive injection phases was not relevant.

The main reasons may be as follows:

- The mechanical weakness of the argillaceous intercalations and bedding joints in the altered rock mass, and especially near the interface with the dam embankments.
- The probable connections with percolation paths that occur dispersedly in the rock mass.
- The low critical hydraulic fracturing pressures that cannot be controlled under the embankments.

7. CONCLUSIONS

The intensive analysis of the data from previous injection and reinforcement works and the highly detailed geological investigations at the start of the new injection curtain have provided a definition of the most suitable injection methods and procedures, which have been described in the previous sections.

Geology, grouting and permeability was continuously monitored to be aware of changes in the bedrock in good time and make appropriate adjustments to procedures based on the performance of the available equipment.

In this way, it was possible to adapt the procedures and reinforce or alleviate the waterproofing treatment on a very heterogeneous massif, with very sensitive characteristics, for the construction of an effective waterproofing curtain.

REFERENCES

[1] Roman, W.M., Hockenberry, A.N., Berezniak, J.N., Wilson, D.B. and Knight, M.A. (2013). Evaluation of grouting for hydraulic barriers in rock. Environmental & Enginnering Geoscience, Vol. XIX, No. 4 November 19, 13 pp.

[2] Paisley, A.C., Wullenwaber, J. and Bruce, D.A. (2017). Practical Aspects of Water Pressure Testingfor Rock Grouting. 5th International Grouting, Deep Mixing, and Diaphragm Walls Conference,International Conference Organization for Grouting (ICOG), Honolulu, Oahu, Hawaii, July 9-12, 12 pp.

[3] Bruce, D.A., Dreese T.L. and Hallahan, C. (2017). Errors, Misunderstandings and Mistakes in Remedial Grouting Projects for Dams. Association of State Dam Safety Officials Annual Conference, San Antonio, TX, September 10-14, 15 pp.

[4] Worden R. H. and Burley S. D. (2003). Sandstone diagenesis: the evolution of sand to stone. In S.D. Burley and Richard H. Worden (Eds). Sandstone diagenesis: recent and ancient. International Association of Sedimentologists Special Publication, 4, Blackwell, Oxford, 3-44. 10.1002/9781444304459 Search in Google Scholar.

[5] Fry, J.J. Beguin and Jorge, Gabriel. (2012). Characterization of Internal erosion susceptibility in Sandstone Dam Foundations". 6th International Conference on Scour and Erosion (ICSE6) Paris, August 27-31, 6 pp.

[6] Stare, D.P., Hockenberry A.N., Dreese T.L., Wilson D.B. and Bruce, D.A. (2012). Protection of Embankments during Drilling and Grouting. Deep Foundation Institute, 4 th International Conference on Grouting and Deep Mixing, New Orleans, LA, February 15-18, 10 pp.

[7] Bruce, D.A., and Gallavresi, F. (1988). The MPSP System: A New Method of Grouting Difficult Rock Formations. Presented at ASCE National Convention, Nashville, TN. May 10-11, 18 pp.

[8] Deere, D.U. (1976). Dams on rock foundations -Some design questions. American Society of Civil Engineers Conference on Rock Engineering for Foundation Slopes. New York, NY: ASCE.

Fifth International Dam World Conference
PORTUGAL • LISBON • LNEC • APRIL 13-17, 2025
dam world 2025

DRONE SURVEY OF AN EMBANKMENT DAM TO DETECT SURFACE CHANGES

Maria João Henriques[1]
LNEC

Hugo Silva
LNEC

ABSTRACT

A point cloud is a set of three-dimensional coordinates, to which color (that of the object's surface) can be added. It's a simple way to reproduce this object (which could be a dam, a building, a breakwater, a street, a room) on the computer. The point cloud can be obtained by laser scanner survey, photogrammetric survey and, in the case of small objects, also by 3D scanning.

The coordinates resulting from laser scanners and photogrammetric surveys are generally obtained with less accuracy than those obtained by classical methods developed within the scope of geodesy and surveying (topography). For this reason, the use of point clouds (and the 3D models created from these) in dams to detect changes, for example for safety control studies, is more suitable to embankment dams as these are works where there is a requirement for slightly lower accuracy of results, on the order of few centimetres. Despite being less precise coordination methods, the laser scanner and photogrammetric methods have a very important advantage in earthworks as they cover the entire surface with a cloud with a high density of points. A localized problem can be easily detected if it has an expression on the surface of the work.

As part of a study aimed at obtaining better knowledge of some details of an embankment dam situated in Portugal, two aerial photogrammetric surveys were carried out, approximately one year apart, with a drone. From these surveys point clouds and 3D models of the dam's surface were created. The communication presents various aspects of the surveys as well as the clouds and models generated.

Keywords: embankment dam, safety, drone survey, point cloud, 3D model

[1]mjoao@lnec.pt, Portugal

1. INTRODUCTION

A point cloud of an object, a structure, etc., is a file with data related to surface points. This data always includes 3D coordinates of points in a given referential, established by the producer of the point cloud. The point cloud is created to reconstruct the surface in a computer. The coordinates may be complemented with information intended to visualize the surveyed surface or even another type of information, quite often intended to facilitate the reconstruction of the surface by the visualization software.

Creating two or more clouds of the same object at different times (epochs) allows one to detect changes in the surface (variation of the geometry) if these have happened. Free software is available to easily explore the data in the point cloud files and present the changes in appealing ways. This paper presents the use of point clouds to detect changes in the surface of an earth dam.

The use of point clouds to analyse the geometry of civil engineering structures or for territorial studies has been developed by LNEC, the Portuguese National Laboratory for Civil Engineering, for many years. The first studies involved the use of laser scanners [1, 2]. In recent years, because of work carried out systematically using drones, they have been used mainly in change detection [3, 4, 5], as is the case of the study here presented, a long-term monitoring.

This paper has six sections. After this introduction, the second section refers to the information that is included in point clouds, and the third section to the common procedures to get these clouds. Regarding change detection, the fourth section refers to some of the most accessible ways to present the changes on the surface. The fifth chapter describes an example of the creation and exploration of point clouds of a Portuguese earth dam, a point cloud created for change detection. The sixth section has the conclusions.

2. THE POINT CLOUD

A point cloud is used to re-create a surface in a computer. In addition to the importance of visualizing the object, creating a surface model can contribute to the analysis of the surface, including detecting changes when there is more than one cloud from the same surface obtained at different times.

In the file that has the point cloud, there are always three-dimensional coordinates for each of the points. These coordinates can be defined in a local reference frame, or in a national reference frame, this choice being made by the producer during the cloud creation procedures.

The most basic form of a point cloud is then 3D coordinates of points, without any other information (Fig. 1A). However, it is more appealing to add chromatic information - or the colour of the point (Fig.1B), or the intensity of a signal (Fig. 1C) - as this makes understanding the

object much easier. Colouring with the intensity of the signal is important when the surveying is done in little or no light.

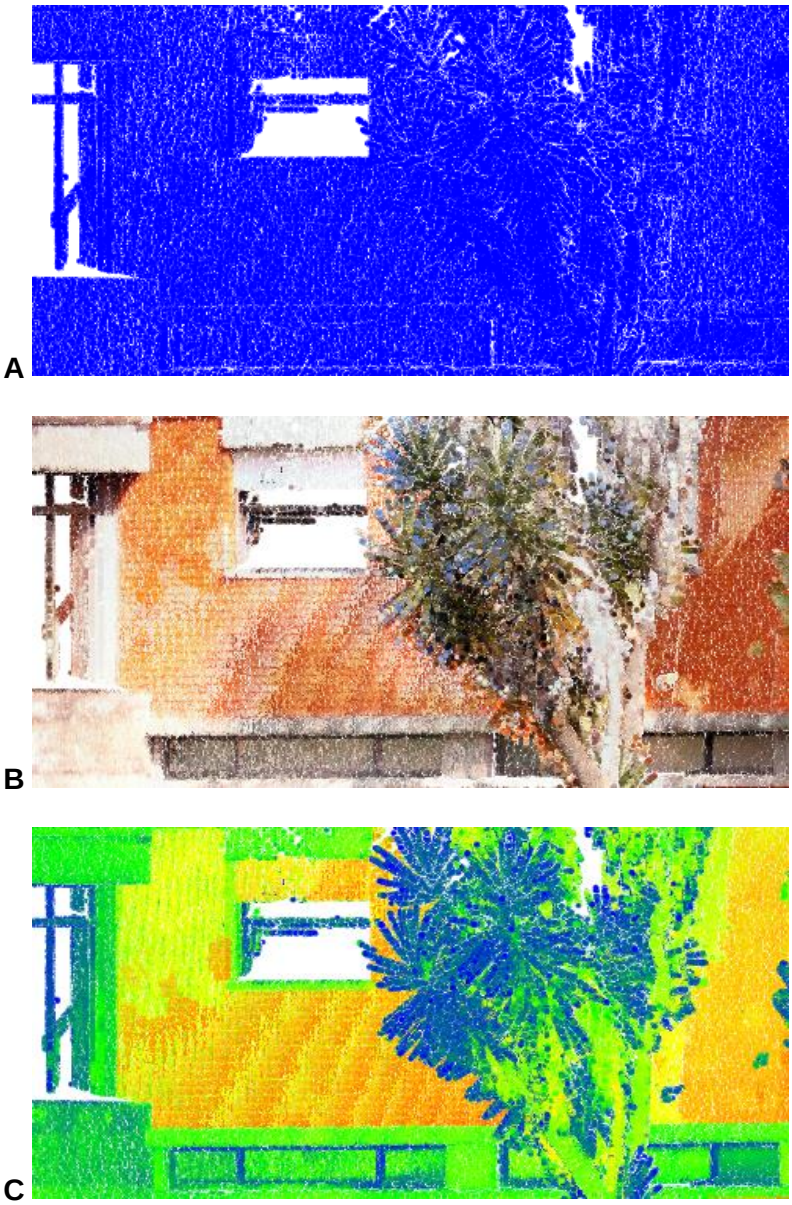

Fig. 1 – Point cloud of a building of LNEC generated by a laser scanner: A – no colour (the points were assigned blue); B – RGB colours; C – intensity (assigned to RGB colours being the blue the least intense and the red the most intense)

Most, if not all, software used to see the point clouds can import data in ASCII format (see Fig. 2). It is, however, preferable to use binary-based formats as they create smaller files that are faster to read. The opening of these files (ASCII or binary) may need interaction with the user. In binary files, there are free formats, the best known of which are LAS (used for point clouds generated by laser scanner equipment) and PLY. In Figure 3 it is possible to notice the varied information that may be associated with each point: in addition to the colour (RGB) and intensity.

Many equipment manufacturers have created their own, closed formats. For these formats, manufacturers provide software to manipulate the data and often make available point cloud viewers at no cost. These viewers usually allow one to carry out simple procedures, such as calculating distances, angles, areas, cylinder diameters, or viewing photographs (Fig. 4) taken on-site by the equipment.

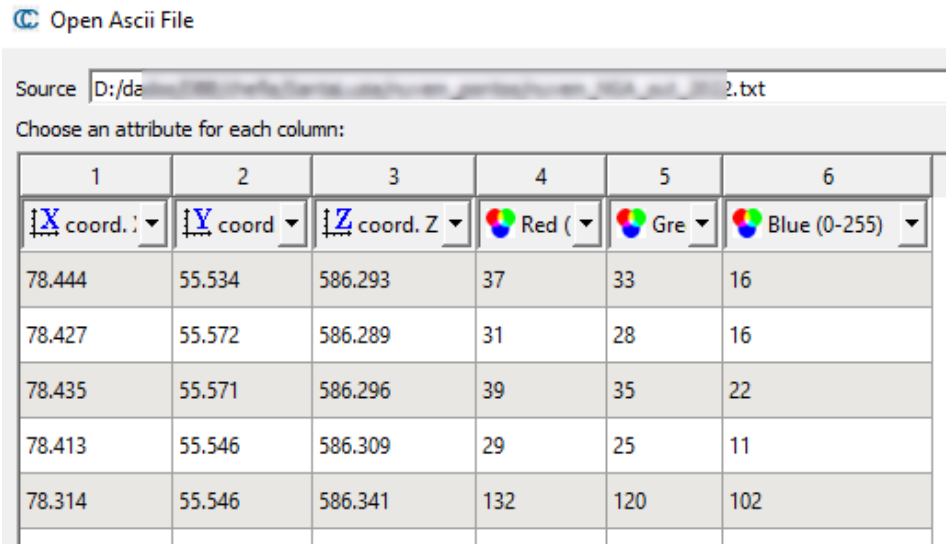

Fig. 2 – Opening an ASCII file using the software Cloudcompare®

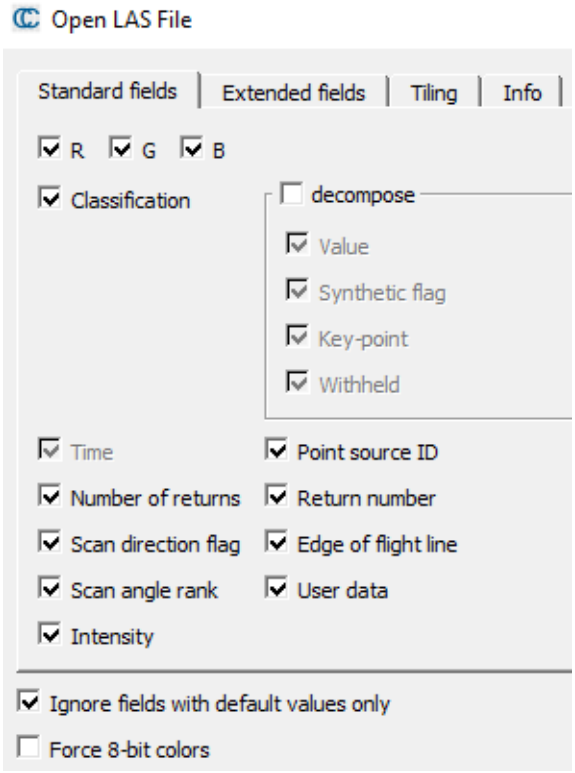

Fig. 3 – Opening an LAS file using the software Cloudcompare®

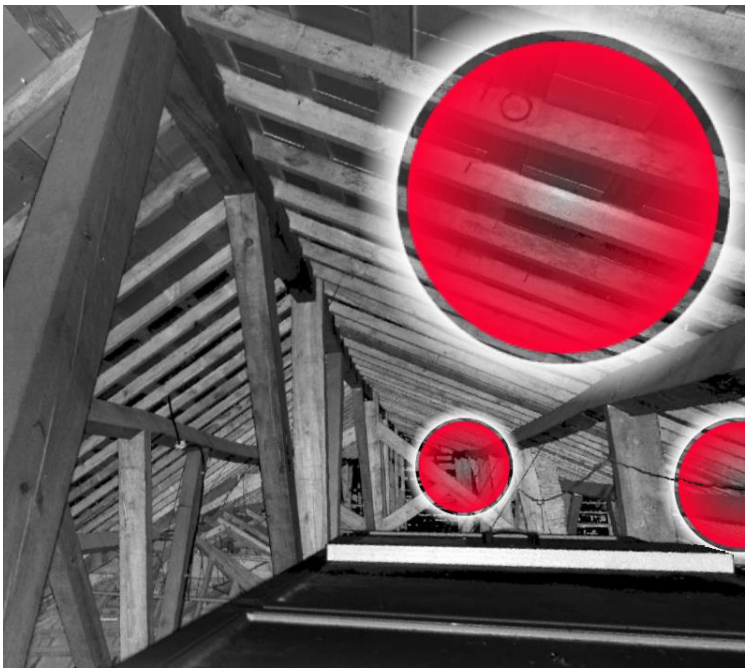

Fig. 4 – Black and white (monochromatic) image taken by a laser scanner seen in the final project of a laser scanner survey: the red circles define locations of the laser scanner during the survey of a wooden structure

3. THE GENERATION OF A POINT CLOUD

It is important to differentiate the equipment that collects the data necessary to create the point cloud from the system that carries that equipment.

The equipment can be divided into two big groups: laser scanners (active sensors because they emit radiation) and digital photographic cameras (passive sensors because they only collect radiation). The cameras can be a normal RGB, multispectral, thermographic, etc..

The carrying devices can be tripods, aeroplanes, helicopters, cars, UAV (most commonly drones), UUV, etc.. UAV stands for Unmanned Aerial Vehicles while UUV stands for Unmanned Underwater Vehicles.

The laser scanners include an emitter of radiation and a receiver. This radiation is most usually infrared or visible laser light, of a class that is eye-safer. The equipment measures the time from transmission of a pulse to its reception (time of flight) and determines the distance to the surface, at a rate that can reach a few millions of measurements per second.

The laser scanners used to scan large areas or structures, also use the information about the direction (azimuth and elevation) in which the radiation was emitted. Combining direction and distance, the system determines 3D coordinates (X, Y, Z). Nowadays, accuracies of some millimetres can be achieved, and one survey (each setting) takes very few minutes.

For small objects that demand very high accuracy (in the order of 0.1 mm) 3D manual laser scanners must be used. These are handheld equipment that integrates not only the laser emitter and receiver but also an inertial system to measure the movements of the scanner.

All the scanners measure the intensity of the signal received and integrate that information into the point cloud data. They can measure without ambient light, including in the darkness.

The scanners can integrate a digital camera to take photos. Based on these photos, post-processing software can assign a colour to the points, which allows one to create a cloud that is much more realistic than a cloud based solely on the intensity of the reflected signal.

The other method to create a point cloud is using many photographs taken from different places. Each photograph must overlap, at least 60% of the image, with another photograph. It is necessary to use photogrammetric software to reconstruct the object's surface. Colour is already included in the cloud. Compared with point cloud laser scanners, point clouds from photographs are less accurate (accuracy is several centimetres) but are less expensive to get (a digital camera is much more affordable than a laser scanner).

If the point cloud is to be connected/integrated with other products or if it is to support point cloud-based variation studies, it is recommended that the point cloud be linked to a reference frame (national or local). This is accomplished by coordinating points, sometimes the equipment, by surveying or other measuring methods. These points need to be identifiable during cloud creation. Figure 5 presents a target commonly used in laser scanner surveys (black triangles printed on a sheet of paper) and three targets seen in a point cloud. The targets were at different distances from the laser scanner. Figures 6 and 7 present two targets, one artificial and one natural, seen in two aerial photographs. These two targets were used in a photo survey with a digital camera mounted under a drone.

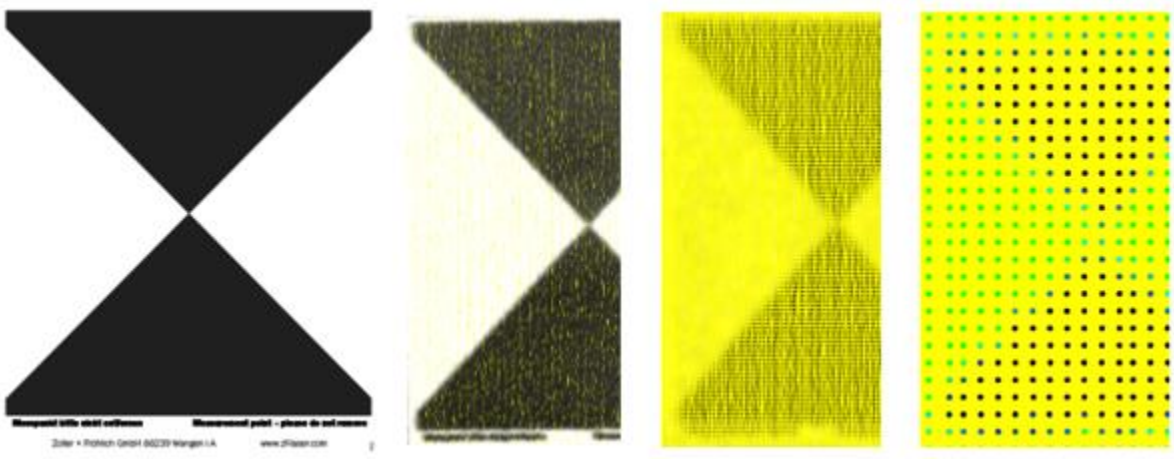

Printed target *Point cloud seen using yellow as the background colour*

Fig. 5 – A printed target and three targets in a point cloud. The targets were at various distances from the laser scanner (2.3 m, 12.0 m and 60.4 m respectively)

Fig. 6 – An artificial target (red arrow)

Fig. 7 – A natural target (a corner of the access cover)

In the case of a photographic survey, is usual to perform two more steps after creating the point cloud. The first is to create a digital surface model, the second and last is to create an orthomosaic, an image that is the result of stitching several orthorectified images (Fig. 8). Orthorectification, which is the removal of image distortions and displacements caused by the relief and the sensor tilt, is applied to each photograph and needs information of the relief, being this obtained from the digital surface model.

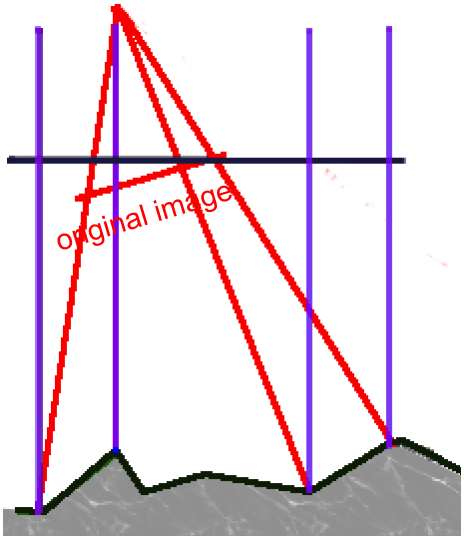

Fig. 8 – In red the original image with the light rays between the surface and the optical center; in black the position of the orthorectified image with, in purple, the light rays parallels

4. DETECTING CHANGES BASED IN POINT CLOUDS

The changes considered in this paper are related to changes in form, in the geometry. For example, a settlement.

To carry out comparisons it is necessary that the object of study is globally in the same position, which is achieved via the reference points that must be coordinated in relation to a stable

reference. This reference can be the country's planimetric and altimetric frame of reference, which is created and maintained by the National Geographic Institute, or it can be a local reference, created specifically for a work.

A shape variation is the result of the displacement of surface elements. In real conditions, it is very rare for displacements to occur either purely horizontally or purely vertically. What is normal is to have three-dimensional displacements, resulting from position variations in the three components (dX, dY, dZ). One can be predominant to the remaining two.

The procedure used by the author to detect the changes in structures like dams, breakwaters, and terrain, has two steps:

1) the first is to create a digital surface model in the form of a matrix, being that the value in each cell is the average of the heights of the points that are within the cell. Each cell has the information concerning an area of s*s, with s being a length defined by the user (5 cm, for instance). The result is a georeferenced image (see Fig. 9). This means that each cell has a location, usually the left upper corner;

2) the second is to use software capable of reading georeferenced images and performing mathematical calculations with the information included in the cells. In the case of the digital surface models, is enough to subtract one image from the other to have the variations in height.

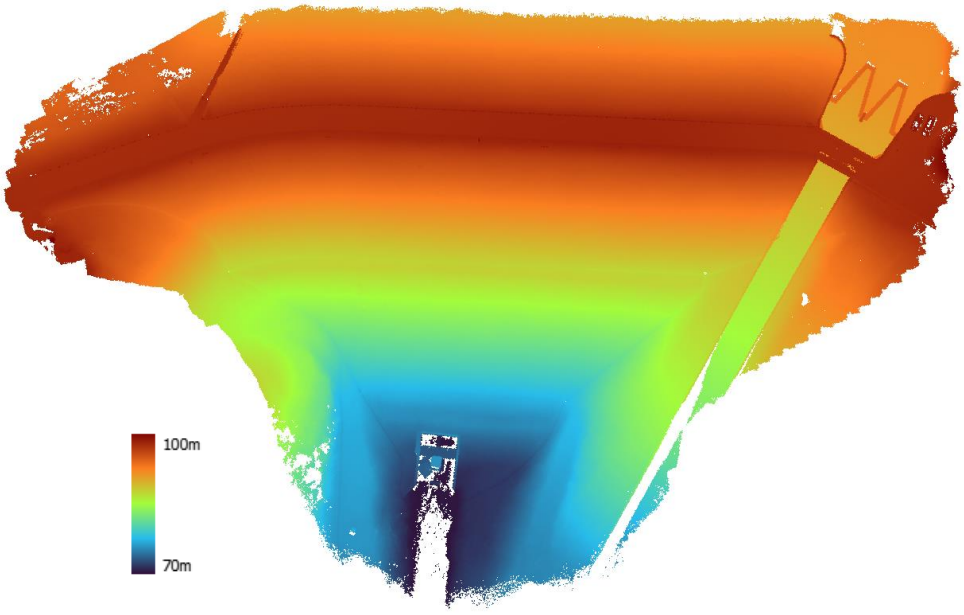

Fig. 9 – Digital surface model of Carril dam artificially colored according to the color scale presented

To illustrate an analysis of differences based on the data of surface models, it was chosen a situation that occurred in Carril dam, which was the displacement of a manhole cover due to works that happened in 2024. Two sections of the orthomosaics of 2023 and 2024 are shown

in Figure 10, while in Figure 11 presents the digital surface models of the area, converted to a colour image using the palette included. Figure 12 presents the result of the comparison between the digital surface models. It used a different palette to highlight the upper or down differences. For instance, the pixels in blue mean that, in 2024, these have a higher height than in 2023.

Fig. 10 – Displacement of a manhole cover between 2023 and 2024

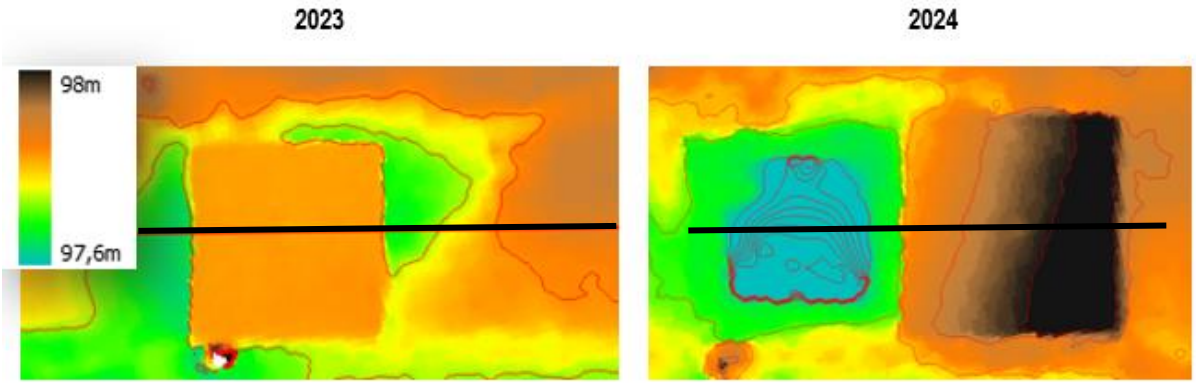

Fig. 11 – Digital surface models colored according to the palette presented

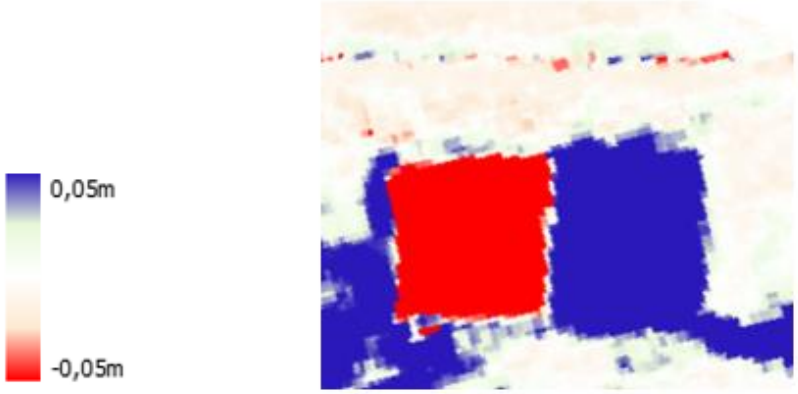

Fig. 12 – Comparison between numerical surface models

A second product of the exploration of the digital surface models is profiles. The two images in Figure 13 include a horizontal black line. This indicates the direction of profiles, profiles that are shown in the chart presented in Figure 11.

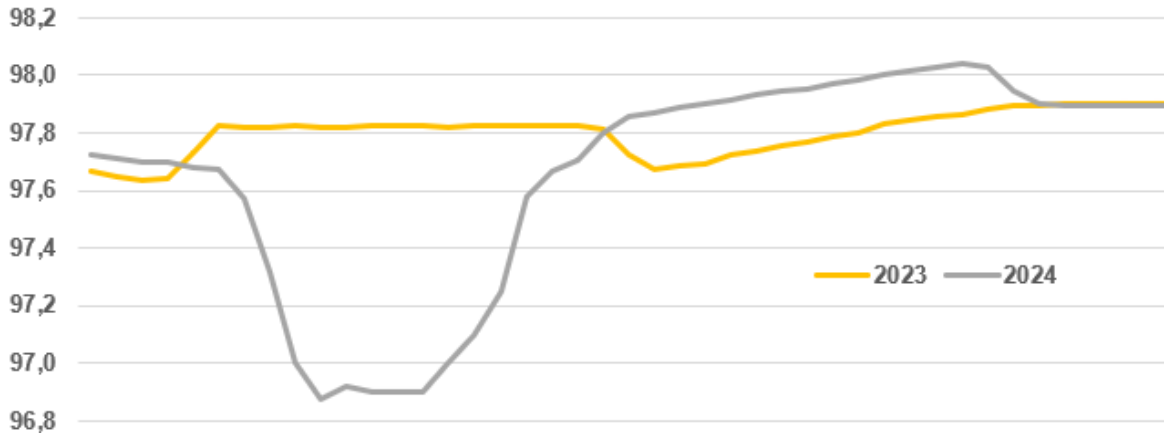

Fig. 13 – Profiles extracted from the digital surface models

Looking at the profile of 2024 of the area inside the manhole, one can notice that this is not very well modelled. The photographs used were from the aerial surveys of a dam (information about these surveys is included in section 5 of this paper). To achieve good modelling, it would have been necessary to take more photographs of the manhole and these from a shorter distance.

5. CREATING A POINT CLOUD AND DETECTING CHANGES IN AN EARTH DAM

The dam chosen to present the use of point clouds in dam control is called Carril, named after a nearby village situated in the centre of Portugal. The Carril Dam is under the jurisdiction of the Commission for Regional Development and Coordination of Lisbon and Tagus Valley. It's an earth dam whose construction ended in 2001. It was built for the irrigation of an area of, approximately, 1000 acres. The maximum height above the foundation is 25 m. Crest development is 188 m. The upstream slope is protected with stones and the downstream slope is covered with earth except the areas around the outlet that are covered with stones.

The dam includes a geodetic surveying system, to monitor the displacements of points on the crest and berm (downstream side). This system allows the determination of displacements with high accuracy. However, to obtain information on the occurrence of changes in areas other than those surrounding the observed points, two photo surveys were carried out to obtain point clouds of the crest and downstream side, the areas of interest for the study [6, 7].

To create the point clouds, it was used photogrammetric methods. The equipment (Fig. 14) was from DJI: the drone (Matrice 300 RTK) and its remote controller, the digital camera (Zenmuse H20), the GNSS RTK base station and four batteries.

Fig. 14 – Drone operator, Matrice 300 RTK drone and, in the background, the GNSS RTK station

In each survey, two flights (Fig. 15) were carried out at a constant height of 15 m above the crest. This implied that the points at the base of the dam were about 40 m away from the drone. The flights were planned so the photos had an overlap (front and side) of 80%, with the camera pointing straight down.

The photo surveys were made in October 2023 and October 2024. In each survey, a total of nearly 1400 photographs were obtained. The two flights took about 55 minutes. The take-off point was on the left side of the dam, in a parking lot next to the crest.

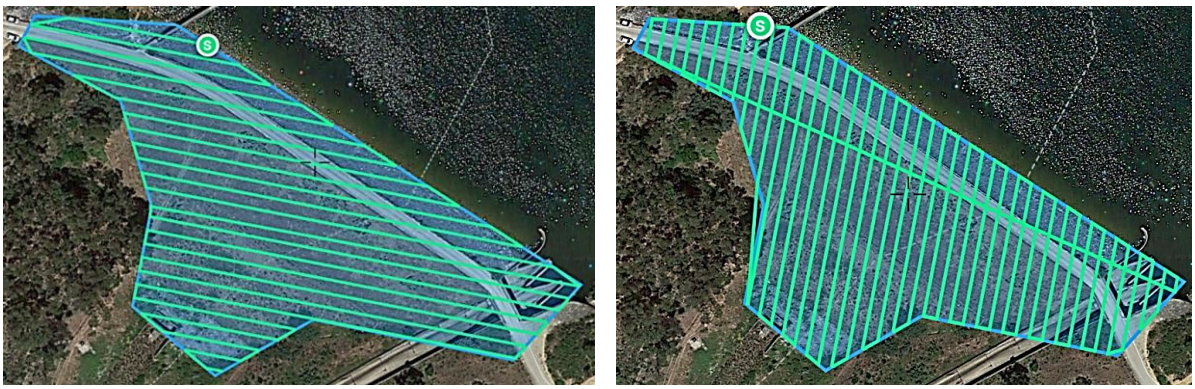

Fig. 15 – Flight plans

To georeferenced the photosurvey, several points were marked. The location of these points (ground control points, GCP) is present in Figure 16. For quality control some extra points (check points, CP) were also marked (Fig. 16). The points (GCP and CP) were materialized by arrows painted on the pavement of the crest, on small structures in concrete or metal, or on stones. The points on the earth were materialized by canvas with arrows. Since the drone has

a GNSS RTK receiver it would have been possible to have less GCP if the data of the drone location, obtained by GNSS RTK, had been included in the processing. The negative aspect of this type of procedure is that the products generated have lower accuracy. For this reason, it was used many GCP to have high accuracy.

The points were coordinated using a total station Leica TC2003 (Fig. 17 and 18). In small surveyed areas, it is more accurate to use a total station than a GNSS receiver to coordinate the points. The reference points used for the coordination were the two pillars of the geodetic surveying system, that has coordinates in the Portuguese Reference Systems used in the mainland.

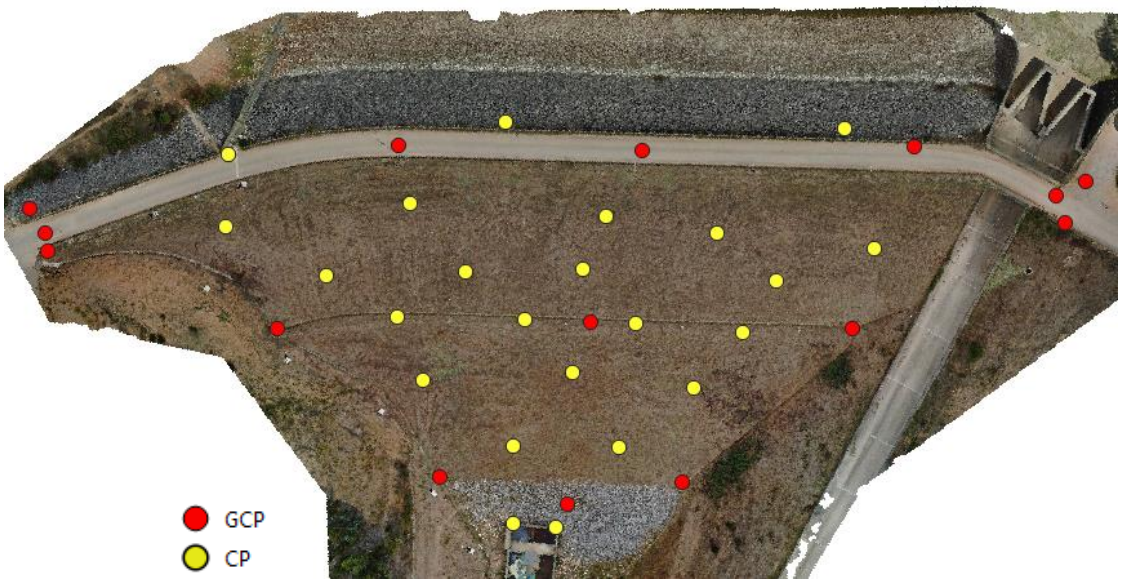

Fig. 16 – Location of the ground control (GCP) and check points (CP) presented on the orthomosaic of 2024

Fig. 17 – Total station Leica TC2003

Fig. 18 – Pole with a prism on the top

It was generated, for each photo survey, a point cloud, two digital surface models (in the forms of a matrix, Fig. 9, and a mesh, Fig. 19 and 20) and an orthomosaic (Fig. 16). It was used the software Agisoft Metashape Pro. The point cloud had around 115 million points and the orthomosaic with 0.7 cm/pixel resolution. It created two matrices: one with a pixel of 1.4 cm (the value proposed by the software) which was used to orthorectify the photos; the other with a pixel of 5 cm, used for the comparison of the numerical surface models.

Fig. 19 – Mesh of Carril dam in 2023, seen from the downstream side

Fig. 20 – Mesh of Carril dam in 2023, seen from the upstream side

In each survey, quality control was carried out. The procedures used, as well as the minimum number of check points needed to perform a good quality check, were the ones included in [8]. For each of the check points (CP) there are two coordinates: 1) the ones obtained in the field, by surveying methods (X_{CP}, Y_{CP}, Z_{CP}); 2) the "photogrammetric" coordinates, from the orthomosaic (X_{ortho}, Y_{ortho}) and point cloud (Z_{cloud}). Based on these coordinates, it is calculated, for each component, the Root Mean Squared Error (RMSE):

$$RMSE_X = \sqrt[2]{\frac{1}{n}\sum (X_{ortho} - X_{CP})^2} \quad (1)$$

$$RMSE_Y = \sqrt[2]{\frac{1}{n}\sum (Y_{ortho} - Y_{CP})^2} \quad (2)$$

$$RMSE_Z = \sqrt[2]{\frac{1}{n}\sum (Z_{cloud} - Z_{CP})^2} \quad (3)$$

where n represents the number of check points. In the surveys, the values obtained were the ones presented in Table 1.

To calculate the uncertainty, it is assumed that the errors are normally distributed. The uncertainty, with a 95% confidence level, is calculated by the equations presented in [8],

$$\text{Planimetric uncertainty} = 2{,}4477 \times 0{,}5 \times (RMSE_X + RMSE_Y), \quad (4)$$

$$\text{Altimetric uncertainty} = 1{,}9600 \times (RMSE_Z)\,. \quad (5)$$

The values obtained are presented in Table 1 and can be considered acceptable for a photogrammetric survey.

Table 1 – Number of check points, root mean squared errors and uncertainties

	Number of CP	RMSE X (cm)	RMSE Y (cm)	RMSE Z (cm)	Planimetric uncertainty (cm)	Altimetric uncertainty (cm)
CP – 2023	22	1,4	1,1	2,1	3,1	4,1
CP - 2024	23	1,1	1,4	2,0	3,1	3,9

The digital surface model in the form of a matrix, explored by the software QGIS, was used to present some features of this dam. Not all of these are important. They are presented here so that one can see the potential of the products created, based on the point clouds.

One curiosity detected is an area with a higher height (about 40 cm) in the crest. It can be noticed in Figures 21 and 22. The chart of Figure 22 has, in the X axis, the distance to the beginning of the crest on the right margin. The Y axis has the heights.

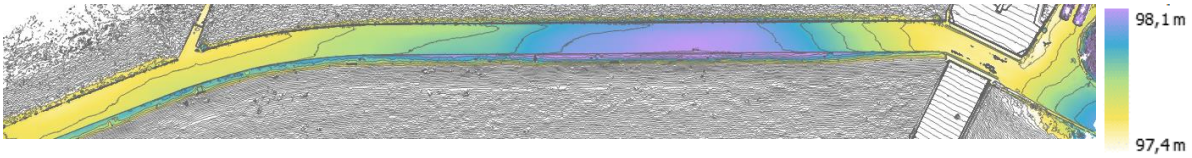

Fig. 21 – Digital surface model of the dam (crest and surrounding areas), artificially coloured, with the inclusion of contour lines spaced 0.1 m

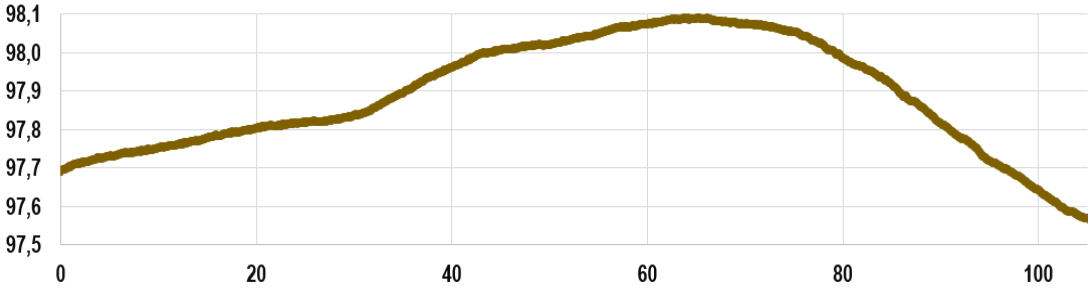

Fig. 22 – Longitudinal, elevated profile, of the central section of the crest

The module Hillshade from QGIS was used to highlight areas with variations in relief. Figures 23 and 24 present some features detected on the downstream side. In the second figure, the marks left by the backhoe used during the cleaning of the dam surface, carried out shortly before the aerial survey of 2023, can be seen. One can also notice the canes that were beginning to grow.

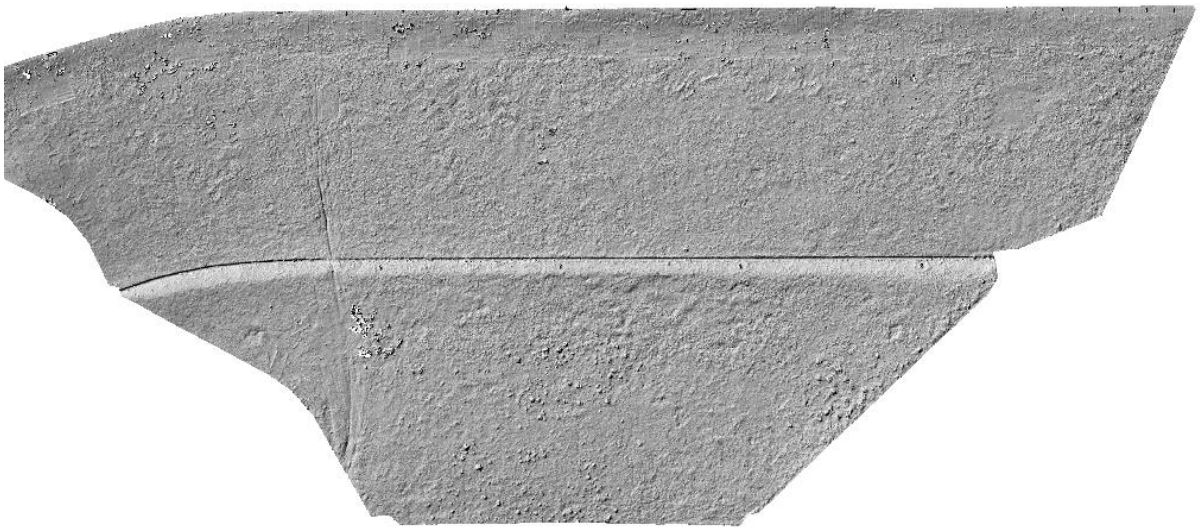

Fig. 23 – Shaded relief of the downstream side

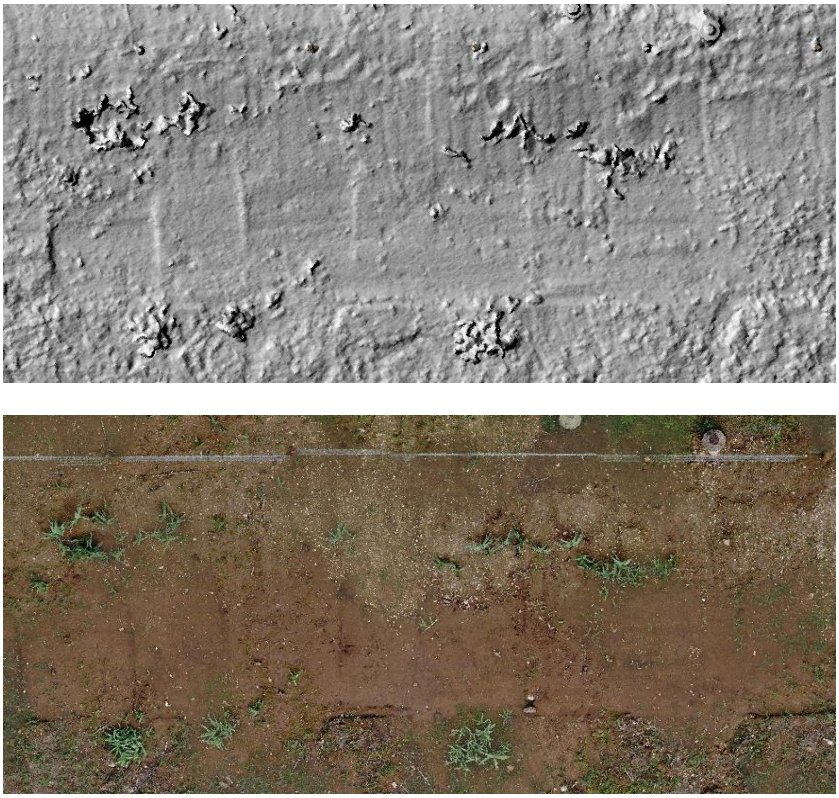

Fig. 24 – Shaded relief of the downstream side near the crest and orthomosaic of the area

The canes and other vegetation are a problem in the detection of changes. Although the vegetation was cleaned before the surveys, in 2023 there was heavy rain and periods of strong winds that postponed the drone survey. That allowed some vegetation to grow. That can be noticed in the comparison of the digital surface models (Fig. 25). The changes detected on the downstream side have as origin the vegetation. This is the normal situation in earth dams.

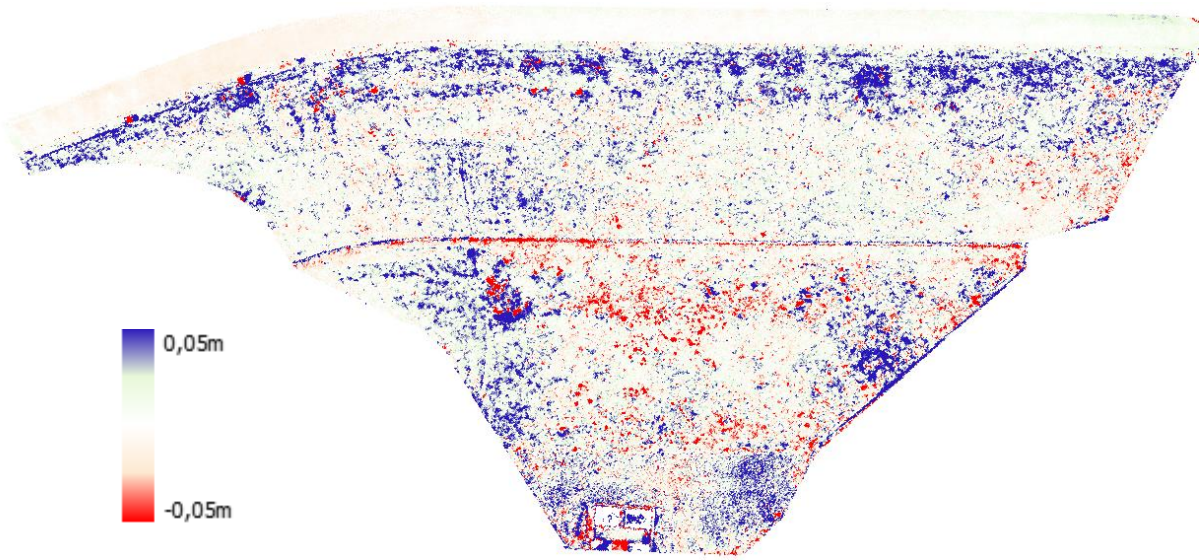

Fig. 25 – Comparison of the digital surface models of 2023 and 2024, crest and downstream side

More interesting is the analysis of the variation of the heights of the pavement of the crest, since small changes can be more easily detected because of the type of surface. The results are presented in Figure 26. To notice that the amplitude of the color scale is different and was created to highlight smaller changes.

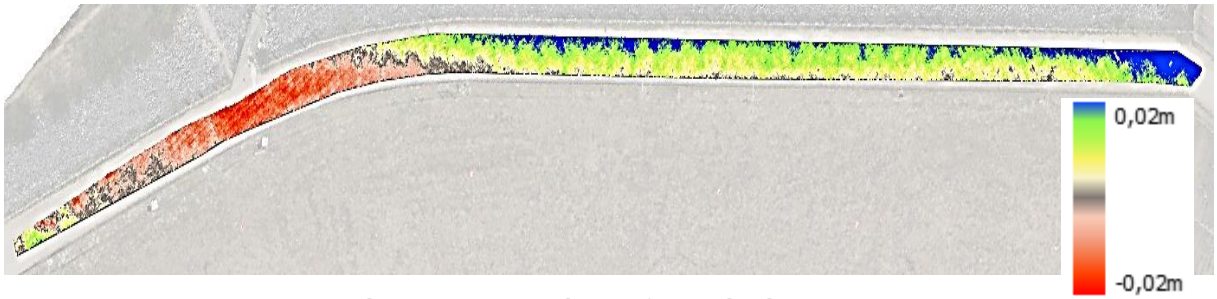

Fig. 26 – Comparison of MNS in the crest

6. CONCLUSIONS

Point clouds are a powerful tool to detect geometric changes of surfaces. In the case of dams two different techniques can be used: laser scanners or digital cameras (photogrammetric methods) [9].

The paper presents the results of exploring two point clouds created from two photogrammetric surveys of an earth dam made with a difference of one year. The photos were taken by a digital camera mounted under a drone. The paper also shortly describes the work done in the field, the drone survey and the coordination of points, this last to georeferenced the products generated and to their quality control.

In the two monitored areas, which were the crest and the downstream side, changes were detected. In the downstream side, these have no meaning as they only reflect different situations in the vegetation cover. The studies carried out at the crest are more interesting as they indicate the existence of a very slight settlement that occurs close to the water intake. Regarding this settlement, it would be interesting to continue following it, eventually applying more exact techniques.

ACKNOWLEDGEMENTS

The authors acknowledge the Commission for Regional Development and Coordination of Lisbon and Tagus Valley for authorizing the dissemination of the work carried out and results obtained at the Carril dam.

REFERENCES

[1] Berberan, A.L. and Baptista, B. (2011). Laser scanning and digital imagery as a tool for dam monitoring and rehabilitation. Dam Maintenance and Rehabilitation II, Proceedings of the 2nd International Congress on Dam Maintenance and Rehabilitation, Zaragoza, Spain.

[2] Berberan, A.L.; Ferreira, I.; Portela, E. and Baptista, B. (2011). Overview on terrestrial laser scanning as a tool for dam surveillance. 6th International Conference on Dam Engineering, Lisboa, Portugal.

[3] Henriques,M.J.; Fonseca,A.; Roque,D.; Lima,J.N. and Marnoto,J. (2014). Assessing the quality of an UAV-based orthomosaic and surface model of a breakwater. FIG Congress 2014, Kuala Lumpur, Malaysia.

[4] Henriques,M.J.; Braz,N.; Roque,D.; Lemos,R. and Fortes,C.J.E.M. (2016). Controlling the damages of physical models of rubble-mound breakwaters by photogrammetric products - Orthomosaics and point clouds. Proceedings of the 3rd Joint International Symposium on Deformation Monitoring, Viena, Austria.

[5] Lemos, R.; Capitão, R.; Fortes, C.J.E.M.; Henriques, M.J.; Silva, L.G.; Martins, T. (2020). A methodology for the evaluation of evolution and risk of breakwaters. Application to Portimão harbor and of Faro-Olhão inlet. Revista de Gestão Costeira Integrada, Volume 20, Issue 2, June 2020, pag. 103-119, DOI: 10.5894/rgci-n298.

[6] LNEC (2004a). Carril dam. Photogrammetric survey carried out in October 2023 (in Portuguese). Report, LNEC, Lisboa.

[7] LNEC (2004b). Carril dam. Photogrammetric survey carried out in October 2024 (in Portuguese). Report, LNEC, Lisboa.

[8] FGFC, 1998 − Geospatial Positioning Accuracy Standards. Part 3: National Standard for Spatial Data Accuracy. Federal Geographic Data Committee, FGDC−STD−007.3−1998.

[9] Bolkas, D.; O'Banion, M.; Prickett, J.; Ellsworth, G.; Rusek, G. and Corson, H. (2022). Comparison of TLS and sUAS point clouds for monitoring embankment dams. 5th Joint International Symposium on Deformation Monitoring (JISDM2022), Valencia, Spain.

Fifth International Dam World Conference
PORTUGAL • LISBON • LNEC • APRIL 13-17, 2025
dam world 2025

A DETAILED SAFETY AND RISK ASSESSMENT OF PEQUENOS LIBOMBOS DAM

Melo, J. F.[1]	Sardinha, R.[2]	Pimenta, L.[3]	Duarte, A.[4]	Freitas, R. M.[5]
LNEC	COBA	COBA	COBA	COBA
Juízo, D.[6]	**Martins, A.[7]**	**Sengo, D.[8]**	**Timba, J.[9]**	**Mabunda, L.[10]**
SALOMON	SALOMON	ARA-Sul, IP	ARA-Sul, IP	DNGRH

ABSTRACT

At the request of the Mozambican National Directorate of Water Program (DNGRH) and as part of the National Climate Resilience Program, a study aimed to evaluate the current safety of the Pequenos Libombos dam and downstream valley was developed by the Consortium COBA/LNEC/SALOMON. The objectives encompassed a range of activities designed to ensure a thorough assessment and enhancement of dam safety, a critical issue to guaranty the integrity and reliability of this key water infrastructure in Mozambique. In this paper, structural and hydraulic-operational safety results are presented, as well as its adaptation to the new Mozambican dam regulations.

The Pequenos Libombos Dam, located on the Umbelúzi River, serves as the primary water supply for Maputo city. It features a 1,540-meter-long and 46-meter-high earthfill structure, with a 100-meter-long central gravity concrete dam where all the appurtenant structures are located.

The study involved a comprehensive evaluation of dam performance, including a review of operational procedures and detailed site inspections. It analyzed existing monitoring data and assessed current safety conditions. A thorough safety assessment identified both structural and non-structural mitigation measures.

The comprehensive assessment approach taken for the Pequenos Libombos dam revealed strengths and weaknesses in current dam safety practices. By implementing the recommended measures, the safety and functionality of these dams will be significantly enhanced.

Key lessons underscored the critical need for regular monitoring and robust risk assessment procedures. This will contribute to the overall resilience and security of the region's water infrastructure and ensure the safety of populations living downstream.

Keywords: Earth and concrete dam, safety assessment, safety regulation.

[1] jfmelo@lnec.pt, Portugal
[2] r.sardinha@cobagroup.com, Portugal
[3] l.pimenta@cobagroup.com, Portugal
[4] a.duarte@cobagroup.com, Portugal
[5] r.m.freitas@cobagroup.com, Portugal
[6] juizo@hotmail.com, Mozambique
[7] amiromartins13@gmail.com, Mozambique
[8] dsengo@yahoo.com, Mozambique
[9] timbanetimba@gmail.com, Mozambique
[10] luismabunda@gmail.com, Mozambique

1. INTRODUCTION

The Dam Safety Assessment of Pequenos Libombos dam was carried out by COBA-LNEC-SALOMON Joint Venture, in the scope of the contract established between the National Directorate of Water Resources Management (DNGRH). These services were developed within the scope of the National Climate Resilience Program (RCRP) of the Government of the Republic of Mozambique, funded by the International Development Association (IDA). These services were carried out between March/2024 and November/2024 and the main activities undertaken were the following:

i. Compilation and analysis of existing documentation
ii. Field inspections.
iii. Dam safety assessment.
iv. Recommendations of structural and non-structural measures needed to enhance dam safety.
v. Training program.

The Pequenos Libombos Dam is a large structure, and as such, it falls under the provisions of the Mozambique Dam Safety Regulation (MDSR) [1]. It is classified as Risk Class I, with Medium Vulnerability and High Potential for Damage. This classification is subject to review every five years and outlines several responsibilities for the Project Owner. Among these, the following priorities will be addressed in the short term: i. Organization of the Technical Archive, ii. Development of the Safety Plan, iii. Organization of the monitoring data, iv. Providing the required information for the development of the External Emergency Plan, v. Identification and Development of structural and non-structural measures for safety improvement and rehabilitation.

This paper focuses on structural safety, hydraulic-operational safety, and the safety of electrical equipment and installations, as well as on the structural and non-structural measures aimed at mitigating the risks of failure and various malfunctions, improving safety conditions, and adapting the dam to the current safety regulations.

Downstream consequences of dam failure and operational flood releases are treated in the paper “Strengthening Key Water Infrastructure in Mozambique: A Risk Assessment of Downstream Valley of Pequenos Libombos Dam”.

2. PEQUENOS LIBOMBOS DAM MAIN CHARACTERISTICS

The Pequenos Libombos Dam, managed by ARA Sul, is situated on the Umbelúzi River in the Boane District of Maputo Province. Constructed between 1983 and 1986, the dam’s first filling occurred from 1986 to 1989. It is a multi-purpose dam primarily intended to provide water

supply to the cities of Maputo, Matola, and Boane, as well as to control flooding, support irrigation, and operate a small hydroelectric plant with an installed capacity of 1.7 MW. The hydroelectric plant operated from 2014 to 2016 but was subsequently suspended due to a drought that intensified water scarcity for other essential uses.

The Pequenos Libombos watershed spans 3,735 square kilometers, of which only 20% lies within Mozambique, with an average annual inflow volume of 350 hm^3. The reservoir's maximum capacity is 393 hm^3, with an operational capacity of 350 hm^3, and it covers an area of 38 km^2 when the water level reaches the Normal Water Level (NWL) of 47 meters. The Maximum Flood Level (MFL) is 49.55 meters, and the minimum operational level is 25 meters.

The dam spans approximately 1,640 meters at the crest level, which sits at an elevation of 51.5 meters. The embankment cross-sections reach a maximum height of 46 meters and extend over 1,540 meters. In the central valley, where the appurtenant structures are located (**Figure 1**), the concrete section measures around 100 meters in length and has a maximum height of 48 meters.

Figure 1 – Appurtenant structures. Upstream and downstream views

The spillway consists of a middle-level outlet with seven spans, each equipped with radial gates (dimensions: width = 7.5 m, height = 5.3 m), positioned with a bottom sill at elevation 24 m and a discharge capacity of 5,600 m^3/s. Additionally, an emergency spillway provides a discharge capacity of 1,200 m^3/s, featuring six free spans at level 47 m and one central span with a 1-meter-high flap gate with the crest at level 46 m. The primary spillway includes a cofferdam gate measuring 7.5 x 11.175 m^2, operated by a gantry.

Two bottom outlets are installed along the left and right concrete walls that separate the earthfill dam from the concrete section, each 110 meters long with a diameter of 1.5 meters. These outlets are equipped with a fixed wheel safety gate upstream (1.3 m x 1.5 m) and a downstream slide gate (1.2 m x 1.3 m) for flow regulation. Each outlet has a maximum discharge capacity of 30 m^3/s at the Normal Water Level (NWL).

The water intake has 4 intake levels, each equipped with 1.4m x 1.4m slide gates. The water is conveyed into a 700 mm diameter conduit. This conduit joins the bottom outlet conduit near its downstream extremity, sharing the same exit structure. The maximum discharge capacity is 1.2 m^3/s.

Currently, 15-30% of the diverted water through the outlets is assigned to environmental purposes.

The occupation of the downstream valley has increased significantly in recent years. When the dam construction was completed, there were no dwellings in the floodplain downstream. Today, however, there is considerable development, including a new residential area that is flooded even with relatively small floods, around 200 m^3/s, as well as a railway bridge crossing the downstream valley.

Figure 2 provides a Google Earth view showing the general layout of the dam, while **Figure 3** offers detailed views of the concrete dam and its associated structures. **Figure 4** and **Figure 5** present the dam's cross-sections.

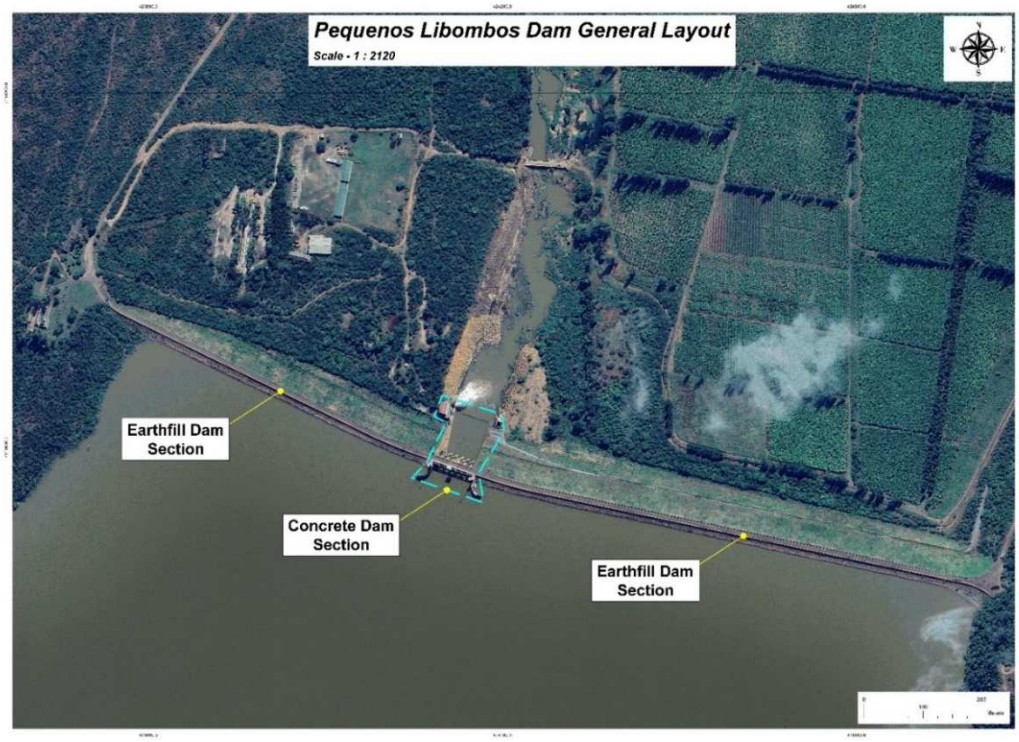

Figure 2 – Pequenos Libombos. View from Google Earth.

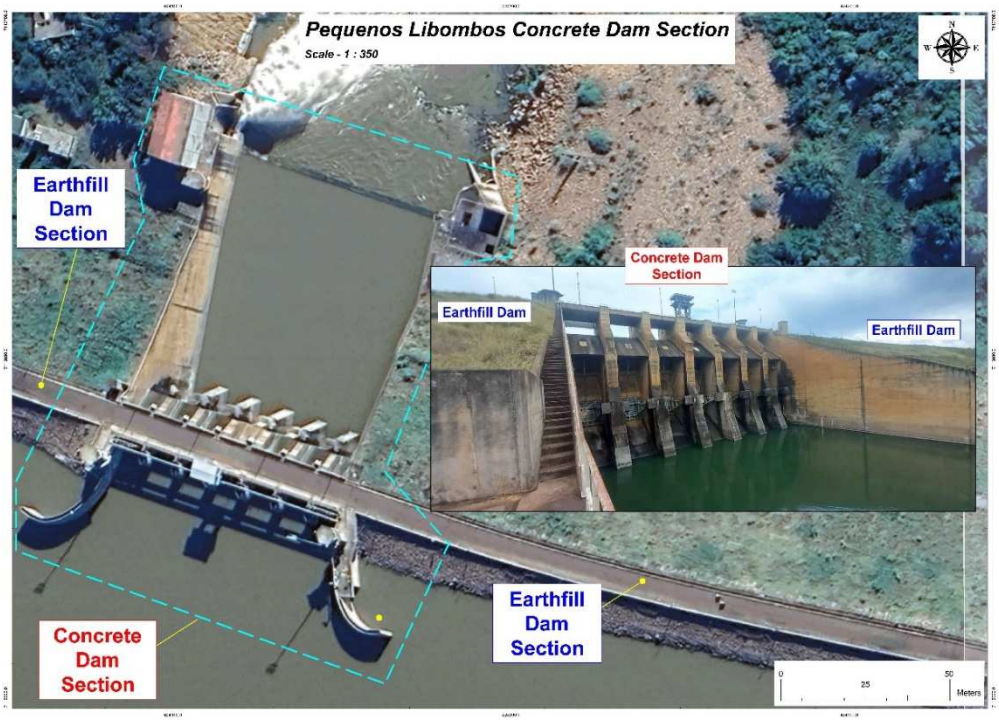

Figure 3 – Pequenos Libombos dam general layout of the appurtenant works.

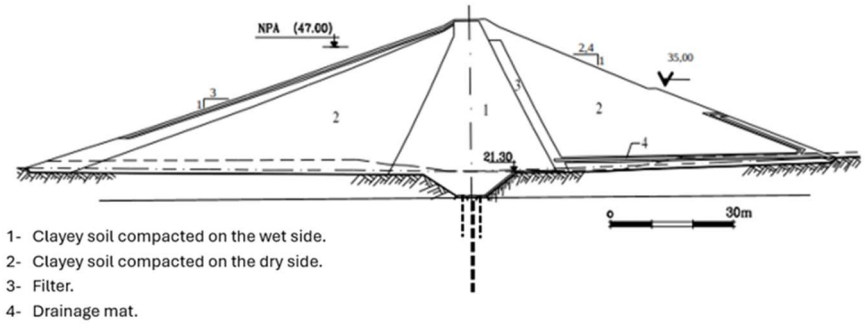

Figure 4 – Typical cross section of Pequenos Libombos dam
(adapted from Portugal et al, 2012 [2], and Maranha das Neves et al, 1985 [3])

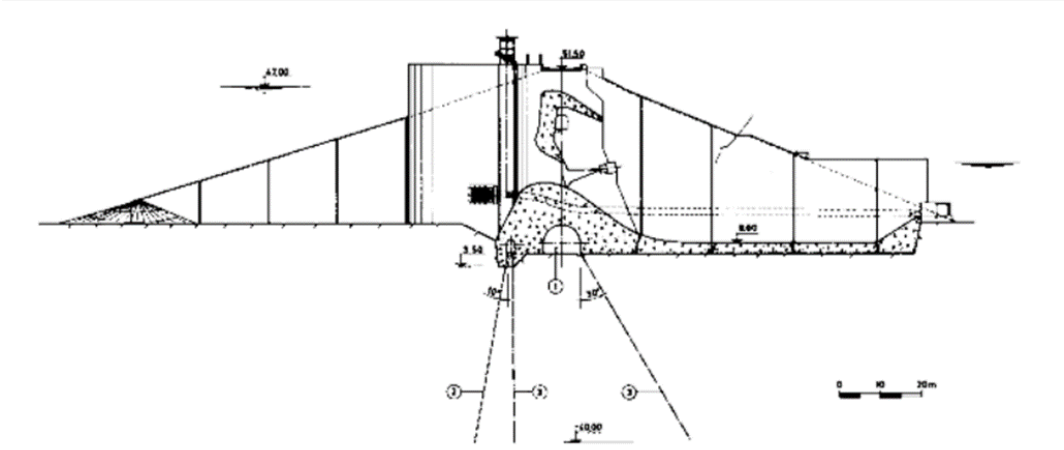

1 – Gallery in the foundation; 2 – Impermeabilization curtain; 3 – drainage curtain

Figure 5 – Typical cross section of Pequenos Libombos spillway (Maranha das Neves et al, 1985)

3. FIELD INSPECTION

A field inspection was carried out following the agenda of the program previously agreed with DNGRH and ARA Sul. A dam Safety Inspection Form was prepared using the World Bank's Good Practice Note on Dam Safety (WB 2020) [4]. Also, a list of issues and aspects to be inspected and/or addressed during the inspection visits and meetings was previously shared with the Client. The following components were covered during the field inspection:

i. Dam body and foundation,
ii. Monitoring systems,
iii. Appurtenant structures. Structural component,
iv. Appurtenant Structures. Hydraulic and hydromechanical components,
v. Electrical equipment and installations,
vi. Downstream valley and environmental constraints.

During the inspection various meetings with the inspection team and the Owner's staff were held, to allow the gathering of information from the resident team and the engineers responsible for the operation and safety of the dam, as well as familiarizing the team with the facilities and the measurement equipment of the monitoring devices. At the end of the inspection visit the main conclusions and recommendations were conveyed, resulting from an initial safety assessment based on the information collected and the inspections carried out on the various components of the project [5].

4. DAM SAFETY ASSESSMENT

The performed dam safety assessment main conclusions [6] are presented on the following subsections.

4.1. Embankment dam body and foundation

Figure 6 and **Figure 7** presents general views of the earth dam and crest.

Figure 6 – Downstream slope. General view (view towards the right bank).

No indicators of abnormal behaviour in the dam body or its foundation that jeopardize the safety of the dam were identified. To assure longevity of the structure and to correct localised superficial landslides in the downstream face of the dam, it was recommended to improve the slope protection of the downstream slope of the embankment and to rehabilitate the asphalt road surface in certain sections of the crest. It was also recommended to assure periodic maintenance activities, mainly regarding the superficial drainage system and the irrigation system.

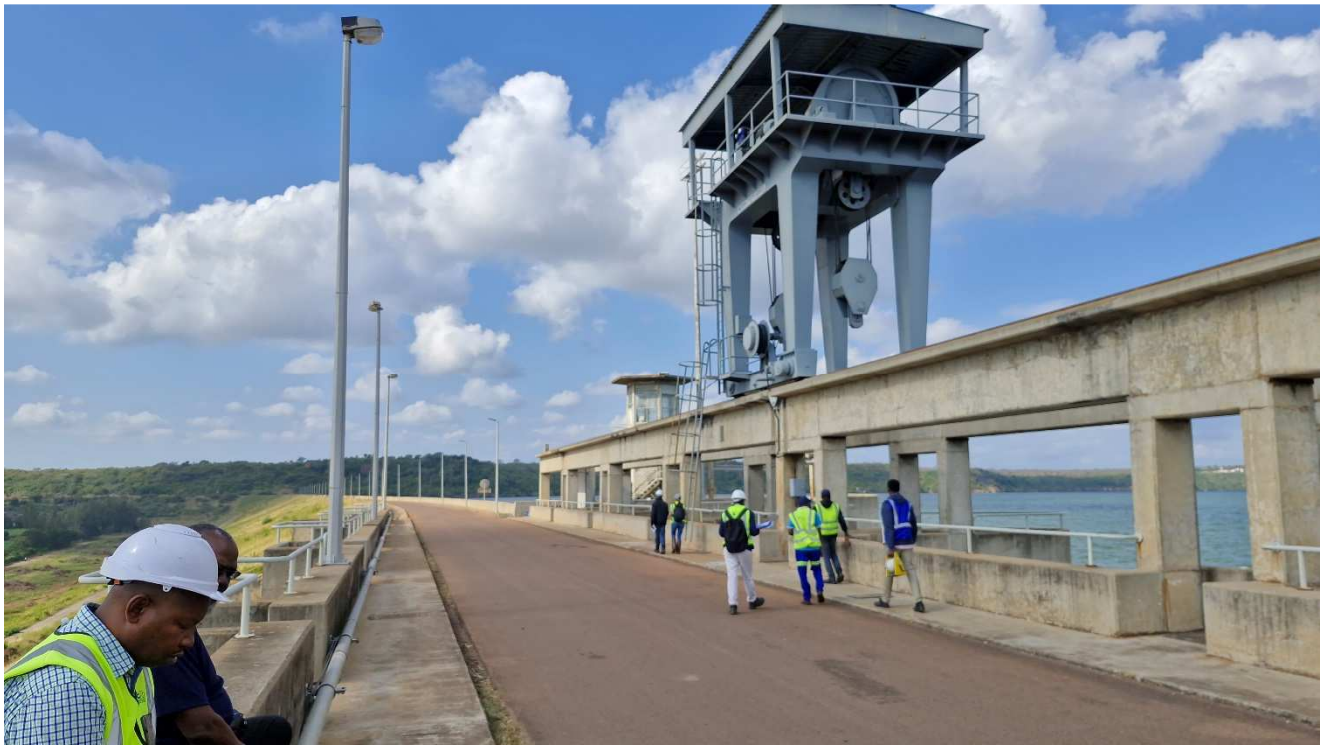

Figure 7 – Crest. General view. Section of the concrete dam (view towards the right bank).

The freeboard is constrained by the combination of factors related to the water level in the reservoir, estimated at the Maximum Water Level (MWL) of 49.55 m, which is assumed to be associated to a millennial flood. The current crest elevation of 51.5 m seems barely adequate to accommodate the wave run-up caused by a typical wind speed of 60 km/h (a modest value), a residual creep settlement estimated at 0.14 m, and an allowance of 0.4 m for unquantifiable factors, including seismic effects. However, for a design flood with a 2000-year return period, as specified by the MDSR for the Pequenos Libombos Dam, the current crest elevation can be insufficient.

4.2. Concrete Dam Body

No indicators of abnormal behaviour have been identified in the concrete dam body that houses the hydraulic structures. A routine maintenance plan for the reinforced concrete and metal structures was recommended, to ensure proper functioning and continuous monitoring of existing structural pathologies.

The observed reduction in the inflow rates to the large gallery between 2005-2014, for approximately constant reservoir levels, suggested a potential malfunction due to obstruction in the drainage system, raising the possibility of a concurrent increase in the uplift pressures. The latest monitoring data do not seem to confirm this hypothesis.

Given the importance of the stability of the reinforced concrete portico beam in the operation of the flood gates, an urgent need to repair the identified anomalies given the pattern of their occurrence along the spans was identified. This repair has been done afterwards.

Existing small cracks in the slab (specifically at the oil hydraulic units of the spillway radial gates) must be repaired and consistently monitored. The roof of the command of the regulating gate of the right-side bottom outlet gate needs to be repaired to prevent water accumulation inside. This water has corroded the perimeter of the DN700 bottom outlet pipe where it connects to the concrete base, and retained water must be evacuated to prevent further excessive corrosion.

As far as the metal structure is concerned, most elements need to be completely replaced, while others just need a protective coating. Additionally, the drainage gallery stairway and the stairs providing access to the spillway gates require rehabilitation, including the incorporation of resting platforms, particularly for the stairway leading to the control room of the right-side bottom outlet regulating gate.

4.3. Monitoring system, procedures and data

The observation procedures are centralized at the dam site and well-organized, allowing for the quick access and interpretation of the variables subject to periodic readings. There is no immediate transmission of observation data to either the Authority or the Mozambique Engineering Laboratory (MEL), as specified by the MDSR.

The operators are knowledgeable and familiar with the procedures for data reading and analysis, but the technical means at their disposal, namely hardware and software, urgently require improvements. Readings from the observation devices are performed by a team from ARA-Sul stationed at the dam site.

Regarding the surface marks in the embankment dam, the last known campaign dates from 1991. Maximum settlements were recorded in the central area of the valley where the embankment heights are greater, as expected. At that time, the maximum settlement on the downstream bench at elevation 35 was 64 mm. At the crest, the maximum settlement was 140 mm downstream (marks at elevation 50.5 m) and 112 mm upstream (marks at elevation 48 m).

A drone survey is recommended to obtain a quick assessment of the current elevations along the crest, allowing the reassessment of the dam's current freeboard. After this survey, it will be necessary to resume the readings of the superficial displacements of the dam.

In the concrete dam there are no devices to monitor movements, either in the dam body or in its foundation.

The hydraulic piezometers installed in the embankment body and its foundation generally show water levels consistent with the water level in the reservoir and their location. However, it is worth noting the limited number of piezometers installed and in operation. The water levels measured in the relief wells exhibit a similar behaviour (**Figure 8** and **Figure 9**).

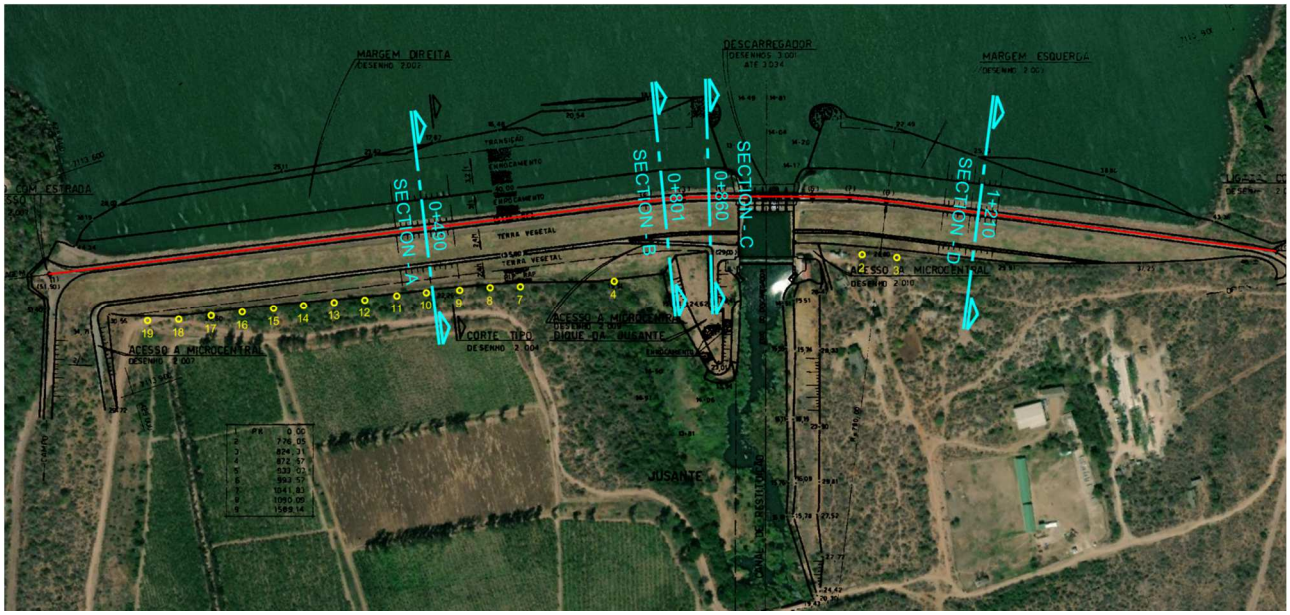

Figure 8 – Location plan of the monitoring cross-sections (A to D) and the relief wells situated downstream of the dam toe (yellow circles)

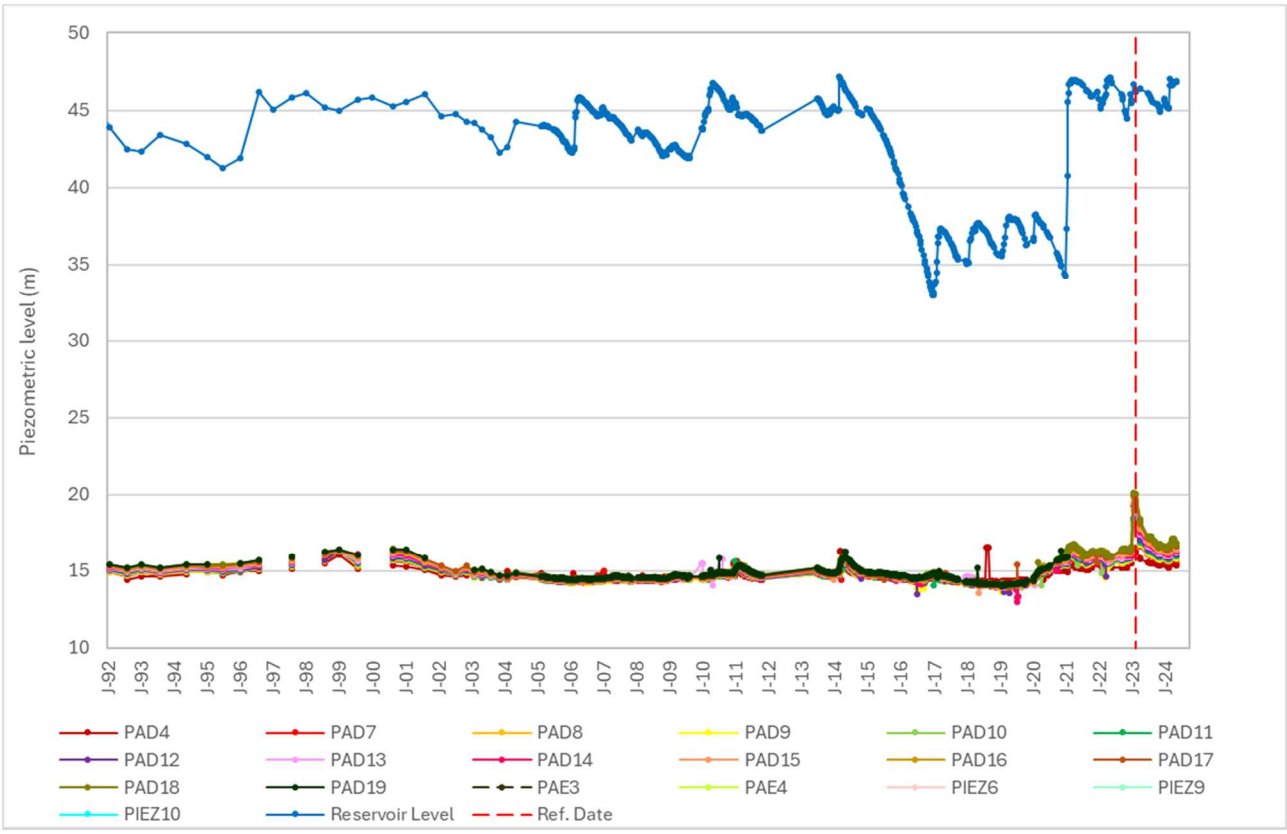

Figure 9 – Relief wells. Variation in piezometric levels from January 1992 to June 2024

Concerning the flows measured in the drains located in the longitudinal galleries of the concrete dam, the behaviour has fluctuated over time. Between 2005 and 2014, while total flows in the small gallery remained approximately constant, in the large gallery the trend was towards a decrease in total flows. From 2014 to 2017, total flows in both galleries decreased, following the drop in reservoir water levels, stabilizing between 4 and 7 l/min from 2017 to 2021, with relatively stable reservoir water levels, ranging from approximately 35 to 37.5 m. The sharp rise in reservoir water levels at the beginning of 2021, to around elevation 47 m, was accompanied by an increase in total flows in both galleries, though the values remained lower than those previously recorded for similar reservoir water levels. Finally, in March 2023, with the reservoir water near level 47, there was an exceptional increase (of unknown cause) in the total flows in both galleries (reaching values of around 39 l/min in the large gallery and around 34 l/min in the small gallery), followed by a sharp decrease for similar water levels in the reservoir, standing at around 25 l/min and 20 l/min, respectively, higher than the total flows recorded in the past for similar water levels (**Figure 10**).

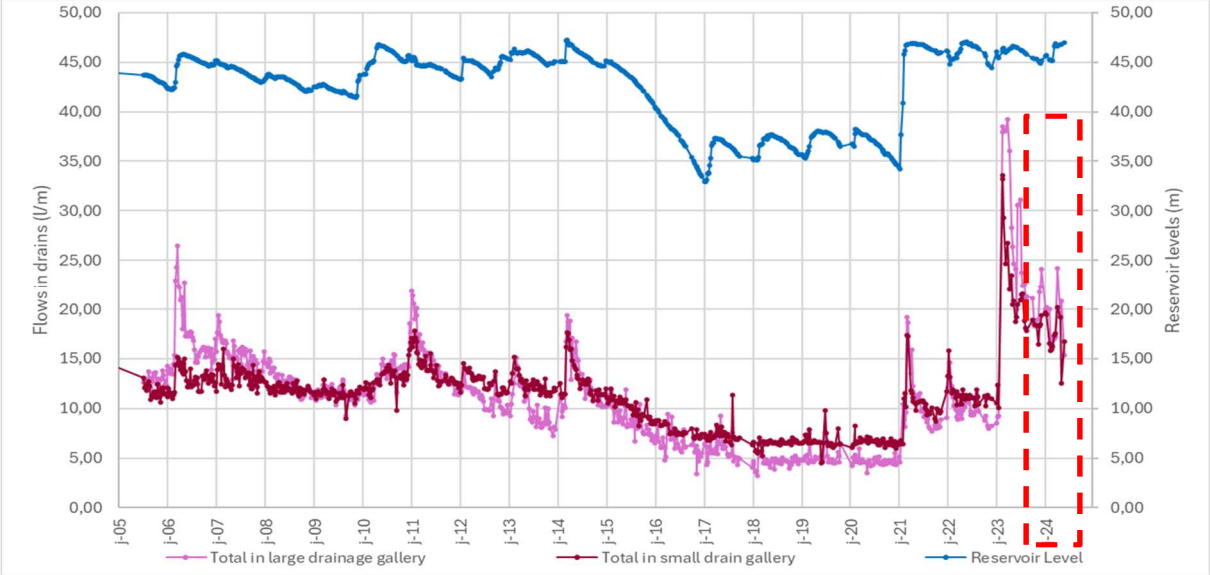

Figure 10 – Total flows in the small gallery and in the large gallery

Given that no significant variation was recorded in the readings from the piezometers with manometers installed in the gallery in March 2023 (**Figure 11**), it is possible that a drain cleaning intervention occurred, which could explain the sudden increase in the flows of the drains described above. These piezometers also did not register any pressure increases during the period when the trend in the drains showed a reduction in measured flow rates, with the reservoir levels remaining approximately constant. Therefore, the concern regarding a potential rise in uplift pressures in the foundation of the concrete dam does not appear to be supported by the integrated analysis of the monitoring devices' data, considering the readings up until 2023.

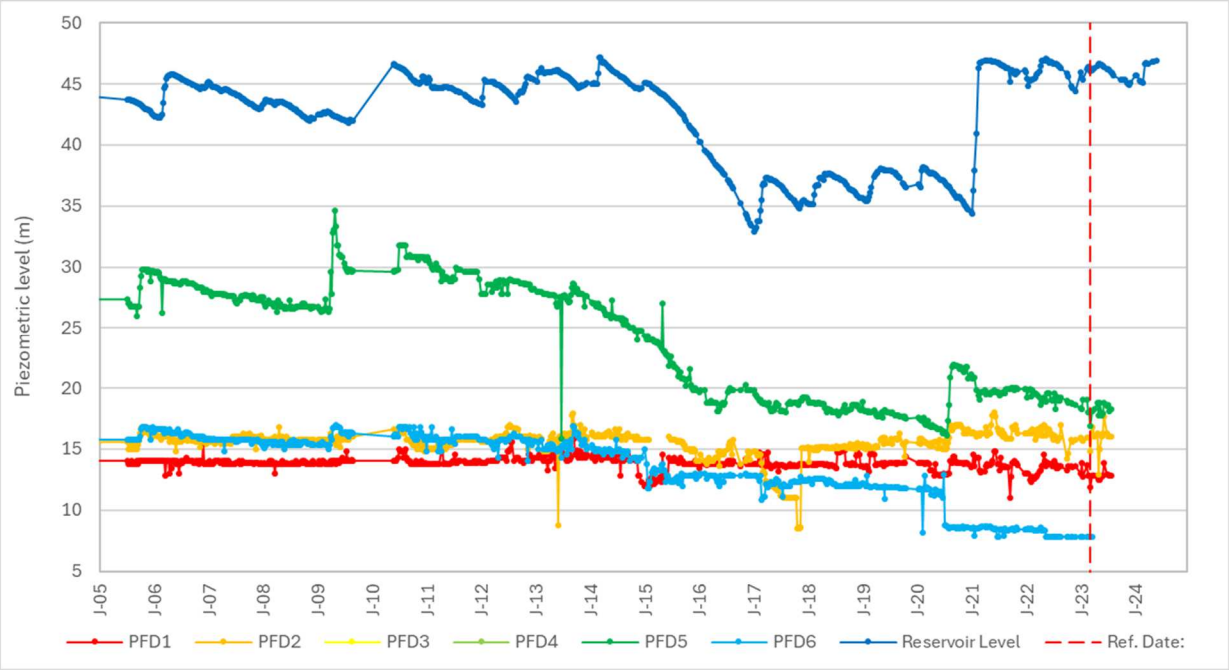

Figure 11 – Variation in piezometric levels in the spillway foundation

The monitoring data provided to the Consortium has been organized and compiled into an Excel file, which has been supplied to the Client and includes the respective analysis. This file can be used to upload and analyse the results of future reading campaigns.

4.4. Appurtenant structures. Spillway design and verification floods

The Pequenos Libombos Dam's spillway must comply with Mozambique's safety regulation (MDSR), which specifies a 2,000-year return period flood as the design flood and a 5,000-year return period flood for verification. Previous studies analysed extreme events such as the Probable Maximum Flood (PMF) and 10,000-year floods but did not address the MDSR's specific requirements for the 2,000-year and 5,000-year floods.

Those studies revealed, anyhow, that the PMF and 10,000-year floods could result in overtopping, highlighting the need for updated hydrological studies for 2,000-year and 5,000-year return period floods, as well as an assessment of the spillway system's functionality during scenarios of gate failure or power supply loss.

4.5. Appurtenant structures. Hydromechanical equipment

The following critical issues concerning the hydromechanical equipment were identified during the site inspections.

- Gantry Crane Inoperability: The crane, essential for maintenance and emergency operations of the radial gates, was non-functional during the visit, severely limiting the ability to address gate failures during floods.

- Bottom Outlet System Corrosion: Extensive corrosion was observed in the bottom outlet, embedded parts, penstock, and interconnecting gallery pipes, presenting a high rupture risk under operating pressures.
- Outdated Equipment: The dam's systems reflect 1986 technology without significant upgrades, leaving critical components vulnerable to wear and inefficiency. Remote gate operation is currently unavailable, demanding modernized control systems for safety and reliability.

4.6. Electrical equipment and installations

Since 1988/89, the dam had no major work done on the existing electrical installations. The only intervention known is the installation of new dataloggers equipment to record data, which is then sent by a radio communication system for data processing, exterior lighting installation in dam access and some maintenance repairs as usual are needed.

The technicians and engineers' dam team provided comprehensive support and information during the site inspection visit focused on dam safety. During the visit, it was possible to assess the state and condition of the electrical, control, and communications systems.

A significant set of safety issues has been identified and is listed in Chapter 5, along with the defined rehabilitation measures.

5. PROPOSED SAFETY MEASURES AND INTERVENTIONS

Under the scope of the assignment the following structural and non-structural safety measures and interventions were recommended. These arise, from dam safety assessment studies [7] and the requirements of the current dam safety legislation in Mozambique (MDSR).

Technical Archive of the Project

The Technical Archive of the Project should be organized and complemented to include: i) Dam's classification; ii) Dam's Safety Plan (Observation Plan, Operating Rules, Internal Emergency Plan and Environmental Safety Plan); iii) documents from operation; iv) documents from construction phases; v) rehabilitation design documents; vi) design studies; vii) preliminary studies.

Additionally, the technical record of the project should be prepared to be available at the dam site, paginated and sealed, for the purpose of recording inspection reports and significant events related to safety, observed during operations, and recorded by the Director of Operations.

Embankment dam body and foundation

It is necessary to improve the surface coating of the downstream slope of the embankment dam and to rehabilitate the asphalt road surface in certain sections of the crest, keep the drainage gutters unobstructed and repair the irrigation system.

The freeboard is presently constrained by the combination of factors related to the water level in the reservoir, estimated at the Maximum Water Level (MWL) of 49.55 m, which supposedly corresponds to a millennial flood. The current crest elevation of 51.5 m seems barely adequate to accommodate the wave run-up caused by a typical wind speed of 60 km/h (a modest value), a residual creep settlement estimated at 0.14 m, and an allowance of 0.4 m for unquantifiable factors, including seismic effects. However, for a design flood with a 2000-year return period, as specified by the MDSR for the Pequenos Libombos Dam, the current crest elevation can be insufficient.

Concrete Dam body

No significant indicators of anomalous behaviour have been identified in the concrete dam body housing the hydraulic structures. Nevertheless, it remains important to periodically undertake the unblocking and rehabilitation of the foundation drains in the concrete dam body and to install monitoring devices, such as plumb lines and extensometers, to assess the structure's behaviour over time.

It is important to establish a routine rehabilitation plan for the reinforced concrete and metal structures to ensure proper functioning and to ensure continuous monitoring of structural pathologies. Although not significant, the reported pathologies should be corrected to prevent further damages.

Monitoring system, procedures and data

It is recommended to review the monitoring plan considering the current dam safety regulations of Mozambique, the behaviour of the dam which has been in operation for 37 years, and the results of the inspection visit carried out. **Table 1** and **Table 2** below present the recommendations made for the monitoring plan review. The recommendations regarding the monitoring of the concrete dam (**Table 2**) follow the guidelines established by Hidroprojeto [8] and LNEC [9].

Table 1 – Monitoring plan review recommendations. Embankment dam cross-sections

Monitoring parameter	Device	Reading frequency	Instrumented profiles and location of the devices
Vertical and horizontal displacements	Surface Marks/High-precision geometric levelling	Annual	Upstream and downstream of the crest. Replacement or rehabilitation of existing ones.
Pore pressures	Hydraulic piezometers	Monthly	At the dam body and foundation. Rehabilitation of the existing ones and installation of new ones covering additional cross-sections both in right and left banks.
Seepage flows	Relief wells	Monthly	At the toe of the dam. Rehabilitation of existing ones.

Table 2 – Monitoring plan review recommendations. Concrete dam cross-section

Monitoring parameter	Device	Reading frequency	Instrumented profiles and location of the devices
Horizontal displacements	Reverse plumb line	Semestral	Left wing wall
Vertical displacements	Surface Marks/High-precision geometric levelling	Annual	Crest
Vertical displacements	Foundation Extensometers	Semestral	At the ends of the small gallery
Relative movements between blocks	Three-dimensional extensometer bases	Monthly	At all joints in the small gallery
Uplift pressures	Hydraulic piezometers with manometers	Monthly	Small gallery: one piezometer per block downstream of the drainage system and Rehabilitation of the existing ones or substitution
Uplift pressures	Hydraulic piezometers with manometers	Monthly	Large gallery: one piezometer per block upstream of the drainage system and Rehabilitation of the existing ones or substitution
Flow Rates	Drains	Monthly	Rehabilitation or Replacement of existing ones.

Appurtenant structures

The proposed safety measures and interventions resulting from the inspection and safety assessment include hydrological studies, infrastructure upgrades, and flood mitigation measures.

In terms of hydrological studies, the development of flood hydrographs for 2,000-year and 5,000-year return periods is recommended, along with the review and verification of compliance with flood capacity requirements designated by MDSR.

Regarding infrastructure upgrades, comprehensive inspections and refurbishments of the corroded bottom outlet system are necessary. Additionally, the gate operation and monitoring systems should be modernized to ensure remote control functionality. Restoring the operational status of the gantry is also imperative to facilitate emergency interventions, improving the dam's safety conditions.

For flood mitigation, risks associated with overtopping due to the probable maximum flood (PMF) or 10,000-year return period floods should be assessed, and mitigation measures must be developed. Furthermore, adjustments to the guide curves and recalculations of the dam’s freeboard and crest elevation must be performed to comply with revised flood levels and safety requirements.

Electrical equipment and installations

The Pequenos Libombos dam is equipped with a range of electrical installations and equipment that have been in operation for several years, show signs of wear, and are in humid environments.

The difficulty of replacing protective equipment in the event of a breakdown or damage is a reality, compounded by long waiting times for the purchase and delivery of replacement materials. In some cases, the equipment is not even replaced because the market doesn’t have similar equipment to offer.

During the site inspection, it was observed that the facilities critical to the electrical operation of the Pequenos Libombos dam, such as the HV/LV substation and the generator room, need intervention. In HV/LV substation, the switchgear and HV/LV transformer presents signs of corrosion and without any safety equipment. The generator room was poorly maintained or in deteriorating condition. As a result, we recommend replacing the equipment, fully renovating the buildings, and enhancing safety within these areas. Additionally, exterior periodic cleaning around these buildings is crucial for fire prevention, particularly due to their proximity to the HV/LV substation and generator room. The HV/LV substation and generator room should be restricted access to qualified technicians. The generators and switchboards need to be urgently replaced or repaired, and the technical room should be fully renovated.

The electrical panels are in working order and generally well-maintained inside. However, they are equipped with long-standing equipment that is difficult to replace, and the cabinets are showing signs of corrosion.

The power cables will have to be replaced as they have been in place since the dam began operating. New signal cables will have to be installed.

The lighting, sockets and fire safety installations should be renewed or installed.

The SCADA supervision system at the dam has not been installed. It is recommended to implement a Supervision System that enables technicians to remotely monitor (either locally or from a distance) a range of events and operations, as well as record critical events for planning repairs and inspections. Remote operation of the Pequenos Libombos dam should be conducted with caution and always with the presence and expertise of the Pequenos Libombos dam team.

The CCTV system should be implemented together with the control system.

It is also very important to carry out regular electrical checks, operations and inspections. The lack of records and the absence of an electrical project is commonplace. There should be a space dedicated to the technical archive with all the documents on the electrical activities carried out, from design, maintenance, inspections and equipment manufacturers' manuals.

Continuous training in the areas of electrical systems, instrumentation, automation, supervision, and IT should be prioritized. Additionally, the creation of a technical space for recording operations and a dedicated electrical workspace should be considered.

It is also recommended that the entire electrical installation be new, renovated in a phased manner to maintain the proper functionality of the Pequenos Libombos dam.

6. CONCLUSIONS

A Dam Safety Assessment of the Pequenos Libombos Dam, in operation since 1986, was carried out by the COBA-LNEC-SALOMON Joint Venture. Based on the findings of this assessment, the activities to be implemented for risk management of the dam are outlined below. As mentioned in the Introduction, this paper does not address aspects related to downstream consequences, environmental risks, or emergency planning.

Regarding the likelihood of failure, important key vulnerabilities related to hydromechanical equipment must be corrected, namely corroded bottom outlet systems and outdated control mechanisms.

For the dam risk prevention, the following measures are considered necessary:

- Development and implementation of up-to-date operation standards,
- Periodic staff training,
- Routine maintenance activities,
- Routine hydromechanical equipment tests,

- Routine electrical tests,
- Installation of two new generators with canopies.

The revision of the monitoring plan for the Pequenos Libombos Dam is mandatory, due to the requirements of the current regulatory framework in Mozambique, as well as the absence of displacement monitoring devices for the concrete dam body and its foundation, along with deficiencies and the inoperability of a significant set of instruments in both the foundation and the dam body of the earth dam.

Also, in accordance with the MDSR, the maximum flood level should be reviewed for both the design flood and the verification flood. This review must incorporate flood routing analyses to determine the dam's response under these conditions. Consequently, the freeboard calculations and the dam's minimum crest elevation must also be revised, and meanwhile, the guide curves may have to be adjusted so that safety requirements defined in the regulation are duly complied with.

A topographic survey of the dam using drone technology was recommended to obtain information in the short term that supports the evaluation of the dam's freeboard.

At hydromechanical level the following critical issues were identified and are to be refurbished as soon as possible:

- Bottom Outlet System,
- Outdated Equipment.

It is relevant to mention that the Gantry Crane was rehabilitated in December 2024 and so reducing the future priority refurbishment needs.

Finally, regarding the electrical equipment and installations, a significant set of rehabilitation and upgrade interventions must be implemented in the short term. This is an area often overlooked in dam risk and safety assessments, yet it plays a crucial role in preventing and mitigating various failure risks, particularly those related to the operation of the hydromechanical equipment.

REFERENCES

[1] MDSR (2017), "Mozambique Dam Safety Regulation"

[2] Portugal, J. C., Marcelino, J., Modelos de Comportamento da Barragem dos Pequenos Libombos em Moçambique, 2011, Proceedings do XI CNG, Sociedade Portuguesa de Geotecnia (2012), 18p.

[3] Maranha das Neves, E., Costa Pereira, A. S., Veiga Frade, J. T., Tratamento da Fundação da Barragem de Pequenos Libombos, Revista Geotecnia (1085), Vol 45, pág 59-74.

[4] The World Bank (2020) Good Practice Note on Dam Safety.

[5] COBA, LNEC and SALOMON (2024), “Inspection Report. Pequenos Libombos Dam”, Product 2 of the *Consulting Services for Dam Safety Assessment of Pequenos Libombos and Massingir Dams*

[6] COBA, LNEC and SALOMON (2024), “Technical Report. Pequenos Libombos Dam”, Product 2 of the *Consulting Services for Dam Safety Assessment of Pequenos Libombos and Massingir Dams*

[7] COBA, LNEC and SALOMON (2024), “Safety Assessment Report. Pequenos Libombos dam”, Product 3 of the *Consulting Services for Dam Safety Assessment of Pequenos Libombos and Massingir Dams*

[8] Hidroprojeto (1986), “Plano de Observação da Zona de Betão da Barragem dos Pequenos Libombos”

[9] LNEC (2005), “Barragem dos Pequenos Libombos. Avaliação da Segurança em Novembro de 2004 e Revisão do Plano de Observação”. Proc. 0403/001/14990.

Fifth International Dam World Conference
PORTUGAL • LISBON • LNEC • APRIL 13-17, 2025
dam world 2025

A DETAILED SAFETY AND RISK ASSESSMENT OF MASSINGIR DAM

Sardinha, R. [1]	Melo, J. F. [2]	Pimenta, L. [3]	Duarte, A. [4]	Freitas, R. M. [5]
COBA	LNEC	COBA	COBA	COBA
Juízo, D. [6]	**Martins, A. [7]**	**Miguel, F. [8]**	**Cuna, I. [9]**	**Mabunda, L. [10]**
SALOMON	SALOMON	ARA-Sul, IP	ARA-Sul, IP	DNGRH

ABSTRACT

At the request of the Mozambican National Directorate of Water Program (DNGRH) and as part of the National Climate Resilience Program, a study aimed to evaluate the current safety of the Massingir dam and downstream valley was developed by the Consortium COBA/LNEC/SALOMON. The objectives encompassed a range of activities designed to ensure a thorough assessment and enhancement of dam safety, a critical issue to guaranty the integrity and reliability of this key water infrastructure in Mozambique. In this paper, structural and hydraulic-operational safety results are presented, as well as its adaptation to the new Mozambican dam regulations.

The Massingir Dam, the second largest in Mozambique, is situated on the Elephants River, a tributary of the Limpopo River. This 4,500-meter-long and 47-meter-high earthfill dam primarily supports irrigation in the Lower Limpopo Valley. Concluded in 1976, Massingir dam has a history of anomalous structural and hydraulic-operational behaviors and has already had several rehabilitation interventions.

The study involved a comprehensive evaluation of dam performance, including a review of operational procedures and detailed site inspections. It analyzed existing monitoring data and assessed current safety conditions. A thorough risk assessment identified both structural and non-structural mitigation measures.

The comprehensive assessment approach taken for the Massingir dam revealed strengths and weaknesses in current dam safety practices. By implementing the recommended measures, the safety and functionality of this dam will be significantly enhanced.

Key lessons underscored the critical need for regular monitoring and robust safety assessment procedures. This will contribute to the overall resilience and security of the region's water infrastructure and ensure the safety of populations living downstream.

Keywords: Earth dam, safety assessment, safety regulation.

[1] r.sardinha@cobagroup.com, Portugal
[2] jfmelo@lnec.pt, Portugal
[3] l.pimenta@cobagroup.com, Portugal
[4] a.duarte@cobagroup.com, Portugal
[5] r.m.freitas@cobagroup.com, Portugal
[6] juizo@hotmail.com, Mozambique
[7] amiromartins13@gmail.com, Mozambique
[8] fnandomiguel1234@gmail.com, Mozambique
[9] ivancunaa@yahoo.com.br, Mozambique
[10] luismabunda@gmail.com, Mozambique

1. INTRODUCTORY CONSIDERATIONS

A comprehensive dam safety assessment for the Massingir Dam was conducted as part of a contract between the National Directorate of Water Resources Management (DNGRH) and the Joint Venture COBA-LNEC-SALOMON. This work was developed under the National Climate Resilience Program (RCRP) of the Government of the Republic of Mozambique, with funding from the International Development Association (IDA). The studies were based on a thorough analysis of all the foundational documentation, the original design, and the rehabilitation projects, the monitoring data, the results of inspection site visits to the dam and the downstream valley, as well as expedited support calculations.

The Massingir dam is a large dam, thus falling under the provisions of the Mozambique Dam Safety Regulation (MDSR) [1] , classified as Risk Class I, with High Vulnerability and High Potential Damage. This classification, which should be reviewed every 5 years, establishes several responsibilities for the Project Owner, among which, the following will be prioritized in the short term [2]:

- Organization of the Technical Archive of the Project.
- Development of the Safety Plan (including the Observation Plan, the Operating Rules, the Internal Emergency Plan and the Environmental Safety Plan).
- Organization of the archive of data and results from the monitoring devices reading campaigns, which should be sent to Mozambique Engineering Laboratory (MEL) immediately upon their acquisition.
- Providing the necessary information to the Regional Authority on Dam Safety (RADS) for the preparation of the External Emergency Plan.
- Development and implementation of structural and non-structural measures and interventions for safety improvement and rehabilitation, defined within the scope of the safety assessment studies undertaken.

Massingir Dam is the second largest dam in Mozambique and is managed by Ara Sul. It is located on the Elephants River, a tributary of the Limpopo River, in Massingir District, approximately 12 km upstream from its confluence with the Chimwedzis River in Gaza Province. The dam serves multiple purposes, primarily for the irrigation of 90,000 hectares, flood control, hydroelectric power generation (not yet implemented), and water supply for the town of Massingir.

The Massingir catchment area covers 67504 km^2 with an average annual affluent volume of 1800 hm^3. The maximum total capacity of the reservoir is 2844 hm^3 (being the operational capacity of 2784 hm^3) and the flooded area 150.78 km^2 (0,64 km^2 in South Africa) at level 125

m, the Normal Retention Level (NRL). The Maximum Flood Level (MFL) of the original design is at 126.45 m (subsequently revised to the elevation 128.5 m) and the Minimum Operating Level at 90 m.

Figure 1 shows a Google Earth view of the Massingir Dam.

Figure 1 – Massingir dam general view (google earth).

The dam is a zoned earth-fill dam, with a crest length of approximately 4,596 m and a maximum height of 47 m. Its construction began in 1971 under the Government of Portugal and was partially completed in 1977, after Mozambique gained independence. The Massingir Dam's hydraulic infrastructure includes a main spillway with six radial gates, designed to handle 10,500 m^3/s at the Maximum Water Level (MWL) of 128.5 m. An auxiliary spillway equipped with Hydroplus fuse gates, commissioned in 2015, adds a discharge capacity of up to 10,000 m^3/s for reservoir levels reaching 131.0 m. The bottom outlet system, located on the right bank, complements the dam's discharge capacity, ensuring operational and flood management flexibility. Due to issues stemming from armed conflict during this period and a lack of funding, the six spillway gates were not installed at the time of completion, nor was the powerhouse constructed.

The geological and geotechnical conditions of the foundation influenced the overall design of the dam and were the root cause of the problems that emerged after the initial filling began. The first filling of the reservoir began after the dam's partial completion in November 1977, the

same year when significant foundation issues were identified, the right bank being the most affected zone. These issues included piping and extensive water passes along large sections of the foundation.

In the early 1980s, rehabilitation studies were carried out, leading to the execution, on the right bank, along the downstream foot of the dam, of a drainage ditch measuring approximately 1.5 km and with several transversal ditches, crossing the foundation, aiming to improve local drainage and stability conditions.

Due to concerns about the dam's integrity, and because the gates of the spillway were not installed, the reservoir's maximum water level was restricted to elevation 110 for many years. During the year 2000, floods rose the reservoir level to elevation 124 for several hours what immediately worsened the percolation and internal erosion of the foundation. Following these exceptional floods, a review of the hydrological studies confirmed that the spillway was unable to pass the design flood.

Between 2004 and 2006, the following rehabilitation interventions were carried out.

- Foundation grouting along two sections of the right bank (between Pk 1800 and 2500, and between Pk 3000 and 3200) and of the left bank, at the lower elevations (between Pk 3500 and 3800), with three rows, each with primary holes spaced of 12 m, secondary holes and tertiary holes, execution control was made by GIN method, the grout take was generally low.
- Execution of a downstream berm at the dam toe at the righ-bank, inverted filter, and stabilizing berms on the downstream natural ground for stability strengthening purposes.
- Execution of additional relief wells for seepage control, bringing the total to nearly 100 relief wells currently in operation. However, and despite this significant number of relief wells, seepage through the foundation remains uncontrolled.
- Rehabilitation of the riprap of the upstream slope of the dam.
- Raising of the crest of the embankment dam by 1 m, and installation of a concrete parapet wall on the upstream alignment of the crest (the crest over the spillway was not raised).
- Rehabilitation of the monitoring devices.
- Installation of the 6 radial gates on the main spillway (18 m wide x 10.5 m high).
- Repair of hydro-mechanical equipment of the bottom outlets.

After these rehabilitation works, in 2008, during the reservoir filling – specifically at the second filling stage, around elevation 122.5 meters (reached on April 7) – an accident occurred on May 22 at the bottom outlets, resulting in an uncontrolled release of water. Rehabilitation and reconstruction works of the bottom outlets were only completed in 2016. Meanwhile, an auxiliary spillway was added at higher elevations on the left bank in 2015.

Notwithstanding all the rehabilitation interventions, normal retention level (NRL) of 125 m has not yet been achieved. In fact, water levels above 121 m have been reached only sporadically,

and continue to cause uncontrolled water passages through the foundation of the dam on the right bank.

This paper focuses on structural safety, hydraulic-operational safety, and the safety of electrical equipment and installations, as well as on the structural and non-structural measures aimed at mitigating the risks of failure and various malfunctions, improving safety conditions, and adapting the dam to the current safety regulations. Downstream consequences of dam failure and operational flood releases are treated in the paper “Strengthening Key Water Infrastructure in Mozambique: A Risk Assessment of Downstream Valley of Massingir Dam”.

2. STRUCTURAL SAFETY ASSESSMENT OF THE DAM

2.1. Main characteristics of the dam

Massingir dam is composed of three typical cross-sections, primarily determined by the characteristics of the foundation soils (**Figure 2** and **Figure 3**).

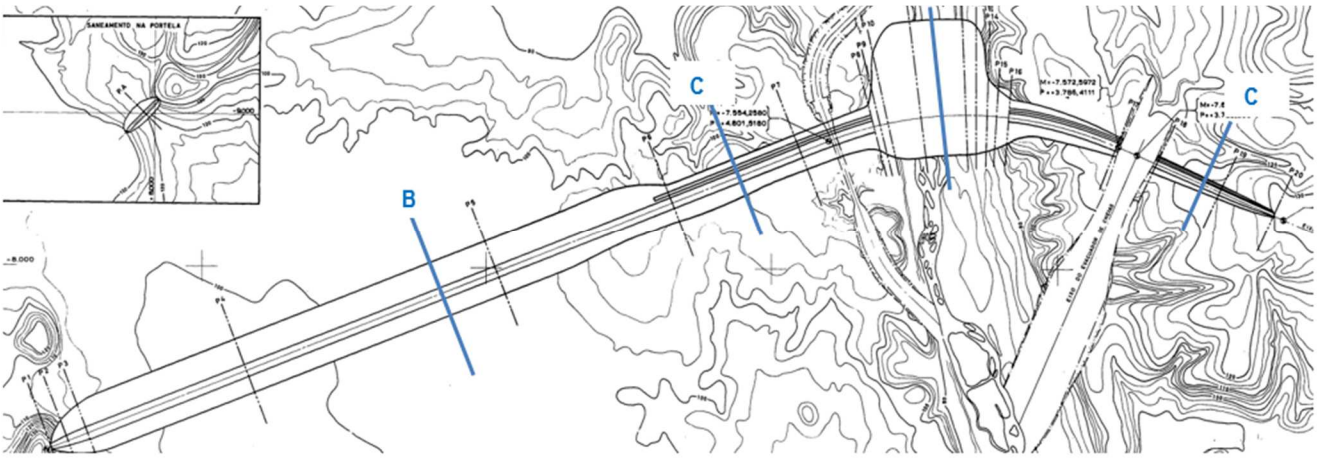

Figure 2 – Plan view of the original layout of the dam (adapted from [3])

The cross section of the dam on the central valley (cross-section A) is founded on a thick layer of low-strength, highly permeable alluvium, treated with vibroflotation to a depth of 15 m, in addition to the creation of relief wells downstream of the insertion of the dam into the foundation.

Cross-section A has a crest width of 12 m, initially located at elevation 130. The upstream slope has a variable steepness, between 1:2 (V:H) at higher elevations and 1:3.5 (V:H) at lower elevations. Below elevation 88, a clay blanket is in place, extending for approximately 350 m from the dam axis. The downstream slope also has a variable steepness (1:2 and 1:2.5) and includes four berms of different widths.

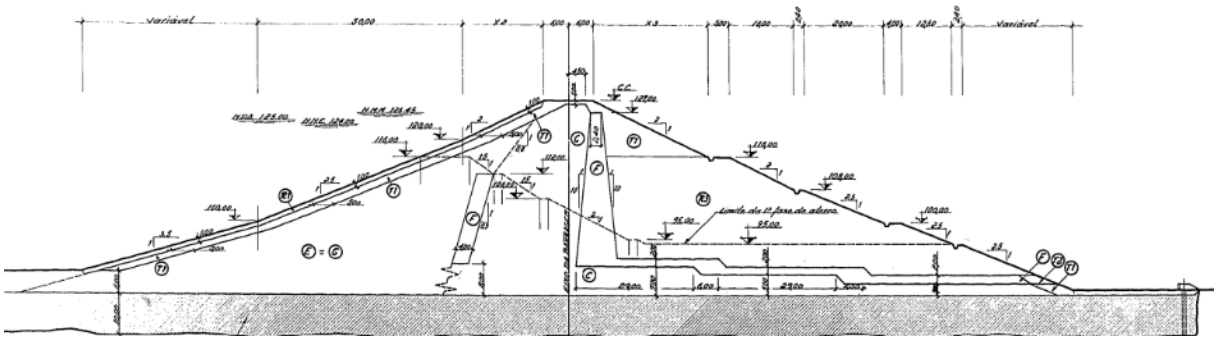

Cross-section A

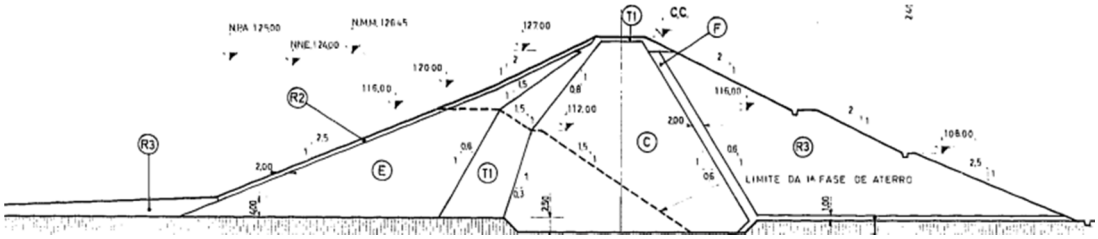

Cross-section B

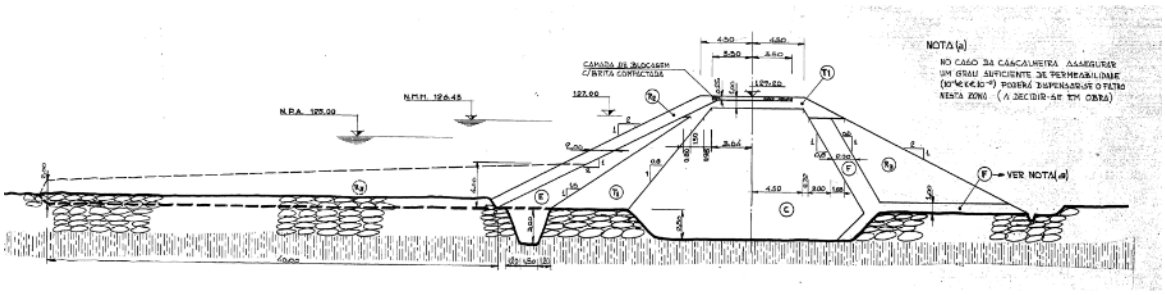

Cross-section C

Figure 3 – Cross-sections of Massingir dam [3]

Cross-section A includes a central clay core slightly inclined towards the upstream side, which is separated from the downstream shoulder – primarily composed of rock materials from excavation – by a chimney filter. This filter extends sub horizontally beneath the downstream shoulder, with a thickness of 2 m, and rests on a clay layer, in a highly unusual layout. Upstream of the core, a subvertical filter below elevation 112 separates the core from the upstream shoulder, which consists of sandy-clay materials. The upstream shoulder is protected by a 1-meter-thick rip-rap layer, placed over a transition layer of clayey gravel.

Cross-section B has a crest width of 9 m, located originally at elevation 129.6. The upstream slope has a variable steepness of 1:2 (V:H) at higher elevations and 1:2.5 (V:H) at lower elevations. The downstream slope has a constant steepness of 1:2 and includes two berms of different widths.

Cross-section B features a large central clay core with slopes of 1:0.8 (V:H) upstream and 1:0.6 (V:H) downstream. The core is separated from the downstream shoulder – mainly

composed of rock materials from excavations – by a chimney filter with a thickness of 1 m, which extends sub horizontally beneath the downstream shoulder and contacts the foundation. A transition zone of gravelly clay materials separates the core from the upstream shoulder, which is made of sandy-clay materials and protected by a 2-meter-thick (measured horizontally) rip-rap layer. The clay core extends into the foundation, composed of silty-clay soils, through a cut-off trench approximately 3 m deep. At the upstream toe, a 40-meter-long layer of granular material was placed to prevent the alteration of the foundation soil and to minimize swelling effects of the clay.

Cross-section C is very similar to Section B in both its external geometry and internal zoning. The main differences are the absence of an upstream granular blanket in Section C and the presence of two cut-off trenches: one beneath the core, like that of Section B, and another upstream, beneath the cofferdam embankments. This section is found on gravelly materials.

2.2. Dam design

The dam design studies covered the necessary safety checks, having been developed based on the knowledge and calculation methods available at the time, which were naturally much more limited than those currently available to dam engineering.

In **Table 1**, the main conclusions regarding the design calculations carried out during the original design are presented.

Based on the freeboard design studies, the dam's crest elevation was determined using the maximum design flood level (126.45 m), with an additional wave run-up of 2.38 m calculated for a wind speed of 100 km/h, plus 1 m to account for potential seismic effects. This resulted in an elevation of 129.83 m, rounded-up to 130 m in the central valley where the dam has its greatest height. Furthermore, the crest elevation was increased by a maximum of 0.80 m to accommodate potential creep deformations of the dam-foundation system.

The freeboard calculation is constrained by the combination of actions related to the water level in the reservoir, equal to the Maximum Water Level (MWL), currently estimated at 128.5 m. The crest elevation defined in the rehabilitation project, 131 m, appears insufficient to accommodate the wave run-up caused by a typical wind speed of 60 km/h (a modest value) – ranging from 2.39 to 2.69 m, depending on the adopted methodology – a residual creep settlement, estimated between 0.12 and 0.15 m – and an allowance of 0.5 m for non-quantifiable factors, including seismic effects.

The re-evaluation of the freeboard should be carried out alongside an assessment of the hydraulic operation of the spillways – both primary and auxiliary – for the design flood (T=2000 years) and the verification flood (T=5000 years), in accordance with the MDSR. This process

must also include a reassessment of the freeboard, considering the potential existence of varying crest elevations along the length of the dam.

Table 1 – Design calculations. Summary

Calculations	Results	Observations
Global stability analysis under static conditions	Minimum global safety factor during rapid drawdown = 1.02. Minimum global safety factor during full storage = 1.82	Minimum global safety factor during rapid drawdown lower than the recommended. Minimum global safety factor during full storage higher than the recommended.
Global stability analysis under seismic conditions	Minimum global safety factor during full storage = 1.30	Conservative minimum global safety factor. However, since the seismic amplification appears to be lower than expected, the actual safety factor will be lower.
Amplification of seismic action	Horizontal peak acceleration on the dam base foundation: 0,14g. Horizontal peak acceleration on the crest: 0,18g	The peak acceleration value at the dam's foundation level appears to be close to the value that would be obtained for the SMP and type D ground (EC8). The amplification of the seismic action along the height of the dam is lower than expected, considering the characteristics of the embankments and foundation soils.
Hydraulic stability	Only the values of the hydraulic head were calculated.	It is expected that the water levels established in the foundation will differ from those in the body of the dam, due to the different permeability coefficients, which is not inferred from the calculation results.

2.3. Monitoring system and data

The monitoring systems at Massingir Dam currently faces significant deficiencies. The system lacks adequate organization and technological support for efficient data analysis and timely communication with relevant authorities, such as ARA-Sul and other safety monitoring entities. Although there is an ongoing civil works project aimed at rehabilitating piezometers and other monitoring devices, numerous critical issues remain unresolved.

The absence or malfunctioning of critical monitoring and measurement equipment, as highlighted by the MDSR, severely hampers the ability to assess the performance and safety of the Massingir Dam. The significant deficiencies in the quantity, functionality, and placement of these devices underscore the urgent need for corrective actions to be implemented in the short term. Also, there is no immediate transmission of monitoring data to either the Authority or the MEL, as specified by the MDSR.

The operators are knowledgeable and familiar with the procedures for data reading and analysis, but the technical means at their disposal, namely hardware and software, urgently require improvements.

Additionally, the process for measuring the relief wells must be changed to ensure the necessary health and safety conditions at work of the operators. For measuring the inflows to the relief wells, operators must enter these wells and descend ladders to the depth where the measurements are taken. During this process, operators face life-threatening dangers due to the presence of venomous snakes, scorpions and spiders that shelter inside (**Figure 4**). The high number of observation relief wells also makes this task physically exhausting, in addition to being hazardous.

Figure 4 – Relief wells in the right bank

Table *2* provides a summary of the devices installed at Massingir Dam and their current condition.

Since the surface displacements of the dam have not been recorded for a long time, and there is no reference reading of the marks installed in 2015, a topographic survey using drone technology should be conducted to obtain a quick assessment of the current elevations of the crest, necessary for a substantiated evaluation of the dam's freeboard. After this survey, it will be necessary to resume the readings of the superficial displacements of the dam.

The limited number of piezometers installed in the dam body and its foundation constrains the reliability of the seepage network analysis.

Table 2 - Monitoring devices installed and operational conditions

Device	Location	Total	Not operational	Observations
Surface marks	embankments and spillway	17	17	-Surface displacements of the embankment are not currently being monitored due to the lack of appropriate measurement equipment. -New markers were installed in 2015; however, they have not yet been used.
Open-tube Piezometers	Drainage channel	60	20	- Measurements are conducted weekly. -Some piezometers are obstructed by small debris due to the lack of proper protection for the housing boxes. -Ongoing works are in place to clear obstructions and rehabilitate the affected equipment.
	Dam body (Downstream Slope)	20	5	
	Left and right bank	12	0	
Electrical Piezometers	Dam body	21	0	- Measurements are conducted weekly. -Good condition.
Relief Wells	Drainage channel	77	19	-Measurements are taken every 15 days. -Some relief well chambers are damaged, submerged or compromised. -Relief wells on the left bank are not being measured due to overgrown vegetation and the presence of snakes. -Ongoing efforts are focused on rehabilitating the damaged equipment, clearing the overgrown vegetation, and installing a new Total flow meter.
	Drainage channel (new wells)	30	4	
Gallery Drains	Gallery	37	0	- Measurements are conducted weekly.
Level Scale	Water intake and spillway	2	-	-Daily readings are taken at 7:00, 9:00, 12:00, 15:00, and 17:00, with increased frequency and continuous monitoring during the rainy season. -Equipment is in good condition.
Level Gauge	Water intake and spillway	2	2	-

On the contrary, the measurement of piezometric levels and inflows downstream of the dam's toe provides a comprehensive view of the dam's performance in terms of foundation flow in the right bank.

As shown in **Figure 5**, the piezometric levels are read in 60 wells, between Stakes 0+212 and 2+112. The piezometric readings indicate a greater pressure near the higher levels of right abutment and in the vicinity of Stakes 2+000 where an upper limit is reached, at VD41. On 30/10/2023, the piezometric level at VD41 was 105.52 m, while the reservoir was at an elevation of 120.34 m.

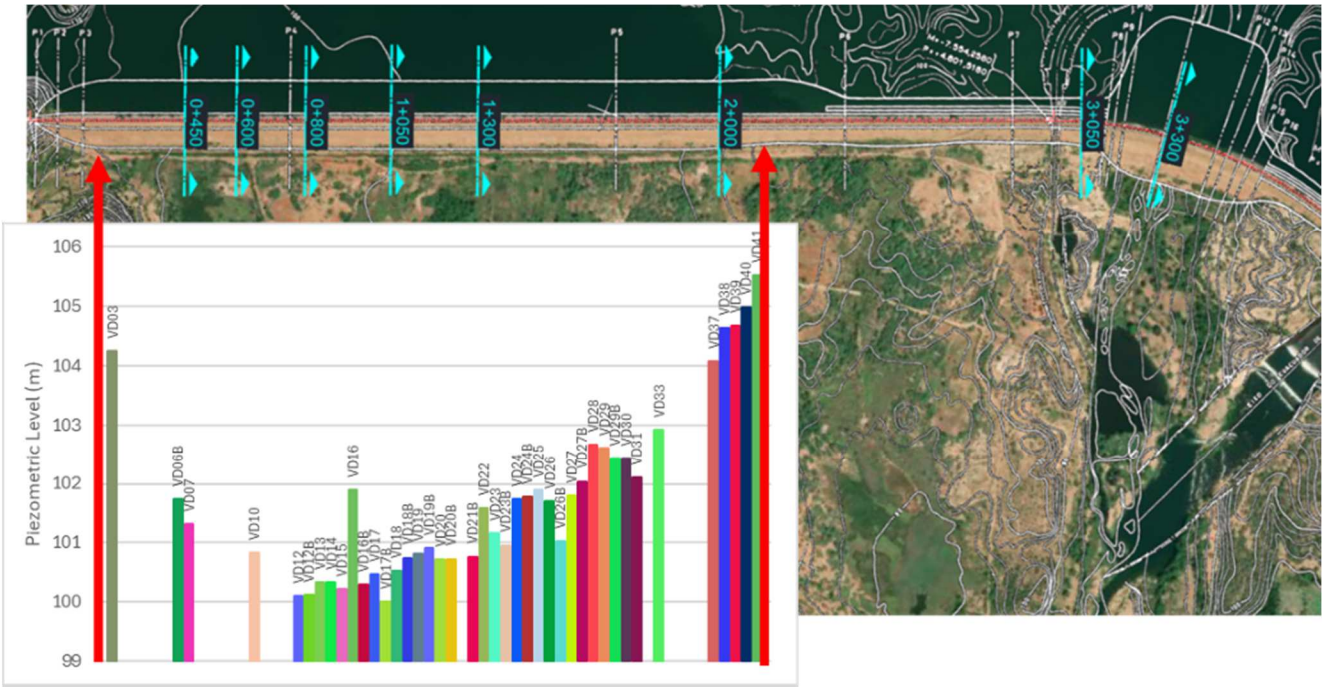

Figure 5 – Piezometric levels measured downstream of the dam on 2023-10-30

Figure 6 shows the history of the readings taken between January 2006 and October 2023. In the period between 2014 and 2022, the data is somewhat inconsistent; however, from 2022 onwards, the measurements show greater consistency. Nevertheless, it is possible to identify a gradual increase in piezometric levels when comparing the initial data with the most recent.

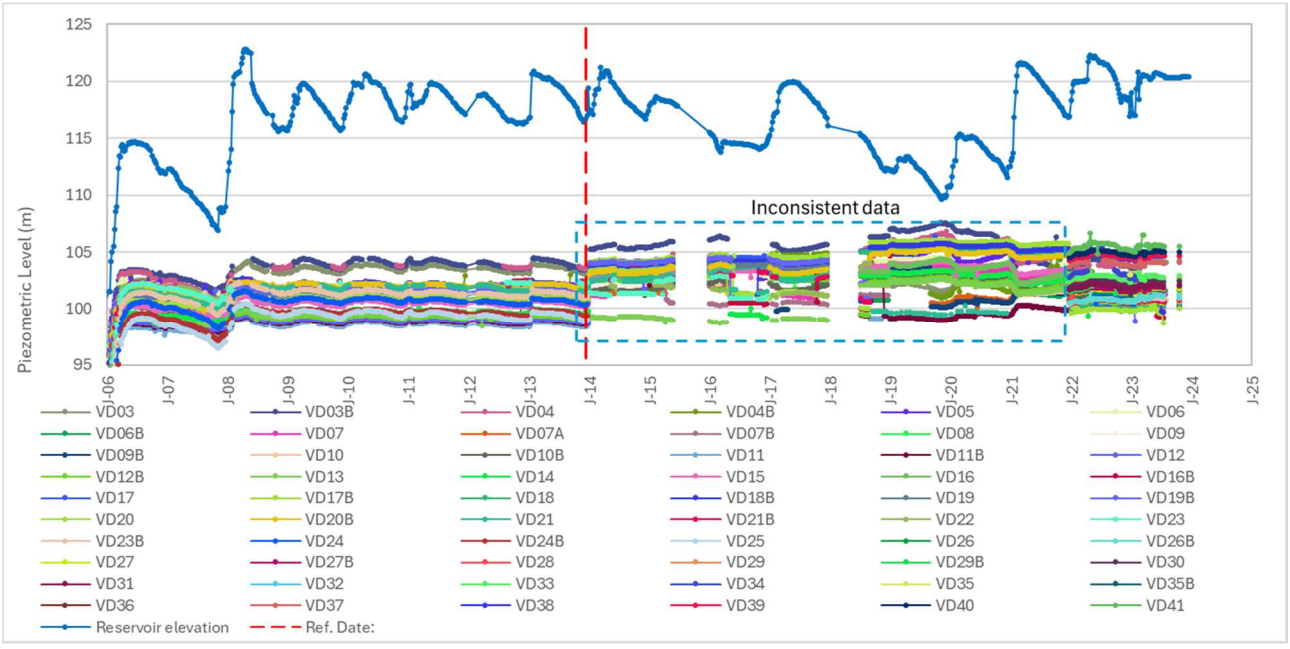

Figure 6 - Historical piezometric levels downstream of the dam, between 2006 and 2023

Concerning the flow rates measured in the relief wells - there are a total of 74 devices in operation at right bank, distributed between stakes 0+200 and 2+025 - these devices show a downward trend, as can be seen in **Figure 7**.

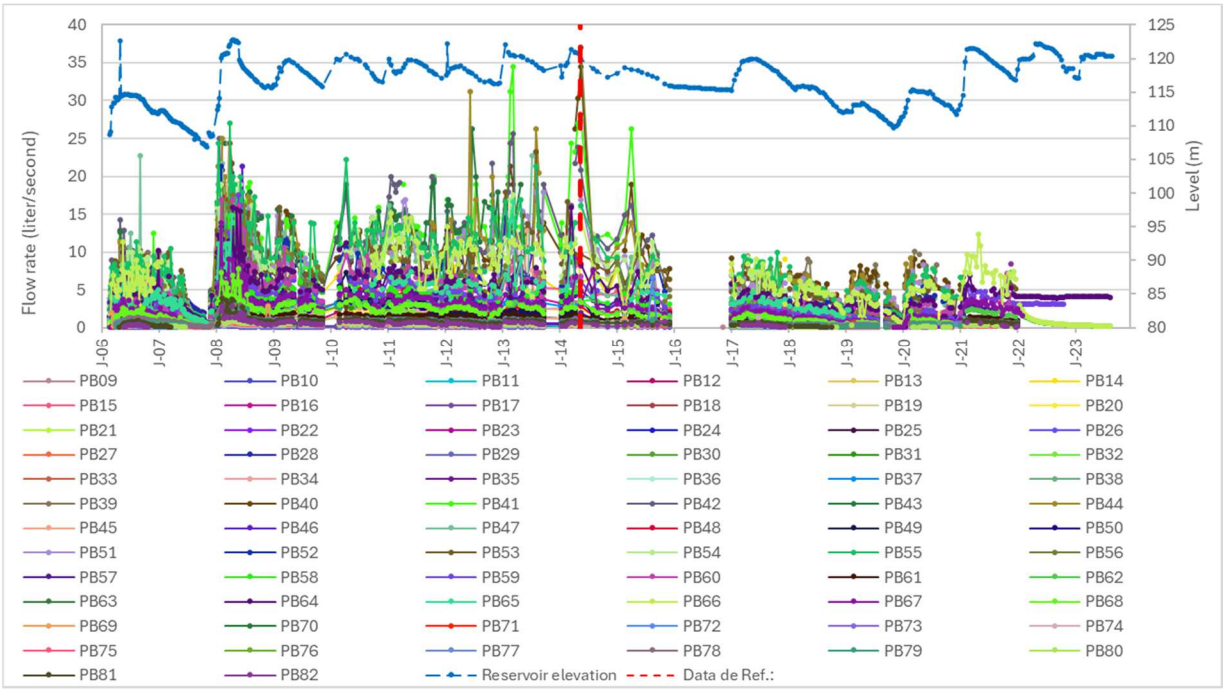

Figure 7 - History of the flows in the relief wells, between 2006 and 2023

Figure 8 shows the location and the values of the measured flows on 2020-10-20, when the reservoir was at an elevation of 113.12 m. The flows are significantly higher in the central area of the right bank (pattern that repeats for other reading dates), in contrast to the piezometric levels, which are higher at the extremities. This phenomenon may be associated with the clogging of drains near the areas with higher piezometric levels.

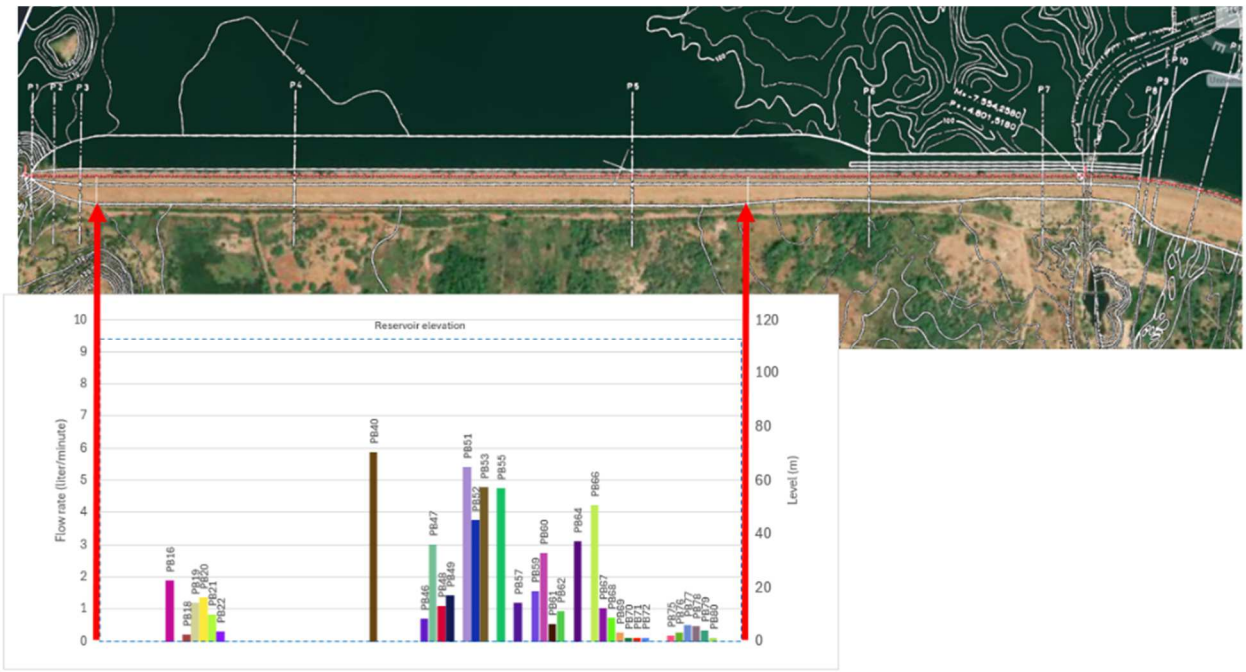

Figure 8 - Measured flows in the relief wells on 20/10/2020

For the analysis of the total flows percolating through the foundation of the dam on the right bank, periods were selected in which readings were taken from at least 60 relief wells. **Figure 9** presents a graph of the total flow observed in these wells, showing a directly proportional relationship between flow behaviour and reservoir levels. Based on the most reliable data series, the trend curve that best represents the relationship between flows and reservoir levels was analysed. As shown in **Figure 10**, the estimated flow for current reservoir levels is approximately 344 l/s. At the Normal Retention Level (125 m), the flow is estimated at 784 l/s, and at the Maximum Flood Level (128.5 m), the flow is projected to reach around 1,394 l/s.

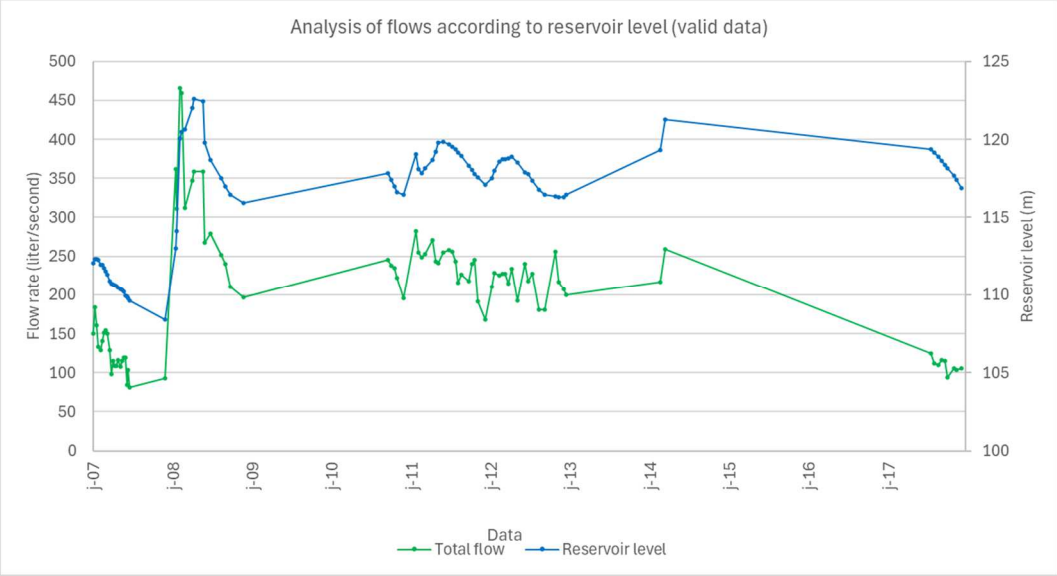

Figure 9 - Total flows on the right bank versus reservoir water level

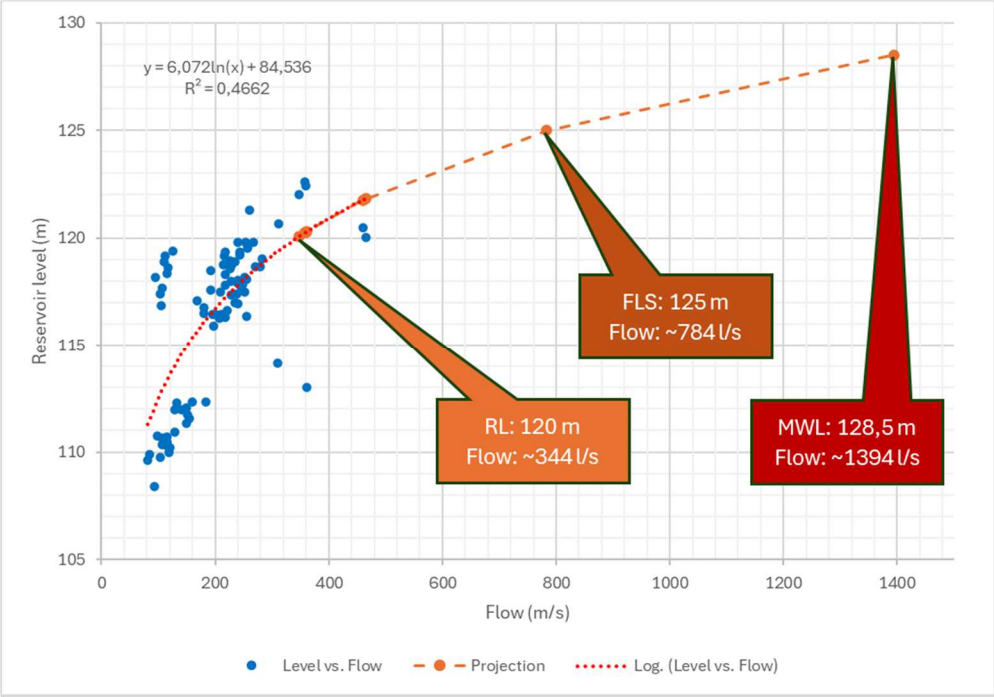

Figure 10 – Extrapolated flows downstream of the dam on right bank

Considering that the wells are distributed over approximately 1,900 meters and the flow occurs along this entire length, a specific flow rate of about 25 l/min/m is observed at a reservoir level of 125 m, and around 44 l/min/m at a level of 128.5 m. These values represent a potentially hazardous condition, further aggravated by the fact that these are average values, as significantly higher flow rates are observed in sections with greater inflows to the relief wells

2.4. Dam performance and failure modes

In what concerns the results of the site inspections [4], there are currently no indicators of anomalous behaviour in the dam body that threatens its safety. However, the monitoring data show that there are preferential seepages through the foundation on the right bank, water levels at the toe of the dam exceeding natural ground levels, and significant total and partial flows. The medium and long-term effects of these conditions on the foundation soils and the dam body cannot be underestimated, as they may trigger internal erosion processes that could compromise the integrity of the dam-foundation system, potentially resulting in the downstream release of a catastrophic flood wave.

Although preferential water pathways through the foundation have been identified since the first filling of the reservoir, the monitoring data proves that they remain unresolved despite stabilization and drainage interventions, including stabilizing berms, filter/drainage zones at the toe of the dam, and the installation of additional relief wells. Despite the large number of relief wells installed at the downstream toe of the dam on the right bank, around 100, there are still uncontrolled preferential seepage paths.

The most common failure mechanisms in earth dams, in order of importance, are overtopping erosion (usually due to inadequate or failed operation of spillways), internal erosion, and loss of integrity due to foundation failure. Although most dam failures occur within the first 10 years of operation, around 70%, a still significant percentage, 30%, happens during the later operational period.

For the Massingir Dam, from a risk assessment perspective, it is important to note that the reservoir has not yet reached full capacity. The water level has only exceeded 120 m (5 m below the Normal Retention Level) for brief periods, primarily during flood events. Additionally, for reservoir water levels above elevation 121, even if occasional and occurring over short periods, resurgences appear at the dam's toe, at the transition between the central valley section of the dam and the right bank dike.

The estimated inflow rates at the base of the dam on the right bank, based on monitoring data, are approximately 790 l/s at level 125 m and 1,400 l/s at level 128.5 m. These values imply the need for implementing effective impermeabilization solutions and temporarily limiting the maximum operating level until these measures are carried out.

Level 121 was established for the temporary maximum operating level at Massingir reservoir. This level must be validated using the observational method. Once this level is reached in the reservoir, the inflows to the relief wells should be monitored weekly (or, if feasible, twice a week) for a period of two months. If the flow reading remains constant, elevation 121 can be temporarily used for normal operation of the reservoir. If an increase in inflow is observed while the reservoir level remains at elevation 121, this value should be reduced by 1 m (to elevation 120) and the validation procedure should be repeated.

Additionally, in the event of floods that temporarily raise the water level in the reservoir, supplementary measurements of the inflows to the relief wells should be taken, and the increase in flows should be analyzed for flood levels. This will enable timely decision-making, if necessary, through the operation of the main spillway gates or the bottom outlets.

3. HYDRAULIC AND OPERATIONAL SAFETY

3.1. Characteristics of appurtenant structures

The main spillway features a 475 m-long concrete chute with a 3% slope, transitioning from a width of 128 m to 100 m, then expanding to 170 m at its end. The ogee-type crest is set at elevation 115.0 m and controlled by six radial gates measuring 18.0 m in width and 10.5 m in height. The downstream stilling basin includes energy dissipation components such as baffle blocks and an end sill.

The auxiliary spillway, located on the upper left bank, includes a 151.9 m-long crest at elevation 120.0 m, fitted with 14 Hydroplus fuse gates, each 10.85 m wide and 5.85 m high. This spillway operates progressively for reservoir levels exceeding 127.5 m.

The bottom outlet system comprises two conduits, each 7 m in diameter and 300 m long, capable of discharging 800 m^3/s per conduit. The conduits include radial gates for flow regulation and connect to a stilling basin for energy dissipation.

Figure 11 – Downstream view of the spillway crest and detail of a spillway gate

Figure 12 – View of the Auxiliary Spillway

Figure 13 – Bottom outlet intake tower

3.2. Hydraulic and operational safety assessment

The Mozambican dam safety regulation MDSR requires design floods with a 2,000-year return period and verification floods with a 5,000-year return period for Class I embankment dams like Massingir. Prior to the construction of the auxiliary spillway, past studies assessed the dam's performance for the 10,000-year flood and the Probable Maximum Flood (PMF), revealing that the main spillway alone was insufficient to prevent water levels from approaching the embankment dam crest (130.5 m). While the installation of the auxiliary spillway has significantly enhanced the dam's flood discharge capacity, further hydrological and hydraulic studies are needed to verify its compliance with MDSR standards.

Key safety concerns include the non-operational status of the spillway gantry crane, bottom outlet, and remote-control system, all critical for safe flood management. Thus, the following equipment must be refurbished in a short term.

- The gantry crane requires complete redesign, followed by supply and installation. A new gantry crane specification guiding the future tender must be done compatible with the current civil structure and the hydromechanical equipment to be maneuvered.
- The Bottom Outlet and Water Intake Systems were non-operational when the inspection took place due to gate seal problems. Meanwhile, both bottom outlets have been put into operation. However, to ensure that these outlets are restored to full functionality, it is necessary to proceed with in a reasonable short period with the following steps:
    - A thorough inspection to all equipment,
    - Replacement of obsolete or deficient equipment and components.

The remote-control system, installed in 2006, has been non-functional since 2008. It is recommended to either repair this system or implement a new, reliable remote-control mechanism to improve operational efficiency and comply with Mozambican regulatory requirements.

Additionally, downstream erosion in the outlet channel requires frequent monitoring to prevent potential structural deterioration.

3.3. Electric equipment and installations safety assessment

The Massingir dam is equipped with a range of electrical installations and equipment that have been in operation for several years, show signs of wear, and are located in humid environments.

The difficulty of replacing protective equipment in the event of a breakdown or damage is a reality, compounded by long waiting times for the purchase and delivery of replacement materials. In some cases, the equipment is not even replaced because the market doesn´t have similar equipment to offer. .

During our site inspection, we observed that the facilities critical to the electrical operation of the Massingir dam, such as the HV/LV substation and the generator room, were poorly maintained or in deteriorating condition. As a result, we recommend replacing the equipment, fully renovating the buildings, and enhancing safety within these areas. Additionally, exterior cleaning around these buildings is crucial for fire prevention, particularly due to their proximity to the HV/LV substation, generator, and control room.

Access to the Massingir dam control room is through the generator room, and its proximity results in mechanical and electrical noise, compromising people’s safety. The generator room should be a dedicated technical space with separate access, restricted to qualified technicians. The generators and switchboards need to be urgently replaced or repaired, and the technical room should be fully renovated.

The SCADA supervision system at the Massingir dam has not been installed. It is recommended to implement a Supervision System that enables technicians to remotely monitor (either locally or from a distance) a range of events and operations, as well as record critical events for planning repairs and inspections. Remote operation of the Massingir dam should be conducted with caution and always with the presence and expertise of the Massingir dam team.

The electrical panels are in working order and generally well-maintained inside. However, they are equipped with long-standing equipment that is difficult to replace, and the cabinets are showing signs of corrosion.

The power cables will have to be replaced as they have been in place since the Massingir dam began operating. New signal cables will have to be installed.

The lighting, sockets and fire safety installations should be renewed or installed.

The CCTV system should be implemented together with the control system.

It is also very important to carry out regular electrical checks, operations and inspections. The lack of records and the absence of an electrical project is commonplace. There should be a space dedicated to the technical archive with all the documents on the electrical activities carried out, from design, maintenance, inspections and equipment manufacturers' manuals.

Continuous training in the areas of electrical systems, instrumentation, automation, supervision, and IT should be prioritized. Additionally, the creation of a technical space for recording operations and a dedicated electrical workspace should be considered.

It is also recommended that the entire electrical installation be new, renovated in a phased manner to maintain the proper functionality of the Massingir dam.

4. CONCLUSIONS AND RECOMMENDATIONS

After 47 years of operation of the Massingir Dam, considering its history of issues since the beginning of its operation, as well as the analysis of the dam's design criteria and calculations, a comprehensive review of all safety checks of the dam-foundation system is strongly recommended based on the methods and models currently available in dam engineering and aligned with the MDSR. Freeboard calculations and the minimum crest elevation of the dam - which is not constant throughout its entire length - must also be reviewed and, if necessary, a design for raising the entire crest of the dam should be developed.

These calculations should be supported by a geotechnical exploration campaign to characterize the material properties, and by monitoring data to be collected following the rehabilitation of the actual monitoring systems in progress. In fact, the presence of a significant number of out-of-service monitoring devices limits the overall assessment of the safety implications of excessive and preferential seepage through foundation.

Regarding internal erosion mechanisms, it is recommended to use specialized detection techniques to monitor changes in the seepage network, such as temperature, resistivity, or electrical current measurements. This data will be crucial for informing the design of impermeabilization and flow control solutions for the dam foundation, namely in the right bank. It will also be important to assess percolation through the foundation in the central valley area and in the left bank, where the inflow rates to the relief wells are not being recorded.

From the analysis of all the information consulted and collected, and considering the extensive stabilization and drainage works at the toe of the dam on the right bank – stabilizing berms, filter/drainage zones at the toe of the dam, and an extremely high number of relief wells, as well as impervious treatment of the foundation by injection of cement grouts in some sections of longitudinal development – the solution that appears to be most suitable for controlling the excessive flows percolating through the foundation and reducing the risk of internal erosion is a diaphragm wall.

The foundation of the right bank dike consists of two distinct alluvial zones: an upper clayey layer and a lower sandy layer with gravel. The alluvium rests on a Cretaceous substratum, whose upper fringe is decompressed and weathered. The impermeabilization of these alluvial deposits cannot be achieved through cement grout injection, as it lacks the ability to penetrate the pores.

The detailing of the diaphragm wall solution (characteristics, depth, execution and control techniques), as well as the selection of its location in the cross-sectional profile to optimize execution lengths and minimize operational impacts, requires additional baseline information and detailed design studies. Together with the design of the foundation impermeabilization solution, the dam Observation Plan should be reviewed and complemented accordingly.

Complementary hydrological studies should also be undertaken to establish the maximum peak flows and hydrographs for floods with return periods of 2,000 years and 5,000 years. These updated studies, together with flood-routing and hydraulic analyses, are critical for assessing the dam’s capacity to safely manage extreme flood events and ensuring compliance with MDSR requirements.

Concerning the appurtenant structures, updated flood-routing studies, a new and functional spillway gantry crane, gate remote-control system and maintenance of hydromechanical components are essential to ensure regulatory compliance and safe operation.

Regarding the hydromechanical equipment the following must be refurbished:

- The gantry crane requires complete redesign, followed by supply and installation.
- The bottom outlet inspections and replacement of obsolete or deficient equipment and components.
- The remote-control system, installed in 2006, has been non-functional since 2008.

The safety assessment studies for the Massingir dam culminated in the definition of a set of studies and projects, topographical and geological-geotechnical surveys, and rehabilitation interventions aimed at mitigating risks and ensuring the dam's compliance with the current safety regulations and their associated safety requirements. A work schedule and a preliminary budget estimate were established, along with implementation priorities and terms of reference for carrying out the studies, projects, and supporting works [5].

Table 3 presents the list of studies to be carried out and their priority classification and **Table 4** the list and priority classification of the surveys to support the studies and the rehabilitation interventions.

Table 3 – Priority classification for the studies and projects

Studies to support the implementation of both structural and non-structural measures.	Priority Classification
1. TECHNICAL ARCHIVE OF THE PROJECT	
1.1 Identification and organization of technical documents and data for the various phases of the dam's lifecycle	1
1.2 Elaboration of the Dam Safety Plan	3
2. COMPLEMENTARY HYDROLOGICAL AND HYDRAULIC STUDIES	2
3. COMPLEMENTARY DAM-FOUNDATION STUDIES	
3.1 Geological-geotechnical investigation program	1
3.2 Comprehensive review of all safety checks of the dam-foundation system (global stability analysis under static and seismic conditions, and seepage studies through the dam and foundation)	2
3.3 Detail design for the foundation waterproofing solution (cut-off wall), including report, calculations, technical specifications, drawings, and budget estimate	3
3.4 Possible detail design for the dam crest raising, including report, calculations, technical specifications, drawings, and budget estimate	3
4. HYDROMECHANICAL EQUIPMENT (Design and Technical Specifications)	1
5. ELECTRICAL EQUIPMENT AND INSTALLATIONS (Design and Technical Specifications)	1

1	< 3 months
2	< 6 months
3	< 9 months

Table 4 – Priority classification for the topographical and geotechnical surveys and for the rehabilitation works

Implementation of structural and non-structural measures.	Priority Classification
1. DRONE-BASED TOPOGRAPHIC SURVEY OF THE DAM	1
2. DRONE/LIDAR and SONAR/ADCP-BASED TOPOGRAPHIC AND BATHYMETRIC SURVEYS OF DOWNSTREAM VALLEY	1
3. PROGRAM OF ADDITIONAL INVESTIGATION WITH IN SITU AND LABORATORY TESTS TO CHARACTERIZE THE MECHANICAL AND HYDRAULIC PROPERTIES OF THE DAM'S EMBANKMENTS AND FOUNDATION, INCLUDING DETECTION TECHNIQUES OF INTERNAL EROSION PHENOMENA	1
4. MONITORING DEVICES	
4.1 Mapping of dam's monitoring devices in operation/local repairs	1
4.3 Installation of the monitoring devices specified in the revised observation plan	2
5. DAM-FOUNDATION REHABILITATION WORKS	3
6. INSTALLATION OF WARNING AND ALERT SYSTEMS, COMMUNICATION MEANS, AND OTHERS DEFINED IN THE INTERNAL EMERGENCY PLAN	3
7. INTERVENTIONS IN THE HYDROMECHANICAL EQUIPMENT	2
8. INTERVENTIONS IN THE ELECTRICAL EQUIPMENT AND INSTALLATIONS	2

1	< 4 months
2	< 12 months
3	< 24 months

REFERENCES

[1] MDSR (2017), “Mozambique Dam Safety Regulation”

[2] COBA, LNEC and SALOMON (2024), “Technical Report. Massingir dam”, Product 2 of the *Consulting Services for Dam Safety Assessment of Pequenos Libombos and Massingir Dams*

[3] COBA, 1974, Drawings from the Technical Assistance to construction.

[4] COBA, LNEC and SALOMON (2024), “Inspection Report. Massingir dam”, Product 2 of the *Consulting Services for Dam Safety Assessment of Pequenos Libombos and Massingir Dams*

[5] COBA, LNEC and SALOMON (2024), “Safety Assessment Report. Massingir dam”, Product 3 of the *Consulting Services for Dam Safety Assessment of Pequenos Libombos and Massingir Dams*

Fifth International Dam World Conference
PORTUGAL • LISBON • LNEC • APRIL 13-17, 2025
dam world 2025

DESIGN OF RAGHAI EMBANKMENT DAM IN A COMPLEX GEOLOGICAL AND GEOTECHNICAL FRAMEWORK (TUNISIA)

V. Rebelo[1] COBA	**J. Antunes**[2] COBA	**A.Morgado**[3] COBA	**A.El Ghali**[4] University of Carthage
A.Yahia[5] SCET Tunisie Consultant	**S. Pinto**[6] TETRAPLANO	**F. Naguindás**[7] COBA	**R. Khlifi**[8] DGBGTH

ABSTRACT

The Raghai Dam is located in northwestern Tunisia, near the Algerian border, approximately 9 km from Ghardimaou, on Oued Raghai, a left-bank tributary of the Medjerda River. Owned by the Direction Générale des Barrages et des Grands Travaux Hydrauliques, the dam's primary purposes are irrigation and the supply of drinking water, ensuring that water provision meets consumption demands.

The site presents significant topographical and geological challenges. Topographically, its location in a wide valley near the border limits site selection and water level. The reservoir will have a capacity of 30 million cubic meters, covering 149 hectares. Geologically, the foundation is complex due to lithological heterogeneity and tectonic deformation, forming a mosaic of tilted and sheared blocks. This required specialized design and calculation measures. The Numidian flysch formation, consisting of fractured sandstone and argillite layers of varying thickness, introduces variable permeability and deformability to the foundation. Additionally, the scarcity of construction materials in the region and environmental constraints on their extraction further complicated the project. The bedrock, composed of intercalated sandstone and clay layers, made sourcing aggregates infeasible.

To address these challenges, a zoned rockfill dam using locally available materials was chosen. The dam, rising 60 meters above the Oued bed, includes a central clay core with fine materials sourced from the reservoir and downstream areas. Rockfill for the upstream and downstream shells will come from a limestone quarry, with the total dam volume estimated at 1.9 million cubic meters.

Foundation treatment aims to reduce percolation, particularly through fractured sandstone layers. A cement-based grout curtain, injected from the dam gallery, targets depths of 30–45 meters. The spillway, designed to handle a maximum flow of 954 cubic meters per second, is located on the left bank. It features a 55-meter-long free-flow spillway, a 55-meter collector channel, and a 424-meter discharge channel ending in a stilling basin.

This study outlines the design approach and criteria for constructing a dam in a geologically complex environment, necessitating comprehensive site investigations and innovative solutions.

Keywords: embankment, geological, foundation, materials, site investigation.

[1]v.rebelo@cobagroup.com, Portugal
[2]j.antunes@cobagroup.com, Portugal
[3]a.morgado@cobagroup.com, Portugal
[4]absabselghali@gmail.com, Tunisia
[5]ali.yahia@gmail.com, Tunisia
[6]s.l.pinto@cobagroup.com, Portugal
[7]f.naguindas@cobagroup.com, Portugal
[8]rabii_khlifi@yahoo.com, Tunisia

1. INTRODUCTION

The Raghai Embankment Dam is an essential element of Tunisia's "Programme de Stockage de l'Eau et de la Protection Contre les Inondations (SPCI)," which focuses on enhancing water resource management and mitigating flood risks. Designed to serve dual purposes - potable water supply and irrigation - the dam is strategically positioned along the Oued Raghai, a tributary of the Medjerda River. The Medjerda is the longest river in Tunisia and plays a pivotal role in the region's hydrological network. By regulating the flow of the Oued Raghai, the dam will provide critical water storage capabilities, contributing to agricultural productivity and ensuring a reliable water supply for surrounding communities.

The project represents a synergy of multidisciplinary studies, including topographical surveys, hydrological analyses, and geotechnical investigations. The unique challenges posed by the site's geological and climatic conditions underscore the need for innovative engineering solutions. This paper presents an overview of these challenges, and the strategies employed to address them, offering insights into the development of resilient infrastructure in complex environments.

2. SITE CHARACTERISTICS

2.1. Location and Accessibility

The Raghai Embankment Dam is located in the Jendouba governorate of northwest Tunisia, near the border with Algeria (Fig. 1). The dam site lies approximately 9 kilometers west of Ghardimaou and is accessible via the RN6 highway, followed by a local road leading to the village of Ouchtata. The project spans multiple administrative sectors, including Es-Sraia, Mrassen, and Er-Rakha, highlighting its regional significance.

The location's proximity to the Algeria-Tunisia border introduces transboundary hydrological considerations, as 40% of the Oued Raghai's catchment area is situated in Algeria. This cross-border nature necessitates cooperative management of water resources and inflow monitoring to ensure sustainable operation.

2.2. Topography

The dam site's topography is characterized by steep slopes and narrow valleys, with the Oued Raghai's thalweg situated at an altitude of 283.3 meters above sea level. These topographical constraints limit the choice of dam sites, necessitating careful evaluation to optimize the structure's location. Detailed topographical surveys (Fig. 2) have been conducted to assess the site's suitability, including its elevation profiles and slope stability.

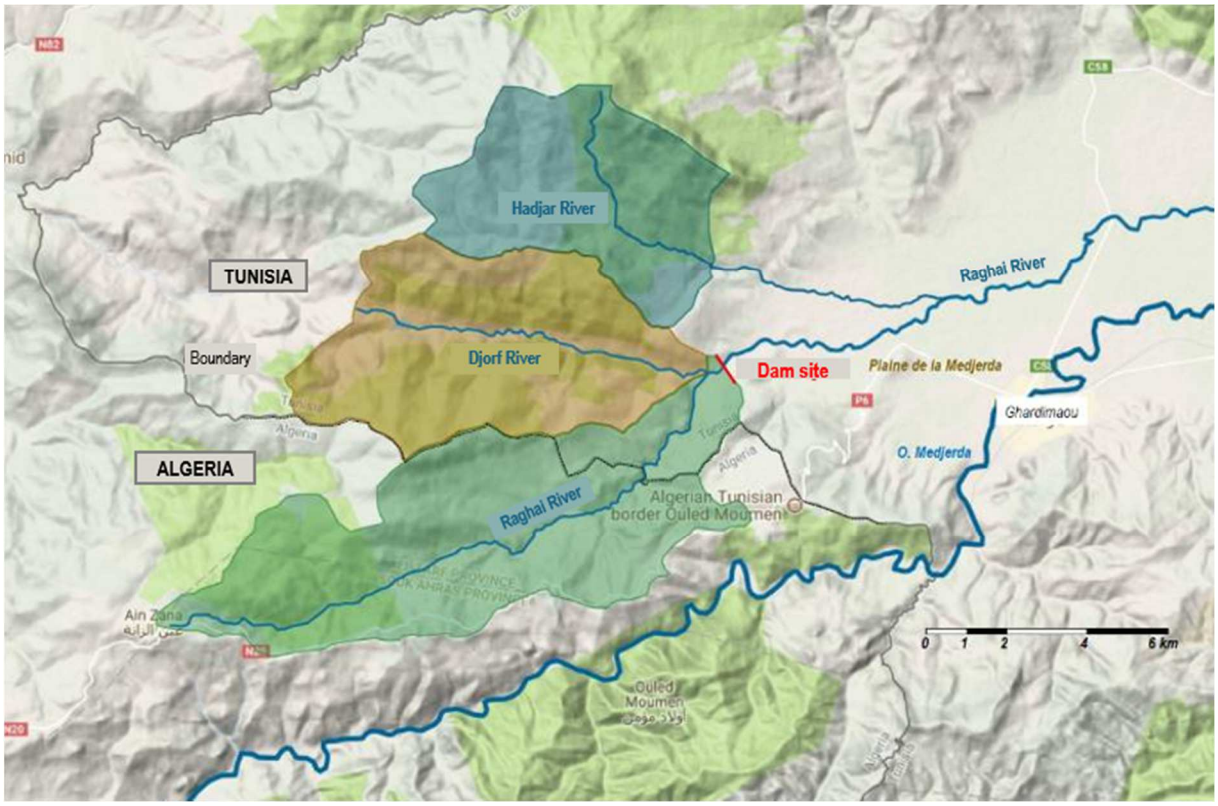

Fig. 1 - Watersheds and hydrographic network of the study area

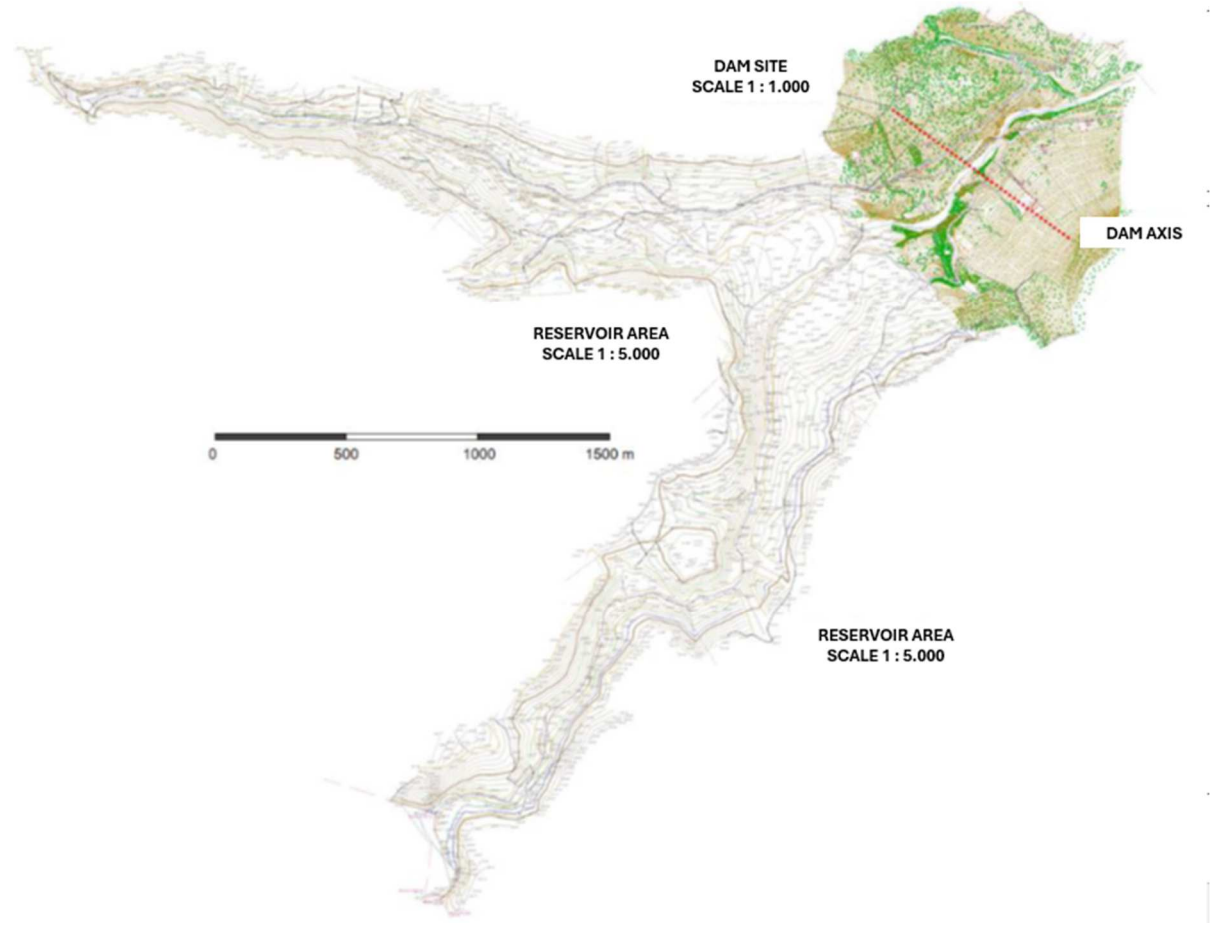

Fig. 2 - Topographic survey of the reservoir and dam area

The surrounding terrain's steepness and rugged nature also present challenges for construction logistics, requiring tailored approaches to access roads, material transport, and workforce mobilization.

2.3. Climatic Data

The climatic conditions of the region significantly influence the dam's operational design. The estimated annual evaporation rate is 1400 mm, which represents a critical factor in calculating reservoir losses and determining storage efficiency. Temperature and precipitation patterns in the region reveal a marked seasonality. January typically accounts for 15.2% of total annual precipitation, making it the wettest month, while July contributes less than 1%, rendering it the driest (Table 1).

Table 1 - Monthly Rainfall Distribution

	Sep	Oct	Nov	Dec	Jan	Fev	Mar	Avr	Mai	Jun	Jul	Août
Ghardimaou	7,0%	8,4%	11,2%	12,7%	12,8%	11,5%	11,6%	10,2%	8,0%	3,2%	1,1%	2,5%
Sraya	4,4%	9,5%	12,1%	15,9%	14,5%	12,7%	11,1%	10,8%	6,0%	2,2%	0,6%	1,3%
Raghai	5,5%	7,0%	11,3%	14,9%	15,7%	12,5%	11,9%	10,4%	6,3%	2,4%	0,5%	1,5%
El Feija	4,1%	7,7%	9,3%	15,7%	17,7%	14,0%	12,7%	9,7%	5,4%	2,1%	0,5%	1,2%
Moyenne	5,3%	8,2%	11,0%	14,8%	15,2%	12,7%	11,8%	10,3%	6,4%	2,5%	0,7%	1,6%

The climatic conditions also impact construction schedules, as heavy rainfall during the wet season may affect excavation and material transport. Engineering strategies, such as temporary drainage systems, are incorporated to manage weather-related delays during construction phases.

2.4. Hydrological Data

2.4.1. Catchment Overview

The Oued Raghai drains a catchment area of approximately 90 km², 40% of which lies within Algerian territory. This transboundary characteristic adds complexity to water resource management and necessitates coordinated monitoring efforts. The river's flow is driven primarily by seasonal rainfall, which is concentrated in the wet months between November and April.

2.4.2. Seasonal Flow Characteristics

On average, the catchment contributes an annual inflow of 17.38 hm³ to the proposed reservoir. However, more than 75% of this volume is delivered during the wet season. Monthly inflow analysis reveals that peak contributions occur in January and February, coinciding with

the highest rainfall periods. Conversely, the dry season (May to October) sees drastically reduced flows, often approaching zero during the driest months.

2.4.3. Flood Analysis and Modelling

Flood risk is a critical design consideration for the Raghai Dam. Advanced hydrological models, including the HEC-HMS system, were employed to simulate flood behaviour under various return periods. The peak discharges estimated are presented in Table 2.

Table 2 - Estimated Peak Discharges

T (years)	Raghai	
	Q_{max} (m^3/s)	Volume (hm^3)
10	224	4,4
20	296	5,8
100	469	9,2
200	543	10,7
500	706	14,3
1000	781	15,9
2000	856	17,5
5000	954	19,6

The flood modelling results informed the design of key hydraulic structures, ensuring their capacity to handle extreme events. The spillway, in particular, has been dimensioned to safely discharge the maximum expected flow, mitigating risks to downstream areas.

2.4.4. Sediment Transport and Deposition

The catchment's geological characteristics and land use patterns influence sediment transport into the reservoir. Annual sediment inflow is projected to be significant, leading to an estimated reduction in reservoir capacity from 30.0 hm^3 to 25.0 hm^3 over 50 years. A dead storage zone of 5.0 hm^3 has been allocated to trap sediments. Upstream erosion control measures, such as reforestation and terracing, aim to reduce sediment yield. Periodic dredging is also planned to maintain operational capacity.

2.4.5. Hydrological Variability and Adaptation

The catchment exhibits significant interannual variability in rainfall and inflows, with potential for prolonged droughts and episodic heavy rainfall. Dynamic water release schedules are used to balance irrigation and potable water needs. Real-time monitoring of inflows and reservoir levels helps optimize storage and respond effectively to these fluctuations.

2.4.6. Rainfall-Runoff Dynamics

Empirical studies and rainfall-runoff modelling highlight the rapid response of the catchment to intense precipitation events. The use of intensity-duration-frequency (IDF) curves and unit hydrograph techniques provided the necessary data to design robust stormwater management systems. For instance, short-duration storms can generate peak runoff within hours, emphasizing the need for efficient flood routing mechanisms.

By incorporating these hydrological insights, the Raghai Dam is designed to be a resilient and sustainable infrastructure capable of addressing the region’s water management challenges effectively.

2.5. Geological and Geotechnical Framework

The Raghai dam site is located in the southwestern end of the Numidian Flysch domain, characterized by alternating sandstone and clay/claystone layers. This domain extends into eastern Algeria and is recognized as a thrust-nappe zone.

The dam's foundation (Fig. 3) sits upon a sandstone-clay-siltstone substratum, specifically the "Numidian Flysch" unit dating back to the Upper Oligocene-Aquitanian age. This flysch comprises a prograding megasequence formed from deep-sea fan deposits, including massive channels, mass flows, slumps, and turbidites.

Overlying this substratum are unconsolidated clay-silty deposits, likely of Pliocene-Early Quaternary age, and conglomeratic layers with pebbles and olistoliths, potentially from the Holocene. These recent deposits fill the valley and cover most of the dam's reservoir area.

Structurally, the Raghai dam axis displays significant complexity. While outcrops are limited, the area exhibits dense, multidirectional fracturing. This fracturing is linked to the region's tectonic history, where the Tell Atlas domain's NE-SW trending structures intersect with E-W faults associated with the Tunisian Atlas. This complex architecture stems from the continuation of deeply tectonized blocks reaching the surface.

Lithologically, the foundation zone is predominantly clayey, especially on the right bank (Fig. 4). These are slope deposits formed by gravity and cover the lower valley. These ancient colluviums contain sandstone blocks, likely detached from higher slopes and embedded at various levels within the sedimentary layers or trapped in depressions created by tectonic collapse.

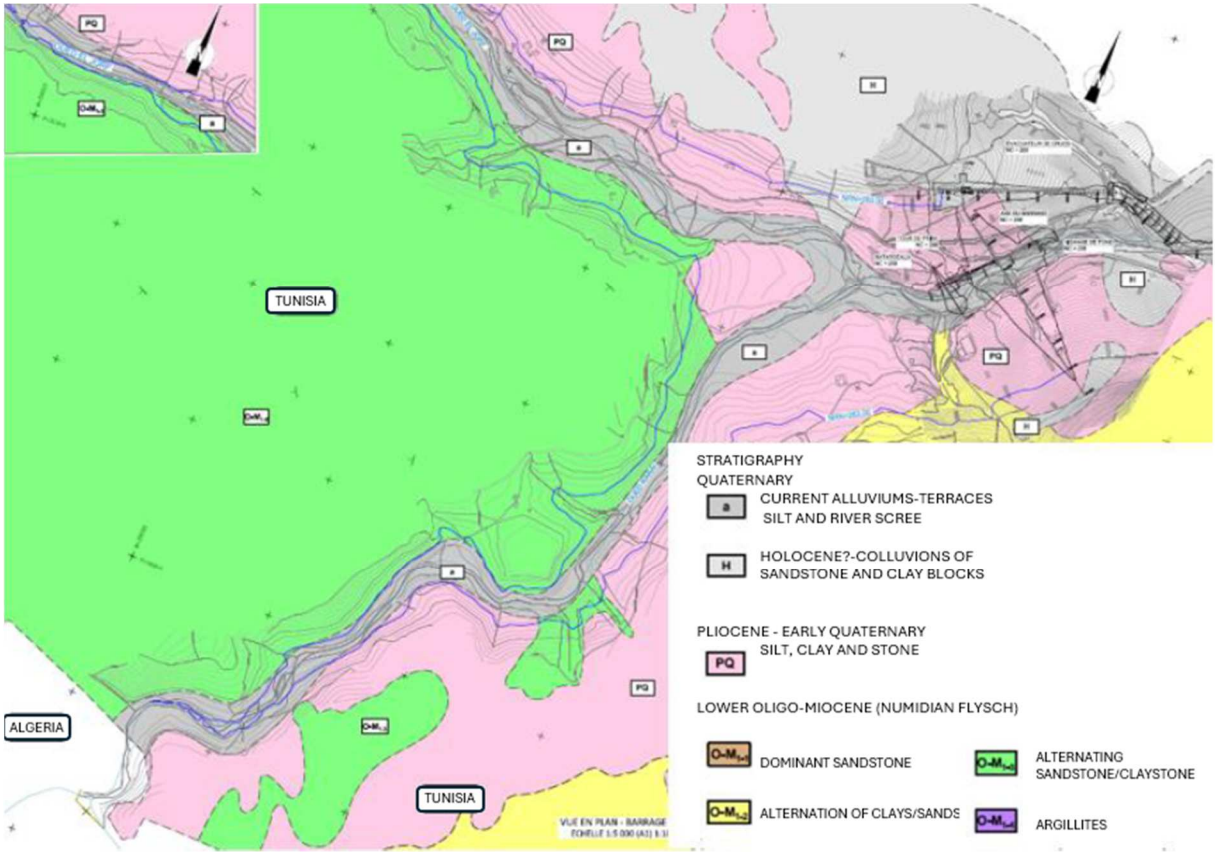

Fig. 3 – Extract of geological plan

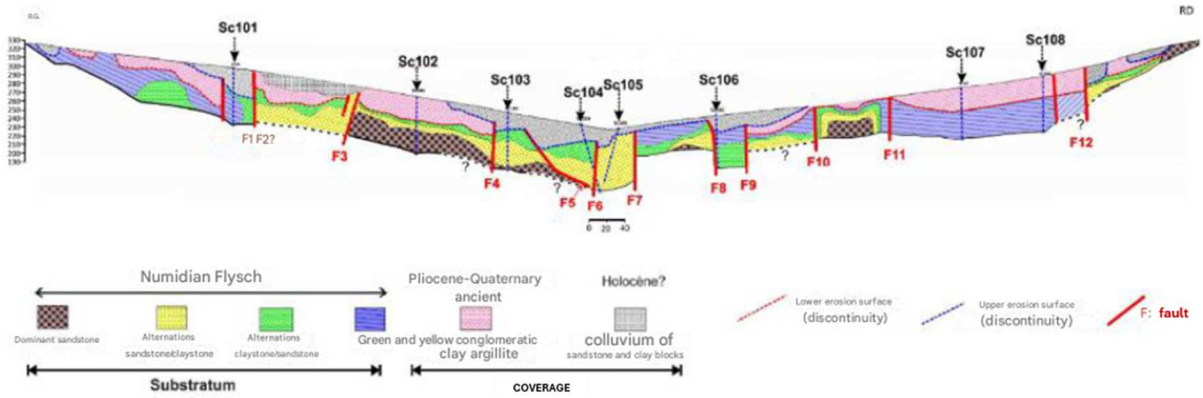

Fig. 4 – Geological section at the level of the foundation of the Raghai dam

3. SITE INVESTIGATION WORKS

Various site investigation works were carried out at the Raghai dam site to characterise the geological and geotechnical conditions of the dam foundation and the surrounding areas. The aim of this work was to assess the suitability of the foundation, identify potential borrow areas and evaluate the availability of construction materials. The site investigation work was carried out in different phases, including the Preliminary Study phase and the Detailed Design phase [1].

During the Preliminary Study phase, the aim was to gain a preliminary understanding of the foundation conditions. This phase involved methods such as the excavation of 31 trial pits using a backhoe and a further 4 trial pits dug by hand. Samples were taken for laboratory tests. Additionally, boreholes, pressiometer tests and electric and seismic profils were executed.

The Detailed Design phase involved additional geotechnical investigation works to complement the geological and geotechnical model. This included boreholes, Standard Penetration Tests (SPT), water absorption tests (Lugeon and Lefranc tests), pressiometer tests, trial pits and seismic profils.

Site investigation works revealed that the dam's foundation is composed of alluvium, colluvium and a fractured bedrock. The bedrock near the dam consists of sandstone intercalations and clay/claystone layers. The presence of dense fractures and the heterogeneity of the foundation materials required treatment to ensure stability and reduce seepage.

Additional geotechnical investigation work during the Construction Design phase, to address specific issues and refine the understanding of site conditions, will be executed.

4. GEOTECHNICAL CHARACTERISTICS

4.1. Geotechnical zonation

The geotechnical zonation along the dam foundation, the axis of the spillway and the axis of the temporary diversion/bottom outlet was defined by considering mainly quantitative aspects, to the extent that the geotechnical investigations carried out allowed for obtaining a minimum number of parameters that are sufficiently representative of each geotechnical zone.

The geotechnical zonation considers, essentially, several characteristics that are at the basis of the decisions in terms of excavation for the dam foundation and foundation treatment.

Based on all the available elements, namely lithology, recovery percentage, RQD percentage, SPT blows, the results of pressuremeter tests and permeability tests, the dam foundation and the ancillary works foundation were divided into 3 designated geotechnical zones (ZG) and characterized as follows:

Geotechnical Zone 3 (ZG3)

Consisting of the most superficial part of the foundation soils, essentially composed of loose materials (alluvium, recent colluvium, and gravel from the plains) and, eventually, weathering soils of the sandstone-claystone rock mass.

The values of the SPT tests carried out in the colluvium are highly variable between 13 blows and >50, due to its less consistent clayey matrix and the sandstone blocks with refusal results.

The recovery percentage is generally greater than 90% and the RQD % is highly variable, generally between 0 and 40%; according to the ISRM classification, it is a strongly to very strongly fractured (F4 to F5) rock mass, generally moderately to completely weathered (W3 to W5).

The pressuremeter modulus (Em) varies between 100 and 300 MPa, exceptionally between 300 and 350 MPa around the low elevations of the right bank and in the area of the water intake tower.

Geotechnical Zone 2 (ZG2)

ZG2 is composed of sandstone and shale formations, with an alternation of materials. The SPT tests show variable values, ranging from 20 – 50 blows, characteristic of sandstone blocks. The area offers acceptable conditions for the foundation of an earth dam, with adequate strength, deformability, and permeability values between 4 to 20 UL. The recovery percentage is above 95%, and the RQD varies between 0 to 40%, indicating a heavily to very heavily fractured rock mass, generally moderately to highly weathered. The pressuremeter modulus (Em) varies between 100 and 300 MPa, exceptionally between 300 and 350 MPa.

Along the axis of the dam, this geotechnical zone has a variable thickness. On the left bank, it reaches depths in the order of 20 to 25 m and in the bottom of the valley a depth of 35 to 40 m. On the right bank, the ZG2 varies between 10 and 40 m deep, except for the higher elevations where this horizon is found at a depth of greater than 60 m.

At the spillway axis, the ZG2 reaches a depth in the order of 10-20 m and is also present under the foundation slab of the stilling basin with a minimum thickness of 5 m. Along the axis of the bottom outlet this depth is highly variable, between 20 and more than 40 m (in the foundation of the water intake).

Geotechnical Zone 1 (ZG1)

Composed of the sandstone-claystone rock mass, which presents acceptable foundation conditions for the dam, even if it occasionally has areas with significant permeability values.

The recovery percentage is generally greater than 95% and the RQD rate varies between 0 and 40%, exceptionally greater than 40%; according to the ISRM classification, it is a moderately to strongly fractured (F3 to F4) rock mass, generally moderately weathered (W3), and may occasionally reach higher RQD values, which may reach 100%. According to the ISRM classification, it is a rock mass that is, in general, moderately to highly weathered (W3 to W5).

4.2. Hydraulic zonation

The hydraulic zonation (HZ) considers the permeability of the rock mass based on Lugeon tests. This analysis as allowed to identify two different horizons, the Hydraulic Zone 2 (HZ2) values range from 4 UL (Lugeon Units) up to DT (total loss), with values frequently found between 4 and 20 UL. On the other hand, the Hydraulic Zone 1 (HZ1) has values up to 3 UL, with exceptions that can reach up to 4 UL. Along the axis of the dam, the thickness of the HZ2 zone varies between 30 and 45 m; exceptionally, at the high levels of the right bank, the thickness is reduced to 20-25 m due to the more clayey bedrock.

Along the axis of the spillway this limit is around 15 m deep, but in part of the spillway foundation it can reach more than 35 m.

Along the axis of the temporary diversion/bottom discharge the thickness of the HZ2 is around 30 m, but around the water intake tower this value is over 45 m.

4.3. Dam foundation conditions

The foundation soils are essentially composed of loose materials (recent and old colluvium) and, possibly, weathering soils from the sandstone-clay/claystone rock mass.

The results of the Lefranc tests show that the geological formations are not very permeable, except for the particular zone at the bottom of the valley, in the foundation of the clay core, where the soil corresponds to the sandstone-clay rock mass, with Lugeon-type water absorption test values of 12 UL.

The mechanical characteristics recorded in the pressuremeter boreholes are good overall, with limiting pressures (Pl) of 4 MPa above a depth of 4m. The analysis of the results of the pressuremeter modulus (Em) allow to identify 3 distinct units. Unit 3 defined by values below 100 MPa, Unit 2 with values between 100 and 300 MPa and Unit 1 with Em > 300 MPa. On the left bank and at higher levels of the right bank, Unit 3 reaches a depth between 2 and 13m, overlaying Unit 2 which varies between 15 and 25m. Unit 1 was not registered in pressuremeter boreholes SP203 and SP208. Along the remaining right bank, Em values are higher at shallower depths, with Unit 3 thickness varying between 2 and 4m immediately superimposed on Unit 1, which sometimes still begins within ZG3.

In geotechnical terms, these are materials with a RQD of less than 20% (generally zero), with a recovery percentage of over 90%, generally of low strength, corresponding to the ZG3 zone. Occasionally, at the bottom of the valley, the core foundation corresponds to the ZG2 zone.

In general, after excavation of the upper 2.5 m, the ground presents suitable foundation conditions for an embankment dam.

4.4. Foundation conditions for hydraulic structures

The foundations of the spillway structure and the stilling basin are made up of sandstone and clay, with RQD values of zero in the highly fractured clay and sandstone layers (F5) and varying between 60 and 100% in the less fractured sandstone layers (F2 to F3 – wide to moderate spaced fractures). The percentage of recovery is over 95% and the foundation is in ZG1.

Along the spillway channel, the bedrock is mainly composed of massive formations. However, there may also appear some colluvium composed of silty clays with sandstone blocks. The foundation varies between geotechnical zones ZG2 and ZG1.

The results of water absorption tests show that, according to permeability coefficients, the more clayey soils are classified as not very permeable. The sandstone formations show water absorption test values varying between ≤ 3 and 10 UL and are characterised as not very permeable to permeable.

The mechanical characteristics recorded with the pressuremeter tests are good overall, with limiting pressures in excess of 4 MPa above the depth of 2 m and above 9 m at the SP211 pressuremeter borehole in the stilling basin. Unit 3 (of the pressuremeter modulus) in the area of the spillway structure is 1 to 2 m thick, and 8 m thick in the stilling basin. Unit 2 ends at a depth of 15-16 m along the structure and at 2 m in the area of the stilling basin. The foundations of these structures are located in Unit 1 with values more than 300 MPa.

The geological and geotechnical information gathered along the axis of the temporary diversion/bottom drain shows that the foundation of the structure is generally found in the clay and sandstone bedrock. The more clayey formations show zero RQD. In the sandstone strata this value varies generically between 0 and 40% but can reach 100% in areas showing a degree of fracturing between F3 and F4 (moderate to close spaced fractures). The recovery percentage is over 95%.

In general, most of the ground for the foundation is in ZG2, with the intake tower in ZG1 and the stilling basin in ZG3.

In a particular area of the water intake tower foundation, located at a depth of between 33 and 40 m, the bedrock shows weaker geotechnical characteristics, classified as ZG3, where highly weathered clay and sandstone have been intersected.

The results of the water absorption tests show that, according to their coefficient of permeability, the more clayey and argillaceous soils are classified as not very permeable. Sandstone formations have water absorption test values ranging from ≤ 3 to >40 UL and are characterised as low permeability to permeable.

In the area of the water intake tower foundation, the mechanical characteristics recorded by the SP214 pressuremeter are generally good, with limiting pressures in excess of 4 MPa above a depth of 4m. The thickness of Unit 3 of the pressuremeter modulus (Em) is 4 m and Unit 2 is 2 m, so the foundation of this structure is located in Unit 1 (Em > 300 MPa), which begins at a depth of 6m. The weakest zone identified in borehole S202 is also observed by a drop in the limiting pressures recorded from a depth of 30m.

At the intersection of the bottom discharge with the axis of the dam, the SP203 pressuremeter borehole recorded pressure modulus values <100 MPa (Unit 3) down to 8m. From this depth onwards, the results obtained correspond to Unit 2 until the end of the borehole. The values are generally higher than 200 MPa.

5. CONSTRUCTION MATERIALS

5.1. Fine soils to be used for the core

In the Raghai dam reservoir, the exclusively clayey and clayey silt deposits found in the trial pits and boreholes have very small thicknesses, between 1 and 3 metres (borrow areas E1 and E3 in the reservoir), with an average thickness of around 2 metres.

Considering the information gathered from the site investigation trial pits and refraction seismic profiles in borrow area E6 (near the El Hadjar stream), an average thickness of 2.5 m was considered for the clay-silt strata in order to estimate the volume available in these two zones.

In the ZEA5 zone, located downstream of the dam, the information provided by the trial pits carried out revealed an average thickness of 1.7 m of fine materials available.

To guarantee the watertight function of the core in safe conditions with regard to cracking and stress transfer phenomena, a percentage of fines greater than or equal to 40% is recommended for the materials to be used for the core. Ideally, the fine materials should be plastic with a plasticity index of more than 14% but less than 35%. This type of material was found in part of the borrow areas analysed, mentioned above.

In fact, clayey, silty, clayey sand or silty sand soils from the CH, CL, MH, SC and SM groups were identified, with a percentage of fines often exceeding 60% (high plasticity inorganic clays). Most of the soils identified belong to the CH group. Most of the fines are highly plastic, with liquidity limits often exceeding 51% and plasticity indexes of 14% to 35% or slightly higher.

Soils with a plasticity index of up to 35% are favoured for the core. Higher plasticity clays should be reserved for the contact areas between the core and the foundation rock mass and the concrete works. The maximum allowed size for the core materials will be 4 mm (D100 = 4

mm). It will not be acceptable to have a percentage greater than 65% of solid particles with a size equal to or less than $1x10^{-3}$ mm.

According to the results of the mineralogical analyses, the clays in borrow area E6 will be those with the most significant potential for expansibility, which can be easily controlled by properly managing the placement of these clays in the core backfill. During the execution phase, the clays with the highest values of expansibility pressure should be reserved for sections with an embankment height of more than 15 metres. Since the stresses imposed by the embankments planned for the core will be high, no problems are anticipated.

Due to the high liquidity limits and plasticity indexes, it will be necessary to carry out trial layers at the start of the construction of the dam core embankment with these fine materials in order to draw conclusions about the optimum conditions for placement on site.

As far as the available volume is concerned, considering a previous stripping thickness of 0.2 m to 0.4 m, and assuming an average exploitation thickness of around 2 m in borrow zones E1 and E3, it was estimated that the volume of fine material available in the reservoir will be around 307,000 m³.

In borrow area E6, next to the El Hadjar stream, considering an exploitable area of 180,000 m² and an average exploitable thickness of 2.5 m, the total volume of fine material available will be around 450,000 m³.

In the ZEA5 zone, considering an exploitable area of 125,000 m² and an average exploitable thickness of 1.7 m, the total volume of fine material available will be around 212,500 m³.

5.2. Rockfill

Since the quantity and quality of rock materials in the reservoir (at the Preliminary Study phase) did not meet the needs of the project, the rockfill for the shoulders will have to come from a quarry outside the reservoir.

A potential quarry has been identified about 20 kilometres south of the dam site, on the Jebel Changoura hill. The limestone at Jebel Changoura is a moderately hard to hard limestone, of poor to good quality, with characteristics suitable for the dam's shoulders.

The poor-quality rock should be reserved for internal recharge and the better quality rock should be used for external recharge.

Very good quality rock should be reserved for the protective rockfill of the upstream slope of the dam and the manufacture of materials for the filters and drains.

In order to guarantee good compaction characteristics, the rockfill for the inner shoulders should have a large grain size, with a percentage of fines of less than 15%, and a percentage of material retained on the 3/4' ASTM series sieve (20 mm) of more than 25%.

The inner areas of the upstream and downstream shoulders of the dam will be made up of poorer quality materials from the Jebel Changoura quarry. These are granular materials with an extense granulometry with a percentage of fines, after compaction, less than or equal to 15%.

The outer areas of the upstream and downstream shoulders of the dam will be made up of better-quality quarry materials. These are granular materials - coarse sands, gravels and fine to medium pebbles - of extensive granulometry with a percentage of fines, after compaction, less than or equal to 5%.

5.3. Filters, drains, aggregates for concrete and protective rockfill

The site investigation works carried out in the area of the future reservoir indicates the absence of coarse materials of quality for the production of filters, drains, aggregates for concrete and protective rockfill "rip rap". Those materials will therefore come from quarries or exploration areas outside the reservoir.

These materials will come from the Jebel Changoura quarry after crushing and screening the best quality material (fresh to slightly weathered limestone without clay minerals or pyrite).

The materials for the aggregates for concrete, in particular the sands, could be obtained from the crushing of good quality materials from Jebel Changoura, to be confirmed with information to be obtained from the complementary site investigation work and the complementary tests for the Construction Design phase (alkali-reactivity potential), provided that, in order to achieve the strengths required for the class of concrete used in the works, the source rock for the concrete aggregates must be chosen with a minimum dry uniaxial compressive strength of 50 MPa.

6. SEISMIC CONSIDERATIONS

The older earthquakes in the historical series have a major impact on the results obtained.

Given the low number of historical events obtained from Tunisia for statistical analysis, the minimum magnitude for the collection of earthquakes chosen was 3.0 (very low for this type of work) and the search radius was extended to 300 km.

From the data analysis, it can be concluded that there is only one event at a distance equal to or less than 100 km from the dam site, with a magnitude greater than 5 (Thibar earthquake,

Tunisia (1920) with M = 5, and a maximum deterministic horizontal acceleration of 0.028g for the 69 km distance from the dam site.

The nearest earthquake, with a significant magnitude, is the Zaghouan earthquake (M = 6.2 and a deterministic maximum horizontal acceleration of 0.02g for the 157 km distance from the dam site).

The vast majority of earthquakes in the region with an epicentral distance (ED) < 300 km are of magnitude less than 5.0.

From the deterministic approach based on magnitudes, epicentral distances and using the Ambraseys attenuation law applied to the list of historical events to reach the dam site, we obtained a maximum value of agR of 0.12g for a reference return period TLR, of 294 years.

According to the risk classification of the dam, the dam is classified as ‘Class I’, and the life span of the structure was considered to be 100 years.

According to the agR value of 0.12g, the estimated acceleration for a return period of T = 145 years (0.09g), as well as the estimated acceleration for a return period of T = 475 years (0.14g), are lower than the value of the Tunisian standard (RPT 1. 1 – 2009 [2]), so the corresponding spectrum for designing the structures in each case will be the spectrum of the regulatory reference acceleration for Ghardimaou - agR value of 0.15g (T=475 years).

7. CHOICE OF RESERVOIR CAPACITY

The height of the reservoir was determined as part of the parametric study of the dam during the Preliminary Design phase, with the aim of optimising the cost per cubic metre of exploitable water. However, this capacity is limited by the border with Algeria and the restriction not to flood Algerian territory. The normal water level (NL) elevation was set at level 283 m, the highest possible considering these restrictions. The dam has been designed so that the reservoir can be raised in the future if necessary. Reservoir main characteristics are presented in Table 3.

It is important to emphasise that the reservoir's storage capacity is lower than the optimum capacity that would be defined on the basis of the river's average inflows. This limitation is due to the proximity of the border with Algeria. Changes in inflows due to climate change will not significantly affect the economic viability of the dam, as the reservoir will not reach its maximum capacity even with current inflows. However, the construction of the transfer from El Hadjar could increase the inflow to the reservoir if necessary.

The climate series do not indicate long-term trends in rainfall and runoff. The data from the Jendouba and Beni M'Tir stations, which are close to the dam site, show some natural irregularity, but no significant upward or downward trends in inflows.

Table 3 - Characteristics of the reservoir

Average annual inflow	17.38 hm^3
Normal water level (NL)	283 m
Volume of reservoir at NL	30.0 hm^3
Average volume / inflow ratio	1,7
Surface area of reservoir at NL	149.0 ha
High water level (T = 5000 years)	286.38 m
Volume of reservoir at high water level	36.0 hm^3
Surface area of reservoir at design flood level	167.0 ha

8. DESIGN AND CONSTRUCTION

8.1. Chosen Layout

The retained layout scheme for the Raghai Dam, presented in Fig. 5, considered topographical and geological conditions, optimisation of construction costs and experience with other dam projects in Tunisia.

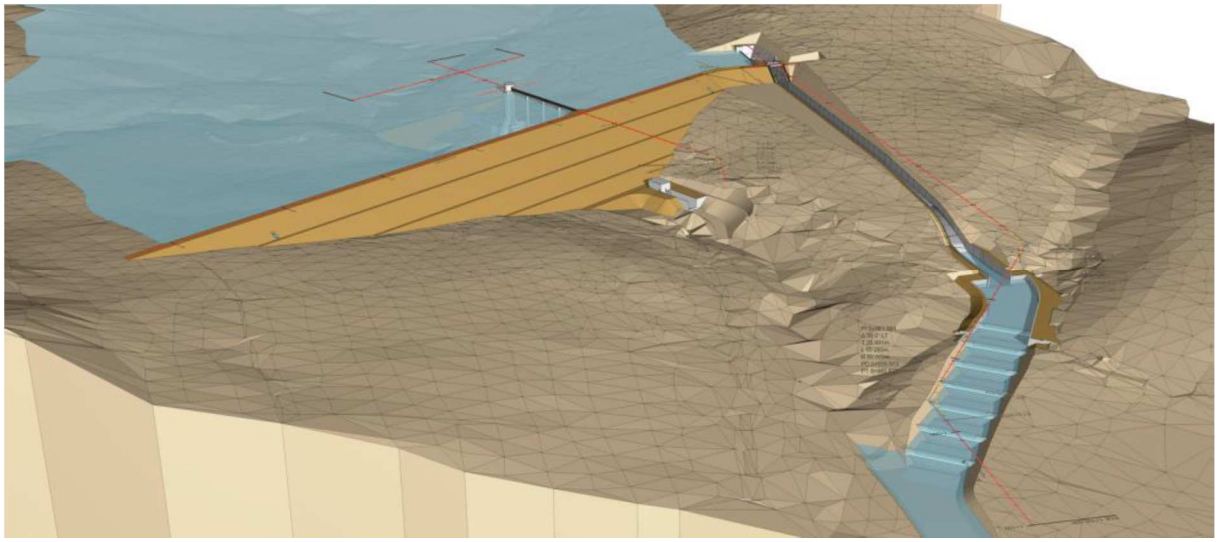

Fig. 5 - Project Layout

8.2. Dam Structure

The Raghai Embankment Dam features a central clay core flanked by rockfill shoulders. Key dimensions include a crest elevation of 288.0 m, a height of 53 m above the riverbed, and a crest width of 9.2 m. The total volume of the dam body is approximately 1.9 million m^3.

8.3. Injection and Monitoring Gallery

A gallery located in the foundation of the dam is foreseen, designed to inject a waterproofing curtain into the rock mass and monitor the behaviour of the foundation over time. This gallery is crucial to ensuring the safety of the dam, given the geological complexity of the site.

8.4. Diversion tunnel

A diversion tunnel will be built on the left bank to divert the water course during the construction of the dam. Once the dam is completed, the tunnel will be used to allocate the bottom discharge gallery.

8.5. Intake and Bottom Discharge Tower

The water intake tower is planned to be located on the left bank, 100 metres upstream from the dam axis, which combines the functions of temporary diversion, bottom discharge and water intake. The location of the tower on the left bank was determined by the most favourable geological conditions found there.

8.6. Spillway

The spillway, to be located on the left bank, comprises of a free sill with a side entrance, a rectangular discharge channel and an energy stilling basin (Fig. 6). The spillway was designed to convey a flood with a return period, T, of 5000 years.

The selection of these elements was based on a detailed analysis of site conditions, taking into account issues such as topography, geology, the availability of construction materials and the project's needs in terms of water storage, flood control and dam safety.

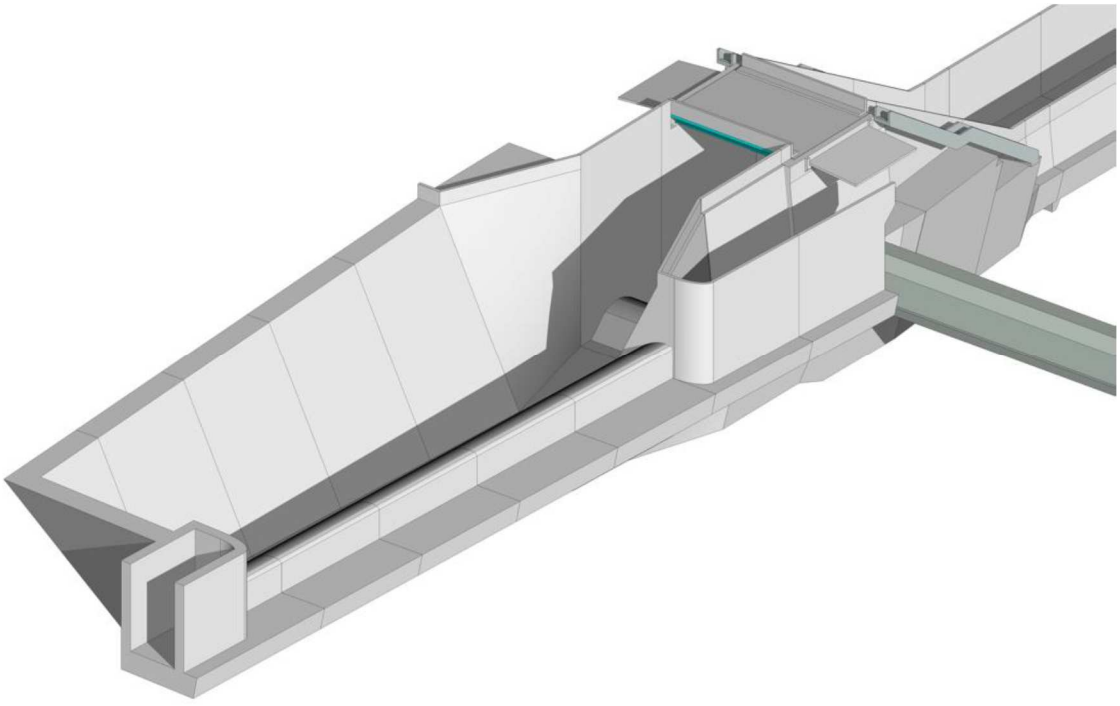

Fig. 6 - 3D view of the lateral structure at the entrance of the spillway and exit of the rectangular channel

8.7. Technical Justification for the Injection Gallery

The injection and monitoring gallery is fundamental to guaranteeing the safety of the dam. Its need arises from the geological complexity of the site, which has permeable and deformable materials at the dam foundation. The gallery makes it possible to monitor the effectiveness of the waterproofing curtain and detect any problems in the foundation after the dam has been put into operation.

The gallery runs along the axis of the dam at the foundation and crosses the bottom discharge, as shown in Fig. 7. The culvert is made of reinforced concrete and has a horseshoe-shaped cross-section. The inner section is 2.50 m wide and varies in height up to a maximum of 2.75 m, with a circular vault of 2.50 m diameter. The outer section varies with the height of the embankment above the culvert.

Longitudinally, the gallery is made of 12.0 m sections, separated by shrinkage joints with 0.30 m wide waterproofing strips. The maximum longitudinal slope is 23%. The intersection of the culvert with the temporary diversion culvert was optimised considering the morphology of the valley, the hydraulic conditions and the ramps to facilitate inspection and maintenance. The culvert should be well excavated into the rock and in areas without rock loose material should be excavated and replaced with concrete.

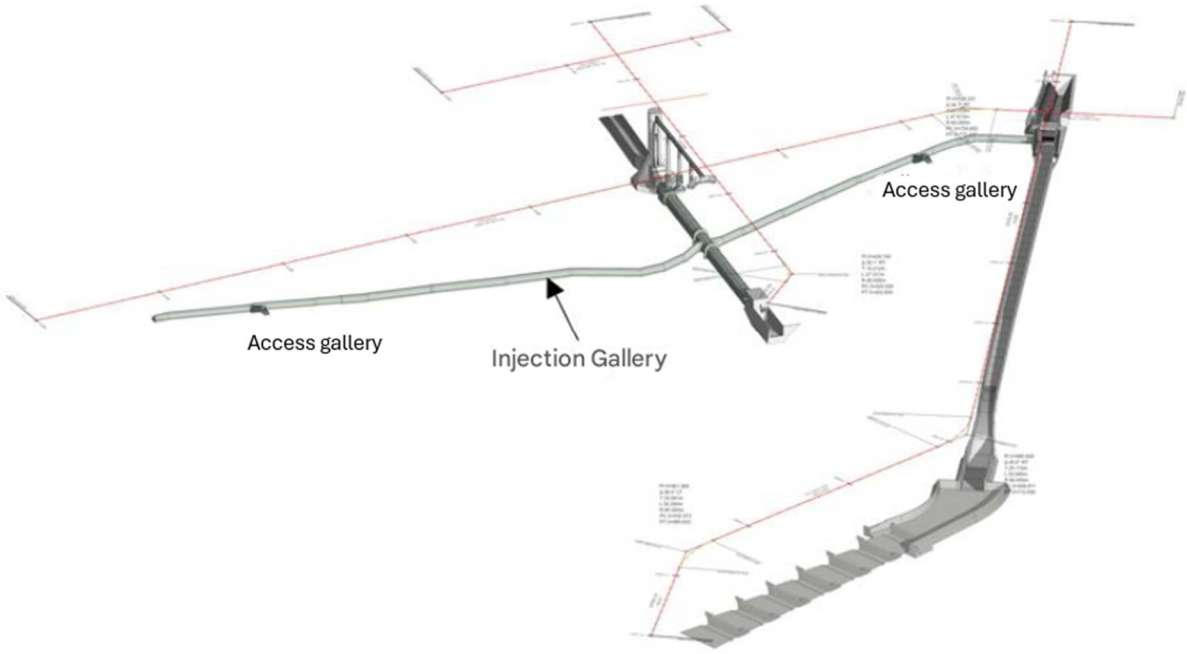

Fig. 7 - Insertion of the injection gallery in the hydraulic scheme

It is recommended that most of the injection work be carried out before the culvert is built, although it can continue during the construction of the embankment. Piezometers will be installed in the foundation from the base of the gallery to monitor the hydrostatic pressure

during the operation of the dam. This data, together with the water level in the reservoir and rainfall, provides information on the effectiveness of the waterproofing curtain.

Mainly, the injection and monitoring gallery is crucial to the long-term safety of the Raghai Dam. The gallery enables not only the creation of a waterproofing curtain in the foundation, but also its continuous monitoring. It also makes it easier to carry out maintenance and repair work on the foundation, ensuring the dam's stability over time.

8.8. Dam design

The dam comprises a rockfill embankment with a clay core, a choice dictated by the geology of the site and the availability of materials. The impermeable core is relatively thin to optimise the use of the available clay, and the safety of the foundation is ensured by limiting hydraulic gradients.

The profile of the dam is shown in Fig. 8, with a central, symmetrical core, inclined at 1V:0.45H. The dam's foundation is composed of rock interspersed with clays, requiring a sealing trench to cross the valley's alluvial deposits. The core will be protected with upstream and downstream filters, 3 m wide, crucial part of the dam's internal drainage system.

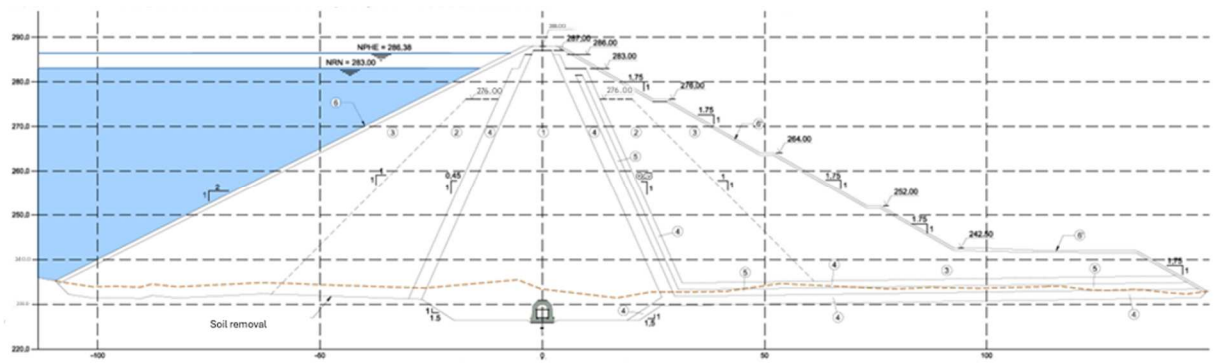

Fig. 8 – Proposed type profile for the dam (Normal Water Level 283 m)

The materials used in the construction of the dam, include:

- Material (1): Clay soils for the impermeable core.
- Material (2): Large-grained soils, rock-fill soils and rock-fill for the internal areas of the upstream and downstream shoulders.
- Material (3): Rockfill from quarries for the outer areas of the upstream and downstream shoulders.
- Material (4): Sand for the filter.
- Material (5): Gravel for the drain.
- Material (6) and (6'): Sandstone or limestone rockfill for the rip-rap.

The grain size curves of the materials used in the construction of the dam are presented in Fig. 9.

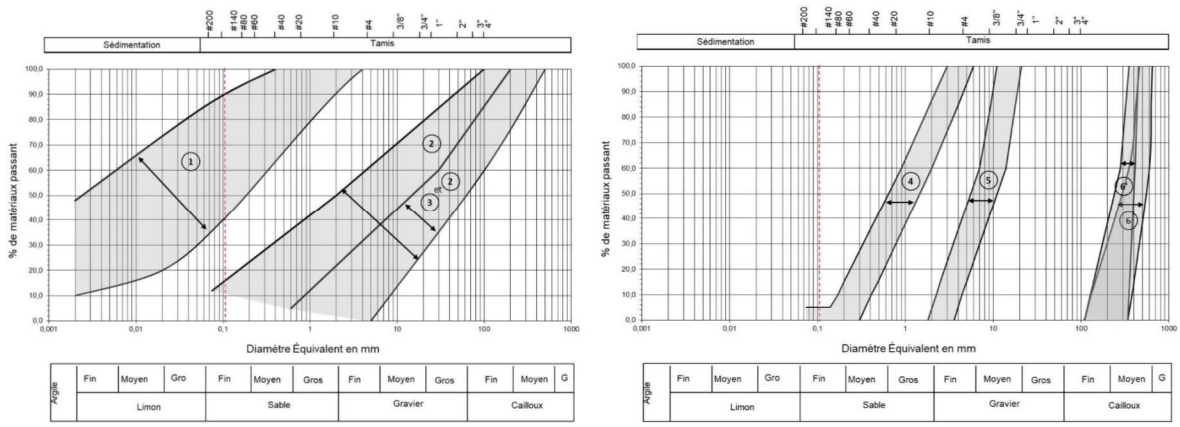

Fig. 9 – Materials for the embankment

Regarding the provenance of the materials, the core is to be built with materials from the borrow areas identified and possibly from excavations. The filters and drains will be built with sands and gravels from selected quarries. The shoulders will be built with rockfill from quarry supplemented with materials from excavations.

The dam's freeboard, calculated using the USBR methodology (2012) [3], considers the height of the waves and the elevation of the water due to the wind. Fetch lengths considered for calculating the freeboard ranged from 0.37 to 1.42 km.

8.9. Settlement analysis

The main objective is to assess the deformations that the embankment will undergo and to verify the possibility of stress transfer between the different materials that make up the dam structure, particularly between the clay core and the shoulders zones.

In order to guarantee the safety of the structure, the slopes of the core slopes were studied so as to avoid the transfer of tensions between the core and the recharge areas. In addition, the maximum displacements expected for the embankment, both during construction and when it is first filled, make it possible to estimate long-term displacements and implement compensation measures if necessary.

The settlements were analysed using the finite element method, using the commercial software SigmaW 2021.3 (GeoStudio Professional). The model considered the most unfavourable scenario, with the reservoir's water level at 283 m (Normal Water Level) and the highest section of the dam.

The calculation parameters used, based on laboratory tests results, are shown in Table 4.

Table 4 – Stress-deformation analysis. Mechanical characteristics of dam materials

Material		γ_d (kN/m³)	*E* (MPa)	*v*	*c'* (kPa)	ϕ' (º)
nº	Description					
1	Core	19	20	0,40	10	25
2	Internal shoulders	21	35	0,32	0	40
3	External shoulders	21	40	0,28	0	42
4	Filter	20	30	0,25	0	35
5	Drain	21	40	0,25	0	45
6	Protection Riprap	22	50	0,25	0	48

The construction simulation was divided into three main stages:

1. Initial site conditions: Before construction begins.
2. Foundation excavation: Removal of loose material and preparation of the foundation.
3. Construction simulation: Incremental process in 15 phases, representing the placement and compaction of the different embankment materials.

The model results indicate a maximum vertical displacement of the embankment of around 0.46 m (Fig. 10), corresponding to around 1% of the dam's height. This displacement will be compensated for by the subsequent layers of the embankment, resulting in a residual displacement of practically zero at the end of construction.

With regard to the foundation, the expected settlements are minimal (around 0.05 m), in line with the model results. This value corresponds to approximately 0.1% of the dam's height. Fig. 10 shows the results of the analysis, displaying total displacements and average total stresses at the end of construction.

The study also simulated the first filling of the reservoir, a critical phase in which significant movements in the dam body can occur. The simulation assumed instantaneous filling up to the Normal Water Level, and the results indicate a maximum horizontal displacement of 7.7 cm in relation to the centre core axis. The horizontal displacement on the slope surface and in the core varies between 0.10 and 0.12 m, while the vertical displacement on the slope surface is 0.12 m.

Due to long-term settlements, it is recommended to implement a counter-slope at the top of the dam, with a value of 0.50 m, in the sections where settlements are most significant.

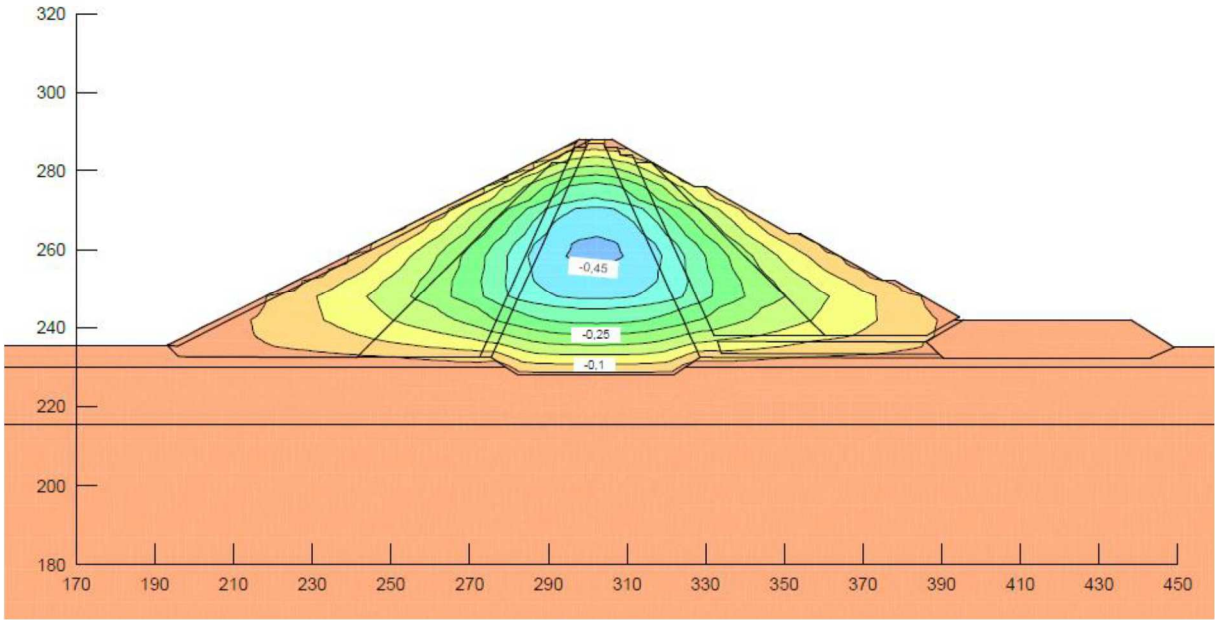

Fig. 10 – Construction model. Total settlements

8.10. Stability analysis

The analysis was conducted using the limit equilibrium method, by means of Slide software (Rocscience), and considers the most critical profile of the dam, located at the bottom of the valley. During construction, stability is checked considering the mechanical characteristics of the materials and the foundation, resulting in a minimum safety factor of 1.56, which guarantees the safety of the structure.

In the exploration phase, stability was assessed for different scenarios, including normal water level, earthquake occurrence and rapid drawdown. Design basis (SBE) and safety (SES) earthquakes are considered, and the results indicate satisfactory safety factors for normal water level and rapid emptying, even in seismic situations. The performed analyses demonstrate safety factors greater than 1.0, except in the situation of normal water level with earthquake. However, even in this scenario, the expected displacements are considered to be of small magnitude, not putting the safety of the dam at risk.

8.11. Foundation treatment

The site's foundation is characterised by a complex geological structure, with the presence of clayey slope deposits, mainly on the right bank, and a substratum made up of sandstone-claystone lithological units (Numidian flysch). This geological complexity, in particular the

presence of fractured sandstone levels, makes it essential to treat the foundation in order to guarantee the safety and good performance of the dam.

The main objectives of foundation treatment are:

a) Consolidation treatment: Although the stress-strain analyses indicate acceptable settlement values for the dam body and the water intake tower, the geological heterogeneity of the foundation requires consolidation treatment, especially in the area on the right bank where clay deposits with sandstone blocks were found. This treatment will be carried out using cement injections, with the aim of strengthening the weaker soils and homogenising the deformability characteristics of the foundation.
b) Waterproofing treatment: To reduce percolation through the foundation, especially in fractured sandstone areas, a waterproofing treatment is planned. This treatment will consist of a curtain of cement grout injection, executed from an injection gallery located at the base of the dam. The injection gallery, with a length of 180 m and a diameter of 6 m, will allow the execution of injection holes along the entire dam foundation. The effectiveness of the waterproofing treatment will be assessed through water absorption tests carried out in the injection holes, allowing the injection plan to be adjusted depending on the permeability of the soil.

9. CONCLUSION

The Raghai Dam project faced several significant challenges, mainly related to the complex geological conditions of the site and the limited availability of suitable construction materials. The heterogeneity of the substrate, composed of sandstone-clay-claystone lithological units (namely the “Numidian flysch”) with fractured levels, represented an important challenge to guarantee the safety and impermeability of the dam foundation. Additionally, the scarcity of good quality clay materials in the reservoir area forced the search for alternatives for the construction of the dam's waterproof core.

To overcome these challenges, the project adopted a series of efficient solutions. The geological complexity of the foundation was mitigated through the implementation of a consolidation treatment using cement injections and a waterproofing treatment using a cement grout injection curtain. The location and depth of the injections were carefully planned and adjusted based on data from water absorption tests, ensuring the effectiveness of the treatments. To address the limitation of clay materials, the project team conducted extensive research to identify suitable clay borrow zones outside the reservoir area. Additionally, the optimization of the dam's design, with a relatively thin impermeable core, made it possible to minimize the amount of clay required for construction. The choice of a rockfill embankment

with a clay core also contributed to the flexibility of the project, allowing the use of rock materials from nearby quarries.

10. ACKNOWLEDGEMENTS

The authors express their gratitude to the Ministère de l'Agriculture, des Ressources Hydrauliques et de la Pêche (Direction Générale des Barrages et des Grands Travaux Hydrauliques) from Tunisia for granting permission to publish this paper.

The authors would like to extend their thanks to SCET TUNISIE for their collaboration and support within the dam design by COBA-SCET TUNISIE-AHT Group consultants joint venture.

REFERENCES

[1] COBA-SCET TUNISIE-AHT Group. (2024). « Programme de Stockage de l'Eau et de la Protection Contre les Inondations », Phase 3 (Avant-Projet Détaillé). Rapport de Synthèse. Ministère de l'Agriculture, des Ressources Hydrauliques et de la Pêche. Direction Générale des Barrages et des Grands Travaux Hydrauliques (DG/BGTH), Tunisia.

[2] Project National de Reduction du Risque Sismique, République Tunisienne (2009). Règles Parasismiques Applicables aux bâtiments RPT 1.1.

[3] The United States Bureau of Reclamation (2012). Design Standards No. 13: Embankment Dams (Ch. 6: Freeboard)

Fifth International Dam World Conference
PORTUGAL • LISBON • LNEC • APRIL 13-17, 2025
dam world 2025

Calucuve Dam – Geotechnical Conditions and Design

Ricardo Sardinha[1]	Hesham Badry[2]	Lurdes Pimenta[3]	Rui Abreu[4]	Daniel Leite[5]	Hugo Custódio[6]	Febin Naguindás[7]
COBA	DAR	COBA	COBA	COBA	COBA	COBA

ABSTRACT

At the request of MOTA ENGIL AFRICA, COBA and DAR consortium developed the design for the construction of the Calucuve Dam, located in Cunene Province, Angola. This design is part of a Design and Build Contract between MOTA ENGIL ANGOLA and the Ministry of Water and Energy of Angola (MINEA). This paper addresses the major geotechnical aspects of the dam's design and construction.

This article presents the constraints of the general lay-out of the Calucuve dam, the criteria and methodologies that based the dimensioning of its main components and also the adaptations carried out during the construction phase. This article refers mainly to the geological and geotechnical conditions and design as well as the adaptations to the geotechnical design made during the construction phase, resulting from the actual conditions encountered.

The embankment dam features a crest length of approximately 2184 meters and the dam body, with a maximum height of 31.6 meters, has a zoned earthfill cross-section. Internally, the dam's cross-section features a central core, protected by upstream and downstream filters. The outer slopes are protected by rockfill, both upstream and downstream.

Materials identified for construction include clayey sands with ferruginous concretions, selected for the dam's the stabilizing shoulders, and clayey-sandy deposits, for the core.

The channel spillway with a frontal weir, located on the left bank, extends approximately 1,862 meters. It includes an unlined approach channel, an entrance structure with a labyrinth weir, a downstream channel, and a stilling basin. The unlined return channel downstream of the stilling basin is about 1,465 meters long.

The hydraulic circuit is located in the centre of the valley and is composed by an intake tower, with multiple-level intakes. Downstream this structure, follows a concrete gallery with approximately 170 m long, inside which the water intake and bottom outlet circuits are installed.

Keywords: earth dam, design, construction.

[1] r.sardinha@cobagroup.com, Portugal
[2] Hesham.Badry@dar.com, Egipt;
[3] l.pimenta@cobagroup.com, Portugal
[4] r.abreu@cobagroup.com, Portugal
[5] d.leite@cobagroup.com, Portugal
[6] h.custodio@cobagroup.com, Portugal
[7] f.naguindas@cobagroup.com, Portugal

1. CALUCUVE DAM GENERAL LAYOUT

The total length of the dam crest is approximately 2184 m. The axis is composed by a linear development of about 1997 m, followed, in the left bank, by a curve facing upstream over a stretch of 277 m with a radius of 400 m.

All hydraulic structures were placed along the straight section of the dam axis as showed in **Figure 1**. The gallery for the river diversion system, bottom outlet, and water intake is in the central section of the axis, while the spillway is located at the dam's left abutment.

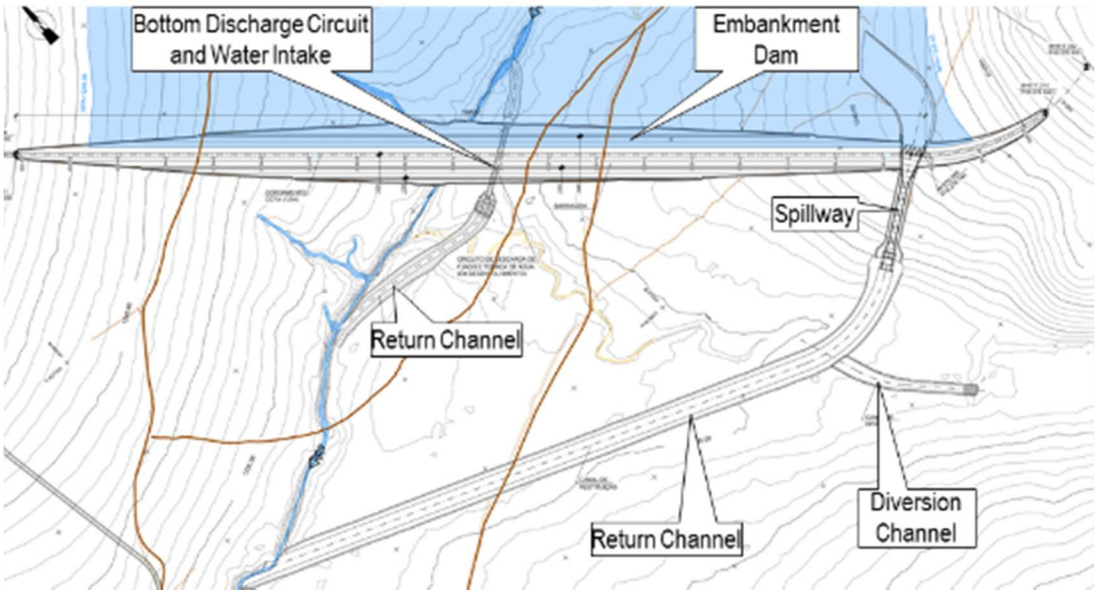

Figure 1 - General layout of the Calucuve dam

A zoned earth fill dam type was adopted, given the morphology of the valley - with a span-to-height ratio of approximately 91 (a crest extent of 2184 m and a maximum height of 24 m above the natural ground) - and the availably of earthfill materials on site (**Figure 2**). The maximum height of the dam above the foundation level is 31.6 m. The valley is slightly asymmetrical, with gentle slopes.

The crest height of 1254.00 m was determined based on freeboard calculation studies, considering the combined effects of typical wind conditions and the maximum flood level (MFL) of the reservoir. The estimated long-term settlement of the dam was accounted for. The crest is 8.0 m wide. The upstream slope of the dam has an inclination of 1:2.5 (V:H) and the downstream slope an inclination of 1:2.25 (V:H) above the rockfill dam toe (1236.00 m), and 1:1.8 (V:H) below. To protect the upstream slope against wind wave erosion, a layer of selected rockfill was designed. The downstream slope is also protected by a riprap layer to prevent erosive actions of precipitation and runoff.

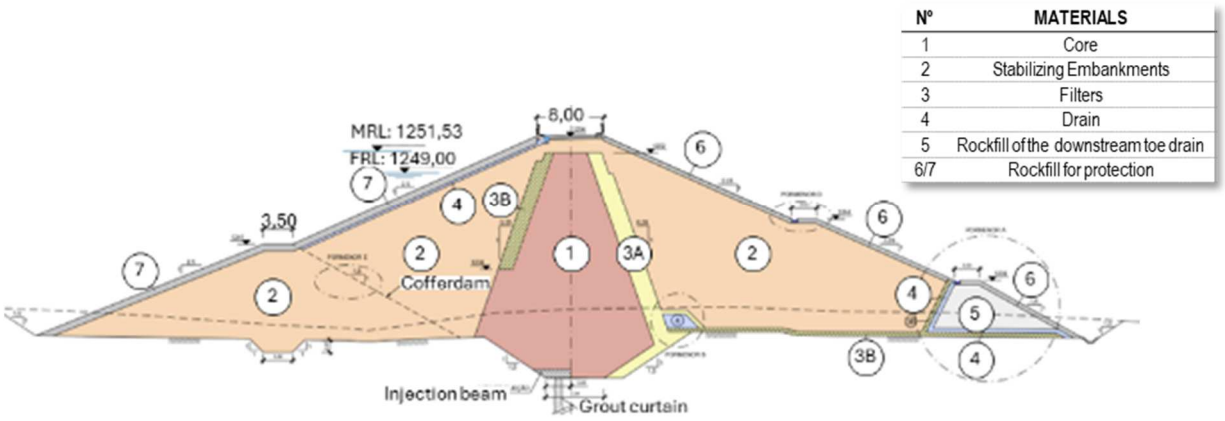

Figure 2 - Typical section of the Calucuve dam

At the intersection of the critical filter with the foundation, downstream of the core, a longitudinal drainage trench collects the flow percolated through the dam core and partially through the foundation. The longitudinal trench is connected to nine transversals trenches that convey the water downstream. Additionally, a filter blanket separates the stabilizing downstream shoulder from the foundation.

The core is embedded in the foundation through a cutoff trench (with a protective filter downstream). The chosen depth was determined based on geological and geotechnical data, following the removal of foundation soils with medium to high permeability, as well as decomposed rock masses, where cement grout injection is not feasible. The cofferdam is located within the upstream part of the dam, with its crest at elevation 1241.

The spillway (**Figure 3** and **Figure 4**) is located on the left bank with a total length of 1862 m. It comprises an approach channel (115 m), a 282 m reinforced concrete section with a labyrinth weir, an open channel downstream of the control sill ending in a dissipation basin, and a 1465 m excavated channel downstream of discharged the flows to the river.

The labyrinth weir is a reinforced concrete U-shaped structure located at an elevation of 1245.50 m, measuring 46 m in length and 51 m to 34.4 m in width. The labyrinth includes 3.5 m high, 0.4 m thick walls, with aeration systems to improve flow conditions. A 42 m long viaduct, with a 1.6 m thick ribbed deck, spans over the spillway, supported by a pillar aligned with the spillway axis, to minimize flow disruption and withstand debris impact during floods. Downstream, the U-shaped channel transitions into a dissipation basin USBR Type III, 18 m wide and 36.4 m long.

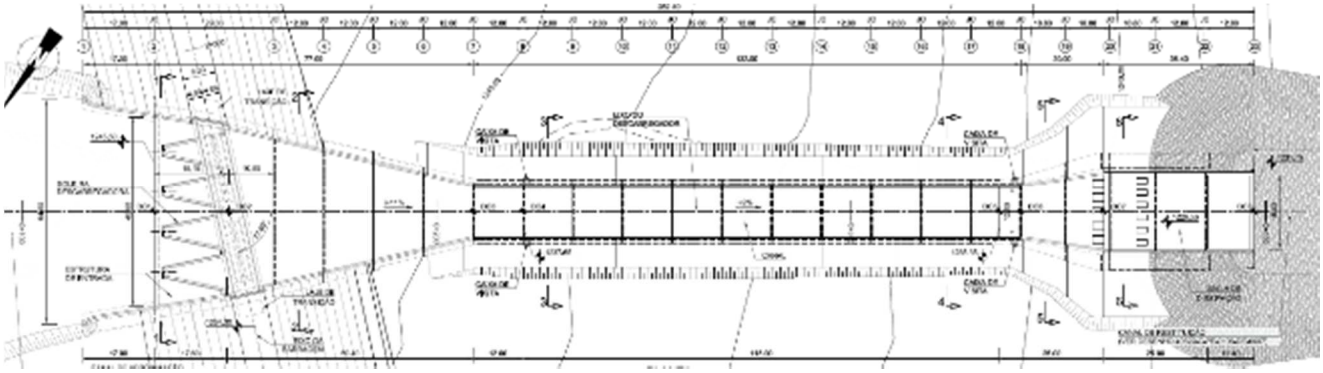

Figure 3 – Calucuve Dam Spillway. Plan View.

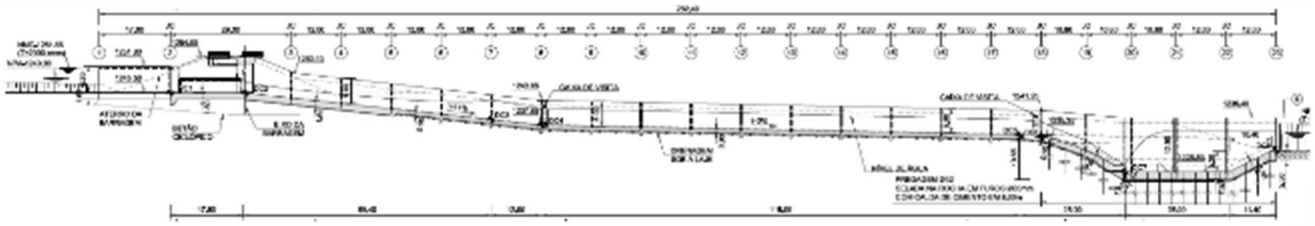

Figure 4 – Calucuve Dam Spillway. Longitudinal profile.

The water intake tower is designed to supply downstream water with a maximum discharge of 2.65 m³/s. It features a dry intake design with openings at multiple levels, allowing water to flow directly into the transport pipes without entering the tower. The tower is located above the diversion gallery and houses the control systems for the intake and bottom outlet valves. A 1000 mm vertical intake pipe connects to multiple level intakes, ensuring functionality regardless of reservoir water depth. The tower is accessible via a bridge for maintenance and operations. The bottom outlet circuit, with 1800 mm in diameter, is located at the base of the intake tower.

2. GEOLOGICAL AND GEOTECHNICAL CONDITIONS

The dam site is located in the western part of the Continental Massif, in the "Central Plateau" of Angola. This area is characterized by a denudation relief with intense erosion phenomena, formed over Archean and Lower Proterozoic rocks.

From a geotechnical perspective, the study area is primarily developed on the oldest crystalline rocks of the lower complex (Lower Precambrian), which are related to the final phase of the structuring of the continental crust that were deposited in depressions and rifts. These are mainly thick volcano-terrigenous sequences affected by intense magmatism, which, according to the literature, are part of structures known as “greenstone belts”.

In lithostratigraphic terms, the region is essentially characterized by magmatic and volcano-sedimentary formations of the Lower Precambrian, as well as Cenozoic sedimentary deposits (**Figure 5**).

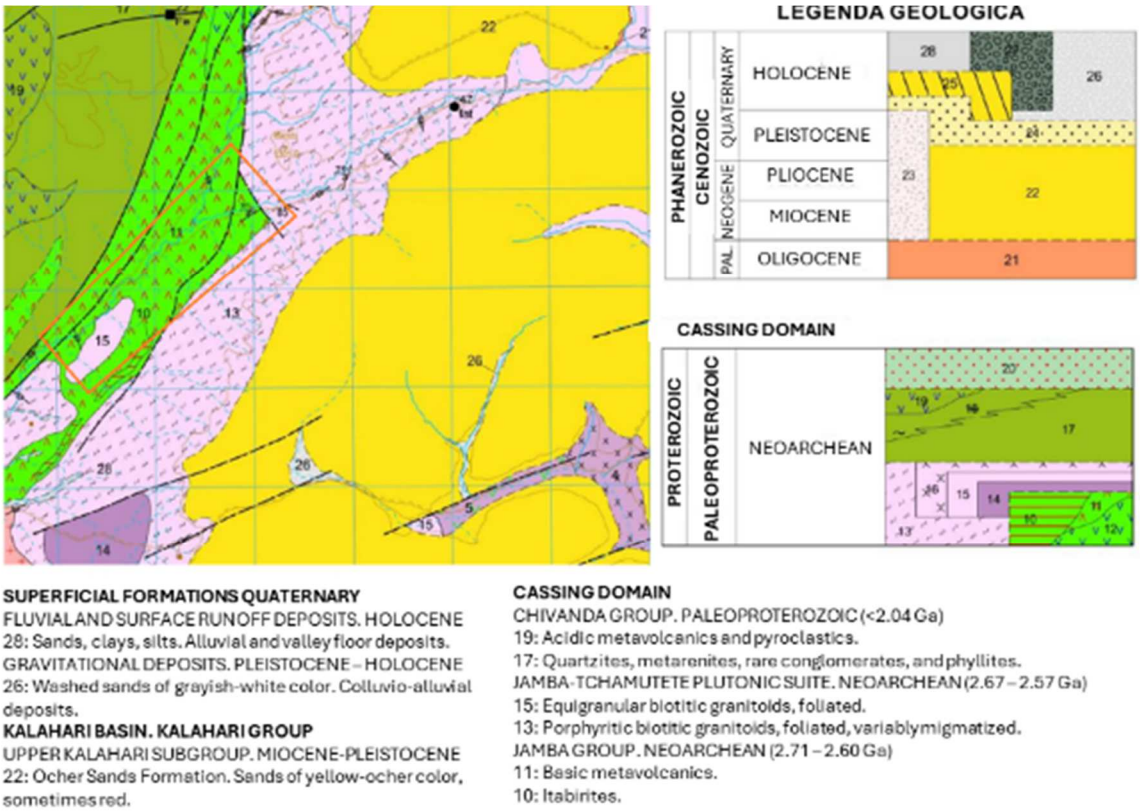

Figure 5 - Extract from the Geological Map of Angola

Figure 6 shows the plan and the longitudinal geotechnical section of the dam.

In general, the foundation of the dam consists of:

- A layer of topsoil (Tv) with a variable thickness between 0.3 and 1.5 meters,
- Alluvial and valley floor deposits (Al1), composed of fine to medium sands, silty to clayey, sometimes with ferruginous concretions, with thicknesses ranging from 1.5 to 6.0 meters,
- A layer of fine to medium clayey sands with ferruginous concretions (Ca2+Qi), with thicknesses varying from 0.8 to 3.0 meters,
- Eluvial and substrate alteration deposits (De), with thicknesses ranging from 2.0 to 12.0 meters, composed of material resulting from the alteration of the underlying rock formations.
- The bedrock, composed of basic metavolcanics (AMVB).

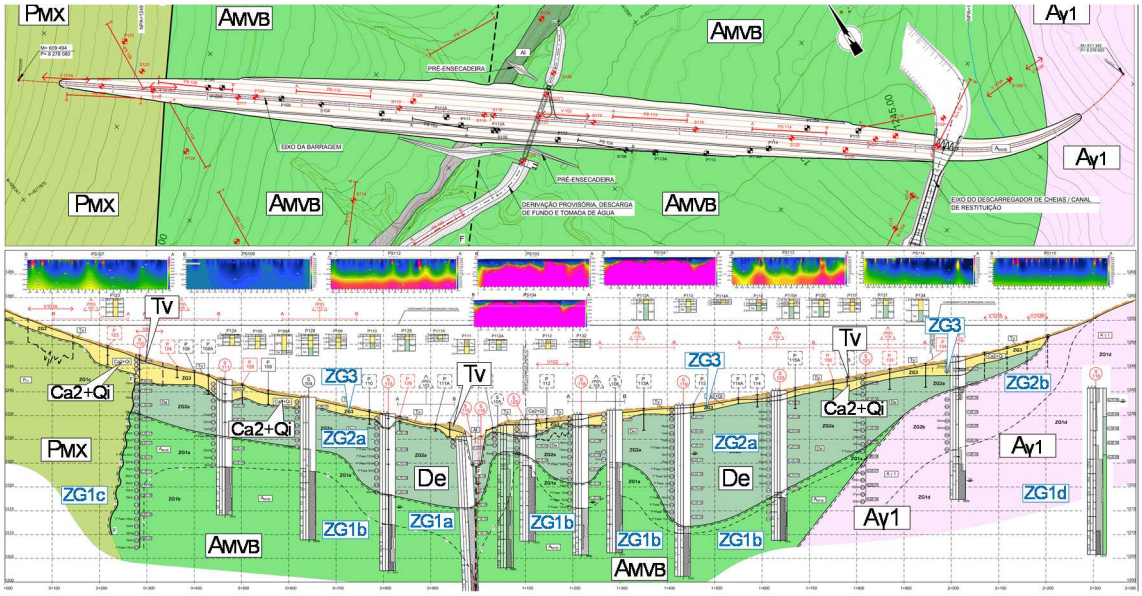

- **Figure 6 - Plan and longitudinal geotechnical section of the dam (vertical scale increased by 10x)**

The geotechnical zoning of the dam's and appurtenant structures foundation was established based on the area's geological and geotechnical characteristics, dam type, and foundation needs. This zoning considered physical, mechanical, and hydraulic properties, including seismic wave velocity, weathering, fracturing, and borehole data such as RQD, core recovery, N_{SPT} values, permeability, and water absorption tests.

Data from 23 exploratory boreholes, spaced around 96 m apart along the dam axis, supplemented the investigations. These boreholes included continuous coring, water absorption tests (Lugeon type), in rock masses, and Lefranc permeability tests, in soils.

Three primary geotechnical zones (ZG1, ZG2, and ZG3) were identified, with ZG1 being the highest quality zone. Seven subzones were also defined. Generally, lower-quality materials (ZG3) are near the surface, while ZG1 and ZG2 are found at greater depths. The geotechnical zoning summary is presented in **Table 1**.

Table 1 - Geotechnical zoning of the dam foundation – Most frequent values

Geotechnical Zone		Formation	Description	NSPT	W_n (SIMR)	F_n (SIMR)	RQD (%)	Longitudinal seismic wave velocity, V_p (m/s)	Permeability	
									k(m/s)	Lugeon Units (UL)
ZG3		Tv / Co+Al / Ca2+Qi	Topsoil, sandy-silty-clayey alluviums and fine to medium clayey sand with rusty concretions, sometimes with angular pebbles.	22-50	-	-	-	< 600	4x10-7 to 4x10-5	-
ZG2	a	From	Eluvial deposits and alteration of the substrate, of sandy clay to silty-clayey sandy nature, yellowish brown to greenish, very compact.	53-60	W4-5	-	-	1000-2500	2x10-7 to 7x10-6	-
ZG1	b	Aγ1	Fine to coarse silty-clay sand	41-60	W4-5	F4-5	-	-	3x10-6 to 1x10-5	-
	a	AMVB	Severely altered and fractured basic metavulcanites	>60	W4-5 to W3	Variable (F4-5 to F2)	Variable (<60)	>2500	3x10-7 to 4x10-6	8 to 37
	b	AMVB	Basic Metavulcanites	-	W1-2	F3 to F1	80-100	>3000	-	<5
	c	PMX	Metarenites, mica-schists, quartzites, rare conglomerates and phyllites	>60	W4-5 to W3	F4-5	-	-	3x10-6 to 7x10-6	3 to 37
	d	Aγ1	Equigranular biotitic granitoids, foliate	-	W1-2	F3 to F1-2	41-100	-	-	<3

Note: Surface deposits: Tv – Vegetable soil; Co+ Al - Alluvial and valley-bottom deposits: sands, clays, silts and gravel; TERTIARY: Ca2+Qi - Ochre sand formation: Yellow-ochre sands, sometimes red; From - sandy clay to silty-clay sand yellowish to greenish gray; PROTEROZOIC - P_{MX} - Metarenites, mica-schists, quartzites, conglomerates and phyllites; ARCHAIC:$_{MBV}$ - Basic Metavulcanites; Aγ1 – Equigranular biotitic granitoids, foliate.

3. DAM DESIGN. MAIN CRITERIA AND ADOPTED METHODOLOGIES

3.1. Dam foundation

Based on geological and geotechnical conditions, the foundation soil was deemed suitable after removing the topsoil (0.2 to 1.0 m thick) and the most decompressed or permeable materials from geotechnical zone ZG3. This preparation ensured the dam core could be founded on ZG2a and ZG1c soils, at depths of 3.0 to 9.3 m below natural ground level, zones with lower permeability (10^{-7} to 10^{-6} m/s), ensuring a stable and impervious foundation for the core. The upstream and downstream shoulders were founded at higher elevations, on ZG3 and ZG2a, where suitable resistance and deformability formations were identified.

A grout curtain was defined along the dam axis to minimize water seepage through the foundation, consisting of a single row of vertical injection holes and reaching depths of 9 to 25 meters below the cutoff trench base. Most of the curtain is embedded in a low-permeability mass, on ZG1b) and its execution followed standard procedures, starting with primary holes and concluding with Lugeon permeability tests. To optimize grout composition and injection pressures, two testing blocks were primarily implemented, each with 48-meter-long.

In highly fractured areas, containment and consolidation curtains were added to improve resistance, reduce soil deformability, and enhance the sealing curtain's performance. These curtains, 6 to 9 meters long and spaced 3 meters apart, were spaced 1.5 meters from the grout curtain. This treatment was specifically applied in fractured and decomposed zones, including intersections with the temporary diversion gallery, bottom outlet, and spillway.

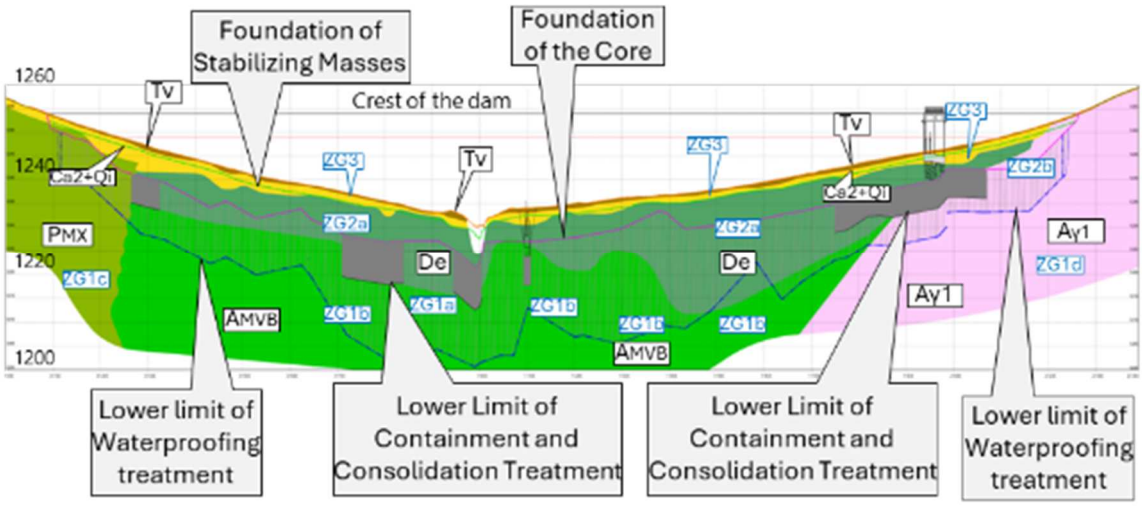

Figure 7 - Foundation treatment. Longitudinal profile (vertical scale increased 10x)

3.2. Construction materials

Figure 8 shows the particle size range of the materials used for the construction of the dam.

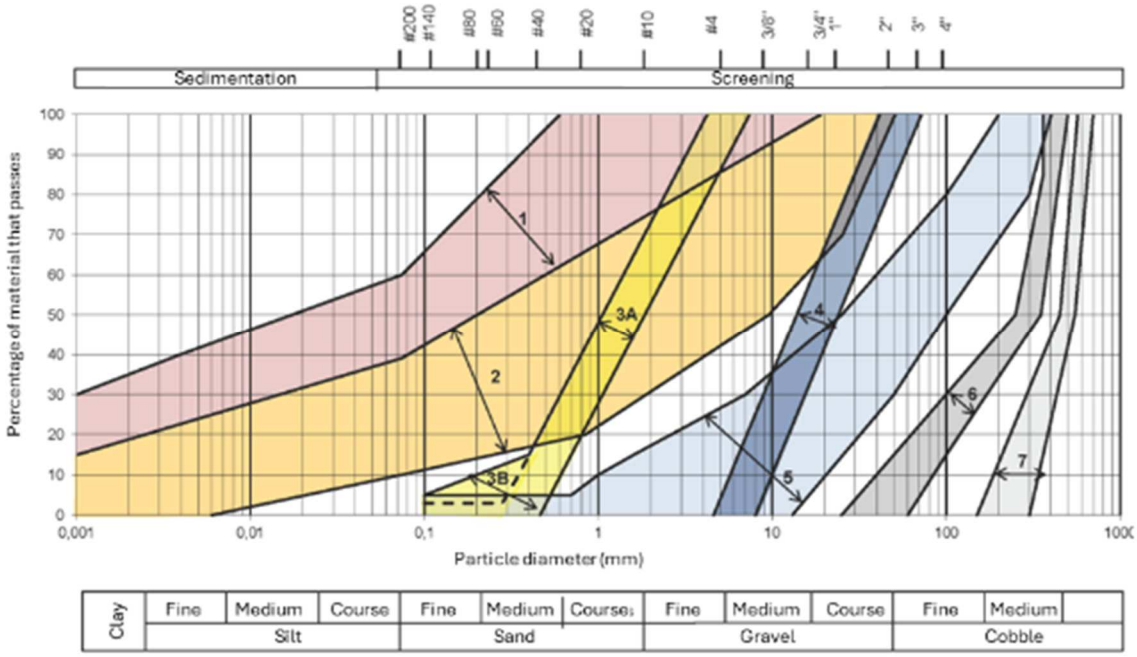

1 – Core, 2 - Stabilizing Embankments, 3 – Filters, 4 – Drain, 5 - Rockfill of the toe drain, 6/7 - Rockfill for protection

Figure 8 - Grain size distribution ranges of construction materials of the Dam

Material 1 - Core Materials

The core consists of compacted clayey-sandy to silty-clayey soils, primarily sourced from eluvial deposits and weathered bedrock. These materials exhibit fine content (passing #200 sieve, ASTM) between 40-60%, liquid limit below 35%, and plasticity index ranging from 9% to 15%. In contact zones (foundation and concrete structures), fine content was defined between 50 and 60% with a plasticity index between 12% and 15%. Mechanical and hydraulic parameters: cohesion (c') = 10 kPa, internal friction angle (φ') = 32°, permeability coefficient = $1x10^{-7}$ m/s.

Material 2 - Dam Shoulders

These are sandy to clayey soils, often with ferruginous concretions. After compaction, fine content ranges between 10% and 39%, with a plasticity index of 5% to 15%. Mechanical and hydraulic parameters: cohesion (c') = 0 kPa, internal friction angle (φ') = 36°, permeability coefficient = $1x10^{-6}$ m/s.

Materials 3A and 3B - Filter

Filters are designed to ensure compatibility with core materials, preventing internal erosion. Fine content percentage less than 3% (Material 3A) and 5% (Material 3B), with permeability coefficients estimated of $5x10^{-5}$ m/s.

Material 4 – Drains

Drains are coarse-grained materials designed to ensure efficient water flow and filtration. Mechanical and hydraulic parameters: internal friction angle (φ') = 38°, permeability coefficient = 10^{-2} m/s.

Material 5 - Downstream Rockfill Materials

Rockfill for the downstream toe includes coarse gravel and blocks for high compaction and stability. Fine content is 0-5%, with permeability coefficient of 10^{-5} m/s.

Materials 6 and 7 - Protective Rockfill Materials

Upstream rockfill (Material 7) protects against wave action, while downstream rockfill (Material 6) protects against precipitation and runoff. Upstream material follow specifications based on wave height and site-specific conditions, with gradations and rock quality ensuring durability and stability.

3.3. Freeboard

A crest elevation of **1254.00 m** was established, ensuring a normal freeboard of 5.0 m (full supply level on the reservoir (FSL) and exceptional wind of 160 km/h) and a minimum freeboard of 2.45 m (maximum water level (MWL) and frequent wind of 80 km/h), meeting conservative safety criteria considering settlement of the dam in the long term and unquantifiable factors.

3.4. Global Stability Studies

Checks for collapse due to global stability loss, both under static and seismic conditions, were carried out for the most critical profile in terms of dam height and its foundation.

The calculation situations considered the specifications outlined in the Terms of Reference, summarized in **Table 2**, incorporating the global safety factors approach and the minimum values defined.

Table 2 - Calculation Situations

Design Scenario	Description	Reservoir Water Level	Seismic Action
1	Construction	-	-
2	Normal Operation	FSL	-
3	Rapid Drawdown	FSL	-
4	Normal Operation with MEE	FSL	MEE

FSL – Full Supply Level; MWL – Maximum Water Level; SEE – Maximum Expected Earthquake

The adopted mechanical parameters are presented in **Table 3**.

Table 3 - Global Stability Collapse Safety Check. Mechanical Parameters

MATERIALS	Colour/Nº	Resistance Parameters		
		γ_h (kN/m³)	ϕ' (º)	c' (kPa)
Stabilizing Masses	2	22	36	0
Core	1	21	32	10
Filters	3	18	36	0
Drain	4	18	38	0
Rockfill	5, 6 e 7	21	43	0
Organic Soil (Tv)	-	18	32	0
ZG3 – Superficial Foundation (Ca2+Qi)	-	18	32	0
ZG2 – Intermediate Foundation (De)	-	19	35	15
ZG1a – Deep Foundation (A_{MVB})	-	21	25	100
ZG1a – Deep Foundation (A_{MVB})	-	21	25	200

Static stability analysis

The safety check for collapse due to global stability loss under static conditions was performed using the Morgenstern-Price method. This method conducts a limit equilibrium analysis to determine the safety factor against rupture along circular sliding surfaces, using the GeoStudio 2023 program, in the SLOPE/W module.

Circular, superficial, intermediate, and deep surfaces were studied. The most unfavourable surface for each analysed case was determined by defining a mesh of centres and varying radii, which were defined by lines tangential to the circles.

For the full storage and rapid drawdown phases, pore pressures were accounted for by defining piezometric lines, estimated through percolation studies conducted using the finite element method and the software SEEP/W.

The global safety factors obtained for the analysed profile are shown in **Table 4**.

Table 4 - Global Safety Check for Collapse due to Loss of Global Stability of PK 0+975 Profile. Static Situation. Results.

Analyzed Situations		Global Safety Factor			
		Reference	Sliding Surfaces		
			Superficial	Intermediate	Deep
Construction Phase	Mounting Slope	1,3	2,0	2,1	2,6
	Downstream Slope	1,3	2,1	2,3	2,8
Full Storage	Downstream Slope	1,5	2,0	2,1	2,3
Rapid Drawdown	Mounting Slope	1,3	1,8	2,0	2,3

Figure 9 and **Figure 10** present examples of the sliding surfaces studied , respectively, for full storage phase (downstream slope) and rapid drawdown phase (upstream slope).

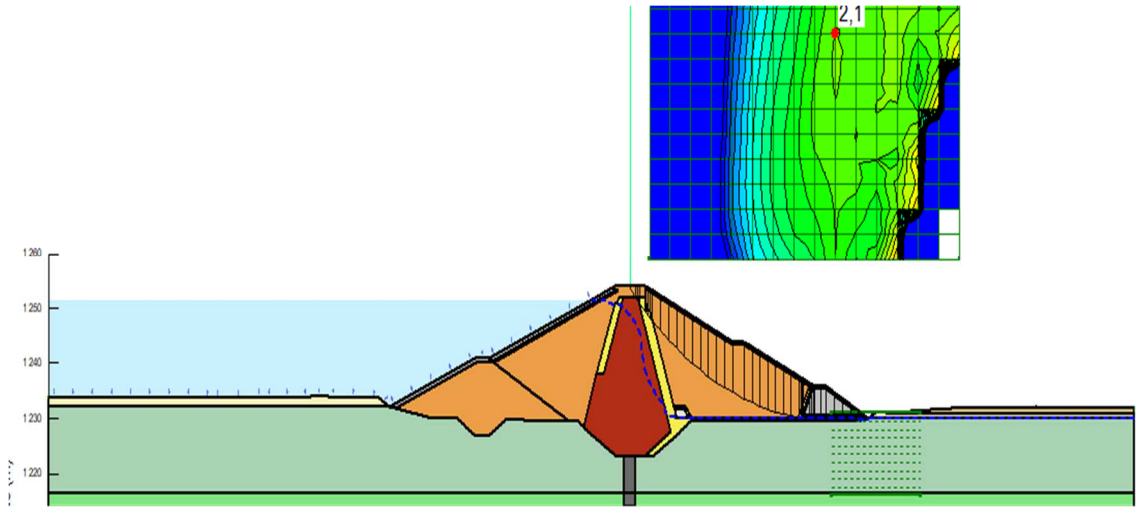

Figure 9 – Static Stability Check. Full Storage Phase. Downstream Slope. Intermediate Rupture Surface.

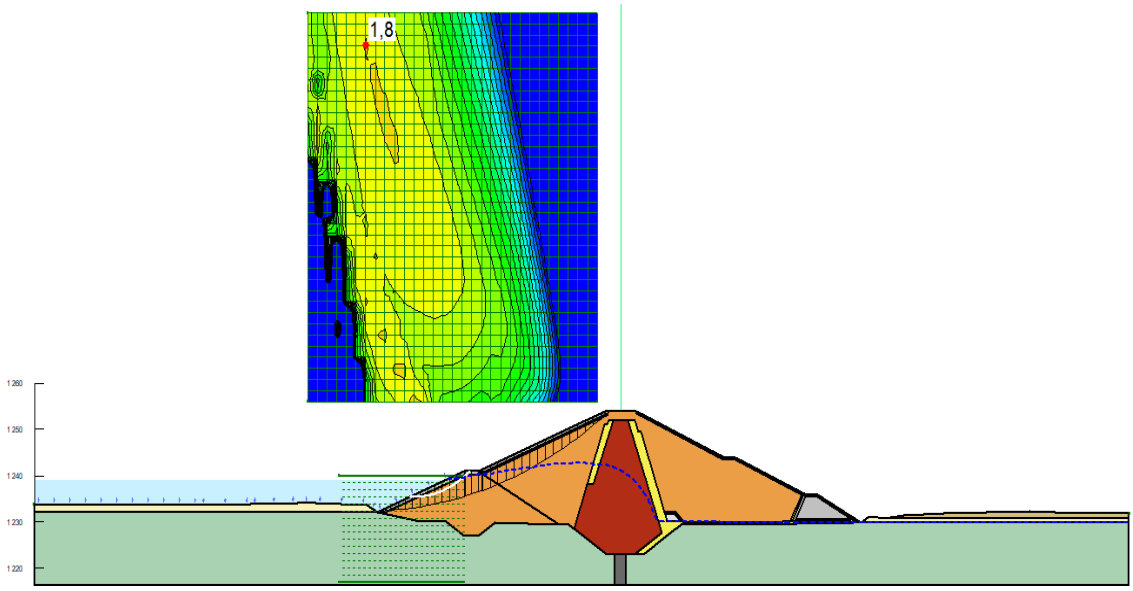

Figure 10 – Static Stability Check. Rapid Drawdown Phase. Upstream Slope. Superficial Rupture Surface.

Given the low seismicity of the site, global stability was verified under seismic conditions using pseudo-static analyses and the obtained global factors of safety were not conditioning.

3.5. Seepage Studies

The seepage studies were conducted using the finite element method and the software SEEP/W to analyse water flow through the dam body and foundation. The goal was to estimate seepage flows, determine the piezometric line within the embankment, and assess safety against hydraulic failure modes.

Six main cross-sections were analysed, selected based on the hydrogeological heterogeneity of the foundation. A triangular mesh with third-order integration was used for discretization. **Figure 11** illustrates one of the sections analysed (Pk 0+975), highlighting the segmentation of the mesh triangles and the materials used in the modelling.

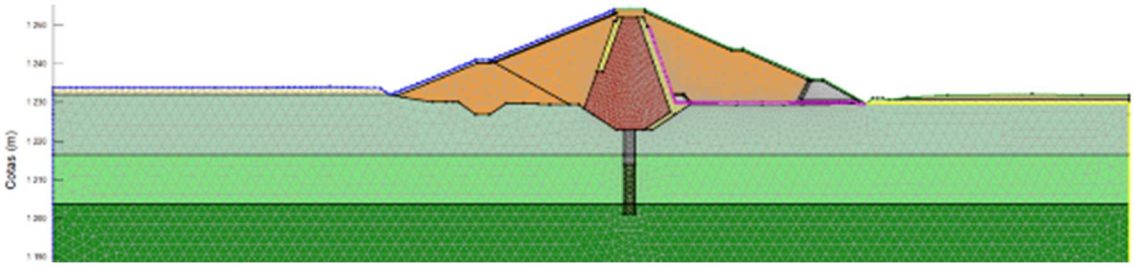

Figure 11 - PK 0+975 Profile Finite Element Mesh – (8265 triangles and 16766 nodal points)

Table 5 presents the permeability coefficients adopted for each material.

Table 5 - Permeability characteristics of embankment and foundation materials.

MATERIALS	Collor/Nº	Permeability Coefficient k (m/s)
Stabilizing Masses	2	1,0E-06
Core	1	1,0E-07
Filters	3	5,0E-05
Drain	4	1,0E-02
Rockfill	5, 6 e 7	1,0E-05
Organic Soil (Tv)	-	2,0E-08
ZG3 – Superficial Foundation	-	4,0E-07
ZG2a - Intermediate Foundation	-	5,0E-06
ZG2a – Injection curtain zone		1,5E-07
ZG1a - Deep Foundation	-	5,0E-06
ZG1a – Injection curtain zone		1,5E-07
ZG1b - Deep Foundation	-	1,0E-07
ZG1b – Injection curtain zone		1,0E-08
ZG1c - Deep Foundation	-	5,0E-06
ZG1c – Injection curtain zone		1,5E-07

The results include equipotential lines, hydraulic gradients, and seepage flow estimates under situations with and without foundation treatment. The treatment significantly reduced seepage, demonstrating its effectiveness in ensuring the structure's safety.

$$i = \left({}^{\Delta H}/_{L}\right) = 0{,}046$$

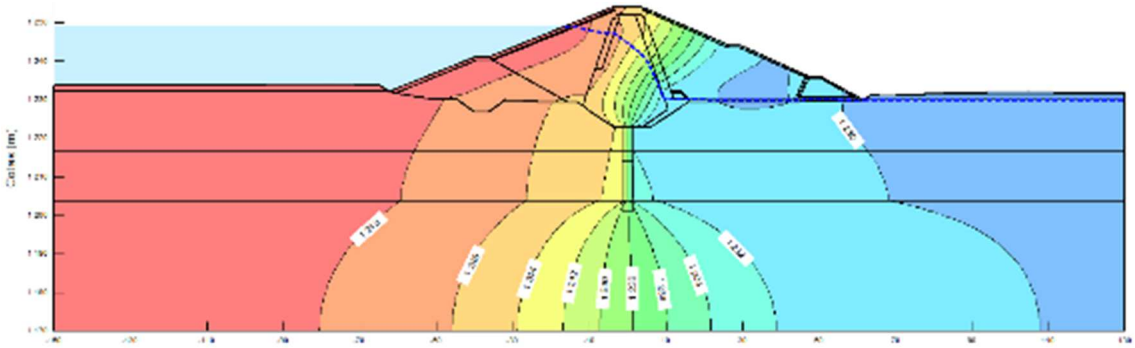

Figure 12 - Seepage studies. Equipotential lines and phreatic surface (section PK 0+975).

The most critical outflow gradient is observed at section PK 1+875, with a value of 0.197, resulting in a safety factor (FS) of 5.08.

The internal drainage system (**Figure 9**) – composed of the chimney filter, the longitudinal drainage trench downstream of the core and the nine transversal trenches – was designed to ensure efficient capture and drainage of percolated flows, with appropriate safety factors to prevent internal erosion and maintain the stability and integrity of the dam body and based on the results of the percolation studies.

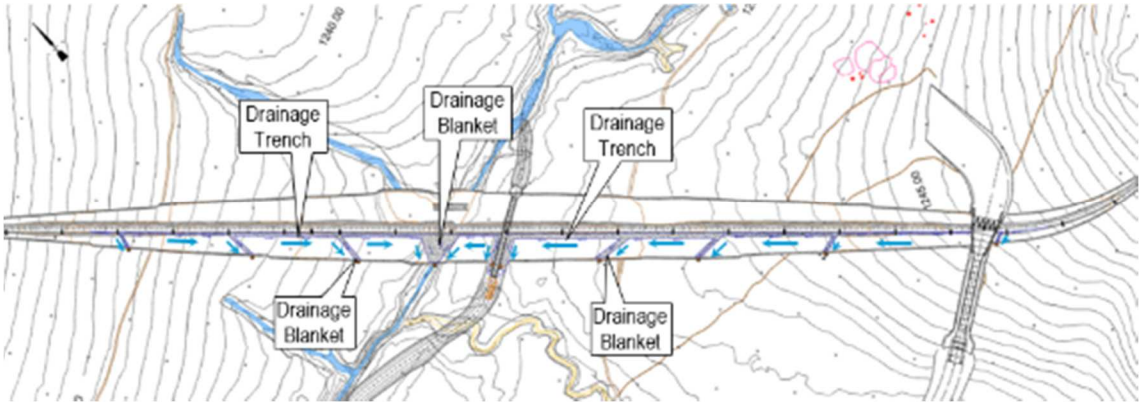

Figure 13 - Internal Drainage System Design

4. ADAPTATIONS CARRIED OUT DURING CONSTRUCTION PHASE

During the construction phase, a significant set of adaptations related to construction materials and waterproofing treatment were made, which are described below.

Additional borrow areas

During the design phase, four potential borrow areas were identified for material extraction for the construction of the core and the stabilizing shoulders. In general, these areas were found to contain materials with availability and characteristics suitable for dam construction.

At the beginning of the construction phase, after the completion of demining activities and some complementary investigation work, an additional potential borrow area was identified. This area exhibited characteristics suitable for the materials of the shoulders, offering better exploitation conditions. In general terms, this borrowing area comprises materials with more granular characteristics compared to the areas identified in the project, involving a greater exploration thickness, higher homogeneity, and consequently, a larger extraction volume (**Figure 14**).

Figure 14 - General appearance of the materials excavated in the additional borrow area.

Dispersive soils

The design initially anticipated the use of eluvial and weathered substrate deposits, characterized as clayey-sandy to sandy-silty-clayey (De), for the dam core. In the design phase, the hypothesis identified it the initial stage of design was later confirmed during the construction phase through supplementary laboratory tests: these materials exhibited moderate to low dispersive behavior, particularly the materials with high percentages of fine content and plasticity.

In fact, some samples of these materials exhibited dispersion values ranging from 10% to 54%, using the Double Hydrometer Method, and were classified as ND3 (slightly dispersive) and ND4 (moderately to slightly dispersive) in the Pinhole Method.

Under these conditions, based on the results of dispersity tests (Double Hydrometer and Pinhole tests) and identification tests, it was recommended that the use of these materials in the core be limited to soils with percentages of fine content below 60%, liquid limit below 35%, and plasticity index below 15% (**Figure 15** and **Figure 16**) which corresponded to the materials classified as non-dispersive.

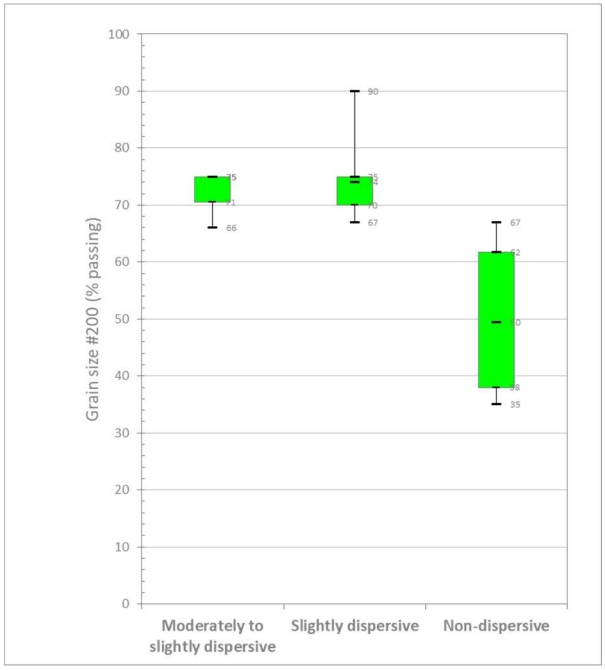

Figure 15 - Relationship between the percentage of fine materials (#200 ASTM) and the dispersivity potential of “De” materials.

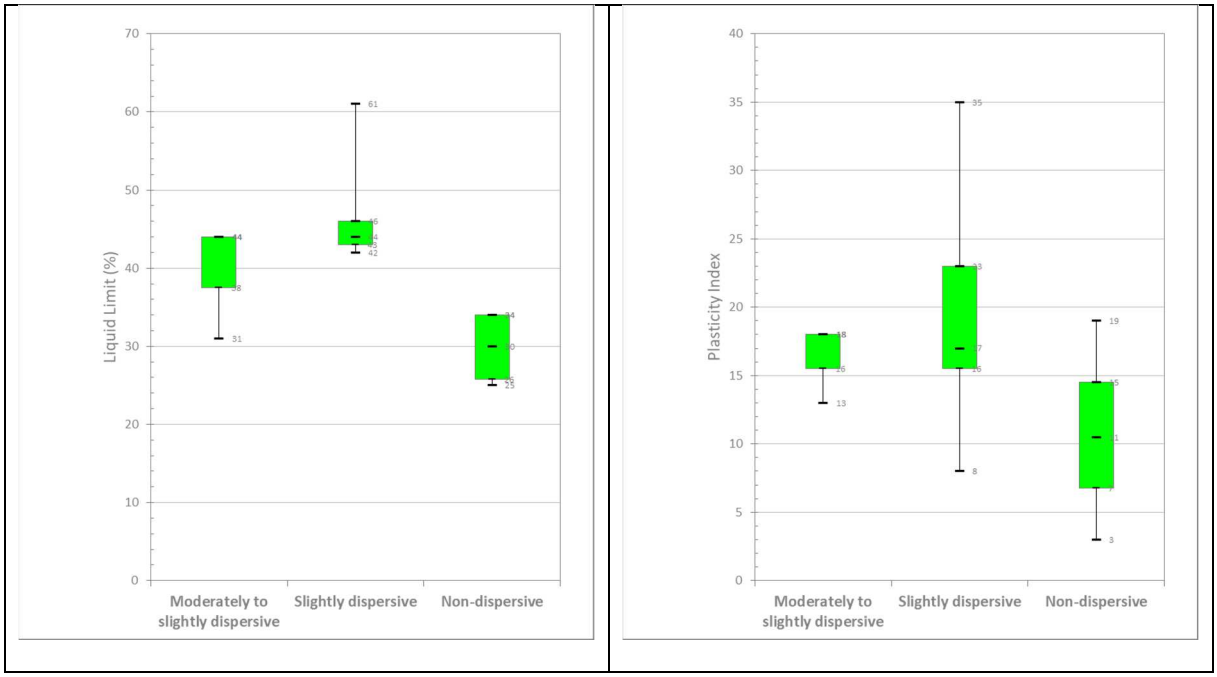

Figure 16 - Relationship between Atterberg limits and dispersivity potential of "De" materials.

These identification tests, commonly used in construction control, allowed the selection of the materials to be used in the dam construction, avoiding the use of potentially dispersive materials.

Filter materials

Regarding materials for filters, drains, aggregates for concrete, and protective riprap, two potential areas for quarry development were identified. One was located on the left bank, upstream of the dam axis, and the other was within the reservoir area, approximately 9.5 km from the dam site.

During the construction phase, following a detailed analysis of the characteristics of the available rock materials, their exploitation constraints and required volumes, it was deemed more appropriate to rely on existing quarries in the region.

The use of materials from these active quarries and sand pits also faced challenges related to obtaining grain sizes that fit the defined ranges. It was necessary to test different mixtures of natural materials (river sand) and materials produced in the quarries, as well as to adapt the design ranges.

Foundation treatment

Foundation treatment followed standard best practices, the criteria defined in the technical specifications, and the approved methodologies for injection, grout types, and quality control.

It is worth noting that the foundation treatment included preliminary geotechnical drilling and exploratory boreholes to confirm the geological-geotechnical complexity and the hydrological characteristics of the area with significant spatial variability.

The foundation levels of the core's cutoff trench were adjusted during the construction phase based on the results of the additional prospecting and the primary boreholes for the waterproofing treatment, to extend the cutoff trench to an injectable zone of the bedrock, that is, bypassing the more altered and fractured layers where cement grout slurries had no penetration.

The injectability and slurries were tested in trial blocks, with excavations carried out to confirm the slurry penetration (**Figure 17**).

Figure 17 - Slurry penetration confirmation in an excavation pit slope.

Additionally, given the geotechnical heterogeneity identified, a decision was made to systematically perform quaternary injection boreholes, regardless of the stopping criteria for tertiary injection boreholes, to minimize the possibility of localized zones with higher permeability.

From the analysis and interpretation of the collected data, particularly regarding permeability results and cement grout absorption recorded in the injection boreholes, it was noted that the impermeabilization curtain reached the limit of the low-permeability massif (generally less than 3 UL, occasionally less than 5 UL). A general decrease in grout absorption was observed from primary/secondary boreholes (frequently absorption values between 20-40kg/m to more than 40 kg/m) to tertiary/quaternary boreholes (down to absorption values below 10-20 kg/m, often less than 5 kg/m), demonstrating the efficiency of the adopted methodology. This efficiency was accompanied by a reduction in Lugeon absorption values, decreasing from values

commonly ranging between 10 and 40 Lugeons, in general, in the primary/secondary boreholes to values frequently below 3 to 5 Lugeons in the tertiary/quaternary boreholes.

Excavations

Currently, the Calucuve Dam is at an advanced stage of construction. The following images, taken in May and August 2024, highlight the progress of the works. In these photos, it is evident that the upstream cofferdam is nearly completed, while the embankments of the dam's core in the *cut-off* area are undergoing compaction (**Figure 18**). Photo a) presents an aerial view of the general layout of the dam, where the spillway excavations on the left abutment and the dam's implementation can be observed. Photo b) and Photo c) show the compaction work on the dam's core in the cut-off zone. Photo (d) shows a view from the top of the upstream cofferdam, with the diversion gallery visible in the background.

During the excavations for earthworks and for the hydraulic structures, geological and geotechnical mapping of the excavation faces was carried out. These activities validated, in general terms, the geological and geotechnical model developed during the design phase, with no significant variations being identified.

Figure 18 - Photos of the ongoing construction of the Calucuve Dam

5. CONCLUSIONS

The Execution Project of the Calucuve Dam has shown positive results, with the dam currently under construction and demonstrating good geotechnical performance. The geological and geotechnical conditions of the site have been carefully assessed and addressed, aiming to ensure the safety and durability of the structure. The dam's foundation was improved by constructing a cut-off curtain along the dam axis to reduce water seepage, as well as containment and consolidation curtains in highly fractured areas. These treatments have been rigorously implemented, ensuring the dam's efficiency and safety.

6. REFERENCES

[1] COBA (2024). Projeto 2. Barragem 128 - Calucuve. Projecto de Execução. Volume 1. Tomo 2 – Estudo Geológico Geotécnico nº 40622-C-PE-0102-ME-B

[2] COBA (2024). Projeto 2. Barragem 128 - Calucuve. Projecto de Execução. Volume 1. Tomo 3 – Corpo da Barragem. Documento nº 40622-C-PE-0103-ME-C

[3] COBA (2024). Projeto 2. Barragem 128 - Calucuve. Projecto de Execução. Volume 1. Tomo 7 – Tratamento de Fundação nº 40622-C-PE-0107-ME-B

[4] ICOLD (2016). Bulletin Nº. 148: Selecting Seismic Parameters for Large Dams – Guidelines (2016)

[5] CPRB - Comissão Portuguesa dos Regulamentos de Barragens (2018), "Regulamento de segurança de barragens" (RSB), Decreto-Lei Nº 21/2018, 28 de março

[6] CPRB - Comissão Portuguesa dos Regulamentos de Barragens (2019), "Documentos Técnicos de Apoio (DTA) ao RSB".

Fifth International Dam World Conference
PORTUGAL • LISBON • LNEC • APRIL 13-17, 2025
dam world 2025

DESIGN, SUPERVISION, AND TECHNICAL ASSISTANCE TO CONSTRUCTION OF IRCL SOUTHERN EXPANSION

Joana Antunes[1]	Lucas Repsold[2]	Lúcia Almeida[3]	Ricardo Sardinha[4]
COBA	COBA	COBA	COBA

ABSTRACT

COBA developed the Design for the construction of the Southern expansion of Cerro do Lobo mine tailings facility (IRCL). The contracted services with SOMINCOR also included the Construction Supervision and Technical Assistance to Construction. In this paper, the major aspects of the design, construction supervision and technical assistance to construction of the dike are addressed. The challenge of this project arises from the complexity and scale of the infrastructures while assuring that no mining activities were interrupted throughout construction.

The project involved constructing a containment dike with soil-rock fill, including a low permeability element, drainage system, instrumentation, and auxiliary infrastructure such as access roads, drainage channels, and tailings transport pipelines.

The project expanded the existing tailings deposition area from 187.9 hectares by an additional 18.5 hectares. The excavation of the dike supplied both the required volume for deposition and construction materials for the embankment.

The dike has a variable total height, reaching a maximum of 20 meters above the foundation, with a crest width between 12.5 and 15 meters and a total length of 1920 meters.

The foundation soil consists of Schist and Greywacke intercalations, and the excavation was carried out using mechanical equipment and explosives.

The downstream slope has a 1V:2H inclination with rip-rap protection, while the upstream slope has a 1V:2.5H inclination protected by a low permeability system of bentonite geocomposite and HDPE geomembrane anchored by trenches.

The drainage system includes internal drains for foundation water and anoxic drains for deposit water, directing them to the collector system for treatment and reuse. The instrumentation system comprises settlement plates, topographic marks, inclinometers, extensometers, total pressure cells, hydraulic piezometers, vibrating wire piezometers, and a telemetry system.

Project supervision controlled material quality, adherence to the 3-year deadline, and budget compliance. Geological mapping, topographic surveying, and safety management were also performed on-site by the COBA team.

Keywords: Tailings dam, Cerro do Lobo, embankment, soil-rock fill, geomembrane.

[1]j.antunes@cobagroup.com, Portugal

1. INTRODUCTION

As part of the Expansion of the Mining Tailings Facility at Cerro do Lobo for the Zinc Expansion Project (PEZ) by Sociedade Mineira de Neves Corvo (SOMINCOR), COBA has developed a design for the construction of the Southern expansion of the Cerro do Lobo mine tailings facility (IRCL) dike. This expansion has increased the deposition area from 187.9 hectares to 206.4 hectares, thereby enhancing the tailings disposal capacity from 33.3 million cubic meters to 50 million cubic meters.

The tailings deposition method at SOMINCOR involves depositing from perimeter berms (Fig. 1). This process is conducted by levels contained by the perimeter berms, with an average usable elevation of 2 m. Upon completing each level, the surfaces are progressively covered with waste rock, which is pushed from the berms inward. This supports the construction of the next level's perimeter berm, which is executed 40 m apart from the previous one, resulting in an overall slope of 5%. The berms are constructed with waste rock, featuring external slopes of 1:4 (V:H) and inner slopes of 1:2.5 (V:H).

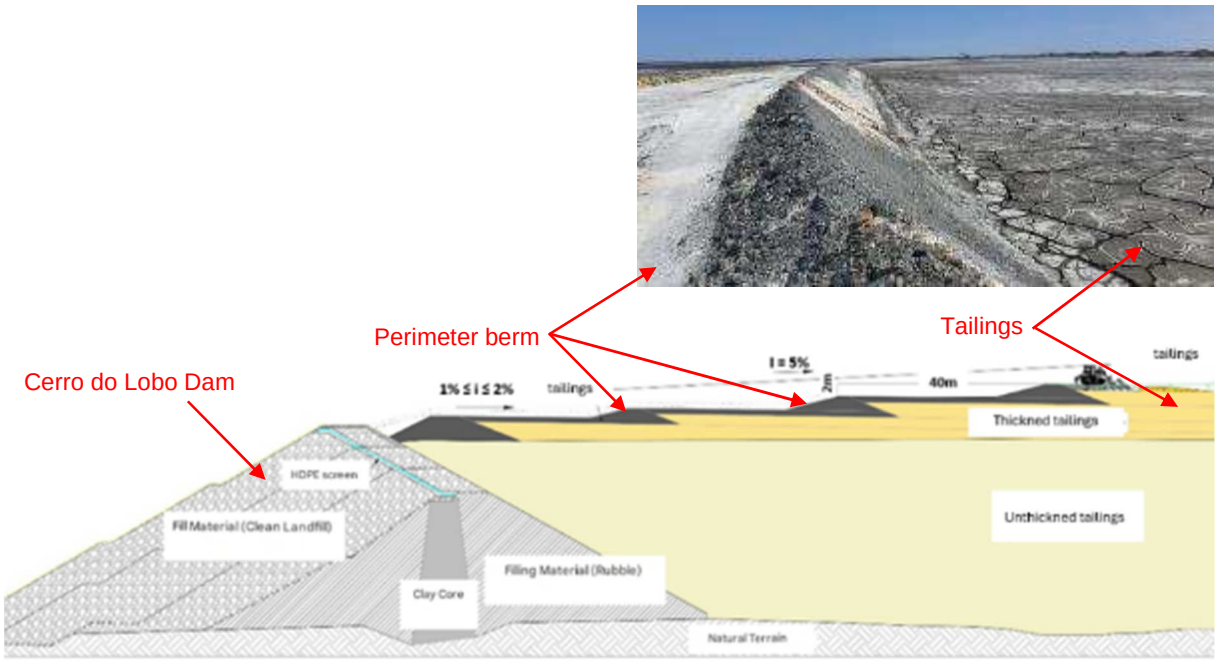

Fig. 1 - Tailing deposition method adopted at SOMINCOR

The IRCL Expansion Project, as illustrated in Fig. 2, will employ the same deposition method currently used at this facility. The project involves the construction of a new Southern containment dike to facilitate a horizontal expansion of an additional 10% area. Furthermore, it includes a vertical increase from the current five levels at level 255 to a total of thirteen levels, elevating the deposit to 282.5 meters. This expansion will be constructed using the remaining materials from the terrain excavation and foundation regularization.

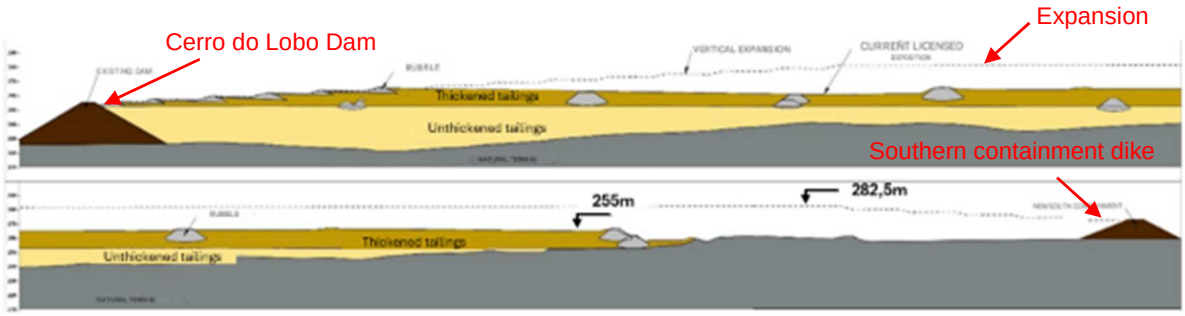

Fig. 2 - North-South Section through Cerro do Lobo Dam and the Southern containment dike

The project layout, shown in Fig. 3, includes a drainage system for acid water and run-off water, which involves the construction of four control reservoirs (Southwest, Northwest, North, and East Reservoirs). Additionally, the project covers the construction of auxiliary infrastructures to support IRCL operations, including access roads, drainage channels, and tailings transport pipelines.

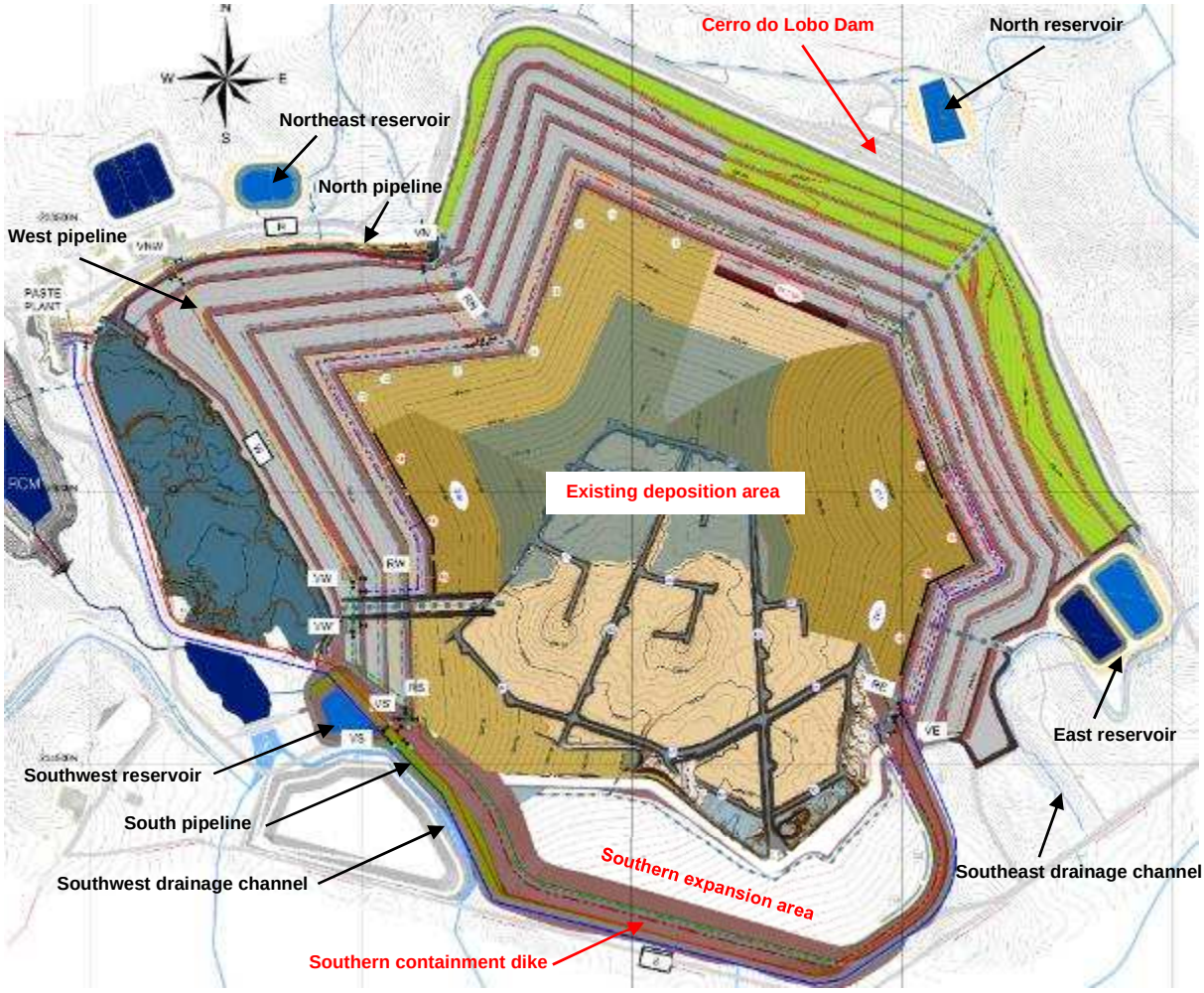

Fig. 3 - General Plan of IRCL deposition area

Given the scope and complexity of this project, this paper will address only the key aspects related to the construction of the Southern containment dike.

2. EARTHWORKS

The Earthworks chapter outlines the excavation and foundation preparation processes associated with the construction of the Southern containment dike for the IRCL expansion project. It presents the excavation methods and foundation preparation. Additionally, the chapter discusses the various typical cross-sections of the embankment, the materials used for construction, and the experimental landfills conducted to proper compaction and performance of the dike structure. Fig. 4 presents a general plan of the Southern expansion area and Fig. 5 presents the corresponding aero-photogrammetric survey after the construction of the Southern containment dike (January 2024).

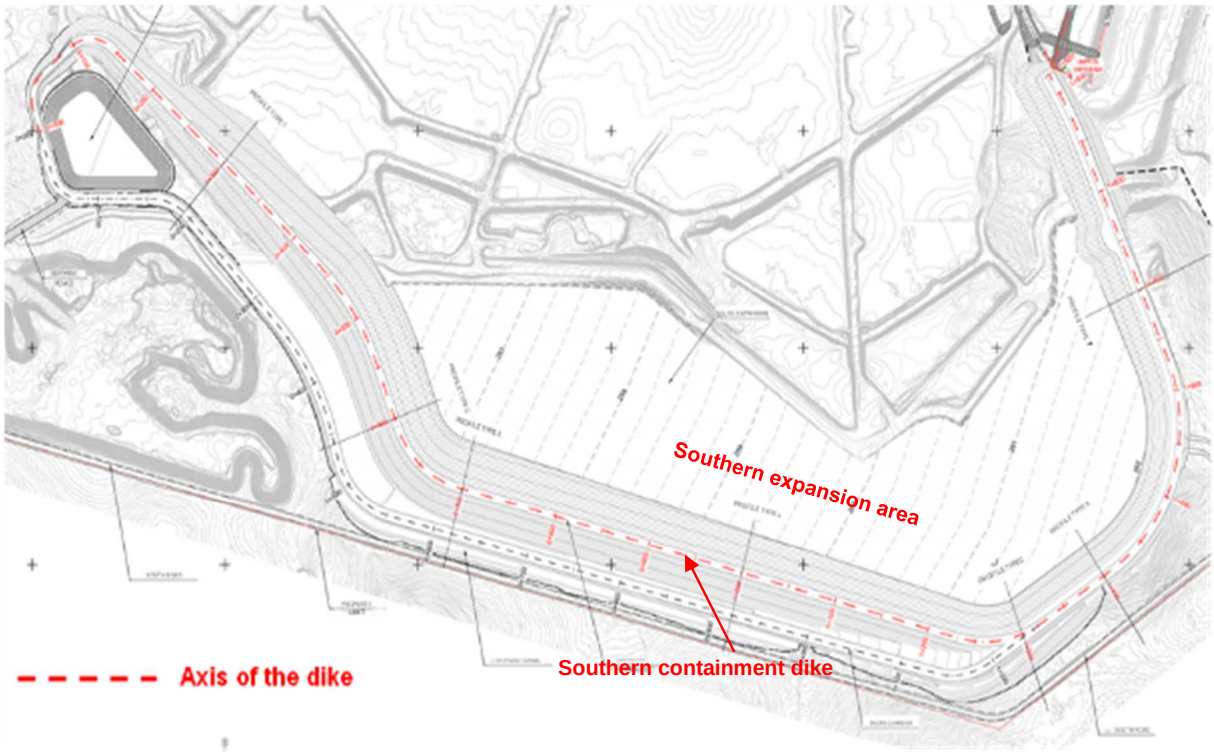

Fig. 4 - General plan of the Southern expansion area

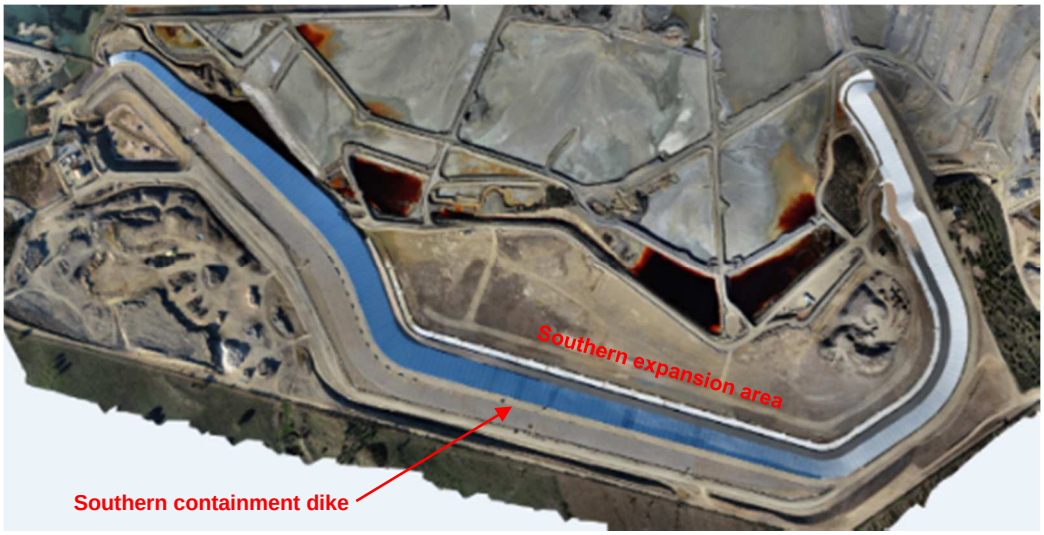

Fig. 5 - Aero-photogrammetric survey of the Southern expansion area (January, 2024)

2.1 Excavations

The excavations were conducted utilizing mechanical equipment and controlled explosives. The geological survey identified moderately weathered Schists and Greywackes (classified as W2-3) at the surface, with a degree of fracturing ranging from F3 to F4. These materials were generally assessed to be rippable.

Excavations on the most resistant materials were conducted using explosives. During these excavations, accelerometers were employed to monitor vibration levels. The allowable maximum peak vibration velocity was set at 10.0 mm/s. This threshold value for peak vibration velocity was never exceeded.

2.2 Foundation

The foundation preparation was executed with careful consideration of the soil's characteristics and density. All rippable rocks and loose soils were removed. The discontinuities in the rock mass, including secondary faults or fractures often filled with fine material, were treated to reduce permeability. Figure 6 illustrates an example of foundation preparation, where a depression was filled with cyclopean concrete.

Fig. 6 - Cyclopean concrete filling of depression on the foundation of the Southern containment dike

2.3 Typical cross-sections

Figure 7 shows a typical schematic cross-section of the embankment. The embankment's height varies, with a maximum height of 20 meters above the foundation. The crest width is between 12.5 and 15 meters at an elevation of 272.2 meters. The downstream slope has an inclination of 1V:2H and is protected with rip-rap. The upstream slope has an inclination of 1V:2.5H and is protected with a low permeability system. This system consists of a bentonite geocomposite and an HDPE geomembrane, secured by anchor trenches. Figure 8 provides a general view of the Southern containment dike after construction.

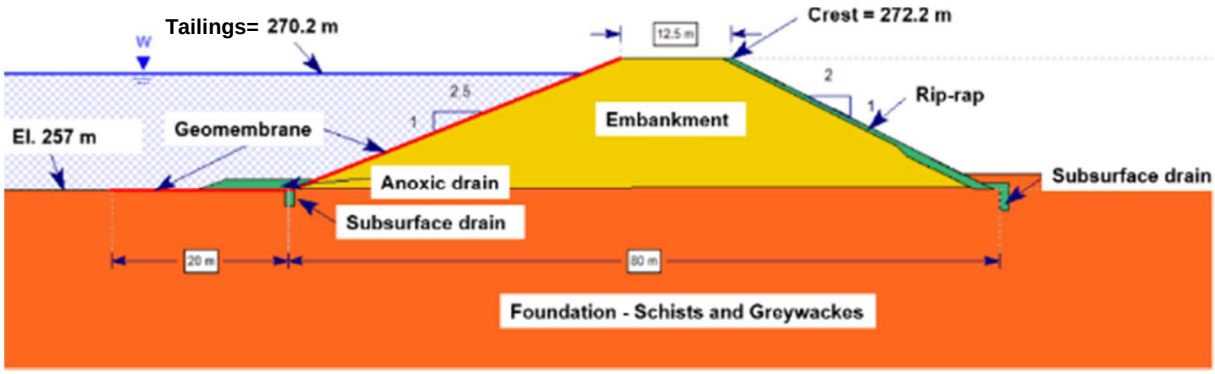

Fig. 7 - Typical schematic cross-section of the embankment (Pk 1+000)

Fig. 8 - General view of the Southern containment dike (January 2024)

The embankment was constructed using both available materials and those from site excavation. Materials obtained through mechanical excavation were processed, while those from explosive excavation were used directly. Figure 9 presents a general view of the earthworks.

Fig. 9 – General view of earthwork's

Figure 10 illustrates the various cross-sections developed during construction to maximize the utilization of available materials. Three distinct typical cross-sections of the dike were designed.

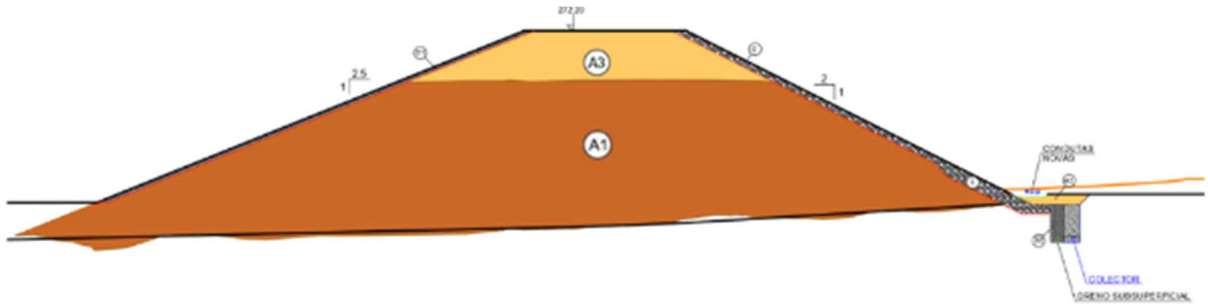

Fig. 10 - Cross-sectional profile of the South Confinement Dike

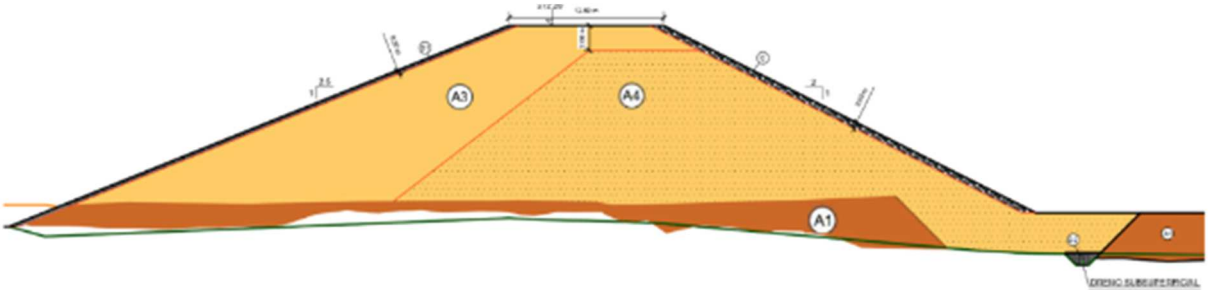

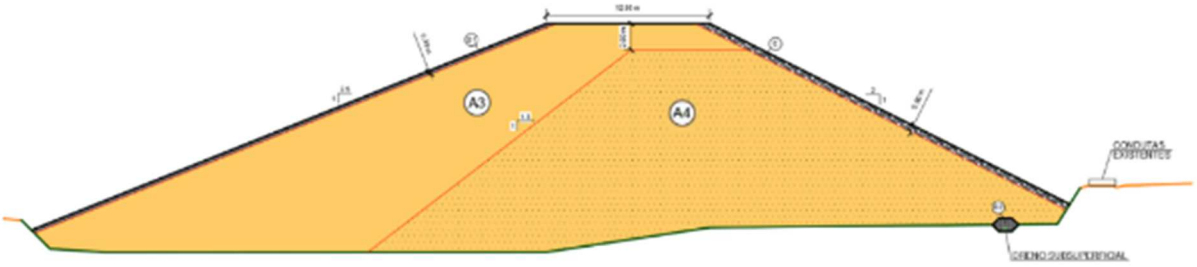

Fig. 11 - Cross-sectional profile of the South Confinement Dike

2.4 Dike materials

The construction of the dike involved utilizing various materials for different sections of the embankment. Table 1 and Fig. 11 illustrate the distinct materials used and their corresponding granulometric curves.

Table 1 - Materials used in the construction of the dike

Material designation	Material description	Site of application
A1	Soil-rockfill mixture	Embankment
A3	Soil-rockfill mixture	Embankment
A4	Rockfill with a wide range of particle sizes	Embankment
Bago de arroz	Crushed stone	Drainage system
Brita 4/12	Crushed stone	Drainage system
C	Rockfill	Downstream slope
H	Sand	Low permeability system
D1	Sand	Drainage system
D2	Crushed stones mixture	Drainage system

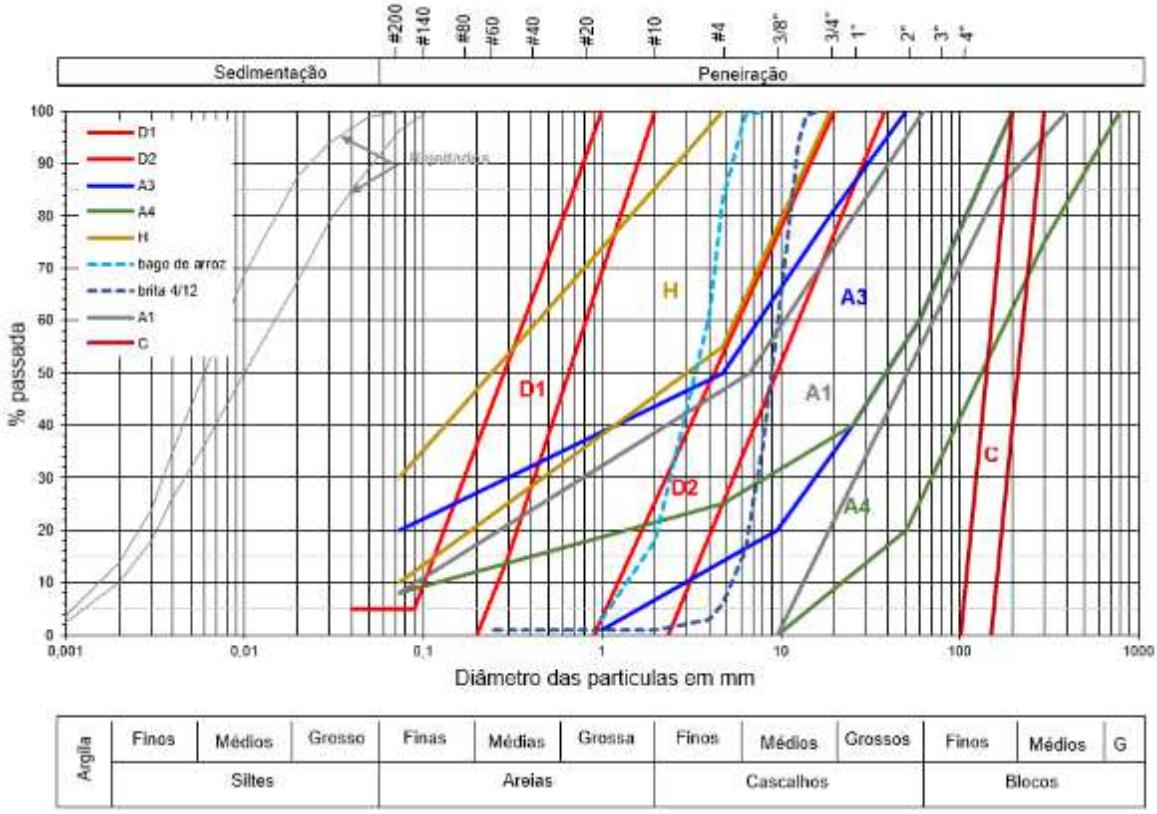

Fig. 12 - Granulometric curves of landfill materials

2.5 Embankment experimental study

The construction of the embankment commenced with an experimental study on material type A1. Given the material characteristics, an experimental section of embankment was conducted with a strip measuring 10 meters in width, 50 meters in length, and 0.80 meters in thickness. This layer was compacted using eight passes of a cylinder roller, and macro tests were performed on each layer after the sixth and eighth passes. To monitor settlements following compaction, eight topographic markers were installed. When settlement stabilization was not achieved after the initial eight passes, two additional passes were conducted, followed by two more macro tests.

Upon incorporating the use of available on-site materials in the cross-section, including processed materials from mechanical excavation and unprocessed materials from explosives excavation, new experimental embankments were subsequently constructed.

For the type A3 material (soil-rockfill mixture from processed material resulting from excavations with mechanical means), two embankment strips were considered, each 10 meters wide and 50 meters long, with thicknesses of 0.40 meters and 0.60 meters. These layers were compacted with a total of 8 passes. The compaction process was monitored in each strip after 6 and 8 passes using 4 sand bottle tests and 2 macro tests near the sand bottle

test locations. For the 0.60-meter-thick layer, the sand bottle tests were conducted at two depths: 5 centimeters from the surface and at the midpoint of the layer. Figure 13 illustrates a macro test being performed.

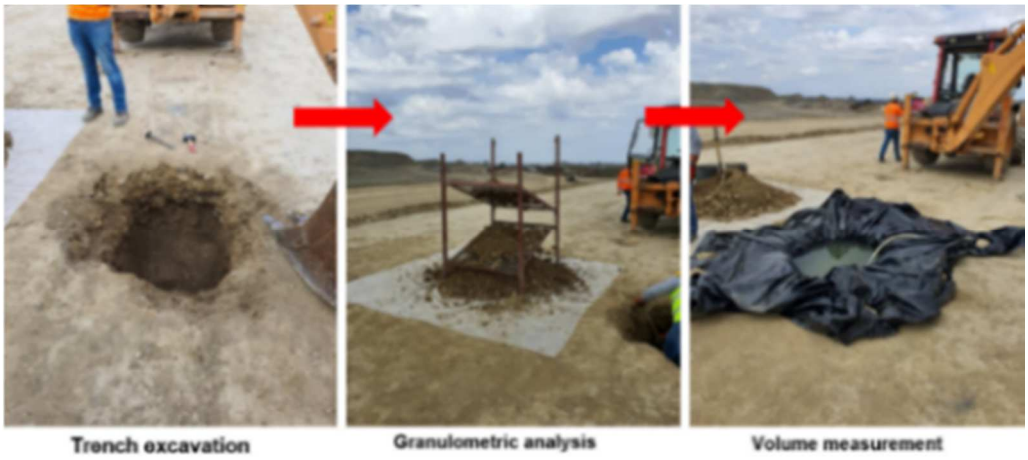

Fig. 13 – Execution of a macro test in A3 material type

For the type A4 material, which consists of a soil-rockfill mixture derived from unprocessed excavation material using explosives, an embankment strip measuring 10 meters in width, 50 meters in length, and 0.80 meters in thickness was evaluated. During the construction of this embankment strip, all blocks exceeding 0.60 meters in size were removed. The layer underwent compaction with a total of eight passes. One macro test was conducted after the sixth pass and two additional macro tests following the eighth pass. Similar to the procedure employed for the A1 type material, leveling marks were installed to monitor settlements. If the settlements had not stabilized after eight passes with the roller, an additional two passes would be performed along with two more macro tests. The materials were thoroughly watered throughout the process.

The experimental embankments in these materials enabled the evaluation of procedures for placement, irrigation, and compaction of landfill layers, as well as the respective control tests. Table 2 summarizes the key parameters obtained from the experimental landfills.

Table 2 - Parameters obtained from experimental landfills

Material	Parameter		
A1	Unit weight	γ (kN/m3)	21
	Optimum moisture content		watered abundantly
	Void ratio	e	≤ 0,18
	Percentage of fines (#200)		≤ 8 %
	Layer thickness (cm)		80
	Number of passes of the vibratory cylinder		8
A3	Unit weight	γ (kN/m3)	22,1
	Optimum moisture content	Wot (%)	5,6
	Percentage of fines (#200)		≤ 20 %
	Layer thickness (cm)		50
	Number of passes of the vibratory cylinder		8
	Optimum moisture content		Wot – Wot + 2%
	Compaction degree		98% of the reference Proctor
A4	Unit weight	γ (kN/m3)	21
	Optimum moisture content		watered abundantly
	Percentage of fines (#200)		≤ 8 %
	Void ratio	e	≤ 0,18
	Layer thickness (cm)		80
	Number of passes of the vibratory cylinder		10

3. LOW PERMEABILITY SYSTEM AND DRAINAGE SYSTEMS

This chapter presents the low permeability system and drainage systems associated with the construction of the IRCL Southern containment dike. The low permeability system consists of a bentonite geocomposite and a HDPE geomembrane, both installed in the upstream slope. To capture the remaining acid waters resultant from the tailings deposition process, an internal and an external drainage system, composed of subsurface drain, anoxic drain and collector drain, were implemented.

3.1 Low permeability system

Figure 13 illustrates the general layout of the low permeability system, with the area to be waterproofed highlighted in blue. At the base of the reservoir, the geomembrane was extended horizontally between 10 meters to 20 meters to enhance the seepage path.

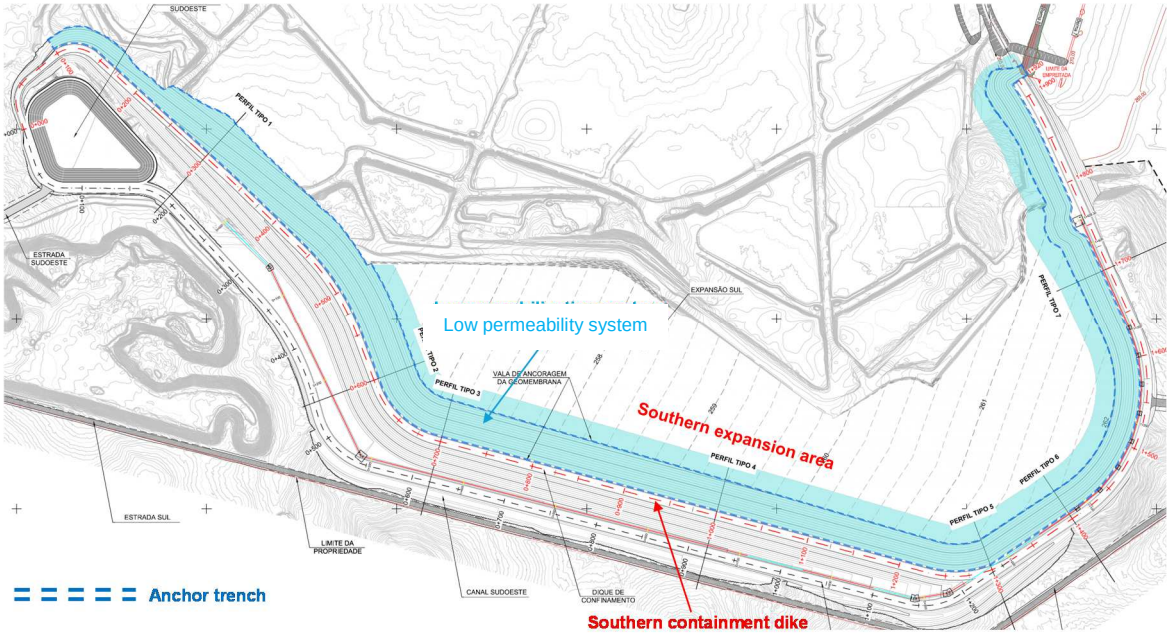

Fig. 14 - General low permeability system layout

The low permeability system of the dike embankment was achieved with bentonite geocomposite (GCL), formed by a layer of bentonite confined between two layers of geotextile, with very low permeability and self-sealing capacity, on which a smooth high-density polyethylene geomembrane (HDPE), 2.5 mm thick, and white outer face was installed, both fixed by anchor trenches. Fig. 15 presents a typical cross-section of the crest, illustrating the low permeability system and Fig. 16 illustrates the installation process.

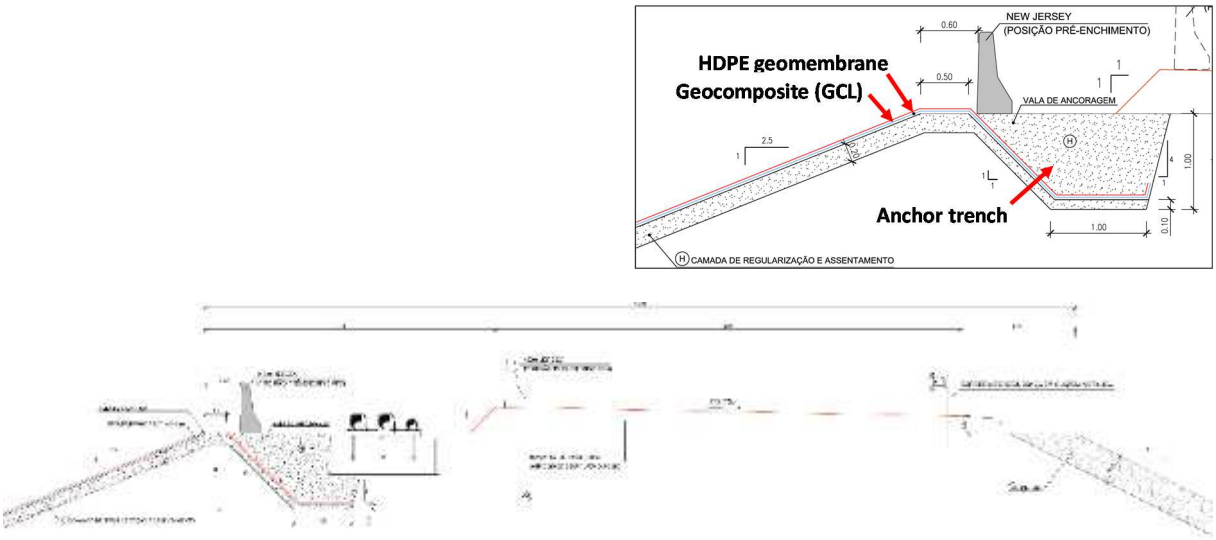

Fig. 15 - Typical cross-section of the crest illustrating the low permeability system

Fig. 16 – General view of the installation process of the low permeability system

The seals of the low permeability system were welded by double fusion welding, whenever possible, or by extrusion where double welding could not be applicable.

Both non-destructive and destructive tests were conducted to evaluate the welds. The non-destructive tests included the air pressure test and the spark test. The air pressure test, commonly used for linear geomembrane welds, was performed on all double welds created by fusion (Fig. 17). The spark test, on the other hand, was applied to all welds made by extrusion.

Fig. 17 - Pressure air test carried out in welding between geomembrane panels

For destructive testing, pull-out tests and shear tests were performed on samples taken from the existing welds. The pull-out test evaluates the weld strength, while the shear test assesses how the welding process impacts the strength of the geomembrane near the weld.

All damage to the geomembrane, whether detected during testing or caused by the removal of samples for destructive testing, was repaired using fusion-welded double-track patches, which were subsequently tested, or through extrusion welding.

3.2 Drainage system

The drainage system has subsurface drains for foundation percolates and an anoxic drain within the deposit, with all collected water directed to a collector system. Figure 17 shows the overall plan, and Figure 18 provides a typical cross-section.

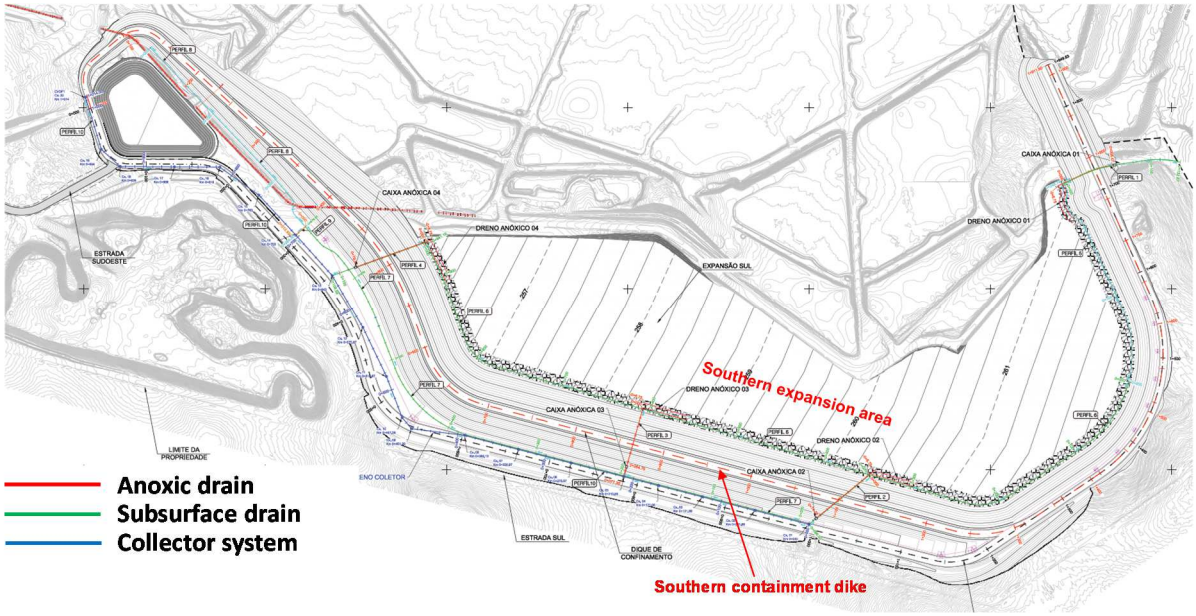

Fig. 18 - General drainage system layout

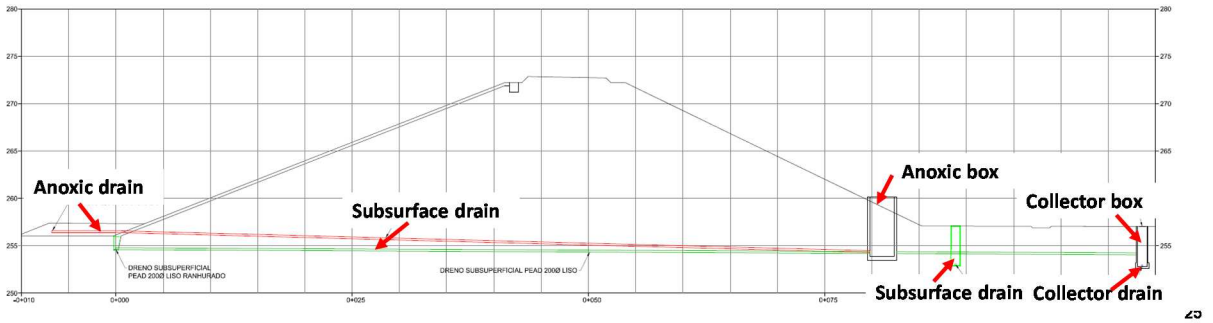

Fig. 19 - Typical cross-section of drainage system

The anoxic drain is situated near the base of the upstream slope of the dike and serves to lower the internal water level of the deposit. This drain operates while saturated, aiding in reducing the formation of precipitates that might obstruct its flow. It consists of three layers: a drainage layer (D2 material type, which includes HDPE drainpipes), a filter layer (D1 material type), and a mechanical protection layer ("Bago de arroz" material type). A protective geotextile is placed between the anoxic drain and the low permeability system. Figure 19 shows a typical cross-section of the anoxic drain, while Figure 20 illustrates its construction process.

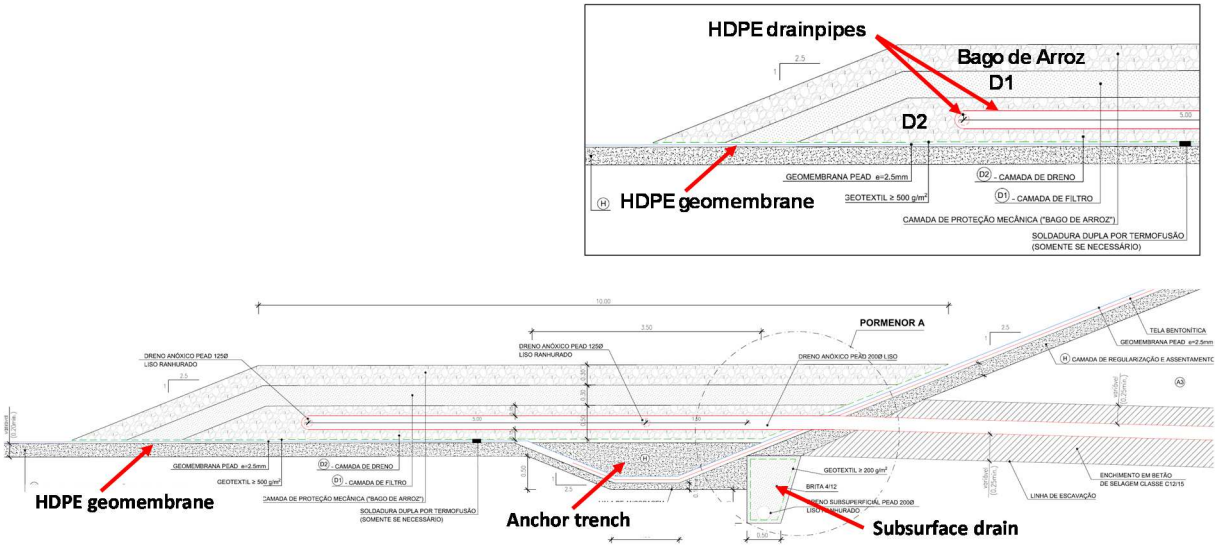

Fig. 20 - Typical cross-section of anoxic drain

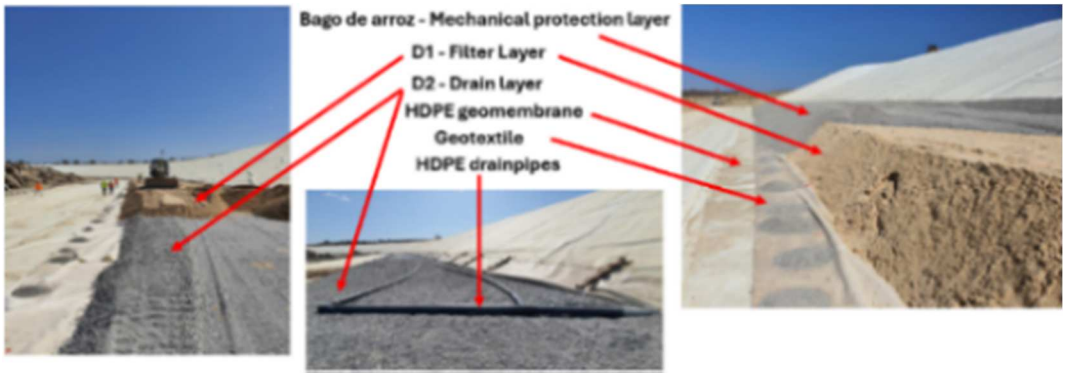

Fig. 21 – General view of the execution of anoxic drain

The subsurface drain, shown in Fig. 21, is positioned on the upstream side of the embankment. It is designed to intercept contaminated water that percolates through the foundation beneath the low permeability system. The drain consists of a drainpipe and crushed stone, enclosed in geotextile.

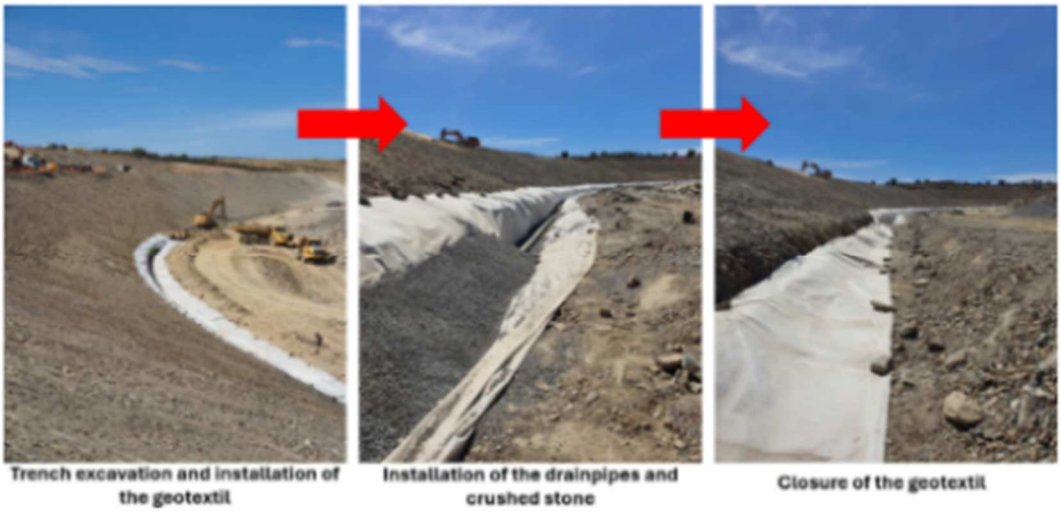

Fig. 22 - General view of the execution of subsurface drain in the upstream side of the dike

At the downstream base of the dike, another subsurface drain was installed, similar to the one on the upstream side, to intercept infiltrations from the tailings deposit. Its primary function is to limit the percolation of contaminated water into the water diversion channel of the Southern corridor.

The water gathered by the system, which includes the anoxic and subsurface drains, is routed to the collector drain. This drain follows the downstream side, parallel to the dike embankment, and directs the water to the Cerro da Mina Reservoir for treatment and industrial reuse. Figure 22 illustrates the construction of the downstream subsurface drain and the collector system.

Fig. 23 - General view of the execution of the collector system

4. INSTRUMENTATION SYSTEM

To monitor the behaviour of the structure during construction and post-construction, monitoring devices were installed on the dike. Fig. 24 illustrates the general monitoring plan. The monitoring system includes 4 settlement plates (PA), 52 topographic markers (M), 3 inclinometers/extensometers (I), 3 total pressure cells (VHP), 4 hydraulic piezometers (PZ), 4 vibrating wire piezometers (PCV), and a telemetry system.

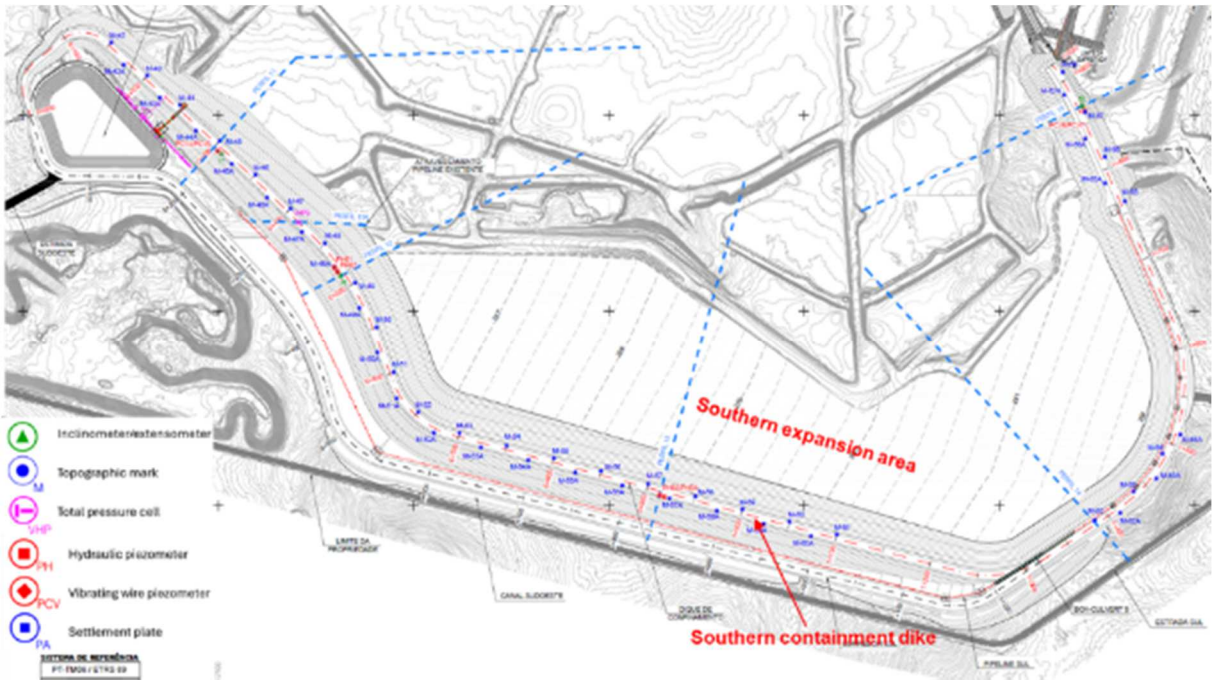

Fig. 24 - General monitoring plan

Figure 24 shows a typical cross-section indicating the locations of the observation devices, while Figure 25 provides an overview of these devices positioned on the crest of the dike. The vibrating wire piezometers installed at the foundation level enable the monitoring of the drainage system and the verification of seepage into the dike.

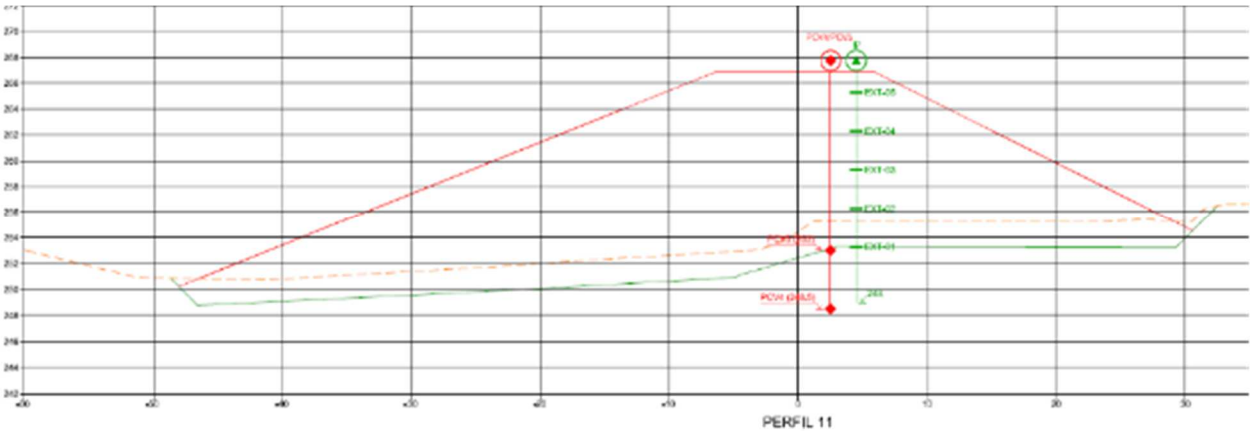

Fig. 25 – Observation devices placed in a typical cross-section

Fig. 26 – General view of the observation devices on the crest of the dike

A pre-existing pipeline required reinforcement with structural concrete to cross the embankment dike and was monitored throughout the construction process to ensure continuous operation. Settlement plates (PA), pressure cells (one horizontal and one vertical at elevation 258), and a vibrating wire piezometer (VHP) were installed along the pipeline, as shown in Figure 26. The observed settlements were minimal and did not compromise the pipeline's functionality (Fig. 28). Once the dike was completed, the pipeline was sealed and deactivated.

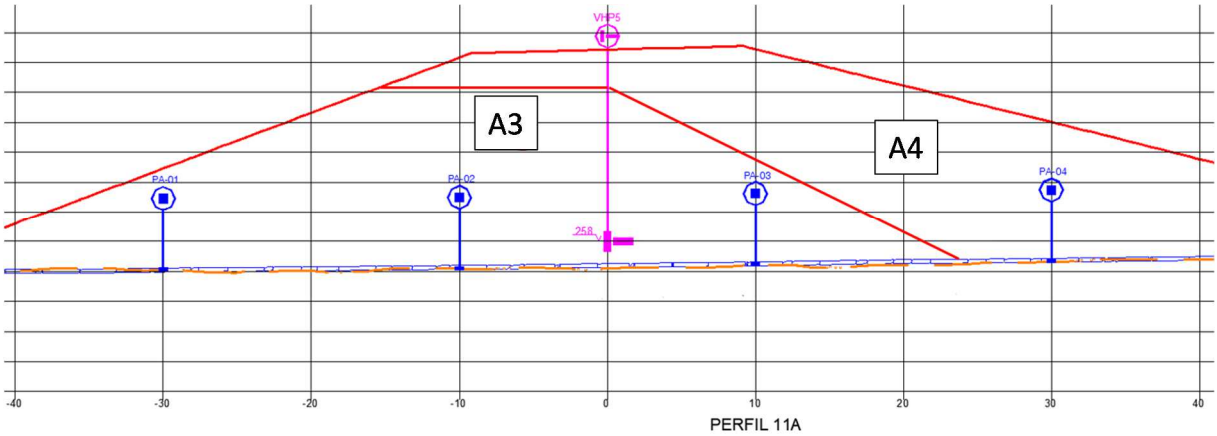

Fig. 27 - Location of the settlement plates along the existing pipeline

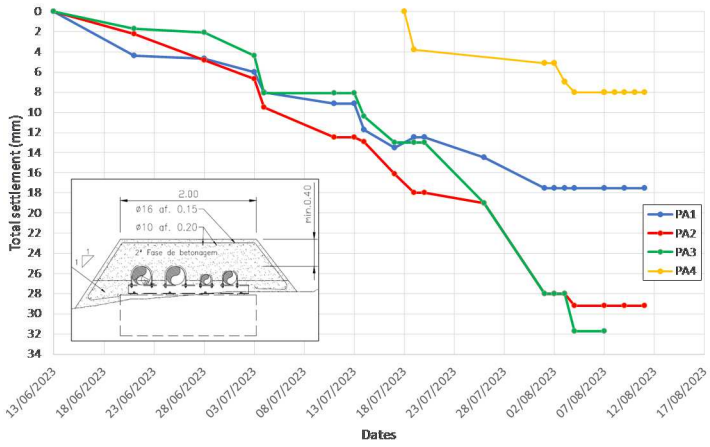

Fig. 28 – Total settlement of the settlement plates

The topographic marks were placed at the crest of the dike to measure surface displacements (both in altimetry and planimetry), establishing two alignments: one on the upstream side and the other on the downstream side of the dike crest. Additional benchmarks were also included to improve the accuracy of the topographic survey (Fig. 30 and Fig. 30).

Fig. 29 – (a) Typical topographic marks, (b) benchmarks

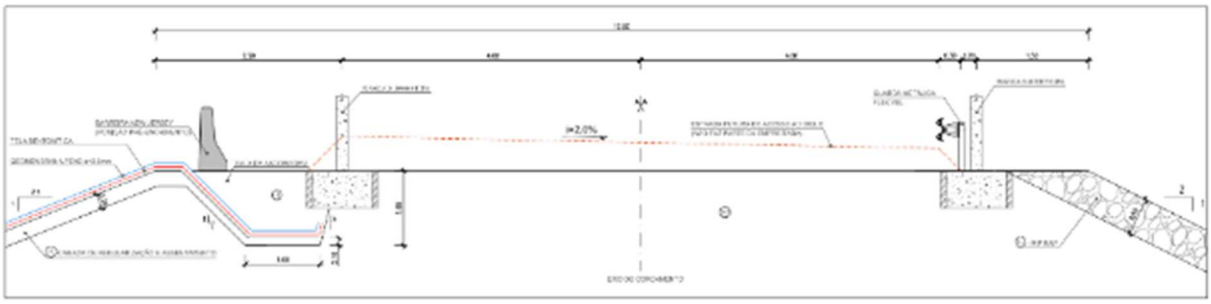

Fig. 30 - Position of the topographic marks on a typical cross-section of the dike

The inclinometers were installed to measure horizontal internal displacements within the dike and were coupled with magnetic rings (extensometers) to monitor internal settlements of the embankment. Both the inclinometers and the positioning of the extensometers were carried out as the landfill was being constructed (Fig. 31a).

The hydraulic piezometers were installed at the foundation and at the embankment-foundation interface. The PH61 and PH62 piezometers were installed and extended as the embankment was built, initially incorporating only a hole for anchoring in the foundation. The PH63 and PH64 piezometers were fully installed after the completion of the landfill (Fig. 31b).

The vibrating wire piezometers were positioned at the foundation and at the embankment-foundation interface (Fig. 31c). These devices were initially calibrated with factory settings, followed by a zeroing reading taken for a known water column, as recorded in the respective installation sheet. Since vibrating wire piezometers were already in use at the tailings facility, those installed as part of the Southern expansion were integrated into the existing telemetry system (Fig. 31d).

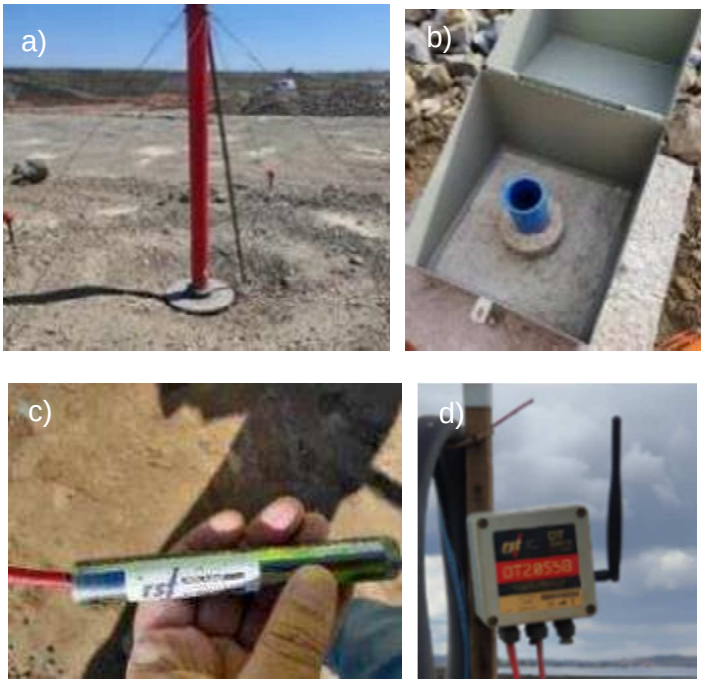

Fig. 31 – Overview of the observation devices: a) inclinometer/extensometer, b) hydraulic piezometer, c) vibrating wire piezometer, d) telemetry system

5. CONCLUSION

The construction of the Southern expansion of the Cerro do Lobo mine tailings facility (IRCL) presented a complex and demanding challenge, requiring careful coordination and a robust design approach. COBA's design, supervision, and technical assistance provided essential solutions to the successful implementation of the expansion, which increased the tailings deposition capacity while maintaining uninterrupted mining activities.

The project focused on the construction of the Southern containment dike, which required earthworks, the use of varied construction materials, and the implementation of a highly efficient low permeability and drainage system. Through the detailed analysis of soil-rock fill materials, earthworks, and foundation preparations, the team achieved the dike's stability and functionality. The utilization of mechanical and explosive excavation techniques, complemented by rigorous quality control and safety management, guaranteed the successful completion of this phase of the project.

The design of the dike's cross-sections, with its variable height and protective slopes, was tailored for optimal performance under varying site conditions and materials. The extensive use of bentonite geocomposite and HDPE geomembrane for the low permeability cover system played a key role in minimizing water percolation, ensuring the long-term stability and environmental safety of the tailings storage area.

Additionally, the drainage system, including subsurface drains and anoxic drains, was carefully integrated to manage potential acid water generation and minimize environmental impact. The collected water was directed to a centralized collector system, facilitating reuse and treatment, in line with SOMINCOR's commitment to sustainable mining practices.

The integration of a comprehensive instrumentation system, with settlement plates, inclinometers, piezometers, and a telemetry system, was crucial in monitoring the structure's behaviour during construction and post-construction.

In conclusion, the Southern expansion of the Cerro do Lobo tailings facility incorporates technology and robust construction methods, which increase the tailings storage capacity. This supports SOMINCOR’s long-term operational objectives while ensuring the safety and sustainability of the facility.

Fig. 32 - Southern expansion area at the beginning of the operation activities (January 2024)

REFERENCES

[1] Australian National Committee on Large Dams ANCOLD (ANCOLD) (2012 and 2019 addendum). Guidelines on Tailings Dams. Planning, Design, Construction, Operation and Closure;

[2] Canadian Dam Association CDA (CDA) (2013). Dam Safety Guidelines;

[3] Hoek, E. Practical Rock Engineering. Canadá, 2007;

[4] ICOLD (1994). Embankment Dams Granular Filters and Drains. Bulletin 95;

[5] Matos Fernandes, M. de (2015) Mecânica dos Solos – Introdução à Engenharia Geotécnica Volume 2. Porto: FEUP Edições, ISBN 978-972-752-178-4;

[6] NP EN 1990 – Bases para projetos de estruturas (EC0);

[7] NP EN 1991 – Bases de projeto e ações em estruturas (EC1);

[8] NP EN 1992 – Projeto de Estruturas de Betão (EC2);

[9] NP EN 1993 – Projeto de Estruturas de Aço (EC3);

[10] NP EN 1994 – Projeto de Estruturas mistas Aço-Betão (EC4);

[11] NP EN 1997 – Projeto Geotécnico (EC7);

[12] NP EN 206-1 – Betão: Especificação, desempenho, produção e conformidade;

[13] NP EN 13670-1 – Execução de estruturas de betão. Parte 1: Regras Gerais;

[14] NP EN 197-1 - Cimento. Parte 1: Composição, especificações e critérios de conformidade para cimentos correntes;

[15] NP EN 197-2 - Cimento. Parte 2: Avaliação de conformidade;

[16] NP EN 13251 - Geotêxteis e produtos relacionados. Características requeridas para a utilização em obras de terraplenagem, fundações e estruturas de suporte;

[17] NP EN 13256 - Geotêxteis e produtos relacionados. Características requeridas para a construção de túneis e obras subterrâneas;

[18] Ortigão, A. et al. (2018). A few lessons from two dams and an excavation instrumentation projects. International Symposium on Field Measurements in Geomechanics, 16-19 July 2018, PUC-Rio, p. 1-20, Rio de Janeiro;

[19] Regulamento de Segurança de Barragens (RSB) (2018). Decreto-Lei n.º 21/2018. Diário da República n.º 62/2018, Série I de 2018-03-28, Lisboa.

Fifth International Dam World Conference
PORTUGAL • LISBON • LNEC • APRIL 13-17, 2025
dam world 2025

THE USE OF SENTINEL-1 RADAR IMAGES ASSOCIATED WITH THE INSAR TECHNIQUE TO MONITOR SURFACE DISPLACEMENTS OF A DAM IN BRAZIL.

Deivid R. Viana
Universidade Federal do Rio de Janeiro

Marcos B. Mendonça[1]
Universidade Federal do Rio de Janeiro

Wagner B. Silva
Exército Brasileiro

Carlos H. O. Rocha
Eletrobras

ABSTRACT

Disasters related to dam failures have major impacts on society and can involve human, material and environmental damages. Decision-making in dam risk management depends on a plan for monitoring the mechanical performance of these structures. This study addresses the application of the interferometry technique using synthetic aperture radar (InSAR) to monitor surface displacements of dams. The study presents the monitoring of displacements of the crest and downstream slope of an earth and rockfill dam at a hydroelectric power plant in Minas Gerais State, Brazil. A set of 13 images and data from the Sentinel-1 radar sensor were used to estimate surface displacements of the dam from January to December 2019. Despite the limitations of the imaging technique, the results made it possible to infer a general behaviour regarding displacements, after comparing to geometric leveling, which confirms the potential for using InSAR as a complementary technique for monitoring slope displacements. It was observed that the spatial distribution of coherence in pairs of interferometric images was an important parameter indicating the influence of vegetation and proximity to water on data quality.

Keywords: Remote Sensing, Interferometry, Synthetic Aperture Radar, Mass Movements, Dams.

[1]mbm@poli.ufrj.br, Brazil.

1. INTRODUCTION

In Brazil, since 1960, there have been 140 cases of accidents in dams and their reservoirs [1]. Given the potential for high impacts resulting from dam failures, implementing dam safety measures is very important for decision-making on risk reduction actions. According to Menescal [2], a dam is considered safe when the hazards related to the dam's performance on life, health, property or the environment remain at acceptable risk levels. One of the main actions to monitor a dam is instrumentation, which in turn consists of measuring, mainly, displacements, stresses, discharge and piezometry [3].

Contextualizing land surface displacement monitoring, new measurement technologies have been developed using instruments installed directly on the ground or remotely [4, 5]. One of these technologies is remote sensing using the InSAR technique - synthetic aperture radar interferometry - which enables the acquisition of displacement data using temporal analysis.

Given the relatively innovative nature of InSAR technology for monitoring ground displacements, this paper aims to contribute to the discussion of its applicability, based on an experiment applied to the case of an earth and rockfill dam located in the southeast of Brazil. Given the specific nature of the subject, which is not usually covered in the classic geotechnical literature, the paper also presents some basic concepts and InSAR technique fundaments before the case study.

2. INSAR TECHNOLOGY

2.1. Interferometric waves

Interferometry is a technique applied to various areas of science and engineering. It can be defined as a technique for obtaining information from the superposition of electromagnetic waves emitted by sensors [6]. Since interference is a general phenomenon between waves, interferometry applies to various fields, such as mapping the earth's surface, detecting environmental changes, monitoring coastal areas and detecting moving targets, among other applications [7]. A wave (Figure 1) is characterized by amplitude, a measure of the height of the wave for a positive value and a negative value, frequency, the number of cycles per second, and phase, which is a quantity whose values are contained in the intervals [0, 2π] and which describes the direction of movement and the position or displacement of a point of vibration on the sinusoid in relation to a reference position [8]. Two waves are said to be in phase difference when, at any instant of time taken as a reference, the angular values of the two are different, Figure 2 [9].

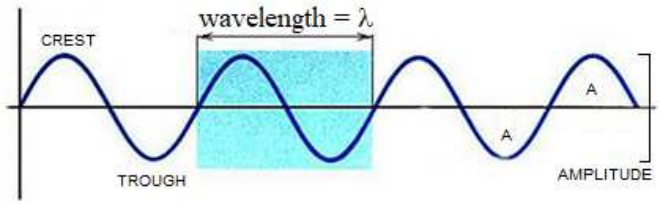

Figure 1 - Elements of waves

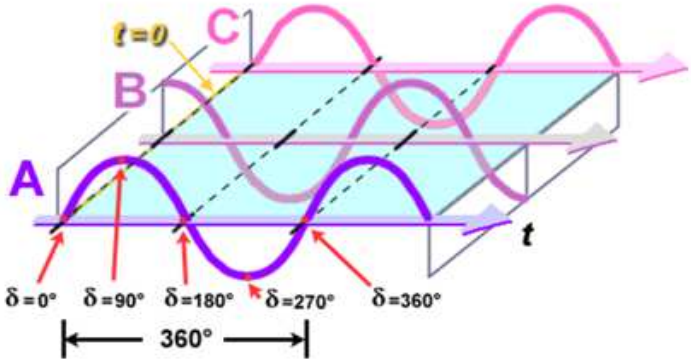

Figure 2 - Schematic representation of the phase in sine waves in a time interval t=0. Waves A and B are 90° out of phase while A and C are in phase

2.2. The SAR system

In the field of remote sensing, interferometry is used for three-dimensional imaging of the Earth's surface using Synthetic Aperture Radars (SAR) [10]. This technique involves combining two or more radar images of the same surface of interest, making it possible to obtain precise measurements from the interaction of the wave emitted by the radar and the imaged surface, thus making it possible to extract altimetric information. Figure 3 illustrates the geometry of the recording of a surface of interest at different times.

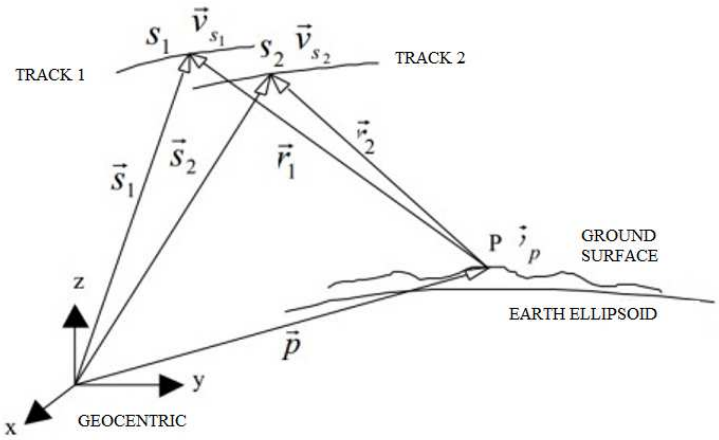

Figure 3 - Geometry of radar sensor imaging

S1 and S2 describe the radar sensors, Vs1 and Vs2 the displacement vector, P and p' the points of interest on the surface and r1 and r2 the distance between the radar and the point of interest, P. Among the characteristics of the electromagnetic waves emitted by radar, basically the information on the phase difference, differential interferometry, when imaging the surface at different times, describes the possible variations in the elevations of the imaged terrain, characterizing surface movements. Differential interferometry (DInSAR) is then based on calculating the phase difference of these waves in each pixel that forms the interferometric image, considering two images acquired at different times [11]. Because of its qualities, the SAR system has been used to image targets, monitor structures and mass movements on large mapping scales [12].

The waves emitted by the radar system use a band of the electromagnetic spectrum known as microwaves, between 225 MHz and 36 GHz, which allows the detection of different elements on the surface [13]. Figure 4 shows an image generated by the Sentinel-1 radar sensor covering an area of approximately 5,000km².

As important as the phase difference or other characteristics of SAR imaging, the coherence information, which is a measure of the variance of the interferometric phase obtained during processing, makes it possible to measure the level of correlation of two corresponding signals, referring to the same pixel of the images that form the interferometric pair or interferogram [14]. Coherence therefore may expresses the quality of the interferometric pair and, consequently, the reliability of the results.

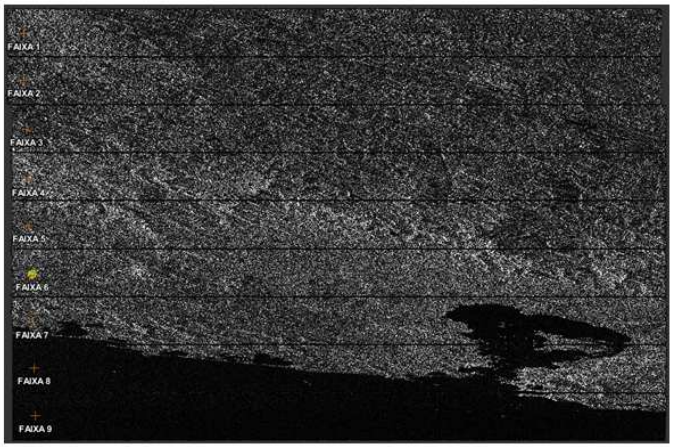

Figure 4 – Example of SAR image generated over a region of interest

2.3. SAR processing

As already mentioned, the main measure used in InSAR to verify displacements is the phase difference. The difference between the phases found in two shots, subject to the appropriate corrections, makes it possible to analyze the displacements on a given surface [15]. The

process of obtaining terrain displacement from knowledge of the phase difference involves the steps listed below:

a) Registration of the interferometric pair images

The InSAR configuration of repeated passes is based on the acquisition of two or more images at different times when only partial orbit information is known. This relative lack of knowledge causes a geometric incompatibility between the two images of the interferometric pair, especially in the case of passes at different times. Coregistration serves to minimize this problem, making the two images coincide geometrically (Figure 5) and favoring both the interferogram generation process and coherence estimation [16];

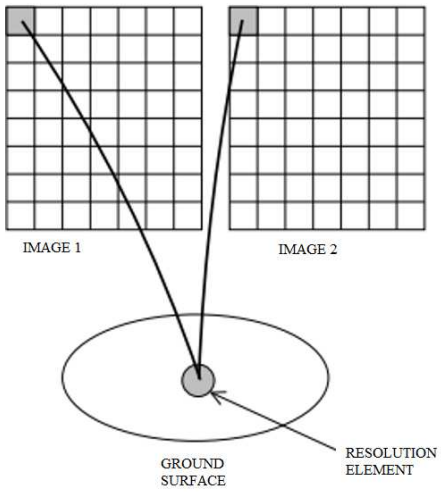

Figure 5 - Image co-registration

b) Generation of the interferogram (interferometric image)

Two registered images whose pixels describe the signal corresponding to the same element of the imaged surface allow the generation of an image resulting from the phase difference, pixel by pixel, called an interferogram [17]. The interferogram consists of an image containing phase information obtained by multiplying the pixel values of the first image (master), by the conjugates of the complex pixel values of the second image (slave).

c) Coherence image generation

According to the Canada Center for Remote Sensing (CCRS), interferometric coherence indicates, in the interferometric pair, whether a target surface has coherent or incoherent behavior, i.e. whether the signal of the waves received by the radar corresponds positionally to the two images of the evaluated pair. The coherence value ranges from zero, when there is

no correlation, to 1, when the correlation is perfect. Table 1 shows the coherence ranges and their respective quality classifications [18].

Factors that influence coherence in interferometric pairs include: density of vegetation cover (changes in vegetation position and wind action on vegetation); proximity to bodies of water; variations in the moisture content of targets; distance between satellites (baseline) in the same orbit when acquiring images; long time intervals between acquisitions.

Table 1 - Interferometric coherence thresholds for cartographic applications

Coherence	Quality
0,0 - 0,3	Low
0,3 - 0,5	Moderate
0,5 - 0,7	Good
0,7 - 1,0	Excellent

d) Removal of the flat earth phase

The so-called flat-earth phase contribution caused by the imaging geometry itself in the interferometric phase needs to be removed, keeping only the component of the phase related to the topography of the terrain.

e) Phase noise reduction

The quality of interferometric phase information can be degraded by existing noise from image acquisition to processing, compromising its application in certain research. Examples include speckle noise, thermal noise and special decorrelation [19].

f) Phase Unwrapping

The interferometric phase represented in the interferogram is ambiguous, represented from 0 to 2π, which implies that the number of cycles that the electromagnetic radiation has completed on its way back to the antenna is unknown, and this fact must be removed by transforming the relative phase into an absolute phase. This need to calculate the absolute phase causes a specific type of interferometric processing to be carried out, defined as “phase splitting”.

g) Generation of the displacement map.

When determining the displacement of targets, observations are made at different times t2 > t1, where the displacement vector D corresponds to what happened in the period t1-t2. Combinations are then made between the images to generate interferograms over the region of interest [20].

3. MATERIALS AND METHODS

The subject of this study is an earth and rockfill dam that makes up a complex of hydroelectric dams for power generation, 75 meters high and 358 meters long (Figure 6). The dam was spatially identified by extracting the coordinates shown in Table 2, using georeferenced optical images (Figures 8a and 8b). The points of interest were determined, coinciding with the existing surface markers (Figure 7) used for topographic monitoring of surface vertical displacements, installed on the crest and berms of the dam.

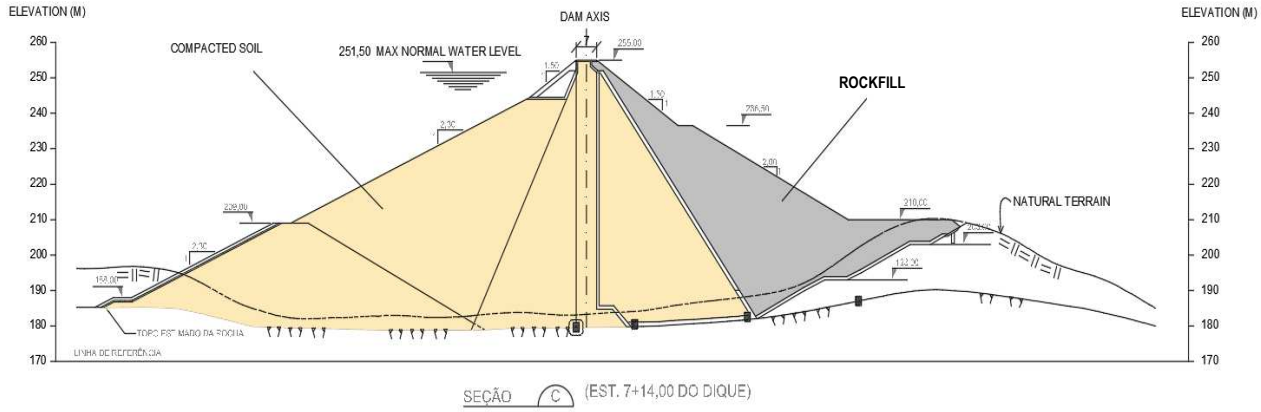

Figure 6 - Highest cross-section of the dam

Table 2 - Spatial identification of points of interest

POINT	LONG	LAT	LOCATION
RN-DE2-01	-42,8830	-21,9552	CREST
MS-DE2-01	-42,8826	-21,9550	
MS-DE2-02	-42,8822	-21,9548	
MS-DE2-03	-42,8819	-21,9546	
MS-DE2-06	-42,8816	-21,9544	
MS-DE2-07	-42,8813	-21,9543	
MS-DE2-10	-42,8811	-21,9541	
RN-DE2-02	-42,8807	-21,9540	
MS-DE2-04	-42,8822	-21,9552	BERM 1 (intermediate)
MS-DE2-08	-42,8819	-21,9550	
MS-DE2-11	-42,8815	-21,9548	
MS-DE2-05	-42,8812	-21,9547	BERM 2 (bottom)
MS-DE2-09	-42,8809	-21,9546	
MS-DE2-12	-42,8804	-21,9542	

Figure 7 - Existing surface landmark

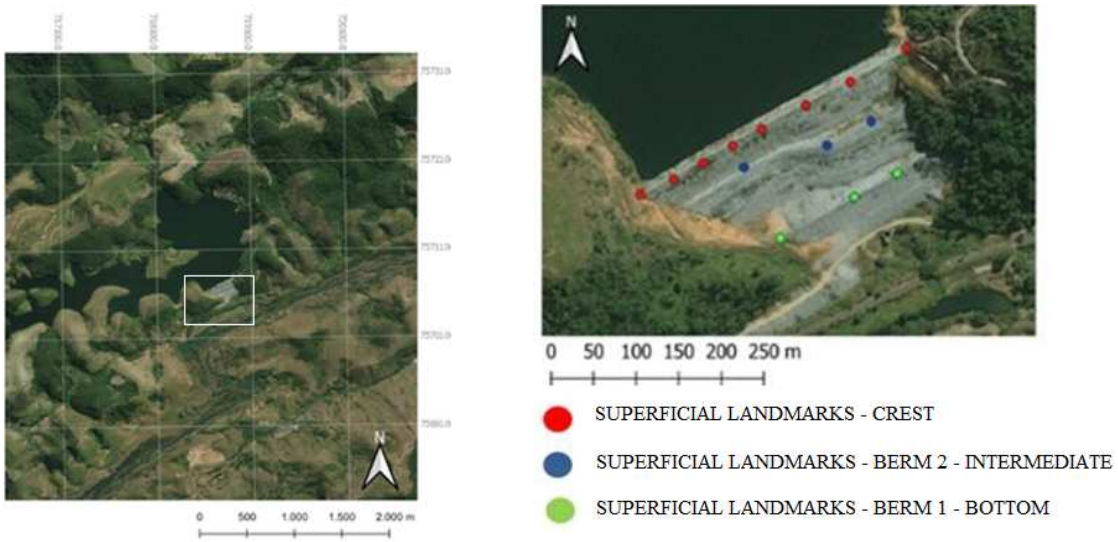

(a) **(b)**

Figure 8 - Images of the dam - a) Region where the dam is located with an indication of the area of interest; b) Image of the dam with the location of the existing surface markers.

The work was carried out by acquiring images from the European Space Agency's (ESA) Sentinel-1 radar sensor for 2019 to form the interferometric pairs. The SAR sensor of the Sentinel series is capable of obtaining both daytime and nighttime images, since its operating frequency is in the 8 to 4 GHz range or 3.8 - 7.5 cm, Band C. The radar supports HH+HV, VV+VH and HH polarization with a spatial resolution of 5 meters and a radiometric resolution of 10 bits. It has a heliocentric orbit, an altitude of 693 km and an inclination of 98.18°.

Processing was carried out using SNAP software version 6.0, which enabled information to be extracted on possible surface displacements by comparing pairs of images taken by the radar. The software used for image processing allows the operation to be automated, enabling several images to be analyzed simultaneously. Considering an annual period, the reference image (slave), dated January 17, 2019, was compared with other images, resulting in two

parameters for assessing surface displacements in the vertical direction: the coherence estimate (COH) and the surface displacements (DISPLAC) themselves. The pixels of the interferogram, defined as points of interest (POI), contain the location of the surface landmarks installed on the crest and surface of the dam berms. After interferometric processing, the displacement data was compared with the data generated by geometric leveling monitoring, provided by the dam owner.

4. RESULTS AND DISCUSSIONS

The analysis of the displacements obtained from the interferometric process considers the coherence indices for each point of interest on the dam's surface. The factors that influence the determination of the coherence index in interferometric pairs (see section 2.3) are present in the study region, as it is a region with dense vegetation cover, with the slope of the dam close to the body of water, as well as variations in rainfall and humidity. The interferometric pairs generated in the processing showed coherence indices between 0.09 and 0.87 at the points of interest, as shown in Figure 9.

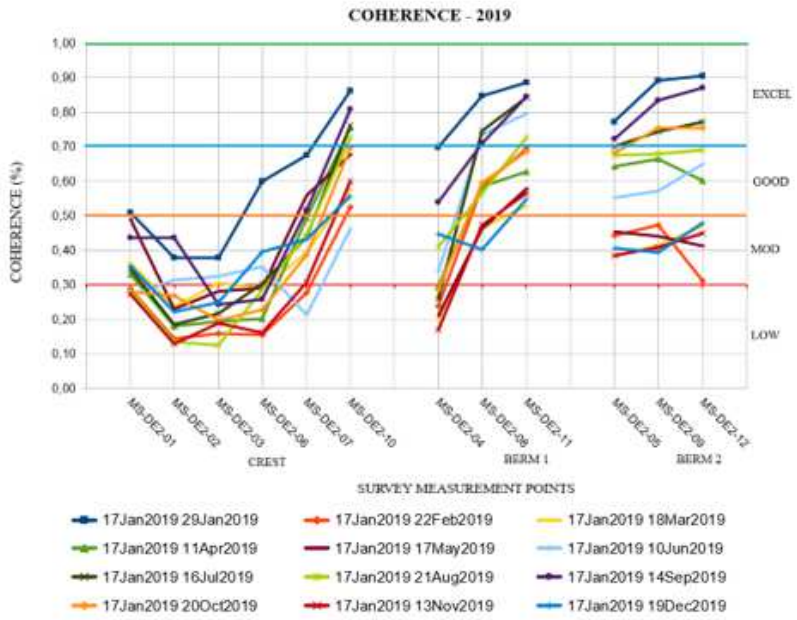

Figure 9 - Coherence indices at the points of interest over the period analyzed.

To qualify the data according to the CCRS classification shown in Table 1, the coherence indices of the interferometric pairs were evaluated. For this study, a filter was adopted, considering a minimum coherence value equal to or greater than 0.70 (excellent quality, see Table 1) to accept the displacement data. As a result, 26 surface landmark displacement data were generated with admissible coherence, classified as excellent quality. Table 3 shows the results of the displacements of the points of interest after applying the filter.

In general, the comparison between the InSAR and geometric leveling results showed similar qualitative behavior concerning the displacements of the surface landmarks. Fig. 10 shows the behavior of the displacements relating to the crest, berm 2 (middle) and berm 1 (bottom). The values measured by the two techniques for crest and berm 2 were close, with a better performance for berm 2 where the shape of the settlement distribution was more in line with that observed by geometric leveling. Greater differences were observed between the results for berm 1.

Table 3 - Coherence values (COH) of the interferometric pair and surface displacements (DISPLAC) in millimeters of the points of interest

SURFACE LANDMARKS	2019															
	INTERFEROMETRIC PAIR															
	17Jan2019 29Jan2019		17Jan2019 22Fev2019		17Jan2019 11Abr2019		17Jan2019 10Jun2019		17Jan2019 16Jul2019		17Jan2019 21Ago2019		17Jan2019 14Set2019		17Jan2019 20Out2019	
	COH	DISPLAC	COH	DISPLAC	COH	DISPLAC	COH	DISPLAC	COH	DISPLAC	COH	DISPLAC	COH	DISPLAC	COH	DISPLAC
MS-DE2-10	0,86	2,90			0,75	2,00					0,73	4,90	0,81	0,20	0,70	3,40
MS-DE2-04	0,70	0,60														
MS-DE2-08							0,73	1,60	0,75	0,20			0,71	0,10		
MS-DE2-11	0,89	0,90	0,70	4,60			0,79	1,20	0,84	0,00	0,73	4,40	0,84	0,10		
MS-DE2-05	0,77	-1,20							0,70	0,00			0,72	0,60		
MS-DE2-09	0,89	-0,40							0,74	0,40			0,84	0,10	0,75	1,20
MS-DE2-12	0,91	-1,30							0,77	0,90			0,87	0,60	0,75	2,80

(a)

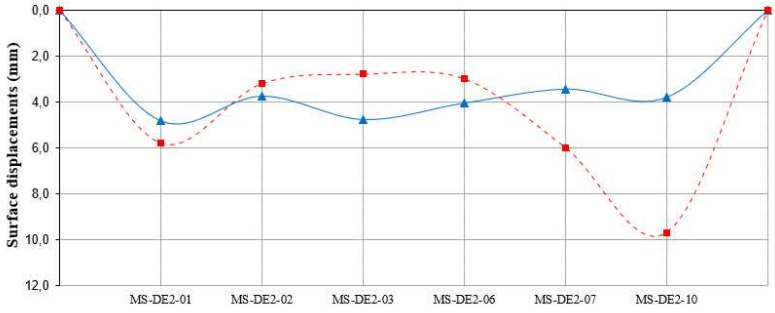

SUPERFICIAL LANDMARKS - Crest

INSAR 08/21/2019 - GEOMETRIC LEVELLING 08/27/2019

(b)

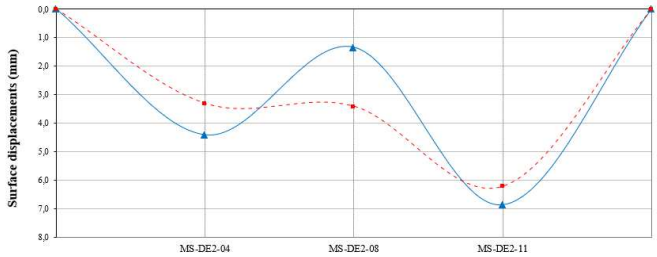

SUPERFICIAL LANDMARKS - Berm 2 (intermediate)

INSAR 08/21/2019 - GEOMETRIC LEVELLING 08/27/2019

(c)

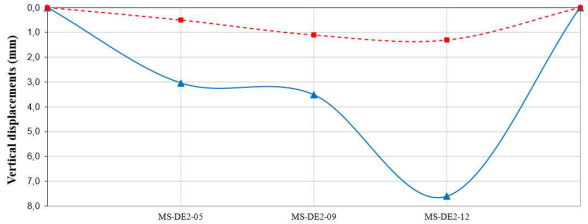

SUPERFICIAL LANDMARKS - Berm 1 (bottom)

INSAR 08/21/2019 - GEOMETRIC LEVELLING 08/27/2019

Figure 10 - Comparison of InSAR displacements versus geometric leveling of points of interest – a) dam crest; (b) Berm 1 (intermediate); (c) Berm 2 (bottom)

5. CONCLUSIONS AND FINAL CONSIDERATIONS

The application of InSAR technology in the case studied proved to be very useful in providing important complementary data for monitoring slope displacements over time, with the advantage that it is relatively easy to create a time series with shorter time intervals, which in the case of the Sentinel-1 mission is 12 days, although it is necessary to consider the limitations mainly related to the quality of the images.

The InSAR technique, combining data from pairs of synthetic aperture radar images and a digital elevation model, proved to be satisfactory for obtaining information on the surface displacement of the predetermined targets (surface landmarks) of the structure analyzed, which consisted of an earth and rockfill dam, represented by settlement and uplifts (positive and negative values, respectively).

In general, it should be noted that the principles of the technique allow the generation of elevation maps and deformation maps with kilometric extensions and millimetric precision for displacements, which, together with the possibility of increasing the frequency of monitoring surface displacements compared to topography, represents a significant gain for the geotechnical monitoring of natural terrain and the structures built on it, such as dams, roads and buildings.

However, some factors limit the application of the InSAR technique. The most severe of these is temporal de-correlation, due to the non-coherent displacement of the scatterers that make up a target, evidenced by the existence of landmarks with low coherence, aggravated by the existence of an envelope made up of dense vegetation and the reservoir's water depth.

Considering the inherent limitations of the technique, with its appropriate controls and corrections, the results of the work, using an earth and rockfill dam as a case study, confirmed the feasibility of using InSAR as a complementary technique for monitoring slope displacements. Other work carried out on hydroelectric dam structures confirms the applicability of the technique, Al-Husseinawi et al [21] demonstrated the monitoring of the Darbandikhan dam in northeastern Iraq to assess its stability after a 7.3 Mw earthquake, Milillo et al [22] monitored the seasonal deformation induced in the Pertusillo dam (Basilicata, Italy) using multitemporal SAR data analysis, in addition, preventive work such as the early detection of the instability of the Mosul dam with InSAR led to a maintenance plan to stabilize the dam's foundation before it became a disaster [23], and SENTINEL-1 SAR data was used for dynamic monitoring of ground displacement in the Tuscany region of Italy [24].

The results presented here are part of a study of the geotechnical behavior of the dam based on the evolution of the dam's displacements over two years, which will be the subject of study in future work.

ACKNOWLEDGMENTS

We thank the National Council for Scientific and Technological Development (CNPq - Processo: 302835/2022-9) and Eletrobras for supporting the development of this study.

REFERENCES

[1] Comitê Brasileiro de Barragens – CBDB (2023). Disponível em: < http://www.cbdb.org.br> Acesso em: 23 ago 2023.

[2] Menescal, R. A. (2009). Gestão de segurança de barragens no Brasil: proposta de um sistema integrado, descentralizado, transparente e participativo. Tese de Doutorado. Universidade Federal do Ceará. Curso de Pós-Graduação em Engenharia Civil.

[3] Fontenelle, A. S. (2007). Proposta Metodológica de Avaliação de Riscos em Barragens no Nordeste Brasileiro–estudo de caso: barragens do estado do Ceará. Universidade Federal do Ceará, Fortaleza.

[4] Nadim F., Lacasse S (2008) Strategies for mitigation of risk associated with landslides. In: Sassa K, Canuti P (eds), Landslides – Disaster Risk Reduction, Berlin, Heidelberg: Springer Berlin Heidelberg, pp. 31–61

[5] Zaki, A., Chai, H. K., Razak, H. A., Shiotani, T. (2014). Monitoring and evaluating the stability of soil slopes: a review on various available methods and feasibility of acoustic emission technique. Comptes Rendus Geoscience, v. 346, n. 9-10, p. 223-232.

[6] Allen, C. T. (1995). Interferometric synthetic aperture radar, IEEE Geoscience and Remote Sensing Society Newsletter, n. 96, pp. 6-13.

[7] Bunch, B, Bunch, B. H., Hellemans, A. (2004). The history of science and technology: a browser's guide to the great discoveries, inventions, and the people who made them, from the dawn of time to today. Houghton Mifflin Harcourt.

[8] Van Der Sanden, J. J. (1997). Radar remote sensing to support tropical forest management. 1997, 330 p. Doctoral Thesis - Wageningen Agricultural University. Series 5. Tropenbos-Guyana, Georgetown. 1997. ISBN: 90-5485-778-1

[9] Gaboardi, C. (2002). Utilização De Imagem de Coerência Sar para Classificação do Uso da Terra: Floresta Nacional do Tapajós. 2002. 137p. (INPE-9612-TDI/842). São José dos Campos: INPE.

[10] Romeiser, R., Thompson, D. R., “Section 2: Fundamentals”. (2002). In: KoRIOLiS – Study on concepts for Radar interferometry from satellites for Ocean (and Land) applications (In german: Studie zu Konzepten für Radar-Interferometrie über Ozeanen (und Land) im Rahmen zukünftiger Satellitenmissionen).

[11] Goldstein, R. M., Zebker, H. A. (1987). Interferometric Radar Measurements of Ocean Surface Currents, Nature, v. 328, n. 6132, pp. 707-709.

[12] Lillesand, T.M., Kiefer, R.W. (1994). Remote sensing and image interpretation. 3rd ed. John Wiley and Sons, New York.

[13] Schrader, S.; Pouncey, R. (1997). Erdas Field Guide. 4. ed. Atlanta: Erdas Inc, 1997. 656p.

[14] Zebker, H. A. (2000). Studying the Earth with interferometric radar. Computing in Science and Engineering, v. 2, n. 3, p. 52–60.

[15] Goldstein, R. M., Zebker, H. A., Werner, C. L. (1998). Satellite radar interferometry: two-dimensional phase unwrapping. Radio Science 23 (4), 713-720.

[16] Tomiyasu, K. (1978). Tutorial review on synthetic aperture radar (SAR) with application to imaging of the ocean surface. Proceedings of the IEEE. V. 66, No. 5, pp. 563-584.

[17] Nievinski, F. G. (2004). Interferometria por radar de abertura sintética (InSAR).

[18] CCRS. (1999) Fundamentals of Remote Sensing. A Canada Centre for Remote Sensing Tutorial.

[19] Gens, R. (1998). Quality assessment of SAR interferometric data. Doctoral Thesis. Hannover: Technishe Universität Hannover. 119 p.

[20] Sandwell, D.T., Price, E.J. (1998). Phase gradient approach to stacking interferograms. Journal of Geophysical Research 103 (B12).

[21] Al-Husseinawi, Y., Li, Z., Clarke, P., Edwards, S. (2018). Evaluation of the stability of the Darbandikhan Dam after the 12 November 2017 Mw 7.3 Sarpol-e Zahab (Iran–Iraq border) earthquake. Remote Sensing, v. 10, n. 9, p. 1426.

[22] Milillo, P., Perissin, D., Salzer, J. T., Lundgren, P., Lacava, G., Milillo, G., Serio, C. (2016). Monitoring dam structural health from space: Insights from novel InSAR techniques and multi-parametric modeling applied to the Pertusillo dam Basilicata, Italy. International Journal of Applied Earth Observation and Geoinformation, v. 52, p. 221-229.

[23] Annunziato, A.; Andredakis, I.; Probst, P. (2016). Impact of Flood by a Possible Failure of the Mosul Dam; EUR 27923 EN; European Commission: Brussels, Belgium.

[24] Raspini, F., Bianchini, S., Ciampalini, A., Del Soldato, M., Solari, L., Novali, F., Casagli, N. (2018). Continuous, semi-automatic monitoring of ground deformation using Sentinel-1 satellites. Scientific reports, v. 8, n. 1, p. 7253.

Fifth International Dam World Conference
Portugal • Lisbon • LNEC • 13-17 April, 2025
dam world 2025

EVALUATION OF A GEOPHYSICAL STUDY INVOLVING ELECTRICAL RESISTIVITY AND SPONTANEOUS POTENTIAL TESTS FOR PIPING IDENTIFICATION ON THE WATER DAM ON MATO GROSSO DO SUL - BRAZIL

Yuri Mestnik[1]
CGT Eletrosul

André Batistella Ribeiro[2]
CGT Eletrosul

ABSTRACT

It is the evaluation of a geophysical study involving electrical resistivity and spontaneous potential tests, carried out simultaneously on an earth dam for water storage, used to identify anomalies in the body of the dam and/or preferential percolation pathways in the mass. The aim was to relate the results obtained to the real field situation, in order to validate these tests as non-destructive sources of information in earth dams.

Keywords: geophysical survey, spontaneous potential, electrical resistivity.

[1]yuri.mestnik@eletrobras.com, Brasil
[2]andre.ribeiro@eletrobras.com, Brasil

1. INTRODUCTION

In light of humanity's constant need for water and the seasonality of nature's cycles, dams play a crucial role in human development, being capable of both providing water and serving as containment and storage for materials resulting from human activity. Hundreds of thousands of dams are present worldwide, and specifically in Brazil, many of them lack adequate maintenance and monitoring (ANA [1]; FISHER, CAMP, KRZHIZHANOVSKAYA [2]; JANSEN [3]; MELLO [4]; 2023, 2016, 1983, 2021), highlighting the need for rapid verification methods to assess their condition, integrity, and capacity to adequately fulfil their intended purpose.

Preventive identification of anomalies can avert disasters. Cost-effective and quick-response investigation methods, such as geophysical testing, represent a promising approach for identifying pathologies in dams. Geophysical investigations, such as electrical resistivity and spontaneous potential discussed here, can be applied to dams and are capable of enhancing the understanding of the integrity of these structures.

1.1. Objective

The implementation of geophysical tests to verify the relationship between low resistivity zones from electrical resistivity and spontaneous potential tests can indicate the presence of moisture zones in earth dams or preferential water flow paths, assisting in predicting anomalies and disasters. This article aims to address the use of electrical resistivity tests and spontaneous potential tests as non-destructive sources of information regarding the presence of anomalies, moisture, and preferential water paths in earth dams, presenting a practical case study based on real field conditions

1.2. Justification

In light of the existing dams in Brazil, where, as indicated by the 2022 Dam Safety Report from Brazilian National Water Agency (Agência Nacional de Água - ANA [1]), thousands of dams lack sufficient information for evaluating their basic characteristics, such as embankment height, reservoir capacity, potential damage associated, or risk category. Given this situation, cost-effective and non-destructive investigation methods become an excellent source of information that can help identify anomalies that may compromise the integrity of these structures.

This study aims to evaluate geophysical investigation methods, specifically electrical resistivity and spontaneous potential, in a practical case of investigation as a potential means of data acquisition, serving as a basis for application in other dams to obtain information regarding the integrity of these structures.

2. DEVELOPMENT

A dam, whether earth, concrete, rock, or composite, is a structure built for the purpose of water accumulation, ensuring human and animal consumption, irrigation, recreation, tourism, energy generation, industry, navigation, flood control, aquaculture, and mining. Its construction is particularly important due to water scarcity during dry periods and the consequent need for water storage for human survival, making it a significant driver of human growth over time.

It is possible to find ruins of ancient dams, dating back over 3,000 years BC, such as the Jawa Dam in Jordan or the Saad al Kafara Dam in Helwan, Egypt (2,900 years BC). In Brazil, the earliest records of dams date back to the Imperial era: by order of King Dom Pedro II, the Cedro-Quixadá Reservoir was constructed between 1890 and 1906 in Ceará state (PEREIRA [5], 2023).

Today, millions of people live downstream of dams, making safety programs critically important for maintaining the integrity of these structures. Multidisciplinary teams comprising engineers, geologists, and others are essential for reducing uncertainties and ensuring the safety not only of dam structures but also of the populations that depend on them (JANSEN [3], 1983, p. 89).

According to Jansen [3] (1983, p. 94), there are over 150,000 dams worldwide that pose hazards in the event of failure, with an estimated more than two thousand collapses since the 12th century, resulting in over 8,000 fatalities.

Mello [4] (2021, p. 72) states that accidents and incidents in dams can be explained in more than one plausible way, with a common issue being the lack of necessary information to clarify the mechanisms that caused them, resulting in difficulty in safely determining the nature and sequence of agents and events that led to the accident. Statistics from recorded accidents and incidents indicate that, out of a total of 185 cases, only 15 occurred during the construction phase of the dam, meaning without water in the reservoir; the remaining records occurred during filling or operation (with water in the reservoir) or were cascade accidents arising from a succession of events (MELLO [4], 2021, p. 151).

Currently, there are tens of thousands of dams in Brazil. The 2022 Dam Safety Report from Agência Nacional de Águas e Saneamento Básico - ANA – Brasil (ANA [1], 2023, pp. 25-27) indicates that, out of a total of 23,977 registered dams in Brazil, 13,438 lack sufficient information. Given the lack of knowledge about the conditions of more than 13,000 catalogued dams, geological investigation methods become essential for identifying anomalies and prioritizing interventions in earth dams. Even among the classified dams, there are numerous questions and uncertainties regarding their integrity and their ability to fulfil their intended purpose safely.

In the survey conducted by Mello [4] (2021, p. 153), it was identified that 48% of the catalogued dam accidents are related to earthworks, impacting the dam during or after its construction. However, due to the lack of accurate and comprehensive cataloguing of accidents and incidents in dams, whether large (over 15 meters in height) or not, there may be an extremely significant underrepresentation of incidents involving earth dams. The study and understanding of these structures are essential for predicting and correcting accidents, thereby preventing more serious problems and greater financial expenditures, as well as the loss of lives.

2.1. Literature review

There are numerous study methods that, depending on their intended purpose, are more recommended or inappropriate. After its construction, an earth dam is monitored through piezometers, topographic markers, water level gauges, flow meters, as well as routine visual inspections that provide direct and superficial information about signs of settlement and the behavior of water within the embankment (SILVA [6], 2019, p. 1).

This monitoring, often constant and systematic, sheds light on a superficial condition of the dam or the point parameters of its interior, as piezometers do not cover the entire length of the dam, but they are very effective in detecting anomalies. The importance of detecting an anomaly can indicate a potentially serious problem (FISHER, CAMP, KRZHIZHANOVSKAYA, 2016 [2], pp. 146-153).

Several studies highlight geophysics as a valuable tool for surface investigations. Typically, geophysical tests are commonly conducted during the initial stage of general site characterization and project feasibility. In dams, the application of geophysical investigation methods becomes a powerful non-destructive tool for their characterization, enhancing the extrapolation of point data from direct research methods, allowing for quick and cost-effective assessments of large areas. They are capable of detecting anomalies such as infiltrations and erosions at an early stage, enabling intervention before a catastrophic failure occurs, the consequences of which can be enormous and difficult to quantify (SILVA [6], 2019; SOUZA and GANDOLFO [7], 2021; ROCHA, BRAGA, RODRIGUES [8], 2019).

Geophysical tests consist of investigating the subsurface using various tools with specific characteristics that contribute to the elucidation of knowledge for specific purposes in engineering, geology, mining, navigation, fishing, among others. Their indirect and non-destructive application provides rapid insight into the main elements of the area of interest, offering a good cost-benefit ratio.

There are numerous study methods that, depending on their intended purpose, are more recommended or inappropriate. Geophysical tests are commonly conducted during the initial

phase of general characterization and feasibility of engineering projects (SOUZA and GANDOLFO [7], 2021).

After the construction of an earth dam, especially when the design information is lacking, identifying problems and anomalies becomes difficult. The absence of adequate monitoring, even with an effective and systematic inspection routine, can conceal potential collapses in the structure. As Rocha, Braga, and Rodrigues [8] (2019) state, "due to the increase in severe accidents involving dam failures in Brazil, [...] the pursuit of developing new alternatives for investigation and monitoring technologies contributes to the prediction of anomalies."

Geophysical tests are a form of investigation that can shed light on the desired knowledge, clarifying and identifying regions in a dam that require attention or intervention.

Geophysics is an interesting alternative for monitoring flow lines in earth dams, given the contrast in physical properties between zones with water percolation and the intact materials surrounding them. The assessment of visible surface aspects resulting from harmful processes to the integrity of a dam structure, such as the presence of gullies or signs of sliding, combined with geophysical testing and the direct monitoring of instrumentation, can provide a thorough evaluation, thereby complementing the assessment of the structure (RODRIGUES [9], 2018).

Among the various existing investigation methods, we highlight the main non-destructive investigation techniques, which can be executed individually or in combination, with their results contributing to a more effective diagnosis:

Seismic methods

- Seismic refraction
- Seismic reflection
- Surface wave – MASW, SASW and HVSW
- Borehole testing

Electrical methods

- Electrical resistivity
- Induced Polarization
- Spontaneous potential

Electromagnetic Methods

- Ground Penetrating Radar (GPR)

The use of geophysical tests has been successfully applied in various parts of the world, such as in a dam in Warren County, Missouri, USA, another located in Zaria, northwestern Nigeria, and here in Brazil, we can mention the dam of the Governador José Richa Hydroelectric Power

Plant (PR), another located in Cordeirópolis (SP), and the BR dam, located in Tapira, MG (ROCHA et al. [10], 2019).

2.2. Instrument and data collection

This study presents the field surveys conducted in the fourth quarter of 2023, utilizing a Terrameter LS device manufactured by ABEM Instruments (Image 1), along with four cables, each with 32 take-outs. Two cables had a spacing of 3 (three) meters between take-outs, while the other two cables had a spacing of 5 (five) meters. This setup constitutes an automated multi-electrode system.

The survey was carried out over a length of 13,415 meters, encompassing 36 study sections of electrical resistivity and spontaneous potential, both conducted simultaneously in the body of the dam, as represented on the map.

Image 1 – Equipment Terrameter LS ABEM

Between nine and thirteen sections were conducted on each structure at the downstream face, as the reservoir is located at the upstream face. The survey was carried out parallel to the axis of the dam.

2.3. Geophysical tests of electrical resistivity and spontaneous potential in the dam

This study presents an investigation conducted on an existing dam structure completed in 2012, located in the state of Mato Grosso do Sul, intended for electricity generation; it draws a parallel between the results obtained and the existing anomalies in the embankment. The methods employed in the study are electrical resistivity and spontaneous potential.

Electrical resistivity is an efficient and low-cost investigation method, widely used not only in earth dams but also in other types of structures such as concrete dams. It should be performed in conjunction with other investigation methods and, when possible, compared with existing monitoring data from the structures; it is an excellent investigative tool applicable in nearly all situations (ZORZI and RIGOTI [11], 2011).

The electrical resistivity method involves injecting a known intensity of electrical current into the ground using electrodes. The potential difference measured between the electrodes, resulting from the passage of this current, is used to calculate electrical resistivity (SOUZA and GANDOLFO [7], 2021). The method utilizes the physical parameter of electrical resistivity, which is a fundamental property of the geological environment, based on the premise that a homogeneous lithological medium exhibits the same resistivity. This allows for the identification of changes in the physical characteristics of soils correlated with a wide range of variations in resistivity values.

For the Electrical Walkover survey, arrangements that allow for the study of lateral variation of the physical parameter at various depth levels can be used, thus achieving better characterization of materials both horizontally and vertically, including configurations such as Wenner, Schlumberger, Dipole-Dipole, Pole-Dipole, Gradient, among others. The arrangement used was of the Schlumberger type, which consists of positioning the four electrodes symmetrically with respect to the midpoint of the array.

Alternatively, Spontaneous Potential involves measuring the natural electric potential difference in the ground, generated by electrochemical and electromagnetic processes (SOUZA and GANDOLFO [7], 2021). The test takes advantage of the fact that soil heterogeneity polarizes, becoming true "electric cells" that generate electric currents in the subsurface. Groundwater flow is the most influential agent in the mechanism of spontaneous potential generation.

2.4. Data processing

In the data processing of the electrical walkover, to achieve better convergence of the results, recursive Jacobian inversion was employed with filtering and removal of spurious resistivities to stabilize the error to the smallest possible range, resulting in good convergence in the approach.

During the data extraction in the field, point adjustments were also made for values of resistivity that were clearly erroneous due to poor contact between the electrode and the ground, ensuring that the counting of the first electrode started from the same origin.

The larger errors are associated with the discrepancies in resistivities arising from more distant sections, due to the deviations in the path of the electric current, which are characteristic of heterogeneous masses.

To obtain the two-dimensional profiles from the resistivity variations for each survey campaign, the software Res2Dinv was used. The analysis took into account and correlated the water levels upstream and downstream of the structures, as well as the water levels from the piezometers and water level gauges measured concurrently with the tests.

Considering the integrity of the dam and its primary characteristic of water storage, the geophysical analysis focused on identifying voids and preferential water percolation zones, taking into account the resistivity values as shown in Table 1 below.

Table 1 – Reference resistivity values used in geophysical surveys

Rock type	Resistivity (ohm.m)		
	Telford (1990)	**Loke (1999)**	**Braga (2002)**
Clay	100-133	1-100	300-5.000
Silt	670-1.330	-	1.000-8.000
Sand	33-6.700	200-8.000	-
Basalt	1.000-1.000.000	200-100.000	>10.000
Water	0,5-300	1-100	50-100

Regions that exhibited resistivity values below 50 ohm·m in the electrical walkover are identified as Low Resistivity Zones (*Zonas de Baixa Resistividade - ZBR*) and are associated with the presence of water, moisture, or clay. For High Resistivity Zones (*Zonas de Alta Resistiviade - ZAR*), the values found were above 1,000 ohm·m and are associated with more compacted portions of the dam body or the presence of sound rock when located below or downstream of the dam body (natural terrain).

2.5. Characteristics of the dam

The dam is located in the Paraná Basin region, within a Paleo-Mesozoic basin (LACERDA [12], 2006). This area is characterized by the occurrence of basalts from the Serra Geral Formation, dating to the Jurassic-Cretaceous period, with a color ranging from black to gray-green, microcrystalline, and containing lenses of pink sandstone with medium granulation, hardened by the thermal effects of the flows. Overlying the basalt are sandstones from the Cretaceous period, belonging to the Caiuá and Santo Anastácio formations (Bauru Group). These are fine to medium and coarse sandstones, generally weathered into brownish-red sandy soils, with fragments and blocks of ferruginous sandstone. Along the waterways, there are restricted alluvial deposits from the Quaternary period (LACERDA [12], 2006).

In the foundation area of the dam, basalts are present and primarily outcropping at the bottom of the river valley, while sandstones are deposited over the basalt in the higher portions of the terrain.

Residual and/or colluvial soils from the Caiuá sandstone predominate in the project. These soils are classified as silty sands or silt-clay soils, mostly containing no more than 15% fines in their composition.

The section of the dam that is composed of compacted soil throughout the mass, with slopes of 1.00 (vertical): 2.00 (horizontal) on the upstream face and 1.00 (vertical): 2.50 (horizontal) on the downstream face, starting from the foundation terrain, resting on dense basalt bedrock, with a height of 19 meters. Above this elevation, the slope changes to 1.00 (vertical): 2.10 (horizontal) for an additional eight meters, resulting in a maximum dam height of 27 meters, with a freeboard of three meters above the average water level.

At the axis of the structure, there is a vertical filter of compacted sand extending from the foundation to the maximum normal water level of the dam's lake (3 meters below the crest of the dam). A drainage blanket has been designed in the downstream area to allow the water that percolates through the dam body to flow, capturing water that seeps through the vertical filter, as well as capturing the flow from the foundation. The dam also features a toe drain and a trench that collect the flows from the vertical and horizontal drains, managing the outflow and ensuring the stability conditions of the downstream face of the dam. In the rocky section, the flow is captured by a pipe that directs the water to a flow meter.

Dam is a compacted sandy-silt soil embankment, rolled with a sheep's foot roller in 20 cm layers, with the grain size curve presented in Graphic 1 below.

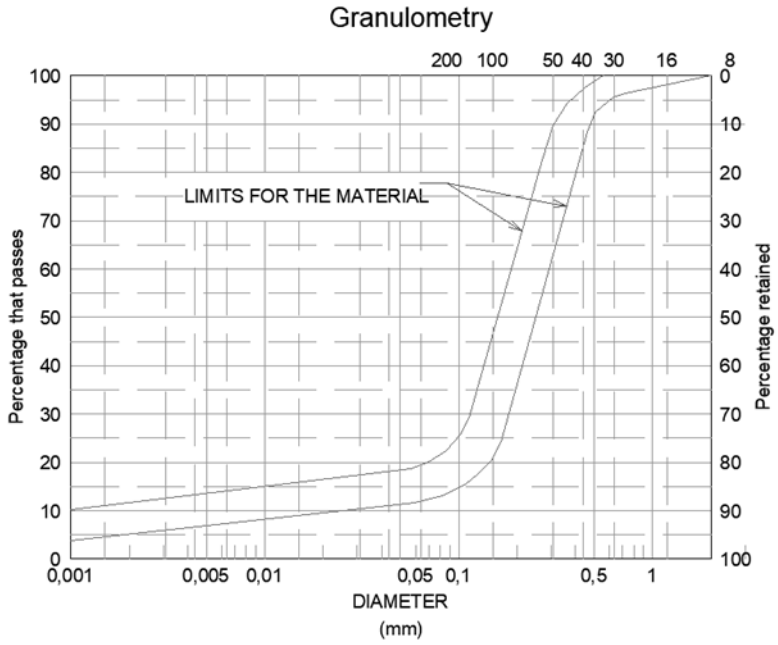

Graphic 1 – Grain size distribution curve

The Figure 1 below shows the cross-section of a typical section of the dam, indicating the slopes of the upstream and downstream faces, elevations, and water level, as well as vertical and horizontal filters and the bedrock. Figure 2 then presents the plan view of the dam, with the locations of the piezometers and reference benchmarks.

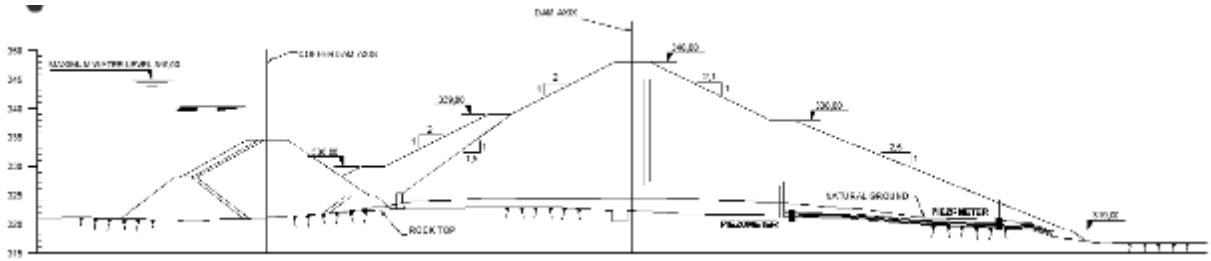

Figure 1 – Schematic drawing of the dam section

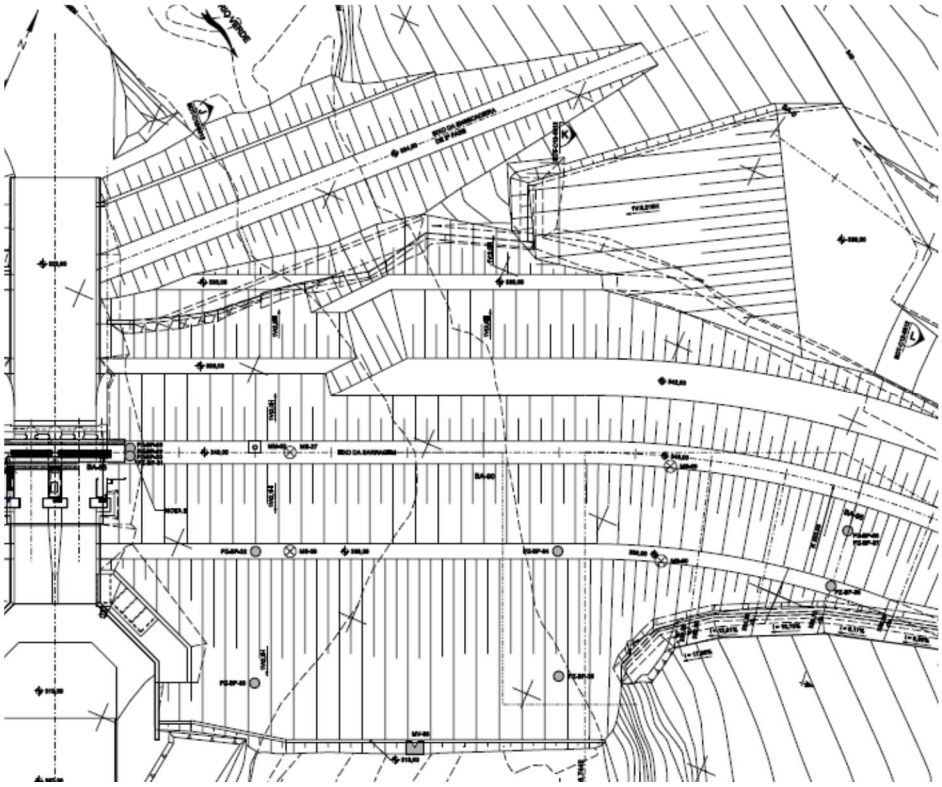

Figure 2 – Dam drawing – plan view

This section of the dam extends for 300 meters from the axis of the spillway and is situated on the riverbed, as can be inferred from Figure 2. The upstream cofferdam was initially constructed to allow for the execution of the dam and is currently submerged in the reservoir, therefore not subject to investigation.

2.6. Instrumentation for monitoring

The studied region is monitored by water level gauges and piezometers, divided into four monitoring sections: one in contact with the spillway, another located far from the riverbed – the region to the right of Figure 3 below, along the curve the dam makes along its axis, a third in the central region of the massif, and a fourth near the riverbed and the spillway.

The piezometers located furthest from the riverbed show readings ranging between elevations 334.6 and 334.7 meters; in the central section of the dam, the piezometric level varies between

elevations 319.2 and 320.1 meters; in the region closest to the riverbed (to the left of Figure 3 below), the piezometric level varies between elevations 319.2 and 321.0 meters. The piezometers installed in contact with the dam spillway show readings ranging between elevations 333.1 and 337.4 meters.

The water level gauge installed downstream of the section furthest from the riverbed shows readings varying between elevations 335.15 meters – 12.85 meters below the top of the dam at elevation 348.00 meters.

2.7. Location of the campaigns

The highlighted section is located on the left bank of the river course, outside the channel of the original water body. A total of 10 reading campaigns were conducted, encompassing campaigns one to nine and campaign 31. All campaigns were carried out parallel to the axis of the dam, starting from the bank closest to the river axis and ending at the farthest edge, following the line of the dam crest.

Figure 3 presents the location of the electrical walkover sections on the dam.

Figure 3 – Schematic design of the monitoring campaigns at the dam

Campaigns one and two were conducted at the crest of the dam, one upstream of the axis and the other downstream. The remaining campaigns were carried out on the downstream slope, advancing into the natural terrain immediately downstream of the dam.

2.7.1. Results of the campaigns

Figures 4, 5, and 6 present only the electrical walkover campaigns for sections L2 and L3, conducted at the crest of the dam, downstream of the vertical filter, as well as campaign L31, carried out downstream of the dam in natural terrain.

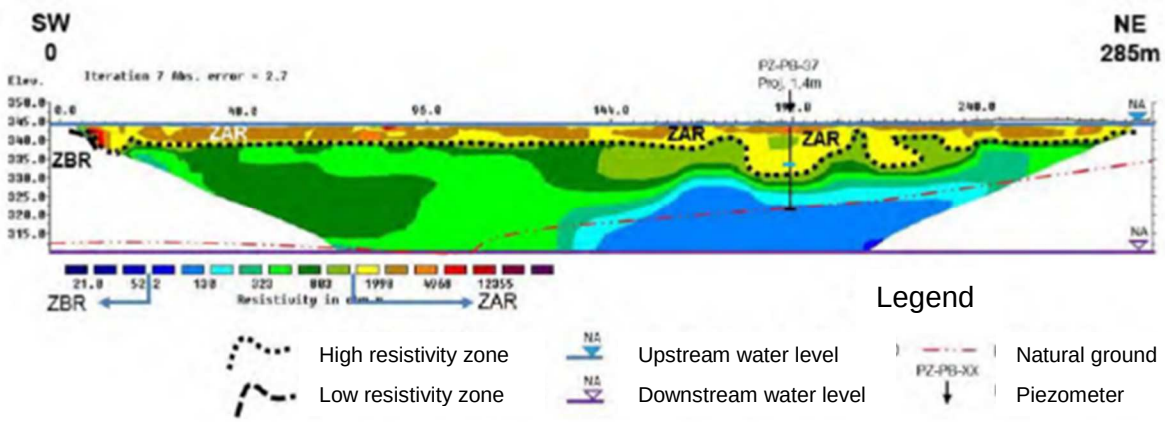

Figure 4 – Section L2

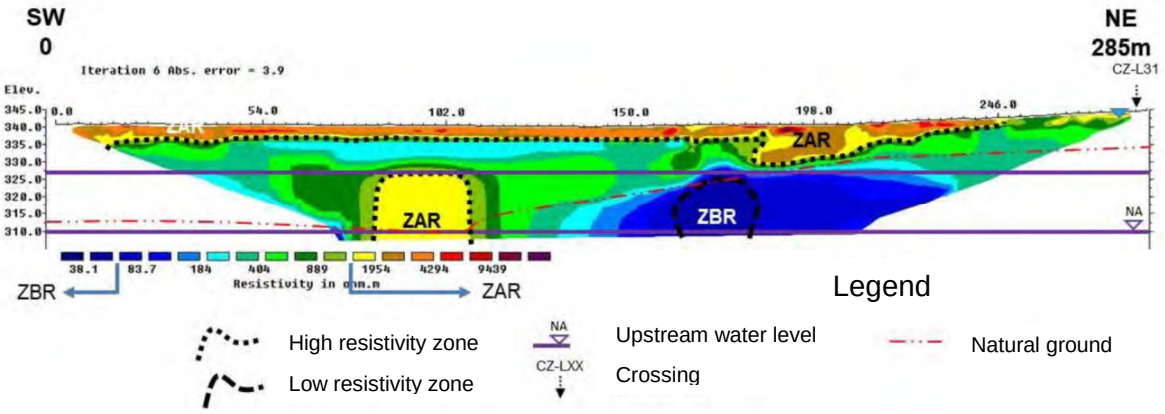

Figure 5 – Section L3

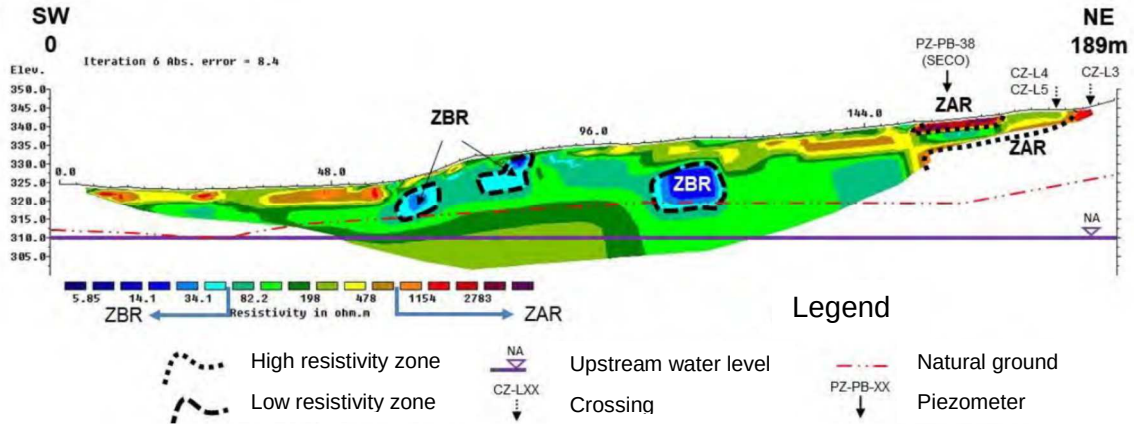

Figure 6 – Section L31

The other electrical walkover campaigns are shown in the three-dimensional modelling indicated in Figure 7, while all spontaneous potential campaigns are presented in the three-dimensional modelling of Figure 8.

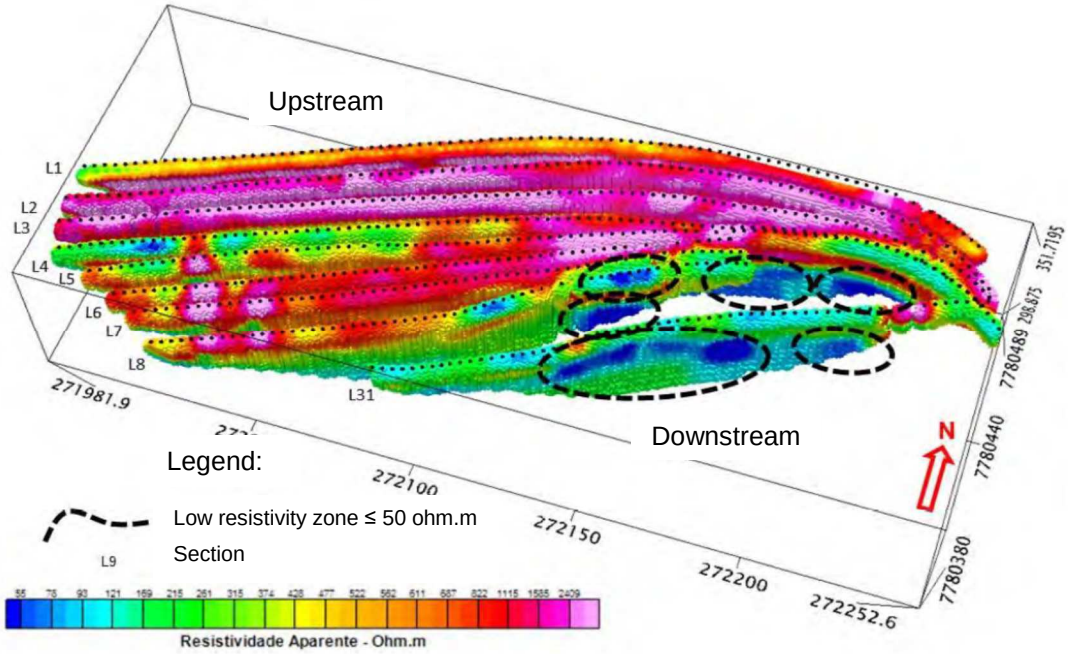

Figure 7 - Three-dimensional electroresistivity modelling of the dam

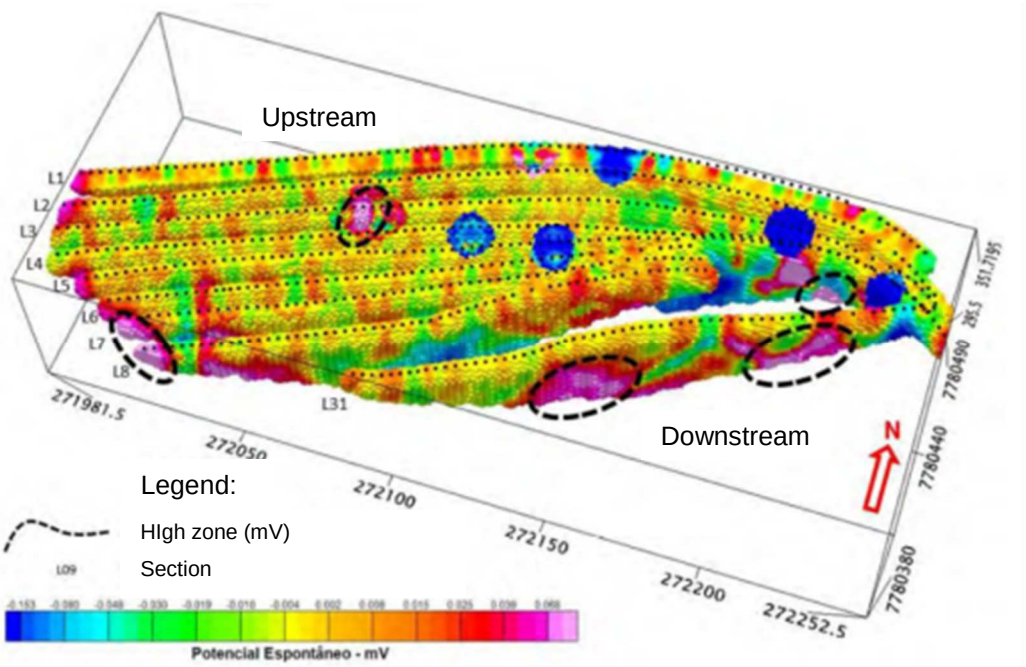

Figure 8 - Three-dimensional spontaneous potential modelling of the dam

2.7.2. Analysis

2.7.2.1. Electroresistivity test

It is possible to observe a low resistivity zone (LRZ) with values below 50 Ohm·m, varying from 9 to 57 meters in depth (blue zone in Figure 4). The low resistivity obtained, located below the

foundation level of the dam, may indicate the presence of clay and/or moisture. Notably, in campaign L31 (Figure 3), there is an LRZ just below the base of the dam.

The high resistivity zones (HRZ) are predominantly located in the sections near the top of the studied area; in the surface portion of the diagram, this reflects a greater compaction of the material, which constitutes the body of the earth dam.

The readings from the monitoring instruments, conducted concurrently with the campaigns, indicated water levels at the contacts located at the interface between the dam and the foundation, while the instruments situated in the natural terrain remained dry. These readings served as a basis for the calibration of the models.

2.7.2.2. Spontaneous potential test

The characterization of a potential preferential water percolation zone is indicated by regions with spontaneous potential values greater than 0.1 mV.

Figure 8 highlights in light pink the areas with spontaneous potential values above 0.1 mV, which may be associated with preferred water flow zones. These are identified in section L3 near the central portion; in section L4, also in its central part; and at the confluence in sections L5, L7, and L8 near their beginnings, as well as in the central part of section L31.

2.7.2.3. Cross-correlation electroresistivity X spontaneous potential tests

A zone with high spontaneous potential values associated with low resistivity zones may indicate a preferred flow region, which can be defined through this association of information.

From Figures 7 and 8, it is possible to correlate Figure 9, which aims to overlay the geophysical surveys of electrical resistivity and spontaneous potential into a single image.

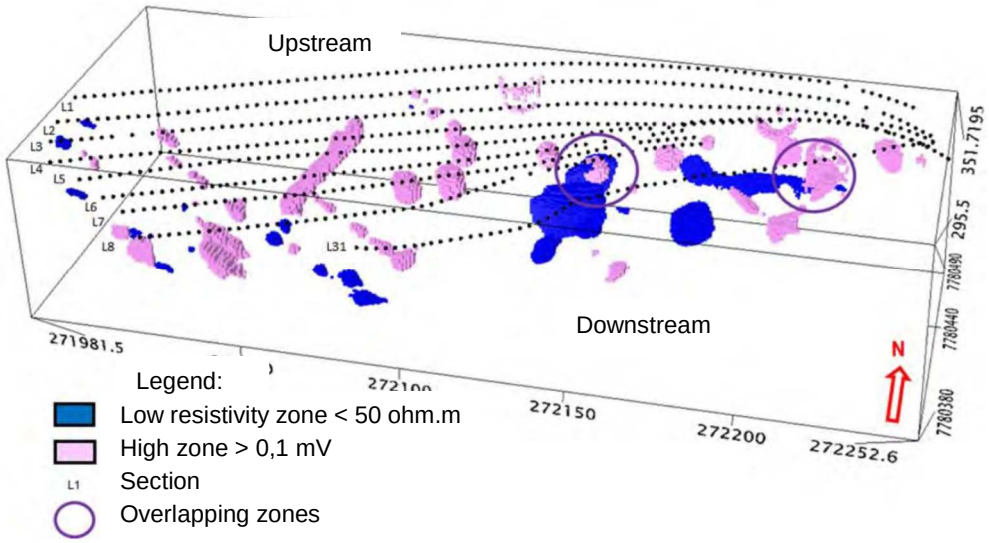

Figure 9 – Modelling of the dam for regions with electroresistivity less than 50 ohm.m and spontaneous potential greater than 0.1 mV

Figure 9 highlights with a circle the areas of interest for both electrical resistivity and spontaneous potential, indicating regions with preferential flow. It is important to note that the highlighted area is located below the foundation line of the dam.

2.7.3. Analysis of local conditions

As shown in Figure 9, there is a region of higher moisture/presence of water indicated by a circle, located in the natural terrain beneath the body of the dam, as highlighted in Figure 10 below.

Figure 10 – Natural downstream slope of the dam

Locally, in the highlighted low resistivity region, we can observe an area characterized by greener vegetation and wetter soil, with water seeping toward the riverbed. This spring is located below the foundation of the dam structure, in a cut area of the natural terrain, where an inverted filter was constructed to direct the water flow to a flow meter that is systematically monitored.

Figure 11 below shows the flow meter built in the area of the water spring identified in the presented surveys.

Figure 11 – Flow meter

As a solution for the water resurgence, an inverted filter was constructed, involving local excavation, placement of a geotextile membrane, sand, and gravel, to direct the water resurgence to a flow meter with constant monitoring, which are around 0,5 l/s. After reshaping the terrain, the meter was surrounded by a channel to prevent surface water from rainfall from interfering with the flow measurements.

3. CONCLUSIONS

Geophysical surveys are an effective means of investigation for dams, providing a quick and economical overview of the dam's overall condition and integrity.

When electrical resistivity surveys are conducted in conjunction with another test, such as spontaneous potential, we obtain a complementary and highly accurate diagnosis of the dam's characteristics, potential anomalies that could lead to a catastrophe, and, importantly, the behavior and flow of water within the structure. This serves as a crucial reference for understanding anomalies. While a single test can diagnose possible pathological manifestations, providing timely opportunities for the operator to act, constant and periodic monitoring can offer an evolving overview of the issues, allowing for intervention and correction before an accident occurs, significantly reducing recovery costs.

3.1. Test results

In the case presented in this document, a region of low resistivity highlighted in blue in figures 3, 4, 5, and 6 was observed, associated with areas of high spontaneous potential shown in Figure 8. These zones were identified through electrical resistivity surveys conducted using the Terrameter LS model during electrical resistivity and spontaneous potential measurements. The results revealed areas of low resistivity corresponding to zones of high spontaneous potential, which may indicate the presence of moisture or flow.

3.2. Condition of the dam

In the site, a region with greener and more lush vegetation (Figure 10) was observed, featuring a water spring downstream of the dam, on the natural slope, both located below the foundation elevation of the dam, which has been identified since the dam's construction according to records.

In light of this situation, and to facilitate periodic monitoring, a flow meter (Figure 11) was constructed to channel this water spring, allowing for weekly monitoring and thus providing an accurate diagnosis of the situation, which remains stable.

Thus, the electrical resistivity survey combined with spontaneous potential measurements serves as an efficient means of diagnosing the behavior of the soil within the mass of a dam,

resulting in an important observational tool capable of reliably and economically diagnosing anomalies in the body of a dam.

REFERENCES

[1] ANA - Agência Nacional de Águas e Saneamento Básico (Brasil). Relatório de segurança de barragens 2023 /Agência Nacional de Águas e Saneamento Básico. - Brasília: 2024 - CDU 627.82(047). Site: https://www.snisb.gov.br/portal-snisb/api/file/download/714/4/rsb_2023_2024_06_27_11_01_28.pdf

[2] FISHER, Wendy D.; CAMP, Tracy. K; KRZHIZHANOVSKAYA, Valeria V. Anomaly detection in Earth dam and leave passive sesmic data using support vector machines and automatic feature selection. Article in Journal of Computational Science. 2016. DOI 10.1016/j.jocs.2016, 11,016. Page 146 a 153.

[3] JANSEN, Robert B. Dams and Public Safety – A Water Recources Technical Publication – U. S. Departament of Interior - Bureau of Reclamation, 1983

[4] MELLO, Flavio Miguez de, GUIDICINI, Guido, SANDRONI, Sandro Salvador – Lições aprendidas com acidentes e incidentes em barragens e obras anexas no Brasil – Livro eletrônico 2021 - ISBN 978-65-990860-1-4

[5] PEREIRA, Geraldo Magela. Material didático do curso de Pós-Graduação Lato Sensu da Universidade Federal da Bahia - Especialização em Segurança de Barragens: Aspectos Técnicos e Legais, 2023

[6] SILVA, Roberto Albuquerque. Geofísica aplicada à caracterização da barragem de rejeito de mineração B1, Cajati, São Paulo. Dissertação de Mestrado (Geologia). Dissertação de Mestrado submetida ao Programa de Pós-graduação em Geologia, Instituto de Geociências, da Universidade Federal do Rio de Janeiro – UFRJ, como requisito necessário à obtenção do grau de Mestre em Ciências (Geologia). 2019

[7] SOUZA, Luiz Antonio Pereira de e GANDOLFO, Otavio Coaracy Brasil – Geofísica aplicada à geologia de engenharia e meio ambiente: manual de boas práticas. Primeira edição. ABGE – Associação Brasileira de Geologia de Engenharia e Ambiental. São Paulo, 2021 ISBN 978-65-88460-02-3

[8] ROCHA, Demetrius Cunha Gonçalves; BRAGA, Marco Antonio da Silva; RODRIGUES, Camila Alves. Geophysical methods for BR tailings dam Research and monitoring in the mineral complexo f Tapira – Minas Gerais, Brasil. Revista Brasileira de Geofísica (2019) 37(3) páginas 276-289 – 2019 Sociedade Brasileira de Geofísica ISSN 0102-261X

[9] RODRIGUES, Camila Tavares. Geofísica aplicada à investigação da barragem de rejeito BR, do complexo de mineração de Tapira, Minas Gerais. Trabalho de final de curso de geologia. Instituto de Geociências da Universidade Federal do Rio de Janeiro, como requisito necessário à obtenção do título de Bacharel em Geologia. Rio de Janeiro. 2018.

[10] ROCHA, Demetrius Cunha Gonçalves; BRAGA, Marco Antonio da Silva; RODRIGUES, Camila Alves. Geophysical methods for BR tailings dam Research and monitoring in the mineral complexo f Tapira – Minas Gerais, Brasil. Revista Brasileira de Geofísica (2019) 37(3) páginas 276-289 – 2019 Sociedade Brasileira de Geofísica ISSN 0102-261X

[11] ZORZI, Roberto Rafael e RIGOTI, Augustinho - Aplicação de métodos geoelétricos para monitoramento da barragem de concreto da UHE Gov. José Richa. Boletim Paranaense de Geociências - Universidade Federal do Paraná - Volume 64-65 (2011) 48-58.

[12] LACERDA FILHO, Joffre Valmório de; BRITO, Reinaldo Santana Correia de; SILVA, Maria da Glória da; OLIVEIRA, Cipriano Cavalcante de; MORETON, Luiz Carlos; MARTINS, Edson Gaspar; LOPES, Ricardo da Cunha; LIMA, Thiers Muniz; LARIZZATT, João Henrique; VALENTE, Cidney Rodrigues - Geologia e recursos minerais do estado de Mato Grosso do Sul. CPRM; SEPROTUR/MS; EGRHP/MS, 2006. Site: https://rigeo.sgb.gov.br/handle/doc/10217

Fifth International Dam World Conference
PORTUGAL • LISBON • LNEC • APRIL 13-17, 2025
dam world 2025

SLOPE STABILIZATION ON THE LEFT BANK UPSTREAM OF THE CANIÇADA DAM – CONSIDERATIONS ON CONSTRAINTS, QUALITY AND MAINTENANCE OF GROUND-ANCHORED STRUCTURES

Carvalho, Mariana[1]
LNEC

Esteves, Carlos[2]
EDP

Caldeira, Laura[3]
LNEC

ABSTRACT

The Complementary Spillway of the Caniçada dam is located on the left bank of the Cávado River next to the dam's abutment, with works finished in 2018. Significant excavations reaching 70 m maximum height, were carried out for the construction of the spillway entrance.

The stabilization solutions involved several multi-anchored reinforced concrete walls at different levels, using permanent ground anchors. The construction faced particularly challenging periods, both in terms of design solutions and work supervision, and were adapted according to the terrain specificities identified as the work progressed.

Regarding the ground anchors installation, in accordance with the applicable standards, preliminary tests were conducted on sacrificial anchors at the initial stage construction, and the respective results were analysed.

As part of the work's quality control, recommendations were issued for the conditioning and storage of the anchors and their components on-site. For the anchors stored on-site, periodic visual inspections, verification measurements, and control of the conditions and characteristics of the anchors and their components were carried out with random sampling.

The anchor holes drilling involved Lugeon type permeability tests, the results of which led to the ground treatment of several areas, using cement injections.

All permanent anchors were subjected to load tests and their lock-off was controlled. The protection of the anchor heads complied with the manufacturer's recommendations.

The paper focuses on the implementation of six anchored walls, M2 and M4 to M8, specifically regarding the various stages leading to the execution of the respective ground anchors.

Results of various load tests, some recommendations issued to ensure the quality of the solutions, and adaptations and/or procedures corrections based on the information collected throughout the project are presented. Additionally, the monitoring system of the structures implemented for the construction and operation phases is described, and some of the results obtained are presented.

Keywords: Ground anchors, test load, lift-off, protection, monitoring.

[1] marc@lnec.pt, Portugal
[2] carlos.esteves@edp.pt, Portugal
[3] laurac@lnec.pt, Portugal

1. INTRODUCTION

This paper presents a brief work description for the construction of the spillway intake on the left bank of the Caniçada dam, namely the quality control inspection procedures, the features regarding aspects to check anchors reception, their storage and transport on site, the technician's guidance, particularly, the follow up of the installation process, anchors sealing and injections, as well as anchor load tests and their head assembly, lock-off and protection.

This work it is based in the technical support made for the technology selection, on technical assistance done during the works for execution of the ground anchors [1] [2], of the retaining walls M2 and M4 to M8 (Fig. 1), for the complementary spillway of Caniçada dam construction.

The paper also describes the anchor load tests, their results analysis and interpretation, namely for the investigation tests, suitability tests, reception tests, anchors lock-off and lift-off tests. Additionally, the monitoring system of the structures implemented for the construction and operational phases is described, and some of the results are presented.

2. FRAMEWORK AND BRIEF WORK CHARACTERIZATION

Caniçada hydroelectric scheme is in the Cávado River, which flows through the north-western Portugal, being part of the hydro electrical system of Cávado-Rabagão-Homem, owned and operated by EDP since 1955. The scheme consists of a double-curvature arch dam with a maximum height of 76 m (see Fig. 1 - left), it's hydraulic safety devices which were originally a spillway located in the central part of the dam body and a bottom outlet (Fig. 1) and an underground hydraulic circuit and powerhouse.

To meet the updated requirements of the Portuguese Dam Safety Legislation (RSB 2007), a new complementary spillway was constructed between 2014 and 2018 near the left dam abutment. This new safety structure consists of an intake equipped with two radial gates, followed by a 200 m long tunnel excavated about 30 m beneath the dam abutment, and a ski jump outlet (Fig. 1- right).

The construction of the intake of the new spillway involved significant excavations, reaching a maximum height of 70m. Two zones with different geological conditions were identified during construction: i) in one of them, which includes walls M2, M4, and M5, the rock mass has, from a depth of 15 meters, reasonable geomechanical quality and moderate weathering and fracturing, although near the surface the quality deteriorates, evolving into a highly weathered to decomposed rock mass and residual soil; ii) in the other zone, where walls M6, M7 and M8 are located, the rock mass is mainly composed of granitic residual soil to decomposed rock with intercalations of boulders.

Fig. 1 – Photo of Caniçada dam (left) and layout of new complementary spillway (right)

Stabilization measures were applied as the excavations progressed, starting at the higher elevations, and gradually progressing downwards. The stabilization solutions adopted were, generally, of two types: i) shotcrete with wire mesh and rockbolts; and ii) concrete walls with permanent anchors.

The Fig. 2 depicts the progress of the intake structure construction works on November 2016 and the anchors walls designation, executed for the excavation's stabilization. Walls M7 and M8 are located below the frequent water level of the reservoir, so specific measures were required to protect their ground anchors.

Fig. 2 – Construction works on the intake structure for the new spillway (November 2016)

3. OVERVIEW OF THE ANCHORED RETAINING WALLS

3.1. Design solutions

Walls M2, M4, M5, M6, M7 and M8 are retaining structures reinforced concrete with permanent ground anchors at different levels, with service loads of 400 kN and 650 kN, varying on their location.

The vertical wall M2 is in the highest part of the slope and has five levels of anchors in the highest section (Fig. 3). In total, 82 ground anchors were installed in the M2 wall. Walls M7 and M8 differ from the others in that they are submerged for the most frequent reservoir water

level. For this reason, and with a view to protecting the anchor heads of these two walls against corrosion, they were surrounded with concrete in the final phase of construction. Geometrical and mechanical characteristics of the six retaining walls and their ground anchors are summarized in Table 1. Fig. 3 illustrates the cross section of anchored retaining walls.

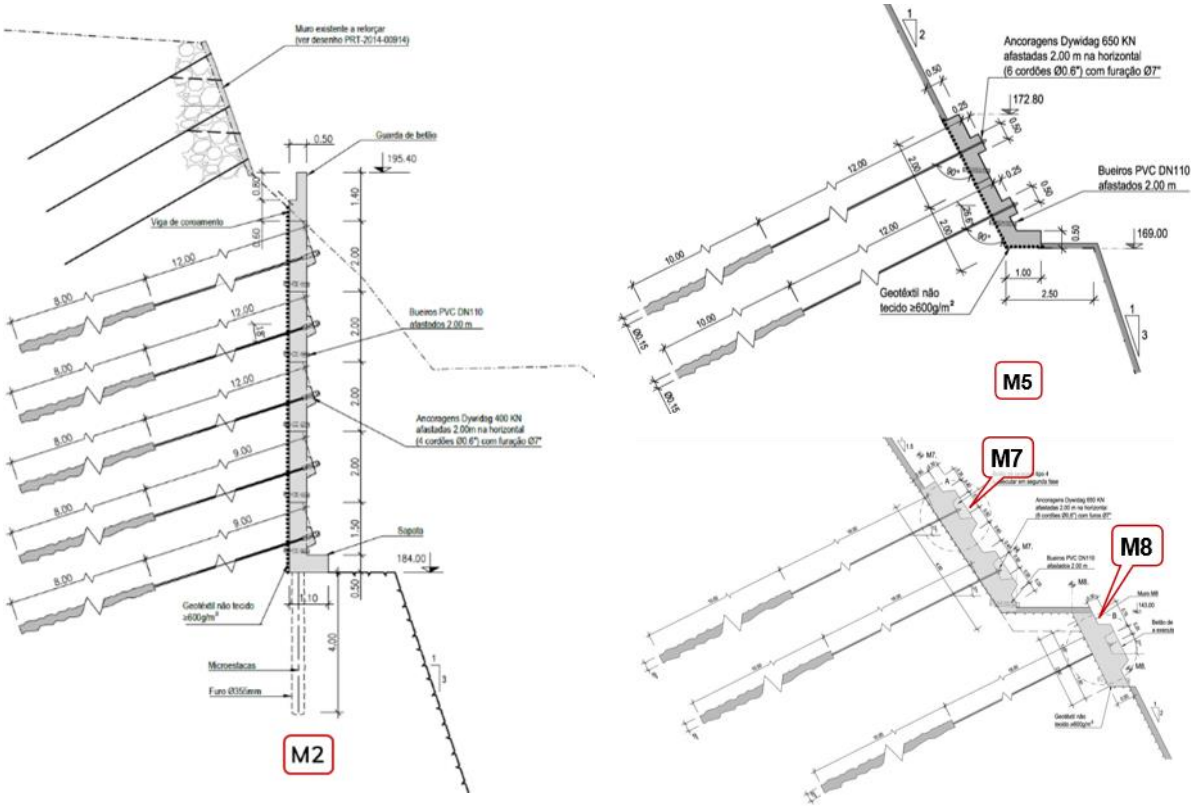

Fig. 3 – Cross section of anchored retaining walls M2, M5 a M7 and M8 [3]

Table 1 – Main characteristics of the retaining walls and ground anchors

	Retaining wall				Ground anchors				
	Tilt (º)	Máx. height (m)	Length (m)	Elev. (m)	P (kN)	α (º)	Levels	Total	Monitored
M2	90	11,40	46,8	195,4-184,0	400	18,0	5	82	12
M4	45	3,18	16,6	187,2-184,0	650	20,0	2	12	2
M5	88	3,95	34,9	173,0-169,0	650	26,6	2	33	6
M6	33,7	2,72	35,5	156,7-154,0	650	32,0	2	33	8
M7	63	4	29,0	147,0-143,0	650	27,0	2	28	3(1)
M8	63	2	29,9	143,0-141,0	650	27,0	1	15	2(1)

Note: P – service load; α – inclination with horizontal; (1) – only during construction.

3.2. Anchor system

The permanent anchors, its accessories and pre-stress equipment were supplied by Dywidag DSI. The selected system was permanent anchor with Double Sheathing TWIN-Corr System

(Fig. 4). Double Corrosion Protection (DCP) is achieved by strands that are greased, individually sheathed and covered by one corrugated sheathing at the factory. Additional protection of the bonded length by a second, concentric corrugated sheathing – two plastic sheathings in the bonded length as well, with the bonded length pregrouted.

The fixed anchor length has sleeve pipes, for multi-stage pressure grouting, with post-grouting valves spaced out 1 m. The system's spacers and centralizers were installed in such a way as to prevent movement, ensure the required cover, the borehole full filling, the tendon elements centrality, and, that the anchor elements and their system corrosion protection components were positioned correctly. On the outside of the covering, the centralizers are made of corrosion-resistant material [4].

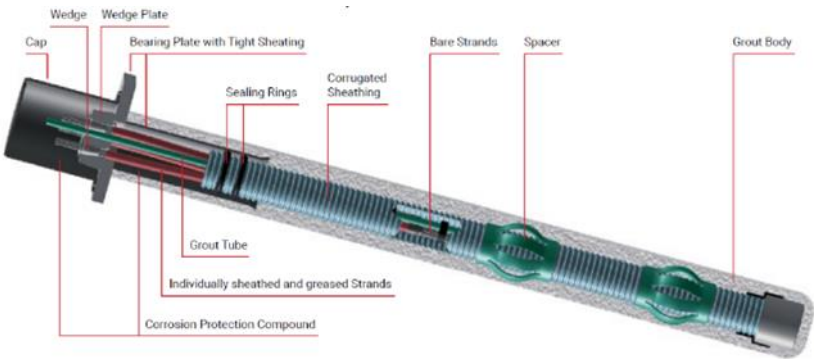

Fig. 4 – Permanent anchor with double sheathing, TWIN-Corr System [5]

The anchor tendon prestressing steel was Y1860 S7, with six strands Ø 15.3 mm (0.6"). The ultimate load P_{tk}, the load at yield $P_{t0,1k}$, elastic modulus (E_t) and the strand cross sectional area (A_t), were obtained from the test certificates for each coil. The ground anchors system corresponds to EN 1537 requirements.

The fixed length grout body of the anchors had initially been designed for lengths between 8 and 13 m. Given the characteristics of the ground found at the site, it was necessary to adapt the value initially predicted in some areas.

3.3. Permanent anchors execution

The ground anchors were located with topographic support and in accordance with the specifications' requirements. Their execution included the following phases: Phase 1) placement; Phase 2) Positioning; Phase 3) Drilling, with a diameter of 172 to 200 mm, by rotopercussion with a downhole hammer (MFF), and direct circulation of compressed air; Phase 4) water injection tests, in the fixed anchor length isolated by a packer installed in the borehole, over the free anchor length. If, in phase 4, the water loss was:

- Phase 4.1) less than 2 Lugeon Units (LU) => borehole apt for the anchor installation.

- Phase 4.2) greater than 2 LU => pre-grouting the fixed anchor length, with a grout mixture of w/c=0.8, until reaching a maximum water loss of 100 l/m or a maximum pressure of 10 Bar, redrilling and restart Phase 4.

In Phase 5), and within the period of 8 hours after phase 4 completion, the anchor was introduced into the borehole; Phase 6) primary grouting and high-pressure multi-stage grouting; Phase 7) load test and controlled lock-off. Each of those phases comprised the recording, in daily parts and sheets, of the data and occurrences verified during the respective execution operations.

4. ANCHORS' QUALITY CONTROL

4.1. Operational execution and anchor load tests procedure

The procedures for each of the walls, for the anchor's execution and for their load tests were prepared as prescribed in EN1537:1999, according to test Method 1. Before the anchor's execution, these procedures were presented by the contractor and revised to include the required information and documentation to ensure that the normative documents requirements were met. The procedures were carried out for the test and production anchors, as well as for investigation tests, suitability tests, acceptance tests and for the lock-off.

4.2. Anchors reception and storage at the site

The anchors' reception control, done through random sampling, had the collaboration of LNEC. For this activity, LNEC created the record control sheet and the recommendations for control, packaging and anchors storage, as well as for the respective components. The criteria and parameters evaluated during the reception control, stated in record control sheet, were intended to allow to be assessed, by visual inspection, the anchors components general conditions (Fig. 5), and allow the detection of any: i) imperfections; ii) nonconformities; iii) geometric incompatibility and/or inadequacy; and iv) planar irregularities, among others.

The stainless-steel wedges, with 3 segments connected by circular spring, were packed in transparent bags, appropriately identified. Upon the reception of the wedges, sealing rings, caps or centralizers, no anomalies were detected. The placement and dimensions of the external protection elements were also checked.

Damage was identified in the corrugated sheathing (Fig. 6) in anchors partially placed on gravel at the site. The need to provide anchors external protection was highlighted, given that long exposure to sunlight could result in premature ageing of the system's plastics and rubbers. Some wedge plates were very rusty, which was considered a poor protection indicator. Inside

caps and trumpets, deposits of debris and water were observed. Indications were given to avoid these situations and to ensure the adequate anchors' storage and of their components.

Fig. 5 – Checking wedges (a); their seats accommodation on the wedge plate (b); protective cap (c), (e); anchor system components (c); checking Individually sheathed accommodation (d); cap, bearing plate and trumpet (e); sealing rings (c), (f); checking anchor system (f), (g); anchors storage (h)

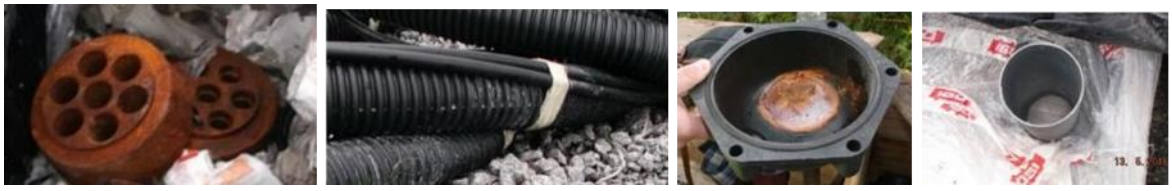

Fig. 6 – Anchors storage at the site: example of anomalies observed in the corrugated sheathing, inside of the cap and trumpet

4.3. Anchor load cells

Load cells hydraulic vibrating string transducers were installed, with temperature transducer, from Glotzl, with 750 kN and 1000 kN nominal load values. The cells were installed in anchors with service load of 400 kN, in the M2 wall, and 650 kN, in the M4 to M8 walls.

The cells reception included load tests to verify their behaviour. Those program tests were previously defined and included an incremental loading and unloading cycle, with simultaneous monitoring of the load cell and of the calibrated work's prestress system. These tests were carried out on anchors available on site. With the data of the equipment calibration certificate,

correlations were obtained that allowed us to verify that, in those cells, there was no evidence of having behaviour problems.

The load in the cell was generally higher than that of the prestress system. Nevertheless, this difference was small, and the load variation did not exceed 2%, particularly regarding the service load. Thus, these results did not indicate inappropriate behaviour of the cells.

4.4. Water injection tests

With the aim of verifying the permeability and behaviour of the ground to water percolation, tests were carried out. Those tests involved the water injection under pressure, through a borehole in the fixing anchor length, measuring the water loss quantity over a period, under a constant injection pressure. Previously, it was checked whether the ground to be tested was saturated.

If the ground was not saturated, the water injection was carried out at low pressure, for 5 minutes, assuming that the constant flow rate corresponds to the ground saturation. If the flow rate decreased, the pressure increased until the flow rate stabilized. The test was done after saturation.

The program test had 5 cycles of pressure. The cycles maximum pressure was 1, 2.5, 5, 2.5 and 1 bar. The pressure was held until reaching a constant flow rate, for 10 minutes, at each level, and then the flow rate (l/min.) was the respective absorption. By the absorption and pressure values obtained, in each section tested, the permeability of the tested ground was assessed. It was assumed that the test results corresponded to “full flow”, that is, high permeability of the ground, if the 1st pressure level (1 bar) was not reached.

To guarantee the tests quality, they had two operators, one controlling the injection circuit, and the other filling out the test sheet, taking readings from the hydrometer, pressure gauges and control chronometer.

4.5. Cement grout

The cement grouts were produced on site (Fig. 7).

Fig. 7 – Grout production base (a); collecting samples (b); moulds for test specimens, for compressive strength tests (c); Marsh cone test, to evaluate the grout viscosity (d)

In grouts preparation, with the total amount of water already in the mixer in operation, cement was added at an appropriate rate to avoid creating lumps, until reaching the predicted water to cement ratio (w/c), mixed for 5 minutes, and then transferred to the shaker. This preparation was repeated until the required grout quantity was available.

For sealing the anchor, that is, the primary injection, the grout had a ratio of w/c=0.30, and an additive was added. For bulb injections, the grout had a w/c of 0.40.

4.6. Anchors head

The anchor head includes the placement of the bearing plate, wedge plate, wedges to lock-off the tendon and prestress application. The external protection of the anchor's head was concrete and/or a cap (section 3.2). An anchor head transfers the anchor load to the substructure and thus to the structure. The head must allow the application of loads, such as test and blocking loads and, if required, reloaded or unloaded. It must allow us to reach 100% of the reinforcement's characteristic load value. According to EN1537, the anchor head must be able to adjust to the expected deformations for the work lifetime and to withstand angular deviations in relation to the normal direction of the head, therefore, the respective requirements and demands have been previously established.

An efficient corrosion protection system was adopted, avoiding water access or other metallic anchors components corroding agents. Thus, the anchor head protection used was from the certified system "Twin Corr" (Fig. 4), which recommends the head external protection by the placement of a plastic cap over the bearing plate, and to cover the wedge plate and strands and the application of an anti-corrosion compound, in accordance with Dywidag's recommendations to guarantee adequate protection conditions.

The transition zone protection, between the back of the head and the free length, is very exposed to constructive aspects, so the installation of the head components determines adequate control, and it must be checked and ensured: i) the trumpet overlap with the corrugated tube; ii) the size of the overlapping areas of the protection elements; iii) the sealing rings adequate placement; iv) filling the empty spaces on the back of the head with appropriate materials; and, v) the correct positioning and alignment of all components.

It was recommended that, after lock-off, efforts be made to apply anti-corrosive protections, eventually temporary, to ensure the good condition of the external anchor's components.

To apply the head protection system, the work consisted of: i) removing the temporary protective material; ii) measuring the strands length to be maintained and cutting the excess; iii) brush and clean the external area, to remove rust from the external surface; iv) filling with corrosion protection compound the internal region of the head, in the trumpet, starting from the

central hole of the wedge plate; v) application and fixing the caps, with stainless steel screws and respective sealing o' ring; and vi) filling with compound the inside of the cap.

In M7 and M8 walls, the anchors remain immersed and subject to variation in the reservoir water level, an additional external protection with a concrete coating was recommended. To provide a higher protection efficiency guarantee, those anchors had monitoring only before applying the external coating.

4.7. Prestressed system and test equipment

The equipment proposed by the contractor for the load tests is presented in Fig. 8, like the prestressing application system, the load cell and the displacement measuring devices.

Fig. 8 – Complementary Spillway of Caniçada Dam: layout of an anchor load test

The equipment was previously calibrated, and its suitability and state requirements validated.

In the investigation and suitability tests, the load was measured simultaneously in the load cell and in the pressure gauge of the prestressing system, which made it possible to obtain correlations between the data of those systems, allowing redundancy and reducing errors.

4.8. Irregularities exhibited with the anchors lock-off

During the acceptance tests, radial striations appeared on the protective material of the outer surface of the bearing plate, showing paint radial deformation (Fig. 9). This anomaly indicated a deficiency in the protection layer of the bearing plate or their deformation due to bending. Therefore, this anomaly was analysed to clarify whether the steel plasticization in the plates occurred, due to deformation resulting from bending, since the hole size in the reaction structure was significant. As a result, it was decided to reduce the holes in diameter (Fig. 10).

Fig. 9 – Visual aspect of anchors bearing plate of the M2 and M4 walls, in 2014

Fig. 10 – Aspect of the structural element, before (M4) and after (M2) hole diameter reduction

A photographic survey was carried out, which allowed the identification of several head anchors with the same phenomenon, on walls M2 and M4. In this scenario, the deflection corresponding to the deformation of these plates was measured, monitoring the evolution of their deformation, and lift-off tests were carried out on anchors with bearing plates deformed. It was, also, intended to evaluate the condition of the inside components head.

With the anchors lift-off tests, in the M2 wall, damages to the bearing plates external protection and corrosion phenomenon were identified. Therefore, the immediate implementation of protective actions against corrosion of the anchor head was recommended. It was also recommended that in the anchors where the deformation evolution of the bearing plates was monitored, the measurements should be carried out before cleaning the plates and after the protection product application. Thus, in order to minimize the effects of the intervention that could raise possible doubts.

The recorded deformations did not show the existence of plastic deformations in the bearing plates. However, it was noted that if gradual deformations increase happens during structure lifetime, significant load losses can occur, which results in an inadequate anchor's behaviour. In this framework, it was recommended to monitor the deformation of the bearing plates of M2 and M4 walls during the work, in order allow to check their behaviour at this stage.

5. GROUND ANCHORS EXECUTION

5.1. Drilling

Following the installation and positioning of the equipment, the boreholes were drilled using destructive methods (Fig. 11), as described in section 3.3, with the lengths specified for each anchor, plus an additional of 50 cm.

Fig. 11 – General aspect of the drilling equipment

5.2. Ground treatment

Before inserting the anchor into the borehole, permeability tests were carried out according to the procedure described in section 4.4. In cases where the value exceeded 2 UL in the bond length, cementitious grouting was carried out for ground treatment. A water/cement ratio of 0.8 was adopted with a simple packer located in the borehole at the depth corresponding to the top of the injection zone. The criteria adopted for stopping the injections were a maximum grout absorption of 100 l/m or an injection pressure of 1 MPa (10 bar). Following this injection, all procedures were repeated until results met the specified criteria. Subsequently, within less than 8 hours, the anchor was introduced into the borehole, followed by subsequent injection operations to form the anchor bulb.

5.3. Anchor transportation and installation

The transport operations from the yard to the site (Fig. 12) were carried out in accordance with the recommendations provided. During the anchor's insertion into the boreholes, a visual inspection of the external components conditions was simultaneously carried out (Fig. 13).

Fig. 12 – Operations associated with the transport of anchors from the yard to the site

Fig. 13 – Anomaly control and correction operations. Anchor's introduction in the borehole

The identified damages were repaired, and centralizers with anomalies were repositioned and/or replaced. Additionally, the identification and characteristics of each anchor were checked, with the information recorded in the respective logs.

5.4. Primary grouting

The filling of the borehole interior with cement grout, with a water/cement ratio of 0.3, was carried out at pressures below 2 bar, from the bottom upwards, through hoses connected to the primary injection tube. This phase was concluded when the grout flowed back to the borehole mouth with a clean appearance, like that of the introduced grout, i.e., from the plant. Six hours after the sealing was completed, the bond length injections were performed.

5.5. Bond length grouting

The cement grout (section 4.5), with a water/cement ratio of 0.4, was injected with increasing pressure until the injection valves opened and the primary injection grout ruptured. Controlled volumes of grout were injected through the valves, with the following criteria adopted to stop the injection (Fig. 14): i) grout consumption exceeding 200 kg of cement/150 litres of grout, without a significant increase in pressure; and/or ii) reaching a pressure of 3 MPa. When the injection was suspended due to the mentioned consumption, the interior of the tube was flushed to allow, after at least 6 hours, the repetition of the described operation as many times as necessary until a pressure of 3 MPa was reached.

Fig. 14 – Anchors grouting and correction of the positioning of the steel tendons at the borehole upper end - transition from the free length to the anchor head

To ensure proper monitoring and prompt response to site issues, the daily drilling logs, permeability test results, and records of grout injection operations were made available following each operation. Analysis of that information led to procedure adaptations/ratifications.

The following was observed during installation of tendons: i) high values of grout consumption during injections; ii) a higher number of injections in walls M7 and M8; iii) the need to modify construction procedures based on the values obtained in the Lugeon tests; and iv) difficulties that sometimes required the casing of the boreholes. In the anchors of walls M2, M7, and M8, high consumption was generally observed, which was an indication of voids in the ground. The consumption reduction at the anchors lower levels may be explained by the upper levels

previous injections. The contractor defined procedures to fill the zone of transition between the anchor head and the free length, i.e., the void space behind the distribution plate, between the trumpet tube and the reaction mass borehole. This approach, implemented to reduce the size of the negative space, was accepted as a contingency solution, as Dywidag confirmed its suitability, particularly regarding its guarantee of proper functioning over the lifetime. The distribution plates for the anchors of wall M6 were supplied with larger dimensions than those for walls M2, M4, and M5, to ensure adequate plate strength.

5.6. Remarks

Despite the high number of injections in some locations, there were difficulties in ensuring the efficiency of the ground waterproofing according to the adopted criteria. Thus, when the permeability tests did not meet the established water absorption criteria, it was deemed appropriate to modify procedures. For the anchors of walls M7 and M8, borehole casing was essential, and permeability tests were therefore dispensed with. The initially obtained values in these permeability tests, the high grout consumption, and the large number of injections performed also necessitated changes in construction procedures, particularly in injection methods. Given the difficulty in executing the anchors of walls M7 and M8, it is considered essential to closely monitor these structures throughout their lifetime to safeguard and ensure the timely detection of any anomalies and/or pathologies arising from their complexity.

6. LOAD TESTS AND LOCK-OFF

Load tests were carried out on all anchors, with suitability tests performed on the instrumented anchors and acceptance tests on the remaining ones.

6.1. General description

The procedures and test programs adopted are described in section 4.1, having been established in accordance with EN1537:1999. The load tests involve applying tension to the free end of the tendons and measuring the corresponding displacements. The load application occurred at least 5 days after the last injection (section 5.5), i.e., when the grout strength was greater than or around 27 MPa.

The load tests begin with the installation of the head components and the jack, on a load transfer plate, to apply the initial load, which is lower than the reference load (P_a), enabling the installation of the test or blocking equipment.

In the investigation and suitability tests, the measurement of the tendons displacements was carried out with two digital deflectometers, installed on two diametrically opposed strands, defining a plane close to the vertical axis of the anchor (Fig. 8). The measurement of the piston

and wall displacements was also done with deflectometers. The deflectometers were installed on magnetic bases, placed on a fixed support located outside the test influence zone, and connected to the strands, the wall, and the jack piston with invar steel wires, with a weight at the opposite end. The resolution of the deflectometers was 0.01 mm, and the measurement range was from 0 to 200 mm, meeting the requirements of EN1537:1999.

Table 2 identifies the type of load tests performed on the anchors of each wall, as well as the respective maximum and blocking loads.

Table 2 – Ground anchors load tests

Structure	Investigation test	P_p (kN)	Suitability test	P_p (kN)	Acceptance test	P_p (kN)	P_0 (kN)
M2	2	1250	12	550	70	550	440
M4			2	900	10	900	715
M5			6	900	27	900	715
M6	3 + 2	1250	8	900	25	900	715
M7			5	894	23	894	715
M8			2	894	13	894	715

After each test, the jack was removed, the wedges were placed in the seats of the respective perforated plate, the jack and monitoring equipment were reinstalled, and the reference load (P_a) was applied, followed by a gradual increase in load, as specified in the lock-off program, up to the respective load P_0, with the wedges being driven in. The entire sequence was accompanied by measurements, including the unloading phase, down to P_a, after lock-off.

6.2. Investigation tests

LNEC analysed the results obtained from the investigation tests performed on anchors executed close to the area of walls M2, M4, and M5, and collaborated in conducting the investigation tests of three anchors close to wall M6 (Fig. 15).

Fig. 16 shows an example of the results obtained in the investigation tests using the conventional testing system, and Fig. 17 shows the results with the automatic data acquisition testing system developed by LNEC.

Fig. 15 – Investigation tests of anchors A1, A2, and A3, close to wall M6

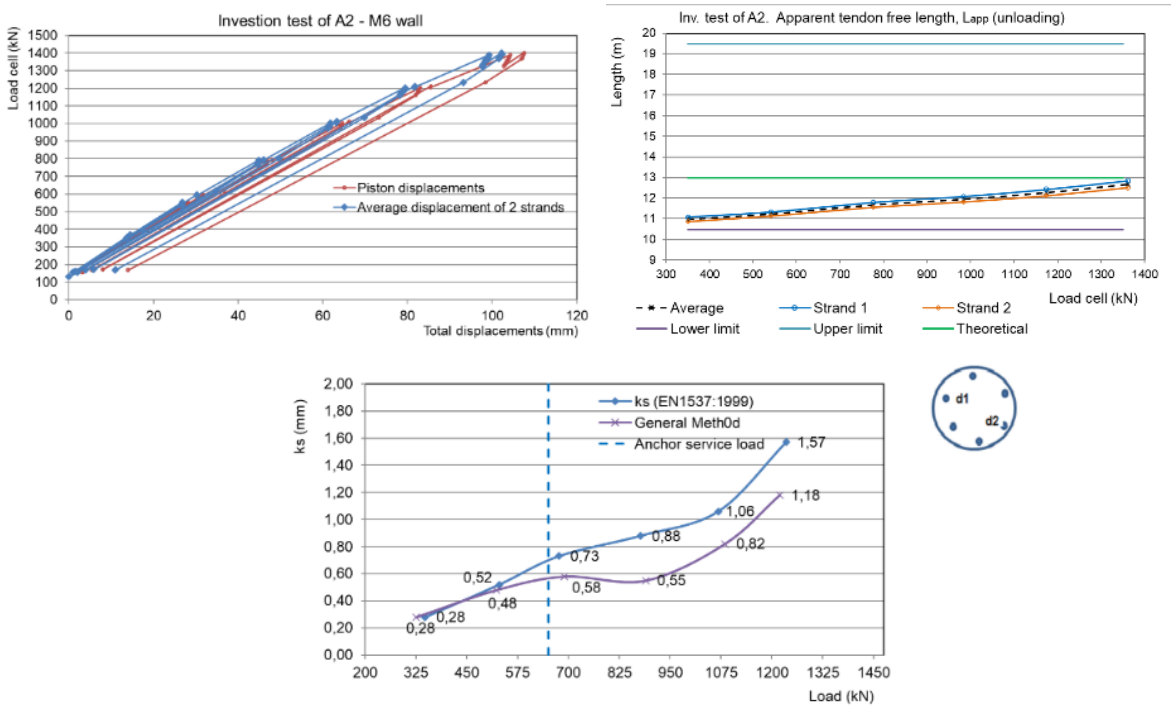

Fig. 16 – Graphs relating displacements and apparent free length and k_s with load, in the investigation test of anchor A2 of wall M6

The k_s values obtained in the 2nd investigation test, with the automatic data acquisition system (SEA) and the conventional testing system (SEC), are of the same order of magnitude for the same load level, except at the 6th level, where the value obtained with the SEA is higher. However, the results obtained confirm that the anchor does not show creep issues at the service load level.

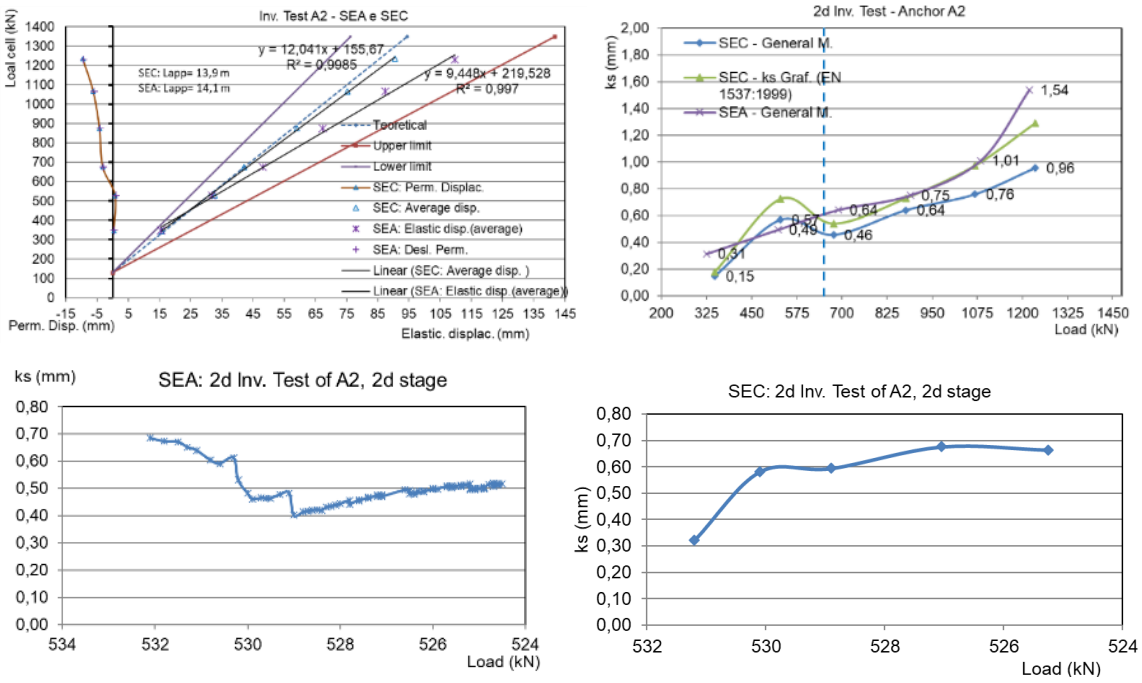

Fig. 17 – Graphs relating permanent and elastic displacements and k_s with load, in the investigation test of anchor A2 of wall M6

6.3. Suitability and acceptance tests

In the anchor instrumented with load cells, for monitoring and controlling the evolution of loads, the performance of suitability tests was planned. The test procedures, as well as the respective program, were established for method 1 (EN1537:1999). Fig. 18 shows images of ongoing load tests, and Fig. 19 exemplifies the graphical representation of results.

Fig. 18 – Equipment used for suitability and acceptance tests

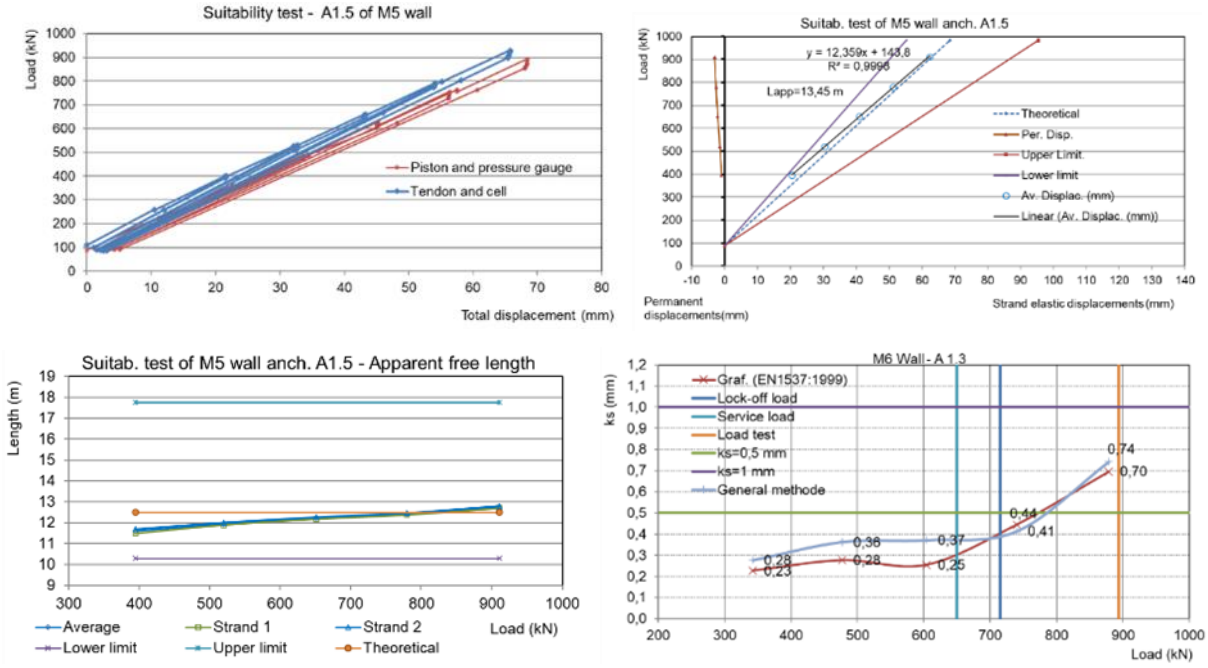

Fig. 19 – Example of results obtained from suitability tests

The procedure adopted in the acceptance tests consisted of observing the displacements in the jack piston and the wall, and the pressure of the pre-stressing system manometer. Fig. 20 show the k_s values obtained from the data of the two different monitoring systems.

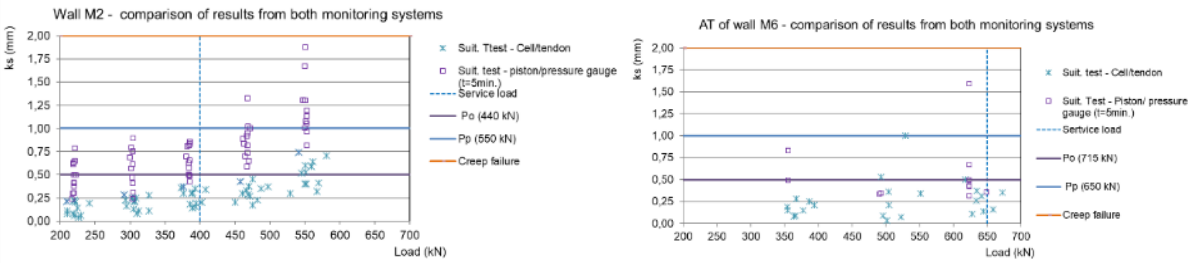

Fig. 20 – Example of creep displacement rate (k_s) obtained in the load tests

6.4. Lock-off

Lock-off of instrumented anchors included recording the pressure value of the pre-stressing system and the cell and measuring the supplementary free length.

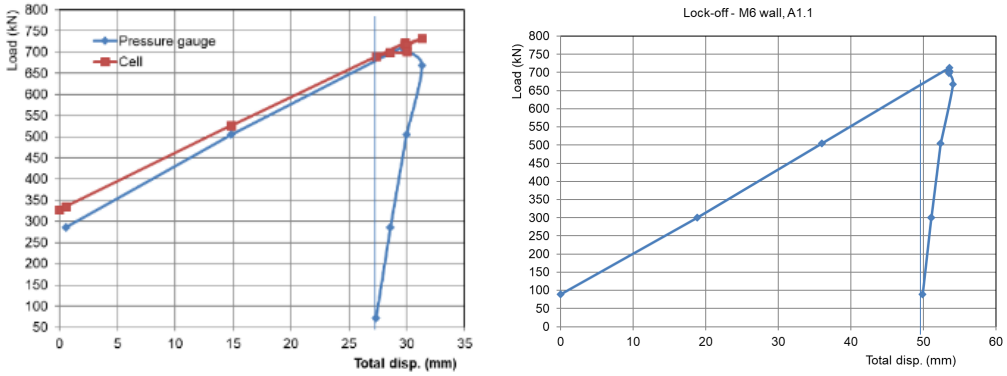

Fig. 21 – Anchors lock-off (graph on the left side refers to anchor with load cell)

Occasionally, during lock-off, load losses were recorded, leading to a new load increase. In some anchors of walls M2 and M4, radial streaks were observed in the protective material of the external surface of the distribution plate. This irregularity was associated with the deficiency of the protective layer of the distribution plate, i.e., the inability of the plate's protective material to withstand the surface stresses from the anchor head load in the most stressed area. Therefore, it was considered prudent to analyse this situation, as the size of the reaction mass hole was significant relative to the characteristics of the distribution plates. To evaluate the situation in a timely manner, photographic reports were made, identifying several anchors on the first level of wall M2 with the same type of irregularity. Additionally, during an inspection, signs of deformation were identified in several anchor plates on the first four levels of wall M2. In wall M4, despite the prior reduction of the holes with grout, deformation was also observed in the distribution plates.

To analyse the cause of the problems previously described, LNEC recommended measuring the deflections of the distribution plates of the anchors and conducting load verification tests on selected anchors where deformations in the distribution plate were observed. Thus, in wall M2, two distinct zones of anchors with deformed plates were identified, located at opposite ends of the wall. Therefore, it was considered necessary to perform two lift-off tests, one in

each zone. It was also intended to assess the condition of the elements positioned inside the heads of the two tested anchors.

6.5. Lift-off and lock-off tests

The anchors where the lift-off tests were performed were selected based on the level of deformation of the distribution plates and their accessibility. Therefore, the lift-off tests were carried out on anchors A4.2 and A1.4 (Fig. 22 e Fig. 23) of wall M2, with the collaboration and recommendations of LNEC.

Fig. 22 – Lift-off test of anchor A4.2 (left side) and preparation for lift-off test of anchor A1.4 (right side), on wall M2

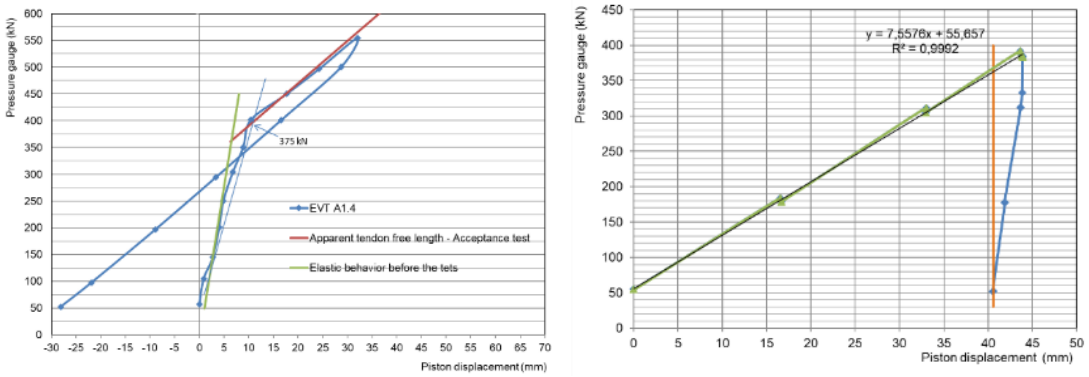

Fig. 23 – Lift-off and new lock-off of anchor A1.4, on wall M2

During the lift-off test of anchor A4.2, it was observed that: i) the two upper wedges loosened during the load increase phase from 300 kN to 350 kN; and ii) the two lower wedges loosened between 400 kN and 450 kN. From this, it was inferred that the load was higher on the two lower strands of the tendon. The installed anchor load, considering the observed behaviour, was 400 kN.

During the anchor A1.4 lift-off test, it was observed that three out of the four wedges loosened between 350 kN and 400 kN, and the last wedge loosened at a load close to 450 kN. This allowed the assumption that this anchor had a more uniform load distribution than anchor A4.2. According to the test results, the installed load on anchor A1.4 was 375 kN.

The load value applied during the new lock-off of each anchor considered: i) the installed load value obtained from the respective lift-off test; ii) the monitored load values in the instrumented anchors located near each anchor; iii) the average load values observed in the anchors at each level of wall M2; and iv) the design load value of 400 kN for the anchors of wall M2. Thus, the new lock-off loads were 440 kN and 390 kN for anchors A4.2 and A1.4, respectively. The installed load value on anchors A4.2 and A1.4, after new lock-off, was 416.7 kN and 362.5 kN, respectively. These values were considered compatible with those obtained in the lift-off tests and the monitored anchors on wall M2.

7. LOAD TESTS RESULTS ANALYSIS

The results of the two investigation load tests conducted for the anchors of wall M2 showed that for the service loads, 400 kN and 600 kN, the value of the creep coefficient, k_s, complied the European Standard EN1537:1999 and that the anchors exhibited appropriate behaviour in terms of their mechanical performance. The results also indicated that there were no significant benefits in adopting 13 m for the bond length instead of 8 m, as both values exhibited the same type of behaviour up to the maximum load of the load tests.

The results of the three investigation load tests on anchors of wall M6 indicated that the anchors exhibited appropriate mechanical behaviour and that the creep coefficients complied with the European Standard EN1537:1999. Furthermore, given the mechanical behaviour observed, there were no significant benefits in constructing anchors with a bond length longer than 10 m.

The k_s values obtained in the suitability load tests comply with the criteria of European Standard EN1537:1999, particularly for the service and lock-off loads of the anchors. It can be observed that the k_s values obtained by LNEC in the acceptance tests are higher than those resulting from the creep stages of the suitability tests. However, from the analysis of results, it should be noted that the data obtained in most acceptance tests have: i) a significantly shorter observation time during the load stages compared to that adopted for the suitability tests; and ii) results obtained from the displacement of the piston and load from the prestressing system pressure gauge generally have lower accuracy than the data obtained in the suitability tests.

Additionally, the higher values of k_s obtained from the acceptance tests can also be explained by the fact that the respective load stages occurred at a higher load level than defined in the program, particularly for the anchors of walls M4 and M5.

The obtained results indicate that the anchors of the walls have mechanical and creep characteristics suitable for the project requirements, in accordance with EN1537:1999 [3].

The apparent free length (L_{app}) was within the limits and in accordance with the criteria of EN1537:1999 and did not indicate the occurrence of friction in the anchors.

The permanent displacements did not indicate the occurrence of rupture, being less than 10 mm in about 90% of the anchors, of which, in 35%, were less than 3 mm. The recorded displacements after the lock-off had the same order of magnitude in anchors with the same characteristics.

In accordance with the obtained values, the applied lock-off load proved to be adequate, as it allowed for the installation of loads near the service load in most of the anchors. This fact generally can also be confirmed by the load values observed in the monitored anchors.

8. MONITORING AND MAINTENANCE

The observation data of the instrumented anchors in the walls recorded during the construction phase does not indicate the existence of load losses due to creep behaviour. The recorded load variations are associated with the construction phasing, namely excavation lowering and the application of prestress in nearby anchors, as well as with seasonality. For example, anchor A2.9 on wall M7, where high k_s values were obtained, shows the same type of behaviour as the other monitored anchors of wall M7.

Fig. 24 illustrates the evolution of the installed load in anchors of walls M2 and M6. Generally, there was a decrease in load during an initial period, corresponding to the excavation phase, followed by a reasonable stabilization where annual cyclic load variations are observed, which should be explained by the effect of seasonality.

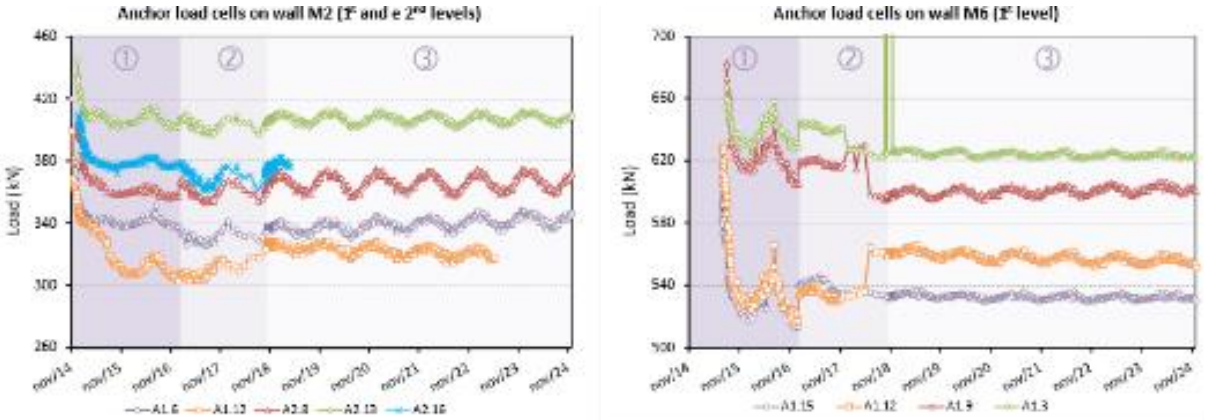

Fig. 24 – Loads on anchors of wall M2 (left side) and M6 (right side)

During the initial monitoring period (indicated in the graphs with ①), the determination of the anchor load value was done more expediently and without correction for temperature variation effects. Subsequently, from period ②, the load value began to be calculated from the polynomial of the respective cell's calibration curve and took also into account the mentioned

thermal effect. From period ③, the load cell readings started to be taken through the Automatic Reading System, i.e. without human intervention.

The monitoring of the project's behaviour is governed by the respective Observation Plan [6]. This document stipulates the execution of regular campaigns for reading load cells and other monitoring devices, as well as for visual inspection. The integrated analysis of the information obtained in the campaigns is essential to identify potential anomalies and anticipate the necessary measures to maintain the project's safety. The analyses carried out within the scope of the most recent revision of the Observation Plan [6] concluded that the project's behaviour in these initial years is generally adequate and within expectations.

9. REMARKS AND CONCLUSIONS

Complying with the European Standard EN1537 [3] in the execution of permanent anchors is complex, demanding, and costly, requiring proper and timely planning of activities, particularly regarding the requirements for conditioning, transportation between different work sites, and protection. Additionally, there are requirements for specialized workforce with expertise in various areas of geotechnics.

The importance of quality control during the execution of the work is emphasized, particularly regarding activities associated with the reception of anchors and their monitoring devices, their conditioning, transportation, installation, execution, testing, and lock-off. This control proved to be important in identifying anomalies and minimizing the risk of damage

Given the grout consumption recorded during the injections performed, the number of injections required, the need to modify construction procedures, particularly injection procedures, the values obtained in the Lugeon tests, and the difficulties encountered during the execution of the anchors of walls M2, M4, M5, and M6, it was considered necessary to closely monitor the work throughout its lifetime. This procedure aims to safeguard and ensure the timely detection of any anomalies and/or potential pathologies arising from the complexity of the work and the formations of the ground in which the work is done.

REFERENCES

[1] LNEC (2017) - Spillway intake on the Caniçada dam. Technical assistance on the execution of the ground anchors of the walls M2, M4, M5 and M6. Report 233/2017-DG/NGUT.

[2] LNEC (2017) - Spillway intake on the Caniçada dam. Technical assistance on the execution of the ground anchors of the walls M7 and M8. Report 347/2017-DG/NGUT

[3] AQUALOGUS (2013) – Spillway intake on the Caniçada dam. Execution design.

[4] EN1537:1999 (1999) – Execution of special geotechnical works - Ground anchors.

[5] DYWIDAG – Geotechnical Product Range. DYWIDAG Strand Anchors. Permanent Anchor with Double Sheathing - Twin-Corr System.

[6] EDP (2023) – Structural safety dams' control. Caniçada dam. Observation Plan Update.

SUPPORTERS

apa
agência portuguesa do ambiente

U.PORTO
FEUP FACULDADE DE ENGENHARIA
UNIVERSIDADE DO PORTO

NOVA
FACULDADE DE
CIÊNCIAS E TECNOLOGIA

1 2 9 0
FACULDADE DE
CIÊNCIAS E TECNOLOGIA
UNIVERSIDADE D
COIMBRA

edp

SOMINCOR
Sociedade Mineira de Neves-Corvo, S.A.
a subsidiary of lundin mining

CIGB
ICOLD
CBDB
Comitê Brasileiro de Barragens

LECM
澳門土木工程實驗室
LABORATÓRIO DE ENGENHARIA CIVIL DE MACAU
Civil Engineering Laboratory of Macau

CDA ACB
Canadian Dam Association
Association canadienne des barrages

Sociedade
Portuguesa
de Geotecnia

ORDEM
DOS
ENGENHEIROS

https://dw2025.lnec.pt/home
damworld@lnec.pt

AV DO BRASIL 101 • 1700-066 LISBOA • PORTUGAL
tel. (+351) 21 844 30 00
lnec@lnec.pt **www.lnec.pt**